

Advancing with Nonmetallic Materials:

A Compendium of NEXCEL Publications 2022-2025

(Volume I)

Preface

It is with great pleasure that we present this collection of research, *Advancing with Nonmetallic Materials: A Compendium of NEXCEL Publications 2022-2025*. This c*ompendium* brings together 112 research papers, all published by the researchers of NEXCEL project teams over a productive four-year period. It should be noted that 26 papers of them were originally published in Chinese and are presented as such to preserve the integrity of the authors' work. Readers can refer to the English abstracts of them to grasp the key contributions and conclusions. The remaining 86 papers were kept and presented in English.

The years 2022-2025 represented a phase of intense exploration and significant advancement in nonmetallic materials for NEXCEL. In a world marked by rapid transformations and complex challenges, materials transition to higher efficiency, more resilience and more intelligence is crucial for meeting sustainability goals and construction needs. The works compiled here stand as a testament to our commitment to generating knowledge that is not only academically sound but also practically applicable.

This Compendium is more than a simple archive of publications; it is a curated map of our intellectual journey. To facilitate the readers to navigate this substantial body of work, we organized the papers into two volumes and six chapters:

VOLUME I

- Chapter 1: FRPs & Advanced Composites (48 papers)

VOLUME II

- Chapter 2: Special Mortars & Concrete (19 papers)
- Chapter 3: Pavement for Roads & Bridges (16 papers)
- Chapter 4: Construction Chemicals (10 papers)
- Chapter 5: Waterproofing & Repair Materials (5 papers)
- Chapter 6: Insulation & Composite Cladding (14 papers)

Each chapter synthesizes key findings and traces the innovation of thought within its focus area, offering readers a coherent narrative of progress and discovery across multiple projects.

The primary aim of this Compendium is twofold. First, it serves to consolidate the core outcomes of our diverse research portfolio, providing a comprehensive

overview of NEXCEL's contributions to its fields of expertise. We hope this synthesis will reveal connections between different projects, highlight emerging materials, and identify promising avenues for future nonmetallic deployment.

Second, and equally important, this Compendium is conceived as a vital channel for interaction and exchange with our valued stakeholders. To our founding sponsor Aramco, our operating archive China Building Materials Academy (CBMA), sponsors, project partners, strategic partners, and the broader academic and practitioner communities: these pages contain the tangible outputs of our shared mission. We invite you to engage with these findings, critique them, build upon them, and explore their practical application scenarios. True impact is achieved not in isolation, but through exchange and partnership. It is our sincere hope that the insights contained herein will inform policy, inspire innovation, enhance professional practice, and stimulate further collaborative ventures.

We extend our deepest gratitude to the dedicated researchers, project staff, and contributing authors whose expertise and hard work are the key foundation of this Compendium. We also acknowledge the unwavering support of our partners, and funders, whose trust and resources made this research possible.

As we look beyond, we envision this Compendium as a springboard for the next phase of our work. May it facilitate the wider dissemination and application of our collective outcomes, strengthening existing partnership and forging new ones as we continue to pursue a promising future for the construction sector.

Prof HOU Diyang

Chairman of NEXCEL Technical Advisory Committee

Feb 2026

© 2026 NEXCEL
This Compendium has been compiled from PDF files provided by the individual authors of each paper. The copyrights of all included papers in this Compendium remain with their original authors. Any questions regarding the content or intellectual property should be directed to its authors. NEXCEL is not responsible for the intellectual property or accuracy of the individual papers.

Contents

VOLUME I

Chapter 1: FRPs & Advanced Composites

1. **Analysis-oriented model for FRP tube-confined concrete: 3D interpretation of biaxial tube behaviour (2022TDA1-1)** **1**

   Zhiyuan Li, Peng Feng, Jia-Qi Yang

2. **Strengthening RC beams with mid-span supporting prestressed CFRP plates: An experimental investigation (2022TDA1-1)** **10**

   Jia-Qi Yang, Peng Feng, Bin Liu, Husheng Wang, Weiping Zhao, Lili Hu

3. **Application of ultra-lightweight and large-scale pultruded for external frame beam in high-rise buildings (2022TDA1-1) - *in Chinese*** **22**

   QIN Heng, LIU Tianqiao, YU Taofeng, YI Shusheng, XIONG Jinfeng, FAN Yanjun, FENG Peng

4. **A binary resin system of epoxy and phenol-formaldehyde for improving the thermo-mechanical behavior of FRP composites (2022TDA1-1)** **29**

   TianQiao Liu, Ruibao Wang, Shilong Zhen, Peng Feng

5. **Non-linear behaviors of pultruded GFRP composites (2022TDA1-1)** **41**

   TianQiao Liu, Shilong Zhen, Ruibao Wang

6. **Flexural performance of curved-pultruded GFRP arch beams subjected to varying boundary conditions (2022TDA1-1)** **53**

   TianQiao Liu, Peng Feng, Yulei Bai, Shangcong Bai, Jia-Qi Yang, Fei Zhao

7. **Comparative study of standard stroke load design of communication poles and towers in China, America and Europe (2022TDA4-1) - *in Chinese*** **66**

   Wu Haipeng, Sun Yunlong, Liu Xinyi, Zhang Yunfeng, Xie Tieqin

8. **Improving performance of GFRP joints using bolted/mortise-tenon hybrid method (2022TDA4-1)** **70**

   YIN Yue, WU Haipeng, SUN Yunlong

9. **Mixed-alkali effect on thermal property and elastic behavior in borosilicate glasses (2022PHD-1)** **78**

   XIE Xianmao, ZHOU Hemin, KE Xuefei, WANG Xiaowei, WANG Yadan, ZHANG Jiayan, QIAO Ang, TAO Haizheng

10. **Strength retention rate distribution model and reliability analysis of FRP stirrups (2023TDA4-1) - *in Chinese*** **86**

    Jiang Jiafei, Lv Jiahao, Xue Weichen

11. **Shear behavior of two-span continuous concrete deep beams reinforced with GFRP bars (2023TDA4-1)** **93**

Fei Peng, Yuhang Cai, Weijian Yi, Weichen Xue

12. **Calculation method of the flexural tensile strength of the GFRP stirrups based on the database (2023TDA4-1) - *in Chinese*** **106**

Bai Haoyang, Xue Weichen, Jiang Jiafei

13. **Transfer learning-based confinement strength prediction of concrete confined by FRP transverse reinforcements (2023TDA4-1)** **113**

Fei Peng, Yazhong Li, Weichen Xue

14. **Flexural Behavior and Design of Ultrahigh-Performance Concrete Beams Reinforced with GFRP Bars (2023TDA4-1)** **127**

Fei Peng, Jidong Deng and Weichen Xue

15. **Experimental Investigation on Pure Torsion Behavior of Concrete Beams Reinforced with Glass Fiber-Reinforced Polymer Bars (2023TDA4-1)** **140**

Haoyang Bai , Jiafei Jiang , Weichen Xue and Xiang Hu

16. **A modified softened truss model and strength prediction formula for fiber-reinforced polymer reinforced concrete members under pure torsion (2023TDA4-1)** **161**

Eslam M Saleh, Jiafei Jiang and Weichen Xue

17. **Experimental investigation on post-fire mechanical properties of glass fiber-reinforced polymer rebars (2023TDA5-1)** **185**

Chanachai Thongchom, Lili Hu , Penpichcha Khongpermgoson Sanit-in, Denise-Penelope N. Kontoni, Nitipong Praphaphankul, Koravith Tiprak and Suphanut Kongwat

18. **Static and fatigue behavior of CFRP strengthened spiral welded steel tubes subjected to four-point bending (2023TDA5-1)** **207**

Andre Cahyadi Salim, Yining Zhang, Lili Hu, Chengjian Shao

19. **Novel adaptive prestressed CFRP-reinforced steel column: Concept and behavior (2023TDA5-1)** **224**

Xu Liang, Lili Hu, Terrance Lim

20. **Novel high-temperature resistant GFRP bars with DOPO-modified vinyl ester: Design, performance, and application (2023TDA5-1)** **242**

Xu Liang, Terrance Lim, Xiaoqing Zhao, Lili Hu, Qiaolong Yuan, Zhiwei Wang

21. **Long-term Behavior of High Performance GFRP Bars, International Conference on Advances in Engineering and Technology for sustainable development (2023TDA5-1)** **259**

Terrance Lim, Tao He, Lili Hu

22. **High-temperature mechanical properties of GFRP bars Experimental database and novel degradation models (2023TDA5-1)** **266**

De-Xin Duan, En-Ci Liu, Yu-Qing Zhang, Wan-Yang Gao

23. **Novel bamboo-raft-type floating structure (BRT-FS) assembled by FRP reinforced concrete tubes: Conceptual design and analysis (2023PHD-1)** **287**

Chongfeng Xie , Peng Feng

24. Mesoscale simulation method for preplaced aggregate concrete based on physics engine (2023PHD-1) **303**

Chongfeng Xie, Xiwang Chen, Jia-Qi Yang, Charun Bao, Peng Feng

25. Experimental investigation on transverse tension-tension fatigue behavior of pultruded GFRP unidirectional lamina (2023PHD-8) **323**

Qinglin Gao, Haohui Xin, Youyou Zhang

26. Prediction of fatigue crack propagation in center cracked steel plate strengthened with partially covered CFRP strip (2023PHD-8) **338**

Jielin Liu, Xiao-Ling Zhao, Haohui Xin, Youyou Zhang

27. Probabilistic fatigue stiffness variation of angle-ply GFRP composites considering stress ratio effect (2023PHD-8) **349**

Qinglin Gao, Haohui Xin, Claudio ´ Horas, Ayman S. Mosallam, Yuqing Liu, Filippo Berto, Jianxun Ma, Qing Sun, Jos´e A.F.O. Correia

28. Effects of aggregates and fibers on the strength and permeability of concrete exposed to low vacuum environment (2024TDA-1) **366**

Zhaofei Long, Guangcheng Long, Zhuo Tang, Minghui Shangguan, Ce Gao, Meihui Yi, Zhenhui He, Yutong Zhang

29. Hydration and microstructure evolution of cement paste in low vacuum environments (2024TDA-1) **384**

Minghui Shangguan, Youjun Xie, Guangcheng Long, Zhaofei Long, Fan Wang, Yue Chen, Ce Gao, Zhuo Tang

30. Regulating drying shrinkage behavior of cement-based materials in low vacuum environments and developing a predictive model (2024TDA-1) **399**

Zhaofei Long, Guangcheng Long, Yue Chen, Minghui Shangguan, Jilin Wang, Yuting Zhang, Meihui Yi, Ce Gao, Zhuo Tang

31. Acoustic emission-based flexural fracture analysis of polyethylene fiber reinforced ultra-high performance concrete under low vacuum environment (2024TDA-1) **419**

Zhaofei Long, Guangcheng Long, Lei Peng, Yuting Zhang, Lixing Wang, Xiaodong Wang, Jilin Wang, Minghui Shangguan, Zhuo Tang, Jionghuang He

32. Enhancing Concrete Performance in Low Vacuum Environments: Strategies and Mechanisms (2024TDA-1) **433**

Zhaofei Long, Jionghuang He, Guangcheng Long, Lixing Wang, Yuting Zhang, Zhuo Tang and Youjun Xie

33. Seismic behavior of full-scale PEN FRP-concrete-steel double skin tubular columns (2024SFP-2) **448**

Shang-Cong Bai, Kai-Di Peng, Yu-Lei Bai, Jia-Xing Ma

34. Seismic performance and shear strength of HECC/RC beam-column joints with simplified reinforcement (2024SFP-2) **462**

Yu-Lei Bai, Shi-Yan Zhang, Wei-Hao Mao, Ze-Yuan Liu, Luo-Bin Zuo, Yao Ding

35. **Seismic performance of short concrete columns reinforced with steel-FRP composite bars and GFRP stirrups (2024SFP-2)** 486

Yulei Bai, Xiaoyong An, Guolin Wang, Hua Rong, Yufeng Zhang, Jun Tao

36. **Seismic Performance of Embedded GFRP Tube-Concrete Composite Exterior Beam-Column Joints(2024SFP-2) - *in Chinese*** 507

Bai Yulei, Liu Zeyuan, Xing Yasen, Zhang Xiao, Meng Xianlei, Zhang Shiyan

37. **Design preparation and mechanical properties of glass fiber reinforced thermoplastic self-anchor plate cable exposed in alkaline solution environment (2024SFP-4)** 517

Zhonghui Zhang, Qikang Ji, Zhengyue Guo, Chenggao Li, Rui Guo, Jingwei Tian, Zhuo Zhang, Taipeng He, Guijun Xian

38. **Study on the durability of compression behavior for glass fiber-reinforced polypropylene thermoplastic composite bars in various aging environments (2024SFP-4)** 531

Ping Zhou, Shaoce Dong, Chenggao Li, Deao Kong, Yanbo Bai, Guijun Xian, Qingrui Yue

39. **Design, preparation and mechanical properties of novel glass fiber reinforced polypropylene bending bars (2024SFP-4)** 550

Guijun Xian, Ping Zhou, Yanbo Bai, Junqi Wang, Chenggao Li, Shaoce Dong, Rui Guo, Jinhao Li, Haoqiang Du, Jian Zhong

40. **Long-term properties evolution and life prediction of glass fiber reinforced thermoplastic bending bars exposed in concrete alkaline environment (2024SFP-4)** 562

Guijun Xian, Yanbo Bai, Ping Zhou, Junqi Wang, Chenggao Li, Shaoce Dong, Rui Guo, Jingwei Tian, Jinhao Li, Jian Zhong, Taipeng He, Zhuo Zhang

41. **Multifunctional phosphorus-containing imidazoliums endowing one-component epoxy resins with superior thermal latency, heat resistance, mechanical properties, and fire safety (2024PHD-4)** 581

Jingsheng Wang, Jun Wang, Shuang Yang, Xi Chen, Kaiwen Chen, Gen Zhou, Xian Liu, Lin Xu, Siqi Huo, Pingan Song, Hao Wang

42. **Development of single-component epoxy resin with superb thermal stability, flame retardancy, smoke suppression, and latency via Cu-based phosphorus/imidazole-containing complex (2024PHD-4)** 595

Jingsheng Wang, Jun Wang, Shuang Yang, Chaoqun Wu, Xi Chen, Kaiwen Chen, Pingan Song, Hao Wang, Siqi Huo

43. **Phosphorus-derived imidazolium salts with varied oxidation states:Tailoring latency, mechanical properties, and flame retardancy in single-component epoxy resins (2024PHD-4)** 607

Jingsheng Wang, Jun Wang, Shuang Yang, Guoping Ding, Renxin Xu, Wei Liu, Jiuxiao Sun, Kaiwen Chen, Liu Duan, Jiaqi Wang, Hao Wang, Siqi Huo

44. **A pull-out equivalent telescopic layered failure model of carbon fiber bundles in seawater sea-sand cementitious matrix (2024PHD-5)** 620

Jiarong Liu, Dawei Zhang, Yewangzhi Tao, Zhiyu Xie

45. Effect of ICCP on tensile performance and piezores effect of CFRCM plates (2024PHD-5) **637**

Jiarong Liu, Dawei Zhang, Yewangzhi Tao, Zhiyu Xie, Bo Yi

46. Effect of ICCP on bond performance and piezoresistive effect of carbon fiber bundles in cementitious matrix (2024PHD-5) **651**

Yewangzhi Tao, Jiarong Liu, Dawei Zhang, Zhiyu Xie, Jiaxin Hong

47. Effect of ICCP on tensile performance of carbon fiber bundles in seawater sea-sand cementitious matrix (2024PHD-5) **668**

Jiarong Liu, Dawei Zhang, Yewangzhi Tao, Zhiyu Xie, Jiaxin Hong

48. Effect of shear connection degree on static behavior of externally prestressed FRP-concrete hybrid beams: Experimental and numerical study (2024PHD-6) **689**

Weichen Xue, Dawei Yan, Shiqian Zhang, Jiafei Jiang

Engineering Structures 272 (2022) 114987

Contents lists available at ScienceDirect

Engineering Structures

journal homepage: www.elsevier.com/locate/engstruct

Analysis-oriented model for FRP tube-confined concrete: 3D interpretation of biaxial tube behaviour

Zhiyuan Li [a], Peng Feng [a], Jia-Qi Yang [b,*]

[a] Department of Civil Engineering, Tsinghua University, Beijing 100084, China
[b] School of Mechanics and Civil Engineering, China University of Mining and Technology (Beijing), Beijing 100083, China

ARTICLE INFO

Keywords:
Filament-wound FRP tube
Biaxial behaviour
Analysis-oriented model
Confined concrete
Concrete-filled FRP tube

ABSTRACT

Filament-wound fibre-reinforced polymer (FRP) tubes are an emerging FRP product employed in various FRP-concrete composite structures, such as concrete-filled FRP tubes (CFFTs). Due to the fibre orientations in the tube wall, the filament-wound FRP tube exhibits biaxial behaviour under simultaneous axial compression and hoop expansion, causing relaxation of the confining stress. Therefore, the conventional hoop tension test may result in overestimation of the confining stiffness. In this paper, the biaxial behaviour of FRP tubes is theoretically investigated using classical laminate theory in conjunction with an analysis-oriented model for FRP-confined concrete. The geometrical meaning of the biaxial tube behaviour is interpreted intuitively using the 3D geometrical approach previously proposed by the authors. For the convenience of analysis and design, this paper proposes a simplified approach to rectify the confining stiffness that considers both elastic and nonlinear biaxial effects. The predicted results show good agreement with the collected test data.

1. Introduction

Fibre-reinforced polymer (FRP) composites have been widely used in civil and infrastructure engineering due to their light weight, high tensile strength and anti-corrosion properties [1,2]. Specifically, FRP composites have proven to be effective materials that can provide confinement to concrete under compression. When confined by FRP, the confining stress acting on the concrete increases with its lateral expansion during axial compression; this scenario is classified as passively confined. With proper design, FRP-confined cylinders can have a bilinear stress–strain curve when subjected to axial compression due to the passive nature of the confinement. FRP tubes are usually manufactured by the filament winding technique so that the fibre directions are symmetrical about the tube axis. In practice, the FRP tube acts as both the confining material and mould, which is convenient for construction. Moreover, the FRP tubes can isolate the concrete and internal reinforcements from the external aggressive environment, which renders concrete-filled FRP tubes (CFFTs) suitable for coastal/marine structures. To date, various composite structural members have been proposed by researchers based on the concept of CFFTs [3–13,43].

As an important fundamental of CFFTs, the behaviour of FRP-confined concrete has been investigated by researchers worldwide during previous decades. A comprehensive database of the test results and a review of analytical models are provided in [14,15]. Basically, analytical models can be classified into design-oriented models [16,17] and analysis-oriented models [18–20]. Design-oriented models assume the expressions of the axial stress–strain curve and calibrate key parameters with test results. These models are concise and easy to apply and hence are suitable for design checks. A series of studies conducted by the authors' research team [20–22] proposed a 3D geometrical approach, with which the mechanism of analysis-oriented models can be revealed. As analysed by Yang and Feng [20], analysis-oriented models can be decomposed into three equations:

$$\text{1st equation}: \quad f(\varepsilon_c, \sigma_l, \sigma_c) = 0 \tag{1-1}$$

$$\text{2nd equation}: \quad g(\varepsilon_c, \sigma_l, \varepsilon_l) = 0 \tag{1-2}$$

$$\text{3rd equation}: \quad h(\varepsilon_l, \sigma_l) = 0 \tag{1-3}$$

The *1st equation* represents the relationship among the axial strain (ε_c), confining stress (σ_l) and axial stress (σ_c), which is also known as the actively confined concrete model. This equation forms a 3D surface in the ε_c-σ_l-σ_c coordinate system (herein *axial stress coordinate system*). The 1st equation proposed by Yang and Feng [20] is as follows:

* Corresponding author.
E-mail address: yangjiaqi@cumtb.edu.cn (J.-Q. Yang).

https://doi.org/10.1016/j.engstruct.2022.114987
Received 28 April 2022; Received in revised form 9 August 2022; Accepted 18 September 2022
Available online 27 September 2022
0141-0296/© 2022 Elsevier Ltd. All rights reserved.

$$\frac{\sigma_c}{f_{cc}'^*} = \frac{\left(\frac{\varepsilon_c}{\varepsilon_{cc}^*}\right) \bullet r}{r - 1 + \left(\frac{\varepsilon_c}{\varepsilon_{cc}^*}\right)^r} \tag{2-1}$$

$$r = \frac{E_c}{E_c - \frac{f_{cc}'^*}{\varepsilon_{cc}^*}} \tag{2-2}$$

$$\frac{f_{cc}^*}{f_{co}'} = 1 + 3.33\left(\frac{\sigma_l}{f_{co}'}\right)^{0.9} \tag{2-3}$$

$$\frac{\varepsilon_{cc}^*}{\varepsilon_{co}} = 1 + 17.4\left(\frac{\sigma_l}{f_{co}'}\right)^{1.07} \tag{2-4}$$

where E_c is the elastic modulus of concrete, and $f_{cc}'^*$ and ε_{cc}^* are the peak axial stress and the corresponding axial strain of concrete under a specific level of lateral confining stress, respectively. The 2nd equation represents the relationship among the axial strain (ε_c), confining stress (σ_l) and lateral strain (ε_l), which is the key of most analysis-oriented models that predict the lateral expansion of confined concrete. An example provided by Yang and Feng [20] for the 2st equation is:

$$\left(\frac{\varepsilon_c}{\varepsilon_{co}}\right) = 0.85\left\{\left[1 + 0.75\left(\frac{-\varepsilon_l}{\varepsilon_{co}}\right)\right]^{0.7} - exp\left[-7\left(\frac{-\varepsilon_l}{\varepsilon_{co}}\right)\right]\right\}\left[1 + 193\left(\frac{\sigma_l}{f_{co}'}\right)^{1.72}\right]^{1.07} \tag{3}$$

Noting that ε_c is positive for axial compression, and ε_l is negative for lateral expansion. This equation defines a 3D surface in the ε_c-σ_l-ε_l coordinate system (herein *lateral strain coordinate system*). With these two equations, the four-variable concrete state point (ε_c, ε_l, σ_l, σ_c) is constrained on the two 3D surfaces in the corresponding coordinate systems. The 1st and the 2nd equations are solely dependent on the concrete property. Problems of path dependency can be solved by modifying these two equations [21,23–25].

The 3rd equation represents the relationship between the lateral expansion (ε_l) and the confining stress (σ_l), which depends on the material property of the confining material and the geometry of the confined concrete cylinder. Specifically, for linear elastic FRP-confined concrete cylinders, the 3rd equation is always given as:

$$\sigma_l = \frac{2E_{frp}t_{frp}}{D}\varepsilon_l = E_l\varepsilon_l \tag{4}$$

where E_{frp} is the elastic modulus of the FRP, t_{frp} is the thickness of the FRP jacket, D is the diameter of the concrete cylinder, and E_l is the confining stiffness. The form of the 3rd equation given by Eq. (4) disregards the biaxial behaviour of the FRP jacket, which is applicable for FRP sheet wrapped concrete cylinders as there is no obvious biaxial behaviour when all the fibres are oriented along the hoop direction. However, an error will be introduced when analysing CFFTs because the biaxial behaviour of the FRP tube is not negligible. It is demonstrated in [26–30] that the angle between the fibres and the tube axis (θ) have a strong influence on not only the biaxial behaviour but also the strength and failure mode of the FRP tube. In practice, the confining stiffness E_l for an FRP tube is obtained by hoop tension tests, including the split-disk tests [4,31–33] and strip tension tests [34], as suggested by ASTM D2290-12 [35]. In addition, Xie et al. [36] conducted hydraulic pressure tests and compression tests on bare glass fibre-reinforced polymer (GFRP) tubes to determine their mechanical properties. In the current hoop tension test methods, the tensile load is applied in only the hoop direction, while the boundary condition for the axial direction is free, which does not match the actual stress state in a CFFT. The FRP tube in a CFFT undergoes compression in the axial direction and tension in the hoop direction. In this stress state, the tube has a trend of relaxation in the hoop direction during the loading process, which means the Poisson's effect introduces extra hoop expansion of the tube. Therefore, the current test and analysis methods overestimate the confining stiffness. In this regard, the biaxial behaviour of FRP tubes needs to be investigated in detail, and it is necessary to make proper modifications to the current design method.

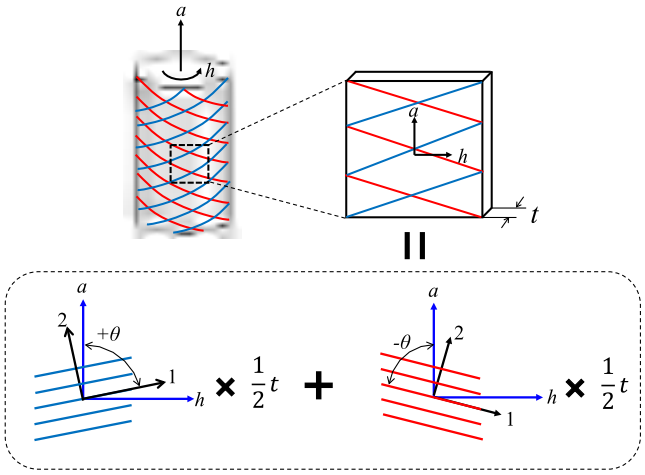


Fig. 1. Simplification of the $\{\pm\theta\}_n$ filament-wound tube.

This paper is a follow-up work of a series of studies on analysis-oriented models for FRP confined concrete conducted by the authors' group [20,21]. In Ref. [20], the authors decomposed the analysis-oriented model into three generalized equations (Eqs. (1-1)–(1-3)) and proposed specific forms of Eqs. (1-1) and (1-2) for normal strength concrete. Ref. [21] modified the 1st and 2nd equations (Eqs. (1-1) and (1-2)) to model the path dependency of high-strength concrete. In this study, the authors further developed the 3D geometric approach by modifying the 3rd equation (Eqs. (1)–(3)) so that the biaxial behaviour of the confining material is interpreted intuitively. The biaxial behaviour of filament-wound FRP tubes is then investigated via classic laminate theory. After that, the influence of the biaxial behaviour of the FRP tube on the total stress–strain response of the CFFT is plotted in 3D coordinates. Finally, the influence of the biaxial behaviour is quantified, and a modification to the design methods is proposed accordingly.

2. 3D interpretation of the 3rd equation

As discussed in the previous section, the biaxial behaviour of the FRP tube is not negligible. Therefore, the σ_l provided by the FRP tube is not only dependent on the hoop strain (ε_h) but also influenced by the axial strain (ε_c). Therefore, the 3rd equation is modified to:

$$h(\varepsilon_l, \varepsilon_c, \sigma_l) = 0 \tag{5}$$

Hence, the 3rd equation forms a 3D surface in the lateral strain coordinate system. Usually, $\varepsilon_l = \varepsilon_h$ due to the compatibility between the tube and the concrete. However, this condition may not be applicable when the lateral expansion of the tube is larger than that of the concrete. For example, in the beginning of the loading stage, if the effective Poisson's ratio of the tube is higher than that of the concrete, then $\varepsilon_l < \varepsilon_h$, indicating that there is a gap formed between the tube and the concrete. Nevertheless, the influence on the overall behaviour is minor, which will be discussed in the following part of this section.

2.1. Confinement models for linear elastic FRP composites

The filament-wound FRP tube is anisotropic dependent on the fibre orientation. Hence, classical laminate theory [37] is adopted herein for the analysis. According to the manufacturing process, the fibres are oriented $\pm\theta$ to the tube axis with almost the same fibre amount, which is usually denoted as $\{\pm\theta\}_n$ in the composite material industry. Therefore, the tube wall can be decomposed into two unidirectional

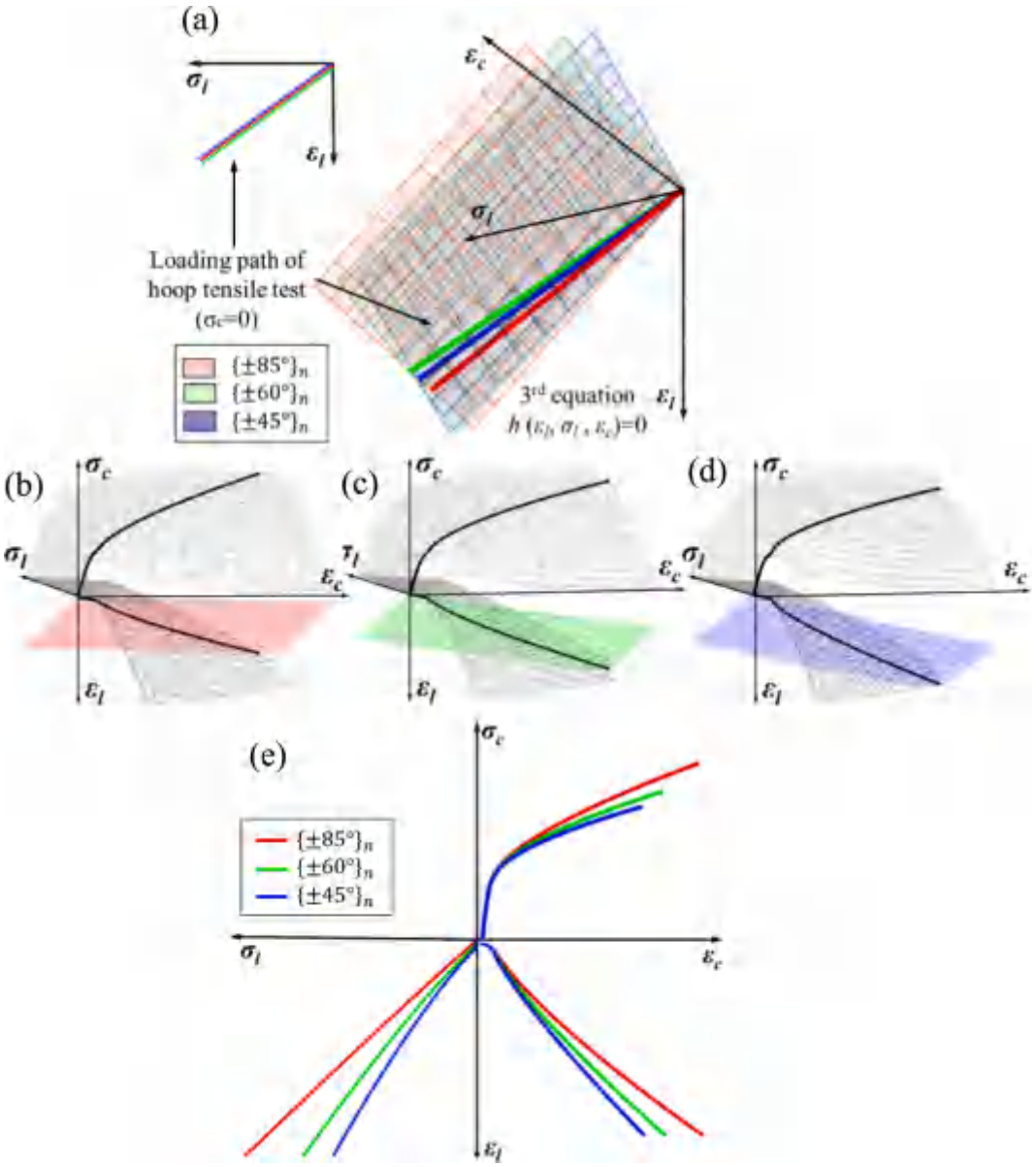


Fig. 2. Concrete confined by linear elastic FRP tubes.

laminates, each having half of the tube thickness, as shown in Fig. 1. The local coordinates for each laminate are defined as direction-1, which is parallel to the fibres, and direction-2, which is perpendicular to the fibres. The two axes a and h in the global coordinates denote the axis and hoop directions of the FRP tube, respectively. The laminates shown as blue and red in Fig. 1 are denoted as laminates with + θ and -θ, respectively. For each laminate, the localized stress and strain can be written in vector form:

$$\boldsymbol{\varepsilon}_{local} = [\varepsilon_1, \varepsilon_2, \varepsilon_6]^{\boldsymbol{T}} \tag{6}$$

$$\boldsymbol{\sigma}_{local} = [\sigma_1, \sigma_2, \sigma_6]^{T} \tag{7}$$

$$\boldsymbol{\sigma}_{local} = [\boldsymbol{Q}]\boldsymbol{\varepsilon}_{local} \tag{8}$$

where [Q] is the stiffness matrix of the unidirectional laminate:

$$[\boldsymbol{Q}] = \begin{bmatrix} \dfrac{E_1}{1-\upsilon_{12}\upsilon_{21}} & \dfrac{\upsilon_{21}E_1}{1-\upsilon_{12}\upsilon_{21}} & 0 \\ \dfrac{\upsilon_{12}E_2}{1-\upsilon_{12}\upsilon_{21}} & \dfrac{E_2}{1-\upsilon_{12}\upsilon_{21}} & 0 \\ 0 & 0 & G_{12} \end{bmatrix} \tag{9}$$

Similarly, the expressions for the global stress and strain are:

$$\boldsymbol{\varepsilon}_{global} = [\varepsilon_a, \varepsilon_h, 0]^{\boldsymbol{T}} \tag{10}$$

$$\boldsymbol{\sigma}^{\theta}_{global} = \left[\sigma^{\theta}_a, \sigma^{\theta}_h, \tau^{\theta}\right]^{T} \tag{11}$$

Note that the superscript θ in $\boldsymbol{\sigma}^{\theta}_{global}$ and its components represents the stress contribution of the laminate with a fibre angle of θ. If the superscript is omitted, it denotes the total stress and its components in the global coordinate system. Using the transforming matrix $T(\theta)^{-1}$, the stress and strain in one laminate can be expressed in the global coordinate system:

$$\boldsymbol{\varepsilon}_{local} = (\boldsymbol{T}(\theta)^{-1})^{T}\boldsymbol{\varepsilon}_{global} \tag{12}$$

Table 1
FRP tube properties.

Orientation	E_a (MPa)	E_h (MPa)	ν_{ah}	ν_{ha}	D/t (mm)	E_l (N/mm)
$\{\pm 85°\}_n$	8329	44,080	0.337	0.064	0.054	1200
$\{\pm 60°\}_n$	8129	21,763	0.842	0.345	0.110	
$\{\pm 45°\}_n$	10,719	10,719	0.638	0.638	0.224	

$$\boldsymbol{T}(\theta)^{-1} = \begin{bmatrix} \cos^2\theta & \sin^2\theta & -2cos\theta sin\theta \\ \sin^2\theta & \cos^2\theta & 2cos\theta sin\theta \\ cos\theta sin\theta & -cos\theta sin\theta & \cos^2\theta - \sin^2\theta \end{bmatrix} \tag{13}$$

$$\boldsymbol{\sigma}_{local} = [\boldsymbol{Q}]\boldsymbol{\varepsilon}_{local} = [\boldsymbol{Q}](T(\theta)^{-1})^T\boldsymbol{\varepsilon}_{global} \tag{14}$$

$$\boldsymbol{\sigma}^{\theta}_{global} = T(\theta)^{-1}\boldsymbol{\sigma}_{local} = T(\theta)^{-1}[\boldsymbol{Q}](T(\theta)^{-1})^T\boldsymbol{\varepsilon}_{global} \tag{15}$$

Assuming that the total thickness of the tube wall is t and each laminate has a thickness of $t/2$, the total global stress is:

$$\begin{aligned}\boldsymbol{\sigma}_{global} &= \left(\frac{1}{2}t\boldsymbol{\sigma}^{\theta}_{global} + \frac{1}{2}t\boldsymbol{\sigma}^{-\theta}_{global}\right)\frac{1}{t} \\ &= \left\{\frac{1}{2}T(\theta)^{-1}[\boldsymbol{Q}]\left(T(\theta)^{-1}\right)^T + \frac{1}{2}T(-\theta)^{-1}[\boldsymbol{Q}]\left(T(-\theta)^{-1}\right)^T\right\}\boldsymbol{\varepsilon}_{global} \\ &= [\overline{\boldsymbol{Q}}]\boldsymbol{\varepsilon}_{global}\end{aligned} \tag{16}$$

where the equivalent stiffness matrix $[\overline{\boldsymbol{Q}}]$ yields:

$$\begin{aligned}[\overline{\boldsymbol{Q}}] &= \begin{bmatrix} \overline{Q}_{11} & \overline{Q}_{12} & 0 \\ \overline{Q}_{21} & \overline{Q}_{22} & 0 \\ 0 & 0 & \overline{Q}_{66} \end{bmatrix} \\ &= \frac{1}{2}T(\theta)^{-1}[\boldsymbol{Q}]\left(T(\theta)^{-1}\right)^T + \frac{1}{2}T(-\theta)^{-1}[\boldsymbol{Q}]\left(T(-\theta)^{-1}\right)^T\end{aligned} \tag{17}$$

Finally, the elastic modulus and Poisson's ratio expressed in the global coordinate system can be extracted from $[\overline{\boldsymbol{Q}}]$:

$$E_a = (\overline{Q}_{11}\overline{Q}_{22} - \overline{Q}_{12}\overline{Q}_{12})/\overline{Q}_{22} \tag{18}$$

$$E_h = (\overline{Q}_{11}\overline{Q}_{22} - \overline{Q}_{12}\overline{Q}_{12})/\overline{Q}_{11} \tag{19}$$

$$\upsilon_{ah} = \overline{Q}_{12}/\overline{Q}_{22} \tag{20}$$

$$\upsilon_{ha} = \overline{Q}_{12}/\overline{Q}_{11} \tag{21}$$

where E_a and E_h are the elastic modulus of the FRP tube in the axial direction and hoop direction, respectively; ν_{ah} is Poisson's ratio for the strain in the hoop direction when stressed in the axial direction; and ν_{ha} is Poisson's ratio for the strain in the axial direction when stressed in the hoop direction. Notably, E_h is the result obtained from the hoop tension test, and E_a can be obtained from the axial compression test on the FRP tube [38]. According to the generalized Hooke's law:

$$\sigma_h = \frac{1}{1-\nu_{ah}\nu_{ha}}(\nu_{ha}E_a\varepsilon_c + E_h\varepsilon_l) \tag{22}$$

Substituting Eq. (22) into Eq. (4) and considering the compatibility condition, the 3rd equation $h(\varepsilon_l, \varepsilon_c, \sigma_l) = 0$ for the filament-wound FRP tube yields:

$$\sigma_l = \begin{cases} \dfrac{2t}{D}\dfrac{1}{1-\nu_{ah}\nu_{ha}}(\nu_{ha}E_a\varepsilon_c + E_h\varepsilon_l), \varepsilon_l = \varepsilon_h \\ 0, \varepsilon_l < \varepsilon_h \end{cases} \tag{23}$$

Based on the above discussions, the behaviour of FRP, tube-confined concrete is presented in Fig. 2 using a 3D geometrical approach. In this demonstration, the FRP tubes are chosen to be $\{\pm 85°\}_n$, $\{\pm 60°\}_n$ and $\{\pm 45°\}_n$. All the demonstrated tubes have the same set of laminate properties with $E_{11} = 44800$ MPa, $E_{22} = 8350$ MPa, $\nu_{12} = 0.058$, $\nu_{21} = 0.311$ and $G_{12} = 3300$ MPa, which are typical values for GFRP composites [37]. The axial and hoop properties of the tubes calculated by Eqs. (18)–(21) are listed in Table 1. For comparison, the three tubes have the same confining stiffness E_l by varying the diameter-to-thickness ratio (D/t). As shown in Fig. 2a, all three surfaces of the 3rd equation are flat and inclined to the axes, indicating the elasticity and biaxial behaviour of the materials. The traces of the state points for the hoop tension test are also marked with thick lines on the corresponding surface in Fig. 2a. As can be observed from the figure, the three traces are not in the same plane, although their projections on the ε_l-σ_l plane coincide, suggesting that even if the hoop tension tests yield the same results of E_l, the behaviour of the tubes with different fibre orientations can be different. The solving process of the stress–strain curve are shown in Fig. 2b-2d. The curves plotted in the ε_l-σ_l quadrant of Fig. 2e show the relationship between the lateral strain and the confining stress, which can be regarded as the actual confining stiffness. Due to the biaxial behaviour, the ε_l-σ_l curves are nonlinear, especially when θ is small. Noting that the three plotted cases have the same E_l, the following inference can be drawn: directly adopting the hoop tension test E_h into Eq. (4) to calculate E_l will introduce error into the final analytical results, regardless of whether design-oriented models or analysis-oriented models are utilized. Therefore, proper modification of the current design methods is needed.

In summary, the biaxial behaviour of filament-wound FRP tubes is influenced by the fibre angle θ. When θ approaches 90°, the biaxial effect is minimal. In contrast, with the decrease in θ, the biaxial effect of the tube becomes nonnegligible. Even with the same hoop tension test results of E_l, FRP tubes with different θ values exhibit different confining behaviours.

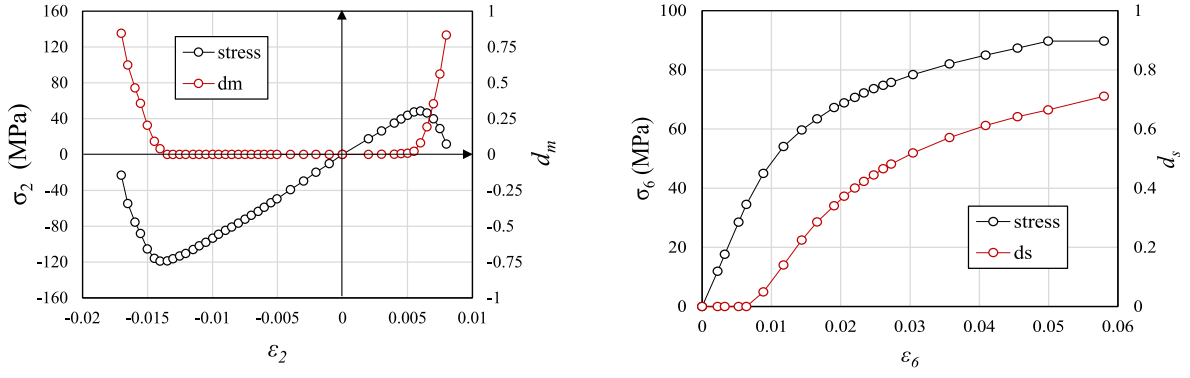


Fig. 3. Nonlinear behaviour of laminate: (a) transverse stress–strain behaviour; (b) shear stress–strain behaviour.

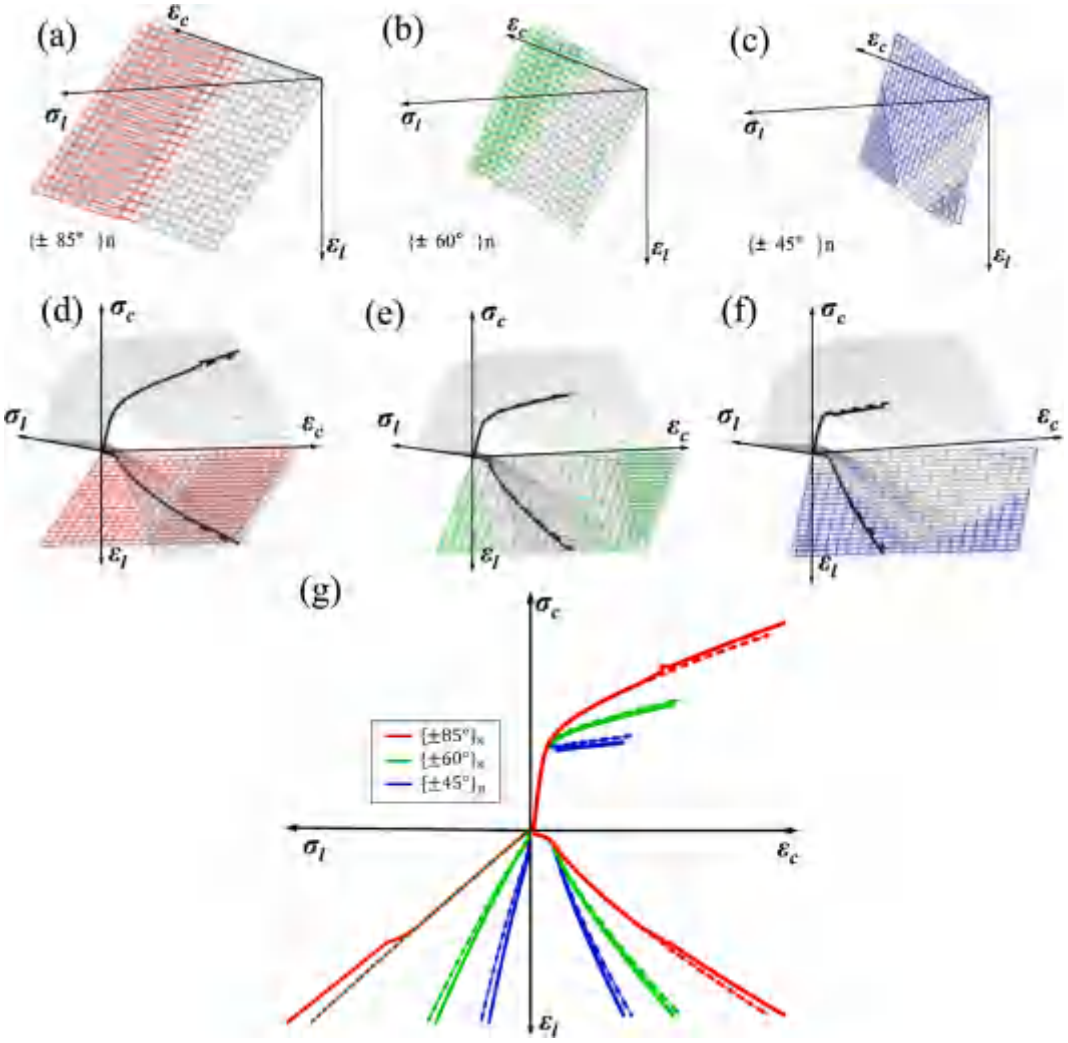


Fig. 4. Concrete confined by a nonlinear FRP tube.

2.2. Confinement models for nonlinear FRP composites

Another major difference between filament-wound FRP tubes and FRP sheet wraps is the nonlinear behaviour of the FRP tube. Apart from the nonlinear confining effect caused by the elastic biaxial behaviour, the nonlinearity of the epoxy resin can also cause nonlinear behaviour of the tube because of the shearing of the laminates. For the FRP sheet wraps, all the fibres are oriented parallel to the hoop direction. Hence, the shear effect is minimal. However, for the filament-wound tubes, since the fibre directions are inclined to the hoop direction, the laminates are subjected to in-plane shear when the hoop direction is under tension. Therefore, the influence of the epoxy resin property becomes nonnegligible, leading to nonlinear behaviour of the FRP tube. To model the material nonlinearity caused by the epoxy resin, the local stiffness matrix [Q] originally presented by Eq. (9) is updated to:

$$[\boldsymbol{Q}_d] = \frac{1}{D}\begin{bmatrix} E_1 & (1-d_m)\upsilon_{21}E_1 & 0 \\ (1-d_m)\upsilon_{21}E_1 & (1-d_m)E_2 & 0 \\ 0 & 0 & (1-d_s)GD \end{bmatrix} \tag{24}$$

$$D = 1-(1-d_m)\upsilon_{21}\upsilon_{21} \tag{25}$$

where $[\boldsymbol{Q}_d]$ is the constitutive matrix considering nonlinearity. d_m and d_s are damage variables for epoxy resin in transverse tension/compression and shear, respectively. Test results [39] have shown that the epoxy in transverse compression and tension exhibits different behaviour. Therefore, the expression for d_m is given by:

$$d_m = \begin{cases} d_m^c, \varepsilon_2 < 0 \\ d_m^t, \varepsilon_2 \geq 0 \end{cases} \tag{26}$$

where d_m^c is the damage variable for compression and d_m^t is the damage variable for tension. These two variables are calculated from the test results [39] by $d_m = 1-\frac{\sigma_2}{E_2\varepsilon_2}$. The test results and calculated damage variables are shown in Fig. 3a. Similarly, the damage variable $d_s = 1-\frac{\sigma_6}{G\varepsilon_6}$ obtained from [40] is shown in Fig. 3b. The damage variables are discrete points and $[\boldsymbol{Q}_d]$ is calculated numerically by linear interpolating from the discrete values.

According to the above discussions, the behaviours of CFFTs considering the nonlinear tube effect are plotted in Fig. 4. The three FRP tubes demonstrated in the figure have the same elastic properties as those described in Fig. 2. Fig. 4a, b and c show the nonlinear 3rd equations for $\{\pm 85^\circ\}_n$, $\{\pm 60^\circ\}_n$ and $\{\pm 45^\circ\}_n$ FRP tubes, respectively. The nonlinear surface of the 3rd equation is plotted as coloured meshes. The elastic 3rd equations with the same fibre orientation are also plotted in the lateral strain coordinate system as grey meshes for comparison. As shown in Fig. 4a, the $\{\pm 85^\circ\}_n$ tube exhibits a weaker nonlinear effect, and the elastic and inelastic surfaces almost coincide. With a decrease in θ, the difference between the elastic surface and the nonlinear surface becomes more obvious, as observed in Fig. 4b and c. With the same values of ε_l and ε_c, the nonlinear surfaces of the 3rd equation always yield a lower confining stress than their elastic counterparts. The state traces for FRP tube-confined concrete considering the nonlinear

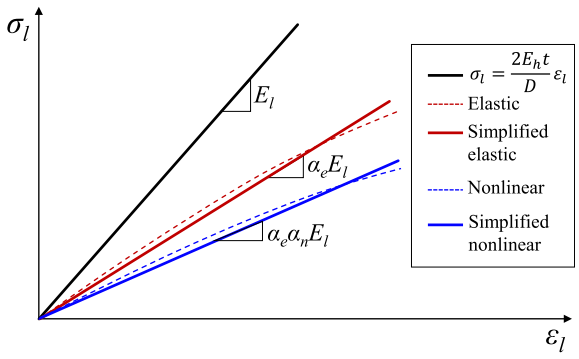


Fig. 5. Schematics for calibrating α_e and α_n.

behaviour of the tube are shown in Fig. 4d, e and f for $\{\pm 85°\}_n$, $\{\pm 60°\}_n$ and $\{\pm 45°\}_n$ FRP tubes, respectively. The solid and dashed curves represent the state traces of nonlinear and elastic confinement, respectively. The two types of state traces for the $\{\pm 85°\}_n$ tube coincide, as shown in Fig. 4d. For the $\{\pm 60°\}_n$ and $\{\pm 45°\}_n$ FRP tubes shown in Fig. 4e and 4f, respectively, the traces of nonlinear confinement have considerable reductions from their elastic counterparts. The projections of the state traces are plotted in 2D coordinate systems in Fig. 4g. The nonlinear and elastic traces are presented by solid and dashed curves, respectively. For the $\{\pm 85°\}_n$ tube, the stress–strain curve for nonlinear confinement is slightly higher than that for elastic confinement when ε_c is at a higher level, which means that when the epoxy resin is damaged, the $\{\pm 85°\}_n$ tube has a less biaxial effect. A reasonable explanation for this phenomenon is that the biaxial effect is mainly caused by Poisson's effect of the epoxy resin when the fibre orientation is close to 90°. When the epoxy resin is damaged, the hoop stress–strain response is highly dependent on the fibre, which exhibits similar behaviour to the FRP sheet-wrapped cases. For the $\{\pm 60°\}_n$ and $\{\pm 45°\}_n$ tubes, the biaxial effects are controlled by not only the Poisson's ratio of the epoxy resin but also the orientation of the fibres. Therefore, the nonlinear behaviour of the tube leads to a smaller confining stiffness and a lower axial stress.

In summary, a modelling technique for the nonlinear behaviour of filament-wound FRP tubes is proposed in this part. For tubes with smaller θ, the nonlinear behaviour of the tube introduces extra reductions to the axial stress–strain behaviour of the CFFT, which has not been considered in current design methods. On the other hand, experimental studies of the nonlinear behaviour of FRP composites are still limited. Hence, the variables assumed in this part are not firm enough and still need further investigation. Nevertheless, the analytical results clearly demonstrate the influence of the nonlinear effect, which is recommended for consideration in design for safety reasons.

Table 2
Values of α_e.

θ (°)	E_l (MPa)					
	400	800	1200	2000	2800	4000
85	0.958	0.930	0.906	0.867	0.838	0.803
70	0.945	0.871	0.812	0.724	0.657	0.587
60	0.941	0.801	0.702	0.569	0.481	0.392
50	0.842	0.644	0.525	0.384	0.304	0.231
45	0.742	0.544	0.431	0.304	0.235	0.175

3. Proposed modifications for design

The confining stiffness E_l is an important factor in both design- and analysis-oriented models. As previously discussed, adopting the hoop tension test result of E_h into Eq. (4) will overestimate the actual confining stiffness due to the biaxial and nonlinear behaviour of the FRP tube, especially when θ approaches 45°. To overcome this limitation, a simple modification to the confining stiffness is proposed:

$$E_{l,mod} = \alpha_e \alpha_n E_l = \alpha_e \alpha_n \frac{2E_h t}{D} \tag{27}$$

where $E_{l,mod}$ is the modified confining stiffness; α_e and α_n are the modification factors for the elastic and nonlinear biaxial behaviours, respectively; E_h is the hoop elastic modulus of the FRP tube obtained from the hoop tension test; t is the thickness of the FRP tube; and D is the concrete cylinder diameter. The modified confining stiffness can be used in both analysis-oriented and design-oriented models when analysing FRP tube-confined concrete.

For convenience of design, E_l and θ are chosen as the independent variables to calculate α_e and α_n. With known E_l and θ, the procedures for calibrating α_e and α_n are presented in Fig. 5 and stated as follows: (1) Solve for D/t using Eq. (4); (2) Substitute D/t into Eq. (23) and solve for the ε_l-σ_l relationship by combining Eq. (23) and the 2nd equation proposed by [20], as shown by the dotted red curve in Fig. 5; (3) Calculate α_e by fitting the dotted red curve into $\sigma_l = \alpha_e E_l \varepsilon_l$, as shown by the solid red line in Fig. 5; (4) Solve for the ε_l-σ_l relationship using the approach mentioned in section 2.2, which is presented by the dotted blue curve in Fig. 5; (5) Calculate α_n by fitting the dotted blue curve into $\sigma_l = \alpha_e \alpha_n E_l \varepsilon_l$, as shown by the solid blue line in Fig. 5. By repeating the above-mentioned steps (1)-(5) with various combinations of E_l and θ, the values of α_e and α_n for typical FRP tubes are determined and plotted in Fig. 6. It should be noted that Fig. 5 is only a schematic for explaining the calibrating process. In many cases the dotted red and blue curves are close to each other and therefore the value of α_n approaches 1.0. This result verifies the phenomenon that for the tubes with $\theta \leq 60°$, it is less efficient to increase the confining stiffness by simply increasing the tube

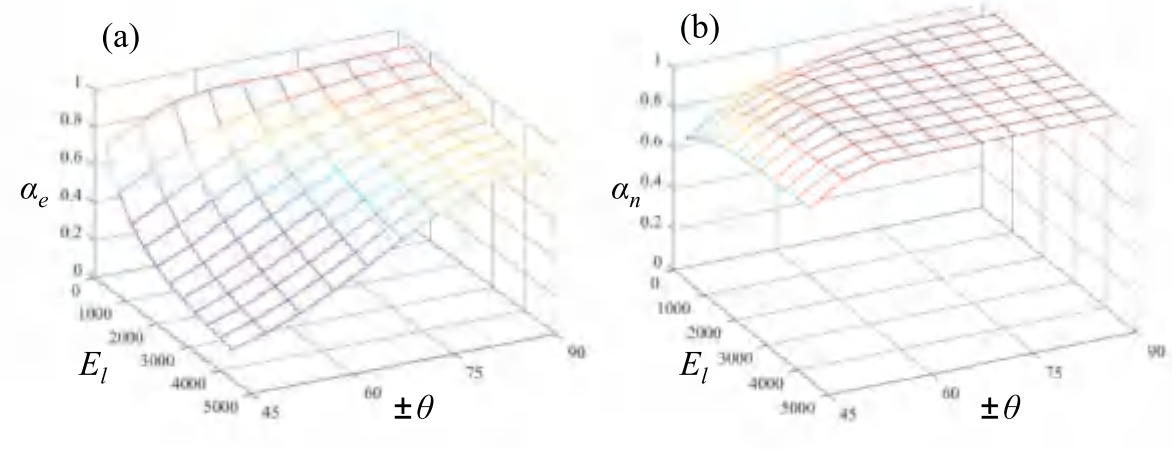


Fig. 6. Distribution of α_e and α_n.

Table 3
Values of α_n.

θ (°)	E_l (MPa)					
	400	800	1200	2000	2800	4000
≥80	1.000	1.000	1.000	1.000	1.000	1.000
70	0.978	1.000	1.000	1.000	1.000	1.000
60	0.919	0.959	0.985	1.000	1.000	1.000
50	0.799	0.852	0.881	0.915	0.935	0.952
45	0.700	0.756	0.785	0.817	0.833	0.846

thickness [26,41,42]. Regarding the nonlinear effect, for the tubes with $\theta \leq 80°$, the nonlinear behaviour of the FRP tube will introduce an extra reduction up to 30 %, especially when E_l is smaller. The values for α_e and α_n are also listed in Tables 2 and 3, which are convenient for design. The values for arbitrary E_l and θ can be interpolated from these tables. Notably, only α_e has a firm theoretical basis, while the determination of α_n is empirical. Therefore, applying α_e is essential for analysis, and it is recommended by the authors to apply α_n for safety reasons.

4. Model verification

The test data from Zhang et al. [41] are selected herein to verify the proposed model because it is one of the few systematic studies on FRP tube confined concrete that satisfies the following conditions: (1) winding angles and tube thickness are included as test variables, which are the concern of this research; (2) the specimens are circular stub columns under axial compression, so that the concrete is uniformly confined by the FRP tube; and (3) the confined concrete is NSC. Thus, the path-independent assumption is valid for simplicity [20]. In Zhang et al. [41], all test specimens have a diameter of 200 mm and height of 400 mm. Three winding angles (±80°, ±60°, ±45°) and two nominal tube thicknesses (4 mm and 6 mm) are tested. The concrete cylinder strengths f'_{co} are 25 MPa and 59 MPa. The laminar properties of the FRP tube are back calculated with the hoop tension test results and the axial compressive test results obtained from the $\{\pm 80°\}_n$ tube presented in Zhang et al. [41]. The back calculating process employs a tri-and-error method: first, assume the range of the fibre volumetric ratio and elastic modulus of glass fibre and epoxy resin, then adjust the aforementioned parameters to fit the axial and hoop properties of $\{\pm 80°\}_n$ tube. Studies conducted by the authors' group show that the hoop tension test introduces more errors to the material properties when θ is small, and the test method needs to be improved. Therefore, the hoop tension tests on the $\{\pm 60°\}_n$ and $\{\pm 45°\}_n$ tubes are not reliable. Relevant research outcomes are under preparation and will be published elsewhere.

Three analytical results are plotted in Fig. 7 to show a comparison with the test results: (1) the prediction from Yang and Feng's [20] model by adopting $E_{frp} = E_{h,test}$ in Eq. (4); (2) the prediction from the model presented in section 2.2 considering nonlinear behaviour of the tube, which is denoted as the precise model; and (3) the prediction from Yang and Feng's [20] model considering $E_l = E_{l,mod}$ in Eq. (4) for the 3rd equation, which is denoted as the simplified model.

As shown in Fig. 7, the results from both the precise model and simplified model are lower than the prediction of Yang and Feng's [20] model. The curves of the precise model predictions are not smooth, representing the damaging process of the epoxy resin. For the tubes with higher value of θ (F60 and F80), the load jumps up when the epoxy resin is damaged. This is because the damage of resin terminates the Poisson's effect of the tube and hence the confining stiffness is increased. However, this phenomenon is only in theory and rarely observed, because in the tests the damage always occurs at local point and is followed by progressive failure of the tube, which is beyond the capacity of analysis-oriented models. With the decrease in θ and increase in t, the difference among the three models becomes more obvious. Overall, Yang and Feng's [20] predictions overestimate the axial stress in most cases, and the simplified model yields closer predictions of the test results.

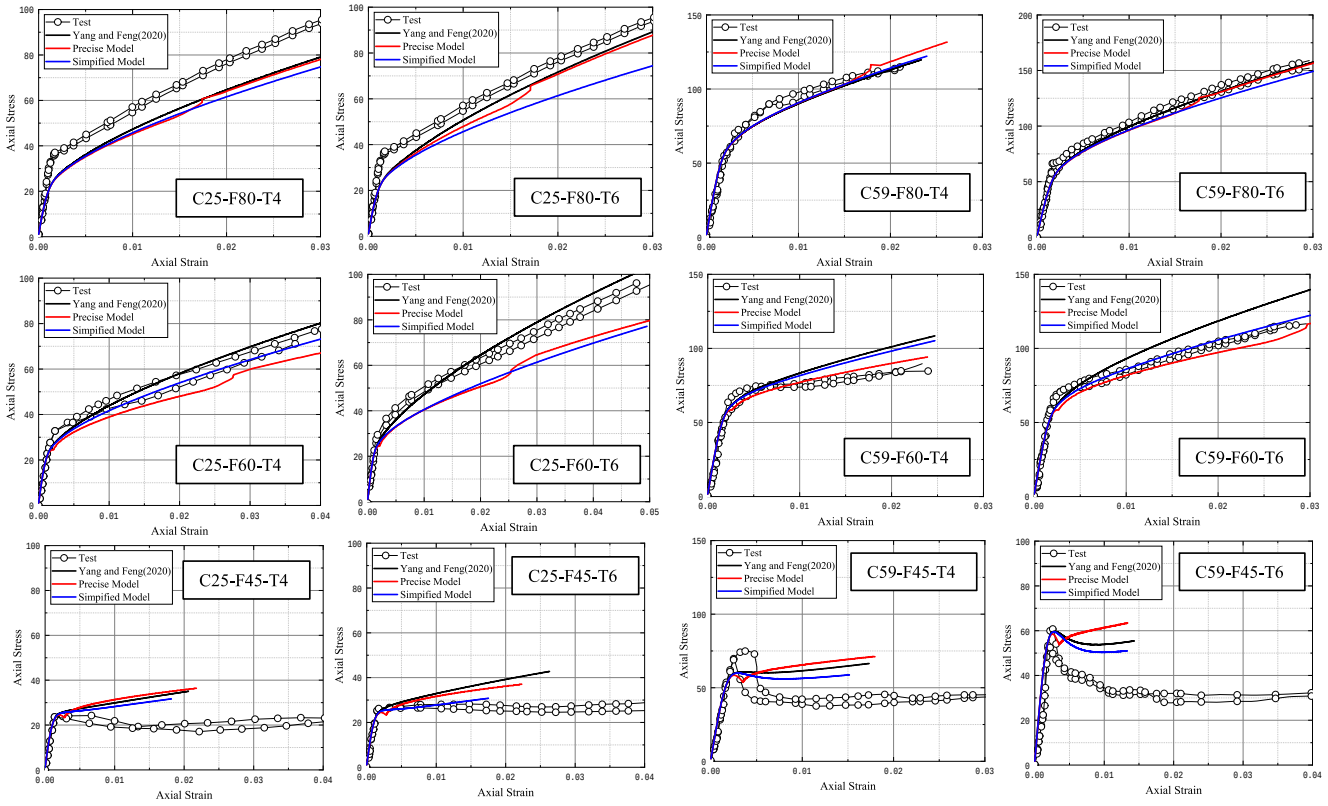


Fig. 7. Model verification.

5. Conclusions

In this research, the biaxial behaviour of filament-wound FRP tubes is analysed with classical laminate theory. The influences of the biaxial confining effect on the stress–strain behaviour of CFFTs are presented using the 3D geometrical approach. An analysis-oriented model for CFFTs considering both the elastic and nonlinear biaxial behaviour of the FRP tube is proposed. A simplified approach for modifying the confining stiffness is also proposed for engineering applications. According to the discussions presented in this paper, the following conclusions can be drawn: (1) The biaxial behaviour of the confining material causes relaxation of the confining stress. Neglecting this effect can cause overestimation of the confining stiffness and eventually overestimation of the strength of the confined concrete. (2) According to classical laminate theory, the biaxial behaviour of filament-wound FRP tubes is highly dependent on θ. When θ approaches 90°, the biaxial effect is minimal. In contrast, with the decrease in θ, the biaxial effect becomes more obvious. Therefore, FRP tubes with $\theta \geq 85°$ is most preferable for CFFTs or other kinds of FRP-concrete composite columns to ensure the confining effect. (3) The filament-wound FRP tubes exhibit nonlinear behaviour before failure due to the nonlinearity of epoxy. In this paper, techniques for modelling the nonlinear behaviour of such a tube are proposed, and key parameters are calibrated with existing test data. (4) Based on the proposed modelling method, a simplified approach is proposed to modify the confining stiffness. This approach is able to consider the biaxial effect caused by both the elastic and nonlinear behaviours of FRP tubes.

Nevertheless, the limitations of this study need to be further investigated: First, there is a lack of systematic studies on the biaxial behaviour of filament-wound FRP tubes. The results of this paper are mainly based on theoretical analysis and limited test results. More detailed test data are necessary to verify or improve the proposed model. Second, the hoop tension test is currently widely adopted to determine the mechanical properties of filament-wound FRP tubes. However, this test method may lead to incorrect results in some cases, which should be further investigated in the future. Moreover, direct biaxial test of FRP tubes (i.e., the tubes are under controllable axial load and internal pressure) needs to be carried out to verify the proposed confining stress model.

CRediT authorship contribution statement

Zhiyuan Li: Conceptualization, Methodology, Writing – original draft, Software, Validation. **Peng Feng:** Methodology, Writing – review & editing, Funding acquisition, Supervision. **Jia-Qi Yang:** Conceptualization, Methodology, Writing – original draft, Funding acquisition, Supervision.

Declaration of Competing Interest

The authors declare that they have no known competing financial interests or personal relationships that could have appeared to influence the work reported in this paper.

Data availability

Data will be made available on request.

Acknowledgements

This work is supported by the National Natural Science Foundation of China (No. 51908322, No. 51978379 and No. U2106219), the Fundamental Research Funds for the Central Universities (No. 2021XJLJ01), the Nonmetallic Excellence and Innovation Centre for Building Materials (No. 2022TDA1-1), the Yueqi Distinguished Scholar Program of China University of Mining and Technology, Beijing (No. 2602021RC59), and the research fund for new faculty members provided by the School of Mechanics and Civil Engineering, China University of Mining and Technology (Beijing).

References

[1] Teng JG, Chen JF, Smith ST, Lam L. FRP-strengthened RC structures. London, UK: Wiley; 2002.
[2] Teng JG, Chen JF, Smith ST, Lam L. Behaviour and strength of FRP-strengthened RC structures: a state-of-the-art review. Struct Build 2003;156(1):51–62.
[3] Mirmiran A, Shahawy M. A new concrete-filled hollow FRP composite column. Compos B Eng 1996;27(3-4):263–8.
[4] Zhang B, Teng JG, Yu T. Experimental behavior of hybrid FRP–concrete–steel double-skin tubular columns under combined axial compression and cyclic lateral loading. Eng Struct 2015;99:214–31.
[5] Wang J, Feng P, Hao T, Yue Q. Axial compressive behavior of seawater coral aggregate concrete-filled FRP tubes. Constr Build Mater 2017;147:272–85.
[6] Yu T, Zhao H, Ren T, Remennikov A. Novel hybrid FRP tubular columns with large deformation capacity: concept and behaviour. Compos Struct 2019;212:500–12.
[7] Dang Z, Feng P, Yang JQ, Zhang Q. Axial compressive behavior of engineered cementitious composite confined by fiber-reinforced polymer. Compos Struct 2020; 243:112191.
[8] Feng P, Li Z, Zhang S, Yang JQ. Steel slag aggregate concrete filled-in FRP tubes: volume expansion effect and axial compressive behaviour. Constr Build Mater 2022;318:125961.
[9] Feng P, Li Z, Wang J, Liu TianQiao. Novel joint for pultruded FRP beams and concrete-filled FRP columns: conceptual and experimental investigations. Compos Struct 2022;287:115339.
[10] Wang Z, Feng P, Zhao Yi, Yu T. FRP-confined concrete core-encased rebar for RC columns: concept and axial compressive behavior. Compos Struct 2019;222: 110915.
[11] Hu L, Feng P, Lin H, Yang JQ, Qiang H. Seismic performance of composite shear walls with embedded FCCCs in boundary elements. Compos Struct 2021;257: 113126.
[12] Cheng S, Feng P, Bai Y, Ye LP. Load-strain model for steel-concrete-FRP-concrete columns in axial compression. J Compos Constr 2016;20:04016017.
[13] Feng P, Cheng S, Bai Y, Ye L. Mechanical behavior of concrete-filled square steel tube with FRP-confined concrete core subjected to axial compression. Compos Struct 2015;123:312–24.
[14] Ozbakkaloglu T, Lim JC. Axial compressive behaviour of FRP-confned concrete: Experimental test database and a new design-oriented model. Compos B Eng 2013; 55:607–34.
[15] Ozbakkaloglu T, Lim JC, Vincent T. FRP-confned concrete in circular sections: review and assessment of stress–strain models. Eng Struct 2013;49:1068–88.
[16] Lam L, Teng JG. Design-oriented stress–strain model for FRP-confined concrete. Constr Build Mater 2003;17(6-7):471–89.
[17] Teng JG, Jiang T, Lam L, Luo YZ. Refinement of a design-oriented stress–strain model for FRP-confined concrete. J Compos Constr 2009;13(4):269–78.
[18] Teng JG, Huang YL, Lam L, Ye LP. Theoretical model for fiber-reinforced polymer-confined concrete. J Compos Constr 2007;11(2):201–10.
[19] Jiang T, Teng JG. Analysis-oriented stress–strain models for FRP–confined concrete. Eng Struct 2007;29(11):2968–86.
[20] Yang JQ, Feng P. Analysis-oriented models for FRP-confined concrete: 3D interpretation and general methodology. Eng Struct 2020;216:110749.
[21] Yang JQ, Feng P. Analysis-oriented model for FRP confined high-strength concrete: 3D interpretation of path dependency. Compos Struct 2021;278:114695.
[22] Feng P, Yang JQ, Li Z. FRP confined concrete: what, why, and how? In: Ilki A, Ispir M, Inci P, editors. 10th international conference on FRP composites in civil engineering CICE 2021 lecture notes in civil engineering. Cham: Springer; 2021. p. 37–45.
[23] Ho JCM, Ou XL, Chen MT, Wang Q, Lai MH. A path dependent constitutive model for CFFT column. Eng Struct 2020;210:110367.
[24] Lai MH, Song W, Ou XL, Chen MT, Wang Q, Ho JCM. A path dependent stress-strain model for concrete-filled-steel-tube column. Eng Struct 2020;211:110312.
[25] Lai MH, Liang YW, Wang Q, Ren FM, Chen MT, Ho JCM. A stress-path dependent stress-strain model for FRP-confined concrete. Eng Struct 2020;203:109824.
[26] Hain A, Motaref S, Zaghi AE. Influence of fiber orientation and shell thickness on the axial compressive behavior of concrete-filled fiber-reinforced polymer tubes. Constr Build Mater 2019;220:353–63.
[27] Kaddour AS, Soden PD, Hinton MJ. Failure of ±55 degree filament wound glass/ epoxy composite tubes under biaxial compression. J Compos Mater 1998;32(18): 1618–45.
[28] Soden PD, Kitching R, Tse PC, Tsavalas Y, Hinton MJ. Influence of winding angle on the strength and deformation of filament-wound composite tubes subjected to uniaxial and biaxial loads. Compos Sci Technol 1993;46(4):363–78.
[29] Carroll M, Ellyin F, Kujawski D, Chiu AS. The rate-dependent behaviour of ± 55° filament-wound glass-fibre/epoxy tubes under biaxial loading. Compos Sci Technol 1995;55(4):391–403.
[30] Meijer G, Ellyin F. A failure envelope for ±60° filament wound glass fibre reinforced epoxy tubulars. Compos Part A Appl Sci Manuf 2008;39(3):555–64.
[31] Chen JF, Li SQ, Bisby LA, Ai J. FRP rupture strains in the split-disk test. Compos B Eng 2011;42(4):962–72.
[32] Teng JG, Zhao JL, Yu T, Li LJ, Guo YC. Behavior of FRP-confined compound concrete containing recycled concrete lumps. J Compos Constr 2016;20:04015038.

[33] Zhang B, Yu T, Teng JG. Behavior and modelling of FRP-concrete-steel hybrid double-skin tubular columns under repeated unloading/reloading cycles. Compos Struct 2021;258:113393.
[34] Zhou JK, Lin G, Teng JG. Compound concrete-filled FRP tubular columns under cyclic axial compression. Compos Struct 2021;275:114329.
[35] ASTM D2290-12. Standard test method for apparent hoop tensile strength of plastic or reinforced plastic pipe by split disk method. West Conshohocken, PA: ASTM; 2012.
[36] Xie P, Lin G, Teng JG, Jiang T. Modelling of concrete-filled filament-wound FRP confining tubes considering nonlinear biaxial tube behaviour. Eng Struct 2020;218:110762.
[37] Feng P, Lu X, Ye LP. Application of fiber reinforced polymer in construction: experiment, theory and methodology. Beijing, China: China Architecture & Building Press; 2011.
[38] GB/T5350-2005. Fiber-reinforced thermosetting plastic composites pipe: determination for longitudinal compressive properties. Beijing, China: The Standards Press of China; 2005.
[39] Tang ZW, Wang CC, Yu YL. Failure response of fiber-epoxy unidirectional laminate under transverse tensile/compressive loading using finite-volume micromechanics. Compos B Eng 2015;79:331–41.
[40] Li S, Xu M, Yan S, Sitnikova E. On the objectivity of the nonlinear along-fibre shear stress–strain relationship for unidirectionally fibre-reinforced composites. J Eng Math 2021;127(1).
[41] Zhang B, Hu X-M, Zhao Q, Huang T, Zhang N-Y, Zhang Q-B. Effect of fiber angles on normal- and high-strength concrete-filled fiber-reinforced polymer tubes under monotonic axial compression. Adv Struct Eng 2020;23(5):924–40.
[42] Vincent T, Ozbakkaloglu T. Influence of fiber orientation and specimen end condition on axial compressive behavior of FRP-confined concrete. Constr Build Mater 2013;47:814–26.
[43] Dang Z, Li Z, Feng P. Axial compressive behaviour of UHPC confined by FRP. Composite Structures 2022;300:116110.

Engineering Structures 272 (2022) 115022

Contents lists available at ScienceDirect

Engineering Structures

journal homepage: www.elsevier.com/locate/engstruct

Strengthening RC beams with mid-span supporting prestressed CFRP plates: An experimental investigation

Jia-Qi Yang [a,*], Peng Feng [b], Bin Liu [a], Husheng Wang [a], Weiping Zhao [a], Lili Hu [c]

[a] School of Mechanics and Civil Engineering, China University of Mining and Technology (Beijing), Beijing 100083, China
[b] Department of Civil Engineering, Tsinghua University, Beijing 100084, China
[c] State Key Laboratory of Ocean Engineering, School of Naval Architecture, Ocean and Civil Engineering, Shanghai Jiao Tong University, Shanghai 200240, China

ARTICLE INFO

Keywords:
CFRP
Prestress
Reinforced concrete beam
Strengthening

ABSTRACT

This paper proposes a novel strengthening method for reinforced concrete (RC) beams using prestressed carbon fibre-reinforced polymer (CFRP) plates. In the proposed method, the CFRP plate is stressed by adjusting the position of the mid-span deviators. The strengthening process is fast and easy to apply because there is no need for hydraulic jacks or adhesives. To investigate the behaviour of the strengthened RC beams, a series of tests were conducted on both intact and damaged beams with different strengthening configurations, and the full range behaviours of the beams are reported in detail. According to the test results, the maximum stress of the CFRP plate reached 1500 MPa, and the beam strength was enhanced up to 43%. Some of the strengthening schemes achieved good ductility. As a result, the proposed strengthening method is found to be effective and can be further developed into a pseudoplastic CFRP strengthening system.

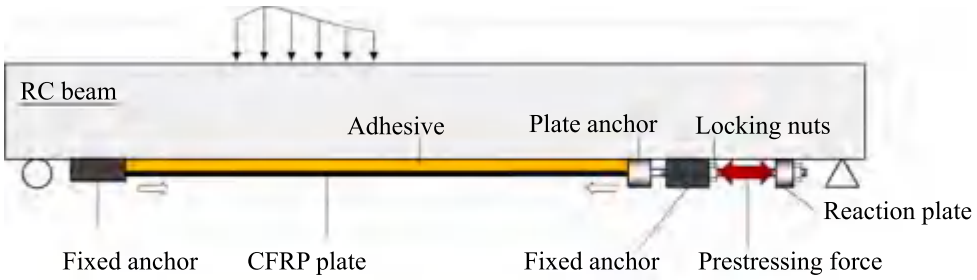
1. Introduction

Flexural strengthening of reinforced concrete (RC) structural members is an important application of fibre-reinforced polymers (FRPs) in civil and structural engineering [1]. The topic has been a concern for decades, and different flexural strengthening techniques have been studied and applied at sites worldwide. The basic form of flexural strengthening is to bond FRP sheets or plates on the tension face of the RC beam, i.e., the externally bonded (EB) technique. The behaviours and failure modes of the EB-strengthened RC beams were investigated thoroughly. Among various failure modes, the intermediate crack-induced debonding of the soffit FRP plate (IC debonding) is the most common and predictable [2]. Hence, codes or standards of many countries calculate the ultimate strength of strengthened beams according to this failure mode [3–8]. In the IC debonding failure mode, the beam strength is limited by the bond strength of the FRP-to-concrete interface [9,10], and the FRP is usually at a low stress level at the ultimate state. To predict the interfacial behaviour between the FRP and concrete, two types of models, namely, the bond strength models [11] and bond-slip models [12], were proposed, based on which numerical analysis can be conducted [13–15]. In addition to the premature brittle failure caused by IC debonding, the EB technique is not able to enhance the beam stiffness in the serviceability limit state since the FRP stress will not be activated until cracks propagate on the concrete beam [16]. To overcome the limitations of the EB technique, several approaches have been proposed and investigated. The first approach is to improve the bond quality. The near surface mounted (NSM) technique [17,18] mounts FRP strips or rods in the grooves cut on the concrete surface. Similarly, bond strength and bond-slip models were proposed for design and analysis [19,20]. Another way of improving the bond quality is the application of anchors, which introduces extra anchorages to the bonded interface [21–25].

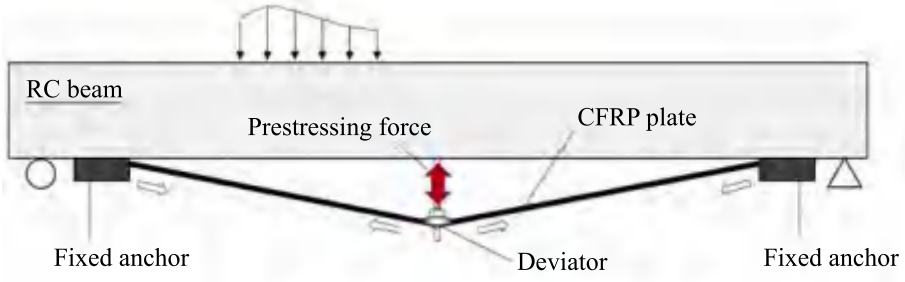
Another important approach to improve the strengthening efficiency is the utilisation of the prestress technique [26]. The prestress system can be either pretensioned or posttensioned in conjunction with EB or NSM techniques, and anchorage systems can be used simultaneously [27–32]. In particular, pultruded carbon fibre-reinforced polymer (CFRP) plates are preferred materials in posttensioned EB prestressing systems, and this technique has already been adopted in the structural strengthening industry [33–36]. The posttensioned EB prestressing system for RC beams is shown schematically in Fig. 1a. The strengthening system consists of two fixed anchors and a tensioning device. Prior to prestressing, epoxy adhesive is applied on the bond surface. A hydraulic jack is then placed between the fixed anchor and the reaction

* Corresponding author.
E-mail address: yangjiaqi@cumtb.edu.cn (J.-Q. Yang).

https://doi.org/10.1016/j.engstruct.2022.115022
Received 15 June 2022; Received in revised form 19 August 2022; Accepted 24 September 2022
Available online 3 October 2022
0141-0296/© 2022 Elsevier Ltd. All rights reserved.



(a) EB prestressing technique



(b) Proposed mid-span jacking prestressing technique

Fig. 1. Concept of mid-span jacking prestressed CFRP plate strengthening system.

plate to apply the tension stress in the CFRP plate. When the jacking force reaches the target value, the nuts in the tensioning device are fastened. Finally, the hydraulic jack is released, and the stress in the CFRP plate is held by the two fixed anchors. Although accepted by the industry, this method still has some room for improvement. First, the size of the tensioning device limits the flexibility of design. There needs to be enough space between the tensioning device and the beam support, resulting in a limited prestressed beam length, and may lead to local shear failure. Second, the application of the strengthening method requires epoxy adhesives, with the curing period usually lasting for at least 72 h [30], which may result in negative externalities, especially for strengthening transportation infrastructures.

To further improve the aforementioned strengthening system, the authors propose a novel prestressing method to strengthen RC beams with CFRP plates. A schematic of the proposed method is shown in Fig. 1b. The method is classified as an external unbonded posttensioned prestressing technique, which usually employs FRP bars or tendons as prestressing materials [37–39]. In the proposed method, both ends of the CFRP plate are fixed on the soffit of the beam, and the tensile stress in the CFRP plate is applied by driving the deviator away from the beam. This method is inspired by [40–44], which was originally proposed to strengthen steel structures. The prestressing process is fast and easy to apply without the use of hydraulic jacks. It provides an alternative solution for the quick strengthening or repair of civil infrastructures. To investigate the effectiveness of the proposed method, a series of experimental tests were conducted. Five intact or damaged RC beams were strengthened by the proposed method with different configurations, and the full range behaviours of the strengthened beams, including preloading, prestressing and reloading, are reported in detail. The flexural strengths of the strengthened beams were enhanced up to 43%, and some of the schemes also achieved ductile failure modes. The proposed method is proven to be effective, and the results show that it has the potential to be further developed into a pseudoplastic CFRP strengthening system.

2. Experimental setup

2.1. Details of the test beams

The experimental program consisted of five simply supported RC beams, including one plain beam and four strengthened beams. All test beams were identical in geometry. The cross sections for all beams were rectangular with a width (B) of 250 mm and a height (H_b) of 400 mm. The total span (L) of the beams was 4000 mm. The longitudinal reinforcements had two 18 mm tension bars and two 12 mm compression bars. The stirrups were 8 mm in diameter with a constant spacing of 100 mm through the beam. All beams were cast with the same batch of commercial ready-mix concrete. Details of the RC beams are shown in Fig. 2.

For the strengthened beams, the CFRP plates were fixed on the soffit of the beam by corrugated anchors [45]. The centre-to-centre distance between the two corrugated anchors was 3400 mm. The deviator

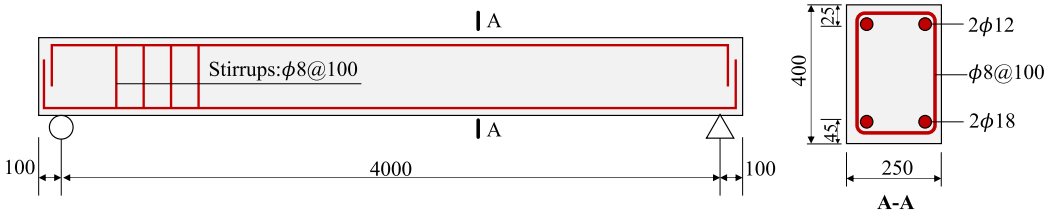
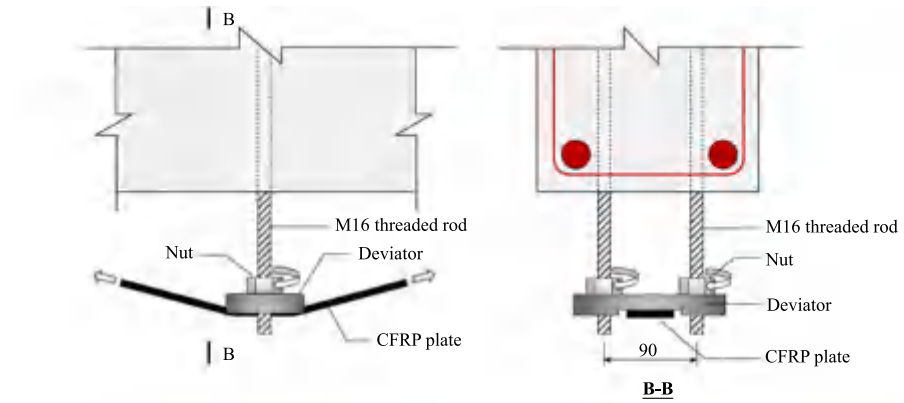
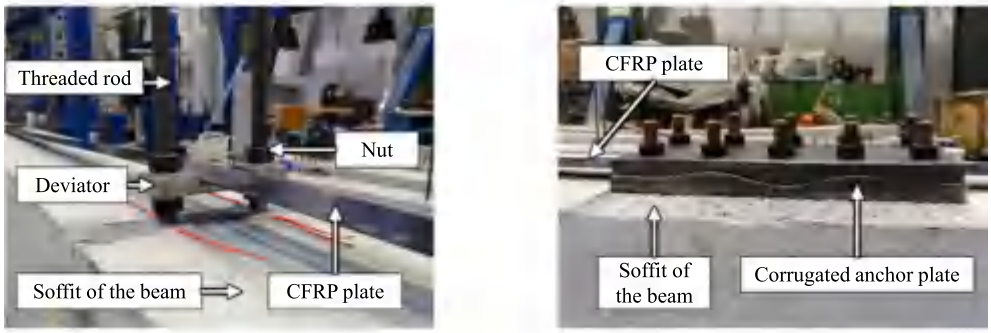


Fig. 2. Details of the RC beams (unit in mm).

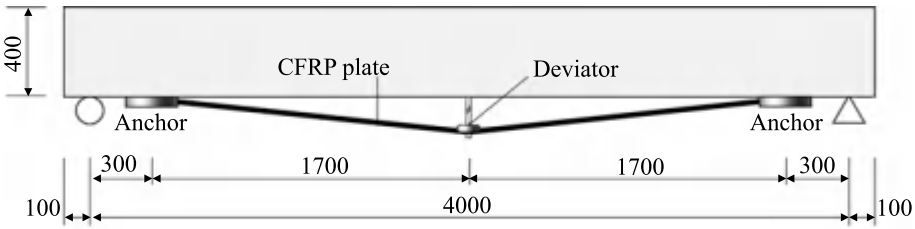


(a) Design of deviators

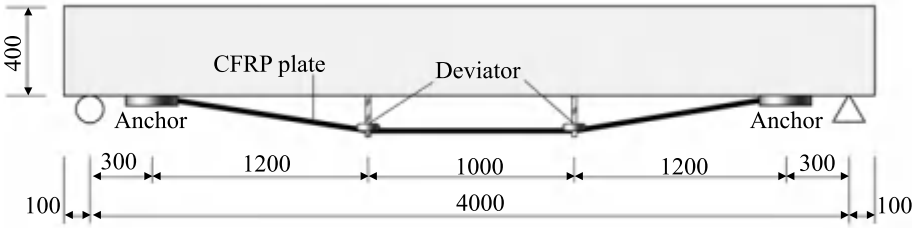


(b) Picture of deviator (c) Corrugated anchor

Fig. 3. Details ofdeviators and anchors.



(a) Scheme 1



(b) Scheme 2

Fig. 4. Strengthening schemes.

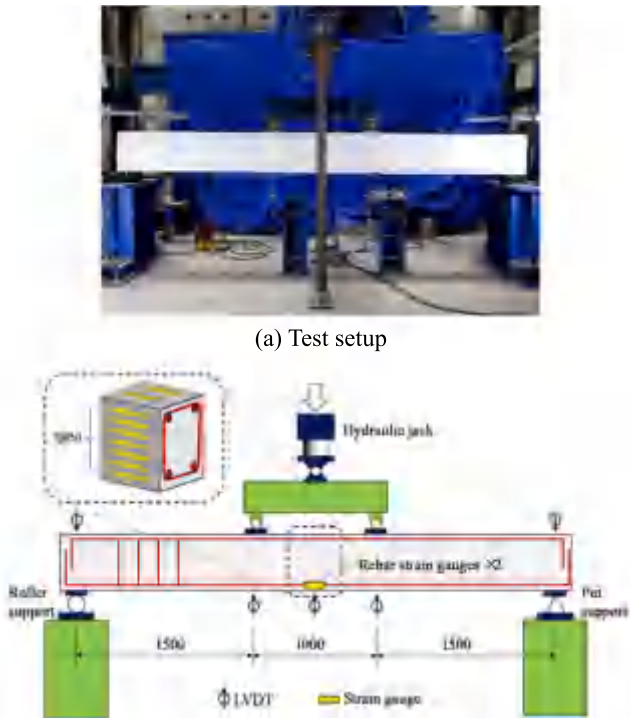
consisted of two M16 threaded rods that were embedded in the concrete during casting and a deviator plate with a slot and rounded corners to relieve the stress concentration. The prestress in the CFRP plate was applied by turning the nuts to drive the deviator away from the soffit of the beam. Details of the deviators and anchors are shown in Fig. 3.

Two strengthening schemes were designed and tested, as shown schematically in Fig. 4. For scheme 1, there was one deviator in the mid-span. For scheme 2, the deviators were located under the two loading points. Each scheme was applied to an intact beam and a damaged beam. Therefore, the control beam was labelled B0, and the intact beams strengthened by scheme 1 and scheme 2 were labelled B1 and B2, respectively, and are referred to as strengthened beams in this paper.

Table 1
Properties of steel bars.

Diameter (mm)	f_y (MPa)		f_u (MPa)	
	Mean	s.d.	Mean	s.d.
8	509.6	14.7	601.6	9.3
12	435.2	11.6	608.4	9.7
18	466.0	19.3	657.8	27.3

s.d. = standard deviation



(a) Test setup

(b) Details of instrumentation

Fig. 5. Test setup and instrumentation.

The damaged beams repaired by scheme 1 and scheme 2 were labelled B1R and B2R, respectively, and are referred to as repaired beams in the following sections.

2.2. Material properties

The commercial ready-mix concrete is of grade C40. Five 150 mm cubes were tested, and the average cube strength (f_{cu}) taken from four valid datapoints was 60.0 MPa (standard deviation, s.d. = 3.1 MPa). The elastic modulus (E_c) and prism strength (f_c) were obtained from compression tests on three 150 × 150 × 300 mm prisms in accordance with GB/T 50081–2019 [46]. The average E_c and f_c were 37.8 GPa (s.d. = 3.5 GPa) and 52.0 MPa (s.d. = 0.7 MPa), respectively. Five specimens for each specification of steel bars were tested in accordance with GB/T 1499.2–2018 [47]. The yield strength (f_y) and ultimate strength (f_u) are listed in Table 1. The pultruded CFRP plate had a width (b_{frp}) of 50 mm and a thickness (t_{frp}) of 1.4 mm. The tensile strength (f_{frp}) and tensile modulus (E_{frp}) were provided by the manufacturer and were 3064 MPa and 160 GPa, respectively.

2.3. Instrumentation and test procedures

The beams were tested under symmetrical four-point bending with a constant moment region (CMR) of 1,000 mm and shear spans of 1500 mm. The test setup is shown in Fig. 5a. Five LVDTs were installed to measure the displacements at the mid-span, two loading points and two supports. Two strain gauges were installed on the tension steel bars at the mid-span, and the average value of these two gauges was taken as the strain of the tension bars (ε_s). To measure the strain distribution of the section in the mid-span, nine 100 mm concrete strain gauges were installed on one side and the top of the beam. Details for the LVDTs and strain gauges are shown in Fig. 5b. The locations of the strain gauges on the CFRP plate are shown in Fig. 6. The strain gauges were installed between the anchor and deviators. The strain of the CFRP plates (ε_{frp}) presented in the following sections of this paper are averaged from all gauges on one CFRP plate. The stress of the CFRP plate (σ_{frp}) can be calculated with $\sigma_{frp} = E_{frp}\varepsilon_{frp}$ accordingly.

The load was applied by a manually controlled hydraulic jack. For control beam B0, the loading procedures were as follows. (1) Before the tension rebar yielded ($\varepsilon_s \leq 2262 \times 10^{-6}$), the load was applied at 5 kN for each level. When a target load level was reached, the hydraulic jack was held until all the data were stable, and then the load was increased to the next level. (2) After the rebar yielded and before the mid-span deflection reached 30 mm, the load was applied in a displacement-controlled manner such that the mid-span deflection was 5 mm for each load level. (3) When the mid-span deflection was > 30 mm, the deflection for each load level was increased to 10 mm until the compressive strain of concrete (ε_{cu}) reached 0.0033. The prestressing procedures for the strengthened beams (B1 and B2) were as follows: (1) one end of the CFRP plate was fixed on one corrugated anchor; (2) the CFRP plate was tightened on the other end by hand while locking the second anchor; and (3) the nuts of the deviators were turned to stress the CFRP plate until reaching the target ε_{frp}. According to a preliminary trial of prestressing, the target ε_{frp} was set to 5000×10^{-6} for all strengthened or repaired beams, with a corresponding prestress level of 800 MPa and a nominal prestressing ratio of 26%. This value was relatively low because of the problem of the anchors, which will be discussed later in this paper. After prestressing, the test beams were loaded following the same procedures as B0. The repaired beams (B1R and B2R) were loaded to 80 kN following the same preload procedures as B0, and then the load was released. The preload was set as the ultimate strength of the plain beams calculated from the design values of the materials [48]. After the preloading stage, the prestress was applied according to the same procedures of B1 and B2, and the load was applied following the same procedures as B0 until compression failure of the concrete. It should be noted that the deviator rods of B1 were bended during the prestressing process. To prevent accident, the prestressing was stopped after σ_{frp} reached 765 MPa. The loading stage begun after ε_{frp} was stabilized (σ_{frp} = 709 MPa). Therefore, the short-term prestress loss for B1 is 7.3%. There was no short-term prestress loss observed in the other three prestressed beams.

3. Experimental results

3.1. Load-deflection behaviours and failure modes

The total load (P) versus mid-span deflection (δ_m) responses for the test beams are shown in Fig. 7. The curves for scheme 1 and scheme 2 beams are plotted separately in Fig. 7a and 7b, together with that of B0 for comparison. Moreover, to present the load–deflection responses during the prestressing process, the initial part of the curves with $\delta_m <$ 20 mm are magnified and plotted in the figures. As shown in the figures, B0 behaved as a typical balanced reinforced concrete beam with stages of elastic, crack propagating and post yield. For strengthened beams (B1 and B2), the load–deflection responses consisted of five stages: (1) the prestressing stage, in which δ_m increased in the negative direction while the load remained zero; (2) the precracking stage, when P increased linearly with δ_m and there was no crack observed on the beam; (3) the cracking stage, in which the load also increased linearly with δ_m but with a lower stiffness, and the cracks propagated towards the top of the beam

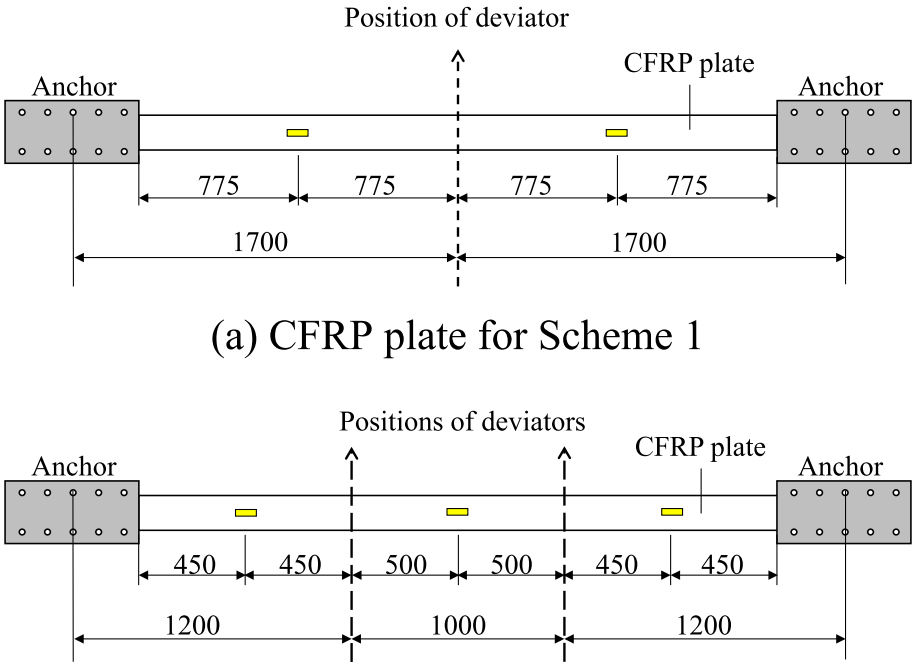


Fig. 6. Strain measurement of CFRP plates.

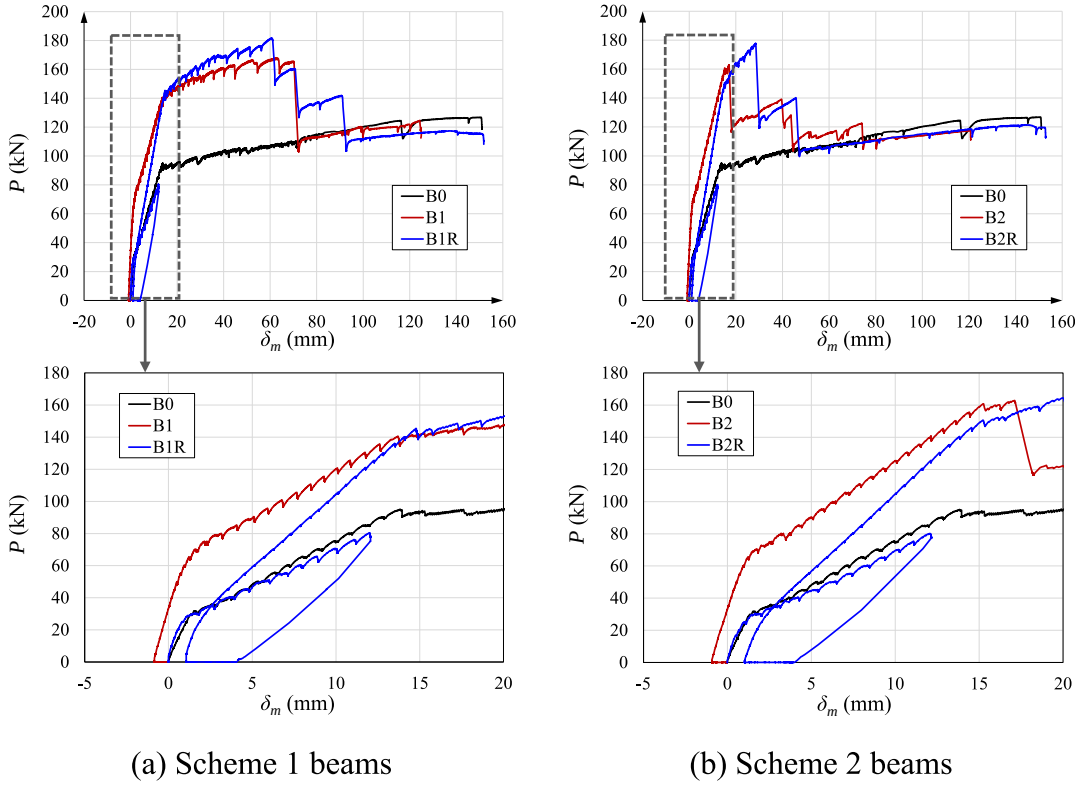


Fig. 7. Load-deflection behaviour of test beams.

(In this stage, the strain gauges data showed that the steel bars remained elastic.); (4) the yielding stage started with the steel bars yielding, and the stiffness of the load–deflection curve further decreased (The increase in load was mainly contributed by the CFRP plate); and (5) when the CFRP plate failed, the load dropped suddenly. After the entire CFRP ruptured, the load–deflection curve almost coincided with B0. The repaired beams (B1R and B2R) had the same behaviour as B0 in the preloading stage. After the preload was released, there was irrecoverable deflection in the mid-span. The application of prestress in the CFRP plates reduced the residual deformation. Except for the absence of the

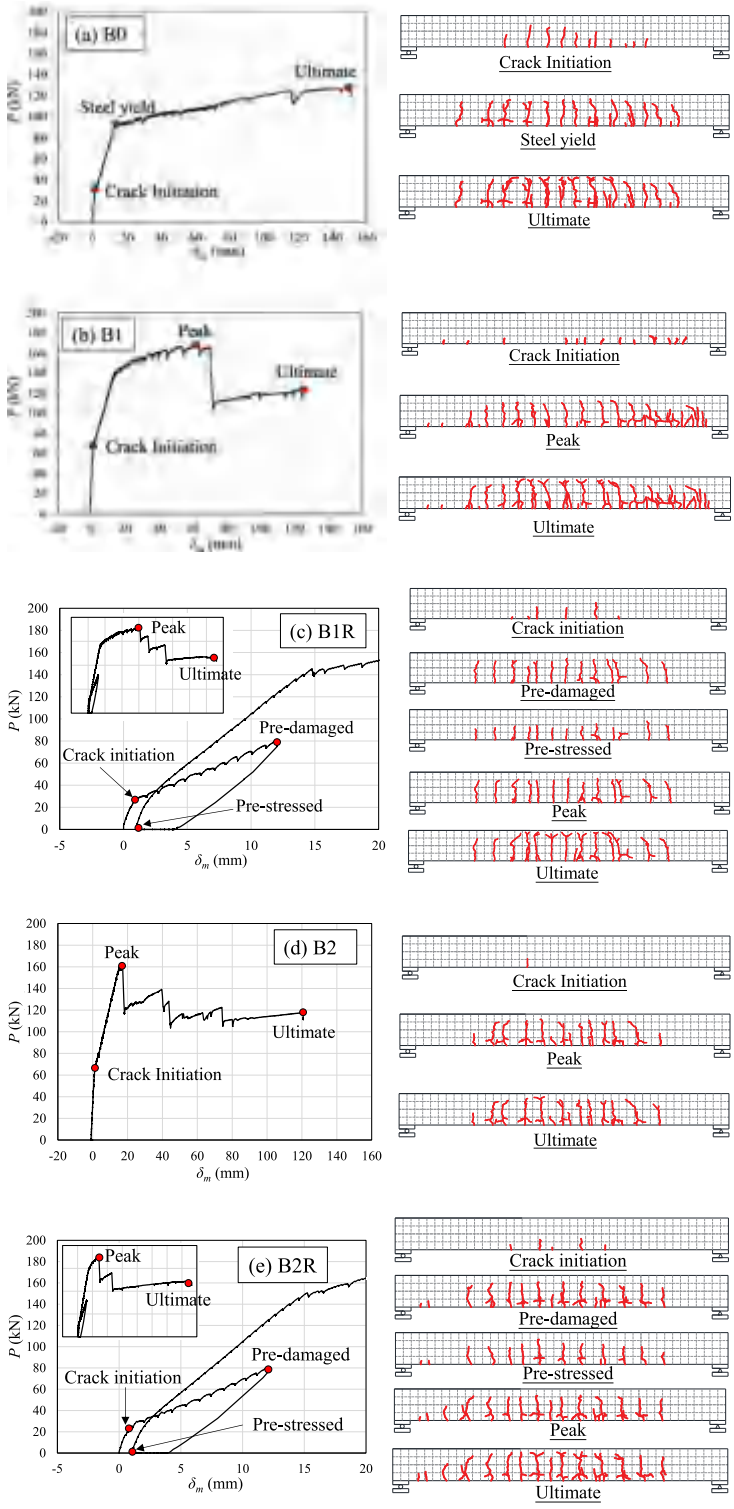
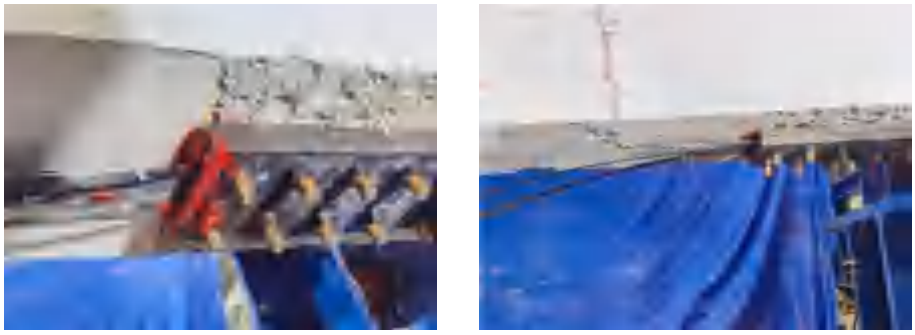


Fig. 8. cracking propagation of test beams.

precracking stage, the behaviour of the repaired beams was the same as that of the strengthened beams.

The crack patterns for all test beams are shown in Fig. 8. Key points are highlighted on the load–deflection curves, and the corresponding crack pattern is plotted. As shown in the figure, the crack spacing for all beams was approximately 200 mm for all beams, indicating that the unbonded prestressing system did not change the crack spacing. For B0, when cracks first appeared, they propagated to 200 mm in the vertical direction. However, for the strengthened beams, the heights of the cracks at the crack initiation point were less than 100 mm. When entering the yielding stage, the cracks for all beams were widened, but their height did not increase significantly. In this stage, the maximum height of the cracks for all beams was approximately 325 mm, and the critical intermediate crack was always below one of the loading points. For the repaired beams, the prestress could not totally close all cracks. However, it successfully reduced most of the crack heights from 300 mm



(a) Plate splitting (b) Plate rupture

Fig. 9. Failure of CFRP plates.

Table 2
Test results.

ID	P_{cr} (kN)	δ_d (mm)	δ_{ps} (mm)	P_y (kN)	δ_y (mm)	P_{max} (kN)	δ_{max} (mm)	$\sigma_{frp,u}$ (MPa)	$\frac{P_{max}}{P_{max,0}}$	$\frac{\delta_{max}}{\delta_y}$
B0	35.0	–	–	95.1	13.83	126.9	149.85	–	1.00	10.84
B1	50.0	–	−0.84	140.7	13.71	167.9	62.77	1042	1.32	4.58
B1R	30.0	3.98	−2.91	145.4	14.76	181.8	60.80	1079	1.43	4.12
B2	65.0	–	−0.91	143.7	12.67	162.9	17.11	1288	1.28	1.35
B2R	25.0	3.83	−2.81	150.7	15.23	177.8	28.43	1539	1.40	1.87

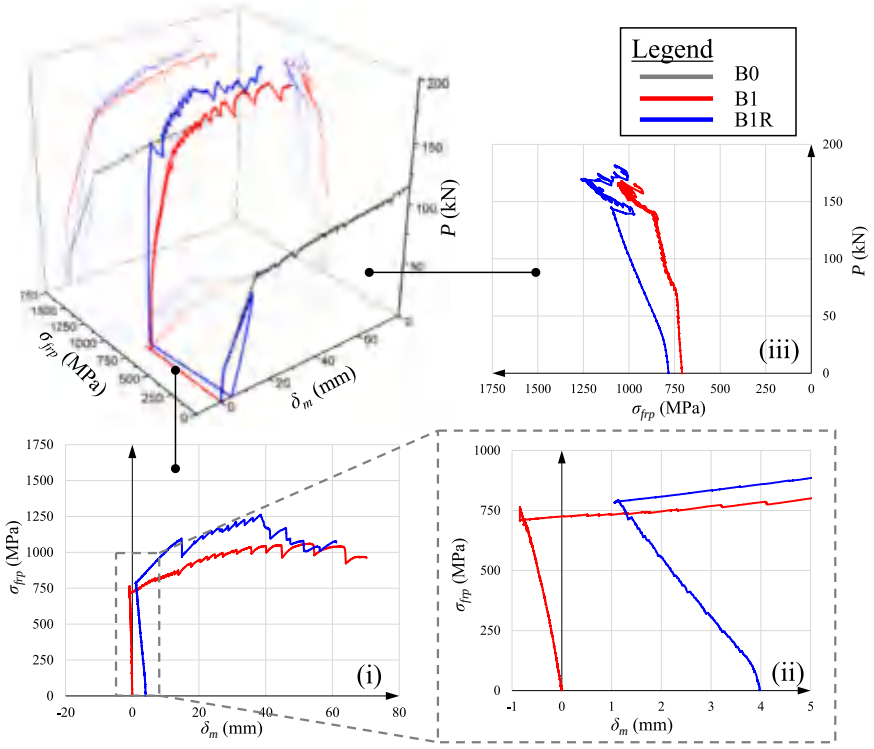
to 200 mm, as shown in Fig. 8c and 8e.

After the peak strength points, the CFRP plate in the strengthened and repaired beams split and partially ruptured, as shown in Fig. 9a. However, part of the CFRP plate still worked, and the whole plate failed progressively. Therefore, the postpeak load–deflection curves had several plateaus, as shown in Fig. 7. After the CFRP plate entirely ruptured (Fig. 9b), the load finally dropped back to the same level as B0. The progressive failure of the CFRP plate was attributed to the uneven distribution of the anchor pressure, which needs further improvement in the future. Possible solutions for this problem are: (1) adjusting the pretightening force/moment of the nuts on the anchor plate; (2) apply adhesives on the interfaces between the CFRP plate and the corrugated anchor plates; and (3) modify the configuration of the corrugated anchor plates [49]. At the ultimate state, the vertical cracks bifurcated at the crack tip, and concrete wedges were formed on the top of the beam; then, the RC beams lost their strength.

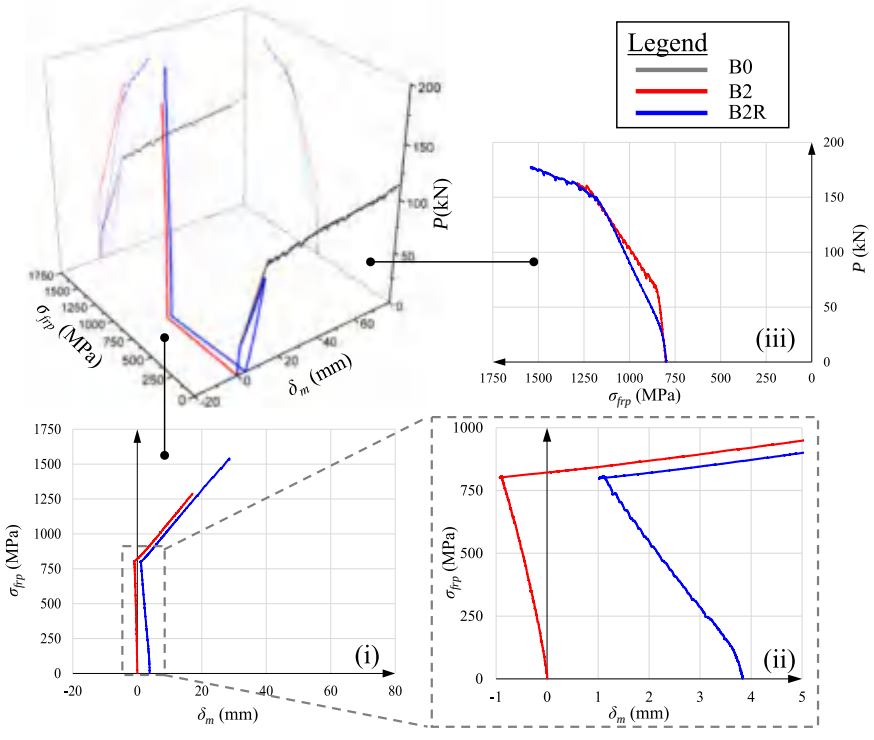
The quantitative test results are listed in Table 2. In the table, P_{cr} is the cracking load for the test beams. For plain RC beams (B0, B1R and B2R), the average cracking load was 30 kN. When prestressed, the cracking loads increased to 50 kN for B1 and 65 kN for B2, indicating that the prestressing system enhanced the cracking strength by at least 60%. The cracking loads were recorded when the cracks first appeared. At the first turning point shown on the load–deflection curve (Fig. 8b), the cracking load for B1 was also 65 kN. Therefore, the strengthened beams remained uncracked under the original designed service load. δ_d represents the irrecoverable mid-span deflection in the preload stage, which is only valid for the repaired beams, and δ_{ps}, noted as negative values, are the deflections due to prestressing. For the repaired beams, δ_d recovered by approximately 73%. P_y and δ_y are the yield load and the corresponding deflection, respectively. The yield point is determined with the farthest point method [50–52]. By checking the strain gauge results, ε_s at the yield points for the test beams is approximately 2200×10^{-6}, which confirms the validity of the farthest point method. P_{max} and δ_{max} are the peak load and the corresponding deflection, respectively. The strengths of the strengthened and repaired beams were enhanced up to 43% compared with B0. The strength enhancements for repaired beams were higher than their strengthened counterpart by approximately 10%. The maximum stresses of the CFRP plates before failure ($\sigma_{frp,u}$) are also listed in Table 2. Unfortunately, the stress level in the CFRP plates was low compared with the ultimate strain, which was caused by problems with the anchors. Nevertheless, it resulted in significant strength and stiffness enhancement of the beams. The results imply that if the performance of the anchors is improved, the efficiency of the proposed strengthening method will be further increased. Regarding the ductility factor (δ_{max}/δ_y), scheme 1 beams performed much better than scheme 2. In fact, visible bending of the threaded rods in the deviators for B1 and B1R was observed during the yielding stage. When the rods bent, the stress in the CFRP plate no longer increased monotonically with the deflection, which resulted in a longer plateau of the yield stage for B1 and B1R. Although unexpected, this phenomenon provides inspiration for future research. If the reaction force in the deviator can be designed as elasto-plastic, the strain in the CFRP plate will be maintained at a higher level with relatively large beam deformation. Using this mechanism, the use of linear elastic material is able to achieve pseudoplastic behaviours.

3.2. CFRP stress development

To better understand the strain development of the CFRP plate, the full range load–deflection-strain relationships are plotted in 3D coordinate systems, as shown in Fig. 10. This method is referred from [53–55], which is able to present complex relationships among multiple variables intuitively. The coordinate system consists of three axes: mid-span deflection (δ_m, unit in mm), the total load (P, unit in kN), and the tensile stress of the CFRP plate (σ_{frp}, unit in MPa). The spatial trajectory shows the history of the external load and the beam response. Each point on the 3D trajectory represents a certain status of the beam (δ_m, σ_{frp}, P). The projection of the trajectory on the δ_m–P plane is the typical load–deflection curve, which is shown in Fig. 7. The projection of the trajectory on the δ_m–σ_{frp} plane shows the plate stress development with the change in the beam deflection, which is noted as plot (i) and plot (ii), and plot (ii) is a highlight of plot (i) with -1 mm $< \delta_m <$ 5 mm, showing the deflection change during the prestressing stage. The projection of the trajectory on the σ_{frp}–P plane shows the relationship between the CFRP stress and the total load, which is noted as plot (iii). The trajectory of B0 is also plotted in 3D space for comparison. The trajectories for B0 and the



(a) Scheme 1



(b) Scheme 2

Fig. 10. Full range load-stress–deflection behaviours.

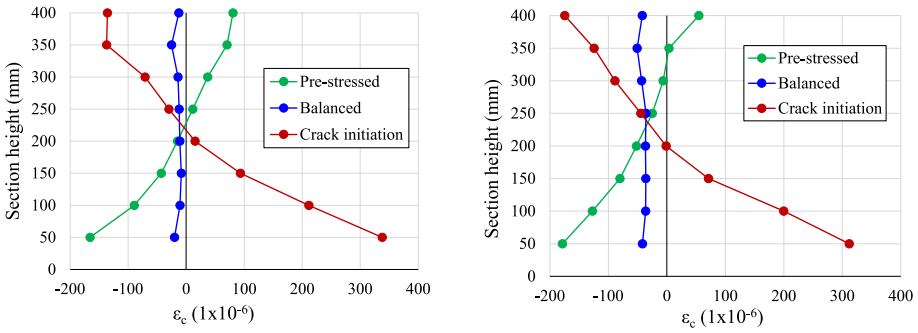


Fig. 11. Section strain distribution.

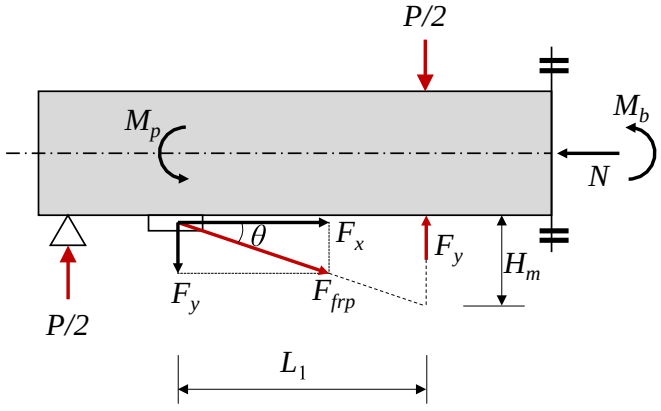


Fig. 12. Freebody diagram.

preloading stages of B1R and B2R lie on the $\sigma_{frp} = 0$ plane, representing the absence of the CFRP plate. It should also be noted that only the trajectories of the strengthened and repaired beams before CFRP failure are plotted for analysis.

The prestressing processes are clearly presented by the plots (i) and (ii). When no external load was applied, δ_m decreased with increasing prestress, indicating that the beam was bending upwards. The curves of strengthened beams (B1 and B2) initiate from the origin. For the repaired beams (B1R and B2R), the curves start from the points of residual mid-span deflection. The slopes of the δ_m–σ_{frp} curves in the prestressing stage for strengthened beams are higher than those of their repaired counterpart, indicating that the initial stiffness of the damaged beam is lower than that of the intact beams. As shown in the plot (i) in Fig. 10, the stress in the CFRP plate changed almost linearly with the deflection before steel yielded, regardless of the prestressing stage or the loading stage. For the strengthened beams, on the other hand, the curves in plot (i) have turning points when cracks are initiated. Prior to this point, the contribution of CFRP stress to the total load was minor. After cracking, the development of CFRP stress accelerated, indicating the stress redistribution of cracked RC beams.

After the steel yielded, as shown in Fig. 10b, σ_{frp} in scheme 2 beams (B2 and B2R) still grew linearly with δ_m until the CFRP failed. Meanwhile, the σ_{frp}–P curves entered the third linear ascending stage, showing that the contribution of CFRP stress to the load increment increased rapidly due to the yield of steel bars. In this stage, however, σ_{frp} of scheme 1 beams (B1 and B1R) was maintained between 900 and 1250 MPa and did not change monotonically with δ_m due to bending of the deviator rods. This enabled the load–deflection curves to have even lower stiffnesses and longer plateaus, which has been discussed in the previous sections. Therefore, it is a promising approach to achieving large deformation and ductile failure modes of CFRP-strengthened/repaired RC beams that design the deviator to have an elasto-plastic behaviour, which is able to maintain the CFRP stress at a higher value with the ever-increasing beam deflection.

The mid-span section strain distributions for B1 and B2 are shown in Fig. 11. Three stages, namely, prestressed (after prestressing the CFRP plate), balanced ($\delta_m = 0$ in the loading stage) and crack initiation, are plotted. The positions of the neutral axis for B1 and B2 are 225 mm and 250 mm, respectively. Therefore, the prestressing efficiency of scheme 2 is higher than that of scheme 1. For the balanced states, the sections were uniformly compressed, with the corresponding load for B1 and B2 at 35 kN. This verified the enhancement of the cracking loads of the strengthened beams.

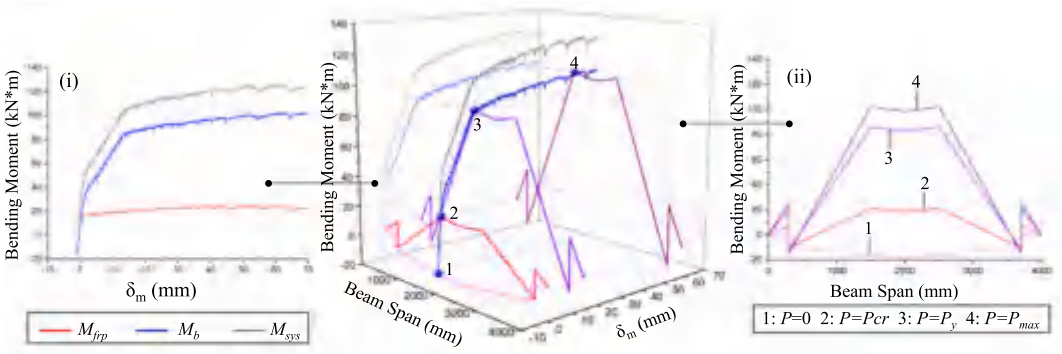
3.3. Bending moment analysis

The bending moment distribution is analysed using the Freebody diagram shown in Fig. 12. If the beam-and-CFRP system is taken as the analysis object, the bending moment diagram is a trapezoid with the maximum value of $M_{sys} = 0.5PL_s$ in the CMR, as shown by the dashed curves in Fig. 13, where M_{sys} is the total bending moment of the beam-and-CFRP system, P is the tested total external load, and L_s is the length of the shear spans, which is 1500 mm for all test beams. When considering the bending moment on the RC beam, the applied load, the reaction force and the prestress force are all treated as external actions on the beam. Hence, the bending moment of the beam (M_b) can be solved. First, the geometry of the system can be calculated as:

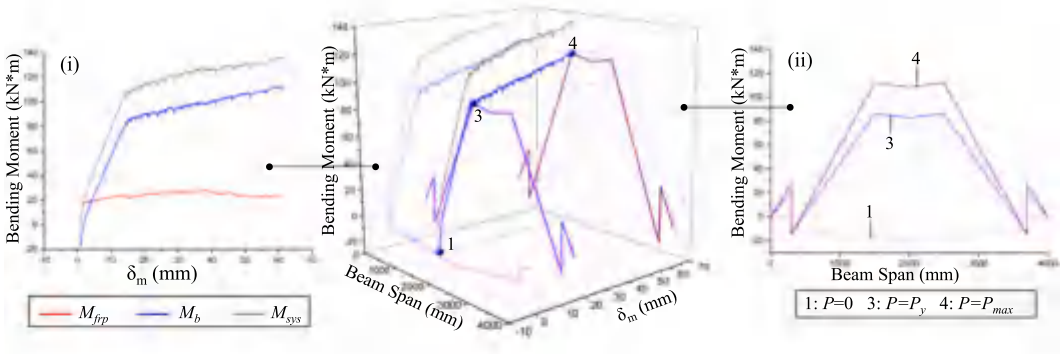
$$H_m = L_1\sqrt{\varepsilon_{frp,p}^2 + 2\varepsilon_{frp,p}} \tag{1}$$

$$\theta = \tan^{-1}\left(\frac{H_m}{L_1}\right) \tag{2}$$

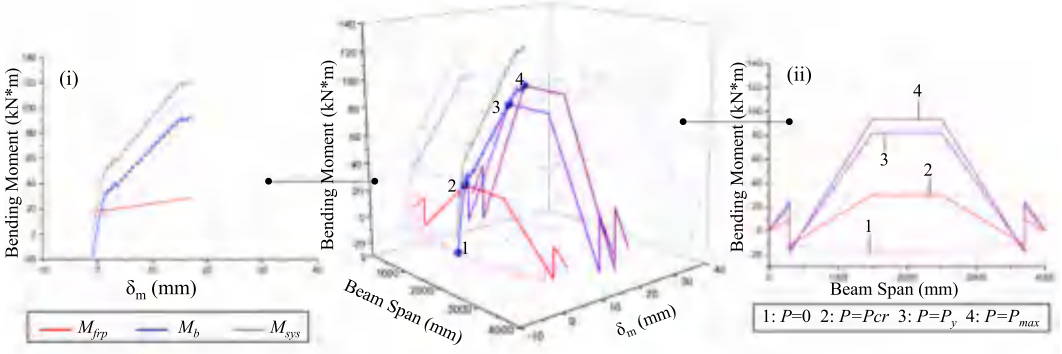
where H_m is the distance between the deviator and the soffit of the beam. Since the prestressing process had significant disturbance on the deviator, there was no device installed to measure the displacement of the deviator plate during prestressing. After finished prestressing, H_m was measured with a ruler, which was approximately 17–20 cm for B1 and B1R, and 12–15 cm for B2 and B2R. These values are close to the calculated H_m (170 mm and 120 mm for Scheme 1 and Scheme 2 beams, respectively) and have minor influence on the final result due to the geometrical relations. Therefore, the calculated values are employed for analysis. L_1 is the distance from the deviator to the centre of the anchor, which is 1700 mm for scheme 1 and 1200 mm for scheme 2. $\varepsilon_{frp,p}$ is the target prestressing strain on the CFRP plate, which is 5000×10^{-6} for all beams. It should be noted that in the following steps H_m is treated as a constant because the axial deformation of the rods is small and hence can be ignored. Even for the rods bent during the test, the vertical displacement of the deviator is small compared with its horizontal



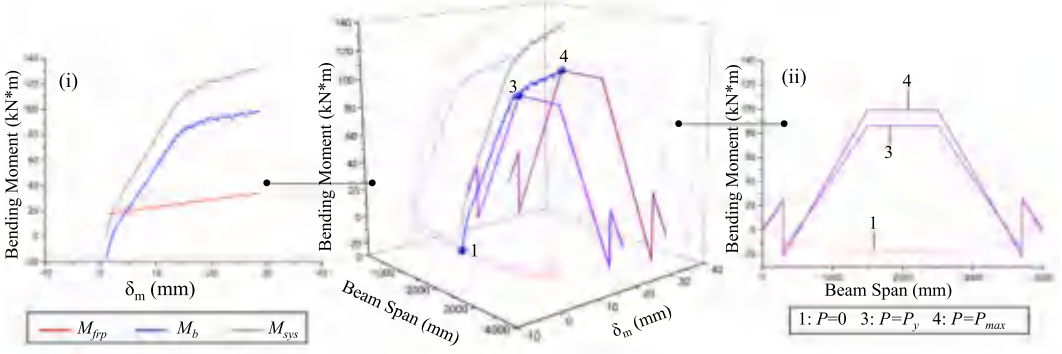
(a) B1



(b) B1R



(c) B2



(d) B2R

Fig. 13. Bending moment diagrams.

Table 3
Internal forces at critical sections.

ID	$P = 0$			$P = P_{cr}$					$P = P_y$					$P = P_{max}$				
	N	M_{frp}	M_b	N	M_{frp}	M_b	M_{sys}	M_b/M_{sys}	N	M_{frp}	M_b	M_{sys}	M_b/M_{sys}	N	M_{frp}	M_b	M_{sys}	M_b/M_{sys}
B1	50.1	16.0	−16.0	51.5	16.5	21.0	37.5	56%	60.9	19.5	86.0	105.5	82%	74.1	23.7	102.2	125.9	81%
B1R	54.5	17.5	−17.5	–	–	–	–	–	70.1	22.4	86.7	109.1	79%	75.2	24.1	112.3	136.4	82%
B2	55.8	17.9	−17.9	57.1	18.3	30.2	48.8	62%	81.5	26.1	81.9	108.0	76%	89.7	28.7	93.5	122.2	77%
B2R	55.6	17.8	−17.8	–	–	–	–	–	84.9	27.2	85.8	113.0	76%	107.2	34.3	99.1	133.4	74%

Notes: the unit for N is in kN, the unit for bending moment in kN*m

displacement. Given the geometry, the forces acting on the beam yield:

$$F_{frp} = E_{frp} b_{frp} t_{frp} \varepsilon_{frp} \tag{3}$$

$$F_x = F_{frp} \cos\theta \tag{4}$$

$$F_y = F_{frp} \sin\theta \tag{5}$$

$$M_p = \frac{1}{2} F_x H_b \tag{6}$$

where F_{frp} is the force in the CFRP plate and ε_{frp} is the strain of the CFRP plate obtained from the test results. M_p is the concentrated moment caused by the horizontal component of F_{frp}, and H_b is the height of the beam section (400 mm). According to the force equilibrium, the axial force in the beam (N) is equal to F_x. The bending moment diagrams of the RC beam (M_b) are shown in Fig. 13. The figures are also shown in a 3D form, representing the variation of the bending moment over the beam length as well as the development of mid-span deflection. The blue spatial curve is the M_b at the section of the loading point, while the grey curve represents the M_{sys}. Two 2D projections for the bending moments are plotted as well, which are denoted as plot (i): the bending moment at critical section with respect to δ_m; and plot (ii): the bending moment distribution over the beam length at different stages. The resisting moment contributed by the CFRP plate (M_{frp}) is marked as red curve in plot (i), which is calculated by $M_b + M_{frp} = M_{sys}$. Four stages of M_b are plotted for B1 and B2, namely, (1) prestressed ($P = 0$), (2) crack initiation ($P = P_{cr}$), (3) yield point ($P = P_y$) and (4) peak strength ($P = P_{max}$). For the repaired beams, there is no cracking initiation stage in the plotted bending moment diagrams. As shown in Fig. 13, in most stages, the maximum bending moment occurs at the loading points regardless of positive or negative bending. Therefore, the beam sections at the loading points are selected as critical sections, and their internal forces at different load levels are listed in Table 3. At the $P = 0$ stage, the bending moment of the beam was contributed solely by the prestress in the CFRP plate, and there was a negative bending moment region between the two anchors, as shown in Fig. 13. At the cracking initiation point, the M_b of B2 was higher than that of B1 because the prestressed CFRP plate could produce a higher axial force (N), indicating that scheme 2 is more effective in cracking prevention. With the increase in the external load, the M_b/M_{sys} ratios increased. At the yield points and the maximum load point, the M_b/M_{sys} ratios were stable and ranged between 74% and 82%. As shown in plots (i) of Fig. 13a and b, due to the bending of the deviator rods, M_{frp} remained at approximately 20 kN*m, resulting in a longer yield plateau of M_{sys}. For the Scheme 2 beams which are shown in Fig. 13c and d, M_{frp} increase linearly with δ_m and failed by CFRP plate splitting or rupture.

4. Conclusions

In this paper, a novel strengthening method for RC beams with mid-span jacking prestressed CFRP plates is proposed. Details of the experimental tests of RC beams strengthened or repaired by two types of schemes are reported. The greatest increase in strength was 43% compared to the control beam, and the cracking load for the prestressed beams was enhanced at least 67%. The stiffness and strength of the damaged beams were recovered and further enhanced. The proposed prestressing method has been proven to be effective. Three main conclusions can be drawn from the test results.

1. Although the ultimate stress of the CFRP plate for the scheme 1 beams was lower than that of the scheme 2 beams, the single-point strengthening system (scheme 1) was more effective in enhancing the strength and ductility.
2. The CFRP plate contributed 20%-25% of the overall resisting bending moment in the post yield stage, but the strength enhancement for the strengthened/repaired beams was 28%-43%. This indicates that the axial force provided by the CFRP plate and the supporting forces from the mid-span deviators increased the flexural resistance of the RC beam.
3. The unexpected bending of the deviator rods maintained the stress of the CFRP plate at a higher level and hence led to a longer yield plateau of the overall load–deflection response.

There are also some limitations of this series of tests that need improvement and further investigation in the future.

1. The effectiveness of the corrugated anchors was low and resulted in premature splitting of the CFRP plate. If the performance of the anchors can be improved, the effectiveness of the strengthening system will be increased significantly.
2. The bending of the deviator rods relaxed the stress in the CFRP plate in the yielding stage, thus achieving the ductile failure mode of the beam. This mechanism is worthy of further investigation. It is a promising approach to developing a CFRP strengthening system with ductile failure modes by designing the deviator to be elastoplastic with optimum stiffness and yield strength.
3. The performance of the proposed strengthening method is dependent on not only the layout of the deviator but also the load distribution. Therefore, more tests and detailed numerical analyses need to be carried out in the future to establish a proper design method.
4. For the present design, it needs at least two workers for prestressing. Also, monitoring the plate strain is necessary during the prestressing process. These may bring inconvenience in practical strengthening projects. Therefore, the design of the deviators needs to be improved for on-site application.

CRediT authorship contribution statement

Jia-Qi Yang: Conceptualization, Methodology, Investigation, Writing – original draft, Funding acquisition. **Peng Feng:** Conceptualization, Writing – review & editing, Supervision, Funding acquisition. **Bin Liu:** Investigation. **Husheng Wang:** Investigation. **Weiping Zhao:** Supervision. **Lili Hu:** Conceptualization, Writing – review & editing.

Declaration of Competing Interest

The authors declare that they have no known competing financial

interests or personal relationships that could have appeared to influence the work reported in this paper.

Data availability

Data will be made available on request.

Acknowledgements

This work is supported by the National Natural Science Foundation of China (No. 51908322), the Fundamental Research Funds for the Central Universities (No. 2021XJLJ01), the Nonmetallic Excellence and Innovation Centre for Building Materials (No. 2022TDA1-1), the Yueqi Distinguished Scholar Program of China University of Mining and Technology, Beijing (No. 2602021RC59), and the research fund for new faculty members provided by the School of Mechanics and Civil Engineering, China University of Mining and Technology (Beijing).

References

[1] Teng JG, Chen JF, Smith ST, Lam L. FRP-strengthened RC structures. London, UK: Weily; 2002.
[2] Teng JG, Smith ST, Yao J, Chen JF. Intermediate crack-induced debonding in RC beams and slabs. Constr Build Mater 2003;17(6–7):447–62.
[3] GB 50608-2020. Technical standard for fibre reinforced polymer (FRP) in construction. Beijing, China: China Planning Press; 2020. (in Chinese).
[4] T/CECS 146-20232. Technical specification for strengthening concrete structures with carbon fibre reinforced polymer. Beijing, China: China Architecture & Building Press; 2022. (in Chinese).
[5] ACI 440.2R-02. Guide for the design and construction of externally bonded FRP systems for strengthening concrete structures. Farmington Hills, MI: American Concrete Institute; 2002.
[6] CSA S806-02. Design and construction of building components with fibre-reinforced polymers. Ontario, Canada: Canadian Standards Association; 2002.
[7] Fib Bulletin No.14. Externally bonded FRP reinforcement for RC structures. Lausanne, Switzerland: International Federation for Structural Concrete (fib); 2001.
[8] JSCE CES41. Recommendations for upgrading of concrete structures with use of continuous fibre sheets. Tokyo, Japan: Japan Society of Civil Engineers; 2001.
[9] Smith ST, Teng JG. FRP-strengthened RC beams. I: review of debonding strength models. Eng Struct 2002;24(4):385–95.
[10] Smith ST, Teng JG. FRP-strengthened RC beams. II: Assessment of debonding strength models. Eng Struct 2002;24(4):397–417.
[11] Chen JF, Teng JG. Anchorage strength models for FRP and steel plates bonded to concrete. J Struct Eng 2001;127(7):784–91.
[12] Lu XZ, Teng JG, Ye LP, Jiang JJ. Bond–slip models for FRP sheets/plates bonded to concrete. Eng Struct 2005;27(6):920–37.
[13] Lu XZ, Teng JG, Ye LP, Jiang JJ. Intermediate crack debonding in FRP-strengthened RC beams: FE analysis and strength model. J Compos Constr 2007;11(2):161–74.
[14] Chen GM, Teng JG, Chen JF. Finite-element modelling of intermediate crack debonding in FRP-plated RC beams. J Compos Constr 2011;15(3):339–53.
[15] Chen GM, Teng JG, Chen JF, Xiao QG. Finite element modeling of debonding failures in FRP-strengthened RC beams: A dynamic approach. Comput Struct 2015;158:167–83.
[16] Oehlers DJ, Muhamad R, Ali MM. Serviceability flexural ductility of FRP RC beams: a discrete rotation approach. Constr Build Mater 2013;49:974–84.
[17] Nanni A. North American design guidelines for concrete reinforcement and strengthening using FRP: principles, applications and unresolved issues. Constr Build Mater 2003;17(6–7):439–46.
[18] De Lorenzis L, Teng JG. Near-surface mounted FRP reinforcement: An emerging technique for strengthening structures. Compos B Eng 2007;38(2):119–43.
[19] Zhang SS, Teng JG, Yu T. Bond strength model for CFRP strips near-surface mounted to concrete. J Compos Constr 2014;18(3):A4014003.
[20] Zhang SS, Teng JG, Yu T. Bond–slip model for CFRP strips near-surface mounted to concrete. Eng Struct 2013;56:945–53.
[21] Kalfat R, Al-Mahaidi R, Smith ST. Anchorage devices used to improve the performance of concrete structures retrofitted with FRP composites: a state-of-the-art review. J Compos Constr 2013;17:14–33.
[22] Wu YF, Wang Z, Liu K, He W, Wang Z. Numerical Analyses of Hybrid-Bonded FRP Strengthened Concrete Beams. Comput-Aided Civ Infrastruct Eng 2009;24(5):371–84.
[23] Smith ST, Hu S, Kim SJ, Seracino R. FRP-strengthened RC slabs anchored with FRP anchors. Eng Struct 2011;33(4):1075–87.
[24] Smith ST, Zhang H, Wang Z. Influence of FRP anchors on the strength and ductility of FRP-strengthened RC slabs. Constr Build Mater 2013;49:998–1012.
[25] Yang JQ, Smith ST, Wang Z, Lim YY. Numerical simulation of FRP-strengthened RC slabs anchored with FRP anchors. Constr Build Mater 2018;172:735–50.
[26] Aslam M, Shafigh P, Jumaat MZ, Shah SN. Strengthening of RC beams using prestressed fibre reinforced polymers–A review. Constr Build Mater 2015 May;1(82):235–56.
[27] Mukherjee A, Rai GL. Performance of reinforced concrete beams externally prestressed with fiber composites. Constr Build Mater 2009;23(2):822–8.
[28] Wight RG, Green MF, Erki MA. Prestressed FRP sheets for poststrengthening reinforced concrete beams. J Compos Constr 2001;5(4):214–20.
[29] Wang WW, Dai JG, Harries KA. Intermediate crack-induced debonding in RC beams externally strengthened with prestressed FRP laminates. J Reinf Plast Compos 2013;32(23):1842–57.
[30] Wang WW, Dai JG, Harries KA, Bao QH. Prestress losses and flexural behaviour of reinforced concrete beams strengthened with posttensioned CFRP sheets. J Compos Constr 2012;16(2):207–16.
[31] El-Hacha R, Soudki K. Prestressed near-surface mounted fibre reinforced polymer reinforcement for concrete structures—a review. Can J Civ Eng 2013;40(11):1127–39.
[32] Hosseini MM, Dias SJ, Barros JA. Behavior of one-way RC slabs flexurally strengthened with prestressed NSM CFRP laminates–Assessment of influencing parameters. Compos Struct 2020;245:112259.
[33] You YC, Choi KS, Kim J. An experimental investigation on flexural behavior of RC beams strengthened with prestressed CFRP strips using a durable anchorage system. Compos B Eng 2012;43(8):3026–36.
[34] Yang DS, Park SK, Neale KW. Flexural behaviour of reinforced concrete beams strengthened with prestressed carbon composites. Compos Struct 2009;88(4):497–508.
[35] Peng H, Zhang J, Shang S, Liu Y, Cai CS. Experimental study of flexural fatigue performance of reinforced concrete beams strengthened with prestressed CFRP plates. Eng Struct 2016;127:62–72.
[36] Xue W, Tan Y, Zeng L. Flexural response predictions of reinforced concrete beams strengthened with prestressed CFRP plates. Compos Struct 2010;92(3):612–22.
[37] Matta F, Nanni A, Abdelrazaq A, Gremel D, Koch R. Externally post-tensioned carbon FRP bar system for deflection control. Constr Build Mater 2009;23(4):1628–39.
[38] Wang X, Shi J, Wu G, Yang L, Wu Z. Effectiveness of basalt FRP tendons for strengthening of RC beams through the external prestressing technique. Eng Struct 2015;101:34–44.
[39] Recupero A, Spinella N, Colajanni P, Scilipoti CD. Increasing the capacity of existing bridges by using unbonded prestressing technology: a case study. Adv Civ Eng 2014;2014.
[40] Ghafoori E, Motavalli M, Nussbaumer A, Herwig A, Prinz GS, Fontana M. Design criterion for fatigue strengthening of riveted beams in a 120-year-old railway metallic bridge using pre-stressed CFRP plates. Compos B Eng 2015;68:1–3.
[41] Hu L, Feng P, Gao W, Wang Y. Flexural behaviour of light steel purlins reinforced by prestressed CFRP laminates. Thin-Walled Structures. 2022;174:109125.
[42] Hu L, Feng P. Theoretical analysis and design of prestressed CFRP-reinforced steel columns. J Compos Constr 2022;26(3):04022029.
[43] Hu L, Feng P, Meng Y, Yang J. Buckling behaviour analysis of prestressed CFRP-reinforced steel columns via FEM and ANN. Eng Struct 2021;245(5):112853.
[44] Hu L, Feng P. Prestressed CFRP-reinforced steel columns under axial and eccentric compression. Compos Struct 2021;268:113940.
[45] Li W. Study on carbon fibre reinforced polymer parallel-plate cables and corrugated-plate anchorages. Beijing: Tsinghua University; 2016. Master thesis.
[46] GB/T 50081-2019. Standard for test methods of concrete physical and mechanical properties. Beijing, China: China Architecture & Building Press; 2019. (in Chinese).
[47] GB/T 1499.2-2018. Steel for the Reinforcement of concrete- Part 2: Hot rolled ribbed bars. Beijing, China: China Standard Press; 2018. (in Chinese).
[48] GB 50010-2010. Code for design of concrete structures (2015 edition). Beijing, China: China Architecture & Building Press; 2016. (in Chinese).
[49] Ding G, Feng P, Wang Y, Ai P. Novel pre-clamp lap joint for CFRP plates: Design and experimental study. Compos Struct 2022;302:116240.
[50] Feng P, Qiang HL, Ye LP. Discussion and definition on yield points of materials, members and structures. Engineering Mechanics. 2017;34(3):36–46. https://doi.org/10.6052/j.issn.1000-4750.2016.03.0192. in Chinese.
[51] Feng P, Cheng S, Bai Y, Ye L. Mechanical behaviour of concrete-filled square steel tube with FRP-confined concrete core subjected to axial compression. Compos Struct 2015;123:312–24.
[52] Feng P, Yang JQ, Li Z. FRP confined concrete: What, why, and how? In: International Conference on Fibre-Reinforced Polymer (FRP) Composites in Civil Engineering 2021 Dec 8. Cham: Springer. p. 37-45.
[53] Yang JQ, Feng P. Analysis-Oriented Models for FRP-Confined Concrete: 3D Interpretation and General Methodology. Eng Struct 2020;216:110749.
[54] Yang JQ, Feng P. Analysis-oriented model for FRP confined high-strength concrete: 3D interpretation of path dependency. Compos Struct 2021;278:114695.
[55] Li Z, Feng P, Yang JQ. Analysis-oriented model for FRP tube-confned concrete: 3D interpretation of biaxial tube behaviour. Eng Struct 2022;272:114987.

DOI:10. 19936/j. cnki. 2096-8000. 20230128. 012

超轻大尺寸复合材料拉挤型材在高层建筑外挂构架梁中的应用研究

秦 珩[1]，刘天桥[2*]，于涛峰[1]，易树声[1]，熊进凤[3]，范艳君[4]，冯 鹏[5]

（1. 雄安万科绿色研发有限公司，雄安 071800；2. 北京工业大学，北京 100124；
3. 南京斯贝尔复合材料仪征有限公司，仪征 211048；4. 沈阳汇斯安装有限公司，沈阳 110141；
5. 清华大学，北京 100084）

摘要：提出了一种基于复合材料拉挤型材的新型高层建筑外挂构架梁。结合实际工程问题，设计并制备了大尺寸拉挤型材外挂构架梁，通过有限元数值模拟分析验证了拉挤型材构架梁的力学性能。对构架梁的安装施工方法进行了介绍，并和传统钢结构方案进行了经济性比较。提出的拉挤型材外挂构架梁可以大幅降低结构自重（仅为同类型钢结构的四分之一），提高结构的环境耐腐性能，并有效减少施工相关的措施费。

关键词：复合材料拉挤型材；高层建筑；外挂构架梁

中图分类号：TB332 **文献标识码**：A **文章编号**：2096-8000(2023)01-0100-07

Application of ultra-lightweight and large-scale pultruded GFRP profile for external frame beam in high-rise buildings

QIN Heng[1], LIU Tianqiao[2*], YU Taofeng[1], YI Shusheng[1], XIONG Jinfeng[3], FAN Yanjun[4], FENG Peng[5]

(1. Xiong'an Vanke Green R&D Co., Ltd., Xiong'an 071800, China;
2. Beijing University of Technology, Beijing 100124, China;
3. Nanjing Spare Composite Yizheng Co., Ltd., Yizheng 211048, China;
4. Shenyang Huisi Installation Engineering Co., Ltd., Shenyang 110141, China;
5. Tsinghua University, Beijing 100084, China)

Abstract: A new type of external frame beam for high-rise buildings is proposed based on pultruded glass fiber reinforced polymer (GFRP) composite profiles. Combined the practical engineering problems, the external hanging frame beam of large size pultruded profiles is designed and prepared. In addition, a series of finite element analyses were conducted to evaluate and validate the mechanical performance of proposed GFRP beam. Then, the installation/construction method was introduced in detail. Last but not least, the proposed GFRP frame beam was compared with steel counterpart in terms of the material usage and economic performance. It is observed that the proposed GFRP frame beam is able to reduce the self-weight of the frame structure by 75%, improve the environmental durability of the structure and decrease the construction-related costs.

Key words: pultruded FRP profiles; high-rise buildings; external frame beam

1 引 言

玻璃纤维增强复合材料拉挤型材(Pultruded Glass Fiber Reinforced Polymer, PGFRP)具有轻质、高强、耐腐等特点，在国内与国际土木工程建设中展现出了强大的应用潜力[1-6]。拉挤型材得益于高度自动化的生产工艺(如图 1 所示)，其材料力学性能较强，生产稳定性较高，目前可制成任意截面和任意长度[7-8]。值得指出的是，拉挤型材已成为实现复材结构大型化的不二选择[9-11]，其代表性工程应用包括冷却塔、人行桥、风机叶片等(如图 2 所示)。

收稿日期：2022-10-08
基金项目：非金属材料创新中心研发类项目（2022TDA1-1）
作者简介：秦珩（1969—），男，教授级高级工程师，学士，主要从事建筑工业装配式技术方面的研究。
通讯作者：刘天桥（1989—），男，校聘教授，博士，主要从事复合材料拉挤型材及其新型结构方面的研究，liu_tianqiao@bjut. edu. cn。

(C)1994-2023 China Academic Journal Electronic Publishing House. All rights reserved. http://www.cnki.net



图 1　拉挤工艺示意图[4]

Fig. 1　Schematic of pultrusion process[4]



图 2　复材拉挤型材大型化应用范例

Fig. 2　Large-scale applications of pultruded GFRP composites

拉挤型材虽具有出色的力学性能,但较高的材料成本极大地限制了其在实际工程中的应用,除风力发电机叶片属于近十年迅速发展的市场热点外,其他典型应用(例如冷却塔和人行桥)自二十世纪八九十年代便已兴起,在近二十年来仍未获得市场的广泛接受。在材料成本的制约下,如何发挥拉挤型材轻质、高强、耐腐,以及便于施工的综合优越性,便成为扩大其建筑领域应用的关键。

本文以某地高层建筑工程应用为出发点,采用复合材料拉挤型材,研发设计了一种新型外挂构架梁。本文提出的外挂构架梁相较原钢结构方案大幅降低了结构自重,有效节省了施工时间及成本,充分满足了建筑立面的风貌要求。本文首先对遇到的工程问题进行了阐述;其次,对拉挤型材的生产制备过程进行了介绍;然后,开展了有限元数值模拟,对提出的拉挤型材外挂构架梁的力学性能进行了研究和评价;最后,对拉挤型材外挂构架梁取得的综合效益进行了分析。本文提出的外挂构架梁进一步挖掘并扩大了拉挤型材在我国建筑领域的应用潜力。

2　工程概况

本文以青岛市某小区在工程建设中遇到的痛点展开研究。依据当地建筑规划设计要求,小区 6 幢高层建筑需分别设置 3 组外挂构架梁,跨度均为 17.5 m,分别位于建筑第 10 层、19 层及 27 层(屋面机房层)(如图 3 所示),其中第 10 层构架梁建筑设计高度为 4.25 m,第 19 层和 27 层构架梁建筑设计高度为 3.65 m。

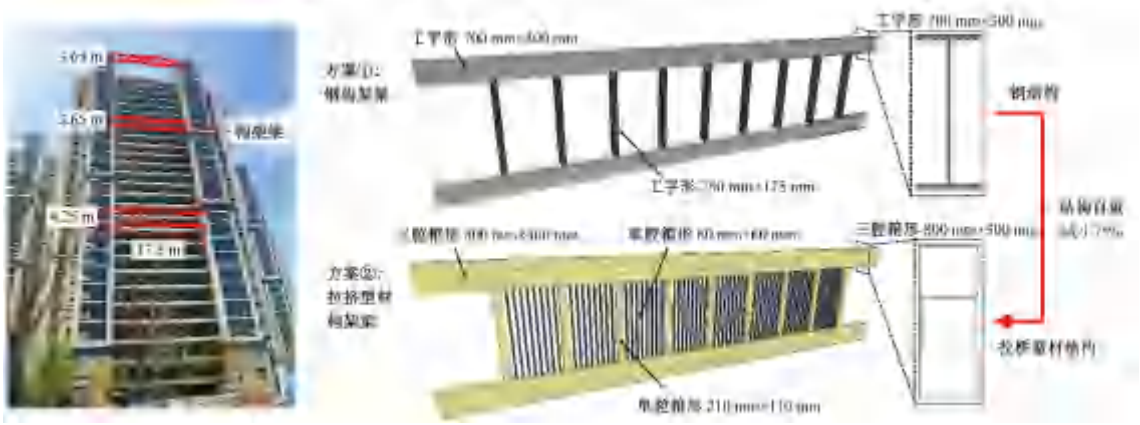


图 3　方案比选:钢结构 vs. 拉挤型材结构

Fig. 3　Scheme comparison: steel structure vs. pultruded GFRP structure

传统外挂构架梁设计方案常使用钢结构(如图 3 所示),但钢构架梁方案在本项目中存在以下痛点:①工字形钢梁自重过大(总重约 6 t),吊装安装需使用 8 t 起重重量的塔吊,而此时小区内主体结构以及地下车库等均已完工,地库顶面覆土回填也已完成,施工场地狭小,工期紧张,分项工程在地面交叉作业,现状场地难以架设大型塔吊;②若采用吊臂长度大于 100 m 的重型汽车吊吊装钢构架梁,需对地下车库顶板做临时支撑加固处理,且重型汽车吊的设置会对地库顶面的管网、景观、道路造成较大破坏,影响项目整体交付节点;③钢构架梁高空吊装就位后,需在高空继续开展人工作业,包括人工安装外包铝板、装饰格栅等构件,而此时高空作业缺少安装操作面,存在较大安全隐患;④传统钢构架梁方案造价过高,尤其是措施费较高,极大提高了项目成本;⑤钢构架梁方案施工周期较长,难以满足交付节点;⑥小区临近海岸线,钢构架梁易受碱性侵蚀环境影响而发生材料锈蚀破坏,后期要求较高频率的保养

(C)1994-2023 China Academic Journal Electronic Publishing House. All rights reserved.　http://www.cnki.net

和维护,且维护工程施工难度较大。

为降低构架梁结构自重、简化高空作业流程、减小施工操作面面积、降低构架梁施工对小区附属设施的影响,以及提高构架梁的环境耐腐性能,本文团队结合有限的场地条件和工程机械(即 2 台起重重量为 1.5 t 的提升机),创新性地使用复合材料拉挤型材设计研发了一种新型建筑外挂构架梁(如图 3 所示),本文提出的拉挤型材外挂构架梁在满足了结构设计强度和刚度的基础上,还成功减小了 75%的结构自重,充分保障了本项目的顺利实施。

3 材料制备

本项目使用的复合材料拉挤型材包括三种截面尺寸:主梁为 800 mm×300 mm×10/3.5 mm(高×宽×壁厚)三腔箱形截面、立柱为 210 mm×110 mm×4 mm 单腔箱形截面、格栅为 60 mm×60 mm×4 mm 单腔箱形截面,材料组成为无碱玻璃纤维和不饱和聚酯树脂,纤维质量含量约为 70%,材料均由本文团队成员之一的南京斯贝尔复合材料仪征有限公司生产制备,制备流程如图 4 所示。拉挤型材主梁截面的初设计尺寸达到了 800 mm×300 mm×10 mm(高×宽×壁厚),在复合材料领域内属于“大截面”,为进一步减轻结构自重,对型材壁厚(10 mm)进行了优化(优化后尺寸如图 4 所示):首先,在满足强轴方向弯曲性能的基础上,减小了中间两道翼缘板的壁厚(从 10 mm 减小到 3.5 mm);然后,在满足弱轴方向弯曲性能的基础上,减小了上、下两个腔体的腹板厚度(从 10 mm 减小到 3.5 mm);最后,截面重量减小了 38%[(27 200 mm^2−16 761 mm^2)/27 200 mm^2]。

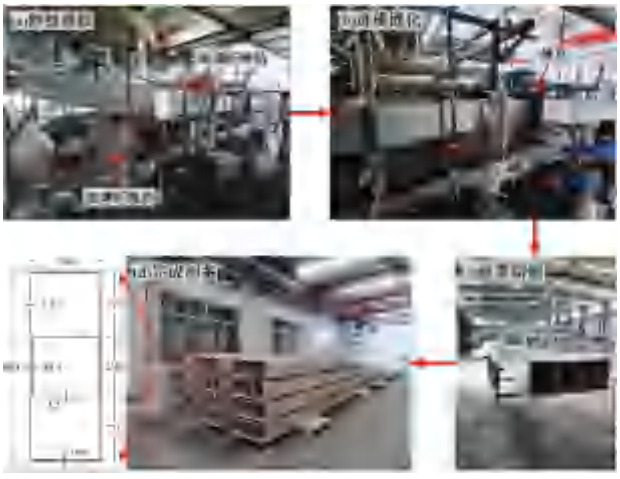


图 4 材料制备流程图

Fig. 4 Material manufacturing process

在材料制备过程中,首先,依据截面尺寸(800 mm×300 mm)对拉挤生产线进行了设计,使用了 60 t 牵引机和1 800股 9 600 tex 玻璃纱线;其次,在纱线浸胶过程中对树脂颜色进行了调配,以满足建筑设计中关于颜色的要求;然后,在进模固化过程中使用了 120℃和 155℃的固化温度,并使用了 110℃和 130℃的侧面辅助加温技术,以保证大截面拉挤型材充分固化并形成设计强度;最后,依据设计长度对拉挤型材进行切割。在出厂前,对拉挤型材进行了力学性能测试,测试结果见表 1。在纵向拉伸强度和弹性模量方面,材料力学性能达到了 GB/T 31539《结构用纤维增强复合材料拉挤型材》[12] 和 CECS 692《复合材料拉挤型材结构技术规程》[13] 中规定的 M30 级的要求。

表 1 复合材料拉挤型材力学性能汇总

Table 1 Mechanical properties of pultruded GFRP profiles

力学性能	数值
纵向拉伸弹性模量 $E_{L,t}$/MPa	30 000
横向拉伸弹性模量 $E_{T,t}$/MPa	7 000
面内剪切模量 G_{LT}/MPa	2 750
层间剪切模量 *ILSM*/MPa	2 750
主泊松比 υ_{LT}	0.30
副泊松比 υ_{TL}	0.07
纵向拉伸强度 $F_{L,t}$/MPa	400
横向拉伸强度 $F_{T,t}$/MPa	45
纵向压缩强度 $F_{L,c}$/MPa	300
横向压缩强度 $F_{T,c}$/MPa	70
面内剪切强度 F_{LT}/MPa	45
层间剪切强度 *ILSS*/MPa	45

4 数值模拟

本文开展了有限元数值模拟,对提出的新型拉挤型材外挂构架梁的力学性能进行了研究和评价。有限元模型如图 5 所示,材料力学性能如表 1 所示。模型使用了壳单元(S4R)模拟主梁(800 mm×300 mm×10/3.5 mm 三腔箱形截面)和立柱(210 mm×110 mm×4 mm 单腔箱形截面)。格栅(60 mm×60 mm×4 mm 单腔箱形截面)不计入受力构件,其承担的风荷载假设由主梁承担,并将格栅区整体面积的一半保守地作为迎风面的计算面积。各构件之间采用共节点的方式连接。构架梁总跨度为17 500 mm,端部牛腿支撑段长度为1 200 mm,拉挤型材主梁与钢支座由螺栓进行连接,形成端部固结体系。依据 GB 50009《建筑结构荷载规范》[14],荷载组合采用 1.3×恒载+1.5×风载,其中拉挤型材密度为 2.0×10^3 kg/m^3,风

(C)1994-2023 China Academic Journal Electronic Publishing House. All rights reserved. http://www.cnki.net

载为 1.05 kN/m^2(1.5×0.70 kN/m^2),格栅部分的风载由主梁承担,因此主梁承担风载为 1.78 kN/m^2[(1.05+0.73) kN/m^2]。通过网格敏感性分析发现,采用 100 mm 和 20 mm 的网格尺寸时,构架梁跨中最大位移分别为 37.10 mm 和 37.42 mm,差异小于 1%,因此采用了兼顾计算精确度和成本的 100 mm 网格尺寸。

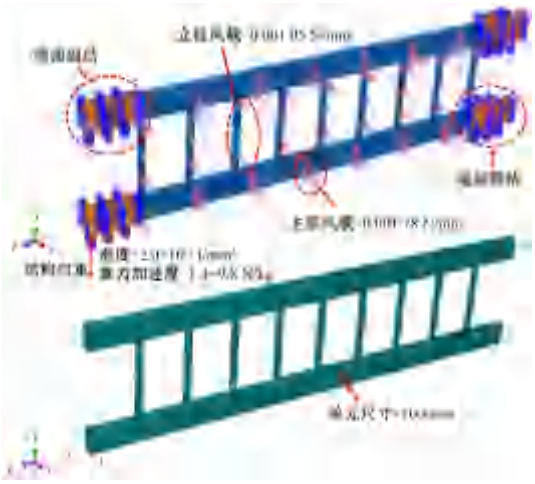
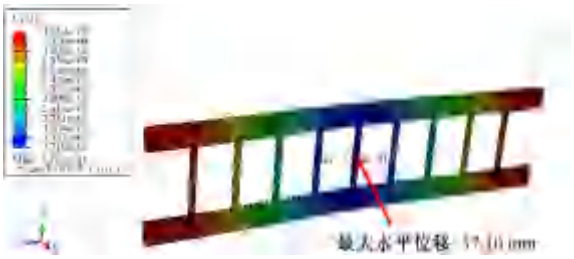


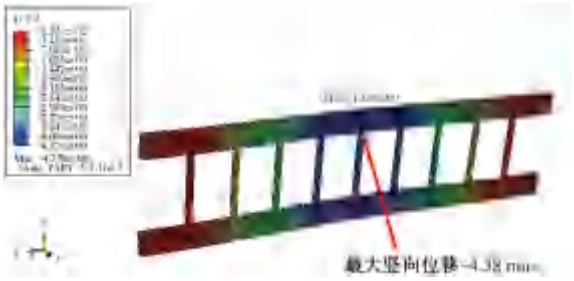
图 5　有限元模型荷载与网格划分示意图

Fig. 5　Diagram of load and meshing of finite element model

有限元数值模拟结果如图 6 所示。首先,在风载作用下的水平位移为构架梁结构设计的关键控制因素,模拟发现拉挤型材构架梁最大水平位移为 37.10 mm,如图 6(a)所示,小于规范限值 42.50 mm (L/400),满足设计要求;同时,传统设计方案中的钢构架梁在风载作用下最大水平位移为 37.49 mm,与拉挤型材构架梁相近(差异仅为 1%),因此拉挤型材构架梁与钢构架梁具有相同的抗弯刚度。其次,拉挤型材构架梁在重力作用下的最大竖向位移仅为 4.38 mm,如图 6(b)所示,约为构架梁跨度的万分之三,远小于设计限值(L/200)。同时,拉挤型材构架梁最大纵向拉伸和压缩应力分别为 30.64 MPa 和 34.70 MPa,如图 6(c)所示,其应力水平约为 8% 和 12%(材料纵向拉伸和压缩强度分别为 400 MPa 和 300 MPa),结构主应力水平远小于其材料强度值。值得指出的是,剪切性能为拉挤型材力学性能中的弱项,其剪切强度通常仅为材料纵向强度的十分之一左右[15-17],模拟发现构架梁中最大剪切应力为 32.39 MPa,如图 6(d)所示,应力水平约为 72%(材料面内剪切强度为 45 MPa),因此构架梁剪切强度也满足设计要求。综上所述,有限元数值模拟结果充分验证了拉挤型材构架梁在弯曲刚度和弯曲强度方面均满足相关设计要求。



(a)水平位移 U1



(b)竖向位移 U2



(c)纵向应力 S11



(d)剪切应力 S12

图 6　有限元数值模拟结果(位移放大 10 倍)

Fig. 6　Results of finite element modeling (deformation amplified by a factor of 10)

拉挤型材由于材料弹性模量较低,仅为钢材的四分之一到三分之一,且为薄壁构件形式,因此拉挤型材构件易在达到其材料强度之前便发生屈曲失稳,以本文所述梁构件为例,其典型屈曲模式包括翼缘板和腹板局部屈曲[18-19]、梁整体屈曲[20-21]以及局部和整体屈曲的耦合作用[22-23],因此稳定性常成为控制拉挤型材结构设计的关键因素[24]。本文在上述材料强度分析的基础上,进行了主梁的稳定性分析,结果如图 7 所示。在有限元模拟中,使用单位荷

(C)1994-2023 China Academic Journal Electronic Publishing House. All rights reserved.　http://www.cnki.net

载 1 N/mm²模拟水平方向的风荷载,梁的边界条件及材料力学性能与上述分析保持一致。通过有限元稳定性分析,得到主梁一节临界屈曲荷载为0.001 88 N/mm²,大于设计荷载0.001 78 N/mm²,因此主梁稳定性满足设计要求。

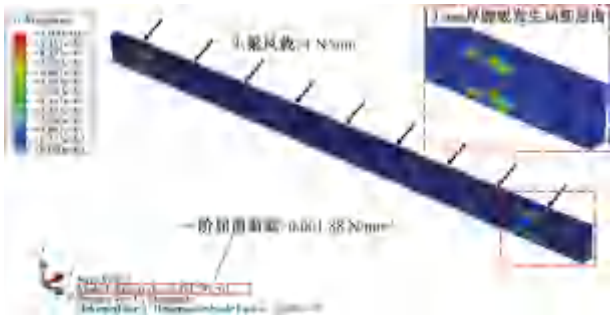


图 7 有限元稳定性分析结果
Fig. 7 FEM stability analysis results

5 安装施工

拉挤型材外挂构架梁的安装工程由本文团队成员之一的沈阳汇斯安装有限公司负责实施。拉挤型材构架梁的安装施工主要包括五个分项工程:现场组装、整体吊装、移入支座(钢支座预先安装完成)、螺栓锚固、竣工验收,如图 8 所示。



图 8 现场施工流程图
Fig. 8 On-site construction process

(1)现场组装:首先,在作业面位置将拉挤型材上、下主梁按图纸尺寸水平铺设在地面上,使用排尺标注 9 根立柱及格栅的安装位置,其中立柱间距为 1 695 mm;其次,使用角铁与镀锌螺栓将拉挤型材立柱与主梁进行连接锚固(如图 9 所示);最后,在立柱之间安装拉挤型材格栅板,格栅与上、下主梁采用镀锌螺栓连接锚固。在构架梁中,立柱的作用主要集中在装饰部分,其竖向和水平力学性能对构架梁贡献较小,立柱部分仅占构架梁迎风面积的 15%左右,而 75%的迎风面积为主梁部分,因此图 9 中所示的螺栓连接可以充分保证立柱与主梁在设计荷载作用下力的传递机制。



图 9 次梁与主梁螺栓连接
Fig. 9 Bolted connection between main and secondary beams

(2)整体吊装:首先,在两个机房屋面位置各安装 1 台提升机用于吊装作业(如图 10 所示),并安装 2 部吊篮用于工人安装使用;其次,使用 2 台提升机将拉挤型材构架梁整体吊至钢支座位置。

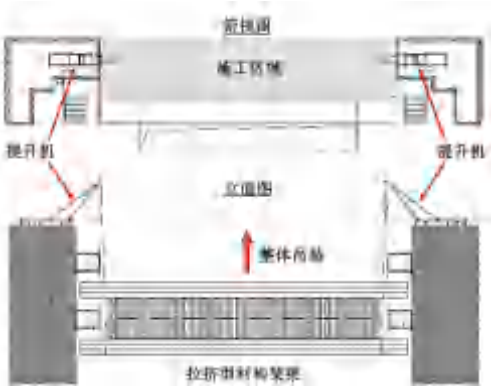


图 10 整体吊装示意图
Fig. 10 Schematic of lifting process

(3)移入支座:工人借助吊篮将拉挤型材上、下主梁水平推入钢支座内,然后使用1 200 mm×1 020 mm×14 mm(长×宽×厚)钢板对钢支座的开口面进行封堵(钢支座对拉挤型材主梁形成封闭式约束),钢构件与拉挤型材主梁之间的缝隙用 3 mm 厚拉挤型材板填塞密实。在构架梁设计中,仅通过钢支座对主梁提供竖向支撑,立柱在构架梁竖向力学性能中的贡献可以忽略不计。

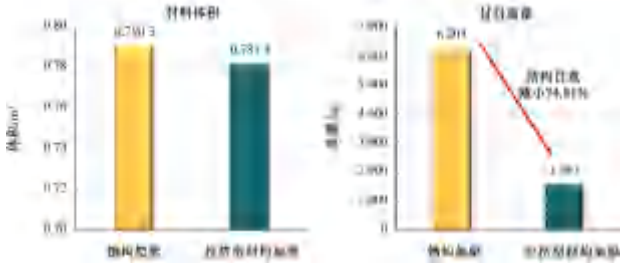
(4)螺栓锚固:使用钢螺栓将拉挤型材主梁与钢牛腿进行连接锚固,其中横向使用 M12×385 mm 螺栓(在宽度方向贯穿主梁),竖向使用 M12×80 mm 螺栓。

(C)1994-2023 China Academic Journal Electronic Publishing House. All rights reserved. http://www.cnki.net

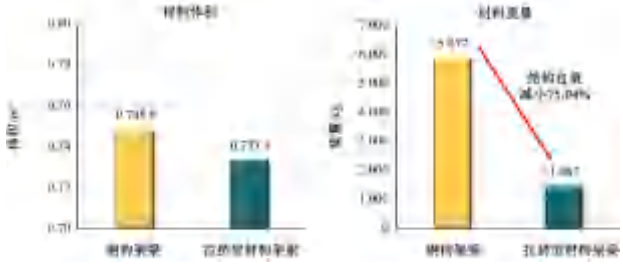
(5)竣工验收:在完成两端钢支座局部防锈、喷漆处理后,对拉挤型材构架梁施工效果进行验收,并对外墙保温层中由于构架梁磕碰导致的轻微破损部位进行维修整改。

6　方案对比

本文提出的新型拉挤型材高层建筑外挂构架梁,旨在减小构架梁的结构自重,从而攻克自重较大的传统钢构架梁可能带来的施工难题。本文计算分析了新型拉挤型材构架梁和传统钢构架梁的结构自重,结果如图 11 所示。此小区共使用了两种建筑高度的构架梁,分别为 4.25 m 和 3.65 m,从图 11 可以看出,钢构架梁和拉挤型材构架梁的材料体积用量相近,差异约为 2%,但钢材的密度约为拉挤型材的 4 倍(7.85/2.00),因此拉挤型材构架梁结构自重相较钢构架梁减小了 75%左右。以 1 幢建筑为例,包含 1 座 4.25 m 高构架梁和 2 座 3.65 m 构架梁,钢结构方案总重为 17.96 t,拉挤型材方案总重为 4.50 t。



(a)4.25 m 高构架梁
(a)4.25 m high architectural beam



(b)3.65 m 高构架梁
(b)3.65 m high architectural beam

图 11　材料用量对比:钢构架梁 vs.拉挤型材构架梁
Fig. 11　Comparison of material consumptions: steel architectural beam vs. pultruded GFRP architectural beam

大幅减小的结构自重不但降低了对工程机械的荷载要求,缓解了对施工场地的空间要求,还提升了安装施工的效率,节省了人工和时间成本。以 1 幢建筑为例,拉挤型材构架梁方案实际施工工期为 15 d,主要工程机械为 2 台 1.5 t 起重重量的提升机;而钢构架梁方案施工工期预计约为 90 d,主要工程机械为 2 台 250 t 起重重量的汽车吊(起吊高度约 80 m)。经设计单位与施工单位测算,对比两种方案,拉挤型材方案可为此项目节省措施费约 500 万元。

7　结　论

本文提出了一种基于复合材料拉挤型材的新型高层建筑外挂梁,有效降低了构架梁结构自重,简化了高空作业流程,减小了施工操作面面积,并降低了构架梁施工对小区附属设施的影响,更重要的是提高了构架梁的环境耐腐性能。主要结论如下:

(1)复合材料拉挤型材构架梁结构自重仅为同类型钢结构的四分之一,对施工机械要求较低,同时拉挤型材的环境耐腐性能较强,后期维护所需成本较小。在本项目中,拉挤型材构架梁共节省施工措施费约 500 万元。

(2)复合材料拉挤型材构架梁为大断面拉挤型材,在设计中建议进行截面优化,以满足力学性能要求并降低材料成本,在生产制备中建议针对截面几何特性进行工艺优化,如使用辅助加温固化技术保障大断面拉挤型材充分且均匀固化并形成预期力学性能。

(3)复合材料拉挤型材首次应用于高层建筑外挂结构体系,在结构性能和经济效益两方面均展现出了优异的效果。因此,本文提出的拉挤型材外挂构架梁体系具有相当的应用潜力,有望在建筑领域内推广。

参考文献

[1] 叶列平, 冯鹏. FRP 在工程结构中的应用与发展[J]. 土木工程学报, 2006(3): 24-36.

[2] 刘伟庆, 方海, 方园. 纤维增强复合材料及其结构研究进展[J]. 建筑结构学报, 2019, 40(4): 1-16.

[3] HOLLAWAY L C. A review of the present and future utilisation of FRP composites in the civil infrastructure with reference to their important in-service properties[J]. Construction and Building Materials, 2010, 24(12): 2419-2445.

[4] CROMWELL J R, HARRIES K A, SHAHROOZ B M. Environmental durability of externally bonded FRP materials intended for repair of concrete structures[J]. Construction and Building Materials, 2011, 25(5): 2528-2539.

[5] VEDERNIKOV A, SAFONOV A, TUCCI F, et al. Pultruded materials and structures: A review[J]. Journal of Composite Materials, 2020, 54(26): 1-37.

[6] LIU T Q, LIU X, FENG P. A comprehensive review on mechanical properties of pultruded FRP composites subjected to long-term environmental effects[J]. Composites Part B: Engineering, 2020, 191, 107958.

(C)1994-2023 China Academic Journal Electronic Publishing House. All rights reserved.　http://www.cnki.net

[7] 陈博. 国内外复合材料工艺设备发展述评之五：拉挤成型[J/OL]. 复合材料科学与工程：1-19[2022-09-28]. https://doi.org/10.19936/j.cnki.2096-8000.20211028.032.
[8] LIU T Q, FENG P, WU Y, et al. Developing an innovative curved-pultruded large-scale GFRP arch beam[J]. Composite Structures, 2021, 256: 113111.
[9] 冯鹏. 复合材料在土木工程中的发展与应用[J]. 玻璃钢/复合材料, 2014(9): 99-104.
[10] 张为军, 田野, 覃兆平, 等. 桥梁用大截面 FRP 拉挤型材的结构设计与试验研究[J]. 玻璃钢/复合材料, 2013(Z3): 55-60.
[11] 田野, 冯鹏,覃兆平, 等. FRP 拉挤型材桁架桥结构体系的研究与应用[J]. 玻璃钢/复合材料, 2012(S1): 139-142.
[12] 结构用纤维增强复合材料拉挤型材：GB/T 31539—2015[S]. 北京：中国标准出版社, 2015.
[13] 清华大学, 中冶建筑研究总院有限公司. 复合材料拉挤型材结构技术规程：CECS692—2020[S]. 北京：中国建筑工业出版社, 2020.
[14] 建筑结构荷载规范：GB 50009—2012[S]. 北京：中国建筑工业出版社, 2012.
[15] ZHANG J, ZHOU P, GUAN C, et al. An ultra-lightweight CFRP beam-string structure[J]. Composite Structures, 2021, 257: 113149.
[16] 邹星星, 陈军, 姜慧, 等. 高抗剪强度 FRP 型材组合梁成型工艺及试验研究[J]. 土木工程学报, 2016, 49(4): 40-47.
[17] LIU T Q, YANG J Q, FENG P, et al. Determining rotational stiffness of flange-web junction of pultruded GFRP Ⅰ-sections[J]. Composite Structures, 2020, 236: 111843.
[18] KOLLÁR L P. Local buckling of fiber reinforced plastic composite structural members with open and closed cross sections[J]. ASCE Journal of Structural Engineering, 2003, 129(11): 1503-1513.
[19] LIU T Q, VIEIRA J D, HARRIES K A. Predicting flange local buckling capacity of pultruded GFRP Ⅰ-sections subject to flexure[J]. Journal of Composites for Construction, 2020, 24(4): 04020025.
[20] ASCIONE F, LAMBERTI M, RAZAQPUR G. Modifications of standard GFRP sections shape and proportions for improved stiffness and lateral-torsional stability[J]. Composite Structures, 2015, 132: 265-289.
[21] LIU T Q, VIEIRA J D, HARRIES K A. Lateral torsional buckling and section distortion of pultruded GFRP Ⅰ-sections subject to flexure[J]. Composite Structures, 2019, 225: 111151.
[22] INSAUSTI A, PUENTE I, AZKUNE M. Interaction between local and lateral buckling on pultruded Ⅰ-beams[J]. ASCE Journal of Composites for Construction, 2009, 13(4): 315-324.
[23] SCHAFER B W. Local, distortional, and euler buckling in thin-walled columns[J]. ASCE Journal of Structural Engineering, 2002, 128(3): 289-299.
[24] LIU T Q. Stability behavior of pultruded glass-fiber reinforced polymer Ⅰ-sections subject to flexure[D]. Pittsburgh: University of Pittsburgh, 2017.

(上接第 25 页)

[7] WANG Y, CHEN X G, YOUNG R, et al. Finite element analysis of effect of inter-yarn friction on ballistic impact response of woven fabrics[J]. Composite Structures, 2016, 135: 8-16.
[8] KINVI-DOSSOU G, BOUMBIMBA R M, BONFOH N, et al. A numerical homogenization of E-glass/acrylic woven composite laminates: Application to low velocity impact[J]. Composite Structures, 2018, 200: 540-554.
[9] VALLONS K, BEHAEGHE A, LOMOV S V, et al. Impact and post-impact properties of a carbon fibre non-crimp fabric and a twill weave composite[J]. Composites Part a Applied Science and Manufacturing, 2010, 41: 1019-1026.
[10] 王涛, 侯玉亮, 铁瑛, 等. 基于 ECPL 模型的平纹机织复合材料低速冲击多尺度模拟[J]. 振动与冲击, 2020, 39(20): 295-304.
[11] 张洁皓, 段玥晨, 侯玉亮, 等. 基于渐进均匀化的平纹编织复合材料低速冲击多尺度方法[J]. 力学学报, 2019, 51(5): 1411-1423.
[12] SHISHEVAN F A, AKBULUT H. Low-velocity impact behavior of carbon/basalt fiber-reinforced intra-ply hybrid composites[J]. Iranian Journal of Science and Technology-Transactions of Mechanical Engineering, 2019, 43: 225-234.
[13] 陈继刚, 薛亚红, 闫世程. 二维机织复合材料弹性常数的有限元法预测[J]. 复合材料学报, 2016, 33(8): 1702-1709.
[14] 王涛. 基于多尺度方法的平纹机织复合材料低速冲击损伤研究[D]. 郑州：郑州大学, 2020.
[15] UDHAYARAMAN R, MULAY S S. Multi-scale approach based constitutive modelling of plain woven textile composites[J]. Mechanics of Materials, 2017, 112: 172-192.
[16] 张松俊. 基于多尺度模型的二维三轴编织复合材料的损伤破坏机理研究[D]. 长沙：湖南大学, 2018.
[17] HASHIN Z. Failure criteria for unidirectional fiber composites[J]. Journal of Applied Mechanics, 1980, 47: 329-334.
[18] HOU J P, PETRINIC N, RUIZ C, et al. Prediction of impact damage in composite plates[J]. Composites Science and Technology, 2000, 60(2): 273-281.
[19] HOU Y L, TIE Y, LI C, et al. On the damage mechanism of high-speed ballast impact and compression after impact for CFRP laminates[J]. Composite Structures, 2019, 229: 111435.
[20] 吴盼, 阎建华, 俞建勇, 等. 碳纤/环氧复合材料层合板低速冲击损伤机理研究[J]. 玻璃钢/复合材料, 2016(3): 31-37.
[21] 杨光猛, 赵美英, 万小朋. 平纹编织复合材料层板高速冲击损伤机理研究[J]. 玻璃钢/复合材料, 2018(4): 21-26.
[22] 张晨曦, 娄源峰, 铁瑛, 等. 基于渐进均匀化多尺度方法的 CFR 平纹机织材料冲击后压缩损伤研究[J].复合材料科学与工程, 2021(10): 5-12.
[23] GODA I, GIRARDOT J. A computational framework for energy absorption and damage assessment of laminated composites under ballistic impact and new insights into target parameters[J]. Aerospace Science and Technology, 2021,115: 106835.

(C)1994-2023 China Academic Journal Electronic Publishing House. All rights reserved. http://www.cnki.net

Construction and Building Materials 389 (2023) 131790



Contents lists available at ScienceDirect

Construction and Building Materials

journal homepage: www.elsevier.com/locate/conbuildmat





A binary resin system of epoxy and phenol-formaldehyde for improving the thermo-mechanical behavior of FRP composites

TianQiao Liu [a,*], Ruibao Wang [a], Shilong Zhen [a], Peng Feng [b]

[a] Department of Civil Engineering, Beijing University of Technology, Beijing, China
[b] Department of Civil Engineering, Tsinghua University, Beijing, China

ARTICLE INFO

Keywords:
FRP composites
Binary resin system
Thermo-mechanical behavior
Phenol-formaldehyde
Epoxy

ABSTRACT

A binary resin system combing epoxy and phenol–formaldehyde is proposed for improving the thermo-mechanical behavior of FRP composites. Five types of FRP plates with varying resin recipes were fabricated through compression molding process. Thermo-mechanical tests were conducted at various temperatures to evaluate the glass transition temperature and the mechanical properties of FRP plates. Owing to the cross-linking occurred between epoxy and phenol–formaldehyde, proposed binary resin system is able to increase the glass transition temperature as well as to improve the mechanical properties of FRPs. Predictive models are recommended to assist the practical design of FRPs with binary resin system.

1. Introduction

Fiber reinforced polymer (FRP) composites have seen an increasing number of practical applications and theoretical developments in the field of civil engineering worldwide [1–4]. To date, one of the main issues hindering the widespread applications of FRPs in civil engineering is the relatively poor thermo-mechanical behavior of the material [5–8]. The resin, in particular, is observed to have a greater impact on thermal behavior of FRPs over the fiber [9]. The most-commonly used fibers and resins of FRPs in civil infrastructures are glass fibers and thermoset resins, and the resins include unsaturated polyester, vinyl ester, epoxy, phenol–formaldehyde, and polyurethane [9]. The selection between different resin systems is primarily dependent on the specific functionality pre-designed for FRPs. Epoxy is known to have the best mechanical performance because of the carbon–oxygen double bond at both ends of its molecular chain (see Fig. 1), and phenol–formaldehyde typically has the highest thermal stability owing to its relatively stiffer molecular structure (i.e., aromatic ring and its bond) (see Fig. 1). Admittedly, epoxy is often preferred over phenol–formaldehyde for those structures servicing around ambient temperatures (i.e., 20–40 °C), such as wind turbine blades, pedestrian bridges, etc. However, phenol–formaldehyde might be the only solution when high service temperature is of critical design concern, such as the evacuation platform in subway tunnel.

For those outdoor applications such as wind turbines and pedestrian bridges, there is often little/minimum requirement on service temperature of FRPs, and naturally, the mechanical behavior is of the highest interest, whereas for those indoor applications such as evacuation platforms in tunnels, the thermal behavior of material often turns out to be the controlling factor in design, as the mechanical aspect can be more conveniently accomplished. Unsurprisingly, almost all existing FRP applications are limited within outdoor scenarios, especially for those large-scale structures, including bridges, cooling towers, and frame structures [10]. In order to improve the thermo-mechanical behavior of FRP composites as well as to further expand their possible applicability in civil infrastructures, this work focuses on the resin system of FRP composites, since it is the resin that essentially determines the overall thermo-mechanical behavior of material. Specifically, a binary resin system combining epoxy and phenol–formaldehyde is investigated. The motivation driving the use of this binary resin system is not only the good thermo-mechanical properties, but also the good economic performance; that is, the common epoxy and phenol–formaldehyde can economically outperform the high-quality epoxy.

In this work, binary resin system with varying resin fractions is investigated along with two control resin systems (i.e., pure epoxy and pure phenol–formaldehyde), and the thermal behaviors of five types of materials are evaluated through dynamic mechanical analysis. Then, thermo-mechanical tests, including tension and compression tests, are conducted on five types of FRPs to measure their residual properties at varying temperatures, from 20 up to 100 °C. Additionally, scanning electron microscope is used to observe the possible degradation of

* Corresponding author.
E-mail address: liu_tianqiao@bjut.edu.cn (T. Liu).

https://doi.org/10.1016/j.conbuildmat.2023.131790
Received 12 October 2022; Received in revised form 22 April 2023; Accepted 12 May 2023
Available online 18 May 2023
0950-0618/© 2023 Elsevier Ltd. All rights reserved.

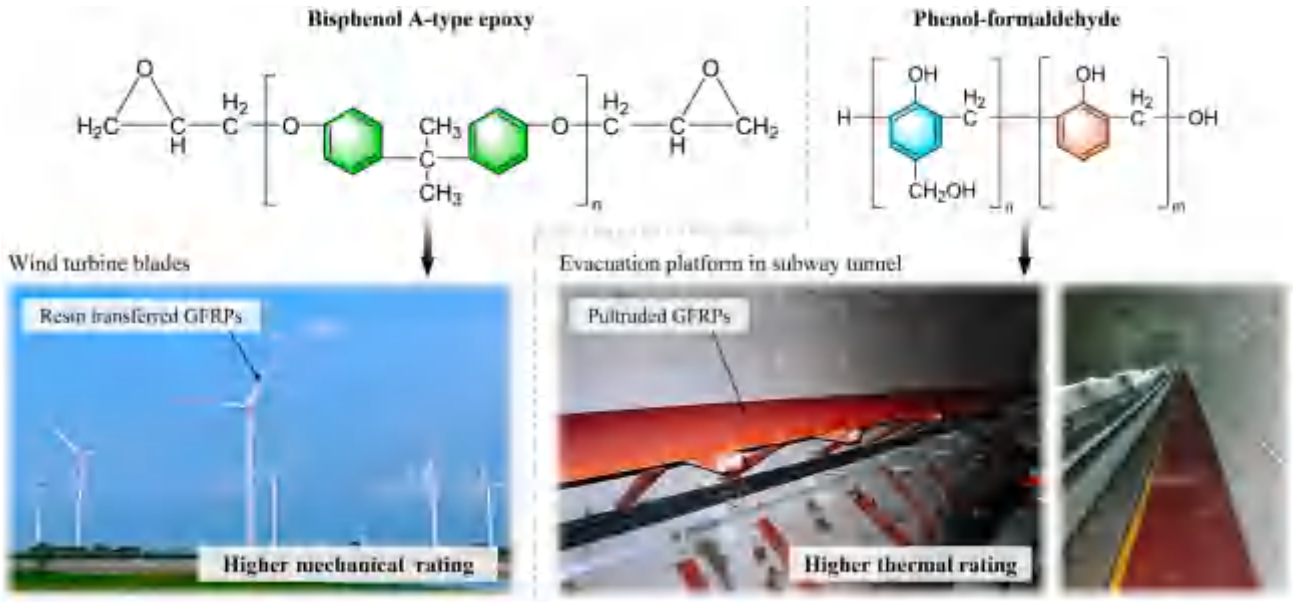


Fig. 1. Molecular structures and typical applications of epoxy and phenol–formaldehyde resins (Photo of evacuation platform in subway tunnel by courtesy of Beijing Composite Materials Co., Ltd. and Nanjing Spare Composite Yizheng Co., Ltd.).

materials at micro-level. Analytical studies are also conducted to develop predictive models for the glass transition temperature of FRPs made of binary resin system as well as for the residual properties of FRPs at high temperatures.

2. Thermal behaviors

2.1. Experimental tests

In this work, FRP composite plates made of binary resin systems of epoxy (EP) and phenol–formaldehyde (PF) were fabricated and tested, as shown in Fig. 2. Both the EP and PF resins were provided by Shaanxi Taihang Fire Retardant Polymer Co., Ltd. In particular, bisphenol A-type EP resin (model E-51)—as the representative of its type—was adopted, and a resole-type PF resin (model THC-400) was used. Three binary resin systems with varying resin fractions (measured by weight) were investigated, including 50% PF + 50% EP, 62.5% PF + 37.5% EP, and 75% PF + 25% EP. Moreover, two control resin systems were also made for comparison purpose, including 100% EP and 100% PF. Additionally, orthotropic glass fabrics (model SW210A-92a) manufactured by Nanjing Fiberglass Research & Design Institute Co., Ltd. were used. Glass fabric has 16/28 fiber yarns in warp direction and 12/28 yarns in weft

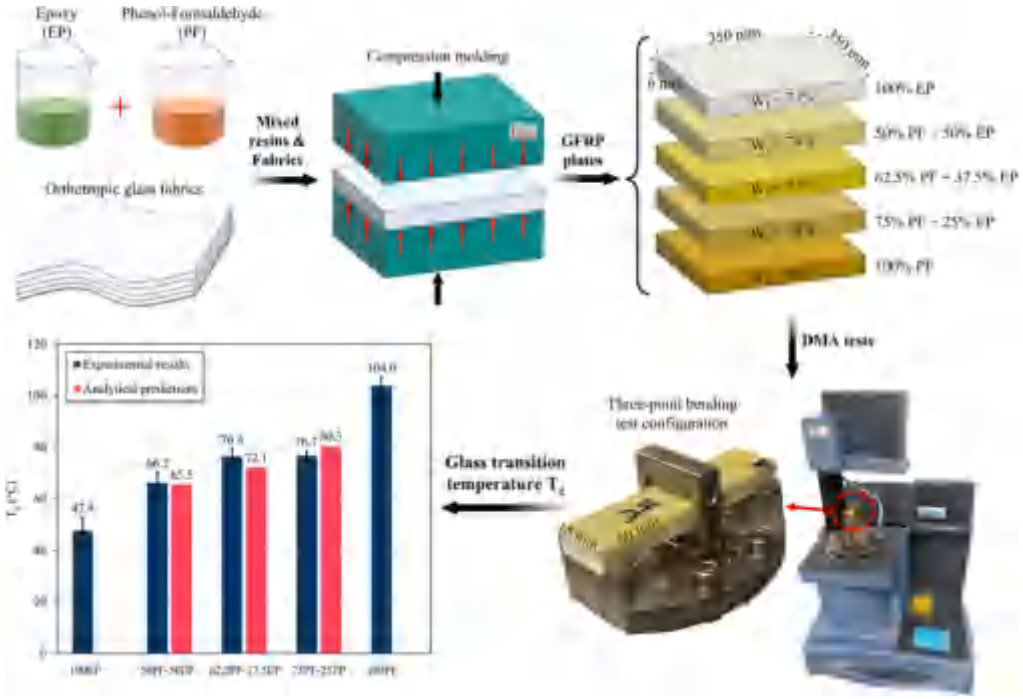
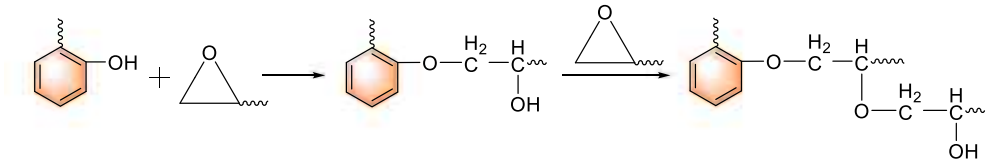


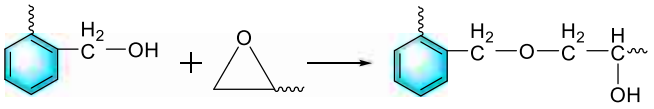
Fig. 2. Schematic of thermal tests of binary resin systems.

direction. Glass fabrics and resin systems were combined and cured through compression molding process following manufacturer's guide; specifically, all materials were pressurized around 10 MPa and heated/cured via three stages, including 120 °C for 1.5 h, 150 °C for 1.5 h, and 180 °C for 3 h. A total of 15 FRP composite plates with five different recipes were fabricated, each recipe having three identical plates and all plates having geometries of 350 × 350 × 6 mm (length × width × thickness). Five types of FRP plates were denoted as 100EP, 50PF-50EP, 62.5PF-37.5EP, 75PF-25EP, and 100PF. Considering the glass fabrics have different mechanical properties in their warp and weft directions, they were layuped in an orthotropic manner in consecutively layers in all plates, such that a quasi-isotropic behavior in the plane of length by width was achieved. The resulting fiber weight fractions W_f of five types of FRP plates were measured through burn-off tests, and the observed W_f were found to fall in a close range of 73–80%.

Typically, PF resin chemically reacts with EP resin in two methods, as shown in Eqs. (1) and (2). First, the phenolic hydroxyl group of PF resin could react with carbon–oxygen double bond of EP resin through cross-linking (see Eq. (1)); second, the hydroxymethyl group of PF resin can react with carbon–oxygen double bond of EP in the same way with phenolic hydroxyl group (see Eq. (2)). Both reactions could lead to increased molecular weight of resin system and consequently, result in improved thermal stability. In fact, PF resin is often used as the catalyst for EP resin and vice versa; thus, the binary resin system proposed in this work is chemically feasible and practically workable.



(1)



(2)

Thermal behavior of FRP composites is typically evaluated by means of glass transition temperature T_g, which indicates the onset of a polymer transitioning from glassy state into rubbery state [11]. In addition, T_g can be measured through various test methods, including differential scanning calorimetry (DSC), thermo-mechanical analysis (TMA) and dynamic mechanical analysis (DMA), and those test methods are designed to measure different responses of polymers subjected to different conditions [12]. Thus, the observed T_g by different methods can vary from one to another. In this regard, the DMA test was adopted in this work (see Fig. 2), since DMA can better reflect the thermo-mechanical behavior of FRP composites having relatively high stiffness, such as the present FRP plates to be used in structural purposes in civil engineering. Specifically, a three-point bending test configuration was adopted through model Q800 from TA Instrument. The coupon geometries were 50 × 15 × 6 mm (length × width × thickness), and the heating rate was set to 5 °C/min. The tested temperature range was from room temperature 20 °C up to 250 °C.

In DMA test, three thermo-mechanical responses were obtained, including storage modulus E', loss modulus E'', and damping factor $tan\delta$, as shown in Fig. 3. It is seen that storage modulus yields the lowest T_g value (44.2 °C, in this case), and damping factor yields the highest T_g value (65.9 °C, in this case); the difference may be up to 49%. Considering the strict safety requirement in civil engineering, the operating temperature of construction materials should be determined such that the storage modulus is kept constant [13]; thus, in this work the T_g value determined by storage modulus E' is used. In addition, each type of FRP plate was repeatedly tested for three times. The DMA results are shown in Table 1.

As expected, FRP plates with 100% PF resin have the highest T_g (avg. = 104.0 °C) and those plates with 100% EP resin have the lowest T_g (avg. = 47.8 °C). More importantly, the binary resin systems uniformly exhibited improved thermal behaviors; that is, specimens 50PF-50EP, 62.5PF-37.5EP, and 75PF-25EP all enabled increased T_g values as compared to specimen 100EP, and the T_g values were increased by 38.5%, 59.9% and 60.4%, respectively.

2.2. Analytical investigations

In order to assist the thermal design of FRP composites with binary resin system, the predictive model for glass transition temperature T_g was investigated. In general, two main approaches are available in the field, one at micro-level and the other one at macro-level. First, glass transition temperature, as a macro-level measurement of polymers, is affected by numerous micro-level properties of material, including molecular weight and size, number of flexible bonds and hydroxyl groups, polymeric structure (i.e., cross-linking and chain stiffness), and constitutive additives and fillers [14–18]. Based on those micro-level properties, a series of theoretical and empirical models were developed for predicting T_g value of polymers and their diluent systems [11,14–18]. The first approach depends greatly on the micro-level properties of FRPs. Nonetheless, for civil engineering practitioners, this type of information is often not available or interpretable.

The second approach is based on macro-level properties of FRPs. In particular, the rule-of-mixture and its derivatives are commonly implemented for co-polymer systems [12,19–20], and this type of approach only requires the macro-level properties of two constitutive resins. Among all existing models, Fox equation [20] draws a great attention as it expresses as an explicit equation in a simple-form (i.e., inverse rule-of-mixture), as shown in Eq. (3).

$$\frac{1}{T_g} = \frac{w_1}{T_{g,1}} + \frac{w_2}{T_{g,2}} \tag{3}$$

where T_g is the predicted glass transition temperature of binary resin system; $T_{g,1}$ and w_1 are the glass transition temperature and weight fraction of the 1st constitutive resin; and $T_{g,2}$ and w_2 are the glass transition temperature and weight fraction of the 2nd constitutive resin.

Using Fox equation, T_g values of FRP plates with three binary systems were calculated. The results are shown in Table 1. It is seen that the greatest difference between analytical predictions $T_{g,pred}$ and experimental results $T_{g,exp}$ is less than 10%, thus showing a good accuracy of Fox equation.

Contrary to Fox equation, Gordon-Taylor equation (and its derivatives) was developed based on direct rule-of-mixture [12], as shown in Eq. (4).

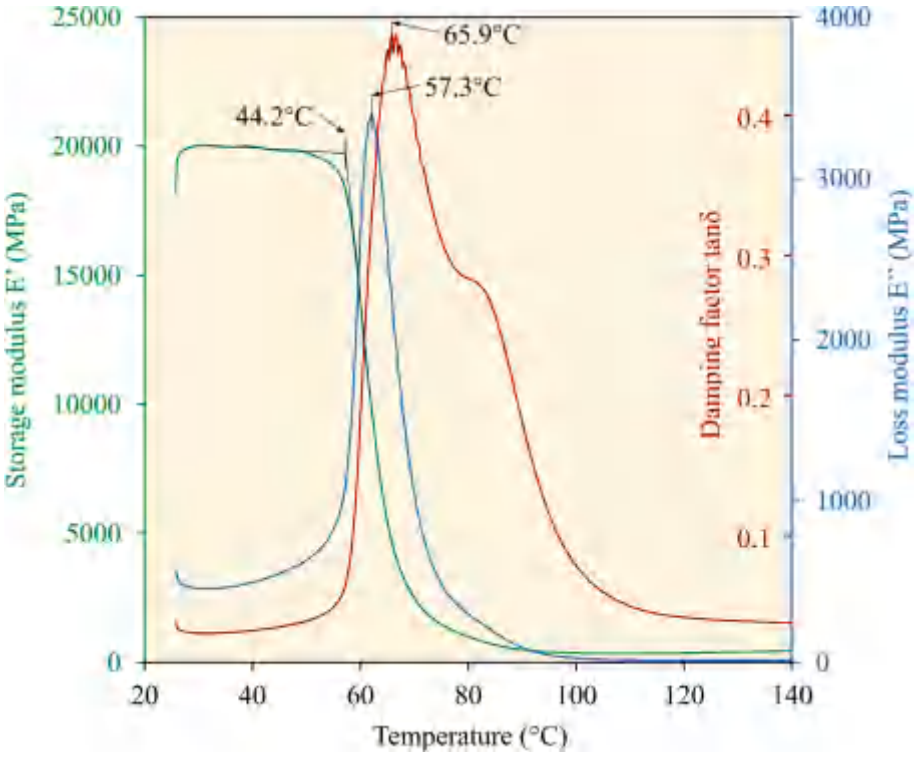


Fig. 3. Exemplar of T_g values determined by DMA test (specimen 100EP).

Table 1
Glass transition temperatures determined by DMA tests.

Specimens		Experimental results		Analytical predictions		
		$T_{g,exp}$ (°C)	Avg. $T_{g,exp}$ (°C)	COV	$T_{g,pred}$ (°C)	$T_{g,pred}$ $T_{g,exp}$
100EP	−1	48.6	47.8	0.07	–	–
	−2	50.5				
	−3	44.2				
50PF-50EP	−1	67.4	66.2	0.06	65.5	0.97
	−2	69.5				0.94
	−3	61.5				1.06
62.5PF-37.5EP	−1	77.4	76.4	0.04	72.1	0.93
	−2	72.9				0.99
	−3	78.9				0.91
75PF-25EP	−1	78.7	76.7	0.02	80.3	1.02
	−2	75.0				1.07
	−3	76.3				1.05
100PF	−1	102.7	104.0	0.05	–	–
	−2	99.9				
	−3	109.3				

$$T_g = \frac{w_1 T_{g,1} + k_{GT} w_2 T_{g,2}}{w_1 + k_{GT} w_2} \tag{4}$$

where k_{GT} is the empirical coefficient to be calibrated with experimental data, accounting for unequal contributions of constitutive resins. If assuming $k_{GT} = 1$ and $w_1 + w_2 = 1$, Gordon-Taylor equation directly reduces to $T_g = w_1 T_{g,1} + w_2 T_{g,2}$, which is the typical expression of direct rule-of-mixture. Compared with Fox equation, Gordon-Taylor equation requires a regression of experimental data. Thus, in this work the Fox equation is recommended considering its satisfactory accuracy as well as the excellent applicability.

3. Thermo-mechanical behaviors

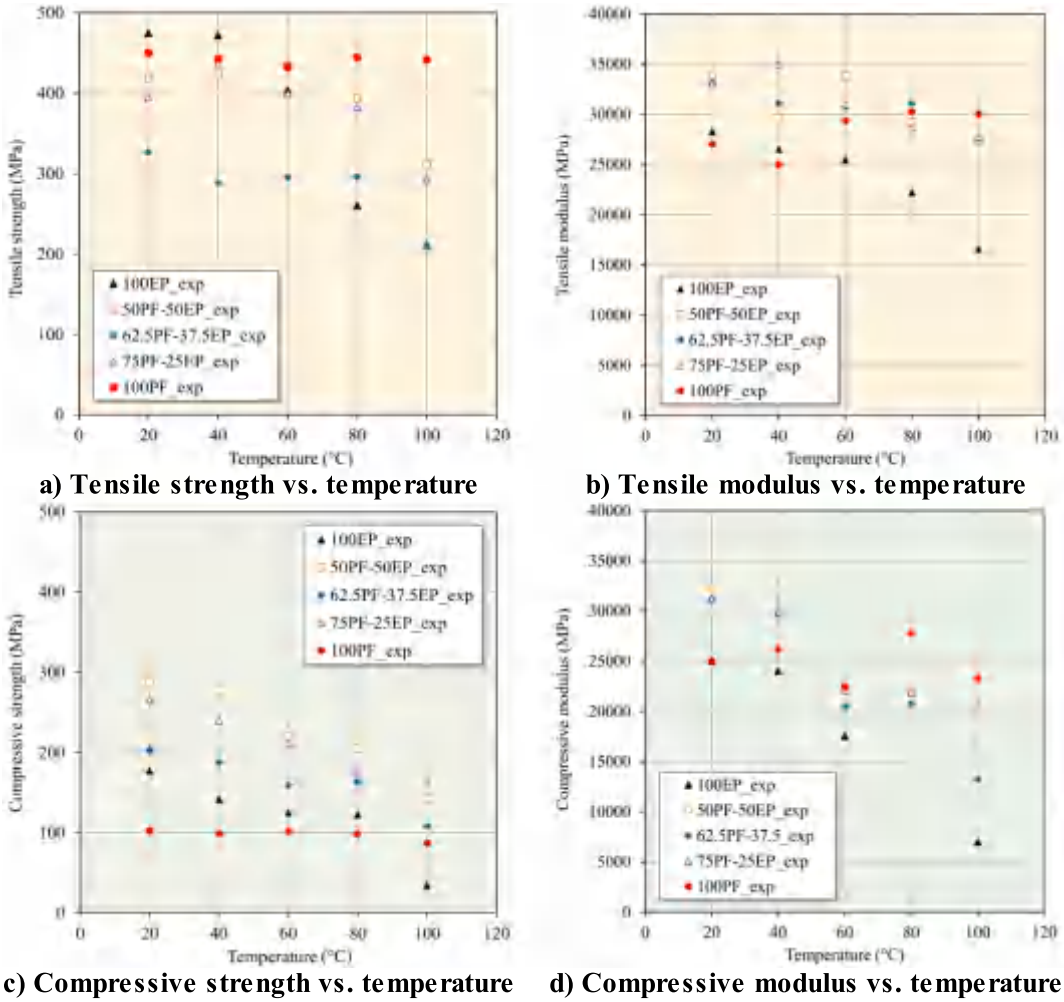
3.1. Experimental tests

A series of thermo-mechanical tests were conducted to measure the degradations of FRP plates with different resin systems. Both tension and compression tests were conducted in acccordance with ASTM D3039 [21] and D6641 [22], as shown in Fig. 4. A universal testing mechine (Instron 8801) with maximum capacity of 100 kN was used. To heat the FRP specimens, a furnace with maximum heating temperature of 150 °C was adopted. The heating rate was set to 5 °C/min. A total of five different temperatures were studied, including 20 (i.e., room temperature), 40, 60, 80, and 100 °C. The temperature range of interest (i.e., from 20 to 100 °C) was determined so as to cover the highest possible service temperature that civil infrastrctures might encounter in real scenarios [23]. The temperature beyond 100 °C up to 1000 °C may involve special treatment to materials such as fire-proof measurements, and this type of design is typically required for extreme limit states, which is not the focus of this work. When reaching the interested temperature, specimens were held at that temperature for at least one hour before mechanical tests. In addition, a remote thermometer was used to measure the surface temperature of specimen, ensuring the specimen (at least at surface level) reached the desired temperature.

Five types of FRP plates—100EP, 50PF-50EP, 62.5PF-37.5EP, 75PF-25EP, and 100PF—were cut into specified geometries per ASTM standards, and each type of material was repeatedly tested for six times. Experimentally determined tensile strength F_t and moduli E_t, and compressive strength F_c and moduli E_c are shown in Fig. 5. Detailed experimental data (i.e., average value of six repeated tests) and representative stress–strain curves are shown in Appendix A. In addition, coefficient of variations (COV) of all experimental data are calculated and presented in Appendix A. It is noted that for specimen 100EP at 80 °C (see Table A.2), the reported data of compressive modulus 21,508 MPa is deemed abnormal and ineffective in this case, as it shows a highly-unreasonable trend of degradation at this temperature. Given the



Fig. 4. Thermo-mechanical test set-ups.



a) Tensile strength vs. temperature **b) Tensile modulus vs. temperature**

c) Compressive strength vs. temperature **d) Compressive modulus vs. temperature**

Fig. 5. Experimentally determined thermal–mechanical properties of FRP plates.

COV of this test is relatively small, it is suspected that a system-related error might have occurred, such as an incorrect set-up in measurement devices or a mis-selection of specimens. Thus, this data is not shown in Fig. 5 and not used in following sections.

It is seen that specimen 100EP dramatically degraded with increasing temperature; that is, when temperature was increased from 20 to 100 °C, the average tensile and compressive strength were respectively dropped by 56% (i.e., from 475 to 211 MPa) and 80% (i.e., from 177 to 35 MPa), and average tensile and compressive moduli were respectively decreased by 41% (i.e., from 28,305 to 16587 MPa) and 72% (i.e., from 25,027 to 6987 MPa). As expected, specimen 100PF showed little degradation in terms of both tensile and compressive properties when temperature was increased from 20 to 100 °C; specifically, tensile modulus was even increased by 11% (i.e., from 27,053 to 30020 MPa), and tensile and compressive strength were decreased by 2% (i.e., from 450 to 442 MPa) and 16% (i.e., from 103 to 87 MPa), and compressive modulus was slightly dropped by 7% (i.e., from 25,022 to 23262 MPa). Despite of having higher initial mechanical properties, epoxy has much poorer thermal behavior as compared to phenol–formaldehyde (i.e., T_g of EP was lower than PF by 54%). Consequently, FRP plates with EP resin exhibited lower mechanical behavior as compared to the PF counterparts even at intermediate temperature, namely 40–60 °C. In fact, at temperature of 60 °C, FRPs with PF resins could outperformance their EP counterparts in terms of tensile and compressive moduli, and tensile strength. On the other hand, those FRP plates made with binary resin systems showed intermediate degradation in terms of tensile and compressive properties, and such degradation generally becomes more severe with increasing EP fraction. It is worth noting that all those specimens with binary resin systems showed better thermo-mechanical properties over specimen 100EP.

Surprisingly, all the binary resin systems were found to be able to enhance the mechanical properties of FRP plates when compared with both specimens made with 100% EP and 100% PF resins. First, when compared with specimen 100EP, all binary resin-specimens have higher tensile and compressive moduli and greater compressive strength at all temperatures. Second, when compared with specimen 100PF, binary resin-specimens can also exhibit higher tensile and compressive moduli for temperatures up to 40 °C and greater compressive strength for all temperatures. This finding, to the best knowledge of authors, has not been reported in available literature. This finding can be evidenced by the chemical reactions occurred between EP and PF resins. Based on Eqs. (1) and (2), the cross-linking between EP and PF resins effectively increased the molecular weight as well as improved the molecular structure of the binary resin system, which reasonably led to enhanced mechanical properties of FRP composites.

To support the above finding, the effect of slightly different fiber weight fractions W_f was also discussed. First, specimens 50PF-50EP and 75PF-25EP ($W_f = 74\%$) have similar fiber content with specimen 100EP ($W_f = 73\%$), and their fiber-dominated behaviors (i.e., F_t and E_t) are presumably similar to each other. However, the tensile moduli E_t of 50PF-50EP and 75PF-25EP are higher than those of 100EP for all temperatures under investigation; and only the tensile strength F_t of 50PF-50EP and 75PF-25EP are lower than those of 100EP. Second, as for the resin-dominated behaviors (i.e., F_c and E_c), all the compressive moduli as well as the compressive strength of 50PF-50EP and 75PF-25EP are higher than those of 100EP for all temperatures, thus showing a positive effect of the binary resin systems. Third, specimen 100PF has the highest fiber content ($W_f = 80\%$) and its mechanical behavior is presumably higher than any other specimens. However, the tensile and compressive moduli of 100PF are comparable to specimen 100EP, and they are lower than those of specimens with binary resin systems.

Based on those experimental observations, it can be concluded that the effect of slightly different fiber weight fractions does not have a noticeable impact on the thermo-mechanical behaviors of FRPs being addressed. Furthermore, the enhanced mechanical properties of specimens 50PF-50EP, 62.5PF-37.5EP, and 75PF-25EP can be attributed to the proposed binary resin system.

3.2. Analytical investigations

Analytical study was conducted to develop the predictive model for the thermo-mechanical degradation of FRP plates addressed in this work. In available literature, a total of six models have been proposed as representatives, as shown in Table 2. Mahieux et al. [24] first proposed to use Weibull distribution to predict FRP degradation subjected to temperature effect. Later, Bisby [25] proposed a sigmoid function to predict the degradation of FRP composites. Then, a third order polynomial function was proposed by Kulcarni and Gibson [26] to capture the degradations of FRPs. Additionally, Gibson et al. [27] used a hyperbolic function for the same purpose, and their function is essentially the same with the sigmoid function by Bisby [25] if assuming no decomposition of resin occurred (i.e., $R_n = 1$). Based on existing models and experimental data, Wang et al. [28] and Feng et al. [29] proposed a series of simple-formed trilinear functions as the lower bound solutions of FRP thermal–mechanical degradations.

In general, those models can be categorized into three types: 1) hyperbolic tangent function [25,27]; 2) third order polynomial [26]; and 3) trilinear function [28,29]. Those three types of models are schematically shown in Fig. 6. First, the hyperbolic tangent function (see FRP_3 in Fig. 6) is known to be able to capture the entire degradation process of FRPs subjected to increasing temperature, from glassy state ($T < T_g$) to rubbery state ($T_g < T < T_m$) and eventually to melting state ($T_m < T$). Indeed, the shape function of this model is similar to that of the storage modulus (see Fig. 3), and the T_g value in this model, though not precisely used as T_g (i.e., $T_{central}$ is used instead and $T_{central}$ is numerically close to T_g), is approximately located at the central point of the function (see $T_{g,3}$ in Fig. 6). The most advantageous feature of hyperbolic tangent model is the capability of capturing the entire thermal–mechanical degradation of FRPs from room temperature to melting temperature.

Second, the third order polynomial function (see FRP_1 and FRP_2 in Fig. 6) is also able to simulate all states of FRPs subjected to increasing temperature, including glassy state, rubbery state, and melting state; in fact, a third order polynomial function can be readily calibrated into a hyperbolic tangent-like function based on sufficient experimental data. The main difference between third order polynomial and hyperbolic tangent functions is that the former also permits the simulation of one single state instead of all three states of materials. For instance, FRP_1 in Fig. 6 is at the glassy state in the temperature range of interest, and FRP_2 is at the rubbery state. Their degradation behaviors can be approximated by the first half part of the hyperbolic tangent function (i.e., $T < T_{g,1}$ and $T_{g,2} < T \ll T_m$).

Third, the trilinear function (see FRP_4 in Fig. 6) is developed based on the key points such as the property at room temperature $P_{initial}$, the property at melting temperature P_R, room temperature $T_{initial}$, glass transition temperature T_g, and melting temperature T_m. Trilinear function is reported to provide lower bound solutions to thermal–mechanical degradation of FRPs.

In this work, specimen 100EP was tested far beyond its T_g, by a factor of 2 ($\approx 100 / 47.8$) and specimen 100PF was only heated near its T_g; on the other hand, specimens 50PF-50EP, 62.5PF-37.5EP, and 75PF-25EP were heated above their T_g while not yet entered their melting stage. With experimental observations respected, the third order polynomial function was adopted so as to predict the degradation behavior of all types of FRP plates, as shown in Eq. (5). The coefficients determined based on experimental data (i.e., a_1, a_2, and a_3) are presented in Appendix B. The R^2 values are also shown in Appendix B. The normalized residual properties obtained from experimental tests and analytical predictions are presented in Fig. 7.

Table 2
Existing predictive models for thermal–mechanical degradations of FRP composites.

Authors	Predictive models	Reviewed by
Mahieux et al. [24]	$P_T = P_R + (P_{initial} - P_R)exp\left[-\left(\frac{T}{T_{initial}}\right)^m\right]$ T is the particular temperature of interest; $T_{initial}$ is the room temperature; P_T is the particular property at temperature T; $P_{initial}$ is the value of that property at room temperature $T_{initial}$; P_R is the residual value of that property at melting temperature T_m; m is the Weibull exponent to be calibrated with experimental data.	Chowdhury et al. [30] Correia et al. [31]
Bisby [25]	$\frac{P_T}{P_{inital}} = \frac{1+a}{2} + \left(\frac{1-a}{2}\right)tanh[-b(T-c)]$ a, b, and c are the coefficients to be calibrated with experimental data.	Wang et al. [28] Yu and Kodur [32] Nguyen et al. [33]
Kulcarni and Gibson [26]	$\frac{P_T}{P_{initial}} = 1 - \left[a_1\left(\frac{T-T_{initial}}{T_g-T}\right) + a_2\left(\frac{T-T_{initial}}{T_g-T}\right)^2 + a_3\left(\frac{T-T_{initial}}{T_g-T}\right)^3\right]$ a_1, a_2, and a_3 are the coefficients to be calibrated with experimental data.	Chowdhury et al. [30]
Gibson et al. [27]	$P_T = R_n\left(\frac{P_{initial}+P_R}{2} + \left(\frac{P_{initial}-P_R}{2}\right)tanh[k_m(T-T_{central})]\right)$ R_n is a power law modification factor accounting for resin decomposition, $R_n = 1$ when no decomposition occurred; $R_n = 0$ when resin completely volatized; $T_{central}$ is the temperature around which the curve is symmetrical; $T_{central}$ is not necessarily equal to T_g; k_m is an empirical coefficient to be calibrated with experimental data.	Wang et al. [28] Chowdhury et al. [30] Correia et al. [31] Nguyen et al. [33]
Wang et al. [28]	$\frac{P_T}{P_{initial}} = A - \frac{(T-B)^n}{C}$ A, B, and C are the coefficients to be calibrated with experimental data.	Correia et al. [31] Nguyen et al. [33]
Feng et al. [29]	$P_T = \begin{cases} P_{initial} & T \le T_s \\ \frac{P_R - P_{initial}}{T_g - T_s}(T - T_{initial}) + P_{initial} & T_s < T < T_g \\ P_R & T_g \le T \le T_r \end{cases}$ T_s is the temperature indicating the beginning of degradation of storage modulus; T_g is the glass transition temperature determined by damping factor; T_r is the temperature indicating the beginning of residual plateau of storage modulus.	–

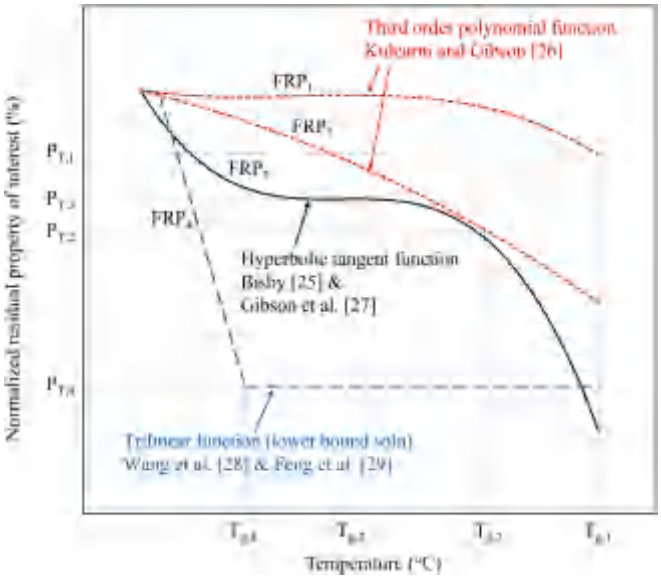


Fig. 6. Schematic of existing predictive models.

$$\frac{P_T}{P_{initial}} = 1 - \left[a_1\left(\frac{T-T_{initial}}{T_g-T}\right) + a_2\left(\frac{T-T_{initial}}{T_g-T}\right)^2 + a_3\left(\frac{T-T_{initial}}{T_g-T}\right)^3\right] \quad (5)$$

A total of 20 sets of functions were data-fitted. As a result, 13 functions have R^2 values greater than 0.95, and 4 functions have R^2 values in between of 0.85 and 0.95; and the rest 3 functions have R^2 values of 0.64 ($E_{t,pred}$ of 50PF-50EP), 0.62 ($F_{t,pred}$ of 100PF), and 0.11 ($E_{c,pred}$ of 100PF). The relatively lower R^2 values were attributed to the highly scattered experimental data. For instance, the worst fitting case occurred for E_c prediction of specimen 100PF; in this case, a relatively higher variation of experimental data and an abnormal trend of degradation are observed, though E_c value is eventually reduced by 7% from 20 to 100 °C.

Except for those three cases, the third order polynomial function is observed to be able to provide accurate predictions for the five types of FRP plates being addressed. From Fig. 7, it can be seen that the third order polynomial function is capable of capturing the degradations of materials at various states, such as glassy state, rubbery state, and melting state. For those materials experienced all three states (i.e., 100EP), the third order polynomial function could provide similar predictions with hyperbolic tangent function, such as the F_t, F_c, and E_c predictions for specimen 100EP, and for those materials only experienced the first one (i.e., 100PF) or two states (i.e., three binary resin systems), the third order polynomial can also capture their degradations with satisfactory accuracy.

3.3. SEM observations

In addition to thermo-mechanical tests conducted at macro-level, scanning electron microscope (SEM) was also used to evaluate the possible material degradation at micro-level. It is noted that SEM tests are aimed to provide a qualitative assessment of material degradations such that previous analyses can be physically validated. All five types of FRP plates were extracted from the intact parts of coupons tested previously in tension or compression. The SEM photos taken from specimens experienced thermal-conditioning of 20 and 100 °C are shown in Fig. 8. Comparing all five types of FRPs, specimen 100EP exhibited the most severe damage. As shown in Fig. 8a, epoxy resin at 20 °C did not show any noticeable damages, while at 100 °C, epoxy showed massive softening/deformation due to pyrolysis. On contrary, specimens 50PF-50EP, 62.5PF-37.5EP, 75PF-25EP, and 100PF, did not show such softening/deformation. In addition, from Fig. 8c, specimen 62.5PF-37.5EP at 100 °C showed some pores in resin, while the cause remains unknown. In all

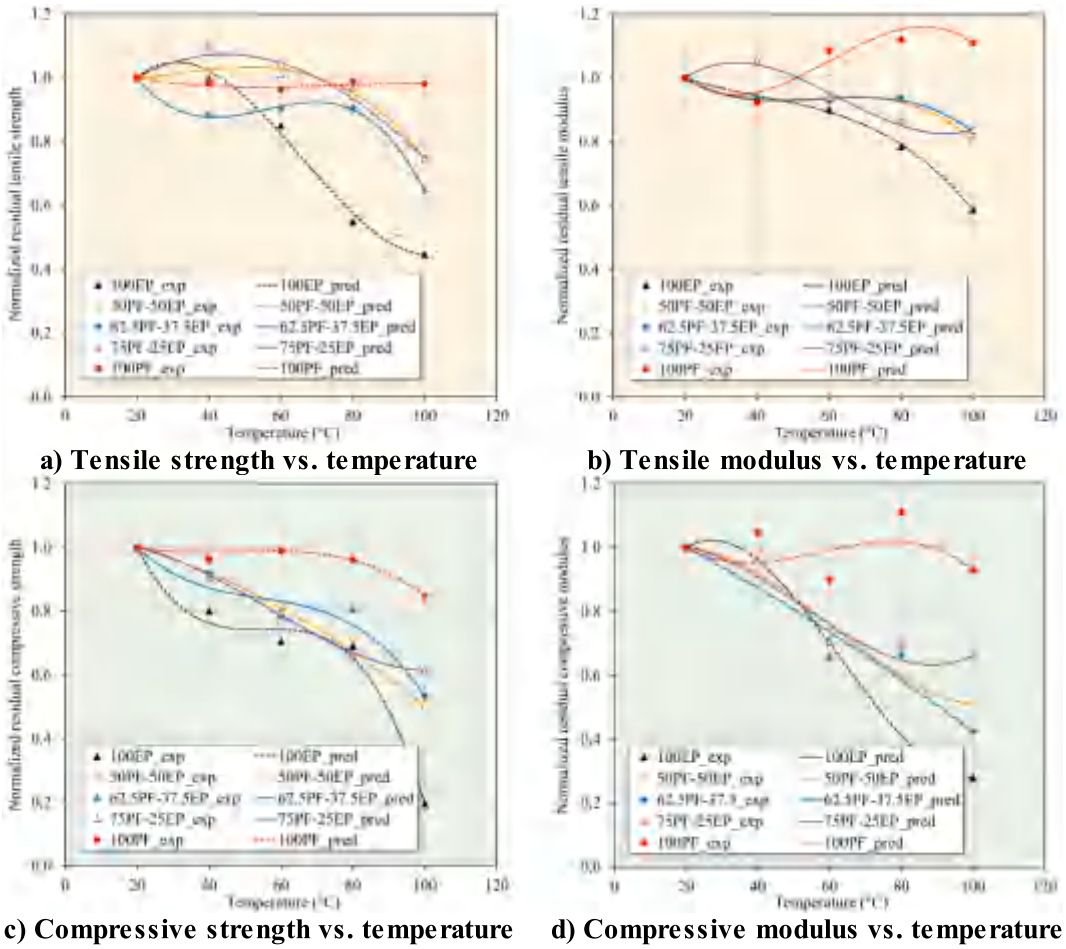


Fig. 7. Normalized residual properties of FRP plates.

other specimens, no evident degradations were identified. Generally, SEM tests support the above finding that PF resin and binary resin systems could greatly enhance the thermal behavior of FRP composites.

4. Discussions

The thermal behavior of all FRP composites was investigated in the temperature range between room temperature and 100 °C, and the FRP plates were fabricated through a manually-controlled compression molding process. In this process, manual work is needed to form the desired layups of fabrics, and resin in liquid form is also applied manually. By nature of this process, the obtained materials are expected to have some extent of imperfections such as varying fabric orientations, fabric undulations, variations in resin thickness and the non-uniform fiber–matrix interface across the plate. Moreover, a non-unform heating of compression mold is almost inevitable, lead to varying degree of curing across FRP plate. All the coupons for thermo-mechanical experiments are randomly extracted from the FRP plate, and consequently, coupons are to have some extent of variations. This is evidenced by the relatively large COVs in some tests, such as specimen 100EP's compressive strength and modulus at 100 °C with COVs of 0.39 and 0.36 (see Table A.2). With that being said, material imperfections may lead to possible variations in observed mechanical properties. For instance, at 20 °C, specimens 100EP and 100PF have higher tensile strength, while for tensile modulus, compressive strength and compressive modulus, specimens 100EP and 100PF generally have lower values. Despite of having inevitable material imperfections, the trend of material degradation is successfully captured. In order to mitigate the effects of material imperfections, highly-automated manufacturing processes are recommended, such as pultrusion.

The temperature range addressed in this work could sufficiently cover most civil engineering-related FRP applications; however, for those structures/applications exposed to extremely high temperatures, the binary resin system may not render the most effective approach. This method is greatly dependent on the thermal behavior of phenol–formaldehyde, and naturally, for those cases where the service temperature exceeds the glass transition temperature of PF, other methods should be considered such as fire-retardant additives or fireproof coatings. The scope of this work is designed to focus on the "normal-high" temperature, rather than "extreme-high" temperature.

The Fox equation and third order polynomial function were recommended in this work for predicting the glass transition temperature of binary resin systems and the degradation behavior of FRPs subjected to increasing temperature. The use of those two methods is mainly stemmed from their powerful applicability. Fox equation is explicit in its expression and can be readily adopted in practice. Third order polynomial is capable of simulating FRP degradation at any states, including glassy state, rubbery state, and melting state. It must be noted that all predictive models for thermal–mechanical degradation behavior introduced in this work are essentially shape functions to simulate the experimentally observed behavior of materials, and thus, they can, to an extremely limited extend, provide theoretical explanation of degradation mechanism. In order to understand the fundamental degradation mechanism of FRP composites, studies are to be done at micro-level of materials. At this moment, the findings drawn from this work could satisfactorily meet the requirement of practical design in civil engineering.

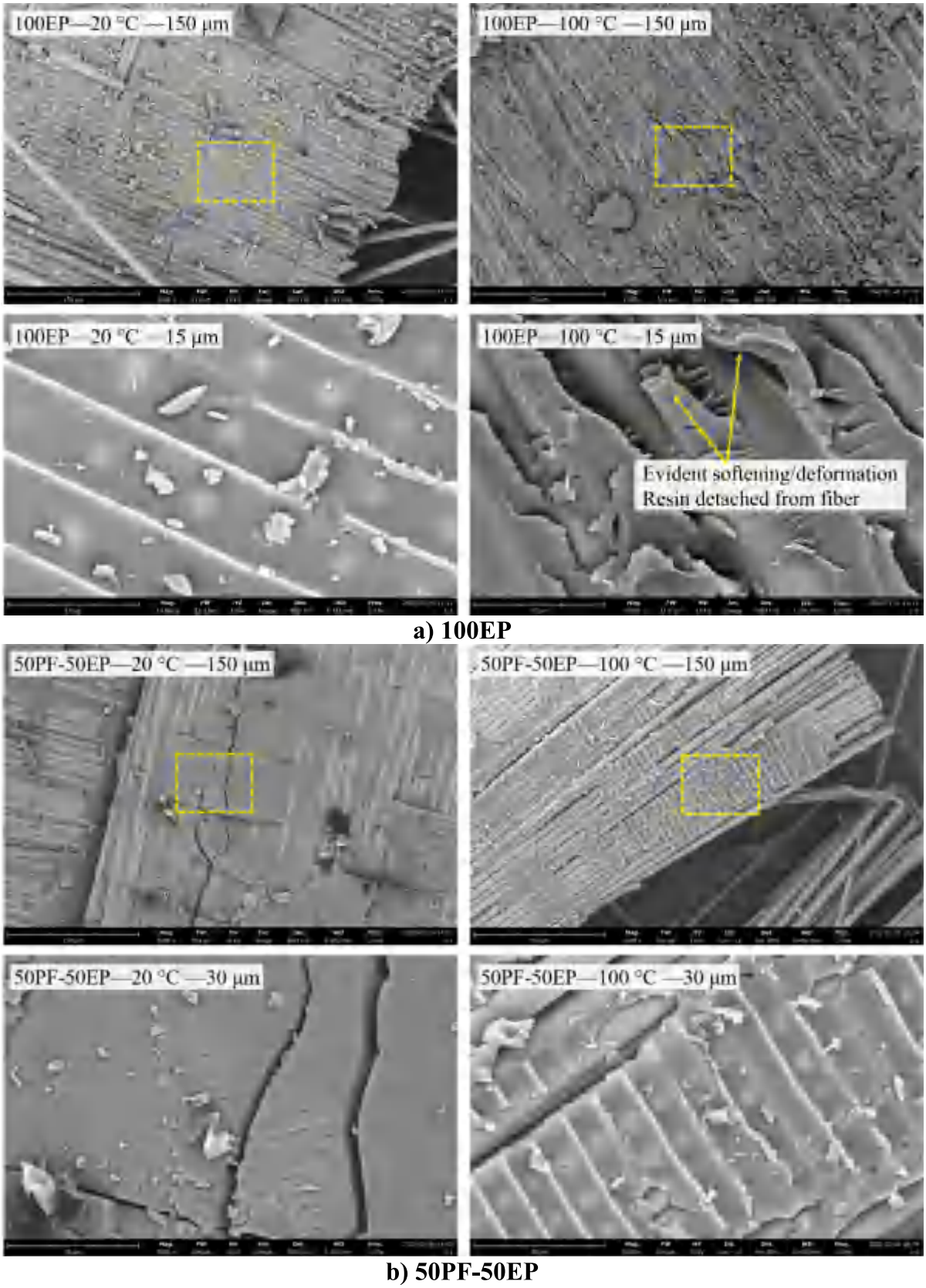
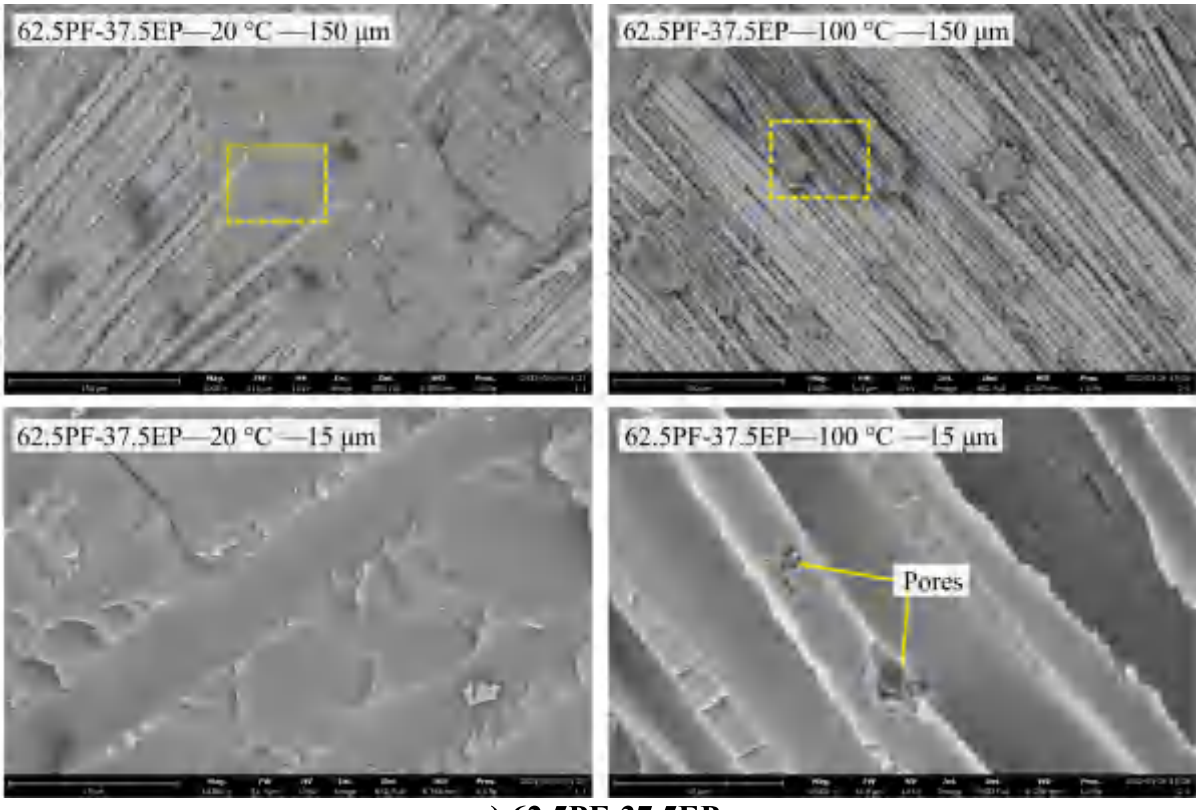
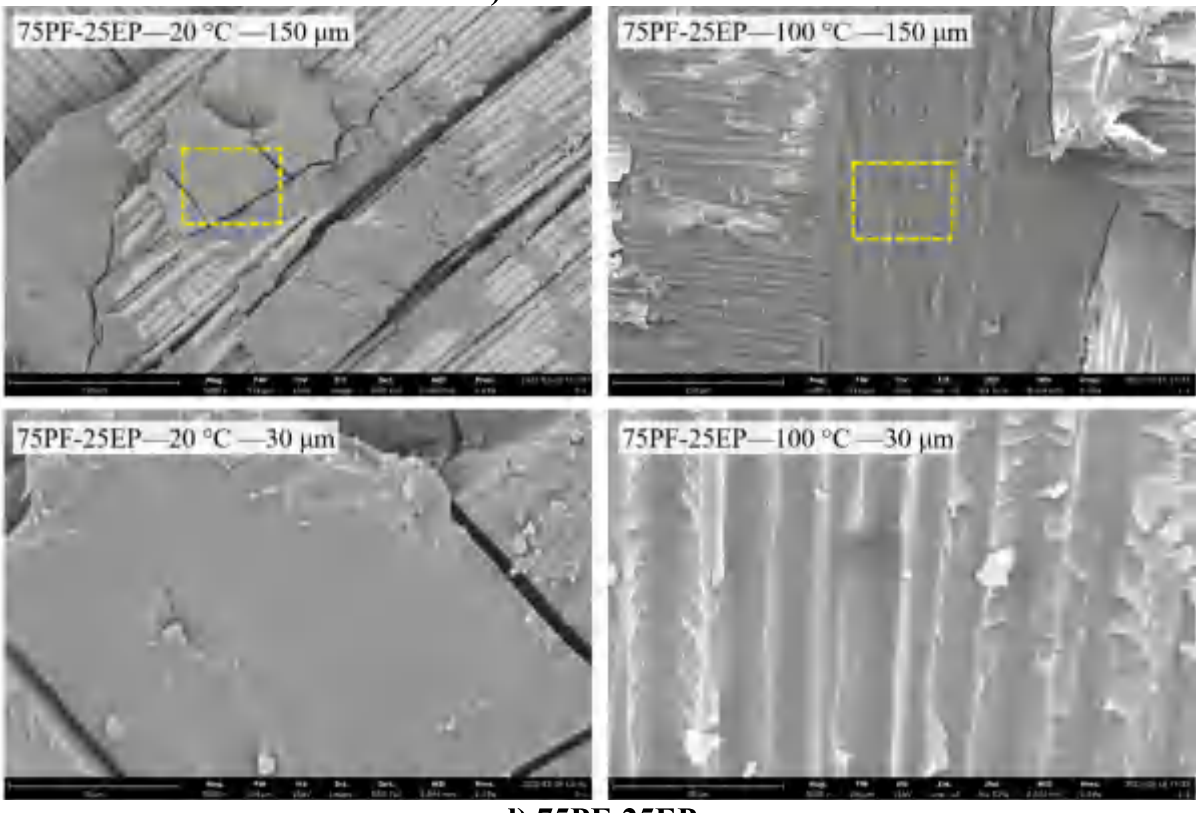


Fig. 8. SEM photos of FRP plates tested at 20 and 100 °C.

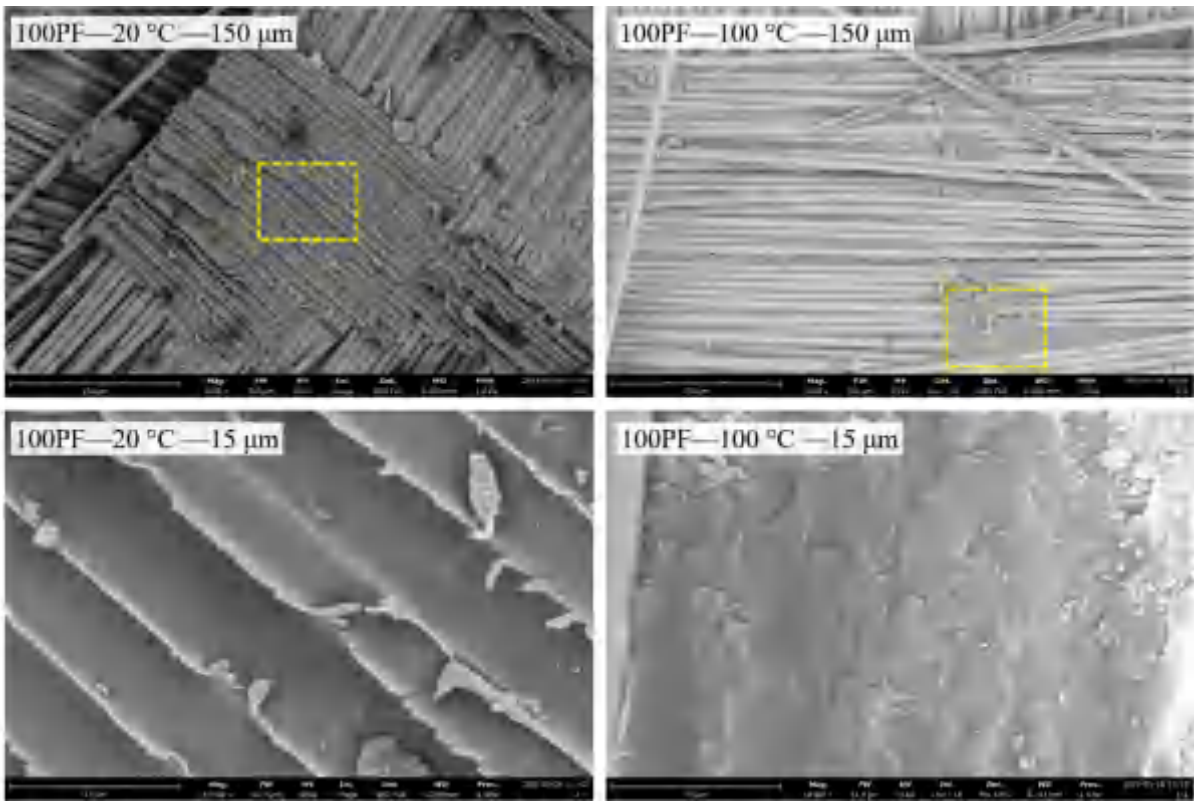


c) 62.5PF-37.5EP



d) 75PF-25EP

Fig. 8. (*continued*).



e) 100PF

Fig. 8. (*continued*).

The binary resin systems were observed to enhance the initial mechanical properties of FRP composites at room temperature. When compared to control specimen made with pure EP resin, the binary resin system (50PF-50EP, for instance) could increase the resin-dominated properties by up to 29% for compressive modulus and 62% for compressive strength; and note that specimens 100EP and 50PF-50EP have almost the same fiber content, namely 73% and 74%. The enhanced mechanical properties are attributed to the cross-linking occurred between EP and PF resins.

5. Conclusions

In this work, a binary resin system combing epoxy and phenol–formaldehyde was proposed for improving the thermo-mechanical behavior of FRP composites. Five types of FRP plates with varying resin recipes were fabricated through compression molding process. A series of experimental tests were conducted to evaluate the thermal and thermo-mechanical behaviors of FRPs. Following conclusions can be drawn from this work.

First, the proposed binary resin system is a chemically feasible and practically workable method to improve the thermal behavior of FRP composites. Compared with control specimen 100EP, the glass transition temperature was increased by up to 60% for binary resin system of 75PF-25EP. Increased thermal behavior greatly expanded the operating temperature range of FRP composites to be used in civil infrastructures. Fox equation is proposed as a quick and accurate method to calculate the resulting glass transition temperature of FRPs with binary resin system.

Second, the proposed binary resin system could also improve the mechanical properties of FRP composites. Compared with the control specimen 100EP, almost all binary resin-specimens show increased compressive strength, and tensile and compressive moduli at all temperatures. Compared with control specimen 100PF, all binary resin-specimens also show increased compressive strength at all temperatures as well as increased tensile and compressive moduli by up to 40 °C. The enhanced properties are mainly due to the improved molecular weight and structure formed in cross-linking reaction.

Last but not least, the third order polynomial function is recommended for predicting the thermo-mechanical behavior of FRP composites. Owing to its versatility, third order polynomial could satisfactorily simulate the FRPs at any states, including glassy state, rubbery state, and melting state. Third order polynomial is particularly effective for those materials servicing within their glass transition temperatures, and in this range, other methods such as hyperbolic tangent function might fail to provide accurate fitting.

CRediT authorship contribution statement

TianQiao Liu: Conceptualization, Formal analysis, Funding acquisition, Investigation, Methodology, Project administration, Writing – original draft. **Ruibao Wang:** Methodology, Visualization. **Shilong Zhen:** Methodology, Visualization. **Peng Feng:** Methodology, Writing – review & editing.

Declaration of Competing Interest

The authors declare that they have no known competing financial interests or personal relationships that could have appeared to influence the work reported in this paper.

Data availability

Data will be made available on request.

Acknowledgements

This research was supported by Nonmetallic Excellence and Innovation Center for Building Materials (No. 2022TDA1-1). The experimental tests were conducted at Beijing University of Technology and Chongqing Polycomp International Corporation (CPIC). The authors sincerely thank Ms. Zhong Hai (CPIC) and Ms. Wang QiuPing (CPIC) for their assistance with the thermo-mechanical tests. The authors also thank Mr. Jia ChenHui (Beijing Composite Materials Co., Ltd.) for his advice on mechanism of chemical reactions. The authors also thank Shaanxi Taihang Fire Retardant Polymer Co., Ltd for their help with material fabrication.

Appendix A. Supplementary data

Supplementary data to this article can be found online at https://doi.org/10.1016/j.conbuildmat.2023.131790.

References

[1] L.C. Hollaway, A review of the present and future utilisation of FRP composites in the civil infrastructure with reference to their important in-service properties, Constr. Build. Mater. 24 (12) (2010) 2419–2445.
[2] J.R. Cromwell, K.A. Harries, B.M. Shahrooz, Environmental durability of externally bonded FRP materials intended for repair of concrete structures, Constr. Build. Mater. 25 (5) (2011) 2528–2539.
[3] A. Vedernikov, A. Safonov, F. Tucci, P. Carlone, I. Akhatov, Pultruded materials and structures: a review, J. Compos. Mater. 54 (26) (2020) 4081–4117.
[4] Y. Yi, D. Zhu, M.Z. Rahman, G. Shuaicheng, S. Li, Z. Liu, C. Shi, Tensile properties deterioration of BFRP bars in simulated pore solution and real seawater sea sand concrete environment with varying alkalinities, Compos. B Eng. 243 (2022), 110115.
[5] J.-J. Zeng, Y. Zhuge, S.-D. Liang, Y.-L. Bai, J. Liao, L. Zhang, Durability assessment of PEN/PET FRP composites based on accelerated aging in alkaline solution/seawater with different temperatures, Constr. Build. Mater. 327 (2022) 126992.
[6] P. Mazzuca, J.P. Firmo, J.R. Correia, E. Castilho, Influence of elevated temperatures on the mechanical properties of glass fibre reinforced polymer laminates produced by vacuum infusion, Constr. Build. Mater. 345 (2022) 128340.
[7] S. Huang, E.V. Bachtiar, L. Yan, B. Kasal, Bond behaviour and thermal stability of flax/glass hybrid fibre reinforced polymer–timber structures connected by polyurethane, Constr. Build. Mater. 322 (2022) 126456.
[8] A.S. Azevedo, J.P. Firmo, J.R. Correia, C. Chastre, H. Biscaia, N. Franco, Fire behaviour of CFRP-strengthened RC slabs using different techniques–EBR, NSM and CREatE, Compos. B Eng. 230 (2022), 109471.
[9] T.Q. Liu, X. Liu, P. Feng, A comprehensive review on mechanical properties of pultruded FRP composites subjected to long-term environmental effects, Compos. B Eng. 191 (2020), 107958.
[10] T. Liu, Stability Behavior of Pultruded Glass-fiber Reinforced Polymer I-Sections Subject to Flexure, University of Pittsburgh, 2017. Doctoral dissertation.
[11] R. García-Domenech, J.V. de Julián-Ortiz, Prediction of indices of refraction and glass transition temperatures of linear polymers by using graph theoretical indices, J. Phys. Chem. B 106 (6) (2002) 1501–1507.
[12] W. Brostow, R. Chiu, I.M. Kalogeras, A. Vassilikou-Dova, Prediction of glass transition temperatures: binary blends and copolymers, Mater. Lett. 62 (17–18) (2008) 3152–3155.
[13] E.J. Bosze, A. Alawar, O. Bertschger, Y.I. Tsai, S.R. Nutt, High-temperature strength and storage modulus in unidirectional hybrid composites, Compos. Sci. Technol. 66 (13) (2006) 1963–1969.
[14] T.S. Chow, Molecular interpretation of the glass transition temperature of polymer-diluent systems, Macromolecules 13 (2) (1980) 362–364.
[15] J. Schut, D. Bolikal, I.J. Khan, A. Pesnell, A. Rege, R. Rojas, L. Sheihet, N.S. Murthy, M.J. Kohn, Glass transition temperature prediction of polymers through the mass-per-flexible-bond principle, Polymer 48 (20) (2007) 6115–6124.
[16] R.G.M. Van Der Sman, Predictions of glass transition temperature for hydrogen bonding biomaterials, J. Phys. Chem. B 117 (50) (2013) 16303–16313.
[17] W.S.W. DeRieux, Y. Li, P. Lin, J. Laskin, A. Laskin, A.K. Bertram, S.A. Nizkorodov, M. Shiraiwa, Predicting the glass transition temperature and viscosity of secondary organic material using molecular composition, Atmos. Chem. Phys. 18 (9) (2018) 6331–6351.
[18] C. Higuchi, D. Horvath, G. Marcou, K. Yoshizawa, A. Varnek, Prediction of the glass-transition temperatures of linear homo/heteropolymers and cross-linked epoxy resins, ACS Appl. Polymer Mater. 1 (6) (2019) 1430–1442.
[19] A.R. Katritzky, P. Rachwal, K.W. Law, M. Karelson, V.S. Lobanov, Prediction of polymer glass transition temperatures using a general quantitative structure–property relationship treatment, J. Chem. Inf. Comput. Sci. 36 (4) (1996) 879–884.
[20] P.C. Hiemenz, T.P. Lodge, Polymer Chemistry, CRC Press, 2007.
[21] ASTM D3039, Standard Test Method for Tensile Properties of Polymer Matrix Composite Materials, ASTM International, West Conshohocken, PA, 2014.
[22] ASTM D6641, Standard Test Method for Compressive Properties of Polymer Matrix Composite Materials Using a Combined Loading Compression (CLC) Test Fixture, ASTM International, West Conshohocken, PA, 2014.
[23] S.K. Foster, L.A. Bisby, Fire survivability of externally bonded FRP strengthening systems, J. Compos. Constr. 12 (5) (2008) 553–561.
[24] C.A. Mahieux, K.L. Reifsnider, S.W. Case, Property modeling across transition temperatures in PMC's: Part I. Tensile properties, Appl. Comp. Mater. 8 (4) (2001) 217–234.
[25] L.A. Bisby, Fire Behaviour of Fibre-Reinforced Polymer (FRP) Reinforced or Confined Concrete, Queen's University, Kingston, 2003.
[26] A.P. Kulcarni, R.F. Gibson. Non-destructive characterisation of effects of temperature and moisture on elastic moduli of vinyl ester resin and E-glass/vinyl ester resin composite. In Proceedings of the American Society of composites, 18th annual technical conference, Florida, 2003.
[27] A.G. Gibson, Y.S. Wu, J.T. Evans, A.P. Mouritz, Laminate theory analysis of composites under load in fire, J. Compos. Mater. 40 (7) (2006) 639–658.
[28] K. Wang, B. Young, S.T. Smith, Mechanical properties of pultruded carbon fibre-reinforced polymer (CFRP) plates at elevated temperatures, Eng. Struct. 33 (7) (2011) 2154–2161.
[29] P. Feng, J. Wang, Y. Tian, D. Loughery, Y. Wang, Mechanical behavior and design of FRP structural members at high and low service temperatures, J. Compos. Constr. 20 (5) (2016) 04016021.
[30] E.U. Chowdhury, R. Eedson, L.A. Bisby, M.F. Green, N. Benichou, Mechanical characterization of fibre reinforced polymers materials at high temperature, Fire Technol. 47 (4) (2011) 1063–1080.
[31] J.R. Correia, M.M. Gomes, J.M. Pires, F.A. Branco, Mechanical behaviour of pultruded glass fibre reinforced polymer composites at elevated temperature: experiments and model assessment, Compos. Struct. 98 (2013) 303–313.
[32] B. Yu, V. Kodur, Effect of temperature on strength and stiffness properties of near-surface mounted FRP reinforcement, Compos. B Eng. 58 (2014) 510–517.
[33] P.L. Nguyen, X.H. Vu, E. Ferrier, Characterization of pultruded carbon fibre reinforced polymer (P-CFRP) under two elevated temperature-mechanical load cases: residual and thermo-mechanical regimes, Constr. Build. Mater. 165 (2018) 395–412.

CICE2023 11TH INTERNATIONAL CONFERENCE ON FRP COMPOSITES IN CIVIL ENGINEERING

NON-LINEAR BEHAVIORS OF PULTRUDED GFRP COMPOSITES

TianQiao Liu, Beijing University of Technology, China, liu_tianqiao@bjut.edu.cn
Shilong Zhen, Beijing University of Technology, China, S202264059@emails.bjut.edu.cn
Ruibao Wang, Beijing University of Technology, China, 17861100522@emails.bjut.edu.cn

ABSTRACT
In this paper, the non-linear behaviors of pultruded glass fiber reinforced polymer (GFRP) composites were experimentally investigated. In particular, GFRP short columns and GFRP bolted connections were focused, aiming to evaluate the progressive failure of material in the manner of compression and shear failure. The obtained experimental observations demonstrated that the continued end-section crushing and shear-out failure could lead to the non-linear behaviors of GFRPs after reaching their peak loads. The non-linear behaviors of GFRP composites may be of great value for meeting the design requirement for extreme loading conditions.

KEYWORDS
Pultruded GFRP composites; Non-linear behaviors; Progressive failures; Short Columns; Bolted connections

INTRODUCTION

Pultruded glass fiber reinforced polymer (GFRP) composites have been increasingly adopted in the field of civil engineering worldwide (Vedernikov et al. 2020; Liu et al. 2021). Typical applications of pultruded GFRPs may include pedestrian bridges, cooling towers, wind turbine blades, photovoltaic supports, and many other frame structures (Hollaway 2010; Liu et al. 2020). Those applications, in general, are aimed to take advantages of GFRPs in terms of their high strength- and stiffness-to-weight ratios, excellent corrosion resistance, superior fatigue performance, etc. In civil engineering, the structural members or systems are often required to have certain ductile capacities, which, however, is a commonly-known weakness of pultruded GFRPs. Indeed, pultruded GFRPs are widely reported to behave in a linear-elastic manner up to failure, often in form of a sudden-brittle failure by reaching either strength or stability limit state (Guades et al. 2014; Liu et al. 2019). Evidently, this type of failure mode is not favored in practice, as it permits little time for emergence reaction. In this regard, enabling a 'non-linear' structural behavior for pultruded GFRP members or structures may potentially improve their applicability in the field.

In past decades, many studies have actually observed various extent of non-linearities in pultruded GFRPs. The earliest study may date back to 1990s when Mosallam and Bank (1992) conducted a static test on a 1.83-m-high by 2.74-m-wide portal frame constructed with pultruded GFRP I-sections. In this test, non-linear load-deflection and moment-rotation responses were identified, which were attributed to the progressive failure of GFRP profiles (including the connections) as well as local buckling of flexural member. Indeed, progressive failure/damage of material may have a significant impact on the overall structural behavior of GFRP members/structures. Such progressive failure is stemmed from the microscopic composition of GFRPs; that is, cracking in fiber and matrix may progressively propagate along certain directions, thus leading to non-linear behavior of pultruded GFRPs at macroscopic level (Fascetti et al. 2021; Zhu et al. 2023). For instance, a simple joint made with only pultruded GFRPs can exhibit a non-linear behavior, due to the inherent progressive damage of material (Qureshi et al. 2015). Additionally, pultruded GFRPs may exhibit non-linear load-displacement curves due to the progressive damage at web-flange junction when subjected to transverse tensile load (Zhu et al. 2023). Moreover, progressive failure can also be realized by certain structural configurations, such as the mortise-and-tenon joint for pultruded GFRP beams and concrete-filled GFRP columns (Feng et al. 2022). This joint was constructed with multiple types of materials with different mechanical properties and found to show a highly non-linear behavior in terms of the moment-rotation response.

The progressive failure of pultruded GFRPs may be determined by many factors. At microscopic level, the fiber volume fraction, resin matrix, and initial material imperfections (i.e., microcracks and voids)

could affect the progressive failure of GFRPs (Haj-Ali and Kilic 2002). In this case, mechanical properties of those GFRPs with low fiber volume fractions may be greatly controlled by the relatively soft resin matrix that tends to behave in a non-linear manner. On the other hand, at macroscopic level, the progressive failure of GFRPs typically becomes more prominent when subjected to high load/strain level (Xin et al. 2017; Zhang et al. 2018), compressive or shear force (Al-saadi et al. 2019), and/or off-axis loading condition (Haj-Ali and Kilic 2002; Zhang et al. 2018). The high load/strain level could facilitate the microcracks or voids to be further opened-up or closed-off; the compressive or shear strength of GFRPs is dominated by properties of matrix; and the off-axis loading condition could transition the fiber-dominant behavior to matrix-dominant behavior. In general, resin matrix is found to have a relatively greater impact on the non-linear behavior of GFRPs.

In this work, the non-linear behaviors of pultruded GFRP composites are focused with the purpose of further exploring their engineering applicability. Inspired by previous studies, structural behaviors of pultruded GFRP short columns and bolted connections are experimentally investigated, since it is the compressive and shear behaviors of GFRPs that have shown the most prominent non-linearities. In addition, this work adopts the latest pullwound GFRP composites with hybrid roving architectures, thus permitting further investigations on the effect of fiber-matrix architecture on the structural behaviors of GFRPs. Pullwinding process and pullwound GFRP box-sections are shown in Figure 1. A total of five types of GFRPs are addressed in this work, including four pullwound box-sections (denoted as Box-1, -2, -3, and -4), and one pultruded box-section (denoted as Box-5). The mechanical properties of all five GFRPs have been measured in the previous study of present authors, as shown in Table 1, and all the details regarding the materials can be seen in Liu et al. (2023).

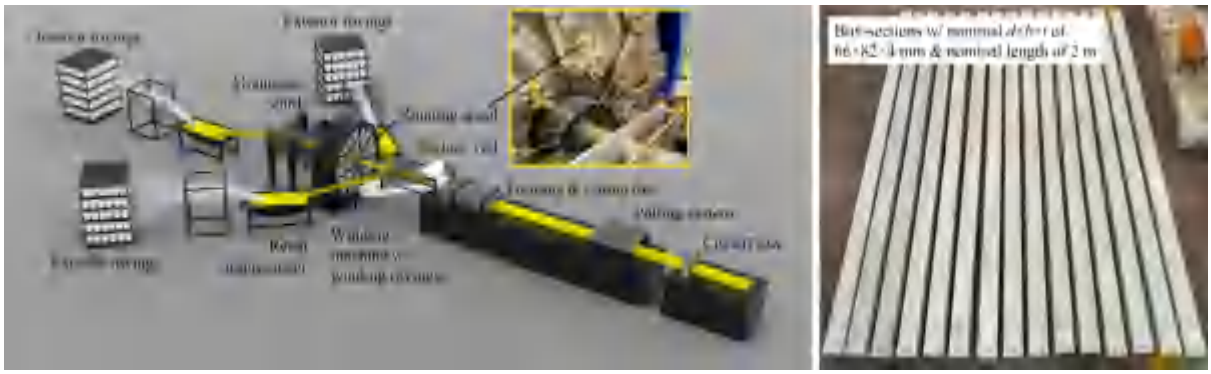


Figure 1: Pullwinding process and pullwound box-sections (Liu et al. 2023)

Table 1: Mechanical properties of pullwound and pultruded GFRP profiles (Liu et al. 2023)

Specimen	$V_{f,total}$	Winding Angle θ	Ratio of $V_{f,winding}$ to $V_{f,total}$	Experimentally- and analytically-determined mechanical properties (MPa)										
				E_{Lt}	F_{Lt}	E_{Lc}	F_{Lc}	E_{Tt}	F_{Tt}	E_{Tc}	F_{Tc}	G_{LT}	F_{LT}	v_{LT}
Box-1	54.5%	84°	11.6%	31983	669	44003	459	15091	117	43020	445	4855	75.8	0.31
Box-2	54.5%	84°	42.8%	23421	481	38254	382	20370	340	37044	386	3564	62.8	0.30
Box-3	54.5%	84°	43.4%	27642	523	37354	375	20472	345	41207	348	3578	57.4	0.28
Box-4	54.5%	72°	32.5%	24604	491	35133	307	14099	256	40268	428	4213	80.8	0.29
Box-5	54.5%	n.a. (pultruded)		34215	779	39755	437	13128	34	36474	421	4531	71.9	0.33

GFRP SHORT COLUMNS

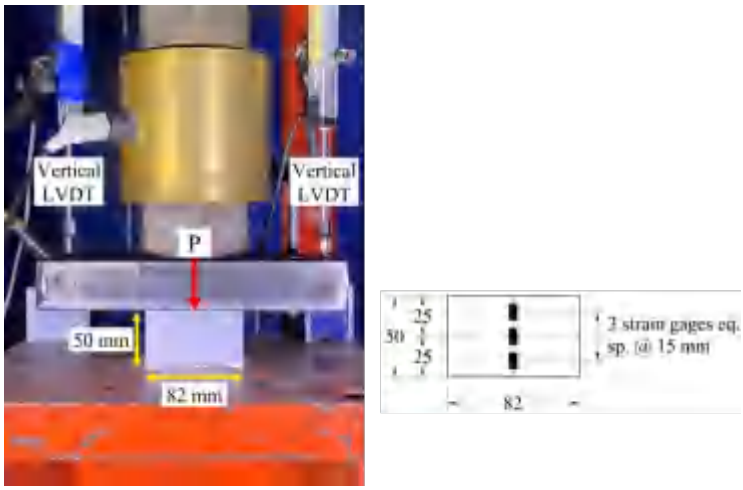
Materials and Test Set-Ups

The pullwound and pultruded GFRP short columns were made to have two types of heights, namely 50 and 400 mm, and they were both extracted from the intact part of those beams previously tested by present authors (Liu et al. 2023). The short column (SC) specimens were denoted as, for example, SC-50-1-1 for SC specimen with height of 50 mm, made of Box-1 material (see Table 1), and the first specimen of its type. The test set-ups of SC specimens are shown in Figure 2. A hydraulic jack with capacity of 1000 kN was used to apply the load to the top section of all SC specimens in the manner of displacement-control at a rate of 1 mm/min. During the tests, the ultimate failure of all specimens cannot be obtained within a rational deformation region (due to the progressive failure to be discussed in

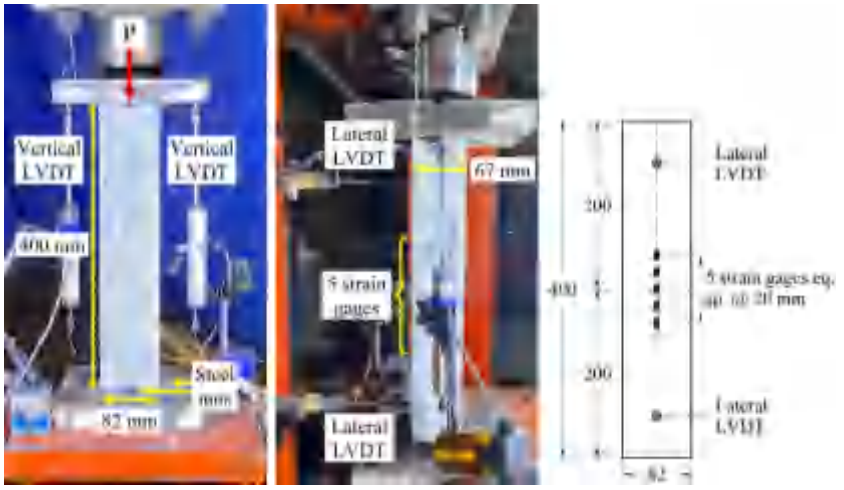
following sections), and thus, all SC-50 specimens were loaded to a vertical deformation of 5 mm (at least), and all SC-400 specimens were loaded to a vertical deformation of 10 mm (at least). When the pre-designated vertical deformation was reached, the test was manually stopped.

A total of 15 SC-50 specimens were tested, namely three identical tests for each type of materials (i.e., Box-1, -2, -3, -4, and -5, as shown in Table 1). The SC-50 specimens were placed directly in between of a steel platform and the steel loading plate, as shown in Figure 2a. Given the friction between GFRPs and steel plates, no lateral movements were observed at the top and bottom sections of specimens. Thus, the boundary conditions of SC-50 specimens can be deemed as fixed conditions at both ends, except that the top end is allowed to move downward. To monitor the vertical deformation of SC-50 specimen, two linear variable differential transformers (LVDT) were installed at the loading plates, denoted as vertical LVDTs, and the average values of those two LVDTs were taken as the vertical deformation of specimen. In addition, to monitor the strain changes during the tests, digital image correlation (DIC) was used focusing on the front web plate having nominal width of 82 mm, and three strain gages were installed at the opposite web plate, spaced at 15 mm at the center.

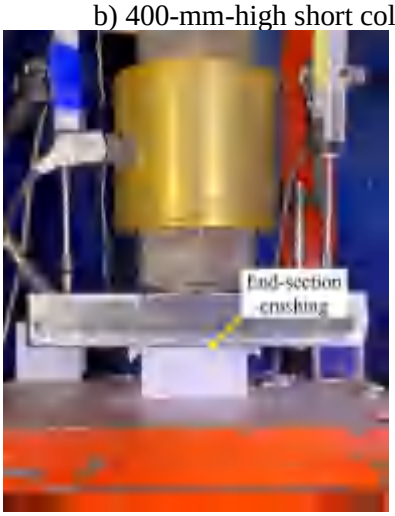
A total of 13 SC-400 specimens were tested, namely three identical tests for each type of materials except for Box-1 having only one specimen. For SC-400 specimens, eight steel nuts were welded at the bottom platform and the top loading plate (four nuts at each side), to restrain the possible lateral movements of specimen, as shown in Figure 2b. Therefore, the boundary conditions of SC-400 specimens were kept the same with those of SC-50 specimens. Similar to SC-50 specimens, two vertical LVDTs were installed at the top loading plate to monitor the vertical deformation of specimen, and DIC and strain gages were respectively installed at front and back web plates of specimen to monitor the strain changes. In addition, two lateral LVDTs were installed near the top and bottom sections of SC-400 specimen to monitor the possible lateral movements.



a) 50-mm-high short column test (denoted as SC-50 specimens)



b) 400-mm-high short column test (denoted as SC-400 specimens)









c) Failure modes of 50-mm-high column d) Failure modes of 400-mm-high column

Figure 2: Test set-ups and failure modes of short column specimens

Test Results of Short Columns

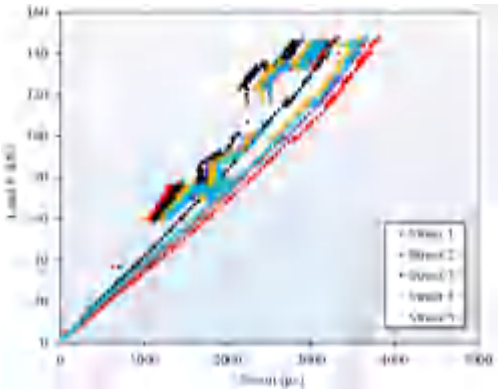
The failure modes of all SC-50 and -400 specimens are shown in Figures 2c and 2d, respectively, and the corresponding test results are presented in Table 2. In addition, the representative load-strain and load-lateral displacement curves of a SC-400 specimen are shown in Figure 3. From Figures 2c and 2d, it can be seen that all GFRP SC specimens failed due to end-section crushing. For relatively shorter specimens SC-50, excessive end-section crushing may also lead to damage of web plates at high load levels. On the other hand, for all SC-400 specimens, no damage was observed at web plates and only end-section crushing was observed. From Figure 3, the load-strain curves are linear until reaching the peak load P_{exp}, showing that there is no local buckling occurred during the test, and the load-lateral displacement curves show limited lateral displacements at both top and bottom ends of SC-400 specimen, with the greatest lateral displacement of 1.10 mm before reaching the peak load P_{exp}. Thus,

both the strains and lateral displacements can demonstrate that buckling and lateral flexure were not occurred in this test, which further validates the dominant failure mode of end-section crushing (i.e., a strength limit state).

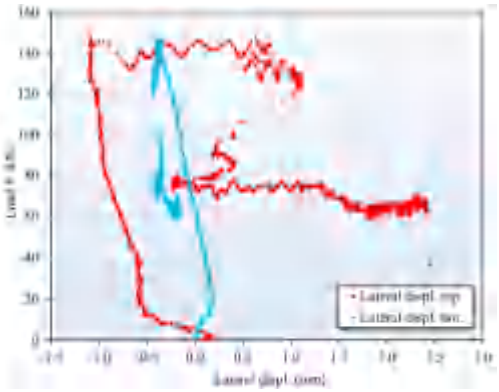
Table 2: Experimental results of short columns

Specimen	d (mm)	b (mm)	t (mm)	P_{exp} (kN)	Avg P_{exp} (kN) (COV)	Δ @ P_{exp} (mm)	Δ_{max} (mm)	$F_{Lc,exp}$ (MPa)	$F_{Lc,coupon}$ (MPa)	$F_{Lc,exp}$ / $F_{Lc,coupon}$	Avg $F_{Lc,exp}$ / $F_{Lc,coupon}$ (COV)
SC-50-1-1	67.80	82.38	4.79	199	184 (0.07)	1.40	7.21	148	459	0.32	0.30 (0.07)
SC-50-1-2				188		1.67	8.51	140		0.30	
SC-50-1-3				169		1.59	6.00	125		0.27	
SC-400-1-1				182		5.43	17.80	135		0.29	
SC-50-2-1	67.81	82.24	4.75	152	142 (0.07)	1.89	10.75	114	382	0.30	0.28 (0.07)
SC-50-2-2				130		2.70	10.03	97		0.25	
SC-50-2-3				154		1.71	8.14	115		0.30	
SC-400-2-1				145		3.34	17.01	109		0.28	
SC-400-2-2				135		3.86	16.61	101		0.26	
SC-400-2-3				134		3.91	19.48	100		0.26	
SC-50-3-1	67.56	82.32	4.82	127	139 (0.08)	1.63	9.20	94	375	0.25	0.27 (0.08)
SC-50-3-2				143		1.56	10.16	106		0.28	
SC-50-3-3				125		1.81	10.87	93		0.25	
SC-400-3-1				148		3.31	14.42	110		0.29	
SC-400-3-2				150		6.55	16.71	111		0.30	
SC-400-3-3				142		3.22	16.99	105		0.28	
SC-50-4-1	67.83	82.41	4.87	155	153 (0.06)	1.54	11.37	113	307	0.37	0.36 (0.06)
SC-50-4-2				147		1.78	11.27	108		0.35	
SC-50-4-3				148		1.77	12.72	108		0.35	
SC-400-4-1				147		3.02	17.69	108		0.35	
SC-400-4-2				125*		3.93	16.70	91		0.30	
SC-400-4-3				169		3.74	17.25	123		0.40	
SC-50-5-1	67.54	81.82	4.70	244	243 (0.03)	1.73	11.37	186	437	0.43	0.42 (0.03)
SC-50-5-2				242		1.55	11.48	184		0.42	
SC-50-5-3				252		1.47	11.79	192		0.44	
SC-400-5-1				248		3.03	17.70	188		0.43	
SC-400-5-2				230		3.20	17.30	175		0.40	
SC-400-5-3				239		3.16	14.49	182		0.42	

* This data is deemed as an outlier, and thus, is removed.



a) Load-strain curves

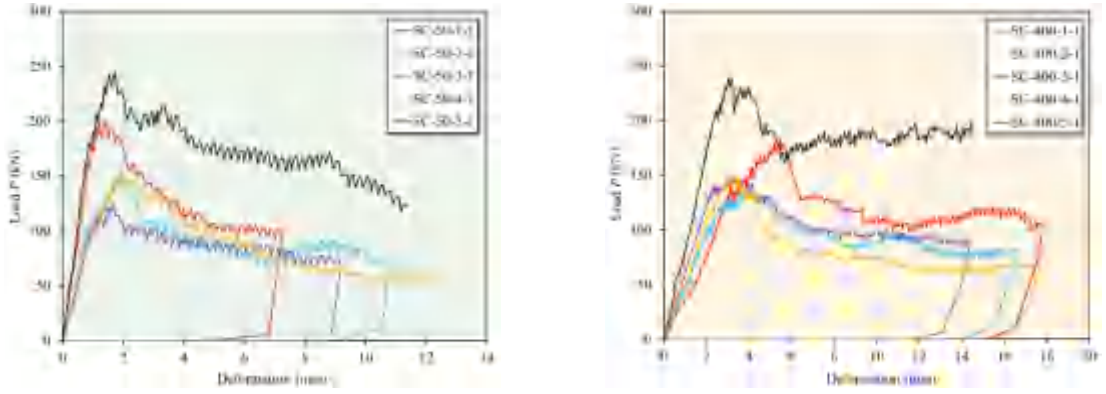


a) Load-lateral displacement curves

Figure 3: Representative load-strain and load-lateral displacement curves of short column specimen (SC-400-4-1)

From Table 2, it is seen that the coefficients of variance (COV) of the average strength P_{exp} of SC-50 and SC-400 specimens are all less than 0.10, showing a good consistency between the SC specimens with two heights. Moreover, the compressive strength of those specimens made with Box-5 material is the highest, namely 243 kN, which is followed by Box-1 of 184 kN, Box-4 of 153 kN, Box-2 of 142 kN, and Box-3 of 139 kN. Such a trend actually does not agree with the longitudinal compressive strength $F_{Lc,coupon}$ measured from small-scale coupon tests. Additionally, the compressive strength of five types of materials were calculated based on experimental results of short columns, denoted as $F_{Lc,exp}$ in Table 2. It is seen that the values of $F_{Lc,exp}$ are only about 0.27~0.42 of $F_{Lc,coupon}$. Evidently, there is a discrepancy between the material strength measured at coupon level and that measured at structural member level. It is noted that Wu et al. (2022) recently reported a similar discrepancy, with strength ratio of 0.37. The influential factors to this issue might include the local stress concentration and material imperfections (Wu et al. 2022), which, from another angle, can be considered as a scale effect between coupons and structural members.

The representative load-deformation curves of specimens SC-50 and SC-400 are shown in Figure 4. All the load-deformation curves are generally linear until reaching their peak loads. Then, the loads dropped by about 18~31%, and after the sudden drop, the loads were able to be maintained at a relatively high level, though they were gradually decreasing. With the failure mode of end-section crushing identified, it can be concluded that it is the progressive failure of material, in the manner of compression failure, led to the non-linear behavior of GFRP short columns after their peak loads. The high non-linearity of GFRP short columns observed in this work is different from those GFRP short columns reported by Alajarmeh et al. (2021) and Aksoylu et al. (2022), in which only the linear-elastic behavior with sudden brittle failure was observed.



a) 50-mm-high short column b) 400-mm-high short column

Figure 4: Representative load-deformation curves of short column tests

GFRP BOLTED CONNECTIONS

Materials and Test Set-Ups

The structural behaviors of pullwound and pultruded GFRP bolted connections (BC) were investigated following ASTM D5961 (2017). A total of two types of BC specimens were fabricated, with the first one fabricated following the standard coupon of ASTM D5961, denoted as BC-plate specimens, and the second one designed by present authors based on ASTM D5961, denoted as BC-box specimens. A total of 15 BC-plate specimens were tested, with three identical tests for each type of materials (i.e., Box-1, -2, -3, -4 and -5, as shown in Table 1), and a total of 24 tests were conducted on 12 BC-box specimens, and each box specimen was tested twice, each at one web plate having nominal width of 82 mm. Test set-ups are shown in Figure 5. All BC specimens were single bolted with 6-mm-diamter steel bolt fastened by a torque of 7 N·m. An MTS universal testing machine with capacity of 300 kN was used to apply the tensile load to the bolted connection in the manner of displacement-control at a rate of 2 mm/min. DIC was used to monitor the strain change around the bolt. The pullwound composites

have winding rovings placed close to transverse direction, which is expected to be able to improve the shear strength of bolted connections; nonetheless, the winding roving layer is found not in good contact with the longitudinal rovings, as reported by Liu et al. (2023). With that being said, the small-scale BC-plate specimen having standard width of 36 mm would cut off the winding rovings, and the winding roving layer may be pulled off from the coupon in the tests, compromising the shear strength of pullwound composites. In this regard, BC-box specimens were fabricated, with one side having a single bolt (i.e., test region) and the other side having four bolts (i.e., grip region). This BC-box specimen has winding rovings going around all the four web plates, and presumably, the winding rovings cannot be easily pulled off from the section, thus ensuring the expected shear strength of pullwound composites. In addition, all tests were manually stopped when reaching the vertical deformation of 5 mm (at least) (measured by loading machine) for BC-plate specimens and 10 mm (at least) for BC-box specimens.



a) Plate specimen (denoted as BC-plate)



b) Box specimen (denoted as BC-box)

Figure 5: Test set-ups of bolted connections

Test Results of Bolted Connections

The typical failure modes of BC-plate specimens are shown in Figure 6. It can be seen that for BC-plate specimens the shear-out failure is the dominant failure mode, and for pullwound specimens—BC-plate-1, BC-plate-3, and BC-plate-4—winding rovings were pulled out from the specimens simultaneously with the shear-out of longitudinal rovings, which agrees with the findings from previous work of authors that winding rovings are not in good contact with longitudinal rovings due to the lack of resin at the interface. Provided the winding rovings were pulled out, the shear strength of pullwound composites is compromised.

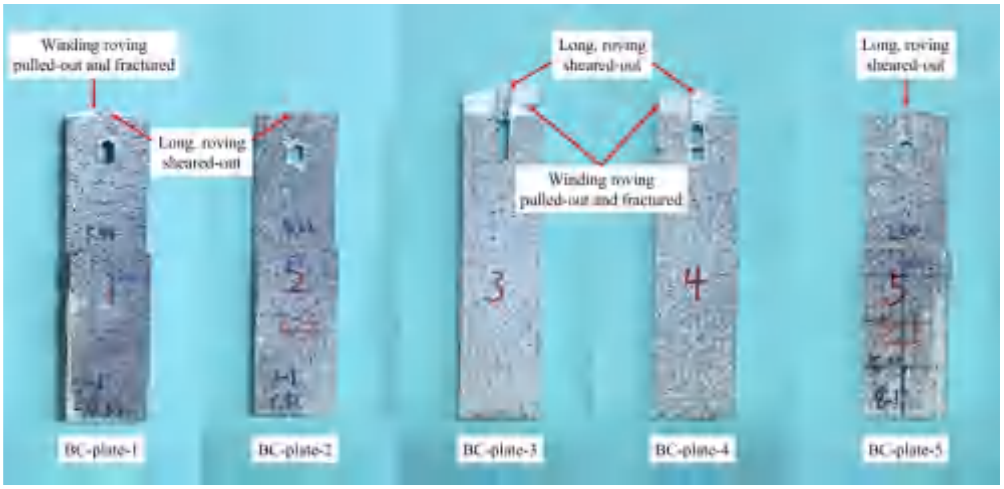
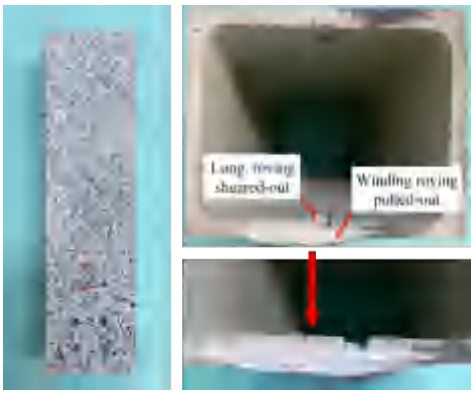


Figure 6: Typical failure modes of BC-plate specimens

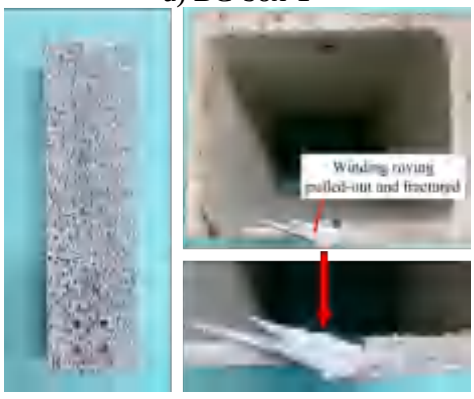
The typical failure modes of BC-box specimens are shown in Figure 7. It is observed that the longitudinal rovings first sheared out from sections, meanwhile the winding rovings continued sustaining the load. Then, winding rovings were gradually pulled out from the section. For BC-box specimens, the interface failure between different roving layers is not as prominent as that occurred for BC-plate specimens. In fact, for BC-box specimens the pull-out of winding rovings occurred after the shear-out of longitudinal rovings, and this can be evidenced by the length of pull-out and shear-out exhibited in Figures 6 and 7. In Figure 6, the length of pull-out of winding rovings and shear-out of longitudinal rovings are almost the same (see BC-plate-3 and BC-plate-4 in Figure 6), while in Figure 7, the length of shear-out is greater than that of pull-out (see BC-box-1 in Figure 7). Thus, winding rovings enabled an improved shear strength of GFRP bolted connections.



a) BC-box-1



b) BC-box-2



c) BC-box-3



d) BC-box-4



e) BC-box-5

Figure7: Typical failure modes of BC-box specimens

Test results of all BC-plate and BC-box specimens are shown in Table 3. It is noted that the thickness *t* of plates under investigation are slightly different from one to another. Despite of having different plate thickness, it is seen that all BC-box specimens have higher shear-out strength $R_{sh,exp}$ than their corresponding BC-plate specimens, except for one case of BC-plate-1 and BC-box-1. Given the same geometry of bolted connection, such an increase in shear strength can be attributed to the effective winding rovings.

Table3: Experimental results of bolted connections

Specimen	Thickness *t* (mm)	$R_{sh,exp}$ (kN)	Avg. $R_{sh,exp}$ (kN) (COV)	$F_{LT,coupon}$ (MPa)	$R_{sh,pred}$ (kN)	$R_{sh,pred}$ / $R_{sh,exp}$
BC-plate-1-1	4.79	8.26	7.97 (0.04)	75.8	7.62	0.92
BC-plate-1-2	5.39	7.97			8.58	1.08
BC-plate-1-3	4.58	7.67			7.29	0.95
BC-box-1-1a	5.30	6.81	7.06 (n.a.)		8.44	1.24
BC-box-1-1b	4.90	7.30			7.80	1.07
BC-plate-2-1	4.22	5.20	5.49 (0.05)	62.8	5.57	1.07
BC-plate-2-2	5.70	5.48			7.52	1.37
BC-plate-2-3	5.89	5.78			7.77	1.34
BC-box-2-1a	4.40	4.15*	6.90 (0.16)		-	-
BC-box-2-1b	5.60	1.09*			-	-
BC-box-2-2a	5.30	6.16			6.99	1.14
BC-box-2-2b	4.70	7.40			6.20	0.84
BC-box-2-3a	5.20	8.24			6.86	0.83
BC-box-2-3b	4.10	5.79			5.41	0.93
BC-plate-3-1	4.77	5.89	5.49 (0.07)	57.4	5.75	0.98
BC-plate-3-2	4.56	5.41			6.77	1.25
BC-plate-3-3	4.33	5.17			5.22	1.01
BC-box-3-1a	6.20	8.59	7.95 (0.14)		7.47	0.87
BC-box-3-1b	4.80	3.04*			-	-
BC-box-3-2a	5.50	6.71			6.63	0.99
BC-box-3-2b	5.00	8.56			6.03	0.70
BC-plate-4-1	4.55	8.20	8.69 (0.05)	80.8	7.72	0.94
BC-plate-4-2	5.04	9.16			8.55	0.93
BC-plate-4-3	4.35	8.71			7.38	0.85

Specimen	Thickness t (mm)	$R_{sh,exp}$ (kN)	Avg. $R_{sh,exp}$ (kN) (COV)	$F_{LT,coupon}$ (MPa)	$R_{sh,pred}$ (kN)	$R_{sh,pred}$ / $R_{sh,exp}$
BC-box-4-1a	5.40	10.45	11.04 (0.09)		9.16	0.88
BC-box-4-1b	5.00	8.28*			-	-
BC-box-4-2a	4.60	11.45			7.81	0.68
BC-box-4-2b	5.00	12.25			8.48	0.69
BC-box-4-3a	5.40	10.03			9.16	0.91
BC-box-4-3b	5.40	8.58*			-	-
BC-plate-5-1	5.33	7.47	7.16 (0.07)	71.9	8.05	1.08
BC-plate-5-2	5.27	7.40			7.96	1.08
BC-plate-5-3	5.24	6.61			7.91	1.20
BC-box-5-1a	5.40	10.00	9.46 (0.09)		8.15	0.82
BC-box-5-1b	4.60	8.79			6.95	0.79
BC-box-5-2a	5.50	9.93			8.30	0.84
BC-box-5-2b	5.50	10.69			8.30	0.78
BC-box-5-3a	5.60	8.51			8.46	0.99
BC-box-5-3b	4.30	8.85			6.49	0.73

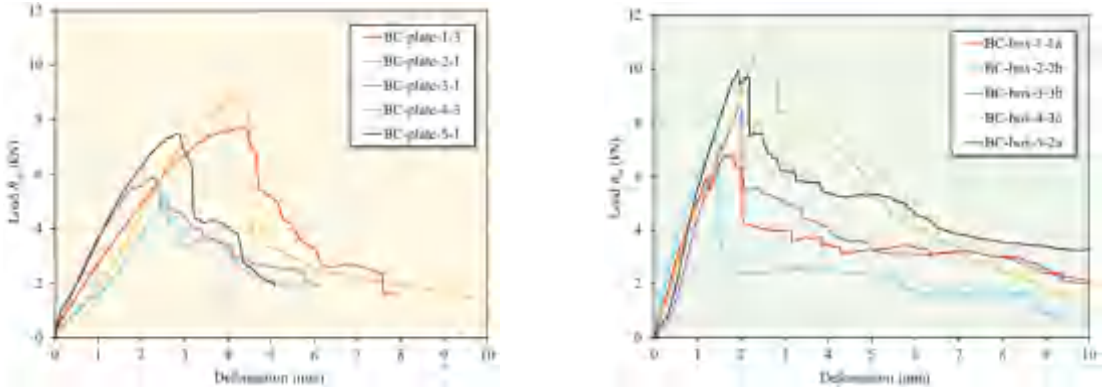
* This data is deemed as an outlier, and thus, is removed.

In addition, the shear-out strength R_{sh} of all BC specimens are calculated according to ASCE (2010), as shown in Eq. 1, and the predicted $R_{sh,pred}$ are shown in Table 3.

$$R_{sh} = 1.4\left(e_1 - \frac{d_n}{2}\right) tF_{LT} \quad \text{Eq. 1}$$

Where e_1 is the end distance, in this case e_1 = 18 mm; d_n is the nominal hole diameter, in this case d_n = 6 mm; t is the plate thickness; and F_{LT} is the in-plane shear strength of GFRP.

Figure 8 shows the representative load-deformation curves of BC-plate and BC-box specimens. It can be seen that all BC specimens exhibit a linear-elastic behavior until the peak loads. Then, the load suddenly dropped due to the partial shear-out of longitudinal rovings. With the cracks continued propagating, the loads continued decreasing; nonetheless, specimens BC-box-1, BC-box-2, BC-box-3 and BC-box-5 were able to maintain their loads for relatively high deformations. The progressive failure of GFRPs, in the manner of shear failure, actually enabled the non-linear behavior of GFRP bolted connections (Feng et al. 2021).



a) BC-plate specimens b) BC-box specimens

Figure 8: Representative load-deformation curves of bolted connections

DISCUSSIONS

This paper is aimed to report the experimental program of an ongoing work on non-linear behavior of pultruded GFRP composites. Corresponding analytical and numerical programs are to be conducted. Based on the experimental observations reported in this paper, it can be concluded that pultruded GFRP members, at macroscope level, could exhibit various extent of non-linearities when subjected to compression or shear force. Such a non-linear behavior is believed to be resulted from the synergistic effect of fiber-matrix architecture, fiber volume fractions, loading conditions, plate slenderness ratios, and material initial imperfections. In order to quantify the effect of each above factor, comprehensive numerical program must be conducted.

Existing design guides, such as ASCE (2010), EUR27666 (2016), CECS-692 (2020), have generally prescribed pultruded GFRP profiles as a linear-elastic material with brittle failure mode. Undoubtedly, this method is to yield conservative designs, whereas it has been greatly limiting the possible applications of this type of material. In many scenarios, steel structures are designed only allowing the linear-elastic behavior of material, and the plasticity is only designed for extreme loading conditions, such as high-degree earthquakes. Following the design philosophy of steel, the non-linear behavior of pultruded GFRPs may be of great potential for meeting the requirement for extreme loading conditions, though pultruded GFRPs are still designed with their linear-elastic properties for normal conditions. To achieve this goal, a number of experimental data is needed to support the development of design methods.

GFRP structural profiles, to date, can be manufactured with various techniques other than pultrusion, such as pullbraiding (Lebel and Nakai 2012), pullwinding (Liu et al. 2023), and curved-pultrusion (Liu et al. 2021). Through these techniques, hybrid roving architecture and non-linear structural geometry can be readily realized, both of which might permit non-linear behaviors of GFRP structures. Nonetheless, little work has been done on those new GFRP structural members as compared to the conventional pultruded GFRP profiles.

CONCLUSIONS

In this paper, the non-linear behaviors of pultruded GFRP composites were investigated through two series of experimental tests, one on GFRP short columns and the other one on GFRP bolted connections. These two experimental tests were designed to evaluate the progressive failure of GFRPs in the manner of compression and shear failure. Based on the experimental observations, the continued end-section crushing and shear-out failure could lead to the non-linear behaviors of GFRPs after reaching their peak loads, thus enabling high extent of deformation capacities (i.e., also known as the quasi-plastic behaviors). The observed non-linear behaviors of GFRP composites may be able to meet the requirement for structural members subjected to extreme loading conditions, which would greatly expand the possible applications of GFRP composites.

CITATIONS

Aksoylu, C., Özkılıç, Y. O., Madenci, E., Safonov, A. (2022). Compressive behavior of pultruded GFRP boxes with concentric openings strengthened by different composite wrappings. *Polymers*, 14(19), 4095.

Alajarmeh, O., Zeng, X., Aravinthan, T., Shelley, T., Alhawamdeh, M., Mohammed, A., Nicol, L., Vedernikov, A., Safonov, A., Schubel, P. (2021). Compressive behaviour of hollow box pultruded FRP columns with continuous-wound fibres. *Thin-Walled Structures*, 168, 108300.

Al-Saadi, A. U., Aravinthan, T., Lokuge, W. (2019). Effects of fibre orientation and layup on the mechanical properties of the pultruded glass fibre reinforced polymer tubes. *Engineering Structures*, 198, 109448.

American Society of Civil Engineers. (ASCE). (2010). *Pre-Standard for Load and Resistance Factor Design (LRFD) of Pultruded Fiber Reinforced Polymer (FRP) Structures*.

ASTM D5961. (2017). *Standard Test Method for Bearing Response of Polymer Matrix Composite Laminates*. ASTM International, West Conshohocken, PA.

China Association for Engineering Construction Standardization (CECS). (2020). *Technical specification for pultruded fiber reinforced polymer composite structure*, CECS-692. (In Chinese)

EUR27666. (2016). *Prospect for new guidance in the design of FRP* (Ascione, L., Caron, J. F., Godonou, P., Van IJselmuijden, K., Knippers, J., Mottram, T., Oppe, M., Gantriis Sorensen, M., Taby, J., Tromp, L.), Publications Office of the European Union.

Fascetti, A., Feo, L., Abbaszadeh, H. (2021). A critical review of numerical methods for the simulation of pultruded fiber-reinforced structural elements. *Composite Structures*, 273, 114284.

Feng, P., Wu, Y., Ding, Y., Liu, T. Q., Tian, Y. (2021). Quasi-plastic flexural behavior of adhesive-bolt hybrid connection for large scale pultruded GFRP frame. *Engineering Structures*, 238, 112200

Feng, P., Li, Z., Wang, J., Liu, T. (2022). Novel joint for pultruded FRP beams and concrete-filled FRP columns: Conceptual and experimental investigations. *Composite Structures*, 287, 115339.

Guades, E., Aravinthan, T., Islam, M. M. (2014). Characterisation of the mechanical properties of pultruded fibre-reinforced polymer tube. *Materials & Design*, 63, 305-315.

Haj-Ali, R., Kilic, H. (2002). Nonlinear behavior of pultruded FRP composites. *Composites Part B: Engineering*, 33(3), 173-191.

Hollaway, L. C. (2010). A review of the present and future utilisation of FRP composites in the civil infrastructure with reference to their important in-service properties. *Construction and Building Materials*, 24(12), 2419-2445.

Lebel, L. L., Nakai, A. (2012). Design and manufacturing of an L-shaped thermoplastic composite beam by braid-trusion. *Composites Part A: Applied Science and Manufacturing*, 43(10), 1717-1729.

Liu, T. Q., Feng, P., Tang, J., Liu, X. (2023). Pullwinding Technique for Realizing Hybrid Roving Architecture in Pultruded GFRP Composites. Composite Structures, 305, 116483.

Liu, T. Q., Feng, P., Wu, Y., Liao, S., Meng, X. (2021). Developing an innovative curved-pultruded large-scale GFRP arch beam. *Composite Structures*, 256, 113111.

Liu, T. Q., Liu, X., Feng, P. (2020). A Comprehensive Review on Mechanical Properties of Pultruded FRP Composites Subjected to Long-Term Environmental Effects. *Composites Part B: Engineering*, 191, 107958.

Liu, T. Q., Vieira, J. D., Harries, K. A. (2019). Lateral torsional buckling and section distortion of pultruded GFRP I-sections subject to flexure. *Composite Structures*, 225, 111151.

Mosallam, A. S., Bank, L. C. (1992). Short-term behavior of pultruded fiber-reinforced plastic frame. *Journal of Structural Engineering*, 118(7), 1937-1954.

Qureshi, J., Mottram, J. T., Zafari, B. (2015). Robustness of simple joints in pultruded FRP frames. *Structures*, 3, 120-129.

Vedernikov, A., Safonov, A., Tucci, F., Carlone, P., Akhatov, I. (2020). Pultruded materials and structures: A review. *Journal of Composite Materials*, 0021998320922894.

Wu, C., Tian, J., Ding, Y., Feng, P. (2022). Axial compression behavior of pultruded GFRP channel sections. *Composite Structures*, 289, 115438.

Xin, H., Mosallam, A., Liu, Y., Wang, C., Zhang, Y. (2017). Analytical and experimental evaluation of flexural behavior of FRP pultruded composite profiles for bridge deck structural design. *Construction and Building Materials*, 150, 123-149.

Zhang, S., Caprani, C., Heidarpour, A. (2018). Influence of fibre orientation on pultruded GFRP material properties. *Composite Structures*, 204, 368-377.

Zhu, Y., Fascetti, A., Feo, L., Mosallam, A. S., Penna, R. (2023). Experimental and numerical characterization of pultruded GFRP structural elements with stiffened Web-Flange junctions. *Composite Structures*, 303, 116383.

ACKNOWLEDGEMENT

This work was supported by Nonmetallic Excellence and Innovation Center for Building Materials (No. 2022TDA1-1).

CONFLICT OF INTEREST

The authors declare that they have no conflicts of interest associated with the work presented in this paper.

DATA AVAILABILITY

Data on which this paper is based is available from the authors upon reasonable request.

Engineering Structures 308 (2024) 117962



Contents lists available at ScienceDirect

Engineering Structures

journal homepage: www.elsevier.com/locate/engstruct



Flexural performance of curved-pultruded GFRP arch beams subjected to varying boundary conditions

TianQiao Liu [a,b,*], Peng Feng [c], Yulei Bai [a,b], Shangcong Bai [a], Jia-Qi Yang [d], Fei Zhao [e]

[a] Department of Civil Engineering, Beijing University of Technology, Beijing, China
[b] State Key Laboratory of Bridge Engineering Safety and Resilience, Beijing University of Technology, Beijing, China
[c] Department of Civil Engineering, Tsinghua University, Beijing, China
[d] School of mechanics and civil engineering, China university of Mining and Technology, Beijing, China
[e] School of Civil Engineering and Architecture, Hainan University, Haikou, China

ARTICLE INFO

Keywords:
Curved-Pultruded GFRP Arch Beam
Beam-String Structure
Flexural Performance
Progressive Failure
Web Crippling Behavior

ABSTRACT

The low stiffness of pultruded glass fiber reinforced polymer (pGFRP) flexural members has been one of the main issues limiting their possible applications ever since this type of material was invented. In this regard, curved-pultrusion technique is adopted in this work to produce GFRP arch beams, and a new GFRP beam-string structure is proposed. Specifically, experimental, numerical, and analytical programs were conducted to investigate the flexural performance of curved-pultruded GFRP arch beams subjected to varying boundary conditions. The flexural strength and stiffness were successfully enhanced by up to 27% and 109%, respectively, which was attributed to the arch mechanism enabled by proposed GFRP beam-string structure. In addition, the progressive failure of GFRP material and the imperfect load-transfer between GFRP arch beam and tension string were investigated through finite element modeling. Then, web crippling strength of GFRP arch beams was predicted with modifications to an existing model, and internal forces of beam-string were analyzed. The GFRP beam-string structure proposed in this work effectively sheds light on possible approach to improve the flexural stiffness of pGFRP members, and with successful demonstration of this work, it is rationally believed that possible applications of curved-pultruded GFRP members can be greatly broadened.

1. Introduction

Pultruded glass fiber reinforced polymer (pGFRP) composites have received an increasing number of interests from construction, automotive, and energy industries all over the world in past two decades [1–5]. Favorable features of pGFRPs that really impress the industries include the high strength- and stiffness-to-weight ratios, excellent corrosion resistance, and superior fatigue performance [6–9]. To date, one of the main issues limiting further applications of pGFRPs is the relatively low modulus of elasticity of material, which is often interpreted as the low stiffness when speaking of structural members. The low stiffness is typically manifested in two aspects, stability and deflection [10]. Stability behaviors (i.e., buckling) of pGFRP members have been extensively investigated by many researchers, and the stability limit state can be readily satisfied provided appropriate plate/member slenderness ratios and/or additional restraints [11–17]. On the other hand, deflection limit state is often found to be the dominant factor in practical design of pGFRP beams, since flexural members may suffer from excessive deflections under service loads [18].

Conventional pultrusion technique only permits straight profiles and enlarging the cross-sectional geometry might render the only approach to improve the flexural stiffness, if excluding the composite action by pGFRPs and other types of materials [19–24]. In this regard, the present authors [25] have proposed to adopt the curved-pultrusion technique to enable a camber in beams (see Fig. 1a), such that the adverse deflections can be mitigated and the clearance under beams can be ensured. Using curved-pultruded GFRP profiles, a pedestrian bridge spanning over 20 m has been designed and constructed in Beijing, China in 2021, as shown in Fig. 1b. The bridge consists of 20 I-beams, each having geometries of 600 × 200 × 20 × 15 mm (depth × width × flange thickness × web thickness). It is noted that the boundary condition of this bridge is close to simply-supported, and thus, the cambered pGFRP beam (referred to as curved-pultruded GFRP arch beam or short as GFRP arch beam in this work) behaves essentially in the same manner with a simply-supported

* Corresponding author at: Department of Civil Engineering, Beijing University of Technology, Beijing, China.
E-mail address: liu_tianqiao@bjut.edu.cn (T. Liu).

https://doi.org/10.1016/j.engstruct.2024.117962
Received 7 January 2023; Received in revised form 27 February 2024; Accepted 31 March 2024
0141-0296/© 2024 Elsevier Ltd. All rights reserved.

straight beam.

The most attractive feature of curved-pultruded GFRP profiles, from the perspective of authors, may lie in the possible arch mechanism and its excellent structural performance, especially the improved flexural stiffness. To enable the arch mechanism, in this work a pair of steel tension strings are introduced to curved-pultruded GFRP arch beam, thus making it a beam-string structure, as shown in Fig. 2. In available literature, a CFRP beam-string structure has been reported, which demonstrates an excellent structural efficiency in terms of strength-to-weight ratio [26]. With that said, the flexural performance of simply-supported GFRP arch beam (as control specimen) and the GFRP beam-string structures with varying tensions in strings are investigated. First, a series of experimental program is carried out with respect to 1) small-scale coupons for defining the mechanical properties of material and 2) large-scale beams for determining the flexural strength and stiffness of curved-pultruded GFRP arch beams. Second, finite element modeling is conducted to evaluate and validate the flexural behaviors of beams observed in experimental tests. Third, analytical program is conducted to calculate the ultimate strength as well as internal forces of GFRP arch beams. The GFRP beam-string structure proposed in this work successfully demonstrates an effective approach for enhancing the flexural stiffness as well as increasing the possible span length of pultruded GFRP beams/structures.

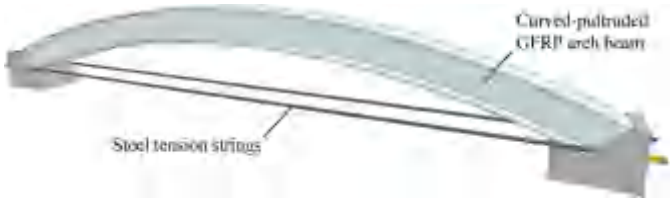
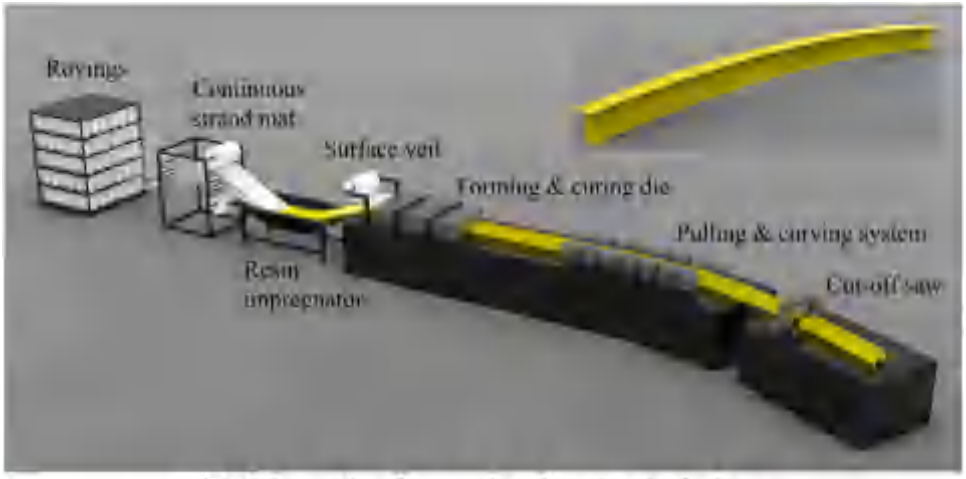


Fig. 2. Proposed GFRP beam-string structure.

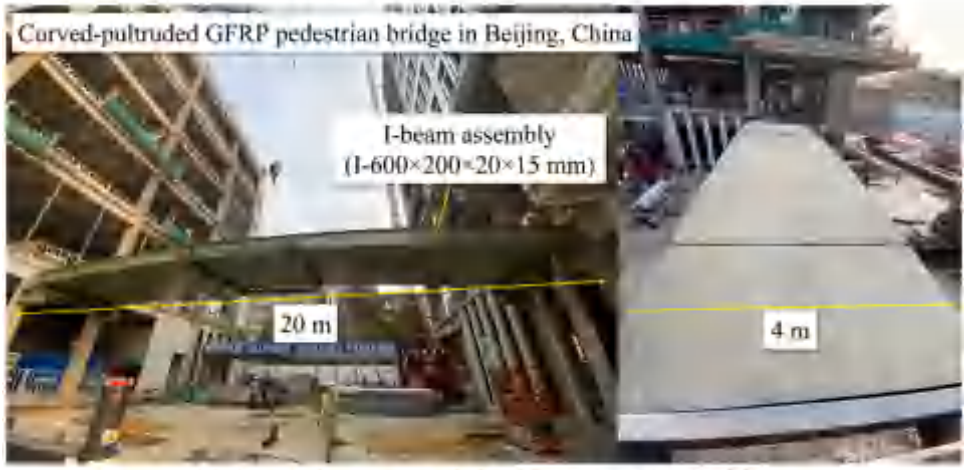
2. Experimental program

2.1. Materials

In this work, the curved-pultruded GFRP arch beams are in form of an I-section with geometries of 100 × 100 × 10 mm (depth × width × plate thickness), and they are manufactured by XingTai HongBang Composites Manufacturing Co., LTD., in China. The GFRP materials consist of E-glass fibers and epoxy resin. A series of material characterization tests were conducted to measure the mechanical properties and fiber volume fraction of material. ASTM standard tests as well as the standard coupon geometries were adopted, including D3039 [27] for tensile properties, D6641 [28] for compressive properties, D5379 [29] for in-plane shear properties, D7264 [30] for flexural properties, and D2584 [31] for fiber volume fraction. Those coupons were randomly extracted from top and bottom flanges. Test set-ups and representative



(a) Schematic of curved-pultrusion technique



(b) Curved-pultruded GFRP pedestrian bridge

Fig. 1. Curved-pultrusion technique and its bridge application [25].

failure modes are presented in Fig. A.1. in Appendix A. It is noted that non-standard coupons with geometries of 80 × 15 × 10 mm (length × width × thickness) were used for measuring the transverse tensile properties, and these coupons were extracted from web plate.

The experimentally-determined mechanical properties and fiber volume fraction of GFRP materials are summarized in Table 1. All types of properties were successfully obtained with coefficients of variation (COV) less than 0.10, except for in-plane shear modulus and minor Poisson's ratio. With that said, the mechanical properties of top and bottom flanges of curved-pultruded GFRP I-section were about the same, despite of having different curvatures from manufacturing process. In addition, an abnormal data is found for longitudinal tensile strength, which is only 574 MPa, even smaller than longitudinal compressive strength, 647 MPa. This is mainly due to the failure mode observed in 10-mm-thick longitudinal coupons, which is dominated by longitudinal delamination—an interface- and/or matrix-dominated failure mode. According to ASTM D3039, standard coupon thickness is taken equal to as-received thickness of GFRP profiles; however, the thick coupon addressed in this work is observed not to exhibit the fiber-dominated failure mode (i.e., fiber fracture). In this regard, many FRP practitioners often use a milling machine to cut the longitudinal coupon thinner (in thickness direction) or narrower (in width direction) depending on whether the through-thickness architecture is of critical design concern. Although the thinner/narrower coupon can be conveniently tested, the obtained results are susceptible to be at the high-end because of the size effect. In addition, ASTM D638 [32] prescribes to use dob-boned coupons, while it also suggests testing continuous fiber reinforced polymer composites per D3039 (see Note 4 in Section 1.3 of D638). In order to address this issue, standard tests need to be revised in order to accommodate the thick/high-strength materials for heavy-duty purposes emerged in recent years, such as the 20-mm-thick flange plate of bridge I-girder (see Fig. 1b), and the spar cap plates having tensile strength exceeding 1000 MPa. In this work, the longitudinal flexural strength, 808 MPa, is taken as the longitudinal strength of material, and this value is used throughout the following analyses.

2.2. Flexural tests

A total of 12 GFRP arch beams having radius of curvature of 2586 mm were tested under three-point bending test configuration, as shown in Fig. 3. All beams were seated at a pair of customized steel supports. The steel support was designed to accommodate the curvature of beams as well as to allow the anchorage of steel tension strings. Three beams were tested without tension strings; thus, they were simply-supported arch beams and taken as control specimens. The other nine beams were tested with tension strings, making them beam-string structures. Given beam-string structure is a self-balanced structural system, the beam-string specimens were also subjected to simply-supported boundary condition. The average clear span of all beams is 1800 mm with variance of ± 20 mm, and the calculated arch rise is 162 mm with variance of ± 5 mm. The steel strand has diameter of 12.7 mm, elastic modulus of 195 GPa, ultimate tensile strength of 1860 MPa, and design tensile strength of 1320 MPa [33], and they were anchored at mid-height of beam end-sections. All tests were controlled within the design tensile strength of steel strands such that only the elastic behavior of steel strands was to be considered.

A hydraulic jack with maximum capacity of 500 kN was employed to apply the load in manner of displacement-control at rate of 2 mm/min. A steel bearing plate having thickness of 3.5 mm and a rubber plate having thickness of 5 mm were used to spread the point-load to the region of 75 × 100 mm (beam length × width) to avoid possible stress concentration. The rubber plate was also used in between of GFRP arch beams and steel supports to avoid stress concentration. Moreover, wood stiffeners were used at mid- and end-sections, aiming to enhance the load-carrying capacity of beams subjected to concentrated loads. A linear variable differential transformer (LVDT) was installed at mid-span of beams to monitor the vertical displacement during the tests. Eight strain gages were installed near mid-span of six GFRP arch beams (i.e., three control specimens and three beam-string specimens) to measure the possible flange local buckling behavior and validate the plane section assumption. The layout of strain gages is illustrated in Fig. 4. Additionally, a pair of load transducers were installed at one end of all beam-string specimens to measure the actual tensile force in steel strands during tests. Two pairs of steel lateral supports were installed at third span of all specimens to prevent the possible lateral torsional buckling. In addition, the side plates of customized steel supports were also designed to prevent the beam-ends from possible lateral torsions. Thus, all beam specimens were exempt from out-of-plane deformations.

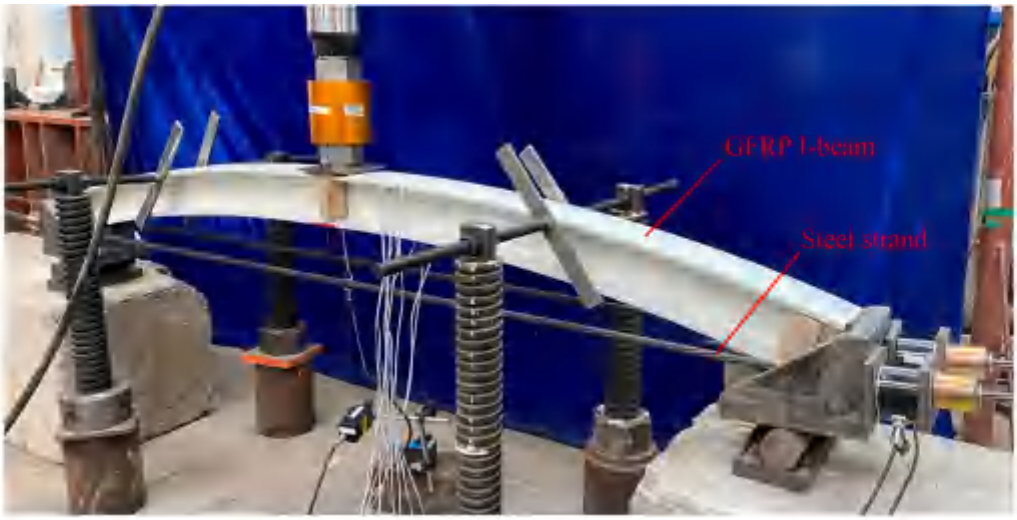
A total of four different boundary conditions were investigated in this work, and 12 specimens were categorized into four groups, with each group having three identical specimens for validating the repeatability of tests. Specifically, three control specimens were only subjected to simply-supported boundary conditions, and thus, they are denoted as specimens SS-1, − 2, and − 3. Three (out of nine) beam-string specimens were tested without pre-tensioning of steel strands such that their tension strings were relaxed before tests; these specimens are denoted as BS-relaxed-1, − 2, and − 3. In addition, another three beam-string specimens were tested with steel strands pre-tensioned to about 0% of their ultimate tensile strength to remove the relaxed part of tension strings; these specimens are denoted as BS-0%− 1, − 2, and − 3. The last three beam-string specimens were tested with steel strands pre-tensioned to about 5% of their ultimate tensile strength, aiming to investigate the effect of pre-tensioning of tension strings on the flexural behavior of GFRP arch beam; these specimens are denoted as BS-5%− 1, − 2, and − 3. All specimens were deemed failed (and tests were stopped) when sudden-catastrophic failure was occurred, and dramatic drop of load was observed.

Table 1
Experimentally-determined mechanical properties of GFRP material.

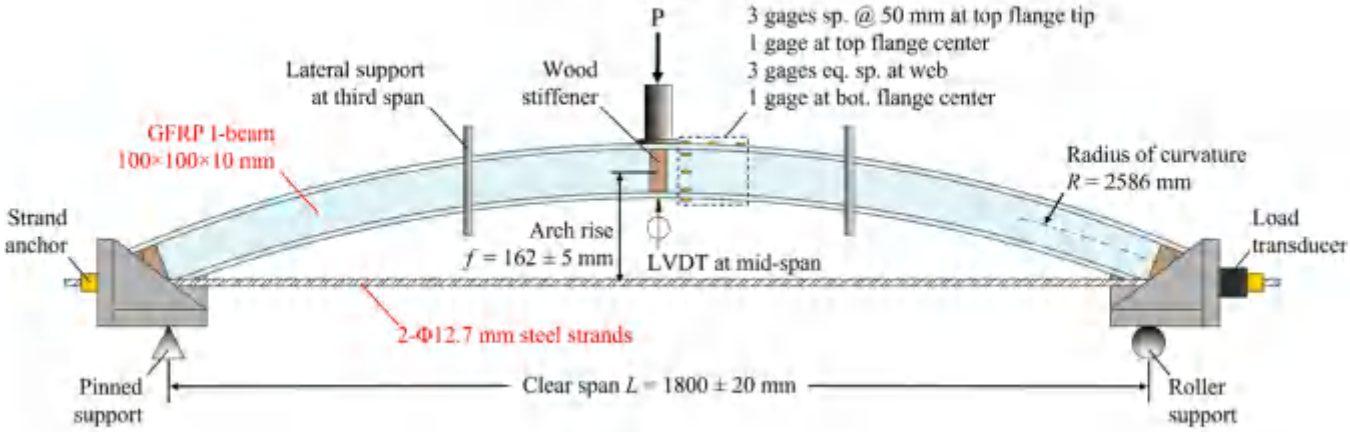
Mechanical properties	Values	COVs
Longitudinal tensile strength F_{Lt} (MPa)	574	0.08
Longitudinal tensile modulus E_{Lt} (MPa)	47208	0.04
Transverse tensile strength F_{Tt} (MPa)	45	0.09
Transverse tensile modulus E_{Tt} (MPa)	14765	0.03
Longitudinal compressive strength F_{Lc} (MPa)	647	0.03
Longitudinal compressive modulus E_{Lc} (MPa)	44770	0.06
Transverse compressive strength F_{Tc} (MPa)	152	0.02
Transverse compressive modulus E_{Tc} (MPa)	13305	0.06
Longitudinal flexural strength F_{Lb} (MPa)	808	0.07
Longitudinal flexural modulus E_{Lb} (MPa)	46763	0.05
In-plane shear strength F_{LT} (MPa)	84	0.09
In-plane shear modulus G_{LT} (MPa)	4573	0.15
Major Poisson's ratio υ_{LT}	0.29	0.03
Minor Poisson's ratio υ_{TL}	0.10	0.15
Fiber volume fraction V_f	0.59	0.01

2.3. Test results

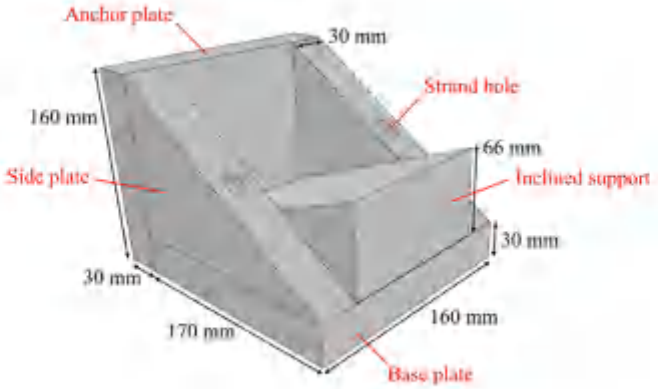
Experimentally-determined ultimate loads, maximum displacements, and linear stiffness of GFRP arch beams subjected to varying boundary conditions are presented in Table 2. It is noted that self-weight of GFRP arch beam, 56 N/m, is neglected in calculation of ultimate load, since its contribution to flexural strength of beam is less than 0.05% of observed value, and also, the stiffness is defined in form of strength-to-displacement ratio. From Table 2, it is seen that all the BS specimens exhibited higher flexural strength and stiffness as compared to SS counterparts; moreover, such an improvement in flexural performance tends to become more prominent with the increasing pre-tensioning in tension strings. Specimens BS-5% exhibited the highest flexural strength and stiffness, increased by 27% and 109%, respectively, as compared to control specimens; that is, with only 5% of pre-tensioning the proposed beam-string system is able to double the flexural stiffness of GFRP arch



(a) Overall view



(b) Schematic view



(c) Customized steel support

Fig. 3. Three-point bending test configuration.

beam.

Taking specimen BS-relaxed-1 as example, representative top flange and cross-sectional strains are shown in Fig. 4. From Fig. 4a, it is observed that all flange strains behaved almost in a linear-elastic manner until failure; thus, flange local buckling is not of concern in this case, and the same behavior is also observed in all other specimens. From Fig. 4b, it is seen that strain distribution generally increased linearly with the sectional height; thus, plane section assumption can be

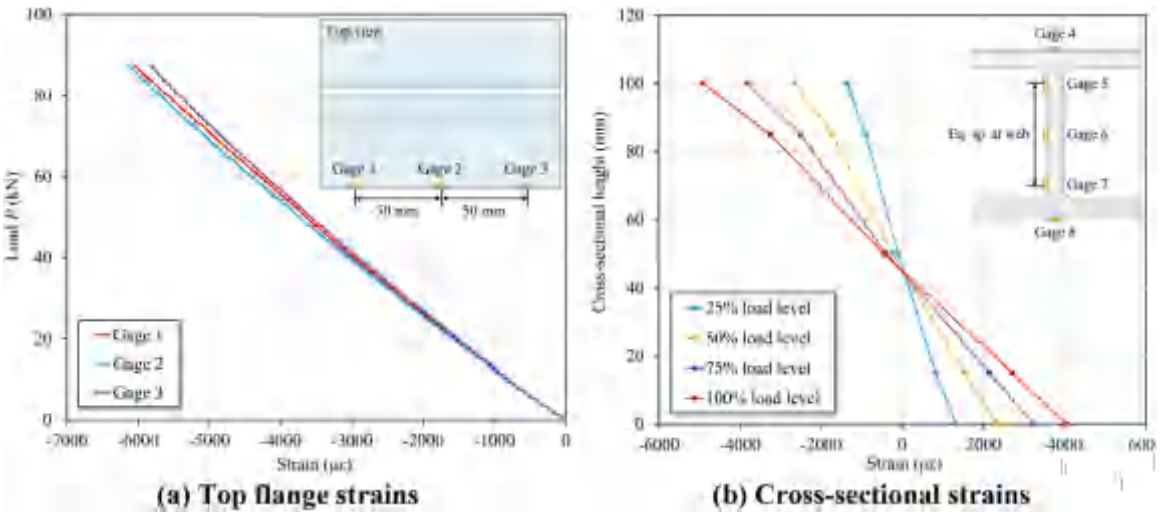


Fig. 4. Representative top flange and cross-sectional strains (BS-relaxed-1).

Table 2
Experimentally- and numerically-determined flexural performance of GFRP arch beams.

Specimens	Experimental results					Numerical results				
	Ultimate Load P (kN)	Avg. P (kN) (COV)	Max. displ. Δ (mm)	Linear stiffness K (kN/m)	Avg. K (kN/m) (COV)	Ultimate Load P (kN)	$\frac{P_{FEM}}{P_{exp}}$	Max. displ. Δ (mm)	Linear stiffness K (kN/m)	$\frac{K_{FEM}}{K_{exp}}$
SS-1	60.68[a]	79.40[b]	42.10	1462	1475	83.89	1.38[a]	59.31	1436	0.98
SS-2	83.00	(-)	58.95	1481	(0.01)		1.01			0.97
SS-3	75.80		55.31	1468			1.11			0.98
BS-relaxed-1	88.58	88.12[b]	44.40	2270	2176	89.40	1.01	44.47	2109	0.93
		(-)			(0.04)					
BS-relaxed-2	59.98[a]		31.61	2233			1.49[a]			0.94
BS-relaxed-3	87.65		44.09	2119			1.02			1.00
BS-0%– 1	97.99	97.97	62.07	2070	2407	101.68	1.04	43.75	2496	1.21
BS-0%– 2	100.55	(0.03)	54.00	2801	(0.18)		1.01			0.89
BS-0%– 3	95.35		58.30	2012			1.07			1.24
BS-5%– 1	100.36	100.56	37.21	3068	3079	104.32	1.04	31.17	2998	0.98
BS-5%– 2	97.81	(0.03)	38.01	3036	(0.01)		1.07			0.99
BS-5%– 3	103.52		34.61	3122			1.01			0.96

[a] This is an outlier due to premature failure of specimen;
[b] Outlier is not considered in calculation of the average load.

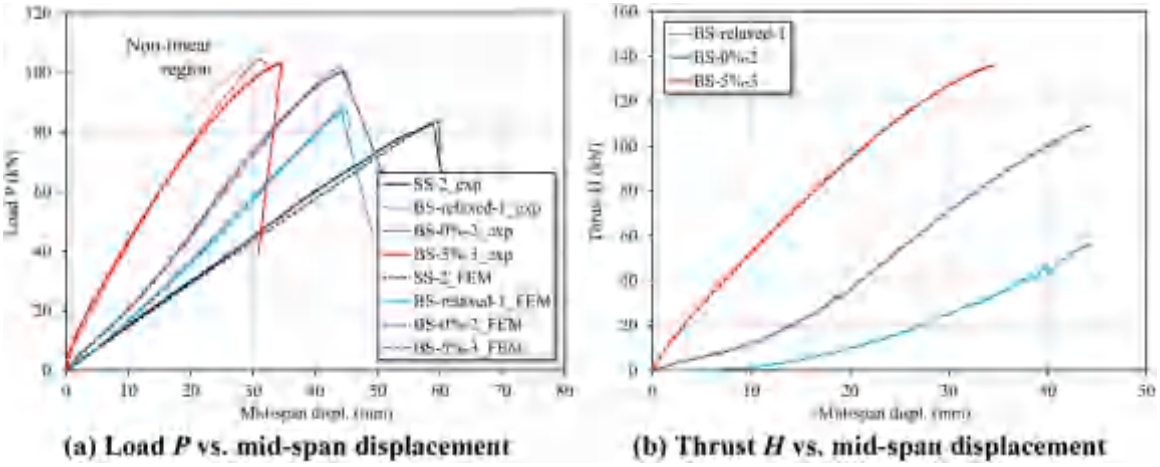


Fig. 5. Representative load-displacement and thrust-displacement curves.

validated.

Load-displacement and thrust-displacement curves of the four specimens having the highest loads from each type of boundary conditions are taken as the representatives, as shown in Fig. 5(i.e., solid lines with subscripts of exp). From Fig. 5a, it is seen that BS-5%− 3 exhibited the highest flexural strength and stiffness, followed by BS-0%− 2, BS-relaxed-1, and SS-2. Moreover, the load-displacement curves of all specimens are observed, to noticeable extent, to show a slightly non-linear behavior. Such a non-linear behavior is susceptibly attributed to the inherent geometric and material non-linearities of GFRP arch beam as well as the initial imperfections of test set-up.

The non-linear behavior is also evidenced by the measured tensile force of tension strings (i.e., thrust H in Fig. 5b). It is noted that the thrusts shown in Fig. 5b are the sum of two steel strands, and they are zeroed against their initial values before applying the load P. This is due to the fact that the possible camber of beams induced by pre-tensioning of strands was not restrained, and the resulting reaction at mid-span of beams was released. Thus, all beam-string specimens were self-balanced, and the structural behaviors of interests are those observed after applying the load P. With that said, the observed thrust of three BS specimens clearly show different behaviors. Initially-relaxed tension strings are seen not to take up the load until the GFRP arch beam experienced a vertical displacement almost 10 mm. With steel strands straightened (i.e., pre-tensioned to 0%), tension strings are able to take up the load simultaneously with deformation of GFRP arch beam; however, the load of tension strings is much lower than that pre-tensioned to 5%. Moreover, considering the widely-recognized linear-elastic behavior of steel strands, the observed thrusts indicate an imperfect load-transfer mechanism in the present configuration of beam-string system; that is, the measured thrusts (by load transducers at steel support) are susceptible to be affected by imperfections of test set-ups and the effective thrusts transferred to GFRP arch beams may be lower than measured values. The non-linear behavior of GFRP arch beams as well as the load-transfer mechanism between GFRP arch beams and steel strands are investigated in the following numerical program.

Taking specimen BS-relaxed-1 as example, typical failure modes of GFRP arch beams are shown in Fig. 6. Additionally, failure modes of other types of specimens (i.e., SS, BS-0%, and BS-5%) are also provided, as shown in Fig. A.2. in Appendix A. Based on experimental observations, the first shear crack occurred at top flange-web junction under load point. With the loss of integrity of flange-web junction, web plate started to take over almost all the load and web crippling failure occurred near the load point, which is marked by tear-apart-like crack at web. Then, shear crack propagated along with the flange-web junction until reaching the end-sections of beam. All cracks occurred within an extremely short period, and the sound was similar to gunshot. These cracks are generally observed in all specimens, and they were not necessarily occurred following the same order for every specimen.

3. Numerical program

3.1. Finite element modeling

Finite element (FE) modeling was conducted via ABAQUS to simulate and validate the flexural behavior of curved-pultruded GFRP arch beams subjected to varying boundary conditions. Two types of models were constructed: the first one only modeling GFRP arch beam and the second one modeling both GFRP arch beam and steel strands, as shown in Fig. 7. The material properties were taken as those shown in Table 1. 2D shell element S4R was used to model the GFRP arch beam and 3D solid element C3D8R was used to model the steel strands. With mesh convergence tests, characteristic element sizes of 5.0 and 1.8 mm were respectively determined for shell and solid elements. All FE models were built mimicking the experimental set-ups, thus having simply-supported boundary condition and a concentrated displacement load at mid-span. In addition, the central surface region of 75 × 100 mm (beam length × width) was coupled in all degrees of freedom with respect to the load point so as to simulate the effect of steel bearing plate. In the first FE model, horizontal thrust H was taken as the actual tensile forces measured from experimental tests (i.e., specimens BS-relaxed-1, BS-0%−2, and BS-5%−3) and it was applied at the roller-end of beam. In the second model, steel strands were constrained together with GFRP

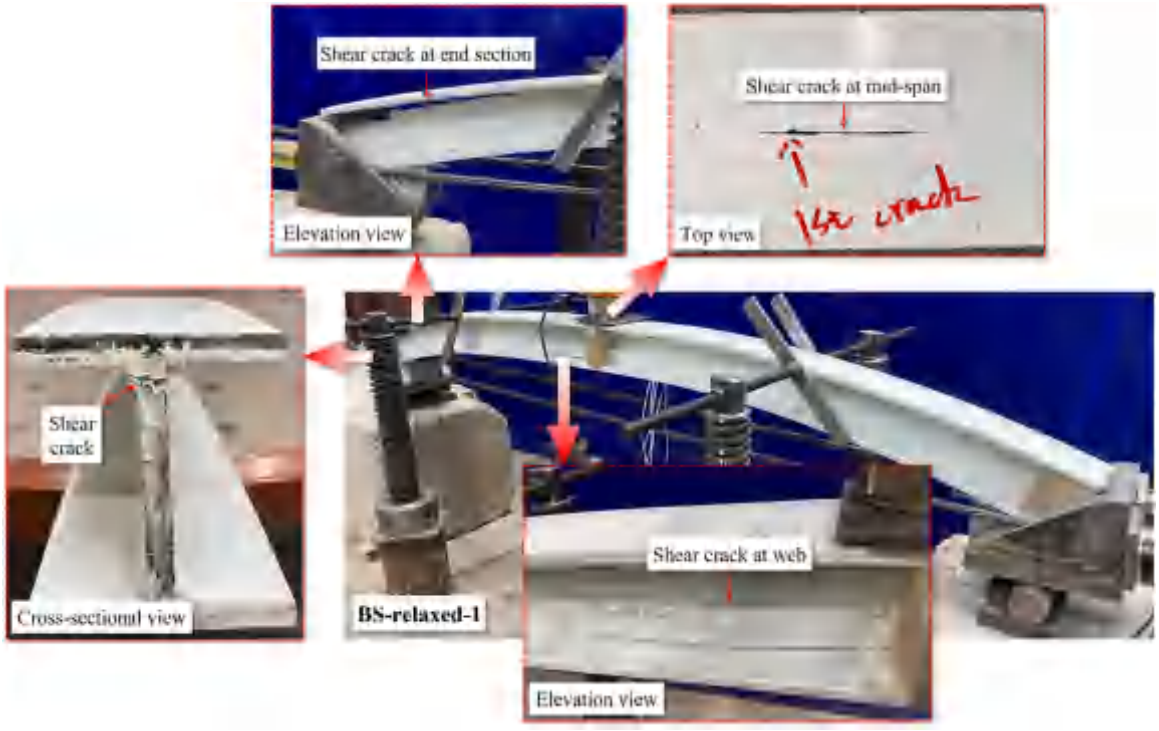


Fig. 6. Representative failure modes of GFRP arch beam (specimen BS-relaxed-1).

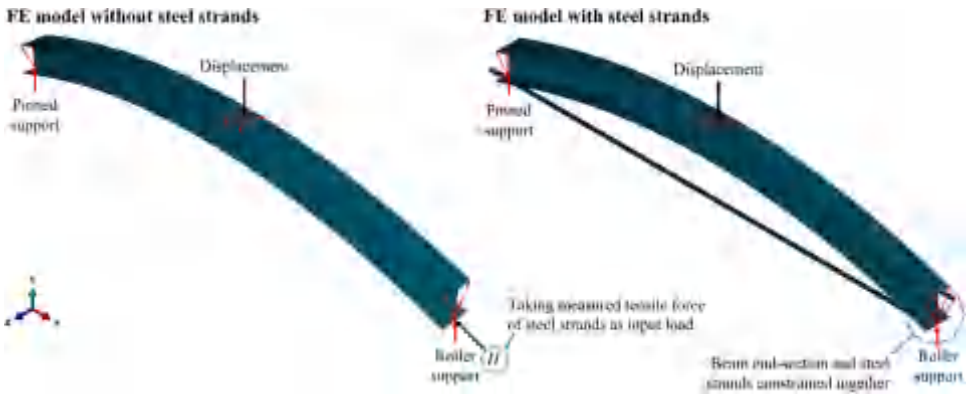


Fig. 7. Finite element models.

arch beam at both ends, thus permitting a perfect load-transfer mechanism. Comparing the two models, the first one is expected to yield a better agreement with experimental results since an imperfect load-transfer between GFRP arch beam and steel strands has been identified, and such an imperfect load-transfer can be observed by specimens BS-relaxed-1 and BS-0%− 2 in Fig. 5b. Thus, the first model is focused in this section for validating the experimental results, meanwhile the second model is to validate the analytical results presented in next section.

In order to simulate the non-linear flexural behavior as well as identifying the failure/damage modes of GFRP arch beams, progressive failure was modeled in ABAQUS using Hashin damage criterion, which consist of three components, including damage initiation, damage evolution, and damage stabilization [34]. Damage initiation considers fiber- and matrix-dominated damages and determines the onset of four modes: 1) fiber tension; 2) fiber compression; 3) matrix tension; and 4) matrix compression [35,36], as expressed in Eqs. 1–4. Note that σ_{11}, σ_{22}, and σ_{12} are the three components of effective stress tensor σ, and α is the coefficient accounting for the contribution of shear stress to fiber tension damage mode. In addition, the longitudinal and transverse shear strength are approximately assumed to be equal to in-plane shear strength F_{LT}. Then, damage evolution is to reduce the stiffness of material based calculated damage variables, and in this process, the tensile and compressive fracture energies in fiber- and matrix-dominated directions must be specified so as to calculate the damage variables, including G_{ft}, G_{fc}, G_{mt}, and G_{mc} (subscripts f and m indicate fiber and matrix, and t and c indicate tensile and compressive) [37]. Last but not least, damage stabilization is to alleviate the convergence difficulties through four viscosity coefficients corresponding to tensile and compressive behavior in fiber- and matrix-dominated directions [37]. Detailed expressions regarding damage evolution and stabilization have been extensively addressed by previous studies (e.g., [36] and [37]), and therefore, they are not repeatedly discussed herein.

$$\text{Fiber tension}: \left(\frac{\sigma_{11}}{F_{Lt}}\right)^2 + \alpha\left(\frac{\sigma_{12}}{F_{LT}}\right)^2 = 1 \sigma_{11} > 0 \tag{1}$$

$$\text{Fiber compression}: \left(\frac{\sigma_{11}}{F_{Lc}}\right)^2 = 1 \sigma_{11} < 0 \tag{2}$$

$$\text{Matrix tension}: \left(\frac{\sigma_{22}}{F_{Tt}}\right)^2 + \left(\frac{\sigma_{12}}{F_{LT}}\right)^2 = 1 \tag{3}$$

$$\text{Matrix compression}: \left(\frac{\sigma_{22}}{2F_{LT}}\right)^2 + \left[\left(\frac{F_{Tc}}{2F_{LT}}\right)^2 - 1\right]\frac{\sigma_{22}}{F_{Tc}} + \left(\frac{\sigma_{12}}{F_{LT}}\right)^2 = 1 \tag{4}$$

Representative data of fracture energies and viscosity coefficients available in literature are summarized in Table 3. The present work empirically adopted the highest fracture energies pertaining to fiber from literature (i.e., $G_{ft} = G_{fc} = 100$ N/mm) and proposed a new set of fracture energies for matrix based on regression of current experimental data (i.e., $G_{mt} = G_{mc} = 14$ N/mm). It is noted that experimental tests are required to obtain an accurate characterization of fracture energies of pGFRP profiles, while in this work such type of tests is not conducted. The selected fracture energies are seen to achieve satisfactory accuracy; that is, those data, though empirically determined, are able to provide a general characterization of the properties as well as the imperfections of the material. In addition, viscosity coefficients η are generally obtained through data-fitting process based on experimental results [34,37–40]. Thus, the same method with previous studies was adopted, and in this work, $\eta = 0.001$ for specimens SS and BS-relaxed; $\eta = 0.0035$ for specimen BS-0%; $\eta = 0.0025$ for specimen BS-5%. Taking specimen SS-2 as example, the effects of fracture energies and viscosity coefficients are illustrated in Fig. 8a. In general, the fracture energies and viscosity coefficients adopted in this work are in similar region with existing data.

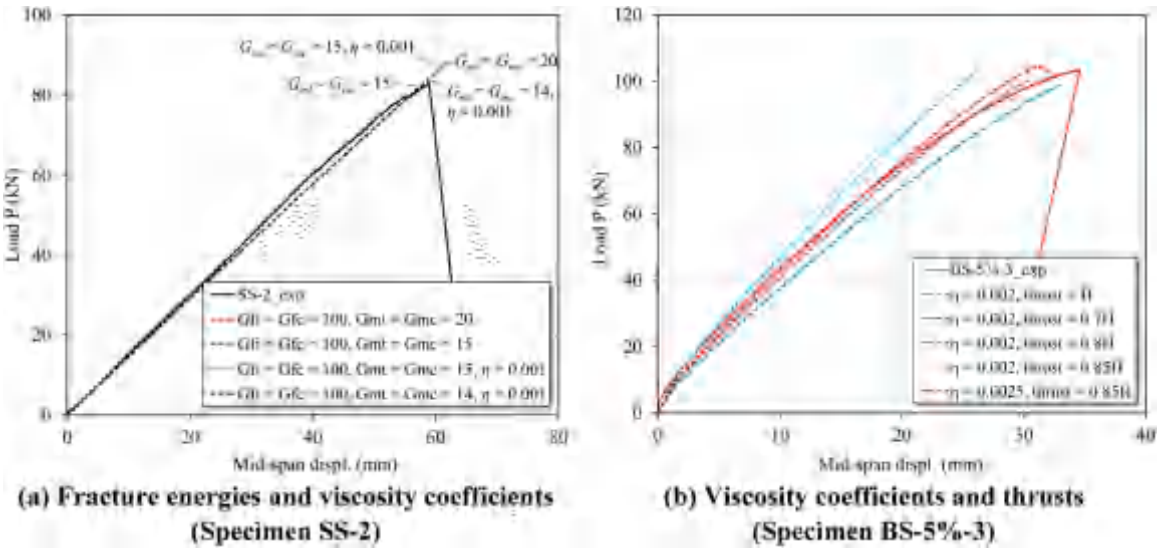
Table 3
Fracture energies and viscosity coefficients in literature and present work.

Authors	Materials[a]	G_{ft} (N/mm)	G_{fc} (N/mm)	G_{mt} (N/mm)	G_{mc} (N/mm)	Viscosity coefficients η
Lapczyk and Hurtado [37]	GF/EP	12.5	12.5	1.0	1.0	$\eta_f = 0.00025$; $\eta_m = 0.005$[b]
Sharma et al. [38]	GF/EP	92	79	0.22	0.61	-
Tarfaoui et al. [39]	CF/EP	100	100	5	5	0.001
Alhawamdeh et al.[34, 40]	GF/VE	92	79	5	5	0.001
Present work	GF/EP	100	100	14	14	0.001; 0.0035; 0.0025

[a] GF indicates glass fiber; CF indicates carbon fiber; EP indicates epoxy resin; VE indicates vinyl ester resin;
[b] Viscosity coefficients η_f and η_m are for fiber and matrix, respectively.

In addition to progressive failure of GFRP material, the load-transfer mechanism between GFRP arch beam and steel strands was investigated. In the tests, the horizontal thrust to GFRP arch beam was realized through a pair of customized steel supports in between of the beam and steel strands. Although the force of strands was measured, a certain extent of loss might exist due to the imperfect transfer of load. Through a parametric study, 20%, 30%, and 15% reductions of recorded forces were identified for specimens BS-relaxed-1, BS-0%− 2, and BS-5%− 3, respectively. Taking specimen BS-5%− 3 as example, the effects of viscosity coefficients and effective thrusts are illustrated in Fig. 8b.

With the progressive failure-related parameters and the losses of thrusts determined, numerically-determined flexural strength and stiffness are obtained, as shown in Table 2. The load-displacement curves of



(a) Fracture energies and viscosity coefficients (Specimen SS-2)

(b) Viscosity coefficients and thrusts (Specimen BS-5%-3)

Fig. 8. Parametric study on fracture energies, viscosity coefficients, and effective thrusts.

four representative specimens are also obtained, as shown in Fig. 5a. In general, FE modeling could satisfactorily predict both the flexural strength and stiffness for GFRP arch beams subjected to varying boundary conditions. For flexural strength, the average ratio of FE modeling and test results is 1.04, with COV of 0.03; and for flexural stiffness, the average ratio of FE modeling and test results is 1.01, with COV of 0.11.

3.2. Failure modes

Using Hashin damage criterion, typical failure/damage modes of GFRP arch beams were simulated, as shown in Fig. 9. In particular, the field outputs DAMAGESHR (i.e., shear damage) and HSNMTCRT (i.e., matrix tension damage) were taken as the main criteria for identifying failure modes, as these two variables directly account for overall shear damage of material and transverse tensile damage of matrix (see Eq. 3). This method has been successfully demonstrated by Alhawamdeh et al. [34,40]. From Fig. 9a, it can be seen that in general, the main failure mode of GFRP arch beam includes the shear damage and matrix tensile damage at top flange-web junction, with the latter being developed into the web. Specifically, in the tests almost all GFRP arch beams are found to start cracking at top flange-web junction near the load point, and this type of failure mode can be accurately simulated by FE modeling, as shown by shear failure in Fig. 9b. Moreover, when flange-web junction loses its integrity, web plate is to take over the load and web crippling failure may occur. This type of failure mode is seen to be similar to tear-apart-like crack, as illustrated by matrix tension damage at web in Fig. 9c. In conclusion, Hashin damage criterion is observed to provide accurate predictions of failure modes for GFRP arch beams addressed in this work.

4. Analytical program

4.1. Flexural strength of GFRP arch beam

Failure mode of all GFRP arch beams is observed to be controlled by shear damage at top flange-web junction and/or web plate. This type of failure mode is characterized as the web crippling of structural members subjected to concentrated loads by ASCE Pre-standard [41]. Web crippling behavior has been investigated by many researchers, including Borowicz and Bank [42], Wu and Bai [43], Wu et al. [44], Fernandes et al. [45,46], and Haloi et al. [47]. The main difference between previous studies lies in the test configuration and observed failure modes. Three-point bending tests on short beams was conducted by Borowicz and Bank [42], while other tests were carried out on pGFRP profiles only subjected to compressive loads. Due to the varying slenderness ratios of web plates being addressed in those tests, three types of failure modes are identified, including through-web shear damage [42], localized junction shear damage [43], and web buckling [45], as shown in Fig. 10. Accordingly, different predictive models are developed with respect to each failure mode. In this work, the flexural test set-up is similar to which Eq. 5 was based off, and through-web shear damage is found to be the dominant failure mode for GFRP arch beams, as shown in Fig. 10d. Thus, the predictive model proposed by Borowicz and Bank [42] was adopted to calculate the web crippling strength, as shown in Eq. 5.

$$P_n = 0.7dt_wF_{ILS}\left(1+\frac{2k+6t_{plate}+b_{plate}}{d}\right) \tag{5}$$

Where d is the section depth; t_w is the web thickness; F_{ILS} is the interlaminar shear strength of material, approximately taken as in-plane shear strength F_{LT} in this case; k is the distance from top of beam to bottom of fillet, measured as 15 mm in this case; t_{plate} and b_{plate} are the thickness and length of bearing plate, respectively measured as 3.5 and 75 mm in this case. It is noted that ASCE adopted Eq. 5 with a conservative modification, namely replacing d with d_w in the second term in parentheses, and d_w is the depth of web plate. The term of $0.7d$ is to simulate the crack length at web, while in this work, it is measured as 0.65–0.68d, as shown in Fig. 10d. Thus, $0.65d$ is used for conservative purpose. Despite of having actual failure mode respected, Eq. 5 is found to over-estimate the web crippling strength observed in this work, by a factor about 1.34. This is mainly due to the non-uniform shear distribution across web plate (in height direction). From FE modeling, it is found that the average shear stress over $0.65d$ region of web plate is about 61 MPa, which is 72% of shear strength of material, as shown in Fig. 11. Thus, Eq. 5 is modified, as shown in Eq. 6.

$$P_n = 0.65dt_w(cF_{ILS})\left(1+\frac{2k+6t_{plate}+b_{plate}}{d}\right) \tag{6}$$

Where c is the coefficient accounting for non-uniform shear distribution across crack region of web plate, taken as 0.72 in this case; and $0.65d$ is the crack length. The predicted web crippling strength, namely flexural strength of GFRP arch beam in this work, is shown in Table 4. Excluding the two outliers (i.e., SS-1 and BS-relaxed-2), the average ratio of analytical predictions and experimental results is 0.97, with COV of 0.10. Additionally, for all beam-strings with pre-tensioned strings (i.e.,

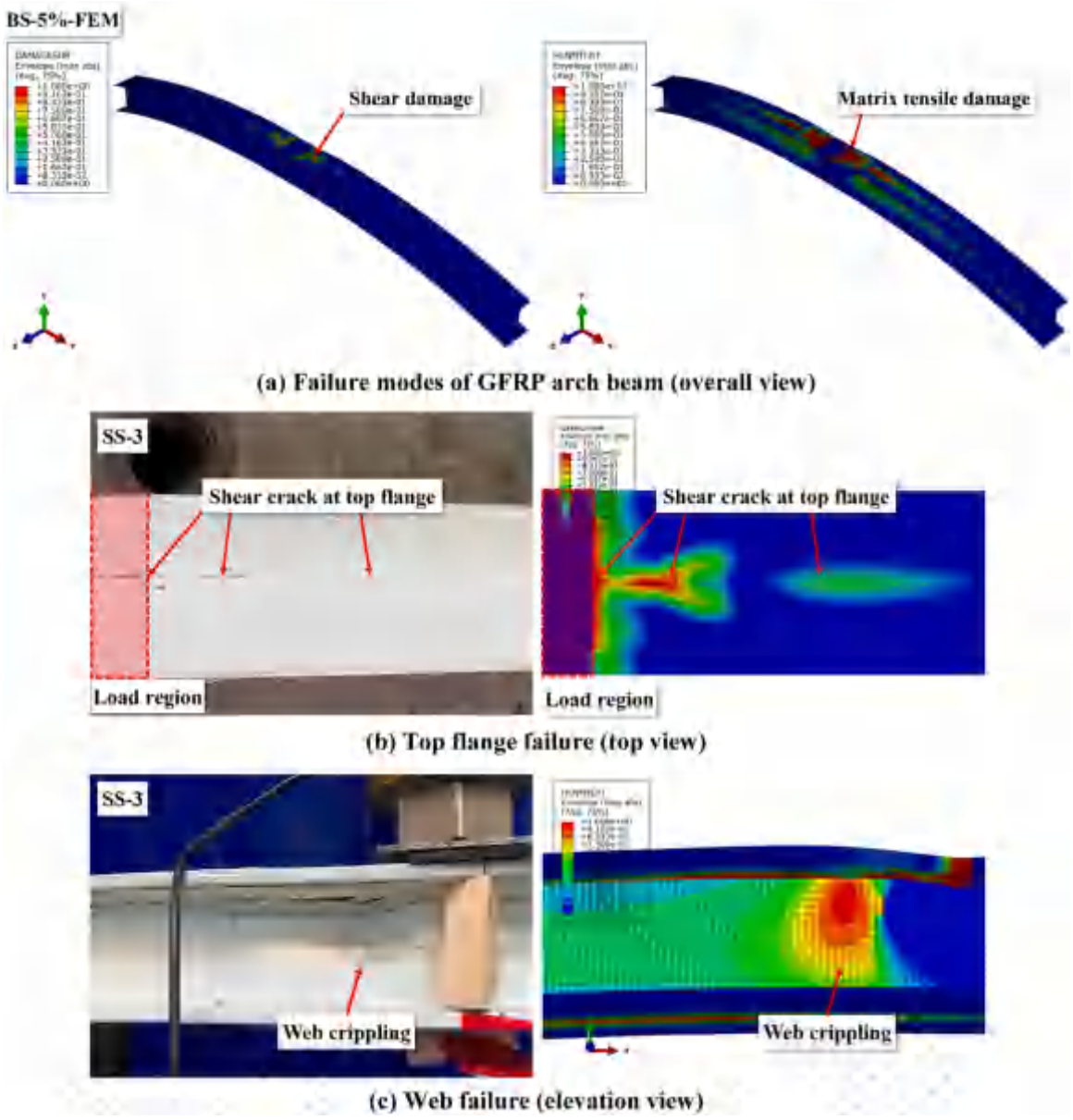


Fig. 9. Typical failure modes simulated by FE modeling.

six specimens of BS-0% and BS-5%), Eq. 6 could uniformly provide conservative predictions, with average ratio of 0.90 and COV of 0.03. Thus, good accuracy of Eq. 6 can be demonstrated.

4.2. Internal forces of GFRP beam-string

In this section, the internal forces of GFRP beam-string are calculated, including internal moment M, shear force Q, and axial force N. To do so, the horizontal thrust H must be solved first. GFRP beam-string is a first-degree indeterminate structure, and the force method can be implemented. The steel strands are replaced with a pair of horizontal forces H, and the free body diagram of GFRP beam-string is obtained, as shown in Fig. 12. The compatibility condition regarding deformation is given in Eq. 7.

$$\delta_{11}H + \Delta_{1P} = 0 \tag{7}$$

Where P is the external load; H is the horizontal force of two steel strands; δ_{11} and Δ_{1P} are the displacements generated by horizontal force H and vertical load P, respectively, and they are calculated through Eqs. 8 and 9. In this case, the displacement due to internal shear force of beam is neglected.

$$\delta_{11} = \int \frac{\overline{M}_1^2}{E_L I_{beam}} ds + \int \frac{\overline{N}_1^2}{E_L A_{beam}} ds + \frac{L}{E_s A_s} \tag{8}$$

$$\Delta_{1P} = \int \frac{\overline{M}_1 M_P}{E_L I_{beam}} ds \tag{9}$$

Where E_L is the longitudinal modulus of GFRP; I_{beam} is the moment of inertia of GFRP arch beam; A_{beam} is the cross-sectional area of GFRP arch beam; E_s is the elastic modulus of steel strand; A_s is the cross-sectional area of two steel strands; M_P is the moment at mid-span generated by external load P; $\overline{M}_1$ is the moment at mid-span generated by a virtual unit load in the direction of H; and $\overline{N}_1$ is the axial force at mid-span generated by a virtual unit load in the direction of H. $\overline{M}_1$ and $\overline{N}_1$ are given as:

$$\overline{M}_1 = -y \tag{10}$$

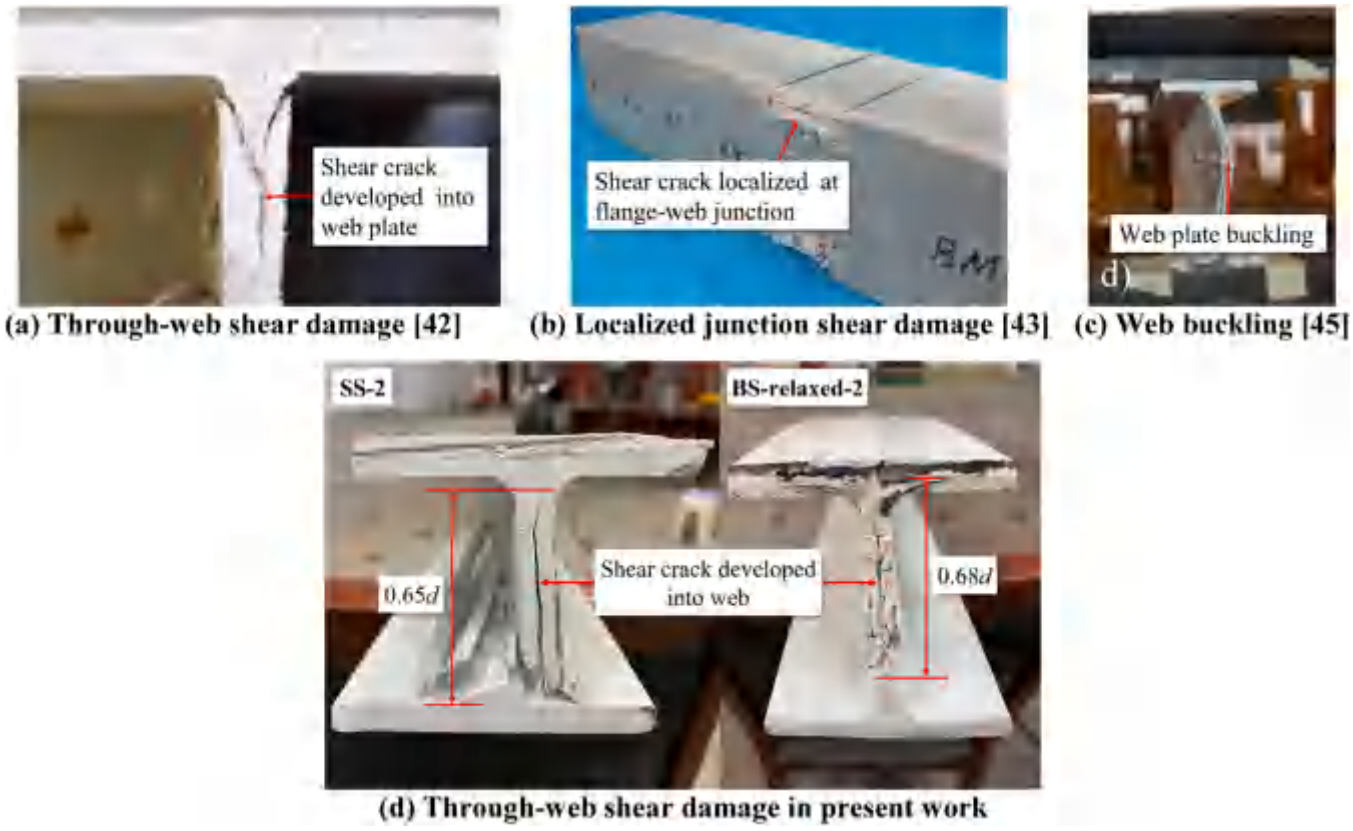


Fig. 10. Typical failure modes of web crippling in literature and present work.

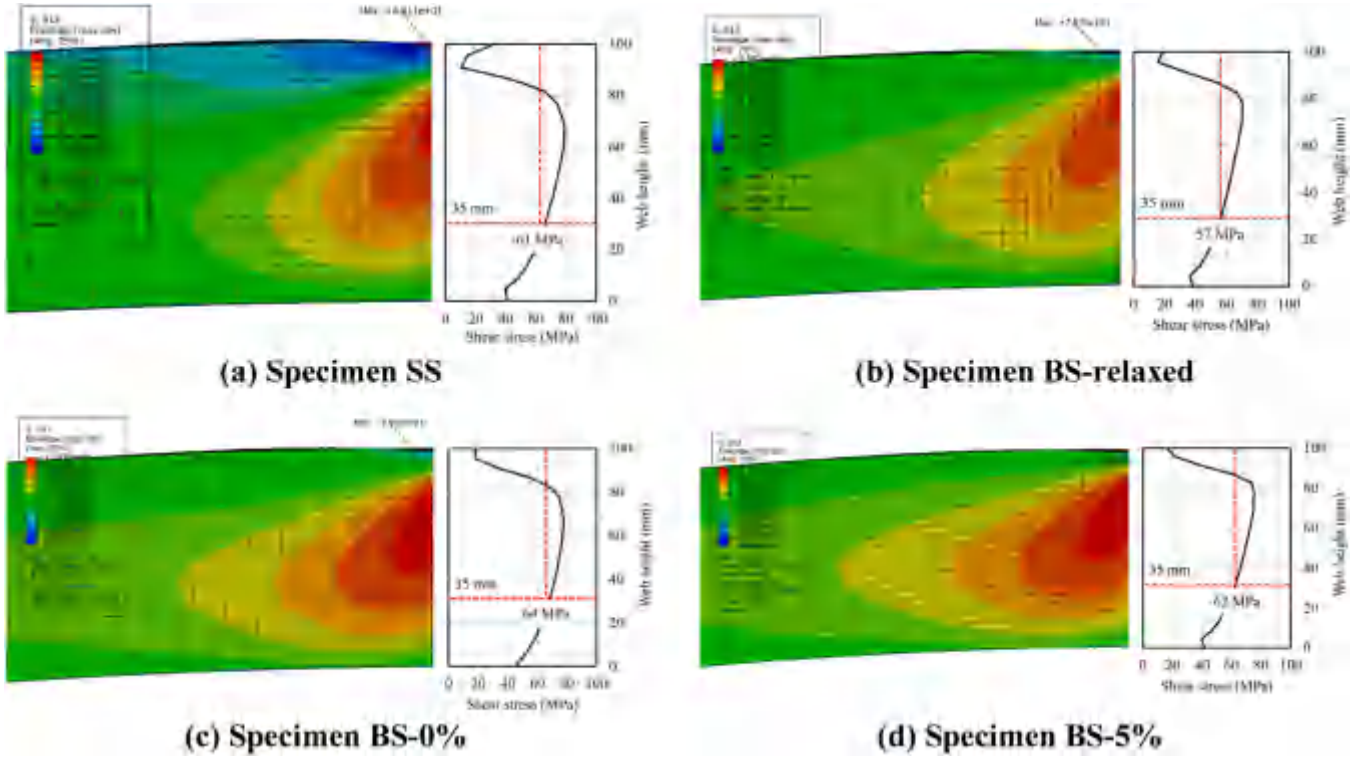


Fig. 11. Non-uniform shear distribution across web plate.

Table 4
Comparison between analytically- and experimentally-determined web crippling strength.

Specimens	Experimental results	Analytical predictions	
	P_{exp} (kN)	P_{pred} (kN)	$\frac{P_{pred}}{P_{exp}}$
SS-1	60.68[a]	89.18	1.47[a]
SS-2	83.00		1.07
SS-3	75.80		1.18
BS-relaxed-1	88.58		1.01
BS-relaxed-2	59.98[a]		1.49[a]
BS-relaxed-3	87.65		1.02
BS-0%− 1	97.99		0.91
BS-0%− 2	100.55		0.89
BS-0%− 3	95.35		0.94
BS-5%− 1	100.36		0.89
BS-5%− 2	97.81		0.91
BS-5%− 3	103.52		0.86

[a] This is an outlier due to premature failure of specimen.

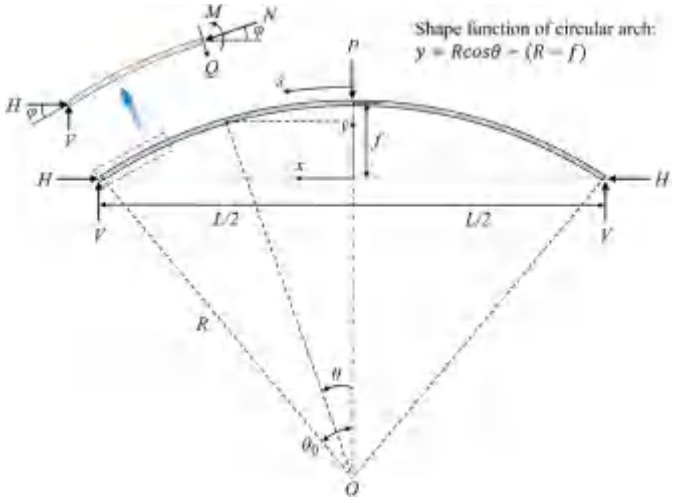


Fig. 12. Free body diagrams of GFRP arch beam (polar coordinate system).

$$\overline{N}_1 = \cos\varphi \tag{11}$$

Where φ is the cross-sectional angle, which is calculated taking the first derivative of shape function y. Then, substituting Eqs. 8–11 into Eq. 7, and taking $ds = Rd\theta$, yields:

$$H = \frac{2\int_0^{\theta_0} \frac{yM_P}{E_L I_{beam}} Rd\theta}{2\int_0^{\theta_0} \frac{y^2}{E_L I_{beam}} Rd\theta + 2\int_0^{\theta_0} \frac{\cos^2\varphi}{E_L A_{beam}} Rd\theta + \frac{L}{E_s A_s}} \tag{12}$$

With the horizontal force H of steel strands determined, the internal forces of GFRP beam-string can be calculated using Eqs. 13–15.

$$M = M_{ss} - Hy \tag{13}$$

$$Q = Q_{ss}\cos\varphi - H\sin\varphi \tag{14}$$

$$N = Q_{ss}\sin\varphi + H\cos\varphi \tag{15}$$

Where M_{ss} and Q_{ss} are the internal moment and shear force of simply-supported GFRP beam; and φ is the cross-sectional angle of GFRP beam. At mid-span (i.e., $\varphi = 0°$), the shear force Q of GFRP beam-string is equal to the shear force Q_{ss} of its simply-supported counterpart; and the axial force N is equal to the horizontal force H.

The second FE model with steel strands (see Fig. 7) is used to validate the analytically predicted horizontal thrust H, as shown in Fig. 13a. Through the load-displacement curves in Fig. 13a, it is seen that the BS model with steel strands has the highest flexural stiffness and behaves in perfectly linear-elastic manner, though its flexure strength is lower than the first model (i.e., BS-5%−3_FEM). The lower strength of second FE model is due to the fact that the progressive failure is not considered. The numerically-predicted ultimate load is 92.91 kN. Taking this value as input for analytical model, horizontal thrust can be calculated, which is 155.92 kN. The difference between analytically- and numerically-predicted thrusts is only about 1.67%, showing an excellent accuracy of analytical model. Then, using this thrust, the internal forces of beam-string (i.e., moment M, shear force Q, and axial force N) can be calculated, as shown in Figs. 13b, 13c, and 13d. The solid lines represent the beam-string structure, and dashed lines represent the simply-supported counterpart. It is seen that beam-string is able to decrease the internal moment due to the enabled arch mechanism, and the internal shear can also be generally reduced while the maximum shear remains the same. For any given external load P, analytically-predicted internal forces of beam-string shall be higher than the actual forces, since the load-transfer mechanism between GFRP arch beam and steel strands is inevitably imperfect for the present structural configuration. Higher internal forces are to result in a conservative design, which is acceptable in practice.

5. Discussions

First, proposed beam-string system is demonstrated to be able to improve the flexural stiffness of GFRP arch beam, by up to 109%. Nonetheless, it is observed that the load-transfer between GFRP arch beam and steel strands is inevitably imperfect. The average loss of thrusts is found to be about 22%. This partially explains the lower flexural stiffness of all beam-strings as compared to the "perfect" FE model (i.e., the second model with steel strands). Although imperfect contacts between components are inevitable, the flexural stiffness of GFRP beam-string is believed to be improved provided the thrust is applied to GFRP arch beam through a more efficient method, and this method must allow the pre-tensioning of tension strings. Thus, future work is needed to develop a new beam-string configuration to achieve a higher efficiency in terms of load-transfer.

Second, varying extent of non-linear-elastic behaviors are observed in GFRP arch beams. Typically, non-linear behavior is attributed to the non-linear geometry of structure and/or non-linear nature of material. The linear load-displacement curve of the "perfect" FE model (i.e., the second FE model with steel strands) successfully demonstrates that the circular geometry of GFRP arch beam is not the main reason for observed non-linear behavior. With that said, it can be concluded that the progressive failure of GFRP material caused the non-linear behavior. Hashin damage criterion with damage evolution and stabilization is found to be able to provide accurate predictions regarding the non-linear flexural behavior of GFRP arch beams. The fracture energies and viscosity coefficients reported in this work could be potentially used to predict the progressive failure of similar materials and structures, meanwhile experimental tests are recommended to be conducted in future work so as to obtain an accurate characterization of fracture energies and viscosity coefficients.

Third, curved-pultruded GFRP arch beams addressed in this work are seen to be controlled by web crippling strength, rather than flexural strength of material. This behavior is similar to conventional pGFRP flexural members subjected to concentrated loads. Indeed, pGFRP members typically tend to fail due to concentrated loads. The horizontal thrusts (and the resulting axial forces) are observed to improve the web crippling strength, by up to 27%. Existing model for web crippling does not consider the arch mechanism of pGFRP members; that is, the effect of horizontal thrust on web crippling remains unknown. In future work, it is recommended to address the effect of interlaminar shear coupled

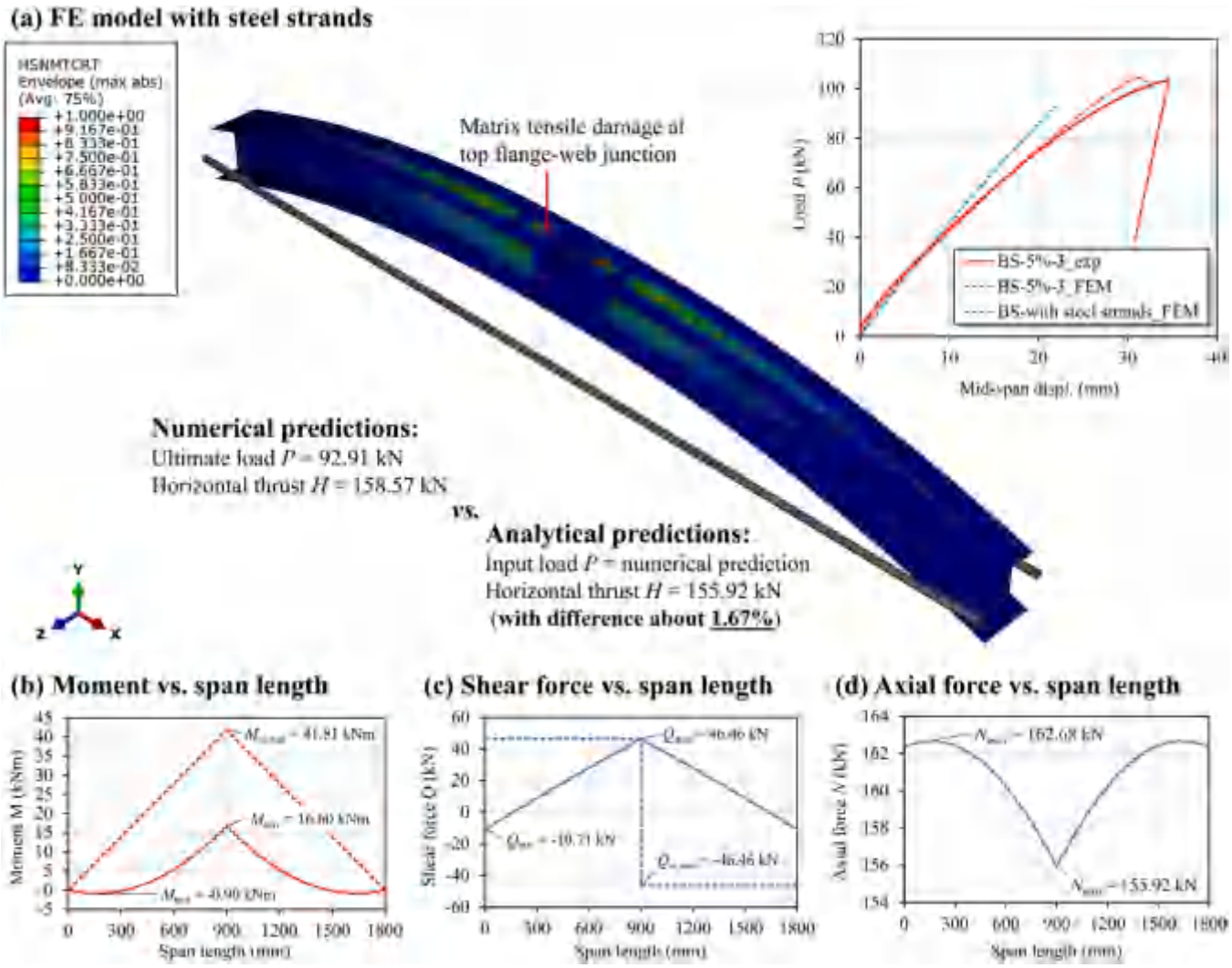


Fig. 13. Comparison of numerical and analytical predictions.

with axial load on web crippling behavior of pGFRP members.

Last but not least, flexural performance of GFRP beam-string is highly dependent on the axial stiffness of tension strings. In this work, a pair of steel strands having diameter of 12.7 mm is adopted and three types of boundary conditions are investigated, including initially-relaxed string (i.e., BS-relaxed), initially-straightened strings (i.e., BS-0%), and pre-tensioned strings (i.e., BS-5%). A small pre-tensioning of 5% could lead to greatly improved flexural stiffness of GFRP arch beam. Thus, it can be readily expected that greater flexural stiffness of GFRP beam-string can be achieved provided a new tension string with higher axial stiffness and/or higher pre-tensioning. Again, the design of tension string shall be incorporated into the design of beam-string configuration. An efficient beam-string configuration with stronger tension string could rationally yield an improved flexural performance of GFRP beam-string.

6. Conclusions

In this work, flexural performance of curved-pultruded GFRP arch beams subjected to varying boundary conditions was investigated through experimental, numerical, and analytical programs. It is observed that the flexural strength and stiffness of GFRP arch beams was successfully enhanced by up to 27% and 109%, respectively. The improved flexural performance was attributed to the arch mechanism enabled by proposed GFRP beam-string structure. In addition, the progressive failure of GFRP material and the imperfect load-transfer between GFRP arch beam and tension string were investigated through finite element modeling. Hashin damage criterion was developed based on experimental data obtained in this work as well as those available in literature, and 22% loss of thrusts (by average) were found in present beam-string configuration. Then, web crippling strength of GFRP arch beams was predicted with modifications to an existing model, and improved accuracy was observed. In addition, internal forces of beam-string were calculated. In future work, it is recommended to develop a new beam-string configuration so as to achieve a higher load-transfer efficiency as well as a higher flexural stiffness.

The GFRP beam-string structure proposed in this work is aimed to shed light on possible approach to improve the flexural stiffness of pGFRP members. Based on the successful demonstration of this work, possible applications of curved-pultruded GFRP members can be greatly broadened, such as the long-span spatial roof structures and heavy-duty vehicle bridges.

CRediT authorship contribution statement

TianQiao Liu: Conceptualization, Formal analysis, Funding acquisition, Investigation, Methodology, Project administration, Software, Visualization, Writing – original draft. **Peng Feng:** Conceptualization, Funding acquisition, Methodology, Project administration, Writing – review & editing. **Yulei Bai:** Writing – review & editing, Methodology. **Shangcong Bai:** Investigation, Methodology. **Jia-Qi Yang:**

Methodology, Writing – review & editing. **Fei Zhao:** Funding acquisition, Methodology, Writing – review & editing.

Declaration of Competing Interest

The authors declare that they have no known competing financial interests or personal relationships that could have appeared to influence the work reported in this paper.

Data Availability

Data will be made available on request.

Acknowledgements

This work was supported by National Key R&D Program of China (2023YFB3711600), National Natural Science Foundation of China (51908321), Nonmetallic Excellence and Innovation Center for Building Materials (2022TDA1-1), Chongqing Construction Science and Technology Plan Project (ChengKeZi2022No.2-1), and Natural Science Foundation of Hainan Province (520RC549).

Appendix A. Supporting information

Supplementary data associated with this article can be found in the online version at doi:10.1016/j.engstruct.2024.117962.

References

[1] Hollaway LC. A review of the present and future utilisation of FRP composites in the civil infrastructure with reference to their important in-service properties. Constr Build Mater 2010;24(12):2419–45.
[2] Cromwell JR, Harries KA, Shahrooz BM. Environmental durability of externally bonded FRP materials intended for repair of concrete structures. Constr Build Mater 2011;25(5):2528–39.
[3] Vedernikov A, Safonov A, Tucci F, Carlone P, Akhatov I. Pultruded materials and structures: A review. J Compos Mater 2020:0021998320922894.
[4] Zou X, Feng P, Bao Y, Wang J, Xin H. Experimental and analytical studies on shear behaviors of FRP-concrete composite section. Eng Struct 2020;215:110749.
[5] Alajarmeh O, Zeng X, Aravinthan T, Shelley T, Alhawamdeh M, Mohammed A, et al. Compressive behaviour of hollow box pultruded FRP columns with continuous-wound fibres. Thin-Walled Struct 2021;168:108300.
[6] Liu TQ, Liu X, Feng P. A Comprehensive Review on Mechanical Properties of Pultruded FRP Composites Subjected to Long-Term Environmental Effects. Compos Part B: Eng 2020;191:107958.
[7] Yang JQ, Feng P. Analysis-oriented models for FRP-confined concrete: 3D interpretation and general methodology. Eng Struct 2020;216:110749.
[8] Hu L, Feng P. Prestressed CFRP-reinforced steel columns under axial and eccentric compression. Compos Struct 2021;268:113940.
[9] Feng P, Wu Y, Ding Y, Liu T, Tian Y. Quasi-plastic flexural behavior of adhesive-bolt hybrid connection for large scale pultruded GFRP frame. Eng Struct 2021;238:112200.
[10] Liu, T.Q. (2017). Stability behavior of pultruded glass-fiber reinforced polymer I-sections subject to flexure (Doctoral dissertation, University of Pittsburgh).
[11] Kollár LP. Local buckling of fiber reinforced plastic composite structural members with open and closed cross sections. ASCE. J Struct Eng 2003;129(11):1503–13.
[12] Tarján G, Sapkás Á, Kollár LP. Stability analysis of long composite plates with restrained edges subjected to shear and linearly varying loads. J Reinf Plast Compos 2010;29(9):1386–98.
[13] Nguyen TT, Chan TM, Mottram JT. Lateral-torsional buckling resistance by testing for pultruded FRP beams under different loading and displacement boundary conditions. Compos Part B: Eng 2014;60:306–18.
[14] Liu TQ, Harries KA. Flange local buckling of pultruded GFRP box beams. Compos Struct 2018;189:463–72.
[15] Liu TQ, Vieira JD, Harries KA. Lateral torsional buckling and section distortion of pultruded GFRP I-sections subject to flexure. Compos Struct 2019;225:111151.
[16] Liu TQ, Vieira JD, Harries KA. Predicting Flange Local Buckling Capacity of Pultruded GFRP I-Sections Subject to Flexure. J Compos Constr 2020;24(4):04020025.
[17] Yang JQ, Liu TQ, Feng P. Enhancing Flange Local Buckling Strength of Pultruded GFRP Open-Section Beams. Compos Struct 2020;244:112313.
[18] Liu TQ, Feng P, Lu X, Yang JQ, Wu Y. Flexural Behavior of Novel Hybrid Multicell GFRP-Concrete Beam. Compos Struct 2020;250:112606.
[19] Deskovic N, Triantafillou TC, Meier U. Innovative Design of FRP Combined with Concrete: Short-Term Behavior. J Struct Eng 1995;121(7):1069–78.
[20] Correia JR, Branco FA, Ferreira JG. Flexural behaviour of multi-span GFRP-concrete hybrid beams. Eng Struct 2009;31(7):1369–81.
[21] Fam A, Honickman H. Built-up hybrid composite box girders fabricated and tested in flexure. Eng Struct 2010;32(4):1028–37.
[22] Gemi L, Madenci E, Özkılıç YO. Experimental, analytical and numerical investigation of pultruded GFRP composite beams infilled with hybrid FRP reinforced concrete. Eng Struct 2021;244:112790.
[23] Chen J, Zhu Y, Wang F, Feng B. Experimental and analytical study of hollow section concrete-filled GFRP tubes in bending. Thin-Walled Struct 2022;177:109297.
[24] Li S, Chan TM, Young B. Behavior of GFRP-concrete double tube composite columns. Thin-Walled Struct 2022;178:109490.
[25] Liu TQ, Feng P, Wu Y, Liao S, Meng X. Developing an innovative curved-pultruded large-scale GFRP arch beam. Compos Struct 2021;256:113111.
[26] Zhang J, Zhou P, Guan C, Liu TQ, Kang WH, Feng P, et al. An ultra-lightweight CFRP beam-string structure. Compos Struct 2021;257:113149.
[27] ASTM D3039. Standard Test Method for Tensile Properties of Polymer Matrix Composite Materials. West Conshohocken, PA: ASTM International; 2017.
[28] ASTM D6641. Standard Test Method for Compressive Properties of Polymer Matrix Composite Materials Using a Combined Loading Compression (CLC) Test Fixture. West Conshohocken, PA: ASTM International; 2014.
[29] ASTM D5379. Standard Test Method for Shear Properties of Composite Materials by the V-Notched Beam Method. West Conshohocken, PA: ASTM International; 2012.
[30] ASTM D7264. Standard Test Method for Flexural Properties of Polymer Matrix Composite Materials. West Conshohocken, PA: ASTM International; 2015.
[31] ASTM D2584. Standard Test Method for Ignition Loss of Cured Reinforced Resins. West Conshohocken, PA: ASTM International; 2011.
[32] ASTM D638. Standard Test Method for Tensile Properties of Plastics. West Conshohocken, PA: ASTM International; 2014.
[33] GB 50010. (2010). Code for Design of Concrete Structures. Ministry of Housing and Urban-Rural Construction of the People's Republic of China General Administration of Quality Supervision, Inspection and Quarantine of the People's Republic of China.
[34] Alhawamdeh M, Alajarmeh O, Aravinthan T, Shelley T, Schubel P, Kemp M, et al. Modelling hollow pultruded FRP profiles under axial compression: Local buckling and progressive failure. Compos Struct 2021;262:113650.
[35] Hashin Z, Rotem A. A fatigue failure criterion for fiber reinforced materials. J Compos Mater 1973;7(4):448–64.
[36] Hashin Z. Failure criteria for unidirectional fiber composites. J Appl Mech 1980;47:329–34.
[37] Lapczyk I, Hurtado JA. Progressive damage modeling in fiber-reinforced materials. Compos Part A: Appl Sci Manuf 2007;38(11):2333–41.
[38] Sharma AP, Khan SH, Parameswaran V. Experimental and numerical investigation on the uni-axial tensile response and failure of fiber metal laminates. Compos Part B: Eng 2017;125:259–74.
[39] Tarfaoui M, El Moumen A, Lafdi K. Progressive damage modeling in carbon fibers/carbon nanotubes reinforced polymer composites. Compos Part B: Eng 2017;112:185–95.
[40] Alhawamdeh M, Alajarmeh O, Aravinthan T, Shelley T, Schubel P, Mohammed A, et al. Design optimisation of hollow box pultruded FRP profiles using mixed integer constrained Genetic algorithm. Compos Struct 2022;302:116247.
[41] American Society of Civil Engineers. (ASCE). (2010). Pre-Standard for Load and Resistance Factor Design (LRFD) of Pultruded Fiber Reinforced Polymer (FRP) Structures.
[42] Borowicz DT, Bank LC. Behavior of pultruded fiber-reinforced polymer beams subjected to concentrated loads in the plane of the web. J Compos Constr 2011;15(2):229–38.
[43] Wu C, Bai Y. Web crippling behaviour of pultruded glass fibre reinforced polymer sections. Compos Struct 2014;108:789–800.
[44] Wu C, Zhang LT, Bai Y, Zhao XL. Web crippling behavior of pultruded GFRP channel sections under transverse bearing load. Compos Struct 2019;209:129–42.
[45] Fernandes LA, Gonilha J, Correia JR, Silvestre N, Nunes F. Web-crippling of GFRP pultruded profiles. Part 1: Experimental study. Compos Struct 2015;120:565–77.
[46] Fernandes LA, Nunes F, Silvestre N, Correia JR, Gonilha J. Web-crippling of GFRP pultruded profiles. Part 2: Numerical analysis and design. Compos Struct 2015;120:578–90.
[47] Haloi J, Singh KD, Borsaikia AC. Effect of web perforation on the performance of pultruded GFRP wide-flange section profile in web crippling under end-two-flange loading configuration. Thin-Walled Struct 2022;175:109187.

中美欧通讯杆塔标准中风荷载设计的对比研究

武海鹏，孙云龙，刘鑫燚，张云峰，谢铁秦

（哈尔滨玻璃钢研究院有限公司，哈尔滨 150028）

摘 要 5G 建设对通讯杆塔的承载提出更高要求，风载荷是通讯杆塔承载力的重要设计组成，对不同标准下风荷载参数的研究分析有着重要的工程意义。本文通过对中、美、欧不同标准中风载荷的参数如地形地貌、荷载动态参数、风压高度变化系数等进行对比，为相关涉外通讯工程的风荷载计算提供参考。同时，探讨了复合材料在通讯杆塔领域中应用的优势。

关键词 5G；风载荷；通讯杆塔；标准；复合材料

Comparative Analysis of Wind Load Specifications for Communication Towers in Chinese, American, and European Standards

WU Haipeng, SUN Yunlong, LIU Xinyi, ZHANG Yunfeng, XIE Tieqin
(Harbin FRP Institute Co., Ltd., Harbin 150028)

ABSTRACT The construction of 5G has higher requirements for the bearing capacity of communication towers, and wind load is an important design component of the bearing capacity of communication towers. The research and analysis of wind load parameters under different specifications has important engineering significance. This article compares the wind load parameters of different specifications in China, American and Europe, such as terrain and topography, load dynamic parameters, and wind pressure height variation coefficient, to provide reference for wind load calculation in related foreign communication engineering. At the same time, the advantages of composite materials in the field of communication towers were explored.

KEYWORDS 5G; wind loads; communication tower; standard; composite materials

1 引言

随着 5G 时代的到来，5G 建设和新基建领域让杆塔建设迎来“新春”。5G 通讯塔相比 3G、4G 的网络平台建设，对通讯塔的高度、天线数量和迎风面积都有了较大的增加，使用地点也要求在旷野、山脉、沼泽、沿海等恶劣地区，这给通讯杆塔整体架构的承载力提出更高的要求[1]。复合材料以比刚度、比强度高、耐腐蚀、便于安装、电绝缘等优点，可以在通讯杆塔领域取代传统的金属材料推广应用。目前，我国通讯塔的高度在 20～42 m甚至更高，对于这类高耸结构，风荷载是重要的设计荷载之一，同时风荷载标准也是各国建筑工程设计的重要依据，深入掌握并正确运用不同地区的标准，尤其是对欧美境外通讯杆塔设计时，工程设计人员应重点关注。

基金项目：非金属材料创新中心研发类项目（2022TDA4－1）
通讯作者：武海鹏，硕士研究生，正高级工程师。研究方向为复合材料结构设计及仿真分析。E－mail：wu_effort@163.com

(C)1994-2024 China Academic Journal Electronic Publishing House. All rights reserved. http://www.cnki.net

本文从中标《建筑结构荷载规范（GB50009－2012）》[2]、欧标《Eurocode 1：Actions on structures－Part 1－4：General actions－Wind actions（EN 1991－1－4－2005）》[3]、美标《Structural Standard for Antenna Supporting Structures，Antennas and Small Wind Turbine Support Structures（TIA－222－H－2018）》[4]出发（以下简称中标、美标、欧标），针对不同标准中关于通讯杆塔风荷载的设计参数进行对比分析。将复合材料应用于通讯杆塔设计，可以根据不同风速下、不同高度杆塔的承载能力，调整铺层角度、铺层数量、铺层顺序等，更好的体现了复合材料杆塔的可设计性。

2　风压计算原理

风压是指垂直于杆塔结构表面上的风荷载标准值。在利用不同标准进行风荷载设计时，通常需要注意对基本风压进行两个方面的换算，时距和重现期。中标标准基本风压对应的基本风速为 B 类地貌离地 10 m 处的 10 min 时距，欧标同样采用的 10 min 时距，美标则采用 C 类地貌离地 10 m 处的 3s 时距。不同时距风速与 3s 时距风速对比如表 1 所示。

表 1　不同时距风速与 3s 时距风速对比

风速时距	10 min	5 min	1 min	10 s	3 s
比值	0.70	0.75	0.85	0.95	1

中、美、欧标中重现期均为 50 年[5-6]，这样保证率基本相同，不会影响到最大风速的统计数值。对于年最大风速概率分布类型，中、美、欧标中均采用极值Ⅰ型概率分布函数分析天气的极端天气现象[7-8]。

3　风荷载计算公式

风荷载值是作为一个独立且重要设计指标，直接参与结构设计中，是一个多参数的表达式，其内部参数相互关联[9-11]。中标标准风荷载值计算公式如公式（1）所示。

$$W_k = \beta_Z \times \mu_s \times \mu_z \times W_0 \tag{1}$$

式（1）中，W_k、W_0 分别为风荷载标准值和基本风压值，KPa；βZ 为高度 z 处的风振系数；μ_s、μ_z 分别为风荷载体型系数和风压高度变化系数。

美标标准基本风压计算公式如公式（2）所示。

$$q_Z = 0.613 \times K_Z \times K_{Zt} \times K_d \times V^2 \times I \tag{2}$$

式（2）中，K_z 为风压变化系数；K_{zt}为地形系数；K_d 为风向系数；V：基本风速；I：结构等级重要性系数。

欧标风速压力计算公式如公式（3）所示。

$$q_p = [1 + 7 \times I_V(z)] \times 0.5 \times \rho \times V_m^2 \tag{3}$$

式（3）中，$I_v(Z)$ 为湍流强度；ρ 为空气密度；V_m^2 为参考高度处的平均速度。

中、美、欧标的风荷载计算公式中，主要涉及到的参数有体型系数、地形地貌、载荷动态参数、风压高度变化系数以及荷载组合系数等。其中对通讯杆塔的体型系数差异有限，以下对其他参数进行分析。

3.1　地形地貌参数

地形的粗糙程度、平整程度直接影响着风速，随着地貌越复杂，越粗糙，平均风速一般会较小，而对于开阔平坦的地形，平均风速相对较大。中标中将地貌分为四类（A/B/C/D），A 类主要指海岸、近海面、沙漠无人地带、湖泊及海岛地区，B 类主要指房屋相对稀疏的乡村镇、田野、丘陵及丛林等，C 类主要指拥有一定密集建筑群的市区，D 类主要指房屋很高以及拥有密集建筑群的一些城市区域。粗糙度分别为 0.12，0.15，0.22，0.30。美标中同样将地貌分为四类，不过 A/B/C/D 与中标中的 D/C/B/A 对应；欧标将地面粗糙度分为 0、Ⅰ、Ⅱ、Ⅲ、Ⅳ五类，其中 0 和Ⅰ类与中标 A 类对应，Ⅱ、Ⅲ、Ⅳ类则对应 B、C、D。

3.2　荷载动态参数

自然风的脉动性对结构是一种典型的动力作用，由平均作用和脉动成分组成。同时通讯杆塔的振型、高度、阻尼特性都会影响此动态作用，且幅值随体表位置变化。所以在不同标准中均需考虑风荷载动力的综合响应。荷载动态参数是考虑在风动力作用下响应的等效静态放大综合系数，中、美、欧中的放大系数[12-13]分别为风振系数 β_Z、阵风影响系数 G_f、结构系数 C_sC_d。中标标准中的风振系数 β_Z，考虑脉动风振的影响，根据随机振动理论计算如公式（4）～公式（7）所示。

$$\beta_Z = 1 + 2gI_{10}B_Z\sqrt{1+R^2} \tag{4}$$

$$B_Z = kH^{\alpha 1}\rho_x\rho_z\frac{\varphi(z)}{\mu_Z} \tag{5}$$

$$R = \sqrt{\frac{\pi}{6\xi(1+x_1^2)}\left(\frac{x_1^2}{}\right)^{\frac{4}{3}}} \tag{6}$$

(C)1994-2024 China Academic Journal Electronic Publishing House. All rights reserved.　http://www.cnki.net

$$x_1 = \frac{30f_1}{k_w W_0},\ x_1 > 5 \tag{7}$$

式中，Bz 是脉动风荷载的背景分量因子，I_{10} 是 10 m 高度名义湍流强度，ζ_1 是结构阻尼比，ρ_x、ρ_z 是脉动风荷载水平、竖直方向相关系数。

美标标准中的阵风影响系数 G_f，针对通讯杆塔类柔性或动力敏感结构计算规定如公式（8）～公式（11）所示。

$$G_f = 0.925\left(\frac{1 + 1.7g_Q I_z \sqrt{g_Q^2 Q^2 + g_R^2 R^2)}}{(1 + 1.7g_v I_z)}\right) \tag{8}$$

$$Q = \sqrt{\frac{1}{(1 + 0.63(\frac{B + h}{L_z})^{0.63})}} \tag{9}$$

$$I_z = C(\frac{33}{Z})^{\frac{1}{6}} \tag{10}$$

$$g_R = [2ln(3600n_1)]^{0.5} + \frac{0.577}{[2\ ln(3600n_1)]^{0.5}} \tag{11}$$

式中，g_Q、g_R 为背景响应影响系数，R 为共振相应参数。

欧标标准中动力影响采用结构系数 C_sC_d 如公式（11）和（12）所示。

$$C_s\ C_d = \frac{1 + 2 \times K_P \times I_v \times (Z_e) \times \sqrt{B^2 + R^2}}{1 + 7 \times I_v \times (Z_e)} \tag{12}$$

$$R^2 = \frac{\pi^2}{2 \times \delta} S_L(Z_e, n_{1,x}) \times K_s(n_{1,x}) \tag{13}$$

式中，I_v 是紊流度，K_P 是峰值系数，B^2 是背景系数，R^2 共振相应系数。

荷载动态参数与风速时距相关，时距越短，阵风特性在风荷载响应影响越大。中标和欧标的时距是 10 min，美标的时距是 3 s，相应考虑调整系数。对于高度较低的通讯杆塔，相同的地形地貌下，荷载动态参数对比是风振系数（中标）＞结构系数（欧标）＞阵风系数（美标）。

3.3 风压高度变化系数

风压高度变化系数，反映了作用在杆塔结构上的风压在不同地形地貌高度的变化规律，中美标准采用指数，欧标采用对数描述风速和高度的变化关系如公式（15）～公式（17）所示。

$$\text{中标}\ \mu_Z^B = 1.000\ (\frac{Z}{10})^{0.30},\ 10m \leqslant z \leqslant 350m \tag{15}$$

$$\text{美标}\ K_z^C = 2.01\ (\frac{z}{z_g})^{\frac{2}{\alpha}},\ 4.57m \leqslant z \leqslant z_g \tag{16}$$

$$\text{欧标}\ C_r(z) = K_r \times ln(\frac{z}{Z_0}),\ z_{min} \leqslant z \leqslant z_{max} \tag{17}$$

同样地貌下，50 m 杆塔的不同标准下的风压高度变化系数比较如图 1 所示。

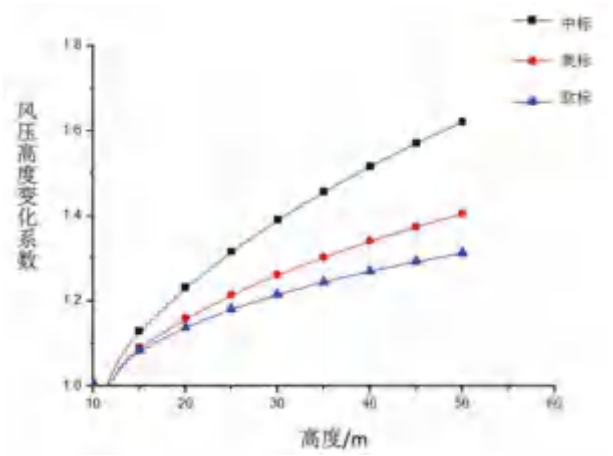


图 1 不同标准风压高度变化系数与高度的关系

从图 1 可以看出，相同地形地貌环境下，中标的风压高度变化系数最大，而欧标最小，这主要是不同标准中关于地貌粗糙度参数差异而造成的。

3.4 不同标准荷载组合值

本文主要分析通讯杆塔的承载力极限状态，下表为中、美、欧标准中起控制的自重静荷载和风荷载的组合进行比较，如表 2 所示。

表 2 不同标准下静载和风载荷的组合对比

标准	组合公式	静载系数	风载系数	风载分项对比
中标	1.2 D + 1.4 W_0	1.2	1.4	1
美标	1.2 D + 1.6 W_0	1.2	1.6	1.143
欧标	1.35 D + 1.5 W_0	1.35	1.5	1.071

注：D 表示通讯杆塔及其附件的自重，W_0 表示作用的通讯杆塔的风荷载。

从表 2 可以看出，通讯杆塔承载中控制作用的风荷载，美标最大 1.6，中标最小 1.4，载荷中的风载荷系数不同标准中差异较大，对最终风荷载产生较大影响。这是由于各国标准建立的体系不同，各个系数的参考的依据不同造成的。

从中、美、欧标中风荷载计算公式参数对比可以看出，对于高度较低的通讯杆塔，地形地貌参数在不同标准中规定大致相同，对杆塔承载力影响较小；荷载动态参数中标最大，美标最小；风压高度变化系数则中标最大，欧标最小；但荷载组合系数中，美标风荷载的分项系数最大，中标最小。综合

(C)1994-2024 China Academic Journal Electronic Publishing House. All rights reserved. http://www.cnki.net

考虑，不同标准对通讯杆塔承载力的影响需具体计算分析。

4　计算对比

为对比不同标准对通讯杆塔变形的影响，分别采用中、美、欧标准对 50 m 单管塔进行风荷载计算。单管塔基本参数，$H=50$ m，$D=1000$ mm，阻尼比 1%。按照中标 B 类粗糙度的开阔地形地貌，基本风速 25 m/s，重现期为 50 年，不同标准下单管塔的风荷载计算值如表 3 所示。

表 3　中美欧标准风荷载计算值对比

类别	15 m	20 m	30 m	40 m	50 m
中标/N	3000	3250	3800	8275	9550
美标/N	4050	6107	6674	13300	15349
欧标/N	9075	9375	9800	20075	20675

根据表 3 的计算结果，对于高度小于 50 m 的通讯杆塔，欧标风荷载计算值最大，中标计算值最小，美标居中。尤其是在高度较低时，欧标计算值近似是中标的 3 倍，随着高度的增加，二者的比值逐渐降低。这主要原因是中标的风振系数沿高度变化趋势要高于美、欧标准。所以对高度小于 50 m 的杆塔，不同标准风荷载的差异不容忽视。

通过对中美欧通讯杆塔标准中风载荷设计公式的风压、地形地貌参数、载荷动态参数、高度变化系数和载荷组合值相对比得出，不同标准中参数值差异较大，工程设计人员不能忽略，同时设计人员可以充分发挥复合材料杆塔的可设计性，以便满足不同标准下的杆塔需求。

5　结语

中、美、欧标准中均采用多参数的形式表征风荷载，主要参数的规定和使用原则基本一致，通过算例结果分析，研究可得以下结论：

（1）中标采用基本风压，美、欧标采用基本风速；

（2）中、美、欧标中风作用的动力影响参数分别是风振系数、阵风影响系数、结构系数，该参数受到结构分类、模态振型等影响，动力参数中标 > 欧标 > 美标；

（3）荷载组合值，风荷载分项系数美标 > 欧标 > 中标，美中标准比值 1.14；

（4）相同地形地貌下，对于高度较低的通讯杆塔，风荷载计算值欧标 > 美标 > 中标，但随着高度的增加比值逐渐减少；

结构风荷载标准值作为多参数表达式，单个参数的差异并不能真实反映荷载标准值的差异。综上所述，对于高低较低通讯杆塔，中、美、欧不同标准下计算风荷载差异较大，不可忽略。

参 考 文 献

[1] 曲方明. 5G 建设过程中通信铁塔的承载能力分析 [J]. 电子技术与软件工程，2021（07）：3－4.

[2] GB50009－2012，《建筑结构荷载规范》[S]. 2012.

[3] EN 1991－1－4－2005，《Eurocode 1：Actions on structures－Part 1－4：General actions－Wind actions》[S]. 2005.

[4] TIA－222－H－2018，《Structural Standard for Antenna Supporting Structures，Antennas and Small Wind Turbine Support Structures》[S]. 2018.

[5] 刘敏，孙义刚，陈娟辉. 基于高层建筑主体结构的中美风荷载计算分析对比 [J]. 邵阳学院学报（自然科学版），2016，13（03）：88－92.

[6] 王敏，何文俊. 欧标风荷载计算及参数取值 [J]. 山西建筑，2019，45（06）：31－32. DOI:10.13719/j.cnki.cn14－1279/tu.2019.06.016.

[7] 吴元元，任光勇，颜潇潇. 欧洲与中国规范风荷载计算方法比较 [J]. 低温建筑技术，2010（06）：63－65.

[8] 吴纯华，浅议中美规范风荷载计算对比 [J]. 低温建筑技术，2010，32（06）：63－65.

[9] 申跃奎，方圆，高宝中. 中美英三国风荷载规范重要参数的比较 [J]]. 钢结构，2014，29（01）：40－43＋7. DOI：10.13206/j.gjg201401011.

[10] 杨坤. 中标、欧标、阿标、南标风荷载规范对比研究 [J]. 建筑结构，2021（21）：124－125.

[11] 黄韬颖，杨庆山. 中美澳风荷载规范重要参数的比较 [J]. 城市建设理论研究（电子版），，2017（21）：124－125. DOI：10.19569/j.cnki.cn119313/tu.201721115.

[12] 周瑞. 中美房屋建筑风荷载计算对比分析 [C] //浙江省建筑设计研究院，东南大学，《建筑结构》杂志社. 第八届工程结构抗震技术交流会论文集. 第八届工程结构抗震技术交流会论文集，2023：297－301. DOI:10.26914/c.cnkihy.2023.036732.

[13] 张军锋，葛耀君，柯世堂. 中美日三国规范高层结构风荷载标准值对比 [J]. 湖南大学学报（自然科学版），2011，38（10）：18－25.

(C)1994-2024 China Academic Journal Electronic Publishing House. All rights reserved.　http://www.cnki.net

Improving performance of GFRP joints using bolted/mortise-tenon hybrid method

YIN Yue*, WU Haipeng, SUN Yunlong

Harbin FRP Institute, Harbin 150036, People's Republic of China

Corresponding-Author: YIN Yue (yinyue@stu.hit.edu.cn)

Abstract. In this study, the effects of different connection methods such as adhesives and bolts on the performance of GFRP joints were compared. A hybrid method based on bolted/mortise-tenon was proposed, and the static strength of joints was studied through experiments and numerical simulations. Static trength testing using glass fiber reinforced polyurethane composites. The results showed that for adhesive-bonded joints, double-lap shear specimens have the highest shear strength. For bolted joints, double-lap specimens also have higher connection strength than single-lap specimens. And the strength of joints using bolts is much greater than that using adhesives. In addition, the bolted/mortise -tenon hybrid joint has a self-locking structure of dovetail and tenon connections, which converts shear strength into structural strength, effectively improves the load-bearing capacity, increases the reliability of the connection, and contributes to higher load-bearing capacity.

1. Introduction

With the development of 5G networks, there is a growing demand for mobile communication[1, 2]. Traditional communication towers are typically made of concrete and steel, which have the drawback of being heavy. This heaviness leads to difficulties in transportation and installation during the construction process, making it challenging to meet the needs of communication stations in remote mountainous areas[3, 4]. Furthermore, as the demand for communication signal coverage increases, the height of communication towers also increases, resulting in an increase in the self-weight of the towers, which has become a driving factor in the structural design of communication stations. Due to their advantages in strength, weight, fatigue resistance, and corrosion resistance, glass fiber reinforced polymer (GFRP) composites are considered ideal building materials that can replace steel[3, 5, 6].

Currently, GFRP composite towers are widely used in various applications such as wind turbine tower frames[7], communication towers[4, 8], and transmission towers[9, 10]. Since communication towers are difficult to transport after assembly, they need to be transported in parts and assembled on-site. Therefore, the connection methods for composites have become a limiting factor for their further application. Currently, the main connection methods for composites include adhesive bonding[11, 12], mechanical fastening[13, 14], and hybrid connections[15-18]. Mortise-tenon connection is the main connection method between wooden components in traditional Chinese architecture, which can effectively transfer loads[19, 20]. Liu et al. [21]studied aluminum mortise-tenon joints and reinforced mortise-tenon joints for electric

vehicle applications. The results showed that the reinforced joint showed the highest load bearing and energy absorption under both the in-plane and out-of-plane bending. This method is ingenious and easy to install, and has good application prospects in modern engineering. However, research on mortise- tenon joints in the field of composites is still limited.

The purpose of this study is to investigate the connection methods for easily installable composite structures, focusing on two main issues. Firstly, to compare the influence of different connection methods on the performance of GFRP joints. Secondly, to design a hybrid method of bolted/mortise-tenon to enhance the performance of GFRP joints.

2. Materials and methods

2.1. Materials

All pultruded profiles used in this study were fabricated using the extrusion machine of Harbin FRP Institute Co., Ltd. E-glass fibers were provided by Shandong Taishan Glass Fiber Co. , Ltd . Isocyanate and Polyether polyolwas provided by Nanjing Jufa New Material Co. , Ltd. Adhesive was provided by Institute of Petroleum Chemistry, Heilongjiang Academy of Sciences. The extrusion traction speed was 150 mm/min. After the process reached a stable state, the unidirectional laminates with a stable cross-section was used for performance testing.

2.2. Characterization

According to GB/T7124, samples of the required dimensions were cut from the unidirectional laminates. Samples include single lap joints, double lap joints, single strap butt joints and double strap butt joints. Tensile tests of the samples were conducted using a hydraulic-driven testing machine (8802, Instron Co. Ltd.) at room temperature (25°C) with a crosshead speed of 1 mm/min. Five samples were tested for each tensile test.

3. Results and Discussion

3.1. Comparison of different adhesives bonded joints

Adhesive bonding is a practical and effective connection technique that joins components into an inseparable whole using adhesive. It has been widely applied in composite joints. Figure 1 shows Four common different forms of joints.

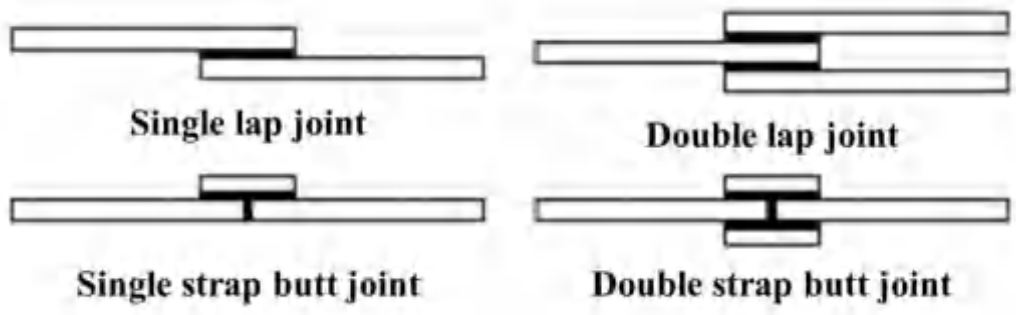


Figure 1 Four common different forms of joints

Four bonded joints with different properties were prepared using GFRP as the adherend, as shown in Figure 2.



Figure 2 Specimens of adhesive bonded joints of GFRP

The tensile shear strength of four different forms of adhesive bonded joints was tested and the results are shown in table1

The shear strength of the four different forms of adhesive bonded joints was tested and the results are shown in Figure 3 and Table 1.

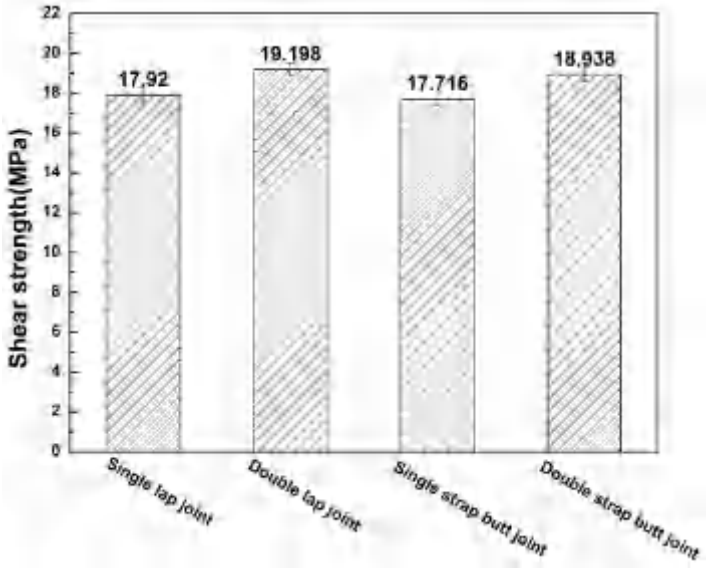


Figure 3 Shear strength of different adhesives bonded joints

Table 1 Detailed data on Shear strength of different adhesives bonded joints

Adhesive bonded joint form	Test Result					Average
Single lap joint	17.56	17.98	18.35	17.45	18.26	17.92
Double lap joint	19.25	19.65	18.87	19.21	19.01	19.20
Single strap butt joint	17.26	17.95	17.45	18.06	17.86	17.72
Double strap butt joint	18.68	18.59	18.76	19.21	19.45	18.94

From Figure 4, it can be observed that the double-lap joint exhibits the highest connection performance, reaching 19.20 MPa. Additionally, double lap joints and double strap butt joints show higher shear strength compared to the single lap joints and single strap butt joints due to uneven shear stress and deformation during testing. The single-lap shear experiences eccentric loading during testing, leading to bending and normal forces, causing adhesive failure.

The factors affecting adhesive strength mainly focus on the bonding area and the strength of the adhesive itself. While a larger bonding area typically results in higher bonding strength, the ultimate joint strength primarily depends on the performance of the adhesive. Additionally,

the performance of the adhesive adhesive is significantly influenced by factors such as the bonding environment and the skill level of the personnel performing the bonding, indirectly affecting the overall structural performance of composite lattice towers. Hence, adhesive bonding is not yet suitable for composite lattice towers.

3.2. Comparison of different bolted joints

Mechanical connection involves locally drilling holes in the components and then connecting them into a whole using fasteners such as rivets, dowel pins, and bolts. Mechanical connection is currently the most widely used method in composites connections, with widespread application and mature technology. Figure 4 shows specimens of different forms of bolted joints.

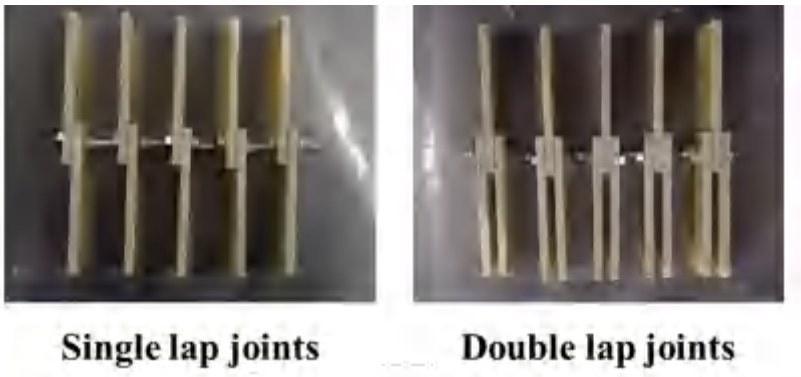


Figure 4 Specimens of different forms of bolted joints of GFRP

The shear strength of the different forms of bolted joints was tested and the results are shown in Table 2 and Figure 5.

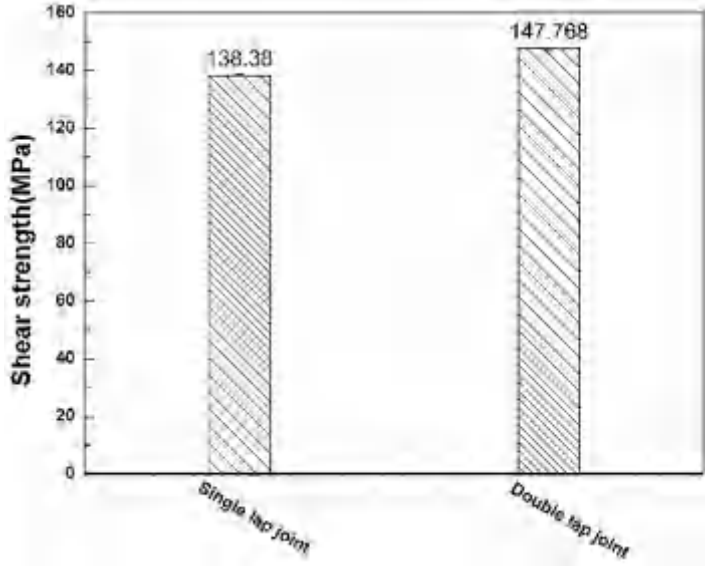


Figure 5 Shear strength of different bolted joints

Table 2 Detailed data on Shear strength of different bolted joints

Bolted joint form	Test Result					Average
Single lap joint	138.95	137.84	138.46	138.16	138.49	138.38
Double lap joint	148.24	147.60	148.88	147.21	146.91	147.78

Figure 5 illustrates that the shear strength of bolted joints exceeds 130 MPa, which is higher than adhesive bonding. However, as bolted joints s typically require pre-drilling,

depending on the drilling method, the stress concentration around the edge of the hole may be different, resulting in differences in shear strength. Initially, when subjected to force, friction between the connected components transfers the load; however, upon surpassing the friction limit, relative slippage between components occurs, resulting in shear forces on the bolts and pressure on the hole walls for load transmission. Moreover, drilling holes in composites weakens their overall strength, and due to the anisotropic nature of composites, severe stress concentration occurs at the hole locations. Hence, while mechanical connections such as bolted connections are widely used and technically mature, there is still significant research space to improve their efficiency and strength.

3.3. Design and performance of GFRP bolted/mortise-tenon hybrid joints

Mortise-tenon connection is a form of interlocking connection used on two components, characterized by its protrusion and recess combination. The mortise and tenon structure is a fundamental connection method in traditional Chinese architecture, furniture, and other wooden structures. While initially associated with wooden structures, mortise and tenon structures have also been applied in stone and metal. By applying the dovetail tenon structure to composites connections, the self-locking and closed structure of the dovetail tenon effectively increases the load-bearing capacity of the connecting components, enhancing connection reliability.

First, a preliminary design and simulation analysis was conducted on the mortise-tenon structure of GFRP, as shown in Figure 6.



Figure 6 Design of mortise and tenon structure specimen of GFRP

With one end constrained and the other end subjected to loading, the simulation results are shown in Figures 7.

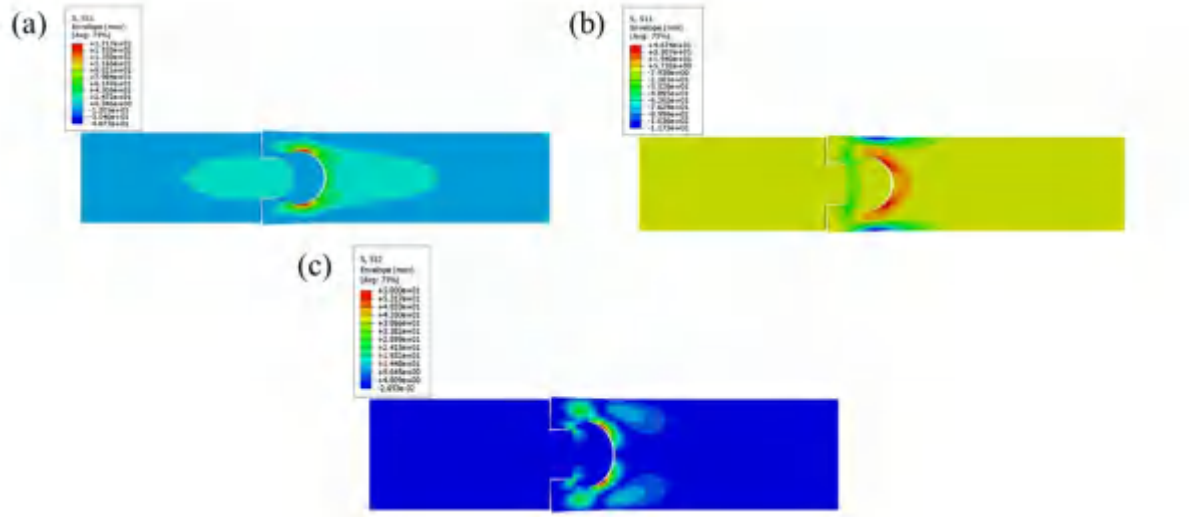


Figure 7 Stress simulation of mortise-tenon joint (a) tensile stress cloud diagram of mortise-tenon joint, (b) compressive stress cloud diagram of mortise-tenon joint and (c) shear stress cloud diagram of mortise-tenon joint

The simulation results indicate that when the mortise and tenon structure is subjected to tension, the maximum stress occurs at the outermost end of the structure, while under compression, the maximum stress occurs at the contact surface of the structure. To eliminate potential structural failure due to maximum stress, a mechanical connection form was introduced to transfer stress positions, enhancing structural stability. The optimized structure is shown in Figure 8.

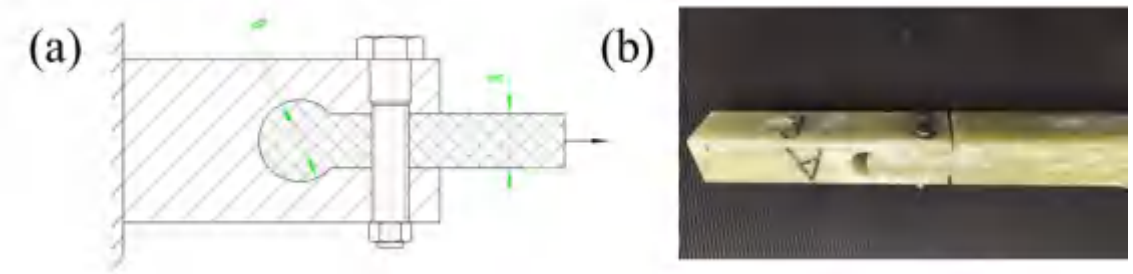


Figure 8 (a)Design drawing and (b)actual picture of bolted/mortise-tenon hybrid joint

After determining the node structure, the tensile strength of the structure was tested, as shown in Figure 9.

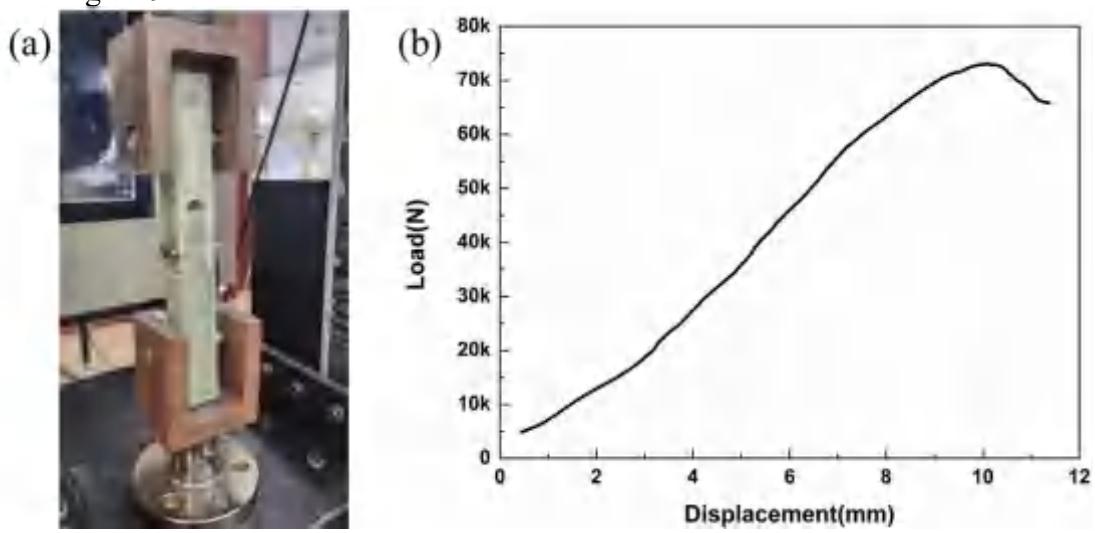


Figure 9 Bolted/mortise-tenon hybrid joint under test and corresponding load-displacement curve

From the load-displacement data, it could be observed that the structure's failure load of the bolted/mortise-tenon hybrid joint reached 71 kN, with a tensile strength of 200 MPa, far exceeding mechanical and adhesive connections. Considering construction environments and conditions, this structure is more suitable for engineering projects.

4. Conclusion

To meet the performance requirements of composite lattice towers for communication and power transmission, and to enhance the strength of GFRP joints, a bolted/mortise-tenon hybrid joint is proposed. Static tests were conducted on three types of specimens: adhesive-bonded joints, bolted joints, and bolted/mortise-tenon hybrid joints. The results indicate that for adhesive-bonded joints, double-lap joints and double-strap butt joints exhibit higher failure strength due to more uniform shear stress and deformation. However, adhesive-bonded joints have the lowest failure strength overall. By reinforcing the mortise-tenon joints with bolts, the bolts transfer the potential failure stress within the mortise-tenon structure, thereby

improving structural stability. Consequently, the hybrid joints demonstrate the highest failure strength.

Acknowlegement
This work was supported by the TDA Program of NEXCEL nonmetallic excellence and innovation center for building materials(2022TDA4-1) .

References

[1] Prasad Rao, N.; Rokade, R. P.; Balagopal, R. Failure investigation of GFRP communication towers. Engineering Failure Analysis 2017, 79, 397-407. DOI: https://doi.org/10.1016/j.engfailanal.2017.05.002.
[2] Gao, H.; Sun, Y.; Lei, X.; Gao, Y.; Liu, H. Mechanical properties and application of glass fiber reinforced polyurethane composites communication lattice tower. Construction and Building Materials 2024, 411, 134180. DOI: https://doi.org/10.1016/j.conbuildmat.2023.134180.
[3] Alshurafa, S.; Alnaafa, M. A.; Polyzois, D. Development of GFRP Guyed Communication Towers. In 10th International Conference on FRP Composites in Civil Engineering: Proceedings of CICE 2020/2021 10, 2022; Springer: pp 1904-1913.
[4] Gao, H.; Sun, Y.; Jian, J.; Dong, Y.; Liu, H. Study on mechanical properties and application in communication pole line engineering of glass fiber reinforced polyurethane composites (GFRP). Case Studies in Construction Materials 2023, 18, e01942.
[5] Sheikh, S. A.; Kharal, Z. Replacement of steel with GFRP for sustainable reinforced concrete. Construction and Building Materials 2018, 160, 767-774. DOI: https://doi.org/10.1016/j.conbuildmat.2017.12.141.
[6] Ramirez-Vazquez, I.; Hernández-Corona, R.; Salgado-Talavera, J. E. Composite materials as an alternative to replace steel members on lattice power transmission towers. Journal of Materials in Civil Engineering 2016, 28 (3), 04015151.
[7] Polyzois, D. J.; Raftoyiannis, I. G.; Ungkurapinan, N. Static and dynamic characteristics of multi-cell jointed GFRP wind turbine towers. Composite Structures 2009, 90 (1), 34-42. DOI: https://doi.org/10.1016/j.compstruct.2009.01.005.
[8] Balagopal, R.; Prasad Rao, N.; Rokade, R. Investigation on buckling behaviour of GFRP angle sections with bolted connections in lattice towers. Journal of The Institution of Engineers (India): Series A 2020, 101, 327-342.
[9] Syamsir, A.; Ean, L.-W.; Asyraf, M. R. M.; Supian, A. B. M.; Madenci, E.; Özkılıç, Y. O.; Aksoylu, C. Recent Advances of GFRP Composite Cross Arms in Energy Transmission Tower: A Short Review on Design Improvements and Mechanical Properties. Materials 2023, 16 (7), 2778.
[10] Adishchev, V. V.; Zubkov, A. S.; Ivanov, A. I.; Maltsev, V. V.; Panichev, A. Y.; Blaznov, A. N. Rational design of steel–GFRP towers for ultracompact overhead power lines. Mechanics of Advanced Materials and Structures 2020, 27 (3), 189-195. DOI: 10.1080/15376494.2018.1472331.
[11] Zhang, Y.; Vassilopoulos, A. P.; Keller, T. Effects of low and high temperatures on tensile behavior of adhesively-bonded GFRP joints. Composite Structures 2010, 92 (7), 1631-1639.
[12] Sousa, J.; Correia, J.; Gonilha, J.; Cabral-Fonseca, S.; Firmo, J.; Keller, T. Durability of adhesively bonded joints between pultruded GFRP adherends under hygrothermal and natural ageing. Composites Part B: Engineering 2019, 158, 475-488.
[13] Jiang, Z.; Wan, S.; Fang, Z.; Song, A. Static and fatigue behaviours of a bolted GFRP/steel double lap joint. Thin-Walled Structures 2021, 158, 107170.
[14] Wang, P.; He, R.; Chen, H.; Zhu, X.; Fang, D. A novel predictive model for mechanical behavior of single-lap GFRP composite bolted joint under static and dynamic loading. Composites Part B: Engineering 2015, 79, 322-330.
[15] Di Franco, G.; Zuccarello, B. Analysis and optimization of hybrid double lap aluminum-GFRP

joints. Composite Structures 2014, 116, 682-693.
[16] Matsuzaki, R.; Shibata, M.; Todoroki, A. Improving performance of GFRP/aluminum single lap joints using bolted/co-cured hybrid method. Composites Part A: applied science and manufacturing 2008, 39 (2), 154-163.
[17] Inbanaathan, P.; Dhinesh, B.; Tamilarasan, U.; Prasanna, B. V.; Dineshkumar, C.; Kiran, S. Characteristics assessment on riveted, bonded and hybrid joints using GFRP composites. Materials Today: Proceedings 2021, 47, 6889-6895.
[18] Fiore, V.; Alagna, F.; Galtieri, G.; Borsellino, C.; Di Bella, G.; Valenza, A. Effect of curing time on the performances of hybrid/mixed joints. Composites Part B: Engineering 2013, 45 (1), 911-918. DOI: https://doi.org/10.1016/j.compositesb.2012.05.016.
[19] Chen, C.; Qiu, H.; Lu, Y. Flexural behaviour of timber dovetail mortise–tenon joints. Construction and Building Materials 2016, 112, 366-377. DOI: https://doi.org/10.1016/j.conbuildmat.2016.02.074.
[20] Yang, Q.; Yu, P.; Law, S.-s. Load resisting mechanism of the mortise-tenon connection with gaps under in-plane forces and moments. Engineering Structures 2020, 219, 110755.
[21] Liu, Q.; Wang, J.; Huang, X.; Wu, T.; Zong, Z.; Li, Q. In-plane and out-of-plane bending responses of aluminum mortise-tenon joints in lightweight electric vehicle inspired by timber structures. Thin-Walled Structures 2018, 127, 169-179. DOI: https://doi.org/10.1016/j.tws.2018.01.033.

DOI https: //doi. org/10.1007/s11595-023-2790-5

Mixed-Alkali Effect on Thermal Property and Elastic Behavior in Borosilicate Glasses

XIE Xianmao[1], ZHOU Hemin[1], KE Xuefei[1], WANG Xiaowei[2], WANG Yadan[2], ZHANG Jiayan[1], QIAO Ang[1,3], TAO Haizheng[1*]

(1. State Key Laboratory of Silicate Materials for Architectures, Wuhan University of Technology, Wuhan 430070, China; 2. AVIC Jonhon Optronic Technology Co. Ltd., Luoyang 471003, China; 3. Wuhan University of Technology Advanced Engineering Technology Research Institute of Zhongshan City, Zhongshan 528437, China)

Abstract: We investigated the mixed alkali effect on the thermal properties and elastic response to temperature in the borosilicate glasses system with the composition of $70.65SiO_2 \cdot 21.09B_2O_3 \cdot 1.88Al_2O_3 \cdot (6.38\text{-}x)Li_2O \cdot xNa_2O$ glasses, where x = 0.00, 1.595, 3.19, 4.785, and 6.38. Except for the expected positive and negative deviations from linearity for the coefficients of thermal expansion, room temperature E and G, we observed a new mixed alkali effect on the response of elastic moduli to temperature. Fourier transform infrared spectra were obtained to elucidate the possible structural origin of the mixed alkali effects. This work provides a valuable insight into the structural and mechanical properties of mixed-alkali borosilicate glasses.

Key words: mixed-alkali effect; borosilicate glass; elastic response to temperature; structural origin

1 Introduction

Mixed alkali effect, or mixed modifier effect, is still one of unsolved basic questions in the glass community, although this effect was firstly discovered in oxide glass by Weber in 1883[1] when investigating the thermometer effect in glasses with more than one alkali modifier. It refers to the phenomenon of nonlinear variation especially in transport properties when a network modifying mobile cation is replaced by a second one[2]. These transport properties, also called dynamic properties, include ionic conductivity, diffusion, and viscosity that go through a minimum or maximum when the mixing ratio of two cations changes[3, 4]. The degree of departure from linearity depends on the compositions, the temperature and frequency of measurement, and especially the discrepancy of size and polarizability of the modifier cations[5].

Despite still lacking a thorough understanding for mixed alkali effect, much progress has been made over the past several decades. Especially, the dynamic structure model, which is based on the energy landscape approach, has helped to establish a more coherent picture[6,7]. Based on the idea of a mismatch effect where sites favorable for one type of cation in the glassy network are unfavorable for the other type of cation, this model elucidates the structural origin of mixed alkali effect, and has been further supported by compelling evidences from extended X-ray absorption fine structure (EXAFS), nuclear magnetic resonance (NMR) and Infrared Spectroscopy[8-10].

Contrary to the similar schematic drawings in the previous studies[8,11,12], by constructing a state-of-the art structural model which reproduces both diffraction and NMR data, recently, Kohara *et al* identified a highly correlated pair arrangement between K and Na ions around non-bridging oxygen atoms in the $22.7R_2O \cdot 77.3SiO_2$ (R = Na and/or K) alkali silicate glasses by using a novel topological analysis technique (persistent homology)[13]. These facts indicate that the correlated pair arrangement could likely be the intrinsic origin of the mixed alkali effect. However, based on the assumption of identically distributed alkali ion throughout the network, another new structural

© Wuhan University of Technology and Springer-Verlag GmbH Germany, Part of Springer Nature 2023

(Received: Apr. 18, 2022; Accepted: July 21, 2023)

XIE Xianmao(谢先茂): E-mail: 1132582532@qq.com

*Corresponding author: TAO Haizheng(陶海征): Prof.; Ph D; E-mail: thz@whut.edu.cn

Funded by National Natural Science Foundation of China (No. 52172007), the Ph D Program Fund of Non-Metallic Excellence and Innovation Center for Building Materials (No.2022SFP6-2), and GuangDong Basic and Applied Basic Research Foundation (No. 2022A1515010312) and Jiangsu Science and Technology Innovation Project for Carbon Peaking and Carbon Neutrality (No.BE2022035)

model based on the topological constraint theory was recently given to elucidate the origin of mixed alkali effect in the $0.30(y\mathrm{Na_2O}+[1-y]\mathrm{K_2O})\cdot 0.70\mathrm{SiO_2}$ glasses[14]. By proposing the composition dependence of constraint energy as a result of network strain due to different cation radii, this model can well explain the experimental observations of the mixed alkali effect in the glass transition temperature, and other performances. Further investigations were conducted on $(25-x)\mathrm{Na_2O}\cdot x\mathrm{K_2O}\cdot 10\mathrm{Al_2O_3}\cdot 65\mathrm{SiO_2}$ aluminosilicate glasses, where alkali ions act as modifiers forming non-bridging oxygen or as charge compensators to $\mathrm{AlO_4}$ units. Among the five major interatomic potentials validated in the classical MD simulations, only the polarizable core-shell (CS) force field model was able to well reproduce the mixed alkali effect in both ionic conductivity and glass transition temperature [15]. By using the van Hove correlation function, the alkali ion jump analysis clearly indicates that the different alkali ions locate at different local surroundings and obstruct each other in the channel, thus constricting their mobility when mixed. Therefore, much contention also remains about the structural origin of mixed alkali effect in glass community. And although there are many investigations on mixed alkali effects on silicate glasses, less effort has been devoted to study such phenomena in mixed alkali borosilicate glasses.

In this work, based on a batch composition from alkali borosilicate glasses (*i e*, electronic sealing glass DM308), we prepared a series of mixed lithium-sodium borosilicate glasses with varying molar ratio r ($[\mathrm{Na_2O}]/([\mathrm{Na_2O}]+[\mathrm{Li_2O}])$) from 0.00 to 1.00. Coefficient of thermal expansion and room temperature and variable temperature moduli were systematically characterized to investigate their composition dependence. Especially, we observed a new mixed alkali effect on the elastic response to temperature. Further Fourier transform infrared spectroscopy (FTIR) measurements were conducted to investigate the structural origin of mixed alkali effect in this series of mixed lithium-sodium borosilicate glasses.

2 Experimental

2.1 Glass preparation

Alkali borosilicate glasses were prepared using the traditional melt-quenching technique. The glasses had nominal molar compositions of $70.65\mathrm{SiO_2}\cdot 21.09\mathrm{B_2O_3}\cdot 1.88\mathrm{Al_2O_3}\cdot(6.38-x)\ \mathrm{Li_2O}\cdot x\mathrm{Na_2O}$, where x = 0, 1.60, 3.19, 4.79, 6.38 molar percent, which correspond to r = 0.00, 0.25, 0.5, 0.75 and 1.00 (r is the molar ratio of $[\mathrm{Na_2O}]/([\mathrm{Na_2O}]+[\mathrm{Li_2O}])$). The raw materials used in glass melting were $\mathrm{SiO_2}$, $\mathrm{H_3BO_3}$, $\mathrm{Al_2O_3}$, $\mathrm{Li_2CO_3}$, and $\mathrm{Na_2CO_3}$ powders. The batches were mixed thoroughly and melted in a $\mathrm{Pt_{90}Rh_{10}}$ crucible at 1 873 K for 1-3 hours. Finally, the melts were cast onto a graphite mold and promptly transferred to a preheated annealing furnace, where they were held at their respective glass transition temperatures for 2 hours to eliminate internal stress. By using the wet chemistry method, chemical compositional analysis indicated that the actual chemical compositions are almost the same to the desired compositions.

2.2 Elastic modulus

To monitor the evolution of elastic properties as a function of temperature, the elastic modulus was measured non-destructively by the GrindoSonic HT1200, which is designed to measure the temperature variation of the elastic properties of materials using impulse excitation technique[16]. The glasses were heated from room temperature to 520 ℃ for each composition. The Young's modulus(E) and shear modulus(G) can be calculated using the following equations:

$$E = 0.946\ 5\left(\frac{mf_{\mathrm{f}}^2}{b}\right)\left(\frac{L^3}{t^3}\right)T \tag{1}$$

$$G = \frac{4Lmf_t^2}{bt}\left(\frac{B}{1+A}\right) \tag{2}$$

where m is the weight of the specimen; f_{f} is the fundamental flexure resonant frequency; f_{t} is the fundamental torsional resonant frequency; b is the width of the specimen; L is the length of the specimen; t is the thickness of the specimen; T, B, and A are the correction factors related to the dimensions of the specimen in calculation.

2.3 Dilatometry properties

By using the thermal dilatometer (type: DIL402PC) made by NETZSCH, coefficients of thermal expansion (CTE, averaged over a temperature range of 50 to 400 ℃) and dilatometric softening temperature (T_{d}, defined as the temperature of maximum expansion, corresponding to the viscosity at about 10^{10} Pa·s), were determined for the polished samples with the size of 5 mm×5 mm×25 mm at an up-scan rate of 5 ℃/min.

2.4 Structural analysis

Atomic-scale structure of the as-prepared glasses was obtained from their Fourier transform infrared

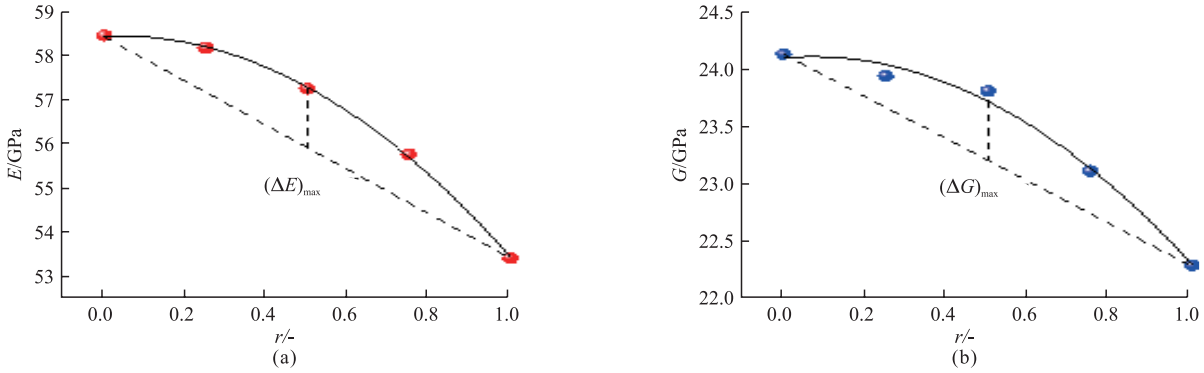


Fig.1 Composition dependence of Young's modulus E (a), shear modulus G (b) at room temperature as a function of the molar ratio r (r is equal to the molar ratio of $[Na_2O]/([Li_2O]+[Na_2O])$) for the $70.65SiO_2 \cdot 21.09B_2O_3 \cdot 1.88Al_2O_3 \cdot (6.38\text{-}x)\ Li_2O \cdot xNa_2O$ glasses (The uncertainties of E and G are both ± 0.01 GPa)

(FTIR) spectra. By using the KBr pellet technique, FTIR absorption spectra of these glasses were collected by the Bruker INVENIO-S FT-IR spectrometer in the range of 400 to 1 600 cm^{-1}. In order to obtain spectra with high quality, the samples were crushed in an agate mortar to obtain particles of micrometer size. Each sample was mixed with KBr in the proportion of 1:100 and pressed with a pressure of 15 MPa to obtain transparent pallets with an approximate thickness of 1 mm.

3 Results

3.1 Mechanical and thermal properties

Similar to mixed alkali effect on microhardness in borate glasses[17], which is as the positive deviation from linearity, here we also observed a positive deviation on E and G in the present glasses as shown in Fig.1. More concretely, with the substitution of Li by Na, a drop of 5.00 GPa in E occurs from 58.40 GPa of the Li-containing end member composition to 53.40 GPa of the Na-containing end member composition.

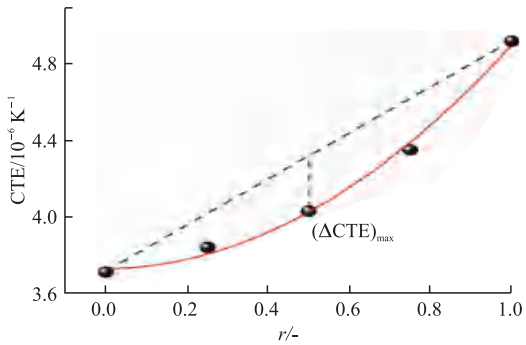


Fig.2 Composition dependence of coefficients of thermal expansion (CTE) between 50 and 400 ℃ for the $70.65SiO_2 \cdot 21.09B_2O_3 \cdot 1.88Al_2O_3 \cdot (6.38\text{-}x)\ Li_2O \cdot xNa_2O$ glasses with different molar ratio r (r is equal to the molar ratio of $[Na_2O]/([Li_2O]+[Na_2O])$ and the uncertainty of CTE is ± 0.2×10^{-6} K^{-1})

And a drop of 2.00 GPa in G appears from 24.20 GPa of Li-containing end member composition to 22.20 GPa of the Na-containing counter-composition. In addition, maximum deviations of 1.35 GPa in E and 0.51 GPa in G from linearity come out at about the equal-molar composition $r = 0.5$.

However, when it comes to the CTE, we observed a negative deviation from linearity (Fig.2). A maximum

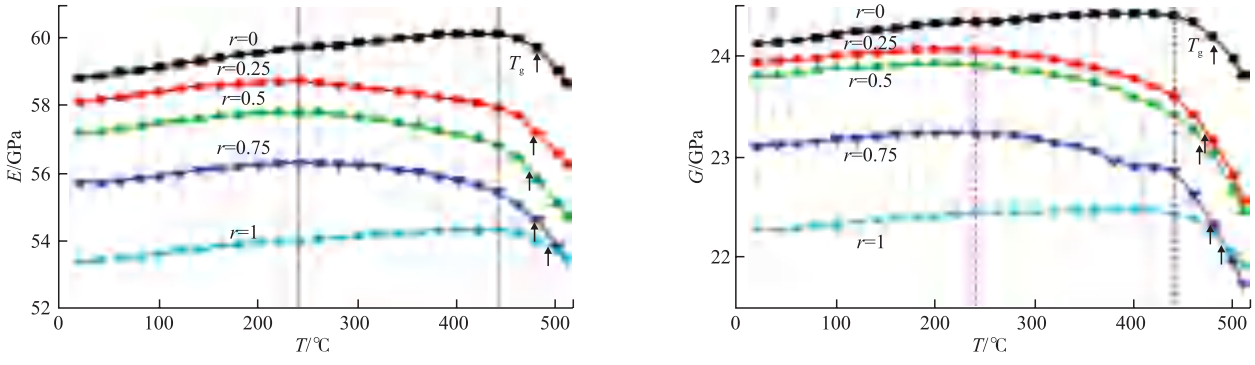


Fig.3 Young's modulus E(a), shear modulus G(b) as a function of temperature with different molar ratio r (r is equal to the molar ratio of $[Na_2O]/([Li_2O]+[Na_2O])$) for the $70.65SiO_2 \cdot 21.09B_2O_3 \cdot 1.88Al_2O_3 \cdot (6.38\text{-}x)Li_2O \cdot xNa_2O$ glasses (The uncertainties of E and G are both ± 0.01 GPa)

deviation (0.3×10^{-6} K^{-1}) in CTE from linearity occurs also at about r = 0.5. And with a gradual increase in r, a big enhancement of about 1.2×10^{-6} K^{-1} turns up from 3.72×10^{-6} K^{-1} of the Li-containing end-member composition to 4.92×10^{-6} K^{-1} of the Na-containing end-member composition.

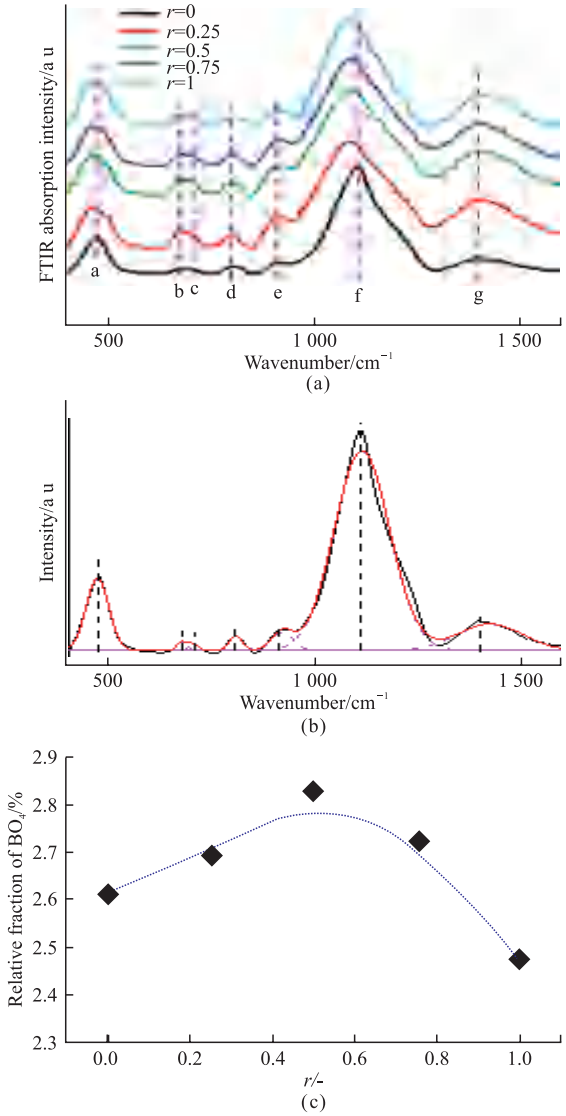


Fig.4 (a) Composition dependence of infrared absorption spectra for $70.65SiO_2\cdot21.09B_2O_3\cdot1.88Al_2O_3\cdot(6.38\text{-}x)\ Li_2O\cdot xNa_2O$ glasses with different molar ratio r (r is equal to the molar ratio of $[Na_2O]/([Li_2O]+[Na_2O])$); (b) Deconvoluted infrared spectrum in the region of 400 - 1 600 cm^{-1} for the glass at r = 0; (c) Composition dependence of the relative fraction (relative to the total integrated area in the region from 400 to 1 600 cm^{-1}) of the infrared band centered at 900 cm^{-1} related to BO_4 units

Finally, we observed a new mixed alkali effect on temperature dependence of E and G in the present glasses (Fig.3). For the two end-member compositions, E and G exhibit the similar increase with the step by step rises in temperature up to 440 ℃. For the Li-containing end-member composition, there are increases of 1.27 GPa in E from 58.81 GPa at 20 ℃ to 60.08 GPa at 440 ℃ and 0.3 GPa in G from 24.12 GPa at 20 ℃ to 24.42 GPa at 440 ℃. Correspondingly, for the Na-containing end-member counterpart, there are increases of 0.94 GPa in E from 53.38 GPa at 20 ℃ to 54.32 GPa at 440 ℃ and 0.16 GPa in G from 22.28 GPa at 20 ℃ to 22.44 GPa at 440 ℃. When it comes to the compositions with r = 0.25, 0.50, and 0.75, a gradual increase of about 0.60 GPa in E and about 0.10 GPa in G occurs from 20 to 240 ℃. However, different from the two end-member compositions, the compositions with r = 0.25, 0.50, and 0.75 exhibit a clear drop in E and G after 240 ℃. That's to say, a drop of 0.80, 1.01, and 0.87 GPa in E and 0.44, 0.50, and 0.79 in G turns up for these compositions with r = 0.25, 0.50, and 0.75 respectively. This observation indicates that the mixture of Li and Na results in a distinct response of E and G to temperature.

Table 1 Characteristic bands of infrared spectrum in Fig.4(a) and their attributions

Band	Wavenumber/cm^{-1}	Assignment
a	470	Bending vibration of the Si-O-Si[18]
b	670	The symmetry stretching vibration of Si-O[19]
c	700	The oxygen bridges between two BO_3[19]
d	800	The symmetric breathing vibration of boroxol ring[20]
e	900	The stretching vibration of the B-O in BO_4 units[21]
f	1 100	The asymmetric stretching vibration of Si-O-Si[22]
g	1 400	The asymmetric stretching vibration of neutral borate triangles, BO_3[22]

3.2 Infrared spectra

In order to investigate the atomic-scale structural underpinnings of the above-mentioned mixed alkali effects on mechanical and thermal properties, the FTIR spectra of the prepared $70.65SiO_2\cdot21.09B_2O_3\cdot1.88Al_2O_3\cdot(6.38\text{-}x)Li_2O\cdot xNa_2O$ glasses were obtained and presented in Fig.4(a). The specific attributions of the characteristic peaks are listed in Table 1. As an example, the infrared spectrum with deconvoluted Gaussian bands and their summation curves of the glass at r = 0 were shown in Fig.4(b). Composition dependence of the relative fraction (relative to the total integrated area in the region from 400 to 1 600 cm^{-1}) of the infrared band centered at 900 cm^{-1} related to BO_4 units is shown in Fig.4(c), which indicates a positive

deviation from linearity with r.

4 Discussion

4.1 Mechanism for mixed-alkali effects on elastic modulus and CTE

Firstly, the atomic packing density, denoted as C_g, was proven by many references to be an important indicator in determining the mechanical properties of oxide glasses, such as elastic modulus, deformation mechanism, and fracture toughness[23-25]. This indictor can be calculated using the following formula[26]:

$$C_g = \rho \frac{\Sigma f_i V_i}{\Sigma f_i M_i} \tag{3}$$

where for the ith constituent with chemical formula A_xB_y, f_i is the molar fraction, M_i is the molar mass; V_i is the theoretical volume,

$$V_i = \frac{4}{3} N_A (x r_A^3 + y r_B^3) \tag{4}$$

where r_A and r_B are the ionic radii, N_A is Avogadro's number. The coordination numbers of two for O, four for Si, four for Al, and six for Li and Na were assumed. According to the Dell-Bray model[27], the content in N_4 of boro-oxygen tetrahedra was calculated. For the present glass system, where $[R_2O] - [Al_2O_3] < [B_2O_3]$, $N_4 = ([R_2O] - [Al_2O_3])/[B_2O_3]$.

A near-linear relationship between the elastic moduli (E and G) and the atomic packing density C_g (Fig.5) with a high goodness of fit (R^2 values of 0.93 for E and 0.91 for G) was clearly observed, which indicates that the compositions with higher Na_2O content have lower packing density and less elastic moduli. This is because alkali metal ions are predominantly present as charge balancing cations in the present alkali borosilicate glasses[28], which serve to balance the negatively charged $[AlO_4]^-$ and $[BO_4]^-$ and occupy the interstices in the glass network. When ions have smaller radii and larger field strength, they are packed more closely together, resulting in a higher packing density of atoms. This increased packing density leads to a greater resistance to deformation under the external force and a higher elastic modulus. However, this indicator is not the cause about the above-mentioned mixed alkali effects appeared in the

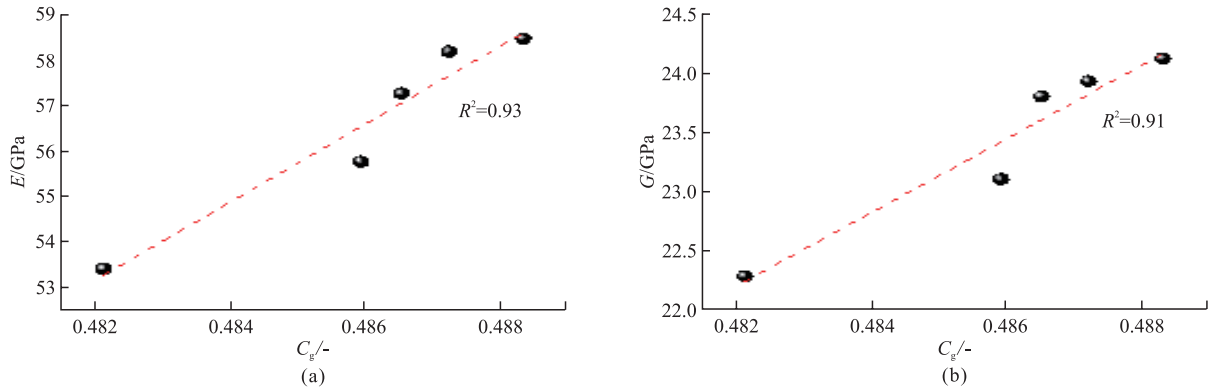


Fig.5 Dependence of Young's modulus E(a) and shear modulus G(b) on the atomic packing density C_g for the $70.65SiO_2 \cdot 21.09B_2O_3 \cdot 1.88Al_2O_3 \cdot (6.38\text{-}x)\ Li_2O \cdot x Na_2O$ glasses

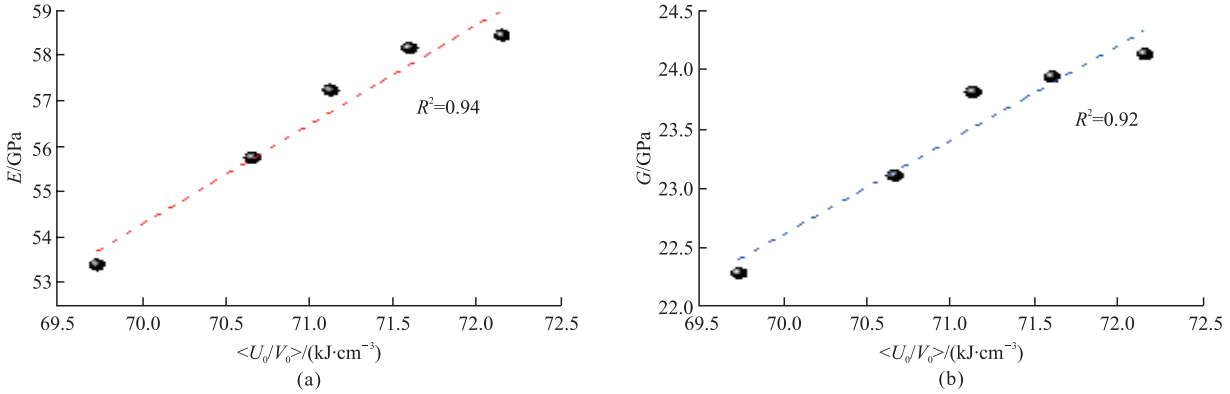


Fig.6 Dependence of Young's modulus E(a) and shear modulus G(b) on the mean-field bond energy density $<U_0/V_0>$ for the $70.65SiO_2 \cdot 21.09B_2O_3 \cdot 1.88Al_2O_3 \cdot (6.38\text{-}x)\ Li_2O \cdot x Na_2O$ glasses

present glass system.

Expect for the atomic packing density, the strength of the chemical bonds is also very important in dominating the elastic modulus of a material[29]. This is especially true for glass, where the bond energy significantly impacts its elastic modulus. However, the amorphous nature of glass results in numerous local variations in bond energy, leading to significant differences in bond energy distribution across various regions. Therefore, an index, *i e*, the average bond energy density ($<U_0/V_0>$), has been proposed[30]. This index can be achieved by calculating the sum of bond energies of all chemical bonds in the glass and dividing it by the volume. It takes into account the enthalpy of dissociation (ΔH_{ai}) of the constituent oxides, their molar fraction, molar mass, and the density of the glass:

$$<\frac{U_0}{V_0}> = \frac{\Sigma f_i \Delta H_{ai}}{\Sigma f_i M_i / \rho} \quad (5)$$

where ρ represents the density of the glass; f_i is the molar percentage of the i component A_xB_y; M_i is the molar mass of A_xB_y; ΔH_{ai} is the molar enthalpy of dissociation of A_xB_y.

For the present alkali borosilicate glasses, a near-linear correlation (Fig.6) exists between this index and the mechanical performances (E and G) with a high goodness of fit (R^2 values of 0.94 in E and 0.92 in G). This near-linear correlation indicates that an increase in the average bond energy density, results in a corresponding increase in both E and G. A higher average bond energy density generally predicts a larger elastic modulus, as it represents the average energy needed to break bonds between adjacent atoms in the glass. Stronger interatomic bonding is the result of a higher bond energy density, making it more challenging for the material to deform in response to applied stress. However, this index also cannot explain why the nonlinear mixed alkali effects mentioned above occurred in the present glass system.

According to previous reports[28], due to larger field strength of Li^+ compared to that of Na^+, more fraction of BO_4 tetrahedra in the B-containing units appears in the Li-containing end-member composition, which can be confirmed by their experimental NMR spectra. This can be explained by the more random distribution of Li ions throughout the glassy network compared to that of Na ions[28]. This can also be confirmed by their FTIR spectra (Fig.4) in the present glasses. The relative fraction of the infrared band centered at about 900 cm^{-1}, which is attributed to vibrations of $[BO_4]$, is higher for the Li-containing end-member composition than that for the Na-containing counter composition. Therefore, the positive deviation of the relative fraction of this infrared band from linearity (Fig.4(c)) as a function of the molar ratio r can be considered as a proof about the structural origin of mixed alkali effect on E and G at room temperature.

Coefficient of thermal expansion (CTE) is a vital thermal property for borosilicate glasses, which is influenced by several factors, including cationic field strength, structural symmetry, and non-bridging oxygen (NBO)[31]. In the present alkali borosilicate glasses, alkali cations serve as charge balancing cations, which fill into the interstices of the glass network. Based on the bond energy theory, it has been observed that alkali metals with larger atomic numbers tend to have weaker R-O bond strength. This is because of their smaller field strength and weaker network constraints[28]. As a result, the pure Na-containing glass exhibits a larger CTE compared to the Li-containing one. Except for SiO_4 glass former, boron polyhedra, which is also an essential network former, should also play a significant role in the present glass system. The transformation of the coordination environment can alter the symmetry of the structure. It is believed[32] that the Na ions in the present glass series are less effective in promoting the conversion of B^{III} to B^{IV} compared to the Li ions. This decrease in structural symmetry ultimately leads to an increase in CTE. Therefore, the positive deviation of the relative fraction of the infrared band centered at about 900 cm^{-1} related to BO_4 units from linearity (Fig.4(c)) as a function of the molar ratio r can be regarded as a proof about the structural origin why the mixed alkali effect on CTE occurs. Certainly, it is worth noting that the relationship between CTE and the structure is complex, and more research is needed to fully understand the mixed alkali effects on thermo-physical properties of borosilicate glasses. Nevertheless, understanding the factors that affect CTE is crucial for the development of new borosilicate glasses with desired thermal properties.

4.2 Understanding the elastic response of borosilicate glass to temperature

Recent studies[33,34] have shown that alloys exhibit the Elinvar effect, wherein their elastic modulus remains constant with increasing in temperature. This discovery has far-reaching implications for the advancement of cutting-edge devices. Moreover, the Elinvar effect has been observed in silicate glass and

sodium-boron glass[35,36], similar to alloys. In this paper, we explored the changes of E and G with temperature. The response of the elastic moduli of borosilicate glasses to temperature should be closely linked to the effect of temperature on the intermediate-range clusters composed of SiO_4, BO_4, and BO_3 polyhedra. On the one hand, the elastic moduli at $r = 0$ and $r = 1$ remain relatively constant with temperature, which could be attributed to the change in silicate ring structure. Specifically, the flexible expansion of the α ring to the rigid expansion of the β-ring may play a role. On the other hand, the variable temperature modulus of boron-containing glass is known to be associated with changes in the intermediate range order (IRO) structure, such as boroxol rings and tetraborate units. In the case of alkali borate glass, the previous investigation suggests that this anomalous behavior may result from a delicate balance between the softening effect of bond weakening in the short-order structure (SRO) and the network hardening effect with temperature in the medium-order structure (IRO)[36]. The hardening of the glass network can occur due to a slight distortion in the network topology or a conformational change of the IRO unit. As shown in Fig.3, increasing temperature should decrease the elastic modulus due to the positive coefficient of thermal expansion. The structural distortion is likely caused by the thermal expansion of the glass, which results in the softening of chemical bonds and rotation of the network.

Molecular dynamics (MD) simulations [37] have shown that pure B_2O_3 glass is comprised of two types of rings with different conformations and stiffness: rigidly expanded β-rings and flexibly expanded α-rings. These rings can undergo transformation into each other under different thermodynamic conditions, which explains why the elastic modulus of pure B_2O_3 glass remains constant with temperature. Based on this hypothesis, we expected that Li-containing ($r = 0$) and Na-containing ($r = 1$) borosilicate glasses might also exhibit similar ring conformation changes. Specifically, as the temperature increases, the flexibly expanded α-ring transforms into the rigidly expanded β-ring, which counterbalances the softening effect of chemical bonds.

Confirmed by the responses of E and G to temperature (Fig.3), the mixture of two alkali cations has a detrimental effect on the Elinvar behavior of borosilicate glasses. This is likely due to the mixed alkali effect, which alters the intermediate range structure in the glass. Although the β-rings provide a strengthening effect, it is not enough to counteract the softening effect of chemical bonds as the temperature increases. As a result, we observed decreases in the elastic moduli of the glasses with increasing temperature. However, more proofs and investigations are needed to elucidate the underlying structural mechanism responsible for this phenomenon.

5 Conclusions

By varying the ratio of Na to Li while maintaining the total alkali content constant, we investigated the impact of mixed modifiers on thermal properties and elastic moduli in borosilicate glasses. The nonlinear evolution of room temperature elastic moduli and CTE with r is attributed to the variance of the ratio of BO_3 and BO_4 due to the mixture of the alkali ions, evidenced by the positive deviation of the relative fraction of the infrared band centered at about 900 cm^{-1} related to BO_4 units from linearity as a function of the molar ratio r. In addition, we observed a new mixed alkali effect on variable temperature elastic behavior in this glassy system, which could be related to the change in intermediate range structure originated from the mixture of sodium and lithium ions. These findings offer experimental evidence for understanding the temperature dependence behavior of the elastic moduli of alkali borosilicate glasses.

Conflict of interest

All authors declare that there are no competing interests.

References

[1] Weber R. Uber Den Einfluß Der Zusammensetzung Des Glases Auf Die Depressions- Erscheinungen Der Thermometer[J]. *Ber. Dtsch. Chem. Ges*., 1883, 21(1): 1 086-1 096

[2] Mohajerani A, Zwanziger J W. Mixed Alkali Effect on Vickers Hardness and Cracking[J]. *J. Non-Cryst. Solids*, 2012, 358(12-13): 1 474-1 479

[3] Rao N S, Bale S, Purnima M, *et al.* Mixed Alkali Effect in Boroarsenate Glasses[J]. *J. Phys. Chem. Solids*, 2007, 68(7): 1 354-1 358

[4] Novy M, Avila-Paredes H, Kim S, *et al.* Communication: Dimensionality of the Ionic Conduction Pathways in Glass and the Mixed-Alkali Effect[J]. *J. Chem. Phys*., 2015, 143(24): 241 104

[5] Uchino T, Yoko T. Sodium and Lithium Environments in Single- and Mixed-Alkali Silicate Glasses. An *ab Initio* Molecular Orbital Study[J]. *J. Phys. Chem. B*, 1999, 103(11): 1 854-1 858

[6] Dyre J C, Maass P, Roling B, *et al.* Fundamental Questions Relating to Ion Conduction in Disordered Solids[J]. *Rep. Prog. Phys*., 2009, 72(4): 046 501

[7] Maass P, Peibst R. Ion Diffusion and Mechanical Losses in Mixed Alkali Glasses[J]. *J. Non-Cryst. Solids*, 2006, 352(42-49): 5 178-5 187

[8] Greaves G N, Ngai K L. Reconciling Ionic-Transport Properties with Atomic Structure in Oxide Glasses[J]. *Phys. Rev. B*, 1995, 52(9): 6 358

[9] Voigt U, Lammert H, Eckert H, *et al.* Cation Clustering in Lithium Silicate Glasses: Quantitative Description by Solid-State NMR and Molecular Dynamics Simulations[J]. *Phys. Rev. B*, 2005, 72(6): 064 207

[10] Kamitsos E, Yiannopoulos Y, Jain H, *et al.* Far-Infrared Spectra of Alkali Germanate Glasses and Correlation with Electrical Conductivity[J]. *Phys. Rev. B*, 1996, 54(14): 9 775

[11] Greaves G. EXAFS and the Structure of Glass[J]. *J. Non-Cryst. Solids*, 1985, 71(1-3): 203-217

[12] Park B, Cormack A. Molecular Dynamics Simulations of Structural Changes in Mixed Alkali (Li-K) Silicate Glasses[J]. *J. Non-Cryst. Solids*, 1999, 255(1): 112-121

[13] Onodera Y, Takimoto Y, Hijiya H, *et al.* Origin of the Mixed Alkali Effect in Silicate Glass[J]. *NPG Asia Mater*., 2019, 11(1): 75

[14] Wilkinson C J, Potter A R, Welch R S, *et al*. Topological Origins of the Mixed Alkali Effect in Glass[J]. *J. Phys. Chem. B*, 2019, 123(34): 7 482-7 489

[15] Lodesani F, Menziani M C, Hijiya H, *et al*. Structural Origins of the Mixed Alkali Effect in Alkali Aluminosilicate Glasses: Molecular Dynamics Study and Its Assessment[J]. *Sci. Rep*., 2020, 10(1): 2 906

[16] Ryou S Y, Lee C S, Cho I S, *et al.* Measurement of Dynamic Elastic Modulus and Poisson's Ratio of Chemically Strengthened Glass[J]. *Materials*, 2020, 13(24): 5 644

[17] Shan Z, Zhang Y, Liu S, *et al.* Mixed-Alkali Effect on Hardness and Indentation-Loading Behavior of a Borate Glass System[J]. *J. Non-Cryst. Solids*, 2020, 548: 120 314

[18] Chinnamat W, Laopaiboon R, Laopaiboon J, *et al.* Influence of Ionic Radius Modifying Oxides on the Elastic Properties of Glasses Using Ultrasonic Techniques and FTIR Spectroscopy[J]. *Phys. Chem. Glasses: Eur. J. Glass Sci. Technol., Part B*, 2017, 58(5): 207-216

[19] Sun Y, Zhang Z. Structural Roles of Boron and Silicon in the CaO-SiO_2-B_2O_3 Glasses Using FTIR, Raman, and NMR Spectroscopy[J]. *Metall. Mater. Trans. B*, 2015, 46(4): 1 549-1 554

[20] Gautam C, Yadav A K, Singh A K. A Review on Infrared Spectroscopy of Borate Glasses with Effects of Different Additives[J]. *ISRN Ceram*., 2012: 1-17

[21] Shao G, Wu X, Kong Y, *et al.* Thermal Shock Behavior and Infrared Radiation Property of Integrative Insulations Consisting of $MoSi_2$/Borosilicate Glass Coating and Fibrous ZrO_2 Ceramic Substrate[J]. *Surf. Coat. Technol*., 2015, 270: 154-163

[22] Winterstein-Beckmann A, Möncke D, Palles D, *et al.* A Raman-Spectroscopic Study of Indentation-Induced Structural Changes in Technical Alkali-Borosilicate Glasses with Varying Silicate Network Connectivity[J]. *J. Non-Cryst. Solids*, 2014, 405: 196-206

[23] Sellappan P, Rouxel T, Celarie F, *et al.* Composition Dependence of Indentation Deformation and Indentation Cracking in Glass[J]. *Acta Mater.*, 2013, 61(16): 5 949-5 965

[24] Frederiksen K F, Januchta K, Mascaraque N, *et al.* Structural Compromise between High Hardness and Crack Resistance in Aluminoborate Glasses[J]. *J. Phys. Chem. B*, 2018, 122(23): 6 287-6 295

[25] Ostergaard M B, Hansen S R, Januchta K, *et al*. Revisiting the Dependence of Poisson's Ratio on Liquid Fragility and Atomic Packing Density in Oxide Glasses[J]. *Materials*, 2019, 12(15): 2 439

[26] Shannon R D. Revised Effective Ionic Radii and Systematic Studies of Interatomic Distances in Halides and Chalcogenides[J]. *Acta Crystallogr., Sect. A*, 1976, 32(5): 751-767

[27] Zheng Q J, Youngman R E, Hogue C L, *et al.* Structure of Boroaluminosilicate Glasses: Impact of $[Al_2O_3]$/$[SiO_2]$ Ratio on the Structural Role of Sodium[J]. *Phys. Rev. B*, 2012, 86(5): 054 203

[28] Januchta K, Bauchy M, Youngman R E, *et al.* Modifier Field Strength Effects on Densification Behavior and Mechanical Properties of Alkali Aluminoborate Glasses[J]. *Phys. Rev. Mater*., 2017, 1(6): 063 603

[29] Januchta K, To T, Bødker M S, *et al.* Elasticity, Hardness, and Fracture Toughness of Sodium Aluminoborosilicate Glasses[J]. *J. Am. Ceram. Soc.*, 2019, 102(8): 4 520-4 537

[30] Rouxel T. Elastic Properties and Short-to Medium-Range Order in Glasses[J]. *J. Am. Ceram. Soc*., 2007, 90(10): 3 019-3 039

[31] Hao J, Zan Q, Ai D, *et al.* Theoretical Calculations of the Thermal Expansion Coefficient of Glass-Ceramic Sealing Materials in Solid Oxide Electrolysis Cell[J]. *J. Non-Cryst. Solids*, 2013, 361: 86-92

[32] Fry A L, George C, Slagle I, *et al.* Field Strength Effect on Structure, Hardness, and Crack Resistance in Single Modifier Aluminoborosilicate Glasses[J]. *J. Am. Ceram. Soc.*, 2022, 106(2): 951-966

[33] He Q F, Wang J G, Chen H A, *et al.* A Highly Distorted Ultraelastic Chemically Complex Elinvar Alloy[J]. *Nature*, 2022, 602(7 896): 251-257

[34] Liu C, Ji Y, Tang J, *et al.* A Lightweight Strain Glass Alloy Showing Nearly Temperature-Independent Low Modulus and High Strength[J]. *Nat. Mater*., 2022, 21(9): 1 003-1 007

[35] Jaccani S P, Huang L. Understanding Sodium Borate Glasses and Melts from Their Elastic Response to Temperature[J]. *Int. J. Appl. Glass Sci*., 2016, 7(4): 452-463

[36] Jaccani S P, Sundararaman S, Huang L. Understanding the Structural Origin of Intermediate Glasses[J]. *J. Am. Ceram. Soc*., 2018, 102(3): 1 137-1 149

[37] Huang L, Kieffer J. Thermomechanical Anomalies and Polyamorphism in B_2O_3 Glass: A Molecular Dynamics Simulation Study[J]. *Phys. Rev. B*, 2006, 74(22): 224 107

文章编号:1007-9629(2024)06-0496-07

FRP箍筋强度保留率分布模型与可靠性分析

江佳斐, 吕佳豪, 薛伟辰*
(同济大学 土木工程学院,上海 200092)

摘要:基于文献数据,采用假设检验法,开展纤维增强复合材料(FRP)箍筋强度保留率分布规律研究.通过Kolmogorov-Smirnov(K-S)检验对比了Weibull分布、正态分布及对数正态分布这3种模型对FRP箍筋强度保留率的拟合优度.结果表明:当FRP箍筋弯折半径(R)与箍筋直径(D)之比(R/D)在常规范围内(3~5)时,对数正态分布为最优分布模型,据此得到95%和50%保证率下FRP箍筋强度保留率分别不小于32.46%和43.79%;中国、美国、日本和加拿大四国规范保留率预测公式计算结果的保证率仅为24.1%~40.3%,偏于不安全.根据中国FRP纵筋与箍筋的强度保证率要求,当R/D=3、4、5时玻璃纤维增强复合材料(GFRP)箍筋强度保留率不小于38.86%、35.68%、46.09%.

关键词:FRP箍筋;强度保留率;分布规律;K-S检验;可靠性
中图分类号:TB332 **文献标志码**:A **doi**:10.3969/j.issn.1007-9629.2024.06.003

Strength Retention Rate Distribution Model and Reliability Analysis of FRP Stirrups

JIANG Jiafei, *LÜ Jiahao*, *XUE Weichen**
(School of Civil Engineering, Tongji University, Shanghai 200092)

Abstract: The hypothesis testing approach was applied to treat the experimental data from the open literature for the establishment of the distribution law of the strength retention rate of fiber reinforced plastic (FRP) stirrups. The goodness-of-fit of three distribution models (Weibull distribution, normal distribution, and lognormal distribution) for the FRP stirrups strength retention rate was compared using Kolmogorov-Smirnov (K-S) test. The results show that the lognormal distribution is the optimal distribution model within the rational range (3-5) of internal radius(R) to bar diameter(D) ratio (R/D). It follows that the strength retention rates of 95% and 50% guarantee rates is no less than 32.46% and 43.79%, respectively. Furthermore, the results show that the reliabilities of calculation results from the retention rate formula used in the Chinese, American, Canadian, and Japanese standards are only between 24.1%-40.3%, which is unconservative. According to the strength guarantee rate requirements of FRP longitudinal reinforcement and stirrups in China, the strength retention rates of glass fiber reinforced plastic(GFRP) stirrups with R/D of 3, 4 and 5 are not less than 38.86%, 35.68% and 46.09%, respectively.

Key words: FRP stirrup; strength retention rate; distribution law; K-S test; reliability

纤维增强复合材料(FRP)筋质量轻、强度高、耐腐蚀性优,可用来替代钢筋,解决混凝土结构中的钢筋锈蚀问题[1-4].FRP筋分为纵筋与箍筋,其中,FRP箍筋在构件抗剪与抗扭性能中发挥了重要作用,其强度设计值是FRP筋混凝土受剪及受扭构件承载力设计计算中的重要参数之一.FRP箍筋是由树脂和纤维复合而成的各向异性弹性材料[5],其弯折段存在纤维应力分布不均匀的特点,且弯折段在混凝土构

收稿日期:2023-07-06; 修订日期:2023-10-24
基金项目:"十四五"国家重点研究计划项目(2022YFB3706504);非金属材料创新中心创新基金资助项目(2023TDA4-1)
第一作者:江佳斐(1984—),女,江苏常熟人,同济大学研究员,博士生导师,博士.E-mail:jfjiang@tongji.edu.cn
通讯作者:薛伟辰(1970—),男,江苏扬州人,同济大学教授,博士生导师,博士.E-mail: xuewc@tongji.edu.cn

(C)1994-2024 China Academic Journal Electronic Publishing House. All rights reserved. http://www.cnki.net

件中往往处于拉压双向应力状态，从而导致FRP箍筋在混凝土中的破坏强度（弯拉强度）低于其直线段抗拉强度且离散性大．为此，国内外学者开展了大量FRP箍筋强度保留率（弯拉强度与直线段抗拉强度之比）的试验研究[6-23]．结果表明：影响FRP箍筋弯拉强度及强度保留率的因素包括箍筋弯折半径（R）、箍筋直径（D）、箍筋弯折半径与箍筋直径之比（R/D）、箍筋类型、生产工艺及质量控制等；普遍认为R/D为主要影响因素，但缺乏基于数据库的相关性分析依据；提出了基于数值回归的强度保留率经验公式，但尚未开展基于强度保留率分布模型的可靠性分析．

鉴于此，本文通过文献调研建立FRP箍筋弯拉强度及强度保留率（S）的数据库，并通过假设检验法确定FRP箍筋强度保留率的最优分布模型．在此基础上进行可靠性分析，并以工程中最为常用的玻璃纤维增强复合材料（GFRP）箍筋为例，提出基于箍筋强度设计要求的箍筋强度保留率的合理取值．

1　数据库的建立

1.1　数据收集与筛选

国内外学者自21世纪初即开展了众多FRP箍筋强度试验研究．本文在公开发表的论文[6-23]中收集整理出159组数据，建立FRP箍筋强度试验数据库，其中试验参数包括：箍筋类型（玻璃纤维增强复合材料（GFRP）、碳纤维增强复合材料（CFRP）、玄武岩纤维增强复合材料（BFRP））、箍筋纤维含量、截面形状、箍筋直径（D，矩形断面厚度，按照文献[10]采用的等效方法换算为等效直径）、箍筋的弯折半径（R）、弯折半径与箍筋直径之比（R/D）、FRP箍筋直线段抗拉强度、箍筋弹性模量及试验方法等．

Imjai等[8]在进行FRP箍筋弯拉强度试验时发现，弯折段前端黏结长度较长会产生应力递减，导致破坏位置出现在非弯折段，此时箍筋破坏强度大于弯拉强度．此外，FRP箍筋的尾部锚固长度也是影响破坏模式的重要参数．El-Sayed等[12]研究了FRP箍筋尾部锚固长度（3D、6D、9D、12D、15D）对破坏模式的影响，得出能充分发挥FRP箍筋弯拉强度的最小尾部锚固长度为6D．FRP箍筋弯拉强度标准测试方法[24]中要求最小尾部锚固长度也为6D．因此，本研究所建数据库剔除了箍筋弯折段前端有黏结和箍筋尾部锚固长度小于6D的数据．此外，部分箍筋试件由于弯折段采用树脂补强措施，其相关数据也被剔除．按照破坏模式一致、试验方法统一和无补强措施的原则，筛选出59组FRP箍筋弯拉强度试验数据，用于分析FRP箍筋强度保留率的分布规律．

1.2　多影响因素的相关性分析

由于影响FRP箍筋强度保留率的参数众多，本研究基于Pearson相关性理论，先对FRP箍筋强度保留率与各影响因素之间的相关性进行分析．

Pearson相关系数（r）又称积差相关系数[25]，是衡量2个变量集合之间线性相关程度的指标，计算式为：

$$r=\frac{\sum_{i=1}^{n}(X_i-\overline{X})(Y_i-\overline{Y})}{\sqrt{\sum_{i=1}^{n}(X_i-\overline{X})^2}\sqrt{\sum_{i=1}^{n}(Y_i-\overline{Y})^2}} \quad (1)$$

式中：X_i、Y_i分别表示变量X和Y的每个具体值；$\overline{X}$、$\overline{Y}$分别表示变量X、Y的所有数据的平均值；n表示变量X与Y的数据量．

r是一个无量纲的统计指标．$r>0$表明变量X与Y正相关；$r<0$表明变量X与Y负相关；$r=0$表明变量X与Y不相关．$|r|$越接近1，两变量之间的相关程度就越密切．变量间相关程度与r的对应关系如表1所示．

表1　变量间相关程度与Pearson相关系数的对应关系
Table 1　Relationship between correlation degree and Pearson correlation coefficient[25]

Correlation degree	$\|r\|$
Uncorrelation	[0,0.3)
Weak correlation	[0.3,0.5)
Significant correlation	[0.5,0.8)
Strong correlation	[0.8,1]

表2为通过Pearson相关性理论计算得出的FRP箍筋强度保留率与各影响因素间的相关系数．由表2可见，R/D的$|r|$最高，为0.63，其他参数的$|r|$均小于0.30，与0.63存在明显差距．这表明FRP箍筋强度保留率与R/D显著相关，其他影响因素对FRP箍筋强度保留率的影响极小，不足以支撑开展数据间的规律分析，可忽略其相关性．因此，本文以R/D作

表2　FRP箍筋强度保留率与各影响因素间的相关性
Table 2　Relationship between strength retention rate of FRP stirrup and various influencing factors

Factor	r
Type of FRP stirrup	0.12
Test method	−0.28
Section shape of stirrup	0.07
Fiber content	0.07
Diameter	−0.24
Bend radius	0.19
R/D	0.63
Tensile strength	0.24
Elastic modulus	0.28

(C)1994-2024 China Academic Journal Electronic Publishing House. All rights reserved.　http://www.cnki.net

为主要变量，进一步分析FRP箍筋强度保留率的分布规律.

1.3 箍筋强度保留率数据库的建立

基于试验数据的筛选原则与相关性分析结果，筛选出的59组数据涵盖了工程中常用的FRP箍筋类型(GFRP、BFRP、CFRP)及箍筋的R/D范围(3～5).详细数据来源[6-8,11-12,21-22]及FRP箍筋保留率如表3所示.

表3 FRP箍筋强度保留率数据库

Table 3 Database of strength retention rate of FRP stirrups

Author	Type of stirrup	Section shape	D/mm	R/mm	R/D	Bend strength/MPa	Tensile strength/MPa	S/%
Li, et al.[6]	CFRP	Rectangle	2.0	8	4	1 086	2 480	43.8
Ahmed, et al.[7]	GFRP	Circular	9.5-19.1	38-76	4	240-712	533-1 538	32.9-58.3
Imjai, et al.[8]	GFRP	Rectangle/circular	3.0-13.5	9-54	3-5	271-464	690-720	36.6-64.4
Shehata, et al.[11]	CFRP	Rectangle/circular	5.0-12.0	20-50	4	345-793	713-1 800	44.1-56.1
El-Sayed, et al.[12]	CFRP	Circular	9.5-12.7	38-51	4	539-761	1 224-1 328	44.0-57.3
WANG, et al.[21]	GFRP	Circular	7.0	20	3	387	1 045	37.0
Lu[22]	BFRP	Circular	6.0-8.0	24-32	4	347-594	1 096-1 604	31.6-39.1

2 结果与讨论

本文采用Weibull分布、正态分布和对数正态分布3种分布模型，对不同R/D情况下FRP箍筋强度保留率数据进行拟合.并通过线性回归分析及Kolmogorov-Smirnov(K-S)检验确定最优分布模型.

2.1 线性回归分析

先将以上3种分布模型的概率累积分布函数表达式线性变换为$y=ax+b$形式，如表4[26]所示；再代入FRP箍筋强度保留率数据，求得相应分布模型中的均值μ、标准差σ及决定系数R^2，并对3种分布模型进行显著性检验，结果见表5. 由表5可见：不同R/D情况下，3种分布模型的R^2均远超工程常用显著性水平$\alpha=0.01$或$\alpha=0.05$时的决定系数临界值.这说明3种分布模型均可表征FRP箍筋强度保留率的分布规律.

表4 3种分布模型的线性变换关系

Table 4 Linear transformation relationship of three distribution models[26]

Distribution model	Cumulative distribution function	y	x	a	b
Weibull	$F(S)=1-\mathrm{e}^{-\left(\frac{S}{\mu}\right)^{\sigma}}$	$\ln\ln\frac{1}{1-F(S)}$	$\ln S$	σ	$\sigma\ln\mu$
Normal	$F(S)=\frac{1}{\sigma\sqrt{2\pi}}\int_{-\infty}^{S}\mathrm{e}^{\frac{-(S-\mu)^2}{2\sigma^2}}\mathrm{d}S$	$\Phi^{-1}\left[F(S)\right]$	S	$\frac{1}{\sigma}$	$-\frac{\mu}{\sigma}$
Lognormal	$F(S)=\frac{1}{\sigma S\sqrt{2\pi}}\int_{-\infty}^{S}\mathrm{e}^{\frac{-(\ln S-\mu)^2}{2\sigma^2}}\mathrm{d}S$	$\Phi^{-1}\left[F(S)\right]$	$\ln S$	$\frac{1}{\sigma}$	$-\frac{\mu}{\sigma}$

Note: $F(S)$ represents the cumulative distribution function of Weibull distribution, normal distribution and lognormal distribution; μ and σ are the mean and standard deviation of different distribution models; a, b represents the slope and intercept of the linear function after linear regression, respectively.

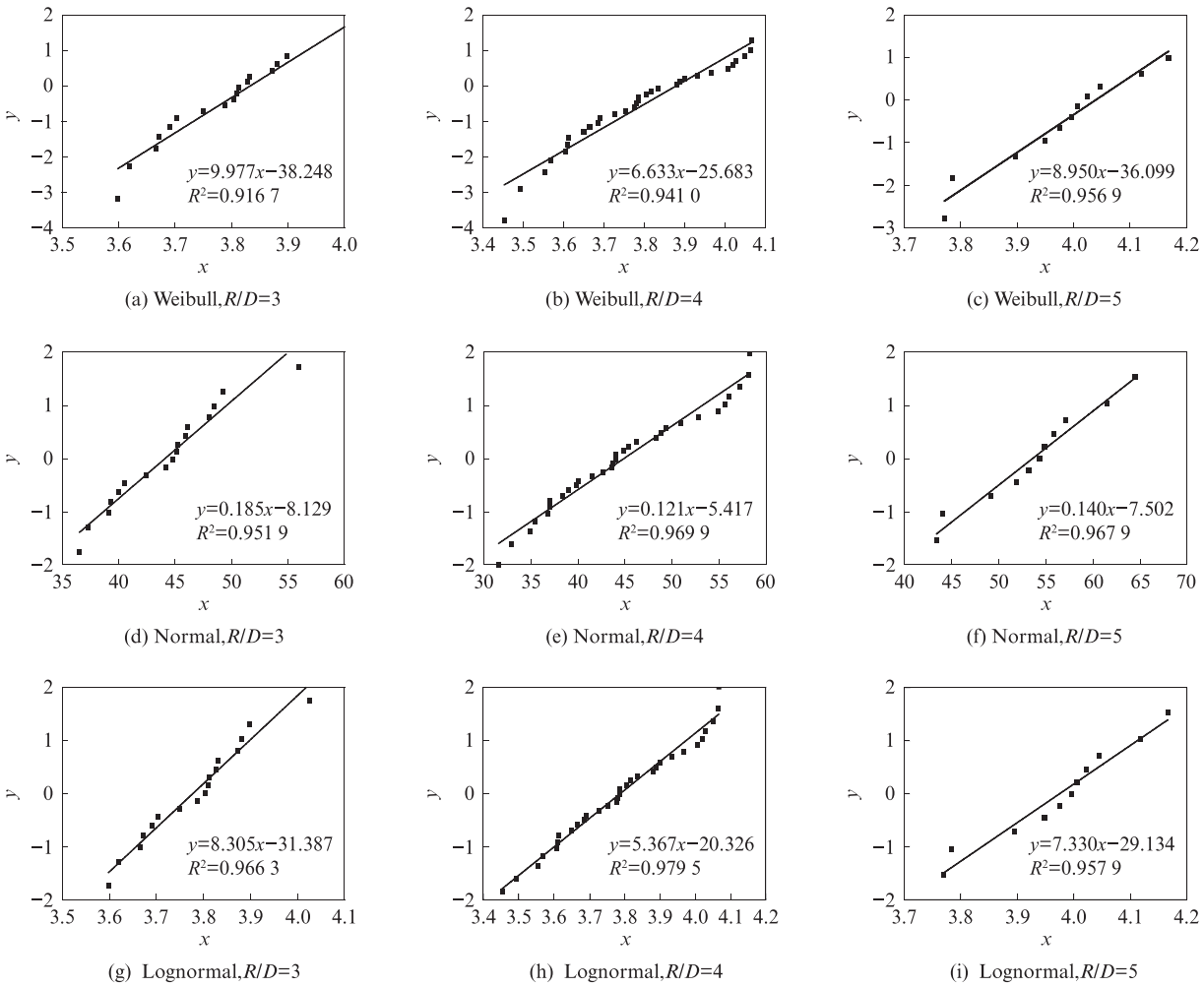
表5 3种分布模型的均值、标准差及显著性检验结果

Table 5 Mean, standard deviation and significance test results of three distribution models

R/D	Weibull			Normal			Lognormal			Critical value of significant level	
	μ	σ	R^2	μ	σ	R^2	μ	σ	R^2	$\alpha=0.01$	$\alpha=0.05$
3	46.22	9.98	0.917	44.04	5.42	0.952	44.11	5.33	0.966	0.575	0.456
4	48.04	6.63	0.941	44.84	8.28	0.970	44.92	8.44	0.980	0.440	0.345
5	56.45	8.95	0.957	53.59	7.14	0.968	53.72	7.36	0.958	0.684	0.553

图1为不同R/D情况下3种分布模型的线性回归结果.由图1可见：当$R/D=3$或$R/D=4$时，3种分布模型中R^2呈现统一规律，即对数正态分布的R^2＞正态分布的R^2＞Weibull分布的R^2；当$R/D=5$时，3种分布模型中R^2值基本相等，这主要跟样本数量有关，$R/D=3$数据量17组，$R/D=4$数据量31组，而$R/D=5$的数据只有11组，表明当样本数量较小时，3种分布模型的R^2值区别不明显.

(C)1994-2024 China Academic Journal Electronic Publishing House. All rights reserved. http://www.cnki.net



(a) Weibull,R/D=3　(b) Weibull,R/D=4　(c) Weibull,R/D=5

(d) Normal,R/D=3　(e) Normal,R/D=4　(f) Normal,R/D=5

(g) Lognormal,R/D=3　(h) Lognormal,R/D=4　(i) Lognormal,R/D=5

图1　不同R/D情况下3种分布模型的线性回归结果

Fig. 1　Linear regression results of three distribution models with different R/D values

2.2　K-S检验

K-S检验[27]是用来检验一组数据是否服从某种理论分布的方法.该方法通过对比统计量D_N与给定显著性水平α下的临界值$D_{N,\alpha}$来确定拟合优度.当$D_N<D_{N,\alpha}$时,分布模型可以表征样本数据的分布规律,且D_N越小,分布模型的拟合优度越高.D_N表达式为:

$$D_N=\max\left[|F_j(S_j)-F(S_j)|\right],1\leqslant j\leqslant N \quad (2)$$

式中:j为按照强度保留率由小到大排序的序号;S_j为序号为j的FRP箍筋强度保留率;N表示样本数据总量;$F_j(S_j)$为由累计分布函数计算得到的强度保留率达到S_j时的失效概率理论值;$F(S_j)$为通过中位秩法计算所得箍筋强度保留率达到S_j时的失效概率,$F(S_j)=(j-0.3)/(N+0.4)$.

选取工程上常用的显著性水平α=0.01和α=0.05,进行不同R/D情况下K-S检验,结果如表6所示.由表6可知:3种分布模型在不同R/D情况下的D_N值均小于$D_{N,\alpha}$;对数正态分布模型中的D_N值在3种R/D情况下最小,为最优分布模型.

表6　K-S检验结果

Table 6　K-S test results

R/D	N	D_N			$D_{N,\alpha}$	
		Weibull	Normal	Lognormal	α=0.01	α=0.05
3	17	0.107	0.086	0.081	0.381	0.318
4	31	0.101	0.070	0.061	0.285	0.240
5	11	0.094	0.097	0.077	0.468	0.391

2.3　最优分布模型确定

线性回归分析与K-S检验结果表明:虽然3种分布模型在一定程度上均可表征FRP箍筋强度保留率的分布规律;但3种分布模型的R^2和D_N值对比分析显示,对数正态分布模型是表征FRP箍筋强度保留率分布规律的最优模型.

3　可靠性分析

3.1　基于对数正态分布模型的可靠性计算

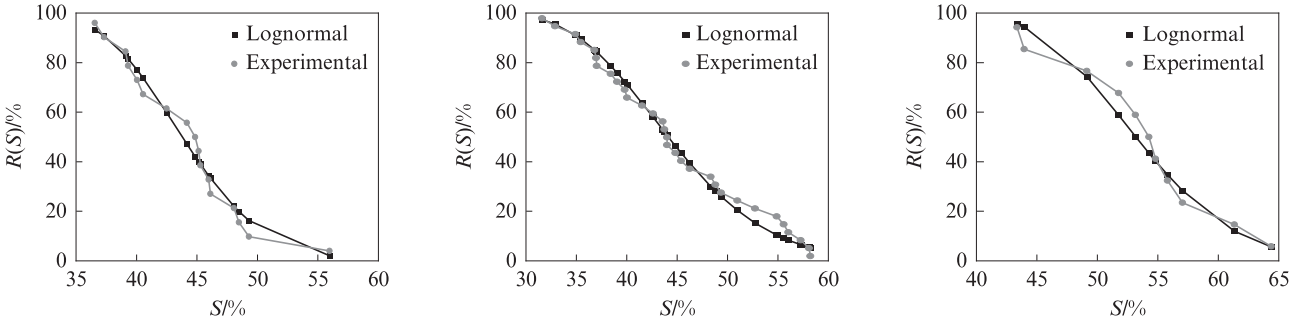
本文基于FRP箍筋强度保留率最优分布模型——对数正态分布模型,采用式(3)计算得到不同R/D情

(C)1994-2024 China Academic Journal Electronic Publishing House. All rights reserved.　http://www.cnki.net

况下FRP箍筋强度的保留率-保证率($R(S)$)曲线，如图2所示.

$$R(S)=1-F(S) \tag{3}$$

根据试验值，将采用中位秩法得到的保留率-保证率曲线也绘于图2. 由图2可见：3种R/D情况下，采用这2种方法得到的曲线吻合度较好.



(a) R/D=3　(b) R/D=4　(c) R/D=5

图2　不同R/D情况下FRP箍筋强度保留率-保证率曲线

Fig. 2　Strength retention rate-reliability curves of FRP stirrup under different R/D values

3.2　现行规范中强度保留率的可靠性分析

中国[28]、美国[29]、日本[30]和加拿大[31]规范中FRP箍筋强度保留率通过式(4)计算得到.

$$\frac{f_{\mathrm{fb}}}{f_{\mathrm{fu}}}=0.05\times\frac{R}{D}+0.3 \tag{4}$$

式中：f_{fb}表示FRP箍筋弯拉强度；f_{fu}表示FRP箍筋直线段抗拉强度.

基于FRP箍筋强度保留率满足对数正态分布规律，本文对各国现行规范中的FRP箍筋强度保留率进行可靠性分析，结果显示：当R/D=4时，各国规范中FRP箍筋强度保留率计算值的保证率仅为24.1%；当R/D=3、5时，FRP箍筋强度保留率计算值的保证率分别为40.3%、39.5%，均小于50%，总体上偏于不安全.

3.3　不同保证率下的FRP箍筋强度保留率

当FRP箍筋强度保留率服从对数正态分布时，在某一保证率下的保留率可按式(5)计算.

$$S=\mathrm{e}^{(z\sigma+\mu)} \tag{5}$$

式中：z为将对数正态分布转换为标准正态分布时对应的参数，可查表确定.

表7列出了3种R/D情况下，当保证率为5%、50%和95%时FRP箍筋强度保留率及其均值. 由表7可知：(1)在较低的保证率下，FRP箍筋强度保留率随着R/D的增加而增大；当保证率不小于50%时，FRP箍筋强度保留率随R/D变化的规律相近，即当R/D=3、4时强度保留率相近，R/D=5时强度保留率显著提升. 其原因在于，当R/D=3、4、5时对数正态分布函数参数不同(表5)，从而导致不同保证率下FRP箍筋强度保留率随R/D变化趋势也略有不同. (2)50%保证率下FRP箍筋强度保留率与均值接近，最大绝对偏差仅为0.25%，最大相对偏差仅为0.57%，说明基于试验均值得到的FRP箍筋强度保留率的保证率为50%；95%和50%保证率下，FRP箍筋强度保留率分别不小于32.46%和43.79%.

表7　不同保证率下的FRP箍筋强度保留率

Table 7　Strength retention rate of FRP stirrup under different reliabilities

R/D	μ	σ	$R(S)$/%	S/%	$\overline{S}$/%
3	44.11	5.33	95	35.90	44.04
			50	43.79	
			5	53.41	
4	44.92	8.44	95	32.46	44.85
			50	44.15	
			5	60.04	
5	53.72	7.36	95	42.50	53.58
			50	53.22	
			5	66.66	

3.4　基于筋材强度设计要求的FRP箍筋强度保留率

本文基于上述提出的FRP箍筋强度保留率分布模型和已有的工程应用最多的GFRP纵筋抗拉强度分布模型[32-33]，采用蒙特卡洛法模拟得到GFRP箍筋弯拉强度分布模型. 当模拟次数达到100万次时，GFRP箍筋弯拉强度数据点的分布规律趋于稳定，并满足对数正态分布，如图3所示. 按照国内规范[28]要求，取95%保证率的GFRP箍筋弯拉强度和GFRP纵筋抗拉强度来计算强度保留率，计算结果表明：当R/D分别为3、4、5时，GFRP箍筋强度保留率分别为38.86%、35.68%、46.09%，其保留率的保证率分别为85.8%、88.9%、85.4%.

(C)1994-2024 China Academic Journal Electronic Publishing House. All rights reserved.　http://www.cnki.net

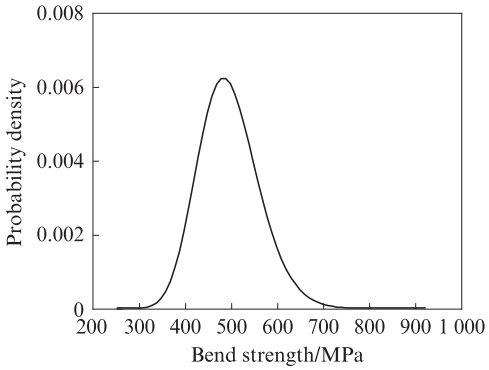


图3　GFRP箍筋弯拉强度分布规律

Fig. 3　Distribution law of bend strength of GFRP stirrups

4　结论

(1)在159组影响FRP箍筋强度保留率试验数据的基础上，基于有效数据筛选原则与相关性分析结果，得到由59组数据构成且按弯折半径R与箍筋直径D之比R/D分组的FRP箍筋强度保留率数据库，用于确定分布模型.

(2)综合线性回归分析和K-S检验结果，研究发现Weibull分布、正态分布和对数正态分布模型均可表征FRP箍筋强度保留率的分布规律，且对数正态分布为最优分布模型.

(3)中国、美国、日本和加拿大现行规范中FRP箍筋强度保留率计算值的保证率均小于50%. 当R/D=3、5时，保证率为40.3%、39.5%；当R/D=4时，保证率仅为24.1%，总体上偏不安全.

(4)根据中国FRP纵筋与箍筋的强度设计要求，当R/D=3、4、5时GFRP箍筋强度保留率分别为38.86%、35.68%、46.09%.

需要说明的是，本文中FRP箍筋强度保留率的相关结论仅适用于采用连续纤维拉挤工艺生产的FRP箍筋，采用模压工艺成型的FRP箍筋强度保留率的可靠性仍需进一步开展相关研究.

参考文献：

[1] 孙亚楠，金祖权，逄博，等. 基于DIC的混凝土嵌入式BFRP筋拔出行为及黏结性能研究[J]. 建筑材料学报，2023，26(1)：45-52.
SUN Yanan，JIN Zuquan，PANG Bo，et al. Pulling-out process and interfacial bonding performance of BFRP bar in concrete based on DIC[J]. Journal of Building Materials，2023，26(1)：45-52.(in Chinese)

[2] 李文超，周广发，温福胜，等. 混凝土环境中GFRP筋性能衰退的规律及机理[J]. 建筑材料学报，2023，26(2)：156-162.
LI Wenchao，ZHOU Guangfa，WEN Fusheng，et al. Degradation law and mechanism of GFRP bars in concrete environment[J]. Journal of Building Materials，2023，26(2)：156-162.(in Chinese)

[3] 付凯，薛伟辰. 人工海水环境下GFRP筋抗拉性能加速老化试验[J]. 建筑材料学报，2014，17(1)：35-41.
FU Kai，XUE Weichen. Accelerated aging tests for evaluations of tensile properties of GFRP bars under artificial seawater environment[J].Journal of Building Materials，2014，17(1)：35-41.(in Chinese)

[4] 王伟，薛伟辰. 碱环境下GFRP筋拉伸性能加速老化试验研究[J]. 建筑材料学报，2012，15(6)：760-766.
WANG Wei，XUE Weichen. Accelerated aging tests for evaluations of tensile properties of GFRP rebars exposed to alkaline solution[J].Journal of Building Materials，2012，15(6)：760-766.(in Chinese)

[5] 蔡启明，陆春华，延永东，等. BFRP和GFRP筋剪切性能的温度效应[J]. 建筑材料学报，2022，25(4)：395-400.
CAI Qiming，LU Chunhua，YAN Yongdong，et al. Temperature effect on shear properties of BFRP and GFRP bar[J]. Journal of Building Materials，2022，25(4)：395-400.(in Chinese)

[6] 李彪，杨勇新，岳清瑞，等. 复合材料箍筋力学性能试验研究[J]. 施工技术，2018，47(20)：4.
LI Biao，YANG Yongxin，YUE Qingrui，et al. Experimental study on mechanical properties of composite stirrups [J]. Construction Technology，2018，47(20)：4.(in Chinese)

[7] AHMED E A，EL-SAYED A K，SALAKAWY E，et al. Bend strength of FRP stirrups：Comparison and evaluation of testing methods[J]. Journal of Composites for Construction，2010，14(1)：3-10.

[8] IMJAI T，GUADAGNINI M，PILAKOUTAS K，et al. Bend strength of FRP bars：Experimental investigation and bond modeling[J]. Journal of Materials in Civil Engineering，2017，29(7)：04017024.

[9] SPADEA S，ORR J，NANNI A，et al. Wound FRP shear reinforcement for concrete structures[J]. Journal of Composites for Construction，2017，21(5)：04017026.

[10] LEE C，KO M，LEE Y，et al. Bend strength of complete closed-type carbon fiber-reinforced polymer stirrups with rectangular section[J]. Journal of Composites for Construction，2014，18(1)：04013022.

[11] SHEHATA E，MORPHY R，RIZKALLA S，et al. Fibre reinforced polymer shear reinforcement for concrete members：Behaviour and design guidelines[J]. Canadian Journal of Civil Engineering，2000，27(5)：859-872.

[12] EL-SAYED A K，El-SALAKAWY E，BENMOKRANE B，et al. Mechanical and structural characterization of new carbon FRP stirrups for concrete members[J]. Journal of Composites for Construction，2007，11(4)：352-362.

[13] 原野，王震宇，王代玉，等. 配置新型封闭缠绕式GFRP箍筋混凝土梁的受剪性能试验[J]. 复合材料学报，2022，39(11)：5074-5085.
YUAN Ye，WANG Zhenyu，WANG Daiyu，et al. Experimental study on the shear performance of concrete beams reinforced with new type closed winding GFRP stirrups[J]. Acta Materiae

(C)1994-2024 China Academic Journal Electronic Publishing House. All rights reserved.　http://www.cnki.net

Compositae Sinica, 2022, 39(11):5074-5085.(in Chinese)

[14] El-TAHAN M, GALAL K, HOA V S, et al. New thermoplastic CFRP bendable rebars for reinforcing structural concrete elements [J].Composites:Part B Engineering,2013,45(1):1207-1215.

[15] TAHIR M. 封闭式CFRP条带箍筋约束混凝土柱的受压性能研究[D].哈尔滨:哈尔滨工业大学, 2021.
TAHIR M. Study on the compressive behavior of concrete columns confined with close-type CFRP strip ties [D]. Harbin: Harbin Industrial University, 2021.(in Chinese)

[16] 林锋. 弯折部位锚固长度对BFRP箍筋抗剪强度影响试验分析[J]. 重庆建筑, 2010, 9(11):26-28.
LIN Feng. Influence of the anchorage length on folded part to shear strength of the BFRP stirrups[J]. Chongqing Architecture, 2010, 9(11):26-28.(in Chinese)

[17] 李明,张黎飞,李斌,等. GFRP箍筋弯折强度试验及理论研究[J]. 公路与汽运,2021(6):131-136.
LI Ming, ZHANG Lifei, LI Bin, et al. Experimental and theoretical study on bending strength of GFRP stirrup [J]. Chongqing Architecture, 2021(6):131-136.(in Chinese)

[18] 陈博文. GFRP复合螺旋箍筋约束混凝土柱受压力学性能研究[D].郑州:郑州大学,2021.
CHEN Bowen. Research on compressive mechanical behavior of concrete columns confined by GFRP composite spiral stirrups [D]. Zhengzhou:Zhengzhou University, 2021.(in Chinese)

[19] 董恒磊. 配置GFRP纵筋与新型箍筋的混凝土墩柱约束机理与抗震性能[D]. 哈尔滨:哈尔滨工业大学, 2020.
DONG Henglei. Confinement mechanism and seismic performance of concrete piers reinforced with GFRP rebars and innovative ties [D]. Harbin:Harbin Industrial University, 2020.(in Chinese)

[20] 涂雅筝. BFRP箍筋约束混凝土柱轴心受压力学性能研究[D].郑州:郑州大学,2020.
TU Yazheng. Research on compressive mechanical behavior of concrete columns confined by BFRP stirrups [D]. Zhengzhou: Zhengzhou University, 2020.(in Chinese)

[21] 王川,欧进萍.热塑性FRP筋折弯成型工艺及其混凝土拔出试验研究[C]//第六届全国FRP学术交流会论文集.北京:中国土木工程学会,2009:102-107.
WANG Chuan, OU Jinping. Study on the bending techniques of fiber reinforced thermoplastic polymer rebar and pulling out experiment of concrete[C]//Proceedings of the Sixth National FRP Academic Exchange Conference. Beijing:Civil Engineering Society,2009:102-107.(in Chinese)

[22] 鲁静. 混凝土结构用热塑性FRP筋基本力学性能研究[D].南京:东南大学,2018.
LU Jing. Evaluation of fundamental mechanical properties of thermoplastic FRP bars for concrete structure [D]. Nanjing: Southeast University, 2018.(in Chinese)

[23] BYWALSKI C, DRZAZGA M, KAŹMIEROWSKI M, et al. Shear behavior of concrete beams reinforced with a new type of glass fiber reinforced polymer reinforcement:Experimental study [J]. Materials, 2020, 13(5):1159.

[24] Canadian Standard Association. Specification for fiber-reinforced polymers:CSA S807-19[S]. Toronto:CSA Group, 2019.

[25] 吴娜, 刘子晖, 樊淑娴, 等. 基于Pearson相关性的小电阻接地有源配电网接地保护[J].电测与仪表, 2021, 58(4):136-143.
WU Na, LIU Zihui, FAN Shuxian, et al. Grounding protection of low resistance grounding active distribution network based on Pearson correlation [J]. Electrical Measurement & Instrumentation, 2021,58(4):136-143.(in Chinese)

[26] 赵永翔, 孙亚芳, 高庆, 等. 分析常用7种统计分布的统一线性回归方法[J].机械强度,2001,23(1):102-106.
ZHAO Yongxiang, SUN Yafang, GAO Qing, et al. Unified linear regression method for the analysis of seven commonly used statistical distributions[J]. Journal of Mechanical Strength, 2001, 23(1):102-106.(in Chinese)

[27] 李湘郡. 基于复合材料强度分布的结构可靠度评估[D].南京:东南大学,2020.
LI Xiangjun. Assessment of structural reliability based on strength distribution of composite material [D]. Nanjing: Southeast University, 2020.(in Chinese)

[28] 中华人民共和国住房和城乡建设部. 纤维增强复合材料建设工程应用技术规范:GB 50608—2020[S]. 北京:中国标准出版社, 2020.
Ministry of Housing and Urban-Rural Development of People's Republic of China. Technical standard for fiber reinforced polymer (FRP) in construction: GB 50608—2020[S]. Beijing: China Standards Press, 2020.(in Chinese)

[29] American Concrete Institute. Guide for the design and construction of structural concrete reinforced with fiber reinforced polymer (FRP) bars:ACI 440.1 R-15[S]. Farmington Hills:American Concrete Institute, 2015.

[30] Japan Society of Civil Engineers. Recommendation for design and construction of concrete structures using continuous fiber reinforcing materials:JSCE—1997[S]. Tokyo:Japan Society of Civil Engineers, 1997.

[31] Canadian Standards Association. Canadian Highway Bridge Design Code :CAN/CSA S6-19[S]. Toronto:CSA Group,2019.

[32] NEOCLEOUS K, PILAKOUTAS K, WALDRON P, et al. Structural reliability for fiber reinforced polymer reinforced concrete structures[J]. Special Publication, 1999, 188:65-74.

[33] 薛伟辰,王圆,方志庆,等. 黏砂变形GFRP筋与约束混凝土之间的黏结性能[J].建筑材料学报,2013,16(1):6-12.
XUE Weichen, WANG Yuan, FANG Zhiqing, et al. Bond behavior between sand coated GFRP rebar and confined concrete [J]. Journal of Building Materials,2013,16(1):6-12.(in Chinese)

(C)1994-2024 China Academic Journal Electronic Publishing House. All rights reserved. http://www.cnki.net

Engineering Structures 290 (2023) 116367



Contents lists available at ScienceDirect

Engineering Structures

journal homepage: www.elsevier.com/locate/engstruct





Shear behavior of two-span continuous concrete deep beams reinforced with GFRP bars

Fei Peng [a,b,*], Yuhang Cai [b], Weijian Yi [a,b], Weichen Xue [c]

[a] Key Laboratory of Building Safety and Energy Efficiency of the Ministry of Education, Hunan University, Changsha 410082, China
[b] College of Civil Engineering, Hunan University, Changsha 410082, China
[c] Department of Structural Engineering, Tongji University, Shanghai 200092, China

ARTICLE INFO

Keywords:
Fiber-reinforced polymer (FRP)
Deep concrete beam
Digital image correlation (DIC)
Arch action
Shear strength

ABSTRACT

To investigate the shear behavior of reinforced concrete (RC) continuous deep beams with glass fiber reinforced polymer (GFRP) bars, four large-scale beams with a constant shear span-to-overall depth ratio of 1.2 and different GFRP shear reinforcement ratios were tested. Digital image correlation technology was used to track the kinematics of diagonal shear cracks in the shear span. It was found that the moment redistribution in the deep beams was very limited. A tie-arch action was confirmed in the tested deep beams with the crack propagation and the strains developed in longitudinal reinforcements. For the beams without GFRP stirrups, the aggregate interlock contribution constituted 46.3% of the total shear resistance. For the beams with GFRP stirrups, however, the shear contribution of aggregate interlock was less significant. As the GFRP shear reinforcement ratio increased from 0% to 0.47%, the failure mode changed from shear compression failure to compression strut failure. As the shear GFRP reinforcement ratio increased from 0.24% to 0.32% and 0.47%, the load-carrying capacity increased by 35.5% and 73.5%, respectively. The minimum required GFRP shear reinforcement in ACI 440.1R-15 was ineffective for the tested GFRP-RC continuous deep beams in terms of shear capacity enhancement and shear crack control. Finally, a database of shear tests on continuous GFRP-RC beams was collected to assess the ability of strut-and-tie methods in three code guidelines.

1. Introduction

Deep reinforced concrete (RC) beams, which are commonly defined as having a shear span-to-effective depth ratio less than 2.0, are widely used as transfer girders in high-rise buildings or bent caps in bridges, at which their safety is generally crucial for the safety of the whole structure [1,2]. When exposed to aggressive environments, such structural concrete beams suffer from severe deterioration due to the corrosion of steel bars. One feasible solution to the corrosion-induced problem is replacing steel with nonmetallic fiber-reinforced polymer (FRP) bars [3,4]. However, compared with steel, FRP bars possess different mechanical properties such as linear stress-strain relationship until failure and lower modulus of elasticity that make the design provisions for steel-RC deep beams may be not directly applicable to FRP-RC deep beams.

Continuous deep RC beams, which are more common in practice, behave differently from simply supported ones due to the coexistence of high shear and hogging moment at the same region, namely, the intermediate support, which adversely affects the efficiency of interior struts. Moreover, due to the indetermination and large stiffness, continuous deep beams are sensitive to differential support settlements, resulting in additional moments and shear forces [5–7]. Therefore, the shear design provisions derived from the simply supported deep beam may be inadequate for continuous deep beams [8–10].

Over the last two decades, research efforts have been made to investigate the shear behavior of FRP-RC deep beams, primarily focusing on the simply supported beam [11–19]. Limited research studies, however, have been carried out to investigate the shear behavior of continuous FRP-RC deep beams [10,20]. Zinkaah et al. [20] tested nine two-span deep beams reinforced with glass FRP (GFRP) bars, including four beams without shear reinforcement and the rest with web GFRP reinforcements. It was found that an increase in the web GFRP reinforcement ratio from 0% to 0.4% improved the load-carrying capacity by 10% and 18% for beams with a shear span-to-overall depth ratio of 1.0 and 1.7, respectively. Mohamed et al. [10] evaluated the shear behavior of nine GFRP-RC continuous deep beams without shear

* Corresponding author at: Key Laboratory of Building Safety and Energy Efficiency of the Ministry of Education, Hunan University, Changsha 410082, China.
E-mail address: pengf@hnu.edu.cn (F. Peng).

https://doi.org/10.1016/j.engstruct.2023.116367

Available online 29 May 2023
0141-0296/© 2023 Elsevier Ltd. All rights reserved.

reinforcement. It was found that the shear capacity decreased with an increase in the shear span-to-depth ratio. Both of the above mentioned studies concluded that the strut-and-tie model (STM) provisions provided in ACI 318-14 [21] overestimated the shear capacity of the continuous GFRP-RC deep beams [10,20]. In contrast, the STM equations in CSA S806-12 [22] significantly underestimated the capacity of continuous GFRP-RC deep beams. It should be noted that the available experiments on GFRP-RC continuous deep beams mainly focus on beams without transverse reinforcements. Limited studies, however, have dealt with GFRP-RC beams with stirrups. Therefore, new research for full-scale deep beams is needed for development or validation of shear design methods for GFRP-RC continuous deep beams.

The strut-and-tie method (STM) is widely accepted by design standards and researchers for the design and analysis of RC deep beams. This method is based on the lower-bound theorem of plasticity, requiring the satisfaction of the force equilibrium and yield conditions. Since FRP is a linear elastic material up to failure without yielding stage, the application of the STM for FRP-RC deep beams should be further studied. Recently, several shear mechanical models, such as the two-parameter kinematic approach proposed by Mihaylov [23] and the cracking strut-and-tie model proposed by Chen et al. [24], emphasize the importance of the aggregate interlock to the shear transfer mechanisms of FRP-RC deep beams. With the advances in the knowledge of Digital Image Correlation (DIC) technique, it is possible to measure the opening and slip of diagonal shear cracks throughout the test, allowing for evaluation of the role of aggregate interlock action.

In summary, available experimental investigations on the shear behavior of continuous FRP-RC deep beams are very limited. New experimental research on full-scale members is needed for understanding of the shear failure mechanism of continuous FRP-RC deep beams and development or validation of the shear design method of such beams. In this paper, four large-scale beams, with an overall depth of 600 mm, are tested under shear loading. The test results are presented in terms of crack pattern, failure mode, shear strength, load-deflection, load-strain behavior and critical shear crack behavior. Based on the tracked kinematics of the major diagonal shear crack through DIC technique, the shear contribution of aggregate interlock action is quantified. In addition, this paper compares and evaluates the accuracy and applicability of several existing design guidelines for continuous GFRP-RC beams.

2. Experimental program

2.1. Test specimens

Four large-scale two-span continuous concrete deep beams reinforced with GFRP bars were constructed and tested to failure in the Structural Laboratory at Hunan University. All beams had a rectangular cross section of 250 mm in width and 600 mm in height. Each beam measured 5040 mm long with an extra 1080-mm end length to ensure the anchorage length. All specimens had a constant shear span-to-overall depth ratio (a/h) of 1.2 and were designed to fail in shear according to current design guidelines [3,22]. Each beam was longitudinally reinforced with eight GFRP bars at the bottom and top. The test parameter was the ratio of GFRP shear reinforcement ρ_v. The details of the beams are summarized in Table 1. Fig. 1 shows the dimensions and reinforcement details of a typical beam (G180). The provided shear reinforcement ratio of 0.24% in Specimen G240 was close to the minimum shear reinforcement requirement specified in ACI 440.1R-15 [3].

2.2. Material properties

All specimens were constructed using ready-mixed normal weight concrete with a maximum aggregate size of 20 mm. Standard cubes with 150 mm edges were tested according to the Chinese standard GB/T 50,081 [25] to determine the concrete compressive strength. The measured cube compressive strength on the day of testing was 40.3 MPa.

The GFRP bars had a sand-coated and helically wrapped surface and were manufactured by Dextra Manufacturing Co. Ltd. In this study, three types of GFRP bars (Fig. 2) were used: No. 19 GFRP bars for bottom and top flexural reinforcements, straight No. 10 GFRP bars for horizontal web reinforcement, prebent No. 10 GFRP bars for stirrups. The GFRP stirrups had a height of 540 mm, a width of 190 mm, and an internal bend radius r_b of 28.5 mm ($r_b = 3d_b$, where d_b is the diameter of the bar). This satisfies the minimum r_b/d_b requirement specified in 440.1R-15 [3] and CSA S806-12 [22]. The tensile properties and bend strength of GFRP bars were determined as per ASTM D7205 [26] and D7914/D7914M [27], respectively. Table 2 lists measured mechanical properties which were calculated using nominal cross-sectional areas. Additionally, the 10-mm-diameter steel stirrups placed every 100 mm were provided in the overhang part.

2.3. Instrumentation

To measure strains in the bottom and top flexural reinforcement, electrical resistance strain gauges (ERSGs) were installed on the longitudinal GFRP bars to monitor the reinforcement strains. Fig. 1 shows the location of the ERSGs mounted on the bottom and top GFRP bars. In addition, the ERSGs were attached to the stirrups along the assumed centerline of the inclined strut, as shown in Fig. 1. Beam deflections were measured using linear variable displacement transducers (LVDTs) at different locations (that is, at midspan in each span, and at end and middle supports), as shown in Fig. 1. Crack widths were measured by hand-held microscopes with an accuracy of 0.01 mm. Each beam was instrumented with a load cell to measure the reactions at the interior support.

In addition, two-dimensional DIC techniques were used to capture the kinematics of the cracks because of their ability of full-field measurement of the crack development during the entire testing [28]. For the DIC measurements, two 24.1 megapixel DSLR cameras with 3984 pixels by 2656 pixels resolution, which was set to a focal length of 36 mm, were used to capture images of the side of the tested beams. The position and DIC test area for each camera are shown in Fig. 3. One camera, which was installed on a tripod at approximately 2.5 m from the specimen, was used to capture the kinematics of shear cracks between the loading points. The other camera, which was installed on a tripod at approximately 4.0 m from the specimen, was used to capture the crack development of the entire tested beam.

Table 1
Specimen design details and test results.

Specimen	s_v (mm)	ρ_v (%)	$P_{cr,f}$ (kN)	P_{cr} (kN)				P_u (kN)	Δ_u (mm)	Failure mode
				W-interior	W-exterior	E-interior	E-exterior			
GN	–	–	660	943	934	938	1195	1235	1.60	SC
G240	240	0.24	681	1052	930	1026	1164	1179	2.40	SC
G180	180	0.32	702	1208	1208	984	901	1598	3.58	C
G120	120	0.47	732	1201	1130	1246	1086	2045	5.11	C

Note: W-interior is west interior shear span; SC is shear compression failure; and C is compression strut failure.

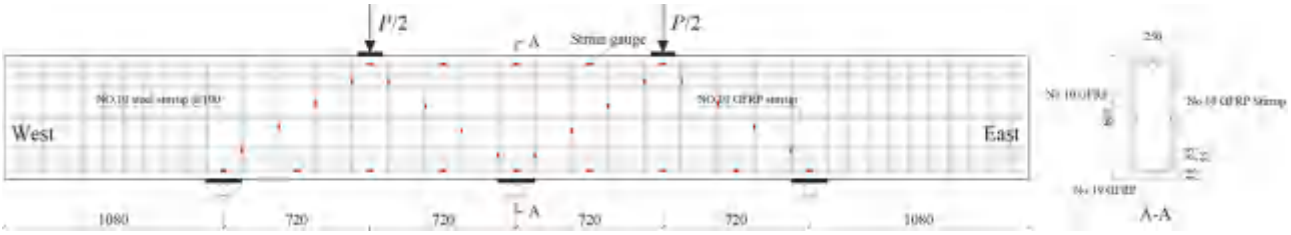


Fig. 1. Dimensions and reinforcement details of typical specimen G180 (dimensions in mm).

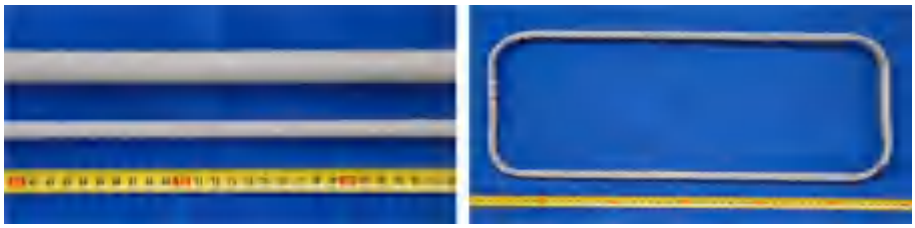


Fig. 2. GFRP reinforcements used in this study.

Table 2
Mechanical properties of GFRP reinforcement.

Material	Nominal cross-sectional area (mm^2)	Ultimate strength (MPa)	Bend strength (MPa)	Elastic modulus (GPa)	Ultimate tensile strain
No. 10 GFRP	71	1094	602	53	2.06%
No. 19 GFRP	284	1081	–	55	1.97%

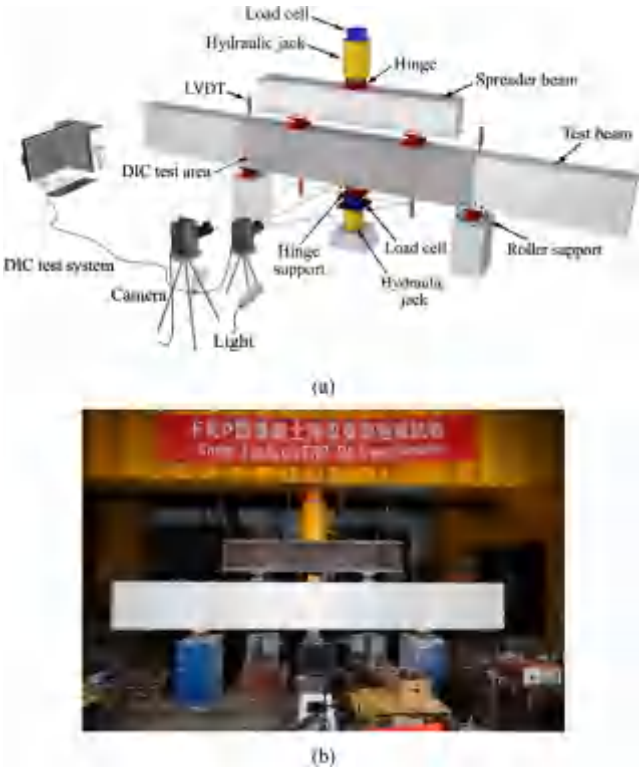


Fig. 3. Test setup: (a) scheme proposal; and (b) final test setup.

2.4. Test set-up and procedure

The continuous GFRP-RC beams were supported on one hinged support at the middle and two roller supports at both ends. Testing was done at the Hunan University Structural Engineering Lab. A 3200 kN-testing machine was used to apply a monotonic concentrated load that was transmitted to the beam through a rigid steel spreader beam. The load was applied in 25 kN increments up to the calculated cracking load. After cracking, 50 kN increments were used. According to the strut-and-tie model, the plate width directly affects the diagonal strut width and hence the shear strength of the deep beam. For continuous deep beams, the interior support bears the greatest reaction force. To avoid premature failure of nodes, the dimension of the bearing steel plates in the direction of the span length was 0.3 h for the support plates and 0.2 h for the loading plates. It should be mentioned that the designed dimension was in accordance with the research conducted by Li et al. [29]. The thickness of all bearing plates was 20 mm.

2.5. Support settlements

Unlike simply supported deep beams, the continuous deep beams are sensitive to differential support settlements which causes additional moment and shear [5,7,9]. The sources of the relative support settlements were the elastic deformation of the bearing steel plates and the bed of the testing system. In this study, the displacements of three supports were recorded, and it was checked whether the three supports were on a line at each interval. If differential support settlements were observed, the load was then applied using a hydraulic jack placed at the intermediate support to ensure that the three supports were on the same level during the entire loading.

3. Test results and discussion

3.1. Crack pattern and failure mode

For each beam, Fig. 4 shows the cracking pattern development registered by DIC system at four chosen load levels. Generally, the GFRP-RC deep beams exhibited four distinguished phases: flexural cracking, flexural-shear levels cracking in the exterior shear span, diagonal shear cracking in the interior shear span, and failure of the inclined struts. During the test, vertical cracks initiated in the hogging moment zone. Then, flexural cracks developed in the sagging moment zone. As loading progressed, flexural-shear cracking formed in the exterior shear span.

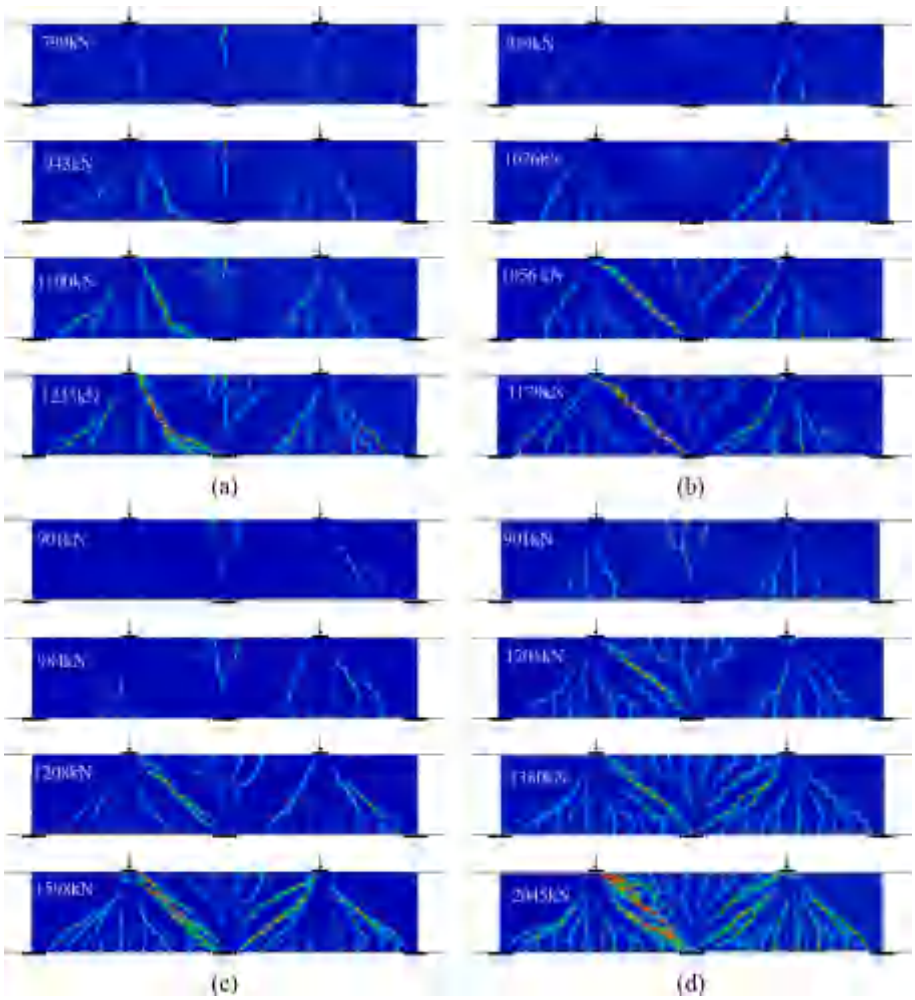


Fig. 4. Cracking pattern development registered by DIC system: (a) GN; (b) G240; (c) G180; and (d) G120.

Subsequently, a typical major diagonal shear crack propagated suddenly between one of the loading points and the middle support accompanied by a loud noise, highlighting the brittle behavior of the specimens reinforced with GFRP bars. This major shear crack is not developed from the flexural crack but is similar to the web-shear crack in prestressed concrete I-beams. With further loading, additional diagonal shear cracks propagated in the shear spans and the diagonal crack kept widening with increasing load until failure.

As shown in Fig. 4, the crack propagation was significantly influenced by the GFRP shear reinforcement ratio. Just before failure, there is no significant difference in the distribution of cracks between Specimens GN and G240, which indicates that the minimum required GFRP shear reinforcements specified in ACI 440.1R-15 [3] are ineffective for control of shear crack distribution. As the GFRP shear reinforcement ratio increased, more diagonal shear cracks were developed in the shear span. This is expected because the close-spaced GFRP transverse reinforcement can better control the crack distribution. According to CSA S806-12 [22], the spacing of such crack control reinforcements shall not exceed 200 mm for GFRP bars.

The last cracking pattern propagated in the interior shear span before failure for each specimen is shown in Fig. 5. As expected, all beams failed in shear, as shown in Fig. 6. Table 1 lists the final failure mode of each beam. Specimens GN and G240 exhibited a shear compression failure, where crushing of concrete at the tips of the diagonal shear crack was noticed. Specimens G180 and G120 failed due to compression strut failure after the formation of parallel diagonal cracks in the compression strut zone. Failure of all the specimens with GFRP stirrups was associated with rupture in the bent portion of the stirrups, as shown in Fig. 6. This is because bending GFRP bars to form stirrups significantly reduces the strength at the bend portions due to the unidirectional characteristics of GFRP and localized stress concentration at the bend [30].

3.2. Shear strength and moment redistribution

Table 1 summarizes the total shear cracking load P_{cr} in each shear span and the ultimate load P_u (excluding self-weight). Due to the slight difference between the modulus of elasticity of GFRP bars and that of concrete, the presence of GFRP shear reinforcement in the deep beams had a slight effect on the load corresponding to the first main diagonal crack compared to their unreinforced counterpart. Also, there was no significant difference in the shear strength between Specimens GN and G240, indicating that the minimum required GFRP stirrups according to ACI 440.1R-15 [3] were ineffective to improve the ultimate shear strength of continuous deep beams. When GFRP shear reinforcement was provided, the maximum force of Specimens G180 and G120 was higher than that of Specimen G240 by 35.5% and 73.5%, respectively. This is expected because increasing the GFRP shear reinforcement ratio can improve the mechanism of shear transfer by GFRP stirrups and enhance the confinement of the concrete of the interior strut which transfers a considerable part of the applied load to the support.

Fig. 7 shows the total applied load against measured elastic interior reactions. The elastic intermediate reaction was calculated elastically to be 0.688 from the total load. Before the propagation of the first flexural

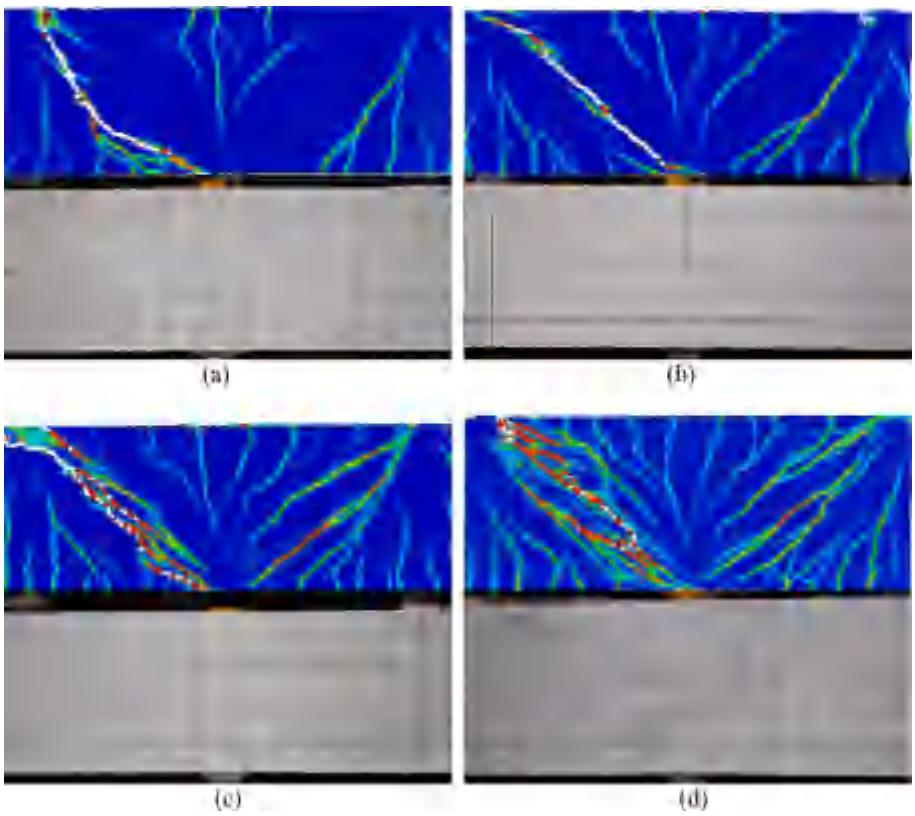


Fig. 5. Cracking pattern of interior shear span at the onset of the maximum shear capacity: (a) GN; (b) G240; (c) G180; and (d) G120.

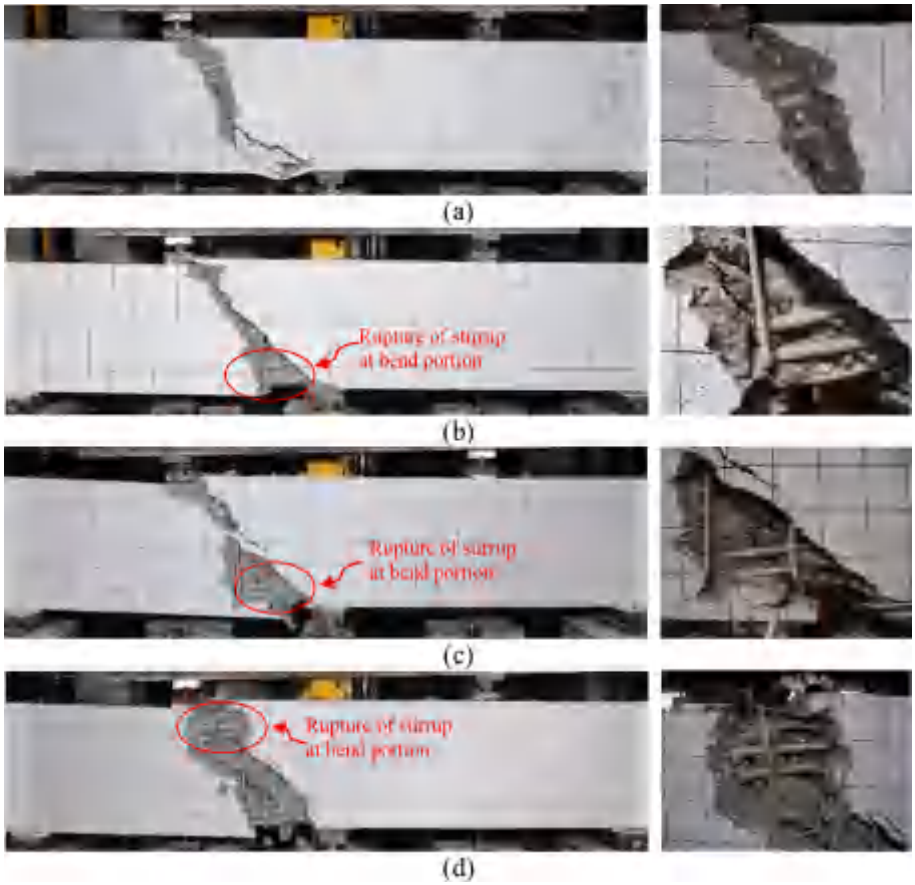


Fig. 6. Failure mode for each beam: (a) GN; (b) G240; (c) G180; and (d) G120.

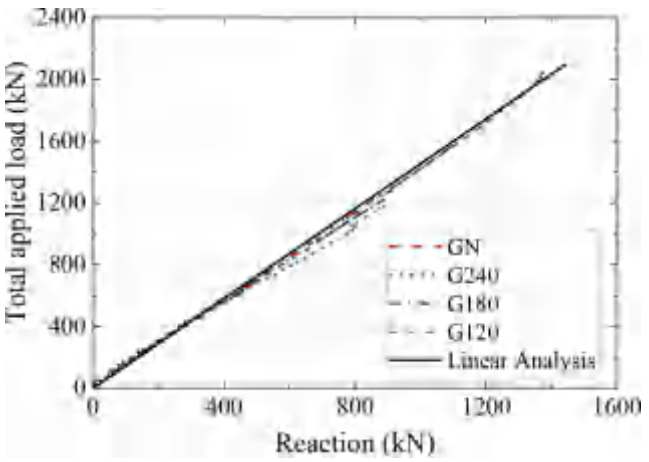


Fig. 7. Interior support reaction against total load.

crack, the measured intermediate reaction in all beams showed similar values to the elastic reaction. After the formation of cracks in the hogging and sagging moment regions, the measured intermediate reaction slightly deviated from the elastic one depending on the development of the cracks in the test beams. At failure, the ratio of the load transferred to the intermediate support to the total applied load ranged from 0.67 to 0.74, indicating the moment redistribution in the tested GFRP-RC continuous deep beams is limited. Similar findings were reported for continuous steel-RC deep beams [5] and FRP-RC deep beams [10,20].

3.3. Load-deflection curves

The total applied load versus midspan deflection for all test beams is plotted in Fig. 8. Before flexural cracking, the load-deflection behavior of test beams was similar where the deflection was of very small values. After cracking, a reduction in the stiffness of the test beams was observed. Table 1 summarizes the total applied loads when the vertical flexural cracks appeared in the beams ($P_{cr,f}$). The flexural cracking load of each beam was almost identical. In Fig. 8, three characteristic points, including flexural cracking and formation of the major diagonal crack in both interior shear spans, are noted. Generally, the occurrence of diagonal cracks in the interior shear span caused a sharp decrease in the beam stiffness and an increase in the beam deflection. As observed, all specimens exhibited significant reserve strength after the diagonal cracks were fully developed, even for the specimen without stirrups. The ratio of the ultimate shear capacity to the shear load at which the critical shear crack formed ranged from 1.15 to 1.70. Table 1 shows the ultimate midspan deflection (Δ_u) for all beams. The presence of GFRP stirrups can significantly increase the maximum deflection at failure. The ultimate midspan deflection of Specimen G240 was 50% higher than that of Specimen GN, although their ultimate shear strength was almost the same. It can be noted that increasing the GFRP shear reinforcement ratio significantly increased the maximum deflection at failure.

3.4. Strains in reinforcement

The strain distribution of the flexural reinforcement along the shear span is an indicator of whether and to what extent a tie-arch action is developed [13]. Figs. 9 and 10 show the strain distribution of GFRP bars in the bottom and top layers for each specimen, respectively. Generally, the developed strains in the reinforcement were very small until the formation of the flexural cracks. Later, a rapid increase in the strains at the locations of the flexural cracks was observed, representing the distribution of the bending moment of such loading configuration. As inclined cracks were formed, however, the bottom reinforcement strains at the shear span increased rapidly until they were approximately the same magnitude as the strains at mid-span. This may be due to the reduction of aggregate interlock effect and the development of the arching behavior with the opening of the inclined crack, indicating that an arch mechanism formed in the tested beams [30]. In addition, the strains in the bottom reinforcement over the intermediate support changed dramatically from compression to tension. At failure, the formation of the tie action was confirmed by the nearly uniform reinforcement strain distribution in the shear span. Moreover, the strain profiles for all test specimens confirmed the development of the arch action. As observed,

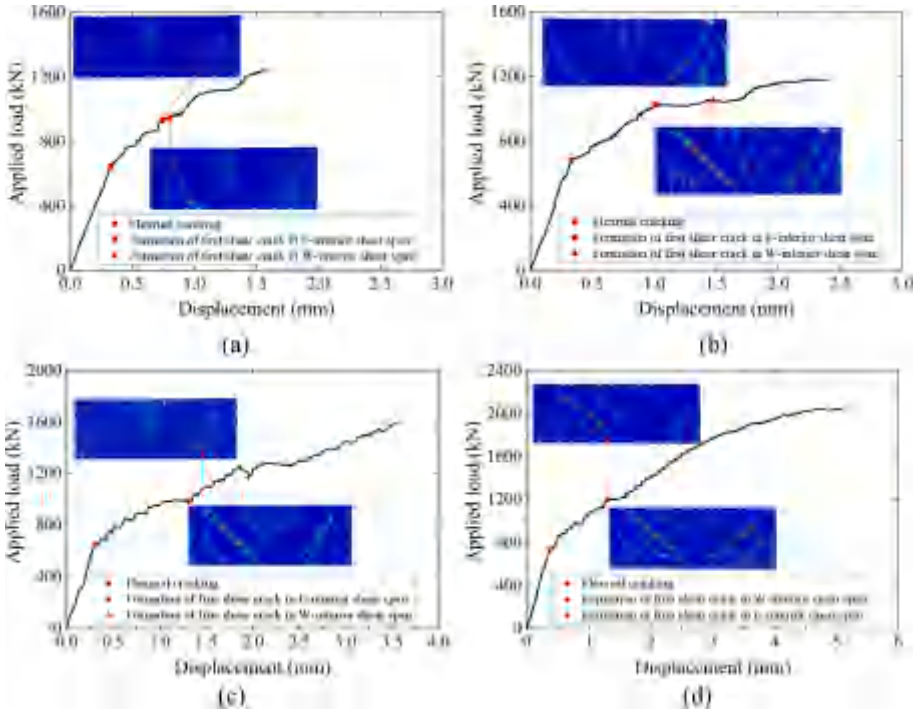


Fig. 8. Applied load-deflection at midspan: (a) GN; (b) G240; (c) G180; and (d) G120.

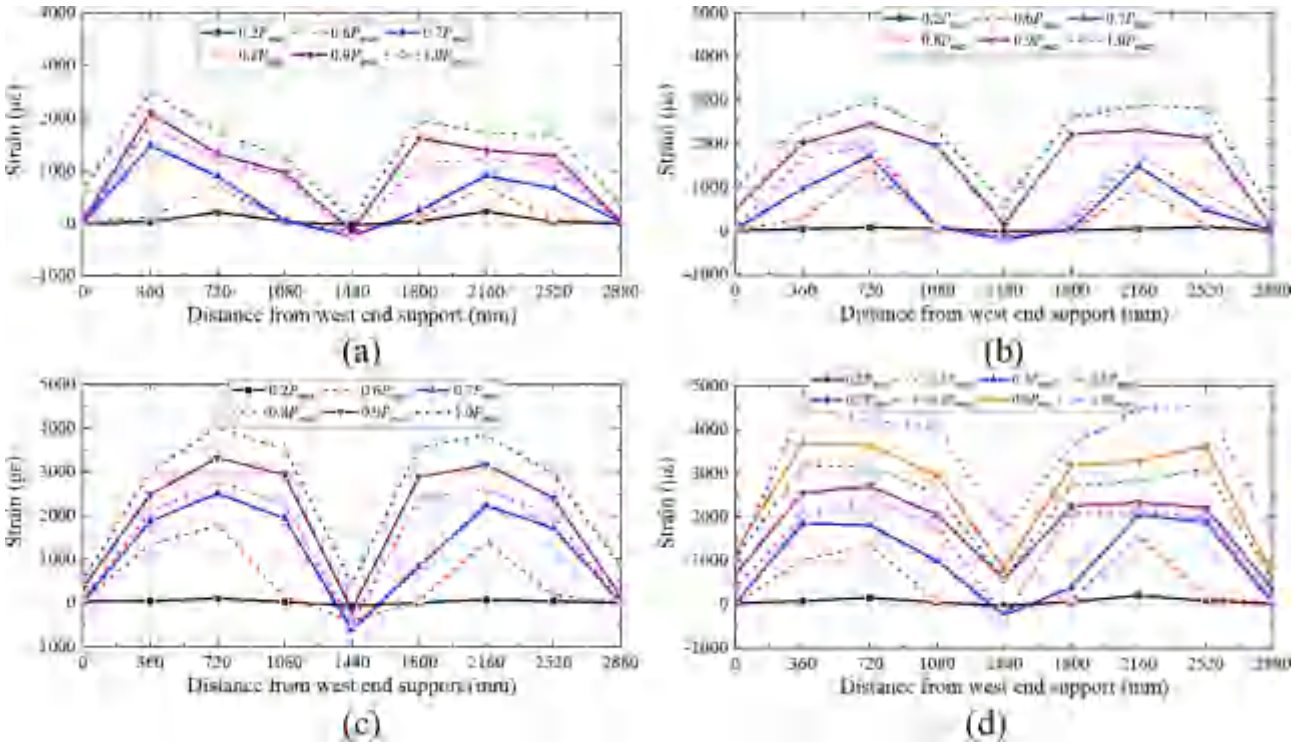


Fig. 9. Strain distribution along longitudinal bottom reinforcement: (a) GN; (b) G240; (c) G180; and (d) G120.

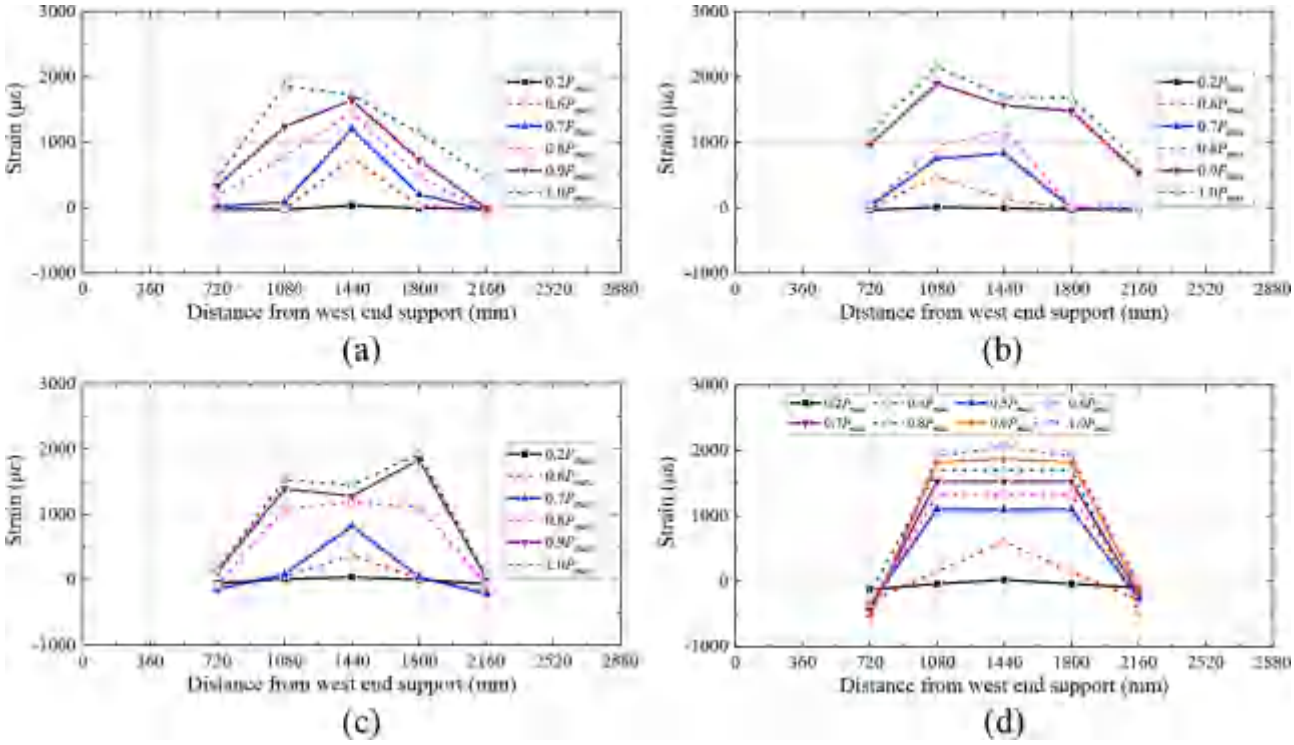


Fig. 10. Strain distribution along longitudinal top reinforcement: (a) GN; (b) G240; (c) G180; and (d) G120.

the maximum strain in top reinforcement was much lower than that in bottom reinforcement. A similar finding was also reported in continuous steel-RC deep beams with a symmetrical reinforcement scheme [31]. This phenomenon can be explained by comparing the horizontal force equilibrium in Fig. 11**(b)** with that in Fig. 11 **(c)**. The horizontal component of the total compressive force of the exterior strut can partially balance the horizontal component of the total compressive force of the interior strut, which lessens the stress in the top tie. CSA S806-12 [22] limits the tensile strength of the longitudinal FRP reinforcement to 65% of its ultimate tensile strength. In this study, the measured maximum bottom reinforcement stress in Specimen GN, G240, G180, and G120 were 12%, 15%, 20%, and 23% of its ultimate

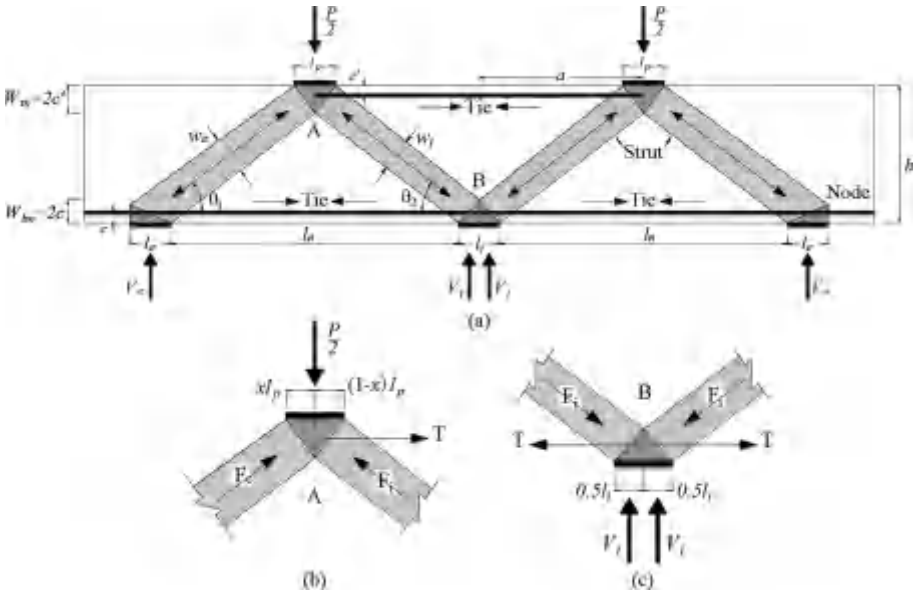


Fig. 11. Strut-and-tie model for continuous deep beams: (a) Schematic STM; (b) joint A for loading point, (c) joint B for intermediate support.

tensile strength, respectively, which were lower than the stress limit specified in CSA S806-12.

3.5. Strain in transverse reinforcement

Fig. 12 shows the applied total load versus the strain in GFRP stirrups measured from the west interior shear span. Before shear cracking, the stirrup strains were trivial. After the formation of the diagonal shear crack, however, the stirrup strains increased rapidly, which is evident from Fig. 12. A light increase in applied load resulted in a significant increase in the stirrup strain, which indicates that there is significant redistribution of stresses between GFRP stirrups and concrete. It should be mentioned that several strain gauges installed on the stirrups broke due to a sudden significant strain increase after the formation of the major diagonal shear crack. Fig. 13 shows the measured maximum strain distribution of stirrups. As observed, the maximum stirrup strain in the exterior shear span was less than that in the interior shear span in which failure took place. This is expected because the interior shear span is subjected to higher shear forces.

Currently, most design guidelines limit the usable strain of GFRP stirrups to control shear crack widths. For example, CSA S806-12 specifies a strain limit of 0.005 for GFRP stirrups. Alternatively, ACI 440.1R-15 and GB 50608 specify a lower strain value of 0.004. In the truss-based model, the stresses in GFRP stirrups are typically assumed constant. Therefore, the average stirrup strain in the shear span at the ultimate limit state may be more critical from a design perspective [30]. For the beams with GFRP stirrups, Table 3 lists the measured maximum and average stirrup strains in each span at the ultimate state. The

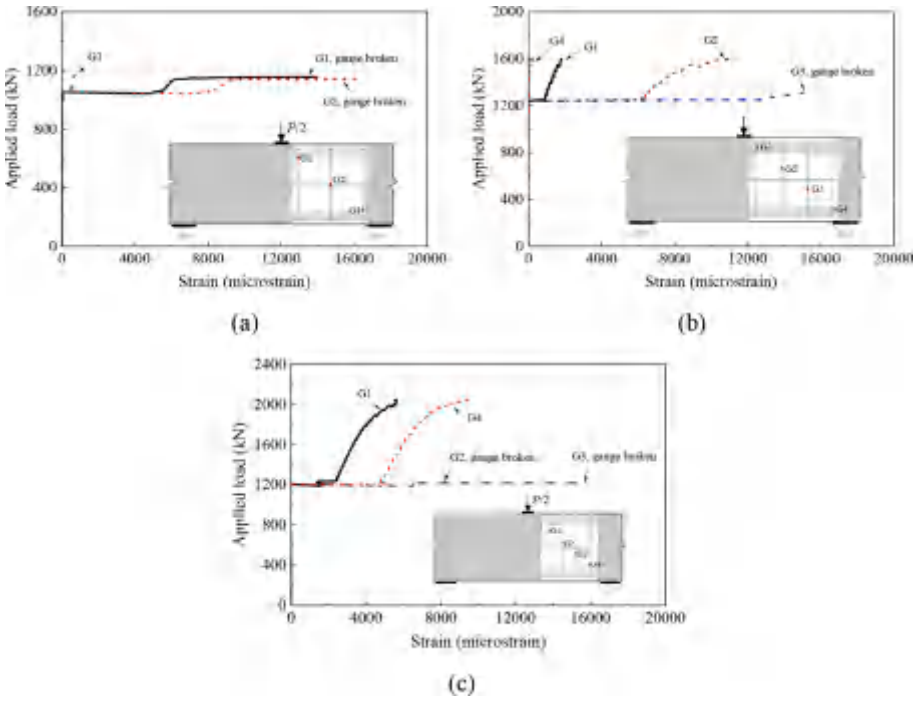


Fig. 12. Strain response in stirrups in west interior shear span: (a) G240; (b) G180; and (c) G120.

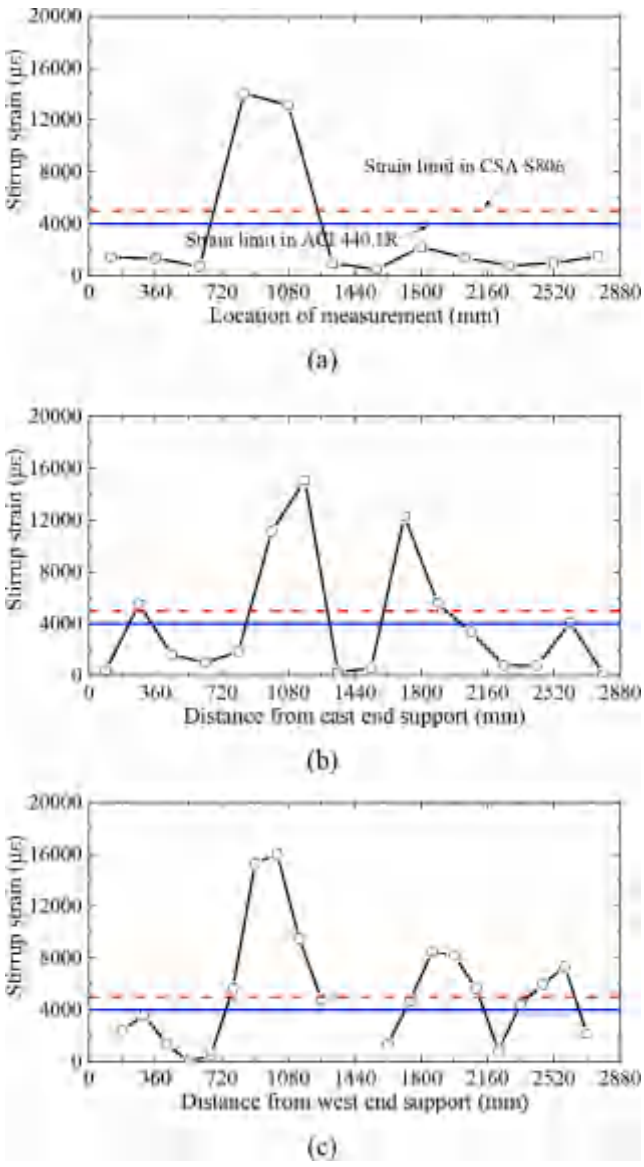


Fig. 13. Strain distribution of stirrups at ultimate limit state: (a) G240; (b) G180; and (c) G120.

Table 3
Strain in GFRP stirrups.

Specimen	Maximum strain (με)		Average strain at ultimate state (με)		Strain at shear cracking in W-interior (με)	
	W-interior	E-interior	W-interior	E-interior	Maximum	Average
G240	14,046	2213	9380	1359	7262	4134
G180	15,079	12,298	7075	5462	11,498	4882
G120	16,016	8498	10,246	5675	8025	5265

average strain in the west interior shear span ranged from 7075 to 10,246 με, indicating the conservatism of the strain limits specified in current design codes. Also, the average stirrup strain in the interior east shear span was less than that in the interior west shear span where failure took place. The average measured GFRP stirrup strains in the east interior shear span were 5462 and 5675 με in G180, and G120, respectively, which were much higher than the 1359 με in G240. This is because the minimum required GFRP stirrups according to ACI 440.1R-15 [3] were ineffective to improve the ultimate shear strength of continuous deep beams. Table 3 also lists the average stirrup strain at the formation of the diagonal shear crack in the interior west shear span. The average strain ranged from 4134 to 5265 με, which was slightly higher than the strain limit of 4000 με specified in ACI 440.1R-15.

3.6. Major diagonal shear crack width

In this study, the two-dimensional DIC system was used to measure the width and slip of the major diagonal shear crack during the entire testing. The measured crack width from the hand-held microscopes with an accuracy of 0.01 mm confirmed the accuracy of the DIC measurement. Fig. 14 shows the width and slip variation along the major diagonal shear crack of each beam at three chosen load levels. As observed, the crack slip generally was smaller than the crack width. Fig. 15 shows the width of the major diagonal shear crack measured at mid-height in the west interior span as a function of the applied load. At the formation of the major diagonal shear crack in the west interior span, the maximum crack width of Specimens G240, G180, and G120 was suddenly increased from zero to 0.77, 0.80, and 0.60 mm, respectively. This is due to the relatively low elastic modulus of the GFRP stirrups. At failure, the maximum crack width of Specimens GN, G240, G180, and G120 was 1.59, 1.66, 1.45, and 1.75 mm, respectively.

3.7. Aggregate interlock effect

In several shear strength models for FRP-RC deep beams, aggregate interlock action is acknowledged as one of the main shear transfer mechanisms [23,24]. Many mechanical models have been developed to estimate the aggregate interlock effect. In this study, the two-phase model proposed by Walraven [32] was used to quantify the tangential and normal stress between cracks:

$$\tau_{ag} = -\frac{f_c}{30} + \left[1.8w^{-0.80} + \left(0.234w^{-0.707} - 0.20\right)f_c\right]\Delta \quad (1)$$

$$\sigma_{ag} = -\frac{f_c}{20} + \left[1.35w^{-0.63} + \left(0.191w^{-0.552} - 0.15\right)f_c\right]\Delta \quad (2)$$

where τ_{ag} and σ_{ag} are shear and normal stress acting on crack, respectively; f_c is concrete compressive strength; and w and Δ are crack width and slip, respectively.

Based on the measured crack width and slip along the major diagonal shear crack, the shear contribution of aggregate interlock then can be estimated by

$$V_{ag} = b\cdot\left(\int_{x=0}^{l_{cr}} \tau_{ag}\sin\alpha(x)\cdot dx - \int_{x=0}^{l_{cr}} \sigma_{ag}\cos\alpha(x)\cdot dx\right) \quad (3)$$

where $l_{cr}$is crack length.

For the beams without GFRP stirrups (GN), the aggregate interlock contribution constituted 46.3% of the total shear resistance. The role of aggregate interlock is less important for specimens with GFRP stirrups. The estimated aggregate interlock contribution of Specimens G240, G180, and G120, constituted 8.4%, 8.9%, and 12.8% of the total shear resistance, respectively. This can be attributed to a steeper inclination of the major diagonal shear crack formed in Specimen GN (Fig. 5**(a)**), and large opening of the major diagonal shear reduces the probability that aggregate particles interlock.

4. Evaluation of shear design equations

Strut-and-tie method (STM) for RC beams is based on the lower-bound theorem of plasticity. Although GFRP is an elastic and brittle material without yielding, the measurements in this study have confirmed the development of the tie-arch action in the GFRP-RC deep beams. In this section, the ability of the STM in ACI 318-2019 [1], EC2-

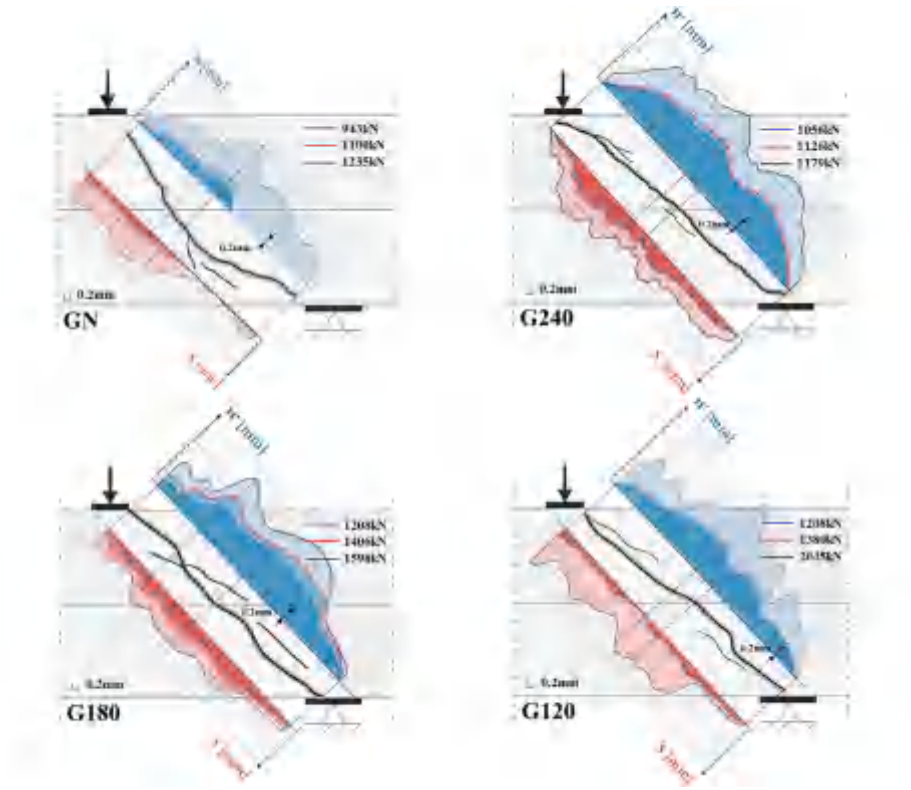


Fig. 14. Major diagonal shear crack width and slip.

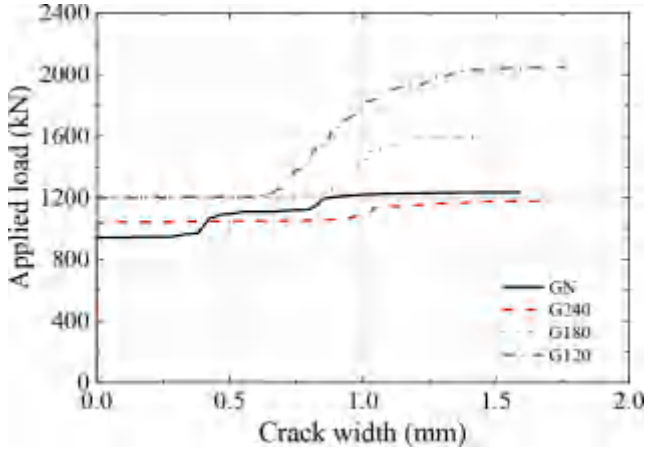


Fig. 15. Major diagonal shear crack width measured at mid-height.

2004 [33], and CSA-S806-2012 [22] to be adapted for GFRP-RC continuous deep beams is evaluated. The STM for a two-span continuous concrete deep beam is shown in Fig. 11. The internal (V_I) and external (V_E) shear strengths of the continuous deep beam due to the failure of the concrete strut can be calculated as follows:

$$V_I = \upsilon f_c' b w_I \sin\theta \tag{4}$$

$$V_E = \upsilon f_c' b w_E \sin\theta \tag{5}$$

where υ is the concrete effectiveness factor; b is the beam width; w_E and w_I are the average widths of the exterior and the interior concrete struts, respectively; and θ is the angle between the strut and the longitudinal axis of the beam.

The widths of the interior, w_I, and exterior, w_E, struts can be calculated as follows:

$$w_I = \frac{(2c + 2c')\cos\theta + [0.5l_I + (1-\chi)l_p]\sin\theta}{2} \tag{6}$$

$$w_E = \frac{(2c + 2c')\cos\theta + (l_E + \chi l_p)\sin\theta}{2} \tag{7}$$

where c is the distance from the bottom face of the beam to the centroid of the bottom reinforcements; c' is the distance from the top face of the beam to the centroid of the top reinforcements; l_I and l_E are the width of the interior and exterior support plate, respectively; l_p is the width of the loading plate; and χ is the ratio of the end reaction to the load applied on one span.

As presented earlier in Fig. 7, the experimental and elastic analysis results show that the load transferred to the intermediate support was about 70% of the load-carrying capacity. Therefore, the value of χ was taken to be 0.3. Accordingly, the total failure load P can be calculated as follows:

$$P = \min\left(\frac{2V_E}{\chi}, \frac{2V_I}{1-\chi}\right) \tag{8}$$

To apply the STM in the three code provisions, only the effectiveness

Table 4
Strut effectiveness factor.

Provision	Strut effectiveness factor (υ)
ACI 318-19	$\upsilon = 0.85\beta_s$ $\beta_s = 0.75$ for struts with minimum distributed reinforcement $\beta_s = 0.4$ for struts without minimum distributed reinforcement
EC2-2004	$\upsilon = 0.6\left(1 - \frac{f_c'}{250}\right)$
CSA-S806-2012	$\upsilon = \frac{1}{0.8 + 170\varepsilon_1} \leqslant 0.85$ $\varepsilon_1 = \varepsilon_f + (\varepsilon_f + 0.002)\cot^2\theta$

factor υ was changed and taken according to Table 4. To assess the STM provisions, a total of 22 two-span GFRP-RC deep beams were collected from different sources as given in Table 5. The shear span-to-overall depth ratio of deep beams in the database ranged from 0.88 to 1.76. The cylinder compressive strength of concrete ranged from 32.3 MPa to 56.6 MPa. The range of load capacity of test specimens was 548 to 2,050 kN. In all beams, the failure was governed by crushing of the concrete strut.

Fig. 16 compares experimental and calculated results for the total failure load. All material reduction and safety factors in the shear strength equations were set equal to 1.0. Generally, the STM specified in EC2 overestimates the shear capacity of GFRP-RC deep beams with an average experimental-to-predicted capacity ratio (P_{exp}/P_{pred}) of 0.92 and a coefficient of variation (COV) of 0.28. This could be attributed to the fact that EC2 underestimates the effect of concrete softening in inclined struts, which is caused by the existence of high tensile strains in the longitudinal GFRP bars [34]. The STM in ACI 318-2019 provides the most accurate prediction in terms of mean value. This finding differs from the observations made by Mohamed et al. [10] and Zinkaah et al. [20] who concluded that ACI 318-14 overestimated the shear capacity of the continuous GFRP-RC deep beams. This is because the latest version of ACI 318 reduced the strut effectiveness factor. The STM in CSA S806, however, provides the most conservative prediction, with a mean P_{exp}/P_{pred} of 2.00 and a COV of 0.35. This may be because this method exaggerates the effect of concrete softening in the inclined strut, as it recommends calculating the effective strength of the concrete strut based on the modified compression field theory which was first developed by Vecchio and Collins [35] for slender beams.

5. Conclusions

To investigate the shear behavior of continuous concrete deep beams reinforced with GFRP bars, four full-scale beams are constructed and tested in this study. Based on the analysis of the experimental results, the following conclusions can be drawn:

1. All beams exhibit brittle shear failure after the formation of diagonal shear cracks in the interior shear span. As the GFRP shear reinforcement ratio increases from 0% to 4.7%, the failure changes from shear compression failure to compression strut failure.
2. The development of the tie-arch action is confirmed by the crack propagation and the strains developed in the top and bottom longitudinal reinforcements.
3. For the beams without GFRP stirrups, the aggregate interlock contribution constitutes 46.3% of the total shear resistance. The role of aggregate interlock is less important for specimens with GFRP stirrups (the contribution to the shear strength by the aggregate interlock effect ranges from 8.4% to 12.8%).
4. The shear capacity of GFRP-RC beams increases with the increase of the shear GFRP reinforcement ratio. Compared to the specimens with a shear GFRP reinforcement ratio of 0.24%, the shear capacity of the specimens with a shear GFRP reinforcement ratio of 0.32% and 0.47% is increased by 35.5% and 73.5%, respectively.
5. The moment redistribution in the GFRP-RC continuous deep beams is limited. At failure, the ratio of the load transferred to the intermediate support to the total applied load ranges from 0.67 to 0.74.
6. The minimum required GFRP stirrups according to ACI 440.1R-15 are ineffective in terms of shear capacity enhancement and shear crack control.
7. The STM design equations in the CSA S806-12 highly underestimate the shear capacity of the GFRP-RC continuous beams, with an average P_{exp}/P_{pred} of 2.0. On the other hand, the STM design equation in EC2-2004 is unconservative, with an average P_{exp}/P_{pred} of 0.92. The STM in ACI 318-2019 provides the most accurate prediction, with an average P_{exp}/P_{pred} of 1.07 and COV of 0.25.

CRediT authorship contribution statement

Fei Peng: Conceptualization, Funding acquisition, Formal analysis, Supervision, Methodology, Software, Writing – original draft, Writing –

Table 5
Comparisons between theoretical and experimental shear capacity of continuous GFRP-RC deep beams.

Reference	Specimen	h (mm)	a/h	f'_c (MPa)	Flexural reinforcement			Horizontal web reinforcement		Vertical web reinforcement		P_{exp} (kN)	V_I (kN)
					ρ_{lb} (%)	ρ_{lt} (%)	E_{fl} (GPa)	ρ_h (%)	E_{fh} (GPa)	ρ_v (%)	E_{fv} (GPa)		
Mohamed et al. 2021	DB-1.0-1.2	590	0.88	49.0	1.00	1.20	63	—	—	—	—	1166	368
	DB-1.0-1.0	590	0.88	48.0	1.00	1.00	63	—	—	—	—	1382	434
	DB-1.0-0.8	590	0.88	49.0	1.00	0.80	63	—	—	—	—	1902	584
	DB-1.5-1.2	590	1.32	49.0	1.00	1.20	63	—	—	—	—	1119	386
	DB-1.5-1.0	590	1.32	49.0	1.00	1.00	63	—	—	—	—	1310	438
	DB-1.5-0.8	590	1.32	49.0	1.00	0.80	63	—	—	—	—	1450	487
	DB-2.0-1.2	590	1.76	47.0	1.00	1.20	63	—	—	—	—	946	325
	DB-2.0-1.0	590	1.76	47.0	1.00	1.00	63	—	—	—	—	1020	350
	DB-2.0-0.8	590	1.76	48.0	1.00	0.80	63	—	—	—	—	1148	397
Zinkaah et al. 2019	G1-300-N	300	1.00	56.6	1.40	1.40	47	—	—	—	—	937	323
	G1-300-W	300	1.00	55.3	1.40	1.40	47	0.40	63	0.40	63	1006	336
	G1-600-N	600	1.00	56.6	1.40	1.40	47	—	—	—	—	1388	479
	G1-600-W	600	1.00	53.6	1.40	1.40	47	0.40	63	0.40	63	1439	502
	G1-800-N	800	1.00	56.6	1.37	1.37	44	—	—	—	—	1957	674
	G1-800-W	800	1.00	53.6	1.37	1.37	44	0.40	63	0.40	63	2050	720
	G1.7-300-N	300	1.70	52.5	1.40	1.40	47	—	—	—	—	548	196
	G1.7-300-W	300	1.70	52.1	1.40	1.40	47	0.40	63	0.40	63	640	214
	G1.7-600-W	600	1.70	52.1	1.40	1.40	47	0.40	63	0.40	63	1001	353
This study	GN	600	1.20	32.3	1.77	1.77	55	—	—	—	—	1235	428
	G240	600	1.20	32.3	1.77	1.77	55	—	—	0.24	53	1179	438
	G180	600	1.20	32.3	1.77	1.77	55	—	—	0.32	53	1598	556
	G120	600	1.20	32.3	1.77	1.77	55	—	—	0.47	53	2045	688

Note: ρ_{lb} and ρ_{lt} are bottom and top flexural reinforcement ratio, respectively; ρ_h and ρ_v are horizontal and vertical web reinforcement ratio, respectively; E_{fl} is elastic modulus of flexural reinforcement; and E_{fh} and E_{fv} are elastic modulus of horizontal and vertical web reinforcement, respectively.

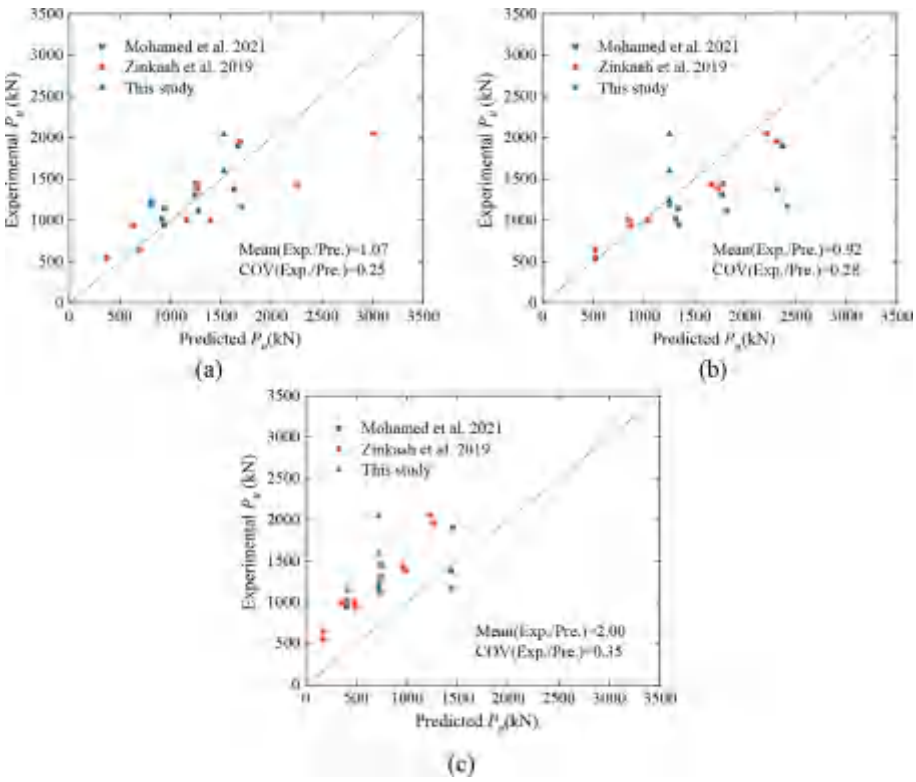


Fig. 16. Comparison between experimental and predicted load-carrying capacity: (a) ACI 318-2019; (b) EC2-2004; and (c) CSA-S806-2012.

review & editing. **Yuhang Cai:** Software, Data curation, Investigation, Writing - original draft. **Weijian Yi:** Methodology, Writing - review & editing. **Weichen Xue:** Conceptualization, Writing - review & editing.

Declaration of Competing Interest

The authors declare that they have no known competing financial interests or personal relationships that could have appeared to influence the work reported in this paper.

Data availability

Data will be made available on request.

Acknowledgement

The authors gratefully acknowledge the financial support provided by the National Natural Science Foundation of China (No. 52008165), the Natural Science Foundation of Hunan Province (No. 2021JJ40082), and the Program Fund of Non-Metallic Excellence and Innovation Center for Building Materials (2023TDA4-1).

References

[1] ACI 318-19. Building code requirements for structural concrete and commentary. Farmington Hills (MI): American Concrete Institute; 2019.
[2] Ismail KS, Guadagnini M, Pilakoutas K. Numerical investigation of the shear strength of RC deep beams using the microplane model. J Struct Eng 2016;142(10): 04016077.
[3] ACI 440.1R-15. Guide for the design and construction of structural concrete reinforced with FRP bars. Farmington Hills (MI): American Concrete Institute; 2015.
[4] Peng F, Xue W, Xue W. Database evaluation of shear strength of slender fiber-reinforced polymer-reinforced concrete members. ACI Struct J 2020;117(3): 273–81.
[5] Yang KH, Chung HS, Ashour AF. Influence of shear reinforcement on reinforced concrete continuous deep beams. ACI Struct J 2007;104(4):420–9. https://doi.org/10.14359/18772.
[6] Chen H, Yi W-J, Ma ZJ, Hwang H-J. Shear Strength of Reinforced Concrete Simple and Continuous Deep Beams. ACI Struct J 2019;116(6):31–40.
[7] Zhang N, Tan K-H. Effects of support settlement on continuous deep beams and STM modeling. Eng Struct 2010;32(2):361–72. https://doi.org/10.1016/j.engstruct.2009.09.019.
[8] Rogowsky DM, MacGregor JG, Ong SY. Tests of reinforced concrete deep beams. ACI Struct J 1986;83:614–23.
[9] Ashour AF. Tests of reinforced concrete continuous deep beams. ACI Struct J 1997; 94:3–11.
[10] Mohamed A, Mahmoud K, El-Salakawy EF. Shear capacity of glass fiber-reinforced polymer-reinforced concrete continuous deep beams without web reinforcement. ACI Struct J 2021;118(3):85–99. https://doi.org/10.14359/51729354.
[11] Nehdi M, Omeman Z, EL-Chabib H. Optimal efficiency factor in strut-and-tie model for FRP-reinforced concrete short beams with (1.5<a/d<2.5). Mater Struct 2008; 41(10):1713–27. https://doi.org/10.1617/s11527-008-9359-9.
[12] El-Sayed AK, El-Salakawy EF, Benmokrane B. Shear strength of fibre-reinforced polymer reinforced concrete deep beams without web reinforcement. Can J Civil Eng 2012;39(5):546–55. https://doi.org/10.1139/l2012-034.
[13] Andermatt MF, Lubell AS. Behavior of concrete deep beams reinforced with internal fiber-reinforced polymer—experimental study. ACI Struct J 2013;110: 585–94.
[14] Kim DJ, Lee J, Lee YH. Effectiveness factor of strut-and-tie model for concrete deep beams reinforced with FRP rebars. Compos Part B Eng 2014;56:117–25.
[15] Farghaly AS, Benmokrane B. Shear behavior of FRP-reinforced concrete deep beams without web reinforcement. J Compos Constr 2013;17(6):04013015.
[16] Mohamed K, Farghaly AS, Benmokrane B. Strut efficiency-based design for concrete deep beams reinforced with fiber-reinforced polymer bars. ACI Struct J 2016;113(4):791–800. https://doi.org/10.14359/51688476.
[17] Mohamed K, Farghaly AS, Benmokrane B. Effect of vertical and horizontal web reinforcement on the strength and deformation of concrete deep beams reinforced with GFRP bars. J Struct Eng 2017;143(8):04017079.
[18] Abu-Obaida A, El-Ariss B, El-Maaddawy T. Behavior of short-span concrete members internally reinforced with glass fiber–reinforced polymer bars. J Compos Constr 2018;22(5):04018038. https://doi.org/10.1061/(asce)cc.1943-5614.0000877.
[19] Abed F, EL Refai A, Abdalla S. Experimental and finite element investigation of the shear performance of BFRP-RC short beams. Struct 2019;20:689–701.
[20] Zinkaah OH, Ashour A, Sheehan T. Experimental tests of two-span continuous concrete deep beams reinforced with GFRP bars and strut-and-tie method evaluation. Compos Struct 2019;216:112–26. https://doi.org/10.1016/j.compstruct.2019.02.078.
[21] ACI 318-14. Building code requirements for structural concrete and commentary. Farmington Hills (MI): American Concrete Institute; 2014.
[22] CSA S806-12, Design and construction of building components with fiber reinforced polymers, Mississauga, Ontario, Canada, Canadian Standards Association; 2017.

[23] Mihaylov BI. Two-parameter kinematic approach for shear strength of deep concrete beams with internal FRP reinforcement. J Compos Constr 2017;21(2):04016094.
[24] Chen H, Yi W-J, Ma ZJ, Hwang H-J. Modeling of shear mechanisms and strength of concrete deep beams reinforced with FRP bars. Compos Struct 2020;234:111715.
[25] GB/T 50081-2019, Standard for test methods of concrete physical and mechanical properties, Ministry of Housing and Construction, People's Republic of China; 2019.
[26] ASTM D7205-06. Standard test method for tensile properties of fiber reinforced polymer matrix composite bars. ASTM International, West Conshohocken, PA; 2011.
[27] ASTM D7914-21. Standard specification for strength of fiber reinforced polymer (FRP) bent bars in bend locations. ASTM International, West Conshohocken, PA; 2021.
[28] Peng F, Xue W. Experimental investigation on shear behavior of FRP post-tensioned concrete beams without stirrups. Eng Struct 2021;244:112835.
[29] Li Y, Chen H, Yi WJ, Peng F, Li Z. Effect of member depth and concrete strength on shear strength of RC deep beams without transverse reinforcement. Eng Struct 2021;241:112427.
[30] Peng F, Xue W. Effect of transverse reinforcement on shear response of fiber-reinforced polymer post-tensioned concrete beams. ACI Struct J 2022;119(5):31–42.
[31] Khatab MAT, Ashour AF, Sheehan T, Lam D. Experimental investigation on continuous reinforced SCC deep beams and Comparisons with Code provisions and models. Eng Struct 2017;131:264–74. https://doi.org/10.1016/j.engstruct.2016.11.005.
[32] Walraven JC. Fundamental analysis of aggregate interlock. J Struct Div 1981;107(11):2245–70.
[33] EC2-2004. Eurocode 2: Design of concrete structures: Part 1-1: General rules and rules for buildings. European Committee for Standardization, Brussels, Belgium; 2004.
[34] Dhahir MK. Shear strength of FRP reinforced deep beams without web reinforcement. Compos Struct 2017;165:223–32.
[35] Vecchio FJ, Collins MP. Modified compression-field theory for reinforced concrete elements subjected to shear. ACI J Proc 1986;83:219–31. https://doi.org/10.14359/10416.

基于数据库的玻璃纤维增强复合材料箍筋弯拉强度计算方法

白浩阳, 薛伟辰, 江佳斐
(同济大学 土木工程学院, 上海 200092)

摘 要:玻璃纤维增强复合材料箍筋弯拉强度试验主要研究弯折半径与直径之比对弯拉强度的影响,直线段抗拉强度对弯拉强度的影响研究较少。本文基于 ACI 440.3R-12 中 B.5 试验方法,开展 3 组(9 个弯拉试件)不同直线段抗拉强度的玻璃纤维增强复合材料箍筋弯拉强度试验研究。3 组试件直线段抗拉强度分别为 530(A 组)、850(B 组)和 1 100 MPa(C 组),弯折半径与箍筋直径之比均为 3。试验结果表明:所有试件均发生玻璃纤维增强复合材料箍筋弯折段被拉断的破坏模式;A、B、C 组试件弯拉强度分别为 325、445 和 530 MPa。本文系统收集了国内外已有 93 个弯拉试件,并结合本文 9 个弯拉试件建立了玻璃纤维增强复合材料箍筋弯拉强度试验数据库。基于数据库统计分析,提出了保证率不小于 95%的玻璃纤维增强复合材料箍筋弯拉强度计算方法。

关键词:玻璃纤维增强复合材料箍筋; 玻璃纤维增强复合材料箍筋弯拉强度; 直线段抗拉强度; 弯折半径; 玻璃纤维增强复合材料箍筋弯拉强度试验; 数据库; 保证率; 计算方法
DOI:10.11990/jheu.202304017
网络出版地址:https://link.cnki.net/urlid/23.1390.U.20231007.1121.006
中图分类号:TU532 **文献标志码**:A **文章编号**:1006-7043(2024)02-0223-08

Calculation method of the flexural tensile strength of the glass fiber-reinforced polymer stirrup based on the database

BAI Haoyang, XUE Weichen, JIANG Jiafei
(College of Civil Engineering, Tongji University, Shanghai 200092, China)

Abstract: Tests for the flexural tensile strength of glass fiber-reinforced polymer (GFRP) stirrups mainly concentrate on the impact of the ratio of the bending radius to the diameter on the flexural tensile strength of GFRP stirrups. However, the influence of the tensile strength of the straight portion on the flexural tensile strength of GFRP stirrups has seldom been studied. In this study, three groups (nine specimens in total) with different tensile strengths of the straight portion were examined to investigate the flexural tensile strength of GFRP stirrups using the B.5 test method from ACI 440.3R-12. The tensile strengths of the straight portion were 530 MPa for group A, 850 MPa for group B, and 1 100 MPa for group C, and the ratio of the bending radius to the stirrup diameter was 3. The findings revealed that GFRP stirrups ruptured at the bending portion in all specimens. The flexural tensile strengths of the specimens of groups A, B, and C were 325, 445, and 530 MPa, respectively. Moreover, a database was established with 93 systematically collected specimens in the literature at home and abroad and 9 specimens for testing of the flexural tensile strength. A method of calculating the flexural tensile strength of GFRP stirrups with a guaranteed rate of more than 95% was proposed based on the statistical analysis of the database.

Keywords: glass fiber-reinforced polymer (GFRP) stirrup; flexural tensile strength of GFRP stirrup; tensile strength of straight portion; bend radius; test for the flexural tensile strength of GFRP stirrup; database; guarantee rate; calculation method

纤维增强复合材料(fiber reinforced polymer, FRP)筋具有高强度、耐腐蚀、高强重比等优点,在侵蚀环境下混凝土结构中的应用日益广泛[1-2]。玻璃纤维增强复合材料(glass fiber reinforced polymer, GFRP)筋是目前工程中最常应用、经济性最高的 FRP 筋。在 GFRP 筋混凝土结构中,GFRP 筋可分为 GFRP 纵筋和 GFRP 箍筋。

常见矩形 GFRP 箍筋可分为:组合封闭型

收稿日期:2023-04-10. **网络出版日期**:2023-10-07.
基金项目:非金属材料创新中心创新基金项目(2023TDA4-1).
作者简介:白浩阳,男,博士研究生;
薛伟辰,男,教授,博士生导师.
通信作者:薛伟辰,E-mail:xuewc@tongji.edu.cn.

GFRP 箍筋、搭接封闭型 GFRP 箍筋、连续缠绕封闭型 GFRP 箍筋、螺旋型 GFRP 箍筋。组合封闭型 GFRP 箍筋由 2 根非封闭 GFRP 箍筋,通过非封闭段重合叠加而成组合封闭 GFRP 箍筋。搭接封闭型 GFRP 箍筋在生产过程中,由已浸润树脂 GFRP 筋连续缠绕于模具上形成一整段 GFRP 箍筋,待固化成型后切割形成搭接封闭型 GFRP 箍筋。搭接封闭型 GFRP 箍筋具有生产工艺简单、生产效率高等优点。搭接封闭型 GFRP 箍筋搭接段长度较长,材料消耗量较大。与搭接封闭型 GFRP 箍筋相比,连续缠绕封闭型 GFRP 箍筋没有搭接封闭段,具有全封闭、构造简单、材料利用率高、纤维在弯折段褶皱扭结少等优点。连续缠绕封闭型 GFRP 箍筋在生产时,由单股已浸润树脂玻璃纤维束连续缠绕于模具上形成单根连续缠绕封闭型 GFRP 箍筋。此外,在连续缠绕封闭型 GFRP 箍筋生产时,还可将已浸润树脂的玻璃纤维束逐层缠绕在桶状模具上形成 GFRP 管材;待 GFRP 管材固化成型后,将 GFRP 管材切割形成单根全封闭 GFRP 箍筋。连续缠绕封闭型 GFRP 箍筋需针对不同尺寸箍筋制作不同模具,模具重复利用率较低。与搭接型封闭型 GFRP 箍筋生产工艺相似,螺旋型 GFRP 箍筋在生产时,由已浸润树脂 GFRP 筋连续缠绕于模具上形成螺旋型 GFRP 箍筋。螺旋型 GFRP 箍筋具有生产工艺简便,生产效率高等优点。

目前,国内外已完成 GFRP 筋混凝土构件受剪、受扭试验结果表明[3-10]:GFRP 箍筋弯折段拉断破坏是一种较为常见的箍筋破坏模式;GFRP 箍筋弯折段抗拉强度(简称弯拉强度)低于直线段抗拉强度。GFRP 箍筋弯折段既承受轴向拉力,又承受混凝土对其产生横向压力,使弯折段处于复杂受力状态。此外,GFRP 箍筋弯折段内侧纤维褶皱扭结和弯折段截面变形,这些原因都会导致弯拉强度明显低于直线段抗拉强度。由于 GFRP 箍筋弯折段抗拉强度低于直线段抗拉强度,在现有 FRP 混凝土结构设计规范 ACI 440.1R-15[11]、GB 50608-2020[12]、CSA S6:19[13]和 JSCE[14]中,计算 GFRP 筋混凝土结构抗剪、抗扭承载力时,均需计算 GFRP 箍筋弯拉强度。美国 ASTM D7957/D7957M-17[15]规范规定:GFRP 箍筋弯拉强度不应小于直线段抗拉强度的 60%。加拿大 CSA S807:19[16]规范规定:GFRP 箍筋弯拉强度不应小于直线段抗拉强度的 46%。目前,国内 GFRP 筋材规范还未对 GFRP 箍筋弯拉强度试验方法和弯拉强度最低限值做出明确规定。

1 GFRP 箍筋弯拉强度研究进展

1.1 GFRP 箍筋弯拉强度试验方法

目前,GFRP 箍筋弯拉强度试验方法主要有 4 种。第 1 种是 ACI 440.3R-12[17]中 B.5 方法(简称 B.5 试验方法)。如图 1(a)所示,B.5 试验方法考虑混凝土与箍筋之间粘结作用影响。第 2 种是 ACI 440.3R-12[17]中 B.12 试验方法(简称 B.12 试验方法)。如图 1(b)所示,B.12 试验方法采用夹具加载方式,忽略混凝土与箍筋之间粘结影响。已有研究表明[18],采用 B.12 试验方法得到的箍筋弯拉强度只占采用 B.5 试验方法得到弯拉强度的 60%左右。这是由于箍筋表面不平整,弯折段与夹具贴合不紧密,导致弯折段应力分布不均匀。第 3 种方法是 CSA S807:19[16]推荐 Pullout 试验方法。如图 1(c)所示,Pullout 试验方法将 GFRP 箍筋弯折段埋入混凝土中,弯折段一端直线段锚固在混凝土中,另一端直线段伸出混凝土,作动器拉拔伸出端。第 4 种方法是 JSCE-E[19]中试验方法(简称 JSCE 试验方法)。如图 1(d)所示,JSCE 试验方法采用夹具加载方式,忽略混凝土与 GFRP 箍筋之间粘结作用影响。JSCE 试验方法与 B.12 试验方法相比,采用 JSCE 试验方法可测试箍筋弯折角度(Bending angle)范围在 0°~180°的箍筋弯拉强度。目前,在已发表的 GFRP 箍筋弯拉强度试验文献中,普遍采用 Pullout 试验方法。

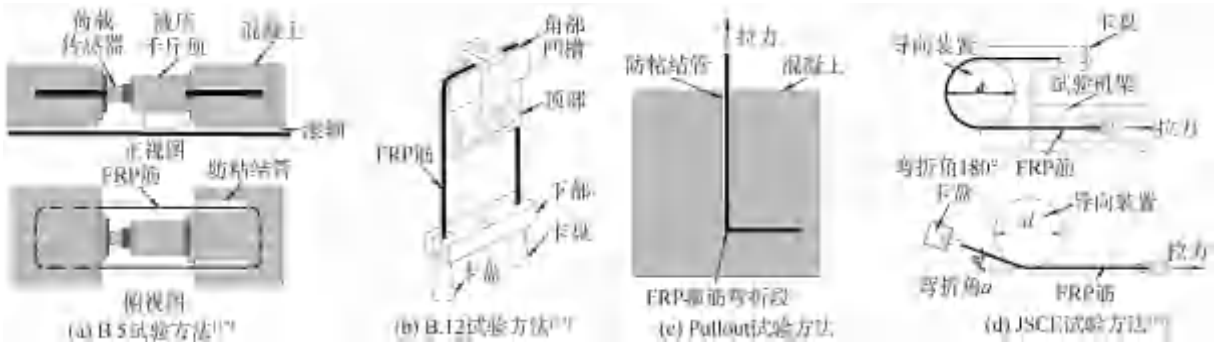


图 1 GFRP 筋弯拉强度试验方法

Fig. 1 Test methods for tensile strength of GFRP stirrup at bend

1.2　GFRP 箍筋弯拉强度试验研究进展

目前,已有 GFRP 箍筋弯拉强度试验研究主要针对弯折半径与箍筋直径之比(r/d)、埋深长度与箍筋直径之比(l_d/d)、尾部长度与箍筋直径之比(l_t/d)等参数开展(如图 2)。

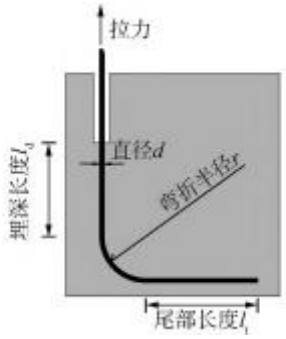


图 2　GFRP 箍筋弯拉强度试验主要参数

Fig. 2　The main parameters of tensile strength of GFRP stirrup at bend

Ehsani 等[20]采用 Pullout 试验方法开展了 36 个试件的 GFRP 箍筋弯拉强度试验研究。试验主要研究尾部长度(l_t: 12 inch, 20 inch),弯折半径与箍筋直径之比(r/d: 0, 3)和埋深长度与箍筋直径之比(l_d/d: 1, 4, 7, 10, 13, 16)对 GFRP 箍筋弯拉强度的影响。试验结果表明:弯折半径与箍筋直径之比为 0 时($r/d=0$),GFRP 箍筋在弯折段发生剪切破坏,GFRP 箍筋弯拉强度仅为直线段抗拉强度的 16%左右;弯折半径与箍筋直径之比为 3 时($r/d=3$),且埋深长度与箍筋直径之比大于 4($l_d/d>4$),箍筋在直线段被拉断。为了研究 GFRP 箍筋弯折半径与箍筋直径之比(r/d)、埋深长度与箍筋直径之比(l_d/d)以及尾部长度与箍筋直径之比(l_t/d)对 GFRP 箍筋弯拉强度的影响,Imjai 等[21]采用 Pullout 试验方法开展了 60 个 GFRP 箍筋的弯拉强度试验研究。试验结果表明:大部分试件 GFRP 箍筋拉断发生在弯折段;GFRP 箍筋弯拉强度随箍筋弯折半径与箍筋直径之比增加而提高;当 GFRP 箍筋弯折半径与箍筋直径之比大于 3 时($r/d>3$),GFRP 箍筋弯拉强度不小于直线段抗拉强度的 40%。

此外,为了研究 B.5 和 B.12 试验方法对 GFRP 箍筋弯拉强度的影响,Ahmed 等[18]分别采用 B.5 和 B.12 试验方法开展了 9 个试件的 GFRP 箍筋的弯拉强度试验研究。GFRP 箍筋直径 d 为 9.5 mm、15.9 mm 和 19.1 mm,弯折半径与箍筋直径之比均为 4($r/d=4$)。试验结果表明:9 个 GFRP 箍筋均在弯折段被拉断;采用 B.5 方法测得直径 9.5 mm GFRP 箍筋、直径 15.9 mm GFRP 箍筋以及直径 19.1 mm GFRP 箍筋的弯拉强度分别是直线段抗拉强度的 58%、68%和 58%;采用 B.12 方法测得到直径 9.5 mm GFRP 箍筋、直径 15.9 mm GFRP 箍筋以及直径 19.1 mm GFRP 箍筋的弯拉强度分别是直线段抗拉强度的 35%、40%和 41%;采用 B.12 方法得到 GFRP 箍筋弯拉强度比采用 B.5 方法得到的弯拉强度低 37%,这是由于 GFRP 箍筋表面不平整,使得 GFRP 箍筋弯曲部分与夹具贴合不紧密,导致弯折段局部应力集中。

综上所述,目前在已有 GFRP 箍筋弯拉强度试验中,埋深长度 l_d 和尾部长度 l_t 主要影响弯拉强度试验破坏模式;GFRP 箍筋弯拉强度随弯折半径与箍筋直径之比 r/d 增大而提高。GFRP 箍筋弯拉强度试验研究主要还存在以下几点问题:

1)已有 GFRP 箍筋弯拉强度试验中专门针对弯折段拉断破坏模式设计的试验较少;

2)针对不同直线段抗拉强度对 GFRP 箍筋弯拉强度影响的试验较少,直线段抗拉强度对弯拉强度影响具体量化关系不明确。

1.3　GFRP 箍筋弯拉强度计算方法研究进展

目前,已有 GFRP 箍筋弯拉强度计算公式大多基于 FRP 箍筋弯拉强度试验数据所提出,还未有针对 GFRP 箍筋弯拉强度试验数据,提出 GFRP 箍筋弯拉强度的计算方法。

日本规范 JSCE[14]基于 16 个碳纤维增强(carbon fiber reinforced polymer, CFRP)箍筋、16 个芳酰胺纤维增强聚合物(aramid fiber reinforced polymer, AFRP)箍筋、6 个 GFRP 箍筋和 1 个维尼伦纤维增强聚合物(vinylon fiber reinforced polymer, VFRP)箍筋弯拉强度试验数据(如图 3)回归得到圆形截面 FRP 箍筋弯拉强度经验公式:

$$f_{\text{bend}} = \left(0.05\frac{r}{d} + 0.3\right)\cdot f_{\text{fu}} \tag{1}$$

式中:f_{bend} 为 FRP 箍筋弯拉强度;f_{fu} 为 FRP 箍筋直线段抗拉强度;r 为 FRP 箍筋弯折半径;d 为 FRP 箍筋直径。

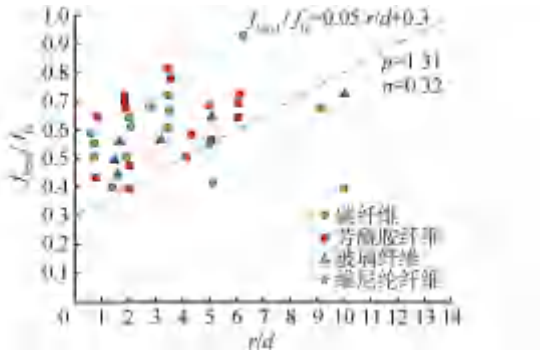


图 3　日本规范 JSCE[14] FRP 箍筋弯拉强度试验结果

Fig. 3　Test results of tensile strength of FRP stirrup at bend in JSCE[14]

美国 ACI 440.1R-15[11]规范、中国 GB 50608-2020[12]规范和加拿大 CSA S6:19[13]规范中 FRP 箍

筋弯拉强度计算方法均采用日本 JSCE 规范[14]中 FRP 箍筋弯拉强度计算公式。日本规范 JSCE[14]基于 AFRP、CFRP、GFRP 和 VFRP 箍筋弯拉强度试验数据,提出 FRP 箍筋弯拉强度计算公式。该计算公式未根据 GFRP 箍筋弯拉强度试验数据提出相应的 GFRP 箍筋弯拉强度计算方法。此外,上述试验采用 JSCE 试验方法获得 AFRP、CFRP、GFRP 和 VFRP 箍筋弯拉强度,JSCE 试验方法采用夹具加载方式,忽略混凝土与箍筋粘结性能影响,与箍筋在混凝土中实际受力状态不符。

美国 ACI 440.4R-04 规范[22]公式基于 Currier[23]开展的 AFRP 和 CFRP 箍筋弯拉强度试验数据提出圆形截面 FRP 箍筋弯拉强度计算方法:

$$f_{\text{bend}} = \varphi_{\text{bend}} \cdot f_{\text{fu}} \tag{2}$$

$$0.25 \leqslant \varphi_{\text{bend}} = \left(0.05\frac{r}{d} + 0.11\right) \leqslant 1.0 \tag{3}$$

式中:φ_{bend} 为 FRP 箍筋弯拉强度折减系数;f_{fu} 为 FRP 箍筋直线段抗拉强度;f_{bend} 为 FRP 箍筋弯拉强度;r 为 FRP 箍筋弯折半径;d 为 FRP 箍筋直径。与日本 JSCE[14]规范公式相比,ACI 440.4R-04[22]公式在直线回归公式基础上提出了双折线回归公式,给出了 $r/d<3$ 时,FRP 箍筋弯拉强度下限值。此外,该公式基于少量 AFRP 和 CFRP 箍筋弯拉强度试验数据提出 FRP 箍筋弯拉强度,尚未覆盖 GFRP 箍筋的试验数据。

常见 FRP 箍筋是圆形截面,但部分封闭缠绕 FRP 箍筋的截面为矩形。Lee[24]基于截面面积相等原则,将矩形截面等效为圆形截面,并结合 14 个矩形截面封闭缠绕型 CFRP 箍筋弯拉强度试验结果,提出了矩形截面 FRP 箍筋弯拉强度计算方法:

$$f_{\text{bend}} = (0.07R/d_{\text{fe}} + 0.45) \cdot f_{\text{fu}} \leqslant f_{\text{fu}} \tag{4}$$

$$d_{\text{fe}} = 2\sqrt{w_{\text{f}}t_{\text{f}}/\pi} \tag{5}$$

式中:R 为 FRP 箍筋弯折半径;d_{fe} 为等效圆形截面 FRP 箍筋直径;f_{bend} 为 FRP 箍筋弯拉强度;f_{fu} 为 FRP 箍筋直线段抗拉强度;w_{f} 为矩形截面 FRP 箍筋宽度;t_{f} 为矩形截面 FRP 箍筋厚度。该公式基于少量 CFRP 箍筋弯拉强度试验数据而提出 FRP 箍筋弯拉强度计算方法,未根据 GFRP 箍筋弯拉强度试验数据提出相应的 GFRP 箍筋弯拉强度计算方法。

Imjai 等[25]基于 Tsai-Hill 破坏准则,并考虑到 FRP 箍筋弯折处截面变形影响,提出 FRP 箍筋弯拉强度计算方法:

$$\sigma_1 = \frac{\sqrt{1-\left(\dfrac{\tau_{12}}{\tau_{\max}}\right)^2}}{\sqrt{1+\dfrac{\pi d\psi}{4r}+\left(\dfrac{\pi d\psi}{4r}\right)^2\left(\dfrac{\sigma_{1\max}}{\sigma_{2\max}}\right)^2}}\sigma_{1\max} \tag{6}$$

$$\psi = \frac{d}{d_b} \leqslant 1 \tag{7}$$

式中:ψ 为截面变形折减系数;d 为 FRP 箍筋直线段直径;d_{b} 为 FRP 箍筋弯折段宽度(如图 4);σ_1 为 FRP 箍筋弯折段轴向拉应力;$\sigma_{1\max}$ 为 FRP 箍筋直线段抗拉强度;$\sigma_{2\max}$ 为 FRP 箍筋横向抗压强度;$\tau_{\max}$ 为 FRP 箍筋粘结强度;τ_{12} 为 FRP 箍筋平均粘结应力;r 为 FRP 箍筋弯折半径。该公式基于 Tsai-Hill 破坏准则提出,其中相关材料参数缺少试验数据进行验证。此外,该公式中弯折段相关应力较难测得。

综上所述,已有 GFRP 箍筋弯拉强度计算方法多为基于有限 FRP 箍筋弯拉强度试验数据回归得到的经验公式。GFRP 箍筋弯拉强度计算方法存在以下几点问题:

1)不同学者提出 FRP 箍筋弯拉强度计算方法基于不同纤维种类的 FRP 弯拉强度试验结果,未针对 GFRP 箍筋弯拉强度试验数据提出相应的 GFRP 箍筋弯拉强度计算方法;

2)大多数学者提出 FRP 箍筋弯拉强度计算方法采用数据回归分析方法,未考虑保证率因素。



图 4 FRP 箍筋弯折段应力状态[25]

Fig. 4 Stress State for bent portion of FRP stirrup[25]

2 GFRP 箍筋弯拉强度研究

2.1 GFRP 箍筋弯拉强度试验研究

本文基于 B.5 试验方法开展了 3 组 9 个 GFRP 箍筋的弯拉强度试验(如图 5),研究 GFRP 箍筋直线段抗拉强度(f_{fu})对弯拉强度(f_{bend})的影响。3 组箍筋直线段抗拉强度分别为:530 MPa(A 组)、890 MPa(B 组)和 1 100 MPa(C 组)。弯折半径与箍筋直径之比采用实际工程中常用比值 3(r/d = 3),GFRP 箍筋直径均为 10 mm(d=10 mm)。

如图 6 所示,9 个试件发生 GFRP 箍筋弯折段拉断破坏,箍筋直线段未被拉断,混凝土未发生劈裂破坏。如表 1 所示,A、B、C 组箍筋弯拉强度平均值 $f_{\text{bend,exp}}$ 分别为 325、445、530 MPa,直线段抗拉强度由

530 MPa 提高到 1 100 MPa,提高率为 106%,弯拉强度由 325 MPa 提高到 530 MPa,提高率为 63%,弯拉强度与直线段抗拉强度基本呈线性增长关系(如图 7)。弯拉强度与各自直线段抗拉强度之比 $f_{bend,exp}/f_{fu}$ 分别为 61%、52%、48%,随直线段抗拉强度增加而降低。弯拉强度与各自直线段抗拉强度之比均大于 40%,这与加拿大 CSA S807:19[16] 规范规定:GFRP 箍筋弯拉强度不应小于直线段抗拉强度的 46%较为吻合。

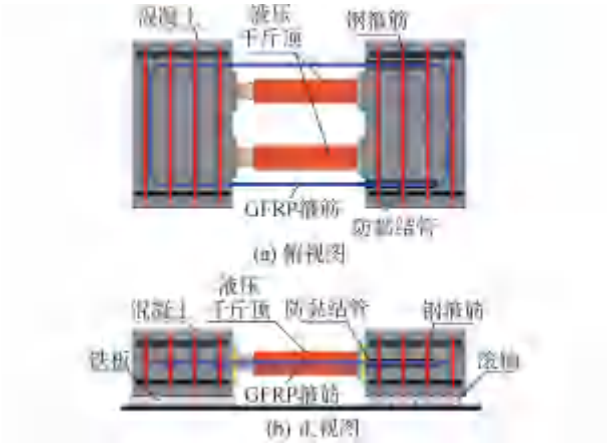


图 5　加载装置

Fig. 5　Test setup



图 6　破坏形态

Fig. 6　Failure pattern

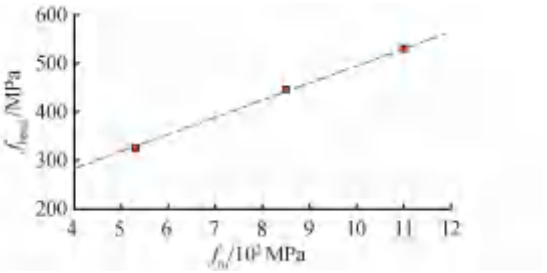


图 7　弯拉强度与直线段抗拉强度关系

Fig. 7　Relation between tensile strength of GFRP stirrup at bend and tensile strength of straight portion

表 1　GFRP 箍筋弯拉强度试验结果

Table 1　Tests results of tensile strength of GFRP Stirrup at bend

文献		试件	d/mm	r/d	f_{fu}/MPa	实测值 $f_{bend,i}$/MPa	平均值 $f_{bend,exp}$/MPa	$f_{bend,exp}/f_{fu}$/%
文献[26]	A 组	G-10-3-A1	10	3	530	391	325	61
		G-10-3-A2				326		
		G-10-3-A2				259		
文献[27]	B 组	G-10-3-B1	10	3	850	444	445	52
		G-10-3-B2				441		
		G-10-3-B3				450		
文献[28]	C 组	G-10-3-C1	10	3	1 100	580	530	48
		G-10-3-C2				498		
		G-10-3-C3				512		

2.2　GFRP 箍筋弯拉强度计算方法

考虑到 GFRP 箍筋与混凝土粘结作用影响,本文从已有 GFRP 箍筋弯拉强度试验中筛选出采用 B.5 和 Pullout 试验方法的试验数据[3-6,18,26-28,30-33],并结合本文试验数据,建立具有 102 个 GFRP 箍筋弯拉试件的数据库。ACI 440.1R-15[11]、GB 50608-2020[12]、CSA S806-12[29] 等规范规定:GFRP 箍筋弯折半径与箍筋直径之比不应小于 3($r/d \geq 3$)。本文剔除数据库中弯折半径与箍筋直径之比小于 3($r/d<3$)的试件、非弯折段拉断破坏模式的试件以及异常数据的试件,综合考虑各国规范中 GFRP 筋抗拉强度保证率因素,提出保证率不小于 95%的 GFRP 箍筋弯拉强度计算方法:

$$f_{bend} = \phi \cdot f_{fu} \tag{8}$$

$$\phi_{min} \leqslant \phi = k\frac{r}{d} + b < 1.0 \tag{9}$$

式中:ϕ 为弯拉强度折减系数;ϕ_{min} 为弯拉强度折减系数最小值;r 为弯折半径;d 为 GFRP 箍筋直径。如图 8 所示,$\phi_{min}=0.4$,$k=0.1$,$b=0.04$。

本文主要评价指标有 GFRP 箍筋弯拉强度试验值与计算值之比($f_{bend,exp}/f_{bend,cal}$)的平均值 μ,标准差 σ,变异系数 c_v。计算结果如表 2 所示,平均值 μ 为 1.38,标准差 σ 为 0.24。

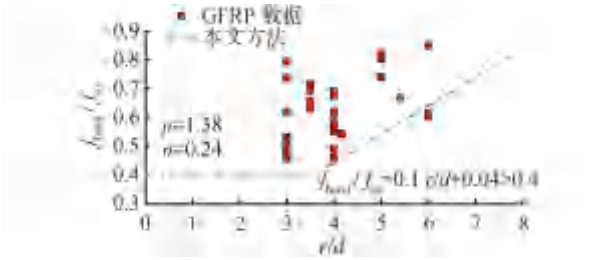


图 8 GFRP 箍筋弯拉强度试验点分布图

Fig. 8 Distribution diagram of test points and calculation formulas

表 2 $f_{bend,exp}/f_{bend,cal}$ 统计表

Table 2 Statistics of $f_{bend,exp}/f_{bend,cal}$

评价指标	μ	σ	c_v	最大值	最小值
$f_{bend,exp}/f_{bend,cal}$	1.38	0.24	0.17	1.99	0.94

3 结论

1)GFRP 箍筋弯拉强度分别与弯折半径与箍筋直径之比、GFRP 箍筋直线段抗拉强度成正比;GFRP 箍筋埋深长度和尾部长度主要影响 GFRP 箍筋弯拉强度试验破坏模式。

2)本文开展了 3 组不同直线段抗拉强度的 GFRP 箍筋弯拉强度试验研究,直线段抗拉强度提高 106%,弯拉强度提高 63%,弯拉强度与直线段抗拉强度基本呈线性增长关系;弯拉强度与直线段抗拉强度之比 $f_{bend,exp}/f_{fu}$ 和直线段抗拉强度 f_{fu} 成反比。

3)基于 102 个 GFRP 箍筋弯拉强度试验数据库统计分析,提出了保证率不小于 95% 的 GFRP 箍筋弯拉强度计算方法,计算值与试验值之比平均值为 1.38,标准差为 0.24。

参考文献:

[1] 薛伟辰, 康清梁. 纤维塑料筋在混凝土结构中的应用[J]. 工业建筑, 1999, 29(2): 19-21.
XUE Weichen, KANG Qingliang. Application of fiber reinforced plastics in concrete structures[J]. Industrial construction, 1999, 29(2): 19-21.

[2] 叶列平, 冯鹏. FRP 在工程结构中的应用与发展[J]. 土木工程学报, 2006, 39(3): 24-36.
YE Lieping, FENG Peng. Applications and development of fiber-reinforced polymer in engineering structures[J]. China civil engineering journal, 2006, 39(3): 24-36.

[3] KURTH M C. Zum querkrafttragverhalten von betonbauteilen mit faserverbundkunststoff-bewehrung [D]. Aachen: Rheinisch-Westfälischen Technischen, 2012: 73-87.

[4] AHMED E A. Shear behaviour of concrete beams reinforced with fibre-reinforced polymer (FRP) stirrups [D]. Quebec: Université de Sherbrooke, 2009: 131-140.

[5] MORPHY R. Behaviour of fibre reinforced polymer (FRP) stirrups as shear reinforcement for concrete structure[D]. Manitoba: University of Manitoba, 1999: 73-97.

[6] IMJAI Thanongsak. Design and analysis of curved FRP composites as shear reinforcement for concrete structures [D]. Sheffield:University of Sheffield, 2007: 76-83.

[7] JOHNSON D. Investigation of glass fibre reinforced polymer reinforcing bars as internal reinforcement for concrete structures[D]. Toronto: University of Toronto, 2009: 61-87.

[8] MOHAMED B H M, BENMOKRANE B. Torsion behavior of concrete beams reinforced with glass fiber-reinforced polymer bars and stirrups[J]. ACI structural journal, 2015, 112(5): 543-552.

[9] MOHAMED H M, CHAALLAL O, BENMOKRANE B. Torsional moment capacity and failure mode mechanisms of concrete beams reinforced with carbon FRP bars and stirrups[J]. Journal of composites for construction, 2015, 19(2): 04014049.

[10] HADHOOD A, GOUDA M G, AGAMY M H, et al. Torsion in concrete beams reinforced with GFRP spirals[J]. Engineering structures, 2020, 206: 110174.

[11] ACI Committee 440. Guide for the design and construction of structural concrete reinforced with FRP bars (ACI 440.1R-15)[S]. Farmington Hills: American Concrete Institute, 2015.

[12] 中华人民共和国住房和城乡建设部. 纤维增强复合材料建设工程应用技术规范: GB 50608-2020[S]. 北京:中国计划出版社, 2020.
Ministry of Housing and Urban-Rural Development of the People′ Republic of China. Technical standard for fiber reinforced polymer in construction: GB 50608-2020[S]. Beijing: China Planning Press. 2020.

[13] Canadian Standards Association (CSA). Canadian highway bridge design code (CSA S6:19)[S]. Rexdale: CSA Group, 2019.

[14] Japan Society of Civil Engineers. Recommendations for design and construction of concrete structures using continuous fibre reinforced materials[S]. Tokyo: JSCE, 1997.

[15] American Society for Testing and Materials. Standard specification for solid round glass fiber reinforced polymer bars for concrete reinforcement: ASTM D7957/D7957M-17[S]. West Conshohocken: ASTM International, 2017.

[16] Canadian Standards Association (CSA). Specification for fibre-reinforced polymers (CAN/CSA S807:19)[S]. Toronto: CSA Group, 2019.

[17] ACI Committee 440. Guide test methods for fiber-reinforced polymers (frps) for reinforcing or strengthening

concrete structures (ACI 440.3R-12)[S]. Farmington Hills: American Concrete Institute, 2012.

[18] AHMED E A, EL-SAYED A K, EL-SALAKAWY E, et al. Bend strength of FRP stirrups: comparison and evaluation of testing methods[J]. Journal of composites for construction, 2010, 14(1): 3-10.

[19] Japan Society of Civil Engineers. Test method for flexural tensile properties of continuous fiber reinforcing materials (JSCE-E 531-1995)[S]. Tokyo: JSCE, 1995.

[20] EHSANI M R, SAADATMANESH H, TAO S. Bond of hooked GFRP rebars to concrete[J]. ACI materials journal, 1995, 92(4): 391-400.

[21] IMJAI T, GUADAGNINI M, PILAKOUTAS K. Bend strength of FRP bars: experimental investigation and bond modeling[J]. Journal of materials in civil engineering, 2017, 29(7): 04017024.

[22] ACI Committee 440. Prestressing concrete structures with FRP tendons (ACI 440.4R-04 Reapproved 2011)[S]. Farmington Hills: American Concrete Institute, 2004.

[23] CURRIER. Deformation of prestressed concrete beams with FRP tendons[D]. Laramie: University of Wyoming, 1995: 54-82.

[24] LEE C, KO M, LEE Y. Bend strength of complete closed-type carbon fiber-reinforced polymer stirrups with rectangular section[J]. Journal of composites for construction, 2014, 18(1): 1-11.

[25] IMJAI T, GUADAGNINI M, PILAKOUTAS K. Mechanical performance of curved FRP rebars-part Ⅱ: analytical study[C]//Proceedings of the 1st Asia-Pacific Conference on FRP in Structures APFIS. Hong Kong, 2007: 339-344.

[26] 夏康. GFRP 箍筋弯拉强度研究[D]. 上海: 同济大学, 2014: 17-27.
XIA Kang. The research on the bending strength of GFRP Stirrup[D]. Shanghai: Tongji University, 2014:17-27.

[27] 彭飞. FRP 筋混凝土梁、柱构件承载力计算理论[D]. 上海: 同济大学. 2019:137-144.
PENG Fei. Theoretical studies on calculation of ultimate capacity of concrete beams and columns with FRP reinforcements[D]. Shanghai: Tongji University, 2019: 137-144.

[28] 白浩阳. GFRP 箍筋弯拉强度试验报告[R]. 上海, 同济大学, 2020.
BAI Haoyang. Bend strength of GFRP stirrups[R]. Shanghai, Tongji University, 2020.

[29] Canadian Standards Association (CSA). Design and construction of building structures with fibre-reinforced polymers (CAN/CSA S806)[S]. Mississauga: CSA Group, 2012.

[30] MORPHY R, SHEHATA E, RIZKALLA S H. Bent effect on strength of CFRP stirrups[C]//Proceedings of the Third International Symposium on Non-Metallic (FRP) Reinforcement for Concrete Structures. Sapporo, 1997: 19-26.

[31] VINT L, SHEIKH S. Investigation of the bond properties of alternate anchorage schemes for GFRP bars[J]. ACI structural journal, 2014, 112(1): 59-68.

[32] SHEHATA E, MORPHY R, RIZKALLA S. Fibre reinforced polymer shear reinforcement for concrete members: behaviour and design guidelines[J]. Canadian journal of civil engineering, 2000, 27(5): 859-872.

[33] NAGASAKA T, FUKUYAMA H, TANIGAKI M. Shear performance of concrete beams reinforced with FRP stirrups[C]//ACI Symposium Publication. Farmington Hills, 1993: 789-812.

本文引用格式:

白浩阳,薛伟辰,江佳斐. 基于数据库的 GFRP 箍筋弯拉强度计算方法[J]. 哈尔滨工程大学学报,2024,45(2):223-229.
BAI Haoyang, XUE Weichen, JIANG Jiafei. Calculation method of the flexural tensile strength of the glass fiber-reinforced polymer stirrup based on the database[J]. Journal of Harbin Engineering University,2024,45(2):223-229.

Engineering Structures 310 (2024) 118116



Contents lists available at ScienceDirect

Engineering Structures

journal homepage: www.elsevier.com/locate/engstruct



Transfer learning-based confinement strength prediction of concrete confined by FRP transverse reinforcements

Fei Peng [a,b,*], Yazhong Li [b], Weichen Xue [c]

[a] Key Laboratory of Building Safety and Energy Efficiency of the Ministry of Education, Hunan University, Changsha 410082, China
[b] College of Civil Engineering, Hunan University, Changsha 410082, China
[c] Department of Structural Engineering, Tongji University, Shanghai 200092, China

ARTICLE INFO

Keywords:
Confined concrete
Fiber-reinforced polymer (FRP)
Transverse reinforcements
Confinement strength
Machine learning (ML), Transfer learning

ABSTRACT

Although several confinement strength models have been proposed for concrete confined by fiber-reinforced polymer (FRP) transverse reinforcements, these models show considerable scatter and discrepancies in the estimation of experimental data. Machine learning (ML) techniques may present an alternative prediction approach, but challenges arise due to insufficient experimental data. This study, therefore, develops a transfer learning-based model for predicting the confinement strength of concrete confined by FRP transverse reinforcements. Firstly, a literature review was conducted to collect a target dataset of FRP-confined concrete columns and a source dataset of steel-confined concrete columns used for knowledge transfer. Subsequently, a transfer learning algorithm was proposed to construct an ML confinement strength model for FRP-confined concrete. Finally, the performance of the proposed model was compared to that of six ML models and seven physics-based models. The model evaluation based on one-time random split indicated that the proposed model provided more accurate predictions for the confinement strength than other models considered in this study, achieving an R^2 of 0.9089 on the test dataset. Shuffle split evaluation demonstrated that the proposed model exhibited superior stability and robustness compared to other models considered. Based on the proposed transfer learning-based model, the importance of the input parameters was obtained, further confirming the robustness of the proposed model.

1. Introduction

The deterioration in reinforced concrete (RC) structures due to corrosion of steel reinforcements is one of the major challenges in marine and coastal construction [1]. RC compression members are often the most critical elements in a structure. Despite effective engineering design and preventive techniques, steel reinforcing bars are prone to corrosion over time, especially transverse reinforcements which have a thinner concrete cover compared to longitudinal reinforcing bars [2]. A viable solution to the corrosion-induced issue is to replace the steel reinforcements with corrosion-resistance fiber-reinforced polymer (FRP) [3–6]. Numerous studies have explored the mechanical performance of FRP-RC columns [4,6–15]. These studies have confirmed the feasibility of utilizing FRP bars as a practical substitute for conventional longitudinal and transverse steel reinforcements in RC columns, notwithstanding their linear stress-strain relationship until failure and a lower modulus of elasticity compared to steel.

In the past decade, valuable studies have been conducted on the axial compressive behavior of concrete confined by FRP transverse reinforcements (ties, spirals, or hoops) [9–23]. These studies have revealed that suitable confinement of the concrete core using FRP ties, spirals, or hoops can efficiently enhance both strength and ductility. Unlike steel-confined concrete columns, where the ultimate confining pressure is determined based on the yield strength of steel and the confining pressure is assumed to be constant which occurs at relatively early stages of concrete deformation, the ultimate confining pressure in FRP-confined concrete continuously increases with transverse strain until failure [10]. Thus, it is crucial to consider the continuous variation in the level of FRP confining pressure when developing a confinement model.

Several physics-based models have been proposed to assess the confinement strength of concrete confined by FRP transverse reinforcements [10–13,24–27]. However, these models encounter considerable scatter and discrepancies in the estimation of experimental data. One of the causes for this discrepancy can be related to the

* Corresponding author at: Key Laboratory of Building Safety and Energy Efficiency of the Ministry of Education, Hunan University, Changsha 410082, China.
E-mail address: pengf@hnu.edu.cn (F. Peng).

https://doi.org/10.1016/j.engstruct.2024.118116
Received 27 February 2024; Received in revised form 10 April 2024; Accepted 25 April 2024
Available online 7 May 2024
0141-0296/© 2024 Elsevier Ltd. All rights reserved.

Nomenclature

Abbreviations	*meanings*
A_{core}	Area of concrete core (mm^2)
A_{tf}	Area of transverse reinforcement (mm^2)
$a_{20\text{-}index}$	Model predictivity within a 20% variation
CI	Confidence interval
COV	Coefficient of variation
d	Diameter or edge of column section (mm)
d_{core}	Core dimension to centerline of outer transverse reinforcements (mm)
d_t	Diameter of transverse reinforcements (mm)
E_t	Elastic modulus of transverse reinforcements (GPa)
$error^t$	Error of $model^t$
f_{cc}'	Maximum confined concrete strength (MPa)
f_{co}'	Maximum unconfined concrete strength (MPa)
f_{fb}	Bend strength of FRP transverse reinforcement (MPa)
f_{fu}	Ultimate tensile strength of transverse reinforcements (MPa)
f_{fv}	Stress of FRP transverse reinforcement at concrete axial peak stress (MPa)
f_l'	Effective lateral confining pressure (MPa)
f_{lx} (f_{ly})	Lateral confining stress in x (y) direction (MPa)
f_y	Yield strength of steel transverse reinforcements (MPa)
FB	Fractional Bias, disparity between experimental and predicted values
h^t	Prediction array of *Learner* at t^{th} iteration
h^t_{weak}	Prediction array of *WeakLearn* at t^{th} iteration
k_e	Confinement effectiveness coefficient computed referring to [28]
kl	Effective length of column (mm)
kl/r	Slenderness ratio of column
l^t_i	i^{th} instance loss of tth base learner
m	Size of target dataset
$model^t$	Model generated by *Learner* at t^{th} iteration
MAE	Mean absolute error
MAPE	Mean absolute percentage error
N	Size of dataset
n	Size of source dataset
N_{20}	Number of instances where $0.8 \leq y_i/\ y_i^* \leq 1.2$
r	Radius of gyration of cross section (mm)
r_p	Pearson correlation coefficients
r_b	Internal radius of bend in FRP reinforcement (mm)
R^2	Coefficients of determination
R^2_{train}	R^2 determined on training dataset
R^2_{test}	R^2 determined on test dataset
RMSE	Root mean square error
S	Number of iterations
SD	Standard deviation
Shape	Shape of column cross-section. 0 =rectangular, 1 =circular
s_t	Pitch of transverse reinforcements (mm)
T	Concatenate dataset, which combines source and target dataset
w^t	Instance weight array at t^{th} iteration
w^t_i	Weight of ith instance at t^{th} iteration
y_i	Experimental value
y_i^*	Predicted value
y_{mean}	Mean value of all y_i
Z_t	Normalizing constant
β_t	Positive constant less than 1
ε_{fu}	Ultimate tensile strain of FRP transverse reinforcement
ρ_{st}	Ratio of volume of FRP transverse reinforcement to volume of confined concrete core
ρ_{ve}	Effective ratio of lateral FRP reinforcement computed referring to [26]

variation in determining the ultimate stress in FRP transverse reinforcements. For instance, Afifi et al. [10,11] suggested a strain limit of 0.004 for Glass FRP (GFRP) or Carbon FRP (CFRP). Alternatively, Karim et al. [13] suggested a ratio of hoop rupture strain to the ultimate tensile strain of 0.333 for GFRP. However, Sankholkar et al. [12] concluded that the ratio ranged from 0.45 to 0.77, with a mean of 0.62. In addition to the lack of consensus on the ultimate stress of FRP transverse reinforcements, it is noteworthy that existing physics-based confinement models were either modified versions of the steel-based Mander Model [28] or the external FRP-based confinement equations based on limited experimental data, which often limits the accuracy of these models.

Recently, machine learning (ML) has emerged as a promising alternative approach to solving structural engineering problems, providing optimal accuracy and efficiency compared to physics-based models [8,29–31]. For example, Sayed et al. [30] built ML models for predicting the axial capacity of FRP-wrapped RC columns, with a dataset comprising 170 columns. Bakouregui et al. [31] constructed the extreme gradient boosting (XGBoost) model to predict the axial capacity of concrete columns longitudinally reinforced with FRP bars based on a dataset of 283 specimens. Based on a database of 241 tests, Tarawneh et al. [8] proposed an artificial neural network-based model capable of predicting the axial capacity and slenderness limit for FRP-RC columns.

Unlike physics-based models, ML models have the capability to determine the relationships between the input variables (features) and target variables (labels) [32] without the need for prior assumptions of the underlying physics [33]. For structural engineering problems, the features typically correspond to design parameters, and the labels denote mechanical performances. Although ML models have proven their effectiveness in the realm of structural engineering, they still encounter two major challenges. Firstly, training ML models requires big data [34], which is not always available for structural engineering problems. This scarcity of data may result in overfitting issues [35], wherein models perform well only on the training dataset and struggle to establish a general predictive rule for unseen data [36]. Secondly, comprehending the rationale behind the decision-making process of black-box ML models often proves challenging, and the lack of interpretability of ML models hinders their application in various structural engineering problems [37,38].

To address the challenge of overfitting due to limited data, various strategies are proposed, including regularization techniques [35,39], cross-validation [40], physics-informed ML [34,41], and transfer learning [42]. Regularization techniques help to control the complexity of the model and prevent it from fitting noise in the training data, leading to better generalization performance on unseen data. Cross-validation is a technique used to evaluate the performance of an ML model by splitting the dataset into multiple subsets or folds. By integrating domain-specific knowledge and constraints from physical laws into the ML models, the physics-informed ML models can learn from data and extrapolate information more effectively. Transfer learning aims to acquire 'knowledge' from source tasks and apply the knowledge to a target task [43]. The source task, while distinct but related, can furnish valuable insights to establish a dependable model for the target task [44]. In this study, the target task is the prediction of the FRP-confined concrete strength. An appropriate source task involves the valuable studies conducted on steel-confined concrete strength [28,45–49]. Utilizing supplementary data from the source task may effectively address the challenge of insufficient data encountered by the target task.

To address the challenge posed by the lack of interpretability of ML models, several outcome explanation methods have been developed [50–52]. Here, 'outcome explanation' provides interpretations for the outcome of the black-box ML models [53], increasing the credibility of the model. For structural engineering problems, SHapley Additive exPlanations (SHAP) [52] is commonly used to establish trust for ML models [31,38,54,55]. For example, Tahmassebi et al. [38] proposed a scalable-interpretable modeling framework based on the SHAP approach, which can be applied to a variety of structural engineering problems.

Thus, the present study attempts to propose a transfer learning-based model for determining the confinement strength of concrete confined by FRP transverse reinforcements. Firstly, a literature review is conducted to collect a target dataset of FRP-confined concrete columns, and a source dataset of steel-confined concrete columns. On this basis, a transfer learning algorithm is proposed to develop an ML confinement strength model for FRP-confined concrete. Then, the performance of the proposed approach is compared to that of six ML models based on existing algorithms and seven available physics-based models. Finally, feature importance analyses and SHAP are used to interpret the output of the proposed transfer learning-based model.

2. Datasets

An intensive literature review was conducted to collect two datasets used in this study. A dataset of concrete columns confined by FRP transverse reinforcements served as the target dataset. A dataset of concrete columns confined by steel transverse reinforcements served as the source dataset, providing 'knowledge' in transfer learning.

2.1. Target dataset - concrete columns confined by FRP transverse reinforcements

The literature review yielded a nonexclusive database of 132 concrete columns confined by FRP transverse reinforcements [9–21,27]. To provide a reliable dataset, several control and filtering criteria below were applied.

(1) Only short columns were considered, excluding tests on slender columns. The slenderness ratio (kl/r, where kl and r represent the effective length and radius of gyration of cross-section, respectively) distinguishes between short and slender columns. According to ACI 318-19 [56], the slenderness limit for unbraced steel-RC columns is 22, indicating that second-order effects can be disregarded for columns with $kl/r \leq 22$. FRP-RC columns are anticipated to have a slenderness limit lower than 22 due to the lower elastic modulus of FRP compared to steel [57]. Several studies have been conducted to estimate the slenderness limit for FRP-RC columns [8,58,59]; however, there is currently no consensus on this limit. For instance, ACI CODE-440.11-22 [60] specifies the slenderness limit as 17 for unbraced FRP-RC columns. Based on an experimental database and buckling analysis, Abdelazim et al. suggested a slenderness limit of 18 [59]. In this study, apart from 24 columns tested by Afifi et al. [10,11], which had a slenderness of 20, all other columns had a slenderness ratio less than 17. It should be noted that the specimens tested by Afifi et al. were confined by steel collars at each end region, resulting in the effective length kl being less than the measured total length of the columns.
(2) Only columns with solid sections were considered, and tests on hollow section columns were omitted from the dataset.
(3) Only columns confined by FRP transverse reinforcements were included in the database, whereas those confined by hybrid transverse reinforcements, FRP sheets, or FRP tubes were excluded from the dataset.
(4) Only columns constructed using plain concrete were considered. Columns constructed using fiber-reinforced concrete or geopolymer concrete were removed from the dataset

After applying the filtering criteria, a total of 106 columns, including 55 circular columns and 51 rectangular columns, remained in the dataset, as shown in Table 1. This filtered dataset is referred to as the target dataset. The distribution of parameters in the target dataset is described in Fig. 1. These parameters included the diameter or edge of column section d, diameter of FRP transverse reinforcements d_t, pitch of transverse reinforcements s_t, ultimate tensile strength of transverse reinforcements f_{fu}, elastic modulus of transverse reinforcements E_t, maximum unconfined concrete strength f_{co}', and maximum confined concrete strength f_{cc}'.

2.2. Source dataset - concrete columns confined by steel transverse reinforcements

A dataset comprising 114 concrete columns confined by steel transverse reinforcements [28,45–49] was collected, referred to as the source dataset. It is important to note that an improperly organized source dataset, such as an excessively noisy dataset, may result in 'Negative transfer'. This negative transfer implies that the knowledge transfer has an adverse impact on target learning [43]. To mitigate the risk of negative transfer, there is a need for a dataset characterized by high quality and low variance. For this reason, the control and filtering criteria outlined in Section 2.1 were consistently applied throughout the process of collecting experimental results for the source dataset, with a focus on steel reinforcements rather than FRP ones. The distribution of parameters in the source dataset is described in Fig. 2. In addition to the parameters such as d, d_t, s_t, f_{co}', and f_{cc}', Fig. 2 also presents the yield strength of transverse reinforcements f_y.

3. Existing machine learning algorithms

The ML algorithms considered in this study fall into two main categories: traditional ML algorithms and transfer learning algorithms. Traditional ML algorithms learn patterns and features directly from the data within a specific task. Transfer learning algorithms, on the other hand, focus on transferring knowledge from one or more source tasks to a target task. Typically, traditional ML algorithms assume that the training and testing datasets are drawn from the same distribution and feature space [43]. Transfer learning algorithms are not bound by this same distribution assumption. They can use data from diverse source tasks to mitigate issues such as insufficient data when modelling for the target task.

In this study, four traditional ML algorithms, including Random Forest (RF) [61], EXTremely RAndomized Trees (Extra Trees) [62], Adaptive Boosting for regression (AdaBoost.R2) [63], eXtreme Gradient Boosting (XGBoost) [64] were examined. Additionally, two transfer learning algorithms, including TrAdaBoost.R2 [44] and Two-stage

Table 1
Summary of the target dataset.

Reference	Amount	Section shape	Transverse reinforcement type
Hadi et al.[9]	2	Circular	GFRP
Afifi et al.[10]	12	Circular	GFRP
Afifi et al.[11]	12	Circular	CFRP
Sankholkar et al.[12]	25	Circular	GFRP
Karim et al.[13]	4	Circular	GFRP
Tobbi et al.[14]	5	Rectangular	GFRP
Tobbi et al.[15]	16	Rectangular	GFRP and CFRP
Zhang et al.[16]	12	Rectangular	Basalt FRP (BFRP)
Tahir et al.[17]	9	Rectangular	GFRP
Li et al.[18]	9	Rectangular	BFRP

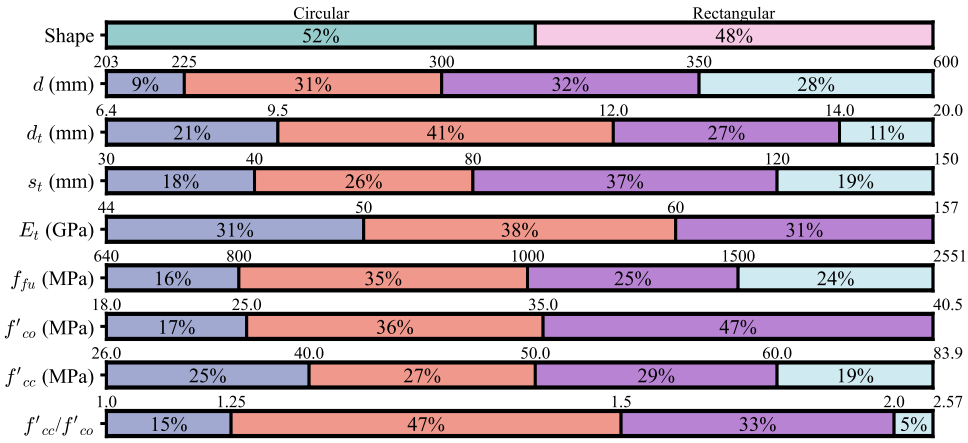


Fig. 1. Distribution of parameters for the target dataset.

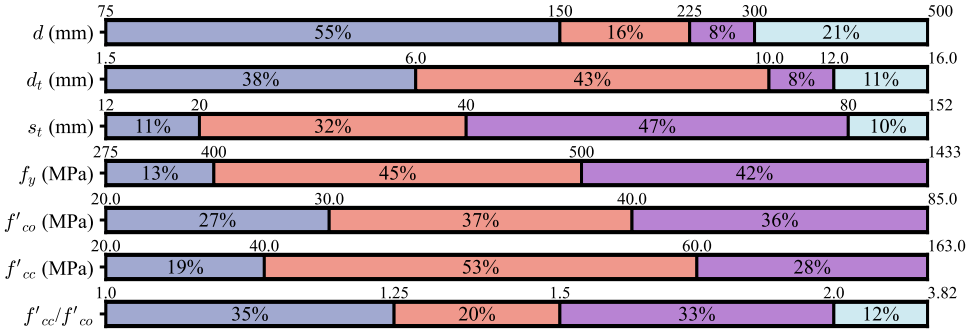


Fig. 2. Distribution of parameters for the source dataset.

TrAdaBoost.R2 [65] were considered.

3.1. Random forest

Random Forest (RF) is a Bagging-based algorithm used for both classification and regression tasks [61]. It's renowned for its robustness to outliers and noise. The fundamental concept behind Bagging [66] involves the random construction of multiple subsets from a training dataset. Then, diverse base learners (typically in the form of decision trees) are built on these distinct subsets, thereby mitigating the risks of overfitting. RF enhances Bagging by introducing random feature selection, preventing over-reliance on specific features.

3.2. Extra trees

Extra Trees, an abbreviation for Extremely Randomized Trees, is another Bagging-based algorithm that offers a balance between accuracy and computational efficiency [62]. Similar to Random Forests, Extra Trees builds multiple decision trees and merges their predictions. On the other hand, the difference between Random Forest and Extra Trees lies in the process of selecting split points for building each tree. The split points in Extra Trees are chosen randomly, while Random Forest employs an exhaustive search approach for selecting them. Compared to Random Forests, Extra Trees is less likely to overfit a dataset, but it may have a slightly higher bias [67].

3.3. XGBoost

XGBoost [64], short for Extreme Gradient Boosting, is an optimized distributed gradient boosting algorithm, known for its fast implementation and high performance. Boosting [68] improves the model performance by iteratively adjusting each base learner based on the feedback from preceding base learners. XGBoost extends traditional gradient boosting by incorporating several enhancements. For example, it provides parallel tree boosting, offering a rapid and accurate solution to many data science problems.

3.4. AdaBoost.R2

AdaBoost, short for Adaptive Boosting, is a Boosting-based algorithm initially developed for binary classification [69]. In this study, the regression variant of AdaBoost, known as AdaBoost.R2 [63], was considered. By adjusting the weights of each training sample in the dataset and combining the predictions of the base learners, AdaBoost.R2 creates a strong ensemble model. To achieve the weight adjustment process, AdaBoost.R2 obtains the ith instance loss l_i^t after training the tth base learner. Here, 'instance' denotes a sample from the dataset, and its associated loss l_i^t reflects the discrepancy between the true and predicted values. Eq. (1) is then employed to update the instance weight of the tth base learner.

$$w_i^{t+1} = w_i^t \beta_t^{1-l_i^t} \tag{1}$$

where w_i^t and w_i^{t+1} are weights of ith instance at t^{th} and $t+1$st iteration, respectively; and β_t is positive constant less than 1.

An accurately predicted instance has a lower l_i^t than inaccurately predicted instances, leading to a faster reduction of its weight. Consequently, inaccurately predicted instances receive increased attention as the iterations go on. AdaBoost.R2 leverages this approach to enhance its generalization performance on the entire dataset. Nevertheless, instances of noise are prone to be recognized as inaccurately predicted instances. By paying more attention to such instances, AdaBoost.R2 may be sensitive to noise and outliers [70].

3.5. TrAdaBoost.R2

TrAdaBoost [44] is an extension of the AdaBoost algorithm that incorporates transfer learning techniques. By leveraging knowledge from the source dataset, it has the ability to train high-quality models even when there is insufficient target data. In this study, the regression variant of TrAdaBoost, known as TrAdaBoost.R2, was considered. TrAdaBoost.R2 makes use of source instances by adjusting their weights. Accurately predicted source instances contribute to improving the model performance on the target dataset. The weights of these useful instances experience an increase consequently. On the other hand, the weights of inaccurately predicted instances are reduced. For target instances, TrAdaBoost.R2 follows the same schedule as AdaBoost.R2. However, findings from research conducted by Pardoe and Stone [65] indicate that the weights of useful instances in the source dataset tend to reduce to zero eventually. This phenomenon may be not favorable for acquiring knowledge from the source dataset.

3.6. Two-stage TrAdaBoost.R2

Two-stage TrAdaBoost.R2 is an extension of the TrAdaBoost.R2 algorithm proposed by Pardoe and Stone [65]. To address the issues identified in the original TrAdaBoost.R2, a control mechanism for the total weight of source and target instances is proposed. Specifically, Two-stage TrAdaBoost.R2 adjusts instance weights in two stages for each iteration. In the first stage, the weights of source instances are adjusted, utilizing cross-validation. In the second stage, the method used for adjusting target instance weights is consistent with the instance weight adjustment approach employed by AdaBoost.R2, while the weights of all source instances are frozen. The output of Two-stage TrAdaBoost.R2 is the prediction generated by the best model in the second stage.

4. Proposed transfer learning algorithm

In this study, an examination of the performance of the Two-stage TrAdaBoost.R2 algorithm uncovered three issues. Firstly, the output of Two-stage TrAdaBoost.R2 relies on AdaBoost.R2, as the models for generating predictions are all built by AdaBoost.R2. The limitations of AdaBoost.R2, such as sensitivity to outliers, may be passed on to Two-stage TrAdaBoost.R2. Secondly, the incorporation of cross-validation into the training process introduces additional computational cost for model training and hyperparameter searching. Thirdly, there is a potential risk of overfitting to generate output with a single learner.

To address these issues, a novel transfer learning algorithm was proposed based on TrAdaBoost.R2 and Two-stage TrAdaBoost.R2. The pseudo-code of this algorithm is illustrated in Fig. 3. A weak ML algorithm (weak learner, *WeakLearn*) and another ML algorithm (*Learner*) are used to construct the proposed algorithm. The *WeakLearn,* utilized for weight adjustment, is intentionally designed as a less complex model to mitigate the risk of overfitting [71]. On this basis, the decision tree, a frequently employed weak learner in Boosting-based algorithms [63,64,69], was selected as the *WeakLearn* in this study. The decision trees can capture specific patterns in the data and are typically computationally efficient, allowing for the training of a large number of them without incurring excessive computational costs. The *Learner*, which can refer to an arbitrary algorithm, provides prediction in each iteration. In this study, RF was chosen as *Learner*. The choice of RF as the *Learner* was based on a thorough hyperparameter searching process. Initially, we considered four ML algorithms (RF, Extra Trees, AdaBoost.R2, and XGBoost) as potential *Learner* candidates. Following an extensive search, the results demonstrated that RF outperformed other algorithms.

Like Two-stage TrAdaBoost.R2, the proposed algorithm acquires 'knowledge' from the source task by adjusting the weights of source instances. The reweighting process is depicted in Fig. 4. In each iteration of the proposed algorithm, the total weights of target instances and

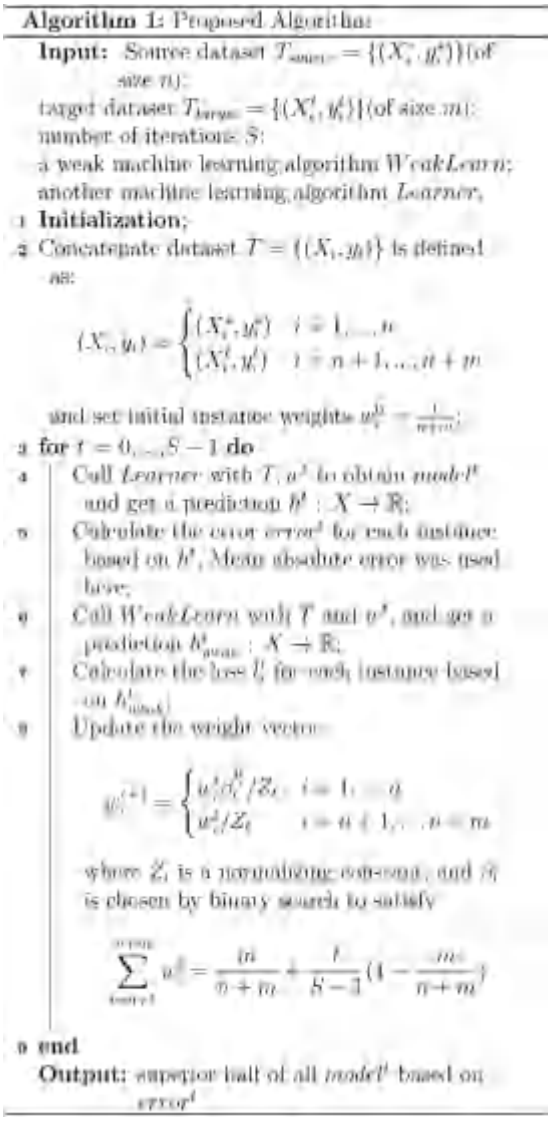


Fig. 3. Pseudo-code for the proposed algorithm.

source instances are calculated from Eqs. (2) and (3), respectively.

$$\sum_{i=n+1}^{n+m} w_i^t = \frac{m}{n+m} + \frac{t}{S-1}\left(1 - \frac{m}{n+m}\right) \tag{2}$$

$$\sum_{i=1}^{n} w_i^t = 1 - \sum_{i=n+1}^{n+m} w_i^t \tag{3}$$

where m and n are number of target instances and source instances, respectively; S is number of iterations; and w_i^t is i^{th} instance weight in iteration t.

For the weights of each instance, the weights of source instances are modified based on the performance of *WeakLearn*. On the other hand, each target instance within the same iteration carries the same weight. The weight manipulations for source and target instances are shown in Eq. (4).

$$w_i^{t+1} = \begin{cases} w_i^t \beta_t^{l_i^t} / Z_t & i = 1, \ldots, n \\ w_i^t / Z_t & i = n+1, \ldots, n+m \end{cases} \tag{4}$$

where β_t is chosen by binary search to satisfy Eq. (2); l_i^t is i^{th} instance loss of $WeakLearn_t$; and Z_t is normalizing constant to ensure total weight equal to 1.

In specific terms, the proposed algorithm incorporates three

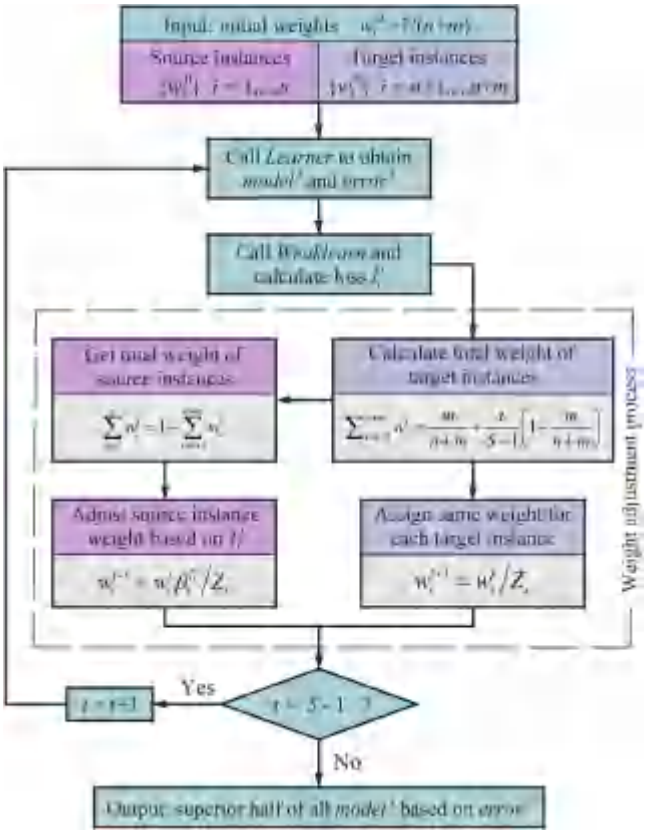


Fig. 4. Reweighting process for the proposed algorithm.

modifications to Two-stage TrAdaBoost.R2. Firstly, the proposed algorithm provides users with the flexibility to select an arbitrary ML algorithm as the *Learner*. This flexibility enables the proposed algorithm to harness the advantages of various traditional ML algorithms. Importantly, altering the *Learner* does not affect the overall convergence of the proposed algorithm on the source dataset (see Appendix A). Secondly, instead of using cross-validation in the model training process, the proposed algorithm directly derives evaluation metrics from the training dataset to reduce computational costs during training. Thirdly, the output of the proposed algorithm relies on the superior half of the *Learner*s rather than an optimal *Learner*. This is done to mitigate overfitting issues, as averaging the predictions of different *Learner*s reduces the risk of selecting an incorrect prediction as the final output [72].

5. Development of machine learning models

In this study, the ML models are categorized into traditional ML models and transfer learning-based models. Four traditional ML models (RF, Extra Trees, AdaBoost.R2 and XGBoost) were built using the target dataset. On the other hand, three transfer learning-based models (TrAdaBoost.R2, Two-stage TrAdaBoost.R2 and the proposed model) were developed utilizing both the source and target datasets. Fig. 5 presents an overview of the modelling process. The application of these models was facilitated by using and extending the well-established ML package scikit-learn [73].

5.1. Feature selection

When incorporating all design parameters of confined concrete columns as features, the high-dimensional space of features may lead to issues such as sparse instance distribution. This phenomenon, known as the curse of dimensionality [74], poses a significant challenge for ML models. To address this issue, design parameters that contribute minimally to the model output were intentionally excluded during the feature selection process. Based on existing physics-based models and experimental findings [9–27], seven features were selected in this study. These features included the area of concrete core A_{core}, unconfined concrete strength f_{co}', diameter of transverse reinforcements d_t, pitch of transverse reinforcements s_t, ultimate tensile strength of transverse reinforcements f_{fu}, modulus of elasticity of transverse reinforcements E_t, and column cross-section shape *Shape*. For *Shape*, a binary assignment was applied— a value of 1 denoted a circular cross-section, while a value of 0 was assigned to rectangular columns.

The linear regression between each feature and the label (f_{cc}') is shown in Fig. 6. Despite the limitations of linear fitting, meaningful correlations between some of the features and the labels were observed. For instance, as s_t increased, the confined concrete strength tended to decrease as shown in Fig. 6(d). This observation indicated that a smaller pitch led to better confinement, which is in line with the outcomes of physics-based models. The Pearson correlation coefficients (r_p) between the features are shown in Fig. 7. A higher value of $|r_p|$ indicates a stronger linear relationship between the two features, and features with $|r_p|$ greater than 0.5 denote a notable linear relationship [75]. In the context of ML modelling, the presence of correlated features in the

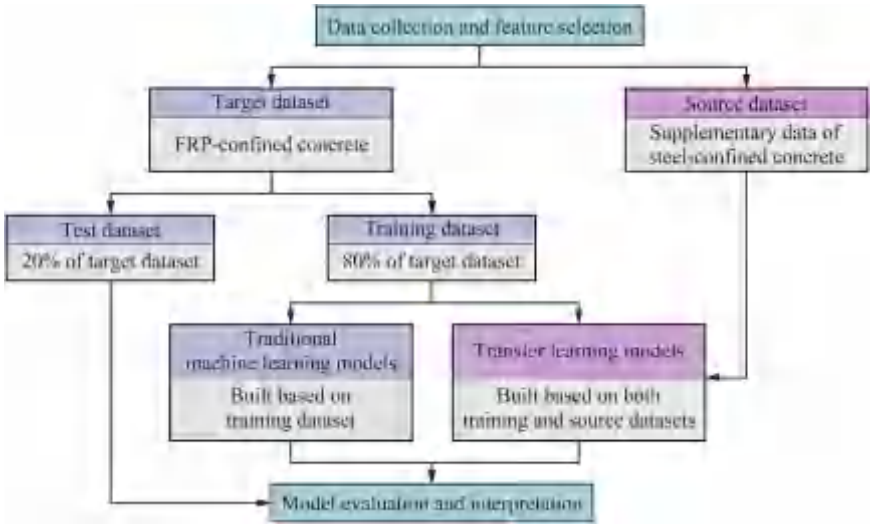


Fig. 5. Overview of the modelling process.

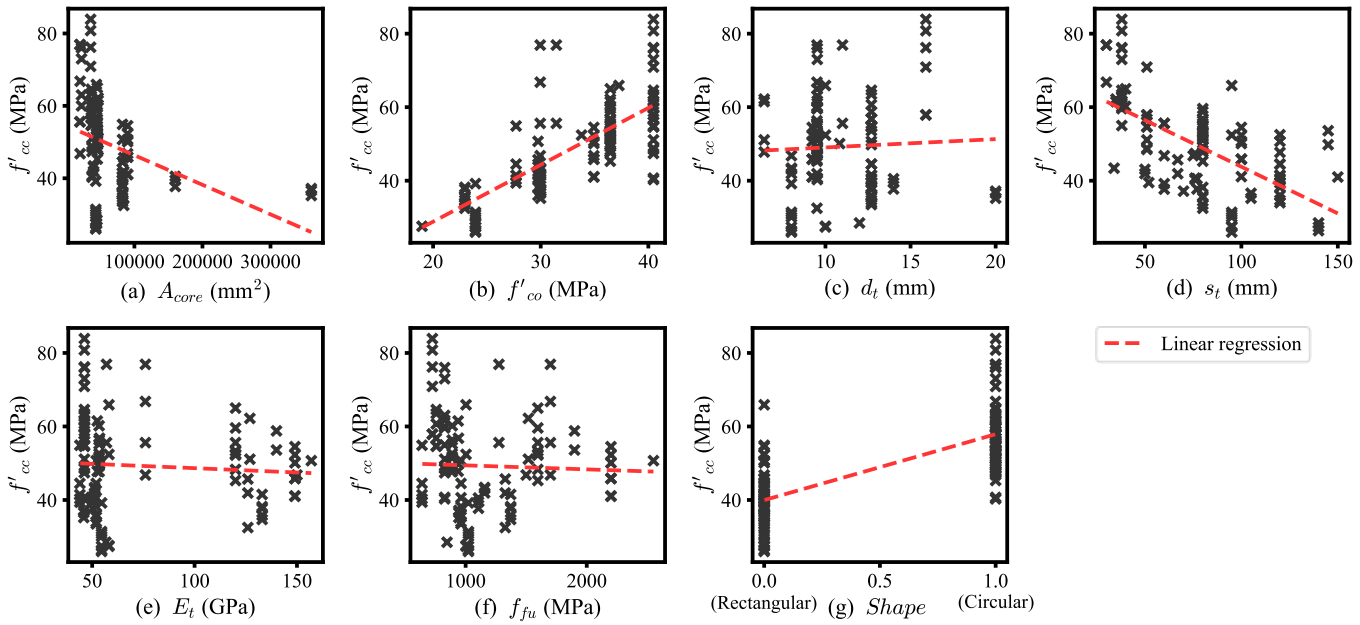


Fig. 6. Linear regression of f_{cc}' versus features in the target dataset.

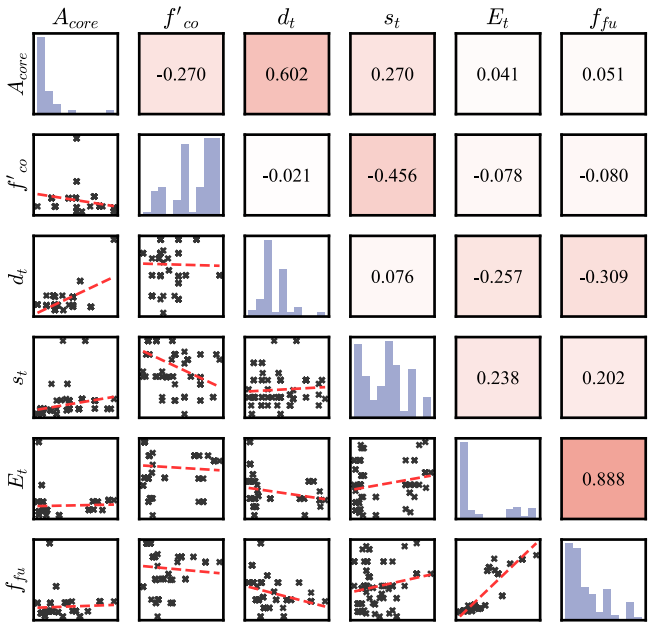


Fig. 7. Correlations between features in the target dataset.

dataset may give rise to issues of collinearity. The collinearity issues may cause the ML model to be sensitive to slight changes in the dataset and pose challenges to the interpretability of the models [76]. In this study, only two pairs of features exhibited notable linear relationships. The strong correlation between E_t and f_{fu} (r_p=0.888) was expected because FRP reinforcement possesses a linear stress-strain relationship up to failure. On the other hand, the correlation between d_t and A_{core} (r_p=0.602) may be a consequence of limited data in the target dataset. Generally, most features exhibited values of $|r_p|$ below 0.5, indicating the insignificance of collinearity in this study.

5.2. Dataset splitting

In this study, the target dataset was randomly split into a training dataset (80%) and a test dataset (20%). The training dataset was used for hyperparameter searching and model training, while the test dataset was exclusively reserved for performance evaluation. The source dataset, which was used for constructing transfer learning-based models, served solely for hyperparameter searching and model training.

For the target dataset, two splitting techniques were employed: one-time random split and shuffle split. Due to its simplicity and computational efficiency, one-time random split has been widely used to assess the performance of ML models [8,31,37,39]. However, it may not yield a robust estimation of the model's performance, as it relies on a single partition of the data. Unlike the one-time random split, shuffle split involves conducting multiple random splits for a more robust evaluation of ML models [38,40]. In this study, 1500 shuffle split iterations were performed to ensure the convergence of statistical analysis results.

5.3. Hyperparameter searching

Hyperparameters are external configuration settings used in the process of training ML models, which are not learned from the data. The choice of hyperparameters is a critical factor influencing model performance. In this study, for models with low-dimensional hyperparameters (RF and Extra Trees), grid search was employed to systematically explore all possible combinations. On the other hand, for models with high-dimensional hyperparameters (AdaBoost.R2, XGBoost, and the transfer learning models), random search was selected for its enhanced computational efficiency [77]. In the search process, a 5-fold cross-validation was applied. The 5-fold cross-validation divides the training dataset into five distinct subsets. Within each fold, one subset is designated as a validation subset, while the remaining four subsets serve for model training. Notably, for the transfer learning-based models, the source dataset is employed for model training in each fold, as shown in Fig. 8. The search range of hyperparameters and their optimized values for each model are presented in Appendix B. Default values were assigned to hyperparameters not explicitly listed.

6. Model evaluation

6.1. Evaluation metrics

Various statistical metrics were employed to evaluate and compare the performances of predictive models, including coefficients of deter-

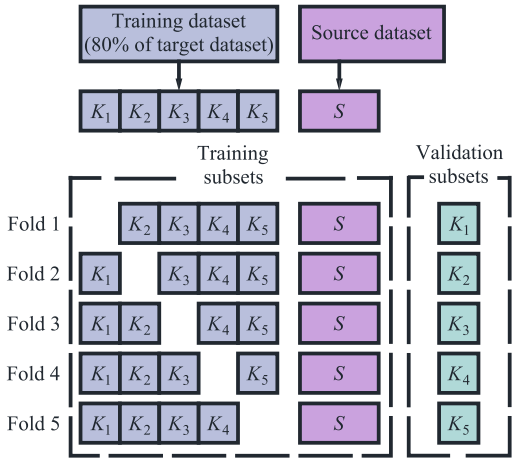


Fig. 8. Overview of the 5-fold cross-validation.

mination (R^2), root mean square error (RMSE), mean absolute error (MAE), and mean absolute percentage error (MAPE) [78], which are commonly used in ML (see Eqs. (5)–(8)). These metrics were chosen for their recognized utility in assessing model performance across different domains. R^2 measures the model's goodness of fit, with values closer to 1.0 indicating better fit. RMSE quantifies the average error magnitude, while MAE provides a straightforward assessment of accuracy. Additionally, MAPE evaluates accuracy as a percentage of observed values.

$$R^2 = 1 - \frac{\sum_{i=1}^{N}(y_i - y_i^*)^2}{\sum_{i=1}^{N}(y_i - y_{mean})^2} \tag{5}$$

$$RMSE = \sqrt{\frac{\sum_{i=1}^{N}(y_i - y_i^*)^2}{N}} \tag{6}$$

$$MAE = \frac{1}{N}\sum_{i=1}^{N}|y_i - y_i^*| \tag{7}$$

$$MAPE = \frac{1}{N}\sum_{i=1}^{N}\left|\frac{y_i - y_i^*}{y_i}\right| \tag{8}$$

where y_i and y_i^* are experimental and predicted values, respectively; and y_{mean} is mean value of all y_i.

Two supplementary metrics, $a_{20\text{-}index}$ and fractional bias (FB) [79], were also utilized to ensure model validity (see Eqs. (9)-(10)). The $a_{20\text{-}index}$ is a performance metric that evaluates the predictivity of a model within a 20% variation [79]. FB quantifies the disparity between experimental and predicted values, with values closer to 0 indicating minimal disparity [79].

$$a_{20-index} = \frac{N_{20}}{N} \tag{9}$$

$$FB = \frac{2\sum_{i=1}^{N}(y_i - y_i^*)}{\sum_{i=1}^{N}(y_i + y_i^*)} \tag{10}$$

where N_{20} is number of instances where $0.8 \le y_i/\ y_i^* \le 1.2$.

In the case of physics-based models, the mean, standard deviation (SD), and coefficient of variation (COV) values of the ratio of predicted-to-experimental confined concrete strength were utilized as evaluation metrics.

6.2. Model evaluation based on one-time random split

The confined concrete strength f_{cc}' predicted by each ML model versus the experimental results are illustrated in Fig. 9. Table 2 lists the statistical metrics for each model. In Table 2, R^2_{train} and R^2_{test} are determined on the training dataset and test dataset, respectively. As observed, the proposed model was more predictive than other ML models, in terms of R^2_{test}. The proposed model achieved the highest R^2_{test} of 0.9089, indicating a good performance in confinement strength prediction of concrete confined by FRP transverse reinforcements. For the model error on the test dataset, the proposed model exhibited the lowest values for RMSE, MAE, and MAPE—specifically, 4.396 MPa, 3.547 MPa, and 7.25%, respectively. Moreover, the proposed model attained an $a_{20\text{-}index}$

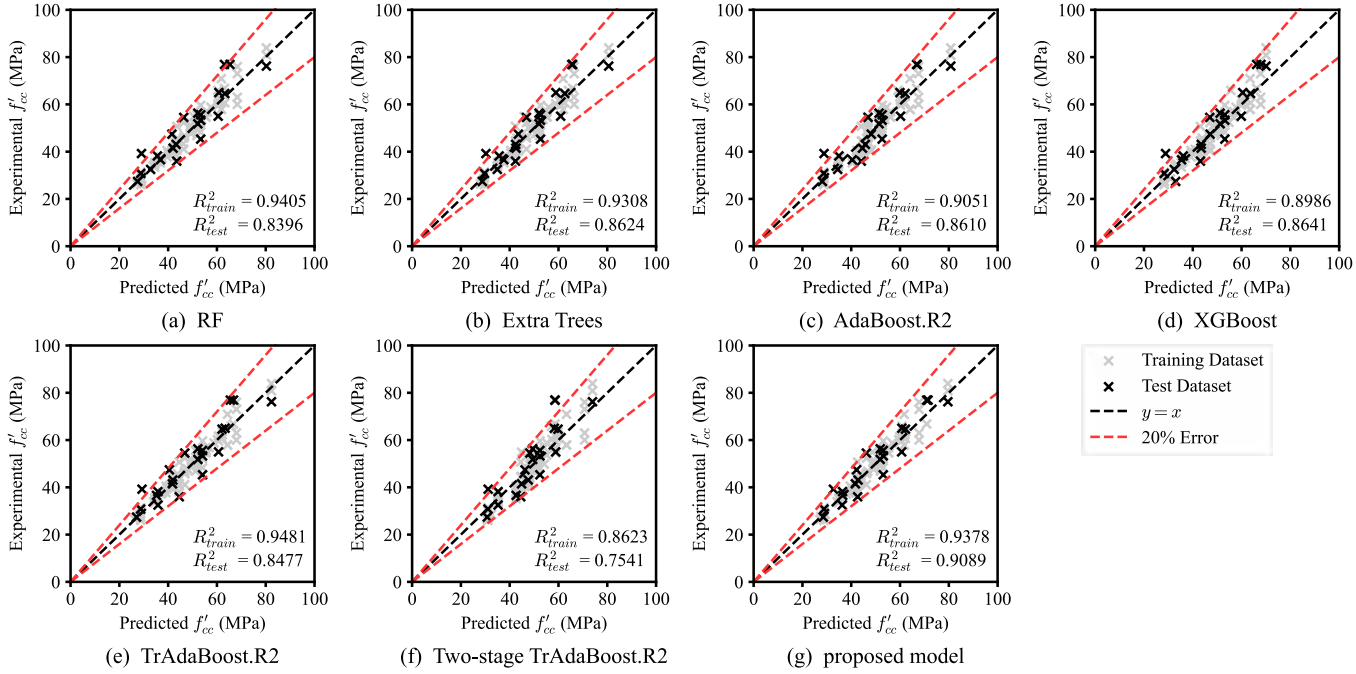


Fig. 9. Comparison of predicted and experimental f_{cc}': (a) RF; (b) Extra Trees; (c) AdaBoost.R2; (d) XGBoost; (e) TrAdaBoost.R2; (f) Two-stage TrAdaBoost.R2; and (g) the proposed model.

Table 2
Performance of machine learning models on the training and test datasets.

Models	Training dataset	Test dataset					
	R^2_{train}	R^2_{test}	RMSE (MPa)	MAE (MPa)	MAPE (%)	$a_{20\text{-}index}$ (%)	FB (%)
RF	0.9405	0.8396	5.834	4.230	8.10	91	3.61
Extra Trees	0.9308	0.8624	5.403	4.248	8.25	95	3.05
AdaBoost.R2	0.9051	0.8610	5.431	4.459	9.01	95	1.93
XGBoost	0.8986	0.8641	5.371	4.160	8.51	95	3.31
TrAdaBoost.R2	0.9481	0.8477	5.686	4.415	8.81	95	2.69
Two-stage TrAdaBoost.R2	0.8623	0.7541	7.223	5.547	10.82	86	3.90
Proposed model	0.9378	0.9089	4.396	3.547	7.25	100	1.87

value of 100%, indicating all samples had a difference between the predicted value and experimental value within ± 20%. In terms of FB, the proposed model exhibited the least disparity in predicting confinement strength (FB=1.87%).

It is worth mentioning that, for the training dataset, RF and TrAdaBoost.R2 exhibited similar performance compared to the proposed model. When considering the test dataset, however, the value of R^2_{test} obtained from the proposed model (R^2_{test} =0.9089) was higher than that obtained from RF (R^2_{test} =0.8396) and TrAdaBoost.R2 (R^2_{test} =0.8477). The improved accuracy of the proposed model on the test dataset revealed that the proposed algorithm can effectively address the issue of insufficient data.

In addition to the ML models, seven physics-based models [10,12,13,24–27] (see Table 3) were also compared against the experimental results. The first four equations were proposed for circular columns, and the subsequent three were developed for rectangular columns. Fig. 10 plots the confined concrete strength f_{cc}' predicted by physics-based models versus the experimental results. Table 4 presents the mean, standard deviation (SD), and coefficient of variation (COV) for each physics-based model and the proposed transfer learning-based model. Overall, the proposed transfer learning-based model exhibited the best performance with the least bias and variance for both circular and rectangular columns. For the circular columns in the test dataset, the values of mean and COV for the proposed model were 0.986 and 0.081, respectively. For all circular columns, these values were 0.999 and 0.063, respectively. In comparison, the optimal physics-based model for all circular columns was the approach proposed by Karim et al. [13], which attained mean and COV values of 1.013 and 0.125, respectively. For the rectangular columns, similar results can be drawn. This highlights the robustness and accuracy of the proposed model, representing a promising advancement in predicting the confinement strength of FRP-confined concrete.

Table 3
Summary of the physics-based models for concrete confined by FRP transverse reinforcements.

References	Confinement strength equations
Afifi et al.[10]	$f'_{cc}=f'_{co}\left[1.0+4.4547\left(\frac{f'_l}{f'_{co}}\right)^{0.723}\right], f'_l=\frac{1}{2}k_e\rho_{st}f_{fb}, f_{fb}=\min\begin{cases}\left(0.05\frac{r_b}{d_t}+0.3\right)f_{fu}<f_{fu}\\0.004E_t\end{cases}$
Sankholkar et al. [12]	$f'_{cc}=f'_{co}+1.31f'_l, f'_l=\frac{1}{2}k_e\rho_{st}\times 0.62E_t\varepsilon_{fu}$
Karim et al.[13]	$f'_{cc}=\frac{f'_{co}+5f'_l}{f'_{co}+0.5f'_l}\times f'_{co}, f'_l=\frac{1}{2}k_e\rho_{st}\times 0.33f_{fb}$
Almomani et al. [24]	$f'_{cc}=f'_{co}+1.7389f'_l, f'_l=\frac{1}{2}k_e\rho_{st}f_{fb}$
Tobbi et al.[25]	$f'_{cc}=f'_{co}\left[1.0+1.23\left(\frac{f'_l}{f'_{co}}\right)^{0.71}\right], f'_l=k_e(f_{lx}+f_{ly})/2$
Tahir et al.[26]	$f'_{cc}=f'_{co}\left[1.0+1.02\left(\frac{f'_l}{f'_{co}}\right)^{0.631}\right], f'_l=k_e\rho_{ve}f_{fb}, f_{fb}=\left(0.05\frac{r_b}{d_t}+0.3\right)f_{fu}<f_{fu}$
Zhang and Deng [27]	$f'_{cc}=f'_{co}\left[1.0+2.84\left(\frac{f'_l}{f'_{co}}\right)^{0.39}\right], f'_l=k_e\frac{A_{tf}f_{fv}}{s_t\times d_{core}}, f_{fv}=0.3\times\left(\frac{E_tk_e\rho_{st}}{f'_{co}}\right)^{1.57}+26.6$

6.3. Model evaluation based on shuffle split

A statistical analysis was performed to assess the performance of various ML models based on 1500 shuffle split iterations. Table 5 presents the statistical parameters of R^2_{test} for each ML model. In this table, the 'Confidence Interval (95%)' refers to the generalization confidence interval (CI) at a 95% statistical significance level. As observed, the proposed model achieved the highest mean R^2_{test} value of 0.8269, with its lower bound of the 95% CI value (0.6523) exceeding those of the other models. This observation implied that the proposed model demonstrated greater stability and robustness compared to other ML models.

To further compare the performance of the proposed model against physics-based models, the optimal physics-based models for rectangular columns (Tobbi et al. model [25]) and circular columns (Karim et al. model [13]) were selected for comparative analysis. Fig. 11 shows the histogram of R^2_{test} for the proposed model. The proposed model achieved a lower bound of 0.6523 for 95% CI of R^2_{test}, surpassing the values obtained by the optimal physics-based models (R^2 =0.6108 and R^2 =0.4482 for rectangular and circular columns, respectively). This indicated that, at a 95% confidence level, the proposed model exhibited a superior goodness of fit compared to the physics-based models.

7. Model interpretation

Model interpretation plays an important role in establishing trust for black-box ML models. In this study, feature importance and SHAP [52] were used to interpret the output of the proposed transfer learning-based model. The feature importance used in this study was permutation importance [61]. It involves comparing the model's accuracy before and after randomly shuffling the values of each feature. A greater performance drop indicates a higher permutation importance for a given feature. SHAP, which is based on game theory, investigates how each feature affects the prediction.

In the proposed model, the last *Learner* was used to interpret the whole model to alleviate the impact of the source instances. This choice was made as the last *Learner* was built exclusively on the target dataset, while the remaining *Learner*s were constructed utilizing both the target and source instances. Fig. 12 presents the permutation importance of each feature. It was observed that the unconfined concrete strength f_{co}' and pitch of transverse reinforcements s_t were the most important features for the confined concrete strength f_{cc}' prediction of concrete confined by FRP transverse reinforcements, which proved the robustness of the proposed model. Fig. 13 presents the SHAP summary plot for the impact of each feature. It was observed that the f_{co}' remained the most significant feature, followed by s_t. This observation was in line with the explanation provided by permutation importance. Analysis of SHAP

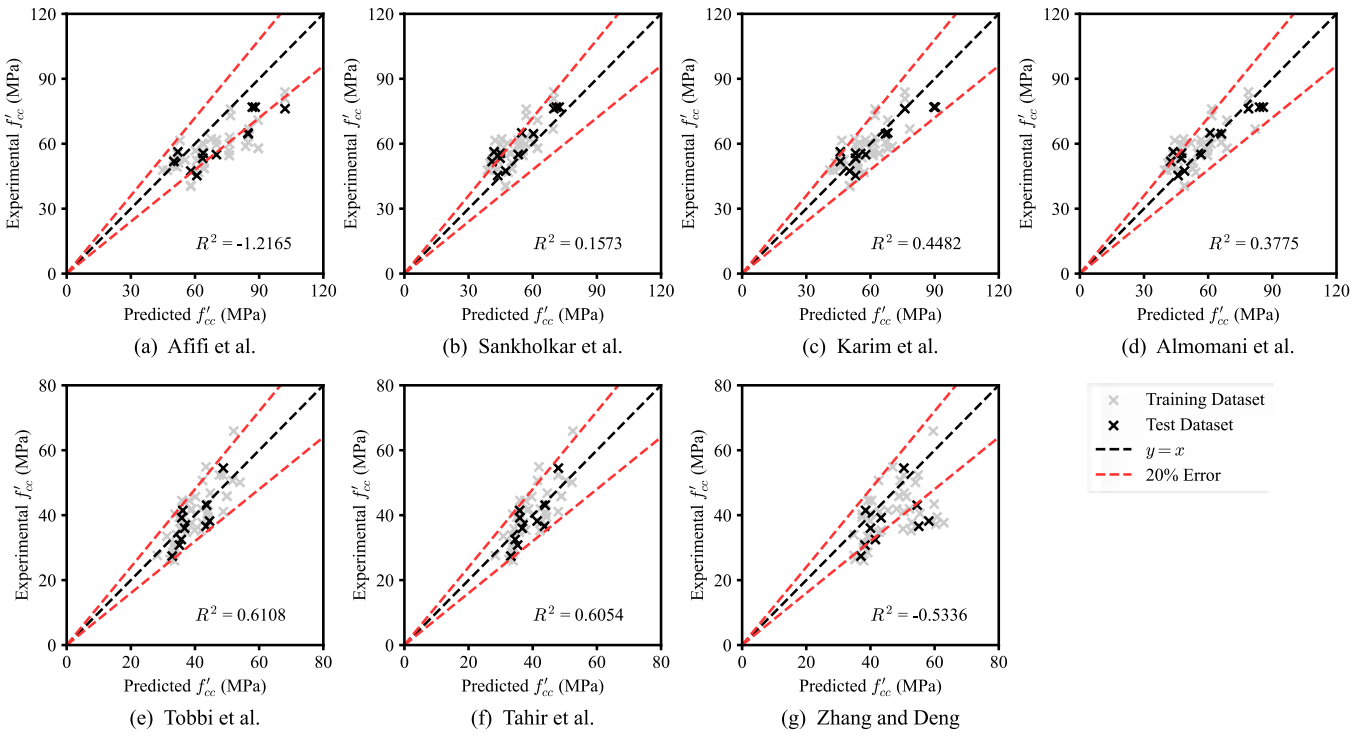


Fig. 10. Comparison of predicted and experimental f_{cc}': (a) Afifi et al.; (b) Sankholkar et al.; (c) Karim et al.; (d) Almomani et al.; (e) Tobbi et al.; (f) Tahir et al.; and (g) Zhang and Deng.

Table 4
Performance of the physics-based models and the proposed model.

Cross-section	Models	Test dataset			All data		
		MEAN	SD	COV	MEAN	SD	COV
Circular	Proposed model	0.986	0.080	0.081	0.999	0.063	0.063
	Afifi et al.[10]	1.192	0.132	0.111	1.192	0.166	0.139
	Sankholkar et al.[12]	0.889	0.078	0.087	0.895	0.111	0.124
	Karim et al.[13]	1.030	0.106	0.103	1.013	0.127	0.125
	Almomani et al.[24]	0.969	0.105	0.109	0.963	0.131	0.136
Rectangular	Proposed model	0.991	0.103	0.104	1.002	0.071	0.070
	Tobbi et al.[25]	1.051	0.119	0.113	1.023	0.128	0.125
	Tahir et al.[26]	1.040	0.118	0.113	1.014	0.130	0.128
	Zhang and Deng[27]	1.224	0.198	0.162	1.186	0.214	0.180

Table 5
Generalization performance of machine learning models: R^2_{test} perspective.

Models	Mean	Confidence Interval (95%)	
		Lower bound	Upper bound
RF	0.8132	0.6124	0.9255
Extra Trees	0.8173	0.6152	0.9237
AdaBoost.R2	0.7937	0.5843	0.9063
XGBoost	0.7943	0.5982	0.9042
TrAdaBoost.R2	0.7916	0.5479	0.9147
Two-stage TrAdaBoost.R2	0.7314	0.4600	0.8855
Proposed model	0.8269	0.6523	0.9238

values indicates that high f_{co}', ultimate tensile strength of transverse reinforcements f_{fu}, and diameter of transverse reinforcements d_t led to an increase in the model output, while high s_t was associated with a reduction in the model output. This was in good agreement with the outcomes of physics-based models (see Table 3). In several physics-based models [10,12,27], the elastic modulus of FRP E_t is an important parameter that affects the prediction of the confined concrete strength. However, the analysis of permutation importance and SHAP

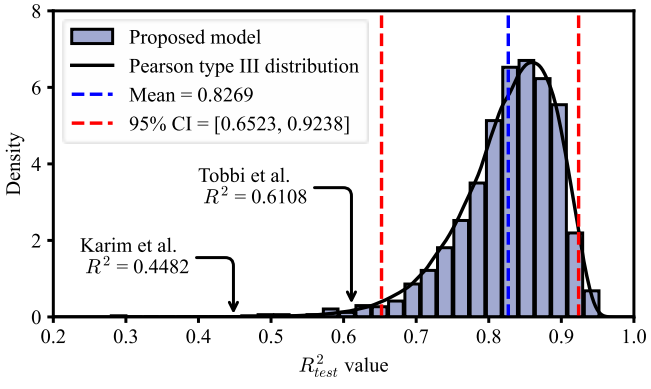


Fig. 11. Histogram of R^2_{test} for the proposed model.

values revealed that the influence of the E_t on the model output was relatively insignificant. A similar finding was reported by Tobbi et al. [15], who found that when employing identical transverse reinforcement layouts (s_t and d_t), the compressive strength of GFRP-confined

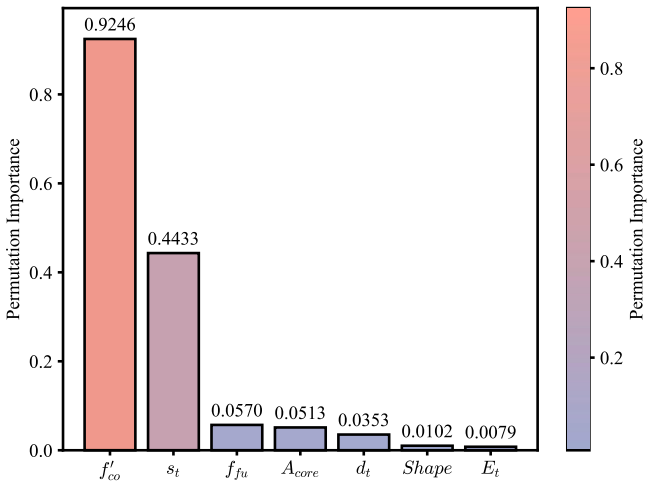


Fig. 12. Permutation importance of the proposed model.

concrete columns closely resembled that of CFRP-confined columns, despite the fact that the elastic modulus of GFRP was far less than that of CFRP.

8. Conclusions

This study develops a transfer learning-based model to predict the confinement strength of concrete confined by FRP transverse reinforcements. The following conclusions can be drawn from the study:

1. A transfer learning algorithm is introduced to acquire additional 'knowledge' from distinct but related research domains. The proposed algorithm can effectively address the issue caused by insufficient data in this study. In the training dataset, RF, TrAdaBoost.R2 and the proposed model exhibit comparable performance. In the test dataset, however, the proposed model outperforms with an R^2 of 0.9089, surpassing the values of 0.8396 and 0.8477 achieved by RF and TrAdaBoost.R2, respectively.
2. The model evaluation based on one-time random split indicates that the proposed model is the optimal choice among the seven ML models considered in this study for predicting the confinement strength of concrete confined by FRP transverse reinforcements. On the test dataset, it achieves the lowest RMSE, MAE, MAPE, and FB values of 4.396 MPa, 3.547 MPa, 7.25%, and 1.87%, respectively. Meanwhile, it yields the highest R^2 and $a_{20\text{-}index}$ values of 0.9089% and 100%, respectively.
3. The proposed model demonstrates superior performance in comparison to the seven physics-based models considered in this study. For the circular columns in the test dataset, the mean and COV of the ratio of predicted-to-experimental confined concrete strength for the proposed model are 0.986 and 0.081, respectively. For all circular columns, these values become 0.999 and 0.063. Conversely, the optimal physics-based model proposed by Karim et al. produces mean and COV values of 1.013 and 0.125, respectively. Similar conclusions can be drawn for rectangular columns.
4. The proposed model exhibits superior stability and robustness compared to other ML models considered. The model evaluation based on shuffle split reveals that the proposed model achieves the highest mean R^2_{test} value of 0.8269, with its lower bound of the 95% CI value (0.6523) exceeding those of the other ML models. Meanwhile, the obtained lower bound surpasses the values obtained by the physics-based models.
5. Based on the proposed model, the interpretations indicate that the most influential design parameters affecting confined concrete strength are the unconfined concrete strength and the pitch of transverse reinforcements.
6. The proposed model can be updated to consider additional experimental results. By updating the target dataset, the proposed algorithm allows for the reconstruction of the model.

CRediT authorship contribution statement

Fei Peng: Conceptualization, Investigation, Funding acquisition, Methodology, Supervision, Writing – original draft, Writing – review & editing. **Yazhong Li:** Writing – original draft, Formal analysis, Methodology, Investigation. **Weichen Xue:** Conceptualization, Writing – review & editing.

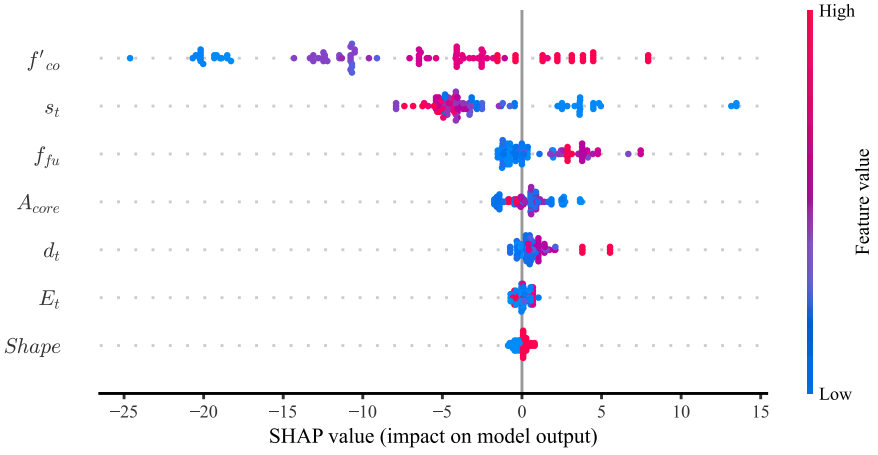


Fig. 13. SHAP summary plot of the proposed model.

Declaration of Competing Interest

The authors declare that they have no known competing financial interests or personal relationships that could have appeared to influence the work reported in this paper.

Data availability

The code and datasets used in this study are available on the GitHub page (https://github.com/PengFeiLab/Transfer-learning-based-model-for-FRP-confined-concrete-strength).

Acknowledgements

The authors gratefully acknowledge the financial support provided by the Program Fund of Non-Metallic Excellence and Innovation Center for Building Materials (2023TDA4–1), National Natural Science Foundation of China (No. 52008165), and Fundamental Research Funds for the Central Universities (No. 531118010497).

Appendix A

The loss for the proposed algorithm consists of two components: the loss on the source dataset and the loss on the target dataset. For the loss on the source dataset, the proof can be derived from the Hedge(β) algorithm provided in [69]. Within each iteration of Hedge(β), the instance weights are adjusted based on Eq. (A1).

$$w_i^{t+1} = w_i^t \beta^{l_i^t} \tag{A1}$$

where β is constant with value ranging between 0 and 1.

The proposed algorithm uses a similar strategy (see Eq. (4)) to identify the instances in the source dataset that are favorable for training. According to a relevant proof provided by Freund and Schapire [69], if the initial weight of each source instance is set equally, the upper bound of loss for the proposed algorithm on the source dataset can be expressed as Eq. (A2).

$$L_{Source} \leqslant \frac{\ln(1-\beta)}{1-\beta} \min_i L_i + \frac{1}{1-\beta} \ln N \tag{A2}$$

where L_{source} is loss of proposed algorithm on source dataset; $\min_i L_i$ is term associated with loss obtained from *Learner*.

Eq. (A2) indicates that the loss of the proposed algorithm on the source dataset depends on the loss obtained from the *Learner*. Altering the *Learner* impacts the values of $\min_i L_i$ and β, while the overall convergence remains constant. In the context of loss on the target dataset, Eq. (A3) specifies that each target instance within the same iteration carries the same weight. This observation implies that the loss for target instances remains unaltered, and the value of this loss is dependent on the performance of *Learner*.

$$w_i^t = \frac{1}{m}\left[\frac{m}{n+m} + \frac{t}{S-1}\left(1 - \frac{m}{n+m}\right)\right] \quad i = n+1, \ldots, n+m \tag{A3}$$

Appendix B

See Table B1.

Table B1
Hyperparameter searching of the machine learning models.

Models	Hyperparameters	Search range	Optimized value
RF	n_estimators	[200]	200
	max_features	[3,7]	7
	max_depth	[5,15]	11
	criterion	['squared_error', 'absolute_error', 'poisson', 'friedman_mse']	'poisson'
Extra Trees	n_estimators	[200]	200
	max_features	[3,7]	6
	max_depth	[5,15]	5
	criterion	['squared_error', 'absolute_error', 'poisson', 'friedman_mse']	'poisson'
XGBoost	n_estimators	[200]	200
	max_depth	[5,15]	15
	learning_rate	[0,10]	1.5583
	reg_alpha	[0500]	21.469
	reg_lambda	[0500]	446.24
AdaBoost.R2	n_estimators	[200]	200
	loss	['linear', 'square', 'exponential']	'linear'
	learning_rate	[0,10]	0.7740
TrAdaBoost.R2	*learner*	Decision Tree	Decision Tree
	max_depth	[5,15]	15
	criterion	['squared_error', 'absolute_error', 'poisson', 'friedman_mse']	'friedman_mse'
Two-Stage TrAdaboost.R2	steps	[10,20]	20
Proposed Model	*WeakLearn*	Decision Tree	Decision Tree
	Learner	[RF, Extra Trees, AdaBoost.R2, XGBoost]	RF
	max_depth (*WeakLearn*)	[5,15]	15

(*continued on next page*)

Table B1 (*continued*)

Models	Hyperparameters	Search range	Optimized value
	criterion (*WeakLearn*)	['squared_error', 'absolute_error', 'poisson', 'friedman_mse']	'friedman_mse'
	n_estimators	[200]	200
	max_features	[3,7]	7
	max_depth	[5,15]	12
	criterion	['squared_error', 'absolute_error', 'poisson', 'friedman_mse']	'absolute_error'

Note: n_estimators is number of decision trees in model; max_features is number of features to consider when looking for best split; max_depth is maximum depth of decision trees; criterion is function to measure the quality of a split; learning_rate is weight applied to each regressor at each boosting iteration; reg_alpha and reg_lambda are L1 and L2 regularization term on weights, respectively; loss is loss function to use when updating weights after each iteration; and steps is number of steps in Two-Stage TrAdaboost.R2.

Appendix C. Supporting information

Supplementary data associated with this article can be found in the online version at doi:10.1016/j.engstruct.2024.118116.

References

[1] Zhu J, Weng K, Huang B, Xu L, Dai J. Ultra-high-strength engineered cementitious composites (UHS-ECC) panel reinforced with FRP bar/grid: development and flexural performance. Eng Struct 2024;302:117193.
[2] Kharal Z. PhD thesis. University of Toronto. Towards Underst Seism Behav GFRP Confin Concr Columns 2019.
[3] ACI 440.1R-15. Guide for the design and construction of structural concrete reinforced with FRP bars. Farmington Hills (MI). American Concrete Institute; 2015.
[4] Peng F, Xue W. Reliability analysis of eccentrically loaded concrete rectangular columns reinforced with fiber-reinforced polymer bars. Acids Struct J 2019;116(4).
[5] Peng F, Cai Y, Yi W, Xue W. Shear behavior of two-span continuous concrete deep beams reinforced with GFRP bars. Eng Struct 2023;290:116367.
[6] Tarawneh AN, Dwairi HM, Almasabha GS, Majdalaweyh SA. Effect of fiber-reinforced polymer-compression reinforcement in columns subjected to concentric and eccentric loading. Acids Struct J 2021;118(3):187–97. https://doi.org/10.14359/51730526.
[7] Salah-Eldin A, Mohamed HM, Benmokrane B. Structural performance of high-strength-concrete columns reinforced with GFRP bars and ties subjected to eccentric loads. Eng Struct 2019;185:286–300. https://doi.org/10.1016/j.engstruct.2019.01.143.
[8] Tarawneh A, Almasabha G, Murad Y. ColumnsNet: neural network model for constructing interaction diagrams and slenderness limit for FRP-RC columns. J Struct Eng 2022;148:04022089. https://doi.org/10.1061/(ASCE)ST.1943-541X.0003389.
[9] Hadi MNS, Karim H, Sheikh MN. Experimental investigations on circular concrete columns reinforced with GFRP bars and helices under different loading conditions. J Compos Constr 2016;20(4):04016009.
[10] Afifi MZ, Mohamed HM, Benmokrane B. Theoretical stress–strain model for circular concrete columns confined by GFRP spirals and hoops. Eng Struct 2015;102:202–13.
[11] Afifi MZ, Mohamed HM, Chaallal O, Benmokrane B. Confinement model for concrete columns internally confined with carbon FRP spirals and hoops. J Struct Eng 2015;141(9):04014219. https://doi.org/10.1061/(ASCE)ST.1943-541X.0001197.
[12] Sankholkar PP, Pantelides CP, Hales TA. Confinement model for concrete columns reinforced with GFRP spirals. J Compos Constr 2018;22(3):04018007.
[13] Karim H, Sheikh MN, Hadi MNS. Axial load-axial deformation behaviour of circular concrete columns reinforced with GFRP bars and helices. Constr Build Mater 2016;112:1147–57. https://doi.org/10.1016/J.CONBUILDMAT.2016.02.219.
[14] Tobbi H, Farghaly AS, Benmokrane B. Concrete columns reinforced longitudinally and transversally with glass fiber-reinforced polymer bars. Acids Struct J 2012;109:551–8.
[15] Tobbi H, Farghaly AS, Benmokrane B. Behavior of concentrically loaded fiber-reinforced polymer reinforced concrete columns with varying reinforcement types and ratios. Acids Struct J 2014;111:375–86. https://doi.org/10.14359/51686528.
[16] Zhang P, Chen B, Liu Y, Tu Y, Gao D, Zhao J, Sheikh SA. Experimental study on the axial compression behavior of columns confined by BFRP ties. Compos Struct 2021;258:113302. https://doi.org/10.1016/j.compstruct.2020.113302.
[17] Tahir M, Wang Z, Ali KM. Axial compressive behavior of square concrete columns confined with CFRP strip ties using wet lay-up technique. Constr Build Mater 2019;200:282–92. https://doi.org/10.1016/J.CONBUILDMAT.2018.12.127.
[18] Li P, Jin L, Fan L, Liang J, Du X. Compressive stress-strain behavior and model for geometrical-similar BFRP-RC square columns. Eng Struct 2023;293:116704.
[19] Pantelides CP, Gibbons ME, Reaveley LD. Axial load behavior of concrete columns confined with GFRP spirals. J Compos Constr 2013;17(3):305–13.
[20] Luca AD, Matta F, Nanni A. Behavior of full-scale glass fiber-reinforced polymer reinforced concrete columns under axial load. Acids Struct J 2010;107:589–96.
[21] El-Gamal S, AlShareedahb O. Behavior of axially loaded low strength concrete columns reinforced with GFRP bars and spirals. Eng Struct 2010;216.
[22] Jiang J, Xiao P, Li B. A novel triaxial test system for concrete under passive confinement. J Test Eval 2018;46(3):913–23. https://doi.org/10.1520/JTE20160547.
[23] Xiong H, Li B, Jiang J. Load path dependence of strain and stress for confined concrete. Mag Concr Res 2016;68(12):604–18. https://doi.org/10.1680/jmacr.15.00175.
[24] Almomani Y, Tarawneh A, Alawadi R, Taqieddin ZN, Taha S, Sheikh NA, Momani Z. Confinement model for circular concrete columns transversely reinforced with GFRP spirals and hoops. Results Eng 2023;17:100918.
[25] Tobbi H, Farghaly AS, Benmokrane B. Strength model for concrete columns reinforced with fiber-reinforced polymer bars and ties. Acids Struct J 2014;111:789–98.
[26] Tahir M, Isleem HF, Wang Z. Axial compressive stress-strain model for hybrid-reinforced concrete columns confined with FRP ties. Mag Concr Res 2022;175(3):215–29.
[27] Zhang X, Deng Z. Experimental study and theoretical analysis on axial compressive behavior of concrete columns reinforced with GFRP bars and PVA fibers. Constr Build Mater 2018;172:519–32. https://doi.org/10.1016/J.CONBUILDMAT.2018.03.237.
[28] Mander JB, Priestley MJN, Park R. Theoretical stress–strain model for confined concrete. J Struct Eng 1988;114(8):1804–26.
[29] Feng Y, Zhang X, Feng S, Chen H, Zhao Y, Chen Y. Improved SOLOv2 detection method for shield tunnel lining water leakages. J Intell Constr 2023;1(1):9180004.
[30] Sayed YAK, Ibrahim AA, Tamrazyan AG, Fahmy MFM. Machine-learning-based models versus design-oriented models for predicting the axial compressive load of FRP-confined rectangular RC columns. Eng Struct 2023;285:116030.
[31] Bakouregui AS, Mohamed HM, Yahia A, Benmokrane B. Explainable extreme gradient boosting tree-based prediction of load-carrying capacity of FRP-RC columns. Eng Struct 2021;245:112836. https://doi.org/10.1016/j.engstruct.2021.112836.
[32] Mitchell TM. Machine Learning. New York: McGraw-Hill,; 1997.
[33] Zhang Q, Barri K, Jiao P, Salehi H, Alavi AH. Genetic programming in civil engineering: advent, applications and future trends. Artif Intell Rev 2020;54:1863–85.
[34] Karniadakis GE, Kevrekidis IG, Lu L, Perdikaris P, Wang S, Yang L. Physics-informed machine learning. Nat Rev Phys 2021;3:422–40.
[35] Ying X. An overview of overfitting and its solutions. J Phys Conf Ser 2023;1168:022022.
[36] Dietterich T. Overfitting and undercomputing in machine learning. ACM Comput Surv 1995;27(3):326–7. https://doi.org/10.1145/212094.212114.
[37] Zhang Q, Vandenbossche JM, Alavi AH. An evolutionary computational method to formulate the response of unbonded concrete overlays to temperature loading. Eng Comput 2022;39(2):523–40. https://doi.org/10.1108/EC-11-2020-0641.
[38] Tahmassebi A, Motamedi M, Alavi AH, Gandomi AH. An explainable prediction framework for engineering problems: case studies in reinforced concrete members modeling. Eng Comput 2021;39(2):609–26.
[39] Tarawneh A, Saleh E, Almasabha G, Alghossoon A. Hybrid data-driven machine learning framework for determining prestressed concrete losses. Arab J Sci Eng 2023;48:13179–93.
[40] Mai HVT, Nguyen MH, Ly HB. Development of machine learning methods to predict the compressive strength of fiber-reinforced self-compacting concrete and sensitivity analysis. Constr Build Mater 2023;367:130339.
[41] Jiao P, Wang Z, Alavi AH. Maximizing triboelectric nanogenerators by physics-informed AI inverse design. Adv Mater 2023;36(5):2308505.
[42] Pak H, Paal SG. Evaluation of transfer learning models for predicting the lateral strength of reinforced concrete columns. Eng Struct 2022;266:114579.
[43] Pan SJ, Yang Q. A survey on transfer learning. IEEE T Knowl Data En 2010;22(10):1345–59. https://doi.org/10.1109/TKDE.2009.191.
[44] Dai W, Yang Q, Xue G, Yu Y. Boosting for transfer learning. ACM Int Conf Proc Ser; 2007. p. 193–200. https://doi.org/10.1145/1273496.1273521.
[45] Sheikh SA, Toklucu MT. Reinforced concrete columns confined by circular spirals and hoops. Acids Struct J 1993;90:542–53. https://doi.org/10.14359/3949.
[46] Ahmad SH, Shah SP. Behavior of hoop confined concrete under high strain rates. J Proc 1985;82:634–47. https://doi.org/10.14359/10373.

[47] Ahmad SH, Shah SP. Stress-strain curves of concrete confined by spiral reinforcement. 484–40 J Proc 1982;79. https://doi.org/10.14359/10922.
[48] Assa B, Nishiyama M, Watanabe F. New approach for modelling confined concrete. I: Circular columns. J Struct Eng 2001;127(7):743–50.
[49] Sharma UK, Bhargava P, Kaushik SK. Behavior of confined high strength concrete columns under axial compression. J Adv Concr Technol 2005;3(2):267–81.
[50] Ribeiro MT, Singh S, Guestrin C. Why should I trust you?": explaining the predictions of any classifier. Proc 22nd ACM SIGKDD Int Conf Knowl Discov Data Min 2016:1135–44.
[51] Ribeiro MT, Singh S, Guestrin C. Anchors: high-precision model-agnostic explanations. In Proceedings of the 32nd. AAAI Conf Artif Intell (AAAI'18 2018: 1527–35.
[52] Lunderberg SM, Lee S. A unified approach to interpreting model predictions. Adv Neural Inf Proces Syst 2017;4765:74. https://dl.acm.org/doi/10.5555/3295222.3295230.
[53] Guidotti R, Monreale A, Ruggieri S, Turini F, Giannotti F, Pedreschi D. A survey of methods for explaining black box models. ACM Comput Surv 2018;51(5):1–42.
[54] Chen J, Zhao X. A general integrated machine learning pipeline: Its concept, main steps and application in shear strength prediction of RC beams strengthened with FRCM. Eng Struct 2023;281:115749. https://doi.org/10.1016/j.engstruct.2023.115749.
[55] Hu S, Wang W, Lu Y. Explainable machine learning models for probabilistic buckling stress prediction of steel shear panel dampers. Eng Struct 2023;288: 116235.
[56] ACI 318-19. Building code requirements for structural concrete and commentary. Farmington Hills (MI). American Concrete Institute,; 2019.
[57] Xue W, Peng F, Fang Z. Behavior and design of slender rectangular concrete columns longitudinally reinforced with fiber-reinforced polymer bars. Acids Struct J 2018;115(2):311–22. https://doi.org/10.14359/51701131.
[58] Zadeh HJ, Nanni A. Flexural stiffness and second-order effects in fiber- reinforced polymer-reinforced concrete frames. Acids Struct J 2017;114(2):533–43.
[59] Abdelazim W, Mohamed HM, Afifi MZ, Benmokrane B. Proposed slenderness limit for glass fiber-reinforced polymer-reinforced concrete columns based on experiments and buckling analysis. Acids Struct J 2020;117(1):241–54. https://doi.org/10.14359/51718073.
[60] ACI 440.11-22. Building code requirements for structural concrete reinforced with glass fiber-reinforced polymer (GFRP) bars—code and commentary. Farmington Hills (MI. American Concrete Institute,; 2023.
[61] Breiman L. Random forests. Mach Learn 2001;45:5–32.
[62] Geurts P, Ernst D, Wehenkel L. Extremely randomized trees. Mach Learn 2006;63: 3–42.
[63] Drucker H. Improving regressors using boosting techniques. Proc Mach Learn Res 1997;107:15. ⟨https://dl.acm.org/doi/10.5555/645526.657132⟩.
[64] Chen T, Guestrin C. XGBoost: a scalable tree boosting system. Proc ACM SIGKDD Int Conf Knowl Discov Data Min 2016:785–94. https://doi.org/10.1145/2939672.2939785.
[65] Pardoe D, Stone P. Boosting for regression transfer. ICML - Proc Int Conf Mach Learn 2010:863–70. ⟨https://dl.acm.org/doi/10.5555/3104322.3104432⟩.
[66] Breiman L. Bagging predictors. Mach Learn 1996;24:123–40.
[67] Ghazwani M, Begum MY. Computational intelligence modeling of hyoscine drug solubility and solvent density in supercritical processing: gradient boosting, extra trees, and random forest models. Sci Rep 2023;13:10046.
[68] Schapire RE. The strength of weak learnability. Mach Learn 1990;5:197–227.
[69] Freund Y, Schapire RE. A decision-theoretic generalization of on-line learning and an application to boosting. J Comput Syst Sci 1997;55(1):119–39.
[70] Rätsch G, Onoda T, Müller KR. Soft margins for Adaboost. Mach Learn 2001;42(3): 287–320.
[71] Wickramaratna J, Holden S, Buxton B. Performance degradation in boosting. Int Workshop Mult Classif Syst 2001:11–21.
[72] Sagi O, Rokach L. Ensemble learning: a survey. Wiley Inter Rev Data Min Knowl Discov 2018;8(4):e1249. https://doi.org/10.1002/widm.1249.
[73] Pedregosa F, Varoquaux G, Gramfort A, Michel V, Thirion B, Grisel O, et al. Scikit learn: machine learning in python. J Mach Learn Res 2011;12:2825–30.
[74] Bellman R. Dynamic programming. Princeton, N.J.: Princeton University Press; 1957.
[75] Cohen J. Statistical power analysis for the behavioral sciences. 2nd ed..,. Routledge; 1988.
[76] Dormann CF, Elith J, Bacher S, Buchmann C, Carl G, Carré G, et al. Collinearity: a review of methods to deal with it and a simulation study evaluating their performance. Ecography 2013;36(1):27–46. https://doi.org/10.1111/J.1600-0587.2012.07348.X.
[77] Bergstra J, Bengio Y. Random search for hyper-parameter optimization. J Mach Learn Res 2012;13:281–305. https://dl.acm.org/doi/10.5555/2188385.2188395.
[78] Botchkarev A. A new typology design of performance metrics to measure errors in machine learning regression algorithms. Inter J Inf Knowl Manag 2019;14:45–76. https://doi.org/10.28945/4184.
[79] Naser MZ, Alavi AH. Error metrics and performance fitness indicators for artificial intelligence and machine learning in engineering and sciences. Arch Struct Constr 2023;3:499–517. https://doi.org/10.1007/s44150-021-00015-8.

Flexural Behavior and Design of Ultrahigh-Performance Concrete Beams Reinforced with GFRP Bars

Fei Peng, Ph.D.[1]; Jidong Deng[2]; and Weichen Xue, Ph.D.[3]

Abstract: The combination of glass fiber–reinforced polymer (GFRP) and ultrahigh-performance concrete (UHPC) to form structural members has generated significant interest due to their excellent durability and mechanical properties. This paper presents the flexural behavior and design methodology of GFRP-reinforced UHPC beams. Eight reinforced UHPC beams were tested to failure, varying in longitudinal reinforcement type (steel and GFRP), flexural reinforcement ratio, and steel fiber volume fraction (1% and 2%). Two flexural failure modes, including crack localization followed by rupture of GFRP (tension failure) and progressive crushing of UHPC followed by rupture of GFRP (compression failure), were observed in the tested GFRP-reinforced beams. Substitution of steel bars with GFRP bars resulted in delayed crack localization and a significant improvement in flexural strength by 54.9% and ultimate displacement by 55.7%. Increasing the GFRP reinforcement ratio showed a trend of increased flexural capacity, ultimate deformation, and energy dissipation capacity. Increasing the steel fiber volume in UHPC improved the flexural capacity of the tension failure–controlled beam, but had a slight effect on the flexural capacity of the compression failure–controlled beam. In addition, two different models were used to calculate beam deflection, and were compared with experimental results at the service load levels. Considering the fiber-bridging mechanism, a flexural strength model for GFRP-reinforced UHPC beams was developed. Finally, a minimum reinforcement ratio was proposed to ensure progressive failure of GFRP-reinforced UHPC beams. DOI: 10.1061/JCCOF2.CCENG-4392. © 2024 American Society of Civil Engineers.

Author keywords: Glass fiber–reinforced polymer (GFRP); Ultrahigh-performance concrete (UHPC); Beam; Flexural behavior; Flexural strength.

Downloaded from ascelibrary.org by HUNAN UNIVERSITY on 04/24/24. Copyright ASCE. For personal use only; all rights reserved.

Introduction

Ultrahigh-performance concrete (UHPC) is a cement-based composite material that is renowned for its durable performance owing to its low permeability resulting from its dense and discontinuous pore structure, a minimum compressive strength of 120 MPa, and a minimum sustained postcracking tensile strength of 5 MPa (MCS-EPFL 2016; ASTM 2017; El-Helou and Graybeal 2022). These features have made UHPC a desirable candidate for various structural applications (Hung et al. 2021). Despite the high strength and durability of UHPC, reinforced UHPC (R-UHPC) flexural members with steel bars may exhibit undesirable structural behavior. Once the steel reinforcement yields, cracks tend to localize at a single plane because of fiber pullout or rupture, a phenomenon known as crack localization (Shao et al. 2021; El-Helou and Graybeal 2022). After crack localization, the loss of the UHPC fiber-bridging resistance mechanism leads to a reduction in the load-carrying capacity of the member, ultimately leading to the rupture of steel bars (Fig. 1), which significantly compromises the structural ductility and deformability of the structural member (Yoo et al. 2017; El-Helou and Graybeal 2022; Saqif et al. 2022; Shao and Billington 2022; Peng et al. 2023a). This can be attributed to the decrease in stiffness of the steel after yielding, resulting in an inadequate increase in the force carried by the steel to compensate for the fiber-bridging loss (Peng et al. 2023a). As a result of crack localization, R-UHPC flexural members often exhibit low structural ductility and deformability, with the ratio of the midspan deflection to shear span length sometimes as low as 1.8% (Yoo et al. 2017; Shao and Billington 2022). To address the issue of low structural ductility caused by crack localization, Peng et al. (2023a) recommended a minimum flexural reinforcement ratio that is much higher than what is required in conventional or high-strength concrete flexural members.

Unlike steel bars, fiber-reinforced polymer (FRP) bars exhibit a linear stress–strain relationship until failure, without undergoing yielding. The substitution of steel bars with FRP bars in UHPC beams has the potential to compensate for the initial fiber-bridging loss and, consequently, delay crack localization. In addition to its linear behavior, the FRP bar has properties such as excellent corrosion resistance, a high strength-to-weight ratio, excellent fatigue resistance, and a lower modulus of elasticity than steel (Peng and Xue 2019; Mehany et al. 2022). Owing to their brittle nature and lower modulus of elasticity, conventional concrete beams reinforced with FRP bars exhibit limited ductility, larger crack width, and greater deflection when compared with steel-reinforced concrete (RC) beams with a similar flexural reinforcement ratio (Peng et al. 2023b). In recent years, a combination of FRP bars and UHPC to

[1]Associate Professor, Key Laboratory of Building Safety and Energy Efficiency of the Ministry of Education, Hunan Univ., Changsha 410082, China; Associate Professor, College of Civil Engineering, Hunan Univ., Lushan S Rd., 1, Changsha 410082, China. ORCID: https://orcid.org/0000-0003-2542-4259. Email: pengf@hnu.edu.cn

[2]Master's Candidate, College of Civil Engineering, Hunan Univ., Lushan S Rd., 1, Changsha 410082, China. Email: dengjidong@hnu.edu.cn

[3]Professor, Key Laboratory of Performance Evolution and Control for Engineering Structures of the Ministry of Education, Tongji Univ., Siping Rd., 1239, Shanghai 200092, China; Professor, Dept. of Structural Engineering, Tongji Univ., Siping Rd., 1239, Shanghai 200092, China (corresponding author). ORCID: https://orcid.org/0000-0002-9779-5676. Email: xuewc@tongji.edu.cn

Note. This manuscript was submitted on May 24, 2023; approved on February 20, 2024; published online on April 23, 2024. Discussion period open until September 23, 2024; separate discussions must be submitted for individual papers. This paper is part of the Journal of Composites for Construction, © ASCE, ISSN 1090-0268.

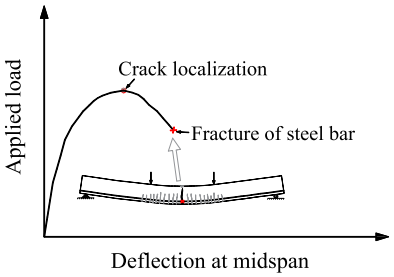


Fig. 1. Typical failure path of steel-reinforced UHPC beam.

form FRP-reinforced UHPC structural members has attracted wide interest (Yoo et al. 2016; Sturm et al. 2020; Cao et al. 2022a, b; Tan et al. 2022; Zeng et al. 2023; Liang et al. 2023; Mahaini et al. 2023). This combination not only fully utilizes the high tensile strength of FRP and the ultrahigh compressive strength of UHPC, it also significantly improves the ductility and serviceability performance of FRP-RC members (Yoo et al. 2016). Moreover, the combination of FRP bars and UHPC has the potential to enhance the blast resistance of reinforced concrete, owing to the self-centering nature of FRP and the increased toughness of UHPC (Yan et al. 2022).

Currently, several experimental studies have been undertaken to investigate the flexural behavior of UHPC beams reinforced with FRP bars (Yoo et al. 2016; Cao et al. 2022a, b; Mahaini et al. 2023). Yoo et al. (2016) found a transition in failure mode from glass fiber–reinforced polymer (GFRP) rupturing to concrete crushing with an increase in the GFRP reinforcement ratio. In addition, increasing the GFRP reinforcement ratio led to enhancements in postcracking stiffness, flexural capacity, and ductility. Similar findings were also reported by Cao et al. (2022a, b) and Mahaini et al. (2023). It is noteworthy that previous research (Yoo et al. 2016; Cao et al. 2022a, b; Mahaini et al. 2023) mainly focused on the impact of the FRP reinforcement ratio on the flexural behavior of the R-UHPC beams. Existing evidence (Saqif et al. 2022; Shao and Billington 2022) suggests that the flexural performance of R-UHPC beams is significantly dependent on the fiber volume fraction. However, the effect of the fiber volume fraction on the flexural behavior of FRP-reinforced UHPC beams remains unexplored.

As UHPC possesses distinct mechanical properties different from conventional concrete, the flexural design approach developed for conventional concrete beams reinforced with FRP bars may not be applicable to FRP-reinforced UHPC beams. The addition of fibers in UHPC effectively bridges the flexural cracks, and therefore, the crack-bridging mechanism can enhance the postcracking stiffness and contribute a significant proportion of the flexural resistance of R-UHPC beams (Peng et al. 2022a, b; Fang et al. 2023). Using conventional concrete specifications to design R-UHPC beams, where the concrete's tensile resistance is neglected in the flexural strength calculation and a degraded tension stiffening model is assumed in the deflection calculation, is not consistent with the flexural behavior of R-UHPC beams (El-Helou and Graybeal 2022; Peng et al. 2022a, b; Fang et al. 2023). Due to the ultrahigh compressive strength and relatively high ultimate compressive strain of UHPC, the use of the American Concrete Institute (ACI) stress block parameters may be nonconservative for over-reinforced UHPC beams with FRP bars (Mahaini et al. 2023). However, a design guide for R-UHPC flexural members with FRP bars has not been established as yet.

Based on the aforementioned discussions, it can be concluded that FRP-reinforced UHPC members have attracted wide interest owing to their high durability and mechanical properties. However, there is a lack of sufficient experimental studies concerning the flexural behavior of UHPC beams reinforced with FRP bars. Moreover, a flexural design method for FRP-reinforced UHPC beams has not been established as yet. The objective of this study is to investigate the flexural behavior of GFRP-reinforced UHPC beams and to develop a flexural strength design approach for the beams. Eight beams are tested to address the flexural behavior of GFRP-reinforced UHPC beams. The test results are presented and discussed in terms of failure modes, flexural strength, crack width, deflection, strains in UHPC and reinforcement, ductility, and energy dissipation capacity. In addition, this paper develops a flexural strength design framework for GFRP-reinforced UHPC beams.

Experimental Program

Test Specimens

A total of eight R-UHPC beams were fabricated and tested in this study. Among them, one beam was reinforced with steel bars, while the remaining beams were reinforced with GFRP bars. All beams had a rectangular cross section with dimensions of 120 mm width and 200 mm height. Each beam measured 2,000 mm long with an additional 100-mm end length. Table 1 illustrates the detailed information on the specimens. The test parameters included the internal reinforcement type (steel and GFRP), the GFRP reinforcement ratio, and the steel fiber volume fraction (1% and 2%). Fig. 2 illustrates the dimensions and reinforcement details of the test beams. The theoretical flexural capacity of the specimens was calculated using a sectional analytical procedure developed in the following section. In this study, two failure modes, including rupture of tensile GFRP bars (tension failure) and crushing of UHPC (compression failure), were expected.

Material Properties

The UHPC material utilized in the study was proprietary. Table 2 lists the concrete mix proportions. The steel fibers employed in the UHPC were straight and had a length of 13 mm, a diameter of 0.2 mm, and a supplier-provided minimum tensile strength of 2,000 MPa. The mechanical properties of the UHPC were evaluated per GB/T 31387 (CNS 2015) and T/CBMF 37 (CCPA 2018). To determine the UHPC compressive strength, six cubes measuring $100 \times 100 \times 100$ mm were tested for each batch. The elastic modulus of UHPC was determined by testing six prism specimens measuring $100 \times 100 \times 300$ mm, and the tensile behavior of the UHPC was determined using six direct tensile dog-bone-shaped specimens with a cross-sectional area of 50×50 mm and a length of 368 mm. Table 3 summarizes the measured average UHPC material properties, while Fig. 3 illustrates the tensile stress–strain behavior of the UHPCs. As observed, the UHPC with 2% fibers exhibited a low strain-softening behavior, whereas the UHPC with 1% fibers showed a strain softening–hardening behavior. Flexural reinforcements were provided using No.10 GFRP bar and No.10 steel bar. The GFRP bar had a sand-coated and helically wrapped surface, and its tensile properties were determined by testing five samples according to ASTM D7205/D7205M-21 (ASTM 2021). Fig. 4 shows the GFRP bar used in this study. Table 4 lists the measured mechanical properties of the steel and GFRP bars, which were calculated based on nominal cross-sectional areas.

Instrumentation

Electrical resistance strain gauges were installed on longitudinal bars to monitor the flexural reinforcement strains. The vertical

Downloaded from ascelibrary.org by HUNAN UNIVERSITY on 04/24/24. Copyright ASCE. For personal use only; all rights reserved.

Table 1. Specimen design details and summary of results

Specimen	Longitudinal bar	ρ (%)	V_f (%)	M_{cr} (kN · m)	M_n (kN · m)	M_u (kN · m)	Δ_{cr} (mm)	Δ_{peak} (mm)	Δ_u (mm)	E_{tot} (kN · mm)	E_{el} (kN · mm)	μ_e	Failure mode
UH-G2-vf2	2 No. 10 GFPR bar	0.77	2	11.6	39.3	39.3	1.49	47.55	47.55	3,587	294	6.61	FR
UH-G3-vf2	3 No. 10 GFPR bar	1.16	2	11.1	50.0	48.0	1.23	48.88	50.72	5,425	574	5.22	B
UH-G4-vf2	4 No. 10 GFPR bar	1.72	2	11.1	49.6	44.8	1.22	44.48	52.21	5,873	597	5.42	CC&FR
UH-G5-vf2	5 No. 10 GFPR bar	2.11	2	8.4	52.3	49.6	1.27	41.68	59.32	7,458	706	5.78	CC&FR
UH-S3-vf2	3 No. 10 Steel bar	1.16	2	8.9	32.3	25.8	1.05	16.91	32.58	2,660	257	5.68	SR
UH-G2-vf1	2 No. 10 GFPR bar	0.77	1	8.2	35.5	35.0	0.77	43.52	44.30	3,463	352	5.42	FR
UH-G3-vf1	3 No. 10 GFPR bar	1.16	1	8.4	43.2	42.1	0.99	40.86	40.98	3,706	5,656	3.77	FR
UH-G5-vf1	5 No. 10 GFPR bar	2.11	1	8.4	53.0	50.9	0.90	45.52	48.43	5,438	722	4.27	CC&FR

Note: FR = FRP rupture; CC = concrete crushing; SR = steel rupture; and B = balanced failure.

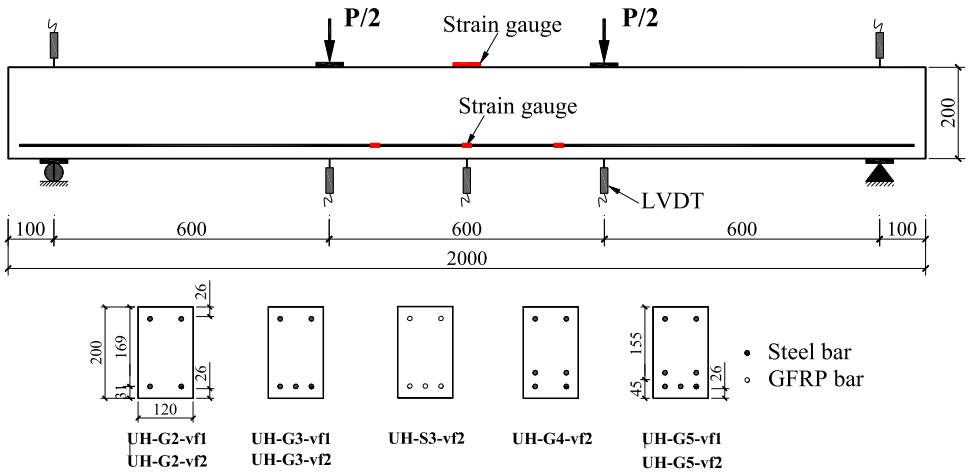


Fig. 2. Dimensions and reinforcement details of test specimens (unit: mm).

Table 2. Concrete mix proportions dimensions: kg/m^3

Cement	Water	Silica fume	Silica sand	Silica powder	Water-binder ratio	Steel fiber (%)
877	175	219	964	267	0.20	1.0–2.0

Table 3. Mechanical properties of UHPC

Material	Elastic modulus (GPa)	Compressive strength (MPa)	Tensile strength (MPa)
UHPCvf2	44.1 ± 0.6	142.4 ± 3.5	8.5 ± 0.3
UHPCvf1	42.6 ± 0.7	130.1 ± 2.4	6.9 ± 0.2

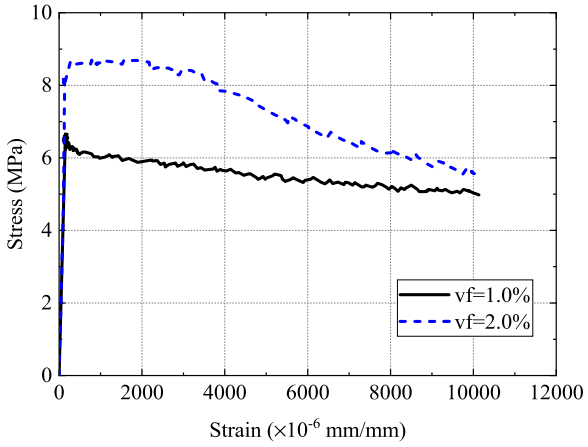


Fig. 3. Tensile stress–strain curve of UHPC.

deflections along the beam were measured using five linear variable displacement transducers (LVDTs) at midspan, loading points, and supports, as shown in Fig. 2. The hand-held microscopes with an accuracy of 0.01 mm were used to measure crack widths. Additionally, two-dimensional digital image correlation (DIC) techniques were utilized to capture the development of the cracks (Peng and Xue 2021). For the DIC measurements, a 24.1-megapixel DSLR camera with 3,840 × 2,160 pixels resolution was installed on a tripod at a distance of approximately 2.8 m from the specimen.

Test Setup and Procedure

The R-UHPC beams were subjected to four-point bending over a clear span of 1,800 mm, as shown in Fig. 2. The loading was monotonically applied by a 500 kN-testing machine. Initially, the load was applied in 5 kN increments until reaching the calculated cracking load. Subsequently, 10 kN increments were employed. When the load reached 80% of the predicted load-carrying capacity, displacement control was implemented to apply the load until final failure at a rate of 1 mm/min.

Test Results and Discussion

Failure Mode and Flexural Capacity

The UHPC beam reinforced with steel bars (UH-S3-vf2) experienced multiple cracking, yielding of the tensile steel bars, followed by crack localization, and eventually rupture of the steel bars. In UH-S3-vf2, crack localization occurred at a single plane, and the crushing of UHPC in the compression zone was very limited. For

Downloaded from ascelibrary.org by HUNAN UNIVERSITY on 04/24/24. Copyright ASCE. For personal use only; all rights reserved.



Fig. 4. GFRP bar used in this study.

Table 4. Mechanical properties of reinforcement

Material	Yield strength (MPa)	Ultimate strength (MPa)	Elastic modulus (GPa)	Ultimate tensile strain (%)
No. 10 GFRP bar	—	997 ± 18	50 ± 0.8	2
No. 10 steel bar	479 ± 15	621 ± 20	205 ± 1.6	18

the GFRP-reinforced UHPC beams, conversely, an increase in the flexural reinforcement ratio (ρ) resulted in a higher number of localized cracks forming in the pure flexure region. This behavior can be attributed to the improved capacity of beams with higher ρ values to compensate for the loss of the fiber-bridging mechanism, allowing additional localized cracks to form (Peng et al. 2023a). With an increase in ρ, the failure mode transitioned from rupture of GFRP bars after crack localization to crushing of UHPC. The failure modes of each specimen are listed in Table 1. Specimens UH-G2-vf2, UH-G2-vf1, and UH-G3-vf1 failed because of the rupture of the GFRP (tension failure) before the crushing of the UHPC, while Specimens UH-G4-vf2, UH-G5-vf2 and UH-G5-vf1 failed as a result of the sequential progressive crushing of the UHPC (compression failure) followed by the rupture of the GFRP bars. Specimen UH-G3-vf2 failed in a balanced manner, where rupture of GFRP bars in tension and crushing of UHPC in compression almost simultaneously happened.

The cracking patterns at the peak load, just before failure, and final failure are illustrated in Figs. 5(a–c), respectively. For the tension failure–controlled beams, few warning signs were available before failure, and the damage of UHPC in the compression zone was limited. For compression tension failure–controlled beams, however, evident warning signs were observed, with relatively more localized cracks and progressive damage of compressive UHPC. Therefore, when designing GFRP-reinforced UHPC beams, to increase the chances of sufficient warning before failure, it is recommended to consider failure after progressive crushing of UHPC to enhance the likelihood of detecting sufficient warning signs before failure occurs.

During the testing process, the R-UHPC beams were visually observed until the first crack appeared and the flexural cracking moment was recorded. The flexural cracking moment (excluding self-weight) was also verified from the load–midspan deflection and load–strain relationships. Table 1 summarizes the flexural cracking moment M_{cr}, peak moment M_n, and ultimate moment M_u for all tested beams. Here, the ultimate moment corresponds to the applied moment at which it decreases to 80% of the peak moment or the moment at failure, whichever is larger.

Crack Pattern and Crack Width

The cracking behavior of the GFRP-reinforced UHPC beams can be characterized by three distinguished stages: microcracking formation, stabilized microcracking, and localization cracking. The crack patterns of the test beam at $0.6M_n$ (where M_n is the measured flexural capacity) are shown in Fig. 6. It was observed that UH-G3-vf2 developed more flexural cracks than UH-S3-vf2, indicating that substitution of steel bars with GFRP bars resulted in more cracks in the beams. This is because UH-G3-vf2 exhibited a much higher flexural capacity than UH-S3-vf2.

Fig. 7 displays the applied moment versus crack width relationships for each beam. In the case of the beam with steel bars (UH-S3-vf2), a sudden increase in crack width occurred after yielding of tensile steel. This can be explained by a decrease in the stiffness of the steel bars after yielding and the formation of a single localized crack in the pure bending region. Since GFRP exhibits linear elastic behavior until failure, crack localization can be delayed, and hence, a sudden increase in the crack width was not observed in the GFRP-reinforced beams before reaching the peak load. However, after the peak load, the crack width significantly increased owing to crack localization. There was a trend that increasing the GFRP reinforcement ratio decreased the crack width at the same load level. For the over-reinforced UHPC beams (UH-G5-vf1 and UH-G5-vf2), reducing the steel fiber volume fraction from 2% to 1% had a minor effect on the maximum crack width. For the under-reinforced UHPC beams (UH-G2-vf1 and UH-G2-vf2), reducing the steel fiber volume fraction from 2% to 1% resulted in wider and more visible flexural cracks. This impact of fiber volume fraction on cracking behavior was observed in the R-UHPC beams with steel bars (Shao and Billington 2022). According to ACI CODE-440.11-22 (ACI 2022), the maximum permissible crack width for GFRP-reinforced concrete members is 0.7 mm. In this study, the measured maximum crack widths for GFRP-reinforced UHPC beams with 2% fibers reached 0.7 mm after almost 71%–78% of the maximum load, which was typically higher than the service loads. Therefore, the GFRP-reinforced beams made with strain-hardening UHPC generally satisfied the crack width criteria specified in ACI CODE-440.11-22 (ACI 2022) at the serviceability levels.

Load–Deflection Curves

The applied load–midspan deflection curves for all tested beams are plotted in Fig. 8. Among them, the UHPC beam reinforced with steel bars (UH-S3-vf2) exhibited a linearly elastic load–deflection response until cracking occurred at a load of 29.6 kN. As the applied load increased, the beam's flexural stiffness gradually decreased because of the development of dense and closely distributed microcracks. Subsequently, the load–midspan deflection response became approximately linear until the yielding of the steel bars, which can be defined as the stabilized microcracking stage (Peng et al. 2022a). The tensile steel bar yielded at an applied load of 97.0 kN. After yielding, the stiffness of the beam was considerably degraded. The beam reached its maximum capacity when subjected to an applied load of 107.6 kN and a midspan deflection of 16.91 mm. Fig. 5(a) shows the crack pattern of the

Downloaded from ascelibrary.org by HUNAN UNIVERSITY on 04/24/24. Copyright ASCE. For personal use only; all rights reserved.

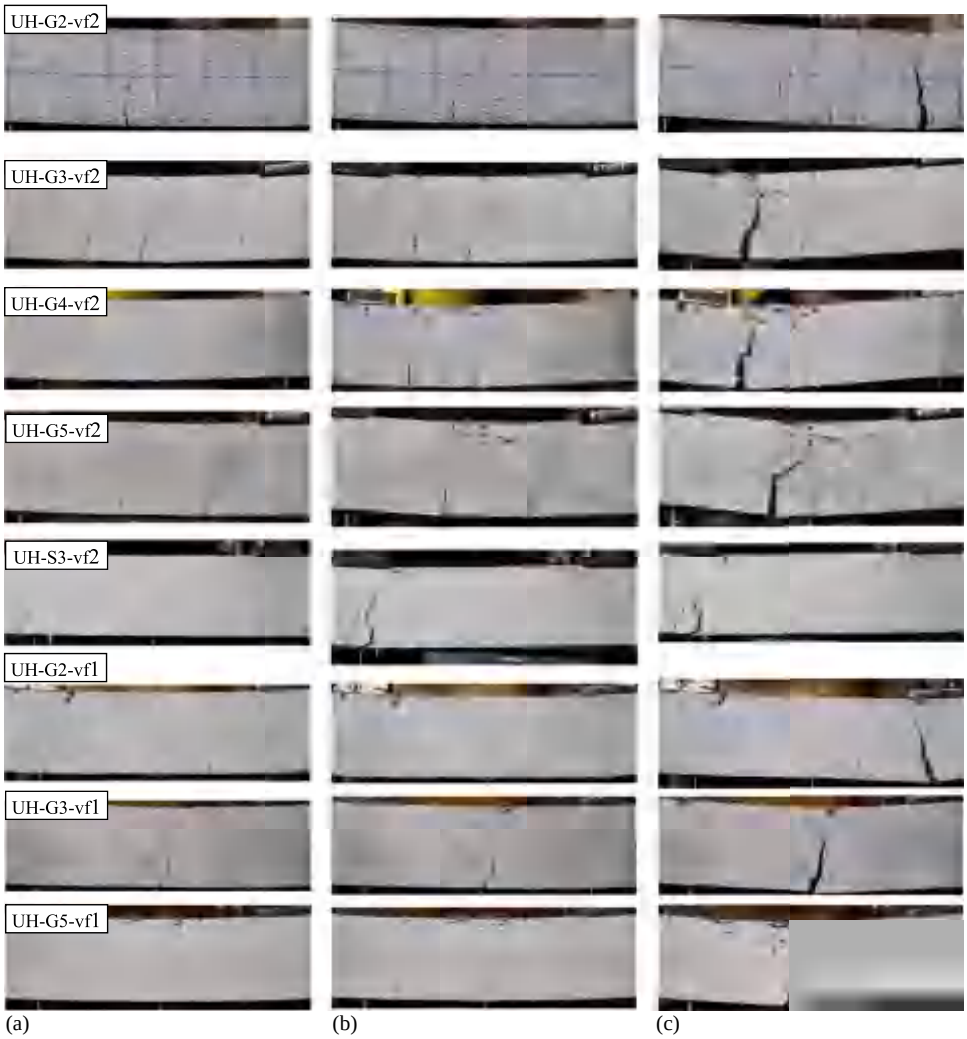


Fig. 5. Crack pattern and failure mode: (a) at peak load; (b) near failure; and (c) final failure.

steel-reinforced UHPC beam at the peak load. As observed, a solitary localized crack was formed, a phenomenon commonly referred to as crack localization (El-Helou and Graybeal 2022; Fang et al. 2023). After crack localization, the load-carrying capacity of the beam continuously decreased. This is because the increase in the force carried by the steel fails to compensate for the fiber-bridging loss as the fibers experience pullout or rupture.

For GFRP-reinforced UHPC beams, the load−deflection response exhibited an approximately linear behavior characterized by a steep slope before cracking. As a result of successively cracking, the flexural stiffness of the beams gradually decreased. After the formation of microcracks, the load–midspan deflection response became approximately linear until the peak load was reached. The beams failing due to GFRP rupture showed typical bilinear load–deflection relationships, and very limited postpeak behavior was observed in these specimens. However, the beams failing due to gradual crushing of UHPC exhibited obvious postpeak behavior, which was not found in conventional concrete beams reinforced with GFRP bars (El-Nemr et al. 2013). This phenomenon is attributed to the presence of steel fibers in the UHPC, which effectively mitigate the brittleness of the concrete under compression. As a result, instead of experiencing a rapid loss of strength following the crushing of conventional reinforced concrete beams, UHPC exhibits a gradual compression-softening behavior. The UHPC fiber-bridging loss owing to crack localization resulted in an abrupt decrease of approximately 10.5% and 8.8% in the applied load in Specimens UH-G4-vf2 and UH-G5-vf2, respectively. After the crack localization-induced applied load reduction, the applied load marginally increased as the displacement increased until the GFRP bars ruptured, indicating that the fiber-bridging mechanism was very limited at this stage. Notably, a similar phenomenon was experimentally observed in prestressed UHPC beams with steel strands (El-Helou and Graybeal 2022; Fang et al. 2023).

Strains in Reinforcement and UHPC

The midspan strains in the tensile flexural reinforcements versus the applied moment are shown in Fig. 9. Prior to cracking, the reinforcement strains were trivial. After cracking, the strain increased rapidly. Because the final failure of all GFRP-reinforced UHPC beams was rupture of GFRP, the measured maximum strains in the GFRP reinforcements approached their ultimate tensile strain. Fig. 10 presents the compressive concrete strains measured at the midspan in relation to the applied load for all test beams. Prior to cracking, all strain gauges exhibited a linear behavior. After cracking, the applied load–UHPC strain behavior of GFRP-reinforced UHPC beams became approximately linear until the peak load was reached. The maximum concrete compressive strain in Specimens UH-G3-vf2, UH-G2-vf2, UH-G2-vf1, and UH-G3-vf1 was 2,477, 3,910, 3,412, and 3,996 $\mu\varepsilon$, respectively. These values

Downloaded from ascelibrary.org by HUNAN UNIVERSITY on 04/24/24. Copyright ASCE. For personal use only; all rights reserved.



Fig. 6. Crack patterns of each beam at $0.6M_n$.

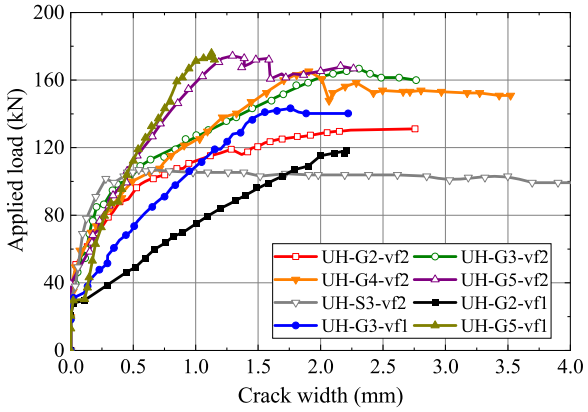


Fig. 7. Maximum crack width.

were lower than the ultimate compressive strain of UHPC. For specimens that failed because of the crushing of the UHPC, the maximum UHPC compressive strain ranged from 4,507 to 5,243 $\mu\varepsilon$, which is much higher than the assumed ultimate compressive strain of normal concrete in flexural design. Additionally, the maximum UHPC compressive strain in UH-G5-vf2 was higher than that in UH-G5-vf1, which is expected because the use of a higher steel fiber fraction results in an increase in the ultimate UHPC compressive strain.

Moment–Curvature Behavior

Fig. 11 illustrates the moment–curvature behavior of the tested beams. The tension failure–controlled GFRP-reinforced UHPC beams exhibited an approximately bilinear moment–curvature relationship, while those that failed due to progressive crushing of UHPC exhibited postpeak ductility behavior. Furthermore, the compression failure–controlled beams had significantly larger ultimate curvatures than the tension failure–controlled beams, indicating that the compression failure mode is a preferred failure mode. When crushing of UHPC controlled the failure, an increase in the fiber content resulted in a higher ultimate curvature. For example, the ultimate curvature of Specimen UH-G5-vf2 was 96% higher than that of Specimen UH-G5-vf1, indicating that increasing the fiber content is beneficial to the deformability of the compression-controlled beams. This is because the use of a higher steel fiber fraction can improve the ultimate compressive strain and toughness of UHPC.

Ductility and Energy Dissipation Capacity

Ductility is a crucial index that evaluates the ability of a structure or a structural member to undergo inelastic deformation before reaching failure. Typically, ductility can be defined in a displacement-based manner or an energy-based manner for a structural member (Patil et al. 2020). The displacement ductility is typically defined as the ratio of the displacement at the ultimate state to the displacement at yielding of tensile bars. However, for UHPC beams reinforced with GFRP bars that exhibit a linear stress–strain relationship until rupture, such displacement-based ductility cannot be quantified (Patil et al. 2020). In this study, the ductility of GFRP-reinforced UHPC beams is indirectly measured through an energy-based ductility index that is defined as the ratio of total energy to elastic energy, as illustrated in Fig. 12. Naaman and Jeong (1995) recommended the following equation to calculate the ductility index, μ_e:

$$\mu_e = \frac{1}{2}\left(\frac{E_{tot}}{E_{el}} + 1\right) \quad (1)$$

where E_{el} = elastic energy, which is equal to A_2 in Fig. 12; and E_{tot} = total energy under the load–deflection curve, which is equal to $(A_1 + A_2 + A_3)$ in Fig. 12. The estimated elastic energy, total energy, and deformation factor are summarized in Table 1. As observed, the compression failure–controlled beams dissipated more energy before failure than the tension failure–controlled beams, indicating that compressive failure is a more favorable mode of failure in contrast to tension failure.

Discussion of Test Results

Effect of Reinforcement Type

The applied load–midspan deflection curves for two UHPC beams reinforced with different types of internal reinforcing bars are depicted in Fig. 8(a). Prior to cracking, the load–deflection curves of the two beams are nearly identical. After cracking, the UHPC beam reinforced with steel bars exhibits significantly higher flexural stiffness. This is because the modulus of elasticity of steel bars is approximately four times that of GFRP bars. Replacing steel bars with GFRP bars results in a 54.9% increase in flexural capacity and a 55.7% increase in ultimate displacement. This difference can be attributed to the decrease in stiffness of the steel bars after yielding, which means the force carried by the steel bars cannot increase sufficiently to counterbalance the reduction of the tensile stress carried by the fibers during pullout. By contrast, because GFRP bars do not yield, the force carried by the GFRP bars increases to compensate for the loss of the fiber-bridging mechanism, thereby maintaining stiffness until peak load is reached. Similar findings were also reported in CFRP-prestressed UHPC beams (Sturm et al. 2020). Due to premature failure of crack localization

Downloaded from ascelibrary.org by HUNAN UNIVERSITY on 04/24/24. Copyright ASCE. For personal use only; all rights reserved.

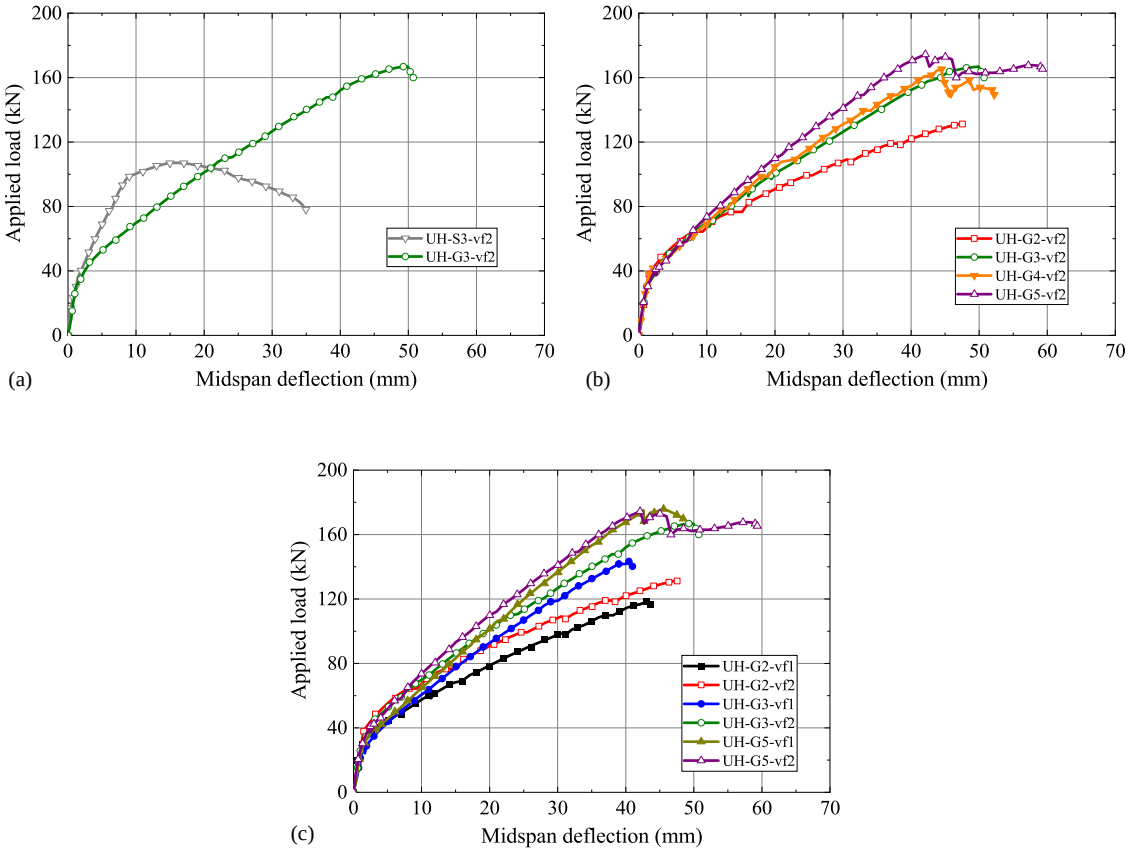


Fig. 8. Applied load–deflection at midspan: (a) effect of reinforcement type; (b) effect of reinforcement ratio; and (c) effect of fiber volume fraction.

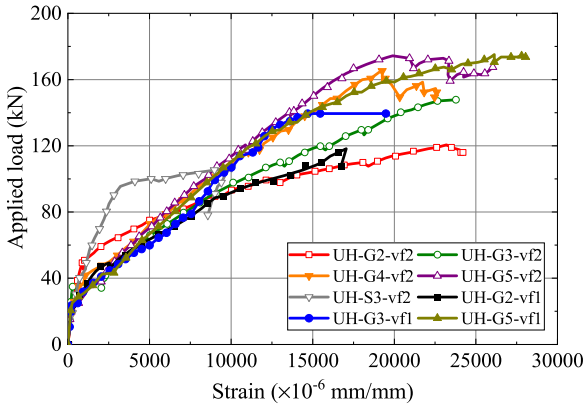


Fig. 9. Applied load–strain in flexural reinforcements.

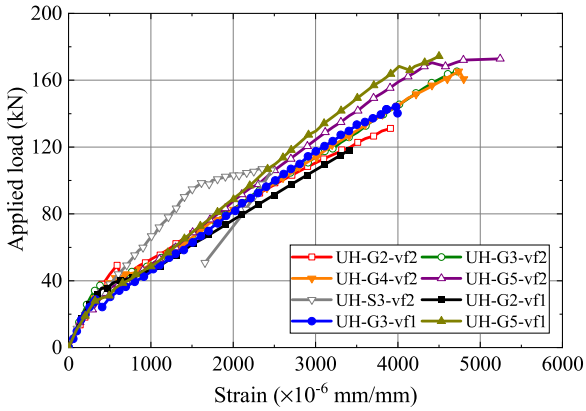


Fig. 10. Strain responses in concrete at the midspan.

followed by rupture of steel bars, the ultimate deflection of Specimen UH-S3-vf2 is 36% lower than that of its GFRP-reinforced counterpart (UH-G3-vf2). As a result, UH-S3-vf2 exhibits the lowest total energy dissipation upon failure, only about 51.0% of that dissipates in UH-G3-vf2. Although there is no yield for GFRP bars, the estimated energy-based ductility index of UH-G3-vf2 is comparable with that of UH-S3-vf2, as observed in Table 1. This is because more flexural cracks are developed in UH-G3-vf2 compared with UH-S3-vf2, as shown in Fig. 6.

Effect of Reinforcement Ratio

Increasing the GFRP reinforcement ratio changes the failure mode from rupture of GFRP to progressive crushing of UHPC. The effect of the GFRP reinforcement ratio ρ on the applied load–midspan deflection curves is plotted in Fig. 8(b). As observed, the cracking loads are minimally affected by the GFRP reinforcement ratio. However, there is a trend that the flexural capacity increases with increasing the GFRP reinforcement ratio. When the ρ increases from 0.77% to 1.16% and 2.11%, the flexural capacity of the beams with a 2% fiber volume fraction increases by 27.2% and 33.0%, respectively, and the flexural capacity of the beams with a 1% fiber volume fraction increases by 21.8% and 49.4%, respectively. There is a trend that a higher ρ results in increased energy dissipation. When the ρ increases from 0.77% to 1.16% and 2.11%, the total energy dissipation of the beams with a 2% fiber volume fraction increases by 51% and 108%, respectively. This is attributed to a much higher load-carrying and

Downloaded from ascelibrary.org by HUNAN UNIVERSITY on 04/24/24. Copyright ASCE. For personal use only; all rights reserved.

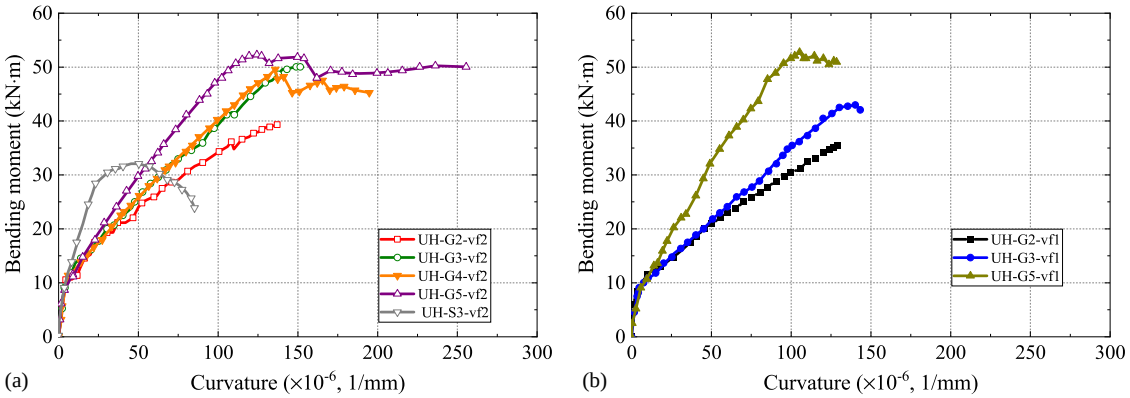


Fig. 11. Moment–curvature response: (a) V_f = 2.0%; and (b) V_f = 1.0%.

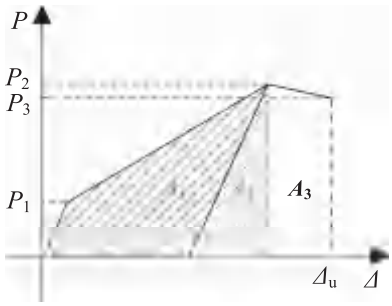


Fig. 12. Definition of ductility index.

deformability capacity of the beam with a higher ρ. However, no general trend can be identified in the energy-based ductility index related to the variation of GFRP reinforcement ratios, as observed in Table 1.

Effect of Steel Fiber Volume Fraction

Available studies have shown that reducing the fiber volume fraction in UHPC altered the failure path from crack localization to gradual crushing of UHPC (Shao and Billington 2022; Peng et al. 2023a). For the tested GFRP-reinforced UHPC beams with a reinforcement ratio of 1.16%, however, reducing the fiber volume fraction from 2.0% to 1.0% altered the failure path from balanced failure (simultaneous rupture of GFRP bars and crushing of UHPC) to tension failure (crack localization followed by GFRP rupture). This is because GFRP bars exhibit a linear stress–strain relationship up to failure without yielding, which can compensate for the fiber-bridging loss and therefore delay crack localization. Fig. 8(c) shows the load–deflection curves with different fiber volume fractions. As observed, increasing the fiber volume fractions enhances the postcracking stiffness of GFRP-reinforced UHPC beams. This is because steel fibers in UHPC can sustain postcracking tensile stress and effectively resist crack development, and increasing the fiber fraction increases the tensile strength and tensile ductility of UHPC. When the failure is governed by rupture of GFRP, as the fiber volume fraction increases from 1.0% to 2.0%, the flexural capacity of the beam with GFRP reinforcement ratio of 0.77% and 1.16% is increased by 10.9% and 15.8%, respectively. When the failure is governed by progressive crushing of UHPC (ρ = 2.11%), however, the variation in fiber volume fraction has minimal impact on the load capacity. This phenomenon indicates that the fiber contribution is negligible for compression-failure controlled beams. From Fig. 8(c), it can be observed that increasing fiber content improves the values of the ultimate deflection because of the higher ultimate compressive strain of UHPC. As observed in Table 1, an increase in the fiber content results in a higher ductility index for GFRP-reinforced UHPC beams. This is expected because the energy is consistently consumed during the process of fiber pullout and stretching.

Table 5. Comparison of experimental and predicted results

Specimen	$M_{cr}/M_{cr,pred}$	$M_n/M_{n,pred}$		ρ/ρ_b		Δ_s (mm)	$\Delta_{s,pred}/\Delta_s$	
		Including fibers	Excluding fibers	Including fibers	Excluding fibers		Peng et al. (2022a)	ACI CODE-440.11-22 (ACI 2022)
UH-G2-vf2	1.14	1.02	1.55	0.69	0.51	9.56	1.18	2.33
UH-G3-vf2	1.09	1.06	1.33	1.03	0.87	14.22	1.18	1.62
UH-G4-vf2	1.09	1.05	1.10	1.38	1.28	13.62	1.13	1.55
UH-G5-vf2	0.82	1.01	1.05	1.62	1.57	13.23	1.07	1.44
UH-S3-vf2	0.87	0.98	1.73	—	—	3.30	0.91	1.15
UH-G2-vf1	0.99	0.98	1.40	0.65	0.61	10.90	1.10	1.66
UH-G3-vf1	1.02	0.95	1.15	0.97	0.92	13.41	1.15	1.55
UH-G5-vf1	1.02	1.06	1.07	1.72	1.67	16.63	0.98	1.32
Mean	1.00	1.05	1.30	—	—	—	1.09	1.58
Standard deviation	0.103	0.040	0.234	—	—	—	0.093	0.325

Note: Δ_s = midspan deflection at the service load of $0.5M_n$.

J. Compos. Constr., 2024, 28(4): 04024019

Downloaded from ascelibrary.org by HUNAN UNIVERSITY on 04/24/24. Copyright ASCE. For personal use only; all rights reserved.

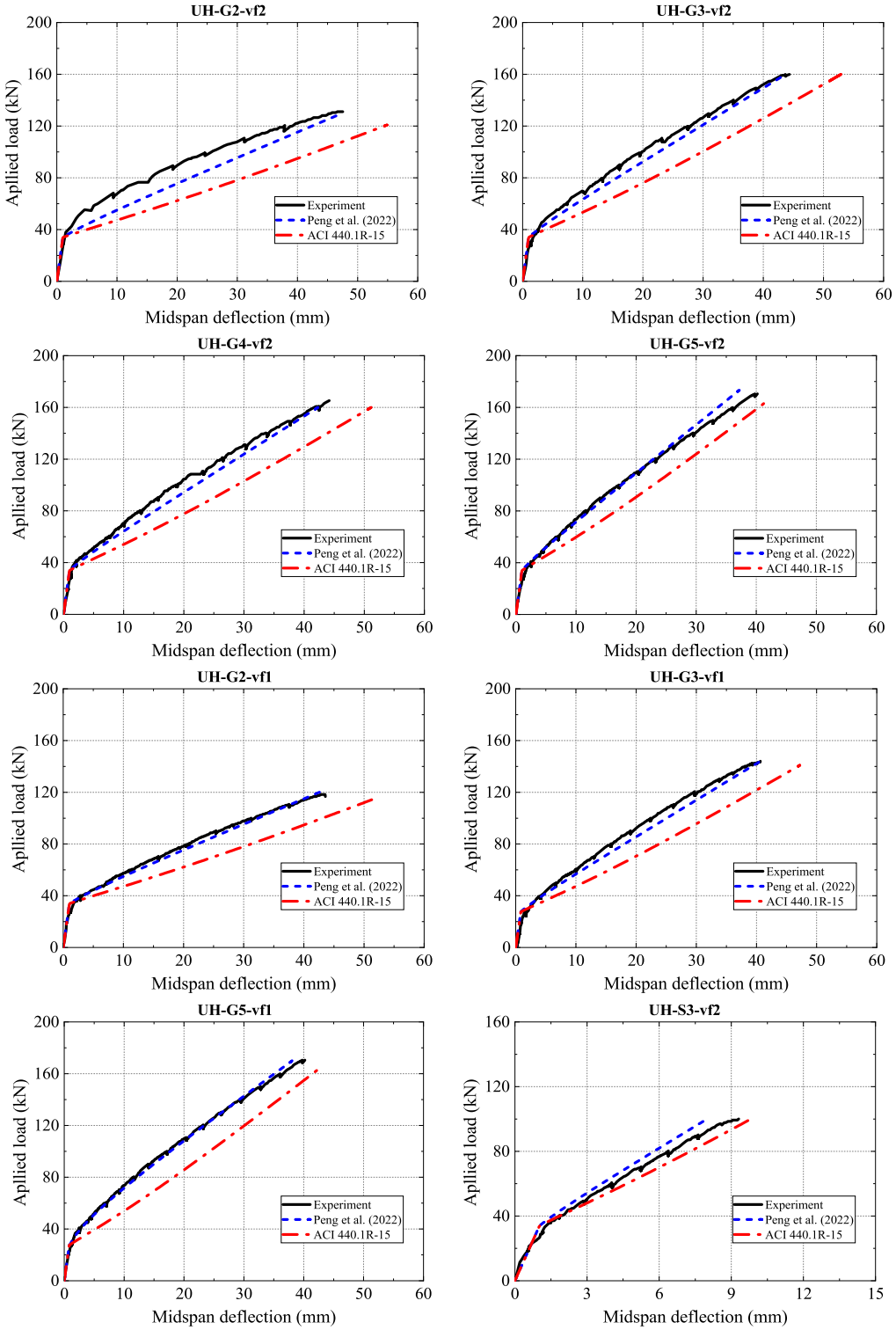


Fig. 13. Comparison of load–deflection curve.

Analytical Comparisons

Cracking Moment

According to Peng et al. (2022a), the cracking moment of R-UHPC beams can be predicted by

$$M_{cr} = \frac{\zeta f_{tu} I_g}{y_t} \quad (2)$$

where f_{tu} = ultimate tensile strength of UHPC; I_g = gross moment of inertia of the uncracked section; y_t = distance from neutral axis to extreme tension fiber; and ζ = plastic influence coefficient, and can be taken as 1.5 (Peng et al. 2022a).

Table 5 compares the experimental and predicted cracking moments. Overall, the predictions demonstrate good agreement with the measured results. The average and standard deviation of the ratio of experimental to predicted cracking moment are 1.00 and 0.103, respectively.

Downloaded from ascelibrary.org by HUNAN UNIVERSITY on 04/24/24. Copyright ASCE. For personal use only; all rights reserved.

Deflection

The first author previously proposed an integration-based effective moment of inertia, I_e, to predict the instantaneous deflection of steel-reinforced UHPC flexural members (Peng et al. 2022a). In this approach, a full tension-stiffening response is assumed, and consequently, the effective moment of inertia I_e can be estimated by (Peng et al. 2022a)

$$I_e = \frac{I_{cr}}{1 - \gamma\left(1 - \frac{I_{cr}}{I_g}\right)\frac{M_{cr}}{M_a}} \le I_g \tag{3}$$

where M_a = applied bending moment; I_{cr} = transformed moment of inertia of the cracked section; and γ = a factor that depends on the boundary conditions and the type of applied load.

For a simply supported R-UHPC beam subjected to symmetric four-point bending, the factor γ can be estimated using the following equation:

$$\gamma = \frac{3(L/a)^2 - 4(M_{cr}/M_a)^2}{3(L/a)^2 - 4} \tag{4}$$

where a = shear span; and L = clear span.

Based on the findings of the research conducted by Bischoff (2005), ACI CODE-440.11-22 (ACI 2022) recommends the following equation to calculate the effective moment of inertia:

$$I_e = \frac{I_{cr}}{1 - \gamma\left(1 - \frac{I_{cr}}{I_g}\right)\left(\frac{M_{cr}}{M_a}\right)^2} \le I_g \tag{5}$$

Then, the deflection of a flexural member can be calculated using classical structural analysis. For a simply supported beam under symmetric four-point bending, the midspan deflection can be calculated by

$$\Delta = \frac{PL^3}{48E_cI_e}\left[3\left(\frac{a}{L}\right) - 4\left(\frac{a}{L}\right)^3\right] \tag{6}$$

where P = applied load; and E_c = elastic modulus of UHPC.

Fig. 13 illustrates a comparison between the predicted load–midspan deflection curves and the experimental curves for the tested beams. As observed, the predicted deflections obtained from Peng et al.'s method align with the test results, while the effective moment of inertia equation provided in ACI CODE-440.11-22 (ACI 2022) is overly conservative for GFRP-reinforced UHPC beams. This is because ACI CODE-440.11-22 (ACI 2022) underestimates the tension stiffening in reinforced UHPC beams (Peng et al. 2022a). Table 5 compares the measured and predicted values for the midspan deflection at the service load of $0.5M_n$. The approach proposed by Peng et al. can consistently and accurately predict the deflection of GFRP-reinforced UHPC members. The mean and standard deviation of the predicted-to-measured deflection ratio obtained from Peng et al.'s approach are 1.09 and 0.093, respectively, while the mean and standard deviation of the ratio obtained from ACI CODE-440.11-22 (ACI 2022) are 1.58 and 0.325, respectively.

Flexural Strength

An analysis procedure is developed to predict the flexural capacity for FRP-reinforced UHPC beams. Fig. 14 illustrates the distribution of strain and stress within the FRP-reinforced UHPC section. The procedure is based on the principles of strain compatibility, equilibrium of forces, and the utilization of assumed stress–strain models for the materials involved. Failure occurs when the strain

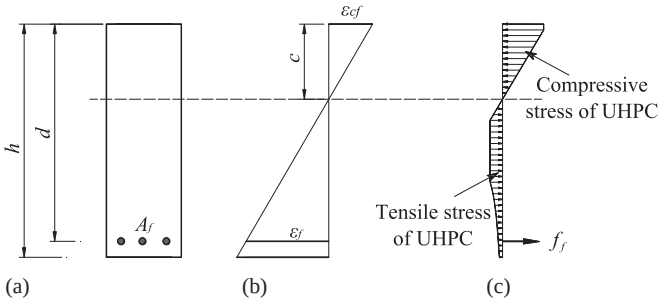


Fig. 14. Distribution of strain and stress across the normal cross section: (a) cross section; (b) strain; and (c) stress.

in the extreme compressive UHPC fiber reaches its ultimate compressive strain ε_{cu} or the tensile strain in GFRP reaches its ultimate tensile strain ε_{fu}. Because of the inclusion of steel fibers, the ultimate compressive strain of UHPC is higher than the value of 0.003 recommended by ACI CODE-440.11-22 (ACI 2022). The ultimate compressive strain ε_{cu} can be determined through experiment. In this study, an ultimate compressive strain ε_{cu} of 0.0045 was used based on the measured results.

In the analysis procedure, the stress–strain relationship of GFRP is assumed to be linear elastic until failure, while mild steel bars are modeled to exhibit an elastic-perfectly plastic response. For UHPC in compression, an elastic-perfectly plastic stress–strain curve can be used as an idealized representation (Shao and Billington 2022; Fang et al. 2023), as shown in Fig. 15(a). The tensile stress–strain behavior of UHPC is characterized by a trilinear relationship (Fang et al. 2023), as shown in Fig. 15(b):

$$\sigma = \begin{cases} E_c\varepsilon, & \text{for } 0 \le \varepsilon \le \varepsilon_{t,cr} \\ f_{cr} + \dfrac{(\varepsilon - \varepsilon_{t,cr})}{(\varepsilon_{t,loc} - \varepsilon_{t,cr})} \times (f_{tu} - f_{cr}), & \text{for } \varepsilon_{t,cr} \le \varepsilon \le \varepsilon_{t,loc} \\ \dfrac{(\varepsilon_{t,lim} - \varepsilon)}{(\varepsilon_{t,lim} - \varepsilon_{t,loc})} \times f_{tu}, & \text{for } \varepsilon_{t,loc} < \varepsilon \le \varepsilon_{t,lim} \end{cases} \tag{7}$$

where f_{cr} = cracking tensile strength of UHPC; $\varepsilon_{t,cr}$ = cracking tensile strain of UHPC; $\varepsilon_{t,loc}$ = UHPC localization strain at which the tensile stress begins to continuously decrease with the increase of the strain; and $\varepsilon_{t,lim}$ = UHPC tensile strain at which the tensile stress is reduced to zero.

The strains $\varepsilon_{t,loc}$ and $\varepsilon_{t,lim}$ can be determined either through direct material testing of uniaxial tensile UHPC specimens or through inverse analysis of material testing conducted on small-scale UHPC beams subjected to flexure. In cases where such tests are not available, a minimum localization strain of 0.0025 can be assumed (El-Helou et al. 2022). The strain $\varepsilon_{t,lim}$ is estimated by Gowripalan and Gilbert (2000) as follows:

$$\varepsilon_{t,lim} = \frac{l_f}{1.2h} \tag{8}$$

where l_f = length of steel fiber; and h = depth of the beam section.

Table 5 presents a comparison between the experimental and predicted flexural capacities. Overall, the predictions demonstrate good agreement with the test results. The average of the ratio of experimental-to-predicted flexural capacity is 1.05, with a standard deviation of 0.040. To highlight the effect of steel fibers on flexural strength and failure mode prediction, a sectional analysis was conducted on the same beam, assuming zero tensile resistance of UHPC ($f_{tu} = 0$). The results of this analysis are also presented in Table 5. It is evident that neglecting the contribution of fibers leads to an underestimation of the flexural strength of FRP-reinforced UHPC beams, particularly in cases where the FRP reinforcement ratio is relatively low.

Downloaded from ascelibrary.org by HUNAN UNIVERSITY on 04/24/24. Copyright ASCE. For personal use only; all rights reserved.

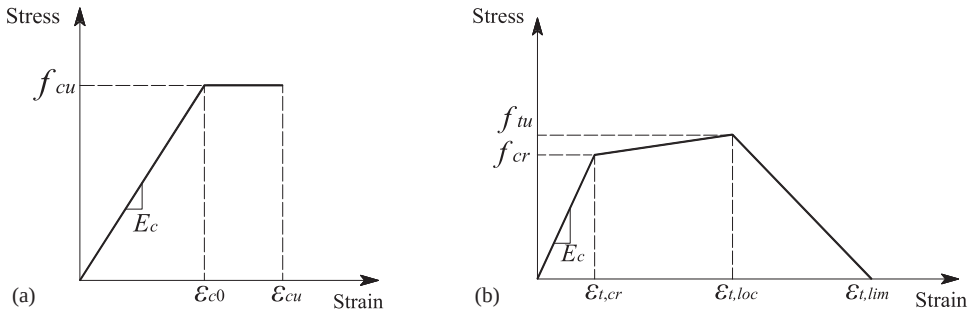


Fig. 15. Schematic stress–strain diagrams of UHPC: (a) compression; and (b) tension.

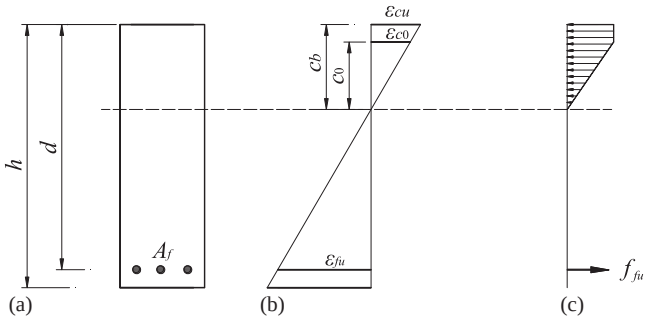


Fig. 16. Distribution of strain and stress across the normal cross section at balanced condition: (a) cross section; (b) strain; and (c) stress.

The flexural strength of an FRP-reinforced UHPC beam is heavily dependent on whether the failure is controlled by rupture of FRP or crushing of UHPC. The balanced failure condition between FRP rupture and UHPC crushing is obtained when the strains in the UHPC and FRP simultaneously reach their maximum values. If the reinforcement ratio ρ is less than the balanced reinforcement ratio ρ_b, FRP rupture governs the failure. Otherwise, UHPC crushing governs. Table 5 lists the ratio of provided-to-balanced reinforcement (ρ/ρ_b). Herein, the balanced reinforcement ratio is obtained from the proposed analysis procedure, taking into account the tensile resistance of UHPC. As listed in Table 5, the proposed method for recognizing failure modes provides accurate predictions regarding the failure mode of GFRP-reinforced UHPC beams.

Minimum Flexural Reinforcement Ratio

The FRP-reinforced UHPC beam with a relatively low reinforcement ratio typically fails in flexure because of FRP rupture after crack localization, which may lead to catastrophic failure and low deformability. Compared with the failure due to FRP rupture, the progressive failure due to crushing of UHPC is a more favorable failure mode. To ensure a progressive failure, a minimum reinforcement ratio is required. Theoretically, if the reinforcement ratio is higher than the balanced reinforcement ratio, the failure is controlled by progressive crushing of UHPC. Therefore, the balanced reinforcement ratio can be considered the minimum reinforcement ratio. However, there is currently no straightforward equation available for determining the balanced reinforcement ratio of FRP-reinforced UHPC sections.

Under balanced failure condition, the ultimate tensile strain of FRP ε_{fu} is attained. Under this scenario, the localized flexural crack typically exhibits wide openings. If the tensile resistance of UHPC is neglected, Figs. 16(b and c) illustrate the strain and stress distributions across the depth of a section under the balanced condition, respectively. Under the assumption that the cross section remains planar and orthogonal to the beam axis after bending deformation, the following equation is obtained:

$$\frac{\varepsilon_{fu}}{d - c_b} = \frac{\varepsilon_{cu}}{c_b} = \frac{\varepsilon_{c0}}{c_0} \tag{9}$$

where ε_{c0} = UHPC compressive strain at which the compressive strength is reached; d = effective depth; c_b = depth of the neutral axis; and c_0 = depth between the neutral axis and the position where ε_{c0} is located, as shown Fig. 16(b).

When the tensile resistance of UHPC is neglected, Eq. (10) is obtained based on the equilibrium of internal forces:

$$A_f f_{fu} = \frac{1}{2} f_{cu} b c_0 + f_{cu} b (c_b - c_0) \tag{10}$$

where A_f = area of tensile FRP reinforcements; b = beam width; and f_{cu} = compressive strength of UHPC.

Then, the minimum flexural reinforcement ratio can be calculated by

$$\rho_{min} = \frac{f_{cu}}{f_{fu}} \frac{\varepsilon_{cu}}{\varepsilon_{cu} + \varepsilon_{fu}} \left(1 - \frac{\varepsilon_{c0}}{2\varepsilon_{cu}}\right) \tag{11}$$

where f_{fu} = ultimate tensile strength of FRP.

Table 5 compares the predicted and actual failure modes when the tensile resistance of UHPC is neglected. As observed, ignoring the UHPC tensile resistance may lead to an incorrect prediction of failure mode. For example, Specimen UH-G3-vf2 with $\rho/\rho_b = 0.87$ actually failed in a balanced failure manner. This is because the balanced ratio given by Eq. (11) is slightly higher than the actual balanced ratio since it neglects the fiber-bridging mechanism. In design practice, Eq. (11) can be considered the minimum reinforcement ratio required to ensure progressive failure of FRP-reinforced UHPC beams.

Conclusions

In this study, eight beams are constructed and tested to investigate the flexural behavior of UHPC beams reinforced with GFRP bars. In addition, a flexural strength design framework is developed for GFRP-reinforced UHPC beams. Based on the experimental and analytical results, the following conclusions can be drawn:

1. As the GFRP reinforcement ratio increases, the failure mode of GFRP-reinforced UHPC beams transitions from tension failure to compression failure. In addition, reducing the fiber volume fraction from 2.0% to 1.0% alters the failure path from balanced failure to tension failure.
2. With the same reinforcing ratio, replacing steel bars with GFRP bars results in a 54.9% increase in flexural capacity and a 55.7% increase in ultimate displacement. This is because the use of GFRP bars as flexural reinforcement in UHPC beams can effectively delay crack localization.

Downloaded from ascelibrary.org by HUNAN UNIVERSITY on 04/24/24. Copyright ASCE. For personal use only; all rights reserved.

3. There is a trend that increasing the GFRP reinforcement ratio ρ results in an increase in the flexural capacity. When the ρ increases from 0.77% to 1.16% and 2.11%, the flexural capacity of the beams with a 2% fiber volume fraction increases by 27.2% and 33.0%, respectively.
4. When the failure is controlled by rupture of GFRP bars, as the fiber volume fraction increases from 1.0% to 2.0%, the flexural capacity of the beam with GFRP reinforcement ratio of 0.77% and 1.16% is increased by 10.9% and 15.8%, respectively. When the failure is controlled by progressive crushing of UHPC, however, the fiber volume fraction has a negligible effect on flexural capacity.
5. The effective moment of inertia equation proposed by Peng et al. (2022a) provides consistent predictions of the instantaneous deflection of GFRP-reinforced UHPC beams, while the equation specified in ACI CODE-440.11-22 (ACI 2022) is too conservative for GFRP-reinforced UHPC beams. At the service load of $0.5M_n$, the average and standard deviation of the predicted-to-measured deflection ratio obtained from Peng et al.'s approach is 1.09 and 0.093, respectively, while the average and standard deviation of the ratio obtained from ACI CODE-440.11-22 (ACI 2022) are 1.58 and 0.325, respectively.
6. The developed model for predicting the flexural capacities of GFRP-reinforced UHPC beams yields close predictions to the experimental results. The mean value of the experimental-to-predicted flexural capacity ratio obtained from the developed model is 1.05, with a standard deviation of 0.040.
7. Neglecting the UHPC tensile resistance underestimates the flexural strength of GFRP-reinforced UHPC beams, especially for the cases where the reinforcement ratio is low. In addition, neglecting the UHPC tensile resistance may lead to an incorrect prediction of the failure mode of GFRP-reinforced UHPC beams. A minimum flexural reinforcement ratio [Eq. (11)] is proposed to ensure progressive failure owing to gradual crushing of UHPC for FRP-reinforced UHPC flexural members.
8. The findings presented in this study are derived from a limited number of beam samples, each representing a given configuration. Further research on full-scale members is needed to develop and validate the flexural design method for FRP-reinforced UHPC beams.

Data Availability Statement

All data, models, and codes generated or used during the study appear in the published article.

Acknowledgments

The authors gratefully acknowledge the financial support provided by the National Natural Science Foundation of China (Nos. 52008165 and 52130806) and the Program Fund of Non-Metallic Excellence and Innovation Center for Building Materials (2023TDA4-1).

Notation

The following symbols are used in this paper:

A_f = area of tensile FRP reinforcements;
a = shear span;
b = beam width;
c_b = depth of the neutral axis;
c_0 = depth between the neutral axis and the position where ε_{c0} is located;
d = effective depth;
E_c = elastic modulus of UHPC;
E_{el} = elastic energy;
E_{tot} = total energy;
f_{cr} = cracking tensile strength of UHPC;
f_{cu} = compressive strength of UHPC;
f_f = tensile stress in FRP;
f_{fu} = ultimate tensile strength of FRP;
f_{tu} = ultimate tensile strength of UHPC;
h = depth of the beam section;
I_{cr} = transformed moment of inertia of the cracked section;
I_g = gross moment of inertia of uncracked section;
I_e = effective moment of inertia;
L = clear span;
l_f = length of steel fiber;
M_a = applied bending moment;
M_{cr} = cracking moment;
$M_{cr,pred}$ = predicted cracking moment;
M_n = maximum moment;
$M_{n,pred}$ = predicted maximum moment;
M_u = ultimate moment;
P = applied load;
V_f = steel fiber volume fraction;
y_t = distance from neutral axis to extreme tension fiber;
σ = stress in UHPC;
ε = strain in UHPC;
ε_{cf} = UHPC strain at the extreme compression fiber of the section;
ε_{cu} = ultimate compressive strain of UHPC;
ε_{c0} = UHPC compressive strain at which the compressive strength is reached;
ε_f = tensile strain in FRP;
ε_{fu} = ultimate tensile strain of FRP;
$\varepsilon_{t,cr}$ = cracking tensile strain of UHPC;
$\varepsilon_{t,loc}$ = localization strain of UHPC;
$\varepsilon_{t,lim}$ = UHPC tensile strain at which the tensile stress is reduced to zero;
Δ = midspan deflection;
Δ_{cr} = cracking deflection;
Δ_{peak} = deflection corresponding to the maximum capacity;
Δ_s = service deflection;
$\Delta_{s,pred}$ = predicted service deflection;
Δ_u = ultimate deflection;
μ_e = energy-based ductility index;
ζ = plastic influence coefficient;
ρ = flexural reinforcement ratio;
ρ_b = balanced reinforcement ratio;
ρ_{min} = minimum FRP reinforcement ratio required to ensure progressive failure; and
γ = factor that depends on the boundary conditions and the type of applied load.

References

ACI (American Concrete Institute). 2022. Building code requirements for structural concrete reinforced with glass *fi*ber-reinforced polymer (GFRP) bars—Code and commentary. ACI CODE-440.11. Farmington Hills, MI: ACI.

ASTM. 2017. Standard practice for fabricating and testing specimens of ultra-high performance concrete. ASTM C1856/C1856M. West Conshohocken, PA: ASTM.

Downloaded from ascelibrary.org by HUNAN UNIVERSITY on 04/24/24. Copyright ASCE. For personal use only; all rights reserved.

ASTM. 2021. Standard test method for tensile properties of *fi*ber reinforced polymer matrix composite bars. ASTM D7205/D7205M-21. West Conshohocken, PA: ASTM.
Bischoff, P. H. 2005. "Reevaluation of deflection prediction for concrete beams reinforced with steel and fiber reinforced polymer bars." J. Struct. Eng. 131 (5): 752–767. https://doi.org/10.1061/(ASCE)0733-9445(2005)131:5(752).
Cao, X., Y.-C. Ren, K. Qian, F. Fu, X.-F. Deng, and W.-J. Zhang. 2022a. "Size effect on flexural behavior of ultra-high-performance concrete beams with different reinforcement." Structures 41: 969–981. https://doi.org/10.1016/j.istruc.2022.05.062.
Cao, X., Y.-C. Ren, L. Zhang, L.-Z. Jin, and K. Qian. 2022b. "Flexural behavior of ultra-high-performance concrete beams with various types of rebar." Compos. Struct. 292: 115674. https://doi.org/10.1016/j.compstruct.2022.115674.
CCPA (China Concrete & Cement-based Products Association). 2018. Fundamental characteristics and test methods of ultra-high-performance concrete. T/CBMF37. Beijing: China Building Materials Industry Press.
CNS (China National Standard). 2015. Reactive powder concrete. GB/T31387. Beijing: China Standards Press.
El-Helou, R. G., and B. A. Graybeal. 2022. "Flexural behavior and design of ultrahigh-performance concrete beams." J. Struct. Eng. 148 (4): 04022013. https://doi.org/10.1061/(ASCE)ST.1943-541X.0003246.
El-Helou, R. G., Z. B. Haber, and B. A. Graybeal. 2022. "Mechanical behavior and design properties of ultra-high performance concrete." ACI Mater. J. 119 (1): 181–194.
El-Nemr, A., E. A. Ahmed, and B. Benmokrane. 2013. "Flexural behavior and serviceability of normal- and high-strength concrete beams reinforced with glass fiber-reinforced polymer bars." ACI Struct. J. 110 (6): 1077–1087.
Fang, Z., X. Tian, and F. Peng. 2023. "Flexural strength of prestressed ultra-high-performance concrete beams." Eng. Struct. 279: 115612. https://doi.org/10.1016/j.engstruct.2023.115612.
Gowripalan, N., and I. R. Gilbert. 2000. Design guidelines for ductal prestressed concrete beams. Sydney, NSW, Australia: Univ. of New South Wales.
Hung, C.-C., S. El-Tawil, and S.-H. Chao. 2021. "A review of developments and challenges for UHPC in structural engineering: Behavior, analysis, and design." J. Struct. Eng. 147 (9): 03121001. https://doi.org/10.1061/(ASCE)ST.1943-541X.0003073.
Liang, K., L. Chen, Z. Shan, and R. K. L. Su. 2023. "Experimental and theoretical study on bond behavior of helically wound FRP bars with different rib geometry embedded in ultra-high-performance concrete." Eng. Struct. 281: 115769. https://doi.org/10.1016/j.engstruct.2023.115769.
Mahaini, Z., F. Abed, Y. Alhoubi, and Z. Elnassar. 2023. "Experimental and numerical study of the flexural response of ultra high performance concrete (UHPC) beams reinforced with GFRP." Compos. Struct. 315: 117017. https://doi.org/10.1016/j.compstruct.2023.117017.
MCS-EPFL (Maintenance, Construction and Safety of Structures-Écolepolytechnique fédérale de Lausanne). 2016. Recommendation: Ultra-high performance *fi*bre reinforced cement-based composites (UHPFRC). Lausanne, Switzerland: MCS-EPFL.
Mehany, S., H. M. Mohamed, and B. Benmokrane. 2022. "Flexural strength and serviceability of GFRP-reinforced lightweight self-consolidating concrete beams." J. Compos. Constr. 26 (3): 04022020. https://doi.org/10.1061/(ASCE)CC.1943-5614.0001208.
Naaman, A. E., and S. M. Jeong. 1995. "Structural ductility of concrete beams prestressed with FRP tendons." In Non-metallic (FRP) reinforcement for concrete structures, edited by L. Taewere, 379–386. London: E. & F.N. Spon.
Patil, G., M. Chellapandian, and S. S. Prakash. 2020. "Effectiveness of hybrid fibers on flexural behavior of concrete beams reinforced with glass fiber-reinforced polymer bars." ACI Struct. J. 117 (5): 1–14. https://doi.org/10.14359/51725844.
Peng, F., J. Deng, Z. Fang, and Z. Tang. 2023a. "Ductility evaluation and flexural failure mode recognition of reinforced ultra-high performance concrete flexural members." Structures 51: 1881–1892. https://doi.org/10.1016/j.istruc.2023.03.127.
Peng, F., J. Deng, and W. Xue. 2023b. "Design provisions for flexural strength of hybrid reinforced concrete beams with fiber-reinforced polymer and steel bars." ACI Struct. J. 120 (1): 49–59.
Peng, F., Z. Fang, and S. Cui. 2022a. "Deflection calculation for reinforced ultra-high-performance concrete beams based on effective moment of inertia." ACI Struct. J. 119 (4): 263–275. https://doi.org/10.14359/51734523.
Peng, F., and W. Xue. 2019. "Reliability analysis of eccentrically loaded concrete rectangular columns reinforced with fiber-reinforced polymer bars." ACI Struct. J. 116 (4): 275–284. https://doi.org/10.14359/51715634.
Peng, F., and W. Xue. 2021. "Shear behavior of post-tensioned concrete beams with draped FRP tendons and without transverse reinforcement." J. Compos. Constr. 25 (4): 04021027. https://doi.org/10.1061/(ASCE)CC.1943-5614.0001128.
Peng, F., W. Yi, and Z. Fang. 2022b. "Design approach for flexural strength of reinforced ultra-high-performance concrete members considering size effect." ACI Struct. J. 119 (1): 281–294. https://doi.org/10.14359/51734140.
Saqif, M. A., Y.-S. Tai, and S. El-Tawil. 2022. "Experimental and computational evaluation of the ductility of UHPC beams with low steel-reinforcement ratios." J. Struct. Eng. 148 (7): 04022077. https://doi.org/10.1061/(ASCE)ST.1943-541X.0003378.
Shao, Y., and S. L. Billington. 2022. "Impact of UHPC tensile behavior on steel reinforced UHPC flexural behavior." J. Struct. Eng. 148 (1): 04021244. https://doi.org/10.1061/(ASCE)ST.1943-541X.0003225.
Shao, Y., C.-C. Hung, and S. L. Billington. 2021. "Gradual crushing of steel reinforced HPFRCC beams: Experiments and simulations." J. Struct. Eng. 147 (8): 04021114. https://doi.org/10.1061/(ASCE)ST.1943-541X.0003080.
Sturm, A. B., P. Visintin, R. Seracino, G. W. Lucier, and D. J. Oehlers. 2020. "Flexural performance of pretensioned ultra-high performance fibre reinforced concrete beams with CFRP tendons." Compos. Struct. 243: 112223. https://doi.org/10.1016/j.compstruct.2020.112223.
Tan, H., Z. Hou, Y. Li, and X. Xu. 2022. "A flexural ductility model for UHPC beams reinforced with FRP bars." Structures 45: 773–786. https://doi.org/10.1016/j.istruc.2022.09.052.
Yan, J., Y. Liu, F. Bai, X. Ni, Y. Xu, Z. Yan, and F. Huang. 2022. "Dynamic response of GFRP-reinforced UHPC beams under close-in blast loading." Mater. Des. 223: 111140. https://doi.org/10.1016/j.matdes.2022.111140.
Yoo, D.-Y., N. Banthia, and Y.-S. Yoon. 2016. "Flexural behavior of ultra-high-performance fiber-reinforced concrete beams reinforced with GFRP and steel rebars." Eng. Struct. 111: 246–262. https://doi.org/10.1016/j.engstruct.2015.12.003.
Yoo, D.-Y., N. Banthia, and Y.-S. Yoon. 2017. "Experimental and numerical study on flexural behavior of ultra-high-performance fiber-reinforced concrete beams with low reinforcement ratios." Can. J. Civ. Eng. 44 (1): 18–28. https://doi.org/10.1139/cjce-2015-0384.
Zeng, J.-J., S.-P. Chen, P. Feng, Z. Yan, K.-D. Peng, J.-G. Dai, and T.-H. Fan. 2023. "FRP bar-reinforced ultra-high-performance concrete plates with a grouting sleeve connection: Development and flexural behavior." Eng. Struct. 287: 116164. https://doi.org/10.1016/j.engstruct.2023.116164.

Downloaded from ascelibrary.org by HUNAN UNIVERSITY on 04/24/24. Copyright ASCE. For personal use only; all rights reserved.

buildings

MDPI

Article

Experimental Investigation on Pure Torsion Behavior of Concrete Beams Reinforced with Glass Fiber-Reinforced Polymer Bars

Haoyang Bai, Jiafei Jiang *, Weichen Xue * and Xiang Hu

College of Civil Engineering, Tongji University, Shanghai 200092, China; baihaoyang@tongji.edu.cn (H.B.); hu_xiang@tongji.edu.cn (X.H.)

* Correspondence: jfjiang@tongji.edu.cn (J.J.); xuewc@tongji.edu.cn (W.X.)

Abstract: The failure mechanism of torsional concrete beams with fiber-reinforced polymer (FRP) bars is essential for developing the design method. However, limited experimental research has been conducted on the torsion behavior of concrete beams with FRP bars. Therefore, the pure torsion test of four large-scale FRP-RC beams (2800 mm × 400 mm × 200 mm) was conducted to investigate the influence of the stirrup ratio (0, 0.49%, and 0.98%) and longitudinal reinforcement ratio (3.01%, 4.25%) on torsion behavior. The test results indicated that three typical failure patterns, including concrete cracking failure, stirrup rupturing failure, and concrete crushing failure, were observed in specimens without stirrups (stirrup ratio 0), partially over-reinforced specimens (stirrup ratio 0.49%), and over-reinforced specimens (stirrup ratio 0.98%), respectively. The tangent angle of spiral cracks at the midpoint of the long side of the cross-section was approximately 45° initially for all specimens. The torque–twist angle curves exhibited a linear and bilinear behavior for specimens without stirrups and specimens with stirrups, respectively. As the stirrup ratio increased from 0 to 0.98%, torsion capacity increased from 24.9 kN·m to 27.8 kN·m, increased by 12%, ultimate twist angle increased from 0.0018 rad/m to 0.0403 rad/m. As the longitudinal reinforcement ratio increased from 3.01% to 4.25%, the torsion capacity increased from 27.8 kN·m to 28.3 kN·m, and the ultimate twist angle decreased from 0.0403 rad/m to 0.0244 rad/m. Based on test results, the stirrup strain limit of 5200 με and spiral crack angle of 45° was suggested for torsion capacity calculation. In addition, based on the database of torsion tests, the performance of torsion capacity provisions was assessed.

Keywords: fiber-reinforced polymer; concrete beam; torsion test; torsion capacity; failure pattern; spiral crack angle

check for updates

Citation: Bai, H.; Jiang, J.; Xue, W.; Hu, X. Experimental Investigation on Pure Torsion Behavior of Concrete Beams Reinforced with Glass Fiber-Reinforced Polymer Bars. *Buildings* **2024**, *14*, 2617. https://doi.org/10.3390/buildings14092617

Academic Editors: Eugeniusz Koda, Duc-Kien Thai, Yiyi Zhou and Zhengyi Kong

Received: 9 July 2024
Revised: 15 August 2024
Accepted: 21 August 2024
Published: 23 August 2024

Copyright: © 2024 by the authors. Licensee MDPI, Basel, Switzerland. This article is an open access article distributed under the terms and conditions of the Creative Commons Attribution (CC BY) license (https://creativecommons.org/licenses/by/4.0/).

1. Introduction

Corrosion of steel reinforcement is one of the main factors for the deterioration of concrete structures. The corrosion problem has found an innovative solution in the form of substituting steel reinforcement with fiber-reinforced polymer (FRP) reinforcement in concrete structures [1]. Due to characteristics of high tensile strength, corrosion resistance, high specific strength (strength-to-weight ratio), etc., FRP bars have been increasingly applied in concrete structures subjected to harsh environments [2,3]. In FRP-reinforced concrete structures, FRP reinforcement can be divided into longitudinal FRP reinforcement and transverse FRP reinforcement (i.e., FRP stirrups). FRP longitudinal reinforcement mainly provides flexural resistance, while FRP stirrups mainly provide torsional and shear resistance. Regarding the mechanical properties of FRP stirrups, studies have shown that rupture of FRP stirrups occurs at the bend generally, and the tensile strength of FRP stirrups at the bend is less than the tensile strength of straight portion, typically about 40% of the tensile strength of straight portion [4]. The specific value of the tensile strength of the stirrup to the tensile strength of the straight portion ratio (i.e., strength retention rate) is mainly related to the ratio of the bend radius to stirrup diameter. Such a feature determines the

diverse behavior of concrete beams reinforced with FRP stirrups compared with that of steel-reinforced concrete beams (steel-RC beams).

The torsion behavior of steel-RC beams was investigated experimentally in terms of stirrup ratio and concrete strength [5–7]. Some researchers conducted studies on the influence of stirrup ratio on the torsion behavior of fiber-reinforced polymer bars reinforced concrete (FRP-RC) beams. In 2016, Benmokrane et al. [8,9] conducted an early investigation on the torsion behavior of GFRP-RC beams (4000 mm × 600 mm × 250 mm). The stirrup ratios varied from 0% to 0.94%. The test results showed that the specimen without stirrups experienced concrete cracking failure. For specimens with a stirrup ratio between 0.19% and 0.47%, stirrups rupture occurred at the bend. For the specimen with a stirrup ratio of 0.94%, concrete crushing failure occurred. Overall, increasing the stirrup ratio improved torsion capacity. The stirrup ratio increasing 5 times resulted in 1.8 times torsion capacity. Benmokrane et al. [9,10] also conducted a torsion test on CFRP-RC beams. The conclusions were similar to those for GFRP-RC beams. Three typical failure patterns—concrete cracking failure, stirrup rupturing failure, and concrete crushing failure—were realized. A fivefold increase in the CFRP stirrup ratio resulted in a 90% increase in torsion capacity. In 2020, Hadhood et al. [11] investigated the type of transverse reinforcement (rectangular spiral and stirrup) and spiral ratio effect on the torsion behavior of GFRP-RC beams. The results displayed that torsion capacity increased with the stirrup ratio. The torsion capacity of the specimens with GFRP spirals was 16% higher than that of the specimen with rectangular GFRP stirrups, attributed to the confinement of spirals and direct resistance of the crack opening with the stirrup leg perpendicular to the diagonal cracks [12]. They further concluded that with spiral ratios ranging from 0 to 0.89%, the torsion capacity increased by 160%. Additionally, some researchers conducted experimental studies on the torsion behavior of FRP-RC beams, focusing on concrete types, cross-section types, and stirrup types [13–16]. Summarily, the torsion behavior of FRP-RC beams differs from that of steel-RC beams, due to different bond behavior and mechanical properties of reinforcement [17]. However, there are few studies on pure torsion tests of FRP-RC beams, which exhibited little information on the spiral crack angle, crack width, and torque–twist angle behavior. Besides, the effect of longitudinal reinforcement has not been investigated. At last, stacked rollers were used as torsion support for all existing tests which could cause the specimens to twist around the rollers rather than around the center of the specimen's cross-section, changing the true stress state of the specimens and resulting in additional torque.

In terms of tensile strength of stirrups, CSA S6:19 [18], ACI 440.1R-15 [19], AASHTO GFRP-RC 2018 [20], and GB 50608-2020 [21] specify the stirrup strain limit as 4000 με. ACI 440.11-22 [22] and CSA S806-12 [23] specify the stirrup strain limit as 5000 με, which was derived from the shear behavior of FRP-RC beams. However, since the stress state of the stirrup legs in shear members and torsion members differed, the stirrup strain limit should be investigated for FRP-RC members under torsion specifically. Benmokrane et al. [8,10] conducted a comparative analysis based on the test results of GFRP and CFRP-RC beams. The study compared the differences between calculated torsion capacity using different tensile strengths of the FRP stirrup (test value of tensile strength of FRP stirrup at bend: $f_{bend,exp}$; 0.4 times the tensile strength of FRP stirrup of straight portion: $0.4 \cdot f_{fu}$; tensile strength corresponding to the stirrup strain limit ε_{lim} of 5000 με: $0.005 \cdot E_f$) and the test results. The results revealed that using $f_{bend,exp}$ to calculate the torsion capacity of GFRP and CFRP-RC members yielded results closest to the experimental results, with an error of about 4%. However, the conclusion relies on the equation from CSA S806-12. The tensile strength or strain limit of the stirrup still needs investigation.

From the above literature review, the following issues can be summarized:

1. In a few existing torsion tests of FRP-RC members, some points could be improved. For instance, stacked rollers were also used as a torsion support which could cause additional torque. The longitudinal reinforcement was arranged asymmetrically on the cross-section, resulting in uneven stress distribution in the longitudinal bars of

the upper and lower chords of the truss. The crack width and short legs of the stirrup were not measured.

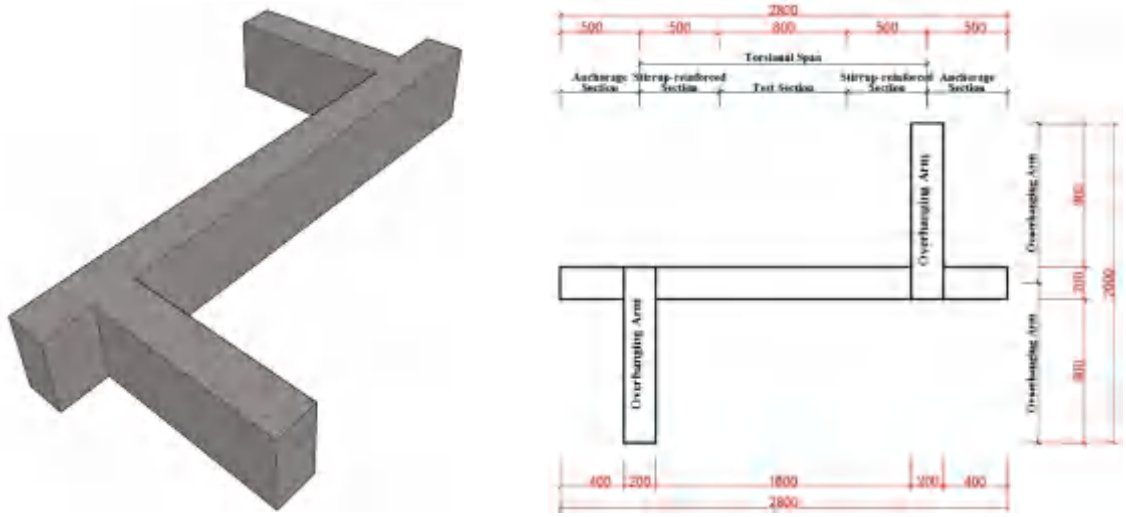
2. Stirrup strain limit and spiral crack angles were summarized and analyzed to provide a suggestion for torsion capacity prediction.
3. A database for torsion tests of FRP-RC members was established and provided to assess the current torsion design provisions.

In this paper, a novel torsion support was designed and fabricated which was suitable for large-scale torsion tests of structural components and could allow the specimens to rotate around the center of the cross-section. This paper conducted a torsion test of four large-scale GFRP-RC beams (2800 mm × 400 mm × 200 mm) reinforced with symmetric longitudinal reinforcement including one specimen without stirrups, and the other three specimens with the variation of stirrup ratio and longitudinal ratio. The influence of longitudinal and transverse reinforcement ratio on the beam's torsion behavior in terms of failure pattern, spiral crack angle, torque–twist angle curve, strain development in reinforcement, concrete strut, etc., was investigated. Based on test results, the stirrup strain limit was suggested for torsion design. In addition, based on the database of torsion tests, the performance of torsion capacity provisions was assessed and the spiral crack angle was suggested for torsion design.

2. Experimental Program

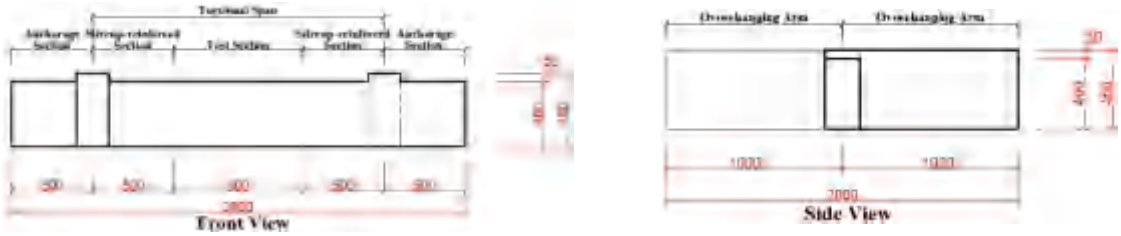
2.1. Test Specimens

Four large-scale GFRP-RC beams with a total length of 2800 mm were designed according to codes CSA S806-12, ACI 440.1R-15, and GB 50608-2020 (as shown in Figure 1). The torsion span was kept constant at 1800 mm in the middle of the beams. The torsion span consisted of one 800 mm long test section in the middle of the torsion span and two 500 mm long stirrups-reinforced sections at both ends. On each side of the beams, an extra 500 mm length anchorage section was set to avoid bond failure before torsion failure. Besides, all beams were equipped with overhanging arms perpendicular to the longitudinal direction associated with the torsion setup. This design allowed the vertical load to be applied to the overhanging arms, enabling torque loading on the main section of the beams.



(**a**) (**b**)

Figure 1. *Cont.*



(**c**) (**d**)

Figure 1. Dimensions of specimens: (**a**) 3D diagram; (**b**) side view; (**c**) front view; (**d**) side view.

Four GFRP-RC beams are categorized into three types of specimens: specimen without stirrups (G-W-12D16-T), partially over-reinforced specimen (G-160-12D16-T), and over-reinforced specimen (G-80-12D16-T, G-80-12D19-T) (as listed in Table 1). The longitudinal reinforcement ratio ρ_l of the specimen without stirrups and the partially over-reinforced specimens was 3.01%. The two over-reinforced specimens had longitudinal reinforcement ratios of 3.01% and 4.25%, respectively. All specimens were reinforced with the longitudinal FRP bars symmetrically on the cross-section. The reinforcement details are illustrated in Figure 2.

Table 1. Specimen design details.

Specimens	Specimen Type	f_c' (MPa)	Stirrup Ratio ρ_t	Longitudinal Reinforcement Ratio ρ_l
G-W-12D16-T	Without stirrups	39	0	3.01%
G-160-12D16-T	Partially over-reinforced	39	0.49%	3.01%
G-80-12D16-T	Over-reinforced	42	0.98%	3.01%
G-80-12D19-T	Over-reinforced	41	0.98%	4.25%

The specimens were denoted with acronyms consisting of letters and numbers, indicating various test parameters. The first letter "G" designated GFRP. The second letter or number represented the type and quantity of stirrups ("W" for without stirrups and "80" for 80 mm spacing GFRP stirrups in the test section). The third letter with a number represented the configuration of longitudinal reinforcement ("12" or "6" for the number of longitudinal GFRP bars, "D16" or "D19" for the diameter of longitudinal GFRP bars). The last letter "T" indicated torque loading.

2.2. Material Properties

All specimens were cast using the target cylinder compressive strength of 40 MPa. The concrete compressive strength was tested according to the Chinese standard GB/T 50081 [24]. The corresponding cylinder concrete compressive strength f_c' (80% of the cube strength) is listed in Table 1. No. 16 and No. 19 GFRP reinforcements were used as longitudinal reinforcement, and No. 10 GFRP reinforcement was used as GFRP stirrups where the internal bend radius r_b was 30 mm. The tensile strength of the longitudinal GFRP reinforcements and GFRP stirrups were tested according to ACI 440.3R-12 [25]. The detailed material properties are listed in Table 2.

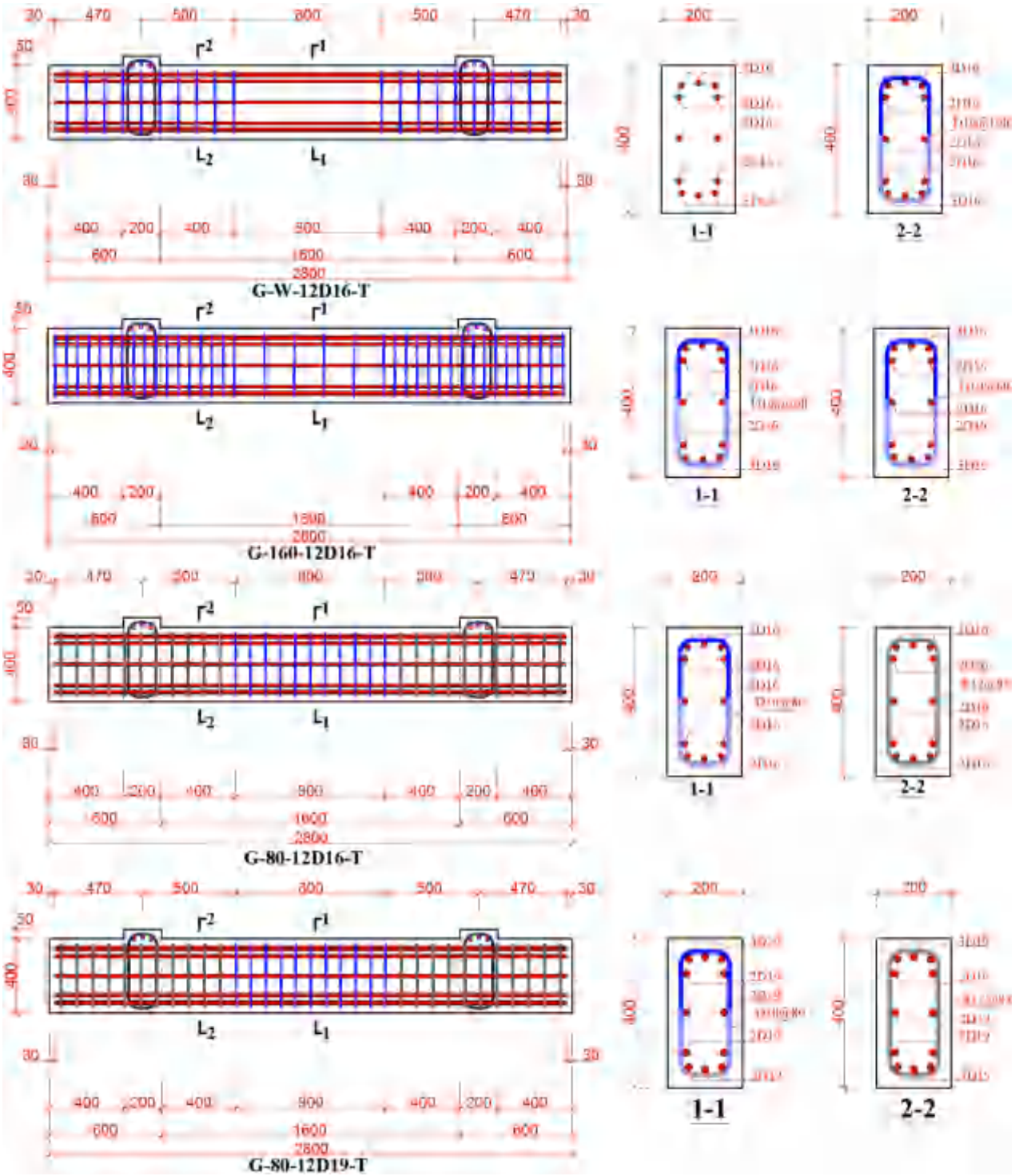


Figure 2. Reinforcement details of specimens.

Table 2. Mechanical properties of reinforcement.

Reinforcement	Nominal Diameter (mm)	Ultimate Strength (MPa)	Bend Strength (MPa)	Elastic Modulus (GPa)
No. 16 GFRP	16	1050	-	62
No. 19 GFRP	19	1090	-	60
No. 10 GFRP	10	1100	486	56

2.3. Test Setup

2.3.1. Loading Mode

The specimens were tested in the Building Structure Laboratory of Tongji University by using a specially designed and fabricated torsion test setup, as shown in Figure 3. The specimens were supported by two torsion supports. During the installation of the specimen, the cross-section center of the specimen coincided with the center of the torsion support to ensure specimens twisted around the center of the cross-section. Two 50-ton electro-hydraulic servo actuators were applied on the overhanging arms to apply torque to the specimens. Both actuators were connected to the same loading system.

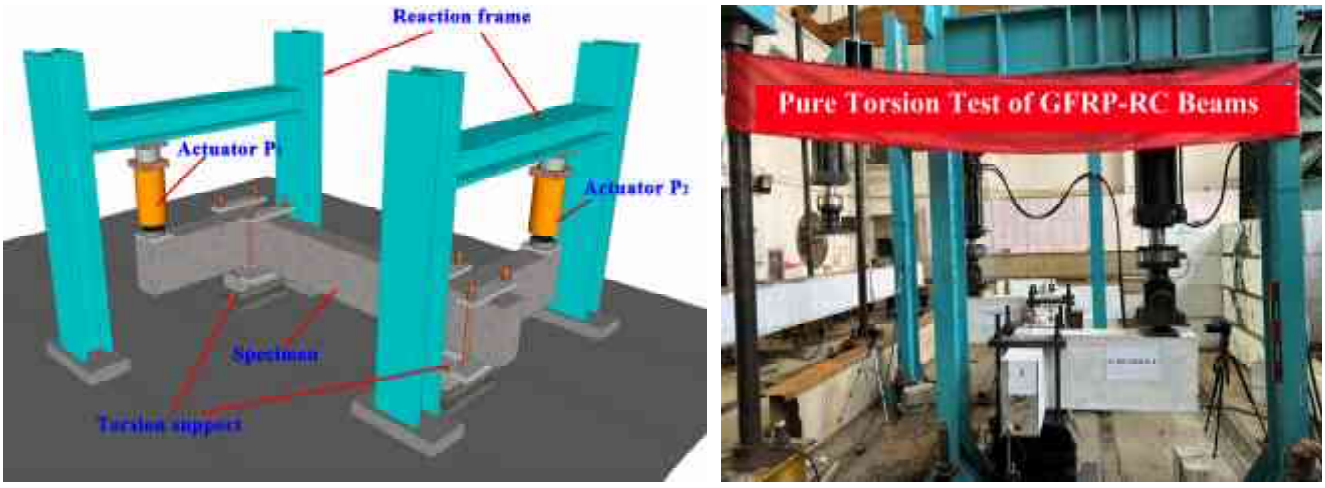
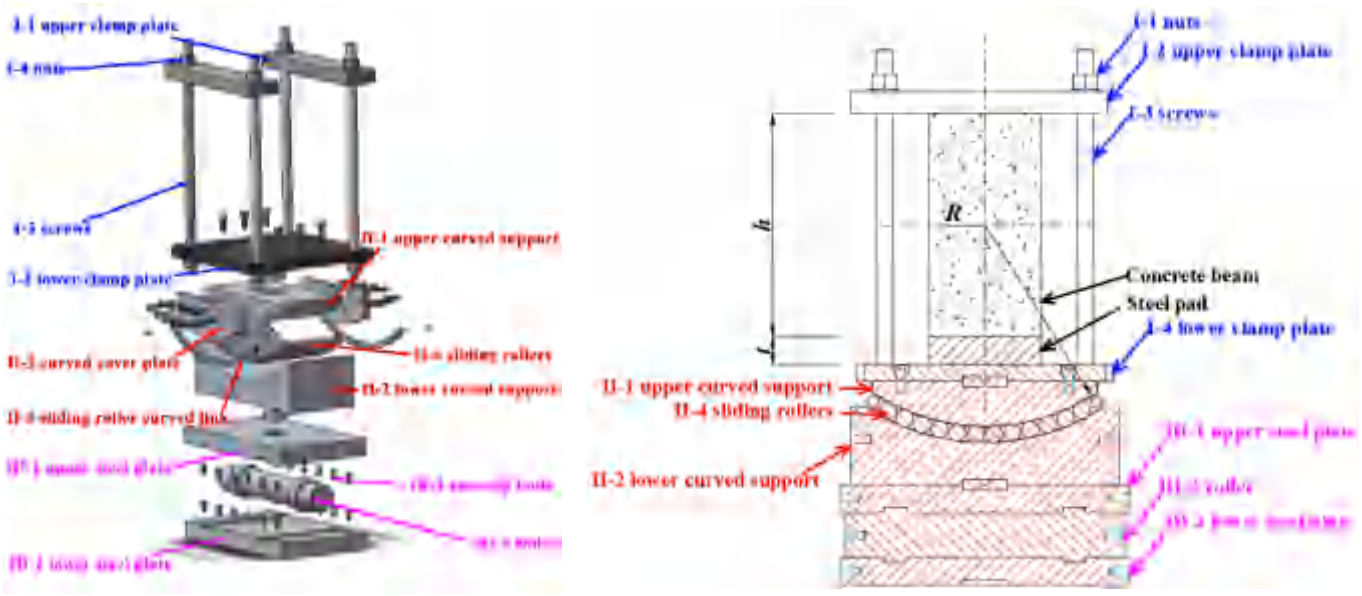


Figure 3. Test setup.

2.3.2. Torsion Support

A torsion support was designed and fabricated for torsion and combined torsion test specially (as shown in Figure 4). This torsion support had been applied for a patent [26]. The torsion support could provide the specimen with freedom of torsion, axial tension, and bending under torsional loads. The features of the torsion support could be summarized as follows:

1. To ensure that the specimens could twist around the center of the cross-section, adjustable height pads were placed between the beam and the lower clamp plate (pad thickness $t = R - 0.5h$, h: the height of cross-section, R: the radius of the upper curved support).
2. To reduce the friction caused by torsion, sliding rollers were installed on the upper and lower curved supports.
3. The anti-slip bolts could be installed on the upper and lower steel plates to prevent the rollers from sliding out during the test. Besides, two sets of key slots and raised circular discs were installed on the upper and lower steel plates and rollers respectively to ensure that the rollers could roll between the upper and lower steel plates in the same direction.

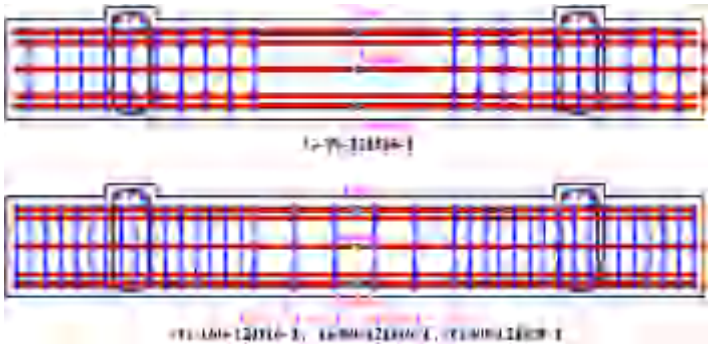


(**a**) (**b**)

Figure 4. Torsion support illustration: (**a**) 3D illustration; (**b**) cross-section.

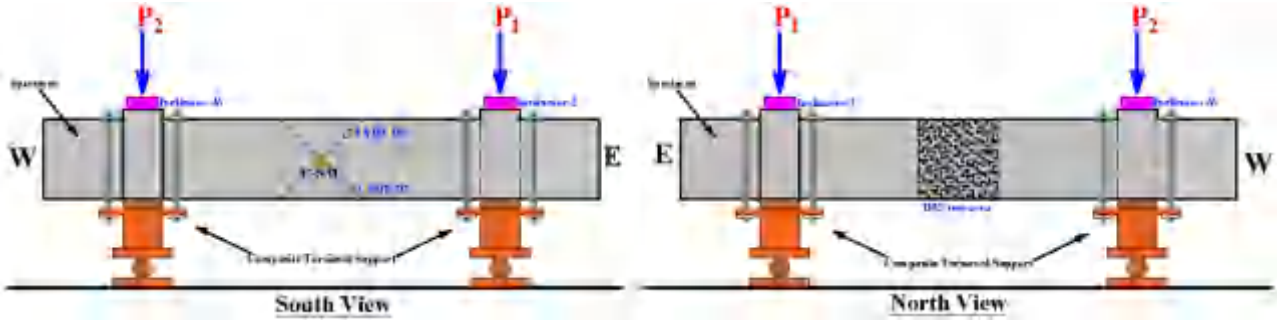
2.4. Instrumentation

The strains in the longitudinal GFRP bars, GFRP stirrups, and concrete were measured by electrical resistance strain gauges (ERSGs) (as shown in Figure 5a). The ERSGs of longitudinal GFRP bars were located in the middle of the torsion span. The ERSGs of GFRP stirrups were installed in the middle of four legs of each stirrups. The ERSGs on the surface of the concrete were placed at 0°, 45°, and 90° to the specimen axis in a rosette shape to measure the local concrete strain state. The linear variable differential transformers (LVDTs) with an accuracy of 0.001 mm were mounted on the surface of the concrete surface. Inclinators with an accuracy of 0.01° were mounted at the top of specimens to measure the twist angle of specimens (as shown in Figure 5b). For the DIC measurement, a camera was employed to capture images of a 400 mm × 400 mm area at the middle of the torsion span on the north side of the specimens.



(**a**)

Figure 5. *Cont.*



(**b**)

Figure 5. Instrumentation: (**a**) instrumentation in GFRP reinforcement; (**b**) instrumentation on the surface of specimens.

3. Results and Discussion

3.1. Overall Responses and Failure Patterns

Throughout the entire test process, no micro-cracks or local concrete crushing was observed in the anchorage zone or on the overhanging arms. The damage of all specimens was concentrated and developed at the test section. Based on the observation of concrete cracking, concrete crushing, and reinforcement behavior, the overall response and failure patterns can be summarized as follows:

1. The specimen without stirrups (G-W-12D16-T) experienced two stages: the uncracked stage and the failure stage. In the uncracked stage, the specimen exhibited visible warping on the surface. When the torque load reached cracking torque, diagonal cracks initiated from the mid-point of two long side surfaces, due to the maximum shear stress at these points. The crack rapidly extended from the midpoint to the top and bottom surfaces of the specimen, forming spiral cracks. With the increase in the width of the cracks on a randomly chosen long side surface of the specimen, the crack opening became significant. Simultaneously, a compressed plastic zone of concrete formed on the other long side surface of the specimen. Meanwhile, the spiral cracks extended to the corners of the specimen, where concrete spalling occurred. Generally, the specimen without stirrups failed immediately after cracking, which exhibited brittle failure as shown in Figure 6a.
2. The specimen with stirrups experienced three stages: pre-cracking stage, cracking stage, and failure stage. Specimens with stirrups exhibited similar behavior in the pre-cracking stage to the specimen without stirrups. In the pre-cracking stage, visible warping was also observed. When the torque load reached cracking torque, diagonal cracks first appeared at the midpoint of long side surfaces. The cracks extended towards the top and bottom surfaces of the specimen, forming spiral cracks on four side surfaces. As the load increased, the number of spiral cracks increased, and the crack width widened. Concrete inclined struts formed between the spiral cracks. In the failure stage, specimen G-160-12D16-T failed due to stirrup rupturing (as shown in Figure 6b), that is, a partially over-reinforced failure pattern. Specimens G-80-12D16-T and G-80-12D19-T failed due to the crushing of concrete strut (as shown in Figure 6c,d), that is, an over-reinforced failure pattern. The cracks on the over-reinforced specimens could be classified into two types: spiral cracks and intersected cracks (as shown in Figure 6c,d). Spiral cracks primarily formed due to torsion stress on the specimen, while intersected cracks primarily occurred due to the crushing of concrete struts.

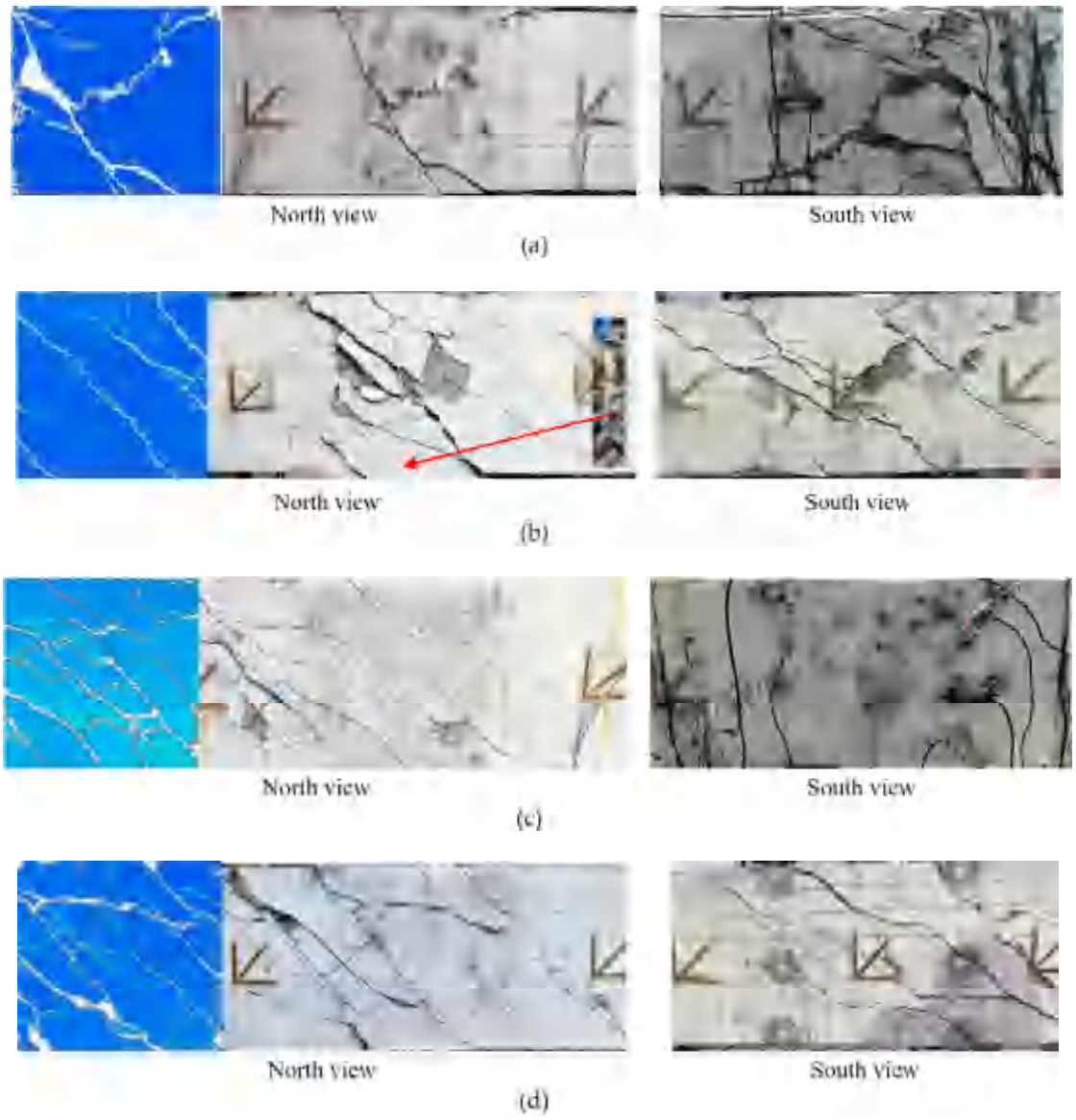


Figure 6. Cracking patterns of specimens at failure: (**a**) G-W-12D16-T; (**b**) G-160-12D16-T; (**c**) G-80-12D16-T; (**d**) G-80-12D19-T.

3.2. Spiral Crack Angle

In terms of spiral crack angle, the spiral crack angle is categorized into two types, as shown in Figure 7: (1) The tangent angle of the spiral crack at the mid-section of the specimen (referred to as the "tangent angle"), and (2) the angle of a straight line between two intersection points between crack and beam edge (referred to as the "secant angle"). The observation reveals the features as follows.

1. For specimens without stirrups, the tangent angle was approximately 45.9°, while the secant angle was 31.8°. After cracking, due to lack of stirrups confinement, the cracks extended longitudinally along the axis of the specimen, resulting in a secant angle smaller than the tangent angle.
2. For specimens with stirrups, the tangent angle was 45.1°, 43.8°, 45.1° for G-160-12D16-T, G-80-12D16-T, and G-80-12D19-T, respectively, and the secant angle ranged from 42.6°, 43.2°, and 46.2° for G-160-12D16-T, G-80-12D16-T, and G-80-12D19-T, respectively. For G-160-12D16-T, which failed due to stirrup rupturing, the axial elongation and crack width were larger than the other two specimens. It resulted in a

slightly smaller of secant angle to the tangent angle. Comparatively, two angles were close to each other for over-reinforced beams, G-80-12D16-T and G-80-12D19-T. All in all, the angle difference was much smaller than that in the beam without stirrups. It can be attributed to the constrain of FRP stirrups.

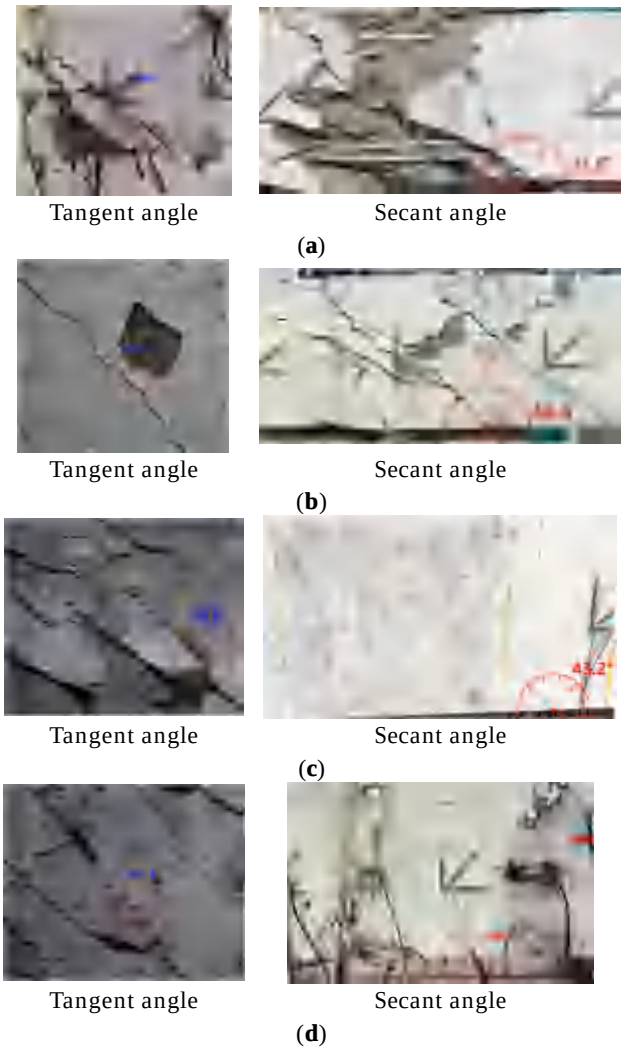


Figure 7. Spiral crack angle: (**a**) G-W-12D16-T; (**b**) G-160-12D16-T; (**c**) G-80-12D16-T; (**d**) G-80-12D19-T.

3.3. Crack Width

The torque–crack width curves of the specimen with stirrups are shown in Figure 8. The features of crack width development can be summarized as follows:

1. Generally, torque–crack width curves showed a rapid increase in crack width after cracking. For the same load, specimen G-160-12D16-T exhibited the widest crack width, while specimens G-80-12D19-T and G-80-12D16-T had smaller crack width. It indicated that the stirrups had a significant influence on the crack width, while the longitudinal reinforcement ratio had a lesser effect.
2. Corresponding to the crack width of 0.5 mm, torques were 23.5 kN·m for specimen G-160-12D16-T, 24.6 kN·m for G-80-12D16-T, and 24.3 kN·m for G-80-12D19-T, respectively. The ratios of the ultimate torque to the torque corresponding to 0.5 mm crack width were 1.09, 1.13, and 1.16, for G-160-12D16-T, G-80-12D16-T, and G-80-12D19-T, respectively. It indicated that the torque corresponding to 0.5 mm crack width was close to torsion capacity, with safety margins ranging from 1.1 to 1.2. Due to the different mechanisms of shear crack formation compared to flexural crack, the shear crack width of FRP-RC members subjected to torsion should be further investigated.

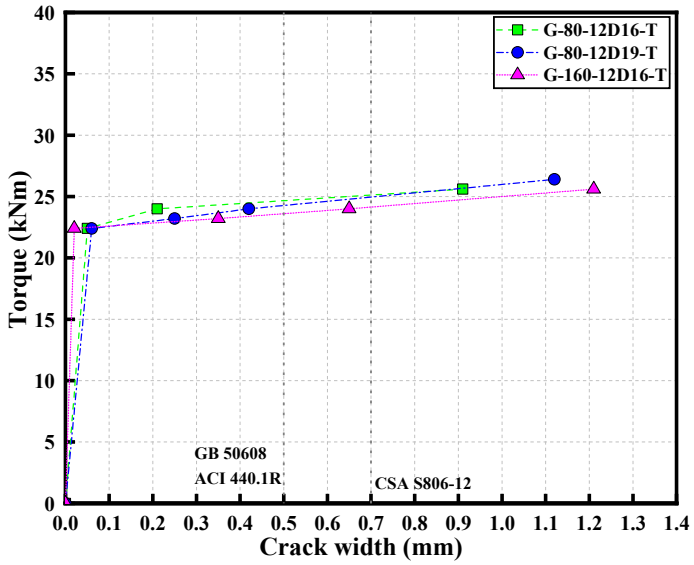


Figure 8. Torque–crack width curves.

3.4. Torque–Twist Angle Behavior

The torque–twist curves of the specimen without stirrups (G-W-12D16-T), the partially over-reinforced specimen (G-160-12D16-T), and the over-reinforced specimens (G-80-12D16-T and G-80-12D19-T) were shown in Figure 9. The features of the torque–twist angle curves of GFRP-RC beams can be summarized as follows:

1. Approximate linear torque–twist angle curves of the specimen without stirrups could be observed. The torque–twist angle behavior has no significant change after cracking. For the partially over-reinforced and over-reinforced specimens, the torque–twist angle curves exhibited bilinear characteristics. In the uncracked stage, the torque increased linearly with the twist until the cracking torque. Afterward, the torque–twist angle curves came into the cracking stage, with the torque increasing slowly until reaching the ultimate torque T_u. After reaching the ultimate torque, the torque–twist angle curves dropped rapidly. The torque–twist angle curves could be divided into three stages: uncracked stage, cracking stage, and failure stage. Similar torque–twist angle behavior of specimens with stirrups was displayed in References [8,10].
2. In terms of torsion capacity, for specimens with the same longitudinal reinforcement ratio, the ultimate torques (i.e., torsion capacity) T_u for G-W-12D16-T, G-160-12D16-T, and G-80-12D16-T were 24.9 kN·m, 25.6 kN·m, and 27.8 kN·m, respectively (as listed in Table 3). As the stirrup ratio increased from 0 to 0.98%, it increased by 12%. It indicated that increasing the stirrup ratio had a certain effect on enhancing the torsion capacity for partially over-reinforced beams. Besides, for over-reinforced specimens with the same stirrup ratio, the torsion capacity was 27.8 kN·m and 28.3 kN·m for specimens G-80-12D16-T and G-80-12D19-T, respectively (listed in Table 3). As the longitudinal reinforcement ratio increased from 3.01% to 4.25%, the torsion capacity increased by 2%, indicating that increasing the longitudinal reinforcement ratio for over-reinforced beams had a less significant effect on enhancing the torsion capacity of over-reinforced specimens.
3. In terms of ultimate twist angle, for the specimen without stirrups G-W-12D16-T, partially over-reinforced specimen G-160-12D16-T, and over-reinforced specimens G-80-12D16-T and G-80-12D19-T, the ultimate twist angles ϕ_u were 0.0018 rad/m, 0.0083 rad/m, 0.0403 rad/m, and 0.0244 rad/m, respectively (as listed in Table 3). For specimens with the same longitudinal reinforcement ratio, increasing the stirrup ratio from 0 to 0.98% resulted in a 21-fold increase in the ultimate twist angle. Increasing the stirrup ratio from 0.49% to 0.98% resulted in a 4.9-fold increase in the ultimate twist angle. It revealed that increasing the stirrup ratio could improve the torsional

deformation capacity significantly. It could be attributed confinement effect from stirrups. For over-reinforced specimens with the same stirrup ratio, increasing the longitudinal reinforcement ratio from 3.01% to 4.25% (an increase of 41%) resulted in a decrease in the ultimate twist angle from 0.0403 rad/m to 0.0244 rad/m (a decrease of 39%). It could be attributed to the dowel effect from the longitudinal bars during the twist.

4. In terms of torsional stiffness, the torsional stiffness in the torque–twist angle curves could be divided into pre-cracking torsional stiffness K_{un} and post-cracking torsional stiffness K_{cr}. The pre-cracking torsional stiffness and post-cracking torsional stiffness can be calculated by Equation (1) and Equation (2), respectively. The pre-cracking torsional stiffness for specimens G-W-12D16-T, G-160-12D16-T, G-80-12D16-T, and G-80-12D19-T were 13,833 kN·m^2, 14,500 kN·m^2, 9269 kN·m^2, and 12,294 kN·m^2, respectively, with an average pre-cracking torsional stiffness of 12,474 kN·m^2 (as listed in Table 3). The variation in pre-cracking torsional stiffness among the four specimens was within 26% of the average value, indicating that the pre-cracking torsional stiffness was significantly influenced by the concrete. For specimens with stirrups, the post-cracking torsional stiffness was 359 kN·m^2, 98 kN·m^2, and 326 kN·m^2 for G-160-12D16-T, G-80-12D16-T, and G-80-12D19-T respectively, which were 2%, 1%, and 3% of their pre-cracking torsional stiffness. In Reference [8] the post-cracking torsional stiffness decreased significantly, which ranged from 1% to 3% of their pre-cracking torsional stiffness.

$$K_{un} = \frac{T_{cr}}{\phi_{cr}} \text{ (Uncracked stiffness)} \quad (1)$$

$$K_{cr} = \frac{T_u - T_{cr}}{\phi_u - \phi_{cr}} \text{(Crack stiffness)} \quad (2)$$

5. In terms of ductility index, the ratio Δ of the ultimate twist angle ϕ_u to the cracking twist angle ϕ_{cr} (ϕ_u/ϕ_{cr}) was proposed to reflect the ductility index of FRP-RC beams. The ductility index can be calculated by Equation (3). The ductility indices for the over-reinforced specimens (G-80-12D16-T and G-80-12D19-T) were 15.5 and 14.4, respectively, with an average ductility index of 14.9 (as listed in Table 3). The longitudinal reinforcement ratio had little effect on the ductility index of over-reinforced specimens. The ductility indices Δ for the specimen without stirrups G-W-12D16-T, the partially over-reinforced specimen G-160-12D16-T, and the over-reinforced specimens (G-80-12D16-T and G-80-12D19-T) were 1.0, 5.2, and 14.9, respectively. The ductility indices of the partially over-reinforced specimen G-160-12D16-T and the over-reinforced specimen G-80-12D16-T were approximately 5 times and 15 times that of the specimen without stirrups G-W-12D16-T, respectively. It indicated that increasing the stirrup ratio could improve the deformation capacity of GFRP-RC beams significantly. Over-reinforced specimens had better ductility than specimens with the other two failure patterns.

$$\Delta = \frac{\phi_u}{\phi_{cr}} \quad (3)$$

Table 3. Summary of test results.

Specimens	ϕ_{cr} (Rad/m)	ϕ_u (Rad/m)	ϕ_u/ϕ_{cr}	T_{cr} (kN·m)	T_u (kN·m)	K_{un} (kN·m^2)	K_{cr} (kN·m^2)	Failure Pattern
G-W-12D16-T	0.0018	0.0018	1.0	24.9	24.9	13,833	-	Concrete Cracking
G-160-12D16-T	0.0016	0.0083	5.2	23.2	25.6	14,500	359	Stirrup Rupturing
G-80-12D16-T	0.0026	0.0403	15.5	24.1	27.8	9269	98	Concrete Crushing
G-80-12D19-T	0.0017	0.0244	14.4	20.9	28.3	12,294	326	Concrete Crushing

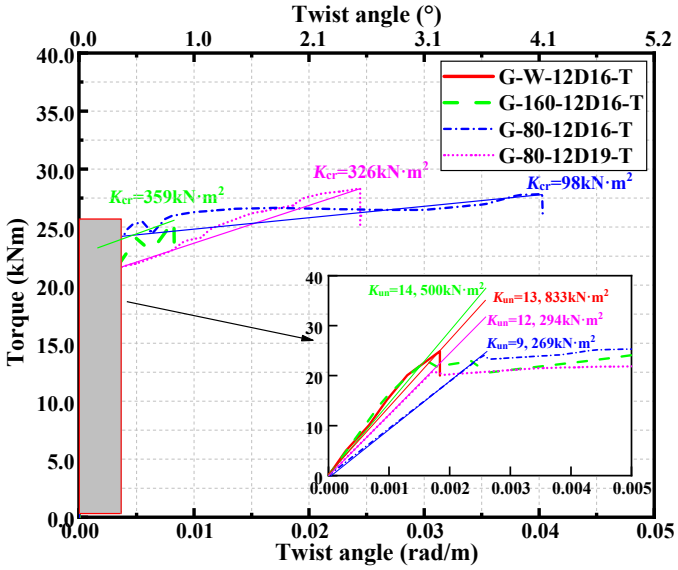


Figure 9. Torque–twist angle curves.

3.5. Strains in Longitudinal Reinforcement

The torque–longitudinal reinforcement strain curves are shown in Figure 10. Strain gauges were concentrated at the upper, middle, and lower longitudinal reinforcement in the mid-span of the specimens. The features of the torque–longitudinal reinforcement strain curves for GFRP-RC beams can be summarized as follows:

1. In terms of specimens without stirrups (G-W-12D16-T), the longitudinal reinforcement strain increased with the torque before the concrete cracked. After cracking, the torque decreased rapidly, and the longitudinal reinforcement strain no longer increased. The longitudinal reinforcement strain corresponding to the ultimate torque was less than 100 με. It indicated that the contribution of the longitudinal reinforcement to the torsion capacity of the specimen without stirrups was weak. Additionally, there were little differences in the strain of the top, middle, and bottom longitudinal reinforcement, indicating that the longitudinal reinforcements at the top, middle, and bottom were in a similar stress state.
2. In terms of specimens with stirrups (G-160-12D16-T, G-80-12D16-T, and G-80-12D19-T), they exhibited different performance in torque–longitudinal reinforcement strain curves. Before cracking, the longitudinal reinforcement strain was less than 100 με. After cracking, the longitudinal reinforcement strain suddenly increased and slowly continued to increase up to the ultimate torque. This showed that before cracking, the axial tension in the longitudinal reinforcement was relatively low. After cracking, there was a redistribution of internal stresses within the specimen, forming a new load transfer mechanism among the longitudinal reinforcement, stirrups, and concrete, leading to the sudden increase in longitudinal reinforcement strain.
3. For specimen G-160-12D16-T, the average longitudinal reinforcement strains corresponding to ultimate torque were 863 με. For specimens G-80-12D16-T and G-80-12D19-T, the average longitudinal reinforcement strains corresponding to ultimate torque were 3018 με and 2042 με, respectively. It revealed that longitudinal reinforcement could provide sufficient tension force sustainably for partially over-reinforced specimens and over-reinforced specimens to form truss mode with longitudinal reinforcement, stirrup, and concrete structures. Comparing partially over-reinforced specimens and over-reinforced specimens, increasing the stirrup ratio could improve the torsion capacity. Higher torsion capacity resulted in more strains in longitudinal reinforcement. In comparison between G-80-12D16-T and G-80-12D16-T, the force transferred by the truss model in longitudinal reinforcement was similar, the average

strain of G-80-12D16-T was higher than that of G-80-12D19-T due to smaller area of longitudinal reinforcement in G-80-12D16-T.

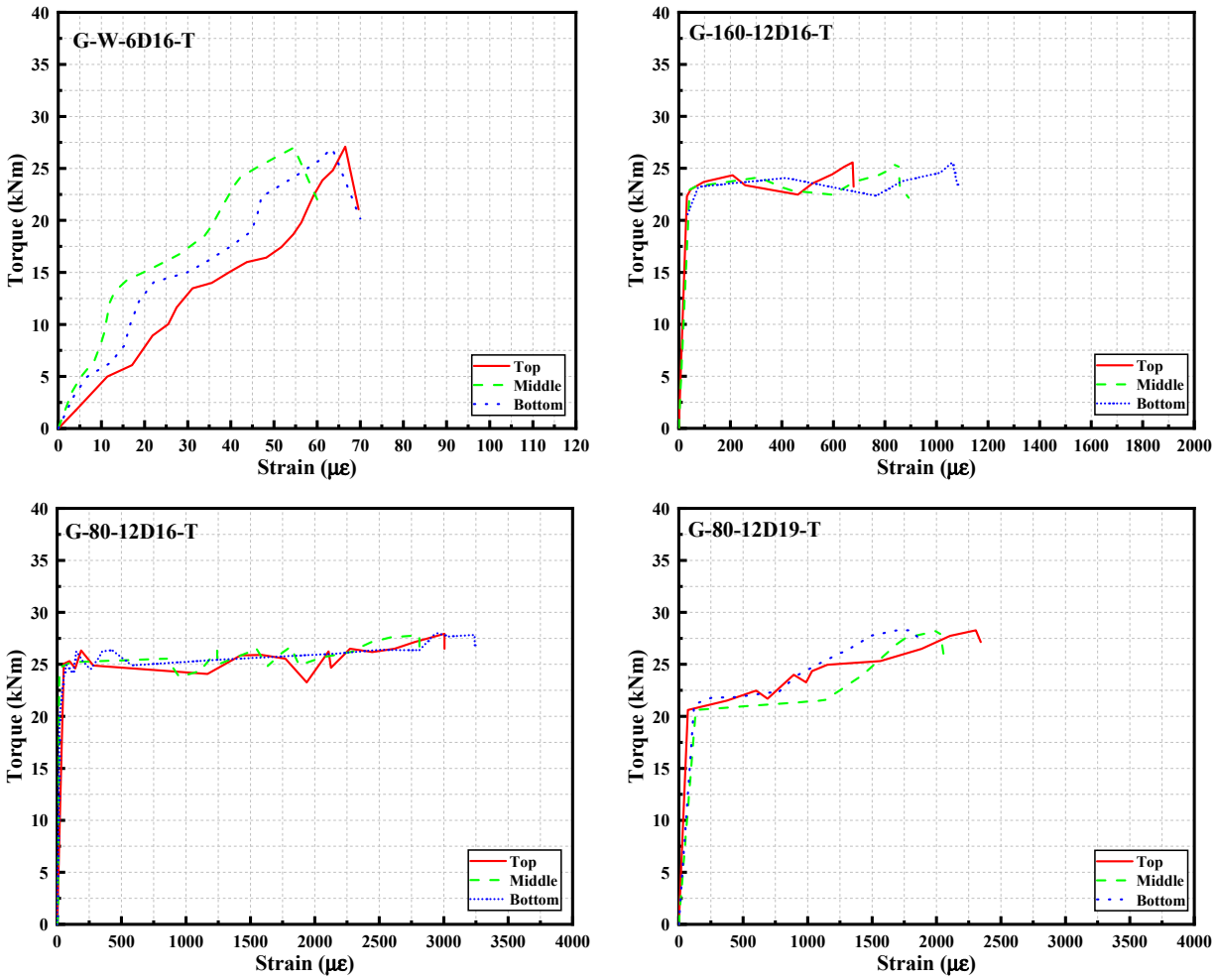


Figure 10. Torque–longitudinal reinforcement strain curves.

3.6. Strains in Transversal Reinforcement

The torque–stirrup strain curves for specimens G-160-12D16-T, G-80-12D16-T, and G-80-12D19-T were shown in Figure 11. The features of the torque–stirrup strain curves can be summarized as follows:

1. Generally, the torque–stirrup strain curves for the specimens G-160-12D16-T, G-80-12D16-T, and G-80-12D19-T exhibited similar behavior. Before concrete cracking, the stirrup strains were relatively small. After concrete cracking, the stirrup strains increased rapidly until they reached the ultimate torque. It indicated that the GFRP stirrups played a minor role before concrete cracking. However, after cracking, the GFRP stirrups could provide a certain enhancement to the torsion behavior of GFRP-RC beams.
2. To compare the strains in different specimens, the average stirrup strain was approximately 3341 με with a standard deviation of 2131 με for specimen G-160-12D16-T. For specimen G-80-12D16-T, the average stirrup strain was approximately 4577 με with a relatively smaller standard deviation of 1664 με. For specimen G-80-12D19-T, the average stirrup strain was approximately 3364 με with a similar standard deviation of 1488 με. The strain distribution in the stirrups of over-reinforced specimens was less dispersed compared to partially over-reinforced specimens. This was mainly because the crack spacing in over-reinforced specimens was smaller than that in partially

over-reinforced specimens, leading to more uniform tensile stress distribution across the stirrup legs in the partially over-reinforced specimen.

3. To compare the strains in short and long stirrup legs, the ratio between strain in the short legs to the strain in the long legs of the GFRP stirrups in the middle of the test section was 0.39, 0.39, and 0.4 for specimen G-160-12D16-T, G-80-12D16-T, and G-80-12D19-T, respectively. Different from only long legs of stirrups cross the diagonal crack appeared in the beams under shear, both the short and long legs of stirrups were intersected by the spiral cracks in beams and participated in torsion resistance.
4. The strain in the long leg of the ruptured stirrup was approximately 7600 με corresponding to 426 MPa, which was $0.88 \cdot f_{bend,exp}$, and $0.39 \cdot f_{fu}$. It indicated that $0.4 \cdot f_{fu}$ specified in CSA S806-12 proved to be reasonable for torsion design, while the stirrup strain limit 4000 με in CSA S9-6:19 and AASHTO GFRP-RC 2018 appeared to be conservative. In this study, the stirrup strain limit was regarded as the average of the ultimate strains of all stirrups that intersected the critical crack for all specimens. The stirrup strain limit of 5200 με was suggested for torsion design. However, due to limited test data, the stirrup strain limit should be further investigated.

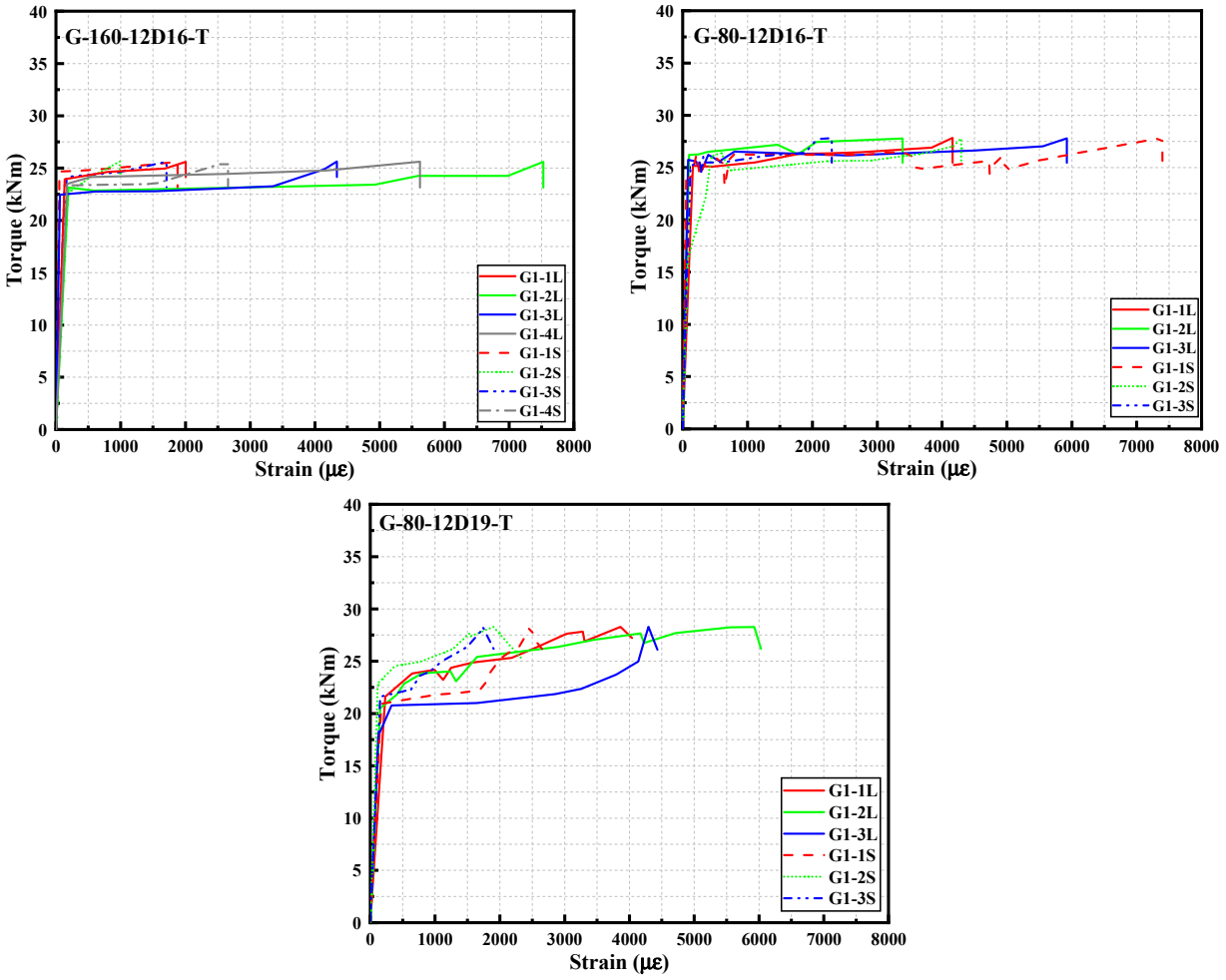


Figure 11. Torque–transverse reinforcement strain curves.

3.7. Concrete Strain

The torque–concrete strain curves (directions: 0-degree, 45-degree, 90-degree, and 135-degree) were illustrated in Figure 12. The features of the torque–concrete strain curves can be summarized as follows:

1. In terms of concrete strains in 0-degree, 45-degree, and 90-degree directions, the torque–concrete strain curves for specimen without stirrups (G-W-12D16-T) and specimen

with stirrups (G-160-12D16-T, G-80-12D16-T, and G-80-12D19-T) exhibited similar behavior. In all three directions, the concrete strain increased linearly with torque. The concrete strain in the 0-degree and 90-degree directions was below 50 με. The concrete strain in the 45-degree direction was approximately 200 με. Calculated with concrete strain in 0-degree, 45-degree, and 90-degree directions, the principle stress angle was about 45° for all specimens. It indicated that the surfaces of the specimens were under a pure shear stress state. The testing setup effectively achieved a pure torsion loading mode for the specimens.

2. In terms of concrete strains in a 135-degree direction, for the specimen without stirrups, the compressive strain was below 200 με because of concrete cracking failure. For the partially over-reinforced specimen G-160-12D16-T, the compressive strain in the concrete at the ultimate torque was approximately 900 με. In contrast, for the over-reinforced specimens G-80-12D16-T and G-80-12D19-T, the compressive strain in the concrete at the ultimate torque was approximately 1500 με and 1200 με, respectively, with an average of 1350 με, which was 1.5 times the compressive strain at the ultimate torque for the partially over-reinforced specimen.

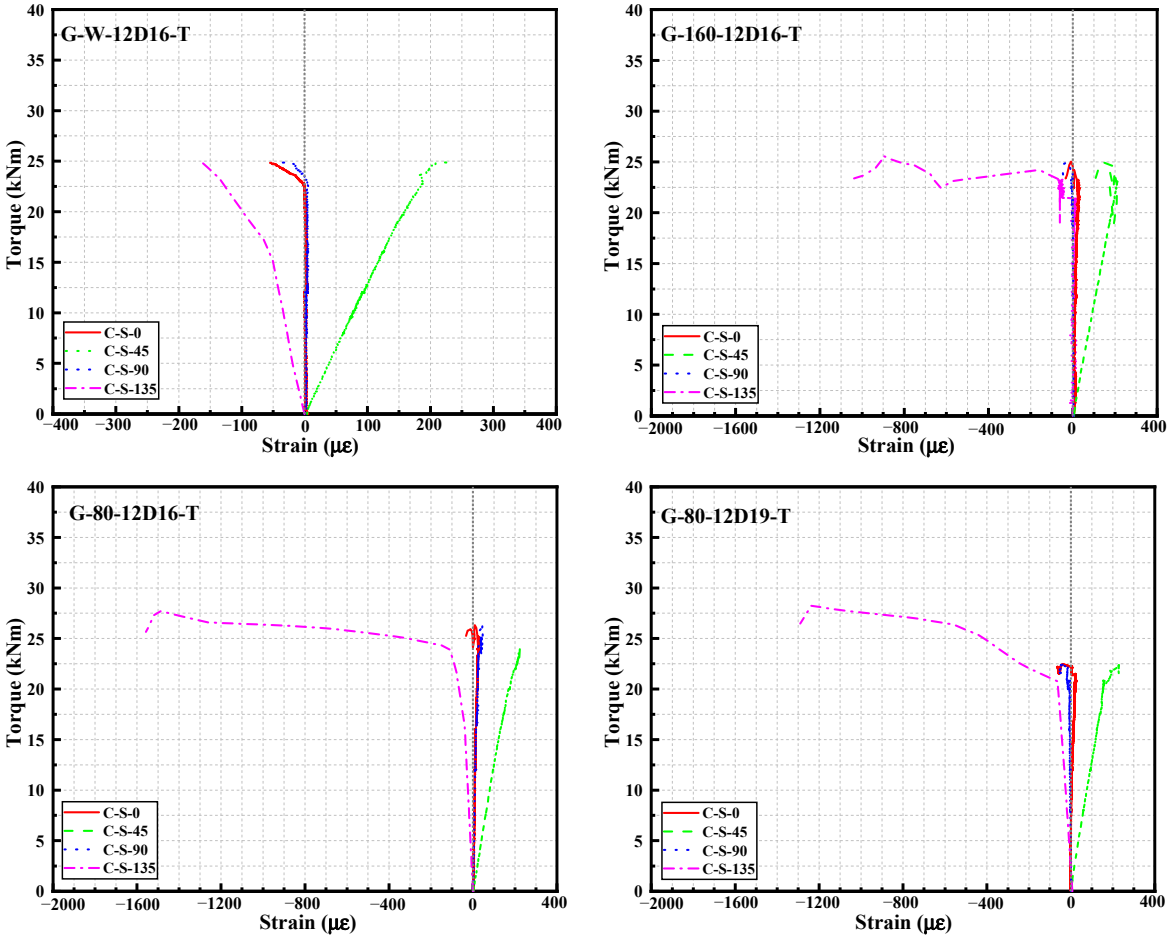


Figure 12. Torque–concrete strain curves.

4. Evaluation of Torsion Design Equations and Design Suggestions

4.1. Evaluation of Torsion Capacity Equations

In terms of the calculation of torsion capacity, the equations were proposed to calculate the torsion capacity for partially over-reinforced FRP-RC beams. For over-reinforced FRP-RC beams, the cross-sectional limit conditions were used to avoid concrete crushing. Available torsion capacity equations from codes CSA S806-12, CSA S6: 19, AASHTO GFRP-

RC 2018, and ACI 440.11-22 were based on the space truss model to calculate torsion capacity of FRP-RC members which failed due to stirrup rupturing.

$$T_u = 2A_0 \cdot \frac{A_{ft1} f_{ft}}{s} \cdot \cot\theta \quad (4)$$

where A_0 referred to the area enclosed by the shear flow centerline; A_{ft1} represented the cross-sectional area of one leg of the stirrup; and f_{ft} represented the tensile strength of FRP stirrups. θ represented the crack angle and s was stirrup spacing.

In this study, four codes, including CSA S806-12, CSA S6: 19, AASHTO GFRP-RC 2018, and ACI 440.11-22, for calculating the torsion capacity of FRP-PC members were considered. To assess the performance of the torsion capacity equations in the above four design guidelines, a database of 32 FRP-RC beams with stirrups was collected from references [8–10,27] to establish a test database of FRP-RC beams under torsion. Of the 32 FRP-RC beams, 19 beams failed due to stirrup rupturing, and 13 beams failed due to concrete crushing. The database information and ratio between the experimental and predicted torsion capacity T_{exp}/T_{pre} are listed in Table 4. All material reduction and safety factors were set equal to 1.0. The crack angle θ was taken as 45°. Table 5 presents the torsion capacity ratio T_{exp}/T_{pre}. The features of the torsion capacity ratio from different codes can be summarized as follows:

1. Generally, the four codes underestimated the torsion capacity of FRP-RC beams. However, CSA S806-12 based on modified compression field theory provided the most accurate predictions with a mean of T_{exp}/T_{pre} 1.48 and a standard deviation of 0.48. It could be attributed that the tensile strength of the FRP stirrup was regarded as $0.4 f_{fu}$ which was greater than $\varepsilon_{lim} \cdot E_f$. The stirrup strain limit ε_{lim} was regarded as 4000 με for CSA S6-19 and AASHTO. and 5000 με for ACI 440.11-22.
2. In terms of failure pattern, all codes provided the more conservative predictions for stirrup rupturing failure with a mean of T_{exp}/T_{pre} over 1.95 compared to the predictions for concrete crushing failure. Particularly, CSA S806-12 provided an unsafety prediction with a mean of T_{exp}/T_{pre} of 0.80. It indicated that the design equations in four codes should be used to calculate the torsion capacity of FRP-RC beams which failed due to stirrup rupturing.
3. CSA S6: 19 provided the most conservative predictions with a mean of T_{exp}/T_{pre} of 3.59. The tensile strength of stirrups specified in CSA S6: 19 was calculated by $\varepsilon_{lim} \cdot E_f$. Additionally, A_0 was 0.85 times the area enclosed by the centerline of the stirrup. The concrete cover was disregarded to calculate the A_0.
4. CSA S6-19, AASHTO, and ACI 440.11-22 underestimated the torsion capacity of the AFRP-RC beam obviously, with a mean of T_{exp}/T_{pre} over 6.18. Especially, the underestimation of torsion capacity occurred in AFRP-RC beams that failed due to stirrup rupturing. The E_f of AFRP bars was similar to that of GFRP bars. However, the f_{fu} of the AFRP bar was about 2 times of the GFRP bars. However, ε_{lim} was used to calculate the tensile strength of stirrups in CSA S6-19, AASHTO, and ACI 440.11-22. The ε_{lim} was underestimated in calculating the torsion capacity of AFRP-RC beams.

Table 4. Comparisons between the experimental and predicted torsion capacity of FRP-RC beams.

Reference	Specimen	h (mm)	b (mm)	ρ_t (%)	Stirrup	Failure Pattern	$T_{u,exp}$ (kN·m)	$T_{u,exp}/T_{u,pre}$			
								CSA S806-12	CSA S6: 19	AASHTO GFRP-RC	ACI 440.11-22
Reference [8]	BG120	600	250	0.47	GFRP	SR	52.7	1.51	3.19	3.01	2.55
	BG180	600	250	0.31	GFRP	SR	41.8	1.79	3.79	3.58	3.03
	BG240	600	250	0.24	GFRP	SR	34.2	1.95	4.14	3.90	3.31
	BG300	600	250	0.19	GFRP	SR	29.9	2.14	4.52	4.27	3.62

Table 4. *Cont.*

Reference	Specimen	h (mm)	b (mm)	ρ_t (%)	Stirrup	Failure Pattern	$T_{u,exp}$ (kN·m)	$T_{u,exp}/T_{u,pre}$			
								CSA S806-12	CSA S6: 19	AASHTO GFRP-RC	ACI 440.11-22
Reference [10]	BC120	600	250	0.47	CFRP	SR	62.9	1.09	1.31	1.24	1.05
	BC180	600	250	0.31	CFRP	SR	49.4	1.29	1.55	1.46	1.24
	BC240	600	250	0.24	CFRP	SR	39.4	1.37	1.64	1.55	1.31
	BC300	600	250	0.19	CFRP	SR	35.7	1.55	1.86	1.75	1.49
Reference [9]	BG60	600	250	0.94	GFRP	CC	56.9	0.81	1.72	1.62	1.38
	BC60	600	250	0.94	CFRP	CC	69.3	0.60	0.72	0.68	0.58
Reference [27]	AFRP	150	115	1.91	AFRP	CC	3.7	0.51	1.26	0.77	1.00
	CFRP	150	115	1.91	CFRP	CC	4.4	0.51	0.52	0.32	0.41
	A1	220	140	0.26	AFRP	SR	8.0	2.10	7.36	6.13	5.89
	A2	220	140	0.27	AFRP	SR	7.2	1.84	6.45	5.20	5.16
	A3	220	140	0.26	AFRP	SR	9.2	2.39	8.38	6.99	6.71
	A4	220	140	0.26	AFRP	SR	8.3	2.16	7.60	6.33	6.08
	A5	220	140	0.26	AFRP	SR	10.1	2.62	9.21	7.67	7.37
	A6	220	140	0.27	AFRP	SR	10.4	2.67	9.38	7.57	7.51
	A7	220	140	0.26	AFRP	SR	11.5	2.99	10.48	8.74	8.38
	A8	220	140	0.27	AFRP	SR	10.4	2.67	9.36	7.56	7.49
	C1	220	140	1.20	CFRP	CC	10.0	0.53	0.82	0.64	0.65
	C2	220	140	0.84	CFRP	CC	9.2	0.69	1.07	0.83	0.85
	C3	220	140	1.01	CFRP	CC	10.0	0.77	1.08	0.87	0.87
	C4	220	140	0.37	CFRP	SR	8.7	1.81	2.57	2.07	2.05
	C5	220	140	0.84	CFRP	CC	13.6	1.01	1.57	1.22	1.25
	C6	220	140	1.20	CFRP	CC	14.7	0.77	1.20	0.93	0.96
	C7	220	140	1.01	CFRP	CC	12.3	0.94	1.32	1.07	1.06
	C8	220	140	0.37	CFRP	SR	10.5	2.20	3.11	2.51	2.49
	C9	220	140	1.20	CFRP	CC	12.8	0.67	1.04	0.81	0.83
This study	G-160-12D16-T	400	200	0.49	GFRP	SR	25.6	0.88	1.73	1.42	1.39
	G-80-12D16-T	400	200	0.98	GFRP	CC	27.8	0.90	1.76	1.45	1.41
	G-80-12D19-T	400	200	0.98	GFRP	CC	28.3	1.63	3.19	2.62	2.56

Note: SR = stirrup rupturing; CC = concrete crushing.

Table 5. Statistics of torsion capacity ratio $T_{u,exp}/T_{u,pre}$.

Code	In Total (32 Beams)		SR (19 Beams)		CC (13 Beams)		GFRP-RC (8 Beams)		CFRP-RC (15 Beams)		AFRP-RC (9 Beams)	
	MEAN	SD	MEAN	SD	MEAN	SD	MEAN	SD	MEAN	SD	MEAN	SD
CSA S806-12	1.48	0.74	1.95	0.56	0.80	0.29	1.45	0.49	1.09	0.49	2.22	0.69
CSA S6: 19	3.59	3.07	5.14	3.11	1.33	0.64	3.01	1.07	1.48	0.66	7.72	2.56
AASHTO GFRP-RC	3.02	2.54	4.37	2.49	1.06	0.56	2.73	1.07	1.23	0.57	6.33	2.19
ACI 440.11-22	2.87	2.46	4.11	2.49	1.06	0.52	2.41	0.85	1.18	0.53	6.18	2.04

Note: SR = stirrup rupturing; CC = concrete crushing; SD = standard deviation.

4.2. Design Suggestions

Based on the collected data from References [8–11] of FRP-RC beams with stirrups under torsion, this study examined the spiral crack angles (tangent angle and secant angle) as depicted in Figure 13. It showed the ratio of ρ_t/ρ_l influenced the spiral crack angle of specimens with stirrups, insignificantly. Statistically, the average tangent angle was 45° with a standard deviation of 0.5, and the average secant angle was 44.2° with a standard deviation of 1.5. Additionally, design codes such as ACI 318-19 [28], EC 2 [29], and ACI 440.11-22 [22] specified using the spiral crack angle of 45 for calculating the torsion capacity. Therefore, the crack angle of 45° was suggested to calculate torsion capacity. Additionally, as mentioned above (Section 3.6), based on the test results, the stirrup strain limit of 5200 με was suggested for torsion design.

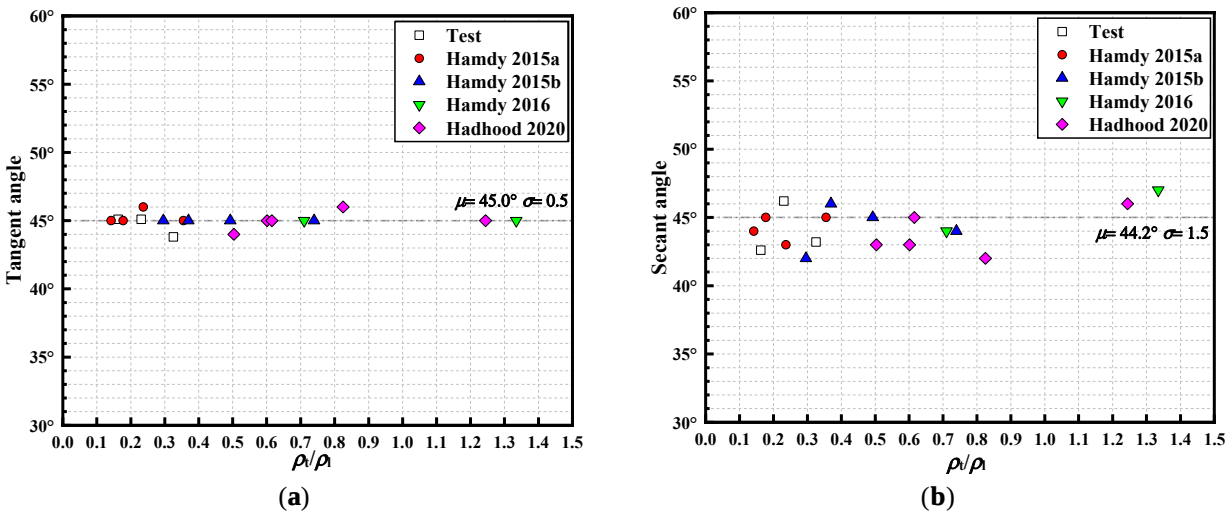


Figure 13. Spiral crack angle of FRP-RC beams with stirrups [8–11]: (**a**) tangent angle; (**b**) secant angle.

5. Conclusions

The four large-scale GFRP-RC beams (2800 mm × 400 mm × 200 mm) reinforced with symmetric longitudinal reinforcement were tested to investigate the influence of longitudinal and transverse reinforcement ratio on the torsion behavior. Based on the analysis of the experimental results, the following conclusions can be drawn:

1. Three typical torsion failure patterns were observed, that is, concrete cracking failure for specimen without stirrups, stirrup rupturing failure for partially over-reinforced specimens, and concrete crushing failure for over-reinforced specimens. The variation of failure patterns can be achieved by the variation of stirrup ratio.
2. Based on test data, the tangent angle of the spiral cracks was approximately 45°. The secant angle for specimens without stirrups was 31.8°, while the angle for specimens with stirrups ranges from 42°~47° with an average value of 44.2°.
3. For specimens with the same longitudinal reinforcement ratio, the torsion capacity of the specimen without stirrups, partially over-reinforced specimens and over-reinforced specimens was 24.9 kN·m, 25.6 kN·m, and 27.8 kN·m, respectively. When the stirrup ratio increased from 0 to 0.98%, the torsion capacity increased by 12%. For specimens with the same stirrup ratio, the torsion capacity was 27.8 kN·m and 28.3 kN·m for G-80-12D16-T and G-80-12D19-T, respectively. The longitudinal reinforcement ratio increased from 3.01% to 4.25%, showing an increase of only 1.8%.
4. For specimens with the same longitudinal reinforcement ratio, the ultimate twist angle ϕ_u of the specimen without stirrups (G-W-12D16-T), partially over-reinforced specimens (G-160-12D16-T) and over-reinforced specimens (G-80-12D16-T) was 0.0018 rad/m, 0.0083 rad/m and 0.0403 rad/m, respectively. The increase in the stirrup ratio could enhance the torsion deformation capacity significantly.

5. The longitudinal reinforcement strain in specimens without stirrups corresponding to ultimate torque was below 100 με, indicating that the axial tensile of the longitudinal reinforcement contributed to the torsion capacity insignificantly. The stirrups of partially over-reinforced specimens ruptured at the bend, with a rupture strain of approximately 7600 με.
6. Regarding the beams with stirrup rupturing failure, CSA S806-12 provided the most accurate predictions with a mean of T_{exp}/T_{pre} 1.95 and a standard deviation of 0.56. CSA S6: 19 provided the most conservative predictions with a mean of T_{exp}/T_{pre} of 5.14 and a standard deviation of 3.11. In terms of torsion design, the crack angle of 45° and stirrup strain limit of 5200 με were suggested.

Author Contributions: Conceptualization, W.X., J.J. and H.B.; methodology, J.J. and X.H.; software, H.B.; writing—original draft preparation, H.B.; writing—review and editing, W.X. and J.J.; funding acquisition, W.X. and J.J. All authors have read and agreed to the published version of the manuscript.

Funding: This research was funded by the National Key Research and Development Program of China (Grant No. 2022YFB3706500), the National Natural Science Foundation of China (Grant No. 52378178 & 52130806), and the Program Fund of Non-Metallic Excellence and Innovation Center for Building Materials (2023TDA4-1).

Data Availability Statement: The original contributions presented in the study are included in the article, further inquiries can be directed to the corresponding authors.

Acknowledgments: The authors gratefully acknowledge the financial support provided by National Key Research and Development Program of China, the National Natural Science Foundation of China and the Non-Metallic Excellence and Innovation Center for Building Materials.

Conflicts of Interest: The authors declare no conflicts of interest.

References

1. Nanni, A.; De Luca, A.; Zadeh, J. *Reinforced Concrete with FRP Bars Mechanics and Design*; CRC Press: New York, NY, USA, 2014; pp. 3–7.
2. Grace, N.; Jensen, A.; Eamon, D. Life-cycle cost analysis of carbon fiber-reinforced polymer reinforced concrete bridges. *ACI Struct. J.* **2012**, *109*, 697–704.
3. Eamon, C.D.; Jensen, E.A.; Grace, N.F. Life-cycle cost analysis of alternative reinforcement materials for bridge superstructures considering cost and maintenance uncertainties. *J. Mater. Civ. Eng.* **2012**, *24*, 373–380. [CrossRef]
4. Imjai, T.; Guadagnini, M.; Pilakoutas, K. Bend strength of FRP bars: Experimental investigation and bond modeling. *J. Mater. Civ. Eng.* **2017**, *29*, 04017024. [CrossRef]
5. Koutchoukali, N.-E.; Belarbi, A. Torsion of High-Strength Reinforced Concrete Beams and Minimum Reinforcement Requirement. *ACI Struct. J.* **2001**, *98*, 462–469.
6. Fang, I.-K.; Shiau, J.-K. Torsional Behavior of Normal- and High-Strength Concrete Beams. *ACI Struct. J.* **2004**, *101*, 304–313.
7. Thomas, T.C.H. Torsion of Structural Concrete A Summary on Pure Torsion. *ACI Symp. Pap.* **1968**, *18*, 165–178.
8. Hamdy, M.; Benmokrane, B. Torsion Behavior of Concrete Beams Reinforced with Glass Fiber-Reinforced Polymer Bars and Stirrups. *ACI Struct. J.* **2015**, *112*, 543–552.
9. Hamdy, M.; Benmokrane, B. Reinforced Concrete Beams with and without FRP Web Reinforcement under Pure Torsion. *J. Bridge Eng.* **2016**, *21*, 04015070.
10. Hamdy, M.; Omar, C.; Benmokrane, B. Torsional Moment Capacity and Failure Mode Mechanisms of Concrete Beams Reinforced with Carbon FRP Bars and Stirrups. *J. Compos. Constr.* **2015**, *19*, 04014049.
11. Hadhood, A.; Gouda, M.G. Torsion in concrete beams reinforced with GFRP spirals. *Eng. Struct.* **2020**, *206*, 110174. [CrossRef]
12. Xiong, H.; Li, B.; Jiang, J. Load path dependence of strain and stress for confined concrete. *Mag. Concr. Res.* **2016**, *68*, 604–618. [CrossRef]
13. Deifalla, A.; Hamed, M.; Saleh, A.; Ali, T. Exploring GFRP bars as reinforcement for rectangular and L-shaped beams subjected to significant torsion: An experimental study. *Eng. Struct.* **2014**, *59*, 776–786. [CrossRef]
14. Zhou, J.; Shen, W.; Wang, S. Experimental study on torsional behavior of FRC and ECC beams reinforced with GFRP bars. *Constr. Build. Mater.* **2017**, *152*, 74–81. [CrossRef]
15. Deifalla, A. Torsional Behavior of Rectangular and Flanged Concrete Beams with FRP Reinforcements. *J. Struct. Eng.* **2015**, *141*, 04015068. [CrossRef]
16. Mostafa, I.T.; Mousa, S.; Mohamed, H.M.; Benmokrane, B. Experimental and Analytical Behavior of GFRP-Reinforced Concrete Box Girders under Pure Torsion. *J. Compos. Constr.* **2024**, *28*, 04023064. [CrossRef]

17. Hu, X.; Xue, W.; Xue, W. Bond properties of GFRP rebars in UHPC under different types of test. *Eng. Struct.* **2024**, *314*, 118319. [CrossRef]
18. *CAN/CSA S6:19*; Canadian Highway Bridge Design Code (CAN/CSA S6:19). Canadian Standards Association: Rexdale, ON, Canada, 2019.
19. *ACI 440.1R-15*; Guide for the Design and Construction of Structural Concrete Reinforced with FRP Bars. ACI Committee: Farmington Hills, MI, USA, 2015.
20. *AASHTO GFRP-RC 2018*; Bridge Design Guide Specifications for GFRP-Reinforced Concrete. American Association of State Highway and Transportation Officials: Washington, DC, USA, 2018.
21. *GB 50608-2020*; Technical Standard for Fiber Reinforced Polymer (FRP) in Construction. China Planning Press: Beijing, China, 2020.
22. *ACI 440.11-22*; Building Code Requirements for Structural Concrete Reinforced with Glass Fiber Reinforced Polymer (GFRP) Bars-Code and Commentary. ACI Committee: Farmington Hills, MI, USA, 2023.
23. *CAN/CSA S806-12*; Design and Construction of Building Structures with Fibre-Reinforced Polymers. Canadian Standards Association: Mississauga, ON, Canada, 2012.
24. *GB/T 50081-2002*; Standard for Test Method of Mechanical Properties on Ordinary Concrete. China Building Industry Press: Beijing, China, 2002.
25. *ACI 440.3R-12*; Guide Test Methods for Fiber Reinforced Polymer Composites for Reinforcing or Strengthening Concrete and Masonry Structures. ACI Committee: Farmington Hills, MI, USA, 2012.
26. Xue, W.; Bai, H.; Hu, X.; Jiang, J. A Composite Torsion Test Loading Device of a Beam Member and a Test Method for Combined Action of Shear and Torsion. *Chinese Patent. CN202211595007.3.* 2022.
27. Razaqpur, A.G.; Bencardino, F.; Rizzuti, L.; Spadea, G. FRP reinforced/prestressed concrete members: A torsion design model. *Compos. Part B Eng.* **2015**, *79*, 144–155. [CrossRef]
28. *ACI 318-19*; Building Code Requirements for Structural Concrete Commentary on Building Code Requirements for Structural Concrete. ACI Committee: Farmington Hills, MI, USA, 2019.
29. *EN 1992-1-1*; Eurocode 2: Design of Concrete Structures- Part 1-1: General Rules and Rules for Buildings. European Committee for Standardization: Brussels, Belgium, 1992.

Disclaimer/Publisher's Note: The statements, opinions and data contained in all publications are solely those of the individual author(s) and contributor(s) and not of MDPI and/or the editor(s). MDPI and/or the editor(s) disclaim responsibility for any injury to people or property resulting from any ideas, methods, instructions or products referred to in the content.

Check for updates

Research Paper

Advances in Structural Engineering

Advances in Structural Engineering
2025, Vol. 28(8) 1489–1512
© The Author(s) 2024
Article reuse guidelines:
sagepub.com/journals-permissions
DOI: 10.1177/13694332241307724
journals.sagepub.com/home/ase
Sage

A modified softened truss model and strength prediction formula for fiber-reinforced polymer reinforced concrete members under pure torsion

Eslam M Saleh[1], Jiafei Jiang[1] and Weichen Xue[1]

Abstract

A modified rotating-angle softened truss model (RA-STM) is proposed for analyzing the torsional behavior of fiber-reinforced polymer-reinforced concrete (FRP-RC) members under pure torsion. In the modified model, a generalized tension stiffening model is developed with consideration of discrepancy in the modulus of reinforcement. Furthermore, a robust numerical model is developed by refining the RA-STM as a system of nonlinear equations instead of a trial-and-error technique, which can significantly improve computational efficiency. The proposed model is verified against the experimental results of FRP-RC members, yielding an average test-to-predicted torsional strength ratio of 1.04 with a coefficient of variation of 11.66%. Moreover, the predicted torque-twist response, reinforcement strain, concrete strain, and failure modes can closely agree with the experimental results. At last, the adapted model is utilized in a parametric study to investigate the influence of key variables on the torsional behavior of FRP-RC members. Nonlinear regression analyses are performed to propose a semiempirical strength prediction formula and balanced stirrup ratio for the FRP-RC members under pure torsion.

Keywords

torsional behavior, rotating-angle softened truss model, tension stiffening, FRP-RC members, torsional strength

Introduction

Fiber-reinforced polymer (FRP) reinforcement is a promising alternative to steel reinforcement because it has exceptional corrosion resistance and high tensile strength (Hu et al., 2023; Mohamed et al., 2015; Mohamed and Benmokrane, 2015; Razaqpur et al., 2015). By incorporating FRP reinforcement, the service life and durability of reinforced concrete (RC) structures can be significantly improved (Deifalla et al., 2014; Karbhari et al., 2003; Peng et al., 2020; Xiong et al., 2016) compared with other advanced materials and techniques (Hu et al., 2024a; Liao et al., 2024; Walraven, 2021). To date, extensive experimental and theoretical studies have been conducted to investigate the axial, flexural, and shear responses of FRP-RC members. Nevertheless, in limited experimental and theoretical studies, behavior and design methods for FRP-RC members under torsion have been studied (Mohamed and Benmokrane, 2015, 2016; Mohamed et al., 2015).

Recently, experimental investigations of the pure torsional response of FRP-RC members have garnered significant attention since the torsional load is a typical loading condition, particularly in spandrel or curved beams (ACI 445, 2013; Majed et al., 2021). Moreover, the behavior of beams under pure torsion is the basis for understanding the failure mechanism of beams under combined torsion, shear, and flexure. The existing investigations focused on examining the influence of different types of concrete (i.e., normal-weight concrete and high-performance concrete) (Mostafa et al., 2023a, 2023b), cross-sectional geometries (solid, hollow, and L-shaped) (Deifalla et al., 2014; Mohamed and Benmokrane, 2015, 2016; Mohamed et al., 2015; Mostafa et al., 2023a), transverse reinforcement ratio (Mohamed and Benmokrane, 2015, 2016; Mohamed et al., 2015;

[1]College of Civil Engineering, Tongji University, Shanghai, China

Corresponding authors:
Jiafei Jiang, College of Civil Engineering, Tongji University, No.1359 Siping Rd, Shanghai 200092, China.
Email: jfjiang@tongji.edu.cn

Weichen Xue, College of Civil Engineering, Tongji University, No.1359 Siping Rd, Shanghai 200092, China.
Email: xuewc@tongji.edu.cn

Mostafa et al., 2024a), and stirrup types (rectilinear and spiral) (Hadhood et al., 2020; Mostafa et al., 2023a, 2024b). The test results show that the torsional behavior of FRP-RC members can be categorized into three stages: before cracking, after cracking, and failure. Before cracking, FRP-RC members exhibit similar linear elastic torque-twist responses mainly related to the concrete resistance itself (Deifalla et al., 2014; Mohamed and Benmokrane, 2015, 2016; Mohamed et al., 2015). After cracking, an interior torque is created by the circulatory shear flow around the perimeter of the cross-section to resist the exterior torque. This shear flow forms diagonal concrete struts balanced by longitudinal and transverse reinforcements, creating space truss action influenced by the mechanical properties of the reinforcement (Hsu and Mo, 2010; Mohamed and Benmokrane, 2015, 2016; Mohamed et al., 2015; Razaqpur et al., 2015). During this stage, it has been found that FRP-RC members experience higher tensile strains in the direction perpendicular to concrete struts compared to steel-RC counterparts, due to the lower Young's modulus of the reinforcement in both the longitudinal and transverse directions (Deifalla et al., 2015; Hadhood et al., 2020; Mohamed and Benmokrane, 2015, 2016; Mohamed et al., 2015). This, in turn, significantly affects the tensile and compressive behavior of concrete struts and the capacity of the beam. At the failure stage, FRP-RC members fail due to either the crushing of concrete struts or the rupture of stirrups, with FRP stirrups exhibiting non-uniform strain distribution (Hadhood et al., 2020; Mohamed and Benmokrane, 2015, 2016; Mohamed et al., 2015; Razaqpur et al., 2015). The test results indicate that as the stirrups ratio increases, the torsional strength improves, along with post-peak stiffness, and the failure mode changes from stirrup rupture to concrete strut crushing. All in all, the test's observations demonstrated that FRP-RC beams under pure torsion have a similar failure mechanism as steel-RC beams, while they have differences in failure modes and ultimate strain in stirrups due to the difference in reinforcement material properties and interaction between reinforcement and concrete.

For further investigating key factors' effects on the torsional behavior of RC beams, extensive theoretical and numerical models have been developed to simulate the torsional mechanisms of RC members. Skew-bending theory (McMullen and Warwaruk, 1967) is the first theory developed for steel-RC beams to predict the torsional capacity by considering the equilibrium of forces along a skew plane at failure. However, this approach cannot directly predict the torsional capacity for FRP-RC beams, as the stress in longitudinal reinforcement, stirrups, and concrete compression struts cannot be directly obtained, while the ultimate stress in steel reinforcement, stirrups, and concrete is obvious. Therefore, this approach has not been adapted for FRP-RC members.

Since the torsional mechanism of FRP-RC beams is more complicated than that of steel-RC beams. The regression analysis technique was adopted for empirical models associated with space truss analogy (STA) (Deifalla, 2021; Deifalla et al., 2015; Mostafa et al., 2024a). However, these models were developed from limited test data (no larger than 15 specimens) of beams that failed due to stirrup rupture. Similarly, some guidelines for designing FRP-RC beams under torsion, such as CSA S806-12 (2021) and CSA S6 (2019), have adopted formulas from the RC structural codes for steel-RC members. These formulas have been modified to account for the reinforcement's mechanical properties, including Young's modulus and stirrup bend strength. However, such modifications may lead to overly conservative predictions in many cases (Hassan and Deifalla, 2016; Mohamed and Benmokrane, 2015, 2016; Mohamed et al., 2015; Mostafa et al., 2024a). Generally, these models have not fundamentally considered the effect of the interaction between concrete and FRP reinforcement and cannot predict the entire torque–twist relationship of FRP-RC members.

Up to now, the most advanced model that can predict the torque-twist curve is based on compression field theory (CFT), which was introduced by treating cracked concrete as a uniform material with distinct stress–strain characteristics. This theory formulates equilibrium, compatibility, and material constitutive laws based on average stresses and strains (Collins and Mitchell, 1980). There are two typical CFT-based approach models: the rotating-angle softened truss model (RA-STM) and the fixed-angle softened truss model (FA-STM). Both models accounted for the softening coefficient of concrete when it is subject to biaxial compression and tensile stressing. The RA-STM model neglects the shear stress along the cracks for simplicity, although some contribution exists due to aggregate interlocking (Pang and Hsu, 1996). To address this, Pang and Hsu (1996) proposed the FA-STM, which incorporates a shear stress component along the crack with fixed angle orientation relative to principal applied loads. However, the solution for FA-STM is significantly more complex than that for RA-STM, and the aggregate interlocking along cracks for FRP-RC members is considerably less significant. This is because larger crack widths in FRP-RC, resulting from the lower axial rigidity and bond performance of FRP reinforcement compared to steel (Hu et al., 2024b; Liang et al., 2023; Mohamed and Benmokrane, 2015, 2016; Mohamed et al., 2015; Xue et al., 2014). And hence, Deifalla (2015) evaluated the torsional behavior of FRP-RC using the Modified CFT . The proposed model assumed that the tension stiffening model of steel-RC members could be applied to FRP-RC members. However, this assumption was contradicted by experimental results that reveal concrete reinforced with FRP reinforcement exhibits

more significant tension stiffening than concrete reinforced with steel bars because of the low modulus of elasticity (Bischoff and Paixao, 2004; Nayal and Rasheed, 2006).

To sum up, the RA-STM approach is suitable for predicting the torsional behavior of FRP-RC beams. However, the existing models have been developed by modifying existing steel-RC torsional models and do not consider the interaction between FRP reinforcement and concrete (Deifalla, 2015, 2021; Deifalla et al., 2015; Hassan and Deifalla, 2016; Mostafa et al., 2024a). Thus, the primary challenge lies in adequately incorporating FRP reinforcement's influence on cracked concrete's constitutive behavior under tension and compression. Secondly, FRP stirrups do not have a yield plateau and exhibit linear elastic behavior until failure. The strain distribution in FRP stirrup legs across cracks is non-uniform, which has been observed in the tests for beams under either pure torsion or shear (Issa et al., 2016; Mohamed and Benmokrane, 2015, 2016; Mohamed et al., 2015). Therefore, it is necessary to incorporate an ultimate characteristic value for the FRP stirrups along the spiral cracks when the stirrup ruptures. Besides, the solution procedure of the original RA-STM relies on an iterative method that requires numerous initial trials to converge to the correct solution. This method is time-consuming and numerically unstable; therefore, it is essential to improve the computational efficiency of this complex model.

To overcome this challenge, a consistent torsional model for FRP-RC members is proposed in this paper. The model validates a constitutive compressive concrete model for FRP-RC members and proposes a generalized tension stiffening approach for FRP- and steel-RC members. In addition, an effective numerical tool is developed as an alternative to the trial-and-error technique. Furthermore, a parametric study is performed to examine the impact of the concrete compressive strength, longitudinal reinforcement ratio, and transverse reinforcement ratio on the torsional behavior of FRP-RC members. Finally, nonlinear regression analyses are performed to propose a strength prediction formula and balanced stirrup ratio.

Modified rotating-angle softened truss model (RA-STM)

The proposed model is based on RA-STM, which integrates the concrete tension stiffening model, thereby significantly influencing the post-cracking response of FRP-RC members (Bischoff and Paixao, 2004; Nayal and Rasheed, 2006). RA-STM can analyze the biaxial compression-tension behavior of concrete while considering the effect of elastic modulus. Thus, the RA-STM model can adapt the impact of reinforcement material on both reinforcement and concrete constitutive models. Moreover, RA-STM's foundational assumptions, such as disregarding dowel action, align well with the behavior of FRP-RC members. Given the lower transverse strength of FRP bars (about 10%–20% of their longitudinal strength) compared to steel bars, dowel action in these members is considered negligible (Liang et al., 2023). The details of the modified RA-STM model are listed in Appendix A.

Refined RA-STM procedure

A new robust numerical model is presented in this section as a replacement for the trial-and-error technique of the original RA-STM model. The solution procedure of the original RA-STM relies on an iterative method that requires numerous initial trials to converge to the correct solution, which is time-consuming and numerically unstable. Therefore, the RA-STM was formulated and solved as a set of nonlinear equations using MATLAB algorithms.

Objective function and primary variables. The original RA-STM neglects the influence of concrete tension stiffening (Hsu and Mo, 1985), leading to a substantial overestimation of deformation (Greene, 2006; Hsu and Mo, 2010). Therefore, for an accurate prediction of the entire load–deformation behavior of the FRP-RC structure, the influence of the concrete tensile stress σ_r must be considered (Greene, 2006; Greene and Belarbi, 2009a). This increases the number of unknown variables and governing equations, that is, 22 unknown variables and 19 governing equations. However, this system of governing equations becomes solvable when ε_{rs} is selected as the increment variable and two known variables ($\sigma_L = \sigma_T = 0$) are used for members under pure torsion. Then, the torque–twist envelope can be traced with an increment of ε_{rs} based on the following procedure.

The equilibrium and compatibility equations and material constitutive laws were used to develop the objective function of the proposed model. This function includes the following independent variables that need to be solved.

$$\begin{bmatrix} F_{RA-STM}(1) \\ F_{RA-STM}(2) \\ F_{RA-STM}(3) \\ F_{RA-STM}(4) \\ F_{RA-STM}(5) \\ F_{RA-STM}(6) \end{bmatrix} = \begin{bmatrix} \sigma_d \cos^2\alpha + \sigma_r \sin^2\alpha + \rho_L f_L \\ \sigma_d \sin^2\alpha + \sigma_r \cos^2\alpha + \rho_T f_T \\ \varepsilon_L + \varepsilon_T - \varepsilon_r - \varepsilon_d \\ \sigma_d - k_1 \zeta f_c' \\ \sigma_r - k_t f_{cr} \\ t_d - \dfrac{A_o}{P_o}\left[\dfrac{(-\varepsilon_d)(\varepsilon_r - \varepsilon_d)}{(\varepsilon_L - \varepsilon_d)(\varepsilon_T - \varepsilon_d)}\right] \end{bmatrix} \quad (1)$$

The objective function, equation (1), is compactly defined as $F_{RA-STM}(x) = 0$, where x represents a vector of primary variables. These primary variables are numerically varied until the objective function approaches zero. In the

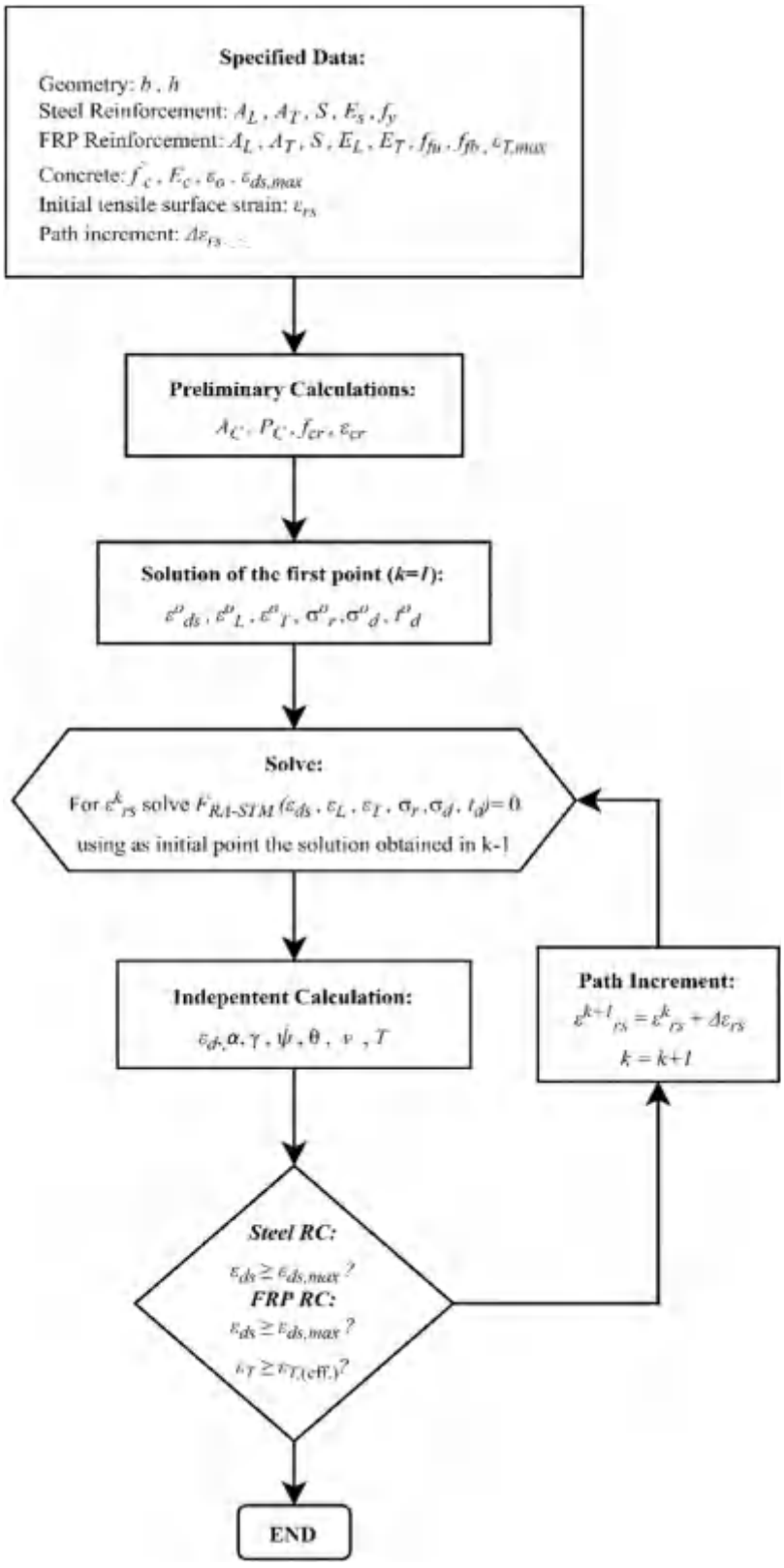


Figure 1. Flowchart for modified RA-STM.

proposed procedure, these primary variables are the concrete compressive principal stress and strain (σ_d and ε_{ds}), as well as the longitudinal and transverse strains (ε_L and ε_T) and the thickness of the shear flow t_d. An initial estimation of these variables (ε^0_{ds}, ε^0_L, ε^0_T, σ^0_d and t^0_d) was made for the first solution point based on Mohr's theory and the theory of elasticity of St. Venant (Hsu and Mo, 2010).

Solution procedure. The flowchart in Figure 1 outlines the steps required to implement the refined RA-STM procedure. The cross-sectional dimensions and reinforcement mechanical properties were given. The longitudinal reinforcement of the unsymmetrical reinforced section was considered to be equivalent to a symmetrical section according to the side panel with lower reinforcement. In an unsymmetrical section, the top panel of the tubed section has less longitudinal reinforcement than the bottom panel. As a result, the ultimate strength of the bottom panel cannot be achieved, and the ultimate shear strength of the top panel becomes critical in determining the ultimate torsional capacity (Rahal, 2007).

A displacement–controlled approach was implemented by entering an initial value for the strain ε_{rs} and path increment $\Delta\varepsilon_{rs}$.The primary variables (ε_{ds}, ε_L, ε_T, σ_d and t_d) were obtained for each increment by solving the objective function $F_{RA-STM}(x) = 0$ using the initial estimates and within an acceptable tolerance of 10^{-8}. These estimates (ε^0_{ds}, ε^0_L, ε^0_T, σ^0_d and t^0_d) were used to calculate only the first solution point (with index k = 1). The objective function $F_{RA-STM}(x)$ is solved using MATLAB's built-in function fsolve. This function is designed for solving systems of nonlinear equations numerically. For the residual solution points, ε_{rs} increased by $\Delta\varepsilon_{rs}$ monotonically for each step ($\varepsilon^{k+1}_{rs} = \varepsilon^k_{rs} + \Delta\varepsilon_{rs}$), and the initial estimation for each increment was set as the solution point from the preceding step. In fact, ε_{rs} varies monotonically from zero, and $\Delta\varepsilon_{rs}$ was selected to ensure that the calculations are performed at the cracking point. The computation process was carried out until failure occurred. The failure criterion of the computational model is based on experimental observations; the failure of FRP-RC members occurs by either stirrup rupture or concrete strut crushing (Hadhood et al., 2020; Mohamed and Benmokrane, 2015, 2016; Mohamed et al., 2015). Therefore, the concrete strut's ultimate compressive strain and the stirrup's ultimate strain define the two failure modes. This failure criterion is discussed later in the paper.

The proposed algorithm ensured both numerical stability and computational efficiency. On an ordinary computer (Intel(R) Core(TM) i5-6200U CPU @ 2.30 GHz), the average processing time for analyzing FRP- or steel-RC members was approximately 5 seconds per beam. As a result, the modified RA-STM proves to be an efficient tool suitable for research purposes and practical applications and simulations.

Compressive stress–strain relationship of concrete

Compared with concrete's uniaxial compression behavior, the response exhibits notable discrepancies if the compression is combined with a tensile strain in the transverse direction. This interaction leads to the primary property of biaxial constitutive models of concrete as the softening of peak stress (Hsu and Mo, 1985, 2010; Vecchio and Collins, 1986).

The commonly adopted base model in RA-STM is proposed by Vecchio and Collins (1986), namely, equation (2), where ζ is the softening coefficient.

$$\sigma_d = \zeta f'_c \left[2\left(\frac{\varepsilon_d}{\varepsilon_o}\right) - \left(\frac{\varepsilon_d}{\varepsilon_o}\right)^2 \right] \tag{2}$$

Vecchio and Collins (1981, 1986) conducted biaxial testing on the panel, revealing that the principal tensile strain ε_r is the primary variable controlling the softening coefficient. Based on their findings, they proposed the characteristic function for ζ as follows

$$\zeta = \frac{1}{0{:}8 + 170\varepsilon_r} \tag{3}$$

Japanese research groups (Izumo et al., 1992; Mikame et al., 1991; Miyahara et al., 1987; Shirai and Noguchi, 1989) further demonstrated the substantial effect of ε_r on the softening coefficient. The group of Prof. Maekawa tested hollow RC cylinders subjected to interior pressure and longitudinal loads, and the suggested softening coefficient is defined as follows (Izumo et al., 1992; Miyahara et al., 1987):

$$\begin{gathered} \zeta = 1{:}0 \text{ when } \varepsilon_r \le 0{:}0012 \\ \zeta = 1{:}15 - 125\varepsilon_r \text{ when } 0{:}0012 \le \varepsilon_r \le 0{:}0044 \\ \zeta = 0{:}6 \text{ when } \varepsilon_r > 0{:}0044 \end{gathered} \tag{4}$$

The group of Prof. Noguchi tested RC panels (Shirai and Noguchi, 1989) and proposed another characteristic

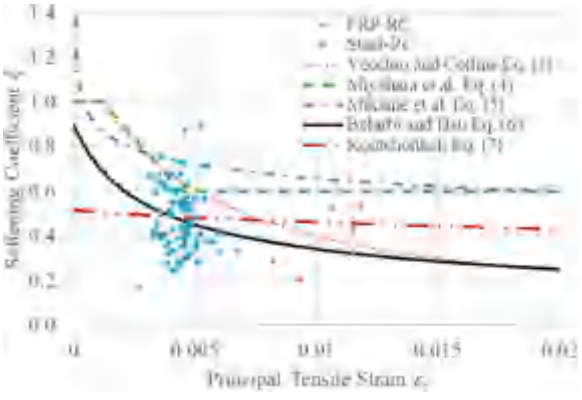


Figure 2. Verification of the influences of tensile strain on softening coefficients.

Table 1. Performance of softening coefficient equations against FRP- and steel-RC members.

		Vecchio and Collins (1986) equation (3)	Miyahara et al. (1987) equation (4)	Mikame et al. (1991) equation (5)	Belarbi and Hsu (1991) Equation (6)	Koutchoukali (1998) Equation (7)
Steel RC	Mean	0.72	0.75	0.64	0.99	0.94
	SD	0.22	0.23	0.19	0.30	0.27
	CV %	30.06	30.52	29.90	29.93	28.50
FRP RC	Mean	1.02	0.65	0.60	1.17	0.92
	SD	0.41	0.23	0.22	0.45	0.32
	CV %	40.60	35.01	36.12	38.52	34.60

function for the softening coefficient (Mikame et al., 1991):

$$\zeta = \frac{1}{0{:}27 + 2{:}71\varepsilon_r^{0{:}167}} \tag{5}$$

Belarbi and Hsu (1991, 1995) thoroughly examined the softening coefficients and found that studying the softening coefficient using small test specimens is complex. Therefore, they conducted extensive test research and proposed an expression of ζ as a function of ε_r as follows:

$$\zeta = \frac{0{:}9}{\sqrt{1 + 600\varepsilon_r}} \tag{6}$$

Koutchoukali (1998) developed a softening coefficient by analyzing more than 100 prismatic members tested under pure torsion. Their study concluded that the softening of strains is not significant, while stress softening was considered as follows:

$$\zeta = \frac{3}{\sqrt{f_c'}\left(1 + 0{:}056\left|\frac{\varepsilon_r}{\varepsilon_d}\right|^{0{:}75}\right)} \tag{7}$$

The above functions for the softening coefficient were all determined from steel-RC members. The low Young's modulus of FRP bars results in relatively high principal tensile strains (Mohamed and Benmokrane, 2015, 2016; Mohamed et al., 2015). This, in turn, may lead to a significant effect on the compressive strength of the concrete strut and beam's capacity compared to those of steel-RC members (Kueres and Hegger, 2020; Mohamed et al., 2015). Since a biaxial constitutive concrete model for RA-STM has yet to be confirmed for FRP-RC members, the softening coefficient was validated based on the global response of FRP-RC members under pure torsion. Among these members, the failure mode was limited to concrete crushing, as the effective concrete compressive strength governs it, more precisely, the softening coefficient ζ (Kueres and Hegger, 2020).

Figure 2 and Table 1 predict the softening coefficient when the theoretical torsional strength $T_{u,th}$ equals the experimental torsional strength $T_{u,exp}$ for the FRP- and steel-RC members and compare the results with the softening coefficients estimated by equations (3)–(7). The results indicate that the softening phenomenon is more significant in FRP-RC members compared to steel-RC members. Moreover, the results demonstrate that the softening coefficient proposed by Belarbi and Hsu (1991), equation (6), effectively captures the softening behavior of FRP- and steel-RC members. Hence, the compression stress-strain model is confirmed for both FRP- and steel-RC members.

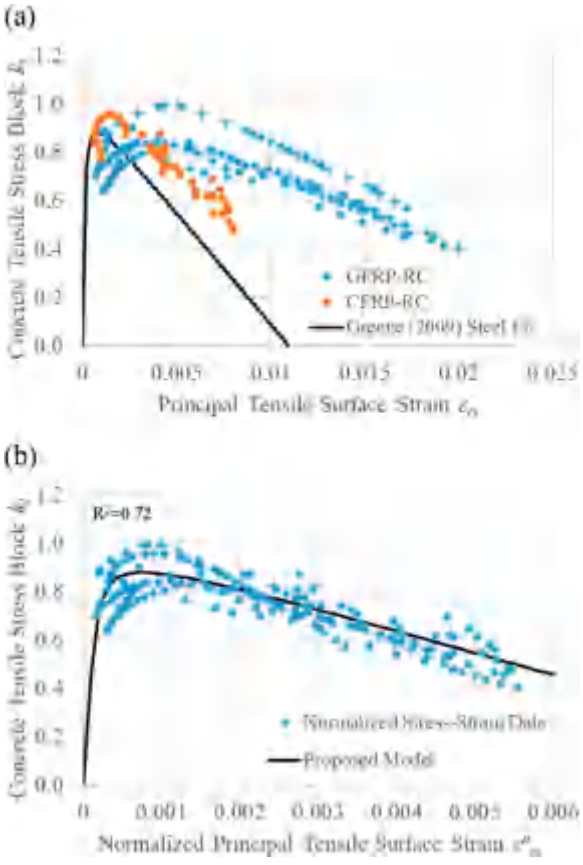


Figure 3. Normalized data and proposed tension stiffening model (a) before normalization, (b) after normalization.

Table 2. Comparison of the modified RA-STM with test results of FRP-RC.

Ref.		Experimental					Average ultimate stirrups strain						Effective stirrups strain		
		Specimen name	$T_{cr,exp}$ (KN.m)	$T_{u,exp}$ (KN.m)	$\theta_{u,exp}$ (Rad/m)	Failure mode[a]	$T_{cr,th}$ (KN.m)	$T_{cr,exp}=T_{cr,th}$	$T_{u,th}$ (KN.m)	$T_{u,exp}=T_{u,th}$	$\theta_{u,th}$ (Rad/m)	$\theta_{u,exp}=\theta_{u,th}$	$T_{u,th}$ (KN.m)	$T_{u,exp}=T_{u,th}$	Failure mode[a]
(Mohamed and Benmokrane, 2015, 2016)	GFRP	BG 60	27.76	56.86	0.075	CC	30.88	0.90	61.53	0.92	0.074	1.01	61.53	0.92	CC
		BG 120	27.46	52.65	0.084	SR	27.97	0.98	52.58	1.00	0.085	0.99	45.53	1.16	SR
		BG 180	26.19	41.75	0.064	SR	26.82	0.98	46.34	0.90	0.091	0.70	37.91	1.10	SR
		BG 240	26.14	34.17	0.057	SR	26.03	1.00	35.45	0.96	0.054	1.04	33.56	1.02	SR
		BG 300	25.98	29.89	0.051	SR	25.90	1.00	31.62	0.95	0.047	1.09	31.08	0.96	SR
(Hadhood et al., 2020)		BGST200	12.9	14.2	0.081	SR	9.70	1.33	14.90	0.95	0.078	1.04	14.90	0.95	SR
(Mohamed and Benmokrane, 2016; Mohamed et al., 2015)	CFRP	BC 60	30.14	69.28	0.041	CC	35.04	0.86	57.37	1.21	0.061	0.67	57.37	1.21	CC
		BC 120	30.45	62.88	0.045	SR	32.86	0.93	49.74	1.26	0.060	0.75	52.70	1.19	CC
		BC 180	29.87	49.4	0.036	SR	31.86	0.94	44.92	1.10	0.063	0.57	48.51	1.02	SR
		BC 240	27.35	39.38	0.0032	SR	31.35	0.87	34.96	1.13	0.002	1.36	40.43	0.97	SR
		BC 300	28.65	35.67	0.0030	SR	31.00	0.92	34.91	1.02	0.002	1.32	34.91	1.02	SR
		Mean						0.97		1.04		0.96		1.05	
		SD						0.13		0.12		0.26		0.10	
		CV %						13.12		11.66		27.02		9.58	

[a]CC = Concrete crushing, SR = Stirrups rupture occurs.

Tension stiffening for FRP-RC members

For an accurate prediction of the entire torsional behavior of FRP-RC members, it is essential to consider tension stiffening (Greene and Belarbi, 2009a), besides the constitutive behavior of concrete struts under compression. Tension stiffening describes the stiffness increment in the post-crack stage due to the transmission of stresses from the reinforcing bar to the boundary concrete. Experimental testing demonstrated that FRP-RC exhibits greater tension stiffening than steel-RC when the reinforcement ratio is the same, which can be attributed to the discrepancy in the modulus of the reinforcement bar and bond performance (Bischoff and Paixao, 2004; Nayal and Rasheed, 2006). Therefore, the tension stiffening models utilized for analyzing steel-RC members under torsion should be modified to account for the use of FRP reinforcement.

To date, there are two different approaches to characterize the tensile stiffening property for RC members under torsion based on smeared cracking: First, the average stress-strain behavior is determined from the biaxial tensile test on the reinforced panels using the special universal panel tester (Belarbi and Hsu, 1994). Second, the indirect calibration approach is based on the adoption of experimental results of RC members under pure torsion since the significant stiffness change in torsion-to-twist angle behavior is largely due to the post-cracking behavior of concrete struts (Greene and Belarbi, 2009a). The deviation between the direct and indirect methods has been demonstrated to be acceptable in the practice of steel-RC members. Due to the lack of in-plane tests for FRP-RC panels, the second approach was implemented to develop a generalized mathematical formula applicable to both FRP and steel reinforcement.

Regarding the base model for the concrete tensile, the principal tensile stress-strain behavior is modeled as the two-segment curve, that is, a linear ascending stage before cracking and a linear descending stage after cracking. Before cracking, the linear expression $\sigma_r = E_c\varepsilon_r$ was adopted, where the modulus of elasticity $E_c = 4700\sqrt{f'_c}$ according to ACI 440.1R-15 (2015). After cracking, the following simple linear expression, originally developed by Greene and Belarbi (2009a), was adopted:

$$\sigma_r = f_{cr}\left(1 - \frac{\varepsilon_r - \varepsilon_{cr}}{\varepsilon_{cr0} - \varepsilon_{cr}}\right) \quad \text{when } \varepsilon_r > \varepsilon_{cr} \tag{8}$$

where ε_{cr0} is a constant that needs to be determined through the calibration approach. f_{cr} is the crack strength to be determined according to the value proposed by Greene and Belarbi (2009a), which is irreverent to the reinforcement and was determined by the regression analysis of 280 data points from the results of steel-RC torsional members based on the RA-STM:

$$f_{cr} = 0{:}5\sqrt{f'_c} \tag{9}$$

Herein, the tensile stress block coefficient k_t, which considers the strain gradient along the cross-section of concrete strut subjected to out-of-plane bending in the shear flow zone, is adopted to determine the tensile behavior of concrete struts as follows:

$$k_t = \frac{\varepsilon_{rs}}{2\varepsilon_{cr}} \text{when } \varepsilon_{rs} \le \varepsilon_{cr} \tag{10a}$$

$$k_t = \frac{\varepsilon_{cr}}{2\varepsilon_{rs}} - \frac{(\varepsilon_{cr} - \varepsilon_{rs})(\varepsilon_{cr} - 2\varepsilon_{cr0} + \varepsilon_{rs})}{2\varepsilon_{rs}(\varepsilon_{cr} - \varepsilon_{cr0})} \text{when } \varepsilon_{rs} > \varepsilon_{cr} \tag{10b}$$

However, the post-cracking descending behavior differs due to variations in reinforcement stiffness. Therefore, a relative stiffness factor E_{re} in the principal tensile direction was proposed, as given by equation (11). The reasonability of this approach has been demonstrated through the experimental behavior between FRP- and steel-RC members under a direct tension test (Bischoff and Paixao, 2004). Herein, the relative stiffness factor for concrete reinforced with two perpendicular bars was determined based on the observation of an initial strut angle of 45° in existing experimental studies (Mohamed and Benmokrane, 2015, 2016).

$$E_{re} = \frac{E_L\rho_L + E_T\rho_T}{E_s(\rho_L + \rho_T)} \tag{11}$$

where ρ_L is the longitudinal reinforcement ratio ($\rho_L = A_L/P_o t_d$) and ρ_T is the transverse reinforcement ratio ($\rho_T = A_T/St_d$). Accordingly, the tensile stress block coefficient in equation (10b) can be normalized by $\varepsilon^n_{rs} = E_{re}(\varepsilon_{rs} - \varepsilon_{cr})$ as follows:

$$k_t = \frac{\varepsilon_{cr}}{2(\varepsilon^n_{rs} + \varepsilon_{cr})} + \frac{\varepsilon^n_{rs}(2\varepsilon_{cr} - 2\varepsilon_{cr0} + \varepsilon^n_{rs})}{2(\varepsilon^n_{rs} + \varepsilon_{cr})(\varepsilon_{cr} - \varepsilon_{cr0})} \quad \text{for } \varepsilon_{rs} > \varepsilon_{cr} \tag{12}$$

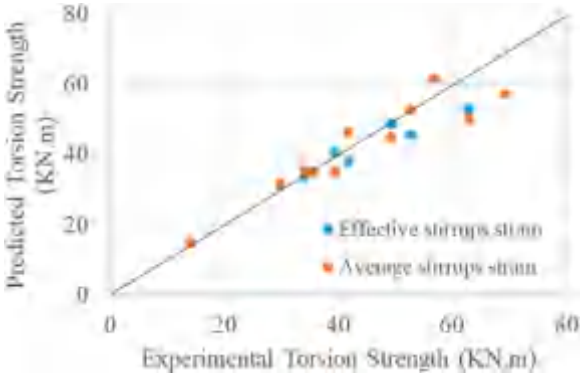


Figure 4. Predicted to experimental torsion strength using the effective and average stirrups strain.

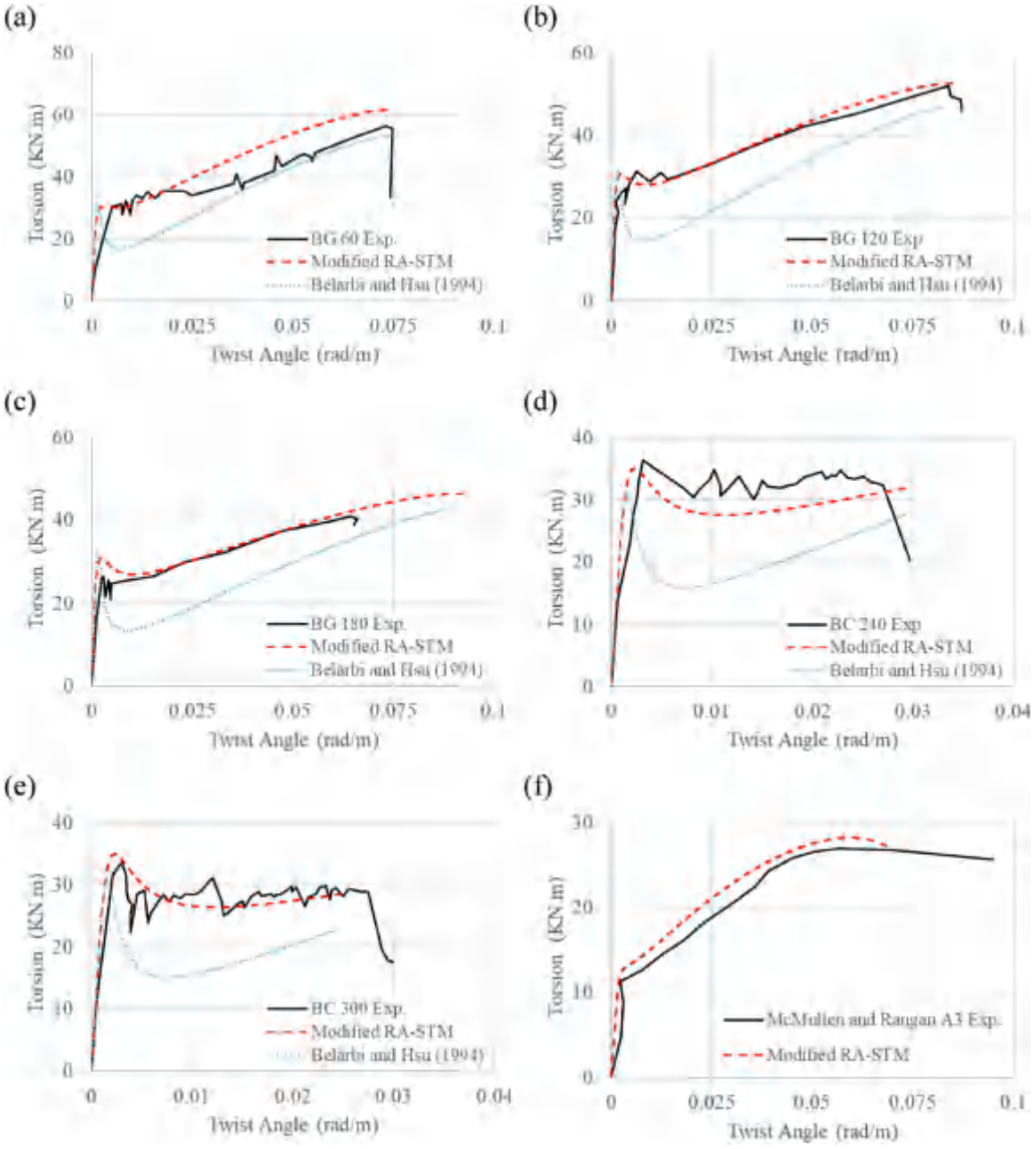


Figure 5. Experimental and predicted torsion behavior using the proposed model of beams (a)–(e) FRP-RC, (f)–(j) Steel-RC.

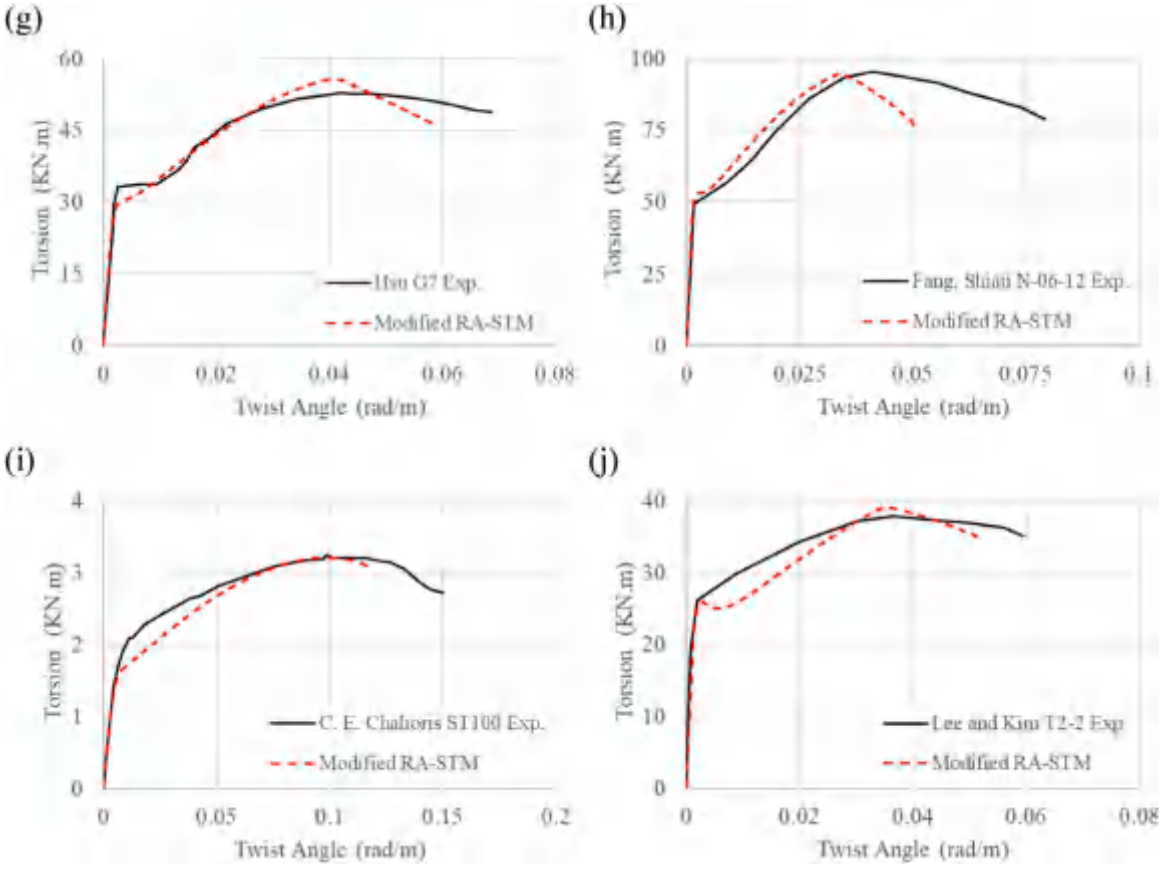


Figure 5. Continued.

For implementing the calibration approach (details presented in Greene, 2006), approximately 190 stress–strain points from four references regarding FRP-RC members (Hadhood et al., 2020; Mohamed and Benmokrane, 2015, 2016; Mohamed et al., 2015) were collected. The determined results of tensile stress-strain curves for FRP-RC members show that tension stiffening is significant and varies with the reinforcement modulus (Figure 3). By introducing the factor E_{re}, the nonlinear regression result shows an acceptable R^2 = 0.72 and the regressed constant value of 0.0055 for ε_{cr0} in equation (12). The feasibility of the generalized tension stiffening model for both FRP- and steel-RC members is further demonstrated in the following section.

Comparison of predictions and experimental results

Since the tension stiffening model considered the effect of reinforcement's modulus, a total of 103 torsion specimens, including FRP- and steel-RC members, were acquired from the literature to evaluate the performance of the modified RA-STM. However, a subset of specimens was excluded from the calibration database based on three criteria: (1) insufficient reinforcement ratio ($T_u \leq T_{cr}$); (2) high-performance concrete members, as the softening coefficient of concrete and the tension stiffening model were validated only for normal-weight concrete; and (3) hollow sections because their experimental torsional properties differ from those of solid sections in terms of cracking response, torsional stiffness, and ductility (Bernardo and Andrade, 2020). Tables 2 and B1 present both experimental and theoretical results for evaluating the behavior of FRP- and steel-RC members, specifically the cracking torque (T_{cr}), ultimate strength (T_u), and twist angle (θ_u). The performance of the model was evaluated by the experiment-to-prediction ratio's mean value ($\bar{x}$), standard deviation (SD), and coefficient of variation (CV).

Cracking and ultimate strength prediction

The results demonstrate the close prediction of cracking torque T_{cr} for FRP- and steel-RC members by the modified RA-STM ($\bar{x}$ = 0:97 for both) while maintaining an acceptable level of variability (CV = 13.12% and 14.36%, respectively). Moreover, the proposed model performs well in predicting the ultimate torque T_u for both FRP- and steel-RC

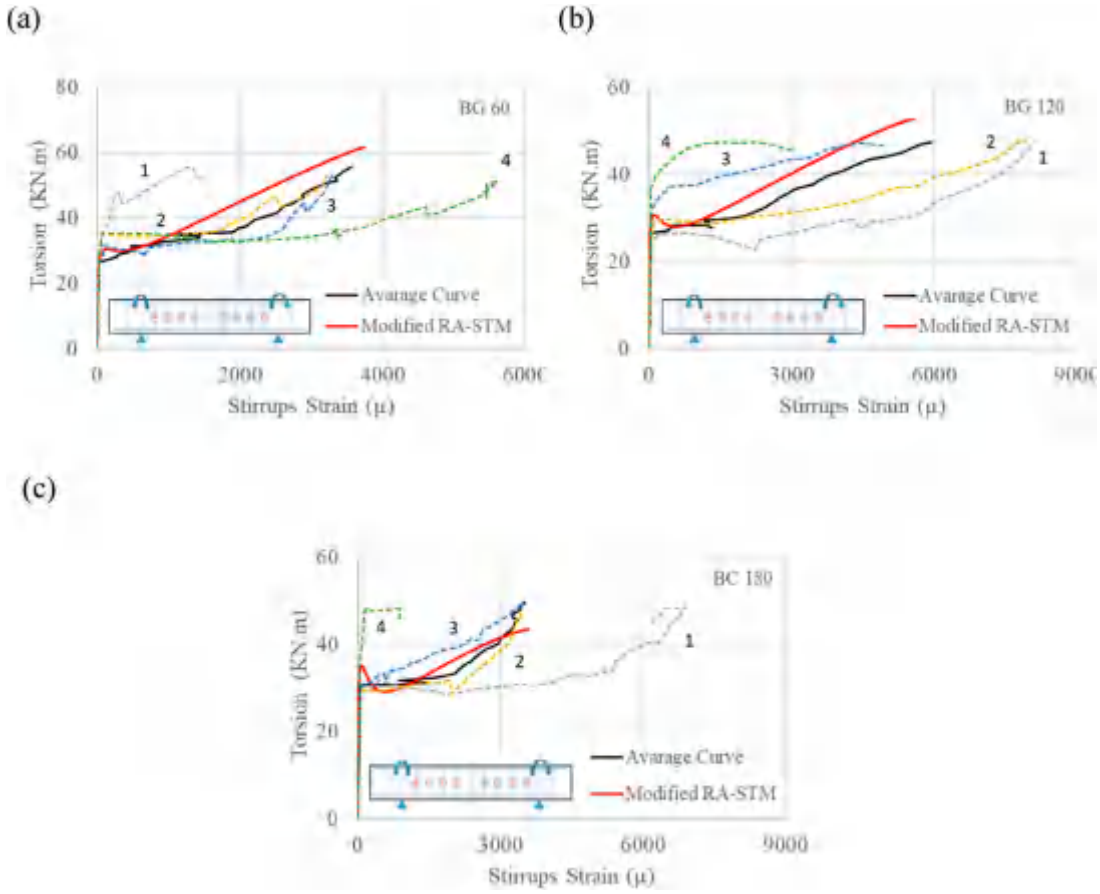


Figure 6. Predicted stirrups stain versus measured stirrup strain and average measured strain of beams (a) BG60, (b) BG120, and (c) BC180.

members ($\bar{x}$ = 1.04 and 1.00, respectively), with an acceptable degree of dispersion (CV = 11.66% and 13.88%, respectively). Furthermore, the prediction of the twist angle is reasonably accurate but shows a relatively high dispersion, with mean values of 0.96 and 1.18, corresponding to CV values of 27.02% and 26.34%, respectively. All in all, the modified RA-STM can accurately predict the torsional behavior of both FRP- and steel-RC members.

Failure mode

Based on experimental observations, the failure of FRP-RC members occurs by either stirrup rupture or concrete strut crushing (Mohamed and Benmokrane, 2015, 2016; Mohamed et al., 2015). Therefore, the concrete strut's ultimate compressive strain and the stirrup's ultimate strain define the two failure modes. The compressive failure strain of concrete was commonly set at 3500 με (Hsu and Mo, 1985, 2010; Mohamed and Benmokrane, 2016), while the stirrup's ultimate strain is the average stirrup strain across multiple cracks according to the smeared cracking concept. If the test results are unavailable, an effective stirrup strain value of $\varepsilon_{T\,(eff:)} = 3962$ με is proposed based on the average values of the available specimens with a CV of 44.7% (Table 2 and Figure 4). If the compared test specimens have the ultimate strain values, the experimental values would be adopted in the model for verification.

The determination of the concrete strut and FRP stirrup's ultimate strain permits the determination of the failure mode of FRP-RC members. Table 2 provides a comparison between the observed and theoretical failure modes for the FRP-RC members. The two main failure modes are identified as follows: the first is when the concrete crushes (CC) without stirrup rupture, and the second is when stirrup rupture occurs (SR). The proposed model accurately detected the failure mode of all GFRP and CFRP specimens except for BC120. In the case of BC120, the model predicted that the concrete was crushed, while the test exhibited that the crushing of the concrete occurred simultaneously with the rupture of the stirrups (Mohamed and Benmokrane, 2016). The difference in the prediction may be caused by the disparity of material properties.

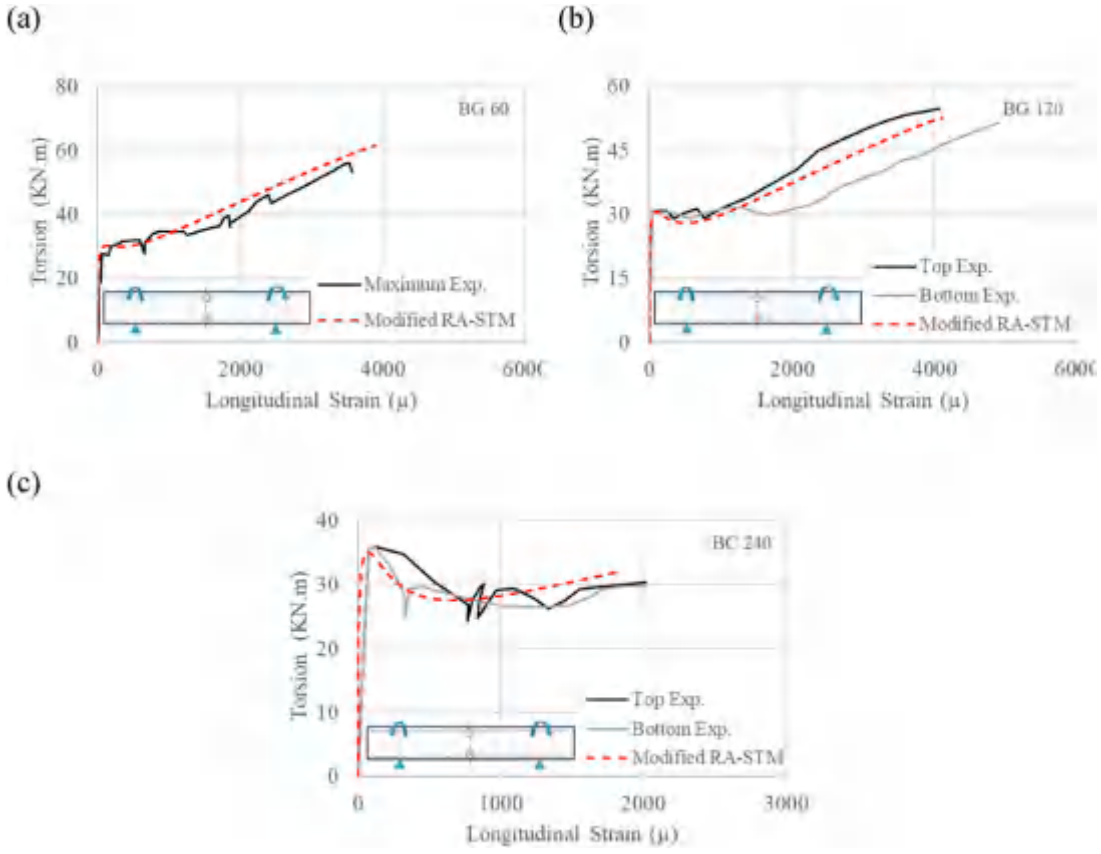


Figure 7. Predicted longitudinal bars stain versus measured strain of beams (a) BG60, (b) BG120, and (c) BC240.

Torsion-to-twist angle response

Figure 5(a)–(j) present the experimental and theoretical curves of torque T and twist angle θ for FRP- and steel-RC members subjected to pure torsion. It can be found that the proposed model accurately captures the overall response of the members throughout all stages, including the cracking and peak load stages.

The tension stiffening model proposed by Belarbi and Hsu (1994) is commonly used in current torsional models for steel-RC members. Figure 5(a)–(e) compare the predictions using the proposed tension stiffening model with the model using the Belarbi and Hsu model (1994) without considering the effect of the bar's modulus. The results confirm the findings of experimental tests showing that FRP-RC members exhibit greater tension stiffening than steel-RC members and the necessity of including the relative stiffness factor E_{re} for the tension stiffening model.

Reinforcement and concrete strain prediction

The modified RA-STM model can also predict the strain of critical reinforcement and concrete zone of FRP-RC members. Figure 6 shows the predicted stirrup strain compared to the measured strain and the average measured strain. In addition, Figure 7 shows the calculated longitudinal strain compared to the measured strain. Furthermore, Figure 8 presents the predicted surface concrete compressive strain compared to the measured strain in the test zone. The comparison results show that the prediction of the proposed model has a good agreement with the experimental observation of the average measured stirrup strain, the longitudinal strain of the reinforcement, and the concrete strain of FRP-RC members.

Parametric study on FRP-RC members

Since the modified RA-STM has been validated against several experimental aspects, it was utilized in a parametric study to examine the impact of critical variables on the torsional strength of FRP-RC members. The specimens in Mohamed et al. (2015) and Mohamed and Benmokrane (2015) were used as reference beams for the parametric analysis. The variables for the parametric study include the concrete compressive strength f_c' ranging from 20 to 50 MPa, transverse reinforcement ratio ρ_T ranging from 0.24% to 1.12%, and symmetrically distributed

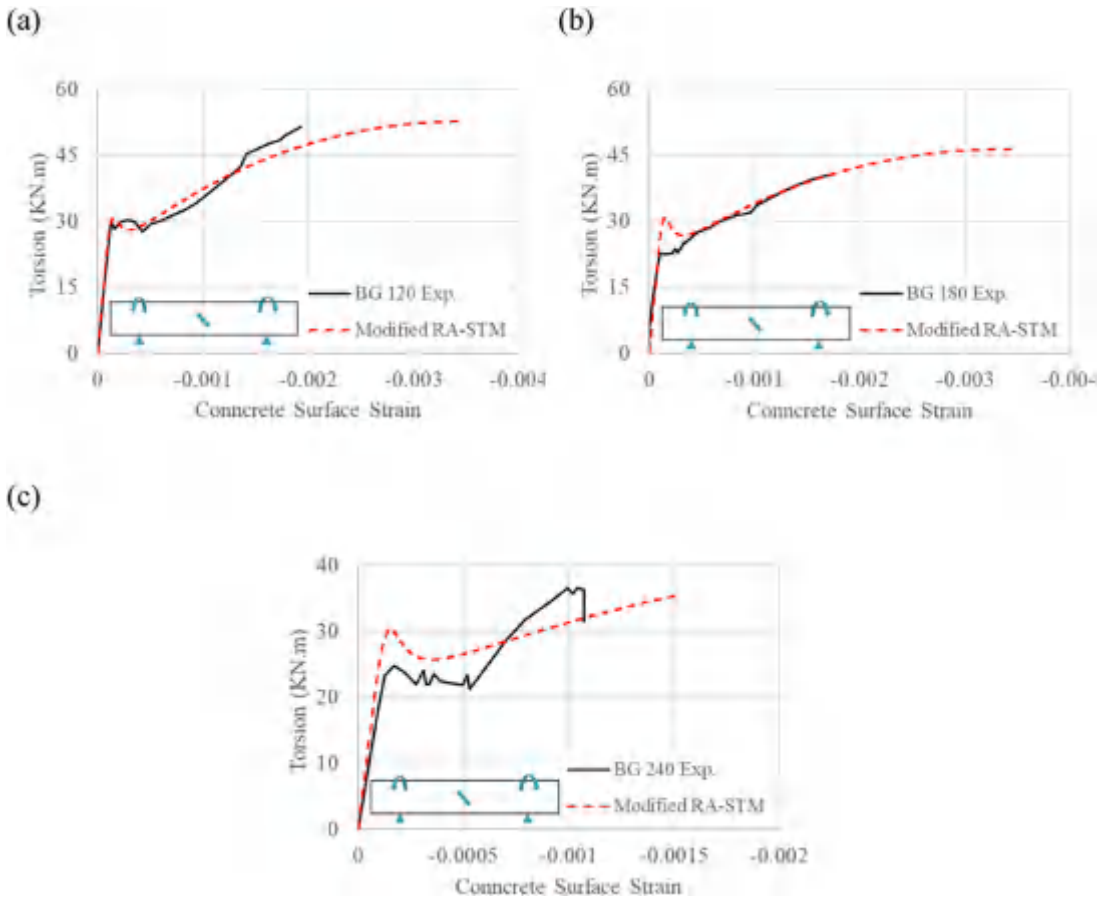


Figure 8. Predicted concrete surface stain versus measured strain of beams (a) BG120, (b) BG180, and (c) BG240.

longitudinal reinforcement ratio ranging ρ_L from 0.41% to 1.31%. The reinforcement ratios in the two directions were different to cover a wide range of diagonal strut angles. The parametric study included about 700 specimens.

Figure 9(a)–(c) demonstrate the effect of stirrups ratio on torsional strength. The results confirm that as the stirrup ratio increases, the resistance also increases and the mode of failure changes from stirrup rupture to concrete strut crushing. This relationship is more pronounced in beams with higher concrete compressive strength.

Figure 10(a)–(c) demonstrate the impact of longitudinal reinforcement ratio on resistance. The figures indicate that beams with a higher longitudinal and transverse reinforcement ratio exhibit greater resistance. Even with constant the stirrup ratio and concrete compressive strength, increasing the longitudinal reinforcement ratio enhances torsional strength, although it has minimal influence on altering the failure mode.

Both Figures 9 and 10 demonstrate the influence of concrete strength on torsional resistance. The results reveal that torsional resistance increases with the increase in concrete compressive strength, accompanied by a transition in failure mode from concrete crushing to stirrup rupture. Moreover, concrete strength exerts a more significant impact when concrete crushing predominates as the failure mode.

The parametric study confirms the experimental findings regarding the failure of FRP-RC members, consistently demonstrating that failure typically occurs due to either stirrup rupture or concrete strut crushing. Notably, longitudinal bar rupture was not observed across varying stirrup ratios, longitudinal bar ratios, or concrete compressive strengths. These results highlight the critical roles of stirrup reinforcement and concrete properties in determining overall torsional performance.

Semiempirical prediction formula for torsional strength

To date, two main types of prediction formulas have been utilized to predict the torsional strength of RC beams. The first type, such as the formula adopted in ACI 318-19 (2019) or CSA S806-12 (2021), is based on the space truss model without accounting for the concrete contribution and the dowel effect. However, some experiments have shown that this type may underestimate the torsional resistance (Hsu, 1968; Rahal, 2013). Accordingly, researchers have

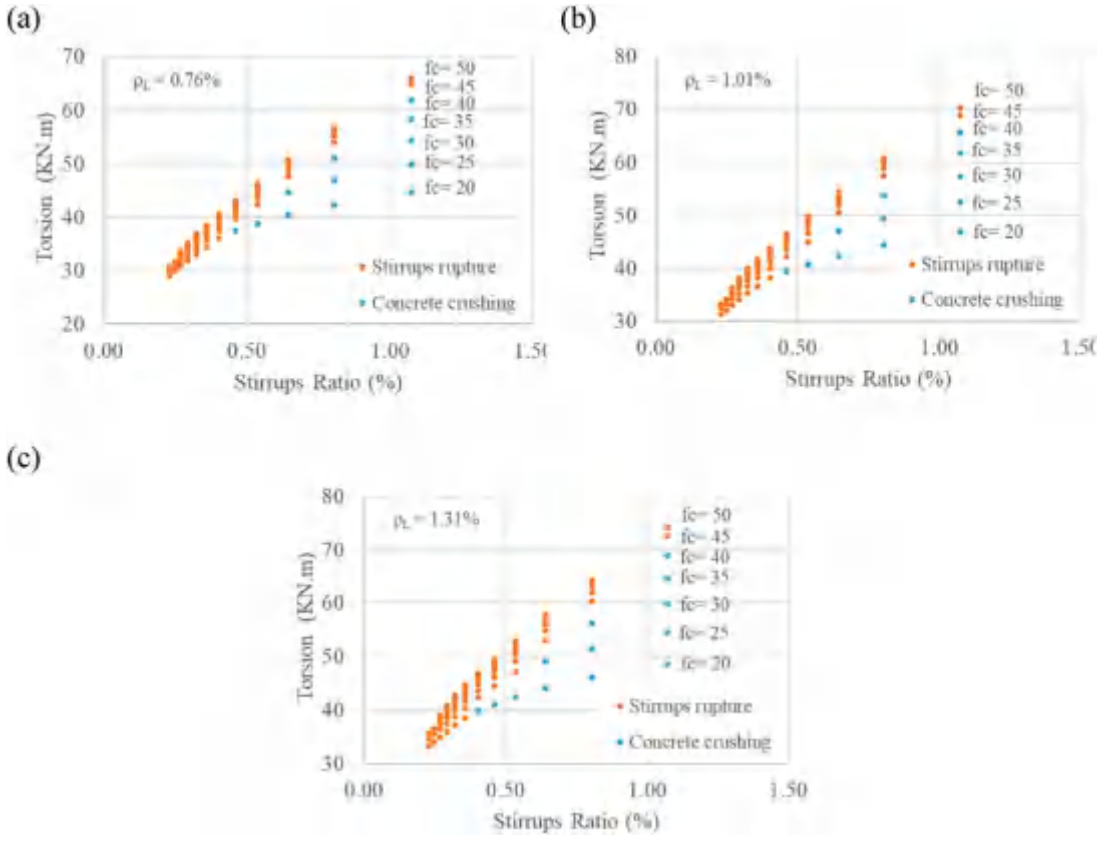


Figure 9. Influence of concrete strength and stirrups ratio on torsion strength of GFRP-RC members (a) $\rho_L = 0{:}76\%$, (b) $\rho_L = 1{:}01\%$, and (c) $\rho_L = 1{:}31\%$.

proposed a different strength calculation formula that takes into account the concrete contribution. This formula has been adopted in some national codes, such as GB 50010-2010 (2015) and the PCI method (2017), to provide a more accurate and cost-effective design (Kuan et al., 2020). Based on the observed torsional behavior of FRP-RC members and the space truss mechanism, a semi-empirical formula was proposed through numerical analysis, accounting for the contributions of both concrete and transverse reinforcement.

Strength prediction formula

The GB 50010-2010 (2015) code predicts torsion strength by considering contributions from both concrete, T_c, and transverse reinforcement, T_s, as follows:

$$T_{u,pre} = T_c + T_s \text{ for FRP stirrup rupture} \tag{13a}$$

where $T_c = \varphi_1 f_t W_t$;
$T_s = \varphi_2 f_{ftb} \frac{A_T A_{cor}}{S} \cot\alpha$;
$W_t = \frac{b^2}{6}(3h - b)$; and
$f_{ftb} = [0{:}05(r_b{=}d_b) + 0{:}3]\, f_{Fut} \le f_{Fut}$:

To prevent crushing of the cross-section, the magnitude of the applied torsion is limited by the following equation for solid sections:

$$\frac{T_{crushing}}{0{:}8\, W_t} = \varphi_3 \beta_c f_{cu} \text{ for concrete crushing} \tag{13b}$$

The coefficients (φ_1, φ_2, and φ_3) are empirical coefficients derived from the experimental data. The factor β_c is a material reduction factor equal to unity. Nonlinear regression analyses were conducted to evaluate these coefficients to propose a strength prediction formula and determine the balanced stirrup ratio.

Using the calculation results from the modified RA-STM and correlation analysis, the distribution of strut angle α was found to be related to the stiffness ratio (λ) of the longitudinal bars to the stirrups, equation (14), and can be represented by a logarithmic function, equation (15), as shown in Figure 11. Through regression analysis, Figure 12, the values of φ_1 and φ_2 were determined to be 0.15 and 1.3, respectively. Using these coefficients, the predicted strength values in equation (13a) align with the results of the parametric study, with a mean value of 1.04 and an acceptable scatter (CV = 8.96%).

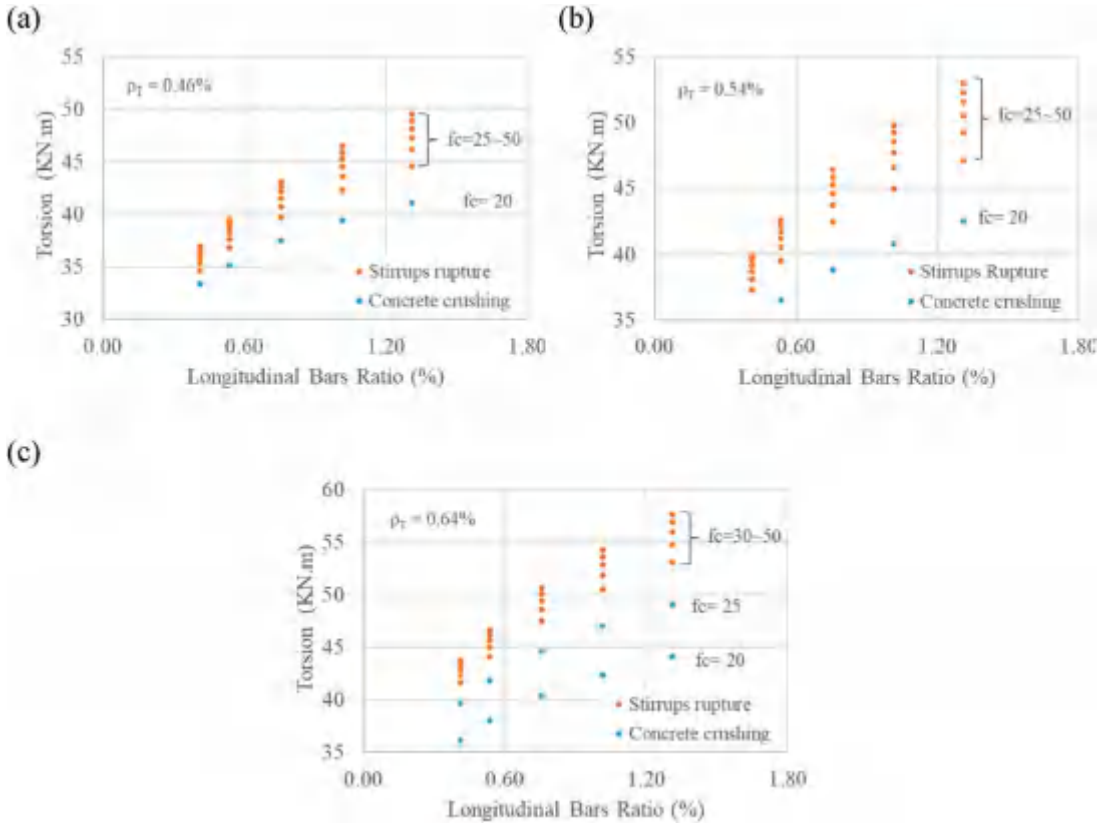


Figure 10. Influence of concrete strength and longitudinal bars ratio on torsion strength of GFRP-RC members (a) $\rho_T = 0{:}46\%$, (b) $\rho_T = 0{:}54\%$, and (c) $\rho_T = 0{:}64\%$.

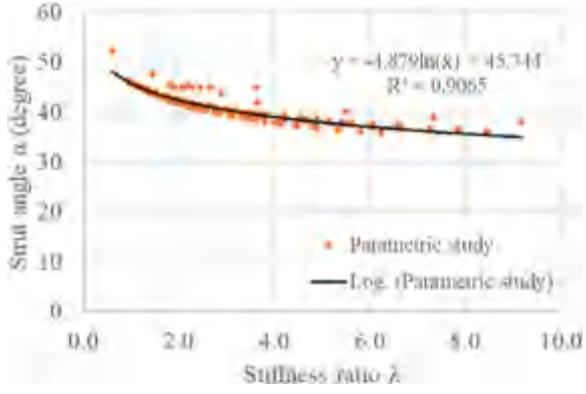


Figure 11. Variation of strut angle with stiffness ratio λ.

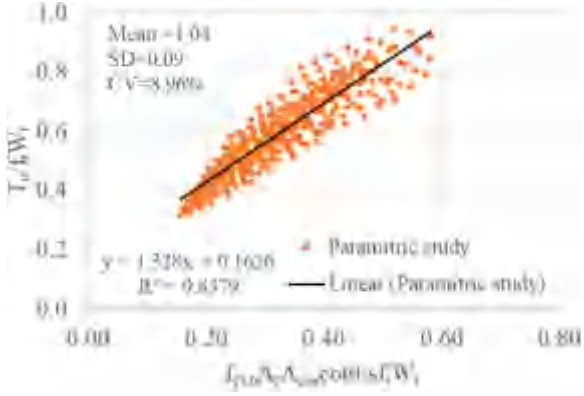


Figure 12. Regression analysis of the proposed formula.

$$\lambda = \frac{E_L A_L S}{E_T A_T u_{cor}} \tag{14}$$

$$\alpha = -4{:}9 \ln \lambda + 45{:}75 \tag{15}$$

The balanced stirrup ratio for the balanced failure mode can be calculated by equating the torsion strength from equation (13a) for FRP rupture failure mode and equation (13b) for concrete crushing failure mode, which is represented as $A_t p_h = (A_c s)$ in equation (16a) as follows:

$$\rho_b = \frac{[0{:}8\,\varphi_3 f_{cu} - \varphi_1 f_t] W_t p_h}{\varphi_2 f_{ftb} A_c A_{cor}} \tan\alpha \tag{16a}$$

Figure 13 shows the transition of the failure mode from stirrup rupture to concrete strut crushing. The value of α

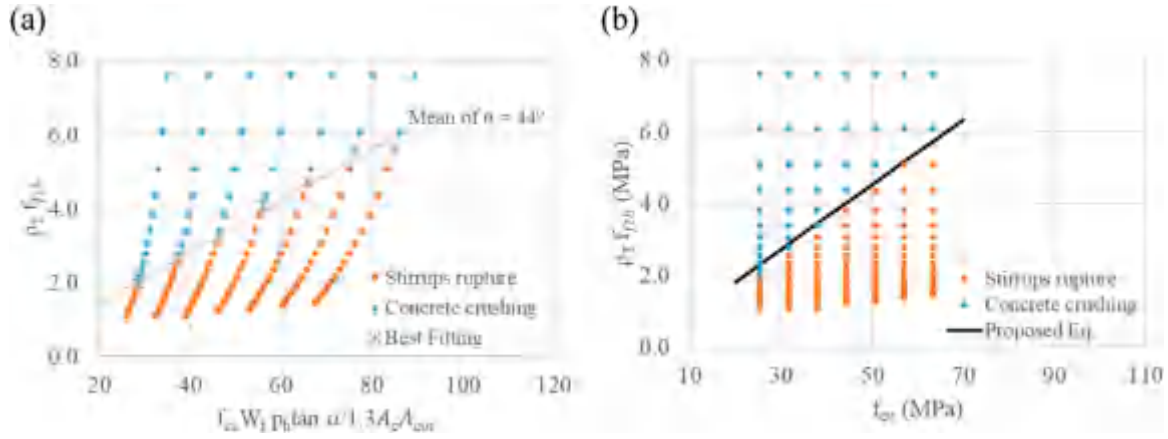


Figure 13. Regression analysis of the balanced stirrups ratio formula (a) exact form equation (16a), (b) simplified form equation (16b).

does not significantly affect the balanced ratio. Since α deviates slightly at approximately 45° at the location of the balanced ratio line, it is set to 45° for simplicity. Assuming that f_t is 1/10 of f_{cu}, the above equation can be presented by substituting the values of φ_1 and φ_2 as follows:

$$\rho_b = \frac{[0{:}8\,\varphi_3 - 0{:}015]\, f_{cu} W_t p_h}{1{:}3 f_{ftb} A_c A_{cor}} \tag{16b}$$

Based on the numerical results (Figure 13), it has been found that the balanced ratio is mainly proportional to the term f_{cu}, which can effectively capture the trend of the balance ratio ρ_b. Through regression analysis, the value of φ_3 was determined to be 0.11. It has also been observed that the resulting function, equation (13b), can predict the low boundary strength of the FRP-RC beam under pure torsion with the failure mode of concrete crushing (Figure 13).

Verification of the proposed formula

This section validate of the performance of the proposed calculation method, ACI 440.1R-15 (2015), and the EN 1992-1-1 (2023) against experimental results and finite element model (FEM) data gathered from literature (Elkheshen et al., 2022; Hadhood et al., 2020; Mohamed and Benmokrane, 2015, 2016; Mohamed et al., 2015).

ACI 440.1R code provision. The current version of the ACI 440.1R-15 (2015) does not include any provision For FRP-RC beams subjected to torsion. However, the design procedure in the ACI 318-19 (2019) used for steel-RC beams can be adapted as follows:

$$T_u = \frac{2A_o A_t f_{fv}}{S}\cot\theta \le 0{:}83\sqrt{f_c'}\left(\frac{1{:}7A_{oh}^2}{P_h}\right) \tag{17}$$

For non-prestressed members, the angle θ is permitted to be 45°. The stress level in the FRP stirrups should not exceed $f_{fv} = 0{:}004E_T \le f_{bFu}$ to control diagonal crack widths during service loads and to prevent failure at the bent portion of the FRP stirrup (ACI 440.1R, 2015).

EN 1992-1-1 (2023). The torsional capacity for steel-RC is calculated according to the EN 1992-1-1 (2023) as follows:

$$T_u = 2A_k t_{ef}\,\tau_{t,Rd} \tag{18}$$

Where A_k denotes the area of the thin-walled cross-section, and the effective wall thickness t_{ef} is defined as

$$t_{ef} = \frac{A}{u} \ge 2c \tag{19}$$

A is the total cross-sectional area, encompassing any internal holes; u denotes the perimeter of the cross-section; and c is the distance from the edge of the member to the centroid of the longitudinal bars.

The torsional shear stress within the equivalent thin-walled tube is described by

$$\tau_{t,Rd} = \min\{\tau_{t,Rd,sw}; \tau_{t,Rd,s}; \tau_{t,Rd,max}\} \tag{20}$$

where $\tau_{t,Rd,sw} = \frac{A_t}{t_{ef}\,s} f_y \cot\theta$ when capacity controlled by yielding of stirrups; $\tau_{t,Rd,sl} = \frac{A_L f_y}{t_{ef}\,u_k \cot\theta}$ when capacity controlled by yielding of longitudinal bars; and $\tau_{t,Rd,max} = \frac{v f_c'}{\cot\theta + \tan\theta}$ when capacity controlled by concrete crushing.u_k represents the perimeter of the thin-walled cross-section, a strength reduction factor of $v = 0{:}6$ is used, and $\theta = 45^o$. The yield stress of stirrups can be replaced by the ultimate tensile bending strength obtained from the B.5 test per ACI 440.3R (2004), while the yield stress of longitudinal bars can be substituted with the tensile strength of FRP bars.

Table 3. Comparison between the proposed approach, ACI 440.1R-15 (2015) and EN 1992-1-1 (2023).

Ref.	Experimental results				Proposed strength prediction approach						ACI 440.1R-15 (2015)		EN 1992-1-1 (2023)	
	Specimen name	$T_{u,exp}$ (KN.m)	ρ_T %	Failure mode[a]	$T_{u,pre}$	$T_{crushing}$	T_{all}	$T_{u,exp}=T_{all}$	ρ_b %	Failure mode[a]	T_u	$T_{u,exp}=T_u$	T_u	$T_{u,exp}=T_u$
(Mohamed and Benmokrane, 2015, 2016)	BG60	56.86	1.07	CC	80.52	70.59	70.59	0.81	0.99	CC	33.6	1.69	94.87	0.60
	BG120	52.65	0.54	SR	51.31	74.58	51.31	1.03	1.05	SR	16.8	3.13	47.43	1.11
	BG180	41.75	0.36	SR	40.35	74.58	40.35	1.03	1.05	SR	11.2	3.72	31.62	1.32
	BG240	34.17	0.27	SR	33.89	70.83	33.89	1.01	0.99	SR	8.4	4.06	23.72	1.44
	BG300	29.89	0.21	SR	30.89	74.58	30.89	0.97	1.05	SR	6.7	4.44	18.97	1.58
(Hadhood et al., 2020)	BGST200	14.2	0.43	SR	14.37	27.18	14.37	0.99	1.01	SR	5.2	2.75	12.83	1.11
(Mohamed and Benmokrane, 2016; Mohamed et al., 2015)	BC60	69.28	1.07	CC	107.67	70.59	70.59	0.98	0.59	CC	56.4	1.23	152.67	0.45
	BC120	62.88	0.56	SR	69.10	69.24	69.10	0.91	0.58	SR	50.8	1.24	79.69	0.79
	BC180	49.4	0.37	SR	52.75	69.24	52.75	0.94	0.58	SR	33.8	1.46	53.13	0.93
	BC240	39.38	0.28	SR	44.08	69.24	44.08	0.89	0.58	SR	25.4	1.55	39.85	0.99
	BC300	35.67	0.22	SR	38.64	69.24	38.64	0.92	0.58	SR	20.3	1.76	31.88	1.12
(Elkheshen et al., 2022)	BF-25	9.42	0.94	-	13.37	7.83	7.83	1.20	0.49	CC	5.1	1.85	15.87	0.59
	BF-30	10.46	0.94	-	13.64	9.40	9.40	1.11	0.58	CC	5.6	1.88	15.87	0.66
	BF-35	11.18	0.94	-	13.91	10.97	10.97	1.02	0.68	CC	6.0	1.86	15.87	0.70
	BF-40	11.73	0.94	-	14.17	12.53	12.53	0.94	0.78	CC	6.4	1.82	15.87	0.74
	BF-45	11.9	0.94	-	14.44	14.10	14.10	0.84	0.88	CC	6.8	1.74	15.87	0.75
	BF-50	12.14	0.94	-	14.71	15.66	14.71	0.83	0.97	SR	7.2	1.69	15.87	0.76
	BC-300	6.28	0.37	-	6.70	7.83	6.70	0.94	0.47	SR	4.9	1.27	6.74	0.93
	BC-400	9.74	0.39	-	10.03	10.97	10.03	0.97	0.45	SR	7.6	1.29	10.34	0.94
	BC-500	13.99	0.41	-	13.63	14.10	13.63	1.03	0.44	SR	10.3	1.35	14.07	0.99
	BF45-S300	6.48	0.31	-	7.39	14.10	7.39	0.88	0.88	SR	4.1	1.58	5.10	1.27
	BF45-S250	6.85	0.38	-	8.20	14.10	8.20	0.84	0.88	SR	4.9	1.39	6.12	1.12
	BF45-S200	8.31	0.47	-	9.38	14.10	9.38	0.89	0.88	SR	6.2	1.35	7.65	1.09
	BF45-S150	9.56	0.63	-	11.25	14.10	11.25	0.85	0.88	SR	6.8	1.40	10.20	0.94
	BF45-S100	12.56	1.88	-	24.39	14.10	14.10	0.89	0.88	CC	6.8	1.84	30.59	0.41
	BF45-S50	14.56	0.94	-	14.79	14.10	14.10	1.03	0.88	CC	6.8	2.13	15.29	0.95
	BF45-S100-D8	7.66	0.75	-	12.91	14.10	12.91	0.59	0.85	SR	7.0	1.10	12.54	0.61
	BF45-S100-D9	8.31	0.94	-	14.79	14.10	14.10	0.59	0.88	CC	6.8	1.22	15.29	0.54
	BF45-S100-D1	8.73	1.15	-	16.70	14.10	14.10	0.62	0.90	CC	6.7	1.31	18.17	0.48
	BF45-S100-D12	9.43	1.64	-	20.53	14.10	14.10	0.67	0.95	CC	6.3	1.49	24.18	0.39
	Mean							0.91				1.89		0.88
	SD							0.14				0.87		0.31
	CV %							15.95				45.89		35.01

[a]CC, Concrete crushing; SR, Stirrups rupture occurs; Missing data are not reported in original reference.

Comparison with experimental and FEM results. This section compares the results obtained from experimental testing and FEM with those obtained from the proposed approach, ACI 440.1R-15 (2015) and the EN 1992-1-1 (2023). According to the design concept, the member's allowable torsional strength (T_{all}) should not exceed $T_{u,pre}$ to prevent FRP stirrup rupture or $T_{crushing}$ to avoid concrete crushing. Table 3 provides the allowable torsional strength based on the lesser of $T_{u,pre}$ or $T_{crushing}$ and the predicted balanced ratio.

The results demonstrate that ACI 440.1R-15 (2015) underestimated the ultimate torsional strength by $\bar{x}$ = 1.89 and CV = 45.59%. Conversely, the EN 1992-1-1 (2023) overestimated the ultimate torsional strength by $\bar{x}$ = 0.88 and CV = 35.01%. Table 3 indicates that the proposed approach's prediction was closer and more consistent with the experimental and FEM results ($\bar{x}$ = 0.91 and CV = 15.95%) when compared with ACI 440.1R-15 (2015) and EN 1992-1-1 (2023). Moreover, the proposed approach aligns well with experimental tests regarding the failure modes of FRP-RC members. Therefore, it can be concluded that the proposed approach is suitable for estimating the ultimate torsional strength of FRP-RC members with reasonable agreement.

Conclusion

This paper adopts the RA-STM to propose a consistent model that comprehensively and effectively analyzes the torsional behavior of FRP-RC members. The traditional RA-STM model is modified by considering the disparate properties of steel and FRP reinforcement. These include generalizing the tension stiffening model, recommending a constitutive model for concrete in compression, and developing new failure criteria for FRP stirrups. This paper enhances practical applications by introducing an efficient computational model to replace trial-and-error techniques. It also proposes a strength prediction formula and a balanced stirrup ratio. Such information can empower practitioners in designing or verifying FRP-RC members subjected to pure torsion. The conclusions can be summarized as follows:

(a) A robust numerical model for the RA-STM was developed by solving nonlinear systems of equations. This approach provides an efficient tool for both research purposes and practical applications, as it allows for predicting the torsional behavior of FRP- and steel-RC members within seconds.
(b) The effective compressive strength of concrete struts in FRP-RC members can be estimated using the strength reduction factor to consider the strain effect. The prediction results demonstrated that the concrete stress–strain model of Vecchio and Collins (1986) associated with the softening coefficient proposed by Belarbi and Hsu (1991) can be used to capture the compressive behavior of concrete in FRP-RC members under pure torsion.
(c) The results affirm the experimental findings showing that FRP-RC members demonstrate greater tension stiffening than steel-RC members, emphasizing the critical role of the tension stiffening model for FRP-RC members.
(d) A generalized tension stiffening model was proposed to capture the diverse post-peak tensile behaviors of concrete in FRP- and steel-RC torsional members. In detail, a relative stiffness factor was introduced to account for the effect of the modulus of longitudinal reinforcement and stirrups on the tension-stiffening phenomenon.
(e) The prediction of modified RA-STM has a good agreement with the experimental results of the torque-and-twist angle curves for the FRP-RC members. It yields an accurate experiment-to-prediction strength ratio with a mean ratio of 1.04 and a coefficient of variation of 11.66%. It can also satisfactorily predict the transverse, longitudinal, concrete strains, and failure modes.
(f) The parametric study reveals that failure in FRP-RC members mostly occurs due to stirrup rupture or concrete strut crushing rather than longitudinal bar rupture, with the variation of the stirrup ratio, longitudinal bar ratio or concrete compressive.
(g) A strength prediction formula and balanced stirrup ratio for FRP-RC members under pure torsion were proposed based on the parametric analysis. The proposed formula has achieved high accuracy in predicting the torsional strength of FRP-RC members compared with the experimental test and FEM results, with an average of 0.91 and a coefficient of variance of 15.95%, along with an accurate prediction of the failure mode.

In summary, the proposed model is applicable to normal-strength solid rectangular members reinforced with GFRP or CFRP reinforcement under pure torsion. However, the corresponding test data for verification is rather limited. Additional experimental research is still needed to investigate other factors that affect the torsional behavior of FRP-RC members. These factors include the types of FRP stirrup, concrete strength, cross-sectional geometry, loading schemes (torsion, torsion-and-shear, torsion-and-bending, torsion-shear-bending), etc. Addressing these aspects can contribute to more comprehensive theoretical modeling, design methods, and code provisions for FRP-RC members.

Declaration of conflicting interests

The author(s) declared no potential conflicts of interest with respect to the research, authorship, and/or publication of this article.

Funding

The author(s) disclosed receipt of the following financial support for the research, authorship, and/or publication of this article: The authors gratefully acknowledge the financial support provided by National Key Research and Development Program of China (Grant No. 2022YFB3706500), the Fund of Non-Metallic Excellence and Innovation Center for Building Materials (2023TDA4-1) and National Natural Science Foundation of China (52378178, 52130806).

ORCID iDs

Eslam M Saleh https://orcid.org/0009-0004-5000-3928
Jiafei Jiang https://orcid.org/0000-0002-8123-8453
Weichen Xue https://orcid.org/0000-0002-9779-5676

References

American Concrete Institute – ASCE Committee 445 (2013) Report on Torsion in Structural Concrete. ACI 445.1R-12. Farmington Hills, MI: ACI.

American Concrete Institute – Committee 318 (2019) Building Code Requirements for Structural Concrete and Commentary. ACI 318-08. Farmington Hills, MI: ACI.

American Concrete Institute – Committee 440 (2004) Guide Test Methods for Fiber-Reinforced Polymers (FRPs) for Reinforcing or Strengthening Concrete Structures. ACI 440.3R-04. Farmington Hills, MI: ACI.

American Concrete Institute – Committee 440 (2015) Guide for the Design and Construction of Concrete Reinforced with FRP Rebars. ACI 440.1R-15. Farmington Hills, MI: ACI.

Belarbi A and Hsu TTC (1991) Constitutive Laws of Softened Concrete in Biaxial Tension Compression. Research report UHCEE 91-2. Houston, Texas: University of Houston.

Belarbi A and Hsu TTC (1994) Constitutive laws of concrete in tension and reinforcing bars stiffened by concrete. ACI Structural Journal 91(4): 465–474. DOI: 10.14359/4154.

Belarbi A and Hsu TTC (1995) Constitutive laws of softened concrete in biaxial tension-compression. ACI Materials Journal 92(5): 562–573. DOI: 10.14359/907.

Bernardo LFA and Andrade JMA (2020) A unified softened truss model for RC and PC beams under torsion. Journal of Building Engineering 32: 101467. DOI: 10.1016/j.jobe.2020.101467.

Bischoff PH and Paixao R (2004) Tension stiffening and cracking of concrete reinforced with glass fiber reinforced polymer (GFRP) bars. Canadian Journal of Civil Engineering 31(4): 579–588. DOI: 10.1139/L04-025.

Canadian Standards Association (2019) Canadian Highway Bridge Design Code. CAN/CSA-S6-19. Mississauga, ON, Canada. CSA Group.

Canadian Standards Association (2021) Design and Construction of Building Components with Fibre-Reinforced Polymers. CAN/CSA S806-02(R2021). Mississauga, ON, Canada. CSA Group.

Chai HK, Majeed AA and Allawi AA (2015) Torsional analysis of multicell concrete box girders strengthened with CFRP using a modified softened truss model. Journal of Bridge Engineering 20(8): B4014001. DOI: 10.1061/(ASCE)BE.1943-5592.0000621.

Chalioris CE and Karayannis CG (2013) Experimental investigation of RC beams with rectangular spiral reinforcement in torsion. Engineering Structures 56: 286–297. DOI: 10.1016/j.engstruct.2013.05.003.

Chiu H-J, Fang I-K, Young W-T, et al. (2007) Behavior of reinforced concrete beams with minimum torsional reinforcement. Engineering Structures 29(9): 2193–2205. DOI: 10.1016/j.engstruct.2006.11.004.

Collins MP and Mitchell D (1980) Shear and torsion design of prestressed and non-prestressed concrete beams. PCI Journal 25(5): 32–100. DOI: 10.15554/pcij.09011980.32.100.

Deifalla A (2015) Torsional behavior of rectangular and flanged concrete beams with FRP reinforcements. Journal of Structural Engineering 141(12): 04015068. DOI: 10.1061/(ASCE)ST.1943-541X.0001322.

Deifalla A (2021) Refining the torsion design of fibered concrete beams reinforced with FRP using multi-variable non-linear regression analysis for experimental results. Engineering Structures 226: 111394. DOI: 10.1016/j.engstruct.2020.111394.

Deifalla A, Hamed M, Saleh A, et al. (2014) Exploring GFRP bars as reinforcement for rectangular and L-shaped beams subjected to significant torsion: an experimental study. Engineering Structures 59: 776–786. DOI: 10.1016/j.engstruct.2013.11.027.

Deifalla A, Khalil MS and Abdelrahman A (2015) Simplified model for the torsional strength of concrete beams with GFRP stirrups. Journal of Composites for Construction 19(1): 04014032. DOI: 10.1061/(ASCE)CC.1943-5614.0000498.

Elkheshen M, Eltahawy R, Shedid M, et al. (2022) Numerical verification for concrete beams reinforced with CFRP subjected to pure torsion. Engineering Structures 268: 114739. DOI: 10.1016/j.engstruct.2022.114739.

EN 1992-1-1 (2023) Eurocode 2: Design of Concrete Structures - Part 1-1: General Rules and Rules for Buildings, Bridges and Civil Engineering Structures. EN 1992-1-1. Brussels: European Committee for Standardization.

Fang I-Kuang and Shiau Jyh-Kun (2004) Torsional Behavior of Normal- and High-Strength Concrete Beams. ACI Structural Journal 101(3): 304–313. doi: 10.14359/13090.

GB 50010-2010 (2015) Code for Design of Concrete Structures. Beijing, China: Ministry of Housing and Urban-Rural Development of the People's Republic of China.

Greene G Jr. (2006) Behavior of Reinforced Concrete Girders Under Cyclic Torsion and Torsion Combined with Shear: Experimental Investigation and Analytical Models. PhD Thesis. Ann Arbor: University of Missouri - Rolla.

Greene G Jr. and Belarbi A (2009a) Model for reinforced concrete members under torsion, bending, and shear. I: theory. Journal of Engineering Mechanics 135(9): 961–969. DOI: 10.1061/(ASCE)0733-9399(2009)135:9(961).

Hadhood A, Gouda MG, Agamy MH, et al. (2020) Torsion in concrete beams reinforced with GFRP spirals. Engineering Structures 206: 110174. DOI: 10.1016/j.engstruct.2020.110174.

Hassan MM and Deifalla A (2016) Evaluating the new CAN/CSA-S806-12 torsion provisions for concrete beams with FRP reinforcements. Materials and Structures 49(7): 2715–2729. DOI: 10.1617/s11527-015-0680-9.

Hsu TTC (1968) Torsion of structural concrete-behavior of reinforced concrete rectangular members. ACI Special Publication SP- 018: 261–306. DOI: 10.14359/17572.

Hsu TTC and Mo YL (1985) Softening of concrete in torsional members - theory and tests. Journal of the American Concrete Institute 82(3): 290–303. DOI: 10.14359/10335.

Hsu TTC and Mo Y-L (2010) Unified Theory of Concrete Structures. Chichester, West Sussex: John Wiley & Sons.

Hu X, Xue W and Lv Y (2024a) Seismic behavior of a new type of precast concrete shear wall using UHPC connections at boundary elements. Engineering Structures 302: 117468. DOI: 10.1016/j.engstruct.2024.117468.

Hu X, Xue Wenyuan, Xue Weichen, et al. (2023) Bond strength of sand-coated deformed GFRP bars in UHPC, HPC, and NC. Construction and Building Materials 403: 133175. DOI: 10.1016/j.conbuildmat.2023.133175.

Hu X, Xue W and Xue W (2024b) Bond properties of GFRP rebars in UHPC under different types of test. Engineering Structures 314: 118319. DOI: 10.1016/j.engstruct.2024.118319.

Ibrahim MS, Gebreyouhannes E, Muhdin A, et al. (2020) Effect of concrete cover on the pure torsional behavior of reinforced concrete beams. Engineering Structures 216: 110790. DOI: 10.1016/j.engstruct.2020.110790.

Issa MA, Thilan O and Mustapha I (2016) Shear behavior of basalt fiber reinforced concrete beams with and without basalt FRP stirrups. Journal of Composites for Construction 20(4): 04015083.

Izumo J, Shin H, Maekawa K, et al. (1992) An analytical model for RC panels subjected to in-plane stresses. In: Concrete Shear in Earthquake. Boca Raton: CRC Press, 206–215. DOI: 10.14359/17572.

Ju H, Han S-J, Zhang D, et al. (2019) Estimation of minimum torsional reinforcement of reinforced concrete and steel fiber-reinforced concrete members. Advances in Materials Science 2019: 1–10. DOI: 10.1155/2019/4595363.

Karbhari VM, Chin JW, Hunston D, et al. (2003) Durability gap analysis for fiber-reinforced polymer composites in civil infrastructure. Journal of Composites for Construction 7(3): 238–247.

Kim M-J, Kim H-G, Lee Y-J, et al. (2020) Pure torsional behavior of RC beams in relation to the amount of torsional reinforcement and cross-sectional properties. Construction and Building Materials 260: 119801. DOI: 10.1016/j.conbuildmat.2020.119801.

Koutchoukali NE (1998) Nonlinear Behavior of Reinforced-Concrete Beams Subjected to Pure Torsion. PhD Thesis. Ann Arbor: University of Missouri - Rolla.

Kuan A, Bruun EPG, Bentz EC, et al. (2020) Alternative design procedures for torsion in ACI 318-19: a comparative study. ACI Special Publication SP- 344: 64–91. DOI: 10.14359/51728291.

Kueres S and Hegger J (2020) Variable strut inclination model for shear design of FRP reinforced concrete members with shear reinforcement. Engineering Structures 206: 110154. DOI: 10.1016/j.engstruct.2019.110154.

Lee JY and Kim SW (2010) Torsional strength of RC beams considering tension stiffening effect. Journal of Structural Engineering 136(11): 1367–1378. DOI: 10.1061/(ASCE)ST.1943-541X.0000237.

Liang X, Peng J and Ren R (2023) A state-of-the-art review: shear performance of the concrete beams reinforced with FRP bars. Construction and Building Materials 364: 129996.

Liao X, Zhang B and Xue W (2024) Cyclic loading response of precast concrete beam-column connections with partially bonded draped prestressing tendon. Engineering Structures 302: 117435.

Majed MM, Tavakkolizadeh M and Allawi AA (2021) Analytical study on torsional behavior of concrete beams strengthened with fiber reinforced polymer laminates using softened truss model. Advances in Structural Engineering 24(8): 1642–1654.

McMullen AE and Rangan BV (1978) Pure tension in rectangular sections-A Re-Examination. In: ACI journal proceedings, 10 October 1978, 511–519. DOI:10.14359/10963.

McMullen AE and Warwaruk J (1967) The torsional strength of rectangular reinforced concrete beams to combined loading. Report for the Department of Civil Engineering, Report no. 2, July, Alberta.

Mikame A, Uchida K and Noguchi H (1991) A study of compressive deterioration of cracked concrete. In: Proceedings international workshop on finite element analysis of reinforced concrete, New York, USA, 1991.

Miyahara T, Kawakami T and Maekawa K (1987) Nonlinear behavior of cracked reinforced concrete plate element under uniaxial compression. Proceedings of JSCE 1987: 249–258.

Mohamed HM and Benmokrane B (2015) Torsion behavior of concrete beams reinforced with glass fiber-reinforced polymer bars and stirrups. ACI Structural Journal 112(5): 543–552. DOI: 10.14359/51687824.

Mohamed HM and Benmokrane B (2016) Reinforced concrete beams with and without FRP web reinforcement under pure torsion. Journal of Bridge Engineering 21(3): 04015070. DOI: 10.1061/(ASCE)BE.1943-5592.0000839.

Mohamed HM, Chaallal O and Benmokrane B (2015) Torsional moment capacity and failure mode mechanisms of concrete beams reinforced with carbon FRP bars and stirrups. Journal of Composites for Construction 19(2): 04014049. DOI: 10.1061/(ASCE)CC.1943-5614.0000515.

Mostafa IT, Mousa S, Mohamed HM, et al. (2023a) Behavior of high-strength concrete (HSC) box girders reinforced with GFRP bars, ties, and spirals under torsion. Engineering Structures 294: 116726. DOI: 10.1016/j.engstruct.2023.116726.

Mostafa IT, Mousa S, Mohamed HM, et al. (2023b) Strength and behavior of glass fiber-reinforced polymer-reinforced concrete box girders without web reinforcement under pure torsion. ACI Structural Journal 120(5): 63–76. DOI: 10.14359/51738836.

Mostafa IT, Mousa S, Mohamed HM, et al. (2024a) Experimental and analytical behavior of GFRP-reinforced concrete box girders under pure torsion. Journal of Composites for Construction 28(1): 04023064. DOI: 10.1061/JCCOF2.CCENG-4212.

Mostafa IT, Mousa S, Mohamed HM, et al. (2024b) Softened membrane torsional model for GFRP-reinforced concrete bridge box girders. Journal of Bridge Engineering 29(3): 04023122. DOI: 10.1061/JBENF2.BEENG-6170.

Nayal R and Rasheed HA (2006) Tension stiffening model for concrete beams reinforced with steel and FRP bars. Journal of Materials in Civil Engineering 18(6): 831–841. DOI: 10.1061/(ASCE)0899-1561(2006)18:6(831).

Pang XB and Hsu TTC (1996) Fixed angle softened truss model for reinforced concrete. ACI Structural Journal 93(2): 197–207.

PCI Design Handbook (2017) PCI Design Handbook: Precast and Prestressed Concrete. Chicago: Precast/Prestressed Concrete Institute.

Peng F, Peng F, Xue W, et al. (2020) Database Evaluation of Shear Strength of Slender Fiber-Reinforced Polymer-Reinforced Concrete Members. ACI Structural Journal 117(3): 273–281. DOI: 10.14359/51723504.

Rahal KN (2007) Combined torsion and bending in reinforced and prestressed concrete beams using simplified method for combined stress-resultants. ACI Structural Journal 104(4): 402–411. DOI: 10.14359/18770.

Rahal KN (2013) Torsional strength of normal and high strength reinforced concrete beams. Engineering Structures 56: 2206–2216. DOI: 10.1016/j.engstruct.2013.09.005.

Rasmussen L and Baker G (1995) Torsion in reinforced normal and high-strength concrete beams part 1: experimental test series. Structural Journal 92(1): 56–62. DOI: 10.14359/1476.

Razaqpur AG, Bencardino F, Rizzuti L, et al. (2015) FRP reinforced/prestressed concrete members: a torsional design model. Composites Part B: Engineering 79: 144–155. DOI: 10.1016/j.compositesb.2015.04.034.

Shirai N and Noguchi H (1989) Compressive deterioration of cracked concrete. Proceedings, Structural design, analysis and testing 1989: 1–10.

Vecchio F and Collins MP (1981) Stress-strain characteristics of reinforced concrete in pure shear, Final report. IABSE colloquium on advanced mechanics of reinforced concrete. International Association for Bridge and Structural Engineering 1981: 211–225.

Vecchio FJ and Collins MP (1986) The modified compression-field theory for reinforced concrete elements subjected to shear. Journal of the American Concrete Institute 83(2): 219–231. DOI: 10.14359/10416.

Walraven J (2021) Synthesized intervention method to prolong service life of reinforced concrete structures: ICCP-SS. Structural Concrete 22(2): 590–592. DOI: 10.1002/suco.202000261.

Xiong H, Li B and Jiang J (2016) Load path dependence of strain and stress for confined concrete. Magazine of Concrete Research 68(12): 604–618. DOI: 10.1680/jmacr.15.00175.

Xue W, Zheng Q, Yang Y, et al. (2014) Bond behavior of sand-coated deformed glass fiber reinforced polymer rebars. Journal of Reinforced Plastics and Composites 33(10): 895–910. DOI: 10.1177/073168441352026.

Appendix A

Equilibrium equations

$$\sigma_L = \sigma_d \cos^2\alpha + \sigma_r \sin^2\alpha + \rho_L f_L \tag{A-1}$$

$$\sigma_T = \sigma_d \sin^2\alpha + \sigma_r \cos^2\alpha + \rho_T f_T \tag{A-2}$$

$$v = (\sigma_r - \sigma_d)\sin\alpha\cos\alpha \tag{A-3}$$

$$T = v(2A_o t_d) \tag{A-4}$$

Compatibility equations

$$\varepsilon_L = \varepsilon_d \cos^2\ \alpha + \varepsilon_r \sin^2\ \alpha \tag{A-5}$$

$$\varepsilon_T = \varepsilon_d \sin^2\ \alpha + \varepsilon_r \cos^2\ \alpha \tag{A-6}$$

$$\frac{\gamma_{LT}}{2} = (\varepsilon_r - \varepsilon_d)\sin\alpha\cos\alpha \tag{A-7}$$

$$\theta = \left(\frac{p_o}{2A_o}\right)\gamma_{LT} \tag{A-8}$$

$$\psi = \theta \sin 2\alpha \tag{A-9}$$

$$\psi = \frac{\varepsilon_{ds}}{t_d} \tag{A-10}$$

$$\varepsilon_d = \frac{\varepsilon_{ds}}{2} \tag{A-11}$$

$$\varepsilon_r = \frac{\varepsilon_{rs}}{2} \tag{A-12}$$

Material constitutive laws

Compressive stress–strain relationship of concrete

$$\sigma_d = k_c \zeta f_c' \tag{A-13}$$

$$k_c = \frac{1}{\varepsilon_{ds}\zeta f_c'}\int_0^{\varepsilon_{ds}} \sigma_d(\varepsilon_d)\mathrm{d}\varepsilon_d \tag{A-14}$$

$$\zeta = f(\varepsilon_d, \varepsilon_r) \tag{A-15}$$

Tensile stress–strain relationship of concrete

$$\sigma_r = k_t f_{cr} \tag{A-16}$$

$$k_t = \frac{1}{\varepsilon_{rs} f_{cr}} \int_0^{\varepsilon_{rs}} \sigma_r(\varepsilon_r) d\varepsilon_r \quad \text{(A-17)}$$

Tensile stress–strain relationship of FRPs reinforcing bars

$$f_L = E_F \varepsilon_L \le f_{Ful} \quad \text{(A-18)}$$

$$f_T = E_F \varepsilon_T \le f_{bFu} \quad \text{(A-19)}$$

Additional equations

$$\varepsilon_r = \varepsilon_L + \varepsilon_T - \varepsilon_d \quad \text{(A-20)}$$

$$\tan^2 \alpha = \frac{\varepsilon_L - \varepsilon_d}{\varepsilon_T - \varepsilon_d} \quad \text{(A-21)}$$

$$\sin^2 (\alpha) = \frac{\varepsilon_L - \varepsilon_d}{\varepsilon_r - \varepsilon_d} = \frac{\varepsilon_r - \varepsilon_T}{\varepsilon_r - \varepsilon_d} \quad \text{(A-22)}$$

$$\cos^2 (\alpha) = \frac{\varepsilon_r - \varepsilon_L}{\varepsilon_r - \varepsilon_d} = \frac{\varepsilon_T - \varepsilon_d}{\varepsilon_r - \varepsilon_d} \quad \text{(A-23)}$$

$$t_d = \frac{A_o}{P_o} \left[\frac{(-\varepsilon_d)(\varepsilon_r - \varepsilon_d)}{(\varepsilon_L - \varepsilon_d)(\varepsilon_T - \varepsilon_d)} \right] \quad \text{(A-24)}$$

Appendix B

Notation

A_c Area enclosed by outside perimeter of concrete cross section (mm^2)

Table B1. Comparison of the modified RA-STM with test results of steel-RC.

Ref.	Specimen name	$T_{cr,exp}$ (KN.m)	$T_{u,exp}$ (KN.m)	$\theta_{u,exp}$ (Rad/m)	$T_{cr,th}$ (KN.m)	$T_{u,th}$ (KN.m)	$\theta_{u,th}$ (Rad/m)	$T_{cr,exp}$=$T_{cr,th}$	$T_{u,exp}$=$T_{u,th}$	$\theta_{u,exp}$=$\theta_{u,th}$
(Hsu, 1968)	B1	20.56	22.26	0.043	18.59	25.51	0.036	1.11	0.87	1.17
	B2	20.00	29.26	0.047	19.92	34.33	0.043	1.00	0.85	1.09
	B3	20.11	37.51	0.052	20.98	40.27	0.045	0.96	0.93	1.13
	B4	21.92	47.34	0.057	22.96	47.23	0.043	0.95	1.00	1.33
	B5	22.60	56.15	0.062	23.80	49.53	0.040	0.95	1.13	1.56
	B6	24.97	61.69	0.065	24.89	52.11	0.037	1.00	1.18	1.74
	B7	20.22	26.89	0.048	19.22	30.15	0.035	1.05	0.89	1.39
	B8	21.81	32.54	–	21.01	35.32	0.033	1.04	0.92	–
	B9	19.66	29.83	0.051	20.08	31.93	0.035	0.98	0.93	1.44
	B10	17.63	34.35	0.055	21.17	35.74	0.034	0.83	0.96	1.61
	G2	30.28	30.28	0.049	28.77	42.75	0.034	1.05	0.71	1.44
	G3	27.12	49.60	0.051	28.76	51.05	0.044	0.94	0.97	1.15
	G4	28.70	64.85	0.054	30.86	59.52	0.042	0.93	1.09	1.29
	G5	29.49	71.97	0.054	31.82	63.32	0.038	0.93	1.14	1.42
	G6	30.96	39.09	0.042	28.28	41.55	0.036	1.09	0.94	1.17
	G7	33.67	52.65	0.045	30.55	55.82	0.041	1.10	0.94	1.10
	G8	33.67	73.44	0.049	31.38	61.54	0.041	1.07	1.19	1.22
	I2	24.86	36.04	0.045	23.20	39.08	0.037	1.07	0.92	1.22
	I3	25.53	45.65	0.047	23.47	38.04	0.032	1.09	1.20	1.48
	I4	28.02	58.07	–	26.36	59.79	0.049	1.06	0.97	–
	I5	28.13	70.73	0.054	28.08	65.90	0.045	1.00	1.07	1.19
	I6	27.57	76.72	0.055	29.89	71.53	0.043	0.92	1.07	1.29
	K1	10.68	12.09	0.044	10.99	16.10	0.054	0.99	0.90	0.98
	K2	12.20	23.73	–	12.08	23.03	0.066	1.04	1.17	–
	K3	12.43	28.47	0.076	12.34	24.29	0.061	1.01	1.17	1.23
	K4	13.11	35.03	0.086	13.15	26.98	0.056	1.00	1.30	1.53
	M1	19.21	30.39	0.044	19.72	30.31	0.038	0.97	1.00	1.15
	M2	20.56	40.56	0.052	20.97	38.50	0.045	0.98	1.05	1.15
	M3	20.68	43.84	0.054	21.05	40.42	0.044	0.98	1.08	1.23
	M4	20.68	49.60	0.058	22.06	43.86	0.040	0.94	1.13	1.43
	M5	21.69	55.70	0.063	23.67	48.57	0.039	0.92	1.15	1.61
	M6	22.71	60.11	–	25.01	52.36	0.038	0.91	1.15	–
	J1	14.01	21.47	0.046	14.52	20.31	0.044	0.97	1.06	1.04
	J2	17.06	29.15	0.052	15.32	24.23	0.040	1.11	1.20	1.29
	J3	16.95	35.25	0.055	17.12	29.58	0.039	0.99	1.19	1.42
	J4	17.96	40.67	0.058	17.90	31.94	0.036	1.00	1.27	1.62
	N1	7.59	9.10	0.076	6.09	9.22	0.062	1.25	0.99	1.22
	N1a	7.03	8.99	0.076	6.04	9.20	0.063	1.16	0.98	1.19
	N2	7.45	14.46	0.086	6.73	12.98	0.072	1.11	1.11	1.19
	N2a	7.50	13.22	0.085	6.56	12.45	0.071	1.14	1.06	1.19
	N3	7.41	12.20	0.082	6.26	11.26	0.074	1.18	1.08	1.11
	N4	7.60	15.70	0.089	6.75	13.28	0.066	1.13	1.18	1.36
	C3	11.86	20.00	–	11.69	22.49	0.052	1.01	0.89	–
	C4	11.86	25.31	0.078	12.56	25.39	0.048	0.94	1.00	1.62
	C5	14.01	29.72	0.085	13.35	27.46	0.045	1.05	1.08	1.89
	C6	13.90	34.23	0.091	14.28	29.55	0.042	0.97	1.16	2.17

(continued)

Table B1. (continued)

Ref.	Specimen name	$T_{cr,exp}$ (KN.m)	$T_{u,exp}$ (KN.m)	$\theta_{u,exp}$ (Rad/m)	$T_{cr,th}$ (KN.m)	$T_{u,th}$ (KN.m)	$\theta_{u,th}$ (Rad/m)	$T_{cr,exp}/T_{cr,th}$	$T_{u,exp}/T_{u,th}$	$\theta_{u,exp}/\theta_{u,th}$
(McMullen and Rangan, 1978)	A2	11.29	22.58	0.069	12.59	22.49	0.045	0.90	1.00	1.55
	A3	12.19	27.77	0.056	13.42	28.18	0.059	0.91	0.99	0.95
	A4	12.53	34.43	0.069	14.40	31.95	0.054	0.87	1.08	1.29
	B2	9.00	20.80	0.057	11.50	20.66	0.048	0.78	1.01	1.17
	B3	8.81	25.59	0.082	12.08	25.42	0.064	0.73	1.01	1.29
	B4	10.16	31.72	0.079	12.94	28.67	0.058	0.79	1.11	1.36
(Fang and Shiau Jyh-Kun, 2004)	N-06-06	43.20	79.70	0.057	50.78	84.87	0.044	0.85	0.95	1.54
	N-06-12	51.80	95.20	0.040	53.20	94.91	0.034	0.97	1.00	1.19
	N-12-12	49.30	116.80	0.047	56.21	114.34	0.036	0.88	1.02	1.32
	N-12-16	57.10	138.00	0.040	58.24	121.88	0.034	0.98	1.13	1.17
	N-20-20	55.00	158.00	0.043	62.40	136.66	0.031	0.88	1.16	1.38
	N-07-10	41.60	111.70	0.054	51.73	92.66	0.036	0.80	1.21	1.51
	N-14-10	41.80	125.00	0.059	54.81	109.16	0.036	0.76	1.15	1.65
	N-07-16	40.00	117.30	0.053	54.46	102.53	0.034	0.73	1.14	1.57
(Chalioris and Karayannis, 2013)	ST200	2.17	2.39	0.051	1.65	2.81	0.108	1.31	0.85	0.47
	ST150	2.01	2.65	0.074	1.68	2.98	0.104	1.20	0.89	0.71
	ST100	2.01	3.25	0.099	1.74	3.21	0.099	1.16	1.01	1.00
(Koutchoukali, 1998)	B5UR1	11.60	19.40	0.038	11.57	21.83	0.059	1.00	0.89	0.65
(Chiu et al., 2007)	NBS-43-44	44.50	60.60	0.033	48.07	60.00	0.029	0.93	1.01	1.14
(McMullen and Warwaruk, 1967)	1-1	5.71	13.78	0.049	7.04	12.06	0.052	0.81	1.14	0.94
	2-1	5.94	20.45	0.058	8.35	18.63	0.067	0.71	1.10	0.87
	3-1	5.65	12.99	0.057	6.88	11.39	0.054	0.82	1.14	1.05
(Lee and Kim, 2010)	T1-1	28.92	32.86	0.033	24.84	34.54	0.037	1.16	0.95	0.89
	T1-2	31.37	45.89	0.039	26.62	47.86	0.042	1.18	0.96	0.94
	T1-3	31.78	54.05	0.042	27.51	56.44	0.050	1.16	0.96	0.85
	T1-4	33.68	62.41	0.058	29.45	64.57	0.046	1.14	0.97	1.26
	T2-2	26.93	38.11	0.038	25.41	39.19	0.035	1.06	0.97	1.09
	T2-3	29.76	50.16	0.050	27.38	52.55	0.039	1.09	0.95	1.26
	T2-4	29.8	56.39	0.049	28.23	58.44	0.043	1.06	0.96	1.14
(Rasmussen and Baker, 1995)	B30.1	7.18	16.62	0.052	8.49	19.20	0.065	0.85	0.87	0.80
	B30.2	6.05	15.29	0.051	8.21	18.13	0.063	0.74	0.84	0.80
	B30.3	6.07	15.25	0.045	8.05	17.52	0.062	0.75	0.87	0.72
(Ju et al., 2019)	MT30-1.32	51.55	57.04	0.031	47.61	67.49	0.030	1.08	0.85	1.03
	MT40-1.89	60.97	98.4	0.028	56.18	111.09	0.043	1.09	0.89	0.70
(Ibrahim et al., 2020)	NSC-S1-C30	11.2	19.71	–	11.13	21.94	0.078	1.01	0.93	–
	NSC-S1-C45	10.8	12.5	–	10.90	20.99	0.076	0.99	0.61	–
(Kim et al., 2020)	S08-3-65	68	123	0.024	83.29	137.14	0.023	0.82	0.90	1.05
	S08-4-90	84	124	0.032	79.56	131.50	0.038	1.06	0.99	0.94
	S08-5-122.5	61	89	0.034	76.94	122.13	0.044	0.79	0.85	0.86
	S10-3-52.5	69	126	0.024	86.29	161.10	0.026	0.80	0.78	0.89
	S10-4-72.5	57	109	0.026	82.07	148.09	0.039	0.69	0.76	0.72
	S10-5-100	70	108	0.023	78.90	134.22	0.043	0.89	0.89	0.60
	S06-3-90	69	101	0.026	79.56	109.51	0.021	0.87	0.92	1.20
	S10-5-90	60	106	0.032	80.00	139.27	0.041	0.75	0.82	0.86
	S08-3-72.5	51	106	0.025	82.07	127.50	0.022	0.62	0.83	1.11
	S12-5-72.5	63	120	0.026	82.59	150.09	0.038	0.76	0.82	0.74
MeanSDCV%								0.97	1.00	1.18
								0.14	0.14	0.31
								14.36	13.88	26.34

S	Center-to-center stirrups spacing (mm)	E_L	Modulus of elasticity of longitudinal reinforcement (MPa)
A_{cor}	enclosed area inside the line of inner surface of the stirrups (mm^2)	γ_{LT}	Smeared shear strain in the L–T coordinate (MPa)
t_d	Thickness of the shear flow zone (mm)	E_T	Modulus of elasticity of stirrups (MPa)
A_o	Gross area enclosed by shear flow path (mm^2)	ε_L	Smeared reinforcement strain in longitudinal direction
T_u	Ultimate torsional moment at section (N·m)	E_s	Modulus of elasticity of steel reinforcement (MPa)
A_L	Longitudinal reinforcement area (mm^2)	ε_T	Smeared reinforcement strains in transversal direction
T_{cr}	Cracking torsional moment (N·m)	E_{re}	Relative regiditey of FRP to steel reinforcement
A_T	Area of one leg of stirrup (mm^2)	ε_{sy}	Yield strain of steel reinforcement
u_{cor}	perimeter of the line of the inner surface of the stirrups (mm)	f_c'	Cylindrical compressive strength of concrete (MPa)
b	Cross-section width (mm)	ε_d	Principal concrete compressive strain
W_t	Plastic section resistance moment subjected to torsion (mm^3)	f_{cu}	Cubic compressive strength of concrete (MPa)
d_b	diameter of the bar (mm)	ε_{ds}	Principal compressive strain at the surface of the concrete strut
α	Angle of inclination of the of the compressive principal strains (degree)		

f_t	Tensile strength of concrete (MPa)
ε_{cr}	Cracking tensile strain of concrete
f_{cr}	Concrete cracking strength (MPa)
ε_r	Principal concrete tensile strain
f_{bFu}	Tensile strength of the bent portion of FRP stirrup (MPa)
ε_{rs}	Principal tensile strain at the surface of the concrete strut
f_{Fut}	Tensile strength of the straight portion of FRP stirrup (MPa)
ε_o	Concrete strain at the peak concrete stress
f_{Ful}	Tensile strength of longitudinal FRP bar (MPa)
ζ	Softening coefficient of the concrete strut
f_L	Smeared reinforcement stress in longitudinal direction (MPa)
θ	Unit twist angle of the member (rad/m)
f_T	Smeared reinforcement stress in transversal direction (MPa)
ρ_L	Reinforcement ratio in the longitudinal direction
f_s	Smeared steel stress (MPa)
ρ_T	Reinforcement ratio in transversal direction
f_{sy}	Yield strength of steel reinforcement (MPa)
σ_L	Smeared normal stress in the longitudinal direction (MPa)
h	Cross-section height (mm)
σ_T	Smeared normal stress in the transversal direction (MPa)
k_c	Compression stress block coefficient
σ_d	Smeared principal compressive stress in the concrete (MPa)
k_t	Tensile stress block coefficient
σ_r	Smeared principal tensile stress in the concrete (MPa)
P_o	Perimeter of the area enclosed by shear flow path (mm)
v	Applied shear stress (MPa)
r_b	radius of the bend (mm)
ψ	Bending curvature of concrete strut in a rectangular section

polymers

MDPI

Article

Experimental Investigation on Post-Fire Mechanical Properties of Glass Fiber-Reinforced Polymer Rebars

Chanachai Thongchom [1], Lili Hu [2,*], Penpichcha Khongpermgoson Sanit-in [3], Denise-Penelope N. Kontoni [4,5], Nitipong Praphaphankul [6], Koravith Tiprak [6] and Suphanut Kongwat [7,8]

1 Department of Civil Engineering, Faculty of Engineering, Thammasat School of Engineering, Thammasat University, Pathumthani 12120, Thailand; tchanach@engr.tu.ac.th
2 State Key Laboratory of Ocean Engineering, School of Naval Architecture, Ocean and Civil Engineering, Shanghai Jiao Tong University, Shanghai 200240, China
3 Department of Civil Engineering, Faculty of Engineering, Kasetsart University Kamphaeng Saen Campus, Nakhon Pathom 73140, Thailand; fengppcs@ku.ac.th
4 Department of Civil Engineering, School of Engineering, University of the Peloponnese, GR-26334 Patras, Greece; kontoni@uop.gr
5 School of Science and Technology, Hellenic Open University, GR-26335 Patras, Greece
6 Department of Civil and Environmental Engineering, Tokyo Institute of Technology, 2-12-1-M1-23 Ookayama, Meguro-ku, Tokyo 152-8552, Japan; praphaphankul.n.aa@m.titech.ac.jp (N.P.); tiprak.k.aa@m.titech.ac.jp (K.T.)
7 Department of Mechanical Engineering, Faculty of Engineering, King Mongkut's University of Technology Thonburi, Bangkok 10140, Thailand; suphanut.kon@kmutt.ac.th
8 Future Automotive Structure Research Group (FASt), Mobility and Vehicle Technology Research Center, King Mongkut's University of Technology Thonburi, Bangkok 10140, Thailand
* Correspondence: lilihu@sjtu.edu.cn

Abstract: Glass fiber-reinforced polymer (GFRP) rebars are commonly used as an alternative to conventional steel reinforcement in a variety of structural applications due to their superior low cost, strength-to-weight ratio, and durability. However, their mechanical properties after exposure to elevated temperatures, particularly in fire-prone environments, remain a significant concern. To address this concern, the present study focuses on investigating the residual tensile behavior, specifically the tensile strength and elastic modulus, of GFRP rebars exposed to high temperatures that are realistically encountered during fire incidents. The temperature range considered in this analysis spans from 100 °C to 400 °C, with a heating rate of 20 °C/min. The fire duration of 1 h is used. This comprehensive analysis is essential for enhancing our understanding of the performance and applicability of GFRP rebars in fire-prone environments. Based on their actual application in the construction industry, five specimens of three different rebar sizes (16, 20, and 25 mm) were examined for the effect of rebar size on tensile behavior after fire exposure. In addition, the effects were investigated of air- and water-cooling methods on residual tensile behavior. The nominal tensile strength, elastic modulus, and ultimate strain of GFRP rebars at ambient temperature are 930 MPa, 50.2 GPa and 1.85%, respectively. The test results indicated that as the temperature increased to 400 °C, the ultimate tensile strength of the GFRP bars decreased by up to 55%, while the ultimate strain increased by up to 44%, regardless of the cooling method. In addition, when rebars of sizes 16–25 mm were subjected to a 400 °C fire treatment, the smaller the rebar, the greater the percentage of ultimate tensile and strain reduction. These findings hold great significance for the utilization of GFRP bars within the construction industry. This study offers valuable insights into the design of fire-resilient structures, emphasizing the importance of considering rebar size and cooling methods due to their impact on the post-fire tensile strength and strain of GFRP rebars.

Keywords: post-fire strength; glass fiber-reinforced polymer (GFRP) bar; tensile strength; tensile behavior; temperature

check for updates

Citation: Thongchom, C.; Hu, L.; Sanit-in, P.K.; Kontoni, D.-P.N.; Praphaphankul, N.; Tiprak, K.; Kongwat, S. Experimental Investigation on Post-Fire Mechanical Properties of Glass Fiber-Reinforced Polymer Rebars. *Polymers* **2023**, *15*, 2925. https://doi.org/10.3390/polym15132925

Academic Editor: Angels Serra

Received: 2 June 2023
Revised: 25 June 2023
Accepted: 29 June 2023
Published: 1 July 2023

Copyright: © 2023 by the authors. Licensee MDPI, Basel, Switzerland. This article is an open access article distributed under the terms and conditions of the Creative Commons Attribution (CC BY) license (https://creativecommons.org/licenses/by/4.0/).

1. Introduction

Reinforcing steel in concrete is a vital material used to enhance structural strength. In addition to its usability, it is crucial to continuously assess its deterioration to evaluate the structure's usability and lifespan. However, the deterioration of reinforcing steel in concrete is influenced by various factors, including its mechanical and physical properties, as well as exposure to environmental conditions and different types of disasters, such as fire resistance and corrosion caused by environments with high concentrations of acids or solutions.

Corrosion of the reinforcements in reinforced concrete (RC) has long been recognized as a major factor in the deterioration of the performance, especially in environments where chlorides are present, such as those found near the ocean or where deicing salts are used [1]. Consequently, structural damage can appear regularly throughout the structure's service life. This damage can manifest as cracking and spalling of the cover concrete, ultimately affecting the RC element's load-bearing and shear capacities [2]. Fiber-reinforced polymer (FRP) corrosion-resistant rebars have been considered to address these issues [3]. Nowadays, FRP are employed in a diverse range of civil engineering applications, including as rebars, plates, sheets and pultruded profiles. The use of pultruded profiles is confronted with challenges pertaining to shape distortions over time [4,5]. Consequently, the rebar form, owing to its inherent stability and dependability, has attracted substantial interest and is extensively deployed in infrastructures such as bridges, buildings, and industrial structures. Furthermore, glass fiber-reinforced plastic (GFRP) rebars have been promoted for use in civil engineering due to their low cost, high strength-to-weight and stiffness-to-weight ratios, and corrosion resistance [6]. Despite the fact that the usage of GFRP rebars has been codified [7–9] and is extensively recognized within the industry [10–12], these materials exhibit an inclination for degradation under severe environmental conditions [13]. Research and real-world applications have demonstrated this material's effectiveness in harsh environments involving seawater and sea sand concrete, seismicity, ultraviolet radiation, and water vapor condensation [14–16]. Nevertheless, concrete reinforced with GFRP rebars exposed to high temperatures or fire requires additional research and analysis to accurately assess the residual capacity of the structure and to understand its behavior in greater depth.

Some research indicates that the mechanical properties of GFRP rebars degrade at high temperatures [17–23]. For example, the tensile strength and elastic modulus of GFRP rebars tested at 325 °C decreased by 55% and 30%, respectively [19]. At 350 °C, the initial tensile strength of both GFRP and carbon fiber-reinforced plastic (CFRP) rebars decreased by 45 and 35%, respectively [18]. Notably, the size effect of GFRP rebars is important when applied in real-world engineering. However, only limited studies have focused on the behavior of GFRP rebars with various diameters. For example, only 13 mm diameter rebars were mentioned in the study by Bisby et al. [17], 10 mm diameter rebars are mentioned in the study by Hamad et al. [19], and 9.5 and 12.7 mm diameter rebars are mentioned in the study by Wang et al. [18]. Thus, additional major evidence is required on the behavior of the various GFRP rebar sizes and cooling methods after high-temperature exposure.

In addition, the published literature on conventional steel-reinforced concrete has discussed how the procedure of cooling the temperature of the structure affects the structural performance after high-temperature exposure. For example, Lee et al. [24] found that the bond strength of specimens cooled with water was greater than that of specimens cooled naturally. The distractive effect of water cooling was greater than that of air cooling, particularly for longer heating durations [25]. The post-fire compressive strength, compressive strength, and modulus of elasticity of concrete reinforced with CFRP wraps were affected by the cooling technique, with water cooled specimens experiencing a greater reduction in strength than air-cooled specimens [26]. However, that study focused primarily on FRP sheet reinforcement and not rebar reinforcement.

To comprehensively clarify the mechanical properties of GFRP rebars under elevated temperature conditions—a prevalent scenario in structures susceptible to fire—and in

consideration of the industry-standard rebar dimensions and cooling techniques, the current investigation examines the residual tensile behavior of GFRP rebars with diameters ranging from 16 to 25 mm. This examination employs both air-cooling and water-cooling methods. In addition, this research probes into the post-fire mechanical properties of GFRP rebars, with an emphasis on failure mode, the stress–strain relationship, tensile strength, and ultimate strain of GFRP rebars. The investigation was conducted using an ASTM D7205/D7205M-06 standard [27] tensile test with different GFRP rebar diameters, cooling methods, and elevated temperatures (100–400 °C). This study evaluated the tensile performance of GFRP rebars embedded in concrete sleeves subjected to high temperatures with varying rebar sizes and cooling techniques using an ASTM D7205/D7205M-06 standard tensile test [27]. The investigated temperature range provided the information necessary for analyses following various fire scenarios. In the evaluation of how various factors affected the tensile behavior of the GFRP rebars, normalization was applied to the tensile test results in addition to the experimental results to observe changes in the mechanical properties after a fire.

2. Experimental Program

This research investigated the post-fire mechanical properties of GFRP rebars, considering rebar size, maximum temperature exposure, and cooling technique. The experiment comprised 27 testing combinations, with a total of 135 specimens. These specimens consisted of three nominal diameters (16, 20, and 25 mm). Each rebar size was subjected to four different maximum temperatures (100, 200, 300, and 400 °C), while some specimens were maintained at ambient temperature (approximately 28 °C) as the control. After heating, the specimens were further divided into two groups to conduct the two different cooling methods of air or water cooling. Then, the specimens were left for 24 h to ensure that all of them reach a steady state at the ambient temperature before conducting the tensile tests.

2.1. Test Specimens

Rebar sizes of 16, 20, and 25 mm were used because they are the most commonly in the construction industry. In terms of the maximum temperature exposure, a literature review [28] reported that once GFRP rebars are exposed to maximum temperatures between 300 °C and 400 °C, their mechanical properties start to degrade. Thus, the mechanical properties after exposure to maximum temperatures of 100, 200, 300, and 400 °C were investigated in the current study and compared to an unexposed specimen. In addition, both air- and water-cooling methods were employed to simulate real-world scenarios involving post-fire reinforcement of GFRP rebars in structures. Specifically, the water-cooling technique represents situations where the structures have been subjected to fire and subsequently extinguished using water from a fire-fighting system. On the other hand, the air-cooling methods simulate portions of the structures that self-extinguished without the use of any external fire-fighting systems.

The 27 testing combinations, with 5 specimens each, are listed in Table 1. The first three combinations namely G16, G20, and G25 have rebar of sizes 16, 20, and 25 mm in diameter, respectively. Specimens in these three combinations were left at ambient temperature (approximately 25 °C), with no added heating or cooling processes performed. On the other hand, the remaining combinations were divided by considering not only the rebar size but also maximum temperature exposure and cooling approach. To clarify, different combinations were exposed to 4 different maximum temperatures (100, 200, 300, and 400 °C) and 2 different cooling techniques (air or water cooling). Therefore, the remaining combinations were composed of $3 \times 4 \times 2 = 24$ combinations amounting to $24 \times 5 = 120$ specimens. For a clear understanding of the testing methods conducted in each combination, the testing combinations were named systematically. "G dd - ttt c" where "dd", "ttt", and "c" indicate the rebar nominal diameter (mm), maximum temperature exposure (°C), as well as whether water cooled (W) or air cooled (A), respectively. For example, "G20-200W" is the group of five replicates for rebars with 20 mm in nominal

diameter that were heated up to 200 °C before conducting the tensile tests after 24 h of water cooling.

Table 1. Test specimens, where RT = room temperature.

Test Code	Diameter (mm)	Temperature (°C)	Cooling Method
G16	16	RT	-
G20	20	RT	-
G25	25	RT	-
G16-100A	16	100	Air
G16-200A	16	200	Air
G16-300A	16	300	Air
G16-400A	16	400	Air
G16-100W	16	100	Water
G16-200W	16	200	Water
G16-300W	16	300	Water
G16-400W	16	400	Water
G20-100A	20	100	Air
G20-200A	20	200	Air
G20-300A	20	300	Air
G20-400A	20	400	Air
G20-100W	20	100	Water
G20-200W	20	200	Water
G20-300W	20	300	Water
G20-400W	20	400	Water
G25-100A	25	100	Air
G25-200A	25	200	Air
G25-300A	25	300	Air
G25-400A	25	400	Air
G25-100W	25	100	Water
G25-200W	25	200	Water
G25-300W	25	300	Water
G25-400W	25	400	Water

All the GFRP rebars were composed of continuous Advantex glass fibers inserted in a vinyl ester matrix using pultrusion. According to the ASTM D792 standard [29], the glass fraction was confirmed as 80.5%. The physical and mechanical properties of GFRP rebars at ambient temperature are shown in Table 2.

Table 2. Physical and mechanical properties of GFRP rebars.

Property	Glass Content	Tensile Strength	Tensile Modulus	Ultimate Strain
Value	80.5% (by mass)	930 MPa	50.2 GPa	0.0185

Figure 1a indicates details of a specimen that was set according to ASTM D7205/D7205M-06 [27]. All the rebars in this research were firmly covered by a steel pipe that was 460 mm long and had a diameter of 48 mm that was filled with mortar at both ends to act as interfaces between rebars and the loading head of the loading machine during the tensile tests. Installing the anchors reduced the stress concentration at the interfaces, which is observed frequently in tensile testing of GFRP rebars; hence, premature tensile failures in the GFRP rebars could be prevented to obtain the full tensile capacity of the specimens. In addition, there was a clear length of rebars between anchors of 380 mm that was heated and attached to a strain gauge to investigate the mechanical properties. The illustration of specimens and anchorages are shown in Figure 1b.

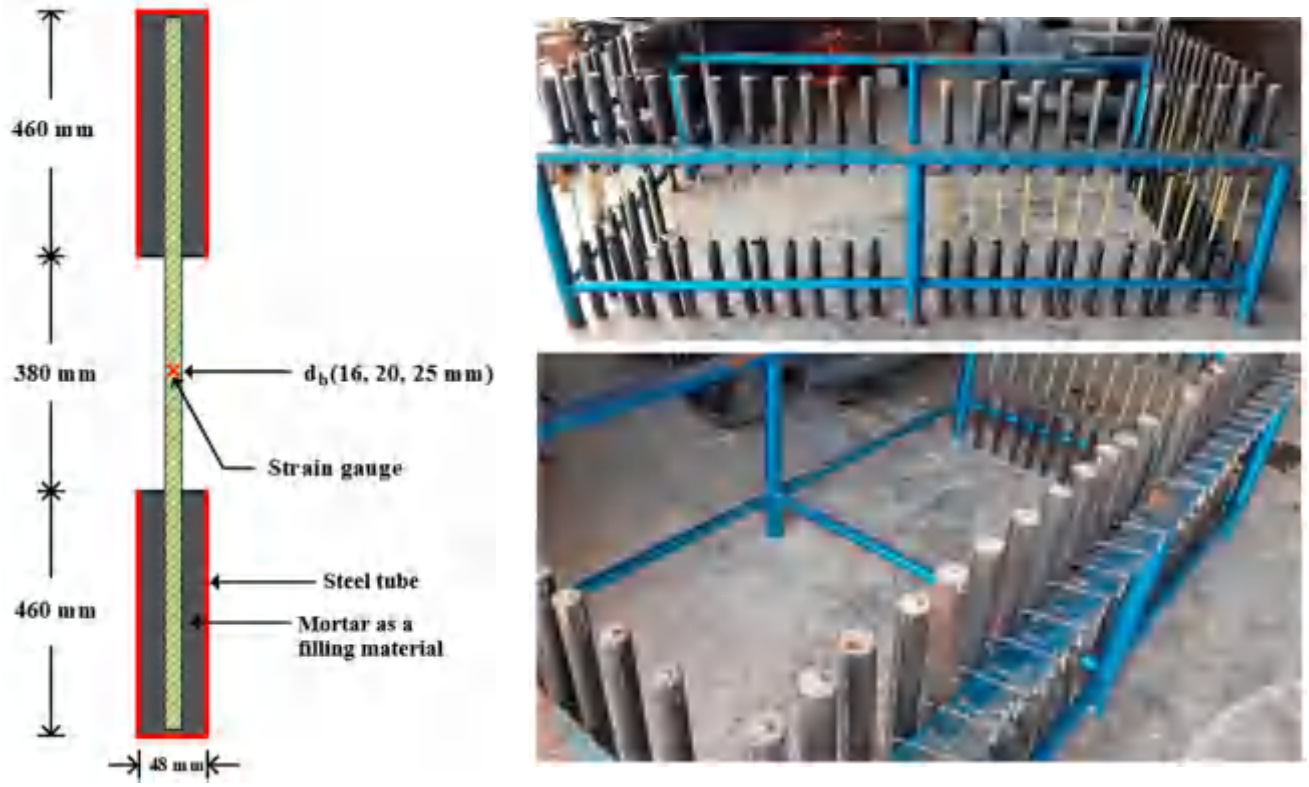


Figure 1. Test specimens: (**a**) details of a specimen (ASTM D7205/D7205M-06 [27]); (**b**) illustration of specimens and anchorages.

2.2. Heating and Cooling

Prior to the experiment, a furnace, capable of heating to 1200 °C, was modified to dimensions of 200 mm, 200 mm, and 200 mm in width, depth, and height, respectively, as shown in Figure 2a to ensure heating occurred only in the desired area. By doing so, the high temperatures were unable to influence and harm the anchors, which played a crucial role during the tensile test as interfaces between the rebars and the loading head of the loading machine.

During the heating process, a GFRP rebar was installed in the modified furnace, as shown in Figure 2b. Then, the specimen was heated to reach the targeted temperature using a heating rate of 20 °C/min [30], as illustrated in Figure 3. After reaching the targeted temperature, the specimen was left for 1 h to simulate a fire at the constant targeted temperature. Then, the designated cooling process was performed on the specimen.



(**a**) (**b**)

Figure 2. Fire testing: (**a**) internal furnace for heating test; (**b**) fire-testing setup.

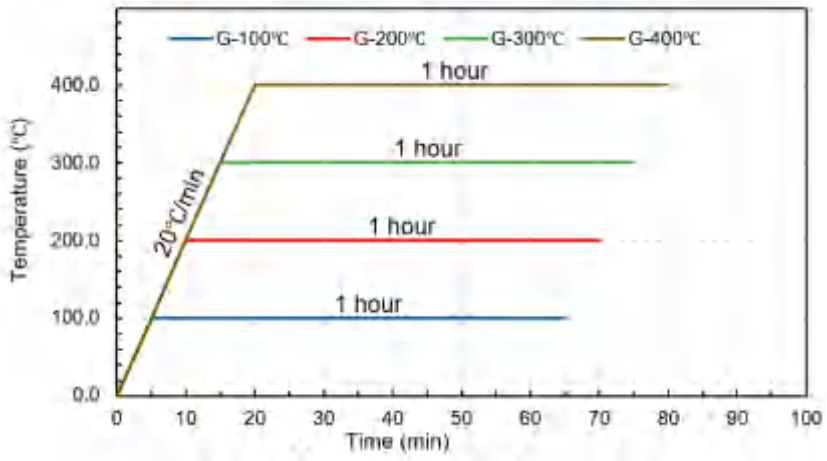


Figure 3. Temperature-time relationship.

Two techniques of cooling were investigated. The first was air cooling, with each specimen left at room temperature of about 25 °C for 24 h after the heating process. The second method used water cooling, where the burnt part of the rebar was submerged in room temperature water immediately after the heating process, and left submerged for 24 h to emulate the influences of cooling on the post-fire mechanical properties of the specimen.

2.3. Tensile Test

After allowing the specimen to cool for 24 h, the standard tensile test according to ASTM D7205/D7205M-06 [27] was conducted, as shown in Figure 4.

First, the anchorage zones of the specimen were firmly attached to the loading head of the loading machine in such a way that slipping during applying the tension force would not occur and the loading direction corresponding to the longitudinal axis of the rebar could be ensured. Next, the burnt rebar surface was polished until a satisfactory level of smoothness was achieved for strain gauge attachment. Finally, before applying the tensile load on the specimen, a strain gauge was attached at the mid-length of the clear range of the rebars for measuring the mechanical properties of the specimen after the fire.

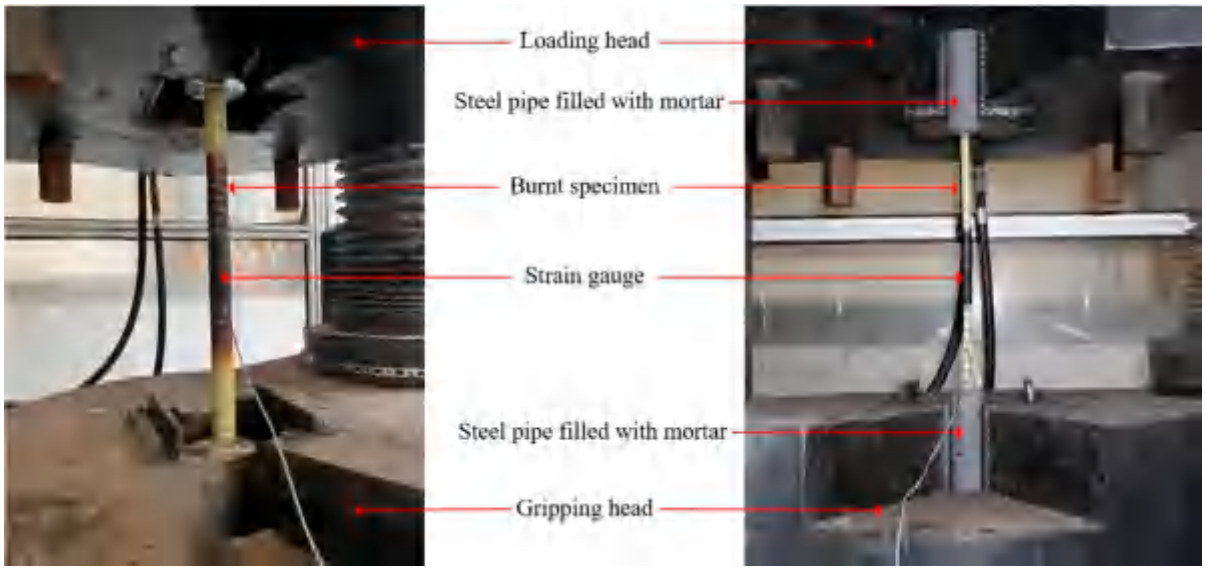


Figure 4. Tensile testing setup.

The tensile test was performed by applying tension force to the specimen through the loading head, which was subsequently increased continuously at a loading rate of 2 mm/min [25] until failure was observed. During the loading process, the tensile stress and tensile strain were recorded to obtain a stress–strain relationship.

3. Results and Discussion

This section presents the results of the tensile tests of the GFRP rebars at elevated temperatures and includes the physical properties and mechanical properties. The physical properties section covers the failure modes of the FRP rebars and changes in the appearance of GFRP rebars under elevated temperatures and after the tensile tests. The mechanical properties section covers the ultimate tensile strength, ultimate strain, and elastic modulus of the GFRP rebars for the evaluated temperature and the normalized mechanical properties. It is noted that, for the purpose of clarity, a normalization approach was employed to facilitate the understanding of the post-fire mechanical properties in relation to the pre-fire properties. The normalization was defined as the ratio of the mechanical properties of the specimen after and before the fire event, was applied to present a clearer picture of the post-fire mechanical properties in comparison to the pre-fire. To illustrate, a value greater than 1.0 in the normalized mechanical properties indicates an improvement in the post-fire properties of the GFRP rebars, whereas a value lower than 1.0 signifies a decrease in the post-fire properties.

3.1. Mode of Failure

After removing the GFRP rebar samples from the heat treatments, samples were observed to have expanded (Figure 5a). This phenomenon may have been attributable to the high values of the resin's coefficient of thermal expansion; this should be noted as the important point since it may contribute to the spalling of concrete under fire conditions. In addition, Figure 5a depicts the GFRP rebars exposed to varying temperatures for the same duration. The rebars exhibited almost no external color change at 100 °C. The surface yellowed when the GFRP rebars were heated to 200 °C and darkened when heated to 300 °C. By the end of their time in the oven at 400 °C, the GFRP rebars had turned an extremely dark color and the surface had turned to ashes in some parts. The hue change was attributable to the decomposition of the polymer matrix during heating. The observed hue shift was clearly correlated with the exposure temperature.

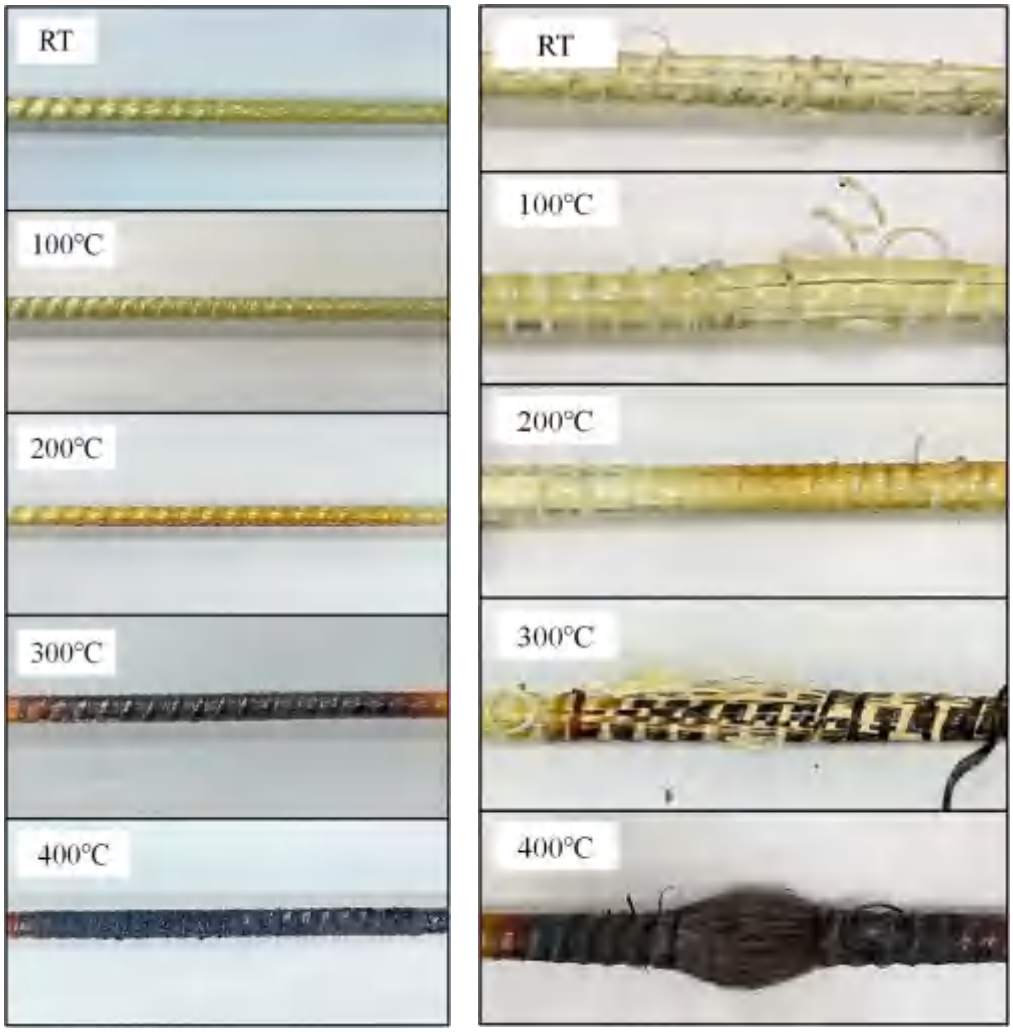


Figure 5. GFRP after fire exposure: (**a**) before tensile test; (**b**) failure mode after tensile test.

In the tensile test, regardless of the elevated temperature or cooling method, all GFRP rebars failed in a similar manner, with fiber rupture at ultimate loads. Due to surface debonding between the fibers and matrix, the failure manifested as a sudden longitudinal central fiber delamination; however, when the GFRP rebars were heated to 300 °C, a similar but more dramatic failure mode was observed, with more fibers collapsing and debonding. At 400 °C, severe delamination was replaced by fiberization. The divergent fibers of each rebar that resulted from the failure are depicted in Figure 5b. Brittle fracture was identified as the predominant mode of failure observed in all the investigated GFRP rebars in this study. This outcome is in accordance with previous studies [31], which have consistently reported the brittle fracture as the common failure mode in GFRP rebars.

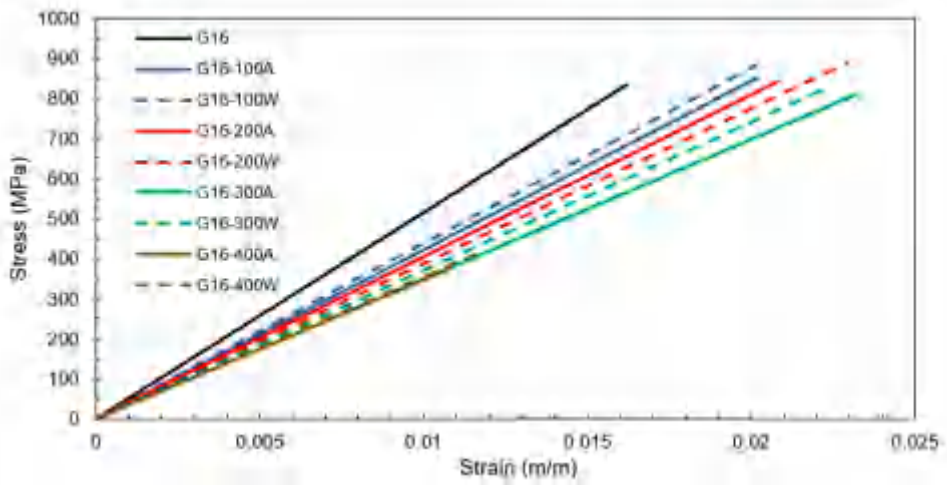
3.2. Mechanical Properties

During the tensile test, the stress and strain of specimens were recorded and the elastic modulus was computed. The average (Avg.), standard deviation (S.D.), as well as the coefficient of variation (COV) of the experimental results are listed in Table 3.

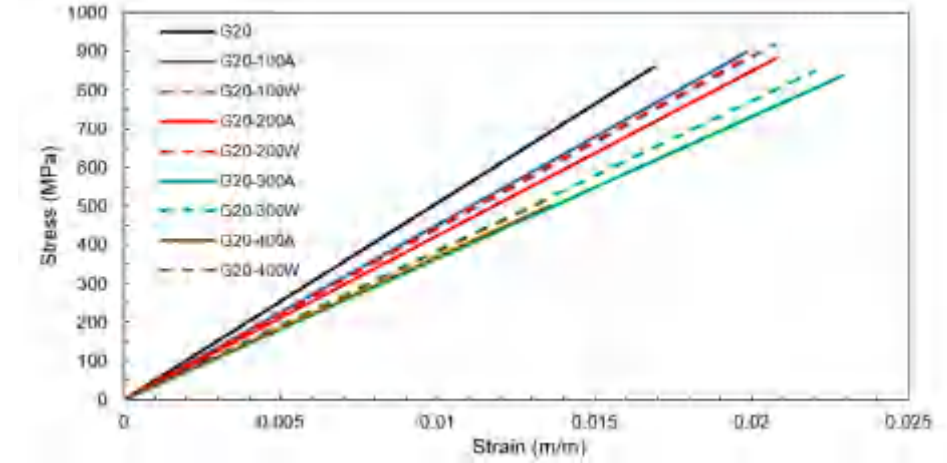
Table 3. Experimental results.

Specimen	Tensile Stress (MPa)			Strain (m/m)			Elastic Modulus		
	Avg. (MPa)	S.D. (MPa)	COV	Avg. (m/m)	S.D. (m/m)	COV	Avg. (GPa)	S.D. (GPa)	COV
G16	833.0	9.9	1.2	0.0162	0.00014	0.9	51.5	0.1	0.1
G20	859.4	10.9	1.3	0.0169	0.00016	0.9	50.9	0.2	0.3
G25	955.1	14.1	1.5	0.0184	0.00066	3.6	52.0	2.6	5.1
G16-100A	849.0	11.3	1.3	0.0218	0.00093	4.6	42.1	1.4	3.3
G16-200A	842.0	2.8	0.3	0.0201	0.00030	1.5	40.1	1.4	3.5
G16-300A	809.5	17.7	2.2	0.0232	0.00206	8.9	35.3	3.7	10.5
G16-400A	375.8	17.5	4.7	0.0108	0.00016	1.5	34.7	2.1	6.2
G16-100W	895.4	58.5	6.5	0.0204	0.00075	3.7	43.9	1.2	2.9
G16-200W	899.5	12.0	1.4	0.0230	0.00019	0.8	38.8	0.8	2.2
G16-300W	829.4	15.6	1.9	0.0224	0.00007	0.3	37.0	0.6	1.6
G16-400W	415.7	9.9	2.4	0.0117	0.00083	7.1	35.5	1.7	4.7
G20-100A	898.5	3.7	0.4	0.0198	0.00024	1.2	45.3	0.7	1.6
G20-200A	883.5	7.9	0.9	0.0208	0.00040	1.9	42.4	0.4	1.0
G20-300A	835.7	5.7	0.7	0.0229	0.00140	6.1	36.5	2.0	5.4
G20-400A	500.9	5.4	1.1	0.0135	0.00048	3.5	37.0	0.9	2.4
G20-100W	917.3	10.6	1.2	0.0207	0.00094	4.5	44.3	1.5	3.4
G20-200W	891.3	9.4	1.1	0.0201	0.00003	0.1	44.4	0.5	1.2
G20-300W	849.0	8.3	1.0	0.0212	0.00073	3.3	38.6	0.9	2.3
G20-400W	518.3	9.1	1.8	0.0136	0.00017	1.3	38.2	1.2	3.0
G25-100A	1004.1	11.6	1.2	0.0225	0.00055	2.5	44.8	1.6	3.6
G25-200A	982.8	4.6	0.5	0.0225	0.00111	4.9	43.8	2.4	5.4
G25-300A	947.1	7.5	0.8	0.0233	0.00091	3.9	40.7	1.3	3.1
G25-400A	590.7	9.0	1.5	0.0150	0.00005	0.3	39.3	0.5	1.2
G25-100W	997.6	36.9	3.7	0.0207	0.00056	2.7	48.0	0.5	1.0
G25-200W	989.3	7.5	0.8	0.0211	0.00062	2.9	46.9	1.0	2.2
G25-300W	950.3	22.3	2.3	0.0218	0.00035	1.6	43.5	1.7	1.6
G25-400W	611.3	9.3	1.5	0.0152	0.000001	0.01	40.3	0.6	1.5

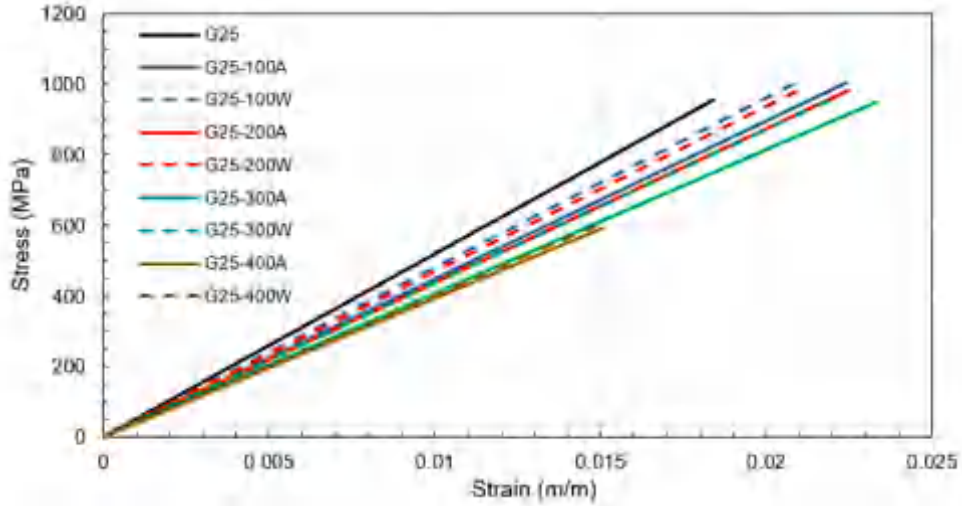
Figure 6a–c illustrate the stress–strain curves for G16, G20, and G25, respectively. Based on the test results, the stress–strain relationship of post-fire GFRP bars increased linearly from the beginning until failure. These results agreed well with Spagnuolo et al. [28], who conducted experiments to investigate the residual mechanical behavior of GFRP bars following exposure to temperature treatments ranging from 100 °C to 700 °C. Notably, their study did not specifically explore the effect of the water-cooling technique.



(**a**)



(**b**)



(**c**)

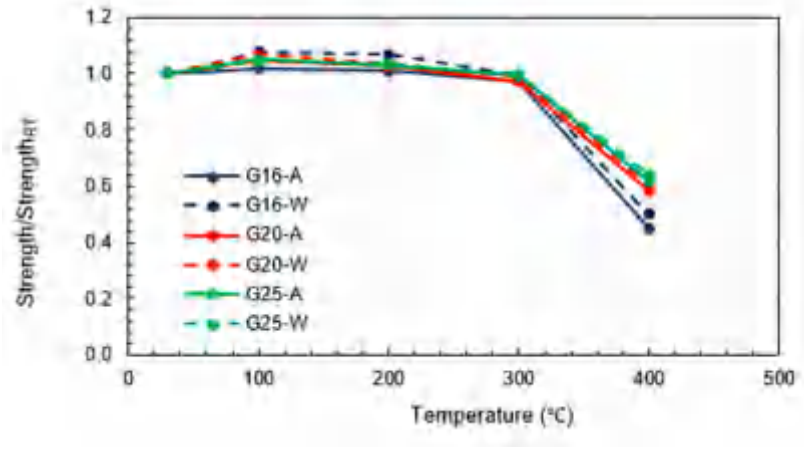
Figure 6. Stress–strain curves for all tested combinations: (**a**) 16 mm (**b**) 20 mm (**c**) 25 mm.

For the maximum temperature exposures of 100 °C, 200 °C, and 300 °C for all rebar sizes and cooling approaches, there was no significant change in the tensile strength compared to the tensile strength of identical-sized rebars before the fire because the maximum temperature exposures did not exceed the critical temperature of between 300 °C and 400 °C; hence, the mechanical properties after being cooled and tested had recovered.

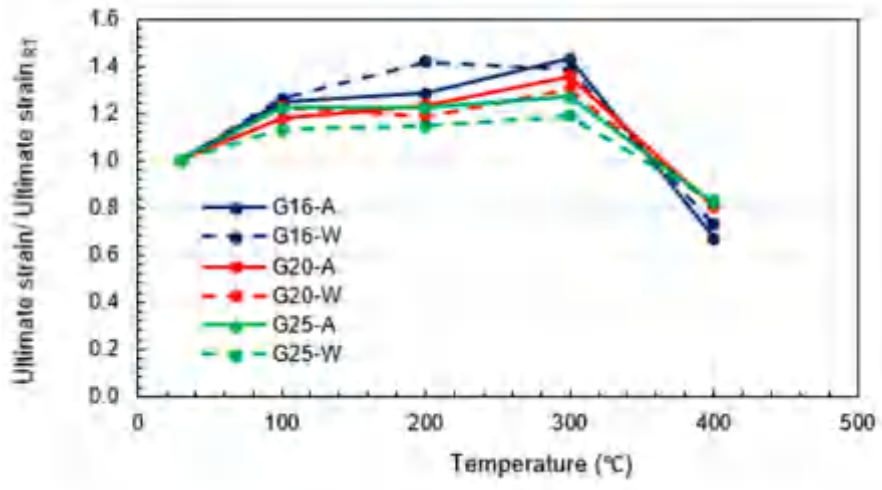
Notably, even though there were slight increments in the tensile strength after exposure to this range of elevated temperatures, these increments might have been inconsistent with the real behavior of the rebars in use because the increases may have been the consequence of better curing of the resin when there was no applied load on the fiber direction of the rebars during the fire, as demonstrated in this study [28]. On the other hand, in cases where the targeted temperature reached 400 °C, the rebars experienced severe damage when they reached the critical temperature range of 300 °C to 400 °C. This resulted in thermal degradation of the polymer and loss of load transfer among the fibers. Consequently, the mechanical properties became non-reversible. This observation is consistent with the findings of a previous study [32] which investigated the tensile, shear, and flexural properties of sand-coated GFRP bars under low temperatures (−100 °C to 0 °C) and elevated temperatures (23 °C to 315 °C). The purpose of that study was to gain insights into the thermal stability of the mechanical properties. Thus, the tensile strengths of G16, G20, and G25 decreased substantially by about 55%, 41%, and 38%, respectively, regardless of the cooling approach, as can be clearly observed from the plot of normalized tensile strength in Figure 7a. Additionally, these numbers implied that the larger the rebar in the range between 16 mm and 25 mm, the smaller the percentage of tensile strength reduction when exposed to 400 °C. It can be seen from Figure 8 that the residual tensile strengths of all rebars after cooling using water were slightly greater than those that were gradually cooled using air.

Considering the ultimate strain, it was clear that all the rebars that were exposed to 100 °C, 200 °C, and 300 °C deformed more than the same-sized rebars before the fire. In other words, rebar ductility increased due to temperature exposure between 100 °C and 300 °C. On the other hand, for maximum temperature exposures to 400 °C, the plot of the normalized ultimate strain in Figure 7b indicates that the ultimate strain of G16, G20, and G25 decreased significantly compared to the pre-fire identical size rebars by about 33%, 20%, and 18%, respectively. Similar to the effects due to the rebar size on the post-fire tensile strength reduction, after exposure to 400 °C, the larger rebars within the range 16–25 mm tended to be more ductile than the smaller rebars in the same range and the percentage of the ductility reduction was relatively lower. In addition, Figure 9 shows that the ultimate strain levels of all rebars after exposure to 400 °C followed by water cooling were more than for the air-cooled rebars, while the ultimate strain levels of the 25 mm rebars after being heated to 100 °C, 200 °C, and 300 °C before being air cooled by air were slightly more than those that were water cooled. However, there was no clear trend observed in the other specimens.

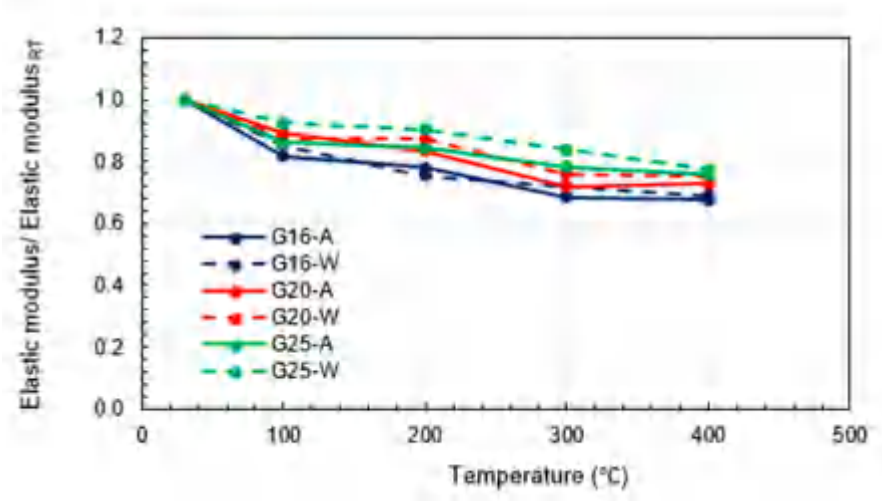
The normalized elastic modulus in Figure 7c demonstrated a clear pattern that as maximum temperature increased, the modulus of elasticity decreased. In addition, some specimens (16 mm and 20 mm rebars heated to 300 °C and 400 °C before being cooled by water as well as all 25 mm water-cooled rebars) had a greater modulus of elasticity compared to those that were air cooled. However, Figure 10 shows that these relationships did not hold true for the 16 mm and 20 mm rebars heated to maximum temperatures of 200 °C and 100 °C, respectively.



(**a**)



(**b**)



(**c**)

Figure 7. Results of all testing combinations normalized by results at room temperature: (**a**) normalized tensile strength, (**b**) normalized ultimate strain, and (**c**) normalized elastic modulus.

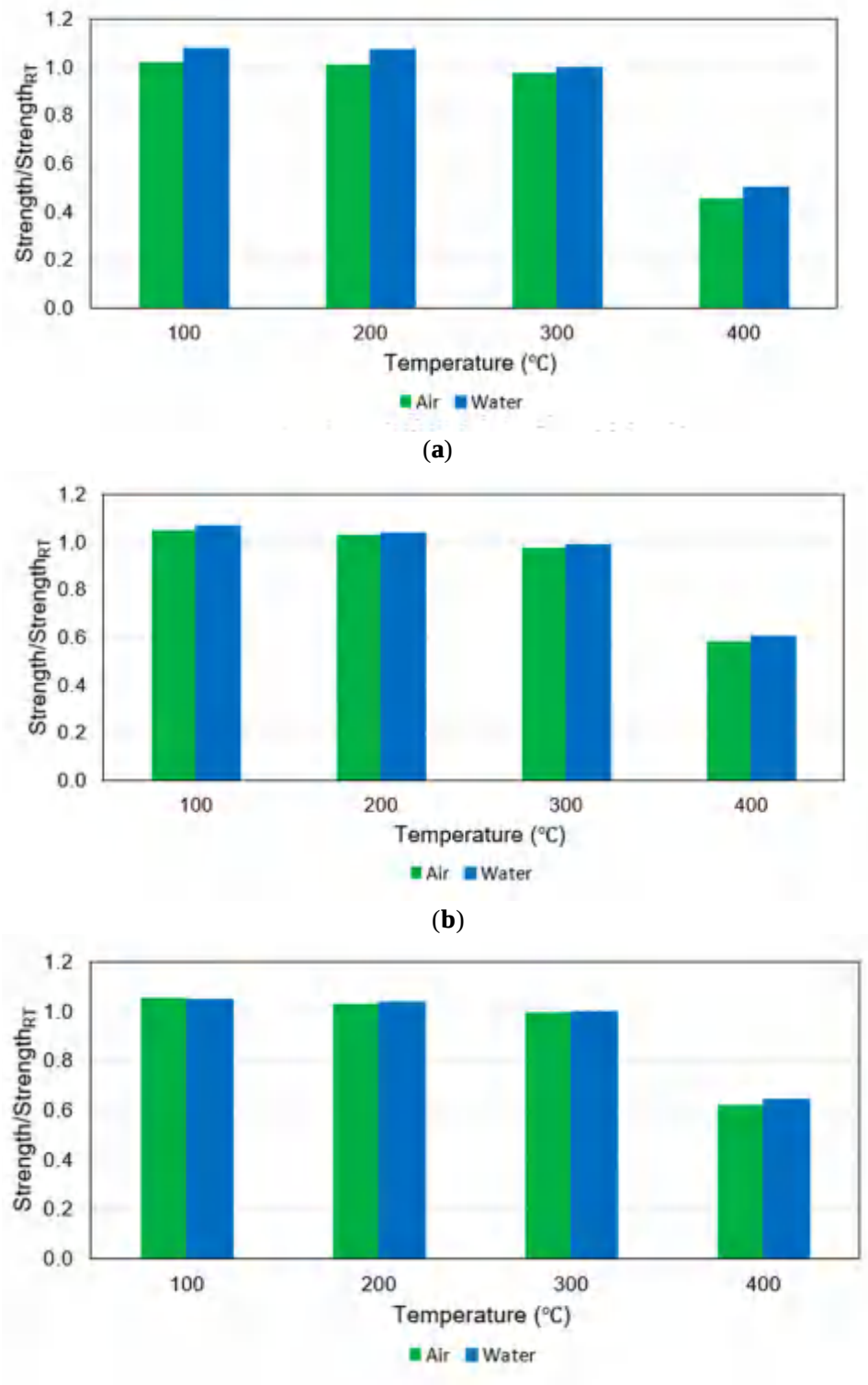
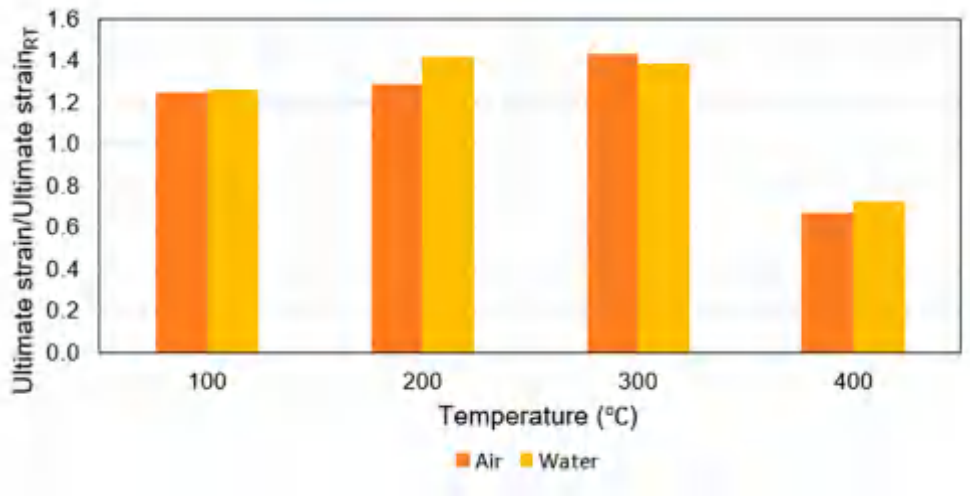
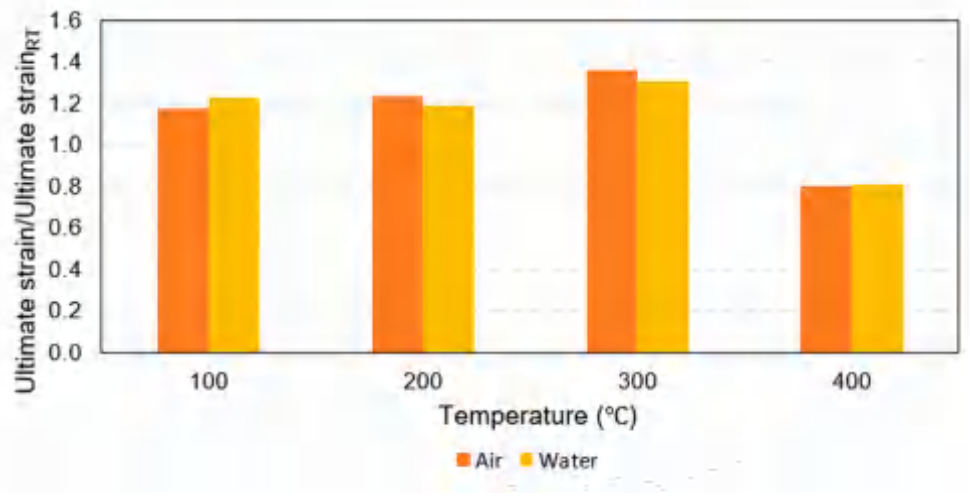


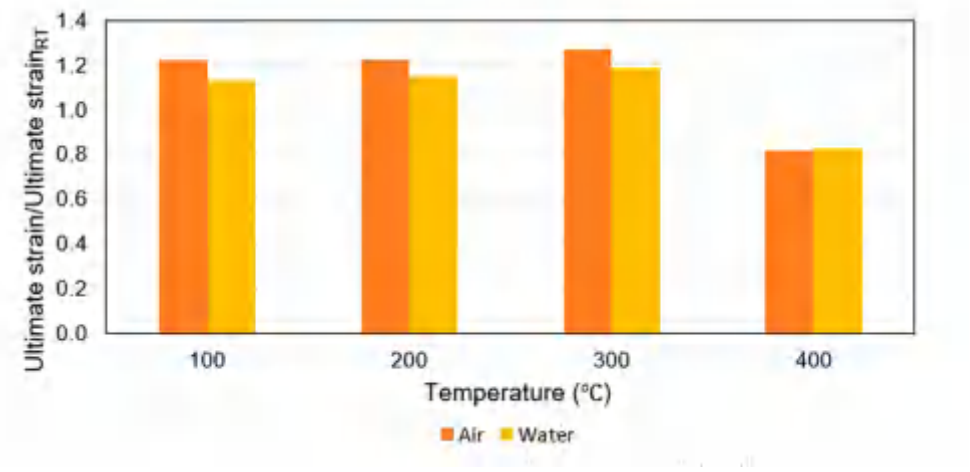
Figure 8. Bar charts of normalized tensile strength: (**a**) 16 mm, (**b**) 20 mm, and (**c**) 25 mm.



(**a**)



(**b**)



(**c**)

Figure 9. Bar charts of normalized ultimate strain: (**a**) 16 mm, (**b**) 20 mm, and (**c**) 25 mm.

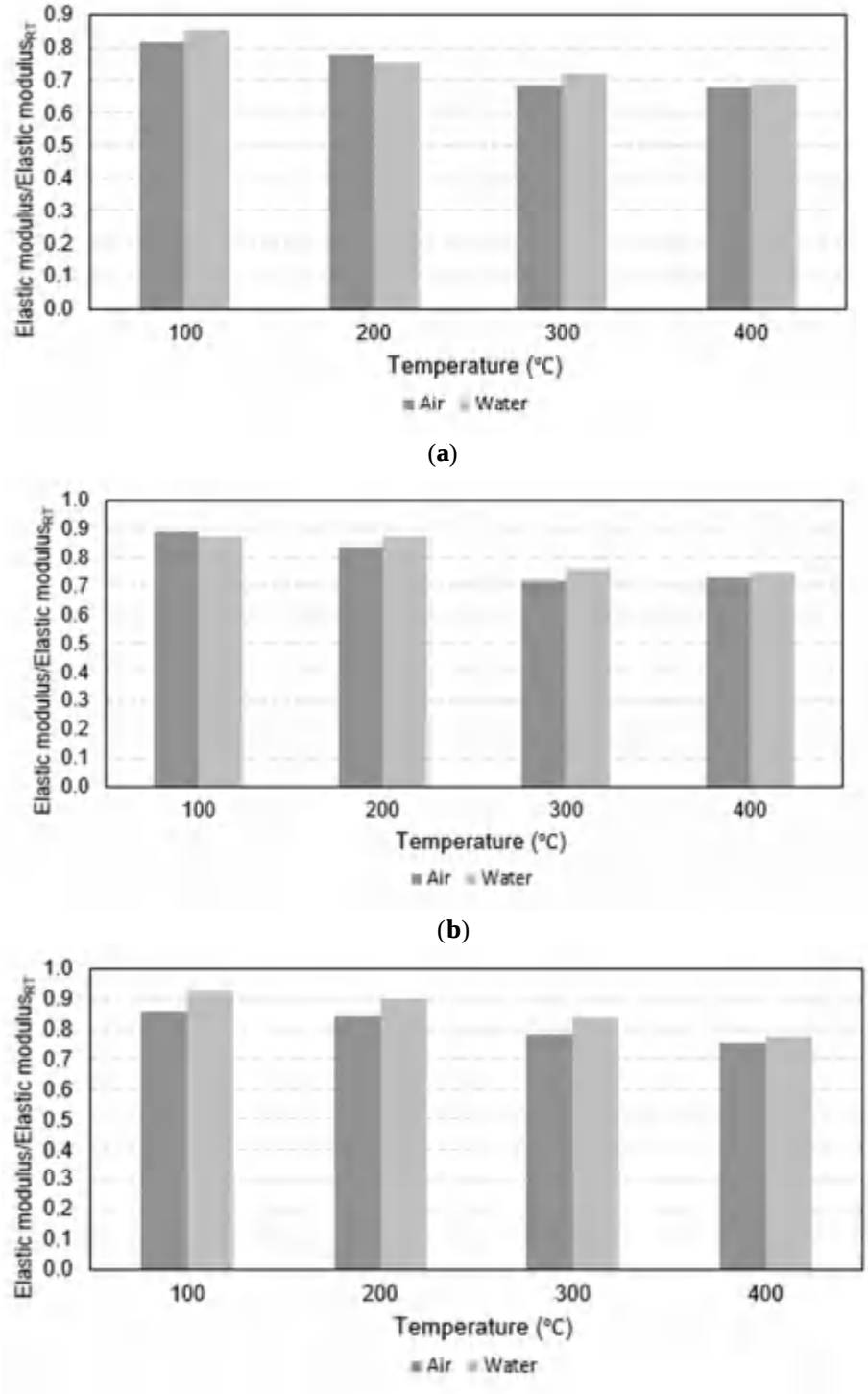


Figure 10. Bar charts of normalized elastic modulus: (**a**) 16 mm, (**b**) 20 mm, and (**c**) 25 mm.

Notably, in the case of traditional steel bars, previous studies such as [33,34] have collected data on the post-fire mechanical properties. It has been observed that the cooling technique exerts a significant influence on these properties. For instance, water-cooled steel bars tend to experience reductions in strength recovery and ductility after exposure to temperatures exceeding 600 °C [33]. However, it is important to clarify that despite a substantial decrease in ultimate strain in water-cooled steel bars by nearly 50%, they still exhibit a notable increase in post-fire strength compared to air-cooled steel bars [34].

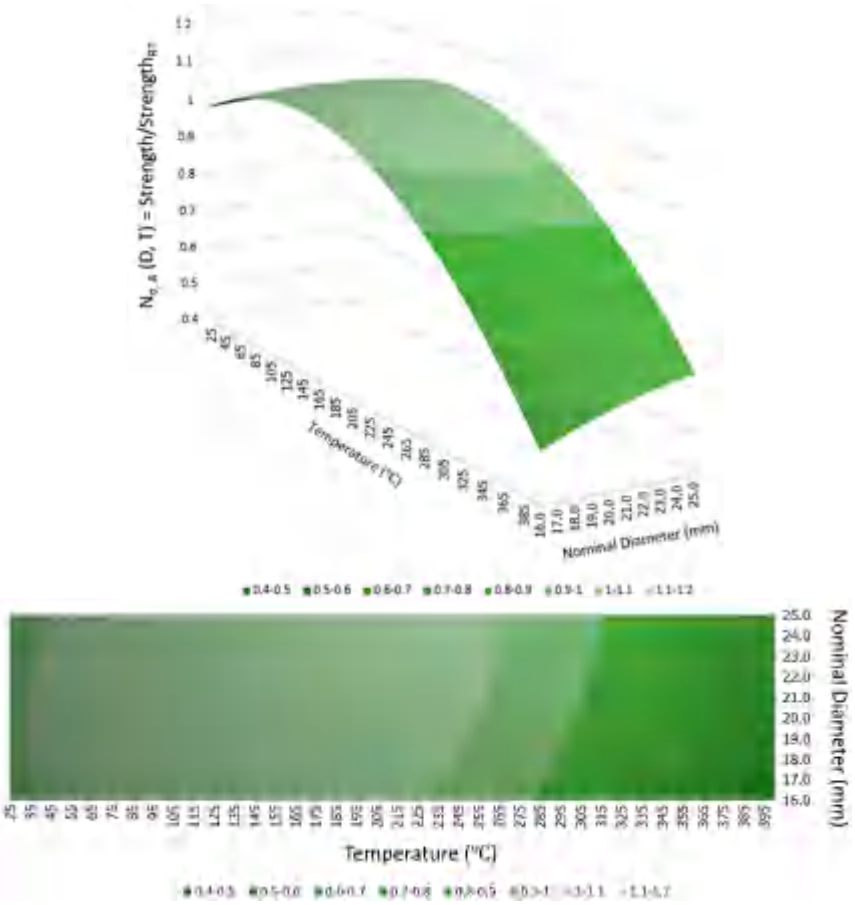
However, even though the same results were observed in all the GFRP rebars exposed to more than 300 °C, the differences were far lower than those investigated for steel bars. Thus, it was not reliable to compare the higher strength of the water-cooled GFRP rebars to the air-cooled ones in post-fire evaluation.

3.3. Variation Model of Post-Fire Mechanical Properties

The mechanical properties of the GFRP rebars were normalized using the pre-fire properties to provide an indication of post-fire mechanical properties variation. These normalized properties, namely $N_{i,j}$ where i denotes strength (σ), ultimate strain (ε), and elastic modulus (E) while j denotes the implemented cooling method (A and W for the air and water cooling method, respectively), were plotted against the maximum fire temperature exposures as well as the nominal diameters in Figures 11 and 12, respectively, for air and water cooling, respectively, to show the more apparent course of the correlation between these two parameters and the dependent variables when implementing different cooling methods. After that, the variation trend was fitted with a quadratic response surface model, as shown in Equation (1):

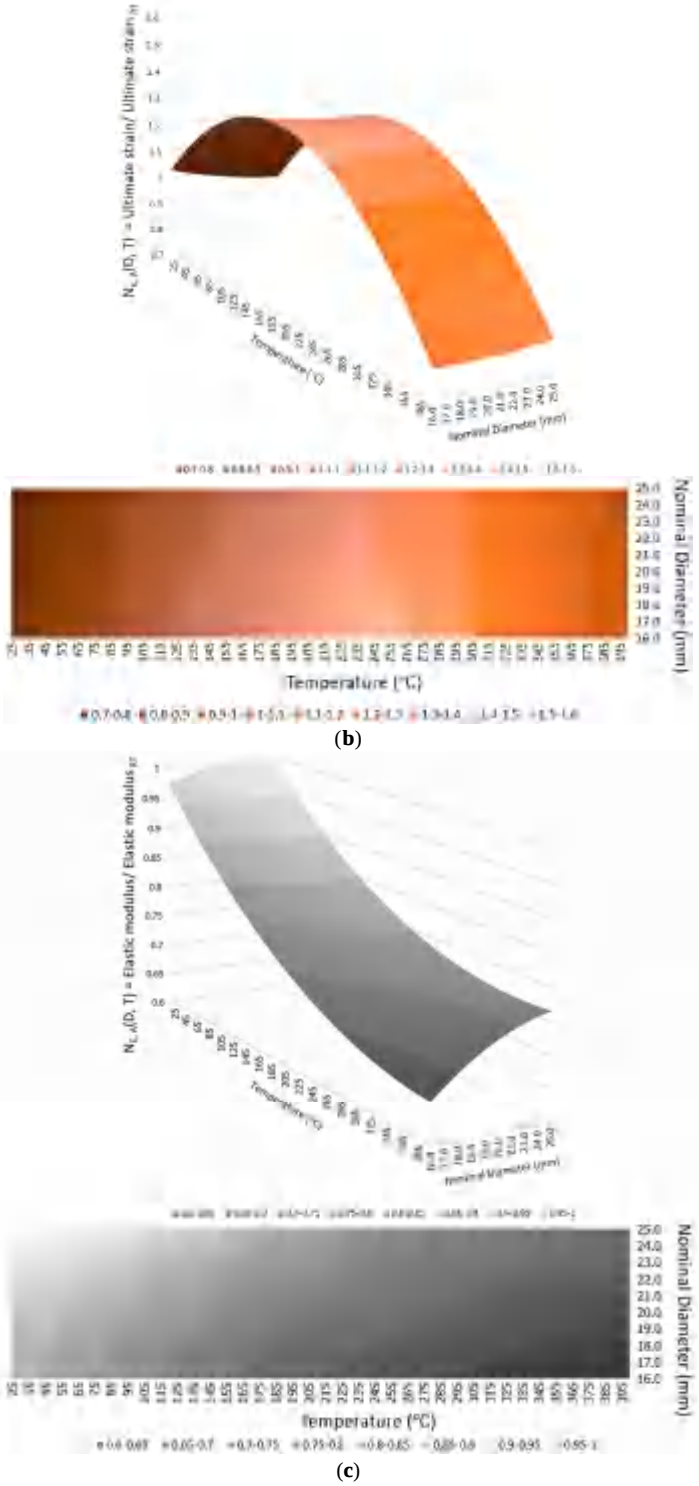
$$N_{i,j}(D,T) = \beta_1 D^2 + \beta_2 T^2 + \beta_3 DT + \beta_4 D + \beta_5 T + \beta_6 \quad (1)$$

where D and T are the nominal diameter (mm) and the maximum fire temperature exposure (°C), respectively. β_1–β_6 are the fitted coefficients of the above quadratic response surface, as listed in Table 4.



(**a**)

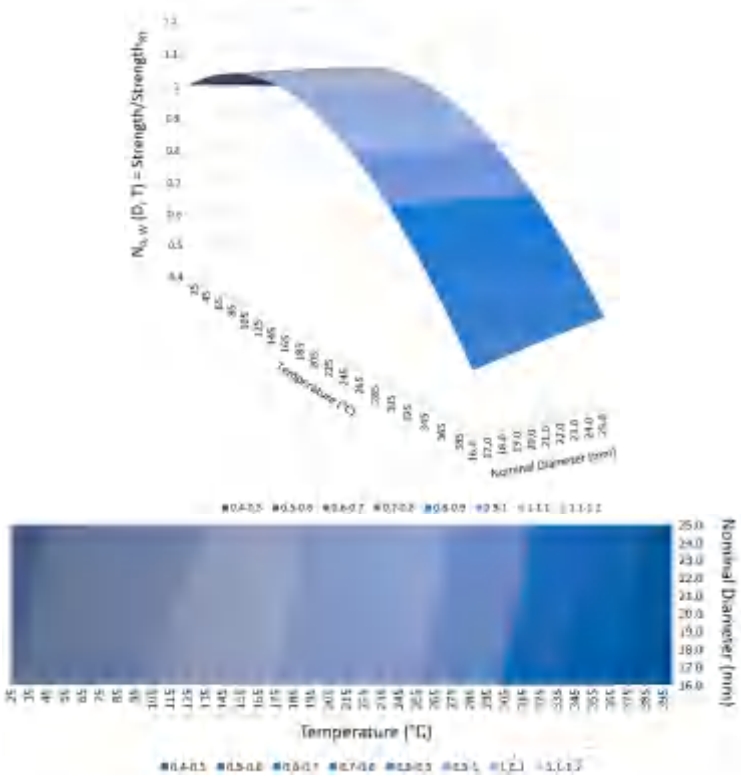
Figure 11. *Cont.*



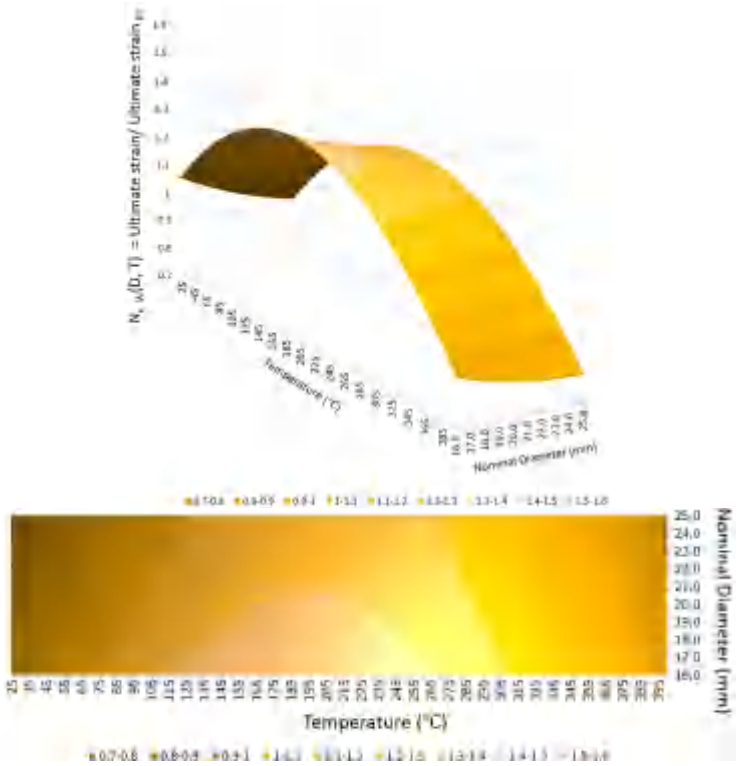
(**b**)

(**c**)

Figure 11. Models of mechanical properties of various nominal diameter GFRP bars after exposure to different maximum fire temperatures followed by air cooling: (**a**) strength variation, (**b**) ultimate strain variation, and (**c**) elastic modulus variation.

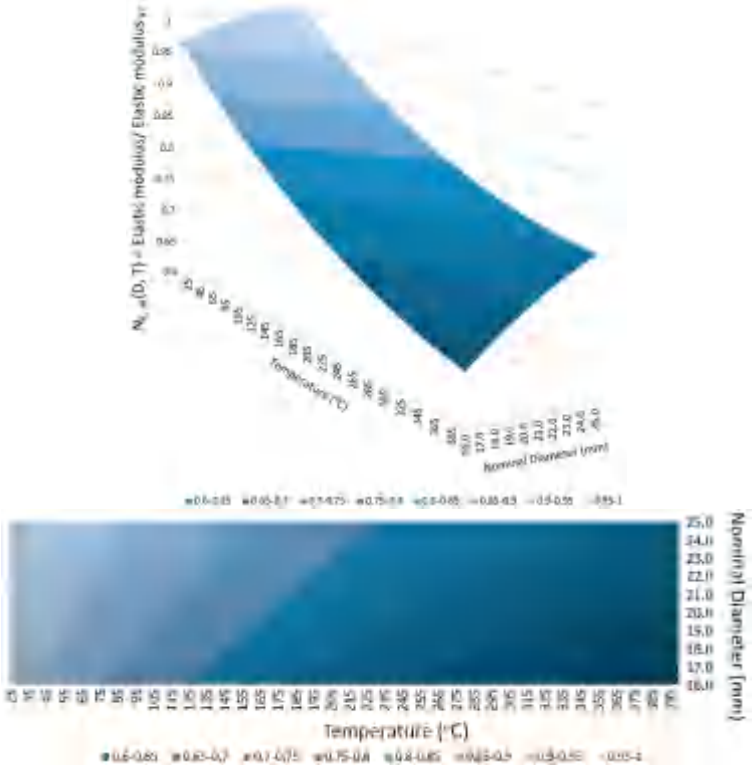


(**a**)



(**b**)

Figure 12. *Cont*.



(**c**)

Figure 12. Models of mechanical properties of various nominal diameters of GFRP bars after exposure to different maximum fire temperatures followed by water cooling: (**a**) strength variation, (**b**) ultimate strain variation, and (**c**) elastic modulus variation.

Table 4. Fitted coefficients of Equation (1), where R^2 = coefficient of determination.

Normalized Mechanical Property	β_1	β_2	β_3	β_4	β_5	β_6	R^2
$N_{\sigma,A}(D,T)$	-7.03×10^{-4}	-7.78×10^{-6}	3.73×10^{-5}	2.65×10^{-2}	1.50×10^{-3}	6.84×10^{-1}	0.93
$N_{\sigma,W}(D,T)$	-1.68×10^{-4}	-8.04×10^{-6}	3.72×10^{-5}	6.98×10^{-4}	1.67×10^{-3}	9.81×10^{-1}	0.94
$N_{\varepsilon,A}(D,T)$	5.75×10^{-4}	-1.28×10^{-5}	3.03×10^{-5}	-3.34×10^{-2}	4.36×10^{-3}	1.30	0.79
$N_{\varepsilon,W}(D,T)$	8.78×10^{-4}	-1.17×10^{-5}	2.07×10^{-5}	-5.14×10^{-2}	4.13×10^{-3}	1.54	0.84
$N_{E,A}(D,T)$	-8.41×10^{-4}	2.00×10^{-6}	2.52×10^{-5}	3.57×10^{-2}	-2.08×10^{-3}	6.58×10^{-1}	0.95
$N_{E,W}(D,T)$	-4.99×10^{-4}	1.33×10^{-6}	2.39×10^{-5}	2.50×10^{-2}	-1.71×10^{-3}	7.23×10^{-1}	0.94

4. Conclusions

This study investigated the post-fire mechanical properties of GFRP rebars, based on rebars with nominal diameters of 16 mm, 20 mm, and 25 mm, maximum temperature exposures between 100 °C and 400 °C, and air-cooling techniques and water-cooling methods. In total, 135 specimens were heated to reach the targeted maximum temperature, followed by continual exposure at that temperature for 1 h before being cooled using the designated cooling approach for 24 h. Finally, tensile tests were conducted on the rebars to obtain the post-fire mechanical properties. The following conclusions were drawn:

The modulus of elasticity of the GFRP rebars decreased as the maximum fire temperature increased compared to the pre-fire modulus of elasticity of the identical-sized rebar.

- Tensile strength reductions were observed in all rebars heated to 400 °C; ductility increased up to 300 °C before decreasing significantly at 400 °C.

- The ductility of GFRP rebars increased due to temperature exposures between 100 °C and 300 °C. However, the ultimate strain decreased significantly after the temperature increased to 400 °C. After exposure to 400 °C, the percentage of tensile strength and ductility reductions decreased as the size of the rebars increased within the range 16–25 mm.
- The post-fire tensile strength of the GFRP rebars that were water cooled was slightly greater than that of the same-sized rebars that were air cooled except for the case of 25 mm bars that were subjected to the maximum temperature of 100 °C. The tensile strength, ultimate strain, and modulus of elasticity of all rebars cooled using water after exposure to temperatures exceeding the critical temperature of between 300 °C and 400 °C, i.e., the case of maximum temperature exposure reach 400 °C in this study were slightly higher than those that had been gradually cooled at ambient temperature. It has been observed that the effects of cooling methods, as observed in this study, are minimal and inconsequential. Furthermore, slight fluctuations in the results were noted.
- The correlations between maximum temperature exposure, rebar nominal diameter, cooling method, and the post-fire mechanical properties were plotted, and variation models were developed by fitting the correlations with the quadratic response surface model. The adoption of this model was based on its capability to provide a reliable reference for design purposes, given its favorable shape.

However, considerations of the physical characteristics, mechanical behavior, and changes in the conditions of reinforcing materials are just some of the important factors that contribute to improving and selecting suitable options for different types of structures. When designing reinforced concrete building elements, it is crucial to consider also the concrete design and to have sufficient concrete cover to ensure proper usage. Incorporating the findings from the study on the behavior of these reinforcing materials into the design process can result in the establishment of appropriate design boundaries. Furthermore, it can lead to a reduction in the consumption of concrete materials by minimizing the concrete cover.

Author Contributions: Conceptualization, C.T. and L.H.; methodology, C.T., P.K.S.-i. and S.K.; validation, C.T., D.-P.N.K., N.P. and K.T.; formal analysis, C.T., N.P. and K.T.; investigation, N.P. and K.T.; writing—original draft preparation, C.T., N.P. and K.T.; writing—review and editing, C.T., L.H., N.P. and K.T.; supervision, L.H., D.-P.N.K., P.K.S.-i. and S.K.; project administration, C.T. and S.K.; funding acquisition, S.K, and L.H. All authors have read and agreed to the published version of the manuscript.

Funding: This research was supported by the Program Fund of Non-Metallic Excellence and Innovation Center for Building Materials (2023TDA5-1) and the Young Elite Scientists Sponsorship Program by CAST (2022QNRC001). This work was also supported by Thammasat University Research Unit in Structural and Foundation Engineering, Faculty of Engineering, Thammasat University, and the Thailand Science Research and Innovation Fundamental Fund fiscal year 2023.

Data Availability Statement: The data presented in this study are available on request from the corresponding author.

Conflicts of Interest: The authors declare no conflict of interest.

References

1. Lu, C.; Yang, J.; Li, H.; Liu, R. Experimental Studies on Chloride Penetration and Steel Corrosion in Cracked Concrete Beams under Drying-Wetting Cycles. *J. Mater. Civil Eng.* **2017**, *29*, 04017114. [CrossRef]
2. Han, C.-G.; Han, M.-C.; Heo, Y.-S. Improvement of residual compressive strength and spalling resistance of high-strength RC columns subjected to fire. *Constr. Build. Mater.* **2009**, *23*, 107–116. [CrossRef]
3. Einde, L.; Zhao, L.; Seible, F. Use of FRP composites in civil structural applications. *Constr. Build. Mater.* **2003**, *17*, 389–403. [CrossRef]
4. Vedernikov, A.N.; Safonov, A.A.; Gusev, S.A.; Carlone, P.; Tucci, F.; Akhatov, I.S. Spring-in experimental evaluation of L-shaped pultruded profiles. *IOP Conf. Ser. Mater. Sci. Eng.* **2020**, *747*, 012013. [CrossRef]

5. Vedernikov, A.; Tucci, F.; Safonov, A.; Carlone, P.; Gusev, S.; Akhatov, I. Investigation on the Shape Distortions of Pultruded Profiles at Different Pulling Speed. *Procedia Manuf.* **2020**, *47*, 1–5. [CrossRef]
6. Debaiky, A.; Cousin, P.; Benmokrane, B. Durability of GFRP bars: A critical review of the literature. *Prog. Struct. Eng. Mater.* **2005**, *7*, 194–209. [CrossRef]
7. *CAN/CSA-S806-02*; Design and Construction of Building Components with Fiber Reinforced Polymers. CSA: Toronto, ON, Canada, 2002.
8. *ACI 440.1R-15*; Guide for the Design and Construction of Concrete Reinforced with FRP Bars. ACI: Dhaka, Bangladesh, 2015.
9. *CNR DT 203-2006*; Guide for the Design and Construction of Concrete Structures Reinforced with Fiber-Reinforced Polymer Bars. CNR: Beijing, China, 2006.
10. Benmokrane, B.; Eisa, M.; El-Gamal, S.; El-Salakawy, E.; Thebeau, D. First use of GFRP bars as reinforcement for continuous reinforced concrete pavement. In Proceedings of the 4th International Conference on FRP Composites in Civil Engineering (CICE2008), Zurich, Switzerland, 22–24 July 2008.
11. Feng, P.; Wang, J.; Wang, Y.; Loughery, D.; Niu, D. Effects of corrosive environments on properties of pultruded GFRP plates. *Compos. Part B Eng.* **2014**, *67*, 427–433. [CrossRef]
12. Alajarmeh, O.; Manalo, A.; Benmokrane, B.; Karunasena, W.; Ferdous, W.; Mendis, P. Hollow concrete columns: Review of structural behavior and new designs using GFRP reinforcement. *Eng. Struct.* **2020**, *203*, 109829. [CrossRef]
13. Bazli, M.; Ashrafi, H.; Oskouei, A.V. Effect of harsh environments on mechanical properties of GFRP pultruded profiles. *Compos. Part B Eng.* **2016**, *99*, 203–215. [CrossRef]
14. Ashrafi, H.; Bazli, M.; Oskouei, A.; Bazli, L. Effect of Sequential Exposure to UV Radiation and Water Vapor Condensation and Extreme Temperatures on the Mechanical Properties of GFRP Bars. *J. Compos. Constr.* **2017**, *22*, 04017047. [CrossRef]
15. Del Zoppo, M.; Di Ludovico, M.; Balsamo, A.; Prota, A.; Manfredi, G. FRP for seismic strengthening of shear controlled RC columns: Experience from earthquakes and experimental analysis. *Compos. Part B Eng.* **2017**, *129*, 47–57. [CrossRef]
16. Wang, Z.; Zhao, X.-L.; Wu, G.; Raman, R.K.; Al-Saadi, S.; Haque, A. Long-term durability of basalt- and glass-fibre reinforced polymer (BFRP/GFRP) bars in seawater and sea sand concrete environment. *Constr. Build. Mater.* **2017**, *139*, 467–489. [CrossRef]
17. Bisby, L.A.; Kodur, V.K.R. Evaluating the fire endurance of concrete slabs reinforced with FRP bars: Considerations for a holistic approach. *Compos. Part B Eng.* **2007**, *38*, 547–558. [CrossRef]
18. Wang, Y.; Wong, P.M.H.; Kodur, V. An experimental study of the mechanical properties of fibre reinforced polymer (FRP) and steel reinforcing bars at elevated temperatures. *Compos. Struct.* **2007**, *80*, 131–140. [CrossRef]
19. Hamad, R.J.A.; Megat Johari, M.A.; Haddad, R.H. Mechanical properties and bond characteristics of different fiber reinforced polymer rebars at elevated temperatures. *Constr. Build. Mater.* **2017**, *142*, 521–535. [CrossRef]
20. Gooranorimi, O.; Claure, G.; De Caso y Basalo, F.; Suaris, W.; Nanni, A. Post-fire behavior of GFRP bars and GFRP-RC slabs. *J. Mater. Civil Eng.* **2018**, *30*, 04017296. [CrossRef]
21. Jarrah, M.; Najafabadi, E.P.; Khaneghahi, M.H.; Oskouei, A.V. The effect of elevated temperatures on the tensile performance of GFRP and CFRP sheets. *Constr. Build. Mater.* **2018**, *190*, 38–52. [CrossRef]
22. Najafabadi, E.P.; Khaneghahi, M.H.; Amiri, H.A.; Estekanchi, H.E.; Ozbakkaloglu, T. Experimental investigation and probabilistic models for residual mechanical properties of GFRP pultruded profiles exposed to elevated temperatures. *Compos. Struct.* **2019**, *211*, 610–629. [CrossRef]
23. Bazli, M.; Abolfazli, M. Mechanical Properties of Fibre Reinforced Polymers under Elevated Temperatures: An Overview. *Polymers* **2020**, *12*, 2600. [CrossRef]
24. Lee, J.; Sheesley, E.; Jing, Y.; Xi, Y.; Willam, K. The effect of heating and cooling on the bond strength between concrete and steel reinforcement bars with and without epoxy coating. *Constr. Build. Mater.* **2018**, *177*, 230–236. [CrossRef]
25. Pul, S.; Atasoy, A.; Senturk, M.; Hajirasouliha, I. Structural performance of reinforced concrete columns subjected to high-temperature and axial loading under different heating-cooling scenarios. *J. Build. Eng.* **2021**, *42*, 102477. [CrossRef]
26. Lenwari, A.; Rungamornrat, J.; Woonprasert, S. Axial Compression Behavior of Fire-Damaged Concrete Cylinders Confined with CFRP Sheets. *J. Compos. Constr.* **2016**, *20*, 04016027. [CrossRef]
27. *Standard D7205*; Standard Test Method for Tensile Properties of Fiber Reinforced Polymer Matrix Composite Rebars. ASTM: West Conshohocken, PA, USA, 2016.
28. Spagnuolo, S.; Meda, A.; Rinaldi, Z.; Nanni, A. Residual behaviour of glass FRP bars subjected to high temperatures. *Compos. Struct.* **2018**, *203*, 886–893. [CrossRef]
29. *Standard D792*; Standard Test Methods for Density and Specific Gravity (Relative Density) of Plastics by Displacement. ASTM: West Conshohocken, PA, USA, 2020.
30. Zhou, F.; Zhang, J.; Song, S.; Yang, D.; Wang, C. Effect of Temperature on Material Properties of Carbon Fiber Reinforced Polymer (CFRP) Tendons: Experiments and Model Assessment. *Materials* **2019**, *12*, 1025. [CrossRef]
31. Al-Salloum, Y.A.; El-Gamal, S.; Almusallam, T.H.; Alsayed, S.H.; Aqel, M. Effect of harsh environmental conditions on the tensile properties of GFRP bars. *Compos. Part B Eng.* **2013**, *45*, 835–844. [CrossRef]
32. Robert, M.; Benmokrane, B. Behavior of GFRP Reinforcing Bars Subjected to Extreme Temperatures. *J. Compos. Constr.* **2010**, *14*(4), 353–360. [CrossRef]

33. Tao, P.Z.; Wang, X.; Uy, B. Stress-Strain Curves of Structural and Reinforcing Steels after Exposure to Elevated Temperatures. *J. Mater. Civil Eng.* **2013**, *25*, 1306–1316. [CrossRef]
34. Lee, J.; Engelhardt, M.; Taleff, E. Mechanical properties of ASTM A992 steel after fire. *Eng. J.* **2012**, *49*, 33–44. [CrossRef]

Disclaimer/Publisher's Note: The statements, opinions and data contained in all publications are solely those of the individual author(s) and contributor(s) and not of MDPI and/or the editor(s). MDPI and/or the editor(s) disclaim responsibility for any injury to people or property resulting from any ideas, methods, instructions or products referred to in the content.

Ocean Engineering 314 (2024) 119685

Contents lists available at ScienceDirect

Ocean Engineering

journal homepage: www.elsevier.com/locate/oceaneng

Research paper

Static and fatigue behavior of CFRP strengthened spiral welded steel tubes subjected to four-point bending

Andre Cahyadi Salim [a,b], Yining Zhang [a,b], Lili Hu [c,*], Chengjian Shao [a,b]

[a] State Key Laboratory of Ocean Engineering, School of Ocean and Civil Engineering, Shanghai Jiao Tong University, Shanghai, 200240, China
[b] Shanghai Key Laboratory for Digital Maintenance of Buildings and Infrastructures, Shanghai Jiao Tong University, Shanghai, 200240, China
[c] Research Institute of Urbanization and Urban Safety, School of Civil and Resource Engineering, University of Science and Technology Beijing, Beijing, 100083, China

ARTICLE INFO

Keywords:
Carbon fiber reinforced polymer
Spiral welded tube
Crack
Fatigue
Strengthening

ABSTRACT

Carbon fiber reinforced polymer (CFRP) has proven to be effective for repairing and strengthening existing structures. Spiral welded steel tubes (SWTs), extensively utilized for steel tube piles in bridges and offshore wind turbines, frequently experience fatigue loadings. This paper explores the spiral welded steel tube's static bending and fatigue behavior with initial damage before and after CFRP strengthening. An initial crack was introduced at the weld toe in the tensile area. Under static loading, CFRP strengthening increased the tube's stiffness and bending capacity by 175.4% and 27.45%, respectively. Under fatigue loading, crack growth was observed in two directions with different rates: circumferentially along the loading direction and along the weld seam, penetrating through the weld and continuing along the loading direction. This highlights how weld geometry and residual stress significantly influence the fatigue crack growth. CFRP strengthening reduced the crack's stress intensity, considerably decreasing the crack growth rate and extending fatigue life by two to three times. Moreover, the CFRP wrapping orientation had significantly impacted fatigue strengthening, with inverse-diagonal wrapping proving to be most effective. The debonding area of the strengthened specimens is also estimated. These findings provide valuable insights for practical engineering applications.

1. Introduction

Steel tubes have been widely utilized due to their excellent multi-directional load-bearing capability, internal space availability, low fluid resistance coefficient, and other advantages (Wu and Wu, 2005; Yin, 2009). For example, major marine infrastructures such as cross-sea bridges, offshore platforms, and large offshore wind turbines have widely employed steel tubes as their pile (Fattah and Al-Soudani, 2015; Audibert and Huang, 2005; Malhotra, 2010). Among various types of steel tubes, including seamless, girth welded, and longitudinal welded tubes, spiral welded steel tubes (SWTs) are particularly popular due to their production process, which involves rolling steel strips into preliminary forms resembling steel tubes at a specific helical angle, followed by spiral submerged arc welding, which offers several advantages. First, it features a flexible production method and cost efficiency. Larger diameter SWTs with diameters reaching up to 3000 mm, thicknesses of up to 25 mm, and lengths of up to 50 m (van Es et al., 2016) can be manufactured from narrower steel plates. Additionally, the same forming equipment can produce steel tubes of various specifications and dimensions without additional instruments (Vasilikis et al., 2016). Second, precise control over tube diameter and roundness ensures consistent quality throughout production. Third, high production efficiency is achieved through fully automated production equipment, allowing continuous manufacturing from entire coils of rolled steel (Yu, 2015). As a result, SWTs have found extensive application across diverse sectors (Aslani et al., 2017). In China, SWTs have been used in many major marine engineering projects, such as Hangzhou Bay Cross-Sea Bridge, the main channel of Ningbo Zhoushan Port, and Jiangsu Xiangshui Offshore Wind Power (Zhang, 2017; Piao et al., 2020).

Research has shown that fatigue failure of steel tubes has become the most common failure mode of offshore structures (Yao, 2013). Fatigue loads caused by sea breezes, seawater fluctuations, wave impacts, and heavy machinery vibrations cause stress concentration, leading to severe casualties and considerable property damage. Liu et al. (2019) found that corrosion fatigue crack propagation in steel tubes within a simulated H_2S environment occurs about 10 times faster than in air. Similarly, Holtam et al. (2010) found that crack growth rates for deep surface

* Corresponding author.
E-mail address: lilihu@ustb.edu.cn (L. Hu).

https://doi.org/10.1016/j.oceaneng.2024.119685
Received 18 August 2024; Received in revised form 16 October 2024; Accepted 29 October 2024
Available online 16 November 2024
0029-8018/© 2024 Elsevier Ltd. All rights are reserved, including those for text and data mining, AI training, and similar technologies.

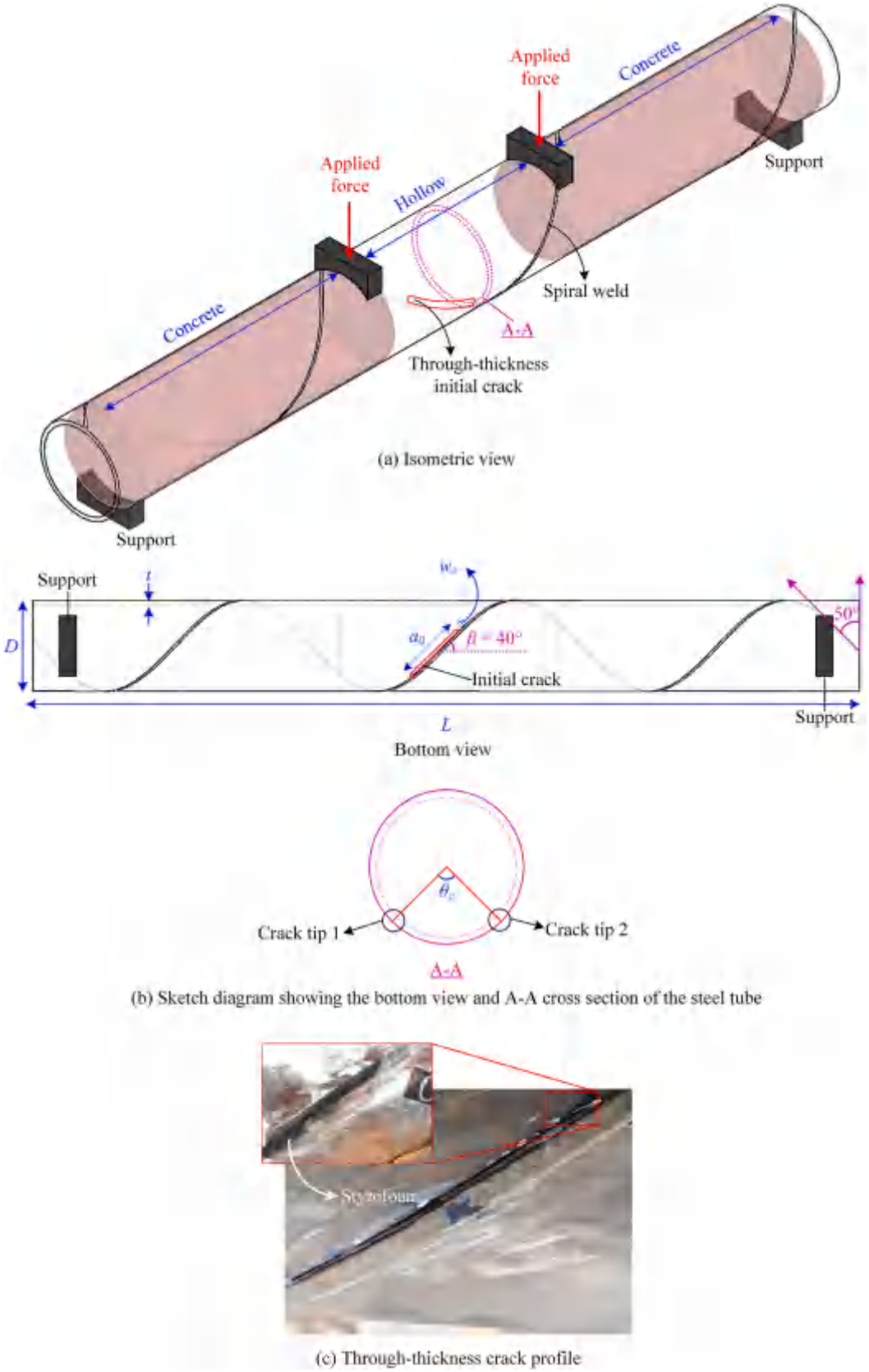


Fig. 1. The sketch diagram and details of the spiral welded steel tube.

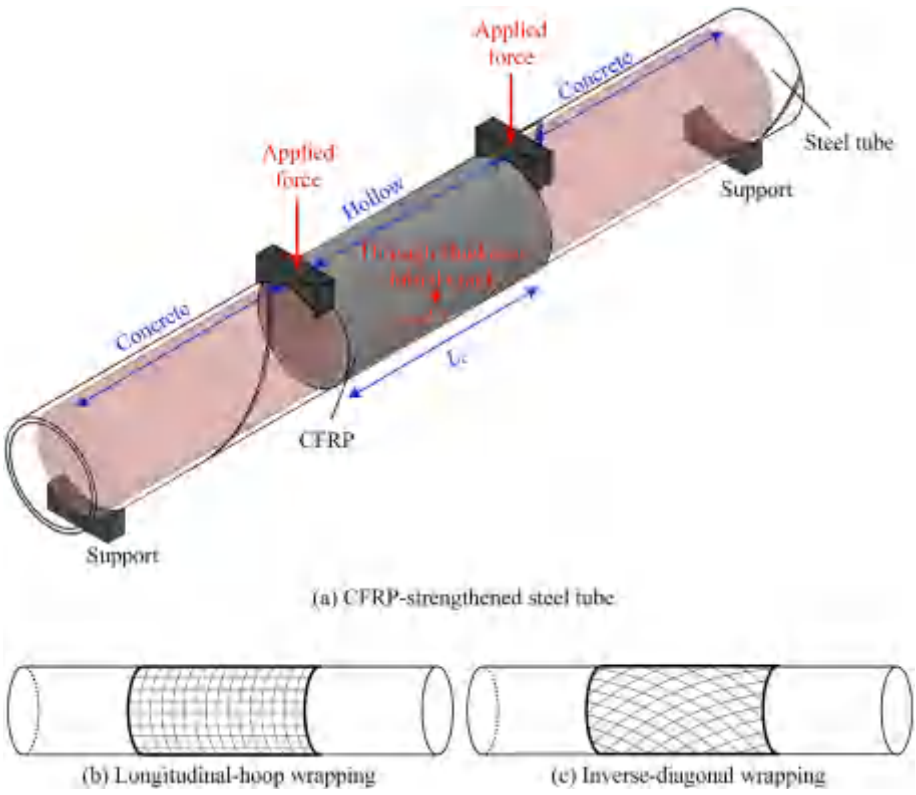


Fig. 2. Sketch diagram of CFRP-strengthened spiral welded steel tube.

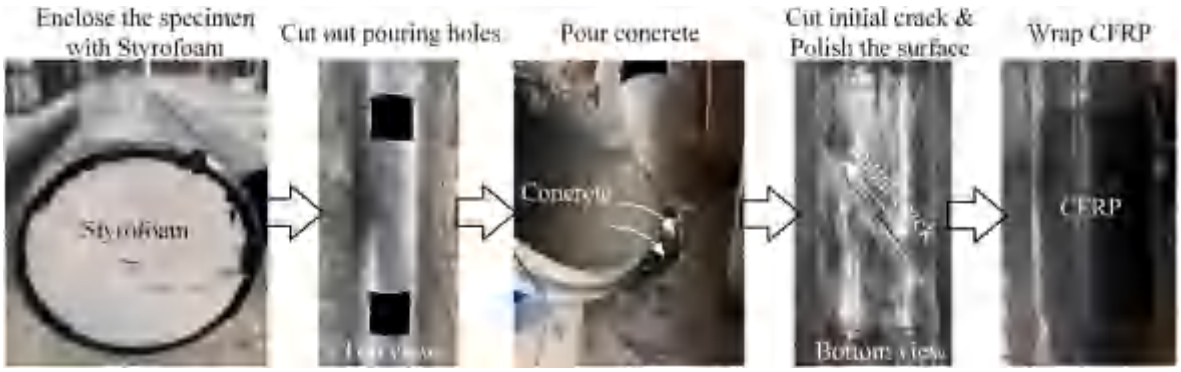


Fig. 3. Manufacturing process of the specimens.

cracks in a sour environment are 5–30 times higher than in air, while shallow surface cracks grow up to 10 times faster than deep surface cracks under the same conditions. Besides external environmental factors, surface imperfections, and residual stress from manufacturing also influence their fatigue behavior (Li et al., 2019a, 2023b; Li et al., 2023). Under flexural fatigue loading, cracks typically form and progress at these defect-prone locations, moving through initiation and growth stages (Ramachandra et al., 2022). These issues also occur in welded tubes, including girth-welded and straight-welded steel tubes. Welding introduces geometrical discontinuities, misalignment, and various defects intrinsic to welded joints, such as crack-like defects, slag inclusions, gas pores, incomplete penetration at the weld root, and undercutting at the weld toes (Cerit et al., 2010; Teng et al., 2002). These imperfections lead to stress concentrations at the defect sites and weld toes. Additionally, welding affects the base metal of the tubes, causing variations in microstructure and mechanical properties between the base metal

Table 1
Test program.

Group	Specimen	Strengthening	L (mm)	Loading type
1	U2500-S	No	2500	Static
	S2000-S-A	Yes, wrapping 4 layers ([0°/90°/0°/90°])	2000	Static
2	U2500-F	No	2500	Fatigue
	S2500-F-A	Yes, wrapping 4 layers ([0°/90°/0°/90°])	2500	Fatigue
	S2500-F-B	Yes, wrapping 4 layers ([-45°/45°/-45°/45°])	2500	Fatigue

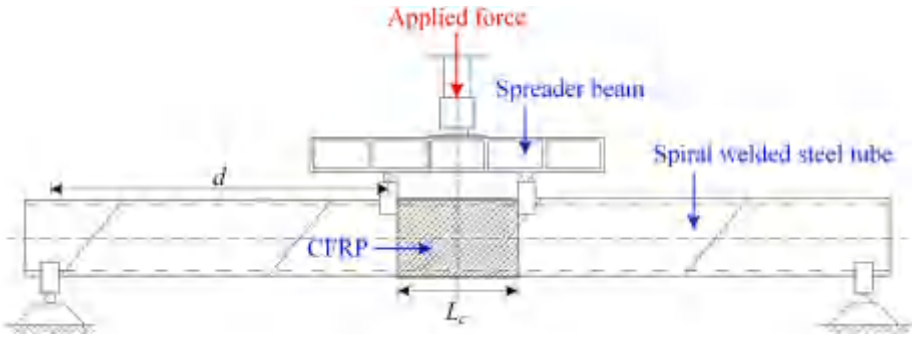


Fig. 4. Schematic view of experimental setup.

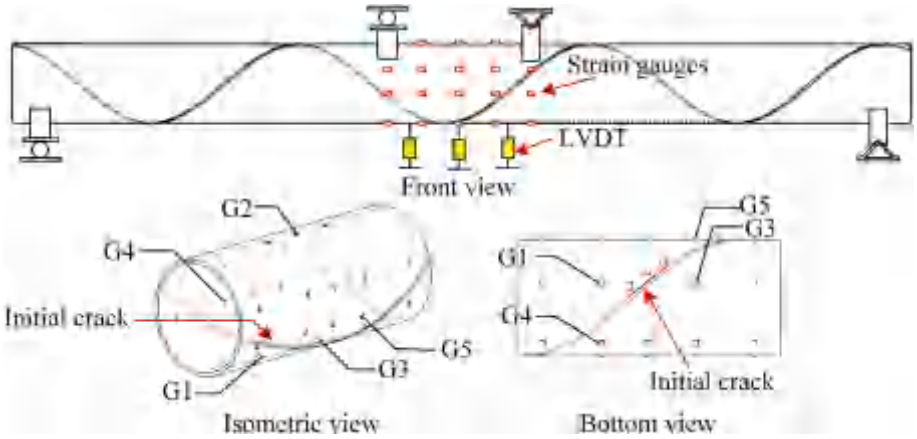


Fig. 5. Schematic view of strain gauge and LVDT placements of static bending loading test.

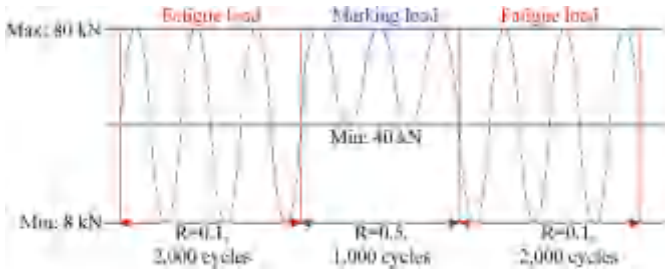


Fig. 6. Fatigue loading spectrum using beach mark loading method.

(BM), the heat-affected zone (HAZ), and the weld seam (Shi et al., 1990; Zhang et al., 2024). Furthermore, welding induces residual stresses and significantly impacting the tubes by causing dimensional changes, altering brittle material behavior, and reducing fatigue life, thereby exacerbating crack propagation (Habibi et al., 2012). It is also found that the performance of welded steel tubes is primarily determined by the welding quality (Han et al., 2022; Yu et al., 2018), and poor weld quality can further degrade fatigue properties. Due to these reasons, welded steel tubes are prone to flexural fatigue loading, with fatigue cracks initiating more easily in weld regions (Turhan et al., 2020; Ancelet et al., 2008; Zhang et al., 2022).

Given SWTs' longer weld seams and thicker walls, they are even more susceptible to initial defects and residual stresses than the steel tubes mentioned above. This makes them more vulnerable to fatigue initiation and crack propagation at weld toes (Nasim et al., 2015). Currently, research on the fatigue performance of SWTs remains limited. Choi et al. (2010) investigated mixed-mode fatigue crack growth in SWTs under four-point bending fatigue, finding that cracks initiated at the weld seam at the bottom of the tube at the neutral axis, extended along the HAZ, and then merged with a new crack which formed in base metal, extending away from the weld area. Fulmer et al. (2012) studied the flexural performance of double-submerged arc welded SWTs and found that while weld fractures occurred under large inelastic deformations, the ultimate failure was due to local buckling, similar to the failure mode in traditional single-seam specimens. However, detailed analysis of SWT's failure modes and crack propagation mechanisms remain underexplored. The spiral weld seam and curved surface of the SWTs may cause cracks to deviate from the principal stress direction, leading to complex stress states such as tension, shear, or tension-shear coupling. Cracks originating from the weld seam can propagate along it or shift perpendicularly into the base material, resulting in intricate fatigue failure patterns. Therefore, a systematic study of SWT fatigue performance under typical loading conditions is essential.

Strengthening steel structures with fiber-reinforced polymer (FRP) has proven to be an effective solution. Traditional retrofitting approaches, such as welding or bolting steel plates, can create additional stress points at the damaged areas, increase the structural self-load, and involve costly and challenging installation and repair processes (Colombi and Fava, 2016). Studies have demonstrated that FRP is highly effective in strengthening steel tubular structures. Under axial loading, FRP can significantly increase the yield and ultimate loads by up to 69.11% and 61.99%, respectively (Liu et al., 2024). Under bending loading, FRP strengthening can increase the maximum bending moment specific energy absorption of square hollow steel tubes by up to 70% and 45%, respectively (Lavayen-Farfan et al., 2022), while increasing the ultimate load of circular steel tubes by approximately 33% (Kabir et al., 2015). Additionally, FRP can reduce the lateral displacement of steel tubes under transverse impact loading by up to 29% (Alam et al., 2017). Furthermore, FRP proves highly effective in strengthening steel structures subjected to fatigue loading, offering significant benefits for

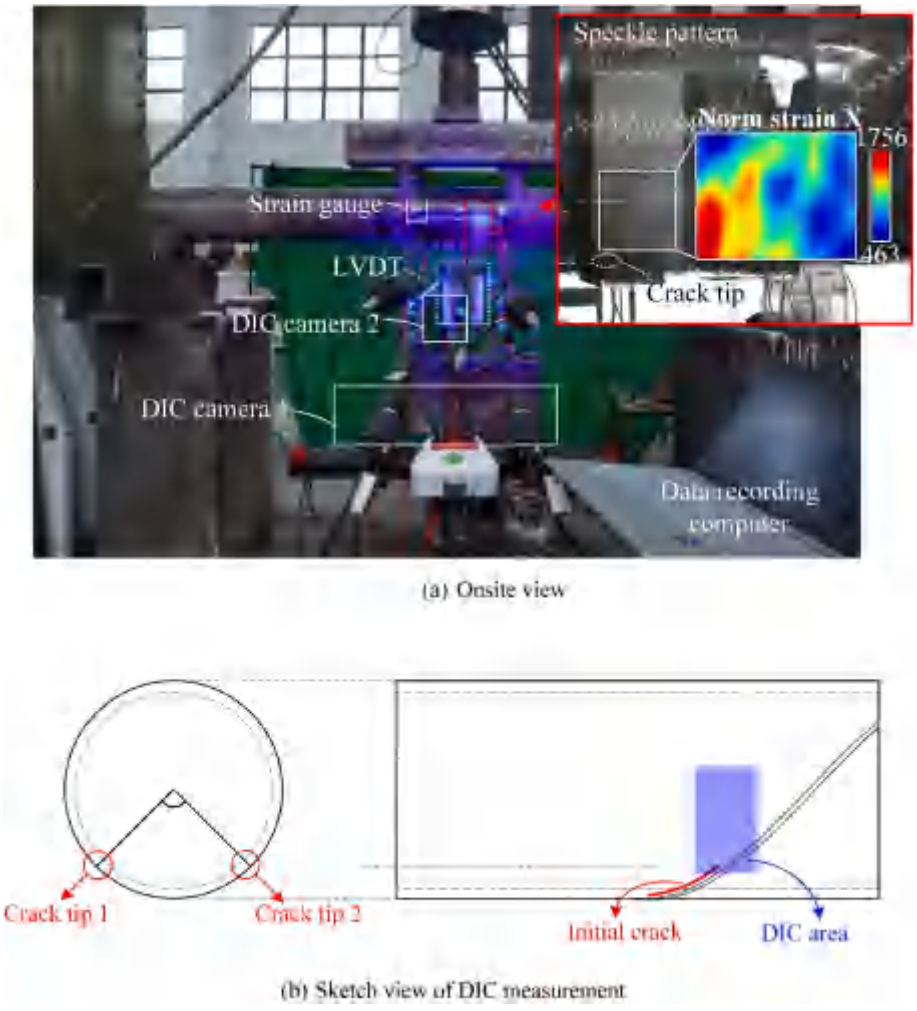


Fig. 7. Data measurement setup for fatigue tested specimens.

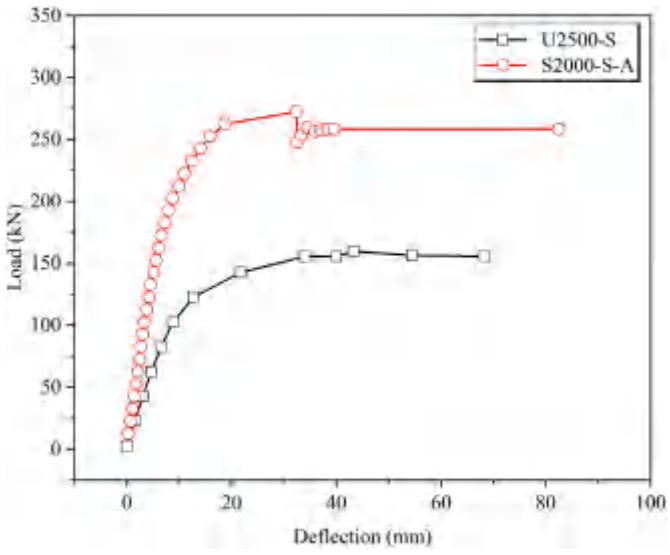


Fig. 8. Vertical load versus deflection of unstrengthened and strengthened specimens.

structures such as steel beams, steel bridges, steel joints, and so on (Hu et al., 2017; Zhao and Zhang, 2007; Teng et al., 2012; Kim and Harries, 2011; Miller et al., 2001; Chen et al., 2012). However, most research on FRP-strengthening of steel structures under fatigue loading primarily focuses on flat steel (Liu et al., 2009; Hu et al., 2016, 2022; Yu et al., 2013; Feng et al., 2014), with relatively minimal attention given to curved steel tubes.

FRP is particularly well-suited for strengthening of SWTs. First, FRP has a high strength-to-weight ratio, reducing the stress concentrations at defect areas without significantly increasing the structure's weight, making it a cost-effective choice for long-distance marine transportation. Second, FRP is resistant to harsh marine environments and effectively protects corrosion-prone steel tubes from degradation (Hulatt et al., 2002; Kootsookos and Mouritz, 2004; Kajorncheappunngam et al., 2002; Zhang, 2018; Zhu, 2015). Third, FRP strengthening is easy to install: the fibers, coated in adhesive, are wrapped around the steel tube's surface. There are limited studies on FRP-strengthened steel tubes, especially SWTs, under flexural fatigue loading. Li et al. (2020) investigated the fatigue behavior of CFRP-strengthened surface-cracked seamless steel tubes. They found that CFRP significantly reduced crack growth rates, and the longitudinal-hoop wrapping direction performed better. However, this study was limited to mode-I surface cracks in seamless pipes. Research on crack propagation in flat FRP-strengthened steel structures does not consider the complexities of curved crack expansion in FRP-strengthened steel tubes. Additionally, the crack propagation in seamless tubes does not fully represent the conditions in SWTs due to the effects of spiral welding. These factors complicate the optimization of FRP layup design and highlight the need for more research on the fatigue behavior of FRP-strengthened SWTs under bending.

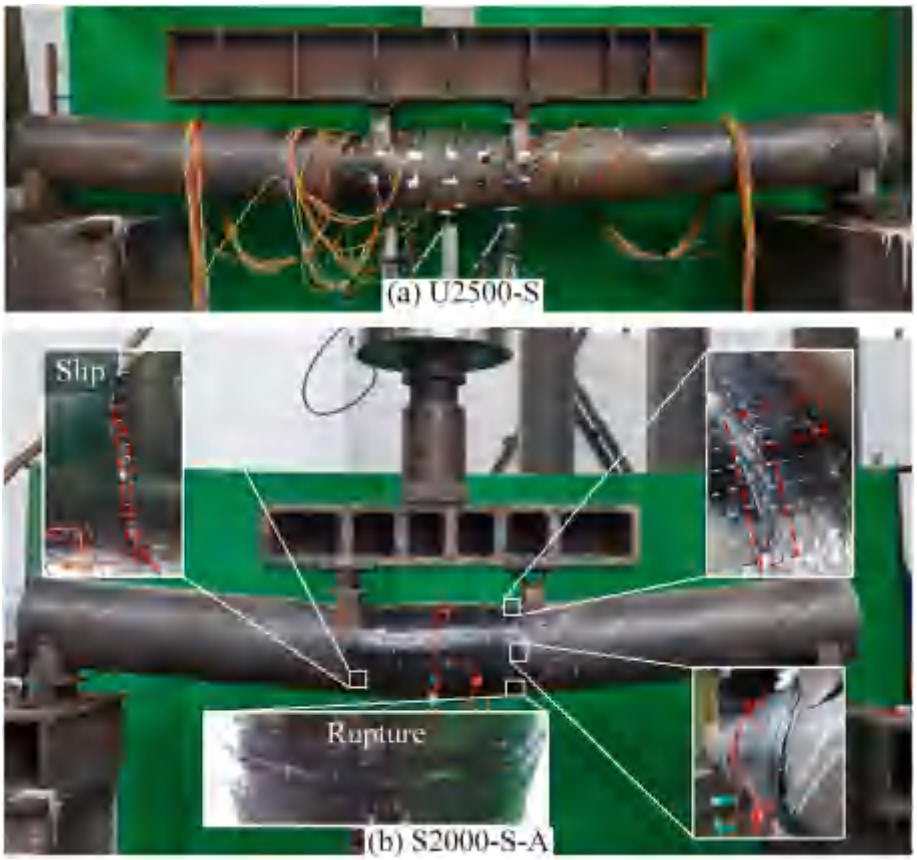


Fig. 9. Overall failure mode of statically loaded specimens.

Due to limited studies on SWTs and the unclear effects of CFRP strengthening on these tubes, this study aims to analyze the bending and fatigue behavior of CFRP-strengthened SWTs comprehensively. First, four-point bending static loading tests were conducted on one unstrengthened specimen, and one strengthened with longitudinal-hoop CFRP to study their flexural behavior. Then, fatigue loading tests were performed on three specimens: one unstrengthened and two CFRP-strengthened specimens with different wrapping orientations (longitudinal-hoop and inverse-diagonal) to investigate the crack propagation behavior of SWTs and evaluate the impact of CFRP strengthening on their fatigue life.

2. Specimen

2.1. Spiral welded tube

SWTs are created by continuously winding a flat steel strip into a spiral shape using a forming machine, with the edges welded together to form a strong and uniform tube. In this paper, the SWTs were welded using the double-sided submerged arc welding (DSSAW) technique. The welding was performed following standard methods used in spiral welded steel tube production to maintain similarities in weld defects and residual stresses.

Due to the limitations of the loading machine, smaller sizes of SWTs were chosen to fit the experimental setup. The wall thickness t of all specimens was 6.5 mm. The length L of the specimens ranged from 2000 mm to 2500 mm, and the diameter D was 219 mm for all specimens. As illustrated in Fig. 1, the SWTs featured a 50° helix angle, and an initial through-wall crack a_0 of 147 mm was positioned along the weld toe at the midspan bottom area. This crack length corresponded to a damage level, defined as the ratio of half crack angle to radius θ_c/π of 0.155, which was considered short, being less than 0.3. This crack size also fell within the range typically observed in real-world scenarios for circumferential through-wall cracks in cylindrical structures such as nuclear pressure vessels, pipelines, and tubular structures. It ensured that the through-wall crack could be detected under regular operating loads, with an additional safety margin to the leak rate. As a result, the crack remained stable both during normal operation and a safe shutdown following seismic loads (Rahman et al., 1998; Lewis and Wang, 2008). The decision to initiate a crack at the weld toe is that this area of SWTs is most prone to fatigue cracks due to initial defects and residual stresses. The initial crack, shown in Fig. 1(c), was created using a 0.8 mm-wide saw cutting disc, resulting in an initial crack width w_c of approximately 1 mm. The white material inside the tube is Styrofoam, visible along the crack length, which confirms that the crack is a through-thickness crack. Artificially introducing the crack ensured consistent crack initiation, avoiding the randomness of natural crack formation, and allowed the focus to remain on the remaining fatigue life of the SWTs. Q235B steel was used as the substrate for the SWTs (Liu et al., 2024), with an elastic modulus of 188 GPa, a yield strength f_y of 367 MPa, and an ultimate strength f_u of 524 MPa.

2.2. CFRP-strengthened spiral welded tube

Fig. 2(a) shows the schematic diagram of the cracked SWTs wrapped with CFRP. The diagram includes: Q235 SWT, concrete, adhesive, and CFRP wrapping. For strengthening, HM-30 CFRP sheets with a thickness of 0.167 mm, an elastic modulus of 240 GPa, and a tensile strength of 3667.5 MPa were used. HM-180C3P epoxy adhesive, which has an elastic modulus of 4.6 GPa and a tensile strength of 59.6 MPa, was applied for bonding. Both CFRP sheets and the epoxy adhesive were sourced from Shanghai Hanma Construction Technology Co., Ltd. It was filled with concrete to prevent local buckling of the steel tube specimen. However, to ensure the concrete did not affect the experimental

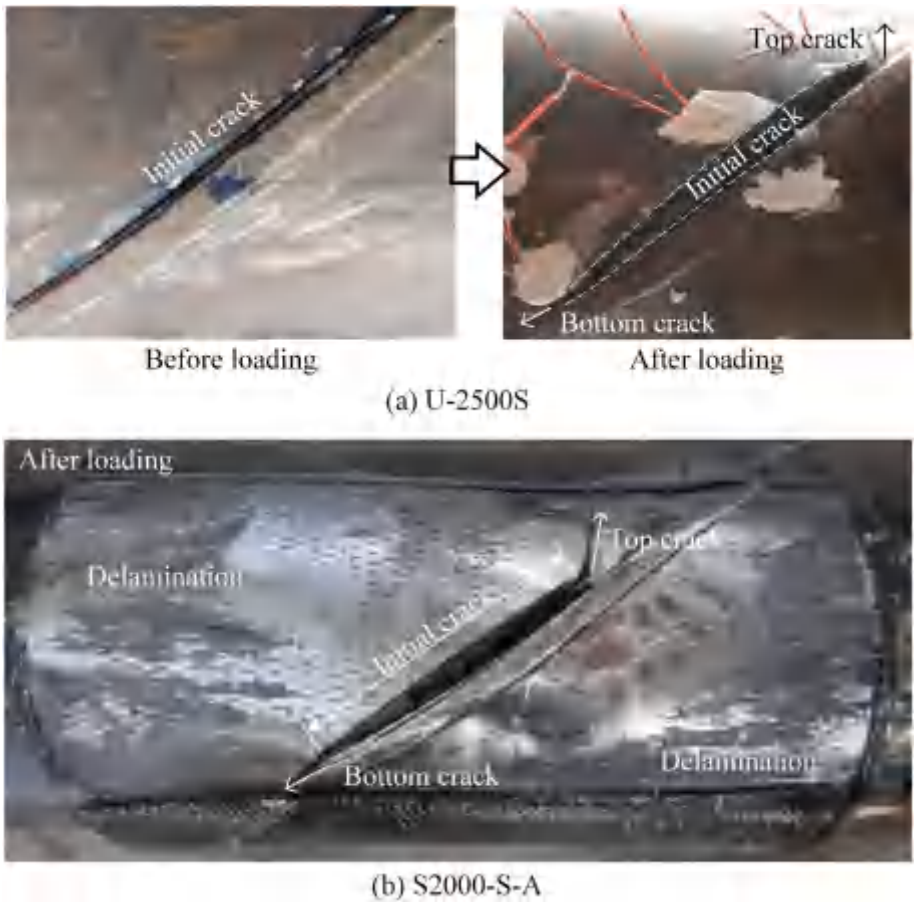


Fig. 10. Failure mode of the statically loaded specimens around the crack region.

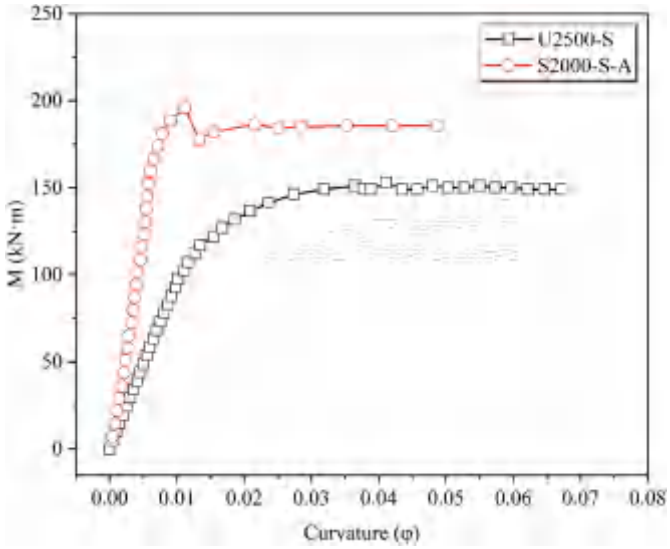


Fig. 11. *M-ϕ* relationship of statically loaded unstrengthened and strengthened specimens.

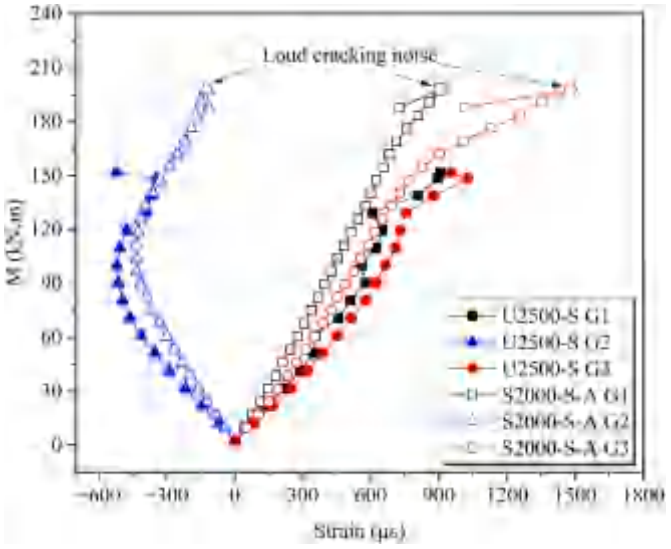


Fig. 12. Strain comparison between unstrengthened and strengthened specimens.

outcomes, the pure bending region of the specimen was left hollow, and the CFRP wrapping was also applied to this part.

Fig. 2(b) and (c) illustrate CFRP wrapping orientations: the longitudinal-hoop wrapping scheme ([0°/90°/0°/90°]), and the inverse-diagonal wrapping scheme ([-45°/45°/-45°/45°]). Four CFRP layers were used for all specimens, with a bond length L_c of 350 mm.

The specimen manufacturing process involved five main steps, as depicted in Fig. 3. First, the specimen's ends and pure bending part were sealed with Styrofoam to prevent the concrete slurry from leaking into unwanted areas. Silicone sealant was applied along the edges to seal any leaks and keep the Styrofoam in place. The Styrofoam, being very light and having negligible stiffness and strength, did not affect the behavior



Fig. 13. Overall failure modes of the fatigue specimens.

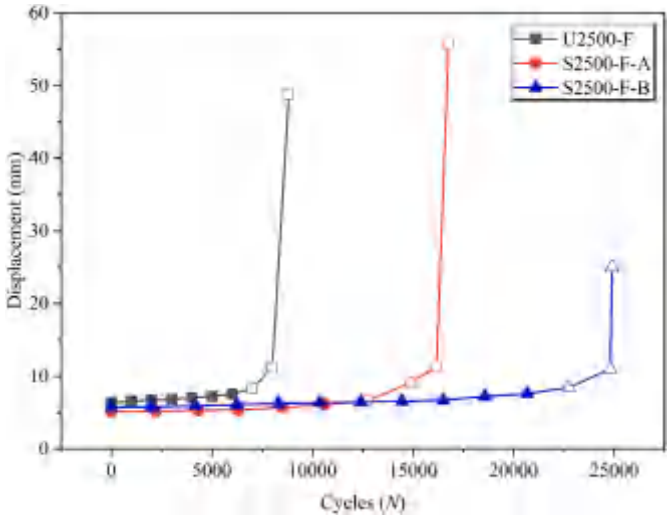


Fig. 14. Displacement versus fatigue cycle of unstrengthened and strengthened specimens.

of the pure bending part. Second, two holes were opened at the top of the steel tubes in the area designated for concrete pouring. Third, concrete was poured into the tubes. Fourth, after curing the concrete for seven days, a through-wall crack was machined along the weld toe at the bottom-middle of the steel tubes. To prepare for CFRP wrapping, the outer surface of steel tubes was polished with an abrasive disc to remove rust and cleaned with alcohol to eliminate residue. Finally, the external surfaces of the cracked steel tubes were wrapped with CFRP sheets, with an overlap of 150 mm, and left to cure at room temperature for seven days to ensure good bonding between the CFRP and the steel tubes.

3. Test program

3.1. Two groups of tests

There are two groups of tests totaling five specimens, and the details and configurations of the specimens are listed in Table 1.

In Group 1, static bending tests were conducted on U2500-S and S2000-S-A specimens to obtain the flexural behavior of unstrengthened and strengthened specimens. The specimen naming convention indicates their strengthening status, length, type of loading, and CFRP wrapping scheme. For example, 'S2000-S-A' denotes a strengthened specimen with a length of 2000 mm, tested under static loading (indicated by 'S'), and using the first CFRP wrapping scheme (denoted by 'A'), which consists of four layers in a longitudinal-hoop pattern.

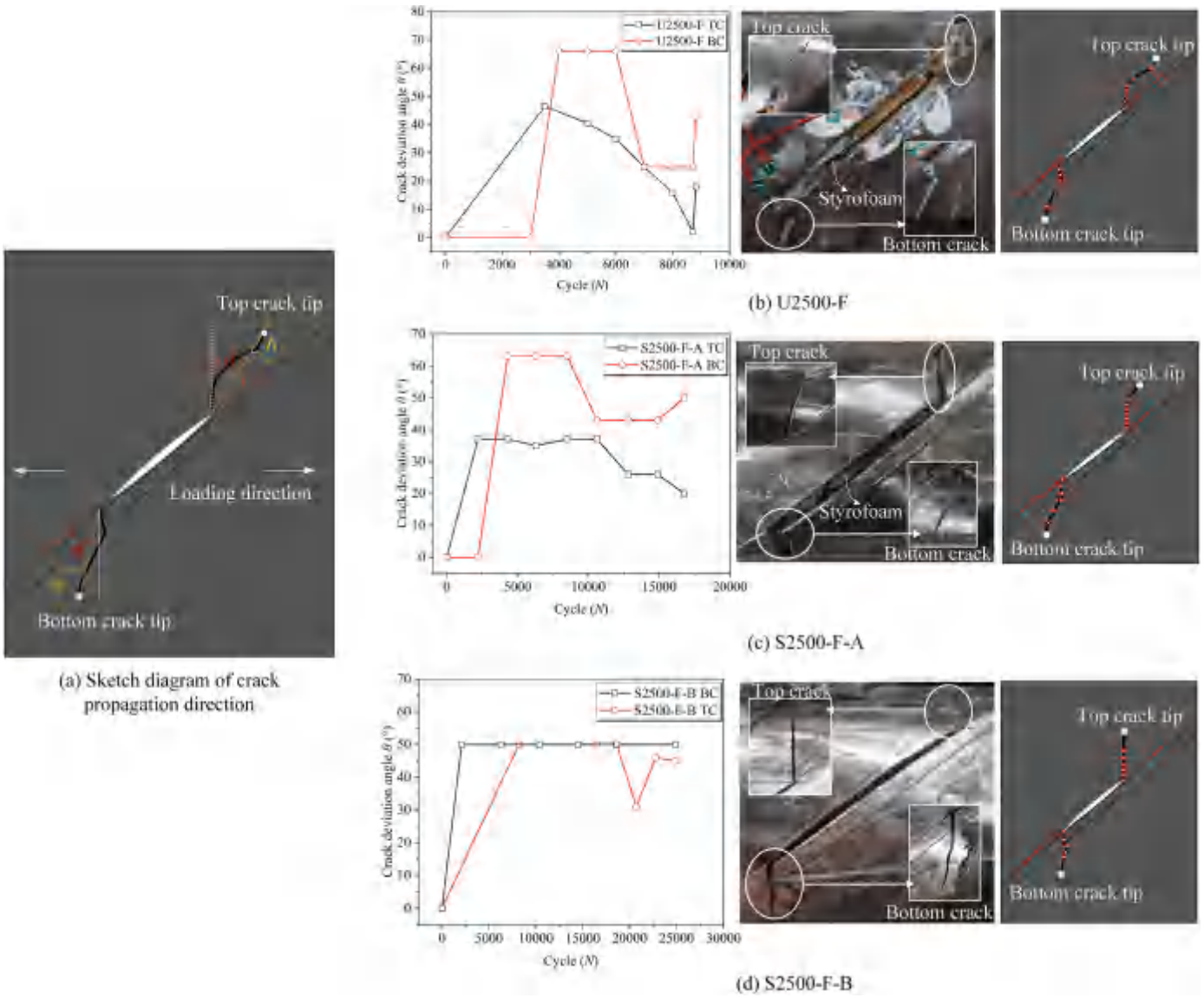


Fig. 15. Analysis of crack propagation behavior of the fatigue specimens.

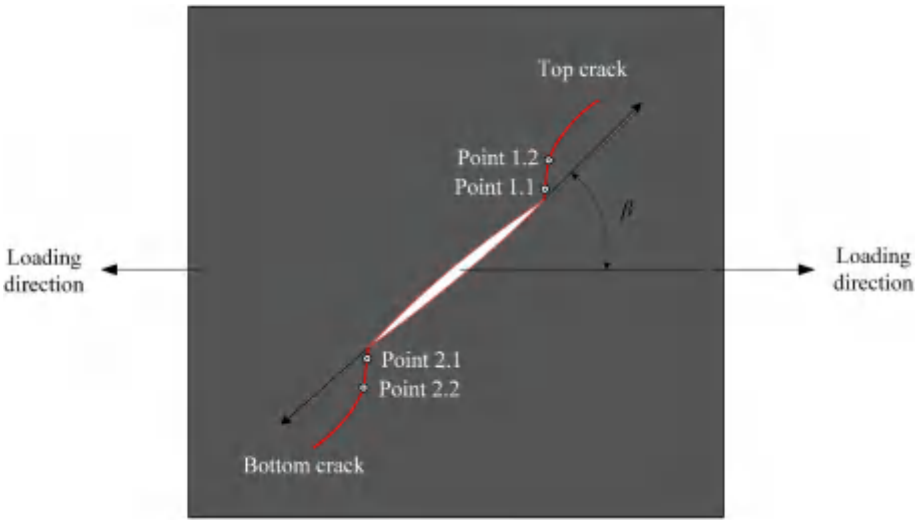


Fig. 16. Inclined crack under uniaxial tension and the corresponding crack propagation path.

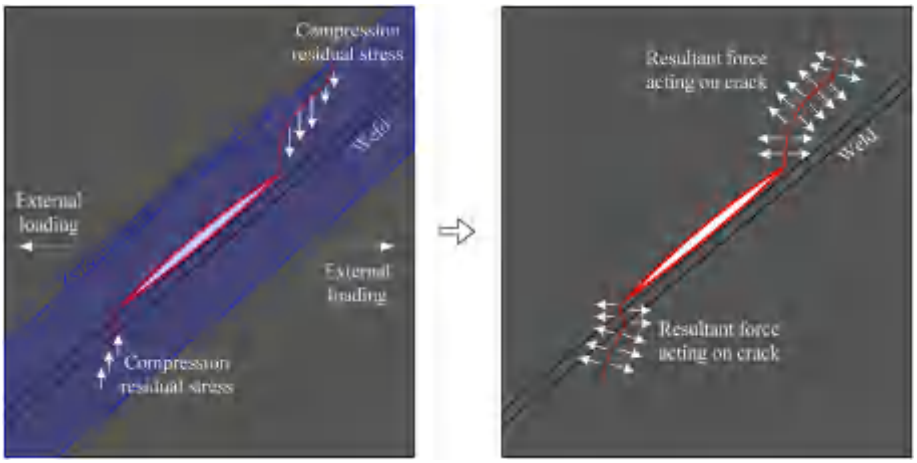


Fig. 17. Schematic view of the forces acting on the crack in specimen U2500-F.

Although the specimens varied in length due to material constraints, this did not affect the comparison of their M–ϕ relationships.

In Group 2, four-point bending fatigue tests (indicated by 'F') were performed on three specimens: U2500-F, S2500-F-A, and S2500-F-B, to evaluate the fatigue behavior and failure modes of the cracked SWTs under flexural fatigue loading. These specimens correspond to the unstrengthened, longitudinal-hoop strengthened, and inverse-diagonal strengthened configurations, respectively.

3.2. Experimental setup

3.2.1. Bending test

Fig. 4 depicts the schematic view of the bending test, which features a simply supported beam with a vertical load applied at the center via a loading jack. This setup symmetrically transfers the load to the specimen through a spreader beam. The load was applied using a four-point bending configuration, ensuring that the area at the bottom of the specimen, where the initial crack was located, would experience a pure bending state. The CFRP bond length L_c and the distance between the two loading supports were set to be 350 and 400 mm, respectively, while the moment arm d varied according to the specimen's length. The tests were conducted using an Instron hydraulic loading machine with a maximum load capacity of 600 kN. The static test specimens were loaded at a rate of 0.05 mm/s until significant deflection was achieved.

As illustrated in Fig. 5, three Linear Variable Displacement Transducers (LVDTs) were positioned along the longitudinal direction on the bottom tension side of the steel tubes to monitor displacements. Thirty strain gauges were also attached to the specimen's surface to monitor the specimen's behavior throughout the experiment. The placement of the LVDTs and strain gauges was identical for both the unstrengthened and strengthened specimens. For the strengthened specimens, the strain gauges were positioned on the surface of the CFRP, which would reflect the strain values of the steel tube if proper bonding was ensured. Data from both the LVDTs and strain gauges were recorded using the data acquisition system software provided by Jiangsu Donghua Testing Technology Company.

3.2.2. Fatigue test

The experimental setup for the fatigue test was identical to that used for the bending test (Fig. 4). All fatigue test specimens were subjected to sinusoidal loading with a maximum load of 80 kN (excluding the self-weight of the concrete and steel tube), resulting in a nominal stress of $0.5f_y$ at the tension edge of the steel tube, a loading frequency of 1 Hz, and a load ratio R of 0.1. For the unstrengthened fatigue specimen, crack growth lengths were monitored using a camera that took a picture every 10 s and was manually recorded every 1000 cycles at each crack tip. In the CFRP-strengthened specimens, where the crack was not visible, the crack propagation rate was recorded using the beach marking method. This method involves changing the load ratio R to 0.5, which was then cycled for 1000 cycles, as shown in Fig. 6. This creates visible markings in the crack interface, facilitating more accurate measurements of fatigue life. Notably, the crack growth during this marking process was minimal compared to when $R = 0.1$; thus, it was excluded from the final calculation of the specimen's overall fatigue life (Hosseini et al., 2019; Furuya, 2016; Li et al., 2020; Li et al., 2020, 2020).

In addition to using LVDTs and strain gauges, two Digital Image Correlation (DIC) systems were positioned near the crack tips, as shown in Fig. 7(a). A black dotted pattern was applied to the area around the initial crack tip and along the anticipated crack propagation path. As shown in Fig. 7(b), the initial crack reached the sides of the tube, and the DIC systems captured strain along the crack's propagation path, focusing on its tip, which is expected to continue along the tube's circumference. The resulting strain contour map corresponds to the red-boxed area. The 3D DIC system model RDIC-STD-DH1200 from Hefei Agile Device Co., Ltd. Was equipped with two cameras with a spatial resolution of 4096 × 3000 pixels, and lenses with a 25-mm focal length were used for data capture and processing. The cameras were connected to a laptop for image acquisition, and the specimens were illuminated using two LED light sources to ensure adequate image contrast. Images were captured every 2000 loading cycles, with 240 photos taken each time to ensure precision. The reference image was calibrated to obtain the physical coordinates of the pixels using the RDIC software package, which calculates the displacement field of the pixels to determine the strain distribution.

4. Bending test results and discussion

4.1. Flexural behavior

Fig. 8 presents the vertical load versus deflection curve at the mid-span of the steel tubes, considering the self-weight of both the concrete and the steel tube. The unstrengthened specimen, U2500-S, exhibited a stable, linear load-deflection relationship up to 102.4 kN, after which it began to yield. It reached a maximum load of 159.4 kN at a deflection of 34 mm. Beyond this point, the load could not be increased further, and the specimen continued to deform, achieving a large displacement of 68 mm. Its failure mode, shown in Fig. 9(a), exhibited typical overall flexural failure without any local buckling. Fig. 10(a) displays the failure mode of U2500-S around the crack region. Under static loading, the top crack extended vertically perpendicular to the loading direction, while the bottom crack propagated along the weld seam.

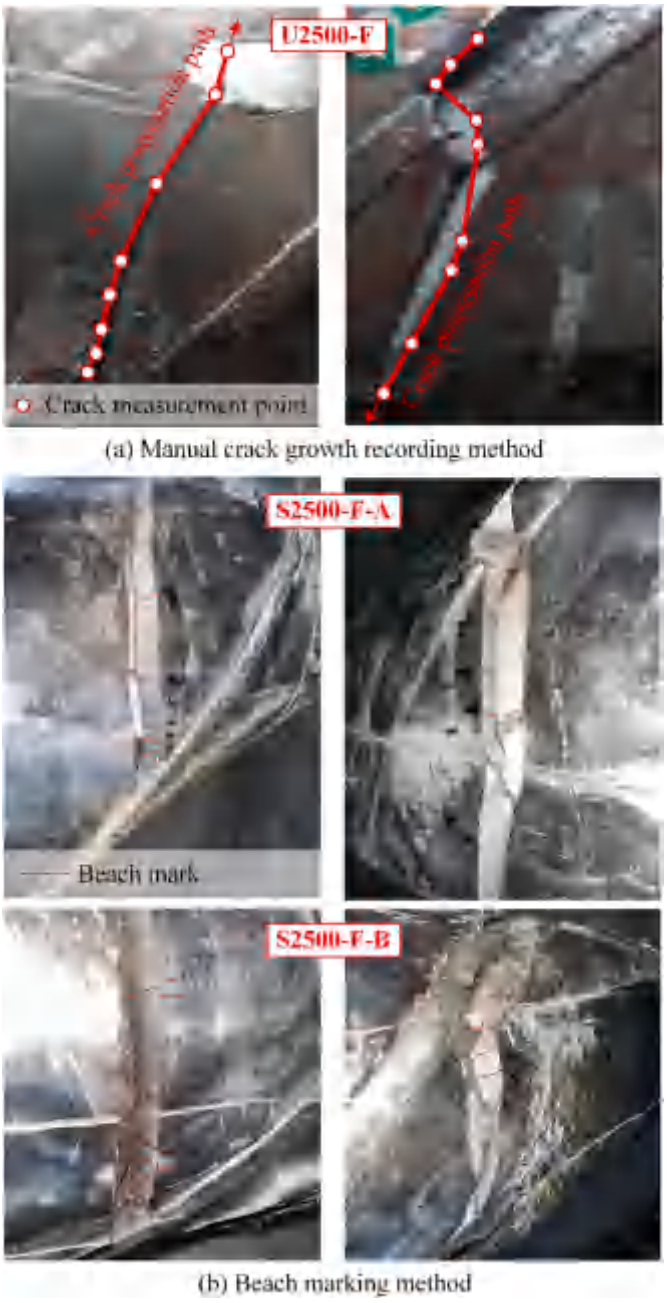


Fig. 18. Crack propagation of unstrengthened and strengthened fatigue specimens.

As shown in Fig. 8, the strengthened specimen S2000-S-A initially displayed a stable, linear load-deflection relationship until approximately 202.4 kN. After this point, the deformation increased more significantly with the load, reaching a peak load of 270 kN at a deflection of 32 mm. Following this, a loud cracking sound was heard, and the load dropped to 247.4 kN. Slip and delamination began with the cracking noise. The load then rose again to 256.4 kN, and a rupture occurred in the CFRP as the specimen reached a displacement of 39 mm. The final displacement for this specimen was 83 mm before the test was concluded. As depicted in Fig. 9(b), no local buckling was observed, similar to the unstrengthened specimen. Fig. 10(b) displays the failure mode of S2000-S-A around the crack region. The tearing of the crack resembled that observed in unstrengthened specimens. Additionally, four distinct failure modes were observed in the CFRP wrapping: delamination and slip in the front-middle surface and rupture in the bottom tensile and top areas of the CFRP wrapping ends. These failure modes were visible after removing the CFRP from the steel surface.

4.2. M-ϕ curve

To assess the strengthening effect of CFRP, Fig. 11 compares the moment M versus curvature ϕ relationship of the unstrengthened specimen U2500-S and the strengthened specimen S2000-S-A, also considering the self-weight of the concrete and the steel tube. The curvature of the midspan section was calculated using the experimental strain data from the top and bottom parts of the midspan. Curvature ϕ can be determined using the plane section assumption and the Euler-Bernoulli theorem (Feng et al., 2017), as described by Eq. (1). Here, H represents the height of the specimen's section. Since the CFRP sheets are significantly thinner than the steel tube, H equals D for both unstrengthened and strengthened specimens.

$$\phi = \frac{\varepsilon_{bot} - \varepsilon_{top}}{H} \tag{1}$$

The stiffness of the SWT was significantly increased after the CFRP wrapping. The slope of the curve in the linear region for the strengthened specimen was 26,258.44 kN m, which was 167.08% higher than the 9831.64 kN m measured for the unstrengthened counterpart. Furthermore, the peak moment of the strengthened specimen reached 197.5 kN m, representing a 27.09% increase compared to the 155.4 kN m peak moment observed in the unstrengthened specimen. This improvement was attributed to the CFRP's mechanism of sharing the tensile stress with the steel tube, which will be discussed in Section 4.3.

4.3. Analysis of strain

Strain at the bottom-left, top-middle, and bottom-right points along the longitudinal direction of the specimen was recorded with strain gauges G1, G2, and G3 (Fig. 5) throughout the static test, as shown in Fig. 12. It can be seen that the CFRP strengthening exhibited more minor strains compared to the unstrengthened counterpart under the same loading, indicating that the CFRP wrapping effectively reduced the stresses in steel. A maximum strain reduction of 28.6% was achieved, as measured by G1, G2, and G3, demonstrating why CFRPs significantly enhanced the flexural capacity and stiffness of the tube.

5. Fatigue test results and discussion

5.1. Fatigue behavior

All specimens' fatigue cracks initiated from the initial crack tips due to high stress concentrations. Initially, the cracks propagated slowly, but their propagation rate accelerated as the number of fatigue loading cycles increased. Eventually, the cracks grew rapidly, approaching their critical crack length, which caused significant flexural deformation of the specimen and ultimately led to its failure. The tests were stopped due to extensive deformation of the specimens, ranging from 48 to 55 mm. However, for specimen S2500-F-B, the experiment was stopped early due to plastic failure upon reaching its critical crack length.

5.1.1. Flexural deformation with fatigue cycles

Fig. 13 presents the final flexural deformation of fatigue specimens. No local buckling was observed. The two strengthened specimens exhibited different failure modes related to the CFRP-steel interface. Specimen S2500-F-A primarily showed slip (debonding) of the CFRP wrapping from the steel surface, while specimen S2500-F-B mainly exhibited CFRP rupture along the 45° fiber orientation. This difference arises from the axial stresses experienced by the tubes (i.e., tensile stress at the bottom part and compressive stress at the upper part). In specimen S2500-F-A, the longitudinal wrapping resists stress more effectively than the hoop wrapping. As the axial stress increases, the adhesive fails,

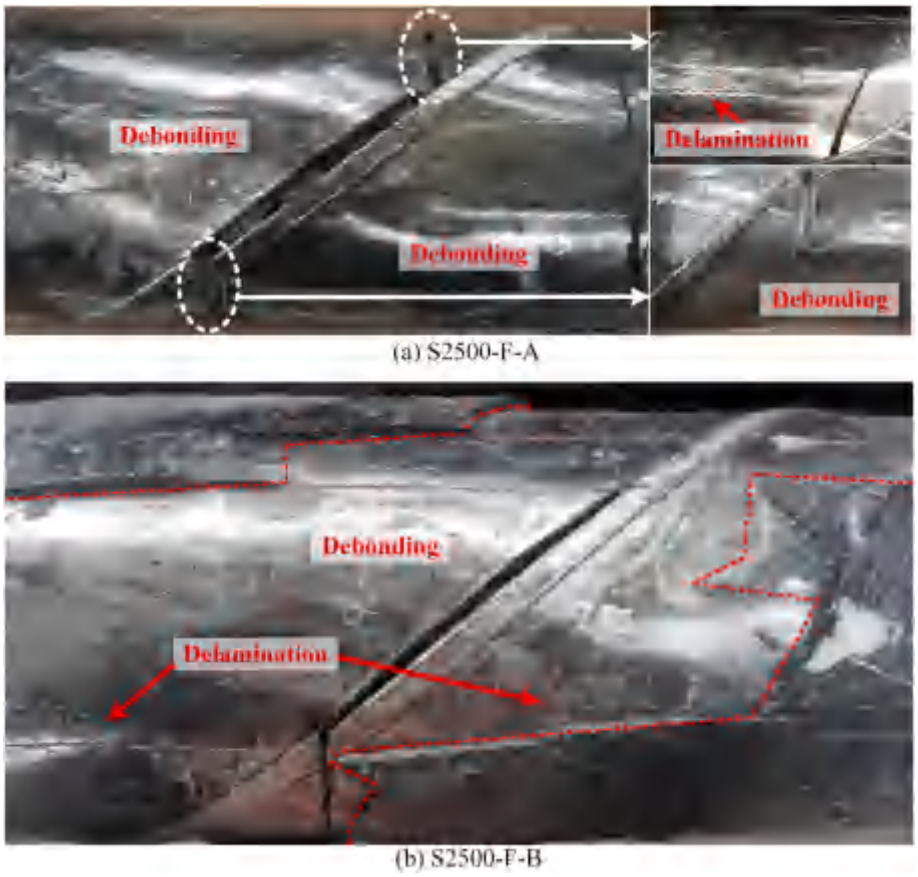


Fig. 19. CFRP-steel interface around the crack region of fatigue specimens.

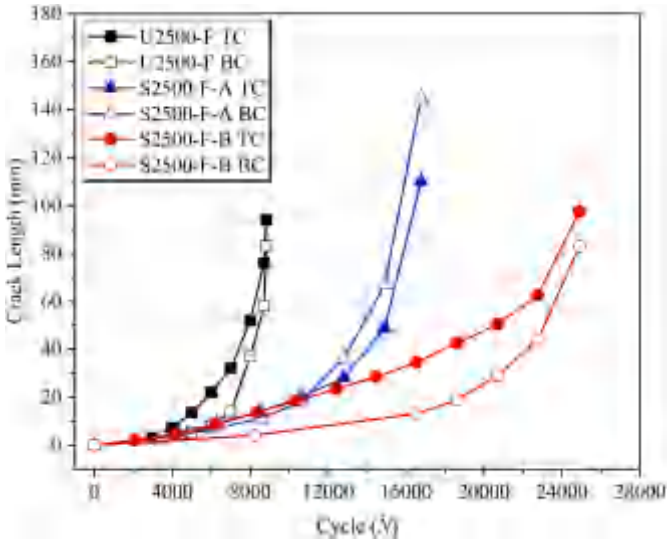


Fig. 20. Fatigue crack versus fatigue cycle graph for strengthened and unstrengthened specimens (TC and BC represent top and bottom cracks, respectively).

leading to debonding. Conversely, in specimen S2500-F-B, the inverse diagonal wrapping at 45° and -45° provides similar resistance in the axial direction, which results in fiber rupture failure at both ends of the CFRP wrapping.

The flexural deformation of the specimens under the fatigue peak load of 80 kN was recorded throughout the entire fatigue testing, as shown in Fig. 14. The whole process can be divided into two stages: initially, the flexural deformation was minimal for all the specimens (first stage), but after accumulating sufficient fatigue damage, the deformation increased rapidly (second stage). In the first stage, the unstrengthened specimen was displaced approximately 6.3 mm. Wrapping the specimen with CFRP increased its initial stiffness, reducing the displacement to 5.1 mm (a 16.4% decrease) for the longitudinal-hoop-wrapped specimen and 5.7 mm (a 6.6% decrease) for inverse-diagonal-wrapped specimens. Additionally, the unstrengthened specimen U2500-F transitioned to the second stage around 6000 cycles, while S2500-F-A transitioned around 12,700 cycles and S2500-F-B around 20,670 cycles, indicating that CFRP wrapping delayed this transition. Notably, the superior bonding of the inverse-diagonal wrapping (Fig. 19) was more effective at resisting stress, maintaining the overall displacement of the specimen more effectively than the longitudinal-hoop-wrapped specimen.

5.1.2. Crack propagation

Fig. 15 shows the crack propagation process of the fatigue specimens. The angle between the weld and the direction perpendicular to the loading direction is denoted as α, and the crack front relative to the initial crack direction is θ. For specimen U2500-F, the top crack tip initially grew perpendicular to the loading direction. However, as the crack length increased, its direction of propagation began to curve. The bottom crack tip initially propagated along the weld toe before penetrating the weld. Following this, the crack grew perpendicular to the loading direction until its propagation direction began to curve. Similar behavior was observed in specimen S2500-F-A, where the bottom crack propagation followed the same pattern. However, the deviation angle of the top crack towards the end of the fatigue cycle was less pronounced than in specimen U2500-F. In specimen S2500-F-B, both crack tips propagated consistently perpendicular to the loading direction.

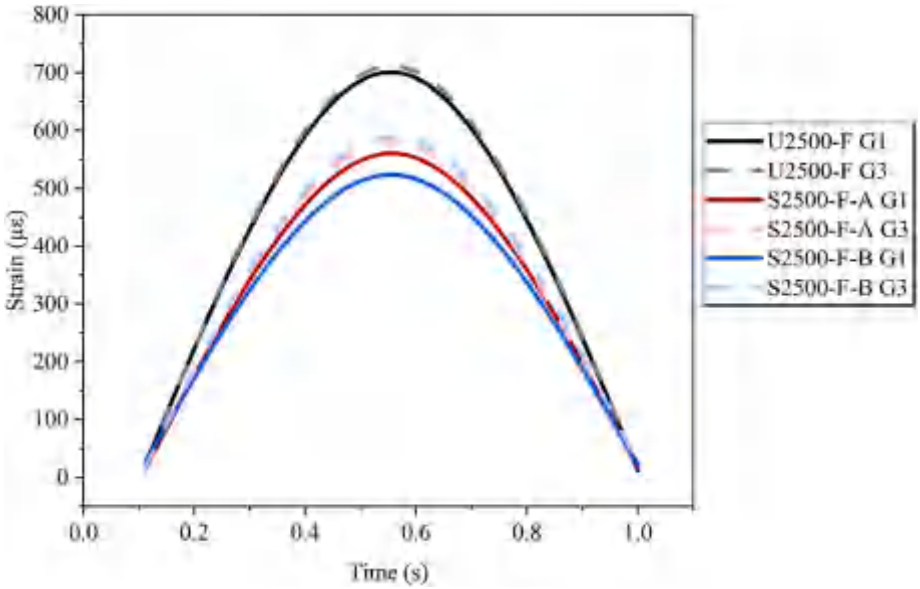


Fig. 21. Strain during the first fatigue cycle loading at various points in the bottom tensile area of the specimens.

With a crack inclination angle β of 40°, less than 45°, K_{II} initially dominated the crack tip. As the crack propagated, K_{II} gradually decreased, and both crack tips transitioned to being K_I-dominated, causing the crack to propagate perpendicularly to the loading direction (Aljabar et al., 2016), as seen in Fig. 16, points 1.1 and 2.1. However, this phase was brief, as the crack soon began to curve, deviating from its expected path, as shown in points 1.2 and 2.2. This deviation was likely attributed to the residual stresses in the SWTs, resulting from the complex manufacturing process, including steel sheet bending and welding. Liu et al. (2024) investigated the distribution of residual stresses in SWTs and found that compressive residual stresses were present near the weld seam and varied with distance from the weld. These compressive residual stresses, combined with external loading, created resultant forces that affected the crack propagation direction, as shown in Fig. 17. Furthermore, CFRP wrapping reduces the deviation in crack propagation angle by resisting shear stress on the crack, thereby limiting the crack curving. As specimen S2500-F-B had inverse-diagonal wrapping, it was more effective in resisting the crack propagation behavior which tends to diverge diagonally, as observed in specimen U2500-F. Thus, the crack propagation direction in specimen S2500-F-B remained relatively perpendicular to the loading direction.

Fig. 18 provides the close-up views of the top and bottom crack geometries of the unstrengthened and strengthened specimens after removing CFRP wrapping. Beach marks were observed at the crack cross-sections of the strengthened specimens. Specimen S2500-F-A exhibited a total of seven beach marks, while specimen S2500-F-B had eleven due to its longer fatigue life. The beach marks became thicker and more pronounced as the number of cycles increased and were more visible in the base metal than the weld metal through which the bottom crack propagated through. As a result, only the last three of seven beach marks on specimen S2500-F-A, and three of eleven beach marks on specimen S2500-F-B, were visible on the bottom crack. The difference can be attributed to the geometry and composition of the weld seam, which differed from the base metal and affected the beach marks' formation. A similar phenomenon has been observed in rib-to-deck welded joints under fatigue loading, where beach marks near the weld toe can only be identified with a stereomicroscope and are sometimes discontinuous due to the randomness of the microstructure near the weld toe (Wang et al., 2019).

The crack propagation process showed that the bottom crack in all fatigue specimens predominantly propagated through the weld seam during most of the fatigue loading cycles. This is evident in Fig. 18(a), where the bottom crack's propagation from the first point to the fifth point took 6000 cycles out of a total fatigue life of 8820 cycles. Similarly, in Fig. 18(b), only the last three of seven beach marks on specimen S2500-F-A and of eleven beach marks on specimen S2500-F-B appeared on the base metal. This indicated that the crack advanced very slowly through the weld seam and accelerated significantly once it exited. The slow propagation through the weld seam is attributed to the increased wall thickness around the weld zone (Hu et al., 2024).

Fig. 19 shows the state of the CFRP-steel interface at the bottom-tensile area of the strengthened specimen after the fatigue loading test, where the initial crack was located. Upon peeling off the CFRPs, two distinct failure modes were observed at the CFRP-steel interface at the crack tips: delamination and debonding. Debonding primarily occurred in the areas where cracks and their propagation were present. At the same time, delamination was found in regions farther from the crack, where the crack propagation had yet to reach. The inverse-diagonal-wrapped specimen S2500-F-B exhibited a stronger CFRP-steel bond than the longitudinal-hoop-wrapped specimen. This was evident in Fig. 19(b), where significant amounts of CFRP laminate remained as it is still tightly bonded to the steel surface, with extensive delamination around the crack geometry. In contrast, the longitudinal-hoop-wrapped specimen, depicted in Fig. 19(a), had no CFRP laminate left around the crack area, as it was no longer tightly bonded to the steel surface. This indicated that the main failure mode was debonding.

5.2. *a-N curve and fatigue life*

Based on the results presented in Section 5.1.2, the crack propagation versus fatigue cycles (*a-N* curve) for both crack tips in all fatigue specimens is shown in Fig. 20. Due to the different paths and experienced stress conditions experienced during fatigue testing, the crack propagation rate varied between the two tips. Initially, the bottom crack propagated more slowly than the top crack. However, once the bottom crack penetrated through the weld, its propagation rate increased significantly, eventually matching or surpassing the top crack. In the inverse-diagonal-wrapped specimen, the bottom crack did not surpass the top crack because the plastic failure stopped the test early.

For the unstrengthened specimen U2500-F, the first 4000 cycles showed relatively linear crack growth. Following this, there was significant crack growth due to accumulated fatigue damage. The propagation rate of the bottom crack was slower because of the weld geometry, which impeded its growth compared to the top crack.

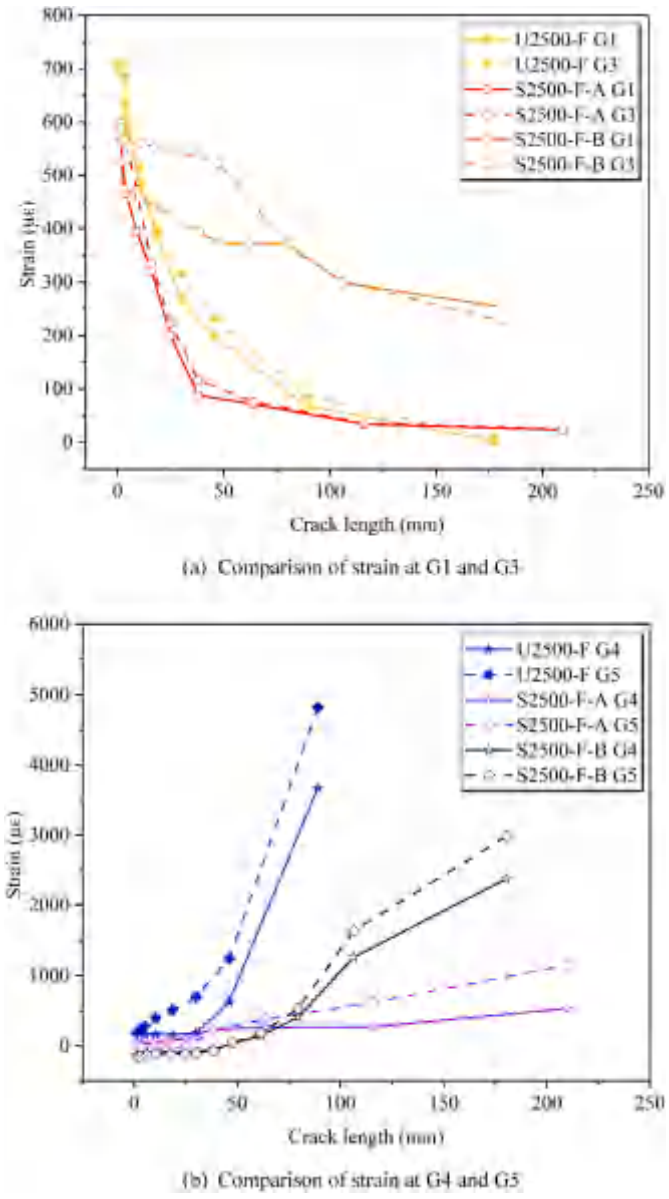


Fig. 22. Strain versus crack propagation length of fatigue specimens.

Ultimately, U2500-F ended with a top crack length of 94 mm, a bottom crack length of 83 mm, a crack mouth opening displacement of 16 mm, and a fatigue life of 8820 cycles.

CFRP strengthening significantly enhanced the fatigue performance of the steel tubes, with inverse-diagonal wrapping demonstrating the most significant improvement. Longitudinal-hoop wrapping increased the fatigue life from approximately 8800 cycles to 16,700 cycles, representing a 90.1% improvement. The crack propagation rate increased significantly after about 8500 cycles. In contrast, inverse-diagonal wrapping extended the fatigue life even further to approximately 24,900 cycles, an 182.7% increase. Notably, the top crack maintained a nearly linear crack propagation rate up to around 20,000 cycles. This enhancement is primarily attributed to the superior bonding of CFRP, as depicted in Fig. 19, which effectively reduced stress intensity through its diagonal fibers. The ±45° fiber orientation likely provided better bonding compared to ±90° wrapping due to the initial crack, positioned along the weld toe with a 50° helix angle, aligning more closely with the fibers, thereby improving load transfer and reducing the risk of interface failure.

Specifically, up to approximately 8500 cycles, the crack propagation rate of the top crack in both strengthened specimens was similar. However, beyond this point, a significant disparity emerged between the two strengthening methods. This suggests that while both methods provided adequate bonding up to 8500 cycles, the bond quality of the longitudinal-hoop-wrapped specimen deteriorated after that.

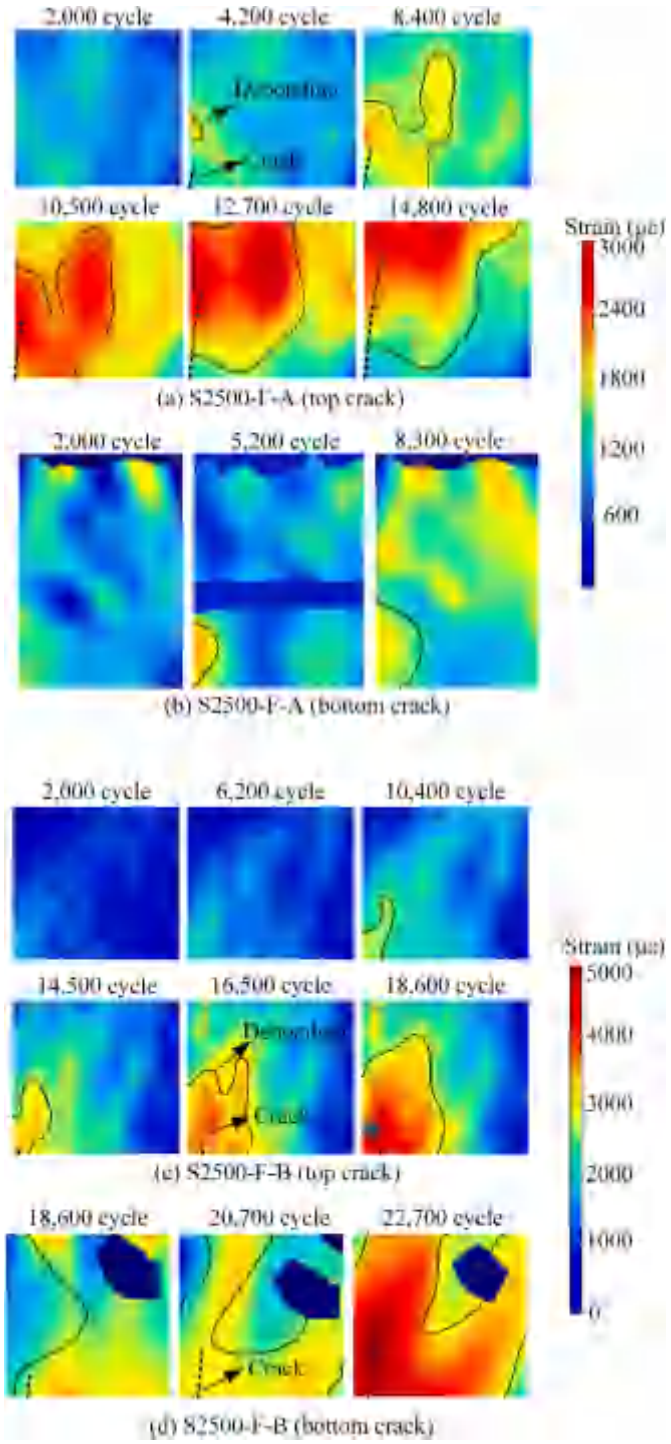


Fig. 23. Debonding and strain contour map of the strengthened fatigue specimens.

5.3. Analysis of strain

The strain data recorded by the strain gauges (G1 and G3) at two different points along the longitudinal tension area during the first

fatigue cycle (from 0 to 80 kN and back to 0 within 1 s) are shown in Fig. 21. Consistent with the observations in Section 4.3, CFRP strengthening resulted in more minor strains compared to the unstrengthened specimens under the same loading conditions. A maximum strain reduction of 25.3% was observed, as measured by G1 and G3. This reduction in strain indicated that CFRP wrapping effectively decreased the stresses in the steel, contributing to extended fatigue life of the steel tube.

Fig. 22 illustrates the variations in strain corresponding to the peak load during fatigue loading of the specimens as the crack propagated. In Fig. 22(a), as the crack length increased, the strain in gauges G1 and G3 decreased. This reduction in strain is because the tensile force initially borne by the regions around these gauges is no longer transferred as the crack grows. Consequently, this region ceased to bear the load. The longer the crack, the larger the area that becomes unloaded, resulting in reduced strain measurements in these gauges. Notably, the specimen S2500-F-B exhibited a relatively more stable and slow decrease in strain as the crack length increased, with the strain in the CFRP sheets remaining higher compared to U2500-F and S2500-F-A. This indicated that the CFRP strengthening in specimen S2500-F-B was more effective than in S2500-F-A. When the steel tube was nearing failure or failing, the CFRP provided additional support by accommodating the stress from the external load, thereby enhancing the steel tube's capacity, stiffness, and fatigue life.

In contrast, Fig. 22(b) shows that the strain in gauges G4 and G5, located away from the crack, increased as the crack length grew due to the expansion of the unloaded area surrounding the initial crack. Both strengthened specimens consistently exhibited lower strain than the unstrengthened specimen throughout the crack propagation. Specimen S2500-F-B displayed an increase in strain with crack length, reflecting its superior stress transfer and effectiveness of CFRP strengthening, while specimen S2500-F-A showed relatively stable behavior.

5.4. Debonding analysis by DIC

As shown previously in Fig. 19, debonding occurred primarily in areas closer to the crack region. The high stress concentration around the crack leads to a significant strain gradient in the CFRP. As the crack propagates, these high strain regions expand, leading to debonding. Because shear stress is transferred outside the debonding region and no shear stress can be transferred inside the debonding region, the debonding region edge is characterized by a high CFRP strain gradient, with a gradient greater than 0.06 με/m considered indicative of the debonding region edge (Zheng and Dawood, 2016; Hu et al., 2021). Using this method, the debonding area is shown in Fig. 23, along with the strain contour maps at various fatigue loading cycles. The strain contours at each fatigue cycle step showed the same behavior: as the number of fatigue cycles increased, the strain and debonding area increased, as indicated by the transition from dark blue to dark red.

In the top crack of the specimens (Fig. 23(a) and (c)), the region near the crack tips exhibited significantly higher strain compared to other areas; the stress concentration followed the crack tip, which gradually shifted due to the crack propagation, reflecting stress redistribution. For the inverse-wrapped specimen S2500-F-B, the crack propagated more slowly, and the experiment was halted early due to plastic failure, preventing the crack from reaching a significant length. Consequently, the stress concentration was less pronounced compared to specimen S2500-F-A. Notably, around 14,500 cycles, the strain and debonding area of specimen S2500-F-A were significantly larger than specimen S2500-F-B, which is why S2500-F-A exhibited a lower fatigue life.

For the bottom crack of the specimens (Fig. 23(b) and (d)), the stress distribution was less clear. This lack of clarity could be attributed to differences in the DIC device used and the influence of the weld seam on strain readings. Therefore, only selected parts along the fatigue cycles are displayed. Fig. 23(b) shows no crack propagation in the contour region early on (at 2000 and 5200 cycles), as the crack had not yet reached this area. By 8300 cycles, the crack tip had propagated slightly to the left, so it was not within the contour. Overall, stresses in the bottom cracks were concentrated at the crack tips, reflecting a pattern similar to the top cracks.

6. Conclusion

This study investigated the static and fatigue behavior of CFRP-strengthened spiral welded steel tubes subjected to four-point bending loading. Five steel tubes were tested, including two unstrengthened and three CFRP-strengthened specimens. The following conclusions were drawn.

(1) All static specimens exhibited overall flexural failure without local buckling. The statically loaded steel tube primarily experienced delamination at the steel-CFRP bond interface, along with ruptures and slips at the ends of the CFRP wrapping. CFRP strengthening significantly improved the stiffness and bending capacity of the steel tubes, increasing stiffness by 175.4% and bending capacity by 27.45% due to CFRP effectively sharing the cross-sectional stress.
(2) The spiral weld's presence influenced each crack tip's propagation behavior differently. The crack tip unaffected by the weld initially grew rapidly perpendicular to the loading direction, before curving at an angle as the crack extended. The other crack tip influenced by the weld seam first traversed the weld toe before shifting to a direction nearly perpendicular to the loading, eventually curved in its propagation. CFRP strengthening was found to reduce this crack curving, with the inverse-diagonal wrapping proving to be the most effective, attributed to its superior ability to resist the diagonal curvature of the crack and the combined effects of compressive residual stress and external loading.
(3) The bottom crack propagated most of its fatigue life through the weld seam. Once it penetrated the weld seam and reached the base metal, its propagation rate increased rapidly, matching or surpassing that of the top crack.
(4) The CFRP strengthening significantly increased the fatigue life of the steel tubes. Inverse-diagonal CFRP wrapping enhanced fatigue life by approximately 182.7% compared to the unstrengthened tube. In contrast, the longitudinal-hoop-wrapped steel tube showed a comparatively lower 90.1% increase in fatigue life. This difference is due to delamination around the bottom-tension area in inverse-diagonal CFRP where the crack developed, while the longitudinal-hoop CFRP experienced debonding in the same location. The DIC effectively captured the strain distribution around the crack tips and estimated the debonding area around them.

CRediT authorship contribution statement

Andre Cahyadi Salim: Writing – original draft, Methodology, Investigation, Formal analysis, Data curation. **Yining Zhang:** Writing – review & editing, Data curation. **Lili Hu:** Writing – review & editing, Supervision, Methodology, Funding acquisition, Conceptualization. **Chengjian Shao:** Writing – review & editing, Supervision.

Declaration of competing interest

The authors declare that they have no known competing financial interests or personal relationships that could have appeared to influence the work reported in this paper.

Acknowledgements

This work was supported by the Young Elite Scientists Sponsorship

Program by CAST (2022QNRC001), and the Program Fund of Non-Metallic Excellence and Innovation Center for Building Materials (2023TDA5-1).

References

Alam, M.I., Fawzia, S., Zhao, X.L., Remennikov, A.M., 2017. Experimental study on FRP-strengthened steel tubular members under lateral impact. J. Compos. Construct. 21 (5). https://doi.org/10.1061/(asce)cc.1943-5614.0000801.

Aljabar, N.J., Zhao, X.L., Al-Mahaidi, R., Ghafoori, E., Motovalli, M., Powers, N., 2016. Effect of crack orientation on fatigue behavior of CFRP-strengthened steel plates. Compos. Struct. 152, 295–305. https://doi.org/10.1016/j.compstruct.2016.05.033.

Ancelet, O., Chapuliot, S., Henaff, G., 2008. Experimental and numerical study of crack initiation and propagation under a 3D thermal fatigue loading in a welded structure. Int. J. Fatig. 30 (6), 953–966. https://doi.org/10.1016/j.ijfatigue.2007.08.010.

Aslani, F., Uy, B., Hur, J., Carino, P., 2017. Behaviour and design of hollow and concrete-filled spiral welded steel tube columns subjected to axial compression. J. Constr. Steel Res. 128, 261–288. https://doi.org/10.1016/j.jcsr.2016.08.023.

Audibert, J.M., Huang, J., 2005. Geophysical and geotechnical design. Handb. Offshore Eng. 1145–1268. https://doi.org/10.1016/b978-0-08-044381-2.50023-0.

Cerit, M., Kokumer, O., Genel, K., 2010. Stress concentration effects of undercut defect and reinforcement metal in butt welded joint. Eng. Fail. Anal. 17 (2), 571–578. https://doi.org/10.1016/j.engfailanal.2009.10.010.

Chen, T., Yu, Q.Q., Gu, X.L., Zhao, X.L., 2012. Study on fatigue behavior of strengthened non-load-carrying cruciform welded joints using carbon fiber sheets. Int. J. Struct. Stabil. Dynam. 12 (1), 179–194. https://doi.org/10.1142/s0219455412004586.

Choi, J.H., Kim, I.H., Koo, J.M., Seok, C.S., 2010. A study on behavior of mixed mode fatigue crack growth of spiral welding part under bending load. In: Vessels Pip. Conf., vol. 1. ASME Press. https://doi.org/10.1115/pvp2010-25972.

Colombi, P., Fava, G., 2016. Fatigue crack growth in steel beams strengthened by CFRP strips. Theor. Appl. Fract. Mech. 85, 173–182. https://doi.org/10.1016/j.tafmec.2016.01.007.

Fattah, M.Y., Al-Soudani, W.H.S., 2015. Bearing capacity of open-ended pipe piles with restricted soil plug. Ships Offshore Struct. 11 (5), 501–516. https://doi.org/10.1080/17445302.2015.1030247.

Feng, P., Hu, L., Qian, P., Ye, L., 2017. Buckling behavior of CFRP-aluminum alloy hybrid tubes in axial compression. Eng. Struct. 132, 624–636. https://doi.org/10.1016/j.engstruct.2016.11.051.

Feng, P., Hu, L., Zhao, X.L., Cheng, L., Xu, S., 2014. Study on thermal effects on fatigue behavior of cracked steel plates strengthened by CFRP Sheets. Thin-Walled Struct. 82, 311–320. https://doi.org/10.1016/j.tws.2014.04.015.

Fulmer, S.J., Kowalsky, M.J., Nau, J.M., Hassan, T., 2012. Reversed cyclic flexural behavior of spiral DSAW and single seam ERW steel pipe piles. J. Struct. Eng. 138 (9), 1099–1109. https://doi.org/10.1061/(asce)st.1943-541x.0000553.

Furuya, Y., 2016. Small internal fatigue crack growth rate measured by beach marks. Mater. Sci. Eng. 678, 260–266. https://doi.org/10.1016/j.msea.2016.09.109.

Habibi, N., H-Gangaraj, S.M., Farrahi, G.H., Majzoobi, G.H., Mahmoudi, A.H., Daghigh, M., Yari, A., Moridi, A., 2012. The effect of shot peening on fatigue life of welded tubular joint in offshore structure. Mater. Des. 36, 250–257. https://doi.org/10.1016/j.matdes.2011.11.024.

Han, Y., Zhong, S., Peng, C., Tian, L., Sun, Y., Zhao, L., Xu, L., 2022. Fatigue behavior of X65 pipeline steel welded joints prepared by CMT/GMAW backing process. Int. J. Fatig. 164, 107156. https://doi.org/10.1016/j.ijfatigue.2022.107156.

Holtam, C.M., Baxter, D.P., Ashcroft, I.A., Thomson, R.C., 2010. Effect of crack depth on fatigue crack growth rates for a C–MN pipeline steel in a sour environment. Int. J. Fatig. 32 (2), 288–296. https://doi.org/10.1016/j.ijfatigue.2009.06.013.

Hosseini, A., Nussbaumer, A., Motavalli, M., Zhao, X.L., Ghafoori, E., 2019. Mixed mode I/II fatigue crack arrest in steel members using prestressed CFRP reinforcement. Int. J. Fatig. 127, 345–361. https://doi.org/10.1016/j.ijfatigue.2019.06.020.

Hu, L., Ding, X., Li, L., Chen, M.T., Zhang, Y., 2024. Fatigue behavior of CFRP-strengthened inclined welded steel plates with initial cracks. Thin-Walled Struct.

Hu, L., Feng, P., Zhao, X.L., 2017. Fatigue design of CFRP strengthened steel members. Thin-Walled Struct. 119, 482–498. https://doi.org/10.1016/j.tws.2017.06.029.

Hu, L., Li, M., Yiliyaer, T., Gao, W., Wang, H., 2022. Strengthening of cracked DH36 steel plates by CFRP sheets under fatigue loading at low temperatures. Ocean Eng. 243, 110203. https://doi.org/10.1016/j.oceaneng.2021.110203.

Hu, L., Wang, Y., Feng, P., Wang, H., Qiang, H., 2021. Debonding development in cracked steel plates strengthened by CFRP laminates under fatigue loading: experimental and boundary element method analysis. Thin-Walled Struct. 166, 108038. https://doi.org/10.1016/j.tws.2021.108038.

Hu, L., Zhao, X.L., Feng, P., 2016. Fatigue behavior of cracked high-strength steel plates strengthened by CFRP sheets. J. Compos. Construct. 20 (6), 04016043. https://doi.org/10.1061/(asce)cc.1943-5614.0000698.

Hulatt, J., Hollaway, L., Thorne, A., 2002. Preliminary investigations on the environmental effects on new heavyweight fabrics for use in civil engineering. Composites, Part B 33 (6), 407–414. https://doi.org/10.1016/s1359-8368(02)00034-3.

Kabir, M.H., Fawzia, S., Chan, T., 2015. Effects of CFRP layer orientation on strengthening of hollow steel elements. J. Croat. Assoc. Civ. Eng. 67 (5). https://doi.org/10.14256/jce.1127.2014.

Kajorncheappunngam, S., Gupta, R.K., GangaRao, H.V., 2002. Effect of aging environment on degradation of glass-reinforced epoxy. J. Compos. Construct. 6 (1), 61–69. https://doi.org/10.1061/(asce)1090-0268(2002)6:1(61.

Kim, Y.J., Harries, K.A., 2011. Fatigue behavior of damaged steel beams repaired with CFRP strips. Eng. Struct. 33 (5), 1491–1502. https://doi.org/10.1016/j.engstruct.2011.01.019.

Kootsookos, A., Mouritz, A.P., 2004. Seawater durability of glass- and carbon-polymer composites. Compos. Sci. Technol. 64 (10–11), 1503–1511. https://doi.org/10.1016/j.compscitech.2003.10.019.

Lavayen-Farfan, D., Butenegro-Garcia, J.A., Boada, M.J., Martinez-Casanova, M.A., Rodriguez-Hernandez, J.A., 2022. Theoretical and experimental study of the bending collapse of partially reinforced CFRP–Steel Square Tubes. Thin-Walled Struct. 177, 109457. https://doi.org/10.1016/j.tws.2022.109457.

Lewis, T., Wang, X., 2008. The T-stress solutions for through-wall circumferential cracks in cylinders subjected to general loading conditions. Eng. Fract. Mech. 75, 3206–3225. https://doi.org/10.1016/j.engfracmech.2007.12.001.

Li, L., Chen, T., Gu, X., Ghafoori, E., 2020. Heat activated SMA-CFRP composites for fatigue strengthening of cracked steel plates. J. Compos. Construct. 24 (6), 04020060. https://doi.org/10.1061/(asce)cc.1943-5614.0001072.

Li, Y., Wang, W., Pan, M., Cao, W., Ma, X., Li, Y., 2023. Fatigue life analysis of high-pressure seamless steel cylinder for hydrogen using autofrettage design. Int. J. Pres. Ves. Pip. 206, 105065. https://doi.org/10.1016/j.ijpvp.2023.105065.

Li, Z., Jiang, X., Hopman, H., 2019. Numerical analysis on the SIF of internal surface cracks in steel pipes reinforced with CRS subjected to bending. Ships Offshore Struct. 15 (10), 1070–1083. https://doi.org/10.1080/17445302.2019.1702769.

Li, Z., Jiang, X., Hopman, H., Zhu, L., Liu, Z., 2020. External surface cracked offshore steel pipes reinforced with composite repair system subjected to cyclic bending: an experimental investigation. Theor. Appl. Fract. Mech. 109, 102703. https://doi.org/10.1016/j.tafmec.2020.102703.

Liu, H., Xiao, Z., Zhao, X.L., Al-Mahaidi, R., 2009. Prediction of fatigue life for CFRP-strengthened steel plates. Thin-Walled Struct. 47 (10), 1069–1077. https://doi.org/10.1016/j.tws.2008.10.011.

Liu, M., Luo, S., Shen, Y., Lin, X., 2019. Corrosion fatigue crack propagation behavior of S135 high–strength drill pipe steel in H_2S environment. Eng. Fail. Anal. 97, 493–505. https://doi.org/10.1016/j.engfailanal.2019.01.026.

Liu, X.Y., Salim, A.C., Ban, H.Y., Hu, L.L., 2024. Behavior of CFRP-strengthened short spiral welded tubes under axial load. Thin-Walled Struct. https://doi.org/10.1016/j.tws.2024.112408.

Malhotra, S., 2010. Design and construction considerations for offshore wind turbine foundations in North America. GeoFlorida 2010. https://doi.org/10.1061/41095(365)155.

Miller, T.C., Chajes, M.J., Mertz, D.R., Hastings, J.N., 2001. Strengthening of a steel bridge girder using CFRP plates. J. Bridge Eng. 6 (6), 514–522. https://doi.org/10.1061/(asce)1084-0702(2001)6:6(514.

Nasim, K., Arif, A.F.M., Al-Nassar, Y.N., Anis, M., 2015. Investigation of residual stress development in spiral welded pipe. J. Mater. Process. Technol. 215, 225–238. https://doi.org/10.1016/j.jmatprotec.2014.08.009.

Piao, L., Zhang, X.Z., Zhu, C.K., 2020. Integrated steel pipe pile manufacturing technology for the main channel of Ningbo Zhoushan Port. World Bridges 48 (3), 40–44. CNKI:SUN:GWQL.0.2020-03-008. (in Chinese).

Ramachandra Murthy, A., Vishnuvardhan, S., Anjusha, K.V., Gandhi, P., Singh, P.K., 2022. Prediction of fatigue crack initiation life in SA312 type 304ln austenitic stainless steel straight pipes with notch. Nucl. Eng. Technol. 54 (5), 1588–1596. https://doi.org/10.1016/j.net.2021.11.011.

Rahman, S., Brust, F.W., Ghadiali, N., Wilkowski, G.M., 1998. Crack-opening-area analyses for circumferential through-wall cracks in pipes—Part I: analytical models. Int. J. Pres. Ves. Pip. 75, 357–373. https://doi.org/10.1016/S0308-0161(97)00081-1.

Shi, Y.W., Chen, B.Y., Zhang, J.X., 1990. Effects of welding residual stresses on fatigue crack growth behaviour in butt welds of a pipeline steel. Eng. Fract. Mech. 36 (6), 893–902. https://doi.org/10.1016/0013-7944(90)90266-j.

Teng, J.G., Yu, T., Fernando, D., 2012. Strengthening of steel structures with fiber-reinforced polymer composites. J. Constr. Steel Res. 78, 131–143. https://doi.org/10.1016/j.jcsr.2012.06.011.

Teng, T.L., Fung, C.P., Chang, P.H., 2002. Effect of weld geometry and residual stresses on fatigue in butt-welded joints. Int. J. Pres. Ves. Pip. 79 (7), 467–482. https://doi.org/10.1016/s0308-0161(02)00060-1.

Turhan, Ş.Ö., Motameni, A., Gürbüz, R., 2020. Fatigue behavior of welded API 5L X70 steel used in pipelines. J. Fail. Anal. Prev. 20 (5), 1554–1567. https://doi.org/10.1007/s11668-020-00959-x.

van Es, S.H.J., Gresnigt, A.M., Vasilikis, D., Karamanos, S.A., 2016. Ultimate bending capacity of spiral-welded steel tubes – part I: experiments. Thin-Walled Struct. 102, 286–304. https://doi.org/10.1016/j.tws.2015.11.024.

Vasilikis, D., Karamanos, S.A., van Es, S.H.J., Gresnigt, A.M., 2016. Ultimate bending capacity of spiral-welded steel tubes – part II: predictions. Thin-Walled Struct. 102, 305–319. https://doi.org/10.1016/j.tws.2015.11.025.

Wang, B., Nagy, W., De Backer, H., Chen, A., 2019. Fatigue process of rib-to-deck welded joints of orthotropic steel decks. Theor. Appl. Fract. Mech. 101, 113–126. https://doi.org/10.1016/j.tafmec.2019.02.015.

Wu, Y.H., Wu, W.Q., 2005. Application and development of steel pipes in structural engineering. Steel Struct 20 (2), 45–49. https://doi.org/10.3969/j.issn.1007-9963.2005.02.014 (in Chinese).

Yao, G.X., 2013. Application of UIT in improving fatigue performance of steel structures in offshore platforms. China Water Transport 8. https://doi.org/10.13646/j.cnki.42-1395/u.2013.08.002 (in Chinese).

Yin, G.M., 2009. The Rapid Development of Steel Pipes in China: A 10-Year Review. Sichuan Science and Technology Press (in Chinese).

Yu, Q.Q., Chen, T., Gu, X.L., Zhao, X.L., Xiao, Z.G., 2013. Fatigue behaviour of CFRP strengthened steel plates with different degrees of damage. Thin-Walled Struct. 69, 10–17. https://doi.org/10.1016/j.tws.2013.03.012.

Yu, W., Fan, M., Shi, J., Xue, F., Chen, X., Liu, H., 2018. A comparison between fracture toughness at different locations of SMAW and GTAW welded joints of primary coolant piping. Eng. Fract. Mech. 202, 135–146. https://doi.org/10.1016/j.engfracmech.2018.09.021.

Yu, X., 2015. Research on Forming Control Technology of Spiral Welded Pipes (Master's Thesis). Shandong University. https://doi.org/10.7666/d.Y2966887 (in Chinese).

Zhang, D., Zhu, H., Zhang, C., Wang, J., Guo, H., 2022. Crack initiation and propagation of defects adjacent to the X65 pipeline spiral weld under axial tensile force. Int. J. Pres. Ves. Pip. 200, 104814. https://doi.org/10.1016/j.ijpvp.2022.104814.

Zhang, X., 2018. Study on the Long-Term Performance of Pultruded Composite Profiles in Marine Environments (Master's Thesis). Tsinghua University (in Chinese).

Zhang, Y., Hu, L., Shen, C., Zhao, X.L., 2024. Study on fatigue behavior of butt-welded high-strength steel connections with surface cracks. Thin-Walled Struct. 200, 111888. https://doi.org/10.1016/j.tws.2024.111888.

Zhang, Y.H., 2017. Key technologies for offshore construction of ultra-large diameter steel pipe piles. China Harbour Constr 37 (3), 57–60. https://doi.org/10.7640/zggwjs201703012 (in Chinese).

Zhao, X.L., Zhang, L., 2007. State-of-the-art review on FRP strengthened steel structures. Eng. Struct. 29 (8), 1808–1823. https://doi.org/10.1016/j.engstruct.2006.10.006.

Zheng, B., Dawood, M., 2016. Debonding of carbon fiber–reinforced polymer patches from cracked steel elements under fatigue loading. J. Compos. Construct. 20, 04016038. https://doi.org/10.1061/(asce)cc.1943-5614.0000694.

Zhu, C., 2015. Study on the Static and Dynamic Performance of FRP-Concrete-Filled Steel Tubular Structures (Ph. D. Thesis). Dalian Maritime University (in Chinese).

Engineering Structures 335 (2025) 120307



Contents lists available at ScienceDirect

Engineering Structures

journal homepage: www.elsevier.com/locate/engstruct





Novel adaptive prestressed CFRP-reinforced steel column: Concept and behavior

Xu Liang [a], Lili Hu [b,*], Terrance Lim [a]

[a] State Key Laboratory of Ocean Engineering, School of Ocean and Civil Engineering, Shanghai Jiao Tong University, Shanghai 200240, China
[b] Research Institute of Urbanization and Urban Safety, School of Future Cities, University of Science and Technology Beijing, Beijing 100083, China

ARTICLE INFO

Keywords:
Active response
Adaptive behavior
Prestressed CFRP plate
Progressive collapse

ABSTRACT

Prestressed carbon fiber reinforced polymer (CFRP) plate reinforcement techniques effectively enhance the structural behavior of steel columns and the active response of such a system ensures the stability of steel columns under the challenges of varying external loads. This paper proposed a novel adaptive prestressed CFRP plates reinforced steel column equipped with actuators for the first time. Its adaptive behavior was achieved by adjusting the actuator length, thereby altering the linear displacement constraint on both sides. Firstly, experimental tests were conducted to investigate the adaptive behavior of specimens with varying slenderness ratios, CFRP plate prestresses, and eccentricities. The results indicated that actuator elongation (AE) significantly increased the stiffness and bearing capacity of the column, and effectively counteracting its deflection. Furthermore, the effect of AE on the structural performance improvement of the column after the first AE was more pronounced for the system with smaller slenderness ratios, CFRP plate prestresses, and eccentricities. Then finite element models were validated against experimental results and parametric studies revealed that higher values of actuator length, CFRP plate prestress, and elastic modulus were advantageous in improving the performance of the steel column. When the elongation timing of actuators was delayed, the elongation speed increased to compensate for the delayed response and larger compressive capacities of the actuators were required. Finally, a practical case demonstrated that an adaptive prestressed CFRP plates reinforced steel column equipped with appropriately designed actuators effectively withstood the rapidly increasing load and prevented the progressive collapse of the frame.

1. Introduction

Structures are generally incapable of perceiving external loads and responding to them. Consequently, factors such as temperature fluctuations, material aging, and external load variation may contribute to structural damage or even failure. Adaptive structures have emerged as a hot topic of research [1,2], offering an alternative by actively counteracting load variations. By actively responding to these fluctuations, adaptive structures pave the way for a more proactive design concept, empowering structures to respond promptly and effectively. Columns, as foundational support elements in diverse engineering structures, play a pivotal role in ensuring structural safety. In particular, columns in buildings facing external threats like seismic events [3], explosions [4], and fires [5] can trigger frame collapse, resulting in significant losses; in bridge structures, vehicle collisions, ship collisions, excessive vehicle loads, or human errors like insufficient design [6] contribute to bridge failures or even progressive collapse. These scenarios underscore the importance of incorporating adaptive measures in columns to enhance structural safety.

Adaptive behavior can be achieved using intelligent materials or actuators. The potential applications of various smart materials have been studied [7], for example, shape memory materials have been used in actuator technology enabling substantial displacements; magneto-rheological fluids are applied for seismic and vibration control owing to their adjustable stiffness; magnetostrictive materials show potential for seismic control. However, integrating these smart materials into real engineering structures remains in the state of fundamental research. Actuators, including linear actuators, and pneumatic muscle actuators, have been applied in a diverse range of structures including string beam structures [8], tensegrity structures [9,10], arches [11], shells [12], pedestrian bridges [2,13,14], trusses [15,16]. Due to precise displacement control and smooth operation, linear actuators are commonly used

* Corresponding author.
E-mail address: hll_1010@163.com (L. Hu).

https://doi.org/10.1016/j.engstruct.2025.120307
Received 6 October 2024; Received in revised form 15 March 2025; Accepted 10 April 2025
Available online 21 April 2025
0141-0296/© 2025 Elsevier Ltd. All rights are reserved, including those for text and data mining, AI training, and similar technologies.

and typically implemented using mechanical devices. The design concept using actuators generally aims to activate the shape control capabilities of the structure to improve its performance. Kmet et al. [10] introduced a newly developed adaptive tensegrity system capable of altering its geometric shape and stress characteristics to adapt to current loading conditions. Senatore et al. [14] optimally designed an adaptive shape cantilever pedestrian bridge deck, a cantilever structure, and trusses based on the minimal energy consumption principle. Zhang et al. [17] conducted experimental and simulation analyses to assess the mechanical performance and active shape control capabilities of the structure, confirming the feasibility of shape control for adaptive cable domes under asymmetric loading conditions. Li et al. [18] studied the arrangement of actuators to replace the struts in truss structures to achieve vibration control objectives. The application of incorporating cables or tendons and actuators on structures has been widely investigated [19–25]. This technique serves to balance loads, incorporate supports, reduce spans, and achieve a more efficient stress distribution and a desired structural response. Xu et al. conducted lots of research [19–21] on the structures with the application of actuators. For example, applying single actuator and double actuators on intelligent prestressed bridges using under slow-moving loads to verify the feasibility of structural deformation and stress control [19]; introducing intelligent prestressing systems into cable-stayed bridges to control the deflection and stress of the main beam to reduce the weight of the structure [20]; integrating actuators in steel truss beams to enhance the bending performance of beam in response to external load variations [21]. Cheng et al. [22] replaced the vertical struts in the original cable-stayed beam structures with adjustable expandable rods to act as actuators and proposed an optimization design method based on structural performance. Shen et al. [8] controlled the struts of cable-stayed beams through a control device, adjusting the length of the actuators based on data from pre-installed sensors to optimize their operational state. Corral et al. [23] and Rooyackers et al. [24] applied a linear actuator situated between the bridge deck and the inclined cable system to achieve adaptive deflection of the bridge under moving loads. Reksowardojo et al. [25] studied the application of external adaptive tensioning systems in high-speed railway bridges.

Steel column buckling under varying external loads can significantly influence structural safety. For instance, in a steel frame system, progressive collapse may be triggered by the initial failure of a buckling column due to accidental loads. This failure can propagate damage to adjacent members, ultimately compromising the integrity of the entire structure and leading to its collapse. To address sudden or unexpected loads, designers should incorporate additional safety factors into their structural calculations. This often involves increasing cross-sectional dimensions of columns. This not only escalates material consumption but also keeps the structure in a low-stress state under normal operational conditions over prolonged periods, resulting in an inefficient utilization of resources. Thus, an innovative adaptive column was developed based on the prestressed carbon fiber reinforced polymer (CFRP) plates reinforced steel column proposed by Hu et al. [26] to address the challenges of steel components under varying external load. In this system, CFRP plates were anchored on both ends of the steel column using mechanical anchorages. The anchorage positions of the device could be installed away from the connections in real structures, ensuring that the reinforcement did not interfere with the existing structural details. Additionally, prestressing chairs at column midspan were replaced with linear actuators to achieve adaptive performance. Firstly, the working principle of adaptive prestressed CFRP plates reinforced steel column was elucidated. Then, six specimens equipped with linear actuators were designed and experiments were conducted following the control strategy to study the adaptive behavior of specimens with varying slenderness ratios, CFRP plate prestresses, and eccentricities. Subsequently, finite element models were established to validate the experimental findings and explore the effect of parameters influencing the linear displacement constraint, including the ratio of actuator length to steel column length, CFRP plate prestress, and elastic modulus of the CFRP plate. Furthermore, the elongation timing on the adaptive response of the system was also studied. Finally, an adaptive prestressed CFRP plates reinforced steel column was designed for a steel frame experiencing progressive collapse, demonstrating that appropriately implementing adaptive columns can help prevent such failures.

2. Design of adaptive prestressed CFRP plates reinforced steel column

2.1. Previous study

Prestressed CFRP plates reinforced steel columns exhibit excellent buckling resistance performance [26–28]. The reinforcement principle is that the system can produce a linear displacement constraint at the midspan of the steel column as it deflects, which reduces the effective length of the steel column, thereby improving its buckling behavior. The constraint effect depends on the parameters of tensile stiffness of CFRP plates, and steel column length to support length ratio. Studies relevant to this system have been comprehensively researched by Hu et al. [26–28] and some critical findings are concluded that the stiffness and buckling capacity of steel columns can be significantly improved by adjusting the relevant parameters that influence the constraint effect. These key findings lay the foundations for designing adaptive prestressed CFRP plates reinforced steel columns.

2.2. Working principle

Prestressed CFRP plates reinforced steel columns have different failure modes depending on the constraint level of linear displacement constraint. The column tends to exhibit a single-wave failure mode with low constraint levels and a double-wave failure mode with high constraint levels. This study focuses on the adaptive column system controlled by the linear displacement constraint, with the columns being hinged at both ends. Actuators are arranged on both sides of the steel column at midspan. The working procedure is illustrated in Fig. 1. The column responds differently under different conditions. First, if the external load induces a deflection smaller than a safe deflection x_s, the column works as a normal prestressed CFRP plates reinforced steel column with the actuator remaining unelongated. Second, if the external load leads to a deflection exceeding x_s, the actuator elongates, which contributes to an increase in CFRP plate stress, leading to an increase of the load-bearing capacity and a reduction of the deflection of the column, until the deflection is below x_s.

2.3. Adaptive implementation method

2.3.1. Adaptive system construction

For the adaptive prestressed CFRP plates reinforced steel column, linear actuators LX712 were utilized to achieve the adaptive response. The installation steps are shown in Fig. 2(a): (1) CFRP plates were fixed at both ends of the steel web using mechanical anchorages secured by high-strength bolts, while epoxy resin was applied on both sides of CFRP plates' ends to ensure bonding with the steel web and anchorage (this method has been verified effectively in previous studies conducted by Hu et al. [27]); (2) one end of the linear actuators was welded to the steel web at midspan, while the other end was connected to a prestressing chair via a bolt, which served to support the CFRP plate (Fig. 2(b)); (3) the actuators were connected to the controlling hardware. The actuators were then controlled to elongate, thereby stretching the CFRP plates, which induced elastic deformation and generated the desired prestress. The onsite photo of such an adaptive system and details of the actuator can also be found in the figure.

2.3.2. Control strategy

The control strategy was determined to maintain the deflection of the

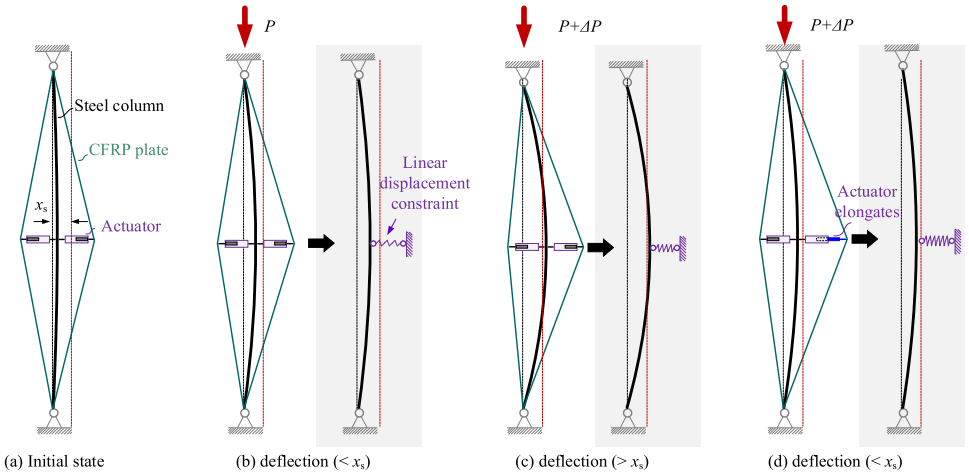


Fig. 1. Working procedure of the adaptive prestressed CFRP plates reinforced steel column.

steel column within a safe threshold (as indicated in Fig. 1). The process was achieved using a remote controller equipped with elongation functionality. Specifically, the control strategy was inherently influenced by the actuators' maximum stroke length (S) and thrust force (T_f). In this study, an incremental load was applied to the columns until column deflection reached x. Then, the load was maintained constant, and the deflection was reduced below x_s by actuator elongation (AE). The initial column deflection was rudimentarily determined to account for both buckling and sufficient operational space for the actuators. The actuator was equipped with instant self-locking capability, ensuring it remained fixed after bearing an external force exceeding its ultimate capacity, thereby allowing the structure to function passively.

3. Experimental tests

3.1. Specimens and test program

Eight specimens were designed, including two pure steel columns and six adaptive CFRP plates reinforced steel columns (Table 1). The naming convention was illustrated using specimens P-S140-e0 and PS0-d7.1-S140-e50 as examples. "P" and "S140" in specimen P-S140-e0 represented the pure steel column and slenderness ratio of 140 mm, respectively, and the suffix "-e0" indicated that the eccentricity was 0 mm. In the case of specimen PS0-d7.1-S140-e50, "PS0-d7.1" signified that CFRP plates were initially slacking and the installment gap d between the actuator and CFRP plate was 7.1 mm. After AE value a_e was 7.1 mm (corresponding actuator length of 307.1 mm), the stress in the CFRP plate began to rise from 0 MPa. All steel columns had a cross-sectional size of the H-steel column with dimensions of 116 mm × 80 mm × 6 mm × 6 mm (height × width × web thickness × flange thickness) and the slenderness ratios of steel columns ranged from 119 to 169. Both ends of the column were welded to a steel plate with dimensions of 500 mm × 500 mm × 6 mm (length × width × thickness) for loading convenience. The width and thickness of CFRP plates were 50 mm and 3 mm, respectively. The elastic modulus, yield strength, and ultimate strength of steel were 203 GPa, 657 MPa, and 734 MPa, respectively. The elastic modulus and ultimate strength of the CFRP plate were 170 GPa and 2800 MPa, respectively. The study included axial and eccentric loading tests, with eccentricities of 50 mm and 100 mm based on the positions of the hinge support notches. Furthermore, CFRP prestress was set as 20 MPa for specimen PS20-d16.5-S140-e50 and the corresponding actuator length on both sides was 318.2 mm. The schematic diagram of the parameters is shown in Fig. 3.

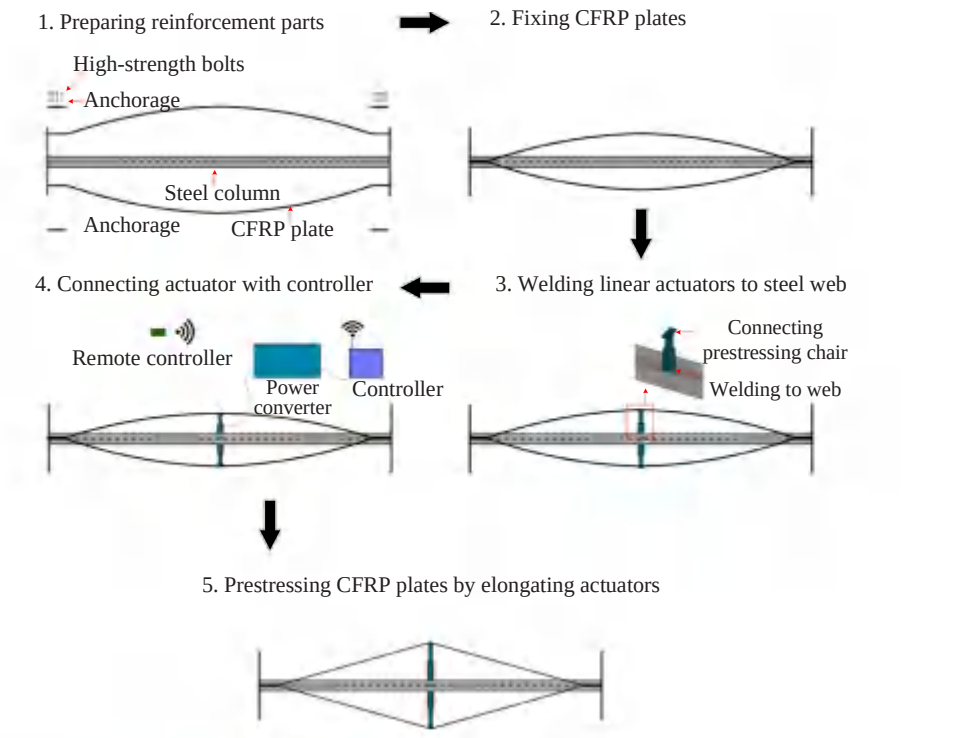
3.2. Loading and measurement

An incremental load was applied on the columns until x reached 10 mm, making the first loading stage. Then, x was reduced to 0 mm by AE on the convex side, defining the first AE stage. During AE, the load on the system was maintained as constant as possible. Subsequently, the external load continued to increase, causing x to reach 5 mm, signifying the second loading stage. The actuator on the convex side was then activated to return the columns to the deflection of 0 mm and this was the second AE stage. In the subsequent stages, the deflection was set as 5 mm taking into account S and T_f. If the column deflected toward the side opposite the initial deflection after AE or loading stages, only the actuator on that side was activated to push the column back to 0 mm. The process was repeated iteratively to collect more valuable data until the actuator reached either S of 100 mm or T_f of 12 kN, which was not necessary in practice. Specimens were loaded horizontally using hydraulic actuators (Fig. 4). Steel plates at the ends of the column were bolted to hinge supports, forming a hinge boundary condition. A force sensor provided feedback on the external load. The hinge supports featured notches spaced 50 mm apart, enabling eccentric loading by aligning the convex-side hinge to different notches (Fig. 4(b)). Dial gauges were arranged perpendicular to steel plates connected with columns at both ends to measure the rotation of the hinge supports. Linear variable differential transformers and dial gauges were set against the prestressing chairs and column web at midspan on both sides to measure displacements of linear actuators and column deflections, respectively. Strain gauges were distributed at various positions on the CFRP plates and steel columns to monitor strain responses.

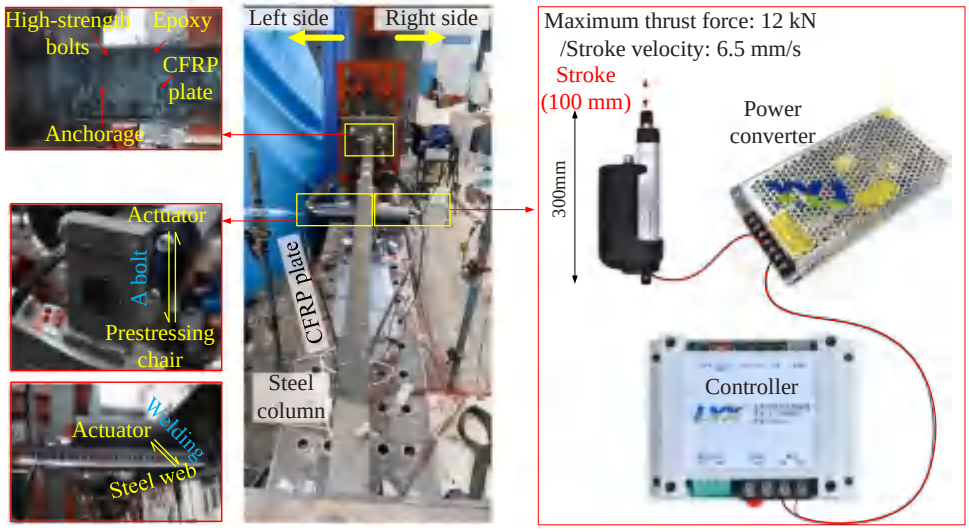
3.3. Results and discussions

Based on the loading process and the similarity in load-deflection curves of all specimens, some general characteristics of the PS0 and PS20 series during experiments are summarized in Fig. 5. The following explanation took the PS0 series as an example to elucidate the whole process. For the pure steel column and specimens of PS0 series, the load-deflection curves for both were almost identical during the first loading stage. This similarity was attributed to the gap between the CFRP plates and the actuator rod, which caused the CFRP plates on both sides to remain slack.

Only the actuator on the deflected side activated to push the column back for all AE stages. During the first AE, the state of CFRP plates at the convex side shifted from slack to tension, and the CFRP plate stress on the convex side started to increase from 0 MPa. As actuators continued to elongate, CFRP plate stress increased and the deflection of the steel column gradually reduced to a safe threshold due to the horizontal force



(a) installation steps



(b) specimen details

Fig. 2. Installation steps and specimen details.

resulting from the stress difference in the CFRP plates on both sides. After the first loading process finished, the CFRP plates and the steel column formed a firm connection, allowing them to jointly bear the external load. During the second loading and second AE stages, CFRP stresses continued to increase.

3.3.1. Load and column deflection relationship

Load-deflection curves of all specimens are shown in Fig. 6. For all the specimens, there was a discernible increase in both stiffness and bearing capacity after the second loading, and the load-bearing capacity increased by nearly 3.78 times compared to that after the first loading (specimen PS0-d7.1-S140-e50). This indicated the effectiveness of AE in improving structural performance. Similarly, an analysis by Corral et al. [23] demonstrated that the adaptive cable-stayed system enhanced the stiffness of a pedestrian bridge after actuator elongation. As shown in Fig. 6(b) for the eccentric loading series, the bearing capacity and initial stiffness of specimens PS20-d16.5-S140-e50 increased by about 2.6 and 4.5 times, respectively, compared to specimen PS0-d7.1-S140-e50, indicating that a higher PS is beneficial for the performance of the steel column. The initial stiffness and load-bearing capacity of specimen PS0-d7.1-S140-e50 were smaller than those of specimen PS0-d10.5-S140-e100, and the bearing capacity before the second AE increased by approximately 139 % and 176 % compared to that after the first AE for specimens PS0-d7.1-S140-e50 and PS0-d10.5-S140-e100, respectively. The results indicated that the effect of AE on bearing capacity improvement after the first AE was more pronounced for columns

Table 1
Specimen design.

Name	$h \times w \times w_t \times f_t$ (mm)	L (mm)	λ	e_0 (mm)	e_i (mm)	d (mm)	PS (MPa)
P-S140-e0	116 × 80 × 6 × 6	2520	140	0	1.42	–	–
P-S140-e50		2520	140	50	1.87		
PS0-d2.1-S119-e0		2150	119	0	0.99	2.1	0
PS0-d0-S140-e0		2520	140		1.87	0	
PS0-d4.7-S169-e0		3050	169		2.36	4.7	
PS0-d7.1-S140-e50		2520	140	50	1.42	7.1	
PS20-d16.5-S140-e50				50	1.90	16.5	20
PS0-d10.5-S140-e100				100	2.41	10.5	0

Note: h, w, w_t, and f_t are the cross-sectional height, width, web thickness, and flange thickness, respectively; L is the steel column length; λ is the slenderness ratio of the steel column; e_0 is the eccentric distance of the column; e_i is the maximum initial imperfection of the column; PS is the CFRP plate prestress.

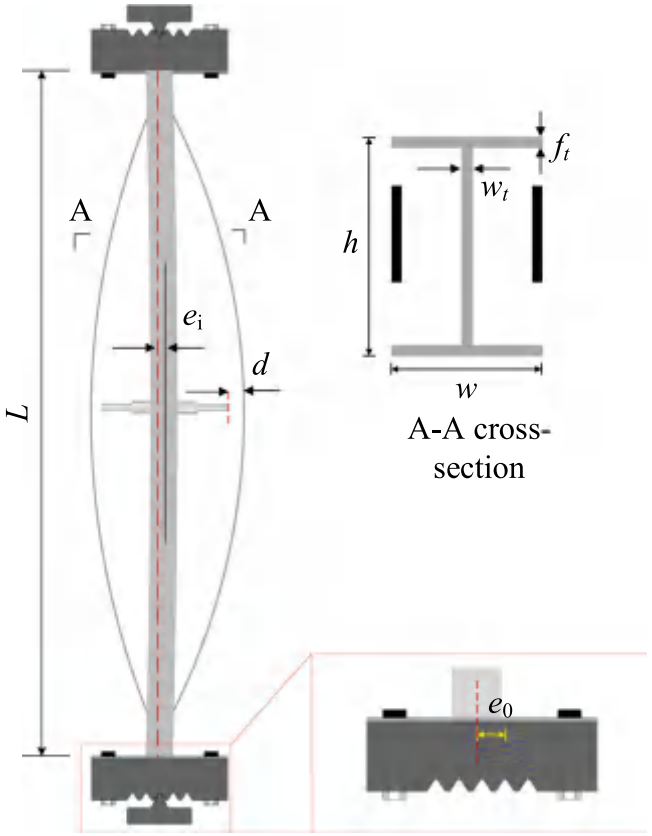


Fig. 3. Schematic diagram of the parameters.

with smaller eccentricities. For specimens with different λ as shown in Fig. 6(c), unexpected perturbations of steel columns occurred during the experiments. The sudden perturbation of the steel column of specimen PS0-d2.1-S119-e0 at the first and second loading processes was due to the unexpectedly rapid loading rate. The external load during the first loading process was reduced to maintain the deflection of the steel column at 10 mm. For specimen PS0-d4.7-S169-e0, the sudden drift of the steel column to the other side was attributed to the unexpectedly rapid elongation rate of the actuator. Then, the actuator on the opposite side was activated to return the steel column to its safe threshold, followed by the subsequent loading process. The load-bearing capacity before the second AE increased by approximately 103.8 % and 60.8 % compared to that after the first AE for specimens PS0-d0-S140-e0, and PS0-d4.7-S169-e0, respectively, indicating that the effect of AE on the bearing capacity improvement of the column after the first AE was more obvious for those with small slenderness ratios.

3.3.2. Deflection and actuator elongation value relationship

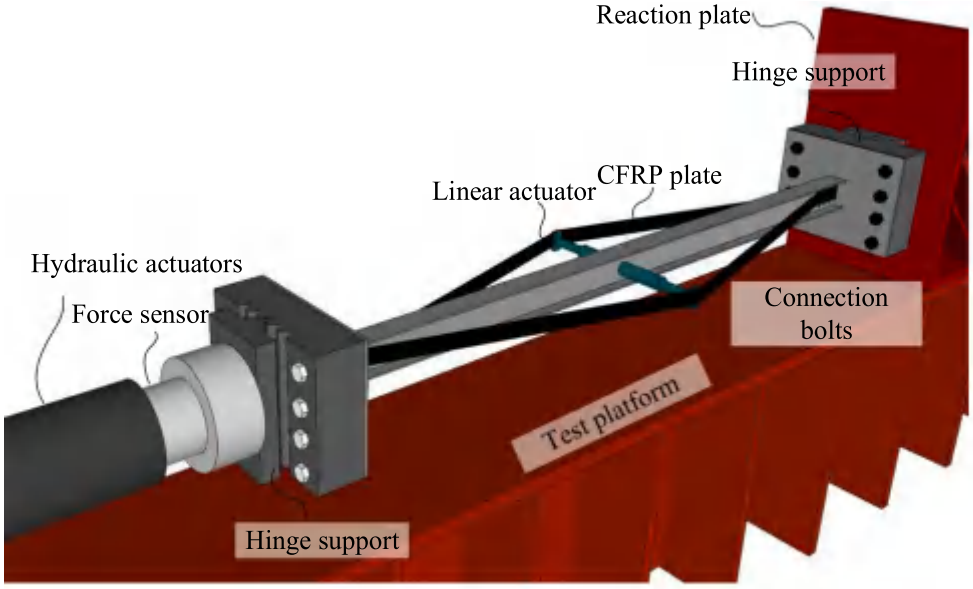
The relationship between column deflection and AE value a_e is shown in Fig. 7. For the S140 series, the specimens exhibited similar loading and AE processes, and specimen PS0-d7.1-S140-e50 was selected to illustrate the behavior (Fig. 8). During the first loading stage and the initial stage of the first AE, CFRP plates on both sides remained slack because d was 7.1 mm. The right actuator elongated 19.5 mm after the close contact between them, with a_e a total of 26.6 mm to push the column back to almost 0 mm. After the second loading, the column deflection was 6.3 mm, and a_e on the right side was 5.8 mm to restore the column during the second AE. For specimens PS0-d2.1-S119-e0 and PS0-d4.7-S169-e0, when the column deflected to the left, only the actuator on that side was activated to push the column back. Taking specimen PS0-d4.7-S169-e0 as an example to illustrate the variation process (Fig. 7(b)), during the first loading stage, the column deflection was 7.0 mm and a_e was 13 mm for the first AE stage. After the second loading stage, the column deflection was 10 mm due to the rapid loading rate, perturbations occurred during the second stage, resulting in a 19.3 mm deflection on the left. Then, only the actuator on the left side elongated and a_e was 16.8 mm to push the steel column to a deflection of 1.91 mm on the right; subsequently, the load continued to increase, resulting in a rightward deflection of 6 mm, and a_e was 3.2 mm on the right to restore the steel column.

3.3.3. CFRP stress and deflection relationship

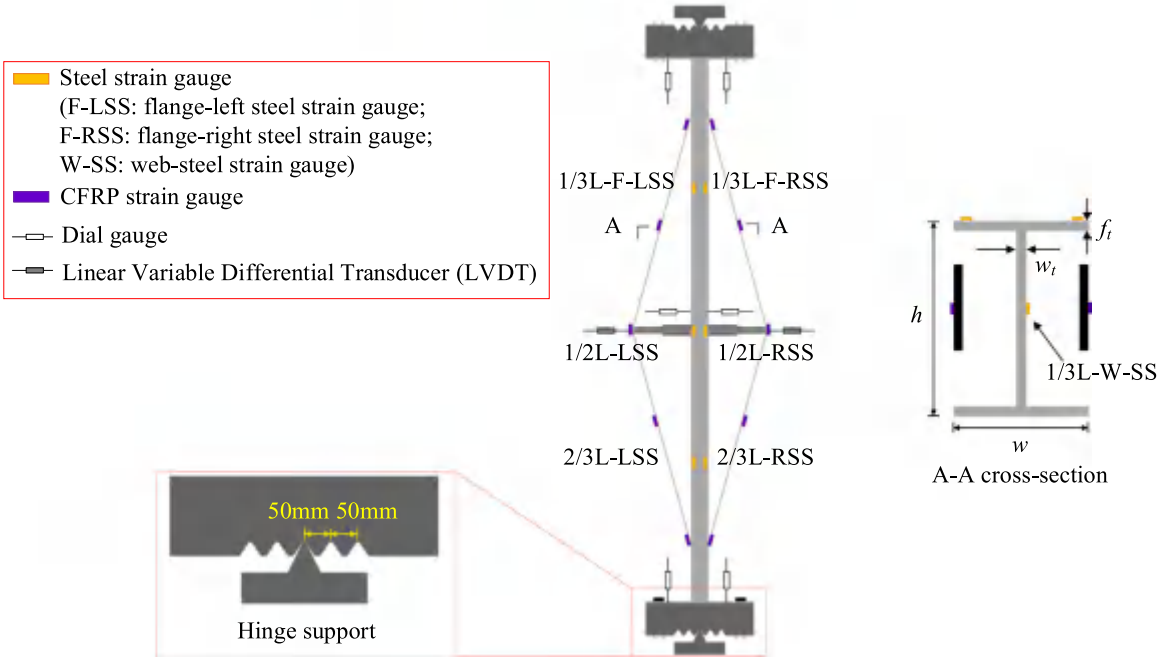
The relationship between CFRP plate stress on the convex side and column deflection for the slenderness ratio of 140 is shown in Fig. 9. CFRP plate stress for the PS0 series on the concave side remained 0 MPa, due to constant slacking throughout the process and CFRP plate stress on the convex side increased in the following loading and AE stages. For specimen PS20-d16.5-S140-e50, before the first loading stage, the CFRP plate stress on the concave side decreased from 20 MPa to 0 MPa, while the stress on the convex side increased from 20 MPa to 106 MPa after the first loading. The CFRP plate on the concave side remained slack during the subsequent stages. The deformation of the steel column caused a corresponding increase in the CFRP plate stress on the convex side. This mechanism effectively exerted a force to push the steel column back toward its original state at different AE stages.

3.4. Summary

AE effectively counteracted the deflection of the steel column, guiding the system toward an adaptive equilibrium. There was a discernible increase in both stiffness and bearing capacity after AE. Specifically, CFRP plate prestress significantly increased the initial stiffness and bearing capacity, which underscored the pivotal role of prestress in enhancing structural performance. Moreover, the effect of AE on increasing the bearing capacity of the column after the first AE was more pronounced in systems with small eccentricities and slenderness ratios. This adaptive mechanism demonstrated the inherent capability of the system to respond and adjust to external forces.



(a) loading diagram



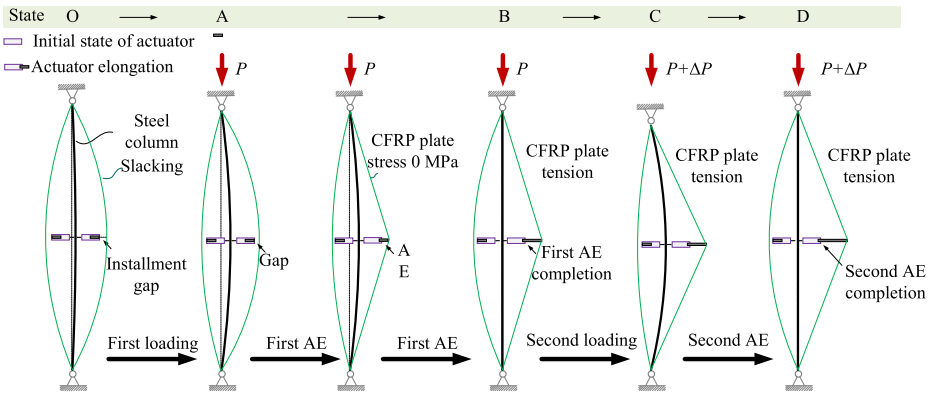
(b) strain and displacement measurement

Fig. 4. Loading diagram and data measurement.

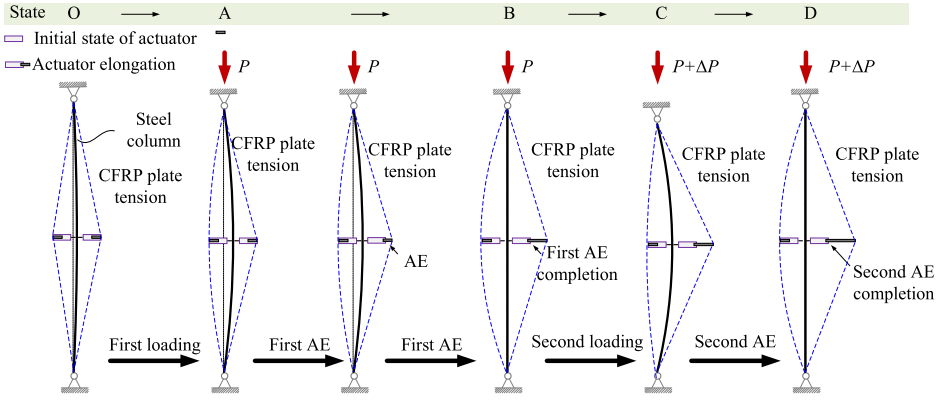
4. Numerical study

4.1. Simulation details

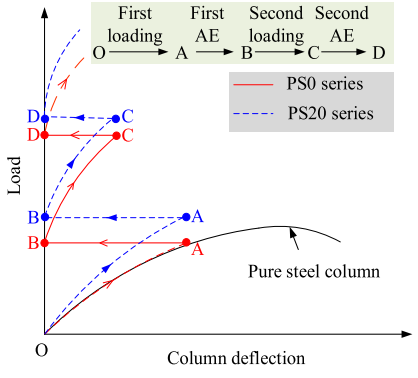
Finite element models were established in this section (Fig. 10) using commercial software ABAQUS [29]. All geometric and material properties were identical to those used in the experiments. The CFRP plate and the steel column were assumed to exhibit linear and linear-elastic behavior, respectively. A four-node shell element (S4R) was utilized to simulate the steel column and CFRP plate, as it was widely used for modeling thin-walled materials. An eight-node linear brick element (C3D8R) was employed for the steel support. Two reference points were established at both ends of the steel column, with the distance between each point and the tip of the steel column matching the hinge support length, identical to that used in the experiments. A 'Rigid Body Constraint' was used to simulate the behavior between the reference points and the steel column. A 'Tie Constraint' was utilized for the connection between the CFRP plates and the steel web to account for the non-slip condition. Furthermore, reference points were created at the geometric center of the steel column and the surface center of the steel support, which were coupled with steel web and steel support, respectively. A 'Translator Connector' was used to link the two reference points to simulate the behavior of AE. A 'Surface-to-Surface Contact' was employed for the interface between the steel support surface and the CFRP plate surface. The mesh sizes for the steel column, the CFRP plate, and the steel support were 10 mm, 7 mm, and 5 mm, respectively. The



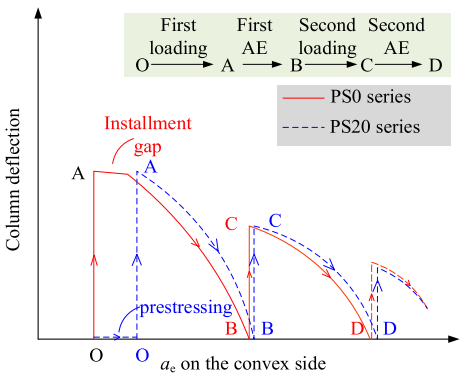
(a) loading and AE process diagram of PS0 series



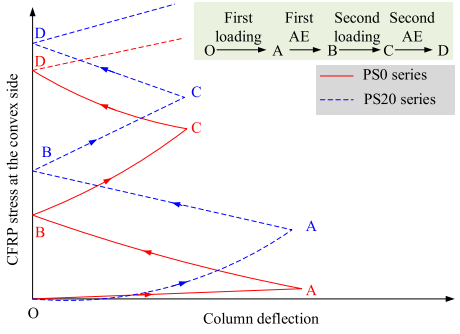
(b) loading and AE process diagram of PS20 series



(c) load-deflection curve

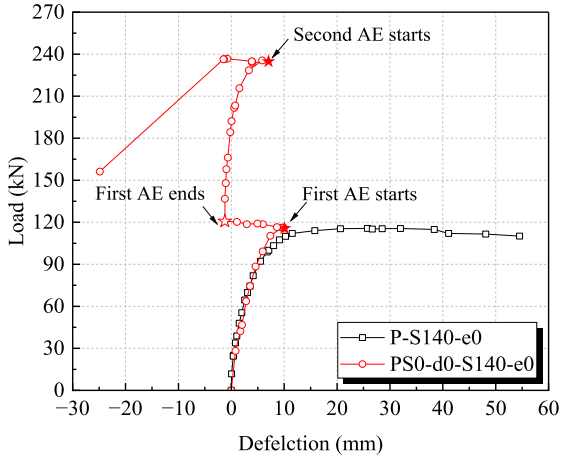


(d) deflection-a_e curve

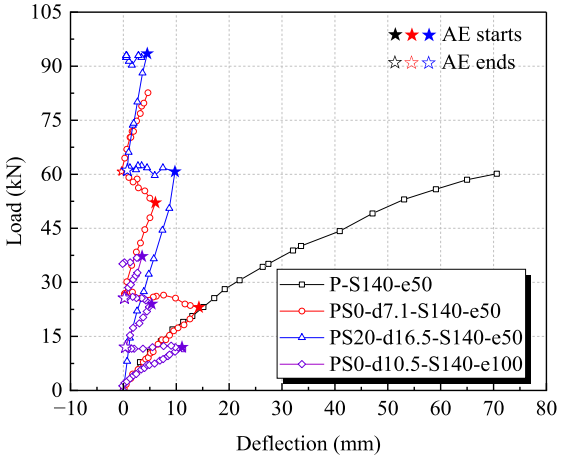


(e) CFRP stress at the convex side-deflection curve

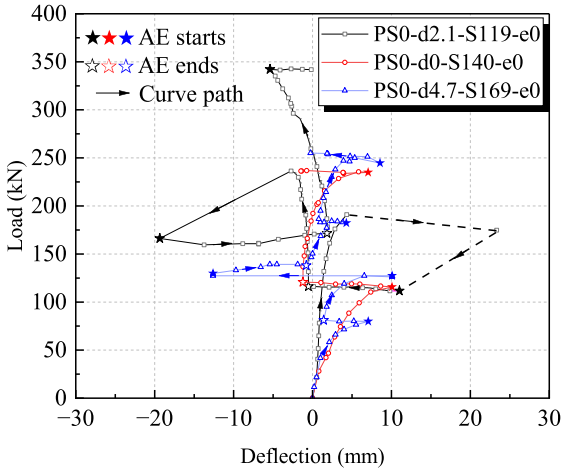
Fig. 5. Loading details and curve path.



(a) typical axial loading specimens

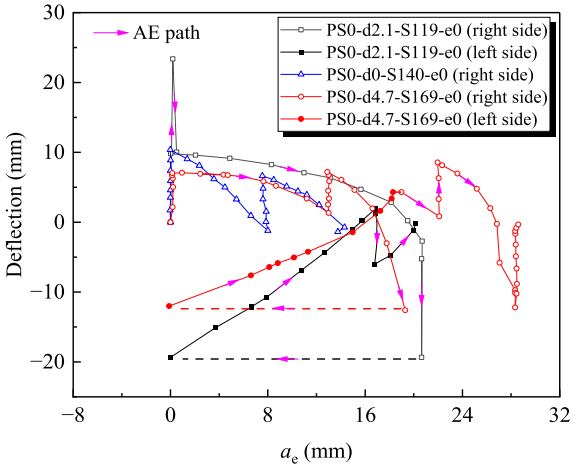


(b) eccentric loading series

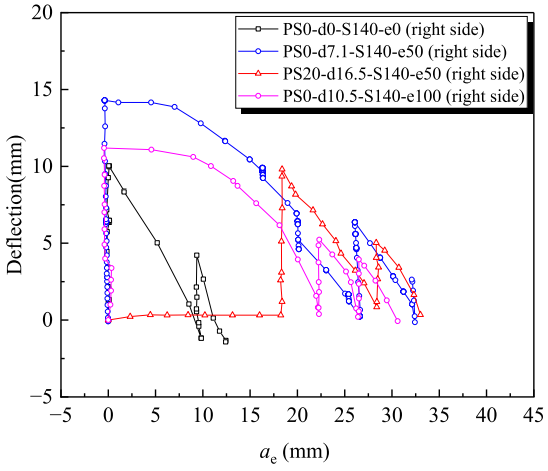


(c) axial loading series with different slenderness ratios

Fig. 6. Load-deflection curves of specimens.



(a) axial loading series



(b) eccentric loading series

Fig. 7. The relationship between column deflection and a_e of all specimens.

boundary conditions were identical to those used in the experiments (Fig. 11). Considering the installation gap between the CFRP plates and actuator rods, the distance was reserved in the finite element model.

The following simulation procedure was implemented. First, a buckling analysis was performed on the steel column to obtain the first buckling mode. The initial geometric imperfection of the steel column was assumed to follow an approximate sinusoidal half-wave distribution, which aligned with the first buckling mode obtained from the

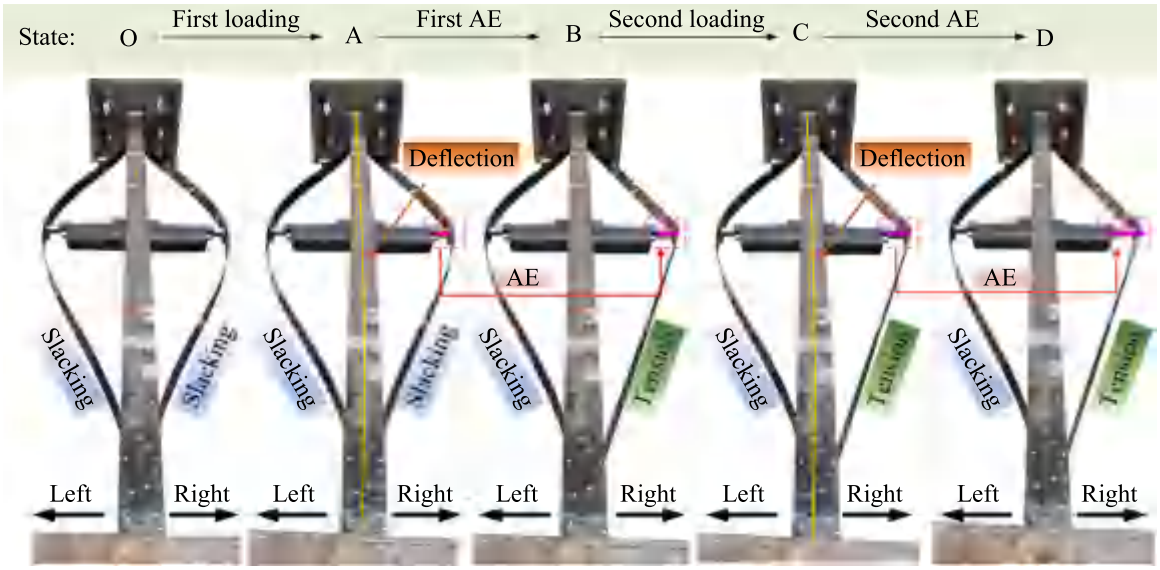


Fig. 8. Loading and process of specimen PS0-d7.1-S140-e50.

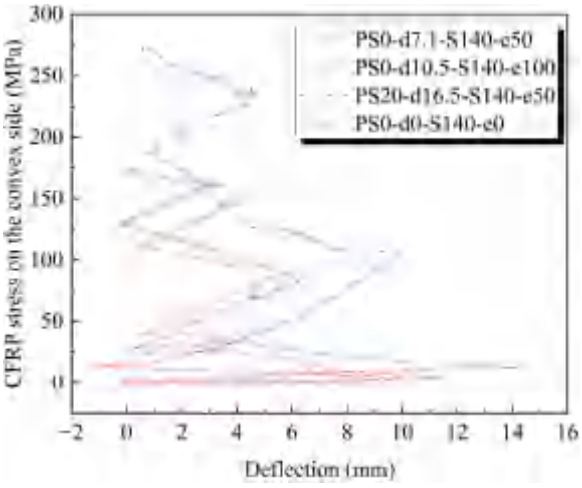


Fig. 9. CFRP plate stress-deflection curve of the S140 series.

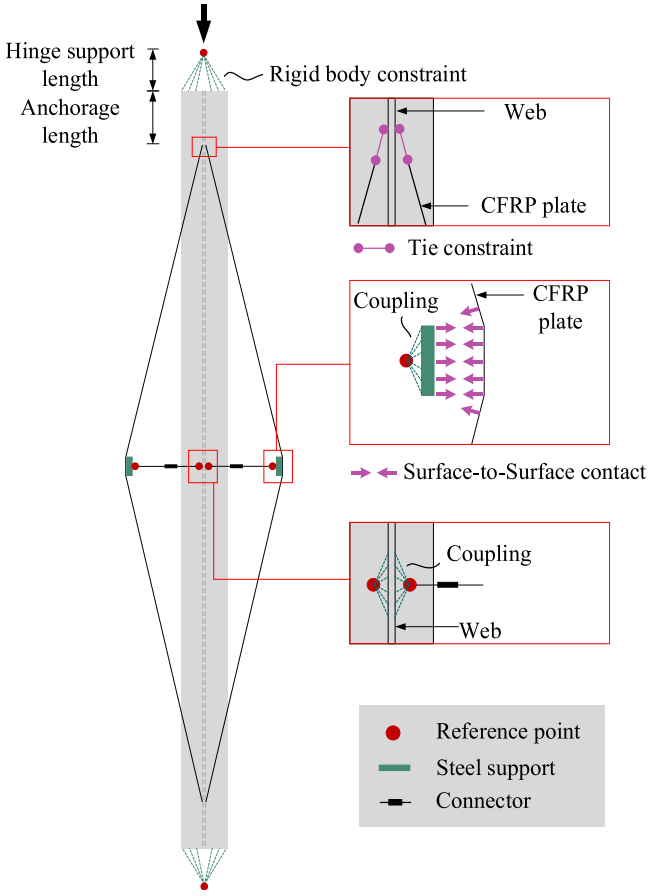


Fig. 10. Constraint relationship.

buckling analysis. The imperfection values were derived from measured data (Table 1) and incorporated into the numerical model; then residual stress was calculated using a classic model by *wang* et al. [30] and applied to the steel column, with the residual stresses in the flanges and web assumed to be independent of each other. The loading process was divided into different steps following experimental procedures.

4.2. Verification

The comparison of different curves between experiments (EXP) and finite element modeling (FEM) of specimens PS0-d7.1-S140-e50, PS20-d16.5-S140-e50, and PS0-d0-S140-e0 is shown in Figs. 12 and 13. The simulation of such dynamic processes was inherently more complex than static simulations. Thus, the Root Mean Square Error (RMSE) method was utilized to thoroughly assess the consistency between the FEM and experimental data. To calculate the RMSE for displacement, the load at each stage was divided into 10 equal parts, and the RMSE was computed for the corresponding displacements. Similarly, for the RMSE of CFRP stress, the displacement at each stage was divided into 10 equal parts, and the RMSE was determined for the stresses. The results were summarized in Table 2. For instance, the maximum RMSE errors for displacement and CFRP stress in specimen PS0-d7.1-S140-e50 were 0.83 mm and 11.2 MPa, respectively. These findings indicated the overall trends between the experimental and numerical results were well aligned. Additionally, the observed discrepancies primarily derived from the installation gap between the CFRP plates and the differences between the ideal and actual boundary conditions.

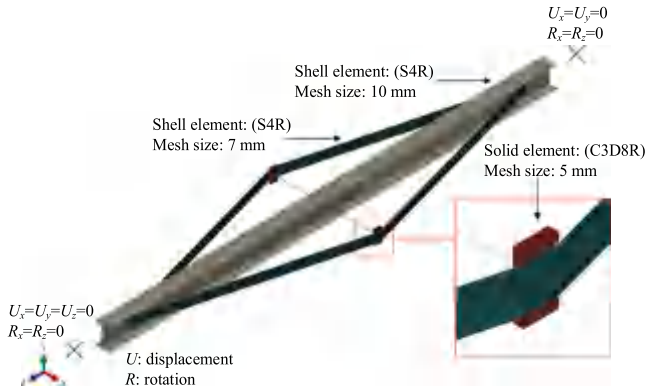


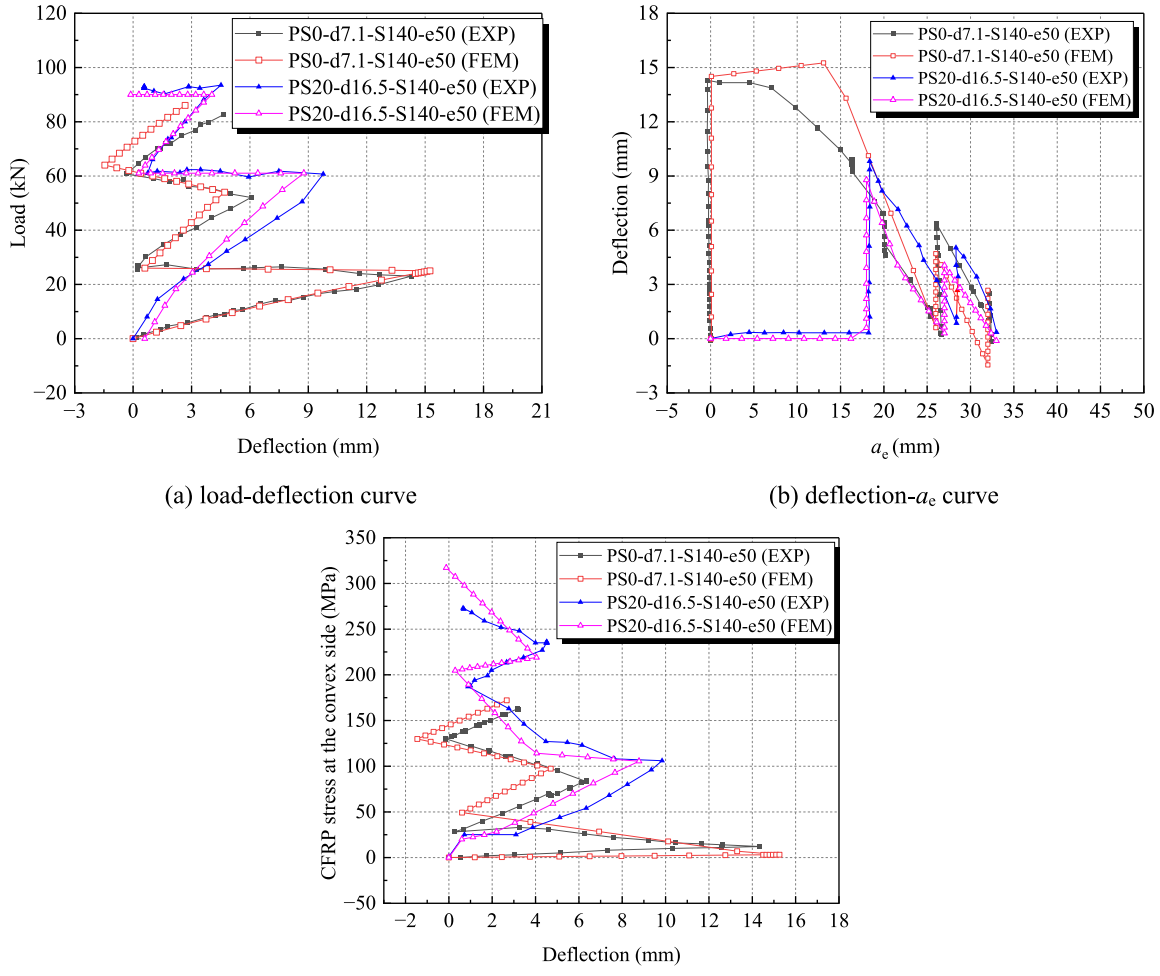
Fig. 11. Meshing and boundary condition.

4.3. Parametric studies

The finite element model of the specimen PS50-d0-S140-e0 was chosen as the basic model to investigate the effect of PS, CFRP plate elastic modulus (E_p), and the actuator length on steel column length ratio (L_a/L_s) on the adaptive behavior of the system. These factors influenced the linear displacement constraint. The initial imperfection was set at 0.1 % of the steel column length, and residual stress was input into the simulation model. Seven models were established, named Models 1–7 in Table 3. For Models 1–3, both sides of the CFRP plate were set at 50 MPa when L_a was 50, 100, and 150 mm, respectively. For Models 1, 4, and 5, both sides of the CFRP plate prestress were set as 50, 80, and 20 MPa, respectively, when L_a was 100 mm. For Models 1, 6, and 7, the CFRP plate prestress on both sides was set as 50 MPa, and E_p was 170 GPa, 210 GPa, and 250 GPa when L_a was 100 mm, respectively. Initially, actuators on both sides elongated to prestress the CFRP plates, but only the actuator on the deflected side operated in the subsequent AE stages. The loading procedure of Models 1–7 is shown in Table 3. Furthermore, it was important to obtain the behavior of such a column under varying external loads at different elongation timing. Thus, the external load was increased to 1.5 times the bearing capacity of the pure steel column (P_{pb}), and the actuators elongated at different deflections of the system simultaneously to push the column back to its original position, as shown in Table 3. The actuator on the deflection side was activated to elongate when the steel column experienced different deflections of 5 mm, 10 mm, and 15 mm for Models 8, 9, and 10, respectively.

4.3.1. Effect of L_a/L_s

Load-deflection curves for specimens with different L_a/L_s and the relationship between L_a/L_s and initial stiffness, as well as load-bearing capacity, are shown in Figs. 14 and 15. For Models 1–3, when L_a/L_s increased from 50/2520–100/2520 and 150/2520, the initial stiffness increased by 90.1 % and 211.1 %, respectively, while the load-bearing capacity increased by 29.9 % and 67.8 %, respectively. The initial



(a) load-deflection curve

(b) deflection-a_e curve

(c) CFRP plate stress- deflection curve

Fig. 12. The comparison between EXP and FEM of specimen PS0-d7.1-S140-e50 and PS20-d16.5-S140-e50.

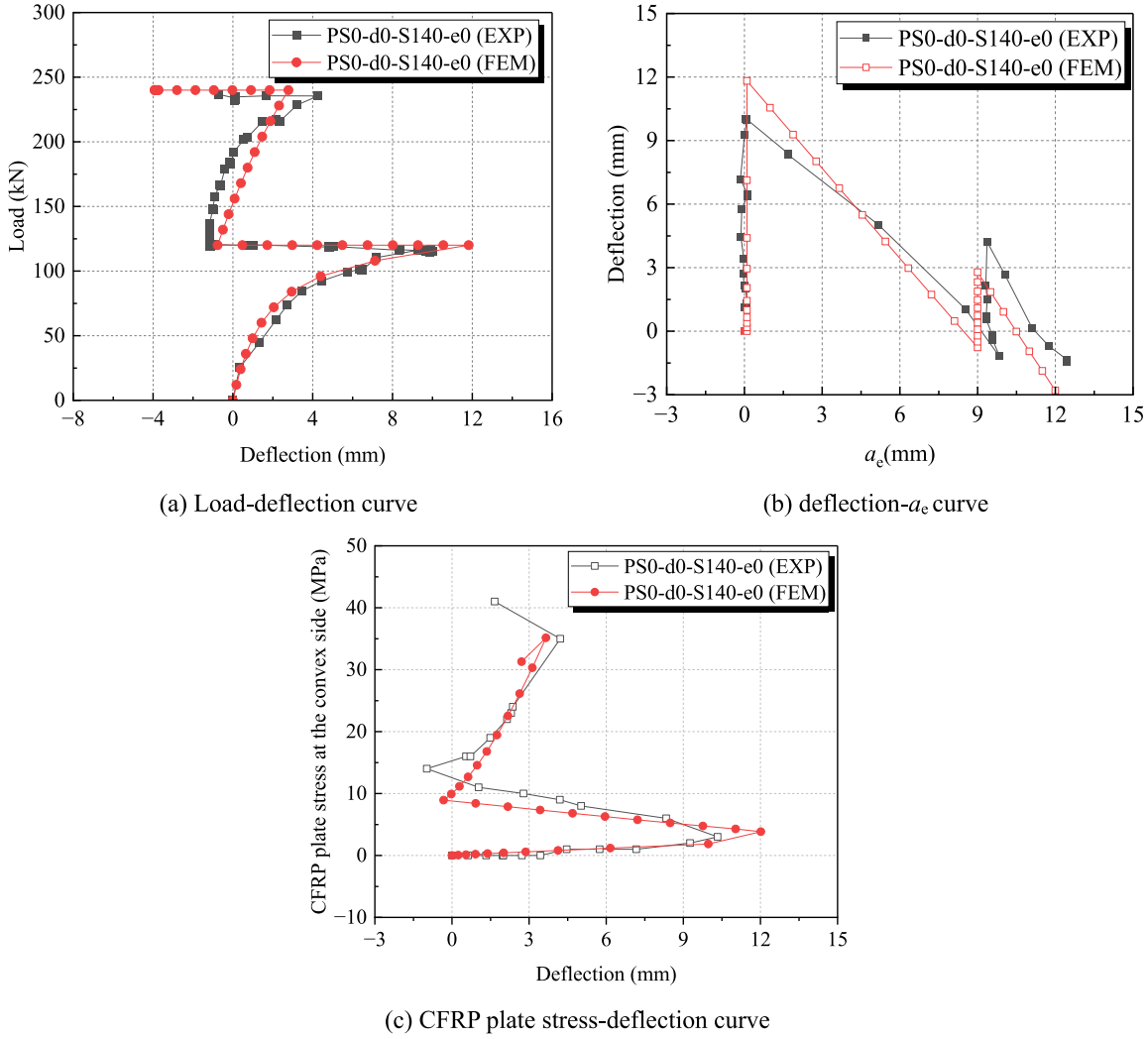


Fig. 13. The comparison between EXP and FEM of specimen PS0-d0-S140-e0.

stiffness after the first AE increased by 25.6 % and 75.4 %, while the load-bearing capacity increased by 31.6 % and 73.4 %, respectively. The results indicated that AE could significantly increase the bearing capacity and initial stiffness with L_a/L_s increasing. The performance of the actuators is illustrated in Fig. 14. a_e at the first and second AE stages decreased as L_a/L_s increased and the decrease in a_e at the first AE was more significant, indicating that smaller a_e can contribute to column shape restoration and larger L_a/L_s had a more positive effect on reducing a_e. The reason was that when L_a/L_s was large, small a_e generated a large increase in CFRP plate stress and a force effectively restoring the column to its original position. This finding aligned with the similar results reported by *Arka* et al. [25], where actuators were applied on a cable-stayed bridge. Furthermore, after the second AE, the load-bearing capacity increased by 12.7 %, 16.5 %, and 18.9 % compared with that after the first AE for models with L_a/L_s of 50/2520, 100/2520, and 150/2520, respectively.

In sum, increasing L_a/L_s can improve the performance of the system, and the effect of AE on improving the structural performance of the column after the first AE was more pronounced in the system with larger L_a/L_s.

4.3.2. Effect of CFRP plate prestress

Load-deflection curves for specimens with different PS and the relationship between PS and initial stiffness, as well as load-bearing capacity, are shown in Figs. 16 and 17. For Models 1, 4, and 5, when PS increased from 20 to 50 and 80, the initial stiffness remained almost unchanged, while the load-bearing capacity increased by 12.5 % and 24.7 %, respectively. The initial stiffness after the first AE decreased by 23.4 % and 37.7 %, respectively, while the load-bearing capacity increased by 6.0 % and 12.6 %, respectively. The results indicated that AE could increase the bearing capacity with PS increasing and had no effect on the initial stiffness before the first AE. The performance of the actuators is illustrated in Fig. 17. As PS increased, a_e at the first and second AE stages decreased, underscoring the role of minor AE in resetting the column shape. Moreover, higher PS values had a notably beneficial impact on reducing a_e. This is because a large PS on the convex side can generate a large force, effectively reinstating the column to its initial position. Thus, with a higher CFRP plate prestress, the actuator required only minimal elongation to achieve the desired restoration. Consequently, the total actuator length could be designed to be shorter, leading to a more compact and space-efficient design. Moreover, after the second AE, the load-bearing capacity increased by 24.4 %, 16.5 %, and 11.6 % compared with that after the first AE stage for models with PS of 20 MPa, 50 MPa, and 80 MPa, respectively.

In sum, increasing PS can increase the bearing capacity of the system and reduce a_e to push the column back, and the effect of AE on improving the structural performance of the column after the first AE was more pronounced in the system with smaller PS values.

Table 2
Displacement variation and CFRP plate stress comparison.

Specimen	Condition	RMSE error of displacement (mm)	RMSE error of CFRP plate stress (MPa)
PS0-d7.1-S140-e50	After the first load	0.21	5.6
	After the first AE	–	5.8
	After the second load	0.83	11.2
	After the second AE	0.51	6.2
PS20-d16.5-S140-e50	After the first load	1.23	8.6
	After the first AE	–	7.8
	After the second load	0.08	5.3
	After the second AE	–	9.8
PS0-d0-S140-e0	After the first load	0.16	1.1
	After the first AE	–	1.8
	After the second load	0.68	4.3
	After the second AE	–	–

Note: RMSE error was not calculated after AE due to overlapping data points.

4.3.3. *Effect of E_p*

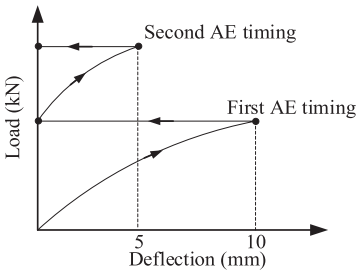
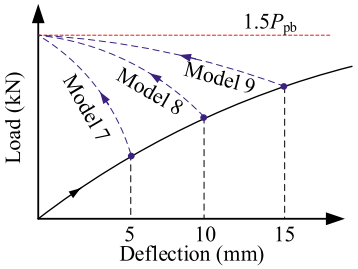
Load-deflection curves for specimens with different E_p and the relationship between PS and initial stiffness, as well as load-bearing capacity, are shown in Figs. 18 and 19. For Models 1, 6, and 7, when E_p increased from 170 to 210 and 250 GPa, the initial stiffness increased by 17.1 % and 42.6 %, respectively; the load-bearing capacity increased by 1.3 % and 1.8 %, respectively. The initial stiffness after the first AE increased 11.9 % and 21.4 %, respectively; the load-bearing capacity increased 3.6 % and 6.2 %, respectively. The results indicated that AE could increase the initial stiffness of the system as E_p increased and had little effect on the increase in bearing capacity. The increase in the initial stiffness was attributed to the linear displacement constraint provided by the CFRP plate at the convex side. The increase in bearing capacity after the first AE was more pronounced compared to before the first AE. This was due to the enhanced stiffness provided by the linear displacement constraint after the first AE, which effectively countered the column deflection. Moreover, after the second AE, the load-bearing capacity increased by 16.5 %, 19.1 %, and 21.5 % compared with that after the first AE for models with E_p of 170 GPa, 210GMPa, and 250 GPa, respectively.

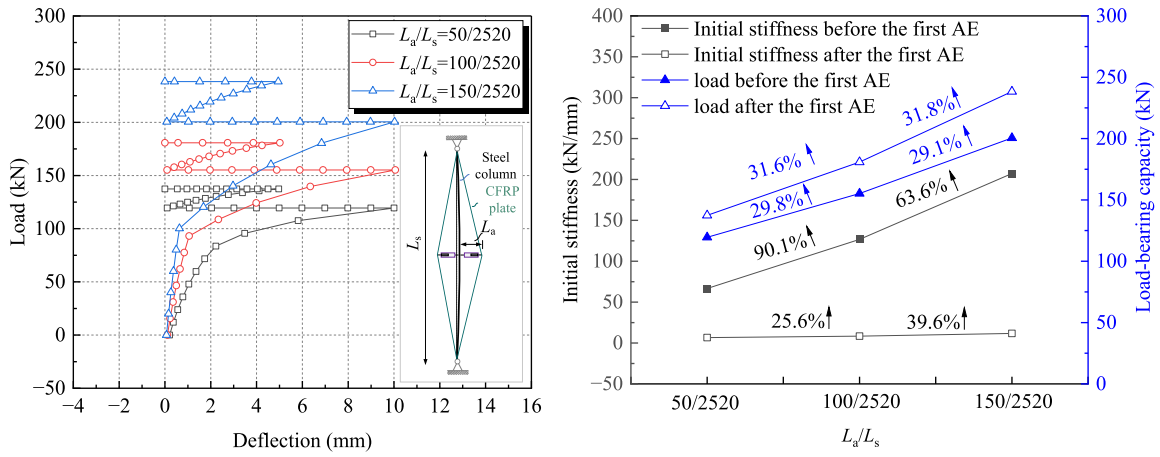
In sum, increasing E_p can enhance both the bearing capacity and initial stiffness of the system, and the effect of AE on improving the structural performance of the column after the first AE was more pronounced in the system with higher E_p.

4.3.4. *Effect of elongation timing*

Elongation timing referred to the activation timing of the actuator. For the same column, the earlier the elongation timing occurred, the smaller the column deformation. In this case, to achieve the same effect of restoring column deformation, the required elongation speed of the actuator varied. Therefore, the elongation timing affected the design and control of the entire intelligent system, which needed studying. In this section, the speed of the external load was assumed to be constant. When the deflection reached 5 mm, the time required for the column to restore to 0 mm deflection was assumed to be 1 second, resulting in an external load speed of 48 kN/s. For deflections of 10 mm and 15 mm, the time for the increasing load was 0.52 s and 0.29 s, respectively. Load-deflection curves and deflection-a_e curves of Models 8–10 are shown in Fig. 20. The results showed that actuator elongation value was the same to restore the column in 1 s, 0.52 s, and 0.29 s corresponding to column defections of 5 mm, 10 mm, and 15 mm, respectively. Thus, the actuator elongation speed was 5.84 mm/s, 11.2 mm/s, and 20.1 mm/s, respectively. Moreover, the maximum compressive forces caused by CFRP plate stress on the actuators were 0.67 kN, 0.97 kN, and 1.51 kN corresponding to column defections of 5 mm, 10 mm, and 15 mm, respectively. The results indicated that when the varying speed of external load and the

Table 3
Model details with different parameters.

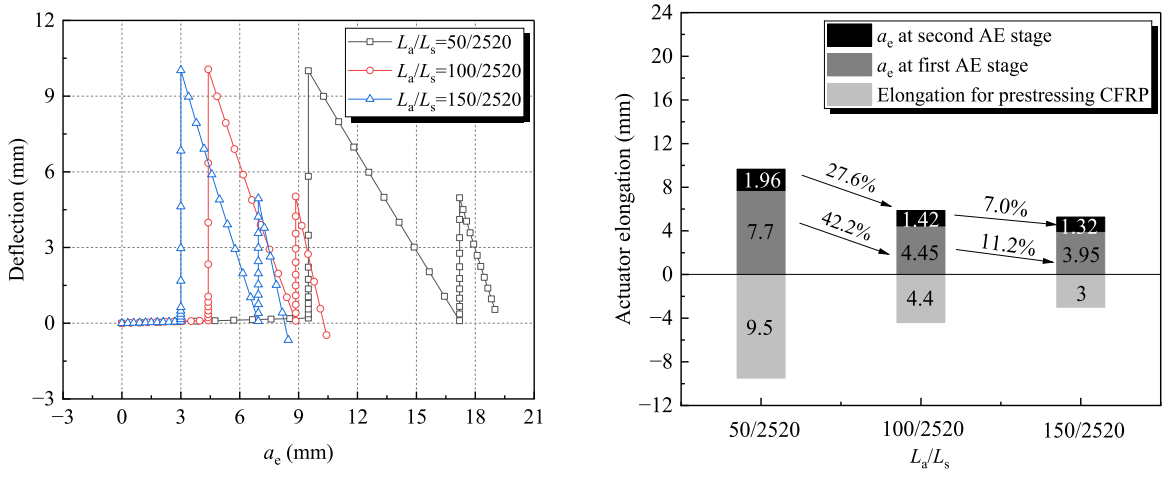
Name	L_a/L_s (mm)	PS (MPa)	E_p (GPa)	Loading pattern and AE timing
Model 1	50/2520	50	170	
Model 2	100/2520	50	170	
Model 3	150/2520	50	170	
Model 4	100/2520	80	170	
Model 5	100/2520	20	170	
Model 6	100/2520	50	210	
Model 7	100/2520	50	250	
Model 8	100/2520	50	170	
Model 9	100/2520	50	170	
Model 10	100/2520	50	170	



(a) load-deflection curve

(b) initial stiffness and load-bearing capacity of models with different L_a/L_s

Fig. 14. Behavior of the system with different L_a/L_s.



(a) deflection-a_e curve

(b) a_e of models with different L_a/L_s

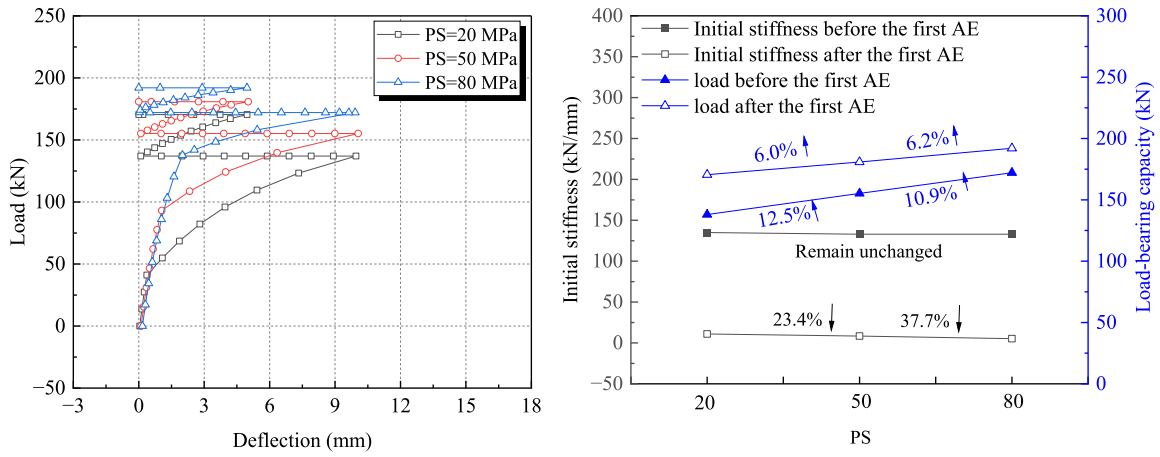
Fig. 15. Behavior of the actuator of models with different L_a/L_s.

destination load were the same, no matter when AE occurred, the elongation value was the same; when the elongation timing was delayed, the elongation speed increased to compensate for the delayed response and larger compressive capacities of the actuators were required.

5. A case study using an adaptive column

This section presents a practical case study. The Ohio Union building, located on the Ohio State University campus, was tested to evaluate its vulnerability to progressive collapse prior to its eventual demolition. *Elsanadedy et al.* [31] analyzed the structure, focusing on the buckling of basement columns to assess its vulnerability to progressive collapse. They subsequently compared these numerical findings with observations, and a refined finite element model was employed to explore potential scenarios involving both sequential and simultaneous column losses. In this case, the actual boundary condition at the bottom of the basement was a hinge support. Beam-column connections were assumed to be fully rigid. The distances between adjacent columns and floors, along with the dimensions of the columns, are shown in Fig. 21. The gravity load of the building was increased to include the superimposed dead load and 25 % of the total design live load. A case involving the instantaneous removal of the columns within the red dashed box in Fig. 21 was studied, which was derived from the numerical results conducted by Elsanadedy et al. [31]. According to their study, the removal of these columns resulted in the failure of multiple ground-story columns, creating a large cantilevered section of the first floor (exceeding 15 m in one direction). This ultimately triggered the progressive collapse of the steel-framed building. In this instance, the axial load fluctuations of the basement columns bearing the largest loads are illustrated in Fig. 21. "Column C2 was the first to reach its axial bearing capacity. If Column C2 had been designed to withstand the escalating load, the steel frame would not have collapsed. Therefore, Column C2 was selected for the design of an adaptive prestressed CFRP-reinforced steel column. It is important to note that the axial bearing capacity of the columns shown in Fig. 22 was calculated using a steel yield strength of 345 MPa and an elastic modulus of 200 GPa, with hinged boundary conditions for the columns. In the study [31], the column buckled when the load reached its axial bearing capacity. In designing the adaptive Column C2, both boundary conditions were assumed to be hinged.

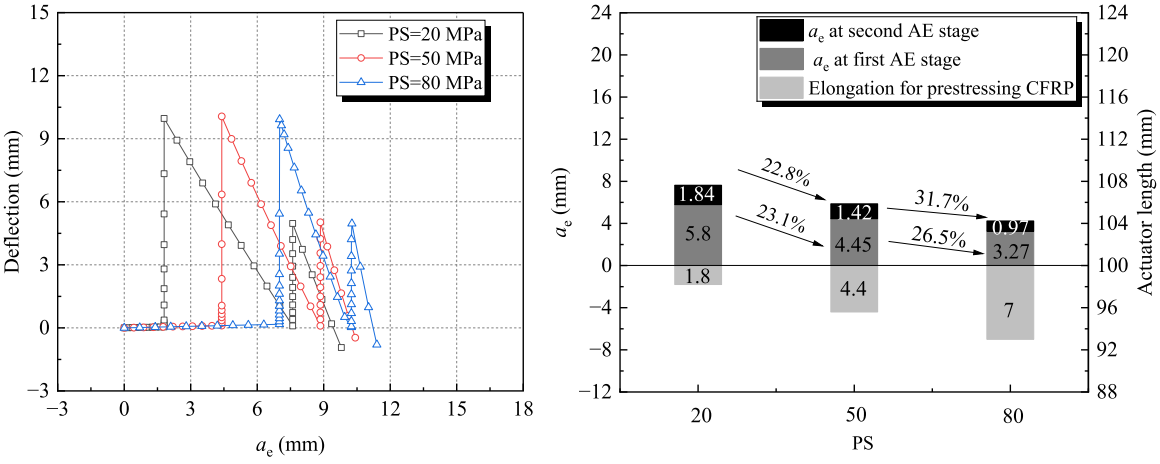
The parameters of the actuator were determined through the following steps, and a flowchart illustrating the process has been added



(a) load-deflection curve

(b) initial stiffness and load-bearing capacity of models with different PS

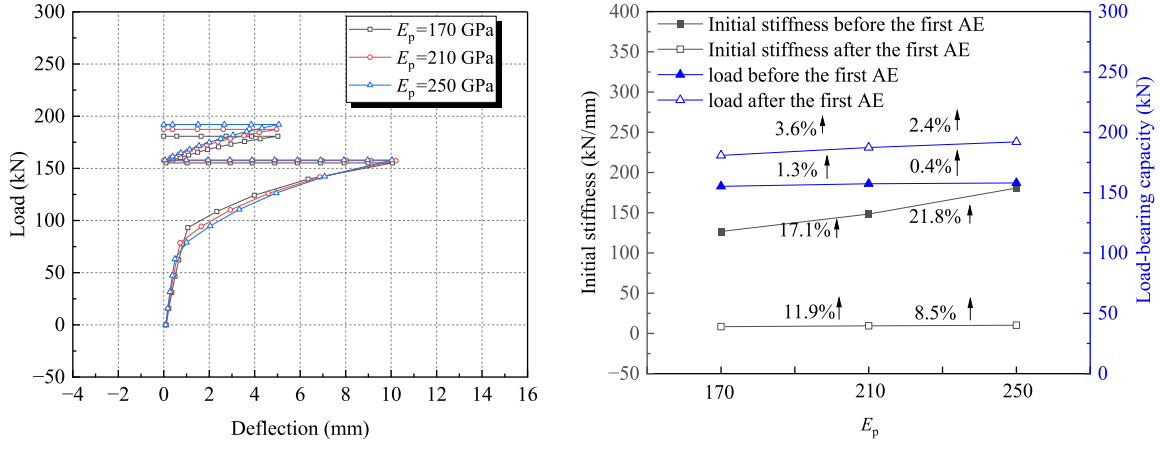
Fig. 16. Behavior of the system with different PS.



(a) deflection-a_e curve

(b) a_e and actuator length of models with different PS

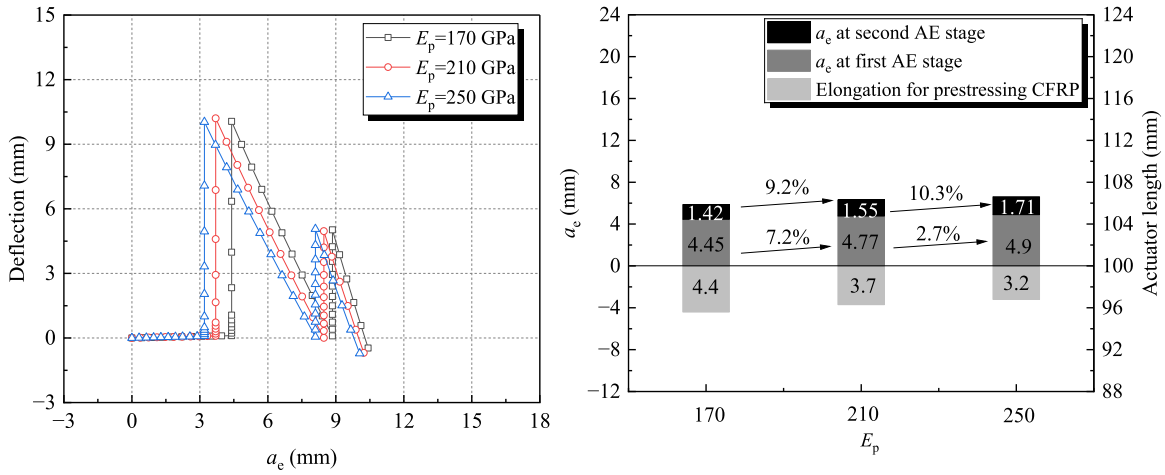
Fig. 17. Behavior of the actuator of models with different PS.



(a) load-deflection curve

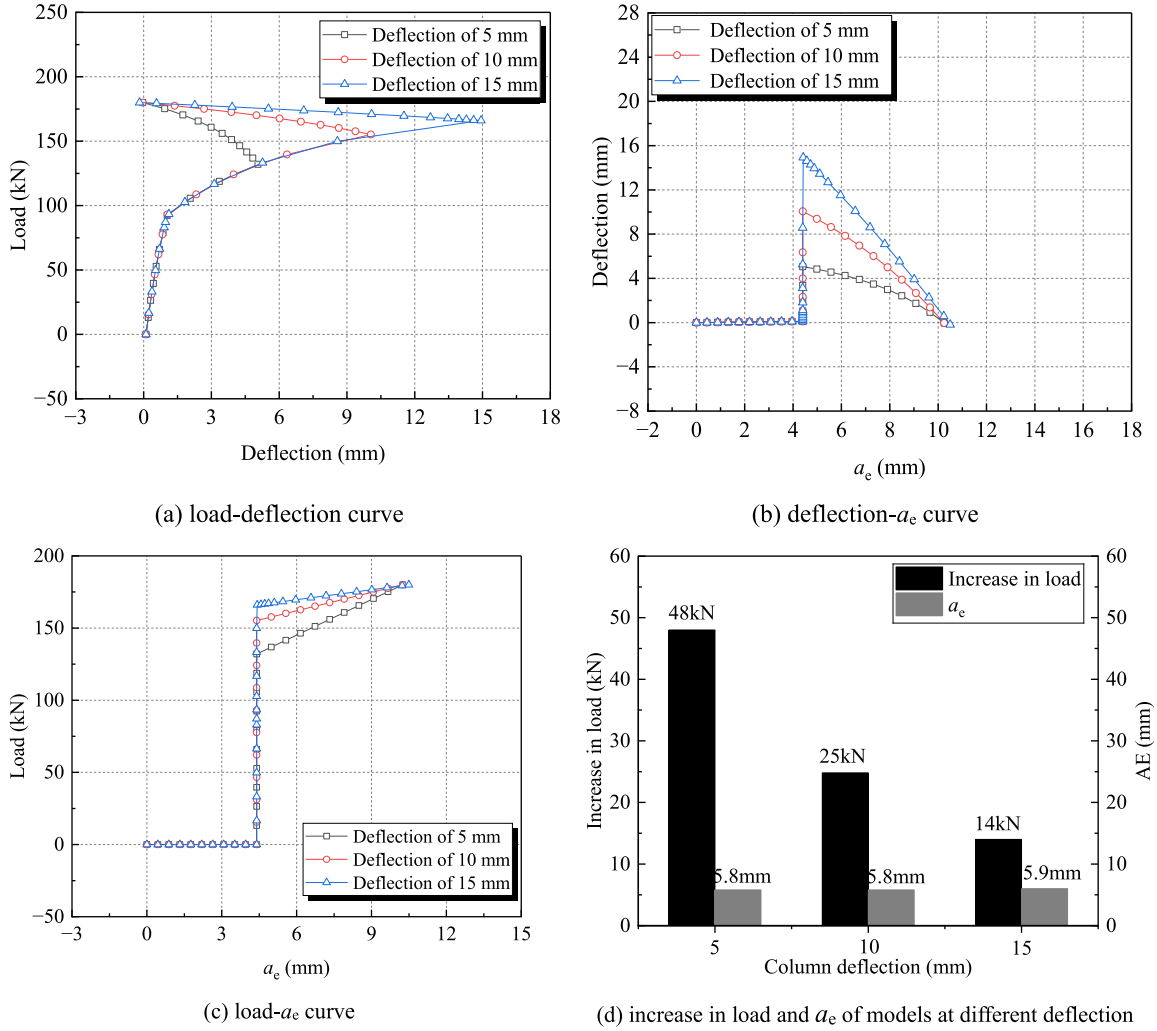
(b) initial stiffness and load-bearing capacity of models with different E_p

Fig. 18. Behavior of the system with different E_p.



(a) deflection-a_e curve (b) a_e and actuator length of models with different E_p

Fig. 19. Behavior of the actuator of models with different E_p.



(a) load-deflection curve (b) deflection-a_e curve

(c) load-a_e curve (d) increase in load and a_e of models at different deflection

Fig. 20. Behavior of the system and the actuator.

as Fig. 23. The geometric dimensions and mechanical properties of the H-steel column, external load, and its varying speed were known parameters. Firstly, the geometric dimensions of the CFRP plates were determined based on the dimensions of the H-steel column, and the initial length of the actuator was determined by spatial constraints. Secondly, the mechanical properties of the CFRP plates, CFRP plate prestress, actuator elongation timing, elongation speed, and compressive capacity of the actuator were preset. Specifically, the mechanical

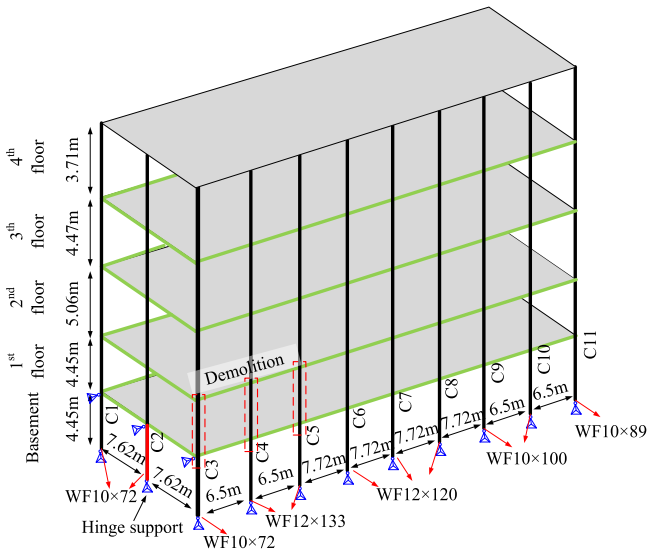


Fig. 21. Details of the Ohio Union Building.

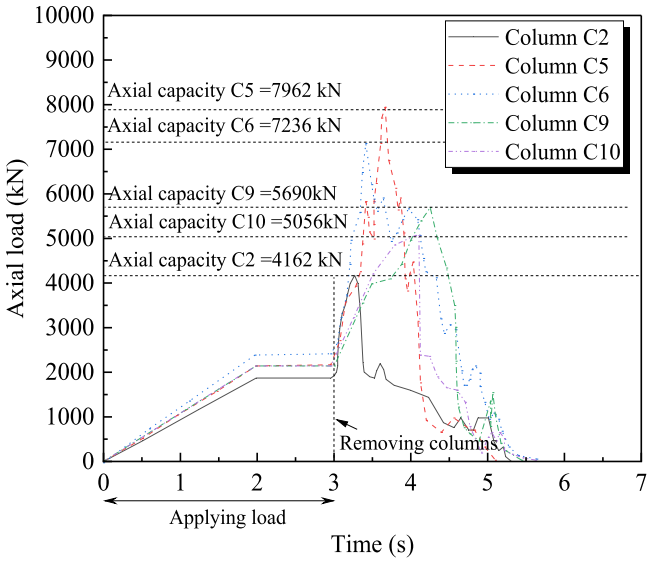


Fig. 22. Axial load-time curve of columns in the basement (data from [30]).

properties of the CFRP plates and the CFRP plate prestress were set as large as possible, while the elongation timing was preset as early as possible, based on the conclusions from Sections 4.3.1, 4.3.2, and 4.3.3. Subsequently, the known parameters, preset parameters, initial imperfections, and residual stresses were input into the finite element model to calculate the final deflection of the steel column after actuator elongation. If the final deflection exceeded the safe deflection threshold, the preset parameters were adjusted and recalculated. Otherwise, the preset parameters were finalized for reinforcing the steel column.

Based on the flowchart, the parameters for reinforcing column C2 were determined. A load combination was applied to the steel frame, causing the axial load on the prestressed CFRP plate-reinforced steel column C2 to increase from 0 kN to 1870 kN. After the instantaneous removal of the columns, the load on the prestressed CFRP plate-reinforced steel column C2 increased from 1870 kN to 4170 kN in just 0.27 s. Firstly, based on the dimensions of the H-steel section of 269 mm × 258 mm × 22 mm × 22 mm (height × width × flange thickness × web thickness), CFRP dimensions were selected as 150 mm × 3 mm (width × thickness). Secondly, the actuator was initially designed with an actuator length of 200 mm and S of 100 mm. Then, the elastic modulus and ultimate stress of the CFRP plate were 170 MPa and 2800 MPa, respectively. The CFRP plate prestress at the convex side was initially set as 200 MPa, resulting in a corresponding actuator length of 222 mm. During this time, only the actuator on the convex side was simultaneously activated to restore the column to a state of zero deflection. After trial calculations, the actuator elongation speed was determined as 64.1 mm/s, and Tf was determined with a minimum value of 8.5 kN. The determined parameters could satisfy the final deflection of steel column of 0 mm when the column removal and actuator elongation were performed simultaneously. It was noteworthy that the design parameters of the actuators were not the only solution but one feasible option. The load-deflection curve and deflection-a_e curve are shown in Fig. 24. The results demonstrated that the designed adaptive column can resist varying external loads and help prevent progressive collapse. When implementing the reinforcement method in practical engineering, the anchorage positions can be installed away from steel connections to avoid interference with existing structural design. In practical applications, the parameter determination process involves numerous interdependent factors with complex interactions. The complexity of the adaptive design also arises from the intricate interaction between the actuators and the reinforced steel. Further research is essential to investigate the influence of multiple parameters on adaptive performance.

6. Conclusions

The following conclusions can be obtained:

(1) A novel adaptive prestressed CFRP-reinforced steel column was proposed for the first time by replacing the prestressing chairs at the column midspan with actuators. Its adaptive behavior was achieved by adjusting the actuator length, thereby altering the linear displacement constraint generated by the stress differences in the CFRP plates on both sides.

(2) AE effectively counteracted the deflection of the steel column, guiding the system toward an adaptive equilibrium. A discernible increase in bearing capacity was observed after AE. Specifically, CFRP plate prestress significantly increased the bearing capacity, underscoring the pivotal role of CFRP plate prestress in enhancing structural performance. The effect of AE on the increase in bearing capacity after the first AE was more pronounced for columns with small eccentricities and slenderness ratios.

(3) Higher values of the actuator length to column length ratio, CFRP plate prestress, and elastic modulus proved beneficial for enhancing the performance of the steel column. Furthermore, AE was unaffected by the timing of elongation and loading rate as long as the target load was determined.

(4) An adaptive prestressed CFRP-reinforced steel column, equipped with appropriately designed actuators within a steel frame, can withstand rapidly increasing loads and help prevent the progressive collapse of the structure.

Moreover, the technology is potential for reinforcing a variety of structural systems, including beams, trusses, and bridges, effectively responding to varying external loads. Additionally, its adaptability makes it suitable for functional components, such as deployable structures, which are widely utilized in both civil engineering (e.g., retractable roofs for sports stadiums) and space engineering (e.g., helium-filled aerostat). In practical applications, the parameter determination process involves numerous interdependent factors with complex interactions. Further research is essential to investigate the influence of multiple parameters on adaptive performance to develop a more comprehensive and practical design methodology.

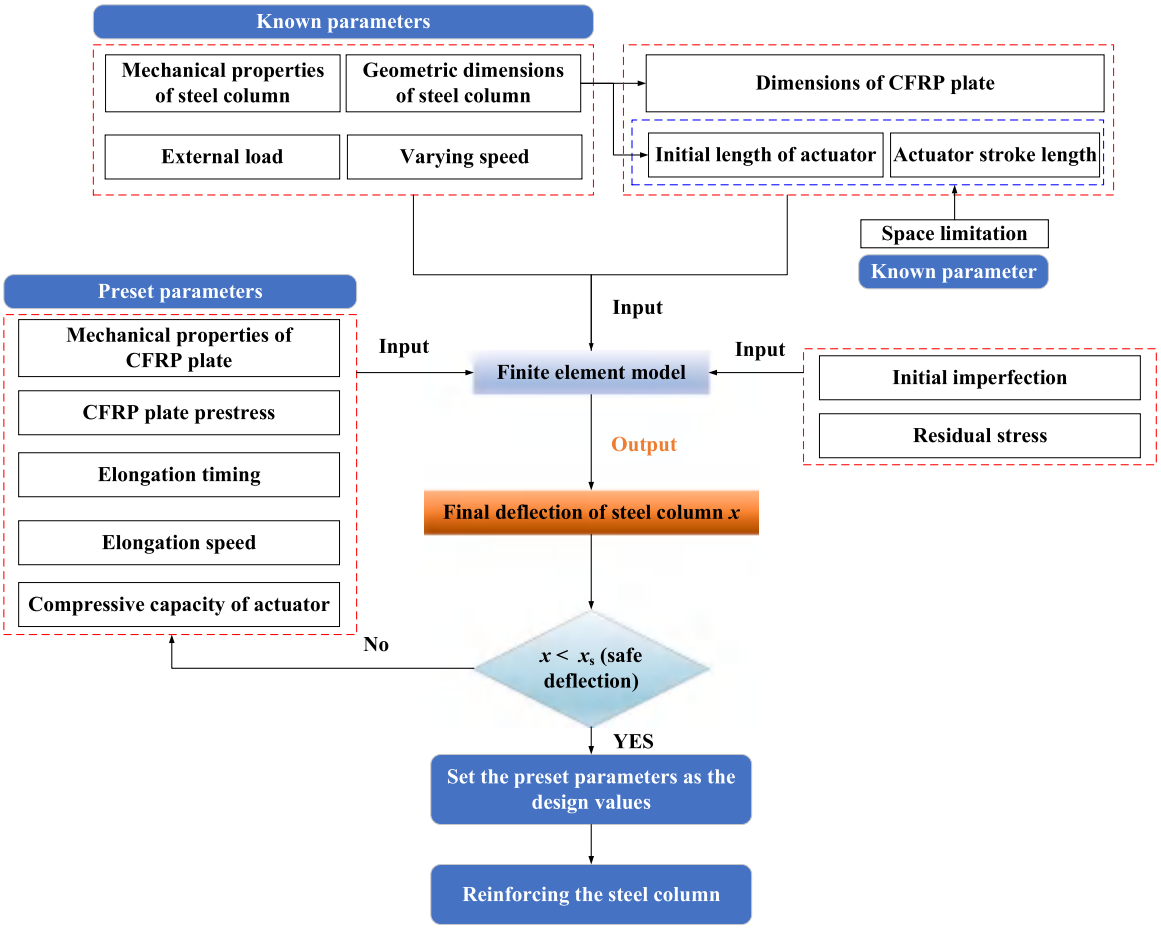
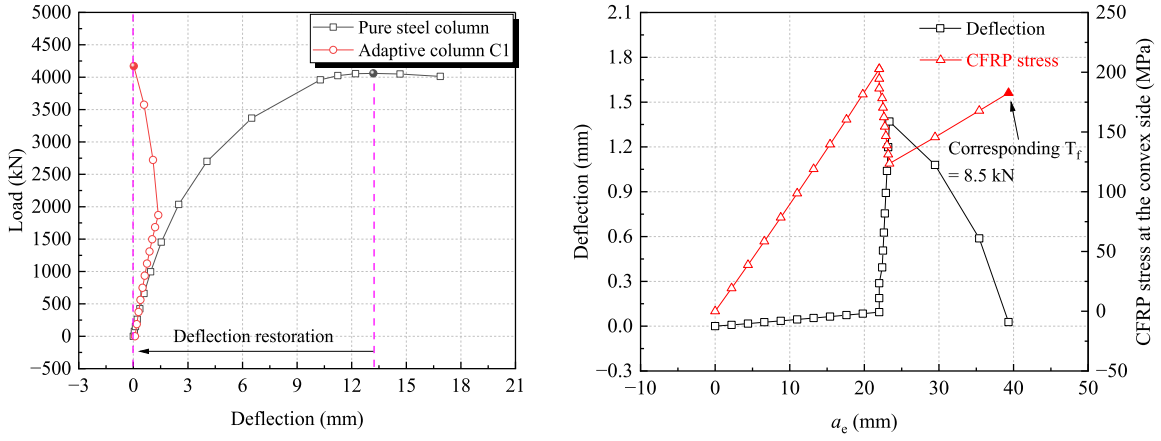


Fig. 23. Flowchart of determining actuator parameters.



(a) load-deflection curve (b) deflection-a_e and CFRP plate stress-a_e curves

Fig. 24. Adaptive response of adaptive column C2.

CRediT authorship contribution statement

Xu Liang: Writing – original draft, Visualization, Validation, Software, Methodology, Investigation, Formal analysis, Data curation. **Lili Hu:** Writing – review & editing, Writing – original draft, Supervision, Project administration, Methodology, Investigation, Funding acquisition, Data curation, Conceptualization. **Terrance Lim:** Writing – review & editing, Validation, Investigation.

Declaration of Competing Interest

The authors declare that they have no known competing financial interests or personal relationships that could have appeared to influence the work reported in this paper.

Acknowledgments

This research was supported by Young Elite Scientists Sponsorship

Program by CAST (2022QNRC001) and the Program Fund of Nonmetallic Excellence and Innovation Center for Building Materials (2023TDA5–1).

Data availability

Data will be made available on request.

References

[1] Soong TT. State of the art review: active structural control in civil engineering. Eng Struct 1988;10:74–84. https://doi.org/10.1016/0141-0296(88)90033-8.
[2] Gennaro S, Philippe D, Pete W. Exploring the application domain of adaptive structures. Eng Strut 2018;167:608–28. https://doi.org/10.1016/j.engstruct.2018.03.057.
[3] Mahmoud YM, Hassan MM, Mourad SA, Sayed HS. Assessment of progressive collapse of steel structures under seismic loads. Alex Eng J 2018;57:3825–39. https://doi.org/10.1016/j.aej.2018.02.004.
[4] Shi YC, Li ZX, Hao H. A new method for progressive collapse analysis of RC frames under blast loading. Eng Struct 2010;32:1691–703. https://doi.org/10.1016/j.engstruct.2010.02.017.
[5] Cao YF, Jiang J, Lu YL, Chen W, Ye JH. Progressive collapse of steel structures exposed to fire: a critical review. J Constr Steel Res 2023;207:107985. https://doi.org/10.1016/j.jcsr.2023.107985.
[6] Derseh SA, Mohammed TA. Bridge structures under progressive collapse: a comprehensive state-of-the-art review. Results Eng 2023;18:101090. https://doi.org/10.1016/j.rineng.2023.101090.
[7] Sobcayk M, Wiesenhutter S, Noennig JR, Wallmersperger T. Smart materials in architecture for actuator and sensor applications: a review. J Intel Mat Syst Str 2022;33:379–99. https://doi.org/10.1177/1045389X211027954.
[8] Shen YB, Cheng HQ, Yang PZ, Luo YZ. A static control algorithm for adaptive beam string structures based on minimal displacement. Math Probl Eng 2023:713768. https://doi.org/10.1155/2013/713768.
[9] Korkmaz S, Ali NBH, Smith IFC. Determining control strategies for damage tolerance of an active tensegrity structure. Eng Struct 2011;33:1930–9. https://doi.org/10.1016/j.engstruct.2011.02.031.
[10] Kmet S, Platko P. Adaptive tensegrity module. II: tests and comparison of results. J Struct Eng 2014;140(9):04014056. https://doi.org/10.1061/(ASCE)ST.1943-541X.0000958.
[11] van Bommel R, Habraken A, Teuffel P. Adaptive arch: active stress minimization in a thin arch structure. Procedia Eng 2016;155:265–74. https://doi.org/10.1016/j.proeng.2016.08.028.
[12] Hunt J, Haase W, Sobek W. Designing adaptive spatial structures. J Int Assoc Shell Sp 2008;49:167–73.
[13] Bleicher A, Schlaich M, Fujino Y, Schauer T. Model-based design and experimental validation of active vibration control for a stress ribbon bridge using pneumatic muscle actuators. Eng Struct 2011;33:2237–47. https://doi.org/10.1016/j.engstruct.2011.02.035.
[14] Senatore G, Reksowardojo AP. Force and shape control strategies for minimum energy adaptive structures. Front Built Environ 2020;6:1–28. https://doi.org/10.3389/fbuil.2020.00105.
[15] Senatore G, Duffour P, Winslow P. Energy and cost assessment of adaptive structures: case studies. J Struct Eng 2018;144(8):04018107. https://doi.org/10.1061/(ASCE)ST.1943-541X.0002075.
[16] PD Xuan, Seung BC. A state-of-the-art on smart materials actuators over the last decade: control aspects for diverse applications. Smart Mater Struct 2022;31:053001. https://doi.org/10.1088/1361-665X/ac5b1e.
[17] Zhang HY, Lu JY, Gong PF, Li N. Mechanical properties and shape-control abilities of a cable dome under asymmetrical loads. J Constr Steel Res 2023;208:108021. https://doi.org/10.1016/j.jcsr.2023.108021.
[18] Li JB, Liu H, Zhang LM. Optimal placement of active members in active vibration control of adaptive truss structures. Acta Aeronaut Et Astronaut Sin 1996;6:118–22. ⟨https://hkxb.buaa.edu.cn/EN/⟩.
[19] Xu WY, Ding HS, Lv ZT. Numerical analysis of design parameters of the smart prestressed beam with two struts. J Southeast Univ 2009;39(06):1174–8.
[20] Xu WY, Ding HS, Lv ZT. The model experiment of smart prestressed structures based on switch control. Eng Mech 2011;28(05):105–10.
[21] Xu WY, Chen LM. Bearing capacity experiment of a smart prestressed steel truss with two structs. Spec Struct 2016;33(06):97–101.
[22] Cheng H.Q. Control theory and design method research of adaptive beam string structure. Zhejiang University 2014. (in Chinese).
[23] Corral MDM, Todisco L. Structural design of responsive under-deck cable-stayed footbridges. Structures 2022;41:1501–14. https://doi.org/10.1016/j.istruc.2022.05.077.
[24] Rooyacker F.A.M., Suiker A.S.J., Habraken A.P.H.W. Dynamic control of adaptive structures. Poster session presented at 20th Engineering Mechanics Symposium, Arnhem, Netherlands, 2017.
[25] Reksowardojo AP, Senatore G, Bischoff M, Blandini L. Design and control of high-speed railway bridges equipped with an under-deck adaptive tensioning system. J Sound Vib 2024;579:118362.
[26] Hu LL, Feng P. Prestressed CFRP-reinforced steel columns under axial and eccentric compression. Compos Struct 2021;268:113940. https://doi.org/10.1016/j.compstruct.2021.113940.
[27] Feng P, Hu LL. Steel columns strengthened/reinforced by prestressed CFRP strips: Concepts and behaviors under axial compressive loads. Compos Struct 2019;217:150–64. https://doi.org/10.1016/j.compstruct.2019.03.038.
[28] Hu LL, Feng P. Theoretical analysis and design of prestressed CFRP-reinforced steel columns. J Compos Constr 2022;26(3):04022029. https://doi.org/10.1061/(ASCE)CC.1943-5614.0001210.
[29] ABAQUS2021. Analysis Users' Manual. Providence, RI, USA: Abaqus Inc; 2021.
[30] Wang YB, Li GQ, Chen SW. Residual stresses in welded flame-cut high strength steel H-sections. J Constr Steel Res 2012;79:159–65.
[31] Elsanadedy H, Sezen H, Abbas H, Almusallam T, Al-Salloum Y. Progressive collapse risk of steel framed building considering column buckling. Eng Sci Technol Int J 2022;35:101193. https://doi.org/10.1016/j.jestch.2022.101193.

Case Studies in Construction Materials 23 (2025) e05022

Contents lists available at ScienceDirect

Case Studies in Construction Materials

journal homepage: www.elsevier.com/locate/cscm

Novel high-temperature resistant GFRP bars with DOPO-modified vinyl ester: Design, performance, and application

Xu Liang [a,b], Terrance Lim [a,b], Xiaoqing Zhao [a,c], Lili Hu [a,c,*], Qiaolong Yuan [d], Zhiwei Wang [e]

[a] Research Institute of Urbanization and Urban Safety, School of Future Cities, University of Science and Technology Beijing, Beijing 100083, China
[b] School of Ocean and Civil Engineering, Shanghai Jiao Tong University, Shanghai 200240, China
[c] Yangtze River Delta Carbon Fiber and Composite Materials Technology Innovation Center, Changzhou 213125, China
[d] School of Materials Science and Engineering, East China University of Science and Technology, Shanghai 200237, China
[e] Zhongfu Carbon Fiber Core Cable Technology Co., Ltd., Lianyungang 222000, China

ARTICLE INFO

Keywords:
High temperature
Modified vinyl ester resin
Fire-resistance
Strength retention
Concrete structures

ABSTRACT

Glass fiber-reinforced polymer (GFRP) bars are used in concrete structures to solve corrosion and durability concerns. While the rapid deterioration of the mechanical properties of GFRP bars at elevated temperatures hinders their widespread application. Thus, in this study, a modified vinyl ester resin with high glass transition temperature (T_g) is developed and used as a matrix material for GFRP bars. The thermal stabilities of the vinyl ester (VE) resin with and without modification, and the tensile performance of the GFRP bars with modified VE at 20℃, 150℃, 300℃, 400℃, and 550℃ were investigated. The results showed that the modified VE had better thermal stabilities and flame-retardant properties; the failure modes of the GFRP bars changed from fiber fracture to hair-like form rupture when temperature increased from ambient temperature to 400℃; at 150℃, 300℃, 400℃, and 550℃, the tensile strength retentions of GFRP bars were 90.6 %, 84.2 %, 68.0 % and 9.9 %, respectively. These findings highlighted the stability of GFRP bars at 400℃, as they still retained a significant portion of their tensile strength at room temperature. This study implemented a real engineering application to demonstrate the practical utility of modified GFRP bars in addressing the fire resistance challenge. Preliminary parameters for GFRP reinforcement were first designed with a concrete cover thickness of 67 mm and a spacing of 500 mm between GFRP bars based on standard requirement. Finite element analysis was subsequently performed to simulate the behavior of the real structure under a 90-minute fire exposure, in compliance with the fire resistance rating requirements for concrete slabs. The results confirmed that GFRP bars retained ability to resist the fire load after steel reinforcement failed, and also highlighted the importance of maintaining adequate concrete cover thickness when using the modified GFRP bars. The study provides critical insights for the broader adoption of fire-resistance GFRP bars in structural engineering, particularly in fire-prone environments.

* Corresponding author at: Research Institute of Urbanization and Urban Safety, School of Future Cities, University of Science and Technology Beijing, Beijing 100083, China.
E-mail address: hll_1010@163.com (L. Hu).

https://doi.org/10.1016/j.cscm.2025.e05022
Received 17 April 2025; Received in revised form 1 July 2025; Accepted 6 July 2025
Available online 7 July 2025
2214-5095/© 2025 The Author(s). Published by Elsevier Ltd. This is an open access article under the CC BY license (http://creativecommons.org/licenses/by/4.0/).

1. Introduction

Reinforced concrete structures often face durability challenges, primarily due to the corrosion of steel reinforcement in harsh environmental conditions [1–3]. To address this issue, glass fiber-reinforced polymer (GFRP) bars used as reinforcement in concrete structures have proven to be an effective solution, providing improved corrosion resistance and extended durability [4,5]. However, the application of GFRP bars in concrete structures is constrained by their susceptibility to high temperatures [6–8]. This is because GFRP bars at elevated temperatures are predominantly influenced by the resin matrix, which degrades rapidly under high-temperature exposure. The softening of the resin reduces stress transfer efficiency between glass fibers and between GFRP bars and concrete [9], thereby compromising mechanical strength and bond properties, which limits the effectiveness of GFRP bars. Two critical thermal properties, i.e., the glass transition temperature (T_g) and decomposition temperature (T_d), are pivotal in determining the thermal stability of GFRP bars. Thermosetting resin such as epoxy and vinyl ester (VE) with T_g typically ranging from 90°C to 120°C and T_d varying between 300°C and 400°C [10,11] are commonly used in GFRP bars. At elevated temperatures, the tensile strength of GFRP bars significantly decreases, reaching approximately 30–45 % of its room temperature value at 400°C [12]. Specifically, VE resin, derived from the esterification of epoxy resin and organic acid, demonstrates excellent chemical resistance, with a mass loss of approximately 0.4 % in alkaline solutions [13]. It offers additional advantages, including fast fabrication cycles, ease of processability, low cost, and adequate mechanical performance, making it an attractive alternative to high-performance epoxy systems [14]. However, the rapid softening of the resin significantly restricts its broader application in GFRP bars under fire conditions.

To enhance the fire resistance of GFRP bars, several strategies have been explored, including applying protective coatings [15], incorporating flame retardants in resin [16], using thermosetting resin matrix [17]. For VE resin, incorporating flame retardants is a fundamental approach that addresses the intrinsic thermal limitations. This method directly targeted the core vulnerabilities of GFRP bars, offering significant advantages such as enhanced retention of mechanical properties at elevated temperatures and improved resistance to thermal degradation. Furthermore, resin modification allowed for tailored improvements in fire performance without necessitating major changes to structural design or construction practices, making it a highly effective and practical strategy for advancing the fire resistance of GFRP bars reinforced concrete structures.

In this study, 9,10-dihydro-9-oxa-10-phosphaphenanthrene-10-oxide (DOPO), a commercially available reactive flame retardant, was incorporated into vinyl ester (VE) resin to create a VE-DP resin system, enhancing its thermal stability and flame-retardant property. The modified GFRP bars, fabricated using the VE-DP resin, were then evaluated for their mechanical properties and failure modes at elevated temperatures. Then, this study demonstrated the practical utility of modified GFRP bars in addressing fire resistance challenges through a real engineering application. Based on standard requirements, the preliminary design parameters for GFRP reinforcement were designed. Finite element analysis (FEA) was subsequently conducted to simulate the behavior of the structure under fire scenarios, validating the feasibility of utilizing fire-resistant GFRP bars.

2. Modified vinyl ester resin

2.1. Production process

DOPO, a phosphorus-based heterocyclic compound with high thermal stability and flame-retardant efficiency, is widely used to enhance the fire resistance of epoxy. It achieves this by releasing active phosphorus species that act as free radical scavengers during combustion [18–20] and promoting the formation of carbonaceous protective layers through dehydration [21]. In this study, DOPO was combined with propargyl, a matrix material known for its excellent thermal stability, low moisture absorption, and superior

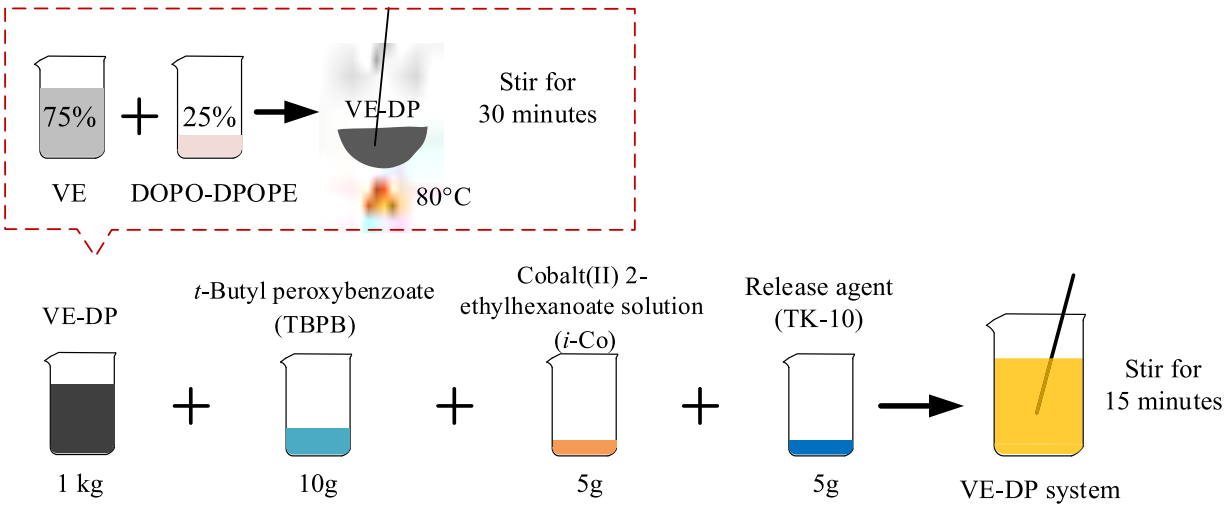


Fig. 1. VE-DP system production process.

physio-mechanical properties [22], to synthesize DOPO-containing dipropargyl ether [1-(6-oxido-6H-dibenz[*c*,*e*] [1,2] oxaphosphorin-6-yl)-1,1-di(4-propargyloxyphenyl)ethane (DOPO-DPOPE)] via Williamson etherification. A DOPO-DPOPE modified vinyl ester resin system (VE-DP) was prepared by heating VE resin and DOPO-DPOPE in a 75: 25 mass ratio at 80°C for 30 min under mechanical stirring, followed by cooling to room temperature (Fig. 1). A curing catalytic system, comprising TBPB, *i*-Co and release agent (TK-10) was mixed with the VE-DP resin at room temperature for 15 min to obtain the modified vinyl ester resin, which was then used for pultrusion.

2.2. Glass transition temperature and thermal stabilities

Dynamic mechanical analysis (DMA) was conducted to obtain the loss tangent (tan δ)-temperature curve and storage modulus-temperature curve, which were used to determine T_g of VE-DP resin, yielding a T_g value of 202°C for the cured resin. The thermal stabilities of the cured VE and VE-DP resins were characterized by thermogravimetry analysis (TGA). The TGA analytical data are listed in Table 1, including the temperature of 5 % weight loss (T_{d5}), residual yield at 600℃ ($Y_{600℃}$) and residual yield at 800℃ ($Y_{800℃}$). The results showed that the T_{d5} and $Y_{600℃}$ of the cured VE-DP resin in nitrogen and air were higher than that of the cured VE resin. Specially, the $Y_{600℃}$ of the cured VE-DP resin in air reached 32.2 %, but the $Y_{600℃}$ of the cured VE resin in air was only 1.2 %. This indicated that the cured VE-DP resin had high thermal-oxidative stability and better carbonization ability, which contributed to improve the fire resistance of the resin [23]. The limiting oxygen index (LOI) of the modified VE resin was tested on the digital oxygen index testers according to the standard GB/T 2406.2–2009 [24], the results of LOI was larger than 27, indicating that VE-DP was flame retardant.

3. High-temperature performances of modified GFRP bars

3.1. Production process of modified GFRP bars

The production process of GFRP bars using modified vinyl ester resin is illustrated in Fig. 2. The process was meticulously designed to optimize performance and durability. Critical factors such as resin impregnation uniformity and curing conditions were carefully considered to ensure the final product met stringent mechanical and thermal requirements. Initially, the glass fiber precursor was impregnated with the modified resin which was thoroughly mixed for 15 min to ensure uniform distribution. Subsequently, the ribs were wrapped at specific angle to set the distance between them. Then the bars passed through a series of three ovens at a consistent speed of 150 mm/min. The curing process for the VE-DP resin, combined with the curing agent, involved a three-stage temperature profile: 25°C for 24 h, followed by 80 °C for 2 h, and finally 100 °C for 2 h. The GFRP bars were fabricated with a nominal diameter of 8 mm, a rib depth of 0.17 mm (Fig. 3), and a glass fiber content of 70 %. Detailed production parameters for the GFRP bars are provided in Table 2.

3.2. Mechanical properties of the modified GFRP bars at elevated temperatures

3.2.1. Test setup and measurement

The two ends of the GFRP bar were secured using a wedge-shaped clamp, which consisted of a triangular pyramid wedge clamp paired with a corresponding sleeve. This wedge grip design demonstrated high anchoring efficiency and ensured no slippage occurred during the testing process. The mechanical properties of the horizontal tensile testing machine were evaluated following a standardized procedure. Initially, the anchors were securely attached to the clamps at both ends of the machine to ensure stable fixation. The GFRP bars were then threaded through the high-temperature test furnace, positioning the furnace at the midpoint of the bars. To create a sealed environment, the surrounding area of the GFRP bars was filled with asbestos. Surface temperatures were measured using thermocouples, which were inserted through holes on the top cover plate and positioned directly on the surface of the GFRP bars. Additionally, strain gauges were carefully applied to the GFRP bars to monitor strain levels. A temperature control box was employed to heat the system, ensuring precise temperature regulation. The temperature control system automatically adjusted the output power based on the difference between the furnace temperature and the target temperature, maintaining accurate thermal control throughout the experiment (Fig. 4). This systematic approach ensured reliable and consistent measurement of the mechanical properties under controlled high-temperature conditions.

3.2.2. Specimens and loading scheme

The steady-state tensile tests of GFRP bars at elevated temperatures were conducted, with five target temperatures (20°C, 150°C,

Table 1
TGA analytic data of the cured resins.

Sample	In nitrogen			In Air		
	T_{d5} (℃)	$Y_{400℃}$ (%)	$Y_{600℃}$ (%)	T_{d5} (℃)	$Y_{400℃}$ (%)	$Y_{600℃}$ (%)
VE	345	72.7	19.8	314	69.3	1.2
VE-DP	351	74.1	27.4	336	77.3	32.2



Fig. 2. Production process of GFRP bar.



Fig. 3. Dimensions of modified GFRP bar (unit: mm).

Table 2
Parameters of modified GFRP bar.

Type	Nominal diameter (mm)	Effective diameter (mm)	Effective cross-section area (mm^2)	Fiber content (%)	T_g (°C)
GFRP bar	8	7.66	46.08	70	202

300°C, 400°C, and 550°C), each tested with two replicate specimens (Table 3). Initially, the GFRP bars were preloaded to 10 % of their ultimate load capacity to verify the normal functioning of the test setup and data acquisition system. After confirming the stability of the measurements, the load was discharged to 0 kN, and the furnace chamber was heated at a controlled rate of 20 °C/min until the target temperature was achieved. To ensure uniform temperature distribution across the cross-section of the bars, the specimens were held at the target temperature for 20 min. Subsequently, the specimens were loaded at a constant displacement rate of 5 mm/min until failure occurred. The loading procedure is shown in Fig. 5.

4. Results and discussion

The failure modes of GFRP bars at temperatures of 20°C, 150°C, 300°C, 400°C, and 550°C are shown in Fig. 6. At 20°C, the failure mode of the GFRP bars was characterized by the rupture of the outer fiber bundles, followed by the bursting failure of the inner fiber bundles. At 150°C, the failure mode transitioned to fiber delamination accompanied by partial softening of the fibers. When the temperature reached 300°C, the GFRP bars inside the furnace exhibited a hair-like failure mode due to resin decomposition, while the bars outside the furnace experienced bundle splitting failure. During the constant temperature process, a small amount of white smoke, resulting from resin decomposition, was observed. At 400°C, the resin of the GFRP bars inside the furnace underwent extensive decomposition, producing significant white smoke, and the failure mode transitioned to hair-like with the material turning dark brown. The GFRP bars outside the furnace continued to exhibit bundle splitting failure. At 550°C, the resin of the GFRP bars inside the furnace completely decomposed, generating abundant white smoke, and the final failure mode was hair-like, revealing the original white color of the glass fibers. These results demonstrated that prior to reaching T_g of the GFRP bars, the failure mode was dominated by fiber bursting. After exceeding the resin decomposition temperature, the failure mode in the heated section involved partial fiber softening and bursting due to resin degradation, while the unheated section retained bundle splitting failure. Once the resin was fully decomposed, the failure mode of the GFRP bars was solely characterized by the softening of the glass fibers. This progression highlighted the critical influence of temperature on the mechanical behavior and failure mechanisms of GFRP bars.

Table 4 presents the ultimate stress values of GFRP bars at various temperatures. For the temperatures of 20°C, 150°C, 300°C, and 400°C, the discrete variations between the two replicate specimens were 3.1 %, 0.9 %, 0.2 %, and 0.8 %, respectively. These results demonstrated remarkably low scatter. Ultimate strength-temperature curve and tensile force-displacement curve are illustrated in Figs. 7 and 8, respectively. The ultimate strength and elastic modulus tested in the ambient temperature were 1236 MPa and 45 GPa, respectively. At 150°C, which was below the T_g of 202°C, the GFRP bar retained 90.6 % of its strength, indicating effective synergy between the resin matrix and the reinforcing fibers. When the temperature increased to 300°C, exceeding T_g, the resin began to soften. The modified vinyl ester resin maintained good thermal stability in air up to 300°C. At this temperature, the GFRP bar retained 84.2 % of its strength, reflecting reasonable thermal stability. The modified VE resin exhibited greater strength reduction from 20°C to 150°C due to secondary relaxations in the imperfect crosslinked network, whereas from 150°C to 300°C, slower degradation occurred as thermal softening was offset by post-curing reactions (e.g., polymerization of residual ethynyl/propargyl ether/chromene groups),

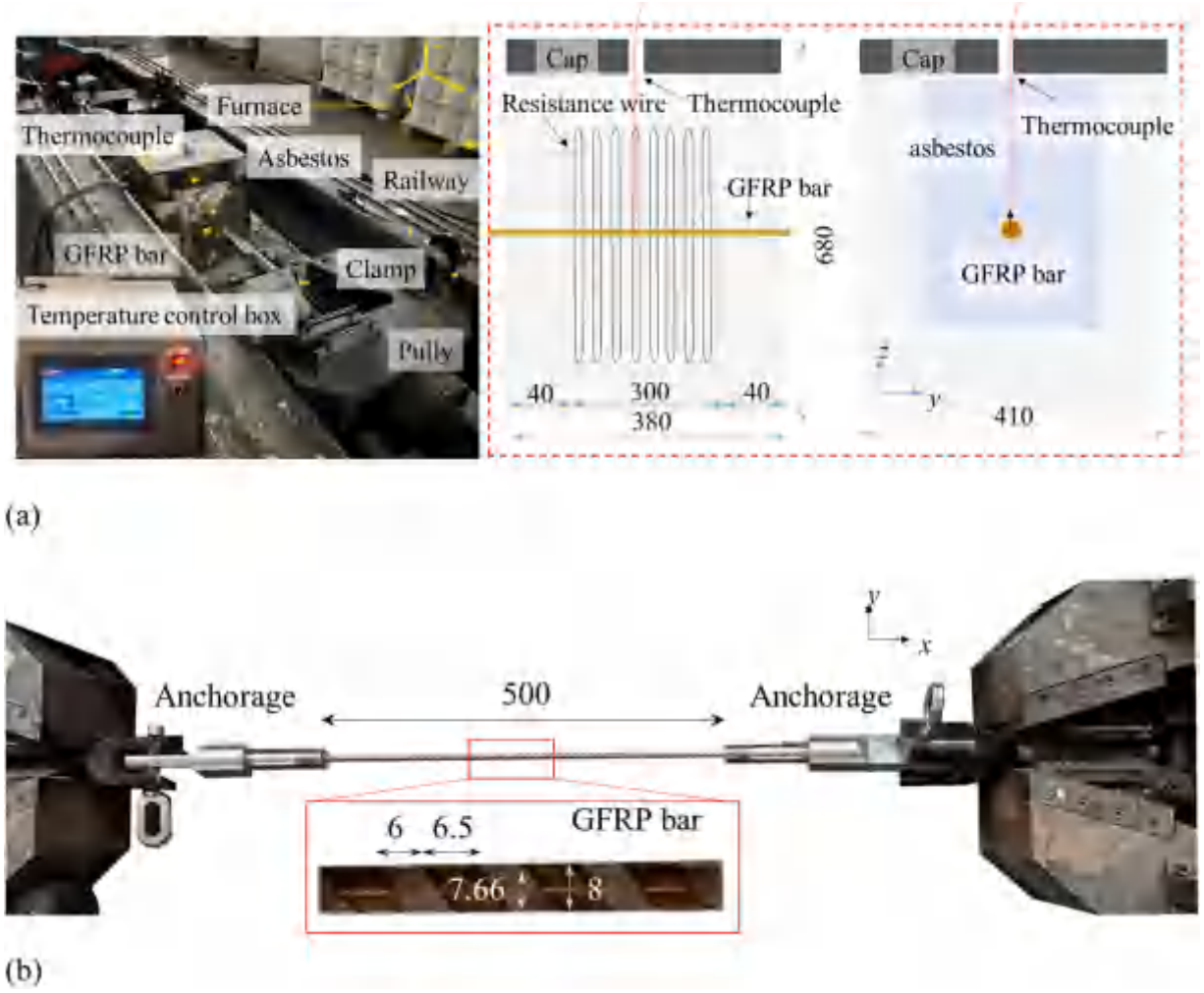


Fig. 4. Experimental details (unit: mm): (a) test setup; (b) GFRP bar specimen.

Table 3
Parameters of high-temperature experiments.

Specimen	Test	Temperature (℃)	Constant temperature time (min)
G20–1 G20–2	Steady-state	20	20
G150–1 G150–2		150	
G300–1 G300–2		300	
G400–1 G400–2		400	
G550–1 G550–2		550	

Note: G20–1 represents a GFRP bar subjected to a temperature of 20°C, where "1" denotes the specimen number.

enhancing crosslinking density and thermal stability. Thus, the modified VE resin exhibited early-stage physical relaxation effects but maintained reasonable thermal resistance upon further heating. At 400°C, the TGA analysis indicated that resin decomposition occurred gradually with increasing temperature, and the GFRP bar retained 68.0 % of its strength. Finally, at 550°C, the resin underwent almost complete decomposition, resulting in a significant reduction in strength, with the GFRP bar retaining only 9.9 % of its original strength. These findings highlighted the critical influence of temperature on the mechanical performance of GFRP bars, particularly in relation to resin degradation and strength retention. Within T_g range of 59°C to 157°C, the tensile strength of GFRP bars decreased to approximately 30–45 % of its original value at 400°C based on the data from [25–30], while the modified GFRP bars in

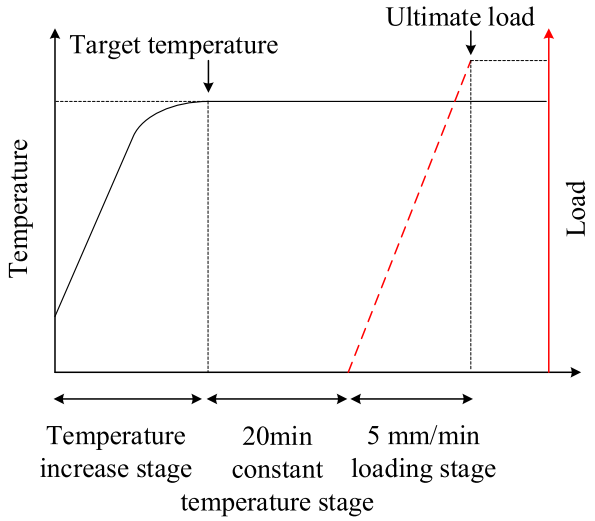


Fig. 5. Loading procedure.

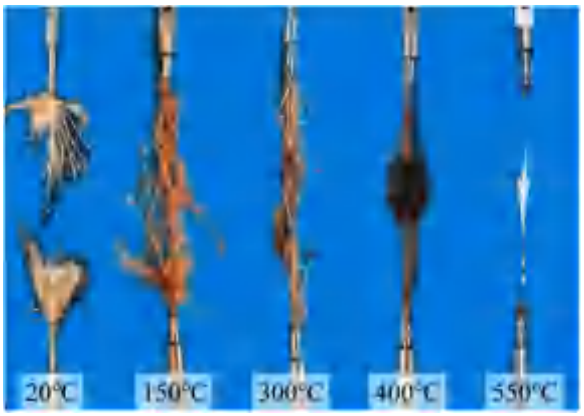


Fig. 6. Failure modes of the modified GFRP bars at different temperature.

Table 4
Ultimate strength and strength retention.

Specimen	Temperature (℃)	Ultimate load (kN)	Ultimate strength (MPa)	Average strength retention (%)
G20–1	20	57.87	1256.40	100.0
G20–2		56.01	1216.01	
G150–1	150	51.83	1125.26	90.6
G150–2		51.37	1115.28	
G300–1	300	47.86	1039.07	84.2
G300–2		47.99	1041.90	
G400–1	400	38.88	844.11	68.0
G400–2		38.56	837.16	
G550–1	550	7.46	161.96	9.9
G550–2		3.68	79.90	

this study retained 68.0 % of its strength under the same conditions, demonstrating significantly enhanced thermal stability and fire resistance. This improvement indicated the effectiveness of the modifications in resin to preserve the mechanical properties of GFRP bars at elevated temperatures.

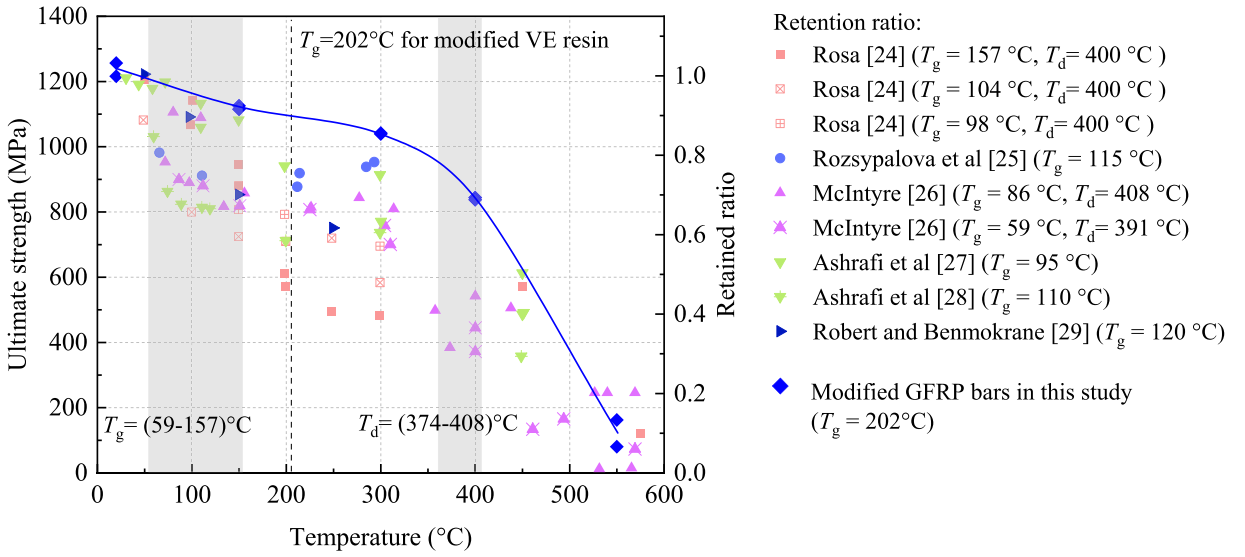


Fig. 7. Ultimate strength-temperature relationship.

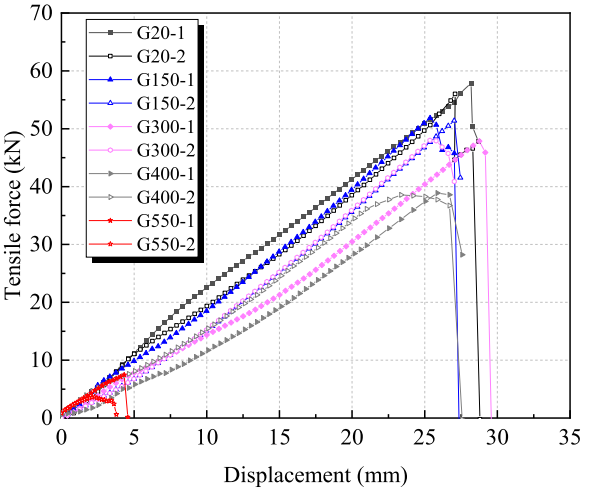


Fig. 8. Force-displacement curve.

5. Application of the modified GFRP bars in real engineering

5.1. Project introduction

This section implemented a real engineering application to demonstrate the practical utility of modified GFRP bars in addressing the fire resistance challenge. For the reinforced concrete frame, the building was designed with a Class 1 fire resistance rating, and the fire resistance limit for the concrete slab requires 1.5 h (90 min) according to GB50016–2014 [31]. Consequently, the GFRP/steel bars reinforced concrete structure (GFRP/steel RC) frame was subjected to a 90-minute fire exposure. In the project as shown in Fig. 9, C30 concrete (with a compressive strength of 28 MPa) and HRB400 steel bars (with a yield strength of 400 MPa) were used. The column cross-sectional dimensions were 400 mm × 400 mm (length × width). Each column was reinforced with eight longitudinal bars, each with a diameter of 8 mm, and stirrups spaced at 200 mm intervals with a diameter of 8 mm. For the beams, the cross-sectional dimensions were 250 mm × 450 mm (width × height). Two steel bars were arranged at both the upper and lower sides of the beam, with diameters of 14 mm and 18 mm, respectively. Stirrups were spaced at 200 mm intervals, each with a diameter of 8 mm (8@200 mm). The slab featured two layers of steel reinforcement. Steel bars were spaced at 200 mm intervals, with diameters of 16 mm and 18 mm (D_s) at the upper and lower sides, respectively (Fig. 10). The concrete cover thicknesses of slab and column/beam were 20 mm and 30 mm, respectively.

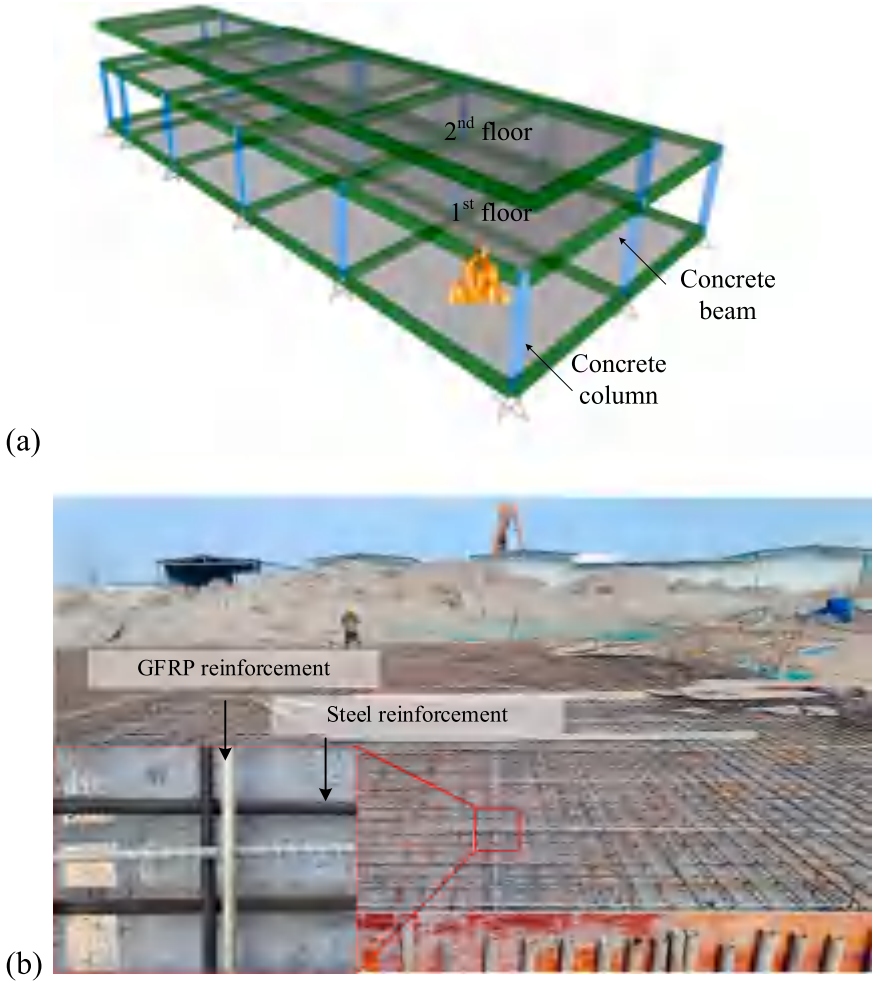


Fig. 9. Description of the real engineering in Lianyungang: (a) three-dimensional model of the fire pump room in Lianyungang, Jiangsu province; (b) onsite construction photo.

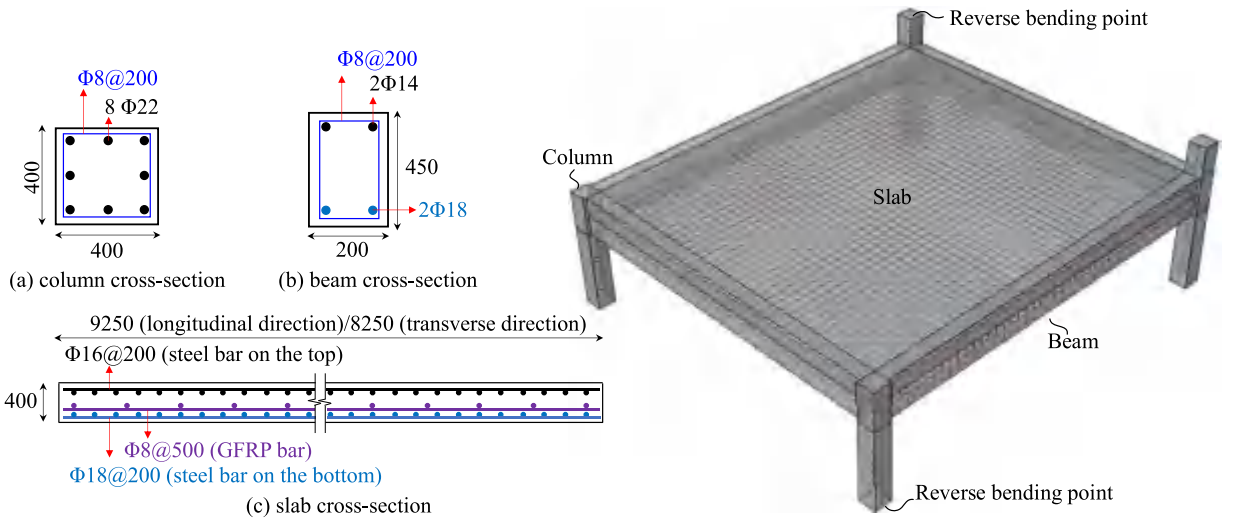


Fig. 10. Details of the reinforced concrete frame (unit: mm).

5.2. Parameter design of GFRP reinforcement

The design parameters for GFRP reinforcement included the concrete cover thickness and the spacing between GFRP bars. The temperature distribution in GFRP bars is significantly affected by the concrete cover thickness, which serves as a thermal insulator, maintaining the reinforcement temperature below critical thresholds for a designated period. According to CSA S806 [32], a concrete cover of 60 mm is required to achieve 2 h of fire resistance. Similarly, ACI 440 [33] specifies a minimum cover of 2 in. (50.8 mm) for GFRP reinforcement in slabs to ensure a fire resistance of 1.5 h. Thus, the preliminary design positioned the GFRP layer above the bottom steel reinforcement in the slab, with a 50 mm vertical spacing between the layers, resulting in a 67 mm concrete cover thickness for the GFRP bars. This configuration was adopted because the thick concrete cover for the GFRP bars restricted their ability to effectively contribute to tensile strength and the bottom steel reinforcement was incorporated to provide the necessary tensile capacity. This hybrid reinforcement strategy optimized structural performance in the slab design. For the GFRP reinforcement spacing, the minimum spacing should be at least 1 in. (25.4 mm) and nominal diameter of GFRP bars (8 mm) and the maximum spacing should not exceed three times slab height (1200 mm) and 500 mm. By comprehensively considering the costs, the spacing between GFRP bars was preliminarily determined as 500 mm. The diameter of GFRP bar used in the project (D_G) was 8 mm as descripted in Section 3.

5.3. FEA of GFRP/steel bars reinforced concrete structure at elevated temperatures

The refined FEA model was developed in ABAQUS [34] to establish concrete beam, column, slab, steel and GFRP reinforcement. The column height was modeled from the bending moment inflection point below and above the slab, considering fixed boundary conditions at both ends. Consequently, the column heights below and above the slab were set at 2250 mm and 700 mm, respectively. When subjected to temperature changes, these slabs experienced thermal expansion or contraction, leading to deformation. However, this deformation was constrained by the beams and columns, preventing the slab from freely expanding or contracting. Traditional approaches often assume fully restrained stiffness, which overly constrains the deformation of structural members and fails to accurately reflect real-world engineering conditions. In contrast, the concept of partially restrained stiffness provides a more realistic simulation of actual restraint conditions. This model accounted for the accompanying deformation of the beams and columns during the slab's deformation process, offering a more accurate representation of the structural interactions. By incorporating these details, the model more realistically captured the restraining effects of the beams and columns on the slab, providing valuable insights into the behavior of GFRP-reinforced structures under fire conditions. The detailed cross-sectional dimensions of steel reinforced concrete (SRC) frame were shown in Fig. 10. In this study, the fire exposure was assumed to act exclusively within the room, affecting the bottom surface of the slab as well as the two side surfaces of the concrete beam and column. Furthermore, the bond between steel bars, GFRP bars and concrete was considered perfect.

5.3.1. Thermal and mechanical properties of materials

The density ρ_c, thermal conductivity λ_c, thermal expansion ε_c, and specific heat c_c of concrete at elevated temperatures θ were determined in accordance with Eurocode 1992–1–2 [35]. The standard differentiates between two types of concrete aggregates: siliceous and calcareous. For this study, concrete with siliceous aggregates was selected. The specific heat of concrete was influenced by its moisture content, which was also considered in the analysis, with the moisture content set at 0 %. The thermal conductivity of normal-weight concrete was determined based on a range between lower and upper limit values. In this study, the upper limit of thermal conductivity was adopted for the analysis.

The calculation equations for ρ_c, c_c, λ_c, and ε_c of concrete were listed as followings Eqs. (1)-(4), respectively.

$$\rho_c(\theta) = \begin{cases} 2300\text{kg/m}^3 & 20^\circ\text{C} \le \theta \le 115^\circ\text{C} \\ 2300 \cdot [1 - 0.02 \cdot (\theta - 115) \big/ 85]\text{kg/m}^3 & 115^\circ\text{C} \le \theta \le 200^\circ\text{C} \\ 2300 \cdot [0.98 - 0.03 \cdot (\theta - 200) \big/ 200]\text{kg/m}^3 & 200^\circ\text{C} \le \theta \le 400^\circ\text{C} \\ 2300 \cdot [0.95 - 0.07 \cdot (\theta - 400) \big/ 800]\text{kg/m}^3 & 400^\circ\text{C} \le \theta \le 1200^\circ\text{C} \end{cases} \tag{1}$$

$$c_c(\theta) = \begin{cases} 900\text{J/(kg} \cdot K) & 20^\circ\text{C} \le \theta \le 100^\circ\text{C} \\ 900 + (\theta - 100)\text{J/(kg} \cdot K) & 100^\circ\text{C} \le \theta \le 200^\circ\text{C} \\ 1000 + (\theta - 200)/2\text{J/(kg} \cdot K) & 200^\circ\text{C} \le \theta \le 400^\circ\text{C} \\ 1100\text{J/(kg} \cdot K) & 400^\circ\text{C} \le \theta \le 1200^\circ\text{C} \end{cases} \tag{2}$$

$$\lambda_c(\theta) = 2 - 0.2451 \cdot (\theta \big/ 100) + 0.0107 \cdot (\theta/100)^2 \text{W} \big/ (\text{m} \cdot \text{K}) \quad 20^\circ\text{C} \le \theta \le 1200^\circ\text{C} \tag{3}$$

$$\varepsilon_c(\theta) = \begin{cases} -1.8 \times 10^{-4} + 9 \times 10^{-6} \cdot \theta + 2.3 \times 10^{-11} \theta^3 & 20^\circ\text{C} \le \theta \le 700^\circ\text{C} \\ 14 \times 10^{-3} & 700^\circ\text{C} \le \theta \le 1200^\circ\text{C} \end{cases} \tag{4}$$

The calculation equations for c_s, thermal conductivity λ_s, and ε_s of steel bars were listed as following Eqs. (5)-(7) according to Eurocode 1992–1–2 [35].

$$c_s(\theta) = \begin{cases} 425 + 7.73 \times 10^{-1} \cdot \theta - 1.69 \times 10^{-3} \cdot \theta^2 + 2.22 \times 10^{-6} \cdot \theta^3 \mathrm{J/(kg \cdot K)} 20^\circ\mathrm{C} \le \theta \le 600^\circ\mathrm{C} \\ 666 - 13002/(\theta - 738)\mathrm{J/(kg \cdot K)} 600^\circ\mathrm{C} \le \theta \le 735^\circ\mathrm{C} \\ 545 + 17820/(\theta - 731)\mathrm{J/(kg \cdot K)} 735^\circ\mathrm{C} \le \theta \le 900^\circ\mathrm{C} \\ 650\mathrm{J/(kg \cdot K)} 900^\circ\mathrm{C} \le \theta \le 1200^\circ\mathrm{C} \end{cases} \tag{5}$$

$$\lambda_s(\theta) = \begin{cases} 54 - 3.33 \times 10^{-2} \cdot \theta \mathrm{W/(m \cdot K)} 20^\circ\mathrm{C} \le \theta \le 800^\circ\mathrm{C} \\ 27.3\mathrm{W/(m \cdot K)} 800^\circ\mathrm{C} \le \theta \le 1200^\circ\mathrm{C} \end{cases} \tag{6}$$

$$\varepsilon_s(\theta) = \begin{cases} -2.416 \times 10^{-4} + 1.2 \times 10^{-5} \cdot \theta + 0.4 \times 10^{-8} \theta^2 20^\circ\mathrm{C} \le \theta \le 750^\circ\mathrm{C} \\ 11 \times 10^{-3} 750^\circ\mathrm{C} \le \theta \le 860^\circ\mathrm{C} \\ -6.2 \times 10^{-3} + 2 \times 10^{-5} \cdot \theta 860^\circ\mathrm{C} \le \theta \le 1200^\circ\mathrm{C} \end{cases} \tag{7}$$

The mechanical properties of concrete, particularly the compressive stress-strain relationship at elevated temperatures, were derived from Eurocode 1992–1–2 [35]. The behavior of concrete was divided into distinct phases: initially, the material exhibited linear elastic behavior when the stress remained below 0.3 times the compressive strength ($f_{c,\theta}$). Beyond this point, the stress-strain curve transitioned into a nonlinear phase until reaching the peak compressive stress. After the peak, the stress gradually decreased in a linear manner until it reached zero. Regarding the tensile behavior of concrete, it was modelled as linear elastic prior to cracking. Following the approach outlined by Ellobody and Bailey [36], the post-cracking behavior was represented using a linearly descending branch in FEA model. This branch described the relationship between tensile stress and crack opening displacement. To ensure numerical stability, a small residual tensile stress ($0.05\,f_t$) was incorporated into the model. Such a tensile stress-crack opening displacement curve is defined in terms of material parameters such as the tensile strength and the fracture energy of the concrete. The tensile strength $f_{t,\theta}$ at temperature θ was taken as $0.1\,f_{c,\theta}$. The "Concrete Damage Plasticity model" was employed in the ABAQUS [34] simulation to capture these behaviors. The compressive stress-strain curve and the tensile stress-crack opening displacement relationship are illustrated in Figs. 11 and 12.

The mechanical properties of steel reinforcement bars were simulated using an elastic-plastic constitutive model. To account for the degradation of material properties at elevated temperatures, reduction factors for both yield strength and elastic modulus were applied, as per the guidelines provided in Eurocode 1994–1–2 [35]. The behavior of the modified GFRP bars was modeled using a linear-elastic constitutive relationship. The ultimate strength of the GFRP bars was directly incorporated into FEA models based on experimentally obtained data. For the elastic modulus at elevated temperatures, it was observed to degrade less significantly with increasing temperatures compared to tensile strength. A classical model was employed to predict the elastic modulus [37]. The reduction factors for steel and GFRP bars was shown in Fig. 13.

5.3.2. *Heat transfer analysis*

Elements adopted in ABAQUS [34] for concrete, steel/GFRP bars were DC3D8 (an 8-node linear heat transfer brick) and DC1D2 (a 2-node heat transfer link), respectively. The Stefan-Boltzmann constant was adopted as $5.669 \times 10^{-14}\,\mathrm{W/mm^2/K^4}$, while absolute zero was defined as $-273.15\,^\circ\mathrm{C}$. Regarding thermal radiation, surface emissivity of the structural element under fire was defined as 0.8. The convection effects were modelled using a surface-based film condition, incorporating the temperature variations defined by the standard ISO fire curve [38]. The convection coefficient for the film condition was set to $25 \times 10^{-6}\mathrm{W/mm^2/^\circ C}$ [39]. The mesh size for the concrete was 80 mm and the mesh sizes were all 100 mm for steel and GFRP bars. Mesh convergence was conducted, confirming the sufficiency of the mesh density for reliable results. In the analysis, fire exposure was applied solely to the bottom surface of the slab, the inner surface of the column, and the beam. The inital temperature of the frame was set as 20 °C, and the frame was subjected to the ISO 834 standard fire curve for a duration of 90 min. The temperature distribution of GFRP/steel RC frame was shown in Fig. 14.

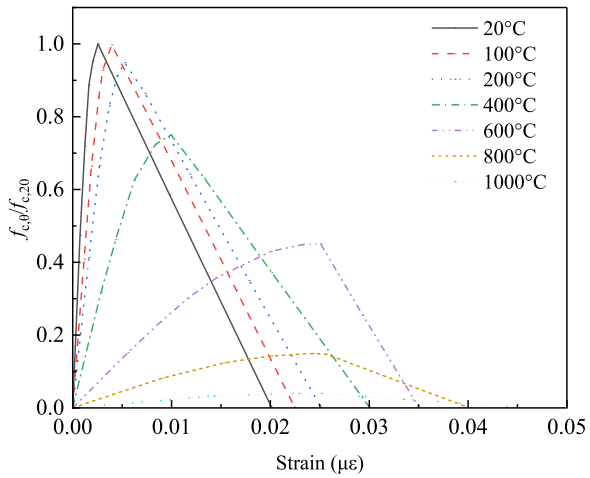


Fig. 11. Normalized compressive stress-strain curve.

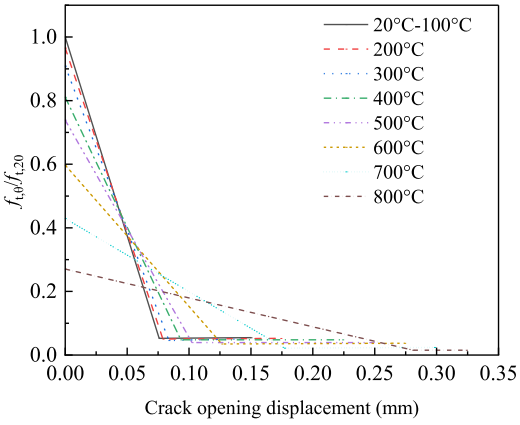


Fig. 12. Normalized tensile stress-crack opening displacement curve.

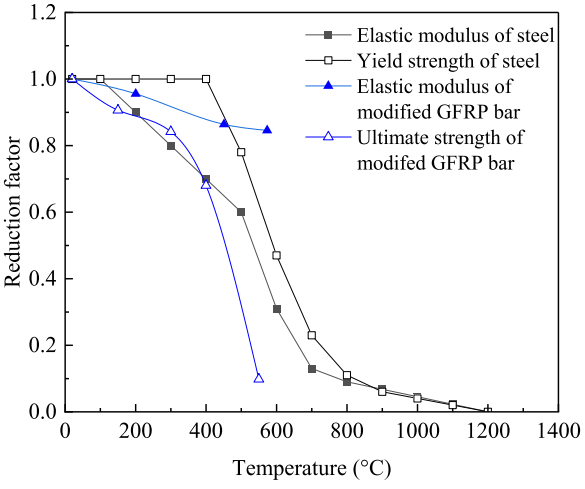


Fig. 13. Reduction factors for mechanical properties of steel and modified GFRP bar.

5.3.3. Sequential coupling analysis

After obtaining the results from the heat transfer analysis, a sequential coupling analysis was performed to evaluate the structural response under the thermal loading. Two steps were set: the first step was to apply load on the slab and the temperature distribution calculated from the heat transfer analysis was set as the second step, which was imported as a predefined field into the structural model. The analysis considered the combined dead and live loads, taken as 9.5 kN/m^2 based on standard GB50009-2012 [40]. This allowed for the simulation of the thermal stresses and deformations induced by the fire exposure. The structural analysis employed the C3D8R element (an 8-node linear brick element with reduced integration) for concrete and the T3D2 element (a 2-node truss element) for steel and GFRP reinforcement. Material properties, including thermal expansion coefficients and temperature-dependent mechanical properties, were assigned to each component to accurately capture their behavior under elevated temperatures. The boundary conditions were defined to simulate realistic structural constraints, with the columns fixed at reverse bending points, while the beams and slabs were allowed to deform freely under thermal loading. The bond between bars and concrete was assumed to be perfect and bars were embedded into the concrete. The analysis focused on evaluating deflections under different temperatures to assess the structural integrity of the reinforced concrete frame under fire conditions. The mesh sizes for materials were the same as those in heat transfer analysis. The results of the sequential coupling analysis provided insights into the influence of GFRP bars on the fire resistance of the structure, particularly in terms of their ability to maintain load-bearing capacity and limit deformations at elevated temperatures. This approach enabled a comprehensive understanding of the interaction between thermal and mechanical effects, offering valuable data for optimizing the design of reinforced concrete structures with GFRP reinforcement in fire scenarios. The final deflections of concrete frame, steel reinforcement, and GFRP reinforcement are shown in Fig. 15.

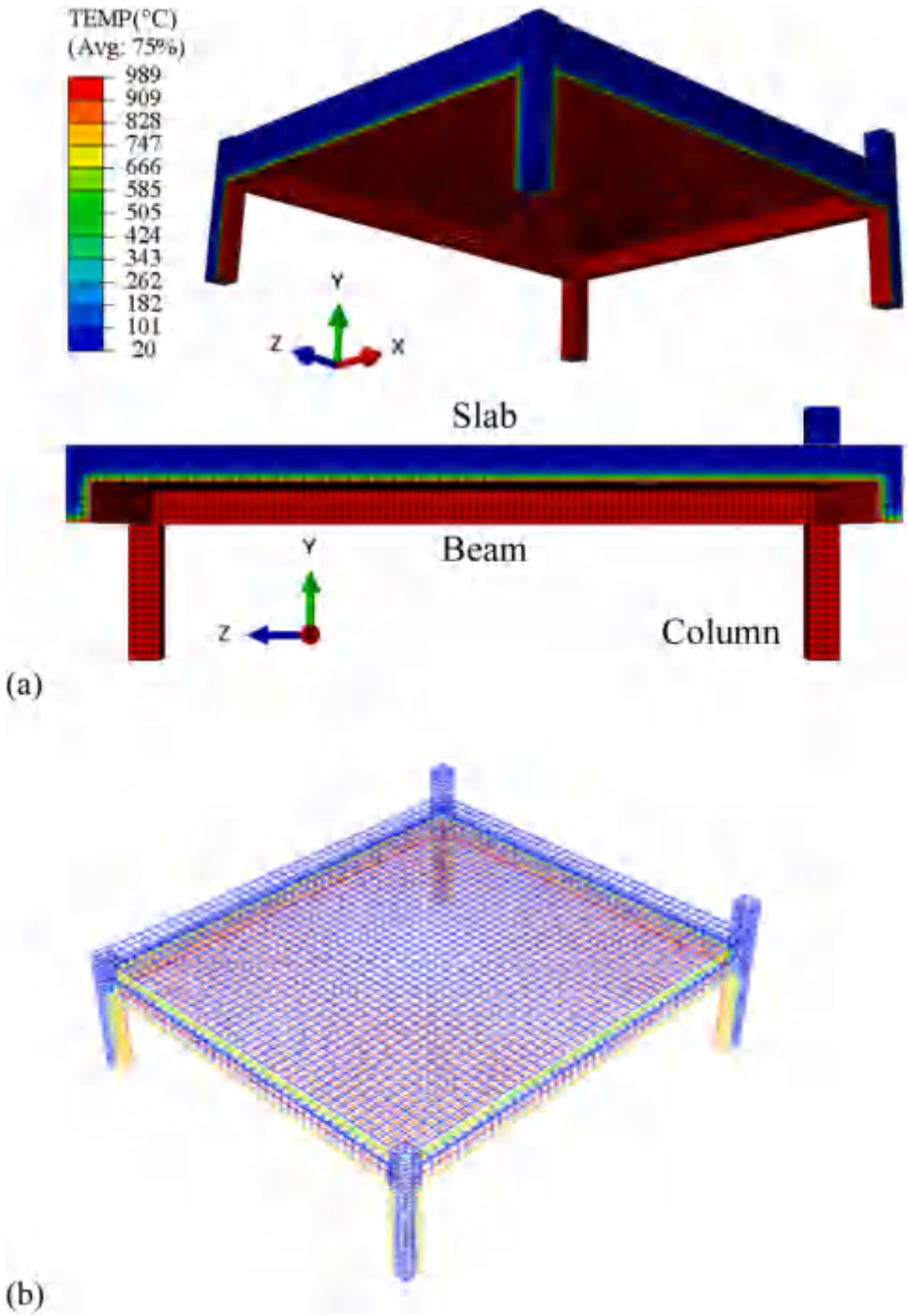


Fig. 14. The temperature distribution of GFRP/steel RC frame after a 90-minute fire exposure: (a) concrete frame; (b) steel and GFRP reinforcement.

5.4. High-temperature performance of GFRP/steel bars reinforced structures

5.4.1. Temperature distribution

Temperature distribution at the critical time corresponding to steel reinforcement failure and after fire resistance time of 90 min was discussed: (1) when the temperature of steel reinforcement exceeded 600°C, its strength and stiffness were significantly degraded, indicating the failure of the steel reinforcement layer. This critical condition was observed at the 39-minute mark, during which the

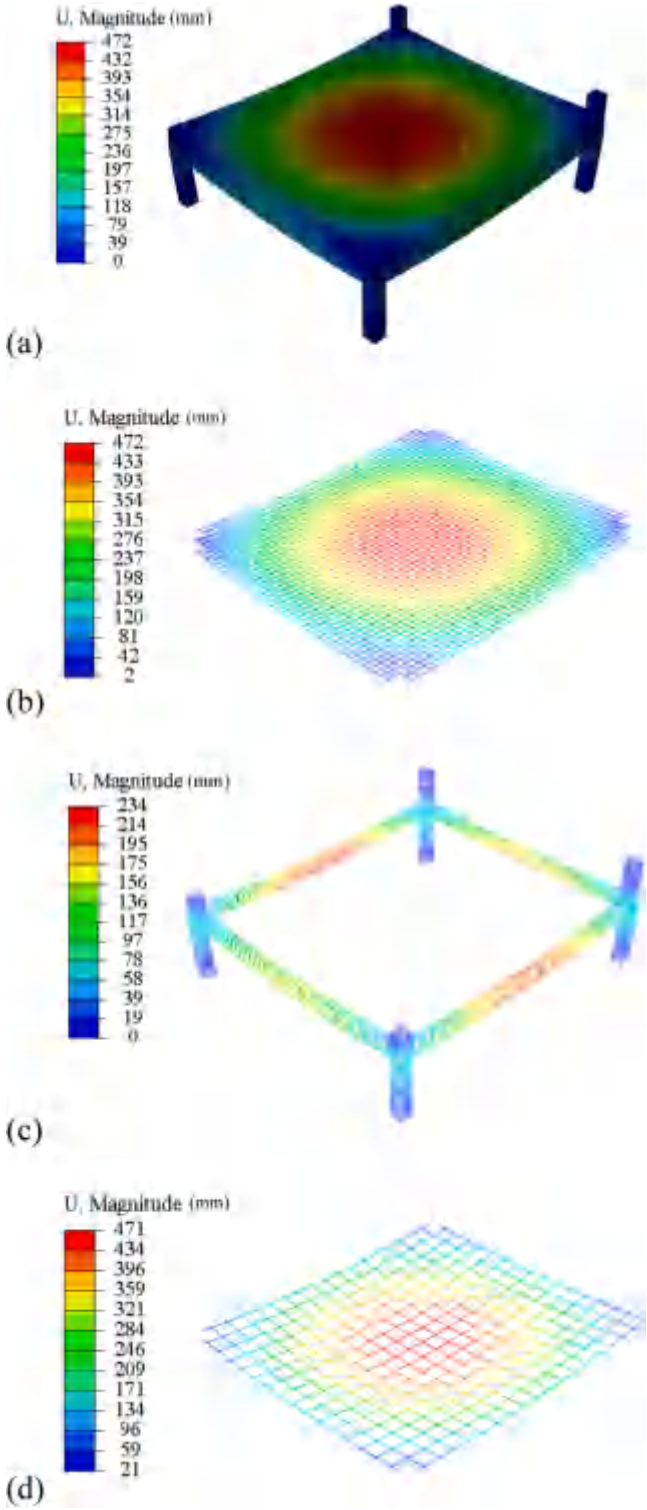


Fig. 15. The deflections of GFRP/steel RC frame after exposed to the ISO 834 curve for a duration of 90 min: (a) concrete frame; (b) steel reinforcement in slab; (c) steel reinforcement layers in columns and beams; (d) GFRP reinforcement layer.

temperatures of the bottom concrete slab and the GFRP bars layer were 420°C and 271°C, respectively. Notably, the temperature of the GFRP bars slightly exceeded T_g of 202°C, they retained 98 % of their initial weight and 90 % of their room temperature strength, indicating minimal degradation of GFRP bars; (2) after exposing the concrete frame to fire for 90 min in accordance with the slab fire

resistance requirement specified in GB50016–2014 [31], the temperature distribution along the height of the slab was analyzed, as illustrated in Fig. 16. The results revealed distinct temperature gradients across different layers of the structural elements. Specifically, the temperatures recorded at distances of 0 mm, 100 mm, and 200 mm from the bottom surface of the concrete slab were 564°C, 331°C, and 65°C, respectively. The temperatures of the bottom and upper steel reinforcement layers were 799°C and 21°C, respectively, while the temperature of the GFRP bars layer was 393°C. TGA results indicated that the modified vinyl ester (VE) resin retained 70 % of its initial weight at this temperature, demonstrating good thermal stability even after the fire resistance period. These findings indicated the ability of GFRP bars to maintain significant residual weight and functional integrity both at the time of steel reinforcement failure and after fire resistance time requirement.

In addition, the temperature distribution of this structure is heavily influenced by the thickness of the concrete cover, as it acts as a thermal insulator, keeping the temperature of the reinforcement below critical levels for a specified duration [41]. Therefore, the influence of concrete cover thickness is also studied. The distance *s* between the GFRP reinforcement layer and the bottom steel reinforcement layer was set at 50 mm (basic model) and 25 mm, resulting in a concrete cover thickness of 67 mm (basic model) and 42 mm for the GFRP bars, respectively.

When the temperature of the bottom steel reinforcement layer reached its critical threshold of 600°C, the corresponding temperatures of the GFRP reinforcement layer were 271°C and 437°C for cover thickness of 67 mm and 42 mm, respectively (Fig. 17). After fire resistance time of 90 mins, the temperatures for the bottom steel reinforcement layer and the GFRP reinforcement layer were 393°C and 601°C for concrete cover thickness of 67 mm and 42 mm, respectively. These results demonstrated that reducing cover thickness significantly increased the temperature of the GFRP bars, indicating the importance of maintaining adequate concrete cover thickness to ensure the fire resistance and structural integrity of GFRP-reinforced concrete elements.

5.4.2. Deflection of the concrete slab

Deflection-distance from one diagonal line end curve and deflection at midpoint-fire exposure time curve are shown in Fig. 18. The deflections of the concrete slab along its diagonal line were obtained at fire exposure times of 10 min, 20 min, 40 min, 60 min, and 90 min, and the cover thickness for GFRP bars was 67 mm. The deflections of the concrete slab at different fire exposure time were as follows: (1) during the initial stages of fire exposure (up to 20 min), the deflection of the GFRP/steel RC frame was marginally lower than that of the steel-reinforced concrete frame. This behavior was attributed to the fact that the temperature of the bottom steel reinforcement layer at this stage was 342°C, at which point the tensile strength of the steel bars remained largely unaffected, and the reduction in the elastic modulus was minimal. Consequently, the bottom steel reinforcement layer preserved its capacity to resist the applied fire load effectively. The deflection difference between GFRP/steel RC slab and SRC slab was 3.6 %; (2) as the fire exposure time increased to 39 mins, the temperature of the bottom steel reinforcement layer reached 600°C and a critical threshold at which the steel bars were deemed to have failed. Beyond this point, the GFRP reinforcement layer played the primary role in resisting the fire load. Consequently, the deflection difference between the GFRP/steel RC and SRC frames increased to 4.12 %; (3) after concrete slab fire resistance time of 90 mins, the deflection difference decreased slightly to 4.0 %, which was attributed to the obvious reduction in the mechanical properties of the GFRP bars after 60 mins. The results confirmed that GFRP bars retained ability to resist the fire load with a concrete cover thickness of 67 mm and a spacing of 500 mm even after steel reinforcement failed, indicating the appropriate parameter design of GFRP bars and the essential role of high-temperature-resistant GFRP bars in enhancing the fire performance of reinforced concrete structures, providing a reliable solution for this project.

6. Conclusion

This study systematically investigated the performance of modified GFRP bars, starting with the resin modification process,

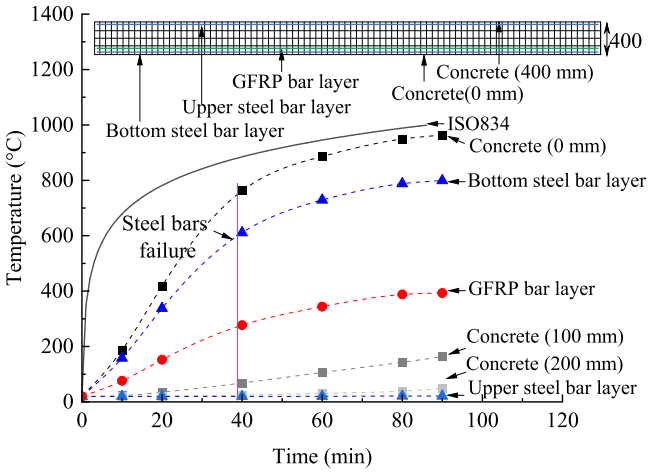


Fig. 16. Temperature distribution of materials in slab.

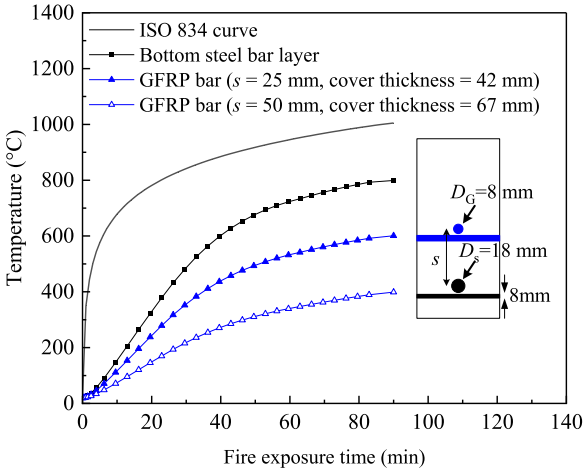


Fig. 17. Temperature distribution of GFRP reinforcement with different concrete cover thickness.

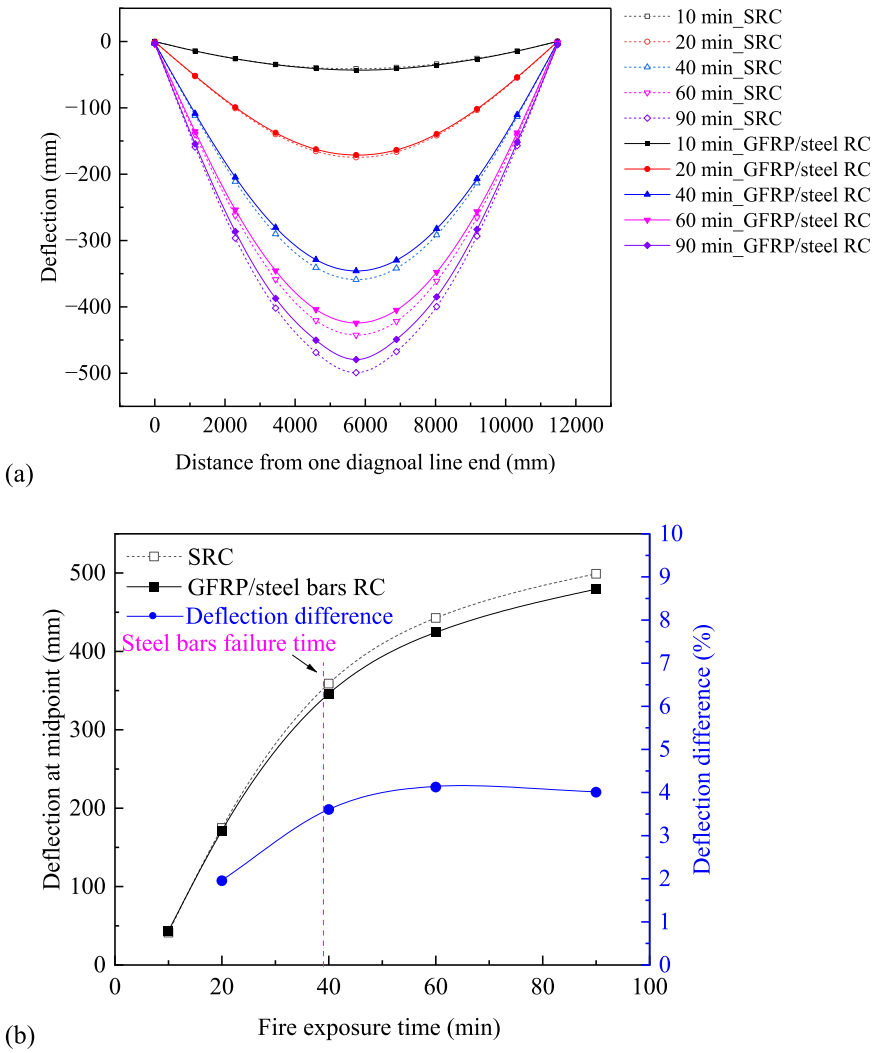


Fig. 18. Deflection of the concrete slab at different fire exposure time: (a) deflection-distance from one diagonal line end curve; (b) deflection at midpoint-fire exposure time curve.

advancing to the fabrication of GFRP bars, and concluding components in concrete slabs, with a primary focus on characterizing their fundamental high-temperature behavior. The following conclusions can be drawn:

(1) Modified vinyl ester resin system exhibited high thermal-oxidative stability and enhanced carbonization capability, significantly improving its fire resistance. The limiting oxygen index of the modified VE resin exceeded 27, confirming its flame-retardant properties. This result underscored the effectiveness of the modified VE resin in enhancing the fire resistance of GFRP bars.

(2) When the temperature was below the glass transition temperature of the GFRP bars, the failure mode was characterized by fiber bursting. At slightly higher temperatures than the resin decomposition temperature, the heated section of the GFRP bars exhibited partial fiber softening and bursting due to resin softening, while the unheated section experienced bundle splitting failure. Once the resin was completely decomposed, the failure mode of the GFRP bars solely involved softening of the glass fibers. In the steady-state experiments, the tensile strength of the GFRP bars decreased as the temperature increased. At temperatures of 150°C, 300°C, 400°C, and 550°C, the retention rates of the tensile strength were 90.6 %, 84.2 %, 68.0 %, and 9.9 %, respectively.

(3) This study demonstrated the practical utility of modified GFRP bars in addressing fire resistance challenges through a real engineering application. Preliminary design parameters for GFRP reinforcement included a concrete cover thickness of 67 mm and a spacing of 500 mm between GFRP bars. FEA was then conducted to simulate the behavior of the structure under a 90-minute fire exposure, in compliance with the fire resistance rating requirements for concrete slabs. The results confirmed that GFRP bars retained their ability to resist fire loads with the designed parameters even after steel reinforcement failed, with a 4.0 % deflection difference observed after fire resistance time. Additionally, the study highlighted the importance of maintaining adequate concrete cover thickness when using high-temperature-resistant GFRP bars. These findings indicated the effectiveness of GFRP reinforcement in minimizing slab deflection and ensuring structural safety of the project under fire conditions.

CRediT authorship contribution statement

Xu Liang: Writing – original draft, Validation, Software, Investigation, Formal analysis, Data curation. **Terrance Lim:** Writing – original draft, Validation, Software, Formal analysis. **Xiaoqing Zhao:** Writing – review & editing, Validation, Investigation, Conceptualization. **Lili Hu:** Writing – review & editing, Validation, Project administration, Methodology, Funding acquisition, Conceptualization. **Qiaolong Yuan:** Writing – original draft, Methodology, Formal analysis, Conceptualization. **Zhiwei Wang:** Visualization, Resources, Methodology, Conceptualization.

Declaration of Competing Interest

The authors declare that they have no known competing financial interests or personal relationships that could have appeared to influence the work reported in this paper.

Acknowledgement

The authors would like to express their gratitude to the Nonmetallic Excellence and Innovation Center for Building Materials (2023TDA5–1) and the Yangtze River Delta Carbon Fiber and Composite Materials Technology Innovation Center for their invaluable support and resources provided during this research.

Data availability

Data will be made available on request.

References

[1] R. Rodrigues, S. Gaboreau, J. Gance, I. Ignatiadis, S. Betelu, Reinforced concrete structures: a review of corrosion mechanisms and advances in electrical methods for corrosion monitoring, Constr. Build. Mater. 269 (2021) 121240, https://doi.org/10.1016/j.conbuildmat.2020.121240.
[2] O. Gooranorimi, A. Nanni, GFRP reinforcement in concrete after 15 years of service, J. Compos. Constr. 21 (2017) 04017024, https://doi.org/10.1061/(ASCE)CC.1943-5614.0000806.
[3] C.H. Lu, S.Q. Yuan, R.G. Liu, Experimental and probabilistic analysis of time to corrosion-induced cover cracking for marine reinforced concrete structures, Corros. Eng. Sci. Technol. 52 (2017) 124–133, https://doi.org/10.1080/1478422X.2016.1213082.
[4] L. Sun, X.Q. Mi, X.S. Zhang, Experimental study on the compression performance of GFRP bars under different corrosion environment, AMM 71-78 (2011) 1711–1714, https://doi.org/10.4028/www.scientific.net/amm.71-78.1711.
[5] C.H. Lu, M.Z. Ni, T.S. Chu, L.Y. He, Comparative investigation on tensile performance of FRP bars after exposure to water, seawater, and alkaline solutions, J. Mater. Civ. Eng. 32 (2020) 04020170, https://doi.org/10.1061/(ASCE)MT.1943-5533.000324.
[6] F.M. Özkal, M. Polat, M. Yağ an, M.O. Öztürk, Mechanical properties and bond strength degradation of GFRP and steel rebars at elevated temperatures, Constr. Build. Mater. 184 (2018) 45–57, https://doi.org/10.1016/j.conbuildmat.2018.06.203.
[7] C.H. Zhou, J.J. Pan, Z. Zhang, Y.H. Zhu, Comparative study on the tensile mechanical behavior of GFRP bars under and after high temperature exposure, Case Stud. Constr. Mater. 16 (2022) 00905, https://doi.org/10.1016/j.cscm.2022.e00905.
[8] Z.K. Wang, K. Wang, J. Zhao, S.B. Wang, E.D. Shumuve, Z.H. Yang, The mechanical properties of GFRP bars embedded in geopolymer concrete after high temperature exposure, J. Build. Eng. 62 (2022) 105355, https://doi.org/10.1016/j.jobe.2022.105355.
[9] S. Solyom, M. Di Benedetti, M. Guadagnini, G.L. Balázs, Effect of temperature on the bond behaviour of GFRP bars in concrete, Compos. Part B Eng. 183 (2020) 107602, https://doi.org/10.1016/j.compositesb.2019.107602.
[10] J. Michels, R. Widmann, C. Czaderski, R. Allahvirdizadeh, M. Motavalli, Glass transition evaluation of commercially available epoxy resins used for civil engineering applications, Compos. Part B Eng. 77 (2015) 484–493, https://doi.org/10.1016/j.compositesb.2015.03.053.

[11] X. Liang, W.Y. Wang, L.L. Hu, P. Feng, Experimental and numerical study on high-temperature performance of prestressed CFRP-reinforced steel columns, Eng. Struct. 301 (2024) 117347, https://doi.org/10.1016/j.engstruct.2023.117347.
[12] M. Haris, E. Xiong, W. Gao, M.A. Samuel, N.U. Sahar, A. Saleem, Strengthening reinforced concrete members using FRP—evaluating fire performance, challenges, and future research directions: a state-of-the-art review, Polymers 17 (2025) 13, https://doi.org/10.3390/polym17010013.
[13] X. Yin, Y. Liu, Y. Miao, G. Xian, Water absorption, hydrothermal expansion, and thermomechanical properties of a vinyl ester resin for fiber-reinforced polymer composites subjected to water or alkaline solution immersion, Polymers 11 (2019) 505, https://doi.org/10.3390/polym11030505.
[14] B. Benmokrane, A.H. Ali, H.M. Mohamed, A. ElSafty, A. Manalo, Laboratory assessment and durability performance of vinyl ester, polyester, and epoxy glass-FRP bars for concrete structures, Compos. Part B Eng. 114 (2017) 163–174, https://doi.org/10.1016/j.compositesb.2017.02.002.
[15] G.F. Ji, G.Q. Li, W. Alaywan, A new fire resistant FRP for externally bonded concrete repair, Constr. Build. Mater. 42 (2013) 87–96, https://doi.org/10.1016/j.conbuildmat.2013.01.008.
[16] M.R. Petersen, A. Chen, M. Roll, S.J. Jung, M. Yossef, Mechanical properties of fire-retardant glass fiber-reinforced polymer materials with alumina tri-hydrate filler, Compos. Part B Eng. 78 (2015) 109–121, https://doi.org/10.1016/j.compositesb.2015.03.071.
[17] J.B. Yang, Y.R. Bai, J.S. Sun, K. Lv, Y.M. Lang, Recent advances of thermosetting resin and its application prospect in oil and gas drilling and production engineering, Geoenergy Sci. Eng. 230 (2023) 212222, https://doi.org/10.1016/j.geoen.2023.212222.
[18] X. Mu, D. Wang, Y. Pan, W. Cai, L. Song, Y. Hu, A facile approach to prepare phosphorus and nitrogen containing macromolecular covalent organic nanosheets for enhancing flame retardancy and mechanical property of epoxy resin, Compos. B. Eng. 164 (2018) 390–399, https://doi.org/10.1016/j.compositesb.2018.12.036.
[19] A. Bifulco, C.–D. Varganici, L. Rosu, F. Mustata, D. Rosu, S. Gaan, Recent advances in flame retardant epoxy systems containing non-reactive DOPO based phosphorus additives, Polym. Degrad. Stab. 200 (2022) 109962, https://doi.org/10.1016/j.polymdegradstab.2022.109962.
[20] Y. Yang, D.-Y. Wang, R.-K. Jian, Z. Liu, G. Huang, Chemical structure construction of DOPO-containing compounds for flame retardancy of epoxy resin: a review, Prog. Org. Coat. 175 (2023) 107316, https://doi.org/10.1016/j.porgcoat.2022.107316.
[21] B. Perret, B. Schartel, K. Stöß, M. Ciesielski, J. Diederichs, M. Döring, J. Krämer, V. Altstädt, Novel DOPO-based flame retardants in high-performance carbon fibre epoxy composites for aviation, Eur. Polym. J. 47 (2011) 1081–1089, https://doi.org/10.1016/j.eurpolymj.2011.02.008.
[22] S.K. Dirlikov, Propargyl-terminated resins-a hydrophobic substitute for epoxy resins, High. Perform. Polym. 2 (1990) 67–77, https://doi.org/10.1177/152483999000200107.
[23] W.J. Zhang, M.T. Zhou, Y.C. Kan, J. Chen, Y. Hu, W.Y. Xing, Synthesis and flame retardant efficiency study of two phosphorus-nitrogen type flame retardants containing triazole units, Polym. Degrad. Stab. 208 (2023) 110236, https://doi.org/10.1016/j.polymdegradstab.2022.110236.
[24] Standardization Administration of the People's Republic of China, GB/T 2406.2-2009 Plastics-Determination of burning behaviour by oxygen index-Part 2: Ambient-temperature test, Standardization Administration of the People's Republic of China (SAC), 2020. (in Chinese).
[25] I.C. Rosa, Fire behaviour of concrete structures reinforced with GFRP bars, Ph.D. thesis, Dept. of Civil Engineering, Instituto Superior Técnico, Univ. of Lisbon, 2022.
[26] I. Rozsypalova, J. Prokes, D. Cairovic, F. Girgle, P. Danek, P. Stepanek, Research on the residual tensile strength of composite reinforcing bars exposed to elevated temperatures, IOP Conf. Ser. Mater. Sci. Eng. 1205 (2021) 012011, https://doi.org/10.1088/1757-899X/1205/1/012011.
[27] E. McIntyre, Fire performance of fibre reinforced polymer (FRP) bars in reinforced concrete: an experimental approach, Ph.D. thesis, Dept. of Civil Engineering, Univ. of Edinburgh, 2019.
[28] H. Ashrafi, M. Bazli, A. Vatani Oskouei, L. Bazli, Effect of sequential exposure to UV radiation and water vapor condensation and extreme temperatures on the mechanical properties of GFRP bars, J. Compos. Constr. 22 (2018) 04017047, https://doi.org/10.1061/(asce)cc.1943-5614.0000828.
[29] H. Ashrafi, M. Bazli, E.P. Najafabadi, A. Vatani Oskouei, The effect of mechanical and thermal properties of FRP bars on their tensile performance under elevated temperatures, Constr. Build. Mater. 157 (2017) 1001–1010, https://doi.org/10.1016/j.conbuildmat.2017.09.160.
[30] M. Robert, B. Benmokrane, Behavior of GFRP reinforcing bars subjected to extreme temperatures, J. Compos. Constr. 14 (2010) 353–360, https://doi.org/10.1061/(ASCE)CC.1943-5614.0000092.
[31] Standardization Administration of the People's Republic of China, GB 20016-2014 Code for fire protection of building, Standardization Administration of the People's Republic of China (SAC), 2014. (in Chinese).
[32] Canadian Standards Association, CSA S806-12 Design and construction of building components with fibre-reinforced polymers, Canadian Standards Association, Mississauga, ON, Canada, 2012.
[33] American Concrete Institute, ACI 440.1R-15 Guide for the design and construction of concrete reinforced with FRP bars, ACI Committee 440, Farmington Hills, MI, 2015.
[34] Abaqus Inc., ABAQUS2021 Analysis users' manual, Abaqus Inc., Providence, RI, USA, 2021.
[35] European Committee for Standardization, Eurocode 2: Design of concrete structures – Part 1-2: General rules – structural fire design, European Committee for Standardization (CEN), Brussels (Belgium), 2004.
[36] E.M. Ellobody, C.G. Bailey, Modelling of unbonded post-tensioned concrete slabs under fire conditions, Fire Saf. J. 44 (2009) 159–167, https://doi.org/10.1016/j.firesaf.2008.05.007.
[37] I.C. Rosa, J. Firmo, J.R. Correia, Experimental study of the tensile behaviour of GFRP reinforcing bars at elevated temperatures, Constr. Build. Mater. 324 (2022) 126676, https://doi.org/10.1016/j.conbuildmat.2022.126676.
[38] International Organization for Standardization, ISO 834-1 Fire resistance tests-Elements of building construction-Part 1: General requirements, ISO, Geneva (Switzerland), 1999.
[39] H. Hajiloo, M.F. Green, GFRP reinforced concrete slabs in fire: finite element modelling, Eng. Struct. 183 (2019) 1109–1120, https://doi.org/10.1016/j.engstruct.2019.01.028.
[40] Ministry of Construction of People's Republic of China, GB 50009-2012 Load code for the design of building structures. Ministry of Construction of People's Republic of China (MCC), 2012. (in Chinese).
[41] A. Zaidi, R. Masmoudi, M. Bouhicha, Numerical analysis of thermal stress-deformation in concrete surrounding FRP bars in hot region, Constr. Build. Mater. 38 (2013) 204–213, https://doi.org/10.1016/j.conbuildmat.2012.08.047.

ACCEPTANCE LETTER FOR PAPER SUBMISSION

Date: June 17, 2025

To: **Terrance Lim,**

We are pleased to inform you that your paper titled "LONG-TERM BEHAVIOR OF HIGH PERFORMANCE GFRP BARS, T. Lim [et al.] (sciencesconf.org:rilemweek2025:600496)" has been accepted for presentation the 79th RILEM Annual Week & ICONS 2025 International Conference on Advances in Engineering and Technology for Sustainable Development.

Please find the reviewers' comments below. Kindly note that accepted full papers will be published in the Springer-RILEM Bookseries (indexed in Scopus and Web of Science). Therefore, it is essential that you strictly adhere to the full paper template, which can be found here: <br data-start="757" data end="760" />https://rilemweek2025.sciencesconf.org/resource/page/id/21

Please upload your revised paper via the submission system no later than June 8, 2025.

We sincerely appreciate your contribution and look forward to welcoming you at the conference!

With our best wishes,



Prof. Van Tuan NGUYEN
Chairman of Scientific committee
79th RILEM Annual week & ICONS 2025
Hanoi, Vietnam
Email: tuannv@huce.edu.vn | Tel: +84 909886386

Long-term Behavior of High Performance GFRP Bars

Terrance Lim[1], Tao He[2], Lili Hu[3][0000-0001-7935-7667].

[1] School of Ocean and Civil Engineering, Shanghai Jiao Tong University, Shanghai, China
[2] Department of Civil Engineering, Tsinghua University, Beijing 100084, China
[3] Research Institute of Urbanization and Urban Safety, School of Future Cities, University of Science and Technology Beijing, Beijing, 100083, China
lilihu@ustb.edu.cn

Abstract. Reinforced concrete is widely used in buildings and infrastructures, but corrosion of steel reinforcement remains a challenge. Glass fiber reinforced polymer (GFRP) bars offer a corrosion-resistant alternative, particularly in harsh environments. Despite their advantages, GFRP bars face limitations in long-term creep behavior, prompting modifications to overcome the weakness and expand their applications. This study explores the creep behavior of modified bars under varying level of sustained loads for at least 500 hours. Based on the observed progression, the creep ratio at the target service life was predicted using an appropriate creep model, yielding values between 5% and 8% for the investigated stress levels of 30% to 60%. The results provide valuable insights that are crucial for advancing the use of newly developed GFRP bars with enhanced properties.

Keywords: GFRP Bar, High Performance, Sustained Load, Long-term, Creep Ratio.

1 Introduction

For years, steel-reinforced concrete has been a cornerstone of construction, widely employed in buildings and infrastructure projects [1]. Yet, the durability of steel reinforcements remains a significant challenge. Steel bars are prone to corrosion, which not only diminishes their strength but also leads to cracking and spalling in the concrete [2,3]. This deterioration undermines the structural integrity and functionality of buildings and infrastructure [4]. Consequently, the lifespan of these structures is often drastically reduced. Premature degradation leads to increased resource use, as structures may need frequent reconstruction or maintenance, compounding their ecological impact [5,6]. Given these challenges, improving the longevity of steel-reinforced concrete remains a critical focus in the construction industry. Enhanced protective measures such as corrosion-resistant coatings, cathodic protection systems [7], and improved concrete mix designs [8] have been implemented to mitigate these issues. However, despite these advancements, corrosion-related deterioration continues to be a persistent problem, driving the need for further research and innovation in structural durability.

In response, fiber-reinforced polymer (FRP) rebars have emerged as a viable alternative to traditional steel rebars, offering superior durability in corrosive conditions [9]. Glass-fiber reinforced polymer (GFRP) bars have gained traction due to their corrosion resistance, high strength, and lightweight properties [10]. In fact, they are much lighter than steel, reducing transportation and handling costs and enabling more efficient design.

While short-term studies and laboratory tests have yielded promising results, their long-term performance—particularly their resistance to creep—remains a significant concern. The presence of sustained load over extended periods has been shown to cause progressive elongation of GFRP profiles, raising questions about their durability and reliability in structural applications [11]. To tackle this issue, a fundamental understanding of the constituent materials of GFRP bars is essential, as modifying these materials is a key approach in improving the overall performance. Since GFRP is a composite material made from combination of fibers and resin, its mechanical behavior is heavily influenced by the properties of both components [12]. In the context of creep, the resin matrix is particularly susceptible due to its viscoelastic nature [13], which allows it to deform gradually under sustained stress. In contrast, the fibers are more rigid and contribute significantly to the material's overall strength [14]. In this initiative, resin modification was conducted to enhance creep resistance. Additionally, fibers were carefully selected to ensure compatibility with the modified resin. However, the interaction between these two components inherently forms a complex mechanism that is not yet fully understood. With additional enhancements through materials modification, it adds another layer of complexity. Therefore, further research is necessary to comprehensively understand the long-term behavior of GFRP bars and encourage their application. In this regard, this paper presents the results of creep investigation on the newly developed GFRP bars, aiming to provide insights into their behavior under sustained loads and to evaluate the effectiveness of material modifications.

2 GFRP Bar

GFRP bars are composed of fibers and resin matrix, pultruded to form a composite material. Careful selection of these composing materials is essential, as they significantly influence the properties of the final product. The resin matrix plays a dominant role in creep performance due to its viscoelastic properties. To improve creep performance, resin modification is essential. In this study, a widely used vinyl ester resin was modified by incorporating a synthesized phosphor-containing aryl propargyl ether compound. This modification significantly enhanced the heat resistance compared to the unmodified resin, justifying its classification as high-performance material. Besides the resin matrix, fibers are another critical component, constituting up to three-quarters of the bar's composition. In this study, TCR glass fibers produced by Taishan Fiberglass Inc. were used. These fibers are known for their excellent high-temperature creep resistance. Since glass fibers are inherently more resistant to creep, the interplay between the fibers and the resin matrix is crucial in determining the

overall creep performance of the bars. Apart from their superior technical properties, TCR fibers also offer better economic advantages compared to other fibers with similar characteristics. The GFRP bars were manufactured using a pultrusion process with involvement of heat to facilitate hardening and curing. The final product of GFRP bar is 8 mm in diameter. The properties of GFRP bar are presented on Table 1.

Table 1. GFRP bar properties.

Fibers Type	Resin Type	Fiber Content (%)	Diameter (mm)
TCR	Modified Vinyl Ester Resin	70	8

3 Experiment

3.1 Tensile Test

A tensile test was conducted prior to the creep test to evaluate the short-term mechanical behavior of the produced bars. The tensile strength of the GFRP rebars was determined by testing two specimens at 20°C, with a controlled loading rate of 5 mm/min until failure. As shown in Fig. 1, the results indicated an ultimate tensile strength of 1256 MPa and an elastic modulus of 45.1 GPa for the GFRP bars.

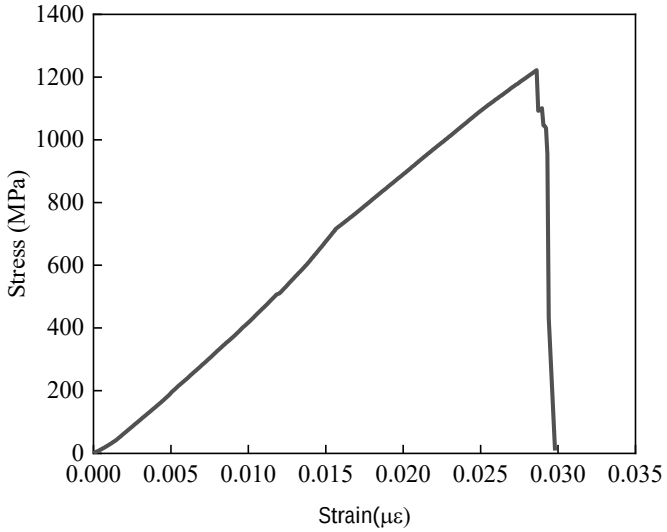


Fig. 1. Stress-strain curve of GFRP bar.

3.2 Creep Test

Creep tests were conducted utilizing a mechanical testing device designed for a sustained period of loading. The device incorporates a load-amplifying mechanism to enhance loading efficiency. Loads were applied using load weights according to the test program for each specimen. The setup is shown in Fig. 2. A specially designed anchorage system, illustrated in Fig. 3, was used to securely attach GFRP bars to the testing machine. The design complies with EN 17129:2018 standard.

The test program is detailed in Table 2. Eight specimens were tested, with two specimens at each stress level. However, some unfit results were excluded from the analysis. The nomenclature of specimens follows this rule: taking "30(1)" as example, number "30" before parentheses indicates the sustained stress level in percentage, and number "1" inside parentheses indicates specimen number within the same category. The creep ratio is calculated as the ratio between creep strain to immediate strain instantly after loading. Creep strain, which is a strain developed during the sustained loading process, is obtained by subtracting the immediate strain from the final recorded strain.

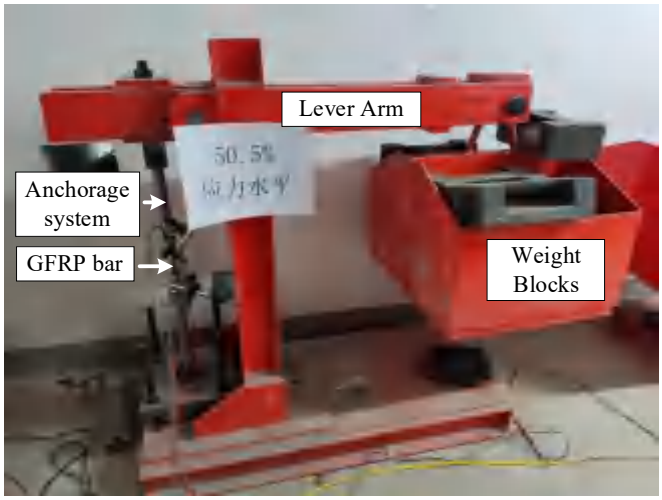


Fig. 2. Anchorage system of GFRP bar for creep test.

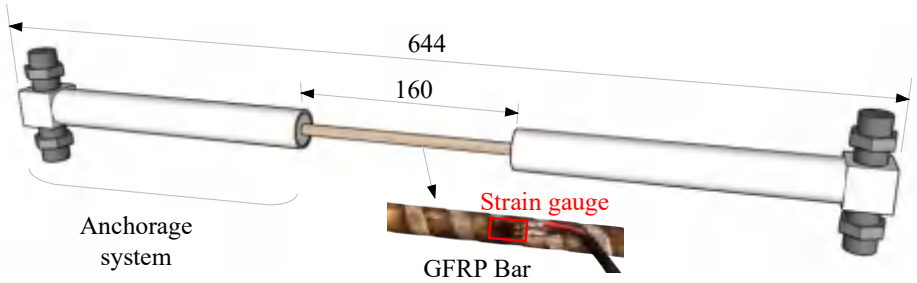


Fig. 3. Anchorage system of GFRP bar for creep test.

Table 2. Creep experiment test program and result.

Specimens	Sustained Stress (% of UTS)	Duration (h)	Creep Ratio (%)
30(1)	30	1393.42	3.63
40(1)	40	528.08	5.85
40(2)	40	1393.42	2.86
50(1)	50	528.08	4.15
60(1)	60	528.08	4.57

The experimental results are presented in Table 2, which illustrates the creep behavior of the tested bars under varying load levels. During the test, no rupture failure was observed, even after extending the loading duration to nearly 1400 hours. However, one of the two data loggers used encountered issues in exporting data, resulting in incomplete records for half of the specimens. Consequently, the reported creep ratios are based on the shortest duration of all tests, which is 528 hours to ensure a logically consistent comparison. In general, the creep ratio tends to increase with the level of sustained stress. Experimental results show that the creep ratio ranges from 3% to 5% for GFRP bars loaded at 30% to 60% of their UTS. This value represents the creep progression under a relatively short-term loading, spanning just over 500 hours.

However, to achieve a significant breakthrough in practical engineering, it is essential to understand the creep behavior over the entire target service lifetime of GFRP bars, which is widely adopted to be 114 years (10^6 hours). Due to practical limitations, conducting a full-length test over such an extended period is unfeasible. Therefore, a statistical approach was employed to identify the most suitable creep model for forecasting behavior at the target service life based on available data. This approach is justified, as the experimental results show that creep behavior has entered the relatively predictable second stage, characterized by a constant creep rate. This stage persists for a prolonged period before transitioning to the third stage, which ultimately leads to rupture. The creep model proposed by D'Antino and Pisani [15], which incorporates a linear viscoelastic relationship, was selected and proved to be accurate for our dataset. The model predicts a creep ratio range of 5% to 8% at 114 years for GFRP bars loaded at 30% to 60% of their UTS.

4 Conclusion

This study addresses the shortcomings of GFRP bars, particularly their creep behavior, as a critical area of investigation. The first step involves modifying the resin matrix to target the underlying causes of creep. Paired with a careful selection of fibers, a new GFRP bar was manufactured and subjected to tensile and creep testing. The results demonstrated that the GFRP bar possesses adequate mechanical properties, with a tensile strength of 1256 MPa. The creep ratio ranged from 5% to 8% at the target service life of 114 years under sustained stress levels of 30% to 60%.

References

1. Allen E, Iano J (2013) Fundamentals of Building Construction: Materials and Methods. John Wiley & Sons, Inc., Hoboken, New Jersey.
2. Fang C, Lundgren K, Plos M, Gylltoft K (2006) Bond behaviour of corroded reinforcing steel bars in concrete. Cement and Concrete Research, 36(10).
3. Kashani M M, Lowes L N, Crewe A J, Alexander N A (2014) Finite element investigation of the influence of corrosion pattern on inelastic buckling and cyclic response of corroded reinforcing bars. Engineering Structures, 75.
4. Ma Y, Zhang J, Wang L, Liu Y (2013) Probabilistic prediction with bayesian updating for strength degradation of RC Bridge Beams. Structural Safety, 44.
5. Broomfield J P (2023) Corrosion of Steel in Concrete. CRC Press, London.
6. Economic Development Research Group Inc. (2011) The Failure to Act: The Economic Impact of Current Investment Trends in Surface Transportation. American Society of Civil Engineers, Reston, Virginia.
7. Koleva D A, Hu J, Fraaij A L A, Stroeven P, Boshkov N,van Breugel K (2006). Cathodic protection revisited: Impact on structural morphology sheds new light on its efficiency. Cement and Concrete Composites, 28(8), 696–706.
8. Wang J, Kim Y J (2023). Evolutionary characteristics of microstructural hydration and chloride diffusion in UHPC. Materials & Design, 225, 111528.
9. Becque J, Patnaik A K, Rizkalla S H (2003b). Analytical models for concrete confined with FRP tubes. Journal of Composites for Construction, 7(1), 31–38.
10. Cadenazzi T, Dotelli G, Rossini M, Nolan S, Nanni A (2019) Life cycle cost and life cycle assessment analysis at the design stage of a fiber reinforced polymer reinforced concrete bridge in Florida. Advances in Civil Engineering Materials 8(2):128-151
11. Gonilha J A, Correia J R, Branco F A (2013a). Creep response of GFRP–concrete hybrid structures: Application to a footbridge prototype. Composites Part B: Engineering, 53, 193–206.
12. Hollaway L C (2011). Key issues in the use of Fibre Reinforced Polymer (FRP) composites in the rehabilitation and retrofitting of concrete structures. Service Life Estimation and Extension of Civil Engineering Structures, 3–74.
13. Ganesh G K B N V S, Hiremath M M, Ray B C, Prusty R K (2021). Improved mechanical responses of GFRP composites with epoxy-vinyl ester interpenetrating polymer network. Polymer Testing, 93, 107008.
14. ACI 440.1R-15 (2015) Guide for the design and construction of concrete reinforced with FRP bars. American Concrete Institute, Farmington Hills, MI.
15. Antino T, Pisani M A (2019a) Long-term behavior of GFRP reinforcing bars. Composite Structures, 227, 111283.

Construction and Building Materials 493 (2025) 143222

Contents lists available at ScienceDirect

Construction and Building Materials

journal homepage: www.elsevier.com/locate/conbuildmat

High-temperature mechanical properties of GFRP bars: Experimental database and novel degradation models

De-Xin Duan [a,b], En-Ci Liu [d], Yu-Qing Zhang [d], Wan-Yang Gao [a,b,c,e,*]

[a] State Key Laboratory of Ocean Engineering, Shanghai Jiao Tong University, Shanghai 200240, China
[b] Shanghai Key Laboratory for Digital Maintenance of Buildings and Infrastructure, School of Ocean and Civil Engineering, Shanghai Jiao Tong University, Shanghai 200240, China
[c] Yunnan Key Laboratory of Building Structure and New Materials, Yunnan Institute of Building Research, Co., Ltd., Kunming 650223, China
[d] Zhongfu Carbon Fiber Core Cable Technology Co., Ltd., Lianyungang 222006, China
[e] Non-Metallic Excellent and Innovative Center for Building Materials, Beijing 100024, China

ARTICLE INFO

Keywords:
GFRP bars
High temperatures
Tensile strength
Elastic modulus
Experimental database
Degradation models

ABSTRACT

Glass fiber-reinforced polymer (GFRP) bars have emerged as a promising alternative to steel reinforcements in concrete structures exposed to aggressive or corrosive environments, primarily due to their superior corrosion resistance and high strength-to-weight ratio. However, the mechanical properties of GFRP bars deteriorate significantly at high temperatures, raising significant concerns about the fire resistance of GFRP bar-reinforced concrete (GFRP RC) members, especially in indoor applications. Despite numerous experimental investigations, the literature still lacks robust and accurate constitutive models capable of predicting the high-temperature degradation behavior of GFRP bars. This study established a comprehensive experimental database comprising 1087 tensile test results of GFRP bars subjected to temperatures ranging from ambient conditions up to 715°C. To address the lack of data on GFRP bars with high glass transition temperatures (T_g), additional high-temperature tensile tests were conducted on 24 GFRP bars with a T_g of 215°C. A critical evaluation of existing predictive models revealed substantial discrepancies between the predicted and observed residual mechanical properties. To identify the key parameters influencing the thermal degradation of the mechanical properties of GFRP bars at high temperatures, an analysis of variance (ANOVA) was performed, focusing on the roles of T_g and the thermal decomposition temperature (T_d). Using the artificial intelligence software Eureqa and the collected experimental database, novel degradation models were developed to predict the residual tensile strength and elastic modulus of GFRP bars at high temperatures. The predictive accuracy and reliability of the proposed models were validated by comparing the model predictions with the corresponding experimental results.

1. Introduction

Since the late 20th century, fiber-reinforced polymer (FRP) composites have been increasingly utilized in structural engineering for both new construction and rehabilitation projects, owing to their exceptional durability and resistance to environmental degradation [1]. Among the various types of FRP products, FRP reinforcing bars (rebars) have emerged as a viable alternative to traditional steel reinforcement, particularly in concrete structures exposed to harsh environments, such as marine settings, deicing salts and chemically corrosive conditions commonly found in bridge decks, parking garages and marine structures [2,3]. The inherent corrosion resistance and electromagnetic neutrality of FRP bars further enhance their applicability in structures that require long service lives and specialized functional constraints [4].

Glass fiber-reinforced polymer (GFRP) bars are among the most widely adopted types of FRP reinforcement due to their cost-effectiveness and favorable mechanical properties, making them a practical alternative to conventional steel bars in various structural applications [5]. Over the past few decades, significant advancements have been made in understanding the structural behavior of GFRP-reinforced concrete (GFRP RC) members through both experimental investigations and numerical modeling (e.g., [5–15]). These efforts have contributed to the development of design guidelines and standards (e.g., [16–18]) that extend traditional reinforced concrete (RC) design methodologies by explicitly considering the unique characteristics of GFRP reinforcement, particularly its linear-elastic behavior

* Corresponding author at: State Key Laboratory of Ocean Engineering, Shanghai Jiao Tong University, Shanghai 200240, China
E-mail address: wanyanggao@sjtu.edu.cn (W.-Y. Gao).

https://doi.org/10.1016/j.conbuildmat.2025.143222
Received 2 December 2024; Received in revised form 12 July 2025; Accepted 16 August 2025
Available online 20 August 2025
0950-0618/© 2025 Elsevier Ltd. All rights are reserved, including those for text and data mining, AI training, and similar technologies.

up to failure and lack of yielding capacity. Unlike steel, GFRP bars exhibit negligible ductility and typically fail in a brittle manner. Consequently, two primary failure modes of GFRP RC flexural members are observed: concrete crushing in compression and rupture of the GFRP bars in tension [6,19,20]. Of these, concrete crushing is generally preferred in design practice due to its more ductile failure process and the presence of identifiable warning signs prior to structural collapse.

A fundamental difference between GFRP and steel reinforcement lies in their performance at high temperatures, particularly under fire exposure [21–24]. Steel-reinforced concrete members generally exhibit superior fire resistance, primarily because the reinforcing steel retains a significant portion of its mechanical properties up to critical temperature thresholds. For example, conventional steel rebars typically maintain approximately 50 % of their ambient yield strength at around 593°C, a value widely referenced in fire-resistance design criteria for RC members [25]. In contrast, GFRP bars, which consist of glass fibers embedded in a thermosetting polymer matrix, are highly susceptible to thermal degradation. Experimental studies have demonstrated that the mechanical performance of GFRP bars, particularly their tensile strength, deteriorates progressively with increasing temperature. Significant losses typically begin near the glass transition temperature (T_g), which usually ranges from 65°C to 120°C. At this stage, the polymer matrix softens and loses its ability to transfer stresses between fibers. Tensile strength reductions of up to 40 % compared to ambient values have been reported within this temperature range [21,24]. Beyond T_g, the degradation may stabilize temporarily before entering a more severe phase as the temperature approaches the thermal decomposition temperature (T_d), which is typically below 500°C. In this regime, tensile strength may decline to as low as 10 %-30 % of its ambient value. This deterioration is primarily attributed to the chemical decomposition of the polymer matrix and the progressive weakening of the fiber-matrix interfacial bond [21,24,26]. Despite the significance of this degradation mechanism for structural fire safety, current design codes and guidelines do not provide temperature-dependent constitutive models for GFRP bars. This absence hinders the accurate evaluation of the fire performance of GFRP RC structural members and is largely due to the limited availability of reliable, validated models capable of capturing the high-temperature mechanical properties of GFRP bars.

This study aims to address this critical gap in the literature by collecting and analyzing a comprehensive experimental database comprising 1087 tensile test results for GFRP bars, covering a temperature range from ambient conditions up to 715°C. One notable shortcoming of the existing data is the limited availability of high-temperature test results for GFRP bars with high glass transition temperatures (T_g). To overcome this limitation, additional tensile tests were conducted on GFRP bars with a T_g of 215°C. The enhanced thermal performance of these bars is primarily attributed to a proprietary polymer matrix, which consists of a vinyl ester core for structural integrity and a phenolic resin layer that improves fire and smoke resistance. Consequently, these high-T_g GFRP bars exhibit superior thermal stability and retain a higher proportion of their mechanical properties at moderately high temperatures, making them particularly suitable for use in fire-exposed structural applications. Given the current lack of high-temperature mechanical property data for high-T_g GFRP bars, the results presented in this study are expected to provide valuable contributions to both research and engineering design practice. A comparative evaluation was conducted to assess the predictive accuracy of existing mechanical property degradation models using the collected database, which revealed significant deficiencies in their accuracy at high temperatures. Furthermore, an analysis of variance (ANOVA) was performed to identify key parameters influencing the mechanical property degradation of GFRP bars at high temperatures, with particular focus on the roles of T_g and the thermal decomposition temperature (T_d). Based on the collected data, temperature-dependent degradation models for tensile strength and elastic modulus were developed using the Eureqa artificial intelligence software [27]. The proposed degradation models were rigorously validated against both the collected database and the newly generated test results for high-T_g GFRP bars. Their predictive accuracy and general applicability suggest their potential use in fire performance assessments and the structural design of GFRP RC members subjected to high temperatures.

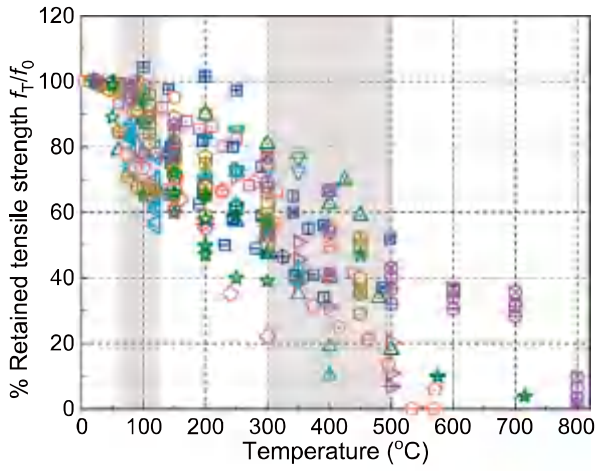
2. Experimental database

2.1. Review of existing test data

Numerous experimental investigations have been conducted to examine the mechanical properties of GFRP bars at high temperatures [28–47]. This section presents a comprehensive review of the existing tensile test data for GFRP bars subjected to steady-state high-temperature environments. The tensile stress-strain responses of GFRP bars consistently exhibit approximately linear elastic behavior until failure across the entire range of investigated temperatures [46,48,49]. The ultimate tensile strength is typically defined as the maximum stress observed prior to failure, while the elastic modulus is derived from the initial linear slope of the stress-strain curve. Fig. 1a and b depict the variations in tensile strength and elastic modulus as a function of increasing temperature, with the percentage of retained strength or modulus defined as the tensile strength or elastic modulus at a given temperature (T) relative to the corresponding value at ambient temperature (T_0). Additionally, the available values of T_g and T_d, along with the respective testing methods, are reported. The shaded regions in Fig. 1 indicate the typical temperature ranges of T_g (65°C-120°C) [24] and T_d (300°C-500°C) [50].

The data presented in Fig. 1 indicate a significant reduction in both tensile strength and elastic modulus as the exposure temperature increases. Given that GFRP bars are primarily composed of E-glass fibers, which exhibit softening and melting points of approximately 830°C and 1070°C, respectively [46], the thermal degradation observed below these temperatures, as illustrated in Fig. 1, is largely governed by the deterioration of the polymer matrix and the fiber-matrix interface. As the polymer matrix softens, its ability to transfer stress between the fibers diminishes, resulting in a progressive decline in mechanical performance. Although both tensile strength and elastic modulus are adversely affected by thermal exposure, the degradation of tensile strength is generally more severe than that of the elastic modulus. This disparity can be attributed to the greater sensitivity of tensile strength to fiber-matrix interfacial debonding and polymer decomposition, which subsequently reduces the effectiveness of load transfer between the fibers under axial loading.

Two distinct degradation phases have been identified in the high-temperature performance of GFRP bars: the **glass transition phase** and the **thermal decomposition phase**. During the glass transition phase, losses in tensile strength typically range from 15 % to 60 %. In the subsequent decomposition phase, further degradation can lead to reductions of 60–95 %. Similarly, the elastic modulus experiences reductions of approximately 5–30 % during the initial phase, which can increase to 20 %-95 % during decomposition. The variations in the degradation behavior of mechanical properties among different GFRP bars can primarily be attributed to differences in the chemistry of the polymer matrix, fiber volume fraction and fiber-matrix interaction. For instance, Kumahara et al. [29] compared GFRP bars fabricated with vinyl ester and polyphenylene sulfide (PPS) matrices. They found that the PPS-based bars exhibited superior thermal stability due to the higher T_g of PPS. Specifically, tensile strength reductions of 40 % and 60 % were recorded for vinyl ester bars at high temperatures of 250°C and 400°C, respectively, while the PPS-based bars retained a significantly higher proportion of their strength at temperatures up to 250°C. Rosa et al. [46] further investigated the influence of surface configurations (ribbed and sand-coated) and thermophysical properties (e.g., T_g and T_d)



Notes:

[a] T_g was determined as the onset temperature of the storage modulus decay from DMA tests.

[b] T_d was identified as the first peak decomposition temperature from TGA tests.

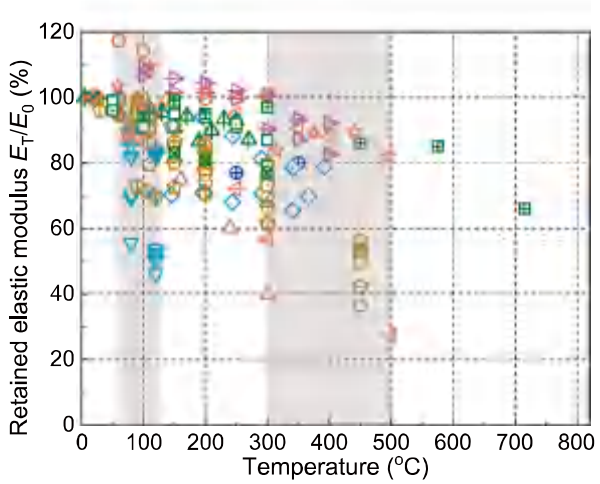
[c] The GFRP bars were embedded in concrete covers prior to high-temperature exposure.

[d] The GFRP bars were immersed in alkaline solutions prior to high-temperature exposure.

"N/A" indicates that the data was unavailable in the original source.

(a)

	T_g	T_d
Rosa *et al.* (2021)	157 °C[a] (DMA)	400 °C[b]
Rosa *et al.* (2021)	157 °C[a] (DMA)	400 °C[b]
Rosa *et al.* (2021)	104 °C[a] (DMA)	400 °C[b]
Rosa *et al.* (2019)	98 °C[a] (DMA)	374 °C[b]
McIntyre (2019)	59 °C[a] (DMA)	391 °C[b]
McIntyre (2019)	86 °C[a] (DMA)	408 °C[b]
McIntyre (2019)	83 °C[a] (DMA)	390 °C[b]
Hajiloo *et al.* (2018)	110 °C (DSC)	412 °C[b]
Hajiloo *et al.* (2018)	114 °C (DSC)	438 °C[b]
Hajiloo *et al.* (2018)	140 °C[a] (DMA)	451 °C[b]
Ashrafi *et al.* (2018)	95 °C (N/A)	N/A
Ashrafi *et al.* (2017)	110 °C (N/A)	N/A
Ashrafi *et al.* (2017)	110 °C (N/A)	N/A
Ashrafi *et al.* (2017)	110 °C (N/A)	N/A
Ashrafi *et al.* (2017)	105 °C (N/A)	N/A
Wang and Zha (2011)	75 °C (DSC)	425 °C[b]
Robert and Benmokrane (2010)	112 °C (DSC)	N/A
Najafabadi *et al.* (2019)[c]	110 °C (N/A)	N/A
Najafabadi *et al.* (2019)[c]	110 °C (N/A)	N/A
Najafabadi *et al.* (2019)[c]	110 °C (N/A)	N/A
Najafabadi *et al.* (2019)[c]	110 °C (N/A)	N/A
Zhou *et al.* (2022)	N/A	N/A
Weber (2008)	N/A	N/A
Zhou (2005)	N/A	N/A
Wang and Kodur (2005)	N/A	N/A
Wang and Kodur (2005)	N/A	N/A
Abbasi and Hogg (2005)[d]	N/A	N/A
Abbasi and Hogg (2005)[d]	N/A	N/A
Abbasi and Hogg (2005)[d]	N/A	N/A
Dimitrienko (1997)	N/A	N/A
Tanano *et al.* (1995)	N/A	N/A
Clarke (1993)	N/A	N/A
Kumahara *et al.* (1993)	N/A	N/A
Kumahara *et al.* (1993)	N/A	N/A



(b)

	T_g	T_d
Rosa *et al.* (2021)	157 °C[a] (DMA)	400 °C[b]
Rosa *et al.* (2021)	157 °C[a] (DMA)	400 °C[b]
Rosa *et al.* (2021)	104 °C[a] (DMA)	400 °C[b]
Rosa *et al.* (2019)	98 °C[a] (DMA)	374 °C[b]
Hajiloo *et al.* (2018)	114 °C (DSC)	438 °C[b]
Hajiloo *et al.* (2018)	140 °C[a] (DMA)	451 °C[b]
Ashrafi *et al.* (2018)	95 °C (N/A)	N/A
Ashrafi *et al.* (2017)	110 °C (N/A)	N/A
Ashrafi *et al.* (2017)	110 °C (N/A)	N/A
Ashrafi *et al.* (2017)	110 °C (N/A)	N/A
Ashrafi *et al.* (2017)	105 °C (N/A)	N/A
McIntyre *et al.* (2014)	59 °C[a] (DMA)	391 °C[b]
Wang and Zha (2011)	75 °C (DSC)	425 °C[b]
Zhou *et al.* (2022)	N/A	N/A
Zhou (2005)	N/A	N/A
Wang and Kodur (2005)	N/A	N/A
Wang and Kodur (2005)	N/A	N/A
Abbasi and Hogg (2005)[d]	N/A	N/A
Abbasi and Hogg (2005)[d]	N/A	N/A
Abbasi and Hogg (2005)[d]	N/A	N/A
Dimitrienko (1997)	N/A	N/A
Tanano *et al.* (1995)	N/A	N/A
Kumahara *et al.* (1993)	N/A	N/A

Fig. 1. Tensile property data collected for GFRP bars at high temperatures: (a) retained tensile strength, and (b) retained elastic modulus (adapted from [46]).

on the high-temperature performance of GFRP bars. Their results confirmed that the degradation of tensile strength was more severe than that of the elastic modulus, particularly near T_g and following the matrix decomposition. At 715°C, the residual tensile strength decreased to approximately 4 % of its ambient value, whereas the elastic modulus maintained roughly 66 % of its initial value.

In addition to material composition, several factors influencing the tensile behavior of GFRP bars at high temperatures include loading conditions, the presence of concrete cover and environmental exposure. Hajiloo et al. [40] investigated the tensile properties of GFRP bars under both steady-state and transient heating conditions, revealing similar degradation trends observed in both scenarios. Najafabadi et al. [43] evaluated the tensile performance of GFRP and carbon FRP (CFRP) bars embedded in concrete when subjected to thermal exposure of up to 800°C. Their results indicated that the presence of concrete cover significantly mitigated direct thermal and oxidative degradation, resulting in improved residual tensile performance compared to the bars that were directly exposed to high temperatures. Abbasi and Hogg [32] explored the combined effects of thermal and alkali exposure on GFRP bars. The specimens were preconditioned in water (pH 7) and an alkaline solution (pH 12.5) at 60°C for durations of 30, 120 or 240 days, followed by tensile testing at temperatures ranging from 20°C to 120°C. Their results demonstrated reductions in tensile strength of 48 %-80 % and reductions in stiffness of 41 %-84 % after exposure to 120°C. In addition, their results highlighted the critical role of polymer matrix integrity and fiber-matrix bond degradation in the deterioration of the mechanical properties of GFRP bars at high temperatures.

The literature review presented above highlights the importance of understanding the thermal-mechanical behavior of the polymer matrix and the degradation of the fiber-matrix interface in influencing the tensile performance of GFRP bars at high temperatures. Despite these insights, existing constitutive models often fail short in accurately predicting the mechanical properties observed during the glass transition and decomposition phases. To enable more precise predictions and modeling, this study collects a comprehensive high-temperature tensile test database comprising 1087 test results for GFRP bars. Table 1 (located in the appendix) summarizes the key experimental parameters and results, including the experimental variables such as (i) exposure temperature, (ii) surface treatment, (iii) bar diameter, (iv) T_g, and (v) T_d. The measured properties include (i) tensile strength at a given temperature (f_T), (ii) tensile strength retention (f_T/f_0), (iii) elastic modulus at a given temperature (E_T), and (iv) elastic modulus retention (E_T/E_0). The database covers a temperature range from 20°C to 715°C, with GFRP bar diameters varying from 4 mm to 18.5 mm. The surface treatments examined include sand-coated (SC) bars with helical wraps, ribbed bars (RB) and helix-wrapped (HW) bars. This database provides a robust foundation for the development and calibration of temperature-dependent degradation models for GFRP bars. Although significant advancements have been achieved in the manufacturing and quality control of GFRP bars over the past three decades, the fundamental constituent materials—E-glass fibers and thermosetting polymers—have remained largely unchanged. Consequently, the thermal degradation trends identified in this study are representative and not significantly influenced by the manufacturing era.

2.2. Tensile testing of high-T_g GFRP bars

2.2.1. Materials

Despite extensive research on the mechanical properties of GFRP bars at high temperatures, limited data are available for GFRP bars fabricated with high-T_g polymer matrices. This study presents the results of tensile tests conducted on thermally resistant helix-wrapped (HW) GFRP bars. The key material properties of the tested bars are summarized in Table 2. The HW GFRP bars were produced by Zhongfu Carbon Fiber Core Cable Technology Co., Ltd. (China) and have a nominal diameter of 12 mm. Each bar consists of an E-glass fiber core (model WS4000) that is impregnated with a high-T_g epoxy matrix, followed by the application of helical wrapping with additional fibers, which occurs post-pultrusion and prior to the thermal curing of the epoxy matrix.

The T_g value of the GFRP bars was determined through dynamic mechanical analysis (DMA) according to ASTM E1640 [51]. The tests were conducted using a TA Instruments Q800 dynamic mechanical analyzer (New Castle, DE; software version V20.24 Build 43). The samples with dimensions of 50 mm× 10 mm x 3 mm were sectioned from the core of the GFRP bar and tested in a dual cantilever configuration. The analysis was performed in a nitrogen atmosphere, maintaining a constant oscillation frequency of 1.0 Hz, a deformation amplitude of 15 μm, and a heating rate of 5 °C/min across a temperature range of 30°C to 200°C. As illustrated in Fig. 2, T_g was determined based on three characteristic temperatures: the onset temperature of the storage modulus (E') drop ($T_{g,onset}$, 215℃), the peak temperature of the loss modulus (E'') (230℃), and the peak temperature of the loss factor ($\tan\delta = E''/E'$) (231℃). Additionally, thermogravimetric analysis (TGA) was performed using a TGA550 instrument (TA Instruments, New Castle, DE) in accordance with ISO 11357 [52]. This analysis was conducted over a temperature range of 20℃ to 700℃ at a constant heating rate of 10℃/min under a nitrogen atmosphere. The onset of decomposition, $T_{d,onset}$, was defined as the temperature at which a 2 % normalized mass loss occurred [38]. The derivative thermogravimetry (DTG) curve, calculated as the first derivative of mass loss with respect to temperature (i.e., DTG = $\Delta mT/\Delta T$), was employed to identify additional indicators of thermal decomposition (see Fig. 3):

- $T_{d,peak}$ represents the temperature associated with the initial peak of the DTG curve, which is identified as the maximum rate of mass loss occurring during the primary decomposition phase of the polymer matrix.
- $T_{d,oxonset}$ is the temperature marking the onset of the secondary degradation phase, which is generally linked to oxidative decomposition.
- $T_{d,oxpeak}$ represents the temperature associated with the second peak in the DTG curve, which indicates the maximum rate of mass loss during oxidative decomposition. These thermophysical parameters collectively describe the multi-stage degradation behavior of the polymer matrix.

2.2.2. Tensile testing

Tensile tests were conducted on HW GFRP bars across a temperature range of 20°C to 550°C under steady-state thermal conditions. Eight temperature levels were selected: 20°C, 150°C, 300°C, 350°C, 400°C, 450°C, 500°C and 550°C. Three replicate specimens were tested at each temperature level. The selection of temperature increments was informed by the T_g (215°C) of the HW GFRP bars. Wider temperature intervals of 150°C were employed below 300°C to capture the gradual degradation, while narrower intervals of 50°C were used beyond 300°C to capture the rapid thermal degradation of mechanical properties.

Each specimen had a total length of 1200 mm and was tested using a 500 kN servo-hydraulic universal testing machine, which was equipped with a high-temperature furnace capable of reaching temperatures up to 1000°C, as illustrated in Fig. 4. To ensure adequate anchorage and to mitigate the risk of premature failures, which could arise from the inherently low transverse strength of GFRP bars, stainless steel sleeves filled with ultra-high-performance concrete (UHPC) were installed at both ends of each specimen. Each steel anchorage measured 380 mm in length and was positioned entirely outside the furnace to prevent thermal exposure during the heating process.

During the experimental procedure, a K-type thermocouple was securely attached to the exposed surface of each specimen to monitor the temperature of the bar accurately. Heating was applied at a controlled rate of approximately 11 °C/min, following the method described by Rosa et al. [46]. Upon reaching the designated target temperature, a

Table 1
Database: details of collected tensile tests of GFRP bars tested at high temperatures.

Reference	Specimenseries	T(°C)	d(mm)	T_g(°C)	T_d(°C)	f_T(MPa)	f_T/f_0(%)	E_T(GPa)	E_T/E_0(%)
Clark [28]	Polystal	20	N/A	N/A	N/A	1670.0	100.0	51.0	100.0
		150	N/A	N/A	N/A	1587.0	95.0	N/A	N/A
		200	N/A	N/A	N/A	1503.0	90.0	N/A	N/A
		300	N/A	N/A	N/A	1336.0	80.0	N/A	N/A
		400	N/A	N/A	N/A	918.0	55.0	N/A	N/A
Kumahara et al. [29]	PPS	20	N/A	N/A	N/A	N/A	100.0	N/A	100.0
		60	N/A	N/A	N/A	N/A	99.3	N/A	117.3
		100	N/A	N/A	N/A	N/A	104.3	N/A	114.1
		140	N/A	N/A	N/A	N/A	97.5	N/A	99.3
		200	N/A	N/A	N/A	N/A	101.4	N/A	99.6
		250	N/A	N/A	N/A	N/A	97.2	N/A	99.9
	Vinyl Ester	20	N/A	N/A	N/A	N/A	100.0	N/A	N/A
		60	N/A	N/A	N/A	N/A	78.9	N/A	N/A
		100	N/A	N/A	N/A	N/A	78.1	N/A	N/A
		140	N/A	N/A	N/A	N/A	78.0	N/A	N/A
		200	N/A	N/A	N/A	N/A	70.1	N/A	N/A
		250	N/A	N/A	N/A	N/A	57.3	N/A	N/A
		300	N/A	N/A	N/A	N/A	47.3	N/A	N/A
		350	N/A	N/A	N/A	N/A	34.9	N/A	N/A
		400	N/A	N/A	N/A	N/A	39.9	N/A	N/A
Tanano *et al.* [30]	Spiral Epoxy	20	N/A	N/A	N/A	N/A	100.0	N/A	100.0
		350	N/A	N/A	N/A	N/A	76.8	N/A	80.0
		250	N/A	N/A	N/A	N/A	84.8	N/A	77.0
Dimitrienko [31]	Epoxy	20	N/A	N/A	N/A	N/A	100.0	N/A	100.0
		100	N/A	N/A	N/A	N/A	70.3	N/A	90.1
		160	N/A	N/A	N/A	N/A	64.1	N/A	75.0
		200	N/A	N/A	N/A	N/A	55.3	N/A	71.1
		240	N/A	N/A	N/A	N/A	35.2	N/A	60.1
		300	N/A	N/A	N/A	N/A	22.2	N/A	40.0
Abbasi and Hogg [32]	G1-unexp	20	12.7	N/A	N/A	366.0	100.0	39.0	100.0
		80	12.7	N/A	N/A	277.0	75.7	27.0	69.2
		120	12.7	N/A	N/A	223.0	60.9	18.0	46.2
	G1-A1	20	12.7	N/A	N/A	346.0	100	36.0	100.0
		80	12.7	N/A	N/A	252.0	72.8	20.0	55.6
		120	12.7	N/A	N/A	193.0	55.8	18.0	50.0
	G1-A2	20	12.7	N/A	N/A	326.0	100	27.0	100.0
		80	12.7	N/A	N/A	242.0	74.2	19.0	70.4
		120	12.7	N/A	N/A	186.0	57.1	19.0	70.4
	G1-A3	20	12.7	N/A	N/A	286.0	100.0	22.0	100.0
		80	12.7	N/A	N/A	236.0	82.5	18.0	81.8
		120	12.7	N/A	N/A	174.0	60.8	18.0	81.8
	G2-unexp	20	12.7	N/A	N/A	416.0	100.0	37.0	100.0
		80	12.7	N/A	N/A	362.0	87.0	33.0	89.2
		120	12.7	N/A	N/A	332.0	79.8	31.0	83.8
	G2-A1	20	12.7	N/A	N/A	349.0	100.0	31.0	100.0
		80	12.7	N/A	N/A	289.0	82.8	28.0	90.3
		120	12.7	N/A	N/A	268.0	76.8	26.0	83.9
	G2-A2	20	12.7	N/A	N/A	333.0	100.0	29.0	100.0
		80	12.7	N/A	N/A	280.0	84.1	26.0	89.7
		120	12.7	N/A	N/A	223.0	67.0	24.0	82.8
	G3-unexp	20	12.7	N/A	N/A	396.0	100.0	41.0	100.0
		80	12.7	N/A	N/A	330.0	83.3	35.0	85.4
		120	12.7	N/A	N/A	246.0	62.1	22.0	53.7
	G3-A1	20	12.7	N/A	N/A	375.0	100.0	39.0	100.0
		80	12.7	N/A	N/A	295.0	78.7	32.0	82.1
		120	12.7	N/A	N/A	240.0	64.0	21.0	53.8
	G3-A2	20	12.7	N/A	N/A	299.0	100.0	33.0	100.0
		80	12.7	N/A	N/A	260.0	87.0	31.0	93.9
		120	12.7	N/A	N/A	210.0	70.2	17.0	51.5
Zhou [33]	GFRP	5	6.0	N/A	N/A	1138.1	100.0	51.5	100.0
		60	6.0	N/A	N/A	1059.2	93.1	51.1	99.2
		90	6.0	N/A	N/A	1046.5	92.0	48.5	94.2
		110	6.0	N/A	N/A	1033.4	90.8	49.7	96.5
		130	6.0	N/A	N/A	1046.4	92.0	49.1	95.3
		150	6.0	N/A	N/A	1003.2	88.1	46.7	90.7
		170	6.0	N/A	N/A	998.9	87.7	48.6	94.4
		190	6.0	N/A	N/A	972.4	85.4	44.6	86.6
		210	6.0	N/A	N/A	981.1	86.2	46.3	89.9
		230	6.0	N/A	N/A	912.5	80.2	48.1	93.4
		250	6.0	N/A	N/A	940.0	82.6	47.9	93.0
		270	6.0	N/A	N/A	776.0	68.2	44.9	87.2
Wang and Kodur [34]	9.5 GFRP	20	9.5	N/A	N/A	561.2	100.0	41.1	100.0
		100	9.5	N/A	N/A	535.4	95.4	40.9	99.7
		250	9.5	N/A	N/A	404.8	72.1	39.0	95.0

(*continued on next page*)

Table 1 (*continued*)

Reference	Specimenseries	T(°C)	d(mm)	T_g(°C)	T_d(°C)	f_T(MPa)	f_T/f_0(%)	E_T(GPa)	E_T/E_0(%)
		350	9.5	N/A	N/A	253.1	45.1	37.2	90.7
		500	9.5	N/A	N/A	88.2	15.7	N/A	N/A
	12.7GFRP	20	12.7	N/A	N/A	586.6	100.0	42.7	100.0
		100	12.7	N/A	N/A	447.3	76.3	37.2	87.1
		200	12.7	N/A	N/A	336.0	57.3	36.8	86.3
		300	12.7	N/A	N/A	315.7	53.8	42.8	100.3
		400	12.7	N/A	N/A	210.4	35.8	37.6	88.1
		500	12.7	N/A	N/A	52.6	9.0	11.8	27.5
Weber [35]	GFRP	20	16	N/A	N/A	1000.0	100.0	N/A	N/A
		200	16	N/A	N/A	898.0	89.8	N/A	N/A
		300	16	N/A	N/A	809.0	80.9	N/A	N/A
		400	16	N/A	N/A	663.0	66.3	N/A	N/A
		400	16	N/A	N/A	624.0	62.4	N/A	N/A
		425	16	N/A	N/A	697.0	69.7	N/A	N/A
		450	16	N/A	N/A	590.0	59.0	N/A	N/A
		480	16	N/A	N/A	339.0	33.9	N/A	N/A
		500	16	N/A	N/A	180.0	18.0	N/A	N/A
Robert and Benmokrane [36]	N/A	25	12.7	112	N/A	756.0	100.0	N/A	N/A
		50	12.7	112	N/A	757.0	99.8	N/A	N/A
		100	12.7	112	N/A	674.0	89.1	N/A	N/A
		150	12.7	112	N/A	532.0	70.7	N/A	N/A
		200	12.7	112	N/A	513.0	68.1	N/A	N/A
		250	12.7	112	N/A	464.0	61.9	N/A	N/A
		300	12.7	112	N/A	405.0	53.6	N/A	N/A
		325	12.7	112	N/A	353.0	46.5	N/A	N/A
Wang and Zha [37]	GFRP	20	8	75	425	1013.4	100.0	52.8	100.0
		60	8	75	425	981.7	96.9	50.2	95.1
		80	8	75	425	948.1	93.6	49.1	93.0
		100	8	75	425	838.7	82.8	50.5	95.6
		120	8	75	425	794.0	78.4	50.8	96.2
		150	8	75	425	769.3	75.9	47.4	89.8
		200	8	75	425	773.4	76.3	41.2	78.0
		250	8	75	425	737.3	72.8	38.1	72.2
		300	8	75	425	739.6	73.0	29.9	56.6
		350	8	75	425	734.4	72.5	N/A	N/A
		400	8	75	425	673.2	66.4	N/A	N/A
McIntyre [38], McIntyre et al. [39]	SRG	20	12	59	391	1057	100.0	62.6	100.0
		59	12	59	391	893.2	84.5	64.8	103.5
		74	12	59	391	819.2	77.5	54.9	87.7
		100	12	59	391	776.9	73.5	61.1	97.6
		111	12	59	391	721.9	68.3	68.4	109.3
		150	12	59	391	687.1	65.0	N/A	N/A
		200	12	59	391	708.2	67.0	63.5	101.5
		315	12	59	391	702.9	66.5	52.1	83.3
		375	12	59	391	333	31.5	55.7	88.9
		440	12	59	391	438.7	41.5	55.9	89.3
		495	12	59	391	142.7	13.5	51.1	81.7
	BPG	20	10	86	408	1467.8	100.0	N/A	N/A
		87	10	86	408	1081.8	73.7	N/A	N/A
		110	10	86	408	967.3	65.9	N/A	N/A
		137	10	86	408	977.6	66.6	N/A	N/A
		150	10	86	408	983.4	67.0	N/A	N/A
		227	10	86	408	968.7	66.0	N/A	N/A
		302	10	86	408	910	62.0	N/A	N/A
		358	10	86	408	594.5	40.5	N/A	N/A
		416	10	86	408	365.5	24.9	N/A	N/A
		570	10	86	408	86.6	5.9	N/A	N/A
	PTG	20	9.5	83	390	1092	100	N/A	N/A
		84	9.5	83	390	989.4	90.6	N/A	N/A
		108	9.5	83	390	976.2	89.4	N/A	N/A
		137	9.5	83	390	845.2	77.4	N/A	N/A
		153	9.5	83	390	768.8	70.4	N/A	N/A
		227	9.5	83	390	729.5	66.8	N/A	N/A
		279	9.5	83	390	755.7	69.2	N/A	N/A
		312	9.5	83	390	618.1	56.6	N/A	N/A
		401	9.5	83	390	542.7	49.7	N/A	N/A
		463	9.5	83	390	231.5	21.2	N/A	N/A
		533	9.5	83	390	1.0	0.1	N/A	N/A
		568	9.5	83	390	1.0	0.1	N/A	N/A
Hajiloo *et al.* [40]	GA−025	25	18.5	110	412	1710.0	100.0	N/A	N/A
	GA−150	142	18.5	110	412	1121.0	65.5	N/A	N/A
	GA−200	190	18.5	110	412	1171.0	62.5	N/A	N/A
	GA−250	231	18.5	110	412	888.6	50.0	N/A	N/A
	GA−300	281	18.5	110	412	832.6	49.0	N/A	N/A
	GA−350	344	18.5	110	412	724.3	40.7	N/A	N/A

(*continued on next page*)

Table 1 (*continued*)

Reference	Specimenseries	T(°C)	d(mm)	T_g(°C)	T_d(°C)	f_T(MPa)	f_T/f_0(%)	E_T(GPa)	E_T/E_0(%)
	GA−400	375	18.5	110	412	705.3	41.0	N/A	N/A
	GB−025	25	18	114	438	1280.0	100.0	62.6	100.0
	GB−150	145	18	114	438	1021.3	80.0	43.9	70.2
	GB−200	196	18	114	438	1049.3	82.0	44.3	70.9
	GB−250	244	18	114	438	1032.6	80.0	42.6	68.0
	GB−300	291	18	114	438	967.0	74.0	44.1	70.4
	GB−350	341	18	114	438	826.3	65.0	41.0	65.5
	GB−375	366	18	114	438	708.0	55.0	43.6	69.7
	GB−400	391	18	114	438	442.5	34.0	N/A	N/A
	GC−025	25	18	140	451	1349.0	100.0	62.9	100.0
	GC−150	145	18	140	451	1012.6	75.0	57.4	91.3
	GC−200	196	18	140	451	904.3	66.0	59.1	94.0
	GC−250	244	18	140	451	788.3	58.0	55.4	88.1
	GC−300	291	18	140	451	798.6	59.0	51.1	81.2
	GC−350	341	18	140	451	810.6	60.0	49.3	78.4
	GC−400	391	18	140	451	749.3	56.0	49.5	78.7
	GC−450	498	18	140	451	687.0	52.0	N/A	N/A
	GC−500	486	18	140	451	498.6	37.0	N/A	N/A
Ashrafi *et al.* [41]	4-Type A	25	4	110	N/A	1438.0	100.0	50.0	100.0
		60	4	110	N/A	1391.0	97.0	49.5	99.0
		90	4	110	N/A	1304.0	91.0	49.3	98.7
		110	4	110	N/A	960.0	67.0	39.7	79.5
		150	4	110	N/A	871.0	61.0	40.0	80.0
		200	4	110	N/A	842.0	59.0	41.1	82.2
		300	4	110	N/A	725.0	50.0	30.5	61.1
		450	4	110	N/A	420.0	29.0	18.2	36.4
	6-Type A	25	6	110	N/A	1274.0	100.0	50.0	100.0
		60	6	110	N/A	1256.0	99.0	49.3	98.6
		90	6	110	N/A	1227.0	96.0	49.0	98.0
		110	6	110	N/A	1034.0	81.0	42.9	85.9
		150	6	110	N/A	918.0	72.0	42.5	85.0
		200	6	110	N/A	841.0	66.0	42.6	85.2
		300	6	110	N/A	780.0	61.0	37.3	74.7
		450	6	110	N/A	503.0	39.0	28.1	56.2
	8-Type A	25	8	110	N/A	1024.0	100.0	50.0	100.0
		60	8	110	N/A	1010.0	99.0	49.9	99.9
		90	8	110	N/A	1005.0	98.0	49.7	99.5
		110	8	110	N/A	890.0	87.0	45.3	90.6
		150	8	110	N/A	811.0	79.0	45.7	91.4
		200	8	110	N/A	700.0	68.0	39.8	79.7
		300	8	110	N/A	645.0	63.0	38.2	76.7
		450	8	110	N/A	410.0	40.0	25.7	51.4
	10-Type A	25	10	110	N/A	971.0	100.0	50.0	100.0
		60	10	110	N/A	964.0	99.0	49.5	99.0
		90	10	110	N/A	955.0	98.0	46.7	93.4
		110	10	110	N/A	903.0	93.0	44.5	89.1
		150	10	110	N/A	862.0	89.0	42.5	85.0
		200	10	110	N/A	750.0	77.0	36.8	73.7
		300	10	110	N/A	727.0	75.0	34.7	69.4
		450	10	110	N/A	490.0	50.0	25.9	51.8
	5-Type B	25	5	110	N/A	2138.0	100.0	150.0	100.0
		60	5	110	N/A	2110.0	98.0	148.9	99.3
		90	5	110	N/A	1987.0	93.0	142.9	95.2
		110	5	110	N/A	1807.0	84.0	136.1	90.7
		150	5	110	N/A	1551.0	72.0	129.6	86.4
		200	5	110	N/A	1400.0	65.0	114.7	76.5
		300	5	110	N/A	1183.0	55.0	109.7	73.1
		450	5	110	N/A	747.0	35.0	74.6	49.7
	5-Type C	25	5	110	N/A	1905.0	100.0	125.0	100.0
		60	5	110	N/A	1895.0	99.0	123.5	98.8
		90	5	110	N/A	1824.0	96.0	120.9	96.7
		110	5	110	N/A	1696.0	89.0	118.3	94.6
		150	5	110	N/A	1410.0	74.0	100.3	80.3
		200	5	110	N/A	1293.0	68.0	97.4	77.9
		300	5	110	N/A	1105.0	58.0	83.4	66.7
		450	5	110	N/A	680.0	36.0	53.0	42.2
	5-Type D	25	5	105	N/A	1632.0	100.0	117.0	100.0
		60	5	105	N/A	1621.0	99.0	111.0	94.8
		90	5	105	N/A	1638.0	100.0	115.5	98.7
		110	5	105	N/A	1574.0	96.0	108.7	92.9
		150	5	105	N/A	1377.0	84.0	101.4	86.6
		200	5	105	N/A	1230.0	75.0	97.6	83.4
		300	5	105	N/A	1080.0	66.0	93.2	79.6
		450	5	105	N/A	851.0	52.0	62.6	53.5
Ashrafi *et al.* [42]	GFRP	15	8	95	N/A	1270.0	100.0	55.0	100.0

(*continued on next page*)

Table 1 (*continued*)

Reference	Specimenseries	T(°C)	d(mm)	T_g(°C)	T_d(°C)	f_T(MPa)	f_T/f_0(%)	E_T(GPa)	E_T/E_0(%)
		30	8	95	N/A	1200.0	98.7	52.7	95.9
		45	8	95	N/A	1180.0	97.4	54.0	98.2
		60	8	95	N/A	1030.0	84.6	51.9	94.5
		75	8	95	N/A	860.0	70.8	49.1	89.3
		90	8	95	N/A	820.0	67.9	40.0	72.8
		105	8	95	N/A	810.0	66.7	39.3	71.4
		120	8	95	N/A	800.0	66.2	38.1	69.3
		150	8	95	N/A	790.0	65.5	39.9	72.6
		200	8	95	N/A	790.0	65.3	38.8	70.6
		300	8	95	N/A	690.0	56.7	33.9	61.7
Najafabadi *et al.* [43]	A−4	25	4	110	N/A	1510.0	100	N/A	N/A
		80	4	110	N/A	1433.0	94.9	N/A	N/A
		150	4	110	N/A	910.0	60.3	N/A	N/A
		300	4	110	N/A	795.0	52.6	N/A	N/A
		400	4	110	N/A	620.0	41.1	N/A	N/A
		500	4	110	N/A	485.0	32.1	N/A	N/A
		600	4	110	N/A	460.0	30.5	N/A	N/A
		700	4	110	N/A	430.0	28.5	N/A	N/A
		800	4	110	N/A	15.0	1	N/A	N/A
	A−6	25	6	110	N/A	1235.0	100	N/A	N/A
		80	6	110	N/A	1207.0	97.7	N/A	N/A
		150	6	110	N/A	959.0	77.7	N/A	N/A
		300	6	110	N/A	835.0	67.6	N/A	N/A
		400	6	110	N/A	668.0	54.1	N/A	N/A
		500	6	110	N/A	451.0	36.5	N/A	N/A
		600	6	110	N/A	420.0	34	N/A	N/A
		700	6	110	N/A	388.0	31.4	N/A	N/A
		800	6	110	N/A	42.0	3.4	N/A	N/A
	A−8	25	8	110	N/A	1041.0	100	N/A	N/A
		80	8	110	N/A	1024.0	98.4	N/A	N/A
		150	8	110	N/A	845.0	81.2	N/A	N/A
		300	8	110	N/A	721.0	69.3	N/A	N/A
		400	8	110	N/A	562.0	54	N/A	N/A
		500	8	110	N/A	422.0	40.5	N/A	N/A
		600	8	110	N/A	375.0	36	N/A	N/A
		700	8	110	N/A	332.0	31.9	N/A	N/A
		800	8	110	N/A	69.0	6.6	N/A	N/A
	A−10	25	10	110	N/A	1003.0	100	N/A	N/A
		80	10	110	N/A	989.0	98.6	N/A	N/A
		150	10	110	N/A	869.0	86.6	N/A	N/A
		300	10	110	N/A	770.0	76.8	N/A	N/A
		400	10	110	N/A	670.0	66.8	N/A	N/A
		500	10	110	N/A	430.0	42.9	N/A	N/A
		600	10	110	N/A	368.0	36.7	N/A	N/A
		700	10	110	N/A	357.0	35.6	N/A	N/A
		800	10	110	N/A	97.0	9.7	N/A	N/A
Rosa *et al.* [44]	SC	20	10	98	374	1045.1	100.0	48.2	100.0
		50	10	98	374	927.5	89.0	47.6	99.0
		100	10	98	374	682.4	65.0	44.1	91.0
		150	10	98	374	623.2	60.0	45.9	95.0
		200	10	98	374	603.7	58.0	45.3	94.0
		250	10	98	374	619.3	59.0	43.7	91.0
		300	10	98	374	598.2	57.0	41.8	87.0
Rosa *et al.* [45,46]	RB-D8	20	8	157	400	1481.7	100.0	57.6	100.0
		50	8	157	400	1463.9	99.0	55.5	96.0
		100	8	157	400	1295.8	87.0	54.9	95.0
		150	8	157	400	1148.3	78.0	56.4	98.0
		200	8	157	400	692.7	47.0	53.9	94.0
		250	8	157	400	597.1	40.0	53.2	92.0
		300	8	157	400	585.2	39.0	45.6	79.0
	RB-D12	20	12	157	400	1380.3	100.0	60.0	100.0
		150	12	157	400	998.5	72.0	59.5	99.0
		200	12	157	400	684.7	50.0	57.2	95.0
		300	12	157	400	660.9	48.0	58.1	97.0
		450	12	157	400	649.4	47.0	51.9	86.0
		575	12	157	400	133.6	10.0	50.9	85.0
		715	12	157	400	49.6	4.0	39.9	66.0
	RBP-D12	20	12	104	400	1184.4	100.0	60.1	100.0
		100	12	104	400	1117.9	94.0	56.5	94.0
		150	12	104	400	783.9	66.0	50.1	83.0
		200	12	104	400	765.6	65.0	48.8	81.0
		300	12	104	400	678.3	57.0	46.2	77.0
Zhou et al. [47]	GFRP	20	8	N/A	N/A	855.8	100.0	26.6	100.0
		100	8	N/A	N/A	832.4	97.3	28.4	106.6
		150	8	N/A	N/A	702.1	82.0	27.0	101.4

(*continued on next page*)

Table 1 (*continued*)

Reference	Specimenseries	T(°C)	d(mm)	T_g(°C)	T_d(°C)	f_T(MPa)	f_T/f_0(%)	E_T(GPa)	E_T/E_0(%)
		200	8	N/A	N/A	616.3	72.0	27.8	104.4
		250	8	N/A	N/A	531.1	62.1	26.5	100.0
		300	8	N/A	N/A	446.5	52.2	26.8	100.6
		350	8	N/A	N/A	366.5	42.8	24.8	93.1
		400	8	N/A	N/A	163.5	19.1	24.5	92.0
		20	12	N/A	N/A	852.4	100.0	21.3	100.0
		100	12	N/A	N/A	810.7	95.1	23.3	109.4
		150	12	N/A	N/A	755.2	88.6	22.5	105.7
		200	12	N/A	N/A	715.8	84.0	21.6	101.5
		250	12	N/A	N/A	618.6	72.6	21.7	101.9
		300	12	N/A	N/A	528.9	62.0	19.2	90.2
		350	12	N/A	N/A	338.5	39.7	18.6	87.4
		400	12	N/A	N/A	87.5	10.3	17.6	82.7

Note: "N/A" indicates data not available in the original source.

Table 2
Properties of the HW GFRP bars.

Type	Nominal diameter (mm)	Tensile strength (MPa)	Elastic modulus (GPa)	Fiber mass content	T_g[a] (°C)	T_d[b] (°C)
HW	12	1598	50	89 %	215	361

Notes:
[a] T_g was determined from the onset of the storage modulus decay using dynamic mechanical analysis (DMA).
[b] T_d was defined as the first peak decomposition temperature under an air environment using thermogravimetric analysis (TGA).

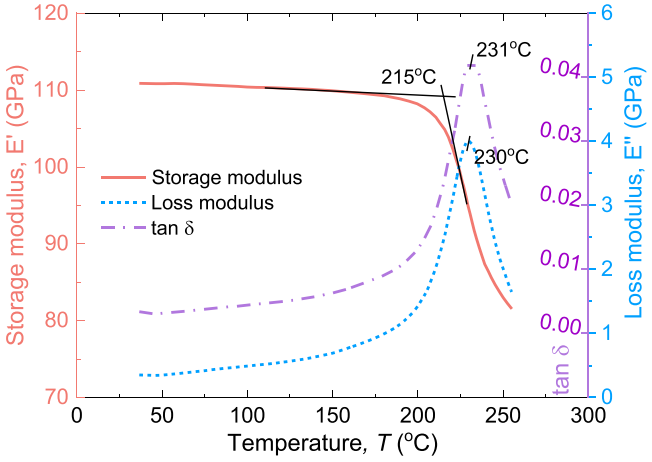


Fig. 2. DMA curves of HW GFRP bars.

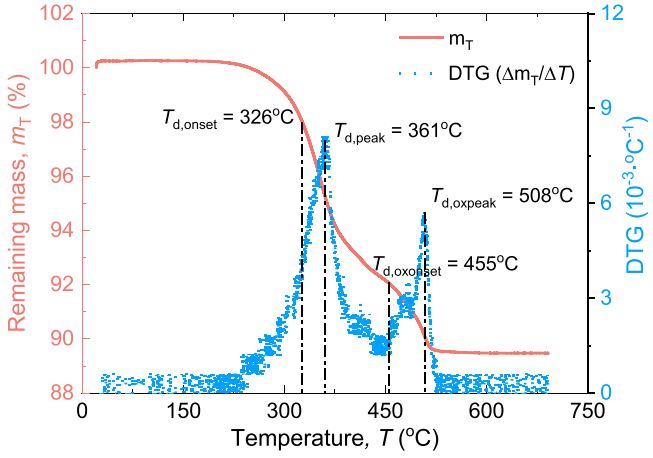


Fig. 3. TGA curves of HW GFRP bars.

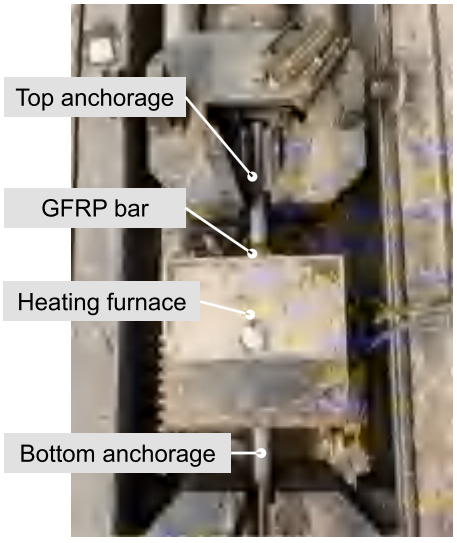


Fig. 4. Test setup for high-temperature tensile testing of HW GFRP bars.

thermal soaking period of 5–10 min was implemented to ensure uniform temperature distribution throughout the cross-section of the bar. To accommodate axial thermal expansion and mitigate stress accumulation, the top anchorage was released during the heating phase. Following the confirmation of thermal equilibrium, tensile loading was applied under displacement control at a constant rate of 5 mm/min until failure occurred.

2.2.3. *Results of high-temperature tensile tests*

Table 3 presents a summary of the average tensile strengths of the HW GFRP bars at various exposure temperatures, along with the corresponding normalized strength reductions relative to the ambient reference strength. The coefficient of variation (CV), expressed as a percentage of the mean, is indicated in parentheses within this table. The results have indicated a distinct temperature-dependent degradation trend in tensile strength, which diverges from trends reported in previous studies. As illustrated in Fig. 5, at moderately high temperatures near the T_g (i.e., 150°C and 300°C), the observed reductions in tensile strength are limited to 2.3 % and 21.7 %, respectively. These relatively low degradation rates suggest an enhanced thermal resistance of the HW GFRP bars within the temperature range below the T_d, particularly under thermal exposure conditions that may be typical for GFRP RC members with adequate concrete cover under fire exposure.

Table 3
Tensile test results of HW GFRP bars at ambient and high temperatures.

Temperature (°C)	Tensile strength (MPa)	Normalized strength reduction (%)
20	1598.0 (4.0 %)	-
150	1563.2 (2.9 %)	2.3
300	1253.3 (5.7 %)	21.7
350	1002.7 (9.0 %)	37.3
400	554.7 (8.1 %)	65.3
450	277.3 (5.5 %)	82.7
500	85.9 (0.3 %)	94.6
550	21.3 (0.3 %)	98.7

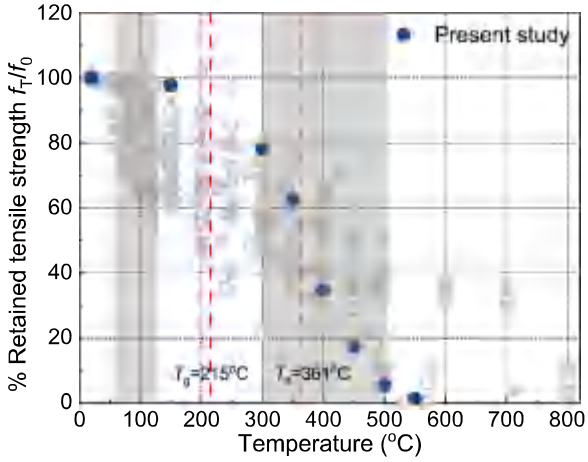


Fig. 5. Normalized tensile strengths of HW GFRP bars as a function of temperature.

In previous studies, GFRP bars typically exhibited a plateau in tensile strength between T_g and T_d. For example, the RB-D12 bars examined in Ref. [46] exhibited negligible strength loss between 200°C and 450°C. In contrast, the HW GFRP bars investigated in the present study show a more continuous and pronounced degradation trend when the temperatures are higher than T_g. This behavior can be primarily attributed to the relatively narrow temperature range, specifically between T_g (215°C) and T_d (361°C), which limits the development of a strength-retaining plateau. The matrix transitions more rapidly from a state of softening to decomposition, resulting in a continuous decline in load-carrying capacity.

The evolution of failure modes for HW GFRP bars subjected to high temperatures is depicted in Fig. 6. When the exposure temperatures were below T_g, such as at 150°C, no visible changes in surface color were observed, indicating a limited thermal impact on the resin matrix. At 300°C, the surface began to darken to a brownish-black hue, signifying the initiation of resin softening. At 350°C, more significant resin degradation was noted, accompanied by dark brown discoloration, and at temperatures of 400°C and above, the nearly complete decomposition of the polymer matrix occurred, resulting in the exposure of the underlying white E-glass fibers.

The mechanical failure modes of GFRP bars exhibited a temperature dependence. At ambient conditions (20°C) and at 150°C (temperatures below T_g), the specimens exhibited typical brittle rupture, characterized by the separation of fiber bundles. At the temperatures increased beyond T_g, the failure transitioned to a more gradual fracture process due to the softening of the resin, which reduced the brittleness of the composite and facilitated partial stress redistribution. At temperatures above 300°C, post-fracture radial expansion of the bar cross-section was observed, indicating progressive fiber breakage. Between 300°C and 500°C, the deteriorated polymer matrix was insufficient for effective load transfer, although the fibers remained partially intact. At 550°C, nearly complete decomposition of the matrix occurred, resulting in the load being carried directly by the fibers, which led to catastrophic fiber fracture under tensile loading. These observations highlight the significant impact of T_g and T_d on the high-temperature tensile performance of GFRP bars. The degradation of structural integrity within the polymer matrix significantly compromises the capacity for stress transfer, thereby accelerating failure. For accurate modeling of the high-temperature behavior of GFRP bars at high temperatures, it is essential to quantitatively incorporate the effects of T_g and T_d into constitutive degradation models.

3. Material properties and degradation model development at high temperatures

3.1. Thermo-mechanical behavior of the polymer matrix in GFRP bars

The thermo-mechanical behavior of the polymer matrix is a critical determinant of the high-temperature performance of GFRP bars. When subjected to high temperatures, the matrix experiences progressive mechanical degradation, primarily due to the thermal dissociation of intermolecular bonds. This degradation adversely affects the matrix's ability to effectively transfer stress between the polymer matrix and the embedded fibers [53,54]. As depicted in Fig. 7, the polymer matrix comprises two fundamental types of intermolecular bonds: primary bonds and secondary bonds. Primary bonds, which include covalent bonds within polymer chains and cross-linking bonds characteristic of thermosetting resins, exhibit high bond dissociation energies (typically ranging from 50 to 200 kcal/mol). These bonds are essential for maintaining the structural integrity and thermal stability of the matrix.

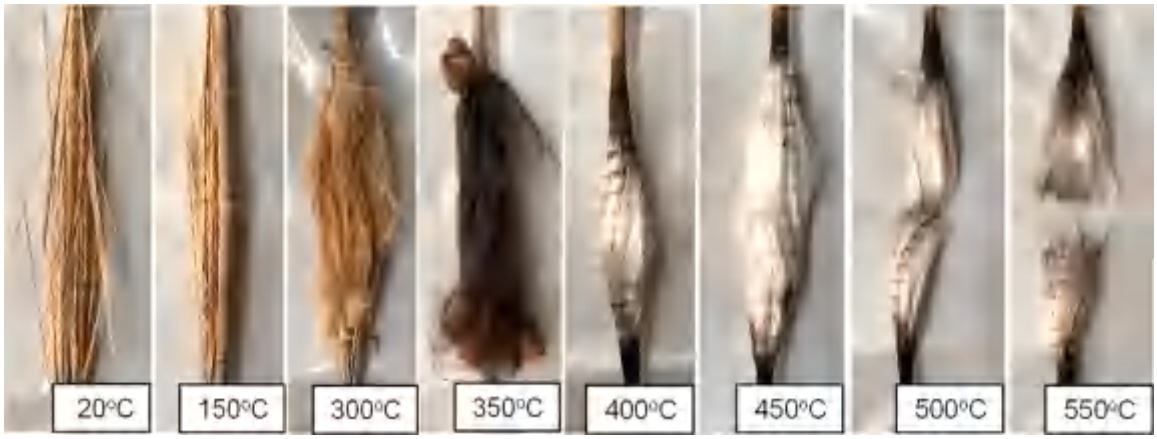


Fig. 6. Failure modes of HW GFRP bars tested at ambient and high temperatures.

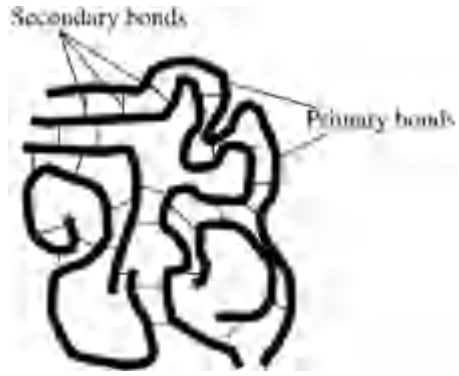


Fig. 7. Schematic representation of the primary and secondary bonding mechanisms within the polymer matrix [55].

Conversely, secondary bonds, such as hydrogen bonds (with dissociation energies of approximately 3–7 kcal/mol), dipole-dipole interactions (around 1.5–3 kcal/mol) and van der Waals forces (approximately 0.5–2 kcal/mol), are significantly weaker and more vulnerable to disruption under thermal loading [54,55].

The high-temperature response of the polymer matrix involves a sequence of temperature-dependent states, which are significantly influenced by two critical temperature thresholds: the T_g and T_d values. The T_g is used to characterize the onset of matrix softening, whereas the T_d describes the initiation of irreversible chemical degradation. These thresholds are essential for understanding and modeling the mechanical behavior of GFRP bars in the context of fire or other high-temperature conditions.

Fig. 8 provides a schematic representation of five distinct thermo-mechanical states of polymer matrices subjected to high-temperature exposure [57,58]:

(a) Glassy state: At temperatures well below the T_g, the polymer matrix exists in a rigid and brittle state, which is characterized by a high elastic modulus and a limited capacity for deformation.

(b) Glass transition region: As the temperature approaches the T_g value, the dissociation of secondary bonds leads to a gradual decrease in stiffness and an increase in ductility. This transition is reversible and represents a transformation from glassy to rubbery behavior.

(c) Rubbery state: At temperatures above the T_g value, the polymer matrix transitions into a viscoelastic state characterized by enhanced molecular mobility. This transition facilitates recoverable large-strain deformations when subjected to mechanical loading.

(d) Viscous flow state: At moderately elevated temperatures

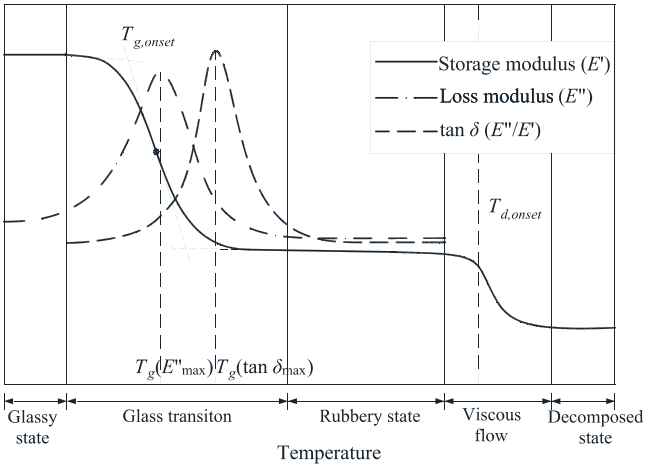


Fig. 8. Thermo-mechanical states of thermosetting polymers during high-temperature exposure [56].

(approximately 1.4 T_g as reported in Ref. [54]), the polymer matrix experiences viscoelastic or viscous flow as a result of disentanglement and partial bond scission. This state is characterized by time-dependent and irreversible deformation.

(e) Decomposed state: At the temperatures approaching or exceeding the T_d value, the cleavage of primary covalent bonds initiates the chemical degradation of the polymer backbone, leading to significant losses of mass, stiffness and load-carrying capacity.

The sequential transitions from a rigid, glassy solid to a fully decomposed material have significant implications for the high-temperature mechanical properties of the GFRP composites, particularly concerning the loss of stiffness and strength within the temperature ranges near T_g and T_d. Consequently, accurate modeling of these thermal effects is crucial for the development of robust degradation models and for ensuring the reliability of GFRP RC members in fire-critical applications.

3.2. Evaluation of existing predictive models

Various degradation models have been proposed in the literature to predict the mechanical properties of FRP composites at high temperatures, including exponential models [48,49,55,59], hyperbolic tangent models [3,60–63] and polynomial models [46,64]. A summary of these models is presented in Table 4 (located in the appendix). For a detailed evaluation, three representative models were selected: those proposed by Saafi [64], Yu and Kodur [62] and Rosa et al. [46]. It is important to note that although the model developed by Yu and Kodur [62] was originally designed for CFRP bars, it is also applicable to GFRP bars due to the similar thermomechanical degradation behavior of their polymer matrices when exposed to high temperatures.

Figs. 9 and 10 illustrate the comparisons between the predicted and experimental values for the tensile strengths and elastic moduli of GFRP bars, respectively. It is important to note that datasets involving GFRP bars that were pre-exposed to alkaline solutions [32] or tested while embedded in concrete [43] were excluded from the model validation. Such factors may introduce additional degradation mechanisms beyond high-temperature exposure, which are not accounted for in the current models. Two statistical indicators, namely the mean value and standard deviation (S.D.), were employed to evaluate the accuracy of the three models. As illustrated in Fig. 9, all three models exhibit significant variability in predicting tensile strengths. The standard deviations in the tensile strength predictions are 34 %, 40 % and 52 % for the models proposed by Saafi [64], Yu and Kodur [62] and Rosa et al. [46], respectively. Furthermore, the mean predictions of Saafi's [64] model and Yu and Kodur's [62] model show large deviations from the experimental values, at 65 % and 111 %, respectively, indicating systematic underestimation or overestimation. In contrast, the degradation trends in elastic modulus (Fig. 10) are generally less severe than those observed for tensile strength, which is consistent with the experimental findings. However, the predictive performance of the existing models remains inconsistent. Saafi's [64] and Yu and Kodur's [62] models tend to underestimate the retained modulus values across the temperature range, while Rosa et al.'s [46] model tends to overestimate them. The standard deviations for elastic modulus predictions are 33 %, 15 %, and 25 % for Saafi [64], Yu and Kodur [62], and Rosa et al. [46], respectively.

Overall, the analysis indicates that the existing predictive models are inadequate for accurately predicting the degradation behavior of mechanical properties in GFRP bars at high temperatures, particularly within the critical thermal transition ranges defined by the T_g and T_d values. As further discussed in Section 3.4 and illustrated in Figs. 15 and 16, these models do not sufficiently capture the nonlinear and stage-dependent deterioration observed in experimental results. These limitations highlight the need for developing new predictive models that explicitly incorporate the thermo-mechanical properties of the polymer matrix and the associated degradation mechanisms.

Table 4
A sum of some representative predictive models for predicting temperature-dependent mechanical properties of GFRP bars.

Reference	FRP type	Predictive model of the tensile strength / elastic modulus	
Mahieux and Reifsnider [55]	FRP composite		$E(T) = (E_1 - E_2)e^{-\left(\frac{T}{T_g}\right)^{m_g}} + E_2 e^{-\left(\frac{T}{T_f}\right)^{m_f}}$ [a]
Saafi [64]	CFRP/AFRP/GFRP bar	CFRPbar : $\frac{f(T)}{f_0} = \begin{cases} 1 & 0 \le T < 100^{\circ}\mathrm{C} \\ 1.27 - 0.0027T & 100 < T \le 475\ ^{\circ}\mathrm{C} \\ 0 & 475^{\circ}\mathrm{C} \le T \end{cases}$ AFRPbar : $\frac{f(T)}{f_0} = \begin{cases} 1 & 0 \le T < 100^{\circ}\mathrm{C} \\ 1.33 - 0.0033T & 100 < T \le 400^{\circ}\mathrm{C} \\ 0 & 400^{\circ}\mathrm{C} \le T \end{cases}$ GFRPbar : $\frac{f(T)}{f_0} = \begin{cases} 1 - 0.0025T & 0 < T \le 400^{\circ}\mathrm{C} \\ 0 & 400^{\circ}\mathrm{C} \le T \end{cases}$	CFRPbar : $\frac{E(T)}{E_0} \begin{cases} 1 & 0 \le T \le 100\ ^{\circ}\mathrm{C} \\ 1.18 - 0.0018T & 100\ ^{\circ}\mathrm{C} \le T < 300\ ^{\circ}\mathrm{C} \\ 1.63 - 0.0033T & 300\ ^{\circ}\mathrm{C} \le T \le 500\ ^{\circ}\mathrm{C} \\ 0 & 500\ ^{\circ}\mathrm{C} \le T \end{cases} =$ AFRP/GFRPbar : $\frac{E(T)}{E_0} = \begin{cases} 1 & 0 \le T \le 100\ ^{\circ}\mathrm{C} \\ 1.25 - 0.0025T & 100\ ^{\circ}\mathrm{C} \le T < 300\ ^{\circ}\mathrm{C} \\ 2 - 0.005T & 300\ ^{\circ}\mathrm{C} \le T \le 400\ ^{\circ}\mathrm{C} \\ 0 & 400\ ^{\circ}\mathrm{C} \le T \end{cases}$
Bisby [3]	CFRP/AFRP/GFRP fibers	CFRP : $\frac{f(T)}{f_0} = 0.45\tanh[-5.83 \times 10\mathrm{e}-3(T-339.54)] + 0.55$ AFRP : $\frac{f(T)}{f_0} = 0.45\tanh[-8.48 \times 10\mathrm{e}-3(T-287.65)] + 0.55$ GFRP : $\frac{f(T)}{f_0} = 0.45\tanh[-8.10 \times 10\mathrm{e}-3(T-289.14)] + 0.55$	CFRP : $\frac{E(T)}{E_0} = 0.475\tanh[-8.68 \times 10\mathrm{e}-3(T-367.41)] + 0.525$ AFRP : $\frac{E(T)}{E_0} = 0.475\tanh[-7.93 \times 10\mathrm{e}-3(T-290.49)] + 0.525$ GFRP : $\frac{E(T)}{E_0} = 0.475\tanh[-7.91 \times 10\mathrm{e}-3(T-320.35)] + 0.525$
Gibson et al. [60]	GFRP laminate	$P(T) = \left[\frac{P_{\text{initial}} + P_{\text{R}}}{2} - \frac{P_{\text{initial}} - P_{\text{R}}}{2}\tanh(k(T - T_c))\right]R^{n}$ [b]	
Bai and Keller [56]	FRP composite	$P_m(T) = P_g(1-\alpha_g) + P_l\alpha_g(1-\alpha_r) + P_r\alpha_g\alpha_r(1-\alpha_d) + P_d\alpha_g\alpha_r\alpha_d$ [c]	
Chowdhury et al. [61]	GFRP coupon	$\frac{f(T)}{f_0} = 0.694 - 0.257\tanh(0.0882(T-47))$	$\frac{E(T)}{E_0} = 0.676 - 0.134\tanh(0.102(T-51))$
Wang et al. [48]	Pultruded CFRP strip	$\frac{f(T)}{f_0} = \begin{cases} 1 - \frac{(T-22)^{0.9}}{200} & 22\ ^{\circ}\mathrm{C} \le T \le 150^{\circ}\mathrm{C} \\ 0.59 - \frac{(T-150)^{0.7}}{490} & 150\ ^{\circ}\mathrm{C} \le T \le 420^{\circ}\mathrm{C} \\ 0.48 - \frac{(T-420)^{1.8}}{76000} & 420\ ^{\circ}\mathrm{C} \le T \le 706^{\circ}\mathrm{C} \end{cases}$	
Wang and Zha [49]	GFRP bar	$\frac{f(T)}{f_0} = \frac{1}{4}e^{-\left(\frac{T-T_0}{75}\right)^4} + \frac{3}{4}e^{-\left(\frac{T-75}{425}\right)^4}$	$\frac{E(T)}{E_0} = \begin{cases} 1 - \frac{T-T_0}{20(75-T_0)}T_0 \le T < 115^{\circ}\mathrm{C} \\ 0.95 - \frac{T-75}{425}T \ge 115^{\circ}\mathrm{C} \end{cases}$
Correia et al. [59]	GFRP pultruded material	$P(T) = \left(1 - e^{Be^{CT}}\right) \times (P_u - P_r) + P_r$ [d]	
Yu and Kodur [62]	CFRP strip/bar	CFRPstrip : $f(T) = 0.56 - 0.44\tanh(0.0052(T-305))$ CFRPbar : $f(T) = 0.54 - 0.46\tanh(0.0064(T-330))$	CFRPstrip : $E(T) = 0.51 - 0.49\tanh(0.0035(T-340))$ CFRPbar : $E(T) = 0.51 - 0.49\tanh(0.0033(T-320))$
McIntyre [38]	GFRP bar	$\frac{f(T)}{f_0} = \alpha_g + k_1(1-\alpha_g)\alpha_d + k_2(1-\alpha_g)(1-\alpha_d)$ [e]	
Hawileh et al. [63]	CFRP/BFRP/Hybrid laminate	CFRPlaminate : $f(T) = 0.594 - 0.405\tanh(0.017(T-117.74))$ BFRPlaminate : $f(T) = 0.795 - 0.205\tanh(0.075(T-190.58))$ Hybridlaminate : $f(T) = 0.67 - 0.33\tanh(0.087(T-192.41))$	CFRPlaminate : $E(T) = 0.545 - 0.455\tanh(0.014(T-60.27))$ BFRPlaminate : $E(T) = 0.86 - 0.140\tanh(0.035(T-163.24))$ Hybridlaminate : $E(T) = 0.705 - 0.295\tanh(0.091(T-196.34))$
Jafari et al. [65]	GFRP laminate	$\frac{f(T)}{f_0} = \begin{cases} 1 & 25 \le T < 45^{\circ}\mathrm{C} \\ a\left(\frac{1}{T^3}\right) + b\left((\log(t))^{0.333}\right) + c & T \ge 45^{\circ}\mathrm{C} \end{cases}$ [f]	
Ashrafi et al. [66]	GFRP laminate	$\frac{f(T)}{f_0} = a\left(\frac{1}{T^3}\right) + b\left(\frac{1}{\left(\log\left(\frac{t_1}{6}\right)\right)^{0.5}}\right) - c\left(\frac{1}{(\log(t_2))^{0.5}}\right) + d$ [g]	$\frac{E(T)}{E_0} = -a(T)^4 + b\left(\frac{1}{\left(\log\left(\frac{t_1}{6}\right)\right)^{0.5}}\right) - c\left(\frac{1}{(\log(t_2))^{0.5}}\right) + d$ [g]
Rosa et al. [46]	GFRP bar	$f_T = 6.69 \times 10^{-7}T^2 - 1.86 \times 10^{-3}T + 1.04$	$E_T = 1.01 - 5.55 \times 10^{-4}T$

Notes:

[a] Subscripts 1 and 2 correspond to specific thermal transitions, namely the glass transition (1) and the flow transition (2). E_i denotes the instantaneous modulus in each thermal region before transition. T_g and T_f are the glass transition temperature and the flow transition temperature, respectively. m_g and m_f are empirical coefficients used to characterize the rate and extent of mechanical degradation across the corresponding transitions.

[b] $P(T)$ represents a temperature-dependent mechanical property (e.g., tensile strength or elastic modulus) at temperature T. $P_{initial}$ and P_R denote the values of this property at ambient temperature and after high-temperature exposure, respectively. The constant k characterizes the breadth of the thermal transition, and T_c is the glass transition temperature. R^n represents the retained resin content (ranging from 0 to 1), where n is a parameter reflecting the sensitivity of $P(T)$ to resin content; $n = 1$ is typically used for resin dominated properties, while $n = 0$ is appropriate for fiber dominated properties.

[c] P_g, P_l, P_r and P_d are the mechanical properties (e.g., modulus) in the glassy, glass transition, rubbery and decomposed states, respectively. α_g, α_r and α_d represent the degree of transformation associated with the glass, glassy-to-rubbery and rubbery-to-decomposed transitions, respectively.

[d] P_u denotes the property at room temperature, while P_r refers to the corresponding value after glass transition but before decomposition. The parameters B and C are empirical shape and scale coefficients, respectively.

[e] α_g and α_d are the normalized reductions in tensile strength at the glassy and decomposed states, respectively, which can be determined through DMA and TGA tests. The coefficients k_1 and k_2 denote the retained tensile strength before glass transition and thermal decomposition, respectively.

[f] The variable t represents the laminate thickness, and a, b, and c are empirical constants in the degradation model.

[g] t_1 is the thermal exposure duration, and t_2 is the laminate thickness. The parameters a, b, c and d are constants that vary depending on the type of laminate under investigation.

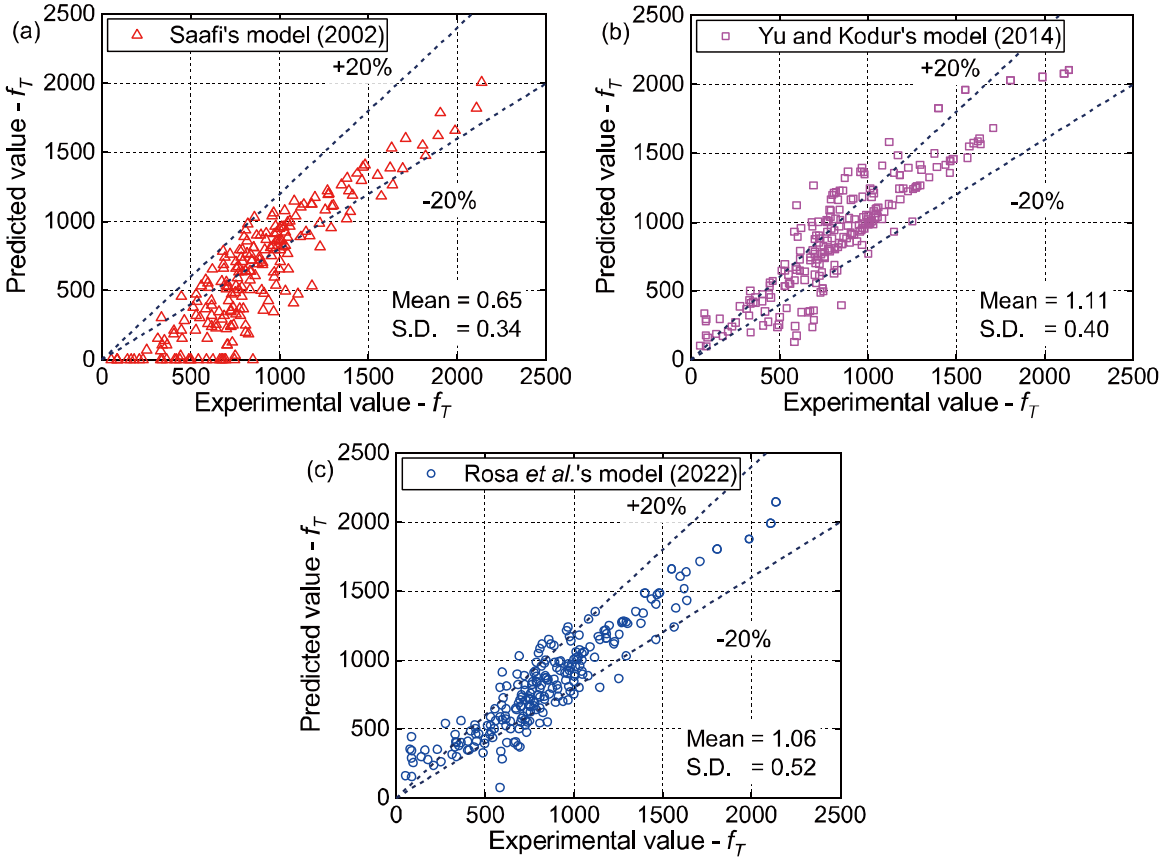


Fig. 9. Comparisons of the predicted and experimental tensile strengths using (a) Saafi's model, (b) Yu and Kodur's model, and (c) Rosa et al.'s model.

3.3. ANOVA analysis

Analysis of Variance (ANOVA) is a widely used statistical method for quantifying the effects of various factors on the degradation of material properties, particularly under high-temperature conditions. In the context of GFRP bars, previous studies such as the one conducted by Ashrafi et al. [41] have employed ANOVA to investigate the effects of temperature, bar diameter and the thermophysical properties of GFRP bars (T_g and T_d), along with their interactions, on the tensile performance of these materials. Their results highlighted the significance of considering these variables and their interactions when evaluating the mechanical property degradation of GFRP bars at high temperatures. In the present study, a two-factor ANOVA was conducted using the established high-temperature tensile test database to evaluate the statistical significance of key parameters affecting the tensile strengths and elastic moduli of GFRP bars under high-temperature conditions. The analysis focused on three main variables, including temperature, T_g and T_d, as well as their interaction effects. Due to the relatively narrow range of bar diameters in the collected database, the influence of bar diameter was excluded as a variable in this analysis.

Tables 5 and 6 summarize the ANOVA results for the tensile strengths and elastic moduli of GFRP bars at high temperatures, respectively. For tensile strength, the p-values associated with temperature, T_g, T_d and their interaction are all below the conventional significance threshold of 0.05, indicating that these variables have statistically significant effects on the tensile strengths of GFRP bars at high temperatures. In the case of the elastic moduli of GFRP bars, both temperature and the thermophysical properties (T_g and T_d) again exhibit statistically significant effects ($p < 0.05$). However, the interaction term shows a higher p-value (> 0.05), suggesting a less pronounced combined influence on the elastic modulus compared to tensile strength. These results highlight the importance of considering the effects of temperature, T_g, T_d and their interaction when developing accurate degradation models for predicting the mechanical properties of GFRP bars at high temperatures.

3.4. Development of new degradation models

The observed reductions in the tensile strength and elastic modulus of GFRP bars at high temperatures are primarily attributed to the reduced efficiency of stress transfer between the glass fibers and the surrounding polymer matrix, rather than the degradation of the glass fibers themselves. As such, any constitutive model intended to represent the high-temperature mechanical behavior of GFRP bars must explicitly account for the temperature-dependent characteristics of the polymer matrix. A foundational framework for modeling the elastic modulus degradation of polymers at high temperatures was established by

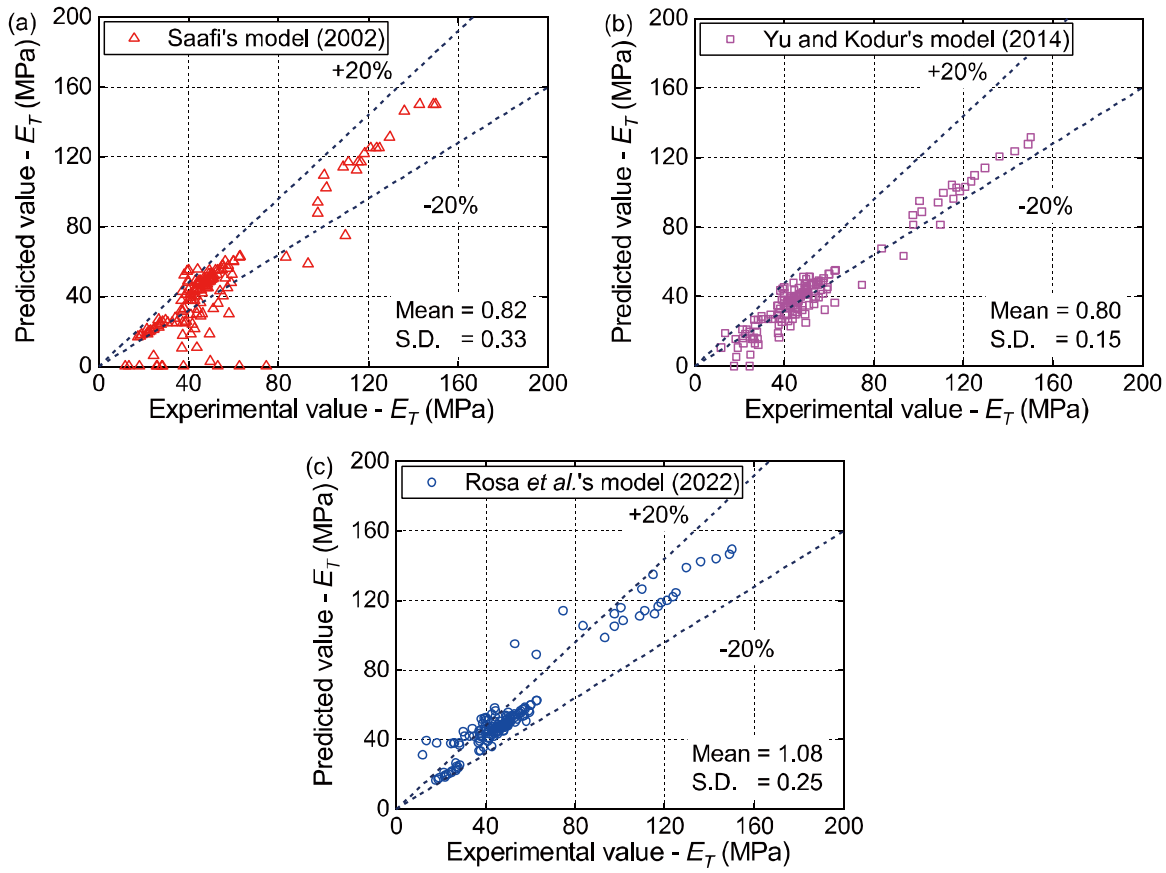


Fig. 10. Comparisons of the predicted and experimental elastic moduli using (a) Saafi's model, (b) Yu and Kodur's model, and (c) Rosa et al.'s model.

Table 5
ANOVA results for tensile strengths of GFRP bars.

Source of variation	SS[c]	df[d]	MS[e]	F[f]	p-value[g]
Bar properties[a]	3742.682	11	340.244	11.934	0.451E−4
Temperature	55434.622	17	3260.860	114.369	0.224E−10
Interaction[b]	7257.114	71	102.213	3.585	0.00691
Error	370.652	13	28.512		
Total	538484.343	113			

Table 6
ANOVA results for elastic moduli of GFRP bars.

Source of variation	SS	df	MS	F	p-value
Bar properties	1922.777	7	274.682	4.864	0.016
Temperature	4016.375	14	286.884	5.080	0.010
Interaction	1508.901	35	43.111	0.763	0.733
Error	508.301	9	56.478		
Total	515379.299	66			

Notes: [a] "Bar properties" refer to the thermophysical properties of GFRP bars (i.e., T_g and T_d).
[b]"Interaction" refers to the interaction effects between temperature and thermophysical properties (T_g and T_d) on the mechanical properties of GFRP bars.
[c]SS (Sum of squares) represents the total sum of squares attributed to each factor in the ANOVA.
[d]df (Degrees of Freedom) indicates the number of independent values that can vary in the dataset.
[e]MS (Mean Square) is the mean square value derived by dividing the sum of squares by the corresponding degrees of freedom.
[f]F (F-ratio) is the ratio of the mean square between groups to the mean square within groups.
[g]The p-value indicates the statistical significance of each factor. A p-value less than 0.05 is typically considered significant.

Mahieux and Reifsnider [55], which uses a Weibull-based statistical formulation to capture the progressive deterioration of secondary bonds during thermal transitions. This model effectively characterizes the modulus degradation across a wide range of polymer systems, including thermosetting, thermoplastic and amorphous polymers, as they transition from the glassy to the rubbery state. The degradation behavior is expressed using a cumulative function representing multiple thermal transition stages:

$$E_T^* = \sum_{i=1}^{N} H_i e^{-\left(\frac{T}{T_i}\right)^{m_i}} \tag{1}$$

In Eq. (1), each T_i denotes the characteristic temperature associated with a specific transition stage. For the polymer matrices commonly used in GFRP bars, such as epoxy and vinyl ester resins, two major transitions are typically observed: the glass transition and the viscous flow of the polymer. Therefore, $N = 2$, and Eq. (1) can be simplified as:

$$E_T^* = \left(E_1^* - E_2^*\right) e^{-\left(\frac{T}{T_1}\right)^{m_1}} + E_2^* e^{-\left(\frac{T}{T_2}\right)^{m_2}} \tag{2}$$

Here, E_i^* represents the elastic modulus at the onset of each transition stage, where E_1^* corresponds to the modulus prior to the glass transition, and E_2^* corresponds to the modulus at the onset of viscous flow (also referred to as the rubbery modulus). The reduction amplitudes $H_1 = E_1^* - E_2^*$ and $H_2 = E_2^*$, along with the Weibull shape parameters m_j (for $j = 1,2$), reflect the statistical nature of the degradation process and are influenced by the polymer properties such as crosslinking density, molecular weight and crystallinity.

Building upon this conceptual basis, a semi-empirical model is

developed herein to characterize the degradation of both tensile strength and elastic modulus of GFRP bars at high temperatures, as expressed in Eq. (3):

$$P_T = (P_0 - P_r)e^{-\left(\frac{T-T_0}{T_g}\right)^n} + P_r e^{-\left(\frac{T-T_0}{T_d}\right)^n} \quad (3)$$

In the above equation, P_0 and P_r denote the initial and residual mechanical properties (either tensile strength or elastic modulus) at ambient temperature and in the rubbery state, respectively. A unified Weibull shape parameter is adopted for both the glass transition and decomposition states. Substituting temperature-dependent terms yields the following expressions for tensile strength and elastic modulus degradation:

$$\frac{f_T}{f_0} = k_1 e^{-\left(\frac{T-T_0}{T_g}\right)^{n_1}} + \left(1 - k_1\right) e^{-\left(\frac{T-T_0}{T_d}\right)^{n_1}} \quad (4)$$

$$\frac{E_T}{E_0} = k_2 e^{-\left(\frac{T-T_0}{T_g}\right)^{n_2}} + \left(1 - k_2\right) e^{-\left(\frac{T-T_0}{T_d}\right)^{n_2}} \quad (5)$$

In the above equations, the dimensionless coefficients $k_1 = (f_0 - f_r)/f_0$ and $k_2 = (E_0 - E_r)/E_0$ quantify the relative reductions in tensile strength and elastic modulus, respectively, where f_0 and f_r represent the tensile strength at ambient temperature and in the rubbery state, and E_0 and E_r are the corresponding elastic modulus values.

A key distinction between the present model and the formulation by Mahieux and Reifsnider [55] lies in the assignment of thermophysical temperatures (i.e., T_g and T_d) of the polymer matrix for the two transition stages. Specifically, for the tensile strength degradation model, the two thermophysical temperatures are defined as $T_{g,onset}$ and $T_{d,onset}$, whereas for the elastic modulus degradation model, they are defined as $T_{g,onset}$ and $T_{d,oxpeak}$. This differentiation reflects the fact that both tensile strength and elastic modulus exhibit significant degradation near $T_{g,onset}$ due to the softening of the polymer matrix, whereas the elastic modulus is less sensitive to temperature increases compared to the tensile strength, as the elastic modulus is more strongly governed by the properties of the glass fibers than by the polymer matrix. As a result, different values for T_d are assigned in the tensile strength and elastic modulus degradation models.

To determine the values of the dimensionless coefficients k_1 and k_2, Eureqa software was employed to perform data-driven regression analysis using the collected high-temperature tensile test datasets containing both the T_g and T_d values. During the regression analysis, the Weibull shape parameters were fixed at $n_1 = 4$ and $n_2 = 4$ as these values provided an appropriate trade-off between model simplicity and predictive accuracy. The rationale and methodology for selecting these Weibull shape parameters are discussed in detail in the following section. As revealed by the ANOVA results presented in Section 3.3, both coefficients exhibit statistically significant correlations with T_g, T_d and their interaction. The regression analysis enabled the determination of the coefficient values that accurately represent the temperature-dependent degradation trends in tensile strength and elastic modulus observed in the test datasets. Accordingly, the following empirical expressions are proposed to quantify the effects of T_g, T_d and their interaction on the thermal degradation behavior:

$$k_1 = 116 \times 10^{-2} + 127 \times 10^{-7} T_g T_d - 303 \times 10^{-5} T_d - 101 \times 10^{-9} T_g^3 \quad (6)$$

$$k_2 = 703 \times 10^{-3} + 142 \times 10^{-7} T_g T_d - 174 \times 10^{-5} T_d - 387 \times 10^{-7} T_g^2 \quad (7)$$

Fig. 11 presents a comparison between the model predictions and the corresponding derived values of k_1 and k_2 using the high-temperature tensile test datasets, demonstrating good agreement with most deviations contained within ±20 %.

Further investigation, as presented in Fig. 12**a**, compares two representative GFRP bar types: RB and RBP. Although the RB bars exhibit a higher T_g and share the same T_d as the RBP bars, their tensile strength of RB degrades more rapidly at high temperatures than its T_g. This observation suggests that the mechanical properties of GFRP bars at high temperatures are influenced not only by T_g and T_d, but also by interfacial properties between fibers and matrix, which are in turn affected by fiber volume or mass content [67]. To account for these effects, an interaction parameter defined as $T_g T_d$ is introduced and its empirical correlation with fiber mass content. Fig. 12**b** shows a positive correlation between fiber mass content and the value of $T_g T_d$. While this interaction parameter not directly representing a specific physical degradation mechanism, this parameter effectively captures the combined influence of thermal transitions and fiber content. Incorporating this interaction parameter is expected to enhance the predictive accuracy of the proposed degradation models, enabling a more comprehensive representation of the combined thermal and compositional effects on the residual tensile strength of GFRP bars at high temperatures.

As previously discussed, the Weibull shape parameters n_1 and n_2 in the degradation model characterize the statistical distribution of material failure in GFRP bars at high temperatures. Initial estimates of $n_1 = 4$ and $n_2 = 4$ were employed to calibrate the degradation coefficients k_1 and k_2, which govern the reductions in tensile strength and elastic modulus, respectively. These initial values yielded model predictions in close agreement with the experimental data. To further optimize the parameter selection, a sensitivity analysis was conducted by varying n_1

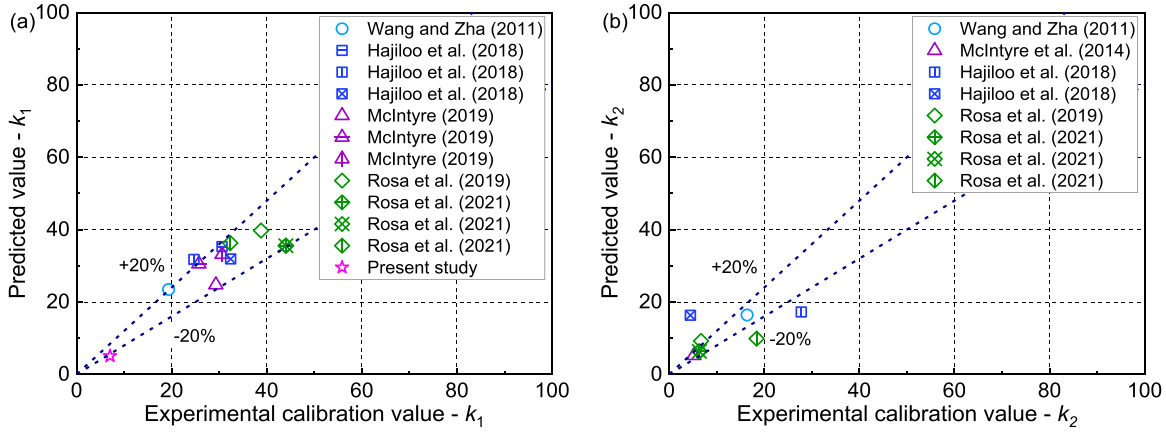


Fig. 11. Comparisons of (a) k_1 and (b) k_2 between the model predictions and the corresponding calibrated values.

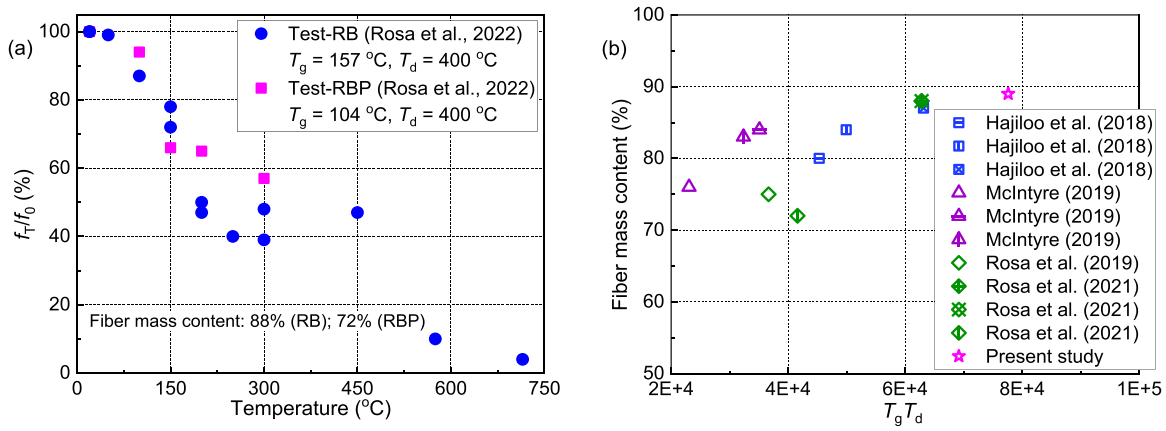


Fig. 12. Factors influencing the tensile strength degradation of GFRP bars at high temperatures: (a) comparison of RB and RBP, and (b) the correlation between fiber mass content and the interaction parameter T_gT_d.

and n_2 across six discrete values (from 1 to 6). The mean and standard deviation (S.D.) of the relative prediction errors were computed to assess the model's performance across the high-temperature tensile test database. As shown in Fig. 13, the parameters combination $n_1 = 4$ and $n_2 = 4$ yielded the lowest prediction errors, with mean prediction ratios approaching one and relatively small standard deviations. These results indicate that the selected Weibull shape parameters provide a statistically reliable representation of the degradation behavior observed experimentally.

Fig. 14 compares the tensile properties predicted by the proposed degradation models (Eqs. (4) and (5)) with the experimental results collected from the literature. The following criteria were applied to selected datasets for model validation: (1) datasets were excluded if both the T_g and T_d values were not reported; (2) for datasets where the T_g value was reported but T_d was not, a representative T_d value of 412.5 °C was assigned. This value was determined as the average value derived from the complete database; and (3) datasets involving additional degradation mechanisms, such as pre-exposure to alkaline environments [43] or testing for GFRP bars embedded in concrete [32], were excluded from the model validation.

Overall, the model predictions show good agreement with the experimental data, demonstrating the effectiveness of the proposed formulations in capturing the degradation behavior of GFRP bars in terms of both tensile strength and elastic modulus at high temperatures. The corresponding mean values and standard deviations (S.D.) of the model predictions are also presented in Fig. 14. It is noted that the predicted average tensile strength is slightly conservative compared to the experimental data, primarily due to the model's assumption of accelerated degradation beyond the decomposition temperature.

Figs. 15 and 16 provide further comparisons between the proposed model and the existing predictive models using 12 well-reported experimental datasets, including six for tensile strength and six for elastic modulus. As shown in Fig. 15, previous studies often observed relatively stable tensile strength variation between T_g and T_d. For example, the RB bars examined in Ref. [46] exhibited minimal strength loss between 200°C and 450°C (see Fig. 15d). In contrast, the HW GFRP bars investigated in this study showed a much more rapid strength reduction beyond T_g (see Fig. 15f), which is attributed to the narrower thermal transition range between softening and decomposition (T_g = 215°C and T_d = 361°C), resulting in a more abrupt degradation of the polymer matrix. In general, the comparisons show that the proposed degradation models are generally good at making predictions across a wide range of experimental data. However, notable discrepancies are observed in Figs. 15d and 16d. In Fig. 15d, the experimental data indicate a nearly constant tensile strength within the 200°C-450°C range, while the model predicts a steeper decline, thereby underestimating the stability period. In Fig. 16d, the model overestimates the elastic modulus degradation at temperatures above 400°C. As shown in Fig. 16, the experimental data on elastic modulus at temperatures above 450°C are limited. Among the entire database, only one dataset includes modulus measurements above this threshold. In that case, the model predicted greater degradation than what was experimentally observed. To enhance the predictive reliability of the proposed model for the elastic modulus degradation, especially at high temperature levels, additional experimental studies are needed, particularly those focusing on the elastic modulus response of GFRP bars at temperatures above 450°C.

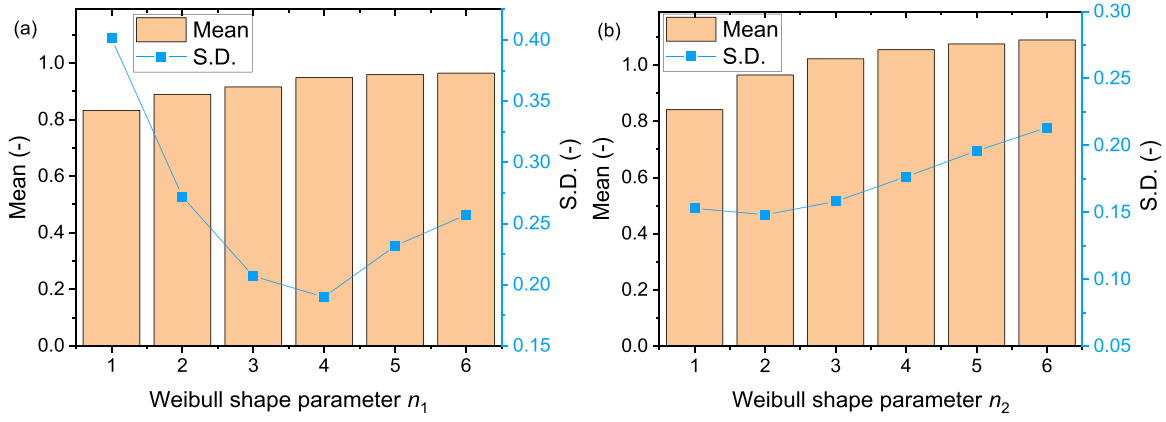


Fig. 13. Mean and S.D. values of the model predictions for tensile property degradation using various Weibull shape parameter: (a) effect of n_1, and (b) effect of n_2.

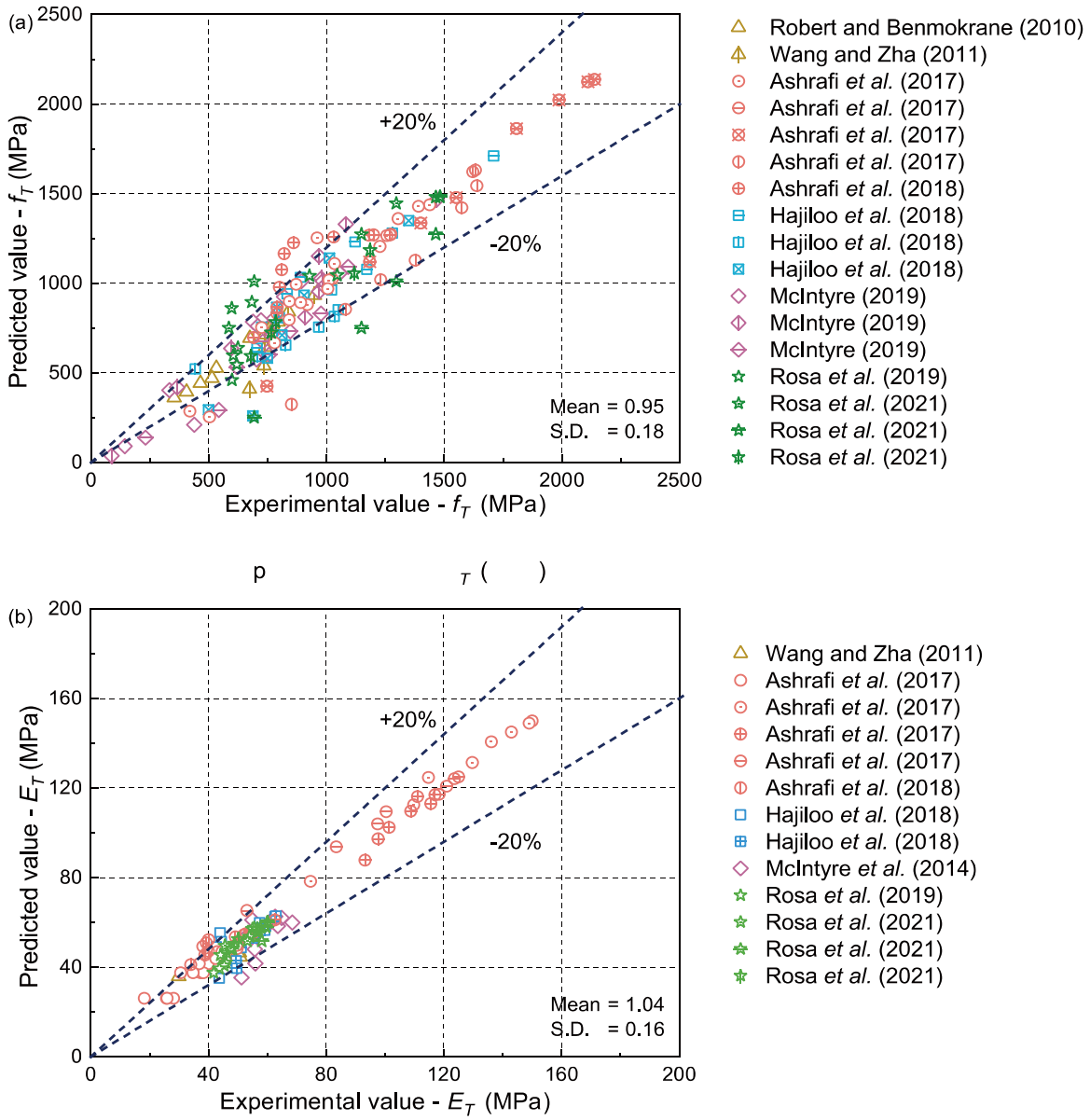


Fig. 14. Comparisons between the predicted and experimental mechanical properties based on the proposed degradation models: (a) tensile strength and (b) elastic modulus.

4. Conclusions

This paper presents a comprehensive database comprising 1087 tensile tests on GFRP bars at both ambient and high temperatures. Additional tensile tests were conducted on HW GFRP bars with a T_g of 215°C. A novel semi-empirical degradation model was developed to predict the mechanical property degradation of GFRP bars at high temperatures, based on a detailed analysis of key influencing parameters such as T_g and T_d. The predictive accuracy of the proposed model was validated against a wide range of existing experimental datasets. The main conclusions of this study are summarized as follows:

(a) High-temperature tensile tests on HW GFRP bars showed that the strength reductions at moderately high temperatures below T_g are slower than those of the conventional GFRP bars reported in the literature. However, these bars exhibited a significantly accelerated reduction in tensile strength beyond T_g. This behavior is primarily attributed to the relatively narrow thermal transition range between T_g and T_d, which results in a rapid transition of the polymer matrix from softening to decomposition.

(b) A semi-empirical degradation model was proposed to predict the degradation of tensile strength and elastic modulus of GFRP bars at high temperatures. This model was established based on both the collected experimental database and the newly conducted tests presented in this paper, with particular focus on T_g, T_d, and their interaction as well as the high temperature as critical parameters. An analysis of variance confirmed the statistical significance of these parameters in influencing the mechanical property degradation of GFRP bars at high temperatures. The proposed model demonstrated good agreement with experimental results and thus can capture the degradation trends in both tensile strength and elastic modulus.

(c) The results reported in this paper highlight the critical importance of accurately determining the T_g and T_d values for GFRP bars, as these two parameters predominantly govern the degradation of their mechanical properties of GFRP bars at high temperatures. For practical applications involving the fire-resistance design of GFRP RC structural members, it is strongly recommended that manufacturers provide both T_g and T_d values to enable reliable evaluation of the residual tensile strength and elastic modulus of GFRP bars at high temperatures during

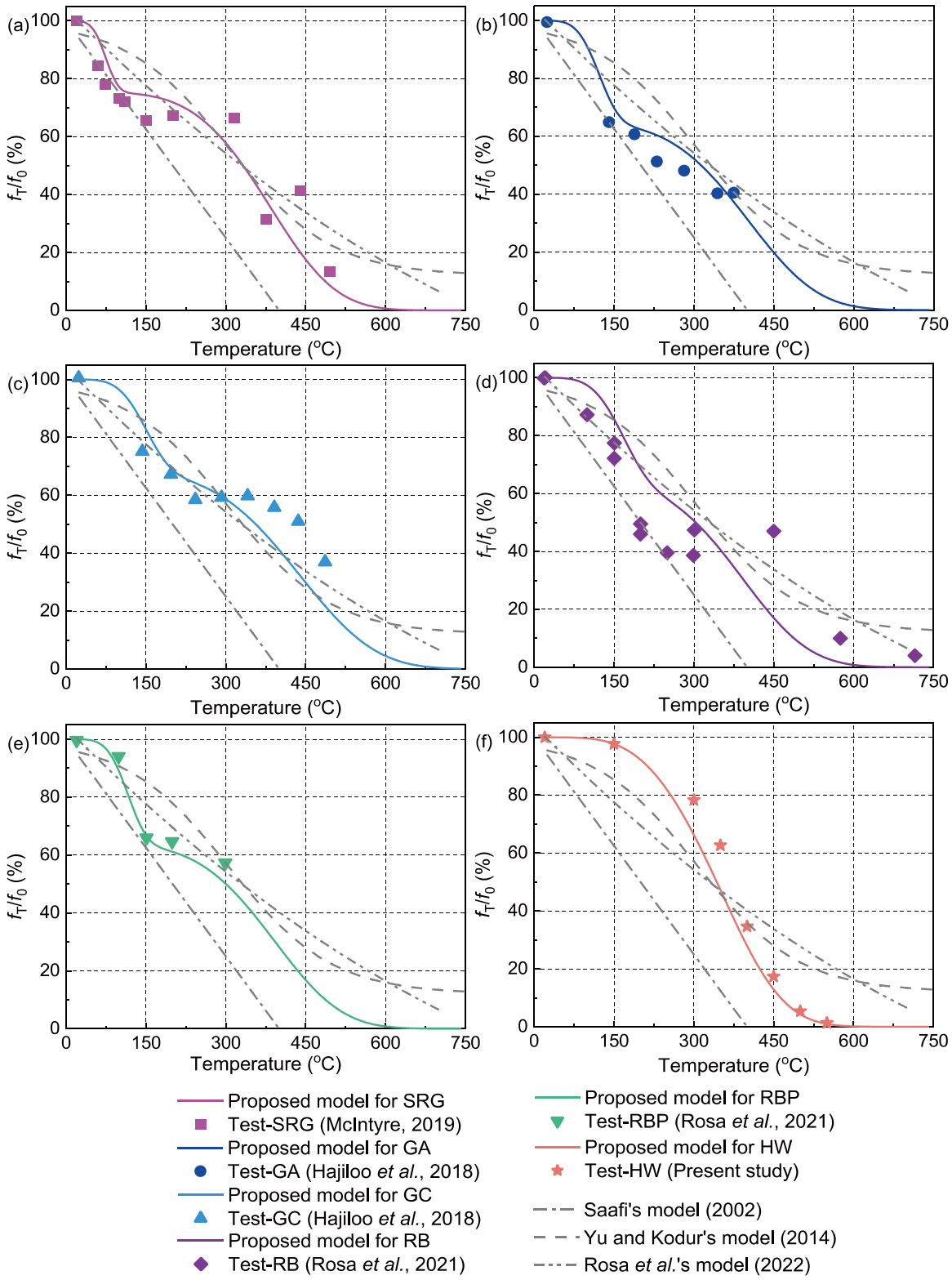


Fig. 15. Comparisons of the temperature-dependent degradation trends in tensile strength between the experimental results and the predictions from the existing models and the proposed degradation model: (a) test-SRG, (b) test-GA, (c) test-GC, (d) test-RB, (e) test-RBP, (f) test-HW.

fire exposure. In the absence of such information, the average values derived from the collected database (e.g., $T_g = 108$ °C, $T_d = 412.5$ °C) may serve as reasonable estimates for preliminary design.

CRediT authorship contribution statement

De-Xin Duan: Writing – original draft, Visualization, Validation, Software, Methodology, Investigation, Formal analysis, Data curation. **En-Ci Liu:** Validation, Resources, Investigation, Data curation. **Yu-Qing Zhang:** Validation, Resources, Investigation, Data curation. **GAO Wan-**

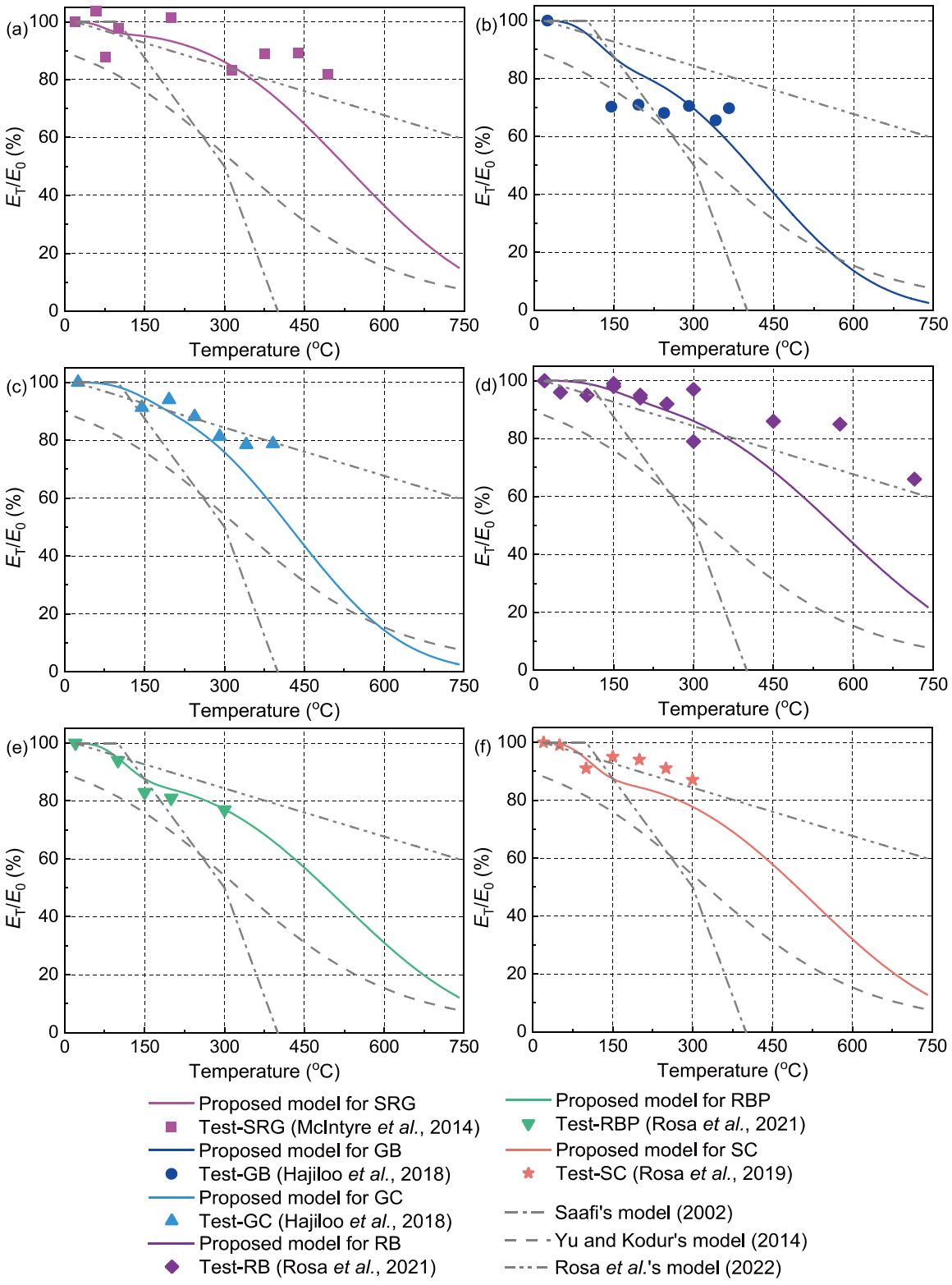


Fig. 16. Comparisons of the temperature-dependent degradation trends in elastic modulus between the experimental results and the predictions from the existing models and the proposed degradation model: (a) test-SRG, (b) test-GB, (c) test-GC, (d) test-RB, (e) test-RBP, (f) test-SC.

Yang: Writing – original draft, Validation, Supervision, Resources, Investigation, Funding acquisition, Formal analysis, Conceptualization.

Declaration of Competing Interest

The authors declare the following financial interests/personal relationships which may be considered as potential competing interests: Wan-Yang Gao reports financial support was provided by National Natural Science Foundation of China (NSFC). Wan-Yang Gao reports financial support was provided by Natural Science Foundation of Shanghai. Wan-Yang Gao reports financial support was provided by Open Foundation of Yunnan Key Laboratory of Building Structure and

New Materials. Wan-Yang Gao reports financial support was provided by Program Fund of Non-Metallic Excellence and Innovative Center for Building Materials. Wan-Yang Gao reports a relationship with Shanghai Jiao Tong University that includes: employment. If there are other authors, they declare that they have no known competing financial interests or personal relationships that could have appeared to influence the work reported in this paper

Acknowledgements

The authors gratefully acknowledge the financial support from the National Natural Science Foundation of China (NSFC) (No. 51978398) and the Natural Science Foundation of Shanghai (No. 23ZR1429200). Additional support was provided by the Open Foundation of Yunnan Key Laboratory of Building Structure and New Materials (No. 2023-JKKF-01) and the Program Fund of Non-Metallic Excellence and Innovative Center for Building Materials (No. 2023TAD5–1).

Data availability

Data will be made available on request.

References

[1] L.C. Bank, Composites for Construction: Structural Design with FRP Materials, John Wiley & Sons, 2006.
[2] A. Nanni, A. De Luca, H.J. Zadeh, Reinforced Concrete with FRP Bars: Mechanics and Design, CRC press, 2014.
[3] L.A. Bisby, Fire Behaviour of Fibre-reinforced Polymer (FRP) Reinforced or Confined Concrete, Queen's University Kingston, Canada, 2003.
[4] A. Zaman, S.A. Gutub, M.A. Wafa, A review on FRP composites applications and durability concerns in the construction sector, J. Reinf. Plast. Compos 32 (2013) 1966–1988.
[5] A. Rimkus, J.A.O. Barros, V. Gribniak, M. Rezazadeh, Mechanical behavior of concrete prisms reinforced with steel and GFRP bar systems, Compos. Struct. 220 (2019) 273–288.
[6] L. Torres, K. Neocleous, K. Pilakoutas, Design procedure and simplified equations for the flexural capacity of concrete members reinforced with fibre-reinforced polymer bars, Struct. Concr. 13 (2012) 119–129.
[7] S. Alsayed, Y. Al-Salloum, T. Almusallam, Performance of glass fiber reinforced plastic bars as a reinforcing material for concrete structures, Compos. Part B Eng. 31 (2000) 555–567.
[8] A.C. Berg, L.C. Bank, M.G. Oliva, J.S. Russell, Construction and cost analysis of an FRP reinforced concrete bridge deck, Constr. Build. Mater. 20 (2006) 515–526.
[9] K. Bouguerra, E.A. Ahmed, S. El-Gamal, B. Benmokrane, Testing of full-scale concrete bridge deck slabs reinforced with fiber-reinforced polymer (FRP) bars, Constr. Build. Mater. 25 (2011) 3956–3965.
[10] E.A. Ahmed, B. Benmokrane, M. Sansfaçon, Case study: design, construction, and performance of the la Chancelière parking Garage's concrete flat slabs reinforced with GFRP bars, J. Compos. Constr. 21 (2017) 05016001.
[11] M.M. Rafi, A. Nadjai, F. Ali, D. Talamona, Aspects of behaviour of CFRP reinforced concrete beams in bending, Constr. Build. Mater. 22 (2008) 277–285.
[12] A. Ashour, Flexural and shear capacities of concrete beams reinforced with GFRP bars, Constr. Build. Mater. 20 (2006) 1005–1015.
[13] M. Theriault, B. Benmokrane, Effects of FRP reinforcement ratio and concrete strength on flexural behavior of concrete beams, J. Compos. Constr. 2 (1998) 7–16.
[14] Y. Liu, H.T. Zhang, T. Tafsirojjaman, A. Ur Rahman Dogar, O. AlAjarmeh, Q.R. Yue, A. Manalo, A novel technique to improve the compressive strength and ductility of glass fiber reinforced polymer (GFRP) composite bars, Constr. Build. Mater. 326 (2022) 126782.
[15] Z. Saleh, M. Goldston, A.M. Remennikov, M.N. Sheikh, Flexural design of GFRP bar reinforced concrete beams: an, Apprais. Code Recomm. J. Build. Eng. 25 (2019) 100794.
[16] ACI Committee 440, Building code requirements for structural concrete reinforced with glass fiber-reinforced polymer (GFRP) bars—Code and commentary, ACI CODE-440.11-22, American Concrete Institute, Farmington Hills, Michigan, USA, 2022.
[17] CSA (Canadian Standards Association), Design and construction of building components with fiber-reinforced polymers. CSA-S806, Canadian Standards Association, Mississauga, Canada, 2012.
[18] fib. Model Code 2010, fib Bulletin 55, The Fédération internationale du béton, Lausanne, Switzerland, 2013.
[19] K. Pilakoutas, K. Neocleous, M. Guadagnini, Design philosophy issues of fiber reinfored polymer reinforced concrete structures, J. Compos. Constr. 6 (2002) 154–161.
[20] V. Gribniak, A. Pérez Caldentey, G. Kaklauskas, A. Rimkus, A. Sokolov, Effect of arrangement of tensile reinforcement on flexural stiffness and cracking, Eng. Struct. 124 (2016) 418–428.
[21] L.A. Bisby, V.K.R.Kodur Evaluating, The fire endurance of concrete slabs reinforced with FRP bars: considerations for a holistic approach, Compos. Part B Eng. 38 (2007) 547–558.
[22] S. Spagnuolo, A. Meda, Z. Rinaldi, A. Nanni, Residual behaviour of glass FRP bars subjected to high temperatures, Compos. Struct. 203 (2018) 886–893.
[23] S. Alsayed, Y. Al-Salloum, T. Almusallam, S. El-Gamal, M. Aqel, Performance of glass fiber reinforced polymer bars under elevated temperatures, Compos. Part B Eng. 43 (2012) 2265–2271.
[24] L.A. Bisby, M.F. Green, V.K.R.Kodur Response, To fire of concrete structures that incorporate FRP, Prog. Struct. Eng. Mater. 7 (2005) 136–149.
[25] R. Park, W.L. Gamble, Reinforced Concrete Slabs, John Wiley & Sons, 1999.
[26] I.C. Rosa, J.P. Firmo, J.R. Correia, L.A.Bisby Fire, Behavior of GFRP-reinforced, Concr. Struct. Memb. a StateArt. Rev. J. Compos. Constr. 27 (2023) 03123002.
[27] R. Dubčáková, Eureqa: software review, Genet Program Evol. Mach. 12 (2011) 173–178.
[28] J.L. Clarke. Alternative Materials for the Reinforcement and Prestressing of Concrete, 1st ed, Blackie Academic, London; New York, 1993.
[29] S. Kumahara, Y. Masuda, H. Tanano, A. Shimizu, Tensile strength of continuous fiber bar under high temperature, Acids Spec. Publ. 138 (1993) 731–742.
[30] H. Tanano, Y. Masuda, T. Kage, H. Fukuyama, I. Nishida, T. Hashimoto, 44 fire resistance of continuous fiber reinforced concrete, in: F.R.P. Non-Metallic (Ed.), Reinforcement for Concrete Structures: Proceedings of the Second International RILEM Symposium, CRC Press, 1995, p. 368.
[31] Y.I. Dimitrienko, Thermomechanical behaviour of composite materials and structures under high temperatures: 1, Mater. Compos. Part Appl. Sci. Manuf. 28 (1997) 453–461.
[32] A. Abbasi, P.J. Hogg, Temperature and environmental effects on glass fibre rebar: modulus, strength and interfacial bond strength with concrete, Compos. Part B Eng. 36 (2005) 394–404.
[33] C.D. Zhou. Fire performance of GFRP reinforced concrete, Research Rep., Dept. of Civil Engineering, Tongji University, China, 2005.
[34] Y.C. Wang, V. Kodur, Variation of strength and stiffness of fibre reinforced polymer reinforcing bars with temperature, Cem. Concr. Compos 27 (2005) 864–874.
[35] A. Weber, Fire-resistance tests on composite rebars. Proceedings of the Fourth International Conference on FRP Composites in Civil Engineering, CICE2008, Zurich, Switzerland, 2008.
[36] M. Robert, B. Benmokrane, Behavior of GFRP reinforcing bars subjected to extreme temperatures, J. Compos. Constr. 14 (2010) 353–360.
[37] X.L. Wang, X.X. Zha, Experimental research on mechanical behavior of GFRP bars under high temperature, Appl. Mech. Mater. 71-78 (2011) 3591–3594.
[38] E.R.E. McIntyre. Fire performance of fibre reinforced polymer (FRP) bars in reinforced concrete: An experimental approach, Ph.D. thesis, University of Edinburgh, UK, 2019.
[39] E.R.E. McIntyre, A. Bilotta, L. Bisby, E. Nigro, Mechanical properties of fibre reinforced polymer reinforcement for concrete at high temperature. Proceedings of the 8th International Conference on Structures in Fire, Tongji University Press, Shanghai, 2014, pp. 1227–1234.
[40] H. Hajiloo, M.F. Green, J. Gales, Mechanical properties of GFRP reinforcing bars at high temperatures, Constr. Build. Mater. 162 (2018) 142–154.
[41] H. Ashrafi, M. Bazli, E.P. Najafabadi, A. Vatani Oskouei, The effect of mechanical and thermal properties of FRP bars on their tensile performance under elevated temperatures, Constr. Build. Mater. 157 (2017) 1001–1010.
[42] H. Ashrafi, M. Bazli, A. Vatani Oskouei, L. Bazli, Effect of sequential exposure to UV radiation and water vapor condensation and extreme temperatures on the mechanical properties of GFRP bars, J. Compos. Constr. 22 (2018) 04017047.
[43] E.P. Najafabadi, A.V. Oskouei, M.H. Khaneghahi, P. Shoaei, T. Ozbakkaloglu, The tensile performance of FRP bars embedded in concrete under elevated temperatures, Constr. Build. Mater. 211 (2019) 1138–1152.
[44] I.C. Rosa, J.P. Firmo, J.R. Correia, J.A.O.Barros Bond, Behaviour of sand coated GFRP bars to concrete at elevated temperature - definition of bond vs. Slip relations, Compos. Part B Eng. 160 (2019) 329–340.
[45] I.C. Rosa, J.P. Firmo, J.R. Correia, P. Mazzuca, Influence of elevated temperatures on the bond behaviour of ribbed GFRP bars in concrete, Cem. Concr. Compos 122 (2021) 104119.
[46] I.C. Rosa, J.P. Firmo, J.R. Correia, Experimental study of the tensile behaviour of GFRP reinforcing bars at elevated temperatures, Constr. Build. Mater. 324 (2022) 126676.
[47] C.H. Zhou, J.J. Pan, Z.H. Zhang, Y.H. Zhu, Comparative study on the tensile mechanical behavior of GFRP bars under and after high temperature exposure, Case Stud. Constr. Mater. 16 (2022) e00905.
[48] K. Wang, B. Young, S.T. Smith, Mechanical properties of pultruded carbon fibre-reinforced polymer (CFRP) plates at elevated temperatures, Eng. Struct. 33 (2011) 2154–2161.
[49] X.L. Wang, X.X. Zha, Experimental investigation into mechanical behavior of GFRP rebars at elevated temperature, J. South China Univ. Technol. (Nat. Sci. Ed.) 39 (9) (2011) 75–81.
[50] M. Bazli, M. Abolfazli, Mechanical properties of fibre reinforced polymers under elevated temperatures: an overview, Polymers 12 (2020) 2600.
[51] ASTM (American Society for Testing and Materials), Standard test method for assignment of the glass transition temperature by dynamic mechanical analysis. ASTM E1640, ASTM, West Conshohocken, Pennsylvania, 2009.
[52] ISO (International Organization for Standardization). Plastics - differential scanning calorimetry (DSC) - Part 1: General principles, ISO 11357-1, Geneve, Switzerland, 2016.

[53] M.F. Ashby, D.R.H. Jones. Engineering Materials 2: An Introduction to Microstructures and Processing, Fourth edition, Elsevier/Butterworth-Heinemann, Amsterdam, 2013.
[54] R.H. Alasfar, S. Ahzi, N. Barth, V. Kochkodan, M. Khraisheh, M. Koç, A review on the modeling of the elastic modulus and yield stress of polymers and polymer nanocomposites: effect of temperature, loading rate and porosity, Polymers 14 (2022) 360.
[55] C.A. Mahieux, K.L. Reifsnider, Property modeling across transition temperatures in polymers: a robust stiffness-temperature model, Polymer 42 (2001) 3281–3291.
[56] Y. Bai, T. Keller, T. Vallée, Modeling of stiffness of FRP composites under elevated and high temperatures, Compos. Sci. Technol. 68 (2008) 3099–3106.
[57] P.-G. De Gennes, Scaling concepts in polymer physics, Cornell university press, 1979.
[58] J.P. Mercier, G. Zambelli, W. Kurz, - factors influencing mechanical properties, Chapter 12, in: J.P. Mercier, G. Zambelli, W. Kurz (Eds.), Introduction to Materials Science, Elsevier, Oxford, 2002, pp. 279–320. Chapter 12.
[59] J.R. Correia, M.M. Gomes, J.M. Pires, F.A. Branco, Mechanical behaviour of pultruded glass fibre reinforced polymer composites at elevated temperature: experiments and model assessment, Compos. Struct. 98 (2013) 303–313.
[60] A.G. Gibson, Y.-S. Wu, J.T. Evans, A.P. Mouritz, Lamina Theory Anal. Compos. Load. fire J. Compos. Mater. 40 (2006) 639–658.
[61] E.U. Chowdhury, R. Eedson, L.A. Bisby, M.F. Green, N. Benichou, Mechanical characterization of fibre reinforced polymers materials at high temperature, Fire Technol. 47 (2011) 1063–1080.
[62] B. Yu, V. Kodur, Effect of temperature on strength and stiffness properties of near-surface mounted FRP reinforcement, Compos. Part B Eng. 58 (2014) 510–517.
[63] R.A. Hawileh, J.A. Abdalla, S.S. Hasan, M.B. Ziyada, A. Abu-obeidah. models for predicting elastic modulus and tensile strength of carbon, basalt and hybrid carbon-basalt FRP laminates at elevated temperatures, Constr. Build. Mater. 114 (2016) 364–373.
[64] M. Saafi, Effect of fire on FRP reinforced concrete members, Compos. Struct. 58 (2002) 11–20.
[65] A. Jafari, M. Bazli, H. Ashrafi, A. Vatani Oskouei, S. Azhari, X.-L. Zhao, H. Gholipour, Effect of fibers configuration and thickness on tensile behavior of GFRP laminates subjected to elevated temperatures, Constr. Build. Mater. 202 (2019) 189–207.
[66] H. Ashrafi, M. Bazli, A. Jafari, T. Ozbakkaloglu. tensile properties of GFRP laminates after exposure to elevated temperatures: effect of fiber configuration, sample thickness, and time of exposure, Compos. Struct. 238 (2020) 111971.
[67] S.H. Kim, H.C. Park, H.M. Jeong, B.K. Kim, Glass fiber reinforced rigid polyurethane foams, J. Mater. Sci. 45 (2010) 2675–2680.

Engineering Structures 318 (2024) 118705



Contents lists available at ScienceDirect

Engineering Structures

journal homepage: www.elsevier.com/locate/engstruct



Novel bamboo-raft-type floating structure (BRT-FS) assembled by FRP reinforced concrete tubes: Conceptual design and analysis

Chongfeng Xie, Peng Feng *

MOE Key Lab of Civil Engineering Safety and Durability, Department of Civil Engineering, Tsinghua University, Beijing, 100084, China

ARTICLE INFO

Keywords:
Bamboo-raft-type
Floating structure
Concrete
Fiber reinforced polymer (FRP)

ABSTRACT

To improve construction efficiency in offshore engineering and extend service life of offshore platforms, a novel bamboo-raft-type floating structure (BRT-FS) assembled by FRP reinforced concrete tubes is proposed. It comprises four fundamental components: concrete tube, carbon fiber-reinforced polymer (CFRP) cable, holding beam, and bellow. This paper presents the structure system and structure design of BRT-FS. Separating load-bearing and buoyant functions ensures structural safety and ease of design. It has broad application perspectives in offshore construction due to its high corrosion resistance, designability, construction efficiency, and low crack control requirement. Furthermore, to obtain the operation conditions of BRT-FS, the mechanical performance is analyzed from two levels, which are hydroelastic analysis and structural analysis. Hydroelastic analysis is conducted under different wave directions, wave periods, water depths, and structural dimensions using a new finite element-boundary element (FE-BE) method. In a specify study case, a sensitive period around 11 s for head sea, around 7 s for oblique wave, around 5 s for beam sea are noted. The hydroelastic response is not significantly affected by water depth or transverse dimension. Structural analysis indicates that the structure can work in clam harbour sea with breakwater protection. Even after concrete tubes crack in higher waves, this new structure can still float with the inside bellows in theory. These preliminary findings confirm the feasibility of this novel structure. Structural details such as tube-tube joints, tube-beam joints, CFRP cable anchorages, and other connections will be further designed and tested in the future.

1. Introduction

Ocean contains a considerable number of resources. The fast-growing marine industries, such as aquaculture, oil, and gas exploitation, reflect enormous economic value[8,16]. Besides, Climate change and urban development have also further fuelled the need to utilize ocean space. Some large floating city concepts, such as Oceanix City, have even been proposed[36]. With the economic development of coastal cities and the progress of ocean engineering technology, floating platforms will enter a boom.

Compared with steel, the construction of floating platforms with concrete is characterized by outstanding durability, high load-bearing capacity, and excellent dynamic performance[27]. Many concrete floating platform concepts have been proposed and even put into application. In 1995, Troll B, the first concrete semi-submersible platform was built in the North Sea, with a displacement of 193,000 tons [10]. Another type of floating concrete structures extensively explored is the EPS-concrete system[18]. Expanded polystyrene (EPS) provides buoyancy, while the concrete frame provides stiffness. Besides these existing structures, several new concepts of modular concrete floating structures have also been proposed. Rectangular or hexagon modules are used to form whole structures through connector systems[12–14,5]. Furthermore, Li et al. introduced fiber-reinforced polymer (FRP) and ultra-high performance concrete (UHPC) into concrete floating structures[22].

In addition to concrete, FRP composite is also an ideal offshore construction material. FRP composite consists of fibers and resin matrix, known for its lightweight, high strength, and corrosion resistance[24]. These properties make it have been applied widely in piles, pipelines, offshore platforms, and other offshore engineering[20,3,38,7].

The disadvantages of steel reinforced concrete structures, such as heavy and easy cracking, limit their wide application in offshore engineering. Replacing steel bars and cables with FRP bars and cables can effectively breakthrough this obstacle. Firstly, glass FRP (GFRP) surpasses steel with a strength-to-density ratio over 5 times higher, while carbon FRP (CFRP) exceeds steel by over 16 times. Employing FRP

* Corresponding author.
E-mail address: fengpeng@tsinghua.edu.cn (P. Feng).

https://doi.org/10.1016/j.engstruct.2024.118705
Received 9 January 2024; Received in revised form 8 June 2024; Accepted 25 July 2024
Available online 1 August 2024
0141-0296/© 2024 Elsevier Ltd. All rights are reserved, including those for text and data mining, AI training, and similar technologies.

composites can effectively decrease the deadweight of platform. Secondly, steel reinforced concrete needs to be provided with a certain thickness of protective layer due to the effects of chloride ion erosion and carbonation. For tidal and splash zones, both Chinese and Norwegian standards specify a concrete protective layer thickness of 50 mm. In practice, this protective layer thickness even extends up to 75 mm[11]. FRP reinforcement can reduce the thickness of protective layer, making thin-walled concrete floating structures possible. Finally, concrete floating structures are more prone to tensile stress compared to land structures, leading to concrete cracking. Significant rusting of the reinforcing steel happens, followed by localized concrete spalling and eventual structural failure. FRP reinforcement can improve the durability of concrete after cracking and avoid accelerated corrosion.

However, it should be noted that the low elastic modulus of FRP reinforcement will not improve the cracking load of concrete structure. Although the durability of structure after cracking is guaranteed, water seepage problem is still a great hidden danger for floating platform. Therefore, it is necessary to develop a specific structural form for FRP reinforced concrete floating structure. On the one hand, tensile stress in the floating structure needs to be reduced through special form. On the other hand, sealing function needs to be stripped from concrete structure to reduce the influence of concrete cracking.

Based on the above considerations, this paper proposes a novel bamboo-raft-type floating structure (BRT-FS) assembled by FRP reinforced concrete tubes, as shown in Fig. 1. The concept is a new very large floating structures (VLFS) type inspired from bamboo raft, a traditional Chinese transport. Longitudinal bamboos are replaced by concrete tubes and transverse bamboos are replaced by UHPC holding beams. Corrosion-resistant FRP composites are employed to improve structural life span. The structure adopts tubular section to form arch effect, diminishing the risk of transverse cracking. Prestressed CFRP plates are arranged inside to reduce the risk of longitudinal cracking. At the same time, foldable bellows are laid inside the tube to separate floating function from bearing function.

In this paper, the structure system and structure design are introduced first. In order to obtain the operation conditions of BRT-FS, the mechanical performance of BRT-FS is analyzed from two levels, which are hydroelastic analysis and structural analysis. According to the special characteristics of BRT-FS, a new finite element-boundary element (FE-BE) method is proposed based on Timoshenko beam element. Hydroelastic analysis is conducted under different wave directions, wave periods, water depths, and structural dimensions. For structural analysis, bending capacity is calculated and checked based on the structural response in hydroelastic analysis.

2. Structure system

BRT-FS is designed to be utilized in nearshore scenarios including tourism, marine aquaculture, photovoltaic power generation, and so on. The platform is anchored to the seafloor by dolphin-fender mooring system, which restricts the horizontal displacement of the structure while releasing the vertical displacement[33]. Due to the limitation of the mooring system, the expected water depth of structure is 10 – 30 m. The wave conditions applicable to the structure will be obtained by

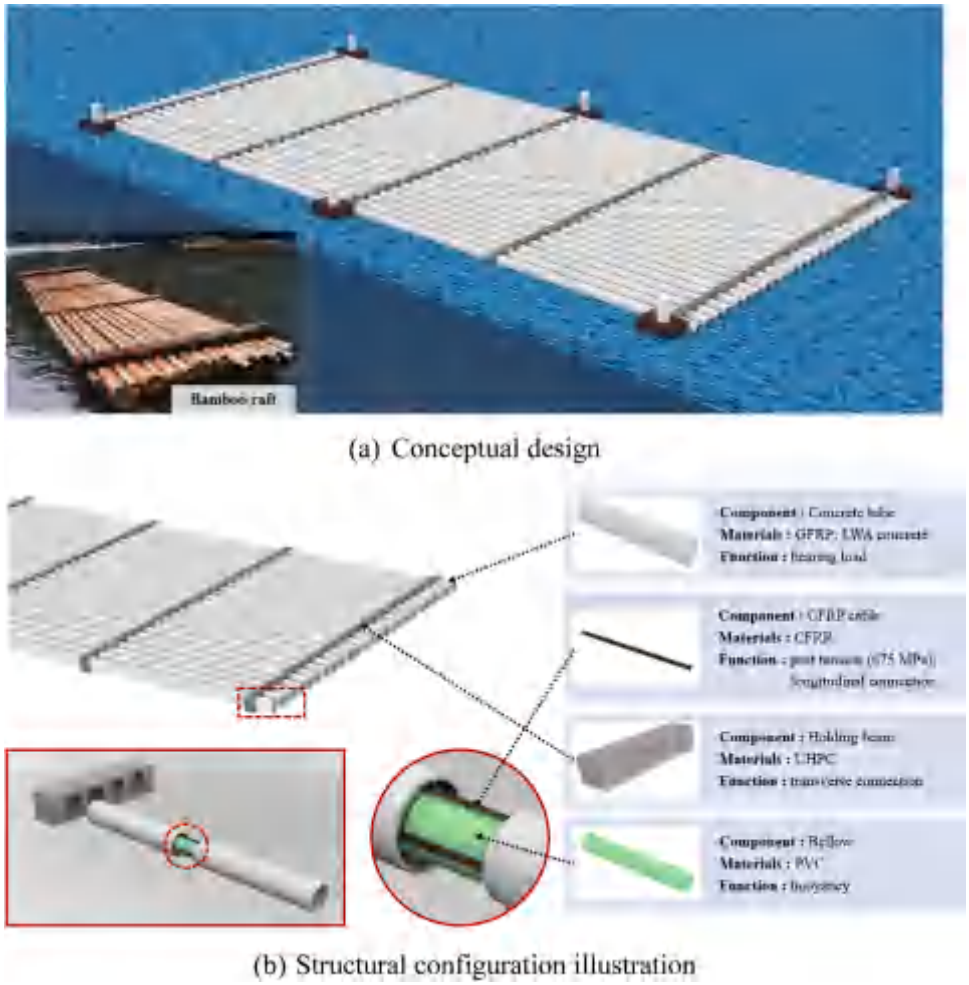


Fig. 1. BRT-FS assembled by FRP reinforced concrete tubes.

hydroelastic analysis and structural analysis in the following sections.

As illustrated in Fig. 1(b), BRT-FS comprises four fundamental components: concrete tube, carbon fiber-reinforced polymer (CFRP) cable, holding beam, and bellow. Concrete tubes are connected in longitudinal direction with post-tensioned CFRP cables and transversely through holding beams. CFRP cables are prestressed to slow down cracking process and ease concrete tube assembly. After post-tension, the ends of short tubes are connected to form a long tube longitudinally, creating rigid tube-tube joints. In lateral direction, rows of concrete tubes are connected through holding beams. In this way, the lateral bending stiffness is obtained. Foldable bellows passing through concrete tubes create an enclosed area with buoyancy by sealing in suitable places.

Two size types are selected for personnel and vehicle applications. Mechanical properties of load-bearing components for both types are listed in Table 1. Moreover, different tube sizes can apply in one structure, realizing high transport efficiency by nesting placement. Note that for brevity, only personnel operation type is considered for further analysis in the paper. Considering personnel demand, the upper design load of the structure needs to exceed 4.5 kN/m^2. This parameter will influence the displacement and size of the structure.

3. Structure design

3.1. Concrete tube

The concrete tubes use glass fiber-reinforced polymer (GFRP) bars and lightweight aggregate concrete (LWAC) as raw materials. GFRP reinforced concrete has similar mechanical properties as normal reinforced concrete[9] but better corrosion resistance[2,4]. Besides, LWAC reduces 20 % the density of normal aggregate concrete, which is beneficial for floating platforms and other projects that are sensitive to structural weight. Concrete tube has a circular section rather than a square section. Advantages include the ability to create an arch effect to resist transverse cracking, the ability to be mass-produced by mandrel vibration, and the ability to obtain a larger cross-sectional area for the same material consumption.

Considering the actual displacement demand of the floating platform, an optimal section size analysis of concrete tubes is carried out to select the proper section dimension. The inner diameter and thickness are optimized to satisfy the topside load demand. In this design, the waterline is considered to be above the center of the concrete tube. A waterline near the tube centerline can increase the waterline area, inhibiting the heave of structure. However, a too close distance between the waterline and centerline will reduce the sturcture displacement. 3/4 of the outer diameter is selected as the maximum draft. The density of seawater is assumed to be 1020 kg/m^3. Considering transportation limitations and load requirements, an outer diameter of 2360 mm and a thickness of 180 mm are selected. In this condition, the maximum topside load is 4.76 kN/m^2. The concrete tube state under empty (minimum draft) and full topside loads (maximum draft) are shown in

Table 1
Mechanical properties of the load-bearing components: concrete tube, CFRP cable, and holding beam.

Components	Dimension		ρ (kg/m^3)	E (GPa)
	personnel operation	vehicle operation		
Concrete tube	inner diameter 2 m thickness 180 mm	inner diameter 3 m thickness 270 mm	2000	30
CFRP cable	100 mm × 5 mm (4)	100 mm × 5 mm (6)	1600	150
Holding beam	0.5 m × 3 m	0.75 m × 4.5 m	2500	40

* For brevity, only personnel operation type is considered for further analysis in the paper.

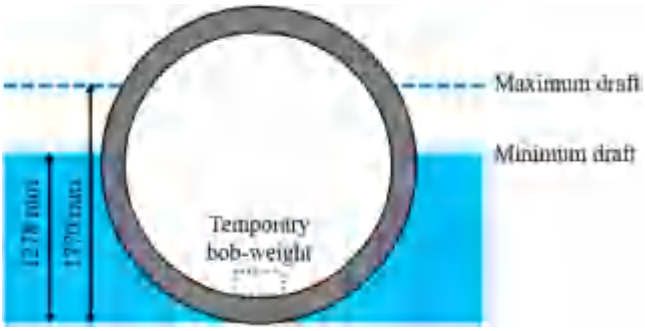


Fig. 2. State of concrete tube under empty (minimum draft) and full topside loads (maximum draft).

Fig. 2. Fig. 3 shows the reinforcement arrangement in a concrete tube. Longitudinal reinforcement is GFRP bars with a diameter of 28 mm. Because concrete tubes undertake bending in the vertical direction, the number of GFRP bars increases at both the top and bottom. Stirrups are 16 mm GFRP bars with intervals of 200 mm. To ease assembly, bob-weight can be added to the tube bottom to restrict the tube from rotation, then removed after assembly. Socket joints are applied to the end of these tubes, which are widely used in concrete drainage tubes.

3.2. CFRP cable

CFRP is a composite material with resin as matrix and carbon fiber as reinforcement. Compared with other FRP, CFRP has prominent characteristics of high strength and corrosion resistance[15]. Therefore, the application of CFRP has attracted increasing attention in ocean engineering[29,39]. As a common CFRP product, CFRP plate cable takes full advantage of high tensile strength and has been utilized as prestressed cable. However, the shear performance of CFRP is poor, making anchorage a crucial problem in its application[1]. Compared with circular section, plate section has higher anchoring efficiency due to the large perimeter-area ratio.

Each CFRP cable is prestressed to 675 MPa (approximately 30 % of the ultimate strength). To avoid damage in CFRP cables caused by external loads, these CFRP cables are arranged inside concrete tubes in circumferential distribution. The anchorage devices are fixed on the inner wall of concrete tubes for post-tensioning. Limited by the huge dimension of BRT-FS, CFRP cables are post-tensioned in sections, each containing two or three concrete tubes. CFRP plate anchorage devices are already a mature product on the market and will not be introduced here.

3.3. Holding beam

Holding beams are made from ultra-high performance concrete (UHPC) with a maximum strength of 200 MPa and better durability than conventional concrete[21]. There is no need to take into account the corrosion problem of UHPC in seawater because its chloride diffusion coefficient is orders of magnitude lower than that of conventional concrete. Holding beams have circle holes for concrete tubes crossing through. The interval of these holes is 2500 mm, leaving 140 mm interspace between concrete tubes. The high strength of UHPC is supposed to be adequate, which is not considered for the bearing capacity check in this paper.

3.4. Construction scheme

The construction of BRT-FS contains six main steps, as Fig. 4 shows:

1) Factory prefabrication. Precast production of concrete tubes and holding beams in a land factory;

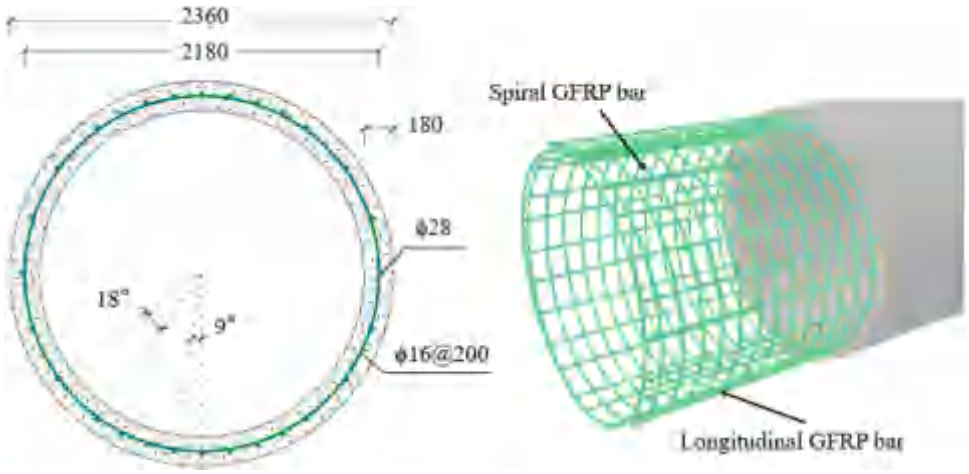


Fig. 3. GFRP reinforcement arrangement in a concrete tube (unit in mm).

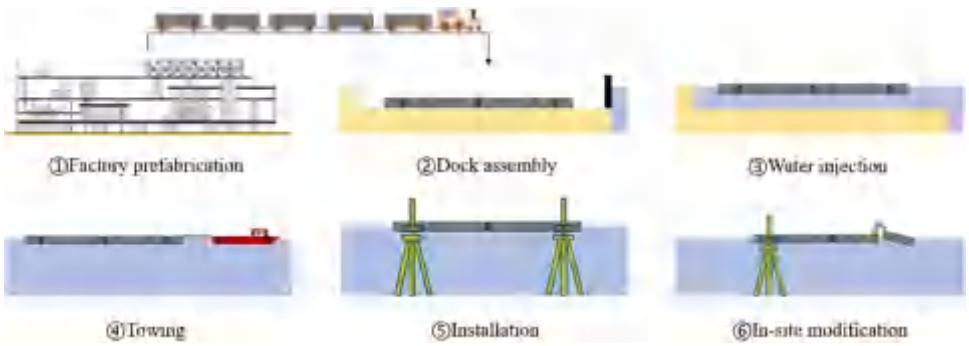


Fig. 4. Construction process of BRT-FS.

2) Dock assembly. Assemble BRT-FS in the dock;
3) Water injection. Inject water into dock to float the structure in seawater;
4) Towing. Tow the assembled module to the intended location;
5) Installation. Install the mooring system and fix it to several holding beams;
6) In-site modification. Repeat steps 1) −6) until the whole structure is completed.

The specific assembly process of BRT-FS is shown in Fig. 5. Firstly, holding beams are placed, which allows concrete tubes to cross through and be fixed into. The ends of the concrete tubes fixed to holding beams are connected by other concrete tubes. Note that, to avoid tube end connections lying in a row which may cause an apparent weakness in certain longitudinal sections, tube-tube joints are arranged in a stagger. Then in concrete tubes, CFRP cables pass through and post-tensioned, and bellows are unfolded. Cushion rubbers are installed at last to support topside modules.

4. Hydroelastic analysis by FE-BE method

4.1. Simplified model

The elasticity of VLFS results in the interaction of fluid field and

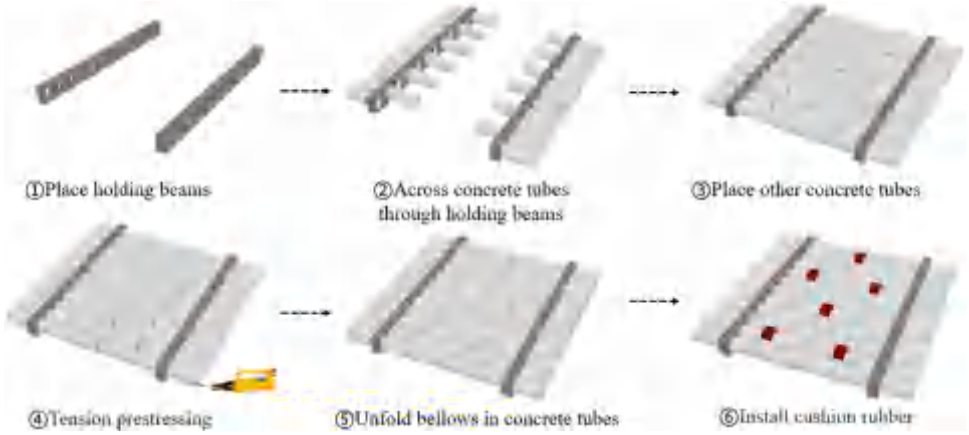


Fig. 5. Assembly process of BRT-FS.

structural deformation. For numerical investigation of the fluid-structure interaction, hydroelastic analysis is required. The state-of-the-art method for solving hydroelastic problem is finite element-boundary element (FE-BE) method[30]. To acquire the structural hydroelastic response including deflection and internal force, FE-BE method is employed in the frequency domain.

The assembled floating structure in water is simplified into the fluid-structure interaction problem as shown in Fig. 6. The structure consists of n tubes in the longitudinal direction and m rows of tubes in the transverse direction. The length of each tube is l. The diameter of each tube is D. The angle between incident wave direction and longitudinal direction is θ_w. The cracking of concrete tubes is suppressed under normal wave conditions. As a result, the mechanical properties of the concrete tubes are considered as linear elastic. The connection between dolphin-fender mooring system and structure is assumed to have vertical freedom and rotation freedom[26].

Seawater is assumed to be an ideal fluid, which is irrotational, incompressible, and non-viscous. The fluid domain is denoted as Ω, and the depth is H. It has no boundary in the x and y direction. The bottom surface ($z = -H$) is the seabed boundary (S_{SB}). The top surface ($z = 0$) is the free boundary (S_F) and the wetted surface of the structure (S_{HB}). S_∞ is the infinite boundary, as shown in Fig. 6(b) and Fig. 6(c). The amplitude of incident wave is A.

Most VLFS feature square cross-sections and can be simplified into Kirchhoff plate and Mindlin plate for hydroelastic analysis[19,26,31]. However, BRT-FS is comprised of cylindrical tubes, and each row of these tubes exhibits a large aspect ratio. In such cases, beam elements are more suitable for hydroelastic analysis than plate elements. Meanwhile, the large size of the concrete tube makes shear deformation and rotational inertia unreasonable to be ignored. As a result, the concrete tubes and holding beams are regarded as Timoshenko beam elements to facilitate calculation, as shown in Fig. 7. For the convenience of hydroelastic analysis, the structural system needs to be transformed into simple geometry. The influence of CFRP cable on the stiffness of concrete tube before cracking is negligible. Structural attachments such as CFRP cables, holding beams, and bellows have low mass ratio and limited dynamic influence on concrete. Hence, only the motion response of concrete tube and holding beam is considered in the analysis of structural motion. For concrete tube element, it has one translational degree of freedom (TDOF) of w_z and one rotational degree of freedom (RDOF) of θ_y. For holding beam element, it has one TDOF of w_z and one RDOF of θ_x.

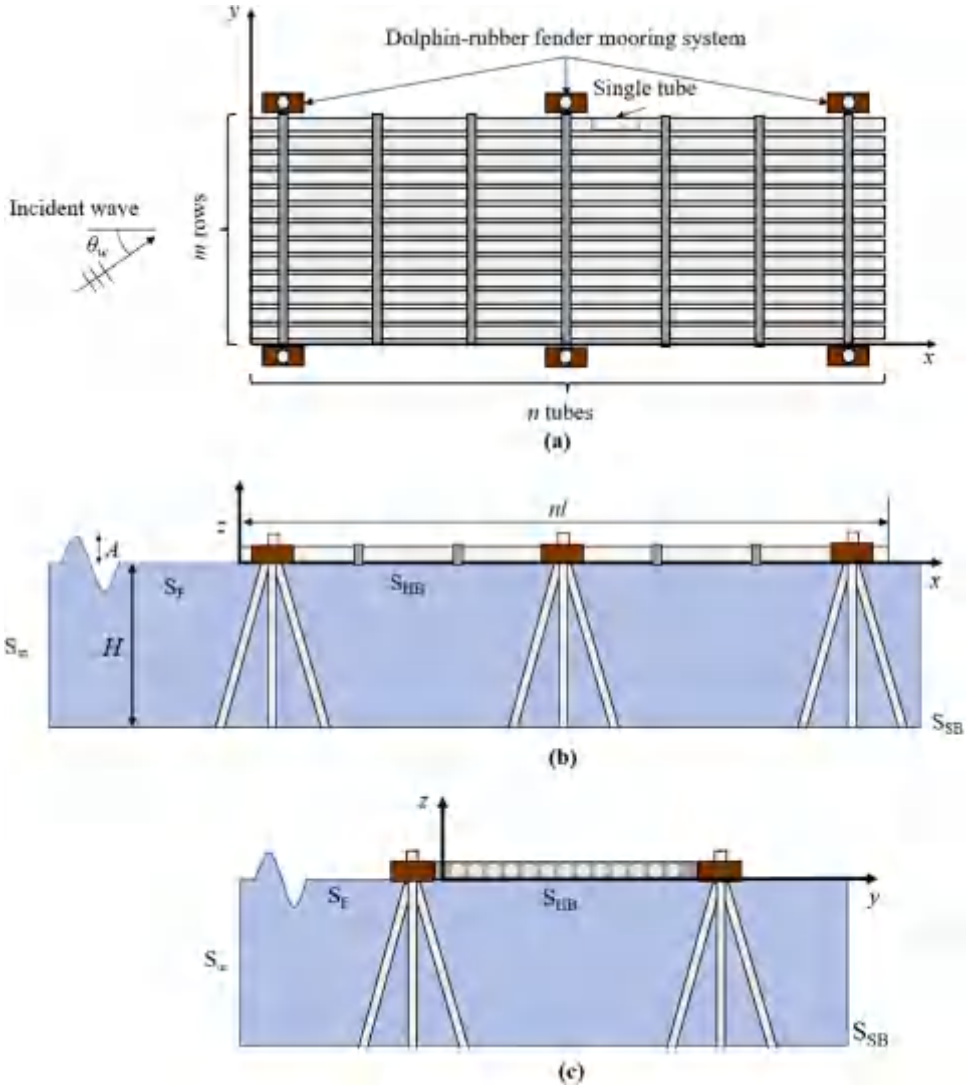


Fig. 6. Schematic diagram of coupled fluid-structure problem: (a) top view; (b) front view; (c) side view.

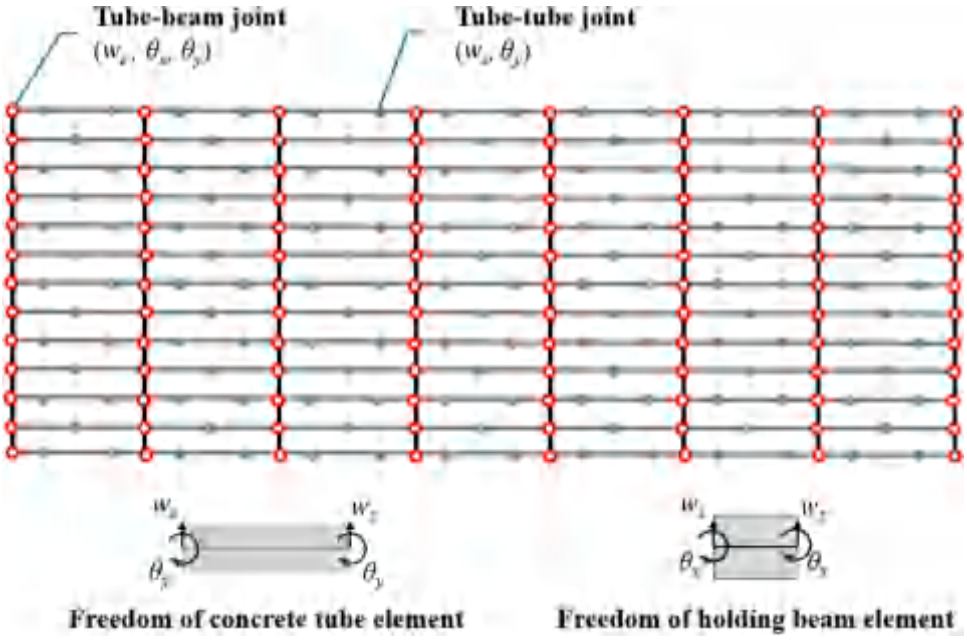


Fig. 7. Simplified structural model of BRT-FS.

The simplified model has two types of joints, tube-tube joint and tube-beam joint. Under normal wave conditions, tube-tube joints are designed not to generate relative rotation, treated as rigid connections. This implies that tube-tube joint has one TDOF and one RDOF. The situation for tube-beam joints is more complicated. The different bending directions of concrete tube and holding beam provide tube-beam joint with one TDOF and two RDOF. Since concrete tubes can rotate freely within the holding beam, the bending of the holding beam will not induce torsion in the concrete tube. Nevertheless, variations in the rotation of different rows of concrete tubes can result in torsion of the holding beams. Twisting spring is utilized to replace the torsional stiffness of holding beam, as shown in Fig. 8. The additional bending moment acting on the joint satisfies Eqs. (1) and (2):

$$\overline{M}_{x,ij} = -G_h K_h\left(\theta_{x,i} - \theta_{x,j}\right)/L_h \tag{1}$$

$$\overline{M}_{x,ji} = -G_h K_h\left(\theta_{x,j} - \theta_{x,i}\right)/L_h \tag{2}$$

where $\overline{M}_{x,ij}$ is the additional bending moment acting on joint i for the twisting spring between joint i and j, which is the same rule for $\overline{M}_{x,ji}$. $\theta_{x,i}$ and $\theta_{x,j}$ are the RDOF in x direction of joint i and j, respectively. G_h is the shear modulus of holding beam. L_h is the interval between concrete tubes. K_h is the equivalent polar moment of inertia of holding beam. For rectangular solid section, K_h is acquired from Eq. (3).

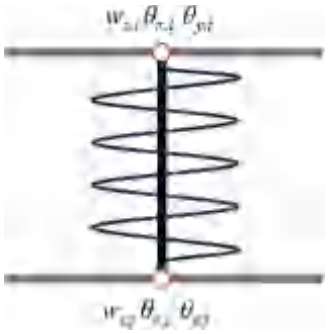


Fig. 8. Tube-beam joint details between joint i and joint j.

$$K_h = d_h {b_h}^3\left[\frac{1}{3} - 0.21\frac{b_h}{d_h}\left(1 - \frac{(b_h/d_h)^4}{12}\right)\right] \tag{3}$$

where d_h and b_h are the depth and width of holding beam cross-section.

4.2. Hydroelastic analysis methodology

4.2.1. Variational equation for plate motion

According to Timoshenko beam theory, the beam motion is described by the vertical displacement w and rotation θ. Shear deformation and rotational inertia are considered compared to Euler-Bernoulli beam theory. Under shear force, the section perpendicular to the neutral axis is no longer perpendicular after deformation. In the local coordinate system x, y, and z axes represent the length, width, and thickness directions of the element, respectively. Denoting ε and γ as axial and shear strains at the intersection point of cross section and neutral axis, which are [35]:

$$\varepsilon = -z\frac{\mathrm{d}\theta}{\mathrm{d}x} \tag{4}$$

$$\gamma = -\theta + \frac{\mathrm{d}w}{\mathrm{d}x} \tag{5}$$

The structure under free boundary condition needs to satisfy the constraint condition that both bending moment and shear force vanish at edges, which means:

$$M = EI\frac{\mathrm{d}\theta}{\mathrm{d}x} = 0 \tag{6}$$

$$Q = \frac{G_c A_c}{\kappa}\gamma = 0 \tag{7}$$

where elastic modulus E, moment of inertia I, and cross-sectional area A_c are defined. G_c and κ are the shear modulus and shear correction factor (6/5 for rectangular section and 10/9 for circle section), respectively. Both concrete tubes and holding beams apply this constitutive equation.

The dynamic equations can be derived from the principle of minimum potential energy. The potential energy U concludes bending strain energy, shear strain energy, work done by twisting spring, and work done by fluid pressure in vertical direction, as shown in Eq. (8). The

kinetic energy T concludes vertical kinetic energy and rotational kinetic energy, as shown in Eq. (9).

$$U=\frac{1}{2}\int_{S_{HB}}\int_0^h \varepsilon E\varepsilon \mathrm{d}z\mathrm{d}\mathbf{x}+\frac{1}{2}\int_{S_{HB}}\int_0^h \gamma\frac{G_c}{\kappa}\gamma \mathrm{d}z\mathrm{d}\mathbf{x}-\frac{1}{2}\sum\left(M_{x,ij}\theta_{x,i}+M_{x,ji}\theta_{x,j}\right)-\int_{S_{HB}} p_z w\mathrm{d}\mathbf{x} \tag{8}$$

$$T=\frac{1}{2}\int_{S_{HB}}\left(\frac{\partial^2 w}{\partial t^2}\right)\rho A_c\frac{\partial^2 w}{\partial t^2}\mathrm{d}x+\frac{1}{2}\int_{S_{HB}}\left(\frac{\partial^2 \theta}{\partial t^2}\right)\rho I\frac{\partial^2 \theta}{\partial t^2}dx \tag{9}$$

where $\mathbf{dx}$ means integral in both longitudinal and transverse directions, while $\mathrm{d}x$ means only integral in longitudinal direction. As the bottom of the concrete tube is cambered instead of flat, the direction of fluid pressure $p(x, y)$ deviates from the z direction. The transverse component of p is much smaller than the vertical component, and its impact on the vertical motion is neglected. Only the influence of the vertical component p_z on the structure is taken into consideration. p_z and p adhere to the relationship depicted in Eq. (10). $\varphi(x, y)$ is the angle between water pressure and vertical direction. In Eq. (11), p can be calculated according to Bernoulli's equation.

$$p_z = p\cos\varphi \tag{10}$$

$$p=-\rho_w\left(\frac{\partial\phi}{\partial t}+gw\right)=i\omega\rho_w\phi-\rho_w g w \tag{11}$$

where ρ_w is the fluid density, g is the gravitational acceleration, and $\phi(x, y)$ is the velocity potential of the fluid at the interface between structure and fluid (S_{HB}).

According to Hamilton's principle, the following equation (after omitting the time factor $e^{-i\omega t}$) is obtained from Eqs. (1), (2), and (8) - (11). The fluid pressure can be decomposed into two parts: hydrodynamic pressure and hydrostatic pressure.

$$\begin{aligned}&\int_{S_{HB}}\int_0^h \delta\varepsilon E\varepsilon \mathrm{d}z\mathrm{d}\mathbf{x}+\int_{S_{HB}}\int_0^h \delta\gamma\frac{G_c}{\kappa}\gamma \mathrm{d}z\mathrm{d}\mathbf{x}-\omega^2\int_{S_{HB}}\delta w\rho A_c w dx-\omega^2\int_{S_{HB}}\delta\theta\rho I\theta dx\\&=-\sum\delta\left(\theta_{x,i}-\theta_{x,j}\right)\frac{G_h K_h}{L_h}\left(\theta_{x,i}-\theta_{x,j}\right)+i\omega\rho_w\int_{S_{HB}}\delta w\phi\cos\varphi\mathrm{d}\mathbf{x}-\rho_w g\int_{S_{HB}}\delta w\cos\varphi w\mathrm{d}\mathbf{x}\end{aligned} \tag{12}$$

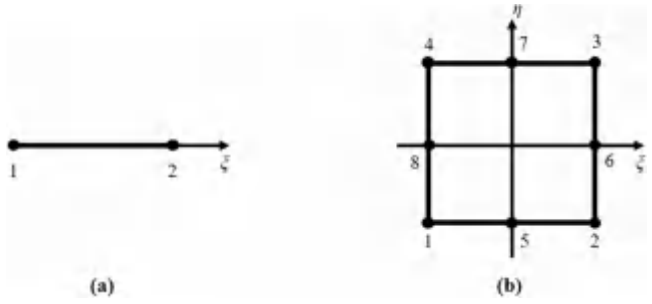


Fig. 9. Isoparameteric elements for structures: (a) beam element; (b) quadratic-serendipity plane element.

4.2.2. Discretization of motion equation by FEM

Finite element method (FEM) is a common method for elastic mechanics. It can transform the structural integral equation into the form of global matrix. The primary structural components experience bending moment and shear force, yet the distribution of vertical fluid action across the width of these components is non-uniform. So beam elements are employed to analyze the deformation and dynamic response, while plane elements are used to consider the vertical fluid action. Beam element contains 2 nodes. Since only a single element is used to calculate fluid action in the concrete tube width direction, a quadratic-serendipity plane element with 8 nodes is adopted for better accuracy. The isoparameteric elements for these two types are shown in Fig. 9.

For each beam element, the displacement field is $\mathbf{w}_b = [w_b \quad \theta_b]^{\mathrm{T}}$, potential field is $\boldsymbol{\phi}_b = [\phi_b \quad 0]^{\mathrm{T}}$. In order to maintain the continuity of displacement and rotation, linear interpolation is used for shape function. The values inside the element can be obtained from the shape function and node values:

$$\mathbf{w}_b = \mathbf{N}_b\hat{\mathbf{w}}_b \tag{13}$$

$$\boldsymbol{\phi}_b = \mathbf{N}_b\hat{\boldsymbol{\phi}}_b \tag{14}$$

where $\hat{\mathbf{w}}_b = [w_{b1} \quad \theta_{b1} \quad w_{b2} \quad \theta_{b2}]^{\mathrm{T}}$ is the nodal displacement vector and $\hat{\boldsymbol{\phi}}_b = [\phi_{b1} \quad 0 \quad \phi_{b2} \quad 0]^{\mathrm{T}}$ is the nodal velocity potential vector. $\mathbf{N}_b$is the shape function:

$$\mathbf{N}_b = \begin{bmatrix} N_{b1} & 0 & N_{b2} & 0 \\ 0 & N_{b1} & 0 & N_{b2}\end{bmatrix}^{\mathrm{T}} \tag{15}$$

where $N_{b1} = (1-\xi)/2$and $N_{b2} = (1+\xi)/2$.

For each plane element, the displacement field is $\mathbf{w}_p = [w_p \quad \theta_p]^{\mathrm{T}}$, potential field is $\boldsymbol{\phi}_p = [\phi_p \quad 0]^{\mathrm{T}}$. Similar to beam element, the values inside the element can be obtained from the shape function and node values:

$$\mathbf{w}_p = \mathbf{N}_p\hat{\mathbf{w}}_p \tag{16}$$

$$\boldsymbol{\phi}_p = \mathbf{N}_p\hat{\boldsymbol{\phi}}_p \tag{17}$$

where $\hat{\mathbf{w}}_p = [w_{p1} \quad \theta_{p1} \quad \cdots \quad w_{p8} \quad \theta_{p8}]^{\mathrm{T}}$ is the nodal displacement vector and $\hat{\boldsymbol{\phi}}_p = [\phi_{p1} \quad 0 \quad \cdots \quad \phi_{p8} \quad 0]^{\mathrm{T}}$ is the nodal velocity potential vector. $\mathbf{N}_p$is the shape function:

$$\mathbf{N}_p = \begin{bmatrix} N_{p1} & 0 & \cdots & N_{p8} & 0 \\ 0 & N_{p1} & \cdots & 0 & N_{p8}\end{bmatrix}^{\mathrm{T}} \tag{18}$$

where

$$N_{pj} = \frac{1}{4}(1+\xi_j\xi)(1+\eta_j\eta)(\xi_j\xi+\eta_j\eta-1) \text{ for corner nodes } j=1,2,3,4 \tag{19}$$

$$N_{pj} = \frac{1}{2}(1-\xi^2)(1+\eta_j\eta) \text{ for mid}-\text{side nodes } j=5,7 \tag{20}$$

$$N_{pj} = \frac{1}{2}(1+\xi_j\xi)(1-\eta^2) \text{ for mid}-\text{side nodes } j=6,8 \tag{21}$$

To calculate elements with different nodes in the coupling equation, the following relationship is established:

$$\widehat{\mathbf{w}}_p = \mathbf{T}\widehat{\mathbf{w}}_b \tag{22}$$

$$\widehat{\boldsymbol{\phi}}_p = \mathbf{T}\widehat{\boldsymbol{\phi}}_b \tag{23}$$

$$\mathbf{T} = \begin{bmatrix} \mathbf{I} & 0 & 0 & \mathbf{I} & \frac{1}{2}\mathbf{I} & 0 & \frac{1}{2}\mathbf{I} & \mathbf{I} \\ 0 & \mathbf{I} & \mathbf{I} & 0 & \frac{1}{2}\mathbf{I} & \mathbf{I} & \frac{1}{2}\mathbf{I} & 0 \end{bmatrix}^{\mathrm{T}} \left(\mathbf{I} = \begin{bmatrix} 1 & 0 \\ 0 & 1 \end{bmatrix}\right) \tag{24}$$

The relationship means velocity potential and displacement is the same in cross-section. The value on mid-side point is the average of the corner point values. The matrices for beam element and plane element have the same dimension through the transformation matrix **T**.

$$\mathbf{M}_d = \int_{\triangle d} \mathbf{N}_b^{\mathrm{T}} \mathbf{m} \mathbf{N}_b \mathrm{d}x \tag{28}$$

$$\mathbf{R}_d = \int_{\triangle d} \mathbf{N}_b^{\mathrm{T}} \mathbf{r} \mathbf{N}_b \mathrm{d}x \tag{29}$$

$$\mathbf{K}_{\mathrm{Iz}d} = \int_{\triangle d} \mathbf{T}^{\mathrm{T}} \mathbf{N}_p^{\mathrm{T}} \mathbf{k}_{\mathrm{Iz}} \mathbf{N}_p \mathbf{T} \mathrm{d}\mathbf{x} \tag{30}$$

$$\mathbf{K}_{rfd} = \int_{\triangle d} \mathbf{T}^{\mathrm{T}} \mathbf{N}_p^{\mathrm{T}} \mathbf{k}_{rf} \mathbf{N}_p \mathbf{T} \mathrm{d}\mathbf{x} \tag{31}$$

where $\mathbf{K}_{fd}$, $\mathbf{K}_{sd}$, $\mathbf{M}_d$, $\mathbf{R}_d$, $\mathbf{K}_{\mathrm{Iz}d}$, $\mathbf{K}_{rfd}$ are respectively element bending, shear, mass, rotational inertia, vertical unit, and restoring force matrices. Δd is the element domain. The matrix $\mathbf{m}$, $\mathbf{r}$, $\mathbf{k}_{\mathrm{Iz}}$, and $\mathbf{k}_{rf}$ are respectively:

$$\mathbf{m} = \begin{bmatrix} \rho A_c & 0 \\ 0 & 0 \end{bmatrix},\ \mathbf{r} = \begin{bmatrix} 0 & 0 \\ 0 & \rho I \end{bmatrix},\ \mathbf{k}_{\mathrm{Iz}} = \begin{bmatrix} \cos\varphi & 0 \\ 0 & \cos\varphi \end{bmatrix},\ \mathbf{k}_{rf} = \begin{bmatrix} \rho_w g \cos\varphi & 0 \\ 0 & 0 \end{bmatrix} \tag{32}$$

where φ is the angle between fluid pressure and vertical direction.

The global twisting string matrix $\mathbf{K}_m$ is the sum of all the local twisting string matrix, which is:

$$\mathbf{K}_{md} = \frac{G_h K_h}{L_h} \begin{bmatrix} \cdots & i & & j & \\ i & 1 & & -1 & \\ & & \cdots & & \\ j & -1 & & 1 & \\ & & & & \cdots \end{bmatrix} \text{(twisting string between joint } i \text{ and joint } j\text{)} \tag{33}$$

$$\mathbf{K}_m = \sum \mathbf{K}_{md} \tag{34}$$

Minimizing Eq. (12) with respect to $\widehat{\mathbf{w}}$, and integrating element matrix into global matrix, the motion equation of the structure can be written as:

$$(\mathbf{K}_f + \mathbf{K}_s + -\omega^2\mathbf{M} - \omega^2\mathbf{R})\widehat{\mathbf{w}} = -\mathbf{K}_m\widehat{\mathbf{w}} + i\omega\rho_w\mathbf{K}_{\mathrm{Iz}}\widehat{\boldsymbol{\phi}} - \mathbf{K}_{rf}\widehat{\mathbf{w}} \tag{25}$$

where $\widehat{\mathbf{w}}$ and $\widehat{\boldsymbol{\phi}}$ are the global vectors of the nodal displacement and velocity potential. $\mathbf{K}_f$ and $\mathbf{K}_s$ are the global bending and shear stiffness matrices using reduced integration; while $\mathbf{M}$, $\mathbf{R}$, $\mathbf{K}_{\mathrm{Iz}}$, and $\mathbf{K}_{rf}$ are the global mass, rotational inertia, vertical unit, and restoring force matrices, respectively. Each global matrix is assembled by the following element matrix using finite element method (calculation procedure for $\mathbf{K}_{fd}$ and $\mathbf{K}_{sd}$ referring to [25]):

$$\mathbf{K}_{fd} = \frac{EI}{l_d}\begin{bmatrix} 0 & 0 & 0 & 0 \\ 0 & 1 & 0 & -1 \\ 0 & 0 & 0 & 0 \\ 0 & -1 & 0 & 1 \end{bmatrix} \tag{26}$$

$$\mathbf{K}_{sd} = \frac{GA_c}{4\kappa l_d}\begin{bmatrix} 4 & 2l & -4 & 2l \\ 2l & l^2 & -2l & l^2 \\ -4 & -2l & 4 & -2l \\ 2l & l^2 & -2l & l^2 \end{bmatrix} \tag{27}$$

The numerical integration for Eqs. (28) - (31) is conducted based on Gauss-Legendre equation. $\mathbf{M}_d$ and $\mathbf{R}_d$ are calculated through two Gaussian points in beam element. $\mathbf{K}_{\mathrm{Iz}d}$ and $\mathbf{K}_{rf}$ are calculated through nine Gaussian points in plane element.

4.2.3. Solution for fluid velocity potential

Boundary element method (BEM) is a common method for solving fluid problem. The linear wave hypothesis is adopted, which means the wave height is very small relative to the wavelength and water depth. The fluid velocity potential satisfies the Laplace equation:

$$\nabla^2\phi(x,y,z) = 0 \text{ in fluid domain } \Omega \tag{35}$$

The boundary conditions of the fluid domain are:

$$\frac{\partial\phi}{\partial z}(x,y,0) = -i\omega w(x,y) \text{ on the wetted surface } S_{\mathrm{HB}} \tag{36}$$

$$\frac{\partial\phi}{\partial z}(x,y,0) = \frac{\omega^2}{g}\phi(x,y,0) \text{ on the free boundary } S_{\mathrm{F}} \tag{37}$$

$$\frac{\partial \phi}{\partial z}(x, y, -H) = 0 \text{ on the seabed boundary } S_{SB} \tag{38}$$

$$\lim_{|\mathbf{x}|\to\infty} \sqrt{|\mathbf{x}|}\left(\frac{\partial(\phi - \phi^{in})}{\partial|\mathbf{x}|} - ik(\phi - \phi^{in})\right) = 0 \text{ on the infinite boundary } S_{\infty} \tag{39}$$

where S_{HB}, S_F, S_{SB}, and S_∞ are defined in Fig. 6 and Section 4.1; $\mathbf{x} = (x, y)$ is the coordinate of fluid particle in Ω; ω and k represent the wave frequecy and wave number satisfying the dispersion equation:

$$k \tanh kH = \frac{\omega^2}{g} \tag{40}$$

$\phi^{in}$is the velocity potential of the incident wave, calculated by the following equation[31]:

$$\phi^{in} = \frac{gA}{\omega}\frac{\cosh k(z+H)}{\cos kH} e^{ik(x\cos\theta_w + y\sin\theta_w)} \tag{41}$$

where A is half of the wave height and H is the depth of fluid domain Ω; while z is the thickness direction of the structure as shown in Fig. 6.

By substituting the boundary conditions (Eqs. (36) - (39)) into Laplace's equation (Eq. (35)) using Green's function, the velocity potential can be expressed as [26]:

$$\phi(\mathbf{x}_s) = \phi^{in}(\mathbf{x}_s) + \int_{S_{HB}} G\left(\mathbf{x}_s, \boldsymbol{\xi}\right)\left[\frac{\omega^2}{g}\phi(\boldsymbol{\xi}) + i\omega w(\boldsymbol{\xi})\right] d\boldsymbol{\xi} \tag{42}$$

where $\mathbf{x}_s = (x, y)$ and $\boldsymbol{\xi} = (\xi, \eta)$ is the source point and field point. G is the Green function satisfying the boundary conditions, which is calculated according to the following equation[23]:

$$G\left(\mathbf{x}, \boldsymbol{\xi}\right) = -\sum_{r=0}^{\infty} \frac{K_0(k_r R)}{\pi H\left(1 + \frac{\sin 2k_r H}{2k_r H}\right)} \cos^2 k_r H \tag{43}$$

where k_r ($r \geq 1$) is positive and satisfies the equation $k_r \tan(k_r H) = -\omega^2/g$. And $k_0 = -ik$ where k is the positive root of $k_r \tanh(k_r H) = \omega^2/g$. R is the distance between source point $\mathbf{x}$ and field point $\boldsymbol{\xi}$. K_0 is the modified Bessel function of the second kind.

The same quadratic-serendipity plane elements with fluid action are adopted in BEM. For the element domain, Eq. (42) can be discretized to:

$$\mathbf{K}_{Id}\widehat{\boldsymbol{\phi}}_p = \mathbf{K}_{Id}\widehat{\boldsymbol{\phi}}_p^{\text{in}} + \frac{\omega^2}{g}\sum_{e=1}^{n_n} \mathbf{g}_{pe}\widehat{\boldsymbol{\phi}}_e + i\omega\sum_{e=1}^{n_n} \mathbf{g}_{pe}\widehat{\mathbf{w}}_e \tag{44}$$

where $\widehat{\boldsymbol{\phi}}_p^{\text{in}}$ is nodal velocity potential vector of incident wave and $\mathbf{g}_{pe}$ is element Green function matrix (calculation procedure for $\mathbf{g}_{pe}$ referring to [34]). Eqs. (22) and (23) are adopted to convert plane element to beam element:

$$\mathbf{T}^{\mathrm{T}}\mathbf{K}_{Id}\mathbf{T}\widehat{\boldsymbol{\phi}}_b = \mathbf{T}^{\mathrm{T}}\mathbf{K}_{Id}\mathbf{T}\widehat{\boldsymbol{\phi}}_b^{\text{in}} + \frac{\omega^2}{g}\sum_{e=1}^{n_n} \mathbf{T}^{\mathrm{T}}\mathbf{g}_{pe}\mathbf{T}\widehat{\boldsymbol{\phi}}_{be} + i\omega\sum_{e=1}^{n_n} \mathbf{T}^{\mathrm{T}}\mathbf{g}_{pe}\mathbf{T}\widehat{\mathbf{w}}_{be} \tag{45}$$

where $\mathbf{K}_{Id}$ is the element unit matrix, which is similar to $\mathbf{K}_{Izd}$:

$$\mathbf{K}_{Id} = \int_{\triangle d} \mathbf{N}_p^{\mathrm{T}}\mathbf{k}_{\mathrm{I}}\mathbf{N}_p d\mathbf{x} \tag{46}$$

$$\mathbf{k}_{\mathrm{I}} = \begin{bmatrix} 1 & 0 \\ 0 & 1 \end{bmatrix} \tag{47}$$

Integrating all n_n element matrices into the global matrix, we can get:

$$\mathbf{K}_{\mathrm{I}}\widehat{\boldsymbol{\phi}} = \mathbf{K}_{\mathrm{I}}\widehat{\boldsymbol{\phi}}^{in} + \frac{\omega^2}{g}\mathbf{G}\widehat{\boldsymbol{\phi}} + i\omega\mathbf{G}\widehat{\mathbf{w}} \tag{48}$$

where $\widehat{\boldsymbol{\phi}}^{in}$is the global nodal velocity potential vector of incident wave, $\mathbf{K}_{\mathrm{I}}$ is the global unit matrix, and $\mathbf{G}$ is the global Green function matrix.



Fig. 11. A case study for BRT-FS.

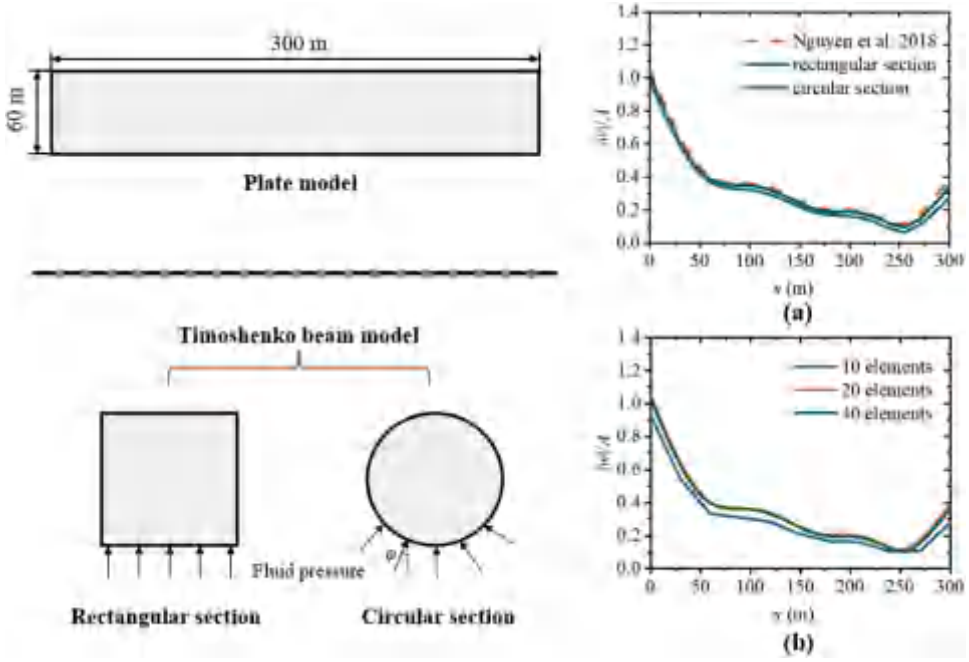


Fig. 10. Simplified validation model of a plate structure subjected to a longitudinal incident wave: (a) comparison between Mindlin plate model and Timoshenko beam model; (b) convergence results.

4.2.4. FE-BE solution method

Finite element-boundary element (FE-BE) method combines the advantages of finite element analysis and boundary element analysis, so it is suitable for solving fluid-structure interaction problems. The structure equation Eq. (25) and fluid motion equation Eq. (48) can be combined to:

$$\left(\mathbf{K}_f + \mathbf{K}_s + -\omega^2\mathbf{M} - \omega^2\mathbf{I} + \mathbf{K}_m + \mathbf{K}_{rf} + \omega^2\rho_w\mathbf{K}_{\mathrm{Iz}}\left(\mathbf{K}_{\mathrm{I}} - \frac{\omega^2}{g}\mathbf{G}\right)^{-1}\mathbf{G}\right)\widehat{\mathbf{w}} = i\omega\rho_w\mathbf{K}_{\mathrm{Iz}}\left(\mathbf{K}_{\mathrm{I}} - \frac{\omega^2}{g}\mathbf{G}\right)^{-1}\mathbf{K}_{\mathrm{I}}\widehat{\boldsymbol{\phi}}^{in} \tag{49}$$

The nodal displacement vector $\widehat{\mathbf{w}}$ is obtained by solving the above equation. Element nodal moment $\mathbf{F}_{Md}$ can be calculated through element bending stiffness matrix as Eq. (50) shows. If the same node exists in different elements, average value is taken as the nodal moment at that node.

$$\mathbf{F}_{\mathrm{Md}} = \mathbf{K}_{fd}\mathbf{w}_d \tag{50}$$

4.3. Model validation

It is necessary to compare the novel hydroelastic model described in this paper to the existing hydroelastic model. However, the majority of the existing hydroelastic models are based on rectangular sections. As a result, validation for both rectangular and circular section will be conducted. For rectangular section, the objective is to confirm the reliability of the transformation matrix **T**. While for circular section, the objective is to compare the differences between rectangular and circular section. Notably, rectangular section and circular section are set to have the same density, width, cross-section area, and moment of inertia, which is not possible in reality.

The validation model is a floating plate with a dimension of 300 m * 60 m * 2 m[26]. The incident wave in the longitudinal direction has a wavelength of 150 m. The water depth is 20 m. Material elastic modulus of the platform is 11.9 GPa with a density of 256.25 kg/m^3. The thickness-to-incident wavelength ratio is 0.0133, which satisfies thick plate assumption[17]. Fig. 10 illustrates the simplified process for the validation model. Because the lateral influence of head sea on the structure is negligible, the floating plate is simplified to Timoshenko beam with a smaller width to make the section closer to circular. For rectangular section, set φ as zero on the wetted surface. Mesh number for the longitudinal direction are 20. After meshing, the structure is analyzed by aforementioned FE-BE approach to solve the hydroelastic response.

The comparison between Mindlin plate model and Timoshenko beam model with rectangular and circular section is shown in Fig. 10 (a). The result indicates that the transformation matrix **T** is reliable and the influence of circular shape is relatively small. Meanwhile, a convergence test is further conducted on the model. Analysis results under various mesh number ranging from 10 - 40 are shown in Fig. 10 (b), which proves the convergence of the model.

4.4. Hydroelastic analysis of BRT-FS

4.4.1. A typical case study for hydroelastic analysis

In this section, a case study of hydroelastic analysis for BRT-FS is

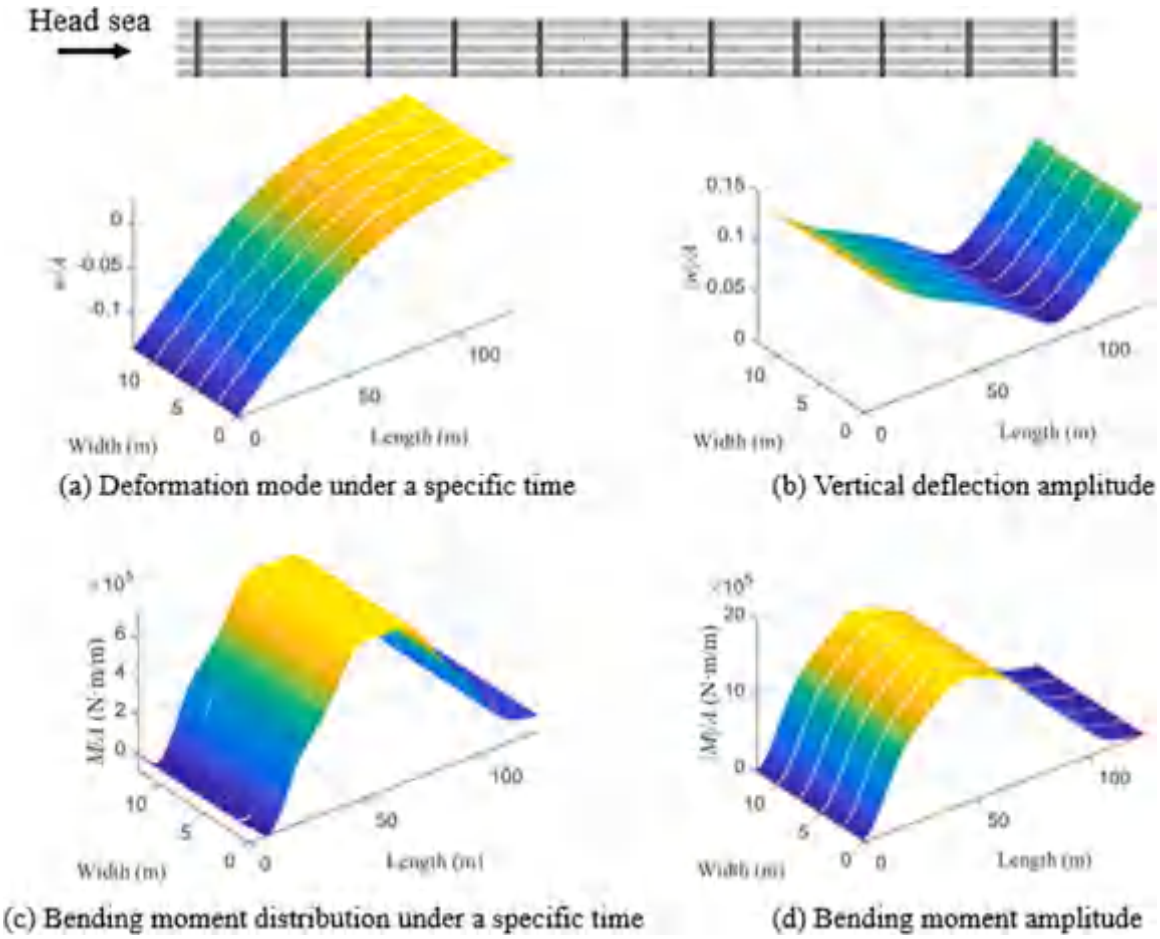


Fig. 12. Hydroelastic responses of assembled floating structure in a unit head sea: (a) and (b) vertical deflection; (c) and (d) bending moment response.

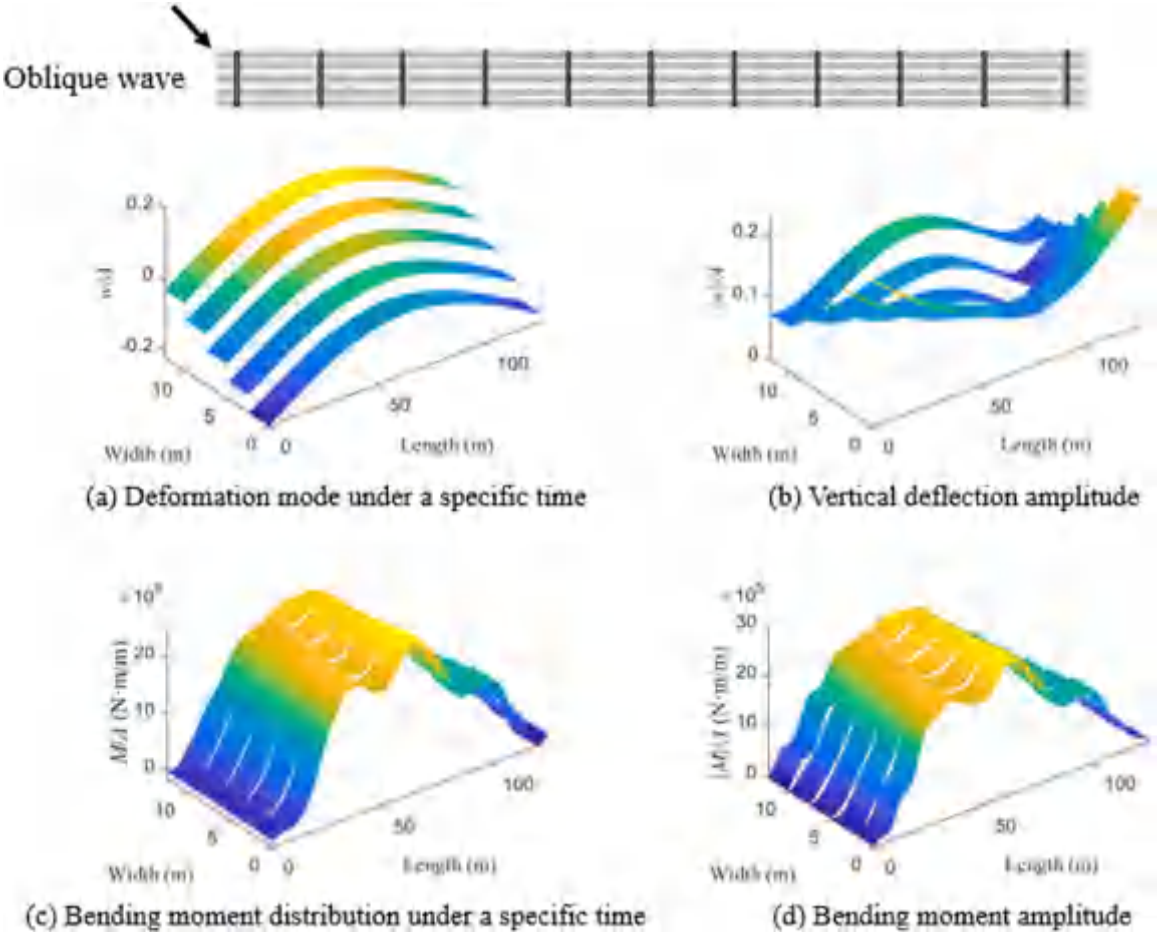


Fig. 13. Hydroelastic responses of assembled floating structure in a unit oblique wave: (a) and (b) vertical deflection; (c) and (d) bending moment response.

investigated. The structure has five rows of tubes joined by holding beams in the transverse direction, with a length of 126 m and a width of 13 m, as illustrated in Fig. 11. Holding beams are installed every two concrete tubes. Each row has 21 tubes of 6 m connected in the longitudinal direction. In Section 2, the design condition of the structure is given in a wide range. A typical wave condition will be selected for analysis in the case study. The influence of wave condition changes on the structural response will be described in the following sections. The typical wave condition has water depth H of 15 m and wave period T of 4 s. Corresponding to the incident-wave period, the wavelength-structural length ratio is 0.20, which means elastic effect on the structural response is remarkable.

The hydroelastic response of the proposed structure is analyzed by the novel hydroelastic model. The influences of GFRP reinforcement bars and CFRP cables on stiffness and density of concrete tubes are ignored. The average density of holding beams is calculated by the total mass without hole mass dividing total volume, which is 1042 kg/m^3. However, the average elastic modulus of holding beams is assumed to be the modulus of UHPC, because the tube-beam joints can enhance the stiffness. Other component property parameters refer to Table 1.

4.4.2. *Influence of wave direction*

Firstly, the hydroelastic response under a unit amplitude of head sea (wave incident direction is the longitudinal direction) is analyzed. The deformation mode of the platform under a specific time (zero phase angle) is indicated in Fig. 12 (a). The y axis is vertical deflection normalized by the wave amplitude A. For each node, take the maximum value during one period as the amplitude. The normalized vertical deflection amplitude is shown in Fig. 12 (b). The vertical deflection is smallest in the middle of structure, increasing linearly until reaching the peak value above 0.1 at both ends. Similarly, Fig. 12 (c) and Fig. 12 (d) show the bending moment distribution at zero phase angle and the normalized bending moment amplitude. There is almost no bending moment at the end of structure in the absence of constraint. A peak bending moment amplitude of 1.6×10^6 N·m/m occurs in the middle of structure, which is the weak area under head sea.

The same method is adopted to calculate the hydroelastic response under the unit oblique wave (the angle between the wave incident direction and longitudinal direction is 45°) and the unit beam sea (the wave incident direction is the transverse direction), as shown in Fig. 13 and Fig. 14. Under oblique wave, the hydroelastic response is quite complex. Different rows tend to exhibit different deformation patterns without holding beam constraints. However, holding beams limit the relative displacement and rotation between different rows. Different rows are forced to exhibit approximate deformation patterns. The maximum vertical deflection response exceeds that in the head sea, reaching 0.238. The moment response amplitude is larger within the third to seventh holding beams, with a peak value of 2.6×10^6 N·m/m, which is greater than that under head sea.

Under beam sea, the dimension along the wavelength direction decreases and the deflection response of the structure increases significantly. The deflections of the same concrete tube row are consistent and the structure remains almost planar at zero phase, indicating a small elastic deformation in this case. It is worth mentioning that in Fig. 13 (a) and (b) the structure appears to be "separated" as a result of significant displacement disparities among different rows. This is due to the fact that the deflection and dimension values are not in the same amplitude and the actual structure does not have such a significant deflection

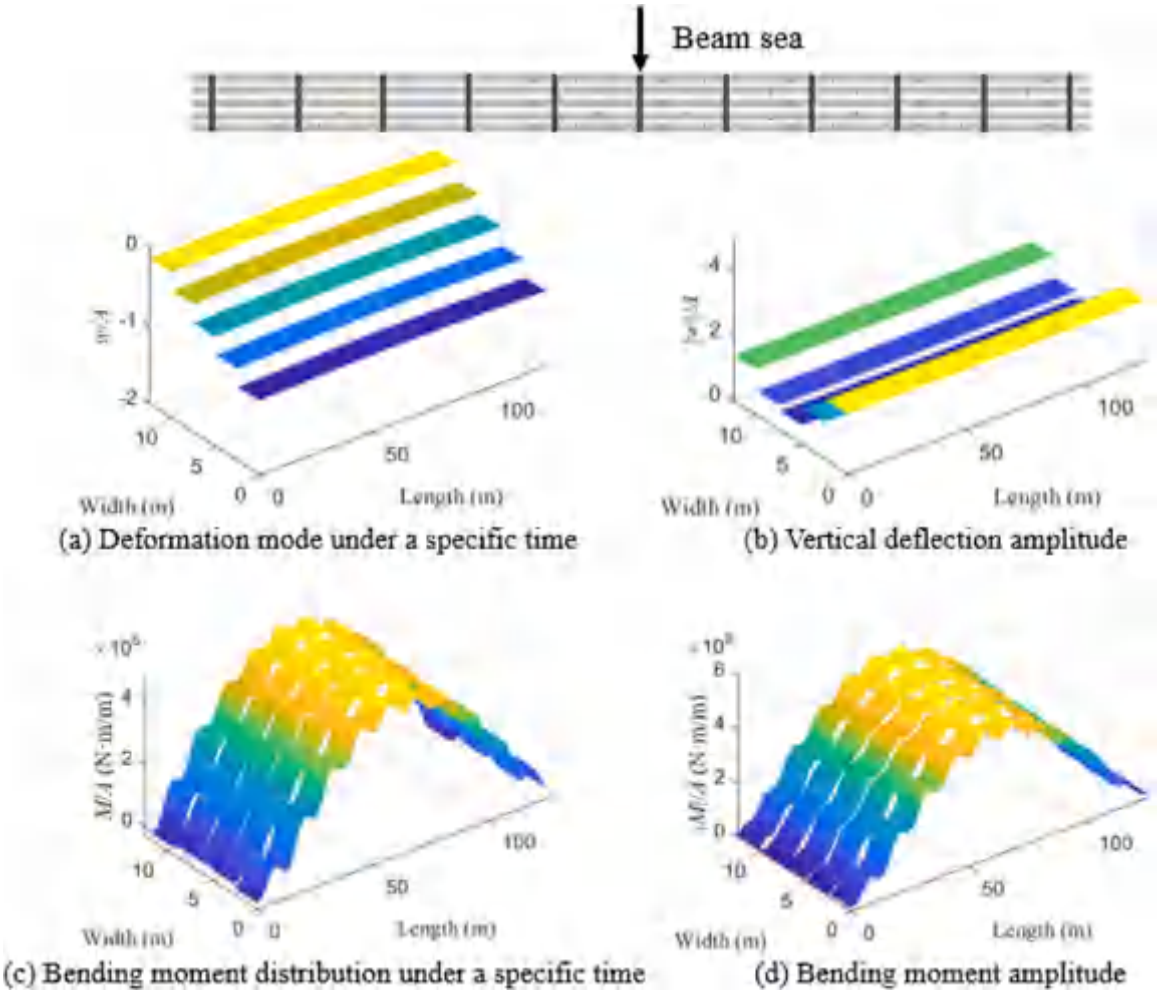


Fig. 14. Hydroelastic responses of assembled floating structure in a unit beam sea: (a) and (b) vertical deflection; (c) and (d) bending moment response.

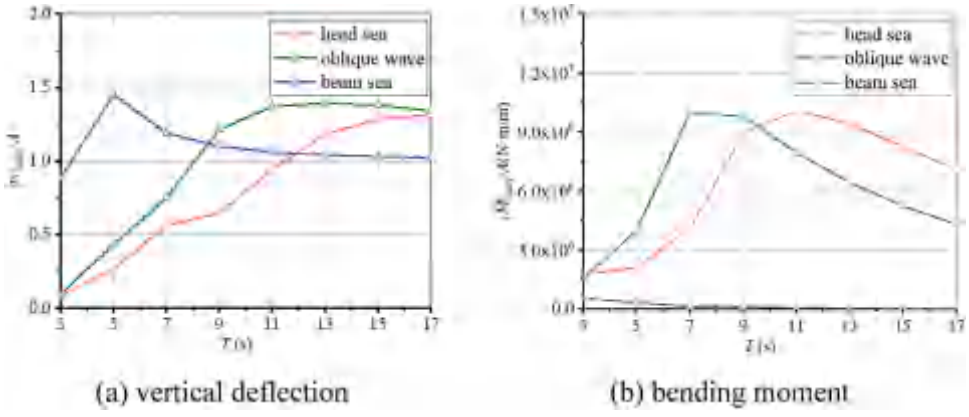


Fig. 15. Structural responses under different wave directions and wave periods (water depth = 15 m).

difference. In addition, the concrete tubes are represented with plane instead of circular section. Although it is shown as a surface discontinuity in Fig. 13 (a), the actual surface of tubes can still be formed as a flat surface. Vertical deflection amplitude in the transverse direction is high on both sides while low in the middle. The maximum deflection amplitude reaches 1.85, which is significantly larger than that in the case of head sea and oblique wave. The peak amplitude of bending moment response under transverse waves is low at 4.8×10^5 N·m/m. The analyses above indicate that oblique waves represent the most hazardous wave condition. Further investigation into other wave conditions and water depth on hydroelastic response of the structure will be conducted in subsequent sections.

4.4.3. *Influence of wave period*

The hydroelastic response to a 4 s wave is discussed in the preceding section. However, the structure will be exposed to broader wave periods during operation. Hydroelastic analysis is conducted over wave periods ranging from 3 to 17 s, corresponding to incident wavelength between

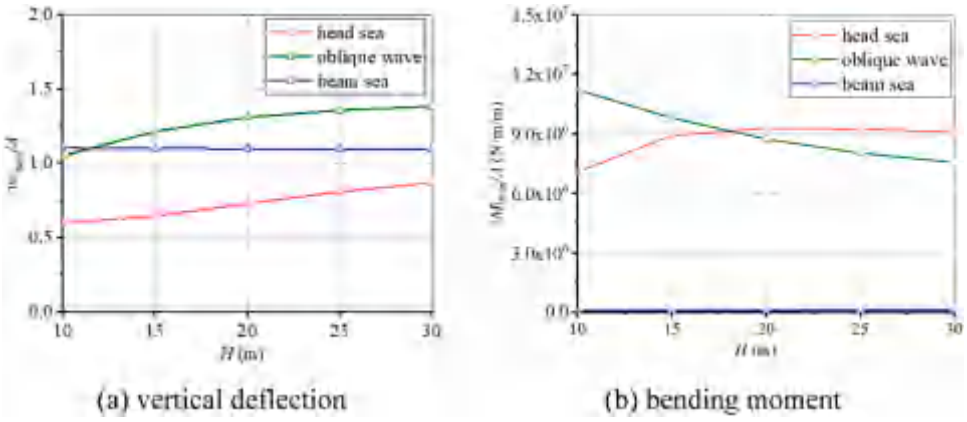


Fig. 16. Structural responses under different water depths (wave period = 9 s).

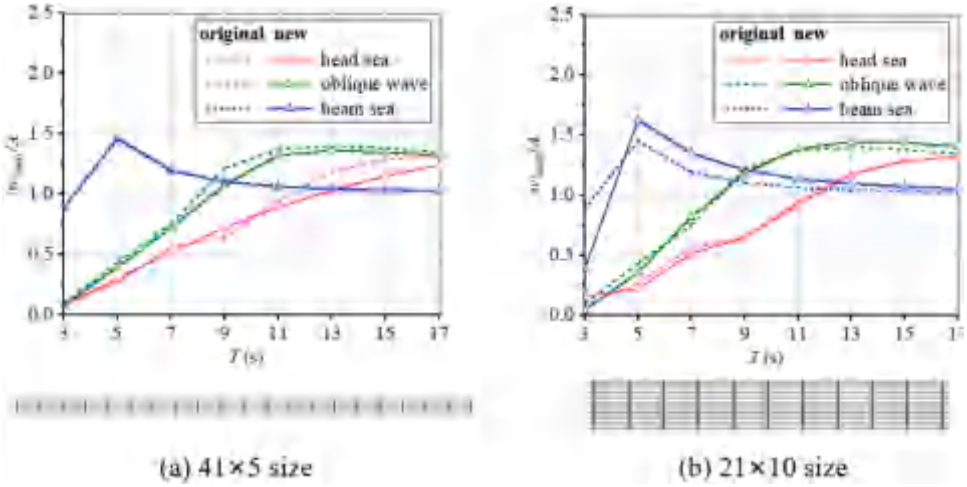


Fig. 17. Structural vertical deflection responses of different size structures (solid lines for new structures and dashed lines for former structure).

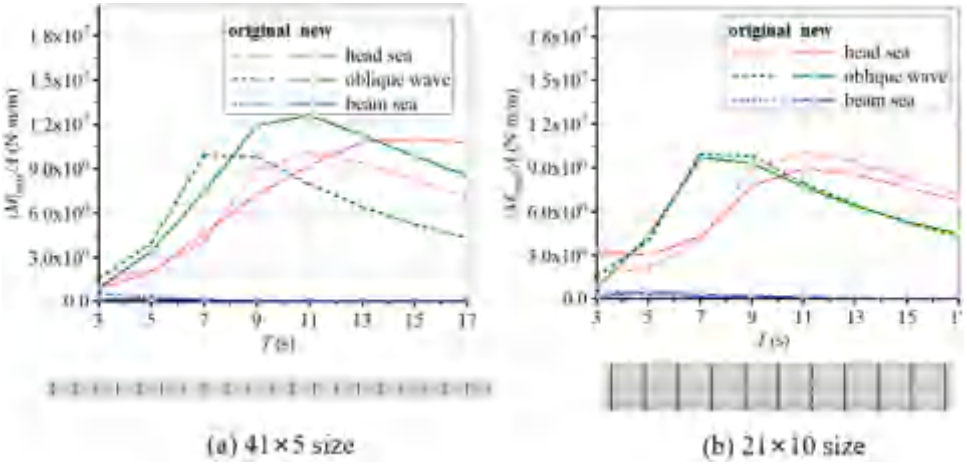


Fig. 18. Structural bending moment responses of different size structures (solid lines for new structures and dashed lines for former structure).

14.0 to 198.9 m. Under each wave period, the maximum value in all the nodes is taken as the structural response amplitude. Fig. 15 shows the structural response amplitudes under different wave directions and wave periods, Fig. 15 (a) and (b) for vertical deflection and bending moment respectively.

The effect of wave period on vertical deflection is mainly concentrated in the short periods less than 9 s. The structure is more sensitive to beam sea in short periods, and the vertical deflection amplitude reaches a peak value of 1.45 in 5 s wave. For long-period waves higher than 11 s, the effects of wave period and wave direction on vertical deflection amplitude are no longer significant. Structural moment response amplitudes under head sea and oblique wave are significantly larger than those under beam sea. The peaks under head sea and oblique wave are close to each other but occur at different wave periods. This

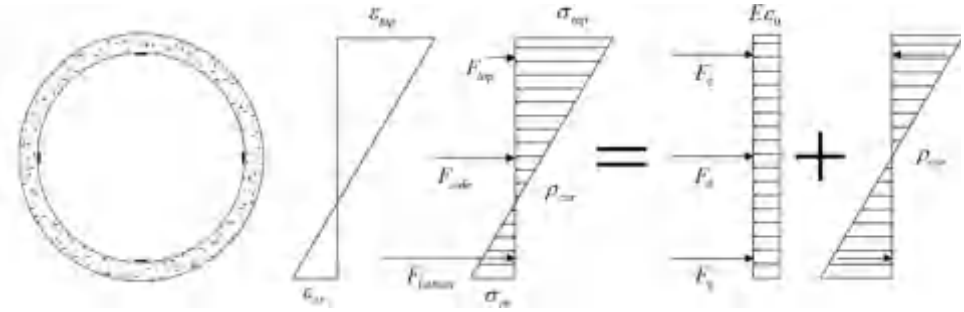


Fig. 19. Strain and stress distribution on the cross-section of a CFRP prestressed concrete tube.

phenomenon of different sensitivity periods has been observed in similar structures[22], which is due to the difference in longitudinal and oblique dimension. The sensitivity period under head sea is around 11 s, whereas that under oblique wave is around 7 s. Overall, when the angle between wave direction and longitudinal direction is less than 45°, the effect on structural response is limited. However, as the angle increases to 90°, a significant difference is observed.

4.4.4. Influence of water depth

The structure is planned to operate in a water depth of 10 – 30 m. Consequently, it is imperative to conduct an analysis considering the influence of varying water depths. When the wave enters shallow water from deep water, wavelength becomes shorter and wave speed decreases, thus the structural response changes. Regarding the influence rule of wave period, the most sensitive wave period 9 s is selected for water depth analysis, and the results are shown in Fig. 16. The effect of water depth on structural response is not obvious. Under oblique wave, vertical deflection is positively correlated with water depth, while bending moment is inversely correlated with water depth.

4.4.5. Influence of structural dimension

In practical use, structures may be designed in different sizes, so the applicability of the new structural model to various structural dimensions needs to be verified. Increase the above structural dimension (21 *5 tubes) to double length (42 *5 tubes) and double width (21 *10 tubes). The hydroelastic responses of the new structures are also studied with the wave range of 3 – 17 s and three wave directions, as shown in Fig. 17 and Fig. 18. The responses of new structures and the original structure are represented by solid and dashed lines, respectively.

Learned that the vertical deflections of the new and original structures show similar trends. The change in vertical deflection amplitude after dimensional change is in the range of 12 %. Bending moment response amplitude is more sensitive to length. After doubling the length, the sensitive period and peak response of the structure under both head sea and oblique wave increase. The maximum moment response amplitude increases by 8.9 % under head sea and 26.6 % under oblique wave. Whereas, after doubling the width, the sensitive period and the peak response remain almost unchanged.

5. Structural analysis

In this section, the bending moment in hydroelastic response calculated above is checked. It is assumed that the structural behavior under normal wave loads satisfies the plane-section assumption and the concrete is in elastic state. The contribution of GFRP rebars to the cracking load is ignored due to the similar elastic modulus to concrete. The strain and stress distributions in the concrete tube section under cracking load are shown in Fig. 19. ε_{cr}, σ_{cr} and, ε_{top}, σ_{top} are the strain and stress for concrete cracking and tube topside, respectively. F_{top} and F_{bottom} represent the forces in the top and bottom CFRP cables.

Stress state of the prestressed tube under bending moment can be combined by two modes, a prestressed tube and a tube under bending moment. In the first mode, no bending moment exists in the concrete tube. In the second mode, neutral plane is the middle plane due to the symmetry of cross-section. Additionally, the curvature of the second mode is the same as prestressed tube. The following equations can be obtained through strain compatibility:

$$F_{top} = F_0 - E_{\mathrm{CFRP}} A_{\mathrm{CFRP}} \left(\frac{d}{2\rho_{cur}} \right) \tag{51}$$

$$F_{bottom} = F_0 + E_{\mathrm{CFRP}} A_{\mathrm{CFRP}} \left(\frac{d}{2\rho_{cur}} \right) \tag{52}$$

$$F_{side} = F_0 \tag{53}$$

where d is the inner diameter and ρ_{cur} is the sectional curvature; ε_0 is the strain in concrete after CFRP cable post-tension; F_0 is the prestress force in CFRP cable; E_{CFRP} and A_{CFRP} are the elastic modulus and cross-section area of CFRP cable.

By combining two modes, the cracking strain can be expressed as follows:

$$\varepsilon_{cr} = \varepsilon_0 + \frac{D}{2\rho_{cur}} \tag{54}$$

ε_{cr} is assumed to be 100 με for concrete, and ρ_{cur} is obtained by Eq. (54). The cracking bending moment is equal to that of the second mode, which is:

$$M_{cr} = \frac{EI}{\rho_{cur}} + E_{\mathrm{CFRP}} A_{\mathrm{CFRP}} \left(\frac{d}{2\rho_{cur}} \right) d \tag{55}$$

By solving Eq. (55), the cracking bending moment 2.6×10^6 N·m is obtained. Assuming ε_0 equals zero to eliminate CFRP prestress, cracking bending moment is only 1.9×10^6 N·m left. Prestressed CFRP cables increase the cracking bending moment by 37 %. Based on the results in hydroelastic analysis, the safety period of head sea is 3–7 s and the safety period of oblique wave is 3–5 s under 1 m wave height. The structure is suitable for calm sea conditions in harbours, where long-period waves are suppressed and wave heights are reduced by breakwaters. To make the structure suitable for harsher wave conditions, the length of the structure can be appropriately reduced. Additionally, increasing the prestress in concrete tubes can help postpone cracks during higher waves. Furthermore, even when the structure is exposed to rare extreme waves, this new structure is designed to be able to float with the bellow even after the concrete tubes crack.



Fig. 20. BRT-FS with WEC hinged connections.

6. Discussion

In the structure component aspects, a large proportion of mature industrial products improves the feasibility of BRT-FS. In the construction aspects, the production of concrete tubes can follow the production process of existing drainage tubes, which also improves the feasibility of BRT-FS. In the mechanical property aspects, the feasibility of normal service under expected working conditions is verified by the calculation mentioned above. As a consequence, the novel BRT-FS can satisfy the nearshore demand including tourism, marine aquaculture, photovoltaic power generation, and so on.

Compared with traditional VLFS, BRT-FS has the following advantages:

- High designability. Diverse shapes and sizes can be designed using small size modules. The structure can be easily expanded or reinforced locally using filament winding to meet special utilization requirements.
- Excellent durability. The main load-bearing components realize "no steel", which can prolong service life and reduce maintenance costs. Moreover, concrete tubes can be recycled conveniently due to modularization.
- Low crack control requirement. The separation of stress and sealing demands can ease design and improve safety. Concrete tubes and bellows function as load-bearing and sealed buoyancy elements respectively, which avoids the floating structures still needing to ensure their sealing performance even under extreme loading conditions.
- High construction efficiency. The production method for concrete tubes is mature and effective, enabling mass production. Additionally, concrete tubes can be transported by trains or vessels, then swiftly installed in dock or offshore.

A further design of this structure with power generation system is also proposed here. It is proved that hinge connections in multi-module configuration can reduce structural hydroelastic response[32,37]. A raft wave energy converter (WEC) shows a similar configuration, which can convert rotation movement between rafts into electricity, as shown in Fig. 20 (a)[6,28]. Combining these two concepts, BRT-FS with WEC hinged connections is formed as shown in Fig. 20 (b). This concept is more environment-friendly which can partially realize self-supply.

7. Conclusions

Inspired by bamboo rafts, a novel BRT-FS assembled by FRP reinforced concrete tubes is proposed in this paper. It has good designability and construction efficiency due to its unique structural design. The durability is improved by the addition of two corrosion-resistant materials, concrete and FRP. The bearing and buoyancy functions are separated to further increase the durability of the structure and ease structural design. Based on existing models, a new hydroelastic model for the novel structure is proposed, whose accuracy is verified. Then structural responses under different wave directions, wave periods, water depth, and structural dimensions are analyzed to find hydroelastic response characteristics. Moreover, the cross-section bearing capacity of the concrete tube is calculated to find use condition for BRT-FS. Based on the analysis results, the following conclusions can be drawn:

1. The simplified model proposed for BRT-FS demonstrates reliability and convergence. The hydrodynamic effect of a circular section is taken into account through the vertical projection of fluid action. The calculation results indicate that the hydroelastic behavior of circular section closely resembles that of square section.
2. BRT-FS will behave different responses under different wave directions. Under head sea, the vertical deflection amplitude is minimal in the middle, while bending moment amplitude reaches maximum at the same location. The vertical deflection distributions under oblique wave and beam sea are different from that under head sea. However, the bending moment distributions remain similar. The maximum vertical deflection response and bending moment response both increase under oblique wave. Under beam sea, the maximum vertical deflection response increase, while the maximum bending moment response decrease.
3. Both vertical deflections and bending moments exhibit similar trends with wave periods in the head sea and oblique wave. These two wave directions have similar peak values, but different sensitive periods. The sensitivity period under head sea is around 11 s, whereas that under oblique wave is around 7 s. The vertical deflection under 5 s beam sea reaches its maximum, while the bending moment is always of a small order of magnitude.
4. Water depth and transverse dimension have no significant influence on the structural response. But an increase in length results in higher peak response and larger sensitive period. The length of the structure needs to be controlled if the applied wave condition is poor.
5. The structural analysis of the section bearing capacity show that the safety period of head sea is 3-7 s and the safety period of oblique wave is 3-5 s under 1 m wave height, which is a clam harbour sea condition. To make the structure suitable for harsher wave conditions, breakwater can be incorporated to suppress high-period wave and reduce wave heights. Furthermore, even when the structure is exposed to rare extreme waves, this new structure is designed to be able to float with the bellow even after the concrete tubes crack. The separation of load-bearing and buoyant functions ensures structural safety and ease of design.

Conclusively, the novel BRT-FS has broad application perspectives in offshore construction due to its high corrosion resistance, designability, construction efficiency, and low crack control requirement. Structural details such as tube-tube joints, tube-beam joints, CFRP cable anchorages, and shear capacity will be further designed and tested in the future.

CRediT authorship contribution statement

Chongfeng Xie: Writing – original draft, Validation, Methodology, Investigation, Formal analysis, Data curation. **Peng Feng:** Writing – review & editing, Supervision, Resources, Project administration, Methodology, Funding acquisition, Conceptualization.

Declaration of Competing Interest

The authors declare that they have no known competing financial interests or personal relationships that could have appeared to influence the work reported in this paper.

Data availability

Data will be made available on request.

Acknowledgments

This research has been supported by the National Key Research and Development Program of China (No. 2022YFC3801800), the National Natural Science Foundation of China (No. U2106219), and the New Cornerstone Science Foundation through the XPLORER PRIZE. The first author Chongfeng Xie was supported by the Program Fund of Non-Metallic Excellence and Innovation Center for Building Materials (No. 2023Ph. D-1).

References

[1] Ai P, Feng P, Lin H, Zhu P, Ding G. Novel self-anchored CFRP cable system: concept and anchorage behavior. Compos Struct 2021;263. https://doi.org/10.1016/j.compstruct.2021.113736.

[2] Al-Khafaji AF, Haluza RT, Benzecry V, Myers JJ, Bakis CE, Nanni A. Durability assessment of 15- to 20-year-old GFRP Bars extracted from bridges in the US. II: GFRP bar assessment. J Compos Constr 2021;25(2). https://doi.org/10.1061/(asce)cc.1943-5614.0001112.

[3] Alabtah FG, Mahdi E, Eliyan FF. The use of fiber reinforced polymeric composites in pipelines: a review. Compos Struct 2021;276. https://doi.org/10.1016/j.compstruct.2021.114595.

[4] Benzecry V, Al-Khafaji AF, Haluza RT, Bakis CE, Myers JJ, Nanni A. Durability assessment of 15- to 20-year-old GFRP Bars extracted from bridges in the US. I: selected bridges, bar extraction, and concrete assessment. J Compos Constr 2021;25(2). https://doi.org/10.1061/(asce)cc.1943-5614.0001110.

[5] Dai J, Hellan Ø, Watn A, Ang KK. Modular Multi-purpose Floating Structures for Space Creation. WCFS2020. Singapore: Springer Singapore; 2022. p. 257–71.

[6] Davey T, Sarmiento J, Ohana J, Thiebaut F, Haquin S, Weber M, et al. Round robin testing: exploring experimental uncertainties through a multifacility comparison of a hinged raft wave energy converter. J Mar Sci Eng 2021;9(9). https://doi.org/10.3390/jmse9090946.

[7] Guades E, Aravinthan T, Islam M, Manalo A. A review on the driving performance of FRP composite piles. Compos Struct 2012;94(6):1932–42. https://doi.org/10.1016/j.compstruct.2012.02.004.

[8] Gulas S, Downton M, D'Souza K, Hayden K, Walker TR. Declining arctic ocean oil and gas developments: opportunities to improve governance and environmental pollution control. Mar Policy 2017;75:53–61. https://doi.org/10.1016/j.marpol.2016.10.014.

[9] Habeeb MN, Ashour AF. Flexural behavior of continuous GFRP reinforced concrete beams. J Compos Constr 2008;12(2):115–24. https://doi.org/10.1061/(ASCE)1090-0268(2008)12:2(115).

[10] Helland K., Jensen B., Martin J., Meaas P. The Troll Oil Floater: The First Concrete Floater Platform. The Fourth International Offshore and Polar Engineering Conference.1994. p. ISOPE-I-94-303.

[11] Helland S, Aarstein R, Maage M. In-field performance of North Sea offshore platforms with regard to chloride resistance. Struct Concr 2010;11(1):15–24. https://doi.org/10.1680/stco.2010.11.1.015.

[12] Jiang D, Tan KH, Dai J, Ang KK, Nguyen HP. Behavior of concrete modular multi-purpose floating structures. Ocean Eng 2021;229. https://doi.org/10.1016/j.oceaneng.2021.108971.

[13] Jiang D, Tan KH, Dai J, Ong KCG, Heng S. Structural performance evaluation of innovative prestressed concrete floating fuel storage tanks. Struct Concr 2019;20(1):15–31. https://doi.org/10.1002/suco.201800032.

[14] Jiang D, Tan KH, Wang CM, Ong KCG, Bra H, Jin J, et al. Analysis and design of floating prestressed concrete structures in shallow waters. Mar Struct 2018;59:301–20. https://doi.org/10.1016/j.marstruc.2018.01.006.

[15] Kafodya I, Xian G, Li H. Durability study of pultruded CFRP plates immersed in water and seawater under sustained bending: water uptake and effects on the mechanical properties. Compos Part B: Eng 2015;70:138–48. https://doi.org/10.1016/j.compositesb.2014.10.034.

[16] Kaiser MJ, Snyder B, Yu Y. A review of the feasibility, costs, and benefits of platform-based open ocean aquaculture in the Gulf of Mexico. Ocean Coast Manag 2011;54(10):721–30. https://doi.org/10.1016/j.ocecoaman.2011.07.005.

[17] Karperaki AE, Belibassakis KA. Hydroelastic analysis of very large floating structures in variable bathymetry regions by multi-modal expansions and FEM. J Fluids Struct 2021;102. https://doi.org/10.1016/j.jfluidstructs.2021.103236.

[18] Koekoek M. Connecting modular floating structures. Gemeente Rotterdam: Netherlands. 2010.

[19] Kyoung JH, Hong SY, Kim BW, Cho SK. Hydroelastic response of a very large floating structure over a variable bottom topography. Ocean Eng 2005;32(17):2040–52. https://doi.org/10.1016/j.oceaneng.2005.03.003.

[20] Li G, Hou C, Shen L. Life-cycle analysis of FRP-strengthened offshore CFST columns suffering from steel corrosion. Compos Struct 2021;277. https://doi.org/10.1016/j.compstruct.2021.114607.

[21] Li J, Wu Z, Shi C, Yuan Q, Zhang Z. Durability of ultra-high performance concrete – A review. Constr Build Mater 2020;255:119296. https://doi.org/10.1016/j.conbuildmat.2020.119296.

[22] Li Z, Chen D, Feng X, Chen J-F. Hydroelastic analysis and structural design of a modular floating structure applying ultra-high performance fiber-reinforced concrete. Ocean Eng 2023;277. https://doi.org/10.1016/j.oceaneng.2023.114266.

[23] Linton CM. Rapidly convergent representations for Green' functions for Laplace' equation. Proc R Soc Lond Ser A: Math, Phys Eng Sci 1999;455(1985):1767–97. https://doi.org/10.1098/rspa.1999.0379.

[24] Liu T, Liu X, Feng P. A comprehensive review on mechanical properties of pultruded FRP composites subjected to long-term environmental effects. Compos Part B: Eng 2020;191. https://doi.org/10.1016/j.compositesb.2020.107958.

[25] Logan DL. First Course in the Finite Element Method, Enhanced Edition, SI Version. Cengage Learning,; 2022.

[26] Nguyen HP, Dai J, Wang CM, Ang KK, Luong VH. Reducing hydroelastic responses of pontoon-type VLFS using vertical elastic mooring lines. Mar Struct 2018;59:251–70. https://doi.org/10.1016/j.marstruc.2018.02.005.

[27] Pérez Fernández R, Lamas Pardo M. Offshore concrete structures. Ocean Eng 2013;58:304–16. https://doi.org/10.1016/j.oceaneng.2012.11.007.

[28] Ruol P, Zanuttigh B, Martinelli L, Kofoed JP, Frigaard P. Near-shore floating wave energy converters: applications for coastal protection. 32nd Int Conf Coast Eng ICCE 2011:2010.

[29] Shao W, Sun Q, Xu X, Yue W, Shi D. Durability life prediction and horizontal bearing characteristics of CFRP composite piles in marine environments. Constr Build Mater 2023;367:130116. https://doi.org/10.1016/j.conbuildmat.2022.130116.

[30] Tay ZY. Artificial neural network framework for prediction of hydroelastic response of very large floating structure. Appl Ocean Res 2023;139:103701. https://doi.org/10.1016/j.apor.2023.103701.

[31] Tay ZY, Wang CD, Wang CM. Hydroelastic response of a box-like floating fuel storage module modeled using non-conforming quadratic-serendipity Mindlin plate element. Eng Struct 2007;29(12):3503–14. https://doi.org/10.1016/j.engstruct.2007.08.015.

[32] Teng B., Gou Y., Wang G., Cao G. Motion response of hinged multiple floating bodies on local seabed. The Twenty-fourth International Ocean and Polar Engineering Conference. OnePetro; 2014.

[33] Ueda S. Mooring systems of the world largest floating oil storage base. In: Bratteland E, editor. Advances in Berthing and Mooring of Ships and Offshore Structures. Springer Netherlands; 1988. p. 461–73. https://doi.org/10.1007/978-94-009-1407-0_32.

[34] Wang CD, Meylan MH. A higher-order-coupled boundary element and finite element method for the wave forcing of a floating elastic plate. J Fluids Struct 2004;19(4):557–72. https://doi.org/10.1016/j.jfluidstructs.2004.02.006.

[35] Weaver W, Timoshenko SP, Young DH. Vibration problems in engineering. Wiley,; 1991. https://books.google.com/books?id=YZ7t8LgRqi0C.

[36] Yang H, Zhao S, Kim C. Analysis of floating city design solutions in the context of carbon neutrality-focus on Busan Oceanix City. Energy Rep 2022;8:153–62. https://doi.org/10.1016/j.egyr.2022.10.310.

[37] Yoon J-S, Cho S-P, Jiwinangun RG, Lee P-S. Hydroelastic analysis of floating plates with multiple hinge connections in regular waves. Mar Struct 2014;36:65–87. https://doi.org/10.1016/j.marstruc.2014.02.002.

[38] Zeng J-J, Feng P, Dai J-G, Zhuge Y. Development and behavior of novel FRP-UHPC tubular members. Eng Struct 2022;266. https://doi.org/10.1016/j.engstruct.2022.114540.

[39] Zhang Y, Liu Z, Xin J, Wang Y, Zhang C, Zhang Y. The attenuation mechanism of CFRP repaired corroded marine pipelines based on experiments and FEM. Thin-Walled Struct 2021;169. https://doi.org/10.1016/j.tws.2021.108469.

Case Studies in Construction Materials 21 (2024) e03687

Contents lists available at ScienceDirect

Case Studies in Construction Materials

journal homepage: www.elsevier.com/locate/cscm

Mesoscale simulation method for preplaced aggregate concrete based on physics engine

Chongfeng Xie [a], Xiwang Chen [a,b,*], Jia-Qi Yang [c], Charun Bao [a], Peng Feng [a]

[a] MOE Key Lab of Civil Engineering Safety and Durability, Department of Civil Engineering, Tsinghua University, Beijing, 100084, China
[b] BCEG Advanced Construction Materials Co., Ltd., Beijing, 100015, China
[c] School of Mechanics and Civil Engineering, China University of Mining and Technology (Beijing), Beijing, 100083, China

ARTICLE INFO

Keywords:
Preplaced aggregate concrete
Physics engine
Expansive agent
Mechanical property
Shrinkage behavior

ABSTRACT

Preplaced aggregate concrete (PAC) has up to 60 % aggregate volume content, making mesoscale modelling difficult. A novel mesoscale simulation method based on physics engine was proposed in this study to accurately simulate the coarse aggregate skeleton of PAC. Unlike in conventional mesoscale simulations, point-to-point contacts between aggregates were formed due to virtual gravity in the physics engine. To verify this novel method, mechanical property and shrinkage behavior tests of PAC were conducted under different aggregate gradings and with different expansive agents. For the mechanical property test, the simulation results were compared with the test results in terms of the aggregate stacking state, failure mode, stress–strain curve, and mechanical property parameters. Repeatability and aggregate shape analyses were performed using finite element (FE) model. A similar comparison between the simulation and test results was also performed for the shrinkage behavior. A shrinkage coefficient reflecting the relationship between grout and PAC shrinkage was proposed. This novel mesoscale simulation method based on physics engine is particularly suitable for PAC. However, it is not limited to PAC and can be applied to the simulation of conventional concrete, thus solving the problem of traditional simulation methods that struggle to achieve a high aggregate fraction.

1. Introduction

Preplaced aggregate concrete (PAC), also known as two-stage concrete, is manufactured by preplacing coarse aggregate inside a formwork following the pouring of flowable grout [1]. Either gravity or the pumping method is utilized in the grout pouring process, depending on the component section depth [2]. As shown in Fig. 1, the aggregates form a skeleton through point-to-point contact, and the grout fills the voids in the skeleton. When the concept of PAC was proposed in the 1930s [3], its application was limited to repair and rehabilitation. Subsequently, with maturity, this technique has been utilized in underwater construction, highly reinforced member fabrication, mass concreting, and shielding structures [4].

Compared with conventional concrete, PAC has many advantages. First, the special construction method eliminates the segregation problem that is particularly common in lightweight aggregate concrete [5]. Second, PAC is suitable for all complex shapes, even without the need for vibration. Finally, the coarse aggregate content (approximately 60 % of the total volume) of PAC is higher than that of conventional concrete [6]. This property provides effective protection for nuclear and biological shield concrete [1]. In

* Corresponding author at: BCEG Advanced Construction Materials Co., Ltd., Beijing, 100015, China.
E-mail address: cxw20@mails.tsinghua.edu.cn (X. Chen).

https://doi.org/10.1016/j.cscm.2024.e03687
Received 8 July 2024; Received in revised form 19 August 2024; Accepted 26 August 2024
Available online 2 September 2024
2214-5095/© 2024 The Author(s). Published by Elsevier Ltd. This is an open access article under the CC BY-NC license (http://creativecommons.org/licenses/by-nc/4.0/).

addition, a high coarse aggregate content indicates low dry shrinkage and thermal cracking [7].

For homogeneous materials, an accurate constitutive model can be easily obtained. However, for non-homogeneous materials, the macro behavior is influenced by various mesoscale behaviors in different parts. As a non-homogenous material, PAC, despite having the same constituent materials as conventional concrete, it has different mechanical mechanisms at the mesoscale level. Consequently, an appropriate mesoscale simulation method is essential for PAC.

Commonly, there are five main methods used to simulate the mesoscale behavior of concrete, which are finite element method, discrete element method, lattice element method, lattice discrete particle method and rigid body spring method[8]. Among them, finite element method belongs to continuum method, while others belong to discrete method. Compared to discrete method, the continuum method offers the advantage of explicitly generating the concrete mesostructure, allowing for a more realistic simulation of the aggregate particle size distribution. This makes the continuum method particularly suitable for parameter analysis. Additionally, the continuum method is relatively mature, with various constitutive equations available to simulate the mechanical behavior of raw materials. Discrete element method, the most common discrete approach, can also be used for concrete mesoscale simulation[9–11]. However, it requires more computational resources compared to the continuum method[8]. Furthermore, since discrete element method typically uses spherical particles as the basic unit, it cannot accurately capture the geometry of the mesostructure.

Finite element (FE) method is adopted for the mesoscale simulation of PAC in this work. This method requires the establishment of a geometric model and mesh. Aggregate placement is a key issue in geometric models. Generally, the aggregate placement method can be categorized into three types: random aggregate placement method [12,13], Voronoi graphic method [14], and CT scanning method [15,16]. For the first two methods, it is difficult to reflect the difference between PAC and conventional concrete. In the third method, the simulation is based on fabricated specimens, which means that parameter analysis is difficult to conduct. It can been seen that it is difficult for traditional methods to accurately represent the unique characteristics of PAC. The physics engine method is an ideal solution for PAC aggregate placement because it creates a gravitational field, enabling simulation of aggregate stacking. This method has been attempted in conventional concrete and asphalt concrete modelling, but it has not yet been integrated with finite element (FE) method [15,17].

The main objective of this paper is to propose a novel mesoscale simulation method for PAC that can precisely simulate the coarse aggregate skeleton. To achieve this, physics engine PhysX was used to simulate the coarse aggregate stacking process. The stacking data was then transferred to an FE model. Unlike in conventional mesoscale simulations, point-to-point contacts were formed owing to virtual gravity in physics engine. Mechanical property and shrinkage behavior tests were conducted under different aggregate gradings and with different expansive agents. This novel mesoscale simulation method was used to simulate the test specimens, and the test and simulation results for the mechanical property and shrinkage behaviors were compared.

2. Model methodology

2.1. Mesoscale simulation framework

Fig. 2 shows the flowchart of the novel mesoscale simulation method for PAC. This method comprises two main steps. The first step is to establish a geometric model in which coarse aggregates are preplaced by physics engine. The geometric model contains aggregate information including shape and location. This information is then transferred to the commercial FE software ABAQUS. The second step is to establish an FE model using the background grid mapping method. The element properties, loads, and boundary conditions are also created in this step. The details of these steps are described in the subsequent sections.

2.2. Preplacement of coarse aggregates in a physics engine

To simulate aggregate stacking, an open-source physics engine PhysX, developed by NVIDIA, was used. This physics engine is applicable to scientific simulations involving Newtonian physics based on discrete element method (DEM) [18]. Several attempts have been made at conventional concrete mesoscale simulations using physics engines [15,19]. However, these attempts only used physics engine to compact aggregates, which meant that the random generation of aggregates was still required. In this study, aggregates were generated directly by physics engine.

Before the aggregate generation, a virtual formwork was established as the boundary. The aggregate size was randomly generated according to the aggregate grading. Ten points were randomly selected on a sphere with diameter d to generate convex polyhedral aggregates. These points must be uniformly dispersed on the sphere to avoid malformed aggregates. Therefore, an aggregate point was



Fig. 1. Casting process of PAC.

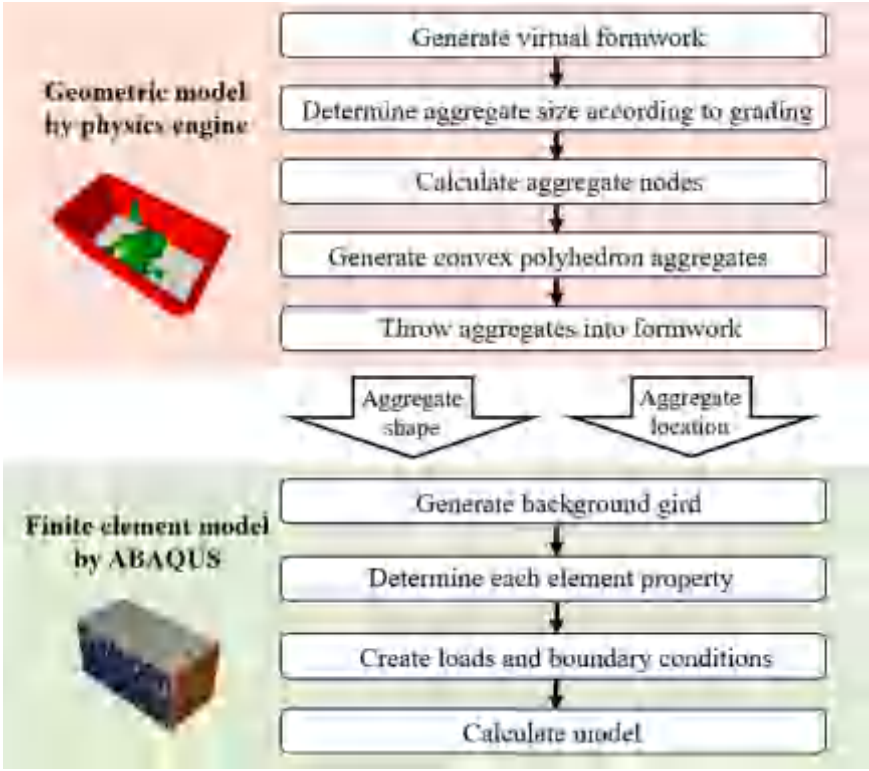


Fig. 2. Flowchart of the novel mesoscale simulation method.

generated at each eighth of the sphere, as shown in Fig. 3. The remaining two aggregate points were randomly generated over the entire sphere. The local coordinates of these points were entered into the physics engine to generate virtual convex polyhedral aggregates. The position, direction, and speed of aggregate throwing were arbitrarily set until they filled the formwork, as shown in Fig. 4. It is important to note that, to ensure that the aggregates fully filled the formwork, some of the aggregates were allowed to overflow from the formwork during the stacking process. Aggregates contained entirely within the formwork were selected based on their positional information. The aggregate information, including aggregate size, global coordinates of aggregate and aggregate nodes, and node numbers of each aggregate face, was output to a text file.

2.3. Discretizing geometric model to FE model

In the discretization process, direct meshing method and background grid mapping method are most commonly utilized [20]. Direct meshing is close to the geometric model information. However, owing to irregular element size and shape, the accuracy of the solution is limited. Background grid mapping method can acquire uniform hexahedral computational grids, which can improve calculation efficiency. However, the similarity between the geometric model and background grid also significantly influences the accuracy of solution. Considering that the aggregate fraction in PAC is high and the minimum aggregate size is small, background grid mapping method was adopted in this study.

Generally, PAC consists of three main phases: aggregate, grout, and interfacial transition zones (ITZ). There are different methods for determining ITZ. The two-phase composite model is the simplest model and ignores the influence of ITZ [5]. To improve accuracy,

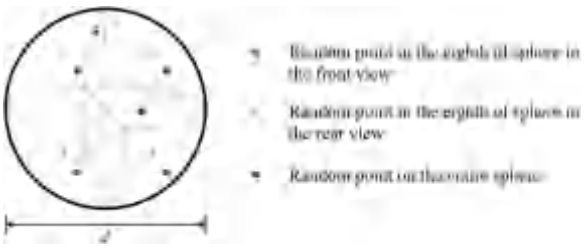


Fig. 3. Random points distribution on the sphere.

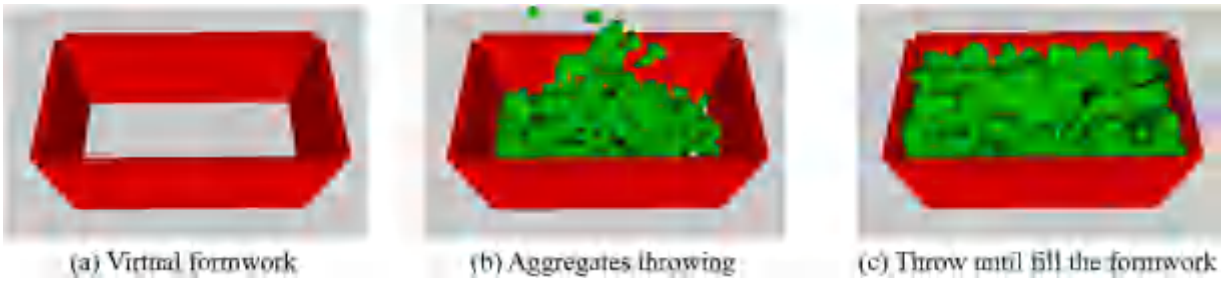


Fig. 4. Aggregate stacking process.

three- and four-phases are also adopted, which is more realistic [21,22]. Compared to conventional concrete, PAC has weaker ITZ, which significantly affects its macro-properties. Therefore, three-phase model including aggregate, grout, and ITZ was adopted in this study.

Background grid mapping procedure is illustrated in Fig. 5. First, background grid was established in ABAQUS using a Python script. Each grid unit was a standard cube. Next, the position of each grid unit node was determined, that is, whether it was in the aggregate, grout, or ITZ. For each grid, the number of nodes in the aggregate was defined as n_a. When $n_a \geq 6$, the grid was defined as an aggregate grid. When $n_a \leq 2$, the grid was defined as a grout grid. When $3 \leq n_a \leq 5$, the grid unit was defined as an ITZ unit. Through background grid mapping, a geometric model with complex shapes was transformed into an easily calculated FE model.

3. Experimental investigation

3.1. Materials and specimens

3.1.1. Raw materials

Coarse aggregate selection is essential in PAC mix design because up to 70 % of the external load is transferred by the aggregate skeleton [23]. Both the shape and grading of aggregate have a significant impact on the grouting, filling, and aggregate content. Bulky rounded or angular aggregates are preferred over flat or elongated aggregates [7]. The void contents of different grading aggregate range from 25 to 50 % [24]. Suitable grading can ensure a production process with lower grout usage. Grout is another important component of PAC. To maintain the strength and flowability of grout, various additives can be added to cement, such as fly ash, limestone powder, silica fume, alkali-activated slag grout, and foamed glass [25–28].

For PAC structures, the maximum coarse aggregate size depends on the dimensions of the structural members. The minimum coarse aggregate size must ensure that the grout flows. Three different coarse aggregate grades were selected for the tests, as listed in Table 1. Fig. 6 demonstrates the coarse aggregate grading curves. The mixing rules are shown in Fig. 7. Grading (A1) is commonly used for conventional concrete. Grading (A2) is composed of grading (A1) and large aggregates. Grading (A3) is a large-sized group without coarse aggregates smaller than 19 mm. The density of aggregates (ρ_a) is 2740 kg/m^3. All the coarse aggregates were washed to keep the surfaces clean, thereby improving the bond between aggregates and grout.

Because the minimum size of the aggregate skeleton was 4.75 mm, sand was not added to the grout. The raw materials included water, cement, additives, and expansive agents. The water–cement (w/c) ratio of the grout was 0.6, which is relatively high. The additive content was 7 % to improve the flowability. Two types of expansive agents were used to compare the effects of different expansive agents on the PAC specimens: calcium sulfoaluminate (CSA) and MgO. The expansion effect of CSA was not evident at a later stage because of the high demand for hydration water [29]. For MgO, the hydration process required less water. Different expansion speeds can be achieved, depending on the hydration reactivity and microstructure [30]. The compressive (f_{gc}) and flexural strengths (f_{gf}) of the grout were obtained from mechanical tests on three 40 × 40 × 160 mm prisms, in accordance with GB/T 29756–2013 [31]. The density (ρ_g) was also measured for each specimen. The average measurement results are listed in Table 2.

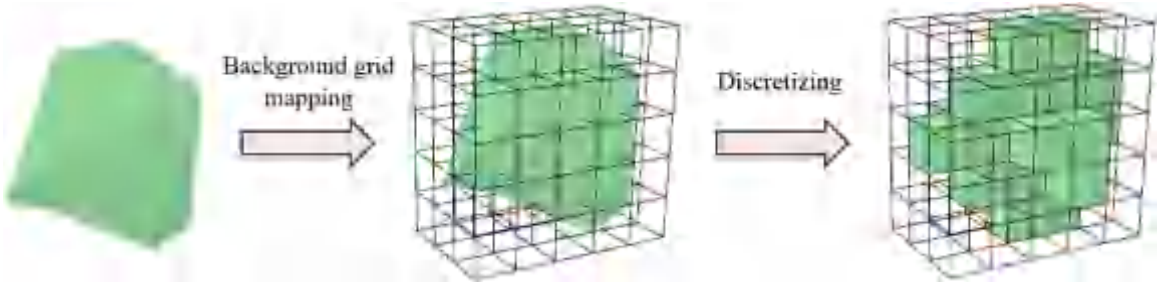


Fig. 5. Background grid mapping procedure.

Table 1
Particle size gradation of coarse aggregates.

Sieve size (mm)	Cumulative percentage passing (%)		
	Grading (A1)	Grading (A2)	Grading (A3)
37.5	–	100	100
31.5	–	90	50
26.5	100	90	50
19	64	57.6	0
16	33	29.7	–
9.5	5	4.5	–
4.75	1	0.9	–

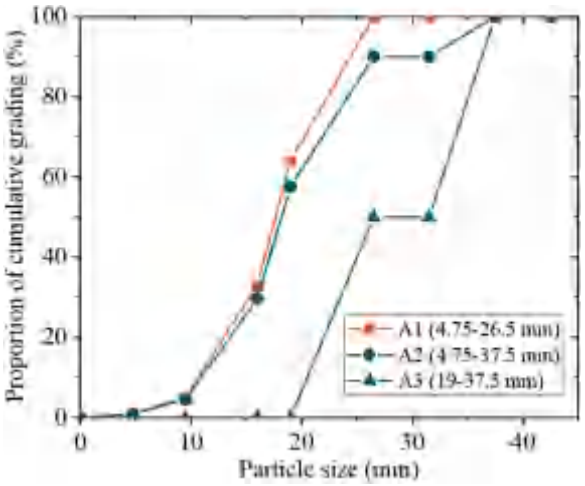


Fig. 6. Cumulative grading curves of coarse aggregates.

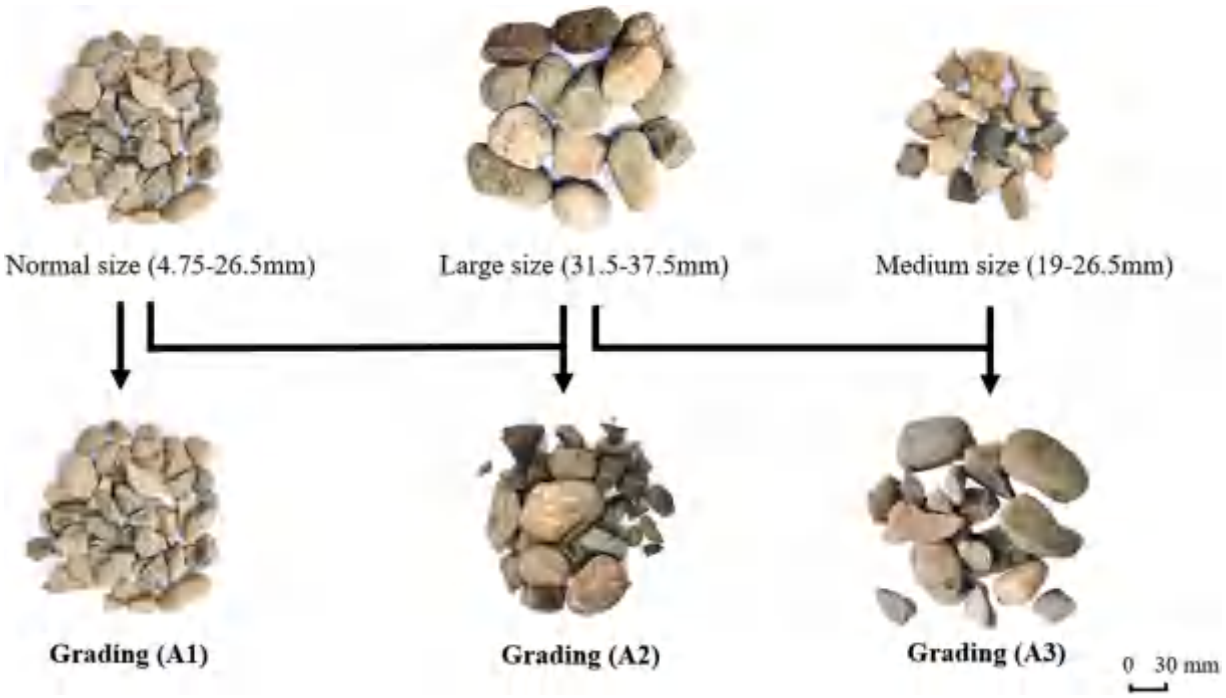


Fig. 7. Mixing rules for coarse aggregates.

3.1.2. Concrete casting

To investigate the compression and shrinkage performance of PAC, two specimen sizes were designed. Three 150 × 150 × 300 mm prismatic specimens were manufactured for the compression test of each PAC type, denoted as Group P. One cylindrical specimen with a diameter of 350 mm and a height of 500 mm was manufactured for the shrinkage test of each PAC type, denoted as Group C. Five types of specimens were manufactured for each group, as listed in Table 3. The influence of aggregate grading and grout type on the A1E0 specimen was studied. The casting process is shown in Fig. 8. To observe the distribution of coarse aggregates in concrete more clearly, the aggregates were dyed red for one of the three specimens in Group P. For Group C, the depth of 800 mm was too deep for a one-time pour. Consequently, the specimen was divided into three parts for separate casting. After all the casting procedures, the specimens were cured at 23 ℃ and a relative humidity of 95 %. The specimens in Group P were removed after 28 d of curing. The specimens of Group C were demolded on the third day, and the shrinkage behavior of concrete under this condition was tested from that day onward. The surface of Group C was smooth after demolding, indicating that full flow of grout was achieved in the aggregate skeleton.

The aggregate fraction is an important parameter that reflects the performance of PAC. For Group C, the coarse aggregate mass m_a was measured. The entire specimen mass M was also measured after curing. The aggregate fraction D_a can be calculated using Eq. (1), and the grout compactness D_g in the aggregate skeleton void can be calculated using Eq. (2).

$$D_a = \frac{m_a/\rho_a}{V} \tag{1}$$

$$D_g = \frac{(M - m_a)/\rho_g}{V - m_a/\rho_a} \tag{2}$$

where V is the volume of the entire specimen based on the standard prism assumption. The calculation results are presented in Table 4. All the specimens had an aggregate fraction level exceeding 50 %. Meanwhile, the selected aggregate grading had no significant impact on the aggregate fraction. Almost all the grout compactness values were above 95 %, reflecting the full flow of the grout.

3.2. Mechanical property test

A concrete compression test was conducted on Group P, in accordance with GB/T 50081–2019 [32]. The effects of the aggregate size and expansive agent type on the compressive performance were investigated. The test setup is illustrated in Fig. 9. Two lateral 100-mm concrete strain gauges and two vertical 150-mm strain gauges were installed on the left and right sides of the specimen. The stress–strain relationship can be obtained by considering the average strain value on both sides as the specimen strain. The loading rate during the test was 0.5 MPa/s. To reduce the impact of non-compact contact between the specimen and machine, the specimen was loaded three times in the initial loading cycle (0.5 MPa to approximately 1/3 of the ultimate load).

3.3. Shrinkage behavior test

The shrinkage properties of Group C were tested. Compared with those of Group P, they had a larger size to reduce the measurement error because concrete dry shrinkage occurs at a very low order of magnitude. The effects of the aggregate size and expansive agent type on shrinkage performance were also investigated. Grout shrinkage tests were performed according to JGJ/T70–2009 [33]. A prismatic specimen with dimensions of 40 × 40 × 160 mm was measured using a digital length comparator for each grout type. The test setup for PAC is shown in Fig. 10. Two dial indicators were placed on both sides using rebars and adaptive screws. The measurement points were located 150 mm from the top and bottom, and the distance between these two measurement points was 500 mm. The average shrinkage value of both sides was considered the specimen shrinkage. Because the specimens required a certain time for hardening, the grout and PAC specimens were demolded three days after casting to initiate the shrinkage measurements. The environment for shrinkage measurement was the same as that for curing. Both the grout and PAC shrinkage tests had a measurement duration of 40 d. Considering that the shrinkage speed was high in the early stages of the test, the shrinkage displacement was measured twice a day for the first 15 d and once a day for the remaining days.

4. Mechanical property simulation discussion

4.1. Aggregate stacking state

The aggregates were randomly placed according to the grading used in the test. The cumulative percentage passing listed in Table 1

Table 2
Properties of grout.

Label	Expansive agent	f_{gc} (MPa)	f_{gf} (MPa)	ρ_g (kg/m^3)
E0	–	35.6	3.05	1754
E1	CSA	38.1	2.51	1757
E2	MgO	38.1	3.73	1779

Table 3
Test specimens for Groups P and C.

Specimen ID	Aggregate grading	Grout type
A1E0	A1	E0
A2E0	A2	E0
A3E0	A3	E0
A1E1	A1	E1
A1E2	A1	E2

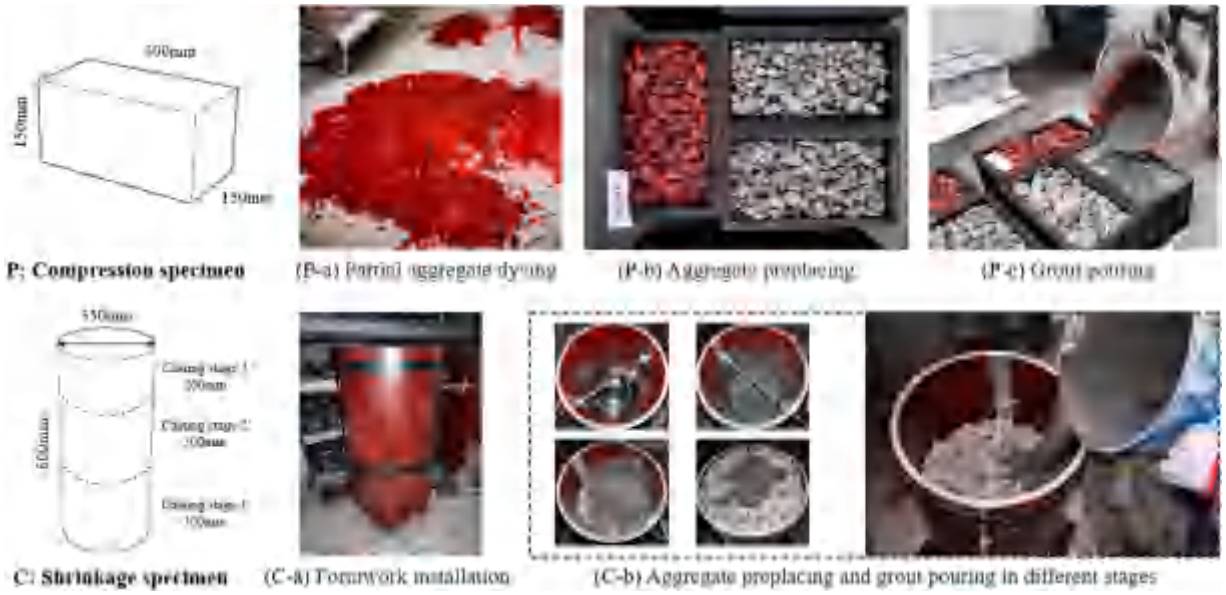


Fig. 8. Concrete casting process of Groups P and C.

Table 4
Aggregate fraction and grout compactness of Group P.

ID	D_a (%)	D_g (%)
A1E0	56.6–58.4	92.2–99.5
A2E0	56.9–58.7	97.5–99.8
A3E0	56.8–57.8	98.3–98.7
A1E1	54.5–57.7	97.2–98.1
A1E2	55.8–58.9	96.7–98.9

*Each type consisted of three specimens. The ranges listed in the table indicate the minimum and maximum values for each of the three specimens.

reflects the total aggregate mass for each grading. It is necessary to convert this into an aggregate quantity distribution based on a single aggregate mass. Assuming that the aggregates were standard spheres, the quantity distribution of each grading interval could then be easily acquired. Based on the distribution, aggregates were randomly generated using the physics engine PhysX. To ensure that the aggregates filled the formwork, they were allowed to scatter outside the formwork. Outside aggregates were removed by range checking when outputting the resulting text files. The aggregate fraction was calculated for each grading.

A stacking-state comparison of the simulation and test results is shown in Fig. 11. The dashed blue line represents the aggregate fraction obtained from simulations. The blue-shaded area represents the aggregate fraction range obtained from the test. As shown, the simulation and test results had similar aggregate stacking states. However, compared to the simulation results, the tested aggregates were more rounded. For gradings A1 and A2 with smaller aggregate sizes, the simulated aggregate fraction was slightly higher. For grading A3 with a larger aggregate size, the simulated aggregate fraction was rather low. This may be because the corner of the convex polyhedron was sharper than the actual aggregate shape. Hence, the space between the aggregates was larger. However, for small aggregates, contact overclosure caused more overlap between the aggregates. This canceled out the sharper shape effect and caused the simulated aggregate fraction to be higher than the actual value.

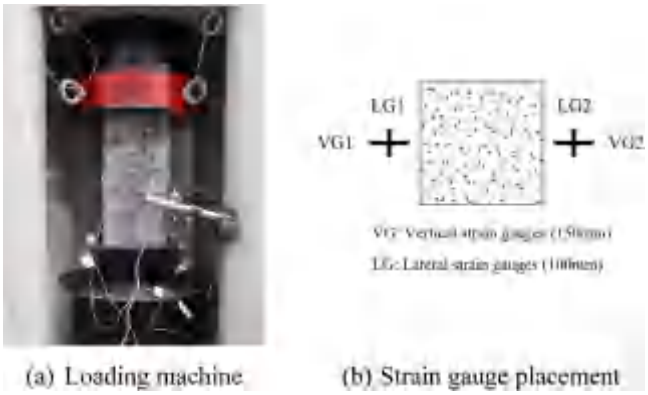


Fig. 9. Compression test setup.

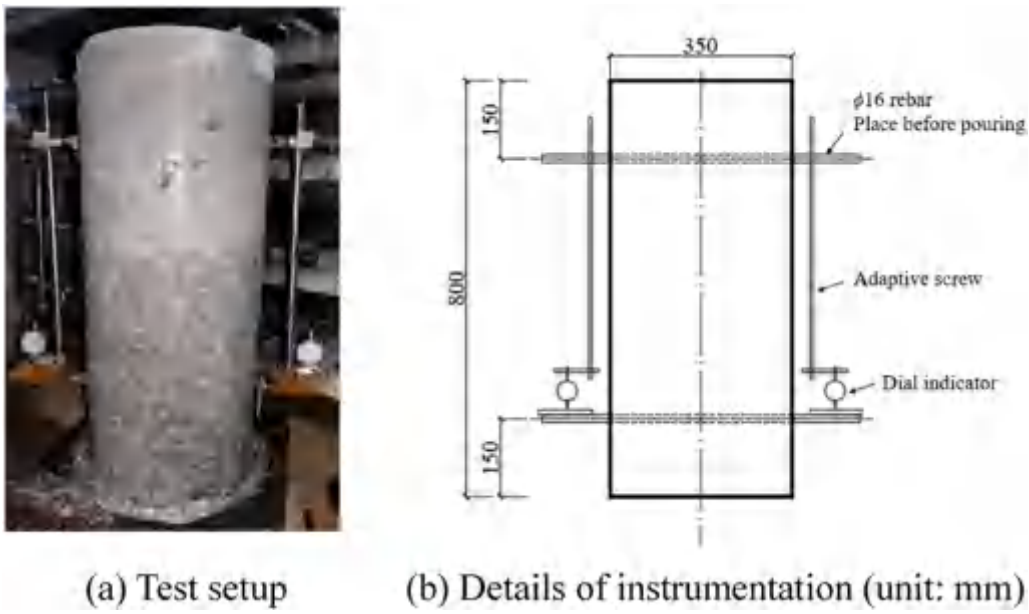


Fig. 10. Shrinkage test setup and instrumentation.

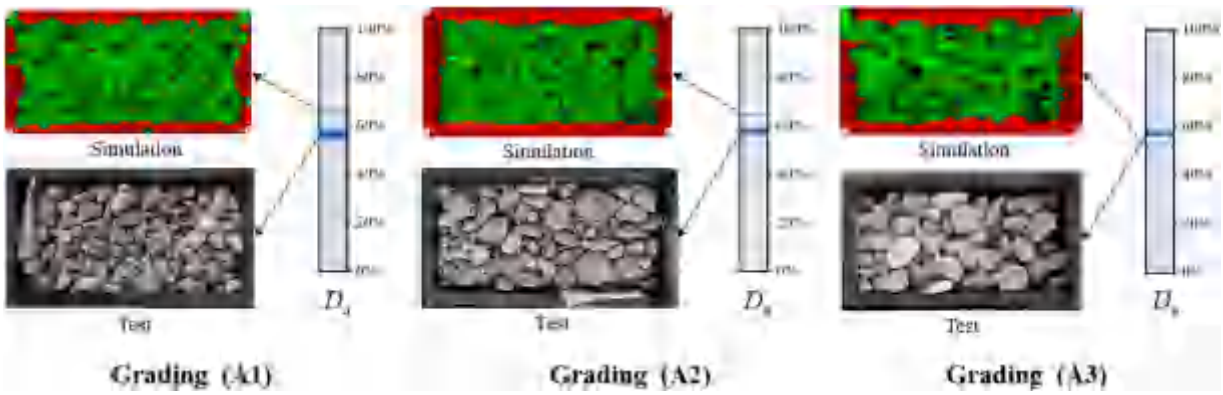


Fig. 11. Aggregate stacking comparison.

4.2. Finite element model

An FE model with dimension of 150 × 150 × 300 mm and the same size as the test specimens was established using the commercial FE software ABAQUS. Considering calculation efficiency and accuracy, the size of the background grid was 3.75 mm. Because the strength of PAC is low, damage occurs in the grout and ITZ rather than in the aggregates. As a result, the elastic constitutive model was used for the aggregates, whereas the elastic-plastic model was used for the grout and ITZ. The parameters determined using the constitutive models are listed in Table 5.

The elastic modulus of the aggregates was defined as 50 GPa using the inverse method [34,35]. For the grout, flexural strength was regarded as the tensile strength. The flexural and compressive strengths were consistent with those listed in Table 2. The mechanical behavior of grout is similar to that of concrete [36]. The concrete damage plastic (CDP) model was adopted in the FE model to simulate the grout damage progress [37,38]. The elastic modulus was calculated based on the stress–strain curve. For the ITZ, the constitutive model was more complex. Compared to grout, the ITZ is more porous because of the wall effect, micro-bleeding, nucleation, and precipitation [39]. Therefore, the mechanical properties of the ITZ are poor. Background electron imaging reveals that the thickness of this area can reach 50 μm [39]. In conventional mesoscale simulation, the thickness of the ITZ is generally between 0.05 and 1 mm [40]. However, the aggregate fraction is higher in PAC. Hence, the ITZ content is higher and the shape of the transition zone is more abnormal. To improve the calculation efficiency and broaden its applicability, the ITZ and grout shared the same mesh sizes in the FE model. The ITZ mechanical parameters were obtained by multiplying the grout mechanical parameters by reduction coefficients [41,42]. The construction procedure of PAC results in an inferior ITZ. Therefore, a larger reduction coefficient was required. Using the inverse method, the reduction coefficients for the elastic modulus, compressive strength, and tensile strength were 1/3, 1/9, and 1/9, respectively. The Poisson's ratios of the aggregate, grout, and ITZ were defined as 0.2.

Considering A1E0 specimen as an example, the FE model is shown in Fig. 12. A sparse region of aggregates formed at the top of the specimen owing to the stacking effect, and an aggregate concentration area was formed at the bottom of the specimen. Because of the high aggregate content in the A1E0 specimen, the grout could only form a relatively small volume inside the specimen. In the longitudinal section, breakpoints existed in the vertical direction of the aggregate skeleton. This implies that there is no integral aggregate skeleton at the 2D level. This phenomenon verifies the necessity of a 3D model. All the nodes on one side were coupled to the reference point, and the axial load acted on the reference point. Meanwhile, only the longitudinal freedom was preserved for the reference point. For nodes on the other side, the longitudinal freedom was constrained. On this constrained surface, the bottom nodes were constrained in the vertical direction, and the back nodes were constrained in the transverse direction. The grout, aggregate, and ITZ were set as C3D8R elements to avoid the shear self-locking effect and improve computational stability.

4.3. Comparison of test and simulation

4.3.1. Failure mode

The failure modes of the test specimens and FE model are shown in Fig. 13. The top, side, and bottom views correspond to the positions of the specimens during casting. For ease of observation, obvious cracks on the specimen are indicated by yellow lines. For each test group, only one of the three specimens is presented, for which the aggregates were dyed. In the FE model, the distribution of equivalent plastic strain is illustrated. Owing to grout shrinkage during specimen curing, the top face of the specimen was uneven. This phenomenon was more obvious in the groups without an expansive agent, namely, A1E0, A2E0, and A3E0. Failure predominantly occurred in the grout and ITZ, validating the assumption that the aggregates were not damaged. The cracks mostly developed longitudinally and attached to the aggregates. Crack propagation was concentrated near the edges and corners, leading to grout detachment. Some specimens exhibited more severe damage at the top face than at the bottom, or vice versa. However, this phenomenon was random. Within some groups, these two opposing phenomena were observed for all three specimens. The results of the FE model agreed well with the test results. Areas near the edges often exhibited higher plastic strains, and noticeable local damage occurred at some corners and edges. However, owing to the limitations of the FE method, simulating the later stage of the concrete spalling process was challenging.

With respect to the effect of aggregate grading, a smaller aggregate size resulted in denser cracks. The damage patterns were essentially the same, with local crack propagation leading to grout spalling in all groups. Regarding the effect of the grout type, differences were only reflected in the top faces of the specimens. The A1E0, A1E1, and A1E2 FE models used the same aggregate data

Table 5
Constitutive model parameters.

Properties	Aggregate	E0	E1	E2	E0 ITZ	E1 ITZ	E2 ITZ
Elastic modulus (GPa)	50[a]	30.9[b]	30.8[b]	30.8[b]	10.3[a]	10.3[a]	10.3[a]
Compressive strength (MPa)	–	35.6[b]	38.1[b]	38.1[b]	4.0[a]	4.2[a]	4.2[a]
Tensile strength (MPa)	–	3.05[b]	2.51[b]	3.73[b]	0.34[a]	0.28[a]	0.41[a]
Dilation angle	–	38°[c]					
Eccentricity	–	0.1[c]					
fb0/fc0	–	1.12[c]					
K	–	0.667[c]					
Viscosity parameter	–	0[c]					

Note: Data "a" were acquired through inverse method; Data "b" were acquired through mechanical tests; Data "c" referred to the literature [37,38].

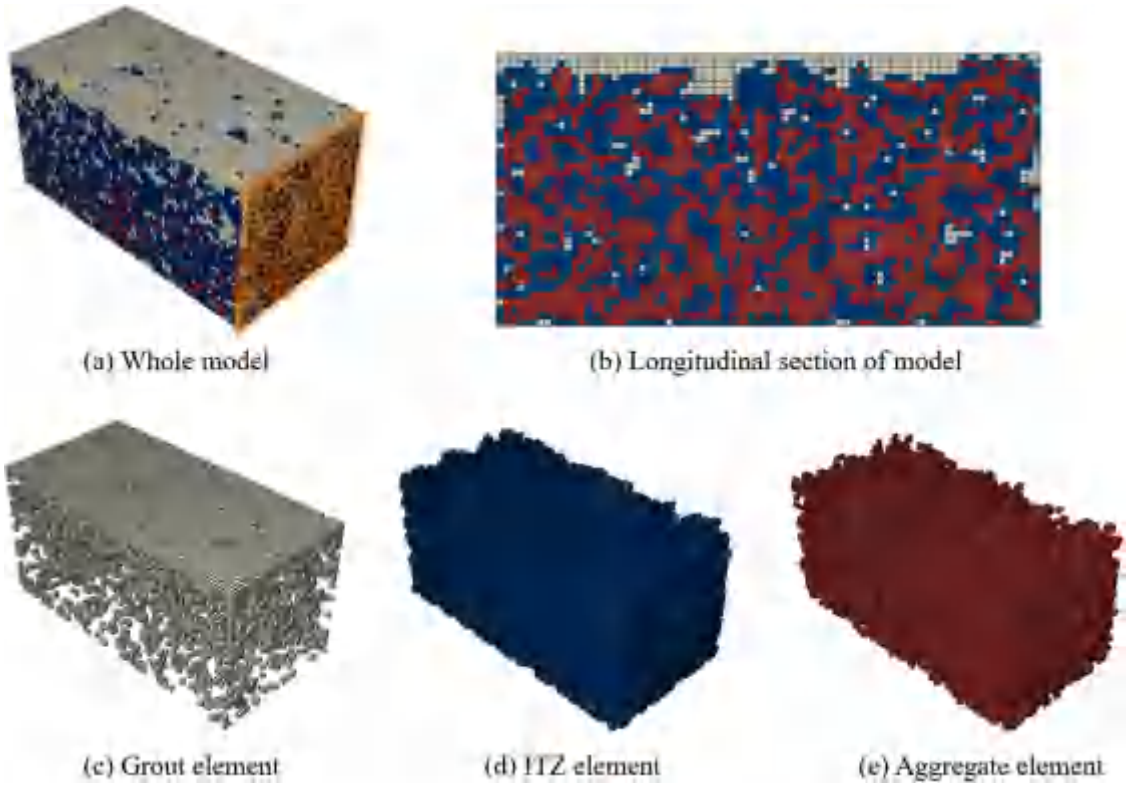


Fig. 12. Mechanical FE model of the A1E0 specimen.

and thus exhibited similar simulated damage patterns. However, owing to the different stress–strain relationships of the different grouts, the ultimate states at the end of the calculation were different.

4.3.2. Stress–strain curve

Fig. 14 shows a stress–strain curve comparison between the test and FE model. The endpoint of the curve corresponds to the moment of strain gauge failure. Therefore, the ultimate strength of the specimen may not be equal to the peak value. In the same group, the elastic modulus at the initial stage were almost identical. However, the stress–strain curves softened as cracks developed. The ultimate strain may also differ significantly within the same group. Taking the A3E0 group as an example, the ultimate strain of A3E0–1 was approximately 140 % higher than that of the other two specimens. This may be due to the poor mechanical properties of the ITZ in PAC. ITZ destruction occurred in the late loading stage, which led to local failure of the specimens. Nonetheless, the overall aggregate skeleton could withstand the load. The stress in the members continued to increase while the stiffness gradually decreased. Owing to the differences in the contact between the aggregates, some specimens quickly suffered global damage, whereas others were still able to sustain the load within a certain deformation. Residual deformation of concrete occurred during the initial loading cycle stage. This phenomenon was particularly evident in the group using grout without an expansive agent. This could be attributed to the plastic deformation of the porous ITZ during the loading cycle. With the addition of an expansive agent, the mechanical properties of the ITZ were improved and plastic deformation was reduced.

For the FE model, the failure process was non-uniform. The model was analyzed using implicit static calculation method, and the localized failure of the grout led to the premature termination of the simulation. Consequently, the stress-strain curve lacked a descending section. The simulation results in the elastic stage were consistent with the test results. However, there were some differences in the plastic stage. This is because it was difficult for the ITZ element to simulate the slip between the aggregates and the grout. Therefore, it exhibited limited ductility. It is noteworthy that the FE calculation results for A1E1 and A1E2 were significantly different from the test results. An increase in the grout strength led to more local brittle failure, which led to a decrease in the ultimate deformation of the model. However, the use of an expansive agent improved the performance of the ITZ, and the ductility of the specimen increased during test. For PAC specimens with an added expansive agent, more test results are required to modify the ITZ property parameters.

*For test specimen A1E0–1, the ultimate stress was incorrectly estimated. During the initial loading cycle, the specimens exhibited wide stress ranges.

4.3.3. Mechanical property parameters

To more clearly compare the differences between the FE and test results, the mechanical property parameters of the test and FE

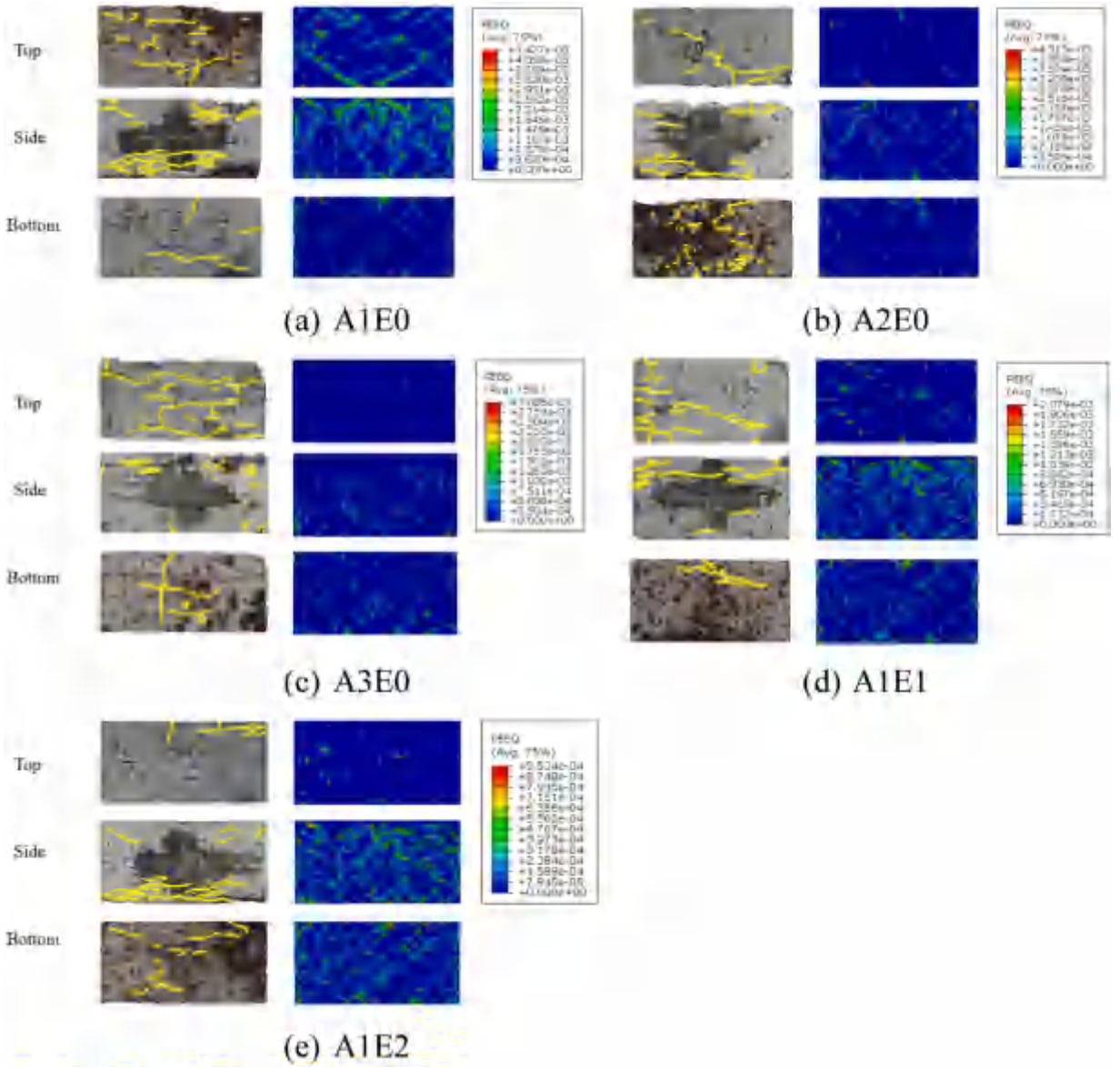


Fig. 13. Comparison of failure modes between the test and FE model.

results are shown in Fig. 15. The standard deviation and mean values were calculated for the test results. The elastic modulus was obtained from the initial stage of the strain–stress curve. Poisson's ratio was calculated from the vertical and lateral strain values at the elastic stage. For the FE model, the vertical strain was obtained from the overall displacement, whereas the lateral strain was obtained from the displacement of the nodes in the middle section at a distance of 100 mm. The test specimen strengths were calculated using the peak force of the loading machine. The peak value of the stress–strain curve was regarded as the strength of the FE model.

When no expansive agent was added to the grout, the variation tendencies of the elastic modulus and Poisson's ratio of the FE model were nearly consistent with the test results. The elastic modulus of the FE model was low in groups with small aggregate sizes. Because the actual ITZ thickness is smaller than the grid size, more aggregate areas are identified as the ITZ, causing a lower elastic modulus. This deviation may be considered acceptable for small aggregate size ranges. The FE results exhibited a relatively high Poisson's ratio compared with the test results. This difference may be because even in the elastic stage, part of the ITZ suffers failure. The failure mode of the CDP model differed from the actual failure mode, leading to a greater volume expansion. A notable discrepancy existed in the simulation of the specimen strength. This discrepancy originated from the correlation between the specimen strength and ductility. Local damage to the aggregate skeleton, which contributes to ductility, is a challenge in FE simulations. This influence was more remarkable in the groups with larger aggregate sizes, which stress–strain curve behaved bilinearly. In practical use, the FE results can be applied as a conservative design value considering the significant discretization of PAC.

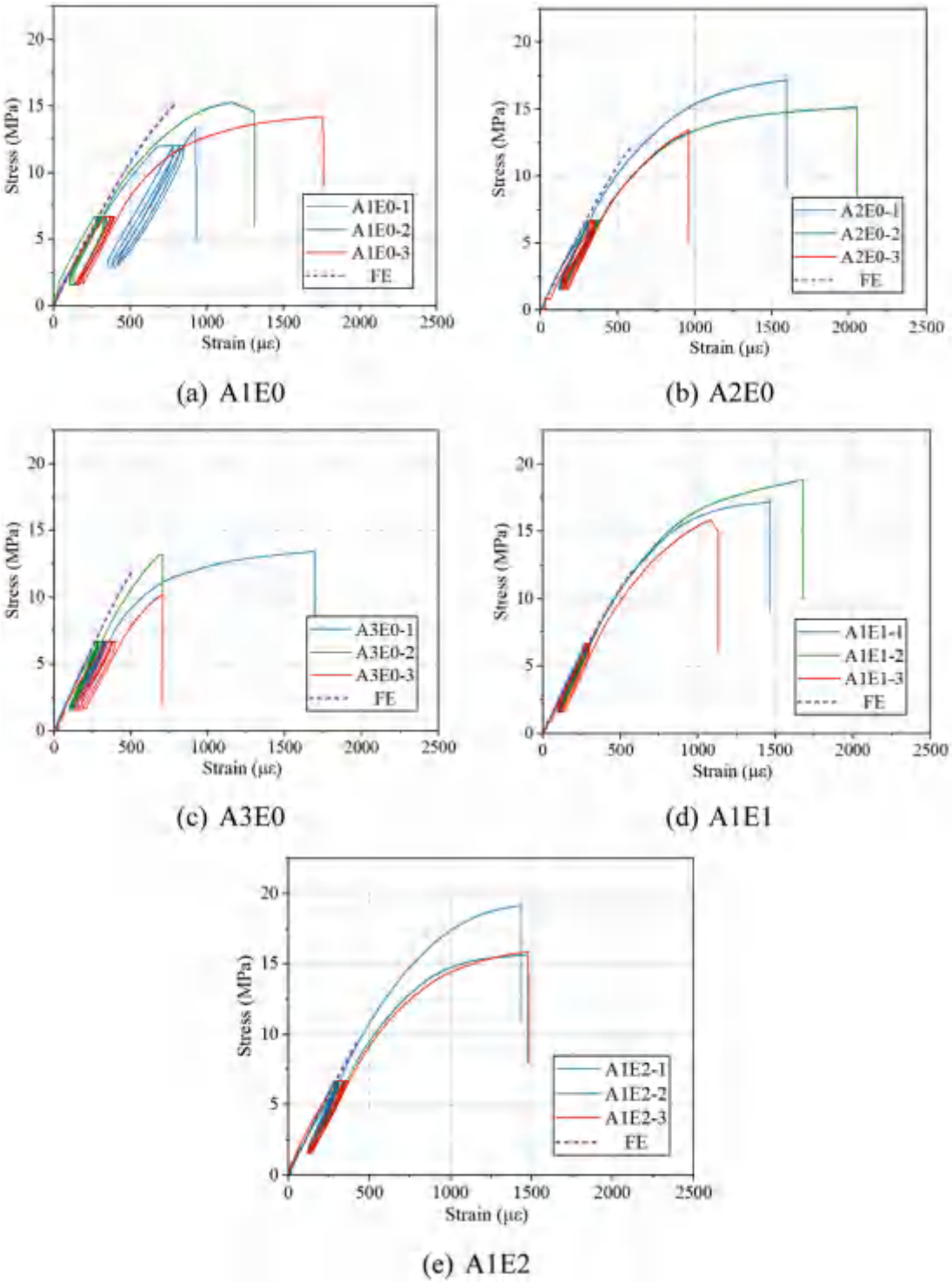


Fig. 14. Stress–strain curve for the test and FE model.

After adding expansive agent to the grout, the mechanical properties of the ITZ were improved. Consequently, the elastic modulus and strength also improved. However, the improved mechanical properties of the ITZ were not properly reflected in the FE model, leading to overestimated simulation results. To reduce this overestimation, additional specimens must be tested using an expansive agent to acquire accurate ITZ mechanical property parameters.

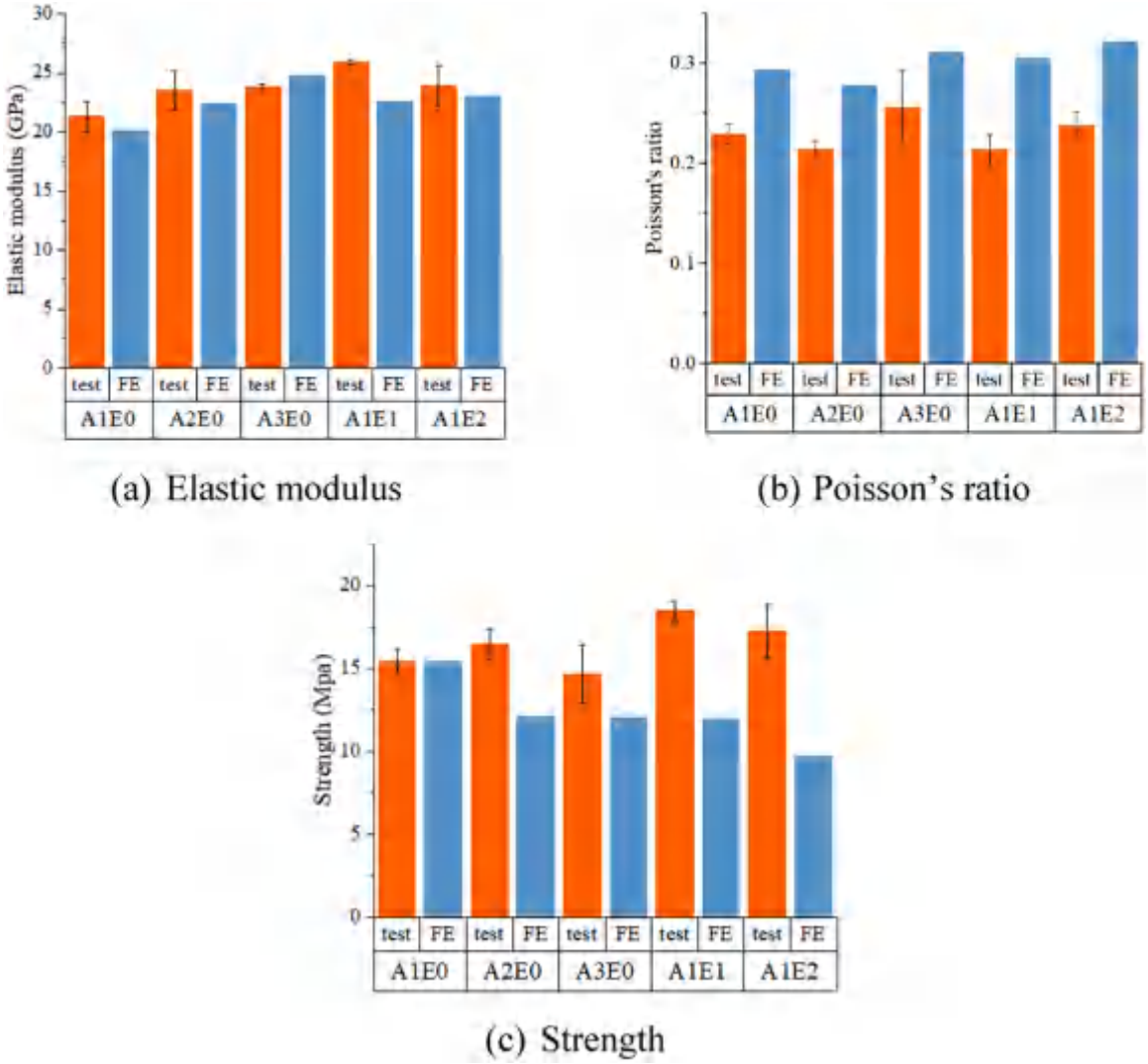


Fig. 15. Mechanical parameters for the test and FE model.

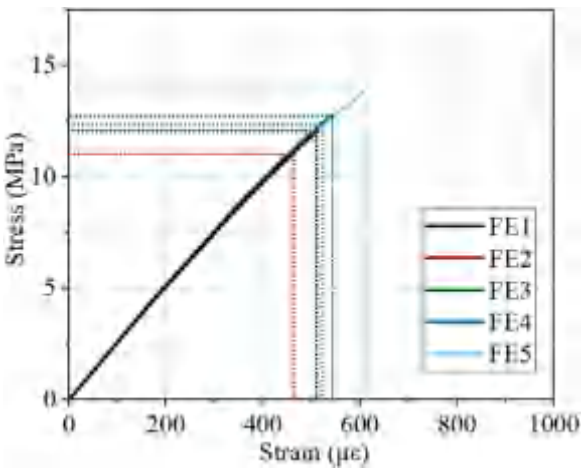


Fig. 16. FE repeatability analysis of A3E0.

4.4. Repeatability analysis

Similar to the test results, randomness existed in the physics engine simulations. A repeatability analysis was conducted on the FE model, the results of which are shown in Fig. 16. For ease of calculation, the analysis was performed based on the A3E0 group, which had the largest aggregate size. FE1 is the A3E0 model analyzed in Section 4.3. The aggregate fractions of all the models were in the range 52.15–54.15 %. The FE model exhibited consistent results in the initial stage. However, after local failure occurred in the model, variations in the ultimate strain and stress were observed. The maximum strength exceeded the minimum strength by 26 %. This inconsistency further verified the inherent randomness of the aggregate skeleton.

4.5. Influence of aggregate shape

To study the influence of flat and elongated aggregate on the PAC properties, FE models with different aggregate shapes were established. During aggregate generation in the physics engine, convex polyhedral points were obtained from ellipsoids rather than from spheres. The lengths of the three axes of ellipsoid are denoted as d_1, d_2, and d_3 ($d_1 \geq d_2 \geq d_3$). The four selected ellipsoidal shapes are listed in Table 6. When sieving the aggregates, the size of the sieve hole corresponded approximately to the minimum cross-sectional area of the aggregates. Therefore, d_3 was equivalent to the sieve size of the aggregates. The stacking state of the aggregates in the formwork is shown in Fig. 17. The aggregate fraction was mainly controlled by d_1. The impact of d_2 on the aggregate fraction was minimal, and its influence was not significant. This suggests that elongated aggregates exert a more pronounced effect on PAC than flat aggregates.

FE models were established based on geometric models. All groups selected the E0 grout without expansive agent added. The stress–strain curves are shown in Fig. 18. The FE models arranged in decreasing order of the elastic modulus are A3e3E0, A3e2E0, A3e4E0, A3e1E0, and A3E0. There was a strong positive correlation between the elastic modulus and single aggregate volume, whereas the correlation with the aggregate fraction was relatively weak. Owing to the poor mechanical properties of the ITZ without expansive agent, the elastic modulus and strength of PAC could be improved by appropriately increasing the volume of a single aggregate.

5. Shrinkage simulation discussion

5.1. Finite element model

The specimen size for the shrinkage behavior test was too large for mesoscale simulation. Therefore, an FE model of the same size as the mechanical properties was chosen to simulate the shrinkage behavior. During the physics engine simulation process, the aggregates were placed vertically. Owing to the different directions of aggregate stacking, the shrinkage and mechanical models of the same aggregate grading had different aggregate fractions. Considering the A1E0 group as an example, the shrinkage FE model is shown in Fig. 19. The grout, ITZ, and aggregates were all considered elastic materials owing to the minimal free shrinkage of PAC. The elastic modulus and Poisson's ratio of the material as well as the boundary conditions and element types were the same as those in Section 4.2. The free-shrinkage process of the grout and ITZ was simulated using a temperature field. Because shrinkage and elastic deformation are both elastic behaviors, the same reduction coefficient as the elastic modulus was used to determine the shrinkage of the ITZ. In other words, the shrinkage of the ITZ was considered to be 1/3 of the grout shrinkage.

5.2. Comparison of test and simulation

5.2.1. Grout shrinkage

The shrinkage measurement results for grouts E0, E1, and E2 are presented in Fig. 20. For consistency with the PAC test, the grout specimens were measured from the third day after casting. For the E0 grout without expansive agent, the relationship between the shrinkage strain and time was approximately linear. After 40 d, the shrinkage strain of the E0 grout reached 452 με.

The addition of the expansive agent significantly reduced the shrinkage strain. In comparison with E1, the shrinkage strain of E2 was smaller and exhibited expansion, indicating a stronger expansion effect of the MgO expansive agent. Furthermore, there were differences in the reaction times of the two expansive agents. The effect of the CSA expansive agent was mild, and the shrinkage strain of the E1 grout stabilized after a rapid increase in the early stages. The influence of MgO persisted for an extended period. The expansion of the E2 specimen continued until 40 d. Meanwhile, the shrinkage strain of specimen E2 exhibited greater fluctuation, reflecting the lower soundness of MgO [30].

Table 6
Shape of ellipsoids in aggregate generation.

ID	d_1: d_2: d_3
A3e1	2: 1: 1
A3e2	2: 2: 1
A3e3	4: 2: 1
A3e4	4: 1: 1

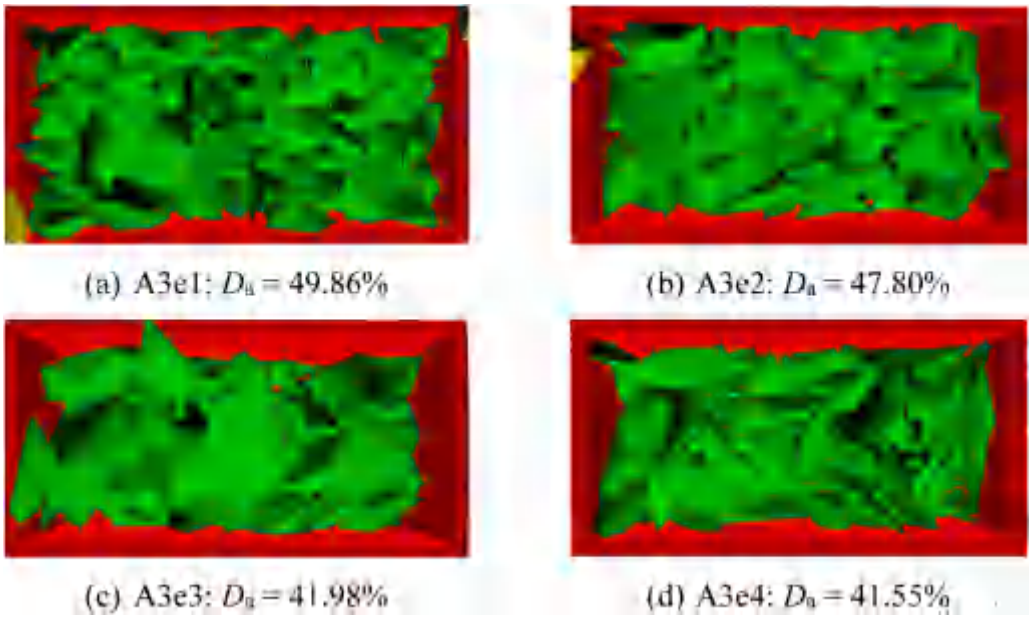


Fig. 17. Stacking state of different aggregate shapes.

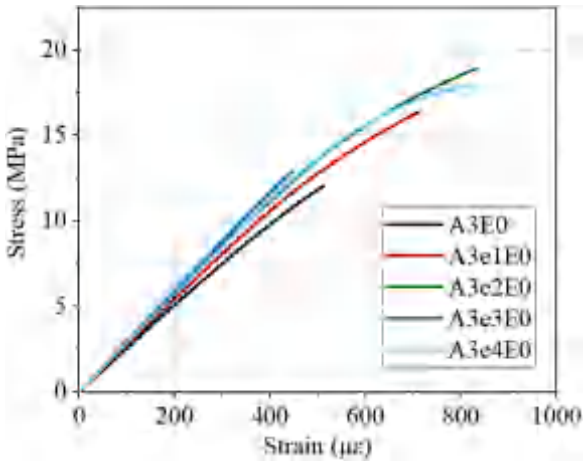


Fig. 18. Stress–strain curve of FE models with different aggregate shapes.

5.2.2. Shrinkage strain curve

The grout shrinkage results were input into the FE model. The shrinkage properties of the ITZ were those of the grout multiplied by a reduction factor of 1/3. Taking the A1E0 model as an example, Fig. 21 shows the calculated longitudinal deformation distribution. Owing to the uneven distribution of the grout and aggregates, the deformation was also uneven in the horizontal and longitudinal directions. To avoid this nonuniformity, the middle 202.5 mm was selected as the measurement section. The average value of the midpoints on the four sides was considered as the deformation value, and the strain was obtained from the deformation at both ends of the measurement section.

Fig. 22 illustrates the shrinkage strains of the test specimens and FE models. Owing to the elastic behavior of the FE model, the shrinkage strain in the overall model was proportional to that of the grout input into the model. A difference was observed between the FE and experimental results. This difference indicates that the grout and PAC specimen shrinkage involved distinct mechanisms. The shrinkage of the PAC specimen without an expansive agent followed a two-stage mode:

Stage I: Steady growth stage. This stage occurred approximately during 0–8 d. During this period, the growth rate of the simulated shrinkage strain was lower than that in the test results. This is due to the accumulation of temperature in the mass concrete [43]. Increasing the temperature promoted evaporation and accelerated shrinkage. However, the FE and test results showed a similar pattern of aggregate grading influence on the shrinkage performance. The early-stage shrinkage of A3E0 was greater than that of A1E0 and A2E0, indicating that larger aggregate sizes lead to increased early shrinkage.

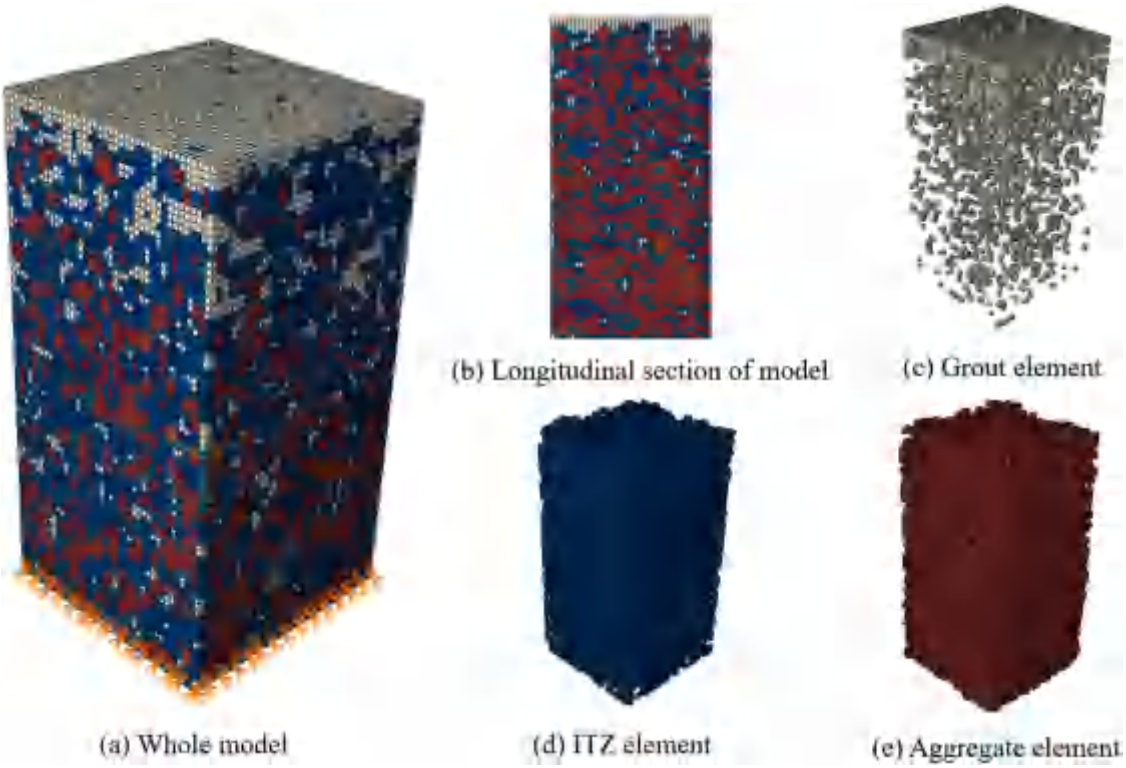


Fig. 19. Shrinkage FE model of the A1E0 specimen.

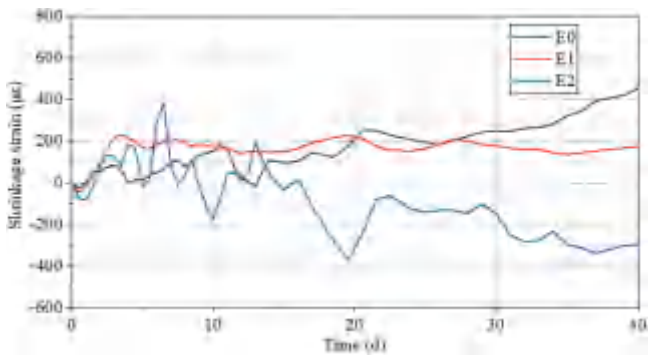


Fig. 20. Shrinkage strain for the E0, E1, and E2 grout.

Stage II: Strain stabilization stage. This stage occurred approximately during 8–40 d. During this period, the change in the shrinkage strain was no longer significant. After the surface moisture evaporated, it was difficult for the internal moisture to evaporate and diffuse because of the large size of the PAC specimens. The internal shrinkage stabilized quickly, and as the surface moisture evaporated, the overall shrinkage stabilized. Small aggregates could form a dense ITZ network, which was conducive to internal moisture diffusion. This led to a lower shrinkage strain in A3E0 compared to A1E0 and A2E0 at this stage.

After the addition of the expansive agent, the shrinkage of PAC was noticeably mitigated and even converted to expansion. The expansive strain caused by the expansive agent was obtained by subtracting the strains of specimens A1E1 and A1E2 from that of the A1E0 specimen, as shown in Fig. 23. Similar to the shrinkage behavior of the grout, the expansion of the A1E2 specimen was higher than that of the A1E1 specimen. In Stage I, the expansion effects of the two expansion agents were superior to those of the simulated results. This may be attributed to the accumulated temperature in PAC, which promoted the reaction of the expansive agent. In Stage II, the accumulated temperature was released, and the expansion rate of the FE models was essentially the same as that of the test models.

The results show that the PAC and grout had different shrinkage conditions. In Stage I, the heat generated from cement hydration was difficult to dissipate, leading to an increase in specimen temperature. This significantly enhanced both the shrinkage strain of grout and the expansion strain induced by the expansive agent. In Stage II, the smaller specific surface area of PAC specimen makes it

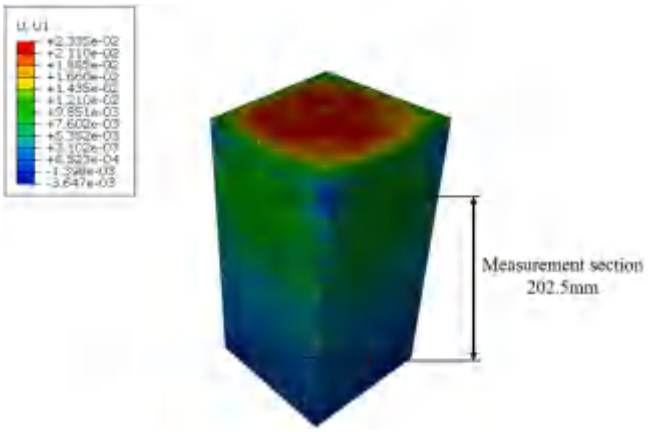


Fig. 21. Longitudinal deformation distribution of the A1E0 model.

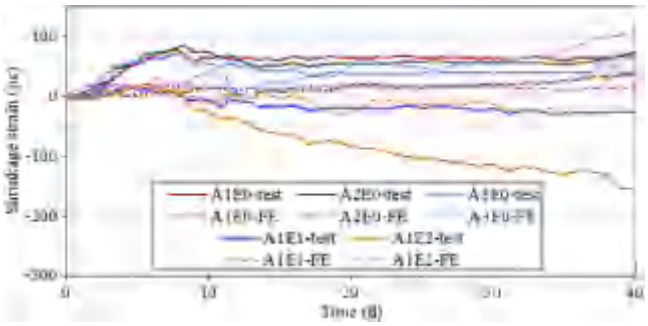


Fig. 22. Shrinkage strain of test specimens and FE models.

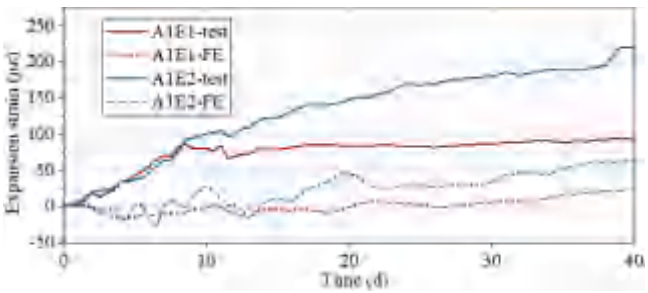


Fig. 23. Expansion strain of test specimens and FE models (only for A1E1 and A1E2).

harder for internal moisture to evaporate, thereby inhibiting shrinkage. Consequently, PAC specimens no longer exhibit continuous shrinkage behavior like grout specimens. At this stage, the expansion strain obtained from the FE model aligned well with experimental results. Therefore, deducing the accurate shrinkage curve of PAC from a single-grout shrinkage curve is challenging. It is essential to establish shrinkage curves for grout tests under different drying and sealing conditions. A more refined FE model can be developed based on the shrinkage conditions and temperature field distribution of the grouts at different locations in the PAC specimens.

5.3. Relationship between aggregate fraction and PAC shrinkage

Although the FE model cannot directly predict the relationship between the PAC shrinkage and grout shrinkage, it can be used to evaluate the relationship when the shrinkage conditions are consistent. By denoting the shrinkage strain of the PAC model as ε_p and the shrinkage strain of grout as ε_g, the shrinkage coefficient α_s can be defined as:

$$\alpha_s = \varepsilon_g / \varepsilon_p \tag{3}$$

Similar to the mechanical property simulation, repeatability and aggregate shape influence analyses of A3E0 were conducted. the aggregate fraction D_a was obtained for each model using the physics engine, and the shrinkage coefficient α_s was calculated for each model by the FE model. Combining the previously calculated shrinkage results of the A1E0, A2E0, and A3E0 models, the relationship between D_a and α_s was obtained, as shown in Fig. 24. The expansive agent had little effect on the grout elastic modulus. It can be considered that under different grout types, the same aggregate grading has the same α_s. The definition of the A3e series was consistent with that described in Section 4.5. α_s increased nonlinearly with an increase in D_a. Satisfying $\alpha_s \to +\infty$ ($D_a = 100$ %) and $\alpha_s = 1$ ($Da = 0$), the fitting curve could be obtained. A3 in the different simulations and different aggregate shapes showed a good fit with the fitting curve.

6. Conclusion

In this study, physics engine was introduced to PAC mesoscale simulation. This novel simulation method addressed the limitations of traditional approaches in accurately simulating the coarse aggregate skeleton. Mechanical property and shrinkage tests were performed on PAC, considering the impact of aggregate size and expansive agents. Test specimens were simulated using this mesoscale simulation method, and the mechanical properties and shrinkage behaviors of the test and simulation were compared. The following conclusions were drawn from this study:

(1) To verify the accuracy of the novel method, the simulated aggregate fraction was compared with the test results. The results showed that the simulated aggregate fraction could reach a high level of 60 % and closely aligned with the test results. The discrepancy could be attributed to the sharp shape effect and the contact coverage. In the FE model, the breakpoints were present in the vertical direction of the aggregate skeleton. This indicates the absence of an integral aggregate skeleton at the 2D level and verifies the necessity of the 3D model. The aggregate shape analysis revealed that the aggregate fraction was primarily influenced by the longest axis of the circumscribed ellipsoid. Elongated aggregates had a more pronounced effect on the aggregate fraction than flat aggregates.

(2) In the mechanical property test, the cracks mostly developed longitudinally and attached to the aggregates. Crack propagation was concentrated near the edges and corners, leading to grout detachment. Because the overall aggregate skeleton could still bear the load after local failure, some specimens exhibited good ductility in the stress–strain curve. The FE model and test specimens exhibited similar variation tendencies in the elastic modulus and Poisson's ratio. However, owing to the limitations of the FE method, simulating the later stage of the concrete spalling process was challenging, which resulted in a lower simulated strength. The aggregate shape influence analysis showed that the elastic modulus of PAC was mainly affected by the volume of the individual aggregates.

(3) The shrinkage of the PAC specimen without expansive agent followed a two-stage mode: Stage I (steady growth stage) and Stage II (strain stabilization stage). Owing to the elastic behavior of the FE model, the shrinkage strain in the overall model was proportional to that of the grout input to the model. Discrepancies existed between the FE and test results, which were attributed to the diverse shrinkage conditions in the curing process, surface area, and interior area. To obtain a more accurate simulation, it is essential to establish shrinkage curves for grout tests under different conditions, such as drying and sealing. The shrinkage coefficient α_s reflecting the relationship between grout and PAC shrinkage was proposed. The relationship between the aggregate fraction and α_s was obtained through a fitting curve, which can be used to assess the impact of different aggregate fractions on PAC shrinkage.

(4) This novel mesoscale simulation method based on a physics engine is particularly suitable for PAC. The simulation yields relatively good results. However, this method is not limited to PAC and can be applied to the simulation of conventional concrete, thus solving the problem of traditional simulation methods that struggle to achieve a high aggregate fraction. However, unlike PAC, gaps exist between the aggregates in traditional concrete. During the aggregates throwing process, these gaps can be considered by expanding the aggregate size.

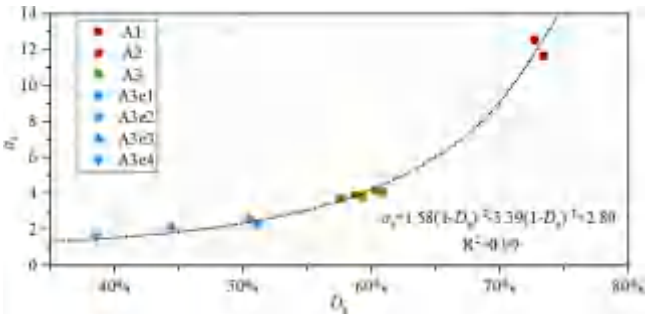


Fig. 24. Relationship between the aggregate fraction and shrinkage coefficient.

CRediT authorship contribution statement

Chongfeng Xie: Writing – original draft, Methodology, Investigation, Conceptualization. **Charun Bao:** Methodology, Investigation. **Xiwang Chen:** Writing – review & editing, Supervision, Conceptualization. **Jia-Qi Yang:** Methodology, Investigation, Conceptualization. **Peng Feng:** Writing – review & editing, Supervision, Funding acquisition.

Declaration of Competing Interest

The authors declare that they have no known competing financial interests or personal relationships that could have appeared to influence the work reported in this paper.

Data availability

Data will be made available on request.

Acknowledgements

This research has been supported by the National Natural Science Foundation of China (No. U2106219), CNPC Offshore Engineering Company Limited (No. 2019B-3203), and the Guoqiang Institute, Tsinghua University (No. 2021GOG1001). The first author Chongfeng Xie was supported by the Program Fund of Non-Metallic Excellence and Innovation Center for Building Materials (No. 2023Ph. D-1).

References

[1] M.F. Najjar, A.M. Soliman, M.L. Nehdi, Critical overview of two-stage concrete: properties and applications, Constr. Build. Mater. 62 (2014) 47–58.
[2] S. Champion, L. Davis, Grouted concrete construction, Reinf. Concrete Rev. (1958) 569–608.
[3] A.S. Abdul Awal, Creep recovery of prepacked aggregate concrete, J. Mater. Civil Eng. 4 (1992) 320–325.
[4] R.J. Vishwakarma, P. Kumari, S.G. Morkhade, P.V. Bahekar, Engineering properties of two-stage concrete: a critical review, Mater. Today Proceedings 77 (2023) 729–733.
[5] J.Y. Yoon, J.H. Kim, Mechanical properties of preplaced lightweight aggregates concrete, Constr. Build. Mater. 216 (2019) 440–449.
[6] H.S. Abdelgader, Effect of the quantity of sand on the compressive strength of two-stage concrete, Magazine Concr. Res. 48 (1996) 353–360.
[7] J. O'Malley, H.S. Abdelgader, Investigation into viability of using two-stage (pre-placed aggregate) concrete in Irish setting, Front. Architecture Civil Eng. China 4 (2010) 127–132.
[8] P.S.M. Thilakarathna, K.K. Baduge, P. Mendis, V. Vimonsatit, H. Lee, Mesoscale modelling of concrete–a review of geometry generation, placing algorithms, constitutive relations and applications, Eng. Fract. Mech. 231 (2020) 106974.
[9] Y. Yu, Y. Zheng, X.-Y. Zhao, Mesoscale modeling of recycled aggregate concrete under uniaxial compression and tension using discrete element method, Constr. Build. Mater. 268 (2021) 121116.
[10] J. Zhou, M. Zheng, Q. Zhan, R. Zhou, Y. Zhang, Y. Wang, Discrete element modelling of the uniaxial compression behavior of pervious concrete, Case Stud. Constr. Mater. 18 (2023) e01937.
[11] Y. Yu, J. Xu, J. Su, L. Xu, Y. Luo, Investigating specimen size and shape effects on compressive mechanical behaviors of recycled aggregate concrete using discrete element mesoscale modeling, Constr. Build. Mater. 438 (2024) 137196.
[12] A. Yin, X. Yang, C. Zhang, G. Zeng, Z. Yang, Three-dimensional heterogeneous fracture simulation of asphalt mixture under uniaxial tension with cohesive crack model, Constr. Build. Mater. 76 (2015) 103–117.
[13] H. Ma, W. Xu, Y. Li, Random aggregate model for mesoscopic structures and mechanical analysis of fully-graded concrete, Comput. Struct. 177 (2016) 103–113.
[14] J. Zhang, Z. Wang, H. Yang, Z. Wang, X. Shu, 3D meso-scale modeling of reinforcement concrete with high volume fraction of randomly distributed aggregates, Constr. Build. Mater. 164 (2018) 350–361.
[15] Y.-j Huang, F.-q Guo, H. Zhang, Z.-j Yang, An efficient computational framework for generating realistic 3D mesoscale concrete models using micro X-ray computed tomography images and dynamic physics engine, Cem. Concr. Compos. 126 (2022).
[16] H.-K. Man, J. Van Mier, Damage distribution and size effect in numerical concrete from lattice analyses, Cem. Concr. Compos. 33 (2011) 867–880.
[17] Z. Tan, F.-q Guo, Z. Leng, Z.-j Yang, P. Cao, A novel strategy for generating mesoscale asphalt concrete model with controllable aggregate morphology and packing structure, Comput. Struct. 296 (2024) 107315.
[18] S. Longshaw, M. Turner, E. Flinch, R. GawthorpeAnalyzing the use of real-time physics engines for scientific simulation: exploring the theoretical and practical benefits for discrete element modeling Proceedings of the 18th Conference on Computational Mechanics (ACME-UK) , 2010.
[19] Z. Zheng, C. Zeng, X. Wei, J. Chen, Parameterized implementation of a triple refined modeling framework for mesoscale concrete, Constr. Build. Mater. 346 (2022).
[20] H. Ouyang, X. Chen, 3D meso-scale modeling of concrete with a local background grid method, Constr. Build. Mater. 257 (2020).
[21] G. Li, Y. Zhao, S.-S. Pang, Four-phase sphere modeling of effective bulk modulus of concrete, Cem. Concr. Res. 29 (1999) 839–845.
[22] Qu, J., Cherkaoui, M., Fundamentals of micromechanics of solids, Wiley Online Library2006.
[23] H.S. Abdelgader, J. Górski, Stress-strain relations and modulus of elasticity of two-stage concrete, J. Mater. Civil Eng. 15 (2003) 329–334.
[24] P.R. Stodola, D. Akers, J. Bennet Jr, A. Cheff, T. Clapp, J. Cope, D. Green, Guide for the use of preplaced aggregate concrete for structural and mass concrete applications, ACI Mater. J. 88 (1992) 650–668.
[25] M. Coo, T. Pheeraphan, Effect of sand, fly ash and limestone powder on preplaced aggregate concrete mechanical properties and reinforced beam shear capacity, Constr. Build. Mater. 120 (2016) 581–592.
[26] M. Tuyan, L.V. Zhang, M.L. Nehdi, Development of sustainable preplaced aggregate concrete with alkali-activated slag grout, Constr. Build. Mater. 263 (2020).
[27] H.S. Abdelgader, M. Kurpińska, M. Amran, Effect of slag coal ash and foamed glass on the mechanical properties of two-stage concrete, Mater. Today Proceed. 58 (2022) 1091–1097.
[28] K.K. Das, E.S.-S. Lam, J.G. Jang, Effects of modified binders on flowability of grout and properties of preplaced aggregate concrete, J. Build. Eng. 68 (2023).
[29] G. Ou, T. Kishi, L. Mo, Z. Lin, New insights into restrained stress and deformation mechanisms of concretes blended with calcium sulfoaluminate and MgO expansive additives using multi-scale techniques, Constr. Build. Mater. 371 (2023).
[30] L. Mo, M. Deng, M. Tang, A. Al-Tabbaa, MgO expansive cement and concrete in China: past, present and future, Cement and concrete research 57 (2014) 1–12.
[31] GB/T 29756–2013, Test methods of physical property for dry-mix mortar, Beijing, China: China Standardization Administration, 2013. (in Chinese).

[32] GB/T 50081–2019, Standard for test methods of concrete physical and mechanical properties, Beijing, China: China Architecture & Building Press, 2019. (in Chinese).
[33] JGJ/T 70–2009, Standard for test method of basic properties of construction motar, Beijing, China: China Industry Press, 2009. (in Chinese).
[34] L. Jin, W. Yu, X. Du, S. Zhang, D. Li, Meso-scale modelling of the size effect on dynamic compressive failure of concrete under different strain rates, Int. J. Impact Eng. 125 (2019) 1–12.
[35] H. Chen, B. Xu, J. Wang, T. Zhou, X. Nie, Y.L. Mo, Parametric analysis on compressive strain rate effect of concrete using mesoscale modeling approach, Constr. Build. Mat. 246 (2020) 118375.
[36] X. Hu, C. Shi, Z. Shi, L. Zhang, Compressive strength, pore structure and chloride transport properties of alkali-activated slag/fly ash mortars, Cem. Concr. Compos. 104 (2019) 103392.
[37] J. Lubliner, J. Oliver, S. Oller, E. Oñate, A plastic-damage model for concrete, Int. J. Solids Struct. 25 (1989) 299–326.
[38] W. Yuan, Y. Xiaojing, W. Kai, H. Tianhai, Expermental study on the stress-strain curve of cementitious grout under uniaxial compression, Ind. Constr. 44 (2014) 909–913. +903. (in Chinese).
[39] Z. Zhu, H. Chen, Overestimation of ITZ thickness around regular polygon and ellipse aggregate, Comput. Struct. 182 (2017) 205–218.
[40] M. Maleki, I. Rasoolan, A. Khajehdezfuly, A.P. Jivkov, On the effect of ITZ thickness in meso-scale models of concrete, Constr. Build. Mat. 258 (2020) 119639.
[41] L. Jin, S. Wan, D. Li, L. Miao, X. Du, Influence of concrete strength and aggregate size on the size effect of shear capacity of RC beam-column joints under monotonic loading: Mesoscale numerical tests, Structures 37 (2022) 671–685.
[42] S.-M. Kim, R.K. Abu Al-Rub, Meso-scale computational modeling of the plastic-damage response of cementitious composites, Cem. Concr. Res. 41 (2011) 339–358.
[43] Y. Hu, J. Chen, F. Zou, M. He, J. Mao, X. Liu, C. Zhou, Z. Yuan, A comparative study of temperature of mass concrete placed in August and November based on on-site measurement, Case Stud. Constr. Mater. 15 (2021) e00694.

Construction and Building Materials 399 (2023) 132527

Contents lists available at ScienceDirect

Construction and Building Materials

journal homepage: www.elsevier.com/locate/conbuildmat

Experimental investigation on transverse tension-tension fatigue behavior of pultruded glass-fiber reinforced polymer (GFRP) unidirectional lamina

Qinglin Gao, Haohui Xin *, Youyou Zhang *

Department of Civil Engineering, School of Human Settlements and Civil Engineering, Xi'an Jiaotong University, Xi'an, Shaanxi, PR China

ARTICLE INFO

Keywords:
Pultruded glass-fiber reinforced polymer (GFRP) lamina
Transverse behavior
Fatigue life
Stiffness variation
Dissipated energy
Cyclic creep strain

ABSTRACT

Inadequate transverse or shear strength is the key factor contributing to the failure of pultruded GFRP structures. In this paper, the static and fatigue performance of 90° pultruded unidirectional GFRP lamina were tested. A series of macroscopic phenomenological models were established to describe the performance variations during cyclic loading, including fatigue life, energy dissipation capacity and cyclic creep strain. The fracture surfaces of specimens were observed by a field-emission scanning electron microscopy (SEM). Experimental results indicated that the transverse fatigue life of GFRP unidirectional lamina can be fitted by *S-N-R* regression equation. The transverse stiffness degradation can be even ignored during fatigue loading. The results also show that the proposed equations can reasonably reflect the growth trend of dissipated energy per unit volume (*UDE*) and successfully predict cyclic creep strain increment of pultruded GFRP during cyclic loading.

1. Introduction

Pultruded glass-fiber reinforced polymer (GFRP) composites have been mainly adopted for new construction in bridge engineering [1–6], mostly due to construction cost restrictions. However, pultruded GFRP products showed up as being exceptionally transversely isotropic due to the characteristics of production process. The ultimate strength of pultruded composites in the pultrusion direction is 15–30 times greater than it in the vertical direction [7,8]. Inadequate transverse or shear strength is the key factor contributing to the failure of pultruded GFRP structures.

Typical failure mode of three common pultruded GFRP products is illustrated in Fig. 1. When the GFRP bridge deck [9] is subjected to a local loading in Fig. 1a, the top flange produces a downward deflection resulting in a transverse tensile stress, and the bridge deck is destroyed for the weak transverse strength. Even when the GFRP column [10] is subjected to axial compression along pultrusion direction in Fig. 1b, the column is pulled apart in the vertical pultrusion direction due to weak transverse properties caused after overall buckling. When the GFRP I-beam is subjected to a mid-span loading, the top flange produces a downward deflection. The stress component along the pultrusion direction eventually leads to transverse tensile failure of the flange-web junction (Fig. 1c).

The aforementioned failure frequently inhibits GFRP components from benefiting from their performance in the direction of pultrusion. It is beneficial to thoroughly comprehend the transverse performance of pultruded GFRP composite, especially long-term behavior, in order to minimize unforeseen damage and advance the use of pultruded GFRP application in engineering. The fatigue problem caused by dynamic stresses in terms of the pultruded GFRP profiles used in bridge constructions is the main issue of the assessment of the engineering durability of GFRP bridges.

The essence of composite fatigue failure is due to the accumulation of internal damage. The small initial defects in the composite will gradually increase under the action of cyclic loading. Microscopic initial defects gradually merge into large defects or cracks, causing the composite to lose its bearing capacity in the area. When the strength of the remaining area gradually decreases to the maximum strength of cyclic loading, the specimen fails completely. It is more convenient for engineering applications to describe the degradation and damage accumulation of composite behavior using a macroscopic model. Experiments [11–14] have shown that the *S-N* curve characterizing the transverse fatigue life is linear in double logarithmic space. The stress ratio has a great influence on the transverse fatigue life [14,15]. M. Kawai et al. [15,16] also described the relationship between fatigue life and fatigue stress based on the constant life diagram. However, the fatigue behavior of pultruded GFRP lamina is still unknown despite the frequent publication of fatigue experimental results in GFRP composites. This is

* Corresponding authors.
E-mail addresses: xinhaohui@xjtu.edu.cn (H. Xin), youyouzhang@xjtu.edu.cn (Y. Zhang).

https://doi.org/10.1016/j.conbuildmat.2023.132527
Received 25 May 2023; Received in revised form 12 July 2023; Accepted 13 July 2023
Available online 27 July 2023
0950-0618/© 2023 Elsevier Ltd. All rights reserved.

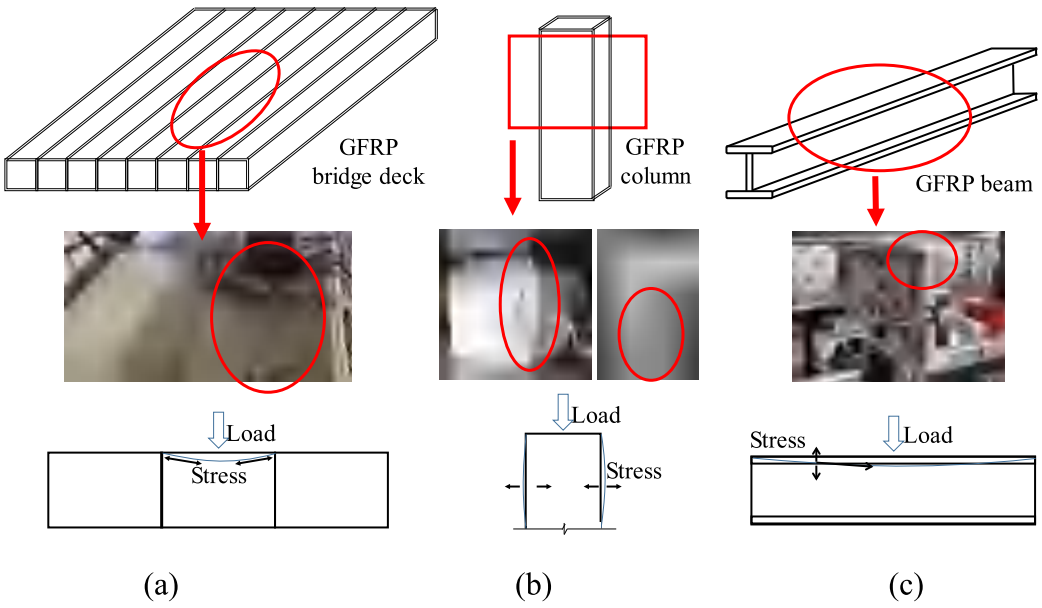


Fig. 1. Failure of GFRP structural component due to transverse weakness [9,10].

Table 1
Fatigue experimental series.

Fatigue experimental series		σ_{max}			
		70 %σ_{ULT}	50 %σ_{ULT}	40 %σ_{ULT}	30 %σ_{ULT}
R	0.1	3 Hz	4 Hz	5 Hz	7 Hz
	0.25		5 Hz		
	0.5	5 Hz	6 Hz		
–	0.75	8 Hz			

because the fatigue behavior of FRP composites is highly reliant on the preparation method and manufacturing process. The pultrusion process used for producing pultruded profiles for construction application has a relatively lower quality control resulting in uneven and unstable reinforcement distribution [7,9]. The phenomenological model's material parameters, which were primarily reported from high-quality laminated composites in the aerospace sector, may be affected in predicting the fatigue behavior of pultruded FRP composites in civil engineering field. Hence, to meet the demands of engineering design, it is therefore necessary to study the fatigue performance of pultruded FRP composites, particularly in the vertical pultrusion direction.

The degradation of transverse fatigue behavior of GFRP composite is mainly characterized by residual stiffness and residual strength. Philippidis & Vassilopoulos [11], Subramanian et al. [17], Echtermeyer et al. [18] proposed several stiffness degradation models related to fatigue cycles based on experimental studies. Yang et al. [19,20] and Wu et al. [21] considered that it is reasonable to use fatigue modulus $F(n)$ instead of secant modulus $E(n)$ to describe the stiffness degradation of a 90° unidirectional lamina. Furthermore, under conditions of high stress ratio, GFRP composites will exhibit non-negligible residual deformation, which is attributed to the creep of polymer materials rather than internal cyclic damage to composites. The above-mentioned model cannot accurately describe the residual stiffness caused by fatigue-creep interaction under different stress ratios. Although Yang [19] and Hashin [22] have proposed some classical residual strength models to describe the fatigue performance degradation of composites, the large number of experiments needed and the numerous factors that affect the fatigue properties that must be taken into account actually limit the research on directly obtaining the FRP residual strength model. To more accurately consider the fatigue behavior of pultruded GFRP composites, it is necessary to modify the existing model.

The energy dissipation capacity of GFRP lamina is represented by the area of the stress–strain loop. The evolution of the hysteresis area per cycle has been studied by researchers [23–25]. Meneghetti et al. [25]

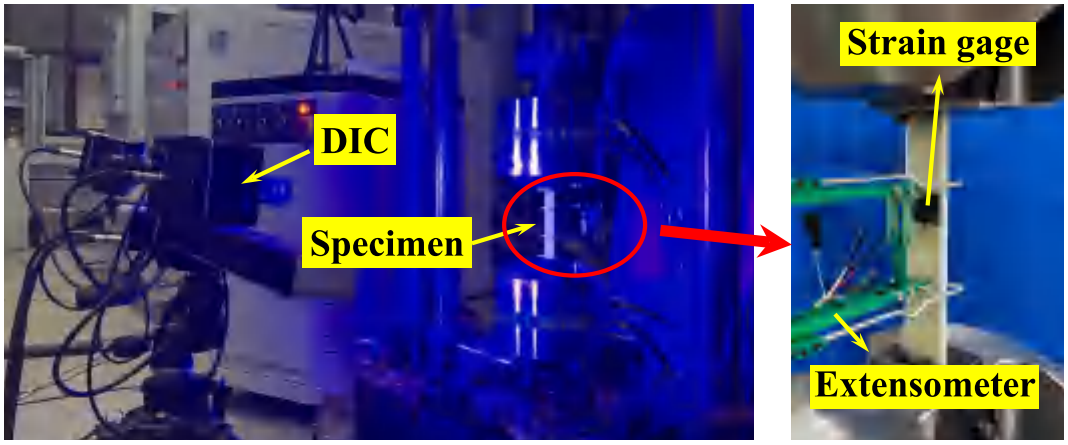


Fig. 2. The arrangement of test instruments.

Table 2
The results of transverse static tension experiments of GFRP unidirectional lamina.

No.	Width/ mm	Thickness/ mm	Area/ mm^2	σ_{ULT}/ MPa	ε_{ULT}/%	E/GPa
S1	25.493	4.460	113.70	49.323	0.369	16.469
S2	25.413	4.513	114.70	50.717	0.395	16.038
S3	25.340	4.487	113.69	46.148	0.336	16.178
S4	25.107	4.547	114.15	48.452	0.375	16.252
S5	25.420	4.487	114.05	51.614	0.440	15.977
AVE				49.251	0.383	16.183
SD				1.898	3.43×10^{-4}	0.173
CV				0.0385	0.0896	0.0107

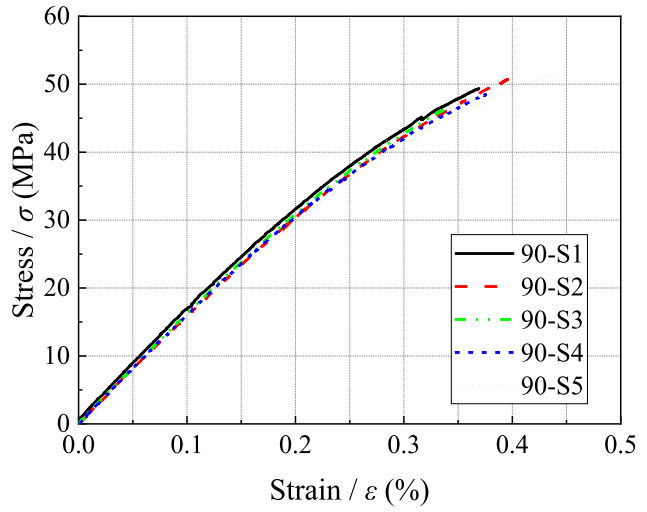


Fig. 3. Stress–strain curves of transverse static tension experiments of GFRP unidirectional lamina.

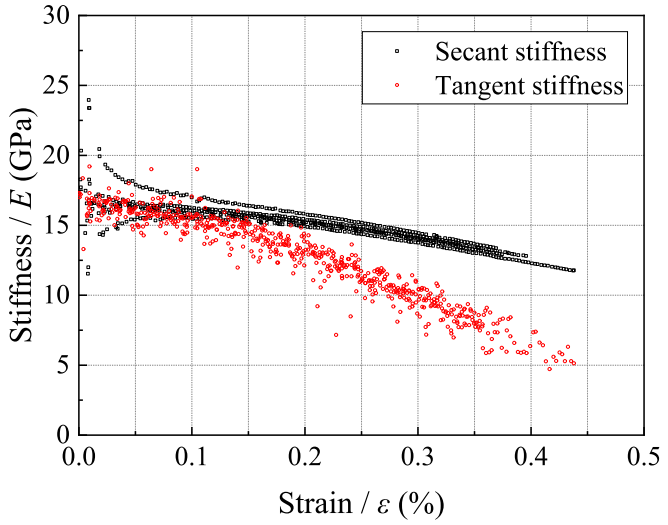


Fig. 4. Tangent modulus and secant modulus of transverse static tension experiments of GFRP unidirectional lamina.

considered the hysteresis energy density per cycle as the fatigue damage index. However, the dissipated energy per cycle of the whole process is replaced by the cyclic dissipated energy at half the total fatigue life. The damage process cannot be judged. In addition, the measurement of energy dissipation capacity does not consider the stress ratio effect. The application of the research to practical engineering is relatively limited.

This paper aims to study the fatigue behavior of pultruded GFRP unidirectional lamina vertical to fiber direction through experiments. Through the transverse tensile static and fatigue experiments, assisted by Digital Image Correlation (DIC) set-up to obtain the strength, fatigue life, performance degradation, energy dissipation capacity and cyclic creep deformation of the specimens. First, the basic mechanical properties of GFRP unidirectional lamina were obtained by static experiment. Second, the *S-N-R* equation, which describes fatigue life, is fitted using constant amplitude fatigue experiments on GFRP lamina under various stress levels and stress ratios. Third, the peak and valley of stress and strain in each cycle are used to evaluate the variation of lamina stiffness with the number of cycles and analyze the composite performance degradation. Fourth, the energy dissipation capacity is calculated by the stress–strain hysteresis loops, and a prediction equation for dissipated energy considering the stress level, stress ratio and number of cycles is established. Fifth, a model describing the increment of fatigue cyclic creep strain with normalized fatigue cycles related to mean stress and stress amplitude is proposed. Finally, the micro fracture surface characteristics of fiber, matrix and interface of GFRP lamina under static and different fatigue stress ratios were observed by field-emission scanning electron microscope (SEM).

2. Experimental procedures

2.1. Fiber and resin

In this work, pultruded E-glass fiber-epoxy unidirectional lamina was used in experiments. To fabricate the specimens, unidirectional E-glass fibers with a density of 9600 TEX were used. The E51 epoxy was used for impregnation of the fibers.

2.2. Specimen preparation

The unidirectional GFRP lamina of 1000 mm × 370 mm × 4 mm is fabricated by pultrusion production. According to the burn-off tests described in GB/T 2577-2005 [26], the achieved fiber volume fraction was 60%. The average density of the pultruded lamina is 2.05×10^3 kg/m^3. For all experiments, rectangular specimens with dimensions of 250 mm × 25 mm × 4 mm (length × width × thickness) were cut from the lamina using a water-jet cutting machine in accordance with Chinese specification [27,28].

2.3. Experimental series

Static tension experiments and tension–tension fatigue experiments of GFRP lamina were conducted in this paper. The static experiment uses displacement control, the loading rate is constant at 0.5 mm/min. Five identical specimens are tested in the static loading. The fatigue experiment uses sinusoidal cyclic load control to study the influence of stress level and stress ratio on fatigue behavior. The loading frequency is adjusted according to the stress amplitude to ensure that the loading rate of fatigue stress is identical, so as to avoid the loading speed effects on fatigue behavior. A total of 8 series of specimens were carried out in the fatigue experiments, including four different stress levels (described by the maximum stress, σ_{max}) and four different stress ratios R (the ratio of the minimum stress, σ_{min}, to the maximum stress, σ_{max}). Four identical specimens were tested in the fatigue loading in each loading series. The specific test series and loading frequency are shown in Table 1.

2.4. Experimental set-up and instrumentation

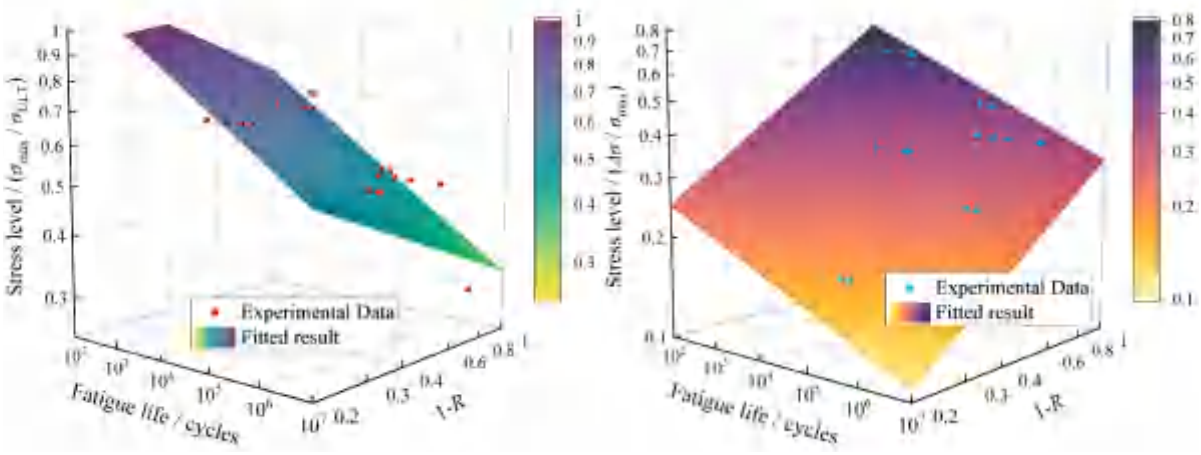
The experiments were conducted using a 100kN fatigue testing machine. The arrangement of test instruments is shown in Fig. 2. The experiments were in an indoor laboratory to ensure a relatively stable environment. The static test uses a 50 mm span extensometer to measure the deformation of the whole test process and strain gauges to measure

Table 3
Fatigue life experimental results.

No.	R	σ_{max}/MPa		Δσ/MPa		N	Runout
		Actual	Normalized ($\sigma_{max}/\sigma_{ULT}$)	Actual	Normalized ($\Delta\sigma/\sigma_{ULT}$)		
90-R0.1–70%-1	0.1	34.476	70%	31.028	63%	1497	
90-R0.1–70%-2	0.1	34.476	70%	31.028	63%	471	
90-R0.1–70%-3	0.1	34.476	70%	31.028	63%	1197	
90-R0.1–70%-4	0.1	34.476	70%	31.028	63%	1559	
90-R0.1–50%-1	0.1	24.626	50%	22.163	45%	32,795	
90-R0.1–50%-2	0.1	24.626	50%	22.163	45%	79,899	
90-R0.1–50%-3	0.1	24.626	50%	22.163	45%	11,134	
90-R0.1–50%-4	0.1	24.626	50%	22.163	45%	49,285	
90-R0.1–40%-1	0.1	19.700	40%	17.730	36%	281,107	
90-R0.1–40%-2	0.1	19.700	40%	17.730	36%	79,756	
90-R0.1–40%-3	0.1	19.700	40%	17.730	36%	976,412	
90-R0.1–40%-4	0.1	19.700	40%	17.730	36%	411,134	
90-R0.1–30%-1	0.1	14.775	30%	13.298	27%	4,000,000	R
90-R0.1–30%-2	0.1	14.775	30%	13.298	27%	4,000,000	R
90-R0.1–30%-3	0.1	14.775	30%	13.298	27%	3,439,321	
90-R0.1–30%-4	0.1	14.775	30%	13.298	27%	4,000,000	R
90-R0.25–50%-1	0.25	24.626	50%	18.470	37.5%	116,100	
90-R0.25–50%-2	0.25	24.626	50%	18.470	37.5%	2,055,271	
90-R0.25–50%-3	0.25	24.626	50%	18.470	37.5%	251,822	
90-R0.25–50%-4	0.25	24.626	50%	18.470	37.5%	525,139	
90-R0.5–50%-1	0.5	24.626	50%	12.313	25%	965,140	
90-R0.5–50%-2	0.5	24.626	50%	12.313	25%	190,125	
90-R0.5–50%-3	0.5	24.626	50%	12.313	25%	620,349	
90-R0.5–50%-4	0.5	24.626	50%	12.313	25%	1,090,473	
90-R0.5–70%-1	0.5	34.476	70%	17.238	35%	8024	
90-R0.5–70%-2	0.5	34.476	70%	17.238	35%	34,372	
90-R0.5–70%-3	0.5	34.476	70%	17.238	35%	878	
90-R0.5–70%-4	0.5	34.476	70%	17.238	35%	41,477	
90-R0.75–70%-1	0.75	34.476	70%	8.619	17.5%	21,640	
90-R0.75–70%-2	0.75	34.476	70%	8.619	17.5%	113,683	
90-R0.75–70%-3	0.75	34.476	70%	8.619	17.5%	167,949	
90-R0.75–70%-4	0.75	34.476	70%	8.619	17.5%	50,918	

Table 4
The fitted parameters of *S-N-R* equation.

Representation form	*A* (95% confidence bounds)	*B* (95% confidence bounds)	*γ* (95% confidence bounds)	R^2	RMSE	ESS
σ_{max}-*N-R*	0.02638(−0.05463,0.1074)	−0.07276(−0.08905,−0.05646)	−3.214(−4.699,−1.728)	0.8153	0.04432	0.05108
Δσ-N-R	0.02638(−0.05463,0.1074)	−0.07276(−0.08905,−0.05646)	10.53(7.994,13.07)	0.9337	0.04432	0.05108



(a) (b)

Fig. 5. The fitted planes of *S-N-R* equation.

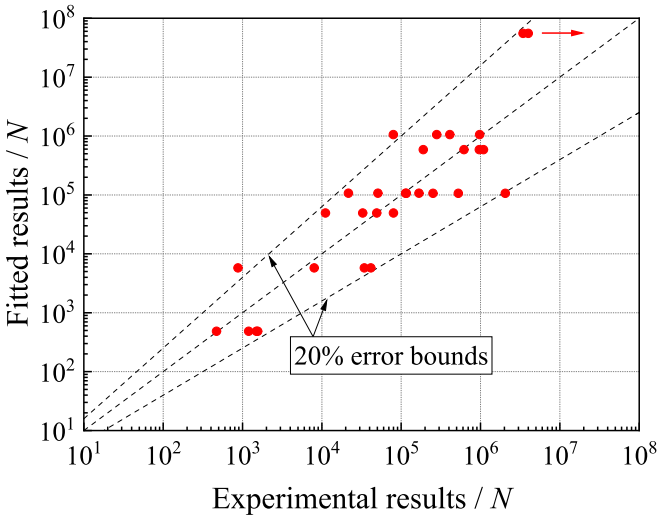


Fig. 6. Comparison of fatigue life experimental results and fitted results.

the elastic modulus. In executing the tests, Digital Image Correlation (DIC) set-up was used to track the spatial distribution of the deformation and measure the strain distribution of the specimen. Furthermore, the fracture surface characteristics of the specimens were observed by SEM after the fatigue test.

3. Experimental results and discussion

3.1. Static behavior

The tensile behavior was experimentally evaluated in accordance to GB 1447-2005 [29]. Table 2 shows the parameters and experimental results of GFRP unidirectional lamina. In the table, AVE is the average value, SD is the standard deviation and CV is the covariance. The results show that the average ultimate strength and ultimate strain of lamina are 49.251 MPa and 0.383%, respectively. The average elastic modulus is 16.183GPa.

Fig. 3 shows the stress–strain curves of GFRP lamina under transverse static tension experiments. The final failure, a classic abrupt brittle fracture, lacks a clear foreshadowing. Furthermore, the transverse behavior of GFRP unidirectional lamina is linear elastic up to 60 % σ_{ULT} and 0.2% strain. When the stress level is high, a small amount of plastic deformation occurs in the material. This nonlinear behavior can also be

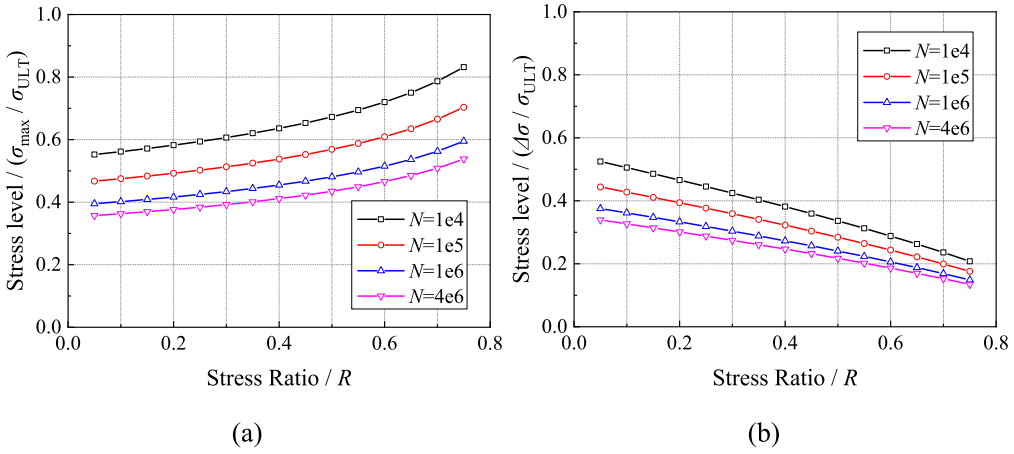


Fig. 7. Stress ratio-stress level curves corresponding to same fatigue life.

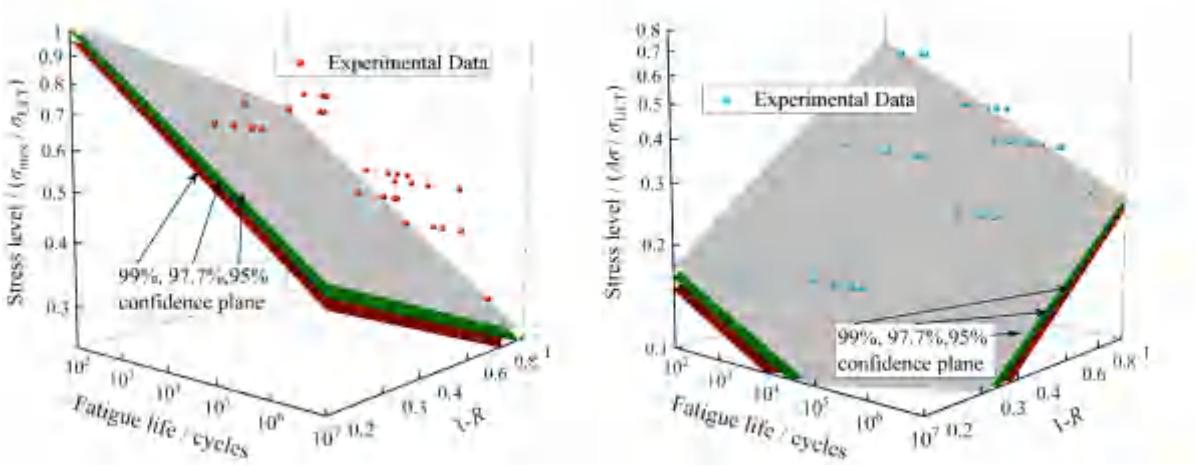


Fig. 8. *S-N-R* planes with different safety confidences.

Table 5
Fitted parameters of *S-N-R* equation with different safety confidences.

Representation form	Confidence	*A*	*B*	*γ*	Regression equation
σ_{max}-*N-R*	99%	−0.05901	−0.08167	−2.626	$\lg(\sigma_{max}/\sigma_{ULT}) = -0.05901 - 0.08167\lg(N) - 0.2961\lg(1 - R)$
	97.7%	−0.04733	−0.08046	−2.707	$\lg(\sigma_{max}/\sigma_{ULT}) = -0.04733 - 0.08046\lg(N) - 0.2983\lg(1 - R)$
	95%	−0.03407	−0.07925	−2.781	$\lg(\sigma_{max}/\sigma_{ULT}) = -0.03407 - 0.07925\lg(N) - 0.2996\lg(1 - R)$
Δσ-N-R	99%	−0.02078	−0.08491	11.785	$\lg(\Delta\sigma/\sigma_{ULT}) = -0.02078 - 0.08491\lg(N) + 0.9158\lg(1 - R)$
	97.7%	−0.01490	−0.08319	11.540	$\lg(\Delta\sigma/\sigma_{ULT}) = -0.01490 - 0.08319\lg(N) + 0.8768\lg(1 - R)$
	95%	−0.00634	−0.08160	11.339	$\lg(\Delta\sigma/\sigma_{ULT}) = -0.00634 - 0.08160\lg(N) + 0.8437\lg(1 - R)$

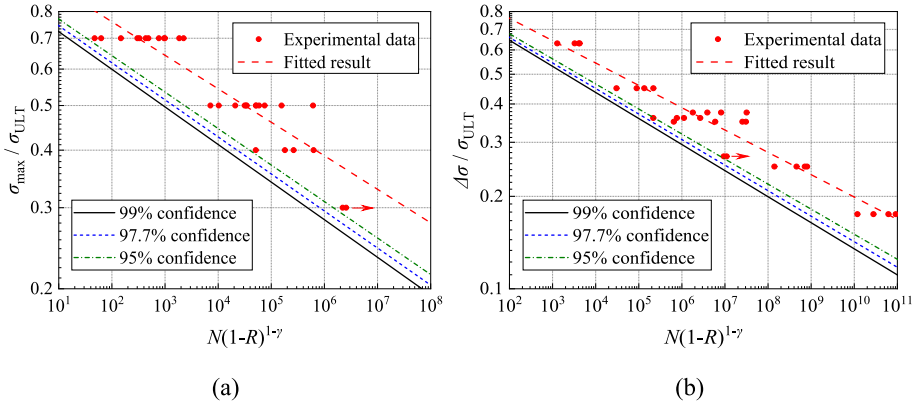


Fig. 9. Fitted $S\text{-}N(1\text{-}R)^{1-\gamma}$ curves with various safety confidences.

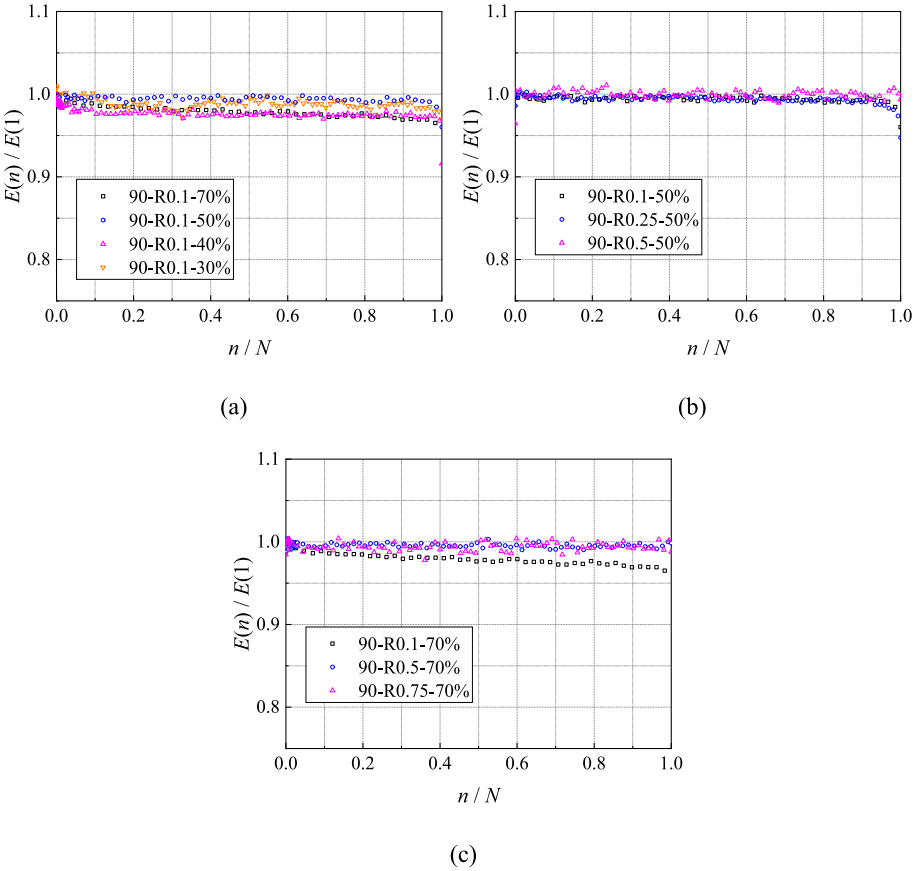


Fig. 10. Stiffness variation of GFRP unidirectional lamina in transverse fatigue experiments.

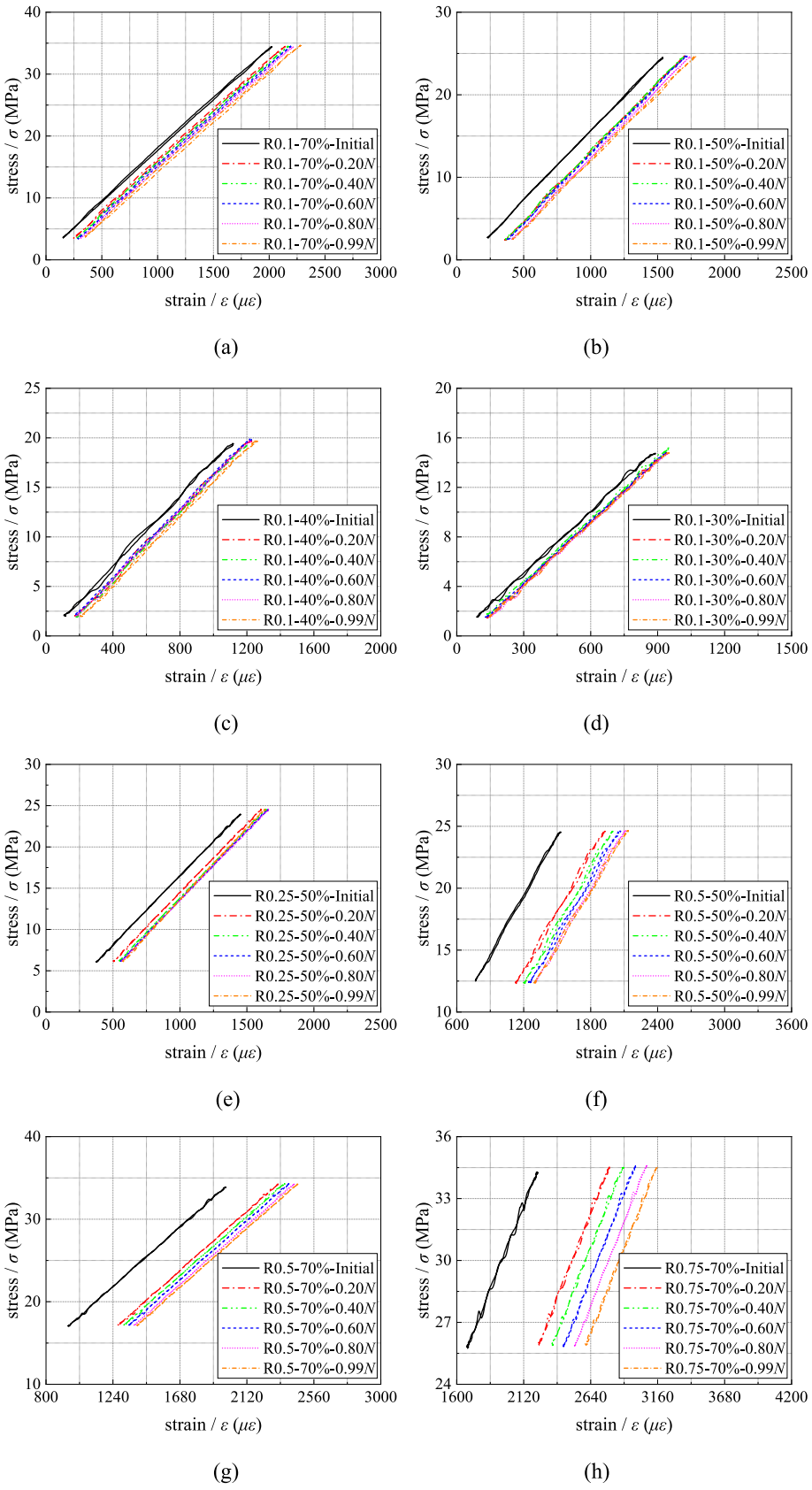


Fig. 11. Stress–strain hysteresis loops and dissipated energy.

Table 6
Dissipated energy of typical cycles (J/m^3).

n/N	Code							
	90-R0.1–70%	90-R0.1–50%	90-R0.1–40%	90-R0.1–30%	90-R0.25–50%	90-R0.5–50%	90-R0.5–70%	90-R0.75–70%
Initial	588.88	122.30	78.38	47.42	94.57	62.98	230.93	51.00
0.20*N*	568.79	170.67	81.10	46.60	96.79	74.94	241.92	43.18
0.40*N*	587.87	151.67	88.35	51.99	93.74	77.30	240.54	60.13
0.60*N*	564.09	158.19	86.44	53.20	109.52	58.82	245.51	49.88
0.80*N*	596.15	159.17	77.10	59.43	117.27	78.51	246.72	47.46
0.99*N*	804.61	234.62	83.56	55.52	128.73	77.19	239.76	54.76

Table 7
Fitted parameters of energy dissipation capacity prediction equation.

λ	α	β	γ	R^2
2011.698	3.067	0.0237	−74.036	0.9240

expressed by calculating tangent stiffness and secant stiffness, as shown in Fig. 4. The secant stiffness of the specimen before failure is still 80% of the elastic modulus, while the tangent stiffness is only about 40% remained.

3.2. Fatigue behavior

3.2.1. Fatigue life

The results of the fatigue experiments are summarized in Table 3. The specimen denomination is in the following form: the first term is 90, which denotes the angle of fiber, the second term shows the magnitude of the stress ratio, the third term shows the normalized maximum fatigue stress and the last term is the specimen number with the same parameter combination. If fatigue loading cycle exceeds four million, the specimen is considered to reach the fatigue failure threshold in this paper.

The relationship between the fatigue life N, the stress level S (which can be the maximum stress σ_{max} or the stress amplitude $\Delta\sigma$) and the stress ratio R of GFRP composite can be expressed in Eq. (1) [30].

$$S = S_0\left[N(1-R)^{1-\gamma}\right]^{-\frac{1}{k}} \tag{1}$$

Where: S_0, γ and k are material parameters.

Dividing both sides of the Eq. (1) by material static tension strength S_{ULT} and taking decimal logarithm with $\lg(S_0/S_{ULT}) = A$ and $-1/k = B$ gives:

$$\lg(S/S_{ULT}) = A + B\lg(N) + B(1-\gamma)\lg(1-R) \tag{2}$$

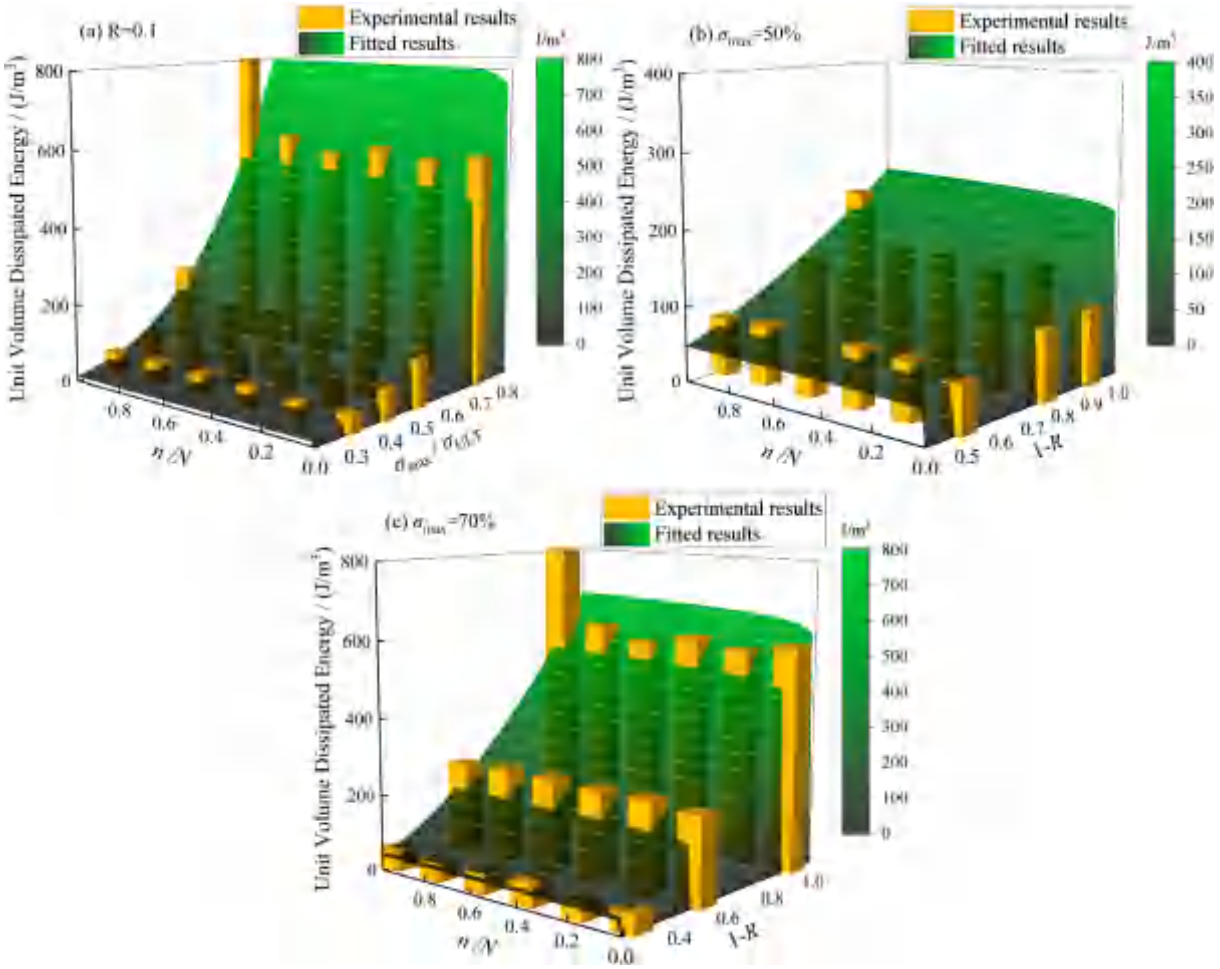


Fig. 12. Energy dissipation capacity of experimental results and equation predictions.

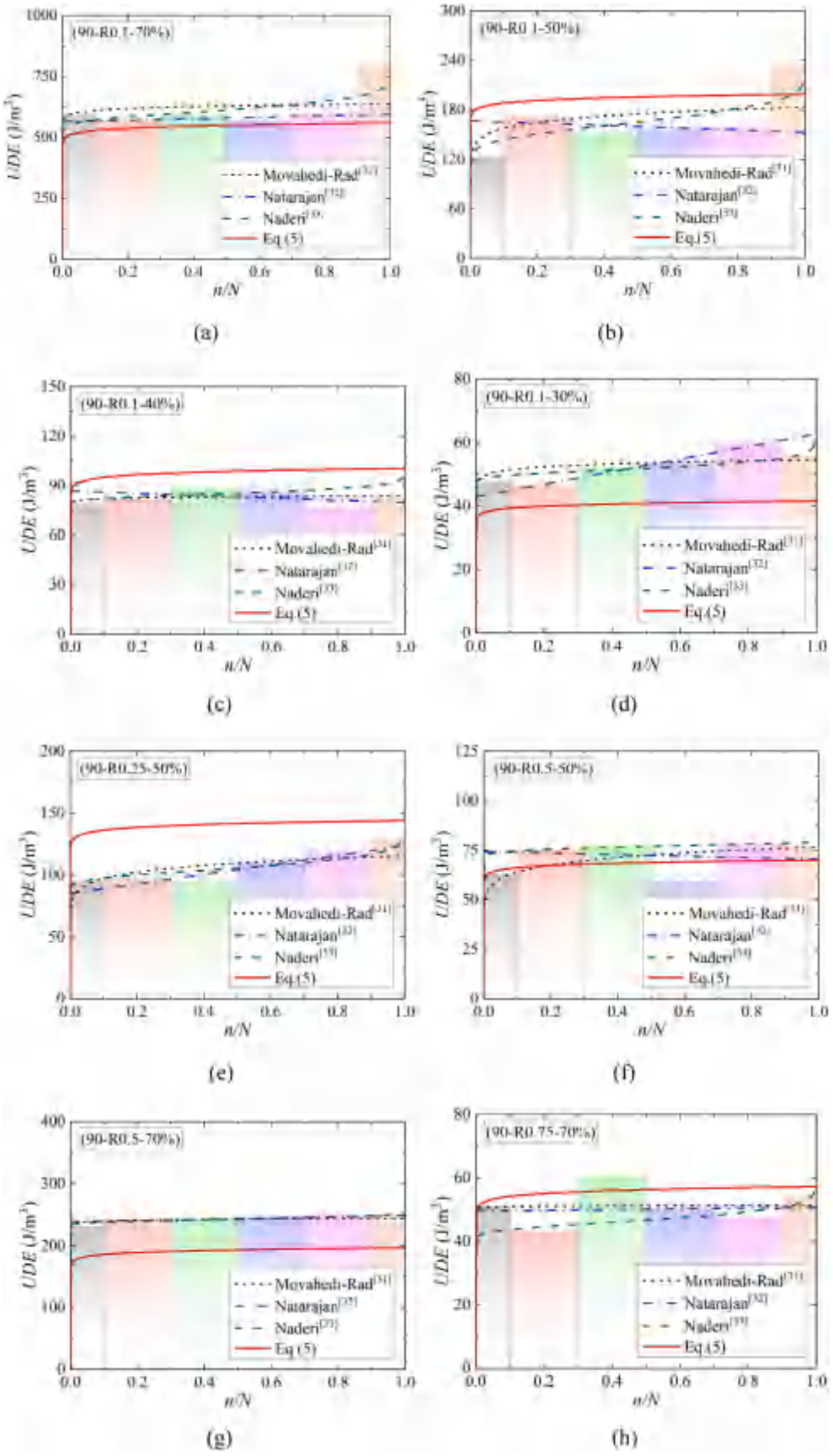


Fig. 13. Comparison of the prediction results of energy dissipation capacity between existing models and proposed model (Eq.5).

Table 8
The average relative error between the prediction models and the experimental results.

Prediction model	Movahedi-Rad [31]	Natarajan [32]	Naderi [33]	Proposed model (Eq. (5))
Average relative error	6.40%	7.03%	6.17%	14.51%

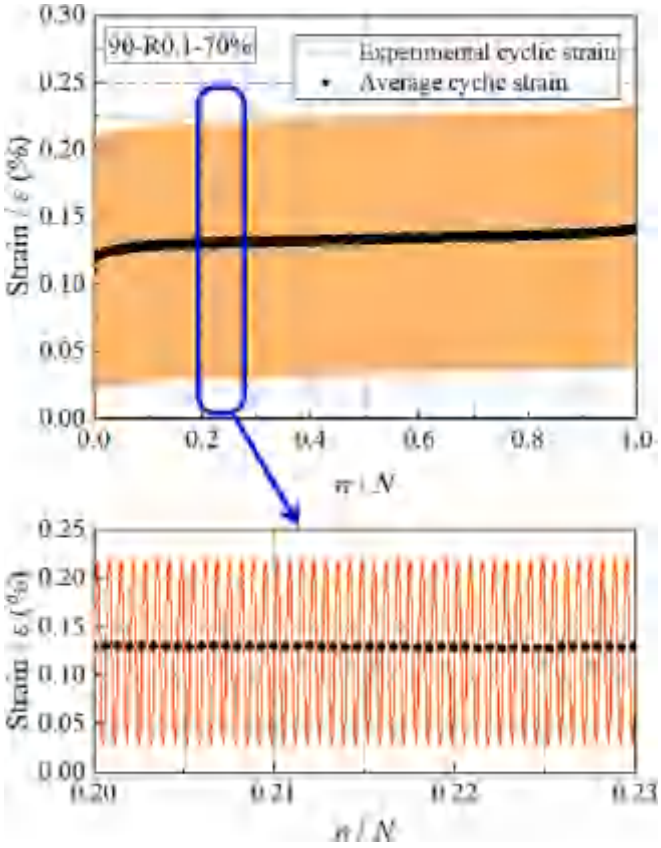


Fig. 14. Typical experimental cyclic strain versus normalized number of cycles.

Table 9
Fitted parameters of cyclic creep strain prediction equation.

m	p	q	v	R^2
0.0220	−0.7930	0.8514	0.2719	0.9562

S/S_{ULT} can be named normalized fatigue load level. The fatigue life results represented by normalized maximum stress and normalized stress amplitude, respectively, in Table 3 are fitted by Eq. (2). The fitted parameters are shown in Table 4. In the logarithmic coordinate system with N as X-axis, 1-R as Y-axis and S as Z-axis. The S-N-R plane is shown in Fig. 5. It can be seen that the coefficient of determination (R^2) of the two representation forms is above 0.8, showing a high correlation between the three parameters. The R^2 of fitted parameters calculated by the stress amplitude is higher. Fig. 6 shows the comparison between the experimental results and the fitted results of the S-N-R equation. The relative error of the two in the logarithmic space is basically within 20%.

Fig. 7 shows the stress level and stress ratio corresponding to same fatigue life obtained by the S-N-R equation. For the stress ratio-stress level curve expressed by σ_{max}, the stress level increases with the stress ratio increasing. For the stress ratio-stress level curve at the same fatigue life, the stress ratio decreases with a roughly linear relationship when $\Delta\sigma$ increases. Specifically, the expected fatigue life expressed by σ_{max} as stress level increases with the increase of R, and the expected fatigue life with $\Delta\sigma$ as stress level decreases with the increase of R.

Given the high dispersion of GFRP composite fatigue life, failure probabilities are generally calculated in practical engineering applications. Fig. 8 shows the S-N-R planes with safety confidences of 95%, 97.7% and 99%. Table 5 shows the corresponding fitted parameters. The results show that the plane position is mainly controlled by the parameter A when the confidence changes, which is reflected in the change of the intercept of the S-axis in the S-N-R logarithmic coordinate system. In addition, the parameters A and B decrease with increasing confidence, and γ increases slightly with increasing confidence.

The fatigue life expressions in Figs. 5 and 8 could be simplified to two dimensions by using $N(1\text{-}R)^{1-\gamma}$ as X-axis and S/S_{ULT} as Y-axis. The expression can show the relationship between experimental data and fitted results more intuitively, as shown in Fig. 9. The fitted results are quite close to all the test samples, indicating the proposed equation is effective. The safety confidence lines also show that the equation can be used to predict the fatigue life of composites with various failure probabilities.

3.2.2. Stiffness variation

The stiffness variation during fatigue cycles is calculated by Eq. (3) using peak and valley values of stress and strain captured by fatigue experiments. The normalized stiffness (the ratio of the nth cycle's stiffness to the first cycle's stiffness, $E(n)/E(1)$) is used to describe the stiffness variation of GFRP unidirectional lamina. Fig. 10 shows the typical fatigue stiffness curves of 8 fatigue experimental series. The X-axis is the normalized fatigue life and the Y-axis is the normalized stiffness. In general, the transverse fatigue stiffness of GFRP unidirectional lamina does not decrease significantly during the whole process of cyclic loading.

$$E(n) = \frac{\sigma_{max}(n) - \sigma_{min}(n)}{\varepsilon_{max}(n) - \varepsilon_{min}(n)} \tag{3}$$

At the initial cyclic stage (about 0.05 N), the stiffness will decrease within 2% After that, the composite stiffness remained stable for a long time without significant change. Finally, the stiffness of the material decreased by about 5% before failure(after 0.95 N).

The experimental results also show that the decrease in stiffness is not related to the stress level, but the stress ratio has an impact on the stiffness variation. As shown in Fig. 10(b) and Fig. 10(c), for the stress ratio $R = 0.1$, the stiffness decrease is visible to the naked eye at the initial stage. With the increase in stress ratio, the decrease in stiffness in the early stage is getting smaller and smaller. The stiffness of the whole process of fatigue loading with $R = 0.5$ and 0.75 is basically not degraded.

3.2.3. Stress–strain loops and dissipated energy

Fig. 11 shows the stress–strain hysteresis loops of typical specimens under cyclic loading at initial, 0.20 N, 0.40 N, 0.60 N, 0.80 N and 0.99 N. When the number of loading cycles reaches 0.20 N, the stress–strain curve shows obvious residual deformation compared with the initial stress–strain curve. When the number of fatigue cycles continues to increase, the increment of residual deformation at low stress ratios ($R = 0.1$ or $R = 0.25$) is not obvious, while the increment at high stress ratios cannot be ignored. Reference [23] believe that the composite is subjected to a high mean stress as a result of a high stress ratio. After long-term fatigue loading, the cyclic creep caused by high mean stress leads to the gradual increase of permanent residual deformation. The specific research on residual deformation will be analyzed in detail in the next section of this paper.

The transverse energy dissipation of the GFRP lamina is represented by the area of the stress–strain hysteresis loop. The areas of the hysteresis loops in Fig. 11 are shown in Table 6. The dissipated energy of the initial loading state is relatively small and the unit cycle's energy only

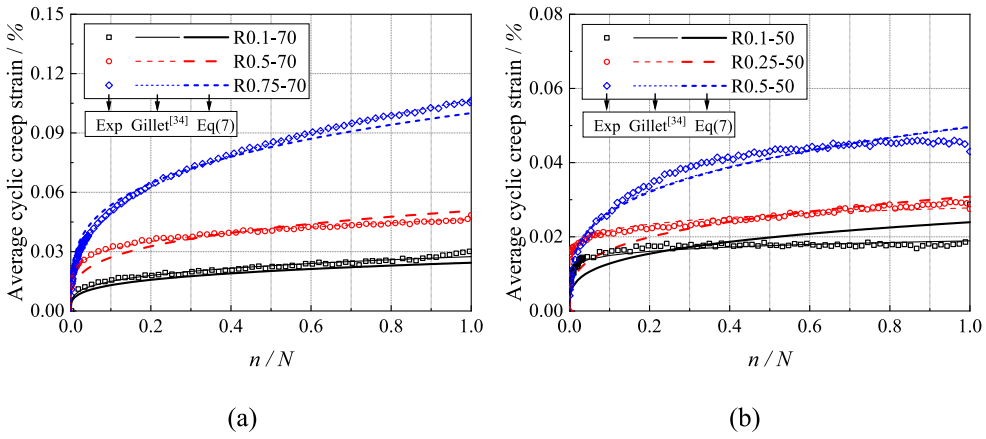


Fig. 15. Comparison of experimental results and fitted results of average cyclic creep strain.

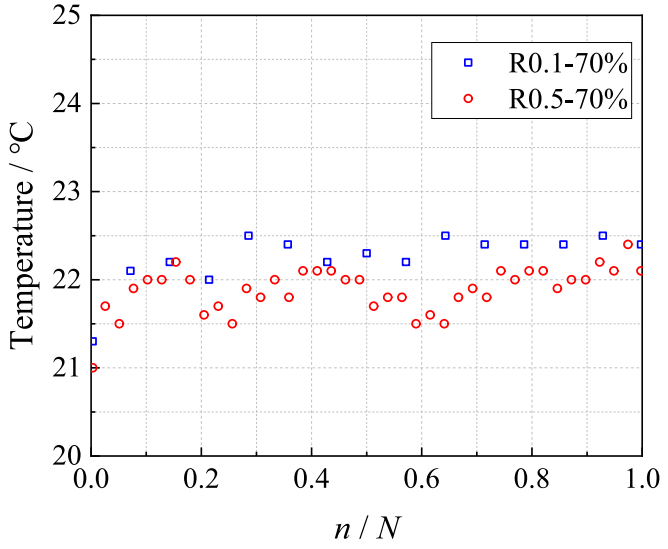


Fig. 16. Typical self-generated temperature versus normalized number of cycles.

increases before fatigue damage.

A power relationship is proposed to express the composite's unit dissipated energy and the number of normalized fatigue cycles or stress level approximately [25,31]. Thus, the relationship among the unit dissipated energy, stress level and normalized fatigue cycles can be described in Eq. (4).

$$UDE = \lambda S^{\alpha}\left(\frac{n}{N}\right)^{\beta} \tag{4}$$

Where, *UDE* is the dissipated energy per unit volume, a, b, λ, α, β are fitted parameters.

The correction term considering the effect of stress ratio is introduced into Eq. (4). Then the prediction equation for dissipated energy considering stress level, stress ratio and the number of normalized fatigue cycles is:

$$UDE = \lambda \sigma_{\max}^{\alpha}\left(\frac{n}{N}(1-R)^{1-\gamma}\right)^{\beta} \tag{5}$$

Where, γ is the fitted parameter related to stress ratio R.

Taking decimal logarithm for both sides of Eq. (5) gives:

$$\lg UDE = \lg\lambda + \alpha\lg\sigma_{\max} + \beta\lg\frac{n}{N} + \beta(1-\gamma)\lg(1-R) \tag{6}$$

Table 7 lists the fitted results of Eq. (6) to the experimental data. The R^2 reaches 0.9240, showing the good fitting effect of the equation. Fig. 12(a) shows experimental results and fitted results for the stress ratio $R = 0.1$ with normalized fatigue life as X-axis, normalized stress level as Y-axis and single-cycle unit volume dissipated energy as Z-axis. Fig. 12(b) and 12(c) show the experimental data and fitted results for stress levels $\sigma_{max} = 50\%$ and 70 %σ_{ULT}, respectively, with 1-*R* as Y-axis. Specifically, the fitted results for stress levels $\sigma_{max} = 30\%$ and 70 %σ_{ULT} are more conservative than the experimental results, while the fitted results for stress levels $\sigma_{max} = 40\%$ and 50 %σ_{ULT} are more radical than the experimental results.

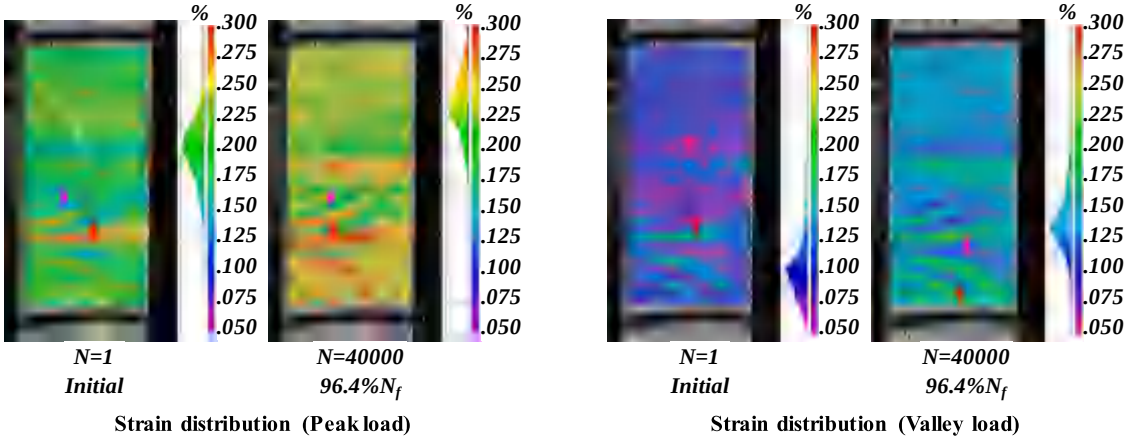


Fig. 17. Typical full-field strain distribution (90-R0.5–70%).



Fig. 18. Typical failure mode and section appearance (90-R0.5–70%).

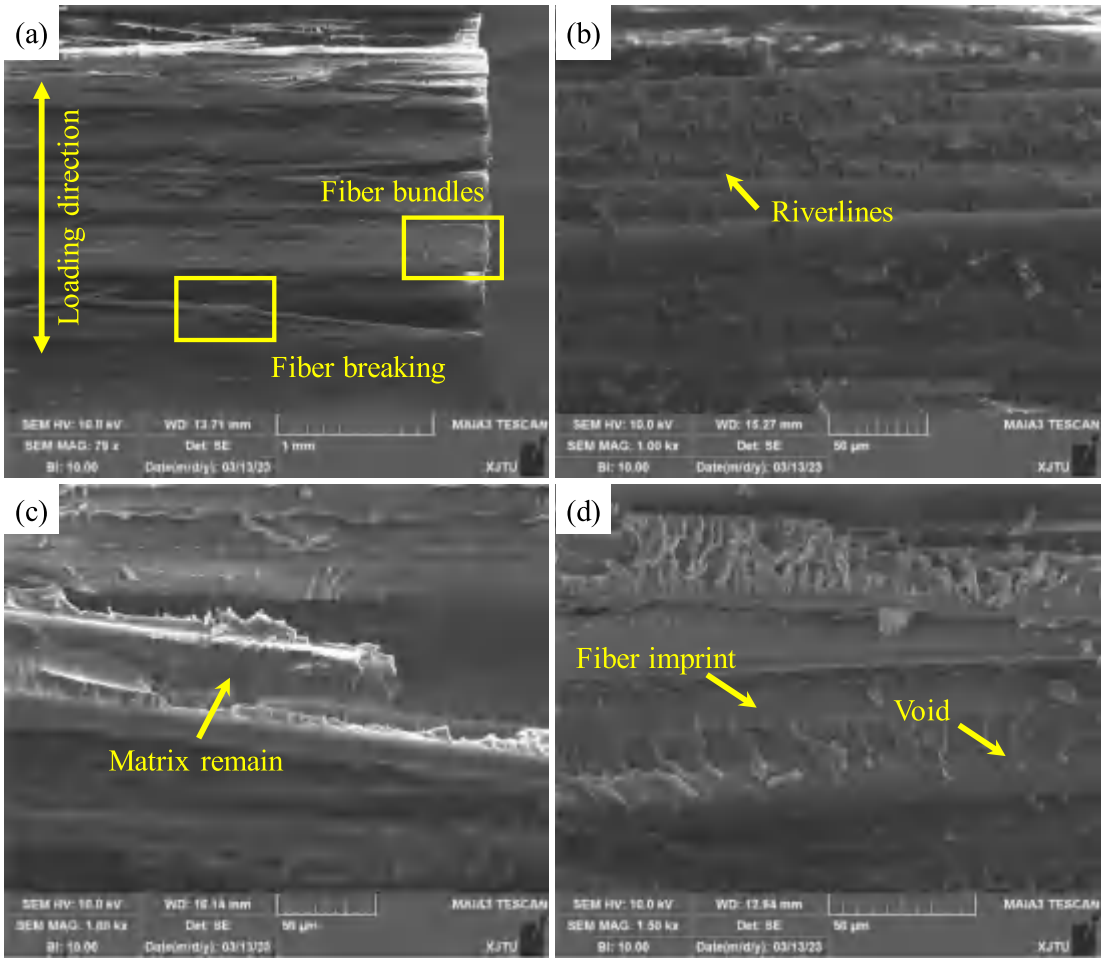


Fig. 19. SEM images of fracture surface for static experiments.

Fig. 13 depicts the predicted results of energy dissipation capacity according to existing models of Movahedi [31], NatarajanV [32] and Naderi [33]. Table 8 shows the average relative error of each model compared with the experimental results. The relative error of the existing models is about 6%~7%. In this study, the effects of stress level and stress ratio on energy dissipation capacity are further considered. The prediction error of the equation proposed on the basis of Movahedi [31] is 14.51%.

3.2.4. Cyclic creep strain

The creep strain of composite materials under cyclic loading with high stress ratios cannot be ignored. The cyclic creep strain of GFRP lamina in the whole process of fatigue test is directly related to the stress level, stress ratio and fatigue cycles. Fig. 14 shows the strain with the number of cycles in the whole process of cyclic loading. The average value of strain in each cycle is taken as the average cyclic strain. In order to express the relationship between cyclic creep strain and fatigue loading directly, the stress level is represented by mean stress σ_m, the stress ratio is represented by stress amplitude σ_a, and the fatigue cycles are represented by normalized fatigue life.

Eq. (7) is proposed to describe the relationship between cyclic creep strain and fatigue life established by analogy with the model between pure creep strain and loading time of GFRP composites. The Eq. (7) is consistent with the equation proposed by Gillet [34] to describe cyclic creep strain without considering the stress states.

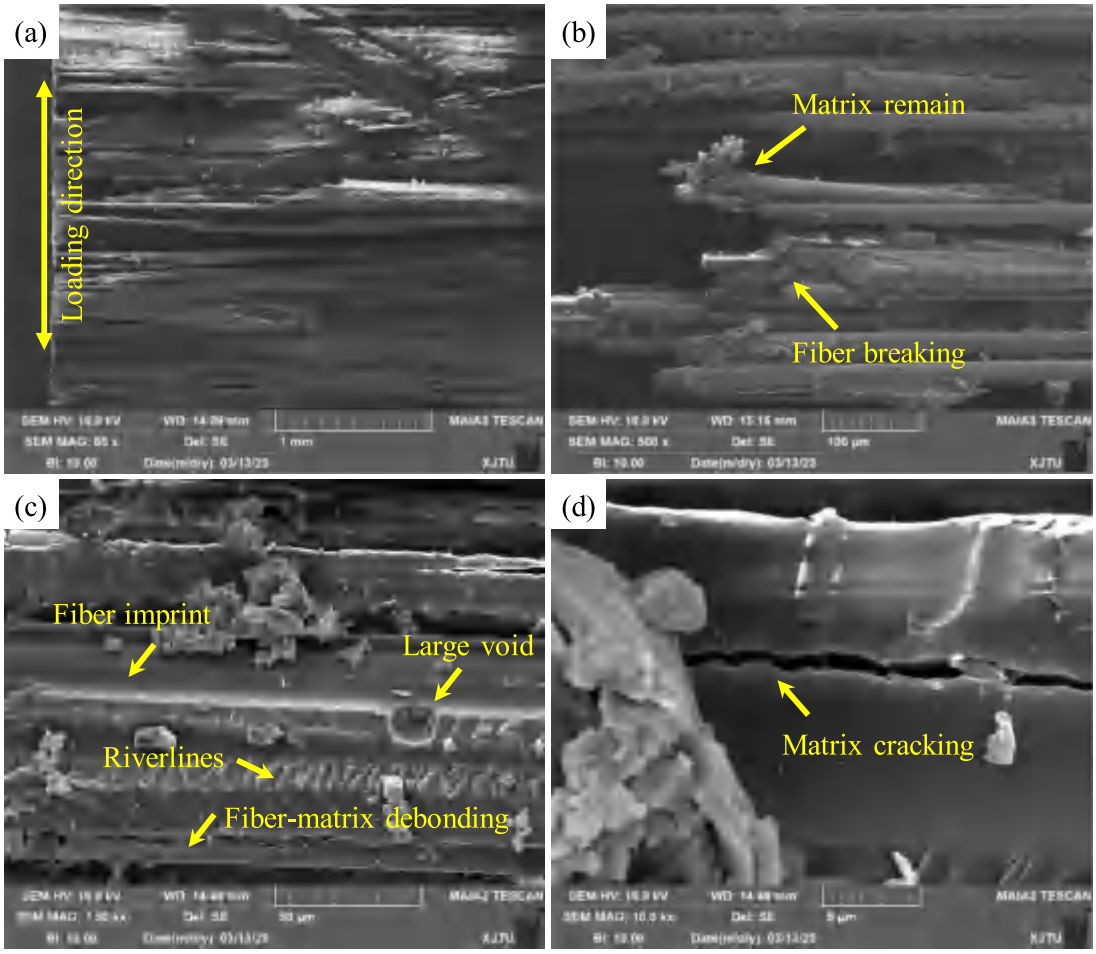


Fig. 20. SEM images of fracture surface when stress ratio is 0.1 (No. 90-R0.1–50%).

$$\varepsilon_c = m\sigma_a^p\sigma_m^q\left(\frac{n}{N}\right)^v \tag{7}$$

Where, ε_c represents the cyclic creep strain, which is calculated by the difference between the strain of the nth cycle and the strain of the first cycle, σ_a and σ_m represent the normalized stress amplitude and mean stress respectively, which are calculated by Eqs. (8) and (9), m, p, q and v are the fitted parameters.

$$\sigma_a = \frac{(1-R)\sigma_{max}}{2\sigma_{ULT}} \tag{8}$$

$$\sigma_m = \frac{(1+R)\sigma_{max}}{2\sigma_{ULT}} \tag{9}$$

Table 9 shows the fitted parameters of Eq. (7). The R^2 is 0.9562, indicating that the equation has a good fitting effect. Fig. 15 shows the comparison between typical specimens' experimental results and fitted results of average cyclic creep strain. The average relative error between the fitted results of the equation proposed by Gillet [34] and the experimental results is 3.07%. When the influence of stress state is considered, the relative error of the equation proposed in this study is slightly increased to 7.36%. In addition, the parameter of σ_a, which describes the stress ratio, is negative, and the parameter of σ_m, which describes the stress level, is positive. That is, when the mean stress and the number of normalized cycles are the same, cyclic creep strain decreases with the increase in stress amplitude. When the stress amplitude and the number of normalized cycles are the same, cyclic creep strain increases with the increase in mean stress.

3.2.5. Fatigue failure mode

Since the resin in GFRP is a kind of polymer material, the friction between the polymers under fatigue loading causes the specimen to generate considerable heat, resulting in an increase in the temperature of the specimen and affecting the fatigue life. Specimens with high stress amplitudes tend to produce greater self-generated temperature. Fig. 16 shows the surface temperature variation of typical specimens obtained by handheld thermography camera during fatigue loading. From the initial to the failure of the fatigue loading, the surface temperature fluctuation caused by self-generated temperature of the specimen is below 2 °C, that is, the temperature is controlled stably in experiments, which has no effect on the fatigue results.

The full-field strain distribution of a typical specimen captured by DIC system is shown in Fig. 17. The strain distribution corresponding to the peak and valley loads at the initial loading stage ($N = 1$) and before failure ($N = 96.4\ \%N_f$) increases uniformly. The generation and development of weakness zone were not observed. The transverse fatigue failure of GFRP lamina is a typical sudden failure.

Fig. 18 shows the typical failure modes of specimens. The fatigue failure modes are basically the same, all of which are transverse cracks and there is no obvious macroscopic damage in other positions. Furthermore, there is a small amount of fiber bridging between the cracks of the specimens after fatigue failure.

Figs. 19–21 depict the typical SEM images obtained from static tension specimens, low-stress ratio fatigue specimens (R = 0.1), and high-stress ratio fatigue specimens (R = 0.75). The images demonstrate that for the static tension loading, in addition to a few bridged fibers breaking, the fibers on the fracture surface remain as fiber bundles (Fig. 19a). The main failure pattern is matrix cracking between fiber

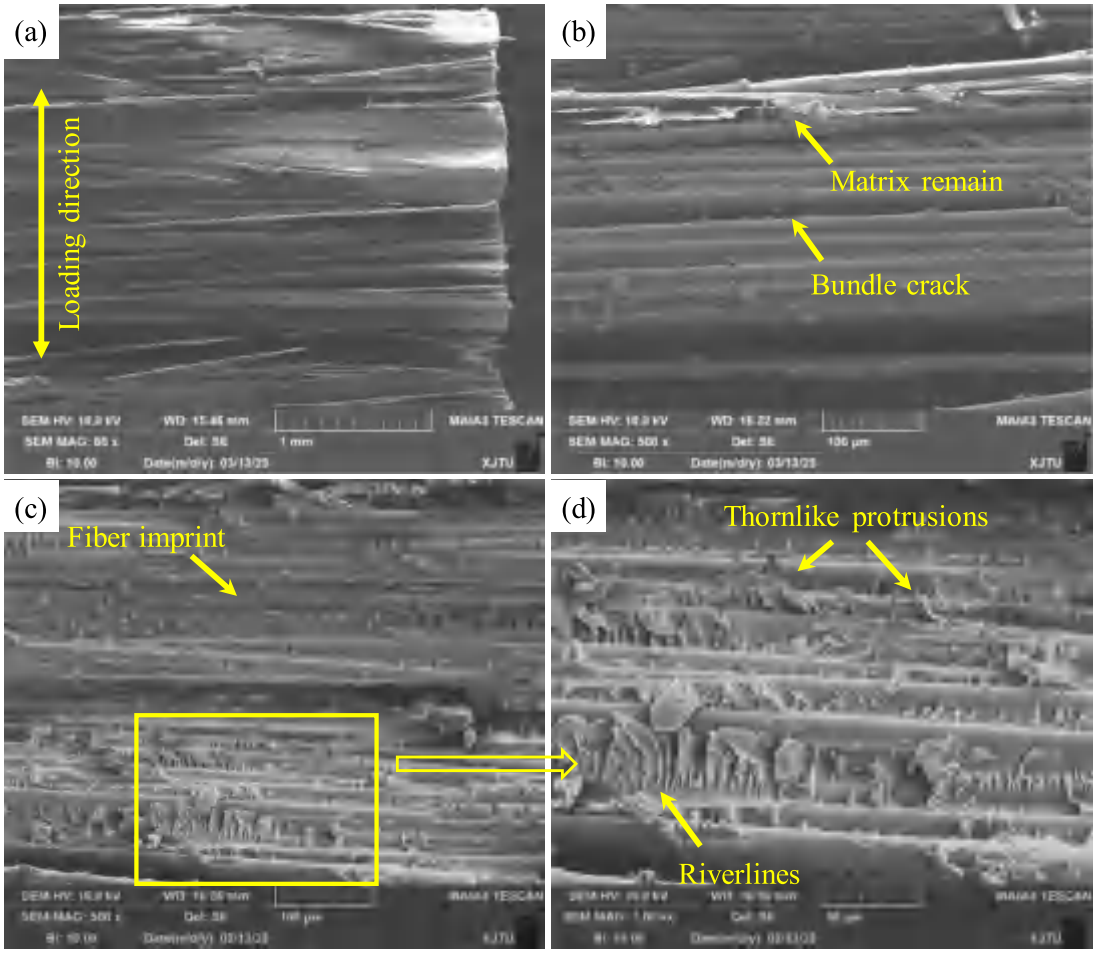


Fig. 21. SEM images of fracture surface when stress ratio is 0.75 (No.90-R0.75–70%).

bundles. The fibers maintain a good bonding condition by relying on the matrix in the bundles. Riverlines perpendicular to the fracture direction appeared on the matrix. (Fig. 19b). The presence of leftover matrix on the broken fibers demonstrates the effectiveness of the bonding between epoxy resin and glass fiber. (Fig. 19c).

For the fracture surface of the specimen under low stress ratio (R = 0.1) fatigue loading in Fig. 20, the fibers can no longer maintain good bonding status inside the bundles. Many interfaces cracks form between the fibers and the resin. A large void (Fig. 20c) due to production imperfection is observed. The fatigue failure under low stress ratio loading is mainly due to micro interface debonding and production imperfection.

The fracture surface of the specimen under high stress ratio (R = 0.75) fatigue loading present characteristics of both static and low stress ratio fatigue experiments, as shown in Fig. 20. Some of the fibers in the bundles have dispersed, and the remaining fibers are still clustered together (Fig. 21b). It is worth noting that matrix thornlike protrusions (Fig. 21d) is discovered on the fracture surface under high stress ratio fatigue loading. The phenomenon is attributed to the creep deformation of resin caused by long-term high mean stress. The phenomenon is attributed to the high mean stress of the resin under high stress ratio. The final failure mode is affected by both fatigue loading and the creep loading provided by high mean stress, which makes the matrix produce a significant creep deformation.

4. Conclusion

In this paper, the fatigue behavior of GFRP unidirectional lamina vertical to fiber direction is studied through experiments. The effects of stress level and stress ratio on fatigue behavior were taken into consideration. A series of macroscopic phenomenological models are established to describe the performance variation of the lamina by measuring the fatigue life, stiffness variation, energy dissipation capacity, and cyclic creep strain during transverse cyclic loading. The following conclusions can be made:

(1) The transverse fatigue life of GFRP unidirectional lamina can be fitted by *S-N-R* equation. The relative error of the experimental results and the fitted results in the logarithmic space is basically within 20%. The expected fatigue life expressed by σ_{max} increases with the increase in stress ratio, and the expected fatigue life expressed by $\Delta\sigma$ decreases with the increase in stress ratio. The *S-N-R* regression equation expressed by $\Delta\sigma$ is better than σ_{max} due to its higher coefficient of determination (R^2).
(2) The transverse fatigue stiffness degradation occurs only at the initial and near-failure stages. The degree of stiffness degradation decreases as the stress ratio increases. The total stiffness degradation is still within 5% until failure.
(3) When the number of fatigue cycles increases, the unit dissipated energy (*UDE*) of GFRP unidirectional lamina increases slightly with the majority of the growth occurring in the initial and last 20% of the fatigue life. A power function equation is proposed to express the relationship between *UDE*, stress level, stress ratio and fatigue cycles. For the proposed equation considering stress ratio effects, it can reasonably reflect the growth trend of *UDE* of GFRP lamina.
(4) The cyclic creep strain basically occurs before the initial 20% fatigue life at stress ratios $R = 0.1$ or 0.25. While in the process of

fatigue loading at a high stress ratio, the cyclic creep strain keeps growing and cannot be disregarded. The cyclic creep strain increases with the increase of mean stress with constant stress amplitude and the number of normalized cycles, and decreases with the increase of stress amplitude with constant mean stress and the number of normalized cycles. By establishing the relationship between cyclic creep strain and mean stress, stress amplitude and fatigue cycles, the purpose of accurately describing the residual deformation of GFRP during cyclic loading is achieved.

(5) The SEM images observation presented that the static experiment failure pattern is primarily matrix cracking between fiber bundles. At low stress ratio fatigue loading, the main failure patterns for GFRP lamina are fiber–matrix debonding or production imperfections, whereas at high stress ratio fatigue loading, thornlike protrusions are observed on the fracture surface. The formation of protrusions is attributed to the creep deformation of the matrix under high mean stress.

CRediT authorship contribution statement

Qinglin Gao: Data curation, Formal analysis, Visualization, Writing – original draft. **Haohui Xin:** Writing – review & editing, Supervision, Supervision, Project administration, Methodology, Investigation, Conceptualization. **Youyou Zhang:** Writing – review & editing.

Declaration of Competing Interest

The authors declare that they have no known competing financial interests or personal relationships that could have appeared to influence the work reported in this paper.

Data availability

Data will be made available on request.

Acknowledgments

The authors gratefully acknowledge the financial support provided by the Program Fund of Non-Metallic Excellent and Innovation Center for Building Materials, (Grants #2023Ph.D-8) and the National Natural Science Foundation (Grants #51808398) of the People's Republic of China. The calculations were performed by using the HPC Platform at Xi'an Jiaotong University. The characterization analysis was provided by Instrument Analysis Center of Xi'an Jiaotong University.

References

[1] A.S. Mosallam, A. Bayraktar, M. Elmikawi, S. Pul, S. Adanur, Polymer composites in construction: An overview. (2015).
[2] C.E. Bakis, L.C. Bank, V.L. Brown, E. Cosenza, J.F. Davalos, J.J. Lesko, A. Machida, S.H. Rizkalla, T.C. Triantafillou, Fiber-reinforced polymer composites for construction-state-of-the-art review, J. Compos. Constr. 6 (2) (2002) 73–87.
[3] T. Keller, Recent all-composite and hybrid fibre-reinforced polymer bridges and buildings, Prog. Struct. Eng. Mater. 3 (2) (2001) 132–140.
[4] A. Vedernikov, A. Safonov, F. Tucci, P. Carlone, I. Akhatov, Pultruded materials and structures: A review, J. Compos. Mater. 54 (26) (2020) 4081–4117.
[5] J.R. Correia, Y. Bai, T. Keller, A review of the fire behaviour of pultruded GFRP structural profiles for civil engineering applications, Compos. Struct. 127 (2015) 267–287.
[6] H.H. Xin, A. Mosallam, Y.Q. Liu, C.Z. Wang, Y.Y. Zhang, Analytical and experimental evaluation of flexural behavior of FRP pultruded composite profiles for bridge deck structural design, Constr. Build. Mater. 150 (2017) 123–149.
[7] H.H. Xin, Y.Q. Liu, A.S. Mosallam, J. He, A. Du, Evaluation on material behaviors of pultruded glass fiber reinforced polymer (GFRP) laminates, Compos. Struct. 182 (2017) 283–300.
[8] H.H. Xin, A. Mosallam, Y.Q. Liu, M. Veljkovic, J. He, Mechanical characterization of a unidirectional pultruded composite lamina using micromechanics and numerical homogenization, Constr. Build. Mater. 216 (2019) 101–118.
[9] H.H. Xin, A.S. Mosallam, Y.Q. Liu, C.Z. Wang, J. He, Experimental and numerical investigation on assessing local bearing behavior of a pultruded GFRP bridge deck, Compos. Struct. 204 (2018) 712–730.
[10] L. Xie, Y. Bai, Y. Qi, C. Caprani, H. Wang, Effect of width–thickness ratio on capacity of pultruded square hollow polymer columns, Proc. Inst. Civil Eng. – Struct. Build. 171 (11) (2018) 842–854.
[11] T.P. Philippidis, A.P. Vassilopoulos, Fatigue of composite laminates under off-axis loading, Int. J. Fatigue 21 (3) (1999) 253–262.
[12] M. Kawai, A phenomenological model for off-axis fatigue behavior of unidirectional polymer matrix composites under different stress ratios, Compos. Part A-Appl. Sci. 35 (7–8) (2004) 955–963.
[13] A. Varvani-Farahani, H. Haftchenari, M. Panbechi, An energy-based fatigue damage parameter for off-axis unidirectional FRP composites, Compos. Struct. 79 (3) (2007) 381–389.
[14] B. Mohammadi, B. Fazlali, Off-axis fatigue behaviour of unidirectional laminates based on a microscale fatigue damage model under different stress ratios, Int. J. Fatigue 106 (2018) 11–23.
[15] M. Kawai, T. Teranuma, A multiaxial fatigue failure criterion based on the principal constant life diagrams for unidirectional carbon/epoxy laminates, Compos. Part A-Appl. Sci. 43 (8) (2012) 1252–1266.
[16] M. Kawai, N. Itoh, A failure-mode based anisomorphic constant life diagram for a unidirectional carbon/epoxy laminate under off-axis fatigue loading at room temperature, J. Compos. Mater. 48 (5) (2014) 571–592.
[17] S. Subramanian, K.L. Reifsnider, W.W. Stinchcomb, A cumulative damage model to predict the fatigue life of composite laminates including the effect of a fiber-matrix interphase, Int. J. Fatigue 17 (5) (1995) 343–351.
[18] A.T. Echtermeyer, B. Engh, L. Buene, Lifetime and Youngs modulus changes of glass/phenolic and glass/polyester composites under fatigue, Composites 26 (1) (1995) 10–16.
[19] J.N. Yang, Fatigue and residual strength degradation for graphite-epoxy composites under tension-compression cyclic loadings, J. Compos. Mater. 12(Jan) (1978) 19–39.
[20] J.N. Yang, L.J. Lee, D.Y. Sheu, Modulus reduction and fatigue damage of matrix dominated composite laminates, Compos. Struct. 21 (2) (1992) 91–100.
[21] W.F. Wu, L.J. Lee, S.T. Choi, A study of fatigue damage and fatigue life of composite laminates, J. Compos. Mater. 30 (1) (1996) 123–137.
[22] Z. Hashin, Cumulative damage theory for composite-materials - residual life and residual strength methods, Compos. Sci. Technol. 23 (1) (1985) 1–19.
[23] A.V. Movahedi-Rad, T. Keller, A.P. Vassilopoulos, Stress ratio effect on tension-tension fatigue behavior of angle-ply GFRP laminates, Int. J. Fatigue 126 (2019) 103–111.
[24] A.V. Movahedi-Rad, T. Keller, A.P. Vassilopoulos, Fatigue damage in angle-ply GFRP laminates under tension-tension fatigue, Int. J. Fatigue 109 (2018) 60–69.
[25] G. Meneghetti, M. Ricotta, G. Lucchetta, S. Carmignato, An hysteresis energy-based synthesis of fully reversed axial fatigue behaviour of different polypropylene composites, Compos. B Eng. 65 (2014) 17–25.
[26] GB/T 2577-2005. Test method for resin content of glass fiber reinforced plastics. Beijing: SAC/TC 39; 2005. (in Chinese).
[27] GB/T 3354-2014. Test method for tensile properties of orientation fiber reinforced polymer matrix composite materials. SAC/TC 435; 2014. (in Chinese).
[28] GB/T 35465.3-2017. Test method for fatigue properties of polymer matrix composite materials Part 3: Tension-tension fatigue. SAC/TC 39: 2017; 2017. (in Chinese).
[29] GB/T 1447-2005. Fiber-reinforced plastics composites-Determination of tensile properties. SAC/TC 39; 2005. (in Chinese).
[30] Q. Gao, H. Xin, A.S. Mosallam, F. Berto, J.A.F.O. Correia, Probabilistic fatigue life analysis considering mean stress effects of fiber reinforced polymer (FRP) composites, Int. J. Fatigue 162 (2022) 106951.
[31] A.V. Movahedi-Rad, T. Keller, A.P. Vassilopoulos, Interrupted tension-tension fatigue behavior of angle-ply GFRP composite laminates, Int. J. Fatigue 113 (2018) 377–388.
[32] V. Natarajan, H.V.S. Gangarao, V. Shekar, Fatigue response of fabric-reinforced polymeric composites, J. Compos. Mater. 39 (17) (2005) 1541–1559.
[33] M. Naderi, A. Kahirdeh, M.M. Khonsari, Dissipated thermal energy and damage evolution of glass/epoxy using infrared thermography and acoustic emission, Compos. B Eng. 43 (3) (2012) 1613–1620.
[34] S. Gillet, T. Jacopin, S. Joann'es, N. Bedrici, L. Laiarinandrasana, Short-term creep and low cycle fatigue unified criterion for a hybridized composite material, Int. J. Fatigue (2022) 106571.

Thin-Walled Structures 189 (2023) 110917



Contents lists available at ScienceDirect

Thin-Walled Structures

journal homepage: www.elsevier.com/locate/tws



Full length article

Prediction of fatigue crack propagation in center cracked steel plate strengthened with partially covered CFRP strip



Jielin Liu [a], Xiao-Ling Zhao [b], Haohui Xin [a,*], Youyou Zhang [a]

[a] Department of Civil Engineering, Xi'an Jiaotong University, Xi'an 710116, China
[b] Department of Civil and Environmental Engineering, The Hong Kong Polytechnic University, Hong Kong, China

ARTICLE INFO

Keywords:
Steel structures
Fatigue strengthening
CFRP strengthening method
Paris law
Extended finite element method (XFEM)

ABSTRACT

Evaluating the fatigue performance of steel members strengthened with carbon fiber reinforced polymer (CFRP) is of great significance for formulating maintenance strategies and making full use of materials. Current analytical models are mainly developed for fully covered CFRP strengthening method without considering different mechanisms at each stage. In this paper, an analytical model considering different stages of crack propagation was proposed to predict the fatigue performance of center cracked steel plates strengthened with partially covered CFRP strips. The strengthening effects of CFRP strips were numerically analyzed based on the extended finite element model (XFEM) calibrated by test data. The validity of the analytical model was checked by several sets of test data and numerical simulations. The results show that the proposed analysis model can reasonably predict the fatigue life of center cracked steel plates strengthened with partially covered CFRP strips. This study may provide a reference for the application of the partially covered CFRP fatigue strengthening method in engineering structures.

1. Introduction

Fiber reinforced polymer (FRP) has a great potential in improving fatigue life of thin-walled steel structures. The work prior to 2013 on fatigue strengthening can be found in Zhao (2013) [1] which covered fatigue strengthening of steel plates and I-section beams, prediction of improved fatigue life using boundary element method and fracture mechanics approach for CCT (center-cracked tensile) steel plates, stress intensity factor for CCT steel plates strengthened by CFRP. Recent research on FRP strengthened steel plates under fatigue loading was summarized in Zhao (2022) [2], which included the work considering the effect of debonding [3], temperatures [4–6] and crack orientation [7], damage level [8,9] and types of adhesives and CFRP prestress [10–12].

Partially covered CFRP strips are often used for local strengthening of structural cracking areas due to limited access or cost saving. The fatigue crack propagation of steel members locally strengthened by partially covered CFRP strips can be generally divided into different stages. As shown in Fig. 1, for example, in center cracked steel plates strengthened with partially covered CFRP strips, fatigue crack propagation can be divided into three stages according to the location of the crack front, namely Stage I, Stage II, and Stage III. In Stage I the crack front does not reach the CFRP strip strengthening area. In Stage II the crack front is in the CFRP strip coverage area. Stage III refers to the stage when the crack front passes through the CFRP strip. For different stages, CFRP strips play different roles. In Stage I, CFRP strips mainly play a role in improving structural stiffness and reducing the stress level. In Stage II, CFRP strips can not only reduce the stress level near the crack front but also limit the crack opening. In Stage III, the steel plate is seriously damaged, and the CFRP strip gradually becomes the main bearing component. The strengthening mechanism of CFRP strips at different stages is different, resulting in different crack propagation mechanisms accordingly. Therefore, to evaluate the fatigue performance of the steel members strengthened with partially covered CFRP strips, the fatigue life of each stage should be predicted separately.

The finite element numerical simulation method can effectively evaluate the fatigue performance of steel members strengthened with CFRP strips. Mohajer et al. [13] used the cyclic cohesive zone model (CZM) to numerically evaluate the pure mode I fatigue crack growth of steel plates strengthened with CFRP strips. Wang et al. [14] evaluated the fatigue crack growth of double-edged cracked steel beams strengthened with CFRP strips based on the linear elastic fracture mechanics method and finite element method. He et al. [15] proposed an isosceles trapezoid bond–slip model and established a finite element model to simulate the bond behavior between steel and CFRP strips. Yu et al. [16] simulated the fatigue crack propagation of CFRP strip strengthened steel plates with edge cracks using the boundary element method. Huang et al. [17] simulated the fatigue crack propagation of the CFRP strips repaired four-point bend specimens based on the

* Corresponding author.
E-mail address: xinhaohui@xjtu.edu.cn (H. Xin).

https://doi.org/10.1016/j.tws.2023.110917
Received 4 March 2023; Received in revised form 4 May 2023; Accepted 2 June 2023
Available online xxxx
0263-8231/© 2023 Elsevier Ltd. All rights reserved.

Nomenclature

The following symbols are used in this paper

a	Half-crack length
As	The sectional area of the steel plate
Ac	Total sectional area of CFRP strips
C_0, m	Material coefficients of Paris law
Es	Elastic modulus of steel plate
Ec	Elastic modulus of CFRP strip
$f(a, Ws)$	Shape factor of stress intensity factor
ΔK_I	Stress intensity factor (SIF) range
ΔK_{init}	The SIF range of the crack front at the beginning of Stage II
ΔK_{end}	The SIF range of the crack front at the end of Stage II
$\Delta K_{end,unrepaired}$	SIF range of unrepaired steel plate with a crack at the end of Stage II
$\Delta K_{I,unrepaired}$	SIF range of unrepaired steel plate with a crack at Stage III
N_f	Fatigue life
n	Number of data for calculating the mean absolute deviation (*MAD*)
P	External load
R	Stress ratio
R_S	Stiffness ratio of CFRP covered areas from the beginning of Stage II to the end
R_L	Location variable of CFRP strips
Ts	Thickness of steel plate
Tc	Thickness of CFRP strips
U	SIF reduction factor in Stage III
U_{init}	SIF reduction factor at the beginning of Stage III
Ws	Width of steel plate
Wc	Width of CFRP strip
Wm	Distance between two adjacent CFRP strips
σ_{load}	Tensile stress caused by fatigue load on steel plates
$\Delta\sigma_{load}$	Tensile stress range of fatigue load on steel plates
σ_{steel}	The actual far-field tensile stress of steel plate to calculate the SIF
$\Delta\sigma_{steel}$	The actual far-field tensile stress range of steel plate under fatigue load
$\bar{\varepsilon}$	Average strain of steel plate section and CFRP section under external load
ρ	Ratio of steel plate stiffness to total stiffness
$\eta_{\Delta K}$	The ratio of the SIF range at the end of Stage II to that at the beginning of Stage II
$\eta_{\Delta K}(a)$	The ratio of the SIF range at Stage II to that at the beginning of Stage II
$\frac{da}{dN}$	Fatigue crack growth rate
μ_i	Truth value
μ_i',	Estimated value
$\alpha_1, \alpha_2, \alpha_3, \alpha_4$	Fitting coefficient

contour integral method. Dong et al. [18] established the extended finite element model (XFEM) to simulate the fatigue crack growth of steel plates repaired with CFRP strips. The above FE analysis did not cover the case shown in Fig. 1 where three stages are involved.

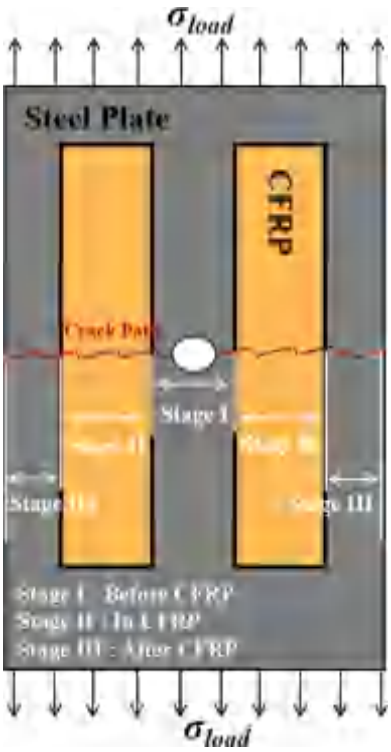


Fig. 1. Center cracked steel plate strengthened with CFRP strips.

Since the stress field at the crack tip is very complex when fatigue crack occurs in the CFRP strip strengthened steel members, it is necessary to analyze the stress of the steel members, adhesive, and CFRP strips and the interaction among them at the same time in order to accurately evaluate the fatigue strengthening effect. The numerical simulation method can accurately evaluate the fatigue performance of the CFRP strip strengthened steel structures, but it is sensitive to mesh and needs a lot of computation time. Compared with the numerical method, the theoretical analysis method can quickly and accurately evaluate the fatigue performance of the CFRP strip strengthened steel structures. Mohabeddine et al. [19] proposed an analytical model to predict the mode I fatigue crack growth of steel Central Cracked Tensile (CCT) specimens repaired with both fully covered and partially covered CFRP strips bonded on the two sides of the plate. In the analysis model, one SIF reduction factor β as a function of stiffness and geometric size is proposed to reflect the reinforcement effect of CFRP strip. Considering the failure mechanism of the partially covered CFRP strips strengthening method, the revised factor is also related to the position of the crack front. Liu et al. [20] proposed a practical SIF formula based on plenty of finite element analysis to predict the fatigue performance of fully covered CFRP strips repaired steel plates. A SIF correction coefficient F_C was introduced in the linear elastic fracture mechanics formula for calculating SIF to reflect the strengthening effect of CFRP strips, which was defined as a function of damage level, stiffness ratio, and width ratio of CFRP strip to steel plate.

Above analytical models in [19,20] is mainly developed for fully covered CFRP strengthening method and have some limitations in predicting the fatigue life of the steel members strengthened with partially covered CFRP strips without considering different mechanism at each stage. Hence, to further improve the fatigue performance theoretical analysis method of steel members strengthened with CFRP strips, a more comprehensive analysis model considering the influence of different stages of crack propagation on the strengthening effect of CFRP strips will be discussed in this paper.

In this paper, an analysis model based on linear elastic fracture mechanics considering different stages of crack propagation was proposed

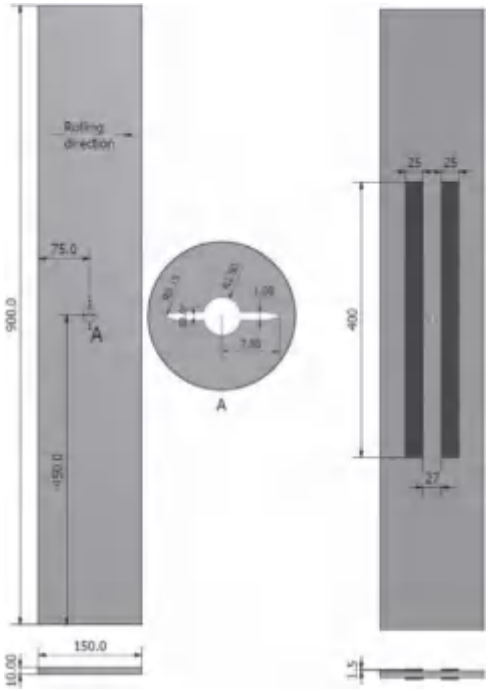


Fig. 2. Geometric dimension of test specimen [21].

to evaluate the fatigue performance of the center cracked steel plate strengthened with CFRP strips. The strengthening effects of CFRP strips were numerically analyzed based on the extended finite element model (XFEM) calibrated by test data. The validity of the analysis model was checked by several sets of test data in the literature and numerical simulation.

2. Numerical analysis

2.1. Numerical simulation

To study the fatigue performance of the center cracked steel plate strengthened with CFRP strips, the fatigue crack propagation was numerically simulated by the extended finite element method. The XFEM model is based on the phantom node method [22] and virtual crack closure technique (VCCT) [23]. The XFEM model includes a set of real nodes and a set of virtual nodes. When cracks occur between nodes, the constraints between real nodes are lost, and the real nodes are connected by virtual nodes to ensure continuity. Through the cooperation between real and virtual nodes, the numerical simulation of fatigue cracks is realized. Virtual node and real node are defined by

Table 1
Mechanical and fatigue properties of S355 steel [21].

Mechanical property		Fatigue properties
Modulus of elasticity 205 GPa	Poisson's ratio 0.3	Material parameter of Paris Law $C_0 = 10^{-13.79}$ $m = 3.401$

Table 2
Mechanical properties of CFRP [21].

Longitudinal modulus of elasticity	Transverse modulus of elasticity	Longitudinal Poisson's ratio	Longitudinal shear modulus	Transverse shear modulus
435 GPa	48.71 GPa	0.245	17.41 GPa	17.41 GPa

the cohesion model [24]. The level set method (LSM) [25] is used to characterize the geometric characteristics of cracks.

The virtual crack closure technique (VCCT) [23] is used to calculate the strain energy release rate. For linear elastic materials, the energy release rate of mode I fatigue crack can be expressed as the product of node force and displacement. The Paris law [26] was used to calculate the fatigue crack propagation rate and implemented in the user-defined subroutine "UMIXMODEFATIGUE" of ABAQUS [27–31].

The validity of the XFEM model is verified by a set of fatigue crack propagation tests of center cracked steel plates strengthened with partially covered CFRP strips in Ref. [21]. The fatigue crack propagation tests were carried out on an unreinforced steel plate and a CFRP repaired steel plate. The geometric dimensions of the specimens are shown in Fig. 2. The central notch length of the steel plate is 15 mm and the length, width, and thickness of CFRP strips are 400 mm, 25 mm, and 1.5 mm, respectively. The material properties of the CFRP strip and steel plate are shown in Tables 1 and 2. A two-component epoxy adhesive of type Araldite 420 A/B was used to bond the CFRP strips to the steel plate. The average thickness of the adhesive is 0.075 mm. According to the manufacturer's report, its elastic modulus and Poisson's ratio are 1495 MPa and 0.35, respectively. The steel plates of both specimens were pre-cracked before the test. Fatigue tests were carried out under a stress ratio of $R = 0.2$, and the maximum external load value is 140.6 kN.

As shown in Fig. 3, the geometric dimension and material properties of the numerical model are consistent with the test. The finite element model's material properties are linear elasticity. One end of the model is fixed, and the other end is constrained in the X and Z axis directions, and cyclic loads are applied along the Y axis direction. To reduce the computational cost, only a semi-structural numerical model was established. The X-axis direction of the symmetrical section is constrained. The element mesh size of the crack propagation zone of the steel plate is 1 mm, and the type is C3D8. The element mesh size of the resin adhesive layer and CFRP strip is 2 mm, and the type is C3D8 and SC8R, respectively. The boundary conditions of the numerical model of the

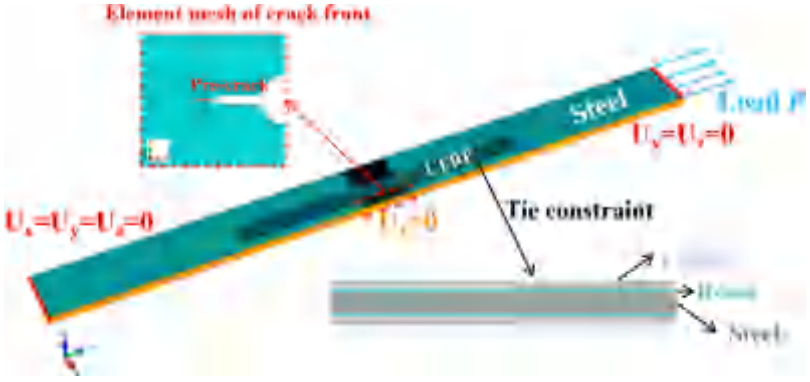


Fig. 3. The XFEM model of the steel plate strengthened with CFRP strips.

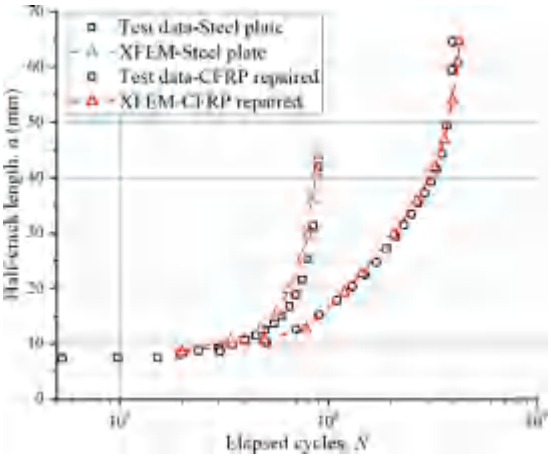


Fig. 4. Comparison of numerical simulation results with test data. *Source:* The experimental results were reproduced from Ref. [21].

un-strengthened steel plate are the same as those of the CFRP strips strengthened steel plate.

Fig. 4 compares the numerical simulation results with the test data. For the unstrengthened specimen, the ratio of the fatigue life of the numerical simulation to the test data is 0.997. For CFRP strengthened specimens, in the later stage of crack propagation, the numerical simulation results are slightly larger than the test data. The ratio of the fatigue life of numerical simulation results to test data is 1.071. This may be due to the fact that the material properties in the finite element model are set to linear elasticity, ignoring the damage of CFRP and the adhesive layer, resulting in conservatively predicted results. In general, the numerical simulation results are in good agreement with the test data, and the numerical simulation based on the XFEM model can reflect the fatigue performance of CFRP strengthened center cracked steel plates. Fig. 5 shows the fatigue crack propagation process of the strengthened steel plate numerical model. In the legend, ' STATUSXFEM ' represents a damage factor in the extended finite element method, which is a dimensionless value. The status of an element is 1.0 if the element is completely cracked and 0.0 if the element contains no crack. If the element is partially cracked, the value of ' STATUSXFEM ' lies between 1.0 and 0.0. According to Fig. 5, the numerical simulation results are reasonable.

2.2. Parametric analysis

To study the fatigue strengthening mechanism of CFRP on centrally cracked steel plates, parametric analysis was carried out based on the validated XFEM model. Fig. 6 shows several main factors affecting the strengthening effect, including the width *Wc* and thickness *Tc* of CFRP strips and the distance between two CFRP strips *Wm*. As shown in Table 3, fifteen strengthening schemes are considered in this paper. Three widths *Wc* of CFRP strips, 25 mm, 35 mm, and 45 mm, are considered. Three kinds of CFRP strip thickness *Tc*, 0.75 mm, 1.5 mm, and 3 mm, are considered. Three kinds of CFRP adjacent distance *Wm*, 27 mm, 54 mm, and 81 mm, are considered. Fifteen types of reinforcement schemes can be divided into five groups based on the width *Wc* and adjacent distance *Wm* of CFRP strips. The first group includes schemes *No*. 1 to *No*. 3, the second group includes schemes *No*. 4 to *No*. 6, and the third group includes schemes *No*. 7 to *No*. 9. The thickness *Tc* and adjacent distance *Wm* of the CFRP are the same in these three groups, but the width *Wc* of the CFRP plate varies, with widths of 25 mm, 35 mm, and 45 mm, respectively, to investigate the influence of the CFRP strip width *Wc* on the reinforcement effect. The fourth group includes schemes *No*. 10 to *No*. 12, and the fifth group includes schemes *No*. 13 to *No*. 15. The width *Wc* and thickness *Tc* of the CFRP in these two groups are the same, but the adjacent distance *Wm* of the CFRP strips varies, to investigate the influence of the strip layout position on the reinforcement effect. Three thicknesses of CFRP strips were considered in each group.

The CFRP bonding reinforcement scheme achieves fatigue reinforcement by reducing the SIF range of the fatigue crack front. Therefore, the finite element model was used to calculate the SIFs of crack fronts for different positions of various reinforcement schemes. Fig. 7 shows the numerical simulation results of the SIF range at the crack front of the five group reinforcement schemes. Fig. 8 compares the numerical simulation results of reinforcement schemes with 1.2 mm-thick CFRP strips in different groups. It is noted that as the thickness of CFRP increases, the stress intensity factor of the crack front gradually decreases, which indicates that as the stiffness of CFRP strips increases, the reinforcement effect is better. In stage I and stage III of crack propagation, the SIF increases with the increase of crack length. However, in stage II, the SIF range stops increasing even decreases with the increase of CFRP

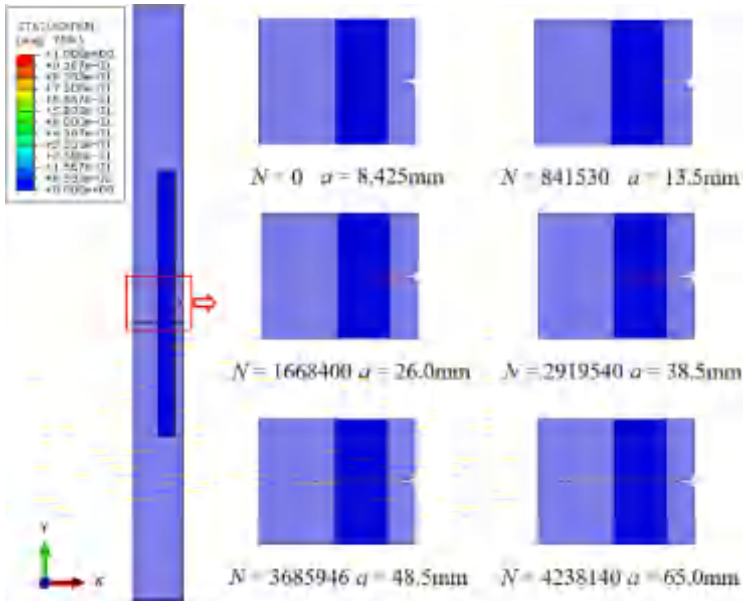


Fig. 5. The fatigue crack propagation of the strengthened steel plate model.

Table 3
Different CFRP strengthening schemes.

No.	Strengthening schemes	Ws (mm)	Ts (mm)	Es (MPa)	Wc (mm)	Tc (mm)	Wm (mm)	Ec (MPa)
1	Ws150-Wc25-Tc075-Wm27				25	0.75	27	
2	Ws150-Wc25-Tc120-Wm27				25	1.2	27	
3	Ws150-Wc25-Tc150-Wm27				25	1.5	27	
4	Ws150-Wc35-Tc075-Wm27				35	0.75	27	
5	Ws150-Wc35-Tc120-Wm27				35	1.2	27	
6	Ws150-Wc35-Tc150-Wm27				35	1.5	27	
7	Ws150-Wc45-Tc075-Wm27				45	0.75	27	
8	Ws150-Wc45-Tc120-Wm27	150	10	205000	45	1.2	27	435000
9	Ws150-Wc45-Tc150-Wm27				45	1.5	27	
10	Ws150-Wc25-Tc075-Wm54				25	0.75	54	
11	Ws150-Wc25-Tc120-Wm54				25	1.2	54	
12	Ws150-Wc25-Tc150-Wm54				25	1.5	54	
13	Ws150-Wc25-Tc075-Wm81				25	0.75	81	
14	Ws150-Wc25-Tc120-Wm81				25	1.2	81	
15	Ws150-Wc25-Tc150-Wm81				25	1.5	81	

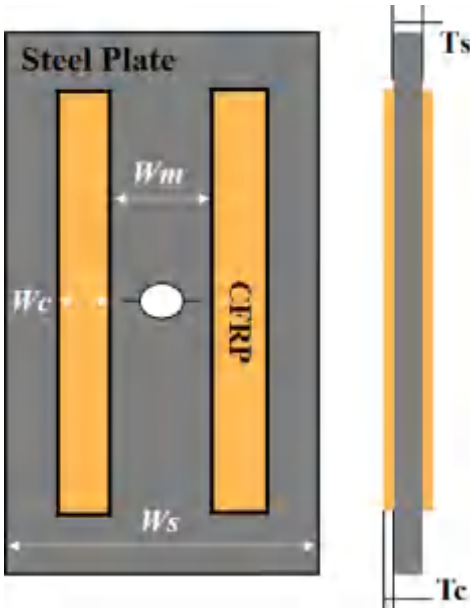


Fig. 6. Illustration of related parameters.

strip thickness. It is noted that the decrease of SIF range is related to the stiffness of CFRP strips and the location of CFRP strips.

3. Theoretical analysis

3.1. Analytical model

3.1.1. Stage I: the crack front before the partially covered CFRP strip

In the crack propagation Stage I, the fatigue crack does not enter the CFRP covered area. The steel plate and CFRP strip bear the external load together, and the internal force of the component can be calculated by the principle of stiffness distribution. As shown in Fig. 9, it is assumed that the average strain of the undamaged steel plate section is $\bar{\varepsilon}$. Since the CFRP strips are bonded to the surface of the steel plate, the average strain of the CFRP strip is also $\bar{\varepsilon}$. The average strain of the steel plate section can be obtained by solving Eq. (1), and the stress can be obtained by Eqs. (2) and (3). Based on linear elastic fracture mechanics, the SIF range can be obtained by Eqs. (4) and (5). As shown in Eq. (6), the fatigue crack growth rate can be calculated using the Paris Law. The fatigue life can be obtained by integrating the fatigue crack growth rate according to Eq. (7).

$$\bar{\varepsilon}(EsAs + EcAc) = \sigma_{load}As \tag{1}$$

$$\sigma_{steel} = \rho\sigma_{load} \tag{2}$$

$$\rho = \frac{EsAs}{EsAs + EcAc} \tag{3}$$

$$\Delta K_I = \Delta\sigma_{steel} f(a, Ws) \tag{4}$$

$$f(a, Ws) = \sqrt{\pi a sec(\frac{\pi a}{Ws})} \tag{5}$$

$$\frac{da}{dN} = C_0(\Delta K_I)^m \tag{6}$$

$$N_f = \int_{ai}^{af} C_0^{-1}\Delta K_I^{-m} da \tag{7}$$

3.1.2. Stage II: the crack front in the partially covered CFRP strip

In the crack propagation Stage II, with the increase of crack length, the stress intensity factor stops increasing and even decreases. To study this phenomenon, reinforcement efficiency $\eta_{\Delta K}$ shown in Eq. (8) was defined, which is expressed as the ratio between the SIF range of the crack front at the end of stage II ΔK_{end} and the SIF range of the crack front at the beginning of Stage II ΔK_{init}. $\eta_{\Delta K}$ can reflect the decrease of the SIF range in Stage II. Because the crack is in the area covered by CFRP, the influence of the CFRP strips on the SIF range of the crack front is complex, and it is difficult to solve the mechanical behavior of the components using derivation of balance equation. To calculate the reinforcement efficiency $\eta_{\Delta K}$, a simple linear regression formula as shown in Eq. (9) was proposed.

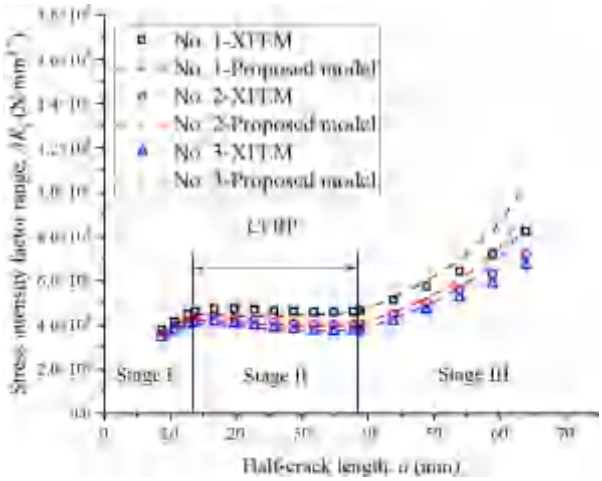
$$\eta_{\Delta K} = \frac{\Delta K_{end}}{\Delta K_{init}} \tag{8}$$

$$\eta_{\Delta K} = \alpha_1 R_S + \alpha_2 R_L + \alpha_3 \tag{9}$$

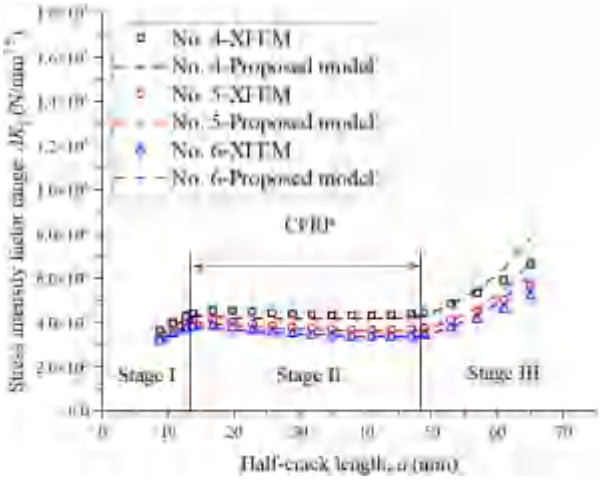
According to the numerical simulation results in Section 2.2, the reduction of the SIF range in Stage II is related to the stiffness and location of the CFRP strips, so the stiffness variable R_S and the CFRP strip position variable R_L as well as three fitting coefficients α_1, α_2 and α_3 were defined in Eq. (9).

As shown in Fig. 10, when the fatigue crack is at the beginning of Stage II, the total stiffness of the CFRP strip coverage area is $EsTsWc+2EcTcWc$, and when the crack is at the end of Stage II, the total stiffness of the CFRP strip coverage area is $2EcTcWc$. The stiffness ratio R_S is defined as the ratio of the former to the latter. R_L is the location variable of CFRP strips, which is equal to the center distance of CFRP strips $Wm+Wc$. As shown in Fig. 11, linear regression analysis is performed on the numerical simulation results based on the validated XFEM model of 15 reinforcement schemes. It is noted that the R-square is 0.8538, which indicates that the fitting results of the proposed linear regression equation are accurate.

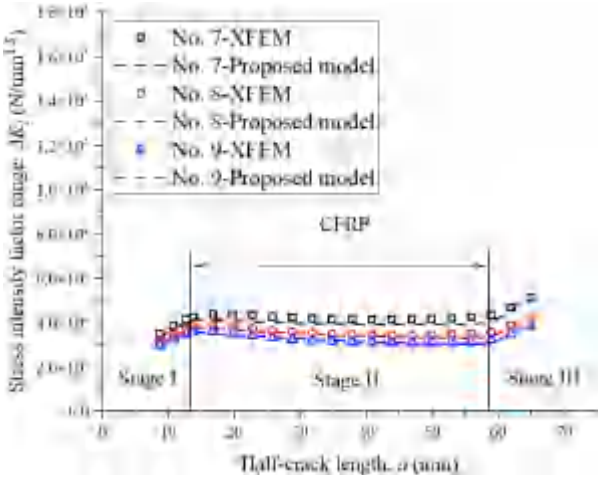
To obtain the ratio of the SIF range in Stage II with different crack lengths to ΔK_{init}, the reinforcement efficiency function $\eta_{\Delta K}(a)$ shown in Eq. (10) is proposed based on polynomial curve fitting. The establishment of Eq. (10) must satisfy two necessary conditions. Firstly,



(a)

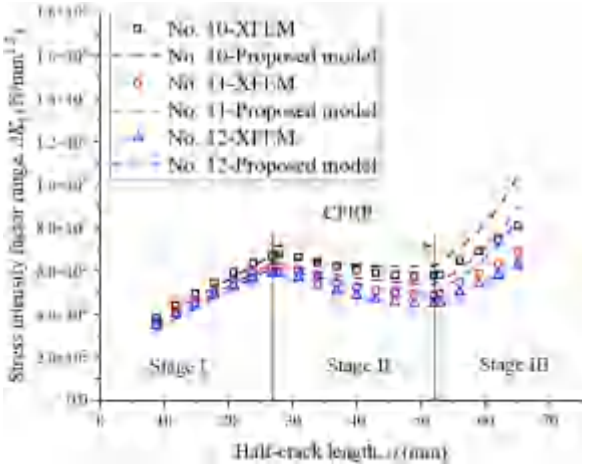


(b)

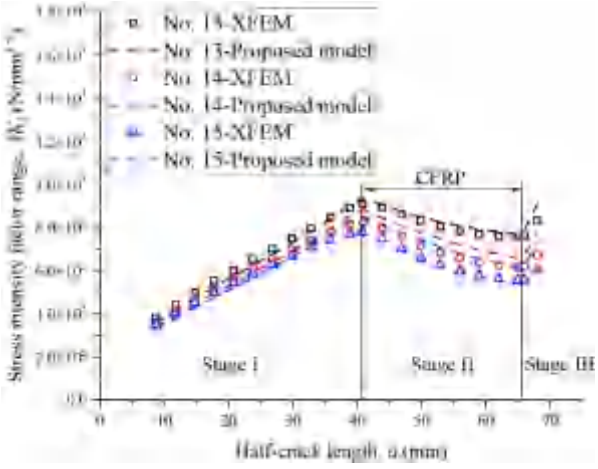


(c)

Fig. 7. SIF range of different strengthening schemes.



(d)



(e)

Fig. 7. (*continued*).

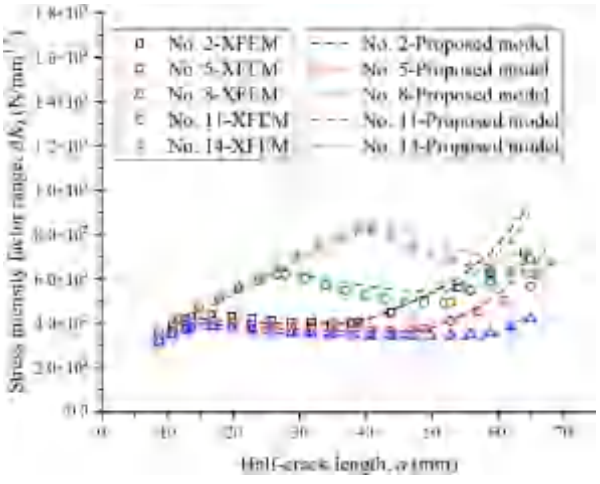


Fig. 8. The influence of different schemes on fatigue strengthening effects.

when the crack front is at the left edge of the CFRP strip, $\frac{a-Wm/2}{Wc}$ is equal to 0, $\eta_{\Delta K}(a)$ is equal to 1. Secondly, when the crack front is at the left edge of the CFRP strip, $\frac{a-Wm/2}{Wc}$ is equal to 1, $\eta_{\Delta K}(a)$ is equal to $\eta_{\Delta K}$. Therefore, it is only necessary to determine a coefficient α_4 to obtain $\eta_{\Delta K}(a)$. Assign values to α_4 from 0, interval 0.02, until 0.5. When α_4 is 0, function $\eta_{\Delta K}(a)$ is a linear polynomial. When α_4 is not 0, function $\eta_{\Delta K}(a)$ is a quadratic polynomial.

For each assignment, a set of $\eta_{\Delta K}(a)$ has been obtained and compared with the numerical simulation result. As shown in Fig. 12, the

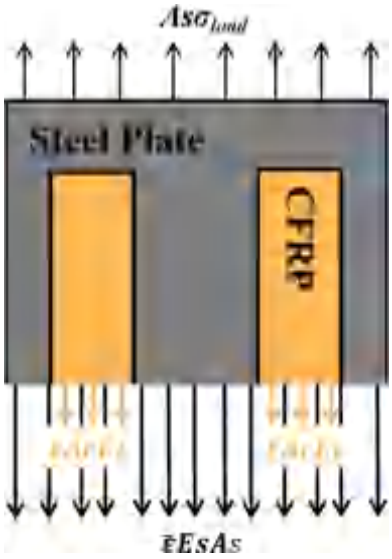


Fig. 9. Stress analysis of components at crack propagation stage I.

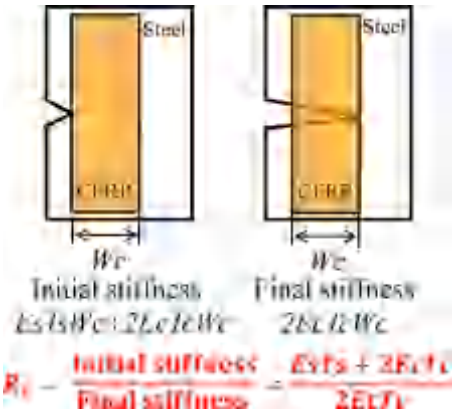


Fig. 10. Ratio of initial stiffness to final stiffness R_S.

mean absolute deviation (*MAD*) was calculated according to Eq. (11). It is noted that when α_4 takes 0.12, *MAD* takes the minimum value of 0.0156, so the value of α_4 is determined to be 0.12. Finally, the SIF range of the crack front at Stage II can be calculated based on Eq. (12). The fatigue crack growth rate can be calculated from Eq. (6), and the fatigue life can be obtained by integrating the crack growth rate.

$$\eta_{\Delta K}(a) = 1 + (\eta_{\Delta K} - 1 - \alpha_4)\left(\frac{a - Wm/2}{Wc}\right) + \alpha_4\left(\frac{a - Wm/2}{Wc}\right)^2 \tag{10}$$

$$MAD = \frac{1}{n}\sum_{i=1}^{n}\left|\mu_i - \mu_i'\right| / \mu_i \tag{11}$$

$$\Delta K_I = \eta_{\Delta K}(a)\Delta K_{init} \tag{12}$$

3.1.3. Stage III: the crack after the partially covered CFRP strip

When the crack front is in Stage III, the CFRP strip gradually becomes the main bearing part of the system. With the increase in crack length, the SIF range increases, and the fatigue crack growth rate increases sharply. As shown in Eq. (13), the fatigue strengthening effect of the CFRP strips can be reflected by a SIF range reduction factor *U*. *U* is defined as the ratio of the SIF range of the crack front of the repaired steel plate to the SIF range of the crack front of the unrepaired steel plate in Stage III. When the crack front is located at the beginning of Stage III, the SIF range reduction factor *U* is defined as the initial reduction factor U_{init} and can be calculated by Eq. (14).

The numerical simulation results in Section 2.2 are analyzed first to study the properties of *U*. Fig. 13 shows the ratio of the SIF range of the repaired steel plate predicted by the XFEM model to the SIF range of the unrepaired steel plate in the 15 reinforcement schemes. The SIF range of the unrepaired steel plate is directly calculated by Eq. (4). In Fig. 13, the abscissa represents the ratio of crack propagation length to total length in Stage III. When the crack front is located at the beginning of Stage III, it is 0, and when the crack propagates to fracture, it is 1. The ordinate represents the SIF range reduction factor *U* corresponding to different crack lengths. It is noted that with the propagation of fatigue cracks, the *U* value reflecting the strengthening effect of CFRP strips tends to decrease, but the degree of reduction is very small. This shows that in Stage III, as the crack front moves away from the CFRP strip, on the one hand, the limitation of the CFRP strip on the crack opening is getting weaker and weaker, resulting in a weakening trend of the reinforcement effect. On the other hand, the stiffness ratio of CFRP in the structure is getting larger and larger, bearing more fatigue load. Under the combined action of these two factors, the reinforcement effect of CFRP tends to decrease with the increase in crack length, but the degree of reduction is not obvious. Fig. 14 compares the average value of *U* in Stage III with the value of U_{init}. Obviously, the gap between the two is very small.

Hence, in analysis model, to simplify the calculation, U_{init} is used instead of *U* to reflect the effect of CFRP strips on the SIF range. Although this will cause a slight error in the SIF range reduction factor at the later stage of Stage III, the fatigue crack propagation is already in an unstable state, and the steel plate fractures after a few loading cycles. Since the fatigue life is very small at this stage and the error of the SIF range reduction coefficient is not significant, the accuracy of the analysis model for the total fatigue life assessment of the steel member is not affected. Finally, in Stage III, the SIF range of the crack front can be calculated by Eq. (15), and the fatigue life can be obtained by integrating the crack growth rate.

$$U = \frac{\Delta K_I}{\Delta K_{I,unrepaired}} \tag{13}$$

$$U_{init} = \frac{\Delta K_{end}}{\Delta K_{end,unrepaired}} \tag{14}$$

$$\Delta K_I = U_{init}\Delta\sigma_{load} f(a, Ws) \tag{15}$$

3.2. Calibration of analysis model

To check the accuracy of the theoretical analysis model, Fig. 7 compares the theoretical analysis results and numerical simulation results of the SIF range of the steel plate using different reinforcement schemes. Table 4 calculates the mean absolute deviation (*MAD*) between theoretical analysis and numerical results based on Eq. (11). In Stage I and Stage II, the theoretical analysis results are in good agreement with the numerical simulation results, and the *MAD* is 3.62% and 4.45% for the 15 strengthening schemes, respectively. In Stage III, there is a slight deviation between the theoretical analysis and numerical results, but for the 15 reinforcement schemes, the *MAD* is 9.84%, which is acceptable. The *MAD* value of the three stages is 5.97%, which indicates that the analytical model has high accuracy.

4. Validation of the analytical model

The fatigue life of the steel plate with different strengthening schemes was further simulated, and several fatigue test data sets from literatures [21,32,33] were collected to check the validity of the analysis model in predicting the fatigue performance of the cracked steel plate strengthened with CFRP.

To reduce the computational cost, several typical reinforcement schemes—*No.* 3, *No.* 5, *No.* 7, *No.* 9, *No.* 11, *No.* 13, and *No.* 15—were selected to carry out numerical simulation of fatigue crack propagation. To validate that the analysis model is suitable for the fatigue performance evaluation of reinforcement schemes with different widths of

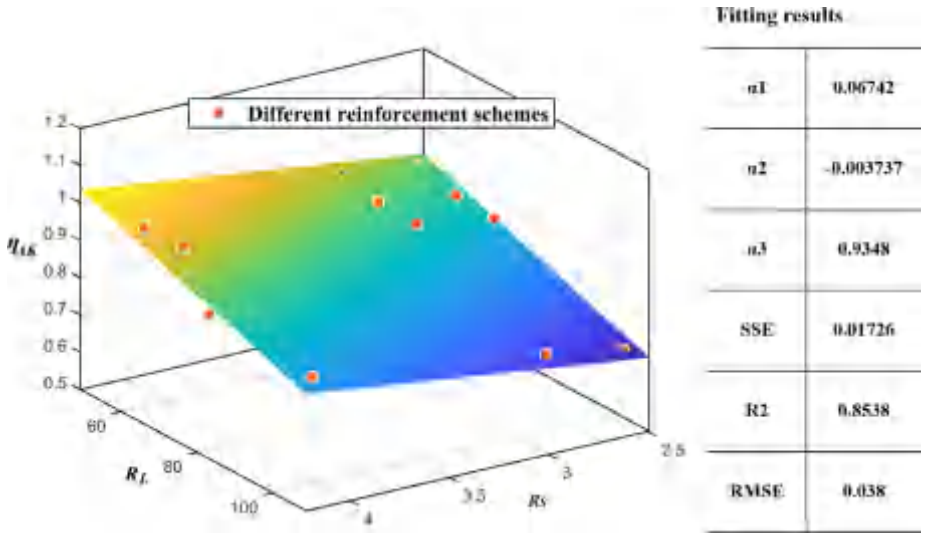


Fig. 11. Linear regression fitting results.

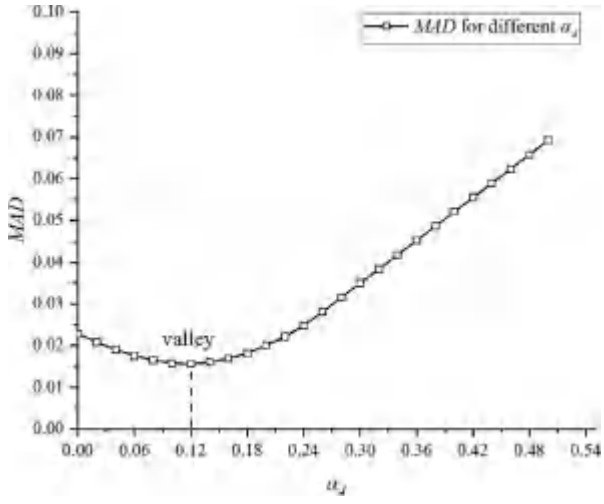
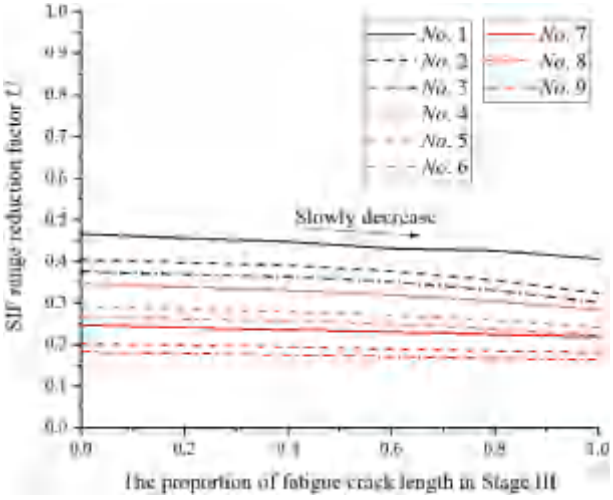


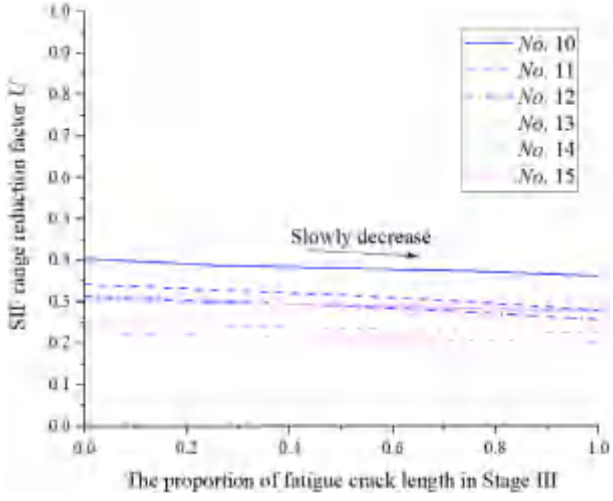
Fig. 12. *MAD* for different α_4.

Table 4
MAD between the SIF range calculated by the proposed model and the XFEM model.

No.	*MAD* (%)			
	Stage I	Stage II	Stage III	All stage
1	4.36	3.99	8.79	5.71
2	3.52	2.29	8.60	4.80
3	3.06	1.46	9.38	4.64
4	4.23	4.66	6.55	5.15
5	3.35	1.94	6.55	3.95
6	2.88	1.00	7.11	3.66
7	4.15	5.73	4.76	4.88
8	3.24	2.29	4.15	3.23
9	2.75	1.40	3.70	2.62
10	3.95	3.89	15.77	7.87
11	3.68	7.02	18.04	9.58
12	3.65	9.36	20.21	11.08
13	3.88	2.32	6.35	4.18
14	3.71	7.87	11.82	7.80
15	3.84	11.49	15.79	10.38
Mean	3.62	4.45	9.84	5.97



(a)From *No.*1 to *No.*9



(b)From *No.*10 to *No.*15

Fig. 13. SIF range reduction factor *U* of different strengthening schemes.

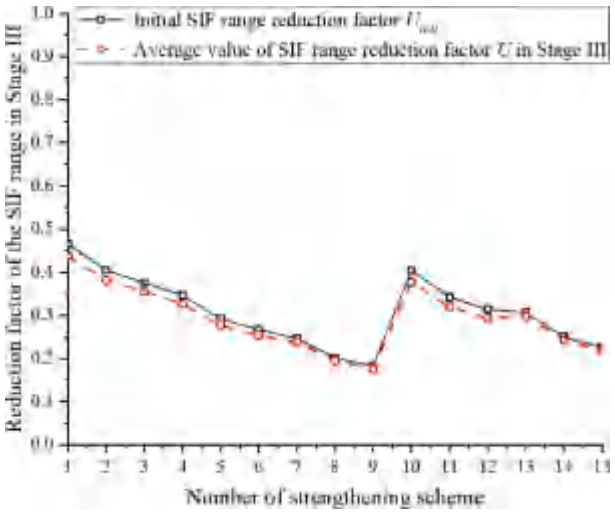


Fig. 14. Reduction factor of the SIF range of Stage III.

Table 5
Geometric dimensions and mechanical properties of steel plates and CFRP strips.

Reference		[21]	[32]	[33]			
Specimen		UHM	Sika S512	ND2	HD2	ND10	HD10
Steel plate	*Es* (MPa)	205	200	200	200	200	200
	Ws (mm)	150	300	90	90	90	90
	Ts (mm)	10	10	10	10	10	10
	2a (mm)	16.85	30	6.8	6.8	14	14
CFRP	*Ec* (MPa)	435	155	177	479	177	479
	Wc (mm)	25	50	25	25	25	25
	Tc (mm)	1.5	1.2	1.4	1.2	1.4	1.2
	Wm (mm)	27	50	40	40	40	40

Table 6
Loading conditions of fatigue test and Paris law coefficients of steel plates.

Reference	Specimen	Fatigue loading		Steel	
		$\Delta\sigma_{load}$ (MPa)	*R*	*C*	*m*
[21]	UHM	75	0.2	$10^{-13.79}$	3.401
[32]	Sika S512	80	0.4	$10^{-12.62}$	3
[33]	ND2 HD2 ND10 HD10	135	0.1	$10^{-12.64}$	3

steel plates and CFRP strips, *No*. 16 and *No*. 17, were supplemented. In these two reinforcement schemes, the width *Ws* of the steel plate is 300 mm, and the thickness *Ts* is 10 mm. In the reinforcement scheme *No*. 16, the width *Wc* of the CFRP strip is 75 mm, the thickness *Tc* is 1.2 mm, and the spacing *Wm* is 54 mm. The width *Wc* of the CFRP strip in the reinforcement scheme *No*. 17 is 50 mm, the thickness *Tc* is 1.2 mm, and the spacing *Wm* is 81 mm.

Tables 5 and 6 show the mechanical properties, geometric dimensions, and relative positions of steel plates and CFRP materials in fatigue tests. It is noted that the reinforcement conditions of the six fatigue tests are different, and the fatigue specimens of different literatures are quite different, which can well prove the validity of the analysis model.

Fig. 15 compares the predicted results of the proposed model with test data and numerical simulation results. Table 7 shows the ratio of the fatigue life predicted by the proposed model to the test data and numerical simulation results. The prediction results of the proposed

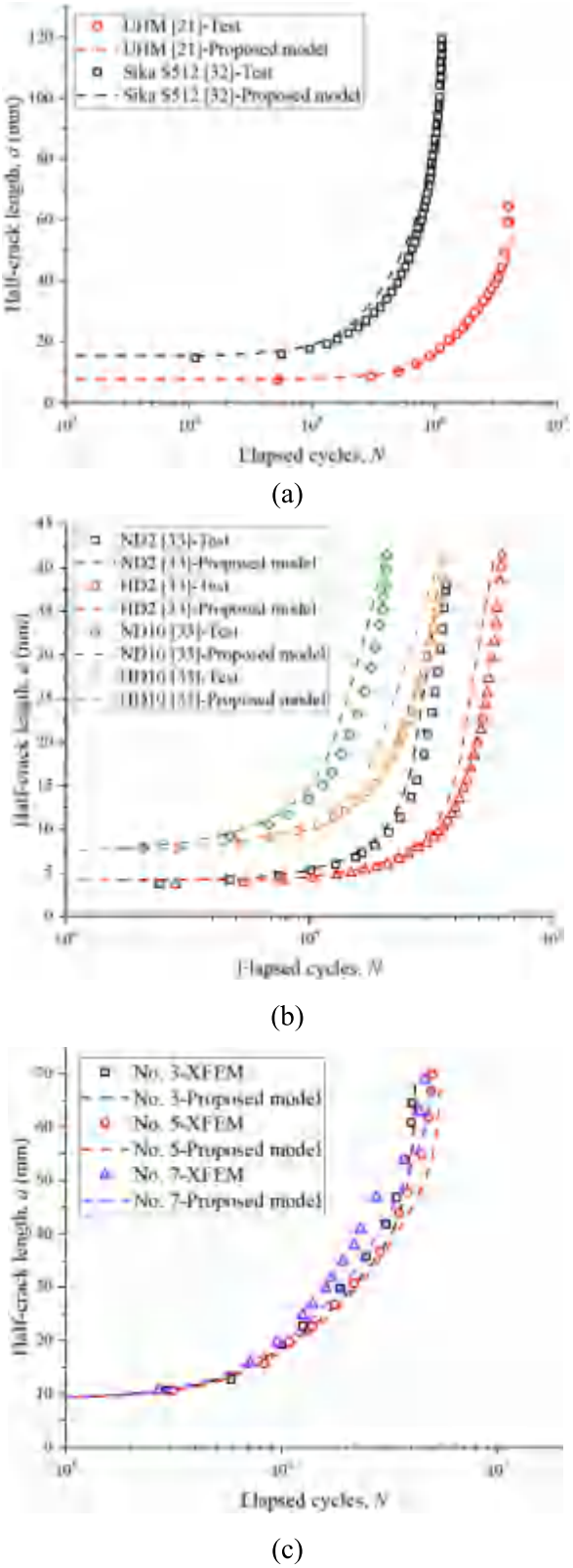
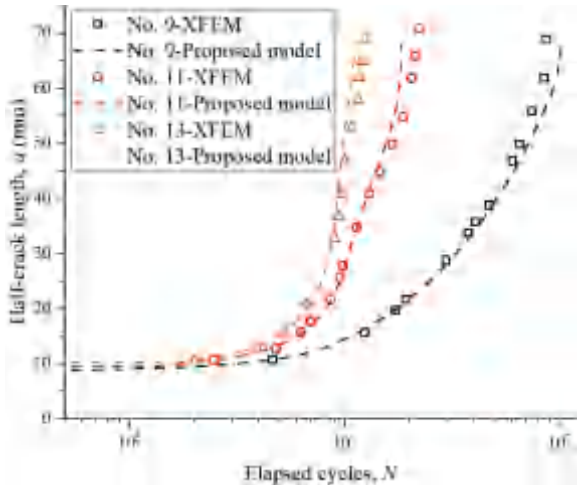
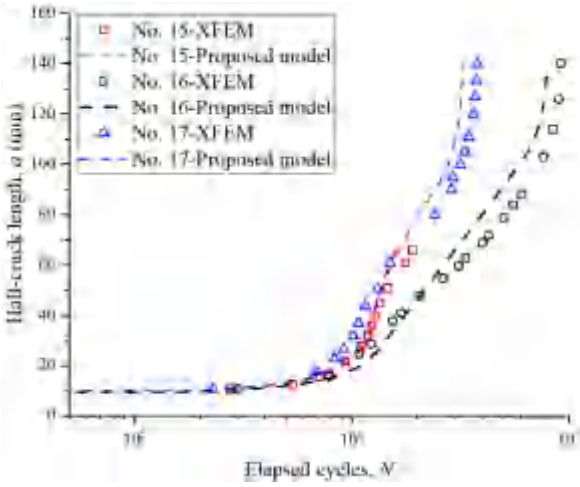


Fig. 15. Fatigue crack growth life of different strengthening schemes.



(d)



(e)

Fig. 15. (*continued*).

Table 7
The ratio of the fatigue life predicted by the proposed model to the test data and simulation results.

Specimen	Test&XFEM	Proposed model	Ratio proposed model/ Test&XFEM
UHM [21]	3.958E+06	4.356E+06	1.101
Sika S512 [32]	1.153E+06	1.206E+06	1.046
ND2 [33]	3.668E+05	3.431E+05	0.936
HD2 [33]	6.222E+05	5.770E+05	0.927
ND10 [33]	2.092E+05	2.016E+05	0.964
HD10 [33]	3.600E+05	3.429E+05	0.952
No. 3	4.038E+06	4.156E+06	1.029
No. 5	4.982E+06	5.400E+06	1.084
No. 7	4.580E+06	4.969E+06	1.085
No. 9	8.688E+06	1.017E+07	1.171
No. 11	2.216E+06	1.844E+06	0.832
No. 13	1.249E+06	1.132E+06	0.906
No. 15	1.953E+06	1.633E+06	0.836
No. 16	9.144E+06	7.897E+06	0.864
No. 17	3.792E+06	3.225E+06	0.850
Mean value			0.972
Coefficient of variation			0.11

model are in good agreement with the test data or numerical simulation results in general. The error between the prediction results of the proposed model and the test data is less than 11%, the error between the prediction results of the proposed model and the numerical simulation results is less than 18%, and the mean error is 2.8%. Fig. 16 visually compares different fatigue life prediction results. It should be noted that the prediction results of the proposed model can all fall within a 18% error interval.

5. Conclusion

In this paper, an analysis model was proposed to predict the fatigue life of the center cracked steel plate strengthened with partially covered CFRP strips. The strengthening effects of different schemes were numerically studied by the validated XFEM model. The validity of the analysis model was checked by numerical simulation and several sets of test data. The following conclusions are drawn:

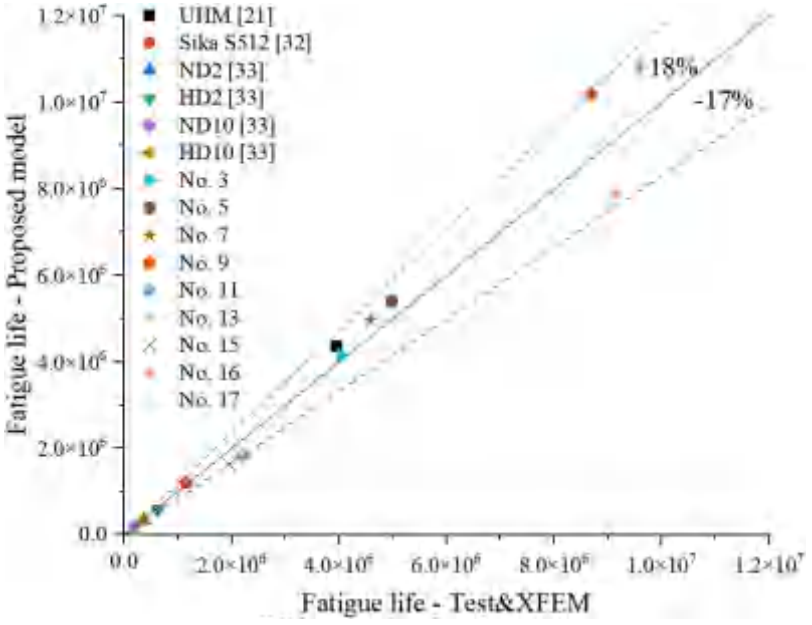


Fig. 16. Comparison of fatigue life predicated by the proposed model with that predicted by the finite element method.

1. The fatigue crack propagation of the center cracked steel plate strengthened with CFRP strips can be divided into three stages, namely Stage I, Stage II, and Stage III. For Stage I and Stage III, with the increase of crack length, the SIF range of the crack front increases gradually, and the stiffness of CFRP strips has a significant effect on SIF range. The larger the stiffness, the smaller the SIF range. For Stage II, with the increase of crack length, SIF range stops increasing and even begins to decrease, and the reduction is related to the stiffness and arrangement position of CFRP strips. Increasing the stiffness of the CFRP strip or the spacing between the CFRP strips can increase the reduction in the SIF range.

2. The accuracy of the SIF range predicted by the analytical model was checked by the validated XFEM model. For the fifteen reinforcement schemes studied, the mean absolute deviations (*MAD*) between the SIF range predicted by the analysis model and the numerical simulation results in Stage I, Stage II, and Stage III are 3.6%, 4.5%, and 9.8%, respectively, and the total *MAD* in all stages is less than 6%.

3. The validity of the analytical model was checked by six sets of fatigue test data and numerical simulation results of fatigue crack propagation. The error between the fatigue life predicted by the proposed model and the test data is less than 11%, the error between the prediction results of the proposed model and the XFEM model is less than 18%, and the mean error is 2.8%.

CRediT authorship contribution statement

Jielin Liu: Validation, Methodology, Data curation, Conceptualization, Formal analysis, Investigation, Visualization, Writing – original draft. **Xiao-Ling Zhao:** Supervision, Validation, Writing – review & editing. **Haohui Xin:** Supervision, Resources, Project administration, Methodology, Validation, Writing – review & editing. **Youyou Zhang:** Supervision, Writing – review & editing.

Declaration of competing interest

The authors declare that they have no known competing financial interests or personal relationships that could have appeared to influence the work reported in this paper.

Data availability

Data will be made available on request.

Acknowledgments

The authors gratefully acknowledge the financial support provided by the Program Fund of Non-Metallic Excellent and Innovation Center for Building Materials (Grants #2023Ph.D-8).

References

[1] X.L. Zhao, FRP Strengthened Metallic Structures, CRC Press, Taylor & Francis Group, Boca Raton, FL, USA, 2013.
[2] X.L. Zhao, Improving fatigue performance of steel members and connections using fibre reinforced polymer, in: The 6th International Conference on Smart Monitoring, Assessment and Rehabilitation of Civil Structures, SMAR 2022, 6–8 September 2022, Shanghai, China, 2022.
[3] Yashar Doroudi, D. Fernando, Ardalan Hosseini, Elyas Ghafoori, Behavior of cracked steel plates strengthened with adhesively bonded CFRP laminates under fatigue loading: Experimental and analytical study, Compos. Struct. 266 (2021) 113816.
[4] P. Feng, L.L. Hu, X.L. Zhao, L. Cheng, S.H. Xu, Study on thermal effects on fatigue behavior of cracked steel plates strengthened by CFRP sheets, Thin-Walled Struct. 82 (2014) 311–320.
[5] Lu Ke, Chuan-Xi Li, Jun He, Qiang Shen, YongMing Liu, Yang Jiao, Enhancing fatigue performance of damaged metallic structures by bonded CFRP patches considering temperature effects, Mater. Des. 192 (2020) 108731.
[6] Lili Hu, Mingyi Li, Tuerxunmaimaiti Yiliyaer, Wanyang Gao, Haitao Wang, Strengthening of cracked DH36 steel plates by CFRP sheets under fatigue loading at low temperatures, Ocean Eng. 243 (2021) 110203.
[7] N.J. Aljabar, X.L. Zhao, R. Al-Mahaidi, E. Ghafoori, M. Motavalli, Nigel Powers, Effect of crack orientation on fatigue behavior of CFRP-strengthened steel plates, Compos. Struct. 152 (2016) 295–305.
[8] N.J. Aljabar, X.L. Zhao, R. Al-Mahaidi, E. Ghafoori, M. Motavalli, Yew-Chin Koay, Fatigue tests on UHM-CFRP strengthened steel plates with central inclined cracks under different damage levels, Compos. Struct. 160 (2017) 995–1006.
[9] N.J. Aljabar, X.L. Zhao, R. Al-Mahaidi, E. Ghafoori, M. Motavalli, Y.C. Koay, Experimental investigation on the CFRP strengthening efficiency of steel plates with inclined cracks under fatigue loading, Eng. Struct. 172 (2018) 877–890.
[10] Tao Chen, Liang Hu, Ning-Xi Zhang, Qian-Qian Yu, Boundary element analysis of fatigue behavior for CFRP-strengthened steel plates with center inclined cracks, Thin-Walled Struct. 125 (2018) 164–171.
[11] Tao Chen, Ling-Zhen Li, Ning-Xi Zhang, Xiaobin Song, Yuya Hidekuma, Fatigue performance test on inclined central cracked steel plates repaired with CFRP strand sheets, Thin-Walled Struct. 130 (2018) 414–423.
[12] Lingzhen Li, Tao Chen, Ningxi Zhang, Yuya Hidekuma, Test on fatigue repair of central inclined cracked steel plates using different adhesives and CFRP, prestressed and non-prestressed, Compos. Struct. 216 (2019) 350–359.
[13] M. Mohajer, M. Bocciarelli, P. Colombi, A. Hosseini, A. Nussbaumer, E. Ghafoori, Irreversible cyclic cohesive zone model for prediction of mode I fatigue crack growth in CFRP-strengthened steel plates, Theor. Appl. Fract. Mech. 110 (2020) 102804.
[14] H.T. Wang, G. Wu, Crack propagation prediction of double-edged cracked steel beams strengthened with FRP plates, Thin-Walled Struct. 127 (2018) 459–468.
[15] J. He, G. Xian, Y.X. Zhang, Numerical modelling of bond behaviour between steel and CFRP laminates with a ductile adhesive, Int. J. Adhes. Adhes. 104 (2021) 102753.
[16] Q.Q. Yu, T. Chen, X.L. Gu, X.L. Zhao, Boundary element analysis of edge cracked steel plates strengthened by CFRP laminates, Thin-Walled Struct. 100 (2016) 147–157.
[17] C. Huang, T. Chen, S. Feng, Finite element analysis of fatigue crack growth in CFRP-repaired four-point bend specimens, Eng. Struct. 183 (2019) 398–407.
[18] J. Dong, Z. Li, H. Pasternak, Y. Ciupack, Reinforcement of fatigue damaged steel structures using CFRP lamellas-part 3: Numerical simulation, Bauingenieur 95 (2020) 362–368.
[19] A. Mohabeddine, J.A. Correia, P.A. Montenegro, J.M. Castro, Fatigue crack growth modelling for cracked small-scale structural details repaired with CFRP, Thin-Walled Struct. 161 (2021) 107525.
[20] R. Liu, T. Chen, L. Li, K. Tateishi, A practical stress intensity factor formula for CFRP-repaired steel plates with a central crack, J. Construct. Steel Res. 162 (2019) 105755.
[21] A. Hosseini, E. Ghafoori, M. Motavalli, A. Nussbaumer, X.L. Zhao, Mode I fatigue crack arrest in tensile steel members using prestressed CFRP plates, Compos. Struct. 178 (2017) 119–134.
[22] T. Rabczuk, G. Zi, A. Gerstenberger, W.A. Wall, A new crack tip element for the phantom-node method with arbitrary cohesive cracks, Internat. J. Numer. Methods Engrg. 75 (5) (2008) 577–599.
[23] R. Krueger, Virtual crack closure technique: History, approach, and applications, Appl. Mech. Rev. 57 (2) (2004) 109–143.
[24] O. Nguyen, E.A. Repetto, M. Ortiz, R.A. Radovitzky, A cohesive model of fatigue crack growth, Int. J. Fract. 110 (4) (2001) 351–369.
[25] G. Ventura, J.X. Xu, T. Belytschko, A vector level set method and new discontinuity approximations for crack growth by EFG, Internat. J. Numer. Methods Engrg. 54 (6) (2002) 923–944.
[26] N. Pugno, M. Ciavarella, P. Cornetti, A. Carpinteri, A generalized Paris' law for fatigue crack growth, J. Mech. Phys. Solids 54 (7) (2006) 1333–1349.
[27] H. Xin, J.A. Correia, M. Veljkovic, Three-dimensional fatigue crack propagation simulation using extended finite element methods for steel grades S355 and S690 considering mean stress effects, Eng. Struct. 227 (2021) 111414.
[28] N. van den Berg, H. Xin, M. Veljkovic, Effects of residual stresses on fatigue crack propagation of an orthotropic steel bridge deck, Mater. Des. 198 (2021) 109294.
[29] J. Liu, H. Xin, X.L. Zhao, Prediction of fatigue crack propagation in center cracked steel plate strengthened with prestressed CFRP strip, Thin-Walled Struct. 183 (2023) 110416.
[30] H. Xin, J. Liu, J.A. Correia, F. Berto, M. Veljkovic, G. Qian, Mixed-mode fatigue crack propagation simulation by means of Geq and walker models of the structural steel S355, Theor. Appl. Fract. Mech. 123 (2023) 103717.
[31] H. Xin, J. Liu, J.A. Correia, F. Berto, M. Veljkovic, Y. Fei, Strengthening effects evaluation on fatigue damage of rib to deck joint in orthotropic steel deck, Eng. Fail. Anal. (2022) 107041.
[32] A. Bassetti, A. Nussbaumer, P. Colombi, Repair of riveted bridge members damaged by fatigue using CFRP materials, Adv. FRP Mater. Civ. Struct. 19 (2000) 33–42.
[33] Q.Q. Yu, X.L. Zhao, R. Al-Mahaidi, Z.G. Xiao, T. Chen, X.L. Gu, Tests on cracked steel plates with different damage levels strengthened by CFRP laminates, Int. J. Struct. Stab. Dyn. 14 (06) (2014) 1450018.

Engineering Structures 304 (2024) 117622



Contents lists available at ScienceDirect

Engineering Structures

journal homepage: www.elsevier.com/locate/engstruct





Probabilistic fatigue stiffness variation of angle-ply GFRP composites considering stress ratio effect

Qinglin Gao [a], Haohui Xin [a], Cláudio Horas [b,*], Ayman S. Mosallam [c], Yuqing Liu [d], Filippo Berto [e], Jianxun Ma [a], Qing Sun [a], José A.F.O. Correia [f]

[a] Department of Civil Engineering, School of Human Settlements and Civil Engineering, Xi'an Jiaotong University, Xi'an, Shaanxi, PR China
[b] CONSTRUCT-LESE, Faculty of Engineering, University of Porto, Portugal
[c] Department of Civil & Environment Engineering, University of California, Irvine, CA, USA
[d] Department of Bridge Engineering, College of Civil Engineering, Tongji University, Shanghai, PR China
[e] Department of Chemical Engineering Materials Environment, University of Rome Sapienza, Rome, Italy
[f] INEGI & CONSTRUCT-LESE, Faculty of Engineering, University of Porto, Portugal

ARTICLE INFO

Keywords:
Fiber-reinforced polymer (FRP)
Stress ratio effects
Fatigue stiffness degradation model
Residual stiffness reliabilities
Bayesian inference

ABSTRACT

Fiber-reinforced polymer (FRP) composites are frequently used in bridges, wind power installations, and marine floating structures, and there is a growing interest in understanding their fatigue behavior. However, due to a considerable dispersion of the fatigue properties of FRP composites, reliable tools for probabilistic prediction of the fatigue stiffness are required. Thus, in this work, it is proposed a method that uses Bayesian inference and Markov Chain Monte Carlo (MCMC) simulations to estimate the degradation of the stiffness in FRP composites. This methodology is suggested not only to predict the fatigue residual stiffness, but also to consider the reliability of such predictions. Currently, the existing models for stiffness degradation in FRP composites need to fit the model parameters separately under different stress ratios. To address this, a correction term is proposed to describe the relationship between the stress level, stress ratio, fatigue cycles, and residual stiffness. The results achieved validate and prove the effectiveness of the suggested stiffness model, which incorporates four material parameters to calculate the residual fatigue stiffness of FRP composites.

1. Introduction

When compared to traditional construction materials, fiber-reinforced polymer (FRP) composites have a range of appealing characteristics, including the high strength-to-weight ratio, superior corrosion resistance, and exceptional fatigue performance. The lightweight nature of FRP composites provides a significant advantage in substantially reducing the structural dead load, particularly for highway bridges, wind power installations, and marine floating structures. Since the early 1990 s, FRP composites have found extensive application as an external strengthening system, in addition to their use in the construction of lightweight civilian and military structures [1–8]. Throughout the service life of bridge structures, FRP composite elements are consistently subjected to fatigue loading from vehicular traffic. The damage to the structure is largely caused by fatigue loading. Thus, it is essential to conduct a detailed assessment of the fatigue behavior of FRP composites, with this being critical to fully leverage the advantageous properties of these materials in several structural applications [8–11].

Damage to FRP composites under fatigue loading typically starts at a very early stage as small-size matrix cracks, which eventually propagate and grow, leading to delamination and gradual mechanical degradation. In general, three types of phenomenological models [12,13] can be used to describe the evolution of the fatigue behavior, namely: i) models for predicting fatigue life; ii) models for estimating residual stiffness; and iii) models for evaluating residual strength. Creating a fatigue life model and a residual strength model requires conducting several destructive tests, with only one data point being obtained from each test. However, developing a residual stiffness model allows for multiple data points to be gathered from a single test without causing relevant damage to the specimen. Thus, stiffness degradation is often applied as an efficient parameter for characterizing fatigue damage in composite structures [14–16].

Prior research [17–20] has illustrated the progression of damage and the reduction in stiffness of FRP composites subjected to fatigue loading.

* Corresponding author.
E-mail address: claudiohoras@fe.up.pt (C. Horas).

https://doi.org/10.1016/j.engstruct.2024.117622
Received 19 October 2023; Received in revised form 26 December 2023; Accepted 4 February 2024
Available online 17 February 2024
0141-0296/© 2024 Elsevier Ltd. All rights reserved.

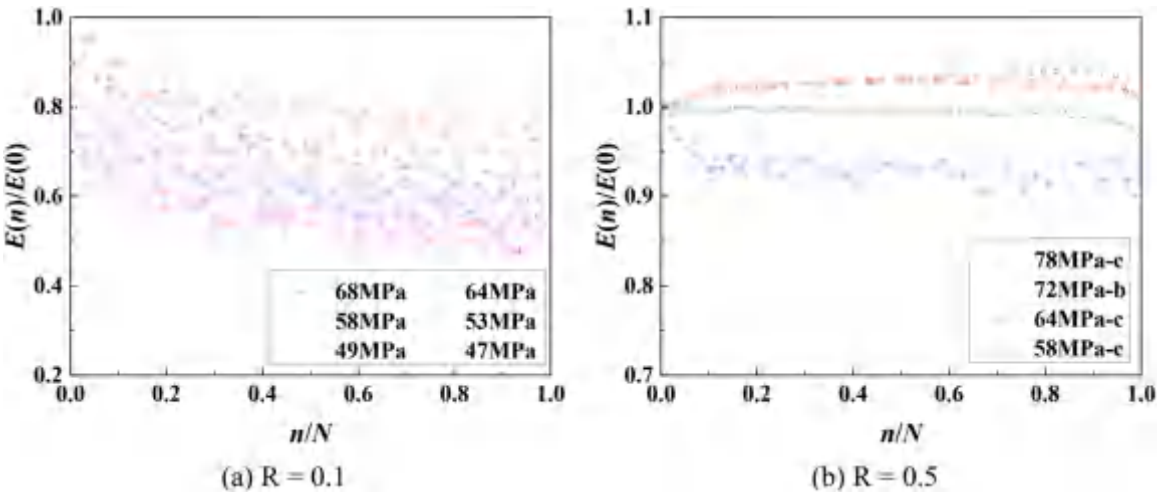


Fig. 1. Experimental data related to the residual stiffness under fatigue loading.

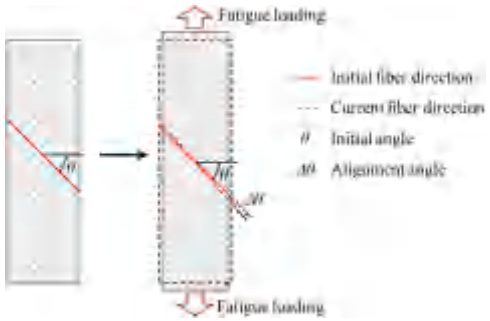


Fig. 2. Schematic diagram illustrating the alignment angle of fibers.

Several models [21–28] have been proposed to describe the concept of residual stiffness from a phenomenological perspective. For example, Yang et al. [21] suggested a statistical model for stiffness degradation in graphite/epoxy laminates, aimed at predicting the residual stiffness in FRP composite laminates exposed to fatigue loading. Papanikos et al. [22] stated an almost linear decline in the stiffness of quasi-isotropic CFRP laminates, and used a linear equation to describe the link between normalized residual stiffness and the normalized number of cycles. Khan et al. [23] developed an analytical model that considers the correlation between fatigue-induced damage and the reduction in stiffness of laminated panels exposed to fatigue loading. Hochard and Thollon [24] introduced a generalized nonlinear cumulative damage model for woven ply laminates, which substitutes the woven ply with two stacked unidirectional plies that correspond to the warp and weft thicknesses. The accuracy of such a model was confirmed after tensile-tensile fatigue testing for several plies and stress ratios. Liu et al. [25] introduced an analytical residual stiffness model to assess the impact of voids on the fatigue of FRP composites. Carraro and Quaresimin [26] formulated a model to describe the degradation of stiffness in composite laminates under several loading conditions, also proposing a damage-based design approach for predicting damage progression and

Table 1
Mechanical properties of the fibers and resin [42].

Property	Modulus, E (GPa)	Poisson's ratio, ν	Shear modulus, G (GPa)
E-glass fibers	72.0	0.30	27.70
Resin	3.50	0.35	1.30

Table 2
Fitted parameters of stiffness variation equation due to the fiber realignment for $R = 0.5$.

Parameters	Fitted results
a_f (95% confidence bounds)	-0.2152 (−0.2650, −0.1653)
b_f (95% confidence bounds)	0.005127 (0.004432, 0.005821)
$c_{1,f}$ (95% confidence bounds)	0.4885 (0.4854, 0.4916)
$c_{2,f}$ (95% confidence bounds)	6.864 (6.747, 6.981)
R^2	0.9883

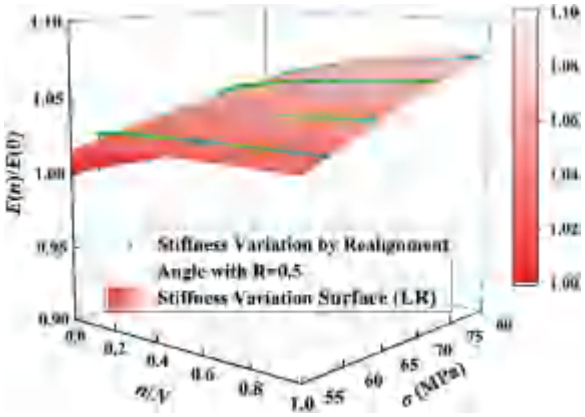


Fig. 4. Stiffness variation due to the fiber realignment for $R = 0.5$.

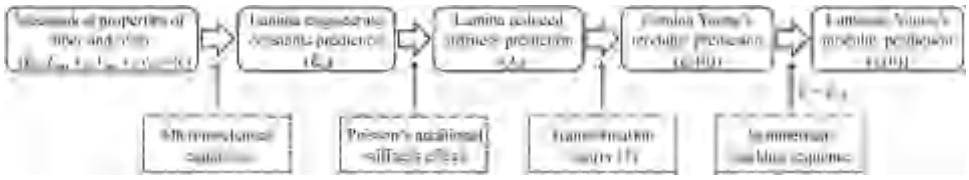


Fig. 3. Flowchart for the micromechanics analysis process.

Table 3
Fitted parameters of normalized residual stiffness model by the LR method.

Parameters	Stress ratio	
	0.1	0.5
a (95% confidence bounds)	-0.5525 (−0.5706, −0.5343)	-0.8910 (−1.069, −0.7132)
b (95% confidence bounds)	0.01440 (0.01406, 0.01474)	0.01697 (0.01404, 0.01990)
c_1 (95% confidence bounds)	2.509 (2.387, 2.631)	0.9246 (0.9114, 0.9378)
c_2 (95% confidence bounds)	2.513 (2.431, 2.596)	4.424 (4.221, 4.626)
R^2	0.8138	0.7172

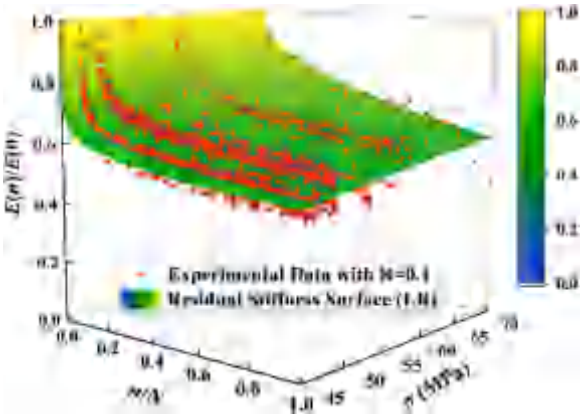


Fig. 5. Normalized residual stiffness results obtained from fitting for $R = 0.1$.

stiffness reduction in composite laminates. Gao et.al. [27] considered the uncertainties of initial strength and initial stiffness, and a pair of probabilistic models of residual strength and residual stiffness were proposed. The performance degradation data of Gr/PEEK $[0/45/90/-45]_{2S}$ laminates were utilized to verify the suggested probabilistic models. Philippidis et al. [28] explored the residual stiffness of composites subjected to fatigue loading at several stress ratios, establishing a correlation between composite stiffness degradation and fatigue life.

Earlier investigations [15,28–31] have emphasized the impact of the stress ratio (R) when evaluating the stiffness degradation of FRP composites. Shokrieh and Lessard [32,33] suggested a generalized model for assessing the residual performance degradation of unidirectional laminates. After analysing the fatigue damage for different stress ratios, a normalized residual performance degradation rule was defined. Nonetheless, it is worth noting that the stiffness degradation model is primarily based on unidirectional FRP composite laminates, and its suitability for multi-directional laminates requires further validation. Additionally, the mesoscale heterogeneity of FRP composites contributes to the dispersion of fatigue test results. When integrating FRP components into any structure, it becomes essential to assess the reliability of the predicted fatigue residual stiffness. Moreover, with the inclusion of the stress ratio, additional material parameters are introduced into the stiffness degradation equation. The analytical probability method is not well-suited for predicting the reliabilities of FRP composites' residual stiffness or determining the allowable stress and fatigue cycles related to a specified stiffness. Consequently, it is necessary to develop an alternative approach using the Monte Carlo method [34] and Bayesian inference [21,35] to get probabilistic estimates of fatigue residual stiffness, while simultaneously proving the validity of the stiffness degradation model of FRP composites.

As mentioned previously, the primary goal of this investigation is to evaluate the stiffness degradation in FRP composite laminates subjected to fatigue loading, taking into account the influence of stress ratios to

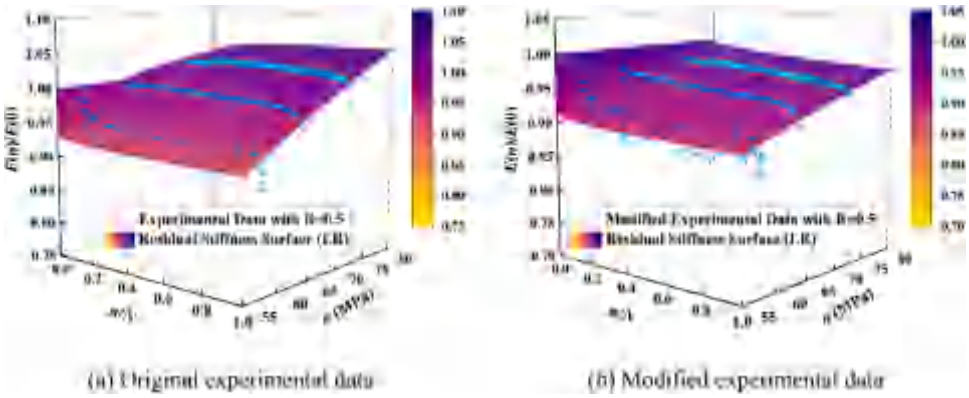


Fig. 6. Normalized residual stiffness results obtained from fitting for $R = 0.5$.

Table 4
Prior distribution of normalized residual stiffness model at different stress levels.

Stress ratio	Stress level	Number of points	Prior distribution						
			A	SE	SD	B	SE	SD	R^2
0.1	47 MPa	3509	0.5064	0.7908×10^{-3}	46.84×10^{-3}	0.1390	0.0245×10^{-3}	1.454×10^{-3}	0.7698
	49 MPa	1843	0.4445	1.5816×10^{-3}	67.90×10^{-3}	0.1577	0.0901×10^{-3}	3.087×10^{-3}	0.6524
	53 MPa	2868	0.4549	0.9184×10^{-3}	49.18×10^{-3}	0.1604	0.0343×10^{-3}	1.837×10^{-3}	0.7628
	58 MPa	370	0.4056	3.3163×10^{-3}	63.79×10^{-3}	0.2426	0.4589×10^{-3}	8.827×10^{-3}	0.7533
	64 MPa	32	0.4538	16.150×10^{-3}	91.36×10^{-3}	0.4632	8.6903×10^{-3}	49.16×10^{-3}	0.8404
	68 MPa	55	0.3818	8.4184×10^{-3}	62.43×10^{-3}	0.3835	3.7863×10^{-3}	28.08×10^{-3}	0.8432
0.5	58 MPa	472	0.1129	0.8163×10^{-3}	17.735×10^{-3}	0.1533	0.2818×10^{-3}	6.122×10^{-3}	0.6374
	64 MPa	129	0.0564	0.6276×10^{-3}	7.1276×10^{-3}	0.1989	0.9571×10^{-3}	10.87×10^{-3}	0.8082
	72 MPa	478	0.0368	0.4056×10^{-3}	8.8677×10^{-3}	0.1977	0.5274×10^{-3}	11.53×10^{-3}	0.4102
	78 MPa	37	0.0360	0.5689×10^{-3}	3.4604×10^{-3}	2.374×10^{-6}	1.6769×10^{-3}	10.20×10^{-3}	0.8723

Table 5
Parameters of normalized residual stiffness reliabilities at different stress levels.

Stress ratio	Stress level	Parameter	Residual stiffness curve	Residual stiffness reliability curve			Parameter	Residual stiffness curve	Residual stiffness reliability curve		
				95.0%	97.7%	99.0%			95.0%	97.7%	99.0%
0.1	47 MPa	*A*	0.5062	0.5842	0.6028	0.6218	*B*	0.1390	0.1390	0.1389	0.1387
	49 MPa		0.4448	0.5568	0.5830	0.6615		0.1577	0.1576	0.1575	0.1569
	53 MPa		0.4548	0.5367	0.5560	0.5763		0.1604	0.1602	0.1600	0.1603
	58 MPa		0.4057	0.5098	0.5347	0.5612		0.2425	0.2410	0.2404	0.2398
	64 MPa		0.4529	0.5969	0.6328	0.6568		0.4647	0.4399	0.4358	0.4194
	68 MPa		0.3818	0.4853	0.5059	0.5305		0.3835	0.3742	0.3676	0.3683
0.5	58 MPa		0.1129	0.1427	0.1499	0.1571		0.1533	0.1527	0.1520	0.1486
	64 MPa		0.05639	0.0684	0.0710	0.0741		0.1991	0.1965	0.1954	0.1965
	72 MPa		0.03682	0.0516	0.0552	0.0587		0.1975	0.1951	0.1951	0.1924
	78 MPa		0.03599	0.0418	0.0433	0.0447		4.580×10^{-4}	7.536×10^{-7}	6.291×10^{-8}	6.544×10^{-7}

compute the reliabilities of fatigue residual stiffness. To achieve this, the Least-squares Regression (LR) method was initially implemented to estimate a normalized residual stiffness model for the composite laminates. Afterwards, a methodology is introduced to compute the parameters of the fatigue stiffness degradation model using Bayesian inference and Markov Chain Monte Carlo (MCMC) simulations, with the results obtained then compared with those from the LR method. Subsequently, Bayesian inference and MCMC simulations are considered to estimate the probabilistic residual stiffness, assuming different levels of stiffness reliabilities. Lastly, the suggested revision term is introduced to the original normalized residual stiffness model. Also, it is important to emphasize that the recommended Bayesian inference and MCMC simulations are employed for predicting probabilistic fatigue stiffness degradation, considering the influence of stress ratios.

2. Fitted normalized residual stiffness model

2.1. Experimental data

The fatigue test results for glass-fiber-reinforced polymer (GFRP) composite laminates, admitting a stacking sequence of $[\pm 45]_{2s}$, have been reported in prior studies [36–38]. This investigation involved a total of 44 specimens to assess the fatigue performance of GFRP laminates. The fatigue tests [36–38] were adopted by loading control with sinusoidal cyclic pattern. The strain was provided by a video extensometer with an acquisition frequency of 160 fps. The fatigue stress levels of the tests were between 47 MPa and 78 MPa with fatigue life ranges from 500 to 10^7 cycles. The fatigue test of each stress level contained repeated tests of four specimens. All fatigue tests were carried out in a chamber with a constant temperature of 20 °C and the same loading rate of 30.5 kN/s was used to avoid the temperature increase during the loading process. Among these specimens, 24 were subjected to a stress ratio (R) of 0.1, while the remaining 20 laminate specimens were tested at a stress ratio of $R = 0.5$. All specimens had dimensions of 250.0 mm × 25.0 mm × 2.3 mm and a fiber volume ratio of 62%. The details of the experiment can be found in Refs [36–38].

All relevant experimental data points for GFRP laminates subjected to a stress ratio (R) of 0.1 [36,38] were measured, and were considered to obtain the fatigue stiffness degradation (as shown in Fig. 1a). For the case of $R = 0.5$, data from typical specimens described in Ref. [37] were used to illustrate the normalized residual stiffness (as shown in Fig. 1b). The normalized stiffness of a typical specimen, as in Fig. 1b, exceeds 1.0 at lower stress levels. Similar results, in which stiffness increases as the number of fatigue cycles grows, has been noted by Radhakrishnan [39]. According to Movahedi-Rad [37], the rise in stiffness can be attributed to the realignment of the fibers during the fatigue loading process. Consequently, the actual fatigue stiffness of angle-ply GFRP laminates results from combining stiffness increase due to fiber realignment and degradation due to cumulative fatigue damage.

2.2. Normalized residual stiffness model

A two-stage model is applied to assess the stiffness changes in angle-ply GFRP laminates, ignoring the third rapid decline stage [36–38,40] in material behavior. Based on Yang's stiffness degradation model [21], a normalized residual stiffness model [41] is derived to relate normalized residual stiffness $E(n)/E(0)$, stress level σ, and normalized fatigue cycles n/N during fatigue loading:

$$\frac{E(n)}{E(0)} = 1 - \left[1 - \left(\frac{\sigma}{c_1\sigma_U}\right)^{1/c_2}\right]\left(\frac{n}{N}\right)^{a+b\sigma} \tag{1}$$

where, n is the number of fatigue loading cycles; N is the fatigue life expressed in number of cycles; $E(0)$ is the initial stiffness; $E(n)$ is the stiffness after n cycles of loading; σ_U is the strength of FRP composites; and c_1, c_2, a, b are the parameters fitted to the model.

For a certain stress level, Eq. (1) can be simplified as follows:

$$\frac{E(n)}{E(0)} = 1 - A\left(\frac{n}{N}\right)^B \tag{2}$$

where, A and B are the fitted parameters.

It is important to note that at a high-stress ratio the mean stress is also high [37,39], which can introduce additional damage to the composite material due to the creep effects during fatigue loading. In addition, for the angle-ply GFRP laminates, the creep will gradually alter the alignment angle of the laminate fibers (see Fig. 2) as the number of fatigue cycles increases, which becomes one of the main reason for the variation of the stiffness of the laminates. Until now, several stiffness degradation models, including the one in Eq. (1), have not taken into account the creep effect, even though previous research has highlighted its substantial influence [37]. Thus, an equation describing the changes in fatigue stiffness caused by the creep effects is introduced, following a similar form of Eq. (1) and illustrated in Eq. (3). This equation takes into account that the fatigue stiffness variation due to the fiber realignment is related to the stress level and fatigue cycles.

$$\frac{E_f(n)}{E_f(0)} = 1 - \left[1 - \left(\frac{\sigma}{c_{1f}\sigma_U}\right)^{1/c_{2f}}\right]\left(\frac{n}{N}\right)^{a_f+b_f\sigma} \tag{3}$$

where, $E_f(n)/E_f(0)$ is the normalized stiffness due to fiber realignment during fatigue loading; $E_f(n)$ is the stiffness variation due to fiber realignment over n loading cycles; and $c_{1,f}$, $c_{2,f}$, a_f, b_f are the fitted parameters.

Thus, the original equation for normalized residual stiffness is proposed to be modified as follows:

$$\frac{E(n)}{E(0)} = 1 - \left[1 - \left(\frac{\sigma}{c_1\sigma_U}\right)^{1/c_2}\right]\left(\frac{n}{N}\right)^{a+b\sigma} - \left[1 - \left(\frac{\sigma}{c_{1f}\sigma_U}\right)^{1/c_{2f}}\right]\left(\frac{n}{N}\right)^{a_f+b_f\sigma} \tag{4}$$

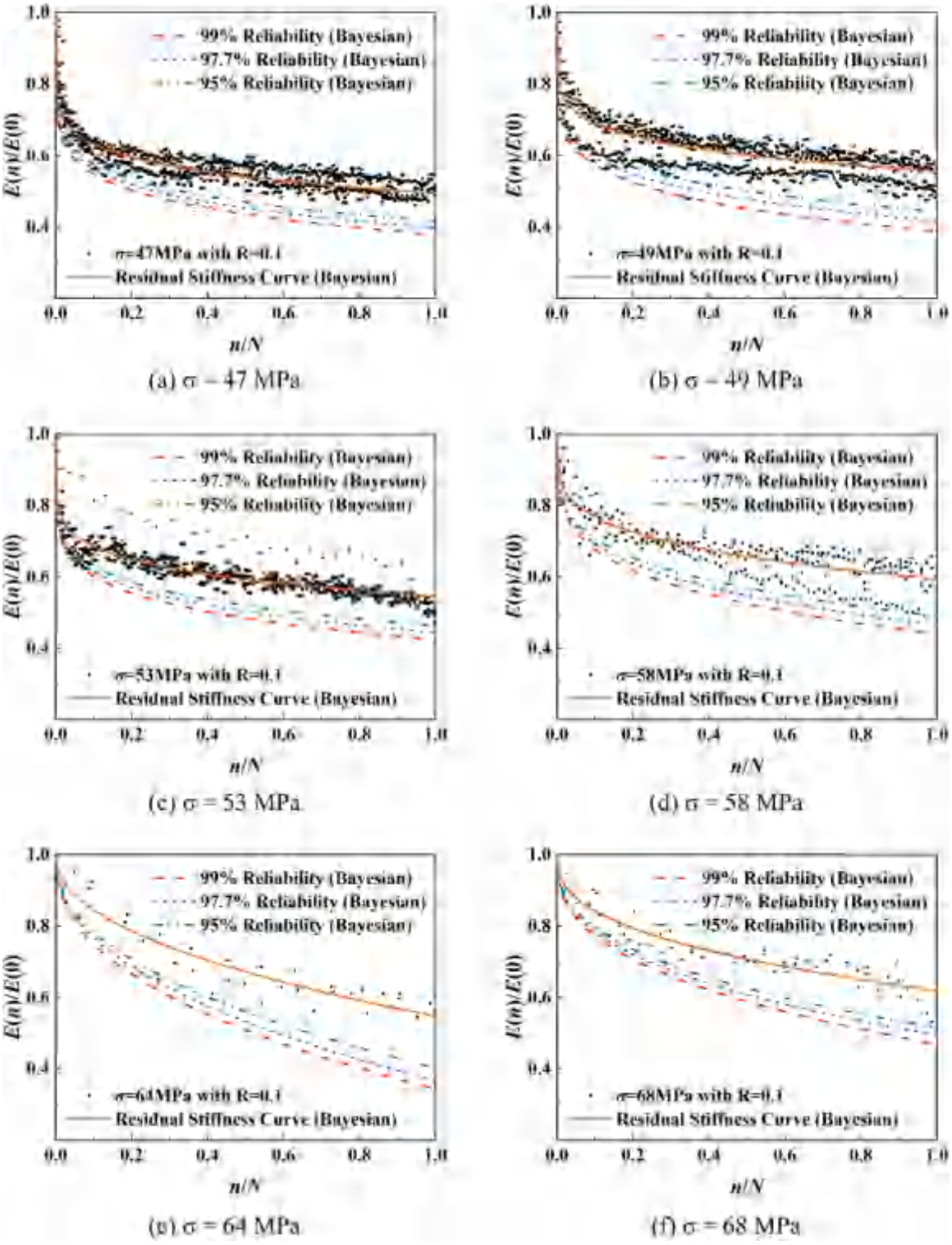


Fig. 7. Normalized residual stiffness curves and several reliability curves for R = 0.1 at different stress levels.

2.3. Stiffness variation due to the fiber realignment

Considering that creep has a minor impact at low-stress ratios and the realignment of fibers is not significant, stiffness variation can be assumed as negligible at $R = 0.1$ [37]. However, for a stress ratio of $R = 0.5$, the influence of the fiber realignment on stiffness should be taken into account. In the prior analysis, the mechanical characteristics of composite laminates are derived from the properties of the fiber, matrix, and interface. Thus, the micromechanics method [42,43] is employed to compute the modulus of FRP laminates as a function of the angle between the fiber direction and the loading direction. The stiffness increment resulting from the fiber realignment is determined to assess its impact on the stiffness of the composite laminate. Fig. 3 provides a flowchart for calculating the laminate's stiffness through micromechanics analysis, and Table 1 details the mechanical properties of both glass fibers and resin [42].

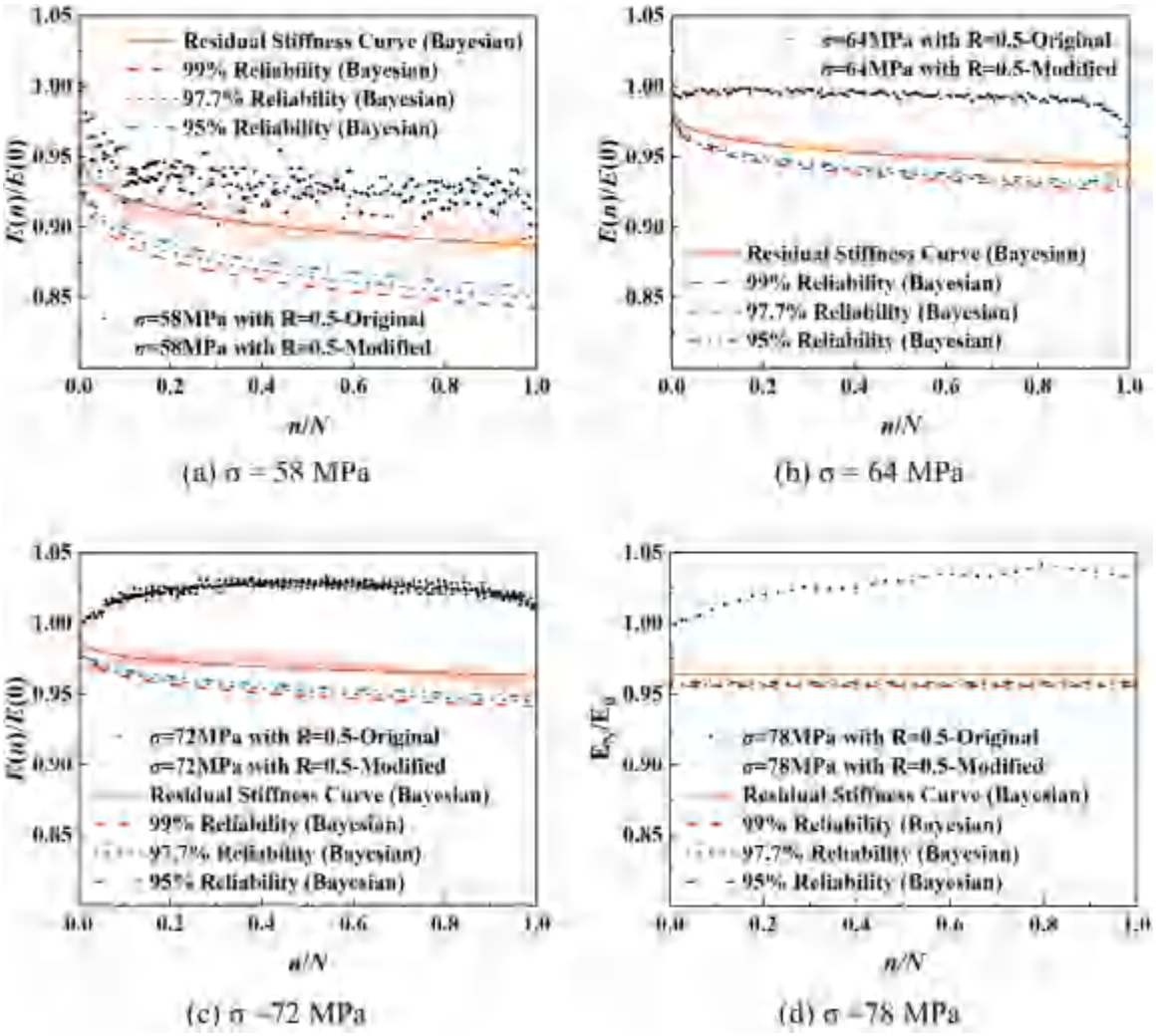


Fig. 8. Normalized residual stiffness curves and several reliability curves for R = 0.5 at different stress levels.

Table 6
Normalized residual stiffness model parameters considering the stress level.

Parameters	Stress ratio	
	0.1	0.5
a (95% confidence bounds)	-0.5522 (−0.5737, −0.5307)	-0.9734 (−1.1320, −0.8150)
b (95% confidence bounds)	0.01431 (0.01391, 0.01472)	0.01843 (0.01583, 0.02104)
c_1 (95% confidence bounds)	2.437 (2.301, 2.574)	0.9277 (0.9162, 0.9391)
c_2 (95% confidence bounds)	2.474 (2.378, 2.569)	4.380 (4.211, 4.550)
R^2	0.9567	0.7788

Table 7
The parameters of normalized residual stiffness reliabilities considering the stress level.

Stress ratio	Parameters	Residual stiffness reliability surface		
		95.0%	97.7%	99.0%
0.1	a	-0.5164	-0.5041	-0.4874
	b	0.01359	0.01334	0.01300
	c_1	8.142	12.44	15.31
	c_2	3.363	3.649	3.649
0.5	a	-0.9594	-0.9671	-0.9958
	b	0.0182	0.01832	0.01876
	c_1	0.9220	0.9214	0.9205
	c_2	3.379	3.205	3.040

The results showed a good agreement between experimental and analytical data. For instance, the experimentally determined stiffness of GFRP laminates is $E_{test}(0) = 24.76$ GPa, and the stiffness predicted by micromechanics analysis is $E_{micro}(0) = 23.13$ GPa, with a minor deviation of 6.6%.

Table 2 presents the parameters obtained by the Least-squares Regression (LR) method for the stiffness variation due to the fiber realignment in accordance with the equation proposed in [44]. Fig. 4 illustrates the corresponding experimental data points and the stiffness variation surface. The coefficient of determination (R^2) is 0.9883. At a maximum stress of 78 MPa, the stiffness increment reaches almost 8%, highlighting the significance of considering the impact of the fiber realignment at high-stress ratios.

2.4. Normalized residual stiffness equations

The correlation between normalized residual stiffness, normalized fatigue cycles, and stress level, derived from laboratory fatigue tests, is established by the LR method. More specifically, Eq. (1) is fitted for a low-stress ratio ($R = 0.1$), while Eq. (4) is fitted for a high-stress ratio ($R = 0.5$). The parameters considered in the fitting of these equations are detailed in Table 3.

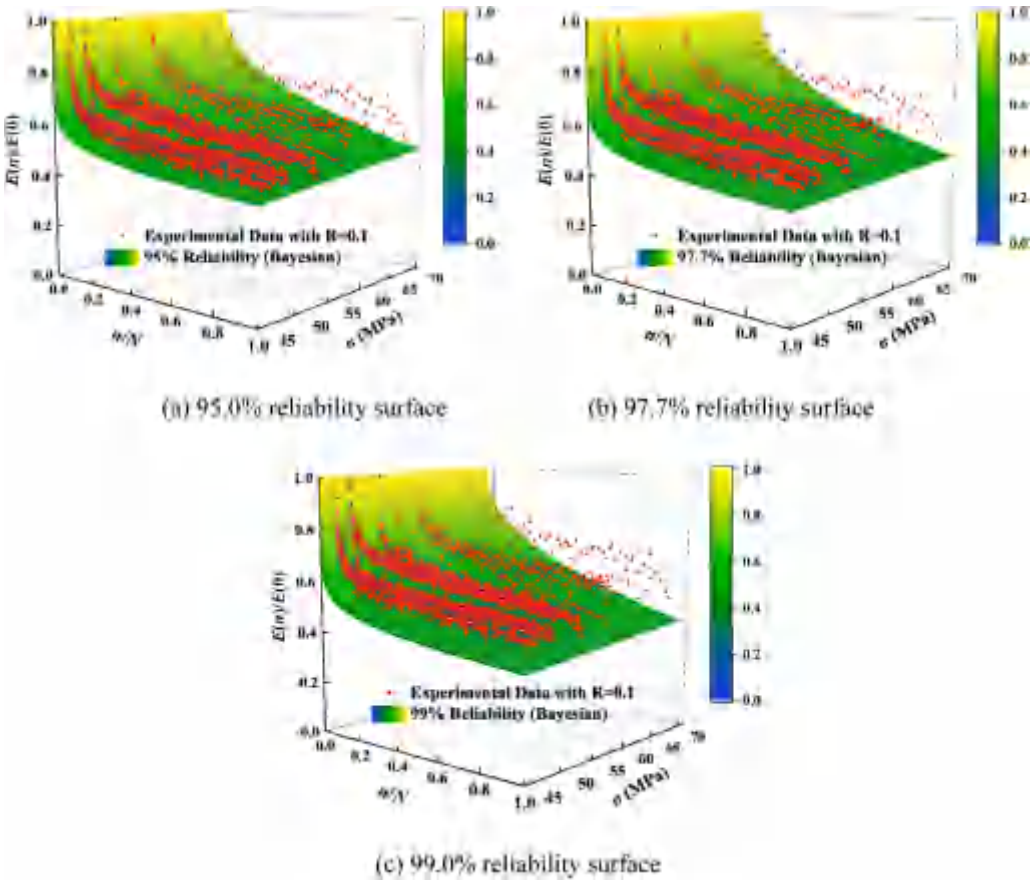


Fig. 9. Several residual stiffness reliability surfaces for $R = 0.1$.

Figs. 5 and 6 offer comparisons between the fitted outcomes and the experimental data points, with stress (σ) on the X-axis, normalized fatigue cycles n/N on the Y-axis, and normalized residual stiffness $E(n)/E(0)$ on the Z-axis. In particular, Fig. 6(a) displays the fitted results based on the original experimental data, while Fig. 6(b) presents the fitted results using modified experimental data that subtracts the stiffness increment due to the fiber realignment from the original experimental data. The results demonstrate coefficients of determination exceeding 0.70, with a noticeable decline in residual stiffness as normalized fatigue cycles increase, particularly at lower stress levels or stress ratios.

3. Probabilistic fatigue residual stiffness evaluation based on Bayesian inference

3.1. Bayesian inference and MCMC simulations

The Bayesian inference model comprises three main components: i) a set of input parameters $x \in \{A, B\}$ to be inferred; ii) a computational forward model $M(x)$; and iii) a set of experimental data $y = E(n)/E(0)$. As the forward model is inherently an approximation of real outcomes, a discrepancy term, ε, is introduced to relate the model predictions, $M(x_i)$, to the actual experimental data, y_i:

$$y = M(x) + \varepsilon \tag{5}$$

The discrepancy term, ε, is defined by the subsequent expression, which follows a Gaussian distribution [45]:

$$\varepsilon \sim N(\varepsilon|0, \boldsymbol{\Sigma}) \tag{6}$$

where, 0 is the mean value of ε, and $\boldsymbol{\Sigma}$ is the covariance matrix.

The discrepancy model, $\pi(y|x)$, for experimental data can be expressed as:

$$\pi(y|x) = N(y|M(x), \boldsymbol{\Sigma}) \tag{7}$$

In practice, the discrepancy represents a measurement error. In the Bayesian framework, it is assumed that the parameters of the discrepancy model follow the prior distribution $\pi(x)$. Then, the posterior distribution of the parameters, $\pi(x|y)$, can be expressed as [45]:

$$\pi\left(x|y\right) = \frac{\pi(y|x)\pi(x)}{\pi(y)} \tag{8}$$

Now, considering a dataset of experimental data denoted as $Y = \{y_1, y_2, \cdots, y_N\}$, the likelihood function of the parameters x is defined as follows [45]:

$$L\left(x, Y\right) = \prod_{k=1}^{N} \pi(y_k, x) \tag{9}$$

The posterior distribution $\pi(x|Y)$ can be further expressed as [45]:

$$\pi\left(x|Y\right) = \frac{L(x, Y)\pi(x)}{Z} \tag{10}$$

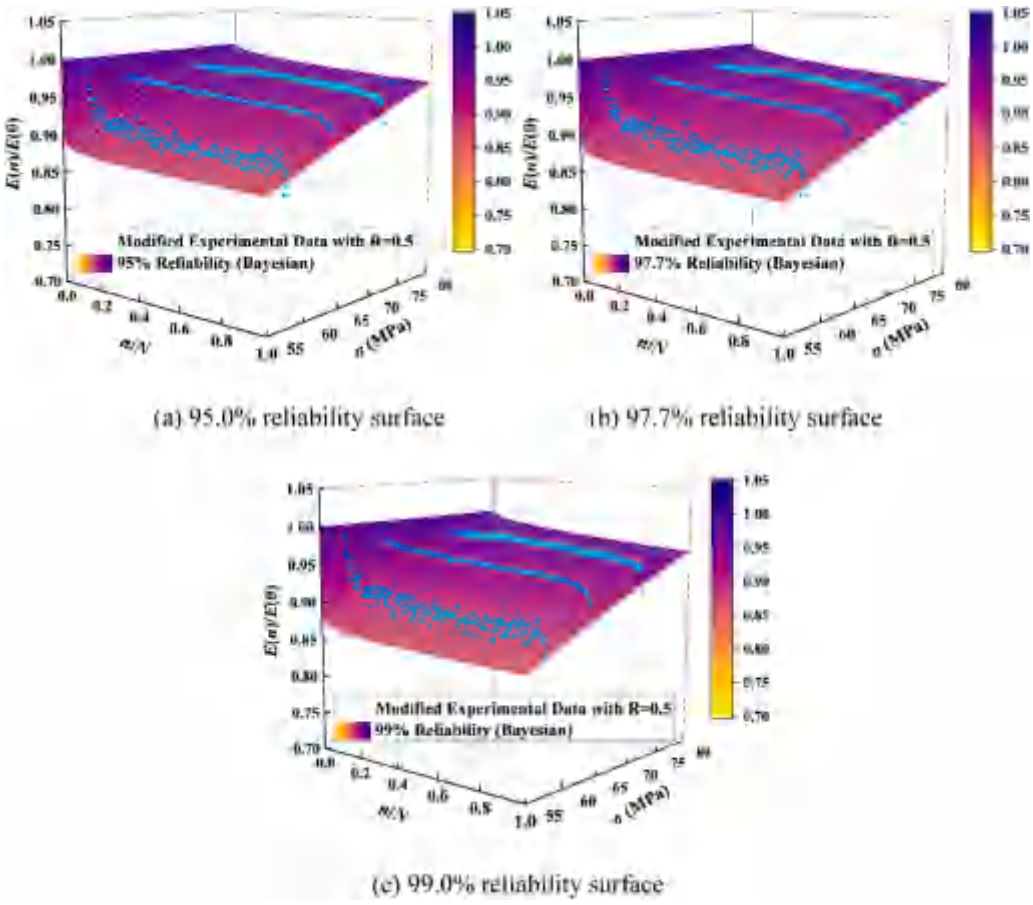
where, Z is the normalized factor defined by the following integral:

$$Z = \int_{\{A,B\}} L(x, Y)\pi(x)dx \tag{11}$$

Replacing Eq. (7) into Eq. (9) results in:

$$L\left(x, Y\right) = \prod_{k=1}^{N} N(y_i|M(x), \boldsymbol{\Sigma}) \tag{12}$$

Also, Eq. (10) can be written as:



(a) 95.0% reliability surface (b) 97.7% reliability surface

(c) 99.0% reliability surface

Fig. 10. Several residual stiffness reliability surfaces for $R = 0.5$.

Table 8
Relative discrepancy between the fitted results considering and without considering the stress level.

Stress ratio	Stress level	Residual stiffness surface	Residual stiffness reliability surface		
			95.0%	97.7%	99.0%
0.1	47 MPa	3.19%	1.97%	1.79%	1.30%
	49 MPa	4.16%	1.58%	0.50%	0.53%
	53 MPa	2.48%	2.09%	2.52%	2.63%
	58 MPa	2.24%	2.88%	2.87%	2.86%
	64 MPa	2.98%	6.48%	8.15%	8.61%
	68 MPa	0.91%	2.71%	3.34%	3.89%
0.5	58 MPa	1.24%	1.66%	1.77%	1.87%
	64 MPa	1.58%	2.24%	2.42%	2.59%
	72 MPa	0.69%	0.55%	0.53%	0.53%
	78 MPa	1.45%	1.52%	1.54%	1.57%

$$\pi\left(x|Y\right) = \frac{1}{Z}\pi(x)\prod_{k=1}^{N} N(y_i|M(x),\mathbf{\Sigma}) \tag{13}$$

Thus, the posterior mean value [45] is formulated as follows:

$$E[x|Y] = \int_{\{A,B\}} x\pi(x|Y)dx \tag{14}$$

If the posterior distribution is an intermediate quantity, the conditional expectation [45] is calculated as:

$$E[h(x)|Y] = \int_{\{A,B\}} h(x)\pi(x|Y)dx \tag{15}$$

The estimation uncertainty can be quantified using the posterior covariance matrix [45]:

$$\mathrm{Cov}[x|Y] = \int_{\{A,B\}} (x - E[x|Y])(x - E[x|Y])^{\mathrm{T}}\pi(x|Y)dx \tag{16}$$

In practice, the posterior distribution presented in Eq. (13) often lacks an analytical solution. To address this issue, MCMC simulations are performed to generate samples from a given probability distribution. The fundamental concept behind MCMC simulations [46,47] involves constructing a Markov Chain, denoted as $(x^1, x^2, \cdots)$, that explores the prior space, $\{A, B\}$, with an invariant distribution equivalent to the posterior distribution of interest.

Within the Markov Chain, the parameter value at time $(n + 1)$ relies on the parameter value of time n (i.e., x(n + 1) will depend on x(n)), independently of $\{x^{(n-1)}, x^{(n-2)}, \cdots, x^{(0)}\}$. If the transition probability, $K(x^{(t+1)}|x^{(t)})$, fulfils the detailed balance condition [46]:

$$\pi\left(x^{(t)}|Y\right)K\left(x^{(t+1)}|x^{(t)}\right) = \pi\left(x^{(t+1)}|Y\right)K\left(x^{(t)}|x^{(t+1)}\right) \tag{17}$$

Thus, the posterior value is the invariant distribution of the Markov Chain. Integrating Eq. (17) results in:

$$\pi\left(x^{(t+1)}|Y\right) = \int_{\{A,B\}} \pi\left(x^{(t)}|Y\right)K\left(x^{(t+1)}|x^{(t)}\right)dx^{(t)} \tag{18}$$

Finally, the expectation can be approximated as shown in Eq. (19) [45] by averaging the $T + 1$ generated sample points $x^{(t)}$ over the iterations.

$$E[h(x)|Y] \approx \frac{1}{T}\sum_{t=1}^{1} h\left(x^{(t)}\right) \tag{19}$$

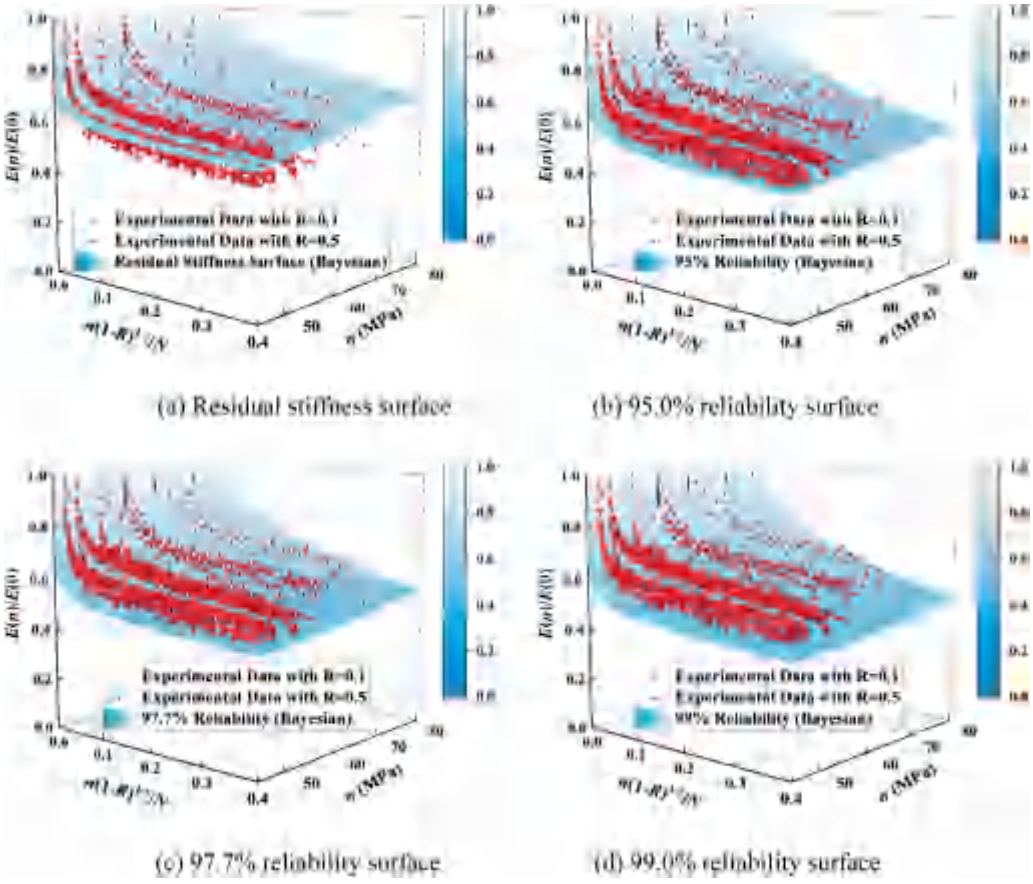


Fig. 11. Fatigue residual stiffness reliability surfaces considering stress ratio effects.

3.2. Probabilistic fatigue residual stiffness prediction based on Bayesian inference at different stress levels

The stiffness data used in this study are derived from two stress ratios. The stress ratio R= 0.1 contains test data at six different stress levels. The stress ratio R= 0.5 contains test data at four different stress levels. In order to ensure that the weight of each test is the same, it is considered that the weight of each stress level in the calculation process is 1/10. The weight of each data point is the product of 1/10 and the reciprocal of the number of data points (the number of data points is 3509 for the case of $\sigma = 47$ MPa with R=0.5, and the weight of single data point is 1/35090). Using Eq. (2), the relationship between normalized fatigue stiffness and fatigue cycles is established at every stress level. In the analysis, the original experimental data are used in the set of normalized stiffness data with an R of 0.1, while the stiffness increase due to the fiber realignment must be considered when $R = 0.5$. To mitigate the impact of the fiber realignment and achieve an accurate representation of degradation of the material performance, the modified experimental data is used in the dataset with $R = 0.5$.

The prior distribution of the experimental data (i.e., parameters mean values, and standard errors) is established through the LR method. It is essential to note that the standard error (SE) serves as a measure of the gap between sample and population mean values, and cannot be used to measure the sample dispersion. Thus, the standard deviations (SD) for both A and B are computed using Eq. (20) as the parameters of the prior distribution. These results are provided in Table 4.

$$SD = \sqrt{n_p} \cdot SE \tag{20}$$

where, n_p represents the count of data points obtained from testing.

The R^2 values for the majority of the prior distribution exceeds 0.6, except for the case of $\sigma = 72$ MPa and $R = 0.5$. In general, a larger dataset leads to reduced SE and greater confidence in the fitted parameters.

In order to generate random samples from the probability distribution, the Affine Invariant Ensemble Algorithm (AIES) [48], which is an enhanced method derived from the standard MCMC algorithm, was used. Table 5 presents the posterior distributions of the parameters calculated with the open-source software program UQLab [45]. The results indicate that the posterior distribution values closely align with the prior distribution values obtained for cases with high number of experimental data points. Nevertheless, some differences may emerge in cases with a lower number of experimental data points, in particular for the case of $\sigma = 78$ MPa with $R = 0.5$, where the value of parameter B exhibits significant variability.

The relationship between normalized residual stiffness and fatigue cycles at different reliability levels was also predicted by implementing the MCMC algorithm and Bayesian inference. Figs. 7 and 8 depict the fitted residual stiffness curves and the corresponding residual stiffness reliability curves for reliability levels of 99.0%, 97.7%, and 95.0%. The parameters of the residual stiffness equation for several reliabilities are presented in Table 5. The results obtained demonstrate that the curves enable a reasonable calculation of GFRP laminates' stiffness degradation, and provide an estimate of the design stiffness at the life expectancy.

3.3. Probabilistic prediction of fatigue residual stiffness based on Bayesian inference considering the stress level

The influence of stress level on stiffness degradation is identified in Eq. (1). The fatigue residual stiffness curves at several stress levels, as described in the previous section, are used to establish fatigue residual stiffness surfaces with respect to stress levels. The parameters for

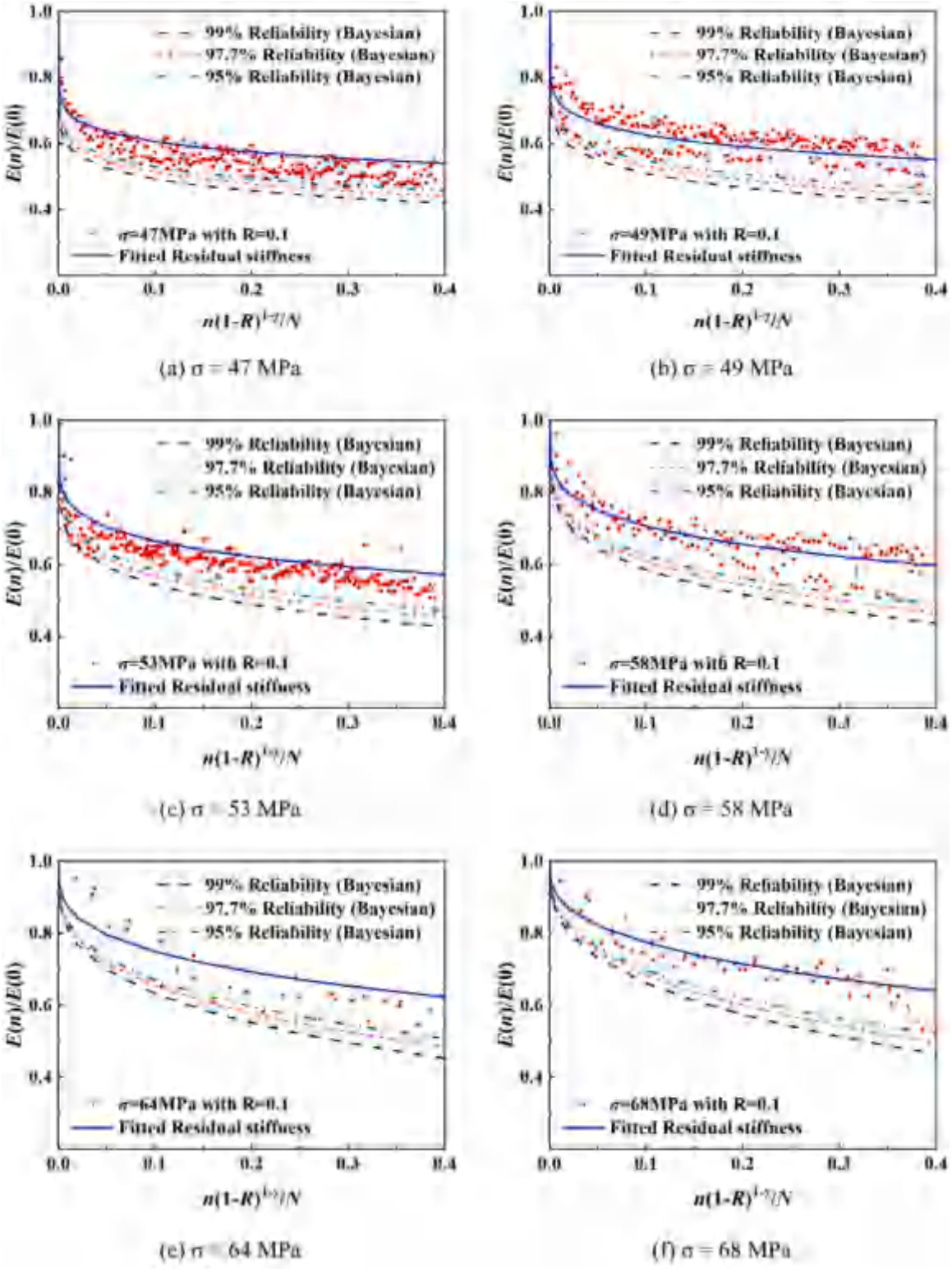


Fig. 12. Fatigue residual stiffness reliability curves at different stress levels for R= 0.1.

normalized residual stiffness are presented in Table 6. It is important to note that the values of these parameters do not exhibit significant differences from the ones previously provided in Table 3, indicating the reasonability of the results derived through Bayesian inference.

Table 7 presents the parameters for residual stiffness reliabilities obtained by Bayesian inferences, including the influence of the stress level. Meanwhile, Figs. 9 and 10 illustrate different residual stiffness reliability surfaces, considering the effect of the stress level. For $R = 0.1$, as reliability increases, the values of the parameters a, c_1, and c_2 also increase, while the value of b decreases. On the other hand, for $R = 0.5$, as the reliability increases, the values of the parameters a, c_1, and c_2 decrease, and the value of b increases slightly.

There is a relative discrepancy between the calculated normalized residual stiffness values that take the stress level into account (Eq. 2) and

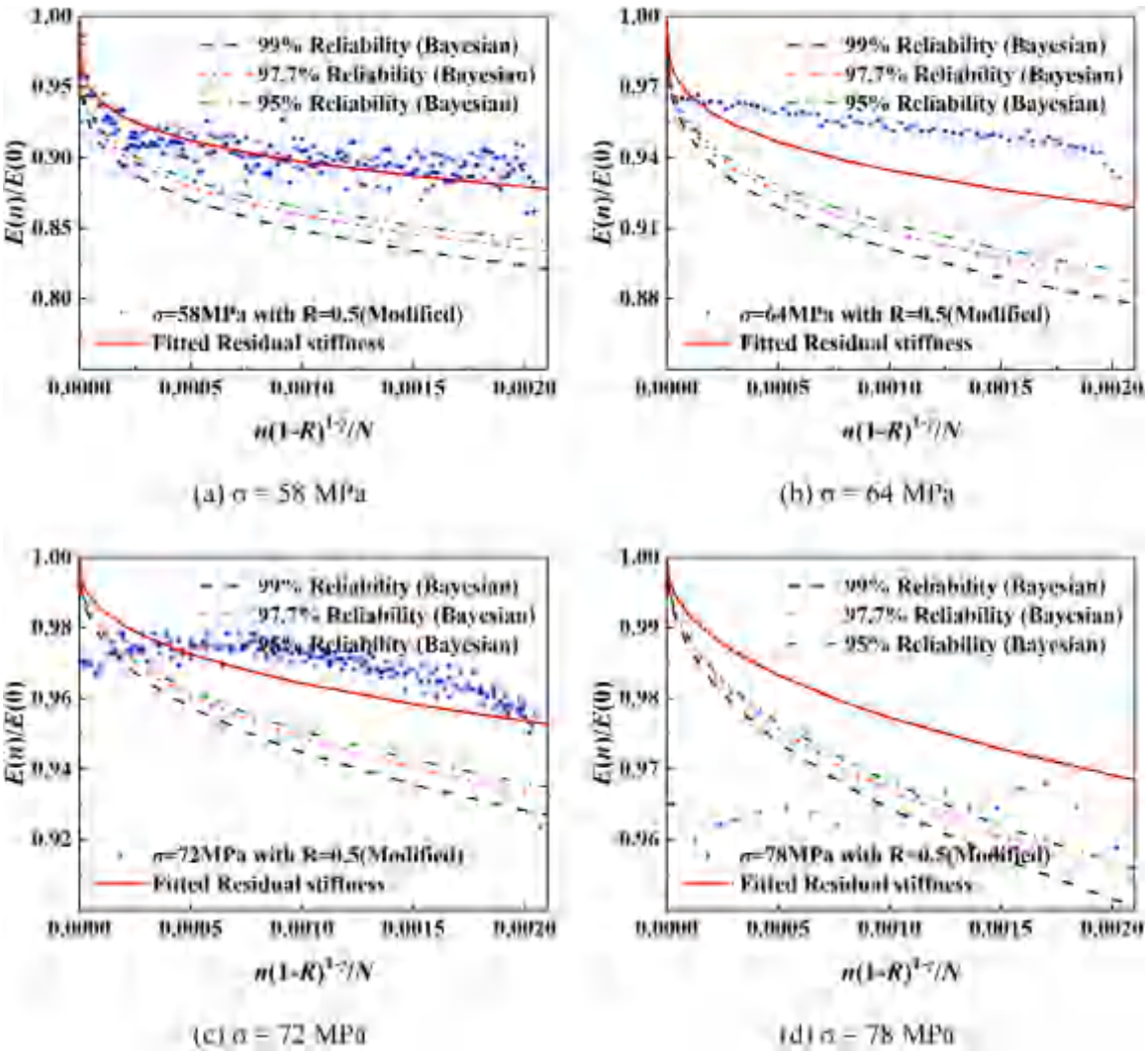


Fig. 13. Fatigue residual stiffness reliability curves at different stress levels for $R = 0.5$.

Table 9
Fatigue residual stiffness reliability parameters considering stress ratio effects.

Surface name	Fitted parameters				
	a	b	c_1	c_2	γ
Residual stiffness surface	-0.3950	0.01074	616.1786	10.0577	-7.9163
95.0% reliability surface	-0.4139	0.01096	0.0500	-2.5110	-8.2882
97.7% reliability surface	-0.4191	0.01106	0.0838	-1.8443	-8.2360
99.0% reliability surface	-0.4265	0.01113	0.1316	-1.2945	-8.3836

Table 10
Conversion results of parameters c_1, and c_2.

Surface name	Fitted parameters	
	m_1	m_2
Residual stiffness surface	0.5280	0.0994
95.0% reliability surface	0.3033	-0.3983
97.7% reliability surface	0.2608	-0.5422
99.0% reliability surface	0.2088	-0.7725

the normalized residual stiffness values obtained without considering the stress level (Eq. 1). The mean relative discrepancy, δ_{AVE}, can be calculated using the following equation:

$$\delta_{AVE} = \frac{1}{k}\sum_{1}^{k}\left|\frac{\left(\frac{E(n)}{E(0)}\right)_s - \left(\frac{E(n)}{E(0)}\right)_c}{\left(\frac{E(n)}{E(0)}\right)_c}\right| \times 100\% \tag{21}$$

where, k is the number of data points; $\left(\frac{E(n)}{E(0)}\right)_s$ and $\left(\frac{E(n)}{E(0)}\right)_c$ are the normalized stiffness of the fitted results considering and without considering the stress level.

Table 8 presents the relative discrepancy between the fitted results when considering the stress level and without the influence of the stress level. When considering the stress level, the mean relative discrepancy of the fitted results is 2.41% in comparison to the results obtained without accounting for the stress level, indicating that the outcomes are not significantly affected by introducing the stress level effect. More specifically, the relative discrepancy for $R = 0.1$ is 3.03%, which is slightly greater than 1.48% for the case when $R = 0.5$. As shown in Table 8, the highest discrepancy is equal to 8.61% and observed at $\sigma = 64$ MPa with $R = 0.1$, while other values are below 4%.

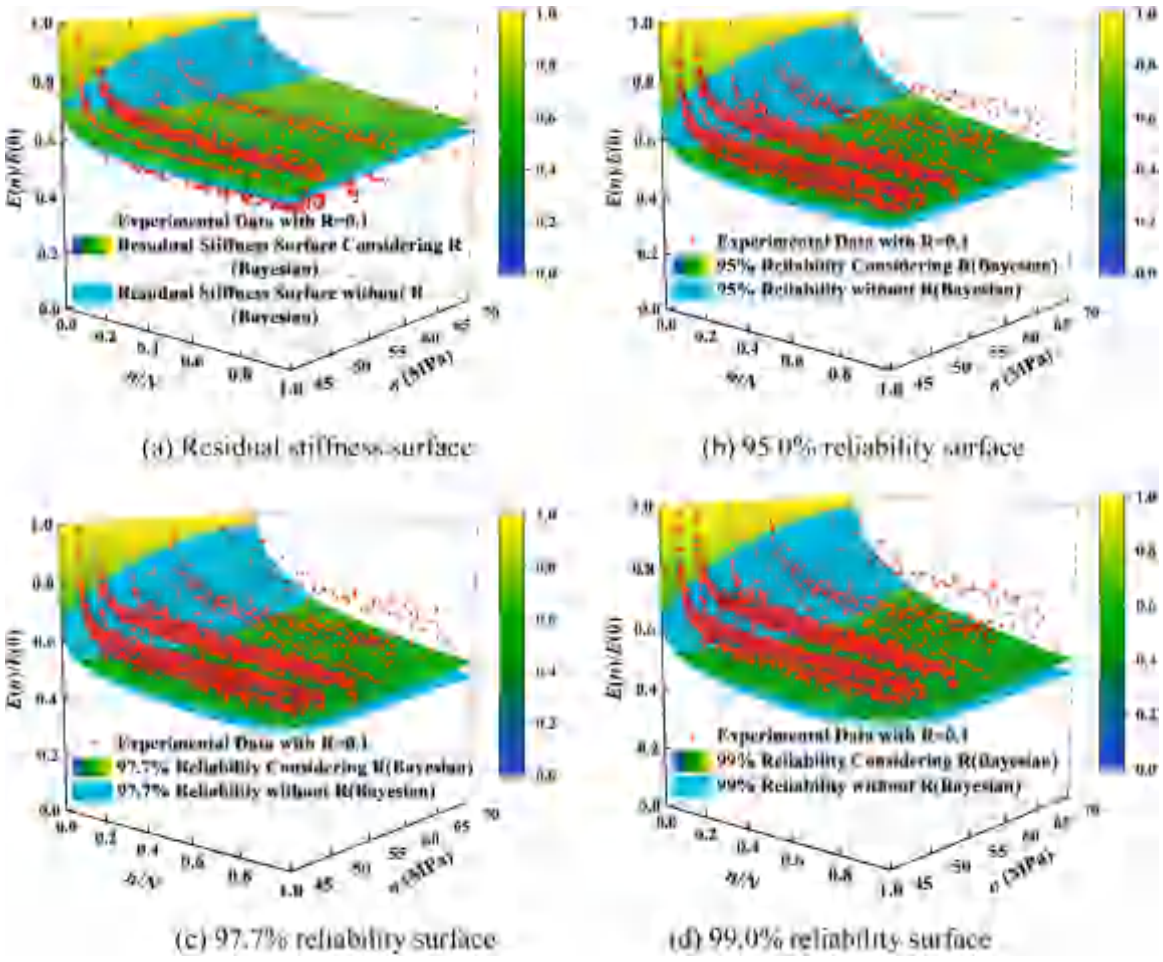


Fig. 14. Comparison of residual stiffness models with $R = 0.1$.

4. Probabilistic assessment of fatigue residual stiffness considering stress ratio effects

4.1. Probabilistic prediction of fatigue residual stiffness considering stress ratio effects

The effect of the stress ratio on the fatigue-induced residual stiffness of GFRP laminates cannot be ignored, even though the original residual stiffness model [41] does encompass this effect. To include such an influence in the original residual stiffness model, an additional term, $(1-R)^{1-\gamma}$, is used as shown in Eq. (22):

$$\frac{E(n)}{E(0)} = 1 - \left[1 - \left(\frac{\sigma}{c_1 \sigma_U}\right)^{1/c_2}\right] \left(\frac{n}{N}(1-R)^{1-\gamma}\right)^{a+b\sigma} \tag{22}$$

where, γ is a material parameter that considers stress ratio effects.

The data points for the residual stiffness model and the surfaces at 95.0%, 97.7%, and 99.0% reliability levels can now be calculated based on the parameters provided in Tables 6 and 7. These data points obtained at several stress ratios can be fitted in MatLab™ [49] using Eq. (22). Fig. 11 illustrates a comparison between the fitted results, different reliabilities and experimental data on a Cartesian coordinate system. In this figure, the X-axis represents the values of σ; the Y-axis represents the values of $n(1-R)^{1-\gamma}/N$; and the Z-axis represents the values of the ratios $E(n)/E(0)$.

On a 2D graph, plotting $n(1-R)^{1-\gamma}/N$ on the X-axis and $E(n)/E(0)$ on the Y-axis, Figs. 12 and 13 present the experimental data and the corresponding residual stiffness curves for various stress levels and stress ratios. This representation offers a more intuitive visualization of the fitted results presented in Fig. 11. Eq. (22) accounts for more material parameters compared to existing stiffness degradation models [15,21,41], which may result in higher fitting deviation. For instance, in Fig. 12 (a), (c) and Fig. 13 (b), (d), differences are shown between the stiffness degradation curve predicted by Eq. (22) and the experimental data. However, given the high dispersion of the stiffness degradation results, it can still be considered that this equation reasonably reflects the trend of the residual stiffness.

The fitted parameters can be found in Table 9. From this table, one can clearly see that the values of the fitted parameters c_1, and c_2 for the residual stiffness model are significantly different of those related to the residual stiffness reliability surfaces. Next, considering the structure of Eq. (22), the parameters c_1 and c_2 will be converted to the fitted parameters m_1 and m_2, as demonstrated in Eqs. (23) and (24). The conversion results are presented in Table 10. At this point, the values of m_1 and m_2 for the residual stiffness model are within the same order of magnitude as the values for the residual stiffness reliability surfaces. As the reliability increases, the values of the fitted parameters m_1 and m_2 decrease.

$$m_1 = (1/c_1)^{1/c_2} \tag{23}$$

$$m_2 = 1/c_2 \tag{24}$$

4.2. Verification of the fatigue residual stiffness considering stress ratio effects

The model proposed in this study (Eq.22) considers the effects of the

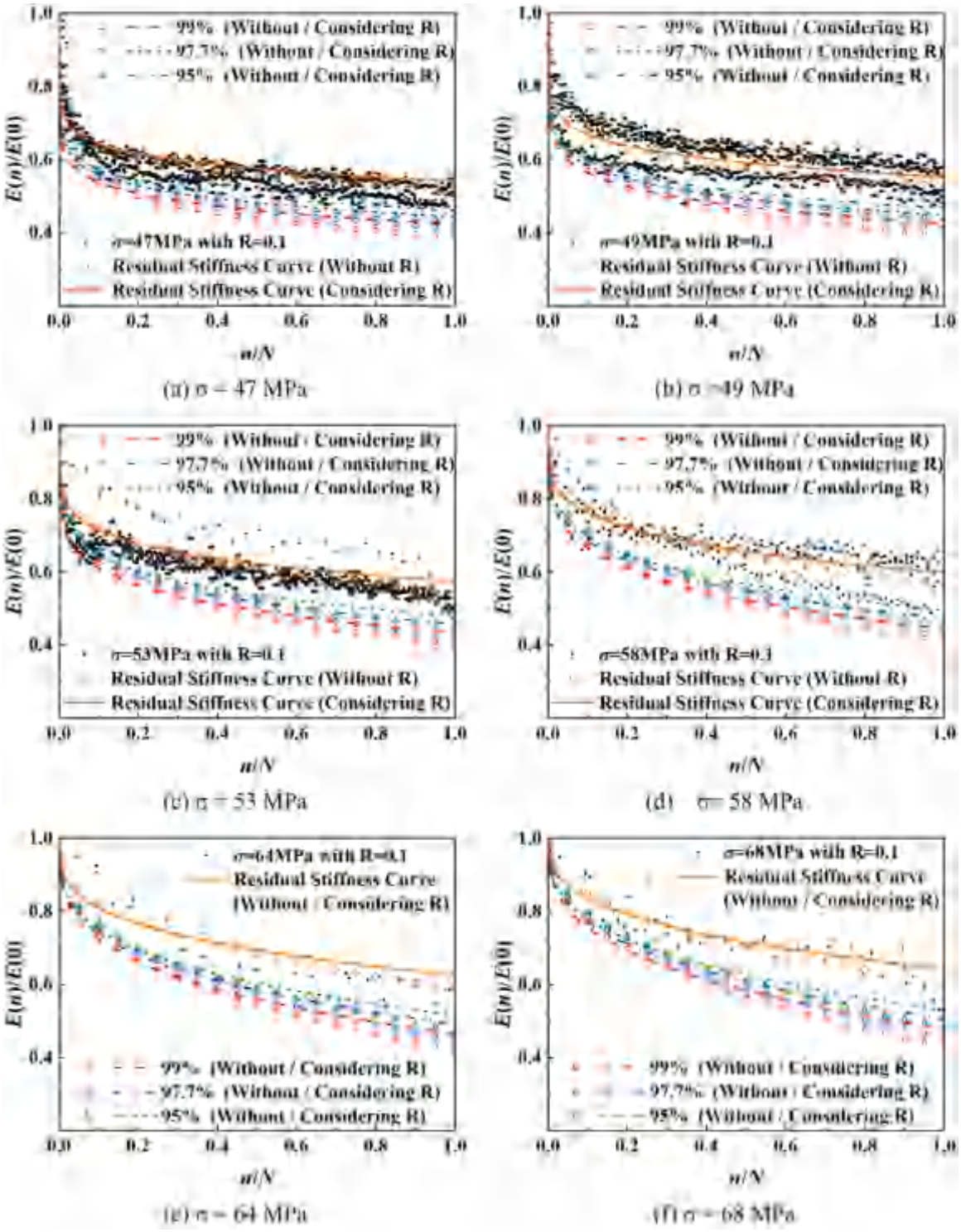


Fig. 15. Comparisons between the output of residual stiffness models at different stress levels for R = 0.1.

stress level, stress ratio and normalized number of cycles on fatigue stiffness. If the fitted result of this model is directly compared with that of the existing models, it cannot reflect the advantage that the proposed model can consider the influence of various factors on the variation of fatigue stiffness. The studies [21,41] have confirmed the accuracy of the Yang's model (Eq.1) in describing stiffness degradation. The validity of the proposed model can be confirmed by comparing the fitting results of the model with the fitting results of the Yang's model.

Figs. 14–17 show comparisons between fitted results obtained from Eqs. (1) and (22). In these figures, the yellow-green surfaces represent the results of the model considering stress ratio effects, while the light-blue surfaces represent the results of the model without considering stress ratio effects. For the case of $R = 0.1$, when the normalized fatigue cycles are less than 0.2, one can state that the model considering stress ratio effects slightly underestimates the residual stiffness. On the other hand, when the normalized fatigue cycles are greater than 0.2, the model tends to slightly overestimates the residual stiffness. Also, for $R = 0.5$, when the stress level exceeds 64 MPa, the results from both

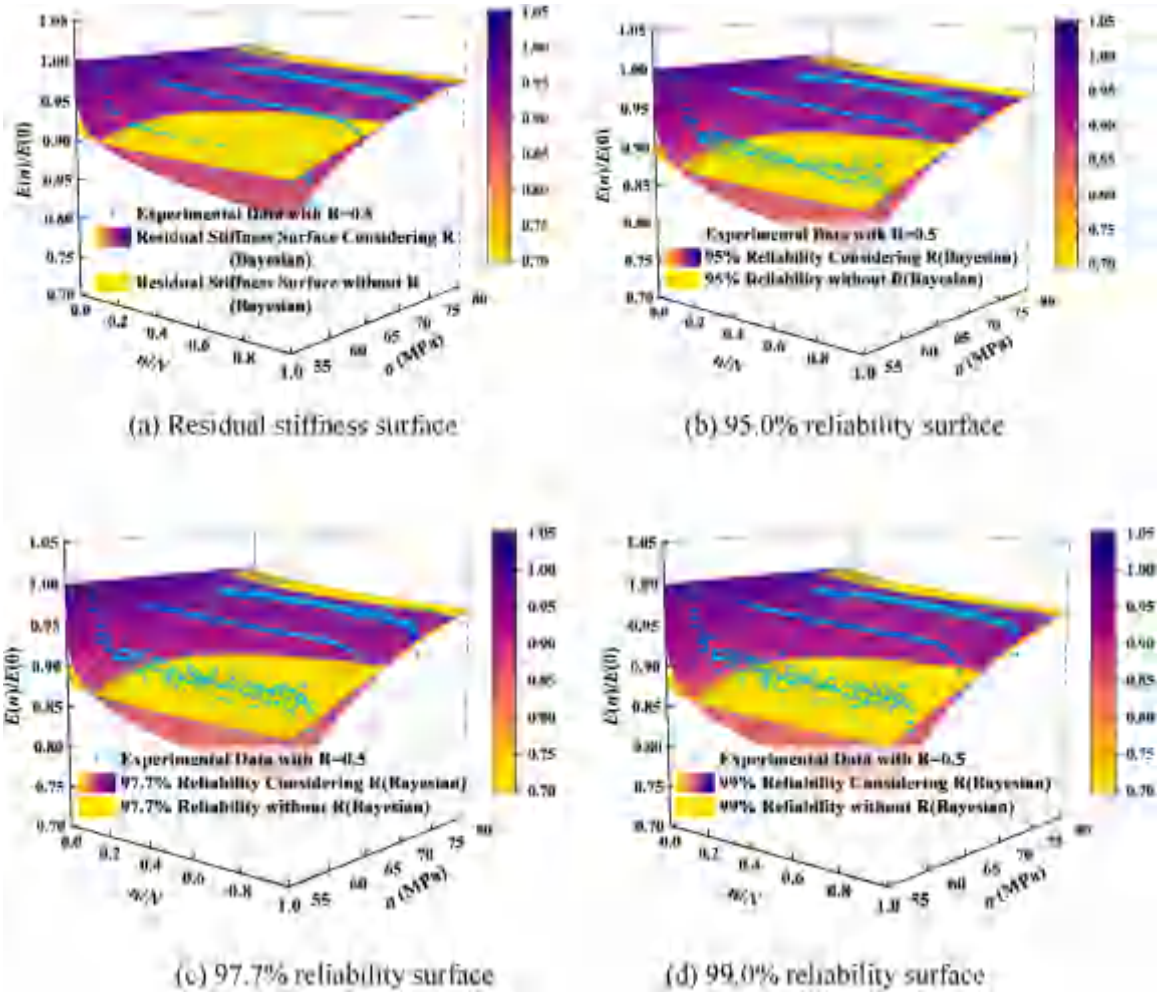


Fig. 16. Comparisons between residual stiffness models for R = 0.5.

models are close. However, for stress levels lower than 64 MPa, the fitted residual stiffness results seems to be more conservative when considering stress ratio effects than when no stress ratio effects are taken into account.

The relative discrepancy between the normalized residual stiffness, considering stress ratio effects (see Figs. 14 and 16), and the normalized residual stiffness at different stress levels (see Figs. 7 and 8) was computed and presented in Table 11. These results show that the mean relative discrepancy between two fitted results is 3.13%. More specifically, the relative discrepancy for $R = 0.1$ is 4.41%, which is greater than the corresponding results obtained when stress ratio effects are not considered (see Table 8). The relative discrepancy with $R = 0.5$ is 1.21%, which is slightly lower than the results without considering stress ratio effects. Also, the discrepancies of the fitted results considering stress ratio effects are close to the corresponding results without considering stress ratio effects, which confirms the validity of Eq. (22). The relative discrepancies at $\sigma = 47$ MPa and 64 MPa with $R = 0.1$ exceed 6%, which may be attributed to experimental results dispersion.

It should be noted that the fatigue stiffness degradation model proposed in this study is based on angle-ply GFRP laminates. The model and probabilistic prediction method can predict the fatigue performance of composites with two-stage or three-stage stiffness degradation trend. However, many factors such as component materials, layers design and manufacturing process will affect the fatigue damage process of laminates. There is still a lack of a unified model to reasonably describe the fatigue degradation mechanism of all FRP composites. It should also be noted that the fiber realignment of the composite material is obvious before and after fatigue loading at high stress ratio. Complementing the fatigue experiments at various stress ratios can establish a relationship between fiber alignment angle, stress level, and stress ratio. The result can also assist in proving the validity of the model in this study.

5. Conclusions

This paper provides a summary of the results from a research study focusing on evaluating the impact of stress ratio on fatigue stiffness degradation of FRP laminates. The study suggests the introduction of a revision (modification) term into the original residual stiffness model to account for the effect of the stress ratio. Furthermore, a technique for evaluating the reliability of fatigue residual stiffness in FRP composite laminates using Bayesian inference and MCMC simulations is proposed. Based on the results of this study, the following conclusions can be drawn:

(1) The relationship between the angle of the fiber realignment and the stiffness variation is established using micromechanics principles. After subtracting the stiffness variation due to the mentioned realignment of fibers, the original normalized residual stiffness model is well fitted for cross-ply symmetrical GFRP composite laminates with a stacking sequence of $[\pm 45]_{2S}$;
(2) The findings suggest that the fitted results of the fatigue residual stiffness, using the Bayesian inference and MCMC simulations, closely align with those obtained through the LR method. When the stress level is taken into account, the fitted results showed a

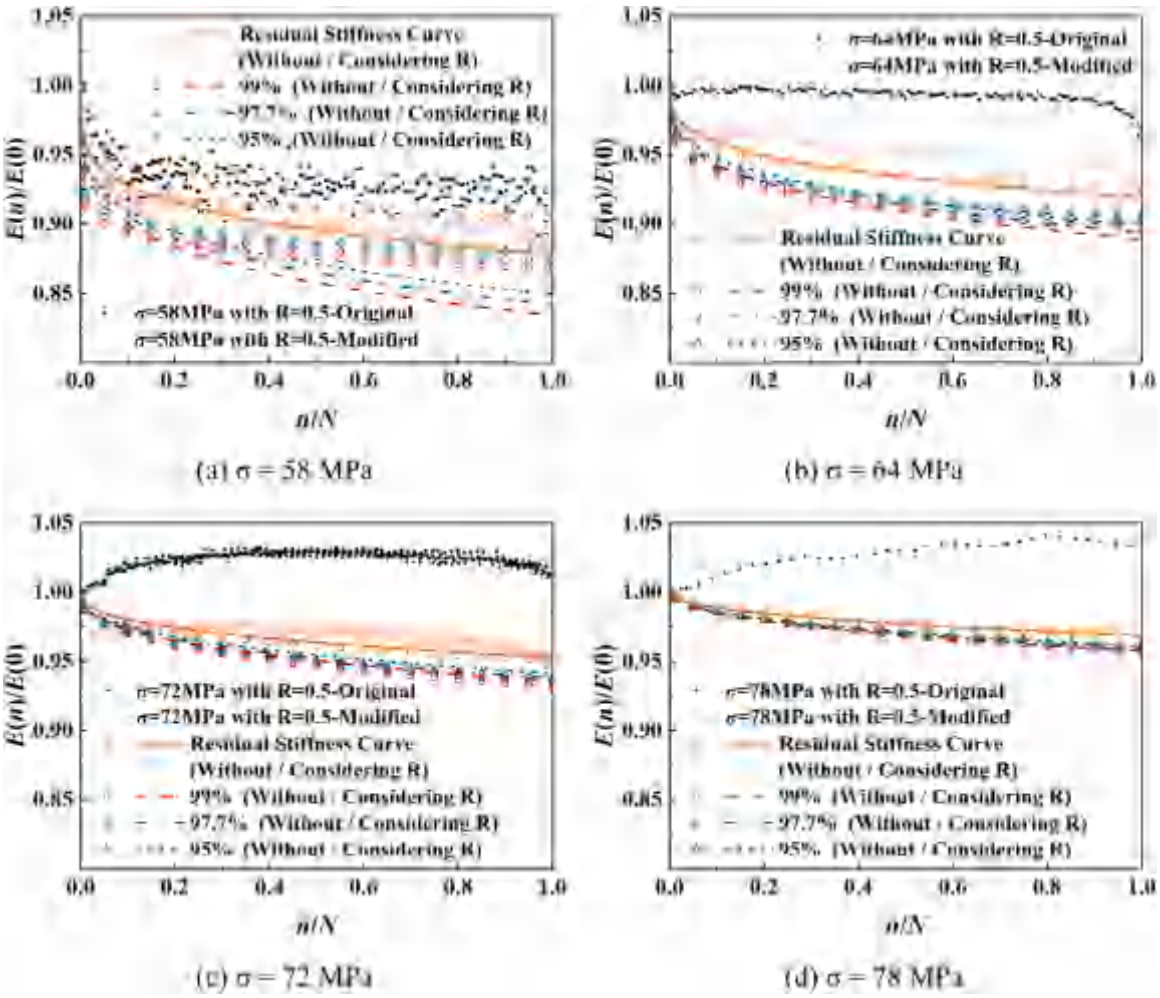


Fig. 17. Comparison of output of residual stiffness models for different stress levels with R = 0.5.

Table 11
Relative discrepancy between the fitted results considering stress ratio effects at different stress levels.

Stress ratio	Stress level	Residual stiffness surface	Residual stiffness reliability surface		
			95.0%	97.7%	99.0%
0.1	47 MPa	5.89%	5.76%	6.13%	5.98%
	49 MPa	1.83%	2.56%	3.58%	4.62%
	53 MPa	4.69%	2.94%	2.82%	1.79%
	58 MPa	0.38%	0.71%	0.76%	0.91%
	64 MPa	5.56%	10.34%	12.48%	12.80%
	68 MPa	1.62%	3.34%	3.67%	4.62%
0.5	58 MPa	0.55%	0.58%	0.62%	0.66%
	64 MPa	1.66%	2.26%	2.45%	2.62%
	72 MPa	0.52%	0.45%	0.47%	0.49%
	78 MPa	1.47%	1.52%	1.52%	1.58%

mean relative discrepancy of 2.41% in comparison with the results obtained without considering stress level effects, which indicates that this method has a negligible effect when stress levels are introduced;

(3) In addition to the normalized residual stiffness model, a revision (modification) term that incorporates stress ratio effects is proposed to predict fatigue stiffness degradation trends. The mean relative discrepancy between the fitted results for the normalized residual stiffness is only 3.13%, considering stress ratio effects and at different stress levels. Consequently, the proposed equations can reasonably predict the residual stiffness of FRP laminates with varying levels of reliability.

CRediT authorship contribution statement

Gao Qinglin: Validation, Methodology, Investigation, Formal analysis, Conceptualization, Writing – original draft. **Xin Haohui:** Writing – review & editing, Writing – original draft, Validation, Supervision, Methodology, Investigation, Formal analysis. **Horas Cláudio:** Writing – review & editing, Validation, Methodology, Formal analysis. **Mosallam Ayman S.:** Writing – review & editing, Validation, Methodology, Formal analysis. **Liu Yuqing:** Validation, Supervision, Methodology, Investigation, Formal analysis, Conceptualization, Writing – review & editing. **Berto Filippo:** Writing – review & editing, Validation, Methodology, Formal analysis. **Ma Jianxun:** Investigation, Validation, Writing – review & editing, Data curation. **Sun Qing:** Data curation, Investigation, Validation, Writing – review & editing. **Correia José A.F.O.:** Writing – review & editing, Validation, Methodology, Formal analysis.

Declaration of Competing Interest

The authors declare that they have no known competing financial interests or personal relationships that could have appeared to influence the work reported in this paper.

Data availability

Data will be made available on request.

Acknowledgments

The authors gratefully acknowledge the financial support provided by the Program Fund of Non-Metallic Excellent and Innovation Center for Building Materials, (Grants #2023Ph.D-8) and the National Natural Science Foundation (Grants #51808398 & 52078362) of the People's Republic of China. The calculations were performed using the HPC Platform at Xi'an Jiaotong University, China. This research was also supported and funded by the base funding - UIDB/04708/2020 and programmatic funding - UIDP/04708/2020 of the CONSTRUCT - Instituto de I&D em Estruturas e Construções - funded by national funds through the FCT/MCTES (PIDDAC). Additionally, this research work was supported by: individual project grant (2020.03856. CEECIND), awarded to José A.F.O. Correia, by Portuguese funds (PIDDAC) through the Portuguese Science Foundation (FCT/MCTES).

References

[1] Ahmed A, Zillur Rahman Md OuY, Liu S, Mobasher B, Guo S, et al. A review on the tensile behavior of fiber-reinforced polymer composites under varying strain rates and temperatures. Constr Build Mater 2021;294:123565. https://doi.org/10.1016/j.conbuildmat.2021.123565.
[2] Fuhrman DM, Rafiee-Dehkharghani R, Lopez MM, Aref A, O'Connor J. Field performance of a new fiber-reinforced polymer deck. J Perform Constr Fac 2015;29:04014162. https://doi.org/10.1061/(asce)cf.1943-5509.0000656.
[3] Liu TQ, Liu X, Feng P. A comprehensive review on mechanical properties of pultruded FRP composites subjected to long-term environmental effects. Compos Part B-Eng 2020;191:107958. https://doi.org/10.1016/j.compositesb.2020.107958.
[4] Tuwair H, Drury J, Volz J. Testing and evaluation of full scale fiber-reinforced polymer bridge deck panels incorporating a polyurethane foam core. Eng Struct 2019;184:205–16. https://doi.org/10.1016/j.engstruct.2019.01.104.
[5] Xin HH, Liu YQ, Mosallam AS, He J, Du A. Evaluation on material behaviors of pultruded glass fiber reinforced polymer (GFRP) laminates. Compos Struct 2017;182:283–300. https://doi.org/10.1016/j.compstruct.2017.09.006.
[6] Xin HH, Mosallam A, Liu YQ, Wang CZ, Zhang YY. Analytical and experimental evaluation of flexural behavior of FRP pultruded composite profiles for bridge deck structural design. Constr Build Mater 2017;150:123–49. https://doi.org/10.1016/j.conbuildmat.2017.05.212.
[7] Mosallam AS, Bayraktar A, Elmikawi M, Pul S, Adanur S. Polymer composites in construction: an overview. SOJ Mater Sci Eng 2015;2:25. https://doi.org/10.15226/sojmse.2014.00107.
[8] Abdi F, Qian ZY, Mosallam A, Iyer R, Wang JJ, Logan T. Composite army bridges under fatigue cyclic loading. Struct Infrastruct E 2006;2:63–73. https://doi.org/10.1080/15732470500254691.
[9] Cameselle-Molares A, Vassilopoulos AP, Keller T. Two-dimensional fatigue debonding in GFRP/balsa sandwich panels. Int J Fatigue 2019;125:72–84. https://doi.org/10.1016/j.ijfatigue.2019.03.032.
[10] Mallick PK, Zhou YX. Effect of mean stress on the stress-controlled fatigue of a short E-glass fiber reinforced polyamide-6,6. Int J Fatigue 2004;26:941–6. https://doi.org/10.1016/j.ijfatigue.2004.02.003.
[11] Movahedi-Rad AV, Keller T, Vassilopoulos AP. Creep effects on tension-tension fatigue behavior of angle-ply GFRP composite laminates. Int J Fatigue 2019;123:144–56. https://doi.org/10.1016/j.ijfatigue.2019.02.010.
[12] Degrieck and J, Van Paepegem W. Fatigue damage modeling of fibre-reinforced composite materials. Appl Mech Rev 2001;54:279–300. https://doi.org/10.1115/1.1381395.
[13] Gao JX, Heng F, Yuan YP, Liu YY. A novel machine learning method for multiaxial fatigue life prediction: improved adaptive neuro-fuzzy inference system. Int J Fatigue 2024;178:108007. https://doi.org/10.1016/j.ijfatigue.2023.108007.
[14] Gao JX, Yuan YP. Probabilistic modeling of stiffness degradation for fiber reinforced polymer under fatigue loading. Eng Fail Anal 2020;116:104733. https://doi.org/10.1016/j.engfailanal.2020.104733.
[15] Ospina Cadavid M, Al-Khudairi O, Hadavinia H, Goodwin D, Liaghat GH. Experimental studies of stiffness degradation and dissipated energy in glass fibre reinforced polymer composite under fatigue loading. Polym Polym Compos 2017;25:435–46. https://doi.org/10.1177/096739111702500602.
[16] Zhang Y, Vassilopoulos AP, Keller T. Stiffness degradation and fatigue life prediction of adhesively-bonded joints for fiber-reinforced polymer composites. Int J Fatigue 2008;30:1813–20. https://doi.org/10.1016/j.ijfatigue.2008.02.007.
[17] Schulte K. Stiffness reduction and development of longitudinal cracks during fatigue loading of composite laminates. Mechanical Characterisation of Load Bearing Fibre Composite Laminates Proceedings of the European Mechanics Colloquium, 182. Brussels, Belg: Elsevier Applied Science Publ; 1985. p. 36–54.
[18] Naik NK. Woven-fibre thermoset composites. Fatigue in composites: science and technology of the fatigue response of fibre-reinforced plastics. Boca Raton Boston New York Washington, DC: Woodhead Publishing Ltd and CRC Press LLC; 2003. p. 296–313.
[19] De Finis R, Palumbo D, Galietti U. Evaluation of damage in composites by using thermoelastic stress analysis: a promising technique to assess the stiffness degradation. Fatigue Fract Eng Mater Struct 2020;43:2085–100. https://doi.org/10.1111/ffe.13285.
[20] Esleman EA, Önal G. Three-point bending fatigue behavior of basaltcarbon-glass/epoxy hybrid composites under saltwater environment. 2496-09 Fatigue Fract Eng Mater Struct 2023;46(7). https://doi.org/10.1111/ffe.14012.
[21] Yang JN, Jones DL, Yang SH, Meskini A. A stiffness degradation model for graphite epoxy laminates. J Compos Mater 1990;24:753–69. https://doi.org/10.1177/002199839002400705.
[22] Papanikos P, Tserpes KI, Pantelakis S. Modelling of fatigue damage progression and life of CFRP laminates. F Fatigue Fract Eng Mater Struct 2003;26(1):37–47. https://doi.org/10.1046/j.1460-2695.2003.00585.x.
[23] Khan Z, Al-Sulaiman FA, Farooqi JK, Younas M. Fatigue life predictions in woven carbon fabric/polyester composites based on modulus degradation. J Reinf Plast Compos 2001;20:377–98. https://doi.org/10.1177/073168401772678706.
[24] Hochard C, Thollon Y. A generalized damage model for woven ply laminates under static and fatigue loading conditions. Int J Fatigue 2010;32:158–65. https://doi.org/10.1016/j.ijfatigue.2009.02.016.
[25] Liu H, Cui H, Wen W, Kang H. Fatigue characterization of T300/924 polymer composites with voids under tension-tension and compression-compression cyclic loading. Fatigue Fract Eng Mater Struct 2018;41:597–610. https://doi.org/10.1111/ffe.12721.
[26] Carraro PA, Quaresimin M. Fatigue damage and stiffness evolution in composite laminates: a damage-based framework. Procedia Eng 2018;213:17–24. https://doi.org/10.1016/j.proeng.2018.02.003.
[27] Gao JX, Heng F, Yuan YP, Liu YY. Fatigue reliability analysis of composite material considering the growth of effective stress and critical stiffness. Aerospace 2023;10:785. https://doi.org/10.3390/aerospace10090785.
[28] Philippidis TP, Vassilopoulos AP. Fatigue design allowables for GRP laminates based on stiffness degradation measurements. Compos Sci Technol 2000;60:2819–28. https://doi.org/10.1016/S0266-3538(00)00150-0.
[29] Manjunatha CM, Jagannathan N, Padmalatha K, Kinloch AJ, Taylor AC. Improved variable-amplitude fatigue behavior of a glass-fiber-reinforced hybrid-toughened epoxy composite. J Reinf Plast Comp 2011;30:1783–93. https://doi.org/10.1177/0731684411426202.
[30] Philippidis TP, Vassilopoulos AP. Stiffness reduction of composite laminates under combined cyclic stresses. Adv Compos Lett 2001;10:113–24. https://doi.org/10.1177/096369350101000302.
[31] Sarfaraz R, Vassilopoulos AP, Keller T. Experimental investigation of the fatigue behavior of adhesively-bonded pultruded GFRP joints under different load ratios. Int J Fatigue 2011;33:1451–60. https://doi.org/10.1016/j.ijfatigue.2011.05.012.
[32] Shokrieh MM, Lessard LB. Progressive fatigue damage modeling of composite materials, part I: modeling. J Compos Mater 2000;34:1056–80. https://doi.org/10.1177/002199830003401301.
[33] Shokrieh MM, Lessard LB. Multiaxial fatigue behaviour of unidirectional plies based on experiments uniaxial fatigue.1. Modelling. Int J Fatigue 1997;19:201–7. https://doi.org/10.1016/S0142-1123(96)00074-6.
[34] Atadero R, Lee L, Karbhari VM. Consideration of material variability in reliability analysis of FRP strengthened bridge decks. Compos Struct 2005;70:430–43. https://doi.org/10.1016/j.compstruct.2004.09.003.
[35] Zhang J, Shields M, TerMaath S. Probabilistic modeling and prediction of out-of plane unidirectional composite lamina properties. Mech Adv Mater Struct 2021;28:2310–26. https://doi.org/10.1080/15376494.2020.1733713.
[36] Movahedi-Rad AV, Keller T, Vassilopoulos AP. Fatigue damage in angle-ply GFRP laminates under tension-tension fatigue. Int J Fatigue 2018;109:60–9. https://doi.org/10.1016/j.ijfatigue.2017.12.015.
[37] Movahedi-Rad AV, Keller T, Vassilopoulos AP. Stress ratio effect on tension-tension fatigue behavior of angle-ply GFRP laminates. Int J Fatigue 2019;126:103–11. https://doi.org/10.1016/j.ijfatigue.2019.04.037.
[38] Movahedi-Rad A.V. Load history effects in fibre-reinforced polymer composite materials. Lausanne, EPFL; 2019.
[39] Radhakrishnan PM, Bharadwaj S, Sudhi G, Ramajeyathilagam K. Effect of stress ratio on the tension-tension fatigue behavior of tungsten carbide nanoparticles toughened GFRP. Fatigue Fract Eng Mater Struct 2023;46(8):2949–65. https://doi.org/10.1111/ffe.14058.
[40] Behera A, Dupare P, Thawre MM, Ballal AR. Effect of fatigue loading on stiffness degradation, energy dissipation, and matrix cracking damage of CFRP [±45]3S composite laminate. Fatigue Fract Eng Mater Struct 2019;42:2302–14. https://doi.org/10.1111/ffe.13065.
[41] Wang DY, Wen WD. Material degradation models of unidirectional laminas subjected to tension-tension or compression-compression fatigue loadings (in Chinese) J Mat Sci Eng 2007;26:256–9. https://doi.org/10.14136/j.cnki.issn1673-2812.2013.05.021.
[42] Barbero EJ (ed.). Introduction to composite materials design. Third edition.,. Boca Raton: CRC Press, Taylor & Francis Group; 2018.
[43] Xin HH, Mosallam A, Liu YQ, Veljkovic M, He J. Mechanical characterization of a unidirectional pultruded composite lamina using micromechanics and numerical homogenization. Constr Build Mater 2019;216:101–18. https://doi.org/10.1016/j.conbuildmat.2019.04.191.
[44] Björck Å. Numerical methods for least squares problems. SIAM; 1996.

[45] Wagner P.R., Nagel J., Marelli S., Sudret B. UQLab user manual-Bayesian inference for model calibration and inverse problems. Report UQLab-V20–113: Chair of Risk, Safety and Uncertainty Quantification, ETH Zurich, Switzerland; 2022.
[46] Robert CP, Casella G. Monte Carlo statistical methods. 2nd ed..,. New York: Springer; 2004.
[47] Liu JS. Monte Carlo strategies in scientific computing. New York: Springer; 2001.
[48] Goodman J, Weare J. Ensemble samplers with affine invariance. Comm Appl Math Com Sc 2010;5:65–80. https://doi.org/10.2140/camcos.2010.5.65.
[49] Optimization Toolbox Release Notes. Natick, MA: The MathWorks, Inc; 2019.

Journal of Building Engineering 97 (2024) 110902

Contents lists available at ScienceDirect

Journal of Building Engineering

journal homepage: www.elsevier.com/locate/jobe

Effects of aggregates and fibers on the strength and permeability of concrete exposed to low vacuum environment

Zhaofei Long [a], Guangcheng Long [a,*], Zhuo Tang [a,**], Minghui Shangguan [a], Ce Gao [b], Meihui Yi [a], Zhenhui He [a], Yutong Zhang [a]

[a] School of Civil Engineering, Central South University, Changsha 410075, China
[b] China Railway Engineering Design and Consulting Group Co., Ltd, Beijing 100055, China

ARTICLE INFO

Keywords:
Low vacuum
Aggregate
Fiber
Strength
Permeability

ABSTRACT

The performance and regulation of concrete in low vacuum environments are receiving increasing attention. This study investigates the effects of aggregates and fibers on the strength and permeability of concrete in a low vacuum environment, using varying gradients of sand ratios (37.5 %, 40 %, and 42 %) and aggregate-to-binder ratios (3.27, 3.92, and 4.14). Three types of non-metallic fibers are utilized: polyethylene (PE), polyvinyl alcohol (PVA), and glass fibers. Evaluations focus on concrete strength, mass loss, gas permeability, capillary water absorption, and porosity. Results indicate that higher sand and aggregate-to-binder ratios enhance both flexural and compressive strength. Fiber incorporation improves flexural and compressive toughness, with PE fibers showing the most significant toughening effect. The low vacuum environment increases the strength of the concrete but reduces its axial compression toughness ratio and increases brittleness, while fiber incorporation helps improve the compression toughness of the concrete. Higher sand and aggregate-to-binder ratios reduce mass loss and accelerate drying equilibrium, while fibers increase mass loss and prolong drying equilibrium, with PVA fibers causing greater mass loss. The pattern of concrete mass loss can be explained by the tortuosity of the moisture diffusion path. Additionally, low vacuum significantly increases the gas permeability of concrete. Enhancing the sand and aggregate-to-binder ratios reduces permeability both before and after low vacuum treatment. Although fibers increase the gas permeability, they help mitigate this increase under low vacuum condition. Capillary water absorption tests reveal that concrete under low vacuum condition has a significantly higher water absorption rate compared to air-drying condition. Increasing sand and aggregate-to-binder ratios reduces water absorption and capillary water content, whereas fibers have the opposite effect. Porosity tests show that moisture migration in a low vacuum environment is mainly related to permeable porosity, while total porosity is more closely related to compressive strength.

1. Introduction

With the rapid advancement of modern technology, economy, and society, the demand for fast, efficient, and safe passenger transport has surged. The novel ultra-high-speed low vacuum tube maglev transportation system addresses these needs [1]. A low

* Corresponding author.
** Corresponding author.
E-mail addresses: longguangcheng@csu.edu.cn (G. Long), zhuo.tang@csu.edu.cn (Z. Tang).

https://doi.org/10.1016/j.jobe.2024.110902
Received 19 June 2024; Received in revised form 4 September 2024; Accepted 29 September 2024
Available online 1 October 2024
2352-7102/© 2024 Elsevier Ltd. All rights are reserved, including those for text and data mining, AI training, and similar technologies.

vacuum environment (100 Pa) paired with maglev technology minimizes air resistance, noise, and wheel-rail friction, enabling speeds of 1000 km/h or more [2]. According to Lenz's law [3], the superconducting magnets of the train induce eddy currents in surrounding metal structures during high-speed travel, generating a magnetic field that opposes the original field, creating magnetic resistance that impedes the motion of the train. Therefore, to reduce magnetic resistance, save costs, and facilitate construction, concrete remains an ideal engineering material for the infrastructure of low vacuum tube maglev systems [4]. However, prolonged exposure to a low vacuum environment can cause rapid drying or dehydration of concrete, leading to shrinkage and cracking risks [5]. The internal microstructure of the concrete becomes unstable, compromising the airtightness, mechanical properties, and durability of vacuum tube structures [6]. Studies have shown that drying shrinkage is a primary cause of physical cracking in conventional concrete during its service life, posing significant challenges throughout the concrete lifecycle [7]. Thus, it is essential to investigate the drying shrinkage behavior and performance evolution of concrete in low vacuum environments and seek measures to improve its performance under these conditions.

When concrete dries, pore water migrates to the surface, causing spatial and temporal variations in water content. Moisture migration in concrete is more complex than in other porous media due to its diverse and evolving pore structure [8]. According to Dalton's law [9], the evaporation rate is inversely proportional to air pressure. Moisture diffusion in concrete pores is driven by the vapor pressure gradient between the pores and the environment. A low-pressure vacuum environment increases this gradient, enhancing moisture diffusion, evaporation, and the risk of cracking [10]. High water content in concrete heightens susceptibility to drying shrinkage; thus, a lower water-cement ratio mitigates these effects and reduces permeability [11]. Studies [7] demonstrate that adding mineral admixtures, shrinkage-reducing agents, fibers, internal curing materials, increasing aggregate content, and adequate wet curing can alleviate drying shrinkage. Mechanisms include enhancing microstructure density, reducing surface and capillary tension, increasing matrix restraint, and maintaining internal relative humidity to reduce tensile stress from shrinkage.

It is important to note that concrete is composed of cement paste and aggregates, and its shrinkage is the result of the interaction between the shrinkable cement paste and the non-shrinkable aggregates [12]. Aggregates are typically considered impermeable materials, so changes in their content will inevitably affect the drying and shrinkage behavior. The drying of concrete is a typical nonlinear moisture diffusion process, and the dilution effect of the aggregates can reduce the effective drying area of the concrete specimen, thereby reducing the moisture diffusion coefficient at any cross-section of the specimen [13]. However, when their content increases to a certain extent, it may accelerate moisture diffusion [13], and their specific mechanism of action in low vacuum environments is still unclear. On the other hand, due to the magnetic resistance effect caused by magnetic induction in metal structures, the use of steel bars, steel strands, and steel fibers in concrete for low vacuum pipelines will be limited. Using non-metallic fibers is an effective way to compensate for the mechanical properties of concrete. Furthermore, studies have reported that the inhibitory effect of fibers on drying shrinkage increases with the strength grade of the concrete, which is crucial for shrinkage inhibition in high-strength concrete [14]. However, previous research has mainly focused on the volumetric stability, mechanical properties, and microstructural evolution of cement-based materials in low vacuum environments [6,15–18]. The impact of aggregates and fibers on moisture transport and the performance of concrete in low vacuum environments remains unclear, and there are almost no related research reports. This requires further study and investigation.

Considering the special application scenarios of low vacuum pipelines and the specific requirements for high air-tightness, low magnetic resistance, and high stability of concrete materials, designing a high-strength, low-permeability concrete is beneficial for achieving the safe and stable operation of high-speed maglev trains. Based on this, under the condition of a low water-to-binder ratio (0.3), this study introduces fly ash (FA), ground granulated blast furnace slag (GGBS), and silica fume (SF) as supplementary cementitious materials to further densify the pores in concrete, reduce permeability, enhance the strength of the interfacial transition zone (ITZ), and minimize cracks caused by autogenous shrinkage and drying shrinkage [19,20]. Ultra-high molecular weight polyethylene (PE) fiber, polyvinyl alcohol (PVA) fiber, and glass fiber are selected as non-metallic toughening fibers. This study explores the influence of sand ratio, aggregate-to-binder ratio, and non-metallic fibers on the strength and permeability of concrete to provide a theoretical basis for the design of high-strength, high air-tightness concrete for use in low vacuum environments.

2. Test program

2.1. Materials

The chemical composition of Portland cement (P.I 42.5) and supplementary cementitious materials were tested using an X-ray Fluorescence Spectrometer (XRF), as detailed in Table 1. Additionally, the particle size distribution of the cementitious materials was measured using a laser particle size analyzer, as displayed in Fig. 1. The densities of PC, FA, GGBS, and SF are 3.12 g/cm^3, 2.4 g/cm^3, 2.85 g/cm^3, and 2.1 g/cm^3, respectively. The fine aggregate is well-graded washed river sand with a fineness modulus of 2.57 and an apparent density of 2660 kg/m^3. The coarse aggregate is hard impact-crushed limestone gravel, comprising two particle sizes: 5–10

Table 1
Performance indexes summary of cementitious materials (wt%).

Binder	CaO	SiO_2	Al_2O_3	Fe_2O_3	SO_3	MgO	TiO_2	Na_2O	K_2O	Ignition Loss
PC	55.45	24.05	5.50	3.63	3.44	1.36	0.29	0.17	1.06	1.38
FA	7.38	51.53	27.68	7.67	1.44	0.91	–	0.83	1.22	5.70
GGBS	33.60	26.10	13.80	14.10	–	8.10	–	0.45	0.81	2.10
SF	0.35	96.90	0.10	0.03	0.90	0.64	–	0.16	0.70	1.20

mm and 10–25 mm, with an apparent density of 2680 kg/m^3. A high-performance polycarboxylate-based superplasticizer (SP) with an approximate water reduction rate of about 30 %, provided by Shanxi Feike New Material Technology Co., Ltd, was employed as a water-reducing agent. The mixing water utilized was sourced from the tap water supply of Changsha City, Hunan. The physical properties of PE, PVA, and glass fibers are shown in Table 2.

2.2. Mix proportions

The high-strength concrete in the experimental design has a water-to-binder ratio of 0.3. Supplementary cementitious materials comprise 38 % of the total binder, with 15 % FA, 20 % GGBS, and 3 % SF. Table 3 presents the composition of each concrete mix. A1, A2, and A3 have sand ratios of 37.5 %, 40 %, and 42 %, respectively. A4 and A5 maintain a sand ratio of 40 %, but their aggregate-to-binder ratios are adjusted to 4.14 and 3.27, compared to A2's 3.92. Mixes B1, B2, and B3 incorporate PE, PVA, and glass fibers compared to A2, respectively, with volume fractions of 0.5 % for PE fibers and 1 % for PVA fibers and glass fibers.

2.3. Test procedures

2.3.1. Specimen preparation

Concrete specimens of various sizes were prepared to test strength and permeability. For compressive strength, 100 × 100 × 100 mm^3 cubic specimens were used. Flexural strength tests employed 100 × 100 × 400 mm^3 prismatic specimens. Cylindrical specimens of 100 mm diameter and 50 mm height were used for mass loss, gas permeability, and capillary absorption tests. Fresh concrete was placed into molds, covered with plastic film to prevent moisture evaporation, and demolded after 24 h of room temperature curing. The specimens then underwent wet curing in a standard room at 20 ± 2 °C and over 95 % humidity for 28 days. After standard curing, the mechanical strength and gas permeability of the specimens were tested. Subsequently, the samples were divided into two groups. one group was exposed to atmospheric air condition for drying, while the other group underwent low vacuum drying treatment. The latter were placed in a custom-designed vacuum drying chamber (Fig. 2) at around 100 Pa pressure, sustained by a vacuum pump, for 56 days. After reaching the specified age, various performance tests were conducted. Detailed testing methods will be elaborated in subsequent sections.

2.3.2. Strength test

Compressive and flexural strength tests of concrete are performed following GB/T 50081-2019 [21]. Fig. 3 illustrates the testing procedure for these strengths. Both tests utilize an electro-hydraulic servo universal testing machine. The uniaxial compression test utilized an Instron 1346, while the four-point bending test was carried out with an Instron 1342. The compressive test loading rate is 0.36 mm/min, with an extensometer used to record longitudinal deformation during compression, facilitating the construction of the stress-strain curve. The flexural test loading rate is 0.09 mm/min, and the method for calculating flexural strength is detailed in Eq. (1).

$$f_t = \frac{F_s l}{bh^2} \tag{1}$$

Where f_t is the flexural strength of the specimen, MPa; F_s is the peak force of the load-displacement curve of the specimen, N; l is the span between the supports of the specimen, mm; b is the width of the specimen, mm; h is the height of the specimen, mm.

2.3.3. Mass loss

First, record the initial mass of each group of specimens after 28 days of standard curing. Then, place the specimens in a vacuum test chamber for low vacuum treatment, and record the mass of the specimens at various exposure times under vacuum: 1 day to 5 days (measured daily), 7 days, 10 days, 14 days, 21 days, 28 days, 42 days, and 56 days. The mass loss rate and drying rate of the specimens

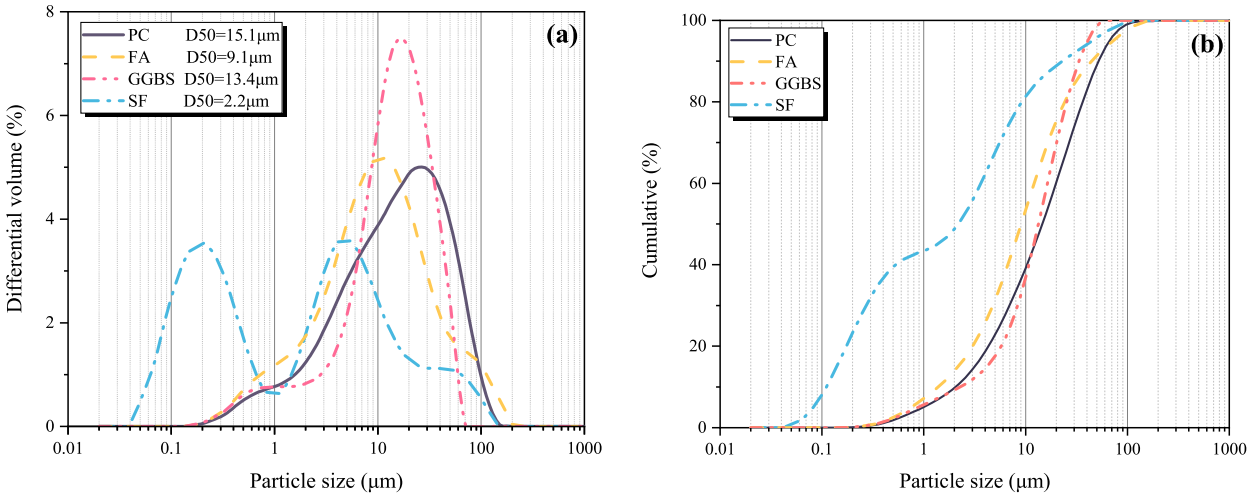


Fig. 1. Particle size distribution of cementitious material: (a) Differential curves; (b) Cumulative curves.

Table 2
Performance indexes summary of non-metallic fibers.

Fiber type	Density (g·cm^{-3})	Length (mm)	Diameter (μm)	Elastic modulus (GPa)	Fracture strength (MPa)
PE fiber	0.97	12	24	122	3100
PVA fiber	1.30	12	40	40	1600
Glass fiber	2.70	12	17.40	85	2000

Table 3
Mix proportions of the concrete specimens.

Mixture	Raw material (kg/m^3)												
	PC	FA	GGBS	SF	Water	Sand	Gravel	S/A	A/B	PE fiber	PVA fiber	Glass fiber	SP
A1	298	72	96	14	144	660	1100	37.50	3.92	–	–	–	4.80
A2	298	72	96	14	144	704	1056	40	3.92	–	–	–	4.80
A3	298	72	96	14	144	740	1020	42	3.92	–	–	–	4.80
A4	292	70	94	14	140	728	1092	40	4.14	–	–	–	5.20
A5	341	82.50	110	16.50	165	670	1010	40	3.27	–	–	–	4.50
B1	298	72	96	14	144	704	1056	40	3.92	4.85	–	–	7.20
B2	298	72	96	14	144	704	1056	40	3.92	–	9.10	–	7.20
B3	298	72	96	14	144	704	1056	40	3.92	–	–	27	7.20

Note: S/A is the sand ratio, %; A/B is the aggregate-to-binder ratio.



Fig. 2. Vacuum test equipment.

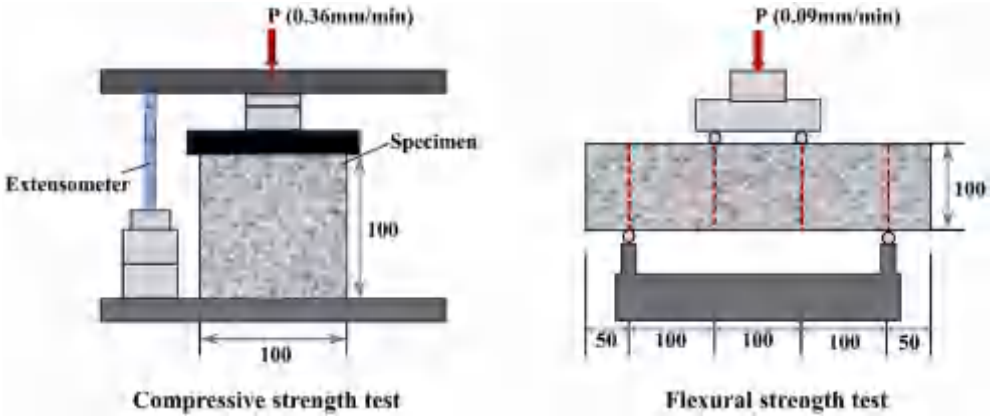


Fig. 3. Loading diagram of concrete strength test: (a) Cube compressive strength test; (b) Four-point flexure test.

are recorded using Eqs. (2) and (3) respectively [15].

$$\Delta w_t = \frac{m_0 - m_t}{m_0} \times 100\% \tag{2}$$

Where $\triangle w_t$ represents the mass loss rate of the specimen at time t during exposure to the low vacuum environment, %; m_0 is the initial mass of the specimen before exposure to the low vacuum environment, g; m_t is the mass of the specimen at time t after exposure to the low vacuum environment, g.

$$\Delta v_t = \frac{m_0 - m_t}{\Delta t \cdot S} \times 10^{-3} \tag{3}$$

Where $\triangle v_t$ represents the drying rate of the specimen at time t during exposure to the low vacuum environment, kg/d/m^2; $\triangle t$ is the time interval, d; S is the surface area of the specimen exposed to the low vacuum environment, m^2.

2.3.4. Gas permeability test

The gas permeability of concrete was tested using the NELD-AV037 gas permeability tester produced by Beijing Neld Intelligent Technology Co., Ltd., based on the Cembureau method [22]. Cylindrical specimens were sealed on the sides with epoxy resin and then placed between the high-pressure and low-pressure zones of the instrument, with the low-pressure zone at atmospheric pressure. It was found that the apparent permeability coefficient of concrete is unstable when the inlet pressure is less than 200 kPa [23]. Therefore, in this experiment, the pressure in the high-pressure zone was set to 300 kPa, with a test duration of 6 h and a sampling interval of 1 min. The apparent permeability of concrete was calculated using Eq. (4) [24].

$$k = 2\mu L \frac{P_2}{{P_1}^2 - {P_2}^2} \frac{Q}{A} \tag{4}$$

Where k represents the gas permeability coefficient, m^2; μ is the viscosity coefficient of air, 1.78 $\times$ 10^{-5} Pa s; L is the thickness of the sample, mm; P_1 is the gas pressure at the inlet, maintained at a constant pressure of 300 kPa; P_2 is the atmospheric pressure, 101 kPa; Q is the gas flow rate, m^3/s; A is the cross-sectional area of the specimen, m^2.

2.3.5. Capillary water absorption test

The specimens, after standard curing, were subjected to air drying and low vacuum drying treatments for 56 days. Specimens for air drying were placed in a curing room with a temperature of 20 °C–25 °C and a relative humidity of 60 %–70 %. Upon reaching the specified drying time, the specimens were removed for capillary absorption tests. The tests were conducted according to ASTM C1585-13 [25]. First, the sides of the specimens were sealed with epoxy resin, and then the side away from the water absorption surface was wrapped with plastic film and secured with rubber bands (to prevent evaporation of absorbed moisture). The mass of the specimen at this time was measured using an electronic balance as the initial mass, after which the capillary absorption test was conducted. The immersion depth of the water absorption surface of the specimen was controlled at 2 ± 1 mm. Upon reaching the specified age, the specimens were removed, dried with a wet towel, and then weighed. The testing cycle was 7 days. The capillary absorption height of the specimens can be calculated using Eq. (5).

$$H = \frac{m_{wt}}{S_w \rho_w} \tag{5}$$

Where H represents the water absorption height, mm; m_{wt} is the absorbed water mass of the specimen at time t, g; S_w is the contact area between the specimen and water, mm^2; ρ_w is the density of water, 0.001 g/mm^3.

2.3.6. Porosity test

The strength and permeability of concrete are closely related to the porosity and pore connectivity within the concrete [26]. Therefore, comparing the total porosity and permeable porosity of different samples can help further understand the reasons for changes in permeability.

The total porosity of concrete is assessed via a nitrogen adsorption and desorption test. Samples obtained post-compressive strength testing, are trimmed to 3–5 mm and immersed in isopropanol to halt hydration. These samples are then vacuum-dried and analyzed using a Builder SSA-4000 specific surface area analyzer for nitrogen adsorption and desorption. The cumulative total pore volume from this test characterizes the total porosity. The permeable porosity is calculated according to the method outlined in ASTM C642-13 [27].

$$\rho = \frac{m_{sat} - m_{dry}}{m_{sat} - m_{sub}} \times 100\% \tag{6}$$

Where ρ is the permeable porosity, %; m_{sat} is the saturated mass of the specimen when fully saturated with water, g; m_{dry} is the absolutely dry mass of the specimen, g; m_{sub} is the mass of the saturated specimen when submerged in water, g.

It should be noted that the absolutely dry mass of the specimen is typically obtained by drying in an oven at a temperature of 105 °C for no less than 24 h. Although this temperature is sufficient to expel capillary water and gel water, high-temperature drying can affect the permeability of concrete by altering its microstructure, increasing the diameter of capillary pores and the number of interconnected pores [28]. To reduce the impact of high temperatures on the concrete microstructure, this test selected 60 °C as the drying temperature for the specimens until they were dried to a constant weight. In fact, the porosity calculated in the end is closer to the

permeable capillary porosity [29].

3. Results and discussion

3.1. Concrete strength

3.1.1. Flexural strength

To explore the impact of sand ratio, aggregate-to-binder ratio, and fibers on the toughness of concrete, the flexural strength of various concrete mixes was tested after 28 days of standard curing. The failure modes are illustrated in Fig. 4, and the load-displacement curves are presented in Fig. 5. As observed in Figs. 4 and 5, both plain concrete and glass fiber-reinforced concrete exhibit brittle failure under bending loads, with the curves abruptly dropping to zero force at the peak load. Conversely, PE fiber-reinforced concrete and PVA fiber-reinforced concrete demonstrate characteristics of plastic failure, where the concrete cracks after reaching the peak load, and the load gradually decreases with the progression of deformation. Notably, the PE fiber-reinforced concrete experienced a slip-hardening phenomenon at a displacement of 0.58 mm, which is related to the excellent crack resistance and bridging provided by PE fibers. It can be seen that there are numerous fibers pulled out and still embedded at the crack opening. PE fibers, with a higher elastic modulus and better ductility compared to PVA fibers and glass fibers, provide superior crack resistance and toughening effects.

According to Eq. (1) and by integrating the area under the load-displacement curves, the flexural strength and energy absorption (E_a) for each group of specimens were obtained, as shown in Fig. 6. It can be concluded that the flexural strength and energy absorption capacity of concrete increase with the increase in sand ratio. Uddin et al. [30] previously reported that at sand ratios of up to 44 %, both compressive and tensile strength of concrete increase. This is because, under the assumption of an appropriate sand ratio, an increase in sand ratio not only helps to fill the voids between coarse aggregates, increasing concrete compactness but also improves the cohesiveness of the paste, which is conducive to reducing concrete segregation and slippage during the loading process. These factors enhance the flexural strength and energy absorption capacity of concrete.

It can also be observed that the flexural strength increases with the increase in aggregate-to-binder ratio, which is due to the high elastic modulus of aggregates alleviating stress concentration under load, thereby increasing the critical stress intensity factor and fracture energy [31]. This also increases the number of aggregate particles in the effective cross-sectional area [32]. The bridging and crack-resistant effects of fibers effectively enhance the flexural toughness of concrete. PE, PVA, and glass fibers increased the flexural strength of concrete by 31 %, 21 %, and 7 %, and raised the E_a by 181 %, 7 %, and 2 % respectively. Among them, PE fibers have the best toughening effect, followed by PVA fibers, while glass fibers have hardly improved the flexural toughness of concrete.

3.1.2. Compressive strength

The compressive strength of concrete was tested after standard curing for 28 days (SC28), low vacuum drying treatment for 28 days (SC28 + VD28), and 56 days (SC28 + VD56), with the test results shown in Fig. 7. As observed, the compressive strength trends of plain concrete align with those from flexural strength tests, showing an increase with higher sand ratios and aggregate-to-binder ratios, consistent with findings by Uddin et al. [33], Yang et al. [34], and Haruna et al. [35]. Conversely, fiber-reinforced concrete, irrespective of fiber type, exhibited reduced compressive strength due to the introduction of fibers, which diminishes interfacial bonding strength and forms a spatial network structure, thereby impairing paste workability [36].

Analysis of concrete strength development under low vacuum condition indicates an increase in strength after 28 days of low vacuum drying. This enhancement can be explained by several factors: (1) Low vacuum induces water evaporation, causing water in

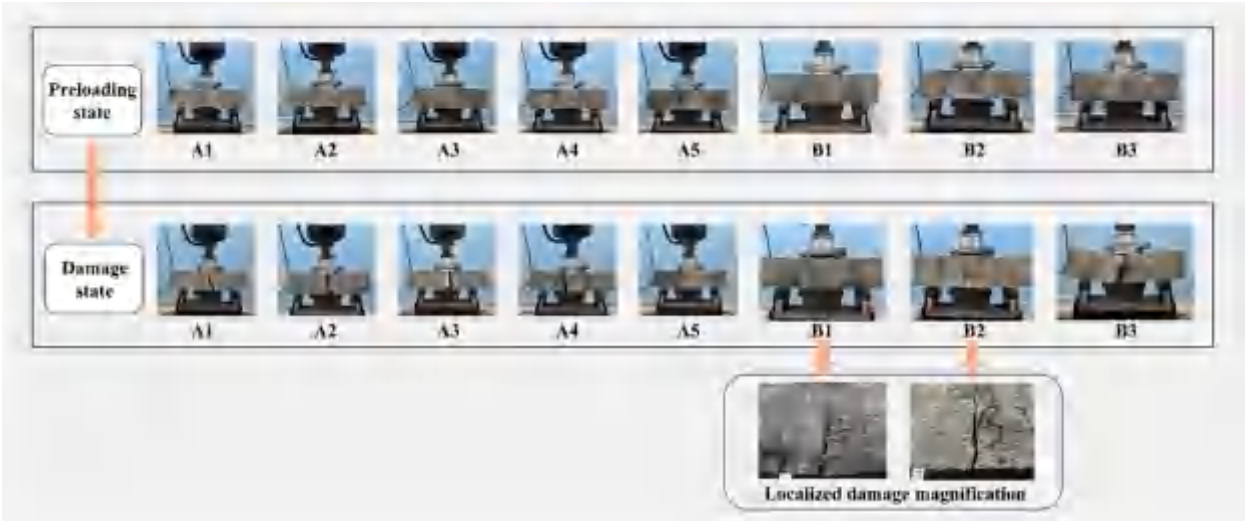


Fig. 4. Four-point bending failure diagram of concrete.

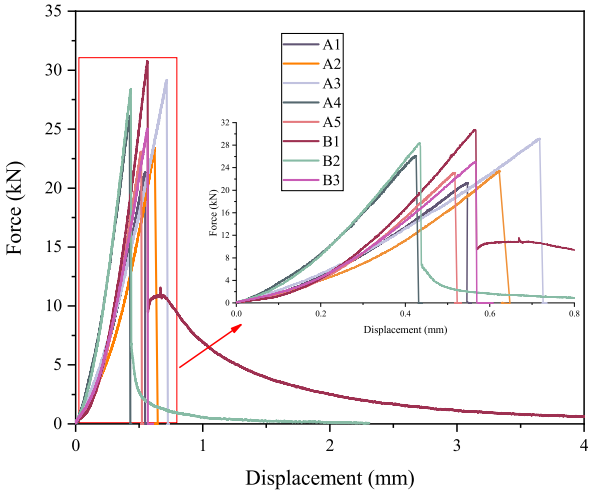


Fig. 5. Force-displacement curves of concrete.

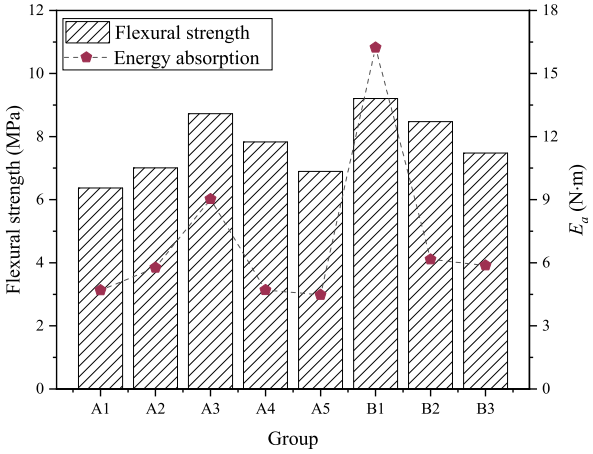


Fig. 6. Flexural strength and energy absorption of concrete.

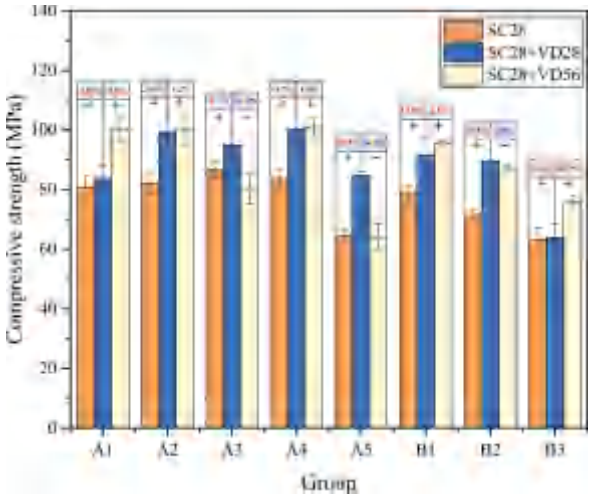


Fig. 7. The cube compressive strength of concrete.

smaller capillary pores to migrate to larger ones, promoting matrix hydration and strengthening concrete [15]. (2) The reduction in pore water during evaporation decreases pore pressure and surface tension, facilitating water penetration into the cement matrix and accelerating hydration [37]. (3) Evaporation also diminishes the dissociation force at crack tips and the viscous effect on cracks, mitigating crack expansion under compressive loads [16]. (4) Continuous low vacuum exposure reduces relative humidity within the concrete, enhancing the diffusion of interlayer water in C-S-H. This leads to a more compact C-S-H molecular structure, where calcium-oxygen and hydrogen bonds in water molecules are replaced by oxygen in C-S-H molecules, reducing the bond length and increasing solid phase strength [38,39].

Further observations reveal that when the low vacuum drying duration reaches 56 days, the strengths of concrete mixes A3, A5, and B2 decreased by 15.5 %, 24.4 %, and 2.8 % respectively, while the strengths of the other mixes continued to increase. The reasons for the increase in concrete strength are similar to those mentioned above, but the reasons for the decrease in strength are different. High sand ratio concrete (A3) has a denser pore structure, reducing the number of large capillary pores and interconnected pores, which makes water migration due to drying more difficult and limits the hydration reaction. Additionally, an increase in sand ratio leads to a reduction in the amount of paste, and the removal of moisture under low vacuum condition may result in a weak structure of hydration products, ultimately leading to a decrease in concrete strength. For concrete with a low aggregate-to-binder ratio (A5), the paste content is high, the porosity is larger, and the excess free paste is more prone to shrinkage and cracking under low vacuum drying condition. The cumulative internal damage under prolonged strong drying leads to the appearance of more cracks, which offset or even exceed the favorable effects of low vacuum condition on the increase in compressive strength. The PVA fiber-reinforced concrete may experience an initial increase in strength followed by a decrease under low vacuum condition, which could be attributed to the water-absorbing fiber network inside that may form channels for water migration, adversely affecting drying shrinkage [40].

Fig. 8 illustrates the typical uniaxial compression failure characteristics of concrete after standard curing and low vacuum treatment. It can be observed that the failure characteristics of concrete before and after low vacuum treatment are similar. Plain concrete exhibits characteristics of brittle failure, with cracks appearing on the specimen surface as strain increases and quickly penetrates to form multiple longitudinal cracks. The specimen is destroyed with a loud "bang" and is accompanied by a large amount of paste and aggregate spalling. Fiber-reinforced concrete, however, exhibits characteristics of plastic failure. Due to the crack-resistant bridging properties of the fibers, the concrete still has a certain bearing capacity after cracking. As strain increases, many microcracks appear around the main crack and gradually widen and densify. The time for the compression loading failure process is significantly extended, and the amount of spalling at the time of failure is significantly reduced compared to ordinary concrete, resulting in better specimen integrity.

Fig. 9 presents the complete stress-strain curves of concrete under uniaxial compression. It can be observed that the stress-strain curves well characterize the failure modes of concrete. Regardless of whether low vacuum treatment was applied, the stress-strain curves of concrete before the peak stress are nearly linear, indicating elastic deformation. The curve for plain concrete drops sharply after the peak strain and the entire descending segment of the curve cannot be obtained due to the sudden bursting of the specimen. The curve for fiber-reinforced concrete descends slowly after the peak load, exhibiting ductile characteristics. It can be noted that the curves of concrete after low vacuum treatment become steeper, indicating an increase in brittleness. To quantitatively analyze the ability of concrete to resist axial compression deformation, the energy absorption value (the integral area of the ascending segment of the stress-strain curve), the energy dissipation value (the integral area of the descending segment of the stress-strain curve), and the axial compressive toughness ratio ($R_{e,1.0}$) were calculated, as shown in Table 4. According to the specification CECS13-2009 [41], the $R_{e,1.0}$ can be calculated using Eq. (7):

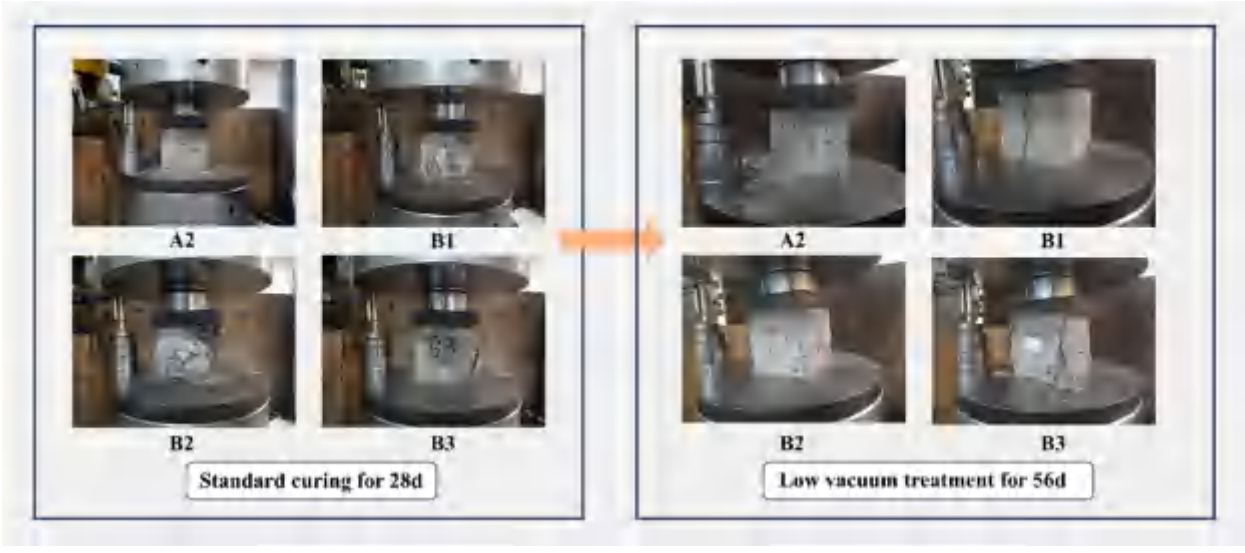


Fig. 8. Uniaxial compression failure diagram of concrete.

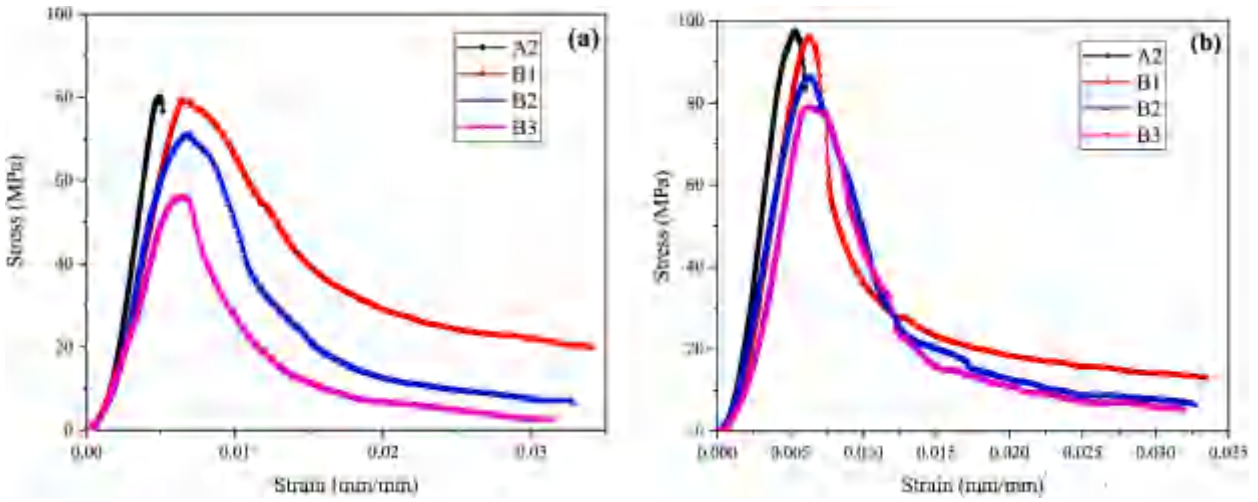


Fig. 9. Stress-strain curves of concrete: (a)SC28; (b) SC28 + VD56.

$$R_{e,1.0} = \frac{W_{1.0}}{F_{max} \times L_0 \times 1.0\%} \tag{7}$$

Where F_{max} is the peak load of the load-deformation curve, kN; L_0 is the gauge length of axial compression deformation measurement, mm; $W_{1.0}$ is the compression work, which is the area under the load-deformation curve of the axial deformation from 0 to $L_0 \times 1.0$ % mm, N·m.

As indicated in Table 4, the peak load of concrete after low vacuum treatment has significantly increased, which leads to an increase in its energy absorption value. It can also be observed that the $R_{e,1.0}$ values for A2, B1, B2, and B3 have decreased by 1.0 %, 5.2 %, 5.5 %, and 5.9 %, respectively. This indicates that the low vacuum environment has reduced the deformation capacity of the concrete, leading to a weakened energy dissipation capability and an increase in brittleness. This corroborates the previous research conclusions [16] and can be further applied to fiber-reinforced concrete. Further observation reveals that fibers help enhance the compressive toughness of concrete, with glass fibers showing the best improvement in toughness, with growth rates of 40 % and 33 % before and after low vacuum treatment, respectively.

3.2. Mass loss

Fig. 10 (a) and (b) respectively show the mass loss rate and drying rate curves of concrete under low vacuum condition. As seen in Fig. 10 (a), the mass loss of concrete increases rapidly in the early stages, and the dependence of the mass loss rate on age gradually decreases. An increase in the sand and aggregate-to-binder ratios reduces the mass loss rate of concrete, indicating an inverse correlation between them; the mass loss rate of fiber-reinforced concrete is greater than that of the control group. In Fig. 10 (b), the drying rate of concrete shows a consistent pattern with the mass loss. Concrete with a high sand and aggregate-to-binder ratio has a lower drying rate than concrete with a low sand and aggregate-to-binder ratio, and the drying rate of fiber-reinforced concrete is greater than that of plain concrete. Literature [15] indicates that when the drying rate is below 2×10^{-3} kg h^{-1} m^{-2} (equivalent to 4.8 × 10-2 kg h^{-1} m^{-2}), concrete reaches a state of drying equilibrium. Table 5 details the drying parameters for each concrete mix. According to Table 5, the maximum drying rate for A5 is the highest, requiring the longest time to reach drying equilibrium, and the mass loss rate corresponding to the drying equilibrium time is also the highest, whereas A4 is the opposite. Compared to the control group, fiber-reinforced has a greater mass loss rate, a higher drying rate, and a delayed drying equilibrium time. The mass loss rate and drying rate of PVA fiber-reinforced concrete are greater than those of PE and glass fiber-reinforced concrete.

The mass loss of concrete under low vacuum condition is attributed to the migration and evaporation of moisture. The sand ratio, aggregate-to-binder ratio, and the incorporation of fibers influence the pathways of moisture migration, as illustrated in Fig. 11.

Table 4
Uniaxial compression stress-strain test results of concrete.

Group		Peak load (kN)	Energy absorption (MPa)	Energy dissipation (MPa)	W (N·m)	$R_{e,1.0}$
SC28	A2	801.72	0.156	–	510.81	0.398
	B1	792.62	0.230	0.930	657.66	0.519
	B2	710.93	0.238	0.541	595.49	0.524
	B3	561.62	0.165	0.335	499.68	0.556
SC28 + VD56	A2	976.07	0.304	–	615.77	0.394
	B1	960.57	0.260	0.627	755.76	0.492
	B2	906.17	0.268	0.567	681.09	0.495
	B3	792.72	0.204	0.523	663.56	0.523

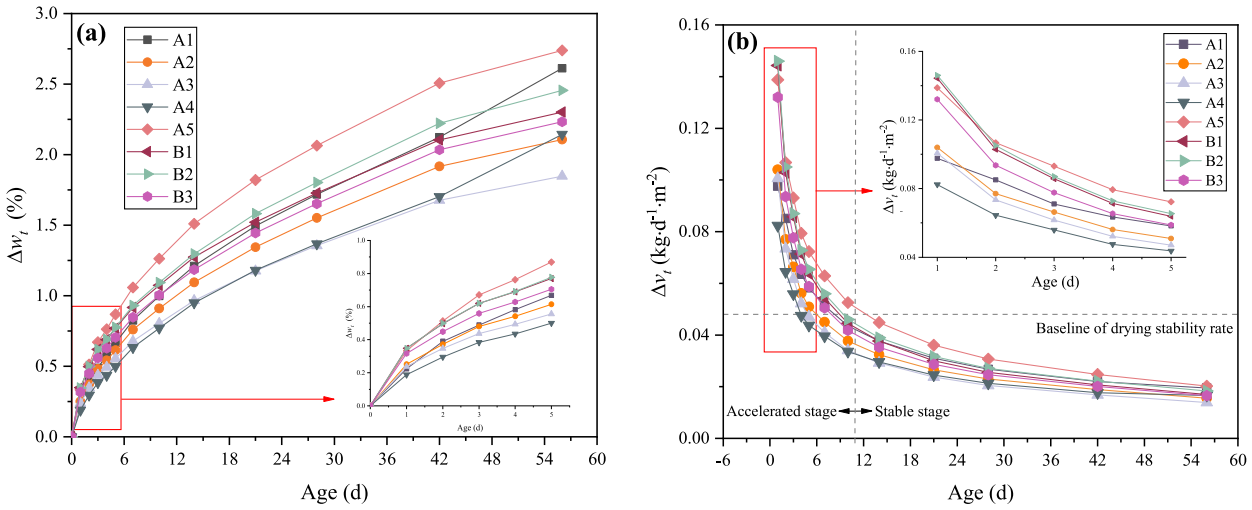


Fig. 10. Mass loss rate and drying rate of concrete: (a) $\triangle w_t$; (b) $\triangle v_t$.

Table 5
Low vacuum drying characteristic parameters of concrete.

Group	Maximum $\triangle w_t$ (%)	Minimum $\triangle v_t$ (kg·d^{-1}·m^{-2})	Maximum $\triangle v_t$ (kg·d^{-1}·m^{-2})	Drying equilibrium time (d)	$\triangle w_t$ of drying equilibrium time (%)
A1	2.612	0.020	0.098	10	0.998
A2	2.107	0.016	0.104	7	0.759
A3	1.847	0.014	0.101	5	0.555
A4	2.144	0.017	0.082	4	0.435
A5	2.739	0.020	0.139	14	1.509
B1	2.302	0.017	0.144	10	1.073
B2	2.455	0.018	0.146	10	1.093
B3	2.233	0.017	0.132	10	1.093

Assuming that moisture in a certain-sized cement stone migrates linearly towards the low vacuum drying environment, the introduction of coarse aggregate will block the wet diffusion path with impermeable aggregate, thereby extending the wet diffusion path and resulting in $L_1 > L_0$. Therefore, the higher the aggregate-to-binder ratio, the longer the wet diffusion path (L_3 being the longest), making moisture migration more difficult and resulting in lower mass loss. When the aggregate-to-binder ratio remains constant,

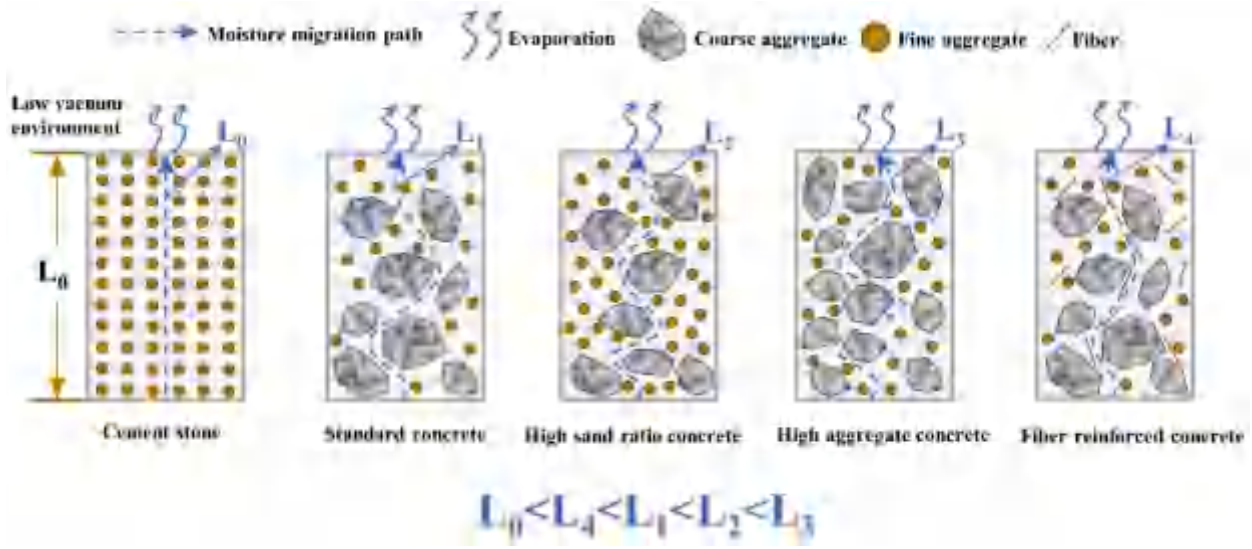


Fig. 11. The schematic diagram of moisture migration in concrete under low vacuum environment.

increasing the sand ratio can further increase the wet diffusion path (L_2>L_1). This is because the smaller size of sand particles can fill the gaps between coarse aggregates, refining the pore structure and reducing the porosity of the ITZ, which in turn lowers the wet diffusion coefficient of concrete [23]. The addition of fibers introduces new fiber-matrix interfaces, which can easily become channels for gas and liquid transport, thus facilitating the removal of moisture under drying conditions [42]. On the other hand, during the concrete casting process, some fiber ends may be exposed on the surface of the specimen, which will further facilitate the removal of moisture under drying condition, ultimately leading to L_1>L_4. Additionally, since PVA fibers are hydrophilic, they absorb moisture from the fresh mortar and release it during the hardening process [40]. Under low vacuum drying, this moisture then migrates out along the fiber network, leading to an increase in the mass loss rate.

It should be noted that although aggregates introduce a tortuous effect on the wet diffusion path, they also introduce a large number of ITZs, which typically have higher porosity and can easily form channels for moisture transport. Therefore, when the sand and aggregate-to-binder ratios exceed a certain value, the ITZs will overlap and connect, forming the main channels for moisture migration, thereby accelerating the loss of moisture. As observed in Fig. 10, when the low vacuum exposure time exceeds 21 days, the mass loss rate of A4 begins to exceed that of A3, especially from 42 days to 52 days, where the mass loss significantly increases. Interestingly, A1 with a high coarse aggregate content also exhibits the same pattern. This suggests that the effect of the ITZ caused by coarse aggregates may be exacerbated, and the low vacuum environment may have triggered the coarsening of the pore structure at the paste-aggregate ITZ, which is well demonstrated by permeability tests.

3.3. Gas permeability

Fig. 12 presents the results of gas permeability tests on concrete before and after low vacuum treatment. It can be observed that the gas permeability of concrete significantly increases after low vacuum treatment, with the gas permeability coefficient increasing by 1-2 orders of magnitude. The increase in permeability is closely related to the porosity, pore tortuosity, and pore connectivity within the concrete [43]. On the other hand, since the ITZ is typically a region rich in coarse hydration products, it has a higher porosity, and microcracks are prone to initiation and propagation, making it a weak zone for strength and a channel for fluid transport [44]. The low vacuum environment may have caused the coarsening of the concrete pore structure and the degradation of the ITZ, leading to an increase in gas permeability, as previously demonstrated in the study [16]. The pore saturation level significantly affects the gas permeability of concrete; Islam et al. [45] pointed out that the gas permeability of water-saturated concrete is nearly zero, and the permeability increases as drying progresses. The low vacuum environment accelerates the migration and evaporation of pore water, and the channels formed by water loss provide pathways for gas permeability, resulting in a significant increase in the gas permeability of concrete. Additionally, microcracks generated by concrete shrinkage under low vacuum condition also provide channels for gas transport [45].

By comparing the gas permeability coefficients of concrete after standard curing, it can be observed that the gas permeability coefficient of concrete decreases with the increase of sand and aggregate-to-binder ratios, which is consistent with the law observed in compressive strength tests. It can also be noted that the gas permeability coefficients of PE fiber-reinforced concrete, PVA fiber-reinforced concrete, and glass fiber-reinforced concrete are 383 %, 24 %, and 156 % higher, respectively than those of the control group, indicating a significant increase in permeability. This is due to the introduction of fibers, which increases the number of new fiber-matrix ITZs, leading to an increase in harmful pores and porosity as a result of the oriented growth of hydration products in the ITZ [46,47]. On the other hand, the incorporation of fibers can reduce the workability of fresh mortar, increase the likelihood of binder agglomeration, impede the flow of aggregates, and increase the difficulty of vibration and compaction, leading to an increase in the number of permeable pores and porosity in the hardened paste, and a reduction in impermeability [48,49]. Additionally, PE fibers and glass fibers are hydrophobic fibers, which have weaker bonding with the matrix compared to the hydrophilic PVA fibers. This weak

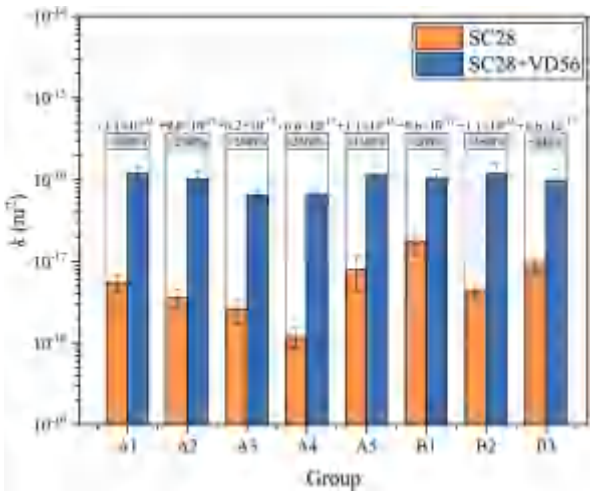


Fig. 12. Gas permeability coefficient of concrete.

interaction may lead to an increase in the porosity of the fiber-cement paste ITZ, providing channels for gas migration [47]. By comparing the gas permeability coefficients of concrete after low vacuum treatment, it can be observed that the gas permeability coefficient also decreases with the increase of sand and aggregate-to-binder ratios. The gas permeability coefficients of fiber-reinforced concrete are not significantly different from those of plain concrete, which may be due to the fibers to some extent restraining the shrinkage cracks caused by low vacuum.

An interesting phenomenon can be found from the above data, the compressive strength of concrete in low vacuum environment obtained a different percentage of increase compared with the standard curing but the gas impermeability of the concrete significantly decreased, which contradicts traditional experience. Therefore, the relationship between compressive strength and the gas permeability coefficient of concrete before and after low vacuum treatment was further compared, as shown in Fig. 13. It can be seen that there is a complex correlation between the compressive strength and the gas permeability coefficient of concrete. The gas permeability coefficient of concrete after standard curing generally falls within the range of 10^{-18} m^2 to 10^{-17} m^2, while the gas permeability coefficient after low vacuum treatment is around 10^{-16} m^2. However, only the compressive strengths of A3 and A5 decrease as their gas permeability coefficients increase after vacuum treatment. The above conclusions indicate that the mechanism by which low vacuum affects the strength of concrete is not directly related to its permeability; the reduction in saturation is likely the direct cause of the increased gas permeability in concrete [15,50]. This also indirectly suggests that changes in the pore structure of concrete under a low vacuum environment are a dynamic and complex process. The capillary water absorption test in the next section further characterizes this process.

3.4. Capillary water absorption

The capillary water absorption heights of concrete under different drying conditions were tested, as shown in Fig. 14 (SC28 + AD56 represents the specimens subjected to air drying). It can be seen that the capillary water absorption height of concrete in both drying environments increases rapidly in the early stages and then significantly slows down after 6 h. Based on the trend of the capillary water absorption curves, the capillary water absorption of concrete can be precisely divided into two stages: the initial absorption stage (0–6 h) and the secondary absorption stage (6 h-7 d). The initial stage of water absorption in concrete is usually controlled by capillary forces and inertial forces, while the secondary stage of water absorption is driven by gel pores, diffusion, and gravity [51,52]. When concrete first contacts water, surface effects promote rapid water absorption; when the air/water interface relaxes to a stable or metastable state within the pore space, the rate of water ingress slows down [51]. For dried specimens, the reabsorption of water can also activate hydration, reducing the critical pore diameter of the matrix and slowing down water adsorption. It is not difficult to observe that the capillary water absorption height of concrete under low vacuum drying is significantly higher than that under air drying condition, indicating that the pore structure of concrete becomes coarser and the number of connected capillary pores increases after low vacuum treatment. Winslow et al. [53] pointed out that pore coarsening may lead to the formation of permeable clusters, resulting in complete connection of the aggregate ITZ, thereby increasing the capillary water absorption rate.

To quantitatively analyze the water absorption rates of concrete with different mix ratios, the two-stage capillary water absorption curves can be segmented and fitted. The slope of each fitted curve in each stage is defined as the capillary sorptivity coefficient, which can be determined by Eq. (8). A schematic of the fitting process is shown in Fig. 15.

$$H = \alpha\sqrt{t} + b \tag{8}$$

Where α is the sorptivity coefficient, mm·s^{-}½; b is the axial intercept of H, which is the correction term considering the surface effect when the sample is in contact with water, mm.

According to the method shown in Fig. 15, the two-stage capillary sorptivity coefficients of concrete with different mix ratios can be calculated, as illustrated in Fig. 16. From Fig. 16, it can be observed that due to surface effects, the initial stage sorptivity coefficient of concrete is higher than the secondary stage sorptivity coefficient. The two-stage capillary sorptivity coefficients of concrete under low vacuum drying condition are significantly higher than those under air drying condition. Under air drying condition, the initial sorptivity coefficient of concrete decreases with the increase in sand and aggregate-to-binder ratios, which is consistent with the findings of Haruna et al. [35]. The incorporation of fibers leads to an increase in the initial sorptivity coefficient. This is attributed to the coarsening of the ITZ caused by the fibers and the formation of smooth, non-tortuous channels within the matrix, which reduce the dynamic resistance of fluid flow, thereby enhancing the water absorption capacity [54]. Furthermore, fibers can enhance the connectivity between surface permeable pores and internal micropores, leading to an increased water absorption rate [49]. Under low vacuum drying condition, increasing the sand ratio and aggregate content also helps to reduce the water absorption rate. An increased proportion of fine aggregate enlarges the area of the ITZ but helps reduce its porosity, whereas coarse aggregate has the opposite effect [23]. Within the gradient designed in this experiment, the increase in sand and aggregate-to-binder ratios both contribute to further densification of the concrete interior, achieving an effective balance between ITZ area and porosity, thereby favoring the reduction of capillary water absorption rate. After low vacuum drying, the initial capillary sorptivity coefficient of fiber-reinforced concrete remains higher than that of plain concrete. It is noteworthy that the sorptivity coefficient in the second stage for PVA fiber-reinforced concrete significantly increases, which is caused by the reabsorption of water by the fiber network within the specimen [40].

The intersection point of the fitted curves for the two-stage capillary sorptivity coefficients can be used to further determine the capillary water content. The calculation method is shown in Eq. (9), and the results are presented in Fig. 17.

$$w_{cap} = \frac{H_i}{h}\rho_w \tag{9}$$

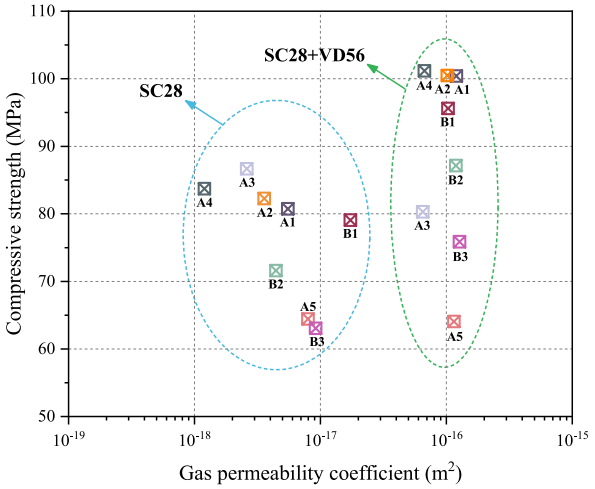


Fig. 13. Compressive strength versus gas permeability coefficient of concrete.

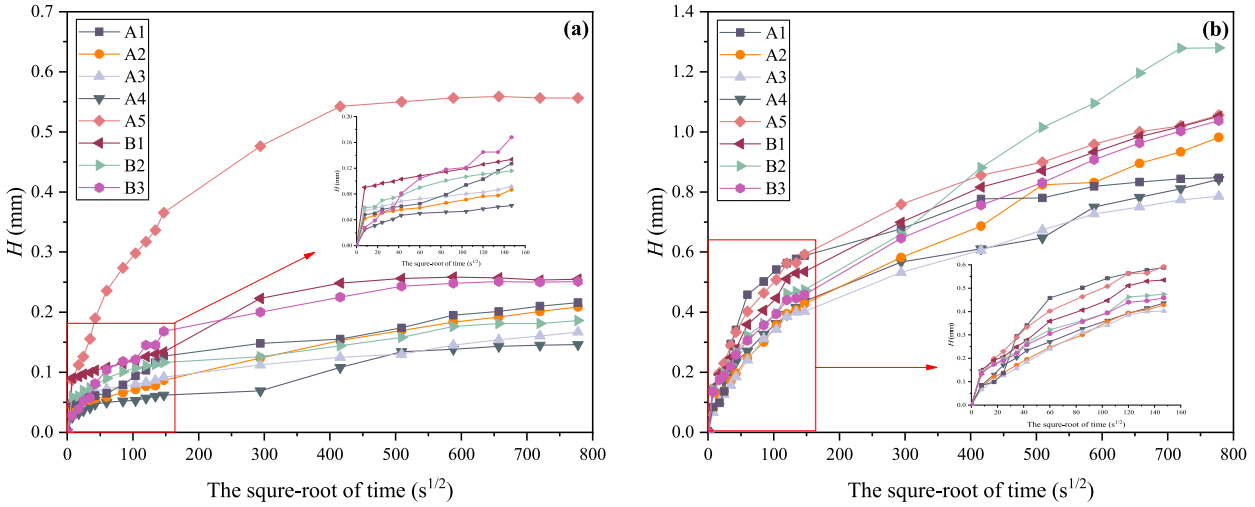


Fig. 14. Capillary water absorption height: (a) SC28 + AD56; (b) SC28 + VD56.

Where w_{cap} is the capillary water content, g/mm^3; H_i is the intersection point of the fitting curve of the capillary sorptivity coefficient of concrete with different proportions, mm; h is the height of the water absorption specimen, mm.

As shown in Fig. 17, under air-drying condition, the capillary water content of concrete decreases with the increase of sand and aggregate-to-binder ratios and increases with the addition of fibers. Under low vacuum drying condition, the change in capillary water content with the sand ratio is consistent with that under air-drying condition, but the capillary water content of concrete with high aggregate content is higher than that of the control group. Overall, the variation in the capillary water content of concrete is consistent with the initial capillary sorptivity coefficient, which is also determined by the capillary forces in the initial stage. By comparison, it can also be observed that the mass loss and capillary water absorption laws of concrete under low vacuum condition are similar, specifically: increasing the sand and aggregate-to-binder ratios reduces the mass loss of concrete under low vacuum condition and decreases the capillary sorptivity coefficient, while the addition of fibers exacerbates the loss of moisture and capillary water absorption behavior of concrete. This indirectly confirms that the moisture evaporation behavior of concrete under low vacuum condition is primarily related to the water in the capillary pores, and the porosity test data in the next section further supports this conclusion.

3.5. Porosity

To better understand how low vacuum environment affects the macroscopic properties of concrete, Fig. 18 depicts the cumulative pore size distribution curves of concrete after low vacuum treatment. Fig. 19 depicts the statistical results for total porosity and permeable porosity. As seen in Fig. 19, the total porosity and permeable porosity of each specimen exhibit a similar pattern of variation. The permeable porosity of concrete decreases with an increase in sand ratio and aggregate-to-binder ratio. Notably, the concrete

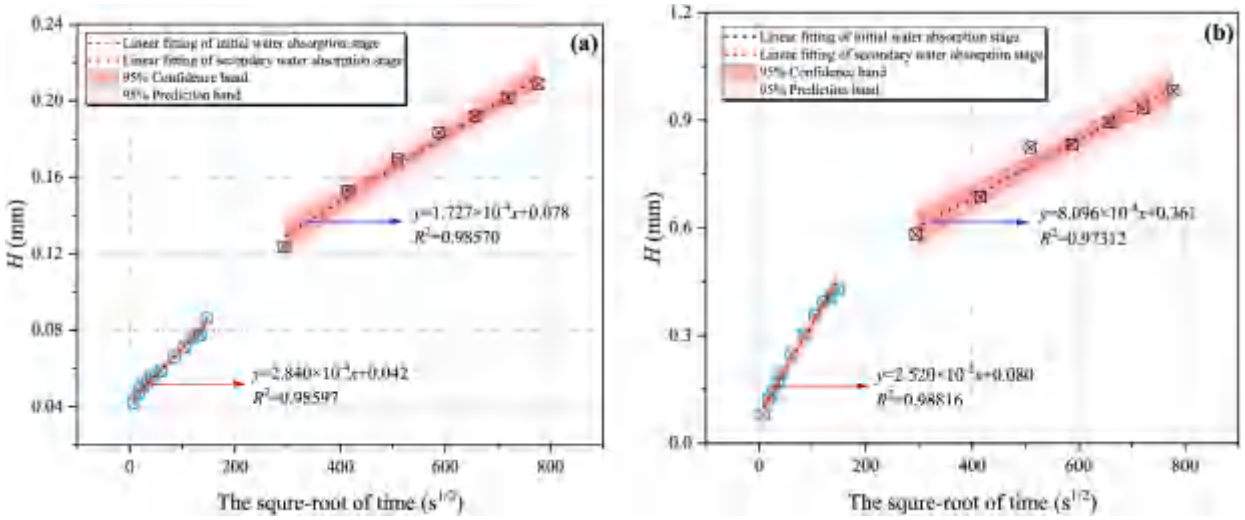


Fig. 15. Schematic of the two-stage fit of the sorptivity coefficient: (a) SC28 + AD56 for A2; (b) SC28 + VD56 for A2.

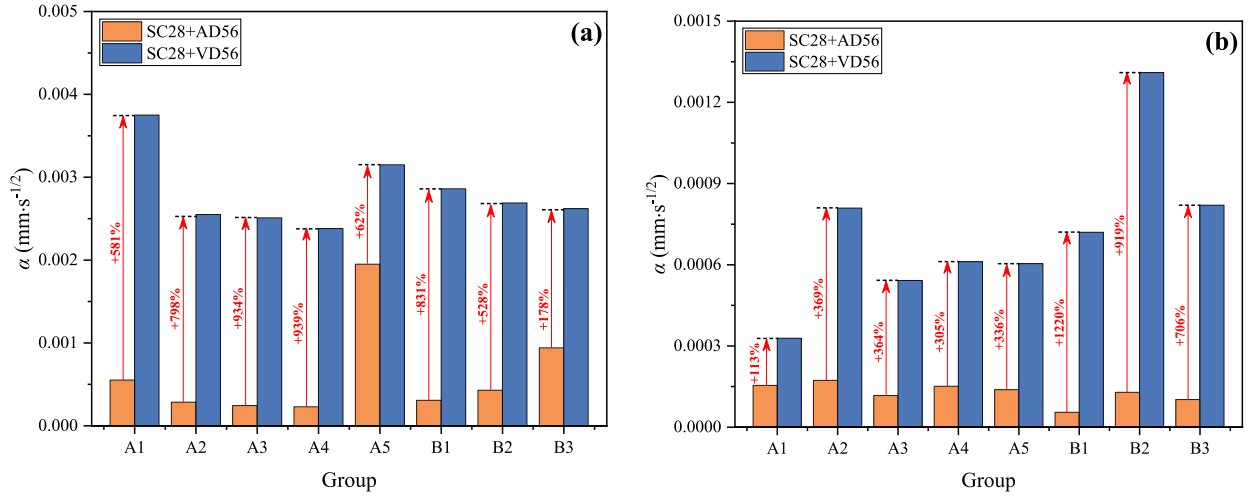


Fig. 16. The sorptivity coefficient of concrete under different drying conditions: (a) Initial water absorption stage; (b) Secondary water absorption stage.

with the lowest aggregate-to-binder ratio has the highest permeability, indicating that an increase in the aggregate-to-binder ratio is beneficial for reducing the permeability of concrete. The permeable porosity of fiber-reinforced concrete is higher than that of the control group. The total porosity initially decreases and then increases with changes in the sand ratio and aggregate-to-binder ratio of concrete; the addition of fibers tends to increase the porosity of concrete to some extent.

Figs. 20 and 21 respectively present the relationship between capillary water content and permeable porosity, and the relationship between compressive strength and total porosity. It can be observed that there is a good positive correlation between permeable porosity and capillary water content, while there is a good negative correlation between total porosity and compressive strength. This indicates that under low vacuum condition, the moisture migration in concrete is primarily related to capillary pores, while the evolution of strength is mainly associated with changes in total porosity. It is noteworthy that within the testing age range, the pore coarsening caused by the low vacuum environment is mainly reflected in the capillary pores near the surface, which leads to an increase in the permeable porosity and higher permeability of the concrete.

4. Conclusion

This study investigated the changes in strength and permeability of concrete exposed to low vacuum environment through tests on strength, mass loss, gas permeability, capillary water absorption, and porosity. It also discussed the effects of aggregate and fibers on concrete properties and water migration mechanisms. The following conclusions can be drawn from the results.

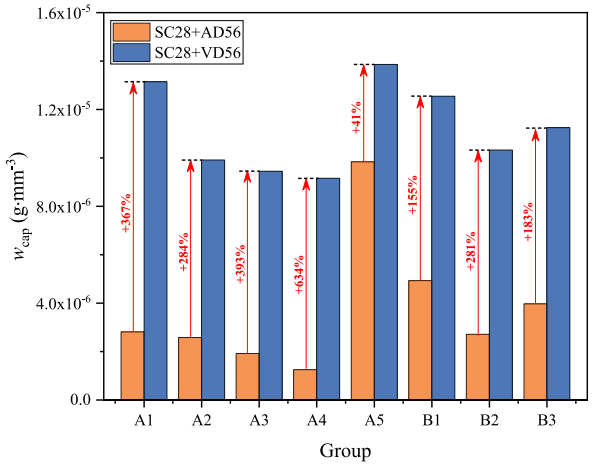


Fig. 17. Capillary water content of concrete under different drying conditions.

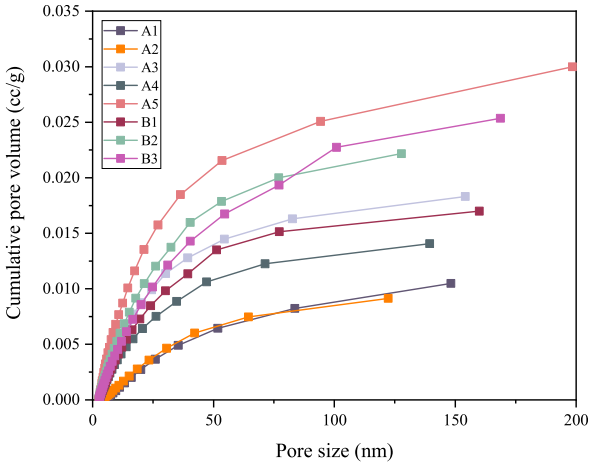


Fig. 18. Cumulative pore volume of concrete after low vacuum treatment.

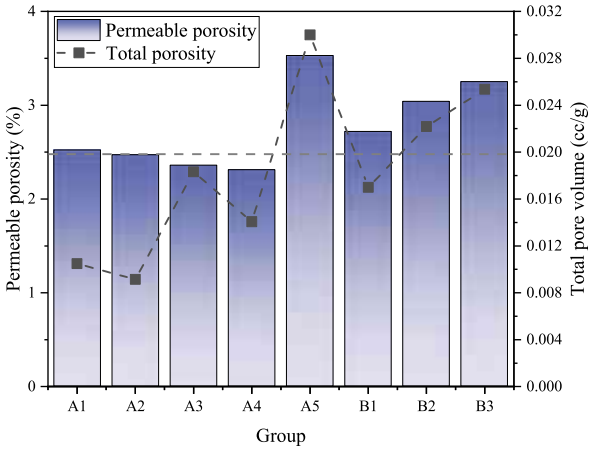


Fig. 19. Statistical results of permeable porosity and total pore volume of concrete.

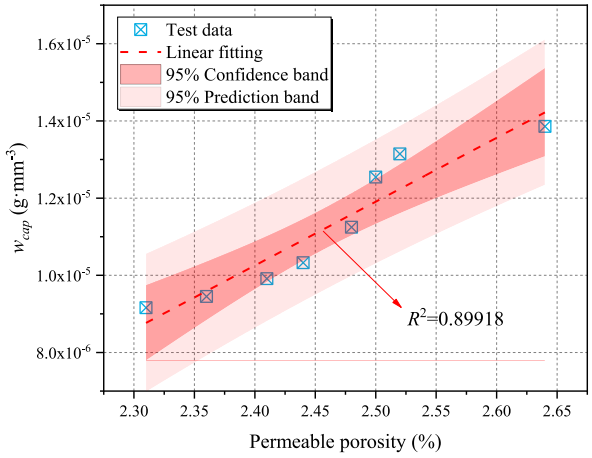


Fig. 20. Permeable porosity versus capillary water content.

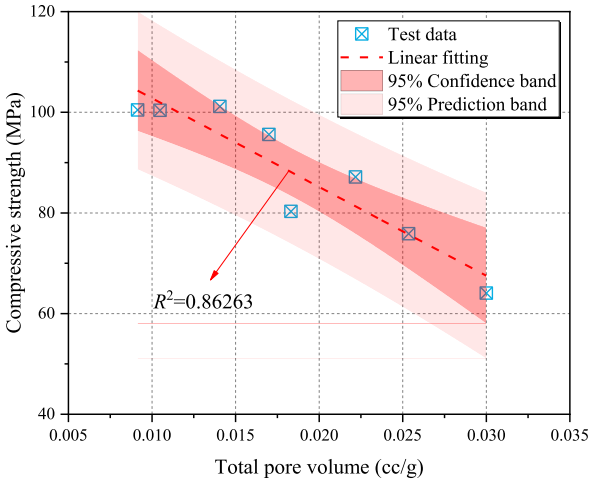


Fig. 21. Total pore volume versus compressive strength.

(1) Increasing the sand ratio and the aggregate-to-binder ratio is beneficial for improving the flexural and compressive strength of standard curing concrete. Fibers significantly contribute to the bending toughness, with PE, PVA, and GF fibers increasing the flexural strength of concrete by 31 %, 21 %, and 7 %. Under low vacuum condition, the strength of concrete increases by 1.3%–26.4 % within the first 28 days, with the strength values showing a positive correlation with the sand ratio and the aggregate-to-binder ratio. After 56 days of exposure, the strength of concrete continues to increase, except for high sand ratio, low aggregate, and PVA fiber-reinforced concrete mixtures. The changes in strength are attributed to the migration, evaporation, and redistribution of moisture. Low vacuum drying leads to a reduction in the axial compression toughness ratio of concrete, increasing its brittleness. Fibers, on the other hand, help improve the compressive toughness of concrete.

(2) The mass loss of concrete under low vacuum is negatively correlated with the sand ratio and the aggregate-to-binder ratio. Fibers increase the mass loss, with PVA fiber-reinforced concrete exhibiting a higher mass loss rate and drying rate compared to PE fiber and glass fiber-reinforced concrete. The tortuosity effect of aggregates can effectively reduce the moisture diffusion coefficient, decrease the drying rate, and expedite the time to reach drying equilibrium. In contrast, fibers introduce new fiber-matrix interfaces, which can form channels for gas-liquid transmission, thereby accelerating moisture evaporation. The ITZ effect of aggregates may adversely affect the long-term performance of concrete in low vacuum environment.

(3) After low vacuum treatment, the gas permeability coefficient of concrete increases by 1-2 orders of magnitude due to reduced saturation from moisture evaporation. Before and after low vacuum treatment, gas permeability decreases with higher sand and aggregate-to-binder ratios. After standard curing, the gas permeability of PE, PVA, and glass fiber-reinforced concrete increased by 383 %, 24 %, and 156 % respectively compared to the control group. After low vacuum treatment, the gas permeability of fiber-reinforced and plain concrete shows little difference, attributed to the crack-resistant mechanism of fibers. The correlation between low vacuum effects on concrete strength and permeability is weak.

(4) Under low vacuum drying, both the height and rate of capillary water absorption are significantly higher than under air drying. Higher sand and aggregate-to-binder ratios reduce the water sorptivity coefficient, while fibers increase it. The variation in capillary water content aligns with the initial sorptivity coefficient, paralleling the mass loss pattern. This indicates that moisture evaporation under low vacuum primarily involves water in capillary pores.
(5) Porosity test results show a strong correlation between total porosity and compressive strength, and between permeable porosity and capillary water content. This suggests that moisture migration in concrete under low vacuum is primarily related to capillary pores, while strength evolution is mainly associated with changes in total porosity.

The impact of low vacuum on concrete drying and pore structure is a dynamic process progressing from the surface inward. Extended exposure to low vacuum can lead to coarser pore structures and decreased stability of hydration products. Future research should focus on long-term performance changes of concrete in low vacuum environments.

CRediT authorship contribution statement

Zhaofei Long: Writing – original draft, Methodology, Writing – review & editing. **Guangcheng Long:** Supervision, Funding acquisition, Conceptualization. **Zhuo Tang:** Supervision, Resources, Writing – review & editing. **Minghui Shangguan:** Investigation, Supervision, Writing – review & editing. **Ce Gao:** Investigation, Project administration. **Meihui Yi:** Formal analysis, Validation. **Zhenhui He:** Visualization, Data curation. **Yutong Zhang:** Software.

Declaration of competing interest

The authors declare that they have no known competing financial interests or personal relationships that could have appeared to influence the work reported in this paper.

Data availability

Data will be made available on request.

Acknowledgments

The authors are grateful to the financial support of the Program Fund of Nonmetallic Excellence and Innovation Center for Building Materials (No. 24TDA-1).

References

[1] Z. Deng, Y. Zhang, B. Wang, W. Zhang, Present situation and prospect of evacuated tube transportation system, J. Southwest Jiao Tong Univ. 54 (5) (2019) 1063–1072, https://doi.org/10.3969/j.issn.0258-2724.20180204 (In Chinese).
[2] F. Michelberger, M. Plavec, K. Pyrek, P. Graf, The Hyperloop Concept Development, Possible Applications and Critical Analysis, Sustainable Rail Transport 4: Innovate Rail Research and Education, Springer International Publishing, Cham, 2021, pp. 341–367, https://doi.org/10.1007/978-3-030-82095-4.
[3] Y. Xin, W. Li, Q. Dong, T. Yang, B. Tian, Q. Li, Superconductors and Lenz's law, Supercond. Sci. Technol. 33 (5) (2020) 055004, https://doi.org/10.1088/1361-6668/ab794b.
[4] J. Park, L. Kim, S. Nam, I. Yeo, Performance evaluation of airtightness in concrete tube structures for super-speed train systems, Mag. Concr. Res. 65 (9) (2013) 535–545, https://doi.org/10.1680/macr.12.00161.
[5] H. Kanamori, S. Matsumoto, N. Ishikawad, Long-term Properties of Mortar Exposed to a Vacuum, vol. 125, Special Publication, 1991, pp. 57–70, https://doi.org/10.14359/2415.
[6] G. Long, Y. Chen, Z. Tang, M. Shangguan, C. Gao, S. Xu, Drying shrinkage behavior of cement mortar under low vacuum conditions, Construct. Build. Mater. 374 (2023) 130933, https://doi.org/10.1016/j.conbuildmat.2023.130933.
[7] N.P. Tran, C. Gunasekara, D.W. Law, S. Houshyar, S. Setunge, A. Cwirzen, A critical review on drying shrinkage mitigation strategies in cement-based materials, J. Build. Eng. 38 (2021) 102210, https://doi.org/10.1016/j.jobe.2021.102210.
[8] N. Jafarifar, K. Pilakoutas, T. Bennett, Moisture transport and drying shrinkage properties of steel-fibre-reinforced-concrete, Construct. Build. Mater. 73 (2014) 41–50, https://doi.org/10.1016/j.conbuildmat.2014.09.039.
[9] S.M. Aldarabseh, P. Merati, An experimental investigation of the potential of empirical correlations derived based on Dalton's law and similarity theory to predict evaporation rate from still water surface, Proc. IME C J. Mech. Eng. Sci. 236 (12) (2022) 6554–6578, https://doi.org/10.1177/09544062211068976.
[10] X. Ge, Y. Ge, Q. Li, X. Cai, W. Yang, Y. Du, Effect of low air pressure on the durability of concrete, Construct. Build. Mater. 187 (2018) 830–838, https://doi.org/10.1016/j.conbuildmat.2018.07.179.
[11] S.T. Yi, T.Y. Hyun, J.K. Kim, The effects of hydraulic pressure and crack width on water permeability of penetration crack-induced concrete, Construct. Build. Mater. 25 (5) (2011) 2576–2583, https://doi.org/10.1016/j.conbuildmat.2010.11.107.
[12] T. Lu, Z. Li, H. Huang, Restraining effect of aggregates on autogenous shrinkage in cement mortar and concrete, Construct. Build. Mater. 289 (2021) 123166, https://doi.org/10.1016/j.conbuildmat.2021.123166.
[13] X. Zhang, P. Gao, Lnfluence of aggregate on dry shrinkage of concrete, Fly Ash Comp. Util. 2 (2014) 3–7 (In Chinese).
[14] B. Barr, S.B. Hoseinian, M.A. Beygi, Shrinkage of concrete stored in natural environments, Cem. Concr. Compos. 25 (1) (2003) 19–29, https://doi.org/10.1016/S0958-9465(01)00044-0.
[15] M. Shangguan, Y. Xie, F. Wang, G. Long, Z. Tang, Y. Chen, S. Xu, H. Li, C. Gao, M. Liu, Effect of low-vacuum environment on the strength and permeability of cement-based materials, Construct. Build. Mater. 400 (2023) 132676, https://doi.org/10.1016/j.conbuildmat.2023.132676.
[16] M. Shangguan, Y. Xie, S. Xu, C. Gao, G. Long, F. Wang, M. Liu, Mechanical properties characteristics of high strength concrete exposed to low vacuum environment, J. Build. Eng. 63 (2023) 105438, https://doi.org/10.1016/j.jobe.2022.105438.
[17] H. Chang, X. Wang, Y. Wang, S. Li, J. Wang, J. Liu, P. Feng, Influence of low vacuum condition on mechanical performance and microstructure of hardened cement paste at early age, Construct. Build. Mater. 346 (2022) 128358, https://doi.org/10.1016/j.conbuildmat.2022.128358.
[18] M. Shangguan, Y. Xie, G. Long, Z. Long, F. Wang, Y. Chen, C. Gao, Z. Tang, Hydration and microstructure evolution of cement paste in low vacuum environments, Construct. Build. Mater. 438 (2024) 137233, https://doi.org/10.1016/j.conbuildmat.2024.137233.
[19] V. Afroughsabet, L. Biolzi, P.J.M. Monteiro, The effect of steel and polypropylene fibers on the chloride diffusivity and drying shrinkage of high-strength concrete, Composer Part B-Eng. 139 (2018) 84–96, https://doi.org/10.1016/j.compositesb.2017.11.047.

[20] M. Mazloo, A.A. Ramezanianpour, J.J. Brooks, Effect of silica fume on mechanical properties of high-strength concrete, Cem. Concr. Compos. 26 (4) (2004) 347–357, https://doi.org/10.1016/S0958-9465(03)00017-9.
[21] GB/T 50081–2019, Standard for Test Methods of Concrete Physical and Mechanical Properties, China Architecture and Building Press, 2019.
[22] J.J. Kollek J J, The determination of the permeability of concrete to oxygen by the Cembureau method—a recommendation, Mater. Struct. 22 (1989) 225–230, https://doi.org/10.1007/BF02472192.
[23] R. Qian, J. Shi, Y. Li, W. Chen, G. Liu, Z. Liu, W. She, Y. Zhang, Investigation on parameters optimization for gas permeability testing of concrete: inlet-gas pressure and confining pressure, Construct. Build. Mater. 250 (2020) 118901, https://doi.org/10.1016/j.conbuildmat.2020.118901.
[24] H. Sogbossi, J. Verdier, S. Multon, New approach for the measurement of gas permeability and porosity accessible to gas in vacuum and under pressure, Cem. Concr. Compos. 103 (2019) 59–70, https://doi.org/10.1016/j.cemconcomp.2019.04.032.
[25] ASTM C1585, Standard Test Method for Measurement of Rate of Absorption of Water by Hydraulic-Cement Concretes, West Conshohocken, Pennsylvania, the United States, 2013.
[26] N. Banthia, A. Biparva, S. Mindess, Permeability of concrete under stress, Cement Concr. Res. 35 (9) (2005) 1651–1655, https://doi.org/10.1016/j.cemconres.2004.10.044.
[27] ASTM C642, Standard Test Method for Density, Absorption, and Voids in Hardened Concrete, West Conshohocken, Pennsylvania, the United States, 2013.
[28] Z.A. Kameche, F. Ghomari, M. Choinska, A. Khelidj, Assessment of liquid water and gas permeabilities of partially saturated ordinary concrete, Construct. Build. Mater. 65 (2014) 551–565, https://doi.org/10.1016/j.conbuildmat.2014.04.137.
[29] M. Romer, Effect of moisture and concrete composition on the Torrent permeability measurement, Mater. Struct. 38 (2005) 541–547, https://doi.org/10.1007/BF02479545.
[30] M.T. Uddin, M.Z.B. Harun, J.A. Joy, M.A. Ahmed, Effect of sand-to-aggregate volume ratio on mechanical properties of concrete. ABSE-JSCE Joint Conference on Advances in Bridge Engineering-IV, 2020.
[31] F.E. Amparano, Y. Xi, Y.S. Roh, Experimental study on the effect of aggregate content on fracture behavior of concrete, Eng. Fract. Mech. 67 (1) (2000) 65–84, https://doi.org/10.1016/S0013-7944(00)00036-9.
[32] B. Akcay, A.S. Agar-Ozbek, F. Bayramov, H.N. Atahan, C. Sengul, M.A. Tasdemir, Interpretation of aggregate volume fraction effects on fracture behavior of concrete, Construct. Build. Mater. 28 (1) (2012) 437–443, https://doi.org/10.1016/j.conbuildmat.2011.08.080.
[33] M.T. Uddin, A.H. Mahmood, Md R.I. Kamal, S.M. Yashin, Z.U.A. Zihan, Effects of maximum size of brick aggregate on properties of concrete, Construct. Build. Mater. 134 (2017) 713–726, https://doi.org/10.1016/j.conbuildmat.2016.12.164.
[34] K.H. Yang, H.Z. Hwang, S. Lee, Effects of water-binder ratio and fine aggregate–total aggregate ratio on the properties of Hwangtoh-based alkali-activated concrete, J. Mater. Civ. Eng. 22 (9) (2010) 887–896, https://doi.org/10.1061/(ASCE)MT.1943-5533.0000091.
[35] S. Haruna, B.S. Mohammed, M.M.A. Wahab, M.S. Liew, Effect of paste aggregate ratio and curing methods on the performance of one-part alkali-activated concrete, Construct. Build. Mater. 261 (2020) 120024, https://doi.org/10.1016/j.conbuildmat.2020.120024.
[36] Y. Wang, F. Liu, J. Yu, F. Dong, J. Ye, Effect of polyethylene fiber content on physical and mechanical properties of engineered cementitious composites, Construct. Build. Mater. 251 (2020) 118917, https://doi.org/10.1016/j.conbuildmat.2020.118917.
[37] V. Baroghel-Bouny, M. Mainguy, T. Lassabatere, O. Coussy, Characterization and identification of equilibrium and transfer moisture properties for ordinary and high-performance cementitious materials, Cement Concr. Res. 29 (8) (1999) 1225–1238, https://doi.org/10.1016/S0008-8846(99)00102-7.
[38] G. Zhang, Z. Li, L. Zhang, Y. Shang, H. Wang, Experimental research on drying control condition with minimal effect on concrete strength, Construct. Build. Mater. 135 (2017) 194–202, https://doi.org/10.1016/j.conbuildmat.2016.12.141.
[39] I. Maruyama, Y. Nishioka, G. Igarashi, K. Matsui, Microstructural and bulk property changes in hardened cement paste during the first drying process, Cement Concr. Res. 58 (2014) 20–34, https://doi.org/10.1016/j.cemconres.2014.01.007.
[40] A. Noushini, K. Vessalas, G. Arabian, B. Samali, Drying shrinkage behaviour of fibre reinforced concrete incorporating polyvinyl alcohol fibres and fly ash, Adv. Civ. Eng. 2014 (1) (2014) 836173, https://doi.org/10.1155/2014/836173.
[41] CECS13-2009, Standard Test Methods for Fiber Reinforced Concrete, China Planning press, 2009.
[42] T. Aly, J. Sanjayan, F. Collins, Effect of polypropylene fibers on shrinkage and cracking of concretes, Mater. Struct. 41 (10) (2008) 1741–1753, https://doi.org/10.1617/s11527-008-9361-2.
[43] D.C. Hughes, Pore structure and permeability of hardened cement paste, Mag. Concr. Res. 37 (133) (1985) 227–233, https://doi.org/10.1680/macr.1985.37.133.227.
[44] Z. Lafhaj, M. Goueygou, A. Djerbi, M. Kaczmarek, Correlation between porosity, permeability and ultrasonic parameters of mortar with variable water/cement ratio and water content, Cement Concr. Res. 36 (4) (2006) 625–633, https://doi.org/10.1016/j.cemconres.2005.11.009.
[45] G.M.S. Islam, S.D. Gupta, Evaluating plastic shrinkage and permeability of polypropylene fiber reinforced concrete, Int. J. Sust. Built Env. 5 (2) (2016) 345–354, https://doi.org/10.1016/j.ijsbe.2016.05.007.
[46] J. Zhang, F. Bian, Y. Zhang, Z. Fang, C. Fu, J. Guo, Effect of pore structures on gas permeability and chloride diffusivity of concrete, Construct. Build. Mater. 163 (2018) 402–413, https://doi.org/10.1016/j.conbuildmat.2017.12.111.
[47] Y. Guo, X. Hu, J. Lv, Experimental study on the resistance of basalt fibre-reinforced concrete to chloride penetration, Construct. Build. Mater. 223 (2019) 142–155, https://doi.org/10.1016/j.conbuildmat.2019.06.211.
[48] B. Zhang, Y. Feng, J. Xie, J. He, T. Yu, C. Cai, D. Huang, Compressive behaviours, splitting properties, and workability of lightweight cement concrete: the role of fibres, Construct. Build. Mater. 320 (2022) 126237, https://doi.org/10.1016/j.conbuildmat.2021.126237.
[49] B. Ali, L.A. Qureshi, Influence of glass fibers on mechanical and durability performance of concrete with recycled aggregates, Construct. Build. Mater. (2019) 116783, https://doi.org/10.1016/j.conbuildmat.2019.116783.
[50] B. Ghanbarian-Alavijeh, A.G. Hunt, Comparison of the predictions of universal scaling of the saturation dependence of the air permeability with experiment, Water Resour. Res. 48 (8) (2012) 1–14, https://doi.org/10.1029/2011WR011758.
[51] N.S. Martys, C.F. Ferraris, Capillary transport in mortars and concrete, Cement Concr. Res. 27 (5) (1997) 747–760, https://doi.org/10.1016/S0008-8846(97)00052-5.
[52] C. Song, C. Jiang, X. Gu, Effects of carbonation on microscopic pore characteristics and water absorption performance of concrete, J. Tongji Univ. 52 (4) (2024) 567–573, https://doi.org/10.11908/j.issn.0253-374x.23129. In Chinese.
[53] D.N. Winslow, M.D. Cohen, D.P. Bentz, K.A. Snyder, E.J. Garboczi, Percolation and pore structure in mortars and concrete, Cement Concr. Res. 24 (1) (1994) 25–37, https://doi.org/10.1016/0008-8846(94)90079-5.
[54] S. Corradetti, L. Biasetto, M.D.M. Innocentini, S. Carturan, P. Colombo, A. Andrighetto, Use of polymeric fibers to increase gas permeability of lanthanum carbide based targets for nuclear physics applications, Ceram. Int. 42 (15) (2016) 17764–17772, https://doi.org/10.1016/j.ceramint.2016.08.104.

Construction and Building Materials 438 (2024) 137233

Contents lists available at ScienceDirect

Construction and Building Materials

journal homepage: www.elsevier.com/locate/conbuildmat

Hydration and microstructure evolution of cement paste in low vacuum environments

Minghui Shangguan [a], Youjun Xie [a], Guangcheng Long [a], Zhaofei Long [a], Fan Wang [a], Yue Chen [a], Ce Gao [b], Zhuo Tang [a,*]

[a] School of Civil Engineering, Central South University, 68 South Shaoshan Road, Changsha, Hunan 410075, China
[b] China Railway Engineering Design and Consulting Group Co., Ltd., 15 Guang'an Road, Beijing 100055, China

ARTICLE INFO

Keywords:
Low vacuum environments
Portland cement
Sulphoaluminate cement
Tricalcium silicate
Microstructure
Hydration

ABSTRACT

Low vacuum is one of the most challenging service environments for cementitious materials, which would affect their hydration and microstructure, and thereby impair strength and durability. In this study, the hydration phases and microstructural evolution of pastes based on Portland cement (PC), sulphoaluminate cement (SAC), and tricalcium silicate (C_3S, the clinker of PC) were investigated under low vacuum conditions. The results show that rapid mass loss could be observed at the initial stage of low vacuum treatment, which was mainly attributed to the dissipation of free water. After that, the mass loss rate was greatly slowed down and maintained at a relatively low level, which was primarily due to the loss of chemical bound water in hydration products. As a result, C_3S samples, with the slowest early hydration procedure, exhibited the highest mass loss, which was followed by PC and SAC samples. The dissipation effect by low vacuum treatment resulted in the inhabitation of cement hydration, and correspondingly the contents of hydration products remained almost constant, or even decreased especially for ettringite (AFt). Moreover, the examination of the hydration product morphology demonstrates that under low vacuum conditions, the needle-like morphology of the hydration product C-S-H transferred gradually from divergence to convergence or underwent collapse, while the AFt crystals experienced degradation and then transformed into an amorphous state. This consequently led to the sample after low vacuum treatment exhibiting increased total volume of pores less than 100 nm and elevated percentage of pores with sizes from 50 nm to 100 nm. Overall, this research holds great scientific significance in guiding the engineering application of concrete in low vacuum environments.

1. Introduction

Concrete, one of the most widely utilized engineering materials globally, has been progressively employed under more severe and extreme environments [1–3]. Taking the evacuated tube transportation systems as an instance, the concrete structures are anticipated to service under low vacuum environments (with the pressure ranging from 10^2 to 10^4 Pa) [4,5]. Previous studies have indicated that long-term exposure to low vacuum environments would induce a series of issues such as mechanical property deterioration [6,7], increased shrinkage [8,9], heightened permeability [10,11], etc. However, the mechanism behind the above degradation of macroscopic properties induced by low vacuum conditions remains obscure.

It is well known that the macroscopic properties of concrete are depended by the microstructure inherent within the material. Microscopically, concrete comprises a complex of cement matrix, aggregates, interfaces, and micro-pores [12]. Among them, aggregates contribute to the deformation resistance of concrete [13]. Previous research of the authors has indicated that low vacuum environments had insignificant effects on aggregates [10]. However, the disparities in deformation between aggregates and cement matrix under low vacuum conditions may increase the potential of microcracking at the concrete interface [10]. The interface typically exhibits coarse crystalline products and a higher porosity, serving as a frequent site for crack initiation and propagation, thereby constituting a region of weakened strength [14]. In a low vacuum environment, the reduction of moisture within the hardened paste led to matrix shrinkage [15]. This resulted in the widening of the interface transition zone and the generation of more microcracks, ultimately leading to increased concrete permeability [10, 15].

* Corresponding author.
E-mail address: zhuo.tang@csu.edu.cn (Z. Tang).

https://doi.org/10.1016/j.conbuildmat.2024.137233
Received 7 May 2024; Received in revised form 17 June 2024; Accepted 24 June 2024
Available online 26 June 2024
0950-0618/© 2024 Elsevier Ltd. All rights are reserved, including those for text and data mining, AI training, and similar technologies.

Cement paste, as a crucial binding material for concrete, is also the principal source of concrete strength. Therefore, studying the microscopic physical and chemical changes of cement paste under low vacuum conditions is crucial for understanding the mechanical properties and durability of concrete materials. Portland cement (PC), characterized by its main clinker components of tricalcium silicate (C_3S), dicalcium silicate (C_2S), tricalcium aluminate (C_3A), and tetracalcium aluminoferrite (C_4AF), stands as the most extensively employed cement series in engineering applications [16,17]. The hardening and strength development of cement pastes from the hydration reaction of cement clinker minerals with water, yielding new products such as calcium silicate hydrate (C-S-H) gel, portlandite (CH), ettringite (AFt), and monosulphoaluminate (AFm) [12]. This process involves a gradual compaction of the microstructure and progressive strengthening. However, in the highly dried environment caused by low vacuum conditions, the moisture within the hardened cement migrates and diffuses outward [18]. Such migration and dissipation of internal moisture during the early stages of incomplete cement hydration or in the later stages of hydration may affect the modification of internal microstructure and the development of cement strength. Therefore, it is crucial to investigate the influence of low vacuum conditions on hydration and microstructure of cement paste.

To the best of the authors' knowledges, there is limited research on the effects of low vacuum environment on cement paste, including on the hydration and microstructure. Cementitious materials often necessitate various drying methods to stop hydration for conducting microscale testing. Consequently, previous investigations into the impact of vacuum on cement microstructure have primarily focused on comparing short-term vacuum drying with alternative drying techniques [19–21]. Zhang and Glasser [22] observed an increase in porosity of sulphoaluminate cement (SAC) and degradation of AFt and AFm in high vacuum environments. Additionally, Collier et al. [23] identified notable differences in the differential thermogravimetry (DTG) curve of vacuum-dried samples compared to those dried with acetone or freeze methods. These differences include an additional minor peak around 75°C, heightened C-S-H peak, and diminished peaks corresponding to CH and calcite ($CaCO_3$) [23]. Despite some scholars having examined the microstructural changes of cement under short-term vacuum drying, studies on the effects of prolonged vacuum drying remain scarce. This prompts a deeper investigation into how extended vacuum exposure influences cement microstructure. Furthermore, the only relevant studies were conducted by Chang et al. [6], who investigated the mechanical properties, phase composition, and multiscale pore structure changes of hardened cement pastes in both low vacuum and normal air environments. The findings indicated that low vacuum conditions led to a reduction in PC gel pores and an increase in overall porosity [6]. Nonetheless, these above studies only concentrate on the hardened pastes subjected to standard curing for 7 days, thus failing to capture the progression of hydration phases and microstructural changes in cement pastes with varying degree of hydration under low vacuum conditions.

Therefore, to address this gap in the literature and provide a comprehensive understanding of the effects of prolonged vacuum exposure on cement microstructure, this study investigated the impacts of low vacuum treatment on the hydration and microstructure of PC, SAC, and C_3S pastes after various ages of standard curing (SC). In specific, the investigation focused on the mass loss of hardened pastes at different periods under low-vacuum conditions. Additionally, the evolution of hydration product types and morphology under various treatments was explored. Besides, the alterations in the specific surface area, porosity, and pore size distribution of hardened cement pastes were analyzed. In addition, the evolution of the two primary hydration products, C-S-H and AFt, under low-vacuum conditions was discussed. The findings of this study are anticipated to offer valuable insights for the engineering utilization of concrete in the extreme environment of low vacuum.

2. Materials and experimental methodology

2.1. Raw materials

Commercially available PC and SAC, complying with Chinese standards, as well as, laboratory-prepared C_3S were utilized in this study. According to the reference of [24], C_3S was synthesized by a solid-state reaction. The mixed and compacted powders of calcium carbonate and silica were first sintered as per the process shown in Fig. 1. Then, the pellets were ground, compacted, and sintered twice to ensure a complete reaction. Finally, the pellets were ground and sieved through a 60 μm mesh.

The particle size distributions of PC, SAC and C_3S are given in Fig. 2. The chemical compositions of raw materials were determined by X-ray fluorescence (XRF) and are presented in Table 1. The X-ray diffraction (XRD) patterns of PC, SAC and C_3S are given in Fig. 3.

2.2. Sample preparation

The water-to-cement ratios (w/c) of 0.45 and 0.3 were used for the preparation of cement paste samples. The nomenclature of samples starts with the cement type (i.e., PC, SAC, and C_3S) and then the w/c ratios (i.e., 0.45 and 0.3). For example, $C_3S0.45$ refers to a sample made with C_3S and a water-to-cement ratio of 0.45. The samples were prepared according to the following process. Deionized water was first added into the mixer, followed by adding cement. The pastes were mixed at 800 rpm for 90 s and then at 1200 rpm for 90 s. Then, pastes were cast in cylindrical plastic moulds with a diameter of 10 mm and cubic iron moulds with a side length of 20 mm. After one day of sealed curing, the pastes were demoulded. Cylinders were cut into thin slices with a thickness of 2 ± 0.2 mm (Fig. 4a).

Subsequently, part of the slice and cube samples were directly exposed to low vacuum environments [15]. The pressure (P) of the low vacuum environment was 100 ± 10 Pa, the temperature (T) was 20 ± 2 °C, and the relative humidity (RH) was 0. Considering the defined range of low vacuum (10^5 to 10^2 Pa) specified in the standard ISO 3529–1: 2019 [25], this choice of low vacuum values was informed by the operating environment of evacuated tube transportation systems and the worst-case conditions. While other part of the samples were cured under standard environments (T=20 ± 2 °C, RH ≥ 95 %) to a certain age (i.e., 7 d or 28 d) and then exposed to low vacuum environments. Further, the rest of the samples were continuously cured under standard environments and served as the control samples. The curing and treatment regimens of samples are shown in Fig. 4b, in which the numerals after B and V represent the days of standard curing and low vacuum treatment, respectively.

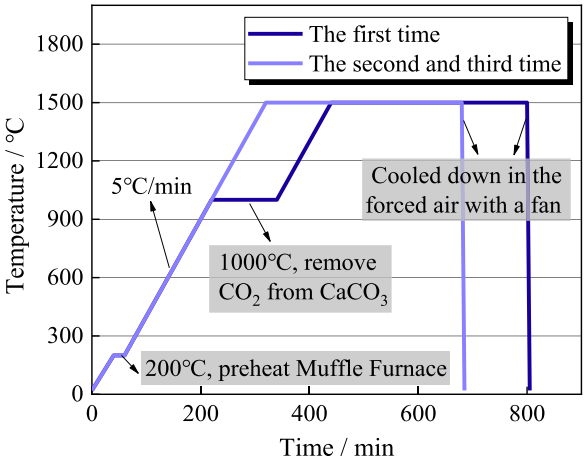


Fig. 1. Sintering process for synthesis of C_3S.

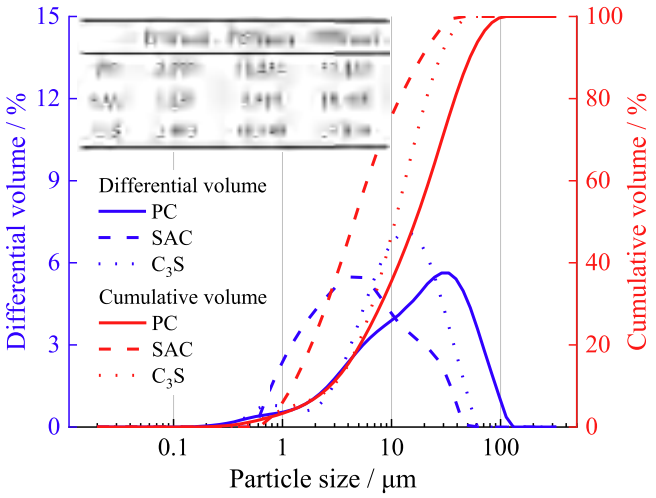


Fig. 2. Particles size distributions of PC, SAC and C_3S.

After the designed curing and treatment regimens, the samples underwent solvent substitution to stop hydration and then were prepared for microscopic tests, including the tests of scanning electron microscopy-energy dispersive X-ray spectroscopy (SEM-EDS), nitrogen adsorption (NAD), XRD, and thermogravimetry analysis (TGA). For SEM-EDS and NAD measurements, the cube samples were cut into small pieces with lengths of about 5 mm and immersed into isopropanol for 7 days to stop the hydration reaction. Then, the pieces were vacuum dried to evaporate isopropanol. For XRD and TGA tests, the dehydrated samples of slices were ground into powder less than 45 μm.

2.3. Methodology

2.3.1. Mass loss

In this study, the mass of 1-day and 7-day cured samples (i.e., B1 and B7) were measured when exposed to low vacuum environments. In specific, the initial mass of the samples after curing was weighed by a balance (the accuracy is 0.0001 g), with the surface being wiped dry. Then, the samples were exposed to low vacuum environments and weighed at certain intervals. Correspondingly, the mass loss (the ratio of the mass variation to the initial mass) and the mass loss rate (mass loss per unit time and surface area) were calculated. The reported mass loss and mass loss rates are the averages of the results obtained from three duplicate samples.

2.3.2. TGA

The degree of hydration was determined using the thermogravimetry curves. The specific decomposition temperatures in curves can be used to identify the hydration products and also determine their contents. TGA tests were conducted by the Setaram Labsys Evo thermogravimetric analyzer. About 20 mg samples were heated from 35 °C to 950 °C at 10 °C/min in atmospheres of nitrogen.

2.3.3. XRD

The X-ray diffraction is a common analytical method for analyzing crystalline, fine-grained materials like cement. The diffraction of X-rays by crystalline materials produces unique diffraction patterns. XRD can quantify the degree of hydration in cement and provide the information on the formation of different products during the hydration process [26]. XRD patterns of raw materials and cement hydration productions were collected by a Bruker D8 Advance diffractometer with a scanning rate of 2°/min from 5° to 65° (2-theta).

2.3.4. NAD

NAD was utilized to assess alterations in specific surface area, porosity, and pore size distribution. NAD were carried out using an SSA-4000 apparatus from Builder Electronic. In this study, about 1.0 g samples were used for all NAD tests.

2.3.5. SEM-EDS

SEM-EDS effectively visualizes the morphological evolution of cementitious materials by scanning the sample surface with an electron beam. SEM pictures of the treated sample after gold coating were acquired using a JEOL JSM-7900 F scanning electron microscope with an acceleration voltage of 20 kV.

3. Results and discussion

3.1. Evolution of appearance and mass during exposure to low vacuum

Fig. 5a demonstrates that all 1-day cured samples remained intact after low-vacuum treatment for 27 days. Conversely, after 7 days of standard curing followed by low-vacuum treatment, a layer of white solids was detached from the surface of the samples. XRD experiments were conducted on the white solid detached from PC at B7+V21, and the results, as shown in Fig. 5b, revealed diffraction peaks highly consistent with the standard card PDF#81–2027 of $CaCO_3$. It can be inferred that the white solids was likely attributable to the carbonation of CH on the surfaces of PC and C_3S or AFt on the surface of SAC during the 7-day curing process [27]. When subjected to low-vacuum environment,

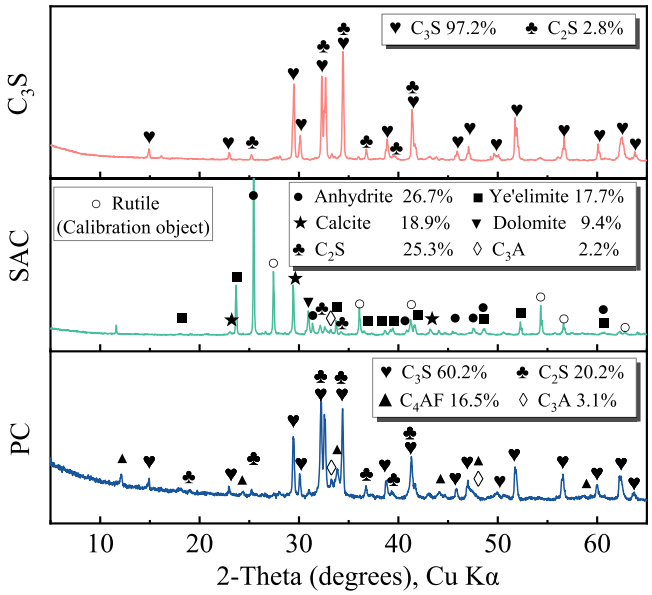


Fig. 3. XRD patterns of PC, SAC and C_3S.

Table 1
XRF compositions of PC, SAC and C_3S (%).

	Na_2O	CaO	SiO_2	MgO	Al_2O_3	Fe_2O_3	P_2O_5	SO_3	K_2O	MnO	Cl
PC	0.22	66.28	19.05	1.77	4.26	3.60	0.25	3.62	0.70	0.24	0.01
SAC	0.09	53.75	8.82	1.85	15.28	1.55	0.08	17.95	0.57	0.02	0.03
C_3S	-	71.04	26.65	2.02	0.21	0.07	-	0.01	-	-	-

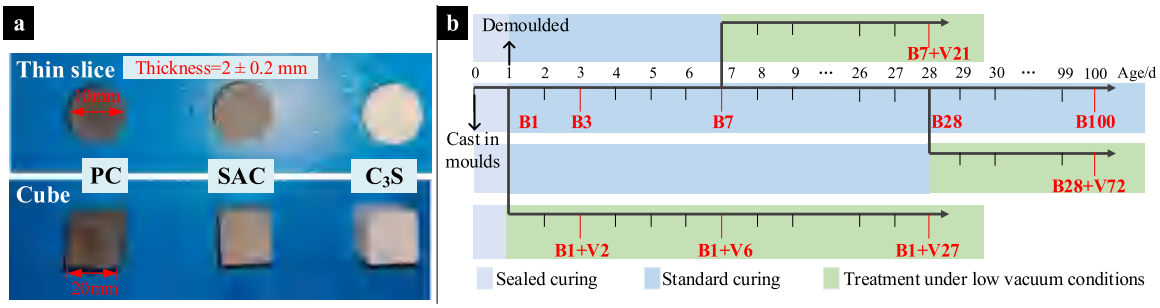


Fig. 4. (a)The samples of different hardened cement paste and (b) the curing and treatment regimens.

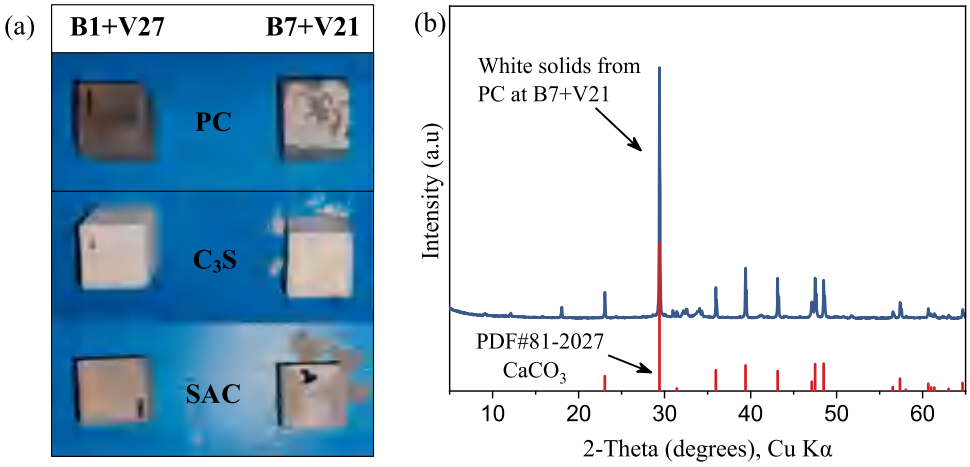


Fig. 5. (a) Appearance of 1-day and 7-day cured samples after exposure to low vacuum; (b) XRD patterns of white solids from PC at B7+V21.

hardened cement paste undergoes shrinkage [9], and the specimens subjected to longer curing ages exhibiting greater strength and elastic modulus, consequently experiencing heightened shrinkage stress [28, 29]. The generated $CaCO_3$ on the surfaces failed to adhere to the interior hardened cement paste tightly due to varying degrees of shrinkage, and then became dislodged during the low-vacuum drying process. Hence, particular attention should be directed towards the potential dust predicament when concrete is exposed to low-vacuum environments in practical engineering applications.

Fig. 6 illustrates the mass loss and mass loss rates for the 1-day and 7-day cured samples when subjected to vacuum treatment. It is obvious that the mass loss of all samples escalated with prolonged exposure to low vacuum, but eventually remained or approached constant. Also, all the mass loss rates reached the peak on the initial day of vacuum exposure (i.e., at 2 days and 8 days of actual age for B1 and B7 samples, respectively), followed by an abrupt decline. However, it is noteworthy that an inflection point (defined as the point where the second derivative of the curve changes sign) appeared in the mass loss curve of SAC samples at the ages of about 14 days (Fig. 6a). Correspondingly, the mass loss rate curve exhibited a secondary peak (Figs. 6b and 6c). This could be attributed to the mass loss before 14 days being predominated by unreacted free water, while some of the crystalline water of AFt in the hydration products began to release in the low vacuum environment after 14 days. This paralleled the findings in the reference of [9], where mortars based on SAC exhibited abrupt contraction and mass loss after 14 days.

The comparison between the samples based on different cement illustrates that C_3S exhibited the shortest periods required for mass stabilizing and the highest mass loss rate, which was followed by PC and SAC. This disparity arose from the variations in the early hydration degree between different cements and correspondingly the water content involved in hydration. The hydration rate of SAC is the most rapid, and therefore a significant amount of water was transferred into bound water or crystalline water in the hydration products, which is difficult to lose in low-vacuum environments. In contrast, the hydration procedure of C_3S is the slowest, and a large amount of free water that has not yet been involved in the reaction is prone to loss under low-vacuum conditions. Furthermore, besides C_3S, PC contains clinkers like C_3A with rapid early-stage reactions, contributing to relatively lesser free water compared to C_3S and thereby relatively smaller mass loss.

The results also indicates that the final mass loss was greater for the samples with w/c=0.45 compared to w/c=0.3. This difference is reasonable as higher w/c ratios entailed a greater content of residual water not utilized for cement hydration [10]. Meanwhile, samples with higher w/c ratios exhibited lower compactness [14], resulting in faster water loss rates in low-vacuum environments. In addition, the 7-day cured samples of PC and C_3S exhibited longer periods required for mass stabilization and a higher final mass loss rate, in comparison with the corresponding 1-day cured samples. This was due to the denser structure of specimens with longer curing periods, as well as the conversion of more free water into bound water, which is more resistant to loss under low-vacuum conditions. Conversely, for SAC samples, the final mass loss of the 7-day cured samples was comparable to that of the 1-day cured samples. This could be attributed to the rapid progression of the hydration reaction in SAC, where most free water in the samples under these two curing periods has been transformed into crystalline water within the hydration products. However, this crystalline water fraction proves unstable under prolonged low-vacuum conditions, rendering it susceptible to loss [9], thereby resulting in the close proximity of the final mass loss between the 1-day and 7-day cured samples.

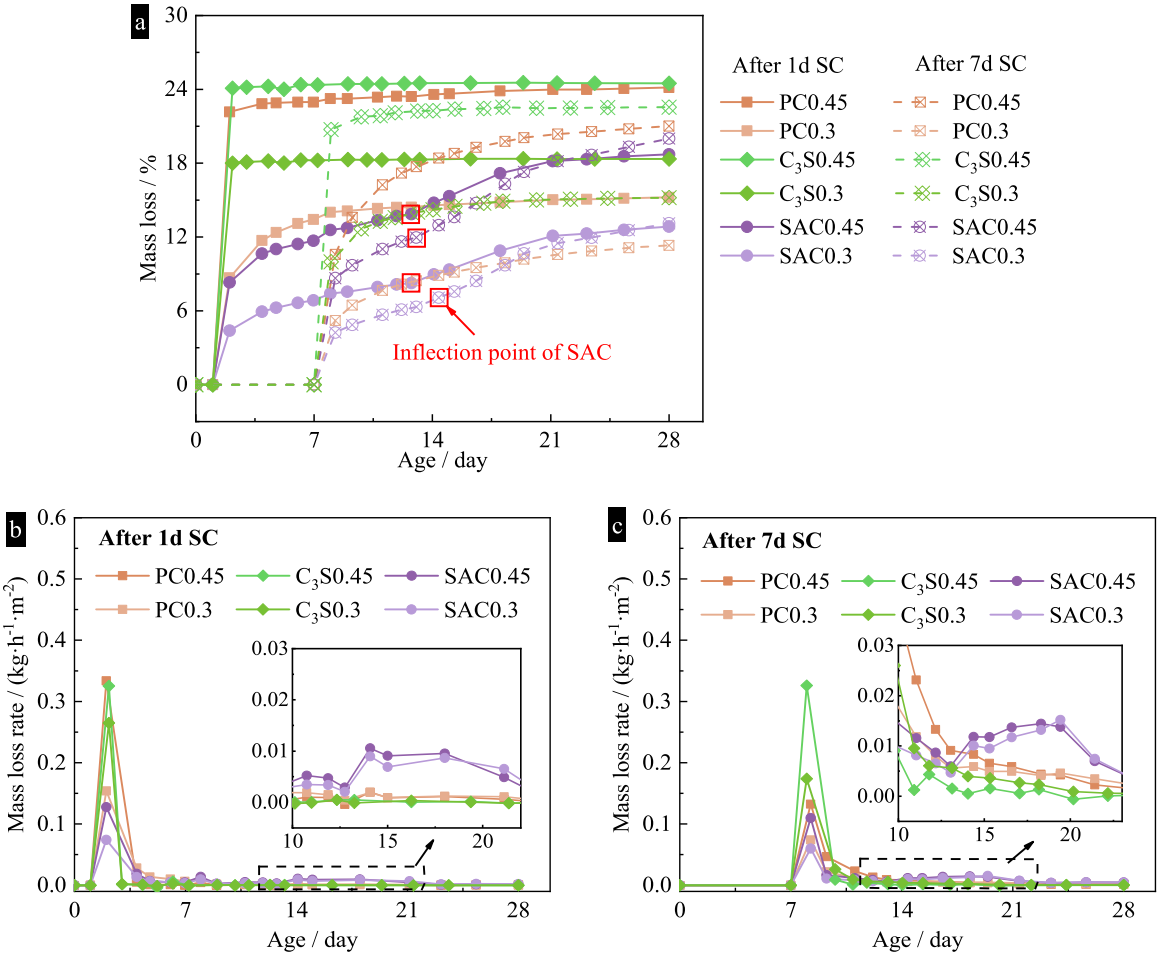


Fig. 6. (a) Mass loss and (b, c) mass loss rates of samples that continued to be exposed to low vacuum after 1 or 7 days of SC.

3.2. Characterization of hydration products

3.2.1. PC

Fig. 7 depicts a typical TG-DTG curve of PC samples. As shown in Fig. 7, three peaks of heat absorption are evident within the temperature range of 35 °C to 950 °C. The initial peak appears around 100 °C, primarily resulting from the dehydration of C-S-H gel, AFt, and AFm. The second peak appears at approximately 450 °C, mainly due to the decomposition of CH. Finally, the third peak, around 700 °C, stems predominantly from the decomposition of $CaCO_3$. On the TG curves, the weight loss at the intervals from 35 °C to 70 °C (free water), 70 °C to 400 °C (C-S-H gel, AFt), 400 °C to 500 °C (CH), and 500 °C to 800 °C ($CaCO_3$) were designated as m_A, m_B, m_C and m_D, respectively. Subsequently, the content of chemical bound water and CH (normalized to binder mass) could be determined according to Eqs. (1–2) [30].

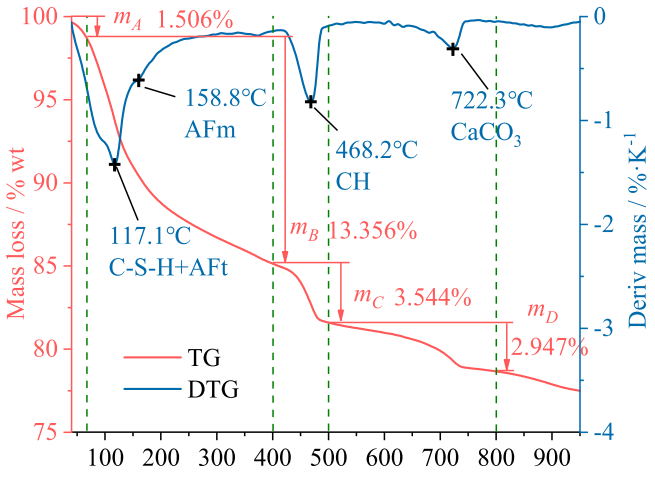


Fig. 7. The TG-DTG curves of PC0.3 sample with B28.

$$m_{H_2O} = m_B + m_C + m_D \frac{M_{H_2O}}{M_{CO_2}} \quad (1)$$

$$m_{CH} = m_C \frac{M_{CH}}{M_{H_2O}} + m_D \frac{M_{CH}}{M_{CO_2}} \quad (2)$$

where, m_{H_2O} is the content of chemical bound water, %; m_{CH} is the content of portlandite, %; M_{H_2O}, M_{CO_2} and M_{CH} are the relative molecular masses of H_2O (18), CO_2 (44) and CH (74), respectively.

The DTG curves and contents of chemical bound water and portlandite for PC0.3 and PC0.45 under various curing and treatment regimens are depicted in Fig. 8. As for the DTG curves, the decomposition peak of $CaCO_3$ was amplified as the curing period increased. This was attributed to the carbonation during the standard curing period. However, subsequent low-vacuum treatment induced a reduction in the decomposition peak of $CaCO_3$. This reduction stemmed from carbonation primarily occurring at the sample surface, where shrinkage stress induced by low-vacuum drying caused detachment of surface $CaCO_3$ (as shown in Fig. 5). However, isolated instances of $CaCO_3$ decomposition peaks were also observable in certain samples with prolonged curing periods, such as B7+V21 in Fig. 8b. The occurrence is likely attributed to the inadvertent introduction of incompletely dislodged surface $CaCO_3$

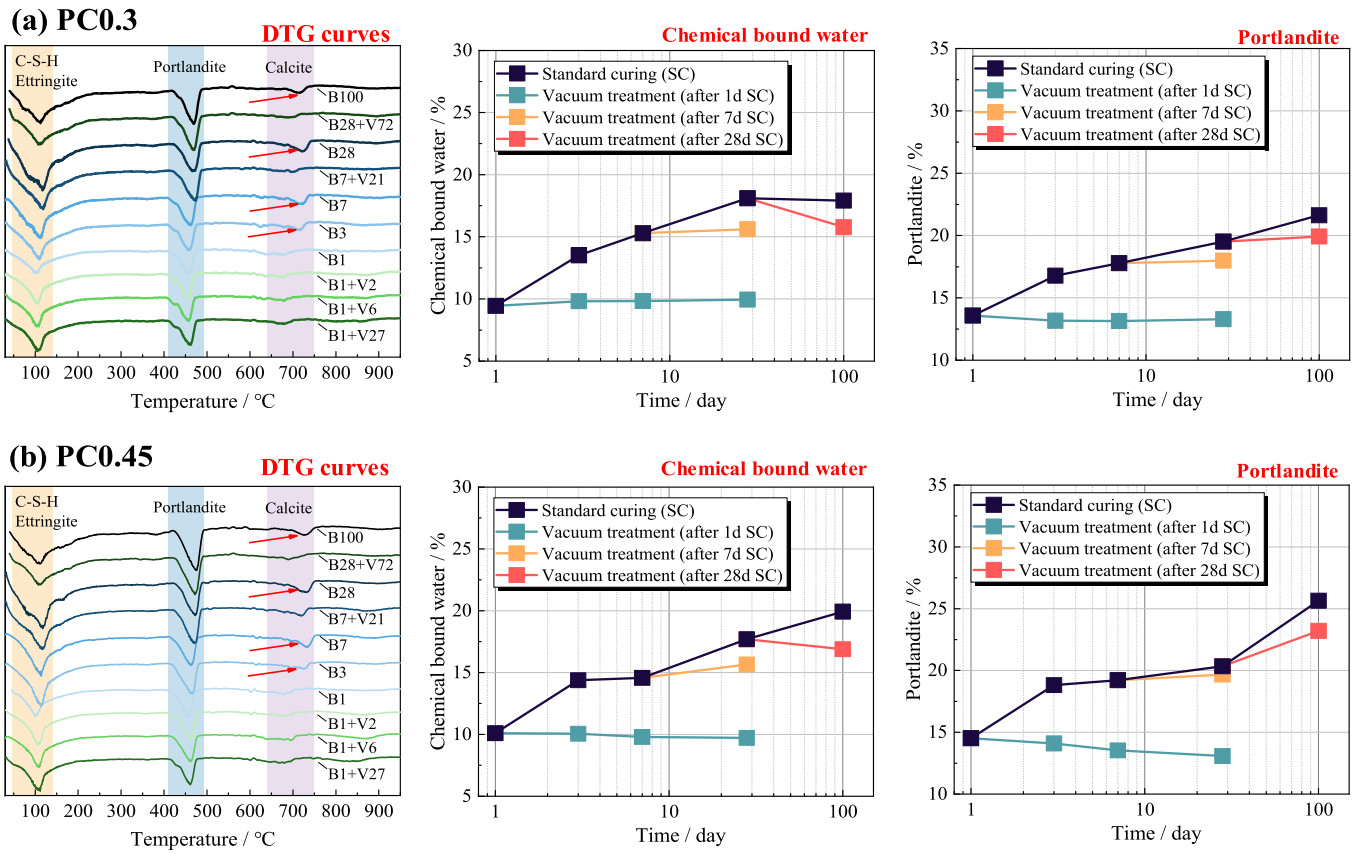


Fig. 8. DTG curves, chemical bound water and portlandite content of (a) PC0.3 and (b) PC0.45 at various curing and treatment periods.

during the sample preparation process.

For the chemical bound water, the content exhibited continued increases with curing periods. While subjected to low-vacuum treatment, the content of chemical bound water ceased to increase, or even decreased. As a result, the content of chemical bound water for the sample under vacuum treatment was obviously lower than that of the sample under continued standard curing to the same ages. However, it should be noteworthy that the effects of low-vacuum treatment on the chemical bound water content were slightly different for the samples with varying curing periods. In specific, the content of chemical bound water of the 1-day and 7-day cured samples essentially ceased to increase and there was no significant decrease after low-vacuum treatment. However, after low-vacuum treatment of the 28-day cured samples, the content of chemical bound water in PC0.3 and PC0.45 decreased by 12.8 % and 4.6 %, respectively. This contrary result can be attributed to the dual effects of low-vacuum treatment on the free water and chemical bound water simultaneously. Although the loss of free water under low-vacuum conditions led to a slowdown or even inhibition of cement hydration, a small portion of free water was not completely lost, and thus, continued to participate in hydration and generate chemical bound water. It, to some extent, could compensate for the loss of the chemical bound water for low-vacuum treatment for 1-day and 7-day cured samples. But for 28-day cured samples, most of the free water had participated in cement hydration reactions. The chemical bound water produced by hydration was less than that lost due to the exposure to low-vacuum conditions, leading to a gradual decrease in its content in the 28-day cured samples.

The variation trend of CH was similar to that of chemical bound water. However, unlike chemically bound water, there was no significant decrease in CH for all samples after low-vacuum treatment. Particularly, following low-vacuum treatment, the CH contents of B28+V72 for PC0.3 and PC0.45 even increased by 2.1 % and 14.1 %, respectively. This suggests that despite the influence on chemically bound water, PC maintains its hydration process, yielding CH. This phenomenon might be attributed to the thorough cement hydration in later stages, resulting in heightened density and a reduced inhibitory effect of low-vacuum conditions on PC hydration.

The XRD patterns of PC0.3 and PC0.45 under various curing and treatment periods are depicted in Fig. 9. Similar XRD results could be detected for the samples with different water-cement ratios, in which in addition to the four unhydrated PC clinkers (i.e., C_3S, C_2S, C_3A, and C_4AF), the crystalline hydration products comprised AFt, CH, and $CaCO_3$. Also, the peak positions of the main hydration phases in samples exhibited no alteration after low-vacuum treatment. This suggested that low vacuum treatment did not alter the phase composition of PC, and thus, no additional chemical reactions occurred under low vacuum environments. However, the peak intensities of phases in the XRD patterns demonstrated certain variations for different samples. In specific, the peak intensities of hydration products CH and AFt gradually increased with curing age, while C_3S and C_2S contents decreased. In contrast, under low vacuum treatment, peak intensities of C_3S, C_2S and hydration products CH remained almost unchanged. Moreover, the peak intensities of AFt were slightly lower in B7+V21 compared to B7, and in B28+V72 compared to B28. This suggested that low vacuum treatment may have induced changes in AFt crystals. Overall, low-vacuum treatment did not alter the type of PC hydration phase, but it impeded further hydration of PC, resulting in alterations in the contents of specific phases.

3.2.2. C_3S

As the C_3S samples with water-cement ratios of 0.3 and 0.45 exhibited similar variation in the DTG curves, only the results of $C_3S0.45$ were presented (Fig. 10). The DTG curves of C_3S resemble those of PC, with three peaks of heat absorption. However, the peak at 100°C

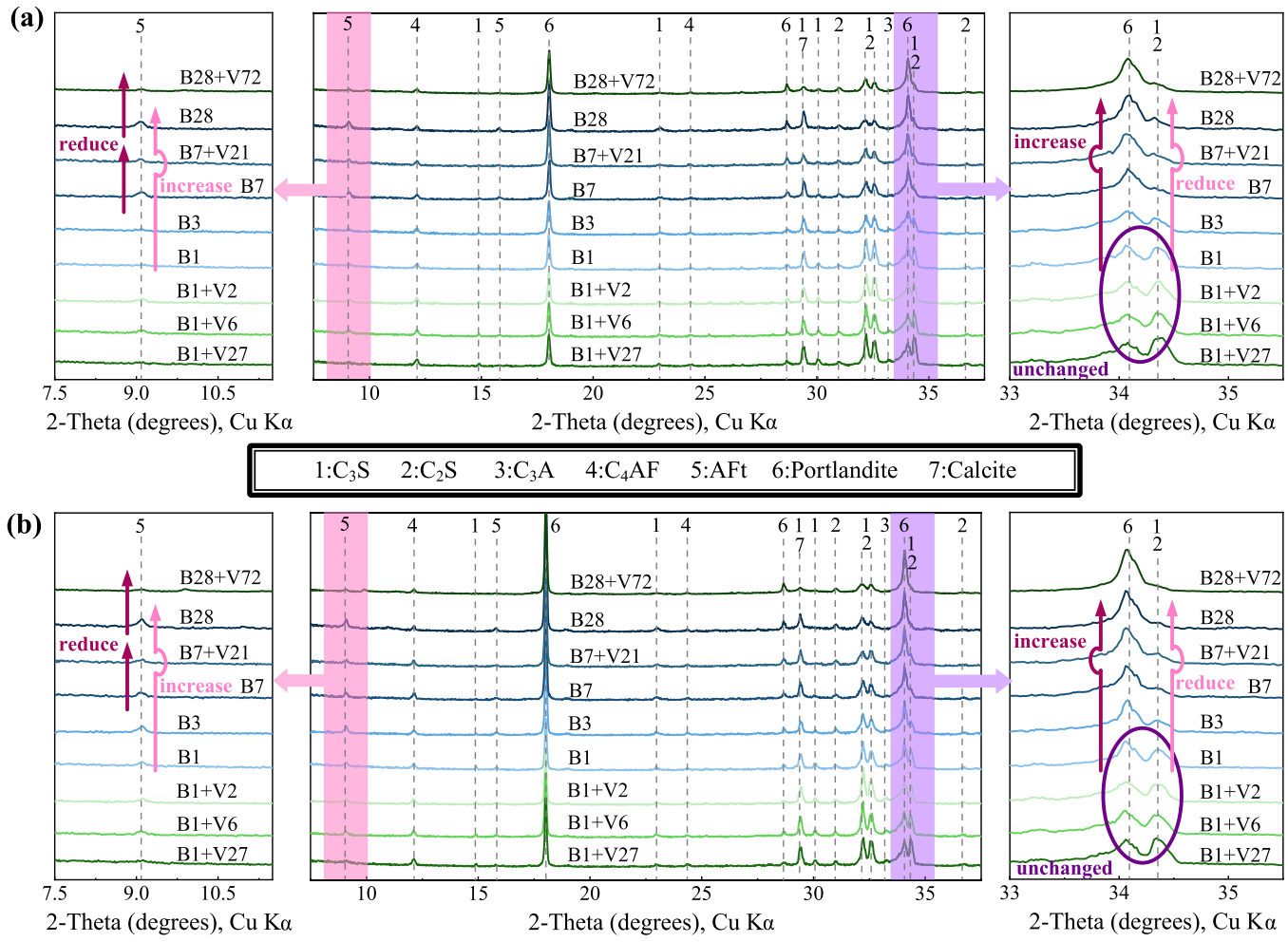


Fig. 9. XRD patterns of (a) PC0.3 and (b) PC0.45 at various curing and treatment periods.

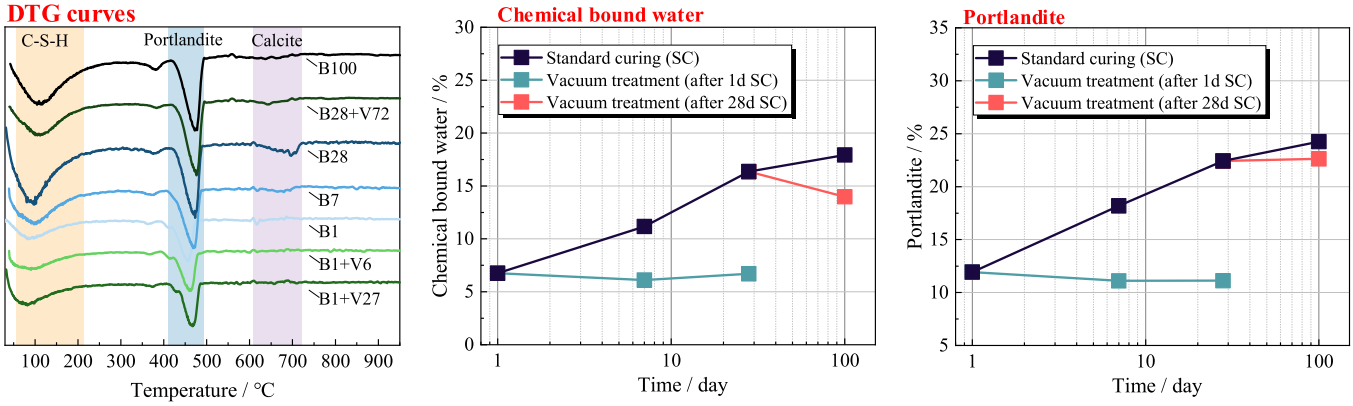


Fig. 10. DTG curves, chemical bound water and portlandite content of $C_3S0.45$ at various curing and treatment periods.

primarily indicates the water loss of C-S-H and does not involve that of AFt and AFm. The decomposition peak of CH at around 450°C increased with the curing period but remained essentially unaltered following low-vacuum treatment. Similar to PC, chemical bound water and CH content could be calculated using Eqs. (1–2). The findings revealed that both escalated with the duration of curing, but they essentially remained unchanged or even decreased following low-vacuum treatment. This implies that low-vacuum treatment notably impeded the hydration process of C_3S.

The XRD patterns of $C_3S0.45$ under various curing and treatment periods are presented in Fig. 11. The crystalline phase hydration products of C_3S primarily comprised CH. Under standard curing conditions, the diffraction peak of CH increased with curing age, whereas C_3S was gradually consumed, resulting in a decrease in the diffraction peak. Conversely, for the samples treated with low vacuum, the diffraction peak intensities of C_3S remained almost constant with age, while those of CH remained stable or even decreased. This indicated that low vacuum was unfavorable for C_3S hydration and CH generation.

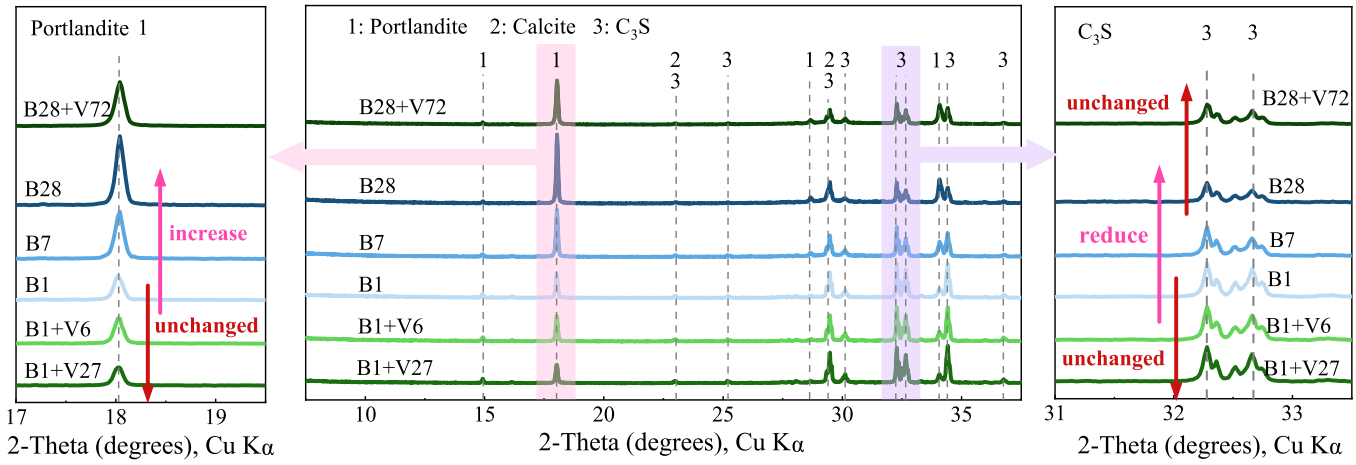


Fig. 11. XRD patterns of $C_3S0.45$ at various curing and treatment periods.

3.2.3. SAC

Fig. 12a depicts a typical TG-DTG curve of SAC samples. The DTG curve of SAC displayed three peaks of heat absorption within the temperature range of 35 °C to 950 °C. The initial peak point appeared around 120°C and represents the dehydration of AFt, which is the principal hydration product of SAC. The second peak point appeared around 250°C, primarily corresponding to the decomposition of aluminum hydroxide (AH_3). Subsequently, the third peak point appeared around 750°C, mainly arising from the decomposition of $CaCO_3$.

Fig. 12b and c present the DTG and TG curves of SAC0.3 and SAC0.45 under various curing and treatment regimens, respectively. Analysis of the DTG curves revealed that the intensity of AFt peak was diminished after vacuum treatment. Correspondingly, the TG curves illustrate that the mass loss of the samples after low vacuum treatment was less at a certain temperature.

The chemical bound water content of SAC under various treatments was further computed using Eq. (1), as depicted in Fig. 13. The chemical bound water content of SAC increased with curing periods. However, following low vacuum treatment, the chemical bound water content of SAC essentially ceased to increase or even decreased. Specifically, B1+V27 of SAC0.3 remained almost unchanged compared to B1, while B1+V27 of SAC0.45 decreased by 15.8 %. Additionally, B28+V72 of SAC0.3 and SAC0.45 decreased by 5.3 % and 19.0 % compared to B28, respectively. The phenomenon indicates that low vacuum treatment inhibited the hydration of SAC cements and resulted in the gradual dissipation of hydration product binding water, especially in samples with higher water-cement ratios.

The XRD patterns of SAC0.45 under various curing and treatment periods are depicted in Fig. 14. Under standard curing conditions, distinct diffraction peaks of AFt are observable alongside unreacted ye'elimite, C_2S, dolomite, anhydrite, and $CaCO_3$ in XRD patterns. AH_3 is present in an amorphous form, hence not detected in the XRD analysis. As observed in the pattern of 1-day cured samples, a substantial amount of AFt was generated in SAC, suggesting a faster hydration rate compared to PC. Moreover, AFt content continued to increase while ye'elimite gradually decreased with increasing curing periods. Low vacuum treatment did not induce the formation of new hydrated phases in SAC. However, a noticeable decrease in the peak intensity of AFt was observed after low vacuum treatment. Compared to B1 and B28, the presence of AFt peaks was essentially invisible in B1+V27 and B28+V72. The findings were consistent with those in the reference of [22], which suggested that the intensity of AFt peaks in XRD weakened or decreased to the background level after vacuum drying at room temperature. This phenomenon occurred due to the gradual dehydration of AFt crystals under low vacuum [22,31]. With prolonged low vacuum

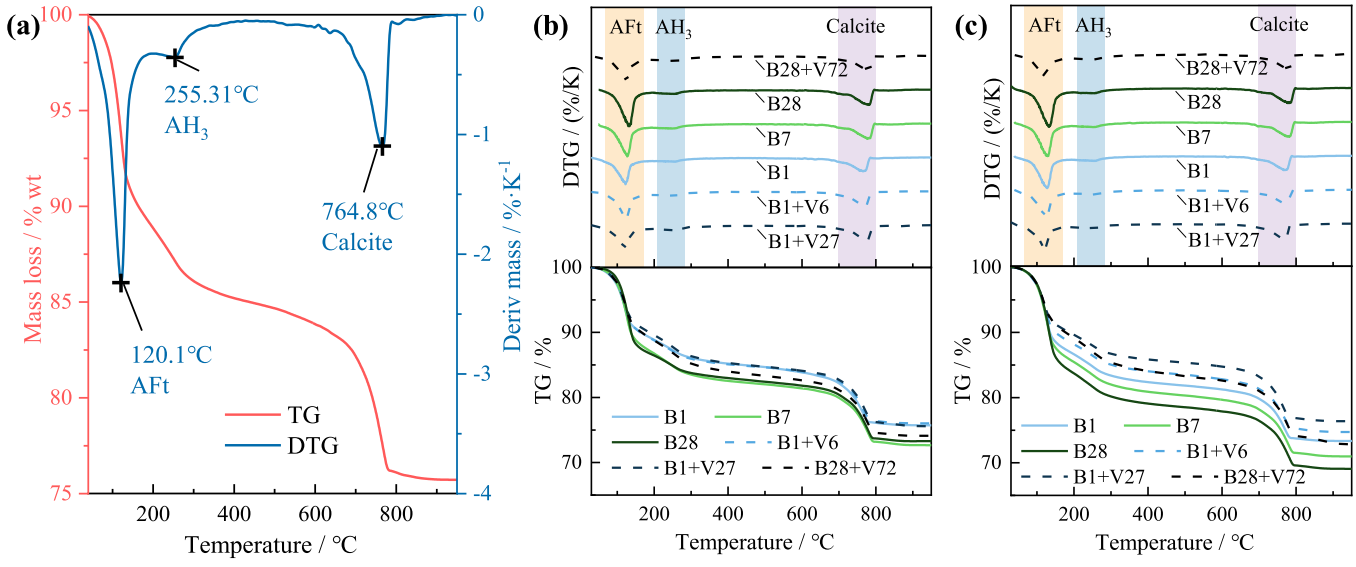


Fig. 12. DTG and TG curves of (a)SAC0.3 with B1, (b) SAC0.3 and (c) SAC0.45 at various curing and treatment periods.

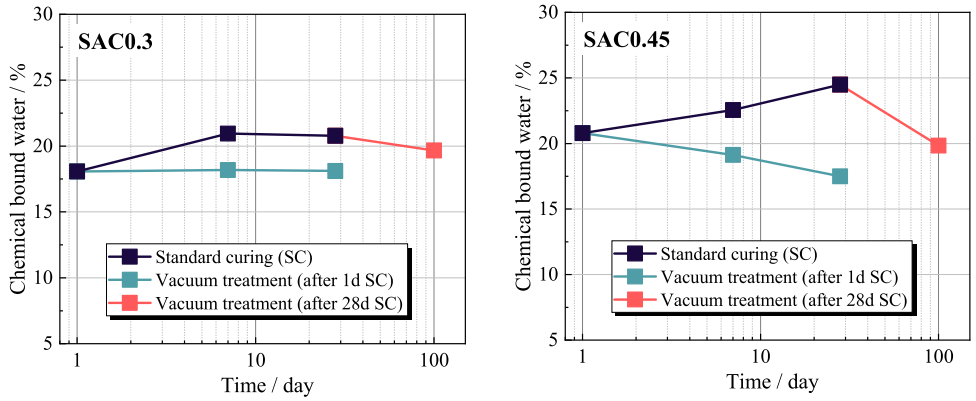


Fig. 13. Chemical bound water of SAC at various curing and treatment periods.

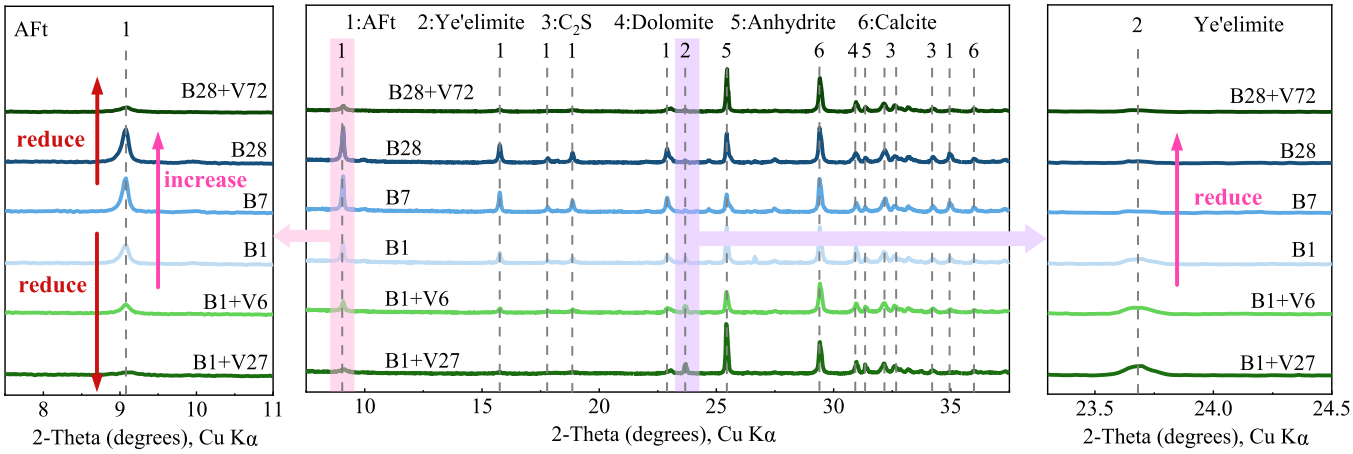


Fig. 14. XRD patterns of SAC0.45 at various curing and treatment periods.

treatment, the number of crystalline water molecules contained in the AFt crystals gradually decreased, leading to structural damage until they became amorphous phases [32–34].

3.3. Pore structure

3.3.1. BET surface area

The specific surface areas of the different samples determined by the Brunauer-Emmett-Teller (BET) method [35] are shown in Fig. 15, in which nitrogen adsorption curves in the relative pressure range of 0.05–0.3 were analyzed. The BET surface area of PC and C_3S increased with the progression of curing periods. This was mainly attributed to the increase of C-S-H gel generated from the hydration, which has a large specific surface area [36]. However, the low vacuum treatment resulted in a reduction in BET surface area, irrespective of the curing periods before the low vacuum treatment. This reduction might stem from the removal of physically adsorbed water or even C-S-H interlayer water by the desiccation of low vacuum [21,37]. It would cause the collapse of C-S-H gel, which allowed the opposing surfaces to come in contact and therefore a decrease in BET surface area [36]. As for the SAC samples, interesting results could be identified. In specific, the BET specific surface area of SAC samples increased when subjected to low vacuum treatment, and was close to or even surpassed that of the samples cured to the same ages. This could be attributed to the dehydration of AFt. The dehydration of AFt could reduce the number of molecules, especially the coordination number of Ca and Al, and consequently cause the rupture of AFt columns, thereby introducing cracks and defects [37].

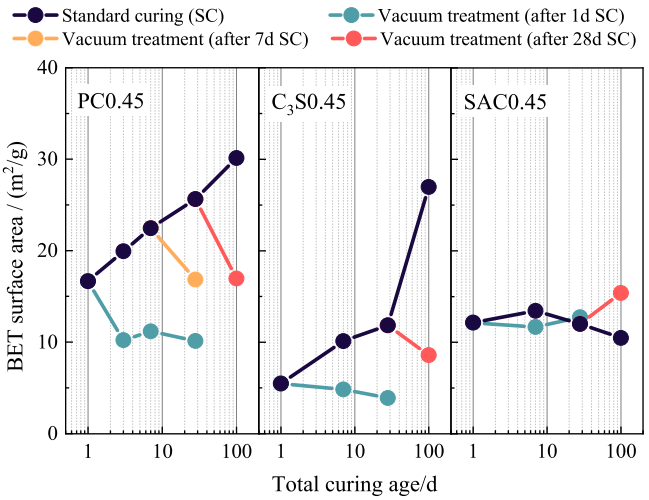


Fig. 15. BET surface area for different samples (w/c=0.45).

3.3.2. Pore size distribution and pore volume

Based on the NAD desorption results, the pore size distribution and pore volume of various samples were computed using the Barrett-Joyner-Halenda (BJH) method [38]. As pore size increased, the sensitivity of the pressure at which capillary coalescence occurs decreased [26]. Consequently, the pore apertures characterized by NAD were confined to a narrow range [39], with maximum pore sizes falling between 100 and 200 nm [26,40]. The International Union of Pure and Applied Chemistry (IUPAC) recommends the BJH method for

determining pore size distribution in the mesopore range (diameters of 2–50 nm) [41]. Hence, the maximum pore size measured in this study was constrained to 100 nm. The measured pore sizes were classified into three ranges: <10 nm, 10–50 nm, and 50–100 nm [21]. Subsequently, the percentage of different pore size volumes (PPSV) and the total pore volume (TPV) were calculated, as illustrated in Fig. 16. Notably, the TPV signified the pores less than 100 nm, which may not accurately represent the overall porosity of the sample.

The TPV of all three cements increased with the progression of curing periods, which was consistent with the findings in previous studies [36]. This could be attributed to the continuous hydration of cement: specifically, the generated hydration products would fill and alter the pores in the way that they are transformed into smaller pores, especially with sizes of 0–100 nm. As for PC and C_3S, although the low vacuum treatment also resulted in the increase of TPV (except for B1+V2 and B1+V6), the TPV of the sample after exposure to vacuum treatment was still lower than that of the corresponding sample cured to the same ages. This increase might be due to prolonged low-vacuum conditions, which remove more moisture and facilitate the entry of nitrogen molecules into additional small pores [21], thereby resulting in an increase in the measured TPV. Based on the results of PPSV, it can be found that the low vacuum treatment caused a decrease in the percentage of pores with a diameter of <10 nm but an increase in the percentage of pores with a diameter of 50–100 nm. This indicated that low-vacuum treatment also caused the collapse or merging of small pores to form larger ones. Moreover, literature indicates that under low humidity conditions, capillary forces cause the convergence of C-S-H gel needles, gradually increasing the gap between neighboring products [42].

For SAC, similar increase in TPV can be observed after the vacuum treatment, but the TPV was higher than that of the corresponding sample cured to the same ages. For instance, the TPV of B1+V6 for PC, C_3S, and SAC was 0.50, 0.49, and 3.45 times higher than that of B7, respectively. The different trends between SAC and PC or C_3S could be attributed to the production of a significant quantity of AFt crystals in SAC, wherein the AFt crystal structure was compromised by the reduction of water molecules in a low-vacuum environment [37,43]. Consequently, this led to shrinkage in SAC cement and the emergence of micro cracks and defects [9].

3.4. Morphology of hydration products

The SEM-EDS images of various cement pastes with a water-cement ratio of 0.45 under different regimens are depicted in Figs. 17–19. For PC samples, 1-day cured samples of PC0.45 before and after low vacuum treatment were presented, as well as the samples with actual age of 28 days but subjected to different treatment regimes. For C_3S and SAC samples, the images of C_3S0.45 and SAC0.45 samples at different magnifications and ages are illustrated, including B1+V27, B28, and B28+V72.

From Fig. 17a-c, it is evident that the PC0.45 with B1 contained a significant abundance of needle-like and fibrous structures, primarily composed of AFt and fibrous C-S-H, while the fibrous formations in B1+V6 and B1+V27 showed no marked increase. It confirms again a deceleration or cessation of the hydration process of PC induced by low

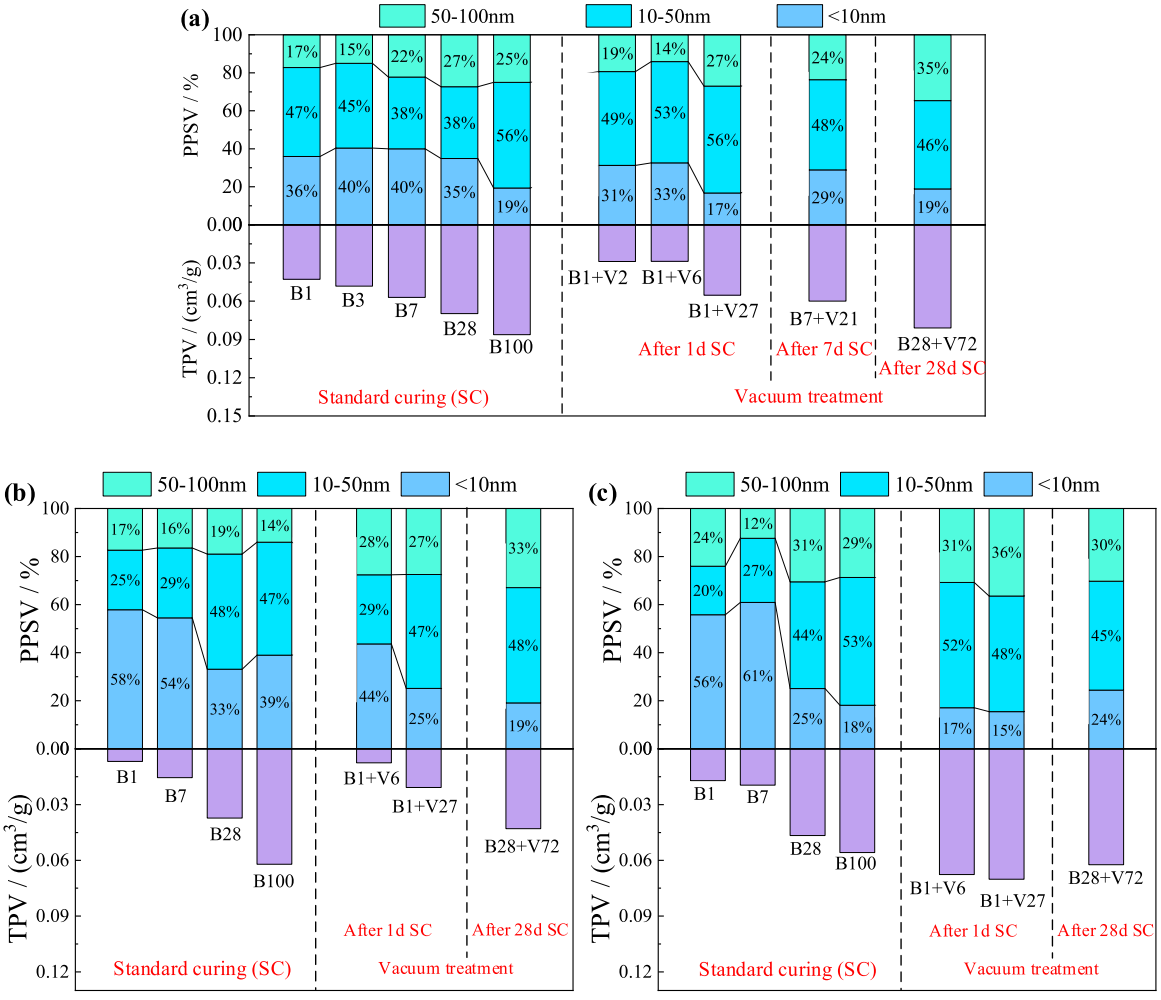


Fig. 16. Percentage of different pore size volume (PPSV) and total pore volume (TPV) for different samples: (a)PC0.45; (b)C_3S0.45; (c)SAC0.45.

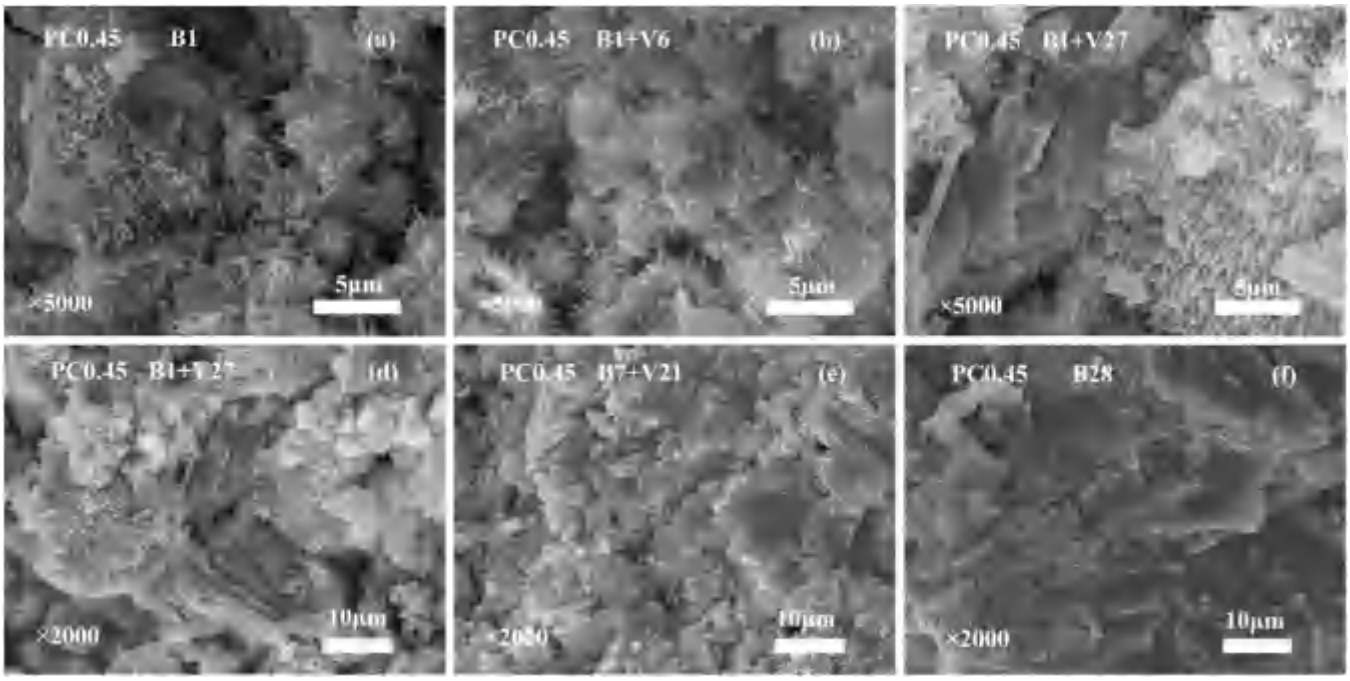


Fig. 17. SEM images of PC0.45 samples (a) (b) (c) after 1-day standard curing and subsequent vacuum treatment for varying durations, and (d) (e) (f) at 28 days of treatment under different treatment methods.

vacuum. Fig. 17d-f compare the microstructures of the specimens at the identical 28-day age but with different treatment regimens. The longer the standard curing period, the hardened paste contained more amorphous hydration products and a denser structure. This was attributed to the thoroughness of cement hydration, which facilitated the continuous filling of pores by the generated products. Additionally, needle-like AFt underwent further hydration to produce AFm.

Previous studies have demonstrated that C-S-H exhibits diverse morphologies under varying drying conditions. Fonseca and Jennings [37] indicated that early-stage C-S-H tends to manifest as fibrous when subjected to rapid drying, whereas it tends toward an amorphous state under slow drying. Besides, Soja et al. [42] observed that specimens maintained under standard curing conditions displayed a prevalence of beehive-like structures within the C-S-H, while prolonged drying under low humidity conditions resulted in isolated, converged, or collapsed peaks within the C-S-H. In this study, the comparison of Fig. 18a-c reveals that, at 500× magnification, the hydrated morphology of C_3S with B1+V27 exhibited numerous loosely packed spherical particles, lacking tight interparticle bonding and featuring a substantial presence of pores. In contrast, B28 and B28+V72 exhibited a profusion of amorphous gel connections between particles, imparting a relatively denser structure to the hardened slurry. Under higher magnification, each spherical particle surface in B1+V27 displayed short fibrous C-S-H strands measuring less than 1 μm, predominantly comprising low-density C-S-H gels encapsulating unhydrated C_3S particles (EDS spots 1 and 2). Conversely, the fibrous C-S-H in B28 appeared elongated, typically exceeding 1 μm, accompanied by the presence of globular and massive products (EDS spot 3). These products intertwined more tightly, forming a more stable slurry structure. This phenomenon arose from the inability of unreacted C_3S particles to continue hydration due to water loss under low vacuum treatment, leading to their encapsulation by a plethora of low-density C-S-H gels. In contrast, continual standard curing promoted the gradual formation of high-density C-S-H gel within the paste, refilling pores between crystals with new C-S-H gel and significantly densifying the sample structure. Comparative analysis of Fig. 18b and c revealed a greater abundance of elongated fibrous C-S-H in B28+V72 compared to B28, with a more heterogeneous distribution and increased presence of pores between different fiber clusters. This phenomenon may have stemmed from the contraction of C-S-H needles under low vacuum treatment, resulting in the interlocking of C-S-H structures and large pores between them.

From Fig. 19, it is evident that at a magnification of 500, SACs of different ages exhibited denser structures compared to C_3S. However, after low vacuum treatment, specimens of B1+V27 and B28+V72 displayed multiple fine microcracks in contrast to B28. Based on the higher magnification, B28 demonstrated a more well-developed crystal structure than B1+V27. Nevertheless, the crystal structure of B28+V72 gradually deteriorated with the emergence of numerous amorphous products. Following standard curing, SAC generated a substantial quantity of highly hydrated AFt crystals (EDS spot 1), contributing to the formation of a relatively dense hardened paste structure. During the low vacuum process, the crystallization water of AFt gradually dissipated, resulting in a mixture of damaged and undamaged AFt (EDS spots 2 and 3).

3.5. Evolution of C-S-H and AFt in low vacuum conditions

The evolution of C-S-H under different treatment conditions is depicted in Fig. 20. At initial, needle-like C-S-H was generated on the surface of C_3S or PC particles. As the curing proceeded, the C-S-H structures grew and merged together, thus the matrix became denser. However, the emergence of more and more gel pores due to the C-S-H generation also led to a gradual increase in the total surface area and pores. Under low vacuum treatment, the hydration was inhibited due to the dissipation of water between particles. In other words, C-S-H could not continue to grow, and new C-S-H could not be generated. As the low vacuum treatment continues, the needles diverged by C-S-H gradually underwent convergence, or C-S-H might also collapse, which could cause smaller pores to form larger ones.

The early achievement of high strength development in SAC was facilitated by the rapid hydration of a substantial amount of ye'elimite, leading to the formation of the crystal structure of AFt. As depicted in Fig. 21, these crystals were typically regarded as hexagonal columnar structures [44]. Depending on the dosage of gypsum added, AFt could

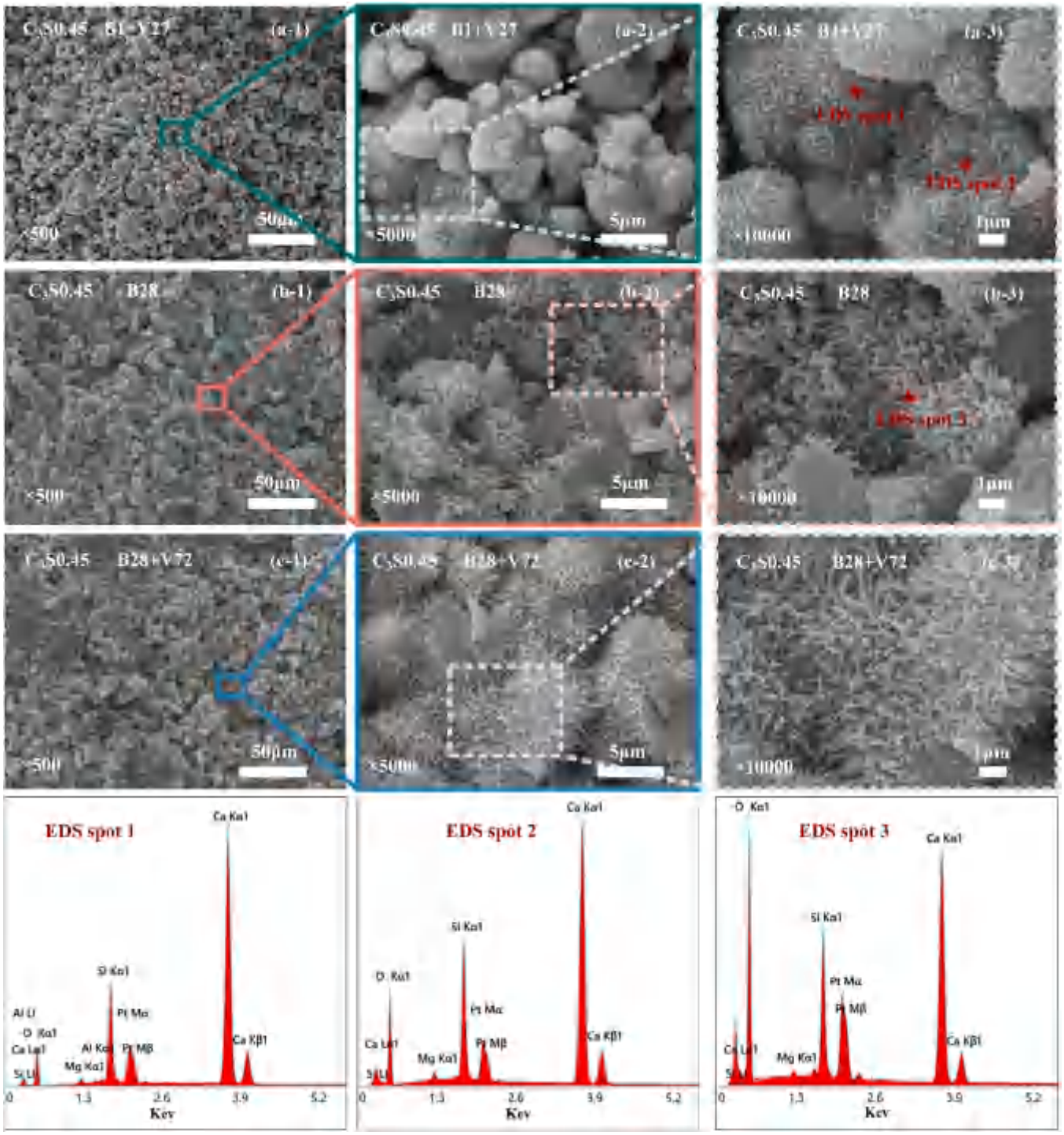


Fig. 18. SEM-EDS images of $C_3S0.45$ samples with (a) B1+V27, (b) B28 and (c) B28+V72.

assume various forms such as needles and short columns. The intense drying effect in a low vacuum environment gradually dissipated the crystallization water of AFt, potentially reducing the coordination number of Ca and Al. Consequently, the AFt crystals underwent degradation and might fragment into multiple parts. Ultimately, some AFt crystals might transition into an amorphous state, resulting in decreased compactness of the hardened pastes.

4. Conclusion

Based on the presented results and discussion, the following conclusions can be drawn:

1. During the initial stage of low vacuum treatment, rapid mass loss of hardened cement paste was evident, primarily attributed to the dissipation of free water. Subsequently, the mass loss rate markedly decelerated and then maintained at a relatively low level, primarily owing to the loss of chemical bound water from hydration products. Given C_3S has the slowest hydration rate, it exhibited the greatest mass loss under low vacuum, which was followed by PC and SAC.
2. The dissipation effect caused by low vacuum treatment leads to the inhibition of cement hydration. Consequently, the contents of

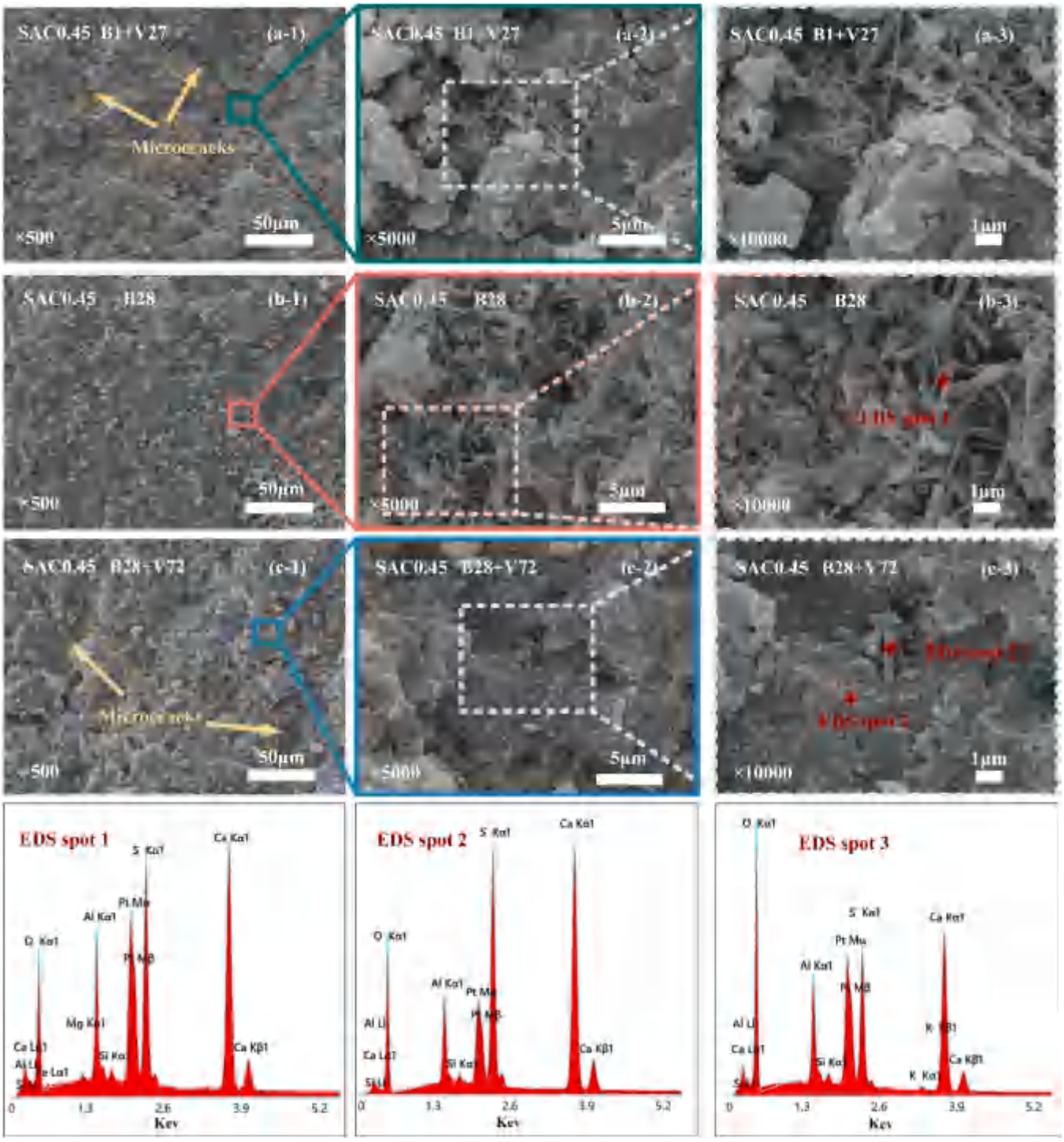


Fig. 19. SEM-EDS images of SAC0.45 samples with (a) B1+V27, (b) B28 and (c) B28+V72.

hydration products remained nearly constant, or even exhibited a decrease, particularly notable in the case of AFt.

3. As the duration of low-vacuum treatment increased, the total pore volume (less than 100 nm) increased, and meanwhile small pores collapsed to form larger ones, leading to an increase in the percentage of pores with sizes ranging from 50 nm to 100 nm. In addition, this was more pronounced in SAC cement in comparison with PC and C_3S pastes.
4. Under low vacuum conditions, the morphology of C-S-H gradually transitions from dispersed needle-like to convergent or collapsed forms, resulting in the enlargement of gel pores. Simultaneously, the crystalline water of AFt crystals gradually dissipates, leading to crystallization degradation. This degradation may cause some of the crystals to evolve into an amorphous state, thereby reducing the compactness of the hardened pastes.

CRediT authorship contribution statement

Ce Gao: Investigation. **Zhuo Tang:** Writing – review & editing, Validation, Supervision. **Fan Wang:** Writing – review & editing. **Yue Chen:** Methodology. **Guangcheng Long:** Methodology, Conceptualization. **Zhaofei Long:** Methodology, Formal analysis. **Minghui**

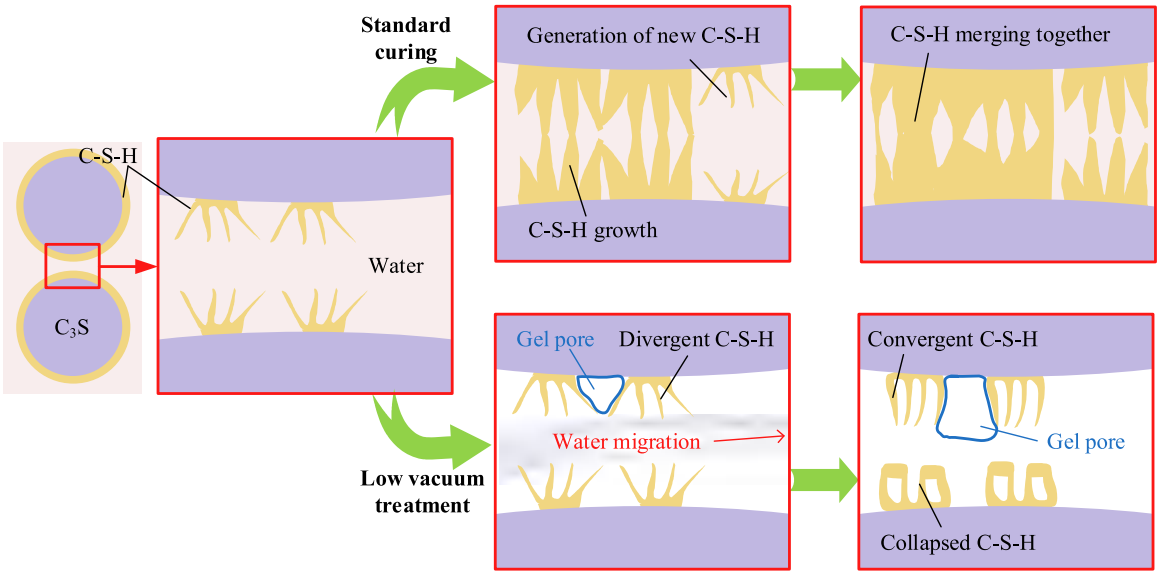


Fig. 20. Evolution of C-S-H under different treatment conditions.

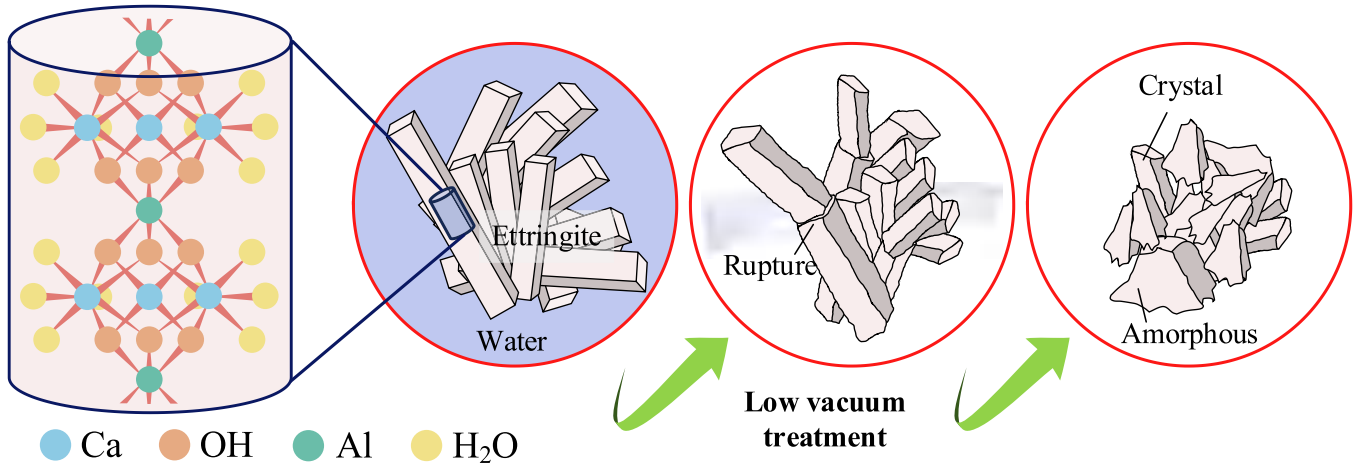


Fig. 21. Evolution of ettringite under low vacuum treatment.

Shangguan: Writing – review & editing, Writing – original draft, Investigation. **Youjun Xie:** Resources, Methodology.

Declaration of Competing Interest

We declare that we have no financial and personal relationships with other people or organizations that can inappropriately influence our work, there is no professional or other personal interest of any nature or kind in any product, service and/or company that could be construed as influencing the position presented in, or the review of, the manuscript entitled, "**Hydration and microstructure evolution of cement paste in low vacuum environments**".

Data availability

Data will be made available on request.

Acknowledgement

This research was supported by the Program Fund of Nonmetallic Excellence and Innovation Center for Building Materials (No. 24TDA-1).

References

[1] S. Zuo, Q. Yuan, T. Huang, K. Zhang, J. Shi, Y. Tan, Microstructural changes of young cement paste due to moisture transfer at low air pressures, Cem. Concr. Res. 164 (2023) 107061, https://doi.org/10.1016/j.cemconres.2022.107061.
[2] S. Zuo, Q. Yuan, T. Huang, Z. Wang, K. Zhang, J. Liu, Rheology and air entrainment of fresh Portland cement mortars in simulated low air pressure environments, Cem. Concr. Compos. 135 (2023) 104848, https://doi.org/10.1016/j.cemconcomp.2022.104848.
[3] X. Lan, X. Zeng, H. Zhu, G. Long, Y. Xie, Experimental investigation on fractal characteristics of pores in air-entrained concrete at low atmospheric pressure, Cem. Concr. Compos. 130 (2022) 104509, https://doi.org/10.1016/j.cemconcomp.2022.104509.
[4] C. Park, D. Cheon, J. Park, Analytical model of fluid flow through closed structures for vacuum tube systems, Math. Probl. Eng. 2015 (2015) 1–6, https://doi.org/10.1155/2015/210727.
[5] C. Park, J. Synn, J. Park, Probabilistic performance assessment of airtightness in concrete tube structures, KSCE J. Civ. Eng. 20 (4) (2016) 1443–1451, https://doi.org/10.1007/s12205-015-0735-z.
[6] H. Chang, X. Wang, Y. Wang, S. Li, J. Wang, J. Liu, P. Feng, Influence of low vacuum condition on mechanical performance and microstructure of hardened cement paste at early age, Constr. Build. Mater. 346 (2022) 128358, https://doi.org/10.1016/j.conbuildmat.2022.128358.
[7] C. Honglei, W. Xiaolong, G. Zhengkun, F. Pan, L.I. Shaowei, L. Jian, Effect of low vacuum environment on the mechanical properties of hardened cement paste, Mater. Rep. 38 (4) (2024) 109–114, https://doi.org/10.11896/cldb.22070290.
[8] Y. Chen, M. Shangguan, G. Long, S. Xu, C. Gao, Study on the drying shrinkage deformation of cement mortar under low vacuum condition and its mechanism (in

Chinese), J. Railw. Sci. Eng. 20 (7) (2023) 2530–2538, https://doi.org/10.19713/j.cnki.43-1423/u.T20221476.
[9] G. Long, Y. Chen, Z. Tang, M. Shangguan, C. Gao, S. Xu, Drying shrinkage behavior of cement mortar under low vacuum conditions, Constr. Build. Mater. 374 (2023) 130933, https://doi.org/10.1016/j.conbuildmat.2023.130933.
[10] M. Shangguan, Y. Xie, F. Wang, G. Long, Z. Tang, Y. Chen, S. Xu, H. Li, C. Gao, M. Liu, Effect of low-vacuum environment on the strength and permeability of cement-based materials, Constr. Build. Mater. 400 (2023) 132676, https://doi.org/10.1016/j.conbuildmat.2023.132676.
[11] M. Liu, Y. Xie, M. Shangguan, G. Long, C. Gao, Effect of low vacuum condition on medium migration performance in concrete, J. Central South Univ. (Sci. and Tech.) 54(09) (2023) 3535-3543 (in Chinese). https://doi.org/10.11817/j.issn.1672-7207.2023.09.014.
[12] P.K. Mehta, P.J.M. Monteiro, Concrete: Microstructure, Properties, and Materials, Prentice Hall, Upper Saddle River, 2013.
[13] X. Du, Z. Li, J. Han, R. Zhang, Effect of isothermal drying process of cement paste, mortar and concrete on compressive strength (in Chinese), J. Chin. Ceram. Soc. 47 (05) (2019) 639–647, https://doi.org/10.14062/j.issn.0454-5648.2019.05.08.
[14] Z. Lafhaj, M. Goueygou, A. Djerbi, M. Kaczmarek, Correlation between porosity, permeability and ultrasonic parameters of mortar with variable water / cement ratio and water content, Cem. Concr. Res. 36 (4) (2006) 625–633, https://doi.org/10.1016/j.cemconres.2005.11.009.
[15] M. Shangguan, Y. Xie, S. Xu, C. Gao, G. Long, F. Wang, M. Liu, Mechanical properties characteristics of high strength concrete exposed to low vacuum environment, J. Build. Eng. 63 (2023) 105438, https://doi.org/10.1016/j.jobe.2022.105438.
[16] H. Taylor. Cement chemistry, vol. 2 ed., Thomas Telford, London, 1997.
[17] H. Ludwig, W. Zhang, Research review of cement clinker chemistry, Cem. Concr. Res. 78 (2015) 24–37, https://doi.org/10.1016/j.cemconres.2015.05.018.
[18] M. Shangguan, Y. Xie, F. Wang, Y. Chen, Z. Tang, G. Long, S. Xu, H. Li, C. Gao, Preparation of coatings for moisture migration control of cementitious materials under low-vacuum environment, Mater. Lett. 355 (2024) 135553, https://doi.org/10.1016/j.matlet.2023.135553.
[19] C. Galle, Effect of drying on cement-based materials pore structure as identified by mercury intrusion porosimetry - a comparative study between oven-, vacuum-, and freeze-drying, Cem. Concr. Res. 31 (10) (2001) 1467–1477, https://doi.org/10.1016/S0008-8846(01)00594-4.
[20] A. Korpa, R. Trettin, The influence of different drying methods on cement paste microstructures as reflected by gas adsorption: comparison between freeze-drying (F-drying), D-drying, P-drying and oven-drying methods, Cem. Concr. Res. 36 (4) (2006) 634–649, https://doi.org/10.1016/j.cemconres.2005.11.021.
[21] Z. Zhang, G.W. Scherer, Evaluation of drying methods by nitrogen adsorption, Cem. Concr. Res. 120 (2019) 13–26, https://doi.org/10.1016/j.cemconres.2019.02.016.
[22] L. Zhang, F.P. Glasser, Critical examination of drying damage to cement pastes, Adv. Cem. Res. 12 (2) (2000) 79–88, https://doi.org/10.1680/adcr.2000.12.2.79.
[23] N.C. Collier, J.H. Sharp, N.B. Milestone, J. Hill, I.H. Godfrey, The influence of water removal techniques on the composition and microstructure of hardened cement pastes, Cem. Concr. Res. 38 (6) (2008) 737–744, https://doi.org/10.1016/j.cemconres.2008.02.012.
[24] X. Li, A. Ouzia, K. Scrivener, Laboratory synthesis of C_3S on the kilogram scale, Cem. Concr. Res. 108 (2018) 201–207, https://doi.org/10.1016/j.cemconres.2018.03.019.
[25] ISO 3529-1, 2019: Vacuum technology - vocabulary - part 1: general terms, Vernier, Geneva, Switzerland.
[26] K. Scrivener, R. Snellings, B. Lothenbach, A practical guide to microstructural analysis of cementitious materials, CRC Press, Boca Raton, Florida, United States, 2016.
[27] V. Rostami, Y. Shao, A.J. Boyd, Z. He, Microstructure of cement paste subject to early carbonation curing, Cem. Concr. Res. 42 (1) (2012) 186–193, https://doi.org/10.1016/j.cemconres.2011.09.010.
[28] J. Zhang, H. Dongwei, S. Wei, Experimental study on the relationship between shrinkage and interior humidity of concrete at early age, Mag. Concr. Res. 62 (3) (2010) 191–199, https://doi.org/10.1680/macr.2010.62.3.191.
[29] P. Lura, K. van Breugel, I. Maruyama, Effect of curing temperature and type of cement on early-age shrinkage of high-performance concrete, Cem. Concr. Res. 31 (12) (2001) 1867–1872, https://doi.org/10.1016/S0008-8846(01)00601-9.
[30] X. Qin, A. Shen, Z. Lyu, L. Shi, J. Yang, H. Liu, Research on water transport behaviors and hydration characteristics of internal curing pavement concrete, Constr. Build. Mater. 248 (2020) 118714, https://doi.org/10.1016/j.conbuildmat.2020.118714.
[31] N.N. Skoblinskaya, K.G. Krasilnikov, L.V. Nikitina, V.P. Varlamov, Changes in crystal structure of ettringite on dehydration. 2, Cem. Concr. Res. 5 (5) (1975), https://doi.org/10.1016/0008-8846(75)90017-4.
[32] N.N. Skoblinskaya, K.G. Krasilnikov, Changes in crystal structure of ettringite on dehydration. 1, Cem. Concr. Res. (1975), https://doi.org/10.1016/0008-8846(75)90093-9.
[33] P.A. Kißling, F. Lübkemann, T. von Bronk, D. Cotardo, L. Lei, A. Feldhoff, L. Lohaus, M. Haist, N.C. Bigall, Influence of low-pressure treatment on the morphological and compositional stability of microscopic ettringite, Materials 14 (11) (2021) 2720, https://doi.org/10.3390/ma14112720.
[34] I. Galan, H. Beltagui, M. García-Maté, F.P. Glasser, M.S. Imbabi, Impact of drying on pore structures in ettringite-rich cements, Cem. Concr. Res. 84 (2016) 85–94, https://doi.org/10.1016/j.cemconres.2016.03.003.
[35] S. Brunauer, P.H. Emmett, E. Teller, Adsorption of gases in multimolecular layers, J. Am. Chem. Soc. 60 (2) (1938) 309–319, https://doi.org/10.1021/ja01269a023.
[36] M.C. Garci Juenger, H.M. Jennings, Wca, The use of nitrogen adsorption to assess the microstructure of cement paste, Cem. Concr. Res. 31 (6) (2001) 883–892, https://doi.org/10.1016/S0008-8846(01)00493-8.
[37] P.C. Fonseca, H.M. Jennings, The effect of drying on early-age morphology of C-S-H as observed in environmental SEM, Cem. Concr. Res. 40 (12) (2010) 1673–1680, https://doi.org/10.1016/j.cemconres.2010.08.007.
[38] E.P. Barrett, L.G. Joyner, P.P. Halenda, The determination of pore volume and area distributions in porous substances. I. Computations from nitrogen isotherms, J. Am. Chem. Soc. 73 (1) (1951) 373–380, https://doi.org/10.1021/ja01145a126.
[39] H. Ma, Z. Li, Realistic pore structure of Portland cement paste: experimental study and numerical simulation, Comput. Concr. 11 (4) (2013) 317–336, https://doi.org/10.12989/cac.2013.11.4.317.
[40] K.K. Aligizaki. Pore structure of cement-based materials: Testing, interpretation and requirements, Taylor and Francis, New York, U.S.A., 2006.
[41] K.S.W. Sing, Reporting physisorption data for gas/solid systems with special reference to the determination of surface area and porosity (Recommendations 1984), Pure Appl. Chem. 57 (4) (1985) 603–619, https://doi.org/10.1351/pac198557040603.
[42] W. Soja, F. Georget, H. Maraghechi, K. Scrivener, Evolution of microstructural changes in cement paste during environmental drying, Cem. Concr. Res. 134 (2020) 106093, https://doi.org/10.1016/j.cemconres.2020.106093.
[43] Q. Zhou, E.E. Lachowski, F.P. Glasser, Metaettringite, a decomposition product of ettringite, Cem. Concr. Res. 34 (4) (2004) 703–710, https://doi.org/10.1016/j.cemconres.2003.10.027.
[44] A.E. Moore, H.F.W. Taylor, Crystal structure of ettringite, Acta Crystallogr. Sect. B 26 (4) (1970) 386–393, https://doi.org/10.1107/S0567740870002443.

Journal of Building Engineering 99 (2025) 111639

Contents lists available at ScienceDirect

Journal of Building Engineering

journal homepage: www.elsevier.com/locate/jobe

Regulating drying shrinkage behavior of cement-based materials in low vacuum environments and developing a predictive model

Zhaofei Long [a], Guangcheng Long [a,*], Yue Chen [a], Minghui Shangguan [a], Jilin Wang [a], Yuting Zhang [a], Meihui Yi [a], Ce Gao [b], Zhuo Tang [a,**]

[a] School of Civil Engineering, Central South University, Changsha, 410075, China
[b] China Railway Engineering Design and Consulting Group Co., Ltd, Beijing, 100055, China

ARTICLE INFO

Keywords:
Drying shrinkage
Low-vacuum environments
Mass loss
Shrinkage mitigation
Prediction model

ABSTRACT

Low-vacuum pipeline transportation is essential for surpassing train speed limits, but the low-vacuum environment can intensify the drying shrinkage of cement-based materials, impacting their structural durability. Leveraging existing shrinkage mitigation strategies, this study examines the influence of various shrinkage-reducing components and surface coating treatments on cement-based materials' shrinkage and mass loss behavior under low-vacuum condition. The findings indicate that the shrinkage strain of mortar and concrete under low-vacuum drying could reach more than 1.35 and 1.2 times that of standard drying, respectively. For mortar, fly ash (FA) and shrinkage reducing admixture (SRA) can minimize shrinkage. Silica fume (SF), nano-silica (NS), polyvinyl alcohol (PVA), and polypropylene (PP) fibers can all reduce the early shrinkage rate to varying degrees. The combined addition of FA, SF, and SRA can significantly alleviate the drying shrinkage behavior of concrete. Surface coating treatments can reduce specimen shrinkage by approximately 20 % and early shrinkage rates by about 30 %. The mass loss test results indicate that under low-vacuum drying condition, the mass loss rate of the mortar can exceed twice that of standard drying condition, with the drying rate being over three times higher. A linear fitting relationship between shrinkage strain and mass loss rate reveals a strong correlation. In low-vacuum environments, specimen shrinkage is less affected by mass loss than in standard drying condition. Shrinkage-reducing components make shrinkage less sensitive to water loss, while coatings increase this sensitivity. A new predictive model for concrete shrinkage strain has been developed based on existing models. This model incorporates the effects of shrinkage-reducing components and low-vacuum environments, demonstrating high precision. The research findings offer valuable insights for the improvement of drying shrinkage performance in low-vacuum environments for cement-based materials.

1. Introduction

Hyperloop considered the fifth mode of transportation in the modern era, integrates vacuum tube technology with magnetic levitation. This combination surpasses the limitations of air resistance, noise, and wheel-rail friction, allowing trains to travel at speeds

* Corresponding author.
** Corresponding author.
E-mail addresses: longguangcheng@csu.edu.cn (G. Long), zhuo.tang@csu.edu.cn (Z. Tang).

https://doi.org/10.1016/j.jobe.2024.111639
Received 29 September 2024; Received in revised form 3 December 2024; Accepted 20 December 2024
Available online 22 December 2024
2352-7102/© 2024 Elsevier Ltd. All rights are reserved, including those for text and data mining, AI training, and similar technologies.

exceeding 1000 km/h. This addresses the demand for rapid and efficient travel [1]. Concrete is widely used as a construction material and offers benefits such as mitigating magnetic resistance, providing flexibility and convenience in construction, and being cost-effective. As a result, it is considered an ideal engineering material for low-vacuum tube magnetic levitation transportation systems [2,3]. However, the low-vacuum environment poses a significant challenge to the long-term performance stability of porous and non-homogeneous conventional concrete materials. Existing research shows that there is a significant drying effect in the plateau low-pressure environments and lower-vacuum conditions. This accelerates the moisture migration and dissipation within the concrete, increasing the shrinkage rate of concrete, generating greater destructive tensile stresses, and even leading to cracking of the concrete structure [4,5]. Long-term exposure to low-vacuum conditions can cause concrete to become dehydrated. This can lead to risks such as shrinkage and cracking, as well as compromising its air tightness, mechanical properties, and durability. Additionally, there may be potential changes in its phase and pore structure [6–9].

Drying shrinkage occurs when hardened cement specimens lose water in dry environments to balance with the external humidity, resulting in volume changes. This process is influenced by the relative humidity (RH) and temperature of the environment, as well as the composition, water-to-binder ratio, and dimensions of the specimens [10]. Under the strong drying effect of a low-vacuum environment, cement-based materials initially lose free water from large capillary pores (>50 nm). The loss of this water does not cause significant volume changes. However, as drying time extends, adsorbed water from smaller capillary pores (<50 nm) and gel pores begins to be lost, resulting in significant shrinkage deformation of the specimens [11]. Traditional long-term performance of concrete in harsh low-vacuum environments is challenging to guarantee. Consequently, effective shrinkage mitigation strategies are urgently needed to enhance the service stability of concrete under low-vacuum drying conditions.

The use of supplementary cementitious materials (SCMs) in certain proportions to replace cement is considered a significant measure to enhance concrete durability and reduce environmental impact, as well as a key factor in designing high-strength, low-shrinkage concrete [12,13]. As a major member of SCMs, fly ash (FA) has been proven to reduce the autogenous and drying shrinkage of concrete [14]. The filling and pozzolanic effects of FA and silica fume (SF) help form a denser structure in the matrix, thereby reducing water loss and long-term shrinkage and creep of concrete [15,16]. Research has reported [17] that ultra-fine ground granulated blast furnace slag (GGBS) and SF can promote the formation of more ettringite crystals and C-S-H gel by cement hydration, thereby enhancing the concrete's resistance to external force deformation. Based on this, the use of a composite cementitious system with cement and SCMs not only helps reduce the shrinkage of cement-based materials but also offers considerable cost and environmental benefits. Additionally, the addition of shrinkage-reducing admixtures [18,19], nanomaterials [20,21], polymers [22,23], and fibers [24,25] to concrete is considered an effective means to regulate drying shrinkage. The related shrinkage reduction mechanisms mainly include lowering the surface tension and capillary tension of the liquid phase, improving the compactness of microstructure, strengthening the interfacial transition zone, bridging cracks, and ultimately reducing the tensile stress caused by shrinkage [26]. It has also been pointed out that surface coating treatments are efficient and cost-effective methods to control water loss in cement-based materials in low-vacuum environments [27].

Based on the existing shrinkage control strategies, this paper employs SCMs, shrinkage-reducing admixtures (SRA), nano-silica (NS), polyvinyl alcohol (PVA), polypropylene fibers (PP), and surface film-forming organic coatings to improve the shrinkage characteristics of cement-based materials in low-vacuum environments. The study investigates the effects of the above mitigation techniques on the shrinkage and mass loss behaviors, as well as the interaction between the two. It is particularly noted that predicting volume changes in concrete structures remains the most effective and economical approach to addressing drying shrinkage issues, providing a basis for further measures to minimize stress development and potential cracking. Compared to concrete structures in normal atmospheric conditions, the shrinkage behavior of concrete in low vacuum environments will be more significant, and the pattern of shrinkage development will be notably different. With the application of mineral admixtures and shrinkage-reducing admixtures, the shrinkage evolution of concrete in low-vacuum conditions becomes more complex, making the shrinkage patterns even more difficult to predict. Currently, although there are numerous models available for predicting concrete shrinkage behavior, models that are specifically applicable to low-vacuum conditions and consider the impact of shrinkage mitigation measures are extremely limited, thereby increasing the discrepancies between different models. It is necessary to develop a predictive method for the shrinkage evolution of concrete in low vacuum environments. In light of this, this paper aims to develop a comprehensive concrete shrinkage prediction model that takes into account the effects of low-vacuum condition and shrinkage-reducing components, to accurately predict and regulate the shrinkage behavior of concrete in such harsh environments.

Table 1
Chemical compositions and physical properties of cementitious materials (wt.%).

Binder	Chemical compositions (wt.%)									Physical properties	
	CaO	SiO_2	Al_2O_3	Fe_2O_3	SO_3	MgO	Na_2O	K_2O	Loss	Specific surface area (m^2/kg)	Density (g/cm^3)
PC	59.70	24.60	7.30	4.00	2.50	3.80	0.60	–	2.50	367	3.12
FA	3.70	52.30	26.30	9.70	0.20	1.20	1.80	–	5.70	450	2.40
SF	0.35	96.89	0.11	0.03	0.91	0.64	0.16	0.69	1.20	20500	2.10
GGBS	33.60	26.10	13.80	14.10	–	8.10	0.45	–	2.10	440	2.85

2. Test program

2.1. Materials

The chemical composition and physical properties of Portland cement (P.I 42.5) and mineral admixtures were tested, as shown in Table 1. Furthermore, the particle size distribution of the cementitious materials was assessed using a laser particle size analyzer, as displayed in Fig. 1. Here, FA and GGBS were sourced from Xiangtan Power Plant and a steel mill in Hunan Province, respectively, meeting the national standards for Class II and S95 grade; SF, provided by Shanghai Aiken Co., Ltd, is a gray powder (SiO_2>95 %). The fine aggregate is well-graded washed river sand with a fineness modulus of 2.57 and an apparent density of 2650 kg/m^3. The coarse aggregate is hard impact-crushed limestone gravel, comprising two particle sizes of 5–10 mm and 10–25 mm, with an apparent density of 2680 kg/m^3. The water reducer was supplied by Jiangsu Sobute New Materials Co., Ltd. The water reducer is a PCA-I polycarboxylate-based high-performance superplasticizer (SP), with a solid content of approximately 40 % and a water reduction rate of up to 30 %. The mixing water utilized was sourced from the tap water supply of Changsha City, Hunan.

The shrinkage-reducing components include SRA, NS, PVA, and PP. The SRA is a polyether-type shrinkage reducing admixture with a solid content of 99 %. NS is a white powder with a specific surface area of 230 m^2/g and a average particle size 20 nm. PVA, a white powder of analytical purity, has a pH of 5–7, a volatility of less than 7 %, and a particle size of 150 μm. It requires pre-mixing in deionized water before incorporation, and the addition of an 880B type defoamer to prevent foam formation. PP has a length of 12 mm, a diameter of 20 μm, a modulus of elasticity of 3.5 GPa, a fracture strength of 460 MPa, and a density of 0.91 g/cm^3.

The surface coatings used were commercially available polyurea coating (PUA), polyurethane coating (PU), and waterborne acrylic coating (WAC). PUA is a blue viscous liquid with a high solid content and slow water evaporation, offering a lower cost. PU possesses a solid content exceeding 65 % and exhibits weather resistance lasting over 2400 h. WAC boasts a tensile retention rate of over 98 %, excellent heat resistance, and is a high molecular weight dense waterproof coating. To enhance the adhesion between the organic coatings and inorganic cement-based materials, a KH-550-type silane coupling agent was used.

2.2. Mix proportions

Mortar and concrete with the same water-to-binder ratio (0.3) were designed to investigate the evolution of drying shrinkage performance of cement-based materials in low-vacuum environments. The binder-to-sand ratio of the mortar was set at 1:2, and the SP dosing was 0.5 %. FA was used as the main shrinkage-reducing material to replace PC by 20 % in equal parts. On this basis, 3 % of SF, 0.3 % of SRA, 1 % of NS, 1 % of PVA, and 4 % of PP were individually added, forming a dual-admixture composite shrinkage-reducing cementitious system. Based on the mortar proportion, three specific concrete ratios were designed, with SP admixture maintained at 0.9 %.CFA was the control group, with FA and GGBS accounting for 30 % of cementitious materials. Compared with the control, CFA-SF added 3 % SF, while CFA-SF + SRA added 3 % SF and 0.3 % SRA. The specific mix proportions of the mortar and concrete are shown in Table 2.

2.3. Test procedures

2.3.1. Specimen preparation

The mortar was prepared using a planetary mixer and poured the fresh slurry into molds measuring 25 mm × 25 mm × 280 mm and compacted by vibrating. After demolding at 1 day, subjected them to standard curing for 2 d. Then, placed the cured mortar samples in

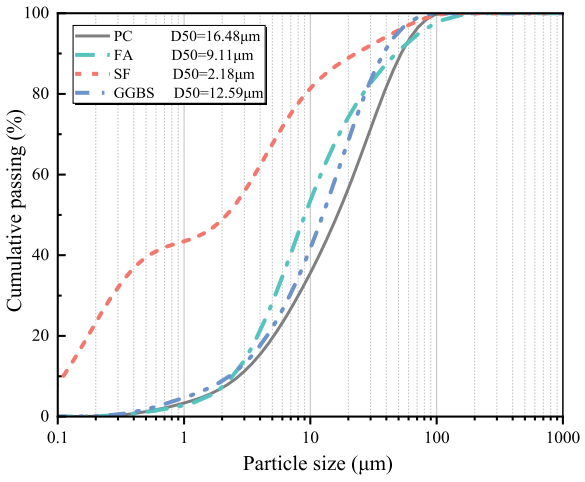


Fig. 1. Particle size distribution of cementitious material.

Table 2
Mix proportions of the mortar and concrete specimens.

Mixture		Raw material (kg/m^3)												
		PC	FA	GGBS	SF	SRA	NS	PVA	PP	Sand	Gravel		Water	SP
											(5–10) mm	(10–25) mm		
Mortar	PC	720	0	–	–	–	–	–	–	1440	–	–	216	3.6
	FA	576	144	–	–	–	–	–	–	1440	–	–	216	3.6
	FA-SF	554.4	144	–	21.6	–	–	–	–	1440	–	–	216	3.6
	FA-SRA	576	144	–	–	2.16	–	–	–	1440	–	–	216	3.6
	FA-NS	576	144	–	–	–	7.2	–	–	1440	–	–	216	3.6
	FA-PVA	576	144	–	–	–	–	7.2	–	1440	–	–	216	3.6
	FA-PP	576	144	–	–	–	–	–	28.8	1440	–	–	216	3.6
	FA-PVA + PP	576	144	–	–	–	–	7.2	28.8	1440	–	–	216	3.6
Concrete	CFA	336	96	48	0	0	–	–	–	680	432	648	144	4.32
	CFA-SF	321.6	96	48	14.4	0	–	–	–	680	432	648	144	4.32
	CFA-SF + SRA	321.6	96	48	14.4	1.44	–	–	–	680	432	648	144	4.32

both standard drying and low-vacuum drying environments for subsequent drying characteristic tests. The low-vacuum drying environment was simulated using a self-made vacuum box with a vacuum pressure of 100 ± 10 Pa and a temperature of 20 ± 2 °C. The standard drying was conducted in a drying chamber with a temperature of 20 ± 2 °C and a RH of 50 %–60 %. For the low-vacuum environment discussed in this paper, the decrease in environmental pressure leads to a reduction in RH, which can be calculated using Eq. (1):

$$RH = \frac{p_{wA}}{p_{ws}} \times 100\% \tag{1}$$

where: P_{wA} is the vapor partial pressure of water in the current environment, Pa; P_{ws} is the saturation vapor pressure of water, 20 °C for 2338 pa.

Assuming that after a certain period, the evaporation rate of water in the low-vacuum environment is consistent with the efficiency of the vacuum pump in removing water vapor, the vapor pressure of water can be approximated to be equal to the environmental pressure. It can be estimated that the RH of concrete in a 100 Pa low-vacuum environment is approximately 4.3 %. An electronic digital thermohydrometer was used to test the evolution of temperature and RH inside the vacuum box, as shown in Fig. 2. It was observed that under continuous low-vacuum condition, the temperature inside the box could be maintained near 20 °C (close to the ambient temperature), while the RH dropped to nearly 5 % (the lowest humidity threshold of the instrument). This indicates that under low-vacuum condition, concrete is almost in an environment with 0 % RH, which will significantly affect the shrinkage behavior of the concrete. Detailed schematic diagrams of these two types of drying environments can be found in Ref. [5].

Concrete was prepared using a double-axis horizontal concrete mixer. Poured the freshly mixed concrete into molds with dimensions of 100 mm × 100 mm × 400 mm and compacted using a vibrating table. After demolding at 1 day, subjected to standard curing for 27 days, and then placed in different environments for drying treatment. When the specimens reached the specified age, corresponding performance tests were conducted.

The coating application was performed after the mortar specimens were standard-cured for 7 d. A glass rod was used to mix the coating with the KH-550 type silane coupling agent for 5 min to ensure uniform mixing. After the dried specimens were sanded and

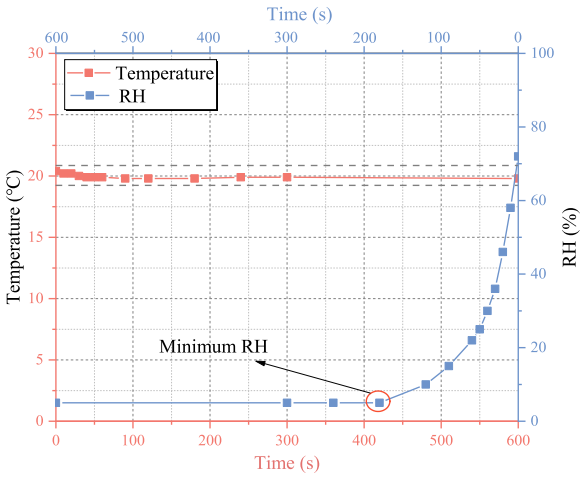


Fig. 2. Evolution of temperature and humidity in low-vacuum chamber.

cleaned, the coating was evenly brushed onto the surface of the PC specimens. Once cured, a second layer of coating was applied, and a film was allowed to form. Subsequently, the coated specimens and a group of specimens without surface treatment were placed in a vacuum chamber and a standard drying chamber for drying treatment, respectively. The preparation and drying process of cementitious materials in the tests are shown in Fig. 3(a) and (b). The specimens subjected to standard drying were labeled as SD, and those subjected to low-vacuum drying were labeled as VD.

2.3.2. Drying shrinkage test

The shrinkage strain of the specimens was calculated using Eq. (2), and the results were averaged over three specimens, with the effective length of the mortar and concrete specimens being 250 mm and 400 mm, respectively. The shrinkage test of specimens is shown in Fig. 3(c).

$$\varepsilon(t) = \frac{L_0 - L_t}{L} \times 100\% \tag{2}$$

where $\varepsilon(t)$ is the drying shrinkage strain when the age of the specimen is t, με; L_0 is the initial length, mm; L_t is the measured length of the specimen at the age of t, mm; L is the effective length of the specimen or the measurement gauge length, mm.

2.3.3. Mass loss test

The test cycle for the mass loss of mortar, concrete, and coating specimens was consistent with the shrinkage test. The initial mass of mortar specimens after standard curing for 3 d and concrete specimens after standard curing for 28 d was recorded using a high-precision electronic balance. Subsequently, the specimens were transferred to their respective exposure environments and tested according to the designed treatment ages. The calculation method for the mass loss rate is shown in Eq. (3), and the final result was the average of the mass losses from three prismatic specimens.

$$\Delta w_t = \frac{m_0 - m_t}{m_0} \times 100\% \tag{3}$$

where $\triangle w_t$ represents the mass loss rate of the specimen at time t during exposure to the low-vacuum environments, %; m_0 is the initial mass of the specimen before exposure to the low-vacuum environments, g; m_t is the mass of the specimen at time t after exposure to the low-vacuum environments, g。

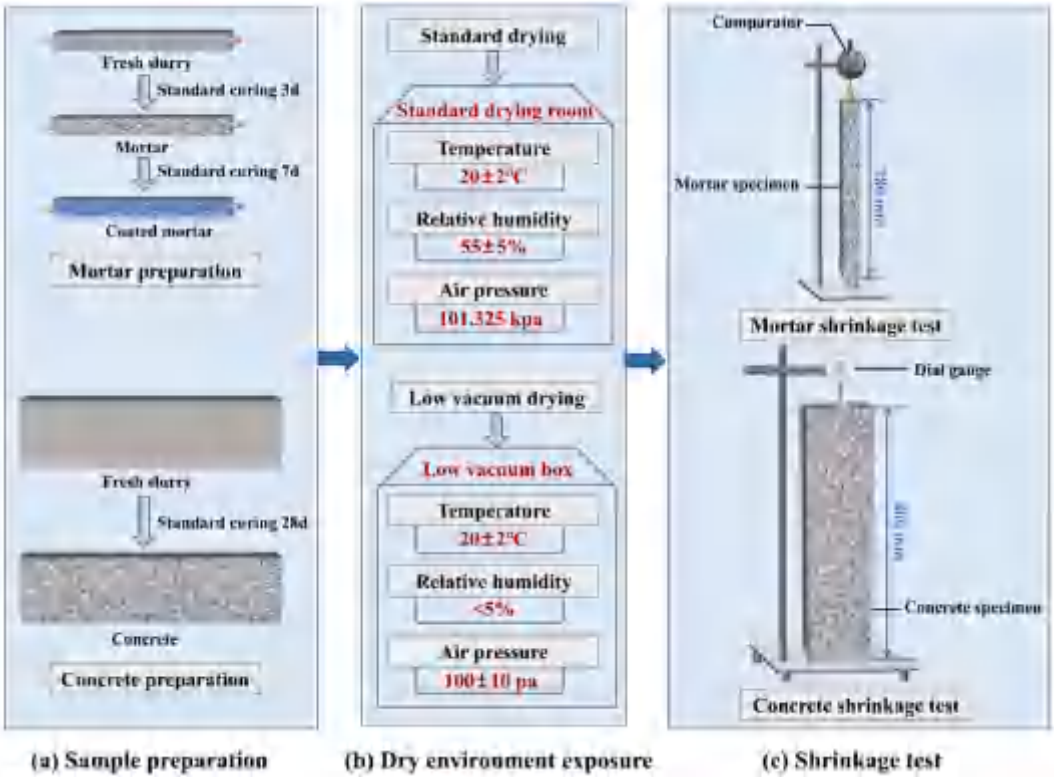


Fig. 3. Schematic diagram of shrinkage test for cementitious materials.

3. Results and discussion

3.1. Drying shrinkage of specimens

Fig. 4 illustrates the results of shrinkage deformation in mortar with different mix ratios under standard drying and low-vacuum drying conditions. As seen in the figure, the shrinkage of mortar under different drying conditions consistently showed a pattern of rapid increase in the early stages followed by a slow increase and eventual stabilization. The early shrinkage rate of mortar in the low-vacuum environment was significantly higher than that in the standard drying environment, leading to a significantly increased final shrinkage value. Compared to standard drying, the shrinkage value of mortar specimens increased by 60 %–140 % after 7 d of low-vacuum drying, and the shrinkage value after 60 d of drying could reach more than 1.35 times the standard. This indicates that the low-vacuum environment intensifies the shrinkage behavior of mortar, ultimately resulting in increased shrinkage deformation.

By comparing mortar specimens with different mix ratios, it was observed that the incorporation of FA effectively alleviated the drying shrinkage under both standard and low-vacuum environments, which reduced the shrinkage by 19 % and 10 % at 7 d, 16 % and 11 % at 60 d, respectively. Based on the FA mix ratio, the addition of SF further reduced the shrinkage before 7 d but increased the shrinkage after 7 d; SRA, however, further alleviated the shrinkage behavior of the matrix, reducing the shrinkage at 7 d and 60 d under SD and VD by 34 %, 16 %, and 18 %, 16 %, respectively. Under standard drying condition, the combination of FA and NS provided the best shrinkage reduction effect, which could reduce the drying shrinkage value of PC by 21 %. However, under low-vacuum drying condition, NS only achieved shrinkage reduction for the first 7 d, and the shrinkage reduction effects of PP and PVA were even weaker than those of NS. Interestingly, the shrinkage of specimens with the combination of PVA and PP was greater than that of the single-addition groups. This may be because when PP is mixed with PVA, PVA increases the viscosity of the paste, which to some extent affects the dispersion of PP [28], resulting in a relatively loose network structure that is not conducive to resisting shrinkage stresses. It should be noted that although different admixtures had varying degrees of alleviation on the final shrinkage values of cement mortar specimens, the overall differences were not significant. The combination of FA + SRA had the smallest shrinkage in the low-vacuum environment, while the combination of FA + PVA + PP failed to improve the shrinkage behavior of the hardened paste.

In summary, FA contributes to the reduction of drying shrinkage in mortar specimens under low vacuum condition. This is because the hydration rate and degree of FA are much lower than that of cement, and the pozzolanic effect takes a long time to manifest, which, due to the inhibition of hydration, leads to a reduction in system shrinkage. On the other hand, the elastic modulus of fly ash particles is also higher than that of cement particles, which can limit the shrinkage of the paste to some extent [29]. SF has shown different shrinkage reduction capabilities under different drying conditions. Ding and Li [30] found that silica fume can lead to earlier cracking in concrete. Under low-vacuum drying, where water evaporation is rapid, this may further cause earlier cracking in silica fume mortar, reducing its ability to resist drying shrinkage. SRA can reduce the interfacial tension in the liquid phase of the capillary, and decrease water evaporation, thereby reducing shrinkage and improving crack resistance [31]. SF and SRA achieve synergistic shrinkage mitigation due to the different mechanisms of shrinkage reduction. NS can accelerate its hydration mechanism and pore refinement effect, reduce the water loss of hardened cement paste, and decrease its drying shrinkage [32]. PVA, as a water-soluble polymer, can react with cement to form new compounds, enhancing the bonding performance between cement particles and between cement paste and aggregate, thus resisting drying shrinkage [33]. However, PVA can delay the early hydration of cement to some extent, which leads to a lower hydration degree in early-age mortar specimens and a reduced ability to resist strong drying under low-vacuum condition [23]. PP can bridge microcracks in the hardened paste to limit water flow and reduce drying shrinkage [34]. However, due to the smooth and hydrophobic nature of PP, especially when its ends are exposed on the specimen surface, water evaporation may accelerate [35]; additionally, PP can promote an increase in the number of meniscus pores, leading to higher capillary stress and increased shrinkage [35].

Fig. 5 presents the drying shrinkage results of concrete under two drying environments. It is evident that the drying shrinkage process of concrete is largely consistent with that of mortar, but due to the constraint effect of coarse aggregate, longer pre-curing time,

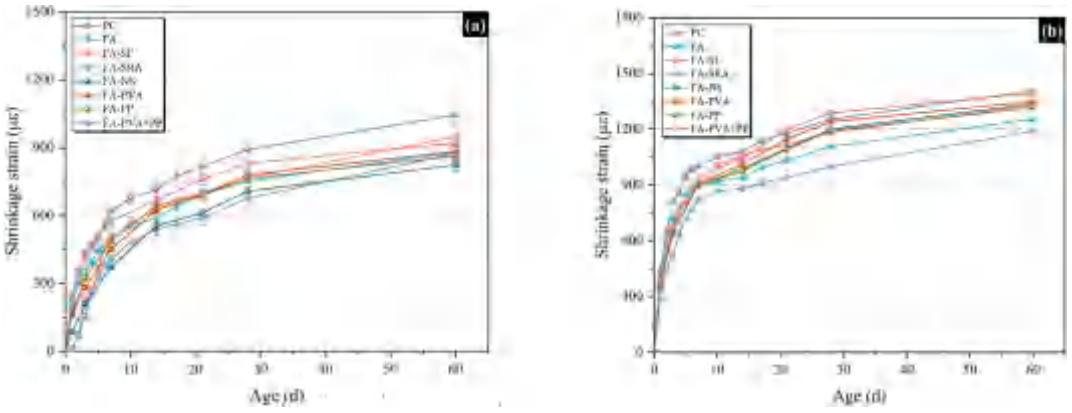


Fig. 4. Drying shrinkage values of mortar: (a) standard drying environment; (b) low-vacuum drying environment.

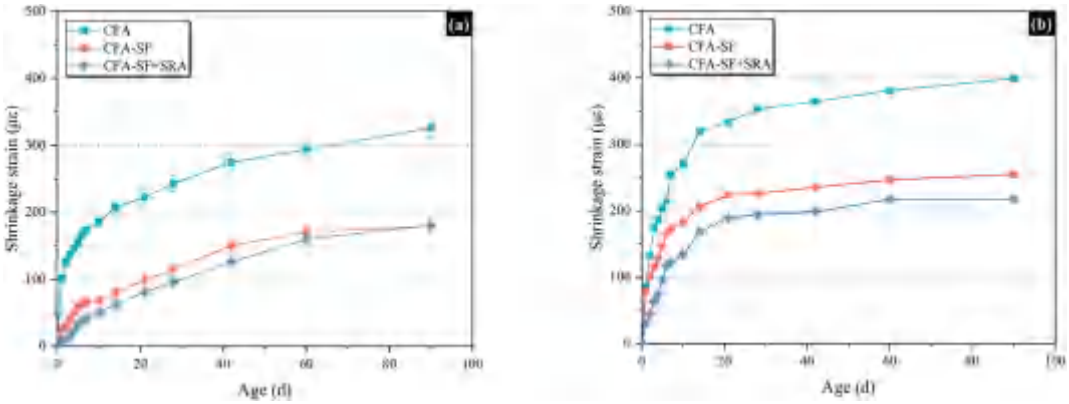


Fig. 5. Drying shrinkage values of concrete: (a) standard drying environment; (b) low-vacuum drying environment.

and size effect [36], the shrinkage is significantly lower than that of mortar. For the standard drying environment, the final shrinkage values of the control and shrinkage-reducing concrete groups were no more than 350×10^{-6} and 200×10^{-6}, respectively; for the low-vacuum drying environment, these values increased to 400×10^{-6} and 250×10^{-6}, respectively. Unlike mortar specimens, SF exhibited a strong shrinkage-reducing effect in concrete, which could reduce the final shrinkage values under SD and VD by 45 % and 36 %, respectively. Furthermore, SRA and SF achieved a synergistic shrinkage-reducing effect, keeping both early and late shrinkage of concrete within a low range. The reason for the difference in the shrinkage-reducing effect of SF may be related to the pre-curing age of mortar and concrete specimens. Mortar was exposed to the drying environment after 3 d of pre-curing, and water began to evaporate from the inside out, continuously losing moisture. Due to the fine nature of SF particles, which increases water demand, its strong pozzolanic effect and pore refinement mechanism can lead to increased mortar drying shrinkage [37]. For concrete, exposure to the drying environment begins at 28 d, by which time the concrete specimens, having undergone sufficient wet curing, have fully established their internal pore structure, with strong resistance to water loss caused by drying. The micro-aggregate and pozzolanic effects of SF are beneficial in strengthening this process, thereby alleviating the drying shrinkage of concrete.

Overall, for shrinkage-reducing components to achieve sufficient shrinkage-reduction effects, cement-based materials need to undergo a longer period of pre-curing. Otherwise, the negative effects brought by the low-vacuum environment may counteract the beneficial impacts of the shrinkage-reduction mechanisms.

Fig. 6 illustrates the drying shrinkage results of coated protective mortar under a low-vacuum environment. It was observed that the drying shrinkage deformation of the specimens significantly increased after low-vacuum exposure compared to those under standard drying condition. The shrinkage strain of the coated specimens decreased noticeably compared to the control group, but the shrinkage reduction effects of different coating materials were not significantly different. PUA coating reduced the 60-day shrinkage by 25 %, while WAC and PU coatings reduced the shrinkage by 22 % and 20 %, respectively, demonstrating the effectiveness of these organic coatings in inhibiting drying shrinkage. Overall, the hydrophobic groups in the organic coatings impart strong hydrophobicity, not only forming a dense barrier structure on the mortar surface [27] but also penetrating the pores of the cement matrix and forming a hydrophobic film [38]. Additionally, the retention of moisture helps in the continued hydration of cement, forming a stable

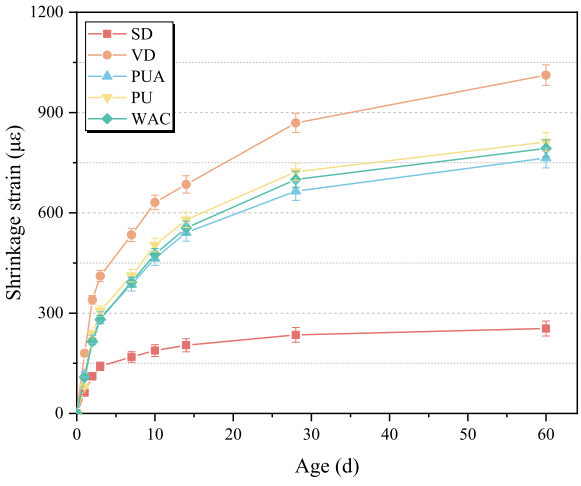


Fig. 6. Drying shrinkage values of coated mortar.

microstructure that resists drying shrinkage deformation. It should be noted that compared to WAC and PU coatings, PUA coatings possess excellent waterproof sealing properties and exhibit good flexibility and elongation characteristics [39,40]. This allows them to adhere better to concrete substrates and resist cracking caused by drying shrinkage, thus providing the best shrinkage reduction effect.

To analyze the shrinkage behavior of cement-based materials in different stages of the whole shrinkage cycle, the shrinkage rate of cement-based materials in different time intervals is calculated, and the calculation method is shown in Eq. (4).

$$\Delta v_\varepsilon(t) = \frac{\Delta \varepsilon(t)}{\Delta t} \tag{4}$$

where Δt is the time interval, d; $\Delta v_\varepsilon(t)$ is the shrinkage rates at different time intervals, με/d.

The calculation results of the shrinkage rate are summarized in Fig. 7. It is evident that the shrinkage rate of cement-based materials under a low-vacuum environment is significantly higher than that under standard drying condition. The patterns of mortar and concrete shrinkage rate in the first 3 d under various drying conditions are generally consistent. After 14 d, the shrinkage rate remains within a very small range, tending to be constant. For mortar, the incorporation of shrinkage-reducing components all reduced the early shrinkage rate of the specimens, with the FA-SRA group having the lowest shrinkage rate, which was 64 % and 35 % lower than that of the PC group under standard and low-vacuum drying, respectively. The FA-PVA + PP group had the least effective shrinkage reduction, with the shrinkage rate only decreasing by 5 % and 17 %, respectively. For concrete, SF and SRA significantly reduced the early drying rate of the specimens, with the CFA-SF and CFA-SF + SRA groups having drying rates 34 % and 63 % lower than that of the CFA group under low-vacuum condition, respectively. However, it is worth noting that although SRA plays a better role in reducing the drying shrinkage of cementitious materials, it is mainly manifested at an early age. It is observed that after 3 d of drying under low-vacuum condition, the drying rate of SRA-containing mortar and concrete is higher than that of their control groups This suggests that the shrinkage reduction effect of SRA on cementitious materials at the later stage is not significant, which is attributed to its inhibitory effect on hydration, and the related inhibitory mechanism has been well explained [41,42]. Consistent with the shrinkage strain law, the three types of coatings have a similar pattern of shrinkage rate development, and the shrinkage reduction effect is not significant among each other, but all of them can reduce the shrinkage rate of the specimens at an early age by about 30 %.

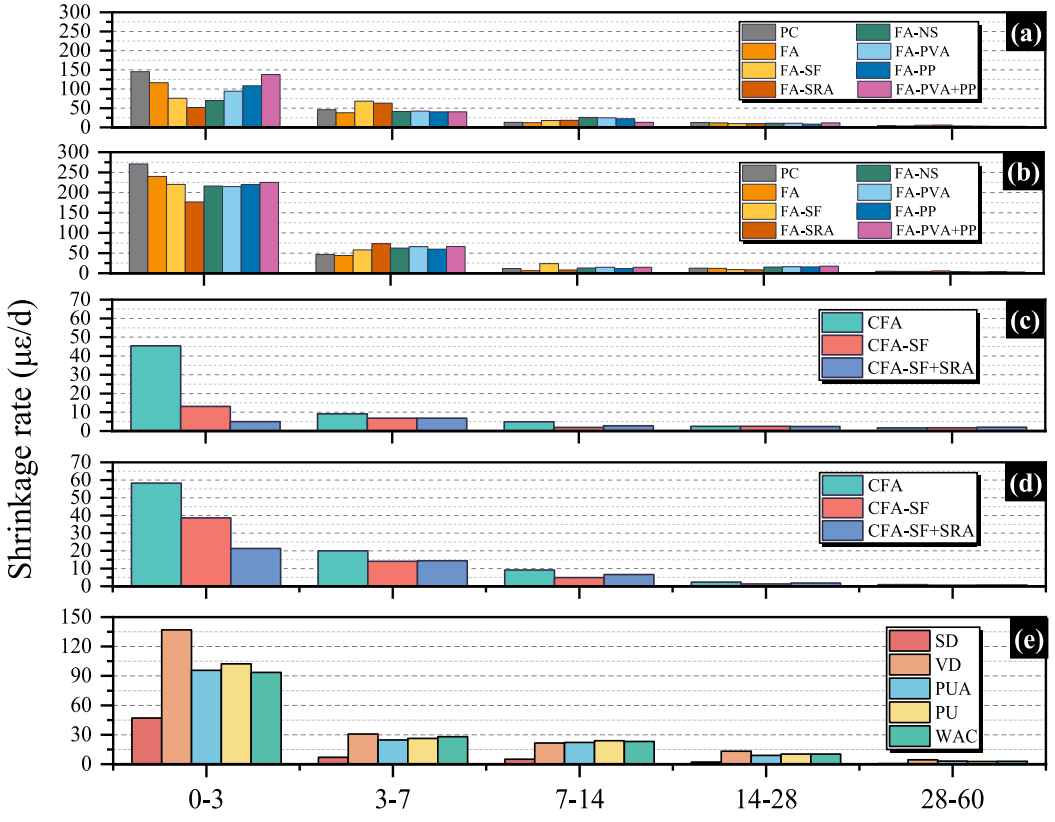


Fig. 7. Shrinkage rates of mortar and concrete under different drying environments: (a) mortar under standard drying; (b) mortar under low-vacuum drying; (c) concrete under standard drying; (d) concrete under low-vacuum drying; (e) coated mortar.

3.2. Mass loss of specimens

Fig. 8 depicts the mass loss results of mortar under standard drying and low-vacuum drying conditions. The results show that mass loss increases rapidly in the first 7 d and tends to stabilize after 28 d, similar to the shrinkage pattern. Under low-vacuum condition, the mass loss rate of mortar can exceed more than twice that under standard drying. Unlike shrinkage, the mass loss of FA group specimens under different drying conditions was higher than that of the PC group. The mass loss rate at 60 d increased by 32 % and 12 % under standard and low-vacuum conditions, respectively. This is mainly because the pozzolanic effect of FA has not yet manifested, leading to a lower hydration degree in the FA group compared to the PC group at the same age. The more porous structure allows moisture to escape more easily in a drying environment. For the standard drying environment, the addition of other shrinkage-reducing components to the FA group can alleviate mass loss to some extent. Among them, the effects of SF and SRA are relatively poor, while NS and PVA perform better, even achieving mass loss rates lower than the PC group.

Under low-vacuum drying conditions, the mass loss of all shrinkage-reducing groups exceeded that of the control group. The addition of other shrinkage-reducing components to the FA group even further exacerbated the mass loss of the mortar specimens, exhibiting a pattern opposite to that under standard drying condition. Compared with the PC group, the mass loss at 60 d increased by 15 %, 25 %, 26 %, 17 %, and 22 % for the FS-SRA, FA-NS, FA-PVA, FA-PP, and FA-PVA + PP groups, respectively. The reason for the above differences might be due to the coarsening of pores caused by the low-vacuum and shrinkage-reducing components, resulting in a higher proportion of large interconnected capillary pores in the matrix. These pores form pathways for moisture loss. While the moisture loss from these pores has little impact on shrinkage, it significantly increases the mass loss rate [10].

Further research on the mass loss results of concrete under different drying environments is shown in Fig. 9. It is observed that the mass loss rate of concrete under low-vacuum drying can exceed more than three times that under standard drying condition. Under standard drying condition, SF significantly reduced the mass loss rate of concrete at 60 d, with a reduction of up to 36 %. The synergistic effect of SF and SRA was not very pronounced. Compared to CFA, the mass loss rates of CFA-SF and CFA-SF + SRA under low-vacuum condition were reduced by 22 % and 31 %, respectively. By comparing with Fig. 5, it is not difficult to find that the shrinkage and mass loss patterns of concrete are generally consistent. Concrete specimens that have undergone a longer period of pre-curing have a more complex pore structure, and the loss of moisture often accompanies the formation of menisci, thus maintaining a good correlation between shrinkage and mass loss.

Fig. 10 presents the mass loss results of different coated mortars under standard drying and low-vacuum drying conditions. By comparing the mass loss of specimens under two environments, it can be observed that the mass loss of the PUA, PU, and WAC groups at 60 d decreased by 25 %, 20 %, and 22 %, respectively, compared to the control group. The outstanding film-forming ability, low permeability to air and water, high crosslinking density, and intermolecular forces of the organic coatings enable them to maintain the moisture of the cement matrix and inhibit the evaporation of water vapor. Additionally, the barrier films formed by organic coatings possess a certain degree of elasticity, allowing them to accommodate slight deformations of the matrix, thereby inhibiting the initiation of microcracks. This results in minimal mass loss, thereby resisting durability issues caused by drying shrinkage.

Similar to the shrinkage rate, the drying rate of cement-based materials over different time intervals was calculated using the method shown in Equation (5).

$$\Delta v_m(t) = \frac{\Delta(\Delta w_t)}{\Delta t} \tag{5}$$

where $\Delta v_m(t)$ is the drying rates at different time intervals, d^{-1}.

The drying rate calculations are summarized in Fig. 11. It can be observed that the overall trend of the drying rate of cement-based materials is similar to the shrinkage rate, being relatively high at an early age and stabilizing after 14 d. NS is most effective in suppressing the development of the drying rate at an early stage, while SF shows opposite effects under different drying conditions.

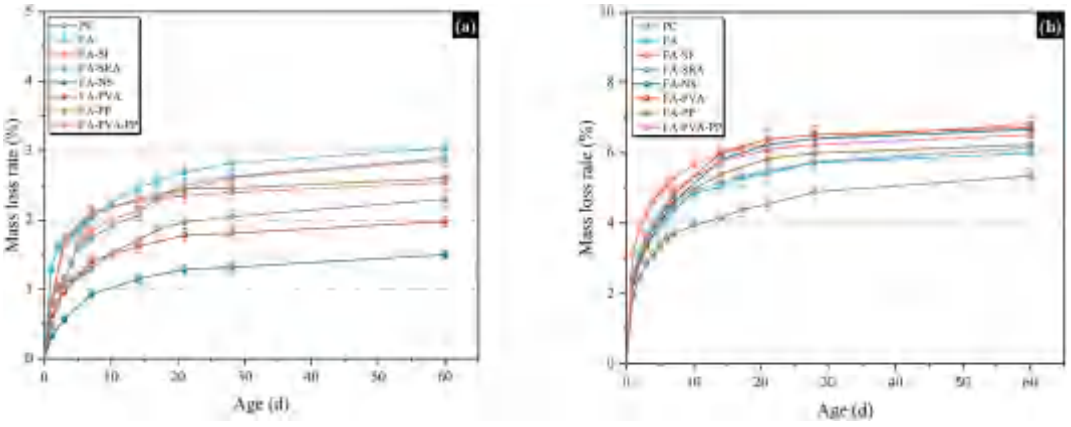


Fig. 8. Mass loss rate of mortar: (a) standard drying environment; (b) low-vacuum drying environment.

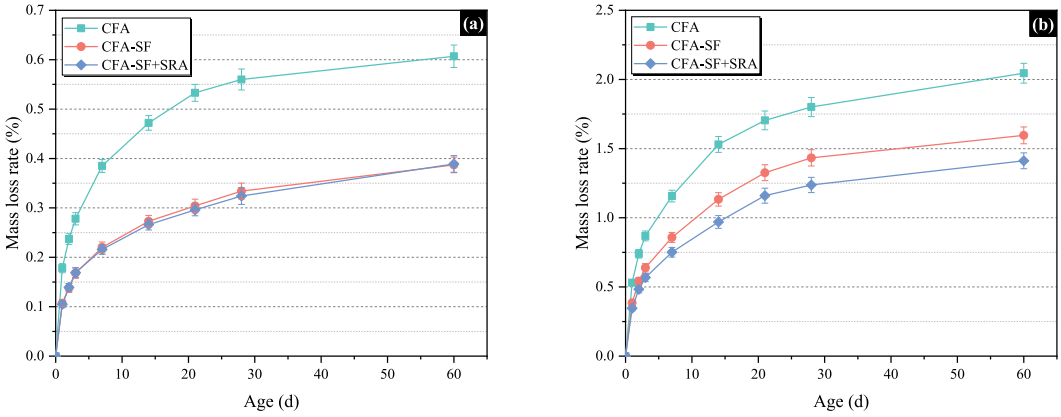


Fig. 9. Mass loss rate of concrete: (a) standard drying environment; (b) low-vacuum drying environment.

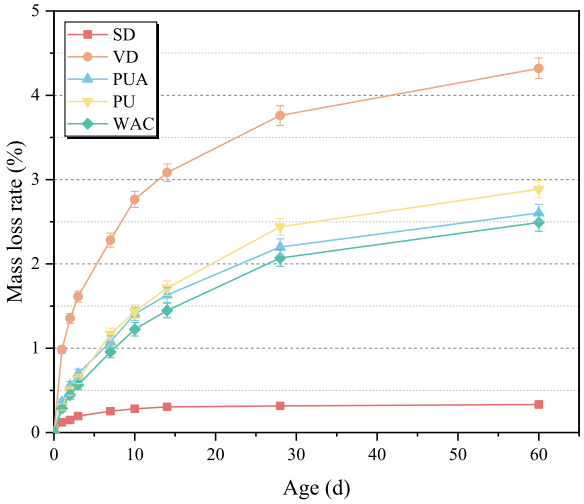


Fig. 10. Mass loss rate of coated mortar.

Combining previous analyses, it appears that SF can only exert its shrinkage-reducing and water-retaining effects when cement-based materials are fully cured and then exposed to dry environments. For instance, SF can reduce the drying rate of concrete from 0 to 3 days by 40 % in standard drying condition and by 26 % under low vacuum. Conversely, the drying rate of mortar from 0 to 3 days is highest under low vacuum, likely due to its morphology and pozzolanic effects. SRA does not significantly enhance the water retention capacity in concrete, whereas coatings effectively reduce the water loss rate of specimens, with no significant differences among the three types of coatings.

3.3. Relationship between drying shrinkage and mass loss

Based on the above conclusions, the shrinkage and mass loss behavior of mortar and concrete in a low-vacuum environment are closely related. It is necessary to further clarify the relationship between them to explore the underlying drying shrinkage mechanism. Fig. 12 summarizes the maximum shrinkage strain and mass loss rate of cement-based materials under standard drying and low-vacuum drying conditions. The results show a good correlation between the maximum shrinkage and mass loss of cement-based materials in a low-vacuum environment. Except for certain mortar specimens, specimens with larger shrinkage values generally correspond to higher mass loss. This correlation is particularly significant for concrete and coated mortar specimens with longer pre-curing periods. Establishing the corresponding relational function will help further understand the drying shrinkage mechanism of cement-based materials under low-vacuum drying conditions.

The relationship between the shrinkage values and mass loss rates of different specimens is shown in Fig. 13. It can be observed that for different specimens, regardless of whether they are under standard drying or low-vacuum drying condition, there is a strong positive correlation between the drying shrinkage and mass loss, a phenomenon that has been well-established in previous studies [5, 43–45]. To further characterize the correlation between the two, the parameter known as the hydrous compressibility factor (CF) [5]

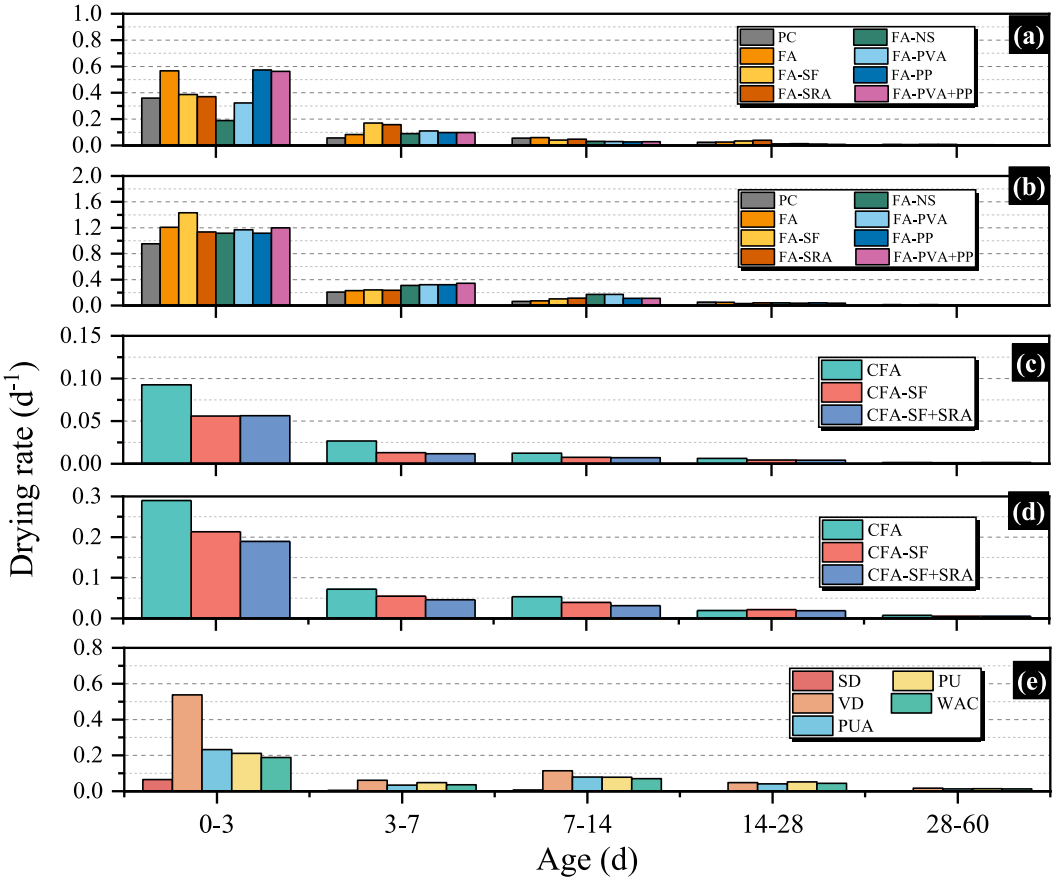


Fig. 11. Drying rates of mortar and concrete under different drying environments: (a) mortar under standard drying; (b) mortar under low-vacuum drying; (c) concrete under standard drying; (d) concrete under low-vacuum drying; (e) coated mortar under low-vacuum drying.

was introduced. A linear fit was performed on the data points in Fig. 13, and the slope of the curve represents the CF, reflecting the intrinsic relationship between the two. The parameter fitting results are shown in Table 3.

As shown in Table 3, there is a good linear relationship between the shrinkage strain and mass loss rate of cement-based materials under different drying environments, with correlation coefficients exceeding 0.95. By comparing the CF values, it can be concluded that the CF values under low-vacuum condition are significantly smaller than those under standard drying condition. The CF value of the mortar is only about 50 % under standard drying condition, while the CF value of the concrete decreases to approximately 40 %. This means that under the same water loss condition, the drying shrinkage deformation of the paste in a low-vacuum environment is smaller. The mass loss is mainly due to the rapid evaporation of water through larger capillary pores on the specimen surface. The presence of large pores leads to a rapid decline in internal RH of the specimen, while not forming sufficiently high capillary stress. According to previous research [9], the coarsening of pores caused by a low-vacuum environment increases the number of large capillary pores. The water loss from these large capillary pores has little impact on shrinkage but increases the mass loss of the specimen, leading to a reduced sensitivity of shrinkage to mass loss for cement-based materials under low-vacuum condition. It is worth mentioning that the RH under low-vacuum condition approaches 0 %, and the sustained large humidity gradient causes the internal humidity of the cement-based materials to gradually decrease to maintain equilibrium. At such low humidity, the interlayer water in the C-S-H gel will also be lost, leading to irreversible shrinkage of the matrix [26]. At this point, the sensitivity of shrinkage to water loss may significantly increase.

Further comparison was made regarding the impact of different shrinkage-reducing components on the CF value. It is evident that the shrinkage-reducing components effectively lower the CF value of cement-based materials, resulting in reduced drying shrinkage and decreased sensitivity to shrinkage under the same water loss condition. For mortar, NS raises the shrinkage sensitivity of specimens under standard drying to the highest level (CF value increased by 90 %) but reduces it to the lowest level (CF value decreased by 90 %) under low-vacuum drying, which is related to its pore refinement mechanism. The nucleation effect of NS promotes the formation of more small capillary pores related to shrinkage [21], increasing the sensitivity of the matrix to water loss. The pore coarsening caused by the low-vacuum environment counteracts the pore refinement effect of NS, reducing the shrinkage sensitivity [5]. SF, SRA, and PVA reduced the CF value by 1.5 %, 5.4 %, and 5.0 % respectively, which helps decrease the shrinkage sensitivity of mortar in low vacuum environments. As expected, the combined use of PP fibers and PVA increased the shrinkage sensitivity of the mortar by 3.5 %. For

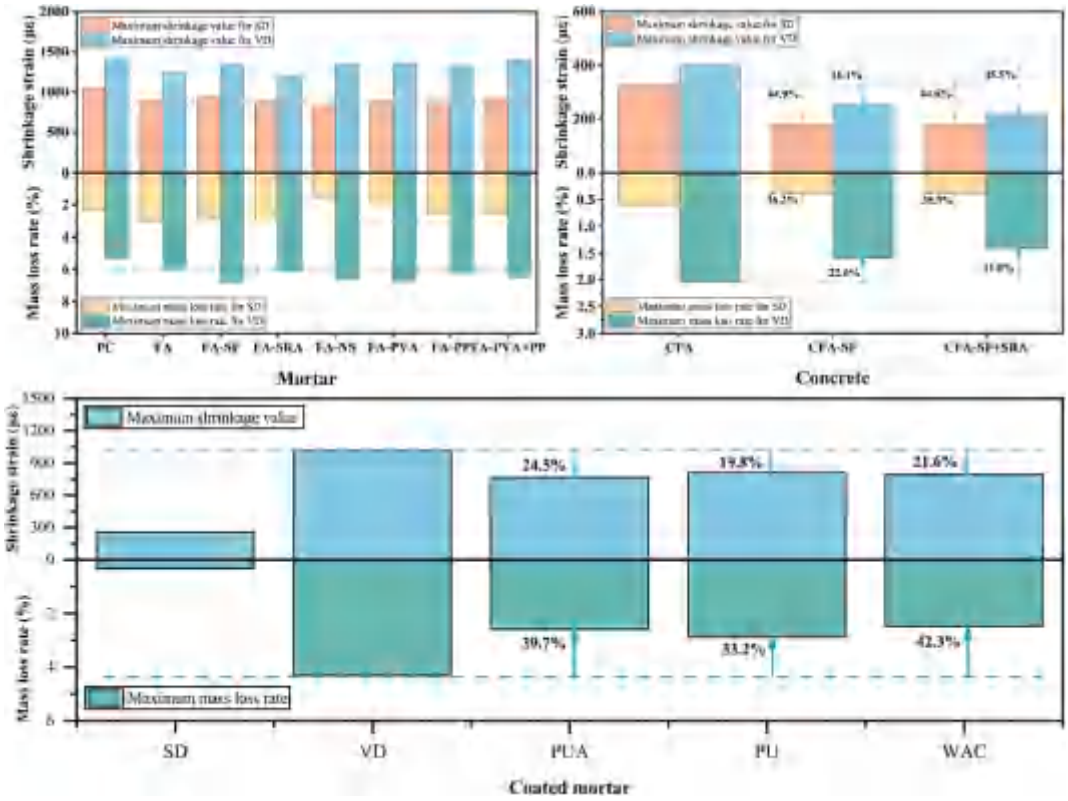


Fig. 12. Statistical results of maximum shrinkage value and mass loss rate.

concrete, SF and SRA can reduce its shrinkage sensitivity in low vacuum environment. Interestingly, the coating increases the shrinkage sensitivity of the specimens. The dense organic film formed on the coating surface can effectively prevent moisture from escaping from the interior of the concrete [38]. As a result, the release of water vapor is slowed over the same period, making it especially difficult for moisture in small pores to disperse. As is well known, the water loss from these size pores will lead to significant drying shrinkage behavior.

3.4. Drying shrinkage prediction model

Based on theoretical and experimental research, commonly used conventional concrete drying shrinkage models include the ACI209R-92 model, Bazant models (B3/B4 models), and GL2000 model [46,47]. The specific information of these models is summarized in Table 4, and the relevant parameter information can be found in Refs. [48–52].

Considering the water-to-binder ratio of 0.3 for the concrete in this study, and combined with previous experimental results [8], it is expected that the average compressive strength of the concrete at 28 d under standard curing can reach 60 MPa. Therefore, it is assumed that the value of f_{cm} (mean compressive strength) is 60 MPa. The values of the other parameters are determined according to the methods in Refs. [51–53]. Fig. 14 shows the comparison between the shrinkage calculation results of the aforementioned models and the experimental shrinkage results of concrete under a low-vacuum environment in this study. The comparison reveals that all four types of models have certain deviations in predicting concrete shrinkage. The ACI209R-92 model and the CEB-FIP-90 model predict results that are too low, which is due to these two models usually applying to dry environments with RH greater than 40 % [48]. However, the RH under a low-vacuum environment is extremely low, which accelerates the shrinkage rate, causing the models to underestimate the shrinkage of the concrete. The B3 and B4 models take into account factors such as the composition of the concrete, environmental conditions, curing time, and structural dimensions, but they underestimate the early shrinkage rate of the concrete under low-vacuum condition and overestimate the later shrinkage rate. The GL2000 model applies to environmental humidity levels down to 20 % and considers the impact of strength factors [54]. Therefore, its predictions are larger compared to other models, but the predictive deviation also increases with age.

To evaluate the applicability of various shrinkage models for high-strength concrete under low-vacuum condition based on the B3 coefficient of variation method proposed by Bazant [49], the specific calculation formula would typically involve the following steps:

$$\overline{w}_j = \sqrt{\frac{1}{n-1}\sum_{i=1}^{n}\left(w_{ij}\Delta_{ij}\right)^2} \tag{6}$$

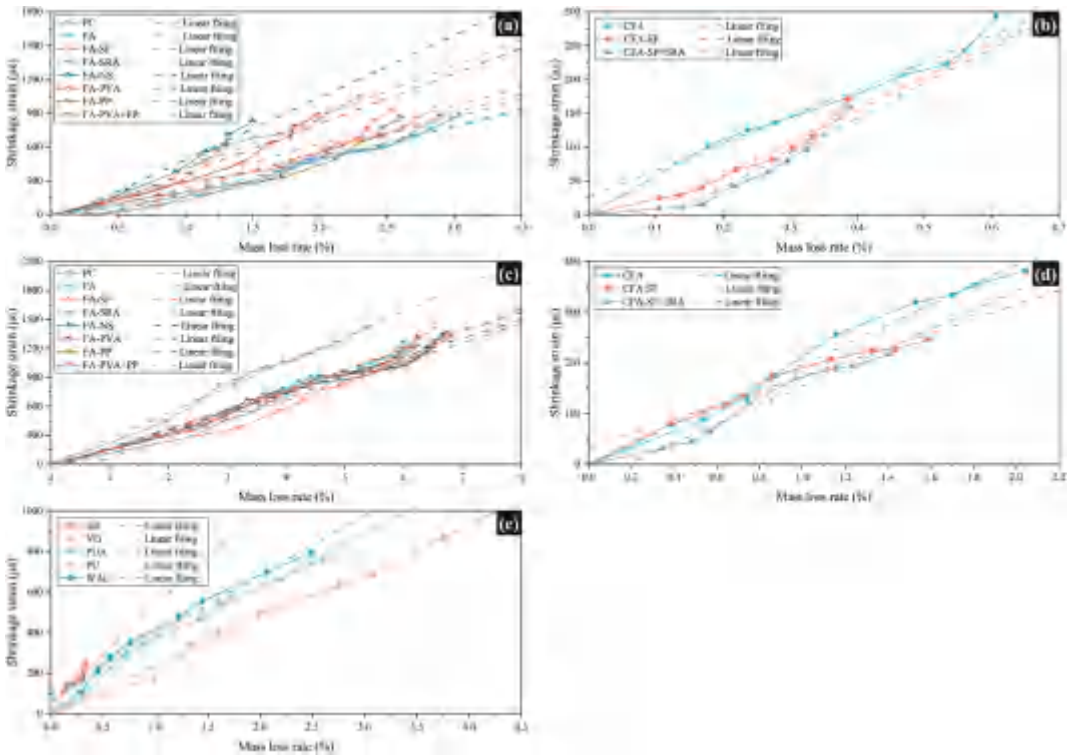


Fig. 13. The relationship between shrinkage value and mass loss rate of specimens under different drying environments: (a) mortar under standard drying; (b) concrete under standard drying; (c) mortar under low-vacuum drying; (d) concrete under low-vacuum drying; (e) coated mortar under low-vacuum drying.

Table 3
Fitting results between drying shrinkage and mass loss rate.

Group		Equation	CF		*B*		R^2	
			SD	VD	SD	VD	SD	VD
Mortar	PC	$y = CF{\cdot}x + B$	458	264	−52	4	0.96992	0.98963
	FA		291	202	−98	−36	0.95275	0.98215
	FA-SF		346	199	−138	−136	0.95862	0.95948
	FA-SRA		303	191	−119	−72	0.95314	0.96914
	FA-NS		554	189	−69	−16	0.97013	0.98101
	FA-PVA		446	192	−83	−42	0.95357	0.98032
	FA-PP		313	202	−72	−38	0.91603	0.98321
	FA-PVA + PP		334	209	−37	−61	0.93986	0.98184
Concrete	CFA		400	198	25	−2	0.96357	0.97631
	CFA-SF		483	142	−39	31	0.94344	0.96776
	CFA-SF + SRA		516	188	−63	−34	0.93486	0.97142
Coated mortar	SD		477		54		0.72126	
	VD		231		5		0.98761	
	PUA		274		72		0.98346	
	PU		257		106		0.95830	
	WAC		295		92		0.97626	

Table 4
Classical shrinkage prediction models for concrete.

Model	Equation
ACI209R-92	$\varepsilon_s(t,t_0)=\left(\frac{t-t_0}{35+(t-t_0)}\right)\varepsilon_{su}$ (Parameters cannot be determined)
B3/B4	$\varepsilon_s(t,t_0) = -k_h\varepsilon_{su,\infty}\tanh\sqrt{\frac{t-t_0}{\tau_{sh}}}$
CEB-FIP-90	$\varepsilon_s(t,t_0) = [160+10\beta_{sc}(9-0.1f_{cm})]\times\beta_{RH}\sqrt{\frac{(t-t_0)}{350\times\left(\frac{2A_c}{100\mu}\right)+(t-t_0)}}$
GL2000	$\varepsilon_s(t,t_0) = 1000K\sqrt{\frac{30}{f_{cm}}}\times\left(1-1.18h^4\right)\sqrt{\frac{t-t_0}{t-t_0+0.15(V/S)^2}}$

Note: $\varepsilon_s(t,t_0)$ is the time-dependent shrinkage strain of concrete, 10^{-6}; t is the age of concrete, d; t_0 is the time when the drying shrinkage test begins, d.

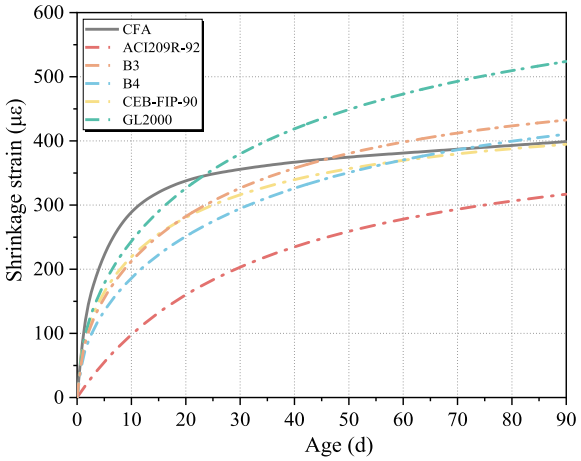


Fig. 14. Comparison of experimental values of drying shrinkage evolution with predicted values from classical models.

$$w_{ij}=\frac{n}{n_d n_1} \tag{7}$$

$$\overline{w}_{total}=\sqrt{\frac{1}{N}\sum_{j=1}^{N}\overline{w}_j^{\,2}} \tag{8}$$

Where n is the total number of data points in the jth group; n_1 is the number of data points in the k-th period; n_d is the number of periods included in the j-th group of data; N is the total number of data groups; Δ_{ij} is the absolute difference between the experimental value and the predicted value from the model for the ith data point in the j-th group; w_{ij} is the weight of the i-th data point in the j-th group; $\overline{w}_j$ is the coefficient of variation for the j-th group of data; $\overline{w}_{total}$ is the total characteristic coefficient of variation.

For a given model, the smaller the $\overline{w}_{total}$, the higher the prediction accuracy and conformity of the model. Table 5 lists the total characteristic coefficients of variation for each model along with their rankings. It can be observed that the CEB-FIP-90 model has the smallest coefficient of variation, indicating the highest prediction accuracy. The B3 model follows closely behind, with a slightly larger but still small coefficient of variation compared to the CEB-FIP-90 model. The B4 model and the GL2000 model have lower prediction accuracy than the first two models, while the ACI209R-92 model has the lowest prediction accuracy.

Overall, the shrinkage of concrete under low-vacuum condition shows a trend of rapid increase in the early stages followed by a slower increase in the later stages. Traditional models not only tend to underestimate the early shrinkage of concrete but also gradually overestimate the long-term shrinkage. This discrepancy arises because most existing shrinkage calculation models primarily account for temperature and humidity parameters while neglecting the impact of low-vacuum (100 Pa) condition on concrete shrinkage, leading to differences between model predictions and actual field measurements. Additionally, when shrinkage-reducing components are incorporated into the concrete, the shrinkage inevitably decreases. The effect of shrinkage-reducing components on shrinkage is difficult for classical models to account for, further increasing the prediction bias.

From the results above, it is evident that current models struggle to accurately predict the shrinkage of concrete under low-vacuum condition, especially for specimens with different shrinkage-reducing components. To develop models that can predict the shrinkage

Table 5
Comparison of the accuracy of different shrinkage prediction models.

Model	Total Characteristic Coefficient of Variation	Rank.
ACI209R-92	139.5	5
B3	47.8	2
B4	64.7	4
CEB-FIP-90	42.6	1
GL2000	64.3	3

evolution of cement-based materials under low-vacuum condition, it is necessary to modify traditional models. Based on previous research, hyperbolic functions, logarithmic functions, and exponential functions have been frequently used to describe the shrinkage deformation of concrete. The specific mathematical expressions can be referred to in Eqs. (9)–(11).

Hyperbolic function

$$\text{model}: \varepsilon_s(t,t_0) = \frac{t-t_0}{a+b(t-t_0)} \tag{9}$$

Logarithmic function

$$\text{model}: \varepsilon_s(t,t_0) = a + b\ln[(t-t_0)+1) \tag{10}$$

Exponential function

$$\text{model}: \varepsilon_s(t,t_0) = \varepsilon_{su}\left(1-ae^{b(t-t_0)}\right) \tag{11}$$

where a and b are empirical parameters.

To further investigate which type of function is more suitable for predicting shrinkage under low-vacuum condition, experimental data were fitted using Eqs. (9)–(11). The fitting results are shown in Figs. 15–17; and the fitting correlation coefficients are summarized in Table 6. It can be observed that all three function models effectively simulate the shrinkage evolution of mortar, concrete, and coated mortar under low-vacuum condition; except for a few specific mixtures, the correlation coefficients (R^2) are mostly greater than 0.9. This indicates that the empirical equations of the three types of functions can be used to predict the time-dependent shrinkage deformation of cement-based materials under low-vacuum condition. Further comparison of different function models in terms of R^2 and residual sum of squares (RSS) reveals that the hyperbolic function provides a higher R^2 and a smaller RSS for predicting shrinkage

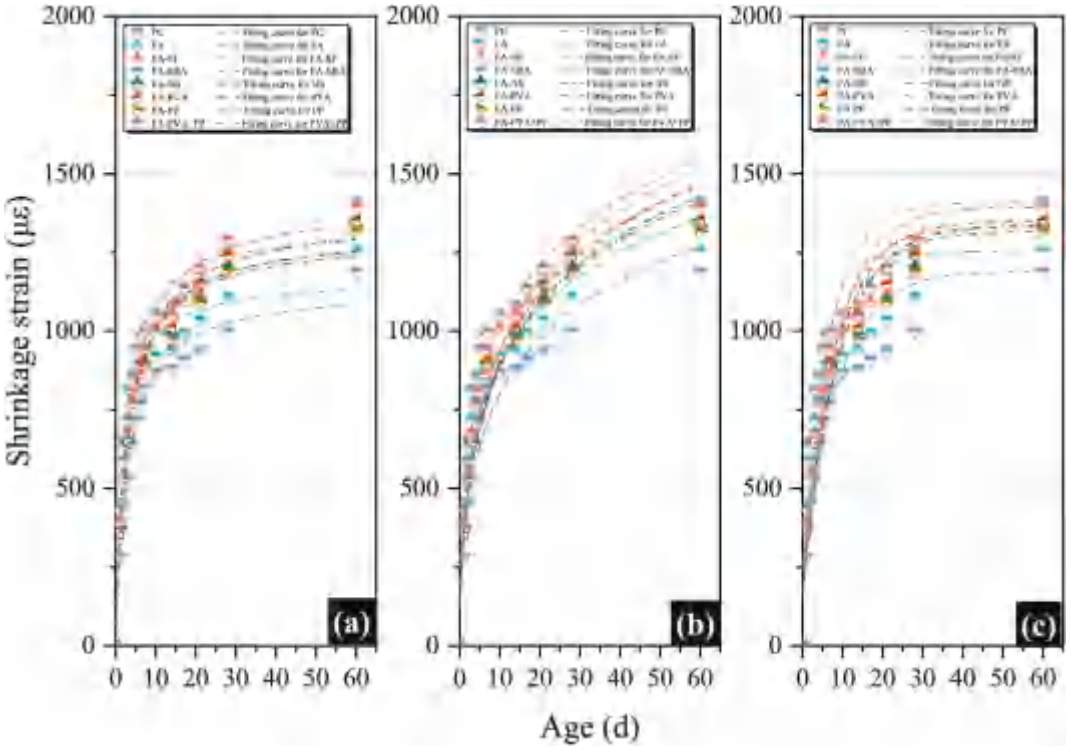


Fig. 15. Fitting of mortar shrinkage under low-vacuum drying condition: (a) hyperbolic function; (b) logarithmic function; (c) exponential function.

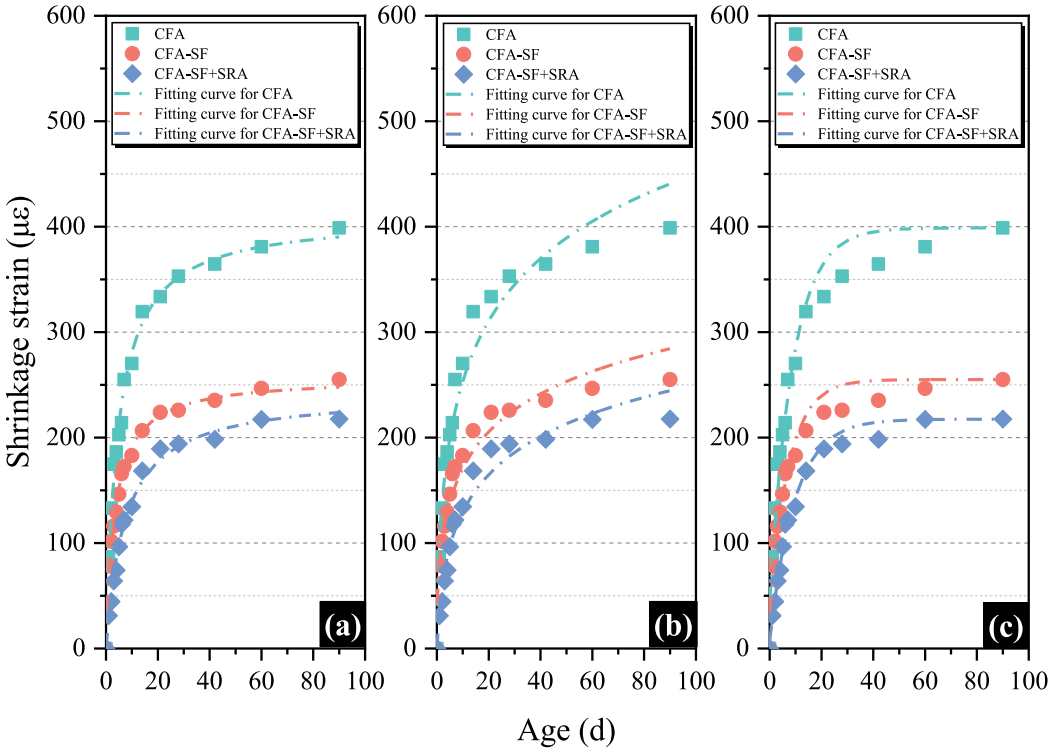


Fig. 16. Fitting of concrete shrinkage under low-vacuum drying condition: (a) hyperbolic function; (b) logarithmic function; (c) exponential function.

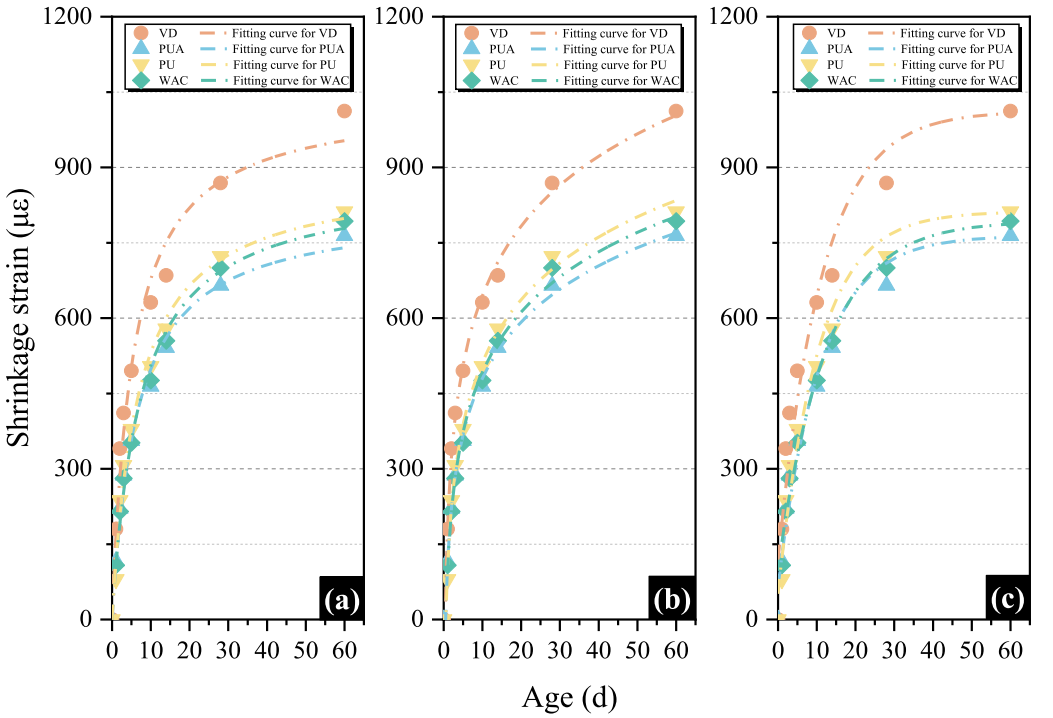


Fig. 17. Fitting of coated mortar shrinkage under low-vacuum drying condition: (a) hyperbolic function; (b) logarithmic function; (c) exponential function.

Table 6
Fitting correlation coefficients of different prediction models.

Group		Correlation coefficient (R^2) and Residual sum of squares (RSS)					
		Hyperbolic function		Logarithmic function		Exponential function	
		R^2	RSS × 10^3	R^2	RSS × 10^3	R^2	RSS × 10^3
Mortar	PC	0.98353	27.8	0.90625	158.2	0.85911	237.8
	FA	0.97688	30.2	0.89344	139.2	0.83019	221.8
	FA-SF	0.99252	12.2	0.94744	85.4	0.92023	129.6
	FA-SRA	0.98198	22.8	0.94289	72.4	0.88219	149.4
	FA-NS	0.98531	20.9	0.96857	44.7	0.92963	100.1
	FA-PVA	0.99031	14.8	0.97057	44.9	0.94717	80.5
	FA-PP	0.98558	20.0	0.96399	50.0	0.92706	101.3
	FA-PVA + PP	0.98876	18.2	0.96789	51.9	0.94564	87.9
Concrete	CFA	0.99322	1.3	0.95964	7.7	0.96280	7.1
	CFA-SF	0.98911	0.8	0.93676	4.5	0.94910	3.6
	CFA-SF + SRA	0.99101	0.6	0.96248	2.7	0.98846	0.8
Coated mortar	VD	0.98207	7.0	0.99782	4.6	0.95218	22.3
	PUA	0.99287	2.2	0.99826	0.7	0.97404	6.9
	PU	0.99215	4.4	0.99675	3.9	0.97464	9.7
	WAC	0.99272	2.4	0.99533	0.5	0.97101	3.5

in mortar and concrete, indicating the highest accuracy. In contrast, the exponential function has the lowest prediction accuracy. Interestingly, the logarithmic function shows higher accuracy in predicting the shrinkage of coated mortar, which may be related to the increased sensitivity of the mortar to shrinkage in low vacuum environments due to the organic coatings. This is consistent with the larger growth rate of the logarithmic function.

Considering that the hyperbolic function yields the best-fitting results, introducing relevant coefficients for the effects of shrinkage-reducing components and low-vacuum condition can achieve accurate predictions of concrete shrinkage deformation under low-vacuum environments. The following section will detail the process of establishing the prediction model.

Due to the behavior of concrete shrinkage under low-vacuum condition, which shows a rapid increase in the early stages and a gradual increase until stabilization in the later stages, fixing a final shrinkage value can prevent the model from continuously deviating in long-term predictions. Based on this, the basic formula for predicting concrete drying shrinkage under low-vacuum condition can be proposed as follows:

$$\varepsilon_s(t,t_0) = K_c K_{LV} \varepsilon_{su} \frac{t-t_0}{a+(t-t_0)} \tag{12}$$

where K_c is the shrinkage-reducing component influence coefficient; K_{LV} is the low-vacuum influence coefficient; a is an empirical parameter; ε_{su} is the final shrinkage value, determined according to the extrapolation formula in Ref. [55]. The specific calculation method is as follows:

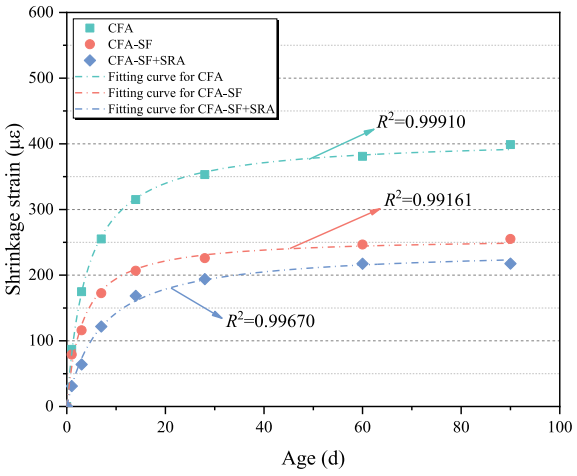


Fig. 18. Comparison of calculated and experimental results of concrete shrinkage model considering the low-vacuum environment and shrinkage-reducing components.

$$\varepsilon_s(t,t_0)=\frac{(t-t_0)}{t_{50}+(t-t_0)}\varepsilon_{su} \tag{13}$$

where t_{50} is the time to reach half of the final shrinkage value, d. By establishing a linear fitting relationship between $1/\varepsilon_s(t,t_0)$ and $1/\varepsilon_{su}$ during the stable shrinkage development stage, the reciprocal of the intercept gives the value of ε_{su}.

Taking CFA as the control group, and considering the addition of SF and SRA as shrinkage-reducing components, which are beneficial for reducing the shrinkage deformation of concrete under low-vacuum condition,

K_c can be approximately expressed by Eq. (14).

$$K_c=\frac{c_s}{c+c_s} \tag{14}$$

where c_s is the dosage of mineral admixtures, and c is the empirical parameter.

Based on previous research and the experimental results of this study, the effect of low vacuum on concrete shrinkage is primarily due to its impact on the RH gradient in the environment and pore solution. Considering that the CEB-FIP-90 model has the highest prediction accuracy, its calculation formula for the humidity influence coefficient is introduced into the low-vacuum concrete shrinkage calculation model, specifically expressed as:

$$K_{LV}=1.55\left[1-\left(\frac{h}{h_0}\right)^3\right] \tag{15}$$

where h is the environmental RH, which is taken as 0.05 in a low-vacuum environment; and h_0 is the 100 % RH, which is taken as 1.

Therefore, the shrinkage strain formula for concrete under low-vacuum condition can be expressed as:

$$\varepsilon_s(t,t_0)=1.55\varepsilon_{su}\frac{c_s}{c+c_s}\left[1-\left(\frac{h}{h_0}\right)^3\right]\frac{t-t_0}{a+(t-t_0)} \tag{16}$$

Using Eq. (16) to fit the experimental data, the fitting results are shown in Fig. 18. As can be seen from the figure, the model fits well, with a correlation coefficient exceeding 0.99. This indicates a significant improvement in accuracy compared to the original hyperbolic model. This fully demonstrates the good predictive adaptability of the optimized shrinkage calculation model in a low-vacuum environment. Specifically, the optimized model considers the combined effects of the low-vacuum environment and shrinkage-reducing components on the shrinkage behavior of concrete, resulting in predictions that closely match actual conditions, thereby enhancing the predictive accuracy and reliability of the model.

4. Conclusion

Through drying shrinkage and mass loss test experiments, this study investigated the shrinkage characteristics of cement-based materials in low-vacuum environments, regulated by various shrinkage mitigation techniques. A model suitable for predicting concrete shrinkage evolution in low-vacuum environments has been established based on existing shrinkage models and experimental data. The results offer new insights into predicting and regulating concrete shrinkage in high-speed maglev low-vacuum tube environments. The conclusions can be drawn as follows.

(1) Low vacuum drying significantly increases the shrinkage of cement-based materials compared to standard drying condition. The shrinkage strain of mortar and concrete after 60 d of drying can reach 1.35 times and more than 1.2 times that of standard drying. Under low-vacuum drying condition, FA can reduce the 7-day and 60-day shrinkage of mortar by 16 % and 11 %, respectively. The addition of SRA can further reduce the 60-day shrinkage by 16 %. NS, PVA, and PP are effective only in reducing shrinkage for the first 7 d, but they can increase long-term shrinkage, with the combined shrinkage effect of PVA and PP being the least effective. SF exhibits a strong shrinkage reduction effect in concrete, reducing the final shrinkage value by 36 % in a low-vacuum environment. Additionally, SRA and SF achieve a synergistic shrinkage reduction effect, controlling both early and long-term shrinkage of concrete to a relatively low range. Organic coatings such as PUA, WAC, and PU can reduce the 28-day shrinkage of specimens by 23 %, 19 %, and 17 %, respectively, demonstrating good shrinkage reduction effects. Shrinkage of cementitious materials under low-vacuum environment mainly occurs in the early stage (0-7d), and the shrinkage rate tends to be close to 0 after 28d, which is maintained at a constant level.

(2) Under low-vacuum drying condition, the mass loss rate of mortar can exceed twice that under standard drying condition, and all shrinkage-reducing groups exhibit greater mass loss than the control group. For concrete, the mass loss rate under low-vacuum drying can exceed three times that of standard drying condition. The incorporation of SF and SRA can reduce the 28-day shrinkage by 42 %. The maximum mass loss rates of PUA, WAC, and PU groups' specimens decreased by 41.5 %, 45 %, and 35 %, respectively, compared to the control group.

(3) The linear fitting results indicate that there is a strong positive correlation between drying shrinkage and mass loss in cement-based materials, and the correlation coefficient can reach more than 0.95. The sensitivity of the shrinkage of cement-based materials to water loss under low-vacuum condition is weaker than that under standard drying condition. Shrinkage-

reducing components decrease the sensitivity to water loss, while coatings increase it. The difference in pore size distribution between the surface and the interior of the specimens is the reason for the non-uniform behavior of shrinkage and mass loss.

(4) A model has been established to predict the time-dependent evolution of concrete shrinkage under low-vacuum drying condition. The model is based on experimentally measured concrete shrinkage data and references classical concrete shrinkage models. The model employs a hyperbolic function, incorporating a shrinkage-reducing component influence coefficient and a low-vacuum influence coefficient to integrate the effects of the shrinkage-reducing component and low-vacuum conditions on shrinkage. The results show that the established shrinkage model has high predictive accuracy, with a correlation coefficient exceeding 0.99 and an error of less than 3 %. This model can serve as an important reference for future calculations of the shrinkage evolution of different concrete components under low-vacuum conditions.

CRediT authorship contribution statement

Zhaofei Long: Writing – review & editing, Writing – original draft, Conceptualization. **Guangcheng Long:** Writing – review & editing, Supervision, Project administration, Funding acquisition. **Yue Chen:** Methodology, Data curation. **Minghui Shangguan:** Supervision, Investigation. **Jilin Wang:** Visualization, Formal analysis. **Yuting Zhang:** Validation, Software. **Meihui Yi:** Data curation. **Ce Gao:** Resources, Project administration. **Zhuo Tang:** Writing – review & editing, Supervision.

Declaration of competing interest

The authors declare that they have no known competing financial interests or personal relationships that could have appeared to influence the work reported in this paper.

Acknowledgments

The authors are grateful to the financial support of the Program Fund of Nonmetallic Excellence and Innovation Center for Building Materials (No. 24TDA-1).

Data availability

Data will be made available on request.

References

[1] F. Michelberger, M. Plavec, K. Pyrek, P. Graf, The Hyperloop Concept Development, Possible Applications and Critical Analysis, Sustainable Rail Transport 4: Innovate Rail Research and Education, Springer International Publishing, Cham, 2021, pp. 341–367, https://doi.org/10.1007/978-3-030-82095-4.
[2] J. Park, L. Kim, S. Nam, I. Yeo, Performance evaluation of airtightness in concrete tube structures for super-speed train systems, Mag. Concr. Res. 65 (9) (2013) 535–545, https://doi.org/10.1680/macr.12.00161.
[3] H. Chang, X. Wang, Y. Wang, S. Li, J. Wang, J. Liu, P. Feng, Influence of low vacuum condition on mechanical performance and microstructure of hardened cement paste at early age, Construct. Build. Mater. 346 (2022) 128358, https://doi.org/10.1016/j.conbuildmat.2022.128358.
[4] X. Ge, Y. Ge, Y. Du, X. Cai, Effect of low air pressure on mechanical properties and shrinkage of concrete, Mag. Concr. Res. 70 (18) (2018) 919–927, https://doi.org/10.1680/jmacr.17.00305.
[5] G. Long, Y. Chen, Z. Tang, M. Shangguan, C. Gao, S. Xu, Drying shrinkage behavior of cement mortar under low vacuum conditions, Construct. Build. Mater. 374 (2023) 130933, https://doi.org/10.1016/j.conbuildmat.2023.130933.
[6] H. Kanamori, S. Matsumoto, N. Ishikawad, Long-term properties of mortar exposed to a vacuum, Lunar Concr. ACI 125 (1991) 57–70, https://doi.org/10.14359/2415.
[7] M. Shangguan, Y. Xie, F. Wang, G. Long, Z. Tang, Y. Chen, S. Xu, H. Li, C. Gao, M. Liu, Effect of low-vacuum environment on the strength and permeability of cement-based materials, Construct. Build. Mater. 400 (2023) 132676, https://doi.org/10.1016/j.conbuildmat.2023.132676.
[8] M. Shangguan, Y. Xie, S. Xu, C. Gao, G. Long, F. Wang, M. Liu, Mechanical properties characteristics of high strength concrete exposed to low vacuum environment, J. Build. Eng. 63 (2023) 105438, https://doi.org/10.1016/j.jobe.2022.105438.
[9] M. Shangguan, Y. Xie, G. Long, Z. Long, F. Wang, Y. Chen, C. Gao, Z. Tang, Hydration and microstructure evolution of cement paste in low vacuum environments, Construct. Build. Mater. 438 (2024) 137233, https://doi.org/10.1016/j.conbuildmat.2024.137233.
[10] İ.B. Topçu, T. Bilir, Experimental investigation of drying shrinkage cracking of composite mortars incorporating crushed tile fine aggregate, Mater. Des. 31 (9) (2010) 4088–4097, https://doi.org/10.1016/j.matdes.2010.04.047.
[11] F. Collins, J.G. Sanjayan, Strength and shrinkage properties of alkali-activated slag concrete containing porous coarse aggregate, Cement Concr. Res. 29 (4) (1999) 607–610, https://doi.org/10.1016/S0008-8846(98)00203-8.
[12] M.C.G. Juenger, R. Siddique, Recent advances in understanding the role of supplementary cementitious materials in concrete, Cement Concr. Res. 78 (2015) 71–80, https://doi.org/10.1016/j.cemconres.2015.03.018.
[13] B.A. Gedam, N.M. Bhandari, A. Upadhyay, Influence of supplementary cementitious materials on shrinkage, creep, and durability of high-performance concrete, J. Mater. Civ. Eng. 24 (4) (2015) 04015173, https://doi.org/10.1061/(ASCE)MT.1943-5533.0001462.
[14] S.A. Kristiawan, M.T.M. Aditya, Effect of high volume fly ash on shrinkage of self-compacting concrete, Procedia Eng. 125 (2015) 705–712, https://doi.org/10.1016/j.proeng.2015.11.110.
[15] D. Dong, Y. Hung, Y. Pei, X. Zhang, N. Cui, P. Zhao, P. Hou, L. Lu, Effect of spherical silica fume and fly ash on the rheological property, fluidity, setting time, compressive strength, water resistance and drying shrinkage of magnesium ammonium phosphate cement, J. Build. Eng. 63 (2023) 105484, https://doi.org/10.1016/j.jobe.2022.105484.
[16] W.A. Al-Khaja, Strength and time-dependent deformations of silica fume concrete for use in Bahrain, Construct. Build. Mater. 8 (3) (1994) 169–172, https://doi.org/10.1016/S0950-0618(09)90030-7.
[17] J. Li, Y. Yao, A study on creep and drying shrinkage of high performance concrete, Cement Concr. Res. 31(8) 1203-1206 https://doi.org/10.1016/S0008-8846(01)00539-7.

[18] J. Saliba, E. Rozière, F. Grondin, A. Loukili, Influence of shrinkage-reducing admixtures on plastic and long-term shrinkage, Cem. Concr. Compos. 33 (2) (2011) 209–217, https://doi.org/10.1016/j.cemconcomp.2010.10.006.
[19] W. Zhang, M. Xue, X. Duan, Y. Jin, F. Su, Effect of polyether shrinkage reducing admixture on the drying shrinkage properties of alkali-activated slag, Cem. Concr. Compos. 136 (2023) 104865, https://doi.org/10.1016/j.cemconcomp.2022.10486.
[20] S.J. Lee, S. Kawashima, K.J. Kim, S.K. Woo, J.P. Won, Shrinkage characteristics and strength recovery of nanomaterials-cement composites, Compos. Struct. 202 (2018) 559–565, https://doi.org/10.1016/j.compstruct.2018.03.003.
[21] Y. Gao, B. He, Y. Li, J. Tang, L. Qu, Effects of nano-particles on improvement in wear resistance and drying shrinkage of road fly ash concrete, Construct. Build. Mater. 151 (2017) 228–235, https://doi.org/10.1016/j.conbuildmat.2017.06.080.
[22] S.C. Kou, C.S. Poon, Properties of concrete prepared with PVA-impregnated recycled concrete aggregates, Cem. Concr. Compos. 32 (8) (2010) 649–654, https://doi.org/10.1016/j.cemconcomp.2010.05.003.
[23] N.B. Singh, S. Rai, Effect of polyvinyl alcohol on the hydration of cement with rice husk ash, Cement Concr. Res. 31 (2) (2001) 239–243, https://doi.org/10.1016/S0008-8846(00)00475-0.
[24] T. Alomayri, M.T. Amir, B. Ali, S.S. Raza, M. Hamad, Mechanical, tidal erosion, and drying shrinkage behaviour of high performance seawater concrete incorporating the high volume of GGBS and polypropylene fibre, J. Build. Eng. 76 (2023) 107377, https://doi.org/10.1016/j.jobe.2023.107377.
[25] K. Aghaee, K.H. Khayat, Design and performance of fiber-reinforced shrinkage compensating eco-friendly concrete, Construct. Build. Mater. 408 (2023) 133803, https://doi.org/10.1016/j.conbuildmat.2023.133803.
[26] N.P. Tran, C. Gunasekara, D.W. Law, S. Houshyar, S. Setunge, A. Cwirzen, A critical review on drying shrinkage mitigation strategies in cement-based materials, J. Build. Eng. 38 (2021) 102210, https://doi.org/10.1016/j.jobe.2021.102210.
[27] M. Shangguan, Y. Xie, F. Wang, Y. Chen, Z. Tang, G. Long, S. Xu, H. Li, C. Gao, Preparation of coatings for moisture migration control of cementitious materials under low-vacuum environment, Mater. Lett. 355 (2024), https://doi.org/10.1016/j.matlet.2023.135553.
[28] M. Li, V.C. Li, Rheology, fiber dispersion, and robust properties of Engineered Cementitious Composites, Mater. Struct. 46 (2013) 405–420, https://doi.org/10.1617/s11527-012-9909-z.
[29] J. Liu, W. Sun, C. Miao, J. Liu, Effect of mineral admixtures on drying and autogenous shrinkage of concrete with low water-to-binder ratio, Journal of Southeast University(Natural Science Edition) 39 (3) (2009) 580–585, https://doi.org/10.3969/j.issn.1001-0505.2009.03.030 (In Chinese).
[30] J. Ding, Z. Li, Effects of metakaolin and silica fume on properties of concrete, ACI Mater. J. 99 (4) (2002) 393–398. https://www.researchgate.net/publication/279902244.
[31] W. Zhang, H. Lin, M. Xue, S. Wang, J. Ran, F. Su, Influence of shrinkage reducing admixtures on the performance of cementitious composites: a review, Construct. Build. Mater. 325 (2022) 126579, https://doi.org/10.1016/j.conbuildmat.2022.126579.
[32] R. Zhang, X. Chen, P. Hou, Z. Ye, Influences of nano-TiO_2 on the properties of cement-based materials: hydration and drying shrinkage, Construct. Build. Mater. 81 (2015) 35–41, https://doi.org/10.1016/j.conbuildmat.2015.02.003.
[33] J. H. Kim, R. E. Robertson, Effects of polyvinyl alcohol on aggregate–paste bond strength and the interfacial transition zone, Adv. Cement Base Mater. 8(2) 66-76 https://doi.org/10.1016/S1065-7355(98)00009-1.
[34] T. Alomayri, M.T. Amir, B. Ali, S.S. Raza, M. Hamad, Mechanical, tidal erosion, and drying shrinkage behaviour of high performance seawater concrete incorporating the high volume of GGBS and polypropylene fibre, J. Build. Eng. 76 (2023) 107377, https://doi.org/10.1016/j.jobe.2023.107377.
[35] T. Aly, J.G. Sanjayan, F. Collins, Effect of polypropylene fibers on shrinkage and cracking of concretes, Mater. Struct. 41 (2008) 1741–1753, https://doi.org/10.1617/s11527-008-9361-2.
[36] J.A. Almudaiheem, W. Hansen, Effect of specimen size and shape on drying shrinkage of concrete, ACI Mater. J. 84 (2) (1987) 130–135, https://doi.org/10.14359/1860.
[37] G.A. Rao, Long-term drying shrinkage of mortar — influence of silica fume and size of fine aggregate, Cement Concr. Res. 31 (2) (2001) 171–175, https://doi.org/10.1016/S0008-8846(00)00347-1.
[38] X. Pan, Z. Shi, C. Shi, T.C. Ling, N. Li, A review on concrete surface treatment Part I: types and mechanisms, Construct. Build. Mater. 132 (2017) 578–590, https://doi.org/10.1016/j.conbuildmat.2016.12.025.
[39] H.A. Toutanji, H. Choi, D. Wong, J.A. Gilbert, D.J. Alldredge, Applying a polyurea coating to high-performance organic cementitious materials, Construct. Build. Mater. 38 (2013) 1170–11779, https://doi.org/10.1016/j.conbuildmat.2012.09.041.
[40] D. Song, Q. Tan, Y.Y.Y. Cao, Y. Hu, Experimental investigation on blast and post-blast performance of reinforced concrete straight-wall arches strengthened with polyurea coating, Construct. Build. Mater. 385 (2023) 131352, https://doi.org/10.1016/j.conbuildmat.2023.131352.
[41] P. Zhan, Z. He, Application of shrinkage reducing admixture in concrete: a review, Construct. Build. Mater. 201 (2019) 676–690, https://doi.org/10.1016/j.conbuildmat.2018.12.209.
[42] I. Mehdipour, K.H. Khayat, Effect of shrinkage reducing admixture on early expansion and strength evolution of calcium sulfoaluminate blended cement, Cem. Concr. Compos. 92 (2018) 82–91, https://doi.org/10.1016/j.cemconcomp.2018.06.002.
[43] R. Jaafri, A. Aboulayt, S.Y. Alam, E. Roziere, A. Loukili, Natural hydraulic lime forblended cement mortars: behavior from fresh to hardened states, Cement Concr. Res. 120 (2019) 52–65, https://doi.org/10.1016/j.cemconres.2019.03.003.
[44] F. Benboudjema, F. Meftah, J.M. Torrenti, Interaction between drying, shrinkage, Interaction between drying, shrinkage, creep and cracking phenomena in concrete, Eng. Struct. 27 (2) (2005) 239–250, https://doi.org/10.1016/j.engstruct.2004.09.012.
[45] H. Samouh, A. Soive, E. Rozière, A. Loukili, Experimental and numerical study of size effect on long-term drying behavior of concrete: influence of drying depth, Mater. Struct. 49 (2016) 4029–4048, https://doi.org/10.1617/s11527-015-0771-7.
[46] R. Goel, R. Kumar, D.K. Paul, Comparative study of various creep and shrinkage prediction models for concrete, J. Mater. Civ. Eng. 19 (3) (2007) 249–260, https://doi.org/10.1061/(ASCE)0899-1561(2007)19:3(249.
[47] L. Bal, F. Buyle-Bodin, Artificial neural network for predicting drying shrinkage of concrete, Construct. Build. Mater. 38 (2013) 248–254, https://doi.org/10.1016/j.conbuildmat.2012.08.043.
[48] ACI Committee 209, Guide for Modeling and Calculating Shrinkage and Creep in Hardened Concrete (ACI 209.2R-08), American Concrete Institute, USA, 2008, p. 44.
[49] Z.P. Bazant, S. Baweja, Creep and Shrinkage Prediction Model for Analysis and Design of Concrete Structures-Model B3, vol. 194, ACI Special Publications, 2000, pp. 1–84.
[50] N.J. Gardner, M.J. Lockman, Design provisions for drying shrinkage and creep of normal-strength concrete, ACI Mater. J. 98 (2) (2001) 159–167, https://doi.org/10.14359/10199.
[51] Z.P. Bažant, M. Jirásek, Creep and Hygrothermal Effects in Concrete Structures, Springer, 2018, https://doi.org/10.1007/978-94-024-1138-6.
[52] Z. Pan, B. Li, Z. Lu, Re-evaluation of CEB-FIP 90 prediction models for creep and shrinkage with experimental database, Construct. Build. Mater. 38 (2013) 1022–1030, https://doi.org/10.1016/j.conbuildmat.2012.07.009.
[53] J. Meng, B. Zhao, J. Liu, Prediction model and influencing factors for concrete shrinkage and creep effects, J. Chang'an Univ. (Nat. Sci. Ed.) 33 (2) (2013) 56–62, https://doi.org/10.1016/10.19721/j.cnki.1671-8879.2013.02.010 (In Chinese).
[54] X. Yang, Research on Prediction Model of Concrete Shrinkage and Creep, Wuhan University (Master's Thesis), Wuhan, China, 2004 (In Chinese).
[55] J.A. Almudaiheem, W. Hansen, Prediction of concrete drying shrinkage from short-term measurements, ACI Mater. J. 86 (4) (1989) 401–408, https://doi.org/10.14359/2178.

Construction and Building Materials 501 (2025) 144333



Contents lists available at ScienceDirect

Construction and Building Materials

journal homepage: www.elsevier.com/locate/conbuildmat



Acoustic emission-based flexural fracture analysis of polyethylene fiber reinforced ultra-high performance concrete under low vacuum environment

Zhaofei Long [a], Guangcheng Long [a,*], Lei Peng [a], Yuting Zhang [a], Lixing Wang [a], Xiaodong Wang [a], Jilin Wang [a], Minghui Shangguan [b], Zhuo Tang [a], Jionghuang He [a,c,**]

[a] School of Civil Engineering, Central South University, Changsha 410075, China
[b] School of Civil Engineering, University of South China, 28 West Changsheng Road, Hengyang, Hunan 421001, PR China
[c] Department of Civil and Environmental Engineering, The Hong Kong Polytechnic University, Hong Kong, China

ARTICLE INFO

Keywords:
Low vacuum
Polyethylene fiber reinforced ultra-high performance concrete
Flexural behavior
Acoustic emission
Damage evolution

ABSTRACT

This study systematically investigates the flexural behavior and damage mechanisms of polyethylene fiber reinforced ultra-high performance concrete (PEFRC) under low vacuum conditions. Based on the dense particle packing model, PEFRC specimens were designed with different fiber contents (0.75–1.50 vol%) and coarse aggregate replacement ratios (ARR: 0, 20 %, 40 %). Through three-point bending tests combined with acoustic emission (AE) technology, a comparative analysis was conducted on the effects of atmospheric drying (AD) and low vacuum drying (VD) on the mechanical properties and damage evolution of PEFRC. The results indicate that the low vacuum environment reduces the post-peak toughness of the specimens. The synergistic effect of fiber (1.5 %) and coarse aggregate substitution (ARR 20 %-40 %) allows PEFRC to retain superior fracture toughness under VD conditions while maintaining cost advantages. AE analyses (ringing counts, AE energy, *b*-values, and AF-RA images) reveal that VD-induced shrinkage exacerbated fiber pullout behavior, leading to an increase in AE signals, a rise in the proportion of shear cracks, and a shortening of the *b*-value warning period. The establishment of a stable fiber-matrix-aggregate synergistic structural system can effectively mitigate VD-induced embrittlement of PEFRC. This study provides critical theoretical and technical support for the development of high-performance concrete with low-vacuum resistance.

1. Introduction

With the increasing exploration of extreme environments by humans, the low vacuum environment has emerged as a frontier focus in the field of engineering. Low vacuum tube transportation systems, such as Hyperloop, are regarded as the harbinger of the next-generation transportation revolution due to their advantages of ultra-high speed, low energy consumption, and low noise [1]. In the realm of deep space exploration, the construction of lunar and Martian bases urgently demands building materials that can withstand extreme vacuum conditions [2]. However, the low vacuum environment poses unprecedented challenges to traditional engineering materials, particularly concrete, which is the most widely used construction material globally. The porous, heterogeneous, and chemically complex structure of concrete is prone to performance instability under vacuum conditions. For instance, moisture loss induced by low pressure can exacerbate shrinkage behavior [3–5], deteriorate pore structure [6–8], and alter phase composition [9–11]. These factors make concrete more susceptible to surface cracking in low vacuum environments, directly threatening the durability and safety of structures. Therefore, optimizing the mix design of concrete to enhance its toughness and crack resistance is crucial for extending the service life of material structures in low vacuum environments.

To improve the drying behavior of cement-based materials, researchers have proposed various control technologies, such as reducing the water-to-cement ratio, using supplementary cementitious materials, increasing aggregate content, employing internal curing materials, and incorporating fibers [12,13]. However, the long-term effectiveness and

* Corresponding author.
** Corresponding author at: School of Civil Engineering, Central South University, Changsha 410075, China.
E-mail addresses: longguangcheng@csu.edu.cn (G. Long), hjh2017@foxmail.com (J. He).

https://doi.org/10.1016/j.conbuildmat.2025.144333
Received 3 April 2025; Received in revised form 14 October 2025; Accepted 30 October 2025
0950-0618/© 2025 Elsevier Ltd. All rights are reserved, including those for text and data mining, AI training, and similar technologies.

multi-scale synergistic mechanisms of these methods under low vacuum conditions still require breakthroughs. Ultra-high performance concrete (UHPC) with an extremely low water-to-cement ratio not only possesses high strength and toughness but also features an ultra-low gas permeability coefficient ($<10^{-18}$ m^2) [14], which offers broad application prospects in engineering construction under vacuum conditions.

Fibers, as materials with high toughness, can prevent the occurrence of autogenous shrinkage and drying shrinkage cracks, making them key materials in the design of UHPC [15]. Steel fibers have long been the mainstream choice for UHPC design. However, it is essential to consider the negative impact of ferromagnetic materials on train magnetic resistance when designing concrete for low vacuum tube systems [16]. Therefore, steel fibers are no longer suitable for such engineering designs. In recent years, ultra-high molecular weight polyethylene (PE) fibers have received widespread attention due to their ultra-high tensile strength (>3000 MPa), elastic modulus (>100 GPa), low density, and aging resistance making them one of the most effective alternatives to steel fibers [17–19]. Compared to traditional organic fibers such as polypropylene (PP) fibers and polyvinyl alcohol (PVA) fibers, PE fibers exhibit higher tensile strength and elastic modulus; when compared to traditional inorganic fibers such as basalt fibers and glass fibers, PE fibers offer better corrosion resistance and lightweight advantages. Previous study [12] has shown that, compared to PVA fibers and glass fibers, PE fiber reinforced concrete (PEFRC) demonstrated higher fracture toughness in low vacuum environments, showcasing unique potential.

Currently, UHPC is predominantly designed using fine aggregates alone [20]. However, the strategic incorporation of a controlled proportion of coarse aggregates offers an efficient method to reduce costs without obviously compromising the performance of PEFRC [21]. The anchoring effect between coarse aggregates and fibers can improve the overall stability and strength of UHPC, aiding in the resistance to shrinkage stresses [22]. However, the inclusion of coarse aggregates may also introduce weakened interfacial transition zones (ITZ), which could reduce the homogeneity of the matrix and affect the workability of the paste [22]. Fiber content also significantly affects the performance of concrete. It becomes difficult to form a continuous three-dimensional network when the fiber content is insufficient. Conversely, an excessively high fiber content may lead to decreased workability and increased porosity [18,23]. Guan et al. [24] pointed out that the UHPC phase composition was complex and highly heterogeneous, so the effect of fiber-aggregate structure on the cracking behaviors cannot be neglected. Therefore, the design of PEFRC with good serviceability under low vacuum conditions, which incorporates coarse aggregates and fibers, heavily relies on the precise control of their contents. To enhance the continuity of the multi-component network formed by the matrix, fibers, and aggregates, polymer bridging methods can be considered [25]. Re-dispersible polymer powder (RDP) can help overcome issues related to low bonding strength, low tensile strength, and low chemical resistance in cement-based materials [26]. Under low vacuum environments, RDP demonstrates enhanced potential for efficient demulsification and film formation due to rapid drying effects, effectively bridging micro-cracks. This approach could improve the bonding at the interfaces between the matrix-fiber and matrix-aggregate on a micro-scale, thereby alleviating the micro-crack propagation caused by vacuum dehydration [27,28].

Acoustic emission (AE), as a highly sensitive and non-destructive in-situ testing method, is widely used to monitor the dynamic damage of materials such as rocks, concrete, and backfill [29–31]. As a quasi-brittle material, concrete generates micro-damage during failure, including crack initiation and growth, crack opening and closure, pore formation, interface failure, and fiber debonding from the matrix [32,33]. This damage propagates energy in the form of elastic waves, allowing AE technology to effectively determine the location and time of damage occurrence. Numerous studies have confirmed that AE characteristic parameters are closely related to the internal damage of concrete specimens, and there are differences in AE characteristics corresponding to different stages of damage [34–36]. Therefore, AE technology can reflect the failure mechanisms of concrete specimens. Xu et al. [37] utilized AE technology to investigate the damage modes of UHPC and quantified the analysis of damage sources and their evolution. Zheng et al. [38] revealed the influence of silica fume on the flexural behavior of UHPC based on AE. Thus, employing AE technology can provide deeper insights into the damage modes of PEFRC under low vacuum conditions.

This study focuses on the performance evolution and design of PEFRC under extremely low vacuum environments based on AE technology. Three-point bending tests were conducted to investigate the effects of atmospheric drying and low vacuum drying on the flexural performance of PEFRC. By integrating AE technology, the study aims to reveal in detail how different drying environments affect the bending behavior of PEFRC. Through a comparison of the mechanical and acoustic characteristics of samples with varying fiber contents and coarse aggregate replacement ratios (ARR), the optimal combination will be identified. This research provides a scientific basis for the development of high-performance concrete materials suitable for engineering applications in low vacuum environments.

2. Test program

2.1. Materials

To design high-strength, high-toughness, and high-density PEFRC, P·I. 42.5 Portland cement (PC) was selected as the primary binding material, complemented by S95 grade slag (GGBS) and ultrafine silica (SF). The oxide content in the binding materials is determined using X-ray fluorescence spectrometry, as detailed in Table 1. RDP, made from dried vinyl acetate ethylene copolymer emulsion with a volatility of < 2 %, was used as a flexibilizer. The employed fine aggregates were composed of quartz sands with varying gradations: 0.125 mm-0.212 mm, 0.212 mm-0.425 mm, and 0.425 mm-0.710 mm. Coarse aggregates are 5–10 mm limestone gravel, replacing part of the fine aggregates. The mixing water was tap water from the laboratory, and a polycarboxylate superplasticizer (SP) with a water-reducing rate of > 25 % was employed. PE fibers (0.97 g/cm^3 density, 12 mm length, 25 μm diameter) with an elastic modulus of 122 GPa, tensile strength of 3100 MPa, and 3.5 % elongation at break were utilized.

2.2. Mix proportions

To prepare PEFRC with high stability and density in low vacuum environments, precise design of raw material composition is essential to ensure dense particle packing and minimize the likelihood of initial defects.

The Modified Andreasen and Andersen (MAA) particle packing model has demonstrated outstanding potential in UHPC design [39–42]. This model takes into account the effects of minimum and maximum particle size and achieves optimal dense packing by adjusting the distribution modulus. The specific design approach is as follows [39]:

$$P(D) = \left(\frac{D^q - D_{\min}^q}{D_{\max}^q - D_{\min}^q}\right) \times 100\% \quad (1)$$

Where $D_{\min}$ is the minimum particle size of the particle system, mm; $D_{\max}$ is the maximum particle size of the particle system, mm; q is the distribution modulus, usually less than 0.25, which is set to 0.23 in this study.

The mixing proportions of different particles within the particle system can be adjusted using the least squares method. The goodness of fit between the actual cumulative packing curve and the theoretical target cumulative packing curve is evaluated using the residual sum of squares (RSS) and the coefficient of determination (R^2), as shown in Eqs.

Table 1
The oxide composition of cementitious materials (wt%).

Binder	CaO	SiO_2	Al_2O_3	Fe_2O_3	SO_3	MgO	TiO_2	Na_2O	K_2O
PC	55.45	24.05	5.50	3.63	3.44	1.36	0.29	0.17	1.06
GGBS	37.18	29.78	14.29	0.40	2.61	6.16	1.95	0.59	0.36
SF	1.4	96.39	0.54	0.11	0.12	0.39	-	0.14	0.54

(2) and (3). A smaller RSS and a larger R^2 indicate a superior particle gradation design and a higher packing density.

$$RSS = \sum_{i=1}^{n} \left(P_{mix}(D_i^{i+1}) - P_{tar}(D_i^{i+1})\right)^2 \quad (2)$$

Where $P_{mix}(D_i^{i+1})$ and $P_{tar}(D_i^{i+1})$ denote the proportion of the actual and target cumulative packing curve for particle between rows i and $i+1$, respectively.

$$R^2 = 1 - \frac{RSS}{\sum_{i=1}^{n} \left(P_{mix}(D_i^{i+1}) - \overline{P}_{mix}\right)^2} \quad (3)$$

Where $\overline{P}_{mix}$ is the average value of the actual cumulative packing proportion for particle.

The particle size distribution curves of the used cementitious materials, polymers, and various grades of quartz sand were obtained using a laser particle size analyzer, as shown in Fig. 1. Based on the MAA model, the target packing curve and the fitted optimized actual packing curve were plotted. It was observed that the two curves exhibited a high degree of fit, with R^2 exceeding 0.99 and an *RSS* of 226, which met the expectations of the previous practice [39,43].

Based on the optimization results of the above MAA model, the mix proportions of PEFRC are shown in Table 2. The water-to-binder ratio was set at 0.18, with the binder materials comprising 65 % PC, 15 % GGBS, and 20 % SF. Considering the dual-edged effect of RDP, which enhances toughness and water retention while also compromising strength [44], its dosage was set at 3 % of the total binder weight. The proportions of quartz sand in the size ranges of 0.125–0.212 mm, 0.212–0.425 mm, and 0.425–0.710 mm were 0.28:0.22:0.50. The aggregate composition varied across mixes: E1 and E2 contained exclusively quartz sand, while E3 and E4 incorporated 20 % gravel replacement of the quartz sand. In E5 and E6, the gravel content increased to 40 % of the total aggregate, replacing the corresponding proportion of quartz sand. Two volume fractions of PE fibers were used: 0.75 % (mixes E1, E3, E5) and 1.50 % (mixes E2, E4, E6), to comprehensively investigate the effects of fiber content and coarse aggregate replacement ratio (ARR) on the flexural properties of PEFRC in low vacuum environments.

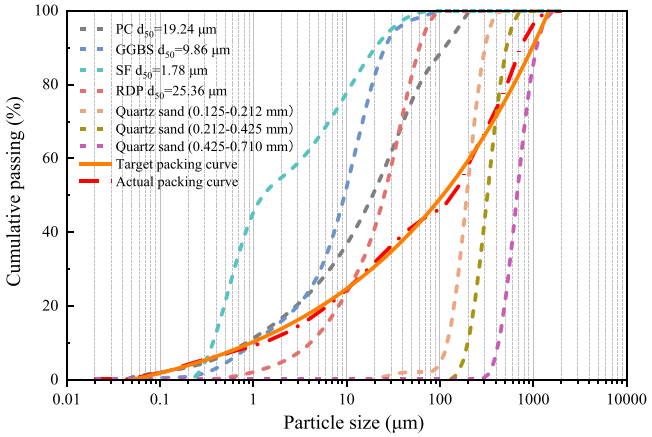


Fig. 1. Particle size distribution of granular system.

2.3. Experimental procedures

2.3.1. Specimen preparation

Based on the mix proportions in Table 2, PEFRC was prepared as follows: First, coarse and fine aggregates along with cementitious materials were dry-mixed for 2 min in a planetary cement mortar mixer. Then, water and a superplasticizer were added, and the mixture was slowly stirred for 120 s. Finally, redispersible polymer powder (RDP) and PE fibers were incorporated, and the mixture was stirred for an additional 2–3 min to obtain the fresh paste. This mixture was then poured into molds measuring 40 mm× 40 mm× 160 mm and vibrated evenly. After demolding, specimens were cured for 28 days and subsequently subjected to atmospheric drying (AD) and low vacuum drying (VD). AD was performed at ambient conditions of 20 ± 2°C and 55–65 % humidity, while VD was conducted in a custom-made low vacuum chamber at a pressure of 100 Pa, maintaining the same temperature as AD, as detailed in reference [12]. Both drying methods lasted for 56 days. After drying, the specimens were removed for mechanical performance testing.

2.3.2. Experimental methods

The dried concrete specimens were subjected to a three-point bending test using an Instron 1342 electro-hydraulic servo press, as shown in Fig. 2. The loading rate was set at 0.30 mm/min, and a displacement gauge was used to record the mid-span displacement for plotting the load-displacement curve. Acoustic emission monitoring was carried out using a six-channel PCI-2 acoustic emission system manufactured by Acoustic Physics Corporation, USA. A Mini 300 acoustic emission sensor was placed at the front of the loading instrument and on the side of the specimen near the midspan to capture the acoustic signals generated during loading. These sound signals were amplified using a preamplifier with a gain of 40 dB, and the amplitude threshold was set to 40 dB to minimize interference and prevent signal loss. The system continuously collected data at a rate of 1 MHz, which was displayed in graphical form on a monitor. The acoustic emission equipment was turned on synchronously after the start of the bending loading, and after the continuous data acquisition, the variation of parameters such as ring count, AE energy, rise time, amplitude, and duration (see Fig. 2) can be obtained with respect to time and loading to evaluate the damage characteristics of the specimen. During the bending tests, three specimens were tested for each group, and the median value along with its corresponding acoustic emission data was selected for comparative analysis.

2.3.3. Calculation method for flexural toughness index

To elucidate the effects of low vacuum environment and material composition on flexural performance of concrete, the flexural toughness index was introduced. Based on ASTM C1018 [45], Fig. 3 depicts the calculation method for the flexural toughness indices (I_5, I_{10}, and I_{20}), with the formulas provided in Eq. (4). A higher value indicates enhanced concrete toughness.

$$I_5 = \frac{S_{OACD}}{S_{OAB}}, I_{10} = \frac{S_{OAEF}}{S_{OAB}}, I_{20} = \frac{S_{OAGH}}{S_{OAB}} \quad (4)$$

Where S_{OAB}, S_{OACD}, S_{OAEF}, S_{OAGH} represent the integrated areas at the corresponding locations on the flexural curve.

Table 2
Mix proportions of the concrete specimens.

Mixture	Raw material (kg/m^3)										
	PC	GGBS	SF	Water	Quartz sand (mm)			Gravel 5–10 mm	RDP	PE fiber	SP
					0.125–0.212	0.212–0.425	0.425–0.710				
E1	682	158	210	189	308	242	550	-	31.5	7.3	42
E2	682	158	210	189	308	242	550	-	31.5	14.6	42
E3	682	158	210	189	246	194	440	220	31.5	7.3	42
E4	682	158	210	189	246	194	440	220	31.5	14.6	42
E5	682	158	210	189	185	145	330	440	31.5	7.3	42
E6	682	158	210	189	185	145	330	440	31.5	14.6	42

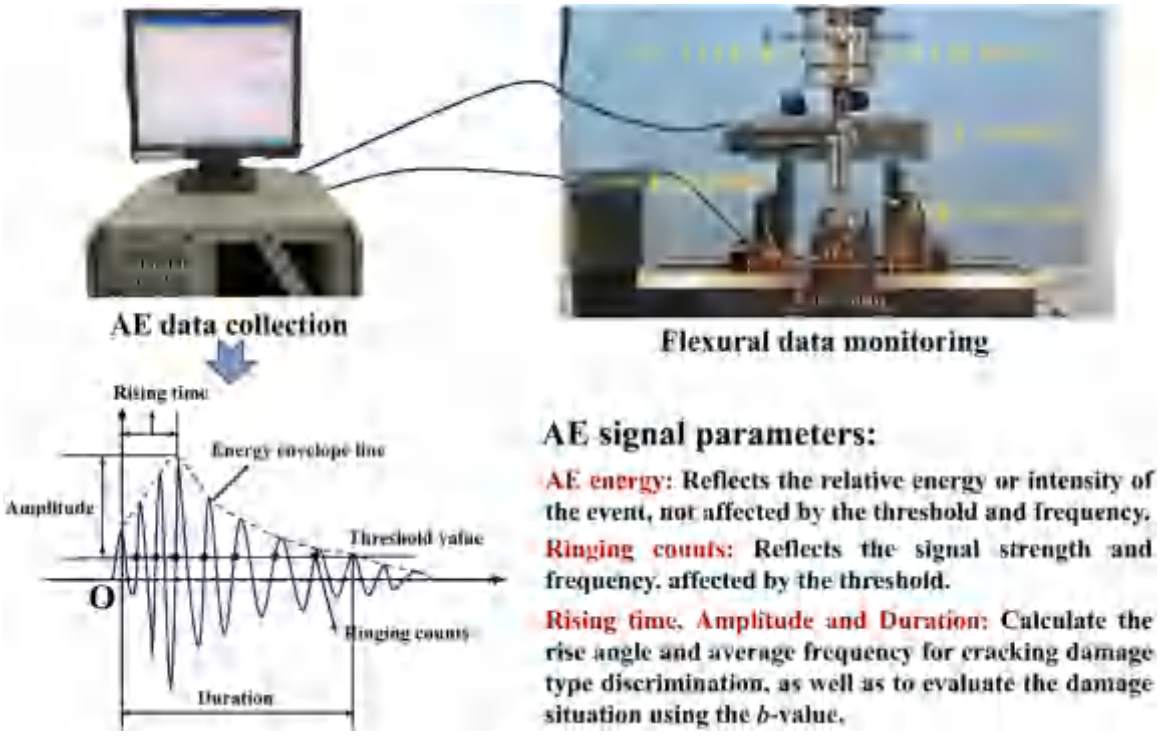


Fig. 2. Schematic diagram of concrete AE test and interpretation of AE parameters.

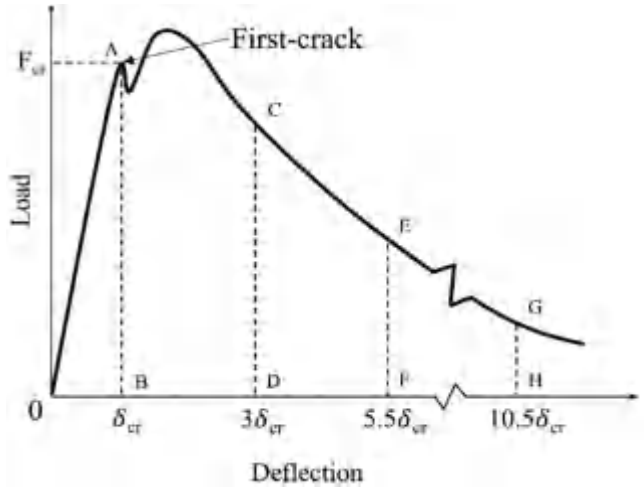


Fig. 3. Schematic diagram of the calculation of the flexural toughness indices of concrete.

3. Results and discussion

3.1. Load-displacement curve

Fig. 4(a) and (b) present typical load-displacement curves for specimens subjected to AD and VD, respectively. The corresponding flexural characteristic values were counted as shown in Table 3. The results indicated that PEFRC exhibited good ductility even after drying in different environments. Increasing the fiber content not only raised the peak load of the specimens but also enhanced the secondary strain-hardening effect post-peak. Under AD conditions, increasing the ARR led to a reduction in the initial cracking load while increasing the softening load. In contrast, under VD conditions, the influence of ARR on the bending performance was related to the fiber volume fraction. For low fiber content (0.75 %), the secondary hardening behavior initially strengthened with increasing ARR but subsequently weakened. For high fiber content (1.5 %), this behavior continued to strengthen with increasing ARR. By observing the fracture morphology of the specimens, it was also found that the main crack propagation in E2, E4, and E6 became increasingly tortuous, indicating that more fibers had formed a tight network with the coarse aggregates, thereby promoting a hardening behavior.

A comparative analysis of AD and VD conditions revealed that the

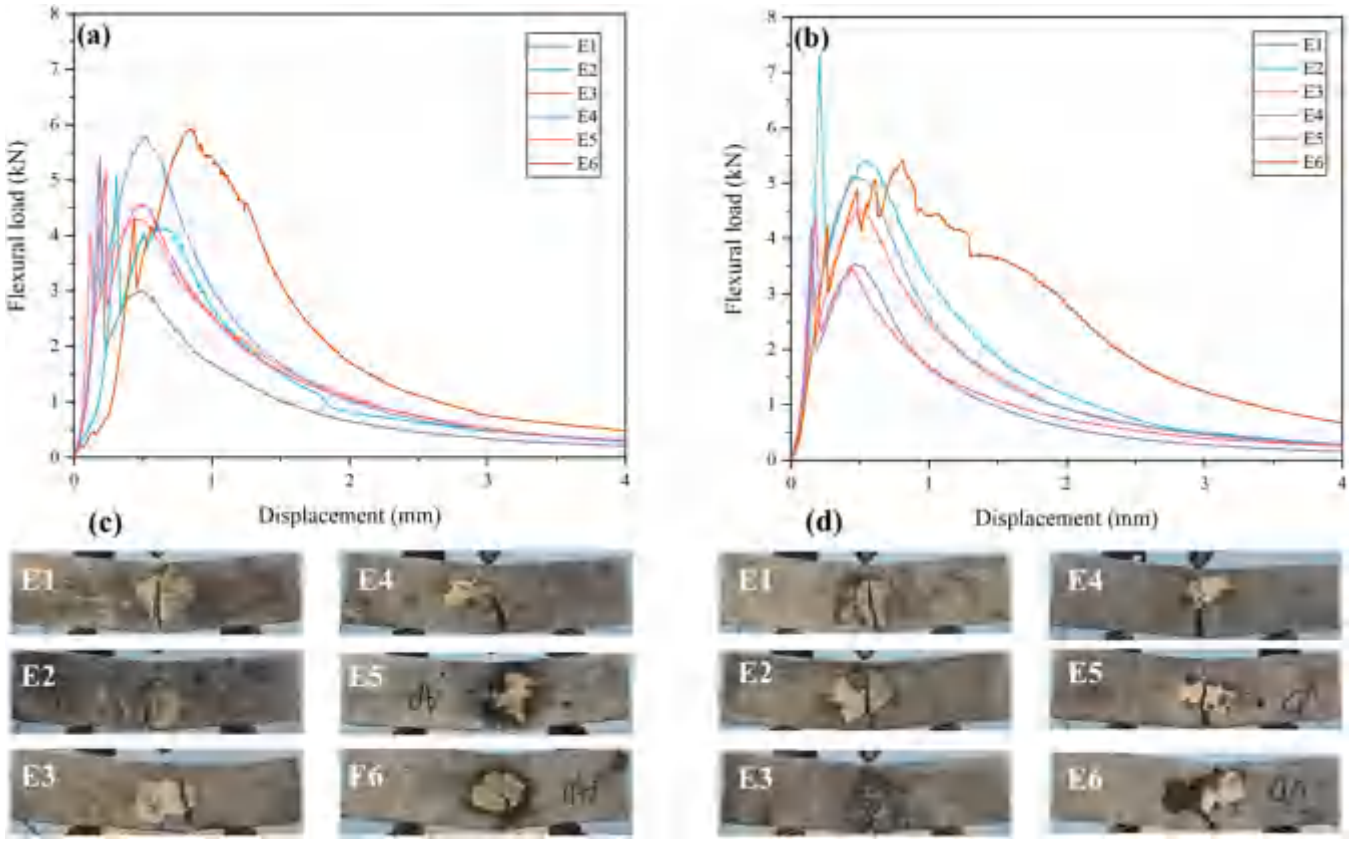


Fig. 4. Typical flexural load-displacement curves and fracture images of specimens at different drying conditions: (a) and (c) show the fracture curve and morphology under AD; (b) and (d) show the fracture curve and morphology under VD.

Table 3
Flexural characteristic values of specimens.

Characteristic values	Initial cracking load (kN)		Initial crack displacement (mm)		Softening load (kN)		Softening displacement (mm)	
Mixture	AD	VD	AD	VD	AD	VD	AD	VD
E1	5.412	4.177	0.187	0.146	3.005	3.534	0.496	0.468
E2	5.089	7.312	0.305	0.207	4.135	5.383	0.653	0.538
E3	4.046	3.585	0.121	0.152	4.296	4.486	0.478	0.487
E4	4.179	4.086	0.173	0.146	5.798	5.103	0.522	0.493
E5	5.220	4.44	0.227	0.179	4.560	3.45	0.498	0.444
E6	4.305	4.22	0.438	0.264	5.914	5.410	0.840	0.813

secondary hardening curve was narrower under VD treatment. This observation indicated that sample softening occurred within a more constrained strain range, leading to reduced post-peak toughness. The effects of VD on the initial cracking and softening points were associated with the fiber volume fraction and ARR. VD generally reduced the initial cracking load in specimens with low fiber volume fractions, while moderately enhancing the softening load (except for E5). For specimens with high fiber content, VD had minimal impact on the initial cracking load but slightly decreased the softening load. Interestingly, specimens E2 showed significant increases in both initial cracking and softening loads following low vacuum drying, likely due to enhanced bond strength at the fiber-matrix interface caused by increased shrinkage under low vacuum conditions. Nevertheless, VD still resulted in reductions in both initial cracking strain and softening strain, thereby increasing the brittleness of specimens. Further observation revealed that specimen E6 exhibited significant peak fluctuations during the hardening stage. This phenomenon may be due to an increased amount of coarse aggregates creating obstacles between the fibers and the matrix, which results in a plugging effect [45] and increased friction between the fibers and the matrix. This effect is even more pronounced under the VD condition.

3.2. Damage characterization based on AE signals

3.2.1. Ringing counts

The AE characteristics are closely related to the internal damage of concrete, and the following analysis will address them sequentially. Based on AE signals, the evolution of load and ringing counts over time is illustrated in Fig. 5. It is evident that the development patterns of the ringing counts captured by the two AE sensors are fundamentally consistent, although there are noticeable differences in the count magnitudes. The sensor in direct contact with the specimen (No. 2 AE probe) recorded more AE signals, despite being farther from the mid-span area. Consequently, the subsequent dynamic damage analysis will utilize AE signals collected from probe No. 2.

Further observations revealed that the moments of significant increases in the ringing counts corresponded to the key stages on the load development curve. The first surge coincided with the initial cracking point, while the second surge corresponded to the softening point. Specifically, the bending behavior of PEFRC could be categorized into

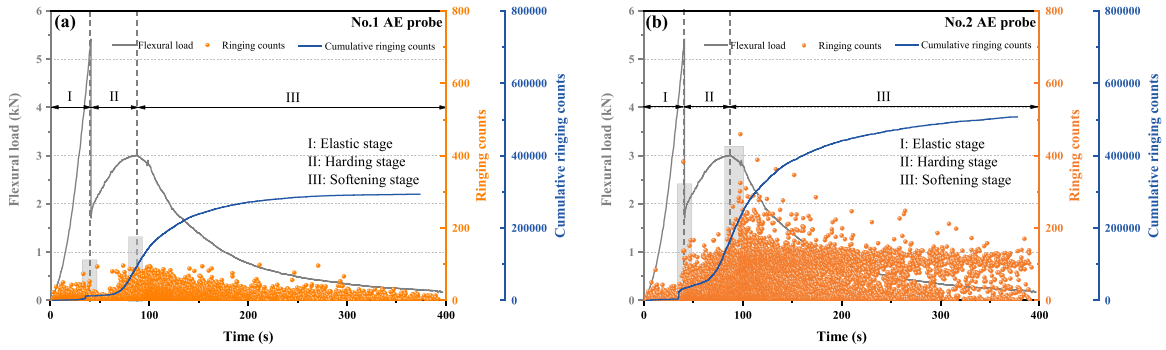


Fig. 5. Characterization of typical flexural curves of specimens based on AE signals: (a) No.1 AE Probe for E1-AD; (b) No.2 AE Probe for E1-AD.

three stages: (I) the elastic stage, (II) the hardening stage, and (III) the softening stage. These stages will be discussed in the following sections.

Based on the aforementioned analysis, the cumulative ringing counts for each group of specimens are summarized in Fig. 6. The cumulative ringing counts evolution exhibited a three-stage S-curve: an initial slow-growth stage, a middle accelerated-growth Stage, and a final deceleration stage approaching gradual stability. In Stage I, the count values were primarily below 100, attributed to both the closure of inherent defects at low stress levels and the initiation/propagation of micro-cracks. In Stages II and III, the ringing counts were predominantly generated from the pull-out behavior of fibers from the matrix. Additionally, distinct sparse hits significantly exceeded the main body of ringing counts, likely caused by partial rupture of PE fibers [46].

Comparing the cumulative ringing counts curves under AD and VD conditions revealed that the curve under VD exhibited a steeper slope in Stage II. This indicated that the fiber pull-out behavior generated more AE signals, which may be attributed to matrix shrinkage [3,5], as it increases the friction during fiber pull-out [45]. Notably, the ringing counts for specimen E5 slightly decreased after VD, which correlated with its lower critical load-bearing capacity.

The increase in fiber content resulted in an increase in ringing counts, which may be attributed to the fact that a higher fiber ratio led to increased pull-out behavior and consequently generated more AE signals. The influence of the ARR on ringing counts was related to the fiber content: in high fiber content groups (E2, E4, and E6), ringing counts increased with higher ARR, while in low fiber content groups, ringing counts initially increased and then decreased with increasing ARR. An increased ARR ratio can provide a more stable skeletal structure, which helped alleviate shrinkage issues caused by low vacuum conditions. Furthermore, the pull-out behavior of fibers, which was hindered by the interference of aggregates, resulting in greater energy. However, specimen E5 exhibited lower ringing counts under both AD and VD conditions. At high ARR ratios, the area of the ITZ between aggregates and mortar also increased. In the absence of sufficient fiber restraint, drying effects can lead to ITZ degradation, resulting in microcracking [47]. This degradation reduced the energy absorption and resistance capacity at the interface, subsequently decreasing the load-bearing capacity and the generation of AE signal.

3.2.2. *AE energy*

Generally, the recorded acoustic emission (AE) energy is nearly equivalent to the fracture energy of concrete in the absence of material attenuation [48]. This fundamental relationship establishes AE energy serves as a reliable indicator for characterizing the fracture process in concrete. Fig. 7 illustrates the evolution of AE energy in relation to the load curve. The evolution patterns of AE energy and ringing counts were largely consistent. The AE energy evolution also exhibited three-stage pattern: (I) gradual development during initial microcrack formation,

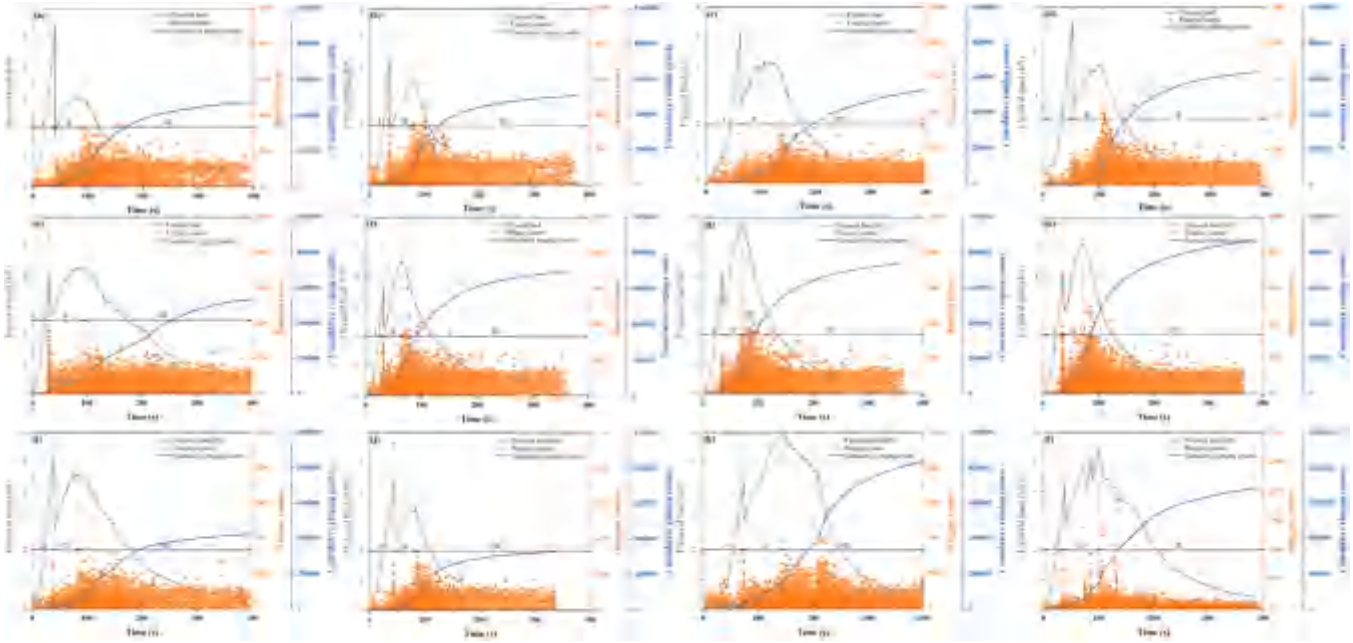


Fig. 6. Flexural load-time curves of the specimens with the acquisition results of ringing counts: (a) E1-AD; (b) E1-VD; (c) E2-AD; (d) E2-VD; (e) E3-AD; (f) E3-VD; (g) E4-AD; (h) E4-VD; (i) E5-AD; (j) E5-VD; (k) E6-AD; (l) E6-VD.

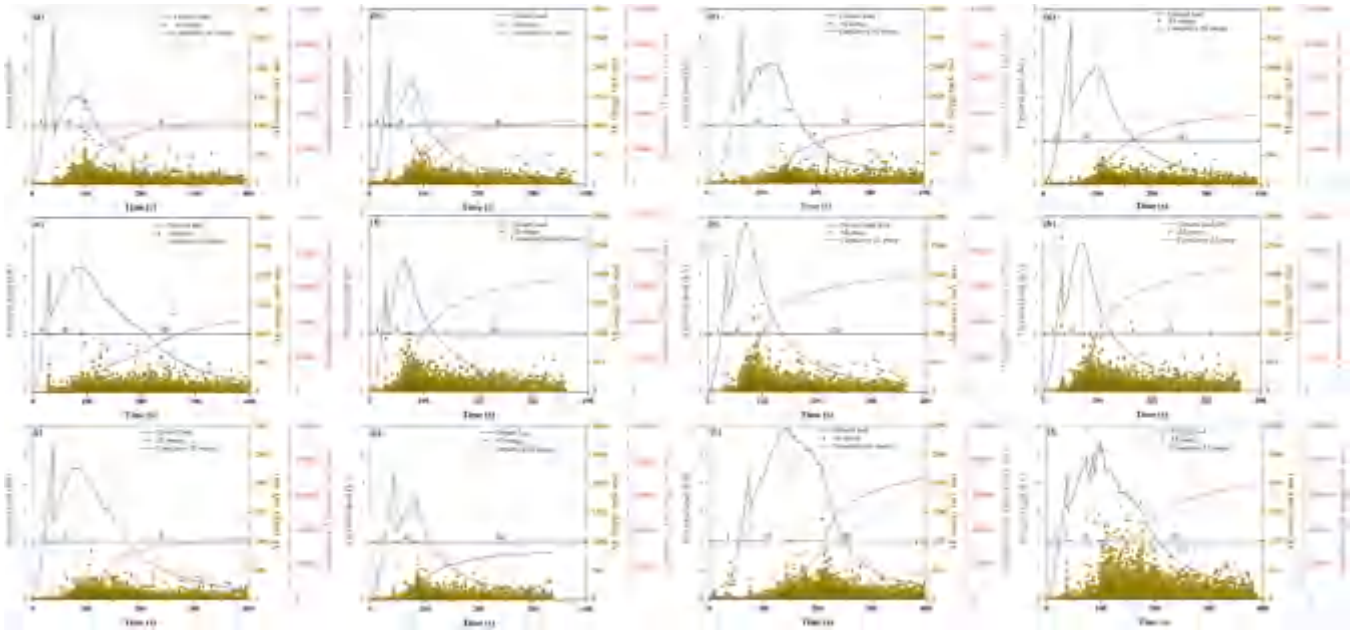


Fig. 7. Flexural load-time curves of the specimens with the acquisition results of AE energy: (a) E1-AD; (b) E1-VD; (c) E2-AD; (d) E2-VD; (e) E3-AD; (f) E3-VD; (g) E4-AD; (h) E4-VD; (i) E5-AD; (j) E5-VD; (k) E6-AD; (l) E6-VD.

(II) rapid accumulation coinciding with stable crack propagation and fiber debonding, and (III) decelerated growth as progressive fiber fracture reduced bridging capacity. Notably, the VD accelerated the accumulation rate of AE energy compared to AD. In addition, both fiber content and ARR influenced AE energy evolution, following similar trends as those observed in ringing counts.

3.2.3. *b*-value analysis

The formation and growth of microcracks within concrete release numerous AE hits of varying amplitudes in the form of elastic waves, as illustrated in Fig. 2. Due to their similarity to seismic waves, the *b*-value analysis method can be employed to detect internal cracking in concrete subjected to flexural loads [37,48]. Specifically, the *b*-value is defined according to the Gutenberg-Richter equation as follows:

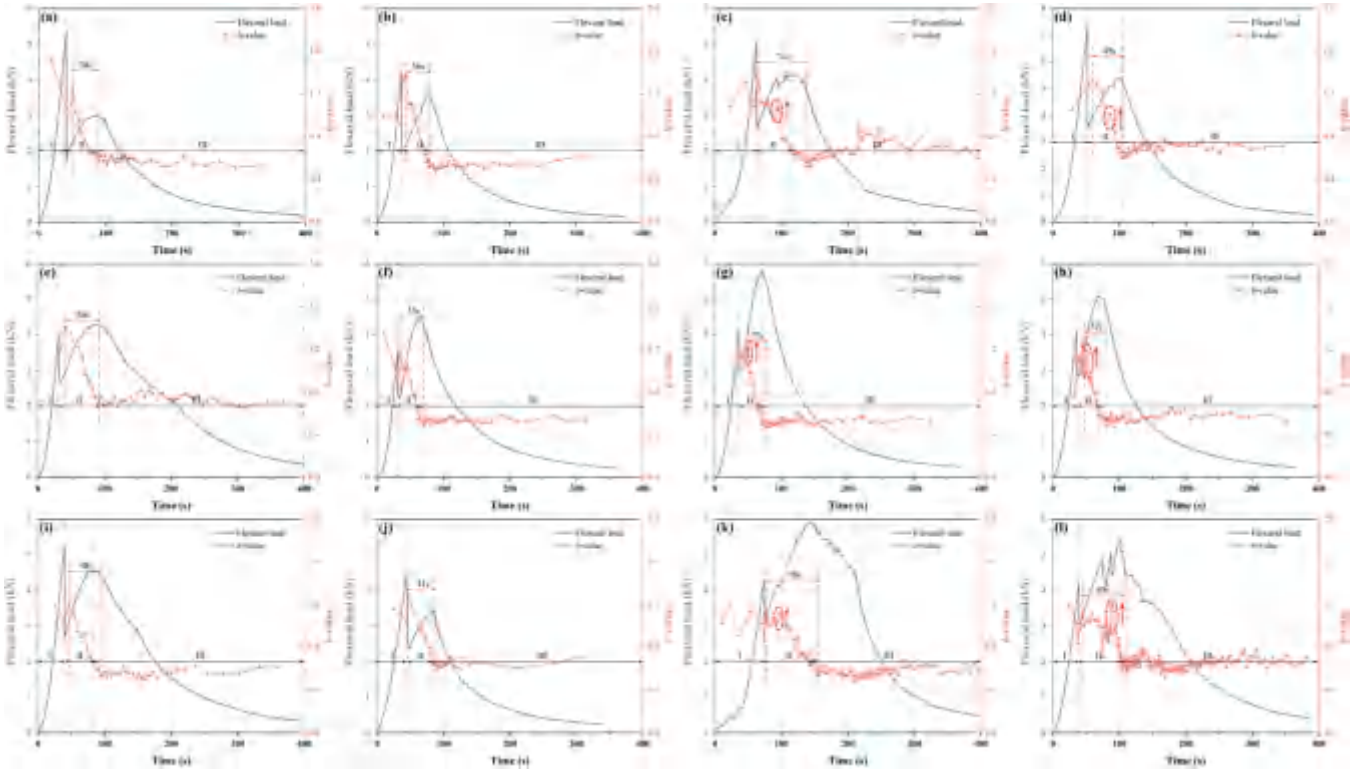


Fig. 8. Flexural load-time curves of the specimens with the acquisition results of *b*-value: (a) E1-AD; (b) E1-VD; (c) E2-AD; (d) E2-VD; (e) E3-AD; (f) E3-VD; (g) E4-AD; (h) E4-VD; (i) E5-AD; (j) E5-VD; (k) E6-AD; (l) E6-VD.

$$\log_{10}N = a - b\left(\frac{A_{dB}}{20}\right) \tag{5}$$

Where A_{dB} is the peak amplitude of AE hits; N is the AE hits with amplitudes exceeding A_{dB}; a is the empirical constant; b is the b-value, representing the slope of the fitted curve; 20 is a constant, the basis of which can be viewed through the literature [49]. The AE data is grouped into sets of 200 hits each (1–200, 201–400, and so on) to analyze the variation of the b-value during the loading process.

Fig. 8 presents the variation of the b-value for PEFRC under flexural loading. Under both AD and VD conditions, the b-value initially increases briefly before rapidly decreasing at the transition between Stage I and Stage II (near the initial cracking point). The initial increase in the b-value is associated with the microcrack initiation and early-stage propagation, which generate low-amplitude AE signals [50]. The sudden drop in the b-value corresponds to the emergence of macrocracks, where microcracks coalesce, releasing a significant amount of high-amplitude signals, indicating that the material has reached critical strength [51–53].

Notably, groups with high fiber content (E2, E4, and E6) exhibited a marked increase in b-value during Stage II, suggesting that the random distribution of PE fibers at the main crack locations effectively mitigated further crack propagation, thereby delaying damage. Interestingly, the trough of the b-value corresponded closely to the softening point of the specimen (the boundary between Stages II and III), providing a basis for determining the failure point of the specimen. Further observations indicated that, after the drop, the b-value fluctuated at a constant level, while its density initially increased and then decreased, indicating a transition from non-steady-state to steady-state crack growth [54]. This phenomenon may be attributed to the progressive disengagement of fibers, resulting in a sustained decrease in AE signals.

The abrupt change in the b-value signal can be interpreted as the moment when the material or structure begins to fail, with the duration of this decline serving as a warning period for material failure [37,55]. As shown in Fig. 8, the warning period of samples under VD was generally shorter than that under AD, indicating that a low vacuum environment reduced the toughness of samples, warranting additional engineering precautions during service. Comparatively, it can be concluded that increasing fiber content can extend the warning period. Specifically, raising the ARR ratio to 40 % can prolong the warning periods to 79 s and 65 s under AD and VD, respectively, significantly enhancing the specimen's performance in dry environments.

Based on the warning period and the critical b-value, the decrease rate in the descending segment of the b-value curve can be further calculated, the results are shown in Fig. 9. A higher b-value decrease rate indicated a more rapid transition between small and large cracks within the specimen. Except for E4, the b-value decrease rate under VD was greater than that under AD, indicating an increased brittleness under VD conditions. The E4 specimen exhibited the most significant decrease rate in b-value among all specimens, with a lower rate under VD compared to that under AD. This suggests that E4 has a higher density, allowing it to accumulate more energy before failure, resulting in a faster crack transition. Notably, the E6 specimen has the lowest b-value decrease rate under both AD and VD, with only minimal differences between the two conditions. This behavior indicates that the mix design of E6 effective mitigated the brittleness resulting from VD. In combination with the above, the E6 specimen demonstrated the highest fracture energy among all tested groups. This suggests that synergistic combination of an elevated coarse aggregate content and increased fiber volume fraction effectively enhances the mechanical performance through optimized load-transfer mechanism.

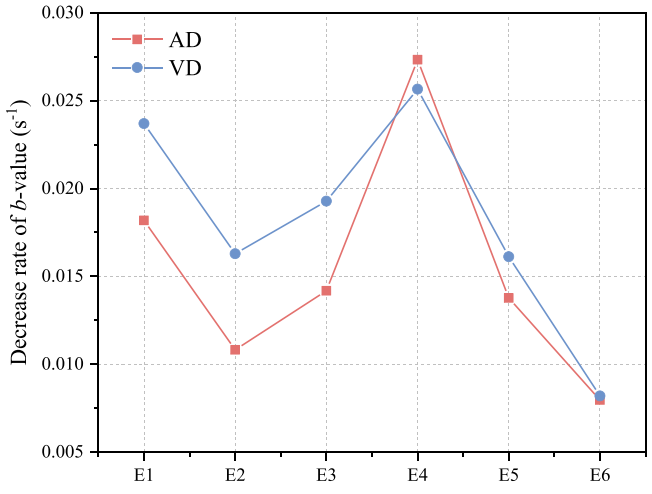


Fig. 9. The decrease rate of the critical b-value of the specimens.

3.2.4. Crack evolution analysis based on AF-RA images

The Japan Concrete Association (JCMS-IIB 5706) correlates the average frequency (AF) and rise angle (RA) to evaluate the cracking failure mechanisms of concrete materials [56]. The calculation methods for AF and RA are presented in Eqs. (6) and (7).

$$RA = \frac{RT}{A} \tag{6}$$

$$AF = \frac{RC}{D} \tag{7}$$

Where RT is the rise time; A is the amplitude; RC is the ringing counts; D is the Duration.

A standardized methodology for determining the AF/RA ratio remains undefined in current literature, and the criteria for classifying cracks vary [57]. Generally, the diagonal line in the AF-RA plot serves as a boundary between tension cracks and shear cracks [56,58]. Tension cracks typically exhibit opposing lateral movements, resulting in AE waveforms characterized by short RT and high AF, while shear cracks display the opposite behavior [54]. Therefore, tension cracks are located above the diagonal line, and shear cracks are below it, as illustrated in Fig. 10(a). However, different concrete specimens exhibit varying failure modes and AE signals, making a uniform classification approach potentially prone to calculation errors [59]. Hence, it is essential to implement intelligent classification of AF-RA signals for different specimens.

This study employs a Kneedle algorithm model [60], which identifies the inflection point by plotting the shear crack ratio against the slope k to determine the critical slope (k_0), as shown in Fig. 10(b) and (c). When the slope exceeds k_0, variations in k have minimal impact on crack classification results, as the curve approaches horizontal. Conversely, when the slope is below k_0, variations in k significantly affect the classification outcomes. Thus, k_0 serves as the slope of the boundary line equation for the AF-RA plot. This method allows for the calculation of the critical slopes at different failure stages of specimens and the proportions of various crack types, as illustrated in Fig. 10(d). Additionally, to visually represent the cracking process of specimens under tensile/-shear mixed modes, the kernel density estimation (KDE) method [61] was utilized. AE hits transition from sparse to concentrated, with colors changing from dark to light.

Fig. 10 presents the fitted results of the critical slopes for various specimens under different drying environments. The results indicated that the k values were generally above 100, while the slope value determined by the diagonal line was merely 10. This division would inevitably result in a higher proportion of tension cracks. Fig. 12 illustrates the inflection point measurements for specimen E1, demonstrating that the Kneedle algorithm accurately identifies the position of the critical slope. Thus, it is reasonable to believe in the validity of the crack classification method employed in this study. The KDE results in

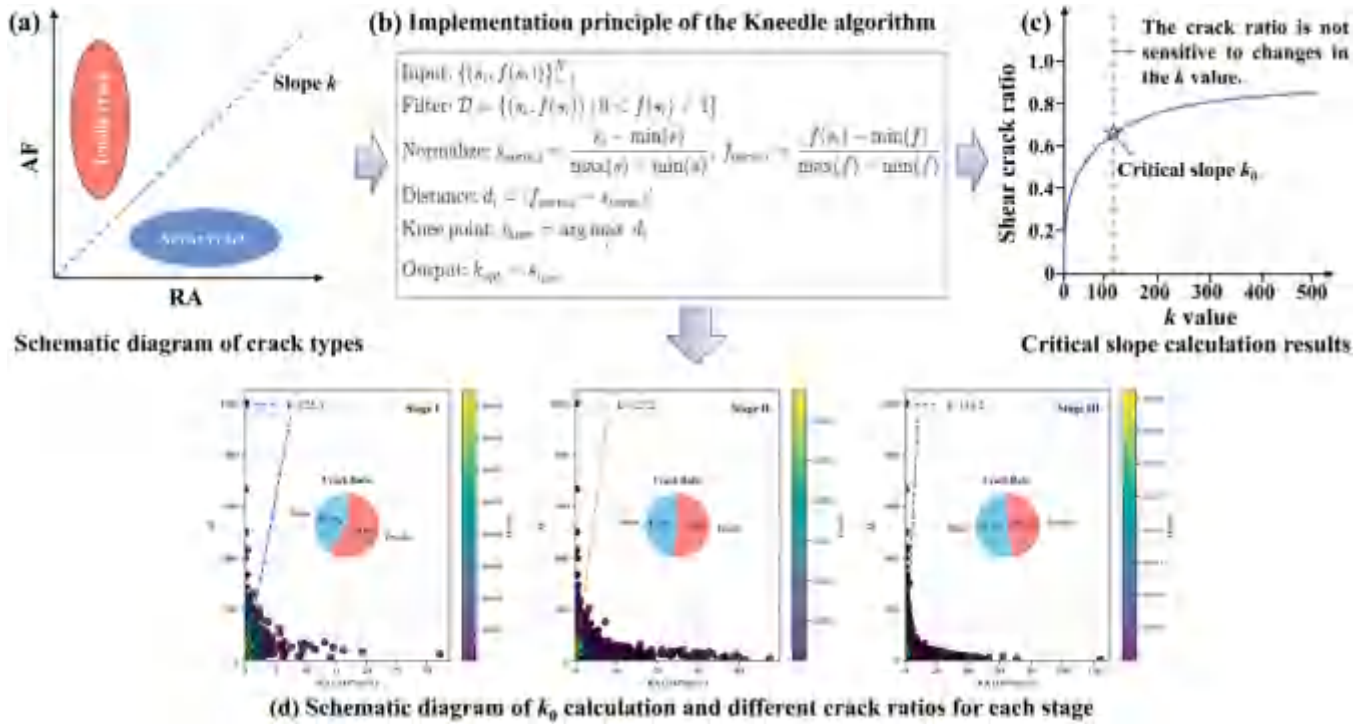


Fig. 10. Schematic diagram of critical slope (k_0) calculation for crack division based on Kneedle algorithm.

Fig. 11 indicated that the tensile crack density was relatively high during Stage I and a gradual decrease in Stages II and III. This suggests that under sustained flexural load, PEFRC undergoes a progressive failure mode transition from tensile-dominated failure to shear-controlled failure mechanisms. The classification results based on the Kneedle algorithm corroborate this observation, which will be elaborated upon in the following sections.

Fig. 13 illustrates the crack proportion based on the Kneedle algorithm. In Stage I, the majority of AE hits were attributed to tension failure (over 50 %), indicating that damage in this stage was predominantly due to tension cracks. During this phase, initial pore compaction and micro-crack initiation occurred, with the matrix bearing the tensile load [62]. Notably, the tension crack proportions for specimens E3 and E5 under vacuum drying (VD) were relatively low, likely due to insufficient fiber reinforcement. Dry shrinkage may have induced the formation of micro-cracks near the ITZ, thereby resulting in a higher occurrence of shear cracks due to initial defects and relative movements between aggregates [60].

In Stage II, the merging of micro-cracks led to the formation of macro-cracks, increasing the proportion of shear cracks. Shear cracks typically developed under high energy conditions and were primarily controlled by the frictional forces at the crack surfaces [32]. The debonding and pullout behaviors of fibers generated significant shear signals [63,64], aligning with the monitoring results of ringing counts and AE energy, as presented in Figs. 5 and 6. In Stage III, the proportion of shear cracks further increased, consistent with the findings of Yang et al. [39]. As crack openings enlarged, the bridging mechanism of PE fibers was fully activated, and the pullout of numerous fibers facilitated the development of shear cracks, a phenomenon that appeared more pronounced under VD conditions. According to previous research [47], VD contributed to an increase in concrete brittleness, thereby increasing the likelihood of shear crack signals throughout all stages compared to concrete under AD conditions.

It is noteworthy that the failure of specimens E4 and E6 was primarily dominated by tension cracks, whereas specimens E3 and E5 were dominated by shear cracks. This indicates that, with a limited fiber volume, increasing the ARR promoted shear failure, a situation that was undesirable in engineering applications. To ensure that components fail in a tensile mode, it is necessary to adjust the fiber volume fraction to an optimal level, as there exists an optimal relationship between fiber volume fraction and ARR ratio. Within the scope of this study, the combination of 1.5 % fiber volume fraction with 20–40 % ARR yields the best overall performance for PEFRC.

3.3. Flexural toughness analysis

By calculating the envelope areas of the load-displacement curves for each stage, the distribution of flexural capacity for each specimen was determined, as shown in Fig. 14. From Fig. 14(a), under AD conditions, the flexural capacity across all stages was positively correlated with fiber content and ARR ratio. Increasing fiber content enhanced the flexural capacity in all stages, particularly in Stage II, where energy absorption was significantly improved due to a stronger bridging effect. However, at low fiber content levels, an ARR exceeding 20 % does not contribute significantly to flexural capacity, indicating that further increases in fiber quantity are necessary.

Fig. 14(b) shows that, compared to AD conditions, the overall flexural capacities of E1, E2, and E6 increased by 21.70 %, 26.59 %, and 24.24 %, respectively, while E3, E4, and E5 experienced decreases of 5.18 %, 9.34 %, and 28.89 %. It is also noted that E2, E4, and E6 exhibited improvements in energy absorption during Stage II, with E6 demonstrating the most significant increase. This further supports the notion that the mix design of E6 represents the optimal configuration for a robust matrix-fiber-aggregate system, effectively enhancing the flexural capacity of concrete in low vacuum environments.

According to ASTM C1018 [65], the flexural toughness indices (I_5, I_{10}, and I_{20}) for each specimen were calculated, as shown in Fig. 15. A higher toughness index indicates better material ductility. It is evident that the development patterns of the toughness indices showed no significant decrease in toughness under VD compared to AD. This optimized formulation represents a notable improvement in flexural performance compared to some prior concrete designs [47]. Additionally, E5 exhibited relatively low flexural toughness, indicating a lower fracture energy, which correlates with its reduced AE signals. In

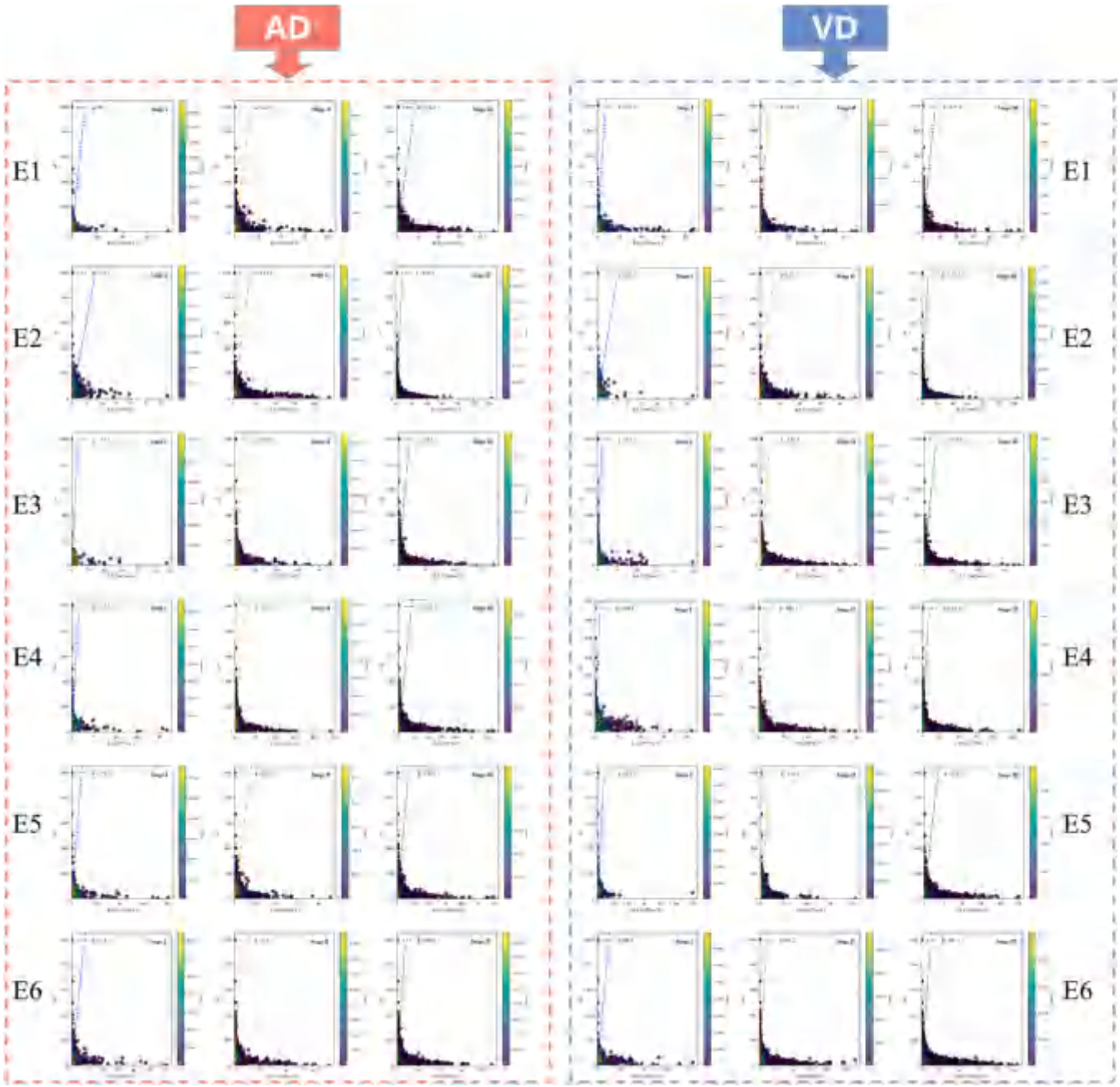


Fig. 11. Fitting calculation of the slope (k) of the flexural RA-AF images of specimens based on the Kneedle algorithm.

contrast, specimens E3, E4, and E6 demonstrated high flexural toughness under low vacuum conditions. Combining the AE data, E4 and E6 showed superior performance in both flexural load capacity and toughness, providing a balance of performance and cost advantages.

3.4. Mechanism analysis

Based on the mechanical and acoustic properties of PEFRC, this study further elucidated the synergistic interactions of the fiber-aggregate network structure under flexural loads and the influence mechanisms of different drying treatments on specimen fracture damage, as shown in Fig. 16. The figure illustrated that the incorporation of fibers and coarse aggregates introduced initial defects, such as increased ITZ and porosity [24]. Fig. 16(a) depicts the crack propagation process in the fracture process zone (FPZ) of specimens without coarse aggregates. It is observed that crack propagation occurred through fiber rupture. As the crack opening increased, the bridging effect of the fibers was progressively activated, leading to a significant number of AE signals due to fiber pull-out. In the absence of coarse aggregates, the crack propagation direction gradually shifted upward along the mid-span. When coarse aggregates were present in the FPZ, microcrack growth tends to bypass or split the coarse aggregates [66]. The high elastic modulus and tensile strength of PE fibers effectively reduced the stress at the crack tip, significantly lowering the probability of crack breakthrough through the aggregates. Instead, cracks primarily propagated along the ITZ surrounding the aggregates, as illustrated in Fig. 16(b). The diversion of cracks increased the surface area of the propagation path, dissipating more energy and resulting in denser AE hits. Overall, the stable three-dimensional fiber-aggregate network effectively utilized the bridging effect of fibers and the crack-blocking capability of the aggregates, effectively alleviating stress concentration phenomena.

Fig. 16(c) illustrates the impact of different drying environments on

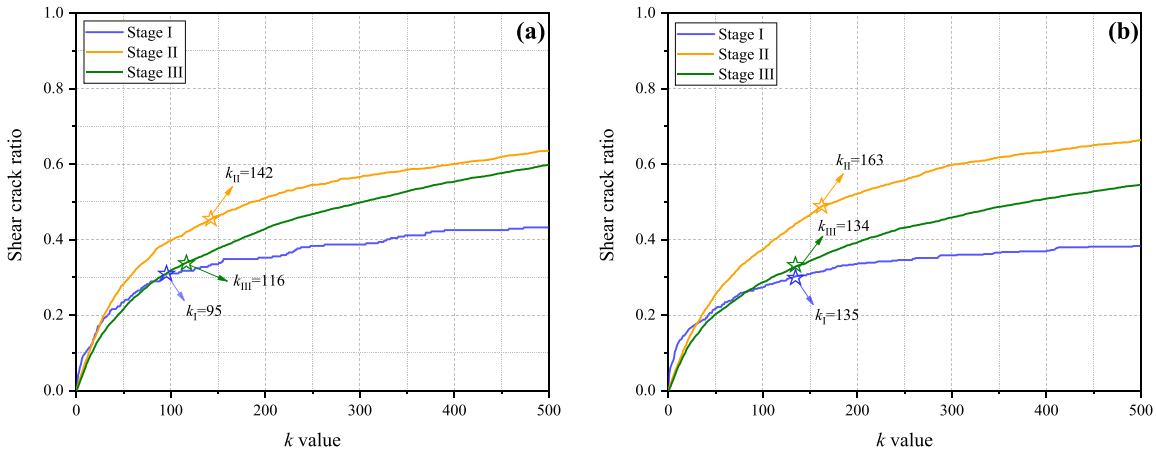


Fig. 12. The variation of flexural shear crack ratio with changes in k value and the fitting results of the k_0: (a) E1-AD; (b) E1-VD.

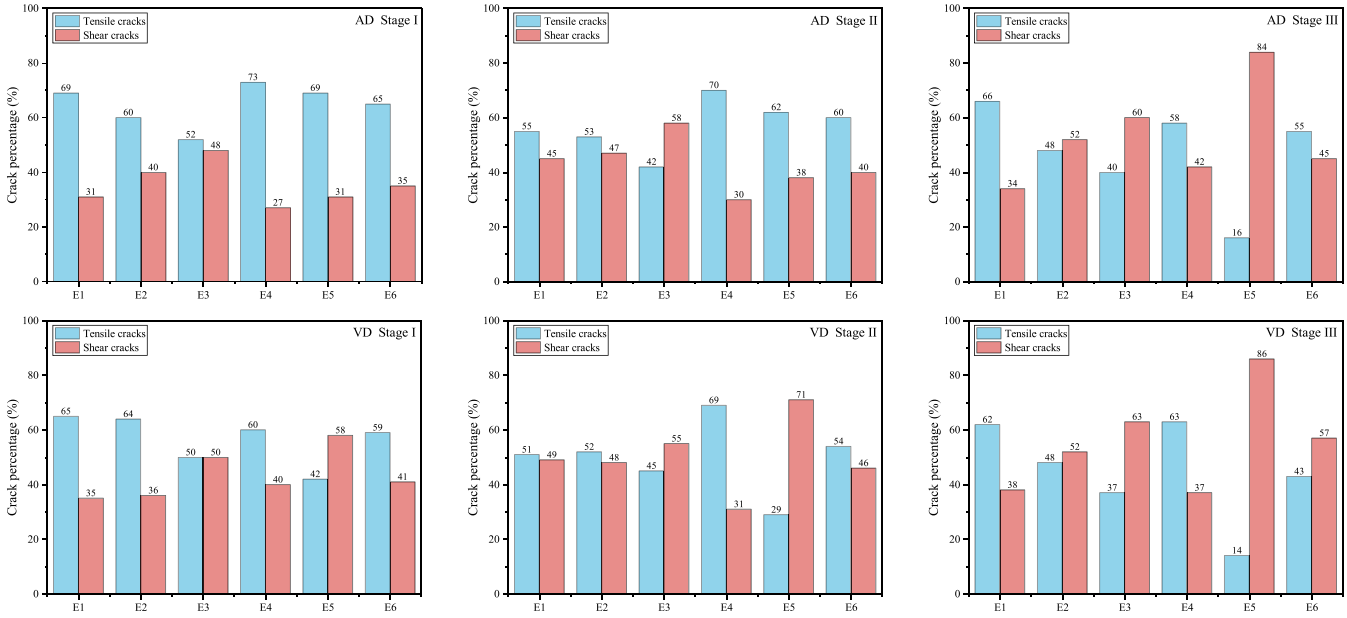


Fig. 13. Flexural tensile crack to shear crack ratio based on Kneedle algorithm discrimination.

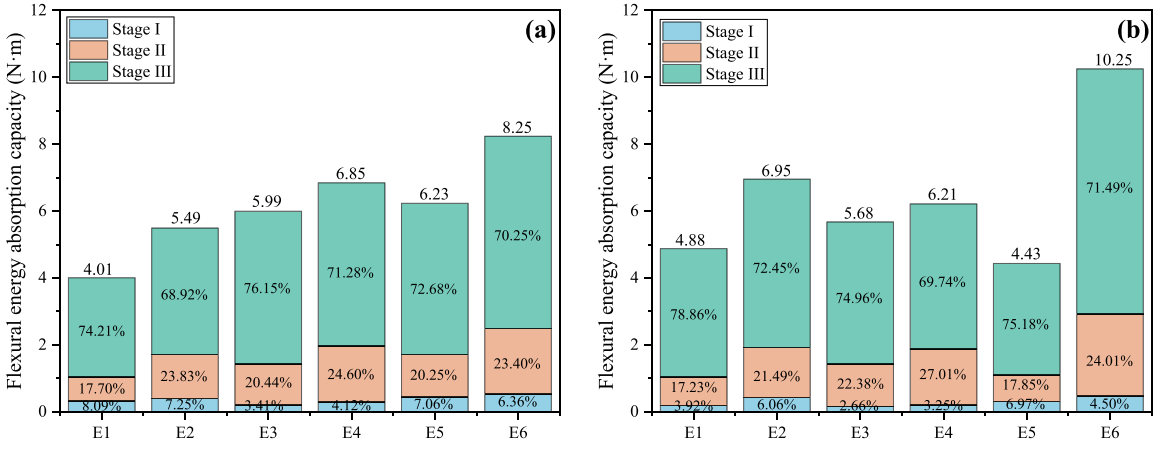


Fig. 14. Flexural energy absorption capacity of specimens in different dry environments: (a) AD; (b) VD.

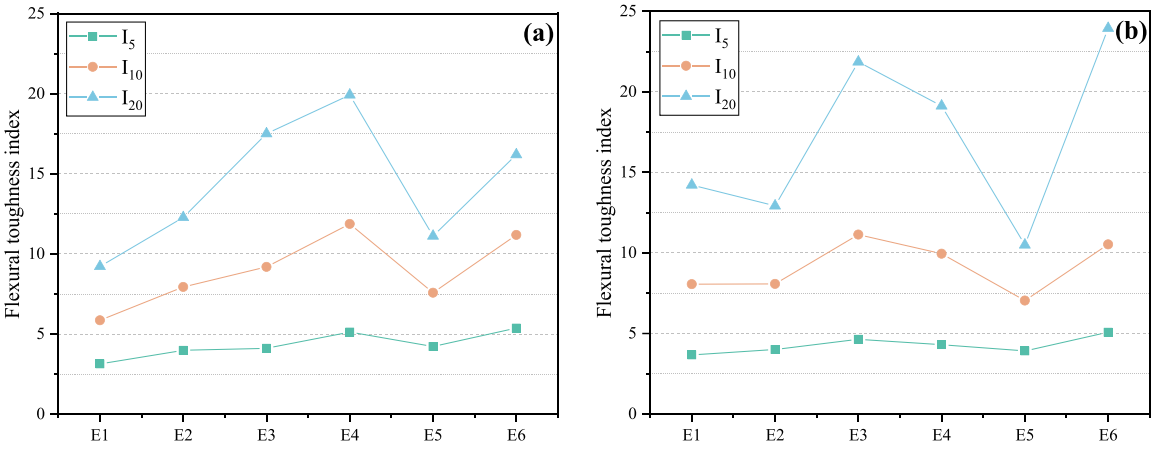


Fig. 15. Flexural toughness index of specimens in different dry environments: (a) AD; (b) VD.

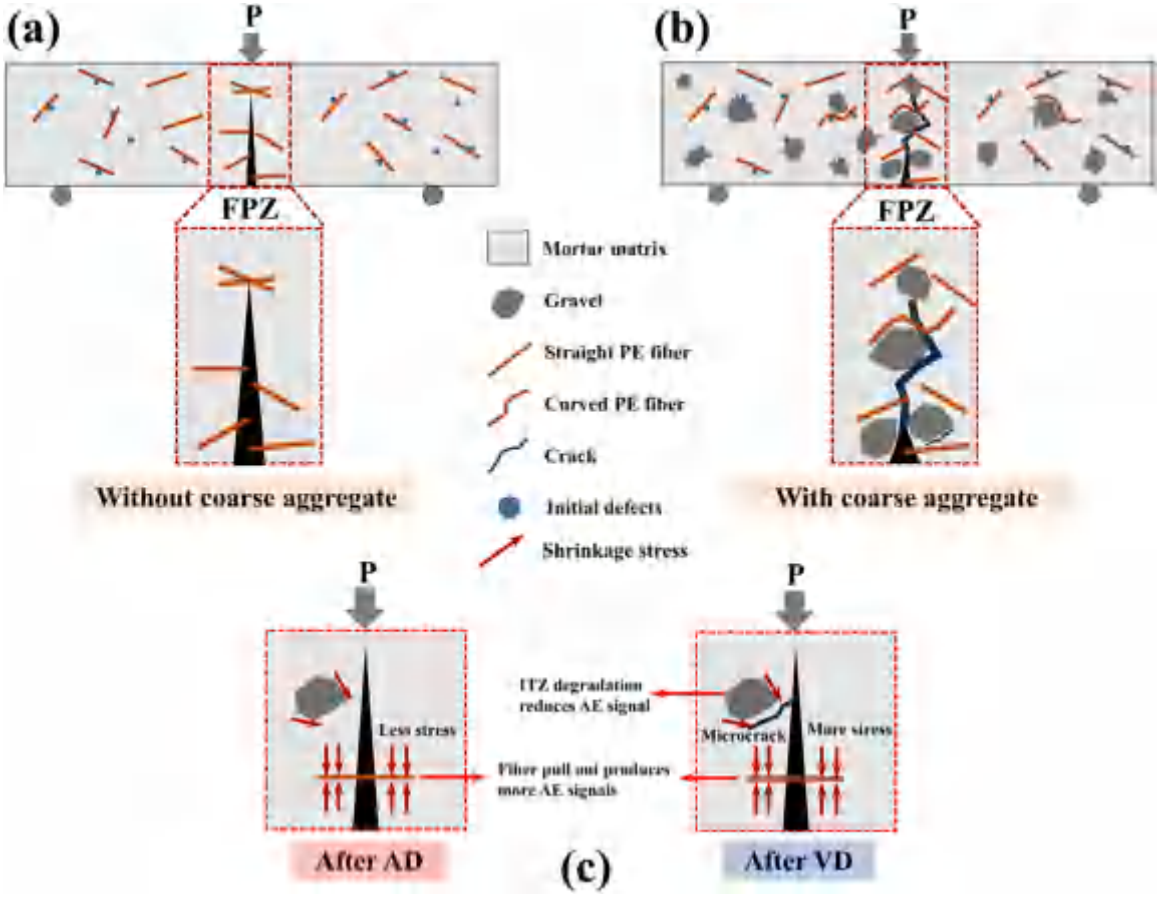


Fig. 16. Schematic diagram of the effect of fiber-coarse structure and low vacuum on flexural fracture characterization.

the flexural behavior of specimens. Drying shrinkage led to a tighter bond between fibers and the matrix, thereby increasing the difficulty of fiber pull-out. This process consumed more energy and generated increased AE signals during the failure process. As previously mentioned, the introduction of coarse aggregates introduced ITZ. Under strong drying conditions (VD), shrinkage can induce microcracking within the ITZ [3,47]. If these microcracks aligned with the propagation path of the FPZ, they may connect with the main crack, reducing the flexural capacity and energy absorption of the specimen (E5) and consequently decreasing AE signals [67]. To mitigate the issue of increased brittleness in the ITZ, a greater amount of fibers was needed to provide confinement (E6), thereby alleviating the propagation of microcracks. This is crucial for enhancing the performance of concrete under VD conditions.

4. Conclusion

This study provided a systematic investigation of the flexural fracture behavior of PEFRC and its mechanism in low vacuum environments based on AE analysis. A synergistic optimization strategy for enhancing fiber-aggregate interactions in PEFRC was proposed, and an innovative application of AE technology for corresponding multi-scale damage

characterization was also presented. The following conclusions can be drawn from the results:

(1) Low vacuum accelerated matrix shrinkage, reducing post-peak toughness of PEFRC. AE analysis revealed intensified fiber-matrix debonding (30 % higher cumulative ringing counts/AE energy) and shortened *b*-value warning periods under VD, indicating accelerated crack transitions. Furthermore, AF-RA image analysis indicated a significant rise in the proportion of shear cracks under VD, directly linking low vacuum environment induced brittleness to altered fracture modes.
(2) Controlling coarse aggregate substitution and coordinating polyethylene fibers improve the performance of PEFRC in low-vacuum environments. E6 (1.5 % fiber + 40 % aggregate) demonstrated superior performance under VD, achieving a 24 % enhancement in fracture energy compared to AD conditions. The mechanism involves coarse aggregates stabilizing shrinkage stress via skeletal frameworks, while fibers bridge cracks, synergistically enhancing the resistance of fracture process zone. This "high fiber-moderate aggregate" principle balanced mechanical strength and interfacial cohesion, offering a cost-effective strategy for low-vacuum resistant concrete.
(3) AE offers multi-scale, quantifiable damage tracking for PEFRC. The ringing counts and AE energy quantitatively characterized the energy dissipation patterns of fiber pullout and matrix cracking. The *b*-value analysis revealed the phenomenon of shortening the warning period of concrete damage in low vacuum environment, providing new indicators for engineering safety monitoring. These innovations advance PEFRC damage mechanism insights and enable high-precision structural health monitoring in extreme environments, providing critical scientific and engineering value.

CRediT authorship contribution statement

Xiaodong Wang: Visualization. **Jilin Wang:** Investigation. **Guangcheng Long:** Supervision, Project administration, Funding acquisition, Conceptualization. **Lei Peng:** Software, Formal analysis. **Yuting Zhang:** Investigation, Data curation. **Lixing Wang:** Validation. **Zhuo Tang:** Supervision, Project administration. **Jionghuang He:** Writing – review & editing, Supervision. **Zhaofei Long:** Writing – review & editing, Writing – original draft, Methodology, Investigation. **Minghui Shangguan:** Data curation.

Declaration of Competing Interest

The authors declare that they have no known competing financial interests or personal relationships that could have appeared to influence the work reported in this paper.

Acknowledgments

The authors are grateful for the financial support of the Program Fund of Nonmetallic Excellence and Innovation Center for Building Materials (No. 24TDA-1).

Data Availability

Data will be made available on request.

References

[1] F. Michelberger, M. Plavec, K. Pyrek, P. Graf, The Hyperloop concept development, possible applications and critical analysis. Sustainable Rail Transport 4: Innovate Rail Research and Education, Springer International Publishing, Cham, 2021, pp. 341–367, https://doi.org/10.1007/978-3-030-82095-4.
[2] Z. Hu, T. Shi, M. Cen, J. Wang, X. Zhao, C. Zeng, Y. Zhou, Y. Fan, Y. Liu, Z. Zhao, Research progress on lunar and Martian concrete, Constr. Build. Mater. 343 (2022) 12117, https://doi.org/10.1016/j.conbuildmat.2022.128117.
[3] G. Long, Y. Chen, Z. Tang, M. Shangguan, C. Gao, S. Xu, Drying shrinkage behavior of cement mortar under low vacuum conditions, Constr. Build. Mater. 374 (2023) 130933, https://doi.org/10.1016/j.conbuildmat.2023.130933.
[4] Y. Sakoi, T. Horiguchi, N. Saeki, Durability of hardened mortar under high-vacuum condition, Cem. Comb. Durable Concr. Proc. Int. Conf. Held Univ. Dundee Scotl. UK (2005).
[5] Z. Long, G. Long, Y. Chen, M. Shangguan, J. Wang, Y. Zhang, M. Yi, C. Gao, Z. Tang, Regulating drying shrinkage behavior of cement-based materials in low vacuum environments and developing a predictive model, J. Build. Eng. 99 (2025) 111639, https://doi.org/10.1016/j.jobe.2024.111639.
[6] N. Hatanaka, T. Ishida, Hydration reaction and strength development of lunar concrete under vacuum condition, SAE Trans. 113 (2004) 324–334.
[7] H. Lin, S. Han, B. Han, S. Liang, H. Ye, H. Liu, P. Feng, Y. Liu, G. Cheng, Development of mechanical properties of concrete in vacuum tunnel of vacuum-based maglev train, Constr. Build. Mater. 445 (2024) 137928, https://doi.org/10.1016/j.conbuildmat.2024.137928.
[8] X. Liu, Z. Si, L. Huang, P. Zhao, Z. Yang, Y. Zhang, R. Wang, Performance of concrete under a low-pressure environment, Constr. Build. Mater. 461 (2025) 139862, https://doi.org/10.1016/j.conbuildmat.2025.139862.
[9] M. Shangguan, Y. Xie, G. Long, Z. Long, F. Wang, Y. Chen, C. Gao, Z. Tang, Hydration and microstructure evolution of cement paste in low vacuum environments, Constr. Build. Mater. 438 (2024) 137233, https://doi.org/10.1016/j.conbuildmat.2024.137233.
[10] S. Zuo, Q. Yuan, T. Huang, K. Zhang, J. Shi, Y. Tan, Microstructural changes of young cement paste due to moisture transfer at low air pressures, Cem. Concr. Res. 164 (2023) 107061, https://doi.org/10.1016/j.cemconres.2022.107061.
[11] C. Zhou, X. Zhang, J. Qiao, J. Feng, Q. Zeng, The deformation of C-S-H gels and its link with dynamic length change of cement pastes upon drying and resaturation, Cem. Concr. Res. 187 (2025) 107693, https://doi.org/10.1016/j.cemconres.2024.107693.
[12] Z. Long, G. Long, Z. Tang, M. Shangguan, C. Gao, M. Yi, Z. He, Y. Zhang, Effects of aggregates and fibers on the strength and permeability of concrete exposed to low vacuum environment, J. Build. Eng. 97 (2024) 110902, https://doi.org/10.1016/j.jobe.2024.110902.
[13] N.P. Tran, C. Gunasekara, D.W. Law, S. Houshyar, S. Setunge, A. Cwirzen, A critical review on drying shrinkage mitigation strategies in cement-based materials, J. Build. Eng. 38 (2021) 102210, https://doi.org/10.1016/j.jobe.2021.102210.
[14] M. Dahal, S. Park, S. Pyo, A modified approach for measuring the air permeability of ultra-high performance concrete (UHPC) under vacuum conditions, Constr. Build. Mater. 401 (2023) 132933, https://doi.org/10.1016/j.conbuildmat.2023.132933.
[15] D.Y. Yoo, S.T. Kang, J.H. Lee, Y.S. Yoon, Effect of shrinkage reducing admixture on tensile and flexural behaviors of UHPFRC considering fiber distribution characteristics, Cem. Concr. Res. 54 (2013) 180–190, https://doi.org/10.1016/j.cemconres.2013.09.006.
[16] F. Cai, D. Zhou, J. Wei, J. Wang, C. Cheng, Y. Zhang, Y. Zhao, Running magnetic resistance of high-Tc superconducting maglev prototype vehicle in an evacuated tube track, Mech. Syst. Signal Pr. 169 (2022) 108635, https://doi.org/10.1016/j.ymssp.2021.108635.
[17] Y.F. Li, C.F. Hsu, J.Y. Syu, F.W. Chen, J.H. Wu, Experimental investigation on the mechanical characteristics of ultra-high-molecular-weight polyethylene (UHMWPE) based fiber-reinforced concrete, Case Stud. Constr. Mater. 21 (2024) e03762, https://doi.org/10.1016/j.cscm.2024.e03762.
[18] Z. Chen, L. Yu, W. Jin, L. Jiang, M. Guo, Effect of ultra-high molecular weight polyethylene fiber on the early mechanical strength and shrinkage crack resistance of concrete, Struct. Concr. 23 (1) (2022) 412–422, https://doi.org/10.1002/suco.202100590.
[19] Y. Wu, M. Chen, D. Chen, X. Zhou, J. He, Modification of ultra-high molecular weight polyethylene fiber to improve mechanical properties of foamed concrete, Constr. Build. Mater. 450 (2024) 138681, https://doi.org/10.1016/j.conbuildmat.2024.138681.
[20] D.Y. Yoo, N. Banthia, Mechanical properties of ultra-high-performance fiber-reinforced concrete: a review, Cem. Concr. Compos 73 (2016) 267–280, https://doi.org/10.1016/j.cemconcomp.2016.08.001.
[21] P.P. Li, Q.L. Yu, H.J.H. Brouwers, Effect of coarse basalt aggregates on the properties of Ultra-high Performance Concrete (UHPC), Constr. Build. Mater. 170 (2018) 649–659, https://doi.org/10.1016/j.conbuildmat.2018.03.109.
[22] T. Feng, M. Jia, W. Xu, F. Wang, P. Li, X. Wang, Y. Tan, J. Jiang, Three-dimensional mesoscopic investigation of the compression mechanical properties of ultra-high performance concrete containing coarse aggregates, Cem. Concr. Compos 133 (2022) 1046788, https://doi.org/10.1016/j.cemconcomp.2022.104678.
[23] T. Uygunoğlu, Effect of fiber type and content on bleeding of steel fiber reinforced concrete, Constr. Build. Mater. 25 (2) (2011) 766–772, https://doi.org/10.1016/j.conbuildmat.2010.07.008.
[24] J. Guan, B. Zhang, C. Xie, L. Li, M. Khan, Meso-fracture model of ultra-high-performance fiber-reinforced geopolymer concrete pertinent to aggregate gradation and fiber spacing, Eng. Fract. Mech. 317 (2025) 110877, https://doi.org/10.1016/j.engfracmech.2025.110877.
[25] B. Tripathi, Effects of polymers on cement hydration and properties of concrete: a review, ACS Omega 9 (2) (2024) 2014–2021, https://doi.org/10.1021/acsomega.3c05914.

[26] N. Tarannum, Km Pooja, R. Khan, Preparation and applications of hydrophobic multicomponent based redispersible polymer powder: a review, Constr. Build. Mater. 247 (2020) 118579, https://doi.org/10.1016/j.conbuildmat.2020.118579.
[27] N.P. Tran, T.N. Nguyen, T.D. Ngo, The role of organic polymer modifiers in cementitious systems towards durable and resilient infrastructures: a systematic review, Constr. Build. Mater. 360 (2022) 129562, https://doi.org/10.1016/j.conbuildmat.2022.129562.
[28] A. Beeldens, D.V. Gemert, H. Schorn, Y. Ohama, L. Czarnecki, From microstructure to macrostructure: an integrated model of structure formation in polymer-modified concrete, Mater. Struct. 38 (6) (2005) 601–607, https://doi.org/10.1007/BF02481591.
[29] K. Du, X. Li, M. Tao, S. Wang, Experimental study on acoustic emission (AE) characteristics and crack classification during rock fracture in several basic lab tests, Int. J. Rock. Mech. Min. Sci. 133 (2020) 104411, https://doi.org/10.1016/j.ijrmms.2020.104411.
[30] M. Ohtsu, Elastic wave methods for NDE in concrete based on generalized theory of acoustic emission, Constr. Build. Mater. 122 (2016) 845–854, https://doi.org/10.1016/j.conbuildmat.2015.12.137.
[31] S. Yin, Y. Zhou, X. Chen, G. Li, A new acoustic emission characteristic parameter can be utilized to evaluate the failure of cemented paste backfill and rock combination, Constr. Build. Mater. 392 (2023) 132017, https://doi.org/10.1016/j.conbuildmat.2023.132017.
[32] F. Sagasta, M.E. Zitto, R. Piotrkowski, A. Benavent-Climent, E. Suarez, A. Gallego, Acoustic emission energy b-value for local damage evaluation in reinforced concrete structures subjected to seismic loadings, Mech. Syst. Sig. Process 102 (2018) 262–277, https://doi.org/10.1016/j.ymssp.2017.09.022.
[33] H. Ren, T. Li, J. Ning, S. Song, Bending damage and fractal characteristics of steel fiber-reinforced concrete under three-point bending test, Constr. Build. Mater. 409 (2023) 134053, https://doi.org/10.1016/j.conbuildmat.2023.134053.
[34] J. Yang, K. Zhao, X. Yu, Y. Yan, Z. He, Y. Zhou, Y. Lai, Fracture evolution of fiber-reinforced backfill based on acoustic emission fractal dimension and b-value, Cem. Concr. Compos 134 (2022) 104739, https://doi.org/10.1016/j.cemconcomp.2022.104739.
[35] D. Ren, B. Liu, S. Chen, D. Yin, M. Yu, H. Liu, L. Wu, Visualization of acoustic emission monitoring of fracture process zone evolution of mortar and concrete beams under three-point bending, Constr. Build. Mater. 249 (2020) 118712, https://doi.org/10.1016/j.conbuildmat.2020.118712.
[36] D. Triantis, S.K. Kourkoulis, An Alternative Approach for Representing the Data Provided by the Acoustic Emission Technique, Rock. Mech. Rock. Eng. 51 (2018) 2433–2438, https://doi.org/10.1007/s00603-018-1494-1.
[37] X. Xu, Z. Jin, Y. Yu, N. Li, Damage source and its evolution of ultra-high performance concrete monitoring by digital image correlation and acoustic emission technologies, J. Build. Eng. 65 (2023) 105734, https://doi.org/10.1016/j.jobe.2022.105734.
[38] Q. Zheng, C. Li, B. He, Z. Jiang, Revealing the effect of silica fume on the flexural behavior of ultra-high-performance fiber-reinforced concrete by acoustic emission technique, Cem. Concr. Compos 131 (2022) 104563, https://doi.org/10.1016/j.cemconcomp.2022.104563.
[39] K. Yang, G. Long, Z. Tang, W. Li, G. Ma, C. Li, Y. Xie, Enhancing the flexural toughness of UHPC through flexible layer-modified aggregates: a novel interfacial toughening strategy, Cem. Concr. Compos 154 (2024) 105770, https://doi.org/10.1016/j.cemconcomp.2024.105770.
[40] R. Yu, P. Spiesz, H.J.H. Brouwers, Mix design and properties assessment of ultra-high performance fibre reinforced concrete (UHPFRC), Cem. Concr. Res. 56 (2014) 29–39, https://doi.org/10.1016/j.cemconres.2013.11.002.
[41] J.N. Wang, R. Yu, D.D. Ji, L.W. Tang, S.C. Yang, D.Q. Fan, Z.H. Shui, Y. Leng, K. N. Liu, Effect of distribution modulus (q) on the properties and microstructure development of a sustainable ultra-high performance Concrete (UHPC), Cem. Concr. Compos 125 (2022) 104335, https://doi.org/10.1016/j.cemconcomp.2021.104335.
[42] R. Yu, P. Spiesz, H.J.H. Brouwers, Development of an eco-friendly ultra-high performance concrete (UHPC) with efficient cement and mineral admixtures uses, Cem. Concr. Compos 55 (2015) 383–394, https://doi.org/10.1016/j.cemconcomp.2014.09.024.
[43] Y. Li, X. Zeng, Y. Shi, K. Yang, J. Zhou, H.A. Umar, G. Long, Y. Xie, A comparative study on mechanical properties and environmental impact of UHPC with belite cement and portland cement, J. Clean. Prod. 38 (2022) 135003, https://doi.org/10.1016/j.jclepro.2022.135003.
[44] X. Kong, J. Pakusch, D. Jansen, S. Emmerling, J. Neubauer, F. Goetz-Neuhoeffer, Effect of polymer latexes with cleaned serum on the phase development of hydrating cement pastes, Cem. Concr. Res. 84 (2016) 30–40, https://doi.org/10.1016/j.cemconres.2016.02.013.
[45] O. Kononova, V. Lusis, A. Galushchak, A. Krasnikovs, A. Macanovskis, 910. Numerical modeling of fiber pull-out micromechanics in concrete matrix composites, J. Vibroeng. 14 (4) (2012) 1852–1861.
[46] H. Ren, T. Li, J. Ning, S. Song, Analysis of damage characteristics of steel fiber-reinforced concrete based on acoustic emission, Eng. Fail. Anal. 148 (2023) 107166, https://doi.org/10.1016/j.engfailanal.2023.107166.
[47] M. Shangguan, Y. Xie, S. Xu, C. Gao, G. Long, F. Wang, M. Liu, Mechanical properties characteristics of high strength concrete exposed to low vacuum environment, J. Build. Eng. 63 (2023) 105438, https://doi.org/10.1016/j.jobe.2022.105438.
[48] R.V. Sagar, B.K.R. Prasad, A Review of recent development in parametric based acoustic emission techniques applied to concrete structures, Nondestr. Test. Eval. 27 (1) (2011) 47–68, https://doi.org/10.1080/10589759.2011.589029.
[49] R.V. Sagar, B.K.R. Prasad, S.S. Kumar, An experimental study on cracking evolution in concrete and cement mortar by the b-value analysis of acoustic emission technique, Cem. Concr. Res. 42 (8) (2012) 1094–1104, https://doi.org/10.1016/j.cemconres.2012.05.003.
[50] J. Xu, X. Niu, Q. Ma, Q. Han, Mechanical properties and damage analysis of rubber cement mortar mixed with ceramic waste aggregate based on acoustic emission monitoring technology, Constr. Build. Mater. 309 (2021) 125084, https://doi.org/10.1016/j.conbuildmat.2021.125084.
[51] J. Xu, X. Niu, Z. Yao, Mechanical properties and acoustic emission data analyses of crumb rubber concrete under biaxial compression stress states, Constr. Build. Mater. 298 (2021) 123778, https://doi.org/10.1016/j.conbuildmat.2021.123778.
[52] D.L. Carnì, C. Scuro, F. Lamonaca, Damage analysis of concrete structures by means of acoustic emissions technique, Compos. Part BEng. 115 (2017) 79–86, https://doi.org/10.1016/j.compositesb.2016.10.031.
[53] D.G. Aggelis, Classification of cracking mode in concrete by acoustic emission parameters, Mech. Res. Commun. 38 (3) (2011) 153–157, https://doi.org/10.1016/j.mechrescom.2011.03.007.
[54] L. Peng, H. Zhao, Z. Tang, Z. Long, G. Long, Research on freeze-thaw damage of Nano-SiO2/steel fiber modified concrete based on acoustic emission technology, J. Railw. Sci. Eng. (2025) 1–12, https://doi.org/10.19713/j.cnki.43-1423/u.T20250440.
[55] A. Behnia, H.K. Chai, T. Shiotani, Advanced structural health monitoring of concrete structures with the aid of acoustic emission, Constr. Build. Mater. 65 (2014) 282–302, https://doi.org/10.1016/j.conbuildmat.2014.04.103.
[56] Monitoring method for active cracks in concrete by acoustic emission, Fed. Constr. Mater. Ind., Japan Fed. Constr. Mater. Ind. Jpn.2003, 2328.
[57] K. Ohno, M. Ohtsu, Crack classification in concrete based on acoustic emission, Constr. Build. Mater. 24 (12) (2010) 2339–2346, https://doi.org/10.1016/j.conbuildmat.2010.05.004.
[58] M.A.A. Aldahdooh, N.M. Bunnori, Crack classification in reinforced concrete beams with varying thicknesses by mean of acoustic emission signal features, Constr. Build. Mater. 45 (2013) 282–288, https://doi.org/10.1016/j.conbuildmat.2013.03.090.
[59] X. Wang, Q. Yue, X. Liu, Crack pattern identification in cementitious materials based on acoustic emission and machine learning, J. Build. Eng. 87 (2024) 109124, https://doi.org/10.1016/j.jobe.2024.109124.
[60] J. Wang, P. Liang, Y. Zhang, X. Yao, G. Yu, B. Guo, Research on classification of rock tensile-shear fracture based on acoustic emission RA-AF values and kneedle algorithm, Chin. J. Rock. Mech. Eng. 43 (S1) (2024) 3267–3279, https://doi.org/10.13722/j.cnki.jrme.2023.0696.
[61] S. Lian, K. Zheng, Y. Zhao, J. Bi, C. Wang, Y. Huang, Investigation the effect of freeze–thaw cycle on fracture mode classification in concrete based on acoustic emission parameter analysis, Constr. Build. Mater. 362 (2023) 129789, https://doi.org/10.1016/j.conbuildmat.2022.129789.
[62] H. Huang, Z. Liu, Q. Qiu, K. Cao, L. Guo, Damage evolution and crack identification of CSG material based on acoustic emission detection technology, J. Build. Mater. (2023). ⟨https://link.cnki.net/urlid/31.1764.tu.20231211.1547.016⟩.
[63] H. Zhang, B. He, X. Zhu, Q. Wang, Z. Jiang, Flexural performance and patterns identification of UHPC subjected to alternating elevated and cryogenic attacks with acoustic emission characterization, Constr. Build. Mater. 364 (2023) 129962, https://doi.org/10.1016/j.conbuildmat.2022.129962.
[64] T. Li, H. Ren, J. Ning, S. Song, R. Tan, Damage mechanism of splitting failure of steel fiber-reinforced concrete based on PCA, J. Vib. Shock 44 (01) (2025) 221–231, https://doi.org/10.13465/j.cnki.jvs.2025.01.022.
[65] ASTM C1018, Standard Test Method for Flexural Toughness and First-Crack Strength of Fiber-Reinforced Concrete (Using Beam with Third-point Loading) American Society of Testing Materials, USA, 1997.
[66] C. Xie, M. Cao, M. Khan, H. Yin, J. Guan, Review on different testing methods and factors affecting fracture properties of fiber reinforced cementitious composites, Constr. Build. Mater. 273 (2021) 121766, https://doi.org/10.1016/j.conbuildmat.2020.121766.
[67] S. Li, B. Chen, Z. Chen, Z. Gao, Performance assessment of basalt fiber reinforced foamed concrete under freeze-thaw conditions using advanced acoustic emission parameters, Constr. Build. Mater. 440 (2024) 137444, https://doi.org/10.1016/j.conbuildmat.2024.137444.

Enhancing Concrete Performance in Low Vacuum Environments: Strategies and Mechanisms

Zhaofei Long[1]; Jionghuang He[2]; Guangcheng Long[3]; Lixing Wang[4]; Yuting Zhang[5]; Zhuo Tang[6]; and Youjun Xie[7]

Abstract: To enhance the service stability of concrete suffering from a low vacuum environment, the effects of silica fume (SF), redispersible latex powder (RDP), and polyethylene fibers (PEF) on concrete strength and permeability were investigated, and the potential mechanisms were analyzed. Results indicated that SF-enhanced concrete demonstrated a higher strength compared to reference concrete. However, the enhancements from SF may be diminished under prolonged low vacuum conditioning, potentially due to the more significant shrinkage induced by such environments. Although the addition of RDP reduced the compressive strength of concrete, it enhanced the flexural strength and reduced gas permeability. Particularly after low vacuum treatment, the flexural strength increased by 27.4% due to accelerated polymer film formation caused by rapid water loss. The addition of PEF enhanced both the compressive and flexural strength of concrete. However, after low vacuum treatment, a notable reduction in the toughness of PEF-reinforced concrete was observed, primarily attributed to the low vacuum environment diminishing the strain-hardening behaviors. The effectiveness of conventional methods for enhancing concrete performance would be altered in a low vacuum environment. Therefore, it is essential to consider these alterations when developing enhancement techniques for concrete under such conditions. DOI: 10.1061/JMCEE7.MTENG-21743. © 2025 American Society of Civil Engineers.

Author keywords: Low vacuum environment; Silica fume (SF); Redispersible latex powder (RDP); Polyethylene fibers (PEFs); Performance evolution.

Downloaded from ascelibrary.org by Central South University on 12/23/25. Copyright ASCE. For personal use only; all rights reserved.

Introduction

The low vacuum tube maglev train, as a revolutionary mode of transportation, has the potential to surpass airplanes and become the fifth mode of transport. The low pressure within the tube effectively reduces air resistance, while maglev technology eliminates wheel-rail adhesion issues (Michelberger et al. 2021). However, the use of traditional steel structures for the tube introduces significant magnetic resistance, hindering train movement and increasing traction energy consumption (Cai et al. 2022). Thus, the nonmetallic properties of concrete make it an ideal alternative material for low vacuum tube maglev infrastructure. Nonetheless, the unique operating conditions of the low vacuum system present new challenges for the long-term safety and durability of concrete structures.

Low vacuum tube maglev trains operate with air pressure maintained below 10 kPa (Wang et al. 2024), requiring the tube structure to have sufficient bearing capacity, good sealing, and excellent operational stability. Recent studies have found that low vacuum environments accelerated moisture loss in concrete, exacerbating shrinkage behavior (Long et al. 2023). Low vacuum also caused pore coarsening (Chang et al. 2022), reduced the stability of hydration products (Shangguan et al. 2024), and decreased impermeability (Shangguan et al. 2023a). These microstructural changes lead to increased brittleness and reduced plastic deformation capacity (Long et al. 2024; Shangguan et al. 2023b). Therefore, designing high-strength, high-toughness, and low-permeability concrete is crucial for ensuring long-term stable service in low vacuum environments. The incorporation of additives such as silica fume (SF), redispersible latex powder (RDP), and fibers has been proven effective in improving these properties under normal curing conditions (Mazloom et al. 2004; Hakeem et al. 2023; Gwon et al. 2018; Hosseinzadeh et al. 2023). However, their performance in low vacuum conditions warrants further investigation.

Supplementary cementitious materials contribute to densification and synergistic hydration in concrete, essential for achieving eco-friendly and high performance (Hosseinzadeh). SF possesses extremely fine particle morphology and a high content of amorphous SiO_2 (Yan and Zhang 2016). Its strong microfiller and pozzolanic effects refine the pore structure; enhance bond strength at the paste-aggregate interface; and reduce porosity, permeability, and bleeding rate (Köksal et al. 2008), as well as improve the mechanical properties and durability of concrete (Afroughsabet and Ozbakkaloglu 2015). Additionally, it reduces long-term shrinkage and creep (Al-Khaja 1994). However, the use of SF in high-strength concrete can lead to increased brittleness (Köksal et al. 2008).

RDP is created from polymer emulsions through spray drying. Upon contact with water, it forms a new emulsion that retains the properties of the original. Once the water evaporates, a hydrophobic and flexible polymer film forms within the mortar, addressing issues of low bonding strength, low tensile strength, and poor chemical resistance in cementitious materials [H. Pak-Harvey and C. L. Mao,

[1]Ph.D. Student, School of Civil Engineering, Central South Univ., Hunan, Changsha 410075, PR China. Email: lzf2033195@163.com
[2]Ph.D. Student, Dept. of Civil and Environmental Engineering, Hong Kong Polytechnic Univ., Hong Kong, PR China. ORCID: https://orcid.org/0000-0002-6995-3075. Email: hjh2017@foxmail.com
[3]Professor, School of Civil Engineering, Central South Univ., Hunan, Changsha 410075, PR China (corresponding author). Email: longguangcheng@csu.edu.cn
[4]Master's Student, School of Civil Engineering, Central South Univ., Hunan, Changsha 410075, PR China. Email: lixing7363@163.com
[5]Master's Student, School of Civil Engineering, Central South Univ., Hunan, Changsha 410075, PR China. Email: miaooao@163.com
[6]Associate Professor, School of Civil Engineering, Central South Univ., Hunan, Changsha 410075, PR China. Email: zhuo.tang@csu.edu.cn
[7]Professor, School of Civil Engineering, Central South Univ., Hunan, Changsha 410075, PR China. Email: xieyj@csru.edu.cn

Note. This manuscript was submitted on February 26, 2025; approved on May 19, 2025; published online on December 17, 2025. Discussion period open until May 17, 2026; separate discussions must be submitted for individual papers. This paper is part of the Journal of Materials in Civil Engineering, © ASCE, ISSN 0899-1561.

"Redispersible acrylic polymer powder for cementitious compositions," US Patent No. US5519084A (1996); Guziak and Maclay 1963]. The core-shell structure of RDP enhances sprayability and dispersibility without compromising crack-bridging and film-forming properties (Tarannum and Pooja 2022). Studies have shown that different types of RDP improve impermeability and are used in a variety of applications, including building binders, concrete repair joints, waterproof mortars, and crack isolation membranes (Jumate et al. 2007; Tarannum et al. 2020; Tao et al. 2022; Caimi et al. 2018). Given that low vacuum environments increase specimen brittleness (Shangguan et al. 2023b) and challenge the stability of hydration products (Shangguan et al. 2024), RDP is a potential additive to enhance the mechanical properties and durability of cement-based materials under such conditions.

Fibers are commonly used to reinforce brittle materials, enhancing the tensile strength, flexural toughness, and ductility of concrete through their crack-bridging effect (Hakeem et al. 2023; Mohammadi et al. 2008). Barr et al. (2003) noted that fibers inhibit drying shrinkage, with the effect being more pronounced in higher-strength concrete, making them crucial for controlling shrinkage in high-strength mixes. Steel fibers are widely used for reinforcing high-strength, high-toughness concrete (Shah and Ribakov 2011), but their use is limited in low vacuum tubes due to the magnetic resistance of metal structures (Cai et al. 2022). Therefore, alternative fibers such as organic, glass, and textile fibers are considered for improving toughness. Polypropylene fiber (PPF) is the most commonly used organic fiber, improving mechanical properties, reducing water absorption (Afroughsabet and Ozbakkaloglu 2015), and reducing the risk of cracking in high-strength concrete (Shen et al. 2023). Compared to PPF, polyethylene fiber (PEF) has a higher elastic modulus and fracture strength, significantly improving tensile strength, strain capacity, and energy absorption, surpassing steel fibers in enhancing ductility (Ye et al. 2021; Choi et al. 2016; Yoo and Kim 2019). As a result, PEF is ideal for designing ultrahigh ductility concrete.

In low vacuum environments, concrete experiences more significant moisture loss, resulting in increased shrinkage and affecting its overall performance. Therefore, understanding the changes in the inherent properties of concrete under such conditions is critical to ensuring the service safety of concrete in low vacuum tunnels. At the same time, evaluating the effectiveness of commonly used enhancement techniques for normal concrete in low vacuum conditions is equally important. This study investigates the effects of SF, RDP, and PEF on the mechanical properties, mass loss, gas permeability, and microstructure of concrete under low vacuum conditions. Furthermore, it aims to uncover the underlying mechanisms involved and provide valuable insights into designing high-stability, high-performance concrete suitable for use in low vacuum environments.

Test Program

Materials

In this experiment, a 42.5-grade ordinary portland cement was employed. The oxide compositions of the cement, (FA), (GGBS), and SF, were determined using XRF technology (Table 1). The particle size distribution of these cementitious materials was measured with a laser particle size analyzer (Fig. 1). The cement has a density of 3.12 g=cm^3 and a specific surface area of 367 m^2=kg. FA has a density of 2.40 g=cm^3; GGBS has a density of 2.85 g=cm^3; and SF has a density of 2.10 g=cm^3 with a specific surface area over 20,000 m^2=kg. The fine aggregate used was well-graded washed river sand with a fineness modulus of 2.65 and an apparent density of 2,660 kg=m^3. The coarse aggregate was hard impact-crushed limestone gravel with a particle size range of 5–25 mm and an apparent density of 2,680 kg=m^3. A high-performance polycarboxylate superplasticizer (SP) was used as the water reducer, achieving a 30% water reduction rate. Tap water from the laboratory was utilized. RDP was derived from [vinyl acetate-ethylene (VAE)] emulsion drying, with volatility below 2%, bulk density of 500 kg=m^3, average particle size (D50) of 85 μm, and PH of 8. Performance parameters of the polyethylene fibers are detailed in Table 2.

Mix Proportions

The water-to-binder ratio for the concrete was fixed at 0.30. In the control group (A0), supplementary cementitious materials comprised 30% of the total binder, with FA at 15%, GGBS at 10%, and SF at 5%. Through investigation, the mechanical properties of high-strength concrete can be maximized when SF is added at around 10% (Yan and Zhang 2016; Fallah and Nematzadeh 2017; Bhanja and Sengupta 2005). Therefore, Group A1 increased the silica fume content from 5% to 10%, designated as the silica fume group; Group A2 introduced RDP at 2% of the total binder, termed the RDP group; and Group A3 incorporated a 1% volume fraction of polyethylene fibers, representing fiber-reinforced concrete. The specific mix proportions for each group of concrete specimens are detailed in Table 3.

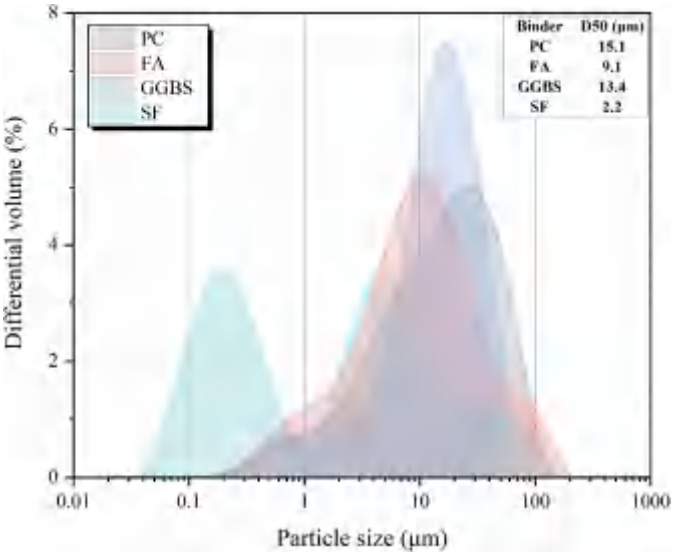


Fig. 1. Particle size distribution of cementitious material.

Table 1. Oxide composition of cementitious materials (wt%)

Binder	CaO	SiO_2	Al_2O_3	Fe_2O_3	SO_3	MgO	TiO_2	Na_2O	K_2O
PC	55.45	24.05	5.50	3.63	3.44	1.36	0.29	0.17	1.06
FA	7.38	51.53	27.68	7.67	1.44	0.91	—	0.83	1.22
GGBS	33.60	26.10	13.80	14.10	—	8.10	—	0.45	0.81
SF	0.35	96.90	0.10	0.03	0.90	0.64	—	0.16	0.70

Table 2. Property indexes summary of polyethylene fibers

Density (g · cm^{-3})	Length (mm)	Diameter (μm)	Elastic modulus (GPa)	Fracture strength (MPa)	Elongation (%)
0.97	30	25	≥122	≥3,100	≤3.5%

Downloaded from ascelibrary.org by Central South University on 12/23/25. Copyright ASCE. For personal use only; all rights reserved.

Table 3. Mix proportions of the concrete specimens

Mixture	Raw material (kg=m^3)									
	PC	FA	GGBS	SF	Water	Sand	Gravel	RLP	PEF	SP
A0	350	75	50	25	147	740	1,050	—	—	5
A1	325	75	50	50	147	740	1,050	—	—	6
A2	350	75	50	25	147	740	1,050	10	—	5
A3	350	75	50	25	147	740	1,050	—	9.7	6

Test Procedures

Specimen Preparation

Following existing standards, a twin-shaft horizontal concrete mixer was used to prepare specimens of different sizes for performance testing. Cube specimens of 100 × 100 × 100 mm^3 were used for compressive strength tests. Prismatic specimens of 100 × 100 × 400 mm^3 measured flexural strength, while 100 × 100 × 300 mm^3 prisms were used for uniaxial compression stress-strain tests. Cylindrical specimens 100 mm in diameter and 50 mm in height were used for mass loss, gas permeability, and capillary absorption tests.

Freshly mixed concrete was placed into molds, covered with plastic film, and cured for 24 hours before demolding. The specimens were then transferred to a curing room for 28 days of standard curing. Post-curing, specimens were divided into two groups for natural drying and low vacuum drying treatments. Natural drying was carried out at room temperature and atmospheric pressure. Low vacuum drying was performed in a custom vacuum chamber achieving 100 Pa pressure (Long et al. 2023). Specimens subjected to natural drying and low vacuum drying were labeled AD and VD, respectively. Specimens dried for 28 days and 56 days were marked as AD28, VD28, AD56, and VD56, respectively.

Strength Test

Concrete compressive and flexural performance tests were conducted using an electrohydraulic servo universal testing machine. The uniaxial compression tests were performed using an Instron 1346 testing machine produced by Instron in the UK, while the four-point bending tests were carried out using an Instron 1342 testing machine. The cube compressive strength tests were controlled by force, with a loading rate of 10 kN=s, as shown in Fig. 2(a).

The concrete flexural tests were conducted using the four-point bending loading method, with a loading rate of 0.09 mm=min, as shown in Fig. 2(b). The flexural strength was calculated using the formula given in Eq. (1); the energy absorption value, which is the area under the force-displacement curve, was calculated using the method described in Eq. (2) (Yang et al. 2020)

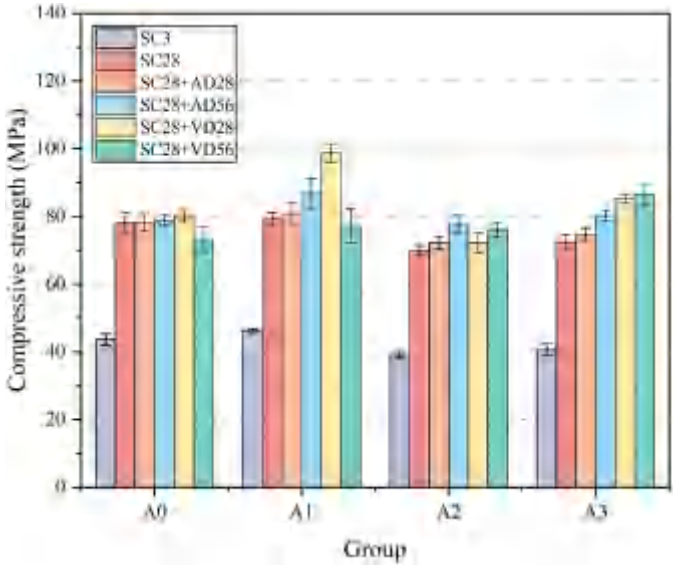


Fig. 3. Cube compressive strength of concrete.

$$f_t = \frac{F_s l}{bh^2} \quad (1)$$

where f_t = the flexural strength of the specimen (Mpa); F_s = the peak force of the load-displacement curve of the specimen (N); l = the span between the supports of the specimen (mm); b = the width of the specimen (mm); and h = the height of the specimen (mm)

$$E_A = \int_0^x F(x)dx \quad (2)$$

where E_A = the energy absorption value (N · m); x = the displacement in the midspan of the specimen (m); and F(x) = the load on the specimen when it undergoes a displacement of x (N).

The compressive stress-strain test was conducted at a loading rate of 0.36 mm=min. An extensometer with a gauge length of 360 mm was used to record the longitudinal deformation of the specimen during compression, allowing for the plotting of the stress-strain curve, as depicted in Fig. 3(c). The axial compressive toughness ratio ($R_{e;1.0}$), representing the compressive toughness of the concrete, was calculated using Eq. (3) (CECS 2009)

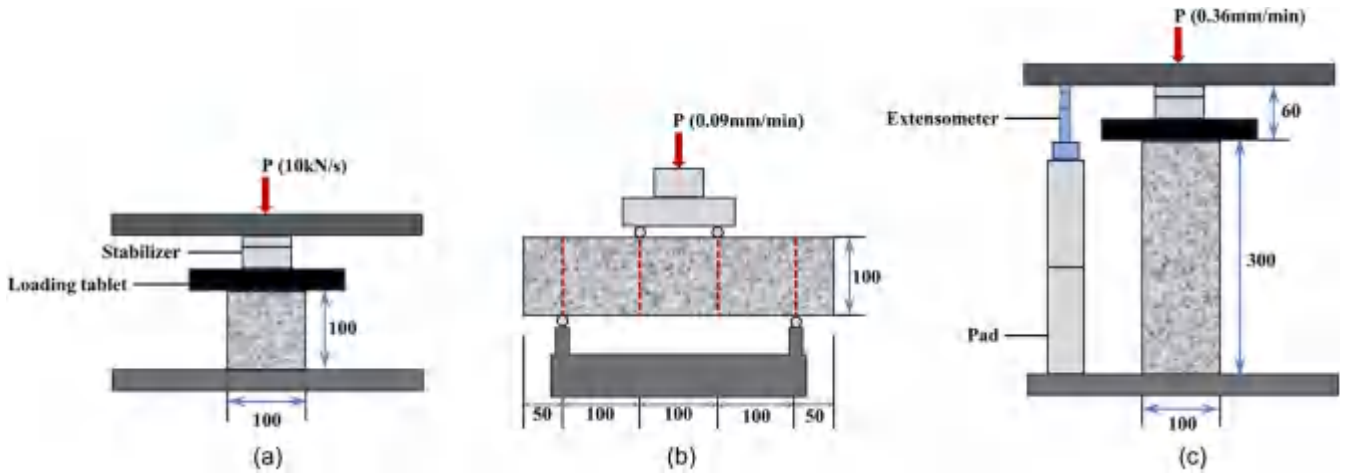


Fig. 2. Loading diagram of concrete strength test: (a) compressive strength test; (b) four-point bending test; and (c) stress-strain test.

Downloaded from ascelibrary.org by Central South University on 12/23/25. Copyright ASCE. For personal use only; all rights reserved.

$$R_{e;1.0} = \frac{W_{1.0}}{F_{max} \times L_0 \times 1.0\%} \quad (3)$$

where F_{max} = the peak load of the load-deformation curve (N); L_0 = the gauge length of axial compression deformation measurement (mm); and $W_{1.0}$ = the compression work, which is the area under the load-deformation curve of the axial deformation from 0 to $L_0 \times 1.0\%$ mm (N · m).

Mass Loss

Initially, the mass of each specimen in various groups was measured using an electronic balance with 0.01 g precision before drying treatment. The mass of each specimen was then recorded at multiple intervals during natural drying and low vacuum drying. The mass loss monitoring period was extended to 56 days. Mass loss was recorded daily for the first 7 days, followed by recordings at 10 and 14 days, then every 7 days until the 56-day mark. The mass loss rate of the specimens was calculated using Eq. (4). The final result is the average value of the three test specimens

$$\Delta w_t = \frac{m_0 - m_t}{m_0} \times 100\% \quad (4)$$

where Δw_t = the mass loss rate of the specimen at time t during exposure to the low vacuum environments (%); m_0 = the initial mass of the specimen before exposure to the low vacuum environments (g); and m_t = the mass of the specimen at time t after exposure to the low vacuum environments (g).

Gas Permeability Test

The effect of drying environment and duration on concrete air permeability was evaluated by measuring the apparent gas permeability coefficient of concrete specimens before and after natural and low vacuum drying using the Cembureau method (Cagnon et al. 2024). The NELD-AV037 gas permeability tester from Beijing Neld Intelligent Technology Co., Ltd. was employed for these tests. Cylindrical specimens were sealed with epoxy resin on the sides and placed between the high-pressure (300 kPa) and atmospheric pressure zones of the device. The test lasted 6 hours with a 1-min sampling interval. The calculation for the apparent gas permeability coefficient is detailed in Eq. (5), with the average value of the three specimens selected as the final result

$$k_a = \frac{2\mu L P_2 Q}{A(P_1^2 - P_2^2)} \quad (5)$$

where k = the gas permeability coefficient (m^2); μ = the viscosity coefficient of air, 1.78×10^{-5} Pa · s; L = the thickness of the sample (mm); and P_1 = the gas pressure at the inlet, maintained at a constant pressure of 300 kPa; P_2 = the atmospheric pressure of 101 kPa; Q = the flow rate measured at the sample outlet (m^3=s); A is the cross-sectional area of the specimen (m^2).

Capillary Water Absorption Test

Following 56 days of natural and low vacuum drying, the cylindrical concrete specimens were subjected to a capillary absorption test following ASTM C1585-20 (ASTM 2020). The sides of the specimens were sealed with epoxy resin, and the opposite side to the water absorption surface was covered with plastic film and secured with rubber bands. The initial mass was recorded using an electronic balance, after which the specimens were immersed in a water tank with a support, ensuring an immersion depth of approximately 3 mm. At specified times, the specimens were removed and gently dried with a wet towel, and the mass post-water absorption was measured. The capillary water absorption was tested over the first 7 days, and the capillary water absorption height was calculated using Eq. (6)

$$H = \frac{m_{wt}}{A\rho_w} \quad (6)$$

where H = the water absorption height (mm); m_{wt} = the absorbed water mass of the specimen at time t (g); A = the contact area between the specimen and water (mm^2); and ρ_w = the density of water, 0.001 g=mm^3.

Nitrogen Adsorption and Desorption Test

The nitrogen adsorption and desorption (NAD) test evaluates changes in the porosity and pore size distribution of concrete. The Builder SSA-4000 specific surface area analyzer was employed for this test, utilizing samples sized between 3 and 5 mm and weighing approximately 1.0 g.

SEM Test

The Bruker S8-TIGER scanning electron microscope (SEM) analyzer was utilized to examine the microstructure of samples extracted from the interior of concrete specimens following compression tests. Before analysis, the base surface of the specimens was polished flat using sandpaper and underwent gold sputtering treatment.

Results and Discussion

Mechanical Properties Development

Compressive Strength

The changes in compressive strength of concrete cubes before and after various drying treatments are presented in Fig. 3. As depicted, SF increased the 3-day and 28-day compressive strength by 5.8% and 1.4%, respectively. Conversely, RDP (Wacker Chemical, Shanghai, China) and PEF (Beijing Tongyizhong New Material Technology, Jingsheng, China) decreased the 3-day strength by 10.2% and 7.1%, and the 28-day strength by 10.5% and 7.3%, respectively. SF can act as a filler and react with calcium hydroxide to form additional C—S—H gel, enhancing concrete strength (Wang et al. 2022). In contrast, RDP would introduce air pores, increasing pore volume and reducing compressive strength (Wang and Wang 2011). The acetate ions from RDP hydrolysis would form complexes with calcium ions in an alkaline environment, inhibiting cement hydration (Kong et al. 2016). Additionally, the low elastic modulus of RDP negatively impacts compressive strength (Ren et al. 2022). PEF addition decreased workability due to fiber agglomeration and reduced interfacial bond strength (Wang et al. 2020; Hu et al. 2022), impairing compressive strength at initial ages. However, the test results indicate that PEF positively impacts the later-stage strength of concrete, demonstrating its effectiveness in resisting drying.

Under natural drying conditions, concrete compressive strength increased continuously with extended drying time. Compared to natural drying, low vacuum drying significantly enhanced strength within the first 28 days. Specifically, samples A0 to A3 exhibited strength increases of 2.8%, 24.7%, 3.3%, and 17.7%, respectively, compared to the 28-day strength of standard-cured concrete. Notably, the compressive strength of A0 and A1 decreased after 56 days of continuous low vacuum drying, while A2 and A3 showed further improvement. The strength enhancement under drying conditions is due to the reduced dissociation forces and viscous effects at crack tips (Shangguan et al. 2023b; Zhang et al. 2017; Maruyama et al. 2014). A recent study reported that in a mature paste with a low water-to-binder ratio and high hydration degree, the negative impact of low vacuum is weaker (Lin et al. 2024). Water removal causes gel pores to close, promoting matrix densification and positively affecting mechanical properties. However, low vacuum drying was more intense than natural drying, resulting

Downloaded from ascelibrary.org by Central South University on 12/23/25. Copyright ASCE. For personal use only; all rights reserved.

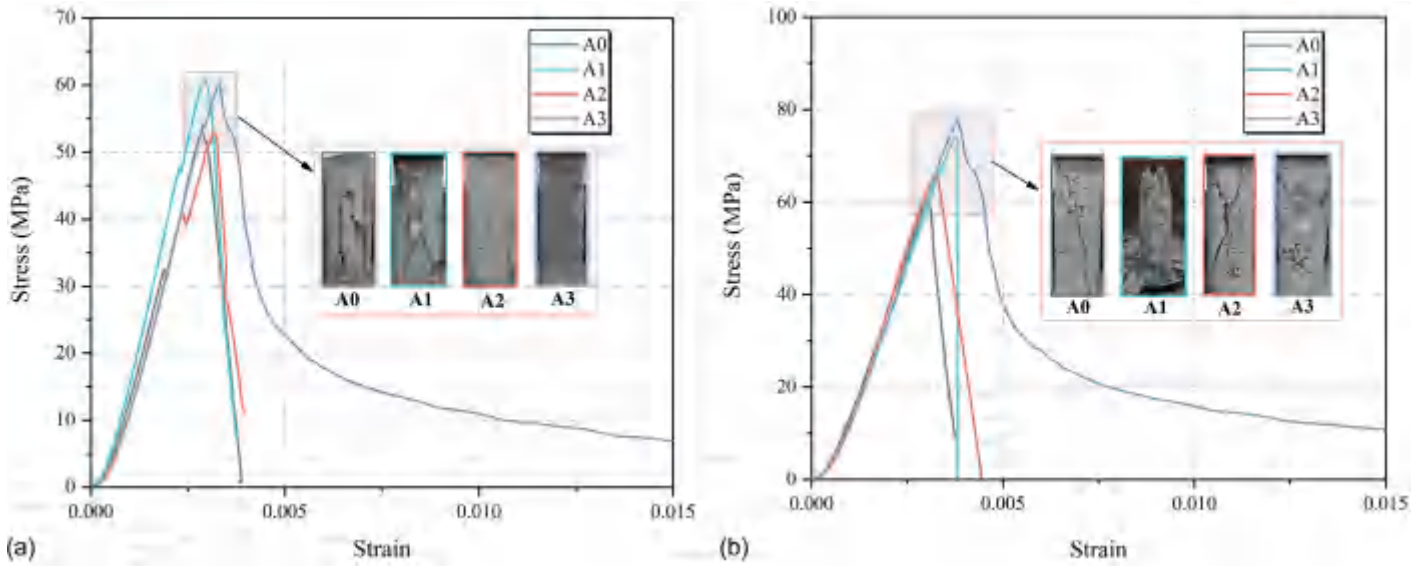


Fig. 4. Stress-strain curves of concrete: (a) SC28+AD56; and (b) SC28+VD56.

in more pronounced cracking from drying shrinkage over time (Long et al. 2023; Shangguan et al. 2023b). The absence of toughness-modulating components in A0 and A1 led to an increased susceptibility to crack propagation, resulting in reduced compressive strength in later stages. Conversely, the flexible polymer film from RDP and the bridging effect of PEF could mitigate the adverse impact caused by drying shrinkage.

Stress-Strain Curves under Uniaxial Compression

Fig. 4 shows the complete stress-strain curves of concrete under uniaxial compression, while Table 4 summarizes the compression characteristic parameters. Under both natural and low vacuum drying conditions, ordinary concrete formed longitudinal and diagonal cracks under compressive loading, rapidly coalescing and causing sudden failure and brittle fracture. Conversely, the presence of PEF increased both the ductility and peak strain value compared to reference concrete. As indicated in Table 4, SF, RDP, and PEF all increased the peak stress of concrete, enhancing its compressive energy absorption capacity. However, SF reduced the energy dissipation capacity under low vacuum drying, with a 0.5% decrease in $R_{e;1.0}$, while RDP and PEF increased $R_{e;1.0}$ by 16.8% and 132.1%, respectively. Overall, RDP and PEF effectively enhanced the compressive toughness of concrete under various drying conditions, whereas SF increased brittleness. Comparing $R_{e;1.0}$ under different drying environments revealed that A0 and A1 had lower $R_{e;1.0}$ under low vacuum drying than natural drying, while A2 and A3 exhibited the opposite trend. This indicates that ordinary and silica fume-enhanced concrete becomes more brittle under low vacuum drying, whereas the addition of RDP and PEF improves compressive toughness in low vacuum environments.

Table 4. Uniaxial compression stress-strain test results of concrete

Group		F_{max} (kN)	Energy absorption (MPa)	Energy dissipation (MPa)	W (N · m)	$R_{e;1.0}$
SC28+AD56	A0	532.01	0.066	0.030	3,486.76	1.821
	A1	605.11	0.083	0.027	3,962.48	1.819
	A2	531.02	0.075	0.024	3,575.48	1.870
	A3	603.27	0.088	0.181	8,140.38	3.748
SC28+VD56	A0	604.34	0.079	0.026	3,787.83	1.741
	A1	740.20	0.126	0.024	4,618.02	1.733
	A2	661.34	0.095	0.040	4,843.44	2.034
	A3	776.61	0.132	0.242	11,296.89	4.041

Flexural Strength

Fig. 5 illustrates the bending failure modes of ordinary and fiber-reinforced concrete under different drying conditions, with the corresponding force-displacement curves shown in Fig. 6. Ordinary concrete underwent brittle failure under bending loads, whereas PEF-reinforced concrete exhibited plastic failure characteristics. The peak load and peak displacement were highest for PEF-reinforced concrete, showing post-peak slip hardening. The main crack openings in the fiber-reinforced specimens revealed numerous uniformly distributed pulled-out and unpulled fibers, demonstrating the excellent crack-bridging performance of PEF.

The flexural strength and energy absorption values for each specimen group were calculated using Eqs. (1) and (2). Following the method in reference (Yang et al. 2024), the flexural toughness index (I_5) of PEF-reinforced concrete before and after low vacuum treatment was obtained and summarized in Fig. 7. After the low vacuum treatment, the flexural strength of samples A0 to A3 increased by 22.1%, 12.3%, 27.4%, and 3.3%, respectively. This improvement is mainly related to the continuous hydration of the matrix from moisture migration and redistribution. The presence of RDP resulted in the highest increase in flexural strength, potentially attributed to the accelerated moisture evaporation under a low vacuum environment. This promoted the rate of polymer film formation and consequently resulted in better bonding between the polymer films and hydrates, which effectively connected with pores and cracks, creating a flexible interlocking network that reduced stress concentration (Tien 2014; Zhu et al. 2011). Moreover, despite fiber-reinforced concrete exhibiting a higher increase in flexural strength and energy absorption after low vacuum drying, its flexural toughness index decreased by 11.2% compared to SC28. This phenomenon may be due to the greater shrinkage caused by the low vacuum conditions, which increased the bonding strength between the fibers and the matrix, thus limiting the slippage during the plastic deformation stage, and ultimately reducing stress hardening. As shown in Fig. 6, the SC28 sample exhibited a significant stress-hardening region, while the stress-hardening region of the SC28+VD56 sample was noticeably reduced. This suggests that the

Downloaded from ascelibrary.org by Central South University on 12/23/25. Copyright ASCE. For personal use only; all rights reserved.

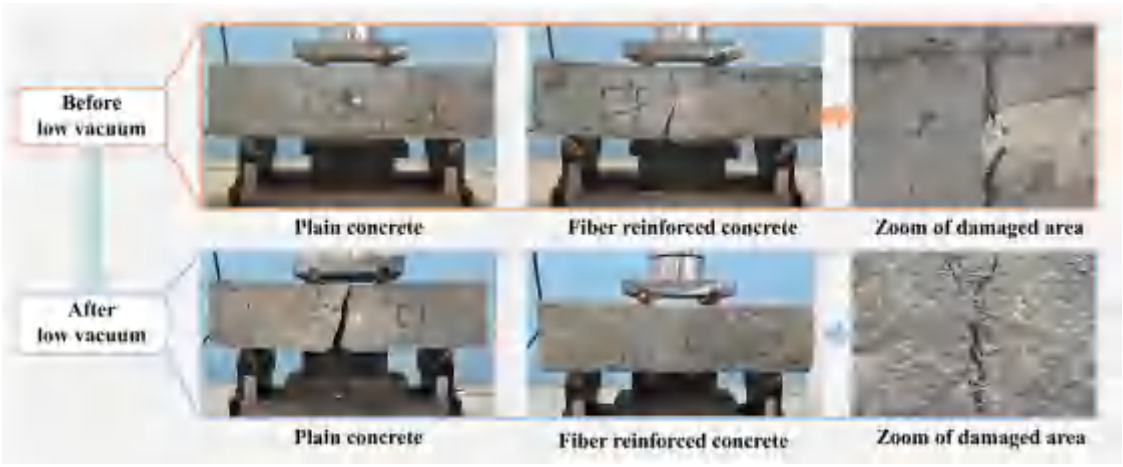


Fig. 5. Four-point bending failure diagram of concrete.

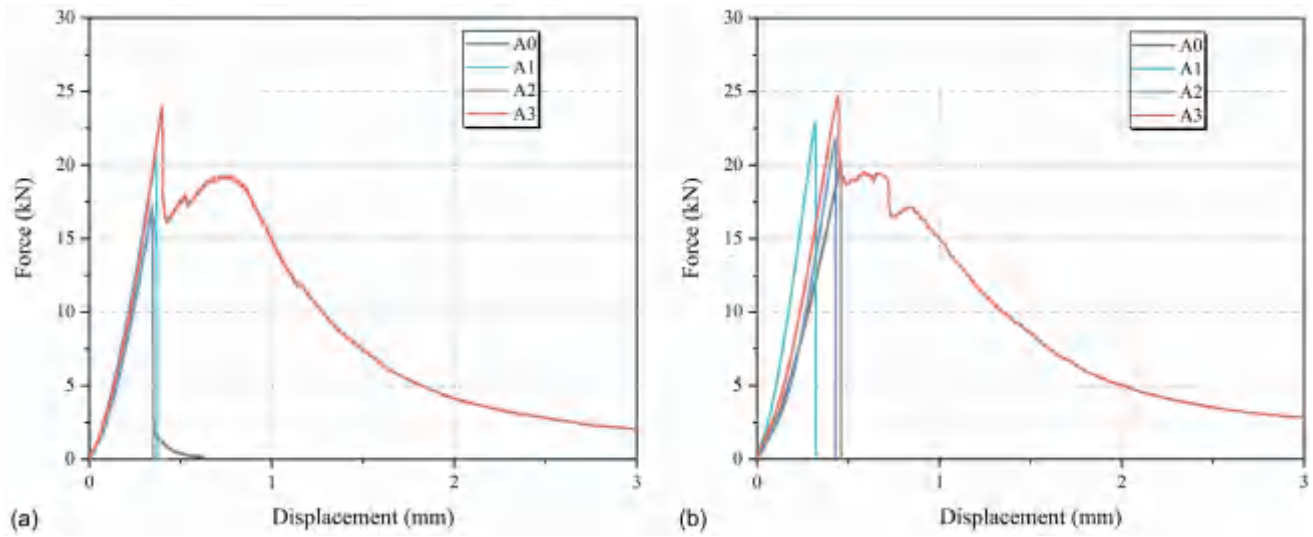


Fig. 6. Force-displacement curves of concrete: (a) SC28; and (b) SC28+VD56.

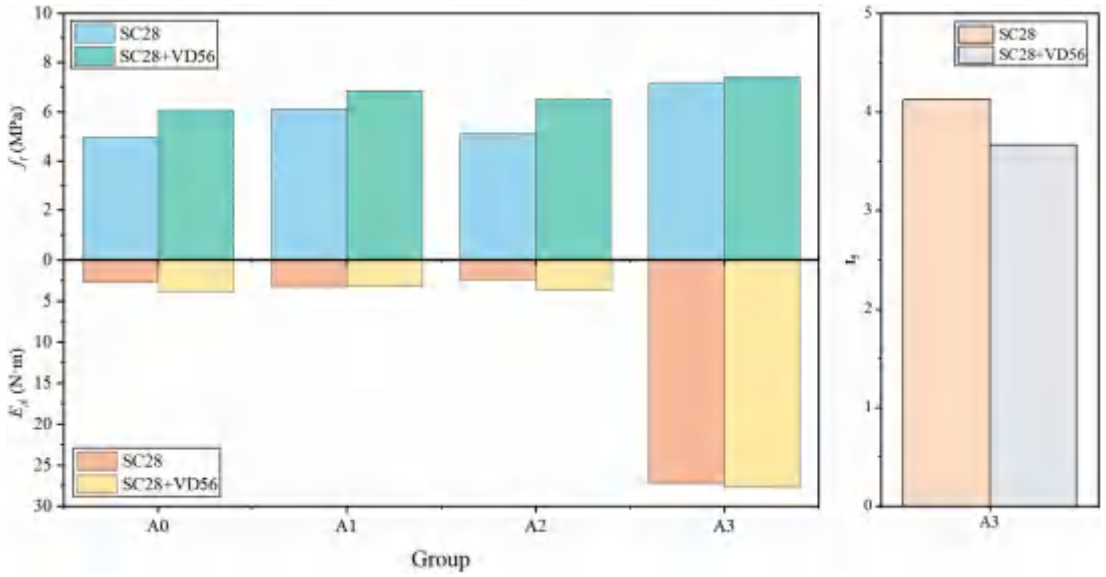


Fig. 7. Flexural toughness of concrete.

Downloaded from ascelibrary.org by Central South University on 12/23/25. Copyright ASCE. For personal use only; all rights reserved.

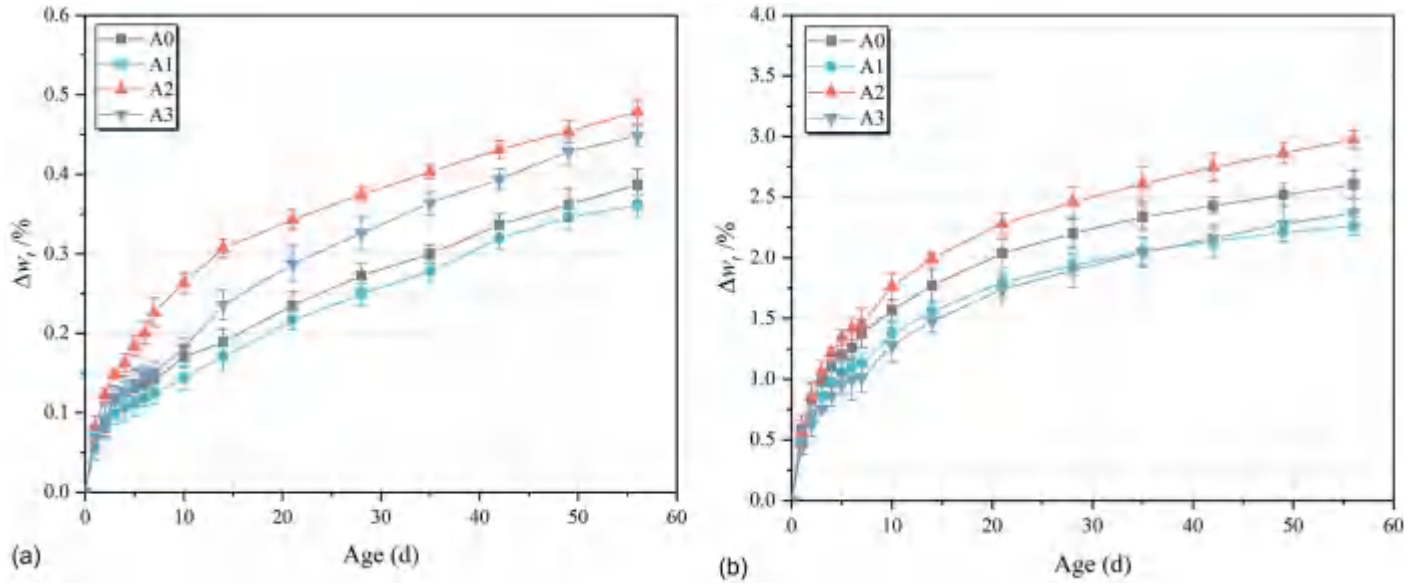


Fig. 8. Mass loss rate (Δw_t) of concrete: (a) SC28+AD56; and (b) SC28+VD56.

flexural toughness of concrete may continue to decline under prolonged low vacuum conditions.

Mass Loss

Fig. 8 illustrates the development curve of the mass loss rate of concrete in different drying environments. Under natural drying and low vacuum condition, concrete initially experiences a rapid increase in mass loss, which then slows and stabilizes after 14 days. In a low vacuum environment, mass loss is particularly pronounced, with the 56-day mass loss rate being 5.3 to 6.7 times higher than under natural drying conditions, and the drying rate being 5.9 to 7.2 times greater. The mass change process of concrete was significantly influenced by environmental humidity. In the initial drying stage, evaporation of free water from capillary pores led to increased mass loss. Low humidity and a large humidity gradient in low vacuum environment promote continuous moisture migration outward, leading to substantially higher mass loss and drying rates compared to natural conditions.

Further observations revealed that SF helps to reduce the mass loss rate of concrete in different drying environments, while RDP increases the final mass loss rate of concrete. PEF increased mass loss under natural drying conditions but reduced it under low vacuum conditions. SF increased the water demand of the paste and refined the pores, thereby reducing free water content in the hardened paste and slowing down mass loss in drying environments (Panjehpour et al. 2011). The increase in mass loss caused by RDP in concrete may be due to two factors. First, RDP increased the number of interconnected pores (Ollitrault-Fichet et al. 1998), providing more pathways for moisture evaporation and migration. Secondly, hydrolysis of RDP molecular groups released carboxyl groups, which reacted with calcium hydroxide to form water molecules, increasing the water content of the matrix (Shi et al. 2023), thus enhancing its sensitivity to drying environments. Under natural drying conditions, the smooth and hydrophobic surface of PEF and the orientation of fiber ends at the specimen surface facilitate outward moisture discharge, leading to increased mass loss (Aly et al. 2008). Under low vacuum drying conditions, intense drying shrinkage could induce more microcracks and shorter moisture diffusion paths. PEF could effectively constrain the crack propagation, thereby reducing mass loss in concrete.

Gas Permeability

The gas permeability coefficients of concrete under different drying conditions are shown in Fig. 9. SF, RDP, and PEF reduced the gas permeability coefficient of concrete cured for 28 days by 48%, 84%, and 85%, respectively. With the exception of A2, gas permeability decreased after 28 days of natural drying and then increased after 56 days. There appears to be a correlation between changes in gas permeability coefficient and mass loss. A greater mass loss corresponded to a larger gas permeability coefficient. Previous studies (Shangguan et al. 2023a; Hughes 1985; Islam and Gupta 2016) indicated that gas permeability in concrete was primarily related to its internal pore structure and pore saturation. Moisture migration in a drying environment forms channels that provide additional pathways for gas permeability. SF, RDP, and PEF could reduce bleeding in fresh paste, explaining their lower gas permeability coefficients compared to the control group at different drying stages. However, shrinkage cracking and pore

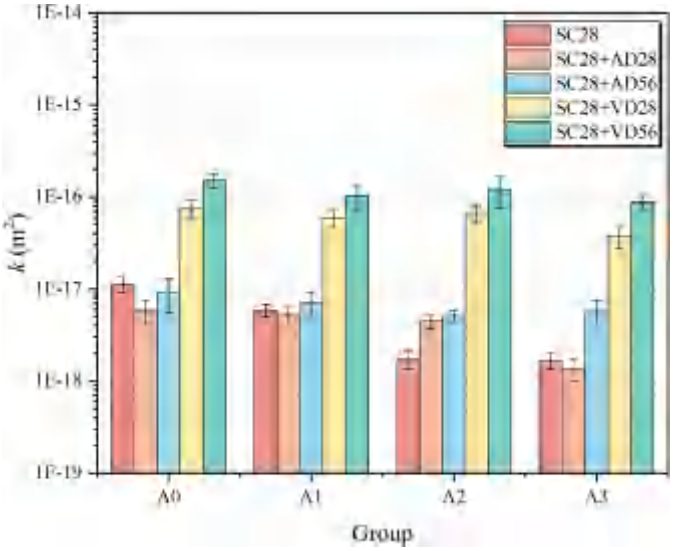


Fig. 9. Gas permeability coefficient (k) of concrete.

Downloaded from ascelibrary.org by Central South University on 12/23/25. Copyright ASCE. For personal use only; all rights reserved.

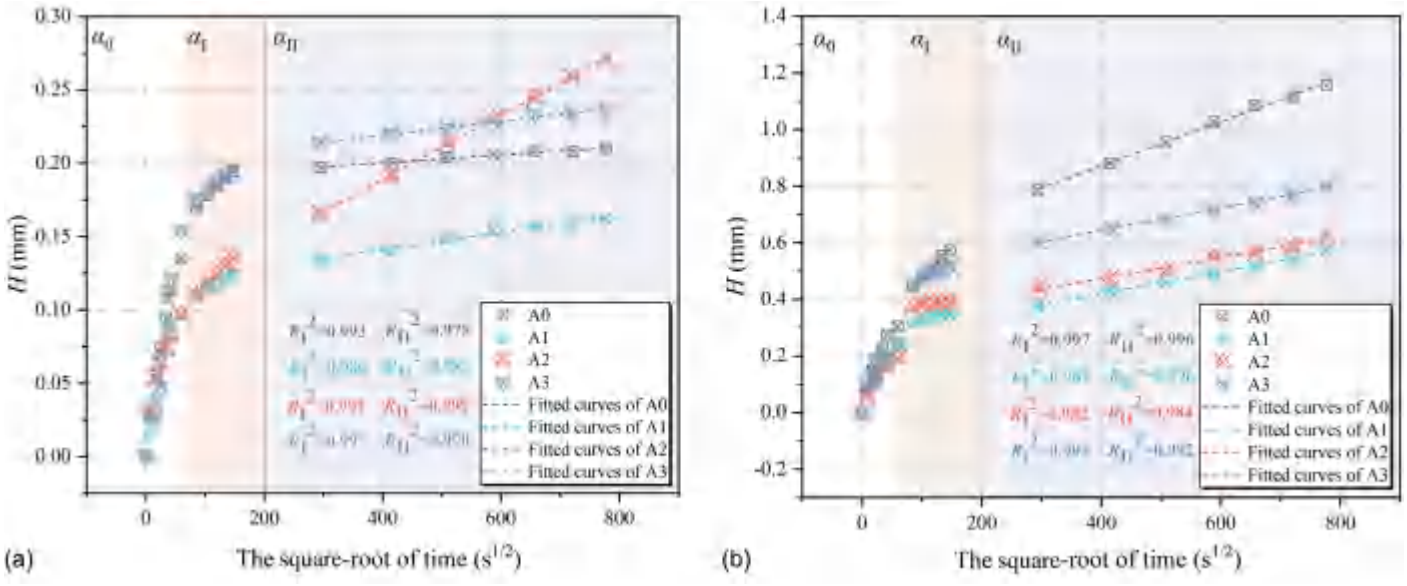


Fig. 10. Schematic of the two-stage fit of the water absorption rates: (a) SC28+AD56; and (b) SC28+VD56.

coarsening caused by low vacuum also increased the gas permeability. The pore refinement effect of SF and the crack-resistance enhancement of PEF could effectively reduce the gas permeability coefficient in low vacuum environments (Güneyisi et al. 2012; Ahmed and Jia 2019). RDP created a high-humidity environment within the matrix, leading to greater mass loss and coarser pores in low vacuum environments, which resulted in the highest increase in gas permeability coefficient.

Capillary Water Absorption

The capillary water absorption height of concrete under different drying conditions is shown in Fig. 10. Initially, the specimens absorbed water quickly, with the rate gradually slowing down. The rapid initial absorption was driven by surface effects and capillary forces, while later absorption was governed by diffusion and gravity (Martys and Ferraris 1997; Song et al. 2024). Fig. 11 indicated that the capillary water absorption height under low vacuum drying was more than three times higher compared to that under natural drying, suggesting an increase in the number of permeable capillary pores due to the low vacuum conditions. After 7 days, SF, RDP, and PEF reduced the capillary water absorption height by 50.6%, 45.9%, and 30.6%, respectively, with SF showing the most significant reduction in water absorption rate.

Further observations revealed that the capillary water absorption height of concrete under the two drying environments can be divided into the initial absorption stage (0–6 hours) and the secondary absorption stage (6 hours to 7 days), each exhibiting characteristics of linear variation. The water absorption rates of concrete specimens can be determined by linearly fitting the capillary water absorption curves for the two stages, as specified by Eq. (7). The fitting results are shown in Fig. 10. It should be noted that due to the surface effect (Martys and Ferraris 1997), concrete specimens rapidly absorb water upon contact, significantly increasing the absorption rate (α_0). Hence, this stage was skipped, and data from the stable absorption period were used for linear fitting to ensure a correlation coefficient greater than 0.98

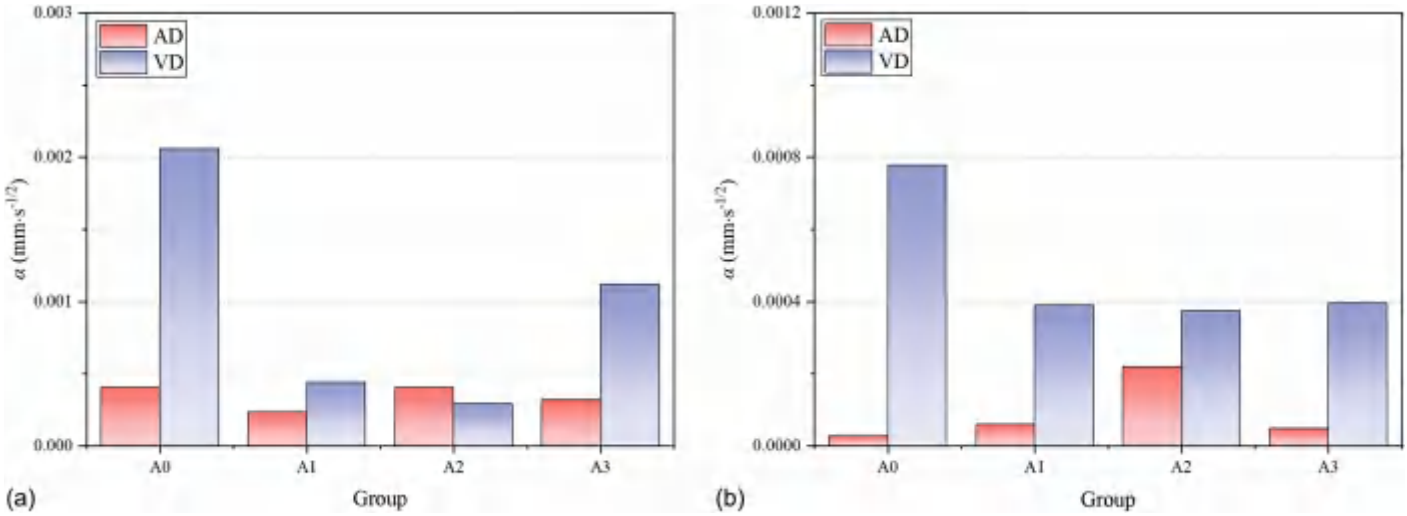


Fig. 11. Capillary water absorption rate of concrete under different drying conditions: (a) initial water absorption stage; and (b) secondary water absorption stage.

Downloaded from ascelibrary.org by Central South University on 12/23/25. Copyright ASCE. For personal use only; all rights reserved.

$$H = \alpha \sqrt{t} + b \quad (7)$$

where α = the water absorption rate ($mm \cdot s^{-1/2}$); and b = the axial intercept of H, which is the correction term considering the surface effect when the sample is in contact with water (mm).

From Fig. 10, it is evident that the fitting of the capillary water absorption rates for the two stages is accurate, and the summarized results are presented in Fig. 11. It shows that the capillary water absorption rates for both stages under low vacuum drying conditions are significantly higher than those under natural drying conditions. SF, RDP, and PEF effectively reduced the capillary water absorption rate of concrete. The filling and pozzolanic effects of SF help reduce surface water penetration. RDP forms an irreversible hydrophobic network during cement hydration, decreasing pore surface wettability and preventing water absorption (Tarannum et al. 2020; Shi et al. 2023). Additionally, low vacuum treatment can promote the rapid evaporation of moisture within the pores, limiting the movement of RDP particles. The surface tension of water and air causes RDP particles to aggregate. The capillary evaporation of water between the particles generates capillary tension, which deforms and fuses the polymer particles into a continuous hydrophobic polymer film (Tarannum et al. 2020), enhancing water resistance. PEF, as a reinforcing component, increases water absorption due to the creation of smooth, nontortuous flow paths that reduce fluid dynamic resistance (Corradetti et al. 2016). Exposed fibers on specimen surfaces enhance connectivity between surface permeable pores and internal micropores, further increasing absorption. It is noteworthy that RDP exhibits inconsistent performance under AD and VD conditions. Under AD, its water resistance is not significant, and the second-stage water absorption rate increases markedly, while under VD, it provides effective waterproofing. The RDP within specimens may form an incomplete film during natural drying, enhancing the connectivity of micropores due to its air-entraining properties, which leads to increased water absorption rates. Conversely, the rapid dehydration caused by low vacuum may make the polymer film denser, reducing the connectivity of micropores and thereby decreasing capillary water absorption efficiency. Overall, all three materials positively impact the reduction of long-term water permeability in concrete under low vacuum conditions.

Pore Structure

Based on the NAD test results, concrete exhibited different nitrogen adsorption isotherms before and after low vacuum treatment (Fig. 12). According to IUPAC classification (Sing 1985), the isotherm in Fig. 12(a) was close to type IV, while Fig. 12(b) was close to type II. The adsorption isotherms showed two stages: an initial slow rise representing micropore filling and monolayer to multilayer adsorption (Zhang and Scherer 2019) and a rapid increase later. Unlike the type IV isotherm, the curve continued to rise as the relative pressure approached 1, indicating the presence of larger pores beyond the testing range of NAD, which aligned with the actual pore size distribution inside the concrete. Observations revealed that the isotherm of concrete after low vacuum treatment approaches the x-axis, with a significantly lower adsorption amount than before low vacuum treatment, indicating an increase in macropores and a decrease in specific surface area after low vacuum drying. It was noted that the samples before low vacuum treatment exhibited a significant hysteresis loop in the isotherm at around 0.5 relative pressure, indicating the presence of interconnected mesopores. This was related to the changes in contact angle during the adsorption and desorption process (Qomi et al. 2021), and it might also be associated with the ink-bottle effect and the cavitation of nitrogen (Maruyama et al. 2018). As relative pressure decreased to the critical point, increased pore wall potential and tensile strength caused the condensed liquid in critical pores (≈4 nm) to evaporate, resulting in the closure of the desorption branch (Feng et al. 2018). After treatment, the hysteresis effect between the adsorption and desorption isotherms becomes weaker, indicating increased pore size within the sample (Zuo et al. 2023). According to the classification of hysteresis loop types (Sing 1985), after low vacuum exposure, the hysteresis loop transitioned from H2-type to H3-type. This indicated an increase in unfilled macropores in the sample, allowing desorption to occur at the onset of the pressure drop. From a microstructural perspective, low vacuum drying caused a collapse of the C—S—H structure, resulting in increased pore connectivity and uniformity, leading to better overlap in the adsorption-desorption cycle process (Shangguan et al. 2024; Zhang and Scherer 2019). This explains why samples dried under low vacuum exhibit increased air permeability and capillary water absorption rates.

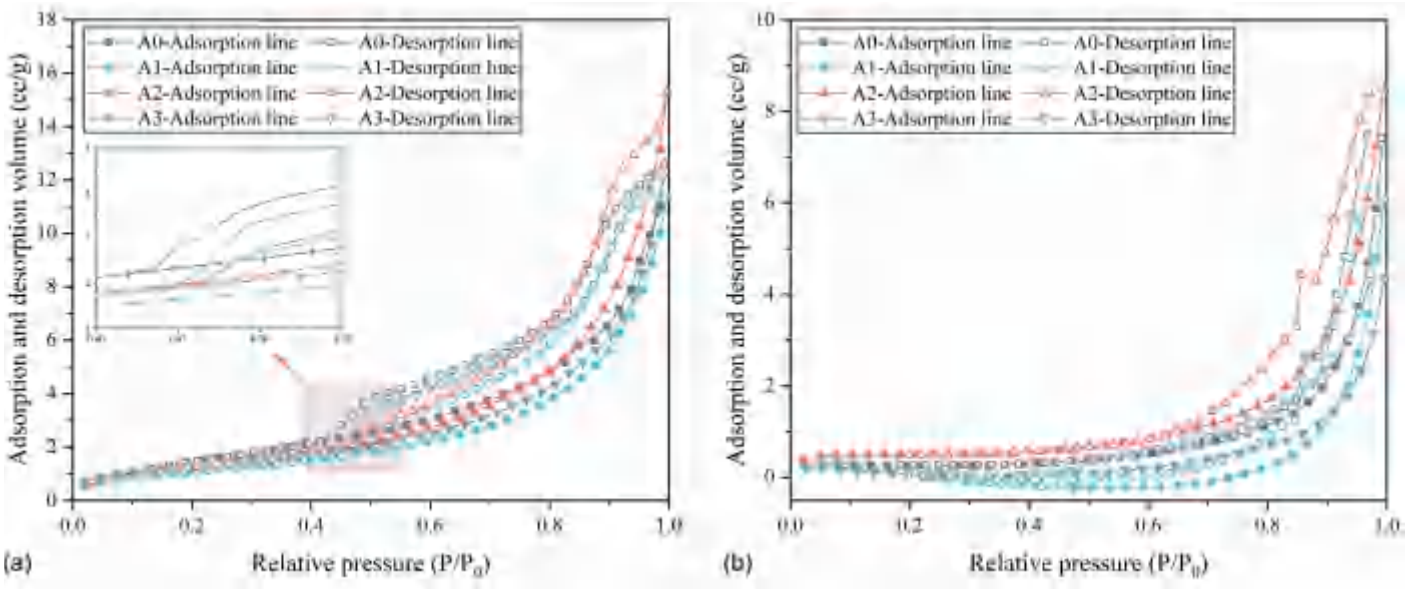


Fig. 12. Nitrogen absorption isotherms of concrete: (a) SC28; and (b) SC28+VD56.

Downloaded from ascelibrary.org by Central South University on 12/23/25. Copyright ASCE. For personal use only; all rights reserved.

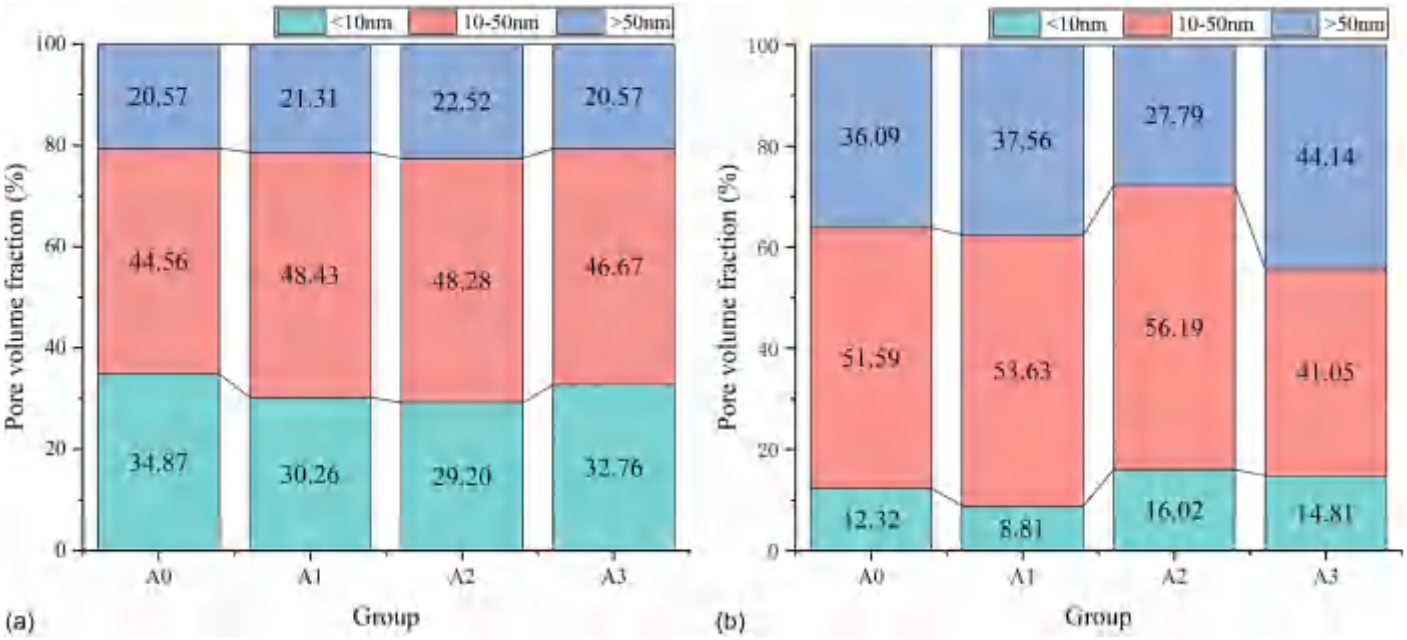


Fig. 13. Pore volume fraction of concrete: (a) SC28; and (b) SC28+VD56.

Based on the Kelvin equation, the pore volume fraction in the range of 2–100 nm before and after low vacuum treatment can be calculated using the Barrett-Joyner-Hallenda (BJH) method, as shown in Fig. 13. According to Fig. 13, the proportion of gel pores (less than 10 nm) in the concrete significantly decreases after low vacuum drying, while the proportion of large capillary pores (greater than 50 nm) noticeably increases. According to previous studies (Long et al. 2023; Shangguan et al. 2023b), the shrinkage and cracking of the matrix under low vacuum conditions can lead to pore coarsening, and this study further supports that finding. It should be noted that nitrogen gas cannot penetrate high-density C—S—H (HD C—S—H), so gel pore data from NAD testing mainly relate to low-density C—S—H (LD C—S—H) (Tennis and Jennings 2000). The significant reduction in gel pore proportion under low vacuum may be due to the transformation from LD C—S—H to HD C—S—H, which has higher solid phase strength, thus supporting the observed increase in concrete's mechanical strength after low vacuum drying.

By comparing the effects of different components on the pore structure under low vacuum conditions, it was found that the addition of SF slightly increased the proportion of large capillary pores, while RDP enhanced the proportions of gel pores and small capillary pores. The inclusion of PEF significantly increased the proportion of large capillary pores, which may be related to the debonding during the fiber pull-out process, specifically the failure at the fiber-matrix interface leading to increased porosity. It is important to note that PEF effectively alleviated the shrinkage and cracking of the concrete, and the following SEM observations provide strong evidence to support this conclusion.

SEM

Figs. 14 and 15 illustrate the changes in the microstructure of concrete before and after low vacuum treatment. The enhancement benefits of SF for the matrix and the interfacial transition zone (ITZ) have been proven (Dong et al. 2021). As shown in Fig. 14, the matrix with SF was more compact, and the distribution of hydration products in the ITZ was more uniform. RDP caused a looser microstructure of ITZ, which was related to the air-entraining and hydration-delaying effects of RDP. The connections between PEF and matrix were observed, which would provide a bridging for restricting the crack propagation. Fig. 15 presented the more compact microstructures of specimens after low vacuum treatment. The dense microstructure of the SF group provided adequate stiffness but may limit the deformation capacity of the hardened paste. Consequently, this group might be more prone to cracking due to variations in shrinkage stress. Due to water evaporation caused by cement hydration and low vacuum, the process of RDP polymer films was promoted, which can fill the defects and pores in concrete. Additionally, it can enhance the bonding between hydration products and the aggregates. The continuous polymer films can improve the integrity and the crack resistance of both the matrix and the ITZ. For PEF-enforced concrete, the aggregate restraint and crack bridging of PEF effectively resisted the shrinkage cracking caused by low vacuum environments.

Further Discussion

Analysis for the Action of SF Suffering from Low Vacuum Environments

The filler effect of SF and its high pozzolanic activity significantly refine the pore structure. Thus, concrete incorporating SF exhibited the lowest gas permeability and capillary water absorption under various drying conditions, as shown in Figs. 9 and 10. Additionally, the extra addition of SF consumed free water in the concrete, thereby reducing moisture loss during the drying process, as illustrated in Fig. 8.

Under low vacuum conditions, the impact of SF on compressive strength has shown noticeable changes over time. As depicted in Fig. 3, the compressive strength increased significantly after 28 days of low vacuum conditioning but decreased obviously at 56 days. This is mainly related to the drying behaviors induced by the low vacuum. A previous study (Shangguan et al. 2023b) found that a low vacuum environment would reduce the moisture content in concrete, which could diminish microcracking caused by water during compression, thus enhancing the compressive strength. The addition of SF further reduced the porosity of the concrete, enhancing this effect. On the other hand, due to the loss of water, the C—S—H restructures into a denser formation, which is beneficial

Downloaded from ascelibrary.org by Central South University on 12/23/25. Copyright ASCE. For personal use only; all rights reserved.

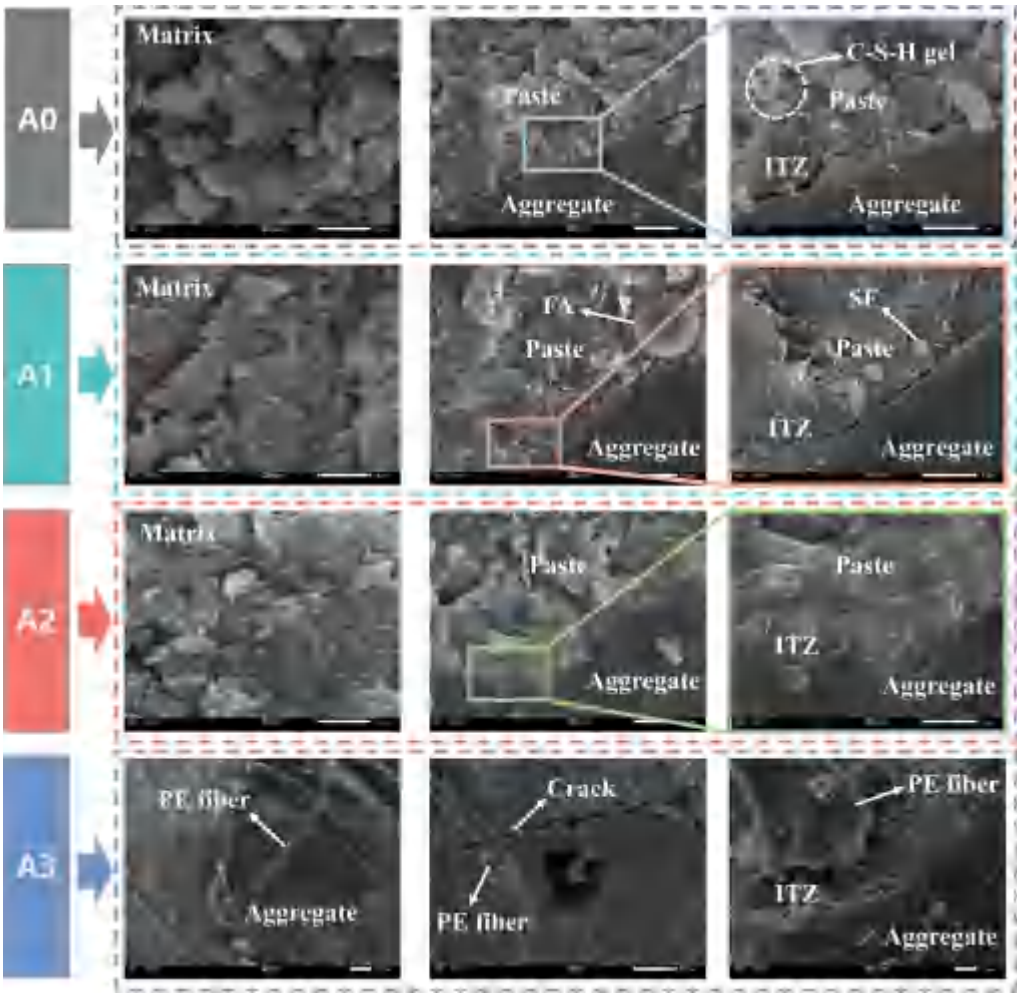


Fig. 14. Micromorphology of samples before low vacuum treatment.

for improving the strength of the matrix, as shown in Figs. 16(b and c). This might explain why the compressive strength of SC28+VD28 was significantly higher than that of other groups. However, research indicated that the pore structure within the cement matrix is refined as hydration progresses, causing more significant shrinkage in the cement paste at later hydration stages (He et al. 2023). According to the Young–Laplace equation, pore refinement leads to greater capillary tension, resulting in the formation of more microcracks, as shown in Fig. 16(a). Correspondingly, the additional inclusion of SF increased the compressive strength, and led to higher shrinkage, especially in the later stages of hydration. This might be the reason for the noticeable decrease in strength of the silica fume-incorporated concrete after 56 days of low vacuum drying.

In summary, the incorporation of SF can enhance pore refinement and elevate the density of concrete. However, it is crucial to consider the increased risk of drying shrinkage resulting from low vacuum environments following pore refinement.

Analysis for the Action of RDP Suffering from Low Vacuum Environments

The RDP is emulsified with water and evenly dispersed throughout the fresh concrete. As hydration progresses, the internal water of the concrete is consumed, allowing the emulsion to reform a polymer film that bridges and fills pores and cracks within the concrete, thereby enhancing its toughness and crack resistance. Consequently, RDP typically increases the flexural strength of concrete, although it may compromise compressive strength due to the inhibition of the hydration process (Tao et al. 2022; Zhao et al. 2011) and the introduction of additional pores by polymer particles (Schulze and Killermann 2001), as shown in Fig. 16(d).

Under low vacuum conditions, the increased loss of moisture in the concrete can accelerate the formation of the polymer film, enhancing the effectiveness of RDP. Thus, RDP-enhanced concrete exhibited a more pronounced increase in flexural strength compared to before vacuum treatment, as shown in Fig. 7. Correspondingly, the gas permeability and capillary water absorption coefficients of RDP-enhanced concrete under low vacuum conditions were significantly lower than those of the control group, as illustrated in Figs. 9 and 10. In short, the function of RDP in concrete primarily relies on its ability to reform polymer films. Low vacuum conditions facilitate this reformation process, thereby enhancing the effectiveness of RDP in concrete.

Analysis for the Action of PEF Suffering from Low Vacuum Environments

The primary purpose of introducing PEF into concrete is to augment its toughness through the crack-bridging and aggregate-constraining effects of the fibers, as shown in Fig. 16(e). Comparative studies indicate that low vacuum environments diminished the effectiveness of PEF in enhancing flexural toughness, primarily through a reduction in strain-hardening behavior. The strain-hardening

Downloaded from ascelibrary.org by Central South University on 12/23/25. Copyright ASCE. For personal use only; all rights reserved.

Downloaded from ascelibrary.org by Central South University on 12/23/25. Copyright ASCE. For personal use only; all rights reserved.

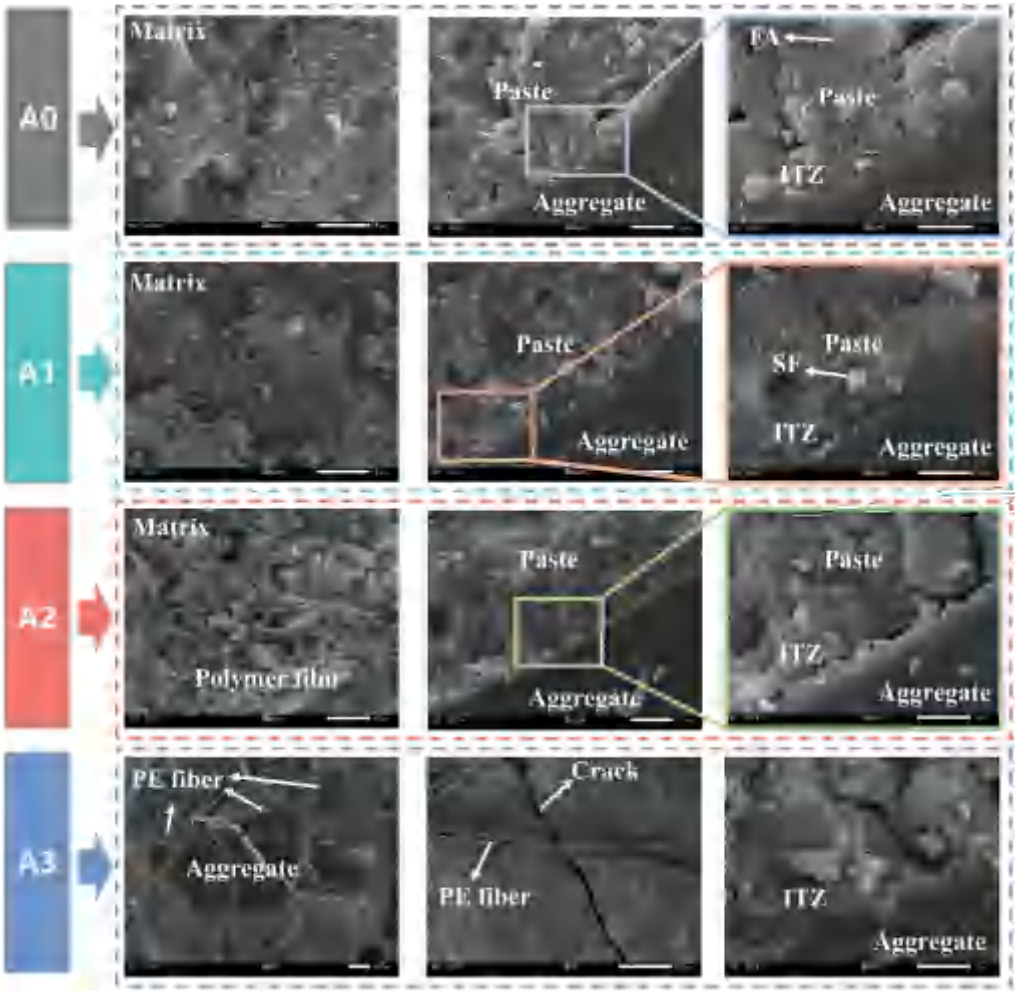


Fig. 15. Micromorphology of samples after low vacuum treatment.

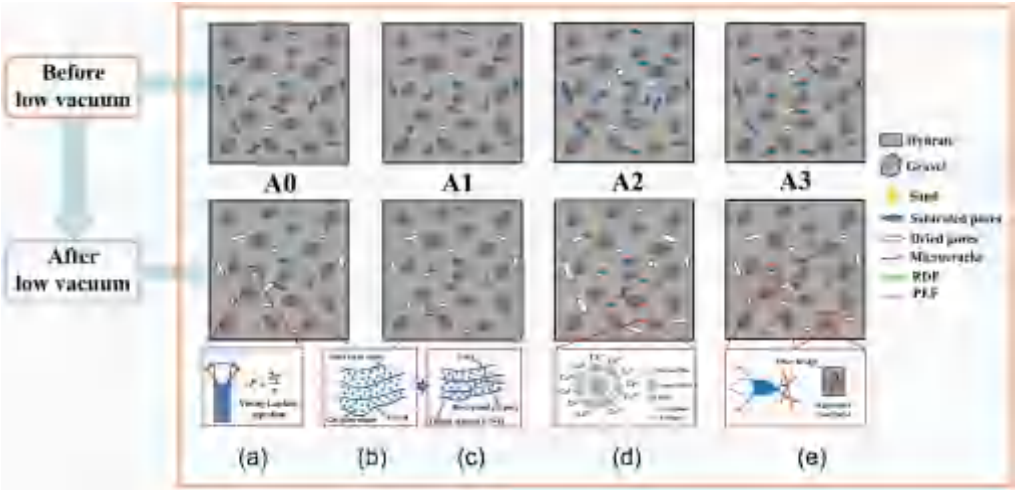


Fig. 16. Mechanisms of SF, RDP, and PEF effects on concrete properties in low vacuum environments.

behavior in fiber-reinforced concrete necessitates adequate bonding strength between the fibers and the matrix. However, excessively strong bonds can also impede the essential bond-slip behavior between fibers and matrix, which is crucial for maintaining strain-hardening behavior (Fantilli et al. 2009). As depicted in Fig. 6, after 56 days of low vacuum treatment, the peak flexural strength of PEF-reinforced concrete surpassed that measured before the treatment. Additionally, a distinct strain-hardening stage was observed in PEF-enhanced concrete before low vacuum treatment. Conversely, after undergoing 56 days in a low vacuum environment, despite an

increase in peak strength, there was a marked absence of strain-hardening behavior post-yielding, resulting in a significant reduction in flexural toughness. This reduction is likely attributable to the considerable matrix shrinkage induced by the low vacuum conditions, which enhances the bond strength between the fibers and the matrix, thereby restricting the bond-slip behavior during the failure process and consequently diminishing the toughness.

Conclusions and Outlook

A comparative study was conducted on the different effects of SF, RDP, and PEF on the evolution of concrete properties under natural and low vacuum drying conditions, and the corresponding influence mechanisms were discussed. Based on the results of this study, the following conclusions can be drawn:

1. The addition of extra SF led to a more refined pore size distribution due to the filling effect and high pozzolanic activity, which induced a denser matrix and a more uniform distribution of hydrates within ITZ. Accordingly, SF-enhanced concrete demonstrated a higher strength compared to reference concrete. Notably, the compressive strength was increased by 24.7% following a 28-day low vacuum treatment. In addition, SF also provided benefits in reducing mass loss, lowering gas permeability, and diminishing capillary water absorption. However, the enhancements from SF may be diminished under prolonged low vacuum conditioning, potentially due to the more significant shrinkage induced by such environments.
2. Although the addition of RDP reduced the compressive strength of concrete, it enhanced its flexural strength. Following 56 days of low vacuum treatment, the flexural strength of the concrete increased by 27.4%, which was significantly higher than that of other groups. This improvement is attributed to the fact that the low vacuum environments accelerate moisture loss and promote polymer film formation, thereby maximizing the effectiveness of RDP. Furthermore, while RDP increased the rate of mass loss in concrete under low vacuum environments, it reduced the gas permeability of RDP-enhanced concrete by 20.7% compared to the reference concrete, demonstrating its potential for improving concrete durability.
3. The addition of PEF enhanced both the compressive and flexural strength of concrete, while concurrently reducing the mass loss, gas permeability, and capillary water absorption in a low vacuum environment. However, after 56 days of low vacuum treatment, a notable reduction in the toughness of PEF-enforced concrete was observed. This reduction was primarily attributed to the low vacuum environment diminishing the strain-hardening behaviors of PEF-reinforced concrete, probably due to the restricted bond-slip behavior between fibers and the matrix.

In low vacuum environments, reduced pressure and humidity can lead to increased water loss from concrete, elevating capillary negative pressure and the risk of cracking, as per the Young–Laplace equation. Using SF for pore refinement may significantly degrade performance when treatment duration is prolonged. It is essential to account for these effects in pore refinement methods. Additionally, low vacuum conditions enhance the reformation of the RDP polymer film, improving its efficacy. However, prolonged exposure to low vacuum may diminish PEF's effectiveness in enhancing concrete toughness, which should be considered in design. This study provides valuable insights for designing highly stable concrete in low vacuum environments. Future research can further explore the effects of combining SF, RDP, and PEF on concrete performance in low vacuum environments.

Data Availability Statement

All data, models, and code generated or used during the study appear in the published article.

Acknowledgments

The authors are grateful to the financial support of the Program Fund of Nonmetallic Excellence and Innovation Center for Building Materials (No. 24TDA-1).

Author Contributions

Zhaofei Long: Methodology; Writing – original draft; Writing – review and editing. Jionghuang He: Conceptualization; Writing – review and editing. Guangcheng Long: Funding acquisition; Project administration; Supervision. Lixing Wang: Formal analysis; Investigation. Yuting Zhang: Software; Validation. Zhuo Tang: Resources; Visualization. Youjun Xie: Supervision.

References

Afroughsabet, V., and T. Ozbakkaloglu. 2015. "Mechanical and durability properties of high-strength concrete containing steel and polypropylene fibers." Constr. Build. Mater. 94 (Sep): 73–82. https://doi.org/10.1016/j.conbuildmat.2015.06.051.

Ahmed, A. A. M., and Y. Jia. 2019. "Effect of using hybrid polypropylene and glass fibre on the mechanical properties and permeability of concrete." Materials 12 (22): 3786. https://doi.org/10.3390/ma12223786.

Al-Khaja, W. A. 1994. "Strength and time-dependent deformations of silica fume concrete for use in Bahrain." Constr. Build. Mater. 8 (3): 169–172. https://doi.org/10.1016/S0950-0618(09)90030-7.

Aly, T., J. Sanjayan, and F. Collins. 2008. "Effect of polypropylene fibers on shrinkage and cracking of concretes." Mater. Struct. 41 (10): 1741–1753. https://doi.org/10.1617/s11527-008-9361-2.

ASTM. 2020. Standard test method for measurement of rate of absorption of water by hydraulic-cement concretes. ASTM C1585-20. West Conshohocken, PA: ASTM.

Barr, B., S. B. Hoseinian, and M. A. Beygi. 2003. "Shrinkage of concrete stored in natural environments." Cem. Concr. Compos. 25 (1): 19–29. https://doi.org/10.1016/S0958-9465(01)00044-0.

Bhanja, S., and B. Sengupta. 2005. "Investigations on the tensile strength of high performance concrete incorporating silica fume." In Proc., 18th Int. Conf. on Structural Mechanics in Reactor Technology. New York: Curran Associates.

Cagnon, H., J. Verdier, A. Nehme, and S. Multon. 2024. "Enhancing permeability measurements: Bridging the gap between pressure and vacuum techniques for steady and transient states." J. Build. Eng. 94 (Oct): 109933. https://doi.org/10.1016/j.jobe.2024.109933.

Cai, F., D. Zhou, J. Wei, J. Wang, C. Cheng, Y. Zhang, and Y. Zhao. 2022. "Running magnetic resistance of high-Tc superconducting maglev prototype vehicle in an evacuated tube track." Mech. Syst. Signal Process. 169 (Apr): 108635. https://doi.org/10.1016/j.ymssp.2021.108635.

Caimi, S., E. Timmerer, M. Banfi, G. Storti, and M. Morbidelli. 2018. "Core-shell morphology of redispersible powders in polymer-cement waterproof mortars." Polymers 10 (10): 1122. https://doi.org/10.3390/polym10101122.

CECS (China Association for Engineering Construction Standardization). 2009. Standard test methods for fiber reinforced concrete. Beijing: Standardization Administration of China.

Chang, H., X. Wang, Y. Wang, S. Li, J. Wang, J. Liu, and P. Feng. 2022. "Influence of low vacuum condition on mechanical performance and microstructure of hardened cement paste at early age." Constr. Build. Mater. 346 (Sep): 128358. https://doi.org/10.1016/j.conbuildmat.2022.128358.

Choi, J. I., K. I. Song, J. K. Song, and B. Y. Lee. 2016. "Composite properties of high-strength polyethylene fiber-reinforced cement and cementless composites." Compos. Struct. 138 (Mar): 116–121. https://doi.org/10.1016/j.compstruct.2015.11.046.

Corradetti, S., L. Biasetto, M. D. M. Innocentini, S. Carturan, P. Colombo, and A. Andrighetto. 2016. "Use of polymeric fibers to increase gas permeability of lanthanum carbide based targets for nuclear physics applications." Ceram. Int. 42 (15): 17764–17772. https://doi.org/10.1016/j.ceramint.2016.08.104.

Dong, F., H. Wang, J. Yu, K. Liu, Z. Guo, X. Duan, and X. Qiong. 2021. "Effect of freeze–thaw cycling on mechanical properties of polyethylene fiber and steel fiber reinforced concrete." Constr. Build. Mater. 295 (Aug): 123427. https://doi.org/10.1016/j.conbuildmat.2021.123427.

Fallah, S., and M. Nematzadeh. 2017. "Mechanical properties and durability of high-strength concrete containing macro-polymeric and polypropylene fibers with nano-silica and silica fume." Constr. Build. Mater. 132 (Feb): 170–187. https://doi.org/10.1016/j.conbuildmat.2016.11.100.

Fantilli, A. P., H. Mihashi, and P. Vallini. 2009. "Multiple cracking and strain hardening in fiber-reinforced concrete under uniaxial tension." Cem. Concr. Res. 39 (12): 1217–1229. https://doi.org/10.1016/j.cemconres.2009.08.020.

Feng, D., X. Li, X. Wang, J. Li, F. Sun, Z. Sun, T. Zhang, P. Li, Y. Chen, and X. Zhang. 2018. "Water adsorption and its impact on the pore structure characteristics of

Downloaded from ascelibrary.org by Central South University on 12/23/25. Copyright ASCE. For personal use only; all rights reserved.

shale clay." Appl. Clay Sci. 155 (Apr): 126–138. https://doi.org/10.1016/j.clay.2018.01.017.
Güneyisi, E., M. Gesoğlu, S. Karaoğlu, and K. Mermerdaş. 2012. "Strength, permeability and shrinkage cracking of silica fume and metakaolin concretes." Constr. Build. Mater. 34 (Sep): 120–130. https://doi.org/10.1016/j.conbuildmat.2012.02.017.
Guziak, L. F., and W. N. Maclay. 1963. "Redispersible latex polymer." J. Appl. Polym. Sci. 7 (6): 2249–2258. https://doi.org/10.1002/app.1963.070070623.
Gwon, S., S. Y. Jang, and M. Shin. 2018. "Microstructure evolution and strength development of ultra rapid hardening cement modified with redispersible polymer powder." Constr. Build. Mater. 192 (Dec): 715–730. https://doi.org/10.1016/j.conbuildmat.2018.10.178.
Hakeem, I. Y., M. Alharthai, M. Amin, A. M. Zeyad, B. A. Tayeh, and I. S. Agwa. 2023. "Properties of sustainable high-strength concrete containing large quantities of industrial wastes, nanosilica and recycled aggregates." J. Mater. Res. Technol. 24 (May): 7444–7461. https://doi.org/10.1016/j.jmrt.2023.05.050.
He, J., G. Long, K. Ma, Y. Yuan, and Y. Xie. 2023. "Comprehensive study on the hydration kinetics, mechanical properties and autogenous shrinkage of cement pastes during steam curing." Cem. Concr. Res. 174 (Dec): 107310. https://doi.org/10.1016/j.cemconres.2023.107310.
Hosseinzadeh, H., A. M. Salehi, M. Mehraein, and G. Asadollahfardi. 2023. "The effects of steel, polypropylene, and high-performance macro polypropylene fibers on mechanical properties and durability of high-strength concrete." Constr. Build. Mater. 386 (Jul): 131589. https://doi.org/10.1016/j.conbuildmat.2023.131589.
Hu, C., L. Li, and Z. Li. 2022. "Effect of fiber factor on the workability and mechanical properties of polyethylene fiber-reinforced high toughness geopolymers." Ceram. Int. 48 (8): 10458–10471. https://doi.org/10.1016/j.ceramint.2021.12.254.
Hughes, D. C. 1985. "Pore structure and permeability of hardened cement paste." Mag. Concr. Res. 37 (133): 227–233. https://doi.org/10.1680/macr.1985.37.133.227.
Islam, G. M. S., and S. D. Gupta. 2016. "Evaluating plastic shrinkage and permeability of polypropylene fiber reinforced concrete." Int. J. Sustainable Built Environ. 5 (2): 345–354. https://doi.org/10.1016/j.ijsbe.2016.05.007.
Jumate, E., D. L. Manea, D. Moldovan, and R. Fechete. 2007. "The effect of hydrophobic redispersible polymer powder in Portland cement based mortars." Procedia Eng. 181: 316–323. https://doi.org/10.1016/j.proeng.2017.02.395.
Köksal, F., F. Altun, İ. Yiğit, and Y. Şahin. 2008. "Combined effect of silica fume and steel fiber on the mechanical properties of high strength concretes." Constr. Build. Mater. 22 (8): 1874–1880. https://doi.org/10.1016/j.conbuildmat.2007.04.017.
Kong, X., J. Pakusch, D. Jansen, S. Emmerling, J. Neubauer, and F. Goetz-Neuhoeffer. 2016. "Effect of polymer latexes with cleaned serum on the phase development of hydrating cement pastes." Cem. Concr. Res. 84 (Jun): 30–40. https://doi.org/10.1016/j.cemconres.2016.02.013.
Lin, H., S. Han, B. Han, S. Liang, H. Ye, H. Liu, P. Feng, Y. Liu, and G. Cheng. 2024. "Development of mechanical properties of concrete in vacuum tunnel of vacuum-based maglev train." Constr. Build. Mater. 445 (Sep): 137928. https://doi.org/10.1016/j.conbuildmat.2024.137928.
Long, G., Y. Chen, Z. Tang, M. Shangguan, C. Gao, and S. Xu. 2023. "Drying shrinkage behavior of cement mortar under low vacuum conditions." Constr. Build. Mater. 374 (Apr): 130933. https://doi.org/10.1016/j.conbuildmat.2023.130933.
Long, Z., G. Long, Z. Tang, M. Shangguan, C. Gao, M. Yi, Z. He, and Y. Zhang. 2024. "Effects of aggregates and fibers on the strength and permeability of concrete exposed to low vacuum environment." J. Build. Eng. 97 (2024): 110902. https://doi.org/10.1016/j.jobe.2024.110902.
Martys, N. S., and C. F. Ferraris. 1997. "Capillary transport in mortars and concrete." Cem. Concr. Res. 27 (5): 747–760. https://doi.org/10.1016/S0008-8846(97)00052-5.
Maruyama, I., E. Gartner, K. Beppu, and R. Kurihara. 2018. "Role of alcohol-ethylene oxide polymers on the reduction of shrinkage of cement paste." Cem. Concr. Res. 111 (Sep): 157–168. https://doi.org/10.1016/j.cemconres.2018.05.017.
Maruyama, I., Y. Nishioka, G. Igarashi, and K. Matsui. 2014. "Microstructural and bulk property changes in hardened cement paste during the first drying process." Cem. Concr. Res. 58 (Apr): 20–34. https://doi.org/10.1016/j.cemconres.2014.01.007.
Mazloom, M., A. A. Ramezanianpour, and J. J. Brooks. 2004. "Effect of silica fume on mechanical properties of high-strength concrete." Cem. Concr. Compos. 26 (4): 347–357. https://doi.org/10.1016/S0958-9465(03)00017-9.
Michelberger, F., M. Plavec, K. Pyrek, and P. Graf. 2021. "The Hyperloop concept development, possible applications and critical analysis." In Sustainable rail transport 4: Innovate rail research and education, 341–367. Cham, Switzerland: Springer. https://doi.org/10.1007/978-3-030-82095-4.
Mohammadi, Y., S. P. Singh, and S. K. Kaushik. 2008. "Properties of steel fibrous concrete containing mixed fibres in fresh and hardened state." Constr. Build. Mater. 22 (5): 956–965. https://doi.org/10.1016/j.conbuildmat.2006.12.004.
Ollitrault-Fichet, R., C. Gauthier, G. Clamen, and P. Boch. 1998. "Microstructural aspects in a polymer-modified cement." Cem. Concr. Res. 28 (12): 1687–1693. https://doi.org/10.1016/S0008-8846(98)00153-7.
Panjehpour, M., A. A. A. Ali, and R. Demirboga. 2011. "A review for characterization of silica fume and its effects on concrete properties." Int. J. Sustainable Constr. 2 (2): 1–7.
Qomi, M. J. A., L. Brochard, T. Honorio, I. Maruyama, and M. Vandamme. 2021. "Advances in atomistic modeling and understanding of drying shrinkage in cementitious materials." Cem. Concr. Res. 148 (Oct): 106536. https://doi.org/10.1016/j.cemconres.2021.106536.
Ren, X., Z. Zhang, M. Xiang, G. Xu, and W. Cao. 2022. "An experimental study on the preparation of soft rock similar materials using redispersible latex powder as a modifier." Molecules 27 (21): 7404. https://doi.org/10.3390/molecules27217404.
Schulze, J., and O. Killermann. 2001. "Long-term performance of redispersible powders in mortars." Cem. Concr. Res. 31 (3): 357–362. https://doi.org/10.1016/S0008-8846(00)00498-1.
Shah, A. A., and Y. Ribakov. 2011. "Recent trends in steel fibered high-strength concrete." Mater. Des. 32 (8–9): 4122–4151. https://doi.org/10.1016/j.matdes.2011.03.030.
Shangguan, M., Y. Xie, G. Long, Z. Long, F. Wang, Y. Chen, and C. Gao. 2024. "Hydration and microstructure evolution of cement paste in low vacuum environments." Constr. Build. Mater. 438 (Aug): 137233. https://doi.org/10.1016/j.conbuildmat.2024.137233.
Shangguan, M., Y. Xie, F. Wang, G. Long, Z. Tang, Y. Chen, S. Xu, H. Li, C. Gao, and M. Liu. 2023a. "Effect of low-vacuum environment on the strength and permeability of cement-based materials." Constr. Build. Mater. 400 (Oct): 132676. https://doi.org/10.1016/j.conbuildmat.2023.132676.
Shangguan, M., Y. Xie, S. Xu, C. Gao, G. Long, F. Wang, and M. Liu. 2023b. "Mechanical properties characteristics of high strength concrete exposed to low vacuum environment." J. Build. Eng. 63 (Jan): 105438. https://doi.org/10.1016/j.jobe.2022.105438.
Shen, D., C. Liu, Y. Luo, H. Shao, X. Zhou, and S. Bai. 2023. "Early-age autogenous shrinkage, tensile creep, and restrained cracking behavior of ultra-high-performance concrete incorporating polypropylene fibers." Cem. Concr. Compos. 138 (Apr): 104948. https://doi.org/10.1016/j.cemconcomp.2023.104948.
Shi, X., B. Ning, J. Liu, and Z. Wei. 2023. "Effects of re-dispersible latex powder-basalt fibers on the properties and pore structure of lightweight foamed concrete." J. Build. Eng. 75 (Sep): 106984. https://doi.org/10.1016/j.jobe.2023.106984.
Sing, K. S. 1985. "Reporting physisorption data for gas/solid systems with special reference to the determination of surface area and porosity (Recommendations 1984)." Pure Appl. Chem. 57 (4): 603–619. https://doi.org/10.1351/pac198557040603.
Song, C., C. Jiang, and X. Gu. 2024. "Effects of carbonation on microscopic pore characteristics and water absorption performance of concrete." [In Chinese.] J. Tongji Univ. (Nat. Sci.) 52 (4): 567–573. https://doi.org/10.11908/j.issn.0253-374x.23129.
Tao, Y., M. K. Mohan, A. V. Rahul, Y. Yuan, G. D. Schutter, and K. V. Tittelboom. 2022. "Stiffening controllable concrete modified with redispersible polymer powder for twin-pipe printing." Cem. Concr. Res. 161 (Nov): 106953. https://doi.org/10.1016/j.cemconres.2022.106953.
Tarannum, N., and K. Pooja. 2022. "Recent trends and applications in the research and development activities of redispersible powder: A vision of twenty-first century." Polym. Bull. 79 (10): 8093–8142. https://doi.org/10.1007/s00289-021-03928-y.
Tarannum, N., K. Pooja, and R. Khan. 2020. "Preparation and applications of hydrophobic multicomponent based redispersible polymer powder: A review." Constr. Build. Mater. 247 (Jun): 118579. https://doi.org/10.1016/j.conbuildmat.2020.118579.
Tennis, P. D., and H. M. Jennings. 2000. "A model for two types of calcium silicate hydrate in the microstructure of portland cement pastes." Cem. Concr. Res. 30 (6): 855–863. https://doi.org/10.1016/S0008-8846(00)00257-X.
Tien, P. V. 2014. "Influence of re-dispersible powder on the properties of mortars." J. Mater. Eng. Struct. 1 (1): 2–10.
Wang, F., X. Sun, Z. Tao, and Z. Pan. 2022. "Effect of silica fume on compressive strength of ultra-high-performance concrete made of calcium aluminate cement/fly ash based geopolymer." J. Build. Eng. 62 (Dec): 105398. https://doi.org/10.1016/j.jobe.2022.105398.
Wang, R., and P. Wang. 2011. "Action of redispersible vinyl acetate and versatate copolymer powder in cement mortar." Constr. Build. Mater. 25 (11): 4210–4214. https://doi.org/10.1016/j.conbuildmat.2011.04.060.
Wang, X., H. Chang, S. Li, Y. Jia, Z. Kong, Y. Wang, J. Liu, and P. Feng. 2024. "Influence of low vacuum and high temperature condition on moisture transport and dry shrinkage of mature concrete." J. Build. Eng. 95 (Oct): 110262. https://doi.org/10.1016/j.jobe.2024.110262.
Wang, Y., F. Liu, J. Yu, F. Dong, and J. Ye. 2020. "Effect of polyethylene fiber content on physical and mechanical properties of engineered cementitious composites."

Downloaded from ascelibrary.org by Central South University on 12/23/25. Copyright ASCE. For personal use only; all rights reserved.

Constr. Build. Mater. 251 (Aug): 118917. https://doi.org/10.1016/j.conbuildmat.2020.118917.
Yan, P., and B. Zhang. 2016. "Mechanical properties of high strength concrete prepared with different densities of silica fume." [In Chinese.] J. Chin. Ceram. Soc. 44 (2): 196–201. https://doi.org/10.14062/j.issn.0454-5648.2016.02.03.
Yang, K., Z. Tang, W. Li, H. Wu, G. Ma, Y. Xiang, Y. Xie, and G. Long. 2024. "A systematic review on the evaluation methods for the flexural toughness of cement-based materials: From classification analysis to case study." J. Build. Eng. 93 (Sep): 109855. https://doi.org/10.1016/j.jobe.2024.109855.
Yang, Y., Q. Zhou, and Y. Deng. 2020. "The reinforcement attributes of multi-scale hybrid fiber throughout the uniaxial compression of ultra-low-weight foamed cement-based composites." Constr. Build. Mater. 242 (May): 118184. https://doi.org/10.1016/j.conbuildmat.2020.118184.
Ye, J., C. Cui, J. Yu, K. Yu, and F. Dong. 2021. "Effect of polyethylene fiber content on workability and mechanical-anisotropic properties of 3D printed ultra-high ductile concrete." Constr. Build. Mater. 281 (Apr): 122586. https://doi.org/10.1016/j.conbuildmat.2021.122586.
Yoo, D. Y., and M. J. Kim. 2019. "High energy absorbent ultra-high-performance concrete with hybrid steel and polyethylene fibers." Constr. Build. Mater. 209 (Jun): 354–363. https://doi.org/10.1016/j.conbuildmat.2019.03.096.
Zhang, G., Z. Li, L. Zhang, Y. Shang, and H. Wang. 2017. "Experimental research on drying control condition with minimal effect on concrete strength." Constr. Build. Mater. 135 (Mar): 194–202. https://doi.org/10.1016/j.conbuildmat.2016.12.141.
Zhang, Z., and G. W. Scherer. 2019. "Evaluation of drying methods by nitrogen adsorption." Cem. Concr. Res. 120 (Jun): 13–26. https://doi.org/10.1016/j.cemconres.2019.02.016.
Zhao, F., H. Li, S. Liu, and J. Chen. 2011. "Preparation and properties of an environment friendly polymer-modified waterproof mortar." Constr. Build. Mater. 25 (5): 2635–2638. https://doi.org/10.1016/j.conbuildmat.2010.12.012.
Zhu, L., Y. Zhao, and S. Chen. 2011. "Tests and studies on the impart of subdivisible sporadic lactoprene powder on dry-mixed mortar properties." [In Chinese.] J. Henan Polytech. Univ. (Nat. Sci.) 30 (3): 336–339. https://doi.org/10.16186/j.cnki.1673-9787.2011.03.012.
Zuo, S., Q. Yuan, T. Huang, K. Zhang, J. Shi, and Y. Tan. 2023. "Microstructural changes of young cement paste due to moisture transfer at low air pressures." Cem. Concr. Res. 164 (Feb): 107061. https://doi.org/10.1016/j.cemconres.2022.107061.

Downloaded from ascelibrary.org by Central South University on 12/23/25. Copyright ASCE. For personal use only; all rights reserved.

Structures 73 (2025) 108345

Contents lists available at ScienceDirect

Structures

journal homepage: www.elsevier.com/locate/structures

Seismic behavior of full-scale PEN FRP-concrete-steel double skin tubular columns

Shang-Cong Bai [a], Kai-Di Peng [b], Yu-Lei Bai [a,c,*], Jia-Xing Ma [d]

[a] State Key Laboratory of Bridge Engineering Safety and Resilience, Beijing University of Technology, Beijing 100124, China
[b] Road & Bridge International Co., Ltd., Beijing 100124, China
[c] Non-Metallic Excellence and Innovation Center for Building Materials, China Building Materials Academy Co., Ltd., Beijing 100024, China
[d] School of Civil Engineering and Architecture, Ningbo Tech University, Ningbo 315100, China

ARTICLE INFO

Keywords:
PEN FRP
FRP-concrete-steel double skin tubular columns (DSTCs)
Large-rupture-strain (LRS)
Seismic behavior

ABSTRACT

This paper presents the first experimental study of the seismic performance of double-skin tubular columns (DSTCs) with polyethylene naphthalate (PEN) FRP tubes. Fiber-reinforced polymer (FRP)-concrete-steel DSTC represents a new type of combined structure. A DSTC has an external FRP tube with an internal steel tube, and concrete fills the gap between the two tubes. DSTCs limit the outward buckling of their steel tubes and have excellent seismic performance. Previous studies have shown that glass FRP (GFRP) fracture controls the ultimate failure of DSTCs with a GFRP tube. Therefore, the fracture strain of the FRP tube is a critical factor for DSTCs. The fracture strain of large-rupture-strain (LRS) FRPs is greater than 5 %, which gives DSTCs an advantage. Six full-scale DSTCs were tested in the paper to investigate the effects of FRP type, PEN FRP thickness and the axial compression ratio as well as the plastic hinge region is filled with concrete on the seismic performance of DSTCs. The experimental results indicate that the seismic performance of DSTCs with PEN FRP is equal to or slightly better than that of GFRP, and the energy dissipation capacity improved by 41.7 %. In addition, decreasing the axial compression ratio, increasing the thickness of PEN FRP, and filling the plastic hinge region with concrete appropriately increased the DSTC seismic performance.

1. Introduction

FRP has been widely used in engineering structures due to its lightweight, high strength, and good corrosion resistance [1–11]. Structures may suffer serious damage during earthquakes [7–10,12–18]. FRP is widely used for seismic retrofitting of existing structures [1,2,5–12,19–21]. For example, Bai et al. [7–11] conducted a series of studies on the seismic behavior of large rupture strain (LRS) FRP-wrapped reinforced concrete (RC) columns, demonstrating the feasibility of using LRS FRP for seismic retrofitting. However, its versatility became evident when FRP was combined with traditional building materials to create high-performance hybrid structures that have become even more popular [3,4,13,16,22–30]. In hybrid structures, each material's advantages should be fully utilized, and any disadvantages should be avoided. Teng et al. [3] proposed a special hybrid structure form, namely the FRP-concrete-steel double skin tubular columns (DSTCs). This hybrid structure consists of an internal steel tube, an external FRP tube, and concrete filling the gap between the two tubes. The structure fully uses the respective advantages of the FRP tube as well as concrete and steel tube. FRP provides restraint to the concrete mainly in the ring direction. In this case, the concrete inhibits the outward buckling behavior of the internal steel tube, and the steel tube provides bending resistance to the hybrid structure. Moreover, FRP tube and concrete also provide corrosion protection to internal steel tube. Therefore, DSTCs are particularly suitable for engineering structures in corrosive environments such as marine environments, areas with heavy pollution, and areas with moist or hot air. In addition, FRP tube and steel tube can be used as formwork for concrete pouring to facilitate construction.

Over the past nearly two decades, many scholars have conducted numerous studies on the axial compressive behavior [22,24,30–33], flexural behavior [4,34], and seismic behavior [13,14,16] of DSTCs using conventional FRPs (e.g., aramid FRP (AFRP), carbon FRP (CFRP), and glass FRP (GFRP)), which have demonstrated excellent structural performance of DSTCs. For example, Teng et al. [3] first proved GFRP-DSTCs' good ductility through tests. Subsequently, Wong et al. [22] conducted a more detailed study on the axial compression behavior

* Corresponding author at: State Key Laboratory of Bridge Engineering Safety and Resilience, Beijing University of Technology, Beijing 100124, China.
E-mail address: baiyulei@bjut.edu.cn (Y.-L. Bai).

https://doi.org/10.1016/j.istruc.2025.108345
Received 21 August 2024; Received in revised form 28 December 2024; Accepted 30 January 2025
Available online 9 February 2025
2352-0124/© 2025 Institution of Structural Engineers. Published by Elsevier Ltd. All rights are reserved, including those for text and data mining, AI training, and similar technologies.

of DSTCs. They found that the axial load-axial displacement curves of DSTCs and the FRP-wrapped RC columns are very similar. Yu et al. [4] investigated the bending behavior of FRP-concrete-steel double skin tubular beams (DSTBs). They found that the bending behavior of DSTBs could be significantly enhanced by moving the internal steel tube to the tensile region of the beam or by using FRP bars as additional longitudinal reinforcement. Zhang et al. [14] conducted the first study on the seismic performance of DSTCs using high strength concrete (HSC) and found that the DSTCs still had good ductility. Existing studies [3,16] have shown that the cause of the ultimate failure of DSTCs is generally due to the fracture of FRP tubes, whereas the fracture strain of conventional FRP tubes is generally less than 3 %. At this moment, the internal steel tube may have yet to be fully utilized. Therefore, to fully utilize the performance of steel tube, there is an urgent need to find an FRP tube with a larger fracture strain to further enhance the DSTC performance.

Recently, a new type of environmentally friendly LRS FRP has received much attention [5,6,25,29,35–37], with a fracture strain of more than 5 %, which is more than three times greater than the fracture strain of GFRP. LRS FRPs are made from waste PET bottles, typically including polyethylene terephthalate (PET) FRP and polyethylene naphthalate (PEN) FRP. Low-carbon and environmentally friendly materials are currently the focus of research and development in most countries, which is conducive to the sustainable use of resources [38,39]. At present, the compression behavior of DSTCs with LRS FRP has been investigated by several scholars [25–27,29]. Yu's research group [25] first conducted an experimental investigation on axial compression performance of DSTCs with LRS FRP tube. They found that the internal steel tube's inward buckling behavior was apparent. Therefore, they further investigated the inhibitory effect of rib stiffeners on the buckling of steel tube [27]. Bai et al. [29] conducted an experimental investigation on the compressive performance of DSTCs with PET FRP tube and recycled aggregate concrete. The results indicated that DSTCs with PET FRP can overcome the disadvantages of recycled concrete. These studies [20–22,24] have shown that LRS FRPs can significantly enhance the ductile behavior of DSTCs. However, to the best of the authors' knowledge, there are no studies on the seismic performance of DSTCs with an LRS FRP tube. Moreover, to date, only one article by Zeng et al. [28] has presented an experimental study on the seismic performance of full-scale DSTCs with basalt FRP and recycled aggregate concrete. However, the study of full-scale columns is crucial for practical engineering applications as well as theoretical modeling.

Against this background, this paper presents the first experimental study on the seismic performance of full-scale DSTCs with LRS FRP. The authors also present a thorough analysis on the effects of FRP types (PEN FRP and GFRP), the thickness of PEN FRP (2.544 mm and 5.088 mm), and the axial compression ratio (0.2 and 0.4) on the seismic behavior of full-scale DSTCs with LRS FRP. The influence of plastic hinge region filled concrete on the seismic performance of full-scale DSTCs using LRS FRP is also studied.

2. Experimental program

2.1. Test specimens

A total of six circular DSTCs were designed for this test, including two GFRP-concrete-steel DSTCs (GFCS-DSTCs) and four PEN FRP-concrete-steel DSTCs (PFCS-DSTCs). They were tested under a combination of constant vertical load and lateral cyclic load to investigate their seismic performance. The outer tube of the DSTC was either a GFRP or PEN FRP with an inner diameter of 400 mm. The GFRP tubes were provided by the manufacturer, and PEN FRP tubes were produced by the wet-layup process. The reason for using the wet-layup process is that the authors could not easily obtain prefabricated PEN FRP tubes with fiber hoop direction. According to Yu et al. [25], the FRP tubes obtained by this method have little effect on the performance of DSTCs. The specific fabrication method of the wet-layup process for PEN FRP tubes are described below. The calculated height h (distance from the loading point to the surface of the foundation) of the DSTCs is 1400 mm. The inner tube of the specimen is a seamless steel tube with an outer diameter D_{so} of 273 mm and a thickness t_s of 8 mm. The diameter-thickness ratio (D_{so}/t_s) is 34.1. The steel tube extends into the 1500 mm × 1000 mm × 500 mm foundation base and is welded to the upper and lower steel plates in the foundation as well as to the steel bars of the foundation. Eight stiffeners are uniformly welded (i.e., spaced at an angle of 45°) between the upper and lower steel plates to prevent the steel tube from breaking away from the foundation (Fig. 1). In order to facilitate loading in the laboratory, a loading head of 700 mm × 500 mm × 400 mm was designed. The longitudinal reinforcement diameter of the loading head and foundation is 16 mm, and the diameter of the stirrup is 8 mm. Fig. 2 shows the specific construction of the specimen.

Details of the specimens are shown in Table 1. The first letter represents the type of FRP (i.e., P is PEN FRP and G is GFRP). The first number represents the FRP tube thickness (2.5, 4 and 5 represent thicknesses of 2.544 mm, 4 mm, and 5.088 mm, respectively). The second number represents the axial compression ratio (0.2 or 0.4), and the final S represents the plastic hinge region filled with concrete. For example, "G4–0.2-S" represents DSTC made of a GFRP tube with a thickness of 4 mm, an axial compression ratio of 0.2, and a plastic hinge region filled with concrete. To compare PEN FRP and GFRP, a set of specimens with similar confinement stiffness $E_{frp1}t_{frp}/R$ (E_{frp1} is the FRP modulus of elasticity; t_{frp} is the thickness of FRP, and R is the inner diameter of the FRP tube) [6–8,10,32] were set, namely G4–0.2 and P5–0.2. The remaining four DSTCs were also set up to investigate the effects of the axial compression ratio (0.2 or 0.4), the thickness of the PEN FRP tubes (2.544 mm or 5.088 mm), and whether or not the plastic hinge region was filled with concrete when testing the seismic performance of the DSTCs.

Fig. 3 shows a schematic diagram of a plastic hinge region filled with concrete. The height of concrete filled in the specimen's plastic hinge region (G4–0.2-S and P2.5–0.2-S) up to 600 mm. The reason for choosing this length is to fill the potential plastic hinge region as much as possible [14]. The remaining four specimens' steel tubes were only filled with concrete in the foundation, with a height of 500 mm.

The fabrication process of the PEN FRP tube follows: (1) concrete was poured using a GFRP tube as the outer formwork; (2) at the end of the concrete curing, the GFRP tube with a height of 600 mm was excised



Fig. 1. Distribution of stiffeners.

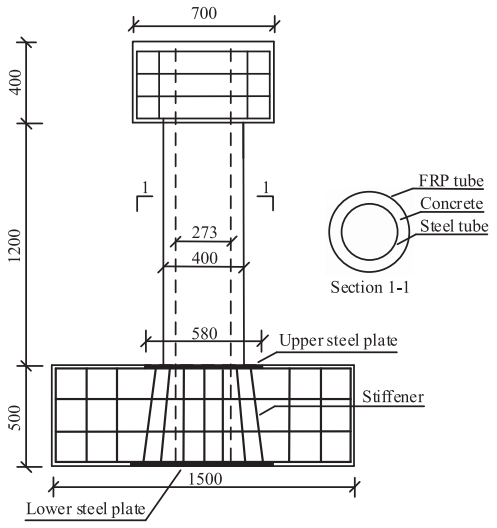


Fig. 2. Dimensions and steel reinforcement details of the specimens (unit: mm).

Table 1
Test details of specimens.

Specimen names	FRP types	Number of FRP layers	t_{frp} /mm	Axial compression ratio	Whether the plastic hinge area is filled with concrete
G4–0.2	GFRP	-	4	0.2	No
G4–0.2-S	GFRP	-	4	0.2	Yes
P2.5–0.2	PEN FRP	2	2.544	0.2	No
P2.5–0.2-S	PEN FRP	2	2.544	0.2	Yes
P5–0.2	PEN FRP	4	5.088	0.2	No
P5–0.4	PEN FRP	4	5.088	0.4	No

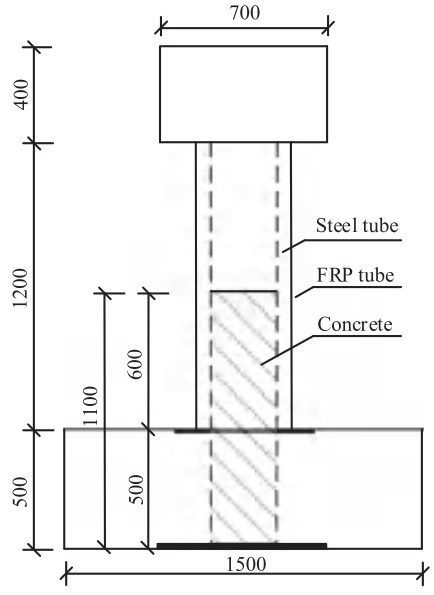


Fig. 3. Steel tube filled with concrete (unit: mm).

starting from the bottom of the column; (3) the PEN FRP was first soaked with epoxy resin adhesive and then rolled and compacted repeatedly with a roller. The step is to allow the epoxy resin completely penetrate into the PEN FRP and squeeze out excess air and epoxy resin. It was then wrapped around the concrete with a wrapping height of 600 mm. To prevent the PEN FRP tube from peeling off during the loading process, the FRP was wrapped around the tube taking up half a circle more (about 628 mm). The PEN FRP wrapping height of 600 mm was chosen to completely cover the plastic hinge region, so that the damage occurs in the confined area of the PEN FRP tube.

2.2. Material properties

2.2.1. Concrete

To facilitate concrete pouring, the specimens were poured into two separate pours. The first pouring of concrete was the foundation, loading head, and between the steel tube and FRP tube interlayer. The second pouring of concrete inside the steel tube required 500 mm for filling only the foundation or 1100 mm for the plastic hinge region. According to ASTM C39/C39M [40], the average compressive strength of the standard cylinders holding the first and second batches of concrete was 25.1 MPa and 29.4 MPa, respectively.

2.2.2. Steel tubes

The steel tubes were made of Q235B grade seamless steel. Based on BS18 [41], the authors cut three tensile specimens from the same batch of steel tubes for testing. The dimensions are shown in Fig. 4. The yield stress, elastic modulus and tensile strength of the steel tubes measured in the test were 265 MPa, 191.2 GPa and 409 MPa, respectively.

2.2.3. FRP tubes

The tests used two FRP tube types, the GFRP tube and PEN FRP tube. According to ASTM D3039 [42], three GFRP coupons and three PEN FRP coupons were made, and the flat coupon tensile was performed. The test results showed that the elastic modulus of the first linear part, the elastic modulus of the second linear part, the tensile strength, and fracture strain of PEN FRP were 27 GPa, 12 GPa, 790 MPa and 6.3 %, respectively. The elastic modulus, tensile strength and fracture strain of GFRP were 33.3 GPa, 573 MPa, and 1.7 %, respectively.

2.3. Instrumentations

Eight 5 mm strain gauges (SGs) were pasted on the steel tube at a distance of 200 mm from the column base with four axial directions (represented by v) and four hoop directions (represented by h). The above SGs were used to measure the strain of steel tubes. Four hoop SGs (represented by H) with a length of 10 mm and eight vertical SGs (represented by V) with a length of 10 mm were pasted on the FRP tube of the same height to monitor the strain change. The rules for numbering the SGs are: the first letter represents the specific location of the SG, and the second letter indicates the orientation of the SG. The SGs on steel tubes are shown in lowercase letters, and the SGs on FRP tubes are shown in uppercase letters. The specific arrangement of the SGs is shown in Fig. 5(a).

Fig. 5(b) shows the detailed arrangement of the linear variable displacement transformers (LVDTs). A total of nine LVDTs (LVDT 1–9) were installed to monitor and measure the displacement of the specimen. Among them, six LVDTs (LVDT 1–6) were installed to monitor the

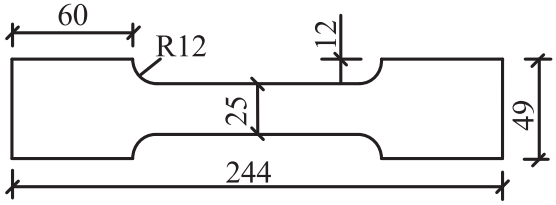


Fig. 4. Tensile specimen of steel tube (unit: mm).

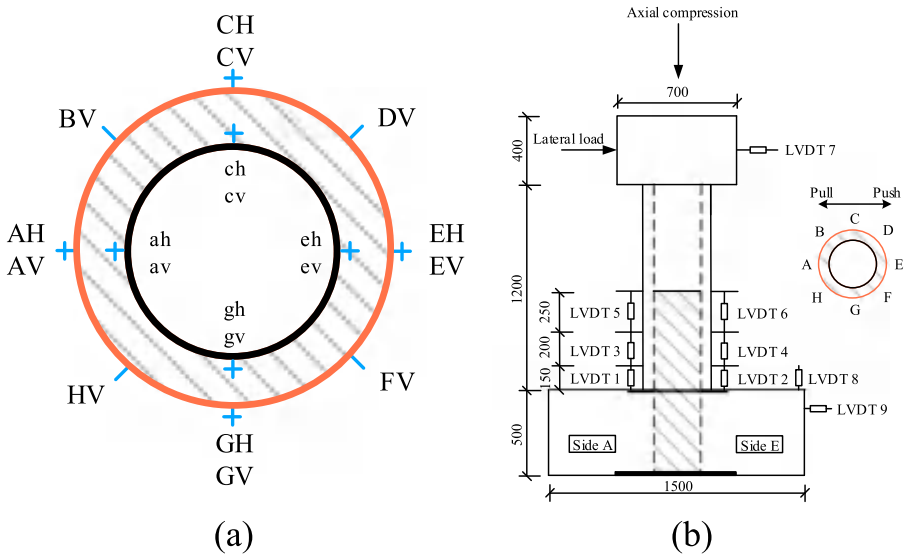


Fig. 5. Details of measurement: (a) Planar layout of strain gauges and (b) layout of LVDTs (unit: mm).

curvature changes of the DSTC within three measurement segments (0–200 mm, 200–400 mm, and 400–600 mm) above the specimen base. LVDT 7 was installed at the loading point to measure the lateral displacement of the specimen. Two LVDTs (LVDT 8–9) were installed at the column base to monitor any movements during the test. In addition, this paper specifies that the push specimen's direction corresponds to the column's E(e) side (Fig. 5(b)), and the pull specimen's direction corresponds to the column's A(a) side (Fig. 5(b)). Unless otherwise indicated, these definitions are used throughout this paper. The remaining positions are also given together, as shown in Fig. 5(b).

2.4. Testing procedures

This experiment was conducted in the State Key Laboratory of Bridge Engineering Safety and Resilience at Beijing University of Technology. A 100 ton horizontal actuator, a 100/200 ton vertical hydraulic jack and a ± 15/20 cm sliding track were used (Fig. 6a). The constant vertical load N_0 is computed using Eq. (1). The contribution of the axial direction of the FRP tube is neglected.

$$N_0 = nN = (f_y A_s + f'_{co} A_c) \quad (1)$$

where N and n are the axial load capacity and the axial compression ratio of the specimen, respectively; f_y and A_s are the yield strength and cross-sectional area of the steel tube, respectively; f'_{co} and A_c are the compressive strength and cross-sectional area of concrete, respectively.

Fig. 6(b) shows the specific loading scheme. First, the axial loading was applied to the specimens. After the loading was stabilized, the lateral loading was then applied. In this test, the specimens were loaded using the displacement loading scheme consistent with Ozbakkaloglu et al. [13] and Zeng et al. [16]. Namely, the drift ratio (the ratio of the lateral displacement Δ of the specimen to the calculated height h) was used to load the specimen step by step, in the order of 1 %, 2 %, 3 %, 4 %, 5 %, 6 %, 7 % and 8 %. Each stage of the drift ratio was cycled three times. The specimen stopped loading when the lateral load dropped substantially.

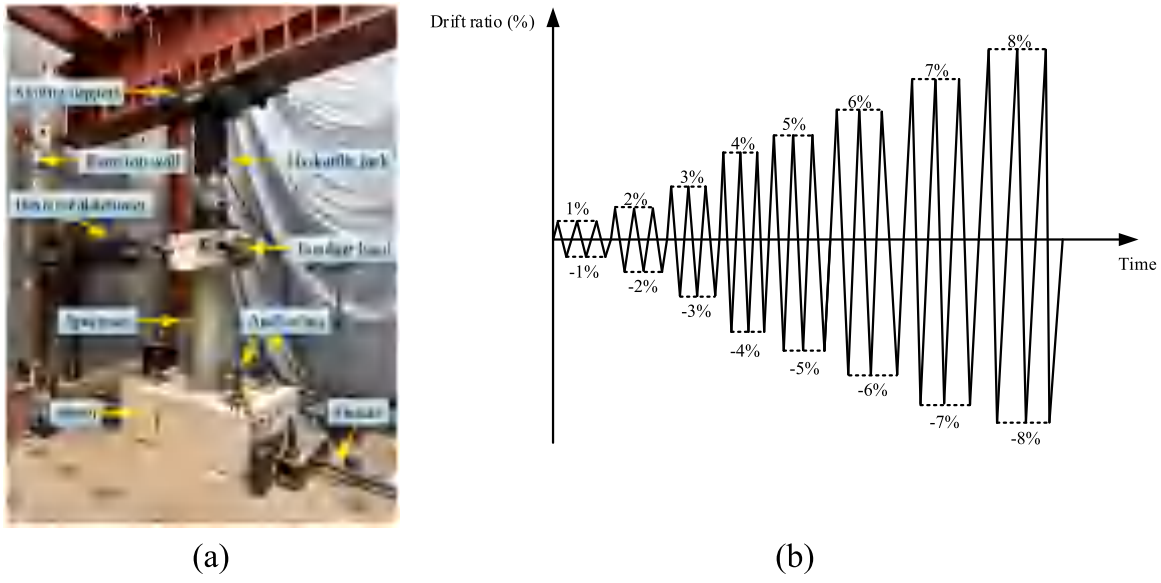


Fig. 6. Instrumentation and testing procedure: (a) Test setup and (b) loading scheme.

3. Results and discussions

3.1. Failure modes

Please note that all lengths appearing below are heights from the foot of the column.

3.1.1. GFCS-DSTCs

The specimens showed no significant damage within three cycles of 1 %. Within a drift ratio of 2 %, the specimens showed horizontal cracks. As the loading proceeded (3 %-5 %), multiple cracks appeared at different heights and continued to develop, eventually converging into multiple large cracks. G4–0.2-S even showed a large crack through the column during loading. The fracture (Fig. 7a) of the GFRP fibers on the G4–0.2 occurred during the final loading cycle (6 %), but the specimen did not show a significant decrease in load capacity. This is because the compression between the GFRP at the bottom of the column and the foundation caused the FRP fibers to fracture, rather than the FRP fibers fracturing under tension. Within a drift ratio of 6 %, the FRP tube on the A side of G4–0.2-S cracked (Fig. 7b). Finally, the bearing capacity of GFCS-DSTCs (G4–0.2 and G4–0.2-S) dropped abruptly after hearing a "thud" sound, and the test was stopped. In addition, G4–0.2-S showed a slight bulging phenomenon in the FRP tube during loading, indicating that the concrete inside the steel tube had a good inhibitory action on the inward buckling of the tube.

At the end of the test, the FRP tube was first stripped and the concrete was largely intact (Fig. 8). G4–0.2 had one large crack (140 mm), and G4–0.2-S had two large cracks (200 and 400 mm). Then, after removing the concrete, G4–0.2 found that the bottom of the steel tube was severely fractured and had buckled inward (Fig. 8a). However, G4–0.2-S only fractured at the bottom of the steel tube and had no significant buckling (Fig. 8b).

3.1.2. PFCS-DSTCs

The failure modes of the four PFCS-DSTCs are significantly different, so they are described separately. However, the final damage phenomenon is similar. When a "thud" sound occurs, the bearing capacity suddenly decreases and the test is stopped.

(1) P2.5–0.2

Within three cycles of 1 %, there was no significant damage to the specimen. Within a 2–4 % drift ratio, multiple cracks appear and continue to develop. Within the 5 % drift ratio, two large cracks appeared and the concrete block inside the FRP tube could be clearly seen (Fig. 7c). FRP cracks continued to increase and widen within a drift ratio of 6–7 %. During the first 7 % drift ratio cycle, the specimen failed.

(2) P2.5–0.2-S

The specimen showed no significant damage within the 1 % drift ratio, and only occasional epoxy resin cracking was heard. Within the 2 % drift ratio, some visible white patches appeared on the FRP tube surface but did not crack. Within a drift ratio of 3 %, white patches between 200 mm and 300 mm of the A side developed to nearly 1/2 the circumference. Within the 4 % drift ratio, FRP cracks appeared between 200 mm and 300 mm on the A side, and multiple visible cracks appeared between 200 mm and 300 mm on the E side. Within the 5 % drift ratio, FRP cracks in the 200–300 mm range on the A side developed rapidly, and the internal concrete could be clearly seen. Within three cycles of 6 %, two large cracks formed between 200 mm and 300 mm of the A side, and both were 1/4 of the column circumference. In the first cycle of 8 %, the specimen failed.

(3) P5–0.2

The specimen did not show significant damage in 1–3 % loading cycles. Within the 4–7 % drift ratio, the FRP tube showed only white patches and did not crack (Fig. 7d). Finally, in the second cycle of 7 %, the specimen failed.

(4) P5–0.4

The specimen showed no significant damage within the 1–2 % drift ratio. Within the 3 % drift ratio, a few white patches appeared on the FRP tube and developed into cracks. Between the 4 % and 6 % drift ratio, multiple cracks appeared and proceeded to develop. In the first cycle of 6 %, the specimen failed.

When the test was completed, the FRP tube was first removed. The P2.5–0.2 concrete was largely intact, while the concrete at the bottom of P2.5–0.2-S, P5–0.2 and P5–0.4 were significantly spalled (Fig. 8). P2.5–0.2 showed two large cracks between 12 mm and 400 mm, and P5–0.2 showed four cracks (45, 190, 385 and 600 mm). The maximum crack width of the P2.5–0.2 was significantly larger than that of the P5–0.2, suggesting that increasing the FRP thickness can enhance the confining effect on the concrete. P5–0.4 showed one crack at 280 mm, with a width greater than P5–0.2. This indicates that increasing the axial compression ratio will increase the damage to the specimen. P2.5–0.2-S, which had one crack at 220 mm, and the width of the crack was significantly smaller than that of P2.5–0.2. It can be seen that filling the plastic hinge region with concrete improved the integrity of the specimen. Subsequently, after removing the concrete, it was found that minor fractures occurred at the bottom of the steel tubes of P2.5–0.2 and P2.5–0.2-S. While severe fractures occurred at the bottom of the P5–0.2 and P5–0.4 steel tubes, the latter had a much lower level of damage. Although P5–0.4 has a higher axial compression ratio, its drift ratio is smaller than that of P5–0.2 (6 % < 7 %), which may explain the more severe tube fracture in P5–0.2. Local buckling occurred in the steel tubes of P2.5–0.2, P5–0.2 and P5–0.4 (Fig. 8). Still, P2.5–0.2-S did not show significant buckling due to the presence of concrete in the steel tube, which is in the plastic hinge region (Fig. 8d).



Fig. 7. Progress of damage in the specimens: (a) FRP tube compression fracture of G4–0.2, (b) FRP tube cracking of G4–0.2-S (c) FRP tube cracking of P2.5–0.2, and (d) FRP tube shows white patches of P5–0.2.

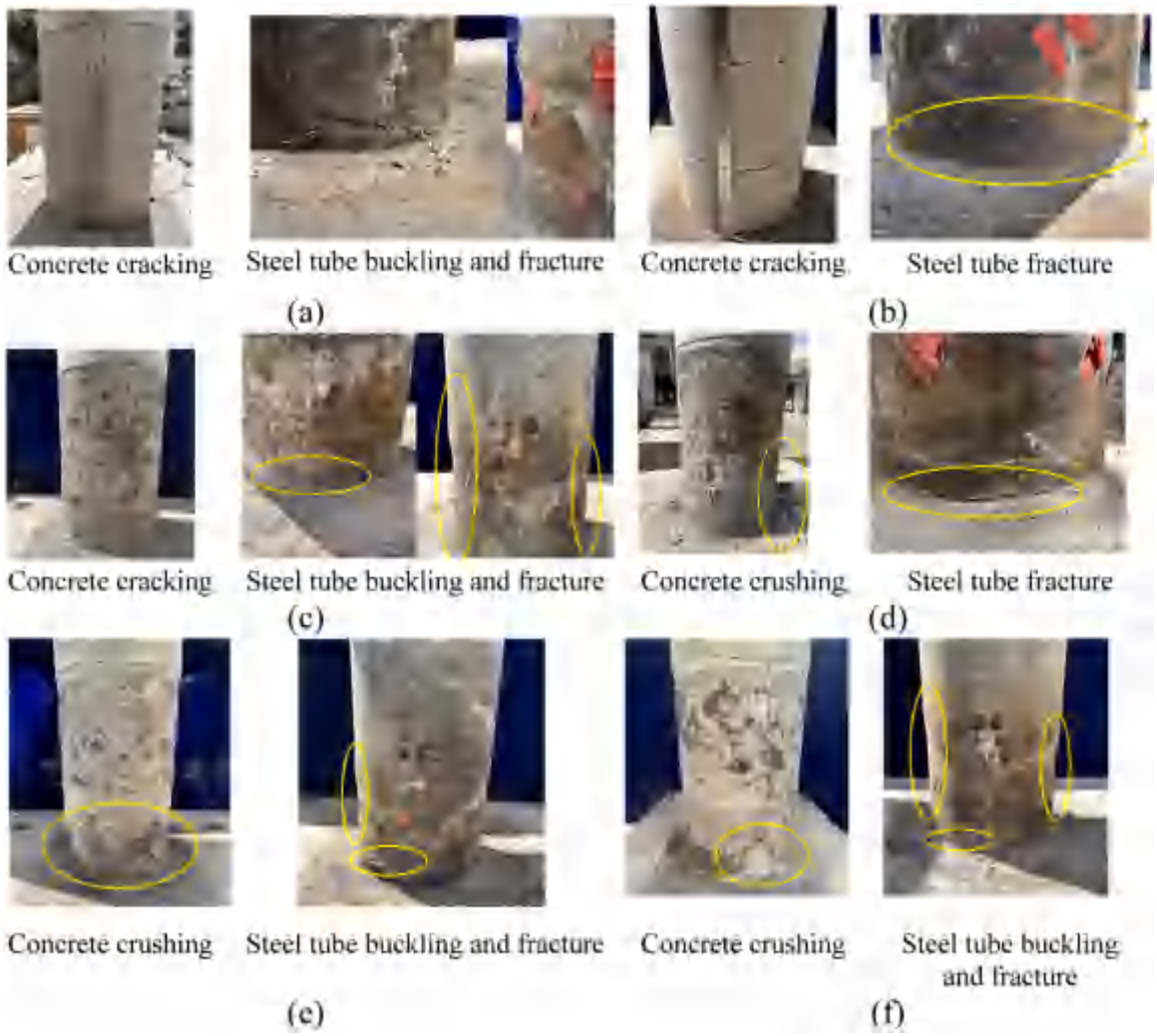


Fig. 8. Specimens after removal of FRP tubes: (a) G4–0.2, (b) G4–0.2-S, (c) P2.5–0.2, (d) P2.5–0.2-S, (e) P5–0.2 and (f) P5–0.4.

3.2. Hysteretic curves

Fig. 9 shows the hysteretic curves of all the specimens as very full, without obvious pinching and shrinking effects, demonstrating good deformation and energy dissipation capacity. All hysteresis curves have similarities. At the initial loading stage (the 1 % drift ratio), the specimens are in the elastic stage, and the hysteresis loop area is small. Within three cycles at the same loading stage, the areas are almost equal. The hysteresis curve is almost linear. The loading and unloading stiffness are almost the same, and no apparent residual deformation exists. As the loading progresses, the steel tube yields and the hysteresis loop area continues to increase, resulting in an increased energy dissipation. The specimen stiffness decreases continuously; the increasing difference between the loading and unloading stiffness leads to a significant increase in residual deformation. The loading continued after reaching the peak lateral load, and the specimens' lateral load decreased insignificantly. Finally, after loading to a drift ratio of 6 %, 7 % or 8 %, the specimens failed due to a rapid decrease in bearing capacity as a result of the steel tubes fracturing.

For the specimens (G4–0.2-S and P2.5–0.2-S) filled with concrete in the plastic hinge region, their hysteresis curves essentially cover the corresponding control specimens (G4–0.2 and P2.5–0.2). It can be seen that for DSTCs, proper filling of steel tubes can improve their seismic performance. This is consistent with the research of Zhang et al. [14]. At the same loading stage, P5–0.4 has a fuller hysteresis loop than P5–0.2, but the former has a faster stiffness degradation. The strength and stiffness of the PFCS-DSTCs increase as the thickness of PEN FRP increases. When the confinement stiffness is the same, the hysteresis curve of P5–0.2 essentially covers G4–0.2, and the strength and deformation capacity of the former is significantly larger than that of the latter. Therefore, LRS FRP is a promising seismic material for full-scale DSTCs used in practical engineering.

3.3. Skeleton curves

The skeleton curve in this paper is an envelope formed by connecting the peak points of the first cycle of each loading level on the specimen hysteresis curve. It can more intuitively reflect the bearing capacity and ductility of the specimens and provide an essential basis for subsequent analysis of the specimen's deformation capacity. Fig. 10 shows the skeleton curves of all the specimens in this test. The specimens show a high stiffness in the test's early stage, and the lateral bearing capacity increases rapidly with the increase of displacement. As the loading level increases, the skeleton curves develop nonlinearly, the lateral load growth rate slows, and the stiffness decreases significantly. In the later stage of the test, the inner steel tubes experienced buckling or fracturing, and the bearing capacity was reduced. However, the degree of reduction was not significant. Before failure, the lateral load on the specimens was relatively stable (i.e., fluctuating within a small range). The DSTCs clearly have better stability in resisting seismic loads.

From Fig. 10(a), we can see that for G4–0.2 and G4–0.2-S as well as P2.5–0.2 and P2.5–0.2-S, the filling of the plastic hinge region with

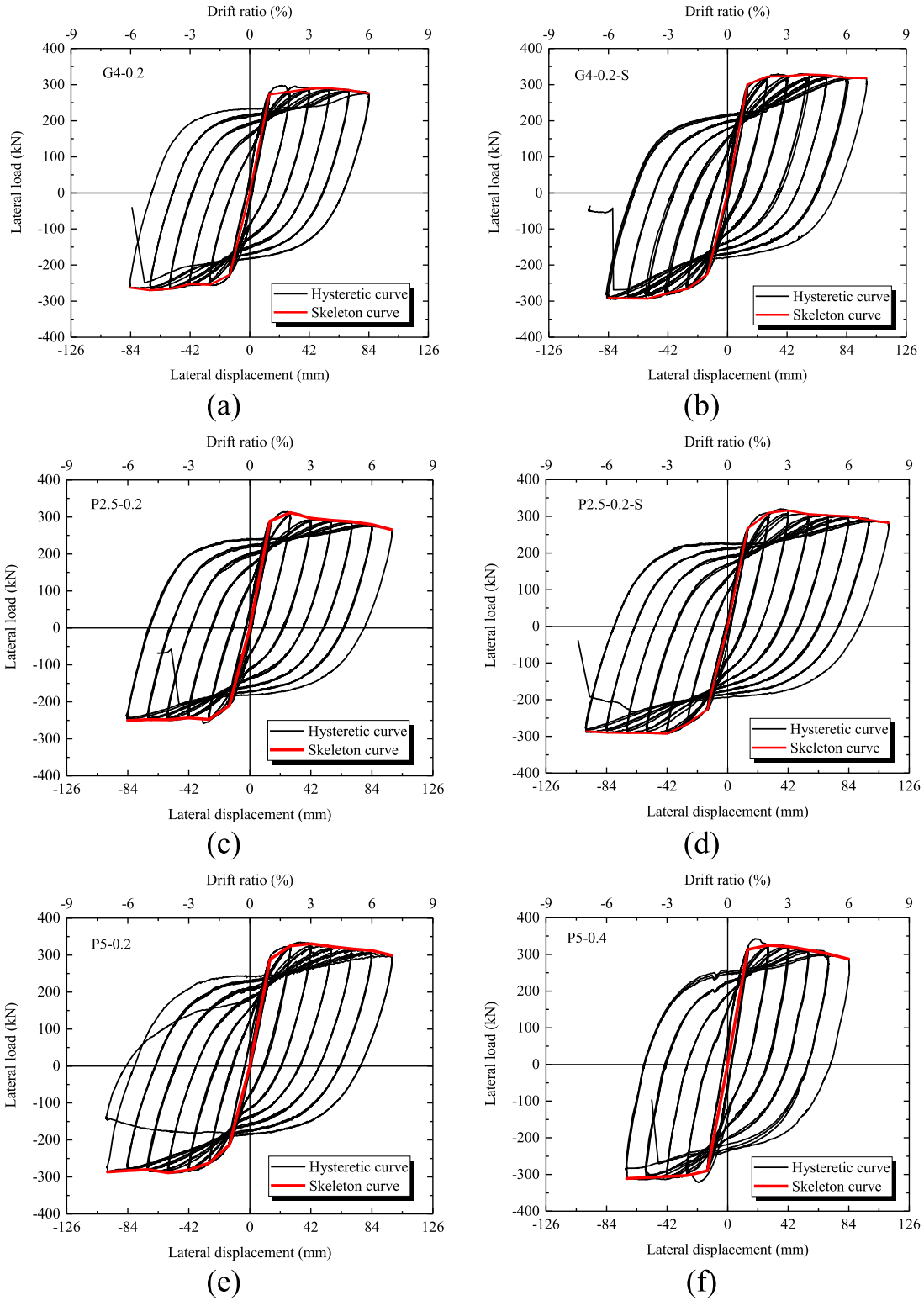


Fig. 9. Hysteresis curves: (a) G4–0.2, (b) G4–0.2-S, (c) P2.5–0.2, (d) P2.5–0.2-S, (e) P5–0.2 and (f) P5–0.4.

concrete improves the peak lateral load and deformation capacity of the DSTCs. The peak strength of G4–0.2-S increases by 10.9 % compared to G4–0.2, and an additional drift ratio is loaded. P2.5–0.2-S has an 8.2 % increase in peak strength over P2.5–0.2 and is loaded with an additional drift ratio. Compared with P5–0.2, the peak strength of P5–0.4 is only 2.6 % higher, indicating that increasing the axial compression ratio does not significantly increase the peak lateral load of the specimen. A larger cross-section and weaker concrete confinement may cause this. For the comparison group with similar confinement stiffness (G4–0.2 vs. P5–0.2), P5–0.2 has a 10.7 % increase in peak lateral load over G4–0.2 and is also loaded with an additional drift ratio (Fig. 10b). It can be seen that the PFCS-DSTCs have higher strength and deformation capacity than GFCS-DSTCs, proving the feasibility of using PEN FRP for DSTCs seismic resistance.

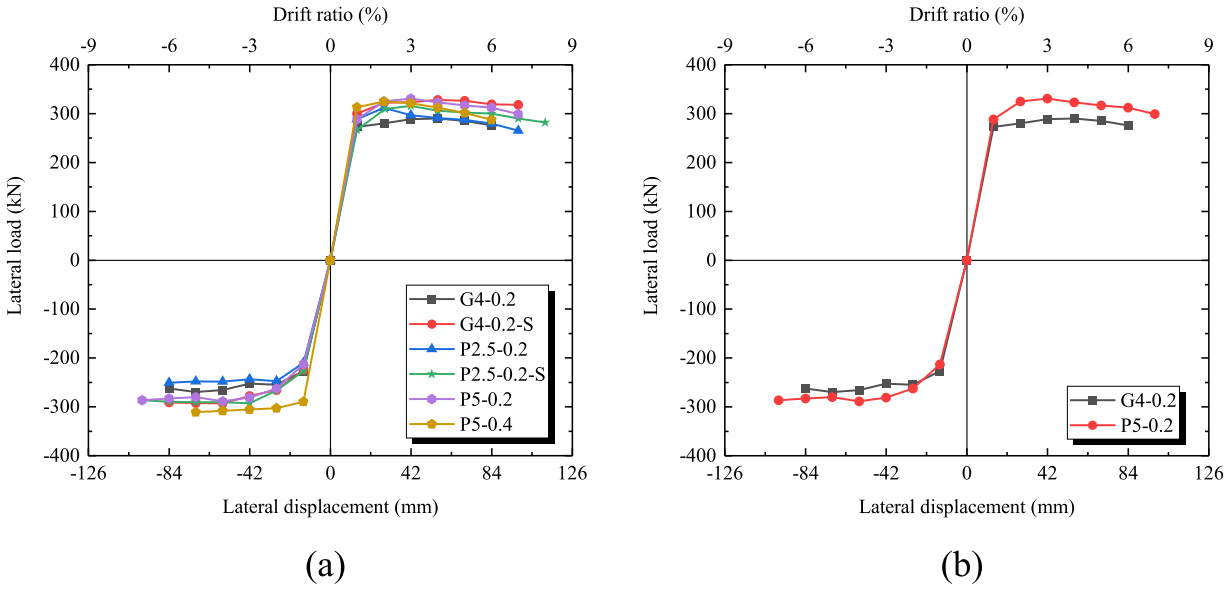


Fig. 10. Skeleton curves: (a) All specimens and (b) G4–0.2 vs. P5–0.2.

For PEN FRP, increasing its thickness (2 to 4 layers) increases the peak lateral load of the specimen by 10.1 %. Therefore, filling the plastic hinge region with concrete, using PEN FRP or increasing the thickness of PEN FRP can increase the specimens' peak lateral load and deformation capacity. At the same time, the axial compression ratio has little influence on the skeleton curves of DSTCs.

3.4. Strength degradation

After a structure or member reaches yield, a pronounced degradation of the bearing capacity occurs under different cycles of the same loading stage. The strength degradation coefficient λ_i at the i-th loading stage can express the degree of specimen strength degradation, which is defined as the ratio of the peak lateral load F_f^i of the last cycle to the peak lateral load F_1^i of the first cycle under each loading stage. The specific calculation formula is as follows:

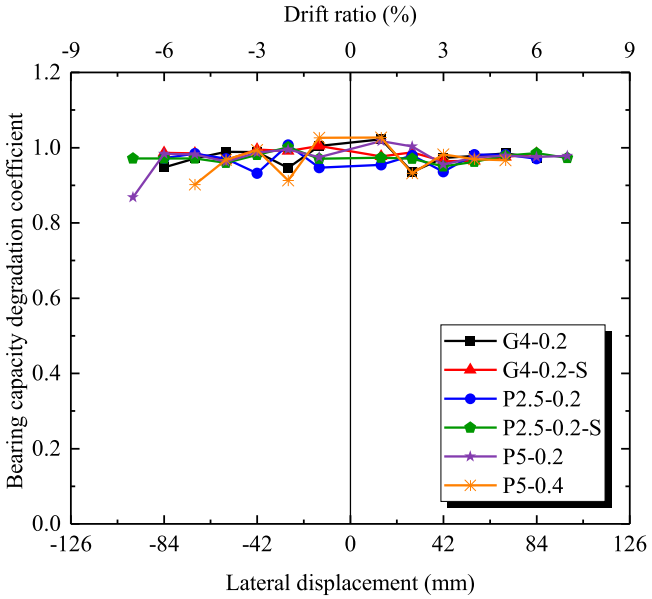


Fig. 11. Strength degradation: All specimens.

$$\lambda_i = F_f^i \Big/ F_1^i \tag{2}$$

Fig. 11 shows the strength degradation curves for all specimens, which shows strength degradation of all specimens as insignificant, as the strength degradation coefficient is greater than 85 %. Hence, DSTCs can significantly improve the specimens' ability to resist damage. In other words, the structure is always in a better stress state, which is conducive to resisting seismic loads, making DSTCs a good structural combination for full-scale columns in practical engineering.

3.5. Stiffness degradation

Under cyclic reciprocation loading, the stiffness of a structure or member will degrade as concrete cracks and steel tubes yield. Therefore, stiffness is an essential indicator of a structure or member's seismic performance. This study defines the slope of the line connecting the positive and negative peak points in the first hysteresis loop of the same loading stage as the stiffness K_i of DSTCs, and the stiffness K_i is calculated as:

$$K_i = \frac{|+F_i| + |-F_i|}{|+\Delta_i| + |-\Delta_i|} \tag{3}$$

where $\pm\Delta_i$ is the positive and negative maximum displacement of the specimen at the i-th loading stage (the first loading cycle); $\pm F_i$ are loads corresponding to the specimen's positive and negative maximum displacements at the i-th loading stage (the first loading cycle).

Fig. 12 shows the stiffness degradation curves for all specimens in this test. Suppose the stiffness corresponding to a drift ratio of 1 % is assumed to be the initial stiffness of the specimens. Then, the initial stiffness for this test is concentrated between 17.8 and 21.3 kN/mm. As the loading proceeds, the specimens' stiffness decreases due to concrete cracking and steel tube buckling. The stiffness degradation rate is fast in the early stage but slows down in the later stage. This indicates that in the later loading stage, the FRP tube plays a limiting role, and can delay the specimens' stiffness degradation. Finally, the specimens' residual stiffness ranges from 1.9 to 4.4 kN/mm.

As can be seen from Fig. 12, if the axial compression ratio is increased (0.2 to 0.4), the initial stiffness of the specimen (P5–0.4) increases, but the stiffness degrades more rapidly as loading proceeds. However, after reaching a drift ratio of 3 %, the rate of stiffness degradation is similar to that of the specimen (P5–0.2) with a low axial

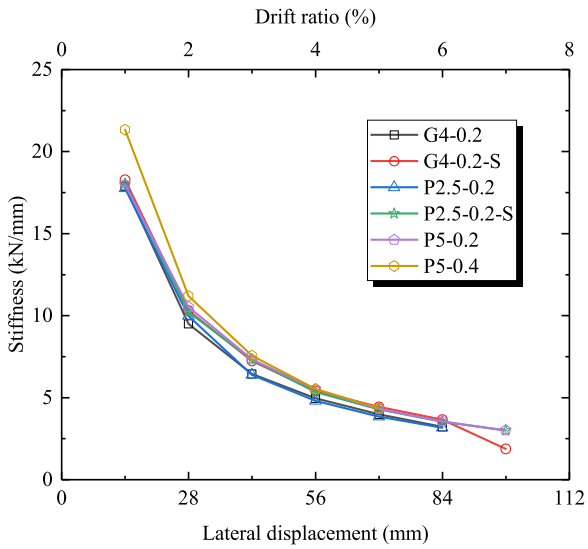


Fig. 12. Stiffness degradation: All specimens.

compression ratio, and the stiffness degradation curves almost overlap. Compared with G4–0.2, the stiffness of P5–0.2 is only slightly higher at each drift ratio, and the stiffness degradation curves are similar. Therefore, PEN FRP and GFRP have similar effects in resisting stiffness degradation. Whether the plastic hinge region is filled with concrete or not and the thickness of the PEN FRP tube have limited influence on the stiffness degradation curves.

3.6. Curvature distribution over the column height

This study used six LVDTs (LVDT 1–6) to measure the deformation along the specimen height (Fig. 5b). The lengths of the measurement segments are 150, 200 and 250 mm, respectively. The average curvature φ_Δ can be calculated from the readings of six LVDTs, which is calculated as:

$$\varphi_\Delta = \frac{\Delta_1 - \Delta_2}{D^* l_{seg}} \tag{4}$$

where Δ_1 and Δ_2 represent the LVDTs values on the symmetric side of the column, respectively; l_{seg} is the length of the measurement segment, which is 150, 200 and 250 mm; D^* is the distance between two LVDTs at the same height. D^* is slightly larger than the diameter of the column, which is 500 mm in this study.

Fig. 13 shows the average curvature distribution calculated using Eq. (4) under different loading stages. The average curvature of each measurement segment is connected with a line and used to show the curvature change of the specimens. The curvature distribution is similar for each specimen. In the initial loading stage, the curvature is linearly distributed along the height of the column and gradually decreases from the bottom up. As the loading proceeds, the curvature is distributed nonlinearly over the column height. The lower curvature develops faster than the column's upper section, and a larger curvature always occurs near the column base. Except for G4–0.2, the curvature distribution of other specimens is approximately symmetrical on both sides of the push and pull. For G4–0.2, when in the range of 0–150 mm, the curvature on the pull side is greater than on push side, possibly due to uneven concrete pouring on the pull side with air bubbles and voids.

Whether GFCS-DSTCs or PFCS-DSTCs, filling the plastic hinge region with concrete makes the curvature distribution more uniform along the column height (Fig. 13b and d). In other words, the plastic hinge region filled with concrete can improve the deformation capacity of DSTCs. Due to the large rupture strain of PEN FRP, the curvature of P5–0.2 is greater than that of G4–0.2 on three cross-sections (Fig. 13a and e), making the deformation of P5–0.2 more evenly distributed along the column height. It can be seen that PEN FRP is noticeably better than GFRP at improving the deformation of specimens. With increasing the axial compression ratio, the curvature of P5–0.4 is smaller than that of P5–0.2 at the same loading stage (Fig. 13e and f). This is because as the axial compression ratio increases, the stiffness of the specimens also increases, making them less prone to deformation. The PEN FRP thickness has no significant effect on the curvature distribution of DSTCs (Fig. 13c and e).

3.7. Moment-curvature curves

The DSTCs bending moment is the moment M at the 75 mm section from the bottom of the column, which is calculated according to Eq. (5), taking into account the second-order effect (P-Δ effect). The column curvature is the average curvature within 150 mm from the bottom of the column, which is expressed as Eq. (4).

$$M = F \times h + N_0 \times \Delta \tag{5}$$

where F is the lateral load, and Δ is the lateral displacement of DSTCs.

Fig. 14 presents the moment-curvature curves for this experiment. And it is stipulated that the positive and negative directions are the directions of pushing and pulling specimen, respectively. Here, the moment-curvature curves usually consist of two stages: (1) the sharp rise stage and (2) the stable development stage. Clearly, after entering the second stage, the bending moment of the DSTCs changes vary little or gradually increases until failure, showing DSTCs' excellent ductile cross-section properties.

To facilitate the analysis of the effect of each studied parameter on the moment-curvature curves, the average moment-curvature curves are given in Fig. 15. This analysis was obtained by averaging the moment-curvature curves in the positive and negative directions. A comparison of P2.5–0.2 and P2.5–0.2-S shows they have similar ultimate curvature, while P2.5–0.2-S has a 12.5 % increase in the peak bending moment. Therefore, filling the plastic hinge region with concrete improved the ability of the specimens to resist the bending moment. After comparing different types of FRP, it was determined that the peak bending moment and ultimate curvature of PEN FRP increased by 6.9 % and 60.4 %, respectively, compared to GFRP. It can be seen that the capacity of PEN FRP to resist bending moment is comparable to GFRP, while the deformation capacity is much higher than GFRP. This indicates that the ductility performance of PEN FRP was fully demonstrated on DSTCs. A comparison of P2.5–0.2 and P5–0.2 shows that the latter's peak bending moment and peak curvature increased by 12.5 % and 23.0 %, respectively. Therefore, increasing the thickness of PEN FRP improved resistance to the bending moment and to the deformation capacity of the PFCS-DSTCs. A comparison of specimens with different axial compression ratios revealed that the larger axial compression ratio specimen (P5–0.4) had a 12.6 % higher peak bending moment and 6.7 % higher ultimate curvature than the smaller axial compression ratio specimen (P5–0.2). Increasing the axial compression ratio had little effect on the deformation capacity of PFCS-DSTCs. This may result from the larger cross-section in this test and a weaker confinement effect of FRP tube.

3.8. Ductility

The ductility of a structure or member is usually defined by its ability to maintain inelastic deformation before damage and without significant reduction in strength. The most common parameter seems to be the ductility coefficient μ_δ, expressed as:

$$\mu_\delta = \frac{\delta_\mu}{\delta_y} \tag{6}$$

where δ_u is the ultimate displacement; δ_y is the yield displacement.

Many scholars [14–16,43] define lateral displacement corresponding to a reduction of the lateral load to 80 % or 85 % of the peak load as the

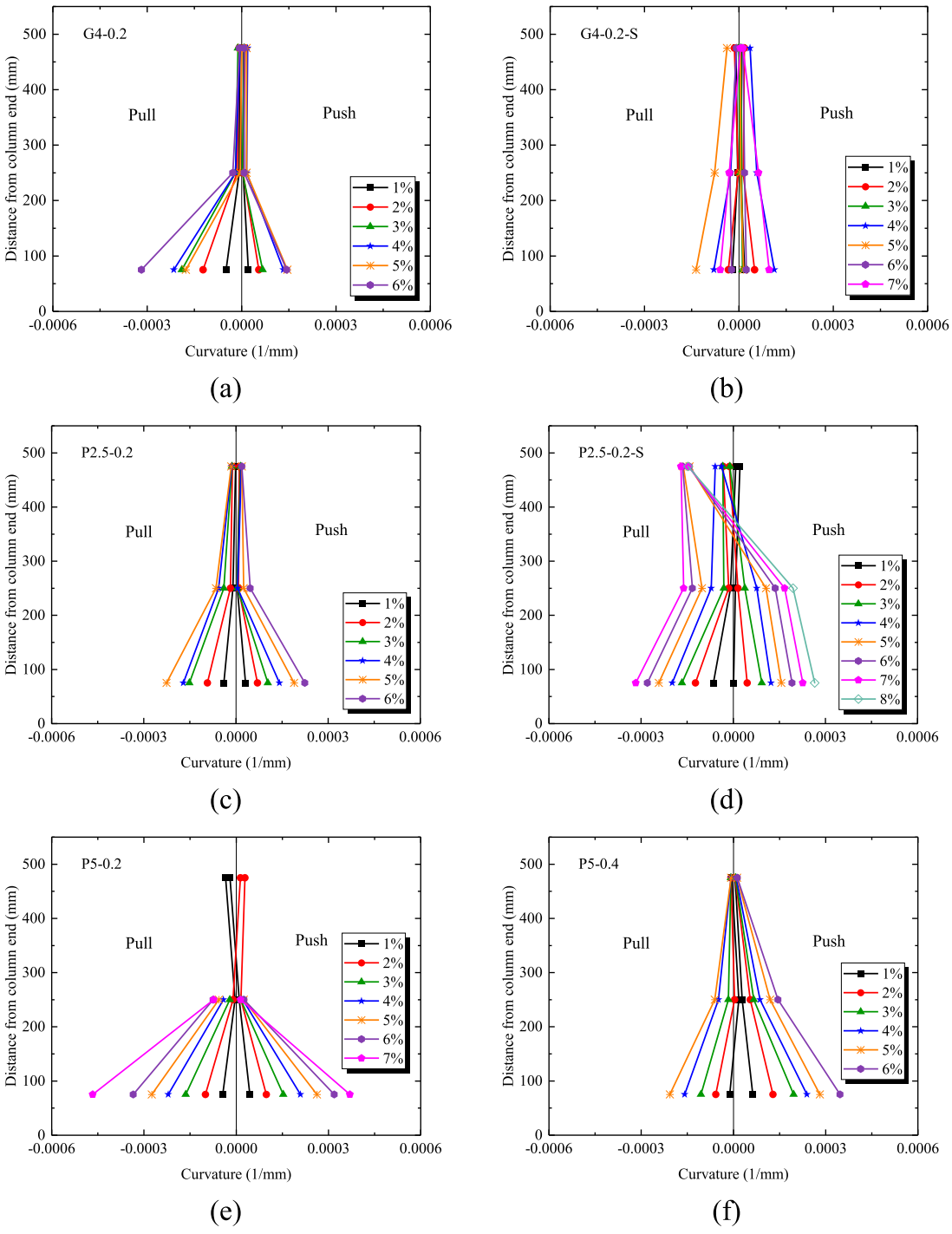


Fig. 13. Curvature distribution: (a) G4–0.2, (b) G4–0.2-S, (c) P2.5–0.2, (d) P2.5–0.2-S, (e) P5–0.2 and (f) P5–0.4.

ultimate displacement. However, the strength of the specimens in this experiment did not significantly decrease before failure. Therefore, the ultimate displacement is defined as the lateral displacement corresponding to the failure of the specimens. Fig. 16 shows the yield point calculated using the equivalent elastic-plastic energy method. F_y is the yield load; δ_{max} and F_{max} are the peak displacement and corresponding lateral load, respectively; F_u is the ultimate load.

Table 2 gives the ductility coefficients for all specimens in this test. The ductility coefficients of all the DSTCs tested in this experiment are greater than 4.0, which is much higher than the ductility coefficient (3.0) of typical RC frame structures. As expected, the ductility coefficients increase with a decreasing axial compression ratio or an increasing thickness of the PEN FRP tube. The ductility coefficient of P5–0.2 increased by 11.9 % compared to G4–0.2, indicating better ductility of DSTCs with PEN FRP tube. However, filling the plastic hinge region with concrete had little effect on the ductility coefficient under the test setup. The G4–0.2, G4–0.2-S, P2.5–0.2 and P2.5–0.2-S had approximate ductility coefficients. The reason for this may be due to the fact that steel tube fractured when the specimens were destroyed, which led to a sudden drop in the bearing capacity. In this paper, the lateral displacement corresponding to the failure is taken as the ultimate displacement, which has a smaller value.

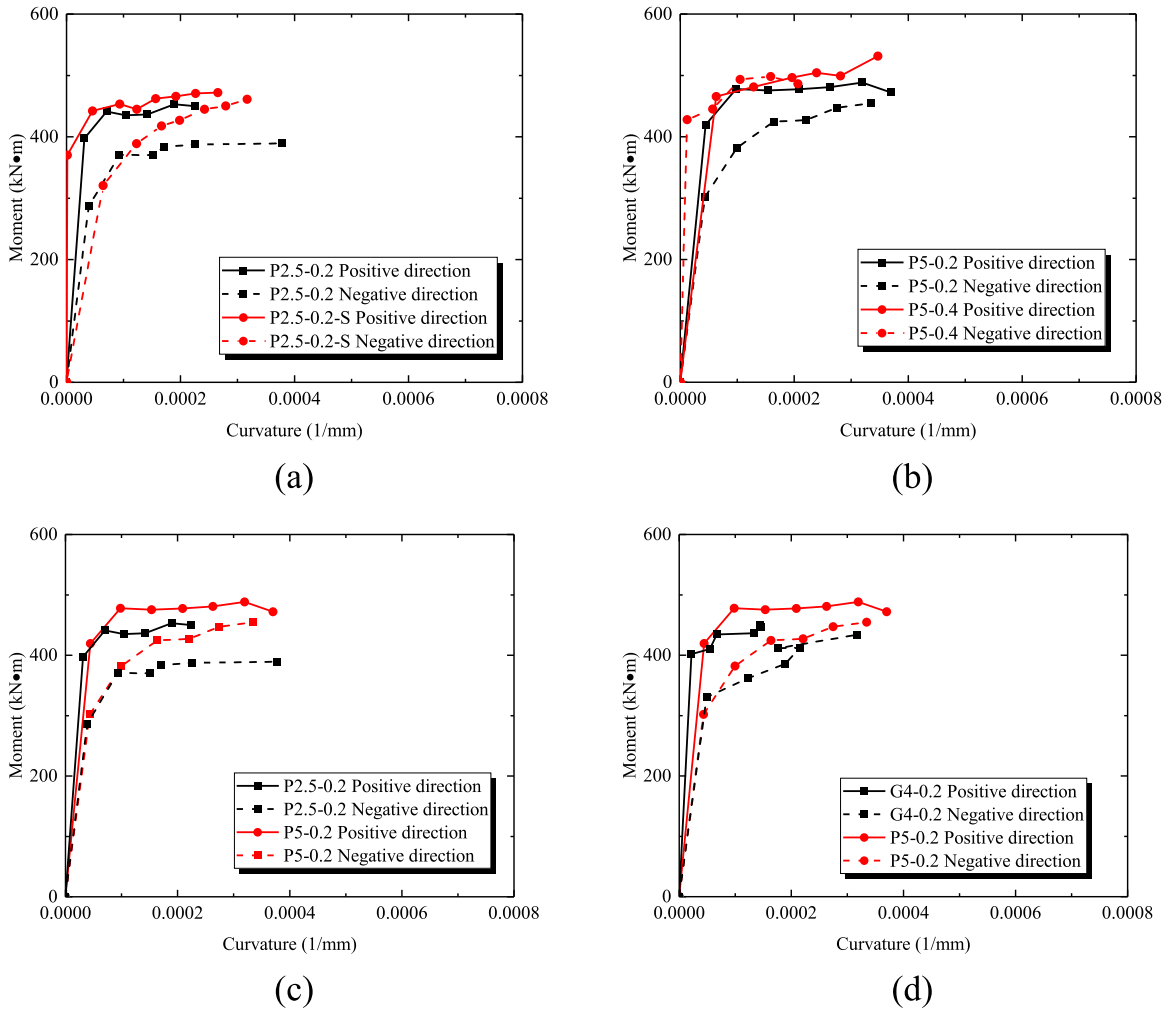


Fig. 14. Comparison of the moment-curvature curves: (a) P2.5–0.2 vs. P2.5–0.2-S, (b) P5–0.2 vs. P5–0.4, (c) P2.5–0.2 vs. P5–0.2 and (d) G4–0.2 vs. P5–0.2.

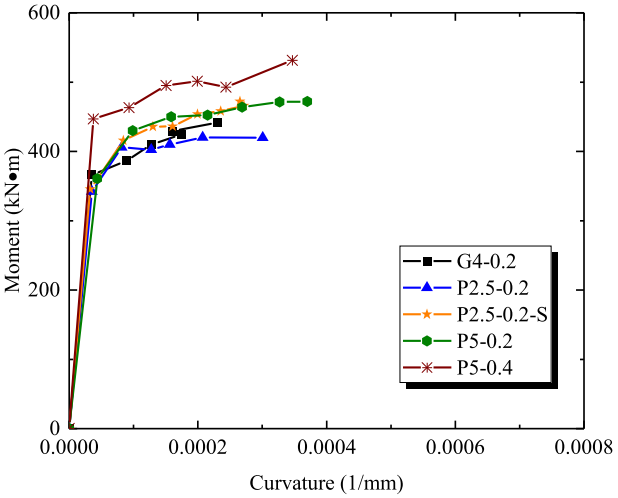


Fig. 15. Average moment-curvature curves.

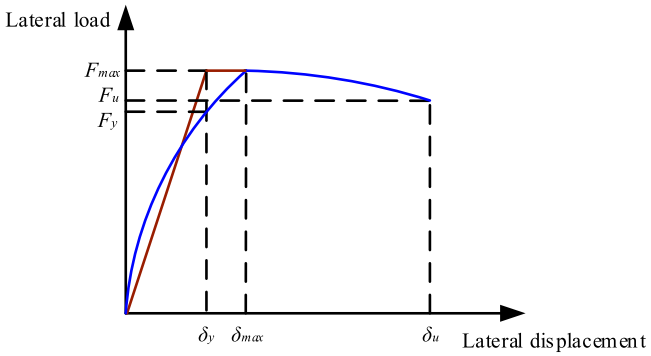


Fig. 16. Equivalent elastic-plastic energy method.

3.9. Energy dissipation

The energy dissipation capacity of a structure or member is its ability to absorb energy under simulated seismic loading; thus, the greater the energy dissipation capacity of a structure or member, the better its seismic performance. The energy consumption of each hysteresis loop is represented by the area of its enclosed region [7,8,29], and the total energy consumption is obtained by adding the areas of all the specimen hysteretic loops [28]. Fig. 17 shows the energy consumption of each hysteresis loop. It can be seen that within a drift ratio of 1 %, the energy consumption of all specimens is almost the same. At this point, the FRP tube has not yet played a role. As loading proceeds, the concrete in the interlayer of FRP tube and steel tube cracks and expands outward. The FRP tube acts as a confinement and the energy dissipation capacity of the structure increases. P5–0.4 has a higher energy consumption of each hysteresis loop than P5–0.2, indicating that increasing the axial

Table 2
Ductility coefficient.

Specimens	Loading direction	δ_y (mm)	δ_u (mm)	u_δ
G4–0.2	Positive	16.7	84.3	5.1
	Negative	22.3	74.1	3.3
	Average	**19.5**	**79.2**	**4.2**
G4–0.2-S	Positive	17.3	98.0	5.7
	Negative	24.5	71.3	2.9
	Average	**20.9**	**84.7**	**4.3**
P2.5–0.2	Positive	16.1	97.8	6.1
	Negative	19.0	48.6	2.6
	Average	**17.6**	**73.2**	**4.3**
P2.5–0.2-S	Positive	19.0	111.4	5.9
	Negative	22.8	65.8	2.9
	Average	**20.9**	**88.6**	**4.4**
P5–0.2	Positive	18.1	97.8	5.4
	Negative	24.6	80.3	4.0
	Average	**21.4**	**89.0**	**4.7**
P5–0.4	Positive	15.0	84.3	5.6
	Negative	16.4	48.0	2.9
	Average	**15.7**	**66.1**	**4.3**

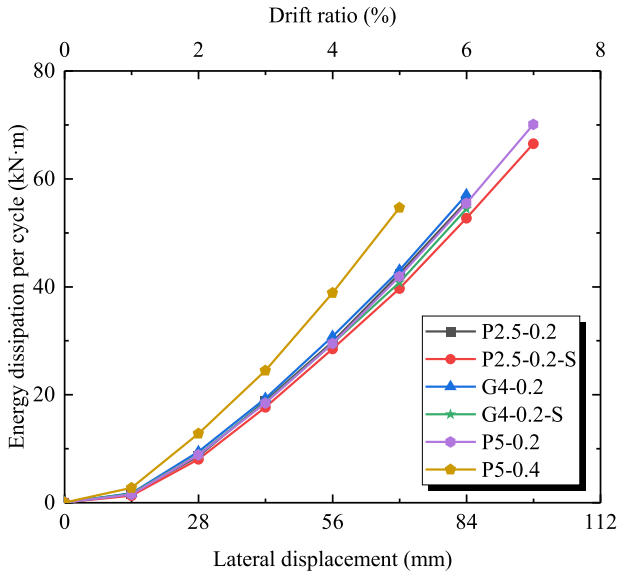


Fig. 17. Energy consumption of each hysteresis loop.

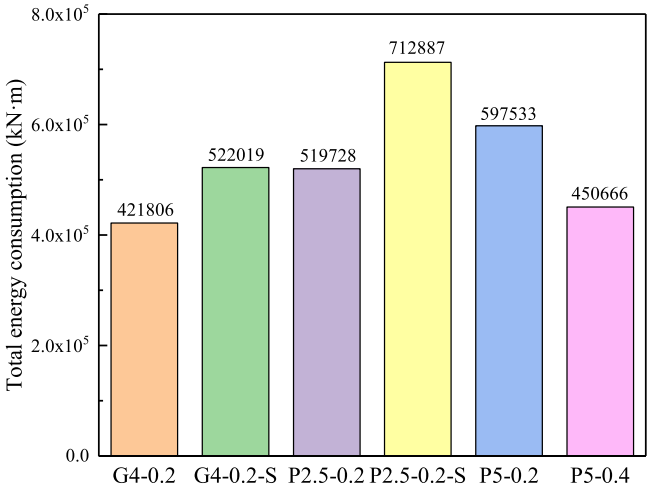


Fig. 18. Total energy consumption of the specimens.

compression ratio increases the energy consumption of the specimen. Fig. 18 plots the total energy consumption for all specimens. The filling of the plastic hinge region with concrete substantially improved the energy dissipation capacity of the specimens. G4–0.2-S increased by 23.8 % compared to G4–0.2, and P2.5–0.2-S increased by 37.2 % compared to P2.5–0.2. P5–0.2 shows a 41.7 % increase in energy dissipation capacity compared to G4–0.2. It can be seen that for DSTCs, using PEN FRP is more advantageous than GFRP in terms of energy consumption. When doubling the thickness of PEN FRP, the energy dissipation capacity increased by 15.0 %. P5–0.4 is 32.6 % lower than P5–0.2. The reason for this is that increasing the axial compression ratio leads to earlier failure of the specimen. Therefore, the total energy consumption of P5–0.4 is lower than that of P5–0.2.

3.10. Distribution of strains in FRP tubes

To investigate the FRP tubes confinement effect, four SGs (AH, CH, EH and GH) monitored the FRP hoop strain at 200 mm above the foundation, as shown in Fig. 5(a). One strain gauge (CH) was in the FRP overlap zone, and three (AH, EH and GH) were outside the FRP overlap zone. Using the drift ratio as the horizontal axis and the hoop strain of the FRP tube as the vertical axis, Fig. 19 plots the hoop strain distribution curves.

The hoop strain of the FRP tube is taken as the maximum strain in three cycles for each loading stage. A positive strain in the Fig. 19 means that the FRP is in tension, and a negative strain means that the FRP is in compression. The hoop strain of the FRP tubes is positive; thus, FRP acts as a confinement for the DSTCs during the loading process. The hoop strain increases with the lateral displacement increases. This suggests that the confinement effect of the FRP tube increases as loading proceeds. Moreover, at the beginning of loading, the FRP tube hoop strain on the A and E sides are symmetric at the vertical axis. At the later loading stage, the FRP hoop strain on the A and E sides gradually separates near the vertical axis due to the development of concrete cracking, steel tube buckling and FRP cracks.

The maximum strains on GFRP tubes (G4–0.2-S) and PEN FRP tubes (P2.5–0.2) are 0.3 % and 1.1 %, respectively. This is much lower than the fracture strain measured in the corresponding flat coupon tensile tests (GFRP is 1.7 %, and PEN FRP is 6.3 %). This is due to the fact that the hoop FRP tubes did not fracture (only localized crimping) during the loading process. This also explains that the failure of the DSTCs was controlled by the failure of the steel tubes, not the FRP tubes.

4. Conclusions

This paper presents an experimental study of the seismic performance of full-scale DSTCs under constant axial load and cyclic lateral load. A total of six circular DSTCs were tested, including four PFCS-DSTCs and two GFCS-DSTCs. Based on the experimental observations and discussions in this study, the following conclusions can be drawn:

(1) The hysteretic curves of all specimens are full. Even at large displacements, the bearing capacity decreases slowly, demonstrating the good deformation and energy dissipation capacity of DSTCs.
(2) Reducing the axial compression ratio, increasing the thickness of the PEN FRP tube, and using the PEN FRP tube can all increase the energy dissipation capacity of DSTCs.
(3) The strength degradation of DSTCs is insignificant, indicating that they can significantly improve the specimen's capacity to resist damage and keep the structure in a better stress state, which is conducive to resisting seismic loads.
(4) The moment-curvature curves remain unchanged in the test's later stage, indicating that the DSTCs have excellent ductility and good seismic behavior.

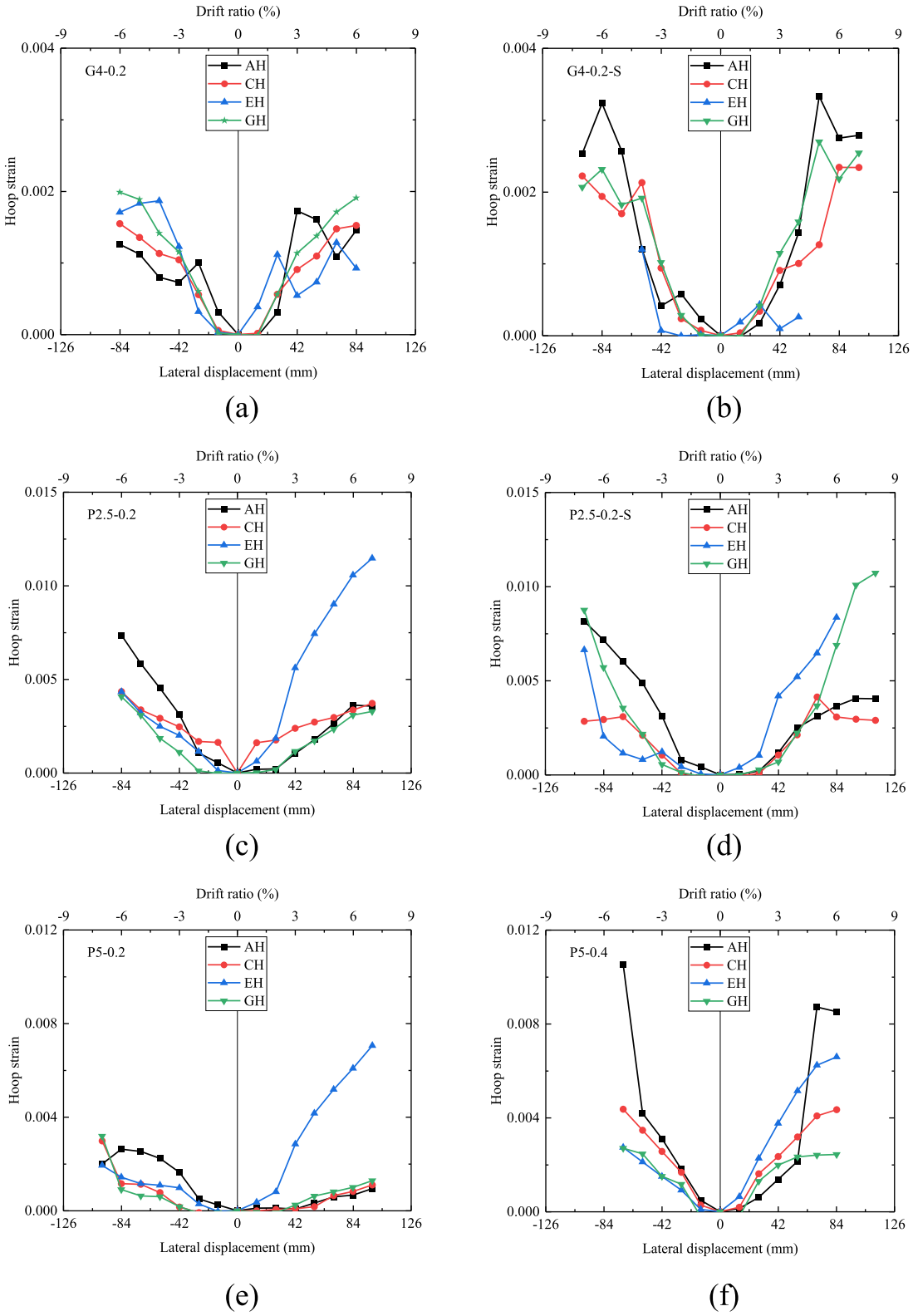


Fig. 19. Hoop strains of FRP tubes: (a) G4–0.2, (b) G4–0.2-S, (c) P2.5–0.2, (d) P2.5–0.2-S, (e) P5–0.2 and (f) P5–0.4.

(5) When the experimental variables are the same, except for material differences (PEN FRP or GFRP), PFCS-DSTCs show 11.9 % improvement in the ductility coefficient and 41.7 % improvement in the total energy consumption compared to GFCS-DSTCs. This indicates that PEN FRP for DSTCs is a good alternative.

CRediT authorship contribution statement

Bai Shang-Cong: Writing – review & editing, Writing – original draft, Methodology, Investigation, Formal analysis, Data curation. **Ma Jia-Xing:** Investigation. **Peng Kai-Di:** Methodology, Investigation. **Bai Yu-Lei:** Writing – review & editing, Supervision, Project administration,

Funding acquisition, Conceptualization.

Declaration of Competing Interest

The authors declare that they have no known competing financial interests or personal relationships that could have appeared to influence the work reported in this paper.

Acknowledgements

The authors are grateful for the financial support received from the National Key Research and Development Program of China (No. 2023YFB2604400), the Natural Science Foundation of Beijing (No. JQ23036), the Program Fund of Non-Metallic Excellence and Innovation Center for Building Materials (No. 24SFP-2), the International Scientific and Technological Cooperation Program of Ningbo (No. 2023H008), and the Key Research and Development Program of Ningbo (No. 2022Z165).

References

[1] Teng J.-G., Chen J.-F., Smith S.T., Lam L. FRP: Strengthened RC Structures. 2002.
[2] Lam L, Teng JG. Design-oriented stress-strain model for FRP-confined concrete. Constr Build Mater 2003;17:471–89.
[3] Teng JG, Yu T, Wong YL, Dong SL. Hybrid FRP-concrete-steel tubular columns: concept and behavior. Constr Build Mater 2007;21:846–54.
[4] Yu T, Wong YL, Teng JG, Dong SL, Lam ES. Flexural behavior of hybrid FRP-concrete-steel double-skin tubular members. J Compos Constr 2006;10:443–52.
[5] Dai J-G, Bai Y-L, Teng JG. Behavior and modeling of concrete confined with FRP composites of large deformability. J Compos Constr 2011;15:963–73.
[6] Bai YL, Dai JG, Mohammadi M, Lin G, Mei SJ. Stiffness-based design-oriented compressive stress-strain model for large-rupture-strain (LRS) FRP-confined concrete. Compos Struct 2019;223.
[7] Bai Y-L, Bai S-C, Mei S-J, Jia J-F. Experimental and numerical study of PEN FRP-strengthened circular RC columns under lateral cyclic loading with high axial compression ratio. Eng Struct 2023;294:116711.
[8] Bai YL, Bai SC, Mei SJ, Jia JF, Yang K. Seismic behavior of RC square columns strengthened with LRS FRP under high axial load ratio. Structures 2023;56.
[9] Mei SJ, Bai YL, Dai JG, Han Q. Seismic behaviour of shear critical square RC columns strengthened by large rupture strain FRP. Eng Struct 2023;280.
[10] Bai Y-L, Zhang Y-F, Sun P-X, Dai J-G, Ozbakkaloglu T. Experimental and numerical study on seismic performance of PEN FRP-jacketed circular RC columns. J Compos Constr 2023;27:04023001.
[11] Bai YL, Yang K, Han Q, Yu H, Zhang YF, Meng QL. Seismic behavior of RC square columns strengthened with large-rupture-strain FRP. J Harbin Inst Technol 2022;54(04):82–91 (In Chinese).
[12] Dai JG, Lam L, Ueda T. Seismic retrofit of square RC columns with polyethylene terephthalate (PET) fibre reinforced polymer composites. Constr Build Mater 2012;27:206–17.
[13] Ozbakkaloglu T, Idris Y. Seismic behavior of FRP-high-strength concrete-steel double-skin tubular columns. J Struct Eng 2014;140.
[14] Zhang B, Teng JG, Yu T. Experimental behavior of hybrid FRP-concrete-steel double-skin tubular columns under combined axial compression and cyclic lateral loading. Eng Struct 2015;99:214–31.
[15] Ouyang LJ, Gao WY, Zhen B, Lu ZD. Seismic retrofit of square reinforced concrete columns using basalt and carbon fiber-reinforced polymer sheets: a comparative study. Compos Struct 2017;162:294–307.
[16] Zeng JJ, Liang SD, Zhuge Y, Zhou JK, Liao JJ. Seismic behavior of FRP-concrete-steel double skin tubular columns with a rib-stiffened Q690 steel tube and high-strength concrete. Thin-Walled Struct 2022;175.
[17] Papavasileiou G, Pnevmatikos N. The cost of retrofitting steel-concrete composite buildings against progressive collapse with steel cables. Int J Progress Sci Technol (IJPSAT 2017;6:103–15.
[18] Papavasileiou G. Optimized design of steel buildings against earthquake and progressive collapse using cables. Int J Progress Sci Technol (IJPSAT 2017;6:213–20.
[19] Jiang T, Teng JG. Analysis-oriented stress-strain models for FRP-confined concrete. Eng Struct 2007;29:2968–86.
[20] Han Q, Yuan WY, Bai YL, Du XL. Compressive behavior of large rupture strain (LRS) FRP-confined square concrete columns: experimental study and model evaluation. Mater Struct 2020;53.
[21] Anggawidjaja D, Ueda T, Dai JG, Nakai H. Deformation capacity of RC piers wrapped by new fiber-reinforced polymer with large fracture strain. Cem Concr Compos 2006;28:914–27.
[22] Wong YL, Yu T, Teng JG, Dong SL. Behavior of FRP-confined concrete in annular section columns. Compos Part B Eng 2008;39:451–66.
[23] Yu T, Wong YL, Teng JG. Behavior of hybrid FRP-concrete-steel double-skin tubular columns subjected to eccentric compression. Adv Struct Eng 2010;13:961–74.
[24] Fanggi BAL, Ozbakkaloglu T. Compressive behavior of aramid FRP-HSC-steel double-skin tubular columns. Constr Build Mater 2013;48:554–65.
[25] Yu T, Zhang SS, Huang L, Chan CW. Compressive behavior of hybrid double-skin tubular columns with a large rupture strain FRP tube. Compos Struct 2017;171:10–8.
[26] Peng KD, Yu T, Hadi MNS, Huang L. Compressive behavior of hybrid double-skin tubular columns with a rib-stiffened steel inner tube. Compos Struct 2018;204:634–44.
[27] Huang L, Zhang SS, Yu T, Peng KD. Circular hybrid double-skin tubular columns with a stiffener-reinforced steel inner tube and a large-rupture-strain FRP outer tube: Compressive behavior. Thin-Walled Struct 2020;155.
[28] Zeng L, Li LJ, Xiao PJ, Zeng JJ, Liu F. Experimental study of seismic performance of full-scale basalt FRP-recycled aggregate concrete-steel tubular columns. Thin-Walled Struct 2020;151.
[29] Bai YL, Zhang YF, Jia JF, Han Q, Gao WY. Compressive behavior of double-skin tubular stub columns with recycled aggregate concrete and a PET FRP jacket. Constr Build Mater 2022;332.
[30] Xie P, Jiang T, Lin G. Behavior of large-scale hybrid FRP-concrete-steel double-skin tubular columns under concentric compression. Thin-Walled Struct 2023;182.
[31] Yu T, Teng JG. Behavior of hybrid FRP-concrete-steel double-skin tubular columns with a square outer tube and a circular inner tube subjected to axial compression. J Compos Constr 2013;17:271–9.
[32] Zhang B, Teng JG, Yu T. Compressive behavior of double-skin tubular columns with high-strength concrete and a filament-wound FRP tube. J Compos Constr 2017;21:04017029.
[33] Yu T, Zhang B, Cao YB, Teng JG. Behavior of hybrid FRP-concrete-steel double-skin tubular columns subjected to cyclic axial compression. Thin-Walled Struct 2012;61:196–203.
[34] Zhao JL, Teng JG, Yu T, Li LJ. Behavior of large-scale hybrid FRP-concrete-steel double-skin tubular beams with shear connectors. J Compos Constr 2016;20.
[35] Bai YL, Mei SJ, Li PD, Xu JJ. Cyclic stress-strain model for large-rupture strain fiber-reinforced polymer (LRS FRP)-confined concrete. J Build Eng 2021;42.
[36] Bai YL, Mei SJ, Chan CW, Li QQ. Compressive behavior of large-size square PEN FRP-concrete-steel hybrid multi-tube concrete columns. Eng Struct 2021;246.
[37] Zeng JJ, Gao WY, Duan ZJ, Bai YL, Guo YC, Ouyang LJ. Axial compressive behavior of polyethylene terephthalate/carbon FRP-confined seawater sea-sand concrete in circular columns. Constr Build Mater 2020;234.
[38] Qaidi SMA, Tayeh BA, Zeyad AM, de Azevedo ARG, Ahmed HU, Emad W. Recycling of mine tailings for the geopolymers production: a systematic review. Case Stud Constr Mater 2022;16:e00933.
[39] Qaidi SMA, Dinkha YZ, Haido JH, Ali MH, Tayeh BA. Engineering properties of sustainable green concrete incorporating eco-friendly aggregate of crumb rubber: a review. J Clean Prod 2021;324:129251.
[40] ASTM C39/C39M. Standard test method for compressive strength of cylindrical concrete specimens. Philadelphia, USA: American Society for Testing and Materials; 2011.
[41] BS 18. Tensile testing of metals (including aerospace materials). London, UK: British Standards Institution; 1987.
[42] ASTM D3039. Standard Test Methods for Tension Properties of Polymer Matrix Composite Materials. West Conshohocken, USA: American Society for Testing and Materials; 2015.
[43] Li B, Lam ESS, Wu B, Wang YY. Experimental investigation on reinforced concrete interior beam-column joints rehabilitated by ferrocement jackets. Eng Struct 2013;56:897–909.

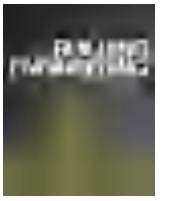
Journal of Building Engineering 108 (2025) 112910



Contents lists available at ScienceDirect

Journal of Building Engineering

journal homepage: www.elsevier.com/locate/jobe



Seismic performance and shear strength of HECC/RC beam-column joints with simplified reinforcement

Yu-Lei Bai [a,b], Shi-Yan Zhang [a], Wei-Hao Mao [c], Ze-Yuan Liu [a], Luo-Bin Zuo [a], Yao Ding [d,*]

[a] Key Laboratory of Urban Security and Disaster Engineering of Ministry of Education, Beijing University of Technology, Beijing, China
[b] Non-Metallic Excellence and Innovation Center for Building Materials, China Building Materials Academy Co., Ltd, China
[c] College of Civil and Transportation Engineering, Shenzhen University, Shenzhen, China
[d] College of Civil Engineering, Chongqing University, Chongqing, China

ARTICLE INFO

Keywords:
Hybrid fiber reinforced ECC (HECC)
Interior beam-column joints
Reinforcement simplification
Seismic performance
Shear strength

ABSTRACT

The application of high-performance materials presents an effective strategy to enhance the performance of structural components. To improve the seismic behavior and ductility of beam-column joints while mitigating reinforcement congestion, a high-performance hybrid fiber reinforced (1 % vol polyethylene fibers and 1 % vol steel fibers) cementitious composite (HECC) was applied in the joint core region. Five HECC/reinforced concrete (RC) composite joint specimens considering stirrup ratio in the core region, axial compression ratio, and HECC strength were designed and tested in this study. The results demonstrated that the application of HECC significantly enhanced the ductility characteristics during shear failure in the joint core region, achieving a shear capacity reserve 34 % greater than that of conventional RC joints. In addition, the specimens maintained structural integrity after failure, with micro-cracks being distributed more uniformly. Unlike RC joints, the contribution of transverse rebars on the bearing capacity of HECC joint was less significant, as evidenced by only a modest 7 % increase in bearing capacity at a 2.10 % stirrup ratio, indicating that the fiber bridging effect of HECC provided a constraint effect similar to that of transverse rebars. Furthermore, existing calculation formulas tend to significantly underestimate the shear capacity of HECC joints. Therefore, a revised formula was proposed to enhance an existing model for HECC beam-column joints by incorporating a synergistic enhancement coefficient. This modification improves accuracy in predicting the shear strength of HECC joints, achieving an average predicted-to-test ratio of 1.013 and a coefficient of variation of 0.096.

1. Introduction

Beam-column joints are critical load-transfer components in reinforced concrete frame structures, playing a significant role in determining the seismic performance of the structure [1,2]. Post-earthquake surveys have revealed that both interior and exterior beam-column joints are highly susceptible to brittle shear failure under seismic loading, primarily due to the complex forces acting within the joint core region. This type of failure not only severely reduces the energy dissipation and bearing capacities of the structure

* Corresponding author.
E-mail address: dingyaohit@126.com (Y. Ding).

https://doi.org/10.1016/j.jobe.2025.112910
Received 15 January 2025; Received in revised form 9 April 2025; Accepted 11 May 2025
Available online 14 May 2025
2352-7102/© 2025 Elsevier Ltd. All rights are reserved, including those for text and data mining, AI training, and similar technologies.

but also causes irreparable damage which triggers tilting or collapse of the building. To mitigate shear failure in the core region and enhance seismic performance, the "strong joint-weak member" principle is adopted in ductile design. Consequently, codes such as ACI 318-19 [3] and GB50010-2010 [4] specify a minimum stirrup ratio in the joint core region to ensure adequate shear strength and ductility. Additionally, for precast reinforced concrete frame structures, stricter design requirements have been established to achieve seismic performance comparable to cast-in-place structures. This leads to reinforcement congestion within the core region, and increases the potential risk to structural safety, particularly in interior beam-column joints of the frame [5].

Engineered Cementitious Composites (ECC), which exhibit strain-hardening behavior and multiple micro-cracking characteristics, is a typical type of fiber reinforced cementitious composite [6]. By incorporating organic short fibers, such as polyvinyl alcohol (PVA), polyethylene (PE), or polypropylene (PP), at a 2 % volume fraction, ECC can achieve compressive strengths ranging from 20 to 80 MPa, tensile strengths of 3–16 MPa, and a tensile strain capacity exceeding 2 % [7–9]. Previous studies [10–12] have demonstrated that compared to conventional reinforced concrete (RC) components, ECC components exhibit smaller shear crack widths and higher shear strength and ductility due to the fiber bridging effect. Additionally, the bond performance between ECC and rebars is significantly enhanced compared to that of conventional concrete [13]. Considering the excellent performance of ECC in shear resistance and bond performance with rebars, researchers have explored its potential as a replacement for conventional concrete in the joint core region to improve joint seismic performance. Experimental studies by Yuan et al. [14] and Said and Abdul Razak [15] demonstrated that ECC significantly improved the shear strength, deformation capacity, and damage tolerance of joints. Notably, even without transverse rebars in the core region, ECC joints exhibited exceptional ductility and load-bearing capacity.

Recent studies have shown that incorporating two or more fibers with distinct physical properties, such as steel fibers (SF) and organic fibers, into the matrix results in Hybrid Fiber Reinforced Cementitious Composites (HECC). This hybrid system enables the fibers to contribute their reinforcing effects at various stages of cracking, thereby enhancing the overall performance of the material [16,17]. Ding et al. [18,19] demonstrated that the bond strength between SF/PE-HECC and deformed rebars were significantly higher than that of PE-ECC, and the critical anchorage length of rebars embedded in SF/PE-HECC was reduced by 40 %. Maheswaran et al. [20] found that introducing PVA/PP-HECC significantly enhanced the shear capacity of beams and shifted the failure mode from brittle shear to ductile flexural failure. Given these benefits, the application of hybrid SF/organic fiber reinforced HECC in the core region of beam-column joints is expected to further improve joint shear performance and optimize the reinforcement configuration in the core region. Recent research [21] demonstrated that, compared to PP-ECC, SF-ECC, and conventional RC joints, the use of SF/PP-HECC in the core region of interior beam-column joints with minimal transverse rebars improved the cracking load, damage tolerance, and ductility of joints, exhibiting superior seismic performance. In multi-story, multi-span frame structures, interior beam-column joints experience bidirectional load transfer from adjacent beams, resulting in greater stress concentration compared to exterior joints. This increases their vulnerability to shear failure. However, existing research on the seismic performance of HECC interior beam-column joints remains limited. Most studies focus on seismic performance indicators such as load-displacement hysteresis curves, ductility, and energy dissipation, while research on the shear bearing capacity of the HECC core region remains scarce. Additionally, although Kantekin and Burak Bakir [22] proposed a joint shear strength prediction equation that accommodates various fiber type, it was derived from a limited statistical sample for HECC joint specimens (i.e., 6 samples). Therefore, further investigation on the shear resistance performance of HECC joints is necessary.

In this study, SF/PE-HECC was used to replace conventional concrete in the core region of interior beam-column joints. Five HECC/RC interior beam-column joint specimens were tested under cyclic loading, with experimental parameters including stirrup ratio, HECC strength, and axial compression ratio. Digital Image Correlation (DIC) technology was employed to analyze the crack patterns and failure modes of the HECC joint core. Based on the experimental results, the effects of various parameters on the seismic performance of the joints, including load-bearing capacity, ductility, energy dissipation, and stiffness degradation, were investigated. Furthermore, by analyzing the transverse rebars strain, damage index, and the shear stress-deformation relationship in the core region, the shear performance of the HECC core region was explored. A modified shear capacity formula for HECC joints was proposed based on existing shear capacity formulas for HECC beam-column joints. This study aimed to leverage the superior mechanical properties of HECC, reduce or even eliminate transverse rebars in the core region, enhance seismic performance, and improve both construction efficiency and quality.

Table 1
Details of specimens.

Specimen	Joint material	Beam rebars			Joint transverse rebars		Column axial compression ratio
		Top	Bottom	Anchorage length	Transverse rebars	ρ_s	
HECC1	H1	8D20	4D20	15*d*	none	0	0.2
HECC2	H1				D10@130	1.05 %	0.2
HECC3	H1				D10@130	2.10 %	0.2
HECC4	H2				none	0	0.2
HECC5	H1				none	0	0.3

Note: H1 and H2 denote two different strength levels of HECC; D10 and D20 denote the rebars with diameters of 10 and 20 mm, respectively; ρ_s is the stirrup ratio in the core region.

2. Experimental program

2.1. Specimen design and fabrication

Five HECC/RC composite interior beam-column joint specimens were designed and fabricated to investigate the effects of stirrup ratio, axial compression ratio, and HECC strength on seismic performance under cyclic loading. Details of each specimen are summarized in Table 1.

Fig. 1 illustrates the geometric dimensions and rebar details of the joint specimens. To ensure shear failure in the core region under cyclic loading, the "strong member-weak joint" design principle was applied. All specimens had columns with a cross-section of 300 mm × 300 mm and a length of 2100 mm. The beam cross-section measured 250 mm × 400 mm, with a length of 1800 mm. The rebar configurations for both beams and columns were identical across all specimens. The column was reinforced with twelve longitudinal rebars with a diameter of 22 mm and four-leg transverse rebars with a diameter of 10 mm and a spacing of 100 mm. Additionally, the beam rebars included eight longitudinal rebars at the top and four longitudinal rebars at the bottom with a diameter of 20 mm, as well as two-leg transverse rebars with a diameter of 8 mm and a spacing of 100 mm.

According to the Chinese code GB50010-2010 [4], with the geometric dimensions and reinforcement details of this study, the minimum calculated stirrup ratio for RC interior beam-column joints is 2.73 %. Considering the improved tensile strength, shear resistance, and anchorage performance of HECC with rebars [23–25], the transverse rebars were simplified in this study. In specimens HECC1, HECC4, and HECC5, transverse rebars were completely omitted from the core region. For specimen HECC2, two-leg transverse rebars with a diameter of 10 mm were adopted at 130 mm intervals, resulting in a stirrup ratio of 1.05 %. Specimen HECC3 used four-leg transverse rebars with the same diameter and spacing, achieving a stirrup ratio of 2.10 %.

Previous studies [18,26,27] have shown that anchorage failure can be effectively prevented in HECC/RC exterior beam-column joints when the anchorage length of the beam longitudinal rebars exceeds 9*d* (*d* is the rebar diameter), owing to the HECC material in the core region possessing a compressive strength of 54.6 MPa and a tensile strength of 6.8 MPa. Additionally, under similar conditions, the code GB50010-2010 specifies a minimum anchorage length of 21*d* [27]. To fully utilize the excellent bonding performance between HECC and rebars and simplify the construction process while ensuring reliable anchorage of beam rebars, the longitudinal rebars at the top of all specimens were extended through the joint. Meanwhile, the bottom longitudinal rebars were anchored straight into the core region with an anchorage length of 15*d*. The beam rebar details in the core region are shown in Fig. 2.

The fabrication process of the specimens is shown in Fig. 3. First, the tied rebars were placed inside wooden molds. Grade C40 strength commercial normal concrete (NC) was then poured into the beams and columns. To enhance the interfacial bonding performance between HECC and NC, a 30 mm-wide groove was reserved at the beam-column interface, in accordance with the design requirements of GB/T51231-2016 [28]. After three days of curing, the HECC was poured into the core region.

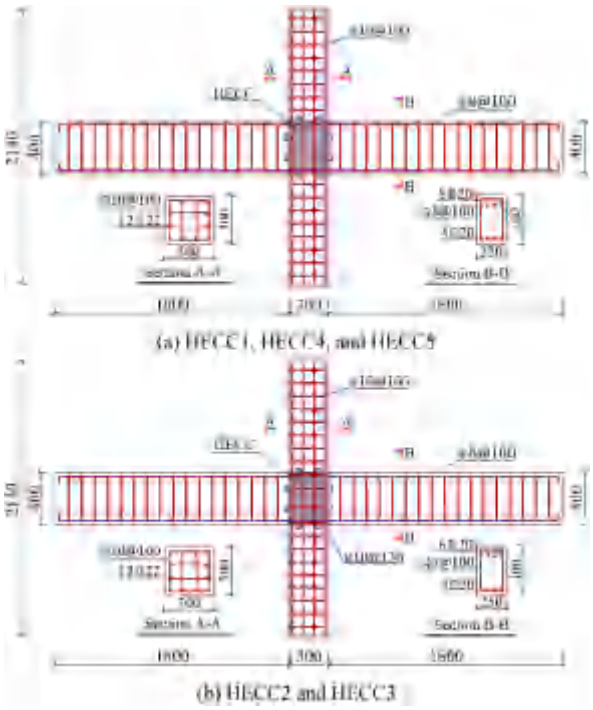


Fig. 1. The geometric dimensions and rebar details of the joint specimens (unit: mm).

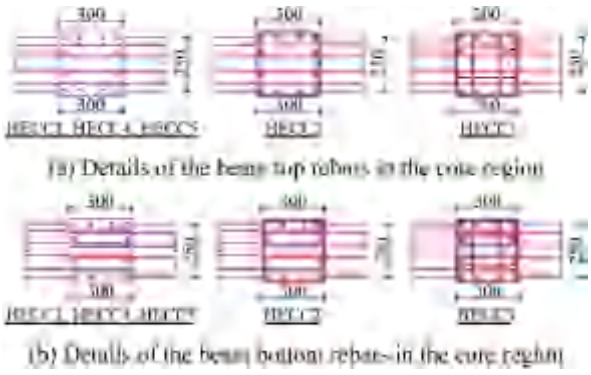


Fig. 2. Rebar configurations in the core region.

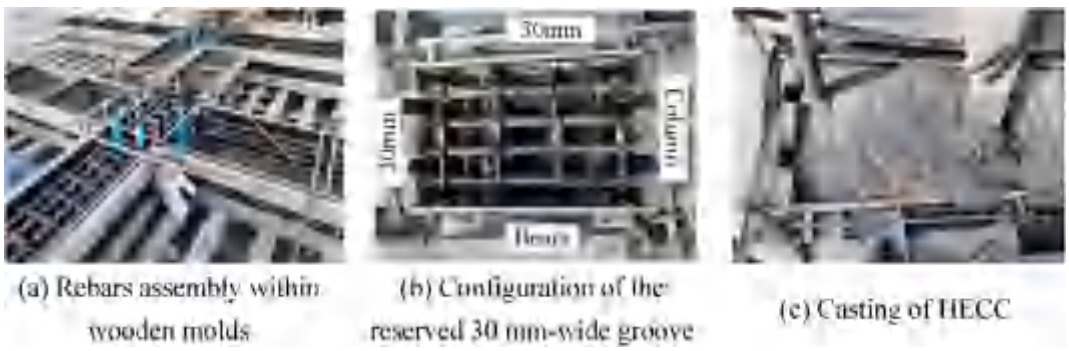


Fig. 3. Fabrication procedure of the specimens.

2.2. Material properties

The HECC used in this study consisted of ordinary Portland cement (P.O. 52.5), limestone powder, silica sand, silica fume, polycarboxylate high-performance water reducer, and water. Additionally, 1 % volume fraction of polyethylene (PE) fibers and 1 % by volume of hooked-end steel fibers (SF) were included. Fig. 4 shows the physical appearance of the two fibers, and their key properties are listed in Table 2. Two HECC strengths, labeled H1 and H2, were achieved by adjusting the water-to-binder ratio. The detailed mix proportions are provided in Table 3.

During the casting of joint specimens, three cubic samples (150 × 150 × 150 mm) were prepared for NC, H1, and H2. Their experimental compressive strengths measured on the day of joint testing were 41.3 MPa, 82.6 MPa, and 51.5 MPa, respectively. The tensile properties of HECC were assessed following the JSCE specifications [29], and the tensile stress-strain relationships are presented in Fig. 5. The tests demonstrated tensile strengths of 7.28 MPa for H1 and 4.03 MPa for H2, with ultimate tensile strain capacities of 2.42 % and 2.63 %, respectively. Additionally, tensile tests were conducted on the rebars used in the joint specimens, and the detailed results are provided in Table 4.

2.3. Test setup and loading procedure

Fig. 6 illustrates the test setup for the beam-column joints. Two hydraulic jacks were placed 1600 mm from the column edges on both the east and west beams. During the test, the jacks moved in opposite directions, inducing the joint to rotate clockwise or



Fig. 4. Surface morphology of two fiber samples.

Table 2
Mechanical properties of PE fibers and SF.

Type of fiber	Length (mm)	Diameter (μm)	Density (kg/m^3)	Tensile Strength (MPa)	Modulus of elasticity (GPa)
PE	18	24	0.97	2400	100
SF	14	220	7.8	2450–2650	200

Table 3
Material mix proportions (kg/m^3) and compressive strengths (MPa) of HECC.

Type	Cement	Limestone Powder	Silica Fume	Sand	HRWR	Water	PE	SF	Water binder ratio	Compressive strength
H1	465	543	112	919	50	194	10	78	0.2	82.6
H2	465	543	112	919	5	390	10	78	0.35	51.5

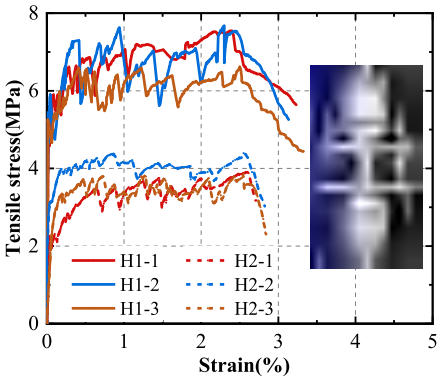


Fig. 5. Tensile stress-strain relationship of the HECC.

Table 4
Tensile properties of the rebars.

Type	Diameter (mm)	Yield strength (MPa)	Ultimate strength (MPa)	Elasticity modulus (GPa)
Longitudinal rebars	20	457	668	196
	22	425	637	208
Transverse rebars	8	428	640	205
	10	451	640	194

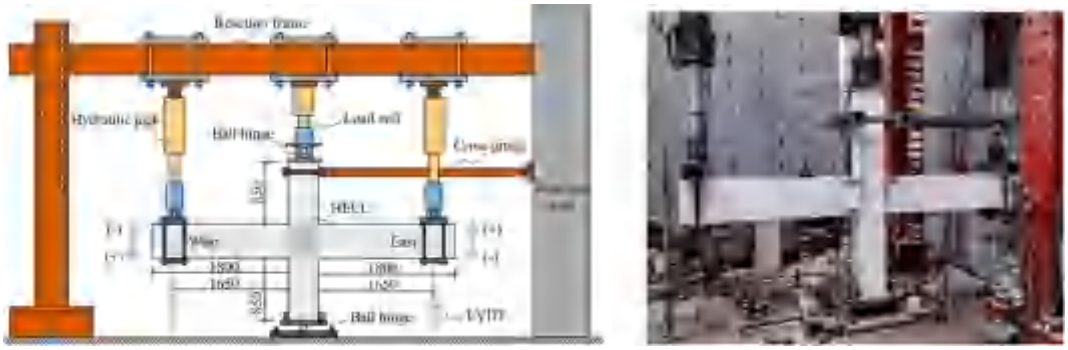


Fig. 6. Test setup.

counterclockwise, with counterclockwise rotation defined as positive direction. The beam ends were supported by rollers, which restricted horizontal movement but allowed vertical movement and rotation within the plane. Hinged supports at the column ends allowed free in-plane rotation. At the top of the column, a 1000 kN hydraulic jack applied constant axial compression loads of 850 kN and 567 kN to specimens with axial compression ratios of 0.3 and 0.2, respectively. Simultaneously, two 1000 kN hydraulic jacks

applied vertical cyclic loads to the beam ends.

The loading protocol followed the cyclic loading procedure recommended by the American Concrete Institute (ACI Committee 374 [30]). A displacement-controlled loading method was applied, with drift ratios of 0.2 %, 0.5 %, 0.75 %, 1 %, 1.5 %, 2 %, 2.5 %, 3 %, 3.5 %, 4 %, and 4.5 %, and two cycles were conducted at each ratio. The cyclic load history is illustrated in Fig. 7. The loading process was terminated when the applied load dropped to 85 % of the peak load.

2.4. Instrumentation and crack mapping

Strain gauges were installed on the longitudinal and transverse rebars to monitor strain during the loading process. Shear deformation in the core region was measured using two LVDTs with a 100 mm capacity, while beam-end displacements (Δ) were recorded with two 300 mm LVDTs, as shown in Fig. 6.

Additionally, Digital Image Correlation (DIC) technology was used to monitor the displacement of the core region. Before the test, black speckle patterns with a diameter of 1 mm were adhered to the back surface of the core region (see Fig. 8). The displacement of those black speckle patterns in the core region was recorded using a Sony A9 digital camera [31] mounted on a tripod. Twelve images were captured during each complete cycle of drift ratios, resulting in approximately 130 images per specimen. The acquired digital images were analyzed using the open-source DIC software Ncorr [32] to evaluate crack characteristics.

3. Experimental results and discussion

3.1. Failure modes

Fig. 9 illustrates the crack pattern and failure mode of all the specimens. As shown in Fig. 9a–e, shear failure occurred in the HECC joint core region of all specimens. The failure process can be divided into three stages: initial cracking, through cracking, and ultimate failure. During the initial cracking stage, the first crack was visually observed at the beam ends when the drift ratio reached 0.2 %, while no cracks were observed in the core region. As the drift ratio increased to 0.5 %, diagonal cracks with a length of 20–30 cm formed in the core region. Under reverse loading at the same drift ratio, shorter diagonal cracks of 5–10 cm appeared in the opposite direction. As the drift ratios reached 1 % and 1.5 %, the number of cracks in the core region increased significantly. When the drift ratio reached 2 %, cracks intersected and formed a main shear crack with a width ranging from 0.3 to 0.4 mm, marking the initiation of the through cracking stage. With further increases in the drift ratio, the main diagonal crack widened. At a drift ratio of 3 %, the specimens entered the failure stage. At this stage, crack progression ceased but existing cracks widened further.

Fig. 9f illustrates the shear failure of a reinforced concrete (RC) joint with a stirrup ratio of 2.00 % [33]. Significant crushing and spalling of the concrete were observed in the core region, resulting in poor overall integrity of the joint. Notably, despite the absence of transverse rebars, the HECC joints can still maintain good structural integrity, with no spalling of HECC observed during the failure process. This superior performance was attributed to the bridging effect of PE and steel fibers in the HECC, which prevented the initiation and propagation of cracks, similarly to the restraining effect of transverse rebars.

In addition, DIC technology was utilized to measure the shear strain distribution, as shown in Fig. 10. Besides, the relationship between the shear strain and the beam-end displacement is shown in Fig. 11. Based on the shear strain distribution of specimens HECC1, HECC2, and HECC3 before reaching a 2 % drift ratio, the core region exhibited dispersed and slight damage (further discussed in Section 3.7), with a maximum strain of only 0.024ε. During this phase, the joint shear force was primarily resisted through diagonal compression struts of the HECC. Upon reaching the through crack stage, HECC1 displayed two distinct regions of concentrated damage, while HECC2 and HECC3 exhibited more dispersed damage. Furthermore, as shown in Fig. 11, the maximum strain growth rate of HECC1 was significantly faster than that of HECC2 and HECC3. This difference can be attributed to the fact that HECC1 relied exclusively on the progressively deteriorating diagonal compression struts of HECC to resist shear forces, which resulted in accelerated damage progression.

In contrast, the transverse rebars in HECC2 and HECC3 provided confinement to the diagonal compression struts of HECC, facilitating the formation of dispersed cracks and decreased shear damage in the core region. At the ultimate drift ratio of 4.5 %, the strains recorded were 0.387ε and 0.283ε for HECC2 and HECC3, respectively, both of which were lower than the corresponding strain

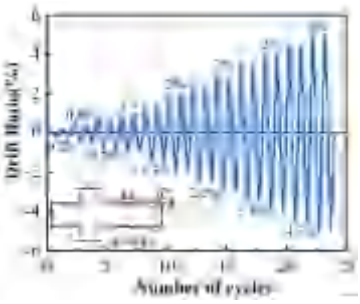


Fig. 7. Cyclic loading history.



Fig. 8. Speckle pattern in the core region.

of 0.414ε observed in HECC1.

Compared to HECC1, HECC4 exhibited more concentrated damage at a drift ratio of 2 % due to reduced material strength in the core region, with a maximum strain of 0.043ε. Upon entering the failure phase (drift ratio of 3 %), the concentrated damage zone expanded, leading to the premature failure of the HECC diagonal strut and subsequently resulting in specimen failure at a drift ratio of 4 %. The shear strain evolution pattern of HECC5 exhibited similar characteristics to that of HECC1. However, the angle (θ) between the primary crack and the horizontal direction in HECC5 was markedly larger than that in HECC1, as shown in Fig. 12. This phenomenon can be attributed to the increased axial compression load at the column ends, which resulted in an enlarged height of the compression zone (h_{c0}) in the column while maintaining a constant beam compression zone height (h_{b0}).

3.2. Hysteresis curves and skeleton curves

Fig. 13 presents the hysteresis and skeleton curves for the west and east beams of each specimen. It can be observed that the shear failure in the joint core region caused varying degrees of pinching in the hysteresis curves across all specimens. Compared with HECC1, the addition of transverse rebars in the core region effectively alleviated the pinching effect in the hysteresis curves of HECC2 and HECC3 specimens. Conversely, due to the reduced strength of HECC in the core region, the hysteresis curve of the HECC4 specimen exhibited a more pronounced pinching effect, accompanied by accelerated peak load degradation. For HECC5, with an increased axial compression ratio at the column ends, the pinching effect in the hysteresis curves was reduced compared to HECC1.

Table 5 summarizes the key experimental results for the specimens, including the yield load P_y and displacement Δ_y, the peak load P_p and displacement Δ_p, the ultimate load P_u and displacement Δ_u, as well as the ductility factor μ. The ultimate load P_u is defined as 85 % of the peak load P_p. A difference in load behavior was observed between the positive and negative loads of the east and west beams, which is attributed to the higher reinforcement ratio at the top of the beam compared to that at the bottom.

The comparison of skeleton curves of each specimen is shown in Fig. 14. The results indicate that increasing the amount of transverse rebars in the core region had minimal impact on enhancing the load-bearing capacity of the joint. For specimen HECC1 without transverse rebars, the peak load under positive loading of the east beam was 118.86 kN. In comparison, specimens HECC2 and HECC3, with stirrup ratios of 1.05 % and 2.10 %, showed slight increases of 3.0 % and 7.0 %, respectively. In contrast, according to Wang et al. [11], when High-Performance Fiber-Reinforced Concrete (HPFRC) was applied in the core region, the joint load-bearing capacity increased by 21.3 % as the stirrup ratio increased from 0 to 2.90 %, indicating that the enhancement effect of transverse rebars on the bearing capacity of HECC joints was less significant. This phenomenon can be attributed to the superior tensile properties and enhanced shear transfer behavior of HECC compared to HPFRC, resulting in decreased reliance on the confinement provided by transverse rebars.

Moreover, when the compressive strength of HECC in the core region decreased from 82.6 MPa to 51.5 MPa (HECC4), the negative peak load of the east beam dropped from 179.4 kN to 146.4 kN, representing a decrease of 18.3 %. When the axial compression ratio at the column ends increased from 0.2 to 0.3, the negative load-bearing capacity of the east beam of HECC5 increased to 183.2 kN, representing a 2.1 % increase. The improved performance can be attributed to the strengthened bond strength of longitudinal rebars and enhanced the constraint on the HECC in the core region under the higher axial compression, which promoted a more favorable shear flow mechanism for joint shear resistance [34].

3.3. Ductility

Ductility is a key indicator for measuring the capacity of a structure to undergo inelastic deformation under external forces. It is typically represented by the displacement ductility factor μ, which is calculated using Eq. (1). The yield point of the specimens was identified using the graphical method shown in Fig. 15 [35].

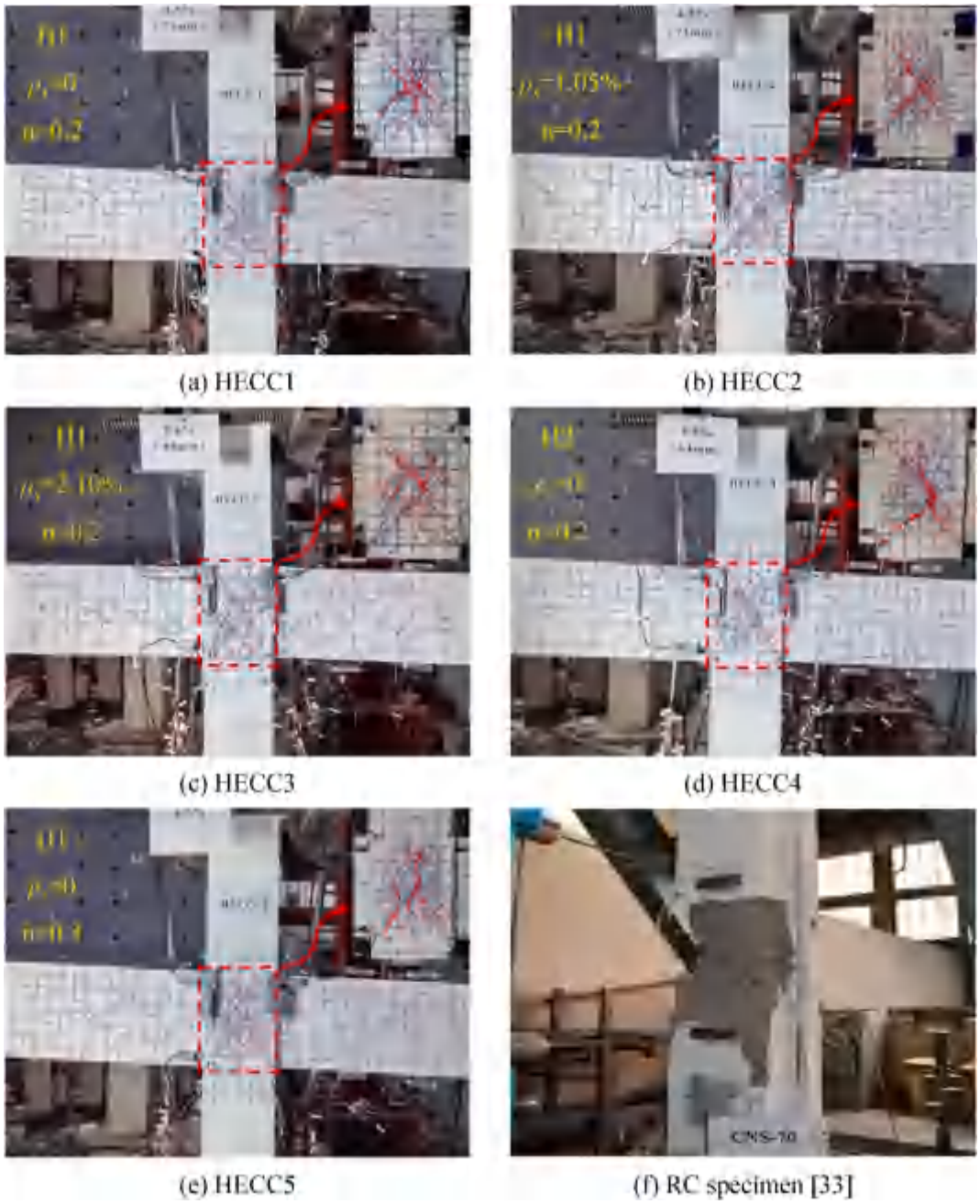


Fig. 9. Failure modes of the specimens.

$$\mu = \frac{\Delta_u}{\Delta_y} \tag{1}$$

The ductility factors (μ) of the specimens are listed in Table 5. The ductility of the joints was assessed by comparing the average ductility factors of the east and west beams under both positive and negative loading. Compared to HECC1 specimen, the average ductility factors of HECC2 and HECC3 were 1.99 and 2.14, with an increase of 4.7 % and 12.6 %, respectively. These results indicate that proper reinforcement of transverse rebars in HECC joints can enhance the deformation capacity of the joints. On the other hand, the ductility decreased when either the HECC strength in the core region was reduced or the axial compression ratio of the column was increased. Compared with HECC1, the HECC4 specimen, which utilized low-strength HECC, demonstrated a 2.6 % decrease in the average ductility factor. Similarly, the HECC5 specimen, characterized by its high axial compression ratio, showed a 4.7 % ductility decrease.

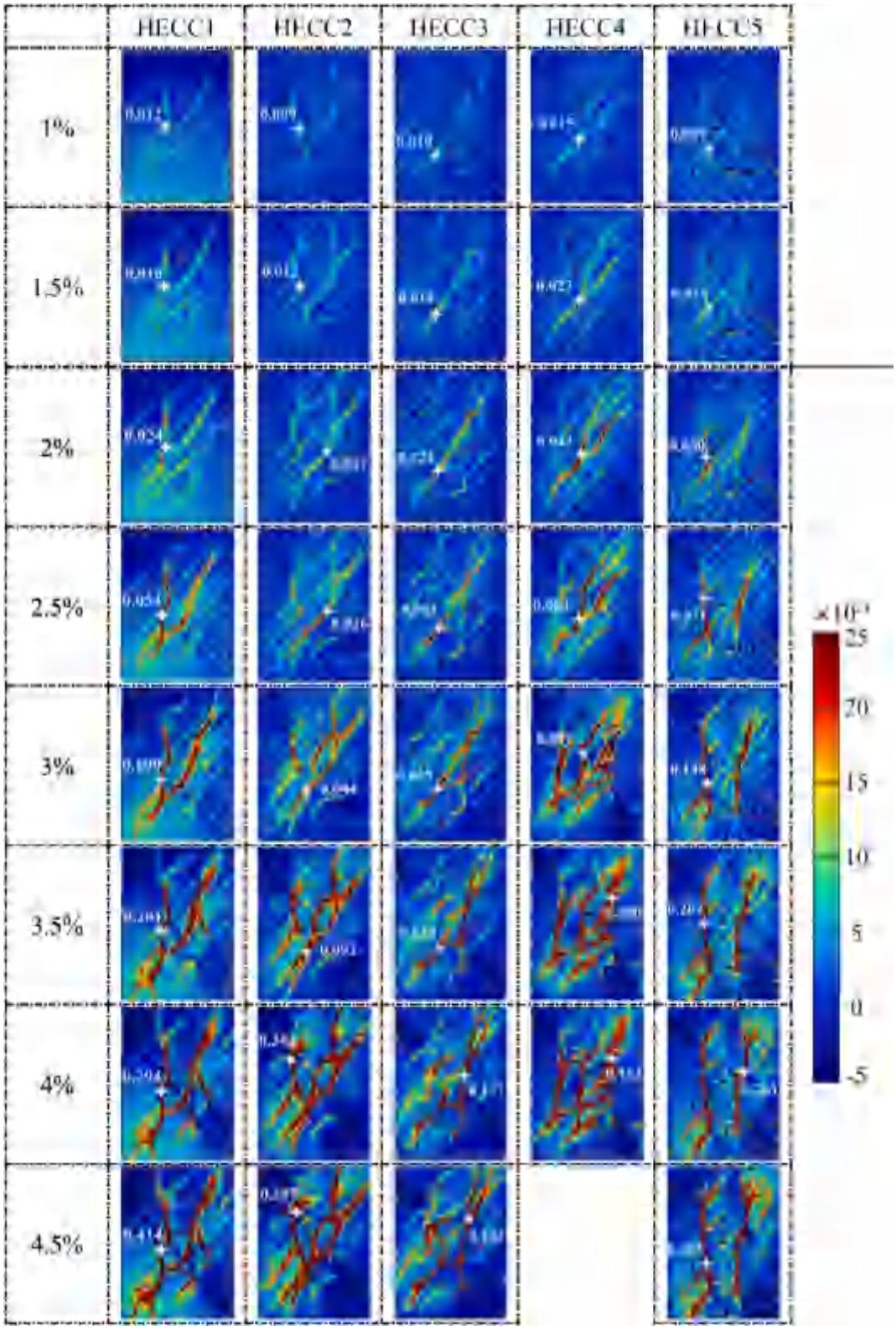


Fig. 10. Shear strain distributions in the core region of the specimens.

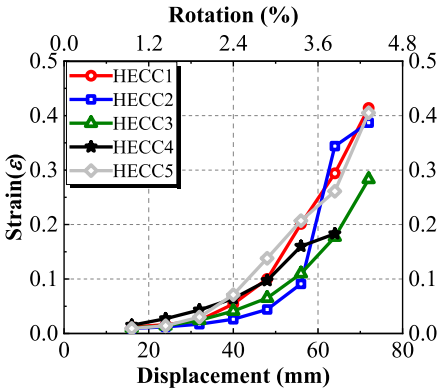


Fig. 11. Relationship between the shear strain and beam-end displacement.

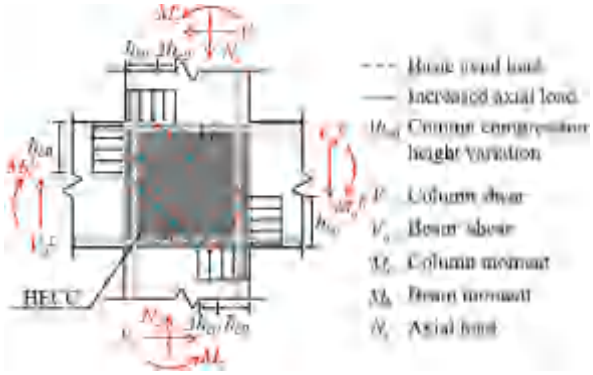


Fig. 12. Variation in the angle of the diagonal compressive strut.

3.4. Energy dissipation capacity

Under cyclic loading, the total energy dissipated by the beam-column joint is equal to the sum of the areas enclosed by each hysteresis loop in the load-displacement curve at the beam ends (denoted as S_1 in Fig. 16). Fig. 17 shows the relationship between the cumulative energy dissipation of each specimen and the beam-end displacement. At a drift ratio of 4 %, the cumulative energy dissipation of specimen HECC1 reached 50.8 kN m, while specimens HECC2 and HECC3 exhibited values of approximately 51.2 kN m. The minimal difference in energy dissipation indicates that increased transverse rebar contributes marginally to the energy dissipation capacity of joints. This can be attributed to the dispersed fibers sustaining tensile forces analogously to transverse rebars. Throughout the process from cracking to failure stages, the strengthening effect of transverse rebar confinement was weakened [11].

The use of low-strength HECC reduced the load-bearing capacity and ductility, weakened the deformation capacity, and resulted in a decrease in the energy dissipation capacity of the specimens. Although the increased axial load at the column ends reduced the ductility of the specimen, the cumulative energy dissipation of HECC5 was increased to 54.0 kN m, representing an improvement of 6.3 %. This can be attributed to the higher axial compression load enhanced the bonding strength between fibers and the matrix after cracks formed in the core region, thereby generating an intensified confinement effect on the cracks [21].

The equivalent damping coefficient h_e is also an essential parameter for assessing energy dissipation capacity [14]. It is determined using Eq. (2), where S_1 and S_2 represent the areas of the shaded regions, as illustrated in Fig. 16.

$$h_e = \frac{1}{2\pi}\frac{S_1}{S_2} \tag{2}$$

The relationship between the equivalent damping coefficient (h_e) and the beam-end displacement is illustrated in Fig. 18. When the drift ratio was less than 1.5 %, h_e values decreased as displacement increased. However, when the drift ratio exceeded 2 %, h_e values began to increase nonlinearly. This initial decrease can be attributed to the fact that the joints remained in the elastic deformation stage before yielding, during which most of the energy was stored rather than dissipated. After yielding, the specimens transitioned into the plastic stage. In this stage, the inelastic deformation became increasingly pronounced, resulting in greater energy dissipation and a gradual rise in the h_e values. Additionally, the differences in h_e values among the specimens were relatively small, and all values were lower than those of specimens associated with beam-end flexural failure, which can reach values up to 0.18 [14,36].

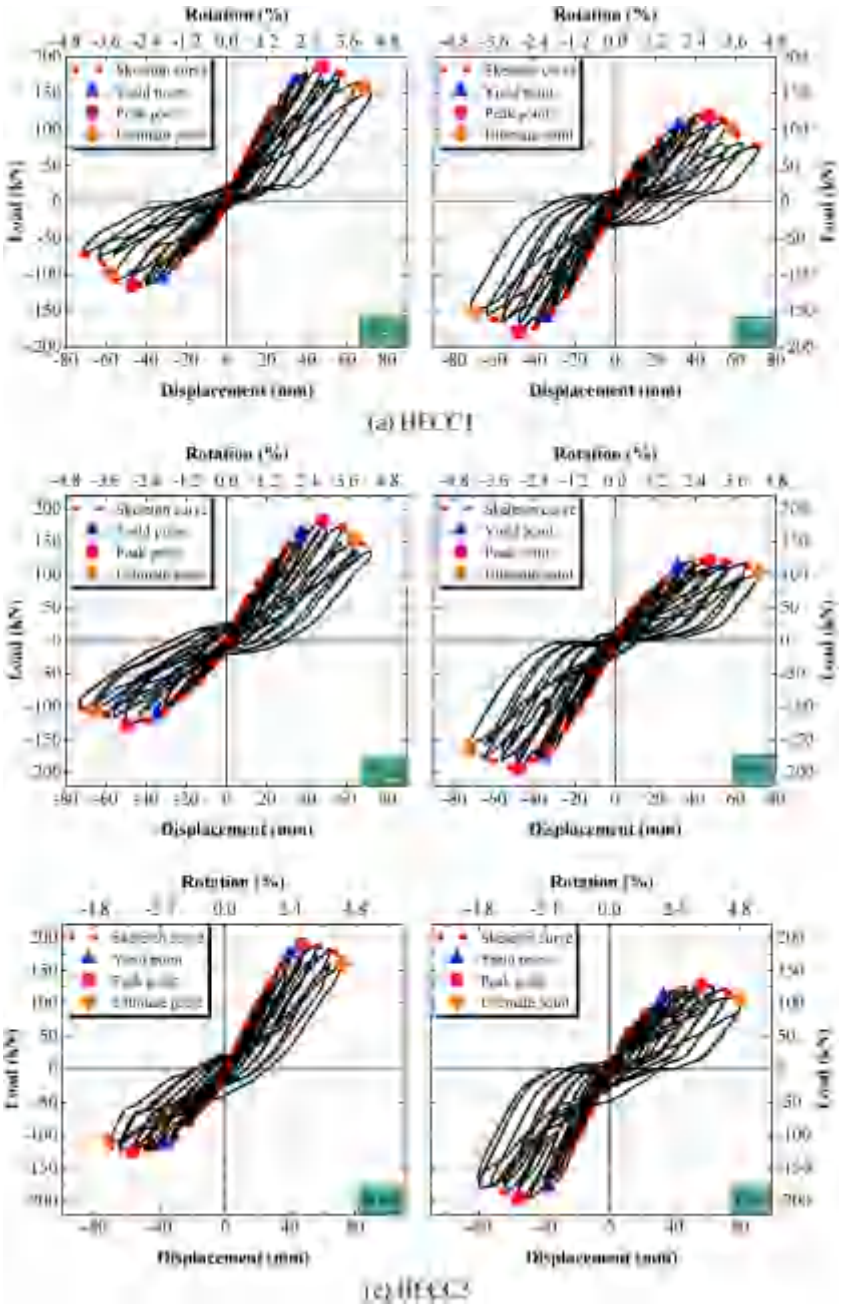


Fig. 13. Hysteresis and skeleton curves of load–displacement for all specimens.

3.5. Stiffness degradation

The secant stiffness K_i under cyclic loading is defined as follows [12,37]:

$$K_i = \frac{|+P_i| + |-P_i|}{|+X_i| + |-X_i|} \tag{3}$$

where $+P_i$ and $-P_i$ denote the positive and negative peak loads during the first cycle of loading at the ith drift ratio, $+X_i$ and $-X_i$ denote the corresponding displacements. Based on Eq. (3), the degradation of secant stiffness under cyclic loading for all specimens is presented in Fig. 19. It can be found that the stiffness of the specimens gradually decreased with increasing displacement. For the HECC1

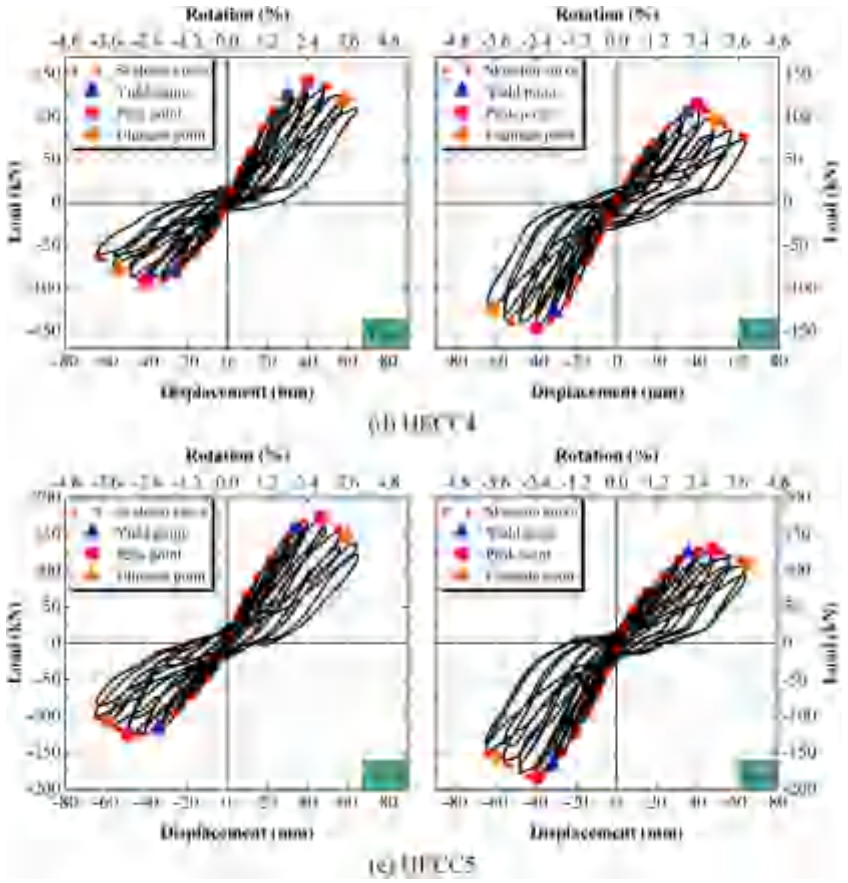


Fig. 13. (*continued*).

Table 5
Summary of key experimental results.

Specimen	Direction		Yield point		Peak point		Ultimate point		Ductility factor μ
			Δ_y (mm)	P_y (kN)	Δ_p (mm)	P_p (kN)	Δ_u (mm)	P_u (kN)	
HECC1	Positive	West	34.34	167.03	47.61	185.82	68.21	157.95	1.98
		East	31.79	105.23	46.89	118.86	58.10	101.03	1.82
	Negative	West	−32.46	−106.35	−46.99	−115.06	−57.71	−97.80	1.77
		East	−34.51	−159.93	−47.73	−179.41	−69.44	−152.50	2.01
HECC2	Positive	West	36.76	161.46	47.76	182.27	63.38	154.93	1.73
		East	31.50	111.33	47.28	122.37	71.71	104.01	2.28
	Negative	West	−34.71	−112.69	−49.74	−127.15	−65.44	−108.08	1.89
		East	−35.29	−174.08	−47.88	−194.39	−72.79	−165.23	2.06
HECC3	Positive	West	40.03	174.79	47.71	189.64	74.52	161.19	1.86
		East	33.38	111.58	56.33	127.15	79.98	108.08	2.40
	Negative	West	−35.94	−112.62	−56.60	−125.58	−77.63	−106.74	2.16
		East	−36.87	−179.09	−55.86	−195.34	–	–	–
HECC4	Positive	West	29.57	124.58	39.83	140.96	57.91	119.82	1.96
		East	34.38	104.89	39.64	113.86	48.55	96.78	1.41
	Negative	West	−26.03	−82.23	−39.77	−92.11	−53.23	−78.30	2.04
		East	−31.03	−128.64	−39.8	−146.42	−61.55	−124.46	1.98
HECC5	Positive	West	33.61	156.33	46.94	172.75	59.32	146.84	1.77
		East	35.50	123.79	47.59	129.06	65.21	109.70	1.84
	Negative	West	−34.24	−117.07	−48.99	−125.90	−58.85	−107.02	1.72
		East	−31.67	−167.48	−39.04	−183.23	−60.01	−155.75	1.90

specimen, the stiffness of the east beam decreased by 66.5 % as the drift ratio increased from 0.5 % to 4 %. In contrast, stiffness reductions for HECC2 and HECC3 were 63.0 % and 58.2 %, respectively. This indicates that the confining action of transverse rebars reduced the rate of stiffness degradation in certain extent.

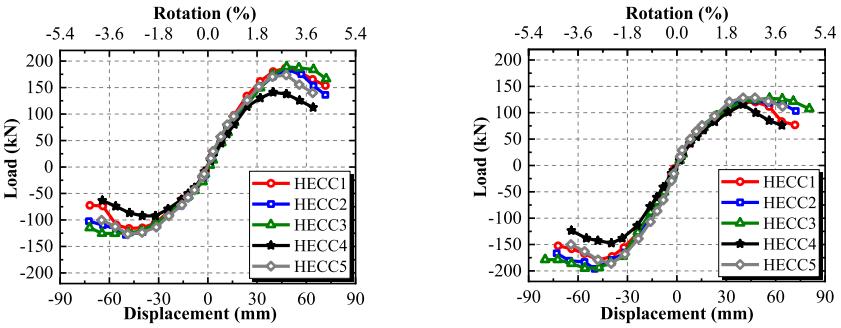


Fig. 14. Load-displacement skeleton curves of the specimens.

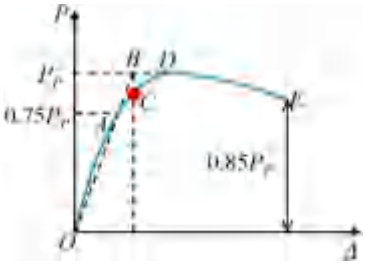


Fig. 15. Graphical method for yield point identification.

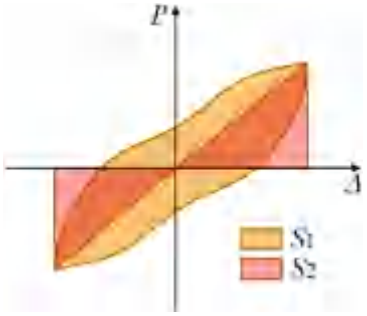


Fig. 16. Energy dissipation and hysteresis behavior.

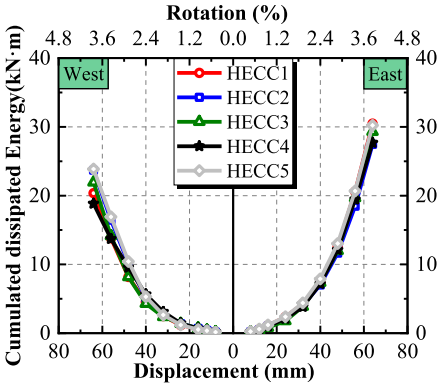


Fig. 17. Cumulative energy dissipation under cyclic displacement.

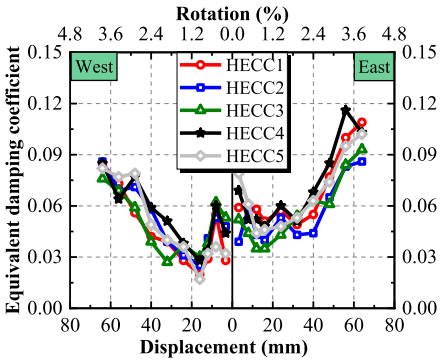


Fig. 18. Equivalent damping coefficient versus displacement curves.

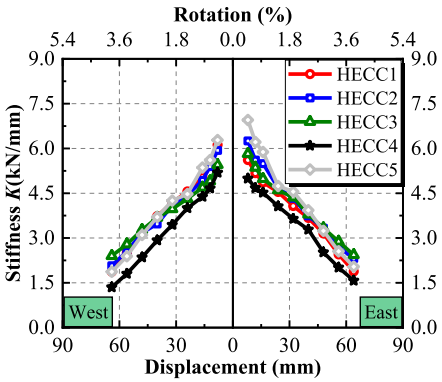


Fig. 19. Secant stiffness under cyclic loading.

Compared to HECC1 specimen, the HECC4 specimen exhibited a combination of lower initial stiffness and a more rapid rate of stiffness degradation. Increasing the axial compression ratio enhanced the initial stiffness of the joints but also accelerated stiffness degradation. Specifically, at a drift ratio of 0.5 %, the stiffness of the east beam in HECC5 was 23.9 % higher than that in HECC1. However, as the drift ratio increased to 4 %, the stiffness of HECC5 decreased by 70.6 %, indicating a faster rate of reduction compared to 66.5 % observed in HECC1. This is primarily because a high axial compression ratio significantly increased the vertical restraint of the specimen during the initial loading stage. However, after the specimen yielded, the high axial compression ratio exacerbated the softening effect in the core region, thereby deteriorating the diagonal compression struts of the HECC, limiting the plastic performance of the joint from achieving full utilization [11].

3.6. Transverse rebars demand

Fig. 20 illustrates the relationship between the strain of transverse rebars in the core region and the displacement of the east beam for specimens HECC2 and HECC3. The strain distribution patterns of transverse rebars in both specimens exhibited similar trends, with

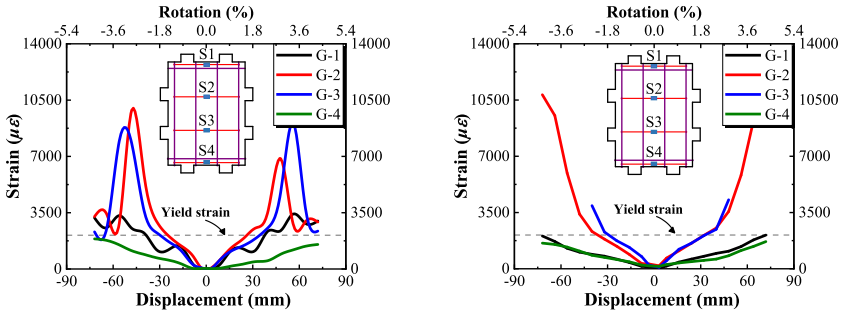


Fig. 20. Strain-displacement relationship of transverse rebars in the core region.

the central transverse rebars (G-2, G-3) experiencing significantly higher strains, while those located at the edges (G-1, G-4) remained within the elastic stage. It is noteworthy that when specimens entered the failure stage (at 3 % drift ratio), the confinement effect of transverse rebars became critical where G-2 and G-3 exhibited significantly increased strain rates.

In order to reflect the positive effect of fiber bridging in ECC on the shear resistance of the joint core region, Zhang and Li [38] proposed an equivalent transverse rebar area considering the influence of ECC cover based on the equivalent constraint effect, which could be calculated as Eq. (4):

$$A_{s,HECC} = \frac{2tb's}{b_c - 2t}\frac{f_t}{f_y} \tag{4}$$

where t denotes the cover thickness of the HECC (=20 mm), b' represents the core dimension of the column core (=260 mm), s denotes the spacing of transverse rebars in the core region (=130 mm), and f_t denotes the tensile strength (=7.28 MPa). b_c represents the column width (=300 mm), and f_y indicates the yield strength of the transverse rebars (=451 MPa).

Therefore, the required net area of transverse rebars for ECC/HECC beam-column joints can be calculated as follows:

$$A_{s,HECC}^{NA} = A_{s,RC} - A_{s,HECC} \tag{5}$$

where $A_{s,RC}$ is transverse rebar required in same strength conventional concrete joint, which can be obtained as Eq. (6) according to GB 50010-2010 [4].

$$A_{s,RC} = \left(V_h - 1.1\eta_j f_t b_j h_j - 0.05\eta_j N\frac{b_j}{b_c}\right)\frac{s}{f_y(h_{b0} - \alpha_s')} \tag{6}$$

where V_h is the experimental shear capacity of HECC joints. η_j is the constraint effect coefficient of orthogonal beams on the joints (η_j = 1), and b_j is the effective joint width, calculated by Eq. (7). h_j is the height of the joint core region ($h_j = h_c$). N denotes the axial load at the column ends.

$$b_j = \begin{cases} \min(b_b + 0.5h_c, b_c) \text{ for } b_b < b_c/2 \\ b_c \text{ for } b_b \geq b_c/2 \end{cases} \tag{7}$$

where b_b is the beam width, and h_c denotes the column depth in the shear direction of the joint.

Based on the experimental results and in conjunction with Eqs. (4)–(6), the calculated $A_{s,HECC}^{NA}$ for HECC1 were 329.1 mm^2. This indicated that under the same reinforcement conditions, the minimum transverse rebar area required to prevent shear failure in the core region of HECC was 329.1 mm^2. In the test, the total cross-sectional areas (A_{svj}) of transverse rebars within the effective calculation width of the joint core region were 157 mm^2 and 314 mm^2 for specimens HECC2 and HECC3, respectively. It can be found that neither configuration meets the minimum required net area for transverse rebars, thereby resulting in insufficient resistance in HECC joints. Therefore, although HECC can reduce congestion in the core area, a certain amount of transverse rebars is still necessary to prevent shear failure.

3.7. Damage index

The damage of HECC/RC composite beam-column joints is evaluated using the damage index (*DI*) proposed by Park and Ang [39], which is defined as:

$$DI = \frac{\delta_M}{\delta_u} + \frac{\beta}{F_y\delta_u}\int dE \tag{8}$$

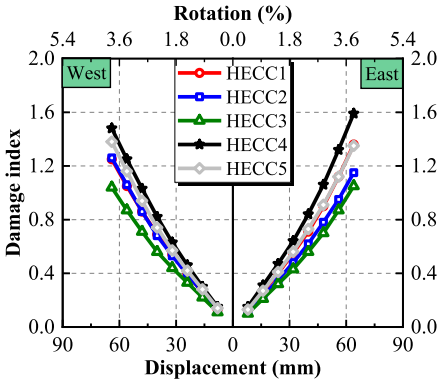


Fig. 21. Comparisons of the damage index in the specimens.

where δ_M denotes the maximum displacement recorded in each loading cycle, and δ_u represents the ultimate displacement at a pre-defined 20 % drop below the peak load P_p of the first cycle under cyclic loading [40]. F_y is the yield strength of the specimen, and the integral term represents the total energy dissipated during cyclic loading. β is the strength reduction parameter, which equals 0.1 for well-reinforced concrete structures [41]. According to the different *DI* values, the damage of joint specimens can be classified into five levels: no damage ($0 < DI \leq 0.2$), slight damage ($0.2 < DI \leq 0.4$), moderate damage ($0.4 < DI \leq 0.6$), severe damage ($0.6 < DI \leq 0.8$), and complete damage ($DI > 0.8$) [42].

Fig. 21 shows the relationship between *DI* and beam-end controlled displacement for all specimens. During the elastic stage, all specimens exhibited the same damage level, categorized as no damage. With an increase in the stirrup ratio, the development of damage was inhibited. When the drift ratio reached 1 %, the specimen entered the stage of slight damage. Specifically, the east beam of specimen HECC1 experienced severe and complete damage at drift ratios of 2.25 % and 2.75 %, respectively. In comparison, specimens HECC2 and HECC3 exhibited severe damage at drift ratios of 2.5 % and 2.75 %, with complete damage occurring at 3 % and 3.25 %, respectively. At a drift ratio of 2.5 %, the *DI* of HECC4 exceeded 0.8, indicating a complete damage stage earlier than HECC1. Under the high axial compression ratio, the joint region experiences intensified stress concentration. Consequently, as shown in Fig. 21, HECC5 exhibits slightly higher damage levels than HECC1 under identical drift ratios.

4. Shear performance analysis and strength prediction

4.1. Shear behavior and deformation characteristics

As shown in Fig. 22, the shear deformation in the core region caused by shear force is expressed as the shear angle γ. Based on the LVDTs installed in the core region (Fig. 6), the shear angle γ is calculated using Eq. (9), where a and b represent the height and width of the core region, respectively. C_1, C_2, C_3, and C_4 denote the deformations along two diagonal directions. During cyclic loading, typical compressive forces from adjacent members acting on the core region are illustrated in Fig. 23. The shear stress v in the core region is calculated using Eq. (10), while the shear force V_h is determined based on the ACI 352R-02 code [43], as shown in Eq. (11).

$$\gamma = \alpha_1 + \alpha_2 = \frac{\sqrt{a^2 + b^2}}{2ab}\left(|C_1 + C_2| + |C_3 + C_4|\right) \tag{9}$$

$$v = \frac{V_h}{b_j h_c} \tag{10}$$

$$V_h = T_1 + C_2 - V_c \tag{11}$$

T_1, C_2, and V_c represent the tensile force in the longitudinal beam rebars, the compressive force in the beam cross-section, and the horizontal shear force in the column, respectively.

Fig. 24 presents the shear stress-shear deformation curves. For the HECC1 specimen, the maximum shear deformation reached 0.0156 rad. In comparison, the maximum shear deformations of HECC2 and HECC3 were 0.0122 rad and 0.0083 rad, respectively, representing decreases of 21.8 % and 46.8 %. This demonstrates that the transverse rebars in the core region effectively restricted shear deformation. Due to the reduced strength of the HECC, the concentrated damage zone within the core region expanded (as shown in Fig. 10), preventing further deformation along the diagonal directions. Consequently, the maximum shear deformation of HECC4 decreased to 0.0089 rad. In contrast, the maximum shear deformation of HECC5 specimen increased to 0.0185 rad. This increase is primarily attributed to the higher axial compression ratio at the column ends, which improved the specimen's load-bearing capacity and consequently resulted in greater shear deformation in the core region.

4.2. Shear strength prediction models and modified formula

Currently, some studies still use the shear strength calculation formulas for conventional RC beam-column joints to predict the shear strength of ECC beam-column joints. However, other researchers have proposed shear strength prediction formulas specifically

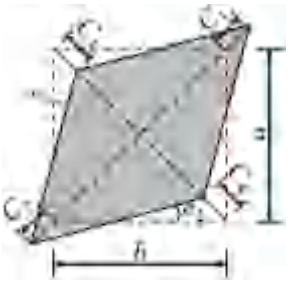


Fig. 22. Shear deformation in the core region.

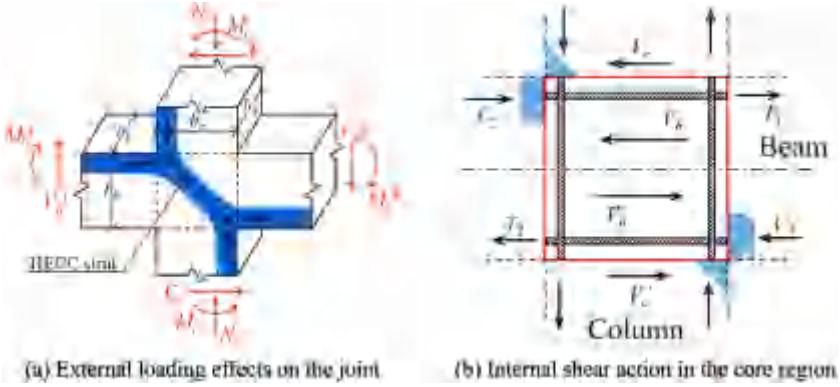


Fig. 23. Joint forces under cyclic loading.

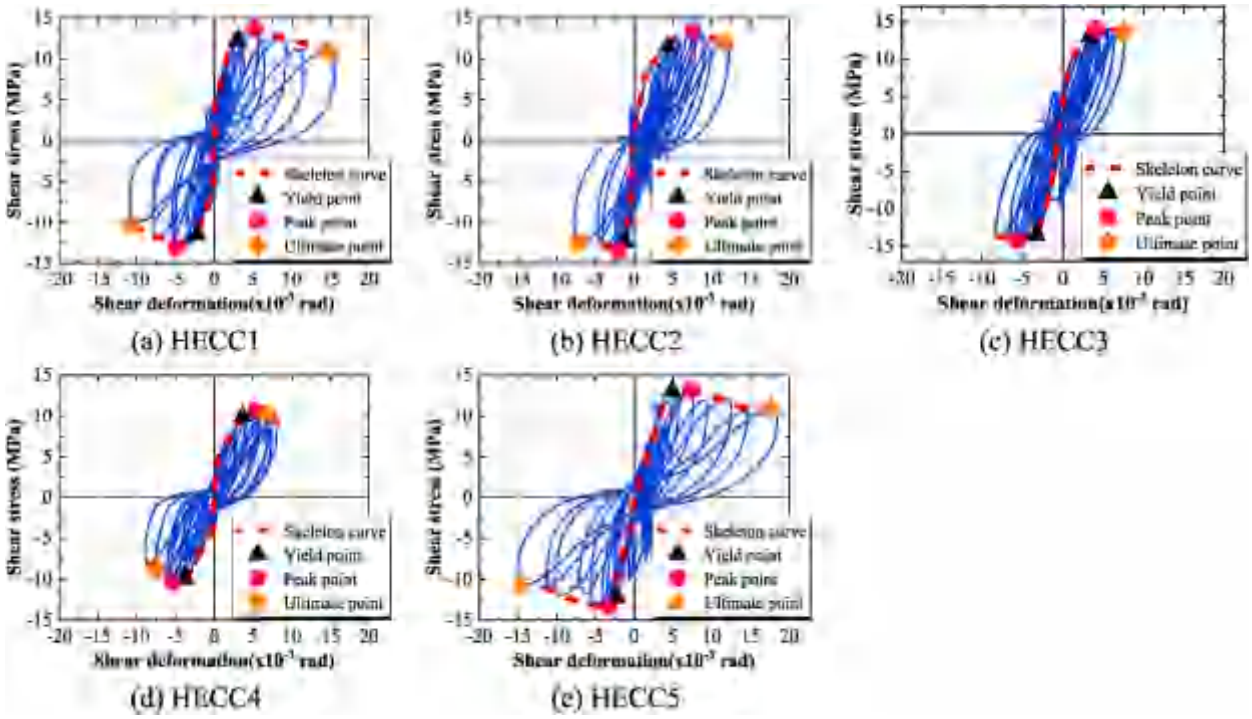


Fig. 24. Shear stress-deformation curve of specimens.

for ECC joints based on methods such as the Strut-and-Tie Model (STM) [44], the Modified Compression Field Theory (MCFT) [45], and Pearson correlation analysis [22]. Kantekin and Burak Bakir [22] were the first to develop a formula designed to predict the shear strength of HECC joints. In this section, the experimental results from this study, along with 24 collected shear strength test values for HECC joints, are compared with predicted shear strength values derived from Kantekin and Burak Bakir's predictive formula [22], the design codes ACI 318-19 [3], GB50010-2010 [4], and Eurocode 8 [46], as well as Kim and LaFave [47] model, recognized for effectively capturing the average shear performance of RC beam-column joints.

4.2.1. ACI 318-19 [3] model

$$V_h^{ACI} = \varphi V_n = \varphi \cdot 0.083\gamma_n \sqrt{f_c'} b_j h_c \tag{12}$$

where φ is the strength reduction factor, with a value of $\varphi = 0.85$. When $b_b \geq b_j$ or the joint is constrained by beams on both sides, $\gamma_n = 15$. Conversely, when $b_b < b_j$, $\gamma_n = 12$. f_c' is the compressive strength of material in joint.

4.2.2. GB50010-2010 [4] model

$$V_h^{GB} = 1.1\eta_j f_t b_j h_j + 0.05\eta_j N\frac{b_j}{b_c} + f_y A_{svj}\frac{h_{b0} - \alpha_s'}{s} \tag{13}$$

4.2.3. Eurocode 8 [46] model

According to Eurocode 8, the joint's shear capacity is determined as the lower value calculated from Eq. (14) and Eq. (15).

$$V_h^{EC,1} = 0.8\eta f_c'\sqrt{1 - \frac{v_d}{\eta}}h_{jc}b_j \tag{14}$$

$$V_h^{EC,2} = \sqrt{\left(\frac{A_{sh}f_y}{b_j h_{jw}} + f_t\right)(f_t + v_d f_c')}h_{jc}b_j \tag{15}$$

where $\eta = 0.6(1\text{-}f_c'/250)$, v_d denotes the normalized axial force of the column, h_{jc} represents the distance between the outer edges of the column's longitudinal rebars, A_{sh} is the total cross-sectional area of the horizontal transverse rebars in the core region, and h_{jw} refers to the distance between the bottom and top longitudinal rebars of the beam.

4.2.4. Kim and LaFave [47] model

Kim and LaFave developed a simplified formula (see Eq. (16)) for predicting the shear strength of RC beam-column joints by leveraging an extensive experimental dataset and employing Bayesian parameter estimation.

$$v_{n,k} = 1.31\alpha_t\beta_t\eta_t(JI)^{0.15}(BI)^{0.30}(f_c')^{0.75} \tag{16}$$

where α_t represents the parameter for in-plane geometry (1.0 for interior joints), β_t denotes the parameter for out-of-plane geometry (1.0 for beam-column joints with no transverse beams), η_t describes joint eccentricity (1.0 for no eccentricity), JI is the transverse reinforcement index of the core region ($JI = \left(\rho_s \cdot f_{yj}\right)/f_c'$), BI is the beam reinforcement index ($BI = \left(\rho_b \cdot f_{yb}\right)/f_c'$).

4.2.5. Kantekin and Burak Bakir [22] model

The shear strength formula for HECC joints, as proposed by Kantekin and Burak Bakir, is expressed as follows:

$$v_{n,K} = \sigma_{cc}\left[1 + \left(0.3\frac{N}{f_c' A_g}\right)\right]\left[\gamma_j\left(\frac{b_b}{h_b}\right)^{1.1}\left(\frac{b_c}{h_c}\right)^{0.2}\left(\frac{h_c}{b_b}\right)^{0.7}RI^{\alpha_j} + 2(\rho_{gross})^{0.5}RI^{\beta_j}\right] \tag{17}$$

where σ_{cc} denotes the cracking strength, calculated using Eq. (18) in accordance with ACI 318-19 [3]. A_g is the total cross-sectional area of the column, and h_b is the beam depth. The stirrup ratio (ρ_{gross}) and fiber reinforcement coefficient (RI) are calculated using Eqs. (19) and (20) [48]. The parameters α_j, β_j, and γ_j are provided in Table 6.

$$\sigma_{cc} = 0.62\sqrt{f_c'} \tag{18}$$

$$\rho_{gross} = \frac{nA_0 l_e}{h_c b_c h_b} \tag{19}$$

$$RI = \sum_{i=1}^{n} k_i V_{fi}\left(\frac{L}{D}\right)_i\left(\frac{f_{ti}}{f_{ts}}\right)^{\alpha_j} \tag{20}$$

where n represents the number of transverse rebar layers in the joint, A_0 denotes the cross-sectional area of a single transverse rebar, and l_e represents the total length of a single transverse rebar. The subscript i refers to the fiber type. The bond coefficient k depends on the fiber type and its surface characteristics. For the end-hooked steel fibers used in this study, k is set to 1.0 [49]. Considering the smooth and straight surface of PE fibers, k is assigned a value of 0.1 [50]. V_{fi} represents the fiber volume fraction, L/D is the fiber aspect ratio, and f_{ti} denotes the tensile strength of the i-th fiber. f_{ts} denotes the tensile strength of the steel fiber. Based on the findings of Almusallam et al. [48] and Cao and Li [51], the tensile stiffness parameter α_j is taken as 0.5.

In order to evaluate the accuracy of the above calculation formulas in predicting the shear strength of HECC joints, the basic

Table 6
Coefficients used in the prediction formula.

Coefficient	Exterior Joints	Interior Joints
α_j	0.25	0.00
β_j	0.75	1.00
γ_j	1.50	2.10

information of the joint specimens from this study and previous studies [52–54] is summarized in Table 7. The experimental and predicted shear strength values are presented in Table 8 and compared in Fig. 25, where this comparison is showed using frequency histograms and normal distribution functions [55]. The results indicate that all three current codes underestimate the shear strength of HECC joints. This discrepancy arises because these codes are based on the shear behavior of RC joints, which cannot be directly applied to HECC joints. In contrast, Kim and LaFave model premised on the presence of transverse rebars in the core region, accurately predicts the shear strength of HECC joints only when transverse rebars are provided.

According to ACI 318-19, Qudah and Maalej [56] defined (v_{test}/v_n)-1 as the shear capacity reserve of ECC joints relative to RC joints with transverse rebars designed and configured according to code requirements. Their study examined the effect of reducing the stirrup ratio in the core region to 50 %, 25 %, and 0 % of the code requirements through experiments. The results showed that the shear capacity reserve of ECC joints ranged from 14 % to 27 %. Based on the calculations in Table 8, the shear capacity reserve of HECC joints is found to reach 34 %, which significantly exceeds that of ECC joints, illustrating that HECC provides a much higher safety margin under seismic loads.

Compared to the three existing codes, although Kantekin and Burak Bakir's predictive formula also underestimates the shear strength of HECC beam-column joints, it exhibits lowest dispersion due to the inclusion of additional parameters. To overcome the limitations of Kantekin and Burak Bakir's [22] predictive formula in underestimating the positive synergistic effect of hybrid fibers [57], a synergistic enhancement coefficient (ζ) of 1.46 is introduced in this study. A modified formula is proposed to predict the shear strength of HECC joints (see Eq. (21)). Fig. 26 presents a comparison between the predictions of the modified formula and experimental results, demonstrating an average (AVG) value of 1.013, and a coefficient of variation (COV) of 0.096. These findings confirm the high accuracy of the modified formula in estimating the shear strength of HECC joints. However, more research should be conducted to investigate more parameters especially hybrid fiber type and fiber volume fraction in future to enhance its accuracy and improve its applicability for predicting the shear strength of HECC joint.

$$v_{n,p} = \zeta \sigma_{cc}\left[1+\left(0.3\frac{N}{f_c' A_g}\right)\right]\left[\gamma_j\left(\frac{b_b}{h_b}\right)^{1.1}\left(\frac{b_c}{h_c}\right)^{0.2}\left(\frac{h_c}{b_b}\right)^{0.7} RI^{\alpha_j} + 2\left(\rho_{gross}\right)^{0.5} RI^{\beta_j}\right] \tag{21}$$

5. Conclusions

In this study, to minimize the reliance on transverse rebars in the core regions of beam-column joints and optimize the reinforcement configuration, HECC was utilized as a replacement for traditional concrete in the joint core regions. To systematically assess the seismic performance of such joints, cyclic loading tests were conducted on five HECC/RC composite beam-column joint specimens. The findings of this study can be summarized as follows.

Table 7
Summary of basic information for joint specimens.

Researcher	Notation	Joint type	Fibers	Beam		Column		Joint transverse rebar	f_c' (MPa)
				b_b (mm)	h_b (mm)	b_c (mm)	h_c (mm)		
This study	HECC1	Interior	PE + SF	250	400	300	300	–	62.78
	HECC2	Interior	PE + SF	250	400	300	300	D10@130	62.78
	HECC3	Interior	PE + SF	250	400	300	300	D10@130	62.78
	HECC4	Interior	PE + SF	250	400	300	300	–	39.14
	HECC5	Interior	PE + SF	250	400	300	300	–	62.78
Wei [52]	SPF1	Interior	PP + SF	150	250	200	200	D8@117	36.35
	SPF2	Interior	PP + SF	150	250	200	200	D8@117	36.64
	SPF3	Interior	PP + SF	150	250	200	200	D8@117	39.83
	SPF4	Interior	PP + SF	150	250	200	200	D8@117	39.20
	SPF5	Interior	PP + SF	150	250	200	200	D8@117	39.80
	SPF6	Interior	PP + SF	150	250	200	200	D8@117	37.90
	SPF7	Interior	PP + SF	150	250	200	200	D8@117	38.73
	SPF8	Interior	PP + SF	150	250	200	200	D8@117	40.27
	SPF9	Interior	PP + SF	150	250	200	200	D8@117	40.62
	SPF10	Interior	PP + SF	150	250	200	200	D8@117	39.91
	SPF11	Interior	PP + SF	150	250	200	200	D8@117	39.88
Han et al. [53]	HyFRCC1	Interior	PVA + SF	150	300	200	200	–	45.52
	HyFRCC2	Interior	PVA + SF	150	300	200	200	–	37.92
	HyFRCC3	Interior	PVA + SF	150	300	200	200	–	37.92
	HyFRCC4	Interior	PVA + SF	150	300	200	200	–	40.40
	HyFRCC5	Interior	PVA + SF	150	300	200	200	–	40.64
	HyFRCC6	Interior	PVA + SF	150	300	200	200	–	32.24
Siva Chidambaram and Agarwal [54]	SJ5	Exterior	PP + SF	130	150	150	150	–	39.00
	SJ6	Exterior	PP + SF	130	150	150	150	–	33.00

Table 8
Comparison of experimental and predicted shear strength values for HECC joints.

Researcher	Notation	v_{test} (MPa)	ACI 318-19		GB50010-2010		Eurocode 8		Kim and LaFave		Kantekin and Burak Bakir		Proposed	
			$v_{n,ACI}$ (MPa)	$v_{test}/v_{n,ACI}$	$v_{n,GB}$ (MPa)	$v_{test}/v_{n,GB}$	$v_{n,Eu}$ (MPa)	$v_{test}/v_{n,Eu}$	$v_{n,k}$ (MPa)	$v_{test}/v_{n,k}$	$v_{n,K}$ (MPa)	$v_{test}/v_{n,K}$	$v_{n,P}$ (MPa)	$v_{test}/v_{n,P}$
This study	HECC1	13.4	8.38	1.60	8.32	1.61	10.41	1.29	0.00	–	7.41	1.81	10.82	1.24
	HECC2	13.5	8.38	1.61	10.27	1.31	12.36	1.09	12.39	1.09	9.01	1.50	13.16	1.03
	HECC3	14.1	8.38	1.68	12.20	1.16	14.01	1.01	13.75	1.03	9.84	1.43	14.36	0.98
	HECC4	10.5	6.62	1.59	4.75	2.21	5.99	1.75	0.00	–	5.85	1.80	8.54	1.23
	HECC5	13.3	8.38	1.59	8.48	1.57	11.27	1.18	0.00	–	7.62	1.75	11.12	1.20
Wei [52]	SPF1	8.17	6.38	1.28	6.22	1.31	7.20	1.13	9.39	0.87	6.10	1.34	8.91	0.92
	SPF2	8.48	6.41	1.32	6.47	1.31	6.86	1.24	9.53	0.89	6.25	1.36	9.12	0.93
	SPF3	8.8	6.68	1.32	6.70	1.31	7.28	1.21	9.56	0.92	6.64	1.33	9.70	0.91
	SPF4	8.57	6.63	1.29	6.65	1.29	7.19	1.19	9.47	0.91	6.40	1.34	9.35	0.92
	SPF5	9.04	6.68	1.35	6.70	1.35	7.27	1.24	9.56	0.95	6.76	1.34	9.88	0.92
	SPF6	8.99	6.51	1.38	6.55	1.37	7.01	1.28	9.28	0.97	6.47	1.39	9.44	0.95
	SPF7	8.72	6.59	1.32	6.61	1.32	7.12	1.23	9.40	0.93	6.54	1.33	9.55	0.91
	SPF8	9.08	6.72	1.35	6.74	1.35	7.33	1.24	9.62	0.94	6.67	1.36	9.74	0.93
	SPF9	8.95	6.74	1.33	6.87	1.30	7.47	1.20	9.67	0.93	6.70	1.34	9.79	0.91
	SPF10	9.04	6.69	1.35	6.54	1.38	6.33	1.43	9.57	0.94	6.46	1.40	9.44	0.96
	SPF11	8.65	6.68	1.29	6.90	1.25	5.85	1.48	9.57	0.90	6.83	1.27	9.97	0.87
Han et al. [53]	HyFRCC1	7.34	7.14	1.03	4.60	1.59	6.55	1.12	0.00	–	5.54	1.33	8.09	0.91
	HyFRCC2	8.09	6.52	1.24	3.83	2.11	5.46	1.48	0.00	–	5.06	1.60	7.38	1.10
	HyFRCC3	7.31	6.52	1.12	3.83	1.91	5.46	1.34	0.00	–	5.06	1.45	7.38	0.99
	HyFRCC4	7.67	6.73	1.14	4.08	1.88	5.82	1.32	0.00	–	5.22	1.47	7.62	1.01
	HyFRCC5	7.71	6.75	1.14	4.11	1.88	5.85	1.32	0.00	–	5.23	1.47	7.64	1.01
	HyFRCC6	7.83	6.01	1.30	3.26	2.40	4.64	1.69	0.00	–	4.66	1.68	6.81	1.15
Siva Chidambaram and Agarwal [54]	SJ5	8.45	6.61	1.28	7.10	1.19	4.73	1.79	0.00	–	6.06	1.40	8.84	0.96
	SJ6	7.77	6.08	1.28	4.95	1.57	3.30	2.35	0.00	–	5.27	1.48	7.69	1.01

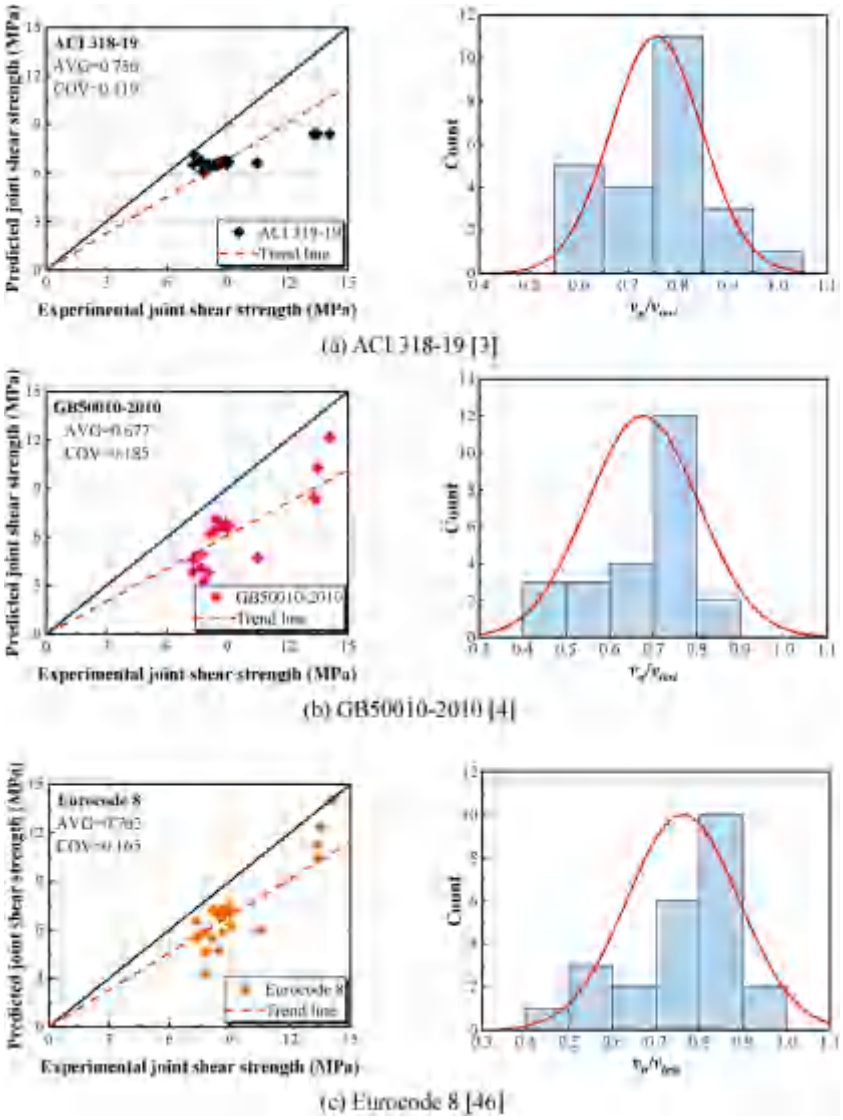


Fig. 25. Comparison of experimental results with predicted values for HECC joints.

1) Even when shear failure occurred in the core region, HECC joints without transverse rebars demonstrated a significantly enhanced ductility compared to conventional RC joints. No matrix spalling was observed after failure, and dense and uniformly distributed cracks were identified using DIC technology. Additionally, HECC joints with lower strength led to a substantial reduction in load-bearing capacity and shear deformation. Despite an increased axial compression ratio at the column ends diminishing ductility, it moderately enhanced load-bearing capacity, energy dissipation, and shear deformation capacity.
2) Unlike RC joint, the enhancement effect of transverse rebars on the bearing capacity of HECC joint was less significant. When the stirrup ratio increased from 0 % to 2.10 %, the bearing capacity of HECC joint only increased by 7.0 %, indicating that the steel-PE hybrid fibers in HECC acting as discrete reinforcement can provide similar confinement to that of transverse rebar.
3) The existing design formulas derived from the shear behavior of conventional RC joints, tended to underestimate the shear strength of HECC joints. Additionally, the shear capacity reserve of HECC joint could reach 34 %, which significantly exceeded that of ECC joint (i.e., 14 %–27 %), indicating that HECC provided a much higher safety margin under seismic loads due to the synergistic effect of steel-polypropylene hybrid fibers.
4) A modified formula, building on Kantekin and Burak Bakir model and introducing a synergistic enhancement coefficient for steel and PE fibers hybridization, was proposed to predicting the shear strength of HECC joints. The proposed model achieves greater precision, as demonstrated by an average predicted-to-test ratio of 1.013 and a coefficient of variation of 0.096, surpassing the accuracy of established models such as ACI 318-19, GB50010-2010, Eurocode 8, and the Kim and LaFave model.

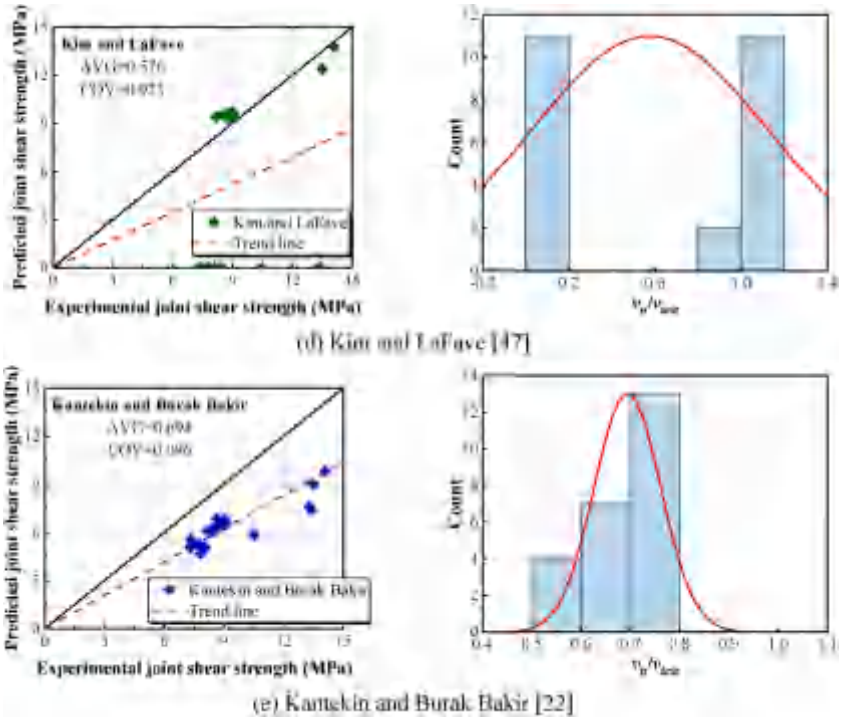


Fig. 25. (*continued*).

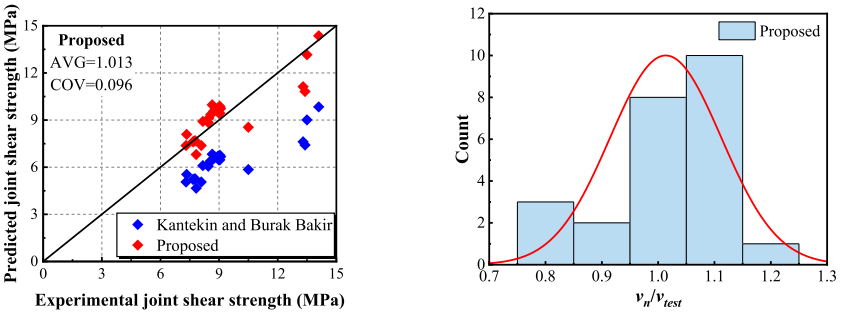


Fig. 26. Comparison of predicted shear strength using the modified formula and experimental results.

Further, more research should be conducted to investigate more parameters especially hybrid fiber type and fiber volume fraction in future to enhance the accuracy and applicability of the proposed model for predicting the shear strength of HECC joint.

CRediT authorship contribution statement

Yu-Lei Bai: Supervision, Resources, Methodology. **Shi-Yan Zhang:** Writing – original draft, Visualization, Formal analysis, Data curation. **Wei-Hao Mao:** Writing – review & editing, Methodology, Conceptualization. **Ze-Yuan Liu:** Investigation. **Luo-Bin Zuo:** Investigation. **Yao Ding:** Writing – review & editing, Supervision, Funding acquisition.

Declaration of competing interest

The authors declare that they have no known competing financial interests or personal relationships that could have appeared to influence the work reported in this paper.

Acknowledgment

The authors are grateful for the financial support received from the National Natural Science Foundation of China (No. 52108114),

the Program Fund of Non-Metallic Excellence and Innovation Center for Building Materials (No. 24SFP-2).

Data availability

Data will be made available on request.

References

[1] H.H. Ghayeb, H.A. Razak, N.H. Ramli Sulong, Performance of dowel beam-to-column connections for precast concrete systems under seismic loads: a review, Constr. Build. Mater. 237 (2020) 117582.
[2] S. Majumder, S. Saha, Quasi-static cyclic performance of RC exterior beam-column joint assemblages strengthened with geosynthetic materials, Structures 29 (2021) 1210–1228.
[3] ACI Committee 318, Building Code Requirements for Structural Concrete (ACI 318-19) and commentary[S], American Concrete Institute, Farmington Hills, MI, 2019.
[4] GB 50010-2010, Code for Design of Concrete structures[S], China Building Industry Press, Beijing, 2010.
[5] A. Ebanesar, H. Gladston, E. Noroozinejad Farsangi, et al., Strengthening of RC beam-column joints using steel plate with shear connectors: experimental investigation, Structures 35 (2022) 1138–1150.
[6] V.C. Li, From micromechanics to structural engineering: the design of cementitious composites for civil engineering applications, Dob. Gakkai Ronbunshu 1993 (471) (1993) 1–12.
[7] V.C. Li, S. Wang, C. Wu, Tensile strain-hardening behavior of polyvinyl alcohol engineered cementitious composite (PVA-ECC), ACI Mater. J. 98 (6) (2001).
[8] J. Zhou, J. Pan, C.K.Y. Leung, Mechanical behavior of fiber-reinforced engineered cementitious composites in uniaxial compression, J. Mater. Civ. Eng. 27 (1) (2015) 04014111.
[9] B.T. Huang, Q.H. Li, S.L. Xu, Fatigue deformation model of plain and fiber-reinforced concrete based on weibull function, J. Struct. Eng. 145 (1) (2019) 04018234.
[10] D. Gu, J. Pan, S. Mustafa, et al., Shear transfer mechanism in reinforced engineered cementitious composite (ECC) beams: quantification of v_s and V_c, Eng. Struct. 261 (2022) 114282.
[11] D. Wang, J. Zhao, Y. Ju, et al., Behavior of beam-column joints with high performance fiber-reinforced concrete under cyclic loading, Structures 44 (2022) 171–185.
[12] H.H. Ghayeb, N.H. Ramli Sulong, H.A. Razak, et al., Enhancement of seismic behaviour of precast beam-to-column joints using engineered cementitious composite, Eng. Struct. 255 (2022) 113932.
[13] J. Cai, J. Pan, J. Tan, et al., Bond behaviours of deformed steel rebars in engineered cementitious composites (ECC) and concrete, Constr. Build. Mater. 252 (2020) 119082.
[14] F. Yuan, J. Pan, Z. Xu, et al., A comparison of engineered cementitious composites versus normal concrete in beam-column joints under reversed cyclic loading, Mater. Struct. 46 (1–2) (2013) 145–159.
[15] S.H. Said, H. Abdul Razak, Structural behavior of RC engineered cementitious composite (ECC) exterior beam–column joints under reversed cyclic loading, Constr. Build. Mater. 107 (2016) 226–234.
[16] P. Hait, R. Mitra, E. Noroozinejad Farsangi, Experimental investigations of resilient hybrid fiber reinforced SCC beam-column subassemblies under cyclic loadings, Structures 41 (2022) 389–403.
[17] S. Wang, L. Xu, Y. Chi, et al., Cyclic tensile behavior of ultra-high performance concrete with hybrid steel-polypropylene fiber: experimental study and analytical model, Compos. Struct. 321 (2023) 117255.
[18] Y. Ding, W.H. Mao, W. Wei, et al., Bond behavior and anchorage length of deformed bars in steel-polyethylene hybrid fiber engineered cementitious composites, Eng. Struct. 252 (2022) 113675.
[19] Y. Ding, J.P. Liu, G. Yao, et al., Cyclic bond behavior and bond stress-slip constitutive model of rebar embedded in hybrid fiber reinforced strain-hardening cementitious composites, Constr. Build. Mater. 369 (2023) 130582.
[20] J. Maheswaran, M. Chellapandian, M.V.R. Sivasubramanian, et al., Experimental and numerical investigation on the shear behavior of engineered cementitious composite beams with hybrid fibers, Materials 15 (14) (2022) 5059.
[21] Z. Tong, L. Xu, C. Wei, et al., Upgrading seismic performance of beam-column joints using steel-polypropylene hybrid fiber: experiment and numerical simulation, J. Build. Eng. 86 (2024) 108681.
[22] Y. Kantekin, Bakir B. Burak, Joint shear strength prediction for fiber reinforced concrete beam-to-column connections, Eng. Struct. 308 (2024) 117959.
[23] J. Ji, Z. Zhang, M. Lin, et al., Structural application of engineered cementitious composites (ECC): a state-of-the-art review, Constr. Build. Mater. 406 (2023) 133289.
[24] J.X. Zhu, L.Y. Xu, B.T. Huang, et al., Recent developments in Engineered/Strain-Hardening Cementitious Composites (ECC/SHCC) with high and ultra-high strength, Constr. Build. Mater. 342 (2022) 127956.
[25] Z. Hu, M. Elchalakani, S. Yehia, et al., Engineered cementitious composite (ECC) strengthening of reinforced concrete structures: a state-of-the-art review, J. Build. Eng. 86 (2024) 108941.
[26] W.H. Mao, J.P. Liu, Y. Ding, et al., Bond-slip constitutive model and numerical analysis for rebar embedded in steel-polyethylene hybrid fiber-reinforced cementitious composites, Constr. Build. Mater. 308 (2021) 125092.
[27] W.H. Mao, J.P. Liu, H.T. Qi, et al., Anchorage characteristics and their impacts on the seismic performance of HECC/RC composites external beam-column joint, Structures 63 (2024) 106469.
[28] GB/T 51231-2016, Technical Standard for Assembled Buildings with Concrete structure[S], China Building Industry Press, Beijing, 2016.
[29] JSCE, Recommendations for Design and Construction of High Performance Fiber Reinforced Cement Composites with Multiple Fine cracks[S], Japan Society of Civil Engineers, Japan, 2008.
[30] ACI Committee 374, ACI 374.2R-13 Guide for Testing Reinforced Concrete Structural Elements under Slowly Applied Simulated Seismic loads[S], American Concrete Institute, Farmington Hills, 2013.
[31] A. Tambusay, B. Suryanto, P. Suprobo, Digital image correlation for cement-based materials and structural concrete testing, Civil Engineering Dimension 22 (1) (2020) 6–12.
[32] J. Blaber, B. Adair, A. Antoniou, Ncorr: open-source 2D digital image correlation matlab software, Exp. Mech. 55 (6) (2015) 1105–1122.
[33] S. Alavi-Dehkordi, D. Mostofinejad, P. Alaee, Effects of high-strength reinforcing bars and concrete on seismic behavior of RC beam-column joints, Eng. Struct. 183 (2019) 702–719.
[34] W. Kassem, Strut-and-tie modelling for the analysis and design of RC beam-column joints, Mater. Struct. 49 (8) (2016) 3459–3476.
[35] R. Park, State of the art report ductility evaluation from laboratory and analytical testing[C]. Proceedings of Ninth World Conference on Earthquake Engineering, 1988, pp. 605–616. Tokyo, Kyoto, Japan.
[36] M hossein Saghafi, H. Shariatmadar, Enhancement of seismic performance of beam-column joint connections using high performance fiber reinforced cementitious composites, Constr. Build. Mater. 180 (2018) 665–680.
[37] B. Dong, J. Pan, J. Cai, et al., Mechanical behaviour of a new ECC-encased CFST column to RC beam connection under cyclic loading, Eng. Struct. 234 (2021) 111915.

[38] X. Zhang, B. Li, Seismic performance of RC beam–column joints constructed with engineered cementitious composites, J. Struct. Eng. 146 (12) (2020) 04020271.
[39] Y. Park, A.H.-S. Ang, Mechanistic seismic damage model for reinforced concrete, J. Struct. Eng. 111 (4) (1985) 722–739.
[40] J. Shafaei, M.S. Zareian, A. Hosseini, et al., Effects of joint flexibility on lateral response of reinforced concrete frames, Eng. Struct. 81 (2014) 412–431.
[41] A. Elenas, K. Meskouris, Correlation study between seismic acceleration parameters and damage indices of structures, Eng. Struct. 23 (6) (2001) 698–704.
[42] R. Sharma, P.P. Bansal, Behavior of RC exterior beam column joint retrofitted using UHP-HFRC, Constr. Build. Mater. 195 (2019) 376–389.
[43] ACI 352R-02, Recommendations for Design of Beam-Column Connections in Monolithic Reinforced Concrete structures[S], American Concrete Institute, Farmington Hills, MI, 2002.
[44] F. Ma, M. Deng, Y. Yang, Experimental study on internal precast beam–column ultra-high-performance concrete connection and shear capacity of its joint, J. Build. Eng. 44 (2021) 103204.
[45] L. Zhang, J. Yao, Y. Hu, et al., Predicting shear strength of steel fiber reinforced concrete beam-column joints by modified compression field theory, Structures 41 (2022) 1432–1441.
[46] CEN. EN 1998–1 Eurocode 8, Design of Structures for Earthquake Resistance. Part 1, General Rules, Seismic Actions and Rules for buildings[S], European Committee for Standardization, Brussels, 2004.
[47] J. Kim, J.M. LaFave, A simplified approach to joint shear behavior prediction of RC beam-column connections, Earthq. Spectra 28 (3) (2012) 1071–1096.
[48] T. Almusallam, S.M. Ibrahim, Y. Al-Salloum, et al., Analytical and experimental investigations on the fracture behavior of hybrid fiber reinforced concrete, Cement Concr. Compos. 74 (2016) 201–217.
[49] S.M. Ibrahim, T.H. Almusallam, Y.A. Al-Salloum, et al., Strain rate dependent behavior and modeling for compression response of hybrid fiber reinforced concrete, Lat. Am. J. Solid. Struct. 13 (9) (2016) 1695–1715.
[50] B. Sagar, M.V.N. Sivakumar, Compressive properties and analytical modelling for stress-strain curves of polyvinyl alcohol fiber reinforced concrete, Constr. Build. Mater. 291 (2021) 123192.
[51] M. Cao, L. Li, New models for predicting workability and toughness of hybrid fiber reinforced cement-based composites, Constr. Build. Mater. 176 (2018) 618–628.
[52] C.M. Wei, A Study on the Seismic Performance of Steel-Polypropylene Hybrid Fiber Reinforced Concrete Frame Joints[D], Wuhan University, 2020.
[53] J.P. Han, W.L. Liu, M. Cui, Experimental investigation on seismic behavior of PVA-steel hybrid fiber reinforced cementitious composite beam-column assemblages, China Civ. Eng. J. 51 (11) (2018) 32–40+52.
[54] Chidambaram R. Siva, P. Agarwal, Seismic behavior of hybrid fiber reinforced cementitious composite beam–column joints, Mater. Des. 86 (2015) 771–781.
[55] M. Mousavi, H.A. Bengar, Investigation of the effect of internal curing as a novel method for improvement of post-fire properties of high-performance concrete, Comput. Concr. 33 (3) (2024) 309–324.
[56] S. Qudah, M. Maalej, Application of Engineered Cementitious Composites (ECC) in interior beam–column connections for enhanced seismic resistance, Eng. Struct. 69 (2014) 235–245.
[57] L. Huang, Y. Chi, L. Xu, et al., Local bond performance of rebar embedded in steel-polypropylene hybrid fiber reinforced concrete under monotonic and cyclic loading, Constr. Build. Mater. 103 (2016) 77–92.

Case Studies in Construction Materials 22 (2025) e04703

Contents lists available at ScienceDirect

Case Studies in Construction Materials

journal homepage: www.elsevier.com/locate/cscm

Seismic performance of short concrete columns reinforced with steel-FRP composite bars and GFRP stirrups

Yulei Bai [a], Xiaoyong An [a], Guolin Wang [b,*], Hua Rong [c], Yufeng Zhang [c], Jun Tao [d]

[a] State Key Laboratory of Bridge Safety and Resilience, Beijing University of Technology, Beijing 100124, China
[b] School of Urban Construction and Safety Engineering, Shanghai Institute of Technology, Shanghai 201418, China
[c] Inspection and Certification Co., Ltd., Central Research Institute of Building and Construction, MCC, Beijing 100088, China
[d] Operation Maintenance Technology Company of China National Nuclear Power Co., Ltd., Hangzhou 311215, China

ARTICLE INFO

Keywords:
SFCB
Short column
Seismic performance
Uniaxial-shear-flexure model (USFM)

ABSTRACT

The steel-FRP composite bar (SFCB) is an ideal reinforcement choice for structures aimed at enhancing durability and resilience. However, research on the seismic applications of SFCBs has primarily focused on flexure-dominated concrete columns, with limited experimental investigation into columns subjected to axial-shear-flexure interaction. To address this gap, quasi-static tests were conducted on six short concrete columns to evaluate their seismic performance. The study examined the effects of key variables, including longitudinal reinforcement type, the spacing of GFRP stirrups, and shear span-to-depth ratios. The results show that all specimens exhibited a shear-flexure failure mode. Compared to the steel-reinforced short column, SFCB-reinforced short columns with an equal stiffness design method demonstrate better seismic performance, including reduced shear-flexure damage, similar initial stiffness, higher load-bearing capacity, and increased resilience. Reducing the GFRP stirrup spacing enhances the shear capacity of SFCB-reinforced columns, thereby reducing shear deformation and improving ductility. A decrease in the shear span-to-depth ratio significantly increases the stiffness and overall load-displacement curves of SFCB-reinforced columns, with a slight improvement in resilience. An analytical model incorporating axial-shear-flexure interaction was developed using the uniaxial-shear-flexure model (USFM) approach and validated by comparing the predicted envelope curves with the experimental results.

1. Introduction

The steel-FRP composite bar (SFCB) is an innovative reinforcement consisting of a ribbed steel core encased in a continuous FRP layer [1,2]. The protective FRP layer of SFCB mitigates structural degradation and reduces the high maintenance costs associated with steel corrosion [3,4]. In contrast to FRP bars of the same fiber material, SFCBs exhibit a higher elastic modulus and greater ductility due to their steel core. These properties effectively address challenges such as significant crack widths, excessive deformations, and brittle failure in FRP bar-reinforced members [5–8]. Additionally, after the steel core yields, the linear elastic FRP layer continues to bear the load, providing stable positive post-yield stiffness. This feature limits the development of plastic strain in the steel core, controlling damage progression and enhancing the structure's post-earthquake repairability [9–12]. Consequently, SFCBs offer a promising

* Corresponding author.
E-mail address: felixwseu@163.com (G. Wang).

https://doi.org/10.1016/j.cscm.2025.e04703
Received 12 March 2025; Received in revised form 13 April 2025; Accepted 22 April 2025
Available online 23 April 2025
2214-5095/© 2025 The Authors. Published by Elsevier Ltd. This is an open access article under the CC BY license (http://creativecommons.org/licenses/by/4.0/).

solution for improving both the durability and resilience of reinforced structures.

Building on the excellent mechanical properties of SFCBs, numerous studies have investigated the seismic behavior of SFCB-reinforced columns, including conventional concrete columns [13–16], precast concrete columns [17], concrete-filled FRP tube (CFFT) columns [18], and engineered cementitious composite (ECC) columns [19,20]. It was concluded from the experimental results that SFCB is highly effective in enhancing the post-yield stiffness of the column and reducing residual deformation. However, all these test specimens are flexure-dominated columns. In practical applications, complex seismic responses and excessive lateral deformations often reduce the shear capacities of reinforced columns, eventually causing shear-flexure failure after the initial flexural response [21–24].

Compared to steel bar-reinforced columns, the lower pre-yield elastic modulus and uncertain transverse shear performance of longitudinal SFCBs may reduce the shear capacity of SFCB-reinforced columns, thereby potentially compromising their ductility. Additionally, the distinctive mechanical characteristics of SFCBs also make the current shear design approaches for steel bar-reinforced or FRP bar-reinforced members unsuitable for direct use [25–28]. The literature review highlights a lack of understanding and comprehensive experimental studies regarding the seismic behavior of SFCB-reinforced columns under axial-shear-flexure interaction, which significantly limits their design and application. Thus, further investigation into the seismic performance of SFCB-reinforced columns with a shear-flexure failure mode is imperative, along with the development of a corresponding theoretical calculation model.

Against this background, this paper presents the first experimental investigation on SFCB-reinforced short concrete columns subjected to axial-shear-flexure interaction. To achieve a more durable reinforcement configuration, GFRP stirrups were used in all specimens. The experimental program included the longitudinal reinforcement type, the spacing of GFRP stirrups, and the shear span-to-depth ratios as the key test variables. The results indicate that under the shear-flexure failure mode, the SFCB-reinforced short column designed with an equal stiffness approach exhibits less damage compared to its steel-reinforced counterpart. As the shear span-to-depth ratio increases, the shear failure characteristics of the SFCB-reinforced short columns diminish, while flexural failure characteristics become more pronounced. Based on the previous analysis of longitudinal SFCB slip by the authors' research group [19] and the uniaxial shear-flexure model (USFM) [29], this study developed a theoretical calculation method that accounts for the axial-shear-flexure interaction for predicting the test skeleton curves of SFCB-reinforced short columns. The findings are expected to inform safer shear design strategies for SFCB-reinforced columns, thereby advancing their design and promoting broader application.

2. Experimental investigation

2.1. Specimens details

A total of six short concrete columns were tested, including five SFCB-reinforced columns and one steel-reinforced column. Details of the specimens are shown in Fig. 1. All columns have a square cross-section of 250 mm × 250 mm (b) and a rigid footing measuring 1400 mm × 400 mm × 500 mm. The concrete cover has a thickness of 22 mm, and the transverse reinforcement consists of 10-mm-diameter GFRP stirrups with a side length of 210 mm. The longitudinal SFCBs in the SFCB-reinforced specimens have a diameter of 22 mm, while the steel-reinforced specimen uses 16-mm-diameter longitudinal steel bars. This configuration was designed to investigate the effect of longitudinal bar types under the equal stiffness design method, where the initial stiffness of SFCBs matches that of steel bars [25,26]. The effective column height (H), defined as the distance between the lateral load application point and the foundation's top surface, was varied among the SFCB-reinforced specimens at 500 mm, 600 mm, and 750 mm, corresponding to shear span-to-depth ratios (H/b) of 2.0, 2.4, and 3.0, respectively. These relatively small shear span-to-depth ratios were chosen to induce a shear-flexure failure mode in the test columns. Additionally, the experimental program also varied the GFRP stirrup spacing, with

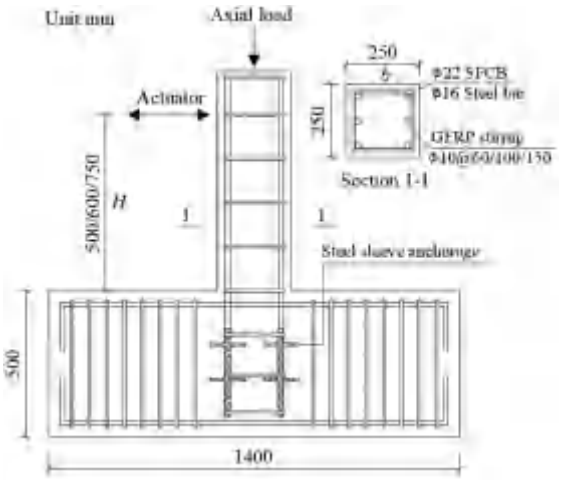


Fig. 1. Specimen size and reinforcement details.

intervals of 60 mm, 100 mm, and 150 mm. Detailed information about the specimens is provided in Table 1. Although individual specimens may exhibit statistical variability, the pronounced influence of the selected parameters ensures that the experimental design remains sufficient for revealing their effect trends. In specimen naming convention, the initial letters "RC" and "SFC" denote steel-reinforced concrete and SFCB-reinforced concrete, respectively. The subsequent numbers, 2.0, 2.4, and 3.0, represent the shear span-to-depth ratios, while the final numbers, 60, 100, and 150, specify the stirrup spacings.

The longitudinal SFCB was anchored in the column footing by inserting it into a 300-mm-long steel sleeve. To enhance the bond strength with the concrete, the steel sleeve was welded to short steel bars. The gap between the sleeve and the SFCB was filled with epoxy resin. Previous experiments have validated the anchorage performance, with results indicating that the failure mode is bar fracture rather than bar slip [12,18].

2.2. Material properties

The test specimens were cast using ready-mixed concrete supplied by a local supplier, with a maximum coarse aggregate size of 25 mm and a slump of 150 mm. Axial compression tests were conducted on three standard cylinders (diameter of 150 mm and height of 300 mm) to determine the concrete properties, as per ASTM C469-22 [30]. The average compressive strength, corresponding axial strain, and the elastic modulus of concrete were 47.3 MPa, 0.00246, and 25.3 GPa, respectively.

The reinforcement samples are shown in Fig. 2. SF22-14 indicates that the SFCB has a diameter of 22 mm, with an inner ribbed steel bar diameter of 14 mm (HRB 400 grade). S16 represents the steel bar with a diameter of 16 mm (HRB 400 grade), and G10 refers to the 10 mm GFRP stirrups. The outer GFRP layer of the SFCB is composed of epoxy resin and glass fibers, which is the same as the material of the GFRP stirrups. The fiber content of the GFRP stirrups ranges from 65 % to 70 %, with an elastic modulus of 42 GPa and an ultimate strength of 750 MPa, as provided by the manufacturer. Tensile tests on three SF22-14 and S16 were conducted per ASTM D7205/D7205M-21 [31], as shown in Fig. 3(a). The resulting stress-strain curves are presented in Fig. 3(b). It can be observed that the steel bars exhibit a distinct yield plateau, while the corresponding segment of the SFCBs shows stable post-yield stiffness. The tensile properties of the test reinforcement are summarized in Table 2.

2.3. Test setup and loading program

The test setup for the quasi-static tests is shown in Fig. 4. A hydraulic jack applied a constant vertical load of 450 kN to the top of the column (i.e., 0.15 axial load ratio). A movable pulley ensured that the hydraulic jack maintained vertical alignment. The column footing was anchored to the rigid ground with an anchoring system to prevent horizontal displacement. A cyclic lateral load was applied using an actuator, and the lateral displacement was recorded with a linear variable differential transformer (LVDT). The loading procedure for the lateral load is shown in Fig. 5. The load is controlled by the drift ratio θ, which is defined as the lateral displacement divided by the effective height of the column. The 2 % drift ratio was adopted as the “major earthquake condition”, in alignment with FEMA P-750 [32] and GB 50011 [33]. Therefore, before reaching the 2 % drift ratio, each loading level was repeated twice to assess the effects of repeated loading. After that, each level was applied only once to minimize testing time. The specimen was considered to have failed at the point where the applied force dropped to 85 % of its peak value.

The arrangement of LVDTs in the lower region of the column is depicted in Fig. 6(a). Four LVDTs, placed on both sides of the column within 300 mm of the base, were used to measure flexural deformation. Additionally, two diagonally positioned LVDTs were employed to measure shear deformation. The horizontal distance between the centers of these two LVDTs is 150 mm, while the vertical distance from the center of each LVDT to the bottom measurement point is 200 mm. The arrangement of strain gauges is shown in Fig. 6(b). A total of eight longitudinal strain gauges were symmetrically placed on the two longitudinal bars along the column centerline, with a spacing of 100 mm. A transverse strain gauge was installed on the GFRP stirrup. For specimens with stirrup spacings of 60 mm, 100 mm, and 150 mm, the strain gauges were positioned 120 mm, 100 mm, and 150 mm from the column base, respectively, to ensure that the stirrup strains could be compared within similar height ranges.

Table 1
Details of the specimens.

Specimen	Height H (mm)	λ	Longitudinal reinforcement		Transverse reinforcement	
			Type	ρ_e*(%)	GFRP stirrup	ρ_v#(%)
RC-2.4-150	600	2.4	6ϕ16(Steel)	1.93	ϕ10@150	1.16
SFC-2.0-150	500	2.0	6ϕ22(SFCB)	1.75	ϕ10@150	1.16
SFC-2.4-150	600	2.4	6ϕ22(SFCB)	1.75	ϕ10@150	1.16
SFC-3.0-150	750	3.0	6ϕ22(SFCB)	1.75	ϕ10@150	1.16
SFC-2.4-100	600	2.4	6ϕ22(SFCB)	1.75	ϕ10@100	1.74
SFC-2.4-60	600	2.4	6ϕ22(SFCB)	1.75	ϕ10@60	2.90

* ρ_e: equivalent longitudinal reinforcement ratio. $\rho_e = (n \times A_b/A) \times (E_1/E_s)$, where n is the number of longitudinal bars. A_b and A are the cross-sectional areas of the longitudinal bar and the column, respectively. E_1 and E_s represent the initial elastic modulus of SFCBs and steel bars, respectively.

ρ_v: Volumetric stirrup ratio.

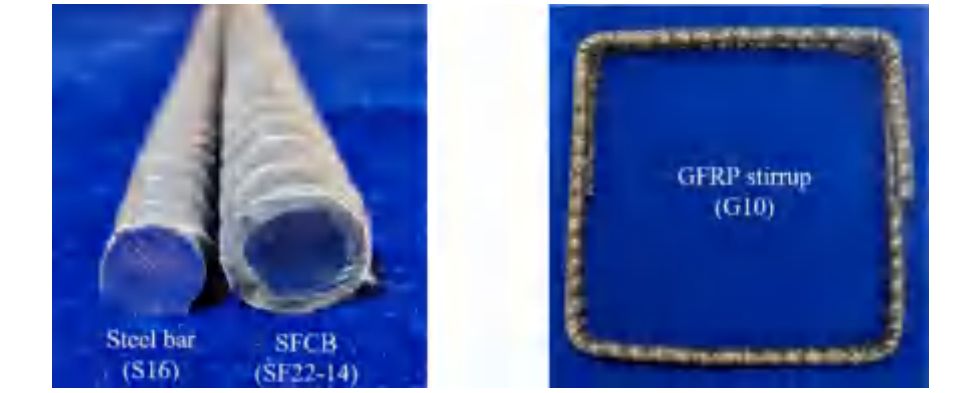


Fig. 2. Photographs of reinforcements.

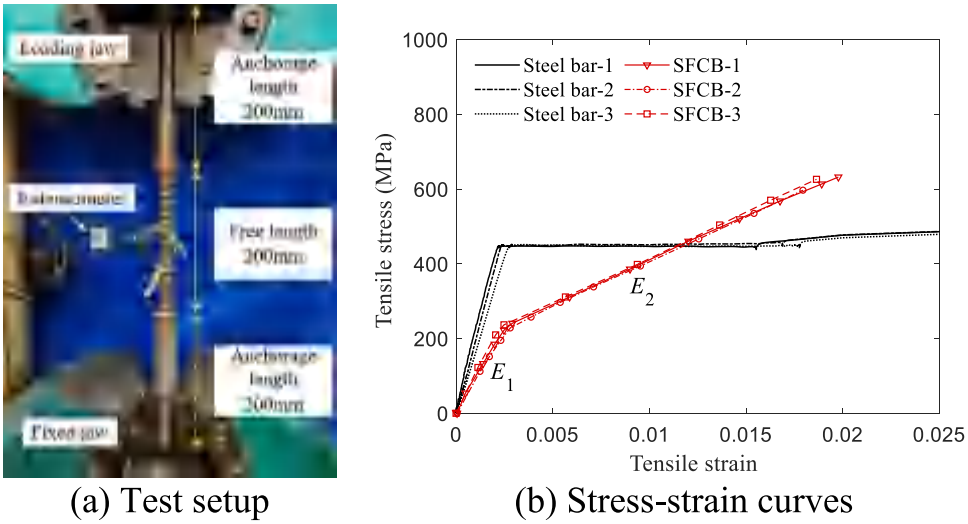


Fig. 3. Tensile test of reinforcements.

Table 2
Tensile properties of reinforcement.

Bar type	f_y (MPa)	ε_y (%)	f_u (MPa)	ε_u (%)	E_1 (GPa)	E_2 (GPa)
Steel bar	448.3	0.236	620.8	23.3	190.0	/
SFCB	249.2	0.273	608.9	1.71	91.3	22.4

3. Experimental results

3.1. Failure modes and crack patterns

The failure modes of each short column at a 2 % drift ratio and ultimate state are shown in Fig. 7. All specimens exhibited the expected shear-flexure failure mode with varying damage characteristics. The steel bar-reinforced specimen RC-2.4-150 displayed a major diagonal shear crack at a 2 % drift ratio (Fig. 7(a)). At a drift ratio of 2.5 %, the major crack widened further, accompanied by a sharp drop in lateral load, demonstrating failure characteristics akin to the highly brittle diagonal tension failure observed in beams.

As shown in Fig. 7(b)–(d), the number of diagonal shear cracks in SFC-2.4-100 and SFC-2.4-60 at a 2 % drift ratio decreased sequentially when the spacing of GFRP stirrups in SFC-2.4-150 was reduced from 150 mm to 100 mm and 60 mm. Additionally, reduced GFRP stirrup spacing led to concrete crushing at the ends of the major shear cracks at the base of SFC-2.4-100 and SFC-2.4-60 in the ultimate state (4 % and 4.5 % drift ratio respectively). This suggests that reducing the stirrup spacing modified the shear-flexure failure characteristics of the short columns, thereby improving the specimens' ductility.

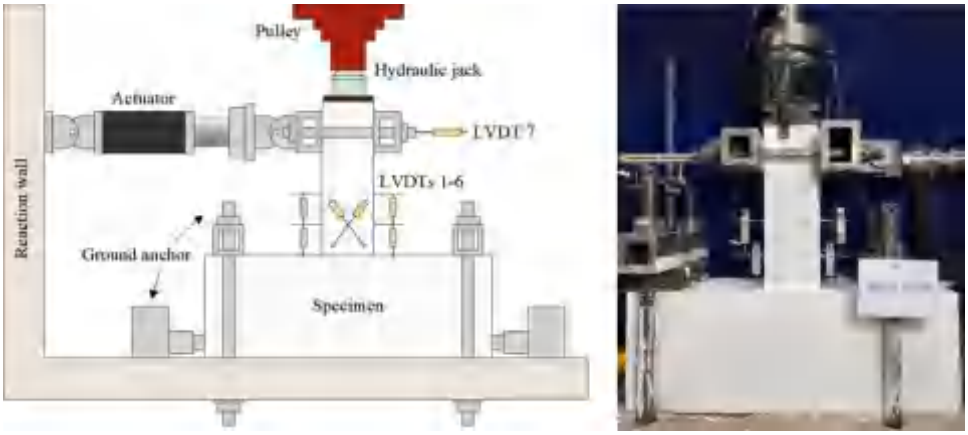


Fig. 4. Test setup.

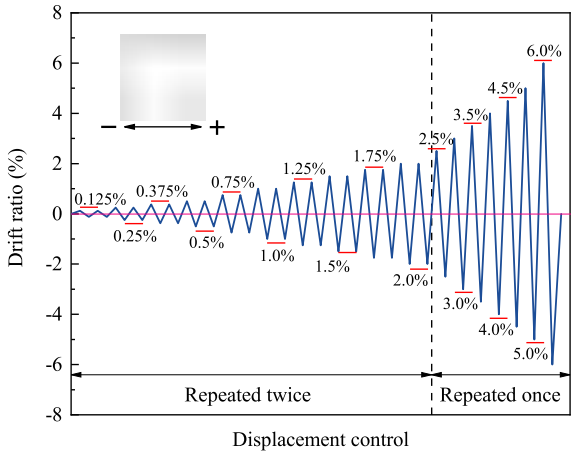


Fig. 5. Lateral loading procedure.

The effect of the shear span-to-depth ratio on the failure pattern is shown in Fig. 7(b), (e), and (f). At a 2 % drift ratio, SFC-2.0-150 had the highest number of diagonal cracks, with inclination angles exceeding 60°. In comparison, the shear crack inclination angles on the surfaces of SFC-2.4-150 and SFC-3.0-150 were smaller, while the number of horizontal flexural cracks increased significantly. This phenomenon is attributed to the larger shear span-to-depth ratios of these two specimens, which amplify the influence of bending moments on their performance. Moreover, the drift ratio corresponding to the ultimate state of SFC-2.0-150 is observed to be greater than that of SFC-2.4-150 and SFC-3.0-150. This is primarily due to its smaller shear span-to-depth ratio, which enhances arch action, increases shear capacity, and delays specimen failure. Further details are discussed in Section 3.3.

After loading, the concrete cover of the SFCB-reinforced short columns was removed to inspect the damaged state of the longitudinal SFCBs. Since the failure modes of the SFCBs were generally consistent across all specimens, SFC-2.4-100 was selected as a representative example for discussion, as shown in Fig. 8. It can be observed that the longitudinal SFCBs exhibited buckling behavior similar to that of steel bars, even though they experienced fracture and splitting failure. This damage characteristic retains the ductile failure traits of steel-reinforced columns while avoiding the brittle failure typically associated with FRP bar-reinforced members. From the perspective of failure modes, this further confirms the feasibility of using SFCBs as a substitute for steel bars in short concrete column applications.

3.2. *Hysteretic curves*

The hysteresis curves of each specimen are depicted in Fig. 9. It is evident that the pinching effect in the hysteresis curve of the SFCB-reinforced short column SFC-2.4-150 is more pronounced than that of the steel-reinforced short column RC-2.4-150. This indicates that the application of SFCBs positively reduces the residual deformation of the columns but adversely affects their energy dissipation capacity. This phenomenon is similar to the behavior of SFCB-reinforced slender columns governed by flexural failure [13,

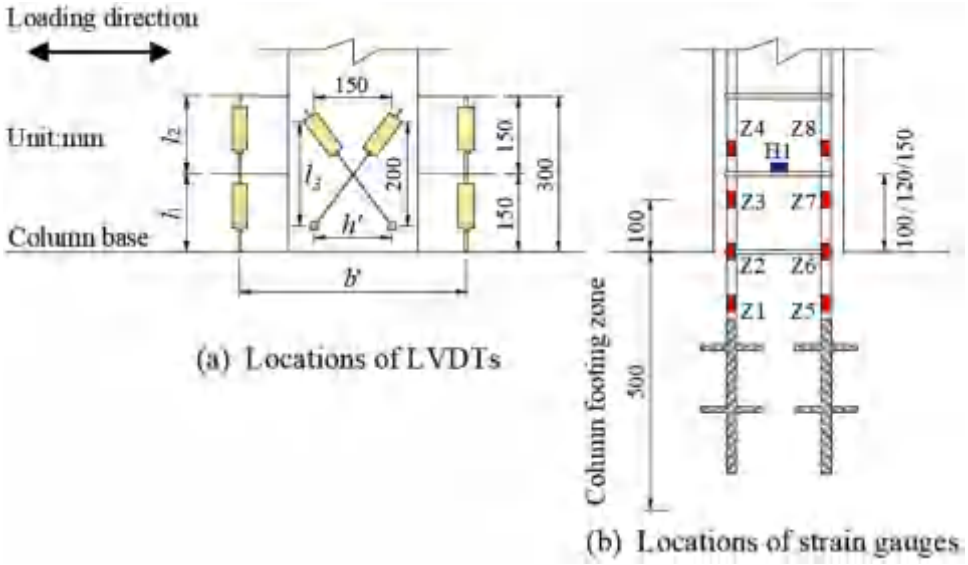


Fig. 6. Layout of LVDTs and strain gauges.

19]. With an reduce in the stirrup spacing, the ductility of SFC-2.4-100 and SFC-2.4-60 improves significantly compared to that of SFC-2.4-150, resulting in a noticeably higher number of hysteresis loops for these two specimens. In addition, the lateral load-bearing capacity and initial stiffness of the short columns decrease markedly as the shear span-to-depth ratio increases. Consequently, the hysteresis loops of SFC-2.4-150 and SFC-3.0-150 exhibit progressively greater inclination compared to the hysteresis loop of SFC-2.0-150.

The hysteresis curves of all columns can be divided into four stages based on four characteristic points: the intact state before the cracking point (Δ_c, V_c), the elastic stage before the yielding point (Δ_y, V_y), the elastoplastic stage between the yielding point and the peak point (Δ_p, V_p), and the softening stage from the peak point to the ultimate point (Δ_u, V_u). The yielding point is determined using the equal energy method [34], and the ultimate load V_u is defined as $0.85V_p$. The lateral displacement and load data corresponding to these characteristic points of each specimen are summarized in Table 3. The influence of various design parameters on the seismic performance of the specimens will be analyzed by comparing these characteristic values and the skeleton curves in the following section.

3.3. Skeleton curves

The comparison of the skeleton curves for the specimens is presented in Fig. 10. The curves for the SFCB specimen SFC-2.4-150 and the steel bar specimen RC-2.4-150 nearly overlap before the cracking point, and this consistency persists up to the yielding point in the positive loading direction (Fig. 10(a)). Thus, it can be concluded that the performance of these two specimens is identical before reaching the service limit state. This observation suggests that the equal-stiffness design method for SFCBs and steel bars is also applicable to short columns governed by shear-flexure failure. Compared to RC-2.4-150, the skeleton curve of SFC-2.4-150 is noticeably higher after the yielding point, with this effect being particularly pronounced in the positive loading direction. The average peak load and peak displacement increased by 7.8 % and 88.1 %, respectively. The substantial improvement in peak displacement reflects the enhanced resilience of the column, a key characteristic of SFCB-reinforced members. This improvement is primarily attributed to the external FRP fibers of the SFCB, which continue to bear the load after the inner steel core yields, significantly enhancing the specimen's post-yield performance. Moreover, the average ultimate displacement of SFC-2.4-150 reaches 16.4 mm, surpassing the 14.8 mm of RC-2.4-150. The experimental results demonstrate that SFC-2.4-150 exhibits performance comparable to that of RC-2.4-150 during the normal service stage, while offering increased safety margins. Therefore, in practical applications, SFCBs can be used as a replacement for steel bars based on the equal-stiffness design principle. According to the market prices provided by the manufacturer, the cost of steel bars is approximately ¥4000/ton, while that of GFRP bars is ¥16,000/ton. Based on this, the unit price of S16 is calculated as ¥6.31/m, and that of SF22-14 as ¥12.06/m. Compared with conventional steel bars, the cost of SFCBs increases by approximately 91 % to achieve the equal-stiffness design. This trade-off results in significantly improved mechanical performance and durability, which is particularly beneficial for critical infrastructure in harsh environments, as it can substantially reduce long-term maintenance costs. In terms of construction practices, the FRP layer cannot be hot-bent or welded, making on-site adjustments less flexible compared to conventional steel bars. As a result, factory prefabrication or specialized cutting equipment is required, which reduces construction adaptability. Therefore, the use of prefabricated SFCB components represents a promising development direction and will be the focus of future research.

Reducing the stirrup spacing has minimal impact on the initial stiffness of SFCB-reinforced short columns but significantly delays

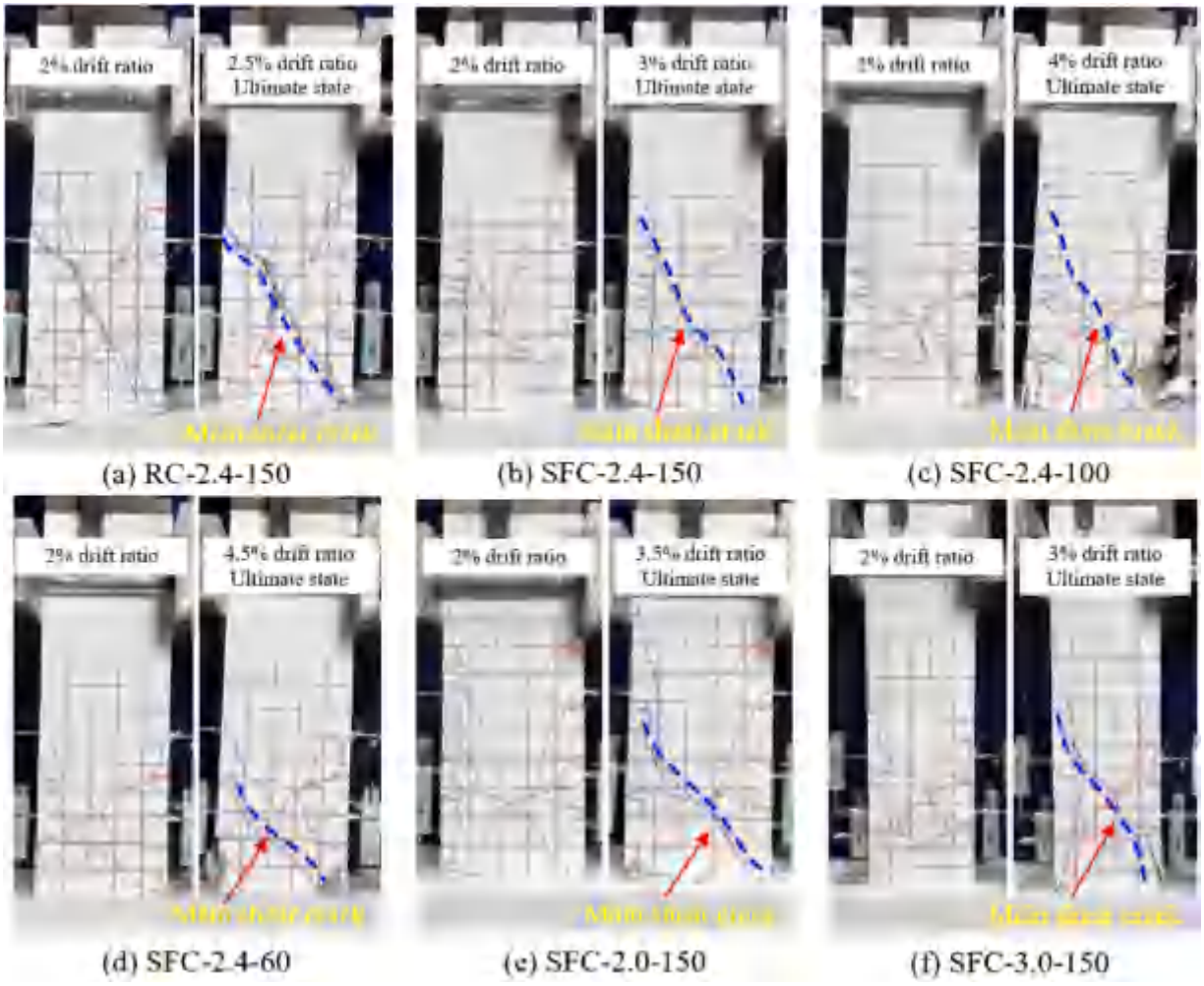


Fig. 7. Failure patterns.



Fig. 8. Damage of longitudinal SFCB.

the cracking process, as shown in Fig. 10(b). Quantitative data in Table 3 indicate that the cracking displacement of SFC-2.4-100 and SFC-2.4-60 is delayed by a 0.125 % drift ratio compared to SFC-2.4-150, with cracking loads increasing by over 20 %. Overall, the skeleton curves of these three specimens are relatively similar, with their yielding and peak points fluctuating within a narrow range. However, the rate of lateral load reduction beyond the peak point decreases with an reduce in stirrup spacing, leading to a notable improvement in ductility. Specifically, the average ultimate displacement of SFC-2.4-100 and SFC-2.4-60 increases by 39.6 % and 57.9 %, respectively, compared to SFC-2.4-150. This phenomenon can be explained by the shear-flexure failure mechanism illustrated in Fig. 11. Shear capacity decreases as lateral displacement increases [35]. If the ultimate point of the test curve appears on the

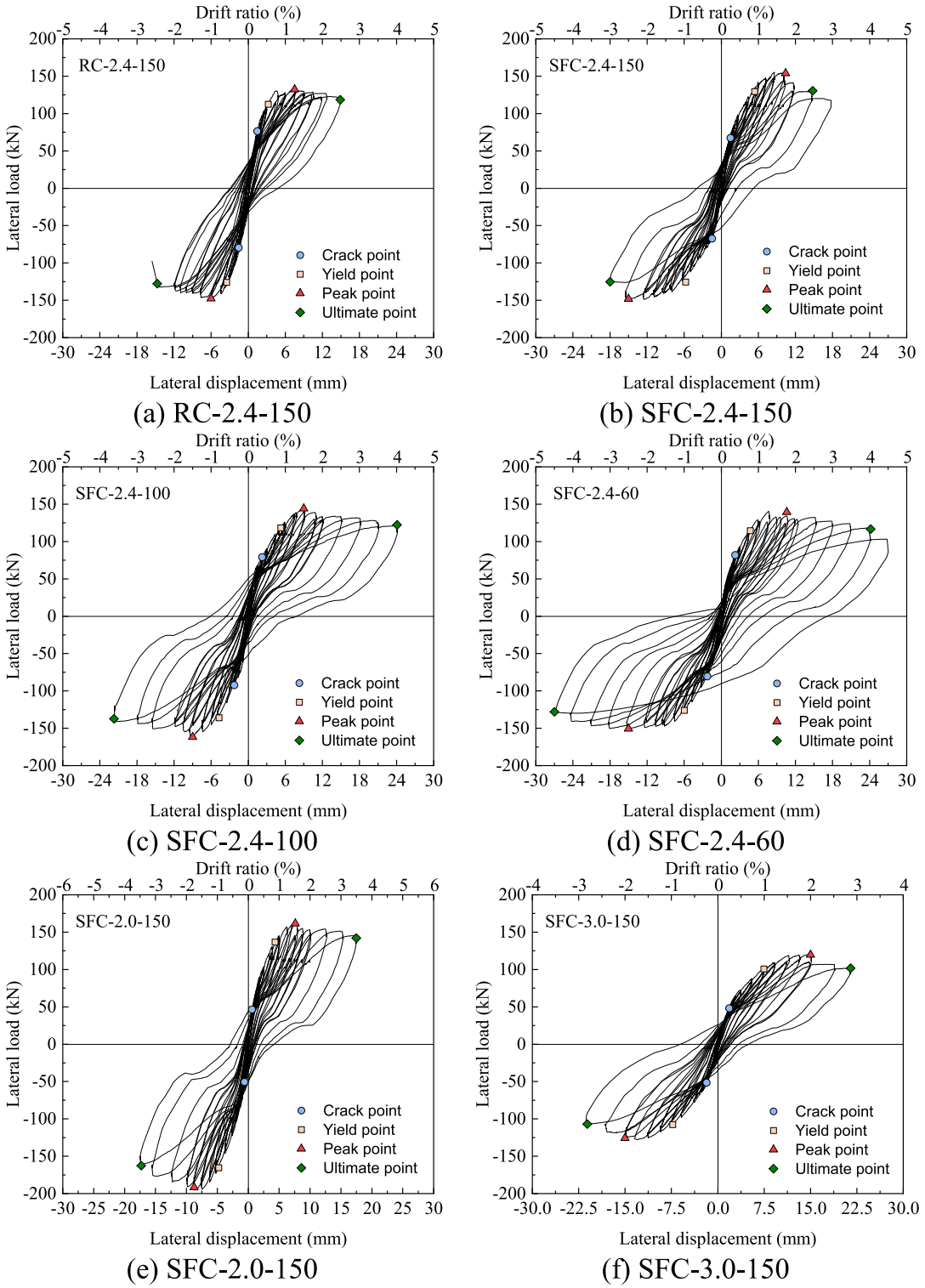


Fig. 9. Hysteresis curves of test columns.

descending branch of the shear capacity envelope, it signifies that the column has reached its maximum flexural strength before shear failure, indicating a shear-flexure failure mode. Conversely, if the ultimate point lies on the beginning segment of the shear envelope, highly brittle shear failure will occur. When the test curve remains below the shear capacity envelope, the column exhibits flexural failure with significant ductility. In this study, reducing the stirrup spacing enhanced the shear capacity of the specimens. For example,

Table 3
Summary of test results.

Specimen	Load direction	Crack point		Yield point		Peak point		Ultimate point	
		Δ_c (mm)	V_c (kN)	Δ_y (mm)	V_y (kN)	Δ_p (mm)	V_p (kN)	Δ_u (mm)	V_u (kN)
RC-2.4-150	+	1.46	76.4	3.24	112.3	7.5	132.4	14.9	118.4
	-	1.54	79.6	3.48	125.9	6	147.8	14.7	127.8
	Average	1.5	78	3.36	119.1	6.75	140.1	14.8	123.1
SFC-2.4-150	+	1.5	67.4	5.41	129.3	10.4	153.8	14.8	130.6
	-	1.5	67.4	5.75	125.5	15	148.2	18	125.2
	Average	1.5	67.4	5.58	127.4	12.7	151	16.4	127.9
SFC-2.4-100	+	2.25	79.1	5.28	118.2	9	144.1	24.1	122.4
	-	2.25	92.3	4.72	136	9	161.7	21.7	137.4
	Average	2.25	85.7	5	127.1	9	152.9	22.9	129.9
SFC-2.4-60	+	2.25	81.8	4.68	114.4	10.6	139.4	24.18	116.8
	-	2.25	80.4	5.98	126	15	150.6	27	128
	Average	2.25	81.1	5.33	120.2	12.8	145	25.59	122.4
SFC-2.0-150	+	0.62	46.5	4.33	136.7	7.61	161.5	17.5	142
	-	0.62	50.5	4.77	165.3	8.75	191.7	17.3	162.6
	Average	0.62	48.5	4.55	151	8.18	176.6	17.4	152.3
SFC-3.0-150	+	1.85	48.1	7.45	100.7	15	119.7	21.5	101.7
	-	1.83	51.5	7.29	107.7	15	125.7	21.3	106.9
	Average	1.84	49.8	7.37	104.2	15	122.7	21.3	104.3

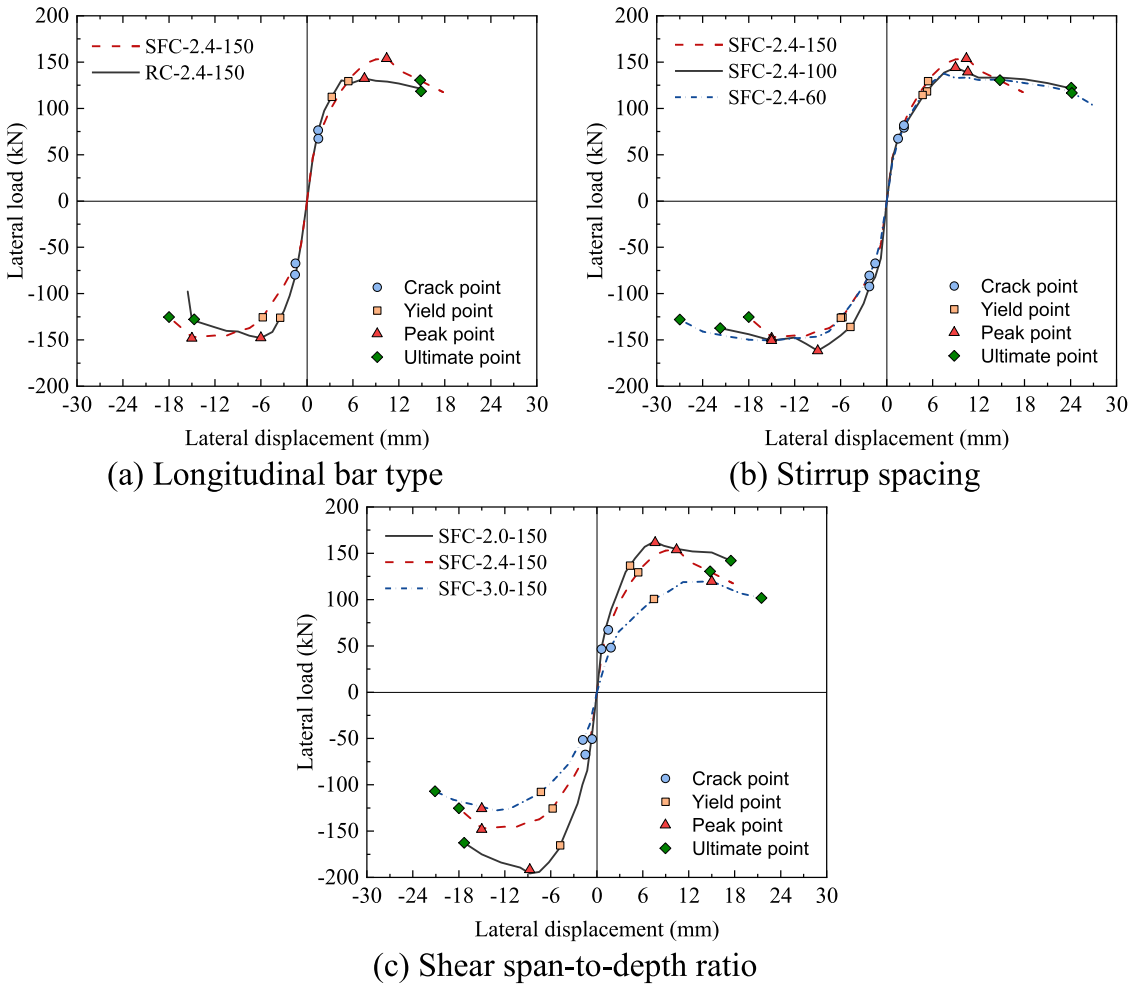


Fig. 10. Skeleton curves.

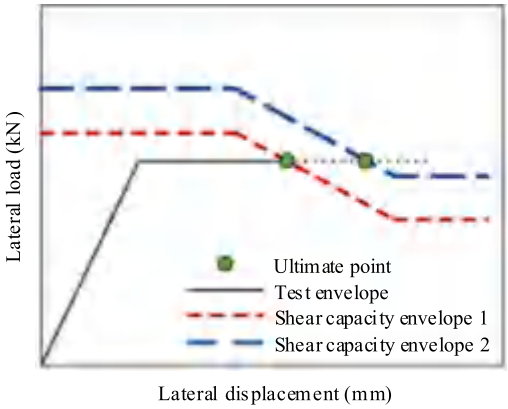


Fig. 11. Mechanism of shear-flexure failure.

reducing the stirrup spacing from 150 mm to 100 mm resulted in shear capacities represented by shear capacity envelopes 1 and 2 in Fig. 11. Consequently, the reduced stirrup spacing significantly improved the ductility performance of the short columns.

The effect of the shear span-to-depth ratio on the skeleton curves of SFCB-reinforced specimens is depicted in Fig. 10(c). The initial stiffness of the specimens decreases significantly as the shear span-to-depth ratio increases, leading to a sequential drop in the overall

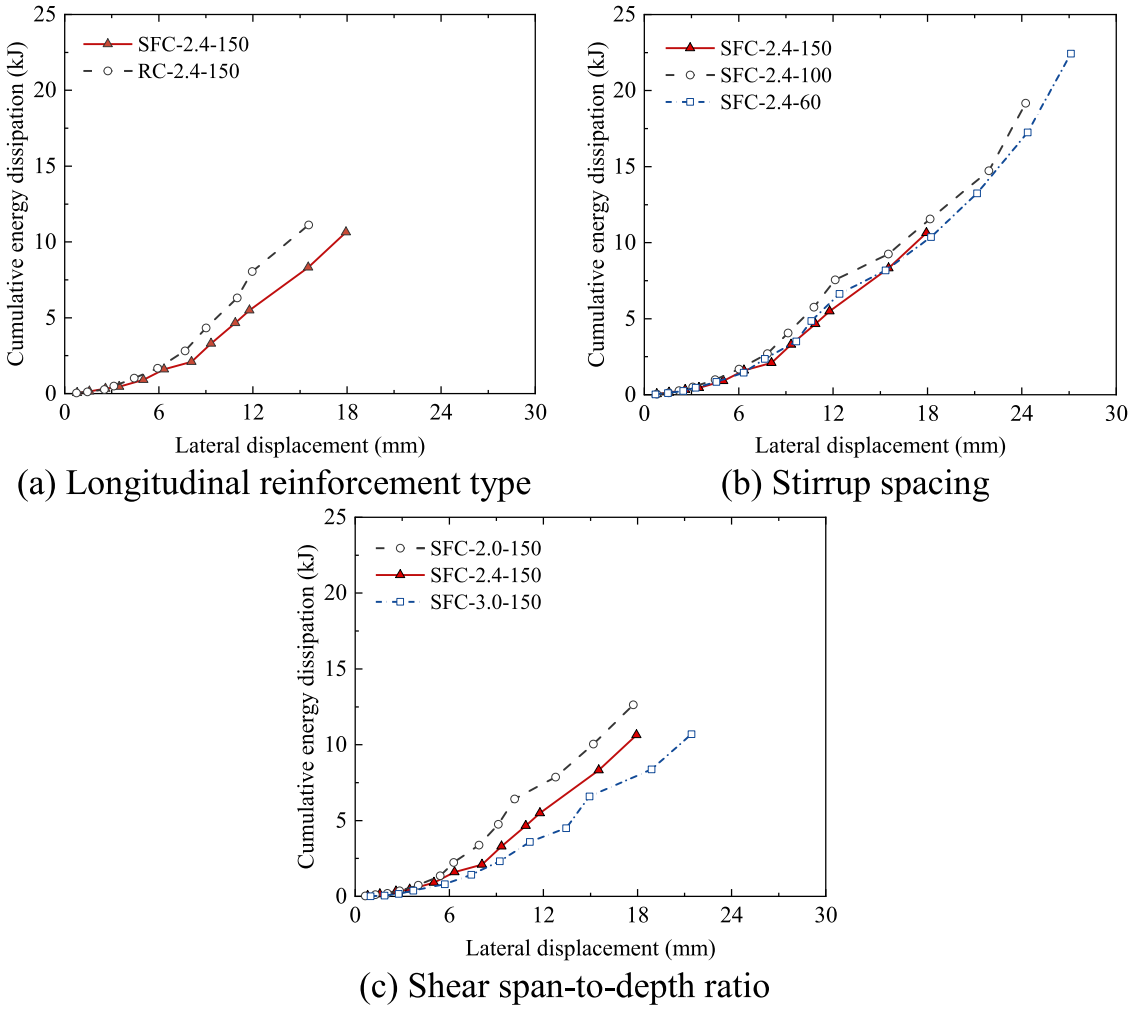


Fig. 12. Energy dissipation.

skeleton curves in the order: SFC-2.0-150 > SFC-2.4-150 > SFC-3.0-150. Specifically, the peak loads of SFC-2.0-150 and SFC-2.4-150 are 43.9 % and 23.1 % higher, respectively, compared to SFC-3.0-150. This result is primarily attributed to the enhanced contribution of the arch mechanism as the shear span-to-depth ratio decreases, which significantly increases the lateral load-bearing capacity. Similar findings were reported in the experiments conducted by Zhang et al. [36] and Dong et al. [37]. Notably, the ultimate drift ratio of SFC-2.0-150 is 38.1 % higher than that of SFC-2.4-150. This increase may be attributed to the enhanced arch mechanism, which places more concrete in a compressive state. This reduces the tensile strain in the longitudinal SFCBs, and thus the specimen's deformation capacity is improved. Similar conclusions were drawn in the study by Li et al. [20], where it was observed that under failure modes dominated by SFCB tensile fracture, increasing the axial load ratio reduced the tensile strain in the longitudinal SFCB, thereby enhancing the ductility of the specimens.

3.4. Energy dissipation

The energy dissipation capacity of each specimen is assessed using cumulative energy dissipation, as shown in Fig. 12. This parameter is calculated as the sum of the areas enclosed by the hysteresis loops at each loading level, showing a steady increase with increasing displacement. Readers may refer to Zhang et al. [19] for further details. Fig. 12(a) compares the energy dissipation capacity of short columns reinforced with steel bars and SFCBs. Before a displacement of 6 mm, RC-2.4-150, and SFC-2.4-150 exhibit similar energy dissipation capacities, as their skeleton curves nearly overlap before the yield point. However, after yielding, the plastic strain of RC-2.4-150 gradually increases, and its hysteresis loops become fuller compared to those of SFC-2.4-150. As a result, under the same loading displacement, RC-2.4-150 exhibits a higher energy dissipation capacity. Nevertheless, SFC-2.4-150 exhibits a larger ultimate displacement compared to RC-2.4-150, resulting in comparable total cumulative energy dissipation capacities of 11.1 kJ and 10.6 kJ, respectively. This suggests that the SFCB-reinforced column enhances seismic resilience without significantly compromising overall energy dissipation capacity, thereby demonstrating its feasibility and advantages for engineering applications.

A smaller stirrup spacing does not significantly enhance the energy dissipation of SFCB-reinforced short columns at the same loading drift, as shown in Fig. 12(b). For instance, at a displacement of 18 mm (the ultimate displacement of SFC-2.4-150), the energy

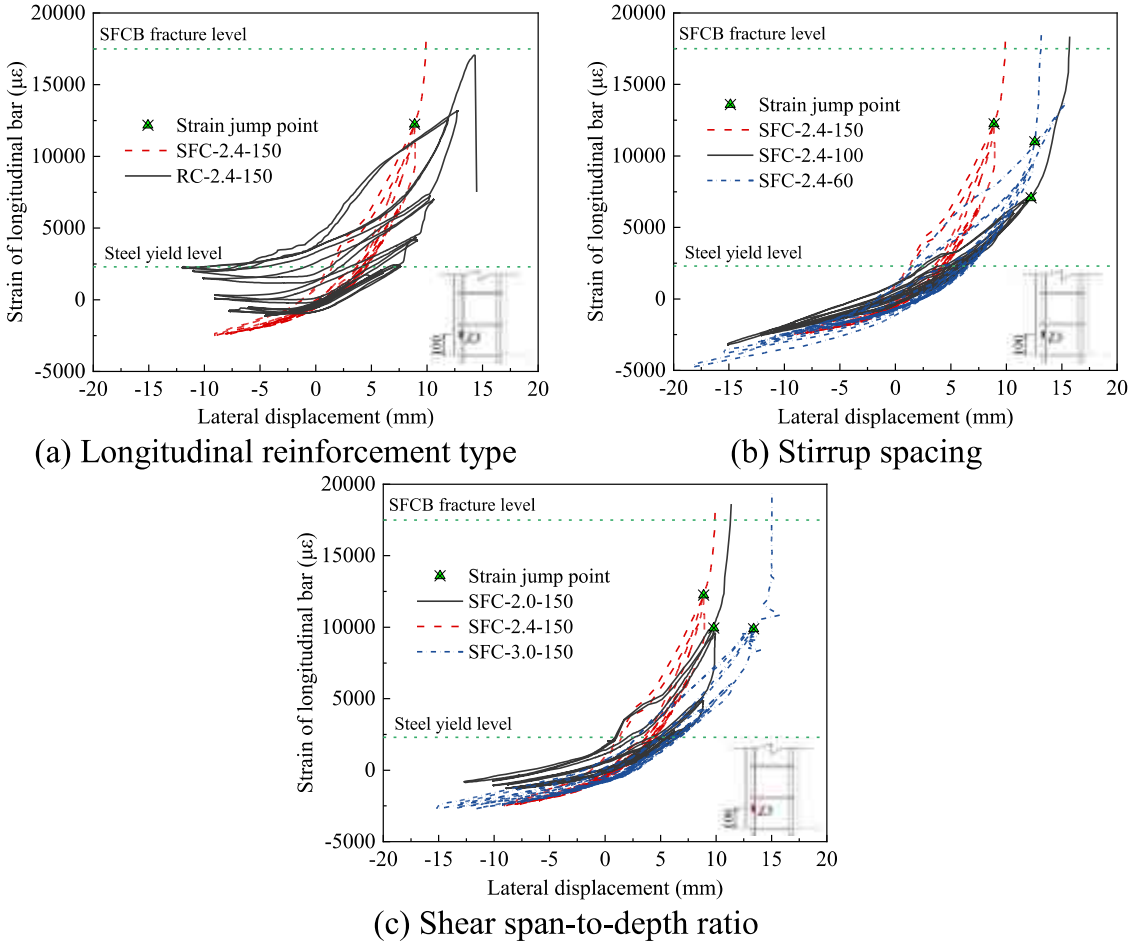


Fig. 13. Strain-displacement response of longitudinal reinforcement.

dissipation differences among SFC-2.4-150, SFC-2.4-100, and SFC-2.4-60 remain within 8.5 %. The improved energy dissipation capacity associated with a smaller stirrup spacing is primarily due to an increase in the ultimate displacement of the test columns, which allows for more hysteresis loops. Fig. 12(c) illustrates that reducing the shear span-to-depth ratio significantly enhances the energy dissipation capacity of the specimens under the same displacement. The energy dissipation capacity of SFC-2.0-150 consistently exceeds that of SFC-2.4-150 and SFC-3.0-150, with the gaps between the curves becoming increasingly pronounced as displacement rises. At a displacement of 18 mm, the energy dissipation capacities of SFC-2.0-150 and SFC-2.4-150 are 58.1 % and 31.5 % higher than that of SFC-3.0-150, respectively. This improvement is attributed to the reduced shear span-to-depth ratio, which increases the initial loading stiffness and the height of the skeleton curve, thereby enhancing energy dissipation during cyclic loading.

3.5. Strain analysis of longitudinal reinforcement

Analyzing the longitudinal reinforcement strain under low-cycle cyclic loading provides deeper insights into the stress state and failure mechanisms of the specimens. This section focuses on the Z3 strain gauge measurements taken at a cross-section located 100 mm above the column base as a representative dataset for analysis. The comparative results are shown in Fig. 13.

From Fig. 13(a), it can be observed that the unloading stiffness of the steel-reinforced short column RC-2.4-150 is significantly lower than its loading stiffness, resulting in much full strain hysteresis loops. In contrast, the unloading stiffness of the SFCB-reinforced short column SFC-2.4-150 shows only a slight reduction compared to its initial stiffness, leading to tighter hysteresis curves. It suggests that the damage to the longitudinal SFCBs is significantly lower than that to the steel bars. This phenomenon explains why the pinching effect in SFC-2.4-150 is more pronounced than in RC-2.4-150. As the stirrup spacing reduces, the fracture of the external GFRP fibers in the longitudinal SFCBs is significantly delayed, as shown in Fig. 13(b). For SFC-2.4-100, the strain jump point occurs at a 2 % drift ratio, whereas for SFC-2.4-60, the strain jump point appears only after reaching the maximum drift ratio of 2.5 % and reloading back to approximately 2 %. These experimental results confirm the reason for the largest ultimate displacement observed in SFC-2.4-60, which is attributed to the latest occurrence of fracture failure in its longitudinal SFCBs. Similarly, the strain jump points in the longitudinal

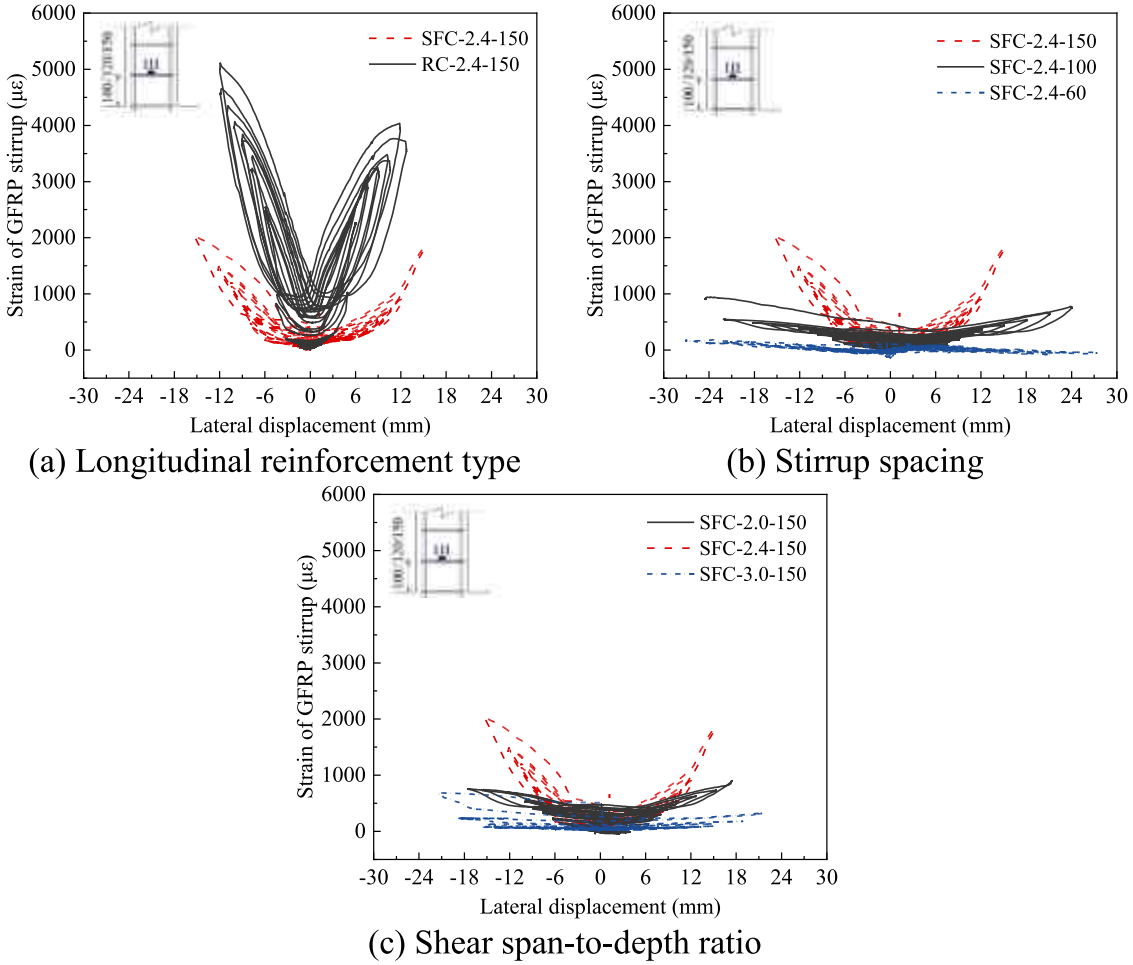


Fig. 14. Strain-displacement response of GFRP stirrup.

SFCBs of SFC-2.0-150 and SFC-3.0-150 occur at larger displacements compared to SFC-2.4-150, as shown in Fig. 13(c). This observation aligns with the comparison of skeleton curves, where SFC-2.4-150 demonstrates the smallest ultimate displacement. The strain analysis of longitudinal SFCB confirms that the failure of the SFCB-reinforced short columns is primarily governed by the tensile fracture of the SFCB. Reducing the shear span-to-depth ratio enhances the arch mechanism of the concrete in short columns, effectively suppressing the rapid increase in longitudinal reinforcement strain. This effect is particularly evident in the later stages of loading, where the longitudinal strain of SFC-2.0-150 is lower than that of SFC-2.4-150 at the same loading displacement. This observation provides quantitative support for the analysis in Section 3.3 regarding the influence of the shear span-to-depth ratio on ultimate displacement.

3.6. Strain analysis of GFRP stirrup

The transverse strain of GFRP stirrups offers valuable insight into the deformation of the core concrete, thereby reflecting the extent of damage in the specimens. Details regarding the arrangement of the stirrup strain gauge H1 are provided in Section 2.3. A comparison of the stirrup strains for the specimens is presented in Fig. 14.

The GFRP stirrup strain of RC-2.4-150 is significantly higher than that of SFC-2.4-150 at the same displacement, as depicted in Fig. 14(a). This indicates that the steel-reinforced short column experiences considerably more severe damage than the SFCB-reinforced short column. The reason lies in the behavior of the longitudinal reinforcement: after yielding, steel bars cannot effectively sustain further loading, whereas SFCBs, with their external FRP fibers, can continue to bear load beyond yielding. This characteristic reduces concrete deformation and slows damage progression, allowing SFCB-reinforced short columns to demonstrate superior damage control capability. Fig. 14(b) illustrates that variations in the stirrup spacing result in distinct stratification of stirrup strain responses. Smaller stirrup spacing correspond to lower stirrup strains at the same displacement. This is attributed to the improved confinement effect and enhanced shear capacity, which effectively suppresses concrete deformation progression. The effect

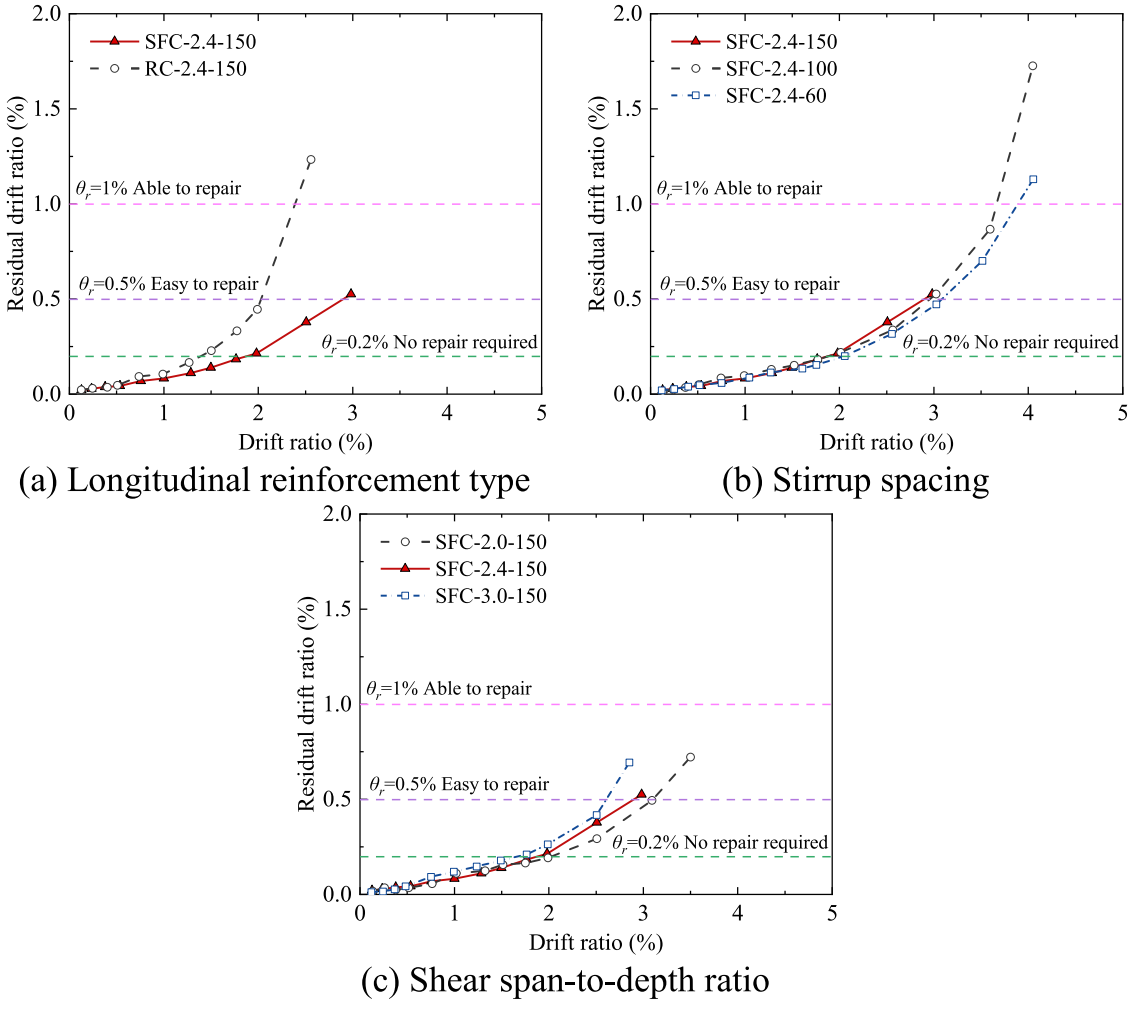


Fig. 15. Residual deformation.

of the shear span-to-depth ratio on GFRP stirrup strain is consistent with the results observed for longitudinal reinforcement strain, as shown in Fig. 14(c). The stirrup strain of SFC-2.4-150 is higher than that of SFC-2.0-150 and SFC-3.0-150, indicating a greater degree of damage in SFC-2.4-150, which results in an earlier ultimate point. These strain test results clearly explain why SFC-2.4-150 exhibits relatively poorer seismic performance compared to the other SFCB specimens.

3.7. Residual deformation

The residual deformation evaluation results categorized by test variables are shown in Fig. 15. A 0.2 % drift ratio corresponds to "no repair required", 0.5 % to "easy to repair", and 1 % to "able to repair". Readers may refer to Zhang et al. [19] for further resilience assessment details.

Fig. 15(a) shows that the residual drift ratio of the specimen RC-2.4-150 is similar to that of SFC-2.4-150 up to the 1 % drift ratio (near the peak point of RC-2.4-150). However, beyond this point, the residual deformation of RC-2.4-150 becomes significantly higher than that of SFC-2.4-150. This can be attributed to the fact that, before the peak, the plastic strain in the steel bars of RC-2.4-150 did not develop significantly, resulting in residual deformation similar to that of SFC-2.4-150. After the peak, the plastic strain in the steel bars of RC-2.4-150 developed extensively, while the external linear-elastic GFRP layer of the SFCB suppressed plastic strain development in its steel core, leading to a greater difference in residual deformation between the two specimens. SFC-2.4-150 remained in a repairable state throughout the pre-ultimate stage, whereas RC-2.4-150 exceeded the maximum repairable limit (1 % residual drift ratio) at an earlier stage. This result underscores the advantages of replacing steel bars with SFCBs in enhancing structural resilience. It demonstrates that SFCB-reinforced columns experience lower repair difficulty after earthquakes, thereby contributing to improved cost-efficiency over the structure's lifecycle.

Fig. 15(b) illustrates that the curves of SFC-2.4-150, SFC-2.4-100, and SFC-2.4-60 are relatively similar, remaining below the "no repair required" level up to a 2 % drift ratio. At the ultimate drift ratio (3 %) of SFC-2.4-150, the residual deformation difference

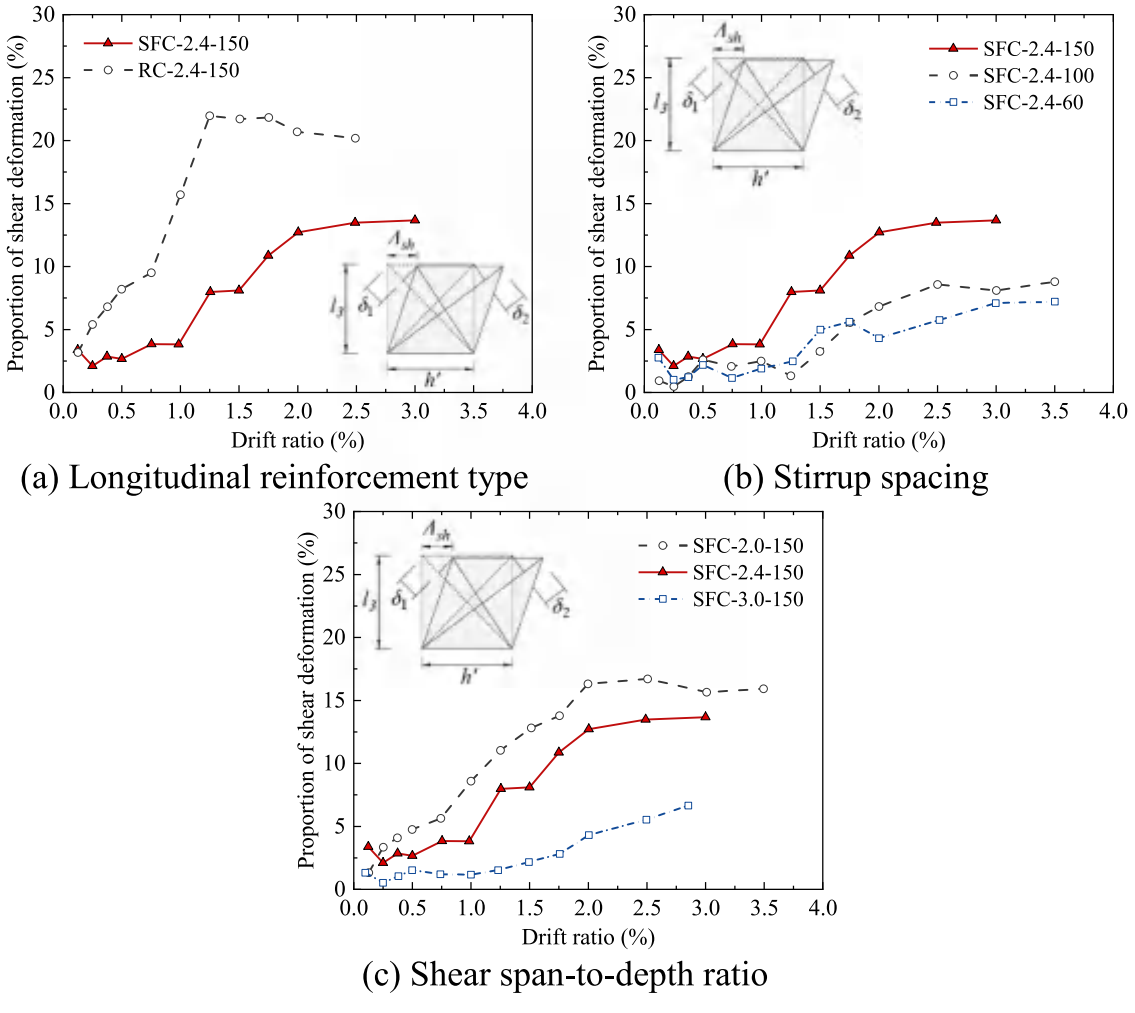


Fig. 16. Proportion of shear deformation.

between SFC-2.4-150 and SFC-2.4-60 is only 1.9 %. This suggests that variations in stirrup spacing have a minimal impact on the resilience of SFCB-reinforced columns. Ensuring compliance with construction requirements during design is sufficient to achieve stable resilience performance. The effect of the shear span-to-depth ratio on resilience is shown in Fig. 15(c). The curves of SFC-2.0-150, SFC-2.4-150, and SFC-3.0-150 are also relatively close, but the gaps between them are slightly larger compared to the stirrup spacing group. In general, a smaller shear span-to-depth ratio results in lower residual deformation. This occurs because, at the same drift ratio, specimens with larger shear span-to-depth ratios experience greater displacements. The non-uniformity of concrete amplifies this effect, making it more susceptible to excessive local deformation and thereby increasing the column's residual deformation.

3.8. Shear deformation

The shear deformation was measured using two LVDTs arranged diagonally in a cross pattern at the bottom region of the column (Fig. 6(a)). The calculation formula is as follows:

$$\Delta_{sh} = \frac{(\delta_1 - \delta_2)\sqrt{l_3^2 + h'^2}}{2h'} \tag{1}$$

where δ_1 and δ_2 represent the compression and elongation measured by the two diagonal LVDTs, respectively; l_3 is the vertical distance from the center of each LVDT to the bottom measurement point; and h' is the horizontal distance between the centers of these two LVDTs.

The proportion of shear deformation to total lateral displacement for the test columns at each loading level is shown in Fig. 16. It should be noted that, since the LVDTs were arranged only in the bottom region of the column rather than along the entire column height, the measured shear deformation does not represent the total shear deformation of the specimens. Nevertheless, the measured values still provide a reflection of the degree of shear deformation in the specimens. Fig. 16(a) reveals that the proportion of shear deformation in the steel-reinforced concrete column is significantly higher than that in the SFCB-reinforced concrete column under the same drift ratio. At a 1.25 % drift ratio, the shear deformation proportion of RC-2.4-150 is 2.75 times that of SFC-2.4-150. This may be attributed to the weaker bond performance between the SFCB and concrete compared to that of steel bar and concrete, resulting in increased slip in SFC-2.4-150. This increased slip induces greater rigid-body rotation, thereby reducing the influence of shear effects.

Fig. 16(b) shows that the shear deformation proportion of SFC-2.4-100 is significantly lower than that of SFC-2.4-150, attributed to the enhanced shear capacity. However, further reducing the stirrup spacing has a limited effect on improving shear capacity. For example, the shear deformation proportion of SFC-2.4-60 is only 9.6 % lower than that of SFC-2.4-100 at a 3 % drift ratio. As the shear span-to-depth ratio increases, the flexural effect becomes more pronounced, while the shear effect diminishes, resulting in a decreased proportion of shear deformation, as shown in Fig. 16(c). At a 3 % drift ratio, the shear deformation proportion of SFC-2.4-150 and SFC-3.0-150 decreased by 12.7 % and 57.3 %, respectively, compared to SFC-2.0-150. Moreover, the failure phenomena presented in Section 3.1 also support these observations. The major shear cracks in RC-2.4-150 were significantly larger than those in the SFCB specimens. With the reduce in stirrup spacing and the increase in shear span-to-depth ratio, the SFCB specimens showed a trend of reduced diagonal cracks or the emergence of more horizontal flexure cracks. Notably, the shear deformation proportion of the steel-reinforced column exceeded 20 %, while it ranged between 5 % and 15 % for the SFCB specimens. Therefore, neglecting shear deformation when predicting the load-displacement response of these short columns would reduce calculation accuracy. The impact of

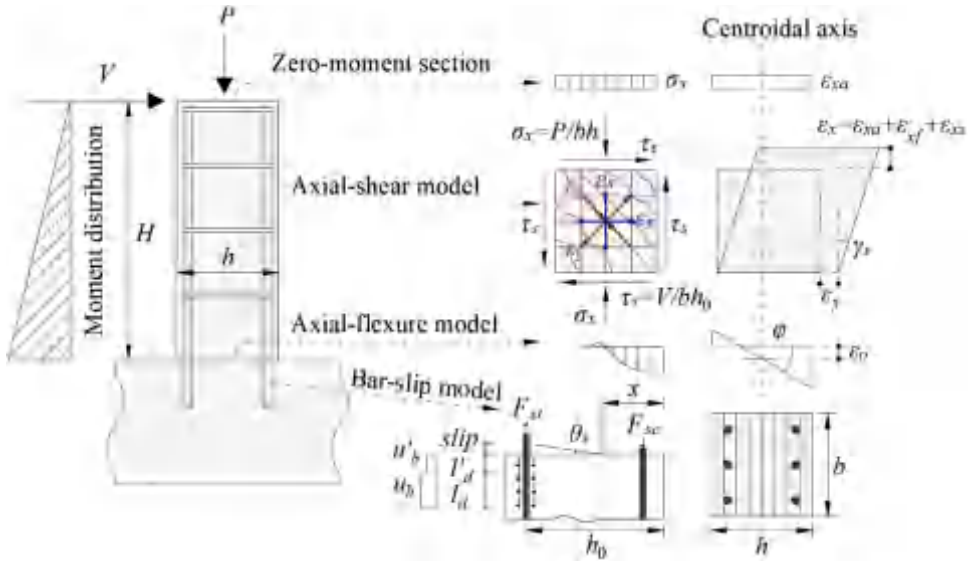


Fig. 17. The USFM method.

ignoring shear deformation will be discussed in Section 4.3.

4. Analytical model of envelope curves

4.1. USFM approach

The accurate prediction of the load-displacement response is crucial for the reasonable design of columns. Through a quantitative analysis of the uniform bond stress of SFCB, the author's research group successfully developed an axial-flexure model that accounts for SFCB slip to calculate the full load-displacement curves of SFCB-reinforced columns [19]. However, this approach neglects shear response, making it unsuitable for columns dominated by shear or shear-flexure behavior. Therefore, this section will adopt the uniaxial-shear-flexure model (USFM) proposed by Mostafaei and Vecchio [29] to incorporate shear effects, further extending the model developed by the author's research group to account for the interaction of axial-shear-flexure, as shown in Fig. 17. The beauty of the USFM method lies in simplifying the axial-shear model based on Modified Concrete Field Theory (MCFT) [38], effectively eliminating the iterative process required in the traditional axial-shear-flexure interaction method [39]. The interaction of axial-shear-flexure is captured through concrete softening and axial deformation. The concrete strength softening factor β is calculated as:

$$\beta = \frac{1}{0.8 + 170\varepsilon_1} \tag{2}$$

where ε_1 is the average principal tensile strain obtained from the axial-shear model.

The total axial strain ε_x considered in the USFM method results from the combined effects of axial, shear, and flexure:

$$\varepsilon_x = \varepsilon_{xa} + \varepsilon_{xs} + \varepsilon_{xf} \tag{3}$$

where ε_{xa}, ε_{xs}, and ε_{xf} represent the axial strain due to axial load, shear mechanism, and flexural mechanism, respectively.

The primary assumption of the USFM is the simplification of the shear model from a biaxial shear element approach to a uniaxial analytical concept, as follows:

$$\varepsilon_2 = 0.5\left(\varepsilon_{2_i} + \varepsilon_{2_{i+1}}\right) \tag{4}$$

where ε_2 represents the average principal compression strain for an element between two sections, i and $i+1$. ε_{2i} and ε_{2i+1} are the uniaxial compression strains corresponding to the resultant forces of the concrete stress blocks at sections i and $i+1$, respectively.

The second assumption of the USFM is the definition of the average axial strain at the centroid:

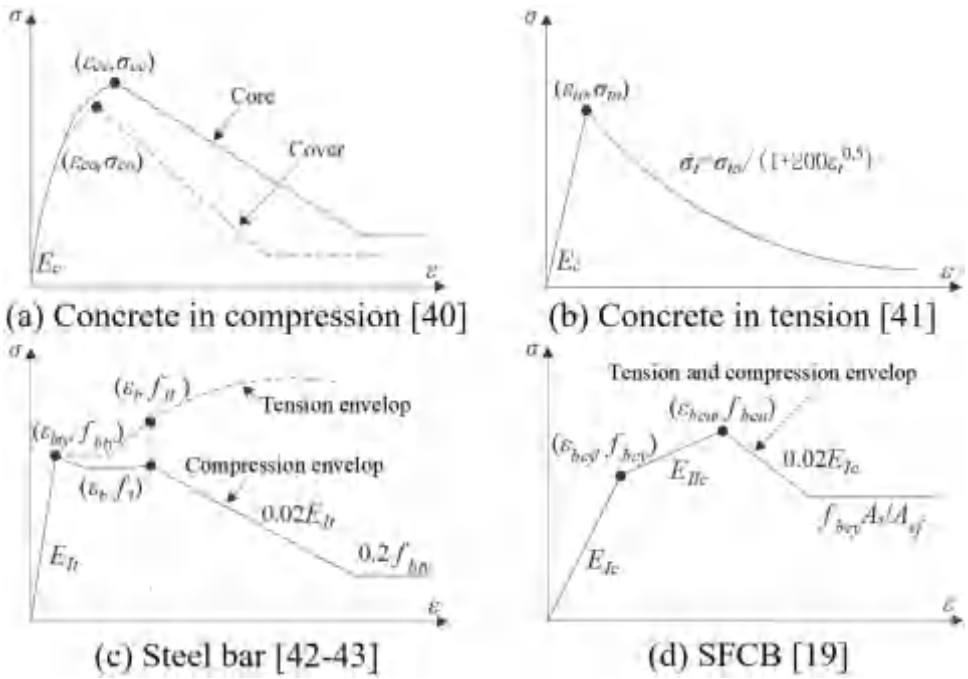


Fig. 18. Stress-strain models of materials [19,40-43].

$$\varepsilon_x = 0.5\left(\varepsilon_{x_i} + \varepsilon_{x_{i+1}}\right) \tag{5}$$

where ε_{xi} and ε_{xi+1} are the axial strains on the centroid of sections i and $i+1$, respectively.

To satisfy the equilibrium conditions, the shear force V and axial load P at each analysis step in both the axial-shear model and the axial-flexure model must be equal. The shear stress τ_s and axial stress σ_x can be calculated as follows:

$$\tau_s = \frac{V}{bh_0} \tag{6}$$

$$\sigma_x = \frac{P}{bh} \tag{7}$$

where b and h denote the section width and depth. h_0 is the effective section depth.

4.2. Material models

The material models for concrete, steel bars, and SFCBs under both tension and compression are depicted in Fig. 18. These relationships are used in sectional analysis to simulate the axial-shear response in the USFM. The concrete compression response is represented by the modified Kent-Park model [40], while the concrete tensile behavior is modeled using the Collin et al. model [41], which considers tensile softening. The tensile and compressive behaviors of steel bars are modeled using the method of Chang and

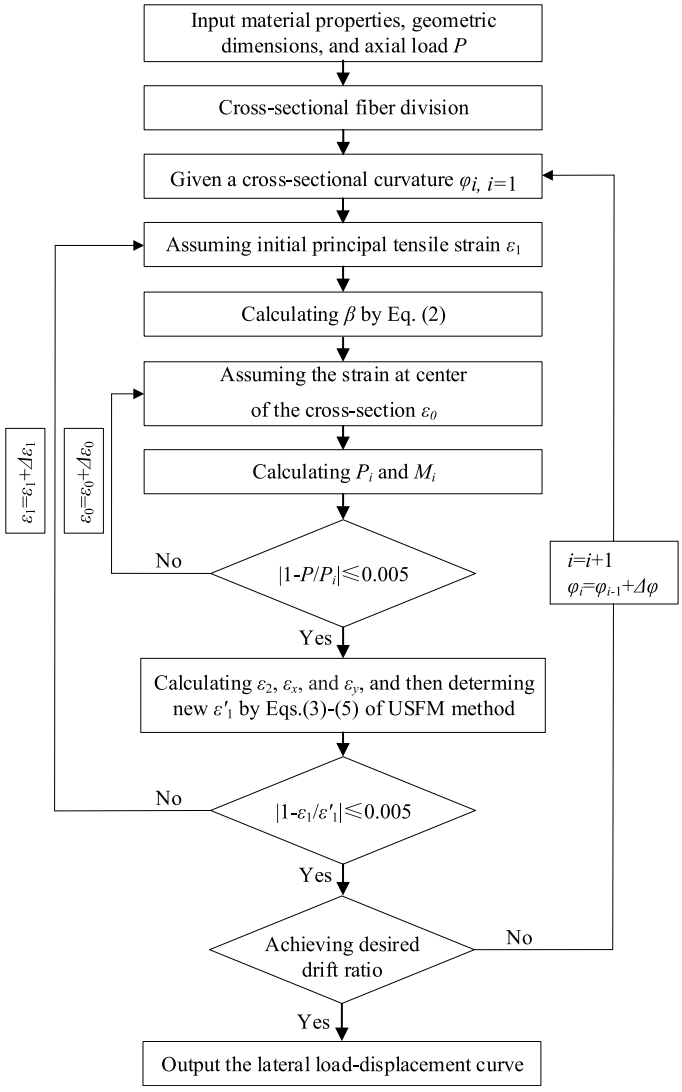


Fig. 19. Flowchart of USFM for lateral load-displacement curves.

Mander [42] and Dhakal and Maekawa [43], respectively. The stress-strain relationship of SFCB is based on a fitted test curve, similar to that of Zhang et al. [19]. Since the specimens in this study are governed by tensile fracture failure of SFCB, an average experimental tensile fracture strain of 1.71 % is used as the ultimate tensile strain for SFCB.

4.3. Deformation calculation

The lateral displacement at the top of the test column consists of flexural deformation Δ_f, pullout deformation Δ_{pul}, and shear deformation Δ_{sh}.

$$\Delta = \Delta_f + \Delta_{pul} + \Delta_{sh} \tag{8}$$

The flexural deformation Δ_f is primarily caused by rotation in the plastic hinge zone of the column:

$$\Delta_f = \begin{cases} \dfrac{\varphi H^2}{3} \varepsilon_b \le \varepsilon_{by} \\ \dfrac{\varphi_y H^2}{3} + (\varphi - \varphi_y) L_p \left(H - \dfrac{L_p}{2} \right) \varepsilon_b > \varepsilon_{by} \end{cases} \tag{9}$$

where φ and φ_y are the section curvature and yielding section curvature, respectively. L_p represents the length of the plastic hinge zone. Following the recommendations of Zhang et al. [19], for RC-2.4-150, $L_p = 0.5\,h$, and other SFCB-reinforced columns, $L_p = 0.6\,h$.

The pullout deformation Δ_{pul} is caused by rigid rotation due to strain penetration and can be calculated using the following equation:

$$\Delta_{pul} = \begin{cases} \dfrac{\varepsilon_b f_b d_b H}{8 u_b (h_0 - x)} \varepsilon_b \le \varepsilon_{by} \\ \dfrac{\varepsilon_{by} f_{by} d_b H}{8 u_b (h_0 - x)} + \dfrac{d_b H}{8 u'_b (h_0 - x)} \left(\varepsilon_b + \varepsilon_{by} \right) \left(f_b - f_{by} \right) \varepsilon_b > \varepsilon_{by} \end{cases} \tag{10}$$

where ε_b and f_b are the longitudinal bar's tensile strain and stress. ε_{by} and f_{by} correspond to the yielding stress and strain, d_b is the longitudinal bar diameter, and x is the depth of compression area. Sezen and Setzler [44] suggest that the average bond stress u'_b can be considered as half of the u_b. According to the study by Zhang et al. [19], the average bond stresses u_b of steel bars and SFCBs are $0.92\sqrt{\sigma_{co}}$ and $0.23\sqrt{\sigma_{co}}$, respectively.

After determining the average principal compression strain ε_2 and average axial strain ε_x at the centroid for each loading step using the USFM method, the shear strain γ_s, and shear deformation Δ_{sh} can be calculated using the following equations:

$$\gamma_s = \frac{2(\varepsilon_x - \varepsilon_2)}{\tan \theta_{cr}} \tag{11}$$

$$\Delta_{sh} = \gamma_s H \tag{12}$$

where θ_{cr} is the crack angle.

The flowchart for predicting the full lateral load-displacement curves of the test short concrete columns is presented in Fig. 19. The experimental skeleton curves for each specimen, along with the predicted curves considering and neglecting shear deformation, are plotted in Fig. 20 for comparison. The initial stiffness of all specimens is overestimated when shear deformation is neglected. This leads to excessive deformation during practical application, which exceeds design expectations and affects the structure's normal operation. Since shear deformation is most significant in the steel-reinforced short column, neglecting the shear effect has the greatest impact on RC-2.4-150. Without considering shear deformation, the secant stiffness of RC-2.4-150 from the initial point to the peak is 36.8 kN/mm, 37.3 % higher than the experimental average value of 26.8 kN/mm. After accounting for shear deformation, the difference between the predicted and experimental values is reduced to just 8.1 %.

The scales of the predicted results to the experimental average results for SFCB-reinforced short columns range from 0.95 to 1.99, with an average of 1.16 and a variable coefficient of 0.19 when shear effects are neglected. When shear deformation is considered, the scales are 0.94–1.32, with an average of 1.07 and a variable coefficient of 0.08. It demonstrates a significant improvement in prediction accuracy for short columns after accounting for shear effects. Therefore, the proposed model can predict the full load-displacement curves of SFCB-reinforced short concrete columns with satisfactory accuracy.

5. Conclusions

This research investigated the seismic behavior of SFCB-reinforced short concrete columns through low-cycle cyclic loading. The following conclusions can be drawn based on the analysis of the results:

(1) Under shear-flexure failure mode, the SFCB-reinforced short column with an equal stiffness design method exhibits less damage than the steel-reinforced short column. Reducing the stirrup spacing alters the shear-flexure failure characteristics of SFCB-reinforced columns, reducing the number of diagonal cracks and leading to concrete crushing at the column base. As the

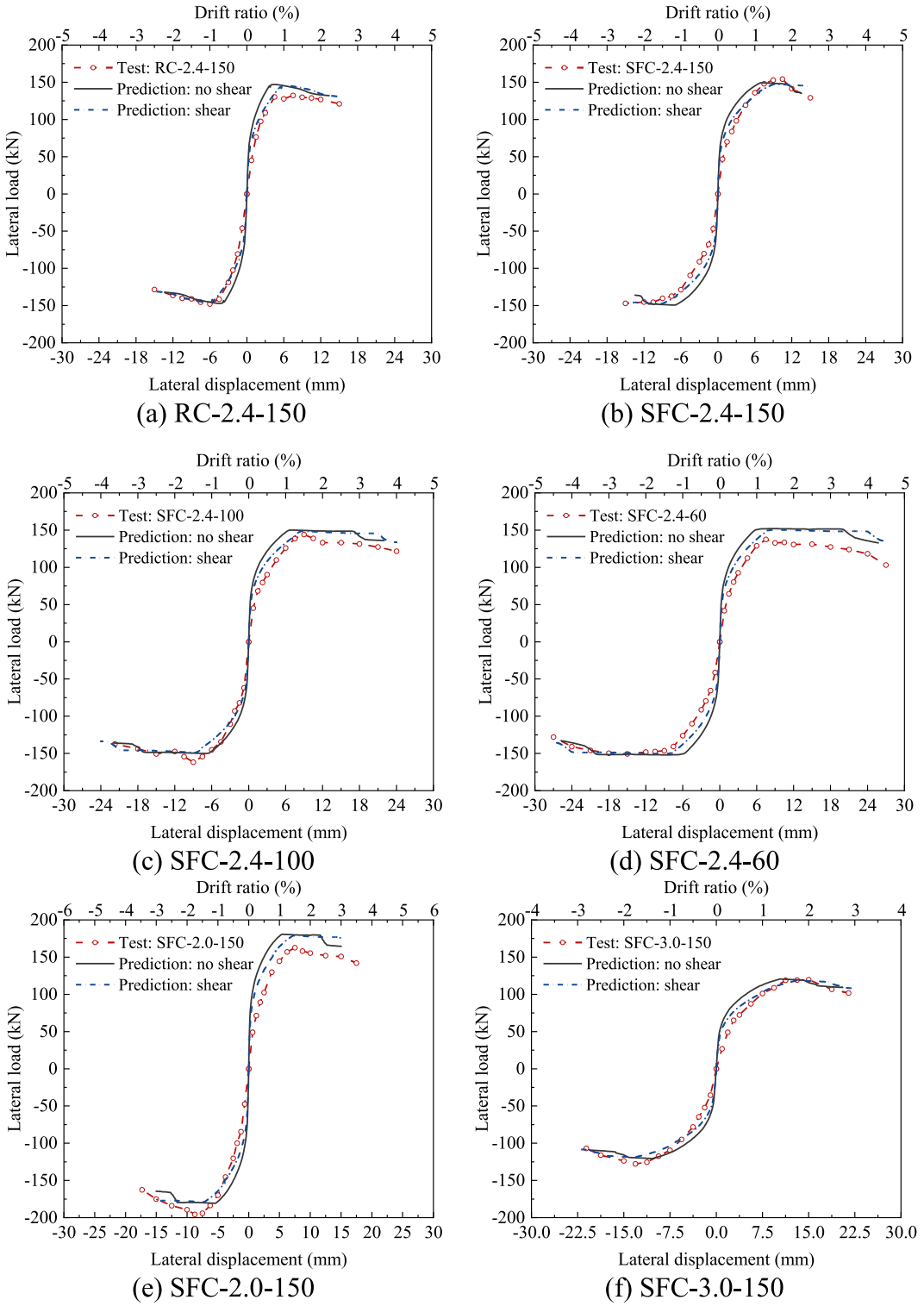


Fig. 20. Comparison of experimental and predicted envelope curves.

shear span-to-depth ratio increases, the shear failure characteristics of SFCB-reinforced short columns weaken, while the flexural failure characteristics strengthen. Additionally, the longitudinal SFCB exhibits buckling behavior similar to that of steel bars, preventing brittle failure of the specimens.

(2) The hysteresis loops of the SFCB-reinforced short column exhibit a significant pinching effect compared to the steel-reinforced short column. After replacing steel bars with SFCBs for equal stiffness, the initial stiffness and total energy dissipation of the SFCB-reinforced short column did not significantly decrease. However, the average peak load and peak displacement increased by 7.8 % and 88.1 %, respectively. The damage to longitudinal reinforcement and GFRP stirrups, as well as the shear and residual deformation, was lower in the SFCB specimen compared to the steel-reinforced specimen. Therefore, the SFCB-reinforced column offers lower repair difficulty and higher cost-effectiveness.
(3) Reducing the stirrup spacing does not significantly affect the shape of the skeleton curves of the specimens, but it substantially enhances shear capacity, thereby greatly increasing ductility. Compared to SFC-2.4-150, the ultimate displacement of SFC-2.4-100 and SFC-2.4-60 increased by 39.6 % and 57.9 %, respectively. The damage to the longitudinal SFCBs and GFRP stirrups also decreases with an reduce in stirrup spacing, although this has minimal impact on resilience. Shear deformation decreases accordingly, but further reduces in stirrup spacing have a limited effect.
(4) As the shear span-to-depth ratio decreases, both the initial stiffness and overall skeleton curves of the specimens increase significantly. Compared to the column with a shear span-to-depth ratio of 3.0, the peak load of columns with shear span-to-depth ratios of 2.0 and 2.4 increased by 43.9 % and 23.1 %, respectively, while energy dissipation increased by 58.1 % and 31.5 %, respectively. Specimens with a larger shear span-to-depth ratio exhibit greater displacement at the same drift ratio, making them more susceptible to excessive local concrete deformation, which reduces resilience. However, shear deformation decreases as the shear span-to-depth ratio increases.
(5) The shear effects in SFCB-reinforced short concrete columns were considered using the USFM method. Building on this, the analytical model developed by the authors' research group, which accounts for SFCB slip, was further extended to predict the skeleton curves of the short columns under axial-shear-flexure interaction, demonstrating reliable accuracy.

CRediT authorship contribution statement

An Xiaoyong: Writing – original draft, Formal analysis, Data curation. **WANG Guolin:** Writing – review & editing, Methodology, Investigation. **Rong Hua:** Writing – review & editing, Methodology, Investigation. **Zhang Yufeng:** Methodology, Investigation. **Tao Jun:** Methodology, Investigation. **Bai Yulei:** Writing – review & editing, Project administration, Funding acquisition.

Declaration of Competing Interest

The authors declare that they have no known competing financial interests or personal relationships that could have appeared to influence the work reported in this paper.

Acknowledgements

The authors are grateful for the financial support received from the Natural Science Foundation of Beijing (No. JQ23036), the National Natural Science Foundation of China (Grant no. 52478294), and the Program Fund of Non-Metallic Excellence and Innovation Center for Building Materials (No. 24SFP-2).

Data availability

Data will be made available on request.

References

[1] G. Wu, Z. Wu, Y. Luo, Z. Sun, X. Hu, Mechanical properties of steel-FRP composite bar under uniaxial and cyclic tensile loads, J. Mater. Civ. Eng. 22 (10) (2010) 1056–1066.
[2] Y. Tang, Z. Sun, G. Wu, Y. Wei, Experimental study on cyclic behavior of SFCBs with different slenderness ratios, J. Mater. Civ. Eng. 33 (8) (2021) 04021204.
[3] Z. Dong, G. Wu, X. Zhao, H. Zhu, J. Lian, Bond durability of steel-FRP composite bars embedded in seawater sea-sand concrete under constant bending and shearing stress, Constr. Build. Mater. 192 (2018) 808–817.
[4] Y. Zhou, Y. Zheng, J. Pan, L. Sui, F. Xing, H. Sun, et al., Experimental investigations on corrosion resistance of innovative steel-FRP composite bars using X-ray microcomputed tomography, Compos. Part B: Eng. 161 (2019) 272–284.
[5] S. Han, A. Zhou, J. Ou, Relationships between interfacial behavior and flexural performance of hybrid steel-FRP composite bars reinforced seawater sea-sand concrete beams, Compos. Struct. 277 (2021) 114672.
[6] S. Han, C. Fan, A. Zhou, J. Ou, Shear behavior of concrete beams reinforced with corrosion-resistant and ductile longitudinal steel-FRP composite bars and FRP stirrups, Eng. Struct. 278 (2023) 115520.
[7] W. Ge, K. Chen, Z. Guan, A. Ashour, W. Lu, D. Cao, Eccentric compression behaviour of concrete columns reinforced with steel-FRP composite bars, Eng. Struct. 238 (2021).
[8] W. Ge, J. Zhu, A. Ashour, Z. Yang, X. Cai, S. Yao, et al., Effect of chloride corrosion on eccentric-compression response of concrete columns reinforced with steel-FRP composite bars, J. Compos. Constr. 26 (4) (2022) 04022042.
[9] C. Su, X. Wang, L. Ding, Z. Wu, Seismic degradation behavior of steel-FRP composite bar reinforced concrete beams in marine environment based on experimental and numerical investigation, Compos. Struct. 313 (2023) 116949.
[10] C. Su, X. Wang, L. Ding, Z. Chen, S. Liu, Z. Wu, Experimental study on the seismic behavior of seawater sea sand concrete beams reinforced with steel-FRP composite bars, Eng. Struct. 248 (2021) 113269.
[11] S. Han, A. Zhou, C. Fan, G. Xiao, J. Ou, Seawater sea-sand concrete columns using durable and ductile steel-FRP composite bars and FRP ties: a promising hybrid scheme for marine engineering, Eng. Struct. 294 (2023) 116731.

[12] Y. Bai, Q. Ma, Y. Zhang, X. Jin, S. Han, Bond behavior and modeling of steel-FRP composite bars in engineered cementitious composites, Case Stud. Const. 20 (2024) e03320.
[13] Z. Sun, G. Wu, J. Zhang, Y. Zeng, W. Xiao, Experimental study on concrete columns reinforced by hybrid steel-fiber reinforced polymer (FRP) bars under horizontal cyclic loading, Constr. Build. Mater. 130 (2017) 202–211.
[14] Z. Sun, G. Wu, Z. Wu, M. Zhang, Seismic behavior of concrete columns reinforced by steel-FRP composite bars, J. Compos. Constr. 15 (5) (2011) 696–706.
[15] A.I. Ibrahim, G. Wu, Z. Sun, H. Cui, Cyclic behavior of concrete columns reinforced with partially unbonded hybrid, Eng. Struct. 131 (2017) 311–323.
[16] A.I. Ibrahim, G. Wu, Z. Sun, Experimental study of cyclic behavior of concrete bridge columns reinforced by steel basalt-fiber composite bars and hybrid stirrups, J. Compos. Constr. 21 (2) (2017) 1–14.
[17] Z. Sun, Y. Zheng, Y. Sun, X. Shao, G. Wu, Deformation ability of precast concrete columns reinforced with steel-FRP composite bars (SFCBs) based on the DIC method, J. Build. Eng. 68 (2023).
[18] Z. Zhang, A. Ashour, W. Ge, Seismic performance of ultra-high performance concrete-filled FRP tube composite columns reinforced with SFCBs: test and modeling, Thin-Walled Struct. 205 (2024).
[19] Y. Zhang, Y. Bai, S. Han, G. Milani, X. Jin, Seismic behavior of novel resilient and corrosion-resistant composite columns using strain-hardening engineered cementitious composites and steel-FRP composite bars, Eng. Struct. 305 (2024).
[20] L. Xu, X. Wang, B. Dong, X. Yang, J. Pan, Seismic behaviors of steel-FRP composite bar-reinforced engineered cementitious composites columns under reversed cyclic loads, Eng. Struct. 316 (2024).
[21] D. Kalliontzis, P.B. Shing, Force-based frame element with axial force-flexure-shear interaction for modeling reinforced concrete members, ACI Struct. J. 118 (3) (2021) 131–146.
[22] S.J. Mei, Y.L. Bai, J.G. Dai, Q. Han, Seismic behaviour of shear critical square RC columns strengthened by large rupture strain FRP, Eng. Struct. 280 (2023) 115679.
[23] Y.L. Bai, W.H. Shi, L.P. Qian, S.Z. Liu, Z.Q. Yang, Flexural behavior of steel-fiber reinforced polymer (FRP) composite bars (SFCBs) reinforced engineered cementitious composite (ECC)-concrete composite beams, Constr. Build. Mater. 457 (2024) 139451.
[24] L.H. Wang, W.H. Shi, L.P. Qian, Y.L. Bai, S.Z. Liu, Z.Q. Yang, Flexural behaviors of GFRP-reinforced engineered cementitious composite (ECC)-concrete composite beams, Eng. Struct. 332 (2025) 120097.
[25] S. Han, C. Fan, A. Zhou, J. Ou, Simplified implementation of equivalent and ductile performance for steel-FRP composite bars reinforced seawater sea-sand concrete beams: equal-stiffness design method, Eng. Struct. 266 (2022).
[26] S. Han, C. Fan, A. Zhou, J. Ou, Shear behavior of concrete beams reinforced with corrosion-resistant and ductile longitudinal steel-FRP composite bars and FRP stirrups, Eng. Struct. 278 (2023) 115520.
[27] ACI 440.1R-15, Guide for the Design and Construction of Concrete Reinforced with Fiber Reinforced Polymers (FRP) Bars, American Concrete Institute, Farmington Hills, MI, USA, 2015.
[28] GB50010-2010, Code for Design of Concrete Structures, China Architecture & Building Press, Beijing, 2015.
[29] H. Mostafaei, F.J. Vecchio, Uniaxial shear-flexure model for reinforced concrete elements, J. Struct. Eng. 134 (9) (2008) 1538–1547.
[30] ASTM C469-22, Standard Test Method for Static Modulus of Elasticity and Poisson's Ratio of Concrete in Compression, ASTM, West Conshohocken, PA, 2022.
[31] ASTM D7205/D7205M-21, Standard Test Method for Tensile Properties of Fiber Reinforced Polymer Matrix Composite Bars, ASTM, West Conshohocken, PA, 2021.
[32] FEMA-P750, NEHRP Recommended Seismic Provisions for New Buildings and Other Structures, Building Seismic Safety Council, Washington, D.C., 2009.
[33] GB50011-2010, Code for Seismic Design of Buildings, China Ministry of Housing and Urban-Rural Development of the People's Republic of China, Beijing, 2016.
[34] Z. Zhang, X. Guo, Z. Yang, Y. Zhou, K. Chen, Q. Sun, et al., Experimental investigation on the seismic performance of square concrete/ECC filled stiffened high-strength steel tubular columns, Eng. Struct. 314 (2024) 118341.
[35] H. Sezen, J.P. Moehle, Shear strength model for lightly reinforced concrete columns, J. Struct. Eng. 130 (11) (2004) 1692–1703.
[36] Y. Zhang, M. Deng, Z. Dong, Seismic response and shear mechanism of engineered cementitious composite (ECC) short columns, Eng. Struct. 192 (2019) 296–304.
[37] H. Dong, J. Qin, W. Cao, L. Zhao, Seismic behavior of circular CFST columns with different internal constructions, Eng. Struct. 260 (2022) 114262.
[38] F.J. Vecchio, M.P. Collins, The modified compression-field theory for reinforced concrete elements subjected to shear, ACI Struct. J. 83 (1986) 219–231.
[39] H. Mostafaei, T. Kabeyasawa, Axial-shear-flexure interaction approach for reinforced concrete columns, ACI Mater. J. 104 (2) (2007) 218.
[40] B.D. Scott, R. Park, M.J. Priestley, Stress-strain behavior of concrete confined by overlapping hoops at low and high strain rates, J. Proc. 79 (1) (1982) 13–27.
[41] M.P. Collins, D. Mitchell, P. Adebar, F.J. Vecchio, A general shear design method, ACI Struct. J. 93 (1) (1996) 36–45.
[42] G.A. Chang, J.B. Mander, Seismic Energy Based Fatigue Damage Analysis of Bridge Columns: Part I-Evaluation of Seismic Capacity Buffalo, National Center for Earthquake Engineering Research, NY, 1994.
[43] R.P. Dhakal, K. Maekawa, Path-dependent cyclic stress–strain relationship of reinforcing bar including buckling, Eng. Struct. 24 (11) (2002) 1383–1396.
[44] H. Sezen, E.J. Setzler, Reinforcement slip in reinforced concrete columns, ACI Struct. J. 105 (3) (2008) 280.

引用格式：白玉磊，刘泽源，邢雅森，等．内置玻璃纤维增强复合材料(GFRP)管-混凝土组合边节点抗震性能研究[J]．工业建筑，2025，55(10)：55-64．BAI Yulei，LIU Zeyuan，XING Yasen，et al. Seismic Performance of Embedded GFRP Tube-Concrete Composite Exterior Beam-Column Joints[J]. Industrial Construction，2025，55(10)：55-64 (in Chinese)．DOI：10.3724/j.gyjzG25082902

内置玻璃纤维增强复合材料(GFRP)管-混凝土组合边节点抗震性能研究*

白玉磊[1]　刘泽源[1]　邢雅森[2]　张　霄[2]　孟宪磊[2]　张石岩[3]

（1. 北京工业大学建筑工程学院，北京　100124；2. 北京建工集团有限责任公司，北京　100055；3. 深圳大学土木与交通工程学院，广东深圳　518060）

摘　要　针对传统混凝土(NC)节点核心区箍筋密集所导致施工拥堵、浇筑缺陷及强震下剪切脆性破坏问题，提出玻璃纤维增强聚合物(GFRP)管-混凝土组合节点形式，并与高延性混杂纤维水泥基复合材料(HECC)联用以替代核心区箍筋并改善界面黏结性能。共设计4个梁柱边节点，参数为核心区材料(NC、HECC)与GFRP管纤维角度(±45°/±60°)。通过循环加载试验，比较了节点的承载力、延性、能量耗散与刚度退化等。结果表明：GFRP管的约束作用显著提升了节点的延性，纤维角度为±45°的组合节点较纤维角度为±60°的组合节点在能量耗散方面提高9.3%；核心区采用GFRP管与HECC的组合节点，由于GFRP管提供侧向约束并分担斜向主拉/压应力，且HECC改善钢筋-基体黏结并抑制裂缝扩展，其延性和刚度保持与传统混凝土节点相当，承载力可提高1.3%，能量耗散提高8.8%。与传统混凝土节点相比，该组合节点可显著减少核心区箍筋用量，为少箍筋高性能节点的应用提供可行路径。

关键词　GFRP管；高延性混杂纤维水泥基复合材料(HECC)；梁柱边节点；抗震性能

Seismic Performance of Embedded GFRP Tube-Concrete Composite Exterior Beam-Column Joints

BAI Yulei[1]　LIU Zeyuan[1]　XING Yasen[2]　ZHANG Xiao[2]　MENG Xianlei[2]　ZHANG Shiyan[3]

(1. *College of Architecture and Civil Engineering, Beijing University of Technology, Beijing* 100124, *China*; 2. *Beijing Construction Engineering Group Co., Ltd., Beijing* 100015, *China*; 3. *College of Civil and Transportation Engineering, Shenzhen University, Shenzhen* 518060, *China*)

Abstract: To address issues such as construction congestion, concrete casting defects, and shear-induced brittle failure in the core region of traditional concrete beam - column joints under severe earthquakes, this study proposes a novel joint system incorporating glass fiber-reinforced polymer (GFRP) tubes combined with high-ductility hybrid fiber-reinforced engineered cementitious composite (HECC). This system is designed to replace stirrups in the joint core and improve interfacial bonding performance. Four exterior beam-column joint specimens were designed, with the core material (normal concrete (NC) or HECC) and GFRP tube fiber orientation (±45° or ±60°) as the main test variables. Quasi-static cyclic loading tests were conducted to evaluate and compare the seismic performance of the joints, including bearing capacity, ductility, energy dissipation, and stiffness degradation. The results demonstrated that the confinement provided by the GFRP tubes sig-

* 非金属材料创新中心创新基金资助(24SFP-2)。

第一作者：白玉磊，博士，教授，主要从事复合材料结构加固研究。

通信作者：张石岩，zsy18834823819@163.com。

收稿日期：2025-08-29

© 2025 工业建筑

中国知网　https://www.cnki.net

nificantly enhanced joint ductility. Specimens with ±45° fiber-oriented tubes exhibited a 9.3% improvement in energy dissipation compared to those with ±60° tubes. Moreover, due to the lateral confinement provided by the GFRP tubes, which helps resist diagonal principal tensile/compressive stresses, and the improved reinforcement-to-matrix bond and crack propagation inhibition offered by the HECC, the joint combining GFRP tubes and HECC in the core region showed comparable ductility and stiffness retention to the conventional concrete joint, along with a 1.3% increase in bearing capacity and an 8.8% improvement in energy dissipation. Compared with traditional concrete joints, the proposed composite joint significantly reduces stirrup usage and construction difficulty, thus offering a viable solution for designing high-performance beam-column joints with minimal transverse reinforcement.

Keywords: GFRP tubes; high-ductility hybrid fiber reinforced ECC (HECC); beam-column exterior joints; seismic performance

0 引 言

混凝土框架结构是建筑领域中最广泛的结构体系之一,梁柱节点作为结构的传力枢纽,其性能直接影响整体的抗震能力与施工效率[1-4]。近年来,随着超高层建筑的发展,传统钢筋混凝土节点(RC节点)面临显著挑战。首先,为满足抗震规范对核心区抗剪承载力的要求,密集箍筋配置常导致钢筋绑扎复杂、施工效率低,并可能导致混凝土浇筑质量缺陷;其次,在强震作用下核心区易发生剪切破坏,显著降低结构延性,导致震后功能失效风险加剧。因此,研发兼具高承载力、优异延性和耗能特性及施工便捷性的节点构造,已成为亟需解决的关键技术难题。

国内外学者针对传统钢筋混凝土梁柱节点开展了广泛研究,提出了3种主要技术路径,以提升节点的抗震性能与承载能力。其一,采用纤维增强复合材料(FRP)片材粘贴节点核心区,这是一种简单有效的加固方式。研究表明:X型、U型、L型、T型等多种粘贴形式可显著提高节点的抗剪承载力[5-8]。然而,复杂空间几何特征导致FRP片材在实际工程中的施工适应性不足,且其耐火性较差,燃烧时释放有毒气体,限制了其广泛应用[9-11]。其二,利用工程水泥基复合材料(ECC)或超高性能混凝土(UHPC)替代节点核心区普通混凝土(NC),可显著提升节点性能。得益于其应变硬化特性,ECC和UHPC能够有效增强节点的剪切承载能力与延性变形能力,从而提高抗震性能[12-14]。然而,受限于材料的高成本及分阶段浇筑的复杂施工工艺,ECC和UHPC的应用对节点箍筋用量的优化效果有限[13]。其三,在核心区内置钢管或FRP管以替代传统箍筋,例如,Yu等[15-17]提出内置芯钢管和钢筋网片的节点构造形式,并通过试验验证了该形式能显著增强节点的抗震性能。但该技术也存在不足之处,例如钢-混凝土界面黏结退化易引发保护层混凝土剥落,且钢管塑性屈服后约束效应显著减弱[18]。Lin等[19]提出了一种基于FRP筋并同时在核心区嵌入FRP管的新型梁柱节点。试验结果表明:该构造能有效提升节点的耗能能力和耐火性,显著改善其抗震性能,但核心区保护层混凝土仍存在不同程度的脱落,且其在传统钢筋混凝土框架中的抗震性能演变规律尚不明确,特别是纤维角度等关键参数对核心区抗震性能的影响亦需进一步研究。

针对FRP管约束混凝土组合结构(Concrete-Filled FRP Tubes,CFFTs)形式,现有研究表明其具有优异的力学性能,且在梁柱节点设计中具有潜在的应用价值。Ozbakkaloglu[20]通过系统试验研究,深入分析了FRP材料的类型、层数以及截面几何形式对CFFTs轴向承载力和延性的影响。研究结果揭示,FRP管的约束效应可显著增强混凝土的抗压强度和延性。进一步地,Bai等[21-22]研究了FRP加固钢筋混凝土柱的抗震性能,通过分析破坏模式、滞回特性及累积耗能,证实随着FRP约束刚度的增加,试件的延性和抗震能力显著提高。在此基础上,Feng等[23]提出了一种复材管约束混凝土核心(FRP-Confined Concrete Core,FCCC)结构,通过内置FRP管形成新型组合体系,有效增强核心混凝土的约束效应并显著提升其延性。

针对传统梁柱节点抗震性能优化中施工适用性和材料耐久性等方面的不足,本研究提出了玻璃纤维增强复合材料(GFRP)管-混凝土组合梁柱节

中国知网 https://www.cnki.net

点形式(图 1)。该节点通过在核心区内置不同纤维角度的GFRP管并结合高延性混杂纤维水泥基复合材料(HECC),旨在提升界面黏结性能和抗震能力,同时减少对传统箍筋的依赖。为验证其抗震性能,设计并开展了 4 组梁柱边节点试件的循环加载试验,包括 1 组传统 RC 节点和 3 组 GFRP 管-混凝土组合节点。试验研究了 GFRP 管纤维角度及核心区是否采用 HECC 对节点抗震性能的影响,重点分析承载力、延性、能量耗散和刚度退化等指标。研究结果验证了 GFRP 管"替代箍筋"这一方式的可行性,为解决传统节点箍筋拥堵问题、发展高性能少箍筋节点提供了新的技术方案与理论依据。

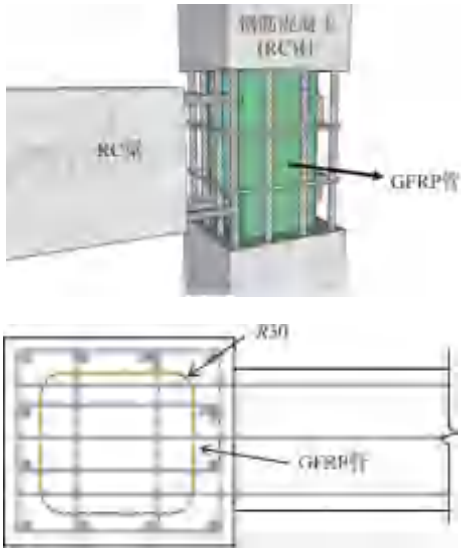


图 1　内置 GFRP 管-混凝土组合节点示意

Fig. 1　Schematic diagram of the embedded GFRP tube-concrete composite joint

1　试验概况

1.1　试件设计

梁柱边节点位于结构的外围,直接影响建筑的外围抗侧力体系的稳定性,为此设计并制作了 4 个梁柱边节点试件(图 2),其中 S-1 为遵循"强节点"原则[24]设计的传统钢筋混凝土对比试件 RC,其核心区配置了加密箍筋。试件 S-2、S-3 和 S-4 则为本研究提出的组合节点,其核心区未配置任何箍筋,用于研究循环加载下 GFRP 管纤维角度及核心区是否采用 HECC 对梁柱节点抗震性能的影响。各试件的详细设计参数见表 1。

按照"强柱弱梁"的设计原则,所有试件的柱截面尺寸为 400 mm×400 mm,柱高 2700 mm,纵筋采用 12 根直径 22 mm 的 HRB400 钢筋。梁截面尺寸为 280 mm×400 mm,梁长 1800 mm,梁顶和梁底各配置 3 根直径 25 mm 的 HRB400 钢筋作为纵筋。梁和柱的箍筋均采用直径 10 mm、间距 100 mm 的 HRB400 钢筋。试件 S-1 遵循"强节点"的设计原则,核心区配置直径 10 mm、间距 100 mm 的四肢箍筋,体积配箍率为 1.85%,其余 3 个试件核心区未配置箍筋,而是采用内置 GFRP 管来增强节点的抗剪性能。根据核心区截面尺寸,选用截面尺寸为 250 mm×270 mm、长度为 450 mm、倒角半径为 30 mm 的 GFRP 管,壁厚采用管材最小制造厚度 3 mm。所有试件的尺寸及配筋如图 2 所示。

表 1　试件的设计参数

Table 1　Design parameters of specimens

编号	核心区材料	GFRP管		核心区配箍率/%	轴压比
		纤维角度	厚度/mm		
S-1	NC	—	—	1.85	0.1
S-2	GFRP管	±60°	3	0	0.1
S-3	GFRP管	±45°	3	0	0.1
S-4	GFRP管+HECC	±45°	3	0	0.1

1.2　内置 GFRP 管组合节点的施工流程

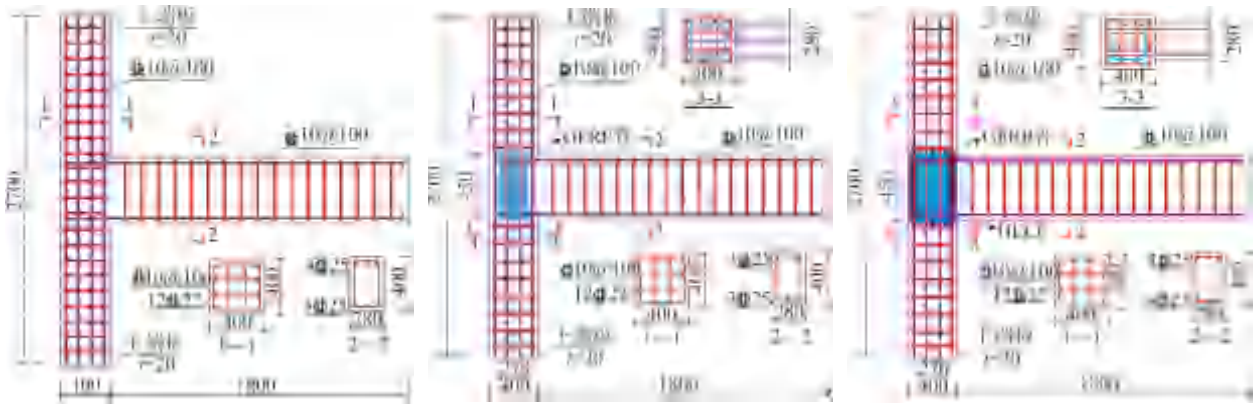
内置 GFRP 管组合节点的施工流程如图 3 所示。首先,根据施工图纸确定梁纵向钢筋在 GFRP 管上的位置并标记,使用比钢筋直径大 2 mm 的钻头进行钻孔。接着,将梁纵向钢筋一端弯折,穿过 GFRP 管后,再弯折另一端。为进一步缓解核心区钢筋拥堵,梁纵向钢筋的弯折长度均控制为 $4d$(d 为钢筋直径)。随后,在木模板中完成梁纵向钢筋的绑扎,并与柱纵向钢筋拼装。最后,将 C40 级 NC 浇筑于所有试件中,并将 HECC 浇筑于试件 S-4 的核心区。

1.3　材料力学性能

本试件 S-4 采用的 HECC 由普通硅酸盐水泥(P·O 52.5)、石灰石粉、硅灰、石英砂、聚羧酸系高性能减水剂和水配制而成,并掺入体积分数为 1% 的聚乙烯纤维(PE)和 1% 的钩端钢纤维(SF)[25]。具体配合比见表 2。浇筑试件时,为 NC 和 HECC 分别预留边长为 150 mm 的立方体试块,并在节点试件试验前进行轴压测试[26],测得 NC 和 HECC 的立方体抗压强度分别为 55.1、78.7 MPa,即 NC 和 HECC 的轴心抗压强度分别为 37.1、55.4 MPa。钢筋拉伸性能依据 GB/T 228.1—2021《金属材料 拉伸试验 第 1 部分:室温试验方法》[27]测定,结果列于表 3。

GFRP 管由哈尔滨玻璃钢研究院有限公司提

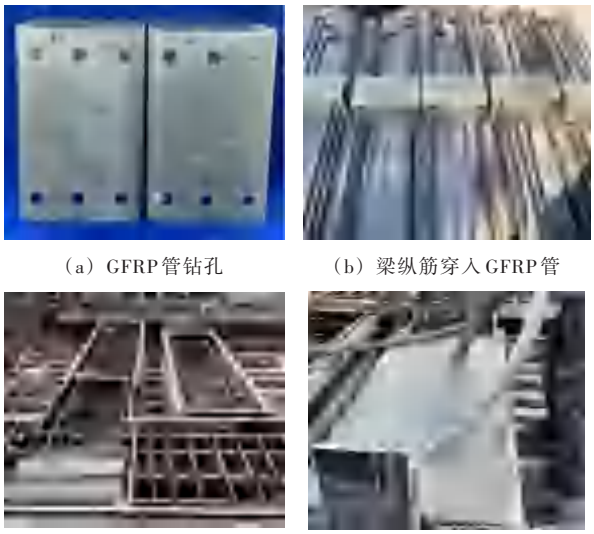
中国知网　https://www.cnki.net



（a）试件S-1　（b）试件S-2、S-3　（c）试件S-4

图2　试件的尺寸及配筋　mm

Fig. 2　Dimensions and reinforcement details of specimens



（a）GFRP管钻孔　（b）梁纵筋穿入GFRP管

（c）钢筋笼绑扎　（d）混凝土浇筑成型

图3　内置GFRP管组合节点的施工流程

Fig. 3　Construction process of the embedded GFRP tube composite joint

表2　HECC的配合比

Table 2　Mix proportions of HECC　kg/m^3

类别	水泥	石灰石粉	硅灰	石英砂	减水剂	水	PE	钢纤维	水灰比
HECC	465	543	112	919	50	194	10	78	0.2

表3　钢筋的拉伸性能

Table 3　Tensile properties of rebars

钢筋类型	d/mm	f_y/MPa	f_u/MPa	E_s/MPa
箍筋	10	421.7	588.6	2.01×10^5
柱纵筋	22	476.9	659.3	2.07×10^5
梁纵筋	25	471.3	637.8	2.05×10^5

注：d为钢筋直径；f_y为屈服强度；f_u为抗拉强度；E_s为弹性模量。

供，采用S2高强玻璃纤维与环氧树脂通过纤维缠绕工艺制备，纤维体积分数为60%。为评估其抗拉性能，选用纤维角度为0°、厚度为5 mm的5块标准GFRP矩形板进行平板拉伸试验[28]，结果如图4所示，平均抗拉强度为1 008.58 MPa，平均弹性模量为47.8 GPa，平均拉伸断裂应变为0.0211。为研究不同纤维角度管材的抗压性能，选用直径100 mm、高度60 mm、厚度5 mm的标准GFRP圆管，分别以纤维角度±45°和±60°各3根进行轴向压缩试验[29]。结果表明：±45°圆管的平均抗压强度为139.8 MPa，峰值应变为0.0198；±60°圆管的平均抗压强度为154.7 MPa，峰值应变为0.0251。

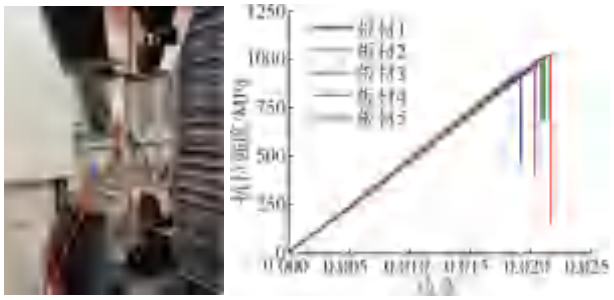


图4　GFRP板的拉伸性能

Fig. 4　Tensile properties of GFRP plates

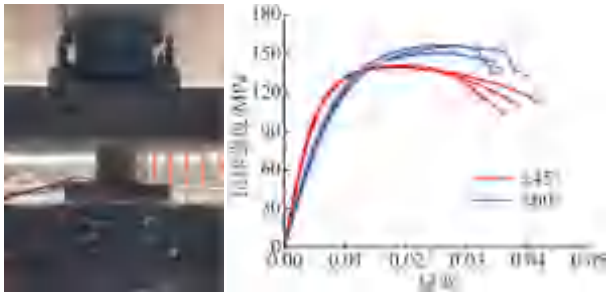


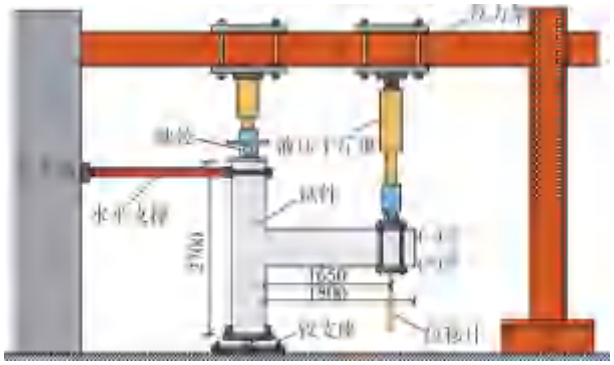
图5　GFRP管的轴压性能

Fig. 5　Axial compressive performance of GFRP tubes

中国知网　https://www.cnki.net

1.4　试验装置及加载制度

梁柱节点试验的加载装置如图 6 所示。梁端通过滚轴与 500 kN 液压千斤顶连接，滚轴限制梁端水平位移，同时允许其在平面内转动；柱端采用铰接，支持平面内自由旋转。一台 500 kN 液压千斤顶置于距柱边缘 1650 mm 的梁端，在试验过程中对梁端施加垂直循环荷载，定义梁端向下荷载为正方向。柱顶采用 1000 kN 液压千斤顶施加 560 kN 恒定轴向压缩荷载，对应柱端轴压比为 0.1，以符合梁柱边节点的设计要求。



（a）加载装置示意，mm



（b）加载现场

图 6　试验加载装置

Fig. 6　Test setup

应变计安装于梁和柱的纵向钢筋上，如图 7 所示，用于实时监测加载过程中的应变。梁端位移（Δ）通过量程为 300 mm 的位移计记录。梁端荷载遵循 ACI 374[30] 推荐的循环加载制度，采用位移控制加载方式，加载位移角（α）依次为 0.25%、0.5%、0.75%、1%、1.5%、2%、2.5%、3%、3.5%、4%、4.5%、5%，每级位移角循环两次，循环加载制度如图 8 所示。试验在施加荷载降至峰值荷载的 85% 时结束。

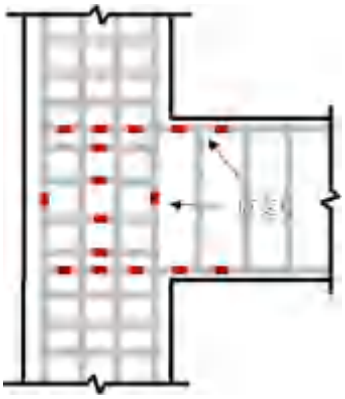


图 7　梁、柱纵筋应变片布置

Fig. 7　Arrangement of strain gauges on beam and column longitudinal reinforcement

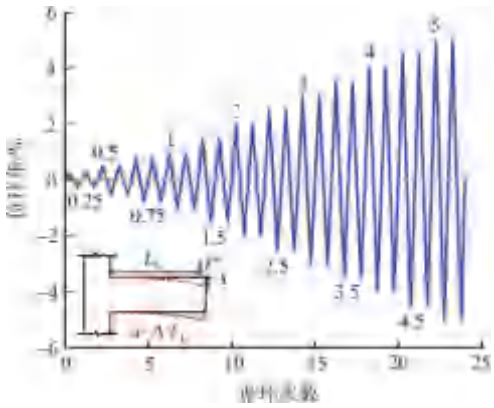


图 8　加载制度

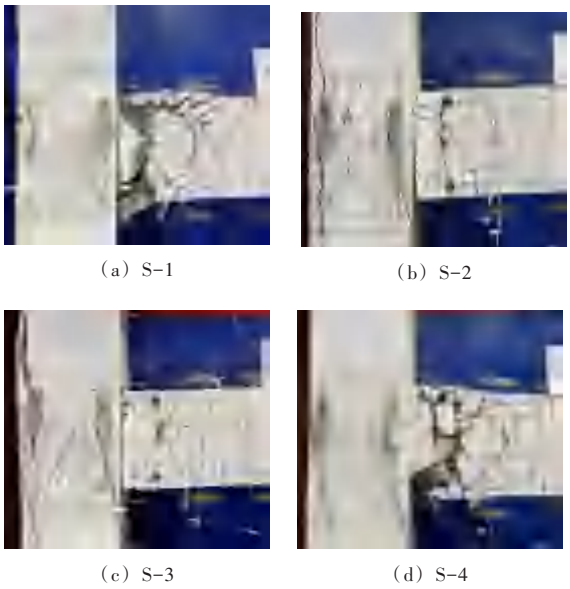
Fig. 8　Loading system

2　试验现象及破坏模式

试件 S-1 的裂缝分布如图 9(a)所示。当位移角为 0.25% 时，梁塑性铰区首先出现裂缝，最大裂缝宽度为 0.25 mm。当位移角为 0.5% 时，核心区出现首条裂缝，宽度仅为 0.1 mm。随着位移角增至 1.5%，梁纵筋发生屈服，梁塑性铰区裂缝逐渐贯穿，最大裂缝宽度为 1.5 mm。当位移角达到 2.5% 时，核心区最大裂缝宽度增至 0.2 mm 后趋于稳定，此时，梁塑性铰区出现大量贯穿裂缝，混凝土被压碎。随着位移角进一步增大，梁塑性铰区混凝土持续压碎并脱落。加载至位移角 5% 时，试验停止，试件 S-1 发生梁端弯曲破坏。

图 9(b)和图 9(c)分别展示了试件 S-2 和 S-3 的裂缝分布，两试件在受力过程中表现出相似的裂缝扩展规律。在位移角为 0.5% 时，梁塑性铰区出现宽度约为 0.4 mm 的裂缝，核心区出现宽度约为 0.1 mm 的初始裂缝。当位移角增至 2% 时，梁纵筋屈服，梁塑性铰区裂缝数量增加，但相较试件 S-1 明显较少，而核心区交叉斜裂缝显著增多，最大宽度

中国知网　https://www.cnki.net



（a）S-1　（b）S-2　（c）S-3　（d）S-4

图9　试件破坏模式

Fig. 9　Failure modes of specimens

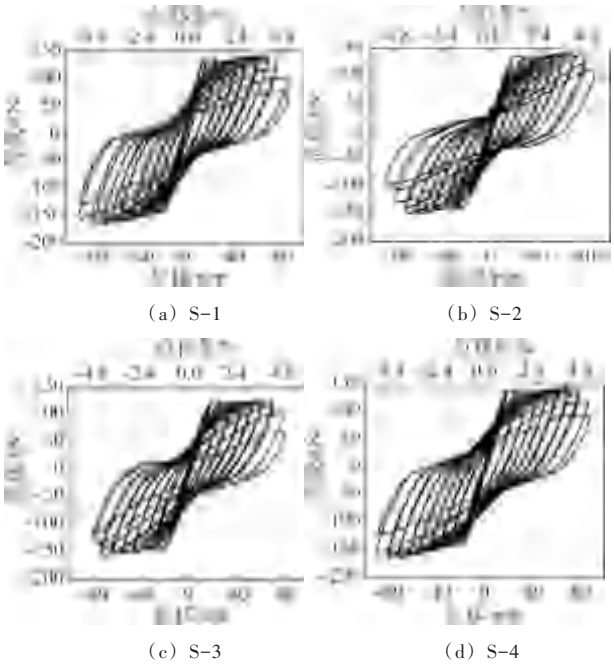
达1.9 mm，同时柱外侧混凝土出现劈裂破坏。随着位移角进一步增大至3.5%，核心区交叉斜裂缝宽度稳定在2.1 mm，而柱外侧混凝土裂缝持续扩展，形成竖向贯穿裂缝，并向柱端延伸。当位移角达到4.5%时，柱外侧混凝土发生剥落破坏，呈楔形特征[3]。加载至位移角为4.5%时，试验停止，试件S-2和S-3均发生锚固破坏。

试件S-4的裂缝分布如图9（d）所示。当位移角为0.5%时，梁塑性铰区首先出现宽度为0.3 mm的裂缝，而核心区无明显裂缝。随着位移角增至0.75%，核心区出现首条斜裂缝，最大宽度仅为0.1 mm。当位移角达到1.5%时，梁纵筋发生屈服，核心区交叉斜裂缝数量增加，最大裂缝宽度增至0.15 mm，梁塑性铰区裂缝逐渐连接贯穿，最大裂缝宽度为0.45 mm。随着位移角进一步增加，核心区交叉斜裂缝数量趋于稳定，最大裂缝宽度保持在0.2 mm，但梁塑性铰区的裂缝向内延伸并显著变宽，混凝土出现明显压碎和脱落现象。直至位移角达到5%时，梁端塑性铰区混凝土大量脱落，试验停止，试件S-4发生梁端弯曲破坏。

3　试验结果分析

3.1　滞回曲线

图10展示了各试件在梁端循环加载下的滞回曲线。值得注意的是，试件S-3在安装过程中因液压千斤顶阀门故障，导致梁端正向受力过早施加，梁上部出现微裂缝，这使得S-3在整个加载期间的正向峰值荷载显著低于其他试件。因此，后续分析主要聚焦于试件的负向加载行为。可以看出，试件S-1和S-4因梁端弯曲破坏，滞回曲线形状较饱满。而试件S-2和S-3因锚固破坏，滞回曲线呈现明显的捏缩效应。与试件S-1相比，S-2和S-3将核心区箍筋完全替换为内置GFRP管，由于GFRP管对外部混凝土的约束作用不足，导致缩短锚固长度的梁纵筋传力受阻，从而使滞回曲线饱满度降低。然而，试件S-4通过将S-2和S-3核心区的混凝土替换为HECC，有效缓解了捏缩效应。



（a）S-1　（b）S-2　（c）S-3　（d）S-4

图10　试件的荷载-位移滞回曲线

Fig. 10　Load-displacement hysteretic curves of specimens

3.2　骨架曲线和延性

表4总结了各试件的试验关键结果，包括屈服荷载P_y、屈服位移Δ_y、峰值荷载P_p、峰值位移Δ_p、极限荷载P_u、极限位移Δ_u、延性系数μ及延性系数平均值$\bar{\mu}$。其中，极限荷载P_u定义为峰值荷载P_p的85%。图11对比展示了各试件荷载-位移骨架曲线。可见，传统RC试件采用核心区加密箍筋配置，其梁负向加载峰值荷载为163.23 kN。相比之下，核心区内置GFRP管的试件S-2和S-3的峰值承载力分别降低7.6%和4.6%，这一现象归因于S-2和S-3的梁纵筋弯折锚固长度较短，导致钢筋与混凝土的黏结性能下降，黏结应力向节点核心区传递受阻，破坏了节点内“剪力流”机制[31]。值得注意的是，试件

中国知网　https://www.cnki.net

表 4　关键试验结果汇总

Table 4　Summary of key test results

编号	方向	Δ_y/mm	P_y/kN	Δ_p/mm	P_p/kN	Δ_u/mm	P_u/kN	μ	$\bar{\mu}$
S-1	正	15.62	129.17	60.29	142.03	76.49	120.72	4.89	4.42
	负	20.00	138.16	65.86	163.23	79.09	138.75	3.95	
S-2	正	17.89	123.02	67.70	142.40	81.82	121.04	4.57	4.20
	负	20.31	127.71	61.46	150.87	77.58	128.24	3.82	
S-3	正	17.15	118.84	67.91	127.64	75.83	108.49	4.42	4.38
	负	17.56	139.60	62.21	155.66	76.23	132.31	4.34	
S-4	正	17.12	136.57	68.77	145.01	81.64	123.26	4.77	4.44
	负	20.75	139.93	78.69	162.91	85.37	138.47	4.11	

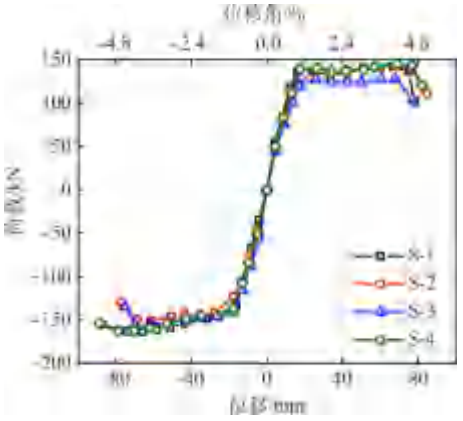


图 11　试件的荷载-位移骨架曲线

Fig. 11　Load-displacement skeleton curves of specimens

S-3 的峰值承载力比 S-2 高 3.1%，这可能是因为，相较于纤维方向为±60°的 GFRP 管，±45°纤维方向的 GFRP 管更加有效地承担了核心区的主拉应力和主压应力。此外，与 S-1 试件相比，采用 GFRP 管与 HECC 组合的试件 S-4 实现了 1.3% 的承载力提升，这表明该组合构造在提供良好延性的同时，也保障了承载能力。

延性是衡量结构在外力作用下非弹性变形能力的关键指标，通常以位移延性系数 μ（$\mu=\Delta_u/\Delta_y$）表示。试件的屈服点采用图 12 所示的 Park 法确定[32]。表 4 列出了各试件的延性系数（μ），通过比较梁在正向和负向加载下的平均延性系数，评估了节点的延性性能。与 S-1 试件相比，S-2 和 S-3 的平均延性系数分别为 4.20 和 4.38，分别降低了 5.0% 和 0.9%。然而，根据毛维浩[31]的研究，相较于 RC 边节点，当核心区采用 HECC 且梁纵筋直线锚固长度为 6d 时，发生锚固破坏的边节点的延性降低了 55.6%。与发生锚固破坏的边节点相比，内置±60°和±45°GFRP 管节点的延性相较于 RC 节点分别提高了 50.6% 和 54.7%，这表明内置 GFRP 管显著提高了内置 GFRP

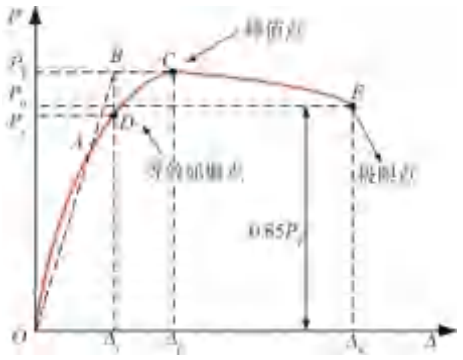


图 12　荷载-位移曲线特征点的确定

Fig. 12　Determination of characteristic points in the load-displacement curve

管-混凝土组合节点的延性。此外，试件 S-4 的平均延性系数为 4.44，与 S-1 相当。

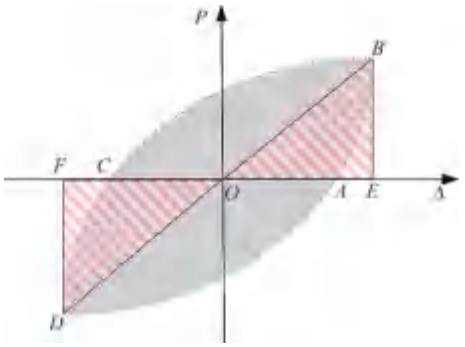


图 13　能量耗散与滞回特性

Fig. 13　Energy dissipation and hysteretic characteristics

3.3　耗能能力

在循环加载下，梁柱节点耗散的总能量为梁端荷载-位移曲线中各滞回环面积之和，如图 13 中的 S_{ABCD}。图 14 显示了各试件累积耗能量与梁端位移的关系。当位移角小于 1.5% 时，各试件处于弹性阶段，累积耗能量相近。当位移角超过 2% 时，试件 S-2 和 S-3 的累积耗能量显著低于 S-1，原因在于其梁纵筋锚固长度较短，导致钢筋与混凝土的传力机制受阻。当加载至位移角 4.5% 时，相较于纤维角度为±60°的 GFRP 管，采用±45°纤维角度的 GFRP 管使试件承载力和延性提高，累积耗能量从 109.7 kN·m 增至 119.9 kN·m，增长 9.3%。试件 S-4 的累积耗能量较 S-1 提高 8.8%，这得益于核心区采用 HECC 材料，PE 和 SF 的相互协同桥连效应增强了与纵筋的黏结性能并抑制了裂缝扩展[31]。

等效黏滞阻尼系数 h_e 是评估结构能量耗散能力的重要参数，其计算式为：

$$h_e = \frac{1}{2\pi}\frac{S_{ABC}+S_{ADC}}{S_{\Delta OBE}+S_{\Delta OFD}} \tag{1}$$

中国知网　https://www.cnki.net

式中：S_{ABC}和S_{ADC}分别为弧面ABC、ADC滞回环的面积，kN/m；$S_{\Delta OBE}$和$S_{\Delta OFD}$分别为三角形ΔOBE、ΔOFD的面积，kN/m，如图13所示。

由式（1）可知，h_e值越大，表明结构滞回曲线越饱满，能量耗散能力越强；反之，h_e值越小，滞回环捏缩越严重，能量耗散能力越弱。

图15展示了试件在不同位移角下第一次循环加载时的等效黏滞阻尼系数h_e。各试件的h_e随位移角的变化趋势基本一致，当位移角小于0.75%时，h_e呈下降趋势；当位移角超过1%时，h_e随位移角增大而非线性增加，这是因为在早期加载阶段，试件处于弹性状态，滞回环呈狭窄梭形，耗能较小；后期随着位移角增大，滞回环逐渐饱满，耗能显著增加。在加载后期，发生梁端弯曲破坏的试件S-1和S-4的h_e保持在0.22以上，高于发生锚固破坏的试件S-2和S-3（分别为0.17、0.20左右）。

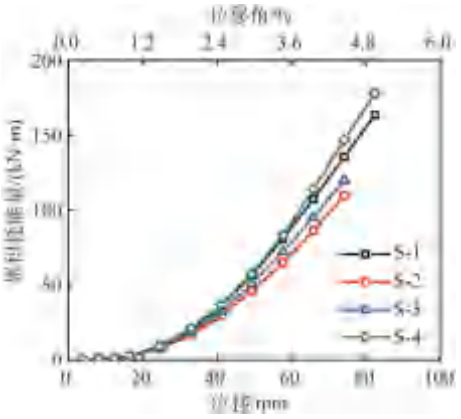


图14 累积耗能曲线

Fig. 14 Cumulative energy dissipation-drift ratio curves

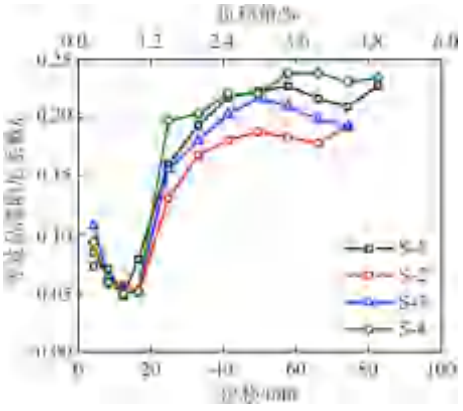


图15 等效黏滞阻尼系数曲线

Fig. 15 Equivalent viscous damping coefficient curves

3.4 承载力退化及刚度退化

承载力退化是指在循环加载下，试件在相同位移角时，最大承载力随加载循环次数的增加而逐渐降低的现象。承载力退化系数计算式为：

$$\lambda_j^i = \frac{P_j^i}{P_j^1} \tag{2}$$

式中：λ_j^i为第j级控制位移下第i圈加载时的承载力退化系数；P_j^i为第j级控制位移下第i圈加载的峰值承载力；P_j^1为第j级控制位移下第1圈加载的峰值承载力。

根据式（2）计算各试件的承载力退化系数λ，其与控制位移的关系曲线如图16所示。结果表明，在梁负向加载时，试件S-1和S-4因发生梁端弯曲破坏，λ值稳定在0.9~1.0，表明循环加载下承载力退化较小，即使梁端变形较大，试件仍能保持较高承载能力。而试件S-2和S-3因发生锚固破坏，当位移角达3%时，梁纵筋锚固不足导致λ迅速下降，当位移角至4.5%时，λ降至0.9以下。

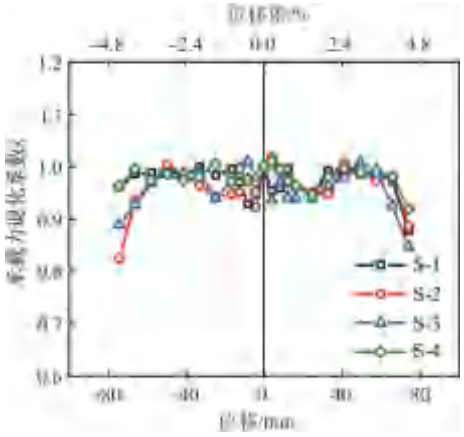


图16 承载力退化曲线

Fig. 16 Strength degradation curves

在循环加载下，试件割线刚度K_i的计算式为：

$$K_i = \frac{|+P_i| + |-P_i|}{|+X_i| + |-X_i|} \tag{3}$$

式中：$+P_i$和$-P_i$分别为第i个位移角循环加载中的正向和负向峰值荷载；$+X_i$和$-X_i$分别为对应的正向和负向位移。

根据式（3），各试件在循环加载下的割线刚度退化情况如图17所示。结果表明，随着梁端位移增加，各试件刚度持续下降，前期下降速率较快，后期退化曲线逐渐趋平。在梁负向加载时，试件S-1的刚度在位移角从0.25%增至4.5%时下降了80.5%。相比之下，试件S-2和S-3的刚度降幅分别为82.7%和80.1%。与±60°GFRP管相比，±45°GFRP管的抗剪作用减缓了试件的刚度退化速率。值得注意的是，即使S-3发生锚固破坏，其刚度退化

中国知网 https://www.cnki.net

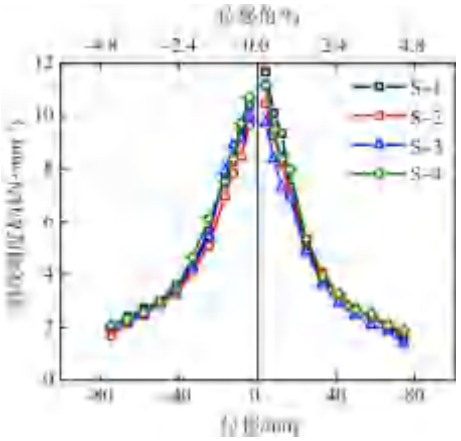


图 17　刚度退化曲线

Fig. 17　Stiffness degradation curves

速率仍低于因梁端弯曲破坏的 S-1 试件。试件 S-4 的刚度退化幅度为 80.6%，与 S-1 相当，表明内置 GFRP 管与 HECC 组合的刚度保持能力可等效于核心区加密箍筋配置。

3.5　钢筋应变分析

图 18 为梁柱交界处附近梁纵筋的应变发展情况。梁纵筋应变-梁端位移曲线呈现 3 个阶段的特征。在位移角小于 0.5%（应变约 1500×10^{-6}）时，曲线呈线性增长。随着位移角增至 1.5%，曲线斜率逐渐减小。当位移角超过 1.5% 时，曲线趋于水平。试件 S-1 和 S-4 的梁纵筋应变最终稳定在（3000~3500）$\times10^{-6}$，而试件 S-2 和 S-3 的应变稳定在（2500~3000）$\times10^{-6}$，这源于梁纵筋与混凝土黏结性能较弱，导致钢筋塑性变形受限。试件 S-4 核心区采用 HECC，增强了钢筋与 HECC 的黏结作用，使梁纵筋受力更充分，其应变值最大。

图 19 为柱外侧纵筋应变随梁端位移的变化。可见，试件 S-1 的柱纵筋应变值在整个加载过程中

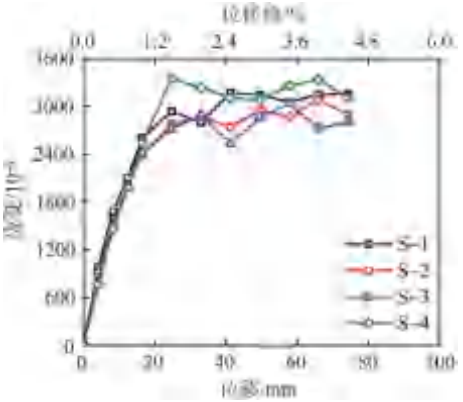


图 18　梁纵筋应变发展

Fig. 18　Strain evolution in beam longitudinal reinforcement

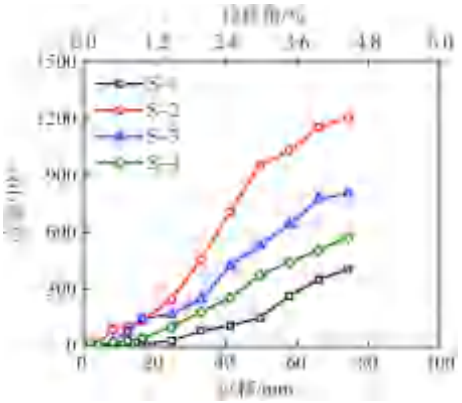


图 19　柱纵筋应变发展

Fig. 19　Strain evolution in column longitudinal reinforcement

较小，这是由于试件 S-1 核心区配有箍筋，箍筋通过横向约束作用，限制了柱纵筋的侧向变形。试件 S-2 柱纵筋的最大应变值为 1198×10^{-6}，而试件 S-3 最大应变值降至 801×10^{-6}，表明相较于纤维角度为 ±60° 的 GFRP 管，纤维角度为 ±45° 的 GFRP 管分担了柱纵筋的应力，这是由于 ±45° 的纤维与梁和柱受压区产生的斜压杆方向一致，有效承担了主应力。在试件 S-3 的基础上，试件 S-4 核心区替换为 HECC，其柱外侧最大应变值进一步降至 573×10^{-6}。

4　结　论

在本研究中，为了减少梁柱节点核心区对传统箍筋的依赖，采用 GFRP 管和 HECC 结合的方式用于节点核心区，为评估此类节点的抗震性能，对 4 组梁柱边节点试件进行了循环加载试验。研究的主要发现如下：

1）相较于传统 RC 节点，无箍筋内置 GFRP 管-混凝土组合梁柱节点因缩短梁纵筋锚固长度，界面黏结性能减弱，破坏了节点“剪力流”机制，导致柱外侧混凝土发生楔形剥落，显著降低承载力和能量耗散能力。然而，GFRP 管的约束作用显著提升了锚固破坏节点的延性，纤维角度为 ±60° 和 ±45° 的节点延性分别提高 50.6% 和 54.7%。

2）相较于纤维角度 ±60° 的 GFRP 管节点，±45° 纤维角度的 GFRP 管节点在能量耗散方面均提升 9.3%，因其纤维方向与核心区斜压杆机制一致，有效承担了主拉应力和主压应力。

3）采用内置 GFRP 管并结合 HECC 的核心区梁柱节点显著降低了对横向钢筋约束和梁纵筋锚固的依赖，其延性与刚度保持性能与传统 RC 节点相当，承载力提升 1.3%，能量耗散能力提高

中国知网　https://www.cnki.net

8.8%。

未来需进一步研究更多参数,特别是GFRP管的纤维角度和厚度,以评估此类节点的抗震性能。

参 考 文 献

[1] 田时雨,任凤鸣,陈光明. 复材新结构梁柱节点:研究现状及展望[J]. 工业建筑,2021,51(6):186-197.

[2] 杨锐,罗开海,黄世敏. 钢筋混凝土框架结构屈服机制研究进展[J]. 建筑结构学报,2024,45(6):1-15.

[3] AAVI-DEHKORDI S, MOSTOFINEJAD D, ALAEE P. Effects of high-strength reinforcing bars and concrete on seismic behavior of RC beam-column joints [J]. Engineering Structures, 2019, 183: 702-719.

[4] 朱立猛,杜岐山,肖红梅,等. 装配式框架柱及梁柱节点抗震韧性研究进展[J]. 建筑结构,2025,55(13):51-58.

[5] EL-AMOURY T, GHOBARAH A. Seismic rehabilitation of beam-column joint using GFRP sheets [J]. Engineering Structures, 2002, 24(11):1397-1407.

[6] WANG G L, DAI J G, BAI Y L. Seismic retrofit of exterior RC beam-column joints with bonded CFRP reinforcement: an experimental study[J]. Composite Structures, 2019, 220: 832-843.

[7] LE-TRUNG K, LEE K, LEE J, et al. Experimental study of rc beam - column joints strengthened using cfrp composites [J]. Composites Part B: Engineering, 2010, 41(1): 76-85.

[8] 吴波,王维俊. 碳纤维布加固钢筋混凝土框架节点的抗震性能试验研究[J]. 土木工程学报,2005,38(4):7-13.

[9] 黄群贤,刘洋,施明峰. CFRP环包加固RC梁柱边节点抗震性能试验研究[J]. 建筑结构学报,2022,43(8):10-18.

[10] 宋天诣,韩林海. 组合结构耐火性能研究的部分新进展[J]. 工程力学,2008,25(增刊2):230-253.

[11] 高皖扬,陆洲导,胡克旭. FRP材料的火灾(高温)性能研究进展[J]. 重庆建筑大学学报,2008,30(6):128-135.

[12] YUAN F, PAN J, XU Z, et al. A comparison of engineered cementitious composites versus normal concrete in beam-column joints under reversed cyclic loading[J]. Materials & Structures, 2013, 46(1/2): 145-159.

[13] DEHGHANI A, MOZAFARI A R, ASLANI F. Evaluation of the efficacy of using engineered cementitious composites in RC beam-column joints[J]. Structures, 2020, 27: 151-162.

[14] SURYANTO B, TAMBUSAY A, SUPROBO P, et al. Seismic performance of exterior beam-column joints constructed with engineered cementitious composite: comparison with ordinary and steel fibre reinforced concrete [J]. Engineering Structures, 2022, 250, 119035.

[15] YU F, WU C, XU B, et al. Study on shear bearing capacity of pvc-cfrp confined concrete column-rc beam exterior joint with core steel tube [J]. Construction and Building Materials, 2024, 410, 131850.

[16] YU F, ZHANG N, NIU D, et al. Strain analysis of PVC-CFRP confined concrete column with ring beam joint under axial compression[J]. Composite Structures, 2019, 224, 111012.

[17] YU F, SONG Z, MANSOURI I, et al. Experimental study and finite element analysis of PVC-CFRP confined concrete column-Ring beam joint subjected to eccentric compression [J]. Construction and Building Materials, 2020, 254, 119081.

[18] 关少钰,白涌滔,刘卫辉,等. 基于统一强度理论的高强钢管混凝土柱压弯屈服准则[J]. 工程力学,2019,36(增刊1):6-12.

[19] LIN G, ZENG J J, LIANG S D, et al. Seismic behavior of novel gfrp bar reinforced concrete beam-column joints internally reinforced with an frp tube [J]. Engineering Structures, 2022, 264, 119380.

[20] OZBAKKALOGLU T. Compressive behavior of concrete-filled frp tube columns: assessment of critical column parameters [J]. Engineering Structures, 2013, 51: 188-199.

[21] BAI Y L, BAI S C, MEI S J, et al. Seismic behavior of rc square columns strengthened with lrs frp under high axial load ratio [J]. Structures, 2023, 56, 104045.

[22] BAI Y L, LIU S Z, MEI S J. Compressive behavior and modeling of concrete wrapped by hybrid low-high elongation capacities frp [J]. Engineering Structures, 2024, 300, 117155.

[23] FENG P, CHENG S, BAI Y, et al. Mechanical behavior of concrete-filled square steel tube with FRP-confined concrete core subjected to axial compression [J]. Composite Structures, 2015, 123: 312-324.

[24] 中华人民共和国住房和城乡建设部. 建筑抗震设计标准:GB 50011—2010[S]. 北京:中国建筑工业出版社,2014.

[25] 刘诗恒. 钢-聚乙烯混杂纤维增强高延性水泥基复合材料(HECC)与钢筋的粘结锚固性能研究[D]. 重庆:重庆大学,2021.

[26] 中华人民共和国住房和城乡建设部. 混凝土物理力学性能试验方法标准:GB/T 50081—2019[S]. 北京:中国建筑工业出版社,2019.

[27] 中国国家标准化管理委员会. 金属材料 拉伸试验 第1部分:室温试验方法:GB/T 228.1—2021[S]. 北京:中国标准出版社,2021.

[28] ASTM D3039. Standard test method for tensile properties of polymer matrix composite materials [S]. West Conshohocken: American Society for Testing and Materials, 2015.

[29] 中华人民共和国国家质量监督检验检疫总局. 纤维增强热固性塑料管轴向压缩性能试验方法:GB/T 5350—2005[S]. 北京:2005.

[30] ACI Committee 374. ACI 374.2R-13 Guide for testing reinforced concrete structural elements under slowly applied simulated seismic loads [S]. Farmington Hills: American Concrete Institute, 2013.

[31] 毛维浩. 钢-聚乙烯混杂纤维水泥基材料及其在梁柱节点中的应用[D]. 重庆:重庆大学,2023.

[32] PARK R. State of the art report ductility evaluation from laboratory and analytical testing [C]//Proceedings of Ninth World Conference on Earthquake Engineering. Tokyo, Kyoto: [s. n.], 1988: 605-616.

中国知网 https://www.cnki.net

Check for updates

Received: 16 February 2024 | Revised: 1 May 2024 | Accepted: 11 May 2024

DOI: 10.1002/pc.28591

RESEARCH ARTICLE

Polymer COMPOSITES WILEY

Design, preparation, and mechanical properties of glass fiber reinforced thermoplastic self-anchor plate cable exposed in alkaline solution environment

Zhonghui Zhang[1] | Qikang Ji[2,3,4] | Zhengyue Guo[2,3,4] | Chenggao Li[2,3,4] | Rui Guo[2,3,4] | Jingwei Tian[2,3,4] | Zhuo Zhang[2,3,4] | Taipeng He[2,3,4] | Guijun Xian[2,3,4]

[1]Institute of Petroleum Engineering and Technology, Shengli Oilfield Company, China Petroleum and Chemical Corporation (SINOPEC), Dongying, China

[2]Key Lab of Structures Dynamic Behavior and Control, Harbin Institute of Technology, Ministry of Education, Harbin, Heilongjiang, China

[3]Key Lab of Smart Prevention and Mitigation of Civil Engineering Disasters of the Ministry of Industry and Information Technology, Harbin Institute of Technology, Harbin, China

[4]School of Civil Engineering, Harbin Institute of Technology, Harbin, Heilongjiang, China

Correspondence
Chenggao Li, 73 Huanghe Road, Nangang District, Harbin 150090, China.
Email: lichenggao@hit.edu.cn

Funding information
Program Fund of Non-Metallic Excellence and Innovation Center for Building Materials, Grant/Award Number: 24SFP-4; Fundamental Research Funds for the Central Universities, Grant/Award Numbers: HIT.OCEF. 2022032, HIT. NSRIF202234; Heilongjiang Natural Science Foundation, Grant/Award Number: LH2021E073

Abstract

The reliable anchorage and long-term durability of high-performance fiber reinforced polymer composites were the decisive factors for engineering applications owing to the anisotropy of materials and the complexity of service environment. In this paper, an innovative glass fiber reinforced polypropylene (GFRPP) self-anchor plate cable was developed to utilize the high toughness/durability of thermoplastic resin and self-anchor load-bearing system. The effects of different reinforcement methods and cable arc angles (10°, 20°, and 30°) on mechanical properties of plate cable were investigated. Water absorption behavior and mechanical properties immersed in alkali solution were tested to evaluate its long-term service behavior. The thermogravimetric and surface morphology analysis were conducted to reveal the performance evolution mechanism. The results showed through the combination of secondary melting, carbon fiber winding confinement and epoxy reinforcements, the splitting failure of transition zone and interlaminar cracking failure of straight zone for plate cable were effectively avoided. The tensile strength retention of plate cable for arc angles of 10°, 20° and 30° were 45.6%, 41.3%, and 34.0% of GFRPP plate, respectively. Larger arc angle increased the curvature of arc-straight transition zone and stress concentration near the straight section, leading to interlaminar splitting failure of plate cable at weak transition zone. The tensile strength of plate cable with the immersion time deteriorated obviously until the lowest retention of 29.7%. The degradation mechanism was mainly due to the etching of glass fibers in alkali solution and the formation of pores and internal defects, including fiber/resin interface debonding and resin swelling. The research results were of significance for solving the anchoring problems and promoting the long-term service reliability in bridge applications.

Highlights

- The mold can realize reliable molding of glass fiber reinforced polypropylene cables after the reinforcements.
- The tensile strength retention of plate cable was up to 34.0%–45.6% of plate.

 © 2024 Society of Plastics Engineers.

- Larger arc angle increased the stress concentration near the straight section.
- Non-polar polypropylene plate was proved to have better hydrophobic performance.
- The degradation mechanism of plate cable in alkali solution was revealed.

KEYWORDS

alkali solution immersion, arc angle, degradation mechanism, forming mold, glass fiber reinforced polypropylene self-anchor plate cable, mechanical properties

1 | INTRODUCTION

Traditional high-strength steel wires or strands have been successfully used in bridge cables with a span of 3000–5000 m. When steel cables were used in bridge structures, two main problems should be considered during the design and service, including large weight and poor corrosion/fatigue resistances.[1–3] On the one hand, high density of steel cables limited the span and bearing efficiency of bridge structures.[4] On the other hand, the corrosion and fatigue problems of steel cables greatly increased the replacement times and maintenance costs.[5] By contrast, fiber reinforced polymer (FRP) composite cable has the advantages of light weight, high strength, corrosion resistance and fatigue resistance.[6–8] Through the popularization and application, the durability and service life of bridge structure can be greatly improved, and the life cycle cost of maintenance and replacement in service can be reduced.[9,10]

When fiber reinforced polymer composites were used in bridge cables, the reliable anchorage[11–13] and excellent durability/fatigue resistances[14–16] were two main issues to be considered in the design of bridge structure to ensure the long-term safety and reliability. For the anchorage performance, it has become a key problem due to anisotropic characteristics of FRP, such as higher tensile strength and lower compressive/shear strength.[17] At present, the anchoring system of FRP mainly divided into mechanical clamping/friction type, bonding type and compound type.[18,19] For the mechanical clamping type, it can be divided into mechanical extrusion type and bonding extrusion type.[20–22] Mechanical extrusion anchorages adopted the conical clamp anchorages similar to prestressed steel strands, and the clamp materials were metal or ultra-high strength concrete. When FRP cables were anchored with clamp anchorage, the clamp in the anchorage zone produced the transverse compression, which led to transverse shear failure of FRP cables before the tensile failure. Bonding extrusion usually adopted resin and cement mortar as loading transfer media to form a conical clamp. FRP cable was anchored under the radial extrusion force. However, larger radial force brought about the stress concentration at the loading end of the anchorage zone, which may cause the early failure of FRP cable. For the mechanical friction type,[23,24] the anchoring methods adopted the expansion material and formed the pre-pressure on the surface of FRP cable to increase the friction force on the surface and realize the effective anchorage. However, the anchoring method still had many shortcomings, such as limited compressive strength of expansive material itself, long anchoring length, large space requirement and higher toughness demand for under fatigue loading. To sum up, there were still many problems to be solved for the above anchoring system in practical engineering owing to coupling effects of complex loading and harsh service environment. Therefore, it was urgent to develop a new, efficient and reliable anchorage system or cable-anchor structure form.

On the other hand, the durability and fatigue performance of FRP cable deserved the attention when considering the complex coupling effects of loading and environment.[7,25] As present, the matrix type of FRP cable was mainly the thermosetting resin, such as epoxy. Thermosetting resin composites (such as epoxy) had the advantages of convenient processing, high production efficiency, high mechanical properties due to low resin viscosity. However, the three-dimensional network cross-linking structure of the thermosetting matrix was easy to cause brittle failure, which also contributed to the lower fatigue life of composites.[26–28] In addition, some active functional groups in thermosetting resins were prone to form hydrogen bonds with water molecules in the service environment, resulting in the durability degradation, such as resin hydrolysis and interface debonding of fiber-resin.[29,30] In contrast, thermoplastic resin (such as polypropylene) has the advantages of high toughness, good durability and fatigue resistance, and so forth.[31–35] Meanwhile, it can also be recycled, economical and environmentally friendly.[36,37] Therefore, using thermoplastic composites instead of thermosetting resin to prepare FRP cables for bridge engineering has great development prospects. At present, limited research focused on the durability of thermoplastic composites. For example, Hou et al.[38] conducted the hygrothermal investigation on glass fiber reinforced thermoplastic composites, including glass fiber reinforced nylon and polyethylene terephthalate, GF/PA and GF/PET with different fiber mass fractions of 20% and 40% immersed into deionized water for 900 h. The experimental results showed that

15480569, 0, Downloaded from https://4spepublications.onlinelibrary.wiley.com/doi/10.1002/pc.28591 by Harbin Institute Of Technology, Wiley Online Library on [22/05/2024]. See the Terms and Conditions (https://onlinelibrary.wiley.com/terms-and-conditions) on Wiley Online Library for rules of use; OA articles are governed by the applicable Creative Commons License

the diffusion rate of water molecules in GF/PA was higher than that in GF/PET. After the immersion, the tensile strength of GF/PA decreased by 65.82% (20 wt%), 51.88% (40 wt%), and that of GF/PET decreased by 44.2% (20 wt%), 49.88% (40 wt%), respectively. Zhou et al.[39] immersed glass fiber reinforced polypropylene (GFRPP) bars in distilled water and alkaline solutions at 21, 40, and 60°C. The water absorption, mechanical properties and microstructure analysis were investigated to evaluate the long-term evolution. The research showed water swelling of GFRPP bars promoted the development of original micropores and cracks, resulting in the continuous intrusion of water molecule. The hygrothermal condition accelerated the formation and development of micro-voids and cracks, which contributed to the degradation of the long-term mechanical properties, as well as fiber-resin debonding and glass fiber etching. Dong et al.[40] evaluated the durability properties of GFRPP bars exposed to the coupling effect of immersion in the simulated SWSC solution (25, 40, and 60°C) and different sustained bending levels (0%, 9.8%, and 29.4%). The degradation of mechanical properties of GFRPP bars was accelerated by higher temperatures, bringing about the extra degradation rates of 0.5%, 9.6%, and 29.3% for flexural strength. High sustained bending stress obviously accelerated the reduction of mechanical properties of GFRPP bars. The degradation mechanism was attributed to the interface debonding between glass fiber and polypropylene and the corrosion of glass fibers. At present, the durability research on thermoplastic composites mainly focused on the conventional component types, such as bar and plate. Aiming at the new type of GFRPP self-anchor plate cable structure proposed in this paper, its long-term durability deserved the attention because of the complex structure and stress state.

In the present paper, an innovative GFRPP self-anchor plate cable structure was developed. The effects of different reinforcement methods and cable arc angles (10°, 20°, and 30°) on mechanical properties of plate cable were investigated. Water absorption behavior and mechanical properties immersing in alkali solution were tested to evaluate its long-term service behavior. The thermogravimetric and surface morphology analysis were conducted to reveal the performance evolution mechanism. The research results were of significance for solving the anchoring problems and promoting the long-term service reliability in bridge applications.

2 | EXPERIMENTAL PROGRAMME

2.1 | Raw materials

In this paper, the raw material used to prepare the plate cable is bidirectional GFRPP composite plate. This plate was from Shandong Tuoyan New Materials Technology Co., Ltd (Zaozhuang, Shaodong) with the width and thickness of 25 mm × 1.6 mm. The plate was prepared through the molding process with the volume fraction (∼70%) of glass fiber. The nominal tensile strength, tensile modulus, flexural strength, flexural modulus of the plate were 400 MPa and 22 GPa, 300 and 15 MPa, respectively.

2.2 | Mold design and assembly

The design idea of mold utilized the principle of heating-melting and cooling molding of thermoplastic resin. The thermoplastic prepreg tape was wound to the molding mold and then placed in a high-temperature furnace to heat up to above the resin melting point temperature. During the melting process, the integrated self-anchor plate cable with stable size, excellent performance and self-locking structure were achieved by imposing constraints. To prepare the bidirectional glass fiber reinforced polypropylene self-anchor plate cable, a novel mold was designed to realize the formation of plate cable by extrusion and constraint under high temperature heating, as shown in Figure 1. The mold was divided into upper forming fixture and lower bearing bottom plate. The upper forming fixture consisted of two cylindrical steel columns, four rectangular steel plates with two transverse bolt holes, two movable extruded steel plates, two semi-circular arc restrained steel plates and two circular steel sheets. The bolt holes of the rectangular steel plates were used for transversely restraining and fixing the movable extruded steel plates and semi-circular arc restrained steel plates. The length of the movable extruded steel plate was the same as the axial distance of the cylindrical steel plate, and the angles between its hypotenuse and horizontal plane were 10°, 20° and 30°, respectively. Semi-circular arc steel plate and circular steel sheet were respectively used for transverse and vertical restraint around the bending part of cylindrical steel column at the both ends to prevent the irregular deformation, such as cable warping. The lower bearing bottom plate had 12 bolt holes and two hollow grooves. The bolt holes were mainly used for fixing the upper forming fixture, and the hollow groove provided a space for the movable extruded steel plate and restricted its transverse movement while fixing the movable extruded steel plate. After the assembly, the overall mold was as shown in Figure 1.

2.3 | Preparation of plate cable

After the size calculation and error estimation, the plates were cut into three lengths of 478, 481, and 486 mm by

15480569, 0, Downloaded from https://4spepublications.onlinelibrary.wiley.com/doi/10.1002/pc.28591 by Harbin Institute Of Technology, Wiley Online Library on [22/05/2024]. See the Terms and Conditions (https://onlinelibrary.wiley.com/terms-and-conditions) on Wiley Online Library for rules of use; OA articles are governed by the applicable Creative Commons License

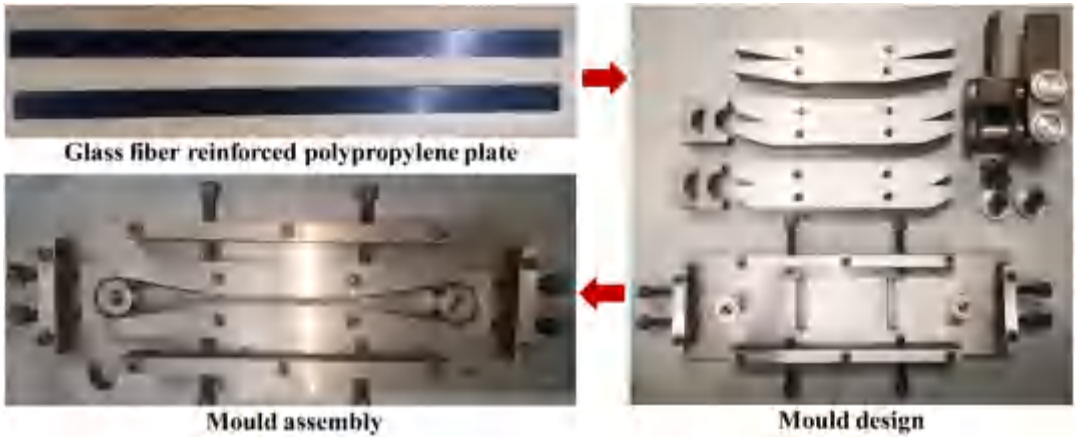


FIGURE 1 Mold design and assembly of glass fiber reinforced polypropylene plate cables.

cutting machine, which corresponded to the plate cables with the angle of arc segment of 10°, 20°, and 30°, respectively. The cutting ends were polished by sandpaper and cleaned by alcohol. The whole preparation process of plate cable mainly included the initial molding process, heating process, cooling process and final molding process. Firstly, the rectangular steel plate and the movable extruded steel plate on the longer side of the upper forming fixture were assembled on the bearing bottom plate, which was convenient for the bending forming of the plate. Then, the intersect position where the hypotenuse and straight edge of the movable extruded steel plate was marked with a marking pen. The overlapping position at the both ends of GFRPP plate was placed in the middle of the straight section to avoid the fracture at the overlapping position. The marked positions were heated by a hot air gun. After the plate was heated and softened, it was placed on the movable extruded steel plate for bending, and can be removed only after it was completely solidified. Then, the bolts on the rectangular steel plate were used to push the movable extruded steel plate and the bending plate to the cylindrical steel columns at both ends, and marked the contact position between GFRPP plate and cylindrical steel columns. Next, the marked positions were heated to soften, and the plates were bent around the cylindrical steel column by a quarter circumference. After this, the plate was taken out and heated until a semicircle semi-finished product. Finally, the semi-finished product was put into a hot oven, and the temperature was set at 185–200°C. After the straight sections of the plate were fused, the mold was taken out and placed to naturally cool to obtain the plate cables, as shown in Figure 2.

2.4 | Exposure condition

In this paper, the short-term and long-term mechanical properties of GFRPP plate cable were further studied. For



FIGURE 2 Sample preparation of glass fiber reinforced polypropylene plate cables.

the long-term evolution, alkaline solution was used as the immersion medium. According to the related research,[41,42] 0.9 g of NaOH, 4.2 g of KOH and 118.5 g of $Ca(OH)_2$ were added to each liter of distilled water to obtain an alkali solution with pH value between 12.6 and 13. The immersion temperature and the longest immersion time were 60°C and 21 days, respectively. The immersion time intervals were 7 and 14 days to analyze the property evolution of plate cables.

2.5 | Water absorption tests

To analyze the effect of water molecules on the mechanical properties of plate cable during the immersion, the water absorption test of glass fiber reinforced polypropylene plate was carried out according to ASTM D5529. Glass fiber reinforced polypropylene plate was cut into 10 specimens with a size of 50 mm × 25 mm × 1.6 mm. After grinding the sample section with the sandpaper, they were marked with an oily marker. Then the samples were dried in an oven at 60°C for 2 days to obtain the samples for water absorption tests. The prepared samples were immersed in alkali solution at 60°C for 1, 2, 3, 5, 7, 10, 15, and 21 days. After regular time interval, the samples were taken out, and the residual moisture and

15480569, 0, Downloaded from https://4spepublications.onlinelibrary.wiley.com/doi/10.1002/pc.28591 by Harbin Institute Of Technology, Wiley Online Library on [22/05/2024]. See the Terms and Conditions (https://onlinelibrary.wiley.com/terms-and-conditions) on Wiley Online Library for rules of use; OA articles are governed by the applicable Creative Commons License

alkali solution on the surface of the sample were cleaned with a dust-free cloth. An electronic balance with an accuracy of 0.1 mg was adopted to obtain the weight of the samples. To more accurately reflect the water absorption performance of materials, each water absorption tests should be completed within 30 min. The water absorption rate at the regular time interval was calculated according to the following Equation:

$$M_t = \frac{W_t - W_0}{W_0} \times 100\%, \quad (1)$$

where, M_t is the water absorption percentage of plate at the time of t. W_t is the weight at the time of t, and W_0 is the initial weight before the immersion.

2.6 | Mechanical properties

The tests of mechanical properties mainly included the tensile test and in-plane shear test. Among them, the tensile properties of glass fiber reinforced polypropylene plate and plate cable were tested. After the tensile failure, an arc segment without fracture failure was selected from the plate cable specimen for in-plane shear test. According to ASTM D 3039, the tensile test of GFRPP plate was conducted through the universal testing machine (DHY-10080) from Shanghai Hengyi Precision Instrument Co., Ltd. and the displacement loading speed was set as 2.0 mm/min. The plates were cut into specimens with dimensions of 200 mm × 25 mm × 1.6 mm. Five tensile tests were repeated to obtain the average tensile strength. A total of 18 groups of specimens were prepared for the tensile tests of plate cables. Among them, the specimens No. 1–3, 4–6 and 7–9 corresponded to the tensile tests of plate cable with the angle of arc segment of 10°, 20° and 30° before the immersion. After the tests, No. 10–18 specimens were prepared from the optimal angle with highest tensile properties, in which No. 10–12, 13–15 and 16–18 specimens were immersed in 60°C alkaline solution for 7, 14, and 21 days, respectively. The tensile test was conducted through the designed tension clamp as shown in Figure 2. To obtain the stress change at the theoretical fracture position, strain gauges were attached to both ends of plate cable and an oblique straight section. The stress–strain curve at the theoretical fracture position was furthermore obtained.

After the tensile test, an arc section of plate cable without fracture failure from each group of specimens was selected and cut with a size of 10 mm × 10 mm × 1.6 mm. At least five specimens were prepared for in-plane shear tests. In addition, the size and number of in-plane shear specimens cut from GFRPP plates were the same as that of plate cables. The prepared specimens were fixed under the shear mold and loaded at the speed of 2 mm/min until the shear failure.

2.7 | Surface morphology tests

Scanning electron microscopy tests were conducted on the fracture surfaces of plate cables before and after the immersion. It was possible to intuitively reflect the morphology changes of cable cross-section, plate delamination and interface debonding. The specimen was cut from fracture surface after the tensile tests into small pieces, and the conductive double-sided adhesive was adopted to stick it onto the aluminum plate. After two rounds of gold spraying treatment for 180 s each time, the scanning electron microscope test specimen was prepared. The electron acceleration voltage of the scanning electron microscope was 30 kV.

3 | RESULTS AND DISCUSSION

3.1 | Effect of reinforcement methods on mechanical properties of plate cable

Before obtaining the mechanical properties of plate cable, the tensile and shear properties of glass fiber reinforced polypropylene plate were obtained as shown in Table 1. The tensile stress–strain curves of plate showed a typical two-stage trend, including the linear ascending stage and subsequent decline stage. Through the slope of the stress–strain curve in the first stage, the elastic modulus of the plate was further obtained. As shown in Table 1, the tensile strength and tensile modulus of glass fiber reinforced polypropylene plate were 365.5 MPa and 16.5 GPa, respectively, which was lower than the nominal value of plate at the factory. Furthermore, the tensile failure modes of plate mainly included the transverse tensile fracture and oblique shear fracture. It should be noted that the above tensile strength was used as the control to evaluate the strength retention of plate cable. In addition, the in-plane shear strength of plate was 42.8 MPa.

After the preparation and installation (Figure 2), the tensile properties of plate cable were tested by a tensile machine. After the tensile properties of plate cable, the insufficient bonding performance of polypropylene resin led to the splitting and overlapping failure in the transition area between straight section and arc section. Furthermore, this failure mode also contributed to the lower load-bearing capacity of plate cable compared to control plate. Therefore, the overlapping interface of

15480569, 0, Downloaded from https://4spepublications.onlinelibrary.wiley.com/doi/10.1002/pc.28591 by Harbin Institute Of Technology, Wiley Online Library on [22/05/2024]. See the Terms and Conditions (https://onlinelibrary.wiley.com/terms-and-conditions) on Wiley Online Library for rules of use; OA articles are governed by the applicable Creative Commons License

TABLE 1 Tensile and shear properties of glass fiber reinforced polypropylene plate.

Sample number	Tensile strength (MPa)	Tensile modulus (GPa)	In-plane shear strength (MPa)
1	360.6	17.5	42.8
2	387.0	16.9	42.3
3	379.2	15.5	42.5
4	367.9	16.8	42.5
5	333.0	16.0	42.3
Average value	365.5	16.5	42.8
Standard deviation	20.8	0.79	0.20

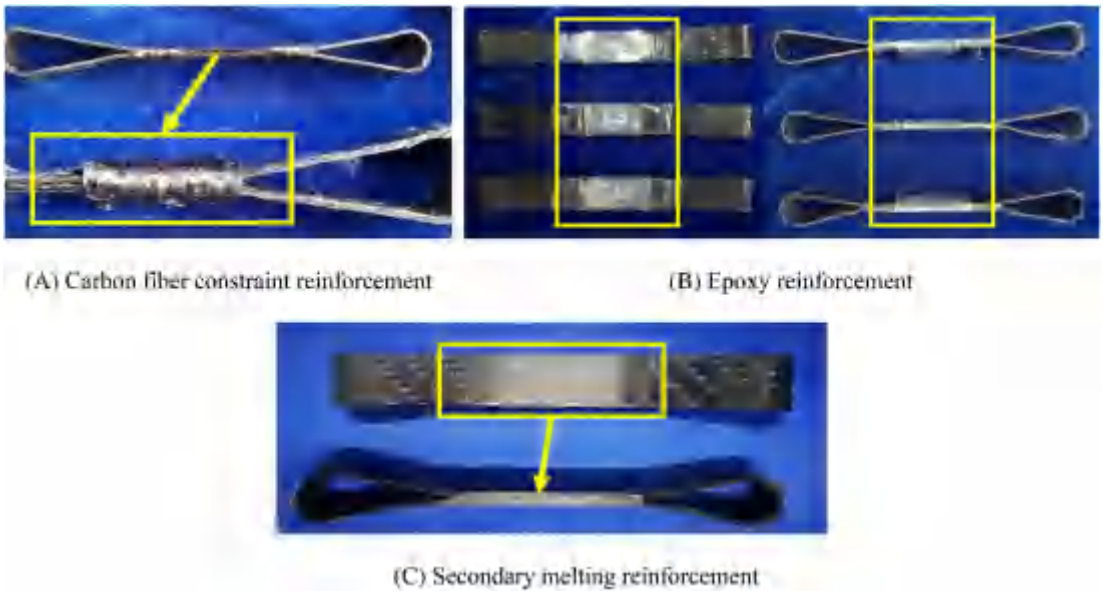


FIGURE 3 Three reinforcement methods of glass fiber reinforced polypropylene plate cables.

straight and arc section was considered as the weak interface layer of plate cable, which was prone to premature interface debonding or peeling failure. It was crucial to reinforce the transition parts between the straight section and arc section to enhance the load-bearing capacity of plate cable. In this paper, three reinforcement methods were selected, including carbon fiber bundle constraint reinforcement, epoxy reinforcement and secondary melting reinforcement, as shown in Figure 3. As shown, for the carbon fiber bundle constraint reinforcement, the carbon fiber bundles were applied to the contact part between straight section and arc section through the winding layer by layer. After this, the prepared epoxy resin was fully impregnated into winding carbon fiber bundles. When the epoxy resin was cured, the constraint reinforcement effect on the plate cable was realized. For the epoxy reinforcement, the reinforcement process was to apply epoxy resin evenly to straight section and straight/arc section contact surface of plate cable. The bonding strength of epoxy was further utilized to reinforce the straight section and straight/arc section contact interfaces to avoid early fracture. For the secondary melting reinforcement, the reinforcement process was to add another composite plate into the straight section of semi-finished plate cable. Three layers of straight section plates were fully heated, melted, cooled and formed to realize the reinforcement effect.

For the carbon fiber bundle constraint reinforcement of plate cables, tensile test showed that there was no splitting phenomenon in the contact part between straight section and arc section. However, the fracture still occurred at the position of fiber winding and extended to the straight position, which also indicated that the fiber winding reinforcement cannot effectively improve the bonding performance of contact parts and straight section. Subsequently, the latter two reinforcement methods were adopted, including following design scheme. The samples No. 1 and 2 adopted the two reinforcement methods at the same time, the samples No. 3 applied epoxy reinforcement method, and No. 4 and 5 applied

15480569, 0, Downloaded from https://4spepublications.onlinelibrary.wiley.com/doi/10.1002/pc.28591 by Harbin Institute Of Technology, Wiley Online Library on [22/05/2024]. See the Terms and Conditions (https://onlinelibrary.wiley.com/terms-and-conditions) on Wiley Online Library for rules of use; OA articles are governed by the applicable Creative Commons License

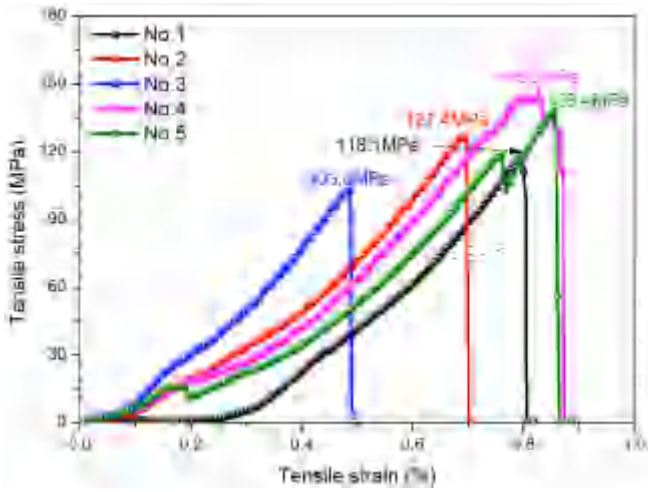


FIGURE 4 Tensile stress–strain curves of glass fiber reinforced polypropylene plate cables for different reinforcement methods.

the secondary melting reinforcement method. Furthermore, the tensile stress–strain curves of the above five cable samples after the reinforcement were shown in Figure 4. As shown, the ultimate tensile stress of specimen No. 3 reinforced with epoxy resin in the straight section was the lowest. The main reason was that the polarity difference between epoxy resin and polypropylene resin led to the bonding inability and weak interface behavior. Furthermore, it can be found that the ultimate tensile strength of plate cable can be significantly improved by secondary melting reinforcement method. This was due to the addition of extra plate can be well fused with the straight section of plate cable at high temperature to realize the reliable lap effect. Through the comparison, the ultimate tensile stress of plate cable made by epoxy and secondary melting reinforcement methods was between the above two values.

In summary, to ensure the molding quality and mechanical properties of plate cable and solve the splitting problem caused by the weak lap interface, this paper adopted the secondary melting reinforcement method to prepare the plate cable. On this basis, carbon fiber winding confinement and epoxy reinforcement at splitting and straight section were also considered to prepare the high-performance plate cable. Furthermore, the prepared plate cables were used to study the effects of arc angle and immersion condition on the mechanical properties.

3.2 | Effect of arc angle on mechanical properties of plate cable

After adopting the above reinforcement methods, the tensile properties of plate cable were obtained and shown in

TABLE 2 Effect of arc angle on tensile strength of plate cable.

Sample number	Tensile strength (MPa)	Tensile strength retention (%)
10°-1	167.4	45.8
10°-2	167.3	45.8
10°-3	165.7	45.3
Average value	166.8	45.6
Standard deviation	1.0	–
20°-1	152.5	41.7
20°-2	154.0	42.1
20°-3	146.3	40.0
Average value	150.9	41.3
Standard deviation	4.1	–
30°-1	121.1	33.1
30°-2	126.4	34.6
30°-3	125.4	34.3
Average value	124.3	34.0
Standard deviation	2.8	–

Table 2. It should be pointed out that the effect of arc angle on tensile strength of plate cable was considered, including 10°, 20°, and 30°. As shown, the tensile strength of plate cable with different arc angles was lower than that of GFRPP plate, and the tensile strength retention for the arc angles of 10°, 20°, and 30° were 45.6%, 41.3%, and 34.0%, respectively. With the increase of arc angle, the tensile strength of plate cable decreased significantly, this was because the larger arc angle increased the curvature of arc-straight transition zone and brought about the stress concentration near the straight section. Furthermore, with the increase of external tensile load, the stress concentration in the transition zone was further intensified. When it exceeded the ultimate interlaminar bonding strength of plate, the progressive cracking occurred, ultimately leading to fiber tensile fracture failure of plate cable at weak transition zone.[43] Figure 5 showed the typical tensile failures of glass fiber reinforced polypropylene plate cables. Two typical failure modes can be found, including tensile fracture failure mode at the cable top and interlaminar splitting failure mode at the transition zone. For the lower arc angle (10° and 20°), the failure mode was mainly the fiber tensile fracture at the cable top. The ultimate properties of plates were fully exerted, resulting in higher strength retention. With the increase of arc angle, the failure mode changed to the interlaminar splitting failure mode in the transition area. This failure mode was mainly dependent on the interfacial bonding properties, which contributed to the low strength retention.

15480569, 0, Downloaded from https://4spepublications.onlinelibrary.wiley.com/doi/10.1002/pc.28591 by Harbin Institute Of Technology, Wiley Online Library on [22/05/2024]. See the Terms and Conditions (https://onlinelibrary.wiley.com/terms-and-conditions) on Wiley Online Library for rules of use; OA articles are governed by the applicable Creative Commons License

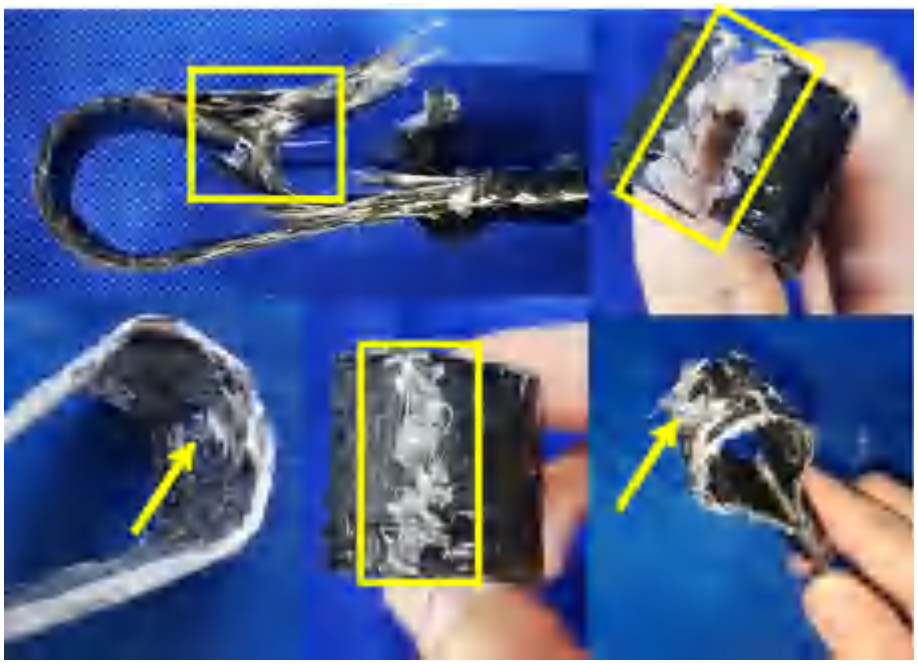


FIGURE 5 Typical tensile failures of glass fiber reinforced polypropylene plate cables.

Figure 6 shows the tensile stress–strain curves of plate cable under different arc angles, and compared them with the stress–strain curves of plates. It can be found that the stress–strain curve of the plate was almost a straight line until the ultimate fracture failure. In contrast, the stress–strain curve of plate cable showed a nonlinear change, and some fluctuations appeared in the tensile curves, which was mainly caused by the local failure by the complex stress condition from the difference between the fiber orientation and loading direction. In addition, the effect of arc angle on tensile stress–strain curves was almost same with the tensile strength. Therefore, the arc angle was recommended to be no more than 20° to obtain the plate cable with high mechanical properties in bridge engineering application.

After the tensile failure of the above plate cable, the in-plane shear properties were tested, and the shear strength was shown in Table 3. Similar to tensile strength, the in-plane shear strength of plate cable was also lower than that of plate. At the same time, with the increase of arc angle, the shear strength decreased with it. Overall, the in-plane shear strength retention was higher than that of tensile strength. The smaller the arc angle of the plate cable, the more reasonable the stress distribution, the greater the in-plane shear strength.

3.3 | Water absorption and diffusion behavior of plate

To reveal the effect of water molecules on mechanical properties, the water absorption and diffusion behavior

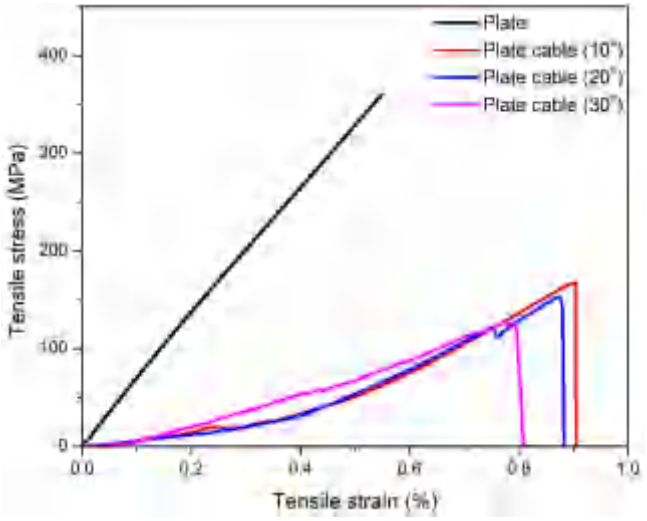


FIGURE 6 Tensile stress–strain curves of glass fiber reinforced polypropylene plate cables at different arc angles.

of plate cable in alkaline solution was further studied with the classical Fick's Law, as follows.

$$\frac{M_t}{M_s} = 1 - \exp\left[-7{:}3 \times \left(\frac{Dt}{h^2}\right)\right]^{0{:}75}, \quad (2)$$

where M_t is the water absorption percentage at time t; M_s is the saturated water absorption percentage; D is the diffusion coefficient; t is the immersion time; h is the thickness of the specimen.

Figure 7 showed the water absorption data and Fick fitting curves of plates immersed at 60°C in alkaline

15480569, 0, Downloaded from https://4spepublications.onlinelibrary.wiley.com/doi/10.1002/pc.28591 by Harbin Institute Of Technology, Wiley Online Library on [22/05/2024]. See the Terms and Conditions (https://onlinelibrary.wiley.com/terms-and-conditions) on Wiley Online Library for rules of use; OA articles are governed by the applicable Creative Commons License

TABLE 3 Effect of arc angle on in-plane shear strength of plate cable.

Sample number	In-plane shear strength (MPa)	In-plane shear strength retention (%)
10°-1	30.3	70.8
10°-2	30.8	72.0
10°-3	29.5	68.9
Average value	30.2	70.6
Standard deviation	0.7	–
20°-1	25.5	59.6
20°-2	26.0	60.7
20°-3	25.0	58.4
Average value	25.5	59.6
Standard deviation	0.5	–
30°-1	23.3	54.4
30°-2	22.8	53.3
30°-3	23.5	54.9
Average value	23.2	54.2
Standard deviation	0.4	–

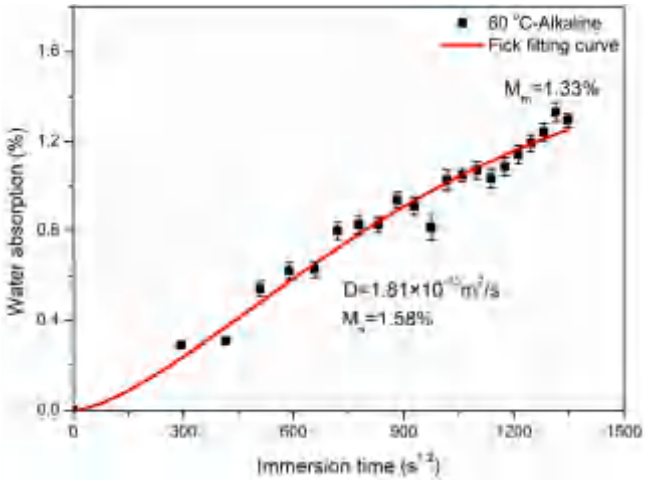


FIGURE 7 Water absorption curves of glass fiber reinforced polypropylene plate at 60°C in alkaline solution.

solution. It can be found that the water absorption of material gradually increased with the immersion time. During the initial immersion of 7 days, the water absorption of plate increased due to the water-absorbing swelling effect of polypropylene resin. At the longest immersion time of 21 days, the material did not reach the water absorption saturation, and the maximum water absorption percentage was 1.33%. Through the fitting, the diffusion coefficient and saturated water absorption of plate were obtained to be 1.81×10^{-13} m^2/s and 1.58%. To further analyze the diffusion behavior of water molecules inside the plates, Table 4 showed the comparison of diffusion coefficient and saturated water absorption of glass fiber reinforced polypropylene or epoxy composites at 60°C. It can be found that the diffusion coefficient of GFRPP straight bars[39] was obviously higher than that of composite plate used in this paper, which was caused by a large number of internal defects in the production process. The formation of defects provided large number of storage and diffusion paths for water molecules, leading to higher diffusion coefficient. On the other hand, compared with GFRPP prepreg tape,[44] the diffusion coefficient of the plate was higher. This was because prepreg tape had a thin thickness and good resin impregnation performance to fibers. Fewer defects lead to a lower diffusion coefficient immersed in distilled water. However, large number of pores and defects formed due to the etching of glass fiber in seawater and sea sand concrete environment, which further improved the saturated water absorption. In addition, by comparing with glass fiber reinforced epoxy (GFREP) plate,[45] GFRPP plate in this paper had lower diffusion coefficient, which meant that polypropylene resin had better hydrophobic performance. In summary, the advantages of self-anchor plate cable developed in this paper for the water absorption and diffusion behavior compared to the other types of composites were summarized as following. The water absorption and diffusion coefficient of glass fiber reinforced polypropylene plate were far lower than that of glass fiber reinforced polypropylene bars due to the efficient molding process and low porosity content. Furthermore, the polypropylene resin had nonpolar functional groups compared with epoxy, which was not sensitive to the immersion of water molecules, contributing to the low diffusion coefficient.

3.4 | Effect of immersion in alkali solution on mechanical properties of plate cable

To analyze the effect of immersion in alkali solution on the mechanical properties of plate cable, the plate cable with the arc angle of 10° was selected to investigate the durability until the longest immersion time of 21 days. Before and after the immersions, the tensile strength and stress–strain curves of plate cable were shown in Figure 8. It can be found that with the increase of immersion time, the tensile strength (Figure 8A) deteriorated obviously. At the longest immersion time of 21 days, the

15480569, 0, Downloaded from https://4spepublications.onlinelibrary.wiley.com/doi/10.1002/pc.28591 by Harbin Institute Of Technology, Wiley Online Library on [22/05/2024]. See the Terms and Conditions (https://onlinelibrary.wiley.com/terms-and-conditions) on Wiley Online Library for rules of use; OA articles are governed by the applicable Creative Commons License

TABLE 4 Comparison of diffusion coefficient and saturated water absorption of glass fiber reinforced polypropylene or epoxy composites at 60°C.

Composites type	Fitting paramaters	Immersion medium		
		Alkaline solution	Distilled water	Seawater and sea sand concrete environment
GFRPP plate in this paper	D (m^2/s)	1.81×10^{-13}	–	–
	M_s (%)	1.58	–	–
GFRPP straight bars[39]	D (m^2/s)	4.22×10^{-13}	2.88×10^{-13}	–
	M_s (%)	1.45	1.91	–
GFRPP prepreg tape[44]	D (m^2/s)	–	1.87×10^{-14}	9.36×10^{-14}
	M_s (%)	–	0.69	3.43
GFREP plate[45]	D (m^2/s)	–	6.80×10^{-13}	–
	M_s (%)	–	–	–

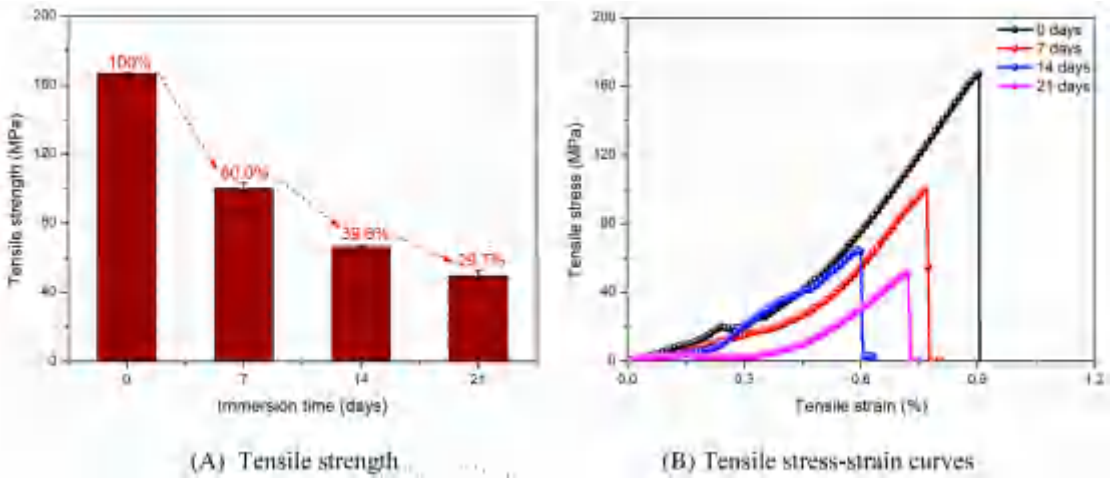


FIGURE 8 Effect of immersion in alkali solution on tensile properties of plate cable of (A) tensile strength and (B) tensile stress–strain curves.

final tensile strength retention was only 29.7%. Generally speaking, the tensile strength of thermoplastic composites mainly depended on the tensile properties of fibers, and the tensile strength degradation of current plate cable was mainly due to the etching of glass fibers in alkali solution. The above chemical etching reaction has been further verified by relevant research,[46] which led to the fracture of Si-O bond and the dissolution of fiber[47] and contributed to the degradation of tensile strength of glass fiber and plate cable.

$$\begin{aligned} &Si-ONa + H_2O \rightarrow Si-OH + NaOH \\ &Si-O-Si + OH^- \rightarrow Si-OH + Si-O \\ &Si-O + H_2O \rightarrow Si-OH + OH^-, \end{aligned} \quad (3)$$

Figure 8B showed the tensile stress–strain curve of plate cable before and after the immersions. It can be found that in addition to the degradation of tensile strength, the ultimate tensile strain of plate cable also deteriorated significantly, which meant that the toughness of the material was further weakened after the immersion. Figure 9 also showed several typical tensile failure modes of cable. Fiber fracture near the top arc section of plate cable was the main tensile failure mode. The possible reason was that the glass fiber here was in a complex stress state due to the difference between fiber orientation and loading direction, which was easier to be destroyed in alkaline solution. From the above phenomenon, it can be known that the section near the arc transitional area had the premature damage due to complex stress and corrosive immersion. When considering the current cable application in practical engineering, the above weak interface should be reinforced to improve the long-term performance.

The effect of immersion in alkali solution on in-plane shear strength of plate cable was also obtained. Compared

15480569, 0, Downloaded from https://4spepublications.onlinelibrary.wiley.com/doi/10.1002/pc.28591 by Harbin Institute Of Technology, Wiley Online Library on [22/05/2024]. See the Terms and Conditions (https://onlinelibrary.wiley.com/terms-and-conditions) on Wiley Online Library for rules of use; OA articles are governed by the applicable Creative Commons License

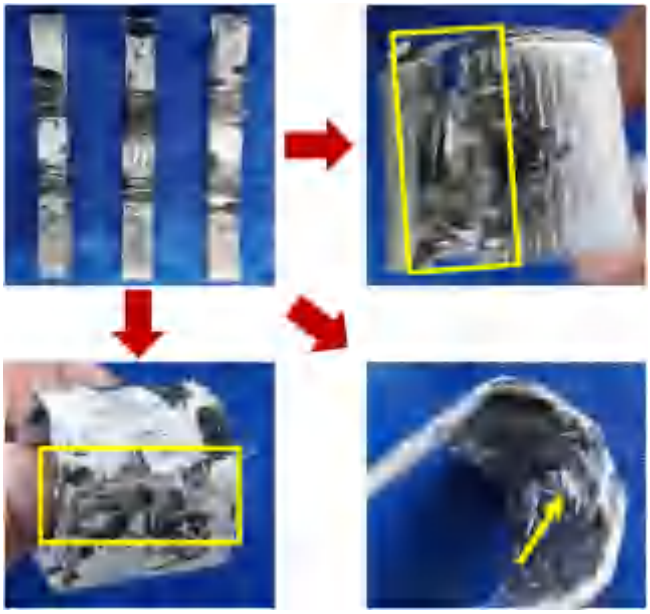


FIGURE 9 Typical tensile failure modes of plate cable after the immersion in alkali solution.

with the evolution of tensile strength, the sensitivity of in-plane shear strength to immersion in alkali solution mainly appeared within the immersion of 7 days, and the strength degradation rate was 24.5%. With the further increase of immersion time, the shear strength did not deteriorate significantly with the strength degradation rate of 71.5% (14 days) and 69.2% (21 days). This was due to the in-plane shear strength was obviously affected by the bonding performance of fiber/resin interface. Better impregnation properties of resin to fiber resulted in higher shear strength retention.

3.5 | Evolution mechanism analysis of plate cable

After analyzing the influence of immersion on mechanical properties of plate cable, the long-term evolution mechanism was further analyzed through the relationship between water absorption and mechanical properties, thermal properties and microscopic morphology. Figure 10 showed the dependence of water absorption on the mechanical properties of plate cable. It can be found that the tensile strength and in-plane shear strength had a linear relationship with water absorption percentage with high degree of fitting. This meant that the degradation of the mechanical properties of plate cable was attributed to the diffusion of water molecules inside the materials. The resin swelling, glass fiber etching and glass fiber/resin interface debonding contributed to the degradation of mechanical properties.[39,48]

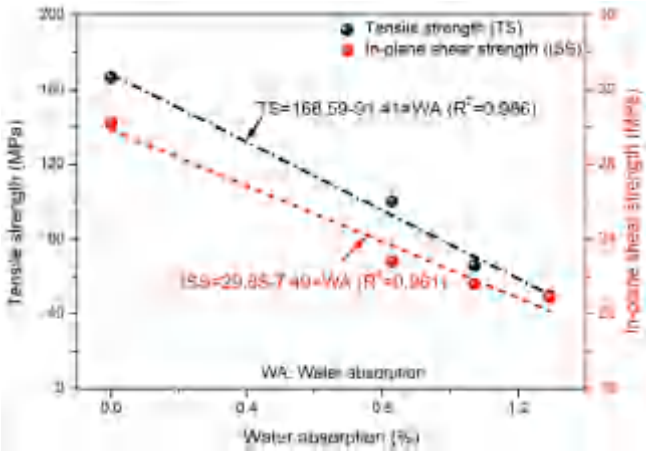


FIGURE 10 Dependence of water absorption on the mechanical properties of plate cable.

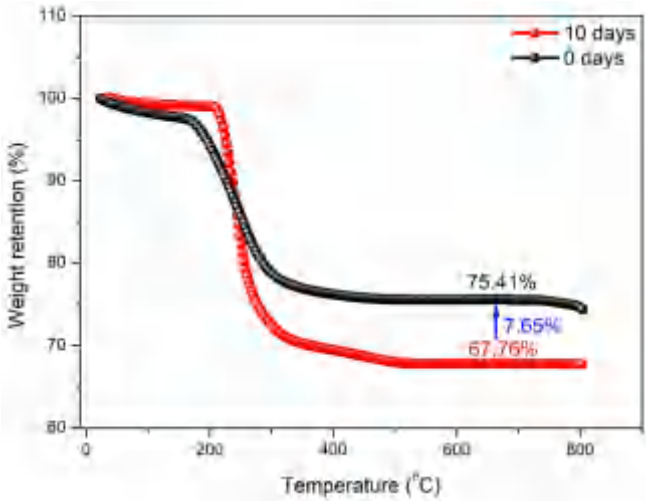


FIGURE 11 Weight retention of plate cable with the temperature before and after the immersions in alkali solution.

Figure 11 conducted the thermogravimetric analysis of plate cable before and after the immersions. It can be found that the weight retention of plate cable presented three stages with the increase of temperature, including the initial slight decline stage, subsequent rapid decline stage and final stable stage. Through the data in the last stage, the mass fraction of glass fiber in the plate cable were 75.41% and 67.76% before and after the immersions. This also meant that the alkaline etching effect led to a decrease of 7.65% in the mass fraction of glass fiber, which also verified the failure mechanism proposed in Equation (3). In addition, the maximum decomposition temperatures obtained by the first order derivative of thermogravimetric curve were 238.85 and 241.63°C before and after the immersions. The above two similar data also indicated that polypropylene resin was not sensitive to alkaline immersion.

15480569, 0, Downloaded from https://4spepublications.onlinelibrary.wiley.com/doi/10.1002/pc.28591 by Harbin Institute Of Technology, Wiley Online Library on [22/05/2024]. See the Terms and Conditions (https://onlinelibrary.wiley.com/terms-and-conditions) on Wiley Online Library for rules of use; OA articles are governed by the applicable Creative Commons License

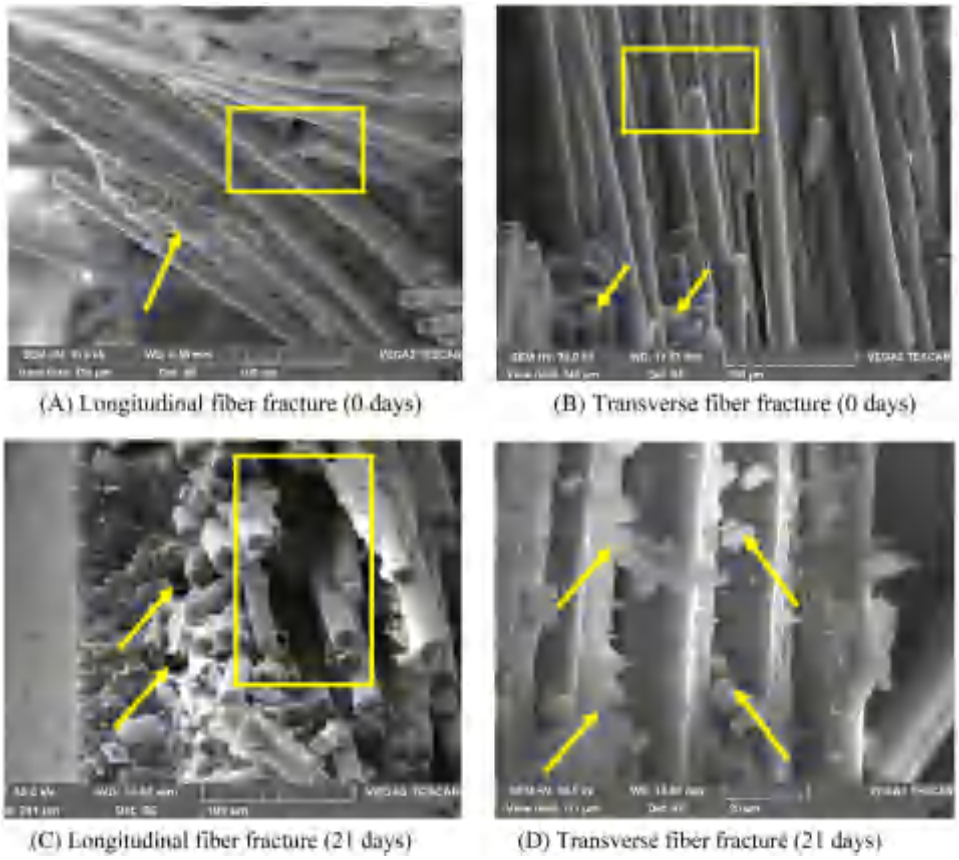


FIGURE 12 Longitudinal and transverse tensile fracture morphology of plate cable before and after the immersions in alkali solution.

Figure 12 showed the longitudinal and transverse tensile fracture morphology of plate cable before and after the immersions in alkali solution. Before the immersion, the glass fibers were filled with large amount of polypropylene resin, which was attributed to the good interface bonding. Longitudinal fiber tensile fracture and transverse fiber shear fracture were the main failure modes of plate cables. After the immersion, obvious pores and defects formed inside the materials. Some fibers were pulled out from the resin and formed the micorvoids, which indicated the debonding of fiber-resin interface. Due to water absorption swelling, the resin morphology became some small particles adhering to the fiber surface. The above-mentioned phenomena further proved that the mechanical properties of plate cable degraded due to the etching effect of alkali solution.

4 | CONCLUSIONS

In the present paper, an innovative mold was developed to realize the forming of glass fiber reinforced polypropylene self-anchor plate cable. Different reinforcement methods were further considered to prepare high performance plate cable. The effects of three cable arc angles (10°, 20°, and 30°) on tensile strength and shear strength of plate cable were investigated. Through immersing in alkali solution for 21 days, the water absorption behavior and mechanical properties were further evaluated. Combined with thermogravimetric and surface morphology analysis, the long-term performance evolution mechanism was furthermore revealed.

The developed mold can realize reliable molding of glass fiber reinforced polypropylene plate cables. Through the combination of secondary melting, carbon fiber winding confinement and epoxy reinforcements, the splitting failure of transition zone and interlaminar cracking failure of straight zone were effectively avoided to prepare high-performance plate cables. The tensile strength retention of plate cable for the arc angles of 10°, 20°, and 30° were 45.6%, 41.3%, and 34.0% of plate, respectively. For the lower arc angle, the failure mode was mainly the fiber tensile fracture at the cable top. Larger arc angle increased the curvature of arc-straight transition zone and stress concentration near the straight section, leading to interlaminar splitting failure of plate cable at weak transition zone.

The diffusion coefficient of polypropylene plate was lower than glass fiber reinforced epoxy plate and glass fiber reinforced polypropylene bars. This was because non-polar polypropylene plate had fewer pores and internal defects, which cannot provide storage space and

15480569, 0, Downloaded from https://4spepublications.onlinelibrary.wiley.com/doi/10.1002/pc.28591 by Harbin Institute Of Technology, Wiley Online Library on [22/05/2024]. See the Terms and Conditions (https://onlinelibrary.wiley.com/terms-and-conditions) on Wiley Online Library for rules of use; OA articles are governed by the applicable Creative Commons License

diffusion path for water molecule, indicating the better hydrophobic performance. With the immersion time, the tensile strength of plate cable deteriorated obviously until the lowest retention of 29.7%. Fiber fracture near the top arc section of plate cable was the main tensile failure mode. The degradation mechanism was mainly due to the etching of glass fibers in alkali solution and the formation of pores and internal defects, including fiber/resin interface debonding and resin swelling.

FUNDING INFORMATION

This work is supported by the Program Fund of Non-Metallic Excellence and Innovation Center for Building Materials (24SFP-4), Fundamental Research Funds for the Central Universities (Grant Nos. HIT.OCEF.2022032 and HIT.NSRIF202234), Heilongjiang Natural Science Foundation (LH2021E073).

CONFLICT OF INTEREST STATEMENT

The authors declare no conflict of interest.

DATA AVAILABILITY STATEMENT

The data that support the findings of this study are available on request from the corresponding author.

ORCID

Chenggao Li https://orcid.org/0000-0002-4338-8944
Guijun Xian https://orcid.org/0000-0002-8540-2580

REFERENCES

1. Li R, Wang H, Miao CQ, Ni Y, Zhang ZX. Experimental and numerical study on the degradation law of mechanical properties of stress-corrosion steel wire for bridge cables. J Constr Steel Res. 2024;212:108294.
2. Miyachi K, Saimoto S, Oki Y. Correlation between corrosion level and fatigue strength of high-strength galvanized steel wires used for suspension bridge cables. Bridge Struct. 2023;19:79-90.
3. Yu Y, Sun ZZ, Wang HK, Gao J, Chen ZW. Time variant characteristic of steel cable considering stress-corrosion deterioration. Constr Build Mater. 2022;328:127038.
4. Yang YQ, Wang X, Wu ZS. Long-span cable-stayed bridge with hybrid arrangement of FRP cables. Compos Struct. 2020;237:111966.
5. Feng B, Wang X, Wu ZS. Fatigue life assessment of FRP cable for long-span cable-stayed bridge. Compos Struct. 2019;210:159-166.
6. Li CG, Xian GJ, Li H. Effect of postcuring immersed in water under hydraulic pressure on fatigue performance of large-diameter pultruded carbon/glass hybrid rod. Fatigue Fract Eng Mater Struct. 2019;42:1148-1160.
7. Lal HM, Uthaman A, Li CG, Xian GJ, Thomas S. Combined effects of cyclic/sustained bending loading and water immersion on the interface shear strength of carbon/glass fiber reinforced polymer hybrid rods for bridge cable. Constr Build Mater. 2022;314:125587.
8. Alocci C, Valvo PS. Feasibility study of a hybrid FRP-steel cable-stayed pedestrian swing bridge. Eng Struct. 2019;189:359-372.
9. Dong SC, Li CG, Xian GJ. Environmental impacts of glass- and carbon-fiber-reinforced polymer Bar-reinforced seawater and sea sand concrete beams used in marine environments: an LCA case study. Polymers. 2021;13(1):154.
10. Yang YQ, Wang X, Wu ZS. Life cycle cost analysis of FRP cables for long-span cable supported bridges. Structure. 2020;25:24-34.
11. Li CG, Guo R, Xian GJ, Li H. Innovative compound-type anchorage system for a large-diameter pultruded carbon/glass hybrid rod for bridge cable. Mater Struct. 2020;53:73.
12. Li CG, Xian GJ. Novel wedge-shaped bond anchorage system for pultruded CFRP plates. Mater Struct. 2018;51:162.
13. Damiani M, Quadrino A, Nisticò N. FRP cables to Prestress RC beams: state of the art vs. a split wedge anchorage system. Buildings. 2021;11(5):209.
14. Xian GJ, Guo R, Li CG, Wang YJ. Mechanical performance evolution and life prediction of prestressed CFRP plate exposed to hygrothermal and freeze-thaw environments. Compos Struct. 2022;293:115719.
15. Li CG, Yin XL, Liu YC, Guo R, Xian GJ. Long-term service evaluation of a pultruded carbon/glass hybrid rod exposed to elevated temperature, hydraulic pressure and fatigue load coupling. Int J Fatigue. 2020;134:105480.
16. Wu WW, He XJ, Yang WR, Wei BY, Alam MS. Durability and microstructure degradation mechanism of FRP-seawater sea-sand concrete structures: a review. Constr Build Mater. 2023;391:131825.
17. Zhou JY, Wang X, Peng ZQ, Wu ZS, Zhu ZG. Evaluation of a large-tonnage FRP cable anchor system: Anchorage design and full-scale experiment. Eng Struct. 2022;251:113551.
18. Li CG, Xian GJ. Design optimization and experimental validation of a novel wedge-shaped bond anchorage system for prestressed CFRP plates. Polym Test. 2019;75:167-174.
19. Liu Y, Zwingmann B, Schlaich M. Carbon fiber reinforced polymer for cable structures-a review. Polymers. 2015;7:2078-2099.
20. Carvelli V, Fava G, Pisani MA. Anchor system for tension testing of large diameter GFRP bars. J Compos Constr. 2009;13:344-349.
21. Correial L, Barris C, França P, Sena-Cruz J. Effect of temperature on bond behavior of externally bonded FRP laminates with mechanical end Anchorage. J Compos Constr. 2019;23:04019036.
22. Schmidt JW, Bennitz A, Täljsten B, Goltermann P, Pedersen H. Mechanical anchorage of FRP tendons: a literature review. Constr Build Mater. 2012;32:110-121.
23. Wang LC, Zhang JY, Xu J, Han QH. Anchorage systems of CFRP cables in cable structures-a review. Constr Build Mater. 2018;160:82-99.
24. Wang X, Xu PC, Wu ZS, Shi JZ. A novel anchor method for multitendon FRP cable: manufacturing and experimental study. J Compos Constr. 2015;19:04015010.
25. Xian GJ, Guo R, Li CG. Combined effects of sustained bending loading, water immersion and fiber hybrid mode on the mechanical properties of carbon/glass fiber reinforced polymer composite. Compos Struct. 2022;281:115060.
26. Li CG, Yin XL, Wang YJ, et al. Mechanical property evolution and service life prediction of pultruded carbon/glass hybrid rod exposed in harsh oil-well condition. Compos Struct. 2020;246:112418.

15480569, 0, Downloaded from https://4spepublications.onlinelibrary.wiley.com/doi/10.1002/pc.28591 by Harbin Institute Of Technology, Wiley Online Library on [22/05/2024]. See the Terms and Conditions (https://onlinelibrary.wiley.com/terms-and-conditions) on Wiley Online Library for rules of use; OA articles are governed by the applicable Creative Commons License

27. Xian GJ, Guo R, Li CG, Hong B. Effects of rod size and fiber hybrid mode on the interface shear strength of carbon/glass fiber composite rods exposed to freezing-thawing and outdoor environments. J Mater Res Technol. 2021;14:2812-2831.
28. Benmokrane B, Ali AH, Mohamed HM, ElSafty A, Manalo A. Laboratory assessment and durability performance of vinylester, polyester, and epoxy glass-FRP bars for concrete structures. Compos Part B: Eng. 2017;114:163-174.
29. Benmokrane B, Elgabbas F, Ahmed EA, Cousin P. Characterization and comparative durability study of glass/Vinylester, basalt/Vinylester, and basalt/epoxy FRP bars. J Compos Constr. 2015;19:04015008.
30. Huang SL, Yan LB, Bachtiar EV, Kasal B. Durability of epoxy and polyurethane bonded timber-hybrid FRP joints under hygrothermal and weathering conditions. J Build Eng. 2022;58:104989.
31. Feng JY, Li N, Wang B, et al. Thermal insulation and mechanical properties of carbon fiber-reinforced thermoplastic polyphthalazine ether sulfone ketone composites reinforced by hollow glass beads. Polym Compos. 2023;44:7941-7952.
32. Han L, Song Y, Qi H, Yang JS, Li S, Liu PA. A comparative study on the mechanical properties of open-hole carbon fiber-reinforced thermoplastic and thermosetting composite materials. Polymers. 2023;15:4468.
33. Bakkal M, Kayihan M, Timur A, et al. Fatigue behavior and self-heating mechanism of novel glass fiber reinforced thermoplastic composite. Adv Compos Mater. 2023;32:899-915.
34. Kwon B, Choe H, Jeong J, Ju H, Kweon JH, Nam YW. Static and fatigue behavior of induction-welded single lap carbon fiber reinforced polyetherketoneketone thermoplastic composite joints. J Compos Mater. 2021;55:4183-4193.
35. Pertuz AD, Díaz-Cardona S, González-Estrada OA. Static and fatigue behaviour of continuous fibre reinforced thermoplastic composites manufactured by fused deposition modelling technique. Int J Fatigue. 2020;130:105275.
36. Wu J, Zhang K, Yang DM. Material extrusion additive manufacturing of recycled discontinuous carbon fibre reinforced thermoplastic composites with different fibre lengths: through-process microstructural evolution and mechanical property loss. Addit Manuf. 2023;78:103839.
37. Zeyrek BY, Aydogan B, Dilekcan E, Ozturk F. Experimental investigation of the recycling of carbon fiber polyetherketoneketone thermoplastic composite. J Thermoplast Compos Mater. 2023;37:1859-1876.
38. Hou ZZ. A Study on the Durability of Glass Fiber Reinforced Thermoplastic Composite. Master thesis, Donghua University. 2019.
39. Zhou P, Li CG, Bai YB, et al. Durability study on the interlaminar shear behavior of glass-fibre reinforced polypropylene (GFRPP) bars for marine applications. Constr Build Mater. 2022;349:128694.
40. Dong SC, Qi X, Tian JW, Zhou P, Li CG, Xian GJ. Durability of glass fiber reinforced thermoplastic polypropylene composite bars under the coupling effect of seawater and sea sand concrete environment and sustained bending. Polym Compos. 2023;45:3194-3209.
41. Hong B, Xian GJ, Li H. Effects of water or alkali solution immersion on the water uptake and physicochemical properties of a pultruded carbon fiber reinforced polyurethane plate. Polym Compos. 2019;40:738-748.
42. Wang B, Li DH, Xian GJ, Li CG. Effect of immersion in water or alkali solution on the structures and properties of epoxy resin. Polymers. 2021;13:1902.
43. Li CG, Zhang YT, Hu SL, et al. Design and mechanical properties of glass fiber reinforced polypropylene polymer composite cableanchor component. Acta Mater Compos Sin. 2022;39(11):5098-5108.
44. Dong SC, Zhou P, Guo R, Li CG, Xian GJ. Durability study of glass fiber reinforced polypropylene sheet under simulated seawater sea sand concrete environment. J Mater Res Technol. 2022;20:1079-1092.
45. Guo R, Xian GJ, Li F, Li CG, Hong B. Hygrothermal resistance of pultruded carbon, glass and carbon/glass hybrid fiber reinforced epoxy composites. Constr Build Mater. 2022;315:125710.
46. Zhang HW. Study on Corrosion Mechanism and Mechanical Properties of GFRP Bars in Alkaline Environment. Master's thesis, Harbin Engineering University. 2015.
47. Lu ZY, Su LZ, Xian GJ, Lu BH, Xie JH. Durability study of concrete-covered basalt fiber-reinforced polymer (BFRP) bars in marine environment. Compos Struct. 2020;234:111650.
48. Sang L, Wang YY, Wang C, Peng XS, Hou WB, Tong LY. Moisture diffusion and damage characteristics of carbon fabric reinforced polyamide 6 laminates under hydrothermal aging. Compos Part A: Appl Sci Manuf. 2019;123:242-252.

How to cite this article: Zhang Z, Ji Q, Guo Z, et al. Design, preparation, and mechanical properties of glass fiber reinforced thermoplastic self-anchor plate cable exposed in alkaline solution environment. Polym Compos. 2024;1-14. doi:10.1002/pc.28591

15480569, 0, Downloaded from https://4spepublications.onlinelibrary.wiley.com/doi/10.1002/pc.28591 by Harbin Institute Of Technology, Wiley Online Library on [22/05/2024]. See the Terms and Conditions (https://onlinelibrary.wiley.com/terms-and-conditions) on Wiley Online Library for rules of use; OA articles are governed by the applicable Creative Commons License

Check for updates

Received: 11 December 2023 | Revised: 18 February 2024 | Accepted: 10 March 2024

DOI: 10.1002/pc.28360

RESEARCH ARTICLE

Polymer COMPOSITES WILEY

Study on the durability of compression behavior for glass fiber-reinforced polypropylene thermoplastic composite bars in various aging environments

Ping Zhou[1,2,3] | Shaoce Dong[1,2,3] | Chenggao Li[1,2,3] | Deao Kong[4] | Yanbo Bai[1,2,3] | Guijun Xian[1,2,3] | Qingrui Yue[5]

[1]Key Lab of Structures Dynamic Behavior and Control, Ministry of Education, Harbin Institute of Technology, Harbin, China

[2]Key Lab of Smart Prevention and Mitigation of Civil Engineering Disasters of the Ministry of Industry and Information Technology, Harbin Institute of Technology, Harbin, China

[3]School of Civil Engineering, Harbin Institute of Technology, Harbin, China

[4]China Railway Construction UnderwaterTunnel Engineering Laboratory, China Railway 14th Bureau Group Co., Ltd., Jinan, China

[5]School of Civil and Resource Engineering, University of Science & Technology Beijing, Beijing, China

Correspondence
Guijun Xian, School of Civil Engineering, Harbin Institute of Technology, 73 Huanghe Road, Nangang District, Harbin 150090, China.
Email: gjxian@hit.edu.cn

Funding information
National Key Research and Development Program of China (2022YFB3706501); Fundamental Research Funds for the Central Universities (Grant No. HIT. OCEF. 2022032 and HIT.NSRIF202234); Program Fund of Non-Metallic Excellence and Innovation Center for Building Materials (24SFP-4); Heilongjiang Natural Science Foundation (LH2021E073)

Abstract

In reinforced concrete structures, GFRP bars are becoming acceptable as internal reinforcement subject to compressive load and hygrothermal environments. The paper presents an experimental study on the compressive behavior, thermodynamic properties, and degradation mechanism of the glass fiber-reinforced polypropylene (GFRPP) bars after aging in distilled water (DW), alkaline solution (AS) and seawater and sea sand concrete (SWSSC) solution at 21, 40, and 60°C up to 120 days. The effect of specimen assembly methods, and slenderness rations (L_u/D_b) on the compressive behavior was evaluated on the control GFRPP bars. After immersion, the compressive strength of the GFRPP bars was significantly affected by the type of solution, immersion time, and temperature. Typically, the compressive strength retention was decreased by 25.8%, 30.0%, and 33.0% at 60°C in DW, AS, and SWSSC solutions, respectively. The degradation mechanism of the compressive behavior of GFRPP bars was revealed through SEM images and FTIR spectroscopy analysis, and the debonding of fiber-resin interfaces, chemical etching of glass fibers, and changes in polypropylene functional groups were confirmed or discovered. Finally, based on the Arrhenius theory, the long-term life prediction of compression strength in three typical service environments was conducted to provide the design guideline for reinforcement concrete.

Highlights

- Effect of specimen assembly and L_u/d_b on compressive behavior of GFRPP bars
- Thermodynamic behavior of the GFRPP bars under different aging environments
- Revealed the degradation mechanism of GFRPP bars under hygrothermal environments
- Predicted the service life of GFRPP bars in typical service environments

KEYWORDS

compressive strength, degradation mechanisms, GFRPP bar, hygrothermal conditions, prediction model

1 | INTRODUCTION

In the last decades, glass fiber-reinforced polymer (GFRP) bars have gained considerable worldwide interest as an effective alternative to steel bars due to their noncorroding, lightweight, high tensile strength and non-conductive properties as reinforcement in concrete members exposed to specific environmental conditions, such as marine and chloride-rich applications.[1–3] Significant research studies have been conducted on GFRP composites to characterize their chemical,[4] physical,[5,6] thermal,[7–9] mechanical,[10–12] and durability properties.[13,14] The cost advantage of GFRP bars being lower than that of steel bars throughout their entire life cycle is also one of the critical advantages.[15] Now these comprehensive and important properties have been specified in ACI 440.3R,[16] ASTM D7957/D7957M,[17] CSA S807,[18] and AASHTO[19] materials specifications and design codes to ensure the proper design, quality, and safety of the GFRP bars reinforcing materials for their utilization as highway barriers, bridges, and concrete pavements.

Although GFRP bars offer several advantages concerning corrosion resistance, they still have quite a few limitations in practical concrete construction applications. One of the application problems is the limitation of bending the currently available GFRP bars that are made of thermoset resin such as epoxy, phenolic, and unsaturated polyester, which can be bent only right after the pultrusion process in the factory.[20] Next, using thermoset resins makes manufacturing complex shapes difficult, generates an inevitable amount of waste during the production process, and prevents recycling of the material at the end of its life cycle.[21] Moreover, due to the molecular structure of thermosetting resins such as epoxy, phenolic, and unsaturated polyester being a three-dimensional cross-linked network structure, the GFRP bars based on them exhibit brittle failure under load, and even the matrix is prone to cracking.[22,23] Additionally, fiber-reinforced thermosetting polymer composites have been used in civil engineering because of their mature preparation technology, lower resin viscosity, and high mechanical properties,[14,24,25] such as epoxy resin-based and polyurethane-based composites. However, a large number of hydrophilic groups in the molecular structure of thermoset resin inevitably undergo hydrolysis and plasticization, resulting in the degradation of the mechanical properties of the thermosetting-based GFRP bars in service.[26] Accordingly, there is a crucial need to develop bendable bars that can be used as shear stirrups or bent to sufficient end anchorage for reinforcement. Thermoplastic composite materials that can be re-melted and cooled at high temperatures have the potential for the applications mentioned above.[22,27–30]

The use of thermoplastic resins as a matrix material in GFRP composites has been growing steadily, especially for automation, aerospace, renewable energy industries, and infrastructure constructions,[21,31] primarily for their recyclability, flexibility, and ability to be processed rapidly. Commonly used thermoplastic matrices for fiber-reinforced polymer composites include polypropylene (PP),[22] polymethyl methacrylate (PMMA),[28] acrylonitrile butadiene styrene (ABS) resin,[32] polyamide (PA),[33] polyphenylene sulfide (PPS),[34] polyetherimide (PET),[35] polyetheretherketone (PEEK),[36] thermoplastic epoxy resin[37] and bioplastics widely applicated in product packaging.[38] Compared to other thermoplastic resins, PP is one of the commodity polymers used in the largest quantities of applications worldwide. Besides being relatively cheap, it has advantages such as being lightweight, moderate strength and deformation, and modifiability.[39] However, PP alone cannot meet the required stiffness and dimensional stability of structural material. Fortunately, glass fiber-reinforced grades have been commercially available on the market for a long time and carbon fiber-reinforced PP is also produced for advanced structural material despite its high price.[40,41] Despite these advantages, manufacturing for thermoplastic-based GFRP bars remains underdeveloped. Volk et al.,[35] conducted on glass-fiber reinforced amorphous polyethylene terephthalate (GFRPET) commingled yarns and found that - with proper design-pultrusion can deliver consistent, high quality (void content <2%) profiles up to at least Φ 40 mm. Alexander et al.[42] pultruded GFRPP bars Φ 6 mm from in-house-made pre-consolidated tapes, demonstrating higher flexural, tensile, and apparent interlaminar shear strength compared to the tapes. All in all, the maturity and improvement of manufacturing equipment and technology of pultrusion have produced high-performance thermoplastic-based GFRP and have also promoted related research toward structural applications.

Almost all of the limited research efforts have aimed at developing bendable thermoplastic-based GFRP bars as an alternative to traditional steel bars used to reinforce concrete structures.[28] Considering GFRP bars have now been increasingly used as longitudinal reinforcement in concrete columns. In the column design and analysis, the contribution of GFRP bars to compression is often ignored or is estimated as a fraction of its tensile strength due to the limited understanding of their compression behavior.[10,43] Moreover, several studies have characterized the compression behavior of the thermosetting-based GFRP using different test methods given the lack of standards and specifications. First of all, direct loading was considered as an initial step in determining GFRP bars' compression strength.[44] However, the results were divergent, and inconsistent strength values were obtained due

15480569, 2024, 9, Downloaded from https://4spepublications.onlinelibrary.wiley.com/doi/10.1002/pc.28360 by Harbin Institute Of Technology, Wiley Online Library on [10/06/2024]. See the Terms and Conditions (https://onlinelibrary.wiley.com/terms-and-conditions) on Wiley Online Library for rules of use; OA articles are governed by the applicable Creative Commons License

to fiber-splitting failure at the ends of GFRP bars. Subsequent studies used steel confinement at the ends of the GFRP bars,[45,46] where unexpected modes of failure appeared such as cutting in the cross-section caused by significant differences in the stiffness of the steel and the transverse direction of the GFRP bars. Moreover, capping the ends of the GFRP bars with hollow steel tubes filled with resin[47] or cementitious grout[10] was reported. These researchers not only obtained the failure mode of the thermosetting-based GFRP bars under compression loading using the above methods but also accurately obtained the compressive strength and modulus value of the bars. However, as far as the authors know, it remains to be verified whether the above-mentioned test methods for the compression behavior of thermosetting-based GFRP bars apply to thermoplastic-based GFRP bars. Furthermore, the application and research of GFRP reinforced concrete showed the presence of water in concrete leads to the hydration reaction of cement leaching out and the formation of alkaline pore solution, which is the most fundamental reason for the performance degradation of GFRP bars during the service period.[22,48] The next instead of the last one, the application and research of GFRP bars reinforced concrete show that,[22,48] the presence of water in concrete leads to the hydration reaction of cement to leaching out and the formation of alkaline pore solution is the most fundamental reason for the performance degradation of the bars during service.

To sum up, to predict the service life of thermoplastic-based GFRP bars, a more comprehensive study of the engineering aspects of failure as well as their compressive behavior under simulated environmental conditions is required.

Thus, this paper investigated the compressive behavior of the GFRPP bars under the effect of deionized water (DW), alkali solution (AS), and seawater-sea sand concrete pore solution (SWSSC) simulating service environments. Firstly, the compression and thermal behavior of the GFRPP bars specimens at different environmental conditions to obtain long-term properties are evaluated. Then, the microstructure analysis was gained to compressive properties' degradation mechanism. Finally, based on the Arrhenius theory, the long-term life prediction of compression strength in three typical service environments was conducted to provide the design guideline for reinforcement concrete.

2 | EXPERIMENTAL PROGRAM OUTLINE

2.1 | Raw materials

The GFRPP bars used in the current study were produced in the Laboratory of Composite Materials and Structures of the Center for Materials Technologies at the Skolkovo Institute of Science and Technology (Skoltech, Moscow, Russia) utilizing the pultrusion technique. The typical pultrusion process, modified for developing the thermoplastic-based GFRP bars, is presented in Figure 1A, and it has also been reported in detail in Reference.[42] The GFRPP bars have a nominal diameter Φ 6.0 mm with smooth surfaces, respectively (Figure 1B). The physical-mechanical properties of the GFRPP bar are shown in Table 1.[22]

2.2 | Design matrix of the specimens

To determine the slenderness ratio (L_u/D_b) of the specimen in the compressive test, the influence of different slenderness ratios ($L_u/D_b = 4$, 8, and 16) on the compression behavior of the GFRPP bars was first studied. Based on the comparative analysis of the compressive strength, stress-displacement curves, and stress–strain curves of the three slenderness ratios, the long-term compressive test was carried out with $L_u/D_b = 8$. Furthermore, five replicates were prepared for each slenderness ratio and condition, as recommended in CSA S807-10 (R2015).

Initially, directly loading GFRP bars was considered in determining their compressive strength. However, the results were divergent, and inconsistent strength values resulted from fiber-splitting failure at the ends of the bars.[3] Therefore, to avoid the above problems, two different methods were attempted when testing the compression performance of GFRPP bars. One capped the ends of the GFRPP bars with a hollow stainless-steel tube filled with a fast-curing epoxy resin, as shown in the Table 2 provides the details on the slenderness ratio (L_u/D_b), unbraced length (L_u), total length (L_t), nominal bar diameter (D_b), and the steel tube/ingot diameter (D_s) of the GFRPP bar specimens.

2.3 | Exposure conditions

The GFRPP bar specimens were completely immersed in DW, AS, and SWSSC solutions inside polypropylene containers. Subsequently, these containers were placed in a constant temperature laboratory (for 21°C condition) and the incubators with temperatures of 40 and 60°C. Except for deionized water (DW) directly provided by the manufacturer, the alkaline solution was prepared using calcium dioxide, potassium hydroxide, and sodium hydroxide according to ACI 440.3R. The simulated SWSSC solution was composed of 0.6 g of NaOH, 1.4 g of KOH, 0.037 g $Ca(OH)_2$, and 35 g NaCl in 1 L of deionized water based on the existing findings.[26,49] Furthermore, the pH values

15480569, 2024, 9, Downloaded from https://4spepublications.onlinelibrary.wiley.com/doi/10.1002/pc.28360 by Harbin Institute Of Technology, Wiley Online Library on [10/06/2024]. See the Terms and Conditions (https://onlinelibrary.wiley.com/terms-and-conditions) on Wiley Online Library for rules of use; OA articles are governed by the applicable Creative Commons License

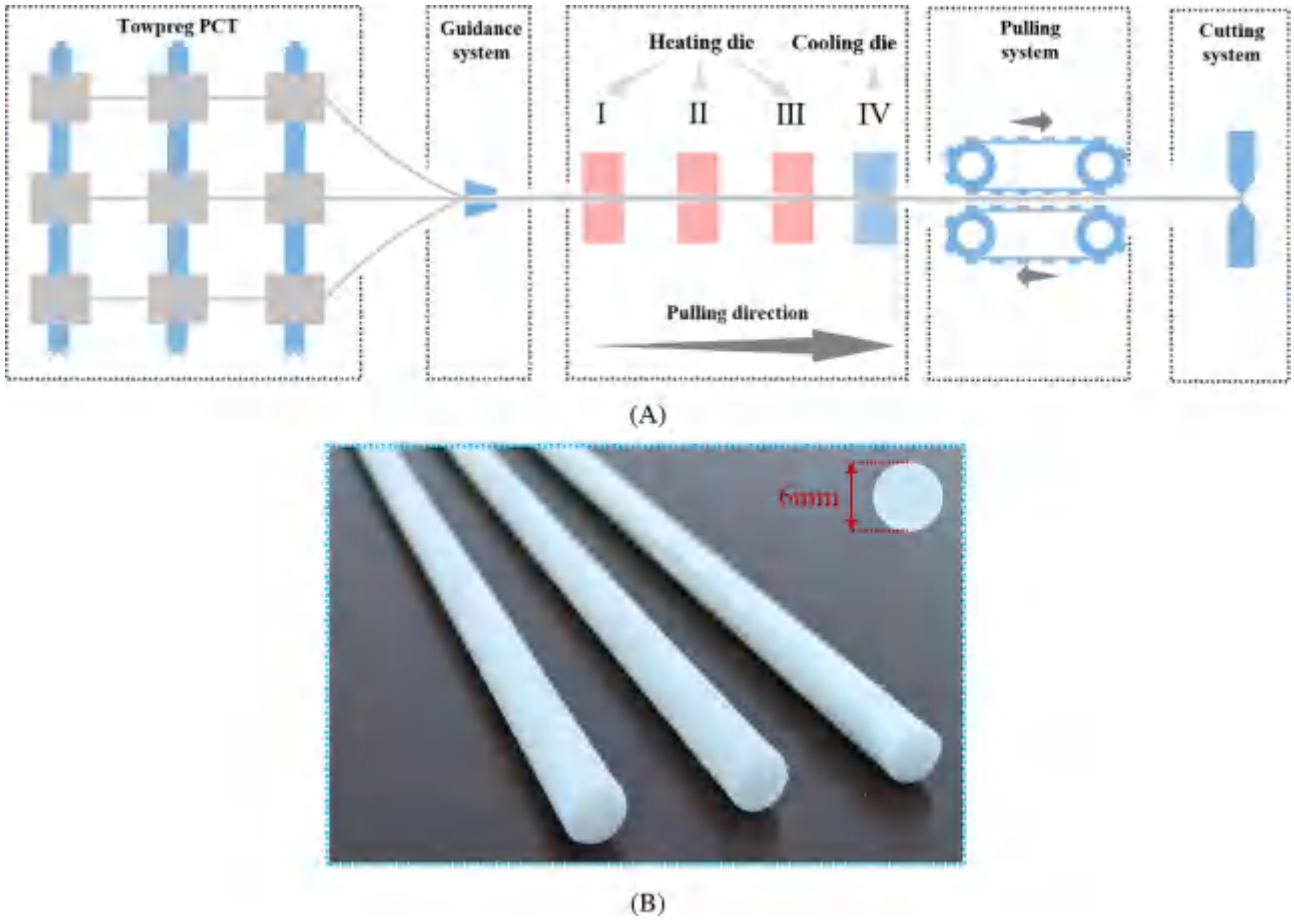


FIGURE 1 (A) Schematic illustration showing a pultrusion process of the GFRPP bars; and (B) GFRPP bars with a diameter of 6 mm used in this investigation.

TABLE 1 Mechanical properties of the investigated GFRPP bars.

Properties	Tensile strength (MPa)	Tensile modulus (GPa)	Ultimate strain (%)	Flexural strength (MPa)	Flexural modulus (GPa)	ILSS (MPa)	TSS (MPa)
Mean	632.0	26.2	2.0	750.0	20.0	17.0	103.5
S.D.	31.4	2.2	0.1	118.0	2.7	1.3	3.7
C.V	5.0	8.4	4.4	15.7	13.5	7.6	3.6

Abbreviations: C.V, coefficient of variation; ILSS, interlaminar shear strength; S.D., standard deviation; TSS, transverse shear strength.

TABLE 2 Specimen matrix.

	Slenderness ratio (L_u/D_b)							
	4		8		16			
Group	L_u (mm)	L_t (mm)	L_u (mm)	L_t (mm)	L_u (mm)	L_t (mm)	D_b (mm)	D_s (mm)
Unconditioned	24.0	48.0	48.0	72.0	96.0	120.0	6.0	22.0
Conditioned	—	—	48.0	72.0	—	—	6.0	22.0

of DW, AS, and SWSSC solutions were measured by applying a high-precision solution pH testing gun to be 7.2, 12.8, and 12.5, respectively.

The GFRPP bar specimens and polypropylene containers were kept at 21, 40, and 60°C for 30, 60, 90, and 120 days of conditioning. Meanwhile, the water level of

15480569, 2024, 9, Downloaded from https://4spepublications.onlinelibrary.wiley.com/doi/10.1002/pc.28360 by Harbin Institute Of Technology, Wiley Online Library on [10/06/2024]. See the Terms and Conditions (https://onlinelibrary.wiley.com/terms-and-conditions) on Wiley Online Library for rules of use; OA articles are governed by the applicable Creative Commons License

the containers was kept constant throughout the study to avoid a pH increase in the solution. In particular, the immersion temperatures were chosen to accelerate the degradation effect of aging, but they were not high enough to produce any thermal-degradation mechanisms.[50] Similarly, the immersed GFRPP bar specimens were tested for compression behavior after drying treatment. Wherein, the procedure was: drying at 60°C for 30 days.

2.4 | Test setup

As illustrated in Figure 2, to obtain the load–displacement behavior of the GFRPP bars accurately, an axial load rate of 1.5 mm/min was adopted by Alajarmeh et al.[50] for GFRP bars under compression testing. The axial strain has been measured employing pasting the axial strain gauges at the mid-height of the GFRPP bars. It is worth noting that the recorded displacements consist of the specimens, the actuator as well as the assembly, instead of the true displacements of the GFRPP bar specimens. Specifically, the actual displacements of the specimens are relatively smaller than the presented ones but exhibit the same trend. It should be acknowledged that the method of attaching a strain gauge on the surface of the GFRPP bar cannot ensure that the compressive process is located on the pressure side of the bar. That is, the starting stage of the curve is line elastic compression. With the pressure and flexion of the bar, the compressed stress release of the side attached to the strain gauge is gradually converted to the tensile side. This brings obstacles to the compilation and analysis of strain data. AlAjarmeh et al.[10] attached the opposite sides of the two of the tested GFRP bars at mid-height to capture the stress–strain behavior. Liu et al.[43] measured the axial and hoop strains by pasting axial and annular strain gauges at the mid-height of the GFRP bars, similarly. Both methods can reduce the possibility of the above situation, but neither can be completely solved. In this study, the calculation of the E_c and ε_c of the GFRPP bars adapted stress–strain curve is a test result with completely compressed. In addition, three failure modes of GFRPP specimens with different L_u/D_b ratios: were presented in Figure 2.

2.5 | Dynamic mechanical analysis test

Dynamic mechanical analysis (DMA, Q800, TA Instruments) was performed on the GFRPP bars before and after immersion in a single cantilever beam clamp loading mode from room temperature to 250°C at 1 Hz and a heating rate of 5°C/min to identify the influence of different test conditions on the mechanical and thermodynamic properties of GFRPP bars. The dimensions of the specimens used for this test were 40 × 5 × 2 mm.

2.6 | SEM and FTIR observations

The surface morphology of GFRPP bars before and after immersion was analyzed using a scanning electron microscope (SEM, VEGA3). Two GFRPP bar specimens were tested for unconditioned and conditioned. The rectangular GFRPP blocks were prepared with a size of 10 × 2 mm^2 and a height of 5 mm. Before testing, the samples were vacuumed and sprayed with gold to increase the electrical conductivity. The test frequency, electric current, and voltage amplitudes were 1000 Hz, 0.7 A, and 30 HV, respectively. Moreover, Fourier transform infrared spectroscopy (FTIR) was used to investigate the characteristic functional chemical groups of the GFRPP bars controlled and conditioned in DW, AS, and SWSSC solutions at 60°C for 30, 60, 90, and 120 days. All the FTIR spectra of this study were obtained in the KBr



FIGURE 2 Mode of failure for the unconditioned GFRPP bars with various L_u/D_b ratios: (A) $L_u/D_b = 16$ (Shear-kinking failure); (B) $L_u/D_b = 8$ (Shear-sliding failure) and (C) $L_u/D_b = 4$(Shear-sliding failure).

15480569, 2024, 9, Downloaded from https://4spepublications.onlinelibrary.wiley.com/doi/10.1002/pc.28360 by Harbin Institute Of Technology, Wiley Online Library on [10/06/2024]. See the Terms and Conditions (https://onlinelibrary.wiley.com/terms-and-conditions) on Wiley Online Library for rules of use; OA articles are governed by the applicable Creative Commons License

matrix and applied with a ThermoFisher Nicolet IS5 Fourier transform infrared spectrometer.

3 | RESULTS AND DISCUSSION

3.1 | Compressive behavior of the GFRPP bars

3.1.1 | Comparison of different specimen assembly methods

The assembly method of GFRPP bar specimens of high-efficiency, reasonable, and accurate is a crucial guarantee for the evolution of the bars' compression performance after immersing solutions. Consequently, compressive strength tests have been conducted on the unconditioned GFRPP bars and the effects of assembly methods of the specimens on compression behavior have been evaluated. The typical stress-displacement curves of the unconditioned GFRPP assembly specimens filled with epoxy resin and constrained with stainless-steel columns are presented in Figure 3, respectively. For all the tested GFRPP bar specimens, a linear stress-displacement relationship was observed at the experiment up to the turning point load, which is the load after which the behavior of the bars becomes non-linear.

For the assembly specimens filled with epoxy resin, the stress-displacement curves of the samples with different L_u/D_b have a significant difference, as shown in Figure 3A. More specifically, the stress-displacement curve of the testing sample with the $L_u/D_b = 16$ is linear before subjecting to compression load to the extreme value. There was no slip throughout the condition. It confirmed that the assembly method with resin filled was a reasonable and feasible preparation method for the GFRPP bar specimens with $L_u/D_b = 16$. Not the same, when the L_u/D_b is 8 and 4, their stress-displacement curve was still linear at the beginning. However, the curve is obvious non-linearity with the characteristics of multi-peak values, when the compression stress value is around 150 MPa. The abnormal feature of the stress-displacement curve was caused by the assembly method of the GFRPP bar specimens. In other words, when the specimens are filled with resin and the compression stress value is about 150 MPa, the GFRPP bar and filled resin interface in the steel tube of the end of the specimen appear to progressive slip under compression loading. In addition, as the L_u/D_b of the GFRPP bar specimens decreases, the stress threshold of slipping will be decreased and the slip stage prolonged.

The typical stress-displacement curves of the mentioned GFRPP bar specimens with $L_u/D_b = 8$, and 4 are presented in Figure 3B. Both ends of the specimens here were constrained with stainless-steel columns. Their stress-displacement curve is linear as a whole stage, and there is little local non-linear turning point on the curve. The minimal slip can be eliminated through the tight assembly of specimens and the addition of strain monitoring systems. Compared with the compression stress-displacement curve of the two assembly methods GFRPP bar specimens, the strength obtained by the test sample

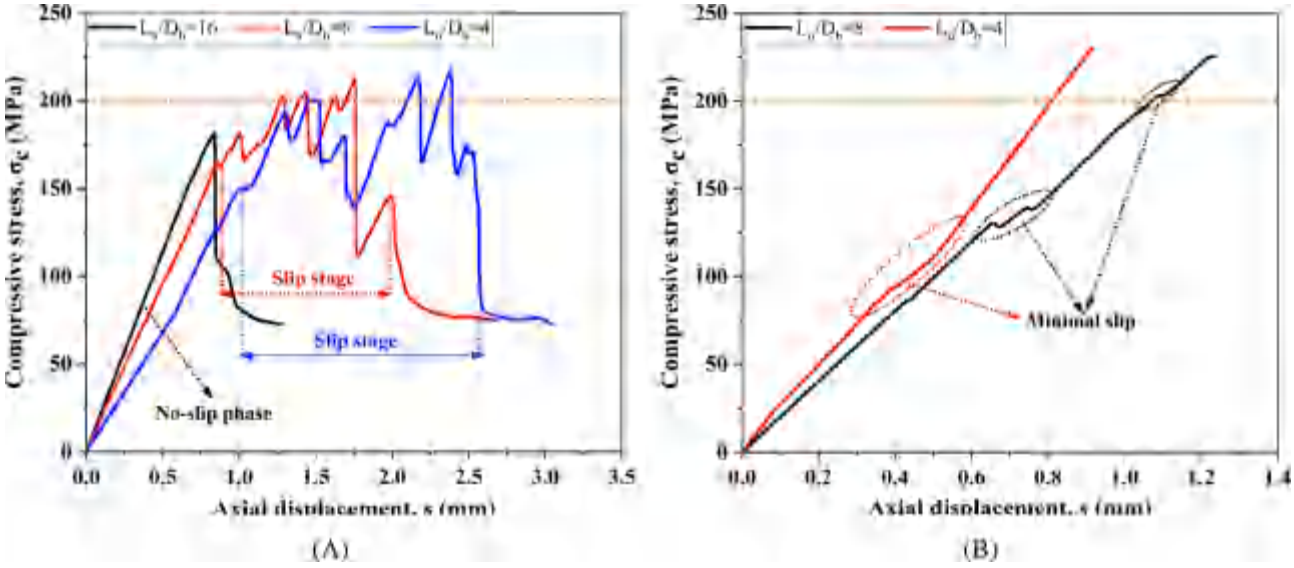


FIGURE 3 The typical stress-displacement curves of the unconditioned GFRPP bar specimens subjected to compression testing using two different assembly methods: (A) The assembly specimens filled with epoxy resin; (B) The specimen with stainless-steel columns constrained.

15480569, 2024, 9, Downloaded from https://4spepublications.onlinelibrary.wiley.com/doi/10.1002/pc.28360 by Harbin Institute Of Technology, Wiley Online Library on [10/06/2024]. See the Terms and Conditions (https://onlinelibrary.wiley.com/terms-and-conditions) on Wiley Online Library for rules of use; OA articles are governed by the applicable Creative Commons License

with stainless-steel columns constrained is 10 ∼ 20% higher than the strength of another type of specimen. In addition, the GFRPP bar specimens with stainless-steel columns have the advantages of simple preparation and the accessories can be reused. It is worth noting that even if the fast-curing epoxy resin was used to fill the stainless-steel tubes to fabricate the GFRPP bar specimens for compression testing, this process requires at least 24 h. Although improving the ambient temperature can accelerate the solidification of epoxy resin, it still cannot meet the GFRPP bar compression testing test required. Since the high-temperature environment can cause the water in the GFRPP-conditioned specimen to evaporate after immersing. In addition, the exposure of the open space for a long time will also result the water volatilization. No matter any form of moisture loss in the conditioned GFRPP bars, it will inevitably produce errors in the test results. Based on these disadvantages, the manufacturing method is applied to prepare all of the subsequent conditioned GFRPP bar specimens.

3.1.2 | Compressive behavior of the GFRPP bars with different slenderness ratios

Under the axial compression load, the typical modes of failure of the traditional thermoset-based GFRP bars depend on the L_u/D_b ratio. These failure modes are categorized as shear-kinking, buckling-splitting, shear-sliding, and shear-softening.[3,10,51] Figure 2 represents the typical modes of failure of the unconditioned GFRPP bars with various L_u/D_b rations. Shear-kinking failure was observed for GFRPP bars with a L_u/D_b ration of 16, which can be described as a severe inclined shear fracture in the cross-section, resulting in the top fractured bar shifting out of the axis as shown in Figure 2A. In this failure mode of mechanism, the tensile strength capacity of the polypropylene (PP) holding the longitudinal glass fibers was exceeded due to the high lateral expansion of the cross-section of the bars under the effect of Poisson's ratio. Before the maximum load, the PP matrix might have developed some micro-cracks, which would have reduced the shear resistance along the cross-section, leading to glass fiber kinking. As shown in Figure 2B,C, as the L_u/D_b ratio decreases, the failure mode has changed from shear-kinking to shear-sliding. This mode of failure occurred due to strong compression and tension stresses at the ends of the GFRPP bar cross-section. In addition, different from the thermoset-based GFRP bars,[3] the failed GFRPP bars with the L_u/D_b ratios of 8 and 4 could not regain their straightness after the load was released with obvious thin longitudinal splitting cracks on the surface of the bars.

The ultimate compressive load (P_c), compressive strength (σ_c), compressive modulus (E_c), and ultimate compressive strain (ε_c) are listed in Table 3. Among them, the compressive modulus (E_c) was calculated as the slope of the linear elastic part of the stress and strain curve. The approach suggested by ASTM D7205/D7205M to determine the tensile modulus of the FRP bars. As mentioned above, the L_u/D_b ratio had a significant effect on the failure mode and the σ_c of the GFRPP bars. When the L_u/D_b ratio increased from 8 to 16, the tested result of the GFRPP bars became unstable. The failure mode shifted from shear-sliding to shear-kinking due to the increased unbraced length of the bars.

As noted in Table 3, this resulted in a reduction of 45.4% in the maximum σ_c value at the L_u/D_b ratio of 8. Moreover, the stress–strain behavior was nonlinear before failure causing the E_c and ε_c of the bars that cannot be calculated reliably. When the L_u/D_b ratio decreased from 8 to 4, except for the failure mode of the GFRPP bars and the ε_c, there was no significant change. The σ_c and E_c decreased by 7.2% and 6.3%, respectively. In addition, the L_u/D_b ratio of 4 showed a higher standard deviation and coefficient of variation of the test results compared to the L_u/D_b ratio of 8. Based on the above discussion, this study used GFRPP bars with a L_u/D_b ratio of 8 to conduct its durability research on compressive behavior. At the same time, the original σ_c, E_c, and ε_c of the GFRPP bars are 223.83 MPa, 31.71 GPa, and 0.68%, respectively. Sadeghian[52] and Khorramian and Alajarmeh et al.[3] adopted the same L_u/D_b ratio to study the compressive behavior of the thermoset-based GFRP bars at room temperature and high temperature. In addition, the study on the compression performance of GFRPP bars with different L_u/D_b ratios first obtains the basic compression performance parameters of the material and determines the compression failure mode. The research results may promote the optimization of the shape parameters of thermoplastic GFRPP reinforcement ribs. Secondly, compared with other L_u/D_b ratios, GFRPP bars have the highest compressive strength when the L_u/D_b ratio is 8. This aspect ratio can be widely recommended and adopted in subsequent compression tests of thermoplastic GFRP bars. Finally, the use of GFRPP bars in reinforced concrete columns and other structures is recommended as a reference when designing the spacing between thermoplastic GFRP stirrups.

3.2 | Durability on compressive behavior of the GFRPP bars

As shown in Figure 4, shear-sliding failure was observed for GFRPP bars with a L_u/D_b ratio of 8 in DW, AS, and

15480569, 2024, 9, Downloaded from https://4spepublications.onlinelibrary.wiley.com/doi/10.1002/pc.28360 by Harbin Institute Of Technology, Wiley Online Library on [10/06/2024]. See the Terms and Conditions (https://onlinelibrary.wiley.com/terms-and-conditions) on Wiley Online Library for rules of use; OA articles are governed by the applicable Creative Commons License

TABLE 3 Compressive properties of the unconditionally tested GFRPP bars with various L_u/D_b ratios.

	Load (N)			Strength (MPa)			Modulus (GPa)			Strain (%)		
Group	Mean	S.D	C.V	Mean	S.D	C.V	Mean	S.D	C.V	Mean	S.D	C.V
$L_u/D_b = 4$	5981.18	491.50	8.22	207.78	12.66	6.09	29.70	1.32	4.44	−0.68	0.09	13.08
$L_u/D_b = 8$	6325.41	273.87	4.33	223.83	9.69	4.33	31.71	1.12	3.53	−0.68	0.06	9.52
$L_u/D_b = 16$	3456.25	368.39	10.66	122.30	13.04	10.66	N/A	N/A	N/A	N/A	N/A	N/A

Abbreviations: C.V, coefficient of variation; S.D, standard deviation.

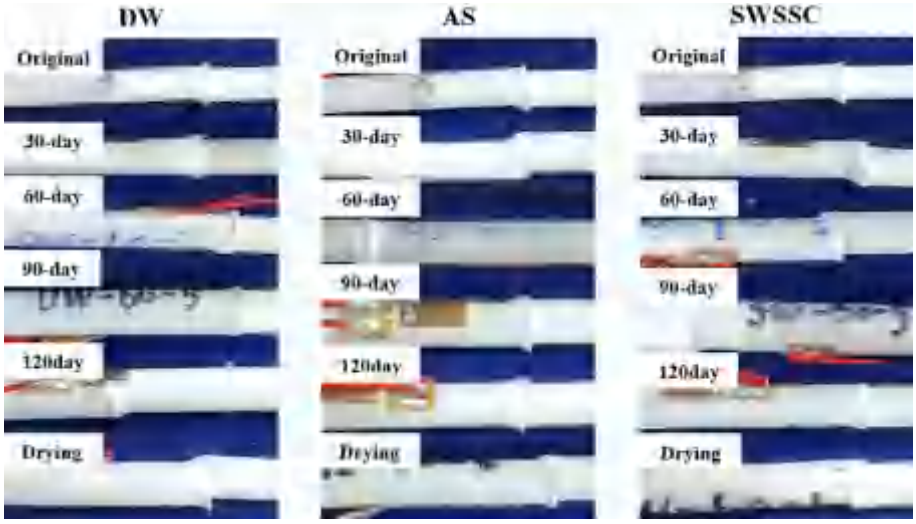


FIGURE 4 Shear-sliding failure of the tested GFRPP bars with L_u/D_b ratio of 8 immersed in DW, AS, and SWSSC at 60°C after different aging times.

SWSSC at 60°C for different immersion times. First of all, the GFRPP bars immersed in the three types of solutions all appeared "texture" distributed along the axis on the bars' surface. The formation of the "texture" is closely related to the manufacturing process of the GFRPP bars. Inevitably, there is glass fiber inside and on the surface of the bars that have not been completely impregnated and coated with PP. After immersing, the blank existing at the interface between the glass and PP is filled with the immersion solution. Specifically, this is since a very small number of glass fibers on the surface of GFRPP bars are not completely covered by polypropylene resin during the manufacturing process, or there are microcracks in the polypropylene matrix that run through the bar's surface and the glass fiber surface. The presence of these defects exposes the glass fibers to the immersing environment, resulting in the formation of white textures under the action of alkaline solutions. The formation mechanism of white texture is explained in section 3.4.3. Noticeably, with the increase of the immersing time, the number of the "texture" has not significantly increased. Furthermore, a layer of the white solid can be observed on the surface of GFRPP bars, which were immersed in AS and SWSSC solutions for 60 days. However, no white layered solid was found on the surface of the GFRPP bars in the DW solution.

In general, compared with the compression behavior of the unconditioned GFRPP bars mentioned above, the immersing solutions and time have no significant impact on the failure mode of the GFRPP bars under compression load. The shear-sliding failure is like a shear-kinking failure, except without a thinner shear plane and less inclination of the longitudinal filament. In the same immersing solution, with the increase of the aging time and immersion temperature, the shear plane thickness in those failure GFRPP bars is reduced. The main reason for this phenomenon is that no matter what kind of immersion solution, it causes a local deserted debonding to the glass fiber-PP resins.[22] Moreover, there is a difference in the transmission of load on the GFRPP bar due to the debonding of the glass fiber-PP interface, which is manifested as a decrease in the compression strength of the bars. Meanwhile, the crushing behavior in the failure mode was weakened.

Figure 5 presents the typical stress–strain behavior of the GFRPP bars after different aging times in DW, AS, and SWSSC solutions at 21, 40, and 60°C with a L_u/D_b ratio of 8. Similar to unconditioned bars, a linear elastic stress–strain behavior was observed in GFRPP bars after 0-4 M (months) immersed in DW solution, as shown in Figures 5A, including test samples of drying after

15480569, 2024, 9, Downloaded from https://4spepublications.onlinelibrary.wiley.com/doi/10.1002/pc.28360 by Harbin Institute Of Technology, Wiley Online Library on [10/06/2024]. See the Terms and Conditions (https://onlinelibrary.wiley.com/terms-and-conditions) on Wiley Online Library for rules of use; OA articles are governed by the applicable Creative Commons License

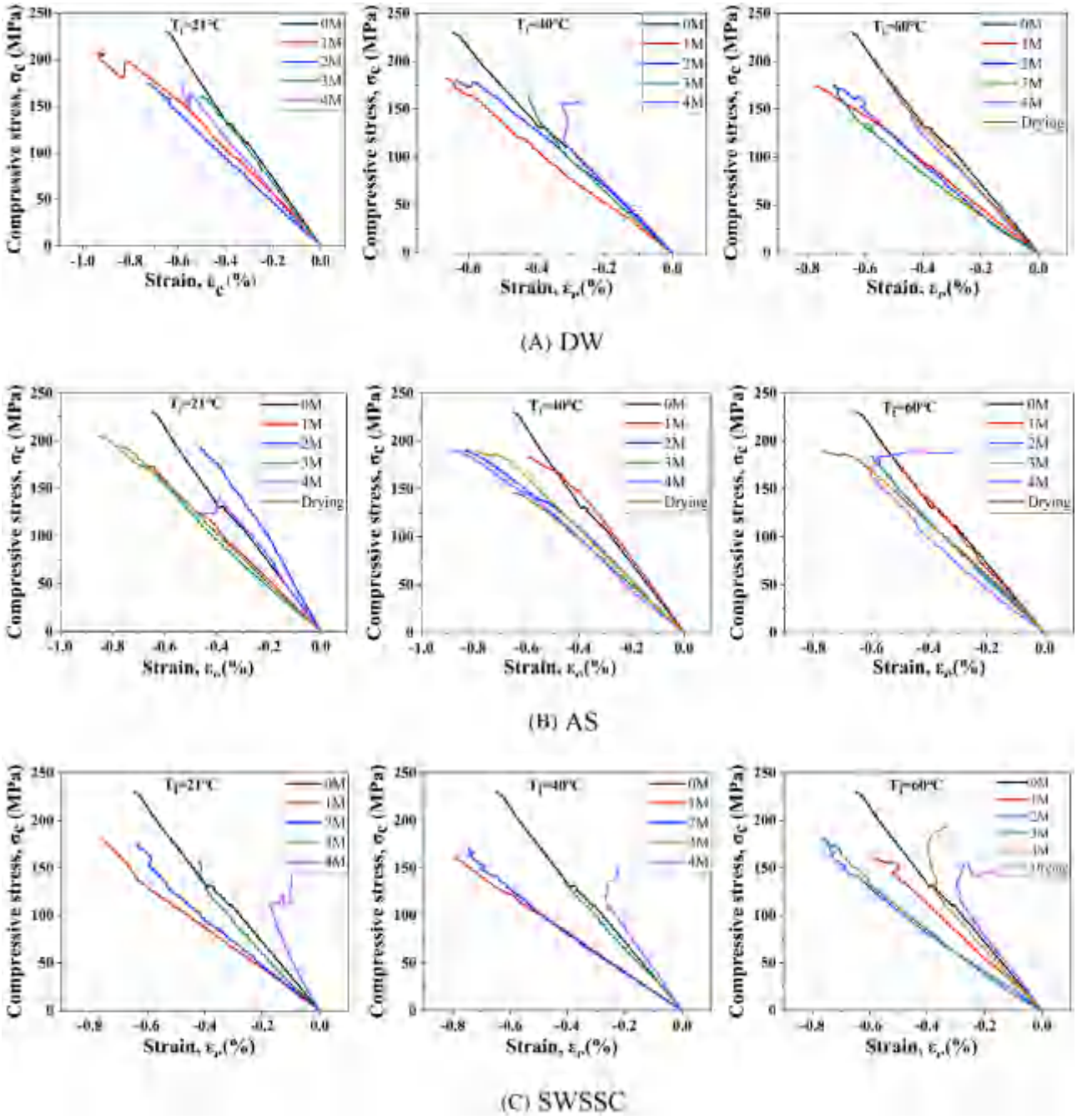


FIGURE 5 The typical stress–strain behavior of the GFRPP bars tested after different aging times in (A) DW; (B) AS and (C) SWSSC solutions at 21, 40, and 60°C.

120 days of immersing. A strain reading was measured by the strain gauge attached to one side of the bars until failure. Combined with data from Table 4, with the increase of the immersing time and temperature, the compressive strength (σ_c) decreased. Among them, after 120 days of 21, 40, and 60°C DW solution immersed, σ_c of the GFRPP bar was reduced by 20.0%, 21.4%, and 25.8%, respectively. Interestingly, σ_c of the bars immersed at 60°C and drying is only decreased by 13.3%, which shows that the loss of the σ_c can be restored partially. On the other hand, the effect of the immersing time and temperature on the compressive modulus (E_c) is weaker than σ_c. the E_c decreased by 9.8%, and the E_c of the GFRPP bars after drying decreased by 7.8%. Moreover, after 120 days of 21, 40, and 60°C DW solution immersed, the ultimate compressive strain (ε_c) of the bars reduced significantly. Those reduction of 22.1%, 17.6%, and 19.1%, respectively. Considering the test error and other potential influencing factors, the effect of immersing temperature on the ε_c was not significant. Similarly, the loss of ε_c for drying GFRPP bars is only 4.4%.

15480569, 2024, 9, Downloaded from https://4spepublications.onlinelibrary.wiley.com/doi/10.1002/pc.28360 by Harbin Institute Of Technology, Wiley Online Library on [10/06/2024]. See the Terms and Conditions (https://onlinelibrary.wiley.com/terms-and-conditions) on Wiley Online Library for rules of use; OA articles are governed by the applicable Creative Commons License

TABLE 4 Compressive strength (σ_c) of the GFRPP bars with $L_u/D_b = 8$ and different conditions.

Conditions	Temperatures (°C)	Time (days)	σ_c (MPa)	S.D (MPa)	C.V (%)	The retention of σ_c (%)
DW	21	0	223.83	9.69	4.33	100
		30	218.28	8.00	3.67	97.52
		60	211.17	20.92	9.91	94.34
		90	185.93	3.36	1.81	83.07
		120	179.00	12.16	6.79	79.97
	40	30	216.63	13.32	6.15	96.78
		60	197.36	5.96	3.02	88.17
		90	183.01	10.59	5.79	81.76
		120	175.93	6.18	3.51	78.60
	60	30	213.68	5.27	2.47	95.47
		60	193.40	7.75	4.01	86.40
		90	182.98	13.19	7.21	81.75
		120	166.03	9.80	5.90	74.18
		Drying	194.02	7.11	3.66	86.68
AS	21	30	206.95	12.16	5.88	92.34
		60	199.29	11.41	5.73	89.04
		90	184.22	13.30	7.22	82.30
		120	173.39	11.10	6.40	77.47
		Drying	197.84	6.33	3.20	88.39
	40	30	202.95	21.54	10.61	90.67
		60	189.18	2.23	1.18	84.52
		90	181.95	9.18	5.04	81.29
		120	173.26	9.18	5.30	77.41
		Drying	190.94	13.96	7.34	85.31
	60	30	191.7	2.95	1.54	85.65
		60	185.86	5.81	3.12	83.04
		90	175.49	8.51	4.85	78.40
		120	156.74	18.95	12.09	70.03
		Drying	187.53	4.89	2.61	83.78
SWSSC	21	30	196.88	11.00	5.59	87.96
		60	183.91	5.67	3.08	82.17
		90	175.77	6.58	3.74	78.53
		120	156.96	5.57	3.55	70.12
	40	30	189.54	5.53	2.92	84.68
		60	178.36	10.02	5.62	79.69
		90	175.23	4.44	2.54	78.29
		120	150.37	8.55	5.69	67.18
	60	30	186.77	6.73	3.60	83.44
		60	177.96	10.98	6.17	79.51
		90	166.23	8.40	5.05	74.27
		120	149.99	2.03	1.35	67.01
		Drying	196.01	7.43	3.79	87.57

15480569, 2024, 9, Downloaded from https://4spepublications.onlinelibrary.wiley.com/doi/10.1002/pc.28360 by Harbin Institute Of Technology, Wiley Online Library on [10/06/2024]. See the Terms and Conditions (https://onlinelibrary.wiley.com/terms-and-conditions) on Wiley Online Library for rules of use; OA articles are governed by the applicable Creative Commons License

Figures 5B presents the effect of conditioning in AS solution at 21, 40, and 60°C on the compression stress–strain behavior of the GFRPP bars, and the detailed results are listed in Table 4. As found, three types of immersing temperatures all show that σ_c of the bars decreased rapidly during initial immersion (∼60 days) and leveled off to tend to be stable up to the end of aging. After immersing at 21, 40, and 60°C in AS solutions for 120 days, the σ_c of the bars was 173.39, 173.26, and 156.74 MPa, respectively. Its E_c evolution is consistent with the laws in the DW solution. Moreover, with the immersion temperature increasing, the ε_c of the GFRPP bars reduction is more significant. It is worth noting that this reduction increased with the increase of immersing temperature. However, for drying GFRPP bars, recovery losses can also increase as the immersing temperature increases. As far as the GFRPP bar exposed in the SWSSC solution, its compressive stress–strain curves at different temperatures and time conditions are shown in Figures 5C. After a 120-day solution immersed at 21, 40, and 60°C, the retention of σ_c the GFRPP bars is 70.12%, 67.18%, and 67.01%. Generally, the σ_c values considerably decreased when the bars were exposed to SWSSC solution higher than others. However, for the GFRPP bars of drying, it is also the highest σ_c in three immersing environments. From our previous study on water absorption of GFRPP bars in two different immersing solutions,[22,53] it can be found that at the same immersing temperature, the water absorption and diffusion rate of GFRPP bars in the SWSSC solution is twice that of AS; However, the saturation absorption rate is the opposite. The main reason for this phenomenon is that the pH value of the AS (12.8) is higher than that of the SWSSC (12.5). From Equation (2),[48] it can be seen that in the same alkaline solution, the higher the pH value of the immersing solution, the more solids precipitate in the solution. Furthermore, these solids to some extent compensate for the rate of the solution's micro-voids inside the GFRPP bars. Because the density of these solid precipitates is higher than that of GFRPP bars and immersion solutions, they also exhibit higher saturation water absorption. Based on the above research results, it can be concluded that the micro-voids in GFRPP bars can be filled to a certain extent in AS solution. But it will not occur during SWSSC.

3.3 | Thermodynamic properties of GFRPP bar

Herein, storage modulus (E′) or dynamic modulus is related to Young's modulus. It is associated with the stiffness of the bar and determines how flimsy a material is. What is more important, E′ is the GFRPP bar a tendency or ability to store energy applied to it. Conversely, loss modulus (E″) or dynamic loss modulus is a viscous response of the GFRPP bar regarded as a tendency to dissipate energy applied to it. Tan δ is regarded as the mechanical damping factor defined as the ratio of loss and storage modulus. Figure 6 shows the effect of temperature on the E′, E″, and Tan $\delta$of the GFRPP bar. For the reason that the glass transition temperature (T_g) of PP is ∼ −10°C, the melting temperature is 165∼180°C.[54,55] Obviously, for the E′, it decreases linearly with the test temperature. This linear relationship is significantly different from the T_g. Therefore, through the method of discontinuous linearity fitting, it can be found that the reduction rates the E′ when the test temperature is higher than T_g is about 5 times the reduction rate at a

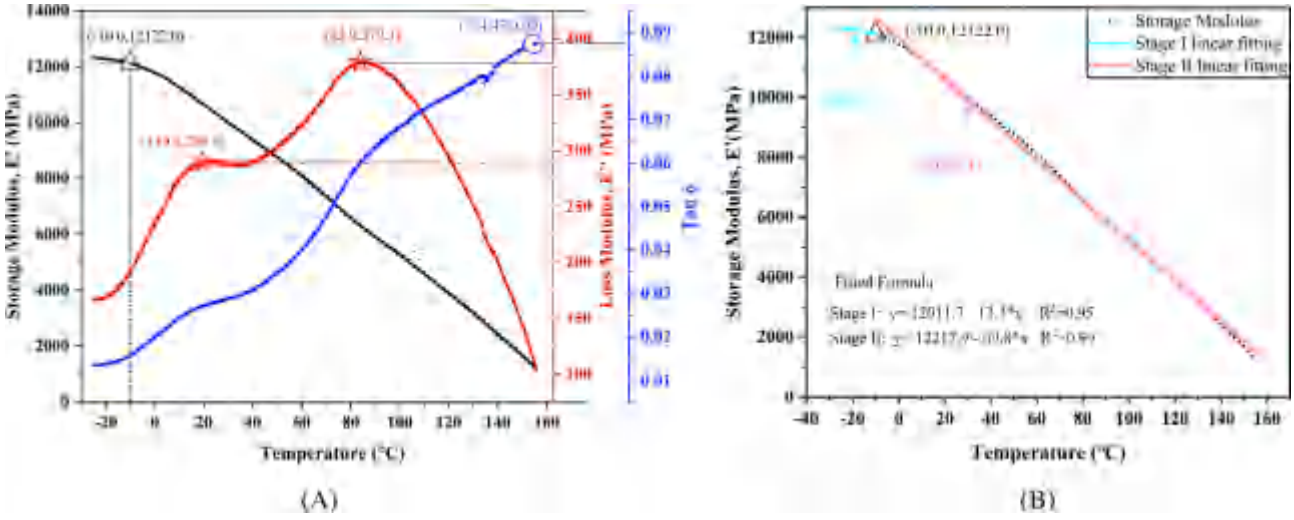


FIGURE 6 The dynamic mechanical analysis curves for the unconditioned GFRPP bars.

15480569, 2024, 9, Downloaded from https://4spepublications.onlinelibrary.wiley.com/doi/10.1002/pc.28360 by Harbin Institute Of Technology, Wiley Online Library on [10/06/2024]. See the Terms and Conditions (https://onlinelibrary.wiley.com/terms-and-conditions) on Wiley Online Library for rules of use; OA articles are governed by the applicable Creative Commons License

temperature less than T_g in Figure 6B. Simultaneously, the values of E″ is first increased, and then decreased within the −25 ~ 155°C temperature range. It has the characteristics of obvious dual peaks when increasing. In addition, when the test temperature is ~84°C, the E″ reaches the maximum value of 379.1 MPa. As the test temperature increases, the Tan δ curve continues to increase non-linearly until the maximum value of 0.09 at 154°C. Based on the above discussion of the unconditioned thermal behavior of the GFRPP bar, the effects of DW, AS and SWSSC solutions on the E′, E″, and Tan δ of the immersed GFRPP bar.

The typical dynamic mechanical analysis curves for the GFRPP bar immersed in the three different solutions for 120 days at 60°C are shown in Figure 7. Previously, Figure 7A represents the comparison of E′ for GFRPP bar before and after immersion. At any given temperature range (30 ~ 155°C), the E′ of bars were lowered after the immersion process. Reduction in E′ is more severe for the bar immersed in SWSSC solution, followed by AS and DW solutions. Quantitatively, the E′ at the 30°C reduced until 796, 864, and 3400 MPa for specimens immersed in DW, AS, and SWSSC solutions respectively. Further, through the linear fitting of the data of this interval, the change rate of the E′ is 69.9, 73.9, and 53.7 for DW, AS, and SWSSC solutions. Compared with the E′ change rate of the control, it increased by 15.7% and 5.7% immersed in DW and AS solutions and reduced by 23.2% in SWSSC solution. The phenomenon shows that the solution of the immersion has reduced the stiffness of the GFRPP bar, the SWSSC solution has the most significant impact, and the others are the same.

Last but not least, Figure 7B shows the comparison of E″ for GFRPP bar before and after immersion. When the testing temperature is less than 60°C, the E″ of the GFRPP bar in the three solutions immersed significantly increased, which is consistent with the E′. Moreover, the difference between the second peak and the first peak (ΔE″) on the curve represents the changes in the amount of E″ in the temperature range of 30 ~ 84.5°C. There is no doubt that the solution immersing caused ΔE″ are reduced, and the viscosity growth rate of the corresponding GFRPP bar is accelerated. From this perspective, the effect of AS and SWSSC solutions on it is very significant, but not for DW. Furthermore, the effects of DW, AS and SWSSC solutions on the Tan δ of the immersed GFRPP bar, are shown in Figure 7C. Tan δ increased sequentially in DW, SWSSC and AS solutions. This indicates the consumption of Tan δ and the pH value of the immersion solution.

3.4 | Degradation mechanism of GFRPP bars

3.4.1 | SEM images

The surface of unconditioned and immersed GFRPP specimens after the compression test is shown in Figure 8. Furthermore, the effect of the aging on the micrographs of the GFRPP bars in Figure 8B-D. Except for a small number of micro-voids and micro-cracks found inside the unconditioned GFRPP bars, as shown in Figure 8A, the surface of the glass fiber is wrapped in PP resin. It shows that glass fiber is adequately impregnated in PP and has a strong bond between them. The obvious debonding of the glass fiber-PP resin interface in DW, AS and SWSSC solutions was observed in Figure 8B,C. Figure 8D was luckily observed after immersing in AS and SWSSC solutions, representing the etching of the glass fiber located on the surface of the micro-voids inside the GFRPP bar.

3.4.2 | FTIR spectral analysis

Some samples were scraped from the control and conditioned GFRPP bar for the FTIR analysis, the result is

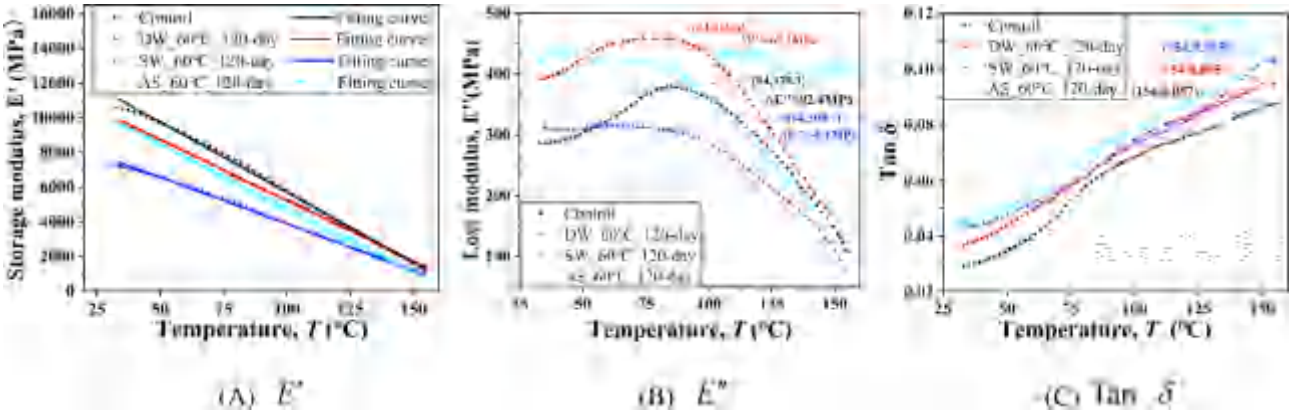


FIGURE 7 Variations of dynamic mechanical behavior for GFRPP bar after exposure to different solutions for 120 days at 60°C.

15480569, 2024, 9, Downloaded from https://4spepublications.onlinelibrary.wiley.com/doi/10.1002/pc.28360 by Harbin Institute Of Technology, Wiley Online Library on [10/06/2024]. See the Terms and Conditions (https://onlinelibrary.wiley.com/terms-and-conditions) on Wiley Online Library for rules of use; OA articles are governed by the applicable Creative Commons License

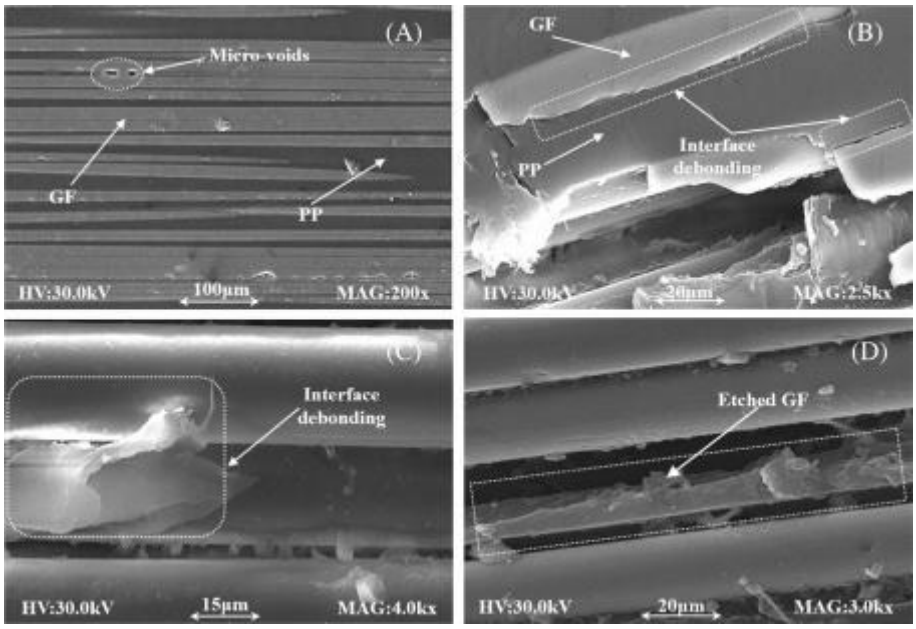


FIGURE 8 Micrographs of the GFRPP bar before and after immersion: (A) unconditioned GFRPP bar; (B) and (C) the debonding of the glass fiber-PP matrix interface of the aging specimens; and (D) glass fiber etching in AS and SWSSC solutions.[53]

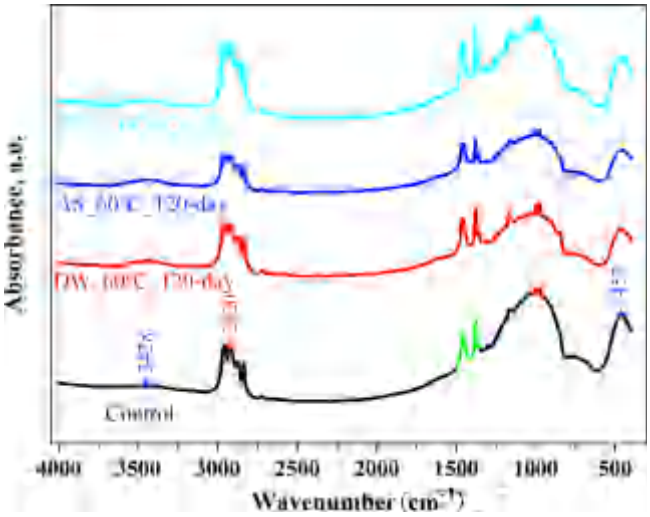


FIGURE 9 Comparison of FTIR spectrum of the GFRPP bars under different aging conditions.

shown in Figure 9. Analysis of FTIR spectra allowed for the identification of the characteristic functional groups occurring in the chemical structure of glass fiber and PP in the GFRPP bar. The proper characteristic is presented in Table 5. 2920 cm^{-1} for PP, which is thought to change little with aging, as corroborated in a study by Brandon et al.[56] Based on research, the peak at 2920 cm^{-1} is defined as the reference peak of the GFRPP bar for FTIR spectrum analysis. Additionally, the peaks at 3428 and 457 cm^{-1} are used to quantitatively characterize the effects of different immersion solutions on the glass fiber.[57] On the other hand, the peaks at 974–998 and 1376–1475 cm^{-1} were analyzed to evaluate the aging of PP.[56]

TABLE 5 Characteristic FTIR absorption bands for GFRPP.[56,57]

Wave number (cm^{-1})	Absorbing group	Type of vibration
3428	-O-H	Stretching vibrations
457	Si(Al)-O-Si	Bending vibrations
2920	$-CH_2$	Asymmetrical stretching
1376 ~ 1457	$-CH_3$	Asymmetrical and asymmetrical stretching
998	$-CH_3$	Asymmetrical rocking
974	C-C-CH_3	Asymmetrical rocking-asymmetrical stretching

The absorbing group of -O-H stretching vibrations corresponding peak (3428 cm^{-1}) shape changes with the immersion solutions are shown in Figure 10A. The area of the closed surrounded by the peak curve and its baseline is used as a quantitative indicator, which is adapted to evaluate the effects of different immersion solutions on the -O-H group of glass fiber in the GFRPP bar. The aging of immersing resulted in the area decreasing. Compared with the unconditional specimen, those areas were reduced by 25.2%, 32.1%, and 53.9% in DW, AS, and SWSSC solutions. Similarly, as shown in Figure 10B, the group of Si(Al)-O-Si (457 cm^{-1}) bending vibrations decreased by 34.6%, 49.6%, and 49.6%. As a result of this, glass fiber is sensitive to immersion solutions. This phenomenon also confirms the occurrence of the above Equation 1, Equation 2, Equation 3.

The group of $-CH_3$ (asymmetrical and asymmetrical stretching and asymmetrical rocking) and C-C-CH_3

15480569, 2024, 9, Downloaded from https://4spepublications.onlinelibrary.wiley.com/doi/10.1002/pc.28360 by Harbin Institute Of Technology, Wiley Online Library on [10/06/2024]. See the Terms and Conditions (https://onlinelibrary.wiley.com/terms-and-conditions) on Wiley Online Library for rules of use; OA articles are governed by the applicable Creative Commons License

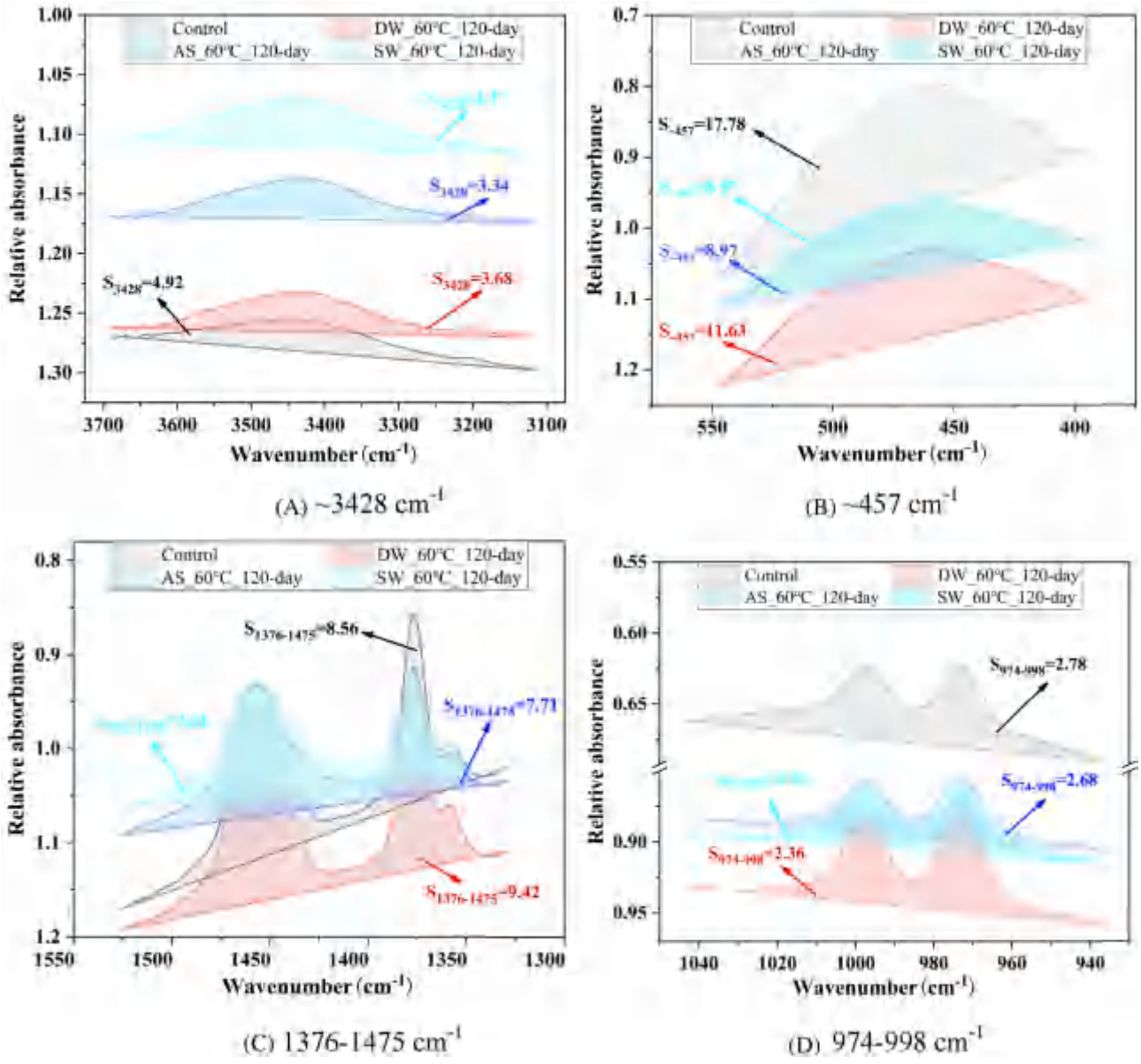


FIGURE 10 Characteristic FTIR spectra of glass fiber and PP: (A) ~3428 cm^{-1} and (B) ~457 cm^{-1} for glass fiber; (C) 1376–1475 cm^{-1} and (D) 974–998 cm^{-1} for PP.

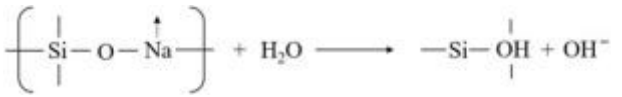
(asymmetrical rocking-asymmetrical stretching) are adapted to compare the influences of the immersion solutions on the PP matrix in GFRPP bar in Figure 10C,D. Compared with glass fiber, the influence of immersing solutions on the PP matrix is less. In particular, the amount of quantitative peak area of -CH_3 (asymmetrical and asymmetrical stretching) in the aging solution changes by less than 10%. If the contact area of the glass and resin in immersing is considered, this effect will be even more significant. The effect of SWSSC immersing environment on -CH_3 (asymmetrical and asymmetrical stretching) is significantly different from DW and AS, which may be caused by Cl^- in SWSSC. Meanwhile, the difference also exists in the absorption curve of -CH_3 (asymmetrical rocking) and C-C-CH_3 (asymmetrical rocking-asymmetrical stretching). In addition, Cl^- in SWSSC has a certain impact on PP functional groups, which has also been confirmed in the study of Brandon.[56]

3.4.3 | The degradation mechanism of GFRPP bar

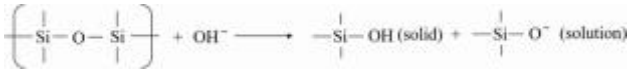
Considering that PP resin is a hydrophobic polymer, the water absorption rate of the isotropic PP sample was 0.03% w/w.[58] This type of water is mainly derived from the reaction of glass fiber and different immersion

15480569, 2024, 9, Downloaded from https://4spepublications.onlinelibrary.wiley.com/doi/10.1002/pc.28360 by Harbin Institute Of Technology, Wiley Online Library on [10/06/2024]. See the Terms and Conditions (https://onlinelibrary.wiley.com/terms-and-conditions) on Wiley Online Library for rules of use; OA articles are governed by the applicable Creative Commons License

solutions. E-glass fiber dissolution in DW solution is termed leaching,[59] as shown by Equation (1). By this chemical response, alkalis are extracted from the glass structures, and the leaching behavior continues as long as alkalis are available in the glass structure. Those alkalis are Ca^{2+}, Al^{3+}, K^{+}, and Mg^{2+}, typically available in fiber composition.[48] There is no doubt that the hydrogen oxides increase the pH values of the immersion solution. When the pH values are higher than 9, the Si networks (Si-O-Si, Si-O-Na, and Si-O-K) of the glass fiber would be affected according to Equation (2).[48] In AS and SWSSC environments, E-glass fibers can degrade directly by Si-O-Si dissolution with hydroxides in Equation (2). As the reaction products (SiO^{-}) of the Equation (2), can further react with water molecules to produce OH^{-} according to Equation (3). In particular, the reactions of Equation (2) and continue to be carried out in AS and SWSSC solutions. These have been confirmed by Figure 8D, Figure 10A, and Figure 10B.



(1)



(2)



(3)

In addition to glass fibers, the changes in functional groups of PP, the debonding of glass fiber- PP interfaces, and the development of existing micro-voids in GFRPP bars[22] have also been confirmed to be these reasons for the degradation of compression behavior of GFRPP bars in hygrothermal environments.

3.5 | Prediction of long-term behavior and service life for compression strength

Several researchers have employed the Arrhenius model for predicting the long-term behavior of GFRP bar.[22,26,60] In terms of the degradation rate, the model was expressed in Equation (4).

$$k = Ae^{(-E_a=RT)} \tag{4}$$

where k: degradation rate of the GFRP bar; A: constant relative to the GFRP and degradation process; E_a: reaction's energy of activation; R: universal gas constant; and T: temperature. The necessary assumption with the model is that only a dominant degradation mechanism of the GFRP operates during aging and that this mechanism will not change with temperature and time.[61] Namely, the degradation rate of the GFRP bar will only be accelerated as the temperature increases. Further, according to the time–temperature equivalence principle of composite materials, the time required for the degradation of the compressive strength of GFRPP bars in different temperature immersion solutions to the same strength retention rate is t_1 and t_2, respectively. This approach generates a time-shift factor (TSF) that can be calculated as shown in Equation (5).

$$TSF = \frac{t_1}{t_2} = \exp\left(\frac{E_a}{R}\left(\frac{1}{T_1} - \frac{1}{T_2}\right)\right) \tag{5}$$

where T_1 and T_2 are exposure temperatures; and t_1 and t_2 are times required to obtain a certain level of decrease in compressive strength at temperatures T_1 and T_2, respectively. Detailed procedures can be found in the literature.[22]

According to Equation (4), the compressive strength retention of GFRPP bars in DW, AS, and SWSSC solutions was fitted with the immersion time, the curves were obtained in Figure 11 What is more important, a coefficient of the determination (R^2) value close to 1.0 was desired. In contrast, ASTM procedures recommend a minimum value of 0.8 for acceptability. The obtained R^2 values were between 0.91 ~ 0.99 in this study. Based on the compressive strength degradation curves of the GFRPP bar obtained above, combined with three typical service environments in Da Lian, Xi Ning, and Xia Men in China. Its average annual temperature in 2020 where be found at https://www.nmc.cn. Furthermore, according to Equation (5), the TSF of the three service environments and the reference temperature of the accelerated in the laboratory can be calculated and determined in Table 6 and Figure 12.

Consequently, the prediction for compressive strength retention as a function of time for immersing in DW, AS, and SWSSC solutions at 9.2°C (Da Lian), 14.8°C (Xi Ning), and 22.0°C (Xia Men), and the general relation between the compressive strength retention levels and the predicted service life at the three areas can be drawn in Figure 12. The predicted time to reach the determined compressive strength retentions for the GFRPP bars aged in DW solution at Da Lian, Xi Ning, and Xia Men are approximately 13.8, 13.1, and 12.3 years for compressive strength retention of more than 45.7%. For the AS solution that simulates the concrete environments, the GFRPP bars aged in it at three

15480569, 2024, 9, Downloaded from https://4spepublications.onlinelibrary.wiley.com/doi/10.1002/pc.28360 by Harbin Institute Of Technology, Wiley Online Library on [10/06/2024]. See the Terms and Conditions (https://onlinelibrary.wiley.com/terms-and-conditions) on Wiley Online Library for rules of use; OA articles are governed by the applicable Creative Commons License

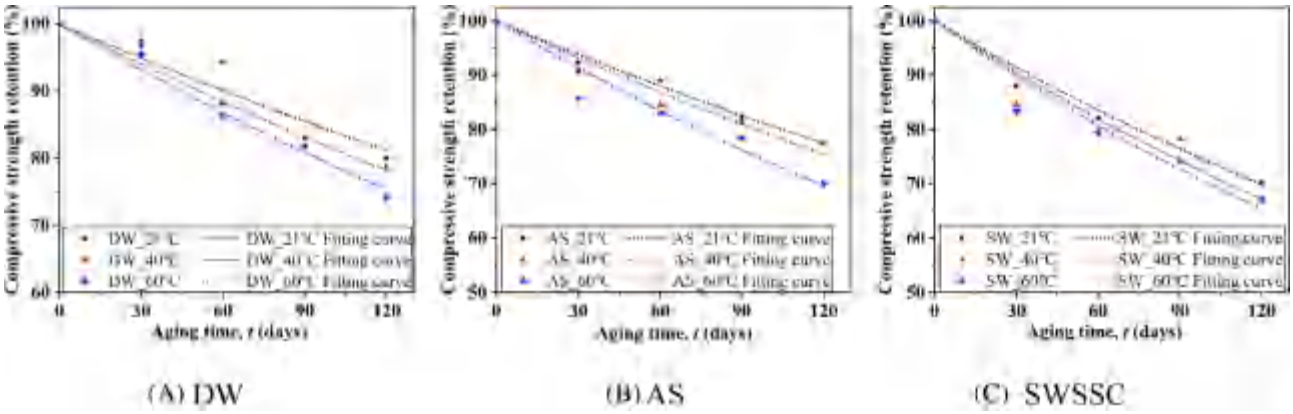


FIGURE 11 Plot of the compressive strength retention of GFRPP bars as a function of time in various immersion solutions.

TABLE 6 Service duration of GFRPP bars in different environments.

		Time-shift factor (TSF)		
Type	T_0 (°C)	Da Lian (9.2°C)	Xi Ning (14.8°C)	Xia Men (22.0°C)
DW	21.0	1.11	1.06	0.99
	40.0	1.31	1.24	1.16
	60.0	1.51	1.43	1.34
AS	21.0	1.13	1.07	0.99
	40.0	1.35	1.27	1.18
	60.0	1.59	1.50	1.40
SWSSC	21.0	1.06	1.03	0.99
	40.0	1.16	1.13	1.09
	60.0	1.26	1.23	1.18

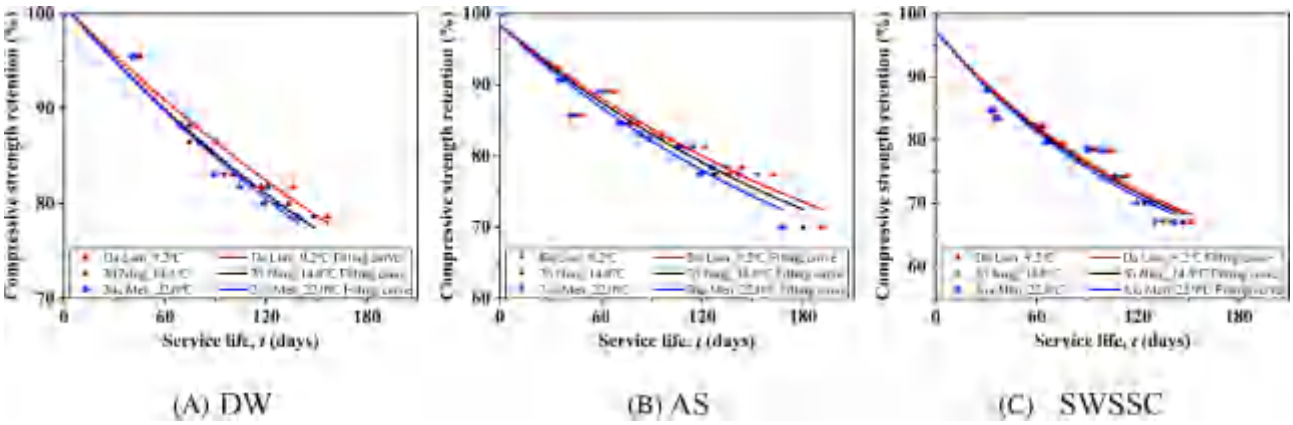


FIGURE 12 Predicted relationship between the retained compressive strength and service life at various cities in China.

areas are approximately 10.7, 10.1, and 9.4 years, respectively, for a compressive strength retention of more than 49.5%. Moreover, the predicted service life of the GFRPP bars aged in SWSSC solutions simulating the sea water and sea sand concrete environment with compressive strength retention rates of less than 52.7% can be estimated as being infinity.

Table 7 presents the service duration of GFRPP bars in different environments. In addition, the stable retention to evaluate the minimum compression strength retention of the GFRPP bars in the immersing environment is obtained. Interestingly, the stable retention in AS and SWSSC solutions is higher than in the DW solution. This phenomenon may be caused by the filling effect of solid generics in the

15480569, 2024, 9, Downloaded from https://4spepublications.onlinelibrary.wiley.com/doi/10.1002/pc.28360 by Harbin Institute Of Technology, Wiley Online Library on [10/06/2024]. See the Terms and Conditions (https://onlinelibrary.wiley.com/terms-and-conditions) on Wiley Online Library for rules of use; OA articles are governed by the applicable Creative Commons License

TABLE 7 Service duration of GFRPP bars in different environments.

Service area	Average annual temperature (°C)	Serving duration (year)			Stable retention (%)		
		DW	AS	SWSSC	DW	AS	SWSSC
Da Lian	9.2	13.8	10.7	7.0	45.7	49.5	52.7
Xi Ning	14.8	13.1	10.1	6.8	45.7	49.5	52.7
Xia Men	22.0	12.3	9.4	6.5	45.7	49.5	52.7

original micro-voids and micro-cracks mentioned in the reaction mentioned by Equation (2). In the end, although the fitting superiority obtained in the predicted model is not less than 0.93, the results obtained in the AS and SWSSC environments are low, and the results in the DW environment are high. These deviations are less than 2.5%, which can also be observed in Figure 12.

4 | CONCLUSIONS

In the present study, new thermoplastic-based GFRPP bars were immersed in DW, AS, and SWSSC solutions simulating different concrete environments to determine the bars' durability as internal reinforcement for concrete structures. The compressive behavior, thermodynamic properties, and microstructural analysis of the control GFRPP bars were studied. Dynamic mechanical analysis (DMA), scanning electron microscopy (SEM), and Fourier transform infrared spectroscopy (FTIR) were used to characterize the durability of the compressive behavior and degradation mechanism of GFRPP bar specimens. Based on the results, the following conclusions are drawn.

A simple and repeatably used anchor with stainless-steel columns constrained for the compressive test of the GFRPP bars was developed. Compared with the anchor method with epoxy adhesives, the newly developed anchor increased the GFRPP bars' compressive strength by 10–20%, without significant slip during testing. The slenderness ratio (L_u/D_b) significantly affects the compressive performance of the tested GFRPP bars. With the L_u/D_b decreasing, the failure mode changes from shear-kinking to shear-sliding.

The compressive strength of the GFRPP specimens was affected significantly by the immersion duration, the pH value of the immersion solution, and immersion temperatures. After 120 days of immersion in DW, AS, and SWSSC solutions at 60°C, degradation in the compressive strength reaches 25.8%, 30.0%, and 33.0%, respectively. The degradation mechanism of the GFRPP bars due to immersion includes glass fiber-resin interface debonding and fiber etching, and the original micro-voids and micro-cracks of the bars accelerate the degradation.

The prediction results show that the long-term compressive strength retention of GFRPP bars immersed in DW was much higher than the other solutions. However, the GFRPP bar exposed in AS and SWSSC solutions has higher stable compression strength retention, which is due to the filling effect of solid products on the micro-voids of the bars and the inhibitory effect of water molecular diffusion.

ACKNOWLEDGMENTS

This work is supported by the National Key Research and Development Program of China (2022YFB3706501), Program Fund of Non-Metallic Excellence and Innovation Center for Building Materials (24SFP-4), Fundamental Research Funds for the Central Universities (Grant No. HIT. OCEF. 2022032 and HIT.NSRIF202234), Heilongjiang Natural Science Foundation (LH2021E073).

CONFLICT OF INTEREST STATEMENT

The authors declare no conflict of interest.

DATA AVAILABILITY STATEMENT

The data supporting this study's findings are available from the authors, upon reasonable request.

ORCID

Chenggao Li https://orcid.org/0000-0002-4338-8944
Guijun Xian https://orcid.org/0000-0002-8540-2580

REFERENCES

1. Allan Manalo BB, Park K-t, Lutze D. Recent developments on FRP bars as internal reinforcement in concrete structures. Concr Aust. 2014;40:10.
2. Manalo A, Maranan G, Benmokrane B, et al. Comparative durability of GFRP composite reinforcing bars in concrete and in simulated concrete environments. Cem Concr Compos. 2020; 109:109.
3. AlAjarmeh O, Manalo A, Benmokrane B, et al. Compression behavior of GFRP bars under elevated in-service temperatures. Construct Build Mater. 2022;314:314.
4. Benmokrane B, Manalo A, Bouhet J-C, Mohamed K, Robert M. Effects of diameter on the durability of glass fiber–reinforced polymer bars conditioned in alkaline solution. J Compos Construct. 2017;21:21.

15480569, 2024, 9, Downloaded from https://4spepublications.onlinelibrary.wiley.com/doi/10.1002/pc.28360 by Harbin Institute Of Technology, Wiley Online Library on [10/06/2024]. See the Terms and Conditions (https://onlinelibrary.wiley.com/terms-and-conditions) on Wiley Online Library for rules of use; OA articles are governed by the applicable Creative Commons License

5. Benmokrane B, Mohamed HM, Manalo A, Cousin P. Evaluation of physical and durability characteristics of new headed glass fiber–reinforced polymer bars for concrete structures. J Compos Construct. 2017;21:21.
6. Mostafa NH, Ismarrubie ZN, Sapuan SM, Sultan MTH. The influence of equi-biaxially fabric prestressing on the flexural performance of woven E-glass/polyester-reinforced composites. J Compos Mater. 2016;50:3385-3393.
7. Alsayed S, Al-Salloum Y, Almusallam T, El-Gamal S, Aqel M. Performance of glass fiber reinforced polymer bars under elevated temperatures. Compos Part B Eng. 2012;43:2265-2271.
8. Laoubi K, Hamadi Z, Ahmed Benyahia A, Serier A, Azari Z. Thermal behavior of E-glass fiber-reinforced unsaturated polyester composites. Compos Part B Eng. 2014;56:520-526.
9. Hilo AK, Abu Talib AR, Acosta Iborra A, Hameed Sultan MT, Abdul Hamid MF. Effect of corrugated wall combined with backward-facing step channel on fluid flow and heat transfer. Energy. 2020;190:190.
10. AlAjarmeh OS, Manalo AC, Benmokrane B, Vijay PV, Ferdous W, Mendis P. Novel testing and characterization of GFRP bars in compression. Construct Build Mater. 2019;225: 1112-1126.
11. Yan F, Lin Z, Yang M. Bond mechanism and bond strength of GFRP bars to concrete: a review. Compos Part B Eng. 2016;98: 56-69.
12. Sultan MTH, Worden K, Pierce SG, et al. On impact damage detection and quantification for CFRP laminates using structural response data only. Mech Syst Signal Process. 2011;25: 3135-3152.
13. Ahmad Sawpan M, Beg MDH. Long-term residual properties and durability of glass fiber reinforced polymer composite exposed to alkaline solution and natural weather for a decade. Polym Compos. 2023;45:1096-1106.
14. Lu Z, Jiang M, Pan Y, Xian G, Yang M. Durability of basalt fibers, glass fibers, and their reinforced polymer composites in artificial seawater. Polym Compos. 1961;2022:43-1973.
15. Cadenazzi T, Dotelli G, Rossini M, Nolan S, Nanni A. Cost and environmental analyses of reinforcement alternatives for a concrete bridge. Struct Infrastruct Eng. 2019;16:787-802.
16. A. C. Institute, Vol. ACI. ACI Committee 440, 38800 Country Club Drive Farmington Hills, U.S.A. 2012. 2012.
17. A. International, West Conshohocken. 2022.
18. C. Group, Rexdale,Ontario,Canada. 2019.
19. A. A. o. S. H. a. T. Officials, Washington, DC. 2018.
20. El-Tahan M, Galal K, Hoa VS. New thermoplastic CFRP bendable rebars for reinforcing structural concrete elements. Compos Part B Eng. 2013;45:1207-1215.
21. Marco Rossini GB, Zoller A, Braghiroli N, Poggi C, Nanni A. The Italian Concrete Days. 2021.
22. Zhou P, Li C, Bai Y, et al. Durability study on the interlaminar shear behavior of glass-fibre reinforced polypropylene (GFRPP) bars for marine applications. Construct Build Mater. 2022; 349:349.
23. El Hajjar RF, Pegoretti A, Movchan A, De Falco P, Pugno NM. The case study of a brittle failure of a mountain bike frame composed by carbon fiber reinforced plastic. Polym Compos. 2023;44:6349-6362.
24. Xian G, Guo R, Li C, Wang Y. Mechanical performance evolution and life prediction of prestressed CFRP plate exposed to hygrothermal and freeze-thaw environments. Compos Struct. 2022;293:293.
25. Lal HM, Uthaman A, Li C, Xian G, Thomas S. Combined effects of cyclic/sustained bending loading and water immersion on the interface shear strength of carbon/glass fiber reinforced polymer hybrid rods for bridge cable. Construct Build Mater. 2022;314:314.
26. Wang Z, Zhao X-L, Xian G, Wu G, Raman RKS, Al-Saadi S. Effect of sustained load and seawater and sea sand concrete environment on durability of basalt- and glass-fibre reinforced polymer (B/GFRP) bars. Corros Sci. 2018;138:200-218.
27. Naito K, Oguma H, Nagai C. Temperature-dependent tensile properties of hybrid carbon/glass thermoplastic composite rods. Polym Compos. 2020;41:3985-3995.
28. Benmokrane B, Mousa S, Mohamed K, Sayed-Ahmed M. Physical, mechanical, and durability characteristics of newly developed thermoplastic GFRP bars for reinforcing concrete structures. Construct Build Mater. 2021;276:276.
29. Dong S, Qi X, Tian J, Zhou P, Li C, Xian G. Durability of glass fiber reinforced thermoplastic polypropylene composite bars under the coupling effect of seawater and sea sand concrete environment and sustained bending. Polym Compos. 2023;45:3194-3209.
30. Tian L, Zhang P, Xian G. Continuous fiber reinforced thermoplastic composite pultrusion with in situ polymerizable methyl methacrylate: a review. Polym Compos. 2023;44:4345-4369.
31. Alshammari BA, Alsuhybani MS, Almushaikeh AM, et al. Comprehensive review of the properties and modifications of carbon fiber-reinforced thermoplastic composites. Polymers. 2021;13:13.
32. Tran TQ, Canturri C, Deng X, Tham CL, Ng FL. Enhanced tensile strength of acrylonitrile butadiene styrene composite specimens fabricated by overheat fused filament fabrication printing. Compos Part B Eng. 2022;235:235.
33. Apitz A, Schmitz J, Hückler A, Schlaich M. New thermoplastic carbon fiber reinforced polymer rebars and stirrups. Struct Concr. 2022;23:923-938.
34. Oshima S, Higuchi R, Kato M, Minakuchi S, Yokozeki T, Aoki T. Cooling rate-dependent mechanical properties of polyphenylene sulfide (PPS) and carbon fiber reinforced PPS (CF/PPS). Compos A: Appl Sci Manuf. 2023;164:164.
35. Volk M, Wong J, Arreguin S, Ermanni P. Pultrusion of large thermoplastic composite profiles up to Ø 40 mm from glass-fibre/PET commingled yarns. Compos Part B Eng. 2021;227:227.
36. Ma X-l, Wen L-h, Wang S-y, Xiao J-y, Li W-h, Hou X. Inherent relationship between process parameters, crystallization and mechanical properties of continuous carbon fiber reinforced PEEK composites. Def Technol. 2022;24:269-284.
37. Wang X, Peng Z, Ding L, Lu J, Zhu Z, Wu Z. Mechanical and bonding behavior of a bendable fiber-reinforced thermoplastic rebar. Construct Build Mater. 2021;302:302.
38. Ibrahim NI, Shahar FS, Sultan MTH, Shah AUM, Safri SNA, Mat Yazik MH. Overview of bioplastic introduction and its applications in product packaging. Coatings. 2021;11:11.
39. Várdai R, Lummerstorfer T, Pretschuh C, et al. Comparative study of fiber reinforced PP composites: effect of fiber type, coupling and failure mechanisms. Compos A: Appl Sci Manuf. 2020;133:133.
40. FP C. Handbook of Polypropylene and Polypropylene Composites. Marcel Dekker; 2003.

15480569, 2024, 9, Downloaded from https://4spepublications.onlinelibrary.wiley.com/doi/10.1002/pc.28360 by Harbin Institute Of Technology, Wiley Online Library on [10/06/2024]. See the Terms and Conditions (https://onlinelibrary.wiley.com/terms-and-conditions) on Wiley Online Library for rules of use; OA articles are governed by the applicable Creative Commons License

41. Shaikh H, Gulrez SKH, Anis A, et al. Progress in carbon fiber and its polypropylene- and polyethylene-based composites. Polym-Plast Technol Eng. 1845;2014:53-1860.
42. Vedernikov A, Minchenkov K, Gusev S, et al. Effects of the pre-consolidated materials manufacturing method on the mechanical properties of pultruded thermoplastic composites. Polymers. 2022;14:14.
43. Liu Y, Zhang H-T, Tafsirojjaman T, et al. A novel technique to improve the compressive strength and ductility of glass fiber reinforced polymer (GFRP) composite bars. Construct Build Mater. 2022;326:326.
44. Chaallal BBO. Physical and mechanical performance of an innovative glass-fiber-reinforced plastic rod for concrete and grouted anchorages. Can J Civil Eng. 1992;20:15-268.
45. Bruun E. GFRP bars in structural design: determining the compressive strength versus unbraced length interaction curve. Can Young Sci J. 2014;2014:22-29.
46. Deitz PEDH, Harik IE, ASCE M, Gesund H, ASCE F. Physical properties of glass fiber reinforced polymer rebars in compression. J Compos Construct. 2003;7:4.
47. Khorramian K. Sadeghian, Pedram. CSCE Annual Conference. Fredericton; 2018.
48. Kamal ASM, Boulfiza M. Durability of GFRP rebars in simulated concrete solutions under accelerated aging conditions. J Compos Construct. 2011;15:473-481.
49. Chen Y, Davalos JF, Ray I, Kim H-Y. Accelerated aging tests for evaluations of durability performance of FRP reinforcing bars for concrete structures. Compos Struct. 2007;78:101-111.
50. Ali AH, Mohamed HM, Benmokrane B, ElSafty A, Chaallal O. Durability performance and long-term prediction models of sand-coated basalt FRP bars. Compos Part B Eng. 2019;157:248-258.
51. Kar NK, Hu Y, Ahn B, Nutt SR. Diametral compression of pultruded composite rods. Compos Sci Technol. 2012;72:1283-1290.
52. Khorramian K, Sadeghian P. Material characterization of GFRP bars in compression using a new test method. J Test Eval. 2021;49:49-1052.
53. Ping ZHOU, Chenggao LI, Shaoce DONG, Guijun XIAN. Interlaminar shear behavior of glass-fibre reinforced polypropylene rod under seawater and sea sand concrete simulation environment. Acta Mater Compos Sin. 2023;41:41.
54. Furushima Y, Schick C, Toda A, et al. Crystallization and melting kinetics of low tacticity polypropylene in relation to preformed nuclei and uncrystallizable defects. Polymer. 2023;269:269.
55. Kim H-S, Kim H-J. Miscibility and performance evaluation of natural-flour-filled PP/PBS and PP/PLA bio-composites. Fibers Polym. 2013;14:793-803.
56. Brandon J, Goldstein M, Ohman MD. Long-term aging and degradation of microplastic particles: comparing in situ oceanic and experimental weathering patterns. Mar Pollut Bull. 2016;110:299-308.
57. Pan L, Guo H, Zhong L, Wang M, Xue P, Yuan X. Influence of surface-modified glass fibers on interfacial properties of GF/PEEK composites using molecular dynamics. Comput Mater Sci. 2021;188:188.
58. Deng H, Reynolds CT, Cabrera NO, Barkoula NM, Alcock B, Peijs T. The water absorption behaviour of all-polypropylene composites and its effect on mechanical properties. Compos Part B Eng. 2010;41:268-275.
59. Nkurunziza G, Debaiky A, Cousin P, Benmokrane B. Durability of GFRP bars: a critical review of the literature. Prog Struct Eng Mater. 2005;7:194-209.
60. Ali HMMAH, Benmokrane B, ElSafty A, Chaallal O. Durability performance and long-term prediction models of sand-coated basalt FRP bars. Composites, Part B. 2019;157:248-258.
61. Won J-P, Park C-G. Effect of environmental exposure on the mechanical and bonding properties of hybrid FRP reinforcing bars for concrete structures. J Compos Mater. 2005;40:1063-1076.

SUPPORTING INFORMATION

Additional supporting information can be found online in the Supporting Information section at the end of this article.

How to cite this article: Zhou P, Dong S, Li C, et al. Study on the durability of compression behavior for glass fiber-reinforced polypropylene thermoplastic composite bars in various aging environments. Polym Compos. 2024;45(9):8555-8573. doi:10.1002/pc.28360

15480569, 2024, 9, Downloaded from https://4spepublications.onlinelibrary.wiley.com/doi/10.1002/pc.28360 by Harbin Institute Of Technology, Wiley Online Library on [10/06/2024]. See the Terms and Conditions (https://onlinelibrary.wiley.com/terms-and-conditions) on Wiley Online Library for rules of use; OA articles are governed by the applicable Creative Commons License

Construction and Building Materials 429 (2024) 136455

Contents lists available at ScienceDirect

Construction and Building Materials

journal homepage: www.elsevier.com/locate/conbuildmat

Design, preparation and mechanical properties of novel glass fiber reinforced polypropylene bending bars

Guijun Xian [a,b,c], Ping Zhou [a,b,c], Yanbo Bai [a,b,c], Junqi Wang [a,b,c], Chenggao Li [a,b,c,*], Shaoce Dong [a,b,c], Rui Guo [a,b,c], Jinhao Li [a,b,c], Haoqiang Du [a,b,c], Jian Zhong [a,b,c]

[a] Key Lab of Structures Dynamic Behavior and Control (Harbin Institute of Technology), Ministry of Education, Harbin, Heilongjiang 150090, China
[b] Key Lab of Smart Prevention and Mitigation of Civil Engineering Disasters of the Ministry of Industry and Information Technology, Harbin Institute of Technology, Harbin 150090, China
[c] School of Civil Engineering, Harbin Institute of Technology, Harbin Heilongjiang 150090, China

ARTICLE INFO

Keywords:
Glass fiber reinforced polypropylene bars
Mechanical properties
Finite element simulation analysis
Bending mechanism
Bending strength model

ABSTRACT

Fiber reinforced thermoplastic composite bars offered the advantages of repeated molding, high toughness, and recyclability, making them a promising alternative to steel bars. For the stirrups applications in concrete structures, it was essential to develop efficient bending technologies for producing high-quality thermoplastic bending bars. In the present paper, the bending properties of glass fiber reinforced polypropylene (GFRPP) composite bars were investigated by experimental and theoretical methods. A novel bending fixture of GFRPP bars was specifically designed for GFRPP bars to ensure the reliable bending of the bars. Finite element simulation was employed to analyze the stress distribution of GFRPP bars, providing valuable insights into their mechanical behavior. Additionally, a bending strength model was developed based on the material mechanics, offering a theoretical framework for understanding and predicting the bending strength of GFRPP bars. Finally, the bending mechanism of bars was further revealed according to experimental and theoretical findings. The results of the study demonstrated that the specially designed bending fixture was successful in minimizing damage to the bending section of the GFRPP bars, leading to a significant improvement in bending strength retention of up to 43.2 %. Furthermore, the theoretical results and experimental test have a good agreement in terms of stress distribution and failure mode. The maximum strain in the transition zone between the straight section and the bending section of the GFRPP bars was nearly double that of the straight section at the same stress levels. With the increase of bending radius to diameter ratio from 3.0 to 7.0, the tensile strength of GFRPP bending bars increased by ~7.9 %. The study identified the transition area between the bending section and straight section of GFRPP bars as the most critical failure point. The strength degradation mechanism during the bending were attributed to the shrinkage and torsion of inner fibers owing to the compression caused the local stress concentration, which caused the inner resin matrix to crack and interface debonding of fiber/resin, leading to the premature tensile failure.

1. Introduction

The corrosion of steel in reinforced concrete structures directly resulted in a decrease in the cross-sectional area and degradation of the mechanical properties of the steel bars [1,2], causing the interface debonding between steel bars and concrete and bringing huge economic losses. For example, according to relevant data [3], the maintenance cost due to steel corrosion was as high as 126 billion US dollars annually, which accounted for approximately 2–4 % of the gross national product worldwide. Currently, various methods such as cathodic protection method, adding corrosion inhibitor and coating on the steel surface have been proposed to address the corrosion issue [4,5]. However, given the intricate and varied environmental conditions, these approaches may not entirely prevent corrosion. Consequently, there was an urgent need to develop new materials to replace steel bars and effectively resolve the corrosion problem.

Fiber reinforced polymer (FRP) composite bars exhibit outstanding corrosion resistance, fatigue performance, high specific strength and

* Correspondence to:73 Huanghe Road, Nangang District, Harbin 150090, China.
E-mail address: lichenggao@hit.edu.cn (C. Li).

https://doi.org/10.1016/j.conbuildmat.2024.136455
Received 27 February 2024; Received in revised form 11 April 2024; Accepted 29 April 2024
0950-0618/© 2024 Elsevier Ltd. All rights reserved.

modulus [6–8], with carbon fiber reinforced polymer (CFRP) being particularly noteworthy [9]. Substituting FRP bars for steel bars in concrete structures could fundamentally address the corrosion issue associated with steel bars and effectively enhance the durability of concrete structures [10–12]. According to matrix type, FRP could be divided into fiber reinforced thermosetting (FRTS) composites [13–15] and fiber reinforced thermoplastic (FRTP) composites [16,17]. Thermosetting resins mainly included the unsaturated polyester, phenolic resin, epoxy resin, polyurethane, etc. [18–22]. Following curing and molding, thermosetting resins developed a network structure through intermolecular crosslinking, resulting in high strength and excellent heat resistance [23]. Nevertheless, challenges such as the absence of no secondary molding, lower fracture toughness and durability, unfriendly environment and difficult recycling were the primary issues associated with thermosetting resins [24–27]. Compared with thermosetting resin, thermoplastic resins have a chain-like molecular structure, exhibiting the characteristics of thermal-softening and cooling-hardening. This reversible process does not involve any chemical alterations, allowing the material to retain its performance even after multiple heating-cooling cycles [28,29]. The above advantages enabled thermoplastic resins to be easily subjected to secondary molding, on-site bending, and exhibit high toughness, exceptional corrosion resistance, as well as superior impact and fatigue resistance [30,31]. Common thermoplastic resins included polyethylene (PE), polypropylene (PP), polyvinyl chloride (PVC), polystyrene (PS), etc. Compared to the other thermoplastic resins, polypropylene resin has abundant raw materials, low cost, easy processing and molding, excellent mechanical and moisture resistance [32–34], which could offer significant advantages in the preparation of high-performance thermoplastic composite bars [35].

Currently, the predominant application of FRP bars in engineering was in the form of thermosetting FRP longitudinal and distributed bars [36,37]. By contrast, the application of thermosetting FRP stirrups was relatively limited owing to the complex prefabrication process, stress incompatibility and poor corrosion resistance. Therefore, the development of thermoplastic FRP stirrups could effectively address the aforementioned issues associated with thermosetting stirrups [38]. In the case of thermoplastic bars, the secondary molding process involved a physical change, ensuring the stability of the bars' chemical properties. Moreover, there was the relative movement between the thermoplastic resin and fiber during the bending process, which reduced the damage to the fiber. After the cooling molding, the interaction between the thermoplastic resin and fiber recovered again to give full play to the mechanical properties of bars.

The preparation and bending performance of thermoplastic bending bars were crucial prerequisites for their engineering application. Additionally, the mechanical properties of the above-mentioned engineering materials could be effectively assessed and monitored through the development of self-monitoring materials, experimental testing, and numerical simulations [39–41]. At present, the researches on bending technology, bending performance and bending mechanism of thermoplastic bars were limited. Wang et al. [42] investigated the effects of bending radius, epoxy resin reinforcement on the tensile strength of glass fiber reinforced polypropylene (GFRPP) bending bars. The experimental results revealed that the strength retention rates were merely 26 % and 28 % when the ratio of bending radius/bars diameter were 2.14 and 2.86. However, the strength could be significantly enhanced by over 20 % through reinforcement with epoxy resin. Lu et al. [43] investigated the effect of fiber and resin type, bars diameter, bending radius on tensile strength of bending bars through adopting ACI440.3 R testing method. The test results indicated that the strength retention of thermosetting and thermoplastic composites after the bending was below 40 %. Moreover, applying epoxy resin coating on the bending parts did not demonstrate a significant reinforcement effect. Wang et al. [44] found the strength retention of bending bars at the bending angles of 30°, 60° and 90° were 59.7 %, 43.9 % and 24.5 %, respectively, and the bending process had the obvious damage on GFRP bars. Ehab A. Ahmed et al. [45] found that the strength retention of bending bars increased from 46 % to 67 % using method B.5, and from 33 % to 41 % using method B.12, respectively, for a bending radius to bar diameter ratio of 4.0. Through the comparison, the strength retention by method B.12 was 30∼40 % lower than that of method B.5. In conclusion, the low bending strength retention of thermoplastic bars in existing research was attributed to factors such as stress concentration, fiber distortion, etc. When the bars were subjected to the oblique section shear loads in concrete as stirrups, the bending part was prone to breakage and damage. Therefore, the development of efficient bending devices was crucial to ensure higher strength retention. Additionally, it was essential to propose bending mechanisms and bending strength models to analyze the bending behavior of thermoplastic bars.

In the present paper, the bending properties of glass fiber reinforced polypropylene (GFRPP) composite bars were investigated using a combination of experimental and theoretical approaches. A novel bending fixture of GFRPP bars was designed based on the principle of heating-melting and cooling-forming of polypropylene. The finite element simulation was employed to analyze the stress distribution during bending and pulling-out process from concrete. The bending strength model of GFRPP bars was proposed to analyze the stress state and failure mode. Finally, the mechanical tests of bending bars were conducted to validate the theoretical and simulation results. By integrating microscopic morphology analysis, the bending mechanism of the bars was further elucidated.

2. Experimental programme

2.1. Raw materials

The material utilized in this study comprised glass fiber reinforced polypropylene (GFRPP) composite bars with the diameter of 6 mm, as reported in [35,46]. It should be noted that the above bars were prepared from glass fiber reinforced polypropylene prepreg sourced from Jushi Group, California, USA, through secondary pultrusion molding. The prepreg consisted of approximately 60 % glass fiber mass fraction, with a tensile strength of 660 MPa, tensile modulus of 47 GPa, flexural strength of 640 MPa, and flexural modulus of 45 GPa. For the composite bars, the tensile strength and modulus were 677.59 MPa and 26.54 GPa, respectively. Furthermore, detailed information regarding the chemical composition of the composite bars could be found in the study by reference [35].

2.2. Bending fixture design and bending method

The bending fixture for GFRPP bars was designed based on the principle of heating-melting and cooling-forming of polypropylene resin. The bending area of bars was heated above the melting point of the resin, and the bending bars with a bending angle were obtained when the resin temperature cooled to room temperature. Fig. 1 illustrated the schematic diagram of bending fixture of glass fiber reinforced

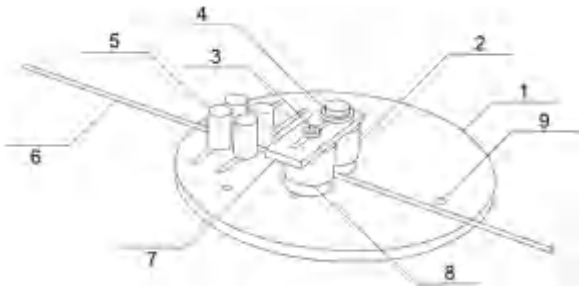


Fig. 1. Schematic diagram of bending fixture of GFRPP composite bars.1-bending disc, 2-center column, 3-rotating column, 4-gasket, 5-fixed column, 6-GFRPP bars, 7-rotating handle, 8-sleeve, 9-support bolt.

polypropylene composite bars, comprising components such as bending disc, central column, rotating column, fixed column, rotating handle, sleeve, gasket and support bolt. The bending process of GFRPP bars involved the setup of the bending equipment and the execution of the bending experiment.

For the installation of the bending equipment, the support bolt was firstly passed through the bolt hole on the outer side of the bending disc, and the extension length of the screw was adjusted to ensure the levelness of the bending disc. Next, the central column was inserted into the reserved bolt hole at the center of the bending disc, with the gasket positioned on the screw from below to secure the central column at the disc's center. Subsequently, the rotating column was inserted into the sleeve and its upper end was extended into the designated track on the rotating handle. After this, the circular hole was aligned with the central column on the opposite side. Finally, the fixed column was placed above the bending disc track to complete the installation of the bending equipment.

For the bending experiment of GFRPP bars, the bending area of bars was firstly wrapped by tin paper and heating strip, and then they were positioned in the semicircular groove located at the lower section of the central column. Subsequently, the fixed column within the curved disc track was utilized to clamp the bars. The bars within the bending region were heated using a pressure regulator. Once the bars softened in the bending area, the handle was rotated to achieve a specific bending angle, and the upper bolt of the central column was tightened. Finally, after the temperature in the bending zone had cooled to room temperature, the bending equipment was removed to obtain the bending bars.

The bending device described above offered several key functionalities. It was designed to be detachable, providing excellent flexibility for practical engineering applications. It could obtain the bending bars with different diameters/angles and bending curvature radius by replacing central columns with different outer diameters. The heating tape winding method ensured uniform heat of thermoplastic bars through accurately controlling of heating temperature. The semicircular groove at the bottom of the central column and sleeve, as well as the inner layer wrapped with tin paper and the outer layer wrapped with heating tape, offered the protection for the bending part of bars, and improved the bending strength retention of bars. Additionally, the rotating sleeve around the rotating column minimized resistance and potential damage to the bars during the bending process, further optimizing the bending operation.

2.3. Preparation of bending bars

The bending process of GFRPP bars could be segmented into: heating softening, bending shaping, and cooling forming. Initially, the silicone tubing was adopted to cover the heated area, limiting the cross-sectional deformation and preventing resin overflow during the bending process. Subsequently, the sleeve silicone tube part of bars was placed tightly into the semi-circular groove at the lower part of the central column and clamped the bars with four fixed columns. The rotating column along the track was employed to clamp the bars and then the bolts above the rotating column was tightened to lock its position. A digital hot air gun equipped with a flat nozzle was used to heat the bending section to 350 °C for 2 minutes. It is essential to note that the inner diameter of the silicone tube used should be equal to the outer diameter of bars to provide the better radial constraints. The sleeve silicone hose length of bars should be slightly longer than the heating length, as shown in Fig. 2,

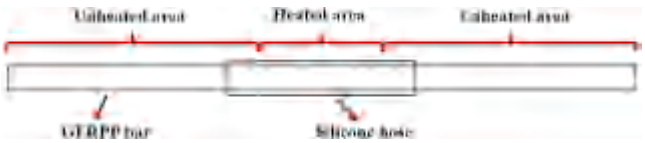


Fig. 2. Bending heating area of GFRPP bars.

to effectively prevent the resin overflow. At the same time, the heating length should be slightly greater than the arc length of bending part. The heating temperature and time were determined by multiple attempts to obtain the optimal bending effect. The higher heating temperature compared to the melting point temperature of polypropylene (around 170 °C), aimed to improve the heating efficiency and resin fluidity when considering the heat loss among the air gun, bars and silicone hose. Once the bars softened, the bending device was employed to bend them to the desired angle. Finally, the silicone hose was removed to obtain bending bars, as shown in Fig. 3. In this paper, three bending radius/bars diameter (r/d) ratios were adopted to be 3.0, 5.0, and 7.0. Three samples in each group were prepared for the tensile tests.

2.4. Mechanical tests of bending bars

2.4.1. Tensile tests

The testing tests of bending bars were based on ACI440.3 R B.12 in the American Concrete Institute Specification [47]. This recommended method was applicable for testing bending bars with various fiber types or resins, regardless of rectangular or circular cross-sections, to preliminarily assess their tensile performance. The bending connection device was further processed, and its schematic diagram was shown in Fig. 4a. The tensile strength test of bending bars was conducted using a universal testing machine (DHY-10080) produced by Shanghai Hengyi Precision Instrument Co., Ltd., as shown in Fig. 4b. The displacement loading speed was set as 1.0 mm/min. During the tests, strain gauges were used to monitor the strain of bending bars at key locations (1, 2, 3…6), as shown in Fig. 3 through the dynamic stress-strain testing and analysis system (DH5921) from Jiangsu Donghua Testing Technology Co., Ltd. It was essential to note that some typical locations mentioned above were selected for strain monitoring, such as the straight section (point 1 and 4) and transition area (point 2, 3, 5 and 6) between straight section and bending section. Additionally, the finite element simulation method was utilized to analyze the stress distribution in arc region. Three repetitive tests were conducted to determine the average bending strength for each condition.

$$S = \frac{P}{2A} \tag{1}$$

where S is the bending strength of bars, P is the maximum tensile load, A is the cross-sectional area of bars.

2.4.2. Short beam shear tests

Short beam shear tests of bending bars were performed according to ASTM D4475 through the universal testing machine (DHY-10080) from Shanghai Hengyi Precision Instrument Co., Ltd. The samples were cut to a total length of 36 mm, and the test span was 30 mm. The loading speed

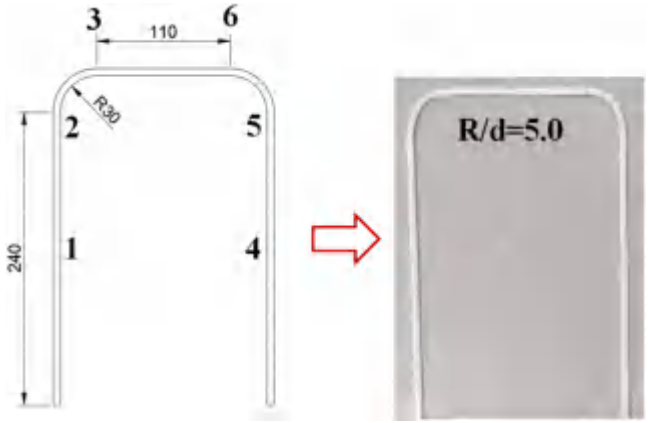


Fig. 3. Schematic diagram and physical diagram of GFRPP bending bars.

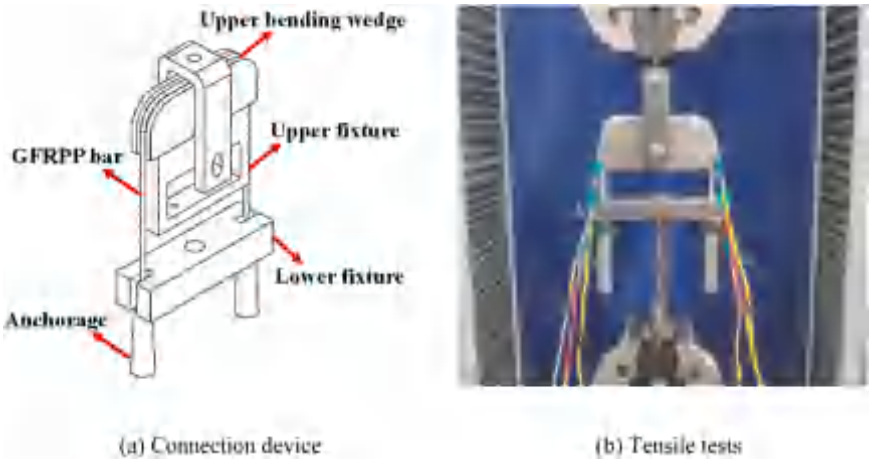


Fig. 4. Bending connection device and tensile tests of GFRPP bending bars of (a) connection device and (b) tensile tests.

was set to 1.3 mm/min. The testing device was shown in Fig. 5. It was noted that the straight sections of bending bars end were selected to conduct the tests for R/d=7.0, while the corresponding lengths of the unbent straight bars were tested as controls. Five repeated tests were conducted to determine the average short beam shear strength for each condition.

$$\tau = \frac{8P}{3\pi D^2} \tag{2}$$

where$\tau$is the short beam shear strength of bars, P is the maximum compressive load, D is the diameter of bars.

2.5. Surface morphology analysis

To investigate the microscopic damage during the bending, the surface morphology analysis of bending bars was conducted through the scanning electron microscope (SEM, VEGA3), as depicted in Fig. 6. Before the test, the samples were vacuumed and sprayed with gold to enhance the electrical conductivity. The SEM parameters were set at a test frequency of 1000 Hz, an electric current of 0.7 A, and a voltage amplitude of 30 kV. This allowed the observation of the fiber and fiber/resin interface in the bending region.

3. Simulation and theoretical analysis of bending properties

3.1. Finite simulation analysis of bending stress

To analyze the effect of bending radius on the stress distribution of GFRPP bars during the bending, finite element simulations were performed using ABAQUS 6.14 software in accordance with the ACI440.3 R B.12 specification. The model was designed to evaluate the stress distribution of GFRPP bars not only during the bending process but also during the pull-out process from a concrete block.



Fig. 5. Short beam shear tests of GFRPP bending bars.



Fig. 6. Physical image of scanning electron microscope.

For the bending process, a two-dimensional finite element model was established to analyze the stress distribution of GFRPP bars. The GFRPP bars had a diameter of 6 mm and an R/d ratio of 5.0, as illustrated in Fig. 3. Bars were considered as the anisotropic materials and its mechanical properties parameters are shown in Table 1. Given that bars deformation was significantly greater than that of steel corner bending wedges for the bending device, the corner bending wedges were modeled as rigid bodies during the modeling to enhance computational efficiency. The contact mode between GFRPP bars and bending wedges was set to "Rough" in the tangential direction and "Hard" in the normal direction, and the separation was considered when the contact was not allowed. The boundary condition was set to fully fix the corner bending wedge and apply horizontal constraints to GFRPP bars in the vertical directions on both sides. A uniformly distributed load of 200 MPa was

Table 1
Mechanical properties parameters of GFRPP bars for the simulation of bending process.

Materials	Modulus of elasticity E_1 (GPa)	Modulus of elasticity E_2 (GPa)	Modulus of shear G_{12} (GPa)	Poisson's ratio ν_{12}
GFRPP	27	3	1	0.2

Note, 1 is along the fiber direction and 2 is perpendicular to the fiber direction.

applied in a downward direction to the two ends of the GFRPP bars.

For the pull-out process from concrete block, the finite element model incorporated the interface bond-slip behavior between GFRPP bars and concrete to analyze the stress state. A 3D finite element model of L-shaped bending bars with a diameter of 6 mm and R/d=5.0 was established and the mechanical properties parameters of GFRPP bars were detailed in Table 2. The bond-slip relationship between GFRPP bars and concrete was simulated using Cohesive elements, while the concrete material parameters were set to C30. A completely fixed boundary condition was applied to the concrete, and an upward displacement of 10 mm at the upper end of the GFRPP bars was imposed for the analysis.

Fig. 7 illustrated the stress cloud diagram and stress distribution of GFRPP bars during the bending process. The analysis revealed that the stress distribution of bars along the longitudinal direction (below point 1) and horizontal direction (on the right of point 4) was relatively uniform, with values of approximately 196 MPa and 6 MPa, respectively. However, the stress distribution in the bending region exhibited uneven changes from point 1–4 as shown in Fig. 7(b). The maximum stress was observed on the inner side of the transition zone between the vertical and the bending areas, reaching a value of 493.6 MPa, which was about 2.5 times the external load. Therefore, it could be predicted that point 2 was the most dangerous point for damage, which will be further verified by the experimental failure mode. For other R/d=3.0 and 7.0, the simulation results demonstrated the similar stress distribution, with maximum stresses of 534.7 MPa and 482.9 MPa, respectively. Notably, the overall stress in the inner side were obviously higher than that in the outer side in the bending area, which was primarily caused by the larger compressive stress owing to fiber twisting effect.

Fig. 8 depicted the stress distribution of glass fiber reinforced polypropylene bending bars during the pull-out process. It could be found that the stress distribution exhibited a similar pattern when considering the bond-slip behavior specified in the test method B.12. The maximum stress was observed on the inner side of the transition area between the bending section and the straight section. Different from the bending process, the external loads were primarily sustained by the vertical bars due to the presence of bonding force, which could delay the transferring of external load from the transition area to the straight section. Additionally, the bonding force between bars and concrete could also balance part of external force, contributing to the decrease of maximum stress. Based on the analysis, the most critical failure point of GFRPP bars appeared in the transition area between the bending section and straight section. Furthermore, the ultimate failure stress could be further reduced owing to bonding protection of concrete. Therefore, reinforcing and repairing GFRPP bars in the bending area was crucial to ensure higher retention of bending strength.

3.2. Theoretical analysis of bending strength

3.2.1. Bending strength model of GFRPP bars

At room temperature, the polypropylene resin within GFRPP bars existed in solid state. When subjected to pure bending load, the stress state within GFRPP bars resembled that of circular cross-section beams. A plane neutral layer in the middle divided GFRPP bars into tension zone and compression zone. As shown in Fig. 9, the linear strain of GFRPP bars was directly proportional to the distance from the fiber to neutral layer, as described by Eq. 3.

$$\varepsilon = \frac{\Delta l}{l} = \frac{y d\theta}{\rho d\theta} = \frac{y}{\rho} \tag{3}$$

where ε is the strain of bars, ρ is the curvature, y is the displacement along the radial direction.

From the mechanics of materials, the maximum normal stress and shear stress of GFRPP bars under pure bending appeared at the farthest point from the neutral axis. Furthermore, the maximum bending normal stress and the maximum shear stress on the cross section were as follows:

$$\sigma_{\max} = \frac{M}{W_z}, \tau_{\max} = \frac{4F_s}{3A} \tag{4}$$

where W_z is bending section coefficient, M is bending moment, F_s is the shear force and A is the cross-sectional area. Based on the above theoretical analysis, it could be inferred that substantial stress was generated within thermoplastic bars for the bending process at room temperature. The significant stress present inside the bars could greatly diminish the strength of the bars following the bending operation.

For GFRPP bars, the maximum strain along the fiber direction typically was within the range of 1–2.5 %. This implied the bending radius required for bending bars was larger to meet the strain requirements at room temperature, leading to practical limitations in applications. Therefore, based on the above analysis, it was not feasible to bend the GFRPP bars at room temperature. In this study, the thermoplastic resin was heated above its melting point. In this molten state, the relative motion between the fiber and resin could occur, effectively reducing the residual stress inside the GFRPP bars. The above bending effect at higher temperature was considered in the subsequent theoretical derivation process.

In this study, the bending angle of GFRPP bars was 90°. To simplify the calculation and ignore the interface shear effect, the theoretical model was treated as planar curved rod in elastic mechanics. The bending bars was considered as a quarter circle with an ideal inner diameter of a and an outer diameter of b, as shown in Fig. 10. During the actual bending failure process, different positions within the bending area did not simultaneously reach the bearing loading limit due to the uneven stress distribution. Instead, failure initially occurred at specific high-stress locations, as indicated in the simulation analysis. Therefore, it was decided to initially utilize the solution of elasticity in polar coordinates to investigate the stress distribution of a planar curved rod in the more universal stress state, as shown in Fig. 10. Here, P_0, Q_0, M_0 were the normal stress, shear stress, and bending moment, e_a and g_a were the normal stress and shear stress on the $r=a$ circular arc surface, e_b and g_b were the normal stress and shear stress on the $r=b$ circular arc surface, respectively. Subsequently, the Tsai-Hill strength criterion was employed to assess the failure status of each point.

The compatibility equation in polar coordinates of elasticity was as following:

$$\nabla^4 \Phi = \left(\frac{\partial^2}{\partial r^2} + \frac{1}{r}\frac{\partial}{\partial r} + \frac{1}{r^2}\frac{\partial^2}{\partial \varphi^2} \right)^2 \Phi = 0 \tag{5}$$

Table 2
Mechanical properties parameters of GFRPP bars for the simulation of pull-out process.

Materials	Modulus of elasticity (GPa)			Modulus of shear (GPa)			Poisson's ratio		
	E_1	E_2	E_3	G_{12}	G_{13}	G_{23}	ν_{12}	ν_{13}	ν_{23}
GFRPP	27	3	3	1	1	0.5	0.2	0.2	0.3

Note, 1 is bars longitudinal direction, 2 is bars radial direction, 3 is bars circumferential direction.

where r is the polar radius, $\varphi$is polar coordinate angle. The following stress function could satisfy the above compatibility equation :

$$\Phi = A_0 \ln r + B_0 r^2 + C_0 r^2 \ln r + D_0 r^2 \varphi + E_0 \varphi + F_0 \varphi \ln r + G_0 \varphi r^2 \ln r + \left(A_1 r^3 + B_1 \frac{1}{r} + C_1 r \ln r\right)\cos\varphi + \left(A_2 r^3 + B_2 \frac{1}{r} + C_2 r \ln r\right)\sin\varphi \tag{6}$$

The relationship between stress function and stress component were determined as following:

$$\sigma_r = \frac{1}{r}\frac{\partial \Phi}{\partial r} + \frac{1}{r^2}\frac{\partial^2 \Phi}{\partial \varphi^2}, \sigma_\varphi = \frac{\partial^2 \Phi}{\partial r^2}, \tau_{r\varphi} = -\frac{\partial}{\partial r}\left(\frac{1}{r}\frac{\partial \Phi}{\partial \varphi}\right) \tag{7}$$

According to the above equation, the corresponding stress component could be obtained as follows.

$$\sigma_r = A_0 \frac{1}{r^2} + 2B_0 + C_0(2\ln r + 1) + 2D_0\varphi + F_0\frac{\varphi}{r^2} + G_0\varphi(2\ln r + 1) + \left(2A_1 r - 2B_1\frac{1}{r^3} + C_1\frac{1}{r}\right)\cos\varphi + \left(2A_2 r - 2B_2\frac{1}{r^3} + C_2\frac{1}{r}\right)\sin\varphi \tag{8}$$

$$\sigma_\varphi = -A_0\frac{1}{r^2} + 2B_0 + C_0(2\ln r + 3) + 2D_0\varphi - F_0\frac{\varphi}{r^2} + G_0\varphi(2\ln r + 3) + \left(6A_1 r + 2B_1\frac{1}{r^3} + C_1\frac{1}{r}\right)\cos\varphi + \left(6A_2 r + 2B_2\frac{1}{r^3} + C_2\frac{1}{r}\right)\sin\varphi \tag{9}$$

$$\tau_{r\varphi} = -D_0 + \frac{E_0}{r^2} - F_0\frac{1-\ln r}{r^2} - G_0(1+\ln r) + \left(2A_1 r - 2B_1\frac{1}{r^3} + C_1\frac{1}{r^3}\right)\sin\varphi - \left(2A_2 r - 2B_2\frac{1}{r^3} + C_2\frac{1}{r^3}\right)\cos\varphi \tag{10}$$

As shown in Fig. 10, the stress boundary conditions were expressed as follows.

$$\begin{aligned} &r = a : \sigma_r = e_a, \tau_{r\varphi} = g_a, r = b : \sigma_r = e_b, \tau_{r\varphi} = g_b \\ &\varphi = 0 : \int_a^b \sigma_\varphi dr = P_0, \int_a^b \sigma_\varphi r dr = M_0, \int_a^b \tau_{r\varphi} dr = Q_0 \\ &\varphi = 90^\circ : \int_a^b \sigma_\varphi dr = P_\alpha, \int_a^b \sigma_\varphi r dr = M_\alpha, \int_a^b \tau_{r\varphi} dr = Q_\alpha \end{aligned} \tag{11}$$

When considering the overall equilibrium condition of bending bars, the combined external force and moment in horizontal direction and vertical direction were both zero ($\sum X = 0, \sum Y = 0, \sum M = 0$). The boundary conditions of$\varphi = 0, \varphi = 90^\circ$were not independent, so the boundary condition of $\varphi = 0$ was adopted to obtain the solution process. The stress component expressions of Eqs. (8) ~ (10) were substituted into the boundary conditions of Eq. (11), and the undetermined coefficients were obtained as follows:

$$A_0 = -\frac{4a^2b^2}{N}\ln\frac{a}{b}\left[M_0 - \frac{a^2b^2}{b^2-a^2}(e_a - e_b)\ln\frac{a}{b} - \frac{1}{2}\left(e_b b^2 - e_a a^2\right)\right] + \frac{a^2b^2}{b^2-a^2}(e_a - e_b) \tag{12}$$

$$B_0 = -\frac{1}{N}\left(2b^2\ln b - 2a^2\ln a + b^2 - a^2\right)\left[M_0 - \frac{a^2b^2}{b^2-a^2}(e_a - e_b)\ln\frac{a}{b} - \frac{1}{2}\left(e_b b^2 - e_a a^2\right)\right] + \frac{e_b b^2 - e_a a^2}{2\left(b^2-a^2\right)} \tag{13}$$

$$C_0 = \frac{2\left(b^2-a^2\right)}{N}\left[M_0 - \frac{a^2b^2}{b^2-a^2}(e_a - e_b)\ln\frac{a}{b} - \frac{1}{2}\left(e_b b^2 - e_a a^2\right)\right] \tag{14}$$

$$D_0 = \frac{g_b b^2 - g_a a^2}{N}\left(2b^2\ln b - 2a^2\ln a + b^2 - a^2\right) \tag{15}$$

$$E_0 = \frac{1}{2}\left(g_a a^2 + g_b b^2\right) + \frac{1}{2N}\left(g_a a^2 - g_b b^2\right)\left[b^4 - a^4 + 4a^2b^2(\ln ab - 1)\ln\frac{a}{b}\right] \tag{16}$$

$$F_0 = -\frac{4a^2b^2}{N}\left(g_a a^2 - g_b b^2\right)\ln\frac{a}{b}, G_0 = \frac{2\left(b^2-a^2\right)}{N}\left(g_a a^2 - g_b b^2\right) \tag{17}$$

$$A_1 = -\frac{1}{2M}(-P_0 + be_b - ae_a), B_1 = \frac{a^2b^2}{2M}(-P_0 + be_b - ae_a),\ C_1 = \frac{a^2+b^2}{M}(-P_0 + be_b - ae_a) \tag{18}$$

$$A_2 = \frac{1}{2M}(Q_0 - ag_a + bg_b), B_2 = -\frac{a^2b^2}{2M}(Q_0 - ag_a + bg_b),\ C_2 = -\frac{a^2+b^2}{M}(Q_0 - ag_a + bg_b) \tag{19}$$

$$N = \left(b^2-a^2\right)^2 - 4a^2b^2\left(\ln\frac{a}{b}\right)^2, M = b^2 - a^2 + \left(a^2+b^2\right)\ln\frac{a}{b} \tag{20}$$

All the coefficients in the Eq. (6) have been obtained. On the premise that the boundary conditions and the shape of bending position (a, b) were determined, the values of the coefficients could be obtained by substituting them into the above Equations. Furthermore, three stress componentsσ_r、σ_φ、$\tau_{r\varphi}$at any point could be obtained by Eq. (7). According to Tsai-Hill strength theory, the failure state corresponding to the stress state of any point in the bending area could be judged. Tsai-

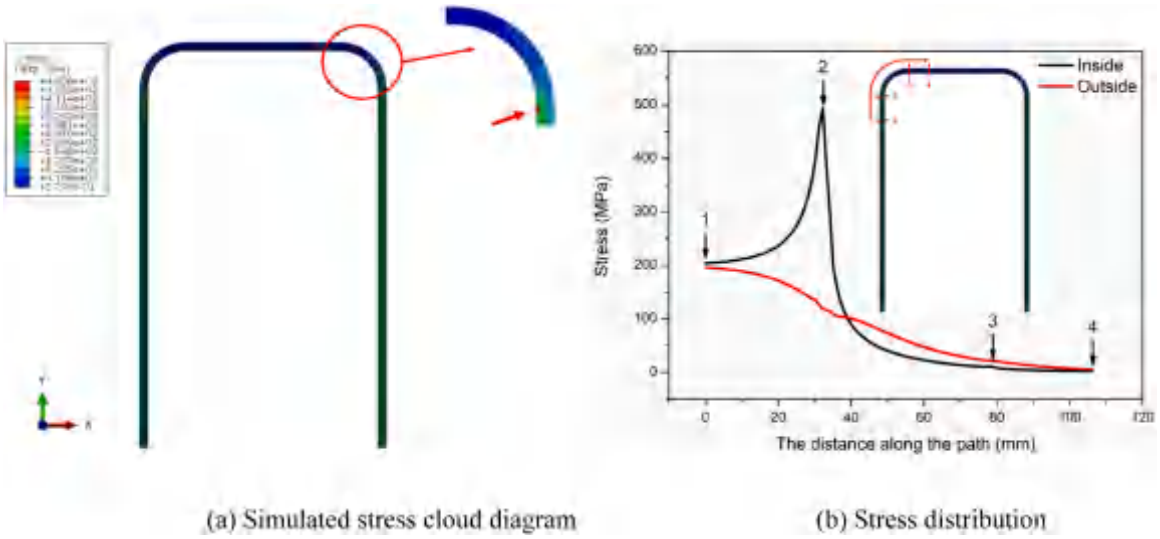


Fig. 7. Stress distribution of GFRPP bending bars during the bending process of (a) simulated stress cloud diagram and (b) stress distribution.

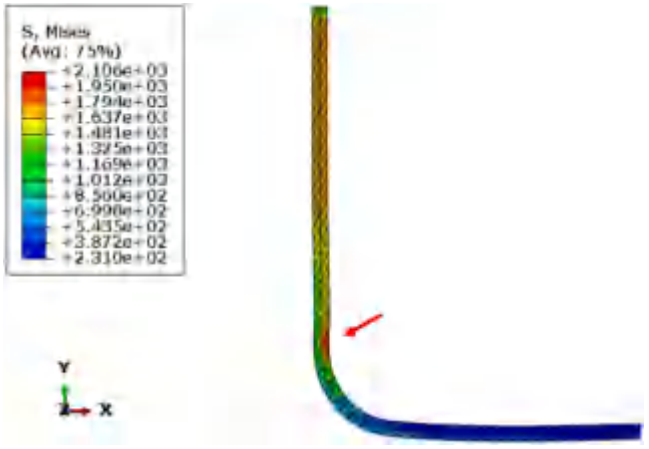


Fig. 8. Stress distribution of GFRPP bending bars during the pull-out process.

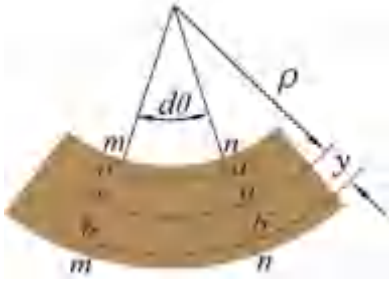


Fig. 9. Schematic diagram of bending stress calculation of GFRPP bars.

Hill strength theoretical expression was shown in Eq. (21). In the equation, the stress of $\sigma_1, \sigma_2, \tau_{12}$ corresponded to σ_r、σ_φ、$\tau_{r\varphi}$ in the above theoretical model, respectively. By substituting three stress components into Tsai-Hill strength theory, the stress state at any point could be obtained. A value less than 1.0 on the left side of the equation indicated a linear elastic state, equality to 1.0 signified the critical state, and a value greater than 1.0 indicated the damage state.

$$\frac{\sigma_1^2}{\sigma_{1\ \max}^2} - \frac{\sigma_1\sigma_2}{\sigma_{1\ \max}^2} + \frac{\sigma_2^2}{\sigma_{2\ \max}^2} + \frac{\tau_{12}^2}{\tau_{\max}^2} = 1 \tag{21}$$

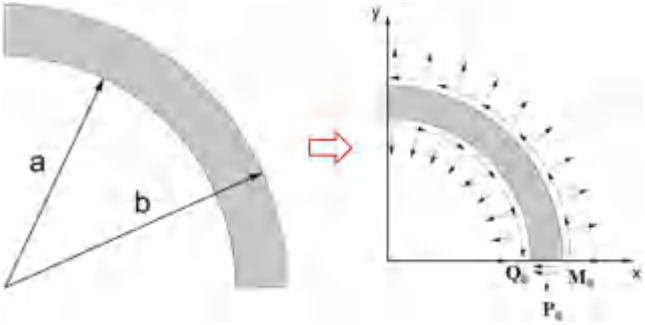


Fig. 10. Mechanical calculation model of GFRPP bending bars.

where $\sigma_{1\ \max}$ is the strength along fiber direction, $\sigma_{2\ \max}$ is the strength perpendicular to fiber direction, $\tau_{\max}$ is in-plane shear strength.

However, there were infinite points in the bending area, so it was impossible to verify each point in the actual operation. To solve this problem, a program for theoretical model was developed by Python program, which could express the region greater than 1.0 on the left side of Eq. (21) to detect the damaged area. At the same time, it was observed that the three stress components σ_r、σ_φ、$\tau_{r\varphi}$ were binary functions with respect to polar diameter r and polar angle φ. Consequently, Python was used to draw the binary function images in the defined domain (i.e., bending region) to obtain the distribution of three stress components in the bending region. Additionally, it was recognized that when the failure area extended across the entire diameter of the bending bars, the ultimate bending damage occurred.

3.2.2. *Bending failure analysis of GFRPP bars*

The theoretical model was applied to analyze the failure state of GFRPP bending bars under the specified boundary conditions as following: e_a=-5 MPa, P_0=200 MPa, and the rest loads were set zero. The inner and outer diameters were a=27 mm and b=33 mm, respectively, and the ultimate strength of $\sigma_{1\ \max}, \sigma_{2\ \max}, \tau_{\max}$ were set as 700 MPa, 50 MPa and 70 MPa, respectively. By substituting these parameters and boundary conditions into Eqs. (12)-(20), the undetermined coefficients were obtained. Subsequently, the shape parameters *a*, *b*, and coefficients were input into the Python program to generate the distribution of three stress components, as depicted in Fig. 11, and the failure zone was shown in Fig. 12. Three stress components presented the uneven stress distribution along the diameter and curvature direction. The main

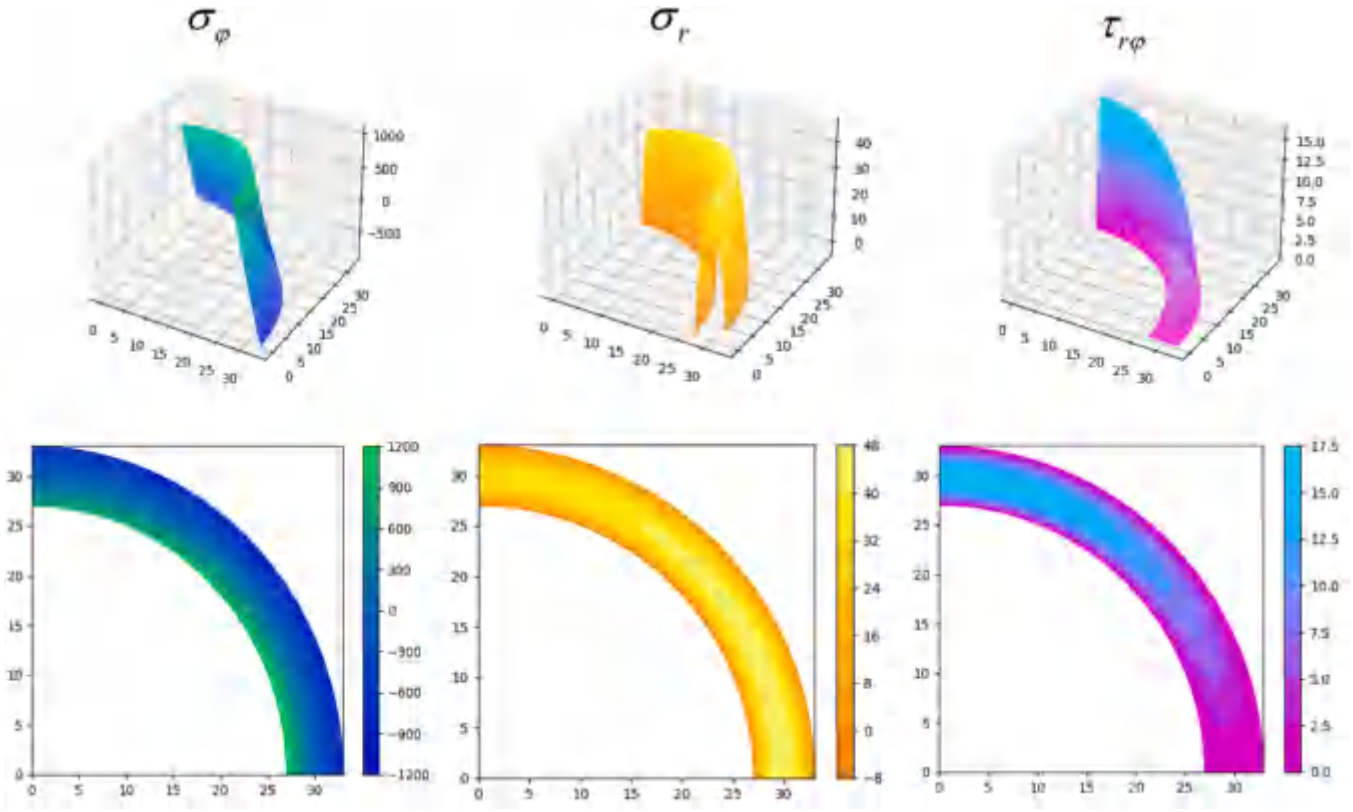


Fig. 11. Distribution of three stress components of GFRPP bending bars.

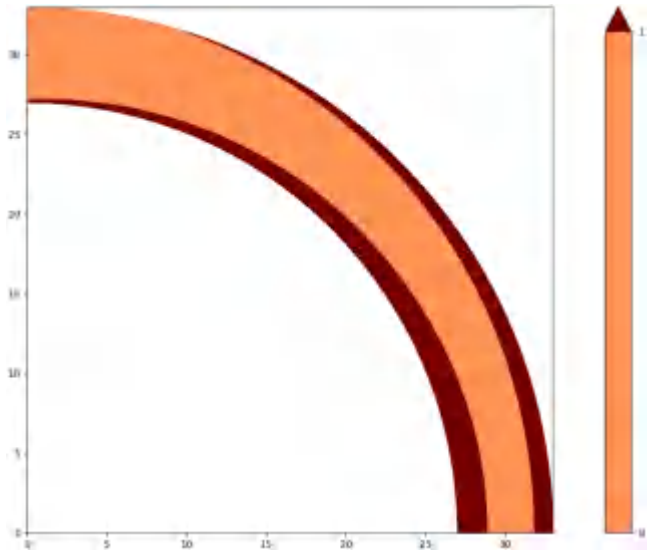


Fig. 12. Ultimate failure mode of GFRPP bending bars.

failure areas of bending bars concentrated on two areas of inner compression and outer tension, which basically consistent with the stress distribution of finite element simulation. Notably, there were no failure areas that penetrated the diameter direction of the GFRPP bending bars.

4. Experimental validation of bending properties

4.1. Tensile properties of GFRPP bending bars

Table 3 presented the tensile results of GFRPP bending bars, while

Table 3
Tensile results of GFRPP bending bars for different R/d.

R/d	Sample number	Failure load (kN)	Tensile strength (MPa)	Average tensile strength (MPa)
3	3–1	13.09	231.48	239.38
	3–2	13.70	242.27	(±6.92)
	3–3	13.82	244.39	
5	5–1	15.35	271.45	287.25
	5–2	15.67	277.11	(±22.64)
	5–3	17.71	313.18	
7	7–1	15.07	266.50	292.79
	7–2	16.27	287.72	(±29.16)
	7–3	18.33	324.15	

Note, the values inside the parentheses represent the standard deviation.

Fig. 13 provided the tensile strength retention after the bending for different R/d ratios. As shown, the average tensile strengths for R/d=3.0, 5.0 and 7.0 were determined to be 239.38 MPa, 287.25 MPa and 292.79 MPa, respectively. Notably, the maximum bending strength retention of bending bars was up to 43.2 %. This higher retention could be attributed to the effectiveness of the developed bending device in mitigating unreasonable stress concentration and fiber distortion, which also further delayed the early shear cracking of arc section. It could be found that as the R/d ratio increased, the ultimate failure load and tensile strength of GFRPP bending bars also increased. This trend could be attributed to the fact that smaller bending radius resulted in a more pronounced distortion of the inner fibers under compression. This distortion led to a more significant stress concentration within the bars, ultimately causing a notable degradation in strength. Conversely, when the bending radius was larger, the effect of the radius on stress concentration diminished, resulting in higher bending strength retention. From the above analysis, it was recommended that the ratio of bending radius to bar diameter should not be less than five to ensure a higher bending strength.

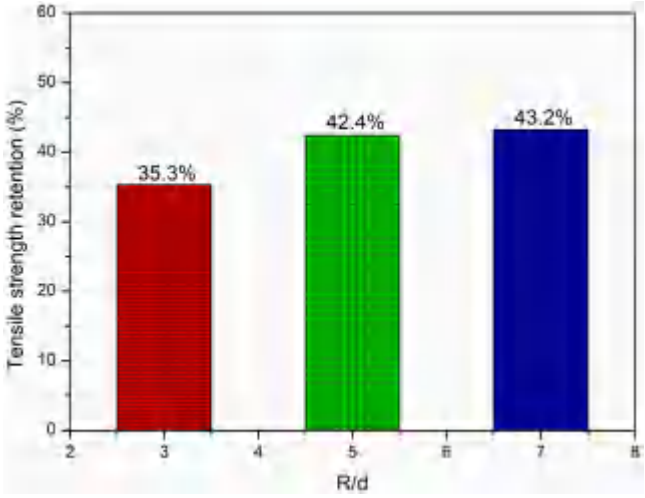


Fig. 13. Tensile strength retention of GFRPP bending bars.

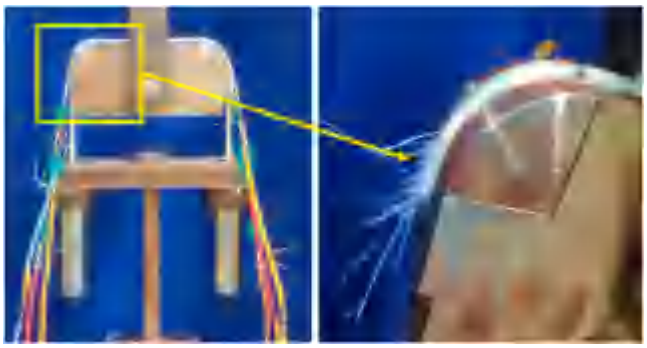


Fig. 14. Tensile failure mode of GFRPP bending bars.

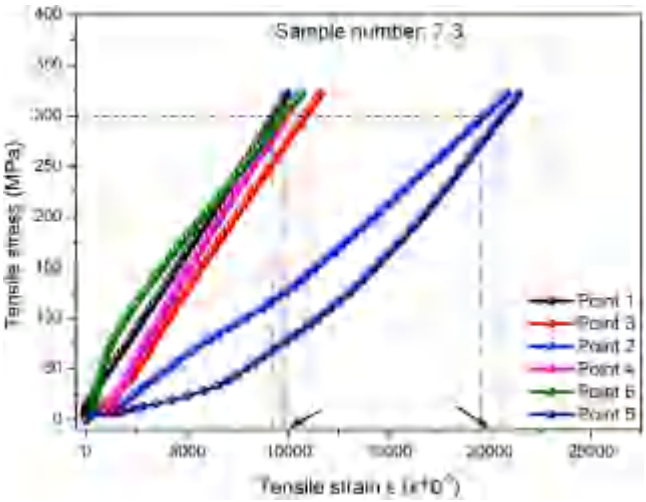


Fig. 15. Tensile stress-strain curves of GFRPP bending bars (R/d=7.0).

Fig. 14 illustrated the tensile failure mode of GFRPP bending bars. It could be found that the predominant failure mode occurred in the transition area between the bending section and the straight section, which was consistent with the results of finite element simulation (Figs. 7 and 8) and theoretical analysis (Fig. 12). This also verified the accuracy of simulation results and theoretical analysis. The discrepancy in tensile strengths between the two bending parts could be attributed to variations in manual bending operations and material inconsistencies, leading to the samples breaking firstly in the section with lower strength. In addition, it could be observed that all bending bars for different R/d were broken in the transition zone between bending parts and straight parts. This consistent failure location highlighted the critical role of the transition area in determining the overall performance and failure behavior of GFRPP bending bars.

Table 4
Short beam shear strength of GFRPP straight bars and bending bars.

Bars type	Failure load (kN)	Short beam shear strength (MPa)	Failure mode
Straight bars	756.85 (±37.41)	17.85 (±0.88)	Shear failure
Bending bars (R/d=7.0)	775.66 (±40.31)	18.29 (±0.95)	Shear failure

To analyze the strain distribution of bending bars during the tension and further verify the accuracy of the theoretical results, strain gauges were applied to the outer surfaces for the No. 7–3 sample as shown in Fig. 3. The resulting strain distribution at different positions during the tensile process were further obtained as shown in Fig. 15. Notably, the strain distributions on both sides of the bending bars were symmetrical with respect to the geometric center of the bars. The stress-strain relationship between the points 1 and 4 in the straight section and the points 3 and 6 at the end of upper bending part exhibited close similarities and approximately displayed linear behavior. When the tensile stress was 300 MPa, the strains at the above four points were about 10,000 με. However, the strains of points 2 and 5 in the transition zone between straight section and bending section exhibited a significant increase with stress. For example, the maximum strain at these points was nearly twice as large as that observed at the other four points at the same stress level of 300 MPa. Ultimately, the failure occurred at the position with maximum strain in the transition zone, aligning closely with the observed failure mode of the specimen (Fig. 14). Through comparing the experimental stress distribution and failure mode (Figs. 14 and 15) with the theoretical/simulated results (Figs. 7, 8 and 12), it was evident that the transition section between the straight section and the bending section emerged as the critical failure position for the bending bars. In engineering applications of bending bars, it was essential to prioritize reinforcement and repair of these critical failure points in the transition zone. Additionally, careful consideration should be given to the selection of bending radius, as it played a significant role in determining the overall performance and failure behavior of the bending bars.

4.2. Short beam shear strength of GFRPP bending bars

In this study, the heating softening length of GFRPP bars was slightly longer than the curve length of the bending part to ensure the smooth transition between bending part and straight part as shown in Section 2.3. Consequently, the straight part at the end of bending part may also undergo the melting and forming process. Taking this into account, the samples of straight bars and straight part at the end of bending bars were selected to conduct tests on short beam shear strength, with the results presented in Table 4. The test outcomes revealed that all specimens were destroyed by interlaminar shear mode. The shear strengths of unbending straight bars and bending bars from the end of bending part were 17.85 MPa and 18.29 MPa, respectively, which indicated that the bending process has no obvious effect on shear strength. This was because the above position was still in the straight section, and fiber distortion did not occur after the melting and forming process. In conclusion, the bending tensile strength and shear strength of bending bars could potentially be enhanced by minimizing fiber distortion during the bending process. By optimizing the bending process to reduce fiber distortion, the overall mechanical properties and performance of bending bars could be further improved.

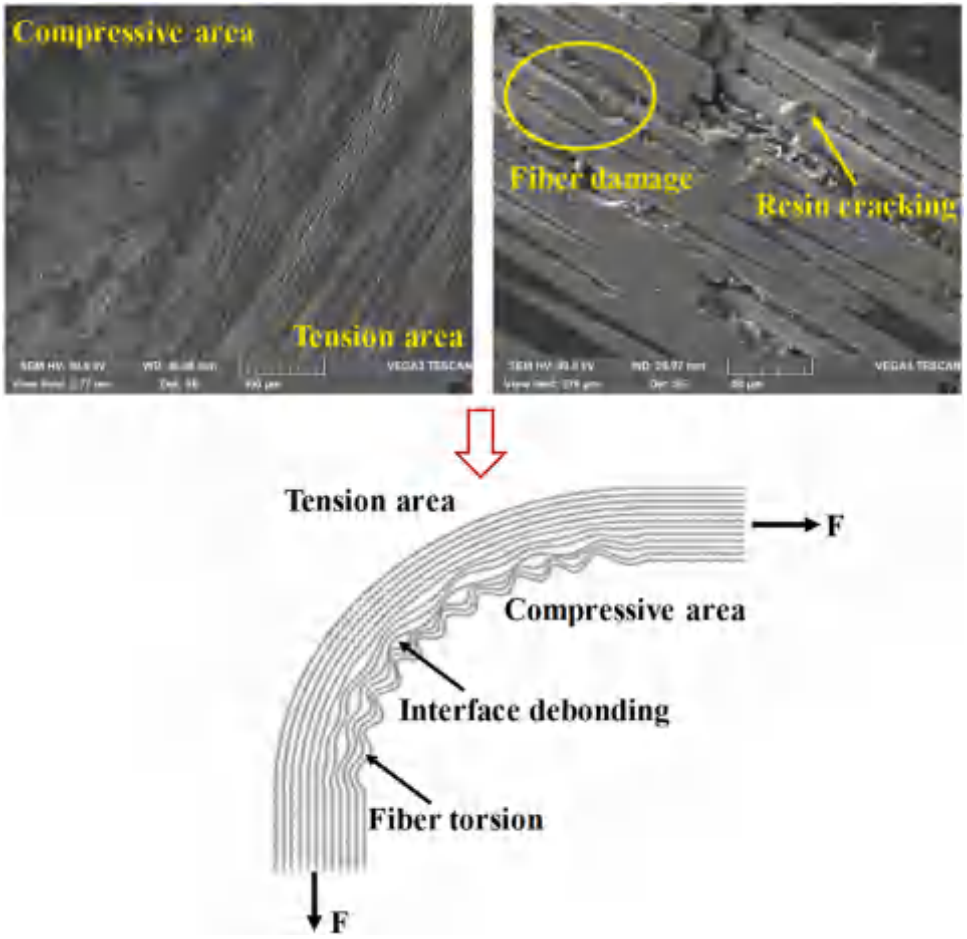


Fig. 16. Microscopic morphology and damage mechanism of GFRPP bending bars after the tensile failure.

4.3. Bending mechanism analysis of GFRPP bars

During the bending process, the polypropylene resin of thermoplastic bars transitioned into a molten state, significantly reducing the internal constraints on the fibers and allowing for sufficient deformation. As a result of the smaller inner diameter and larger outer diameter of the bars, the end face of GFRPP bending bars developed into an inclined section with inner extension and outer retraction. The present bending process was carried out in the central region of the bars, where the non-softened sections on both sides of the softened area imposed constraints. The extension of the inner fibers outward and the retraction of the outer fibers inward were also restricted, leading to compression of the inner fibers and tension of the outer fibers. With the resin in a molten state, the inner fibers struggled to withstand the pressure independently during the bending process, resulting in wrinkling and torsion, as illustrated in Fig. 16. This phenomenon highlighted the complex interplay between material behavior and geometric constraints during the bending of GFRPP bars.

The ratio of the inner length of bending bars to the neutral length in two-dimensional plane was considered to evaluate the extrusion degree$\eta$of the inner fiber as following:

$$\eta = \frac{r_1}{r_2} \tag{22}$$

where r_1 and r_2 are the inner radius and neutral radius of bending bars. The smaller η brought about the more serious shrinkage of inner fiber. Based on the above considerations, when the bending radius was constant, the larger bars diameter led to the lower strength retention after the bending. When the bars diameter remained constant, it was observed that a larger bending radius resulted in higher strength retention. When the bars diameter was constant, the second-order derivative was obtained after substituting the$r_1 = r_2 - \frac{d}{2}$ into Eq. (22), as following:

$$\eta'' = -\frac{d}{r_2^3} < 0 \tag{23}$$

From Eq. (23), it was observed that with the increase of bending radius, η growth rate decreased gradually, and the increase rate of strength retention slowed down, which was consistent with the experimental data. To a certain extent, the parameter η could effectively reflect the effect of bending parameters on bending strength.

Fig. 16 also provided insights into the microscopic morphology and damage mechanism of glass fiber reinforced polypropylene bending bars after the tensile failure. In the longitudinal section view of the bending part, the fibers on the outer side (tension side) remained parallel to the longitudinal section, whereas the fibers on the inner side (compression side) were twisted, causing them to deviate from being parallel to the longitudinal section and instead become perpendicular to the longitudinal section inward. This resulted in a round or oval fiber cross-section in the topography view. At the end of the bending part, GFRPP bars changed from bending form to straight form, and the inner fiber also changed from straight form to shrinkage state. Fiber misalignment, resin cracking and interface debonding were potential issues that may arise the premature tensile failure of bars. Based on the above analysis, the failure mechanism of bending bars could be primarily attributed to the following reason. The shrinkage and torsion of fibers resulted in the local stress concentration, which hindered their ability to effectively withstand external loads. Consequently, when the load was predominantly borne by the resin matrix, it could lead to initial cracking of the

inner resin matrix, thereby diminishing the effective bearing area. Furthermore, the fibers on the outer side may already be subjected to a certain level of tensile stress before encountering external loads, thereby reducing the residual strength of the fibers.

5. Conclusions

In the present paper, the bending properties of glass fiber reinforced polypropylene (GFRPP) bars were investigated by experimental and theoretical methods. A novel bending fixture of GFRPP bars was designed based on the principle of heating-melting and cooling-forming behavior of polypropylene. Finite element simulation was employed to analyze the stress distribution during bending and pulling-out process from concrete. The bending strength model of GFRPP bars was proposed to analyze the stress state and failure mode. Finally, the mechanical properties of bending bars were conducted to validate the theoretical and simulation results. Combined with microscopic morphology analysis, the bending mechanism of bars was further revealed. The following conclusions could be drawn based on the results and discussion.

(1) The bending fixture was proved to be highly effective in minimizing damage to the bending part during the bending process, resulting in the higher retention of bending strength up to 43.2 %, which provided the reliable bending method and high-performance bending bars for the concrete structures as stirrups.

(2) A notable agreement was observed between the theoretical simulations and experimental findings. The results revealed that the most unfavorable failure point of GFRPP bending bars appeared in the transition area between bending section and straight section owing to inner compression and outer tension. Additionally, the protective bonding effect provided by concrete contributed to a reduction in failure stress.

(3) The maximum strain of transition zone between straight section and bending section was nearly double that of the straight section at the same stress level. With the increase of bending radius, the growth rate of extrusion degree for inner fiber decreased gradually, leading to a roughly 7.9 % decrease in tensile strength of bending bars when the bending radius to diameter ratio was from 7.0 to 3.0.

(4) The shrinkage and torsion of inner fibers resulting from compression induced the local stress concentration, which could easily trigger the inner resin matrix to crack and interface debonding of fiber/resin. Moreover, the pre-existing tensile stress on the outer fibers, coupled with fiber distortion, resin cracking, and interface debonding, culminated in the premature tensile failure of bending bars.

Funding

This work is supported by the National Key Research and Development Program of China (2022YFB3706500), Program Fund of Non-Metallic Excellence and Innovation Center for Building Materials (24SFP-4), Fundamental Research Funds for the Central Universities (Grant No. HIT.OCEF. 2022032 and HIT.NSRIF202234), Heilongjiang Natural Science Foundation (LH2021E073).

CRediT authorship contribution statement

Ping Zhou: Software, Methodology, Investigation, Formal analysis. **Yanbo Bai:** Validation, Methodology, Investigation, Data curation. **Junqi Wang:** Writing – original draft, Validation, Software, Investigation, Formal analysis. **Chenggao Li:** Writing – review & editing, Writing – original draft, Supervision, Software, Investigation, Funding acquisition, Data curation. **Shaoce Dong:** Validation, Methodology, Investigation, Data curation. **Rui Guo:** Software, Resources, Methodology, Investigation, Data curation. **Jinhao Li:** Software, Investigation, Formal analysis. **Haoqiang Du:** Validation, Methodology, Investigation, Formal analysis. **Jian Zhong:** Methodology, Investigation, Formal analysis. **Guijun Xian:** Writing – review & editing, Writing – original draft, Supervision, Methodology, Funding acquisition.

Declaration of Competing Interest

The authors declare that they have no conflict of interest.

Data availability

Data will be made available on request.

References

[1] W.J. Ge, J.W. Zhu, A. Ashour, Z.P. Yang, X.N. Cai, S. Yao, W.H. Yan, D.F. Cao, W. G. Lu, Effect of chloride corrosion on eccentric-compression response of concrete columns reinforced with steel-FRP composite bars, J. Compos. Constr. 26 (4) (2022).
[2] S.W. Han, C. Fan, A. Zhou, J.P. Ou, Shear behavior of concrete beams reinforced with corrosion-resistant and ductile longitudinal steel-FRP composite bars and FRP stirrups, Eng. Struct. 278 (2023).
[3] S.D. Cheng, Z.J. Jiang, J.H. You, K. Ma A, Research progress in corrosion and protection of rebars in concrete, Hot Work. Technol. 45 (06) (2016) 14–19.
[4] D.S. Shevtsov, N.L. Cao, I.D. Zartsyn, V.C. Nguyen, Q.Q. Nong, H.Q. Le, D. A. Nguyen, E.S. Komarova, D.A. Zhikhareva, O.A. Kozaderov, A.T. Nguyen, Evaluation of the efficiency of the secondary corrosion protection of steel reinforcement bars in concrete using a bimetallic batch sensor, Int. J. Corros. Scale I 11 (3) (2022) 1228–1237.
[5] Y. Sakakihara, K. Yamagiwa, K. Isoda, S. Okazaki, Electrochemical evaluation of corrosion protection of reinforcing steel bars using sugars, Int J. Geomate 24 (102) (2023) 34–41.
[6] R. Guo, C.G. Li, Y.Z. Niu, G.J. Xian, The fatigue performances of carbon fiber reinforced polymer composites- A review, J. Mater. Res Technol. 21 (2022) 4773–4789.
[7] B.T. Zheng, M. Dawood, Fatigue crack growth analysis of steel elements reinforced with shape memory alloy (SMA)/fiber reinforced polymer (FRP) composite patches, Compos. Struct. 164 (2017) 158–169.
[8] G.J. Xian, R. Guo, C.G. Li, Combined effects of sustained bending loading, water immersion and fiber hybrid mode on the mechanical properties of carbon/glass fiber reinforced polymer composite, Compos. Struct. 281 (2022).
[9] C.G. Li, G.J. Xian, Novel wedge-shaped bond anchorage system for pultruded CFRP plates, Mater. Struct. 51 (6) (2018).
[10] M. Bazli, M. Heitzmann, B.V. Hernandez, Durability of fibre-reinforced polymer-wood composite members: an overview, Compos. Struct. 295 (2022).
[11] D. Zorko, J. Tavcar, R. Sturm, Z. Bergant, Investigation of the durability and performance of autoclave-cured, woven carbon fiber-reinforced polymer composite gears in mesh with a steel pinion, Compos. Struct. 273 (2021).
[12] R. Guo, C.G. Li, G.J. Xian, Water absorption and long-term thermal and mechanical properties of carbon/glass hybrid rod for bridge cable, Eng. Struct. 274 (2023).
[13] H.M. Lal, A. Uthaman, C.G. Li, G.J. Xian, S. Thomas, Combined effects of cyclic/sustained bending loading and water immersion on the interface shear strength of carbon/glass fiber reinforced polymer hybrid rods for bridge cable, Constr. Build. Mater. 314 (2022).
[14] N.A. Abdulla, A state-of art-review of materials, methods, and applications of PVC-FRP-confined concrete, Constr. Build. Mater. 363 (2023).
[15] K. Sanginabadi, A. Yazdani, D. Mostofinejad, C. Czaderski, Bond behavior of FRP composites attached to concrete using EBROG method: a state-of-the-art review, Compos. Struct. 299 (2022).
[16] A.M. Almushaikeh, S.O. Alaswad, M.S. Alsuhybani, B.M. AlOtaibi, I.M. Alarifi, N. B. Alqahtani, S.M. Aldosari, S.S. Alsaleh, A.S. Haidyrah, A.A. Alolyan, B. A. Alshammari, Manufacturing of carbon fiber reinforced thermoplastics and its recovery of carbon fiber: a review, Polym. Test. 122 (2023).
[17] Y.B. Tao, P. Li, J.F. Zhang, S.J. Wang, S.Q. Shi, F.G. Kong, A review of fused filament fabrication of continuous natural fiber reinforced thermoplastic composites: techniques and materials, Polym. Compos. (2023).
[18] C.G. Li, G.J. Xian, H. Li, Effect of postcuring immersed in water under hydraulic pressure on fatigue performance of large-diameter pultruded carbon/glass hybrid rod, Fatigue Fract. Eng. Mater. 42 (5) (2019) 1148–1160.
[19] C.G. Li, G.J. Xian, Design optimization and experimental validation of a novel wedge-shaped bond anchorage system for prestressed CFRP plates, Polym. Test. 75 (2019) 167–174.
[20] A.R. Rozyanty, S.F. Zhafer, Z. Shayfull, I. Nainggolan, L. Musa, L.T. Zheing, Effect of water and mechanical retting process on mechanical and physical properties of kenaf bast fiber reinforced unsaturated polyester composites, Compos. Struct. 257 (2021).
[21] C.L. Zhao, Y. Qin, X.T. Wang, H. Xiao, Coefficient of thermal expansion and mechanical properties of modified fiber-reinforced boron phenolic composites, E-Polymers 22 (1) (2022) 379–388.
[22] M. Ziaie, F. Zamani, S. Homayouni, H. Khaledi, A. Qareqani, M. Ziaie, Numerical and experimental study on mechanical properties of glass fiber-reinforced polymer sandwich structure with polyurethane foam-filled M-shaped core, Polym. Compos. 44 (2) (2023) 1054–1070.

[23] G.J. Xian, R. Guo, C.G. Li, Y.J. Wang, Mechanical performance evolution and life prediction of prestressed CFRP plate exposed to hygrothermal and freeze-thaw environments, Compos. Struct. 293 (2022).
[24] C.G. Li, X.L. Yin, Y.C. Liu, R. Guo, G.J. Xian, Long-term service evaluation of a pultruded carbon/glass hybrid rod exposed to elevated temperature, hydraulic pressure and fatigue load coupling, Int. J. Fatigue 134 (2020).
[25] C.G. Li, X.L. Yin, Y.J. Wang, L. Zhang, Z.H. Zhang, Y.C. Liu, G.J. Xian, Mechanical property evolution and service life prediction of pultruded carbon/glass hybrid rod exposed in harsh oil -well condition, Compos. Struct. 246 (2020).
[26] A. Gupta, M. Singh, J.S. Saini, Effect of nano-silica on fatigue behavior of glass fiber-reinforced epoxy composite laminates: a Weibull distribution approach, Polym. Compos. (2023).
[27] K. Naito, Y. Seki, R. Inoue, Static and fatigue tensile properties of cross-ply carbon-fiber-reinforced epoxy-matrix-composite laminates with thin plies, J. Compos. Sci. 7 (4) (2023).
[28] L. Fu, M.H. Zhang, Z.Y. Zhai, F.Z. Jiang, The influence of preheating temperature on the mechanical properties of injection-overmolded hybrid glass fiber reinforced thermoplastic composites, Polym. Test. 105 (2022).
[29] D. Meinhard, A. Haeger, V. Knoblauch, Drilling induced defects on carbon fiber-reinforced thermoplastic polyamide and their effect on mechanical properties, Compos. Struct. 256 (2021).
[30] V.T. Hoang, B.S. Kwon, J.W. Sung, H.S. Choe, S.W. Oh, S.M. Lee, J.H. Kweon, Y. W. Nam, Postprocessing method-induced mechanical properties of carbon fiber-reinforced thermoplastic composites, J. Thermoplast. Compos 36 (1) (2023) 432–447.
[31] B.C. Kikuchi, F.L.D. Bussamra, M.V. Donadon, R.T.L. Ferreira, R.D.M. Sales, Moisture effect on the mechanical properties of additively manufactured continuous carbon fiber-reinforced Nylon-based thermoplastic, Polym. Compos. 41 (12) (2020) 5227–5245.
[32] K. Ahmed, X.H. Qin, Y. Pang, Y.Y. Shao, S.R. Islam, Y.Q. Yang, H. Hamada, L.C. Yu, Effect of de-sizing on the structural and mechanical properties of carbon fiber reinforced polypropylene composites molded by the novel direct fiber feeding injection molding technology, J. Thermoplast. Compos. 36 (5) (2023) 1847–1876.
[33] V.T. Do, H.D. Nguyen-Tran, D.M. Chun, Effect of polypropylene on the mechanical properties and water absorption of carbon-fiber-reinforced-polyamide-6/polypropylene composite, Compos. Struct. 150 (2016) 240–245.
[34] B. Du, Z.X. Li, H.M. Bai, Q. Li, C.Q. Zheng, J.W. Liu, F. Qiu, Z.H. Fan, H.J. Hu, L. M. Chen, Mechanical property of long glass fiber reinforced polypropylene composite: from material to car seat frame and bumper beam, Polymers 14 (9) (2022).
[35] P. Zhou, C.G. Li, Y.B. Bai, S.C. Dong, G.J. Xian, A. Vedernikov, I. Akhatov, A. Safonov, Q.R. Yue, Durability study on the interlaminar shear behavior of glass-fibre reinforced polypropylene (GFRPP) bars for marine applications, Constr. Build. Mater. 349 (2022).
[36] A. Al-Hamrani, W. Alnahhal, Bond durability of sand coated and ribbed basalt FRP bars embedded in high-strength concrete, Constr. Build. Mater. 406 (2023).
[37] S.W. Han, A. Zhou, C. Fan, G. Xiao, J.P. Ou, Seawater sea-sand concrete columns using durable and ductile steel-FRP composite bars and FRP ties: A promising hybrid scheme for marine engineering, Eng. Struct. 294 (2023).
[38] A. Apitz, J. Schmitz, A. Hückler, M. Schlaich, New thermoplastic carbon fiber reinforced polymer rebars and stirrups, Struct. Concr. 23 (2) (2022) 923–938.
[39] R.J. Huang, Y.F. He, J. Wang, J.D. Zou, H.L. Wang, H.D. Sun, Y.X. Xiao, D. X. Zheng, J.N. Ma, T. Yu, W. Huang, Tunable afterglow for mechanical self-monitoring 3D printing structures, Nat. Commun. 15 (1) (2024).
[40] R. Guo, G.J. Xian, F. Li, C.G. Li, B. Hong, Hygrothermal resistance of pultruded carbon, glass and carbon/glass hybrid fiber reinforced epoxy composites, Constr. Build. Mater. 315 (2022).
[41] C.G. Li, G.J. Xian, H. Li, Tension-tension fatigue performance of a large-diameter pultruded carbon/glass hybrid rod, Int. J. Fatigue 120 (2019) 141–149.
[42] Wang C, Ou JP. Study on the bending technology of fiber reinforced thermoplastic polymer rebar and pulling out experiment of concrete [C]. Proceedings of the 6th National FRP Academic Exchange Conference, 2009: 102-107.
[43] Lu J. Evaluation of fundamental mechanical properties of thermoplastic FRP bars for Concrete Structure[D]. Master's thesis of Southeast University.
[44] L.M. Wang, G.X. Zhang, L.F. Li, B. Hu Y, Experimental and theoretical study on bending strength of GFRP Stirrup, Highw. Automot. Appl. 06 (2021) 131–136.
[45] E.A. Ahmed, A.K. El-Sayed, E. El-Salakawy, B. Benmokrane, Bend strength of FRP Stirrups: comparison and evaluation of testing methods, J. Compos. Constr. 14 (1) (2010) 3–10.
[46] S.C. Dong, P. Zhou, R. Guo, C.G. Li, G.J. Xian, Durability study of glass fiber reinforced polypropylene sheet under simulated seawater sea sand concrete environment, J. Mater. Res Technol. 20 (2022) 1079–1092.
[47] Committee ACI. Guide Test Methods for Fiber-reinforced Polymers (FRP) Composites for Reinforcing or Strengthening Concrete and Masonry Structures, Americould Concrete Institute.

Journal of Building Engineering 91 (2024) 109641

Contents lists available at ScienceDirect

Journal of Building Engineering

journal homepage: www.elsevier.com/locate/jobe

Long-term properties evolution and life prediction of glass fiber reinforced thermoplastic bending bars exposed in concrete alkaline environment

Guijun Xian [a,b,c], Yanbo Bai [a,b,c], Ping Zhou [a,b,c], Junqi Wang [a,b,c], Chenggao Li [a,b,c,*], Shaoce Dong [a,b,c], Rui Guo [a,b,c], Jingwei Tian [a,b,c], Jinhao Li [a,b,c], Jian Zhong [a,b,c], Taipeng He [a,b,c], Zhuo Zhang [a,b,c]

[a] *Key Lab of Structures Dynamic Behavior and Control (Harbin Institute of Technology), Ministry of Education, Heilongjiang, Harbin 150090, China*
[b] *Key Lab of Smart Prevention and Mitigation of Civil Engineering Disasters of the Ministry of Industry and Information Technology, Harbin Institute of Technology, Harbin 150090, China*
[c] *School of Civil Engineering, Harbin Institute of Technology, Heilongjiang, Harbin 150090, China*

ARTICLE INFO

Keywords:
Glass fiber reinforced polypropylene bending bars
Alkaline solution immersion
Mechanical properties
Microscopic analysis
Degradation mechanism
Prediction of service life

ABSTRACT

Glass fiber reinforced polypropylene (GFRPP) bending bars have many advantages, such as high toughness, high durability, repeated molding and recycling, which can be used in concrete structures to replace steel stirrup for solving the problems of corrosion and service life. However, the changes in the properties of GFRPP bending bars during long-term use in alkaline concrete environments require further investigation. In the present study, GFRPP bending bars were immersed in alkaline solution at 20 °C, 40 °C, and 60 °C for as long as 180 d. The water absorption, hydrolysis, mechanical properties, and microscopic properties of the bending bars were evaluated to understand the long-term performance and mechanism of degradation. The bending bars had a higher saturated water absorption percentage and time along with a lower diffusion rate than the straight bars due to the presence of pores and micro-cracks formed during the bending process. The dissolution of the glass fibers in alkaline solution led to the partial mass loss of the GFRPP bars. Compared to the control, the tensile strength retention of the bending bars was 20.6%–56.0 %. The tensile failure mode changed from fiber bursting before immersion to shear fracture after immersion due to the decreased interfacial bonding strength and increased glass fiber brittleness. The primary degradation mechanisms were the etching of glass fibers, interface debonding, and increased void volume (~23.7 %). The bending bars were more seriously eroded than the straight bars due to the twisting of the fibers and imperfect interfaces. The predicted degradation times of the GFRPP bending bars ranged from 1.7 years (Haikou) to 3.9 years (Harbin), corresponding to a stable tensile strength retention of 22.13 %. The results provide a basis for evaluating the durability and service life of GFRPP bending bars and promote the application of GFRPP composite stirrups in concrete structures.

* Corresponding author. 73 Huanghe Road, Nangang District, Harbin 150090, China.
E-mail address: lichenggao@hit.edu.cn (C. Li).

https://doi.org/10.1016/j.jobe.2024.109641
Received 19 February 2024; Received in revised form 9 April 2024; Accepted 17 May 2024
Available online 19 May 2024
2352-7102/© 2024 Elsevier Ltd. All rights are reserved, including those for text and data mining, AI training, and similar technologies.

1. Introduction

Marine engineering is critical to developing the marine economy and safeguarding marine rights and interests. The long-term exposure of steel-reinforced concrete structures to the marine environment may result in the corrosion of steel bars and the cracking and spalling of concrete, thereby degrading the bearing capacity of the concrete structure [1]. For example, the life span of a 90 % steel-reinforced concrete seaport structure is 7–25 years, and the annual loss caused by marine corrosion worldwide is approximately 700 billion US dollars [2]. Therefore, solving the problem of steel corrosion and improving the durability of concrete structures in marine environments are urgent issues.

Fiber reinforced polymer composite are often used to replace steel because of their advantages, such as light weight, high strength, good corrosion resistance and convenient construction, to improve the durability of concrete structures in marine environment [3–5]. Furthermore, the application of fiber reinforced polymer composites in marine systems has been the focus of intensive studies in the last decades, highlighting potential benefits given by the replacement of several steel components, such as ship components, offshore oil and gas composites, marine renewable energy and underwater repairing [6]. For the tailored structures for marine structural applications under mechanical, thermal and fire-induced load scenarios, the processing and production of composites have received much attention to construct quite complex, multi-material, three-dimensional assemblies capable of sustaining extreme loads [7]. At present, thermosetting resins have been used as the matrix of the common composite bars owing to the advantages, such as high strength and modulus, high production efficiency, convenient molding technology, etc. [8,9]. Furthermore, the main application forms of thermosetting composite bar in concrete structure were longitudinal bar and distributed bar [10,11]. However, thermosetting bars were rarely used for stirrups and bending bars. This was because the three-dimensional network crosslinking structure of thermosetting resin bought about high brittleness and inability to multiple molding after the curing, which largely accelerated the formation of damage and defects in the bending area for bending bars. In addition, some active functional groups in thermosetting resins may lead to poor resistance to marine corrosive environment [12–14]. In contrast, fiber reinforced thermoplastic composite bars have the advantages of repeated molding, high toughness/durability, environmental friendliness and recyclability [15–18]. Thus, fiber-reinforced thermoplastic composite bars can overcome disadvantages of thermosetting composites (high preparation cost, low production efficiency, poor toughness, and low recycling rate) to prevent the rapid deterioration in structural performance and short service life caused by steel corrosion in marine environments. Therefore, replacing steel bars with thermoplastic composite bars in concrete structures is a promising approach to ensure long service and safety in marine environments and achieve the goal of maintenance-free or low-maintenance structures.

The resin matrices of thermoplastic composite bars mainly include polyethylene, polypropylene, polyvinyl chloride, and polystyrene [19–21]. Polypropylene resin has the advantages of low cost, abundant production sources, and good mechanical properties, making it suitable for use in thermoplastic composite bars in marine environments. According to the stress state, thermoplastic bars used in concrete structures can be divided into longitudinal bars and bending bars (such as stirrup bars). When applied in bending stirrup bars, thermoplastic composites are advantageous due to their ability to be repeatedly molded [22,23]. Generally, bending stirrups are located at the outermost side of a concrete structure, where they are clearly affected by the external environment. The defects formed in the bending process may accelerate the deterioration caused by the external environment [24]. Therefore, it is necessary to explore the performance evolution and associated mechanism of thermoplastic bending bars exposed to the alkaline environment of concrete.

At present, for the simulation and evaluation of long-term durability of composites in service environment, such as freeze-thaw cycles, elevated temperature, high humidity/moisture levels and high hydrostatic pressure [25,26], the method of accelerated aging in laboratory was generally adopted, and Arrhenius equation was hence employed to correlate the accelerated aging results with the corresponding real service conditions [27]. Furthermore, the existing research work on long-term properties of fiber reinforced thermosetting composites in service environment were conducted through the experimental test, theoretical analysis and numerical simulation [26]. The degradation mechanism of composites, such as fiber etching, resin hydrolysis and interface debonding of fiber/resin can be detected through the microstructure and simulation analysis [25,26]. However, the research on the long-term durability of thermoplastic composites exposed to alkaline environment was limited and only focused on the long-term performance of thermoplastic straight bars or sheets. For example, Chen et al. [28] studied the static tensile properties of basalt fiber reinforced thermoplastic epoxy composite sheets after immersion in acid and alkaline solutions for as long as nine weeks and compared the performance with thermosetting composites. They found that corrosion occurred more rapidly in alkaline solution than in acid solution, and the thermoplastic epoxy composites showed better corrosion resistance than the thermosetting composites. Xiao et al. [29] studied the hygrothermal performance of glass fiber reinforced thermoplastic polyester (PET and PBT) composites and found that resin hydrolysis and cross-section fiber/resin debonding led to the degradation in the mechanical properties of the composites. Furthermore, the PBT composites showed superior hygrothermal performance compared to the PET composites. Wang et al. [30] investigated the durability of glass fiber reinforced polypropylene (GFRPP) composite straight bars at 60 °C in acidic, alkaline, and saline environments. The straight bars were severely corroded in alkaline solution and relatively less corroded in acidic and saline solutions. Sang et al. [31] studied the water absorption and durability of short carbon fiber reinforced PA6 composites in distilled water. After immersion for 336 h, the strength retentions of the PA6 and CF/PA6 composite were around 50 %. Scanning electron microscopy (SEM) indicated that the failure mode changed from matrix cracking to fiber pull-out after immersion, reflecting the weakening of the fiber/resin interface. Benmokrane et al. [32] immersed thermoplastic GFRP and thermosetting GFRP in alkaline solution at 60 °C for 90 d and found that the elastic modulus values of both thermoplastic and thermosetting GFRP were almost 100 % before and after immersion. In contrast, the strength retention of thermosetting GFRP was 90 %, slightly higher than that of thermoplastic GFRP (87 %). In summary, some limited research work has been devoted to the long-term evolution of thermoplastic or

thermosetting composites for the regular sample shape, such as rectangular plate and straight bar. Furthermore, mechanical degradation mechanism related to resin hydrolysis and cross-section fiber/resin debonding has been found. However, the above research findings can not be applied to the performance evaluation of glass fiber reinforced polypropylene composites when considering the coupling effects of complex fiber orientation and alkali solution exposure. Furthermore, the diffusion of water molecules and alkali ion inside the bending part of composites and its effect of long-term degradation were also complicated. Therefore, when considering the performance evolution mechanism and service life of thermoplastic bending bars for stirrup in concrete exposed to alkaline environment, the accelerated aging testing methods should be conducted to clarify the diffusion behavior of water molecules and evolution mechanism of mechanical properties under the exposures of alkaline solution and high temperature.

In the present study, GFRPP composite bending bars were immersed in alkaline solution at 20 °C, 40 °C, and 60 °C to evaluate the long-term performance evolution of composite stirrups in concrete structures. The bidirectional water absorption and hydrolysis adsorption were investigated to analyze the diffusion and form of water molecules. The tensile strength and short-beam shear strength were analyzed to understand the long-term changes in mechanical properties. Thermogravimetric analysis, infrared spectrum and scanning electron microscope tests were conducted to reveal the degradation mechanism of GFRPP bending bars in alkali environment. Based on Arrhenius theory and local annual average temperature, the long-term life of bending bars was predicted in seven typical cities in China. The research findings will provide the understanding for long-term performance evolution mechanism of GFRPP bending bars in alkaline environment, which promoted the application of glass fiber reinforced polypropylene composite stirrups in concrete structures through the durability evaluation and service life prediction.

2. Experimental programme

2.1. Raw materials

GFRPP composite bending bars with diameters of 6.0 mm and bending radius/bar diameter ratios (r/d) of 5.0 were used in this study. It should be pointed out the above bending bar was prepared through the bending process of straight bar. The preparation of bending bars mainly included three processes of heating softening, bending forming and cooling curing. Firstly, the silicone tubes were added the bending areas to prevent resin overflowing. Secondly, a hot air gun was used to heat the bending part, in which the heating temperature was 350 °C and the heating time was 2 min. Finally, the bending device was used to bending the bars to the specified angle. When the thermoplastic resin was cooled to room temperature, the bending bars were obtained. For the straight bar, it was mainly made of glass fiber reinforced polypropylene prepreg with the tensile strength of 660 MPa, tensile modulus of 47 GPa, flexural strength of 640 MPa, and flexural modulus of 45 GPa. The glass fiber weight and volume fractions of GFRPP prepreg tapes were 60 % and 32.77 %, and the nominal densities of glass fiber and polypropylene were 2.5 g/cm^3 and 0.9 g/cm^3, respectively, [15,16].

2.2. Exposure condition

Alkaline solution was used to simulate the alkaline environment of concrete pore liquid as the stirrup application in this paper. Alkaline solution was prepared according to ACI440.3R, and the contents of each component were as follows: $Ca(OH)_2$: 118.5 g, NaOH: 0.9 g and KOH: 4.2 g for per liter of deionized water [33]. pH value of the prepared alkali solution was about 12.6, while the value was measured and adjusted regularly during the exposure to ensure the relative stability. Three immersion temperatures were selected to be 20 °C, 40 °C and 60 °C, and the immersion time intervals for mechanical properties tests were 30 days, 105 days and 180 days, respectively. It should be noted that three temperatures have been selected for laboratory aging acceleration to simulate long-term performance evolution of thermoplastic bending bars in concrete environment. For the selection of the above three temperatures, the single degradation mechanism exposed to the immersion temperature was considered to conduct the long-term service life evaluation through Arrhenius prediction theory. The main consideration for the longest immersion time of 180 days was that the composite underwent enough degradation. At the same time, the choice of temperature and time also referred to the related research work on the durability of fiber reinforced polymer composites [32,34]. In addition, more time intervals were selected for water absorption and hydrolysis adsorption tests of bending bars as follows.

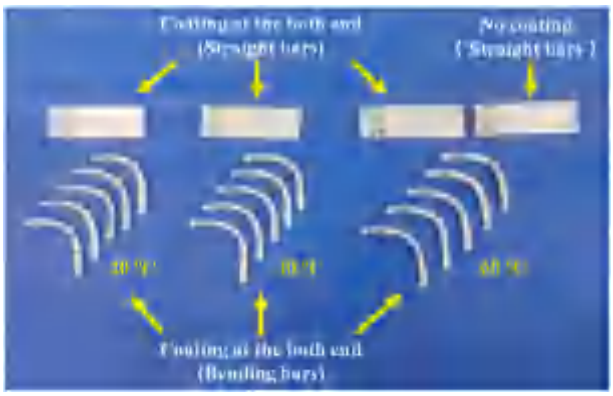


Fig. 1. Water absorption samples of glass fiber reinforced polypropylene bars.

2.3. Water absorption and hydrolysis adsorption tests

Water absorption and hydrolysis adsorption tests of thermoplastic bars were based on ASTM D5529 and related publications [35]. Five straight and bending bars with r/d = 5.0 and length = 100 mm were evaluated at each immersion temperature. Both ends of the bars were coated with epoxy resin to prevent water from entering the bar along the length direction so that one-dimensional radial water absorption could be evaluated [36]. Further, straight bars without epoxy coatings were analyzed at 60 °C as the control group, as shown in Fig. 1. The test equipment was an electronic analytical balance (Tianliang Instrument Co., Ltd., Changshu, China) with a test accuracy of 0.1 mg.

The test process for water absorption was as follows. GFRPP bars were cut using a precision cutting instrument with a cutting length of 100 mm. The bending bar samples were marked on the surfaces of the control bars, bent using the bending process, and cut along the marked positions. After cutting, epoxy resin was applied to both ends of the bars. The bars were then placed in an oven at 60 °C for 2 d to cure the epoxy resin and remove any water molecules remaining on the bar surface [34]. The mass of each bar after drying was recorded as the initial mass W_0. The samples were then placed into a water box containing the prepared alkaline solution. The water box was placed in a constant-temperature water tank at 20 °C, 40 °C, or 60 °C. After immersion in alkaline solution for 0 h, 4 h, 12 h, 24 h, 2 d, 3 d, 5 d, 7 d, 10 d, 14 d, 21 d, 28 d, 35 d, 70 d, 105 d, and 140 d, the samples were removed and weighed using the electronic analytical balance. The mass after immersion time t was recorded as W_t. The water absorption was calculated as:

$$M_t = \frac{W_t - W_0}{W_0} \times 100\% \tag{1}$$

where, M_t is the water absorption percentage of GFRPP bar at the time of t. W_t is the mass at the time of t, and W_0 is the initial mass.

The hydrolysis adsorption performance tests of the GFRPP bending bars and straight bars referred to the literature [36,37]. After immersion in alkaline solution for 140 d, the samples were removed from the water tank and weighed; this mass before drying was recorded as W_{d0}. The samples were then immediately placed into the oven for drying at 60 °C for 20 d followed by 120 °C for 10 d. Thus, the total drying time was 30 d. The samples were removed from the oven and weighed at 1, 3, 7, 10, 14, and 20 d of drying at 60 °C and after 1, 3, 7, and 10 d of drying at 120 °C; these weights were recorded as the mass at drying time t (W_{dt}). The hydrolysis absorption percentage of the bar after drying time t (M_{dt}) was calculated as:

$$M_{dt} = \frac{W_{dt} - W_{d0}}{W_{d0}} \times 100\% \tag{2}$$

2.4. Mechanical properties

The tensile properties of the bars were evaluated based on ACI440.3R B.12 using a universal testing machine (DHY-10080, Shanghai Hengyi Precision Instrument Co., Ltd.). The displacement loading speed was 1.0 mm/min. Three tensile tests were repeated, and the average bending strength was calculated. According to ASTM D4475, short-beam shear tests of the bars were conducted using the same universal testing machine. The length of the sample was 36 mm, and the span was 30 mm. The loading speed was 1.3 mm/min. The average short-beam shear strength was determined from five shear tests.

2.5. Microscopic performance analysis

The surface morphologies of the bars before and after immersion were analyzed by SEM (VEGA3). The samples were vacuumed-coated with gold to improve the electrical conductivity. The SEM frequency and electric current were 1000 Hz and 0.7 A, respectively, and the voltage amplitude was 30 kV.

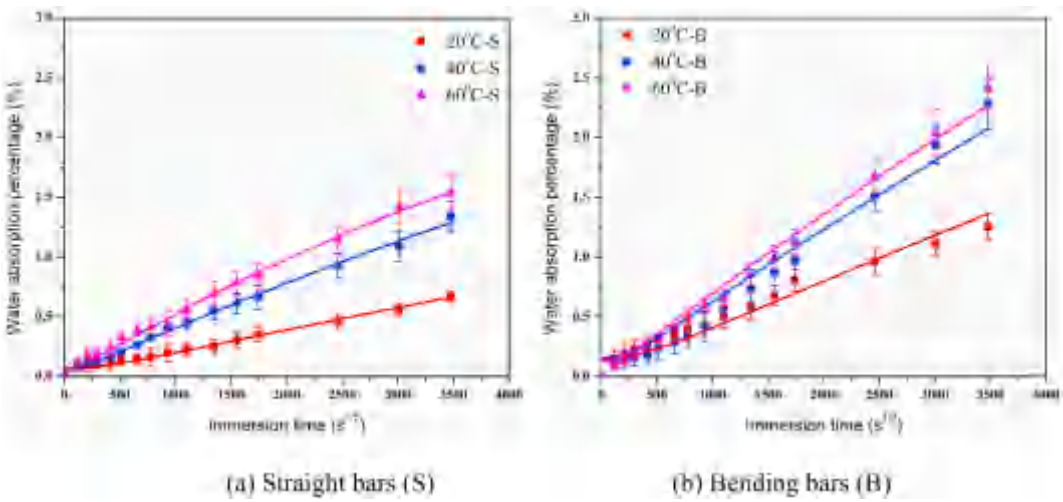


Fig. 2. Water absorption of GFRPP bars with the immersion time in alkali solution of (a) straight bars and (b) bending bars.

TGA was conducted using thermogravimetric analyzer (NETZSCH STA 449C, Hessen, Germany). The mass changes of GFRPP bars before and after immersion in alkaline solution were obtained from room temperature to 800 °C. Powder samples were formed with masses of approximately 10 mg. During testing, air and nitrogen were introduced at a speed of 20 mL/min. The changes in the decomposition rates of the samples at high temperature were also analyzed.

Infrared spectroscopy (PerkinElmer, Waltham, MA, USA) was carried to analyze the changes in functional groups of the GFRPP bars after immersion in alkaline solution. Straight bars were also analyzed under the same conditions as the control. Each spectrum was obtained by scanning 64 times in the wavenumber range of 400–4000 cm^{-1} with a resolution of 4 cm^{-1}.

3. Results and discussion

3.1. Water absorption and hydrolysis adsorption behavior

To analyze the forms of water molecules and water content during immersion, the present work investigated the radial and longitudinal water absorption and diffusion in GFRPP straight and bending bars. The hydrolysis adsorption behavior was further studied to determine the type and content of water molecules inside the bars.

For the GFRPP bars with epoxy resin coated on both sides, the water absorption in alkaline solution can be simulated as the radial water absorption. The relationship between water absorption and immersion time ($t^{1/2}$) under different temperatures in alkaline solution is shown in Fig. 2. The trends in water absorption were essentially the same for the straight and bending bars at the three tested temperatures. The water absorption percentage increased linearly over time during immersion for 140 d, and no clear saturation was observed at the end of testing. As shown in Fig. 3, the water absorption percentage of the bending bars was noticeably higher than that of the straight bars. For example, after immersion for 140 d, the water absorption percentages of the straight bars were 0.67 % (20 °C), 1.34 % (40 °C), and 1.54 % (60 °C), while those of the bending bars were 1.25 % (20 °C), 2.29 % (40 °C), and 2.41 % (60 °C).

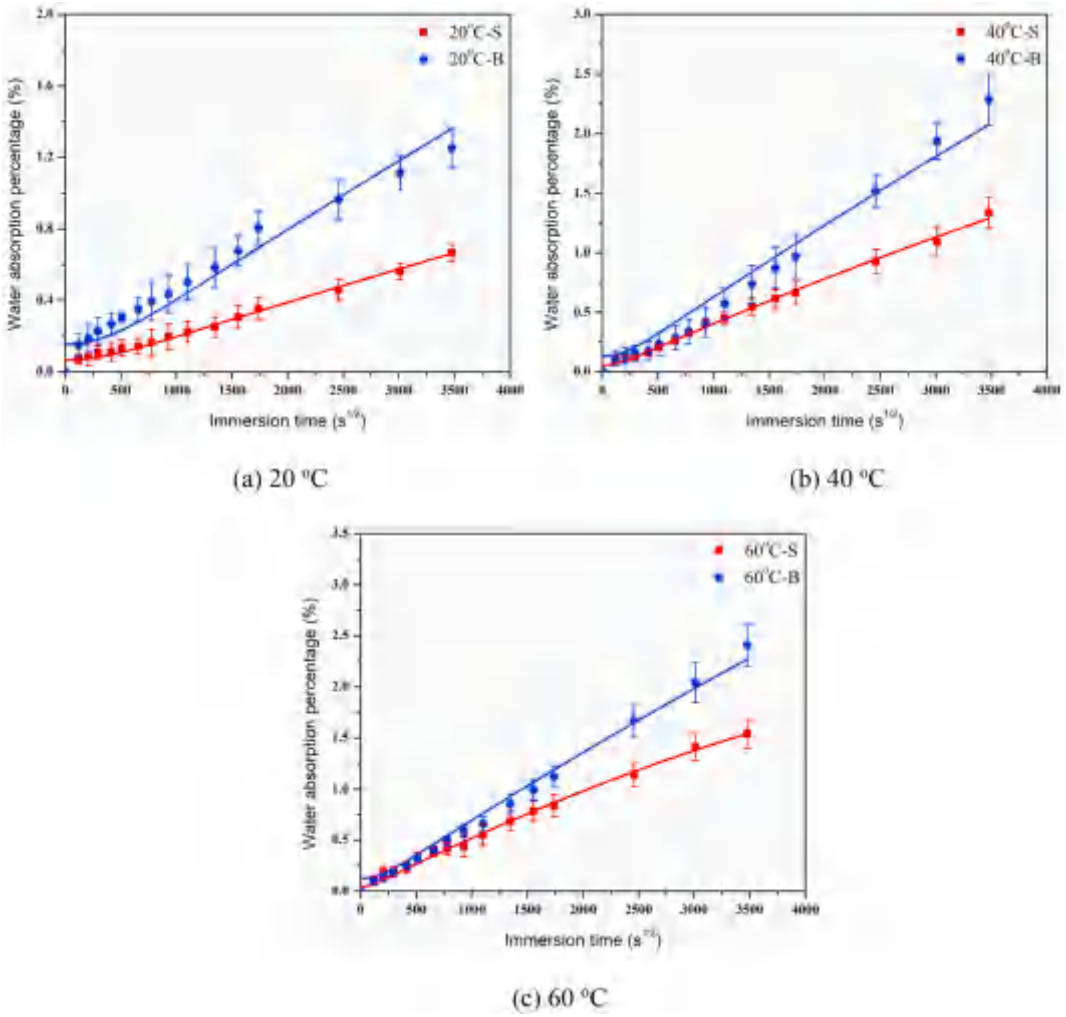


Fig. 3. Water absorption of GFRPP straight and bending bars under different temperatures in alkali solution of (a) 20 °C, (b) 40 °C and (c) 60 °C.

When assuming that the water absorption and diffusion behavior of GFRPP bars conformed to Fick's law [38–40], the water absorption curves of straight and bending bars can be fitted by the following equation, and the fitting curves were shown in Fig. 2, where S was straight bar and B was bending bar.

$$\frac{M_t}{M_m} = 1 - \sum_{n=1}^{\infty} \frac{4}{R^2 \alpha_n^2} \exp\left(-D\alpha_n^2 t\right) \tag{3}$$

where M_t is the water absorption of bar at time t (%), M_m is the saturated water absorption of bar (%), R is the bar radius, and D is the average radial diffusion coefficient, α_n is the nth root of the first kind of zero-order Bessel function, t is the immersion time in alkali solution (s).

Based on Eq. (3), the water absorption data of the straight and bending bars at the three temperatures were fitted using Origin 2018 software. The fitting coefficients (R^2) were all higher than 0.98, indicated that the water absorption and diffusion behavior of GFRPP bars agreed well with Fick's law. The average radial diffusion coefficient D and saturated water absorption M_m obtained by fitting are shown in Table 1. The water absorption and diffusion coefficients of the straights and bending bars increased with the immersion temperature. The diffusion coefficient of bending bars was lower than that of straight bars at the same temperature. The bending area was prolonged during the bending process from the straight to curve shape, which undoubtedly increased the diffusion path of water molecule in the bending area. At the same time, the irregular fiber distribution including the outer tensile fibers and inner compressive fibers in the bending area may hinder the diffusion of water molecules. The saturated water absorption rate was higher for the bending bars than the straight bars due to the pores, micro-cracks, and other defects formed during the bending process; these defects contributed to a water absorption capacity stronger than that of the straight bars.

According to Arrhenius equation [41], the relationship between diffusion coefficient D and immersion temperature T (Kelvin temperature) was determined as follows:

$$D = D_0 \exp\left(-\frac{E_a}{RT}\right) \tag{4}$$

where D_0 is the constant, E_a is the activation energy of water absorption (KJ/mol), R is the universal gas constant (8.314 J/mol/K). Furthermore, the above equation can be transformed as follows:

$$\ln(D) = \ln(D_0) - \frac{E_a}{R}\frac{1}{T} \tag{5}$$

From Eq. (5), $\ln(D)$ and $1/T$ follow a linear relationship. Therefore, the $\ln(D)$ and $1/T$ of the straight and bending bars were linearly fitted, and the resulting E_a values were compared with those of basalt fiber reinforced epoxy (BF/EP) composites [42] and carbon fiber reinforced polyurethane composites (CF/PU) [43], as shown in Fig. 4. The activation energy E_a reflects the energy barrier that must be overcome to absorb water; a larger E_a corresponds to a greater barrier to water absorption. As shown in Fig. 4, the E_a of GFRPP straight bars was higher than those of the CF/PU and BF/EP composites, indicating that polypropylene resin has lower water absorption rate and better water resistance than EP and PU. The bending bars had a noticeably lower E_a than the straight bars because water molecules entered the bending bars more easily due to the pores and interfacial defects formed during the bending process, which provided space for the absorption and diffusion of water molecules. In summary, the bending bars were more susceptible to water absorption and diffusion than the straight bars, which may lead to the rapid degradation of the mechanical properties of bending bars.

To reveal the orientation distribution of water molecules in GFRPP bars, the longitudinal water absorption was studied by analyzing bars with both ends coated and uncoated with epoxy at 60 °C. Without the epoxy resin coating, the water absorption in the GFRPP bars included both radial and longitudinal water absorption. By coating the bar ends with epoxy resin, the radial water absorption was eliminated, and the longitudinal water absorption could be obtained. Fig. 5 shows the comparison of radial and longitudinal water absorption of GFRPP straight bars at 60 °C for the maximum immersion time of 140 days in alkali solution. Through the calculation, the longitudinal water absorption percentage was 2.35 % at the longest immersion of 140 days, which was 52.6 % higher than that of radial water absorption. This indicated the water absorption along the fiber direction (longitudinal direction) was stronger than that perpendicular to the fiber direction (radial direction). This was because the water molecule easily entered the composites along the fiber/resin interface owing to the possible defects and imperfections. In addition, the water absorption in the direction perpendicular to the fiber was easily hindered by the fiber, which increased the diffusion path and reduced the diffusion rate of water molecules in this direction.

After obtaining the radial and longitudinal water absorption, the water absorption concentration distribution of GFRPP straight and

Table 1
Average radial diffusion coefficient and saturated water absorption of GFRPP bars.

Bar type	Fitting paramaters	Immersion temperature (°C)		
		20	40	60
Straight bars	D(m^2/s)	6.48×10^{-15}	3.98×10^{-14}	1.11×10^{-13}
	M_m(%)	3.28	2.77	2.18
Bending bars	D(m^2/s)	4.98×10^{-15}	1.67×10^{-14}	2.35×10^{-14}
	M_m(%)	7.65	6.59	6.17

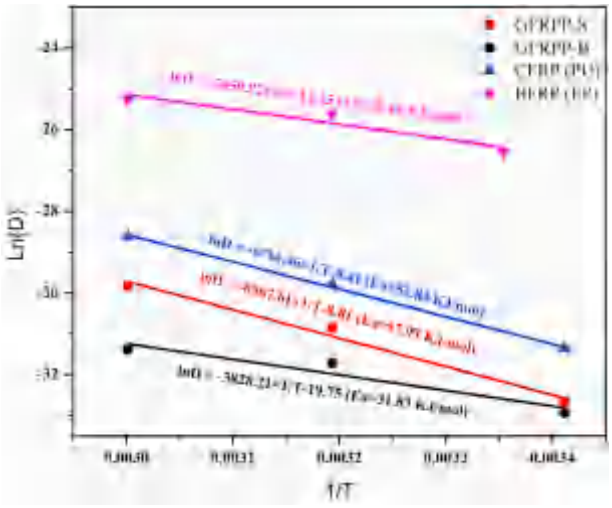


Fig. 4. Dependence of water absorption diffusion coefficient on immersion temperature of GFRPP bars and the other composites.

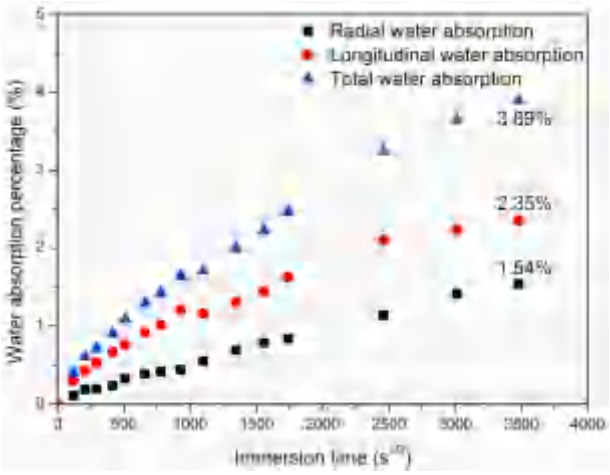


Fig. 5. Comparison of radial and longitudinal water absorption of GFRPP bars at 60 °C.

bending bars were further analyzed. The diffusion of water molecules in the sealed straight bars can be simulated as the radial diffusion process in a cylinder. Meanhwile, the bending bars was regarded as an idealized circular section, and the diffusion equation for straight and benidng bars was also shown as following [44].

$$\frac{\partial C(r,t)}{\partial t}=\frac{1}{r}\frac{\partial}{\partial t}\left(rD\frac{\partial C(r,t)}{\partial r}\right) \tag{6}$$

where $C(r, t)$ is the water absorption concentration at radius position r and immersion time t;D is the average diffusion coefficient (m^2/s). The water absorption process of GFRPP straight bars and bending bars conformed to Fick's law, and the general solution of diffusion Equation (6) was as follows.

$$C(r,t)=u(r)\exp\left(-D\alpha^2 t\right) \tag{7}$$

Through substituting Equation (7) into Equation (6), the following equation can be obtained.

$$\frac{\mathrm{d}^2u(r)}{\mathrm{d}r^2}+\frac{1}{r}\frac{\mathrm{d}u(r)}{\mathrm{d}r}+\alpha^2u(r)=0 \tag{8}$$

Based on the previous work [35], the concentration distributions of GFRPP straight and bending bars were obtained as follows.

$$C(r,t)=1-\frac{2}{a}\sum_{n=1}^{\infty}\frac{J_0(\alpha_n r)}{J_1(a\alpha_n)}\ \frac{1}{\alpha_n}\exp\left(-D\alpha_n^2 t\right) \tag{9}$$

where J_0 is the first kind zero-order Bessel functions, J_1 is the first kind one-order Bessel functions, α_n is the nth root of the first kind of zero-order Bessel function.

According to Eq. (9) and Table 1, the water absorption concentrations of GFRPP straight and bending bars at different radial

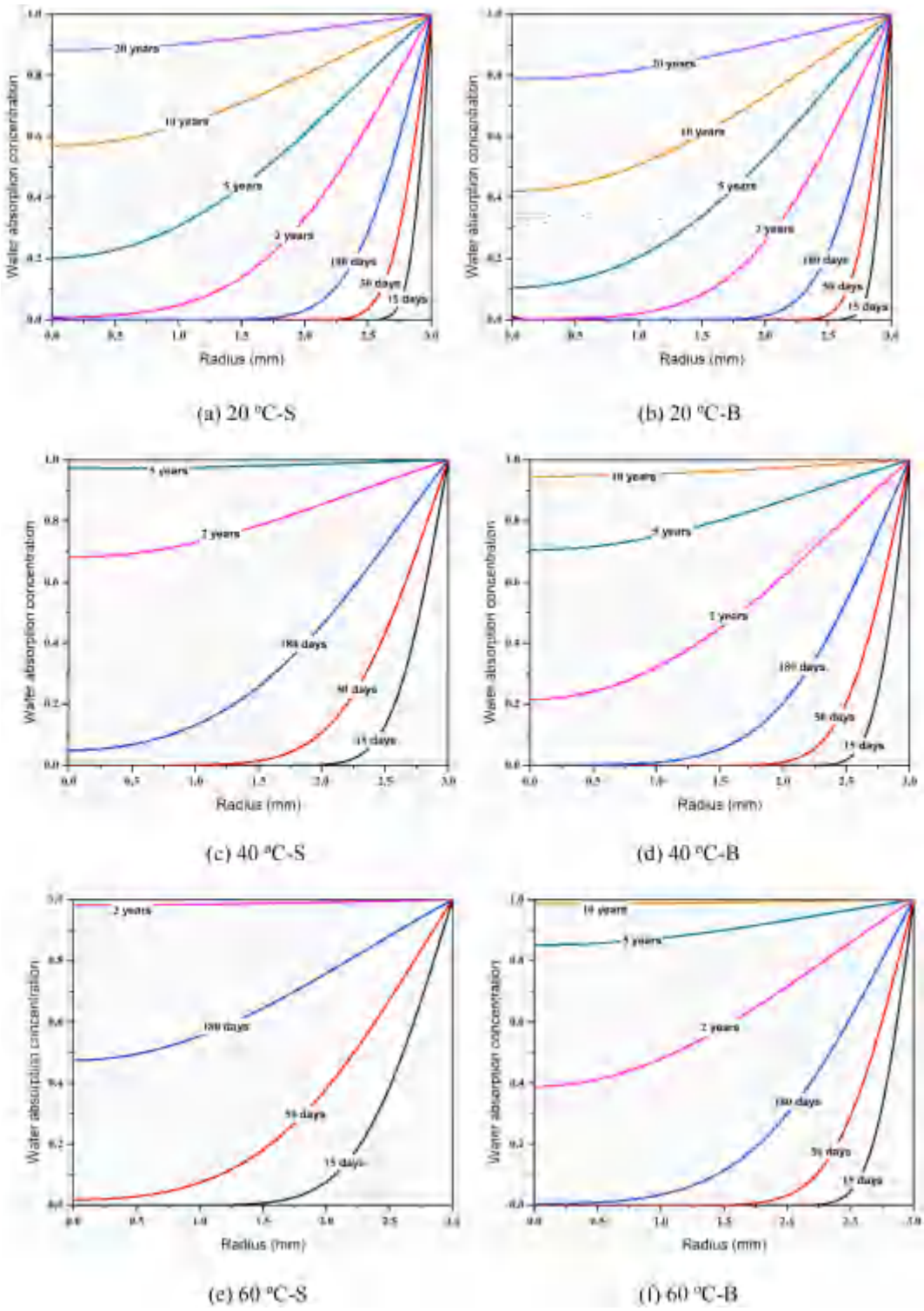


Fig. 6. Water absorption concentration of GFRPP bars with the immersion time in alkali solution of (a) 20 °C-S, (b) 20 °C-B, (c) 40 °C-S, (d) 40 °C-B, (e) 60 °C-S, (f) 60 °C-B. Note that when the water absorption concentration was one, which meant that the saturation condition was reached at this point.

positions and immersion times under the three immersion temperatures were obtained (Fig. 6). The bars were saturated when the center of the bar reached saturation (i.e., the normalized water absorption concentration at $r = 0$ mm was 1.0). The temperature had a significant effect on the diffusion of water molecules inside the bars. As the temperature increased, the diffusion rate of water

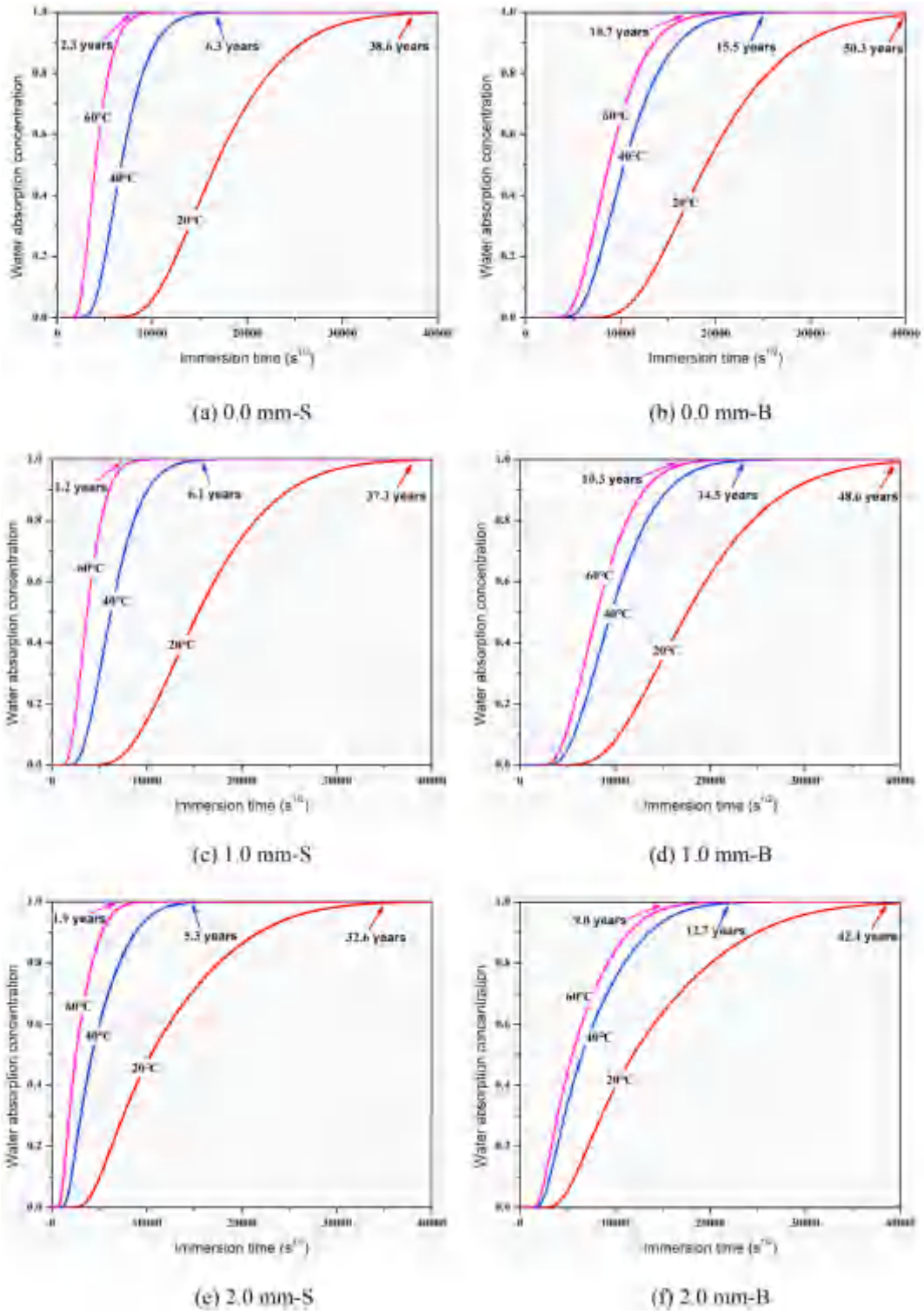


Fig. 7. Water absorption concentration of GFRPP bars with the immersion temperature in alkali solution of (a) 0.0 mm-S, (b) 0.0 mm-B, (c) 1.0 mm-S, (d) 1.0 mm-B, (e) 2.0 mm-S, (f) 2.0 mm-B.

molecules increased, and the time to reach saturation decreased greatly. For example, the saturation times of the straight and bending bars were more than 20 years at 20 °C. When the immersion temperature increased to 60 °C, the saturation times of the straight and bending bars decreased to 2 and 10 years, respectively. For the same temperature, the saturation time of the straight bars was lower than that of the bending bars because the diffusion path of water molecules inside the bending bars was higher due to the effect of fiber bending. Additionally, the large number of pores and defects inside the bending bars provided storage space for water molecules, contributing to the longer saturation time.

The water absorption concentration curve at position (r) and time (t) could obtained using Eq. (9). Three positions ($r = 0.0$, 1.0, and 2.0 mm) were selected to analyze the variation of in absorbed water concentration over time in the straight and bending bars, as shown in Fig. 7. The saturated water absorption times of the corresponding radial positions are summarized in Table 2. When the normalized water absorption concentration at a certain position reached 0.99, saturation was considered to be reached at that position. The diffusion of absorbed water proceeded from the outside to the inside of the straight and bending bars. The concentration of absorbed water was always higher at the outer part than at the inner part, and the outer part reached saturation before the inner part. Increasing the temperature clearly accelerated the water absorption process. For example, the water absorption saturation times of the straight bars were 38.6 years (20 °C), 6.0 years (40 °C), and 2.3 years (60 °C), while those of the bending bars were 50.3 years (20 °C), 15.5 years (40 °C) and 10.7 years (60 °C). When considering the water absorption concentration from 0 to 1, the above-mentioned saturated water absorption times can be used to evaluate the influence of water absorption on the properties of the GFRPP bars.

To further study the forms of water molecules in the bars and mass losses during immersion in alkaline solution, the samples after the water absorption test were placed into an oven for drying. Two drying temperatures (60 °C and 120 °C) were selected; the free water inside the bars was removed at 60 °C, and the bound water was removed at 120 °C. The desorption curves of the GFRPP straight and bending bars are shown in Fig. 8. After drying at 60 °C for 20 d, the sample mass tended to be stable, and the free water content inside the bars could be obtained. After increasing the temperature to 120 °C, the rate of mass loss increased, indicating the loss of bound water. After drying at 120 °C for 10 d, the mass was again stable, indicating that the bound water was mostly removed, and the bound water content could be obtained. The contents and percentages of free and bound water inside the bars are listed in Table 3. The water molecules inside the bars mainly existed in the form of free water. Furthermore, the proportion of free water in the bending bars was higher than that in the straight bars because the pores in the bending bars provided storage space for free water.

From Fig. 8, it was found that the water content of each sample was negative after the drying at 120 °C, which showed that part of mass loss produced in the process of immersion in alkali solution due to the corrosion of glass fiber by alkali. Relevant research [45] showed that Si–O bond of glass fiber reacted with OH ions and water molecules in the alkali solution as follows, which led to the fracture of Si–O bond and the dissolution of glass fiber.

$$Si-ONa+H_2O \rightarrow Si-OH+NaOHSi-O-Si+OH^- \rightarrow Si-OH+Si-OSi-O+H_2O \rightarrow Si-OH+OH^- \quad (10)$$

3.2. Effect of immersion on the mechanical properties of GFRPP bending bars

After immersion for 0, 30, 105, and 180 d at 20 °C, 40 °C, and 60 °C, the tensile strengths and short-beam shear strengths of the GFRPP bending bars were evaluated, and the resulting strength retention rates are shown in Table 4 and Fig. 9. The strength retention rates were calculated based on the values of the straight bars, and the r/d of the bending bars was 5.0. According to a previous study, the strength retention rate of GFRPP bending bars without immersion in alkaline solution was 42.4 % relative to straight bars. The above data were converted into the strength retention rates of bending bars immersed in alkaline solution, as shown in parentheses in Table 4. After immersion for 30, 105, and 180 d, the strengthen retention rates were respectively 56.0 %, 40.2 %, and 31.4 % at 20 °C; 37.3 %, 27.9 %, and 22.8 % at 40 °C; and 29.8 %, 23.7 %, and 20.6 % at 60 °C. It can be found that the tensile strength degradation rate of bending bars was the fastest in the initial immersion of 30 days. This was because the bars had a higher water absorption within the initial immersion of 30 days owing to higher concentration difference between the inner and outer of bending bars, which occupied 40 %–60 % of the maximum water absorption Furthermore, the concentration difference was gradually weakened with the increase of immersion time. Higher temperature and faster water absorption rate may accelerate the etching effect of hydroxide ions on glass fiber and the swelling effect of resin, which led to the fiber degradation, interface debonding and rapid degradation of tensile strength of bending bars. In addition, it can be seen that alkali solution has obvious effect on the tensile strength of GFRPP bending bars. Especially at the initial immersion stage, the strength of GFRPP bending bars decreased rapidly by 44 % after the immersion at 20 °C for 30 days. After the immersion at 60 °C for half a year, the strength of GFRPP bending bars was only 8.7 % of straight bars, which was nearly 80 % lower than that of bending bars. Again, this indicated that alkali solution has a strong erosion effect on GFRPP bending bars, resulting

Table 2
Saturated water absorption time of GFRPP bars for different radial positions.

Bar type	Radial position (mm)	Saturated water absorption time (years)		
		20 °C	40 °C	60 °C
Straight bar (S)	0.0	38.6	6.3	2.3
	1.0	37.3	6.1	2.2
	2.0	32.6	5.3	1.9
Bending bar (B)	0.0	50.3	15.5	10.7
	1.0	48.6	14.5	10.3
	2.0	42.4	12.7	9.0

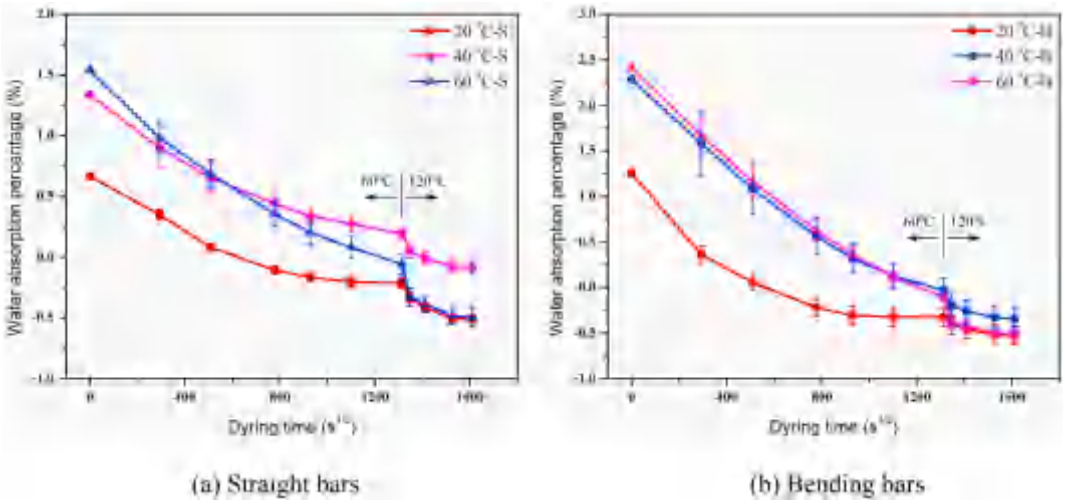


Fig. 8. Desorption curves of water absorption of GFRPP bars with the immersion temperature and time in alkali solution of (a) straight bars and (b) bending bars.

Table 3
Content percentage of free water and bound water of GFRPP bars at different immersion temperatures.

Bar type	Water type	Immersion temperature (°C)		
		20	40	60
Straight bars	Free water	74.6 %	80.1 %	78.7 %
	Bound water	25.4 %	19.9 %	21.3 %
Bending bars	Free water	88.6 %	88.0 %	86.0 %
	Bound water	11.4 %	12.0 %	14.0 %

Table 4
Tensile properties of GFRPP bending bars immersed in alkali solution.

Immersion temperautre (°C)	Immersion time (days)	Average tensile strength (MPa)	Strength retention (%)
20	30	160.93 (±38.47)	23.8 (56.0)
	105	115.48 (±14.31)	17.0 (40.2)
	180	90.13 (±6.91)	13.3 (31.4)
40	30	107.22 (±14.69)	15.8 (37.3)
	105	80.11 (±5.30)	11.8 (27.9)
	180	65.43 (±9.02)	9.7 (22.8)
60	30	85.49 (±10.39)	12.6 (29.8)
	105	68.08 (±6.74)	10.0 (23.7)
	180	59.06 (±5.64)	8.7 (20.6)

Note: The strength retention rate in brackets was relative to the strength retention rate of bending bars without the immersion in alkali solution.

in lower strength retention, especially at higher temperature and longer immersion time.

Fig. 10 shows the tensile failure modes of GFRPP bending bars before and after immersion in alkaline solution. The fracture position appeared at the bending end. Without immersion in alkaline solution, the fracture mode was fiber bursting. After immersion, the fracture surfaces of the bending bars were flusher, and the fracture surface mostly followed the direction of internal bending fibers. The alkaline solution may have entered the bars and weakened the interfacial bonding between the fibers and resin, leading to brittle failure on the interface along the fiber direction due to the brittleness of the glass fibers [30].

Short-beam shear test specimens were obtained from the straight and bending sections at the end of the bending bars. After immersion in alkaline solution at 40 °C for 60 and 180 d, the samples were removed for testing, and the results are shown in Table 5. Compared with short-beam shear strength of the control, those of the straight bars and bending bars immersed in alkaline solution for 60 and 180 d decreased by 21.7 %, 29.1 %, and 18.9 % and 39.2 %, respectively. Overall, the decrease in the short beam shear strength was noticeably lower than that of tensile strength. By comparison, it can be found that the effect difference of immersion on the short shear strength of straight bars and bending bars was negligible, which indicated that the effect of bending process on the long-term shear strength can be neglected.

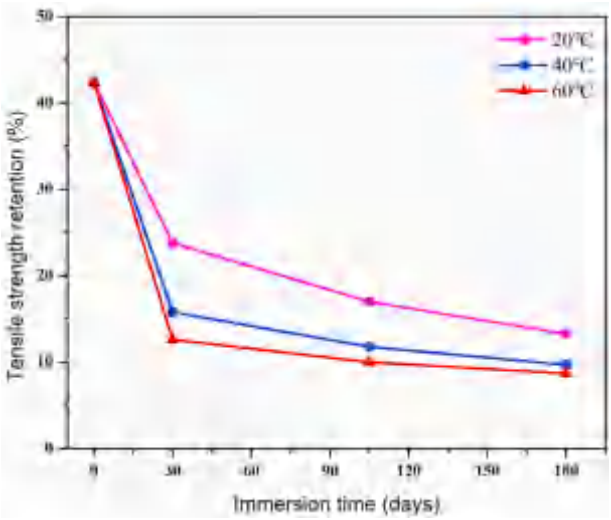


Fig. 9. Tensile strength retention of GFRPP bars with the immersion temperature and time in alkali solution.



Fig. 10. Tensile failure mode of GFRPP bars before and after the immersions in alkali solution.

Table 5
Short beam shear strength of GFRRPP bars after immersing in alkali solution.

Immersion time (days)	Bar type	Short beam shear strength (MPa)
60	Straight bar	13.97 (±0.31)
	Bending bar	14.83 (±1.27)
180	Straight bar	12.66 (±0.31)
	Bending bar	11.13 (±1.30)

3.3. Effect of immersion on the thermal properties of GFRPP bending bars

The thermal properties of GFRPP bending bars before and after immersion were studied. Fig. 11 shows the TGA curves of the bending bars before and after immersion in alkaline solution at 60 °C for three months. The mass degradation at elevated temperature could be divided into three stages. In the first stage, the slight mass loss was mainly attributed to water evaporation inside the samples. When the temperature reached approximately 300 °C, the rate of degradation began to increase clearly. The decomposition temperatures of the bending bars before and after immersion were 297 °C and 357 °C, respectively, corresponding to a mass retention rate of 99.0 %. In the second stage (350°C-490 °C), the mass decomposition rate of the polypropylene resin decreased rapidly. The temperatures of the maximum decomposition rates before and after immersion were 455 °C and 457 °C, respectively, indicating that the alkaline solution had no noticeable effect on the decomposition temperature of polypropylene resin. In the third stage, the resin was completely decomposed, and the mass of glass fibers remained stable. The mass fraction of glass fibers before immersion was appropriately 75.7 % and decreased to approximately 40.9 % after immersion. The ultimate decomposition temperature was approximately 479 °C before and after immersion. The decrease of in the fraction of glass fibers was mainly attributed to etching of the Si–O skeleton of glass fibers by the OH ions in alkaline solution, as shown in Eq. (10).

According to the mass fraction obtained in Fig. 11 and the measured density of GFRPP bar (1.4 g/cm^3), combined with the density

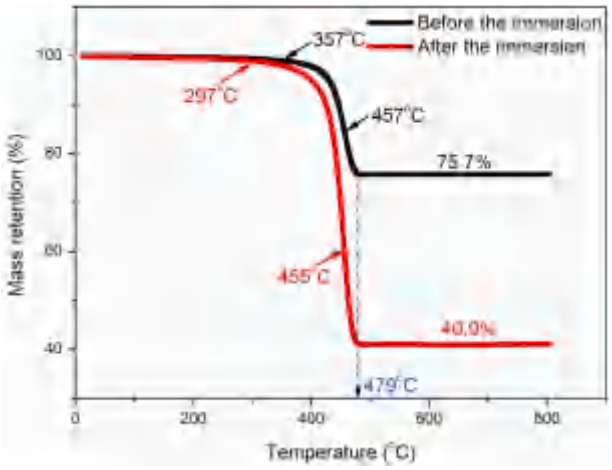


Fig. 11. Thermogravimetric analysis of bending bars before and after the immersions at 60 °C alkali solution for three months.

of glass fiber (2.5 g/cm^3) and polypropylene resin (0.9 g/cm^3), it can be calculated that the internal void volume fraction of bending bars increased by 23.7 % after the immersion when ignoring the change of resin volume during the immersion. The increase in void volume fraction was mainly caused by the etching of the glass fibers and the debonding of the fiber/resin interface.

3.4. Degradation mechanism analysis of GFRPP bending bars

After analyzing the long-term mechanical and thermal performances of the GFRPP bending bars, the degradation mechanism in alkaline solution was investigated by analyzing the changes in functional groups and surface morphology. The infrared spectra of GFRPP straight and bending bars immersed in alkaline solution for three months are shown in Fig. 12, and Table 6 lists the corresponding functional groups and vibration types. The intensities of the characteristic peaks at 1008 and 467 cm^{-1} decreased after immersion, reflecting the etching of the glass fiber network and the reaction of metal oxides with water, respectively. These changes indicate that the glass fibers inside the GFRPP bending bars were eroded in alkaline solution. The infrared peak intensity was higher for the straight bars than the bending bars, demonstrating that the bending bars were more seriously eroded in alkaline solution due to the defects formed during the bending process. The characteristic peaks of polypropylene (2985, 2921, 2873, 2839, 1457, and 1376 cm^{-1}) changed little during immersion, and no new peaks appeared. These findings are in good agreement with the observed thermal properties and confirm that polypropylene was not sensitive to alkaline solution.

SEM was used to observe the surface, cross-sectional, and longitudinal morphologies of GFRPP bending bars before and after immersion in alkaline solution for six months (Fig. 13). The cross-sectional SEM image of the control sample shows a tight fiber/resin interface, indicating good bonding performance. After the immersion, the fiber/resin interface debonding occurred because of alkali solution invading effect. At the same time, cracks and pores appeared inside the bars and the fiber twist phenomenon was more obvious on the compression side of bending part. The above defects formed in the bending part can provide more storage space for water molecules, which also contributed to the higher water absorption (Fig. 3). From the longitudinal-section morphology, it was difficult to keep the elliptical section for the twisted fiber after the immersion. The obvious fiber loss and interface debonding were further

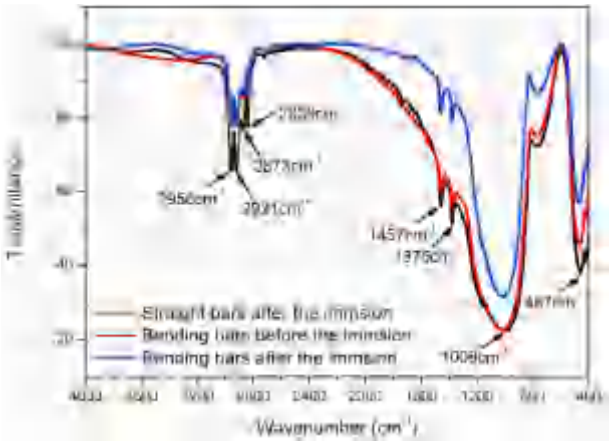


Fig. 12. Functional groups analysis of GFRPP bars before and after the immersion in alkali solution.

Table 6
Functional groups and vibration types of GFRPP bars corresponding to each wavenumber in infrared spectrum.

Wavenumber (cm^{-1})	Functional groups	Vibration types	References
2958	$-CH_3$	Asymmetric stretching vibration	[46]
2921	$-CH_2-$	Asymmetric stretching vibration	[46]
2873	$-CH_3$	Symmetric stretching vibration	[46]
2839	$-CH_2-$	Symmetric stretching vibration	[46]
1457	$-CH_2-$	Bending vibration	[46]
1376	$-CH_3$	Bending vibration	[46]
1008	Si–O	Asymmetric stretching vibration	[47]
467	Si(Al)–*O*–Si	Bending vibration	[46]

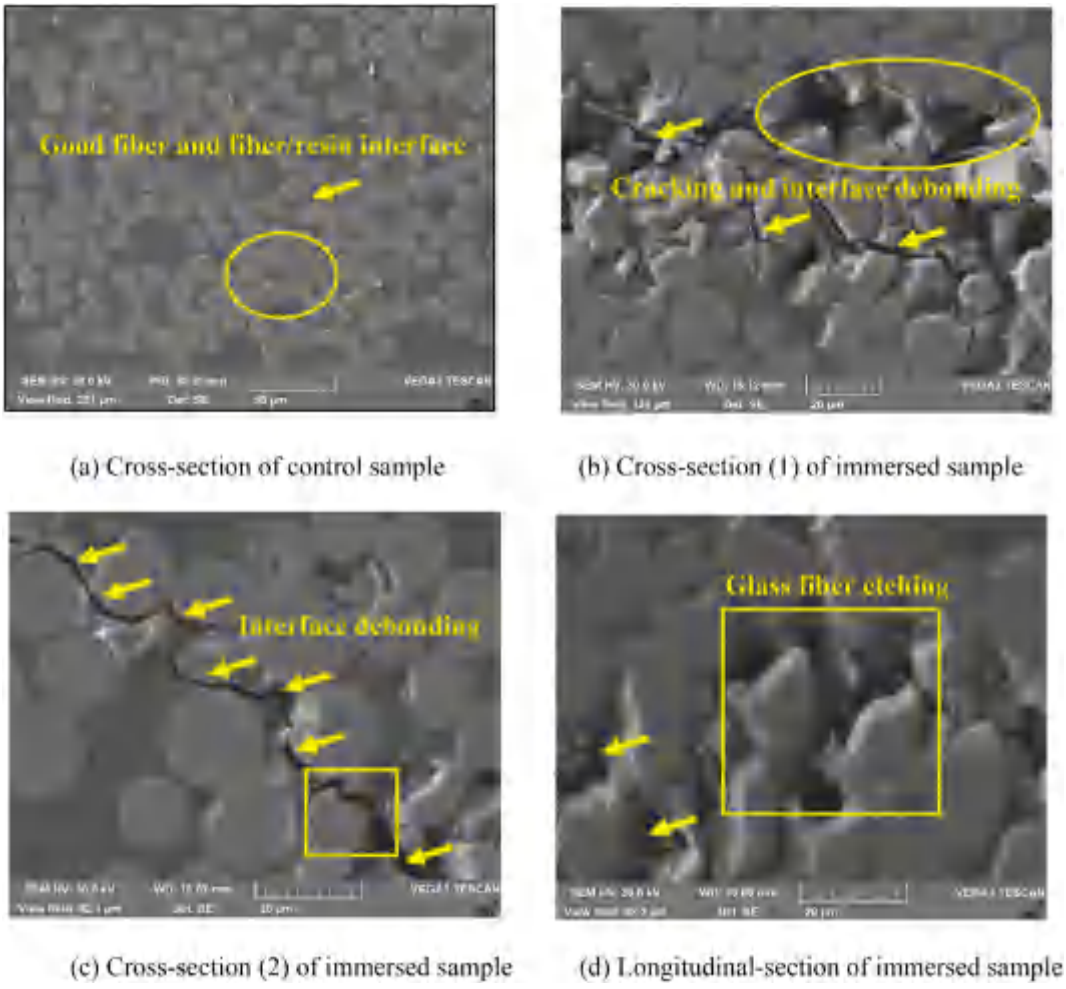


Fig. 13. Surface morphology of GFRPP bending bars before and after the immersions in alkali solution.

observed, which contributed to the degradation of mechanical properties.

3.5. Prediction of long-term service life of GFRPP bending bars

The service life is an important index to evaluate the durability of GFRPP bending bars. Arrhenius theory is an effective framework for predicting the long-term durability of composites based on accelerated aging tests. This method assumes that composite degradation is mainly controlled by a single degradation mechanism that does not change with immersion time and temperature, and the degradation rate increases with increasing immersion temperature [48]. Many theoretical models based on Arrhenius theory have been proposed for predicting the service lives of composites. Considering interface debonding between fiber and resin as the main degradation mechanism, Phani and Bose developed the following theoretical model to predict the service life of CFRP in a hygrothermal environment [49] as follows, and the main degradation mechanism of this model was the interface debonding between fibers

and resins.

$$Y = (100 - Y_\infty)\exp\left(-\frac{t}{\tau}\right) + Y_\infty \tag{11}$$

where Y is the strength retention of GFRPP bars, t is the immersion time, τ is the fitting parameter, and Y_∞ is the strength retention of GFRPP bars with infinite immersion time.

In this study, the intrusion of water molecules and alkaline solution destroyed the interfacial bonding between fibers and resin in the GFRPP bending bars, as verified by SEM microstructure analysis. Furthermore, the bond strength decreased as the water absorption increased until saturated was reached. Based on the above considerations, we applied Eq. (11) to predict the service life of GFRPP bars. According to Arrhenius theory, the relationship between the degradation rate and immersion temperature is as follows:

$$k = A\exp\left(-\frac{E_a}{RT}\right) \tag{12}$$

where k is the degradation rate of the material (reciprocal of immersion time), A is the degeneration constant, E_a is the activation energy (KJ/mol), R is the universal gas constant (8.314 J/mol/K), and T is Kelvin temperature (K). Equation (12) can be transformed into the following equation.

$$\ln\left(\frac{1}{k}\right) = \frac{E_a}{R}\frac{1}{T} - \ln A \tag{13}$$

Equation (13) shows that the natural logarithm of immersion time ($1/k$) is linearly related to the reciprocal of temperature ($1/T$) with slope E_a/R. The time-shift factor (TSF) was defined as follows:

$$\mathrm{TSF} = \frac{t_1}{t_2} = \frac{k_2}{k_1} = \frac{A\exp\left(-\frac{E_a}{RT_2}\right)}{A\exp\left(-\frac{E_a}{RT_1}\right)} = \exp\left[\frac{E_a}{R}\left(\frac{1}{T_1} - \frac{1}{T_2}\right)\right] \tag{14}$$

TSF expresses the relationship between service time and temperature for reaching a certain strength retention. Physically, the TSF expression means that the strength retention reached by time t_1 at T_1 is the same as that reached by time t_2 at T_2.

According to "Building Climate Zoning Standard (GB50178-93)" [50], seven representative Chinese cities under first-class zoning (I–VII) were selected: Harbin (I), Qingdao (II), Shanghai (III), Haikou (IV), Kunming (V), Lhasa (VI), and Urumqi (VII). According to the World Climate and Temperature Database (http://www.climatemps.com/), the annual average temperatures of the above cities in 2022 were 4.3 °C (Harbin), 12.3 °C (Qingdao), 15.8 °C (Shanghai), 23.8 °C (Haikou), 14.6 °C (Kunming), 7.5 °C (Lhasa), and 5.4 °C (Urumqi). The service lives of GFRPP bending bars were estimated at these temperatures.

First, the tensile strengths of the GFRPP bending bars determined in alkaline solution at 60 °C were fitted using Eq. (11). The strength retention of the GFRPP bending bars was obtained through comparison with the strengths evaluated without immersion in alkaline solution. The two fitting parameters Y_∞ and τ were obtained by fitting with correlation coefficients greater than 0.9; their values are listed in Table 7. The parameter Y_∞ was fixed at the value determined at 60 °C, and the fitting parameter τ was then determined at 20 °C and 40 °C. The fitting curves for the GFRPP bending bars are shown in Fig. 14.

By substituting the fitting parameters Y_∞ and τ obtained in Table 7 into Eq. (11), the time t required for the strength retention of the GFRPP bending bars to reach 60 %, 50 %, 40 %, and 30 % at 20 °C, 40 °C, and 60 °C were obtained. Equation (13) was also used to linearly fit the relationship between ln$t$ and $1/T$ (Fig. 15); the corresponding fitting parameters are shown in Table 8. The TSFs between the annual average temperature and service temperature of the seven representative cities were calculated using Eq. (14) and are shown in Table 9.

Based on the TSF, the abscissa of each data point was multiplied by the TSF at the corresponding temperature, and the strength retentions at the three test temperatures were converted into the strength retention at the annual average temperature of the city. The final prediction curves were then fitted, as shown in Fig. 16. Only the cities with the highest and lowest temperatures were selected for plotting in Fig. 16; the corresponding fitting parameters for all cities are shown in Table 10. According to the final master curves, the time required for GFRPP bending bars to completely degrade (i.e., the strength retention decreased to be stable, 22.13 %) in alkali environment was obtained (Table 10). It can be seen that it took 3.9 years (Harbin) and 1.7 years (Haikou) for the tensile strength of GFRPP bending bars to be stable. Compared with the actual service situation, the long-term life prediction by this model may be conservative, this was mainly because the environmental humidity of GFRPP bars in concrete was much lower than that in alkali solution [51], and its degradation rate would be slowed down accordingly. In addition, the relevant data [52] show that the saturated

Table 7
Fitting parameters of long-term life prediction of GFRPP bending bars in alkali solution.

Immersion temperature (°C)	Y_∞	τ	R^2
20	22.13	49.95	0.93
40	22.13	18.60	0.99
60	22.13	12.96	0.99

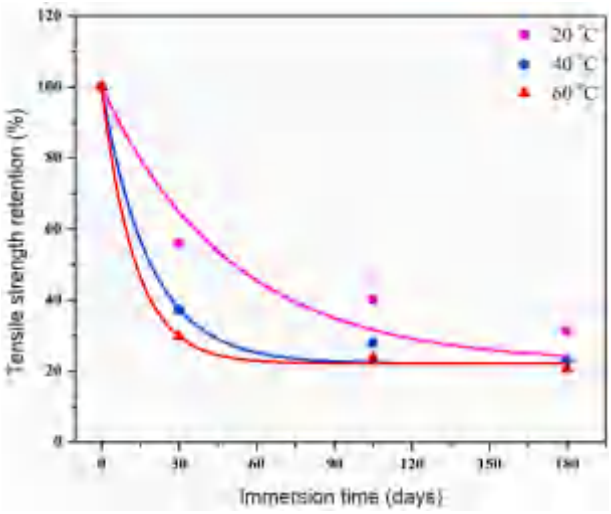


Fig. 14. Fitting curves of long-term life prediction of GFRPP bending bars in alkali solution.

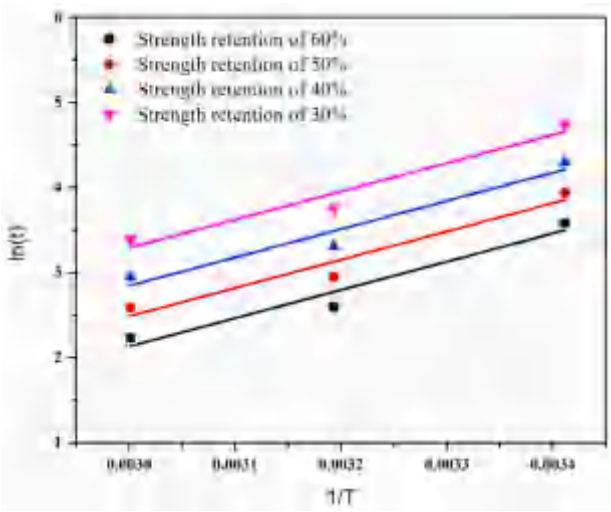


Fig. 15. Arrhenius curve of long-term life of GFRPP bending bars in alkali solution.

Table 8
Linear fitting parameters for long-term life prediction of GFRPP bending bars in alkali solution.

Strength retention (%)	E_a/R	R^2
60	3322.95	0.95
50	3322.95	0.95
40	3322.95	0.95
30	3322.95	0.95

Table 9
Time shift factor (TSF) between annual average temperature and service temperature in each city.

Immersion temperature (°C)	Time shift factor (TSF)						
	Harbin (4.3 °C)	Qingdao (12.3 °C)	Shanghai (15.8 °C)	Haikou (23.8 °C)	Kunming (14.6 °C)	Lhasa (7.5 °C)	Urumqi (5.4 °C)
20	1.90	1.36	1.18	0.86	1.24	1.66	1.81
40	3.92	2.80	2.43	1.78	2.55	3.42	3.74
60	7.41	5.29	4.60	3.37	4.82	6.46	7.06

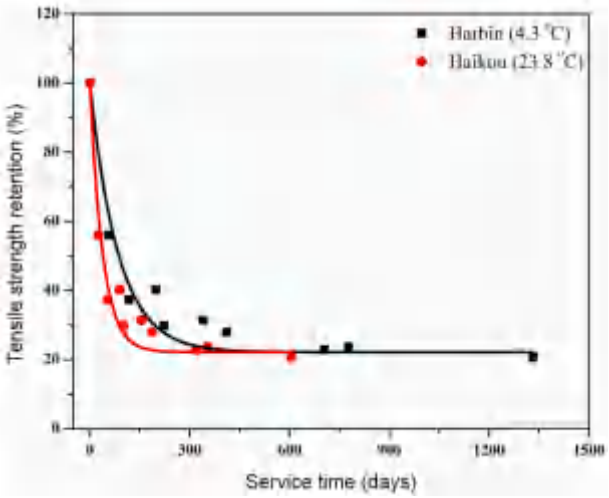


Fig. 16. Principal curves for long-term life prediction of GFRPP bending bar in alkali environment.

Table 10
Main fitting parameters and predicted service lives of GFRPP bending bars in alkaline environments.

City	Annual average temperature (°C)	Y_∞	τ	R^2	Service time of stable strength retention (years)
Harbin	4.3	22.13	84.97	0.95	3.9
Qingdao	12.3	22.13	60.74	0.95	2.8
Shanghai	15.8	22.13	52.72	0.95	2.4
Haikou	23.8	22.13	38.52	0.95	1.7
Kunming	14.6	22.13	55.35	0.95	2.5
Lhasa	7.5	22.13	74.17	0.95	3.4
Urumqi	5.4	22.13	81.01	0.95	3.7

water absorption and diffusion coefficient of polypropylene resin was much lower than that of thermosetting epoxy resin, indicating the excellent corrosion resistance of polypropylene resin. The long-term degradation of GFRPP bars in the present paper exposed to alkali solution was mainly due to the interface debonding of fiber/resin owing to the initial defects during the preparation process. When the resin can better impregnate fibers for the optimized preparation process, the initial defects of GFRPP bars can be reduced to obtain more excellent corrosion resistance.

4. Conclusions

GFRPP composite bending bars were immersed in alkaline solution at 20 °C, 40 °C, and 60 °C to estimate the long-term performance of GFRPP in stirrups for concrete structures. Bidirectional water absorption and hydrolysis adsorption were investigated to analyze the diffusion and existence form of water molecules. The tensile strength and short-beam shear strength were measured to understand the degradation of mechanical properties over the long term. TGA, infrared spectroscopy, and SEM were conducted to reveal the degradation mechanism of GFRPP bending bars in alkaline environments. Based on Arrhenius theory and the local annual average temperature, the service lifetimes of bending bars were predicted in seven cities in China. The main conclusions are as follows.

(1) Due to the presence of pores and micro-cracks formed in the bending process, bending bars had higher saturated water absorption and lower diffusion than straight bars. The longitudinal water absorption capacity was greater than the radial water absorption capacity of bending bards due to the fiber blocking effect. The proportion of free water was higher in bending bars than in straight bars. The dissolution of glass fibers in alkaline solution led to partial mass loss after immersion.
(2) After immersion for up to 180 d, the tensile strength of GFRPP bending bars was reduced by between 20.6% and 56.0 % compared with the control. The tensile failure mode changed from fiber bursting before immersion to shear fracture after immersion due to the decreased interfacial bonding strength and increased glass fiber brittleness. The shear strengths of the straight and bending bars decreased by 29.1 % and 39.2 %, respectively, during immersion.
(3) The degradation of the mechanical properties of GFRPP bars was mainly attributed to the etching of glass fibers, interface debonding, and increase in void volume (23.7 %). The glass fiber etching was related to the destruction of the aluminosilicate network and reaction of metal oxides with water. The bending bars were more seriously eroded than the straight bars due to the abundance of internal defects.

(4) The degradation times of GFRPP bending bars predicted in seven Chinese cities ranged from 1.7 years (Haikou) to 3.9 years (Harbin), corresponding to a stable tensile strength retention of 22.13 %. These estimates are conservative with respect to the actual service conditions (i.e., the lower environmental humidity of GFRPP bars in concrete than in alkaline solution).

Compliance with ethical standards

Funding

This work is supported by the Program Fund of Non-Metallic Excellence and Innovation Center for Building Materials (24SFP-4), Fundamental Research Funds for the Central Universities (Grant No. HIT.OCEF. 2022032 and HIT.NSRIF202234), Heilongjiang Natural Science Foundation (LH2021E073).

CRediT authorship contribution statement

Guijun Xian: Writing – review & editing, Writing – original draft, Validation, Investigation, Funding acquisition. **Yanbo Bai:** Software, Methodology, Investigation, Formal analysis. **Ping Zhou:** Validation, Software, Methodology, Investigation. **Junqi Wang:** Software, Methodology, Investigation, Formal analysis, Conceptualization. **Chenggao Li:** Writing – review & editing, Writing – original draft, Supervision, Methodology, Investigation, Funding acquisition. **Shaoce Dong:** Validation, Software, Methodology, Investigation. **Rui Guo:** Supervision, Resources, Project administration, Methodology. **Jingwei Tian:** Software, Resources, Formal analysis, Data curation. **Jinhao Li:** Validation, Software, Resources. **Jian Zhong:** Software, Methodology, Investigation. **Taipeng He:** Visualization, Software, Resources. **Zhuo Zhang:** Validation, Software, Methodology.

Declaration of competing interest

The authors declare that they have no conflict of interest.

Data availability

Data will be made available on request.

References

[1] K. Wu, S.Y. Qian, H.M. Zheng, Y.K. Zhou, F.Z. Guo, Experimental study and degradation analysis on interfacial shear modulus of steel and steel fiber-reinforced concrete composite structure, KSCE J. Civ. Eng. 26 (2022) 3533–3548.
[2] Wang Shunyi. Summary of Durability Improvement Technology of Port Steel Reinforced Concrete Structure [J]. Port Science and Technology, (5): 35-38 +48.
[3] G.Y. Feng, D.J. Zhu, S.C. Guo, M.Z. Rahman, W.B. Ma, Y. Yi, et al., A comparative study of bare and seawater sea sand concrete wrapped basalt fiber-reinforced polymer bars exposed to laboratory and real marine environments, Construct. Build. Mater. 371 (2023).
[4] Z.Y. Lu, L.Z. Su, G.J. Xian, B.H. Lu, J.H. Xie, Durability study of concrete-covered basalt fiber-reinforced polymer (BFRP) bars in marine environment, Compos. Struct. 234 (2020).
[5] S.Y. Wen, M.L. Cao, Review on degradation behavior of fiber-reinforced polymer bars in marine environments, J. Mater. Sci. (2023).
[6] F. Rubino, A. Nisticò, F. Tucci, P. Carlone, Marine application of fiber reinforced composites: a review, J. Mar. Sci. Eng. 8 (2020).
[7] R.A. Shenoi, J.M. Dulieu-Barton, S. Quinn, J.I.R. Blake, S.W. Boyd, Composite materials for marine applications: key challenges for the future, in: L. Nicolais, M. Meo, E. Milella (Eds.), Composite Materials, Springer, London, 2011.
[8] R. Jeyapragash, V. Srinivasan, S. Sathiyamurthy, Mechanical properties of natural fiber/particulate reinforced epoxy composites - a review of the literature, Mater. Today Proc. 22 (2020) 1223–1227.
[9] G.K. Sathishkumar, M. Ibrahim, M.M. Akheel, G. Rajkumar, B. Gopinath, R. Karpagam, et al., Synthesis and mechanical properties of natural fiber reinforced epoxy/polyester/polypropylene composites: a review, J. Nat. Fibers 19 (2022) 3718–3741.
[10] X.K. Guo, C.S. Xiong, Z.Q. Jin, B. Pang, A review on mechanical properties of FRP bars subjected to seawater sea sand concrete environmental effects, J. Build. Eng. 58 (2022).
[11] D.B. Zhao, J. Pan, Y.W. Zhou, L.L. Sui, Z.H. Ye, New types of steel-FRP composite bar with round steel bar inner core: mechanical properties and bonding performances in concrete, Construct. Build. Mater. 242 (2020).
[12] R. Guo, C.G. Li, Y.Z. Niu, G.J. Xian, The fatigue performances of carbon fiber reinforced polymer composites- A review, Journal of Materials Research and Technology-Jmr&T 21 (2022) 4773–4789.
[13] R. Guo, G.J. Xian, F. Li, C.G. Li, B. Hong, Hygrothermal resistance of pultruded carbon, glass and carbon/glass hybrid fiber reinforced epoxy composites, Construct. Build. Mater. 315 (2022).
[14] G.J. Xian, R. Guo, C.G. Li, Combined effects of sustained bending loading, water immersion and fiber hybrid mode on the mechanical properties of carbon/glass fiber reinforced polymer composite, Compos. Struct. 281 (2022).
[15] S.C. Dong, P. Zhou, R. Guo, C.G. Li, G.J. Xian, Durability study of glass fiber reinforced polypropylene sheet under simulated seawater sea sand concrete environment, Journal of Materials Research and Technology-Jmr&T 20 (2022) 1079–1092.
[16] P. Zhou, C.G. Li, Y.B. Bai, S.C. Dong, G.J. Xian, A. Vedernikov, et al., Durability study on the interlaminar shear behavior of glass-fibre reinforced polypropylene (GFRPP) bars for marine applications, Construct. Build. Mater. 349 (2022).
[17] J.Y. Feng, N. Li, B. Wang, S. Cheng, Q.G. Bao, H.M. Wang, et al., Thermal insulation and mechanical properties of carbon fiber-reinforced thermoplastic polyphthalazine ether sulfone ketone composites reinforced by hollow glass beads, Polym. Compos. (2023).
[18] B.B. Vatandas, A. Usun, N. Yildiz, C. Simsek, O.N. Cora, M. Aslan, et al., Additive manufacturing of PEEK-based continuous fiber reinforced thermoplastic composites with high mechanical properties, Compos. Appl. Sci. Manuf. (2023) 167.
[19] L. Fu, M.H. Zhang, Z.Y. Zhai, F.Z. Jiang, The influence of preheating temperature on the mechanical properties of injection-overmolded hybrid glass fiber reinforced thermoplastic composites, Polym. Test. 105 (2022).
[20] V.T. Hoang, B.S. Kwon, J.W. Sung, H.S. Choe, S.W. Oh, S.M. Lee, et al., Postprocessing method-induced mechanical properties of carbon fiber-reinforced thermoplastic composites, J. Thermoplast. Compos. Mater. 36 (2023) 432–447.
[21] W. Arifin, T. Kuboki, Effects of thermoplastic elastomers on mechanical and thermal properties of glass fiber reinforced poly(3-hydroxybutyrate-co-3-hydroxyhexanoate) composites, Polym. Compos. 39 (2018) E1331–E1345.

[22] H.D. Chen, J.H. Wang, D. Colin, S.X. Li, K. Drechsler, Temperature-Dependent modelling of tension, in-Plane shear, and bending behaviour in non-isothermal thermo-Stamping process simulation of unidirectional UHMWPE fibre reinforced thermoplastic TPU composites, J. Thermoplast. Compos. Mater. 36 (2023) 3891–3918.
[23] A. Margossian, S. Bel, R. Hinterhoelzl, Bending characterisation of a molten unidirectional carbon fibre reinforced thermoplastic composite using a Dynamic Mechanical Analysis system, Compos. Appl. Sci. Manuf. 77 (2015) 154–163.
[24] U. Sachs, R. Akkerman, Viscoelastic bending model for continuous fiber-reinforced thermoplastic composites in melt, Compos. Appl. Sci. Manuf. 100 (2017) 333–341.
[25] V.S. Kathavate, K. Amudha, L. Adithya, et al., Mechanical behavior of composite materials for marine applications–an experimental and computational approach, J. Mech. Behav. Mater. 27 (1–2) (2018) 20180003.
[26] V.S. Kathavate, K. Amudha, N.R. Ramesh, G.A. Ramadass, Failure analysis of composite material under external hydrostatic pressure: a nonlinear approach, Mater. Today Proc. 5 (2018) 24299–24312.
[27] U. Berardi, R.H. Nosrati, Long-term thermal conductivity of aerogel-enhanced insulating materials under different laboratory aging conditions, Energy 147 (2018) 1188–1202.
[28] Siqi Chen, Study on the Method of Improving Corrosion Resistance and Fatigue Behavior of BFRP Composite [D], Southeast University, 2017. Master thesis.
[29] Y.H.W.X. Xiao, L.D. Lu, X.J. Yang, Study on the hygrothermal ageing of glass fiber reinforced thermoplastic polyester composite, Application of Engineering Plastics (9) (2001) 35–37.
[30] C. Wang, J. Ou, Alkali and salt corrosion aging of GFRPP bars, Journal of Disaster Prevention and Mitigation engineering 30 (S1) (2010) 373–377.
[31] L. Sang, C. Wang, Y.Y. Wang, W.B. Hou, Effects of hydrothermal aging on moisture absorption and property prediction of short carbon fiber reinforced polyamide 6 composites, Compos. B Eng. 153 (2018) 306–314.
[32] B. Benmokrane, S. Mousa, K. Mohamed, M. Sayed-Ahmed, Physical, mechanical, and durability characteristics of newly developed thermoplastic GFRP bars for reinforcing concrete structures, Construct. Build. Mater. 276 (2021).
[33] Committee ACI. Guide Test Methods for Fiber-Reinforced Polymers (FRP) Composites for Reinforcing or Strengthening Concrete and Masonry Structures[S]. American Concrete Institute.
[34] Z.K. Wang, G.J. Xian, X.L. Zhao, Effects of hydrothermal aging on carbon fibre/epoxy composites with different interfacial bonding strength, Construct. Build. Mater. 161 (2018) 634–648.
[35] C.G. Li, G.J. Xian, H. Li, Water absorption and distribution in a pultruded unidirectional carbon/glass hybrid rod under hydraulic pressure and elevated temperatures, Polymers 10 (2018).
[36] G.J. Xian, R. Guo, C.G. Li, B. Hong, Effects of rod size and fiber hybrid mode on the interface shear strength of carbon/glass fiber composite rods exposed to freezing-thawing and outdoor environments, Journal of Materials Research and Technology-Jmr&T. 14 (2021) 2812–2831.
[37] C.G. Li, R. Guo, G.J. Xian, H. Li, Effects of elevated temperature, hydraulic pressure and fatigue loading on the property evolution of a carbon/glass fiber hybrid rod, Polym. Test. 90 (2020).
[38] A. Stamboulis, C.A. Baillie, S.K. Garkhail, H.G.H. van Melick, T. Peijs, Environmental durability of flax fibres and their composites based on polypropylene matrix, Appl. Compos. Mater. 7 (2000) 273–294.
[39] R. Guo, C.G. Li, G.J. Xian, Water absorption and long-term thermal and mechanical properties of carbon/glass hybrid rod for bridge cable, Eng. Struct. 274 (2023).
[40] R. Guo, G.J. Xian, C.G. Li, B. Hong, X.Y. Huang, M.Y. Xin, et al., Water uptake and interfacial shear strength of carbon/glass fiber hybrid composite rods under hygrothermal environments: effects of hybrid modes, Polym. Degrad. Stabil. 193 (2021).
[41] V.M. Karbhari, G.J. Xian, Hygrothermal effects on high pultruded unidirectional carbon/epoxy composites: moisture uptake, Compos. B Eng. 40 (2009) 41–49.
[42] Z.Y. Lu, Study on High Temperature Properties of Basalt Fiber Reinforced Polymer Composites [D], Harbin Institute of Technology, 2016. Doctoral thesis.
[43] B. Hong, Study on Water, Alkali and Salt Resistance of Polyurethane-Based CFRP Pultruded Plate, Harbin Institute of Technology, 2018. Doctoral thesis.
[44] J. Crank, The Mathematics of Diffusion[M], Clarendon Press, UK, 1975. Oxford.
[45] Zhang HW. Study on Corrosion Mechanism and Mechanical Properties of GFRP Bars in Alkaline Environment [D]. Harbin Engineering University.
[46] R. Caban, FTIR-ATR spectroscopic, thermal and microstructural studies on polypropylene-glass fiber composites, J. Mol. Struct. 1264 (2022).
[47] Q.X. Wang, Y.N. Ding, N. Randl, Investigation on the alkali resistance of basalt fiber and its textile in different alkaline environments, Construct. Build. Mater. 272 (2021).
[48] J.F. Davalos, Y. Chen, I. Ray, Long-term durability prediction models for GFRP bars in concrete environment, J. Compos. Mater. 46 (2012) 1899–1914.
[49] K.K. Phani, N.R. Bose, Hydrothermal aging of Csm-laminate during water immersion - an acoustoultrasonic study, J. Mater. Sci. 21 (1986) 3633–3637.
[50] GB50178-93, Building Climate Regionalization Standard [S]. General Administration of Quality Supervision, Inspection and Quarantine.
[51] Z.Q. Dong, G. Wu, B. Xu, X. Wang, L. Taerwe, Bond durability of BFRP bars embedded in concrete under seawater conditions and the long-term bond strength prediction, Mater. Des. 92 (2016) 552–562.
[52] P. Zhou, J.W. Tian, C.G. Li, Z.C. Tang, Comparative study of durability behaviors of thermoplastic polypropylene and thermosetting epoxy exposed to elevated temperature, water immersion and sustained bending loading, Polymers 14 (2022).

Chemical Engineering Journal 485 (2024) 149852

Contents lists available at ScienceDirect

Chemical Engineering Journal

journal homepage: www.elsevier.com/locate/cej

Multifunctional phosphorus-containing imidazoliums endowing one-component epoxy resins with superior thermal latency, heat resistance, mechanical properties, and fire safety

Jingsheng Wang [a], Jun Wang [a,b], Shuang Yang [b,*], Xi Chen [b], Kaiwen Chen [a], Gen Zhou [c], Xian Liu [c], Lin Xu [d], Siqi Huo [e,g,*], Pingan Song [e,f], Hao Wang [e]

[a] School of Materials Science and Engineering, Wuhan University of Technology, Wuhan 430070, China
[b] School of Mechanical and Electronic Engineering, Wuhan University of Technology, Wuhan 430070, China
[c] Wuhan East Lake of HiTech Group Co., Ltd, Wuhan, China
[d] Jiangsu LVDAO Pipes and Valves Co., Ltd, China
[e] Centre for Future Materials, University of Southern Queensland, Springfield 4300, Australia
[f] School of Agriculture and Environmental Science, University of Southern Queensland, Springfield Central, 4300, Australia
[g] School of Engineering, University of Southern Queensland, Springfield 4300, Australia

ARTICLE INFO

Keywords:
One-component epoxy resin
Latency
Thermal performances
Mechanical properties
Fire Safety

ABSTRACT

Epoxy resin (EP) possesses a high flammability risk, but the flame retardants applied often reduce other properties. For the sake of large-scale industrial manufacturing, EP and curing agent are increasingly being premixed as one-component system rather than blended immediately prior to application. However, current designs fail to break the trade-off between flame retardancy and mechanical/thermal/optical properties of one-component EPs. Herein, we developed a series of phosphorus-containing imidazolium compounds, named BADM-X (X = 1, 2, 3, and 4), which served as multifunctional latent hardeners for one-component EPs. BADM-1, BADM-2, BADM-3, and BADM-4 were synthesized in ethanol through the neutralization between bisphenol A diphosphate (BAD) and 2-ethyl-4-methylimidazole (EMI) at molar ratios of 1:1, 1:2, 1:3, and 1:4, respectively, which were easy to industrialize. Varying the imidazole content in BADM-X allowed for adjusting the curing reactivity and thermal latency of EP/BADM-X, making it adaptable for various applications. EP/BADM-2, EP/BADM-3 and EP/BADM-4 not only retained excellent optical properties, but also demonstrated increased glass transition temperatures (T_gs) and mechanical performances. The T_g of EP/BADM-2 reached 162.7 ℃, and its tensile and impact strengths increased by 34.8 % and 61.4 % relative to EP/EMI. EP/BADM-X exhibited enhanced fire safety, and the limiting oxygen index (LOI) and vertical burning (UL-94) classification of EP/BADM-2 reached 28.2 % and V-0, respectively. Besides, EP/BADM-2 demonstrated enduring flame-retardant and mechanical performances, thus showing great application potential. Overall, this study introduces a new class of multifunctional latent curing agents for the fabrication of durable fire-safe, high-performance, one-component EPs.

1. Introduction

EPs are renowned for their superior adhesion, chemical resistance, and electrical insulation properties. However, their inherent flammability poses significant safety risks, restricting their applications in industries requiring high fire-safety standards [1–3]. Thus, the necessity to imbue EPs with flame-retardant properties is substantial and immediate. To address this challenge, the phosphorus-containing flame retardants have emerged as a leading solution in recent years [4–7]. These flame retardants are favored for their environmental friendliness and higher thermal stability compared to the traditional halogenated ones [8–11]. The mode-of-action of the phosphorus-based retardants typically involves promoting char formation and quenching high-energy radical in both condensed and gas phases during combustion [12–14]. However, despite the emergence of various highly effective phosphorus-based flame retardants, many of them lead to deteriorations in the thermal and mechanical properties of epoxy resins [15–17]. Therefore, developing flame-retardant EPs without compromising their other properties

* Corresponding authors.
E-mail addresses: ysfrp@whut.edu.cn (S. Yang), Siqi.Huo@unisq.edu.au, sqhuo@hotmail.com (S. Huo).

https://doi.org/10.1016/j.cej.2024.149852
Received 28 November 2023; Received in revised form 18 January 2024; Accepted 18 February 2024
Available online 21 February 2024
1385-8947/© 2024 Elsevier B.V. All rights reserved.

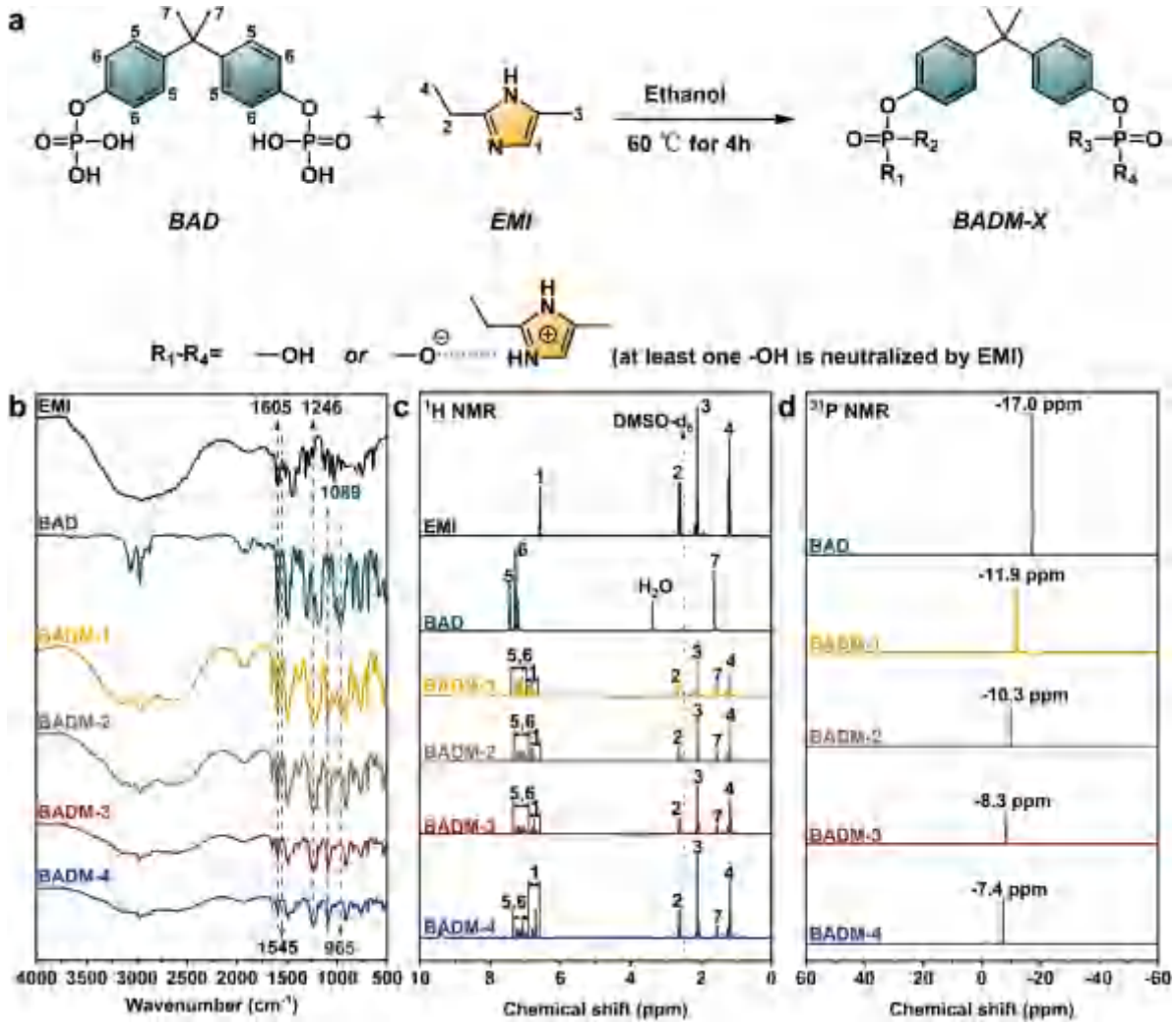


Fig. 1. (a) Synthesis of BADM-X (X = 1, 2, 3 or 4); (b) FTIR spectra of EMI, BAD and BADM-Xs; and (c) ^{1}H and (d) ^{31}P NMR spectra of EMI, BAD and BADM-X.

remains a huge challenge. One-component epoxy systems, comprising EP and latent curing agent, offer distinct advantages in industrial applications. Their ease of processibility, storage, and transport, as well as reduced environmental impact and high production efficiency, make them highly desirable [18–20]. However, the challenge lies in ensuring these EP systems remain inert during storage while being capable of rapidly curing upon activation. Imidazole-based curing agents have gained prominence in one-component EP systems due to their rapid curing abilities [21]. They facilitate the anionic polymerization of EPs, imparting desirable thermal and mechanical properties to the cured product. Nonetheless, the unmodified imidazole suffers from poor thermal latency owing to their high reactivity, leading to premature curing and limited shelf life [19,22].

The synthesis of phosphorus-containing imidazole latent hardeners can address both flammability and latency issues of one-component EPs [23]. The phosphorus-containing groups are typically introduced into imidazole through its 1-position or 3-position nitrogen atom [19,22,23]. For the 1-position nitrogen, the phosphorus-based groups are covalently linked to it *via* the addition or substitution reaction. In our previous works, we [24] reported a cyclotriphosphazene 1-substitued benzimidazolyl (BICP). By the steric hindrance and electron-withdrawing effects of cyclotriphosphazene, the reactivity of the benzimidazolyl group was reduced, so BICP could be used as a flame-retardant latent hardener for EP. As expected, the EP/BICP mixture demonstrated an ultra-long shelf life of 72 days. The EP/BICP thermoset showed improved flame retardancy, with a UL-94 V-0 rating and a LOI of 33.5 %. For the 3-position nitrogen, it can be connected to various P-containing acids by ionic bonds, and such synthesis process is facile and typically only requires green solvents, such as water and ethanol [22,23]. The P-containing groups in the as-synthesized imidazolium can be attached to the EP networks *via* ionic bonds, where it functions as pendant groups to restrict the polymer chain mobility and increase the glass transition temperature (T_g) [25]. Meanwhile, the curing reactivity of the imidazolium is tunable. For instance, Xu *et al.* [22] synthesized an imidazolium diphenylphosphinate (IDPP) for the fabrication of one-component fire-safe epoxy resins. The obtained EP/IDPP mixture showed long-term stability at room temperature. Curing with 15 wt% IDPP, the obtained EP thermoset exhibited a T_g of 172.7 °C, a LOI value of 37.0 % and a UL-94 V-0 classification, indicative of the enhanced heat resistance and fire safety. The reported P-containing imidazolium can simultaneously improve the thermal latency, flame retardancy and heat resistance of one-component EPs, but fails to address the trade-off between flame retardancy and mechanical properties. Hence, it is still a huge challenge to fabricate flame-retardant, advanced one-component EPs with superior heat resistance and mechanical performances.

Bisphenol A diphosphate (BAD), as a phosphorus-based Brønsted acid, can neutralize imidazole. Due to its bisphenol A structure, BAD is expected to possess good compatibility with bisphenol A type epoxy resins [26,27]. Obviously, the compatibility between epoxy resin and curing agent usually determines the overall performances of the corresponding EP thermoset. Consequently, BAD shows a great potential to be used as a raw material to develop multifunctional flame-retardant

Table 1
Formulations of EP thermosets.

Sample	EP (g)	EMI (g)	BADM-1 (g)	BADM-2 (g)	BADM-3 (g)	BADM-4 (g)	Calculated P content (wt%)
EP/EMI	100	6	/	/	/	/	/
EP/BADM-1	100	/	29	/	/	/	2.8
EP/BADM-2	100	/	/	16	/	/	1.4
EP/BADM-3	100	/	/	/	12	/	0.9
EP/BADM-4	100	/	/	/	/	10	0.7

imidazolium for the fabrication of high-performance, one-component EPs, but such work has not yet been reported.

In this work, four phosphorus-containing imidazolium (BADM-X) compounds were designed and synthesized through the neutralization between 2-ethyl-4-methylimidazole (EMI) and bisphenol A diphosphate (BAD) in ethanol. Clearly, such synthesis was a simple and industrializable process, and the imidazole content of the obtained BADM-X could be adjusted by changing the molar ratio of EMI and BAD. These BADM-X compounds were then utilized as multifunctional, flame-retardant latent curing agents for high-performance, one-component EP. Additionally, a thorough investigation was conducted on various aspects of the resultant EP/BADM-X systems, including thermal latency, curing behaviors, optical characteristics, thermal properties, mechanical performances, flame retardancy, smoke suppression and environmental stability. The toughening and flame-retardant mechanisms of BADM-X towards EP thermoset were also comprehensively studied.

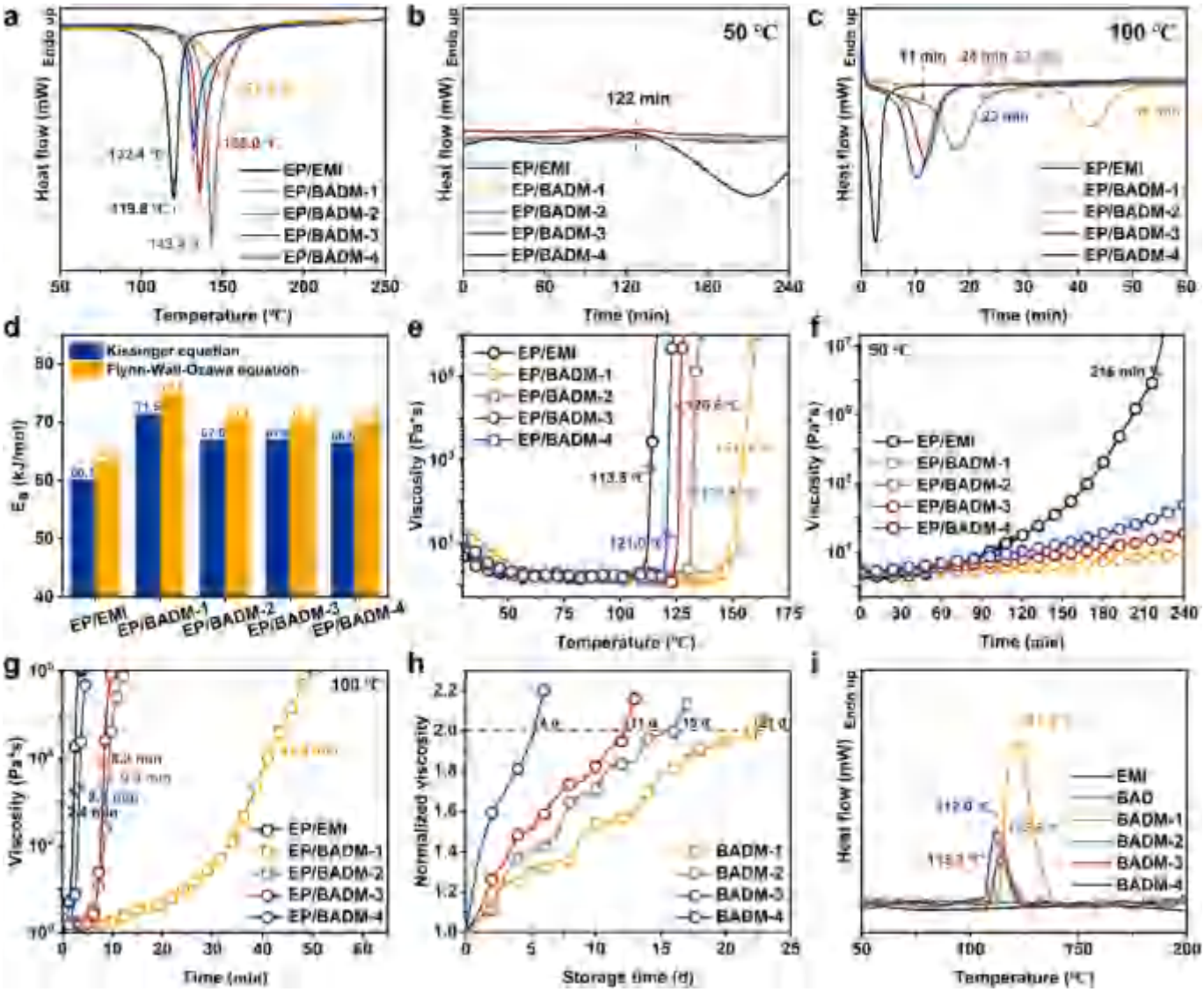


Fig. 2. (a) Non-isothermal DSC curves of EP mixtures; isothermal DSC curves of EP mixtures at (b) 50 and (c) 100 °C; (d) apparent activation energies of EP mixtures; (e) viscosity *vs.* temperature curves of EP mixtures; viscosity *vs.* time curves of EP mixtures at (f) 50 and (g) 100 °C; (h) normalized viscosity curves of EP/BADM-X mixtures during storage at 25 °C; and (i) non-isothermal DSC curves of EMI, BAD and BADM-X.

2. Experiment section

2.1. Synthesis of P/imidazolium-containing latent curing agents (BADM-X)

All P/imidazolium-containing latent hardeners, namely BADM-X (X = 1, 2, 3 or 4), were prepared through a facile self-assembly process in ethanol using bisphenol A diphosphate (BAD) and 2-Ethyl-4-methylimidazole (EMI), as depicted in Fig. 1a. The synthesis of BADM-1 was as follows: Initially, a mixture of BAD (38.8 g, 0.10 mol), EMI (12.1 g, 0.11 mol) and 200 mL ethanol was introduced into a 300 mL three-neck flask. The mixture was then heated to 60 °C and continuously stirred for 4 h. Subsequently, the solvent was removed *via* rotary evaporation. The resultant yellow transparent liquid was washed with water and ethanol for three times, respectively, followed by vacuum-drying at 80 °C for 12 h. The yield of BADM-1 was 84 %. For BADM-2, 3 and 4, the same synthesis was conducted, but the EMI addition was changed into 23.1 g (0.21 mol), 34.1 g (0.31 mol) and 45.2 g (0.41 mol), respectively.

2.2. Preparation of EP thermosets

The formulations of EP thermosets are outlined in Table 1. The EP thermosets, designated as EP/BADM-X (X = 1, 2, 3 or 4) and EP/EMI, were fabricated using BADM-X and EMI as curing agents, respectively. As shown in Fig. S1, all BADM-X exhibited fluidic characteristics with their viscosities ranging from 62.9 to 309.3 Pa*s, and thus they can be readily dissolved in epoxy resin. The fabrication of EP/BADM-X was as follows: Initially, BADM-X was incorporated into epoxy resin and vigorously stirred to form a homogeneous solution at room temperature. Subsequently, vacuum defoaming was carried out, and then the solution was injected into a preheated mold for curing. The curing process for EP/BADM-X involved 80 °C for 1 h, 120 °C for 2 h and 160 °C for 1 h. For EP/EMI, the curing program was changed into 80 °C for 2 h and 140 °C for 3 h.

2.3. Materials and characterization

This section is in the Supporting Information.

3. Results and discussion

3.1. Characterizations of BADM-X

The chemical structures of BADM-X were comprehensively analyzed through Fourier transform infrared (FTIR) spectroscopy, ^{1}H and ^{31}P nuclear magnetic resonance (NMR), and high-resolution mass spectroscopy (MS). The resulting spectra are depicted in Fig. 1b-d and S2. In Fig. 1b, EMI exhibited characteristic peaks at 1605 and 1246 cm^{-1}, corresponding to the stretching vibrations of C = C and C-N groups, respectively [19,23]. Regarding BAD, its FTIR spectrum revealed absorption bands at 3150–3000, 1089 and 965 cm^{-1}, which were attributed to = CH, P-O-C and P-OH groups, respectively [26,27]. Likewise, the FTIR spectra of BADM-X exhibited characteristic peaks related to imidazole and benzene rings, indicating the presence of EMI- and BAD-derived groups in BADM-X. Notably, some significant changes were detected in the FTIR spectra of BADM-X. The absorption peaks corresponding to the P-OH group weakened or even absented in the FTIR spectra of BADM-X as the imidazole content increased. Besides, a new peak of the NH^{+} group emerged at 1545 cm^{-1} [23,28,29]. The emergence of the NH^{+} peak and the weakening of the P-OH peak indicated the successful neutralization reaction between BAD and EMI.

The ^{1}H NMR spectra of EMI, BAD and BADM-Xs are presented in Fig. 1c. For EMI, the chemical shifts observed at 6.57, 2.61, 2.10 and 1.19 ppm belonged to the protons of C = CH–, $–CH_2$-, =C-CH_3 and $–CH_2$-CH_3, respectively [24,30]. Regarding BAD, the chemical shifts from 7.09 to 7.59 ppm were assigned to the protons of benzene ring, and that at 1.63 ppm was attributed to the protons of the -C-CH_3 group. After the reaction of EMI and BAD, several noteworthy changes could be observed in the ^{1}H NMR spectra of BADM-X. Because of the protonation of the 3-position nitrogen atom in imidazole, the signal of H_1 in BADM-X occurred at higher chemical shifts relative to the signal in EMI, and those of H_5 and H_6 moved to lower chemical shifts. Furthermore, Fig. 1d presents the ^{31}P NMR spectra of BAD and BADM-X. The spectra of both BAD and BADM-X showed a single peak, but the chemical shift of the peak displayed an increasing trend as the imidazole content increased. The MS spectra of BADM-1, BADM-2, BADM-3, and BADM-4 are displayed in Fig. S2. The mass-to-charge ratio (m/z) values of BADM-1, BADM-2, BADM-3, and BADM-4 were 499.1670, 609.5064, 719.6605, and 829.8805 $[M + H]^{+}$, respectively, which were close to the theoretical molecular weight of BADM-X. The above results further indicated that varying amounts of phosphonic acid groups in BAD had undergone the neutralization reaction with the 3-position nitrogen in EMI, resulting in the formation of BADM-X.

3.2. Curing behaviors and thermal latency

The curing behaviors of EP/EMI and EP/BADM-X mixtures were investigated *via* differential scanning calorimetry (DSC). The DSC curves and data are presented in Fig. 2a-c and Table S1. As illustrated in Fig. 2a, all EP mixtures exhibited a single exothermic peak, but with different peak curing temperatures (T_ps). The T_ps for EP/BADM-1, EP/BADM-2, EP/BADM-3 and EP/BADM-4 systems increased by about 31, 23, 16 and 12 °C, respectively, in comparison to that of EP/EMI. The result implied that the curing reactivity of BADM-X was lower than that of EMI due to the ionic complexation between BAD and EMI, and it was tunable based on the imidazole content [29]. The curing behaviours of EP mixtures were additionally evaluated through isothermal DSC. As shown in Fig. 2b, EP/EMI exhibited evident exothermic enthalpy after curing at 50 °C for 122 min. In contrast, there were no exothermic peaks in the isothermal DSC curves of EP/BADM-X within 240 min, proving the reduced curing activity and improved thermal latency. When the temperature was raised to 100 °C, BADM-X regained their curing capability (see Fig. 2c). For instance, EP/BADM-1 was completely cured within 55 min, suggesting its rapid curing characteristic at elevated temperatures. Besides, the curing kinetics of EP mixtures were investigated using the non-isothermal DSC tests under various heating rate (β) values, as depicted in Fig. S3a-e. The linear relationships involving $\ln(\beta/T_p^2)$ versus $1/T_p$ and $\ln(\beta)$ versus $1/T_p$ were established according to the Kissinger, Crane and Flynn-Wall-Ozawa equations (see Fig. S3f and g), and the calculated kinetic parameters are listed in Table S2 [2,31]. Apparent activation energy (E_a) is a common index to evaluate the curing activity of resins [2,16,32]. In Fig. 2d and Table S2, the E_a values of EP/BADM-X mixtures (over 66 kJ/mol) exceeded that of EP/EMI mixture (around 60 kJ/mol), further revealing the reduced curing reactivity of EP/BADM-X in comparison to that of EP/EMI. Thereby, the coordination between EMI and BAD inhibited the curing reactivity of imidazole group, endowing EP/BADM-X with improved thermal latency. Moreover, the curing activity of BADM-X was tunable by adjusting the BAD and EMI molar ratio.

The viscosities of EP mixtures under heating were monitored using a dynamic rheometer. Fig. 2e-g illustrate the viscosity curves of all EP/EMI and EP/BADM-X mixtures, with pertinent data summarized in Table S1. In general, the gel temperature (T_v) and gel time denote the respective temperature and time at which the viscosity exponentially increases under heating, signifying the initial formation of the cross-linked network. Clearly, the higher the T_v and the longer the gel time, the better the thermal latency of one-component epoxy resins [2,19,22,29]. As shown in Fig. 2e and f, all EP/BADM-X mixtures displayed higher T_v values and longer gel time (at 50 °C) than EP/EMI. EP/EMI exhibited a low T_v of 113.8 °C and a gel time (at 50 °C) of 216 min. However, the T_v of EP/BADM-1 increased to 151.8 °C, and the gel time (at 50 °C) exceeded 240 min, indicative of enhanced thermal latency and

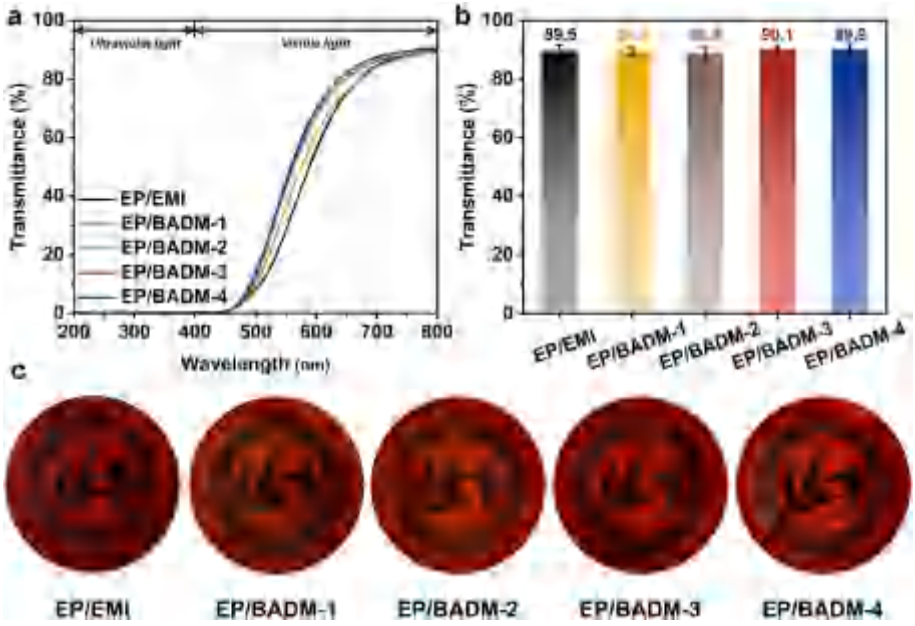


Fig. 3. (a) Ultraviolet–visible transmission spectra, (b) transmittances at 800 nm and (c) digital photos of EP/EMI and EP/BADM films (thickness: 0.15 ± 0.02 mm).

great processibility at 50 °C. Besides, EP/BADM-X displayed the ability to gel rapidly at 100 °C. All EP/BADM-X mixtures solidified within 50 min at 100 °C (see Fig. 2g), which was in line with the DSC result. Additionally, the shelf life of EP/EMI and EP/BADM-X, defined as the time taken for viscosity to double at room temperature, was examined. In Fig. 2h and Table S1, the shelf life of EP/BADM-X (4, 11, 15 and 21 days) was much higher than that of EP/EMI (<1 day). These results highlighted the prolonged shelf life, excellent low-temperature processability and tunable curing activity of EP/BADM-X, enabling them to be widely applied as one-component EPs in high-end industries.

The curing activity and thermal latency of BADM-X were both highly related to the imidazole content. To further explore this relationship, the DSC analyses were conducted on EMI, BAD and BADM-X, as shown in Fig. 2i. Clearly, no obvious endotherms or exotherms were detected when EMI and BAD were heated, respectively. For BADM-X, all exhibited a single endothermic peak in the range of 100–150 °C, likely ascribed to their dissociation. To study the alterations in the chemical structure of BADM-X when heated, BADM-1 was chosen as a representative sample, and its FTIR spectra at room temperature (RT) and 130 °C were compared. In Fig. S3h, the intensity of NH^+ peak at 1545 cm^{-1} reduced, and that of phosphate peak at 965 cm^{-1} increased in the spectrum at 130 °C compared with RT, demonstrating the re-formation of EMI and BAD due to the dissociation of BADM-1. It was deducted that BADM-X initially underwent dissociation during curing, releasing EMI and BAD. Subsequently, the regenerated EMI was involved in the crosslinking of epoxy resin, resulting in the formation of the cured EP. Hence, the dissociation of BADM-X played a crucial role in determining the curing activity. In Fig. 2i, the dissociation temperature of BADM-X increased with reducing imidazole content, and thus BADM-1 possessed the highest dissociation temperature of 121.3 °C among all BADM-X. Thus, EP/BADM-1 showed the highest T_p and T_v, and the longest gel time (at 100 °C) among all EP/BADM mixtures. Taking advantage of the tunable curing activity of BADM-X, EP/BADM-X can adapt to different manufacturing requirements, outperforming the counterparts.

Moreover, the X-ray photoelectron spectroscopy (XPS) tests were conducted on BADM-1 and EP/BADM-1 to investigate the curing mechanism of EP/BADM-X. The high-resolution N1s and P2p spectra are presented in Fig. S4a and b. The N1s spectrum of BADM-1 exhibited a peak at approximately 400.9 eV, which was ascribed to the protonated imidazole group. In contrast, the cured EP/BADM-1 displayed a N1s peak at 401.6 eV, which was attributed to the imidazolium adducts resulting from the addition reaction between the epoxy group and EMI released from BADM-1 [19,22]. This suggested that the released EMI initiated the polymerization of EP. The P2p spectrum of BADM-1 showed a dominant peak at 133.8 eV, which was assigned to the phosphonate anion. This peak persisted in the P2p spectrum of EP/BADM-1, indicating the reestablished ionic interactions between BAD and EMI in the cured EP. Additionally, a newly generated peak at 133.1 eV appeared in the P2p spectrum of EP/BADM-1, which was attributed to phosphate group and phosphonate ester group resulting from the products generated by the addition reaction between EP and BAD. Based on the above analyses, the curing process of EP/BADM-X is proposed in Fig. S4c. Initially, BADM-X underwent dissociation upon heating, releasing EMI and BAD. Subsequently, the liberated EMI initiated the anionic polymerization of EP. Simultaneously, a portion of the highly active alkoxide anions were protonated by the generated BAD during the curing process, leading to a partial termination of the anionic polymerization. Consequently, BAD groups were ultimately affixed to the crosslinked network through forming ionic bonds with imidazole and covalently linking to the EP backbone.

3.3. Optical properties

One-component epoxy resins were frequently utilized in the domain of electronic packaging, and their transparency was critical. Consequently, the impact of BADM-X on the optical performances of epoxy thermoset was examined using ultraviolet–visible (UV–vis) spectrophotometer and digital camera (see Fig. 3). In Fig. 3a and b, the transmittances of the EP/BADM-X films at 800 nm reached approximately 89 %, which were close to that of EP/EMI. Obviously, the good compatibility between EP and BADM-X was responsible for the high visible light transmittance of EP/BADM-X. Moreover, all EP/BADM-X displayed superior UV-shielding capabilities, as evidenced by no transmittance detected in the ultraviolet region (200–400 nm). The UV protection of EP/BADM-X was probably attributed to the absorption of benzene and imidazole groups towards UV light [33,34]. Fig. 3c provides the digital photos of EP/BADM-X films, where the underlying emblems were clearly observable, indicating that BADM-X had good compatibility with EP and thus EP/BADM-X possessed high transparency. In general, EP/

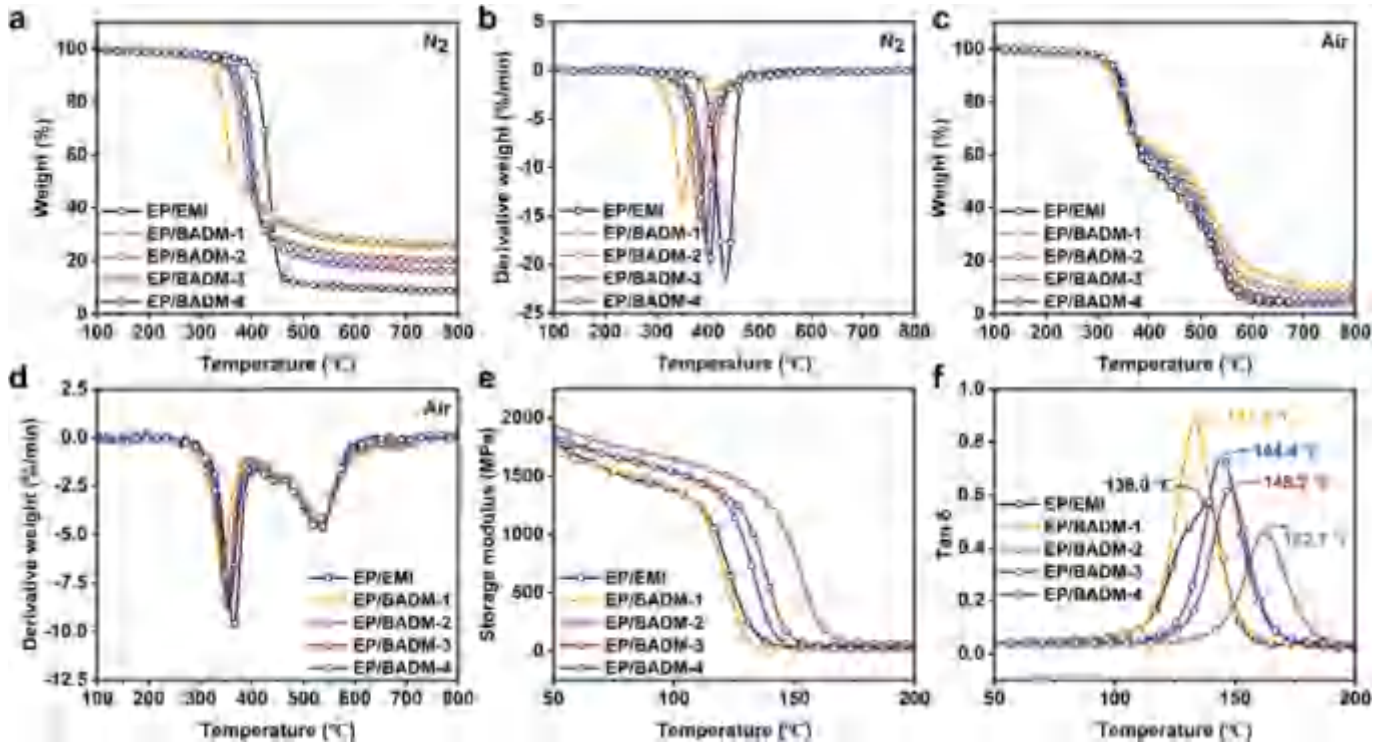


Fig. 4. TG plots in (a) N_2 and (c) air conditions, DTG plots under (b) N_2 and (d) air atmosphere, (e) storage modulus (E') curves, and (f) Tanδ curves of EP/EMI amd EP/BADM-X.

BADM-X exhibited high visible light transmittance and conspicuous UV-protection, presenting huge application potential in the electronic packaging and optics fields.

3.4. Thermal properties

The thermal stability of EP samples was assessed *via* thermogravimetric (TG) analysis under both nitrogen and air atmosphere, with the TG and derivative TG (DTG) curves and data in Fig. 4 and Table S3. In Fig. 4a and b, all samples exhibited one-step degradation process in nitrogen condition. Notably, the temperature at 5 % weight loss ($T_{5\%}$) and the temperature at maximun degradation rate (T_{max}) of EP/BADM-X were lower than those of EP/EMI, and both exhibited a downward trend as the phosphorus content increased (see Table S3). Obviously, it was mainly due to the inferior thermal stability of the phosphorus-containing group in BADM-X [2,35,36]. Besides, EP/BADM-X demonstrated decreased maximum degradation rate (R_{max}) and increased char yield at 800 °C (*CY*) compared with EP/EMI. The R_{max} of EP/BADM-2 decreased from 21.4 %/min of EP/EMI to 15.4 %/min, and the *CY* increased from 8.6 % to 26.2 % by about 2-fold (see Table S3). These findings highlighted the significant enhancement in the charring ability of EP/BADM-X due to the existence of the P-derived group. In air condition, all samples experienced a two-stage decomposition process (see Fig. 4c and d). This process involved the degradation of the network followed by the further decomposition of char residue at elevated temperatures. In Fig. 4c and Table S3, EP/BADM-X displayed slight reductions in $T_{5\%}$, T_{max1} and T_{max2} relative to EP/EMI, which was in line with the TG result in N_2 condition. Additionally, the R_{max} and *CY* values of EP/BADM-X were also much higher than those of EP/EMI. Hence, curing with BADM-X endowed EP with superior char-forming ability, which was conducive to flame retardancy.

Dynamic mechanical analysis (DMA) was employed to evaluate the thermodynamic performances of EP samples, with the curves depicted in Fig. 4e and f. As depicted in Fig. 4f, each of EP samples exhibited one peak, indicating that these samples were all single-phase systems because of the good compability between EP and BADM-X [32]. EP/BADM-1 exhibited a glass transition temperature (T_g) of 133.2 °C, close to 138.0 °C of EP/EMI. In addition, the T_g values of EP/BADM-2, EP/BADM-3 and EP/BADM-4 were 24.7, 10.2 and 6.4 °C higher than that of EP/EMI, respectively. To analyse the reason for the T_g variation, the crosslinking density (υ_e) of EP samples was calculated using the rubbery elastic equation (see Table S4). The υ_e of EP/BADM-1 was significantly reduced compared with that of EP/EMI, indicative of incomplete curing. It was probably because the concentrated release of excess BAD with active phosphate groups during the curing process led to the termination of the anionic polymerization of epoxy resin [37,38]. In contrast, for EP/BADM-2, EP/BADM-3, and EP/BADM-4, the moderate generation of BAD during the curing process contributed to increasing the crosslinking density. The multifunctionality of BAD facilitated the formation of a highly cross-linking network, resulting in increased crosslinking density. The increased υ_e values of EP/BADM-2, EP/BADM-3 and EP/BADM-4 accounted for their increased T_g values and mechanical stiffness (see Fig. 4e and Table S4). Overall, EP/BADM-2, EP/BADM-3 and EP/BADM-4 possessed improved heat resistance, char-forming capacity and mechanical stiffness relative to EP/EMI, but the performances of EP/BADM-1 were deteriorated due to the incomplete curing.

3.5. Mechanical performances

The mechanical properties of EP/EMI and EP/BADM-X were systematically evaluated through tensile, flexural and unnotched impact tests, with the results presented in Fig. 5a-f and Table S5. As shown in Fig. 5a and b, the EP/EMI thermoset exhibited a tensile strength of 51.4 MPa and a tensile modulus of 2685 MPa. For EP/BADM-1, its tensile properties significantly deteriorated relative to EP/EMI, with a 28.0 % reduction in tensile strength. On the contrary, BADM-2, BADM-3 and BADM-4 imparted significant enhancements in the tensile properties of EP thermosets. Specifically, the tensile strength and modulus of EP/BADM-2 reached 69.3 and 3126 MPa, respectively, with 34.8 % and

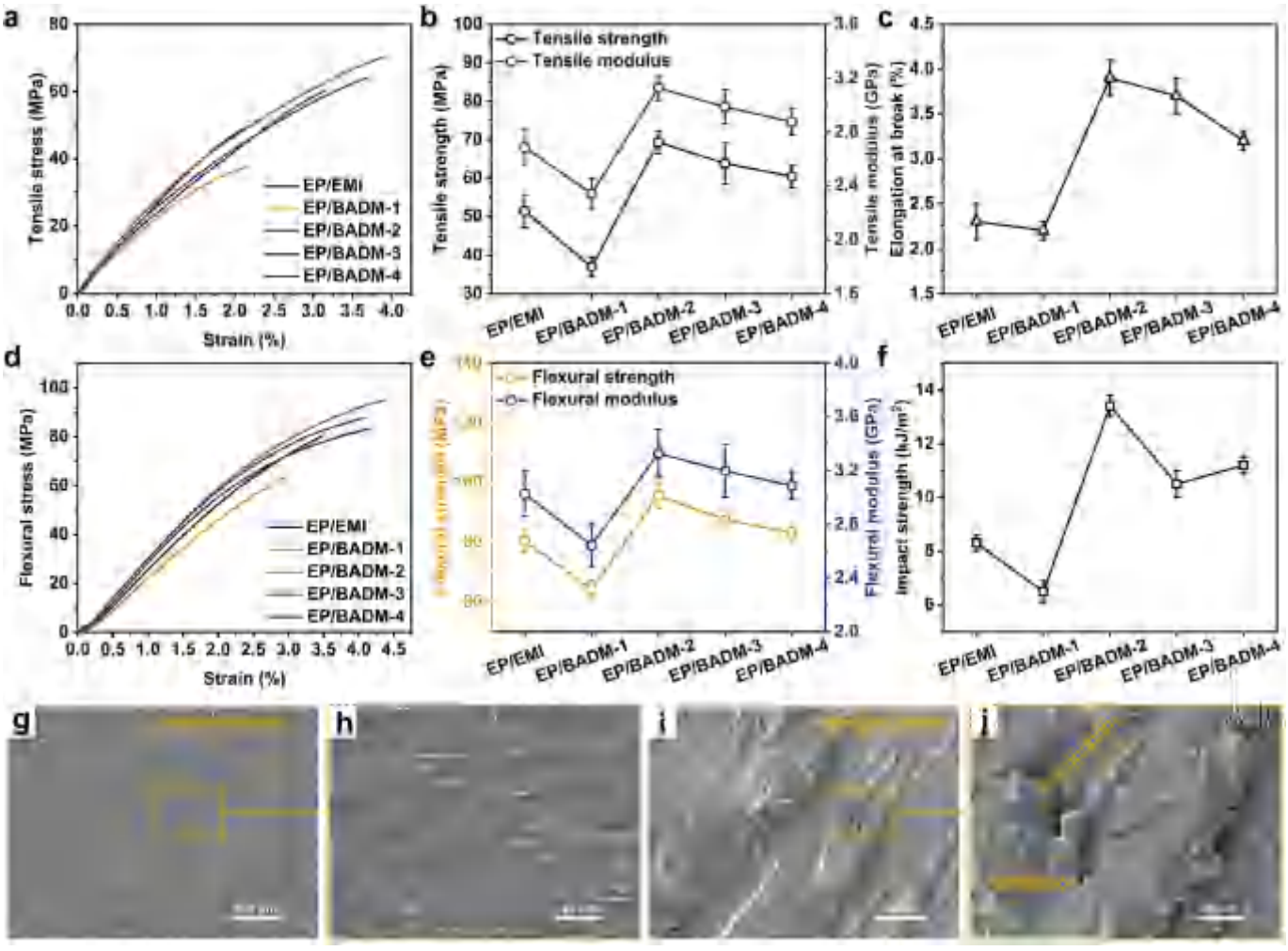


Fig. 5. (a) Tensile stress–strain plots, (b) tensile strengths and moduli, (c) elongations at break, (d) flexural stress–strain plots, (e) flexural strengths and moduli, and (f) impact strengths of EP samples; and SEM images of the fractured surfaces for (g, h) EP/EMI and (i, j) EP/BADM-2 after impact tests.

16.4 % increases in comparison to those of EP/EMI. In Fig. 5d and e, EP/BADM-2, EP/BADM-3 and EP/BADM-4 presented higher flexible strengths and moduli than EP/EMI, further suggesting improved mechanical robustness and stiffness. Notably, the epoxy resins respectively cured by BADM-2, BADM-3 and BADM-4 displayed improved toughness, as evidenced by the increased elongations at break and impact strengths in comparison to those of EP/EMI (see Fig. 5c and f and Table S5). For instance, the elongation at break and impact strength of EP/BADM-2 were 69.6 % and 61.4 % higher than those of EP/EMI. The fractured surfaces of EP/EMI and EP/BADM-2 samples obtained from the impact tests were examined using scanning electron microscope (SEM), and the images are presented in Fig. 5g-j. It was evident that EP/EMI exhibited a flat and smooth fractured surface with minimal deformation, indicative of brittle fracture [39,40]. Conversely, EP/BADM-2 displayed noticeable surface deflection and deformation, signifying plasticization and toughening characteristics.

Based on the above analyses, the reinforcement and toughening mechanisms of BADM-2, BADM-3 and BADM-4 are explicated as follow. On the one hand, the released multifunctional BAD favored the formation of a denser crosslinked network during the curing process, resulting in increased crosslinking density and stiffness. On the other hand, the reestablished ionic bonds between BAD and EMI contributed to the energy dissipation when EP was subjected to the external forces, thus bringing about the enhanced mechanical strength and toughness. Besides, as the BAD content increased gradually from EP/BADM-4 to EP/BADM-2, the improvements in mechanical properties became more pronounced. Consequently, EP/BADM-2 exhibited superior robustness, stiffness, and toughness among all samples.

Table 2
The combustion parameters of EP thermosets.

Sample	LOI (%)	UL-94 rating	TTI [a] (s)	PHRR [a] (kW/m^2)	THR [a] (MJ/m^2)	PSPR [a] (m^2/s)	TSP [a] (m^2)
EP/EMI	20.5	NR	40 ± 2	1018 ± 39	76.8 ± 4.8	0.431 ± 0.036	32.1 ± 0.3
EP/BADM-1	30.8	V-0	24 ± 1	306 ± 13	50.3 ± 2.9	0.183 ± 0.012	26.3 ± 0.6
EP/BADM-2	28.2	V-0	38 ± 2	597 ± 24	57.3 ± 3.5	0.312 ± 0.024	28.8 ± 0.3
EP/BADM-3	27.4	V-1	33 ± 3	617 ± 27	62.9 ± 4.6	0.285 ± 0.017	30.9 ± 0.4
EP/BADM-4	25.7	V-1	38 ± 2	840 ± 26	67.7 ± 1.9	0.378 ± 0.014	31.2 ± 0.4

[a] TTI: time to ignition; PHRR: peak heat release rate; THR: total heat release; PSPR: peak smoke production rate; and TSP: total smoke production.

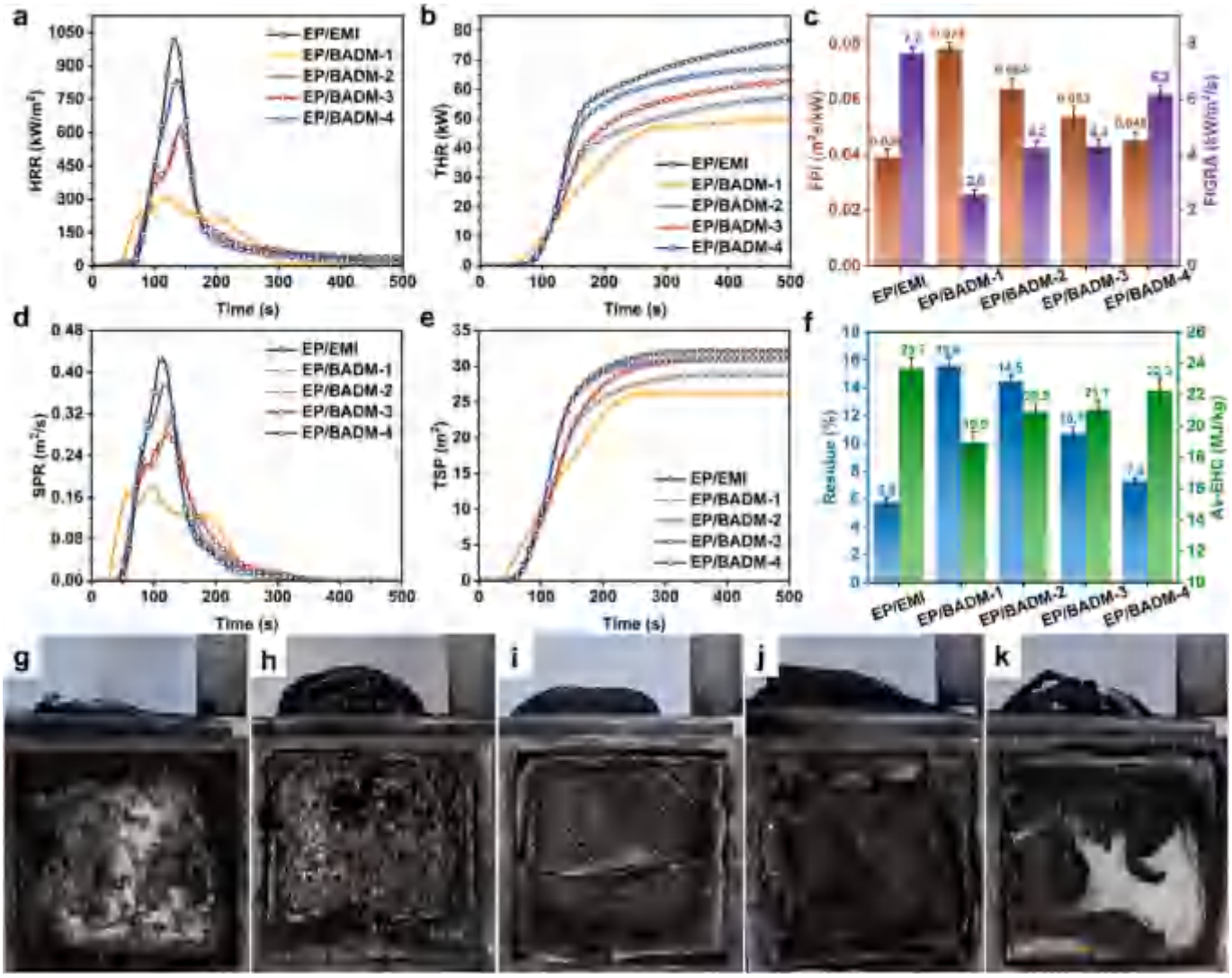


Fig. 6. (a) Heat release rate curves, (b) total heat release plots, (c) fire performance index (FPI) and fire growth rate (FIGRA) values, (d) smoke production rate plots, (e) total smoke production curves, (f) residue and average effective heat of combustion (Av-EHC) values for EP thermosets; and digital photographs of (g) EP/EMI, (h) EP/BADM-1, (i) EP/BADM-2, (j) EP/BADM-3 and (k) EP/BADM-4 chars after cone calorimetry.

3.6. Fire safety

To assess the flame-retardant efficacies of BADM-X, the limiting oxygen index (LOI) and the vertical burning (UL-94) tests of EP/EMI and EP/BADM-X systems were conducted. The data in Table 2 indicated the innate flammability for EP/EMI, of which the LOI value was only 20.5 %. In UL-94 test, EP/EMI burned fiercely and failed to self-extinguish, precluding it from achieving any ratings. By contrast, the EP cured by BADM-1 or BADM-2 self-extinguished within 3 s no matter after first or second ignition, thereby attaining the V-0 classification. Although the P contents of EP/BADM-3 and EP/BADM-4 were reduced, both achieved the UL-94 V-1 level. Furthermore, all EP/BADM-X samples displayed higher LOI values than EP/EMI, and those of EP/BADM-1 and EP/BADM-2 reached 30.8 % and 28.2 %, respectively. Therefore, curing with BADM-X could effectively enhance the flame retardancy of EP, and EP/BADM-1 and EP/BADM-2 were self-extinguishing materials (LOI > 28.0 % and UL-94 rating reaching V-0).

Fig. 6 and Table 2 show the results obtained from the cone calorimetry tests of EP/EMI and EP/BADM-X samples. The intrinsic flammability of EP/EMI was further confirmed by its high PHRR, THR, PSPR, and TSP of 1018 kW/m^2, 76.8 MJ/m^2, 0.431 m^2/s, and 32.1 m^2, respectively (see Fig. 6a, b, d and e and Table 2). The introduction of phosphorus-containing group resulted in notable decrements in the PHRR, THR, PSPR, and TSP for EP/BADM-X. Especially, EP/BADM-1, with the highest phosphorus loading level, showed the most significant reductions in both heat and smoke emissions. Its PHRR, THR, PSPR, and TSP were 69.9 %, 34.5 %, 57.5 %, and 18.1 % lower than those of EP/EMI, respectively. These findings elucidated that the phosphorus-containg group in BADM-X imparted improved flame retardancy and smoke suppression to EP/BADM-X.

FPI and FIGRA are paramount indicators for evaluating the fire safety of materials [23,41,42]. As illustrated in Fig. 6c and Table 2, the FPI values of EP/BADM-X exceeded that of EP/DMP-30, suggesting reduced fire risk [29]. Correspondingly, the FIGRA values for BADM-X-cured EPs were lower than that of EMI-cured EP, further underscoring the enhanced fire safety of BADM-X-cured EPs [24,43]. Moreover, the Av-EHC is routinely utilized to assess the burning degree of gaseous pyrolysis products [15,44]. The Av-EHC values of EP/BADM-X were all markedly lower than that of EP/EMI (see Fig. 6f). For instance, the Av-EHC for EP/BADM-1 reduced from 23.7 MJ/kg of EP/EMI to 19.9 MJ/kg, by 16.0 %. This evidenced that BADM-X pyrolyzed to release phosphorus-based radicals, such as HPO• and PO•, to trap the high-energy radicals from EP during combustion, thereby inhibiting the combustion reactions in the gas phase [45,46]. In Fig. 6f, all EP/BADM-

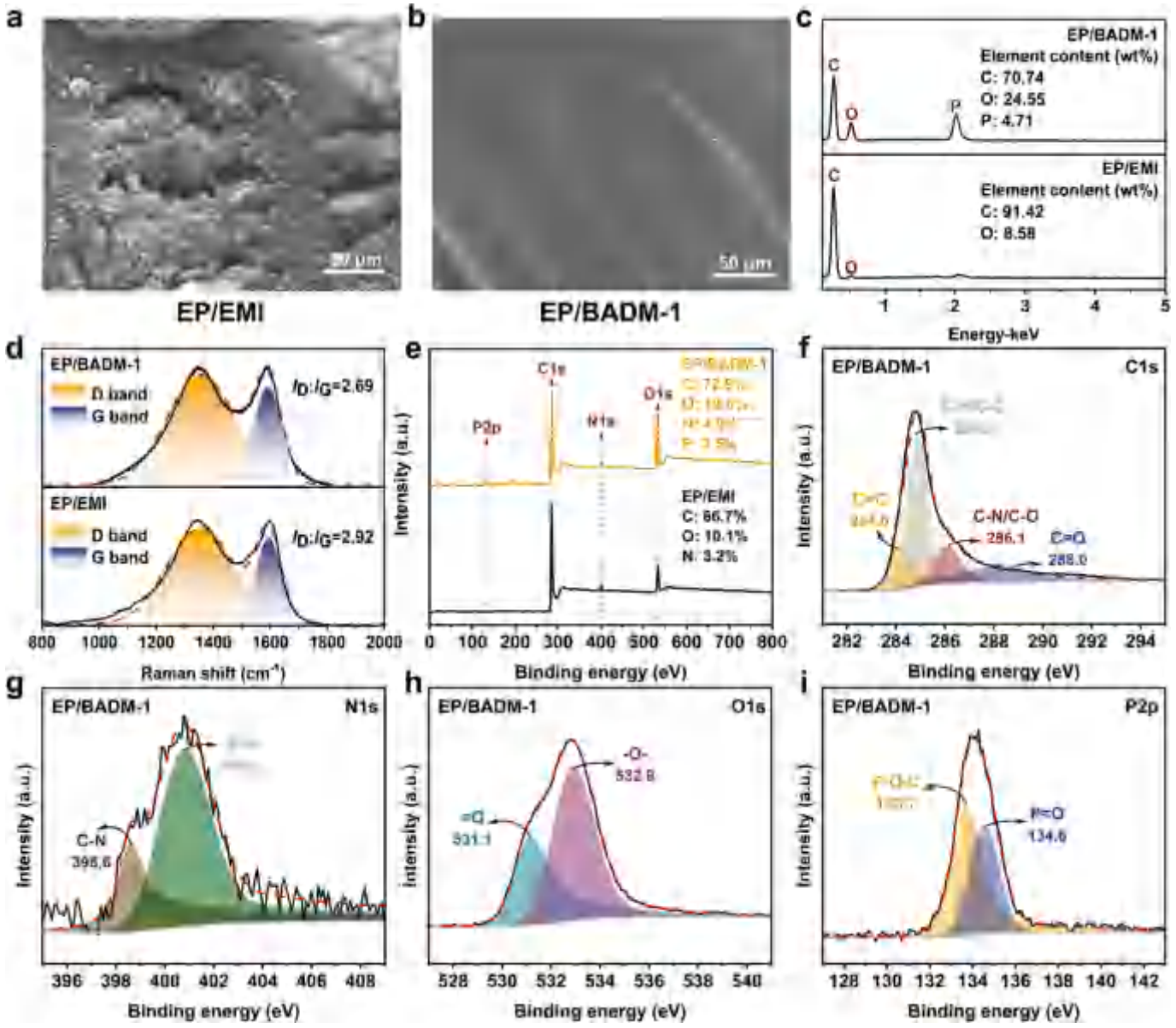


Fig. 7. SEM images of (a) EP/EMI and (b) EP/BADM-1 chars; (c) EDX, (d) Raman and (e) full-scan XPS spectra of EP/EMI and EP/BADM-1 chars; and high-resolution (f) C1s, (g) N1s, (h) O1s and (i) P2p XPS spectra of EP/BADM-1 residue.

X showed higher residues relative to EP/EMI, and EP/BADM-1 had the highest residue among all samples due to its highest P content. This illustrated that the P-based group in BADM-X promoted the char formation in the condensed phase. Additionally, the char residue of EP/EMI was brittle and fragmented (see Fig. 6g), while those of EP/BADM-X demonstrated intumescent and cohesive structures (see Fig. 6h-k), which effectively obstructed the heat release and smoke generation [47,48]. In conclusion, BADM-X significantly boosted the flame retardancy and smoke suppression of EP thermoset through the bi-phase flame retardant effect of the phosphorus-containing group.

Moreover, the flame-retardant and mechanical performances of EP/BADM-2 were assessed in comparison with those of previously reported flame-retardant one-component EP systems (see Table S6) [2,22,24,25,30,49–52]. Our EP/BADM-2 and most of previous flame-retardant one-component EPs achieved high LOI values of > 28.0 % and a UL-94 V-0 rating, confirming that they could be classified into self-extinguishing materials. Notably, compared to its counterparts, our EP/BADM-2 exhibited simultaneous and significant enhancements in tensile strength, elongation at break, and impact strength, indicating the multifunctionality of BADM-2. In general, BADM-2 effectively addressed the trade-off between fire safety and mechanical properties of one-component epoxy systems, making it surpass previous flame-retardant latent curing agents.

3.7. Flame-retardant mechanism

3.7.1. Action in condensed phase

To elucidate the flame-retardant mechanism of BADM-X in the condensed phase, the char residues of EP/EMI and EP/BADM-1 from cone calorimetry were studied using SEM, energy-dispersive X-ray (EDX), Raman spectroscopy, XPS and FTIR. As shown in Fig. 7a, the EP/EMI char revealed a fragmented and porous surface. In contrast, the char layer of EP/BADM-1 presented a more cohesive and intact morphology (see Fig. 7b). The elemental compositions of both chars generated by EDS are presented in Fig. 7c. Compared with EP/EMI char, the phosphorus could be detected in the EP/BADM-1 char, and the oxygen content was sigficantly increased. Clearly, many phosphate-derived pyrolysis products took action in the condensed phase, promoting the

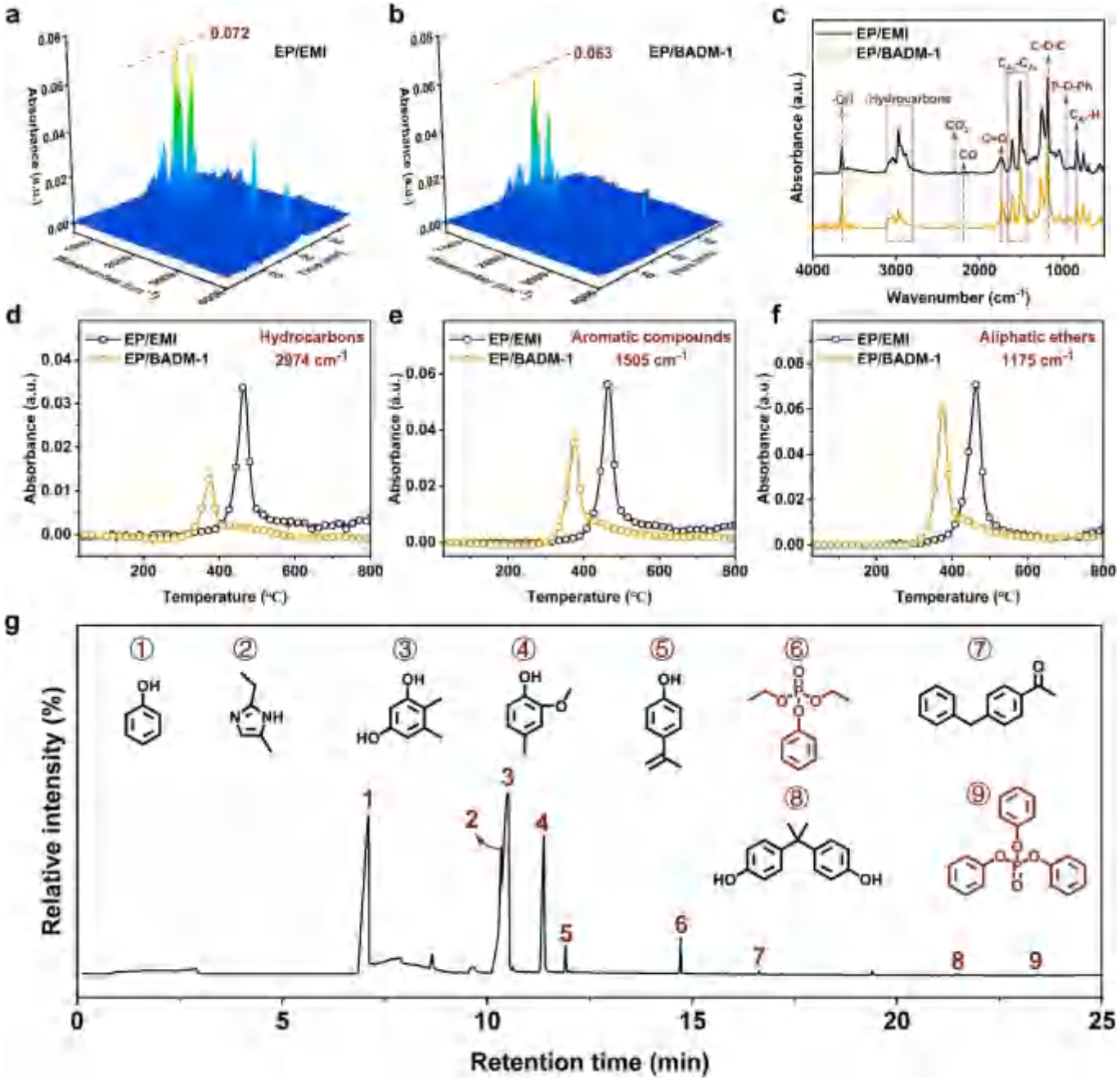


Fig. 8. 3D TG-FTIR spectra of volatiles derived from the decomposition of (a) EP/EMI and (b) EP/BADM-1; (c) FTIR spectra of the volatiles for EP/EMI and EP/BADM-1 at T_{max}; absorbance *vs* temperature curves of EP/EMI and EP/BADM-1 at (d) 2974, (e) 1505 and (f) 1175 cm^{-1}; and (g) total ion chromatogram (TIC) and supposed pyrolysis products of BADM-1.

formation of intact and expanded chars. In the Raman spectra (see Fig. 7d), the assessment of the graphitization level for both chars was conducted by calculating the area ratio of D and G bands (I_D/I_G). Generally, a lower I_D/I_G ratio corresponds to a higher graphitization degree [24,53]. For EP/EMI, the I_D/I_G ratio was 2.92, while that decreased to 2.69 for EP/BADM-1, indicating an increased degree of graphitization since the introduction of phosphorus. The formation of highly graphitized char layers acted as barriers on the matrix surface, which impeded heat transfer and restricted smoke emission [54,55]. This barrier effect significantly enhanced the flame retardancy and smoke inhibition of EP/BADM-1, confirming the condensed-phase function of BADM-1.

The XPS spectra for the chars of EP/EMI and EP/BADM-1 are illustrated in Fig. 7e-i and Fig. S5. In Fig. 7e, the presence of phosphorus element in the residue of EP/BADM-1 indicated that the P-based group in BADM-1 participated in the carbonization during the combustion process. This was in alignment with the EDX results, further substantiating the condensed-phase function of BADM-1. The C1s spectra for both chars demonstrated the presence of four distinct peaks at 284.1, 284.8, 286.1, and 288.0 eV, which were associated with C = C, C-H/C-C, C-N/C-O and C = O bonds, respectively (see Fig. 7f and Fig. S5a) [15]. The N1s spectra for each char revealed the deconvoluted peaks at 398.5 and 400.7 eV, belonging to C-N and N-H structures (see Fig. 7g and Fig. S5b) [2,29]. In the O1s spectra, the peaks around 531.6 and 533.3 eV corresponded to the = O and -O- bonds (see Fig. 7h and Fig. S5c) [16,56]. In Fig. 7i, the P2p spectrum of the EP/BADM-1 char revealed the peaks at 133.7 and 134.6 eV, which were ascribed to P-O-C and P = O bonds, respectively [29,33,35]. Besides, the FTIR spectrum of the EP/BADM-1

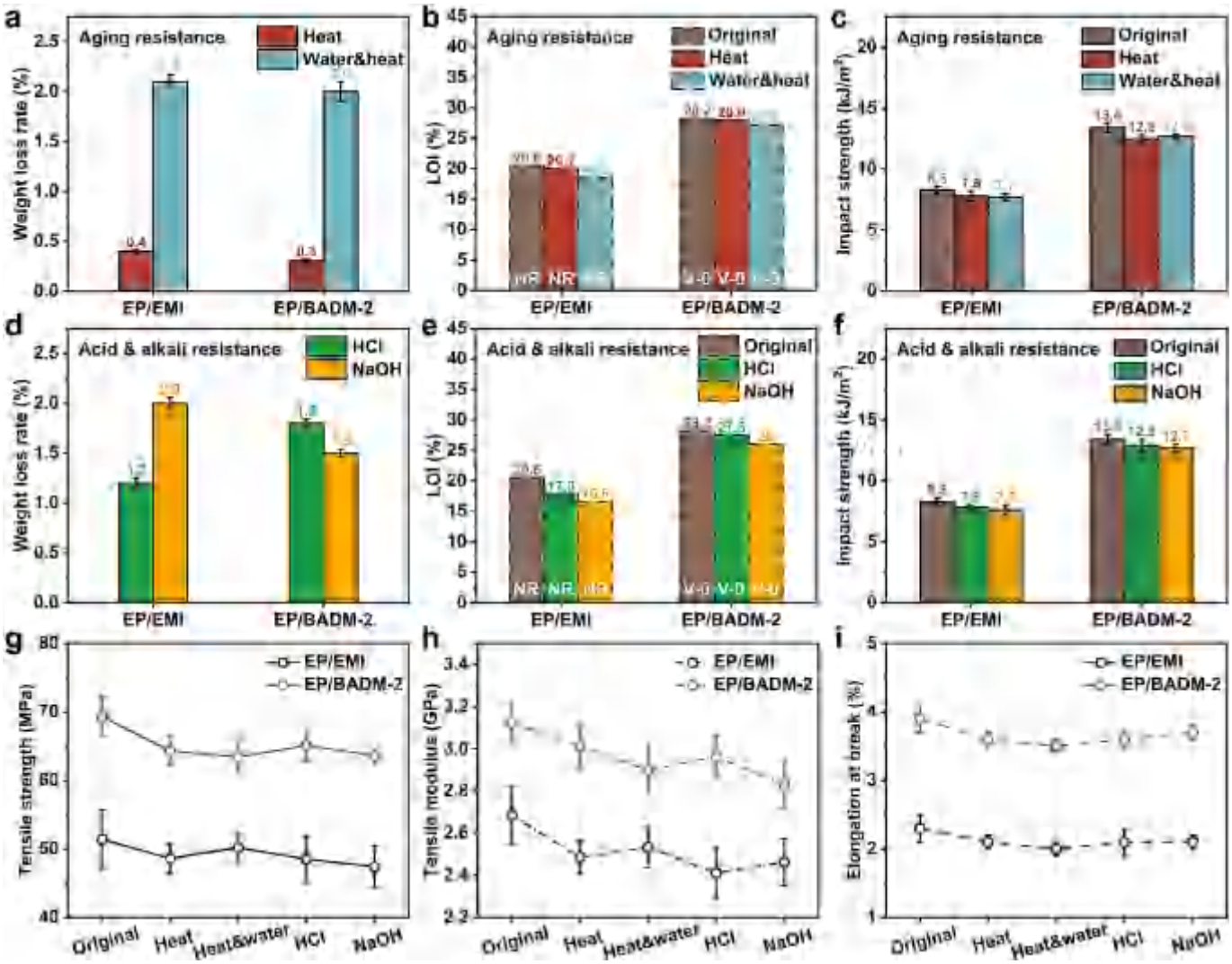


Fig. 9. (a) Weight loss rates of EP/EMI and EP/BADM-2 after aging tests; (b) LOI values and (c) UL-94 ratings of EP/EMI and EP/BADM-2 before and after aging tests; (d) weight loss rates of EP/EMI and EP/BADM-2 after acid and alkali treating tests; (e) LOI values and (f) UL-94 ratings of EP/EMI and EP/BADM-2 before and after acid and alkali treating tests; and (g) tensile strengths, (h) tensile moduli and (i) elongations at break of EP/EMI and EP/BADM-2 before and after durability tests.

char presented additional absorption peaks at 1071 and 942 cm^{-1} compared with the EP/EMI char. These peaks were attributed to the P-O-C and P-O-Ph groups, providing further evidence for the presence of phosphate within the char (see Fig. S5d) [2,57]. These results clearly indicated that the phosphate-based compounds generated by the pyrolysis of BADM-1 participated in the formation of a continuous and intumescent char on the EP surface during burning, which suppressed the heat transfer and smoke emission in the condensed phase.

3.7.2. Action in vapor phase

The TG-FTIR analyses were performed on EP/EMI and EP/BADM-1 to examine the gaseous-phase flame-retardant action of BADM-1, with results displayed in Fig. 8. In Fig. 8a-c, the primary volatile degradation products from EP/EMI and EP/BADM-1 were consistent, comprising water/phenol (3650 cm^{-1}), hydrocarbons (2809–3107 cm^{-1}), carbon dioxide (2296 cm^{-1}), carbon monoxide (2189 cm^{-1}), carbonyl compounds (1725 cm^{-1}), aromatic compounds (1600, 1511, and 826 cm^{-1}) and esters (1169 cm^{-1}) [2,15]. This suggested that the thermal decomposition pathways for EP/EMI and EP/BADM-1 were analogous. However, obviously reduced generation of hydrocarbons, aromatics, and aliphatic ethers from EP/BADM-1 compared with EP/EMI (see Fig. 8d-f) further implied that the phosphorus-containing group of BADM-1 promoted the char formation, consequently inhibiting the release of carbon-based fragments. Significantly, the P-O-Ph peak appeared at 960 cm^{-1} in the FTIR spectrum of the gaseous decomposition products from EP/BADM-1 (see Fig. 8c) [40,44,58], which corroborated the ability of BADM-1 to release the phosphorus-containing fragments into the gas phase. These fragments could further degrade into phosphorus-based radicals, which could capture the active radicals from the EP matrix. Therefore, the phosphorus-containing group of BADM-1 could take action in both condensed and gas phases to retard the combustion of the EP matrix, therefore enhancing flame retardancy and smoke suppression.

Pyrolysis-gas chromatography/mass spectrometry (Py-GC/MS) test was also utilized to identify the pyrolysis products of BADM-1, with the results in Fig. 8g and Fig. S6. In Fig. 8g, the pyrolysis fragments of BADM-1 comprised the bisphenol A-derived compounds (1, 3–5, 7 and 8), 2-ethyl-4-methylimidazole (2) and the phosphate-derived compounds (6 and 9). The pyrolysis route of BADM-1 is graphically summarized in Fig. S7. Initially, the nitrogen-containing fragments (m/z = 95, 82, 68 and 28) along with aromatic derivatives (m/z = 213, 107 and 77) were detected, which resulted from the cleavage of C-N and C-O bonds in BAD and EMI groups. As the pyrolysis progressed, additional fragments containing phosphorus (m/z = 156, 140 and 65) were generated, indicative of the breakdown of the phosphate groups. Such results further demonstrated that BADM-1 generated phosphorus-based

radicals, which were capable of inhibiting the combustion reaction in the gasesous phase during burning.

Based on the above flame-retardant mechanism analyses of EP/BADM-1, the flame-retardant action of BADM-X is proposed in Fig. S8. During combustion, in the vapor phase, the generation of phosphorus-containing radicals and incombustilble nitrogen-based fragments from the thermal degradation of BADM-X played radical-quenching and dilution functions, thereby reducing the burning degree of the volatiles. Concurrently, in the condensed phase, the thermal decomposition of BADM-X yielded phosphate derivatives. These decomposition products promoted the formation of a dense and stable char layer on the matrix surface, effectively obstructing the exchange of heat and reducing the smoke release. Therefore, BADM-X demonstrated a dual-phase flame-retardant action during burning procedure, significantly reinforcing the flame resistance and smoke suppression capabilities of EP.

3.8. Durability of EP samples

Among all EP/BADM-X samples, EP/BADM-2 exhibited the best overall performances, and thus its durability was investigated in this section. The long-term flame retardancy of EP thermosets is crucial for their practical applications. Therefore, the flame retardancy of EP/BADM-2 after acidic, basic, and aging treatments was examined in Fig. 9. The digital photographs of EP/EMI and EP/BADM-2 thermosets before and after treatments are depicted in Fig. S9. Clearly, there were no significant changes in the size and transparency of both EP/EMI and EP/BADM-2 before and after different treatments. As shown in Fig. 9a and d, comparable weight loss rates for EP/EMI and EP/BADM-2 could be observed after different treatments, suggesting that the superior chemical and aging resistance of EP thermoset was effectively retained after the introduction of phosphorus-containing group. In addition, the treated EP/BADM-2 continued to achieve the UL-94 V-0 rating, with only marginal declines in its LOI value, demonstrating durable fire safety (see Fig. 9b and e). The mechanical performances of the treated EP samples were also assessed (see Fig. 9c and f-g and Table S7). Similar to EP/EMI, EP/BADM-2 only displayed marginal reductions in impact strength, tensile strength, tensile modulus and elongation at break after different durability tests, further confirming its superior acid-base and aging resistance. Overall, integrating the phosphorus-containing group into the curing agent contributed to fabricating fire-safe epoxy thermosets with superior environmental stability, which had a great practical value in industries.

4. Conclusion

In this study, four phosphorus-containing imidazoliums (BADM-X) were synthesized as flame-retardant latent hardeners for EP. All BADM-X showed good compatibility with EP, and endowed one-component EP with increased shelf life and enhanced processability due to the ionic complexation between BAD and EMI. The curing temperature and thermal latency of EP/BADM-X could be adjusted through varying the imidazole content of BADM-X. The as-prepared EP/BADM-X systems showed comparable optical performances and improved charring ability relative to EP/EMI. Moreover, BADM-2, BADM-3, and BADM-4 could effectively enhance the mechanical strength, rigidity, and toughness, and glass transition temperature of EP. EP/BADM-X demonstrated significantly enhanced flame retardancy and smoke suppression relative to EP/EMI due to the existence of phosphorus. EP/BADM-2 stood out for its optimal overall performances and outstanding acid, alkali, and aging resistance. Hence, this research delivers an integrated strategy for the creation of high-performance, flame-retardant one-component epoxy resins by an industrially scalable synthesis process.

CRediT authorship contribution statement

Jingsheng Wang: Writing – original draft, Visualization, Methodology, Investigation, Formal analysis. **Jun Wang:** Supervision, Resources, Project administration. **Shuang Yang:** Writing – original draft, Supervision, Project administration. **Xi Chen:** Supervision, Investigation. **Kaiwen Chen:** Formal analysis, Data curation. **Gen Zhou:** Resources. **Xian Liu:** Resources. **Lin Xu:** Validation, Methodology. **Siqi Huo:** Writing – review & editing, Visualization. **Pingan Song:** Writing – review & editing, Visualization, Supervision, Conceptualization. **Hao Wang:** Validation, Project administration, Data curation.

Declaration of competing interest

The authors declare that they have no known competing financial interests or personal relationships that could have appeared to influence the work reported in this paper.

Data availability

Data will be made available on request.

Acknowledgements

This work received financial assistance from Major Program (JD) of Hubei Province (2023BAA028), Australian Research Council Discovery Early Career Researcher Award (DE230100616), and Nonmetallic Excellence and Innovation Center (24PHD-4).

Appendix A. Supplementary data

Supplementary data to this article can be found online at https://doi.org/10.1016/j.cej.2024.149852.

References

[1] S.Q. Huo, Z.X. Zhou, J.W. Jiang, T. Sai, S.Y. Ran, Z.P. Fang, P.A. Song, H. Wang, Flame-retardant, transparent, mechanically-strong and tough epoxy resin enabled by high-efficiency multifunctional boron-based polyphosphonamide, Chem. Eng. J. 427 (2022) 131578, https://doi.org/10.1016/j.cej.2021.131578.
[2] J. Wang, J. Wang, S. Yang, K.W. Chen, Single-component flame-retardant and smoke-suppressive epoxy resins enabled by an aluminum/phosphorus/imidazole-containing complex, Compos. Pt. B-Eng. 253 (2023) 133778, https://doi.org/10.1016/j.compositesb.2023.110571.
[3] J.Y. Zhao, P.J. Liu, J.Y. Yue, H.J. Huan, G.H. Bi, L.P. Zhang, Recycling glass fibers from thermoset epoxy composites by in situ oxonium-type polyionic liquid formation and naphthalene-containing superplasticizer synthesis with the degradation solution of the epoxy resin, Compos. Pt. B-Eng. 254 (2023) 110435, https://doi.org/10.1016/j.compositesb.2022.110435.
[4] S.Q. Huo, P.A. Song, B. Yu, S.Y. Ran, V.S. Chevali, L. Liu, Z.P. Fang, H. Wang, Phosphorus-containing flame retardant epoxy thermosets: Recent advances and future perspectives, Prog. Polym. Sci. 114 (2021) 101366, https://doi.org/10.1016/j.progpolymsci.2021.101366.
[5] S. Gu, S.D. Xu, J.H. Lu, X.L. Pu, Q.R. Ren, Y.F. Xiao, Y.Z. Wang, L. Chen, Phosphonate-influenced Diels-Alder chemistry toward multi-path recyclable, fire safe thermoset and its carbon fiber composites, Ecomat 5 (9) (2023) 12388, https://doi.org/10.1002/eom2.12388.
[6] H.Y. Ma, P.A. Song, Z.P. Fang, Flame retarded polymer nanocomposites: Development, trend and future perspective, Science China-Chemistry 54 (2) (2011) 302–313, https://doi.org/10.1007/s11426-010-4196-4.
[7] P.A. Song, Y. Shen, B.X. Du, Z.H. Guo, Z.P. Fang, Fabrication of fullerene-decorated carbon nanotubes and their application in flame-retarding polypropylene, Nanoscale 1 (1) (2009) 118–121, https://doi.org/10.1039/b9nr00026g.
[8] R.M. Perez, J.K.W. Sandler, V. Altstadt, T. Hoffmann, D. Pospiech, M. Ciesielski, M. Doring, U. Braun, U. Knoll, B. Schartel, Effective halogen-free flame retardants for carbon fibre-reinforced epoxy composites, J. Mater. Sci. 41 (15) (2006) 4981–4984, https://doi.org/10.1007/s10853-006-0134-4.
[9] Z. Li, T. Fu, J.H. Lu, J.H. He, L. Chen, W.D. Li, Y.Z. Wang, Trinity flame retardant with benzimidazole structure towards unsaturated polyester possessing high thermal stability, fire-safety and smoke suppression with in-depth insight into the smoke suppression mechanism, Polymer 275 (2023) 125928, https://doi.org/10.1016/j.polymer.2023.125928.
[10] S. Huo, T. Sai, S. Ran, Z. Guo, Z. Fang, P. Song, H. Wang, A hyperbranched P/N/B-containing oligomer as multifunctional flame retardant for epoxy resins, Compos. Pt. B-Eng. 234 (2022) 109701, https://doi.org/10.1016/j.compositesb.2022.109701.
[11] Y.Q. Sun, S. Shuai, C. Lei, L.N. Liu, P.A. Song, L. Wei, Y.M. Yu, F.Z. Lu, Q. Jun, W. Hao, Flame retardant and mechanically tough poly(lactic acid) biocomposites

via combining ammonia polyphosphate and polyethylene glycol, Compos. Commun. 6 (2017) 1–5, https://doi.org/10.1016/j.coco.2017.07.005.
[12] Y.M. Leng, X. Zhao, T. Fu, X.L. Wang, Y.Z. Wang, Bio-based flame-retardant and smoke-suppressing wood plasticcomposites enabled by phytic acid tyramine salt, ACS Sustainable Chem. Eng. 10 (15) (2022) 5055–5066, https://doi.org/10.1021/acssuschemeng.2c00848.
[13] Y.J. Xu, L.Y. Qu, Y. Liu, P. Zhu, An overview of alginates as flame-retardant materials: Pyrolysis behaviors, flame retardancy, and applications, Carbohydr. Polym. 260 (2021) 117827, https://doi.org/10.1016/j.carbpol.2021.117827.
[14] J.B. Feng, L. Liu, Y. Zhang, Q.S. Wang, H. Liang, H. Wang, P.A. Song, Rethinking the pathway to sustainable fire retardants, Exploration (beijing, China) 3 (4) (2023) 20220088, https://doi.org/10.1002/exp.20220088.
[15] C. Wang, S.Q. Huo, G.F. Ye, P.A. Song, H. Wang, Z.T. Liu, A P/Si-containing polyethylenimine curing agent towards transparent, durable fire-safe, mechanically-robust and tough epoxy resins, Chem. Eng. J. 451 (2023) 138768, https://doi.org/10.1016/j.cej.2022.138768.
[16] Q.S. Yang, J. Wang, X. Chen, S. Yang, S.Q. Huo, Q.F. Chen, P.Z. Guo, X. Wang, F. Liu, W. Chen, P.A. Song, H. Wang, A phosphorus-containing tertiary amine hardener enabled flame retardant, heat resistant and mechanically strong yet tough epoxy resins, Chem. Eng. J. 468 (2023) 143811, https://doi.org/10.1016/j.cej.2023.143811.
[17] J.Y. Zhang, B.W. Liu, Y.Z. Wang, H.B. Zhao, Recent Advances in Halogen-free Flame-retardant Polyurethane Foams, Acta Polymerica Sinica 53 (7) (2022) 842–855, https://doi.org/10.11777/j.issn1000-3304.2022.22062.
[18] B. Hu, J. Wang, J.S. Wang, S. Yang, C. Li, F.Y. Wang, S. Huo, P.A. Song, Z.P. Fang, H. Wang, Flame-retardant single-component epoxy resin cured by benzimidazolyl-substituted cyclotriphosphazene: Storage stability, curing behaviors and flame retardancy, Polym. Degrad. Stab. 204 (2022) 110092, https://doi.org/10.1016/j.polymdegradstab.2022.110092.
[19] Y.J. Xu, J. Wang, Y. Tan, M. Qi, L. Chen, Y.Z. Wang, A novel and feasible approach for one-pack flame-retardant epoxy resin with long pot life and fast curing, Chem. Eng. J. 337 (2018) 30–39, https://doi.org/10.1016/j.cej.2017.12.086.
[20] Y.J. Xue, T.C. Zhang, L.F. Tian, J.B. Feng, F. Song, Z. Pan, M. Zhang, Y.H. Zhou, P. A. Song, A molecularly engineered bioderived polyphosphonate containing Schiff base towards fire-retardant PLA with enhanced crystallinity and mechanical properties, Chem. Eng. J. 472 (2023) 144986, https://doi.org/10.1016/j.cej.2023.144986.
[21] Y.R. Ham, S.H. Kim, Y.J. Shin, D.H. Lee, M. Yang, J.H. Min, J.S. Shin, A comparison of some imidazoles in the curing of epoxy resin, J. Ind. Eng. Chem. 16 (4) (2010) 556–559, https://doi.org/10.1016/j.jiec.2010.03.022.
[22] Y.J. Xu, X.H. Shi, J.H. Lu, M. Qi, D.M. Guo, L. Chen, Y.Z. Wang, Novel phosphorus-containing imidazolium as hardener for epoxy resin aiming at controllable latent curing behavior and flame retardancy, Compos. Pt. B-Eng. 184 (2020) 107673, https://doi.org/10.1016/j.compositesb.2019.107673.
[23] J.S. Wang, S.Q. Huo, J. Wang, S. Yang, K.W. Chen, C. Li, D. Fang, Z.P. Fang, P. A. Song, H. Wang, Green and facile synthesis of bio-based, flame-retardant, latent imidazole curing agent for single-component epoxy resin, ACS Appl. Polym. Mater. 4 (5) (2022) 3564–3574, https://doi.org/10.1021/acsapm.2c00138.
[24] J.W. Cheng, J. Wang, S. Yang, Q.Q. Zhang, S. Huo, Q.X. Zhang, Y. Hu, G.P. Ding, Benzimidazolyl-substituted cyclotriphosphazene derivative as latent flame-retardant curing agent for one-component epoxy resin system with excellent comprehensive performance, Compos. Pt. B-Eng. 177 (2019) 107440, https://doi.org/10.1016/j.compositesb.2019.107440.
[25] J.H. Lu, Y.J. Xu, L. Chen, J.H. Chen, J.H. He, Z. Li, S.L. Li, Y.Z. Wang, Facile fabrication of intrinsically fire-safety epoxy resin cured with phosphorus-containing transition metal complexes for flame retardation, smoke suppression, and latent curing behavior, Chem. Eng. J. 442 (2022) 136097, https://doi.org/10.1016/j.cej.2022.136097.
[26] K.H. Pawlowski, B. Schartel, Flame retardancy mechanisms of triphenyl phosphate, resorcinol bis(diphenyl phosphate) and bisphenol bis(diphenyl phosphate) in polycarbonate/acrylonitrile-butadiene-styrene blends, Polym. Int. 56 (11) (2007) 1404–1414, https://doi.org/10.1002/pi.2290.
[27] W. Zhao, J.P. Liu, Y. Zhang, D.M. Ban, Simple green synthesis of solid polymeric bisphenol A bis(diphenyl phosphate) and its flame retardancy in epoxy resins, Rsc Advances 5 (98) (2015) 80415–80423, https://doi.org/10.1039/c5ra06762f.
[28] Z.M. Zhu, K. Shang, L.X. Wang, J.S. Wang, Synthesis of an effective bio-based flame-retardant curing agent and its application in epoxy resin: Curing behavior, thermal stability and flame retardancy, Polym. Degrad. Stab. 167 (2019) 179–188, https://doi.org/10.1016/j.polymdegradstab.2019.07.005.
[29] J.S. Wang, X. Chen, J. Wang, S. Yang, K.W. Chen, L. Zhu, S.Q. Huo, P.A. Song, H. Wang, High-performance, intrinsically fire-safe, single-component epoxy resins and carbon fiber reinforced epoxy composites based on two phosphorus-derived imidazoliums, Polym. Degrad. Stab. 208 (2023) 110261, https://doi.org/10.1016/j.polymdegradstab.2023.110261.
[30] S. Huo, S. Yang, J. Wang, J. Cheng, Q. Zhang, Y. Hu, G. Ding, Q. Zhang, P. Song, A liquid phosphorus-containing imidazole derivative as flame-retardant curing agent for epoxy resin with enhanced thermal latency, mechanical, and flame-retardant performances, J. Hazard. Mater. 386 (2020) 121984, https://doi.org/10.1016/j.jhazmat.2019.121984.
[31] G. Gerami, R. Bagheri, R. Darvishi, Investigation of isothermal and dynamic cure kinetics of epoxy resin/nadic methyl anhydride/dicyandiamide by differential scanning calorimetry (DSC), J. Therm. Anal. Calorim. 137 (2) (2019) 575–582, https://doi.org/10.1007/s10973-018-7961-9.
[32] Y.Z. Zhao, Y. Chu, Y.J. Xu, P. Zhu, Y.Z. Wang, Highly flame-retardant vinyl ester resins with well-balanced comprehensive performance, Chem. Eng. J. 464 (2023) 142659, https://doi.org/10.1016/j.cej.2023.142659.
[33] L.F. Yu, S.Q. Huo, C. Wang, G.F. Ye, P.A. Song, J.B. Feng, Z.P. Fang, H. Wang, Z. T. Liu, Flame-retardant poly(L-lactic acid) with enhanced UV protection and well-preserved mechanical properties by a furan-containing polyphosphoramide, Int. J. Biol. Macromol. 234 (2023) 123707, https://doi.org/10.1016/j.ijbiomac.2023.123707.
[34] W.J. Yang, Q.K. Zhou, W.H. Pan, S.E. Zhu, C.X. Wei, H.D. Lu, W. Yang, A.C. Y. Yuen, Synthesis of vanillin-based porphyrin for remarkably enhancing the toughness, UV-resistance and self-extinguishing properties of polylactic acid, Chem. Eng. J. 469 (2023) 143935, https://doi.org/10.1016/j.cej.2023.143935.
[35] A.L. Zhang, J.Z. Zhang, L.A. Liu, J.F. Dai, X.Y. Lu, S.Q. Huo, M. Hong, X.H. Liu, M. Lynch, X.S. Zeng, P. Burey, P.A. Song, Engineering phosphorus-containing lignin for epoxy biocomposites with enhanced thermal stability, fire retardancy and mechanical properties, J. Mater. Sci. Technol. 167 (2023) 82–93, https://doi.org/10.1016/j.jmst.2023.06.004.
[36] C.C. Gao, L.H. Guo, P.C. Yuan, Y.J. Qiao, A. Xing, X.Y. Li, Flame retardant, strong and tough, low dielectric epoxy thermoset enabled by a novel bi-DOPO type epoxy with aggregation-induced emission, Chem. Eng. J. 475 (2023) 146241, https://doi.org/10.1016/j.cej.2023.146241.
[37] T. Vidil, F. Tournilhac, S. Musso, A. Robisson, L. Leibler, Control of reactions and network structures of epoxy thermosets, Prog. Polym. Sci. 62 (2016) 126–179, https://doi.org/10.1016/j.progpolymsci.2016.06.003.
[38] L. Philippe, C. Sammon, S.B. Lyon, J. Yarwood, An FTIR/ATR in situ study of sorption and transport in corrosion protective organic coatings - 1. Water sorption and the role of inhibitor anions, Prog. Org. Coat. 49 (4) (2004) 302–314, https://doi.org/10.1016/j.porgcoat.2003.07.002.
[39] Y.D. Wang, L. Ma, J. Yuan, Z.M. Zhu, X.M. Liu, D.S. Li, L.Q. He, F. Xiao, Furfural-based P/N/S flame retardant towards high-performance epoxy resins with flame retardancy, toughness, low dielectric properties and UV resistance, Polym. Degrad. Stab. 212 (2023) 110343, https://doi.org/10.1016/j.polymdegradstab.2023.110343.
[40] F.R. Zeng, X.F. Men, M.J. Chen, B.W. Liu, Q.W. Han, S.C. Huang, H.B. Zhao, Y. Z. Wang, Molecular-micron multiscale toughening and flame retarding for polyurethane foams, Chem. Eng. J. 454 (2023) 140023, https://doi.org/10.1016/j.cej.2022.140023.
[41] X.L. Yu, B.B. Wang, P.F. Jia, Z.T. Yin, G. Tang, X.D. Zhou, T.T. Lu, L.Y. Guo, L. Song, Y. Hu, Effects of graphene nanosheets decorated by cerium stannate on the enhancement of flame retardancy and mechanical performances of flexible polyurethane foam composites, Polym. Adv. Technol. 33 (1) (2022) 290–302, https://doi.org/10.1002/pat.5516.
[42] H. Vahabi, B.K. Kandola, M.R. Saeb, Flame Retardancy Index for Thermoplastic Composites, Polymers 11 (3) (2019) 11030407, https://doi.org/10.3390/polym11030407.
[43] X. Song, Z.P. Deng, C.W. You, R.Y. Sun, F. Song, X.L. Wang, L. Chen, Y.Z. Wang, High-performance and fire-resistant epoxy thermosets derived from plant-derived ferulic acid, Ind. Crops Prod. 187 (2022) 115445, https://doi.org/10.1016/j.indcrop.2022.115445.
[44] X.M. Ding, L. Chen, Y.J. Xu, X.H. Shi, X. Luo, X. Song, Y.Z. Wang, Robust Epoxy Vitrimer with Simultaneous Ultrahigh Impact Property, Fire Safety, and Multipath Recyclability via Rigid-Flexible Imine Networks, ACS Sustainable Chem. Eng. 11 (39) (2023) 14445–14456, https://doi.org/10.1021/acssuschemeng.3c03189.
[45] Y.J. Chen, X.D. Wu, M.Q. Li, L.J. Qian, H.F. Zhou, Mechanically Robust and Flame-Retardant Polylactide Composites Based on In Situ Formation of Crosslinked Network Structure by DCP and TAIC, Polymers 14 (2) (2022) 308, https://doi.org/10.3390/polym14020308.
[46] S.D. Wang, S.H. Lou, P.H. Fan, L. Ma, J. Liu, T. Tang, A novel aromatic imine-containing DOPO-based reactive flame retardant towards enhanced flame-retardant and mechanical properties of epoxy resin, Polym. Degrad. Stab. 213 (2023) 110364, https://doi.org/10.1016/j.polymdegradstab.2023.110364.
[47] R.C. Lian, H.C. Guan, Y.Q. Zhang, M.Y. Ou, Y.P. Jiang, L. Liu, C.M. Jiao, X.L. Chen, A green organic-inorganic PAbz@ZIF hybrid towards efficient flame-retardant and smoke-suppressive epoxy coatings with enhanced mechanical properties, Polym. Degrad. Stab. 217 (2023) 110534, https://doi.org/10.1016/j.polymdegradstab.2023.110534.
[48] Q.R. Ren, S. Gu, Y.Z. Wang, L. Chen, A phosphonate-derived epoxy vitrimer with intrinsic flame retardancy and catalyst-free reprocessability, J. Polym. Sci. (2023) 1–11, https://doi.org/10.1002/pol.20230211.
[49] R.K. Jian, Y.F. Ai, L. Xia, L.J. Zhao, H.B. Zhao, Single component phosphamide-based intumescent flame retardant with potential reactivity towards low flammability and smoke epoxy resins, J. Hazard. Mater. 371 (2019) 529–539, https://doi.org/10.1016/j.jhazmat.2019.03.045.
[50] X. Liu, J.J. Zhou, J.Q. Zhao, S.M. Liu, Design and synthesis of polyetherimides as a flame-retarded thermolatent hardener for high-performance epoxy thermosets, Compos. Pt. B-Eng. 259 (2023) 110754, https://doi.org/10.1016/j.compositesb.2023.110754.
[51] S.M. Liu, J.B. Chen, J.Q. Zhao, Z.J. Jiang, Y.C. Yuan, Phosphaphenanthrene-containing borate ester as a latent hardener and flame retardant for epoxy resin, Polym. Int. 64 (9) (2015) 1182–1190, https://doi.org/10.1002/pi.4890.
[52] Y.J. Xu, L. Chen, W.H. Rao, M. Qi, D.M. Guo, W. Liao, Y.Z. Wang, Latent curing epoxy system with excellent thermal stability, flame retardance and dielectric property, Chem. Eng. J. 347 (2018) 223–232, https://doi.org/10.1016/j.cej.2018.04.097.
[53] J.H. Chen, J.H. Lu, X.L. Pu, L. Chen, Y.Z. Wang, Recyclable, malleable and intrinsically flame-retardant epoxy resin with catalytic transesterification, Chemosphere 294 (2022) 133778, https://doi.org/10.1016/j.chemosphere.2022.133778.

[54] A. Dasari, Z.Z. Yu, G.P. Cai, Y.W. Mai, Recent developments in the fire retardancy of polymeric materials, Prog. Polym. Sci. 38 (9) (2013) 1357–1387, https://doi.org/10.1016/j.progpolymsci.2013.06.006.
[55] J. Gong, X. Chen, T. Tang, Recent progress in controlled carbonization of (waste) polymers, Prog. Polym. Sci. 94 (2019) 1–32, https://doi.org/10.1016/j.progpolymsci.2019.04.001.
[56] G.F. Ye, S.Q. Huo, C. Wang, P.A. Song, Z.P. Fang, H. Wang, Z.T. Liu, Durable flame-retardant, strong and tough epoxy resins with well-preserved thermal and optical properties via introducing a bio-based, phosphorus-phosphorus, hyperbranched oligomer, Polym. Degrad. Stab. 207 (2023) 110235, https://doi.org/10.1016/j.polymdegradstab.2022.110235.
[57] F.K. Chu, S.L. Qiu, Y.F. Zhou, X. Zhou, W. Cai, Y.L. Zhu, L.X. He, L. Song, W.Z. Hu, Novel glycerol-based polymerized flame retardants with combined phosphorus structures for preparation of high performance unsaturated polyester resin composites, Compos. Pt. B-Eng. 233 (2022) 109647, https://doi.org/10.1016/j.compositesb.2022.109647.
[58] T.M. Nguyen-Ha, T.B. Nguyen, T.A. Nguyen, L.H. Pham, D.H. Nguyen, D. M. Nguyen, D. Hoang, E. Oh, J. Suhr, Novel high-performance sustainable polyurethane nanocomposite foams: Fire resistance, thermal stability, thermal conductivity, and mechanical properties, Chem. Eng. J. 474 (2023) 145585, https://doi.org/10.1016/j.cej.2023.145585.

Polymer Degradation and Stability 228 (2024) 110906



Contents lists available at ScienceDirect

Polymer Degradation and Stability

journal homepage: www.journals.elsevier.com/polymer-degradation-and-stability





Development of single-component epoxy resin with superb thermal stability, flame retardancy, smoke suppression, and latency via Cu-based phosphorus/imidazole-containing complex

Jingsheng Wang [a], Jun Wang [a,b], Shuang Yang [b,*], Chaoqun Wu [b], Xi Chen [b], Kaiwen Chen [a], Pingan Song [c], Hao Wang [d], Siqi Huo [d,*]

[a] School of Materials Science and Engineering, Wuhan University of Technology, Wuhan 430070, China
[b] School of Mechanical and Electronic Engineering, Wuhan University of Technology, Wuhan 430070, China
[c] Centre for Future Materials, School of Agriculture and Environmental Science, University of Southern Queensland, Springfield 4300, Australia
[d] School of Engineering, Centre for Future Materials, University of Southern Queensland, Springfield 4300, Australia

ARTICLE INFO

Keywords:
Single-component epoxy resin
Phosphorus-containing mental complex
Thermal stability
Flame retardancy
Smoke suppression

ABSTRACT

To address the growing need for fire-safe single-component epoxy resin (EP) systems, this study introduced a phosphorus-containing copper complex (Cu-DA) as a multifunctional latent curing agent. The Cu-DA complex, synthesized by coordinating copper (II) chloride and a phosphorus-based imidazole, significantly improved the latency, thermal stability, and fire resistance of single-component EP. The obtained EP/Cu-DA-2 mixture with 15.3 wt% Cu-DA showed a 43-day shelf life and a rapid gel time of 22 min at 150 °C, highlighting its superb latency and fast curing. After curing, the resultant thermoset had a high glass transition temperature of 160.9 °C and increased crosslinking density, indicating superior thermal stability. The EP/Cu-DA-3 system with 17.4 wt% Cu-DA achieved a high limiting oxygen index (LOI) of 37.8 % and a UL-94 V-0 rating, reflecting its satisfactory flame retardancy. Furthermore, compared to the control EP system, the total smoke production (TSP) and maximum smoke density (MSD) of EP/Cu-DA-3 were reduced by approximately 28.4 % and 25.8 %, respectively, demonstrating significantly enhanced smoke suppression. The research offers a scalable strategy for developing single-component EP systems with rapid curing, high fire resistance, and great smoke suppression, meeting the demands of industrial applications.

1. Introduction

The ubiquitous use of epoxy resins (EPs) in high-performance sectors necessitates enhanced safety, particularly regarding flammability [1,2]. Traditional EPs are renowned for their exceptional adhesion and mechanical integrity. However, their flammability poses significant risks, limiting their application in safety-critical environments [3-5]. This challenge has spurred extensive research aimed at developing flame-retardant EPs that can meet the stringent safety requirements of industrial applications [6-9]. Two-component EP systems require precise mixing and timely application to prevent premature curing, presenting logistical and operational challenges. Single-component EPs offer a streamlined alternative, eliminating the need for mixing and thereby minimizing waste, potential errors, and simplifying the application process [10,11]. The key to this innovation is the design of latent curing agents, which ensure stability at room temperature and activate at specific temperatures, leading to a robust curing [12,13]. Therefore, the need to create fire-safe single-component EPs focuses on two main objectives: enhancing flame retardancy and improving user-friendliness for diverse industrial applications.

The synthesis of phosphorus (P)-containing imidazole compounds represents an effective pathway in developing flame-retardant single-component EPs [14-16]. This approach involves the strategic modification of the imidazole ring, either at the 1-position or 3-position nitrogen, to incorporate P-based groups known for their superior flame-retardant capabilities [17-19]. One the one hand, these P-based groups can reduce the nucleophilic activity of the tertiary amine nitrogen in the imidazole ring, imparting latent curing characteristics [20,21]. On the other hand, they can covalently integrate into the crosslinking network, endowing the resin with intrinsic flame retardancy

* Corresponding author.
E-mail addresses: ysfrp@whut.edu.cn (S. Yang), Siqi.Huo@unisq.edu.au (S. Huo).

https://doi.org/10.1016/j.polymdegradstab.2024.110906
Received 29 May 2024; Received in revised form 24 June 2024; Accepted 26 June 2024
Available online 29 June 2024
0141-3910/© 2024 Elsevier Ltd. All rights are reserved, including those for text and data mining, AI training, and similar technologies.

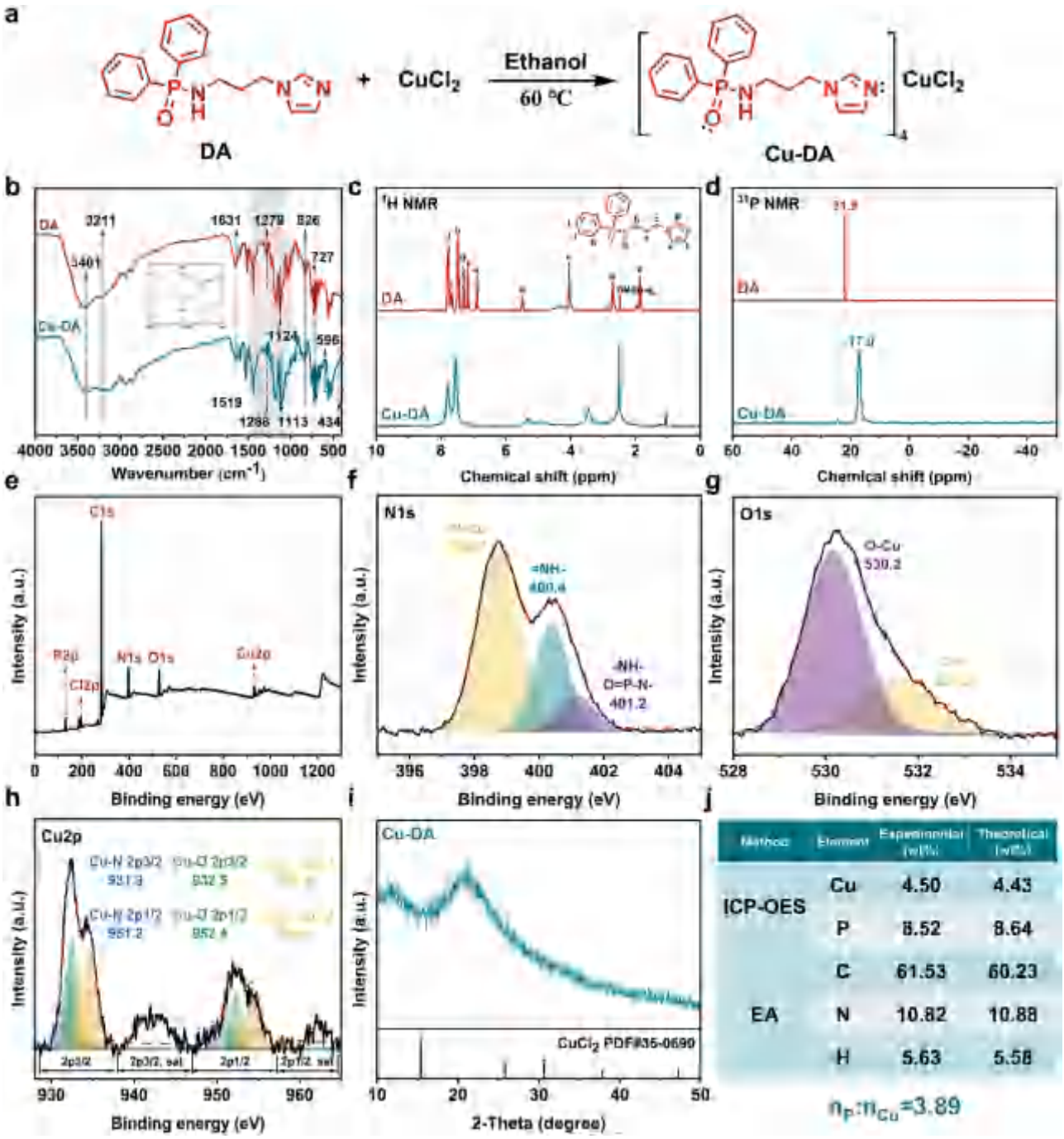


Fig. 1. (a) Synthesis of Cu-DA; (b) FTIR spectra of DA and Cu-DA; (c) ^{1}H and (d) ^{31}P NMR spectra of DA and Cu-DA; (e) full-scan and high-resolution (f) N1s, (g) O1s and (h) Cu2p XPS spectra of Cu-DA; (i) XRD pattern of Cu-DA; and (j) elemental content of Cu-DA obtained by ICP-OES and EA.

[22-24]. Extensive research supports this approach [10,25-28]. For example, Xu et al. [29] developed a novel latent flame-retardant curing agent (DPPIO) for EPs. The EP/DPPIO mixture demonstrated a long storage life and achieved a LOI of 38.0 % and a UL-94 V-0 rating, indicating excellent flame retardancy. Despite these advances, how to enhance smoke suppression remains a challenge. Smoke inhalation and impaired visibility often cause fatalities during fires, highlighting the need for improving smoke suppression [30,31].

Enhancing the carbonization capacity of polymers is an effective strategy to reduce volatile and smoke emissions [32-34]. Metal compounds, known for their catalytic oxidation and carbonization properties, can reduce smoke generation but are ineffective in curbing heat release [35-38]. Combining metal and phosphorus compounds can significantly improve both flame retardancy and smoke suppression [39-43]. Metal cations, as a Lewis acid, can be complexed with P-containing imidazole ligands to prepare complexes, which is an effective way to combine metal- and P-containing groups. In our previous study, we developed a liquid P-containing imidazole (DA) as a flame-retardant latent curing agent for EPs [44]. The resultant EP/DA thermoset demonstrated a LOI of 37.2 % and a UL-94 V-0 rating, indicating enhanced fire safety. However, the latency of EP/DA was insufficient for practical applications, and significant smoke was generated during combustion. Incorporating metal elements is expected to improve the smoke suppression of EP/DA, due to the synergistic effect between metal- and phosphorus-containing groups. Additionally, the coordination between metal cations and DA can further reduce the nucleophilic

Table 1
Formulations of EP thermosets.

Sample	EP (wt %)	DA (wt %)	Cu-DA (wt%)	Calculated P content (wt%)	Calculated Cu content (wt%)
EP/DA	86.2	13.8	/	1.31	/
EP/Cu-DA-1	87.0	/	13.0	1.13	0.58
EP/Cu-DA-2	84.7	/	15.3	1.32	0.68
EP/Cu-DA-3	82.6	/	17.4	1.50	0.77

activity of the imidazole group in DA, thereby improving the latency [45-47]. Therefore, the incorporation of metal ions and phosphorus-containing groups into imidazole is expected to enable the synthesis of imidazole-based latent curing agents with superior flame retardancy and smoke suppression. This innovation could pave the way for the development of high-performance, single-component epoxy resin systems that integrate long-term latency, rapid curing, and high-efficiency flame retardancy and smoke suppression.

In this work, a phosphorus-containing metal complex (Cu-DA) was synthesized through the coordination reaction between copper (II) chloride and DA. The results indicated that incorporating Cu^{2+} significantly reduced the curing activity of DA, allowing EP/Cu-DA to achieve a shelf life of around 43 days and rapid gelation at high temperatures. The thermal stability of the thermosets was improved, and the flame retardancy and smoke suppression were significantly enhanced due to the bi-phase synergistic effect of metal- and phosphorus-containing groups within Cu-DA. This work successfully addresses the limitations of flame-retardant single-component EP/DA system in smoke suppression and latency, and offers a feasible strategy for creating flame-retardant and smoke-suppressive single-component epoxy systems.

2. Materials and methods

2.1. Materials

Bisphenol A-type epoxy resin (E51) with an epoxide value of 0.51 mol/100 g, was supplied by Suzhou Senfeida Chemical Co., Ltd., Jiangsu, China. A phosphorus-containing imidazole (DA) was synthesized based on our previous work [44]. Anhydrous copper (II) chloride and ethanol were purchased from Shanghai Macklin Biochemical Technology Co., Ltd., Shanghai, China.

2.2. Synthesis of Cu-based phosphorus/imidazole-containing complex (Cu-DA)

The preparation method for the Cu-DA complex is depicted in Fig. 1a. Firstly, $CuCl_2$ (0.0074 mol, 1.0 g) was dissolved in 20 mL of

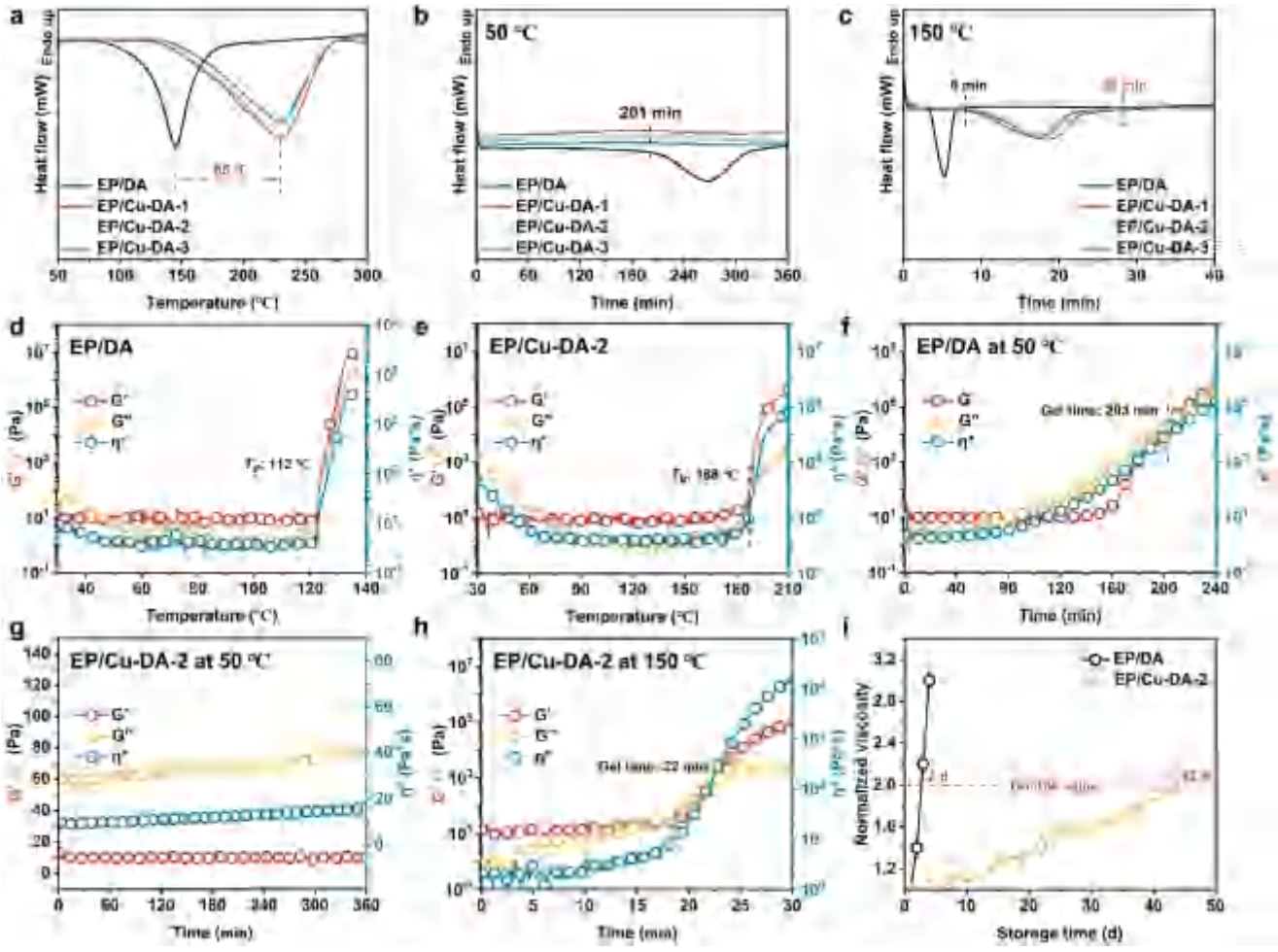


Fig. 2. (a) Non-isothermal DSC curves of EP mixtures; isothermal DSC curves of EP mixtures at (b) 50 and (c) 150 °C; storage modulus (G′), loss modulus (G″), and complex viscosity (η*) curves of (d) EP/DA and (e) EP/Cu-DA-2 mixtures as a function of temperature; G′, G″ and η* plots of (f) EP/DA and (g) EP/Cu-DA-2 mixtures as a function of time at 50 °C; (e) G′, G″ and η* plots of EP/ Cu-DA-2 mixture as a function of time at 150 °C; and (f) normalized viscosity curves of EP/DA and EP/Cu-DA-2 mixtures during storage.

absolute ethanol, named as solution A. DA (0.037 mol, 12.0 g) was dissolved in 100 mL of absolute ethanol to form solution B. Subsequently, solution A was stirred continuously, and then solution B was gradually added. The resultant mixture was stirred at 60 °C for 6 h. Upon cooling naturally to ambient temperature, the solid products precipitated. The crude products were collected via filtration and washed five times with anhydrous ethanol. By drying in a vacuum oven, dark blue solid product, designated as Cu-DA, was gained with a yield of 73 %.

2.3. Preparation of EP thermosets

The EP thermoset formulations are delineated in Table 1. EP/DA and EP/Cu-DA thermosets were fabricated using DA and Cu-DA as curing agents, respectively. For EP/Cu-DA, it was prepared by mixing E51 and Cu-DA at 80 °C for 30 min, and then curing the mixture at 80 °C for 2 h, 130 °C for 2 h, and 180 °C for 1 hour. For EP/DA, it was fabricated by mixing E51 and DA at room temperature, and curing the mixture following the above procedure.

2.4. Characterization

This section is in the Supporting Information.

3. Results and discussion

3.1. Characterizations of Cu-DA

The chemical structure of Cu-DA was thoroughly characterized by using different analytical techniques including Fourier-transform infrared (FTIR) spectroscopy, ^{1}H and ^{31}P nuclear magnetic resonance (NMR), X-ray photoelectron spectroscopy (XPS), X-ray diffraction (XRD), elemental analysis (EA), and inductively coupled plasma optical emission spectrometry (ICP-OES). The results are presented in Fig. 1b-j. In the FTIR spectrum of DA depicted in Fig. 1b, the absorption peaks of benzene ring appeared at 1631, 826, and 727 cm^{-1} [14]. The absorption peaks at 3211, 1279, and 1124 cm^{-1} were assigned to N—H, C—N, and P = O groups, respectively [44,45]. Upon complexation with copper (II) chloride, the peaks at 1279 and 1124 cm^{-1} for DA shifted to 1288 and 1113 cm^{-1} for Cu-DA, suggesting the interaction between DA with Cu^{2+}. It was further supported by the emergence of peaks at 596 and 434 cm^{-1} [41,48,49], corresponding to Cu-O and Cu-N bonds, implying the coordination between the nitrogen of the amine and oxygen of the phosphate with Cu^{2+}. The ^{1}H NMR spectrum of DA, as shown in Fig. 1c, underwent changes upon copper complexation, which was reflected in broadening, weakening, disappearance, and upfield shift of many signals in the spectrum of Cu-DA, likely due to the paramagnetic and shielding effects from the coordination of the nitrogen and oxygen lone pairs with Cu^{2+} cation. Similar phenomenon has also been reported in previous works on copper-imidazole complexes [45,46]. The ^{31}P NMR spectra exhibited analogous signal variations for the Cu-DA complex relative to DA (see Fig. 1d).

XPS analysis, detailed in Fig. 1e, confirmed the presence of C, N, O, P, Cl, and Cu elements in Cu-DA. In the high-resolution N1s spectrum of Cu-DA, as illustrated in Fig. 1f, the deconvoluted peaks at 398.7, 400.4, and 401.2 eV were associated with N—Cu, =NH-, and -NH-/O=P-N- groups, respectively [50,51]. For the O1s region, as shown in Fig. 1g, the peaks at 530.2 and 531.5 eV were assigned to O-Cu and O=P groups, respectively [50,52]. The Cu2p spectrum in Fig. 1h, with peaks at 931.9 and 932.5 eV for Cu2p3/2, and 951.2 and 952.4 eV for Cu2p1/2, confirmed the formation of Cu-N and Cu-O bonds due to the coordination between DA and Cu^{2+} [53]. The appearance of strong satellite peaks of Cu2p indicated +2 oxidation state for copper cation [54]. The XRD pattern in Fig. 1j demonstrated a crystalline phase change upon complex formation between DA and $CuCl_2$. In Fig. 1i, the EA and ICP-OES analyses determined that the P and Cu contents in Cu-DA were 8.52 and 4.50 wt%, respectively, and thus the molar ratio of DA to Cu^{2+} was calculated to be approximately 3.89 : 1. Collectively, these analyses substantiated the successful synthesis of Cu-DA complex, which was composed of four DA molecules complexed with one $CuCl_2$ molecule.

3.2. Curing behaviors and thermal latency

The curing characteristics of EP/DA and EP/Cu-DA mixtures were examined through non-isothermal differential scanning calorimetry (DSC), with results detailed in Fig. 2a–c, Fig. S1a-d, and Table S1. Each epoxy mixture displayed a single exothermic curing peak, but the peak curing temperatures (T_p) for EP/Cu-DA mixtures were substantially elevated compared to that of EP/DA mixture. For instance, the T_p of EP/Cu-DA-1 was 85 °C higher than that of EP/DA, indicating that the reactivity of DA was significantly hindered upon complexation with Cu^{2+} (see Fig. 2a). Isothermal DSC was conducted to further assess the curing behaviors of EP mixtures. The EP/DA mixture exhibited a notable exothermic peak after 200 min at 50 °C. In contrast, EP/Cu-DA mixtures displayed no exothermic peaks within 360 min, highlighting their diminished curing reactivity and enhanced thermal latency (see Fig. 2b). Upon increasing the temperature to 150 °C, EP/Cu-DA mixtures rapidly regained curing ability, completely curing within 28 min (see Fig. 2c). The curing kinetics were analyzed using the Kissinger, Crane, and Flynn-Wall-Ozawa models [55], with the corresponding plots of $\ln(\beta/T_p^2)$ versus $1/T_p$ and $\ln(\beta)$ versus $1/T_p$ presented in Fig. S1e and f. The calculated kinetic parameters are listed in Table S2, and the activation energies (E_a) derived from these models are depicted in Fig. S1g. The E_a, a measure of resin curing difficulty [15], was found to be higher for EP/Cu-DA mixtures (>80 kJ/mol) than that for EP/DA mixture (~67 kJ/mol), further confirming the inhibitory effect of Cu^{2+} on the curing activity of DA. The E_a values obtained from both the Kissinger and Flynn-Wall-Ozawa models were close, suggesting that the curing mechanisms of EP/DA and EP/Cu-DA mixtures adhere to an n-order kinetic model [17]. Collectively, the coordination between DA and $CuCl_2$ within the Cu-DA complex could significantly reduce the curing activity of DA.

Rheological analysis was conducted to investigate the thermal latency of EP mixtures, with the corresponding curves depicted in Fig. 2d-i. As presented in Fig. 2d and e, the η* for both EP/DA and EP/Cu-DA mixtures initially reduced before escalating exponentially with temperature. The intersection points of the G′ and G″ curves, indicative of a viscosity inflection, is denoted as T_v. Significantly, the T_v of EP/Cu-DA-2 was 76 °C higher than that of EP/DA, further validating the reduced curing reactivity of Cu-DA. To evaluate the thermal latency during storage, a rheological assessment at 50 °C was undertaken to mimic adverse storage conditions. The gel time, defined as the time at which G′ and G″ intersect, signifies the initial formation of cross-linking network within EP [12,27,56]. EP/DA reached gelation in 203 min at 50 °C, whereas EP/Cu-DA-2 did not gel within 6 h at this temperature, underscoring its enhanced processability (see Fig. 2f and g). Conversely, EP/Cu-DA demonstrated rapid gelation within 22 min at 150 °C (see Fig. 2h). These findings highlighted the superior storage stability at low temperatures and accelerated curing ability at higher temperatures, which was highly desirable for single-component EP. The viscosity changes for EP/DA and EP/Cu-DA at 25 °C over time were monitored to estimate their shelf life, as shown in Fig. 2i and Table S2. EP/Cu-DA-2 displayed an extended shelf life of 43 days, substantially surpassing that of EP/DA. This indicated the potential of Cu-DA as an effective latent curing agent for single-component EP systems.

DSC, FTIR, and XPS analyses were employed to elucidate the curing mechanism of Cu-DA complexes. In Fig. S1h, Cu-DA displayed a pronounced endothermic transition within 100–180 °C, likely attributable to its dissociation and melting. To delineate the chemical structural evolution upon heating, the FTIR spectra at room temperature (RT) and 150 °C are juxtaposed in Fig. S1i. Notably, the peaks corresponding to Cu-O and Cu-N coordination bonds at 596 and 434 cm^{-1} diminished and vanished in the spectrum recorded at 150 °C, demonstrating the

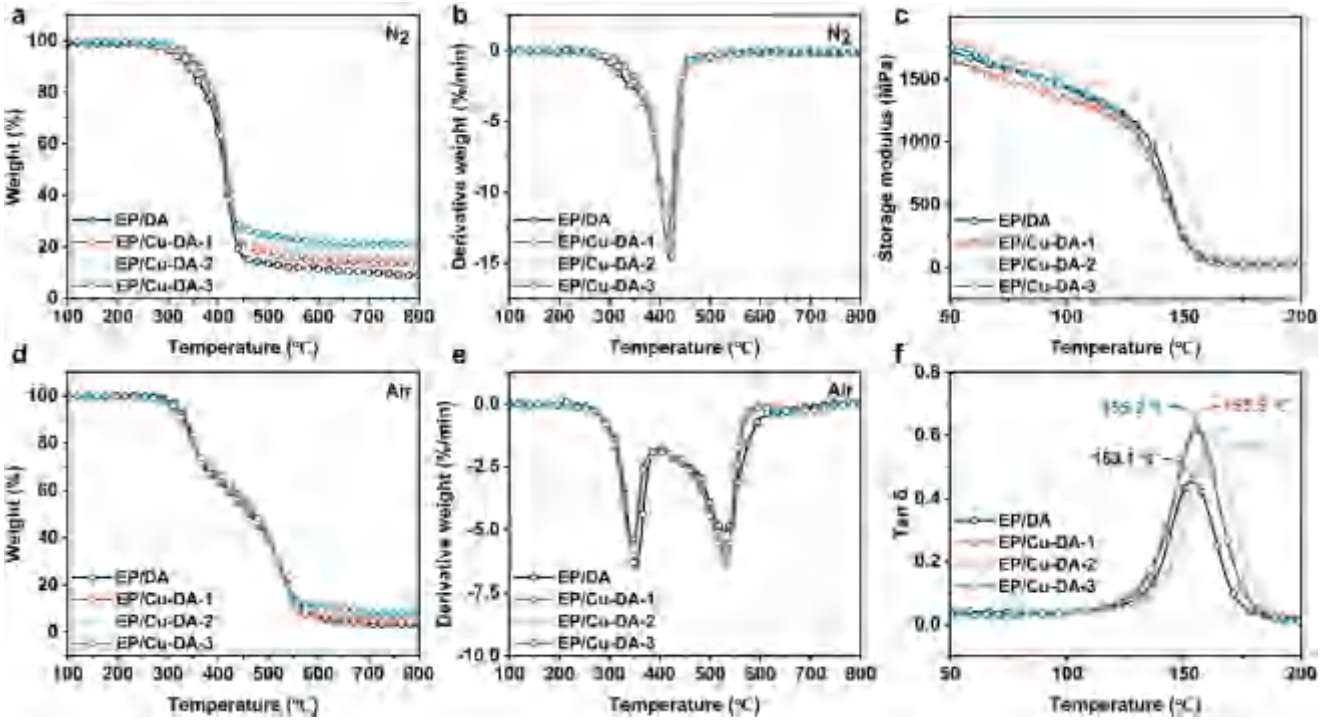


Fig. 3. TGA curves under (a) N_2 and (d) air atmosphere; DTG curves in (b) N_2 and (e) air conditions; (c) storage modulus (*E'*) plots; and (f) Tanδ curves of EP thermosets.

dissociation of DA and $CuCl_2$ within the Cu-DA complex. Fig. S2 presents the N1s, O1s, and Cu2p XPS spectra for Cu-DA and EP/Cu-DA-2 thermosets. Compared with the N1s spectrum of Cu-DA, the peak for N—Cu coordination bond at 398.7 eV dissipated in the N1s spectrum of EP/Cu-DA-2 thermoset, suggesting the dissociation of DA and Cu^{2+} during the curing process (see Fig. S2a). Additionally, the EP/Cu-DA-2 thermoset exhibited two new N1s peaks at 399.4 and 401.8 eV, indicative of secondary amine and imidazolium groups [29]. These groups formed via nucleophilic addition between epoxy group and imidazole, as well as secondary amine within DA. In the high-resolution O1s XPS spectra, the O—Cu peak at 530.2 eV vanished, and a new peak at 533.0 eV emerged, ascribed to the C—O bond of epoxy resin (see Fig. S2b). In the Cu2p spectrum of Cu-DA, peaks at 931.9, 932.5, and 934.5 eV (2p3/2) were indicative of Cu-N, Cu-O, and Cu-Cl (see Fig. S2c), respectively. Conversely, these peaks and the satellite peak of Cu^{2+} vanished in the Cu2p spectrum of EP/Cu-DA-2, replaced by a new peak at 933.3 eV (2p3/2), potentially resulting from Cu^{2+} coordination with alkoxide anions generated from anionic polymerization. Based on that, the proposed curing mechanism for EP/Cu-DA mixture is outlined in Fig. S2d. Initially, DA dissociates from the Cu-DA complexs at elevated temperatures, initiating anionic polymerization and nucleophilic addition between epoxy group and imidazole and secondary amine groups. This process is followed by etherification, leading to epoxy chain propagation. Ultimately, further gelation and polymerization culminate in the formation of crosslinked EP networks. Based on the above analyses, Cu-DA remains inert at low temperatures and rapidly cures epoxy resins at high temperatures, making it an effective latent curing agent for one-component epoxy systems.

3.3. Thermal properties

Thermal stability of EP thermosets was evaluated using thermogravimetric analysis (TGA), with TG and derivative TG (DTG) curves and detailed data presented in Fig. 3 and Table S3. Under nitrogen atmosphere, EP/Cu-DA thermosets demonstrated single-stage degradation, which was similar to EP/DA. Notably, EP/Cu-DA exhibited higher temperature at 5 % weight loss ($T_{5\%}$) compared to EP/DA, signifying superior thermal stability. For instance, EP/Cu-DA-1 diplayed a $T_{5\%}$ of 340.3 °C, surpassing EP/DA by 29 °C. At high temperatures, EP/Cu-DA thermosets showed significant carbonization capabilities, ascribed to the dehydration effect of phosphorus-containing components and the catalytic function of Cu^{2+} [52]. The char yield at 800 °C (*CY*) rose from 8.9 wt% for EP/DA to 20.4 wt% for EP/Cu-DA-3, underscoring the enhanced condensed flame-retardant properties to some extents. Under air atmosphere, EP/Cu-DA-2 and EP/Cu-DA-3 thermosets showed comparable $T_{5\%}$ values, lower maximum mass loss rates, and higher *CY* values compared to those of EP/DA thermoset, further indicating their superb thermal stability (Fig. 3b and e).

Dynamic mechanical analysis (DMA) was utilized to study the thermodynamic properties of EP thermosets, with results depicted in Fig. 3c and f and Table S4. EP/Cu-DA-2 showed the highest storage modulus (*E'*) of 1822 MPa at 50 °C among all EP/Cu-DA thermosets, which surpassed 1730 MPa of EP/DA. Additionally, the glass transition temperature (T_g) for the EP/Cu-DA-2 thermoset was 160.9 °C, higher than 153.1 °C of the EP/DA thermoset. To understand the factors influencing the variations in storage modulus (*E'*) and T_g, the crosslinking density (υ_e) of the EP thermosets was determined using the rubbery elastic equation, with results detailed in Table S4. The crosslinking density (υ_e) values for EP/Cu-DA thermosets, ranging from 2238 to 3163 mol/m^3, consistently exceeded that of the EP/DA thermoset (2241 mol/m^3). This suggested the formation of denser crosslinked networks within the EP/Cu-DA thermosets, likely due to the coordination interactions between Cu^{2+} cations and alkoxide anions [56]. These interactions contributed to the increased storage modulus (*E'*) and glass transition temperature (T_g). In summary, the EP/Cu-DA thermosets demonstrated enhanced heat resistance, char forming ability, and mechanical rigidity compared to the EP/DA thermoset.

3.4. Flame retardancy and smoke suppression

The LOI values and UL-94 ratings for EP thermosets are depicted in Fig. 4a. The EP/DA thermoset achieved a high LOI of 35.3 % and

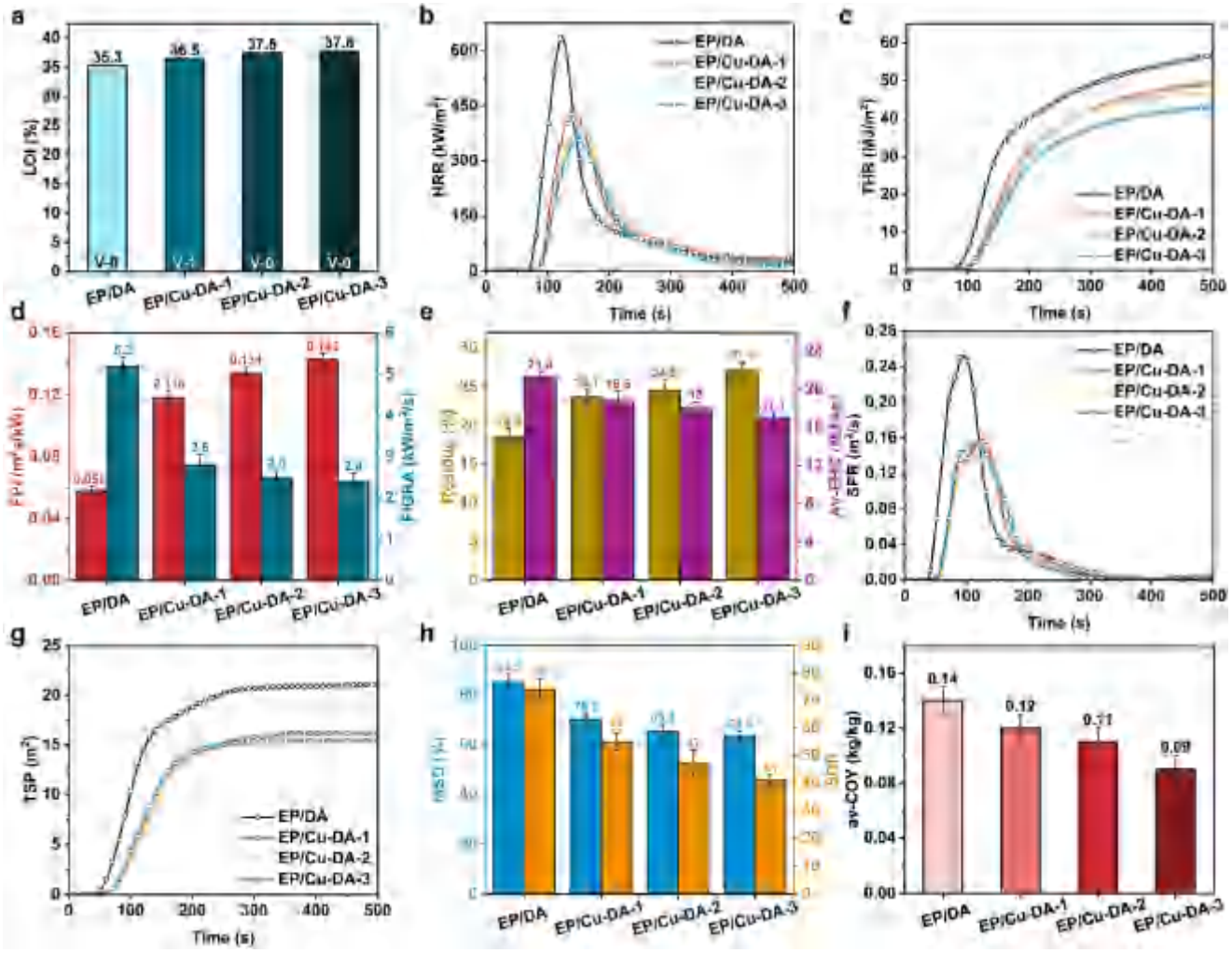


Fig. 4. (a) LOI values and UL-94 ratings, (b) heat release rate plots, (c) total heat release curves, (d) fire performance index (FPI) and fire growth rate (FIGRA) values, (e) Residue and average effective heat of combustion (*Av*-EHC) values, (f) smoke production rate plots, (g) total smoke production curves, (h) maximum smoke density (MSD) and smoke density rating (SDR) values, and (i) average carbon monoxide production rate (av-COY) values of EP thermosets.

Table 2
The combustion parameters of EP thermosets.

Sample	TTI[a] (s)	PHRR[a] (kW/m^2)	THR[a] (MJ/m^2)	PSPR[a] (m^2/s)	TSP[a] (m^2)
EP/DA	37±2	642±16	57.0 ± 2.5	0.252±0.016	21.5 ± 0.2
EP/Cu-DA-1	49±4	415±19	49.4 ± 3.6	0.159±0.030	16.2 ± 0.3
EP/Cu-DA-2	53±5	397±20	46.9 ± 4.0	0.139±0.027	15.3 ± 0.2
EP/Cu-DA-3	51±4	356±11	43.1 ± 2.7	0.153±0.018	15.4 ± 0.2

[a] TTI: time to ignition; PHRR: peak heat release rate; THR: total heat release; PSPR: peak smoke production rate; and TSP: total smoke production.

obtained a UL-94 V-0 rating, ascribed to the phosphorus-containing groups in DA. All EP/Cu-DA thermosets achieved a UL-94 V-0 rating and exhibited modest increases in LOI values. Specifically, the LOI value for EP/Cu-DA-3 reached 37.8 %. Consequently, the EP/Cu-DA thermosets demonstrated enhanced fire safety due to the synergistic effect between metal- and phosphorus-containing groups.

Additionally, cone calorimeter testing was utilized to evaluate the heat and smoke release from EP thermosets during combustion. As detailed in Table 2 and Fig. 4b and c, the EP/DA thermoset, with 1.31 wt % phosphorus content, exhibited low PHRR and THR values of 642 kW/m^2 and 57.0 MJ/m^2, respectively. The incorporation of Cu-DA resulted in significant reductions in both PHRR and THR values relative to those of EP/DA. Notably, EP/Cu-DA-3, containing 1.50 wt% phosphorus and 0.77 wt% copper, achieved the lowest PHRR and THR values of 356 kW/m^2 and 43.1 MJ/m^2 among all EP thermosets, indicative of enhanced flame retardancy.

Besides PHRR and THR, FPI and FIGRA are pivotal in assessing material flammability. Typically, higher FPI and lower FIGRA values denote better flame retardancy [14,30]. As shown in Fig. 4d, EP/Cu-DA-3 demonstrated the highest FPI of 0.143 m^{2}s/kW and the lowest FIGRA of 2.4 kW/m^2/s, underscoring its superior flame retardancy. Generally, *Av*-EHC quantifies the combustion intensity of pyrolysis products in the gaseous phase [10]. The *Av*-EHC values for EP thermosets are presented in Fig. 4e. The EP/DA thermoset showed a low *Av*-EHC value of 21.3 MJ/kg due to the significant quenching effect of DA in the gaseous phase, while those of EP/Cu-DA thermosets further decreased by 11.7 %−19.7 %. Such decreases were attributed to the catalytic carbonization effect of Cu^{2+} during combustion, thereby limiting the release of pyrolysis products into the flame zone. Consequently, EP/Cu-DA thermosets had higher residue values compared to the EP/DA thermoset. Collectively, these findings suggested that Cu-DA effectively promoted carbonization, which in turn suppressed gaseous combustion.

In addition to burn fatalities, casualties from smoke suffocation and poisoning are common in fires, necessitating the assessment of smoke suppression in polymeric materials [30,31]. The smoke-suppressive capabilities of all EP thermosets were evaluated using cone calorimetry

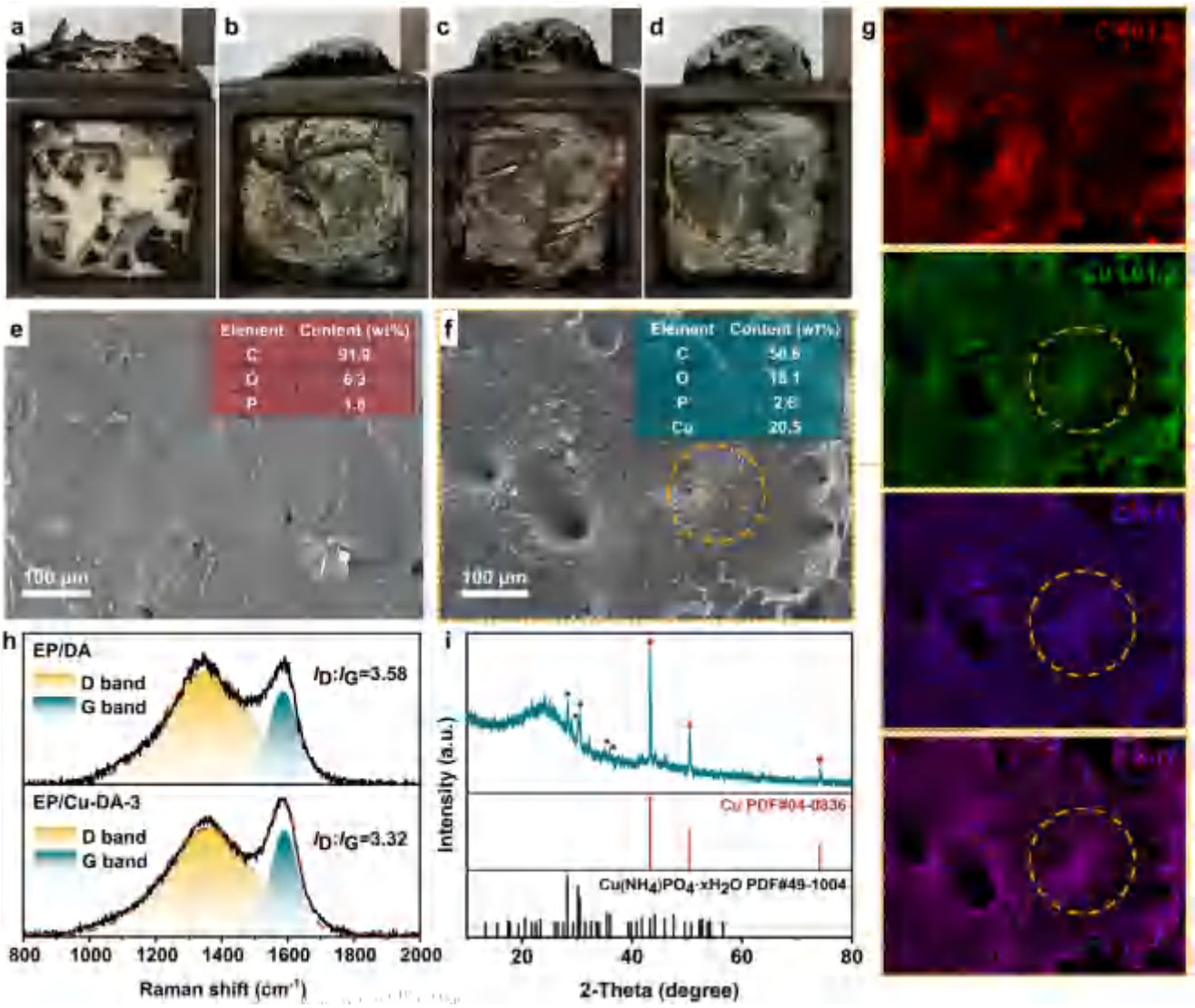


Fig. 5. (a) Digital photographs of (a) EP/DA, (b) EP/Cu-DA-1, (c) EP/Cu-DA-2, and (d) EP/Cu-DA-3 chars; SEM images of (e) EP/DA and (f) EP/Cu-DA-3 chars; (g) C, Cu, O and P elemental mappings of EP/Cu-DA-3 char; (h) Raman spectra of EP/DA and EP/Cu-DA-3 chars; and (i) XRD pattern of EP/Cu-DA-3 char after cone calorimetry.

and smoke density measurements, with findings presented in Fig. 4f-h. EP/Cu-DA thermosets exhibited significantly reduced PSPR and TSP values compared to the EP/DA thermoset. For example, the PSPR and TSP of the EP/Cu-DA-3 thermoset were reduced by 39.3 % and 28.4 %, respectively, relative to those of EP/DA thermoset. Curing with Cu-DA substantially lowered the MSD and SDR values of the EP thermoset. The EP/Cu-DA-3 thermoset demonstrated a 25.8 % decrease in MSD and a 44.6 % reduction in SDR compared to the EP/DA thermoset, showcasing its exceptional smoke suppression. Additionally, the av-COY values for EP/Cu-DA thermosets, ranging from 0.09 to 0.12 kg/kg, were lower than that of the EP/DA thermoset (0.14 kg/kg), suggesting that the copper element significantly contributed to the catalytic oxidation of toxic gases. In summary, EP/Cu-DA demonstrated superior flame retardancy and smoke suppression, with notable reductions in heat, smoke, and CO emissions.

3.5. Flame retardant mechanism

3.5.1. Condensed phase analysis

To clarify the action of Cu-DA in the condensed phase, the micro and macro morphologies and chemical compositions of residual chars from cone calorimetry were analyzed using digital camera, SEM, and EDS, as shown in Fig. 5. The digital photographs of EP/DA and EP/Cu-DA chars after cone calorimetry are displayed in Fig. 5a-d, and the SEM images of the external surfaces of EP/DA and EP/Cu-DA-3 chars are presented in Fig. 5e and f. The residual char from EP/DA thermoset had a compact structure, yet it was nearly completely combusted, as seen in Fig. 5a and e. This may be because the phosphorus group with a low oxidation state in DA primarily exerted flame-retardant effect in the gaseous phase, and its catalytic carbonization ability in the condensed phase was limited. The addition of metal elements compensated for the limited flame-retardant efficiency of DA in the condensed phase, significantly enhancing the carbonization capacities of EP/Cu-DA thermosets. For instance, the char residue from EP/Cu-DA-3 maintained excellent structural integrity and displayed a notable expansion structure with a height of 2 cm. The residual char also exhibited a greenish hue, indicative of the presence of copper element, as shown in Fig. 5d. In Fig. 5f, the external surface of the EP/Cu-DA-3 char was compact and continuous, which contributed to preventing the substrate from the flame. Furthermore, the surface of the residual char was adorned with dendritic crystals enriched with phosphorus, oxygen, and copper, which could improve the thermal stability of the char, as illustrated in Fig. 5g. The

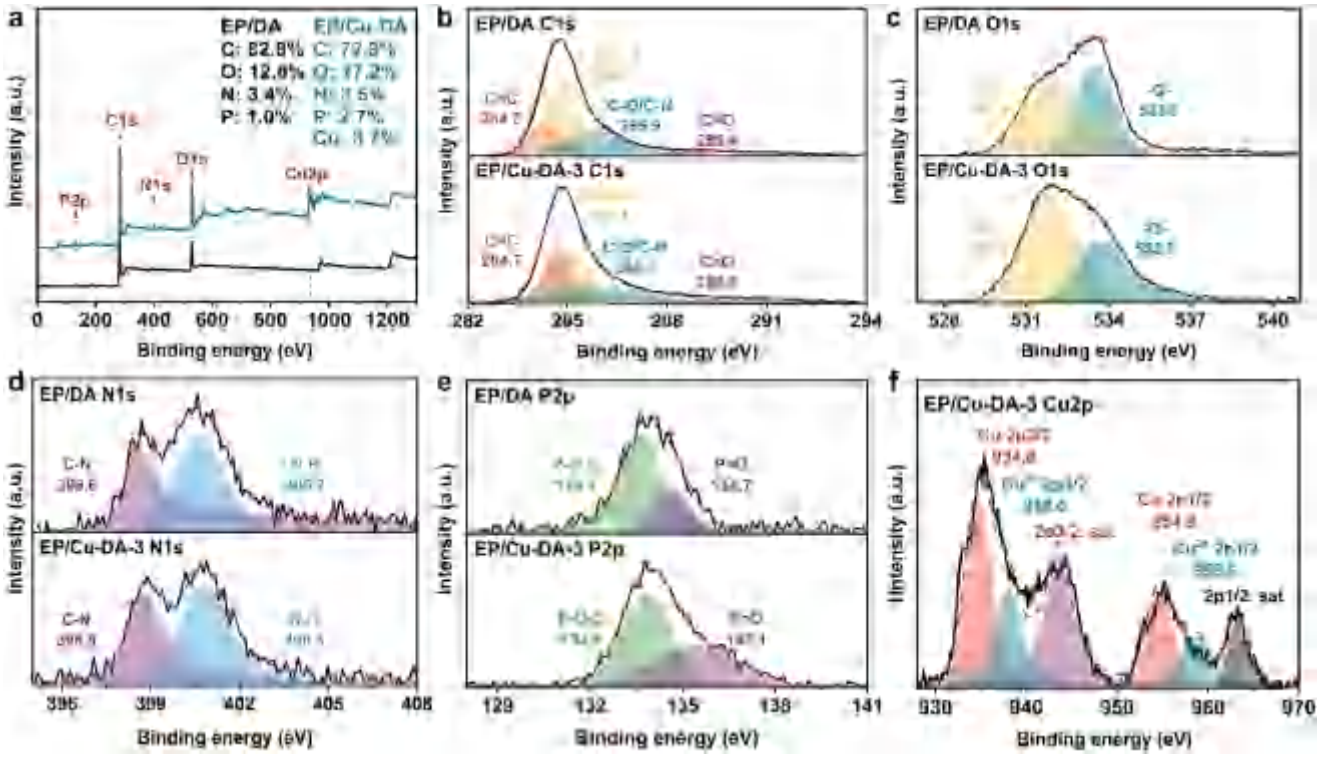


Fig. 6. (a) Full-scan XPS spectra of EP/DA and EP/Cu-DA-3 residues; high-resolution (b) C1s, (c) O1s, (d) N1s and (e) P2p XPS spectra of EP/DA and EP/Cu-DA-3 residues; and (f) high-resolution Cu2p XPS spectrum of EP/Cu-DA-3 char;.

Raman spectra of both EP/DA and EP/Cu-DA-3 chars are shown in Fig. 5h. Both chars displayed the D and G peaks at 1358 and 1587 cm^{-1}, corresponding to the structures of disordered carbon and ordered graphite, respectively [8,40]. A higher area ratio of the D peak to G peak (I_D/I_G) indicated a lower degree of graphitization [56]. The I_D/I_G of EP/Cu-DA-3 char was lower than that of EP/DA char, indicating a higher degree of graphitization and greater thermal stability.

Based on the XRD patterns presented in Fig. 5i, two copper-

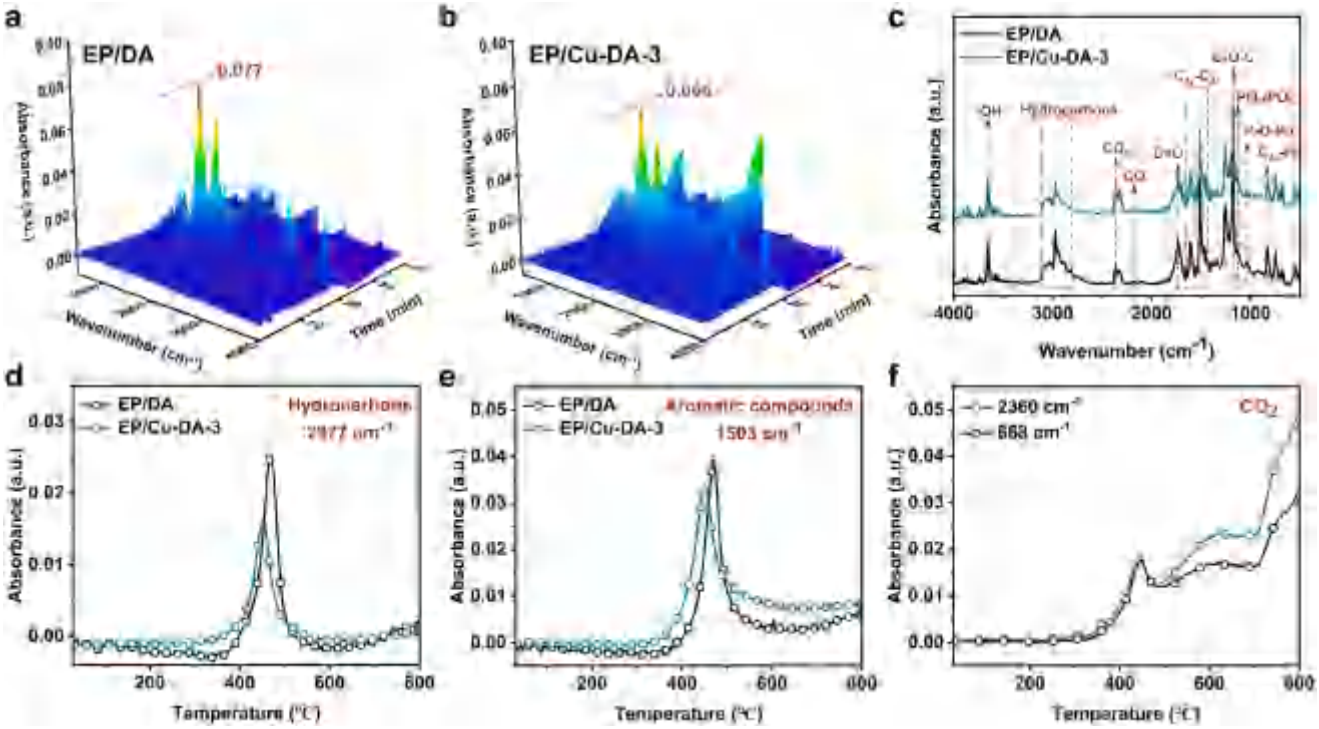


Fig. 7. 3D TG-FTIR spectra of volatiles derived from the decomposition of (a) EP/DA and (b) EP/Cu-DA-3 thermosets; (c) FTIR spectra of the volatiles for EP/DA and EP/Cu-DA-3 thermosets at T_{max}; absorbance vs. temperature curves of EP/DA and EP/Cu-DA-3 thermosets at (d) 2977 and (e) 1503 cm^{-1}; and (f) absorbance vs. temperature curves of EP/Cu-DA-3 thermoset at 2360 and 668 cm^{-1}.

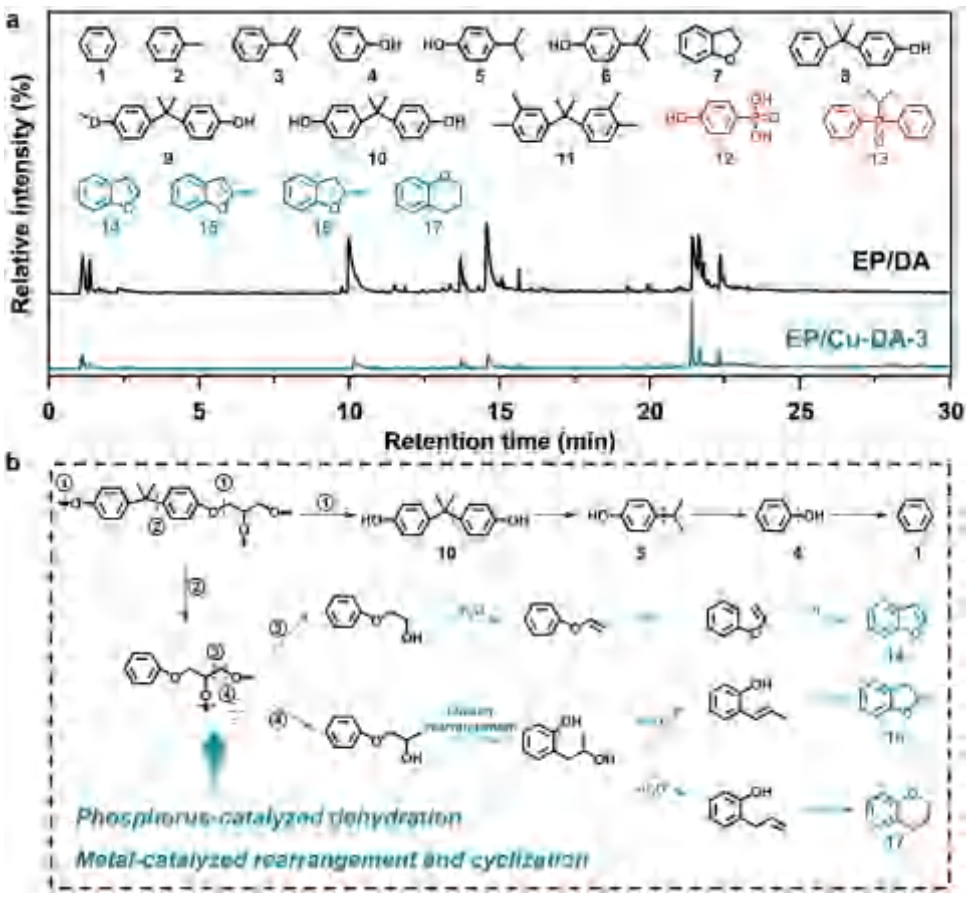


Fig. 8. (a) Total ion chromatograms (TIC) and supposed pyrolysis products, and (b) proposed thermal decomposition pathways of EP/DA and EP/Cu-DA-3 thermosets.

containing compounds, $Cu(NH_4)PO_4{\cdot}xH_2O$ and Cu, were generated following the combustion of the EP/Cu-DA-3 thermoset. During burning, some Cu^{2+} were reduced to Cu_2O or Cu by reductive gases like CO and NO, while some Cu could be re-oxidized to Cu^{2+} by air and volatile products from EP degradation [52]. Fig. 6 displays the XPS spectra for the chars of EP/DA and EP/Cu-DA-3. In Fig. 6a, the detection of copper in the EP/Cu-DA-3 residue signified that copper from Cu-DA contributed to carbonization during combustion. This observation was consistent with the EDS results, further supporting the condensed-phase role of Cu-DA. The C1s spectra for both chars showed four distinct peaks at 284.5, 285.0, 286.0, and 289.5 eV, corresponding to C=C, C-H/C-C, C-N/C-O, and C=O bonds, respectively (see Fig. 6b) [29]. In the O1s spectra, peaks around 531.8 and 533.6 eV were attributed to =O and -O- bonds (see Fig. 6c) [15]. The N1s spectra for each char revealed deconvoluted peaks at 398.7 and 400.8 eV, associated with C-N and N-H structures (see Fig. 6d) [41]. In Fig. 6e, the P2p spectra displayed peaks at 133.8 and 134.9 eV, corresponding to P-O-C and P=O bonds, respectively [10,15]. The Cu2p spectra of the residual char for EP/Cu-DA-3 indicated the presence of both Cu^{2+} and metallic Cu [52]. These changes in the states of copper further confirmed the occurrence of oxidation reactions catalyzed by Cu^{2+} during combustion. These results clearly demonstrated that during combustion, copper-based compounds formed from the pyrolysis of Cu-DA strengthened the condensed-phase flame-retardant effect of DA. They promoted the formation of a continuous and expanded char layer, which inhibited heat transfer and reduced smoke emission.

3.5.2. Gaseous phase analysis

The TG-FTIR analyses were conducted on EP/DA and EP/Cu-DA-3 thermosets to investigate the gaseous-phase flame-retardant action of Cu-DA, with the results shown in Fig. 7. As depicted in Fig. 7a-c, the primary volatile degradation products from both EP/DA and EP/Cu-DA-3 thermosets included water/phenol (3648 cm^{-1}), hydrocarbons (2798–3109 cm^{-1}), carbon dioxide (2360 cm^{-1}), carbon monoxide (2167 cm^{-1}), carbonyl compounds (1726 cm^{-1}), aromatic compounds (1600, 1503, and 830 cm^{-1}), and esters (1174 cm^{-1}) [10,15]. This indicated that the thermal decomposition pathways for both thermosets were similar. Additionally, the presence of P=O absorption peak at 1127 cm^{-1} and P-O-Ph absorption peak at 1034 cm^{-1} in both EP/DA and EP/Cu-DA-3 provided evidence of the generation of phosphorus-containing segments in gaseous phase (see Fig. 7c) [56]. For EP/Cu-DA-3, it showed weaker absorption of hydrocarbons and aromatic compounds than EP/DA (see Fig. 7d and e), demonstrating that more hydrocarbons and aromatic compounds participated in the carbonization reaction during the combustion of EP/Cu-DA, thereby significantly enhancing flame retardancy and smoke suppression. EP/Cu-DA-3 showed a notable increase in the absorption intensity of carbon dioxide (2360 and 668 cm^{-1}) at 600–800 °C (see Fig. 7f). This increase was attributed to the catalytic oxidation effect of copper element at elevated temperatures, promoting the complete combustion of pyrolysis products and the production of carbon dioxide. Within the high-temperature combustion zone, copper element facilitated the full combustion of soot through catalytic oxidation, reducing the amount of smoke particles.

To further elucidate the smoke inhibition behaviors of Cu-DA, pyrolysis-gas chromatography/mass spectrometry (Py-GC/MS) tests were conducted on EP/DA and EP/Cu-DA-3 thermosets. The cleavage products from the chromatogram are shown in Fig. 8a. The pyrolysis products of both thermosets included aromatic compounds and their derivatives (No. 1–7) at the initial pyrolysis stage (retention time:

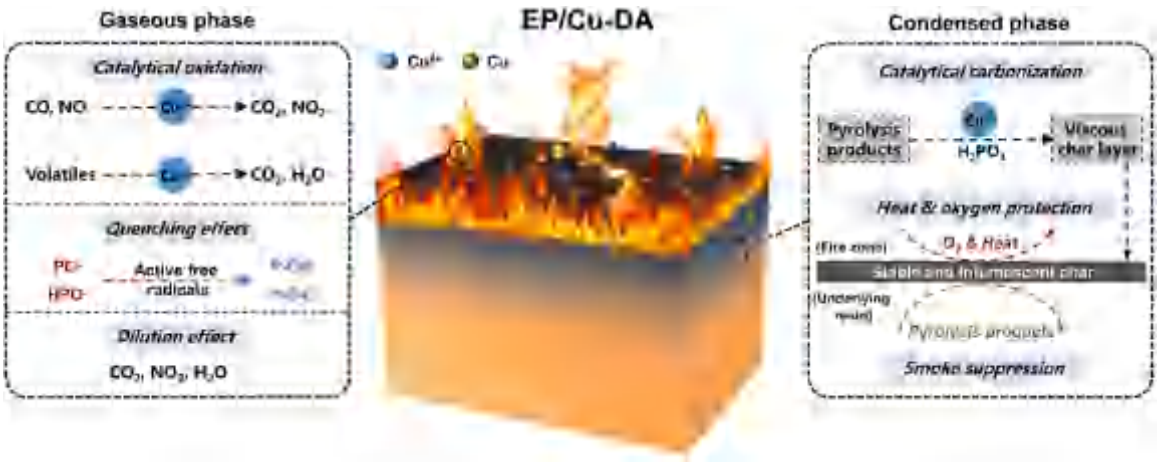


Fig. 9. Proposed flame-retardant action of EP/Cu-DA.

1.6–23.0 min), and bisphenol A and its derivatives (No. 8–11) at the retention time of 23.2–25.0 min. Additionally, P-containing compounds (No. 12 and 13) were detected in both EP/DA and EP/Cu-DA-3 thermosets. Unlike the EP/DA thermoset, the pyrolysis process of EP/Cu-DA thermoset revealed the presence of many fused heterocyclic compounds (No. 14–17). These unique fragments were attributed to the further rearrangement and cyclization of pyrolyzed epoxy segments (see Fig. 8b) [1]. Thus, it was deduced that the presence of Cu-DA promoted the cyclization and rearrangement of EP during pyrolysis under the catalysis of copper-containing groups, contributing to further carbonization rather than releasing volatile products into the gaseous phase.

Based on the above analyses, it was found that the superb fire-safety and smoke-suppression performances of EP/Cu-DA were attributed to the synergistic effect between metal- and phosphorus-containing groups in bi-phase. The flame-retardant action of Cu-DA is proposed in Fig. 9. In gaseous phase, Cu^{2+} promoted the conversion of toxic gases such as CO and NO into CO_2 and NO_2 through catalytic oxidation, thereby reducing the toxicity of the smoke. Additionally, the presence of Cu^{2+} facilitated the further oxidation of volatile organic compounds, producing CO_2 and water. The inert gases generated during the catalytic process, such as CO_2, NO_2, and H_2O, acted as diluents to extinguish the flames. Simultaneously, phosphorus-containing groups decomposed to release phosphorus-containing free radicals. These radicals could quench high-energy free radicals produced during the combustion of the matrix, thereby terminating the chain combustion reactions. In the condensed phase, the catalytic dehydration effect of phosphoric acid, along with catalytic rearrangement and cyclization functions of copper, jointly promoted the carbonization of the matrix, accelerating the formation of a dense and stable char layer. This layer provided excellent thermal and oxidative protection to the underlying matrix and effectively inhibited the release of pyrolysis products into the gas phase. The combined effects of the protective char layer, the reduction in the concentration of flammable gases, and the significant decrease of volatile combustibles, resulted in a signficant improvement in the flame retardancy and smoke suppression of EP/Cu-DA.

4. Conclusion

In summary, to enhance the flame retardancy and smoke suppression of single-component EP, a phosphorus-containing metal complex (Cu-DA) was synthesized through the coordination reaction between copper (II) chloride and DA. EP/Cu-DA system featured temperature-dependent curing behaviors, which can be stored at room temperature for 43 days and cross-linked rapidly at elevated temperatures. The obtained EP/Cu-DA thermoset achieved enhanced thermal stability relative to the control EP system, confirmed by a glass transition temperature of 160.9 °C and an 43 % increase of crosslinking density. Notably, Cu-DA enabled EP thermoset to realize superior flame retardancy and smoke suppression, as evidenced by a high LOI of 37.8 % and a UL-94 V-0 rating. The PHRR, THR, PSPR, TSP, MSD and SDR values were reduced by 44.5 %, 24.4 %, 39.3 %, 28.4 %, 25.8 % and 44.6 %, respectively. During burning, Cu^{2+} facilitated the oxidation of toxic gases and organic volatiles, effectively reducing the toxic components and smoke generation in the gaseous phase. Additionally, phosphorus-containing free radicals generated during pyrolysis captured high-energy free radicals, hindering the combustion process. Concurrently, the synergistic catalytic effect of phosphates and metal ions promoted the formation of a stable char layer, acting as an efficient barrier and significantly suppressing flue gas emissions. This research presents a viable approach for tackling the challenges of limited shelf life, and inadequate flame retardancy and smoke suppression in single-component epoxy resins.

CRediT authorship contribution statement

Jingsheng Wang: Writing – original draft, Investigation. **Jun Wang:** Funding acquisition. **Shuang Yang:** Project administration, Methodology. **Chaoqun Wu:** Supervision. **Xi Chen:** Data curation. **Kaiwen Chen:** Data curation. **Pingan Song:** Funding acquisition. **Hao Wang:** Supervision, Methodology. **Siqi Huo:** Writing – review & editing.

Declaration of competing interest

The authors declare that they have no known competing financial interests or personal relationships that could have appeared to influence the work reported in this paper.

Data availability

Data will be made available on request.

Acknowledgements

We gratefully acknowledge the financial support provided by the Major Program (JD) of Hubei Province (2023BAA028), the Australian Research Council (DE230100616 and DP240102628), and the Nonmetallic Excellence and Innovation Center (24PHD-4). Additionally, we would like to express our sincere appreciation to Shiyanjia Lab (www.shiyanjia.com) for their invaluable contributions to the Py-GC/MS tests.

Supplementary materials

Supplementary material associated with this article can be found, in the online version, at doi:10.1016/j.polymdegradstab.2024.110906.

References

[1] S.Q. Huo, P.A. Song, B. Yu, S.Y. Ran, V.S. Chevali, L. Liu, Z.P. Fang, H. Wang, Phosphorus-containing flame retardant epoxy thermosets: recent advances and future perspectives, Prog. Polym. Sci. 114 (2021) 101366, https://doi.org/10.1016/j.progpolymsci.2021.101366.

[2] O. Dagdag, A. El Bachiri, O. Hamed, R. Haldhar, C. Verma, E. Ebenso, M. El Gouri, Dendrimeric Epoxy Resins Based on Hexachlorocyclotriphosphazene as a reactive flame retardant polymeric materials: a review, J. Inorg. Organomet. Polym. Mater. 31 (8) (2021) 3240–3261, https://doi.org/10.1007/s10904-021-01900-x.

[3] Y. Kim, J.J. Baek, K.C. Chang, H.S. Lim, M. Choi, W. Koh, G. Shin, Influence of Thiol-functionalized Polysilsesquioxane/Phosphorus flame-retardant blends on the flammability and thermal, mechanical, and volatile organic compound (VOC) emission properties of epoxy resins, Polymers (Basel) 16 (6) (2024) 842, https://doi.org/10.3390/polym16060842, 10.1016/j.polymdegradstab.2024.110673.

[4] M. Zhi, X. Yang, R. Fan, S. Yue, L. Zheng, Q. Liu, Y. He, A comprehensive review of reactive flame-retardant epoxy resin: fundamentals, recent developments, and perspectives, Polym. Degrad. Stab. 201 (2022) 109976, https://doi.org/10.1016/j.polymdegradstab.2022.109976.

[5] C. Wang, S.Q. Huo, G.F. Ye, B.T. Wang, Z.H. Guo, Q. Zhang, P.A. Song, H. Wang, Z. T. Liu, Construction of an epoxidized, phosphorus-based poly(styrene butadiene styrene) and its application in high-performance epoxy resin, Compos. Pt. B-Eng. 268 (2024) 111075, https://doi.org/10.1016/j.compositesb.2023.111075.

[6] A. Aljamal, G. Marosi, B. Szolnoki, The utilization of phytic acid as a reactive flame retardant in the preparation of a fully waterborne biobased epoxy system, Fire Mater 48 (4) (2024) 508–521, https://doi.org/10.1002/fam.3199.

[7] J. Sag, D. Goedderz, P. Kukla, L. Greiner, F. Schoenberger, M. Doering, Phosphorus-containing flame retardants from biobased chemicals and their application in polyesters and epoxy resins, Molecules 24 (20) (2019) 3746, https://doi.org/10.3390/molecules24203746.

[8] X. Song, H. Lv, M. Shi, Z. Shao, Y. Wang, Calcium gluconate-based flame retardant towards simultaneously high-efficiency fire safety and mechanical enhancement for epoxy resin, Int. J. Biol. Macromol. 264 (Pt 1) (2024), https://doi.org/10.1016/j.ijbiomac.2024.130409, 130409-130409.

[9] G.F. Ye, S.Q. Huo, C. Wang, Q. Zhang, B.T. Wang, Z.H. Guo, H. Wang, Z.T. Liu, Fabrication of flame-retardant, strong, and tough epoxy resins by solvent-free polymerization with bioderived, reactive flame retardant, Sustain. Mater. Technol. 39 (2024) e00853, https://doi.org/10.1016/j.susmat.2024.e00853.

[10] J.S. Wang, J. Wang, S. Yang, K.W. Chen, Single-component flame-retardant and smoke-suppressive epoxy resins enabled by an aluminum/phosphorus/imidazole-containing complex, Compos. Pt. B-Eng. 253 (2023) 133778, https://doi.org/10.1016/j.compositesb.2023.110571.

[11] Y.F. Fang, B.A. Ma, K. Wei, X.Q. Wang, X.X. Kang, F.S. Liu, Performance of single-component epoxy resin for crack repair of asphalt pavement, Constr. Build. Mater. 304 (2021) 124625, https://doi.org/10.1016/j.conbuildmat.2021.124625.

[12] P.B. Zhang, S.A.A. Shah, F. Gao, H. Sun, Z.C. Cui, J. Cheng, J.Y. Zhang, Latent curing epoxy systems with reduced curing temperature and improved stability, Thermochim. Acta 676 (2019) 130–138, https://doi.org/10.1016/j.tca.2019.03.022.

[13] A.J. Ma, Q.Y. Zhang, H.P. Zhang, Y.Q. Shi, Y. Liu, A novel single component epoxy resin adhesive with microcapsule latent curing agent of 2-phenylimidazole/poly-methyl acrylic glycidyl ester, J. Elastomers Plast. 47 (5) (2015) 439–448, https://doi.org/10.1177/0095244313516888.

[14] J.W. Cheng, J. Wang, S. Yang, Q.Q. Zhang, S. Huo, Q.X. Zhang, Y. Hu, G.P. Ding, Benzimidazolyl-substituted cyclotriphosphazene derivative as latent flame-retardant curing agent for one-component epoxy resin system with excellent comprehensive performance, Compos. Pt. B-Eng. 177 (2019) 107440, https://doi.org/10.1016/j.compositesb.2019.107440.

[15] J.S. Wang, J. Wang, S. Yang, X. Chen, K.W. Chen, G. Zhou, X. Liu, L. Xu, S.Q. Huo, P.G. Song, H. Wang, Multifunctional phosphorus-containing imidazoliums endowing one-component epoxy resins with superior thermal latency, heat resistance, mechanical properties, and fire safety, Chem. Eng. J. 485 (2024) 149852, https://doi.org/10.1016/j.cej.2024.149852.

[16] P.L. Zheng, H.H. Zhao, Q.Y. Liu, P/N synergistic integrated flame retardants with instant cross-linking at high-temperature for flame retardancy and impact resistance of epoxy resins, Polym. Degrad. Stab. 225 (2024) 110817, https://doi.org/10.1016/j.polymdegradstab.2024.110817.

[17] J.S. Wang, S.Q. Huo, J. Wang, S. Yang, K.W. Chen, C. Li, D. Fang, Z.P. Fang, P. A. Song, H. Wang, Green and facile synthesis of bio-based, flame-retardant, latent imidazole curing agent for single-component epoxy resin, ACS Appl. Polym. Mater. 4 (5) (2022) 3564–3574, https://doi.org/10.1021/acsapm.2c00138.

[18] S.Q. Huo, S. Yang, J. Wang, J.W. Cheng, Q.Q. Zhang, Y.F. Hu, G.P. Ding, Q. X. Zhang, P.G. Song, H. Wang, A liquid Phosphaphenanthrene-derived imidazole for improved flame retardancy and smoke suppression of epoxy resin, ACS Appl. Polym. Mater. 2 (8) (2020) 3566–3575, https://doi.org/10.1021/acsapm.0c00577.

[19] Y.X. Xu, J.J. Wang, W.B. Zhang, S.Q. Huo, Z.P. Fang, P.A. Song, D. Wang, H. Wang, A phosphaphenanthrene-benzimidazole derivative for enhancing fire safety of epoxy resins, React. Funct. Polym. 180 (2022) 105390, https://doi.org/10.1016/j.reactfunctpolym.2022.105390.

[20] M.Z. Chai, L. Liu, P.B. Zhang, Y.D. Huang, Long shelf life, intrinsically flame retardant, transparent, high-performance one-component epoxy resin based on phosphorus-containing imidazole derivatives, Polym. Degrad. Stab. 218 (2023) 110587, https://doi.org/10.1016/j.polymdegradstab.2023.110587.

[21] Y.Q. Shi, T. Fu, Y.J. Xu, D.F. Li, X.L. Wang, Y.Z. Wang, Novel phosphorus-containing halogen-free ionic liquid toward fire safety epoxy resin with well-balanced comprehensive performance, Chem. Eng. J. 354 (2018) 208–219, https://doi.org/10.1016/j.cej.2018.08.023.

[22] W. Wang, G. Chen, S.L. Wu, Y. Liu, Q. Wang, Solvent-free synthesis of phosphate-containing imidazole fluid for flame retardant one-component epoxy resin with long pot life, low curing temperature and fast curing rate, J. Appl. Polym. Sci. 140 (8) (2023) e53509, https://doi.org/10.1002/app.53509.

[23] M. Toan, J.W. Park, H.J. Kim, S. Shin, Synthesis and characterization of a new phosphorus-containing furan-based epoxy curing agent as a flame retardant, Fire Mater 43 (6) (2019) 717–724, https://doi.org/10.1002/fam.2723.

[24] S.Y. Zhu, T.T. Zheng, F. Li, L. Wang, Q.R. Jiang, Y. Wei, W.S. Liu, Synthesis of cyclotriphosphazene-containing imidazole as a thermally latent hardener for epoxy resins and its application in carbon fiber reinforced composites, J. Appl. Polym. Sci. 139 (41) (2022) 52980, https://doi.org/10.1002/app.52980.

[25] J.S. Wang, X. Chen, J. Wang, S. Yang, K.W. Chen, L. Zhu, S.Q. Huo, P.A. Song, H. Wang, High-performance, intrinsically fire-safe, single-component epoxy resins and carbon fiber reinforced epoxy composites based on two phosphorus-derived imidazoliums, Polym. Degrad. Stab. 208 (2023) 110261, https://doi.org/10.1016/j.polymdegradstab.2023.110261.

[26] Y.J. Xu, L. Chen, W.H. Rao, M. Qi, D.M. Guo, W. Liao, Y.Z. Wang, Latent curing epoxy system with excellent thermal stability, flame retardance and dielectric property, Chem. Eng. J. 347 (2018) 223–232, https://doi.org/10.1016/j.cej.2018.04.097.

[27] Y.J. Xu, J. Wang, Y. Tan, M. Qi, L. Chen, Y.Z. Wang, A novel and feasible approach for one-pack flame-retardant epoxy resin with long pot life and fast curing, Chem. Eng. J. 337 (2018) 30–39, https://doi.org/10.1016/j.cej.2017.12.086.

[28] Y.J. Xu, X.H. Shi, J.H. Lu, M. Qi, D.M. Guo, L. Chen, Y.Z. Wang, Novel phosphorus-containing imidazolium as hardener for epoxy resin aiming at controllable latent curing behavior and flame retardancy, Compos. Pt. B-Eng. 184 (2020) 107673, https://doi.org/10.1016/j.compositesb.2019.107673.

[29] Y. Xu, J. Wang, Y. Tan, M. Qi, L. Chen, Y. Wang, A novel and feasible approach for one-pack flame-retardant epoxy resin with long pot life and fast curing, Chem. Eng. J. 337 (2018) 30–39, https://doi.org/10.1016/j.cej.2017.12.086.

[30] E. Movahedifar, H. Vahabi, M.R. Saeb, S. Thomas, Flame retardant epoxy composites on the road of innovation: an analysis with flame retardancy index for future development, Molecules 24 (21) (2019) 3964, https://doi.org/10.3390/molecules24213964.

[31] K.P. Song, Y.T. Pan, J. Zhang, P.A. Song, J.Y. He, D.Y. Wang, R.J. Yang, Metal-organic frameworks-based flame-retardant system for epoxy resin: a review and prospect, Chem. Eng. J. 468 (2023) 143653, https://doi.org/10.1016/j.cej.2023.143653.

[32] W.L. Chen, Y. Jiang, R. Qiu, W. Xu, Y.B. Hou, Investigation of UiO-66 as flame retardant and its application in improving fire safety of polystyrene, Macromol. Res. 28 (1) (2020) 42–50, https://doi.org/10.1007/s13233-019-7165-6.

[33] W.Z. Xu, G.S. Wang, J.Y. Xu, Y.C. Liu, R. Chen, H.Y. Yan, Modification of diatomite with melamine coated zeolitic imidazolate framework-8 as an effective flame retardant to enhance flame retardancy and smoke suppression of rigid polyurethane foam, J. Hazard. Mater. 379 (2019) 120819, https://doi.org/10.1016/j.jhazmat.2019.120819.

[34] W.F. Tang, H.M. Zhang, T. Liu, X.L. Li, H. Yang, W.Z. Huang, Y.H. Liao, X.Y. Gu, S. Zhang, Improving the flame retardancy and smoke suppression of ethylene vinyl acetate composites by introducing the hybrid material of Zn/TiO2@AKaol, Polym. Degrad. Stab. 221 (2024) 110673, https://doi.org/10.1016/j.polymdegradstab.2024.110673.

[35] J.W. Li, H.H. Zhao, H.Y. Liu, J.C. Sun, J. Wu, Q.Y. Liu, Y. Zheng, P.L. Zheng, Recent advances in metal-family flame retardants: a review, RSC Adv 13 (33) (2023) 22639–22662, https://doi.org/10.1039/d3ra03536k.

[36] X.B. Chen, Z.Y. Ma, J.G. Zhou, J.T. Wang, X.R. Zhang, R.L. Zhao, J.H. Tong, Thermal degradation characteristics of styrene-butadiene-styrene copolymer asphalt binder filled with an inorganic flame-retarding agent, Polymers (Basel) 14 (18) (2022) 3761, https://doi.org/10.3390/polym14183761.

[37] Z. Li, Z.D. Qin, C.X. Li, G.M. Zhang, A.Z. Zhang, S.S. Li, G.Q. Liang, X. Wang, W. F. Tang, Fabrication of NiO and TiO_2supported nano calcium carbonate and its effect on the flame retardancy and thermal stability of epoxy resin composites, Polym. Degrad. Stab. 210 (2023) 110296, https://doi.org/10.1016/j.polymdegradstab.2023.110296.

[38] J.B. Song, Y.X. Zhang, J. Wang, C. Gu, J.H. Hu, P.H. Yin, X.L. Shi, J. Feng, Self-assembly Fe-Co MOF@BN and epoxy resin nano composites with highly enhanced flame retardancy and smoke suppression properties, Polym. Degrad. Stab. 225 (2024) 110811, https://doi.org/10.1016/j.polymdegradstab.2024.110811.

[39] D.D. Yang, Y. Hu, H.P. Xu, L.P. Zhu, Catalyzing carbonization of organophilic alpha-zirconium phosphate/acrylonitrile-butadiene-styrene copolymer nanocomposites, J. Appl. Polym. Sci. 130 (5) (2013) 3038–3042, https://doi.org/10.1002/app.39224.

[40] T. Sai, Y.K. Su, H.F. Shen, S.Y. Ran, S.Q. Huo, Z.H. Guo, Z.P. Fang, Fabrication and mechanism study of cerium-based P, N-containing complexes for reducing fire hazards of polycarbonate with superior thermostability and toughness, ACS Appl. Mater. Interfaces 13 (25) (2021) 30061–30075, https://doi.org/10.1021/acsami.1c07153.

[41] R.K. Jian, F.Q. Pang, Y.C. Lin, W.B. Bai, Facile construction of lamellar-like phosphorus-based triazole-zinc complex for high-performance epoxy resins, J. Colloid Interface Sci. 609 (2022) 513–522, https://doi.org/10.1016/j.jcis.2021.11.054.
[42] E. Gallo, B. Schartel, U. Braun, P. Russo, D. Acierno, Fire retardant synergisms between nanometric Fe2O3 and aluminum phosphinate in poly(butylene terephthalate), Polym. Adv. Technol 22 (12) (2011) 2382–2391, https://doi.org/10.1002/pat.1774.
[43] W. Xu, X. Wang, Y. Wu, W. Li, C. Chen, Functionalized graphene with Co-ZIF adsorbed borate ions as an effective flame retardant and smoke suppression agent for epoxy resin, J. Hazard. Mater. 363 (2019) 138–151, https://doi.org/10.1016/j.jhazmat.2018.09.086.
[44] S. Huo, S. Yang, J. Wang, J. Cheng, Q. Zhang, Y. Hu, G. Ding, Q. Zhang, P. Song, A liquid phosphorus-containing imidazole derivative as flame-retardant curing agent for epoxy resin with enhanced thermal latency, mechanical, and flame-retardant performances, J. Hazard. Mater. 386 (2020) 121984, https://doi.org/10.1016/j.jhazmat.2019.121984.
[45] B. Yang, Y.Y. Mao, Y.H. Zhang, G.F. Bian, L.Y. Zhang, Y. Wei, Q.R. Jiang, Y.P. Qiu, W.S. Liu, A novel liquid imidazole-copper (II) complex as a thermal latent curing agent for epoxy resins, Polymer (Guildf) 178 (2019) 121586, https://doi.org/10.1016/j.polymer.2019.121586.
[46] J. Brown, I. Hamerton, B.J. Howlin, Preparation, characterization, and thermal properties of controllable metal-imidazole complex curing agents for epoxy resins, J. Appl. Polym. Sci. 75 (2) (2000) 201–217, https://doi.org/10.1002/(sici)1097-4628(20000110)75:2.
[47] A. Omrani, L.C. Simon, A.A. Rostami, M. Ghaemy, Study on curing mechanism of DGEBA/nickel-imidazole system, Thermochim. Acta 468 (1–2) (2008) 39–48, https://doi.org/10.1016/j.tca.2007.11.016.
[48] R. Yan, X. Gao, W. He, R. Guo, R.N. Wu, Z.Z. Zhao, H.Y. Ma, A simple and convenient method to fabricate new types of phytic acid-metal conversion coatings with excellent anti-corrosion performance on the iron substrate, RSC Adv 7 (65) (2017) 41152–41162, https://doi.org/10.1039/c7ra06186b.
[49] S.H. Sumrra, A. Suleman, Z.H. Chohan, M.N. Zafar, M.A. Raza, T. Iqbal, Triazole metal based complexes as antibacterial/antifungal agents, Russ. J. Gen. Chem. 87 (6) (2017) 1281–1287, https://doi.org/10.1134/s107036321706024x.
[50] G.A. Sundaram, S. Kumaravelu, W.L. Tseng, P.V. Pham, A.S.K. Kumar, V. Parimelazhagan, Fine-tuned graphene oxide nanocomposite: harnessing Copper (II)-imidazole complex for enhanced biological responses and balanced photocatalytic functionality, Materials (Basel) 17 (4) (2024) 892, https://doi.org/10.3390/ma17040892.
[51] H. Lee, C. Kwon, C. Keum, H.E. Kim, H. Lee, B. Han, S.Y. Lee, Methane partial oxidation by monomeric Cu active center confined on ZIF-7, Chem. Eng. J 450 (2022) 138472, https://doi.org/10.1016/j.cej.2022.138472.
[52] J. Hong, T. Wu, X. Wang, Z. Lu, J. Zhang, B. Zeng, C. Yuan, L. Dai, Copper-catalyzed pyrolysis of halloysites@polyphosphazene for efficient carbonization and smoke suppression, Compos. Pt. B-Eng. 230 (2022) 109547, https://doi.org/10.1016/j.compositesb.2021.109547.
[53] R. Hardian, P. Pogany, Y.M. Lee, G. Szekely, Molecular sieving using metal-polymer coordination membranes in organic media, J. Mater. Chem. A 9 (25) (2021) 14400–14410, https://doi.org/10.1039/d1ta02601a.
[54] B.R. Pimentel, A. Parulkar, E.K. Zhou, N.A. Brunelli, R.P. Lively, Zeolitic imidazolate frameworks: next-generation materials for energy-efficient gas separations, ChemSusChem 7 (12) (2014) 3202–3240, https://doi.org/10.1002/cssc.201402647.
[55] J. Hu, J. Shan, Z. Tong, Curing kinetics of flame retardant epoxy resin promoted by imidazole grafting graphene oxide, Chem. J. Chinese Univ.-Chinese 38 (10) (2017) 1906–1912, https://doi.org/10.7503/cjcu20170059.
[56] J.H. Lu, Y.J. Xu, L. Chen, J.H. Chen, J.H. He, Z. Li, S.L. Li, Y.Z. Wang, Facile fabrication of intrinsically fire-safety epoxy resin cured with phosphorus-containing transition metal complexes for flame retardation, smoke suppression, and latent curing behavior, Chem. Eng. J. 442 (2022) 136097, https://doi.org/10.1016/j.cej.2022.136097.

Polymer Degradation and Stability 237 (2025) 111325

Contents lists available at ScienceDirect

Polymer Degradation and Stability

journal homepage: www.journals.elsevier.com/polymer-degradation-and-stability

Phosphorus-derived imidazolium salts with varied oxidation states: Tailoring latency, mechanical properties, and flame retardancy in single-component epoxy resins

Jingsheng Wang [a], Jun Wang [a], Shuang Yang [b,*], Guoping Ding [b], Renxin Xu [a], Wei Liu [c], Jiuxiao Sun [d], Kaiwen Chen [a], Liu Duan [a], Jiaqi Wang [a], Hao Wang [e], Siqi Huo [e,*]

[a] School of Materials Science and Engineering, Wuhan University of Technology, Wuhan 430070, China
[b] School of Mechanical and Electronic Engineering, Wuhan University of Technology, Wuhan 430070, China
[c] Bamstone New Material Technology Co. Ltd., Wuhan 430070, China
[d] School of Materials Science and Engineering, Wuhan Textile University, Wuhan 430070, China
[e] School of Engineering, Centre for Future Materials, University of Southern Queensland, Springfield 4300, Australia

ARTICLE INFO

Keywords:
Single-component epoxy resin
Phosphorus-derived imidazolium salt
Thermal latency
Flame retardancy
Mechanical property

ABSTRACT

Single-component epoxy resin (EP) is the premix of EP and latent curing agent, which is highly demanded in industries. However, current single-component EPs struggle to balance storage stability with mechanical properties and flame retardancy. To address this issue, three phosphorus-derived imidazolium salts (MPOx, x = 2, 3, 4) were synthesized using 2-ethyl-4-methylimidazole (EMI) and phosphorus-containing acids with different oxidation states (diphenylphosphinic acid, phenyl hydrogen phenylphosphonate, and diphenyl phosphate). The oxidation state of phosphorus significantly influenced thermal latency of MPOx, with higher oxidation states leading to improved latency. EP/MPO4 achieved the longest shelf life of 42 d at 25 °C. EP/MPO3 and EP/MPO4 exhibited enhanced tensile strength, modulus, and impact resistance compared to EP/EMI, but EP/MPO2 showed poor mechanical properties due to phase separation. All EP/MPOx achieved limiting oxygen index (LOI) exceeding 30 %, with EP/MPO3 showing the highest LOI of 34.0 % and significant reductions in heat release and smoke production. Flame-retardant mechanistic studies revealed a shift from gaseous-phase flame inhibition to condensed-phase promoting carbonization with increasing phosphorus oxidation state. Obviously, MPOx provides a tailored balance of latency, mechanical strength, and flame retardancy, making it a promising solution for advanced single-component EPs in aerospace, electronics, and optical applications.

1. Introduction

EPs are widely used in coatings, adhesives, electronics, and structural composites due to their excellent mechanical properties, thermal stability, and chemical resistance [1,2]. However, their inherent flammability and rapid heat release during combustion significantly limit their application in fields requiring high fire safety standards, such as aerospace, electronics, and construction [3,4]. To address these limitations, researchers have focused on incorporating flame retardants into epoxy resins [5,6]. Traditional halogenated flame retardants, though effective, release toxic and corrosive gases during combustion, posing environmental and health risks [7]. This has spurred interest in halogen-free flame retardants, particularly phosphorus-containing compounds, which exhibit excellent flame-retardant efficiency, low toxicity, and dual-phase flame-retardant mechanisms [8–10]. Phosphorus-based flame retardants function through two primary mechanisms: in the gaseous phase, they release phosphorus-containing radicals that quench high-energy free radicals during combustion; in the condensed phase, they promote the formation of char layers that act as thermal barriers to inhibit heat transfer and prevent further decomposition [11,12]. Importantly, reaction-type phosphorus-based flame retardants, where phosphorus-containing groups are chemically integrated into the resin molecular backbone, exhibit superior performance compared to additive flame retardants [8,13,14]. This chemical integration prevents issues such as leaching or migration of flame-retardant agents while enhancing the long-term stability and flame-retardant

* Corresponding authors.
E-mail addresses: ysfrp@whut.edu.cn (S. Yang), siqi.huo@unisq.edu.au, sqhuo@hotmail.com (S. Huo).

https://doi.org/10.1016/j.polymdegradstab.2025.111325
Received 19 January 2025; Received in revised form 9 March 2025; Accepted 10 March 2025
Available online 11 March 2025
0141-3910/© 2025 Elsevier Ltd. All rights are reserved, including those for text and data mining, AI training, and similar technologies.

efficiency of the cured resin [15]. Developing such flame retardants that not only improve fire safety but also contribute to the structural stability of epoxy resins remains a critical area of research.

The synthesis of latent curing agents is central to the development of single-component epoxy resins, which are highly valued for their extended shelf life, simplified processing, and enhanced storage stability [16,17]. Unlike two-component systems, where curing occurs immediately upon mixing, single-component EPs remain stable under ambient conditions and only cure upon heating [18,19]. Imidazole and its derivatives are widely recognized as highly efficient curing agents for EPs due to their ability to promote rapid anionic polymerization. However, the strong nucleophilicity of imidazole often leads to premature curing during storage, making it unsuitable for single-component systems [20,21]. To address this issue, researchers have focused on chemical modifications of imidazole at the 1- and 3-positions to suppress its nucleophilicity, leveraging electron-withdrawing effects, steric hindrance, or specific interactions with other molecules [22–24]. At the 1-position of imidazole, modifications typically involve introducing functional groups via substitution or addition reactions at the reactive secondary amine [25–27]. Common functional groups include alkyl, benzyl, acetyl, cyanoethyl, and epoxy, which reduce the reactivity of imidazole through steric hindrance or altered electronic properties. For example, alkylimidazoles exhibit reduced nucleophilicity due to the steric bulk of the alkyl chains, while cyanoethyl-imidazoles benefit from the electron-withdrawing nature of the cyano group, enhancing thermal latency [26–29]. At the 3-position of imidazole, modifications leverage the Lewis basicity of the tertiary amine nitrogen to undergo acid-base neutralization or coordination reactions [30,31]. For instance, neutralization with carboxylic acids (e.g., acetic acid, maleic acid, and citric acid) or coordination with transition metal salts (e.g., Zn^{2+}, Co^{2+}, and Cu^{2+}) has been used to create imidazole derivatives with suppressed reactivity and latent curing capabilities [25,32–34]. These tailored modifications not only enhance latency but also allow the introduction of specific functionalities, such as catalytic activity or flame retardancy.

Among these modification strategies, imidazolium salts formed by using imidazole and phosphorus-containing acids show distinct advantages. The acid-base neutralization process is rapid, simple, and environmentally friendly [30,31,35,36]. These salts serve as reaction-type curing agents, where the phosphorus groups are chemically integrated into the EP backbone during curing. This chemical bonding not only prevents the leaching of flame retardants, but also introduces intrinsic flame-retardant properties into the cured EP. Furthermore, the dual functionality of these salts—serving as latent curing agents and flame retardants—makes them highly attractive for the design of advanced single-component EPs [14,19,35]. Besides, the oxidation state of the phosphorus-containing acid used to synthesize imidazolium salts may theoretically influence both the curing behavior and flame-retardant performance of the resulting materials. For flame-retardant performance, it is well-established that phosphorus compounds with lower oxidation states (e.g., phosphinates) are more effective in the gaseous phase by releasing phosphorus radicals, and those with higher oxidation states (e.g., phosphates) are more effective in the condensed phase by promoting char formation [9,11]. Nevertheless, how the oxidation state of phosphorus affects the curing behavior of imidazolium salts remains uncertain. The electron-withdrawing ability of the phosphorus group may theoretically alter the reactivity of imidazole, potentially influencing curing kinetics.

In this work, we synthesized three phosphorus-derived imidazolium salts (MPOx, x = 2, 3, 4) by respectively reacting EMI with three phosphorus-containing acids, including diphenylphosphinic acid (PO2, oxidation state +1), phenyl hydrogen phenylphosphonate (PO3, oxidation state +3), and diphenyl phosphate (PO4, oxidation state +5). These salts were evaluated as flame-retardant latent curing agents for single-component epoxy resins, focusing on their curing behavior, thermal latency, optical properties, mechanical performance, and flame retardancy. Additionally, the influences of phosphorus oxidation state on the curing behavior and flame-retardant mechanism were systematically investigated through experimental analyses and density functional theory (DFT) calculations. By correlating structural variations with curing and flame-retardant behaviors, this work provides valuable insights into the design of high-performance single-component EPs with enhanced thermal latency, mechanical performance, and fire safety.

2. Materials and methods

2.1. Materials

Epoxy resin based on bisphenol A (E51) with an epoxy equivalent weight of 0.51 mol/100 g was supplied by Suzhou Senfeida Chemical Co., Ltd. (Jiangsu, China). Diphenylphosphinic acid (PO2), diphenyl phosphate (PO4), triethylamine, tetrahydrofuran, phenylphosphonic dichloride, dichloromethane, and ethanol were procured from Aladdin Industrial Co., Ltd. (Shanghai, China). 2-Ethyl-4-methylimidazole (EMI) and phenol were purchased from Macklin Biochemical Technology Co., Ltd. (Shanghai, China). Deionized water, used throughout the experimental procedures, was prepared on-site.

2.2. Synthesis of phenyl hydrogen phenylphosphonate (PO3)

The synthetic procedure for PO3 is outlined in Fig. S1a. In a nitrogen-purged 150 mL three-neck round-bottom flask equipped with a mechanical stirrer, reflux condenser, and dropping funnel, phenylphosphonic dichloride (9.8 g, 0.05 mol), triethylamine (TEA, 11.1 g, 0.11 mol), and tetrahydrofuran (THF, 50 mL) were added at ambient temperature. A solution of phenol (4.7 g, 0.05 mol) in THF (30 mL) was then introduced dropwise over a period of 1 hour with continuous stirring. The reaction mixture was kept at room temperature for 2 h before being heated to 75 °C, where it was maintained for an additional 5 h under stirring.

Subsequently, deionized water (1 g, 0.05 mol) was added gradually over 30 min, and the reaction mixture was left stirring overnight to ensure completion. After cooling to room temperature, the solid byproduct, triethylamine hydrochloride, was separated by filtration. The resulting filtrate was transferred to a rotary evaporator and subjected to vacuum distillation at 60 °C under reduced pressure to remove THF, yielding a viscous crude product. This crude product was then dissolved in 50 mL of dichloromethane with gentle stirring for 5 min to ensure complete dissolution. The resulting organic solution was transferred to a separatory funnel and washed three times with 30 mL deionized water to remove any residual water-soluble impurities. Each washing step involved vigorous shaking for 2 min, followed by a 5-min settling period to achieve clear phase separation. The organic layer was then collected and concentrated using a rotary evaporator at 35 °C under reduced pressure to remove dichloromethane. A yellow liquid product was obtained, identified as PO3, with a yield of 76 %. The chemical structure of PO3 was confirmed using Fourier transform infrared spectroscopy (FTIR), proton and phosphorus nuclear magnetic resonance (^{1}H and ^{31}P NMR). The corresponding spectra are displayed in Fig. S1b-d.

2.3. Synthesis of phosphorus-derived imidazolium salts (MPOx)

Phosphorus-derived imidazolium salts, denoted as MPOx (x = 2, 3, or 4), were synthesized via a straightforward self-assembly method in deionized water, using phosphorus-containing acids (PO2, PO3, or PO4) and 2-ethyl-4-methylimidazole (EMI) as the precursors, as illustrated in Fig. 1a.

The preparation of MPO2 was conducted as follows: PO2 (10.9 g, 0.05 mol), EMI (5.5 g, 0.05 mol), and 100 mL deionized water were added to a 150 mL three-neck round-bottom flask. The mixture was stirred continuously at 60 °C for 6 h. After the reaction was completed, the solvent was removed using rotary evaporation. The resulting

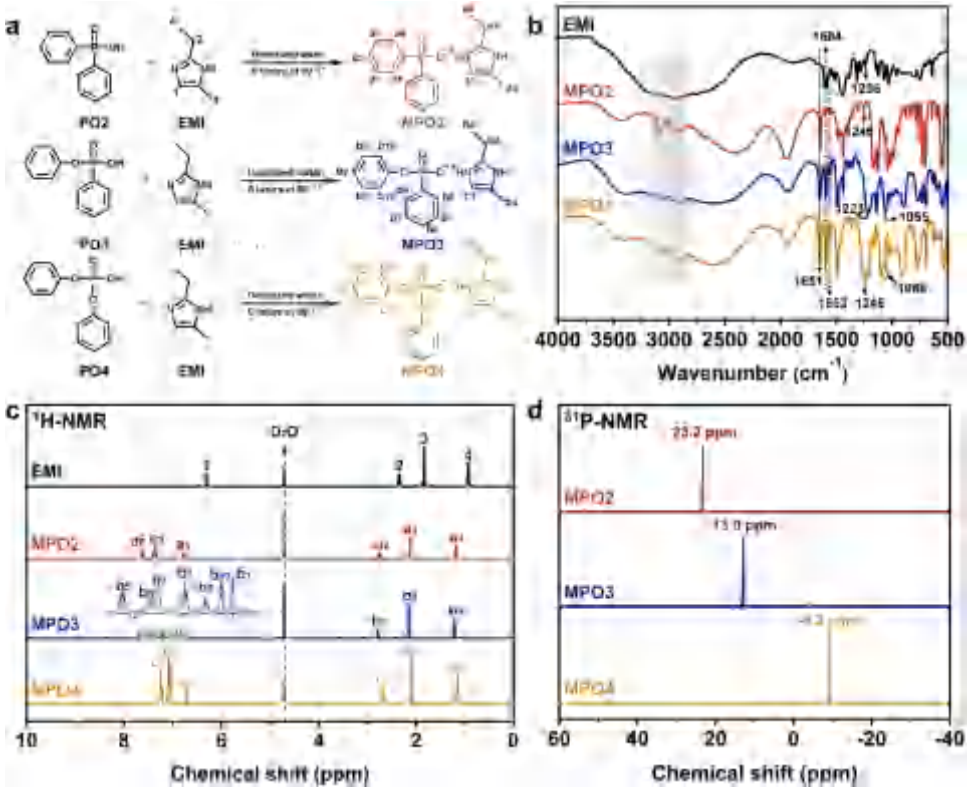


Fig. 1. (a) Synthesis pathway of MPOx (x = 1, 2, or 3); (b) FTIR spectra comparison between EMI and MPOx; and (c) ^{1}H and (d) ^{31}P NMR spectra of EMI and MPOx.

grayish-white powder was washed three times each with water and ethanol, followed by vacuum drying at 80 °C for 8 h. The final yield of MPO2 was 75 %.

For the preparation of MPO3 and MPO4, a similar procedure was followed, except PO2 was replaced by PO3 (11.7 g, 0.05 mol) or PO4 (12.5 g, 0.05 mol), respectively. The resulting products, MPO3 and MPO4, were yellow transparent liquids, with yields of 81 % and 78 %, respectively.

2.4. Preparation of EP thermosets

The compositions of the EP thermoset formulations are presented in Table 1. EP thermosets, labeled as EP/MPOx and EP/EMI, were prepared using MPOx and EMI as curing agents, respectively. These formulations were designed to explore the effect of phosphorus oxidation states in MPOx on the comprehensive performances of EP systems. Each system contains the same mass ratio of EMI to epoxy resin (6 g: 100 g) to keep imidazole content consistent. The similar molecular weights of MPOx variants ensure nearly equal phosphorus content. For the preparation of the EP/MPO2 mixture, to ensure uniformity, the synthesized MPO2 was finely ground and sieved through a 200-mesh sieve to obtain ultrafine powder. In contrast, MPO3 and MPO4, being ionic liquids, exhibited excellent solubility in the epoxy resin, eliminating the need for pre-grinding.

The procedure for fabricating EP/MPOx thermosets was as follows: MPOx was first mixed with the epoxy resin and stirred thoroughly at room temperature until a homogeneous solution was achieved. The mixture was then subjected to vacuum defoaming to remove trapped air and subsequently poured into a preheated mold for curing. The curing protocol for EP/MPOx involved heating at 80 °C for 1 h, followed by 120 °C for 2 h and 160 °C for 1 h. For EP/EMI, the preparation process was identical to that of EP/MPOx, except the curing schedule was adjusted to 80 °C for 2 h and 140 °C for 3 h.

2.4. Characterization

This section is in the Supporting Information.

3. Results and discussion

3.1. Characterizations of MPOx

The chemical structures of MPOx were thoroughly characterized using FTIR, as well as ^{1}H and ^{31}P NMR. The corresponding spectra are shown in Fig. 1b-d. As illustrated in the FTIR spectrum of EMI, characteristic absorption peaks appeared at 3079 cm^{-1} and 2850–3000 cm^{-1}, attributed to the stretching vibrations of =CH, -CH_2, and -CH_3 groups [14,29,37] (see Fig. 1b). Additionally, peaks at 1651, 1604, and 1250 cm^{-1} were assigned to the skeletal vibrations of the imidazole ring [14, 23,38]. After the incorporation of phosphorus-containing acid (POx), the FTIR spectra of all MPOx retained the characteristic absorption bands of EMI, corresponding to methyl, methylene, and the imidazole

Table 1
Formulations of EP thermosets.

Sample	EP (g)	EMI (g)	MPO2 (g)	MPO3 (g)	MPO4 (g)	Calculated P content (wt%)
EP/EMI	100	6	/	/	/	/
EP/MPO2	100	/	18	/	/	1.44
EP/MPO3	100	/	/	19	/	1.44
EP/MPO4	100	/	/	/	20	1.43

ring. New absorption bands around 3150 cm^{-1}, attributed to =CH vibrations in the benzene ring, confirmed the coexistence of EMI and POx groups in MPOx. Furthermore, the FTIR spectra of MPO3 and MPO4 exhibited distinct peaks at 1055 cm^{-1} and 1068 cm^{-1}, respectively, which were associated with the P-O-C stretching vibrations [15,35]. All MPOx also displayed a new absorption band at 1553 cm^{-1}, corresponding to the NH^{+} group [13,39], confirming the occurrence of a neutralization reaction between EMI and POx.

The ^{1}H NMR spectra of EMI and MPOx provided further evidence of structural changes (see Fig. 1c). For EMI, chemical shifts at 6.32, 2.34, 1.83, and 0.93 ppm were attributed to the protons of C═CH-, -CH_2-, =C—CH_3, and -CH_2-CH_3 groups, respectively. After reacting with POx, significant changes were observed in the ^{1}H NMR spectra of MPOx. The chemical shifts corresponding to benzene ring protons appeared between 6.87 and 7.69 ppm, indicating the incorporation of the phosphorus-containing acids. Due to protonation at the nitrogen atom in the imidazole ring, the signals for the imidazole hydrogen shifted downfield compared to EMI. For instance, the proton signal in EMI at 6.32 ppm shifted to 6.78, 6.82, and 6.71 ppm for MPO2, MPO3, and MPO4, respectively. This downfield shift can be attributed to the electron-withdrawing effect of the phosphorus-containing acids, which reduced the shielding effect of electrons around the hydrogen nucleus [13,40]. Moreover, the integral areas of the hydrogen signals in MPOx closely matched their theoretical values, further confirming the structures. ^{31}P NMR analysis showed a single phosphorus resonance for each MPOx at 23.2 ppm (MPO2), 13.0 ppm (MPO3), and -9.2 ppm (MPO4), indicating their high purity and successful synthesis (see Fig. 1d). In summary, the combined FTIR, ^{1}H NMR, and ^{31}P NMR results confirm that the neutralization reaction between EMI and POx successfully occurred, leading to the formation of the phosphorus-derived imidazoliums (MPOx).

3.2. Curing behaviors and thermal latency

The curing behaviors of EP/EMI and EP/MPOx mixtures were investigated using differential scanning calorimetry (DSC). The DSC curves and associated data are presented in Fig. 2a and Table S1. As shown in Fig. 2a, the EP/EMI mixture exhibited a single, symmetric exothermic peak at 119.8 °C, attributed to the addition and etherification reactions between the epoxy group and the secondary amine or imidazole ring of EMI [21,28]. However, the introduction of phosphorus-containing acids significantly altered the curing profiles of EP/MPOx mixtures. The DSC curves showed either two distinct exothermic peaks or an asymmetric profile, reflecting the complex curing behaviors caused by ionic complexation between MPOx and EMI. The peak curing temperatures (T_ps) shifted to 147.2 °C (EP/MPO2), 142.7 °C (EP/MPO3), and 152.0 °C (EP/MPO4), indicating the varying influence of phosphorus-containing acids with different oxidation states on EMI reactivity. Additionally, EP/MPO2 and EP/MPO3 exhibited second exothermic peaks at 171.9 °C and 162.3 °C, respectively. The elevated T_ps of EP/MPOx mixtures compared with EP/EMI highlighted the inhibitory effect of ionic interactions on EMI reactivity, a critical feature for enhancing the thermal latency of these curing systems.

To further investigate the curing mechanism of EP/MPOx mixtures, non-isothermal DSC analyses were performed on MPOx. All MPOx exhibited a single endothermic peak in the range of 75–200 °C, likely

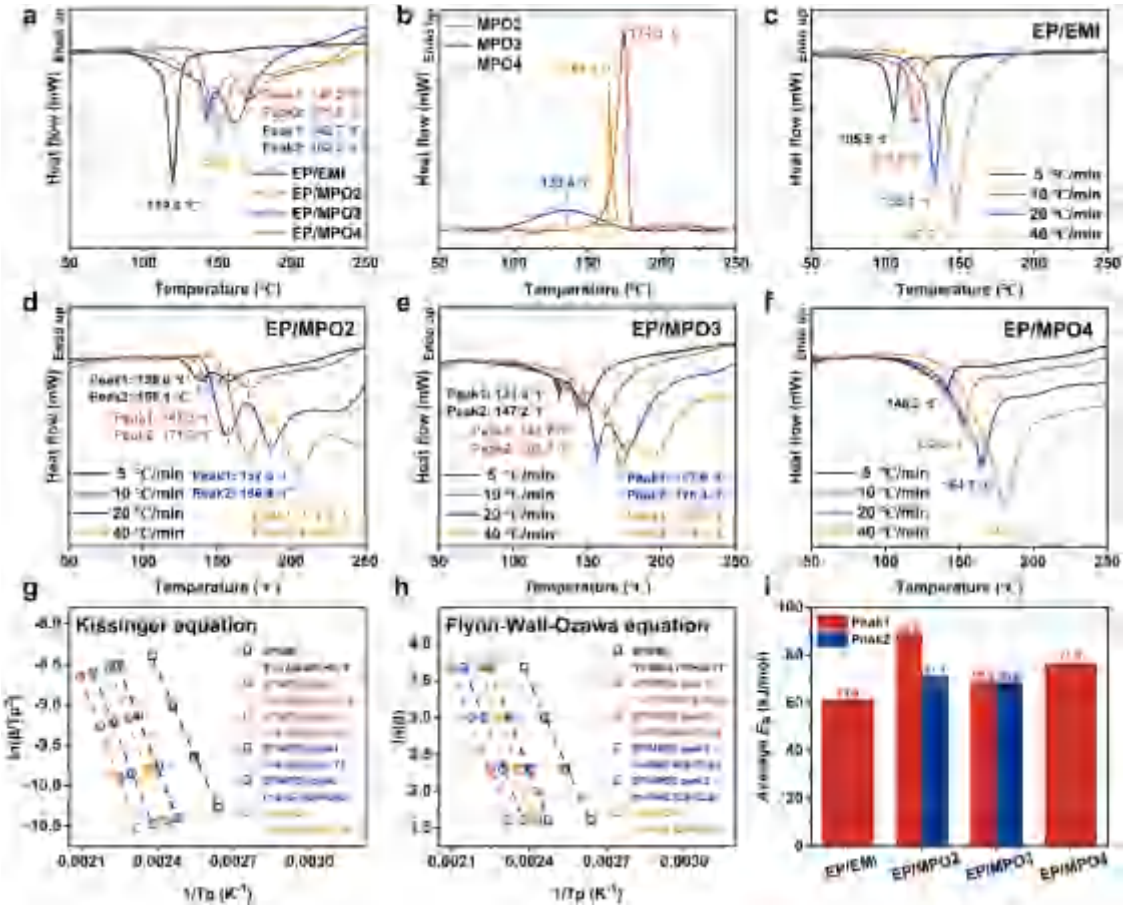


Fig. 2. Non-isothermal DSC curves of (a) EP mixtures and (b) MPOx at the heating rate (β) of 10 °C/min; non-isothermal DSC curves of (c) EP/EMI, (d) EP/MPO2, (e) EP/MPO3, and (f) EP/MPO4 mixtures with different heating rates; (g) linear fitting curves of $\ln(\beta/T_p^2)$ versus $1/T_p$ according to Kissinger equation; (h) linear fitting curves of $\ln(\beta)$ versus $1/T_p$ based on Flynn-Wall-Ozawa equation; and (i) apparent activation energies (E_as) of EP mixtures.

corresponding to melting or dissociation (see Fig. 2b). This endothermic transition aligns closely with the curing temperature range of EP/MPOx mixtures, indicating a direct relationship between MPOx dissociation and curing initiation. Changes in the chemical structure of MPOx during heating were analyzed using FTIR spectroscopy. The FTIR spectra at room temperature (RT) and 130 °C revealed that the NH^+ absorption peaks of MPOx decreased in intensity at 130 °C (see Fig. S2). The C=C bond, unaffected by temperature, served as an internal standard for comparing NH^+ peak areas. The ratio I_{NH+}: $I_{C=C}$ for MPO2 and MPO4 decreased from 0.08 to 0.18 at RT to 0.06 and 0.15 at 130 °C, respectively, while the NH^+ peak for MPO3 disappeared completely at 130 °C. This suggests that the ionic bonding between MPOx and EMI dissociated during heating, releasing free EMI and POx. The released EMI then participated in the crosslinking of epoxy resins, completing the curing process. Therefore, MPOx dissociation played a critical role in determining the curing activity.

To examine differences in curing activity among MPOx, non-isothermal DSC analyses at different heating rates were conducted for EP mixtures (see Fig. 2c-f). The curing kinetics were evaluated using the Kissinger, Crane, and Flynn-Wall-Ozawa models [41–43], with corresponding plots and kinetic parameters summarized in Fig. 2g-h and Table S2. The average activation energies (E_as) are shown in Fig. 2i. E_a, which reflects curing difficulty, revealed that EP/EMI had the lowest E_a of 61.8 kJ/mol among all EP mixtures. After introducing phosphorus-containing acids, E_a increased in the order of EP/MPO2 (peak 1: 88.9 kJ/mol; peak 2: 71.1 kJ/mol) > EP/MPO4 (76.9 kJ/mol) > EP/MPO3 (peak 1: 69.2 kJ/mol; peak 2: 68.8 kJ/mol). These elevated E_as further underscore the inhibitory effects of PO2, PO3, and PO4 on EMI reactivity. The results demonstrate that ionic coordination between EMI and phosphorus-containing acids suppresses the curing reactivity of imidazole groups, with suppression varying according to the oxidation state of the phosphorus-containing acid.

The viscosity changes of EP mixtures during heating were monitored using a dynamic rheometer, providing insights into gelation behavior and thermal latency, key metrics for single-component epoxy resins (see Fig. 3 and Table S3). Gelation temperature (T_v) and gelation time, corresponding to the crossover of storage modulus (G′) and loss modulus (G″) during rheological testing, serve as critical indicators of thermal latency [16]. A higher T_v and extended gelation time signify improved latency, enhancing storage stability and curing control. EP/EMI exhibited a low T_v of 110.1 °C, while EP/MPO2, EP/MPO3, and EP/MPO4 showed elevated T_v values of 180.3, 145.5, and 216.0 °C, respectively, reflecting enhanced thermal latency (see Fig. 3a-d). At 50 °C, simulating challenging storage conditions, EP/EMI gelled within 216 min, whereas EP/MPOx mixtures exhibited no significant viscosity change, demonstrating superior thermal latency (see Fig. 3e-h). At elevated temperatures, EP/MPO2 and EP/MPO3 rapidly gelled within 60 min at 120 °C, while EP/MPO4 required 78 min to gel at 140 °C, demonstrating efficient curing performance at higher temperatures (see Fig. 3i-k). Shelf-life monitoring at 25 °C revealed that EP/EMI exhibited a short shelf life of less than one day. In contrast, EP/MPO2, EP/MPO3, and EP/MPO4 extended shelf lives to 25, 11, and 42 days, respectively (see Fig. 3l). These results highlight the critical role of ionic coordination between POx and EMI in enhancing latency, as MPOx remained inert at low temperatures but effectively initiated curing at elevated temperatures, making them suitable latent curing agents for single-component epoxy systems.

Based on DSC and rheological tests, the curing activity and thermal latency of MPOx varied with the oxidation state of phosphorus-containing acids, following the order of EP/MPO4 > EP/MPO2 > EP/MPO3 for latency improvement. To explore the underlying mechanism, density functional theory (DFT) calculations were performed to examine the electron density fields and electrostatic potentials (ESP) of EMI and MPOx. ESP analysis revealed that tertiary amine nitrogen atoms in EMI and MPOx are regions of high negative charge density, susceptible to electrophilic attack (see Fig. 4a). Additionally, the molecular interaction energy (E_{int}) of MPOx increased with the oxidation state of phosphorus-containing groups: MPO2 (+1, -18.43 kJ/mol) > MPO3 (+3, -21.60 kJ/mol) > MPO4 (+5, -45.04 kJ/mol). The higher oxidation states of phosphorus-containing groups resulted in greater negative charge

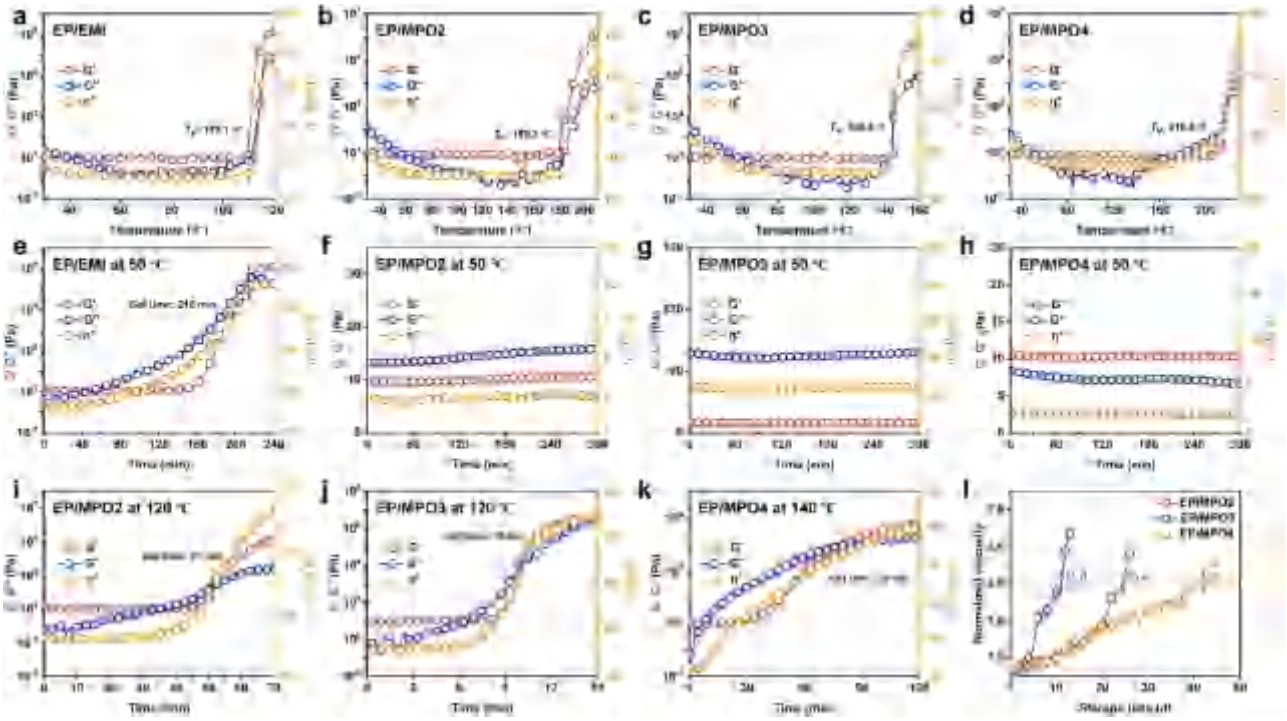


Fig. 3. Temperature-dependent curves of storage modulus (G′), loss modulus (G″), and complex viscosity (η*) for (a) EP/EMI, (b) EP/MPO2, (c) EP/MPO3, and (d) EP/MPO4 mixtures; time-dependent G′, G″, and η* plots at 50 °C for (e) EP/EMI, (f) EP/MPO2, (g) EP/MPO3, and (h) EP/MPO4 mixtures; time-dependent G′, G″, and η* plots at 120 or 140 °C for (i) EP/MPO2, (j) EP/MPO3, and (k) EP/MPO4 mixtures; and (l) normalized viscosity curves for EP/MPOx mixtures during storage.

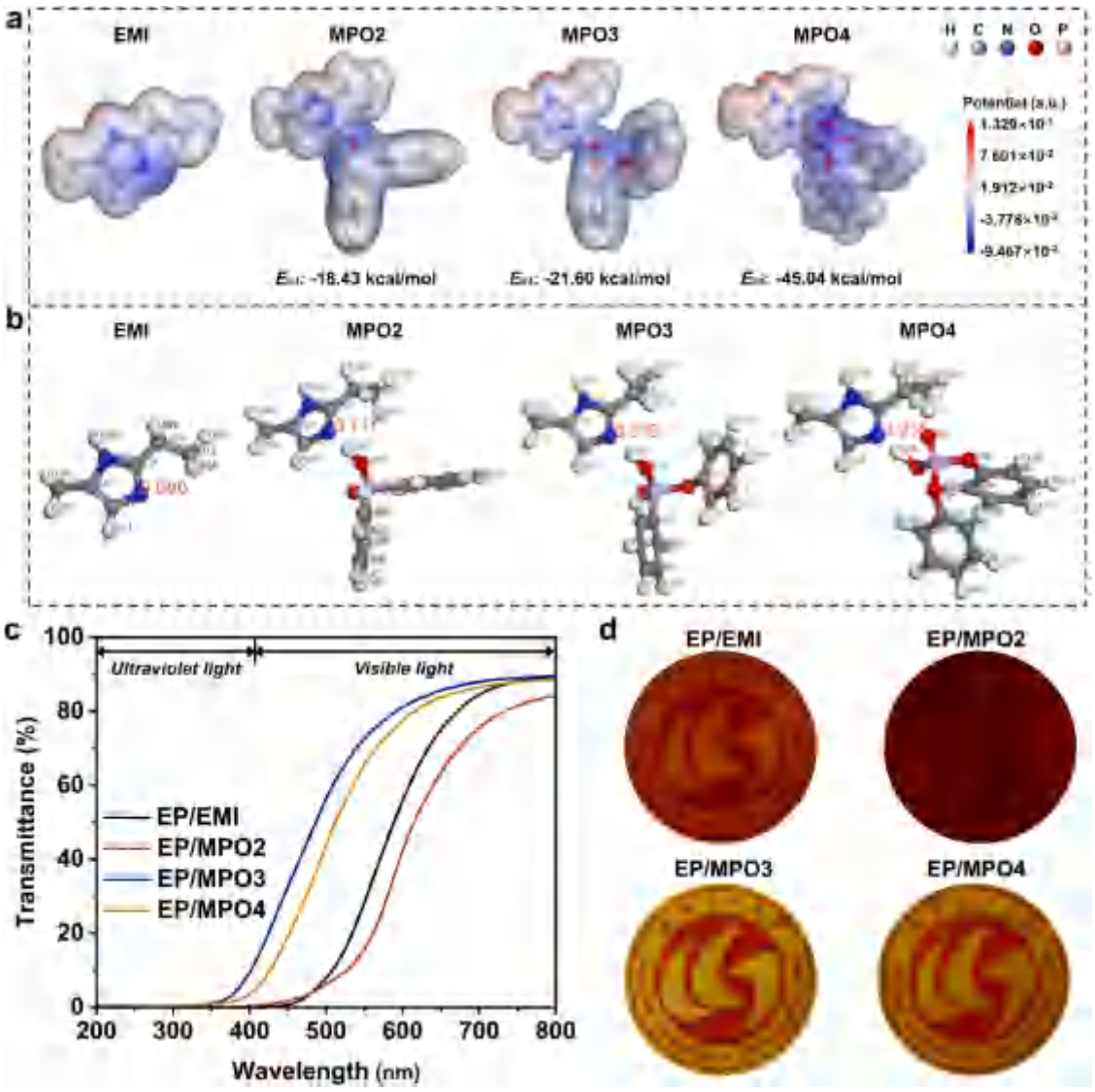


Fig. 4. (a) Calculated electrostatic potentials (ESPs) and interaction energies (E_{int}s) of EMI and MPOx; (b) electrophilic attack indices of atoms in EMI and MPOx; (c) ultraviolet-visible (UV–Vis) transmission spectra; and (d) digital photographs of EP/EMI and EP/MPOx films (thickness: 1.5 ± 0.1 mm).

density, enhancing ionic bond strength with EMI. Moreover, higher oxidation states facilitated stronger hydrogen bonding, further increasing intermolecular interactions. The Fukui function analysis of electrophilic attack indices indicated that the high electrophilic attack indices (highlighted in red) were localized on the tertiary amine nitrogen atoms in EMI and MPOx, indicating their strong electron-donating capability. This property is critical for initiating anionic polymerization of epoxy resins. The indices decreased for MPO3 and MPO4 (0.018 and 0.014, respectively) compared to EMI (0.080), reflecting reduced nucleophilic activity due to the electron-withdrawing effect of phosphorus-containing groups (see Fig. 4b). By contrast, the electrophilic attack index for MPO2 not only did not decrease but increased to 0.111, suggesting stronger nucleophilic activity. The difference between MPO2 and MPO3 or MPO4 may arise from the lower electron-withdrawing ability of PO2 compared to PO3 and PO4. Additionally, the conjugation between the phosphorus atom, two phenyl groups, and oxygen atoms in MPO2 may allow electron density to be partially distributed onto the imidazole ring, increasing the electron density on the tertiary amine nitrogen atom.

Based on the DFT calculation results, EP/MPO2 was expected to exhibit the highest curing activity among all EP systems. However, DSC and rheological results revealed that, compared to EP/EMI, EP/MPO2 demonstrated an extended latency of 25 days and exhibited higher T_p and T_v. This discrepancy may stem from the fact that theoretical calculations do not account for the aggregated state of the curing agents, which affects curing activity. As the only solid curing agent, MPO2 exhibited distinct phase separation with EP. This physical steric hindrance greatly suppressed its curing activity, requiring sufficient energy or time to dissolve MPO2 into EP and overcome physical isolation to initiate curing. In contrast, EMI, MPO3, and MPO4, as liquids with good compatibility with EP, readily initiated curing upon effective collisions. Their curing activity positively correlated with their electrophilic attack indices, following the trend that imidazolium salts with higher oxidation states of phosphorus-containing groups exhibited lower curing activity. These findings suggest that the introduction of phosphorus-containing acids significantly suppresses EMI curing activity due to their electron-withdrawing effects or steric hindrance effects, influencing MPOx curing behavior. Moreover, the suppression varies with the oxidation state of phosphorus-containing acids and the physical state of the resulting imidazolium salts. This provides a valuable basis for designing advanced single-component epoxy systems with tailored latency profiles.

3.3. Optical properties

Single-component epoxy resins are widely utilized in the field of electronic packaging, where their transparency is a critical performance metric. To evaluate the impact of MPOx on the optical properties of epoxy thermosets, ultraviolet-visible spectroscopy and digital imaging were employed. As shown in Fig. 4c, the transmittances of EP/MPO3 and EP/MPO4 films at 800 nm reached approximately 90 %, comparable to that of EP/EMI. Notably, in the visible light region (400–800 nm), EP/MPO3 and EP/MPO4 films exhibited a broad transmittance range exceeding 80 %, indicating their excellent visible light transparency. This high transmittance can be attributed to the good compatibility between EP and MPO3 or MPO4. In contrast, EP/MPO2 exhibited significantly lower transmittance in the visible light region compared to EP/EMI. Furthermore, all EP/MPOx films demonstrated strong UV-shielding capabilities, as evidenced by the low transmittance observed in the ultraviolet region (200–400 nm). This UV protection is likely due to the absorption of UV light by the benzene and imidazole groups present in MPOx. The UV-shielding capability of EP/MPOx offers significant advantages for applications such as protective coatings for UV-sensitive electronics, packaging materials for light-sensitive pharmaceuticals, and outdoor structural components requiring enhanced durability under prolonged UV exposure. The digital photos of EP/MPOx films are presented in Fig. 4d, where the emblems beneath the EP/MPO3 and EP/MPO4 films are clearly visible, further confirming their high transparency and compatibility with EP. However, for the EP/MPO2 film, the emblem underneath is barely discernible, and its transparency is noticeably reduced compared to EP/EMI. Additionally, some particulate dispersed phases were observed in EP/MPO2 films, likely caused by poor compatibility between MPO2 and EP, leading to aggregation. Overall, EP/MPO3 and EP/MPO4 exhibited excellent visible light transparency and significant UV protection, making them highly promising for applications in electronic packaging and optical devices.

3.4. Thermal properties

The thermal stability of EP samples was assessed via thermogravimetric analysis (TGA) under both nitrogen and air atmospheres. The TGA and derivative TG (DTG) curves, along with the data, are shown in Fig. 5 and Table S4. Under nitrogen conditions, all samples exhibited a one-step degradation process. The temperature at 5 % weight loss ($T_{5\ \%}$) and temperature at maximum degradation rate (T_{max}) of EP/MPOx were lower than those of EP/EMI (see Fig. 5a, b and Table S4), primarily due to the inferior thermal stability of the phosphorus-containing groups in MPOx [15,19]. Notably, higher oxidation states of MPOx resulted in further decreases in $T_{5\ \%}$ and T_{max}, indicating poorer thermal stability. Additionally, the maximum degradation rates (R_{max}) of EP/MPOx were significantly reduced compared to EP/EMI (e.g., EP/EMI: 21.4 %/min; EP/MPO2: 16.4 %/min; EP/MPO3: 14.1 %/min; EP/MPO4: 15.5 %/min). This reduction can be attributed to the phosphorus-containing groups promoting the formation of stable char layers. Correspondingly, the char yield at 800 °C (*CY*) for EP/MPOx increased by 1–2 times compared to EP/EMI. Particularly, higher oxidation states of phosphorus in MPOx led to improved charring ability, with EP/MPO4 achieving the highest *CY* of 23.3 wt% (see Table S4). This demonstrates that the P-derived groups in MPOx significantly enhance char formation, with higher oxidation states being more effective. Under air conditions, all samples experienced a two-stage decomposition process, involving the degradation of the network followed by the decomposition of char residues at elevated temperatures (see Fig. 5c and d). Similar to the results under nitrogen, $T_{5\ \%}$, T_{max1}, and T_{max2} for EP/MPOx were slightly lower than those of EP/EMI, consistent with the lower thermal stability of MPOx. Additionally, R_{max} values for EP/MPOx were much lower than that for EP/EMI due to the formation of protective char residues catalyzed by the phosphorus-containing groups. The *CY* values of EP/MPO2, EP/MPO3, and EP/MPO4 under air conditions were 7.2, 9.9, and 10.0 wt%, respectively, further highlighting the superior char-forming ability of MPOx, particularly those with higher oxidation states.

Dynamic mechanical analysis (DMA) was performed to evaluate the thermomechanical properties of EP thermosets, with results shown in Fig. 5e, f and summarized in Table S5. At 50 °C, all EP/MPOx samples exhibited higher storage modulus (*E'*) compared to EP/EMI, indicating the formation of a more rigid and stable network structure. Specifically, *E'* values increased by 14.9 % (for EP/MPO2), 4.0 % (for EP/MPO3), and 30.5 % (for EP/MPO4) relative to EP/EMI (see Fig. 5e). EP/MPO2 and EP/MPO3 also achieved higher glass transition temperatures (T_g) of 145.4 °C and 143.8 °C, respectively, exceeding 138.0 °C for EP/EMI (see

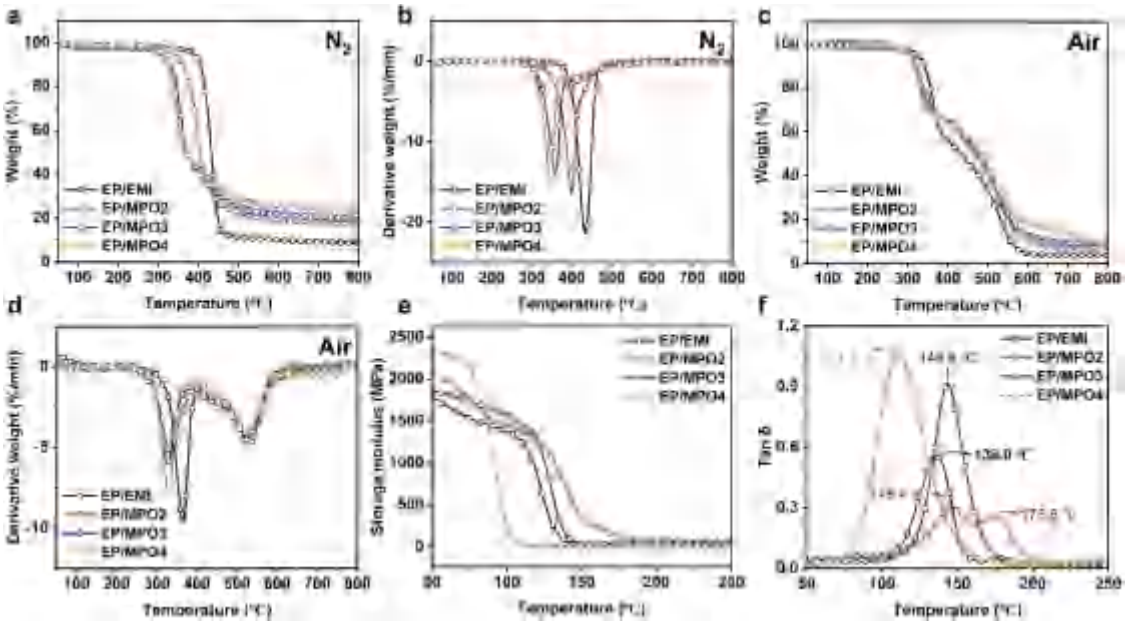


Fig. 5. TGA curves under (a) N_2 and (c) air atmosphere; DTG curves in (b) N_2 and (d) air conditions; (e) storage modulus (*E'*) plots; and (f) Tanδ curves of EP thermosets.

Fig. 5f). Interestingly, EP/MPO2 displayed an additional peak in the Tanδ curve at 175.5 °C, likely due to aggregated MPO2. However, EP/MPO4 exhibited a significant reduction in T_g, dropping to 111.1 °C, despite having the highest E' at 50 °C. This behavior could be attributed to the molecular interactions within the EP/MPO4 network. The high oxidation state of PO4 groups, with more oxygen atoms and higher negative charge density, enhances ionic bonding with imidazolium ions and hydrogen bonding with epoxy resins, leading to increased mechanical rigidity at lower temperatures. However, at elevated temperatures, these ionic and hydrogen bonds are easily overcome, and the rotational freedom of the P-O-C bonds in MPO4 increases molecular flexibility. This allows greater segmental motion within the polymer network, resulting in a lower T_g. In summary, incorporating MPOx significantly improved the char-forming ability of EP thermosets, with higher oxidation states of phosphorus enhancing this effect. Additionally, EP/MPO2 and EP/MPO3 demonstrated superior heat resistance and mechanical rigidity, while EP/MPO4 exhibited reduced thermal stability but the highest rigidity at lower temperatures. These findings reflect the diverse effects of phosphorus-containing compounds with varying oxidation states on the thermal stability and mechanical performance of EP thermosets.

3.5. Mechanical properties

The tensile, flexural, and unnotched impact properties of EP/EMI and EP/MPOx thermosets were analyzed systematically, with results summarized in Fig. 6 and Table S6. As shown in Fig. 6a and c, the EP/EMI thermoset displayed a tensile strength and modulus of 58.1 MPa and 2663 MPa, respectively. However, EP/MPO2 exhibited a 35.5 % reduction in tensile strength compared to EP/EMI, which could be attributed to stress concentrations caused by the aggregation of MPO2 particles in the epoxy matrix. In contrast, the tensile performance of EP/MPO3 and EP/MPO4 was significantly improved. In particular, EP/MPO4 achieved a tensile strength of 87.0 MPa and a tensile modulus of 3378 MPa, representing increases of 49.7 % and 26.8 % relative to EP/EMI. Similar enhancements were observed in flexural properties (see Fig. 6b and d). Both EP/MPO3 and EP/MPO4 exhibited higher flexural strength and modulus compared to EP/EMI. Notably, EP/MPO4 achieved the highest values, with a flexural strength of 130.3 MPa and a modulus of 3573 MPa, corresponding to increases of 31.2 % and 22.3 %, respectively. Additionally, EP/MPO3 and EP/MPO4 thermosets demonstrated improved toughness, evidenced by greater elongation at break and impact strength than EP/EMI (see Fig. 6e and Table S6). For instance, EP/MPO4 exhibited a 65.5 % higher elongation at break and a 74.7 % improvement in impact strength compared to EP/EMI. Conversely, EP/MPO2 showed reduced toughness due to poor compatibility between MPO2 and the epoxy resin.

The enhanced mechanical properties of EP/MPO3 and EP/MPO4 can be attributed to two main factors. First, the introduction of rigid benzene rings in MPOx contributed to increased stiffness and strength. Second, ionic bonds between POx and EMI were reestablished in the crosslinked network of the cured resin, as reported in previous studies on phosphorus-containing imidazolium salts [13,35]. These ionic bonds dissipated energy under external forces, thereby improving both the strength and toughness of the thermosets [30]. Collectively, the mechanical performance of EP thermosets was significantly influenced by MPOx. While MPO2 led to performance degradation due to its poor dispersion, MPO3 and MPO4 notably enhanced tensile, flexural, and impact properties. Among them, EP/MPO4 exhibited the most balanced performance, making it a promising material for applications requiring both mechanical strength and toughness. These results underscore the importance of phosphorus acid structures in tuning the mechanical behavior of epoxy systems.

3.6. Flame retardancy and smoke suppression

To evaluate the flame-retardant performance of MPOx, limiting oxygen index (LOI) and vertical burning (UL-94) tests were performed on EP/EMI and EP/MPOx systems, with results summarized in Table 2. EP/EMI exhibited poor flame resistance, as indicated by its low LOI value of 20.5 %. Additionally, in the UL-94 test, EP/EMI burned intensely and failed to self-extinguish, resulting in no rating. In contrast, the EP/MPOx thermosets showed notable improvements in flame retardancy. Both EP/MPO2 and EP/MPO3 achieved V-0 ratings, while EP/MPO4 attained a V-1 rating. Furthermore, all EP/MPOx thermosets had LOI values exceeding 30 %, with EP/MPO3 achieving the highest LOI at 34.0 %. These results suggest that the incorporation of MPOx effectively enhanced the flame retardancy of EP thermosets.

To further investigate the combustion behavior, cone calorimetry was conducted to measure heat and smoke release. The results,

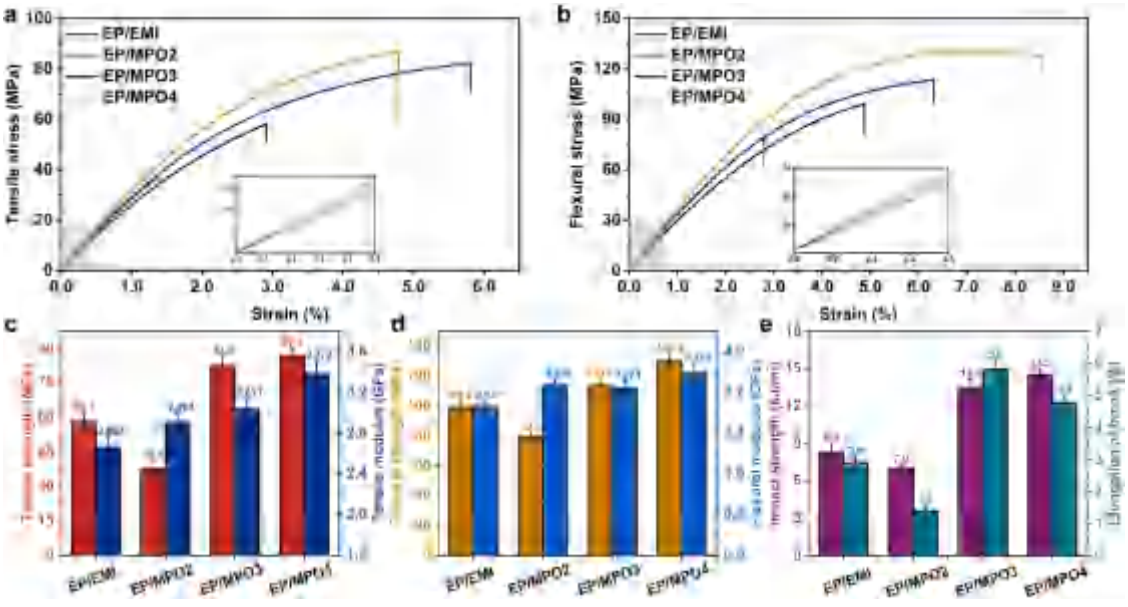


Fig. 6. (a) Tensile stress-strain curves; (b) flexural stress-strain curves; (c) tensile strength and modulus values; (d) flexural strength and modulus values; and (e) impact strength and elongation at break for EP thermosets.

Table 2
The combustion parameters of EP thermosets.

Sample	LOI (%)	UL-94 rating	TTI [a] (s)	PHRR [a] (kW/m^2)	THR [a] (MJ/m^2)	PSPR [a] (m^2/s)	TSP [a] (m^2)
EP/EMI	20.5	NR	40 ± 2	1018 ± 39	76.8 ± 4.8	0.431 ± 0.036	32.1 ± 0.3
EP/MPO2	33.5	V-0	44 ± 2	710 ± 36	60.1 ± 4.6	0.443 ± 0.029	32.6 ± 0.3
EP/MPO3	34.0	V-0	31 ± 3	596 ± 22	50.4 ± 2.2	0.317 ± 0.012	26.6 ± 0.4
EP/MPO4	30.5	V-1	35 ± 2	509 ± 34	54.8 ± 3.4	0.236 ± 0.0031	19.6 ± 1.0

[a] TTI: time to ignition; PHRR: peak heat release rate; THR: total heat release; PSPR: peak smoke production rate; and TSP: total smoke production.

presented in Fig. 7 and Table 2, revealed that EP/EMI had high PHRR and THR values of 1018 kW/m^2 and 76.8 MJ/m^2, respectively, confirming its high flammability. The addition of phosphorus-containing groups significantly reduced these values. For EP/MPO2, EP/MPO3, and EP/MPO4, PHRR decreased by 30.3 %, 41.5 %, and 50.0 %, respectively, while THR was reduced by 21.7 %, 34.4 %, and 28.6 % (see Fig. 7a and b). These reductions demonstrate the effectiveness of MPOx in suppressing heat release during combustion. In addition to PHRR and THR, fire performance index (FPI: TTI/PHRR) and fire growth rate (FIGRA: PHRR/TPHRR; TPHRR: time to PHRR) were used to assess flammability. A higher FPI indicates lower fire risk, while a lower FIGRA suggests slower fire growth [15,23]. As shown in Fig. 7c, the FPI values of EP/MPOx thermosets were higher than that of EP/EMI, indicating improved flame resistance. Meanwhile, FIGRA values for EP/MPO2 and EP/MPO3 were reduced to 6.6 and 5.4 kW/m^2/s, respectively, compared to 7.7 kW/m^2/s for EP/EMI. However, the FIGRA value for EP/MPO4 was slightly higher than that of EP/EMI. This increase may be attributed to its relatively lower thermal stability. During the initial combustion stage, the condensed-phase flame-retardant effect of EP/MPO4 was less pronounced, leading to premature decomposition and a substantial release of volatile combustible products. Consequently, the heat release rate temporarily increased, and the peak heat release occurred earlier.

Since smoke toxicity is a critical factor in fire hazards, smoke production rate (SPR) and total smoke production (TSP) curves obtained from cone calorimetry were analyzed to evaluate smoke suppression in all EP thermosets, as shown in Fig. 7d and e and summarized in Table 2. For EP/MPO2, the PSPR and TSP values were higher compared to those of EP/EMI. This increase may be attributed to the pronounced gaseous-phase quenching effect of MPO2, which led to incomplete combustion of volatile products, forming smoke aerosols. This behavior is commonly observed in phosphorus-based flame retardants with low oxidation states [11,13,35]. In contrast, EP/MPO3 and EP/MPO4 exhibited significant reductions in PSPR and TSP compared to EP/EMI, demonstrating enhanced smoke suppression. Specifically, EP/MPO4 achieved the most substantial reductions, with decreases of 45.2 % and 38.9 % in PSPR and TSP, respectively (see Table 2). The differences in smoke suppression between MPO2 and MPO3/MPO4 are likely due to the

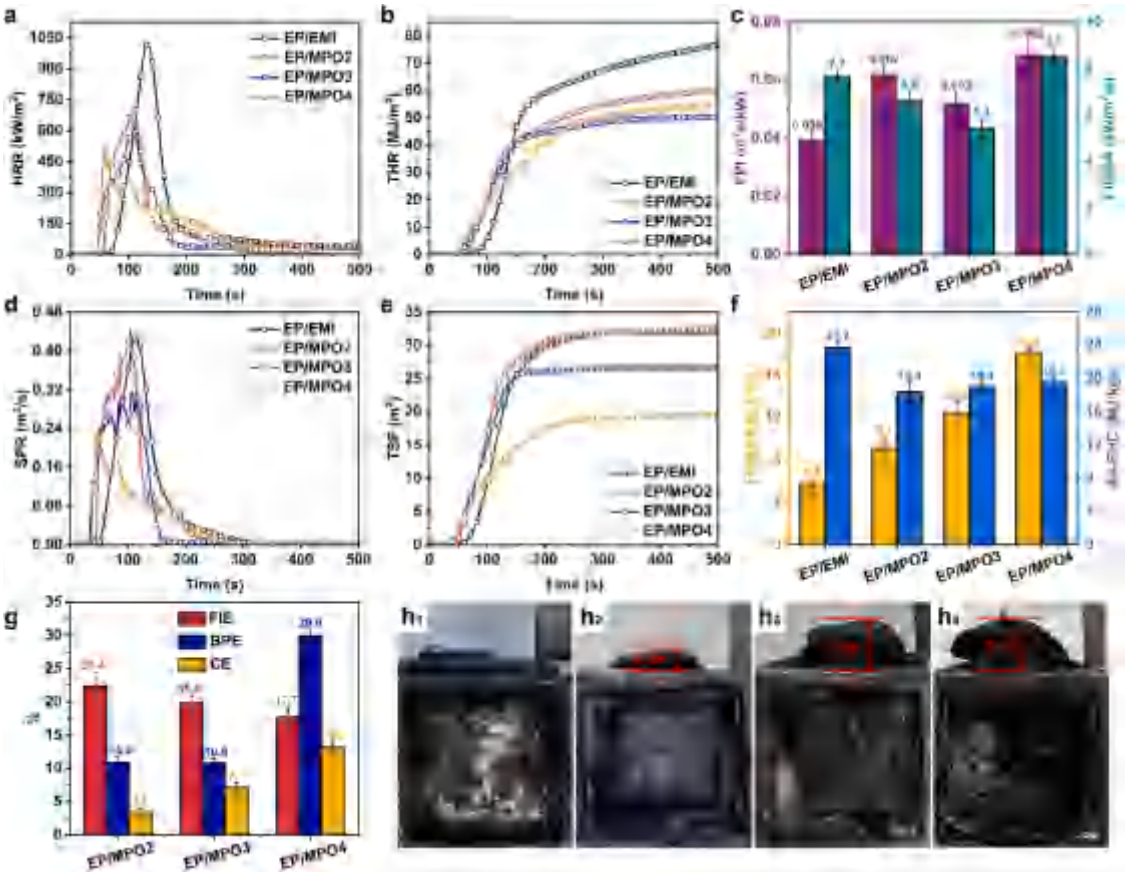


Fig. 7. (a) Heat release rate curves; (b) total heat release plots; (c) fire performance index (FPI) and fire growth rate (FIGRA) values; (d) smoke production rate plots; (e) total smoke production curves; (f) residue and average effective heat of combustion (*Av*-EHC) values; (g) flame inhibition effect (FIE), barrier and protective effect (BPE), and charring effect (CE) of EP thermosets; and digital photographs for (h_1) EP/EMI, (h_2) EP/MPO2, (h_3) EP/MPO3 and (h_4) EP/MPO4 chars after cone calorimetry.

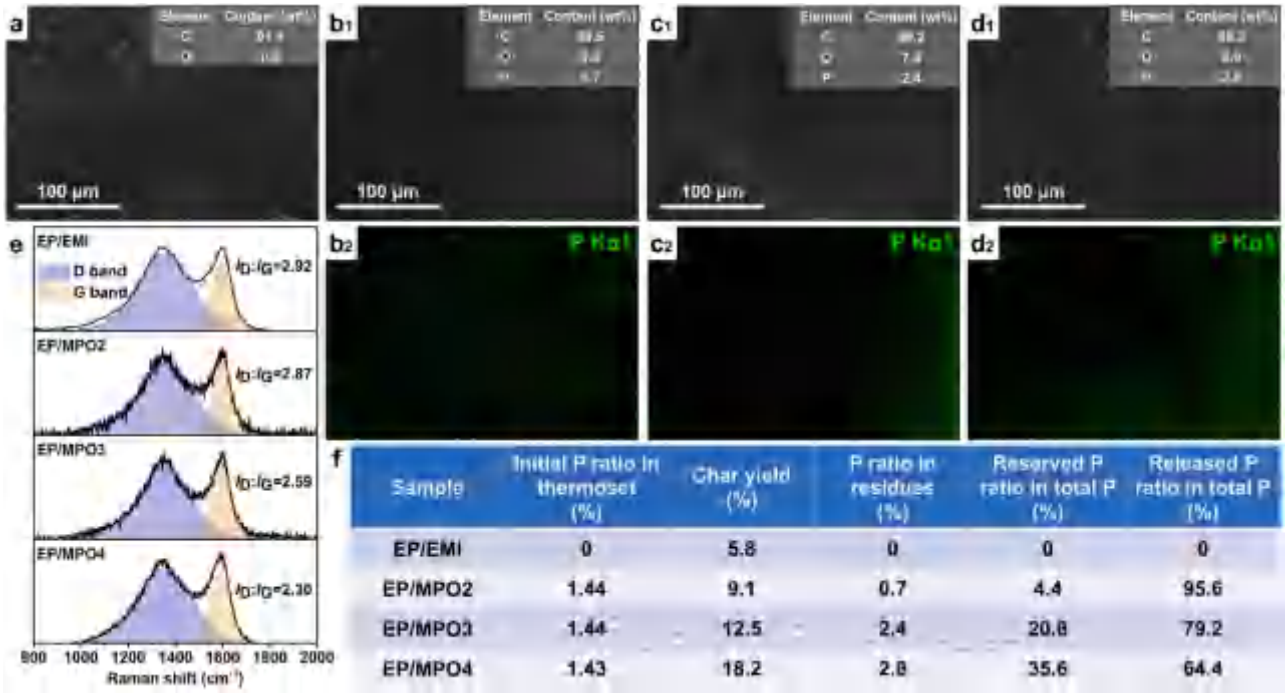
stronger condensed-phase catalytic charring effect of MPO3 and MPO4. On one hand, the pyrolysis products underwent dehydration and carbonization, remaining in the condensed phase rather than releasing into the gas phase to form soot. On the other hand, the generated stable char layer further hindered the release of pyrolysis products [32,44,45]. Correspondingly, EP/MPOx thermosets exhibited higher char residue yields than EP/EMI, as shown in Fig. 7f. Consistent with TGA results, the residue yield increased with the oxidation state of phosphorus. Specifically, the residues for EP/MPO2, EP/MPO3, and EP/MPO4 increased to 9.1 %, 12.5 %, and 18.2 %, respectively, compared to EP/EMI. The morphology of the char residues, depicted in Fig. 7h_1-h_4, also varied significantly. The char residue of EP/EMI was brittle and fragmented (see Fig. 7h_1), whereas those of EP/MPOx thermosets were intumescent and cohesive (see Fig. 7h_2-h_4), effectively reducing heat release and smoke generation. Notably, the char residues of EP/MPO3 and EP/MPO4 reached a thickness of up to 5 cm. Additionally, the average effective heat of combustion (*Av*-EHC) was employed to assess the burning degree of gaseous pyrolysis products [4,26]. As shown in Fig. 7f, the *Av*-EHC values of EP/MPOx thermosets were significantly lower than that of EP/EMI, confirming reduced combustion intensity of gaseous pyrolysis products.

The above results revealed distinct differences in the flame-retardant mechanisms of EP/MPOx in the gaseous and condensed phases. To further quantify these effects, three parameters were calculated: flame inhibition effect (FIE), barrier and protective effect (BPE), and charring effect (CE). Among these, FIE represents the gaseous-phase flame-retardant effect, while BPE and CE correspond to condensed-phase mechanisms [46,47]. The calculated FIE, BPE, and CE values are presented in Fig. 7g. Among all samples, EP/MPO2 exhibited the highest FIE value of 22.4 %, highlighting its strongest gaseous-phase flame--retardant performance. With increasing oxidation state of phosphorus from +1 to +5, the BPE and CE values of EP/MPOx increased progressively, indicating a transition from gaseous-phase to condensed-phase flame-retardant mechanisms. In conclusion, the incorporation of MPOx significantly enhanced the flame retardancy of EP thermosets through bi-phase flame-retardant effects. As the oxidation state of phosphorus increased from +1 to +5, the dominant mechanism shifted from gaseous-phase flame inhibition to condensed-phase char formation. Particularly, EP/MPO3 and EP/MPO4 demonstrated superior condensed-phase flame retardancy and smoke suppression, making them promising candidates for applications requiring both fire safety and reduced smoke toxicity.

3.7. Flame-retardant actions

3.7.1. Condensed phase analysis

To investigate the role of MPOx in the condensed phase, the char residues from cone calorimetry tests were analyzed using scanning electron microscopy (SEM), energy-dispersive X-ray spectroscopy (EDS), Raman spectroscopy, and X-ray photoelectron spectroscopy (XPS). SEM images of EP/EMI and EP/MPOx char residues are shown in Fig. 8a and b_1-d_1, while the corresponding phosphorus (P) elemental mappings of the external surfaces are presented in Fig. 8b_2-d_2. As illustrated in Fig. 8a, the char residue of EP/EMI exhibited a fragmented and porous structure. In contrast, the char layers of EP/MPOx thermosets displayed cohesive and intact morphologies (see Fig. 8b_1-d_1), effectively shielding the underlying matrix from heat and flame exposure. Additionally, the elemental mappings confirmed the presence of phosphorus in the EP/MPOx chars, suggesting that P-containing compounds were involved in the carbonization process. The Raman spectra of the char residues are presented in Fig. 8e, where the degree of graphitization was evaluated by the area ratio of the D and G bands (I_D/I_G). A lower I_D/I_G indicates a higher graphitization degree [16,40]. For EP/EMI, the I_D/I_G was 2.92, which decreased to 2.87 for EP/MPO2 and further to 2.59 for EP/MPO3, indicating that the introduction of phosphorus-containing groups promoted the formation of highly graphitized char layers. These graphitized layers served as thermal barriers, limiting heat transfer and restricting smoke release [4,31]. Moreover, the phosphorus content retained and released during combustion was analyzed using the EDS and cone calorimetry data, as shown in Fig. 8f. Despite having the same initial phosphorus content, the residual P content differed among the EP/MPOx chars. With an increase in the oxidation state of phosphorus (+1, +3, +5), more phosphorus was retained in the condensed phase, while lower oxidation states resulted in more phosphorus being released into



Sample	Initial P ratio in thermoset (%)	Char yield (%)	P ratio in residues (%)	Reserved P ratio in total P (%)	Released P ratio in total P (%)
EP/EMI	0	5.8	0	0	0
EP/MPO2	1.44	9.1	0.7	4.4	95.6
EP/MPO3	1.44	12.5	2.4	20.8	79.2
EP/MPO4	1.43	18.2	2.8	35.6	64.4

Fig. 8. SEM images and phosphorus elemental mappings of char residues for (a) EP/EMI, (b_1, b_2) EP/MPO2, (c_1, c_2) EP/MPO3, and (d_1, d_2) EP/MPO4; (e) Raman spectra showing the graphitization of residual chars; and (f) reserved and released phosphorus ratios determined from cone calorimetry results using EDS analysis.

the gaseous phase. Specifically, EP/MPO2, with the lowest oxidation state (+1), exhibited the highest released P ratio of 95.8 %, while EP/MPO_4, with the highest oxidation state (+5), achieved the maximum reserved P ratio of 35.6 %. These findings further demonstrate that high-oxidation-state phosphorus compounds predominantly enhance condensed-phase flame retardancy, whereas low-oxidation-state phosphorus compounds favor gaseous-phase flame inhibition.

The XPS analysis of EP/EMI and EP/MPOx char residues provided additional insights into their condensed-phase flame-retardant mechanisms. As shown in Fig. 9a-d, the presence of phosphorus in the EP/MPOx chars further confirmed the participation of P-containing groups in the carbonization process, corroborating the EDS results. The C1 s spectra revealed peaks corresponding to C=C (284.1 eV), C—H/C—C (284.8 eV), C—N/C—O (286.1 eV), and C=O (288.0 eV) bonds (see Fig. 9e) [24,26]. The N1 s spectra exhibited peaks at 398.5 eV and 400.7 eV, attributed to C—N and N—H bonds, respectively (see Fig. 9f) [23, 32]. The O1 s spectra showed peaks at 531.1 eV and 532.9 eV, corresponding to =O and -O- bonds (see Fig. 9g) [1,19]. Notably, the P2p spectra of EP/MPOx chars revealed peaks at 133.7 eV and 134.6 eV, assigned to P-O-C and P=O bonds, respectively (see Fig. 9h) [15,35]. These results clearly indicate that phosphate-based compounds derived from the pyrolysis of MPOx contributed to the formation of a continuous and intumescent char layer during combustion. This char layer effectively suppressed heat transfer and smoke generation in the condensed phase. Notably, the condensed-phase flame-retardant effect was more pronounced in EP/MPO3 and EP/MPO4 thermosets due to the higher oxidation states of phosphorus in these systems, which enhanced carbonization and char formation.

3.7.2. Gaseous phase analysis

To investigate the volatile products and clarify the vapor-phase flame-retardant mechanism of MPOx, TG-FTIR analysis was performed. The cumulative absorption of volatile gases is illustrated in the 3D TG-FTIR spectra shown in Fig. 10a-d, while the FTIR spectra at the primary decomposition temperatures of the EP thermosets are displayed in Fig. 10e. The main volatile products typically included water/phenol (3650 cm^{-1}), hydrocarbons (3140–2798 cm^{-1}), carbonyl compounds (1734 cm^{-1}), aromatic compounds (1604, 1509, and 830 cm^{-1}), and esters (1179 cm^{-1}) [46,48]. Additionally, the appearance of P-O-Ph absorption at 952 cm^{-1} in the spectra of EP/MPOx confirmed the involvement of P-containing groups in the gaseous-phase flame--retardant process (see Fig. 10e) [15,23,35]. This result suggests that MPOx released phosphorus-containing radicals during decomposition, which effectively scavenged the high-energy radicals generated in the combustion process, thereby interrupting the combustion chain reactions. Notably, EP/MPO3 and EP/MPO4 exhibited reduced absorption intensities for hydrocarbons, aromatic compounds, and aliphatic ethers compared to EP/EMI (see Fig. 10f-h). This reduction indicates a decreased release of volatile combustible species, thereby diminishing the fuel supply in the gaseous phase. These findings demonstrate that the phosphorus-containing groups in MPOx contribute to flame retardancy by acting in both condensed and gaseous phases, ultimately enhancing the flame-retardant performance of the EP thermosets.

4. Conclusion

This study investigated the effects of three phosphorus-derived imidazolium salts (MPOx, x = 2, 3, 4) as latent curing agents on the overall performance of single-component EPs. The oxidation state of phosphorus played a critical role in determining the latency and flame retardancy of EP/MPOx. DFT calculations revealed that phosphorus acids with higher oxidation states can form stronger ionic and hydrogen bonds with imidazole, leading to enhanced thermal latency. All MPOx maintained efficient curing performance at elevated temperatures. Regarding mechanical properties, EP/MPO3 and EP/MPO4 significantly outperformed EP/EMI, with EP/MPO4 achieving a tensile strength of 87.0 MPa and an elongation at break of 4.8 %. They also exhibited excellent optical transparency, with transmittance of 90 % at 800 nm. EP/MPO3 achieved the highest LOI value of 34.0 % and a UL-94 V-0 rating, with significant reductions in PHRR, THR, and TSP. MPO2

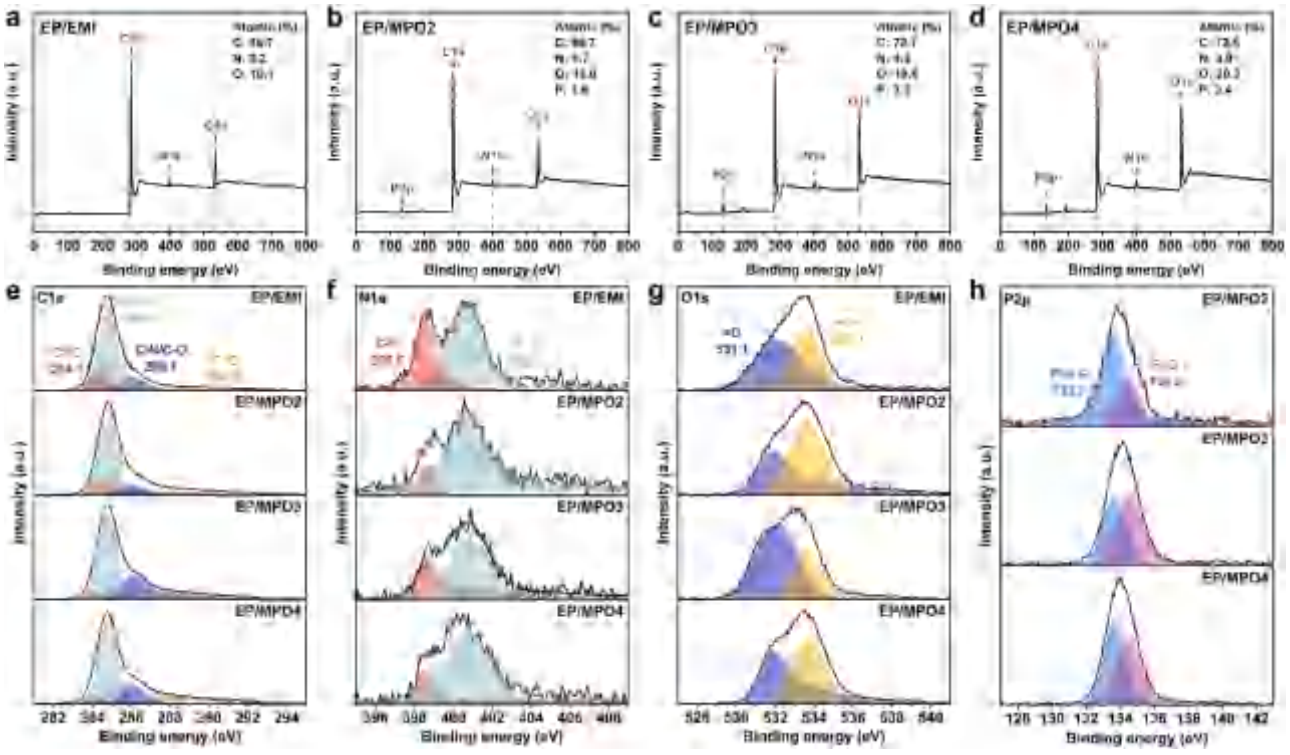


Fig. 9. Full-scan XPS spectra of char residues for (a) EP/EMI, (b) EP/MPO2, (c) EP/MPO3, and (d) EP/MPO4; and high-resolution XPS spectra for (e) C1 s, (f) N1 s, (g) O1 s, and (h) P2p of the char residues.

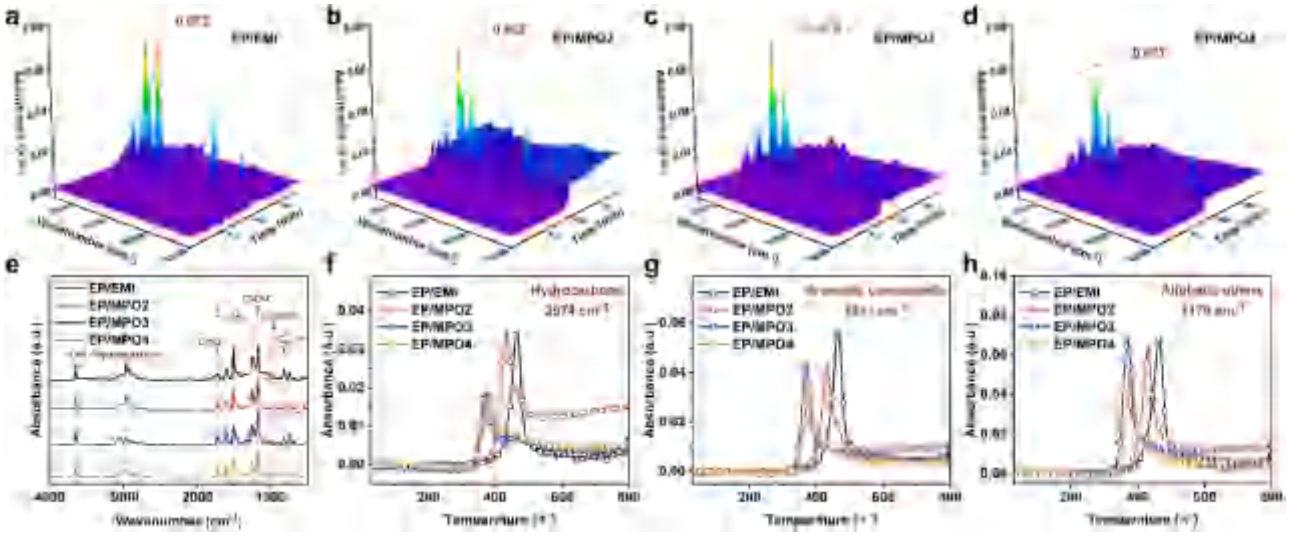


Fig. 10. 3D TG-FTIR spectra of volatiles released during the decomposition of (a) EP/EMI, (b) EP/MPO2, (c) EP/MPO3, and (d) EP/MPO4 thermosets; (e) FTIR spectra of volatiles from EP thermosets at T_{max}; and absorbance vs. temperature curves of EP thermosets at characteristic wavenumbers (f) 2974 cm^{-1}, (g) 1511 cm^{-1}, and (h) 1179 cm^{-1}.

mainly exerted gaseous-phase flame inhibition, while MPO3 and MPO4 promoted condensed-phase char formation, resulting in more effective fire safety and smoke suppression. In summary, MPO3 and MPO4 demonstrated the most balanced performance, combining extended thermal latency, improved mechanical properties, and superior flame retardancy due to the existence of phosphorus in high oxidation states.

CRediT authorship contribution statement

Jingsheng Wang: Writing – original draft, Investigation, Data curation. **Jun Wang:** Supervision, Conceptualization. **Shuang Yang:** Methodology, Funding acquisition. **Guoping Ding:** Supervision, Project administration. **Renxin Xu:** Writing – original draft, Supervision. **Wei Liu:** Resources, Formal analysis. **Jiuxiao Sun:** Writing – review & editing, Funding acquisition. **Kaiwen Chen:** Investigation, Formal analysis. **Liu Duan:** Visualization, Data curation. **Jiaqi Wang:** Visualization, Investigation. **Hao Wang:** Supervision, Methodology. **Siqi Huo:** Writing – review & editing, Writing – original draft.

Declaration of competing interest

The authors declare that they have no known competing financial interests or personal relationships that could have appeared to influence the work reported in this paper.

Acknowledgements

We gratefully acknowledge the financial support provided by the National Natural Science Foundation of China (Grant No. 52473077), the Major Program of Hubei Province (Grant No. 2023BAA028), the Australian Research Council (Grant No. DE230100616), and the Nonmetallic Excellence and Innovation Center (Grant No. 24PHD-4). We also extend our sincere thanks to Shiyanjia Lab (www.shiyanjia.com) for their valuable assistance with the XPS analyses.

Supplementary materials

Supplementary material associated with this article can be found, in the online version, at doi:10.1016/j.polymdegradstab.2025.111325.

Data availability

Data will be made available on request.

References

[1] Q. Chen, S.Q. Huo, Y.X. Lu, M.M. Ding, J.B. Feng, G.B. Huang, H. Xu, Z.Q. Sun, Z. Z. Wang, P.G. Song, Heterostructured Graphene@Silica@Iron Phenylphosphinate for Fire-Retardant, Strong, Thermally Conductive Yet Electrically Insulated Epoxy Nanocomposites, Small. 20 (31) (2024) 10724, https://doi.org/10.1002/smll.202310724.

[2] J. Alongi, Z.D. Han, S. Bourbigot, Intumescence: tradition versus novelty. A comprehensive review, Prog. Polym. Sci. 51 (2015) 28–73, https://doi.org/10.1016/j.progpolymsci.2015.04.010.

[3] K.P. Song, Y.T. Pan, J. Zhang, P.A. Song, J.Y. He, D.Y. Wang, R.J. Yang, Metal-Organic Frameworks-Based Flame-Retardant System for Epoxy Resin: a Review and Prospect, Chem. Eng. J. 468 (2023) 143653, https://doi.org/10.1016/j.cej.2023.143653.

[4] Y.L. Xiao, X.W. Mu, B.B. Wang, W.Z. Hu, J.L. Wang, F. Zhou, C. Ma, Y. Hu, L. Song, A novel phosphorous-containing polymeric compatibilizer: effective reinforcement and flame retardancy in glass fiber reinforced polyamide 6 composites, Compos. Pt. B-Eng. 205 (2021) 108536, https://doi.org/10.1016/j.compositesb.2020.108536.

[5] J.B. Feng, L. Liu, Y. Zhang, Q.S. Wang, H. Liang, H. Wang, P.A. Song, Rethinking the pathway to sustainable fire retardants, Exploration. (Beijing) 3 (4) (2023) 20220088, https://doi.org/10.1002/exp.20220088.

[6] C. Wang, G.F. Ye, Q. Zhang, H. Wang, S.Q. Huo, Z.T. Liu, Closed-Loop Recyclable, Self-Catalytic Transesterification Vitrimer Coatings with Superior Adhesive Strength, Fire Retardancy, and Environmental Stability, ACS. Mater. Lett. 7 (2024) 210–219, https://doi.org/10.1021/acsmaterialslett.4c02235.

[7] M. Zhi, X. Yang, R. Fan, S. Yue, L. Zheng, Q. Liu, Y. He, A comprehensive review of reactive flame-retardant epoxy resin: fundamentals, recent developments, and perspectives, Polym. Degrad. Stab. 201 (2022) 109976, https://doi.org/10.1016/j.polymdegradstab.2022.109976.

[8] H. Duan, Y. Chen, S. Ji, R. Hu, H. Ma, A novel phosphorus/nitrogen-containing polycarboxylic acid endowing epoxy resin with excellent flame retardance and mechanical properties, Chem. Eng. J. 375 (2019) 121916, https://doi.org/10.1016/j.cej.2019.121916.

[9] S.V. Levchik, E.D. Weil, A review of recent progress in phosphorus-based flame retardants, J. Fire Sci. 24 (5) (2006) 345–364, https://doi.org/10.1177/0734904106068426.

[10] T. Sai, X.D. Ye, B.T. Wang, Z.H. Guo, J. Li, Z.P. Fang, S.Q. Huo, Transparent, intrinsically fire-safe yet impact-resistant poly(carbonates-b-siloxanes) containing Schiff-base and naphthalene-sulfonate, J. Mater. Sci. Technol. 225 (2025) 11–20, https://doi.org/10.1016/j.jmst.2024.11.023.

[11] S.Q. Huo, P.A. Song, B. Yu, S.Y. Ran, V.S. Chevali, L. Liu, Z.P. Fang, H. Wang, Phosphorus-containing flame retardant epoxy thermosets: recent advances and future perspectives, Prog. Polym. Sci. 114 (2021) 101366, https://doi.org/10.1016/j.progpolymsci.2021.101366.

[12] C. Wang, S.Q. Huo, G.F. Ye, B.T. Wang, Z.H. Guo, Q. Zhang, P.A. Song, H. Wang, Z. T. Liu, Construction of an epoxidized, phosphorus-based poly(styrene butadiene styrene) and its application in high-performance epoxy resin, Compos. Pt. B-Eng. 268 (2024) 111075, https://doi.org/10.1016/j.compositesb.2023.111075.

[13] Y.J. Xu, X.H. Shi, J.H. Lu, M. Qi, D.M. Guo, L. Chen, Y.Z. Wang, Novel phosphorus-containing imidazolium as hardener for epoxy resin aiming at controllable latent curing behavior and flame retardancy, Compos. Pt. B-Eng. 184 (2020) 107673, https://doi.org/10.1016/j.compositesb.2019.107673.
[14] S. Huo, S. Yang, J. Wang, J. Cheng, Q. Zhang, Y. Hu, G. Ding, Q. Zhang, P. Song, A liquid phosphorus-containing imidazole derivative as flame-retardant curing agent for epoxy resin with enhanced thermal latency, mechanical, and flame-retardant performances, J. Hazard. Mater. 386 (2020) 121984, https://doi.org/10.1016/j.jhazmat.2019.121984.
[15] X.H. Liu, H.J. Wang, B.R. Zeng, X.D. Yi, W.A. Luo, G.R. Chen, Y.T. Xu, C.H. Yuan, L. Z. Dai, Phosphorus-containing curing agents with dynamic bonds endowing epoxy resins with flame retardancy and remolding capability, Compos. Pt. B-Eng. 273 (2024) 111260, https://doi.org/10.1016/j.compositesb.2024.111260.
[16] Y.J. Xu, J. Wang, Y. Tan, M. Qi, L. Chen, Y.Z. Wang, A novel and feasible approach for one-pack flame-retardant epoxy resin with long pot life and fast curing, Chem. Eng. J. 337 (2018) 30–39, https://doi.org/10.1016/j.cej.2017.12.086.
[17] Y.R. Wang, W.S. Liu, Y.P. Qiu, Y. Wei, A One-Component, Fast-Cure, and Economical Epoxy Resin System Suitable for Liquid Molding of Automotive Composite Parts, Materials 11 (5) (2018) 685, https://doi.org/10.3390/ma11050685.
[18] Y.F. Fang, B.A. Ma, K. Wei, X.Q. Wang, X.X. Kang, F.S. Liu, Performance of single-component epoxy resin for crack repair of asphalt pavement, Constr. Build. Mater. 304 (2021) 124625, https://doi.org/10.1016/j.conbuildmat.2021.124625.
[19] M.Z. Chai, L. Liu, P.B. Zhang, Y.D. Huang, Long shelf life, intrinsically flame retardant, transparent, high-performance one-component epoxy resin based on phosphorus-containing imidazole derivatives, Polym. Degrad. Stab. 218 (2023) 110587, https://doi.org/10.1016/j.polymdegradstab.2023.110587.
[20] Y.R. Ham, D.H. Lee, S.H. Kim, Y.J. Shin, M. Yang, J.S. Shin, Microencapsulation of imidazole curing agent for epoxy resin, J. Ind. Eng. Chem. 16 (5) (2010) 728–733, https://doi.org/10.1016/j.jiec.2010.07.011.
[21] Y.R. Ham, S.H. Kim, Y.J. Shin, D.H. Lee, M. Yang, J.H. Min, J.S. Shin, A comparison of some imidazoles in the curing of epoxy resin, J. Ind. Eng. Chem. 16 (4) (2010) 556–559, https://doi.org/10.1016/j.jiec.2010.03.022.
[22] J.S. Wang, J. Wang, S. Yang, C.Q. Wu, X. Chen, K.W. Chen, P.A. Song, H. Wang, S. Q. Huo, Development of single-component epoxy resin with superb thermal stability, flame retardancy, smoke suppression, and latency via Cu-based phosphorus/imidazole-containing complex, Polym. Degrad. Stab. 228 (2024) 110906, https://doi.org/10.1016/j.polymdegradstab.2024.110906.
[23] J.S. Wang, J. Wang, F.Y. Wang, S. Yang, C.Q. Wu, X. Chen, K.W. Chen, P.A. Song, H. Wang, S.Q. Huo, Liquid phosphorus-based bis-imidazole compounds as latent curing agents for enhancing thermal, mechanical, and flame-retardant performances of single-component epoxy resins, Polym. Degrad. Stab. 230 (2024) 111066, https://doi.org/10.1016/j.polymdegradstab.2024.111066.
[24] Y.X. Xu, J.J. Wang, W.B. Zhang, S.Q. Huo, Z.P. Fang, P.A. Song, D. Wang, H. Wang, A phosphaphenanthrene-benzimidazole derivative for enhancing fire safety of epoxy resins, React. Funct. Polym. 180 (2022) 105390, https://doi.org/10.1016/j.reactfunctpolym.2022.105390.
[25] G.A. Sundaram, S. Kumaravelu, W.L. Tseng, P.V. Pham, A.S.K. Kumar, V. Parimelazhagan, Fine-Tuned Graphene Oxide Nanocomposite: harnessing Copper(II)-Imidazole Complex for Enhanced Biological Responses and Balanced Photocatalytic Functionality, Materials 17 (4) (2024) 892, https://doi.org/10.3390/ma17040892.
[26] S.Y. Zhu, T.T. Zheng, F. Li, L. Wang, Q.R. Jiang, Y. Wei, W.S. Liu, Synthesis of cyclotriphosphazene-containing imidazole as a thermally latent hardener for epoxy resins and its application in carbon fiber reinforced composites, J. Appl. Polym. Sci. 139 (41) (2022) 52980, https://doi.org/10.1002/app.52980.
[27] D. Lei, W. Ma, L. Wang, D. Zhang, Preparation of 2-ethyl-4-methylimidazole derivatives as latent curing agents and their application in curing epoxy resin, J. Appl. Polym. Sci. 132 (38) (2015) 42563, https://doi.org/10.1002/app.42563.
[28] S.Q. Huo, J. Wang, S. Yang, C. Li, X.L. Wang, H.P. Cai, Synthesis of a DOPO-containing imidazole curing agent and its application in reactive flame retarded epoxy resin, Polym. Degrad. Stab. 159 (2019) 79–89, https://doi.org/10.1016/j.polymdegradstab.2018.11.021.
[29] W. Yen, K. Chen, M. Yeh, N. Uramaru, H. Lin, F.F. Wong, Investigation of soluble PEG-imidazoles as the thermal latency catalysts for epoxy-phenolic resins, J. Taiwan. Inst. Chem. Eng. 59 (2016) 98–105, https://doi.org/10.1016/j.jtice.2015.08.007.
[30] J.S. Wang, J. Wang, S. Yang, X. Chen, K.W. Chen, G. Zhou, X. Liu, L. Xu, S.Q. Huo, P.G. Song, H. Wang, Multifunctional phosphorus-containing imidazoliums endowing one-component epoxy resins with superior thermal latency, heat resistance, mechanical properties, and fire safety, Chem. Eng. J. 485 (2024) 149852, https://doi.org/10.1016/j.cej.2024.149852.
[31] J.S. Wang, S.Q. Huo, J. Wang, S. Yang, K.W. Chen, C. Li, D. Fang, Z.P. Fang, P. G. Song, H. Wang, Green and Facile Synthesis of Bio-Based, Flame-Retardant, Latent Imidazole Curing Agent for Single-Component Epoxy Resin, ACS. Appl. Polym. Mater. 4 (5) (2022) 3564–3574, https://doi.org/10.1021/acsapm.2c00138.
[32] J.S. Wang, J. Wang, S. Yang, K.W. Chen, Single-component flame-retardant and smoke-suppressive epoxy resins enabled by an aluminum/phosphorus/imidazole-containing complex, Compos. Pt. B-Eng. 253 (2023) 110571, https://doi.org/10.1016/j.compositesb.2023.110571.
[33] B. Yang, Y.Y. Mao, Y.H. Zhang, G.F. Bian, L.Y. Zhang, Y. Wei, Q.R. Jiang, Y.P. Qiu, W.S. Liu, A novel liquid imidazole-copper (II) complex as a thermal latent curing agent for epoxy resins, Polymer. (Guildf) 178 (2019) 121586, https://doi.org/10.1016/j.polymer.2019.121586.
[34] A. Omrani, L.C. Simon, A.A. Rostami, M. Ghaemy, Study on curing mechanism of DGEBA/nickel-imidazole system, Thermochim. Acta 468 (1-2) (2008) 39–48, https://doi.org/10.1016/j.tca.2007.11.016.
[35] S.H. Lou, S.D. Wang, L. Zhang, J. Liu, T. Tang, Intrinsic flame-retardant epoxy resin based on phosphorus-containing liquid imidazole compound: simultaneously improving fire safety, mechanical property and heat resistance, Chem. Eng. J. 493 (2024) 152816, https://doi.org/10.1016/j.cej.2024.152816.
[36] W. Wang, G. Chen, S.L. Wu, Y. Liu, Q. Wang, Solvent-free synthesis of phosphate-containing imidazole fluid for flame retardant one-component epoxy resin with long pot life, low curing temperature and fast curing rate, J. Appl. Polym. Sci. 140 (8) (2023) e53509, https://doi.org/10.1002/app.53509.
[37] J.W. Cheng, J. Wang, S. Yang, Q.Q. Zhang, S. Huo, Q.X. Zhang, Y. Hu, G.P. Ding, Benzimidazolyl-substituted cyclotriphosphazene derivative as latent flame-retardant curing agent for one-component epoxy resin system with excellent comprehensive performance, Compos. Pt. B-Eng. 177 (2019) 107440, https://doi.org/10.1016/j.compositesb.2019.107440.
[38] B. Yang, Y. Wei, Y. Qiu, S. Ramakrishna, Y. Liu, A novel bio-based, flame retardant and latent imidazole compound-Its synthesis and uses as curing agent for epoxy resins, J. Appl. Polym. Sci. 139 (44) (2022) e53079, https://doi.org/10.1002/app.53079.
[39] H. Maka, T. Spychaj, R. Pilawka, Epoxy Resin/Ionic Liquid Systems: the Influence of Imidazolium Cation Size and Anion Type on Reactivity and Thermomechanical Properties, Ind. Eng. Chem. Res. 51 (2012) 5197–5206, https://doi.org/10.1021/ie202321j.
[40] Z. Zhu, L. Wang, X. Lin, L. Dong, Synthesis of a novel phosphorus-nitrogen flame retardant and its application in epoxy resin, Polym. Degrad. Stab. 169 (2019) 108981, https://doi.org/10.1016/j.polymdegradstab.2019.108981.
[41] Y.J. Woo, D.S. Kim, Cure and thermal decomposition kinetics of a DGEBA/amine system modified with epoxidized soybean oil, J. Therm. Anal. Calorim. 144 (1) (2021) 119–126, https://doi.org/10.1007/s10973-020-10159-2.
[42] E. Jiao, K. Wu, Z. Qu, Y. Liu, M. Lu, B. Na N, W. Chen, L. Liang, Preparation and curing kinetics of intrinsic flameretardant epoxy resin system based on polyoxometalates, J. Therm. Anal. Calorim. 146 (3) (2020) 1–14, https://doi.org/10.1007/s10973-020-10075-5.
[43] J. Hu, J. Shan, Z. Tong, Curing Kinetics of Flame Retardant Epoxy Resin Promoted by Imidazole Grafting Graphene Oxide, Chemical Journal of Chinese Universities-Chinese 38 (10) (2017) 1906–1912, https://doi.org/10.7503/cjcu20170059.
[44] C.C. Gao, L.H. Guo, P.C. Yuan, Y.J. Qiao, A. Xing, X.Y. Li, Flame retardant, strong and tough, low dielectric epoxy thermoset enabled by a novel bi-DOPO type epoxy with aggregation-induced emission, Chem. Eng. J. 475 (2023) 146241, https://doi.org/10.1016/j.cej.2023.146241.
[45] Y. Xu, W. Zhang, Y. Qiu, M. Xu, B. Li, L. Liu, Preparation and mechanism study of a high efficiency bio-based flame retardant for simultaneously enhancing flame retardancy, toughness and crystallization rate of poly (lactic acid), Compos. Pt. B-Eng. 238 (2022) 109913, https://doi.org/10.1016/j.compositesb.2022.109913.
[46] G.F. Ye, S.Q. Huo, C. Wang, Q. Zhang, B.T. Wang, Z.H. Guo, H. Wang, Z.T. Liu, Fabrication of flame-retardant, strong, and tough epoxy resins by solvent-free polymerization with bioderived, reactive flame retardant, Sustainable Mater. Technol. 39 (2024) e00853, https://doi.org/10.1016/j.susmat.2024.e00853.
[47] J. Wang, L. Qian, Z. Huang, Y. Fang, Y. Qiu, Synergistic flame-retardant behavior and mechanisms of aluminum poly-hexamethylenephosphinate and phosphaphenanthrene in epoxy resin, Polym. Degrad. Stab. 130 (2016) 173–181, https://doi.org/10.1016/j.polymdegradstab.2016.06.010.
[48] G. Ye, S. Huo, C. Wang, Q. Shi, Z. Liu, H. Wang, One-step and green synthesis of a bio-based high-efficiency flame retardant for poly (lactic acid), Polym. Degrad. Stab. 192 (2021) 109696, https://doi.org/10.1016/j.polymdegradstab.2021.109696.

Engineering Structures 308 (2024) 118052



Contents lists available at ScienceDirect

Engineering Structures

journal homepage: www.elsevier.com/locate/engstruct



A pull-out equivalent telescopic layered failure model of carbon fiber bundles in seawater sea-sand cementitious matrix

Jiarong Liu [a], Dawei Zhang [a,*], Yewangzhi Tao [a], Zhiyu Xie [a,b,c]

[a] Institute of Structural Engineering, Zhejiang University, Hangzhou 310058, China
[b] School of Engineering, Hangzhou City University, Hangzhou 310015, China
[c] Zhejiang Engineering Research Center of Intelligent Urban Infrastructure, Hangzhou, Zhejiang 310015, China

ARTICLE INFO

Keywords:
FRCM
Seawater sea-sand
Pull-out test
Trilinear cohesive material law
Telescopic layered failure model
Piezoresistive effect

ABSTRACT

Based on the excellent mechanical properties and piezoresistive effect of carbon fiber, carbon fiber reinforced cementitious matrix (CFRCM) has been used in the strengthening and self-monitoring research of reinforced concrete (RC) structures. In this study, the assumptions of the telescopic layered model theory of CFRCM were refined. The factors influencing the piezoresistive effect of carbon fibers were subsequently analyzed. Simultaneously, the resistance calculation theory for the pull-out process of CFRCM bundles was established by combining the parallel circuit theory. Based on the above theories, a pull-out equivalent telescopic layered failure model of carbon fiber bundles in the cementitious matrix was developed, considering the trilinear cohesive material law (CML) and the piezoresistive effect. Pull-out tests on carbon fiber bundles in both freshwater standard sand and seawater sea-sand matrices were conducted. This model was successfully used to simulate the piezoresistive effect during the pull-out process of CFRCM bundles with two matrices and different embedded lengths. The number of fiber filaments in each layer, the rupture damage of the fiber filaments during the loading process, and the degree of matrix infiltration into the carbon fibers were calculated. This work lays the foundation for advancing the development of structural strengthening and structural health monitoring.

1. Introduction

Reinforced concrete (RC) structures, widely utilized in civil engineering, may suffer severe deterioration in their mechanical performance and durability over the long-term service [1–4]. Enhancing structural carrying capacity, implementing structural health monitoring, and reducing the frequency of safety accidents are especially important.

Fiber reinforced polymer (FRP) composites, with the advantages of lightweight, high strength, and corrosion resistance, have been widely used to repair and strengthen existing structures [5,6]. However, FRP has disadvantages, such as poor compatibility with concrete, degradation under high temperature and UV exposure, and toxicity [7]. To overcome FRP's durability and applicability issues, fabric reinforced cementitious matrix (FRCM) has gradually gained widespread attention. FRCM is a new composite material composed of fabric and mortar [8,9]. It retains the advantages of FRP while having the following benefits: variable fiber geometry, good compatibility with concrete or masonry substrates, easy installation, good permeability, high-temperature resistance, and reversibility [7,10]. In addition, carbon fiber, with the advantages of high modulus of elasticity, lightweight, good conductivity, and corrosion resistance [11], has been widely studied and applied as CFRCM (Carbon-FRCM) for structural strengthening [12–16].

From a design perspective, the bonding strength of FRCM materials is significant. The theoretical study of the bond-slip relationship in FRCM through pull-out and shear tests has been reported. Various methods such as finite element simulation [17,18], numerical simulation, and analytical closed-form solutions [19–23] have been used to predict the tensile response of FRCM and the bonding performance of FRCM strengthening systems by reproducing the occurrence of multiple cracking in the matrix and debonding at the interface.

The cohesive material law (CML), which describes the relationship between shear stress (τ) and slip (s), elucidates the stress transfer mechanisms at debonded interfaces [24]. Different relationships between τ and s have been proposed in previous studies, each with its shape. For complex CML shapes, such as continuous exponential equations, numerical solution methods are needed [21]. It is worth noting that the trilinear CML employed to describe the bond behavior of

* Corresponding author.
E-mail address: dwzhang@zju.edu.cn (D. Zhang).

https://doi.org/10.1016/j.engstruct.2024.118052

Available online 17 April 2024
0141-0296/© 2024 Elsevier Ltd. All rights reserved.

FRCM-concrete joints typically consists of a rising branch, a softening branch, and a constant branch at the end to account for residual frictional stresses on the boundary surface [25]. Due to its simplicity and ease of computation, the trilinear CML function is widely used to describe the pull-out and shear failure processes of FRCM materials [24]. Relevant studies are as follows: In single-lap shear tests of FRCM bonding with masonry blocks, analytical expressions for load-displacement responses and interface shear stress distribution at different loading stages have been derived, along with the analysis of the influence of bond length, cohesive bond-slip law parameters, and friction on load-displacement responses [23]. Furthermore, a simulation method based on the fundamental principles of the finite difference method has been proposed to calibrate the unknown parameters of the CML for short bond cases [26], and analytical closed-form solutions for the load response of double-sided pull-out boundaries have also been studied [27].

The studies above all adopted the homogenization assumption, treating the carbon fiber as a whole for simulation. However, due to the uneven degree of matrix infiltration into the carbon fiber, the failure modes of the filaments within the cementitious matrix are inconsistent. When the matrix sufficiently infiltrates the gaps between the fiber filaments, there is better bonding between the filaments and the matrix; These fiber filaments are known as the sleeve layer, and they experience rupture failure step by step. In contrast, the inner fiber filaments, known as the core layer fibers, experience pull-out failure due to limited matrix infiltration [28,29]. Consequently, FRCM materials exhibit a telescopic layered failure characteristic.

Therefore, the use of the homogenization assumption presents the following issues: (1) It cannot accurately depict the failure process and mechanisms of carbon fibers in CFRCM; (2) Most studies derive model parameters by fitting experimental data, and these parameters are typically better suited for representing the researcher's test results rather than having general applicability.

Currently, theoretical research on investigating the bonding performance of carbon fibers based on the assumption of telescopic layered failure is limited. A study has considered a discretely infiltrated matrix along the fiber length equivalent to a continuously infiltrated matrix at the free end [28]. Because each layer of fibers experiences different equivalent infiltration lengths of the matrix, they exhibit varying extensional stiffness under load, resulting in a transition of the failure mode of carbon fiber filaments from tensile rupture failure of the outer layer to slippage failure of the inner layer. Based on the failure investigation using the light transmission properties (FILT) test, the arrangement of filaments in Glass-FRCM, and the location and quantity of matrix infiltration have been obtained, and the fiber bundle pull-out failure process was characterized based on the relationship between load response and the number of intact fiber filaments [28]. However, this method does not apply to carbon fibers without light transmission properties. Another study indicates that a fiber bundle can be divided into two layers: the sleeve layer fibers are modeled using a trilinear CML to simulate their load response, while the core layer fibers are represented with a CML having a linear decreasing branch related to friction. The critical parameters of the CML are fitted based on the differences between pull-out test curves with two embedded lengths [27].

In structural health monitoring (SHM), emerging methods such as fiber optic grating and piezoelectric sensors need to be embedded or attached to structures. While they can provide real-time monitoring of damage, they come with drawbacks, including device complexity, high cost, time-consuming installation, poor durability, smaller sensing volume, and a potential reduction in structural mechanical performance [30–32]. Therefore, more advanced SHM technologies are urgently needed for development. The piezoresistive effect of the carbon fiber refers to the phenomenon where its electrical resistance changes with variations in strain [33]. Therefore, carbon fiber, as an intelligent dual-functional material for structural strengthening and self-sensing, eliminates the need for additional sensors to be installed or embedded. As a result, it offers advantages such as lower cost, increased durability, larger sensing volume, and no compromise on mechanical performance [32,34]. Experimental research on continuous carbon fiber bundle, CFRP, and CFRCM has shown that utilizing the piezoresistive effect of carbon fiber to monitor the response (including stress, strain, loads, displacement, and crack damage) of materials and structures is feasible and several methods for SHM based on this principle have already been proposed [32,35–40].

The research on the piezoresistive models used to assess the quantitative relationship between damage to carbon fiber and changes in electrical resistance is as follows: For dry carbon fibers, a parallel circuit model and a Weibull distribution model of fiber strength were used to calculate the resistance change, taking into account the resistance change caused by elastic deformation, rupture, contact of the carbon fiber filaments [41]. Furthermore, the uncertainty of initial rupture, tensile rupture, and contact change in the carbon fiber filaments was analyzed, and their probability distributions were determined. Then, a dynamic random equivalent parallel circuit model and Monte Carlo simulation were used to calculate the resistance of the carbon fiber bundle during the tensile process [42]. For CFRP, a DC circuit model consisting of discrete parallel cells was proposed to explain the resistance evolution [43]. In addition, three factors contributing to the resistance change in CFRP were analyzed, including elastic deformation, the separation of contacting fibers, and the rupture of fibers during loading. An electrical model using parallel circuits, a normal distribution model, a Weibull model, and a piezoresistivity model were developed [44]. Uniquely, based on Maxwell's equation and low-energy theory, a coupled mechanical and electrical model was established, combining the response of the resistivity scalar field and the strain vector field [45]. However, this model does not account for the rupture damage of carbon fiber filaments.

In addition, the advancement of RC concrete projects in certain remote and marine areas is constrained due to the scarcity of freshwater and river sand resources [46,47]. The substitution of freshwater and river sand with seawater and sea-sand is feasible [48,49]. However, the above studies have not addressed the mechanical properties and piezoresistive effects of seawater sea-sand matrix CFRCM. Further investigation is necessary to better utilize seawater and sea-sand resources.

In summary, the current research on numerical models for the failure process of CFRCM mainly relies on the assumption of homogeneity, while analysis using a telescopic layered failure assumption is limited. Additionally, research on the piezoresistive models of continuous carbon fiber materials primarily focuses on dry carbon fibers and CFRP, with rare investigations on CFRCM. More importantly, based on the CFRCM piezoresistive model, a quantitative relationship may be established between the resistivity changes of carbon fiber bundles in the matrix and the load response of the material/structure to conduct a detailed evaluation of the failure process. This could analyze carbon fibers' telescopic layered failure phenomenon in FRCM and achieve damage warning.

In this study, the analytical closed-form solution for the pull-out load response based on the trilinear cohesive material law (CML) was reviewed, and the assumptions of the telescopic layered model theory of CFRCM were refined. The factors influencing the piezoresistive effect of carbon fibers in the matrix, such as elastic deformation, initial rupture, tensile rupture, and contact change, were subsequently analyzed. Simultaneously, the resistance calculation theory for the pull-out process of CFRCM bundles was established by combining the parallel circuit theory. Based on the above theories, an equivalent telescopic layered failure model for pull-out was developed, considering the piezoresistive effect. Then,pull-out tests on carbon fiber bundles in both freshwater standard sand and seawater sea-sand matrices were conducted. This model was successfully used to simulate the pull-out piezoresistive effect. This research lays the foundation for advancing the development of multifunctional systems that combine structural strengthening and structural health monitoring.

2. Pull-out equivalent telescopic layered failure model and trilinear cohesive material law

2.1. Telescopic layered failure model and its basic assumptions

Due to the telescopic failure of the carbon fiber bundle, it can be regarded as a layered system consisting of n layers of sleeve layer filaments and one layer of core layer filaments (Fig. 1). The outermost filament of the sleeve layer (i.e., layer 1) ruptures first, followed by the continuous rupture of the filaments of the neighboring layers. Eventually, the filaments of the core layer are pulled out. Defining the pull-out load response of each fiber filaments layer as $P_{f,i}(u)$, then the total pull-out load response $P(u)$ of the carbon fiber bundle is Eq. (1):

$$P(u) = \sum_{i=1}^{n+1} P_{f,i}(u) \tag{1}$$

Due to the non-uniform infiltration behavior of the matrix along both longitudinal and transverse directions of carbon fiber filaments, accurately determining the contact length and contact area between individual filaments and the matrix presents significant challenges. In the layered failure model, Banholzer [28] consolidated the discretely infiltrated matrix lengths, $L_{dis,k}$, along the longitudinal direction to an equivalent length at the free end to obtain the equivalent infiltration lengths, L_v (Fig. 2). The value of L_v was used to differentiate the rupture sequence of sleeve layer filaments. The larger the L_v of the sleeve layer fiber filaments, the greater the extensional stiffness in the elastic phase of the loading process. Therefore, when the filament reaches the tensile strength, the corresponding slip value is smaller.

Additionally, the non-infiltrated segment length ψ_v was equivalently transposed to the loading end. As a result, the displacement of the fiber filament's end during the loading process was composed of the slip caused by the equivalent infiltrated segment L_v under a bonding-slip state, along with the deformation induced by the free elongation of the non-infiltrated segment ψ_v. The latter was computed through the filament's end load and the stress-strain relationship.

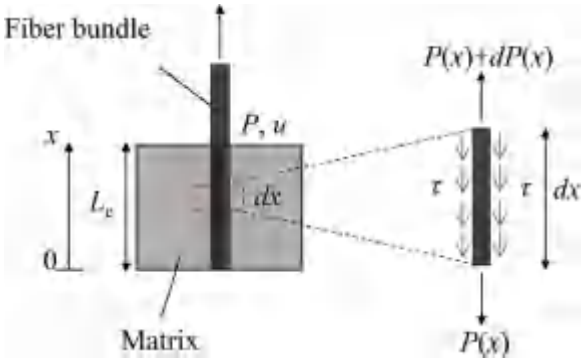


Fig. 3. A single carbon fiber bundle embedded in the cementitious matrix.

In this study, the above equivalent method is retained, and the following assumptions are used:

(1) The sleeve layer fiber filaments are divided into n layers, with the number of filaments in each layer denoted as $N_{s,i}$. The core layer is treated as an equivalent single layer with a filament count of N_{core}. Consequently, a single carbon fiber bundle comprises n+1 layers of fiber filaments.
(2) The combined lengths of infiltrated intervals from all discrete matrix regions are equivalently shifted to the free end.
(3) Due to the challenges in accurately analyzing the relative displacements and load transfer between filaments and between the matrix and filaments, it is assumed that all matrix regions remain fixed. The stress distribution in the filaments is solely determined by the bonding-slip relationship between the matrix and filaments, and load transmission between filaments and filaments is ignored.
(4) In the actual loading process, the fiber filaments discretely infiltrated by the matrix gradually undergo debonding. Thus, Banholzer's assumption of free elongation for the non-infiltrated

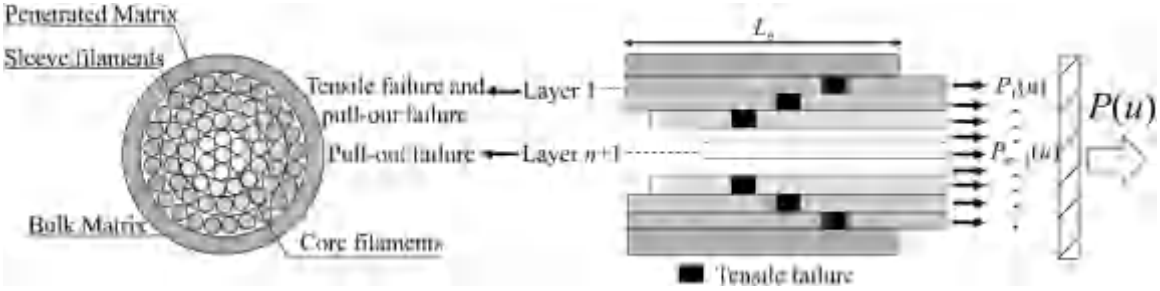


Fig. 1. Schematic diagram of the layered model.

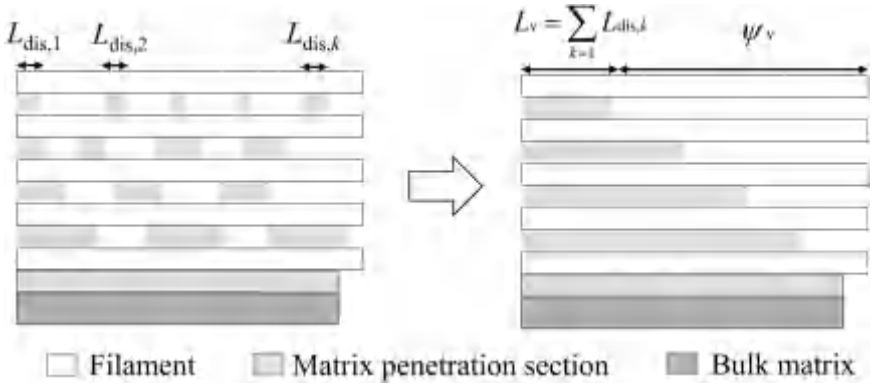


Fig. 2. Schematic diagram of equivalent infiltration length.

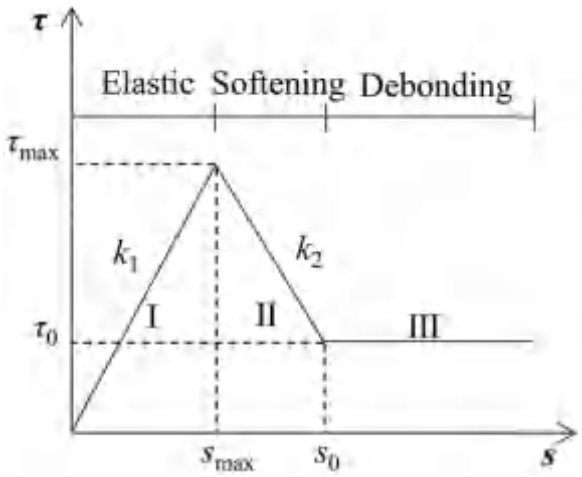


Fig. 4. The trilinear cohesive material law.

section will lead to a large elongation calculation. The elongation of the non-infiltrated segments is significantly influenced by the distribution of the matrix along the fiber's length direction, thereby rendering quantitative calculation unfeasible. In this study, the effect of elastic deformation is taken into account in calculating the resistance of the fiber filaments in the non-infiltrated section, whose strain is equal to the average strain of the equivalent infiltrated section.

2.2. Load-displacement analytical solution based on trilinear CML

Fig. 3 shows a schematic diagram of a carbon fiber bundle embedded in a cementitious matrix. The trilinear CML [23,26,50] (Fig. 4 and Eq. (2)) has been used to analyze the bond-slip relationship at the fiber-matrix interface:

$$\tau = \begin{cases} k_1 s & (0 \le s < s_{\max}) \\ -k_2 s + \dfrac{k_1 + k_2}{k_1}\tau_{\max} & (s_{\max} \le s < s_0) \\ \tau_0 & (s_0 \le s) \end{cases} \tag{2}$$

where τ is the bond stress, in MPa. s is the fiber-matrix slip, in mm. k_1 is the rising slope, in MPa/mm. k_2 is the descending slope, in MPa/mm. $\tau_{\max}$ is the maximum bond stress, in MPa. $s_{\max}$ is the slip under the maximum bond stress, in mm. τ_0 is the residual bond stress, in MPa. s_0 is the slip at the residual bond stress, in mm.

Based on the trilinear CML, during the pull-out process of the carbon fiber bundle, it goes through the following phases sequentially: elastic phase, elastic-softening phase, elastic-softening-debonding phase(for long bond lengths), softening phase(for short bond lengths), softening-debonding phase, and debonding phase. The shear stress distribution and load response are shown in Fig. 5. The detailed development process of each phase can refer to previous studies [23]. The minimum bond length required for the full development of the softening phase is represented by $L_{\text{eff,es}}$ [23,26]. When $L_e > L_{\text{eff,es}}$, the bond length is in the long bond state; when $L_e \le L_{\text{eff,es}}$, the bond length is in the short bond state. $L_{\text{eff,es}}$ is calculated using Eq. (3):

$$L_{\text{eff,es}} = \frac{\arcsin\left(-\frac{\tau_0}{\tau_{\max}}\right) + \frac{\pi}{2}}{\omega_2}, \omega_2 = \sqrt{\frac{ck_2}{EA}} \tag{3}$$

where c is the circumference of the fiber bundle, in mm; E represents the elastic modulus of the fiber bundle, in MPa; and A is the cross-sectional area of the fiber bundle, in mm^2.

According to the assumptions above, the matrix is fixed and immobile. The sleeve layer of a single carbon fiber bundle is divided into n

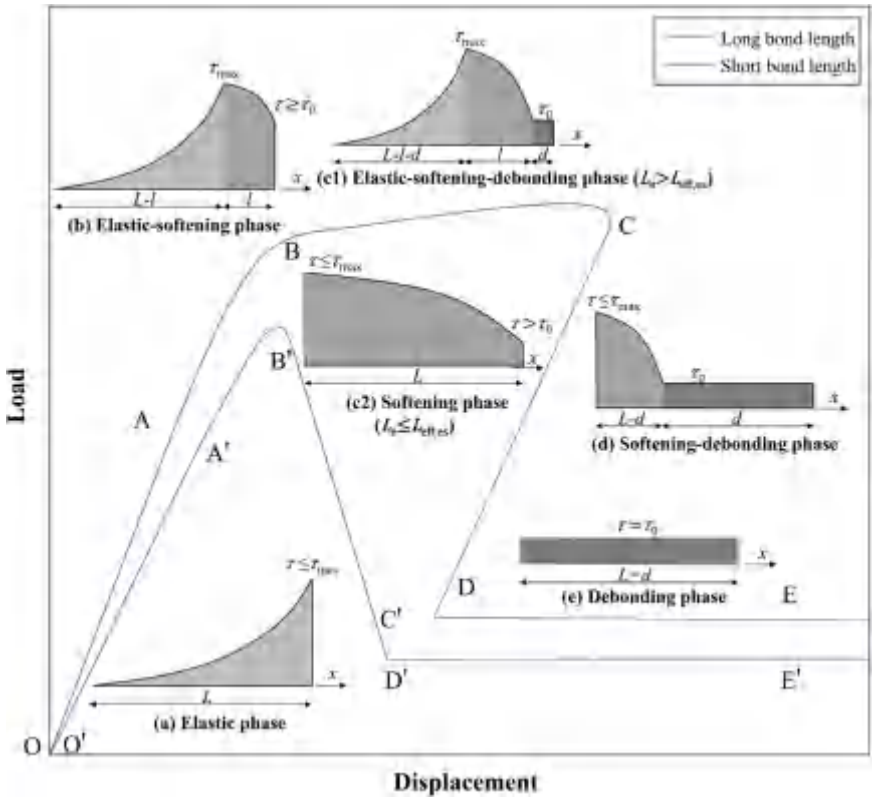


Fig. 5. Typical load-displacement response for a long and short bond length and diagram of shear stress distribution evolution along the length of the carbon fiber bundle during the pull-out process.

layers based on different equivalent infiltration lengths, and the equivalent infiltration length of each layer of fiber is denoted as $L_{v,i}$. Displacement control was used in the loading process. Therefore, after subtracting the elastic deformation of the free segment of the carbon fiber bundle outside the matrix, the average value of the measured loading-end displacement u using LVDTs and the loading-end displacement u_i of each layer of fibers conform to Eq. (4):

$$u = u_i = s_i, i = 1 \cdots n \tag{4}$$

The analytical solution for the relationship between the applied load and the slip of the carbon fiber bundle, based on the trilinear CML, has been reported [23]. Since the layered failure assumption is adopted in this study, the bond-slip process of fiber filaments in each layer is analyzed according to the aforementioned bond-slip process of a fiber bundle. Thus, the relationship between the load $P_i(s_i)$ and slip s_i for each layer of fiber filaments at various development phases can be acquired. Furthermore, the overall elongation of fiber filaments is calculated in this study by subtracting the slip of the loading end from the slip of the free end of the i-th layer of fiber filaments, thereby obtaining the average strain ε_i of the fiber filaments. The relationship between $P_i(s_i)$, ε_i, and s_i is represented in Eqs. (5)-(10). In the layered failure analysis process, the L in Fig. 5 corresponds to the equivalent infiltration length $L_{v,i}$ of fiber filaments in each layer.

It is assumed that the equivalent parameter value of trilinear CML (k_1=0.59 MPa/mm, k_2=0.35 MPa/mm, τ_{max}=0.61 MPa and τ_0=0.085 MPa), obtained by fitting the pull-out curve of the carbon fiber bundle after full impregnation with epoxy resin according to Eqs. (5)-(10), can adequately characterize the bonding performance of the interface between each layer of fiber filaments and the matrix under ideal conditions in CFRCM bundle pull-out simulations. In addition, when the embedded length L_e of the CFRCM bundle pull-out specimen is 30 mm, the average peak loads of specimens with the seawater sea-sand matrix and specimens with the normal matrix are 322 N and 338 N, respectively, with a difference of 4.7 %. Thus, it is evident that the interfacial bonding performance between the carbon fiber bundle and the two types of matrices is highly similar. Consequently, the same parameter values of trilinear CML are used for both matrices.

Elastic phase:

$$\begin{cases} P_i(s_i) = EA\omega_1 \tanh(\omega_1 L_{v,i}) \cdot s_i \\ \omega_1 = \sqrt{\dfrac{ck_1}{EA}} \\ s_{0,i} = \dfrac{P_i(s_i)}{EA\omega_1 \sinh(\omega_1 L_{v,i})} \\ \varepsilon_i = \dfrac{s_i - s_{0,i}}{L_{v,i}} \end{cases} \tag{5}$$

Elastic-softening phase:

$$\begin{cases} P_i(s_i) = EA\omega_2 \cot\varphi \left(s_i - \dfrac{k_1 + k_2}{k_1 k_2}\tau_{max} \right) \\ \varphi = \omega_2 l - \arctan \dfrac{\omega_1}{\omega_2 \tanh(\omega_1 L_{v,i} - \omega_1 l)} \\ s_i = \dfrac{\tau_{max} \sin\varphi}{k_2 \sin(\omega_2 l - \varphi)} + \dfrac{k_1 + k_2}{k_1 k_2}\tau_{max} \\ s_{0,i} = \dfrac{\tau_{max}}{k_1 \cosh(\omega_1 L_{v,i} - \omega_1 l)} = \dfrac{P_i(s_i)\cos(\omega_2 l - \varphi)}{EA\omega_1 \cos\varphi \sinh(\omega_1 L_{v,i} - \omega_1 l)} \\ \varepsilon_i = \dfrac{s_i - s_{0,i}}{L_{v,i}} \end{cases} \tag{6}$$

Softening phase (for short bond lengths):

$$\begin{cases} P_i(s_i) = EA\omega_2 \tan\left(\omega_2 L_{v,i}\right)\left(\dfrac{k_1 + k_2}{k_1 k_2}\tau_{max} - s_i\right) \\ s_{0,i} = \dfrac{k_1 + k_2}{k_1 k_2}\tau_{max} - \dfrac{P_i(s_i)}{EA\omega_2} \dfrac{1}{\sin(\omega_1 L_{v,i})} \\ \varepsilon_i = \dfrac{s_i - s_{0,i}}{L_{v,i}} \end{cases} \tag{7}$$

Elastic-softening-debonding phase (for long bond lengths):

$$\begin{cases} P_i(s_i) = c\tau_0 d + \dfrac{c\tau_{max}\cos\varphi}{\omega_2 \sin(\omega_2 l - \varphi)} \\ \varphi = \omega_2 l - \arctan \dfrac{\omega_1}{\omega_2 \tanh(\omega_1 L_{v,i} - \omega_1 l - \omega_1 d)} \\ s_i = \dfrac{P_i(s_i)d}{EA} - \dfrac{c\tau_0 d^2}{2EA} + \dfrac{\tau_{max}}{k_1} + \dfrac{\tau_{max} - \tau_0}{k_2} \\ -\dfrac{\tau_0}{k_2} = \dfrac{\tau_{max}\sin\varphi}{k_2 \sin(\omega_2 l - \varphi)} \\ s_{0,i} = \dfrac{\tau_{max}}{k_1 \cosh(\omega_1 L_{v,i} - \omega_1 l - \omega_1 d)} = \dfrac{(P_i(s_i) - c\tau_0 d)\cos(\omega_2 l - \varphi)}{EA\omega_1 \cos\varphi \sinh(\omega_1 L_{v,i} - \omega_1 l - \omega_1 d)} \\ \varepsilon_i = \dfrac{s_i - s_{0,i}}{L_{v,i}} \end{cases} \tag{8}$$

Softening-debonding phase:

$$\begin{cases} P_i(s_i) = c\tau_0 d + \dfrac{c\tau_0 \tan(\omega_2 L_{v,i} - \omega_2 d)}{\omega_2} \\ s_i = \dfrac{P_i(s_i)d}{EA} - \dfrac{c\tau_0 d^2}{2EA} + \dfrac{\tau_{max} - \tau_0}{k_2} + \dfrac{\tau_{max}}{k_1} \\ s_{0,i} = -\dfrac{\tau_0}{k_2}\dfrac{1}{\cos(\omega_2 L_{v,i} - \omega_2 d)} + \dfrac{k_1 + k_2}{k_1 k_2}\tau_{max} \\ \varepsilon_i = \dfrac{s_i - s_{0,i}}{L_{v,i}} \end{cases} \tag{9}$$

Debonding phase:

$$\begin{cases} P_i(s_i) = c\tau_0 (L_{v,i} - s_i) \\ \varepsilon_i = \dfrac{P_i(s_i)}{EA} - \dfrac{c\tau_0 L_{v,i}}{2EA} \end{cases} \tag{10}$$

3. Establishment of pull-out equivalent telescopic layered failure model based on piezoresistive effect

3.1. Theoretical logic of pull-out equivalent telescopic layered failure model

Before introducing the telescopic layered failure model based on the piezoresistive effect, it is necessary to clarify the classification and number of fibers. As shown in Fig. 6(a), the resistance of a dry carbon fiber bundle is a parallel circuit composed of the resistance R_u of tens of thousands of intact filaments and the resistance R_c of filaments that have made contact with other filaments after rupturing. During the loading process, the rupture of intact filaments and their subsequent contact with other filaments is a dynamic and random process. Therefore, the circuit of the carbon fiber bundle also changes randomly. Factors affecting the resistance of carbon fiber bundles include the elastic deformation, ruptures (including initial ruptures and load-bearing ruptures), and contact of fibers [42].

The resistance of the carbon fibers in the matrix also conforms to the above characteristics. After the mortar matrix infiltrates the carbon fibers, the fibers are classified based on their initial state and failure mode

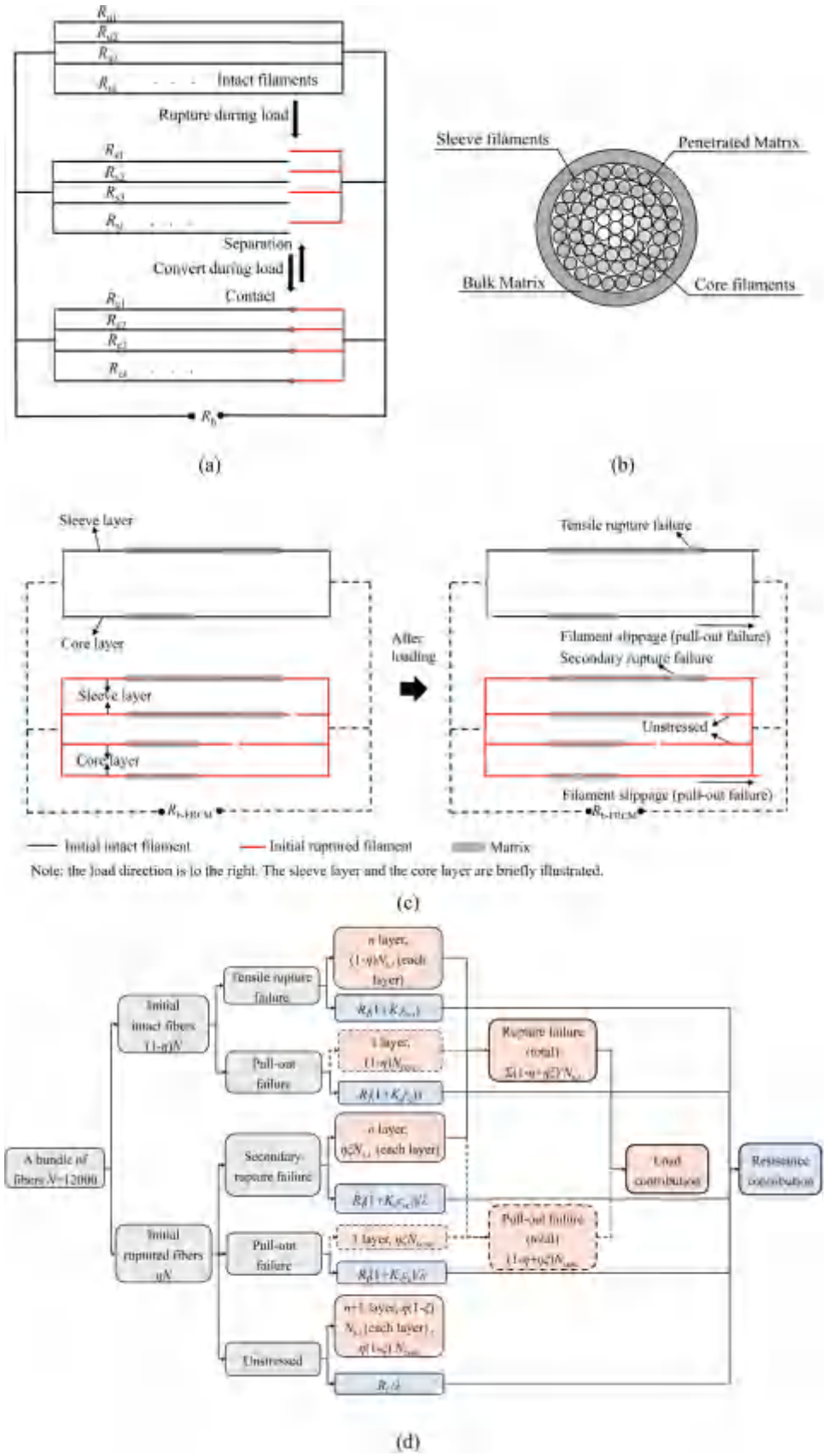


Fig. 6. (a) Dynamic random equivalent parallel circuit model of dry carbon fiber bundle; (b) Telescopic layered failure model; (c) The state and failure modes of the filaments before and after CFRCM loading, and the schematic diagram of the parallel circuit; and (d) Schematic classification of the number of filaments in each layer and their contribution to load and resistance during the CFRCM bundle pull-out process.

in Fig. 6(b)-(d), illustrating the number of filaments in each layer and their contribution to load and resistance. The specific explanation is as follows:

In a fiber bundle used in this study, the total number N of fiber filaments is 12,000. Due to various production, transportation, and fabrication processes, some fiber filaments have already experienced rupture before mechanical testing. These pre-ruptured fibers are defined as initial ruptured fibers, and the proportion of these fibers in the total amount of fibers is defined as the initial rupture ratio η. Hence, the total number of initial intact fibers is $(1\text{-}\eta)N$, while the total number of initial ruptured fibers is ηN.

The initial intact fiber filaments are divided into tensile rupture failure fiber filaments (i.e., sleeve layer, with n layers) and pull-out failure fiber filaments (i.e., core layer) according to their failure modes. It is assumed that the probability of initial rupture of the fiber at each layer is the same. The number of initial intact fibers per layer in the sleeve layer is $(1\text{-}\eta)N_{s,i}$. The contribution to resistance by each layer of fiber filaments is due to elastic deformation before rupture occurs. Meanwhile, the influence of elastic deformation after rupture on resistance is ignored, and only the resistance change caused by filament contact is considered. The ratio of the number of contacting fiber filaments to the total number of ruptured fiber filaments is defined as the equivalent contact ratio λ. The number of initial intact fibers in the core layer is $(1\text{-}\eta)N_{\text{core}}$. The pull-out fiber filaments remain intact throughout, contributing to the resistance change due to elastic deformation.

The initial ruptured fiber filaments can be classified into two types based on the location of the rupture: fibers with initial ruptures occurring inside the matrix and fibers with initial ruptures occurring outside the matrix (i.e., the fiber-free section between the acrylic reinforcing sheet and the matrix), as shown in Fig. 6(c). The secondary rupture reduction factor ξ of the initial rupture fiber filaments is defined as the ratio of matrix length (i.e., fiber embedding length) to the total fiber length where initial rupture may occur, as shown in Eq. (11):

$$\xi = \frac{L_e}{L_e + L_f} \tag{11}$$

where L_e is the length of fiber embedded in the matrix, and L_f is the length of the free segment between the acrylic reinforcement sheet and the matrix.

Fibers that experience initial rupture within the matrix can still transfer load. Based on the failure modes, they can be divided into secondary rupture failure fibers and pull-out failure fibers. The number of these fibers is $\eta\xi N_{s,i}$, and $\eta\xi N_{\text{core}}$, respectively, and their contribution to resistance change theory is the same as that of initial intact fiber filaments.

Fibers that experience initial rupture outside the matrix cannot bear any load. However, because these fiber filaments can still form a current path within the resistance testing section, their contact with other fiber filaments can cause resistance change. The number of these fibers is $\eta(1\text{-}\xi)N$. It is assumed that they are uniformly distributed in the $n+1$ layered system. Therefore, the number of these fibers in each layer of the sleeve layer is $\eta(1\text{-}\xi)N_{s,i}$, and in the core layer is $\eta(1\text{-}\xi)N_{\text{core}}$.

In conclusion, the total number of fibers that fail due to rupture is $\sum_{i=1}^{n}(1-\eta+\eta\xi)N_{s,i}$ and the total number of fibers that experience pull-out failure is $(1\text{-}\eta+\eta\xi)N_{\text{core}}$. These fibers contribute to the load. A more detailed resistance calculation theory will be presented in Section 3.2.

Due to the sensitivity of the CFRCM bundle's resistance to fiber filament rupture and its insensitivity to fiber filament elastic deformation, the loaded end displacement interval corresponding to the occurrence of tensile failure of the fiber filaments in each layer of the sleeve layer is selected as the calculation interval. The relationship curve between the load $P_{f,i}(u_i)$ and the displacement u_i at the loading end of fiber filaments under different equivalent infiltration lengths L_v, obtained based on Eqs. (5)-(10) and the equivalent parameter value of trilinear CML in Section 2.2, is shown in Fig. 7. The ultimate load for a single fiber filament is given by Eq. (12):

$$P_{\text{fu}} = E\varepsilon_u A \tag{12}$$

In reference [26], L_a is defined as the anchorage length, which is the minimum bond length required to reach the tensile capacity of carbon fibers. Similarly, this study defines L_a as the minimum equivalent infiltration length needed for the filament to reach its tensile strength. According to the equivalent parameter values of trilinear CML used in this study, L_a is 7 mm (Fig. 7). When $L_v \geq L_a$, the load borne by fiber filaments during loading can reach the ultimate load P_{fu}, causing filaments to rupture. These fiber filaments are the sleeve layer filaments. When they rupture, the displacement at the loading end of the fiber filament in the i-th sleeve layer is defined as $u_{\text{fu},i}$. When $L_v = L_e$, the fiber filaments in this layer are the first to rupture, and the corresponding displacement $u_{\text{fu},i}$ is defined as $u_{\text{fu,min}}$. When $L_v = L_a$, The fibers in this layer are the last to rupture in the sleeve layer, and the corresponding displacement $u_{\text{fu},i}$ is defined as $u_{\text{fu,max}}$. When $L_v < L_a$, these fibers are no longer ruptured but experience pull-out failure. They are considered core layer fibers and are treated as a whole for load calculations. The average equivalent infiltrated length of the core layer fibers is defined as $L_{v,\text{core}}$. In summary, the displacement calculation range is determined as $[u_{\text{fu,min}}, u_{\text{fu,max}}]$.

3.2. Theory of resistance calculation

According to the theory of parallel circuit resistance calculation (Fig. 6(a)), the resistance of the carbon fiber bundle is as Eq. (13):

$$\frac{1}{R_b} = \sum_{x=1}^{i}\frac{1}{R_{ux}} + \sum_{y=1}^{k}\frac{1}{R_{cy}} \tag{13}$$

where i and k are the number of intact filaments and the number of contacting filaments, respectively; R_{ux} is the resistance of the x-th intact filament, and R_{cy} is the y-th conductive path formed by the contacting filaments.

Assuming that the resistance of all intact filaments before loading and the resistance of the contacting filaments are R_f, and considering the change in resistance of intact filaments due to elastic deformation during the tensile process. Then:

$$R_{ux} = R_f\left(1 + K_s\varepsilon_f\right) \tag{14}$$

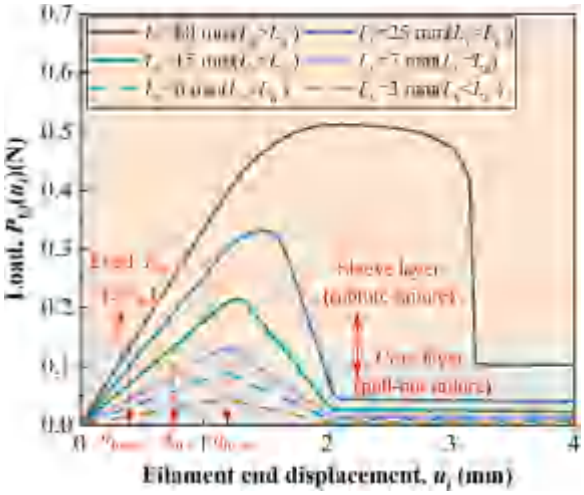


Fig. 7. Load response at the loading end of fiber filaments under different equivalent infiltrating lengths L_v. Note: only some representative values are shown; ε_{fu} is the ultimate strain.

$$\frac{1}{R_b}=\frac{i}{R_f\left(1+K_s\varepsilon_f\right)}+\frac{k}{R_f} \tag{15}$$

$$R_f=\rho_f L_e \tag{16}$$

where R_f is the resistance of a single filament, in Ω; K_s is the sensitivity coefficient with a value of 1.1 [51]; ε_f is the filament strain; ρ_f is the filament length resistivity with a value of 441.733, in Ω/mm.

Combining Eqs. (14)-(16) and Fig. 6(b)-(d), the resistance $R_{b\text{-}s}$ of the sleeve layer fibers, the resistance $R_{b\text{-}c}$ of the core layer fibers, and the resistance $R_{b\text{-}CFRCM}(u)$ of CFRCM bundles at various end displacements u are shown in Eq. (17):

$$\begin{cases}\dfrac{1}{R_{b-s}}=\displaystyle\sum_{i=1}^{n}\left[\frac{(1-\eta)}{1+K_s\varepsilon_{s,i}'(u)}+\frac{\lambda\eta\xi}{1+K_s\varepsilon_{sr,i}'(u)}+\lambda\eta\left(1-\xi\right)\right]\frac{N_{s,i}}{R_f}\\ \dfrac{1}{R_{b-c}}=\left[\dfrac{1-\eta+\lambda\eta\xi}{1+K_s\varepsilon_c'(u)}+\lambda\eta\left(1-\xi\right)\right]\dfrac{N_{core}}{R_f}\\ \dfrac{1}{R_{b-CFRCM}(u)}=\dfrac{1}{R_{b-s}}+\dfrac{1}{R_{b-c}}\end{cases} \tag{17}$$

where $N_{s,i}$ is the number of fiber filaments in the i-th layer of the sleeve layer, N_{core} is the number of fiber filaments in the core layer, and ξ is the secondary rupture reduction factor of the initial rupture fiber. $\varepsilon_{s,i}'$, $\varepsilon_{sr,i}'$, ε_c' represent the equivalent average strains of intact fiber filaments in the i-th layer, the equivalent average strains of initial ruptured fibers in the i-th layer, and the equivalent average strains of core layer fiber filaments used for resistance calculation, respectively. These can be calculated using Eq. (18):

$$\varepsilon_{s,i}'=\begin{cases}\varepsilon_{s,i} & ,u<u_{fu,i}\\ \dfrac{1-\lambda}{\lambda K_s} & ,u\geq u_{fu,i}\end{cases} \tag{18a}$$

$$\varepsilon_{sr,i}'=\begin{cases}\varepsilon_{sr,i} & ,u<u_{fu,i}\\ 0 & ,u\geq u_{fu,i}\end{cases} \tag{18b}$$

$$\varepsilon_c'=\varepsilon_c \tag{18c}$$

where $\varepsilon_{s,i}$, $\varepsilon_{sr,i}$, ε_c are the average strains calculated from the bond-slip relationship Eqs. (5)-(10) for initial intact fiber filaments in the i-th layer, initial ruptured fiber filaments in the i-th layer, and core layer fiber filaments, respectively.

It's worth noting that initial intact fibers bear loads until they reach their ultimate strength, at which point these filaments rupture. Meanwhile, their resistance calculation mode shifts to contact conductivity. For computational convenience, when $u\geq u_{fu,i}$, the fiber filament ruptures, and the influence of elastic deformation on resistance is disregarded, while the resistance change due to contact is considered. To maintain a uniform formula format before and after fiber rupture, $(1-\lambda)/\lambda K_s$ is employed as a replacement for $\varepsilon_{s,i}$. Upon substitution, this portion of resistance changes from $[1+K_s\varepsilon_{s,i}(u)]R_f/[(1-\eta)N_{s,i}]$ to $R_f/[(1-\eta)\lambda N_{s,i}]$.

3.3. Equivalent contact ratio and initial rupture ratio

The resistance solution involves the variation of the equivalent contact ratio λ with the loading process and initial rupture ratio η, so it is necessary to establish the solution method of λ and η. According to the piezoresistive effect law of the CFRCM bundle pull-out process, the change of λ conforms to the following characteristics:

(1) In the elastic phase of the load-displacement curve, the change of resistance is mainly caused by the elastic deformation of the fiber filaments and the change of λ. Since the fiber filaments hardly rupture, the change of λ is small at this phase. Since the initial ruptured fiber filaments may contact or separate due to force, λ may fluctuate slightly or remain constant.
(2) In the softening phase of the load-displacement curve, many fiber filaments rupture, and λ increases significantly.
(3) In the debonding phase of the load-displacement curve, the growth of λ slows down, the slope gradually tends to zero, and λ may even decrease due to the dislodging of contacting filaments in the pull-out process. Based on the above characteristics, the sigmoid function is introduced to describe the change process of λ and its functional form is shown in Eq. (19):

$$f(u)=\lambda(u)=\frac{A}{1+e^{B-C\cdot u}}+D \tag{19}$$

where the four coefficients (i.e., A, B, C, and D) are solved by the following four boundary conditions:

(1) According to Eq. (15), the initial equivalent contact ratio $\lambda(0)$ before loading satisfies Eq. (20):

$$\frac{1}{R_{b-CFRCM}(0)}=\frac{(1-\eta)N}{R_f}+\frac{\lambda(0)\eta N}{R_f} \tag{20}$$

Then:

$$\lambda(0)=\frac{R_f}{\eta N R_{b-CFRCM}(0)}-\frac{1}{\eta}+1 \tag{21}$$

Let $\lambda(0)$=0, which means that the initial rupture number of the carbon fiber bundle is minimized, obtaining η_{min} as shown in Eq. (22):

$$\eta_{min}=1-\frac{R_f}{NR_{b-CFRCM}(0)} \tag{22}$$

Based on the value of η in [42], and considering possible damage to carbon fiber bundle during specimen preparation and transportation, as well as the reduction in computational complexity of the equivalent telescopic layered failure model, this study assumes that the maximum value of η, η_{max}, is 0.45. Therefore, the range of initial rupture ratio η,[η_{min}, η_{max}], is available.

(2) The difference $\Delta\lambda$ between $\lambda(u_{fu,min})$ and $\lambda(0)$ is within ± 5 %, as shown in Eq. (23) when the first fiber filament undergoes tensile rupture:

$$\lambda\left(u_{fu,\,min}\right)=\lambda(0)+\Delta\lambda,\ |\Delta\lambda|\leq 5\% \tag{23}$$

(3) $\lambda(u_{fu,max})$ satisfies Eq. (24) when all fiber filaments undergo tensile rupture:

$$\frac{1}{R_{b-CFRCM}\left(u_{fu,max}\right)}=\frac{\lambda\left(u_{fu,max}\right)(N-N_{core})}{R_f}+\frac{\lambda\left(u_{fu,max}\right)(1-\xi)\eta N_{core}}{R_f}+\frac{\lambda\left(u_{fu,max}\right)\xi\eta N_{core}}{R_f\left(1+K_s\varepsilon_c\left(u_{fu,max}\right)\right)}+\frac{(1-\eta)N_{core}}{R_f\left(1+K_s\varepsilon_c\left(u_{fu,max}\right)\right)} \tag{24}$$

Then：

$$\lambda\left(u_{fu,\,max}\right)=\frac{\frac{R_f}{R_{b-CFRCM}\left(u_{fu,\,max}\right)}-\frac{(1-\eta)N_{core}}{1+K_s\varepsilon_c\left(u_{fu,\,max}\right)}}{N-N_{core}+\frac{\eta\xi N_{core}}{1+K_s\varepsilon_c\left(u_{fu,\,max}\right)}+\eta\left(1-\xi\right)N_{core}} \tag{25}$$

(4) The section with the fastest rate of change of $\lambda(u)$ coincides with the plunging section of the load-displacement curve, where the displacement corresponding to the maximum value of the slope of the $\lambda(u)$ curve is equal to the displacement u_d corresponding to the midpoint of the falling section of the load-displacement curve. Therefore, $\lambda(u_d)$ satisfies Eq. (26):

$$\lambda''(u_d) = 0 \tag{26}$$

3.4. Calculation of fiber filaments number in each layer and simulation of pull-out piezoresistive effect

The embedding lengths L_e (less than 7 mm) of all the fiber filaments of the core layer are less than $L_{eff,es}$ (49 mm), which allows the softening phase to develop fully. Therefore, they are all considered short bond length cases. After the n-th fiber filaments rupture in the sleeve layer, the load-displacement curves of all the fiber filaments in the core layer enter the decreasing section. The number of fiber filaments in the core layer, N_{core}, can be derived from the slope of the descending segment of the load-displacement test curve of the carbon fiber bundle during the softening phase (Eq. (7)). For a single fiber filament, its slope and load in the descending section are denoted as K_{single}, P_{single}, respectively, as shown in Eqs. (27)-(28):

$$K_{\text{sin gle}} = EA\omega_2 \tan\left(\omega_2 L_{v,core}\right) \tag{27}$$

$$P_{\text{sin gle}} = K_{\text{sin gle}}\left(\frac{k_1+k_2}{k_1k_2}\tau_{max} - s_i\right) \tag{28}$$

For a fiber bundle, its slope and load in the descending section are denoted as K_{all} and P_{all}, respectively, as shown in Eq. (29):

$$P_{all} = K_{all}\left(\frac{k_1+k_2}{k_1k_2}\tau_{max} - s_i\right) \tag{29}$$

The relationship between P_{all} and P_{single} satisfies Eq. (30):

$$P_{all} = \left(1-\eta+\xi\eta\right)N_{core}P_{\text{sin gle}} \tag{30}$$

Thus, the relationship between K_{all} and K_{single} satisfies Eq. (31):

$$K_{all} = \left(1-\eta+\xi\eta\right)N_{core}K_{\text{sin gle}} \tag{31}$$

According to Eqs. (27) and (31), the number of the core layer filaments can be given by Eq. (32):

$$N_{core} = \frac{K_{all}}{EA\omega_2 \tan\left(\omega_2 L_{v,core}\right)\left(1-\eta+\xi\eta\right)} \tag{32}$$

According to Eq. (17), the number of layers of fiber filaments (i.e., the number of unknown numbers) is n+1, and the number of formulas is n. To solve for the number of fiber filaments in each layer, it is also necessary to introduce Eq. (33):

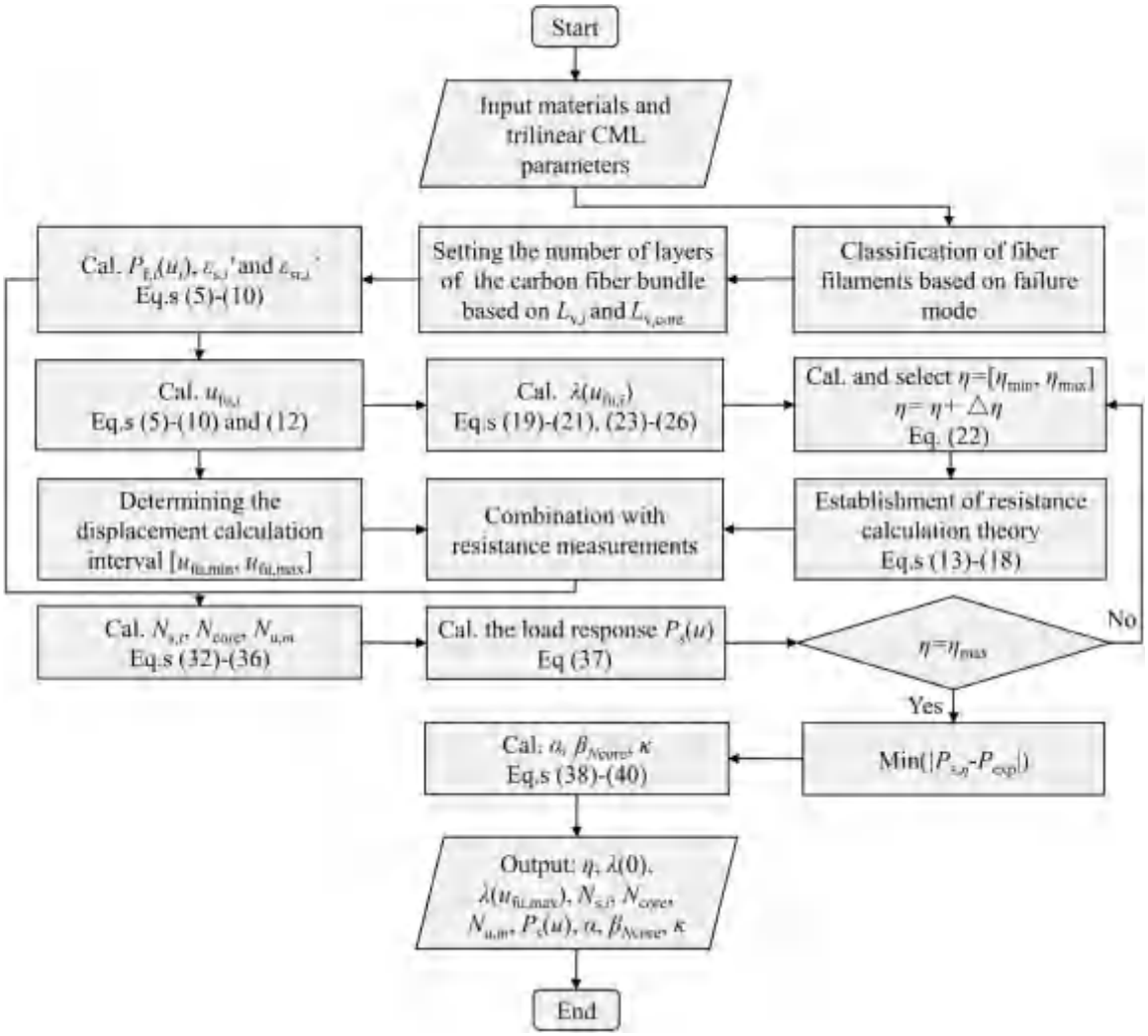


Fig. 8. The theoretical flow of equivalent telescopic layered failure calculation for CFRCM bundle pull-out process based on piezoresistive effect.

$$N_{\text{core}} + \sum_{i=1}^{n} N_{s,i} = N \tag{33}$$

The calculated coefficient of resistance of the j-th layer of fiber filaments at the time of rupture of the i-th layer of fiber filaments is denoted as $k_{i,j}$, and according to Eq. (17), $k_{i,j}$ can be obtained as shown in Eq. (34):

$$k_{i,j} = \begin{cases} \left[\dfrac{(1-\eta)}{1+K_s\varepsilon_{s,j}'(u_{\text{fu},i})} + \dfrac{\eta\xi\lambda(u_{\text{fu},i})}{1+K_s\varepsilon_{\text{sr},j}'(u_{fu,i})} + \eta(1-\xi)\lambda(u_{\text{fu},i})\right]\dfrac{1}{R_f} (i \le n, j \le n) \\ \left[\dfrac{1-\eta+\eta\xi\lambda(u_{\text{fu},i})}{1+K_s\varepsilon_c'(u_{\text{fu},i})} + \eta(1-\xi)\lambda(u_{\text{fu},i})\right]\dfrac{1}{R_f} (i \le n, j = n+1) \end{cases} \tag{34}$$

Therefore, the process of solving for the number of fiber filaments in each layer can be transformed into solving for $\boldsymbol{X}$ in the matrix (Eq. (35)):

$$\boldsymbol{KX} = \boldsymbol{R} \tag{35a}$$

$$K = \begin{bmatrix} k_{1,1} & \cdots & k_{1,n} & k_{1,n+1} \\ \vdots & \ddots & \vdots & \vdots \\ k_{n,1} & \cdots & k_{n,n} & k_{n,n+1} \\ 1 & \cdots & 1 & 1 \end{bmatrix}, X = \begin{bmatrix} N_1 \\ \vdots \\ N_n \\ N_{\text{core}} \end{bmatrix},$$

$$R = \begin{bmatrix} \dfrac{1}{R_{\text{b-CFRCM}}(u_{\text{fu,min}})} \\ \vdots \\ \dfrac{1}{R_{\text{b-CFRCM}}(u_{\text{fu,max}})} \\ N \end{bmatrix} \tag{35b}$$

In addition, the number of intact fiber filaments in the m-th layer, $N_{u,m}$, can be obtained from Eq. (36):

$$N_{u,m} = \left(1-\eta+\eta\xi\right)\left(N - \sum_{i=1}^{m} N_{s,i}\right) \tag{36}$$

The load response $P_{f,i}(s_i)$ of each layer of fiber filaments can be calculated based on the shear stress distribution and bond-slip relationship at each phase (Eqs. (5)-(10)). The load response $P_{f,i}(u)$ for each layer of filaments in the sleeve layer and the load response $P_{f,\text{core}}(u)$ for the filaments of the core layer at the loading end displacement u can be obtained by Eqs. (4)-(10). Finally, the load response of the carbon fiber bundle can be simulated by Eq. (37):

$$P_s(u) = \sum_{i=1}^{n} (1-\eta+\eta\xi) P_{f,i}(u) N_{s,i} + \left(1-\eta+\eta\xi\right) P_{f,\text{core}}(u) N_{\text{core}} \tag{37}$$

In addition, the following key parameters will also be analyzed and discussed in Section 5: the fiber utilization ratio is denoted as α, the core layer fiber ratio is denoted as $\beta_{N\text{core}}$, and the equivalent infiltration ratio is denoted as κ. They can be calculated by Eqs. (38)-(40), respectively:

$$\alpha = \frac{P_{\max}}{P_b} \tag{38}$$

$$\beta_{N_{\text{core}}} = \frac{N_{\text{core}}}{N} \tag{39}$$

$$\kappa = \frac{\sum_{i=1}^{n} N_{s,i} L_{v,i} + N_{\text{core}} L_{v,\text{core}}}{N L_e} \tag{40}$$

where P_b is the ultimate tensile load of a single bundle of fiber bundle, equaling 890 N [42]; $P_{\max}$ is the peak pull-out load of the test.

The above computational flow is shown in Fig. 8. In the simulation process of the piezoresistive effect, a step length is continuously applied to the initial rupture ratio η, and the piezoresistive effect of η in the interval $[\eta_{\min}, \eta_{\max}]$ is calculated until the piezoresistive effect at $\eta = \eta_{\max}$ is simulated. In this way, the load response at different initial rupture ratios can be obtained, and the simulated load response with the smallest difference from the test load response can be selected. The equivalent layer number n of the sleeve layer influences the model's simulation results. The higher the value of n, the more accurate the results. When n is large, the differences in results decrease, but the computational effort increases. After calculation, the simulation results stabilize when n equals or exceeds 50 layers.

4. Experimental program

To apply the equivalent telescopic layered failure model to the CFRCM specimens, this section introduces the experimental procedures and methods. The experimental results will be provided and discussed in Section 5.

4.1. Material properties

The properties of the carbon fiber bundle are presented in Table 1. The matrix includes normal mortar (freshwater ISO standard sand) and seawater sea-sand mortar. Table 2 presents the concentrations of the primary ions identified in seawater. The sand utilized in the normal mortar is a mixture of ISO standard sand with a particle size distribution between 0.5–1 mm and fine sand in the range of 0.25–0.5 mm, in a weight ratio of 2:1. The sea-sand, in its unprocessed state, has its particle size distribution and moisture content outlined in Table 3. The formulation of both normal and seawater sea-sand mortars was proportionally designed aiming to achieve comparable compressive and flexural strengths, as shown in Table 4. The flexural and compressive strengths of the matrix at 28 days were measured according to the specification [52]. Both types of matrices exhibit similar strengths, as shown in Table 5.

4.2. Specimen preparation

The specimen preparation process includes specimen casting, specimen curing, and preparation of the measurement electrodes and acrylic reinforcing sheets, as detailed in previous research [42]. The measurement electrodes are used to measure the resistance change of carbon fibers in CFRCM bundles during the loading process. The schematic diagram of the specimen is shown in Fig. 9. The specimens were labeled as "AB-L_e-X" (Table 6), where AB is the type of matrix, including normal mortar matrix (NM) and seawater sea-sand matrix (SM); L_e is the embedding length of the carbon fiber bundle in the matrix, with values of 60, 90 and 120 mm respectively; X is the number of the parallel specimen. Each experimental group consists of 4–6 specimens. For instance, SM-60–1 represents the first specimen in the series of seawater

Table 1
Properties of the carbon fiber bundle.

Filament number N	Filament diameter (μm)	Elastic modulus E (GPa)	Ultimate tensile strength (MPa)	Ultimate tensile Strain ε_u	Electrical resistivity per unit length ρ_f (Ω/mm)
12,000	7	230	3530	1.1 %	441.733

Table 2
Types and content of seawater ions.

pH	Cl^- (g/L)	SO_4^{2-} (g/L)	Na^+ (g/L)	Mg^{2+} (g/L)	K^+ (g/L)	Ca^{2+} (g/L)
8.02	14.81	1.82	15.74	1.51	1.21	6.35

Table 3
Particle gradation and moisture content of sea-sand.

Sieve residue rates of different particle sizes (%)						Fineness modulus	Moisture content (%)
4.8 mm	2.4 mm	1.2 mm	0.6 mm	0.3 mm	0.2 mm		
0.4	6.7	19.5	34.5	66	96.2	2.2	3.65

Table 4
The mix ratio of two matrices.

The type of matrix	Portland cement (P. O 42.5) (g)	Water (g)	Sand (g)	Redespersible latex powder (Wacker 4115 N)/g	Superplasticizer (MG SKY 8860)/g
NM	100	45	200	1.5	0.15
SM	100	55	207.3	1.5	0.2

Note: NM is freshwater ISO standard sand mortar; SM is seawater sea-sand mortar. The same abbreviations are used below.

Table 5
The Strength of two matrices.

The type of matrix	Curing age	Flexural strength		Compression strength	
		Mean value (MPa)	COV	Mean value (MPa)	COV
NM	28d	4.83	14.3	41.67	5.82
SM	28d	4.70	4.25	39.17	5.01

sea-sand matrix CFRCM with a fiber embedding length of 60 mm.

4.3. Loading and measurement methods

Fig. 10 illustrates the setup consisting of the loading device and measurement system. The loading test was conducted using a Sansi UTM6503 electronic universal testing machine capable of handling loads up to 5 kN. The test was performed at a rate of 0.2 mm/min, with a sampling frequency of 10 Hz. To ensure load transfer, acrylic reinforcement sheets were clamped using a fixture, while the other end was subjected to a counterforce via a frame. Displacement measurements at the load end were taken using two LVDTS, and the collected data was recorded using a Donghua DH3816N-type data collector. The displacement values used in the subsequent calculation process have been deducted by the elastic deformation of the carbon fiber bundle not embedded in the matrix. The electrode measurement method for CFRCM bundles follows [53], and contact resistance has been eliminated. A steady direct current of 1 mA was applied between two measurement points, denoted as point 1 and point 2, while voltage data was gathered using the Donghua collector system at a sampling rate of 10 Hz. According to Ohm's law, the absolute value of the measured voltage corresponded to the CFRCM bundles' resistance value.

5. Results and discussion

5.1. Comparison of piezoresistive effect simulation results with experimental results

The failure modes of the CFRCM specimens are shown in Fig. 11. Due to the uneven infiltration of carbon fiber filaments by the matrix, carbon fiber bundles in both the normal mortar matrix and seawater sea-sand matrix CFRCM specimens exhibited partial fiber filaments tensile rupture failure and partial fiber filaments pull-out failure, also known as telescopic layered failure.

Some typical examples are used to analyze the simulation results. Fig. 12 shows the pull-out piezoresistive effect results in this study, simulated by the equivalent telescopic layered failure model for normal matrix CFRCM bundles (NM-60 series) and seawater sea-sand matrix CFRCM bundles (SM-60 series). The key parameters of the simulation results for the remaining specimens are listed in Table 6. It can be found that the simulated theoretical load-displacement response closely matches the experimental load-displacement response. In addition, the interfacial bonding performance and piezoresistive effect between the carbon fiber bundle and the two types of matrices are similar. Thus, the substitution of freshwater and river sand with seawater and sea-sand is feasible.

In the elastic phase, the number $N_{s,i}$ of ruptured fibers due to pull-out load is relatively small. Many fibers rupture during the softening phase, leading to a sharp decrease in load. In the debonding phase, a few fibers continue to rupture, and the variation trend of the number N_u of intact fibers is consistent with the results reported in [28]. Within the calculation range $[u_{fu,min}, u_{fu,max}]$, the simulated resistance values match the measured values perfectly. For the non-calculation content (e.g., the elastic phase), the resistance values obtained through reverse calculation using the equivalent layered model are consistent with the experimental values. According to Fig. 12(d) and (f), it can be observed that when there is a sudden increase in the resistance curve, there are usually many fiber ruptures, and the number of these ruptured fibers can be calculated using the equivalent telescopic layered failure model. At this point, the simulated load-displacement curve exhibits a sudden drop in load, consistent with the trend in the experimental curve.

In conclusion, when applied to experimental data, the equivalent telescopic layered failure model yields good simulation results. It applies to CFRCM bundles with varying embedding lengths and two types of matrices (i.e. normal matrix and seawater sea-sand matrix) in this study. The variation trend in the simulated number of fiber ruptures aligns with experimental observations and the mechanisms of the pull-out piezoresistive effect.

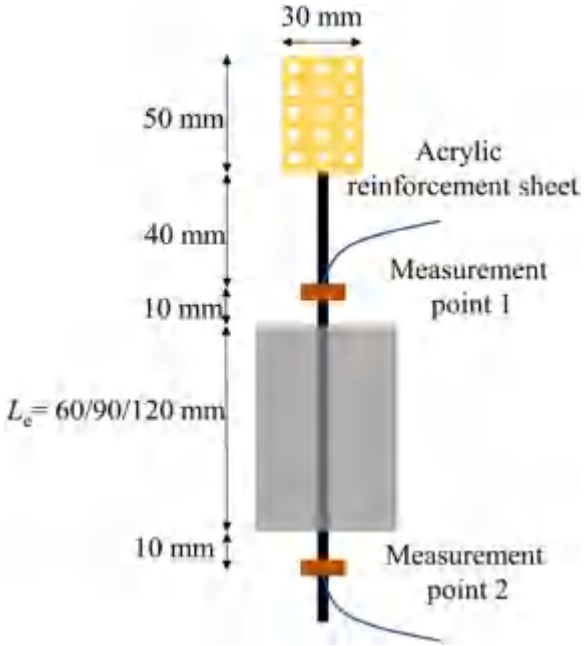


Fig. 9. Schematic diagram of specimen.

Table 6
Key parameters for CFRCM bundles pull-out equivalent layered failure calculation.

Specimens	η	λ (0)	λ ($u_{fu,max}$)	N_{core}	$L_{v,core}$ (mm)	P_{max} (N)	P_{smax} (N)	α	β_{Ncore}	κ
NM-60-1	0.20	0.02	0.26	2075	2.00	601.44	605.03	0.68	0.17	0.58
NM-60-2	0.26	0.17	0.36	3126	6.25	639.86	635.97	0.71	0.26	0.56
NM-60-3	0.26	0.01	0.30	2765	3.75	576.75	560.83	0.63	0.23	0.55
NM-60-4	0.29	0.17	0.56	4897	1.25	538.19	571.33	0.60	0.41	0.38
NM-60-5	0.21	0.25	0.65	3742	3.00	622.79	634.46	0.70	0.31	0.44
NM-60-6	0.41	0.36	0.57	4685	0.75	411.41	425.44	0.46	0.39	0.35
SM-60-1	0.30	0.17	0.21	3508	2.00	512.34	513.91	0.56	0.29	0.49
SM-60-2	0.25	0.01	0.04	4029	2.5	549.99	541.02	0.61	0.33	0.45
SM-60-3	0.25	0.01	0.33	2894	1.75	370.27	390.60	0.44	0.24	0.31
SM-60-4	0.24	0.01	0.09	4056	2.00	478.93	503.82	0.57	0.34	0.45
SM-60-5	0.25	0.01	0.04	2895	1.25	540.06	543.00	0.61	0.24	0.51
SM-60-6	0.27	0.01	0.20	4055	2.5	519.19	511.06	0.57	0.34	0.43
NM-90-1	0.19	0.55	0.74	5952	0.75	469.92	462.06	0.53	0.5	0.25
NM-90-2	0.29	0.69	0.80	4945	1.25	525.90	521.54	0.59	0.41	0.32
NM-90-3	0.28	0.53	0.63	6654	1.50	406.66	423.72	0.46	0.55	0.24
NM-90-4	0.26	0.58	0.74	5763	1.50	536.68	545.09	0.60	0.48	0.31
NM-90-5	0.21	0.70	0.85	5089	1.75	555.13	558.50	0.62	0.42	0.32
NM-120-1	0.22	0.66	0.81	5486	1.75	578.84	580.51	0.65	0.46	0.37
NM-120-2	0.22	0.44	0.77	3771	3.25	778.93	793.95	0.88	0.31	0.50
NM-120-3	0.19	0.78	0.83	3577	2.75	655.36	652.13	0.74	0.30	0.46
NM-120-4	0.26	0.77	0.80	1887	0.50	705.74	743.88	0.79	0.16	0.59

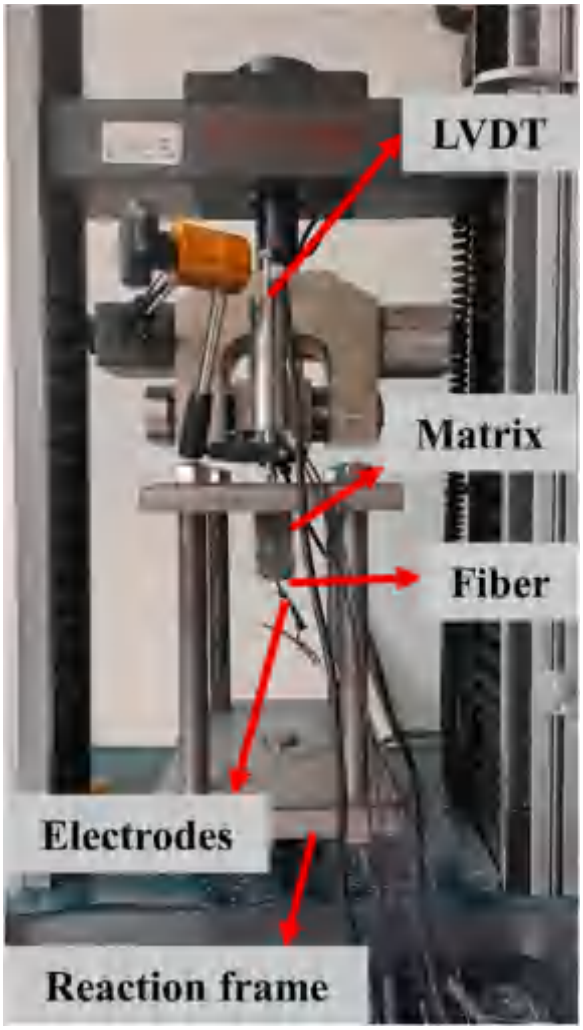


Fig. 10. Loading and measuring device.

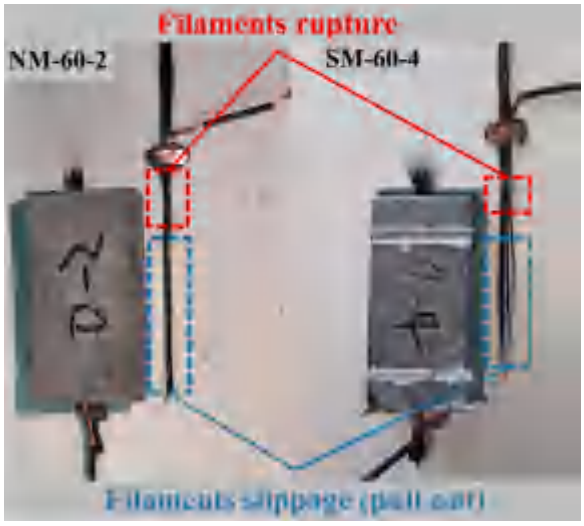


Fig. 11. Failure mode of the CFRCM specimens.

5.2. Analysis and discussion of key parameters

The key parameters of the calculation process for all the above specimens are shown in Table 6. Table 6 demonstrates that the simulated values of peak pull-out loads are very close to the experimental values.

The relationship between α, β_{Ncore}, κ, and η is shown in Fig. 13. From Fig. 13(a)-(c), it can be observed that the fiber utilization ratio α has a linear negative correlation with the core layer fiber ratio β_{Ncore}. The fiber utilization ratio α has a linear positive correlation with the equivalent infiltration ratio κ. However, the correlation between the fiber utilization ratio α and the initial rupture ratio η is insignificant, only displaying a weak correlation. The relationships between these parameters are consistent with experimental results, and further analysis is as follows:

(1) The larger the core layer fiber ratio β_{Ncore}, the more fiber filaments experience pull-out failure, and the smaller the peak load the sleeve layer filaments can withstand. Therefore, the fiber utilization ratio α is lower. When β_{Ncore} approaches 1, α approaches 0.

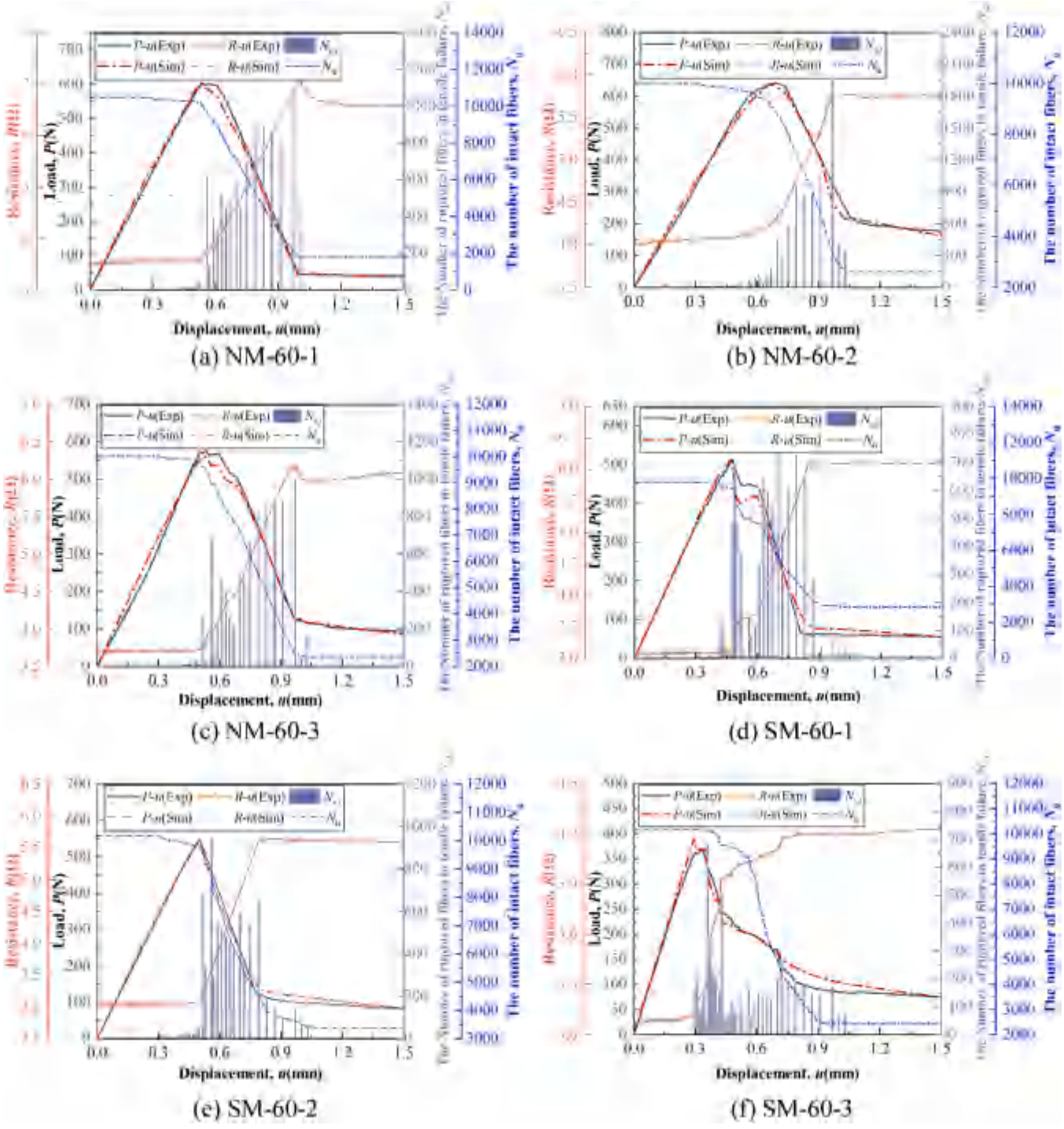


Fig. 12. Simulation results of CFRCM bundle pull-out piezoresistive effects based on equivalent telescopic layered failure model.

(2) A larger equivalent infiltration ratio κ indicates a more thorough infiltration of the carbon fiber bundle by the matrix, resulting in better bond performance between the carbon fiber bundle and the matrix, and higher fiber utilization. When the equivalent infiltration ratio κ reaches 0.7, the fiber utilization ratio α approaches 1. When κ reaches 1, the matrix fully and uniformly infiltrates the carbon fiber bundle, resulting in α being 1.423. This is because the dry carbon fiber bundle has initial ruptures, and these ruptured fiber filaments cannot bear loads during the tensile process of the dry carbon fiber bundle. However, after the fibers are embedded in the matrix, they can continue to bear loads. Therefore, in ideal conditions, the fiber utilization ratio α during the pull-out process of CFRCM bundles can exceed 1, which is higher than the fiber utilization ratio during tensile testing of a fiber bundle.

(3) In the tensile process of the fiber bundle, an increase in the initial rupture ratio η will decrease the fiber utilization ratio α. Therefore, α has a strong negative correlation with η. However, due to the uneven infiltration of the matrix into the fibers, the synergistic load-bearing performance of the fiber filaments decreases, resulting in a lower correlation between the fiber utilization ratio and the initial rupture ratio in CFRCM bundles compared to other

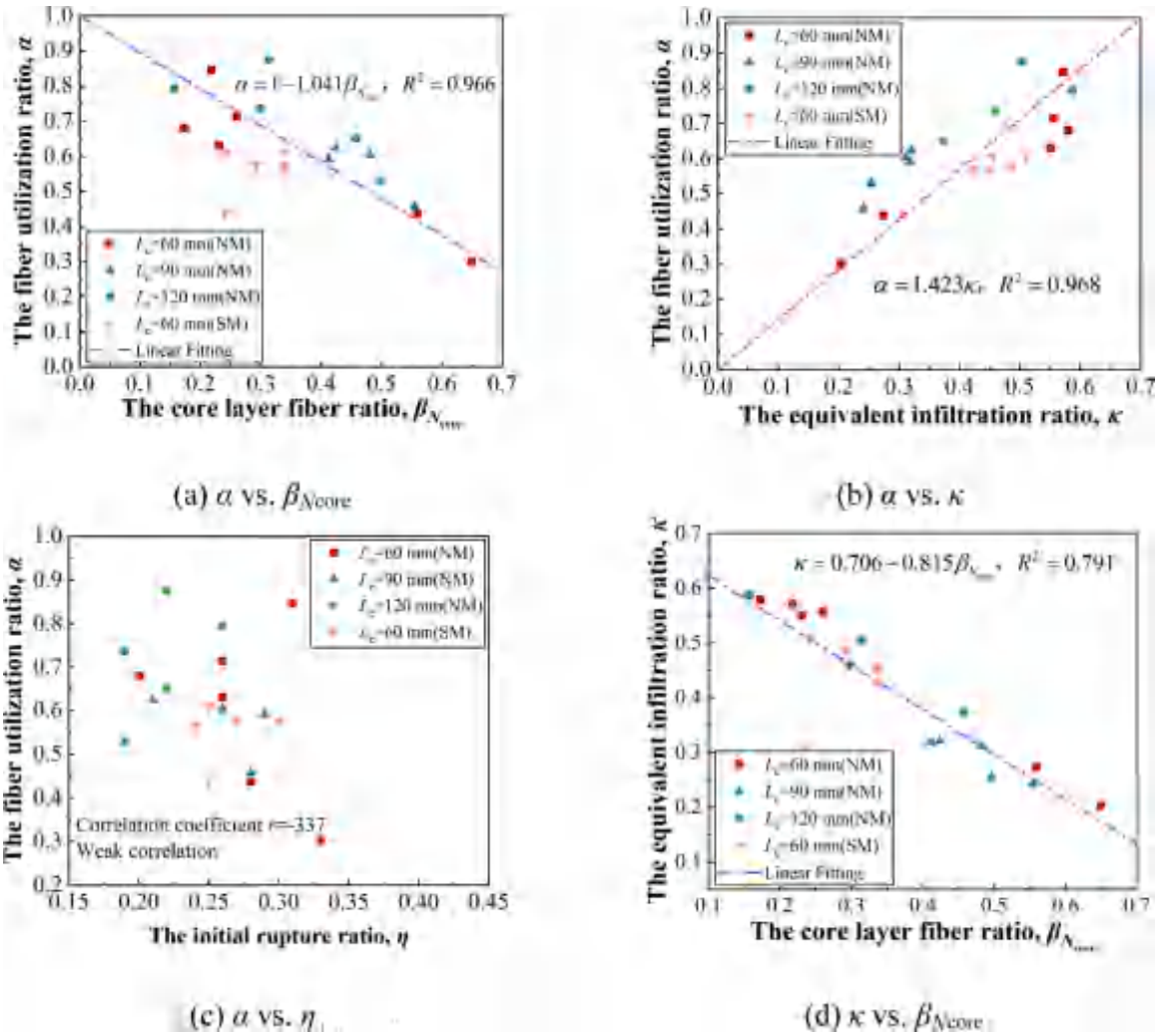


Fig. 13. The relationship between the four parameters α (the fiber utilization ratio), β_{Ncore} (the core layer fiber ratio), κ (the equivalent infiltration ratio), η (the initial rupture ratio). Note: NM is normal matrix (freshwater standard sand mortar); SM is seawater sea-sand mortar.

calculated parameters (Fig. 13(c)). According to Eq. (40), the equivalent infiltration ratio κ is correlated with the core layer fiber ratio β_{Ncore}. As β_{Ncore} increases, κ gradually decreases. This relationship is shown in Fig. 13(d), where a clear linear negative correlation between these two calculated parameters is observed.

In conclusion, the key parameters obtained through model calculations and their correlation analysis are consistent with theoretical logic and experimental results, providing strong support for the reliability of the simulation method. Therefore, the piezoresistive effect has been successfully used to quantitatively evaluate the telescopic layered failure process of carbon fibers in the matrix. The model in this study can more clearly explain the mechanism of the discreteness of the pull-out test results, providing a theoretical basis for how to further improve the fiber utilization ratio in CFRCM.

6. Conclusions

This study reviewed the trilinear cohesive material law and established a theoretical framework for calculating the resistance of CFRCM bundles during the pull-out process. Then, based on the piezoresistive effect, an equivalent telescopic layered failure model for the pull-out process of CFRCM bundles was proposed. The conversion between resistance and load response was achieved, and the model's effectiveness was validated. The relevant conclusions are as follows:

(1) Based on the layered theory, a fiber bundle was divided into n layers of sleeve layers and one core layer. The bonding-slip relationship of these fibers was analyzed using trilinear CML at the fiber filament-matrix interface and its equivalent parameter values.
(2) Factors affecting the resistance of carbon fiber bundles include elastic deformation, contact, and ruptures. Based on these factors and the parallel circuit theory, a resistance calculation theory for CFRCM bundles during the pull-out process was established.
(3) The calculation methods for equivalent contact ratio and initial rupture ratio were proposed. Based on the piezoresistive effect, the equivalent telescopic layered failure model of the CFRCM bundle during the pull-out process could calculate the number of fibers in each layer and the piezoresistive effect, which corresponded well with the load-resistance-displacement curve obtained from experiments. Moreover, this model has also been successfully used to simulate the piezoresistive effect during the pull-out process of CFRCM bundles with two types of matrices and multiple fiber-embedded lengths. The interfacial bonding performance and piezoresistive effect between the carbon fiber bundle and the two types of matrices are similar. Furthermore, it can present the rupture damage of fibers during the loading process, enabling a quantitative evaluation of the loading failure process.

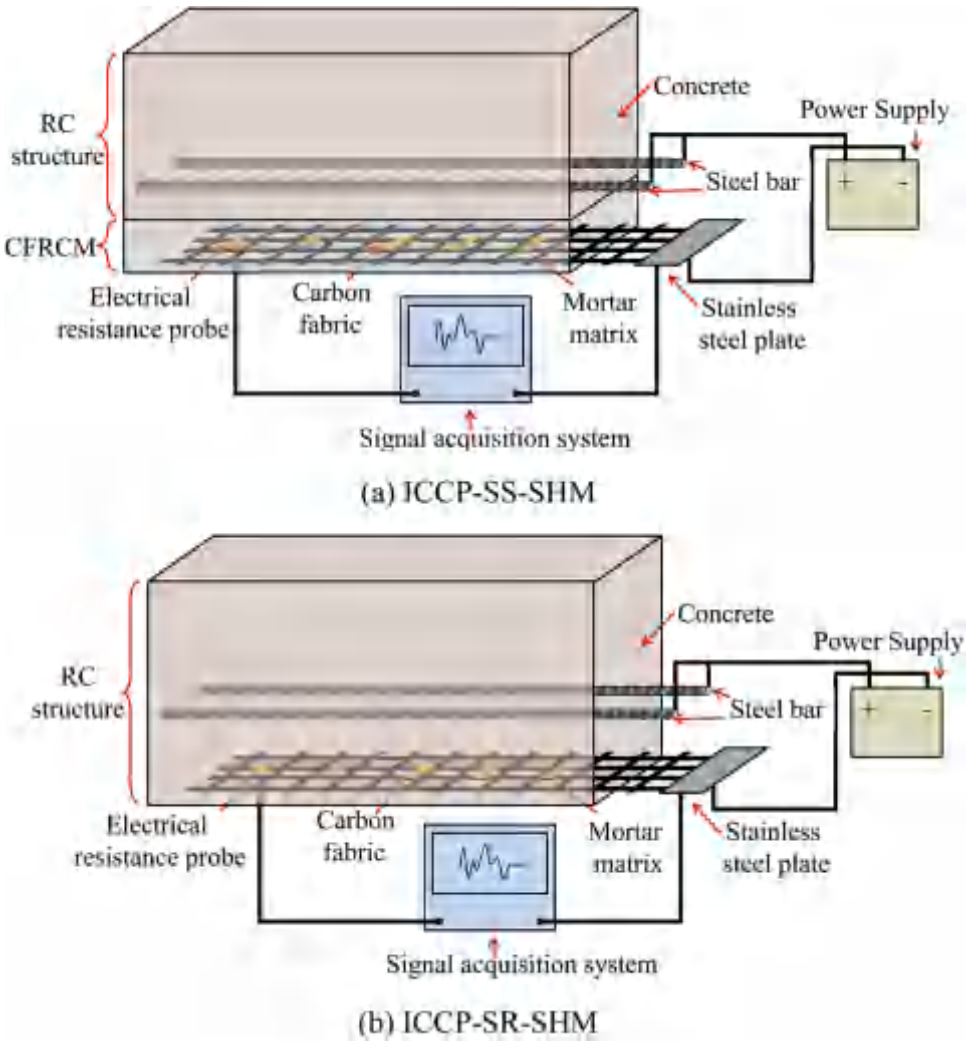


Fig. 14. Schematic diagram of three functional systems.

(4) The relationship between the initial rupture ratio, the core layer fiber ratio, the equivalent infiltration ratio, and the fiber utilization ratio in CFRCM bundles was analyzed. The results showed a strong correlation between the core layer fiber ratio, the equivalent infiltration ratio, and the fiber utilization ratio. The core layer fiber ratio and the equivalent infiltration ratio can be used to describe the degree of fiber infiltration by the matrix quantitatively. This work provides a theoretical basis for how to further improve the fiber utilization ratio in CFRCM.

7. Further research perspectives

If seawater sea-sand can be used not only for strengthening existing RC structures but also for newly constructed RC structures, then seawater sea-sand RC structures will have greater development potential, and the shortage of freshwater river sand resources can be effectively alleviated. For RC structures, structural strengthening (SS) can be achieved through external bonding of CFRCM to RC structures, or by embedding carbon fabrics in concrete to form structural reinforcement (SR).

Interestingly, the application of impressed current cathodic protection (ICCP) technology to RC structures involves using carbon fibers as the anode and steel bars as the cathode. This technology can not only delay the corrosion of steel bars in existing RC structures but also prevent the corrosion of steel bars in newly constructed sea water and sea sand RC structures.

During the service life of RC structures, resistance probes are used for continuous monitoring of the resistance of the carbon fabric. By establishing a quantitative relationship between the rate of change in resistance of carbon fiber bundles in the matrix and the load response of the material/structure based on the telescopic layered failure model established by the piezoresistive effect of CFRCM, it is possible to analyze the detailed evaluation of the damage process, thereby analyzing the telescopic layered failure phenomenon of CFRCM and providing damage analysis and self-monitoring functions. However, this requires consideration of the effect of ICCP on the piezoresistive effect and piezoresistive model.

Ultimately, three functional systems (ICCP-SS-SHM and ICCP-SR-SHM) are proposed, as shown in Fig. 14. This system will involve various design methods and theories for parameters such as multiple fabric reinforcement ratios, the charge densities of ICCP, resistance probe layout intervals, and so on. We welcome readers to follow our subsequent research.

CRediT authorship contribution statement

Jiarong Liu: Writing - review & editing, Writing - original draft, Visualization, Validation, Software, Methodology, Investigation, Formal analysis, Data curation, Conceptualization, Funding acquisition. **Dawei Zhang:** Resources, Project administration, Methodology, Investigation,

Funding acquisition, Supervision, Writing - review & editing. **Yewangzhi Tao:** Conceptualization, Formal analysis, Investigation, Methodology, Sofware, Visualization, Writing -original draft. **Zhiyu Xie:** Writing - review & editing, Methodology, Investigation, Conceptualization.

Declaration of Competing Interest

The authors declare that they have no known competing financial interests or personal relationships that could have appeared to influence the work reported in this paper.

Data availability

Data will be made available on request.

Acknowledgements

The support from the Program Fund of Nonmetallic Excellence and Innovation Center for Building Materials (24PHD-5), and National Natural Science Foundation of China (52078454) is greatly appreciated.

References

[1] Wang Z, Maekawa K, Takeda H, et al. Multi-ion kinetics in pseudo-concrete electrolyte associated with macro-cell corrosion. Cem Concr Compos 2022;133:104690. https://doi.org/10.1016/j.cemconcomp.2022.104690.
[2] Wang Z, Gong F, Maekawa K. Multi-scale and multi-chemo–physics lifecycle evaluation of structural concrete under environmental and mechanical impacts. J Intell Constr 2023;1(1):9180003. https://doi.org/10.26599/JIC.2023.9180003.
[3] Wang Z, Maekawa K. Lifetime assessment of structural concrete – multi-scale integrated hygro-thermal-chemo-electrical-mechanistic approach and statistical evaluation. Struct Infrastruct Eng 2022;18(7):933–49. https://doi.org/10.1080/15732479.2021.1995443.
[4] Li K, Han J, Wang S, et al. Long-term performance of structural concretes in china southeast coastal environments exposed to atmosphere and chlorides. Cem Concr Res 2023;164:107064. https://doi.org/10.1016/j.cemconres.2022.107064.
[5] Zheng A, Zong S, Lu Y, et al. Fatigue performance of corrosion-damaged beams strengthened with FRP grid-reinforced ECC matrix composites. Eng Struct 2022;255:113938. https://doi.org/10.1016/j.engstruct.2022.113938.
[6] Zheng A, Liu Z, Li F, et al. Experimental investigation of corrosion-damaged RC beams strengthened in flexure with FRP grid-reinforced ECC matrix composites. Eng Struct 2021;244:112779. https://doi.org/10.1016/j.engstruct.2021.112779.
[7] Bencardino F, Carloni C, Condello A, et al. Flexural behaviour of RC members strengthened with FRCM: state-of-the-art and predictive formulas. Compos Part B Eng 2018;148:132–48. https://doi.org/10.1016/j.compositesb.2018.04.051.
[8] Pei C, Zeng Y, Kong S, et al. Pull-out performance of anchored carbon-fiber bundles in cementitious matrix. J Compos Constr 2021;25(6):04021057. https://doi.org/10.1061/(ASCE)CC.1943-5614.0001175.
[9] Wu Y, Xie Z, Zhang D, et al. Uniaxial tensile behavior of anchored carbon fabric-reinforced cementitious matrix plates. J Mater Civ Eng 2023;35(8):04023251. https://doi.org/10.1061/JMCEE7.MTENG-14941.
[10] Mandor A, El Refai A. Flexural response of reinforced concrete continuous beams strengthened with fiber-reinforced cementitious matrix (FRCM). Eng Struct 2022;251:113557. https://doi.org/10.1016/j.engstruct.2021.113557.
[11] Zhu H, Zhou H, Gou H. Evaluation of carbon fiber dispersion in cement-based materials using mechanical properties, conductivity, mass variation coefficient, and microstructure. Constr Build Mater 2021;266:120891. https://doi.org/10.1016/j.conbuildmat.2020.120891.
[12] Koutas L, Bousias SN, Triantafillou TC. Seismic strengthening of masonry-infilled RC frames with TRM: experimental study. J Compos Constr 2015;19(2):04014048. https://doi.org/10.1061/(ASCE)CC.1943-5614.0000507.
[13] Wei L, Ueda Tamon, Matsumoto Koji, et al. Experimental and analytical study on the behavior of RC beams with externally bonded carbon-FRCM composites. Compos Struct 2021;273:114291. https://doi.org/10.1016/j.compstruct.2021.114291.
[14] Feng R, Liu Y, Zhu J-H, et al. Flexural behaviour of C-FRCM strengthened corroded RC continuous beams. Compos Struct 2020;245:112200. https://doi.org/10.1016/j.compstruct.2020.112200.
[15] Tetta ZC, Koutas LN, Bournas DA. Textile-reinforced mortar (TRM) versus fiber-reinforced polymers (FRP) in shear strengthening of concrete beams. Compos Part B: Eng 2015;77:338–48. https://doi.org/10.1016/j.compositesb.2015.03.055.
[16] Tran CTN, Nguyen XH, Nguyen HC, et al. Shear performance of short-span FRP-reinforced concrete beams strengthened with CFRP and TRC. Eng Struct 2021;242:112548. https://doi.org/10.1016/j.engstruct.2021.112548.
[17] Bellini A, Bovo M, Mazzotti C. Experimental and numerical evaluation of fiber-matrix interface behaviour of different FRCM systems. Compos Part B Eng 2019;161:411–26. https://doi.org/10.1016/j.compositesb.2018.12.115.
[18] Homoro O, Baranger T, Michel M. 3D finite element modeling of yarn reinforced mineral matrix: comparison of damage behavior with experimental data. Compos Struct 2021;261:113567. https://doi.org/10.1016/j.compositesb.2018.12.115.
[19] Grande E, Imbimbo M, Sacco E. Numerical investigation on the bond behavior of FRCM strengthening systems. Compos Part B Eng 2018;145:240–51. https://doi.org/10.1016/j.compositesb.2018.03.010.
[20] Grande E, Milani G, Imbimbo M. Theoretical model for the study of the tensile behavior of FRCM reinforcements. Constr Build Mater 2020;236:117617. https://doi.org/10.1016/j.conbuildmat.2019.117617.
[21] Milani G, Grande E. Simple bisection procedure in quickly convergent explicit ODE solver to numerically analyze FRCM strengthening systems. Compos Part B Eng 2020;199:108322. https://doi.org/10.1016/j.compositesb.2020.108322.
[22] Grande E, Milani G. Numerical simulation of the tensile behavior of FRCM strengthening systems. Compos Part B Eng 2020;189:107886. https://doi.org/10.1016/j.compositesb.2020.107886.
[23] Carozzi FG, Colombi P, Fava G, et al. A cohesive interface crack model for the matrix–textile debonding in FRCM composites. Compos Struct 2016;143:230–41. https://doi.org/10.1016/j.compstruct.2016.02.019.
[24] Bertolli V, D'Antino T. Modeling the behavior of externally bonded reinforcement using a rigid-trilinear cohesive material law. Int J Solids Struct 2022;248:111641. https://doi.org/10.1016/j.ijsolstr.2022.111641.
[25] Bilotta A, Lignola GP. Effect of fiber-to-matrix bond on the performance of inorganic matrix composites. Compos Struct 2021;265:113655. https://doi.org/10.1016/j.compstruct.2021.113655.
[26] Zhu M, Zhu J-H, Ueda T, et al. A method for evaluating the bond behavior and anchorage length of embedded carbon yarn in the cementitious matrix. Constr Build Mater 2020;255:119067. https://doi.org/10.1016/j.conbuildmat.2020.119067.
[27] Zhu M, Zhu J-H, Ueda T, et al. Bond behavior of carbon fabric reinforced cementitious matrix (FRCM) composites considering matrix impregnation. Compos Struct 2021;262:113350. https://doi.org/10.1016/j.compstruct.2020.113350.
[28] Banholzer B. Bond behaviour of a multi-filament yarn embedded in a cementitious matrix. Bibliothek der RWTH Aachen; 2004.
[29] Cohen Z, Peled A. Controlled telescopic reinforcement system of fabric–cement composites — durability concerns. Cem Concr Res 2010;40(10):1495–506. https://doi.org/10.1016/j.cemconres.2010.06.003.
[30] Goldfeld Y, Quadflieg T, Ben-Aarosh S, et al. Micro and macro crack sensing in TRC beam under cyclic loading. J Mech Mater Struct 2017;12(5):579–601. https://doi.org/10.2140/jomms.2017.12.579.
[31] Luan C, Yao X, Shen H, et al. Self-sensing of position-related loads in continuous carbon fibers-embedded 3D-printed polymer structures using electrical resistance measurement. Sensors 2018;18(4):994. https://doi.org/10.3390/s18040994.
[32] Yosef L, Goldfeld Y. Smart self-sensory carbon-based textile reinforced concrete structures for structural health monitoring. 147592172095112 Struct Health Monit 2020. https://doi.org/10.1177/1475921720951122.
[33] Conor PC, Owston CN. Electrical resistance of single carbon fibres: 5211. Nature 1969;223(5211):1146–7. https://doi.org/10.1038/2231146b0.
[34] Grammatikos SA, Paipetis AS. On the electrical properties of multi scale reinforced composites for damage accumulation monitoring. Compos Part B Eng 2012;43(6):2687–96. https://doi.org/10.1016/j.compositesb.2012.01.077.
[35] Cho JW, Choi JS. Relationship between electrical resistance and strain of carbon fibers upon loading. J Appl Polym Sci 2000;77(9):2082–7. https://doi.org/10.1002/1097-4628(20000829)77:9<2082::AID-APP26>3.0.CO;2-W.
[36] Yang CQ, Wu ZS. Self-structural health monitoring function of RC structures with HCFRP sensors. J Intell Mater Syst Struct 2006;17(10):895–906. https://doi.org/10.1177/1045389X06061520.
[37] Fouad N, Saifeldeen MA. Smart self-sensing fiber-reinforced polymer sheet with woven carbon fiber line sensor for structural health monitoring. Adv Struct Eng 2021;24(1):17–24. https://doi.org/10.1177/1369433220944507.
[38] Wen S, Chung DDL. Piezoresistivity in continuous carbon fiber cement-matrix composite. Cem Concr Res 1999;29(3):445–9. https://doi.org/10.1016/S0008-8846(98)00211-7.
[39] Goldfeld Y, Quadflieg T, Gries T. Sensing capabilities of carbon based TRC beam from slack to pull-out mechanism. Compos Struct 2017;181:294–305. https://doi.org/10.1016/j.compstruct.2017.08.102.
[40] Goldfeld Y, Perry G. AR-glass/carbon-based textile-reinforced concrete elements for detecting water infiltration within cracked zones. Struct Health Monit 2019;18(5–6):1383–400. https://doi.org/10.1177/1475921718808223.
[41] Li H, Zhou W, Ou J. Study on electromechanical behavior of unidirectional carbon fibre sheet without epoxy resin matrix. Adv Struct Eng 2004;7(5):437–45. https://doi.org/10.1260/1369433042863288.
[42] Gong Y, Xie Z, Liu J, et al. Research on piezoresistive effect and random model of carbon fiber bundle. Arch Civ Mech Eng 2023;23(2):128. https://doi.org/10.1007/s43452-023-00672-0.
[43] Park JB, Okabe T, Takeda N, et al. Electromechanical modeling of unidirectional CFRP composites under tensile loading condition. Compos Part A 2002;9. https://doi.org/10.1016/S1359-835X(01)00097-5.
[44] Lv Y, Zhu SR, Li ZQ, et al. The research of modified carbon fiber polymer-matrix composites properties of the mechanism of piezoresistivity. Appl Mech Mater 2011;52–54:1732–6. https://doi.org/10.4028/www.scientific.net/AMM.52-54.1732.
[45] Liu R, Xu Z, Yin J, et al. A coupled mechanical and electrical model concerning piezoresistive effect of CFRP materials. Compos Part B Eng 2016;96:125–35. https://doi.org/10.1016/j.compositesb.2016.04.010.
[46] Ahmed A, Guo S, Zhang Z, et al. A review on durability of fiber reinforced polymer (FRP) bars reinforced seawater sea sand concrete. Constr Build Mater 2020;256:119484. https://doi.org/10.1016/j.conbuildmat.2020.119484.

[47] Wang Z, Yaseen SA, Maekawa K, et al. Performance assessment of seawater fly ash cement paste with integrated physicochemical- geochemical simulation platform and experimental validation. J Build Eng 2023;79:107802. https://doi.org/10.1016/j.jobe.2023.107802.
[48] Mohammed TU, Hamada H, Yamaji T. Performance of seawater-mixed concrete in the tidal environment. Cem Concr Res 2004;34(4):593–601. https://doi.org/10.1016/j.cemconres.2003.09.020.
[49] Xiao J, Zhang Q, Zhang P, et al. Mechanical behavior of concrete using seawater and sea-sand with recycled coarse aggregates. Struct Concr 2019;20(5):1631–43. https://doi.org/10.1002/suco.201900071.
[50] Sueki S, Soranakom C, Mobasher B, et al. Pullout-slip response of fabrics embedded in a cement paste matrix. J Mater Civ Eng 2007;19(9):718–27. https://doi.org/10.1061/(ASCE)0899-1561(2007)19:9(718).
[51] Gong Y, Xie Z, Chen G, et al. Influence of cementitious material infiltration on piezoresistive effect of carbon fiber bundle. J Mater Civ Eng 2023;35(7):04023173. https://doi.org/10.1061/JMCEE7.MTENG-14701.
[52] China Cement Standardization Technical Committee. The national standard of the people's Republic of China: Test method of cement mortar strength(ISO method) (GB/T17671–2021) [S]. Beijing: Standards Press of China, 2021(in Chinese).
[53] Chung DDL. A critical review of piezoresistivity and its application in electrical-resistance-based strain sensing. J Mater Sci 2020;55(32):15367–96. https://doi.org/10.1007/s10853-020-05099-z.

Engineering Structures 313 (2024) 118317



Contents lists available at ScienceDirect

Engineering Structures

journal homepage: www.elsevier.com/locate/engstruct





Effect of ICCP on tensile performance and piezoresistive effect of CFRCM plates

Jiarong Liu [a], Dawei Zhang [a,*], Yewangzhi Tao [a], Zhiyu Xie [a,b], Bo Yi [c]

[a] Institute of Structural Engineering, Zhejiang University, Hangzhou 310058, China
[b] School of Engineering, Hangzhou City University, Hangzhou 310015, China
[c] Guangdong Provincial Key Laboratory of Durability for Marine Civil Engineering, College of Civil and Transportation Engineering, Shenzhen University, Shenzhen 518060, China

ARTICLE INFO

Keywords:
CFRCM
ICCP
Tensile performance degradation
Piezoresistive effect
Crack identification

ABSTRACT

Currently, extensive research has been conducted on carbon fabric–reinforced cementitious matrix (CFRCM) composites, impressed current cathodic protection (ICCP), and the piezoresistive effect in the field of strengthening of reinforced concrete (RC) structures, corrosion protection of steel reinforcement, and structural health monitoring, respectively. This study utilized two types of matrix materials: normal matrix (sand conforming to ISO standard) and seawater sea-sand matrix. The mechanism by which the ICCP procedure affects the degradation of tensile performance in CFRCM plates with these two types of matrix materials was investigated in the study. Additionally, the piezoresistive effects of CFRCM with the two types of matrix materials after the ICCP procedure were analyzed, and the impact of ICCP on the piezoresistive effect was also investigated. By observing the piezoresistive effect of each CFRCM segment, the sequence of crack propagation and an approximate crack location can be inferred. Finally, the tensile performance of CFRCM with charge density was investigated. Leveraging the dual functionality of carbon fiber reinforcement and sensing, this study lays the groundwork for the development of a triple-functional system encompassing impressed current cathodic protection, structural strengthening, and structural health monitoring (ICCP-SS-SHM). Seawater sea-sand has the potential to be used as an alternative to freshwater river sand, which is beneficial for addressing the shortage of freshwater river sand resources.

1. Introduction

The development of concrete projects in remote and coastal areas is greatly limited due to the scarcity of river sand [1]. The feasibility of using seawater and sea-sand as a substitute for freshwater river sand has been explored [2,3]. However, the presence of chloride ions in seawater and sea-sand can cause reinforcement corrosion. Furthermore, in long-term service, reinforced concrete (RC) structures are prone to phenomena such as carbonation, freeze-thaw cycles, and alkali-aggregate reactions, which significantly impact the mechanical properties and durability of RC structures [4,5], ultimately leading to property damage or even casualties. Therefore, considering the safety and reliability of engineering structures, it is crucial to address the challenges of delaying reinforcement corrosion, enhancing structural load-bearing capacity, and implementing structural health monitoring (SHM) to prolong the service life of structures and prevent sudden structural failures.

Carbon fiber has advantages such as high elastic modulus, lightweight, good conductivity, corrosion resistance, etc. [6,7]. In recent years, carbon fabric–reinforced cementitious matrix (CFRCM) has been extensively studied and applied in structural strengthening (SS). CFRCM can significantly enhance the flexural [8,9], shear [10,11], and seismic [12] load-bearing capacity of RC structures. However, it does not address the existing corrosion issues of reinforcements. Impressed current cathodic protection (ICCP) is recognized as one of the most effective methods to address corrosion issues in steel [13]. The principle of ICCP is to provide electrons to the steel reinforcement in the cathodic zone through auxiliary anodes, thereby inhibiting the loss of electrons from the steel reinforcement and achieving the protection of the steel reinforcement. Due to the excellent conductivity of carbon fiber, CFRCM can be used as auxiliary anode material.

A new system called ICCP-SS has been proposed, combining the dual

* Corresponding author.
E-mail address: dwzhang@zju.edu.cn (D. Zhang).

https://doi.org/10.1016/j.engstruct.2024.118317
Received 17 January 2024; Received in revised form 12 May 2024; Accepted 28 May 2024
Available online 1 June 2024
0141-0296/© 2024 Elsevier Ltd. All rights are reserved, including those for text and data mining, AI training, and similar technologies.

functions of impressed current cathodic protection and structural strengthening [14–17]. The ICCP-SS technology can effectively delay the corrosion of steel reinforcement in concrete beams and improve the flexural load-carrying capacity and fatigue life of RC members [16,18,19]. However, it is worth noting that while the corrosion of cathodic steel reinforcement is delayed, the mechanical properties of the auxiliary anode material also deteriorate. With an increase in anode charge density, the mechanical properties of CFRCM weaken due to anodic acidification [20–22]. Meanwhile, anodic polarization reduces the interfacial shear strength between CFRCM and the reinforced beam as the charge density increases [23]. The degradation mechanism of CFRCM is as follows: in an alkaline environment and after ICCP technology, many carbon-hydroxyl radicals are generated near the carbon fiber anode, which reacts with the functional groups of carbon fiber filaments and disrupts the molecular structure of carbon fibers, leading to a decrease in the mechanical properties of carbon fiber [24]. Additionally, the impressed current leads to calcium depletion, which in turn reduces the amount of C-S-H gel surrounding the carbon fibers. Consequently, this results in a decrease in the bond strength between the carbon fibers and the mortar matrix [25].

The reported studies have mainly focused on CFRCM with freshwater and river sand as the matrix components, while research on the performance degradation of CFRCM with seawater and sea-sand as the matrix under ICCP technology is still lacking. Furthermore, the direct correlation between charge density and material performance has not been established yet.

In the field of structural health monitoring (SHM), traditional non-destructive testing techniques such as X-ray, ultrasonic testing, acoustic emission, infrared thermography, or eddy current inspection can reveal localized damage. However, they cannot detect damage instantaneously or monitor damage evolution in real time [26–28]. On the other hand, emerging SHM methods such as strain gauges, accelerometers, fiber optic sensors, and piezoelectric sensors need to be embedded or attached to the structure. Their sensing range is limited, so multiple sensors are required for large structures. Although they can monitor damage in real-time, they have disadvantages such as complex equipment, high cost, time-consuming procedures, the need for specialized personnel, poor durability, and a potential reduction in structural mechanical performance, etc. [29–31]. Therefore, more advanced structural health monitoring technologies are urgently needed to address these limitations.

The piezoresistive effect is a phenomenon where the resistance of a material changes with the applied strain [32]. Self-sensing refers to the ability of structural materials to perceive their health status, such as strain, stress, damage, temperature, humidity, cracks, etc., without the need for additional sensors [33,34]. Carbon fiber possesses the piezoresistive effect, which enable it to have self-sensing capabilities. Therefore, carbon fiber is an intelligent dual-functional material for structural strengthening and self-sensing without the need to install or integrate additional sensors. It offers advantages such as lower cost, enhanced durability, larger sensing volume, and uncompromised mechanical performance compared to materials that rely on embedded or attached sensors [26,31].

There have been numerous studies on the piezoresistive effect of continuous carbon fiber bundles and carbon fiber-reinforced polymer (CFRP) composites, focusing on the relationship between resistance changes and stress, strain, and crack responses of the materials or structures. As tensile strain increases, the resistance change ratio in carbon fiber bundles initially increases linearly and then sharply increases upon fiber rupture [35]. Monitoring residual resistance under static and dynamic loads can be used to assess the level of damage in carbon fibers [35], and the initial linear deformation of the carbon fiber's piezoresistive effect curve can be used to estimate the magnitude of the load [36]. The piezoresistive effect of carbon fiber bundles is mainly influenced by the elastic deformation, rupture, and contact of the filaments. Dynamic stochastic equivalent parallel circuit models based on these factors have been established to quantify the piezoresistive effect of carbon fiber bundles during tensile processes [37]. Three-point bending tests on concrete beams reinforced with CFRP plates have shown a significant correlation between mechanical properties (strain and cracks) and electrical properties within an extensive strain range [38]. Furthermore, CFRP with multiple electrodes can be used to locate damage in different sections of the beam [39]. Additionally, carbon fiber linear sensors can also detect cracking loads and initial debonding between prestressed smart fiber-reinforced polymer plates and RC beams in four-point bending tests [40]. Further research has demonstrated that real-time damage localization and severity analysis of laboratory-scale 3D-printed micro-bridges can be achieved using structural health monitoring algorithms based on the resistance changes of glass-carbon fiber composite materials [41].

Research on the piezoresistive effect of continuous carbon fibers has mainly focused on the field of CFRP, while studies on the self-sensing characteristics of CFRCM are still relatively scarce. The piezoresistive effect of carbon fibers in CFRCM under tensile stress shows similarities to carbon fiber bundles and CFRP [32,36,42,43]. However, due to the uneven impregnation of carbon fibers by mortar, CFRCM exhibits a smaller relative resistance change and higher variability during the failure stage than CFRP. Previous studies on the self-sensing characteristics of glass-carbon hybrid fabric-reinforced beams [29,44–46] have shown qualitative correlations (for cracks) or quantitative correlations (for strains) between the resistance of carbon fibers and the flexural mechanical response of beams under four-point bending and repeated loading-unloading cycles. Carbon fibers can sense the accumulation of cracks, enabling quantitative damage detection.

In summary, the dual-functionality of strengthening-sensing of carbon fibers has been verified, where the resistance changes of carbon fibers during loading can reflect the stress state and damage of both the fibers themselves and the reinforced members. However, there is currently a lack of research on the piezoresistive effect of CFRCM specimens after the application of ICCP. The mechanism of ICCP's effect on the piezoresistive effect is unknown, and the influence of seawater sea-sand (containing chloride) environments on the piezoresistive effect is also unclear. Based on this, further investigation is needed for the analysis of multi-segment piezoresistive effect and damage localization in CFRCM.

This study addresses the issues above by employing two types of matrix materials: normal mortar and seawater sea-sand mortar. Tensile tests were conducted on CFRCM plates to investigate the impact of the ICCP procedure on the tensile performance of CFRCM plates with different matrix materials. The piezoresistive effect of CFRCM plates with the two types of matrix materials after the ICCP procedure was analyzed by monitoring changes in electrical resistance during the loading process. The study leverages the dual-function characteristics of carbon fiber strengthening and sensing, promoting the development of a triple-functional system comprising impressed current cathodic protection, structural strengthening, and structural health monitoring (ICCP-SS-SHM). Moreover, it aims to address the scarcity of freshwater river sand resources.

Table 1
Properties of carbon fiber bundle provided by the manufacturer.

Filament number	Filament diameter (μm)	Density (g/cm^3)	Elastic modulus (GPa)	Ultimate tensile strength (MPa)	Ultimate tensile Strain	Electrical resistivity (Ω·cm)
12,000	7	1.76	230	3530	1.5 %	1.7×10^{-3}

Table 2
Particle gradation and moisture content of sea-sand.

Sieve residue rates of different particle sizes (%)						Fineness modulus	Moisture content (%)
4.8 mm	2.4 mm	1.2 mm	0.6 mm	0.3 mm	0.2 mm		
0.4	6.7	19.5	34.5	66	96.2	2.2	3.65

Table 3
Types and content of seawater ions.

pH	Cl^- (g/L)	SO_4^{2-} (g/L)	Na^+ (g/L)	Mg^{2+} (g/L)	K^+ (g/L)	Ca^{2+} (g/L)
8.02	14.81	1.82	15.74	1.51	1.21	6.35

Table 4
The mix ratio of two matrices.

The type of matrix	Portland cement (P. O 42.5) (g)	Water (g)	Sand (g)	Redespersible latex powder (Wacker 4115 N) (g)	Superplasticizer (MG SKY 8860) (g)
NM	100	45	200	1.5	0.15
SM	100	55	207.3	1.5	0.2

Note: NM is freshwater ISO standard sand mortar; SM is seawater sea-sand mortar. The same abbreviations are used below.

Table 5
The flexural and compressive strengths of the two matrices.

The type of matrix	Curing age	Flexural strength		Compression strength	
		Mean value (MPa)	COV	Mean value (MPa)	COV
NM	7d	4.55	5.23	21.91	6.27
	28d	4.83	14.3	41.67	5.82
SM	7d	4.62	7.58	21.76	3.81
	28d	4.70	4.25	39.17	5.01

2. Experimental program

2.1. Material properties

The carbon fabrics used in this study were provided by Youtejia Company in Wuxi City, Jiangsu Province, China, and the number of filaments of the bundle and the properties of individual filaments are present in Table 1. It's worth noting that the piezoresistive effect of the fabric woven in a bidirectional grid pattern is difficult to characterize. Therefore, unidirectional carbon fiber bundles were adopted to study their piezoresistive effect.

The matrix comprises two types of mortar: normal mortar (made with freshwater standard sand) and seawater sea-sand mortar. The normal mortar used ISO standard sand with a particle size of 0.5–1 mm, and fine sand with a particle size of 0.25–0.5 mm, in a mass ratio of 2:1. The sea-sand used is natural, and its particle grading and water content are provided in Table 2. The main ion concentrations in seawater are presented in Table 3. The design of both normal mortar and seawater sea-sand mortar was based on achieving similar compressive and flexural strengths, as shown in Table 4. To ensure similar flowability between the two types of mortar, it may be necessary to increase the water-to-cement ratio appropriately for the sea-sand mortar. The flexural and compressive strengths (Table 5) of the two matrices were measured according to the specification [47].

Conductive adhesives are utilized in the fabrication of conductive electrodes with the dual purpose of minimizing contact resistance and securely anchoring contact points to enhance electrode stability. This approach aims to prevent the generation of electrical noise during mechanical testing [41].

Table 6
Specimen groups and investigation parameters.

Specimens	Types of mortar and simulated pore solution	I (mA/m^2)	D (day)	Q (10^5 C/m^2)
TN-N	Normal mortar-saturated $Ca(OH)_2$ solution prepared with fresh water	0	0	0
TN-I50-D30		50	30	1.30
TN-I100-D30		100	30	2.59
TN-I150-D30		150	30	3.89
TN-I200-D30		200	30	5.18
TN-I300-D30		300	24	6.22
TN-I400-D30		400	24	8.29
TS-N	Seawater sea-sand mortar-saturated $Ca(OH)_2$ solution prepared with seawater	0	0	0
TS-I75-D40		75	40	2.59
TS-I100-D30		100	30	2.59
TS-I150-D40		150	40	5.18
TS-I200-D30		200	30	5.18
TS-I300-D32		300	32	8.29
TS-I400-D24		400	24	8.29

Due to CFRCM serving as the auxiliary anode material for the ICCP system, a constant current needs to be applied to the carbon fiber bundles. Conductive electrodes were divided into energizing joint electrodes (used in the ICCP procedure for simultaneous energization of multiple carbon fiber bundles), and measuring electrodes (used to measure the resistance of carbon fiber bundles during loading). Measurement electrodes were divided into external measurement electrodes and internal measurement electrodes. The conductive electrodes were categorized into copper adhesive electrodes and silver paste electrodes according to the fabrication materials and processes. Among them, the silver paste electrode was mainly used for seawater sea-sand (containing chlorine) environment internal measurement electrode preparation to ensure the durability of the electrode.

The dual-component epoxy resin-based copper powder conductive adhesive is provided by Shenzhen Xinwei Electronic Materials Co., Ltd. It has a resistivity of 10^{-2}-10^{-3} Ω·mm, tensile strength of 11.8 MPa, and shear strength of 8.2 MPa. It fully cures within 24 h at room temperature. It is used in this study for the fabrication of conductive electrodes in non-seawater environments.

The conductive silver paste is provided by the same manufacturer as the epoxy conductive adhesive. It has a resistivity of 3 mΩ·mm^{-2} and a viscosity of 100–300 pas. It cures at room temperature within 300 min and cures within 30 min when heated to 60–80 °C. It is used in this study for the fabrication of conductive electrodes in seawater (chloride ion-containing) environments, which enhances the durability of the electrodes.

The reasons for using different conductive electrodes in two environments are as follows: To minimize the influence of the electrodes on the tensile testing, the conductive electrode must be thin. In freshwater environments, copper adhesive and two copper sheets are used to prepare the copper paste electrodes. However, in seawater and sea-sand environments, the copper sheet electrodes are susceptible to corrosion by chloride ions. Therefore, silver paste and a single stainless steel sheet are used to prepare the silver paste electrodes, reducing the thickness of the electrodes' impact on the test. Additionally, a thinner layer of epoxy resin is coated on the electrodes to prevent corrosion by chloride ions in seawater. To be further clear, the silver paste electrode and its associated processes endow it with excellent corrosion resistance, making it

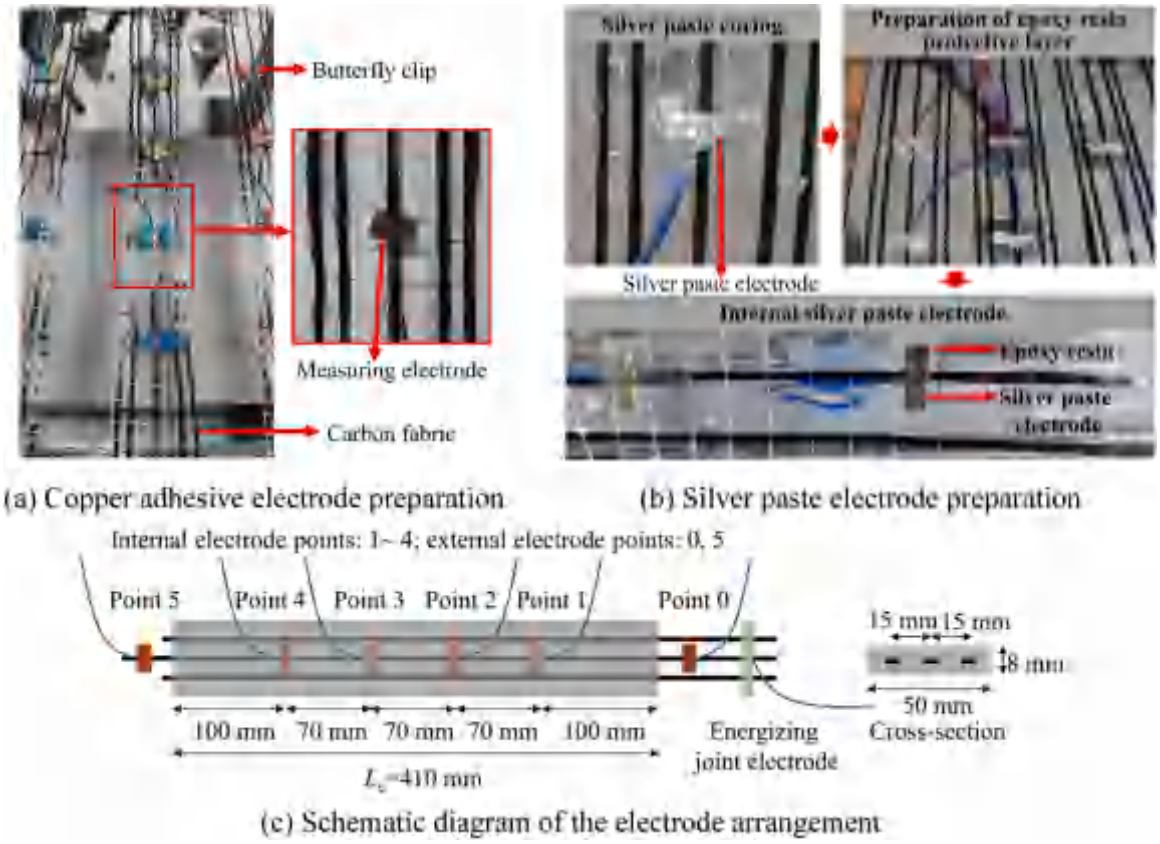


Fig. 1. Conductive Electrode Preparation Process.

suitable for use as an internal electrode in seawater and sea-sand environments. However, due to the more complex preparation process of the silver paste electrode, copper adhesive electrodes are used for both external electrodes in seawater and sea-sand environments and all electrodes in freshwater and normal mortar environments.

2.2. Test specimens and investigated parameters

In this study, the effects of the environment of the ICCP procedure (types of mortar and simulated pore solution), the current density (I), and the duration of the impressed current (D) on the piezoresistive effect of CFRCM plates are investigated. The specimen groups are shown in Table 6. The specimens were labeled as "TE-I-D", where T is the tensile test, and E is the energizing environment: N represents normal mortar and saturated $Ca(OH)_2$ solution prepared with fresh water, and S represents seawater sea-sand mortar and saturated $Ca(OH)_2$ solution prepared with seawater. In the simulated ICCP system, the saturated $Ca(OH)_2$ solution assumed the role of the concrete [22]. For example, TN-I100-D30 represents a set of CFRCM plates with a matrix of normal mortar. It is subjected to an applied current with a current density of 100 mA/m^2 for 30 days. Each experimental group consists of 5 parallel specimens.

Zhu et al. [21,24] quantified the progress of ICCP by utilizing the charge density Q, which represents the total charge per square meter carried by the carbon fiber bundle in contact with the matrix in CFRCM. The calculation of Q is demonstrated in Eq. (1).

$$Q = i_a t \tag{1}$$

where i_a (A/m^2) is the anode current density and t (s) is the duration of the impressed current.

2.3. Specimen preparation

The specimen preparation process includes the following steps: First, electrodes were prepared on carbon fabric, and then the CFRCM panel was poured. Next, an ICCP device was fabricated, and the ICCP procedure was executed. After the ICCP procedure was completed, the CFRCM panel was cut into separate CFRCM plates used for tensile testing.

The electrode fabrication process and arrangement are shown in Fig. 1. The specimens were positioned on the platform, following which lead hammers were suspended at both ends of the carbon fabrics to mitigate the impact of electrode fabrication on the initial co-deformation of the carbon fabrics (Fig. 1(a)). The preparation of conductive copper adhesive electrodes required two copper sheets coated with conductive copper adhesive to be clamped to the carbon fiber bundle and fixed for 4–6 h using butterfly clips. The next step was to remove the butterfly clips, at this point, the conductive copper adhesive electrodes had been successfully made (Fig. 1(a)). The electrode sheet of the silver paste electrode is a piece of 316 stainless steel, and the wire is tinned copper wire. The electrode sheet was first placed under the carbon fabric, with a suitable amount of conductive silver paste evenly applied to it (Fig. 1(b)). It was then curing the conductive silver paste with a 150 °C hot air gun for 1 min. Due to the silver paste's low strength, disconnecting from the electrode sheet under load was easy. Thus, it was necessary to coat the surface of the silver paste electrode with epoxy resin to form a protective layer (Fig. 1(b)). Meanwhile, epoxy resin could also isolate chlorine ions to improve the electrode's durability. The preparation process of the silver paste electrode required strict control over the thickness of the electrode and the epoxy resin protective layer. To explore the method of identifying damage locations in different sections of CFRCM based on the piezoresistive effect, four internal electrodes (1−4) were prepared at the two ends and one-third points of the tensile section of the CFRCM; two external electrodes (0

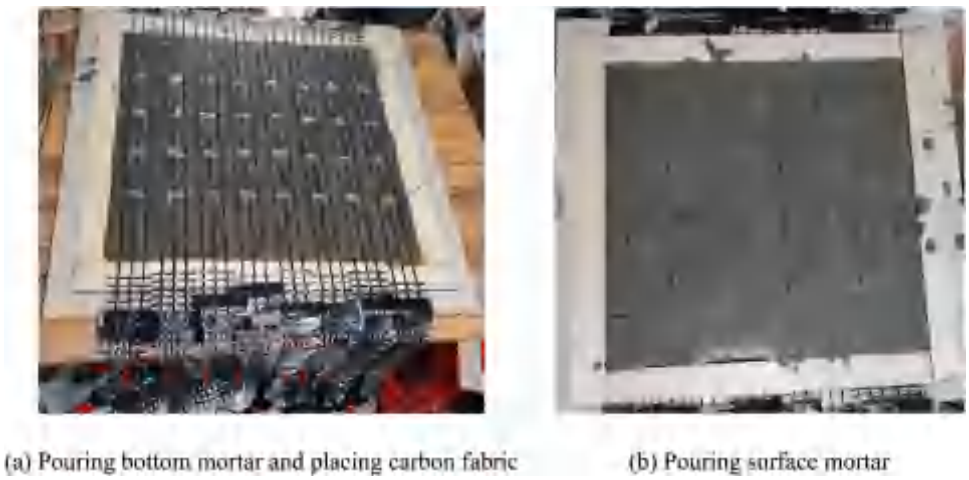


Fig. 2. CFRCM specimen preparation.

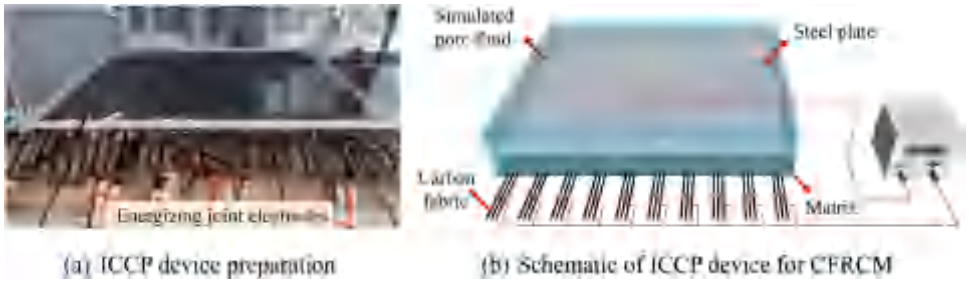


Fig. 3. ICCP device.

and 5) were respectively placed 10 mm away from the surface of the matrix at both ends of the fabric to prevent hindrance from the electrodes to the tensile testing of CFRCM after fabric slippage (Fig. 1(c)).

CFRCM specimens were prepared using the layered pouring method (Fig. 2). Firstly, the bottom layer of 4 mm thick mortar was poured into the mold. Secondly, multiple sets of three bundles of carbon fiber bundles with internal electrodes were placed on the surface of the mortar, and carbon fiber bundles were fixed and tensioned by hanging lead hammers at both ends (Fig. 2(a)). Then, the upper layer of the mold was placed and fixed with a nail gun, and finally, the upper layer of 4 mm thick mortar was poured and properly vibrated (Fig. 2(b)). After 48 h of pouring, the mold was removed, and standard curing (temperature 20 ℃, humidity 95 %) was carried out for 28 days.

The schematic diagram of ICCP device preparation and energization is shown in Fig. 3. The focus of this study is on the impact of ICCP on the performance of anode carbon fabric, rather than analyzing the protective effect of ICCP on cathodic steel reinforcement. Therefore, a steel plate was used as the cathode instead of steel reinforcement in this study to simplify the experimental procedures. Carbon fabrics are the anode, and a 3 mm thick steel plate is the cathode. Joint electrodes were fabricated for the carbon fabrics of each specimen to achieve parallel and simultaneous energization, and the energizing device was bonded to the CFRCM specimen using a nail-free adhesive. Then, the device for the normal mortar specimen was filled with saturated $Ca(OH)_2$ solution prepared with fresh water, and the device for the seawater sea-sand mortar specimen was filled with saturated $Ca(OH)_2$ solution prepared with seawater. A 10 mA constant current DC charge supply was used to provide current to the energizing device, and a closed circuit was formed by connecting the cathode and anode and the solution in the device through the energizing electrodes and wires. The anode carbon fabric lost electrons, and the cathode steel plate got electrons. Cations in the solution migrated to the cathode, and anions were enriched to the anode, forming a stable ICCP protection system.

After the ICCP procedure, CFRCM specimens were cut into individual specimens that met the loading requirements. Since the universal testing machine fixture could not clamp the specimens directly, perforated double-sided steel plates were attached to both ends of the CFRCM specimens to realize the load transfer (Fig. 4(a)). The reinforcing sheets were attached to the surface of the CFRCM specimens using SKO structural adhesive, and the bond length was 100 mm to ensure the bond strength. The schematic diagram of the finished CFRCM specimen used for loading can be seen in Fig. 4(b). The size of CFRCM specimens is as follows [48].

2.4. Loading and measurement methods

The loading device and measurement system are shown in Fig. 5. The loading method follows the procedure described in [48]. The tensile performance loading test was carried out using a Sansi Vertical UTM6503 electronic universal testing machine with a loading range of 5 kN, a loading rate of 0.2 mm/min, and a collection frequency of 10 Hz. A collet conversion was used to clamp the steel plate reinforcing sheet. This type of handle features both rotatable and self-aligning functions, aiming to minimize the bending stress on the specimen. Two LVDTs were used to measure displacement, and the average value was taken.

To eliminate the effect of contact resistance, a four-electrode measurement method based on voltammetry [49] was used to measure the resistance of carbon fiber bundles. A constant DC of 1 mA was passed between measurement point 0 and measurement point 5. According to Ohm's law, the absolute value of the measured voltage is the resistance of the carbon fiber bundle. The displacement and resistance data were recorded using a Donghua DH3816N collector with a sampling frequency of 10 Hz. From this, the full-length resistance of the CFRCM and the resistance data of each section (R_{05}、R_{01}、R_{12}、R_{23}、R_{34}、R_{45})

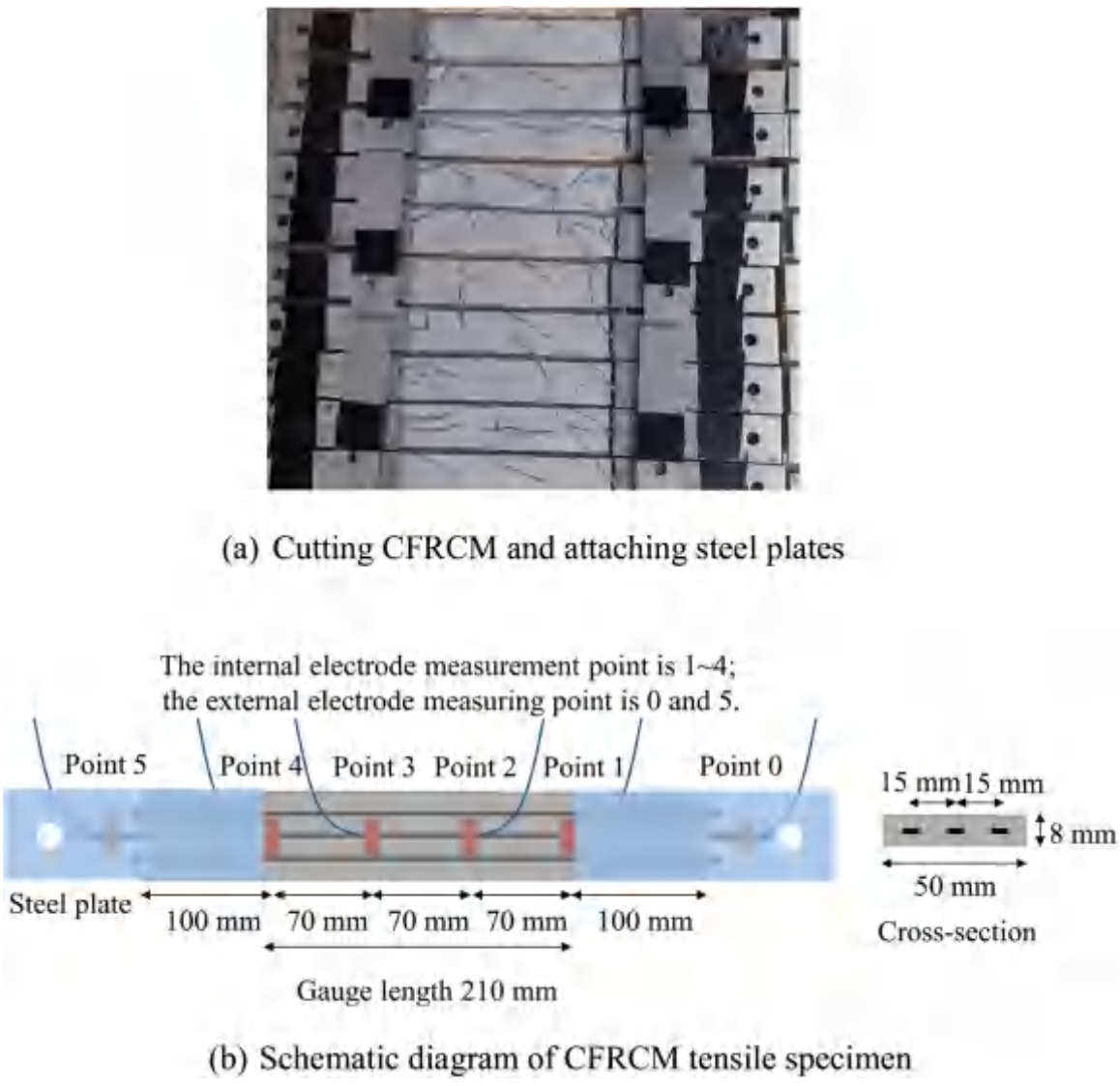


Fig. 4. CFRCM tensile specimen.

were measured during the loading process.

3. Analysis of tensile performance and piezoresistive effect of CFRCM plates after ICCP

3.1. Effect of ICCP on failure mode and load-displacement behavior

According to CFRCM multiple cracking theory and ACK model [50–53], the load-displacement curve of CFRCM without the ICCP procedure in uniaxial tensile can be classified into three phases of elasticity-multiple cracking-strain hardening, as shown in Fig. 6(a)-(b). The load-displacement curves of some representative CFRCM tensile tests are shown in Fig. 7. It should be noted that the cracks in the matrix mentioned below are all macroscopic cracks. It can be seen that the two matrices CFRCM control groups (TN-N and TS-N groups) have significant multiple cracking and strengthening phases, which follow the ACK model.

The changes in the stress state of the fabric and the development of matrix cracks during the tensile process of CFRCM are as follows: When the first crack appears, the load suddenly decreases, and the stress state of the fabric around the crack changes to double-sided pull-out stress. At this point, the fabric transfers the tensile stress to the matrix through the bond with the fabric-matrix interface. The greater the accumulated tensile stress in the matrix away from the crack, the second crack appears when this tensile stress exceeds the cracking stress at that location. At this time, the stress state of the fabric between the two cracks is similar to the tensile stress state of the CFRCM bundle, and the fabric in the rest of the area is still in a pull-out stress state. Similarly, subsequent cracks will gradually form until the distance between adjacent cracks reaches the minimum crack spacing. At this point, the load response curve enters the strain hardening phase. When the fabric reaches the ultimate tensile strength, many filaments rupture, and the CFRCM gradually loses its load-bearing capacity.

After the ICCP procedure, carbon fiber bundles' synergistic stress performance and strength were decreased, and the load decreased instantaneously after matrix cracking. The carbon fabric may enter the telescopic layered phase. At this time, the tensile stress transferred from the carbon fabric to the matrix cannot reach the cracking stress of the matrix. Therefore, only one macroscopic crack appeared in the matrix of all specimens of different charge groups. The failure mode is shown in Fig. 6(c)-(d). The main reasons for this phenomenon are: (1) The inhomogeneity of matrix infiltration into fiber filaments makes the infiltration length of fiber filaments different [54]. Therefore, the extensional stiffness of the filaments under stress is different, which leads to the progressive rupture failure of the sleeve layer filaments and the slippage failure of the core layer filaments, that is, telescopic layered

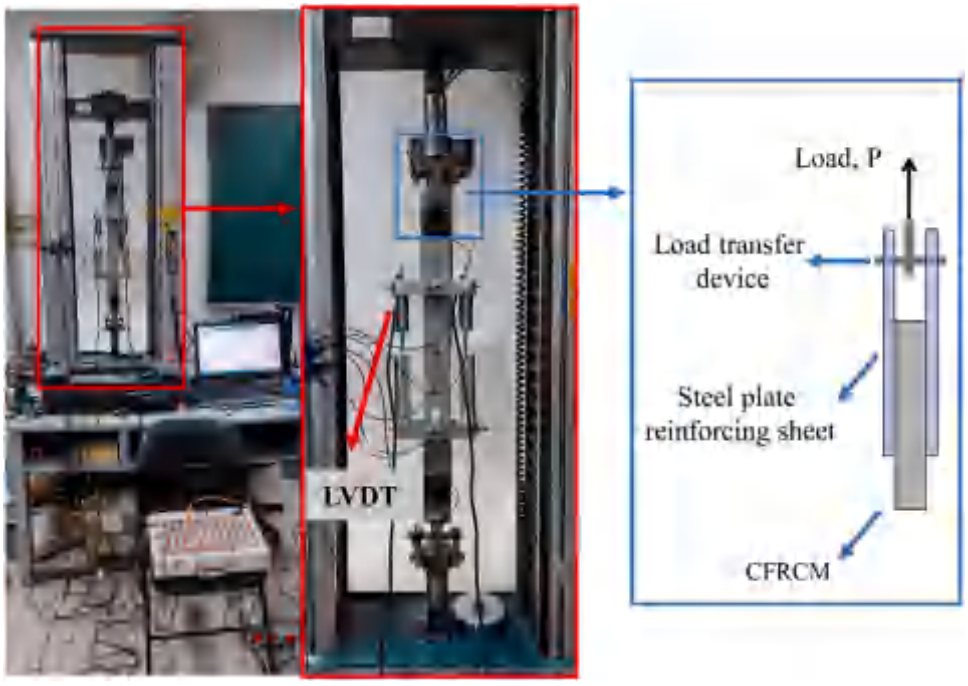


Fig. 5. Loading devices and measuring systems.

failure of the fiber bundle; (2) ICCP makes the fiber filaments deteriorate, and its ultimate strength is greatly reduced. All fiber filaments in a bundle of carbon fiber bundles have poor synergistic force performance, resulting in more severe telescopic layered failure; (3) the three bundles of carbon fiber bundles in CFRCM don't uniformly deteriorate after ICCP. Therefore, there is a stepped failure after cracking, as shown in Fig. 6(d), and there may be one to three-step shapes according to the difference in the synergistic force performance. When the charge density is large (e.g., TS-I600-D32–3 and 4), the instantaneous rupture damage of carbon fabric (Fig. 6(e)) occurs at the instant of matrix cracking due to the severe deterioration of carbon fabric.

3.2. Effect of ICCP on the piezoresistive effect of the loading process

In previous studies [55], the piezoresistive effect of carbon fiber bundle was primarily evaluated using the change in resistance $\triangle R$ and the ratio of resistance change $\triangle R/R$. $\triangle R/R$ was calculated by Eq. (2).

$$\frac{\Delta R}{R} = \frac{R' - R_0}{R_0} \times 100\% \tag{2}$$

where R_0 (Ω) is the reference resistance, and R' (Ω) is the changed resistance value.

Analysis shows that the piezoresistive effect of the CFRCM tensile process is complicated, and the piezoresistive effect of CFRCM specimens with both types of matrices is essentially the same. Thus, two typical specimens were selected to analyze their cracking and failure process and the corresponding changes in the resistance curve. The results of the piezoresistive effect are shown in Fig. 8. R_{05} is the overall resistance change ratio, and R_{01}, R_{12}, R_{23}, R_{34}, and R_{45} are the resistance change rates of each interval. The specimen interval between electrode *i* and electrode *j* is denoted by "*i-j*" in the following. Furthermore, the resistance R_b [37] of carbon fiber bundles during CFRCM loading is shown in Eq. (3):

$$R_b = \frac{R_f(1 + K_s\varepsilon_f)}{N - N_f + \lambda N_f(1 + K_s\varepsilon_f)} \tag{3}$$

where R_f is the resistance of a single fiber filament, K_s is the sensitivity coefficient, ε_f is the fiber filament strain, N_f is the total amount of ruptured filaments, and λ is the fiber filament's contact ratio. Eq. (3) considers the effect of the elastic deformation of filaments, the number of ruptured fiber filaments, and contact change on the resistance during the loading process, and it can be used as an auxiliary means of qualitative analysis in piezoresistive effect analysis.

According to Fig. 8, three cracks appeared in the tensile process of the TS-N-4 specimen, among which Crack I was the main crack. When the matrix cracked at electrode 1, the resistance of R_{01} decreased slightly, and the resistance of interval R_{12} increased slightly. Thus, the direction close to intervals 1–2 can be judged to be the main direction of fiber pull-out. Crack II appeared at electrode 3, and the matrix cracked at both the upper and lower edges of the electrode, resulting in some of the fiber filaments rupturing at both ends of electrode 3. R_{23} and R_{34} increased by 0.8–1.0 %. Crack III then appeared in intervals 2–3, with R_{23} elevated by 0.8 % at the moment of matrix cracking. However, R_{12} and R_{34} both slightly decreased due to the release of stress causing a reduction in the elastic deformation of the fiber bundle. Thereafter, the fiber filaments at both ends of each crack gradually ruptured as the load was elevated. The resistance of the corresponding intervals continued to grow until carbon fiber bundles at crack I were the first to rupture in large numbers, resulting in a sudden increase in resistance, and the resistance of the remaining intervals around the crack decreased due to stress release. After the load in the load-displacement curve developed to the peak load, most of the fiber filaments in the remaining intervals were still in the elastic phase, and the resistance remained almost stable because the load was already low. While the fiber filaments in the main crack section continued to rupture, the overall resistance was mainly affected by the growth of resistance in the main crack section and increased gradually. During the entire tensile process, the change in the overall resistance R_{05} is not significantly affected by the cracking of the matrix but is noticeably influenced by the final failure.

Fig. 9 shows the representative curves of the piezoresistive effect of CFRCM after ICCP (Q=8.29 $\times 10^5$ C/m^2). Due to the severe deterioration of carbon fiber bundles after ICCP, CFRCM showed only one crack during tension. Therefore, the piezoresistive effect process was simpler, the resistance change was small in most intervals, and the mechanism of the piezoresistive effect was not significantly different from that of the control group.

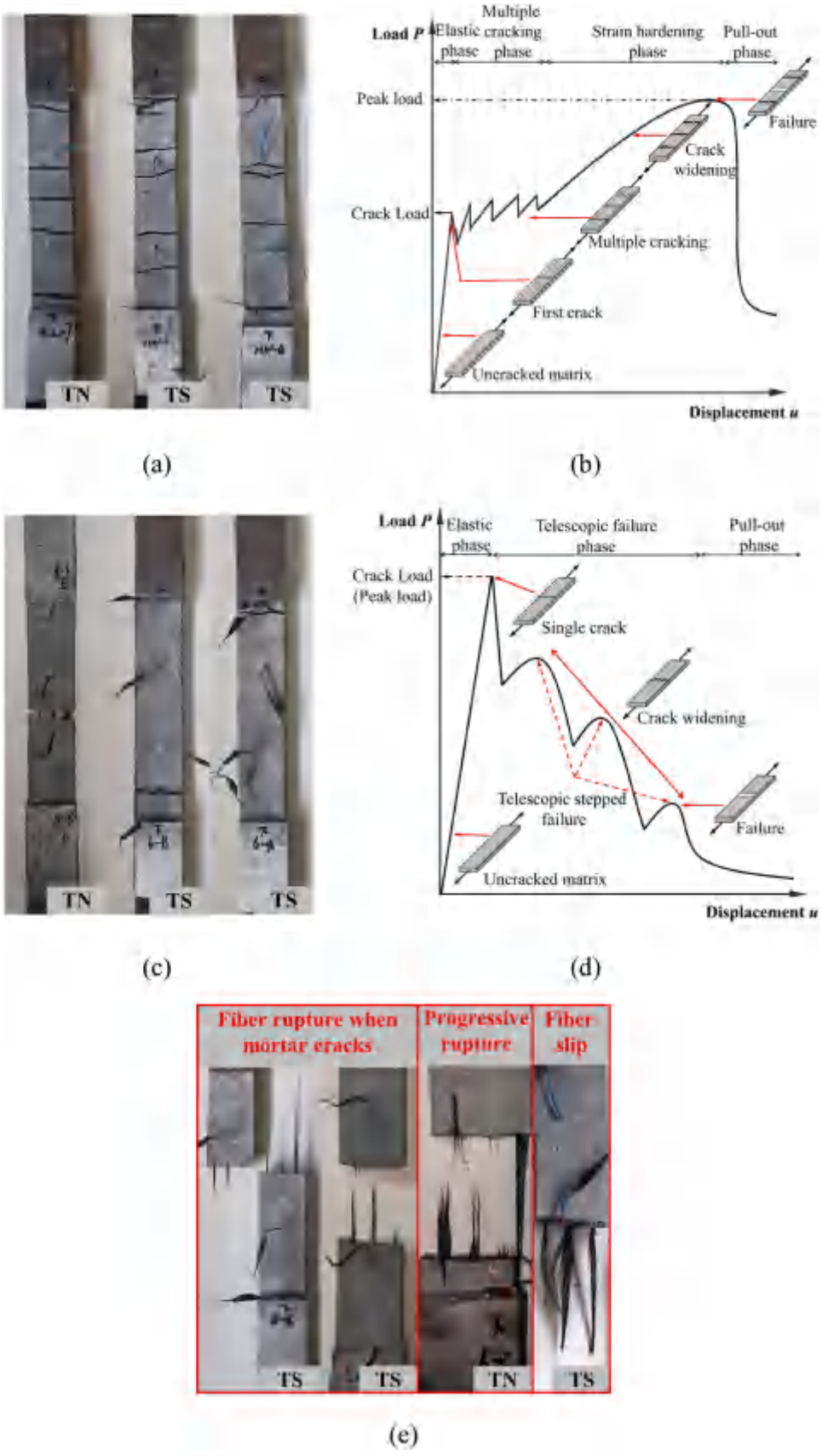
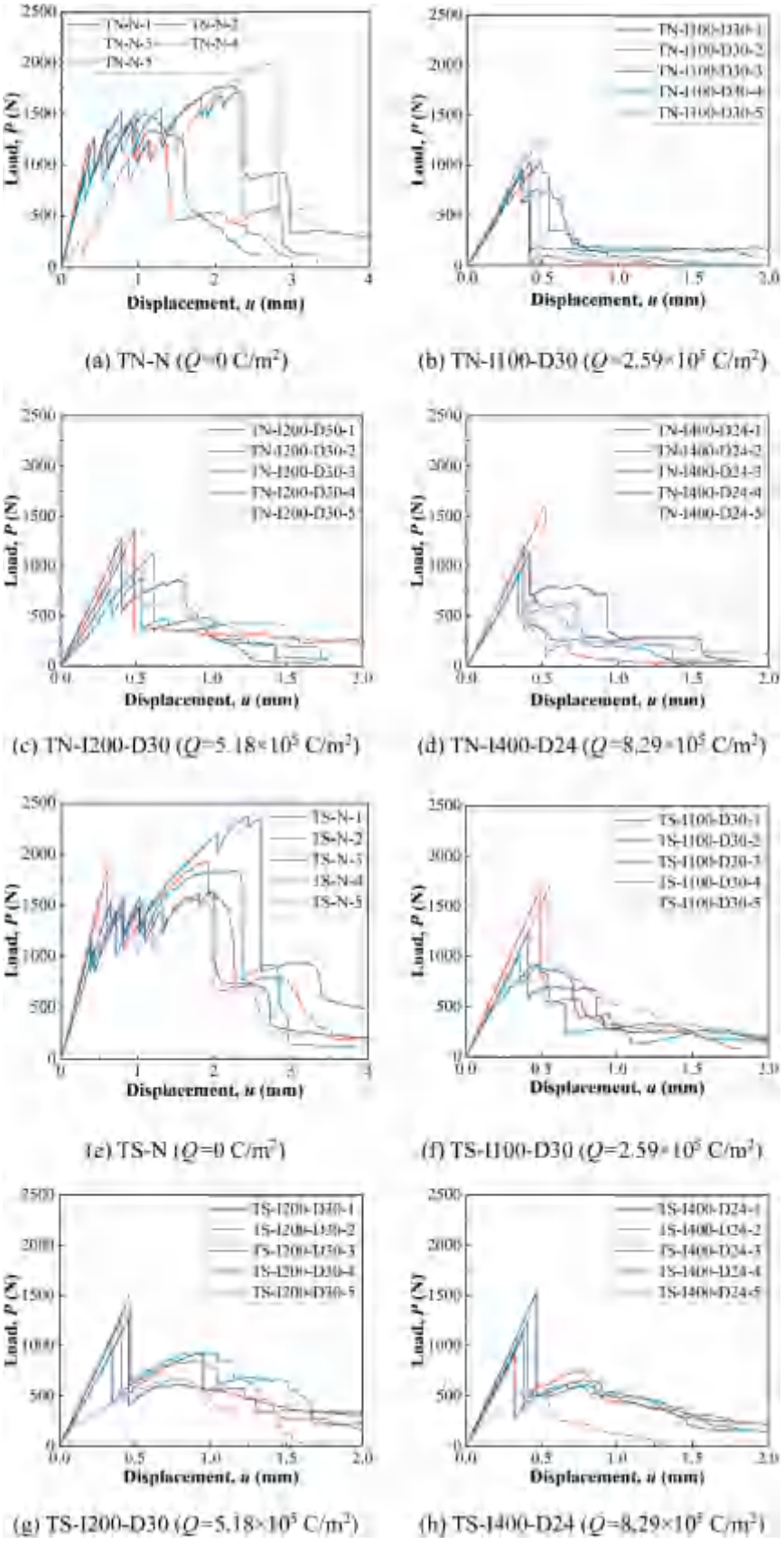


Fig. 6. Failure modes of CFRCM tensile tests before and after ICCP: (a) Multiple cracking of the matrix; (b) Schematic diagram of the ACK model; (c) Single crack of the matrix; (d) Schematic one load-displacement curve of CFRCM specimen after ICCP in the case of a single crack; and (e) Failure modes of carbon fabric.



(a) TN-N (Q=0 C/m^2) (b) TN-I100-D30 (Q=2.59×10^5 C/m^2)

(c) TN-I200-D30 (Q=5.18×10^5 C/m^2) (d) TN-I400-D24 (Q=8.29×10^5 C/m^2)

(e) TS-N (Q=0 C/m^2) (f) TS-I100-D30 (Q=2.59×10^5 C/m^2)

(g) TS-I200-D30 (Q=5.18×10^5 C/m^2) (h) TS-I400-D24 (Q=8.29×10^5 C/m^2)

Fig. 7. Tensile load-displacement curves of CFRCM with two matrices.

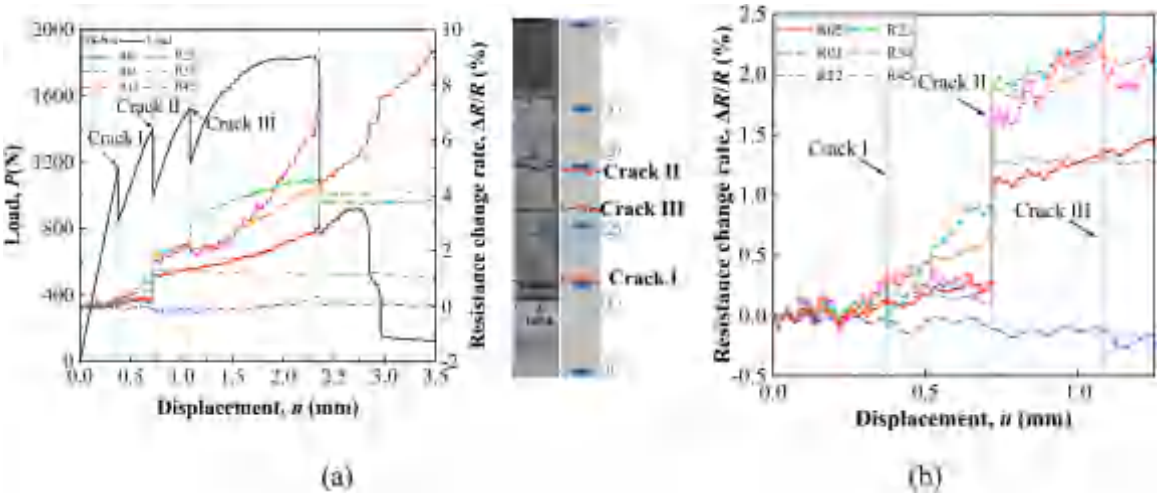


Fig. 8. (a) Piezoresistive effect during the tensile process of TS-N-4; and (b) Details of the piezoresistive effect of TS-N-4 (u=0–1.25 mm).

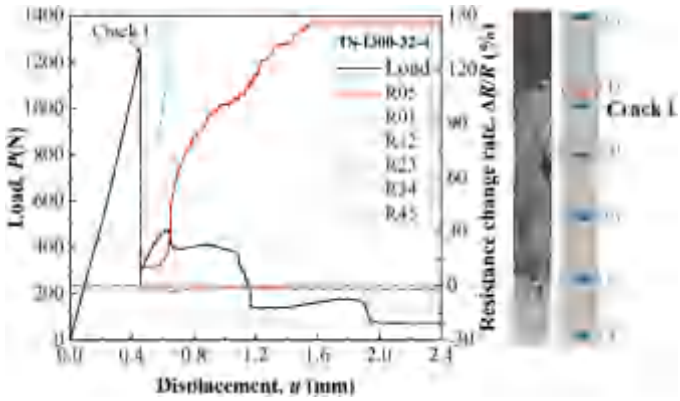


Fig. 9. Piezoresistive effect curves of TS-I300-D32–4 (Q=8.29 ×10^5 C/m^2).

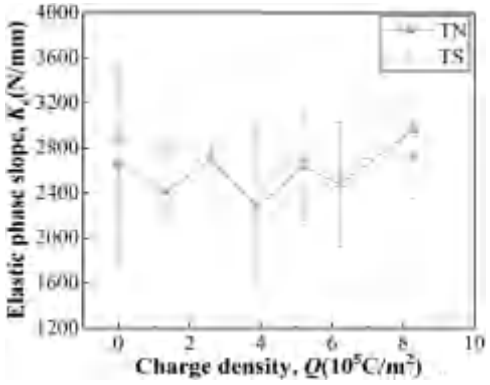


Fig. 10. Trend of the slope of the elastic phase curves of two matrices CFRCM specimens after ICCP.

4. Analysis of the tensile performance of CFRCM after ICCP

The effect of ICCP on elastic phase slope K_e, the peak load P_{max}, and energy dissipation E_p of CFRCM are analyzed in the following section.

4.1. Elastic phase slope

Fig. 10 and Table 7 show the variation of the elastic phase slope K_e of the load-displacement curves concerning the charge density. In the elastic phase, the main load is borne by the matrices, and the effect of ICCP on the tensile performance of the matrices is small, as mentioned before, so K_e remains almost constant with the increase of the charge density.

Table 7
Statistical results of mechanical performance parameters with the growth of charge density for CFRCM specimens with two matrices after ICCP.

Specimens	Q (10^5 C/m^2)	K_e (N/mm) (COV)	σ_{cr} (MPa) (COV)	P_{max} (N) (COV)	E_p (10^{-3} J) (COV)
TN (Normal mortar)	0	2664.78 (0.32)	2.23 (0.51)	1686 (0.14)	2221.83 (0.57)
	1.30	2407.56 (0.19)	2.57 (0.33)	1045.35 (0.17)	340.78 (0.41)
	2.59	2697.73 (0.07)	3.09 (0.19)	1019.6 (0.14)	254.78 (0.28)
	3.89	2271.45 (0.3)	2.25 (0.42)	961.02 (0.31)	261.79 (0.37)
	5.18	2630.45 (0.18)	3.5 (0.31)	1175.8 (0.16)	291.8 (0.20)
	6.22	2477.83 (0.22)	2.85 (0.25)	1030.9 (0.23)	316.21 (0.42)
	8.29	2960.34 (0.08)	3.21 (0.19)	1201.7 (0.21)	240.68 (0.40)
TS (Seawater sea-sand mortar)	0	2887.45 (0.09)	3.37 (0.24)	1876.11 (0.17)	2823.15 (0.36)
	2.59	2745.43 (0.15)	2.9 (0.32)	1284.1 (0.25)	418.05 (0.41)
	5.18	2671.48 (0.14)	2.56 (0.37)	1140.44 (0.19)	372.76 (0.68)
	8.29	2736.29 (0.14)	2.31 (0.44)	1022.76 (0.37)	255.19 (0.31)

4.2. Peak load and crack stress

4.2.1. Effect of charge density

In the ICCP procedure, as the charge density increases, cracking and rupture phenomena occur on the fiber surface, which can significantly affect the mechanical performance of CFRCM.

Fig. 11(a) shows the variation trend of peak load P_{max} with the growth of charge density for CFRCM specimens with two matrices after ICCP, and Table 7 shows the detailed statistical results. From Fig. 7, it can be seen that the control specimens all have multiple cracking and strain hardening phases, the stress of carbon fiber bundles is relatively uniform and the utilization of the fiber is high. While all the ICCP test groups have rapid telescopic layered failure in a certain section after the matrix's first cracking, the fiber filaments' monolithic response is poor.

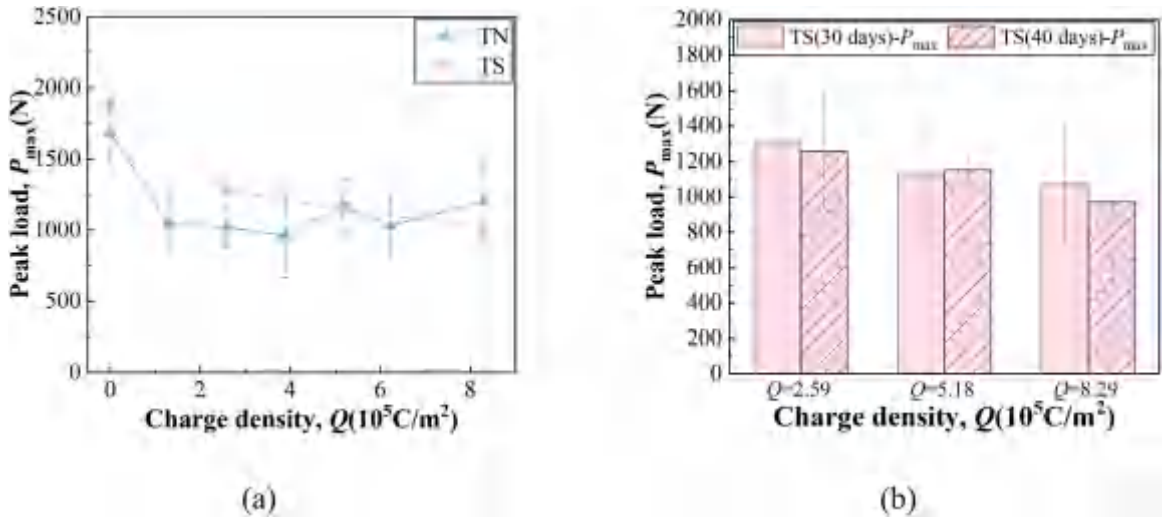


Fig. 11. (a) The trend of peak load P_{max} with the growth of charge density for CFRCM specimens with two matrices after ICCP; and (b) Comparison of peak loads for different energization durations and current densities at the same charge density.

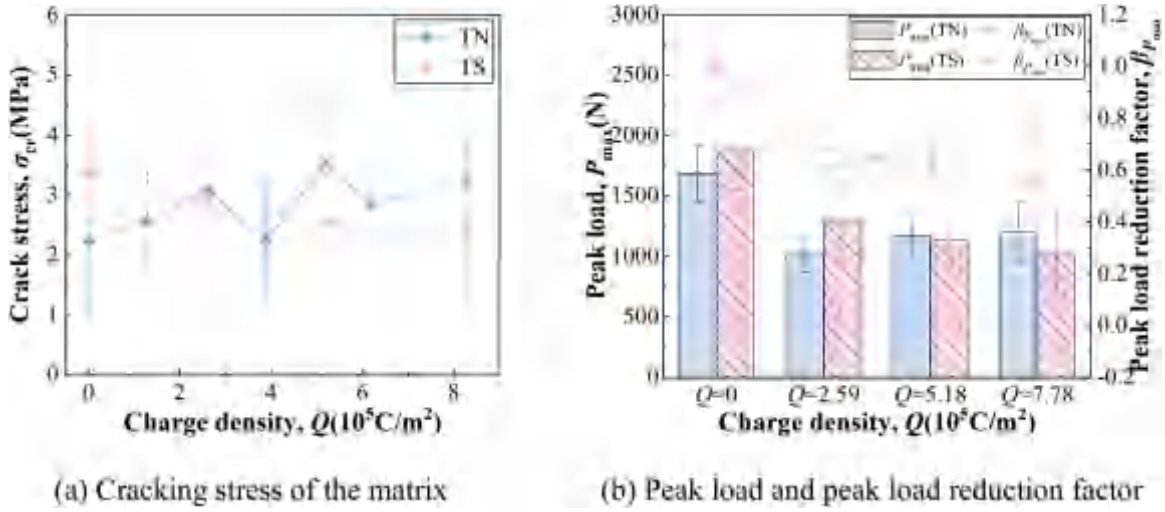


Fig. 12. Effect of matrix type on cracking stress, peak load at the same charge density.

Therefore, as shown in Fig. 11(a), peak loads are significantly greater in the control group than in the ICCP test group. Since the peak load of the ICCP test group is typically the cracking load of the matrix, the variation trend of the peak load is relatively small with the increase of the charge density.

TS series contain comparison tests with the same charge density but different energization durations and current densities. Regarding the tensile performance, a statistical comparison of the peak loads of the TS series of specimens was carried out, and the results are shown in Fig. 11 (b). The results for most of the remaining specimens show that the peak load values for the same series of specimens with different energization durations and current density groups are similar. The degree of ICCP degradation should be assessed by charge density and not only by energization duration or current density.

4.2.2. Effect of the matrix type

The degradation results of cracking stress σ_{cr} of CFRCM after ICCP are shown in Fig. 12(a) and Table 7. The cracking stresses of both matrices are similar and vary around 2.6 MPa, and the effect of ICCP on the tensile performance of the matrix is negligible.

Due to the differences in mechanical performance of the two matrices control specimens, it is not straightforward to compare the effect of different matrix types on ICCP degradation. Therefore, normalized mechanical performance values were calculated. The normalization method involves taking the ratio of the mechanical performance indicator under different charge density conditions to the corresponding indicator of the control group. These ratios are defined as the mechanical performance reduction factors. The discount factor $\beta_{P\max}(Q)$ for the peak load P_{max} is calculated by Eq. (4), respectively. P_{max}, $\beta_{P\max}(Q)$, for the two matrices at different charge densities, are shown in Fig. 12(b). The peak loads of the two types of matrices do not show significant differences with the change in charge density. This is because, after the ICCP procedure, the peak load of CFRCM is usually the cracking load of the matrix.

$$\beta_{P_{max}}(Q) = P_{max}(Q)/P_{max}(0) \tag{4}$$

4.3. Energy dissipation

Pei [6] employed energy dissipation to evaluate the ductility of CFRCM during the loading process. Energy dissipation is determined by the area under the load-displacement curve within the range [0, l_p]. The calculation for energy dissipation is described in Eq. (5).

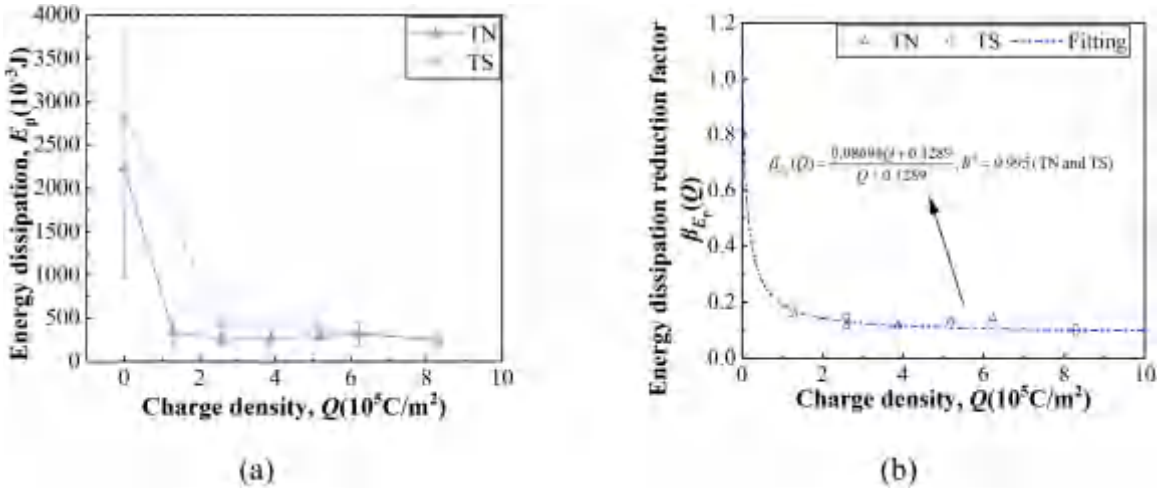


Fig. 13. (a) The variation trends of energy dissipation of CFRCM after ICCP; (b) Fitting results of the energy dissipation discount factor.

$$E_p = \int_0^{l_p} P(u)du \tag{5}$$

where $P(u)$ is the load-displacement response and l_p is the calculated upper displacement limit. In this study, since taking a fixed value for l_p as the interval cannot truly reflect the ductility of the specimen, l_p was defined as the displacement at which the load was reduced to 85 % of the peak load, serving as the upper limit for calculating energy dissipation. It is important to note that l_p should exceed the displacement corresponding to the peak load. The results are shown in Fig. 13(a) and Table 7.

The CFRCM control specimens had higher fiber utilization after cracking due to multiple cracking and strain hardening phases. As a result, the energy dissipation was significantly higher than that of the ICCP test group. Most ICCP test group specimens entered the rapid telescopic layered failure and pull-out phase after matrix cracking. Therefore, the difference in energy dissipation at different charge densities was insignificant. The energy dissipation discount factor $\beta_{Ep}(Q)$ is calculated by Eq. (6).

$$\beta_{E_p}(Q) = E_p(Q) \Big/ E_p(0) \tag{6}$$

After combining the data of two kinds of matrices, the inverse proportional function was used to fit the energy ductility index discount factor $\beta_{Ep}(Q)$. The results of $\beta_{Ep}(Q)$ are shown in Fig. 13(b). Since the energy ductility index is mainly controlled by the failure mode, the difference between different matrix types under the same charge density is not significant. The fitting results have a high degree of goodness of fit.

4.4. Discussions of the variability in experimental results

It's worth noting that the reasons for the relatively large range of results for some specimens in Fig. 10 to Fig. 13 are as follows: Firstly, the initial rupture of filaments for CFRCM before loading is random [37,42]. Moreover, differing initial rupture ratios and contact ratios among various carbon fabrics result in inconsistent effective conduction paths. Consequently, in the ICCP process, despite maintaining a consistent charge density for each fiber bundle, the actual amount of charge transmitted to individual filaments varies. This inconsistency may lead to different filament degradation degrees, ultimately diminishing filaments' collaborative stress performance. Additionally, because of the filaments' small diameter and the narrow gaps between them, achieving complete infiltration of matrix particles into the fiber bundles proves challenging, leading to uneven infiltration in both longitudinal and transverse directions of the matrix [56–58]. Even parallel specimens crafted from the same materials can display variability in bonding performance.

5. Conclusions

In this study, the effect of ICCP on the failure mode and tensile performance of CFRCM composites has been investigated by uniaxial tensile testing. The piezoresistive effect of the CFRCM loading process has been analyzed, and the effect of ICCP on the piezoresistive effect has been explored. Finally, the tensile performance of CFRCM with charge density has been investigated. The main conclusions of the study are as follows:

(1) After the ICCP procedure, the failure mode of CFRCM specimens changed. With the increase of charge density, the failure mode changed from "elasticity-multiple cracking-strain hardening-pull-out failure" to "elasticity-telescopic layered failure-pull-out failure (single crack)". The load-displacement curves in the telescopic layered failure phase showed a step-like failure due to the decrease in the synergistic stress performance of carbon fiber bundles after cracking.
(2) The piezoresistive effects during the tensile phase of the CFRCM specimens with two matrix types are essentially the same. The changes in interval resistance and overall resistance are related to the crack propagation location. When the crack occurs away from the electrode, the segment resistance and overall resistance increase due to instantaneous fiber rupture. When the crack appears at the electrode, the overall resistance change is generally less sensitive, and the resistance on both sides of the crack may decrease or increase. Therefore, based on the piezoresistive effect of each CFRCM segment, the cracks' location and the crack propagation sequence can be inferred.
(3) In the failure phase, the overall resistance of the control group specimens may show segmented growth or instant growth. In contrast, the overall resistance of the ICCP test group shows segmented growth due to carbon fabric telescopic layered failure. The effect of ICCP on the segmented piezoresistive effect during the tensile process of CFRCM specimens is minimal.
(4) After applying ICCP, the slope of the elastic phase remains relatively constant as the charge density increases; in addition, the peak load decreases, but since the peak load is the cracking load of CFRCM, it is not significantly affected by the charge density value. The trend of energy dissipation changes is similar to that of the peak load. The differences in tensile performance of the two matrices before and after applying ICCP are small. Therefore, in the field of CFRCM strengthening and health monitoring,

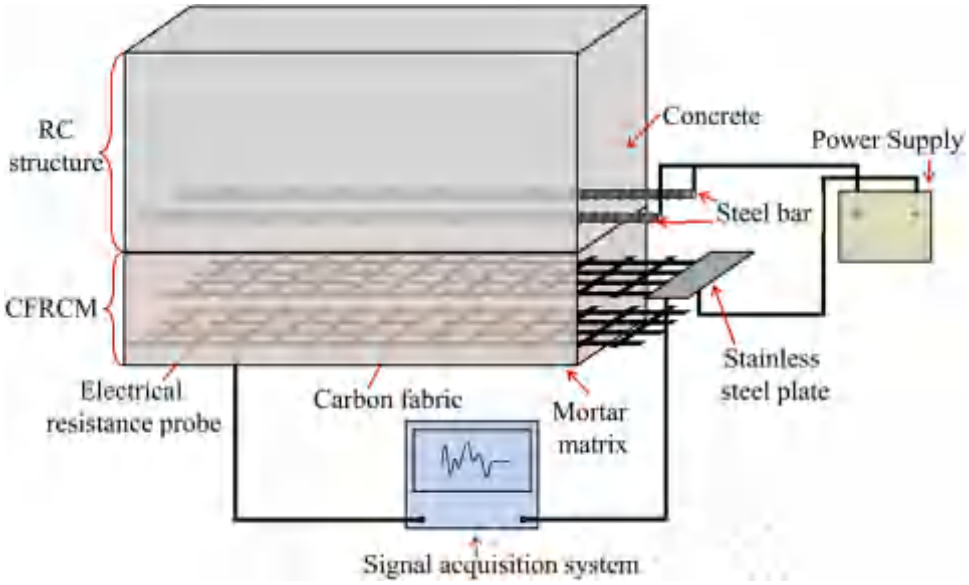


Fig. 14. Schematic diagram of a triple-functional system: ICCP-SS-SHM.

seawater and sea-sand may to some extent serve as a substitute for freshwater river sand.

6. Research prospects

The protective function of ICCP on steel bars in RC structures has been adequately demonstrated in previous research, and there is no need for this study to re-establish it. The focus of this study is on the " Effect of ICCP on tensile performance and piezoresistive effect of CFRCM ", as research related to this is currently rare. Based on Fig. 6(d), Fig. 7, and Fig. 11 (b), it can be observed that under accelerated electrochemical testing (i.e., ICCP testing), a high current density leads to the loss of load-bearing capacity in the CFRCM matrix after a single crack formation, transitioning from ductile failure to brittle failure. For RC structures strengthened with CFRCM, the CFRCM that serves as a strengthening material may experience a loss of load-bearing capacity due to degradation after undergoing ICCP procedures.

Therefore, the solution to the above issue is as follows: the next step of the research will focus on RC structures strengthened with CFRCM containing multiple layers of fabric. Some of the fabrics will serve as anode auxiliary materials for ICCP-SS and self-sensing materials for structural health monitoring, while others will act as load-bearing and self-sensing materials. Conductive electrodes are uniformly arranged on all fabrics to ensure the realization of self-sensing throughout the entire process, including ICCP procedures and loading, corresponding to actual service environments. This will construct an intelligent triple-functional system of ICCP-SS-SHM (Fig. 14). This will involve various design methods and theories concerning parameters such as fabric reinforcement ratio, spacing of resistance probe layout, ICCP charge density, etc. Future research will play a promoting role in the intelligent development of both existing RC structures and newly constructed RC structures for seawater and sea-sand.

CRediT authorship contribution statement

Jiarong Liu: Writing – review & editing, Writing – original draft, Visualization, Validation, Software, Methodology, Funding acquisition, Formal analysis, Data curation, Conceptualization. **Dawei Zhang**: Writing – review & editing, Supervision, Resources, Project administration, Methodology, Investigation, Funding acquisition. **Yewangzhi Tao**: Writing – original draft, Visualization, Software, Methodology, Conceptualization. **Zhiyu Xie**: Writing – review & editing, Methodology. **Bo Yi**: Writing – review & editing, Investigation.

Declaration of Competing Interest

The authors declare that they have no known competing financial interests or personal relationships that could have appeared to influence the work reported in this paper.

Data availability

Data will be made available on request.

Acknowledgments

The support from the Program Fund of Nonmetallic Excellence and Innovation Center for Building Materials (24PHD-5), and National Natural Science Foundation of China (52078454) is greatly appreciated.

References

[1] Ahmed A, Guo S, Zhang Z, et al. A review on durability of fiber reinforced polymer (FRP) bars reinforced seawater sea sand concrete. Constr Build Mater 2020;256:119484. https://doi.org/10/ghfm9f.
[2] Mohammed TU, Hamada H, Yamaji T. Performance of seawater-mixed concrete in the tidal environment. Cem Concr Res 2004;34(4):593–601. https://doi.org/10.1016/j.cemconres.2003.09.020.
[3] Xiao J, Zhang Q, Zhang P, et al. Mechanical behavior of concrete using seawater and sea-sand with recycled coarse aggregates. Struct Concr 2019;20(5):1631–43. https://doi.org/10.1002/suco.201900071.
[4] Xie Z, Zhang D, Huang W, et al. Quantifying fatigue damage in reinforced concrete beams through piezomagnetic effect: a fatigue-magnetomechanical coupling approach. Structures 2024;62:106304. https://doi.org/10.1016/j.istruc.2024.106304.
[5] Lv L, Wang J, Xie Z. Experimental study on axial compression behaviour of steel reinforced concrete-filled steel tube (SRCFST) columns enhanced by steel rings and CFRP. Structures 2024;61:105980. https://doi.org/10.1016/j.istruc.2024.105980.
[6] Pei C, Zeng Y, Kong S, et al. Pull-out performance of anchored carbon-fiber bundles in cementitious matrix. J Compos Constr 2021;25(6):04021057. https://doi.org/10.1061/(ASCE)CC.1943-5614.0001175.
[7] Wu Y, Xie Z, Zhang D, et al. Uniaxial tensile behavior of anchored carbon fabric-reinforced cementitious matrix plates. J Mater Civ Eng 2023;35(8):04023251. https://doi.org/10.1061/JMCEE7.MTENG-14941.
[8] Wei L, Ueda Tamon, Matsumoto Koji, et al. Experimental and analytical study on the behavior of RC beams with externally bonded carbon-FRCM composites. Compos Struct 2021;273:114291. https://doi.org/10.1016/j.compstruct.2021.114291.
[9] Feng R, Liu Y, Zhu J-H, et al. Flexural behaviour of C-FRCM strengthened corroded RC continuous beams. Compos Struct 2020;245:112200. https://doi.org/10.1016/j.compstruct.2020.112200.

[10] Tetta ZC, Koutas LN, Bournas DA. Textile-reinforced mortar (TRM) versus fiber-reinforced polymers (FRP) in shear strengthening of concrete beams. Compos Part B: Eng 2015;77:338–48. https://doi.org/10.1016/j.compositesb.2015.03.055.
[11] Tran CTN, Nguyen XH, Nguyen HC, et al. Shear performance of short-span FRP-reinforced concrete beams strengthened with CFRP and TRC. Eng Struct 2021;242:112548. https://doi.org/10.1016/j.engstruct.2021.112548.
[12] Koutas L, Bousias SN, Triantafillou TC. Seismic strengthening of masonry-infilled RC frames with TRM: experimental study. J Compos Constr 2015;19(2):04014048. https://doi.org/10.1061/(ASCE)CC.1943-5614.0000507.
[13] Feng R, Wang J, Zhu J-H, et al. Fatigue behavior of corroded reinforced concrete continuous beams with multi-intervention system. Eng Struct 2021;231:111748. https://doi.org/10.1016/j.engstruct.2020.111748.
[14] Zhu J, Su M, Huang J, et al. The ICCP-SS technique for retrofitting reinforced concrete compressive members subjected to corrosion. Constr Build Mater 2018;167:669–79. https://doi.org/10.1016/j.conbuildmat.2018.01.096.
[15] Zhu J-H, Wang Z, Su M, et al. C-FRCM jacket confinement for rc columns under impressed current cathodic protection: 2. J Compos Constr 2020;24(2):04020001. https://doi.org/10.1061/(asce)cc.1943-5614.0001006.
[16] Su M, Zeng C, Li W, et al. Flexural performance of corroded continuous RC beams rehabilitated by ICCP-SS. Compos Struct 2020;232:111556. https://doi.org/10.1016/j.compstruct.2019.111556.
[17] Su M, Wei L, Liang H, et al. Fatigue behaviour and design of corroded reinforced concrete beams intervened by ICCP-SS[. Compos Struct 2021;261:113295. https://doi.org/10.1016/j.compstruct.2020.113295.
[18] Su M, Wei L, Zeng Z, et al. A solution for sea-sand reinforced concrete beams. Constr Build Mater 2019;204:586–96. https://doi.org/10.1016/j.conbuildmat.2019.01.146.
[19] Su M, Wei L, Liang H, et al. Fatigue behaviour and design of corroded reinforced concrete beams intervened by ICCP-SS. Compos Struct 2021;261:113295. https://doi.org/10.1016/j.compstruct.2020.113295.
[20] Feng R, Zhang J, Zhu J-H, et al. Experimental study on the behavior of carbon-fabric reinforced cementitious matrix composites in impressed current cathodic protection. Constr Build Mater 2020;264:120655. https://doi.org/10.1016/j.conbuildmat.2020.120655.
[21] Feng R, Zhang J, Zhu J-H, et al. Experimental study on interface bonding fatigue behavior of C-FRCM composites in ICCP. Constr Build Mater 2020;259:119660. https://doi.org/10.1016/j.conbuildmat.2020.119660.
[22] Wei L-L, Zhu J-H, Ueda T, et al. Tensile behaviour of carbon fabric reinforced cementitious matrix composites as both strengthening and anode materials. Compos Struct 2020;234:111675. https://doi.org/10.1016/j.compstruct.2019.111675.
[23] Su M, Wei L, Zhu J-H, et al. Combined Impressed Current Cathodic Protection and FRCM Strengthening for Corrosion-Prone Concrete Structures[J]. J Compos Constr 2019;23(4):04019021. https://doi.org/10.1061/(asce)cc.1943-5614.0000949.
[24] Zhu M, Zhu J-H, Ueda T, et al. Degradation behavior of multifunctional carbon fabric-reinforced cementitious matrix composites under anodic polarization. Constr Build Mater 2022;341:127751. https://doi.org/10.1016/j.conbuildmat.2022.127751.
[25] Zhang EQ, Tang L, Bernin D, et al. Effect of the paste–anode interface under impressed current cathodic protection in concrete structures. Mater Corros 2018;69(8):1104–16. https://doi.org/10.1002/maco.201709908.
[26] Grammatikos SA, Paipetis AS. On the electrical properties of multi scale reinforced composites for damage accumulation monitoring. Compos Part B: Eng 2012;43(6):2687–96. https://doi.org/10.1016/j.compositesb.2012.01.077.
[27] Sebastian J, Schehl N, Bouchard M, et al. Health monitoring of structural composites with embedded carbon nanotube coated glass fiber sensors. Carbon 2014;66:191–200. https://doi.org/10.1016/j.carbon.2013.08.058.
[28] Cheng X, Zhou H, Wu Z, et al. An investigation into self-sensing property of hat-shaped 3D orthogonal woven composite under bending test. J Reinf Plast Compos 2019;38(4):149–66. https://doi.org/10.1177/0731684418808093.
[29] Goldfeld Y, Quadflieg T, Ben-Aarosh S, et al. Micro and macro crack sensing in TRC beam under cyclic loading. J Mech Mater Struct 2017;12(5):579–601. https://doi.org/10.2140/jomms.2017.12.579.
[30] Luan C, Yao X, Shen H, et al. Self-sensing of position-related loads in continuous carbon fibers-embedded 3D-printed polymer structures using electrical resistance measurement. Sensors 2018;18(4):994. https://doi.org/10.3390/s18040994.
[31] Yosef L, Goldfeld Y. Smart self-sensory carbon-based textile reinforced concrete structures for structural health monitoring. Struct Health Monit 2020;1475921720951122. https://doi.org/10.1177/1475921720951122.
[32] Wen S, Wang S, Chung DDL. Piezoresistivity in continuous carbon fiber polymer-matrix and cement-matrix composites. J Mater Sci 2000;35(14):3669–75. https://doi.org/10.1023/A:1004842303468.
[33] Chung DDL. Carbon materials for structural self-sensing, electromagnetic shielding and thermal interfacing. Carbon 2012;50(9):3342–53. https://doi.org/10.1016/j.carbon.2012.01.031.
[34] Park Y-B, Roh HD, Lee IY. Structural health monitoring of CFRPs using electrical resistance by reduced peripheral electrodes. Smart Struct Syst 2021;28(6):737–44. https://doi.org/10.12989/SSS.2021.28.6.737.
[35] Cho JW, Choi JS. Relationship between electrical resistance and strain of carbon fibers upon loading. J Appl Polym Sci 2000;77(9):2082–7. https://doi.org/10.1002/1097-4628(20000829)77:9<2082::AID-APP26>3.0.CO;2-W.
[36] Quadflieg T, Stolyarov O, Gries T. Carbon rovings as strain sensors for structural health monitoring of engineering materials and structures. J Strain Anal Eng Des 2016;51(7):482–92. https://doi.org/10.1177/0309324716655058.
[37] Gong Y, Xie Z, Liu J, et al. Research on piezoresistive effect and random model of carbon fiber bundle. Arch Civ Mech Eng 2023;23(2):128. https://doi.org/10.1007/s43452-023-00672-0.
[38] Wu ZS, Yang CQ, Harada T, et al. Self-diagnosis of structures strengthened with hybrid carbon-fiber-reinforced polymer sheets. Smart Mater Struct 2005;14(3):S39–51. https://doi.org/10.1088/0964-1726/14/3/006.
[39] Yang CQ, Wu ZS. Self-structural health monitoring function of RC structures with HCFRP sensors. J Intell Mater Syst Struct 2006;17(10):895–906. https://doi.org/10.1177/1045389×06061520.
[40] Fouad N, Saifeldeen MA. Smart self-sensing fiber-reinforced polymer sheet with woven carbon fiber line sensor for structural health monitoring. Adv Struct Eng 2021;24(1):17–24. https://doi.org/10.1177/1369433220944507.
[41] Roh HD, Park Y-B. Electromechanical analysis of self-sensing CFRP and its application to real-time non-destructive evaluation. In: Shull PJ, Yu T-Y, Gyekenyesi AL, et al., editors. Nondestructive Characterization and Monitoring of Advanced Materials, Aerospace, Civil Infrastructure, and Transportation IX. Online Only. United States: SPIE; 2020. p. 32. https://doi.org/10.1117/12.2557963.
[42] Gong Y, Xie Z, Chen G, et al. Influence of cementitious material infiltration on piezoresistive effect of carbon fiber bundle. J Mater Civ Eng 2023;35(7):04023173. https://doi.org/10.1061/JMCEE7.MTENG-14701.
[43] Wen S, Chung DDL. Piezoresistivity in continuous carbon fiber cement-matrix composite. Cem Concr Res 1999;29(3):445–9. https://doi.org/10.1016/S0008-8846(98)00211-7.
[44] Goldfeld Y, Quadflieg T, Gries T. Sensing capabilities of carbon based TRC beam from slack to pull-out mechanism. Compos Struct 2017;181:294–305. https://doi.org/10.1016/j.compstruct.2017.08.102.
[45] Goldfeld Y, Ben-Aarosh S, Rabinovitch O, et al. Integrated self-monitoring of carbon based textile reinforced concrete beams under repeated loading in the uncracked region. Carbon 2016;98:238–49. https://doi.org/10.1016/j.carbon.2015.10.056.
[46] Goldfeld Y, Yosef L. Sensing accumulated cracking with smart coated and uncoated carbon based TRC. Measurement 2019;141:137–51. https://doi.org/10.1177/1475921718808223.
[47] China Cement Standardization Technical Committee. The National Standard of the People's Republic of China: Test Method of Cement Mortar Strength(ISO Method) (GB/T17671-2021) [S]. Beijing: Standards Press of China,; 2021 (in Chinese).
[48] ACI 549.6R-20. Guide to Design and Construction of Externally Bonded Fabric-reinforced Cementitious Matrix (FRCM) and Steel-Reinforced Grout (SRG) Systems for Repair and Strengthening Masonry Structures[S]. Farmington Hills, Michigan: ACI,; 2020.
[49] Chung DDL. A critical review of piezoresistivity and its application in electrical-resistance-based strain sensing. J Mater Sci 2020;55(32):15367–96. https://doi.org/10.1007/s10853-020-05099-z.
[50] Aveston J, Kelly A. Theory of multiple fracture of fibrous composites. J Mater Sci 1973;8(3):352–62. https://doi.org/10.1007/BF00550155.
[51] Hegger J, Will N, Bruckermann O, et al. Load–bearing behaviour and simulation of textile reinforced concrete. Mater Struct 2006;39(8):765–76. https://doi.org/10.1617/s11527-005-9039-y.
[52] Zastrau U, Fortmann C, Fäustlin RR, et al. Bremsstrahlung and line spectroscopy of warm dense aluminum plasma heated by Xuv free-electron-laser radiation. Phys Rev E 2008;78(6):066406. https://doi.org/10.1103/PhysRevE.78.066406.
[53] Goldfeld Y., Yosef L. Electrical–structural characterisation of smart carbon-based textile reinforced concrete beams by integrative gauge factors[J/OL]. Strain. https://doi.org/10.1111/str.12344.
[54] Liu J, Zhang D, Tao Y, et al. A pull-out equivalent telescopic layered failure model of carbon fiber bundles in seawater sea-sand cementitious matrix. Eng Struct 2024;308:118052. https://doi.org/10.1016/j.engstruct.2024.118052.
[55] Kang B-G, Hannawald J, Brameshuber W. Electrical resistance measurement for damage analysis of carbon yarns. Mater Struct 2011;44(6):1113–22. https://doi.org/10.1617/s11527-010-9687-4.
[56] Hegger J, Voss S. Investigations on the bearing behaviour and application potential of textile reinforced concrete. Eng Struct 2008;30(7):2050–6. https://doi.org/10.1016/j.engstruct.2008.01.006.
[57] Homoro O, Michel M, Baranger TN. Pull-out response of glass yarn from ettringite matrix: effect of pre-impregnation and embedded length. Compos Sci Technol 2019;170:174–82. Pull-out Response of Glass Yarn from Ettringite Matrix: Effect of Pre-Impregnation and Embedded Length. ⟨https://doi.org/10.1016/j.compscitech.2018.11.045⟩.
[58] Loreto G, Leardini L, Arboleda D, et al. Performance of RC slab-type elements strengthened with fabric-reinforced cementitious-matrix composites. J Compos Constr 2014;18(3):A4013003. https://doi.org/10.1061/(ASCE)CC.1943-5614.0000415.

Cement and Concrete Composites 152 (2024) 105645



Contents lists available at ScienceDirect

Cement and Concrete Composites

journal homepage: www.elsevier.com/locate/cemconcomp



Effect of ICCP on bond performance and piezoresistive effect of carbon fiber bundles in cementitious matrix

Yewangzhi Tao [a], Jiarong Liu [a], Dawei Zhang [a,*], Zhiyu Xie [a,b], Jiaxin Hong [a]

[a] Institute of Structural Engineering, Zhejiang University, Hangzhou, 310058, China
[b] School of Engineering, Hangzhou City University, Hangzhou, 310015, China

ARTICLE INFO

Keywords:
CFRCM
ICCP
Bond performance degradation
Bond performance prediction
Piezoresistive effect

ABSTRACT

The purpose of this study is to lay a foundation for developing a triple-functional system of impressed current cathodic protection, structural strengthening, and structural health monitoring (ICCP-SS-SHM) regarding carbon fabric reinforced cementitious matrix (CFRCM) material performance, and promote the utilization of seawater sea-sand resources to alleviate the shortage of freshwater river sand resources. In recent years, CFRCM, ICCP, and the piezoresistive effect have been widely studied in strengthening reinforced concrete structures, corrosion protection of steel reinforcement, and SHM, respectively. This study used two types of matrix materials: normal matrix (ISO standard sand) and seawater sea-sand matrix. The effect mechanism of the ICCP procedure on the bond performance degradation of CFRCM with the two types of matrix and the bond performance differences between them were investigated through carbon fiber bundle tensile tests and CFRCM bundle pull-out tests. Prediction formulas for bond performance were established based on the different charge densities, mechanical parameters, and resistance parameters, respectively. The piezoresistive effects of CFRCM with the two types of matrix after the ICCP procedure and the effect of ICCP on the piezoresistive effect were analyzed. The seawater sea-sand environment has a positive impact on delaying the degradation of CFRCM by ICCP.

1. Introduction

Existing reinforced concrete structures in service under harsh environments are prone to carbonation and steel corrosion due to long-term physical, chemical, and biological effects. These phenomena severely affect the durability of the structures. Additionally, the development of concrete engineering in remote and coastal areas is greatly limited due to the scarcity of freshwater river sand [1]. Previous studies have shown the feasibility of using seawater sea-sand as a substitute for freshwater river sand [2,3]. However, when seawater sea-sand is directly used in construction, its chloride ions can cause steel corrosion. It is still crucial to find solutions to delay steel corrosion, enhance structural load-bearing capacity, and implement structural health monitoring to reduce or avoid the losses caused by structural failures.

Impressed current cathodic protection (ICCP) is considered one of the most effective methods for addressing steel corrosion [4]. The principle of ICCP is to provide electrons to the steel reinforcement in the cathodic zone through auxiliary anodes, thereby inhibiting the loss of electrons in the steel reinforcement and achieving the protection of the steel. However, ICCP alone cannot enhance the strength of corroded structures. In addition, carbon fiber has advantages such as high elastic modulus, lightweight, good conductivity, and corrosion resistance [5]. In recent years, carbon fabric reinforced cementitious matrix (CFRCM) has been widely studied and applied for structural strengthening (SS) [6–11]. However, it does not address the existing corrosion issues of internal steel reinforcement.

Several studies have combined ICCP and SS techniques to form a new dual-functional system called ICCP-SS (impressed current cathodic protection and structural strengthening) [12–16]. Due to carbon fiber's excellent electrical conductivity and mechanical performance, CFRCM can serve as both an auxiliary anode material and a strengthening material. The ICCP-SS technology has been shown to effectively delay the corrosion of steel reinforcement and improve beams' flexural load-carrying capacity and fatigue life [12–14]. However, it is worth noting that while the corrosion of cathodic reinforcement is delayed, the mechanical performance of the auxiliary anode material also deteriorates. With an increase in anode current density, the acidic environment near the anode causes a decrease in the tensile, flexural, and fatigue mechanical properties of CFRCM under simulated seawater erosion [17–19].

* Corresponding author.
E-mail address: dwzhang@zju.edu.cn (D. Zhang).

https://doi.org/10.1016/j.cemconcomp.2024.105645
Received 17 January 2024; Received in revised form 1 April 2024; Accepted 24 June 2024
Available online 26 June 2024
0958-9465/© 2024 Elsevier Ltd. All rights are reserved, including those for text and data mining, AI training, and similar technologies.

Currently, the reported studies have mainly focused on CFRCM with freshwater river sand as the matrix, and research on the performance degradation of CFRCM with seawater sea-sand as the matrix after the ICCP procedure is still lacking. Additionally, few prediction models or formulas are available to predict the bond performance degradation of CFRCM materials after the ICCP procedure, and a direct link between charge density and material performance has not been established.

In structural health monitoring (SHM), some emerging SHM methods, such as fiber optic grating and piezoelectric sensors, require embedding or attachment to the structure. They have disadvantages such as complex equipment, high cost, time-consuming installation, poor durability, and potential reduction in structural mechanical performance [20–22]. Therefore, there is an urgent need for more advanced structural health monitoring technologies to be developed.

The piezoresistive effect of carbon fibers was first reported in 1969 [23]. When subjected to uniaxial tensile strain, carbon fibers exhibit the piezoresistive effect, which means that the material's resistance increases with increasing strain. Self-sensing refers to the ability of structural materials to perceive their health status, such as strain, stress, damage, temperature, humidity, cracks, etc., without the need for additional sensors [24,25]. The piezoresistive effect of carbon fibers provides them with self-sensing capabilities. Therefore, carbon fibers are smart dual-function materials for structural strengthening and self-sensing. They offer advantages over materials that rely on embedded or attached sensors, including lower cost, more excellent durability, larger sensing volume, and lesser reduction in mechanical performance [22,26].

There have been numerous studies on the piezoresistive effect of continuous carbon fiber bundles and carbon fiber-reinforced polymer (CFRP). These studies primarily focus on the relationship between resistance changes and stress, strain, and crack response of the materials or structures. The resistance change rate of carbon fiber bundles increases linearly with increasing tensile strain and sharply increases upon fiber rupture [27,28]. Monitoring the residual resistance under static and dynamic loads can be used to assess the extent of carbon fiber damage [27], and the initial linear deformation of the piezoresistive effect curve can be used to estimate the applied load magnitude [29]. Furthermore, in terms of structural sensing, the residual resistance of CFRP composites under prestressed conditions can retain information about the maximum tensile strain on the concrete beam and detect hidden crack opening displacements, thus evaluating beam damage [30]. Carbon fiber linear sensors can also detect the cracking load and initial debonding between prestressed smart fiber-reinforced polymer sheets and reinforced concrete surfaces [31]. Real-time damage localization and severity analysis of 3D-printed micro-bridges can be achieved using structural health monitoring algorithms based on the resistance changes of glass-carbon fiber composites [32].

However, studies on the self-sensing characteristics of CFRCM and its strengthening members are still lacking. Due to the non-uniform impregnation of carbon fibers by mortar, the relative resistance change of CFRCM during the failure phase is smaller than that of CFRP, and the variability is greater [33]. Studies on the self-sensing characteristics of glass-carbon hybrid fabric-reinforced beams [20,34–38] have shown qualitative or quantitative correlations between the resistance and flexural mechanical response of carbon fibers under four-point bending and repeated loading-unloading, indicating that carbon fibers can sense crack accumulation, enabling quantitative damage detection. Methods for SHM of fabric-reinforced beams based on engineering specification factors have been proposed [22].

In summary, the dual-function characteristics of strengthening-sensing in CFRCM have been validated. However, there is currently a lack of research on the piezoresistive effect during the loading process of CFRCM specimens before and after the application of ICCP. Specifically, the mechanism of ICCP's effect on the piezoresistive effect is unknown, and the effect of seawater sea-sand (containing chloride) on the piezoresistive effect is unclear.

In this study, the effect of the ICCP procedure on the bond performance of CFRCM bundles with different matrix materials was investigated through carbon fiber bundle tensile tests and CFRCM bundle pull-out tests. In addition, prediction formulas for the bond performance were established based on the charge density, mechanical parameters, and resistance parameters, respectively. The piezoresistive effect of the CFRCM bundles with two types of matrix after the ICCP procedure and the effect of ICCP on the piezoresistive effect were analyzed. This study intends to lay the foundation for developing the tri-functional system of ICCP-SS-SHM in terms of CFRCM material performance. Additionally, it aims to address the shortage of freshwater river sand resources.

2. Experimental program

2.1. Material properties

To investigate the effects of ICCP on the bond performance of carbon fiber bundles and the piezoresistive effect of CFRCM bundles, the ICCP procedures in solution and matrix environments were used in this study, respectively. The solution includes saturated calcium hydroxide solution from fresh water and saturated calcium hydroxide solution prepared from seawater. The matrix includes normal mortar (freshwater-ISO standard sand) and seawater sea-sand mortar. The sand used in the normal mortar consisted of ISO standard sand with 0.5–1 mm particle size and fine sand with 0.25–0.5 mm particle size in a mass ratio of 2:1. The sea sand is natural, and its particle grading and water content are shown in Table 1. The concentration of each major ion of seawater is shown in Table 2. Normal mortar and seawater sea-sand mortar were proportionally designed based on similar compressive and flexural strengths (Table 3). The flexural and compressive strengths of the matrix at 7 and 28 days (Table 4) were measured according to the specification [39].

The number of filaments in the bundle and the physical properties of individual filaments are provided in Table 5. All the performance data, including the electrical resistivity, are provided by Youtejia Company in Wuxi, Jiangsu Province, China.

The performance of the two-component epoxy resin-based copper powder conductive adhesive is provided by SINWE Electronic Materials Co., Ltd. In Shenzhen. It has a resistivity of 10^{-2}-10^{-3} Ω·mm, tensile strength, and shear strength of 11.8 MPa and 8.2 MPa respectively, and it completely cures at room temperature within 24 h. It is used to make conductive electrodes.

2.2. Test specimens and parameters

The main parameters include the environment of the ICCP procedure (types of mortar and simulated pore solution), the current density (I), and the duration of the impressed current (D). The specimen groups are shown in Table 6. The specimens were labeled as "E1ME2-I-D", where E1 is the type of experiment: T represents the tensile test and P represents the pull-out test; M is the type of material; B represents carbon fiber bundle and C represents the CFRCM bundle; E2 is the energizing environment: N represents saturated $Ca(OH)_2$ solution prepared with fresh water or normal mortar and S represents saturated $Ca(OH)_2$ solution prepared with seawater or seawater sea-sand mortar. For example, PCN–I300-D30 represents a set of CFRCM bundle pull-out specimens with a matrix of normal mortar. It is subjected to an applied current with

Table 1
Particle gradation and moisture content of sea sand.

Sieve residue rates of different particle sizes (%)						Fineness modulus	Moisture content (%)
4.8 mm	2.4 mm	1.2 mm	0.6 mm	0.3 mm	0.2 mm		
0.4	6.7	19.5	34.5	66	96.2	2.2	3.65

Table 2
Types and content of seawater ions.

pH	Cl^-(g/L)	SO_4^{2-}(g/L)	Na^+(g/L)	Mg^{2+}(g/L)	K^+(g/L)	Ca^{2+}(g/L)
8.02	14.81	1.82	15.74	1.51	1.21	6.35

Table 3
The mix ratio of two matrices.

The type of matrix	Portland cement (P. O 42.5) (g)	Water (g)	Sand (g)	Redespersible latex powder (Wacker 4115 N)/g	Superplasticizer (MG SKY 8860)/g
NM	100	45	200	1.5	0.15
SM	100	55	207.3	1.5	0.2

Note: NM is freshwater ISO standard sand mortar; SM is seawater sea-sand mortar. The same abbreviations are used below.

Table 4
The Strength of two matrices.

The type of matrix	Curing age	Flexural strength		Compression strength	
		Mean value (MPa)	Coefficient of variation (%)	Mean value (MPa)	Coefficient of variation (%)
NM	7d	4.55	5.23	21.91	6.27
	28d	4.83	14.3	41.67	5.82
SM	7d	4.62	7.58	21.76	3.81
	28d	4.70	4.25	39.17	5.01

a current density of 300 mA/m^2 for 30 days. PCS-I50-D60 represents a set of CFRCM bundle pull-out specimens with a matrix of seawater sea-sand mortar. It is subjected to an applied current with a current density of 50 mA/m^2 for 60 days. In the simulated ICCP system, the saturated $Ca(OH)_2$ solution assumed the role of the concrete [19].

Zhu et al. [18,40] expressed the degree of ICCP proceeding in terms of the charge density Q, which represents the total amount of charge per square meter borne by the carbon fiber bundle in contact with the matrix in the CFRCM. Q is calculated as shown in Eq. (1).

$$Q = i_a t \tag{1}$$

where i_a (A/m^2) is the anode current density of the ICCP procedure and t (s) is the duration of the impressed current.

2.3. Specimen preparation

To accurately measure the resistance of the carbon fiber bundle, each filament must be in contact with each other to form parallel conductive paths. Therefore, it is important to create conductive electrodes with good conductivity and stability. In this study, the conductive electrodes are divided into energizing electrodes and measurement electrodes based on their functions. The energizing electrodes are used to provide a constant current power supply to the carbon fiber bundle during the ICCP process, forming a stable ICCP system with the carbon fiber as the anode and the steel reinforcement as the cathode. The measurement electrodes are used to provide a constant current power supply to the carbon fiber bundle during the loading process while being connected to a data acquisition system to measure the resistance of the carbon fiber bundle.

The preparation process of CFRCM bundle pull-out specimens involves the following sequential steps: Firstly, CFRCM panels were cast, followed by the fabrication of an ICCP device. Once the specimens were prepared with the energizing electrodes, the ICCP procedure was executed on the specimens. Subsequently, the CFRCM panels were cut into CFRCM bundles, and measurement electrodes were created on the carbon fiber bundles. Finally, these specimens were utilized for loading experiments. The preparation process of the carbon fiber bundle tensile specimens after ICCP is similar to the CFRCM bundle pull-out specimens, but there is no need to cast mortar matrix and prepare measurement electrodes. Carbon fiber bundles were soaked in a saturated $Ca(OH)_2$ solution. The details are as follows:

The bottom layer of mortar (15 mm thick) was poured first; then carbon fiber bundles were placed and were kept in a fixed and tensioned state by hanging a lead hammer at both ends; the top layer of the mold was then placed and fixed with a nail gun; finally, the top layer of mortar (15 mm thick) was poured and vibrated (Fig. 1). The standard curing (temperature 20 °C, humidity 95 %) was carried out for 28 days after removing the mold.

For electrode fabrication, two copper sheets coated with conductive copper adhesive were clamped to carbon fiber bundles and fixed using butterfly clips for 4–6 h. Before fabricating the ICCP device (Fig. 2), it was necessary to fabricate energizing electrodes on carbon fiber bundles (Figs. 2 and 3(a)-(b)). In the ICCP system, carbon fiber bundles or CFRCM with two kinds of mortar matrix served as the anode, and steel bars with a diameter of ϕ8 (unit: mm) in parallel served as the cathode. The device was bonded to the matrix using no-nail adhesive, and then different types of solutions were filled into the device. An external direct current of 10 mA was applied. A closed circuit was formed by connecting the cathode, anode, and the solution in the device through energizing electrodes and wires.

After the ICCP procedure, CFRCM panels were cut into multiple independent CFRCM bundles. Specimens were placed on the platform. Subsequently, lead hammers were suspended at both ends of carbon fiber bundles to avoid the influence of the fabrication of electrodes and reinforcing sheets on the initial co-deformation of carbon fiber bundles. If the measurement electrodes were placed close to the matrix during preparation, it would have caused inconvenience in the process and could have led to more severe stress concentration on fibers at the critical interface between the matrix inside and outside, resulting in damage. Additionally, in the pull-out test, there was fiber slippage at the free end, which caused electrode movement. Subsequently, the electrodes formed an anchoring effect at the end of the matrix, affecting the real load response and piezoresistive effect. Therefore, the measurement electrodes were prepared on fiber bundles located 10 mm away from the matrix to address these issues (Fig. 3(b)). After the measurement electrodes were fabricated, two perforated acrylic sheets coated with carbon fiber bundle impregnation adhesive were clamped on both sides of the carbon fiber bundle and left to stand for 24 h. The position of the acrylic reinforcement sheet was 50 mm away from the mortar matrix to ensure that the reinforcement sheet could be securely clamped by the testing machine fixture. The finished specimens are shown schematically in Fig. 3(c)–(d).

2.4. Loading and measurement methods

The loading device and the measurement system are presented in Fig. 4. The tensile test and pull-out test were both carried out using the Sansi UTM6503 electronic universal testing machine, with a range of 5

Table 5
Properties of the carbon fiber bundle.

Filament number	Filament diameter (μm)	Density (g/cm^3)	Elastic modulus (GPa)	Ultimate tensile strength (MPa)	Ultimate tensile Strain	Electrical resistivity (Ω·cm)
12,000	7	1.76	230	3530	1.5 %	1.7×10^{-3}

Table 6
Specimen groups and investigation parameters.

Specimens and number	E1ME2	I (mA/m^2)	D (day)	Q (10^5C/m^2)
TB (1–3)	–	–	–	0
TBN-I100-D65 (1–4)	Carbon fiber bundle tensile specimen-saturated $Ca(OH)_2$ solution prepared with fresh water	100	65	5.62
TBN-I200-D65 (1–4)		200	65	11.23
TBN-I400-D51 (1–4)		400	51	17.63
TBS-I100-D72 (1–4)	Carbon fiber bundle tensile specimen-saturated $Ca(OH)_2$ solution prepared with seawater	100	72	6.22
TBS-I200-D72 (1–4)		200	72	12.44
TBS-I400-D72 (1–4)		400	72	24.88
PCN–N (1–8)	CFRCM bundle pull-out specimen-normal mortar-saturated $Ca(OH)_2$ solution prepared with fresh water	–	–	0
PCN–I50-D30 (1–8)		50	30	1.30
PCN–I50-D60 (1–8)		50	60	2.59
PCN–I100-D30 (1–8)		100	30	2.59
PCN–I100-D60 (1–8)		100	60	5.18
PCN–I150-D30 (1–8)		150	30	3.89
PCN–I150-D60 (1–8)		150	60	7.78
PCN–I200-D30 (1–8)		200	30	5.18
PCN–I300-D30 (1–8)		300	30	7.78
PCN–I400-D30 (1–8)		400	30	10.37
PCS-N (1–8)	CFRCM bundle pull-out specimen-seawater sea-sand mortar- saturated $Ca(OH)_2$ solution prepared with seawater	–	–	0
PCS-I50-D60 (1–8)		50	60	2.59
PCS-I100-D30 (1–8)		100	30	2.59
PCS-I100-D60 (1–8)		100	60	5.18
PCS-I150-D30 (1–8)		150	30	3.89
PCS-I150-D60 (1–8)		150	60	7.78
PCS-I200-D30 (1–8)		200	30	5.18
PCS-I300-D30 (1–8)		300	30	7.78

Note: the numbers in parentheses represent the number of parallel specimens. For example, TBN-I100-D65-1 indicates specimen No. 1 of the four parallel specimens in group TBN-I100-D65. Unfortunately, some specimens were damaged before loading and therefore are not presented in the following text.

kN, a rate of 0.2 mm/min, and a sampling frequency of 10 Hz. In the CFRCM tensile test, acrylic reinforcement sheets at both ends were clamped in the middle by the fixture to apply load to the fiber bundle. To ensure that the fiber bundle was subjected to uniaxial tension, the acrylic-reinforced plates at both ends needed to be vertically aligned for proper centering. In the CFRCM bundle pull-out test, one end of the loading was clamped with acrylic reinforcement sheets through a fixture, and the other end was applied with a counterforce through a frame. The CFRCM bundle pull-out test was conducted using two LVDTS to measure the displacement at the load end. The measured displacement data was recorded using a Donghua DH3816N-type collector with a sampling frequency of 10 Hz. The actual displacement at the loading end was obtained by subtracting the elastic deformation of the fiber's free segment from the measured displacement.

Before the loading process, the insulating tape was applied to the fiber bundle away from the matrix on the acrylic reinforcement sheets (at the far left end in Fig. 3(d)) to prevent the slight current from the testing machine from affecting the resistance measurement data. Additionally, the contact resistance of the electrodes has been eliminated by the four-electrode method. The contact resistance of the specimen was measured using a multimeter through the four-electrode method before the reinforcement sheet of the specimen was made (i.e., before loading), as shown in Fig. 5(a). The principle is as follows.

R_1 and R_2 are the contact resistances of electrodes 1 and 2, and they are calculated by Eq. (2).

$$R_1 = \frac{R_{01} + R_{12} - R_{02}}{2} \tag{2(a)}$$

$$R_2 = \frac{R_{12} + R_{23} - R_{13}}{2} \tag{2(b)}$$

where, R_{01}, R_{12}, R_{02}, R_{23}, and R_{13} represent the measured resistances in each interval. Since the magnitudes of R_{01} and R_{23} do not affect the calculation results of R_1 and R_2, the lengths between intervals 0–1 and 2–3 can be arbitrarily chosen. The contact resistance is considered to remain constant. During loading, a constant direct current of 1 mA passes between the resistance measurement points 1 and 2 (Figs. 3(d) and Fig. 5(b)). According to Ohm's law, the absolute value of the measured voltage is the measured resistance of the carbon fiber bundle R_{12}. Subtracting the contact resistances R_1 and R_2 from R_{12} gives the actual resistance R_{12r} in interval 0–1, as shown in Eq. (3).

$$R_{12r} = \frac{U}{I} - R_1 - R_2 \tag{3}$$

The above method can avoid the issue of limited space in the testing machine that may not accommodate multiple electrodes, while also enhancing the convenience and efficiency of the testing operation. This method is similar to the use of a four-electrode measurement method based on voltammetry [41] for measuring the resistance of carbon fiber bundles.

3. Experimental results

3.1. Carbon fiber bundle tensile test

Fig. 6 shows the load-displacement response of carbon fiber bundles before and after the ICCP procedure in a saturated $Ca(OH)_2$ solution prepared with fresh water and a saturated $Ca(OH)_2$ solution prepared with seawater. After the ICCP procedure, the carbon fiber bundle's peak load and displacement decreased significantly. With an increase in charge density, the degradation of the mechanical properties of the carbon fiber bundle becomes more pronounced. The reasons for this phenomenon are reactions between the carbon fiber bundle surface and oxidized functional groups [40]. This leads to the connection between filaments through oxygen-containing functional groups, gradually damaging the longitudinal structure of the carbon fiber bundle. As a result, the flexural and tensile strength of the carbon fiber bundle decreases, exhibiting brittle characteristics.

3.2. CFRCM bundle pull-out test

3.2.1. Failure mode

The failure modes of the CFRCM bundle pull-out specimens are shown in Fig. 7. Most of the specimens of the normal mortar control group (PCN–N group) suffered fiber rupture failure, and a small portion of the specimens suffered partial fibers rupture-partial fibers slippage failure (referred to as rupture-slippage failure). In addition, all of the specimens of the seawater sea-sand control group (PCS–N group) suffered a rupture-slippage failure (Fig. 7(a)). After the ICCP procedure, both mortar specimens showed fiber embrittlement (Fig. 7(b)), and the fiber embrittlement was more obvious with the increase in charge

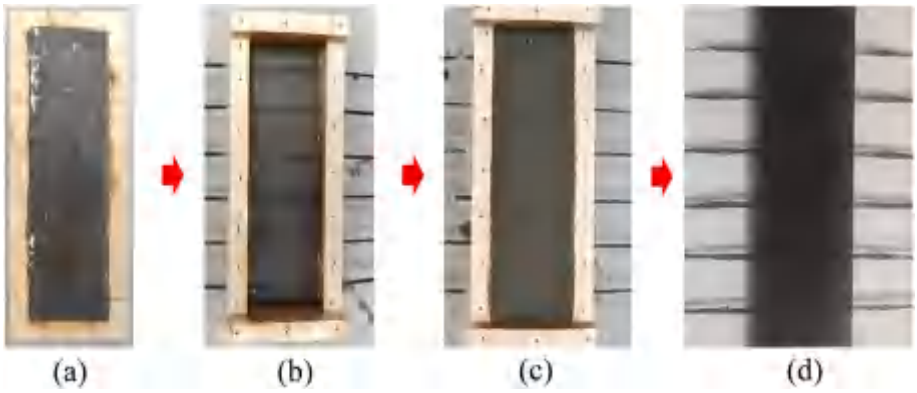


Fig. 1. Specimens fabrication process: (a) Casting bottom mortar; (b) Placing carbon fiber bundle; (c) Casting surface mortar; (d) CFRCM panel.

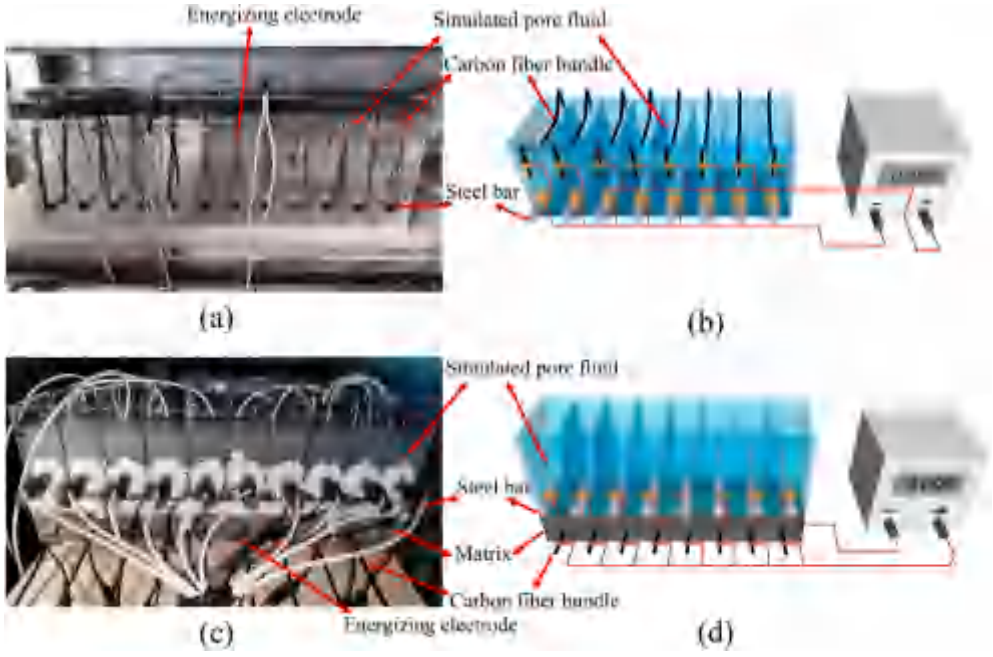


Fig. 2. ICCP system: (a) ICCP device for carbon fiber bundles in solution environment; (b) Schematic diagram of ICCP device for carbon fiber bundles; (c) ICCP device for CFRCM bundles; and (d) Schematic diagram of ICCP device for the CFRCM bundles.

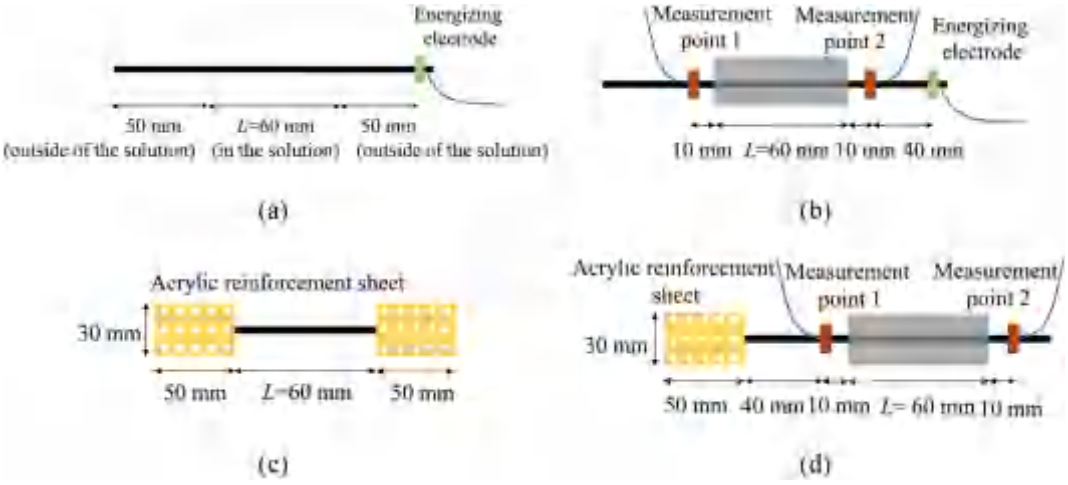


Fig. 3. Schematic diagram of specimens: (a) Electrode arrangement for carbon fiber bundle; (b) Electrode arrangement for CFRCM bundle; (c) Carbon fiber bundle tensile specimen; and (d) CFRCM bundle pull-out specimen.

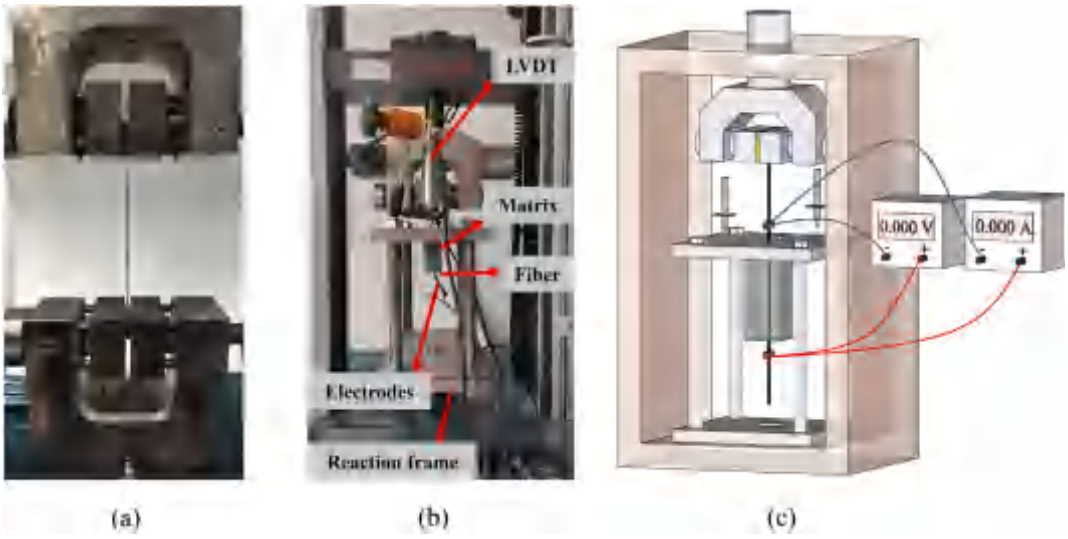


Fig. 4. Loading and measuring device: (a) Carbon fiber bundle tensile test; (b) CFRCM bundle pull-out test; (c) Schematic diagram of pull-out test.

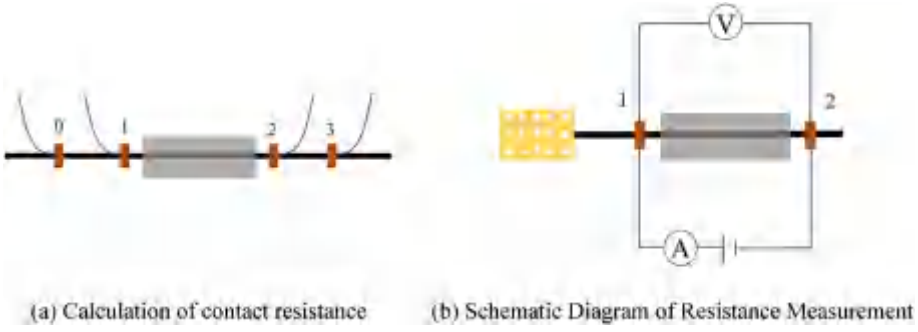


Fig. 5. Principle of contact resistance deduction and resistance measurement.

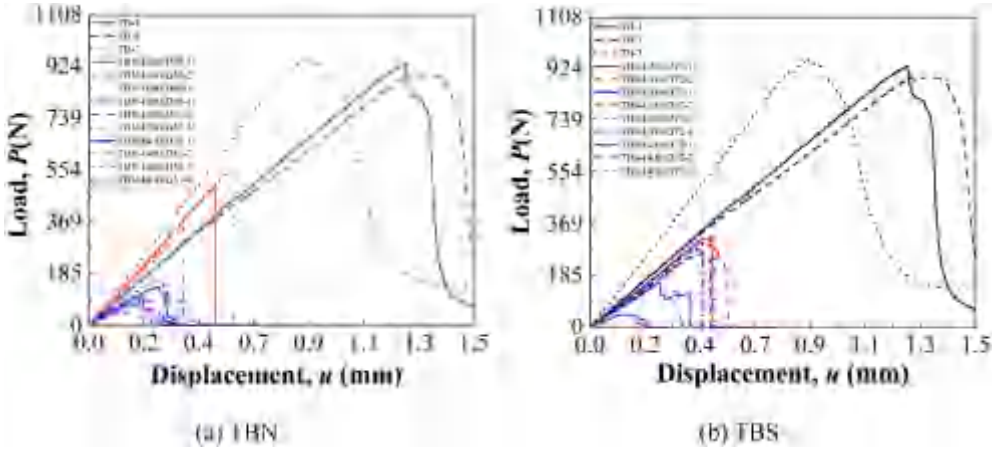


Fig. 6. Load-displacement response of carbon fiber bundle tensile test before and after ICCP.

density.

The reasons for the above phenomena can be explained from a microscopic perspective as follows: After cutting the specimens along the longitudinal and transverse sections and subjecting them to a series of processes including drying, dust removal, fixing, and conductive treatment, the microstructure of the fiber-matrix interface was observed through scanning electron microscope (SEM) in the field emission environment, as shown in Figs. 8 and 9.

According to Fig. 8, regardless of whether the specimens experienced ICCP, there were initial ruptures in the fibers. However, after the ICCP procedure, a significant amount of local damage, peeling, and macro-cracks appeared in the filaments. Therefore, after the ICCP procedure, the specimens exhibited fiber embrittlement.

Due to the inhomogeneous matrix infiltration along the longitudinal and transverse sections of the fibers (Fig. 9(a)), carbon fiber bundles exhibited two different failure modes: rupture failure and rupture-slippage (pull-out) failure. In the CFRCM bundle pull-out test, carbon fiber bundles were subjected to loads mainly from fiber filaments-matrix bonding and filament-filament friction. Among them, the bonding properties of the fiber-mortar interface are the main factor. Fiber

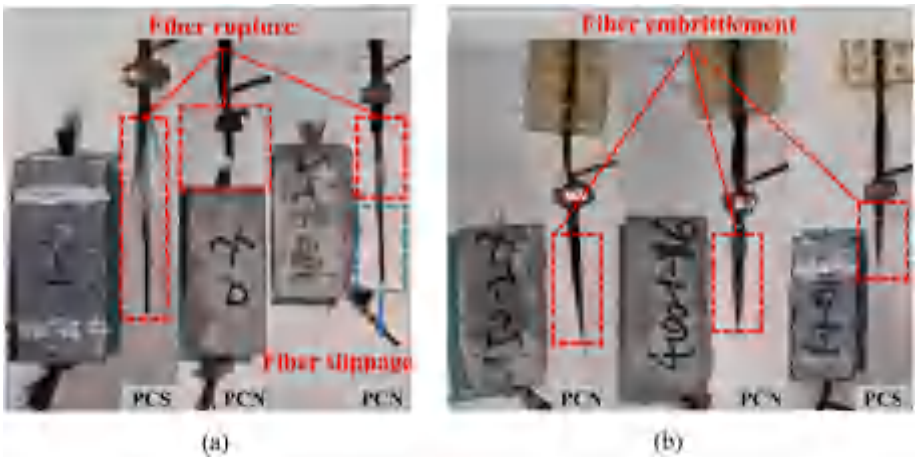


Fig. 7. Failure mode of CFRCM bundles pull-out specimens: (a) without ICCP; and (b) with ICCP.

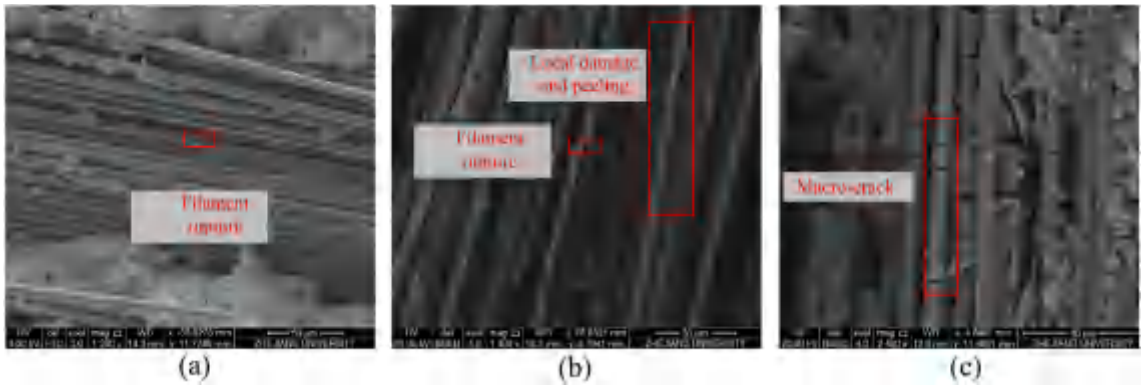


Fig. 8. Microstructure of filament-matrix interface: (a) without ICCP; (b) and (c): with ICCP. Note: the figure originates from specimens before loading.

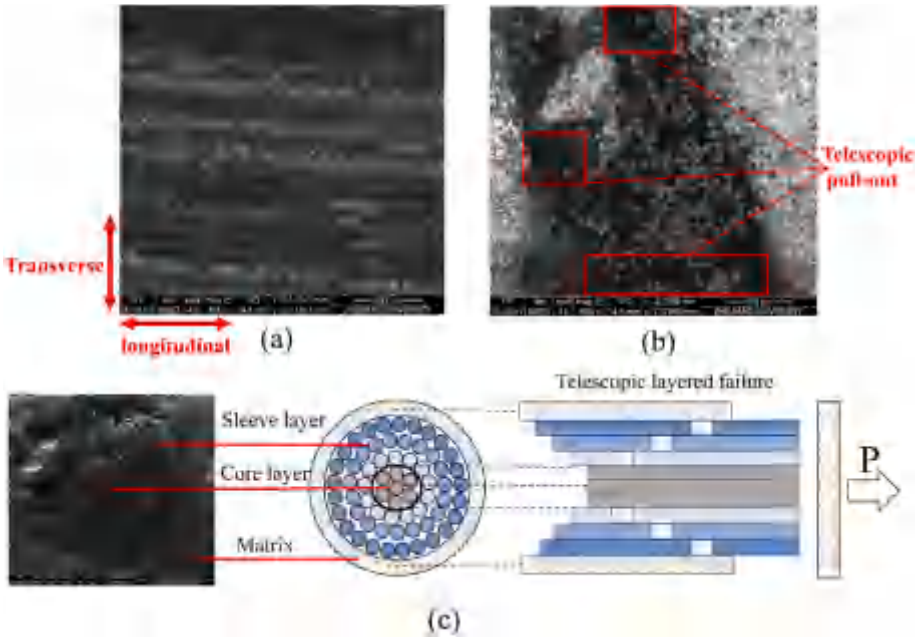


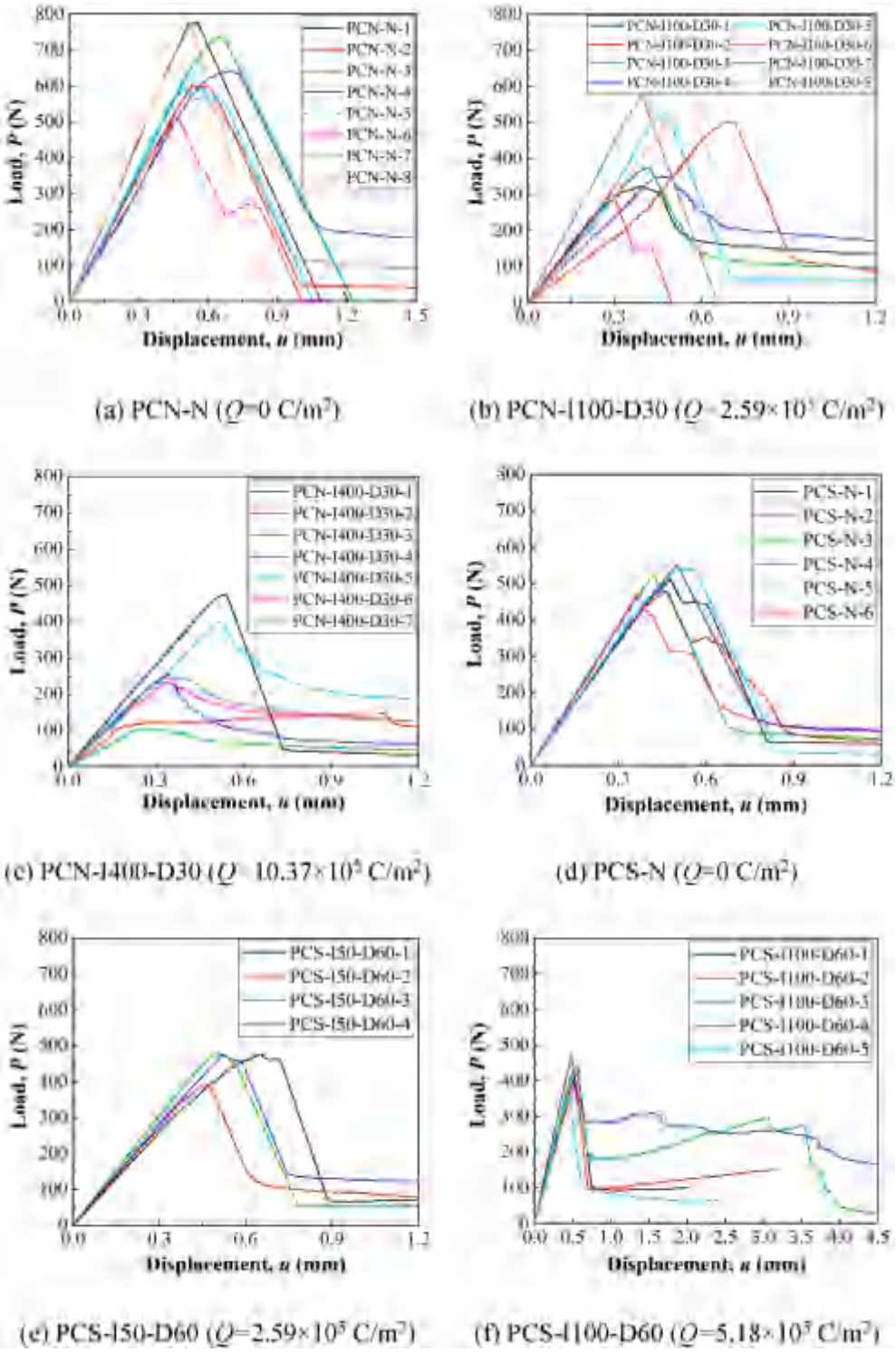
Fig. 9. Telescopic layered failure: (a) Uneven infiltration of the matrix; (b) Telescopic layered failure characteristics during pull-out process; and (c) Schematic diagram of telescopic layered failure. Note: the figure originates from specimens after loading.

filaments that fail due to filament rupture are referred to as sleeve layer fibers, while those that fail due to filament slippage are called core layer fibers. The failure process of the filaments in each layer is as follows: the better-impregnated filaments in the sleeve layer fibers reached tensile strength earlier and ruptured sooner due to faster initial force growth. The closer to the loaded end, the higher the strain of filaments. Due to

the stress concentration of carbon fiber bundles at the edge of the matrix, more fiber filaments ruptured there. The poorly infiltrated filaments in the sleeve layer fibers ruptured later because they reached tensile strength later. Due to the gradual development of interface debonding into the matrix, the location of fiber filament rupture gradually shifts towards the inner matrix. Thus, the sleeve layer fiber filaments show layered rupture failure characteristics. The core layer fibers were not infiltrated by the matrix or the degree of infiltration was limited, resulting in the loading of the fiber filaments cannot reach their tensile strength. As a result, the fiber filaments rapidly debonded, entered the friction phase under loading, and were finally pulled out. The schematic diagram of the telescopic layered failure of the CFRCM bundles is illustrated in Fig. 9(b)–(c).

3.2.2. *Effect of ICCP on load-displacement behavior*

The load-displacement curves of the pull-out tests of PCN and PCS groups are depicted in Fig. 10. The shape of the curves conforms to the three-phase characteristics of elasticity-debonding-friction in the pull-



(a) PCN-N (Q=0 C/m^2) (b) PCN-1100-D30 (Q=2.59×10^5 C/m^2)

(c) PCN-1400-D30 (Q=10.37×10^5 C/m^2) (d) PCS-N (Q=0 C/m^2)

(e) PCS-150-D60 (Q=2.59×10^5 C/m^2) (f) PCS-1100-D60 (Q=5.18×10^5 C/m^2)

Fig. 10. Load-displacement curves of CFRCM bundle pull-out specimens.

out process. With the increase of the charge density, the peak load of the pull-out process of both mortar CFRCM bundles decreased significantly, and the failure mode was gradually changed from fiber rupture failure to fiber rupture-slippage failure. The control specimens of PCN–N and PCS-N, which were not subjected to ICCP, exhibited significantly better collaborative stress carbon fiber bundles than those after ICCP. Meanwhile, the difference between the test curves of each group increased gradually with the increase of charge density. The peak loads of some specimens in the PCN–I400-D30 group are in the range of 400–500 N, but the peak loads of most specimens are in the range of 100–250 N, and the curves are more scattered. Since the peak load and the friction phase load of these curves are close, the curves show the characteristic of "pseudo-ductility". This refers to the small decrease in load after crossing the peak load.

Fig. 10(f) shows that the seawater sea-sand CFRCM bundle pull-out specimens would have irregular load growth segments after most of the sleeve layer fiber filaments have ruptured and the load has dropped abruptly. This phenomenon was more obvious when the charge density was larger. The reasons for this phenomenon may be as follows: 1) Collaborative force performance of the carbon fiber bundle deteriorated, and some of the sleeve layer fiber filaments only gradually began to be stressed and rupture in the pull-out phase; 2) during the ICCP process, seawater, sea sand, and other salt solutes, such as NaCl and $CaCl_2$ in the simulated solution precipitated and crystallized, which leads to an increase in the area of carbon fiber bundles in the local section, and the formation of an anchoring effect in the pull-out process. As a result, the positive stress between the ruptured sleeve layer fibers and the core layer fibers was elevated, resulting in increased friction.

3.2.3. Effect of ICCP on piezoresistive effect

Previous studies [42] mainly used the rate of change in resistance $\triangle R/R$ to evaluate the change in the piezoresistive effect of carbon fiber bundles, and $\triangle R/R$ was calculated by Eq. (4).

$$\frac{\Delta R}{R}=\frac{R'-R_0}{R_0}\times 100\% \tag{4}$$

where R_0 (Ω) is the reference resistance, and R' (Ω) is the changed resistance value.

According to this study (section 4.2.1) and previous research [43–45], the deterioration of CFRCM after ICCP conforms to the principle of equal charge density, and therefore groups with the same charge density were combined with "&" for subsequent analysis (Fig. 12, Table 7). The piezoresistive effect curves of CFRCM bundles during pull-out are depicted in Fig. 11. It can be found that the resistive rate of change curves also show a clear three-phase characteristic, i.e., fluctuating growth-rapid growth-slow growth, which corresponds to the elastic, debonding and friction phases of the load-displacement curves, respectively.

Furthermore, the resistance of carbon fiber bundles during CFRCM loading is shown in Eq. (5):

$$R_b=\frac{R_f(1+K_s\varepsilon_f)}{N-N_f+\lambda N_f(1+K_s\varepsilon_f)} \tag{5}$$

where R_f is the resistance of a single fiber filament, K_s is the sensitivity coefficient, ε_f is the fiber filament strain, N_f is the total amount of ruptured filaments, and λ is the fiber filament's contact ratio. Eq. (5) considers the effect of the number of ruptured fiber filaments and contact change on the resistance during the loading process. It can be used as an auxiliary means of qualitative analysis in piezoresistive effect analysis.

In the fluctuating growth phase, the resistance change was mainly caused by the elastic deformation of fiber filaments and the initial ruptured fibers due to contact changes. The contribution of the elastic deformation of fiber filaments to the growth of the resistance rate of change is in the range of 0.78–1.21 %, and the difference between different specimens is slight, thus leading to a more consistent resistance change curve across specimens in the fluctuating growth phase. At the same time, due to the momentary change in the contact situation between the initial ruptured fiber filaments, they form an effective pathway because of the contact, and the contacting fiber filaments may be disengaged and cannot conduct electricity. Thus, the rate of change of resistance fluctuated. When the resistance growth due to elastic deformation was limited in magnitude, the absolute value change due to this fluctuation was more pronounced. Therefore, the resistance curve as a whole showed a fluctuating growth trend. It's interesting that PCS-I50-D60-3 (Fig. 11) did not initially exhibit a fluctuating upward trend, but rather showed a decreasing trend. The reason for this special case is as follows: Fig. 10(e) indicates that compared to other specimens, the peak load of PCS-I50-D60-3 is lower. This is because the initial rupture ratio of the fiber bundle in this specimen is higher, resulting in more filaments conducting electricity due to random contact during the initial loading stage. According to Eq. (5), a higher contact rate leads to a smaller resistance. Therefore, the decrease in resistance caused by the fiber filament's contact rate λ in this specimen is greater than the increase in resistance caused by elastic deformation, resulting in an initially negative resistance change rate for this curve.

Table 7 and Fig. 12(a) demonstrate the effect of ICCP on the resistance change rate in the elastic phase (fluctuating growth phase). The average values of the resistance change rate $\triangle R_I/R$ of the PCS group specimens in this phase are all around 0.8 %, and the range of the resistance change rate of the PCN group is 0.7–1.84 %. Since the resistance variation caused by contact changes is very small, it can be assumed that the difference between the resistance change of PCN and

Table 7
Effect of ICCP on the rate of change of resistance at different phases of the pull-out process.

The type of matrix	Specimens	Q (10^5C/m^2)	$\triangle R_I/R$		$\triangle R_{III\text{-}0}/(Rtu)$	
			Mean value (%)	Coefficient of variation	Mean value (%/mm)	Coefficient of variation
NM	PCN–N	0	1.51	0.31	−6.65	−1.34
	PCN–I50-D30	1.30	1.13	0.27	−3.23	–
	PCN–I100-D30&I50-D60	2.59	1.60	0.52	10.34	0.91
	PCN–I150-D30	3.89	1.58	0.39	3.14	0.56
	PCN–I200-D30&I100-D60	5.18	1.67	0.37	15.17	1.81
	PCN–I300-D30&I150-D60	7.78	1.84	0.31	17.68	1.12
	PCN–I400-D30	10.37	0.77	0.95	55.81	1.01
SM	PCS-N	0	0.82	0.45	0.77	7.17
	PCS-I100-D30&I50-D60	2.59	0.70	0.19	11.54	0.87
	PCS-I150-D30	3.89	0.91	0.51	74.03	0.71
	PCS-I200-D30&I100-D60	5.18	0.81	0.47	128.78	1.07
	PCS-I300-D30&I150-D60	7.78	0.83	0.82	63.45	1.25

Note: The standard deviation of some specimens is large due to the decrease in resistance in the elastic phase; fiber filaments of some specimens ruptured, so they do not have friction section resistance data. Thus, They have been ignored for statistical purposes.

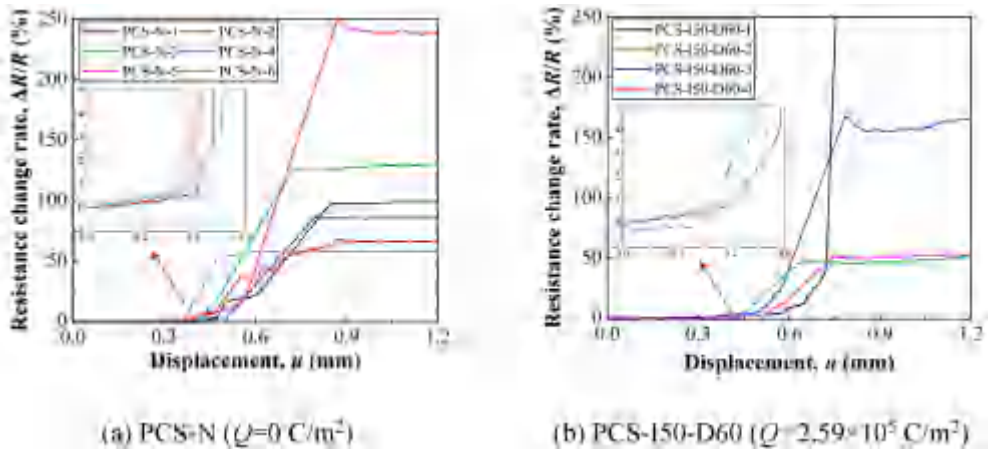


Fig. 11. Piezoresistive effect curves of CFRCM bundles during pull-out.

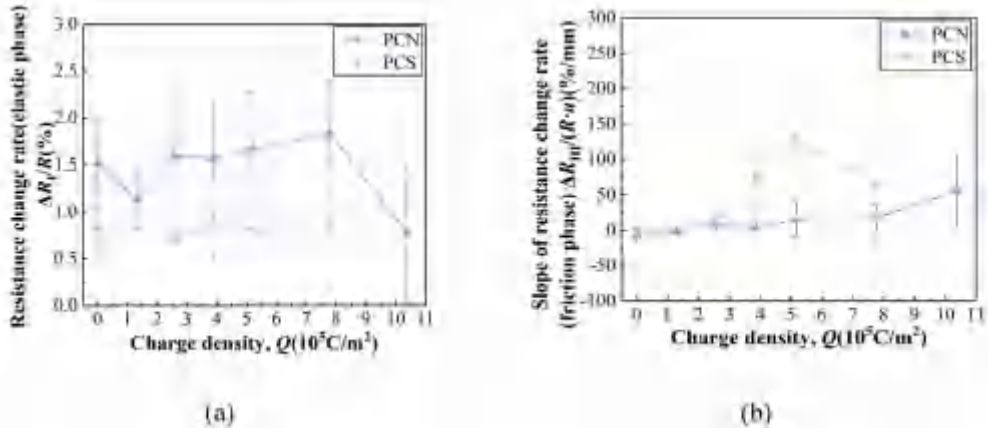


Fig. 12. Effect of ICCP on the rate of change of resistance during CFRCM bundles pull-out process: (a) Rate of resistance change in the elastic phase; (b) Slope of the resistance rate of change curve in the friction phase. Note: PCN refers to specimens with a normal mortar matrix, while PCS refers to specimens with a seawater sea-sand mortar matrix. These notations are also used in the legends of subsequent figures.

PCS group at this phase is insignificant and within the range of contact change fluctuation. Meanwhile, as the charge density increases, $\triangle R_I/R$ remains unchanged. Thus, the effect of ICCP on the piezoresistive effect in the elastic phase (i.e., resistance fluctuation growth phase) of the pull-out process can be neglected.

During the rapid growth phase, the increase in curve resistance was mainly caused by fibers rupturing. Many fiber filaments of the sleeve layer ruptured near the peak load, and the resistance change rate $\triangle R_{II}/R$ varies from 9 % to positive infinity during this phase. This value is not statistically significant for different charge densities because the variation of this value is influenced by the failure and the degree of synergistic stress.

In the slow-growth phase of resistance, the load-displacement curve has entered the friction phase. The core layer fiber filaments were gradually pulled out and the contact with the ruptured filaments was uncertain. At the same time, since the resistance base was already large, the contact ratio change may cause a large resistance change. In addition, it was still possible that a small portion of the sleeve layer fibers may rupture at this phase due to non-collaborative stresses, causing an increase in resistance. The resistive rate of change curve reveals that the slope of the resistive rate of change curve increases significantly in this phase as the charge density increases. Table 7 and Fig. 12(b) show the relationship between the slope of the resistance rate of the change curve concerning the charge density in this phase. The resistance in the friction phase increases significantly with increasing charge density and the growth rate becomes larger. This may be due to the severe fiber degradation and brittleness evident due to ICCP. It is worth noting that the variability in $\triangle R_{III\text{-}0}/(Ru)$ when the charge density is high. This variability is attributed to uncertainties in the rupture of sleeve layer filaments, variations in the contact ratio between sleeve layer and core layer filaments, and the significant degradation effect of excessive charge from ICCP on the filaments.

In conclusion, the effect of ICCP on piezoresistive effect can be schematized in Fig. 13.

3.3. Discussions of the variability in experimental results

In general, the fundamental reason for the relatively large range of results for each specimen in Figs. 6, Fig. 10, and Fig. 11 is that a fiber bundle is not a homogenous and intact material; rather, it is composed of 12,000 individual filaments in this study, and the collaborative stress distribution among these filaments can affect the test results. Furthermore, according to previous references [28,33], the initial rupture, rupture during the loading process of fiber filaments in the fiber bundle, and changes in contact between fiber filaments are all random in tensile and pull-out tests. Detailed explanations are as follows.

3.3.1. The variability in tensile test

For fiber bundle tensile specimens of the same specifications (i.e., all test parameters are the same), the reasons for the differences in their tensile mechanical performance are as follows (Fig. 6):

Firstly, the rupture of carbon fiber filaments is characterized by

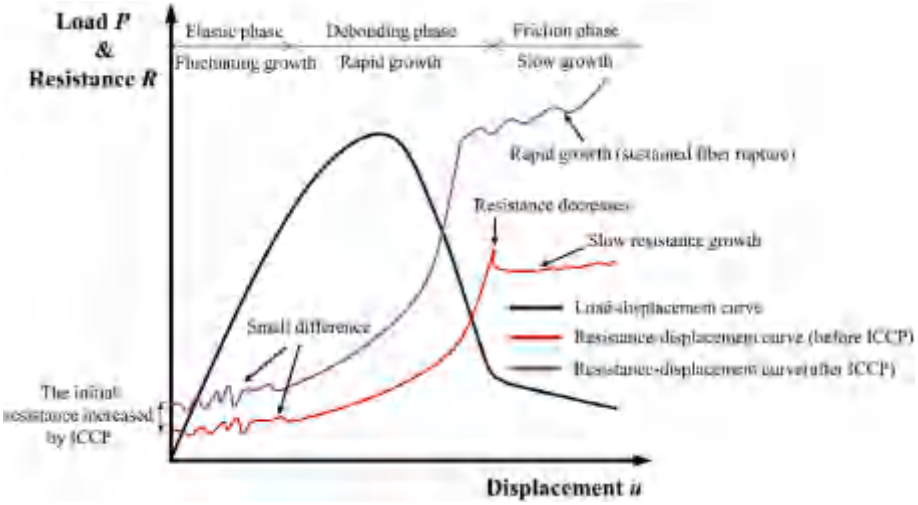


Fig. 13. Schematic diagram of piezoresistive effect of CFRCM bundle pull-out process and the effect of ICCP on piezoresistive effect.

randomness. Carbon fiber filaments are brittle materials that can rupture due to external random disturbances during handling and processing. Therefore, the initial rupture of filaments before loading is random. During the loading process of carbon fiber bundles, based on the weakest link theory of brittle materials [46–48], each filament will rupture at its weakest defect point. Various defects are formed on the surface and inside of carbon fiber filaments due to production processes, and the sizes, shapes, and orientations of these defects are randomly distributed. Therefore, the strength of carbon fiber filaments exhibits a certain degree of dispersion, leading to a certain level of randomness in the tensile rupture of carbon fiber filaments.

Furthermore, there is a disparity in the collaborative stress performance of carbon fiber filaments. Due to initial ruptures in carbon fibers, different carbon fiber bundles have varying initial rupture ratios and contact ratios, leading to an inconsistent number of effective conduction paths. Therefore, in the ICCP procedure, even if the charge density for each fiber bundle remains consistent, the actual amount of charge transmitted to each filament differs. This discrepancy can result in varying levels of degradation of the filaments, thereby reducing the collaborative stress performance of the filaments. Additionally, although in the preparation process of the reinforcement sheets, the ends of the carbon fiber bundles are suspended with a hammer to ensure tension, this method maximizes the collaborative stress performance of all filaments. However, due to the large number of filaments in a bundle and their initial ruptures, it is difficult for the reinforcement sheets to achieve complete collaborative stress for all filaments.

In summary, the randomness of filament rupture and contact, as well as the differences in collaborative stress performance, result in variations in the tensile mechanical properties of carbon fiber bundles.

3.3.2. *The variability in pull-out test*

The reasons for the dispersion in the bond performance (Fig. 10) and the piezoresistive effect (Fig. 11) of CFRCM bundles of the same specifications (i.e., all test parameters being the same) are as follows:

Firstly, since the carbon fiber bundle is embedded in the mortar matrix, the factors affecting the mechanical properties of the carbon fiber bundle mentioned in section 3.3.1 also apply to CFRCM bundle specimens.

In addition, some scholars [33,49,50] and this study have found that due to the small diameter of carbon fibers and the small gaps between their filaments, it is difficult for mortar matrix particles to fully infiltrate the fiber bundles, resulting in uneven infiltration along both the longitudinal and transverse directions of the matrix. According to previous research reports [33,51]: compared to FRP, FRCM exhibited greater variability in mechanical performance. Even parallel specimens made from the same material can exhibit uncertainties in the bonding performance between the fiber bundles and the matrix due to the randomness of mortar infiltration. Depending on the degree of mortar infiltration and filament failure modes, the embedded fiber bundles in the matrix can be divided into sleeve and core layers as shown in Fig. 9 (c) [52]. The location of fiber tensile rupture is random due to different levels of mortar infiltration in the sleeve layer. Additionally, the failure mode of core layer filaments is filament slippage (pull-out failure). Sleeve layer filaments have higher tensile stiffness and strain than core layer filaments, significantly reducing the collaborative load-bearing capacity of the fiber bundle and increasing the variability in load response.

According to previous research [28], the piezoresistive effect of carbon fiber bundles is mainly affected by elastic deformation, rupture (including initial rupture and tensile rupture), and contact of filaments. As mentioned above, the rupture, contact, and separation between filaments during the loading process are randomly changing, leading to random variations in the electrical conductivity path of carbon fiber bundles. In addition, the non-collaborative stress on the filaments can result in the occurrence of a telescopic layered failure phenomenon, causing significant differences in the piezoresistive effect curves during the stage of extensive filament rupture. This phenomenon has been reported [33].

3.3.3. *Methods to reduce the variability in experiment results*

To reduce the variability in experiments, some methods can be employed to modify carbon fibers so that the matrix can more fully penetrate the gaps between filaments and between filaments and the matrix, creating a continuous whole with tens of thousands of filaments and the matrix. This approach not only reduces the uneven stress distribution on the filaments but also improves the bonding performance at the fiber-matrix interface, preventing or reducing the occurrence of telescopic failures. By studying the mechanical properties and piezoresistive effects of modification and ICCP on CFRCM, further research can be conducted to investigate their effects on reducing the variability of various specimens. This has the potential to be significant.

4. Analysis and prediction of the bond performance of CFRCM bundles after ICCP

The effect of ICCP on elastic phase slope K_e, and peak load P_{max} of CFRCM bundle pull-out specimens are analyzed in the following section.

4.1. Elastic phase slope

According to Fig. 14(a) and Table 8, it can be seen that the slope of elasticity phase K_e of CFRCM bundle pull-out specimens shows a linear decrease in the charge density with the deepening of the deterioration effect of ICCP on the carbon fiber bundles. The normalized mechanical index values were calculated to quantitatively analyze the impact of ICCP on the deterioration of bond performance. The normalization method is the ratio of the bond performance indexes at different charge densities to the corresponding indexes of the control group. The elastic phase slope deterioration factor $\beta_{Ke}(Q)$ is calculated by Eq. (6). The fitting results of $\beta_{Ke}(Q)$ and $K_e(Q)$ are shown in Fig. 14(b) and Eq. (7).

$$\beta_{K_e}(Q) = K_e(Q)/K_e(0) \tag{6}$$

$$K_e(Q) = \begin{cases} (1 - 0.03506Q)K_e(0), R^2 = 0.997, \text{PCN} \\ (1 - 0.02042Q)K_e(0), R^2 = 0.997, \text{PCS} \end{cases} \tag{7}$$

4.2. Peak load

4.2.1. Effect of charge density

In the ICCP procedure, as the charge density increases, cracking and rupture phenomena occur on the fiber surface, which can significantly affect the bond performance of the fiber-mortar interface. The specimens of the seawater sea-sand groups showed less curve dispersion due to the relatively lower degree of deterioration (Fig. 15 and Table 8). The peak load P_{max} of both CFRCM specimens showed a linear decreasing trend with the increase of charge density Q.

The two groups, PCN and PCS, have the same charge density but differ in energization duration and current density. According to Fig. 16, the results of most specimens show that when the charge density is the same, the peak loads of CFRCM specimens are similar.

4.2.2. Effect of matrix type

The deterioration factor $\beta_{Pmax}(Q)$ for the peak load P_{max} is calculated by Eq. (8).

$$\beta_{P_{max}}(Q) = P_{max}(Q)/P_{max}(0) \tag{8}$$

The results of peak load P_{max} and deterioration factor $\beta_{Pmax}(Q)$ for both matrices at different charge densities are presented in Fig. 17. The peak load of the control group of CFRCM bundle pull-out test of normal mortar was higher than that of seawater sea-sand mortar, which may be attributed to better degree of infiltration and homogeneity of the normal matrix in the control group. In addition, the peak loads of CFRCM bundles pull-out specimens in the seawater sea-sand group were generally higher than those of normal mortar at different charge densities, which indicated that the uniformity of infiltration and the synergistic stress performance of fiber filaments in the seawater sea-sand group were better than that of the normal mortar. Fig. 17(a) shows that the degradation rate of the bond performance of seawater sea-sand CFRCM after ICCP is significantly lower than that of normal mortar CFRCM, and the seawater sea-sand (chlorine-containing) environment has a positive effect on slowing down the degradation effect of ICCP on carbon fiber bundles. Fig. 17(b) and Eq. (9) quantitatively confirm the

Table 8
Mean values of CFRCM bundle pull-out bond performance and tensile specimens at different charge densities Q.

Specimens	Q (10^5C/m^2)	K_e		P_{max}	
		Mean value (N/mm)	Coefficient of variation	Mean value (N)	Coefficient of variation
PCN	0	1228.83	0.15	649.08	0.15
	1.30	1118.83	0.13	560.14	0.12
	2.59	1088.75	0.22	455.67	0.19
	3.89	1070.63	0.18	396.80	0.19
	5.18	987.72	0.22	402.28	0.26
	7.78	1000.85	0.11	367.17	0.17
	10.37	721.23	0.23	265.81	0.49
PCS	0	1193.18	0.06	511.9	0.06
	2.59	1065.33	0.18	470.22	0.11
	3.89	1116.21	0.09	455.64	0.08
	5.18	1144.68	0.28	426.08	0.10
	7.78	964.53	0.25	368.16	0.18

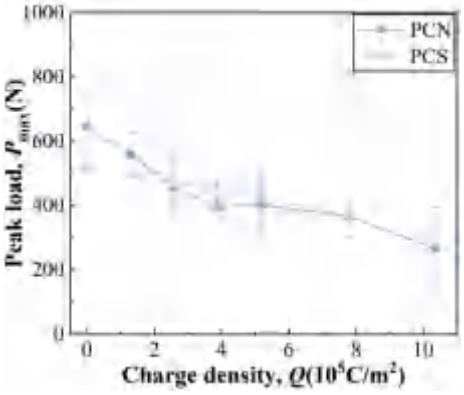


Fig. 15. Effect of the charge density on peak load of CFRCM bundle pull-out specimens.

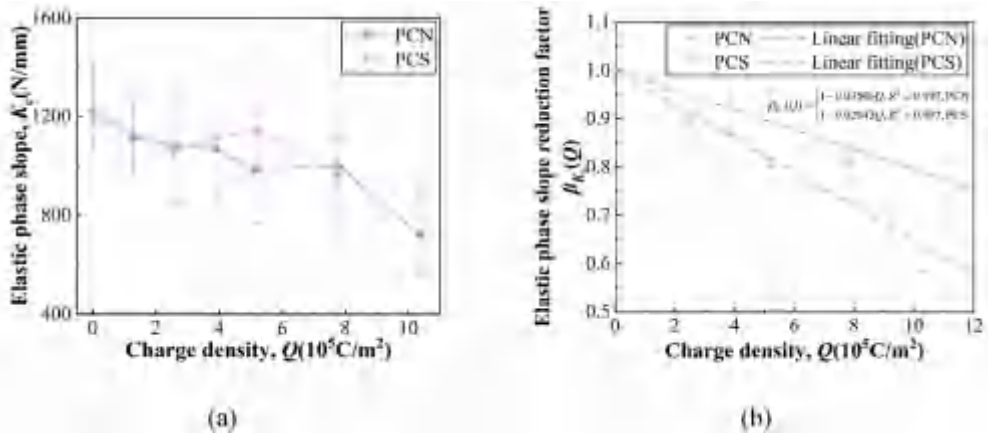


Fig. 14. (a) Elastic phase curve slope versus charge density curves of CFRCM bundle pull-out specimens with two matrices after ICCP; and (b) The fitted prediction formula of the slope discount factor of the elastic phase.

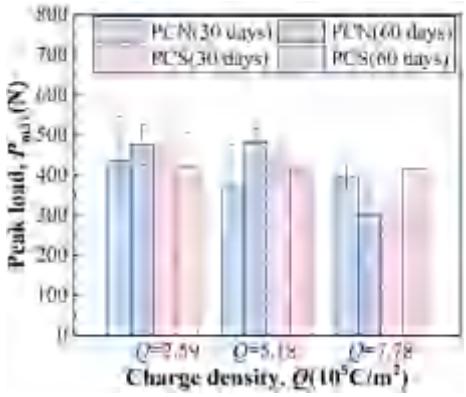


Fig. 16. Peak loads of CFRCM bundles at the same charge density but different energization durations and current densities.

relevant conclusions of Fig. 17(a) and provide the relationship between the peak load and the charge density.

$$P_{max}(Q)=\begin{cases}(1-0.0638Q)P_{max}(0), R^2=0.982, \text{PCN}\\(1-0.0333Q)P_{max}(0), R^2=0.995, \text{PCS}\end{cases} \tag{9}$$

5. Linear correlation analysis and prediction of peak load with mechanical and electrical resistance parameters

CFRCM bundle pull-out specimens are used to explore the linear correlation between their peak loads and mechanical and electrical resistance parameters of the loading process and to fit the prediction formula of the peak load. $|r|$ is the absolute value of Pearson's correlation coefficient.

Table 9 shows the correlation analysis results of the peak load P_{max} during the pull-out process of CFRCM bundles with five parameters, namely, the slope of elastic phase K_e, the rate of change of electrical resistance in the elastic phase $\triangle R_I/R$, the rate of change of electrical resistance in the debonding phase $\triangle R_{II}/R$, the inverse of the initial resistance before loading $1/R_0$, and the inverse of the initial resistance in the pull-out phase $1/\triangle R_{III\text{-}0}$. The larger K_e represents the better consistency of the co-stressing of the fiber filaments. Therefore, the more rapidly the load grows during the pull-out process, the larger the P_{max} usually is. Thus, there is a stronger correlation between P_{max} and K_e for both matrices. With the deepening of ICCP degradation, P_{max} decreases while the resistance of the carbon fiber bundle increases. Thus, P_{max} shows a stronger correlation with $1/R_0$. This study used a dual-parameter surface fitting based on K_e and L/R_0 to predict P_{max}. The fitted prediction Eq. (10) is shown below, with R^2 values of 0.5144 and 0.4975, respectively.

Fig. 18 shows the frequency and distribution of the absolute and relative deviation between the predicted peak load values calculated using Eq. (10) and the experimental values. Due to the large sample size, the Kolmogorov-Smirnov (K–S) test [53] was used here to test the normal distribution. At a significance level of 0.05, the deviations of the predicted results all conform to the characteristics of a normal distribution.

$$P_{max}=\begin{cases}P_b\times\left|\begin{array}{l}\left(3.535\dfrac{K_e}{K_b}-3.798\left(\dfrac{K_e}{K_b}\right)^2+1.586\left(\dfrac{K_e}{K_b}\right)^3\right)\\+\left(1.421\dfrac{L}{R_0}-4.750\left(\dfrac{L}{R_0}\right)^2-11.662\left(\dfrac{L}{R_0}\right)^3\right)\\-0.7062\end{array}\right|, \text{NM}\\P_b\times\left|\begin{array}{l}\left(2.572\dfrac{K_e}{K_b}-1.922\left(\dfrac{K_e}{K_b}\right)^2+0.321\left(\dfrac{K_e}{K_b}\right)^3\right)\\+\left(0.821\dfrac{L}{R_0}-2.271\left(\dfrac{L}{R_0}\right)^2-6.697\left(\dfrac{L}{R_0}\right)^3\right)\\-0.4987\end{array}\right|, \text{SM}\end{cases} \tag{10}$$

where P_b and K_b represent the ultimate tensile load of a single carbon fiber bundle and the slope of the linear elastic stage, which are equal to 890 N and 1481.86 N/mm in this study, respectively. L (dm) is the length of the specimen, and R_0 (Ω) is the initial resistance of the

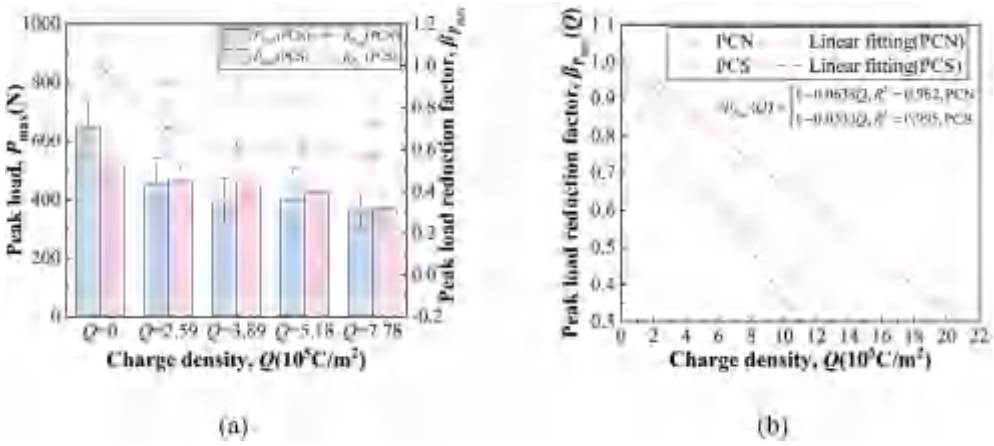


Fig. 17. (a) Effect of ICCP on peak loads of CFRCM pull-out specimens with two matrices; and (b) The fitted prediction formula of CFRCM bundle peak load discount factor after ICCP.

Table 9
Correlation of P_{max} with mechanical and electrical resistance parameters.

Specimens (the type of matrix)	K_e	$1/R_0$	$\triangle R_I/R$	$\triangle R_{II}/R$	$1/\triangle R_{III\text{-}0}$
PCN (NM)	0.69, Stronger correlation	0.68, Stronger correlation	0.07, Uncorrelated	0.41, Moderate correlation	−0.01, Uncorrelated
PCS (SM)	0.63, Stronger correlation	0.69, Stronger correlation	0.08, Uncorrelated	0.12, Uncorrelated	−0.14, Uncorrelated

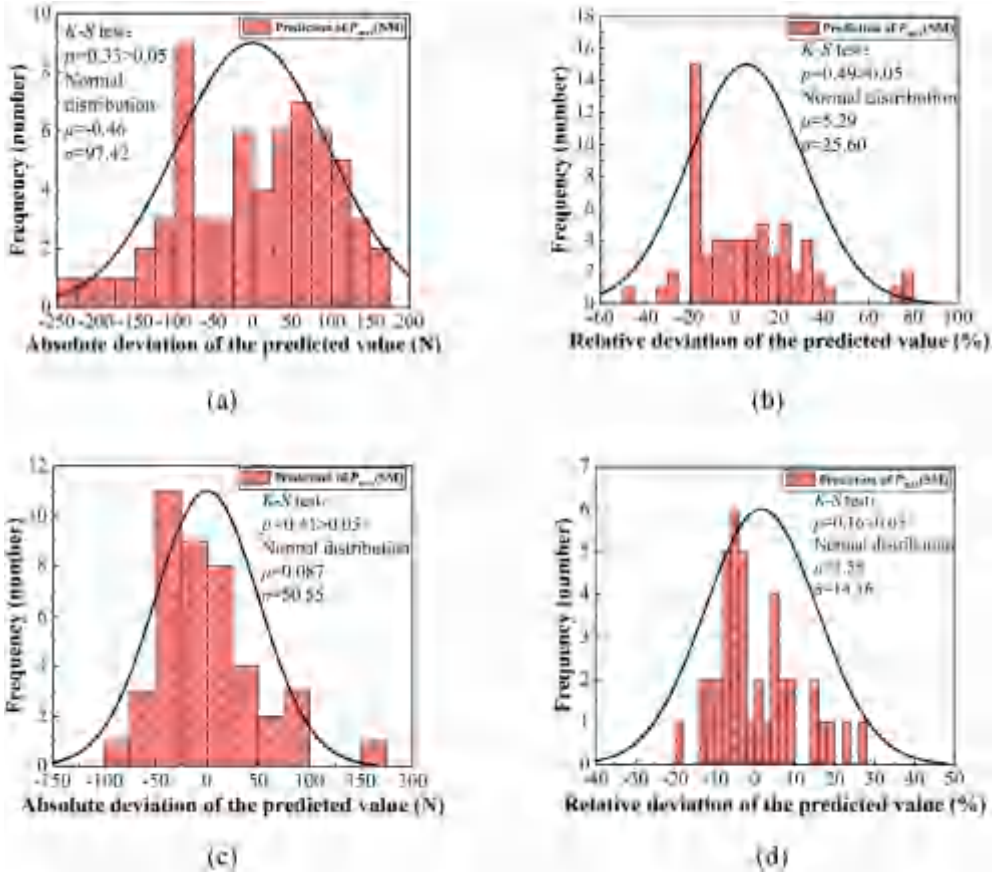


Fig. 18. Prediction of peak load for two types of matrix: absolute error (N) and relative error (%) distribution (test data in this study): (a) Absolute deviation of the predicted value (NM); (b) Relative deviation of the predicted value (NM); (c) Absolute deviation of the predicted value (SM); (d) Relative deviation of the predicted value (SM).

specimen before loading, after ICCP deterioration.

The materials used in this study are the same as those used in the previous study [54]. Therefore, this study validates the effectiveness of Eq. (10) based on the pull-out test results of normal mortar CFRCM bundles without ICCP in Ref. [54]. Three different embedment lengths (60, 90, 120 mm) were included. Due to the limited sample size (16 specimens), the Shapiro-Wilk (*S*–*W*) method was employed for the normal distribution test [53]. The frequency and distribution of predicted absolute deviations and relative deviations are shown in Fig. 19 and the summary of prediction results is presented in Table 10.

According to the prediction results, it can be observed that, at a significance level of 0.05, the deviations of the predicted results follow a normal distribution. When the measured values exceed 622 N, the predicted values tend to underestimate the actual values by a significant margin. This could be attributed to the fact that the samples used for fitting the prediction formula mostly had peak loads below 622 N. Overall, the prediction results are conservative, and the prediction deviations are relatively small when the measured values fall within the range of 250–600 N. This discreteness has already been explained in section 3.3.

In conclusion, the absolute and relative errors of the predicted peak load values follow a normal distribution, with mean values close to or less than 0. The overall prediction results are conservative. Eq. (10) provides a new approach for predicting the peak load of CFRCM bundles. Since only elastic modulus is required, this could lead to possible non-destructive testing of CFRCM.

6. Conclusions

In this study, the effect of ICCP on failure mode, bond performance, and piezoresistive effect of CFRCM bundles have been investigated by carbon fiber bundle tensile tests and CFRCM bundle pull-out tests. The main conclusions are as follows.

(1) After the ICCP procedure, carbon fiber bundles showed embrittlement and decreased tensile strength. The failure mode of the CFRCM bundle pull-out specimens gradually changed from all fiber filaments rupture failure to rupture-slippage failure; the CFRCM bundle pull-out specimens of seawater sea-sand showed the phenomena of secondary growth of the load and pseudo-ductility in the pull-out phase.

(2) The piezoresistive effect of the CFRCM bundle pull-out test is characterized by three phases of fluctuating growth-rapid growth-slow growth, which is consistent with the three phases characteristics of elasticity-debonding-friction of the load-displacement response of the pull-out process. With the charge density increase, the resistance retreat at the end of the rapid growth phase gradually disappears, and the resistance growth rate in the friction stage increases significantly. There is little difference in the piezoresistive effect between the normal matrix CFRCM bundles and the seawater sea-sand matrix CFRCM bundles in the pull-out tests.

(3) After the ICCP procedure, the peak load of CFRCM bundles decreases with the increase in charge density. At the same charge density, the bond performance of specimens with different current densities and energization duration combinations are

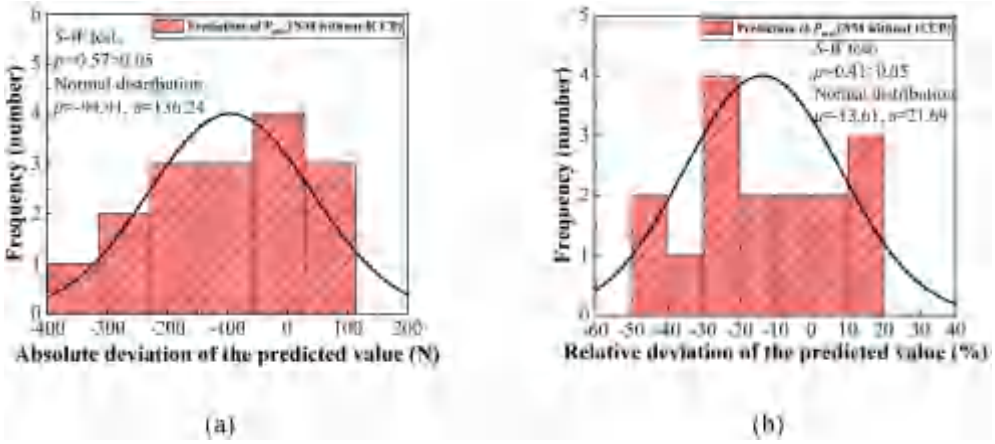


Fig. 19. Prediction of peak load: absolute error (N) and relative error (%) distribution (data source: Chen [54]): (a) Absolute deviation of the predicted value; (b) Relative deviation of the predicted value.

Table 10
Prediction of peak load (data source: Chen [54]).

Gauge length L (mm)	Experiment value (N)	Predicted value (N)	Absolute error (N)	Relative error (%)
60	268.73	302.60	33.87	12.60
	622.79	445.13	−177.66	−28.53
	411.41	407.78	−3.63	−0.88
	538.19	470.37	−67.82	−12.60
	388.79	413.03	24.24	6.23
	752.52	453.69	−298.83	−39.71
90	469.92	342.94	−126.98	−27.02
	340.21	399.62	59.41	17.46
	555.13	517.76	−37.37	−6.73
	525.90	545.21	19.31	3.67
	536.68	290.56	−246.12	−45.86
120	578.84	677.15	98.31	16.98
	778.93	407.39	−371.54	−47.70
	705.74	537.53	−168.21	−23.83
	532.66	453.38	−79.28	−14.88
	655.36	478.99	−176.37	−26.91

similar. Seawater sea-sand environment (chlorine-containing) has a positive effect on delaying the deterioration effect of ICCP: at the same charge density, the deterioration rate of all bond performance of seawater sea-sand CFRCM bundles pull-out are smaller.

(4) Predictive formulas for elastic phase slope, and peak load as a function of charge density have been proposed. They tend to decrease linearly as the charge density increases. A prediction formula was established based on linear correlation analysis between the pull-out specimens' peak load, the initial resistance before loading, and the slope of the elastic stage. The absolute and relative errors of the predicted peak load values follow a normal distribution. The overall prediction results are effective and conservative.

7. Further research perspectives

This study currently investigated the "Effect of ICCP on bond performance and piezoresistive effect of carbon fiber bundles in cementitious matrix" at the material level and proposed predictive formulas for the degradation of mechanical properties based on the piezoresistive effect parameters. On this basis, the next step in the research will focus on establishing a telescopic layered failure model for CFRCM based on the piezoresistive effect and ICCP modification. By quantitatively analyzing and evaluating the damage process through the relationship between the rate of change in resistance of carbon fiber bundles and material/structural load responses, the study aims to achieve detailed damage analysis and self-monitoring capabilities. Ultimately, three functional systems, ICCP-SS-SHM and ICCP-SR-SHM, as illustrated in Fig. 20, are proposed. These systems will involve various design methods and theories related to fabric reinforcement rates, spacing of resistance probe layouts, ICCP charge densities, and other parameters. This research is expected to enhance the longevity and intelligent information development of both existing RC structures and newly constructed ones. Readers are encouraged to follow our future research endeavors.

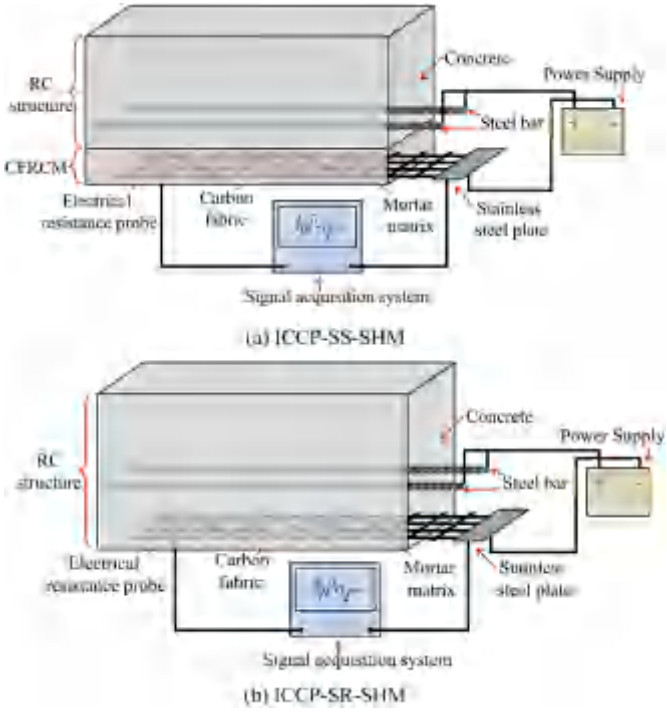


Fig. 20. Schematic diagram of three functional systems.

CRediT authorship contribution statement

Yewangzhi Tao: Writing – original draft, Visualization, Validation, Software, Methodology, Investigation, Formal analysis, Data curation, Conceptualization. **Jiarong Liu:** Writing – review & editing, Writing –

original draft, Visualization, Software, Methodology, Data curation, Funding acquisition. **Dawei Zhang:** Writing – review & editing, Supervision, Resources, Project administration, Methodology, Investigation, Funding acquisition. **Zhiyu Xie:** Writing – review & editing, Methodology. **Jiaxin Hong:** Writing – review & editing, Investigation.

Declaration of competing interest

The authors declare that they have no known competing financial interests or personal relationships that could have appeared to influence the work reported in this paper.

Data availability

Data will be made available on request.

Acknowledgements

The support from the Program Fund of Nonmetallic Excellence and Innovation Center for Building Materials (24PHD-5), and National Natural Science Foundation of China (52078454) is greatly appreciated.

References

[1] A. Ahmed, S. Guo, Z. Zhang, et al., A review on durability of fiber reinforced polymer (FRP) bars reinforced seawater sea sand concrete, Construct. Build. Mater. 256 (2020) 119484.
[2] T.U. Mohammed, H. Hamada, T. Yamaji, Performance of seawater-mixed concrete in the tidal environment, Cement Concr. Res. 34 (4) (2004) 593–601, https://doi.org/10.1016/j.cemconres.2003.09.020.
[3] J. Xiao, Q. Zhang, P. Zhang, et al., Mechanical behavior of concrete using seawater and sea-sand with recycled coarse aggregates, Struct. Concr. 20 (5) (2019) 1631–1643, https://doi.org/10.1002/suco.201900071.
[4] R. Feng, J. Wang, J.-H. Zhu, et al., Fatigue behavior of corroded reinforced concrete continuous beams with multi-intervention system, Eng. Struct. 231 (2021) 111748, https://doi.org/10.1016/j.engstruct.2020.111748.
[5] H. Zhu, H. Zhou, H. Gou, Evaluation of carbon fiber dispersion in cement-based materials using mechanical properties, conductivity, mass variation coefficient, and microstructure, Construct. Build. Mater. 266 (2021) 120891, https://doi.org/10.1016/j.conbuildmat.2020.120891.
[6] L. Wei, Tamon Ueda, Koji Matsumoto, et al., Experimental and analytical study on the behavior of RC beams with externally bonded carbon-FRCM composites, Compos. Struct. 273 (2021) 114291, https://doi.org/10.1016/j.compstruct.2021.114291.
[7] R. Feng, Y. Liu, J.-H. Zhu, et al., Flexural behaviour of C-FRCM strengthened corroded RC continuous beams, Compos. Struct. 245 (2020) 112200, https://doi.org/10.1016/j.compstruct.2020.112200.
[8] Z.C. Tetta, L.N. Koutas, D.A. Bournas, Textile-reinforced mortar (TRM) versus fiber-reinforced polymers (FRP) in shear strengthening of concrete beams, Compos. B Eng. 77 (2015) 338–348, https://doi.org/10.1016/j.compositesb.2015.03.055.
[9] C.T.N. Tran, X.H. Nguyen, H.C. Nguyen, et al., Shear performance of short-span FRP-reinforced concrete beams strengthened with CFRP and TRC, Eng. Struct. 242 (2021) 112548, https://doi.org/10.1016/j.engstruct.2021.112548.
[10] C. Pei, Y. Zeng, S. Kong, et al., Pull-out performance of anchored carbon-fiber bundles in cementitious matrix, J. Compos. Construct. 25 (6) (2021) 04021057, https://doi.org/10.1061/(ASCE)CC.1943-5614.0001175.
[11] Y. Wu, Z. Xie, D. Zhang, et al., Uniaxial tensile behavior of anchored carbon fabric-reinforced cementitious matrix plates, J. Mater. Civ. Eng. 35 (8) (2023) 04023251, https://doi.org/10.1061/JMCEE7.MTENG-14941.
[12] M. Su, L. Wei, Z. Zeng, et al., A solution for sea-sand reinforced concrete beams, Construct. Build. Mater. 204 (2019) 586–596, https://doi.org/10.1016/j.conbuildmat.2019.01.146.
[13] M. Su, C. Zeng, W. Li, et al., Flexural performance of corroded continuous RC beams rehabilitated by ICCP-SS, Compos. Struct. 232 (2020) 111556, https://doi.org/10.1016/j.compstruct.2019.111556.
[14] M. Su, L. Wei, H. Liang, et al., Fatigue behaviour and design of corroded reinforced concrete beams intervened by ICCP-SS, Compos. Struct. 261 (2021) 113295, https://doi.org/10.1016/j.compstruct.2020.113295.
[15] J. Zhu, M. Su, J. Huang, et al., The ICCP-SS technique for retrofitting reinforced concrete compressive members subjected to corrosion, Construct. Build. Mater. 167 (2018) 669–679, https://doi.org/10.1016/j.conbuildmat.2018.01.096.
[16] J.-H. Zhu, Z. Wang, M. Su, et al., C-FRCM jacket confinement for RC columns under impressed current cathodic protection, J. Compos. Construct. 24 (2) (2020) 04020001, https://doi.org/10.1061/(asce)cc.1943-5614.0001006.
[17] R. Feng, J. Zhang, J.-H. Zhu, et al., Experimental study on the behavior of carbon-fabric reinforced cementitious matrix composites in impressed current cathodic protection, Construct. Build. Mater. 264 (2020) 120655, https://doi.org/10.1016/j.conbuildmat.2020.120655.
[18] R. Feng, J. Zhang, J.-H. Zhu, et al., Experimental study on interface bonding fatigue behavior of C-FRCM composites in ICCP, Construct. Build. Mater. 259 (2020) 119660, https://doi.org/10.1016/j.conbuildmat.2020.119660.
[19] L.-L. Wei, J.-H. Zhu, T. Ueda, et al., Tensile behaviour of carbon fabric reinforced cementitious matrix composites as both strengthening and anode materials, Compos. Struct. 234 (2020) 111675, https://doi.org/10.1016/j.compstruct.2019.111675.
[20] Y. Goldfeld, T. Quadflieg, S. Ben-Aarosh, et al., Micro and macro crack sensing in TRC beam under cyclic loading, J. Mech. Mater. Struct. 12 (5) (2017) 579–601, https://doi.org/10.2140/jomms.2017.12.579.
[21] C. Luan, X. Yao, H. Shen, et al., Self-sensing of position-related loads in continuous carbon fibers-embedded 3D-printed polymer structures using electrical resistance measurement, Sensors 18 (4) (2018) 994, https://doi.org/10.3390/s18040994.
[22] L. Yosef, Y. Goldfeld, Smart self-sensory carbon-based textile reinforced concrete structures for structural health monitoring, Struct. Health Monit. (2020) 147592172095112, https://doi.org/10.1177/1475921720951122.
[23] P.C. Conor, C.N. Owston, Electrical resistance of single carbon fibres: 5211, Nature 223 (5211) (1969) 1146–1147, https://doi.org/10.1038/2231146b0.
[24] D.D.L. Chung, Carbon materials for structural self-sensing, electromagnetic shielding and thermal interfacing, Carbon 50 (9) (2012) 3342–3353, https://doi.org/10.1016/j.carbon.2012.01.031.
[25] Y.-B. Park, H.D. Roh, I.Y. Lee, Structural health monitoring of CFRPs using electrical resistance by reduced peripheral electrodes, Smart Struct. Syst. 28 (6) (2021) 737–744, https://doi.org/10.12989/SSS.2021.28.6.737.
[26] S.A. Grammatikos, A.S. Paipetis, On the electrical properties of multi scale reinforced composites for damage accumulation monitoring, Compos. B Eng. 43 (6) (2012) 2687–2696, https://doi.org/10.1016/j.compositesb.2012.01.077.
[27] J.W. Cho, J.S. Choi, Relationship between electrical resistance and strain of carbon fibers upon loading, J. Appl. Polym. Sci. 77 (9) (2000) 2082–2087, https://doi.org/10.1002/1097-4628(20000829)77:9<2082::AID-APP26>3.0.CO;2-W.
[28] Y. Gong, Z. Xie, J. Liu, et al., Research on piezoresistive effect and random model of carbon fiber bundle, Arch. Civ. Mech. Eng. 23 (2) (2023) 128, https://doi.org/10.1007/s43452-023-00672-0.
[29] T. Quadflieg, O. Stolyarov, T. Gries, Carbon rovings as strain sensors for structural health monitoring of engineering materials and structures, J. Strain Anal. Eng. Des. 51 (7) (2016) 482–492, https://doi.org/10.1177/0309324716655058.
[30] Y. Okuhara, H. Matsubara, Memorizing maximum strain in carbon-fiber-reinforced plastic composites by measuring electrical resistance under pre-tensile stress, Compos. Sci. Technol. 65 (14) (2005) 2148–2155, https://doi.org/10.1016/j.compscitech.2005.05.004.
[31] N. Fouad, M.A. Saifeldeen, Smart self-sensing fiber-reinforced polymer sheet with woven carbon fiber line sensor for structural health monitoring, Adv. Struct. Eng. 24 (1) (2021) 17–24, https://doi.org/10.1177/1369433220944507.
[32] H.D. Roh, Y.-B. Park, Electromechanical analysis of self-sensing CFRP and its application to real-time non-destructive evaluation, in: Nondestructive Characterization and Monitoring of Advanced Materials, Aerospace, Civil Infrastructure, and Transportation XIV, United States: SPIE, 2020, p. 32, https://doi.org/10.1117/12.2557963.
[33] Y. Gong, Z. Xie, G. Chen, et al., Influence of cementitious material infiltration on piezoresistive effect of carbon fiber bundle, J. Mater. Civ. Eng. 35 (7) (2023) 04023173, https://doi.org/10.1061/JMCEE7.MTENG-14701.
[34] Y. Goldfeld, O. Rabinovitch, B. Fishbain, et al., Sensory carbon fiber based textile-reinforced concrete for smart structures, J. Intell. Mater. Syst. Struct. 27 (4) (2016) 469–489, https://doi.org/10.1177/1045389X15571385.
[35] Y. Goldfeld, T. Quadflieg, T. Gries, Sensing capabilities of carbon based TRC beam from slack to pull-out mechanism, Compos. Struct. 181 (2017) 294–305, https://doi.org/10.1016/j.compstruct.2017.08.102.
[36] Y. Goldfeld, S. Ben-Aarosh, O. Rabinovitch, et al., Integrated self-monitoring of carbon based textile reinforced concrete beams under repeated loading in the uncracked region, Carbon 98 (2016) 238–249, https://doi.org/10.1016/j.carbon.2015.10.056.
[37] Y. Goldfeld, G. Perry, AR-Glass/Carbon-Based textile-reinforced concrete elements for detecting water infiltration within cracked zones, Struct. Health Monit. 18 (5–6) (2019) 1383–1400, https://doi.org/10.1177/1475921718808223.
[38] Y. Goldfeld, L. Yosef, Sensing accumulated cracking with smart coated and uncoated carbon based TRC, Measurement 141 (2019) 137–151, https://doi.org/10.1016/j.measurement.2019.04.033.
[39] China Cement Standardization Technical Committee, The National Standard of the People's Republic of China: Test Method of Cement Mortar Strength(ISO Method) (GB/T17671-2021), Standards Press of China, Beijing, 2021 (in Chinese).
[40] M. Zhu, J.-H. Zhu, T. Ueda, et al., Degradation behavior of multifunctional carbon fabric-reinforced cementitious matrix composites under anodic polarization, Construct. Build. Mater. 341 (2022) 127751, https://doi.org/10.1016/j.conbuildmat.2022.127751.
[41] D.D.L. Chung, A critical review of piezoresistivity and its application in electrical-resistance-based strain sensing, J. Mater. Sci. 55 (32) (2020) 15367–15396, https://doi.org/10.1007/s10853-020-05099-z.
[42] B.-G. Kang, J. Hannawald, W. Brameshuber, Electrical resistance measurement for damage analysis of carbon yarns, Mater. Struct. 44 (6) (2011) 1113–1122, https://doi.org/10.1617/s11527-010-9687-4.
[43] H. Sun, L. Wei, M. Zhu, et al., Corrosion behavior of carbon fiber reinforced polymer anode in simulated impressed current cathodic protection system with 3% NaCl solution, Construct. Build. Mater. 112 (2016) 538–546, https://doi.org/10.1016/j.conbuildmat.2016.02.141.

[44] E.Q. Zhang, L. Tang, D. Bernin, et al., Effect of the paste–anode interface under impressed current cathodic protection in concrete structures, Mater. Corros. 69 (8) (2018) 1104–1116, https://doi.org/10.1002/maco.201709908.
[45] J.-H. Zhu, L. Wei, G. Guo, et al., Mechanical and electrochemical performance of carbon fiber reinforced polymer in oxygen evolution environment, Polymers 8 (11) (2016) 393, https://doi.org/10.3390/polym8110393.
[46] B.D. Coleman, On the strength of classical fibres and fibre bundles, J. Mech. Phys. Solid. 7 (1) (1958) 60–70, https://doi.org/10.1016/0022-5096(58)90039-5.
[47] G. Zachariev, A statistical theory of the damage of materials: 4, Mod. Mech. Eng. 6 (4) (2016) 129–150, https://doi.org/10.4236/mme.2016.64013.
[48] F.W. Zok, On weakest link theory and weibull statistics, J. Am. Ceram. Soc. 100 (4) (2017) 1265–1268, https://doi.org/10.1111/jace.14665.
[49] J. Hegger, S. Voss, Investigations on the bearing behaviour and application potential of textile reinforced concrete, Eng. Struct. 30 (7) (2008) 2050–2056, https://doi.org/10.1016/j.engstruct.2008.01.006.
[50] O. Homoro, M. Michel, T.N. Baranger, Pull-out response of glass yarn from ettringite matrix: effect of pre-impregnation and embedded length, Compos. Sci. Technol. 170 (2019) 174–182, https://doi.org/10.1016/j.compscitech.2018.11.045.
[51] G. Loreto, L. Leardini, D. Arboleda, et al., Performance of RC slab-type elements strengthened with fabric-reinforced cementitious-matrix composites, J. Compos. Construct. 18 (3) (2014) A4013003, https://doi.org/10.1061/(ASCE)CC.1943-5614.0000415.
[52] B. Banholzer, Bond of a strand in a cementitious matrix, Mater. Struct. 39 (10) (2006) 1015–1028, https://doi.org/10.1617/s11527-006-9115-y.
[53] D. Wang, Multivariate Statistical Analysis and SPSS Application [M], South China University of Technology Press, Guangzhou, 2010.
[54] G. Chen, Mechanism Research on Piezoresistive Effect of Dry Carbon Fiber Bundle and that in CFRCM [D], Zhejiang University, 2020.

Journal of Building Engineering 95 (2024) 110042

Contents lists available at ScienceDirect

Journal of Building Engineering

journal homepage: www.elsevier.com/locate/jobe

Effect of ICCP on tensile performance of carbon fiber bundles in seawater sea-sand cementitious matrix

Jiarong Liu [a], Dawei Zhang [a,*], Yewangzhi Tao [a], Zhiyu Xie [a,b], Jiaxin Hong [a]

[a] Institute of Structural Engineering, Zhejiang University, Hangzhou, 310058, China
[b] School of Engineering, Hangzhou City University, Hangzhou, 310015, China

ARTICLE INFO

Keywords:
CFRCM
ICCP
Tensile performance
Piezoresistive effect
Seawater sea-sand

ABSTRACT

Impressed current cathodic protection (ICCP), carbon fabric reinforced cementitious matrix (CFRCM) composites, and piezoresistive effect have been widely studied in delaying steel bar corrosion, strengthening steel-reinforced concrete structures, and structural health monitoring, respectively. In this study, the effect mechanism of the ICCP procedure on the tensile performance degradation of CFRCM bundles with the two types of matrix (normal matrix (i.e., sand conforming to ISO standard) and seawater sea-sand matrix), as well as the tensile performance differences between them, were investigated through carbon fiber bundle tensile tests and CFRCM bundle tensile tests. The piezoresistive effects of CFRCM with the two types of matrix after the ICCP procedure and the effect of ICCP on the piezoresistive effect were analyzed. Prediction formulas for the tensile performance were established based on the different charge densities. Based on the dual functionality of carbon fiber strengthening and self-sensing, this study lays a foundation for the development of a triple-functional system of impressed current cathodic protection, structural strengthening, and structural health monitoring (ICCP-SS-SHM). The study indicates that seawater sea-sand positively influences the delay of CFRCM degradation through ICCP. This is advantageous in tackling the issue of scarce freshwater river sand resources.

1. Introduction

Reinforced concrete (RC) structures may experience carbonation, freeze-thaw cycles, alkali-aggregate reactions, and steel bar corrosion during long-term service, which severely affect their mechanical and durability properties [1,2]. Moreover, the development of RC concrete projects in some remote and marine areas is limited due to the shortage of freshwater and river sand resources [3]. It is feasible to replace freshwater and river sand with seawater and sea-sand [4,5]. However, the chloride ions in seawater and sea-sand can cause corrosion of the steel bars [6]. Therefore, delaying steel bar corrosion, enhancing the load-bearing capacity of structures, and achieving structural health monitoring are important research topics at present.

Impressed current cathodic protection (ICCP) can prevent or delay steel bar corrosion [7]. The principle is to provide electrons to the steel bars through auxiliary anodes to inhibit the loss of electrons, thereby protecting the steel bars. However, the strength of the corroded structure cannot be enhanced just by applying ICCP. Currently, carbon fabric reinforced cementitious matrix (CFRCM) has been applied to structural strengthening (SS) [8]. It can significantly enhance the flexural [9–11], shear [12–14], and seismic [15,16] capacity of RC structures. However, CFRCM cannot solve the problem of steel bar corrosion. It is worth noting that due to the excellent

* Corresponding author.
E-mail address: dwzhang@zju.edu.cn (D. Zhang).

https://doi.org/10.1016/j.jobe.2024.110042
Received 17 January 2024; Received in revised form 29 February 2024; Accepted 22 June 2024
Available online 25 June 2024
2352-7102/© 2024 Elsevier Ltd. All rights are reserved, including those for text and data mining, AI training, and similar technologies.

electrical conductivity and mechanical properties of carbon fiber, CFRCM can be used as an anode material and a strengthening material.

Given the advantages and disadvantages of ICCP and SS technologies, ICCP and SS have been combined to form a new ICCP-SS intervention technology with both impressed current cathodic protection and structural strengthening functions [17–19]. These research showed that ICCP-SS technology can effectively delay the corrosion of steel bars, thereby improving the flexural load-carrying capacity and fatigue life of simply supported beams and continuous beams, as well as the compressive carrying capacity of pre-corroded reinforced concrete columns. Currently, the ICCP-SS system has been preliminarily applied in engineering, resulting in a 30–40 % increase in the load-carrying capacity of involved bridge piers and beams [20].

However, while the corrosion of steel bars is delayed, the mechanical properties of CFRCM are reduced due to acidification. As the charge density increases, the deterioration of its tensile, flexural, fatigue, and shear properties becomes more obvious [21–24], further affecting the effectiveness of structural strengthening [25].

Currently, there is a lack of research on the mechanical performance degradation of CFRCM using seawater and sea-sand as the matrix after the ICCP process. In addition, there are few prediction models for the degradation of the mechanical performance of CFRCM under different charge densities of ICCP.

In the field of structural health monitoring (SHM), compared with strain gauges, fiber grating sensors, piezoelectric sensors, etc., which need to be embedded or attached to the structure, self-sensing materials have advantages such as lower cost, stronger durability, larger sensing volume, and no decrease in mechanical properties [26,27]. Self-sensing refers to structural materials' ability to sense their health status, such as stress, strain, damage, temperature, humidity, cracks, etc., without the need for additional sensors [28,29]. The piezoresistive effect of carbon fibers is a phenomenon where the rate of change of a material's resistance changes with strain [30]. Therefore, carbon fibers have the intelligent dual function of structural strengthening and self-sensing.

The piezoresistive effects of continuous carbon fiber bundles and carbon fiber-reinforced polymer (CFRP) have been widely studied. The resistance change rate of carbon fiber bundles increases linearly with increasing tensile strain and sharply increases upon fiber rupture. With the increase of tensile strain, the resistance change rate of the carbon fiber bundle first linearly increases and then sharply increases when the fiber ruptures [31]. However, the randomness of the transverse resistance in the CFRP strip causes the total resistance of the carbon fabric to be nonlinear at the initial stage of tensile strain growth [32]. The degree of damage to carbon fibers can be determined by monitoring the residual resistance under static and dynamic loads [31]. The piezoresistive effect of carbon fiber bundles is mainly influenced by the elastic deformation, rupture, and contact of individual fibers. A dynamic stochastic equivalent circuit model based on these factors has been established to quantify the piezoresistive effect during tensile loading of carbon fiber bundles [33]. Furthermore, in terms of structural sensing, three-point bending tests on CFRP-strengthened concrete beams have demonstrated a significant correlation between mechanical properties (strain and cracks) and electrical properties within an extensive strain range [34]. Additionally, CFRP with multiple electrodes can locate the damage in different beam sections [35]. Based on the resistance changes of glass-carbon fiber composite materials, real-time damage location and severity of deformation analysis of 3D-printed miniature bridges have been explored [36].

Research on the piezoresistive effect of continuous carbon fiber composites is mainly concentrated in the field of CFRP. In contrast,

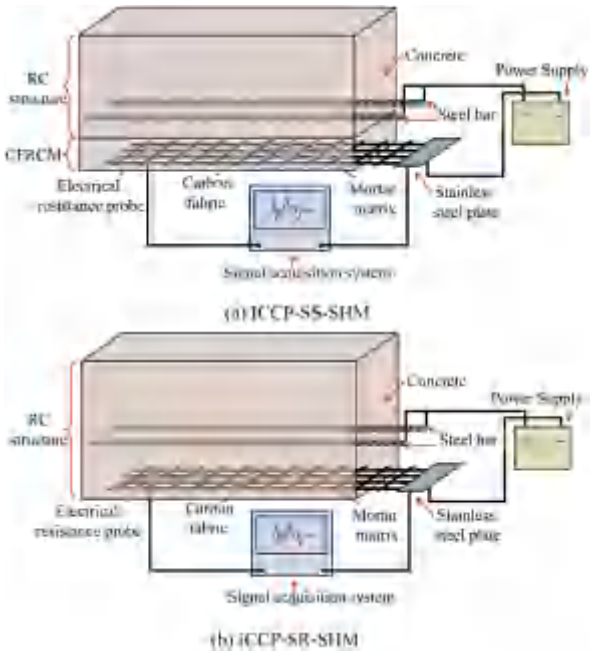


Fig. 1. Schematic diagram of three functional systems.

Table 1
Properties of carbon fiber bundle.

Filament number	Filament diameter (μm)	Density (g/cm^3)	Elastic modulus (GPa)	Ultimate tensile strength (MPa)	Ultimate tensile Strain	Electrical resistivity (Ω·cm)
12000	7	1.76	230	3530	1.5 %	1.7×10^{-3}

research in the field of self-sensing characteristics of CFRCM and its strengthening members is very limited. The piezoresistive effect of carbon fibers in CFRCM under tensile stress exhibits similarities to dry carbon fiber bundles and CFRP [30,37–39]. However, due to the uneven infiltration of carbon fibers by the mortar matrix, the relative resistance change of CFRCM in the damage stage is smaller and more discrete [39]. Existing research shows that there is a correlation between the resistance of carbon fibers and the flexural mechanical response (such as strain and cracks) under four-point bending and repeated loading and unloading of glass-carbon hybrid fabric-reinforced beams, based on which damage detection can be realized [40–43].

In summary, there is currently a lack of research on the piezoresistive effect during the loading process of CFRCM specimens before and after the application of ICCP. In addition, the mechanism of the effect of ICCP and the chloride-containing seawater and sea-sand matrix on the piezoresistive effect is not clear.

Based on the above issues, this study used two types of matrix materials: normal mortar and seawater sea-sand mortar. Through carbon fiber bundle tensile tests and CFRCM bundle tensile tests, the effect of the ICCP procedure on the tensile performance of CFRCM bundles with different matrix materials and the performance differences were investigated. In addition, prediction formulas for the tensile performance were established based on the charge density. The piezoresistive effect of the CFRCM bundles with two types of matrix after the ICCP procedure and the effect of ICCP on the piezoresistive effect were analyzed based on the changes in electrical resistance during the loading process. The aim of this study is to alleviate the problem of freshwater river sand resource shortage. At the same time, it promotes the development of the ICCP, structural strengthening/structural reinforcement, and structural health monitoring (ICCP-SS/SR-SHM) three-function system.

For RC structure, structural strengthening (SS) can be achieved by externally bonding CFRCM to the beam, or by embedding carbon fabrics in the concrete to form structural reinforcement (SR). Applying an impressed current to the steel reinforcement makes carbon fabrics act as the anode and the steel reinforcement as the cathode. During the service life of the structure, resistance probes are employed to sense the resistance of carbon fabrics. Ultimately, based on the piezoresistive effect and piezoresistive model, structural damage identification and self-monitoring functions are realized. Three functional systems, ICCP-SS-SHM and ICCP-SR-SHM, are proposed, as shown in Fig. 1.

2. Experimental program

2.1. Material properties

The properties of carbon fiber bundle are shown in Table 1.

The ICCP procedures were conducted in solution and matrix environments, respectively. The solutions comprised a saturated calcium hydroxide solution derived from freshwater and a saturated calcium hydroxide solution prepared from seawater. The matrices include normal mortar (freshwater-ISO standard sand) and mortar made from seawater sea-sand.

Table 2 displays the concentrations of each major ion found in seawater. The sand employed in the standard mortar is a blend of ISO standard sand with a particle size range of 0.5–1 mm and fine sand with a particle size range of 0.25–0.5 mm, in a mass ratio of 2:1. The sea-sand, in its natural state, has its particle grading and water content detailed in Table 3. The design of both the standard mortar and seawater sea-sand mortar was proportionally based on the principle of achieving similar compressive and flexural strengths (Table 4). The flexural and compressive strengths of the matrix, measured at 7 and 28 days (Table 5), were determined in accordance with the specifications outlined in reference [44].

2.2. Test specimens and parameters

The specimen groups are shown in Table 6. The parameters include the length of the specimen (L), the environment of the ICCP procedure (types of mortar and simulated pore solution), the current density (I), and the duration of the impressed current (D). In the simulated ICCP system, the saturated $Ca(OH)_2$ solution assumed the role of the concrete [23]. The specimens were labeled as "E1ME2-L-I-D", where E1 is the type of experiment: T is the tensile test and P is the pull-out test; M is the type of material: B is carbon fiber bundle and C represents the CFRCM bundle; E2 is the energized environment: N is saturated $Ca(OH)_2$ solution prepared with fresh water or normal mortar and S is saturated $Ca(OH)_2$ solution prepared with seawater or seawater sea-sand mortar. For example, TCN-L100-I300/100-D60 is a set of CFRCM bundle tensile specimens with a matrix of normal mortar and a specimen length of 100 mm. Initially, it is subjected to an applied current with a density of 300 mA/m^2 for 30 days, followed by an applied current with a 100

Table 2
Types and content of seawater ions.

pH	Cl^- (g/L)	SO_4^{2-} (g/L)	Na^+ (g/L)	Mg^{2+} (g/L)	K^+ (g/L)	Ca^{2+} (g/L)
8.02	14.81	1.82	15.74	1.51	1.21	6.35

Table 3
Particle gradation and moisture content of sea-sand.

Sieve residue rates of different particle sizes (%)						Fineness modulus	Moisture content (%)
4.8 mm	2.4 mm	1.2 mm	0.6 mm	0.3 mm	0.2 mm		
0.4	6.7	19.5	34.5	66	96.2	2.2	3.65

Table 4
The mix ratio of two matrices.

The type of matrix	Portland cement (P.O 42.5) (g)	Water (g)	Sand (g)	Redespersible latex powder (Wacker 4115 N)/g	Superplasticizer (MG SKY 8860)/ g
NM	100	45	200	1.5	0.15
SM	100	55	207.3	1.5	0.2

Note: NM is freshwater ISO standard sand mortar; SM is seawater sea-sand mortar. The same abbreviations are used below.

Table 5
The Strength of two matrices.

The type of matrix	Curing age	Flexural strength		Compression strength	
		Mean value (MPa)	COV (%)	Mean value (MPa)	COV (%)
NM	7d	4.55	5.23	21.91	6.27
	28d	4.83	14.3	41.67	5.82
SM	7d	4.62	7.58	21.76	3.81
	28d	4.70	4.25	39.17	5.01

mA/m^2 density for 30 days.

The charge density Q, defined as the total amount of charge per square meter borne by the carbon fiber bundle in contact with the matrix in the CFRCM was used to indicate the degree of ICCP proceeding [22]. Q is calculated as shown in Eq. (1).

$$Q = i_a t \tag{1}$$

where i_a (A/m^2) is the anode current density of the ICCP procedure and t (s) is the duration of the impressed current.

2.3. Specimen preparation

The process of preparing CFRCM bundle tensile specimens unfolds through a series of steps: Initially, CFRCM panels were cast. This was followed by the assembly of an ICCP device. The conductive electrodes were differentiated by their functions, with the energized electrodes used to apply current to the carbon fiber bundles during the ICCP procedure, and the measurement electrodes used to gauge the resistance of the carbon fiber bundles during loading. After outfitting the specimens with energized electrodes, the ICCP procedure was applied. After the ICCP procedure, the CFRCM panels were cut into CFRCM bundles and measurement electrodes were installed on the carbon fiber bundles. These specimens were subsequently used for loading experiments. The preparation process for carbon fiber bundle tensile specimens after ICCP mirrors the process for CFRCM bundle tensile specimens, barring the need to cast a mortar matrix and prepare measurement electrodes. The carbon fiber bundles were immersed in a saturated $Ca(OH)_2$ solution. The process is detailed as follows:

As depicted in Fig. 2, the specimen preparation began with pouring the bottom layer of mortar, which is 10 mm in thickness. Subsequently, carbon fiber bundles were laid out, with a lead hammer at both ends, to maintain a fixed and tensioned state. The top layer of the mold was then positioned and secured using a nail gun. The final step involved pouring the top layer of mortar, also 10 mm thick, followed by vibration. After the mold was removed, the specimen underwent standard curing (at a temperature of 20 °C and humidity of 95 %) for 28 days.

The fabrication of electrodes involved clamping two copper sheets coated with conductive copper adhesive onto carbon fiber bundles. These were then secured using butterfly clips for 4–6 h. Before the assembly of the ICCP device (Fig. 3), it was crucial to fabricate energizing electrodes on the carbon fiber bundles (Figs. 3 and 4(a)-(b)). In the ICCP system, the carbon fiber bundles functioned as the anode, while parallel steel bars with a diameter of φ8 served as the cathode. The device was affixed to the matrix using a no-nail adhesive, followed by the filling of various types of solutions into the device. An external direct current of 10 mA was applied, forming a closed circuit by connecting the cathode, anode, and the solution in the device via energized electrodes and wires.

After the ICCP procedure, CFRCM panels were segmented into several independent CFRCM bundles. Lead hammers were then hung at both ends of the carbon fiber bundles to guarantee the initial co-deformation of the bundles. After the measurement electrodes were created, two perforated acrylic sheets coated with carbon fiber bundle impregnation adhesive were clamped on both sides of the bundle and left to set for 24 h. The completed specimens are depicted schematically in Fig. 4.

Table 6
Specimen groups and investigation parameters.

Specimens	E1ME2	L (mm)	I (mA/m^2)	D (day)	Q (10^5C/m^2)
TB- L150	–	150	–	–	0
TBN-L150-I100-D51	Carbon fiber bundle tensile specimen-saturated $Ca(OH)_2$ solution prepared with fresh water	150	100	51	4.41
TBN-L150-I200-D51			200	51	8.81
TBN-L150-I400-D51			400	51	17.63
TBS-L150-I100-D68	Carbon fiber bundle tensile specimen-saturated $Ca(OH)_2$ solution prepared with seawater	150	100	68	5.88
TBS-L150-I200-D68	CFRCM bundle tensile specimen -normal mortar- saturated $Ca(OH)_2$ solution prepared with fresh water	100	200	68	11.75
TBS-L150-I400-D57			400	57	19.70
TCN-L100-N			–	–	0
TCN-L100-I100-D30			100	30	2.59
TCN-L100-I100-D60			100	60	5.18
TCN-L100-I300-D30			300	30	7.78
TCN-L100-I300/100-D60			300/100	30/30	10.37
TCN-L100-I400-D30			400	30	10.37
TCN-L100-I400/100-D60			400/100	30/30	12.96
TCN-L150-N		150	–	–	0
TCN-L150-I100-D30			100	30	2.59
TCN-L150-I100-D60			100	60	5.18
TCN-L150-I300-D30			300	30	7.78
TCN-L150-I300/100-D60			300/100	30/30	10.37
TCN-L150-I400-D30			400	30	10.37
TCN-L150-I400/100-D60			400/100	30/30	12.96
TCS-L150-N	CFRCM bundle tensile specimen-seawater sea-sand mortar- saturated $Ca(OH)_2$ solution prepared with seawater	150	–	–	0
TCS-L150-I100-D30			100	30	2.59
TCS-L150-I100-D60			100	60	5.18
TCS-L150-I150-D30			150	30	3.89
TCS-L150-I150-D60			150	60	7.78
TCS-L150-I200-D30			200	30	5.18
TCS-L150-I300-D30			300	30	7.78
TCS-L150-I500-D48			500	48	20.74

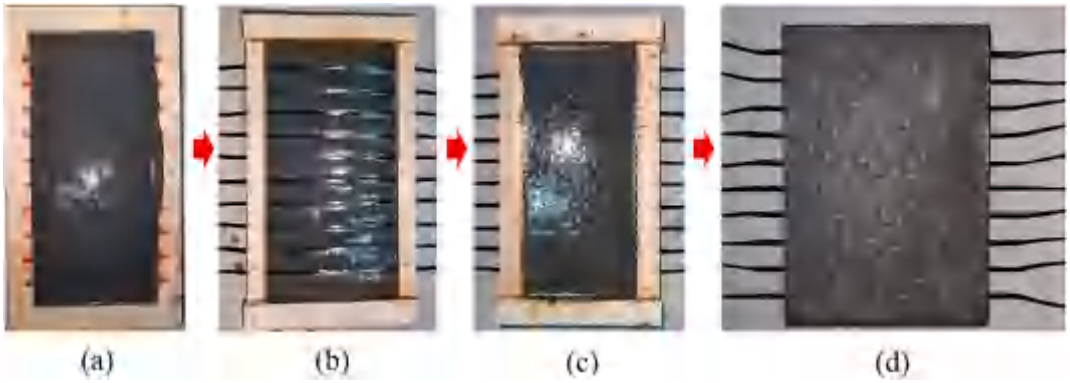


Fig. 2. Specimens fabrication process: (a) Casting bottom mortar; (b) Placing carbon fiber bundle; (c) Casting surface mortar; (d) CFRCM panel.

2.4. Loading and measurement methods

This study's loading and measurement methods are consistent with [39]. The loading device and the measurement system are presented in Fig. 5. The loading test was performed by a Sansi UTM6503 electronic universal testing machine with a range of 5 kN and a rate of 0.2 mm/min. Both ends of the carbon fiber bundle tensile test and the CFRCM bundle tensile test were clamped with acrylic reinforcement sheets through fixtures.

To eliminate the impact of contact resistance, the contact resistances at measurement points 1 and 2 were assessed before loading and subsequently subtracted from the post-loading resistance data. This approach echoes the four-electrode measurement method grounded on voltammetry [45], employed for determining the resistance of carbon fiber bundles. A steady direct current of 1 mA was

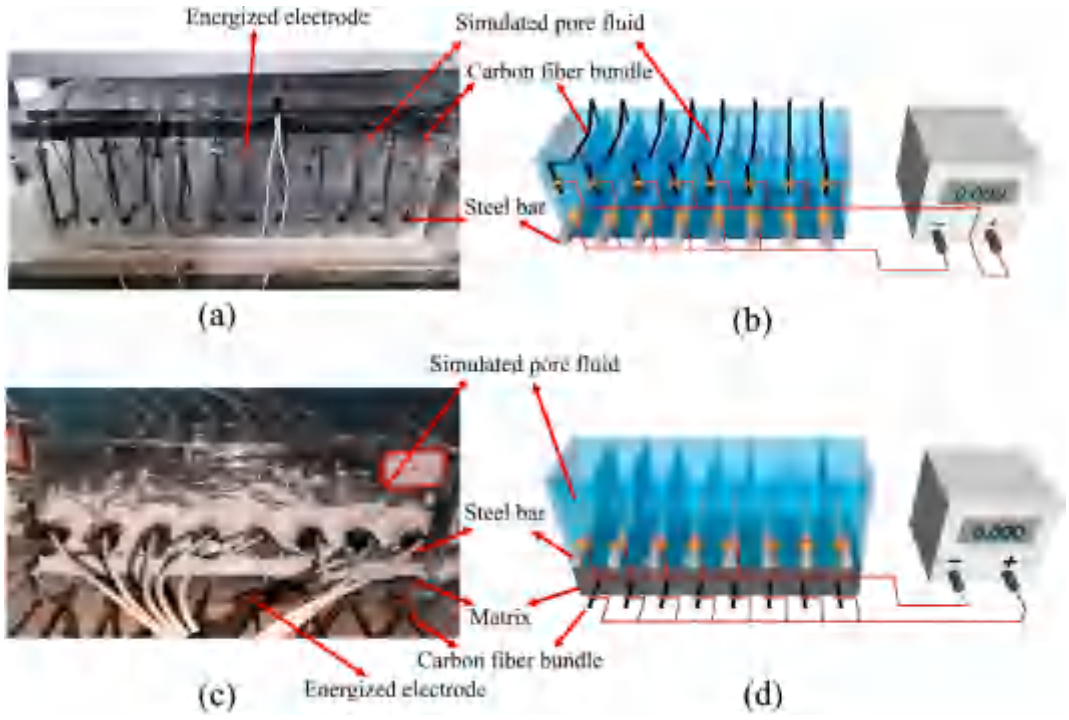


Fig. 3. ICCP system: (a) ICCP device for carbon fiber bundles in solution environment; (b) Schematic diagram of ICCP device for carbon fiber bundles; (c) ICCP device for CFRCM bundles; and (d) Schematic diagram of ICCP device for the CFRCM bundles.

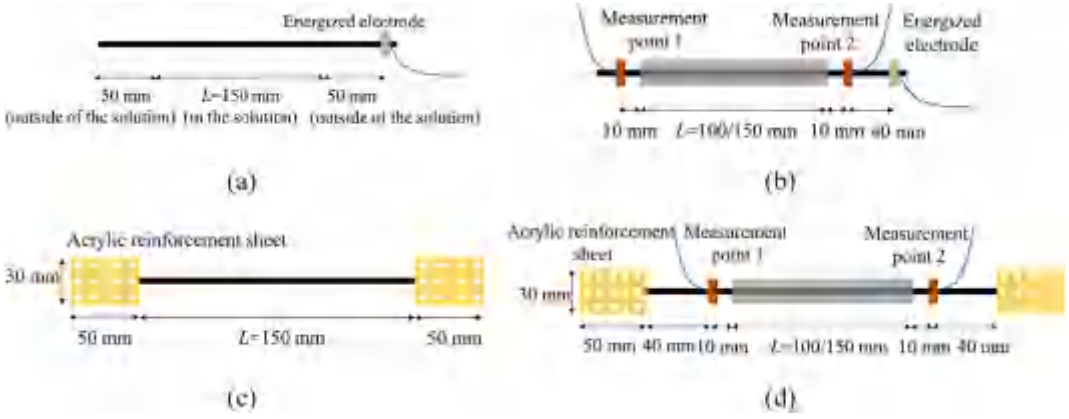


Fig. 4. Schematic diagram of specimens: (a) Electrode arrangement for carbon fiber bundle; (b) Electrode arrangement for CFRCM bundle; (c) Carbon fiber bundle tensile specimen; and (d) CFRCM bundle tensile specimen.

transmitted between resistance measurement points 1 and 2, as depicted in Fig. 4(d). As per Ohm's law, the absolute value of the voltage measured corresponds to the resistance of the carbon fiber bundle.

3. Experimental results

3.1. Carbon fiber bundle tensile test

Fig. 6 illustrates the response of nominal tensile stress to nominal strain for carbon fiber bundles, both before and after the ICCP process, in a saturated $Ca(OH)_2$ solution prepared with fresh water and a saturated $Ca(OH)_2$ solution prepared with seawater. After the ICCP process, there's a notable decline in the carbon fiber bundle's nominal ultimate stress and strain. As the charge density rises, the deterioration of the carbon fiber bundle's mechanical properties becomes increasingly evident. This phenomenon can be explained by Fig. 7: Before undergoing the ICCP procedure, the surface of the carbon fiber bundle is smooth, soft, and has good continuity, which allows it to be bent without causing fiber rupture. After the ICCP procedure, the specific manifestation of fiber brittleness is that the fiber filaments become stiff and stick to each other. Minor bending or stretching can lead to brittle rupture (Fig. 7(a)). With the

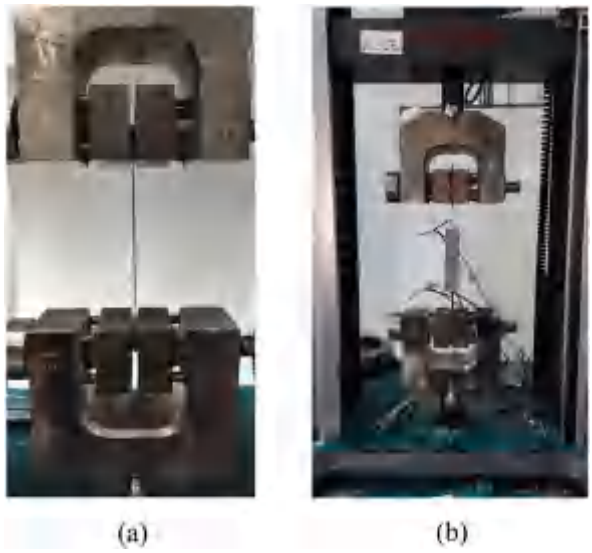


Fig. 5. Loading device: (a) Carbon fiber bundle tensile test; (b) CFRCM bundle tensile test.

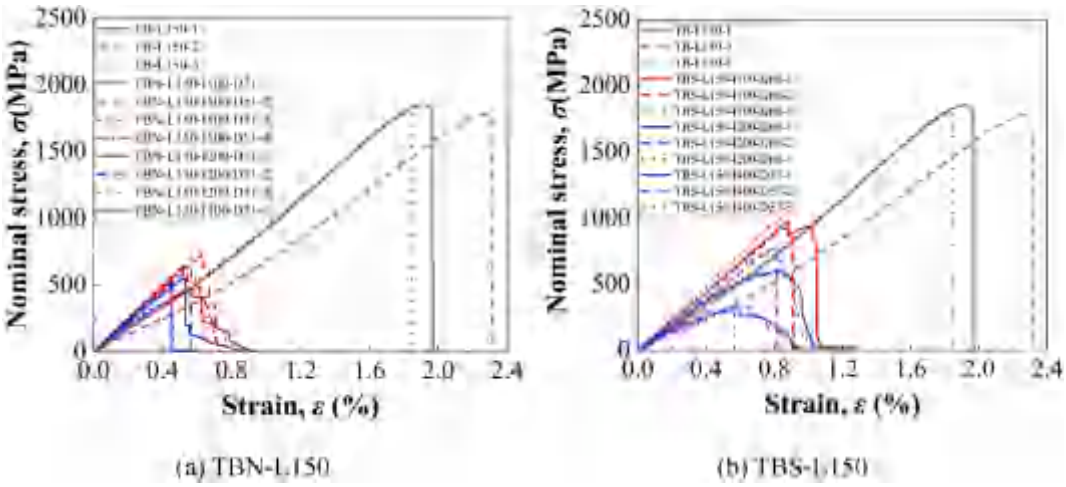


Fig. 6. Nominal stress-strain response of carbon fiber bundle tensile test before and after ICCP.

deepening of the degree of deterioration, the brittle failure characteristics of fiber bundles gradually became obvious (Fig. 7(b)). This phenomenon is attributed to the reactions occurring between the surface of the carbon fiber bundle and oxidized functional groups [46]. These reactions foster connections among filaments via oxygen-containing functional groups, progressively impairing the longitudinal structure of the carbon fiber bundle.

3.2. CFRCM bundle tensile test

3.2.1. Failure mode

The failure mode of CFRCM bundle tensile specimens is shown in Fig. 8. The carbon fiber bundle of CFRCM bundle tensile specimens without ICCP showed telescopic layered failure, and the length of fiber filaments pulled out after rupturing varied in a gradient. All the fiber filaments in the tensile test ruptured and were eventually pulled out. After the ICCP procedure, the pulled-out fibers also show the same brittle characteristics with severe fiber rupture. When the reinforcement sheets at both ends of the carbon fiber bundle were slightly misaligned with each other during the uniaxial tensile test, it may lead to shear damage to the carbon fiber bundle. Moreover, the carbon fiber bundle embedding lengths L used in this study are 100 and 150 mm, and the inhomogeneity of matrix-impregnated carbon fiber bundles greatly impacts the tensile properties of CFRCM bundles. Thus, some of the groups of specimens did not fully show the ultimate strength of carbon fiber bundles.

3.2.2. Effect of ICCP on load-displacement behavior

The load-displacement responses for the CFRCM bundle tensile specimens are illustrated in Fig. 9. The degree of dispersion of the

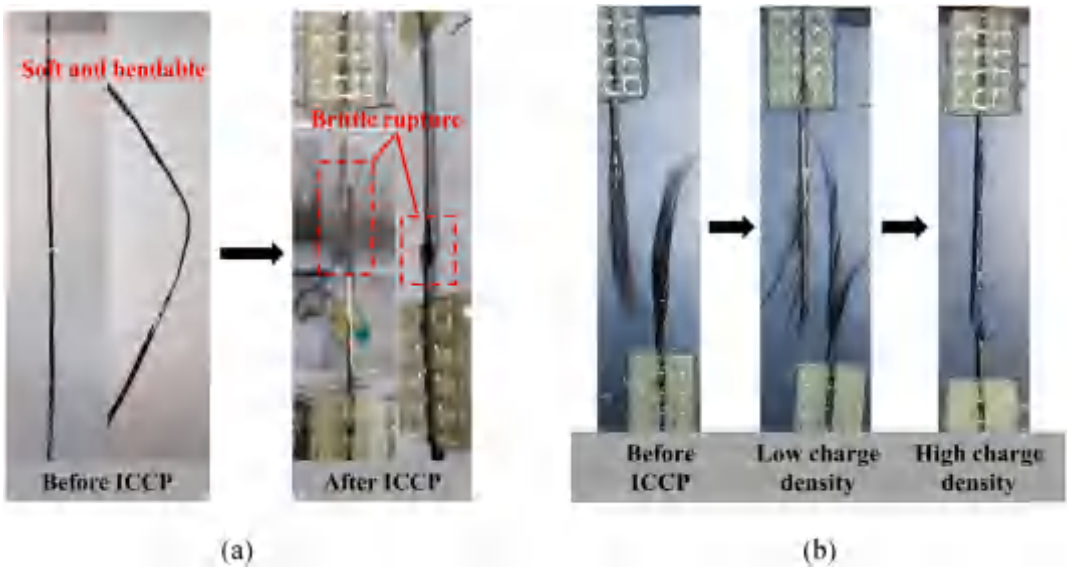


Fig. 7. Effect of ICCP on fiber bundles morphology: (a) Differences in fiber bundles morphology before and after ICCP degradation; and (b) Brittle tensile failure of fiber bundles after ICCP.

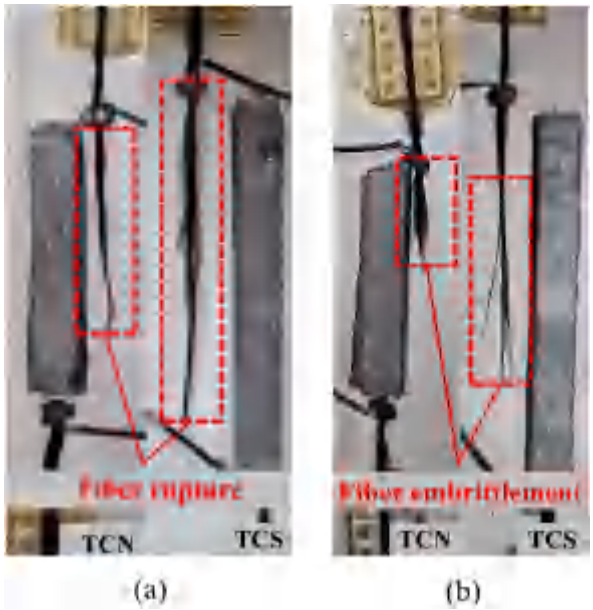


Fig. 8. Failure mode of CFRCM bundle tensile specimens: (a) specimens without ICCP; (b) specimens with ICCP.

curves increases significantly with the charge density increase. Meanwhile, the load-displacement responses of the normal mortar group (TCN) at different charge densities all showed obvious telescopic layered failure phenomena [47]. Due to variations in the degree of matrix infiltration on the filaments, the filaments exhibit different extensional stiffness under loading, resulting in a phenomenon of progressive failure. After the transient rupture of many matrix-impregnated fiber filaments, the remaining fiber filaments continue to carry the load and destroy. Their load-displacement response ductility was significantly higher than that of the seawater sea-sand mortar group (TCS). However, the carbon fiber bundle synergistic stress performance of the seawater sea-sand mortar series is significantly superior to that of the normal mortar series, with generally higher peak loads. When $Q < 5.18 \times 10^5$ C/m^2, the failure modes of CFRCM bundles were all characterized by the sudden rupture of many fiber filaments after reaching the peak load, and the phenomenon of telescopic layered failure was not obvious; when $Q \geq 5.18 \times 10^5$ C/m^2, some specimens gradually appeared obvious telescopic layered failure characteristics.

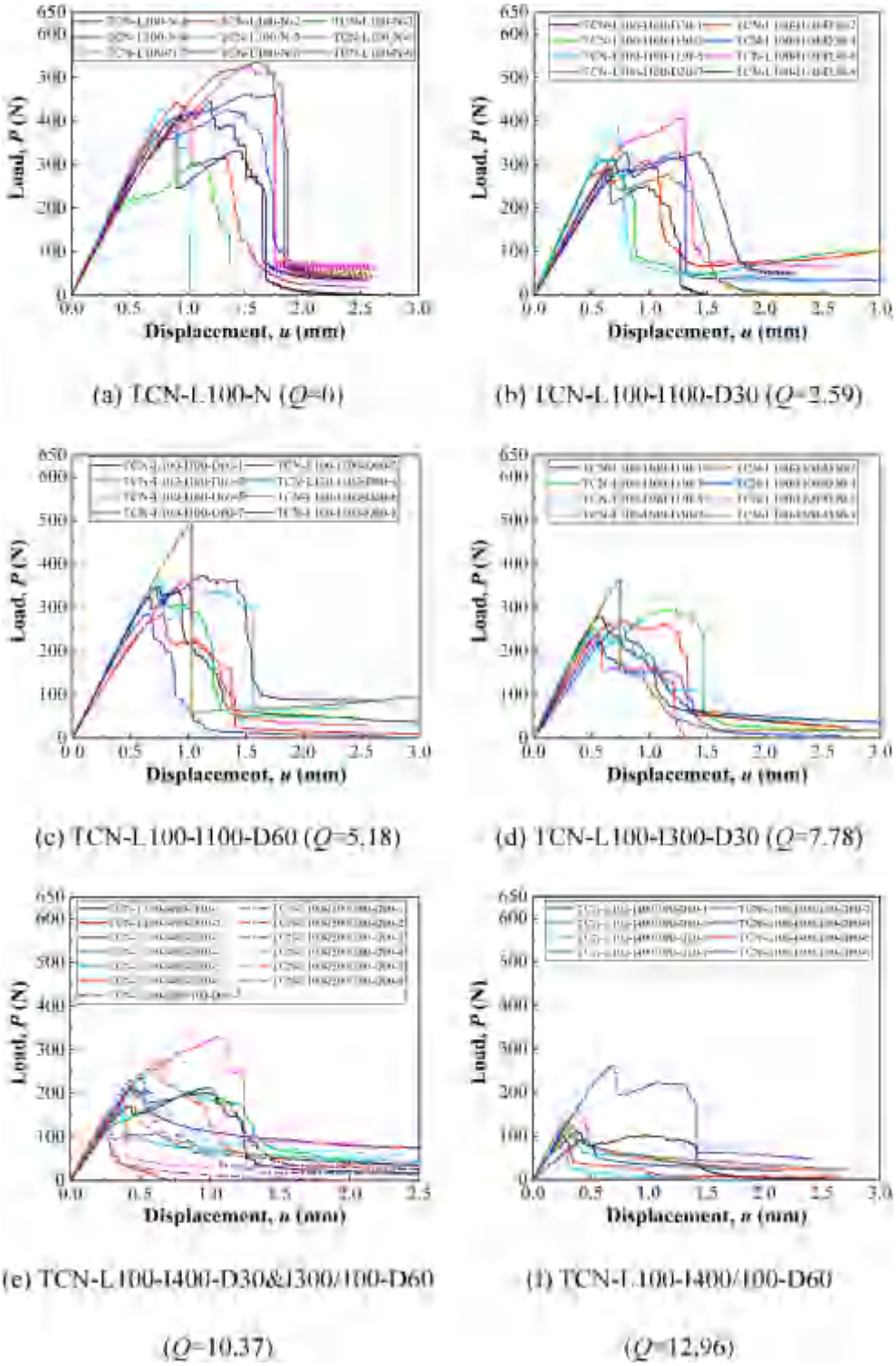
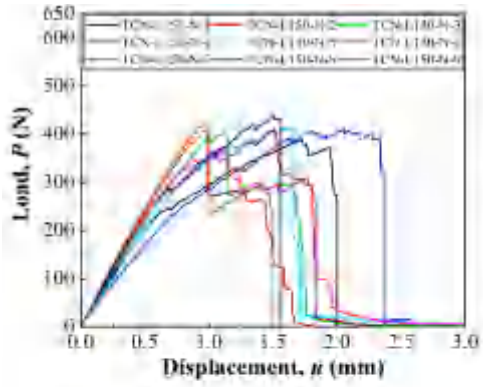
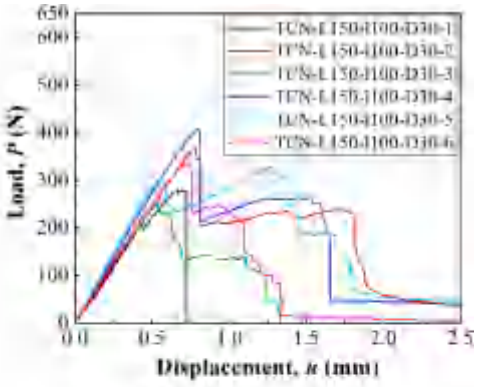


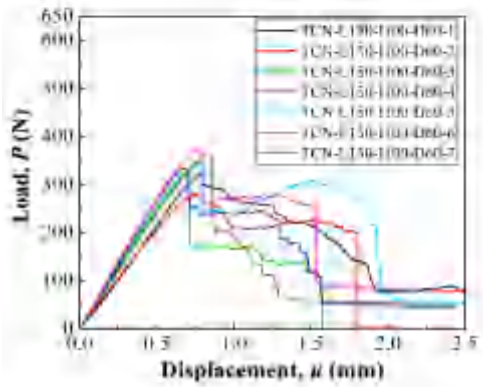
Fig. 9. Load-displacement responses of CFRCM bundle tensile specimens.



(g) TCN-L150-N (Q=0)

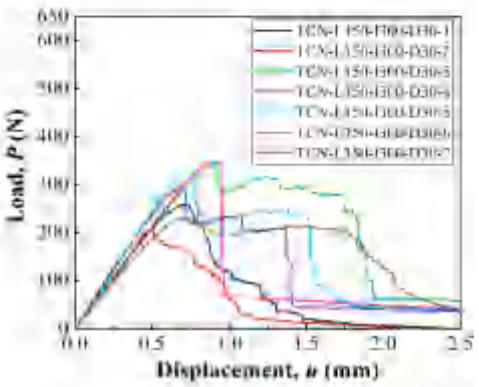


(h) TCN-L150-I100-D30 (Q=2.59)



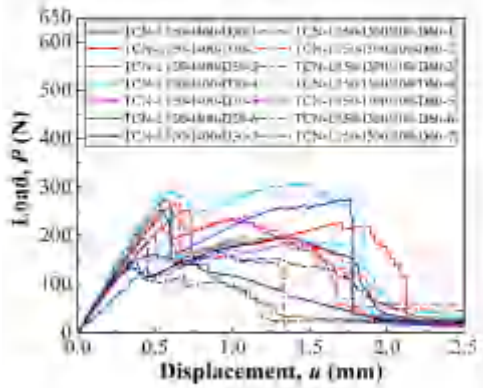
(i) TCN-L150-I100-D60

(Q=5.18)



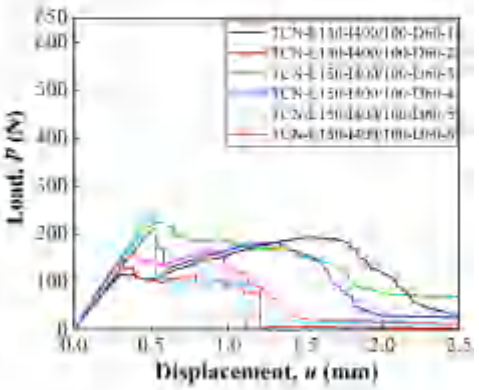
(j) TCN-L150-I300-D30

(Q=7.78)



(k) TCN-L150-I400-D30&I300/100-D60

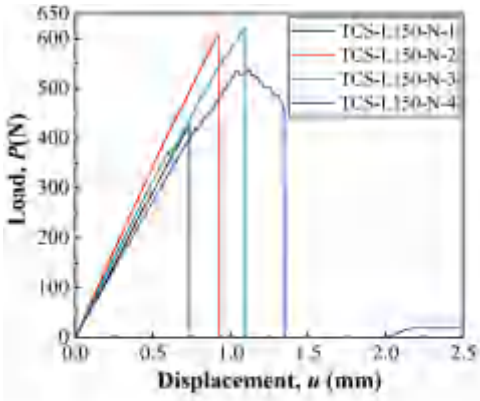
(Q=10.37)



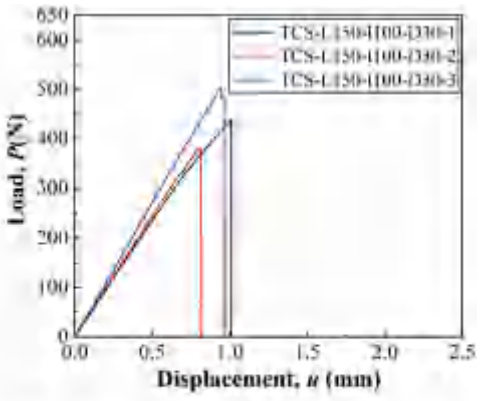
(l) TCN-L150-I400/100-D60

(Q=12.96)

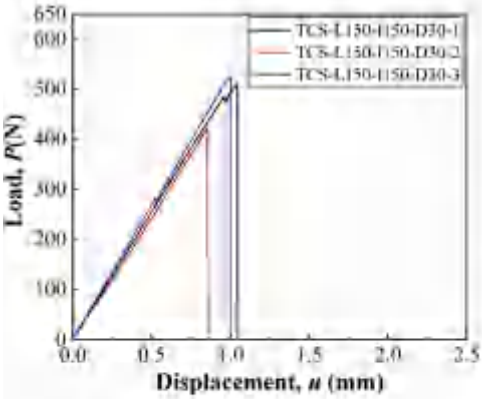
Fig. 9. (*continued*).



(m) TCS-L150-N (Q=0)

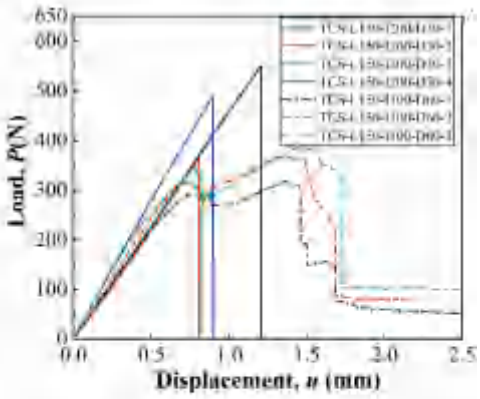


(n) TCS-L150-I100-D30 (Q=2.59)



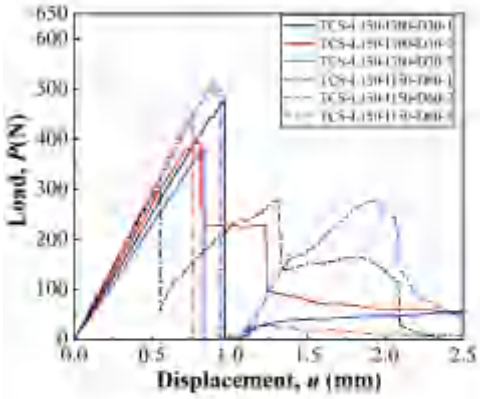
(o) TCS-L150-I150-D30

(Q=3.89)



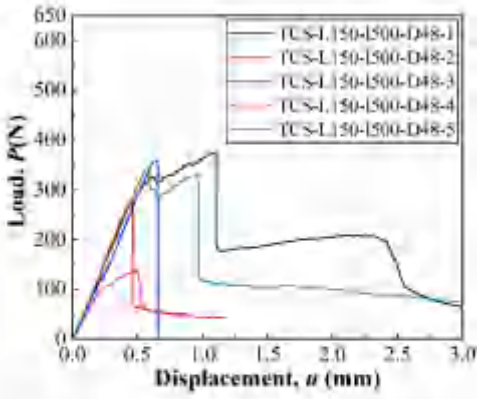
(p) TCS-L150-I200-D30&I100-D60

(Q=5.18)



(q) TCS-L150-I150-D60&I300-D30

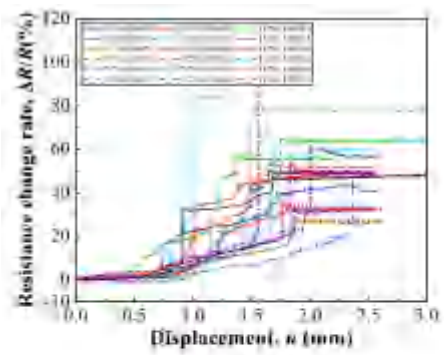
(Q=7.78)



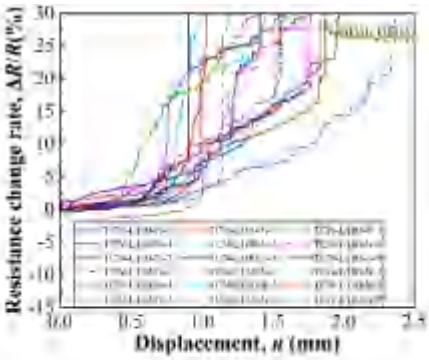
(r) TCS-L150-I500-D48

(Q=20.74)

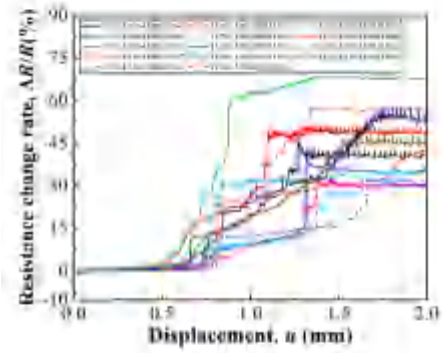
Fig. 9. (*continued*).



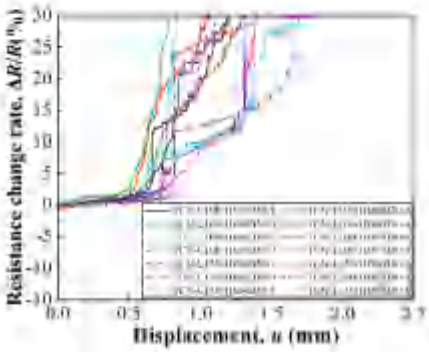
(a) TCN-L100&L150-N (Q=0)



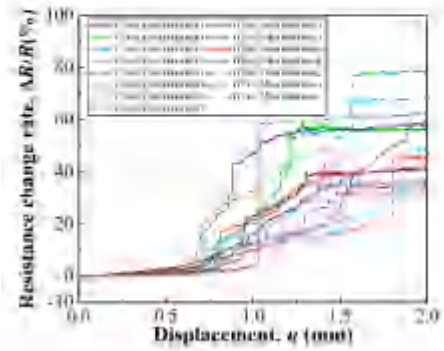
(b) Details of TCN-L100&L150-N



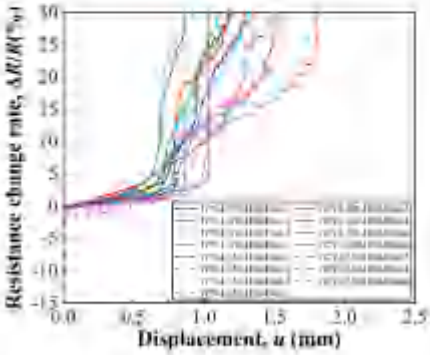
(c) TCN-L100&L150-1100-D30 (Q=2.59)



(d) Details of TCN-L100&L150-1100-D30

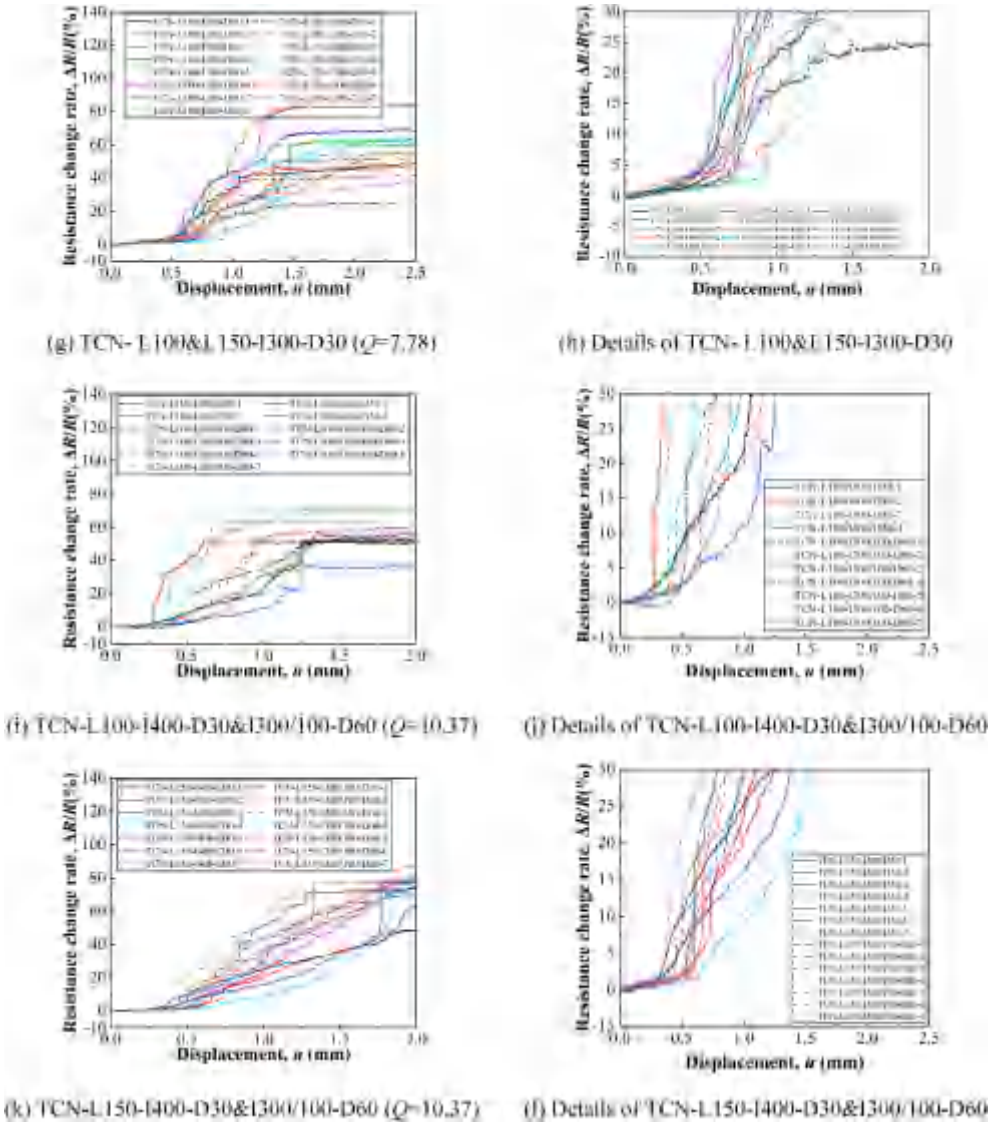


(e) TCN-L100&L150-1100-D60 (Q=5.18)



(f) Details of TCN-L100&L150-1100-D60

Fig. 10. Piezoresistive effect curves of CFRCM bundle tensile process.



(g) TCN-L100&L150-I300-D30 (Q=7.78) (h) Details of TCN-L100&L150-I300-D30

(i) TCN-L100-I400-D30&I300/100-D60 (Q=10.37) (j) Details of TCN-L100-I400-D30&I300/100-D60

(k) TCN-L150-I400-D30&I300/100-D60 (Q=10.37) (l) Details of TCN-L150-I400-D30&I300/100-D60

Fig. 10. (*continued*).

3.2.3. *Effect of ICCP on piezoresistive effect*

The rate of change in resistance $\triangle R/R$ was used to evaluate the change in the piezoresistive effect of carbon fiber bundles [48], and $\triangle R/R$ was calculated by Eq. (2).

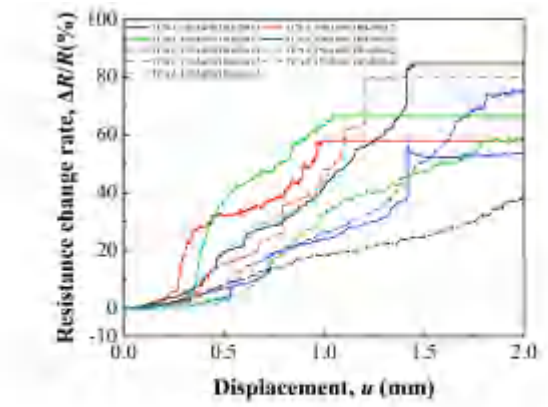
$$\frac{\Delta R}{R}=\frac{R^{'}-R_0}{R_0}\times 100\% \tag{2}$$

where R_0 (Ω) is the reference resistance, and R' (Ω) is the changed resistance value.

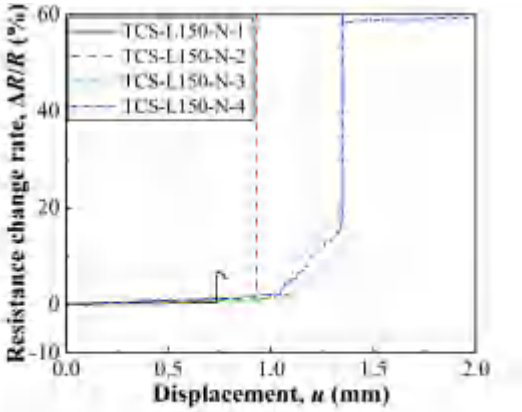
According to previous research [49–51] and this study (section 4.2.1), the deterioration of CFRCM after ICCP conformed to the principle of equal charge densities, and therefore groups with the same charge density were combined with "&" for subsequent analysis (Fig. 10, Fig. 11, and Table 7). According to Fig. 10, there is no essential difference between the piezoresistive effect of specimens with embedding lengths of 100 and 150 mm for the normal mortar group specimens under different charge densities. Therefore, specimens of both lengths were combined and analyzed in this study (Fig. 11, and Table 7).

Piezoresistive effect curves during the CFRCM bundles tensile process (Fig. 11) include a three-phase characteristic, i.e., fluctuating growth-rapid growth-slow growth, which corresponds to the elastic, debonding, and friction phases of the load-displacement curves, respectively.

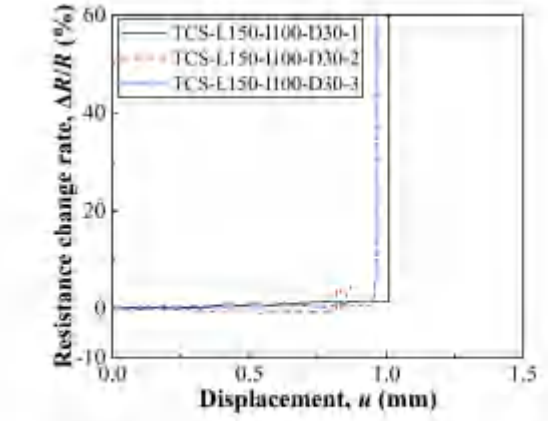
The resistance in the elastic phase exhibited a fluctuating growth, with the range of $\triangle R_I/R$ variation for each group falling between 0.7 % and 1.84 % (Fig. 11 and Table 7). Therefore, the effect of ICCP on the piezoresistive effect in the elastic phase of the tensile



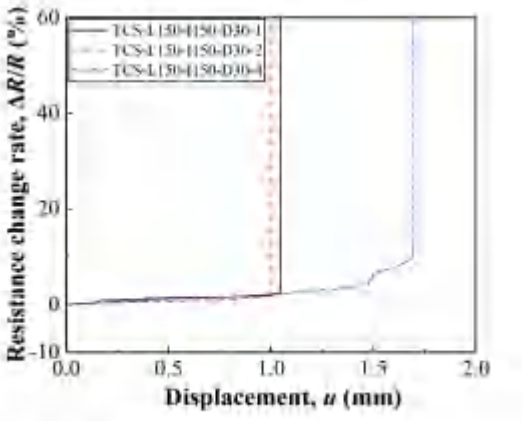
(m) TCN-L100&L150-I400/100-D60 (Q=12.96)



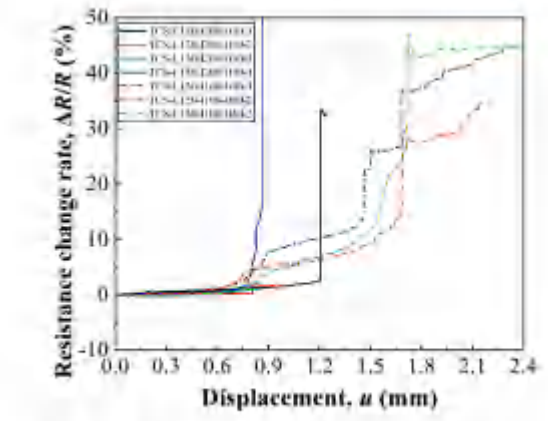
(n) TCS-L150-N (Q=0)



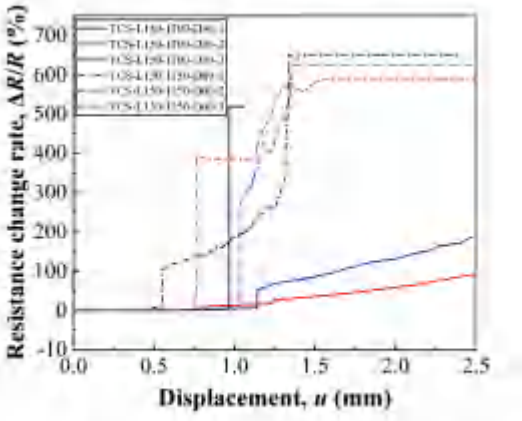
(o) TCS-L150-I100-D30 (Q=2.59)



(p) TCS-L150-I150-D30 (Q=3.89)



(q) TCS-L150-I200-D30&I100-D60 (Q=5.18)



(r) TCS-L150-I150-D60&I300-D30 (Q=7.78)

Fig. 10. (*continued*).

process can be neglected.

With the gradual rupture of fiber filaments, the resistance growth in the rapid growth phase became faster. Since the specimens of normal mortar groups had obvious telescopic layered failure characteristics, the span of the rapid resistance growth phase was larger. However, the specimens of seawater sea-sand groups were mostly concentrated failure of the fiber filaments due to the relatively good

synergistic stress performance. The displacement interval between the end of the elastic phase and the peak load in the seawater sea-sand groups was small (Fig. 9(m)–(r) and Fig. 10(n)-(r)), and the telescopic layered failure of the fibers was not obvious. After reaching the peak load, their loading dropped to zero, which meant that the fiber filaments were all ruptured, so the resistance grew to infinity instantaneously.

Theoretically, no conductive path should be intact when the fiber filaments are ruptured and pulled out. However, due to inadequate infiltration of the matrix into some fiber filaments, rupture location of filaments was closer to the middle of the matrix. These could still form a conductive path by contacting with better infiltrated and earlier ruptured fiber filaments, so resistance values can still be measured. At this time, the changes in the contact between the fiber filaments significantly impact the resistance (as shown in Fig. 10(r) for TCS-L150-I300-D30-2&3). However, most of the specimens could not be measured because the resistance change was beyond the measurement range, so the effect of ICCP on the piezoresistive effect at this phase could not be analyzed.

At present, many scholars have established piezoresistive models of carbon fiber materials, which can calculate the strain according to the resistance or relative resistance change. Based on the model and experimental data, the parameter distribution of the piezoresistive effect can be obtained. Then the strain can be calculated by measuring the resistance. Dry carbon fibers were analyzed using both a parallel circuit model and a Weibull distribution model to calculate resistance changes. These calculations accounted for variations caused by elastic deformation, rupture, and contact of fiber filaments [52]. Additionally, the study examined the uncertainty surrounding initial rupture, tensile rupture, and contact change in fiber filaments, determining their respective probability distributions. Subsequently, a dynamic random equivalent parallel circuit model and Monte Carlo simulation were employed to compute the resistance of the carbon fiber bundle during the tensile process [33]. Additionally, Goldfeld et al. [27,53] utilized integrative gauge factor (GFs) and a non-linear engineering GF to characterize the piezoresistive effect of smart self-sensory carbon-based textile reinforced concrete (TRC) structures, enabling SHM. GFs (strain sensitivity) is equal to the resistance change rate divided by the strain. They assessed the quantitative relationship between resistance changes and strain integration values along the direction of carbon fibers to determine the structural health condition. For each type of sensory carbon fiber, preliminary experiments were conducted to determine its GF values.

In the future, additional tests on CFRCM will be conducted to develop a piezoresistive model for CFRCM, considering scenarios

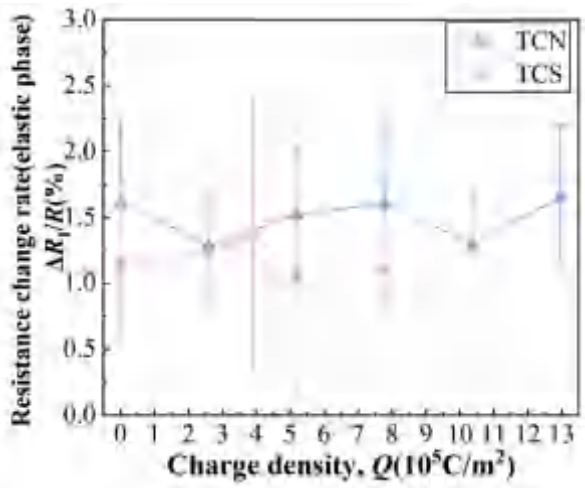


Fig. 11. Effect of ICCP on the rate of change of resistance in the elastic phase of the CFRCM bundles tensile process.

Table 7
Effect of ICCP on the rate of change of resistance in the elastic phase of the CFRCM bundles tensile process.

Specimens	The type of matrix	Q ($10^5C/m^2$)	Mean value of $\triangle R_I/R$ (%)
TCN-L100&150-N	NM	0	1.51
TCN-L100&150-I100-D30		2.59	1.13
TCN-L100&150-I100-D60		5.18	1.60
TCN-L100&150-I300-D30		7.78	1.58
TCN-L100&150-I300/100-D60 &TCN-L100&150-I400-D30		10.37	1.67
TCN-L100&150-I400/100-D60		12.96	1.84
TCS-L150-N	SM	0	0.82
TCS-L150-I100-D30		2.59	0.70
TCS-L150-I150-D30		3.89	0.91
TCS-L150-I200-D30&I100-D60		5.18	0.81
TCS-L150-I300-D30&I150-D60		7.78	0.83

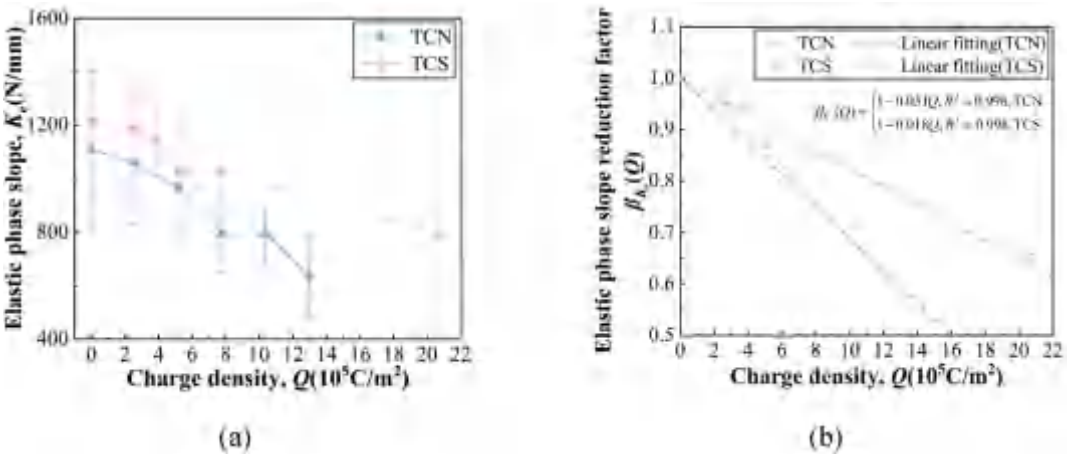


Fig. 12. (a) Elastic phase curve slope versus charge density curves of CFRCM bundle tensile specimens with two matrices after ICCP; and (b) The fitted prediction formula of the slope discount factor of the elastic phase.

Table 8
Mean values of tensile performance of CFRCM bundle tensile specimens at different charge densities Q.

Specimens	Q (10^5C/m^2)	K_e		P_{max}		E_p	
		Mean value (N/mm)	COV	Mean value (N)	COV	Mean value (10^{-3}J)	COV
TCN	0	1110.3	0.27	424.70	0.12	400.73	0.40
	2.59	1057.64	0.21	331.67	0.15	195.16	0.47
	5.18	964.64	0.24	346.60	0.15	163.86	0.53
	7.78	795.7	0.18	279.51	0.18	123.9	0.75
	10.37	794.44	0.14	233.79	0.21	176.97	0.29
	12.96	637.38	0.24	157.87	0.37	71.92	0.97
TCS	0	1215.77	0.12	549.72	0.16	313.82	0.39
	2.59	1186.04	0.12	441.18	0.14	215.18	0.22
	3.89	1148.62	0.08	487.79	0.11	240.26	0.23
	5.18	1024.48	0.21	402.67	0.21	271.2	0.43
	7.78	1030.07	0.11	420.40	0.18	184.31	0.35
	20.74	794.09	0.17	299.81	0.33	147.83	0.68

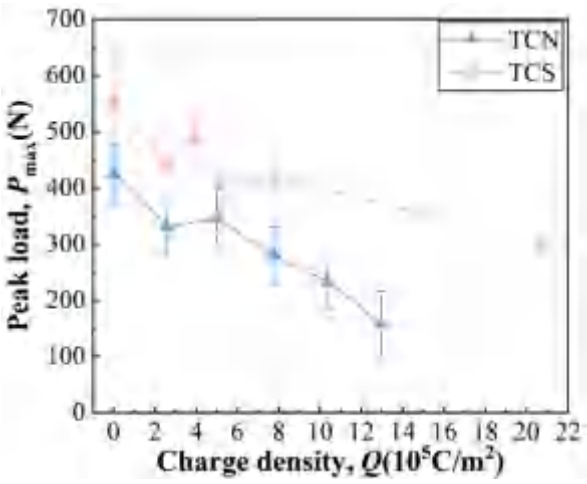


Fig. 13. Effect of the charge density on peak load of CFRCM bundle tensile specimens.

where the initial resistance is both known and unknown. Significantly, leveraging the established CFRCM piezoresistive model, it becomes possible to establish a quantitative relationship between the changes in resistivity of carbon fiber bundles within the matrix and the material/structure's load response. This facilitates a detailed evaluation of the failure process, enabling the analysis of the telescopic layered failure phenomenon in CFRCM and providing a mechanism for damage warning.

4. Analysis and prediction of the tensile performance of CFRCM bundles after ICCP

In the following section, the effect of ICCP on elastic phase slope K_e, the peak load P_{max}, and energy dissipation E_p of CFRCM bundle tensile specimens are analyzed.

4.1. Elastic phase slope

Based on Fig. 12 and Table 8, the slope of the elasticity phase K_e for the CFRCM bundle tensile specimens exhibits a linear decline in charge density as the damaging effects of the ICCP on the carbon fiber bundles intensify. The normalized mechanical index values were calculated to quantitatively analyze the impact of ICCP on the deterioration of tensile performance. The normalization method was the ratio of the tensile performance indexes at different charge densities to the corresponding indexes of the control group. The elastic phase slope deterioration factor $\beta_{Ke}(Q)$ is calculated by Eq. (3). The fitting results of $\beta_{Ke}(Q)$ and $K_e(Q)$ are shown in Fig. 12(b) and Eq. (4).

$$\beta_{K_e}(Q) = K_e(Q)/_{K_e}(0) \tag{3}$$

$$K_e(Q) = \begin{cases} (1 - 0.031Q)K_e(0), R^2 = 0.998, \text{TCN} \\ (1 - 0.018Q)K_e(0), R^2 = 0.998, \text{TCS} \end{cases} \tag{4}$$

4.2. Peak load

4.2.1. Effect of charge density

During the ICCP process, cracks and ruptures appear on the fiber surface, which becomes more pronounced with the increased charge density. This significantly affects the tensile performance of the fiber/mortar interface. According to Fig. 13, the peak load P_{max} of CFRCM bundle tensile specimens demonstrated a linear decline as the charge density Q increased.

The two groups, TCN and TCS, share the same charge density but differ in their energization duration and current density. As illustrated in Fig. 14, for most specimens, it can be observed that the peak loads of CFRCM specimens are similar when the charge density is identical. Additionally, in some series, such as the TCS series ($Q = 5.18 \times 10^5$ C/m^2), there is a significant difference in peak loads between two groups of specimens, which may be due to different failure modes. The fibers in the TCS-L150-I200-D30 series specimens experienced concentrated ruptures, while the fibers in the TCS-L150-I100-D60 series specimens clearly showed a telescopic layered rupture failure.

4.2.2. Effect of matrix type

The deterioration factor $\beta_{Pmax}(Q)$ for the peak load P_{max} is calculated by Eq. (5).

$$\beta_{P_{max}}(Q) = P_{max}(Q)/P_{max}(0) \tag{5}$$

The results of peak load P_{max} and deterioration factor $\beta_{Pmax}(Q)$ for both matrices at different charge densities are presented in Fig. 15. The peak loads of CFRCM bundles tensile specimens in the seawater sea-sand group were generally higher than those of normal mortar at different charge densities, which indicated that the uniformity of infiltration and the synergistic stress performance of fiber filaments in the seawater sea-sand group were better than that of the normal mortar. Since all fiber filaments ruptured during the tensile process, the bonding performance between carbon fiber bundles and matrix can be fully developed, which will make the above differences more obvious. Fig. 15(a) shows that when the charge density is 0–7.78 $\times$ 10^5 C/m^2, the degradation rate of the tensile

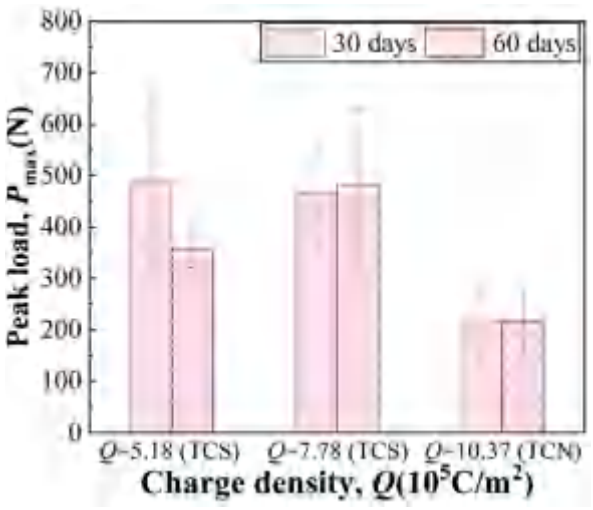


Fig. 14. Peak loads of CFRCM bundles at the same charge density but different energization durations and current densities.

performance of seawater sea-sand CFRCM after ICCP is close to that of normal mortar CFRCM, and the difference in the normalized results of the CFRCM bundle tensile specimens is not obvious. However, Fig. 15(b) and Eq. (6) provide the relationship between the peak load and the charge density. When the charge density is greater than 7.78, the degradation rate of the peak load of seawater sea-sand matrix specimens is lower than that of normal mortar matrix.

The reasons for the above phenomenon can be summarized as follows: The seawater sea-sand (chloride-containing) environment positively slows down the deterioration of carbon fiber bundles caused by ICCP. When the charge density is relatively low, all fiber filaments rupture during the tensile process, making the layered failure phenomenon more obvious. The degree of cooperative stress on the fiber filaments has a greater impact on the peak load, making it challenging to reflect the role of seawater and sea-sand in slowing down the deterioration of carbon fiber bundles caused by ICCP. When the charge density is high, the deterioration of carbon fibers is more serious, making the positive role of seawater and sea-sand more apparent.

$$P_{\max}(Q)=\begin{cases}(1-0.046Q)P_{\max}(0), R^2=0.995, \text{TCN}\\ (1-0.025Q)P_{\max}(0), R^2=0.986, \text{TCS}\end{cases} \tag{6}$$

4.3. Energy dissipation

Energy dissipation, defined as the area of the load-displacement curve in the interval [0, l_p], was used to assess the ductility of CFRCM during loading [54]. It is calculated as in Eq. (7).

$$E_p=\int_0^{l_p} P(u)du \tag{7}$$

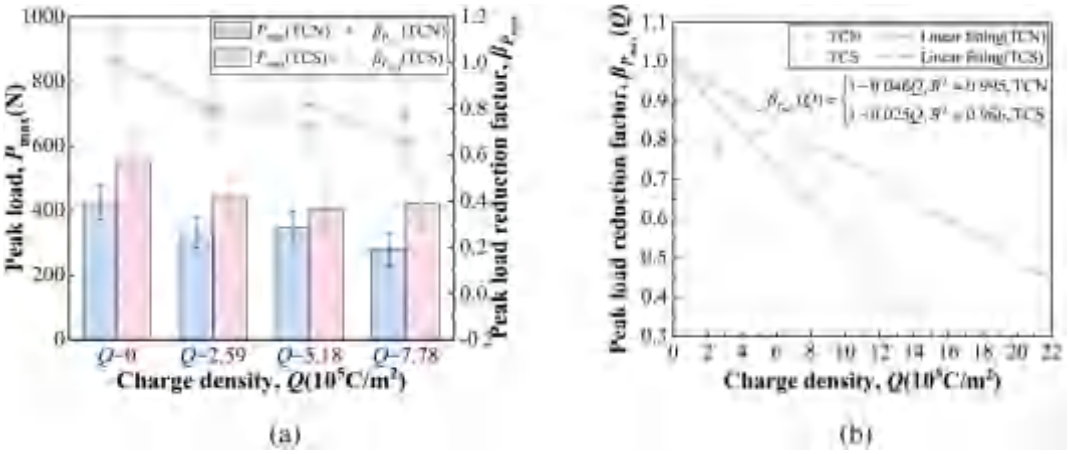


Fig. 15. (a) Effect of ICCP on peak loads of CFRCM bundle tensile specimens with two matrices; and (b) The fitted prediction formula of CFRCM bundle peak load discount factor after ICCP.

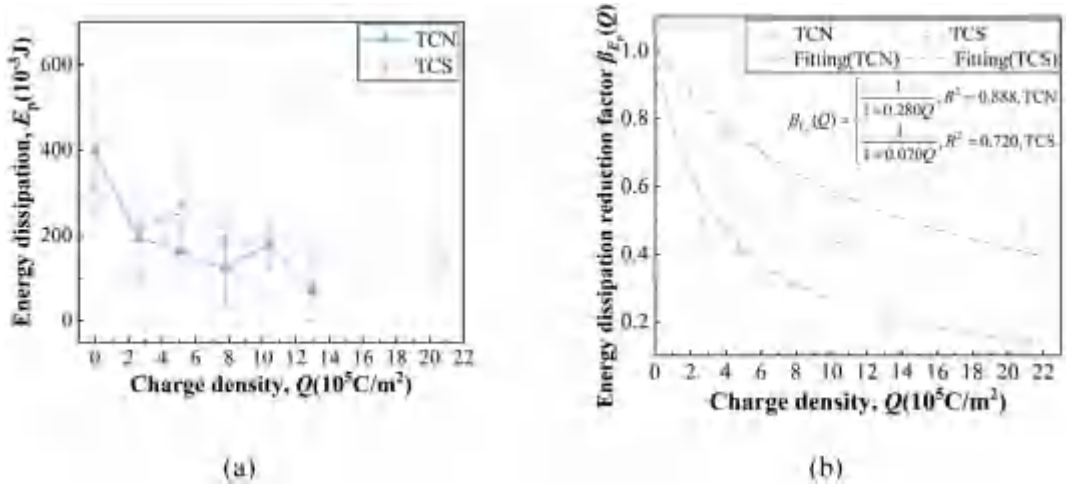


Fig. 16. (a) Energy dissipation change curves of two matrices CFRCM bundle tensile specimens after ICCP; and (b) The fitting prediction formula of energy dissipation discount factors.

where $P(u)$ is the load-displacement response and l_p was taken as the displacement corresponding to the load reduced to 85 % of the peak load as the upper limit of the calculation interval of the energy dissipation.

The results are shown in Fig. 16 and Table 8. The energy dissipation discount factor $\beta_{Ep}(Q)$ is calculated by Eq. (8).

$$\beta_{E_p}(Q) = E_p(Q) \Big/ E_p(0) \tag{8}$$

Energy dissipation shows a nonlinear decreasing trend with the increase in charge density. The inverse proportional function was used to fit the discount factor from different charge densities. The fitting results of $\beta_{Ep}(Q)$ were depicted in Fig. 16(b), and the prediction formula of E_p was shown in Eq. (9).

$$E_p(Q) = \begin{cases} \left(\dfrac{1}{1+0.280Q}\right) E_p(0), R^2 = 0.888, \text{TCN} \\ \left(\dfrac{1}{1+0.070Q}\right) E_p(0), R^2 = 0.720, \text{TCS} \end{cases} \tag{9}$$

5. Conclusions

Based on carbon fiber bundle tensile tests and CFRCM bundle tensile tests, the effects of ICCP on failure mode, tensile performance, and the piezoresistive effect of CFRCM bundles have been investigated. The related research conclusions are as follows.

(1) After the ICCP procedure, the carbon fiber bundles exhibited signs of embrittlement, decreasing tensile strength. With the deepening of the degree of deterioration, the brittle failure characteristics of fiber bundles gradually became obvious. All the fiber filaments in the CFRCM bundle tensile tests ruptured and were eventually pulled out. After the ICCP procedure, the pulled-out fibers also show the same brittle characteristics with severe fiber rupture. With the increase of charge density, telescopic layered failure is more obvious.

(2) The piezoresistive effect during the CFRCM bundle tensile test manifests in three phases: fluctuating, rapid, and slow growth. These phases align with the three-phase characteristics of the load-displacement response: elasticity, debonding, and friction. There is no essential difference between the piezoresistive effect of specimens with embedding lengths of 100 and 150 mm for the normal mortar group specimens under different charge densities. ICCP has little effect on the piezoresistive effect in the CFRCM bundle tensile process, and the resistance growth is mainly determined by the failure and the telescopic layered situation. There is little difference in the piezoresistive effect between the normal matrix CFRCM bundles and the seawater sea-sand matrix CFRCM bundles in the tensile tests.

(3) With the same charge density, specimens exhibiting different current density and energization duration combinations demonstrate similar tensile performance. The seawater sea-sand environment, which contains chlorine, positively influences the delayed deterioration of carbon fiber caused by ICCP. Specifically, at an equivalent charge density, the rate of deterioration for the tensile performance of seawater sea-sand CFRCM bundle tensile specimens is reduced.

(4) Predictive formulas for elastic phase slope, peak load, and energy dissipation as a function of charge density have been proposed.

CRediT authorship contribution statement

Jiarong Liu: Writing – review & editing, Writing – original draft, Visualization, Validation, Software, Methodology, Funding acquisition, Formal analysis, Data curation, Conceptualization. **Dawei Zhang:** Writing – review & editing, Supervision, Resources, Project administration, Methodology, Investigation, Funding acquisition. **Yewangzhi Tao:** Writing – original draft, Visualization, Conceptualization, Methodology, Software. **Zhiyu Xie:** Writing – review & editing, Methodology. **Jiaxin Hong:** Writing – review & editing, Investigation.

Declaration of competing interest

The authors declare that they have no known competing financial interests or personal relationships that could have appeared to influence the work reported in this paper.

Data availability

Data will be made available on request.

Acknowledgements

The support from the Program Fund of Nonmetallic Excellence and Innovation Center for Building Materials (24PHD-5), and National Natural Science Foundation of China (52078454) is greatly appreciated.

References

[1] X. Xu, B. Ran, N. Jiang, et al., A systematic review of ultrasonic techniques for defects detection in construction and building materials, Measurement 226 (2024) 114181, https://doi.org/10.1016/j.measurement.2024.114181.
[2] K. Li, J. Han, S. Wang, et al., Long-term performance of structural concretes in China southeast coastal environments exposed to atmosphere and chlorides, Cement Concr. Res. 164 (2023) 107064 j.cemconres.2022.107064.
[3] A. Ahmed, S. Guo, Z. Zhang, et al., A review on durability of fiber reinforced polymer (FRP) bars reinforced seawater sea sand concrete, Construct. Build. Mater. 256 (2020) 119484, 10/ghfm9f.
[4] T.U. Mohammed, H. Hamada, T. Yamaji, Performance of seawater-mixed concrete in the tidal environment, Cement Concr. Res. 34 (4) (2004) 593–601, https://doi.org/10.1016/j.cemconres.2003.09.020.
[5] J. Xiao, Q. Zhang, P. Zhang, et al., Mechanical behavior of concrete using seawater and seasea-sand with recycled coarse aggregates, Struct. Concr. 20 (5) (2019) 1631–1643, https://doi.org/10.1002/suco.201900071.
[6] J. Xie, J. Wang, M. Li, et al., Estimation of chloride diffusion coefficient from water permeability test of cementitious materials, Construct. Build. Mater. 340 (2022) 127816, https://doi.org/10.1016/j.conbuildmat.2022.127816.
[7] R. Feng, J. Wang, J.-H. Zhu, et al., Fatigue behavior of corroded reinforced concrete continuous beams with multi-intervention system, Eng. Struct. 231 (2021) 111748, https://doi.org/10.1016/j.engstruct.2020.111748.
[8] Y. Wu, Z. Xie, D. Zhang, et al., Uniaxial tensile behavior of anchored carbon fabric-reinforced cementitious matrix plates, J. Mater. Civ. Eng. 35 (8) (2023) 04023251, https://doi.org/10.1061/JMCEE7.MTENG-14941.
[9] U. Ebead, K.C. Shrestha, M.S. Afzal, et al., Effectiveness of fabric-reinforced cementitious matrix in strengthening reinforced concrete beams, J. Compos. Construct. 21 (2) (2017) 04016084, https://doi.org/10.1061/(ASCE)CC.1943-5614.0000741.
[10] R. Feng, Y. Liu, J.-H. Zhu, et al., Flexural behaviour of C-frcm strengthened corroded RC continuous beams, Compos. Struct. 245 (2020) 112200, https://doi.org/10.1016/j.compstruct.2020.112200.
[11] L. Wei, Tamon Ueda, Koji Matsumoto, et al., Experimental and analytical study on the behavior of RC beams with externally bonded carbon-FRCM composites, Compos. Struct. 273 (2021) 114291, https://doi.org/10.1016/j.compstruct.2021.114291.
[12] Z.C. Tetta, L.N. Koutas, D.A. Bournas, Textile-reinforced mortar (TRM) versus fiber-reinforced polymers (FRP) in shear strengthening of concrete beams, Compos. B Eng. 77 (2015) 338–348, https://doi.org/10.1016/j.compositesb.2015.03.055.
[13] O. Awani, T. El-Maaddawy, A. El Refai, Numerical simulation and experimental testing of concrete beams strengthened in shear with fabric-reinforced cementitious matrix, J. Compos. Construct. 20 (6) (2016) 04016056, https://doi.org/10.1061/(asce)cc.1943-5614.0000711.
[14] C.T.N. Tran, X.H. Nguyen, H.C. Nguyen, et al., Shear performance of short-span FRP-reinforced concrete beams strengthened with CFRP and TRC, Eng. Struct. 242 (2021) 112548, https://doi.org/10.1016/j.engstruct.2021.112548.
[15] L. Koutas, S.N. Bousias, T.C. Triantafillou, Seismic strengthening of masonry-infilled RC frames with TRM: experimental study, J. Compos. Construct. 19 (2) (2015) 04014048, https://doi.org/10.1061/(ASCE)CC.1943-5614.0000507.
[16] Y.A. Al-Salloum, N.A. Siddiqui, H.M. Elsanadedy, et al., Textile-reinforced mortar versus FRP as strengthening material for seismically deficient RC beam-column joints, J. Compos. Construct. 15 (6) (2011) 920–933, https://doi.org/10.1061/(ASCE)CC.1943-5614.0000222.
[17] M. Su, C. Zeng, W. Li, et al., Flexural performance of corroded continuous RC beams rehabilitated by ICCP-SS, Compos. Struct. 232 (2020) 111556, https://doi.org/10.1016/j.conbuildmat.2019.01.146.
[18] M. Su, L. Wei, H. Liang, et al., Fatigue behaviour and design of corroded reinforced concrete beams intervened by ICCP-SS, Compos. Struct. 261 (2021) 113295, https://doi.org/10.1016/j.compstruct.2020.113295.
[19] J.-H. Zhu, Z. Wang, M. Su, et al., C-FRCM jacket confinement for RC columns under impressed current cathodic protection: 2, J. Compos. Construct. 24 (2) (2020) 04020001, https://doi.org/10.1061/(asce)cc.1943-5614.0001006.
[20] J. Walraven, Synthesized intervention method to prolong service life of reinforced concrete structures: ICCP-SS: 2, Struct. Concr. 22 (2) (2021) 590–592, https://doi.org/10.1002/suco.202000261.
[21] R. Feng, J. Zhang, J.-H. Zhu, et al., Experimental study on the behavior of carbon-fabric reinforced cementitious matrix composites in impressed current cathodic protection, Construct. Build. Mater. 264 (2020) 120655, https://doi.org/10.1016/j.conbuildmat.2020.120655.
[22] R. Feng, J. Zhang, J.-H. Zhu, et al., Experimental study on interface bonding fatigue behavior of C-frcm composites in ICCP, Construct. Build. Mater. 259 (2020) 119660, https://doi.org/10.1016/j.conbuildmat.2020.119660.
[23] L.-L. Wei, J.-H. Zhu, T. Ueda, et al., Tensile behaviour of carbon fabric reinforced cementitious matrix composites as both strengthening and anode materials, Compos. Struct. 234 (2020) 111675, https://doi.org/10.1016/j.compstruct.2019.111675.
[24] M. Su, L. Wei, J.-H. Zhu, et al., Combined impressed current cathodic protection and FRCM strengthening for corrosion-prone concrete structures, J. Compos. Construct. 23 (4) (2019) 04019021, https://doi.org/10.1061/(asce)cc.1943-5614.0000949.
[25] W. Li, C. Pei, Y. Zhu, et al., Effect of chopped carbon fiber on interfacial behaviors of ICCP-SS system, Construct. Build. Mater. 275 (2021) 122117, 10/gkx6v3.
[26] S.A. Grammatikos, A.S. Paipetis, On the electrical properties of multi scale reinforced composites for damage accumulation monitoring, Compos. B Eng. 43 (6) (2012) 2687–2696, https://doi.org/10.1016/j.compositesb.2012.01.077.
[27] L. Yosef, Y. Goldfeld, Smart self-sensory carbon-based textile reinforced concrete structures for structural health monitoring, Struct. Health Monit. (2020) 147592172095112, https://doi.org/10.1177/1475921720951122.
[28] D.D.L. Chung, Carbon materials for structural self-sensing, electromagnetic shielding and thermal interfacing, Carbon 50 (9) (2012) 3342–3353, https://doi.org/10.1016/j.carbon.2012.01.031.
[29] Y.-B. Park, H.D. Roh, I.Y. Lee, Structural health monitoring of CFRPs using electrical resistance by reduced peripheral electrodes, Smart Struct. Syst. 28 (6) (2021) 737–744, https://doi.org/10.12989/SSS.2021.28.6.737.
[30] S. Wen, S. Wang, D.D.L. Chung, Piezoresistivity in continuous carbon fiber polymer-matrix and cement-matrix composites, J. Mater. Sci. 35 (14) (2000) 3669–3675, https://doi.org/10.1023/A:1004842303468.
[31] J.W. Cho, J.S. Choi, Relationship between electrical resistance and strain of carbon fibers upon loading, J. Appl. Polym. Sci. 77 (9) (2000) 2082–2087, https://doi.org/10.1002/1097-4628(20000829)77:9<2082::AID-APP26>3.0.CO;2-W.
[32] H. Huang, C. Yang, Z. Wu, Electrical sensing properties of carbon fiber reinforced plastic strips for detecting low-level strains, Smart Mater. Struct. 21 (3) (2012) 035013, https://doi.org/10.1088/0964-1726/21/3/035013.
[33] Y. Gong, Z. Xie, J. Liu, et al., Research on piezoresistive effect and random model of carbon fiber bundle, Arch. Civ. Mech. Eng. 23 (2) (2023) 128, https://doi.org/10.1007/s43452-023-00672-0.
[34] Z.S. Wu, C.Q. Yang, T. Harada, et al., Self-diagnosis of structures strengthened with hybrid carbon-fiber-reinforced polymer sheets, Smart Mater. Struct. 14 (3) (2005) S39–S51, https://doi.org/10.1088/0964-1726/14/3/006.
[35] C.Q. Yang, Z.S. Wu, Self-structural health monitoring function of RC structures with HCFRP sensors, J. Intell. Mater. Syst. Struct. 17 (10) (2006) 895–906, https://doi.org/10.1177/1045389X06061520.
[36] H.D. Roh, Y.-B. Park, Electromechanical analysis of self-sensing CFRP and its application to real-time non-destructive evaluation[C], in: P.J. Shull, T.-Y. Yu, A. L. Gyekenyesi, et al. (Eds.), Nondestructive Characterization and Monitoring of Advanced Materials, Aerospace, Civil Infrastructure, and Transportation IX, Online Only, United States: SPIE, 2020, p. 32, https://doi.org/10.1117/12.2557963.
[37] S. Wen, D.D.L. Chung, Piezoresistivity in continuous carbon fiber cement-matrix composite, Cement Concr. Res. 29 (3) (1999) 445–449, https://doi.org/10.1016/S0008-8846(98)00211-7.
[38] T. Quadflieg, O. Stolyarov, T. Gries, Carbon rovings as strain sensors for structural health monitoring of engineering materials and structures: 7, J. Strain Anal. Eng. Des. 51 (7) (2016) 482–492, https://doi.org/10.1177/0309324716655058.

[39] Y. Gong, Z. Xie, G. Chen, et al., Influence of cementitious material infiltration on piezoresistive effect of carbon fiber bundle, J. Mater. Civ. Eng. 35 (7) (2023) 04023173, https://doi.org/10.1061/JMCEE7.MTENG-14701.
[40] Y. Goldfeld, T. Quadflieg, T. Gries, Sensing capabilities of carbon based TRC beam from slack to pull-out mechanism, Compos. Struct. 181 (2017) 294–305, https://doi.org/10.1016/j.compstruct.2017.08.102.
[41] Y. Goldfeld, S. Ben-Aarosh, O. Rabinovitch, et al., Integrated self-monitoring of carbon based textile reinforced concrete beams under repeated loading in the uncracked region, Carbon 98 (2016) 238–249, https://doi.org/10.1016/j.carbon.2015.10.056.
[42] Y. Goldfeld, G. Perry, AR-Glass/Carbon-Based textile-reinforced concrete elements for detecting water infiltration within cracked zones, Struct. Health Monit. 18 (5–6) (2019) 1383–1400, https://doi.org/10.1177/1475921718808223.
[43] Y. Goldfeld, L. Yosef, Sensing accumulated cracking with smart coated and uncoated carbon based TRC, Measurement 141 (2019) 137–151, https://doi.org/10.1016/j.measurement.2019.04.033.
[44] China Cement Standardization Technical Committee, The National Standard of the People's Republic of China: Test Method of Cement Mortar Strength(ISO Method) (GB/T17671-2021) [S], Standards Press of China, Beijing, 2021 (in Chinese).
[45] D.D.L. Chung, A critical review of piezoresistivity and its application in electrical-resistance-based strain sensing, J. Mater. Sci. 55 (32) (2020) 15367–15396, https://doi.org/10.1007/s10853-020-05099-z.
[46] M. Zhu, J.-H. Zhu, T. Ueda, et al., Degradation behavior of multifunctional carbon fabric-reinforced cementitious matrix composites under anodic polarization, Construct. Build. Mater. 341 (2022) 127751, https://doi.org/10.1016/j.conbuildmat.2022.127751.
[47] B. Banholzer, Bond Behaviour of a Multi-Filament Yarn Embedded in a Cementitious Matrix[D], Bibliothek der RWTH Aachen, 2004.
[48] B.-G. Kang, J. Hannawald, W. Brameshuber, Electrical resistance measurement for damage analysis of carbon yarns, Mater. Struct. 44 (6) (2011) 1113–1122, https://doi.org/10.1617/s11527-010-9687-4.
[49] H. Sun, L. Wei, M. Zhu, et al., Corrosion behavior of carbon fiber reinforced polymer anode in simulated impressed current cathodic protection system with 3% NaCl solution, Construct. Build. Mater. 112 (2016) 538–546, https://doi.org/10.1016/j.conbuildmat.2016.02.141.
[50] E.Q. Zhang, L. Tang, D. Bernin, et al., Effect of the paste–anode interface under impressed current cathodic protection in concrete structures, Mater. Corros. 69 (8) (2018) 1104–1116, https://doi.org/10.1002/maco.201709908.
[51] J.-H. Zhu, L. Wei, G. Guo, et al., Mechanical and electrochemical performance of carbon fiber reinforced polymer in oxygen evolution environment: 11, Polymers 8 (11) (2016) 393, https://doi.org/10.3390/polym8110393.
[52] H. Li, W. Zhou, J. Ou, Study on electromechanical behavior of unidirectional carbon fibre sheet without epoxy resin matrix, Adv. Struct. Eng. 7 (5) (2004) 437–445, https://doi.org/10.1260/1369433042863288.
[53] Y. Goldfeld, O. Rabinovitch, B. Fishbain, et al., Sensory carbon fiber based textile-reinforced concrete for smart structures, J. Intell. Mater. Syst. Struct. 27 (4) (2016) 469–489, https://doi.org/10.1177/1045389X15571385.
[54] C. Pei, Y. Zeng, S. Kong, et al., Pull-out performance of anchored carbon-fiber bundles in cementitious matrix, J. Compos. Construct. 25 (6) (2021) 04021057, https://doi.org/10.1061/(ASCE)CC.1943-5614.0001175.

Structures 80 (2025) 109918



Contents lists available at ScienceDirect

Structures

journal homepage: www.elsevier.com/locate/structures



Effect of shear connection degree on static behavior of externally prestressed FRP-concrete hybrid beams: Experimental and numerical study

Weichen Xue [a,*], Dawei Yan [a], Shiqian Zhang [a,b], Jiafei Jiang [a]

[a] College of Civil Engineering, Tongji University, Shanghai 200092, China
[b] China Construction Eighth Engineering Division Co. Ltd., Shanghai 200092, China

ARTICLE INFO

Keywords:
FRP-concrete hybrid beam
Externally prestressed
Shear connection degree
Experiment
FE model
Capacity

ABSTRACT

To address steel corrosion issues in externally prestressed steel-concrete composite beams, a novel externally prestressed FRP-concrete (FRP-PC) hybrid beam is proposed by replacing steel girder, reinforcement, steel strands, and stud with GFRP profiles, GFRP bars, CFRP tendons, and GFRP bolts. The proposed hybrid beam demonstrates considerable potential for large-span bridge applications, due to its lightweight, high strength, excellent corrosion resistance, and ease of construction. Two large-scale simply supported hybrid beams with different shear connection degrees (η = 0.8/1.2) were tested to investigate their static behavior. Test results revealed that FRP-PC hybrid beams suffered FRP shear failure at the upper flange-web joint (η = 1.2) and interfacial connection failure (η = 0.8). Load-deflection curves demonstrated an initial linear elastic phase followed by a stiffness degradation phase. Both load-carrying capacity and stiffness increased with higher shear connection degrees. Despite the presence of significant interfacial slip, indicating partial composite action between the FRP and concrete, the concrete slab and FRP beam maintained identical curvature throughout loading, thereby validating the plane-section assumption. A validated nonlinear finite element model was developed in Abaqus v2017, considering interfacial slip, material isotropy, and FRP damage. A parametric study on 27 hybrid beams was then conducted to evaluate the effects of shear connection degree, concrete strength, prestress level, concrete slab dimensions, and FRP geometry.

1. Introduction

Composite beams made of steel and reinforced concrete (steel-RC) are a common type of structure in building and bridge engineering because of their lightweight, high load capacity, and easy installation [1–3]. Such beams, however, have certain limitations, including lower stiffness, larger deflections, and a tendency to crack in regions of negative moment. To effectively address these limitations, the prestress technique has been applied to form externally prestressed steel-concrete (steel-PC) composite beams [4–9]. Steel-PC composite beams provide several notable benefits over steel-RC composite beams, including reduced overall height and self-weight of the structure, enhanced stiffness with less displacement under service loads, and superior fatigue and fracture performance. In this type of composite beam, external steel strands connect with the beam exclusively via deviators and anchorages. The segment of the strand between adjacent deviators retains a linear profile throughout the loading process. Additionally, the second-order effect becomes a critical consideration due to changes in the eccentricity of the external tendons caused by beam deformation [10]. Moreover, an essential factor in composite beam design is the interaction between the concrete slab and steel beams, which significantly influences their static performance [11]. The composite action could be classified into four types, including partial shear connection, full shear connection, partial interaction and full interaction 74]. The partial and full shear connection depend on whether the interfacial shear forces can be consumed by the shear connectors, while the partial and full interaction depend on whether the interfacial slip between concrete and steel existed. In practical applications, it is hard to reach a full shear connection due to the higher cost of shear connectors and complicated construction.

The serviceability and safety of steel-PC composite beams exposed to harsh or corrosive environments tend to be affected by corrosion of structural steels, steel bars, and steel connectors [12,13]. Fiber-reinforced polymer (FRP) has been proven to be an alternative solution to steel due to its perfect corrosion resistance. FRP has excellent material properties, such as lightweight, high tensile strength, and good

* Corresponding author.
E-mail address: xuewc@tongji.edu.cn (W. Xue).

https://doi.org/10.1016/j.istruc.2025.109918
Received 30 November 2024; Received in revised form 12 July 2025; Accepted 8 August 2025
2352-0124/© 2025 Institution of Structural Engineers. Published by Elsevier Ltd. All rights are reserved, including those for text and data mining, AI training, and similar technologies.

fatigue behavior [14–18]. Currently, FRP, used in new construction, primarily consists of FRP bars, FRP sheets, and FRP profiles. FRP could be divided into glass FRP (GFRP), carbon FRP (CFRP), basalt FRP (BFRP), and aramid FRP (AFRP), based on the fiber types [19,75]. In order to address the issue of steel corrosion, an innovative external prestressed FRP-concrete (FRP-PC) hybrid beam was proposed by replacing steel tendons, steel reinforcement, structural steel, and steel connectors with CFRP tendons, GFRP bars, GFRP profiles, and FRP connectors, respectively [20]. This beam has great potential for application in highway bridges and pedestrian bridges due to excellent mechanical properties such as high ultimate capacity, reduced deformation, good durability, extended elastic behavior under heavier loads, and optimal utilization of material properties [14,21–23].

Shear connectors are important in achieving the composite action between the FRP beam and concrete slab by restraining the relative slip and enabling the interfacial shear force transferring [24]. There are three major types of shear connectors, including epoxy bonding connection [16,25], perforated FRP ribs [26–28], bolts (stainless steel bolts [16,29–32], and GFRP bolts [31]). In comparison with other types of shear connectors, bolts can resist interfacial shear stress in multiple directions and offer benefits such as superior shear strength, fast installation, and economic efficiency [33]. Unlike stainless steel bolts, which often lead to bearing failure in the bolt holes of GFRP flanges and fail to fully exploit shear strength, GFRP bolts are recommended as they maximize shear strength utilization with minimal impact on the specimen's capacity [29,30]. Although studies have been conducted to investigate the shear mechanism of GFRP bolts in hybrid beams and proposed load-slip models and shear capacity calculation methods, the majority of them have focused on push-out tests rather than beam tests [29,31].

Since 1990s, valuable experimental research related to the static behavior of non-prestressed FRP-concrete (FRP-RC) hybrid beams has been made [12,16,17,21–25,30,32,34–48,76], while research on FRP-PC hybrid beams has not yet been reported. Experimental results revealed that FRP-RC hybrid beams exhibited excellent mechanical performance [44,49]. Several failure modes of FRP-RC hybrid beams have been reported: (a) FRP web shear failure [44], (b) shear rupture at the FRP profile's top flange-web joint [21], (c) concrete compressive failure [39], (d) large interfacial slip and failure of shear connector, (e) FRP tensile failure at bottom flange [17] (f) diagonal concrete crack in the shear span [50] and (g) instability of FRP profiles. Saiidi et al. [16] first performed experiments on six 1.0 m graphite/epoxy-concrete hybrid beams with epoxy bonding connection and observed interfacial debonding followed by FRP web shear failure. Thus, the authors suggested to replace epoxy bonding connection with mechanical connectors. Correia et al. [35,51] and Nordin and Täljsten [24] compared the flexural behavior of FRP-RC hybrid beams with either steel bolts or epoxy bonding connection and found that beams with epoxy bonding connection exhibited higher stiffness but lower capacity than beams with steel bolts. Furthermore, Jurkiewicz et al. [12], Nguyen et al. [11,47], and Manalo et al. [39] conducted beam tests to compare the effectiveness of several shear connectors, including bolt, epoxy bonding, and combined connection of bolt and epoxy bonding. Test results indicated that an almost full composite action was achieved by the combined connection. Neagoe et al. [21,52] investigated the static performance of 1.8 m GFRP-RC hybrid beams with a low shear connection degree. Compared to single-pultruded GFRP profiles, these hybrid beams demonstrated enhanced bending resistance and exhibited pseudo-ductile behavior. To improve the shear performance of the FRP web, Zhang [48] proposed two ways, including attaching the FRP beams' web with CFRP sheets and increasing the number of webs. Besides, FRP box section beams are suggested by researchers to provide additional shear strength and prevent the instability phenomenon [24,25,38]. Fam and Skutezky [17] studied the flexural behavior of three 3.1 m GFRP-RC hybrid beams with GFRP bolts and observed that good slip resistance and composite action were achieved by GFRP bolts when it was surrounded by the concrete. El-Hacha et al.[30,53] carried out experiments on four 2.9 m GFRP-ultra-high-performance-concrete (UHPC) hybrid beams with GFRP bolts and found that full composite action could be satisfied by the combined connection of GFRP bolts and epoxy bonding with coarse silica sand aggregates.

Based on experimental findings, finite element models (FEM) were developed to predict the performance of FRP-RC hybrid beams [23,43,54]. Neto [37] and Feng [40] performed linear-elastic finite element (FE) analyses and observed strong consistency between the load-deflection curves obtained from experiments and FEM predictions. Ge et al.[49] proposed a validated non-linear FE model on FRP-RC hybrid beams, considering the orthotropic behavior of the GFRP profile and interfacial slip by the bi-linear traction-separation model. The authors carried out the parametric analysis and found the flexural performance of the hybrid beams can be enhanced by improving interfacial bonding behavior and high-strength concrete.

Currently, standards for FRP-RC/PC hybrid beams have not yet been issued for most countries. Only the Chinese standard GB 50608 provides regulations concerning the flexural capacity, shear capacity, and shear connector capacity of FRP-RC hybrid beams [55]. Design calculation methods, however, have not yet been provided for FRP-PC hybrid beams.

Based on the above literature review, several issues have been identified:

(1) Compared to FRP-RC hybrid beams, the FRP-PC hybrid beam is a novel hybrid beam with potential application in large-span structures due to its improved flexural capacity, enhanced crack and fatigue resistance, and reduced service-load deformation. However, research on FRP-PC hybrid beams is scarce.
(2) Push-out tests on GFRP bolts conducted by both authors and other researchers have confirmed the excellent shear performance of GFRP connectors [29,31,56]. Nevertheless, studies on the static behavior of hybrid beams incorporating GFRP bolts are scarce. While full shear connection can improve structural performance, it often requires closely spaced bolts, which complicates construction and increases costs. To balance performance and practicality, hybrid beams can be designed with partial shear connections (η<1.0). Therefore, the effect of shear connection degree on the static behavior of such hybrid beams warrants further experimental investigation.
(3) Changes in the effective depth of external tendons, caused by vertical deflection of deviators, can lead to increased ultimate stress and second-order effects, complicating the accurate determination of prestressing forces. Limited studies have been reported to investigate the loading history of the external tendon.

Accordingly, monotonic static tests have been conducted on two large-scale simply supported FRP-PC hybrid beams, adopting GFRP bolts with varied shear connection degrees of 0.8/1.2. The failure modes, load-deflection curves, interface slip, and load-strain behavior of FRP-PC beams were investigated. Moreover, a 3D FEM was established by ABAQUS and validated with the test data. Parameter analysis is conducted to investigate the effect of initial prestressing force, shear connection degree, concrete strength, concrete slab thickness and height, FRP flange, and web thickness on the behavior of FRP-PC hybrid

Table 1
Details of FRP-PC hybrid beam specimens.

Specimens	Concrete strength	Spacing of FRP bolts (mm)	Shear connection degree
HB-C30–1.2	C30	180	1.2
HB-C30–0.8	C30	270	0.8

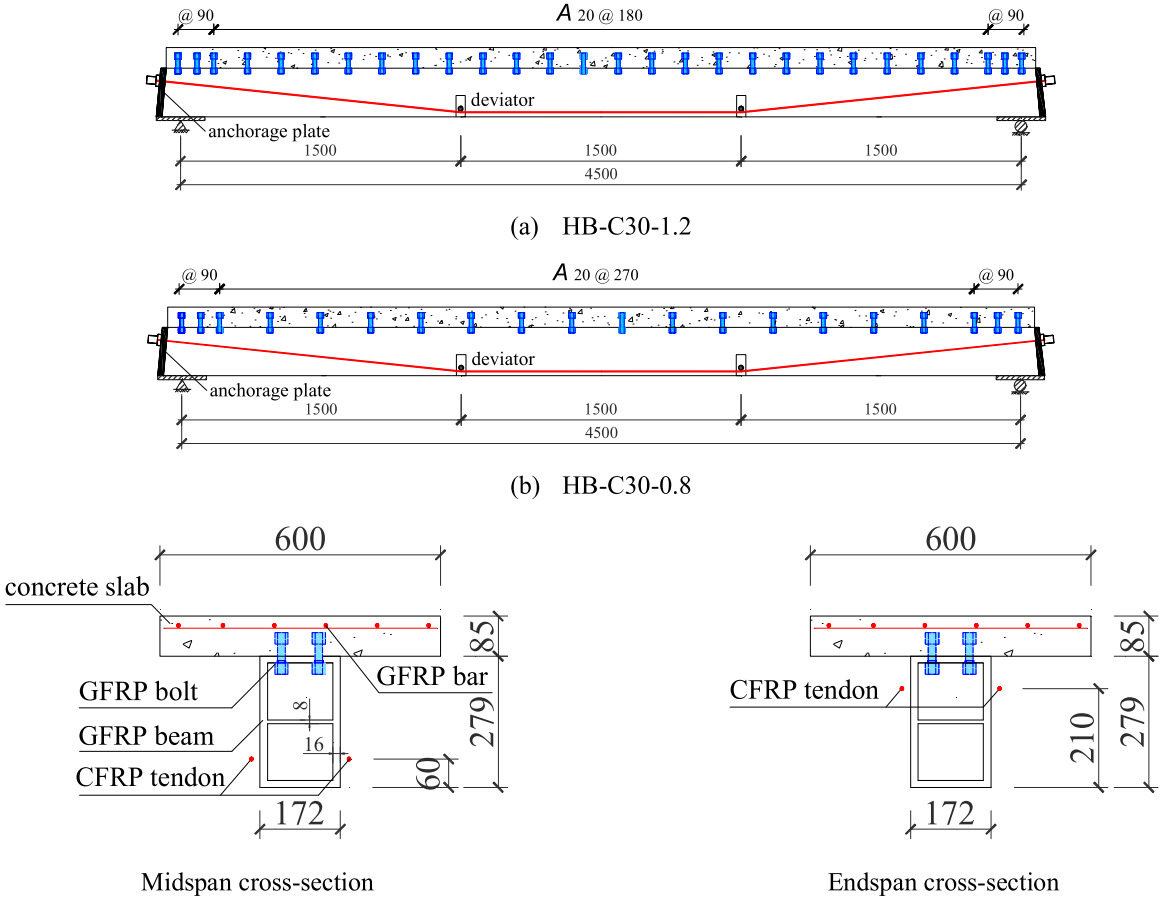


Fig. 1. Dimensions and details of FRP-PC hybrid beams (mm).

beams.

2. Experimental program of FRP-PC hybrid beams

2.1. Specimens design

Two large-scale FRP-PC hybrid beams with a clear span of 4.5 m were designed, fabricated, and tested (Table 1). The details and cross-section dimensions of the beams are shown in Fig. 1. These hybrid beams consisted of an upper reinforced concrete slab, a lower box-shaped GFRP pultruded profile beam, and two bundles of external pre-stressing CFRP tendons. The concrete slab and GFRP beam were connected by 20mm-diameter GFRP bolts. The reinforced concrete slab had a width of 600 mm and a thickness of 85 mm. The GFRP beam was in a cross-section dimension of 260 mm× 160 mm× 16 mm× 15 mm (height × width × web thickness × flange thickness). The span-to-depth ratio of the specimens was 12.4, which satisfied the requirement of PC beams. 9.5 mm diameter GFRP bars were adopted for transverse and longitudinal reinforcements, which were arranged on the concrete slab with a cover spacing of 20 mm to the top surface of the concrete slab. The longitudinal reinforcement ratio was 0.8 % for all beams. It should be noted that the concrete slab was design to be under the compression due to the neutral axial of the hybrid beams in the GFRP section.

Two steel deviators were installed at the side of the GFRP beam by epoxy bonding with a distance of 1500 mm (1/3 clear span) apart from the end of the hybrid beam. The CFRP tendons were tensioned and anchored to the 20 mm thickness end-plates of the hybrid beam with a distance of 210 mm to the bottom of the beams. 150-mm-thick concrete blocks were cast at the support points of beams to prevent local buckling failure of the GFRP web. According to ACI 440.4R-15 [57], the maximum jacking stress of CFRP tendons was limited to 0.6 f_{ftk} (f_{ftk} denotes the ultimate tensile strength of CFRP tendons); thus, the CFRP tendons were prestressed with the same jacking stress ($\sigma_{con} = 0.5\ f_{ftk}$). There are no design standards related to FRP-PC hybrid beams, so the design of the hybrid beams was based on the existing design standards (GB 50917) [58],related to steel-concrete composite beams. In accordance with GB 50917 (Eq. (1)), the shear connection degrees for specimens HB-C30–1.2 and HB-C30–0.8 are 1.2 and 0.8, respectively.

$$\eta = \frac{nN_v}{V_h} = \frac{nN_v}{\min(A_s f_s \quad A_c f_c)} \tag{1}$$

where N_v is the ultimate resistance of the GFRP bolt, it could be calculated according to the research by Xue et al.[59]; n denotes the number

Table 2
Mechanical properties of GFRP beams.

Part	Webs		Flanges	
	Transverse	Longitudinal	Transverse	Longitudinal
Tensile strength σ_{tu}/ MPa	90.83	492	198.7	734
Tensile modulus E_{tu}/ GPa	14.1	35	12.7	38
Compressive strength σ_{cu}/MPa	133.3	306	255	240
Compressive modulus E_{cu}/GPa	20.5	35.6	28.3	22
Shear strength τ_{xy}/ MPa	38		57.5	
Shear modulus G_{xy}/ GPa	10.5		8.8	
Passion ratio	0.12	0.16	0.12	0.3

Table 3
Mechanical properties of GFRP bar and CFRP tendon.

Type of bars	Tensile strength f_u (MPa)	Elastic modulus E (GPa)	Elongation (%)
GFRP A 9.5	951.2	52.3	1.57
CFRP A 12.5	1724	124	1.32

of GFRP bolts in the shear span; V_h denotes the horizontal interfacial shear force when the hybrid beams failed; η denotes shear connection degree ($\eta \geq 1$ denotes a full shear connection, $0 < \eta < 1$ denotes a partial shear connection); A_s represent the cross-sectional area of the FRP profile (analogues to the cross-sectional area of the steel profile in the GB 50917); f_s represents the tensile strength of the FRP profile (analogues to the yield strength of the steel); A_c denotes the cross-sectional area of the concrete slab and f_c represents the compressive strength of concrete slab.

2.2. Material properties

Both specimens were constructed using ready-mixed normal-weight concrete. The specimens were cast with C30 with a compressive strength (f_{cu}) of 37.3 MPa and elastic modulus (E_c) of 31.2 GPa, determined following GB/T 50081. The GFRP beams were produced by Nanjing Spare Composite Co., LTD., in China. The tensile, compressive, and in-plane shear strength of the GFRP beams, as summarized in Table 2, were tested in both parallel and perpendicular-to-fibers directions considering the anisotropic mechanical properties of FRP according to GB/T 1447–2005 [60], GB/T 1448–2005 [61], and GB 3355–2005 [30], respectively. Both the GFRP bars and the CFRP tendon were fabricated by ASLAN FRP. The mechanical properties depended on the B2 test in ACI 440.3R-12 (Table 3) [62]. The ultimate shear strength and shear load-slip (P-S) curves of GFRP bolts were systematically investigated by the authors [31].

2.3. Construction of specimens

The construction process is summarized as follows: (i) installed and fixed the FRP bolts by glue screwing process; (ii) tied the FRP reinforcement and put it into molds; (iii) cast concrete and cured at normal atmospheric temperature for 28 days; (iv) installed deviators by epoxy bonding; (v) placed the beam and tensioned the prestressing tendons (Fig. 2).

2.4. Instrumentations and test setups

All simply supported hybrid beams underwent four-point bending tests, as illustrated in Fig. 3. A hydraulic actuator with a 500 kN capacity applied the vertical load, which was evenly distributed along the loading lines of the hybrid beam using a steel beam and two steel roller supports spaced 1050 mm apart. The load was applied at a constant rate of 0.4 mm/min. Before the main loading, preloading was conducted to verify the functionality of the instrumentation.

Eight Linear variable displacement transducers (LVDTs) of Ld1~Ld8 were employed to record the vertical deflections. A set of LVDTs of Ls1~Lsn were horizontally installed to measure the interfacial relative slip between the concrete slab and the GFRP beams. Five LVDTs of Lq1~Lq5, mounted at the side of the midspan of beams, were used to measure the curvature of hybrid beams. Four strain gauges were bonded on the surface of CFRP tendons at the midspan and shear span to capture the strain increment. Strain gauges were attached to both the concrete slab and GFRP beam surfaces. Besides, strain gauges were used to measure the strain of GFRP bolts along the bolt shank, which were positioned at regular intervals of 360 mm and 270 mm for HB-C30–1.2 and HB-C30–0.8, respectively (Fig. 4).

2.5. Prestressing

The CFRP tendons were tensioned using a hydraulic jack following



Fig. 3. Test setup.



Fig. 2. Construction of FRP-PC hybrid beam.

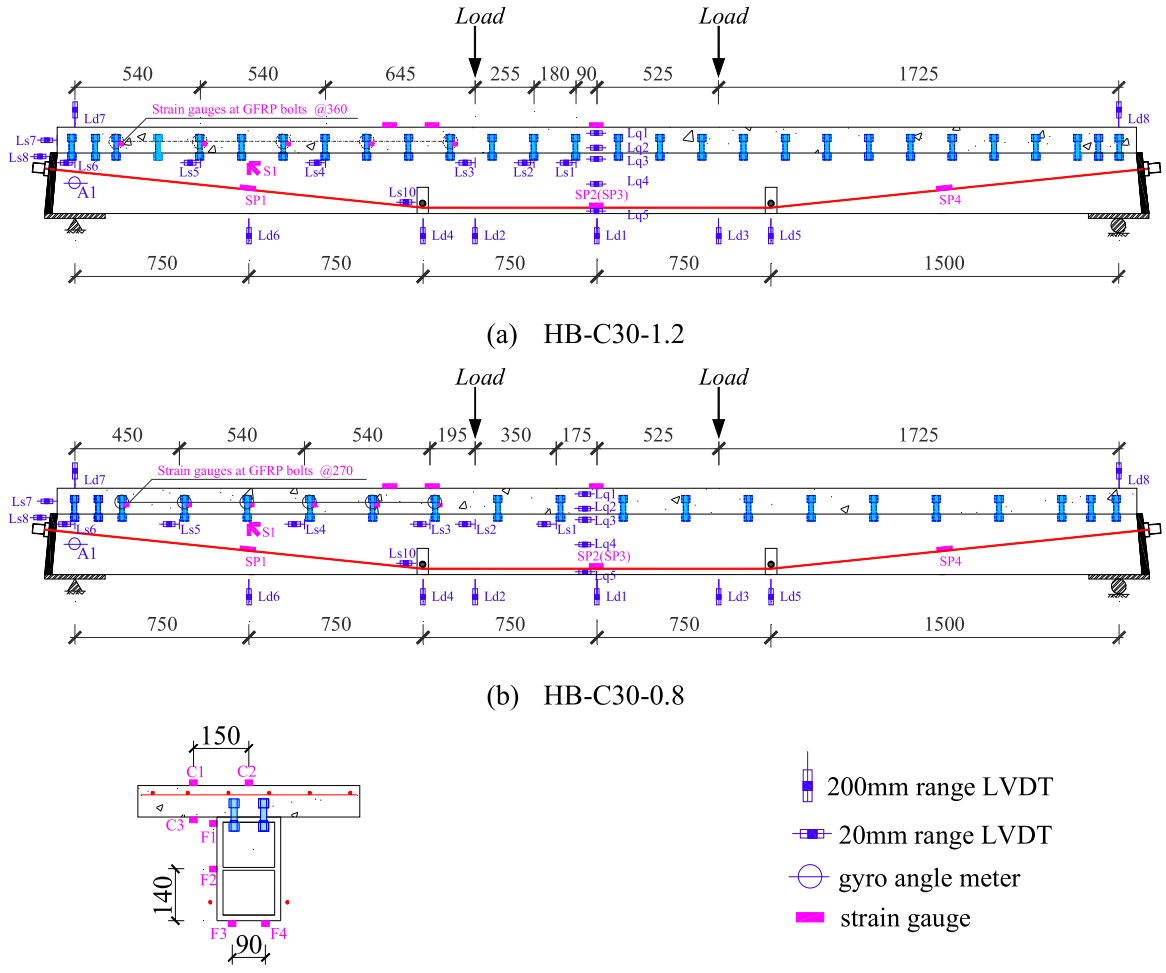


Fig. 4. Instrumentation details.

Table 4
Comparison of the measured value and calculated value of effective prestress force.

Specimens	stretching control stress /MPa	Calculated value of effective prestress / MPa	Measured value after anchorage/ MPa	Measured value after 1 day/MPa
HB-C30–1.2	862	775.2	807.1	792
HB-C30–0.8	862	775.2	811.7	793.7

Note: The effective prestress was calculated regarding [2], taking into account the frictional prestress loss and prestress loss by anchorage retraction.

standard procedures to establish prestresses. The locknuts were installed to prevent CFRP tendons from slipping, and then the jacks were removed when the prestress reached the designed control stress. During the prestressing, the applied stresses were measured by the strain gauge in the CFRP tendons, the oil pressure gauge of the hydraulic jack, and the force transducer to ensure the accuracy of the applied stresses. The results of these measurements were consistent.

After applying the prestress, the specimens were conserved for approximately a day in the laboratory to evaluate the prestress loss due to the relaxation of tendons and anchorage slipping. The measured effective prestress in the CFRP tendons is summarized in Table 4. The prestress losses after 1 day were 1.9 % and 2.2 % for HB-C30–1.2 and HB-C30–0.8, respectively. The calculated effective prestresses of HB-C30–1.2 and HB-C30–0.8 were 96.1 % and 95.5 % of the test values, respectively. The initial camber measured at midspan was 6.1 mm for HB-C30–1.2 and 8.2 mm for HB-C30–0.8. The relative slips measured at the beam ends were 0.10 mm for HB-C30–1.2 and 0.19 mm for HB-C30–0.8.

3. Experimental results

3.1. General behavior and failure modes

Two failure modes were observed, namely shear failure at the upper flange-web joint in the shear span section (HB-C30–1.2) and interfacial connection failure (HB-C30–0.8), as shown in Fig. 5.

For specimen HB-C30–1.2, the concrete slab initially cracked near the loading point at 0.4 P_u (P_u is the ultimate load). As the load increased, more vertical cracks were observed and abnormal noises were heard obviously at the shear span. The specimen failed suddenly with a loud noise and the propagation of the longitudinal shear crack from the end of the beam to the mid-span. The web of the GFRP beam in the compression zone between the loading points instantaneously buckled due to the compression caused by the prestressing of the CFRP tendons. The significant slip occurred at the interface between the concrete slab and the GFRP beam. Additionally, no apparent failure of the GFRP bolts was observed, indicating that the GFRP bolts had excellent shear resistance. As to specimen HB-C30–0.8, the sound of fiber fracture could be heard, and the concrete slab uplifted with the interfacial separation in the shear span due to the pull-out failure of some GFRP bolts when the load increased to P_u.

It should be noted that the shear connection degree for FRP-PC

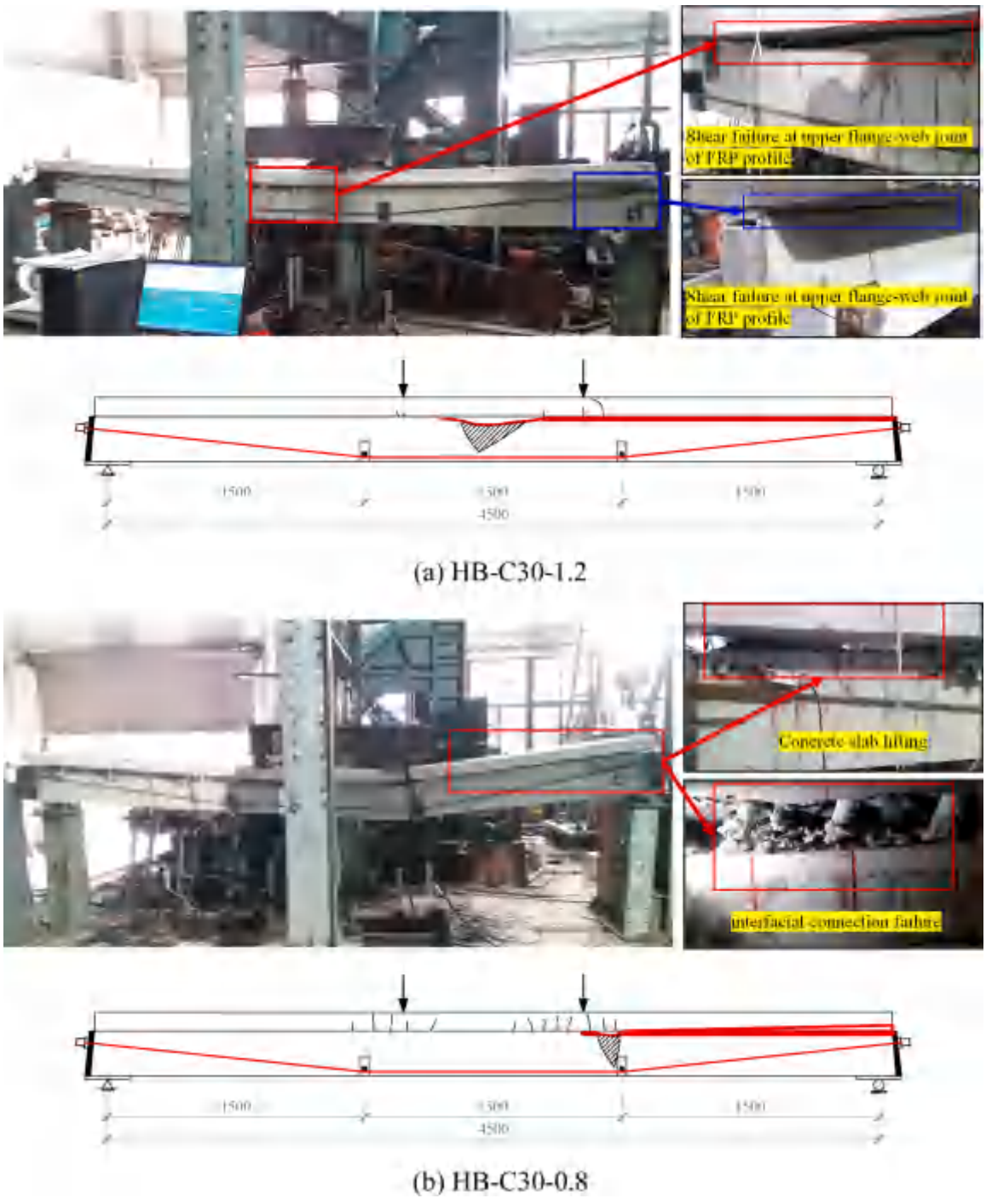


Fig. 5. Failure mode of tested beams.

hybrid beams should not be calculated by Eq.(1). This is because the shear connection degree (Eq. (1)) is defined based on the bending failure of the steel-concrete composite beam (concrete crushing and steel beam yielding in tension). However, both HB-C30–1.2 and HB-C30–0.8 did not suffer bending failure but experienced shear failure at the FRP profile due to the low shear strength of FRP. Therefore, the shear connection degree should be calculated by Eq.(2).

$$\eta = \frac{nN_v}{V_h} \tag{2}$$

3.2. Load-deflection behavior

The load-deflection curves of specimens at the mid-span and loading point are presented in Fig. 6. The flexural test results are summarized in Table 5.

As shown in Fig. 6, load-deflection curves of the FRP-PC hybrid beams can be characterized by two phases, namely, (1) a linear elastic phase ($P \leq 0.4\ P_u$); and (2) a stiffness degradation phase ($P > 0.4\ P_u$). During the linear elastic phase, deflection increased proportionally with load, and the beams exhibited high flexural stiffness. In the stiffness degradation phase, the flexural stiffness gradually decreased due to cracking of the concrete slab. The hybrid beams exhibited no strength

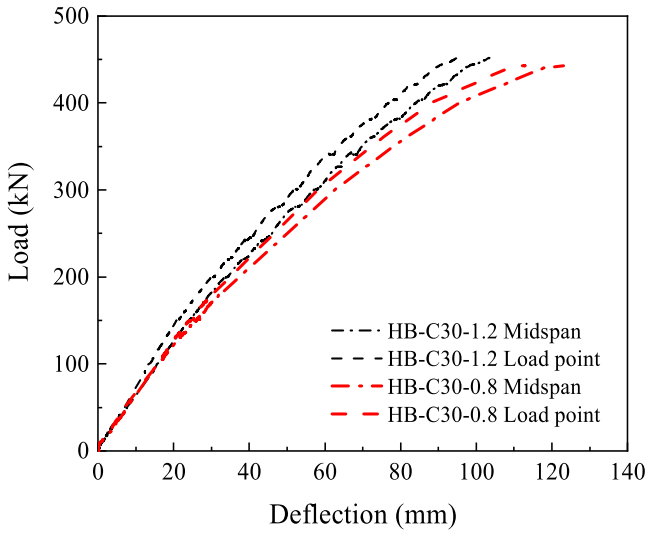


Fig. 6. Load-deflection curves.

degradation during the tests. Furthermore, a reduction in shear connection degree led to decreases in flexural stiffness, cracking load, and ultimate capacity, indicating that the overall composite action was enhanced by increasing the number of GFRP bolts within the shear span.

The reduction of effective depths of tendon versus load curve is shown in Fig. 7. The reduction of effective depths of tendon for specimens in the linear elastic phase was similar, indicating that the second-order effect is minimal at this load level. The reduction of effective depths of CFRP tendons for the specimens of HB-C30–1.2 and HB-C30–0.8 was 13.75 mm and 17.07 mm when the beams failed. This indicated that for specimens with lower shear connection degree, the reduction of effective depth of CFRP tendons was higher and the second-order effect was more obvious.

Fig. 8 shows characteristic values of load and deformation along the hybrid beams. The deflection in the midspan is the largest, and deflection increased rapidly when the load was larger than 0.6 P_u. Referring to Table 5, the ratio of mid-span deflections and span of HB-C30–1.2 and HB-C30–0.8 corresponding to the cracking load are 1/177, and 1/178, which is larger than the allowable value of deformation of beams according to GB 50010 [63] (1/200), Eurocode 2 [64] (1/250–1/300) and ACI 318 [65] (l/240). The Δ_u/L of specimens HB-C30–1.2 and HB-C30–0.8 were 1/46.2 and 1/39.2 when the hybrid beams failed. This indicated that FRP-PC hybrid beams had a large deformation capacity and safety margin. The design of FRP-PC hybrid beams was controlled by the serviceability limit state.

3.3. Load-slip behavior

Fig. 9 presents experimental load-slip curves for hybrid beams at the beam end. Fig. 10 shows the distribution of slips along the half span of the beam under the different characteristic values of load. From these figures, the following findings were concluded:

(1) The interfacial slip between the concrete slab and FRP beams is trivial for all hybrid beams before the load reaches approximately 0.1P_u. Then, the slip increased linearly till the 0.4 P_u. After this threshold, the concrete slab cracked, and the slip increased significantly.

(2) The anti-slipping stiffness of the hybrid beams decreased with the dropping shear connection degree. The relative slips at the ends of the hybrid beam with 1.2 and 0.8 shear connection degrees were approximately 6.9 mm and 10.4 mm, respectively.

(3) As observed from Fig. 10, interface slip was negligible at the initial loading stage and gradually increased with increasing load. The interfacial slip in the pure bending region was smaller than that in the shear span, primarily due to the higher horizontal shear forces acting on the bolt connectors within the shear span. Notably, the slip was zero at mid-span and reached its maximum near the support regions, consistent with previous findings on FRP–concrete hybrid beams [5,11,47]. Furthermore, the maximum slip of HB-C30–0.8 at failure load was approximately 1.49 times larger than that of HB-C30–1.2, as the shear connection degree of HB-C30–0.8 was smaller than that of HB-C30–1.2.

3.4. Strain distribution at the cross-section

The strain at the cross-section of all specimens and the strain development of the CFRP tendons are discussed in this section.

3.4.1. Strain across the cross-section

Fig. 11 illustrates the strain distribution at the mid-span section of the hybrid beams under varying loads. The vertical axis, labeled h, represents the distance from the strain measurement point to the bottom of the FRP beam. The key observations are summarized as follows:

(1) The curvatures of the transverse sections of the FRP beam and concrete slabs were found to be similar, indicating that the plain section assumption was satisfied for the individual layers. Under the same loading conditions, the strain difference between the bottom of the concrete slab and the top flange of the FRP beam in

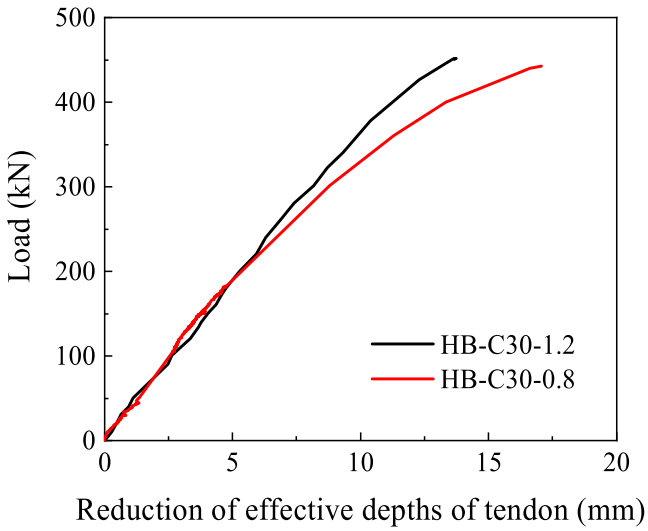


Fig. 7. Load-deviator loss.

Table 5
Summary of flexural test results.

Specimens	P_{cr}(kN)	P_u(kN)	Δ_{cr}(mm)	Δ_u (mm)	S_u(mm)	φ_u (10^{-6} /mm)	Δ_u/L	Failure modes
HB-C30–1.2	190	452	25.48	97.41	6.96	43.2	1/46.2	SF
HB-C30–0.8	180	443	25.32	114.95	10.37	49.7	1/39.2	CF

Notes: P_{cr} is the cracking load; P_u is the ultimate load; Δ_{cr} and Δ_u are the mid-span displacements corresponding to the cracking load and ultimate load, respectively; φ_u is the curvature at the ultimate load; 'SF' means shear failure at upper flange-web joint; 'CF' means interfacial connection failure.

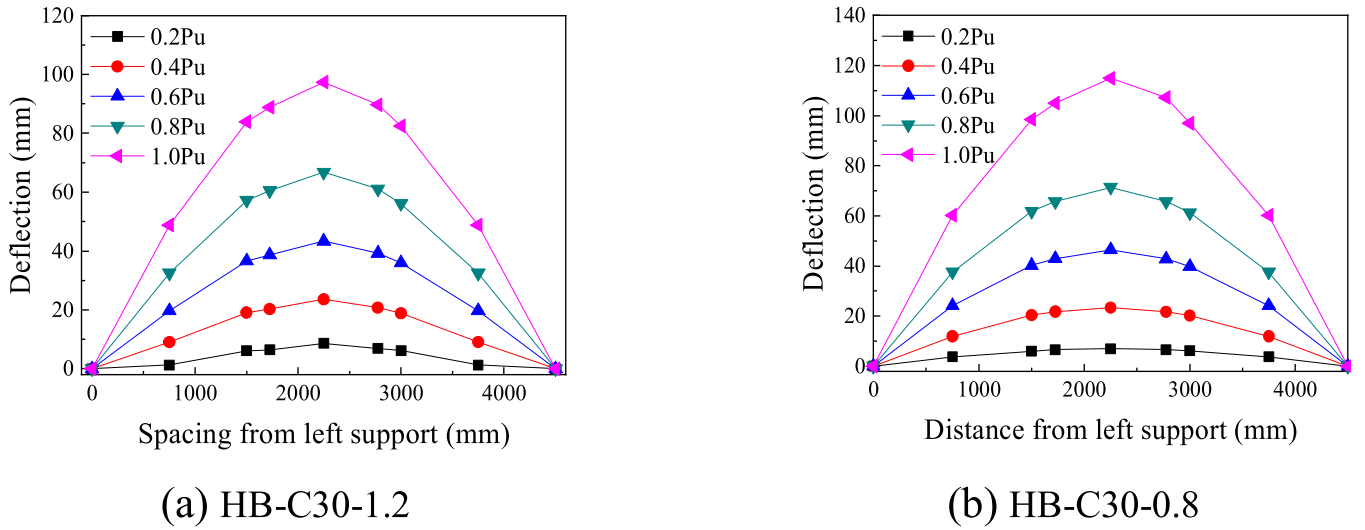


Fig. 8. Deflection along the span.

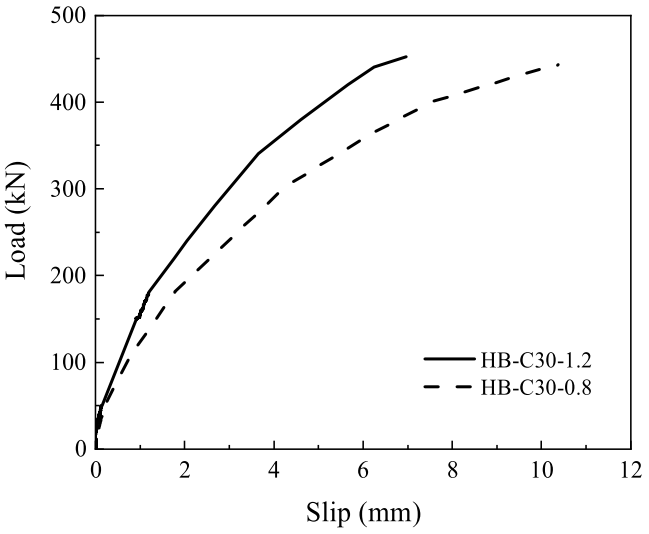


Fig. 9. Load-slip curve at the beam end.

HB-C30–0.8 was greater than in HB-C30–1.2. This can be attributed to the significant interfacial slip resulting from the weaker shear connection.

(2) The ultimate compressive strains measured at the upper edge of the concrete slabs for HB-C30–1.2 and HB-C30–0.8 were −2733 με and −2200 με, respectively, corresponding to approximately 67.5 %–82.5 % of the nominal ultimate strain for concrete as specified in GB 50010. The maximum tensile strains at the bottom flange of the GFRP beam for HB-C30–1.2 and HB-C30–0.8 were 7790 με and 7196 με, both significantly lower than the ultimate strain of 18200 με. Therefore, both the concrete slab and the GFRP beam remained in the elastic state.

(3) The ultimate compressive strain in the longitudinal GFRP bars within the concrete slabs did not exceed −1200 με, and the corresponding compressive stress in these bars was similar to the compressive stress in the concrete with an equivalent cross-sectional area ($E_{bar}\varepsilon_{bar} \approx E_c\varepsilon_c$). This indicated that the contribution of GFRP bars for flexural capacity could be ignored.

3.4.2. *Strain in CFRP tendons*

The strain increment in two bundles of CFRP tendons at midspan as a function of loading for the specimens is shown in Fig. 12.

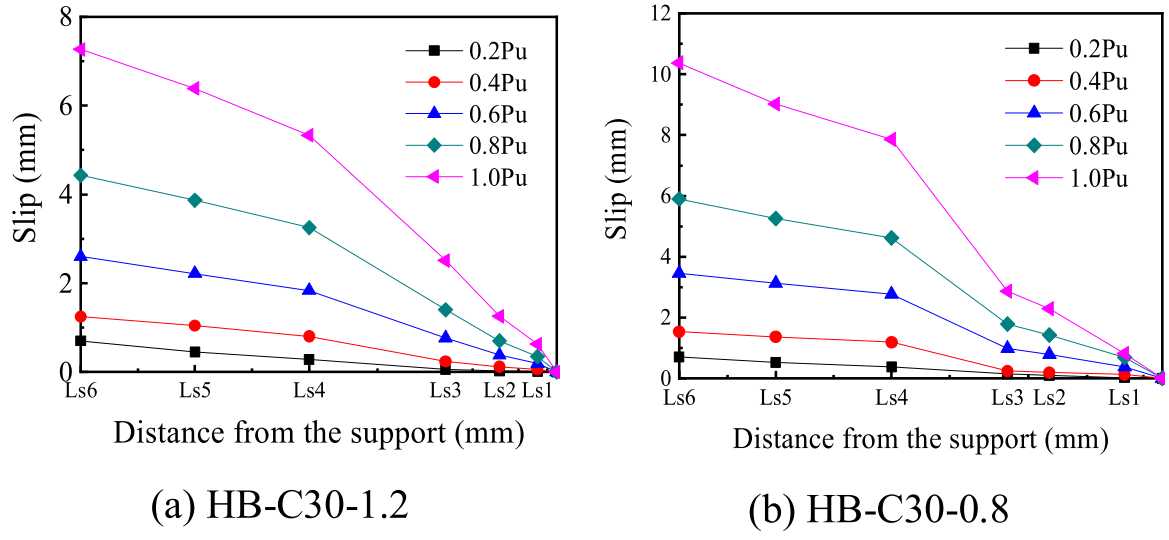


Fig. 10. Distribution of slip along the hybrid beam.

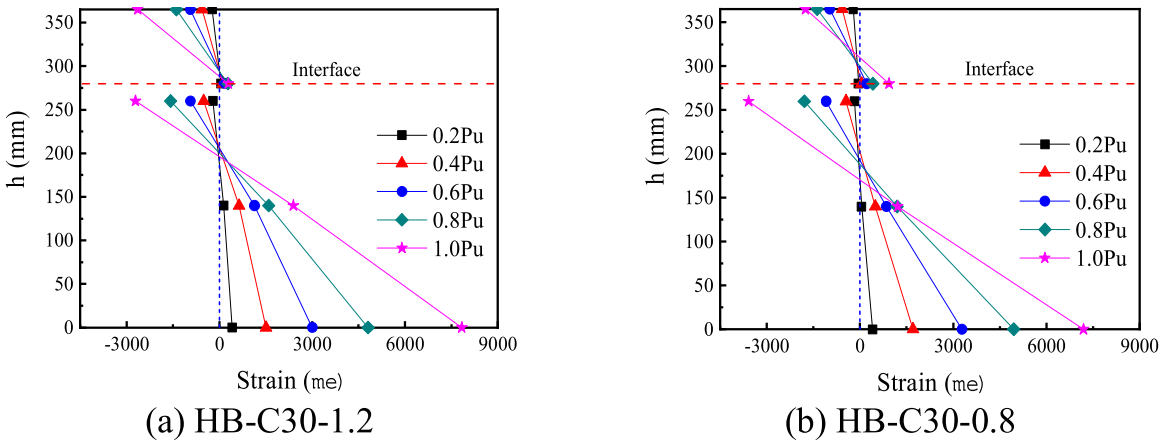


Fig. 11. Strain in cross-section.

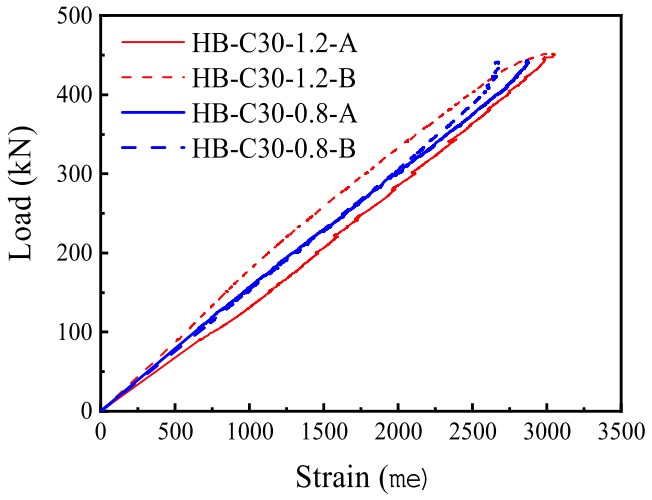


Fig. 12. Relationship between strain increment and load.

It can be concluded that the CFRP tendon strain almost linearly increased with the load. The average stress increments of the CFRP tendons were 373 MPa and 342 MPa for HB-C30–1.2 and HB-C30–0.8, respectively. The CFRP tendons remained elastic when the specimens failed. The stress increments for HB-C30–1.2 and HB-C30–0.8 were 38.2 % and 32.8 % of the initial prestress, respectively. The prestress increment of CFRP tendons for HB-C30–1.2 was 16.5 % greater than that for HB-C30–0.8, which was attributed to the earlier failure of the connection for HB-C30–0.8.

3.4.3. Strain in GFRP bolts

The development of strain on the GFRP bolts along the shear span of beams is shown in Fig. 13. It was observed that the strain of GFRP bolts increased nonlinearly. The highest strain values were in the middle of the shear span. The maximum tensile strain reached the ultimate tensile strain of 12,000 με. This suggests that the bolts experienced both axial and shear forces. For specimen HB-C30–0.8, most strain gauges failed due to the interfacial connection failure of the hybrid beams.

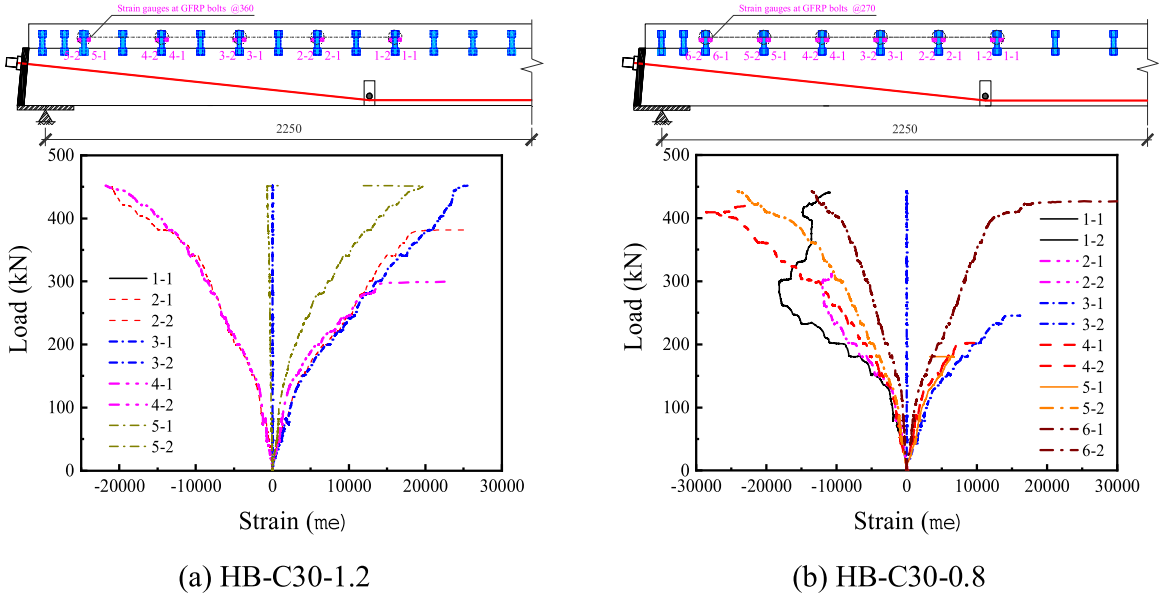


Fig. 13. Load-strain curve for FRP bolted joints.

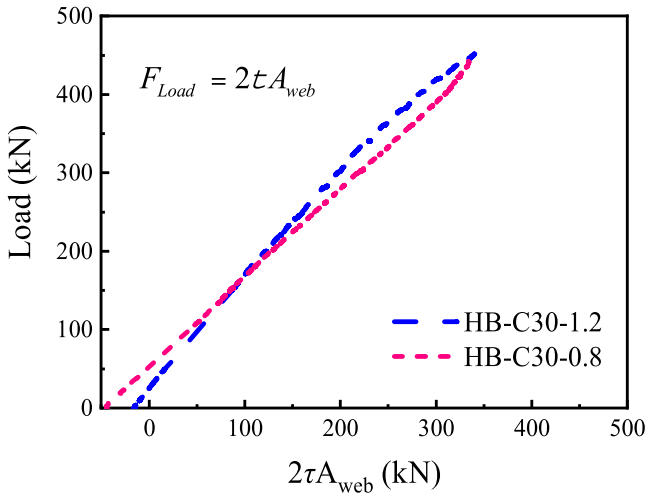


Fig. 14. Load-shear curve of FRP beam web at shear span section.

4. Discussion

4.1. Shear mechanism of GFRP beam webs

Fig. 14 shows the shearing force of the GFRP beam at the shear span measured by the strain gauge rosettes (s_1) as a function of applied loading. It is assumed that the FRP web was subjected to shear uniformly. It is interesting to observe that the shearing bored by the FRP web approximately linearly increased with the applied loading. The shear force undertaken by the FRP beam web occupied the total shearing of the hybrid beam of 79.5 % and 75.6 %, respectively. The vertical component of prestressing of the CFRP tendon was also a contribution to the shearing of the hybrid beam. The vertical components of CFRP tendons when the hybrid beam failed were 23.44 kN and 22.93 kN, and the contribution of CFRP tendons for shear resistance of specimen HB-C30–1.2 and HB-C30–0.8 accounted for 10.37 % and 10.4 %, respectively. This indicated that the contribution of the concrete slab and FRP flange for the shear resistance of the hybrid beams was less than 10 %. Therefore, it is suggested that the shearing is provided by the FRP web when designing the hybrid beam.

4.2. Shear force held by FRP bolts

The shear force on the GFRP bolts at the loading point and the beam's end as a function of the loading is shown in Fig. 15. The shear force of GFRP bolts was calculated by the load-slip model ($\frac{P}{P_u} = \frac{S}{1.94+0.77S}$) in the literature [31]. It was observed that the increase in the shear force of GFRP bolts was trivial before the load reached approximately $0.1P_u$. The shear force of bolts increased with the increase in load. When the specimens failed, the shear forces of GFRP bolts at the loading point for specimen HB-C30–1.2 and HB-C30–0.8 were 80.4 kN and 94.8 kN, which were 61.8 % and 73 % of the ultimate shear capacity of GFRP bolts, respectively. The shear forces of GFRP bolts at the beam end for specimens HB-C30–1.2 and HB-C30–0.8 were 80.4 kN and 94.8 kN, which were 94 % and 104 % of the ultimate shear capacity of GFRP bolts.

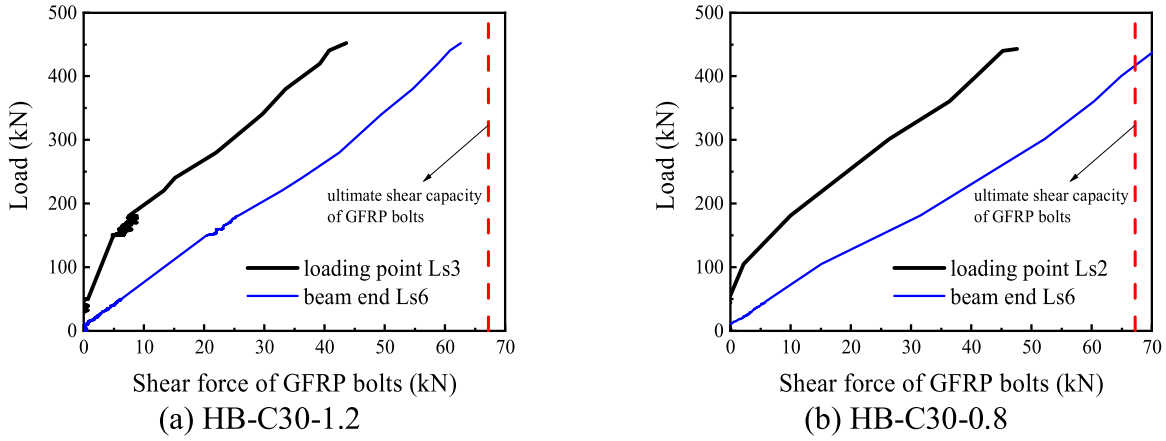


Fig. 15. Connector load-shear curve.

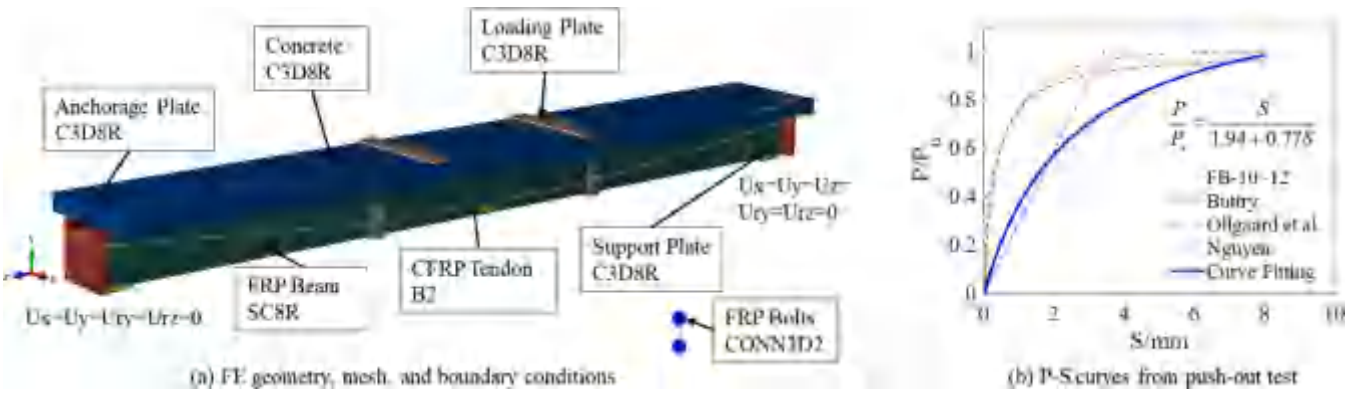


Fig. 16. 3D FE model of FRP-PC hybrid beams.

Table 6
Contact relationship in the FEA models.

Part to part	Type of connection
The lower surface of the concrete slab and the upper surface of the GFRP beam	surface-to-surface contact and hard contact in the normal direction [13]
GFRP reinforcement and the concrete slab	Embedded constraint
The deviators and the FRP beams	tie constrain
The anchorage plate and the FRP beams	tie constrain
CFRP tendons and the anchorage plate	MPC coupling constraint
CFRP tendons and deviators	coupling constraint (all degrees of freedom were restrained except the translation towards the tendons)

Table 7
Material properties of GFRP beams.

Engineering constants		Strength limits		Fracture energy	
E_{11}^{a}	38000	$X^{T\,a}$	734	G_{LT}	12.5
$E_{22}^{a} = E_{33}^{b}$	12700	$X^{C\,a}$	240	G_{LC}	12.5
$\upsilon_{12}^{a} = \upsilon_{13}^{b}$	0.3	$Y^{T\,a}$	198.7	G_{TT}	1
υ_{23}^{c}	0.12	$Y^{C\,a}$	255	G_{TC}	1
$G_{12}^{b} = G_{13}^{b}$	14615	$S^{L\,a}$	57.3		
G_{23}^{b}	5670	$S^{T\,a}$	38		

Note: [a] Obtained from material tests (Section 2.2); [b] Obtained from classical lamination theory [69]; [c] Assumed value; the superscripts C and T denote compression and tension, and the notations X, Y, and S are the longitudinal, transverse, and shear strength values. G_{FT}, G_{FC}, G_{MT}, G_{MC} denotes fracture energies when fiber tensile failure fiber compressive failure, matrix tensile failure and matrix compressive failure occurred [68,69].

5. Finite element analysis

Based on the Abaqus package (*v*2017), a three-dimensional (3D) finite element (FE) model was established to simulate the static behavior of FRP-PC hybrid beams, considering the interfacial slipping, anisotropic behavior of FRP profile, and nonlinear behavior of FRP bolts. The failure behavior of FRP-PC hybrid beams was simulated by a progressive damage analysis.

5.1. FE geometry and mesh

The standard (static, general) solver was adopted. The boundary conditions and mesh generation of the FE model are shown in Fig. 16. The contact relationships for different parts are shown in Table 6.

The concrete slab, supporting/loading plates, and anchorage plates were modeled using 8-node 3D linear reduced integration brick elements (C3D8R). The GFRP beam was modeled by 8-node reduced integration brick continuum stress shell elements (SC8R). A single-layer element approach was adopted for the GFRP beam [49]. The GFRP bolts were modeled by 2-node connector elements (CONN3D2) to simulate the shear force transferring in the Z-direction. The CONN3D2 elements vertically connect a node at the top surface of the compression flange of the GFRP beam to a node at the bottom surface of the concrete slab [47]. The GFRP reinforcements in the concrete slab were modeled by a 2-node linear 3D truss element (T3D2). The CFRP tendons were simulated by a linear and quadratic interpolation beam element (B2). The concrete slab and FRP beam were discretized in 50 mm and 20 mm side elements, respectively. The CFRP tendons adopted 20 mm side elements. Besides, all other parts were discretized in 50 mm side elements. The mesh size used in this model was selected based on the findings from our previous research [66] to balance numerical accuracy and computational cost.

The analysis process consisted of an initial step and two static steps. In the initial step, all the boundary conditions were implemented. In the first static steps, the CFRP tendon stresses were implemented by the cooling method (Eq. (2)), which is predefined as an initial value of the variable temperature in the command predefined field. The stresses were gradually transferred from the CFRP tendons to the hybrid beam through the contact at the anchorage plates and deviators, simulating the stress state of the model after prestressing was applied. In the second loading phase, the hybrid beam had already exhibited the behavior of a prestressed beam, and displacement-controlled loading was then applied to the loading plates.

$$\Delta T = \frac{\sigma_{\mathrm{pre}}}{\alpha A} \tag{3}$$

Table 8
CDP model parameters of NC [70–72].

	ψ	ε	σ_{b0}/σ_{c0}	K_c	μ
concrete	30°	0.1	1.16	0.667	0.005

Note: ψ is the dilation angle, ε is the flow potential eccentricity, σ_{b0}/σ_{c0} is the ratio of the initial equiaxial compressive yield stress to the initial stress, K_c is the ratio of the second stress invariant on the tensile meridian to that on the compressive meridian, and μ is the viscosity parameter.

5.2. Material models

Although the FRP was an isotropic material, the FRP beam was modeled using engineering constants considered orthotropic behavior to reduce the complexity of the model, as shown in Table 7 [47,49,67]. Besides, Hashin Failure model was adopted to stimulate the material properties and GFRP pultruded profile progressive failure (fibers and matrix)[49]. Hashin Failure model considers four failure modes: i.e., fiber tension; fiber compression; matrix tension; and matrix compression. All the values of strength limits for the Hashin failure model were obtained from the material tests (Section 2.2). The values of fracture energy were used to describe the progressive failure of GFRP after it attained the strength limits. As standardized tests for determining the fracture energy of FRP pultruded composites are not yet available, the fracture energy was calculated from the area under the stress-strain curves obtained from the mechanical characterization tests conducted in this study [68,69].

The constitutive law, presented by Chinese standard GB 50010 (Eqs. (3)~(4)) was used.

$$\sigma_c = \begin{cases} \dfrac{\rho_c n}{n-1+x^n} E_0 \varepsilon_c & x \le 1 \\ \dfrac{\rho_c}{\alpha_c (x-1)^2 + x} E_0 \varepsilon_c & x > 1 \end{cases} \tag{4}$$

$$\sigma_t = \begin{cases} \rho_t \left[1.2 - 0.2x^5\right] E_0 \varepsilon_t & x \le 1 \\ \dfrac{\rho_t}{\alpha_t (x-1)^{1.7} + x} E_0 \varepsilon_t & x > 1 \end{cases} \tag{5}$$

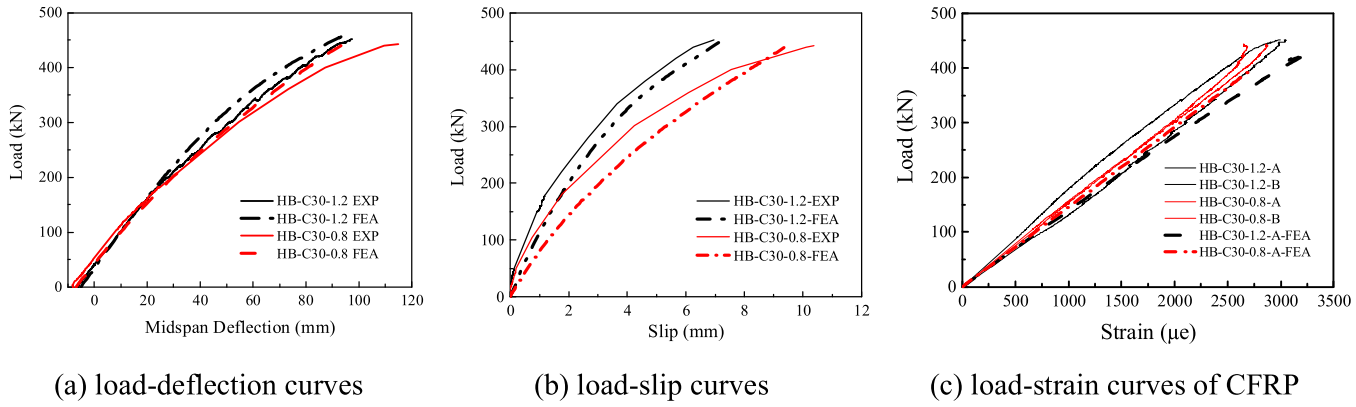
where α_c;$\rho_c = f_{c,r}/(E_c \varepsilon_{c,r})$;$n = E_c \varepsilon_{c,r}/\left(E_c \varepsilon_{c,r} - f_{c,r}\right)$;$x = \varepsilon_c/\varepsilon_{c,r}$; E_0 is the elasticity modulus of concrete; $f_{c,r}$ is the cubic compressive strength; $\varepsilon_{c,r}$ is the peak compressive strain; ε_{cu} is the ultimate compressive strain; α_t; $\rho_t = f_{t,r}/(E_c \varepsilon_{t,r})$;$x = \varepsilon_t/\varepsilon_{t,r}$; $f_{t,r}$ is the axial tensile strength; and $\varepsilon_{t,r}$ is the peak tensile strain.

The tensile and compression concrete damage factor in the CDP model was calculated according to Eq.(5).

$$\begin{cases} d_c = 1 - \sqrt{\dfrac{\sigma_c}{E_0 \varepsilon_c}} \\ d_t = 1 - \sqrt{\dfrac{\sigma_t}{E_0 \varepsilon_t}} \end{cases} \tag{6}$$

The concrete damaged plasticity constitutive (CDP) model was adopted to consider the compressive crushing or tensile cracking of concrete. The specific parameters are shown in Table 8.

CONN3D2 element was assigned by a multi-linear load-slip curve



(a) load-deflection curves (b) load-slip curves (c) load-strain curves of CFRP

Fig. 17. Comparison of the FE values and tested values for hybrid beams.

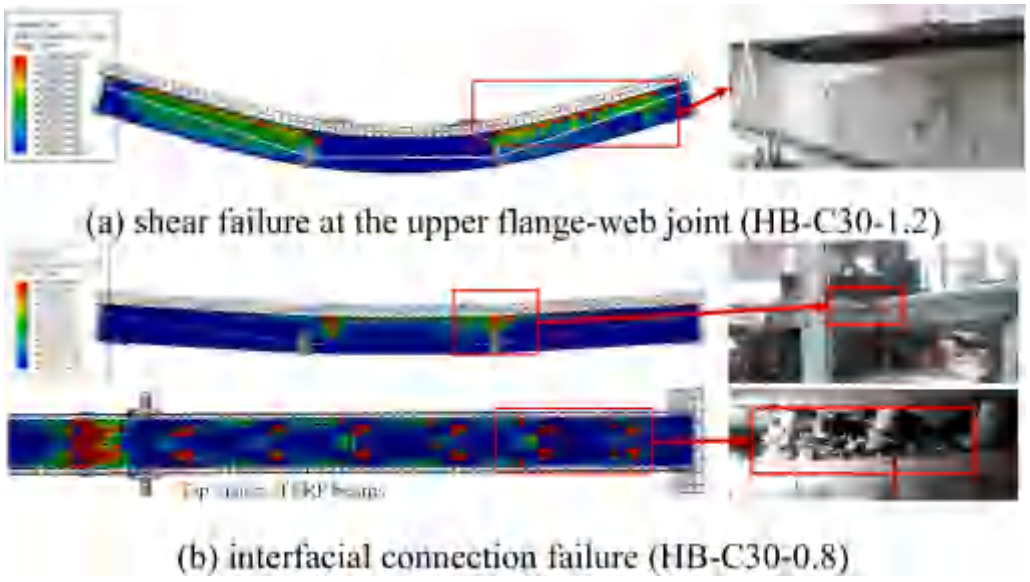


Fig. 18. FEM stress cloud maps.

Table 9
Comparison of stiffness between experimental results and FEA results.

Specimens	*EXP*(kN·m^2)		*FEA*(kN·m^2)		*FEA/EXP*	
	EI_{ela_exp}	EI_{deg_exp}	EI_{ela_FEA}	EI_{deg_FEA}	EI_{ela_FEA} / EI_{ela_exp}	EI_{deg_FEA} / EI_{deg_exp}
HB-C30–1.2	10680.4	7666.5	11513.2	8023.5	1.05	1.08
HB-C30–0.8	9886.8	6314.2	9873.1	7667.3	1.00	1.21

Notes: EI_{ela} denotes the flexural stiffness of hybrid beam in the linear elastic phase ($P \leq 0.4\,P_u$) based on the load-deflection curves according to $EI = M(3l^2\text{-}4a^2)/24\,f$; EI_{deg} denotes the flexural stiffness of hybrid beam in the stiffness degradation phase ($P > 0.4\,P_u$); M denotes the moment; f denotes the midspan deflection; l denotes the length of beams; a denotes the distance from the central load to the beam end.

derived from the push-out test results in the previous research [31] (Fig. 16b). The stress versus strain behaviors of the GFRP reinforcement in the concrete slab, CFRP tendons, steel deviators, and anchorage plate were assumed to be linear due to their undamaged of them till the failure of hybrid beam.

5.3. Verification

The FE model was validated by the experimental results through the comparisons of the load-midspan deflection curves and load-end slip curves as shown in Fig. 17. The FE stress cloud maps were illustrated in Fig. 18. As shown in Fig. 17 and Table 9, the ultimate capacity, overall performance of the FRP-PC hybrid beam could be well predicted by the FE model. The errors between the calculation results and experimental results for the ultimate capacity of the FRP-PC hybrid beam were within 10 %, which could be acceptable. Besides, the predicted stiffnesses for all FE models, except HB-C30–0.8 in the stiffness degradation phase match well with that of experimental specimens with a deviation of no more than 10 %. The deviation may be because the test beams experienced interfacial connection failure and the concrete slab lifting, which results in larger deflection, while the FE model could not simulate the concrete slab lifting. Furthermore, the discrepancy of FE models and experimental beams in the load-slip curves may be caused by the following aspects: (1) The load-slip model of the GFRP bolt shear connector was obtained from the push-out test by curve fitting. The fitted curve is different from the test value. (2) the stress state of the

Table 10
Parameters of the parametric study.

	(1)	(2)	(3)	(4)	(5)
Spacing of FRP bolts	160	180	220	240	260
Initial jacking force	0.4 f_{ftk}	0.5 f_{ftk}	0.6 f_{ftk}		
Concrete strength	C30	C40	C50	C60	
width of concrete slab	400	600	800		
Thickness of concrete slab	70	80	90	100	
Thickness of the web of FRP	12	14	16	18	20
Thickness of the flange of FRP	14	16	18	20	

GFRP bolt shear connector in the push-out test and the beam test is different, and the shear stiffness of the shear connector obtained from the push-out test is lower than that of the beam test. (3) There are deviations between the actual material characteristics and the ideal constitutive relations of concrete, GFRP pultruded profile, GFRP bolts, and CFRP tendon, which are related to the discreteness of the material.

5.4. Parametric analysis

A parametric study was performed on 20 FRP-PC hybrid beams to examine the effects of factors such as shear connection degree, initial prestressing force, concrete strength, tendon eccentricity, and the thickness and width of the concrete slab (Table 10). The details of the specimens involved in the parametric study are summarized in Table 11. In the models, the section of the GFRP beam remained constant (Fig. 19), while the shear connection degree was varied by adjusting the number of FRP shear connectors.

5.4.1. Effect of initial prestressing force

The effect of initial prestressing force on the flexural behavior of FRP-PC hybrid beams is illustrated in Fig. 20 and Table 11.

Increasing the initial prestressing force led to an increase in the initial upward deflection, but the difference in ultimate capacity and load-end slip behavior for specimens prestressed with 0.4–0.6f_{ftk} is within 0.16 % and 2.00 %, respectively. This is due to the fact that the prestressed tendons did not fail when the hybrid beam failed. In this case, it is not very effective in improving the ultimate capacity of the beam by increasing the initial prestressing force.

5.4.2. Effect of concrete strength

The effect of concrete strength on the static behavior of the FRP-PC hybrid beam is shown in Fig. 21 and Table 11 in which the load-midspan deflection and load-end slip curves of the hybrid beam with different concrete strengths are compared.

Increasing the concrete strength significantly increases the loading capacity, flexural stiffness, and slip. Compared to the loading capacity of beams with C30, the loading capacity of beams with C40, C50, and C60 concrete strengths increased by 6.2 %, 10.8 %, and 14.1 %, respectively. The flexural stiffnesses of hybrid beams were almost the same in the elastic bending phase, while in the elastic-plastic bending phase, the flexural stiffness of hybrid beams with lower concrete strength decreased obviously. This is due to more concrete cracks leading to the reduction of flexural stiffness. The hybrid beams with higher concrete strength under the same load exhibited less slip than hybrid beams with

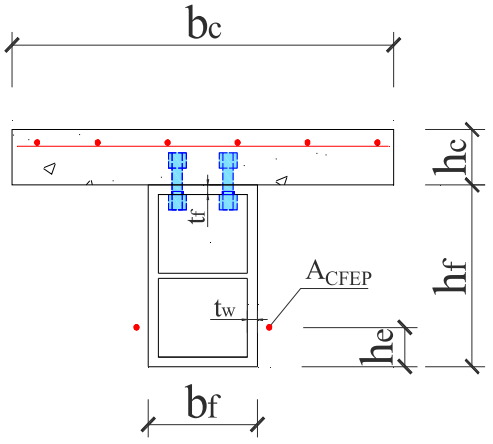


Fig. 19. Cross-section of the FRP-PC hybrid beams.

Table 11
Characteristics of the parametric study models.

Specimens	S_l	σ_{con} (Mpa)	f_c (Mpa)	B_c (mm)	h_c (mm)	t_f (mm)	t_w (mm)	η	Parameters	M_u (kN·m)	Slip(mm)	Failure Mode
HB−1	180	0.5 f_{ftk}	37.3	600	85	15	16	1.17	Concrete strength f_c	369.0	7.75	SF
HB−2	180	0.5 f_{ftk}	30	600	85	15	16	1.17		351.7	7.51	SF
HB−3	180	0.5 f_{ftk}	40	600	85	15	16	0.88		373.5	7.82	SF
HB−4	180	0.5 f_{ftk}	50	600	85	15	16	0.7		389.8	8.08	SF
HB−5	180	0.5 f_{ftk}	60	600	85	15	16	0.58		401.2	8.29	SF
HB−6	180	0.4 f_{ftk}	37.3	600	85	15	16	1.17	initial jacking force σ_{con}	368.5	7.83	SF
HB−7	180	0.6 f_{ftk}	37.3	600	85	15	16	1.17		369.1	7.99	SF
HB−8	160	0.5 f_{ftk}	30	600	85	15	16	1.29	Spacing of FRP bolts	361.9	7.18	SF
HB−9	200	0.5 f_{ftk}	30	600	85	15	16	1.05		349.6	7.61	SF
HB−10	220	0.5 f_{ftk}	30	600	85	15	16	0.94		348.9	8.10	SF
HB−11	240	0.5 f_{ftk}	30	600	85	15	16	0.82		338.8	8.52	SF
HB−12	260	0.5 f_{ftk}	30	600	85	15	16	0.82		329.5	8.32	SF
HB−13	180	0.5 f_{ftk}	30	400	85	15	16	1.75	Concrete slab width b_c	323.4	4.87	SF
HB−14	180	0.5 f_{ftk}	30	800	85	15	16	0.88		363.5	8.53	SF
HB−15	180	0.5 f_{ftk}	30	1000	85	15	16	0.7		370.8	9.15	SF
HB−16	180	0.5 f_{ftk}	30	600	70	15	16	1.42	Concrete slab thickness h_c	330.3	5.25	SF
HB−17	180	0.5 f_{ftk}	30	600	80	15	16	1.24		340.3	7.32	SF
HB−18	180	0.5 f_{ftk}	30	600	90	15	16	1.1		364.1	7.65	SF
HB−19	180	0.5 f_{ftk}	30	600	100	15	16	0.99		390.7	8.04	SF
HB−20	180	0.5 f_{ftk}	30	600	85	14	16	1.17	FRP flange thickness t_f	343.9	7.51	SF
HB−21	180	0.5 f_{ftk}	30	600	85	16	16	1.17		359.8	7.57	SF
HB−22	180	0.5 f_{ftk}	30	600	85	18	16	1.17		377.1	7.62	SF
HB−23	180	0.5 f_{ftk}	30	600	85	20	16	1.17		397.2	7.80	SF
HB−24	180	0.5 f_{ftk}	30	600	85	15	12	1.17	FRP web width t_w	340.4	7.46	SF
HB−25	180	0.5 f_{ftk}	30	600	85	15	14	1.17		345.7	7.42	SF
HB−26	180	0.5 f_{ftk}	30	600	85	15	18	1.17		361.3	7.45	SF
HB−27	180	0.5 f_{ftk}	30	600	85	15	20	1.17		368.8	7.44	SF

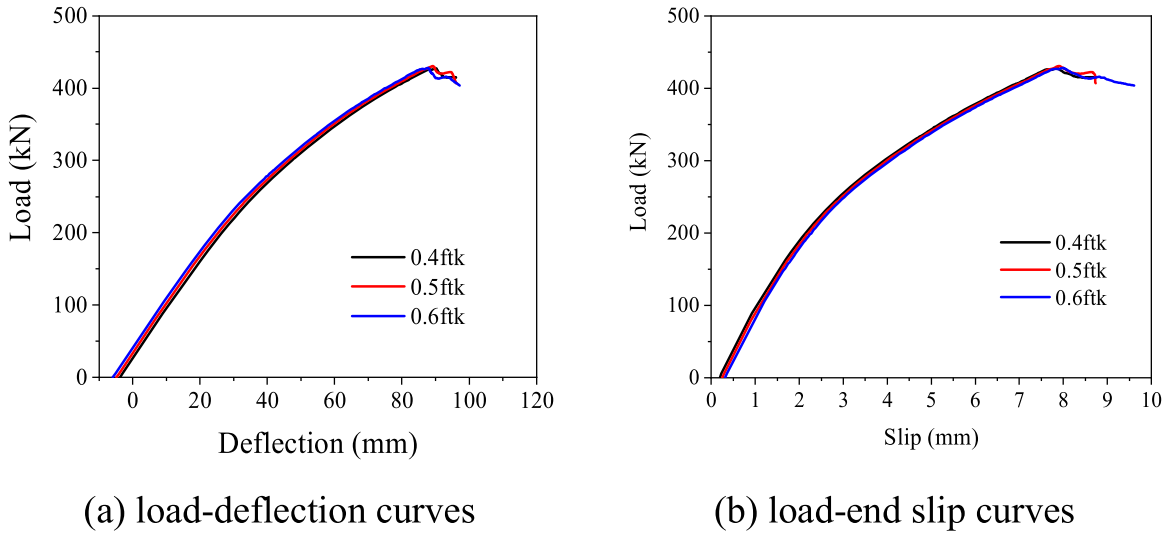


Fig. 20. Effect of initial prestressing force on FRP-PC hybrid beams.

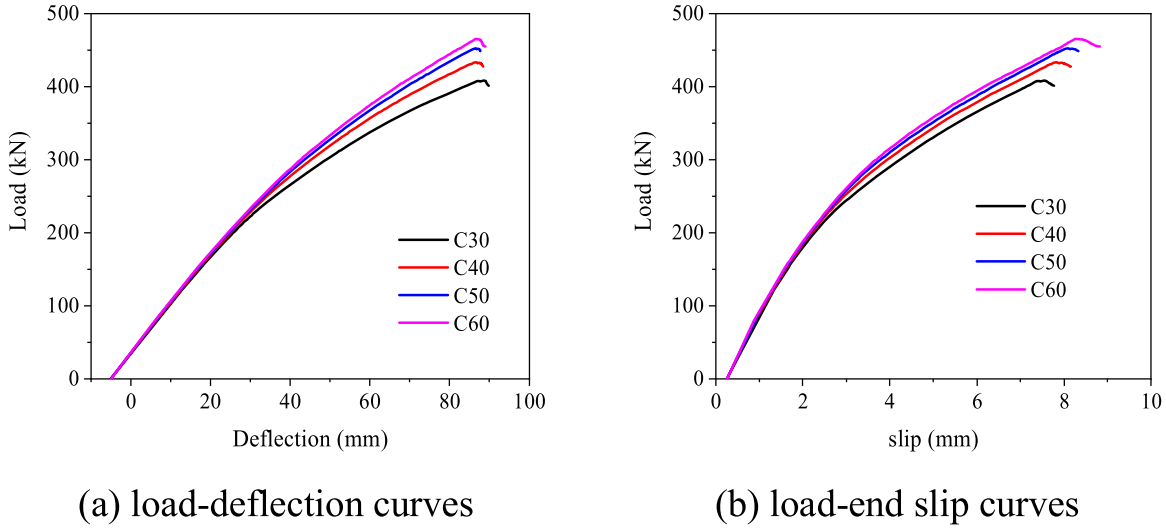


Fig. 21. Effect of concrete strength on FRP-PC hybrid beams.

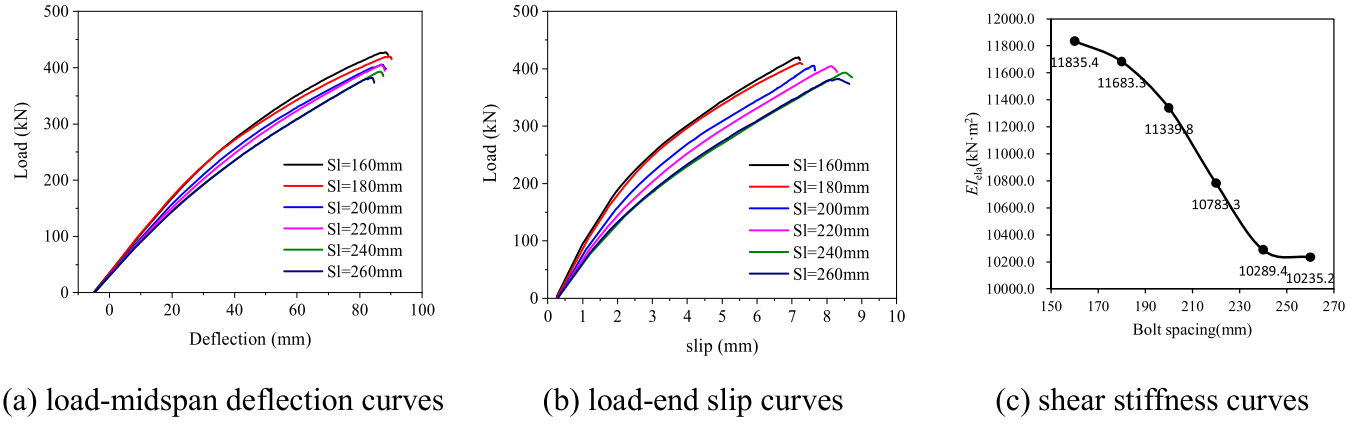


Fig. 22. Effect of concrete slab width and thickness on FRP-PC hybrid beams.

lower concrete strength, which indicated a higher composite action between the FRP profile beams and concrete slabs.

5.4.3. Effect of bolt spacing

This section examines the effect of bolt spacing on the static behavior of FRP-PC hybrid beams. The ultimate capacity, load-slip curves, and

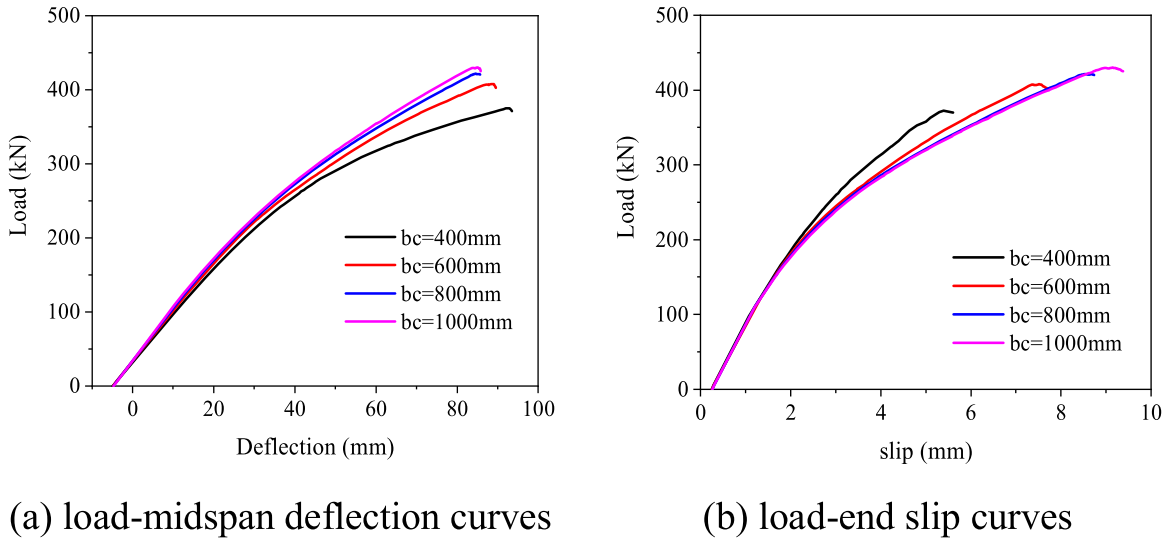


Fig. 23. Effect of concrete slab width on FRP-PC hybrid beams.

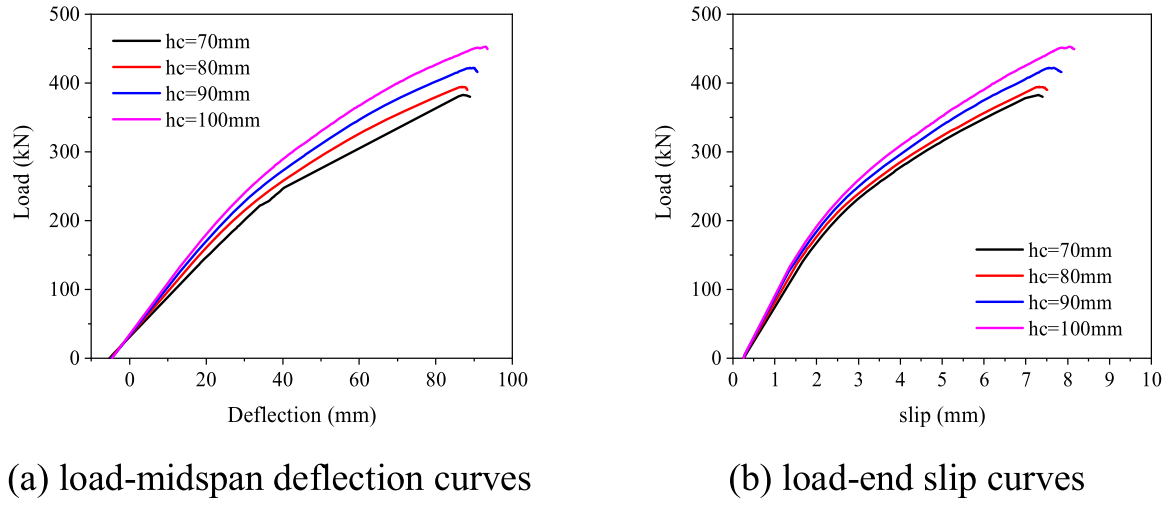


Fig. 24. Effect of concrete slab thickness on FRP-PC hybrid beams.

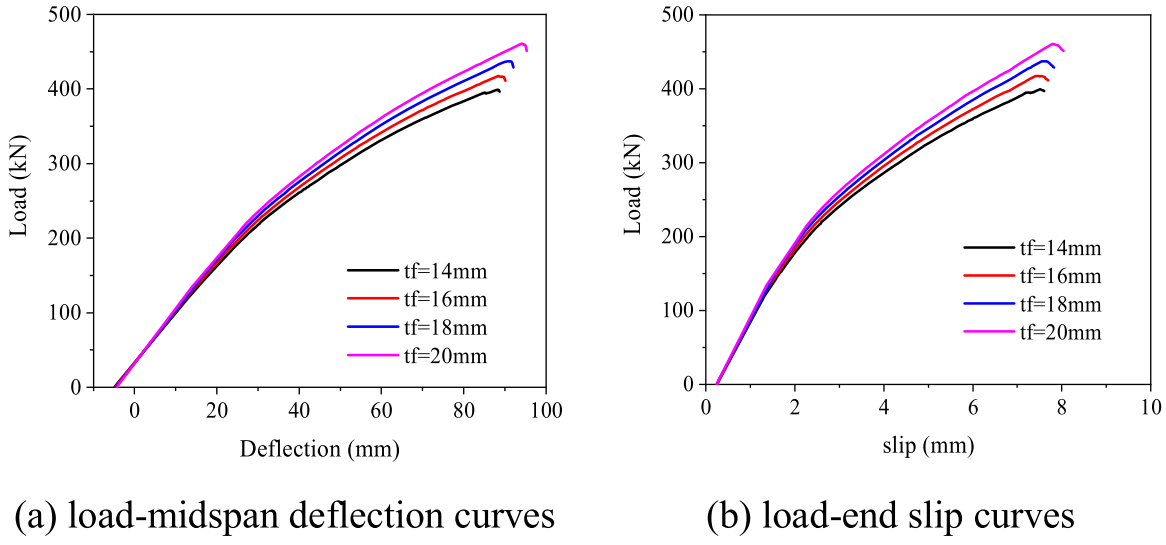


Fig. 25. Effect of concrete slab width and thickness on FRP-PC hybrid beams.

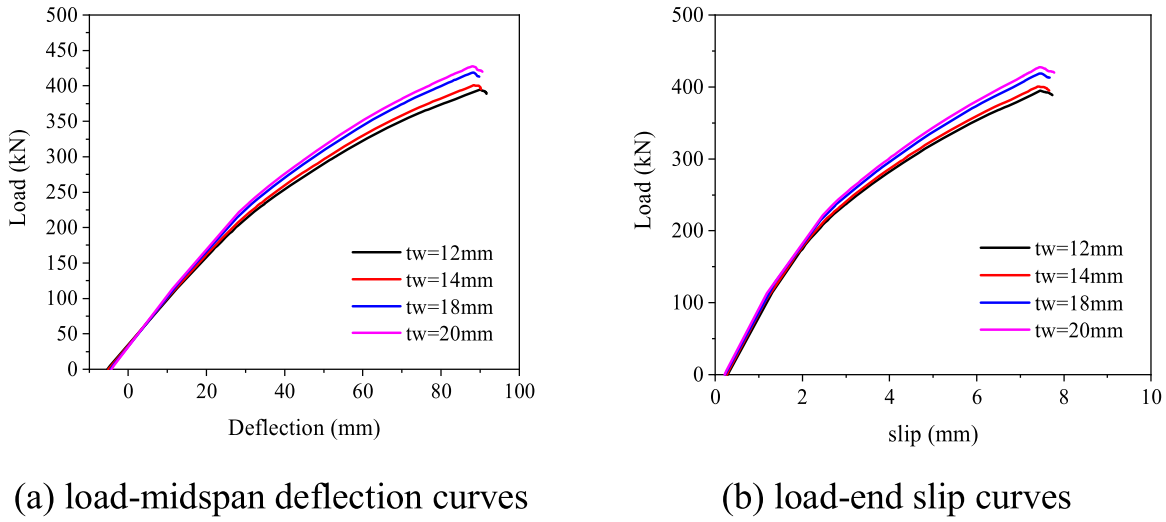


Fig. 26. Effect of concrete slab width and thickness on FRP-PC hybrid beams.

load-deflection curves with a bolt spacing of 160–260 mm are compared in Fig. 22.

As the bolt spacing decreased, the ultimate load and stiffness of the FRP-PC hybrid beams improved, and the interfacial slip decreased. As the bolt spacing increased from 160 mm to 260 mm, the loading capacity decreased by 8.96 %, respectively. This is due to a reduction in bolt spacing, which would increase the composite action, which enhances the flexural performance of the hybrid beam.

All FRP-PC hybrid beams suffered shear failure of FRP when the shear connection degree η varied from 0.82 to 1.29. This indicated that the shear connection degree calculation method of steel-concrete composite beams is not suitable for FRP-PC hybrid beams, which is concluded from the experiment. Because the FRP pultruded profile would not yield and the concrete slabs were hard to attain full-section crushing. Besides, the range of interfacial slip at the serviceability limit state and at the failure is more than 0.2 mm [73] and 1.0 mm [58], respectively. Therefore, this limit for the slip of steel-concrete composite beams did not apply to FRP-PC hybrid beams. It is necessary to consider the partial interaction effects due to the low degree of shear connection and large interfacial slip.

5.4.4. *Effect of concrete slab width and height*

Fig. 23 and Fig. 24 show the comparison of the effect of concrete slab width and concrete slab height.

Increasing the width of the concrete slab led to improvements in the ultimate bearing capacity, flexural stiffness, and ultimate slip of the hybrid beam, while the ultimate deflection gradually decreased. As the concrete slab width increased from 400 mm to 600 mm, 800 mm, and 1000 mm, the ultimate capacities of the hybrid beams increased by 8.8 %, 12.4 %, and 14.7 %, respectively. The width of the concrete slab significantly enhances the bearing capacity of the hybrid beams, although the effect diminishes as the width increases, possibly due to the shear lag phenomenon.

As concrete slab height increases, the ultimate capacity, flexural stiffness, and ultimate deflection increase gradually. As the height of the concrete slab increases, both the moment resistance from concrete pressure and the tension in the GFRP profile rise, as the force value and arm both increase, leading to an increase in the ultimate bearing capacity.

5.4.5. *Effect of FRP flange and web thickness*

Fig. 25 and Fig. 26 show the comparison of the effect of the thickness of the FRP flange and the width.

With the increase in thickness of the FRP flange, the bearing capacity, the flexural stiffness, the ultimate slip and deflection of the hybrid beam increased gradually. Compared to specimens with a flange thickness of 14 mm, the ultimate capacity of specimens with thicknesses of 16 mm, 18 mm, and 20 mm improved by 4.6 %, 9.7 %, and 15.5 %, respectively. This is because an increased FRP flange thickness would increase the contribution of the FRP flange to the bending capacity.

With the increase of thickness of the FRP web, the bearing capacity, the flexural stiffness, and the ultimate slip of the hybrid beam increased, while the ultimate deflection decreased gradually. The ultimate capacity of specimens with thicknesses of 20 mm was 8.3 %, 6.7 %, 4.9 %, and 2.1 % higher than specimens with thicknesses of 18 mm, 16 mm, 14 mm, and 12 mm, respectively. It is important to note that if the flange and web of the GFRP profile are excessively thick, the profile will have a high safety margin, which may not be cost-effective.

6. Conclusions

This paper presents an experimental and numerical investigation on large-scale FRP-PC hybrid beams. The main conclusions are summarized as follows:

(1) Two failure modes were observed in the FRP-PC hybrid beams: (i) FRP shear failure at the upper flange-web junction for beam with shear connection degree of 1.2, and (ii) interfacial connection failure for beam with shear connection degree of 0.8. When the hybrid beam failed, the compressive strain at the top of the concrete slab, the tensile strain at the bottom of the FRP profile, and the strain in the CFRP tendons were all below their respective ultimate limits.
(2) The load-deflection and load-slip curves of the hybrid beams are divided into linear elastic phase and stiffness degradation phase. The ultimate end slip exceeded 6 mm, indicating partial shear connection between the FRP and concrete.
(3) Despite the presence of interfacial slip, the concrete slab and the FRP beam exhibited identical curvature during loading, thereby validating the plane-section assumption. This confirms its applicability as a fundamental assumption in theoretical modeling.
(4) A validated FE model, considering interfacial slip, material isotropy, and FRP damage, was developed and predicted the static behavior of the FRP-PC hybrid beam well in terms of load-deflection curve, failure modes, and interfacial slips.
(5) Increasing the prestressing from $0.40f_{tk}$ to $0.60f_{tk}$ can improve the chamber but not increase the capacity of hybrid beams, because the tendons did not fail. As the bolt spacing decreased from

260 mm (η=1.29) to 160 mm(η=0.82), the capacity increased by 8.96 % due to higher composite action. Increasing the concrete strength, section size of the concrete slab, and the thickness of FRP web and flange can improve the flexural stiffness and the capacity of hybrid beams.

This study provides a foundational understanding of the structural behavior of externally prestressed FRP-PC hybrid beams through comprehensive experimental testing and numerical simulation. The findings contribute to the future development of rational design methods for such hybrid systems. Given the limited number of experimental specimens, further investigations are recommended to evaluate the effects of concrete strength, types of shear connectors, and prestressing levels. Moreover, a design methodology for FRP-PC hybrid beams should be developed, considering the effect of interfacial slip, prestressing loss due to second-order effects and the anisotropic behavior of FRP.

CRediT authorship contribution statement

Jiafei Jiang: Writing – review & editing. **Dawei Yan:** Writing – original draft, Investigation, Formal analysis. **Shiqian Zhang:** Writing – review & editing, Supervision, Investigation, Formal analysis. **Weichen Xue:** Writing – review & editing, Supervision, Methodology, Conceptualization.

Declaration of Competing Interest

The authors declare that they have no known competing financial interests or personal relationships that could have appeared to influence the work reported in this paper.

Acknowledgements

The authors gratefully acknowledge the financial support provided by the National Key R&D Program of China (No. 2022YFC3801800), the National Natural Science Foundation of China (No. 52130806) and Ph.D Scholarship Project supported by NEXCEL (No. 24PHD-6).

References

[1] Faella C, Martinelli E, Nigro E. Steel–concrete composite beams in partial interaction: closed-form “exact” expression of the stiffness matrix and the vector of equivalent nodal forces. Eng Struct 2010;32(9):2744–54.
[2] PENG F, XUE W, et al. Design Approach for Short-Term Deflection of Simple and Continuous Steel–Concrete Composite Beams Considering Interface Slip [J]. Journal of Structural Engineering 2025;151(7).
[3] Xu Y, Liu X, Wang B, Yi X. Residual mechanical properties of composite beams with PBL connectors under fatigue loads. Structures 2023;51:185–95.
[4] Chen L, Qiang X, Jiang X, Bai J. Numerical study of steel–concrete composite beams strengthened by CFRP plates with prestressed unbonded reinforcement system. Eng Fail Anal 2024;157.
[5] El-Sisi AA, Hassanin AI, Shabaan HF, Elsheikh AI. Effect of external post-tensioning on steel–concrete composite beams with partial connection. Eng Struct 2021;247.
[6] Madrazo-Aguirre F, Wadee MA, Ruiz-Teran AM. Non-linear stability of under-deck cable-stayed bridge decks. Int J NonLinear Mech 2015;77:28–40.
[7] Shen J, Groh RMJ, Wadee MA, Schenk M, Pirrera A. Probing the stability landscape of prestressed stayed columns susceptible to mode interaction. Eng Struct 2022;251.
[8] Shen J, Lapira L, Wadee MA, Gardner L, Pirrera A, Groh RMJ. Probing in situ capacities of prestressed stayed columns: towards a novel structural health monitoring technique. Philos Trans R Soc A Math Phys Eng Sci 2023;381(2244).
[9] Wu K, Qiang X, Xing Z, Jiang X. Buckling in prestressed stayed beam–columns and intelligent evaluation. Eng Struct 2022;255.
[10] Peng F, Xue W, Bai L. Flexural behavior of externally prestressed continuous steel-concrete composite beams. J Constr Steel Res 2024;212.
[11] Nguyen H, Zatar W, Mutsuyoshi H. Hybrid FRP-UHPFRC composite girders: part 2-Analytical approach. Compos Struct 2015;125:653–71.
[12] Koaik A, Bel S, Jurkiewiez B. Experimental tests and analytical model of concrete-GFRP hybrid beams under flexure. Compos Struct 2017;180:192–210.
[13] Almeida MMdR, de Souza ASC, de Albuquerque AT, Rossi A. Parametric analysis of steel-concrete composite beams prestressed with external tendons. J Constr Steel Res 2022;189.
[14] Zhu Z, Fang H, Shi H, Yang C, Han J, Chen C. Flexural property study of multiaxial fiber reinforced polymer sandwich panels with pultruded profile cores. ThinWalled Struct 2023;189.
[15] Sánchez-Aparicio LJ, Ramos LF, Sena-Cruz J, Barros JO, Riveiro B. Experimental and numerical approaches for structural assessment in new footbridge designs (SFRSCC–GFPR hybrid structure). Compos Struct 2015;134:95–105.
[16] Saiidi M, Gordaninejad F, Wehbe N. Behavior of Graphite-Epoxy concrete composite beams. J Struct Eng Asce 1994;120(10):2958–76.
[17] Fam A, Skutezky T. Composite T-beams using reduced-scale rectangular FRP tubes and concrete slabs. J Compos Constr 2006;10(2):172–81.
[18] Wang Q, Zhu H, Teng F, Li H. Experimental and analytical studies of the bond between ribbed CFRP bar and aluminum alloy additional ribs anchorage. Eng Fract Mech 2023;290.
[19] Qiang W, Zhu H, Tong Y, Sun Y. Short- and long-term performance of the novel additional aluminum alloy ribs anchored CFRP reinforced pretensioned PC beams. Eng Struct 2022;266.
[20] Wang Q, Zhu H, Zhang B, Tong Y, Teng F, Su W. Anchorage systems for reinforced concrete structures strengthened with fiber-reinforced polymer composites: state-of-the-art review. J Reinf Plast Compos 2020;39(9-10):327–44.
[21] Neagoe CA, Gil L, Perez MA. Experimental study of GFRP-concrete hybrid beams with low degree of shear connection. Constr Build Mater 2015;101:141–51.
[22] Gonilha JA, Correia JR, Branco FA. Structural behaviour of a GFRP-concrete hybrid footbridge prototype: experimental tests and numerical and analytical simulations. Eng Struct 2014;60:11–22.
[23] Gonilha JA, Barros J, Correia JR, Sena-Cruz J, Branco FA, Ramos LF, Goncalves D, Alvim MR, Santos T. Static, dynamic and creep behaviour of a full-scale GFRP-SFRSCC hybrid footbridge. Compos Struct 2014;118:496–509.
[24] Nordin H, Taljsten B. Testing of hybrid FRP composite beams in bending. Compos Part B Eng 2004;35(1):27–33.
[25] Canning L, Hollaway L, Thorne AM. An investigation of the composite action of an FRP/concrete prismatic beam. Constr Build Mater 1999;13(8):417–26.
[26] Zou XX, Feng P, Wang JQ. Perforated FRP ribs for shear connecting of FRP-concrete hybrid beams/decks. Compos Struct 2016;152:267–76.
[27] Huang HL, Li A, Chen L, Zeng CJ, Zhu MQ. Push-Out tests for shear connectors in GFRP-Concrete composite bridge deck slabs. J Adv Concr Technol 2018;16(8):368–81.
[28] Di J, Cao L, Han J. Experimental study on the shear behavior of GFRP-Concrete composite beam connections. Materials 2020;13(5).
[29] Nguyen H, Mutsuyoshi H, Zatar W. Push-out tests for shear connections between UHPFRC slabs and FRP girder. Compos Struct 2014;118:528–47.
[30] El-Hacha R, Chen D. Behaviour of hybrid FRP-UHPC beams subjected to static flexural loading. Compos Part BEng 2012;43(2):582–93.
[31] Xue W, Yan D, Zhang S. Push-out behavior of GFRP bolts shear connectors in FRP-concrete hybrid beam. Eng Struct 2023;294.
[32] Fam A, Honickman H. Built-up hybrid composite box girders fabricated and tested in flexure. Eng Struct 2010;32(4):1028–37.
[33] Xue W, Ding M, Wang H, Luo Z. Static behavior and theoretical model of stud shear connectors. J Bridge Eng 2008;13(6):623–34.
[34] Deskovic N, Triantafillou TC, Meier U. Innovative design of frp combined with concrete - Short-Term behavior. J Struct Eng Asce 1995;121(7):1069–78.
[35] Correia JR, Branco FA, Ferreira J. GFRP-concrete hybrid cross-sections for floors of buildings. Eng Struct 2009;31(6):1331–43.
[36] Correia JR, Branco FA, Ferreira JG. Flexural behaviour of multi-span GFRP-concrete hybrid beams. Eng Struct 2009;31(7):1369–81.
[37] Santos Neto ABdS, La Rovere HL. Composite concrete/GFRP slabs for footbridge deck systems. Compos Struct 2010;92(10):2554–64.
[38] Chakrabortty A, Khennane A, Kayali O, Morozov E. Performance of outside filament-wound hybrid FRP-concrete beams. Compos. Part B Eng. 2011;42(4):907–15.
[39] Manalo AC, Aravinthan T, Mutsuyoshi H, Matsui T. Composite behaviour of a hybrid FRP bridge girder and concrete deck. Adv Struct Eng 2012;15(4):589–600.
[40] Liu T, Feng P, Lu X, Yang J-Q, Wu Y. Flexural behavior of novel hybrid multicell GFRP-concrete beam. Compos Struct 2020;250.
[41] Zhang P, Liu XY, Li QL, Deng EF, Gao DY, Zhang Z, Sheikh SA. Experimental and theoretical studies on the shear performance of innovative box-shape FRP profile-concrete hybrid beams. Structures 2020;28:2772–84.
[42] Zou XX, Feng P, Bao Y, Wang JQ, Xin HH. Experimental and analytical studies on shear behaviors of FRP-concrete composite sections. Eng Struct 2020;215.
[43] Garnevicius M, Gribniak V. Developing a hybrid FRP-concrete composite beam. Sci Rep 2022;12(1):16237.
[44] Zhang P, Qi Y, Zou X, Feng Y, Sheikh SA. Flexural performance of prefabricated FRP-concrete hybrid beam with in-situ-cast UHPC pockets. ThinWalled Struct 2023;185.
[45] Zhang P, Zhang Y, Yang S, Liu Y, Sheikh SA. Experimental tests of FRP-HSC hybrid beams under four-point bending. Adv Struct Eng 2023.
[46] Zhang P, Hu R, Zou XX, Liu Y, Li QL, Wu G, Sheikh SA. Experimental study of a novel continuous FRP-UHPC hybrid beam. Compos Struct 2021;261.
[47] Nguyen H, Mutsuyoshi H, Zatar W. Hybrid FRP-UHPFRC composite girders: part 1-Experimental and numerical approach. Compos Struct 2015;125:631–52.
[48] Zhang P, Lv XL, Liu Y, Zou XX, Li YZ, Wang JQ, Sheikh SA. Novel fiber reinforced polymers (FRP)-ultrahigh performance concrete (UHPC) hybrid beams with improved shear performance. Constr Build Mater 2021;286.
[49] Ge W, Zhang Z, Guan Z, Ashour A, Ge Y, Chen Y, Jiang H, Sun C, Yao S, Yan W, Cao D. Numerical study on flexural and bond-slip behaviours of GFRP profiled-concrete composite beams with groove shear connector. Eng Struct 2023;275.

[50] Zou X, Lin H, Feng P, Bao Y, Wang J. A review on FRP-concrete hybrid sections for bridge applications. Compos Struct 2020:113336.
[51] Correia JR, Branco FA, Ferreira JG. Flexural behaviour of GFRP-concrete hybrid beams with interconnection slip. Compos Struct 2007;77(1):66–78.
[52] Neagoe CA, Gil L. Analytical procedure for the design of PFRP-RC hybrid beams including shear interaction effects. Compos Struct 2015;132:122–35.
[53] Chen DN, El-Hacha R. Damage tolerance and residual strength of hybrid FRP-UHPC beam. Eng Struct 2013;49:275–83.
[54] Kim YJ, Fam A. Numerical analysis of pultruded GFRP box girders supporting adhesively-bonded concrete deck in flexure. Eng Struct 2011;33(12):3527–36.
[55] Bank LC. Reflections on 50 years of pultruded Fiber-Reinforced polymer materials in structural engineering. J Compos Constr 2023;27(5).
[56] Zhang J, Yang T, Du Y, He R, Liu C. Tensile mechanical properties and damage analysis of layered woven GFRP composite bolts. Compos Part B Eng 2024;271.
[57] Institute AC. Guide for the design and construction of structural concrete reinforced with fiber-reinforced polymer (FRP) bars.(ACI 440.1 R-15). Farmington Hills, Michigan: American Concrete Institute; 2015.
[58] M.o.H.a.U.-R . Development, Code for design of steel and concrete composite bridges: GB50917-2013, Beijing China Planning Publishing House.
[59] Weichen Xue, Yan Dawei, Yongsheng WANG, et al. Shear behavior of multi-row perforated GFRP rib shear connectors in GFRP-concrete hybrid beams/desks [J]. Construction and Building Materials 2024;449.
[60] S.A.o.t.P.s.R.o. China. Fiber-reinforced plastics composites-Determination of tensile properties. Standardization Administration of the People's Republic of China; 2005. p. 16.
[61] S.A.o.t.P.s.R.o. China. Fiber-reinforced plastics composites-Determination of compressive properties. Standardization Administration of the People's Republic of China; 2005. p. 8.
[62] Committee A. Guide for test methods for fiber reinforced polymers (FRP) for reinforcing and strengthening concrete structures (ACI 440.3 R-12). ACI Committee 440; 2012.
[63] M.o.H.a.U.-R. Development. Code for design of concrete structures GB 50010. China Architecture & Building Press; 2015.
[64] B. Standard, Eurocode 2: Design of concrete structures, Part, 2004, p. 230.
[65] ACI. ACI CODE-318-19: building code requirements for structural concrete and commentary. American Concrete Institute; 2019.
[66] Yan D, Wang Q. Numerical simulation on structural behavior of FRP profile-concrete hybrid beams with bolt shear connector. Struct Concr 2024.
[67] Aref AJ, Kitane Y, Lee GC. Analysis of hybrid FRP-concrete multi-cell bridge superstructure. Compos Struct 2005;69(3):346–59.
[68] Rahimian Koloor SS, Karimzadeh A, Yidris N, Petru M, Ayatollahi MR, Tamin MN. An Energy-Based concept for yielding of multidirectional FRP composite structures using a mesoscale lamina damage model. Polymers 2020;12(1).
[69] Nunes F, Correia JR, Silvestre N. Structural behavior of hybrid FRP pultruded beams: experimental, numerical and analytical studies. ThinWalled Struct 2016; 106:201–17.
[70] Mansour W, A.Tayeh B, Tam L-h. Finite element analysis of shear performance of UHPFRC-encased steel composite beams: parametric study. Eng Struct 2022;271.
[71] He S, Yang G, Zhou W, Li Q, Dong Y. Evaluation of shear lag effect in HSS-UHPC composite beams with perfobond strip connectors: experimental and numerical studies. J Constr Steel Res 2022;194.
[72] Liang S-L, Yu J, Fang Q. Continuous surface cap model for ultra-high-performance concrete under static and low strain rate loadings: calibration, experiment, and simulation. Int J Impact Eng 2024;185.
[73] L. CCCC Highway Consultants Co , Specifications for Design and Construction of Highway Steel-concrete Composite Bridge: JTG/T D64-01—2015, 2015.
[74] XUE W, YAN D, DAI Y, et al. Experimental research on shear behavior of multiple Perfobond rib shear connectors in steel-concrete composite girder [J]. Structures 2025;71.
[75] HU X, XUE W. Bond properties of GFRP rebars in UHPC under different types of test [J]. Engineering Structures 2024;314.
[76] XUE W, LI Z, LIANG Z, et al. Time-dependent behavior of GFRP-concrete composite slabs under one-year sustained loading: An experimental and numerical study [J]. Construction and Building Materials 2025;489.